Vol. 68, No. 3 / 2022

e: ISSN 2068 – 2239
p: ISSN 2068 – 4215

INMATEH – AGRICULTURAL ENGINEERING

SEPTEMBER - DECEMBER

Managing Editorial Board - INMA Bucharest

INMATEH - Agricultural Engineering **journal is indexed in the next international databases:**
ELSEVIER /SciVerse SCOPUS, CLARIVATE - WEB of SCIENCE- Emerging Sources Citation Index (ESCI), ULRICHS Web: Global Serials Directory, CABI, SCIPIO, Index COPERNICUS International, EBSCO Publishing, Elektronische Zeitschriftenbibliothek

INMATEH - Agricultural Engineering
vol. 68, no.3 / 2022
e-ISSN: 2068 – 2239; p: ISSN: 2068 – 4215

https://inmateh.eu/ *E-mail: inmatehjournal@gmail.com*

Edited by: INMA Bucharest

National Institute for Research-Development of Machines and Installations
Designed for Agriculture and Food Industry - INMA Bucharest
6, Ion Ionescu de la Brad Bvd., sector 1, Bucharest, ROMANIA

CONTENT

ENERGY EFFICIENT DRIVE SYSTEM WITH DIGITAL HYDRAULIC CYLINDER FOR CONSTRUCTION AND AGRICULTURAL MACHINERY
/
SISTEM DE ACTIONARE EFICIENT ENERGETIC CU CILINDRU HIDRAULIC DIGITAL PENTRU MASINI DE CONSTRUCTII SI AGRICOLE

Radu RADOI *[1)], Ionel PAVEL [1)], Polifron CHIRITA [1)], Bogdan TUDOR [1)], Vasilica STEFAN [2)]
[1)]Hydraulics and Pneumatics Research Institute INOE 2000-IHP, Bucharest, Romania
[2)]National Institute of Research – Development for Machines and Installations Designed for Agriculture and Food Industry – INMA Bucharest, Romania
Tel: +40213363991; E-mail: radoi.ihp@fluidas.ro
DOI: https://doi.org/10.35633/inmateh-68-01

Keywords: *digital hydraulic cylinder, efficiency, drive system, simulation*

ABSTRACT
Given the need to reduce greenhouse gas emissions, new energy-efficient solutions can be adopted for construction and agricultural machinery. Such a solution is a digital hydraulic cylinder that uses several active areas and a constant pressure supply with which a gradual variation of the driving force can be obtained. Traditional hydraulic systems have high energy losses due to the need to direct and throttle the flow through different valves. The article presents simulations in the AMESim environment and laboratory experiments of a digital hydraulic cylinder with three active areas. Through numerical simulations, the authors aim to highlight the energy efficiency of a digital hydraulic cylinder compared to a hydraulic cylinder in a conventional drive.

REZUMAT
Avand in vedere necesitatea reducerii emisiilor cu efect de sera, se pot adopta noi solutii eficiente energetic pentru utilajele de constructii si agricole. O astfel de solutie este un cilindru hidraulic digital care utilizeaza mai multe suprafete putandu-se obtine o variere în trepte a fortei de acționare cu presiune de alimentare constanta. Sistemele hidraulice traditionale au pierderi energetice mari din cauza necesitatii de a directiona si strangula debitul prin diferite valve. In articol se prezinta simulari in mediul AMESim si experimentari de laborator ale unui cilindru hidraulic digital cu trei arii active. Prin simularile numerice autorii isi propun sa scoata in evidenta eficienta energetica a unui cilindru hidraulic digital fata de un cilindru hidraulic dintr-o actionare clasica.

INTRODUCTION

Reducing fuel consumption and implicitly carbon emissions in the atmosphere requires the adoption of energy efficient solutions for mobile machinery. In order to reduce unnecessary energy consumption in hydraulic actuations, throttling losses that occur when using proportional valves must be avoided.
For mobile machines, solutions have been adopted to reduce energy consumption, such as load sensing systems (LS) through which hydraulic actuators can be controlled depending on the load variation or secondary control systems (SCS) where the output unit (secondary) is connected to a constant pressure pipeline. The system operates in a high pressure network coupled with a hydraulic accumulator. The purpose of the hydraulic accumulator is to store the energy supplied to the network by the secondary unit when it is reversed (e.g. decelerating a load). When operating under load, the accumulated energy is used to compensate for consumption peaks. While the primary actuations work with an interface through volumetric flow, the systems with secondary control are connected through the specific operating pressure. Systems with secondary control are only suitable for actuations with rotating loads, and for linear actuators other solutions must be used in order not to introduce excessive throttling. One solution is the switching control of hydraulic cylinders with multiple chambers, which can be used to achieve force control by discretely varying the area of the hydraulic cylinder. This solution regarding the parallel connection of the chambers of a digital hydraulic cylinder (DHC), is part of the revised digital hydraulic technologies by Zhang, Q. and Kong, X. *(Zhang et al., 2020). Heemskerk, E. and Bonefeld, R.* studied a semi-binary hydraulic four-chamber cylinder with the aim of improving the force resolution to obtain a more precise control of the cylinder *(Heemskerk et al., 2015)*. For this, one of the cylinder chambers is not connected to the pressure source through a switching valve but with a proportional valve. A study on the use of a multi-chamber cylinder, discretely controlled on/off valves and three pressure lines as

well as a series of useful examples to reach a new level of efficiency in construction machines were outlined by *Heybroek and Norlin, 2015*.

Heybroek and Sahlman developed a highly efficient hydraulic hybrid system for an excavator that uses a multi-chamber cylinder and secondary control, a detailed energy analysis was carried out that explains the energy flow in the hybrid system (*Heybroek et al., 2018*).

Another solution to minimize or completely eliminate the need for proportional valves, thus avoiding throttling losses associated with metering, is through the use of hydraulic transformers, fed from a common pressure line that operates both the working mechanisms and rotary drives from the propulsion system of a front loader (*Heybroek et al., 2012*).

A team from Tampere University of Technology and Aalto University, Espoo in Finland designed, simulated and tested a digital hydraulic multi-pressure actuator with high energy saving potential. It contains a piston pressure accumulator and 4 pressure converters, and the system allows 6 different supply pressure levels that can be connected to the cylinder chambers through on/off valves (*Huova et al., 2017*).

Mäkelä J. determined the traditional, total and regeneration energy efficiencies of the digital hydraulic multi-pressure actuator (DHMPA) used in load-lifting applications in his thesis (*Mäkelä J., 2020*). The efficiency values were determined experimentally. The results showed that DHMPA is feasible to be used in load-lifting applications. *Pedersen* proposed an energy-efficient hydraulic cylinder concept with three pressure lines, which allows reducing throttling losses compared to conventional solutions while maintaining accuracy and control. The final design of the concept was implemented in simulation models to investigate the performance of the developed control system (*Pedersen et al., 2018*).

Changlin, M. and Feng, L. modelled and simulated the mechanism of a variant of DHC, a digital hydraulic cylinder with screw feedback and stepper motor control in order to optimize DHC performance (*Changlin, M. et al., 2020*).

For each machine actuation application, following a complex analysis, modern solutions can be adopted to minimize energy losses. The energy losses of inefficient hydraulic installations lead to the excessive heating of the hydraulic fluid, a fact that can lead to the premature failure of the machines, in addition to the emission of greenhouse gases.

MATERIALS AND METHODS

Digital hydraulic system

A series of laboratory experiments were carried out with a DHC with three active chambers that highlighted the 7 stages of force and speed that can be achieved by connecting the cylinder chambers in parallel. The diagram of the stand can be found in figure 1, and in figure 2 it can be seen the block with 4 valves for connecting the DHC chambers according to the command stages. The surfaces of the active chambers of the cylinder are: 5 cm^2, 13.5 cm^2, 14.7 cm^2, the rod backward chamber having 20.6 cm^2. A pump with a maximum flow rate of 20 l/min and a fastening device for the DHC and the hydraulic load cylinder were used, connecting the rods by means of a force transducer.

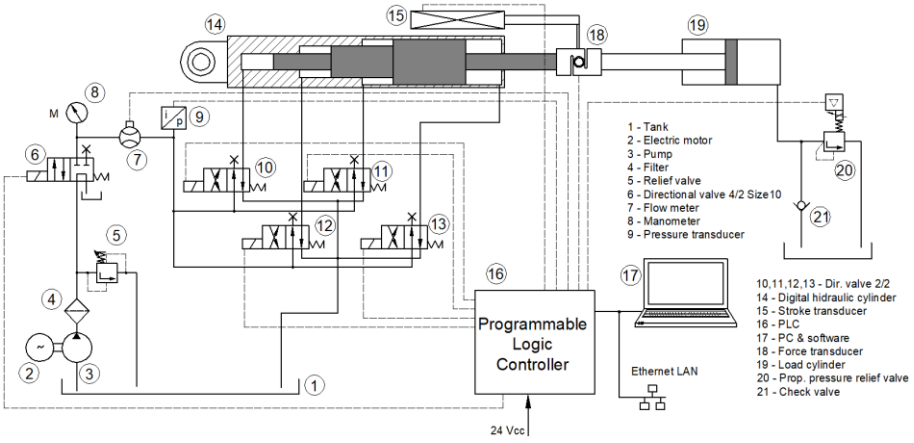

Fig. 1 - Scheme of the test stand for DHC with three chambers

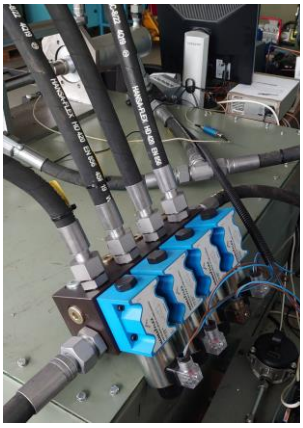

Fig. 2 - Block with 4 valves for connecting DHC chambers

A programmable logic controller was used to control the solenoid valves and to acquire data. The tests were carried out with a virtual instrument application made in the LabView environment. The application communicates with the programmable logic controller through the Modbus TCP/IP protocol, each solenoid of the directional valves, the proportional valve and the transducers having each assigned an address in the programmable logic controller. The test method consisted in the successive command of the electrovalves in order to realize the combinations of the cylinder chambers to obtain a successive increase in the active surface of the DHC. The switching of the stages was done in short times so that the 250 mm stroke of the hydraulic cylinder did not end until all the control stages were achieved. On the diagrams recorded for the force and stroke of the hydraulic cylinder rod, one can see the 7 stages that the three-chamber DHC can achieve. Summing up the combinations of areas of the chambers of the hydraulic cylinder with several lines of pressure, the number of force stages that a DHC can achieve, can be increased. *Dell-Amico, A. and Carsson, M.* investigated an actuation system with a multi-chamber hydraulic cylinder for an excavator arm. The aim of the work was to investigate a cylinder with four chambers with three pressure lines with the generation of 81 force levels, applied to an excavator arm. The different control strategies showed that there is a compromise between accuracy, smoothness of the arm movement and the switching frequencies *(Dell'Amico et al., 2013)*. Figure 3 shows the graphs recorded for the force from the DHC rod for a maximum load set to the load cylinder of 1000 daN. In order to create a gap between steps, the control was deactivated for a short time between steps.

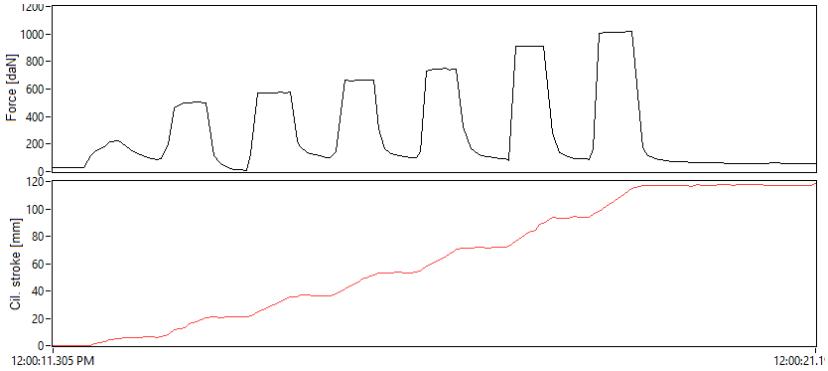

Fig. 3 - Graphs with the variation of the force and stroke of the DHC

In order to determine the energy consumption of the DHC, an actuation system with a digital cylinder with 3 active chambers for advance and a chamber for retraction of the rod was designed and modelled in Amesim (Figure 4). The diameters of the pistons for forward stroke are ∅50 / ∅90 / ∅125, and for backward stroke ∅125. The simulation scheme contains 5 blocks: 1 - ECU, 2 - motor-pump group, 3 - block with valves, 4 - modelled DHC and 5 - load unit. The ECU block: electronic unit control, ensures the command cycle (Figure 5) for obtaining the power levels at the DHC rod. During the simulation, it performs the sequence of the 7 command steps according to Table 1.

Table 1

Energized valves solenoids for different DHC stages

Valve solenoid	DHC Stages							
	Backward	Forward 1	Forward 2	Forward 3	Forward 4	Forward 5	Forward 6	Forward 7
E1		■		■		■		■
E2			■	■			■	■
E3					■	■	■	■
E4	■							

An important issue is related to the structuring of the hydraulic scheme and the appropriate sizing of valves and pipes because in certain situations, e.g. when the cylinder rod is withdrawn and the flow from all the other 3 chambers must be evacuated, high pressure drops may occur. Similarly, when feeding the piston with the smallest area, the speed of the fluid that is evacuated from the other chambers is high and large power losses can occur. The appropriate dimensioning of the exhaust routes to the tank must be taken into account, possibly each valve should have a pipeline directly to the tank or if it is connected to a main pipeline, it should have an increased size.

In the case of conventional actuation systems, there is the situation in figure 6 where the unused power is transformed into heat and eliminated in the environment.

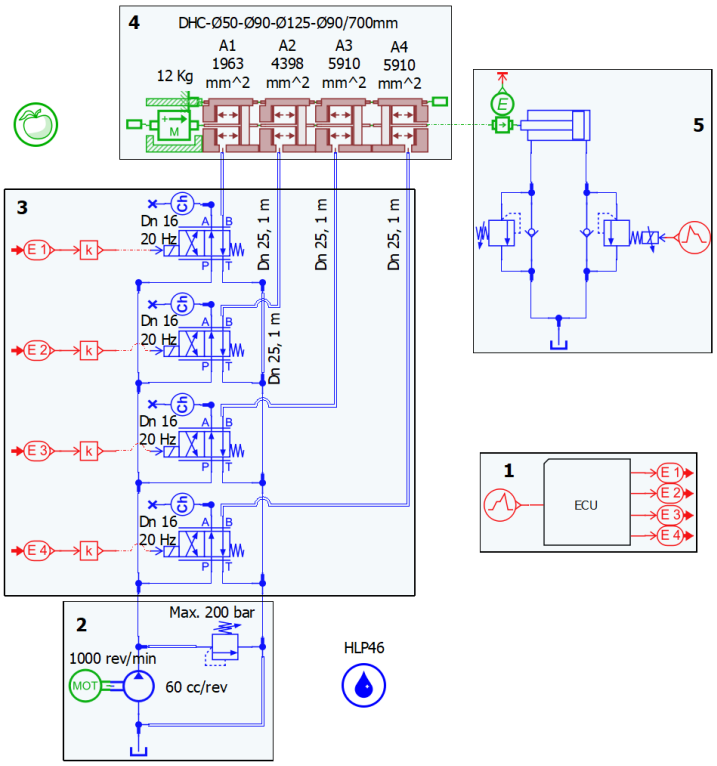

Fig. 4 - The simulation scheme for a drive unit with DHC
1 – electronic control unit ECU; 2 – motor – pump group; 3 – block with valves; 4 – modelled DHC; 5 - load unit

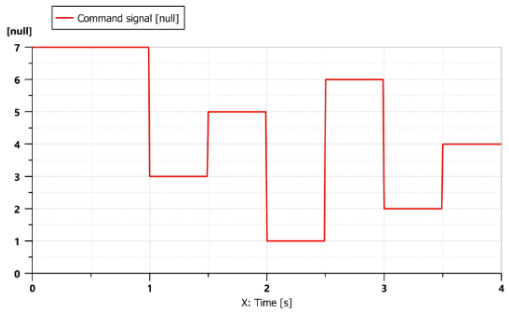

Fig. 5 - Signal for controlling the DHC during simulation

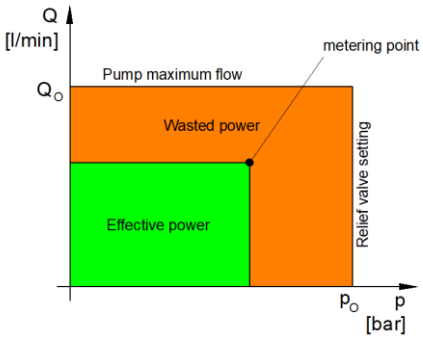

Fig. 6 - Effective power and wasted power

The hydraulic power P of the actuation system can be calculated from the operating pressure p_O and the operating flow rate Q_O provided at the outlet of the pump according to formula (1).

$$P = p_O \cdot Q_O \quad (1)$$

Hydraulic power can also be obtained from the mechanical parameters of the hydraulic motor (DHC), i.e. force F, displacement x or speed $\dot{x}$ according to the formula (2)

$$P = \frac{F \cdot x}{\Delta t} = F \cdot \dot{x} \quad (2)$$

The estimation of the energy consumption E of the actuation system is carried out from flow Q and pressure p, according to the formula (3)

$$E = \int_0^t Q(t) \cdot p(t) dt \quad (3)$$

To determine the total efficiency of the system η_{tot}, the ratio between the output power P_{out} and input power P_{in}, can be calculated as follows:

$$\eta_{tot} = \frac{P_{out}}{P_{in}} \quad (4)$$

At the same time, the total efficiency can be calculated as the product of the volumetric efficiency η_{vol} and the mechanical-hydraulic efficiency η_{mh} according to (5).

$$\eta_{tot} = \eta_{vol} \cdot \eta_{mh} \quad (5)$$

Conventional hydraulic system

In order to evaluate the energy losses from a conventional actuation system with a servo valve, a system like the one in figure 7 was also modelled and simulated. The system is composed of an electric pump that supplies 57 l/min, the system pressure being limited to 250 bar, a servo valve, a hydraulic cylinder with a bilateral rod with bore diameter 100 mm, rod diameter 50 mm and a stroke of 1100 mm. The cylinder rod is coupled with a friction

mass. A speed sensor was also placed in the diagram to measure the speed of the cylinder rod. At the running parameters of the simulation, at additional computations, those for power and energy were checked.

The simulation consisted in obtaining several speed steps at the hydraulic cylinder rod by using a signal source configured in 5 stages according to figure 8.

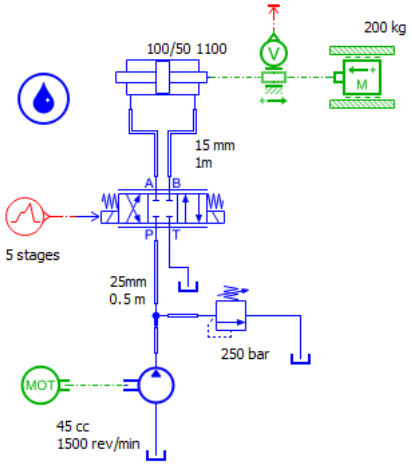

Fig. 7 - Scheme of conventional hydraulic system

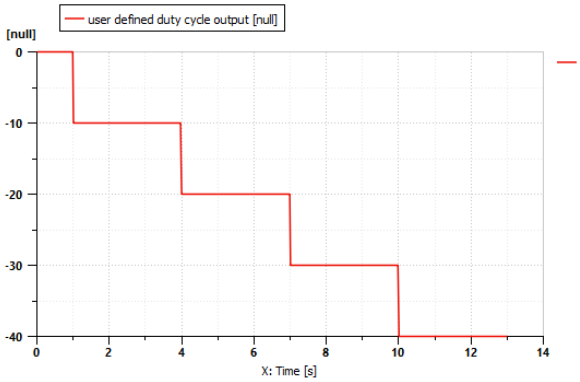

Fig. 8 - Signal for control the servo valve during simulation

RESULTS

The results of the simulations for the digital hydraulic cylinder system and the conventional actuation system are presented below.

Digital hydraulic system

Figure 9 shows the diagrams for the control signals to the solenoids of the block with electrovalves. The shape of the signals corresponds to a typical sequence of the binary states for a 3-bit system.

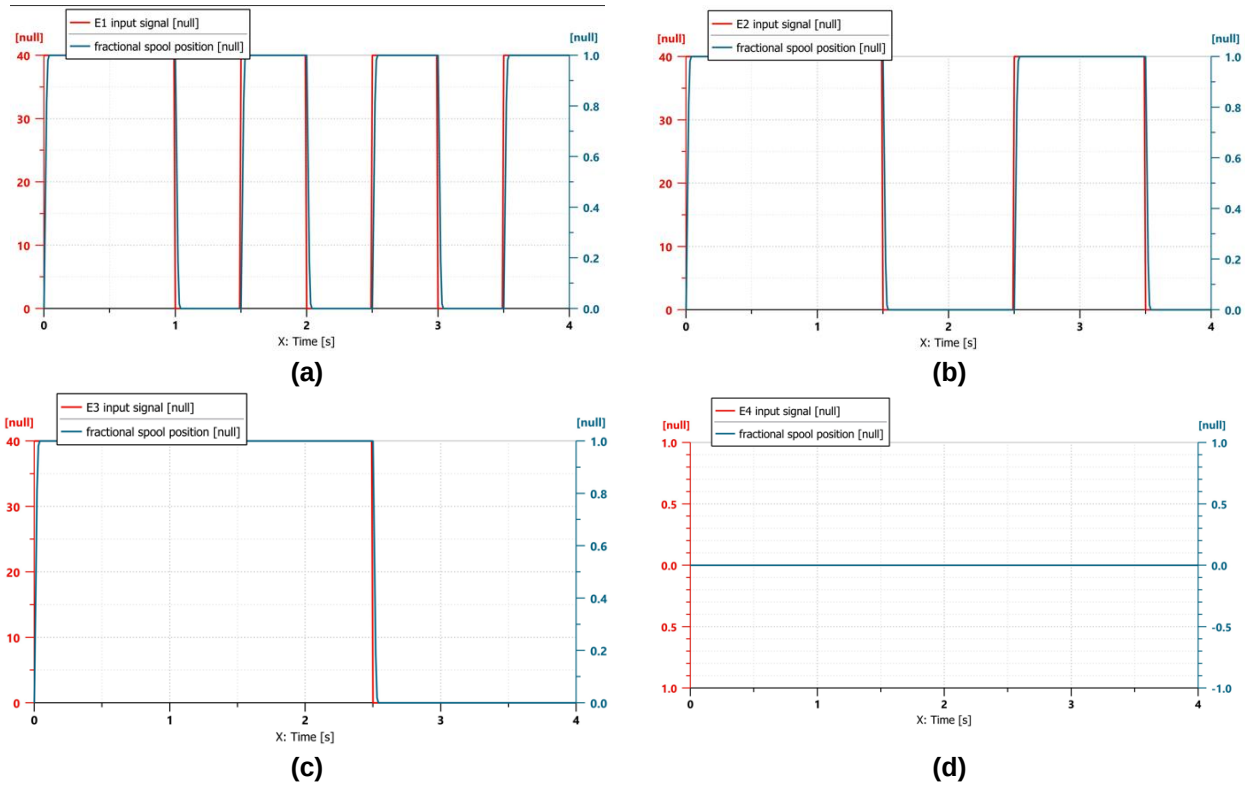

Fig. 9 - Input signals for valves solenoids and fractional spool position

a – E1 solenoid signal / spool position; b – E2 solenoid signal / spool position;
c – E3 solenoid signal / spool position; d – E4 solenoid signal / spool position

Figure 10 shows the pressure variation diagrams in the DHC chambers. The pressure variation in the three active chambers also corresponds to the binary states of the 3-bit system. The pressure variation in chamber A4 is due to a pressure drop that reaches a maximum of 6.4 bar on the hydraulic fluid discharge route to the tank, in correspondence with the movement speed of the DHC piston or the flow rate of hydraulic fluid discharged from the chamber.

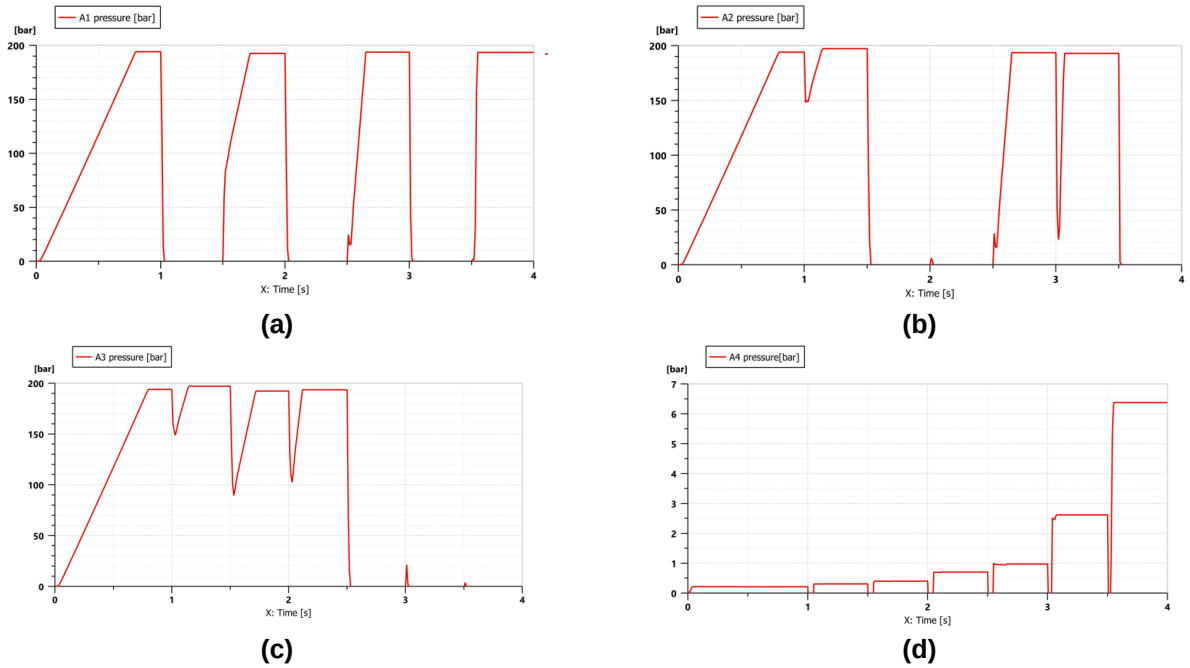

Fig. 10 - Pressure for DHC chambers

a – A1 DHC chamber; b – A2 DHC chamber; c – A3 DHC chamber; d – A4 DHC chamber

The graphs with the variation of the DHC parameters during the simulation can be found in figure 11. In figure 11(a) one can see the movement of the DHC rod. The DHC speed depending on the control step is in figure 11(b). The force exerted on the DHC rod depending on the control stage can be found in figure 11(c), the force obtained being dependent on the level set in the load block by the command transmitted to the valve. In figure 11(d), one can see the DHC acceleration when switching the control stages.

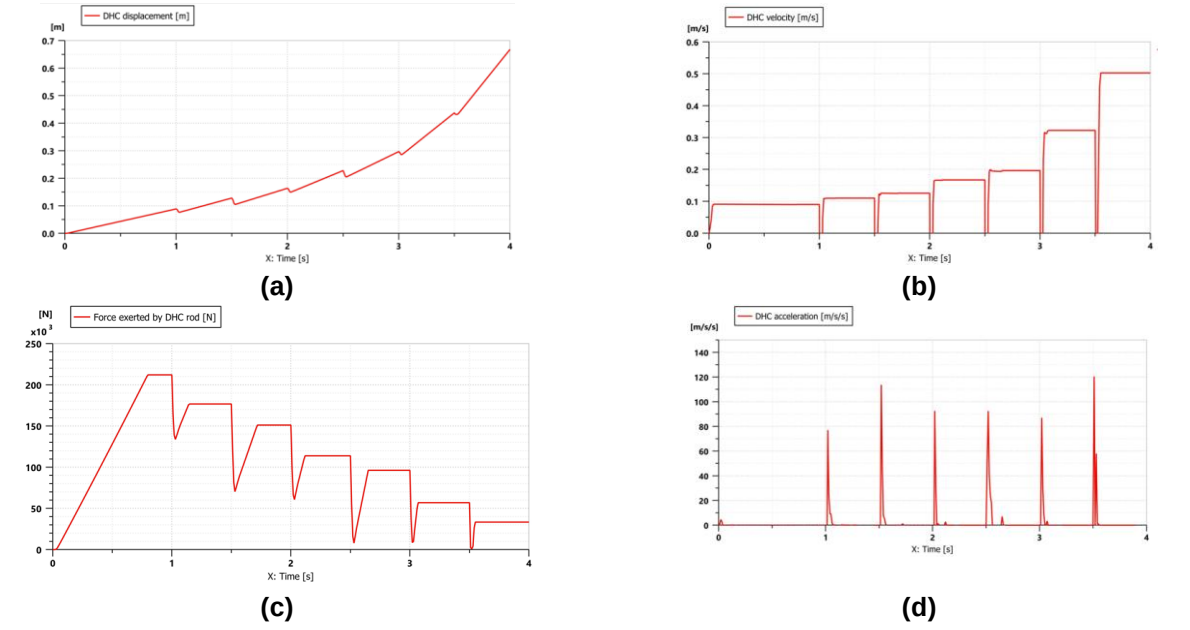

Fig. 11 - The response diagrams of the DHC during the simulation

a – DHC displacement; b – DHC acceleration; c – DHC velocity;
d – Force exerted by DHC

Figure 12 shows the diagrams with shaft speed and torque of the pump. It can be seen that the torque at the pump shaft is constant throughout the simulation, in correspondence with the maximum pressure in the system of approximately 195 bar. Figure 13 shows the graphs with the useful power provided by DCH and the energy consumed during the simulation. The power graph is useful for calculating the efficiency of the DHC drive system. By averaging the power used on each DHC control stage, a useful power of 18.5 kW is obtained. Drive power is 22 kW taking into account also the total efficiency. Using formula (4) results in an efficiency of DHC drive system of 84%, which varies very little with the command stage of the valves block.

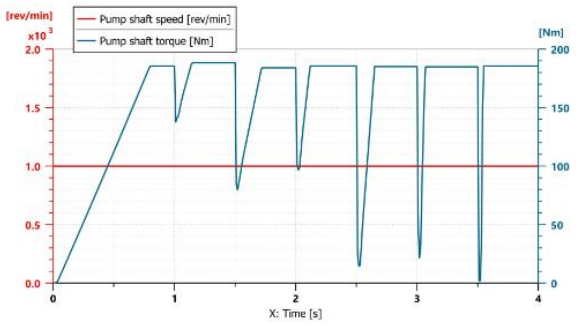

Fig. 12 - Pump shaft speed and torque

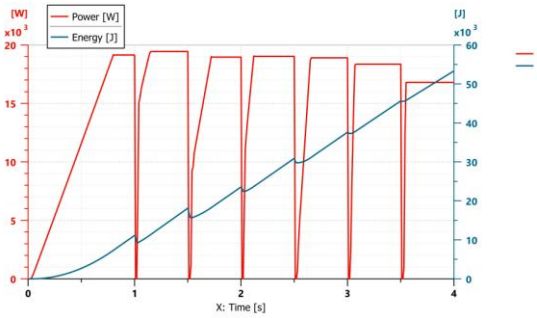

Fig. 13 -The useful power of DCH and the energy consumed

Conventional hydraulic system

In the case of the conventional hydraulic system, the simulation was carried out to obtain speed steps at the rod of a servo cylinder that moves a mass with friction. In order to obtain distinct speed steps during the 1100 mm stroke, the servo valve command was limited to 30%. This fact allowed a precise metering of the flow, which feeds the cylinder, but with the disadvantage of additional throttling losses. After the simulation, the pressure and flow variation at port A of the servo valve was obtained (figure 14). The flow steps obtained for the command stages were 15, 29, 43 and 57 l/min, and the pressure level was at 125 bar. In figure 15, the graphs for the stroke and speed of the piston of the hydraulic cylinder were obtained. Each speed step is found in segments with different slopes on the displacement diagram up to the maximum stroke of the cylinder.

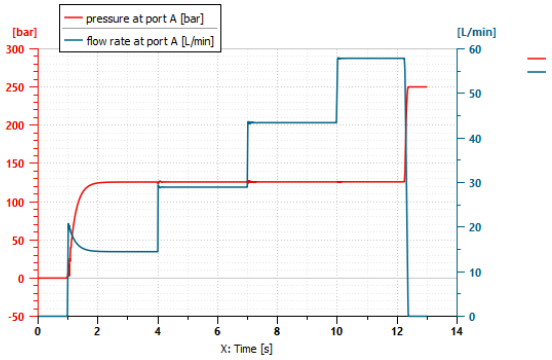

Fig. 14 - Pressure and flow at port A of servo valve

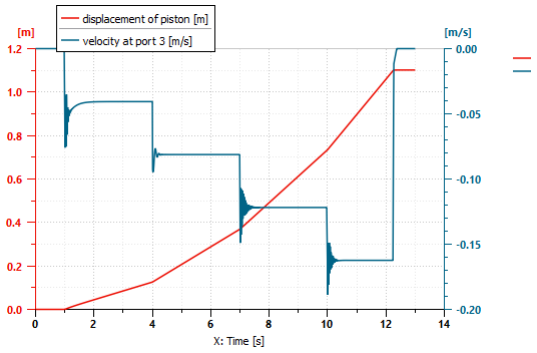

Fig. 15 - Piston stroke and speed of hydraulic cylinder

Figure 16 shows the power and energy dissipated during the simulation by the servo valve. One can see the correspondence with figure 17 in which the power dissipated by the relief valve is in inverted magnitude to the power dissipated by the servo valve.

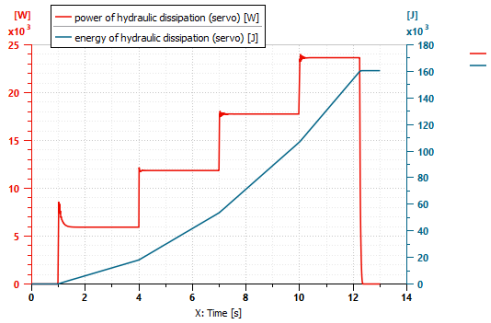

Fig. 16 - Energy and power dissipated by the servo valve at different control stages

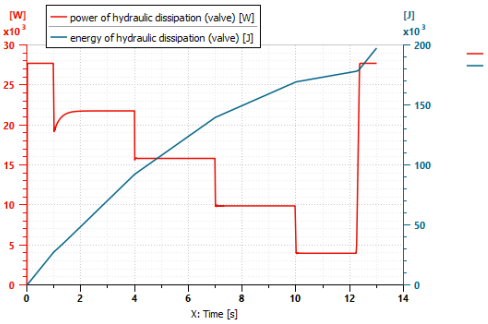

Fig. 17 - Energy and power dissipated by the valve at different control stages

When the metering section from the servo valve is small, the excess flow is discharged through the relief valve, and at maximum command, the power dissipated by the servo valve is maximum, and that dissipated by the relief valve is minimum. Considering the simulation scheme from fig. 7 the maximum efficiency obtained after the simulation was 42.5% for last stage of the simulation.

CONCLUSIONS

Conventional actuation systems involve large power losses of a mechano-hydraulic and volumetric nature. In order to increase the energy efficiency, the linear actuators can be provided with secondary control by using some hydraulic cylinders to which the nominal area can be discreetly adjusted. These actuation systems can be fed at constant pressure by pumps with fixed nominal volume which can be gear pumps that have a low price. The simulation carried out for an actuation system with DHC showed a much better energy efficiency compared to a conventional actuation system. Digital hydraulic cylinders in combination with digital on/off valves and controllers with specialized software can lead to an increase in energy efficiency in actuation systems for construction or agricultural machines. Future work will consider using more pressure lines for DHC and obtaining a greater number of force control steps.

ACKNOWLEDGEMENT

This paper has been funded by the Romanian Ministry of Research and Innovation under NUCLEU Programme, Financial Agreement no. 18N/2019, Ad 14/2021, Project code PN 19-18.01.01, Phase 19 “Research on the realization of mechatronic systems for the control of speeds and forces with digital hydraulic equipment or piezoelectric pneumatic equipment”.

REFERENCES

[1] Changlin, M., Feng, L., Lin, H. and Yangyang, H. (2020). Mechanism Modeling and Simulink Simulation Analysis of Digital Hydraulic Cylinder, *2nd International Conference on Computer Modeling, Simulation and Algorithm Journal of Physics: Conference Series Volume 1624*, IOP Publishing https://doi.org/10.1088/1742-6596/1624/2/022010

[2] Dell’Amico, A., Carlsson, M., Norlin, E., Sethson, M. (2013). Investigation of a Digital Hydraulic Actuation System on an Excavator Arm, *Conference Paper The 13th Scandinavian International Conference on Fluid Power, SICFP2013*, 505-511, Linköping, Sweden, https://dx.doi.org/10.3384/ecp1392a50

[3] Heemskerk, E., Bonefeld, R., and Buschmann, H. (2015). Control of a semi-binary hydraulic four-chamber cylinder, *Proceedings of the 14th Scandinavian international conference on fluid power*. Tampere, Finland. https://researchportal.tuni.fi/files/4075662/SICFP15_proceedings.pdf

[4] Heybroek, K., Norlin, E. (2015). Hydraulic Multi-Chamber Cylinders in Construction Machinery, *Hydraulikdagarna Conference Paper, Linköping, Sweden* http://urn.kb.se/resolve?urn=urn:nbn:se:liu:diva-140877

[5] Heybroek, K., Sahlman, M. (2018). A hydraulic hybrid excavator based on multi-chamber cylinders and secondary control – design and experimental validation, *International Journal of fluid Power Vol.19,* Taylor & Francis, https://doi.org/10.1080/14399776.2018.1447065

[6] Heybroek, K., Vael, G.E.M., and Palmberg, J.-O. (2012). Towards resistance-free hydraulics in construction machinery. *In*: *8th international fluid power conference*. Dresden, Germany. https://www.diva-portal.org/smash/get/diva2:1051345/FULLTEXT01.pdf

[7] Huova, M., Aalto, A., Linjama, M., Huhtala, K., Lantela, T. & Pietola, M. (2017). Digital hydraulic multi-pressure actuator – the concept, simulation study and first experimental results, International Journal of Fluid Power, 18:3, 141-152, https://doi:10.1080/14399776.2017.1302775

[8] Mäkelä, J. (2020). *Energy efficiency of a digital hydraulic multi-pressure actuator for use in load-lifting applications* [Master Thesis, Aalto University School of Engineering], AaltoDoc https://aaltodoc.aalto.fi/handle/123456789/46128

[9] Pedersen, N.H., Jensen, S.C., Hansen, R.H., Hansen, A.H., Andersen, T.O. (2018). Control of an Energy Efficient Hydraulic Cylinder Drive with Multiple Pressure Lines, *Modeling, Identification and Control (MIC), 39(4)*, 245-259, Norsk Forening for Automatisering, http://dx.doi.org/10.4173/mic.2018.4.2

[10] Zhang, Q., Kong X., Yu, Bin, et al. (2020). Review and Development Trend of Digital Hydraulic Technology. *MDPI, Applied Sciences 2020, 10, 579*. https://doi.org/10.3390/app10020579

A PEST ACCURATE SEGMENTATION METHOD BASED ON CRITICAL POINT NONLINEAR ENHANCEMENT
/
基于临界点非线性增强的虫害精准分割方法

JunLin MU [1)], JinXing WANG [*123)], ShuangXi LIU [*123)], Zhen WANG[2)], Hao JIANG [1)], Bo MA[1)], ZhengHui ZHANG[1)], XianLiang HU[4)])[1]

[1)] College of Mechanical and Electronic Engineering, Shandong Agricultural University, Taian 271018, China
[2)] Shandong Province Key Laboratory of Horticultural Machinery and Equipment, Taian, 271018, China;
[3)] Shandong Agricultural Equipment Intelligent Engineering Laboratory, Taian 271018, China;
[4)] Jinan Xiangchen Technology Co., LTD.; Jinan, 250100; China
Tel: +86 05388242336; E-mail: mjl19970127@163.com; shuangxiliu168@163.com
DOI: https://doi.org/10.35633/inmateh-68-02

Keywords: *low contrast image; nonlinear enhancement; pest image; accurate segmentation*

ABSTRACT
The core of intelligent and accurate plant protection of pests is the accurate identification of pest monitoring and early warning model, and the quality of pest sample image is crucial to the model identification accuracy. To solve the problem of complicated background and low contrast colour image samples, in this paper it is proposed a pest accurate segmentation method based on critical point nonlinear enhancement. The segmented image is used as the sample image of the Faster R-CNN model, which can improve the accuracy of the recognition model. Firstly, the original image is segmented by a strong classifier and the image of pest cells with calibrated grids is obtained. Secondly, the Spline adjustment curve is fitted according to the core gray scale range and critical point, and the contrast between pest and mesh in pest monomer image is enhanced based on the Spline adjustment curve. Finally, there are some operations for the enhanced image such as threshold segmentation, contour extraction, morphological transformation and others to obtain the pest image without background interference, and some segmentation experiments are performed to the pest image based on different segmentation methods. The experimental results show that the proposed method can accurately segment the pests in complex background, and the comprehensive evaluation indexes such as recall ratio and precision rate are greater than or equal to 91.5%, which is better than the traditional segmentation method.

摘要
虫害智能精准植保的核心是虫害监测预警模型的精准识别，而虫害样本图像的质量是决定模型识别精度的关键。为解决其图像样本背景复杂、色彩对比度低等问题，本文提出一种基于临界点非线性增强的虫害精准分割方法。将分割后的图像作为 Faster R-CNN 模型的样本图像，提高识别模型精度。首先，使用强分类器对原始图像进行初步分割，获得含标定网格的虫害单体图像；其次，根据核心灰度范围与临界点拟合 Spline 调整曲线，将虫害单体图像基于 Spline 调整曲线增强虫体与网格的对比度。最后，对增强后的图像进行阈值分割、轮廓提取、形态学变换等操作，获得无背景干扰的虫害图像，并基于不同分割方法对虫害图像进行分割试验。试验结果表明：本文所提方法能在复杂背景中准确分割虫体，且查全率、查准率等综合评价指标均大于等于 91.5%，分割效果优于传统分割方法。

[1]*JunLin Mu, M.S. Stud. Eng.; JinXing Wang, Prof. Ph.D. Eng.; ShuangXi Liu, As. Ph.D. Eng.; Zhen Wang, M.S. Stud. Eng.; Bo Ma, M.S. Stud. Eng; ZhengHui Zhang, M.S. Stud. Eng.; Hao Jiang, M.S. Stud. Eng.; XianLiang Hu, As. Ph.D. Eng.*

INTRODUCTION

In the process of planting crops, they are susceptible to various pests. Insect pest has seriously threatened the yield and quality of agricultural products, and spraying pesticide is an important means of effective pest control. How to apply pesticides reasonably and avoiding overuse of pesticides have become an important research content to improve yield and quality (*GuoPing Wen, 2020*). It is a key measure for reducing pesticide waste to construct pest identification model, monitor and warn about pest and assist pesticide spraying. Traditional intelligent pest monitoring lamp can judge and monitor the insect situation by collecting the number and size of insects, but the types of insect pests cannot be accurately detected in this way. However, the monitoring and warning model based on Faster R-CNN can accurately monitor the type and quantity of insect pests. A large number of high-quality sample images without background interference are required to train this model. The quality and quantity of pest sample images directly affect the identification accuracy of the pest monitoring and warning model. At present, due to the lack of high-quality sample images, removing complex background interference and accurate segmentation are crucial to improving the quality of pest sample images. The images studied in this paper are collected by intelligent pest monitoring lamp. Since the traditional intelligent pest monitoring lamp judges the size of the insect body through the calibration grid, insect catching plate needs to be equipped with the calibration grid, which will reduce the image quality. The enterprise has arranged a large number of such equipment and acquired a large number of images. In order to solve the shortage of high-quality sample images in the training of pest model without updating the equipment, the algorithm in this paper starts from dealing with the existing images, and then amplify the pest image samples.

At present, traditional image segmentation methods include threshold segmentation, edge method, artificial neural network method, watershed method, etc. *Peng Huang et al, (2020*), and different segmentation methods adapt to different segmentation conditions. *Chenxi Liu et al, (2019),* segmented rice pests through improved level set algorithm*. Rong et al, (2022),* proposed a method for identifying and counting pests in field yellow plate based on Mask R-CNN, which solved the problem of inaccurate pest identification and counting by improving the feature pyramid network. *Guangqiang Diao, (2014),* segmented pests and diseases images through the study of Region of Interest detection and background segmentation. Scholars both at home and abroad have also conducted a series of studies on low-contrast image segmentation. In foreign countries, *Sarabpreet et al, (2016),* improved image contrast by combining multi-scale top cap filter and H-maximum value, and proposed a curve initialization level set method to extract the nucleus and cell boundary of contact cells. *Mohammad et al., (2018)*, improved the histogram segmentation technology and normalized the whole image to avoid the entropy loss in the process of image enhancement. In China, *Shuangxi Liu et al., (2016),* segmented corn grains dyed longitudinally through the multi-segment threshold segmentation method and obtained images of corn keratin endosperm and farinaceous endosperm. *Chenghui Han et al., (2018),* proposed a flame image enhancement and segmentation algorithm combining Retinex and CV (Chan-Vese) model, which accurately extracted low-contrast flame images in complex background environment and retained the irregular information of target edge.

The gray scale range of the insect body region extracted in this paper overlaps with the gray scale range of the calibrated grid region, resulting in low contrast. Traditional pest segmentation method has non-ideal segmentation effect. In terms of processing low contrast image, the image segmentation method based on deep learning is not ideal because of the lack of original samples. We often enhance its contrast firstly, and then segment it. So, in this article, we put forward a pest accurate segmentation method based on critical point nonlinear enhancement.

Contrast between insect region and calibration grid region is improved by non-linear enhancement method based on critical point, and complete insect pest image without accurate grid background can be extracted from complex background, which reduces the background grid interference to the shape feature extraction, finally the high quality sample image of insect pest is obtained. Thus, the precision of pest monitoring and early warning model is improved, which lays the application foundation for the research of intelligent spray and precise pesticide application.

MATERIALS AND METHODS

Acquisition and preprocessing of original images

The original image samples used in this paper are taken from the intelligent pest monitoring lamp developed by Jinan Xiangchen Technology Co., LTD. The whole machine structure is shown in Fig.1, which is mainly composed of light trap, industrial camera, electronic control unit and insect catching plate. Among

them, the insect receiving plate adopts the background plate with calibration grid, which aims to facilitate the identification and calibration of pest sample size.

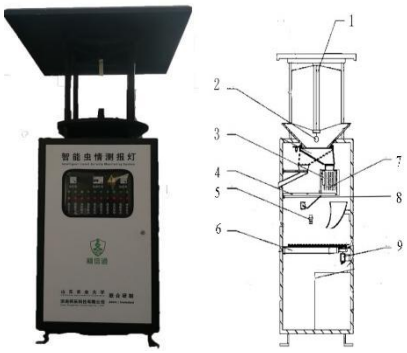

Fig.1 - The overall structure of intelligent pest monitoring lamp

1. Light trap; 2. sex induced core; 3. Insecticidal unit; 4. Electrically controlled turnover board; 5. Industrial camera; 6. Electronic control unit; 7. Oven; 8. Insect catching plate; 9. Driving mechanism

During operation, pests are trapped through light trap and sex induced core, the sex induced core contain insect pheromones. Firstly, pests fall into the pest control unit, and then after being dried in the oven, drop to the electrically controlled turnover board. The electronic control unit controls its turnover, and at the same time, the driving mechanism drives the insect catching plate to rotate, so that the pests randomly drop onto the insect catching plate. Industrial cameras collect pest photos, and upload them to the pest monitoring and early warning model through 5G module for monitoring and warning, which can assist in making pesticide application decisions. Among them, the industrial camera is MV-CE120-10GC plane array camera. The fixed lens is used to collect pest images during operation, with a resolution of 3264×2448.

Original image acquisition

Intelligent pest monitoring lamp has a fixed camera position, and the fixed light source and focal length are adopted to avoid the influence of illumination and sensor on the image gray scale. The images collected by intelligent pest monitoring lamp include the apple pests extracted in this paper: cutworms, cotton bollworm, armyworms, etc., as shown in Fig.2. As can be seen from Fig.2, the collected single photo contains complex background, calibration grid and multiple types of pest samples, and the pest samples are different in size, orientation, position and posture, with little difference in colour and calibration grid, and insects overlap.

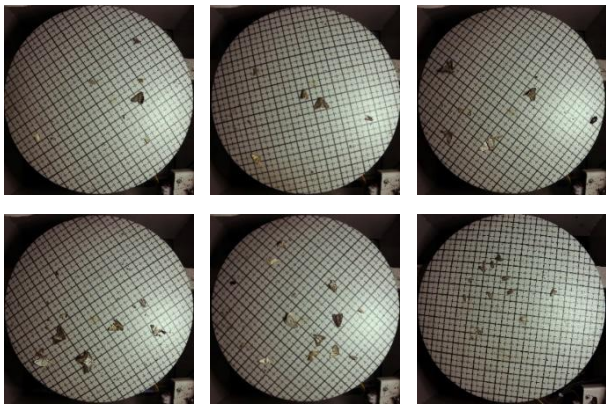

Fig. 2 - Original pest image

Initial Segmentation of Single Pest Image

A strong classifier is generated by Haar-like features and AdaBoost learning algorithm to initially segment single pest and single pest samples containing calibrated grids are obtained. Haar-like feature is a common feature descriptor in the field of computer vision. It is a digital image feature often used in object recognition. Haar-like feature value represents the gray level change of the image. By changing the position and size of the feature template, the image sub-window can list a large number of features to identify the target. As for pests' recognition and segmentation based on Haar-like feature, firstly, Haar-like feature extraction should be carried out on the image, and then the pest feature set and background feature set should be trained to establish a classifier. In order to take into account, the richness and recognition speed of feature sets, four types of Haar-like feature rectangles are set in this paper: A for edge feature, B for linear feature, C for central feature, and D for diagonal feature.

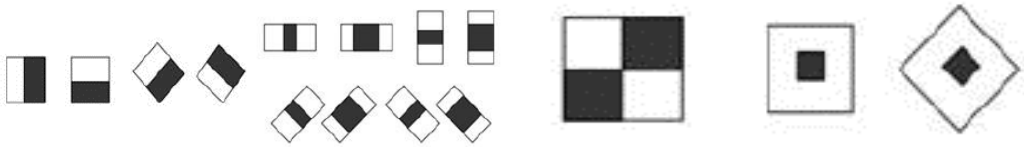

(a) Edge feature (b) Linear feature (c) Central feature (d) Diagonal feature

Fig. 3 - Haar-like feature rectangle

When extracting Haar-like features, the samples are normalized to the same scale of 24 * 24 pixels. Then, the number of Haar-like features is calculated according to Equations (1) ~ (3), and 51664 features are generated for each group of Class A feature rectangles, 28056 features for each group of Class B feature rectangles, 9985 features for each group of class C feature rectangles, and 37600 features for each group of Class D feature rectangles.

$$XY\left[W+1-w\frac{X+1}{2}\right]\left[H+1-h\frac{Y+1}{2}\right] \quad (1)$$

$$XY\left[W+1-z\frac{X+1}{2}\right]\left[H+1-z\frac{Y+1}{2}\right] \quad (2)$$

$$z=w+h \quad (3)$$

Where $W*H$ is the image size; $w*h$ is the characteristic size of rectangle; $X=["W"/"w"]$ is the maximum amplification scale coefficient of the rectangular feature in the horizontal direction; $Y=⌊"H"/"h"⌋$ is the maximum amplification scale coefficient of the rectangular feature in the vertical direction.

After the rectangular features being obtained, in order to improve the calculation speed and strengthen the real-time performance of the algorithm, the integral graph algorithm is introduced to calculate the eigenvalues so as to realize the rapid extraction of Haar-like features. The extracted Haar-like features are input into Adaboost to train and learn.

The Haar-like eigenvalues extracted from the samples to be identified are taken as the input of the strong classifier, and according to the weight of the eigenvalues, the strong classifier gives an evaluation value H to judge whether the samples are insects or not. If H=1, it indicates that the classification result is insect body, which will be segmented and extracted. If H=−1, the detected sample is not insect body. The original image is segmented based on the final generated strong classifier, and the results are shown in Fig.4. It can be seen from Fig.4 that the image after initial segmentation contains not only complete insects, but also the calibration grid, which affects the accuracy of the monitoring and warning model, so the calibration grid needs to be removed.

Fig. 4 - Single insect sample

Critical Point Nonlinear Enhancement

Taking the cutworms as an example, the image after initial segmentation is processed by grayscale processing, gray histogram extraction and watershed algorithm segmentation, and the image shown in Fig.5 is obtained.

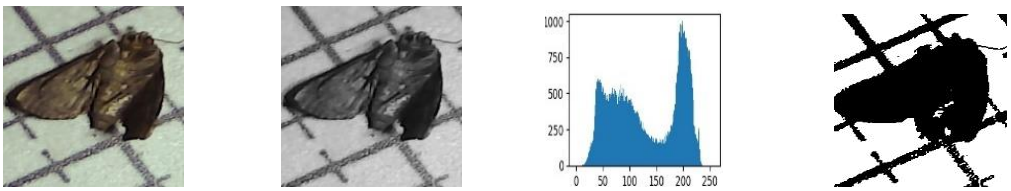

(a) Original pest image (b) Grayscale image (c) Gray histogram (d) Watershed segmentation image

Fig. 5 - Original pest image, Grayscale image, Gray histogram, Watershed segmentation image

Among them, Fig. 5b is a gray image, Fig. 5c is a gray histogram, and Fig. 5d is a watershed algorithm segmentation diagram. As can be seen from Fig. 5c, in the pests gray histogram, the image has bimodal characteristics, and the pixel level of the valley bottom and the peak is significantly different. However, after being segmented by watershed algorithm, due to the low contrast between the calibration grid and the insect body, only the insect body and the calibration grid of the image can be separated with the background, but the insect body and the calibration grid cannot be separated. Therefore, a contrast enhancement method is needed to enhance the contrast between the calibration grid and the insect.

Core Grayscale Range Calculation

The nonlinear enhancement method based on critical point is to increase the dynamic range of gray value by nonlinear adjusting curve, so as to enhance image contrast. According to the gray histogram shown in Fig. 5C, the image gray value after initial segmentation is full of the whole dynamic range, so the image contrast cannot be improved solely by increasing the dynamic range of gray value. The core gray range contains a large number of pixels in the region to be enhanced, and the dynamic range of gray value is small.

Therefore, the dynamic range of gray value is compressed by processing pixels in the core gray range, and then the dynamic range of gray value is increased by nonlinear adjustment curve, finally, the contrast can be enhanced.

Histogram extraction is carried out for the grid region and the insect region respectively, and gray histogram of the grid region and the insect region are obtained as shown in Fig. 6. By analysing the distribution of pixels, it can be seen that pixels in the grid area and the insect area in the gray histogram are concentrated in the middle segment, while less pixels distribute at both ends, and the distribution law is similar to normal distribution. The core of gray level range of grid region and insect body region calculated by the probability density function of normal distribution are (30, 90), (45,130), respectively. Secondly, by gray overlap calculation, the both core grayscale level range is (45, 90). Finally, through nonlinear extension of core grayscale range, contrast between insect body area and calibration grid area is enhanced.

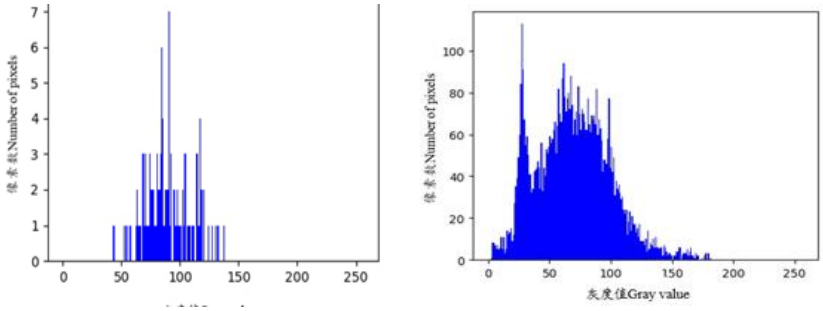

(a) Gray histogram of grid area *(b)* Gray histogram of insect region

Fig. 6 - Gray histogram of insect body and grid area

Critical Point Gray Value Calculation

The single method of nonlinear gray scale expansion for core gray scale cannot achieve the desired enhancement effect, which will result in weak enhancement or over-enhancement phenomenon. In terms of over-enhancement, the gray values of the pixels in the target area and the calibration grid area decrease at the same time, which will lose the features of the target object. However, in terms of weakly-enhancement, the weakening degree of the pixel value of the calibration grid area pixel cannot separate the target object from the background. As shown in Fig.7, threshold segmentation is performed on the enhanced images respectively. It is found that when over-enhancement occurs, however, leading to serious insect region loss at the same time. When weakly-enhancement occurs, the calibrated grid region cannot be separated from the insect region completely, as shown in Fig.8.

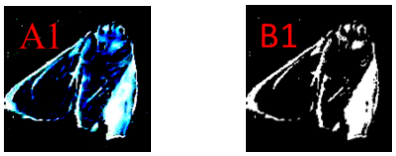

Fig. 7 - Over-enhanced image and its threshold segmentation diagram

Note: A1 is the over-enhanced image, and B1 is the threshold segmentation diagram of the over-enhanced image.

Fig. 8 - Weakly-enhanced image and its threshold segmentation diagram

Note: A2 is a weakly-enhanced image, and B2 is a threshold segmentation diagram of weakly-enhanced image.

In order to reduce weakly-enhancement, the gray value of critical point is required to be within the core gray value range. The nonlinear enhancement of image based on this critical point can maximize the enhancement degree of the insect region features and the suppression degree of the calibrated grid region features, and then achieve the best enhancement effect. In other words, when the gray value of the insect area is less than the critical gray value, the ratio of the total number of enhanced pixel points to the total number of pixel points in the insect region P is obtained; when the gray value of the insect area is greater than the critical gray value, the ratio of the total number of weakened pixel points to the total number of pixel points in the calibrated grid region P is obtained; It is required to maximize the average of P and Q, and the formula is:

$$X=\frac{P+Q}{2} \tag{4}$$

At the same time, in order to prevent over-enhancement in one of the regions and affect the enhancement effect, the critical point should lead to balanced enhancement of the insect region and the grid region, that is, the difference Y between P and Q is the minimum.

$$Y=|P-Q| \tag{5}$$

The comprehensive evaluation index Z is defined as the evaluation index of image enhancement. The larger the Z value is, the better the image enhancement effect is and the higher the contrast is:

$$Z=0.5X+0.5(1-Y) \tag{6}$$

By calculating the evaluation index of image enhancement, the maximum Z-value is 0.826 when the gray value is 80. The critical gray value is finally determined as 80, and its coordinate point in the curve adjustment function is (80, 80).

Spline Curve Fitting

The final Spline nonlinear adjustment curve is generated by Spline curve fitting the critical point coordinates (C, C), origin coordinates (0, 0), (a, 255), (b, 0) and the right-most coordinates of the curve (255, 0), where a is the minimum gray value of the core gray scale range, b is the maximum gray value of the core gray scale range, and c is the critical gray value. The non-linear adjustment curve of Spline is shown as follows:

$$S=\begin{cases}0.00003\ r^4-0.0047r^3+0.1374r^2+6.7948r-10.623 & r<90\\ 0 & r>90\end{cases} \tag{7}$$

Where S is the gray value of pixel points after adjustment, r is the gray value of pixel points before adjustment.

After the image is enhanced by Spline adjustment curve, threshold segmentation is performed on the images before and after the enhancement respectively, as shown in Fig.9. It can be seen from Fig 9b and 9c that, after threshold segmentation of images enhanced by Spline adjustment curve, there is an obvious boundary between the insect area and the calibration grid, while there is no obvious boundary between the calibration grid and the insect of the image without adjustment curve enhancement.

(a) Enhanced image (b) Threshold segmentation (c) Non-enhanced threshold segmentation

Fig. 9 - Enhanced image and its threshold segmentation diagram and non-enhanced image threshold segmentation diagram

Accurate Segmentation of Pest Samples

In the process of different pest sample images, the core gray scale range and critical point of insect area and calibrated grid area are different due to the different gray scale range of insect area. Therefore, in order to achieve better segmentation effect, the gray values at the left and right ends of the core gray scale and critical point gray values should be calculated during the segmentation of different pests. The final Spline nonlinear adjustment curve is generated by Spline curve fitting through (0, 0), (a, 255), (c, c), (b, 0), (255, 0). Finally, the Spline nonlinear adjustment function is used to enhance the contrast between the insect region and the background region, and a high-contrast image is generated for subsequent segmentation.

Image enhancement is performed on the pest samples by nonlinear enhancement method based on the critical point, and threshold segmentation operation is performed on the nonlinear enhanced images and the unenhanced images at the same time. The results are shown in Fig.10. A1~A4 are the images enhanced by Spline nonlinear adjustment curve, B1~B4 are the threshold segmentation images enhanced by Spline nonlinear adjustment curve, and C1~C4 are the threshold segmentation images not enhanced by Spline nonlinear adjustment curve. By comparing B1~B4 with C1~C4, it can be found that, in the image B1~B4 through enhanced threshold segmentation, the pest region is separated from the calibration grid region, while in the image C1~C4 directly through the threshold segmentation, the calibration grid region is not separated from the pest region.

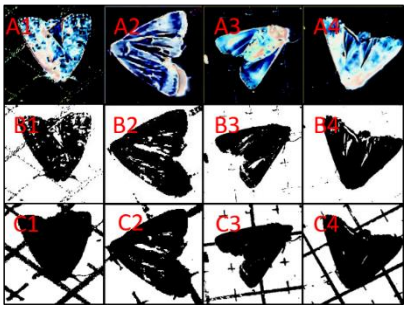

Fig. 10 - Image before and after enhancement and its threshold segmentation results

Note: The first row is a nonlinear enhanced image, and the second row is a threshold segmentation image of the first row. The third row image is the threshold segmentation image without nonlinear enhancement.

Due to different core gray scale range of each insect pest body, different segmentation functions should be created according to the pest species during the creation of segmentation model, that is, different Spline nonlinear adjustment curves should be established. In order to improve the applicability of the segmentation method and meet the requirements of accurate extraction of all kinds of pests, strong classifier will be used to classify the insect images, and different kinds of insect images will be separated by different segmentation models.

Accurate Extraction of Insect Body

The precise pest segmentation process based on critical point nonlinear enhancement is shown in Figure 11. Firstly, through Haar-like feature extraction and strong classifier generated by Adaboost, the pest monomer samples are segmented from the original image and the pest monomer image containing the calibrated grid is obtained. The segmented monomer pest images are classified according to species. Secondly, after being processed by each nonlinear adjustment function, each pest is processed by threshold segmentation. Through comparing the obtained image and the threshold segmentation result, it is found that binary image through piecewise nonlinear enhancement can separate insect body with the calibration grid, which is convenient for subsequent morphological processing. The image segmented by threshold still has a small number of noise interference points, so it is necessary to conduct contour statistics and the images are arranged according to contour size, and only the largest contour, namely the insect contour, is retained at last. For the noise interference inside the pest image, the cavity filling method is used to remove the interference and finally the complete pest binary image is obtained. Finally, the original image is combined with the binary image of insect pest to obtain the sample image only containing insect area. The background and calibration grid are completely removed to achieve accurate segmentation of pest samples.

Since the core gray scale range of each pest is different, different segmentation models should be built according to the pest species when establishing segmentation models, that is, different nonlinear Spline adjustment curves should be built according to the core gray scale range and critical points of images of

different pests. In the process of insect extraction, strong classifier is used to preliminarily classify insect images, and the segmented insect monomer images are classified and screened according to species. Insect images of different species are separated by different segmentation models to improve the applicability of the segmentation method and meet the requirements of accurate extraction of various insect bodies.

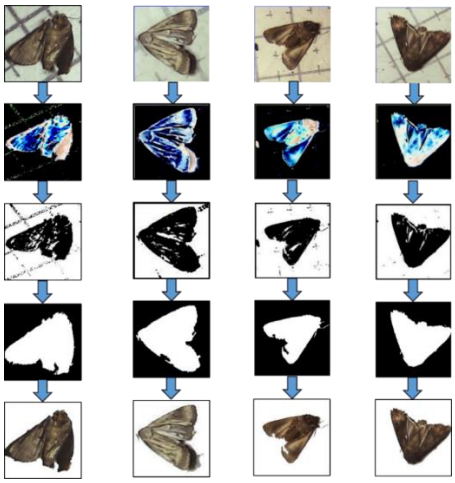

Fig. 11 -Segmentation flow chart

Note: from the top to the bottom, a single sample image Ai, a nonlinear enhancement image Bi, a threshold segmentation image Ci, a two-value image containing the insect contour Di, and no background image at all Ei and Fi (this method and manual segmentation), i=1÷6.

RESULTS

Test Design

In order to test the accuracy of the method proposed in this paper, manual segmentation is used as a reference standard to conduct comparative tests on the same pest image with different segmentation methods. Based on the method proposed in this paper, segmentation tests are carried out on different pest images, and then traditional segmentation methods such as Otsu threshold method, watershed method and regional growth method are used for segmentation tests on the same pest sample images, so as to compare and analyse the performance advantages of the proposed method in pest image segmentation.

Results of Pest Segmentation under Different Segmentation Methods

The proposed method is used to segment the images of 200 samples, including the main apple pests such as cutworms, cotton bollworm, armyworms, and common deer moth. In order to quantitatively evaluate the segmentation effect of pests, two indexes, global recall ratio (G_r) and global precision ratio (G_p), are introduced to evaluate the segmentation effect. Original image I is divided into N area, and its algorithm segmentation results are $M_{seg}=\{m_{seg}^1, m_{seg}^2, \cdots, m_{seg}^N\}$. The reference segmentation image is $H_{seg}=\{h_{seg}^1, h_{seg}^2, \cdots, h_{seg}^N\}$, and recall rate r is the area percentage of the overlap of the region m_{seg} obtained by this algorithm and the matching region h_{seg}^m in the reference segmentation region h_{seg}^m. The accuracy p is the area percentage of the overlapping part of the region m_{seg} obtained by segmentation in this paper and the matching region m_{seg} in the reference segmentation. The calculation formulas of recall rate, recall rate p, global recall rate G_r, global recall rate G_p, and comprehensive evaluation index F_1 are:

$$r_i=\frac{|m_{seg}^i \cap h_{seg}^{m(i)}|}{|h_{seg}^{m(i)}|}\times 100\% \quad (8)$$

$$p_i=\frac{|m_{seg}^i \cap h_{seg}^{m(i)}|}{|m_{seg}^i|}\times 100\% \quad (9)$$

$$Gr=\sum_{i=1}^{N} w_i \cdot r_i \quad (10)$$

$$Gp=\sum_{i=1}^{N} w_i \cdot p_i \quad (11)$$

$$F_1=2rp/(r+p) \quad (12)$$

Where m_{seg}^{i} is the i^{th} region segmented by the algorithm; $h_{seg}^{m(i)}$ is the matching region of the i^{th} region segmented by the algorithm in the reference segmentation graph; r_i is the recall ratio of region i; p_i is precision ratio of region I; w_i is the weighting coefficient, which is defined as:

$$w_i = |m_{seg}^{i}| / |I| \quad (13)$$

Recall ratio is an index to judge whether the segmentation result contains most features of the target region. The more features of target region the segmentation results contain, the higher recall ratio will be. Precision ratio is an index to judge whether the segmentation result can separate the target region from the background region. The less background features the segmentation results contain, the higher the precision ratio will be.

In order to further verify the advantages of the segmentation method in the segmentation of pest background in this paper, 200 pest sample images are taken as the research object, and different segmentation methods such as text method, Otsu threshold segmentation method, watershed method and regional growth method are used to segment the pest images. The results are shown in Fig.12.

Fig. 12 - Processing results of different segmentation methods

Note: A1 ~ A6, B1 ~ B6, C1 ~ C6, D1 ~ D6, E1 ~ E6 and F1 ~ F6 are the original drawing, Otsu threshold method, watershed method, regional growth method, this method and manual segmentation results respectively

In the pest image, the RGB colour of the insect body and the calibration grid is similar. When the Otsu threshold method is used to segment the image, the insect body region and the calibration grid region are seriously adhered, which makes it impossible to segment the insect body and the calibration grid. The watershed algorithm considers the insect region and the grid region as the same region, which can separate the calibration grid and the insect from the background, but cannot separate the calibration grid from the insect. The segmentation effect of the region growth-based segmentation method is basically the same as that of Otsu threshold segmentation method and watershed algorithm, which cannot separate the calibration grid from the insect. In terms of Otsu threshold method segmentation, although the pest area is extracted, it also mistakenly mistook the grid area with similar colour as the insect body, so the target image could not be accurately segmented. The final result obtained by the proposed method has a high similarity with the manual segmentation result, which can accurately segment the image with low contrast between the insect and the calibration grid, and the segmentation effect is more accurate than the traditional segmentation method.

In order to quantitatively evaluate the segmentation results of pest images processed by different segmentation methods, recall ratios, precision ratios and comprehensive index F_1 of pest images processed by different segmentation methods are counted respectively, and their average values are shown in Table 1.

Table 1

Quantitative evaluation of pest image segmentation results based on different segmentation methods

Evaluation index	Otsu threshold method	Watershed method	Regional growth method	Paper method
recall ratio	96.99%	92.24%	79.01%	93.21%
precision ratio	78.87%	86.31%	50.48%	91.74%
F1	87.93%	89.28%	64.74%	92.47%

Test Analysis

According to the analysis of the test data in Table 1, although the watershed algorithm has a high recall ratio and can separate the pest from the background, it cannot separate the calibrated grid from the pest, resulting in a low precision ratio. The F1 values of Otsu method and watershed algorithm are both below 90%, which could not separate the calibration grid from the pest. The accuracy of Otsu method is lower than that of the present method by 5.43% since the calibration grid area is regarded as the insect area. The recall ratio and precision ratio of the region growth method are very low, and it is impossible to separate the background from the pest. Traditional segmentation methods cannot segment the calibrated grid from the insect. The recall ratio, precision ratio and F1 value of the proposed method are all above 91%, which can separate the insect from the background and grid, and the segmentation effect is the best. Traditional segmentation methods can not accurately distinguish the low-contrast insect region from the calibrated grid region. The segmentation accuracy from low to high is region growth method, Otsu threshold segmentation method, watershed method, this method.

The above pest image segmentation experiments show that the method can accurately segment the pests and low contrast image. Different methods of pests and low contrast image segmentation results show that, the method for low contrast image, and the image with serious gray level range overlap between the target area and interference region, can enhance the contrast, and high contrast image is obtained. Its segmentation effect is superior to the traditional segmentation method with higher segmentation accuracy.

CONCLUSIONS

(1) In order to segment low-contrast insect image accurately, an image segmentation method based on critical point nonlinear enhancement method is proposed. Based on the core gray scale range and critical point, the nonlinear enhancement function is fitted by Spline function to realize the image enhancement of the insect region and the grid region. The enhanced image is processed by threshold segmentation to extract the insect image accurately.

(2) The segmentation effect of the proposed method is compared with that of the traditional segmentation method for low-contrast pest images. The results show that the recall ratio and the comprehensive index of the segmentation results obtained by the proposed method are both above 91%, which is the closest segmentation method to manual segmentation and has the best segmentation effect. Although the segmentation accuracy of region growth method, Otsu method and watershed method is improved successively, but none of them can accurately segment the insect and the background grid, and the final image still has grid interference.

(3) The pest images segmented by the method in this paper without background and grid can be used as the original samples for subsequent deep learning, which can greatly improve the accuracy of identification model, and contribute to subsequent pest identification research and provide high-quality raw materials for intelligent identification.

ACKNOWLEDGEMENT

This work was supported by'' National Natural Science Foundation of China (32071908) and China Agriculture Research System of MOF and MARA (CARS-27)''.

REFERENCES

[1] Biswas S., Sil J., (2020), An efficient face recognition method using contourlet and curvelet transform. *Journal of King Saud University-Computer and Information Sciences*, vol.32, issue 6, pp. 718-729;

[2] Diao G.Q., (2014), Study on Segmentation of Rice Disease and Insect Based on Image. *Zhejiang Sci-Tech University*;

[3] Ding L., Zhou X.H., Chen Y.C., (2017), Improved Segmentation of Low-Contrast Lesions Using Sigmoid Edge Model. *China Medical Equipment*, vol.32, issue 11, pp. 66-70+81;
[4] Huang P., Deng Q., Liang C., (2020), Overview of image segmentation methods. *J Wuhan Univ (Nat Sci Ed)*, vol.66, issue 6, pp. 519-531;
[5] Han C.H., Wang H.Q., Hu Y., (2018), Enhancement and Segmentation Algorithm Study for Low Contrast Fire Image. *Computer science and exploration*, vol.12, issue 1, pp. 163-170.
[6] Jonathan L., Evan S., Trevor D., (2015); Proceedings of the IEEE Conference on Computer Vision and Pattern Recognition (CVPR), pp. 3431-3440;
[7] Rong M. X., Wang Z. Z., Ban B., (2022); Pest Identification and Counting of Yellow Plate in Field Based on Improved Mask R-CNN. *Discrete Dynamics in Nature and Society*, vol. 2022, Article ID 1913577.
[8] Liu C.X., Liu D.M., Yang F., (2019), Partitioning Algorithm for rice pest based on improved level set method. *Journal of Ningxia University (Natural Science Edition)*, vol.40, issue 3, pp. 246-254;
[9] Liu S.X., Fu S.H., Wang, J.X., (2019), Quantitative determination of Maize Endosperm Vitreousness Based on Multi－Threshold Segmentation. *Chinese Journal of grain and oil*, vol.31, issue 09, pp. 141-145;
[10] Mohammad F., Mohammad K., (2018), Information preserving histogram segmentation of low contrast images using fuzzy measures. *Optik*, vol.157, pp. 1397-1404;
[11] Sarabpreet K., Sahambi J.S., (2016), Curvelet initialized level set cell segmentation for touching cells in low contrast images. *Computerized Medical Imaging and Graphics,* vol.49, pp. 46-57;
[12] Wen G.P., (2020), Analysis of key point of technique of apple tree cultivation and pest control. *Journal of fruit resources*, vol.1, issue 2, pp. 46-47+51;
[13] Xu Z.H., Song H.Y., Wu Z.M., Xu Z.F., (2021), Research on crop information extraction of agricultural UAV image based on blind image deblurring technology and SVM. *INMATEH Agricultural Engineering*, vol.64, issue 2, pp. 33-42;
[14] Yang B., Ye J.Y., Wang T.Q., (2002), Adaptive thresholding algorithm on low-contrast image. *Sensor Technology*, issue 6, pp. 34-36;
[15] Zhou L.Z., Fang M.G., Lv J., (2019), Study on automatic segmentation method of low contrast tea bud image. *Silkworm tea communication*, issue 6, pp. 22-25;
[16] Zeng Y., Guo L.Y., Zhao J.Y., (2017), Low contrast small target segmentation algorithm based on neighbourhood space feature. *Laser and infrared*, vol.47, issue 4, pp. 507-512.

SIMULATION OPTIMIZATION OF A CONVEYING AND SOIL-REMOVING DEVICE FOR A CORN STALKS PICKING AND PELLETIZING MACHINE
/
秸秆捡拾制粒机输送除土装置仿真优化

Dezhi REN, Xuewei BAI, Wanyuan HUANGI, Huiting CHENG, Yuanjuan GONG, Luji ZHANG, Wei WANG*
College of Engineering, Shenyang Agricultural University, Shenyang/ China
Tel: +86-024-88487119; E-mail: syww@syau.edu.cn; Corresponding author: Wei WANG
DOI: https://doi.org/10.35633/inmateh-68-03

Keywords: *straw pelletizing, conveying & soil removal, discrete element analysis, simulation test, optimization design*

ABSTRACT
RockyDEM is used to simulate the conveying and soil-removing device to determine its optimal structural parameters in order to solve the problem of low soil removal rate and high straw loss rate of the conveying and soil-removing device of the corn stalks picking and pelletizing machinery. Single-factor and multi-factor simulation tests were conducted with soil removal rate and corn stalks loss rate as evaluation indexes, and blade shell clearance, sieve aperture and pitch as influencing factors. The experimental results show that the soil removal rate and the loss of corn stalks have better consistency with the simulation data. Therefore, the procedures of this study can be used for the design and optimisation of conveying and soil-removing device.

摘要
为解决玉米秸秆捡拾造粒机械的输送除土装置除土率低、秸秆损失率高的问题，采用 RockyDEM 对输送除土装置进行模拟，确定其最佳结构参数。 以土壤去除率和秸秆损失率为评价指标，以叶片与壳体的间隙、筛孔和间距为影响因素，进行了单因素和多因素的模拟试验，土壤去除率和秸秆损失率的试验结果与模型的模拟数据显示出良好的一致性。因此，本研究的程序可用于输送和除土装置的设计和优化。

INTRODUCTION
Pelletizing molding is one of the effective ways to improve the comprehensive utilization of corn stalks (*Huo et al, 2019; Wang et al, 2017*). Most of the domestic corn stalks pelletizing equipment is fixed, has high operating costs and low efficiency, so the development of field corn stalks picking and pelletizing technology is an important trend in the comprehensive utilization of corn stalks in the future. Therefore, it is important to design and optimize a kind of conveying and soil-removing device which is suitable for corn stalks pelletizing.

Ulantuya et al, (2016), studied the factors affecting the performance of screw conveyor, and concluded that the influence law of factors, the primary spin velocity and secondary feed into the speed factors were identified and the best combination of parameters. *Fu Qiankun et al, (2018*), designed a vibrating sieve to solve the problem of high soil content after corn stalks picking and baling, taking the soil removal rate and corn stalks loss rate as the test index, which provided a theoretical reference for the design optimization of conveying and soil-removing devices. In summary, the main research methods for screw conveying and screening at home and abroad are discrete element simulation, but there are fewer studies that combine screw conveying and screening.

This study takes the conveying and soil-removing device of corn stalks picker and pelletizer as the research object, combines the screw conveying and sieving, and conducts discrete element simulation analysis: using the blade shell clearance, sieve aperture and pitch as factors, and the soil removal rate and corn stalks loss rate as indicators, the single-factor and ternary quadratic regression orthogonal rotation combination test is designed to determine the optimal structural parameters. A test bench was built for test verification to provide a theoretical basis for the design of the cornstalks picking and pelletizing machine conveying and soil-removing device.

MATERIALS AND METHODS
Test materials and equipment
Simulation and experimental design of the conveying and soil-removing device for the self-propelled ring die granulator, and analysis of the movement pattern of corn stalks and dust in the conveying and soil-removing device by the discrete unit method were carried out.

In order to facilitate the analysis of the influence of the structural parameters of the device on the conveying and dust removal, a single-factor simulation test was conducted using RockyDEM software, and the device was reasonably modified and simplified to be divided into two parts: the casing and the screw conveying shaft. After the introduction, the material properties of the two parts were set, the casing was fixed, the motion of the screw conveyor shaft was set to rotation, and the working speed of the conveying and soil-removing device was set to 1600 r/min based on the working speed of the self-propelled ring die granulator.

The optimal solution of the structural parameters of the conveying and soil-removing device was obtained through the simulation test, and the model of the conveying and soil-removing device test bench was designed according to the optimal structural parameters, and the test bench test was conducted.

Device structure and working principle

The corn stalks picking and pelletizing machine is powered by 117 kW diesel engine, which can complete the functions of corn stalks picking and crushing, conveying and removing soil, and compressing and forming at one time to realize the function of moving dense pellets in the corn stalks field, as shown in Figure 1. The machine can produce about 1.5t of corn stalks pellets per hour, the pellet forming rate reaches 95%, and the pellet density is between 800~1200kg/m^3. In order to improve the corn stalks pellet forming rate and corn stalks pellet density, the corn stalks soil rate needs to be reduced, so the conveying and soil-removing device is optimally designed.

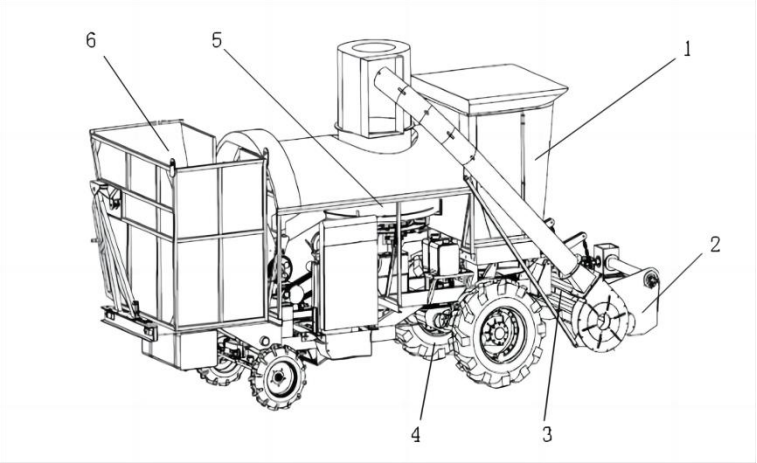

Fig. 1 - Corn stalk granulator

1. Cab 2. Picking Device 3. Conveying and De-Soiling Device 4. Walking Device 5. Molding Device 6. Stock Bin

The structure of the conveying and soil-removing device is shown in Figure 2.

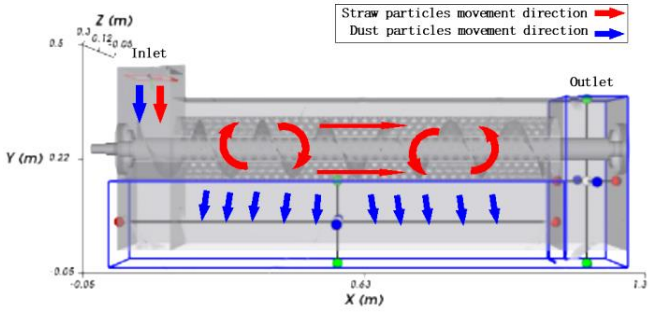

Fig. 2 - Schematic diagram of conveying dust removal device

The corn stalks scattered in the field will be picked up by the picking device with soil, and after being sent into the conveying and soil-removing device, axial movement, tumbling and throwing movement will occur due to the external force exerted by the spiral blade. In the process of movement, the corn stalks and soil are in constant contact with the screen, and the soil is screened out through the screen holes, and the corn stalks are conveyed to the paddle plate, which then throws them to the pelletizing device.

Simulation model and parameter setting

The 4th nodes and internodes of the samples were selected, and the effect of the moisture content of samples on the critical shearing strength was examined at a shearing speed of 15 mm/min.

Samples from different sections of the whole stalk were selected, and the moisture content of each sample was adjusted to 45%±2%, and the effect of the sampling location on the critical shearing strength was examined at a peeling speed of 15 mm/min. The moisture content of the sample in the 4th nodes and internodes were adjusted to 45%±2% to study the influence of the shearing speed on the critical shearing strength. The test was repeated 5 times at each test level, and the variance analysis F value tests were performed at the level of P=0.05.

There are interactions between corn stalks, soil and soil removal device, and the conditions of instantaneous contact and no significant plastic deformation after contact are met in the process of interaction, so the hard sphere contact model is chosen for corn stalks particles and soil particles (*Wang et al, 2017*).

In RockyDEM, the normal force model is set to the Hertzian spring-dashpot model. The normal force model is shown in equation (1).

$$\mathrm{F_n} = \hat{\mathrm{K}}_{\mathrm{H}}\mathrm{S_n^{\frac{3}{2}}} + \hat{\mathrm{C}}_{\mathrm{H}}\mathrm{S_n^{\frac{1}{4}}}\dot{\mathrm{S}}_{\mathrm{n}} \quad (1)$$

$$\hat{\mathrm{K}}_{\mathrm{H}} = \frac{4}{3}E^*\sqrt{R^*} \quad (2)$$

In Equation (1): F_n is the normal force, N. K_H is the stiffness coefficient. C_H is the damping coefficient; S_n is the contact overlap. E^* is the equivalent Young's modulus, Pa. R^* is the equivalent radius, mm.

The equivalent Young's modulus and equivalent radius are shown in equations (3) and (4).

$$\frac{1}{E^*} = \frac{1-v_1^2}{E_1} + \frac{1-v_2^2}{E_2} \quad (3)$$

$$\frac{1}{R^*} = \begin{cases} \frac{2}{L_1} + \frac{2}{L_2} \\ \frac{2}{L} \end{cases} \quad (4)$$

In the Equation (3) and Equation (4): E_1, E_2 is the Young's modulus of the particle-particle or particle-boundary contact; v_1, v_2 is Poisson's ratio; L_1, L_2 is the size of the two particles when the particle is in contact with the particle; L is the size of the particle when the particle is in contact with the boundary.

The damping factor can be found as shown in equation (5).

$$\hat{C}_H = 2\eta_H\sqrt{m^* K_H} \quad (5)$$

In Equation (5): m^* is the effective mass. η_H is the damping ratio of the Hertzian spring-dashpot model.

The effective mass m can be found as shown in equation (6).

$$\frac{1}{R^*} = \begin{cases} \frac{2}{L_1} + \frac{2}{L_2} \\ \frac{2}{L} \end{cases} \quad (6)$$

In Equation (6): L_1, L_2 is the size of the two particles when the particle is in contact with the particle; L is the size of the particle when the particle is in contact with the boundary.

According to the analysis of Antypov and Elliott's study, the damping ratio η is shown by equation (7).

$$\varepsilon = \begin{cases} exp\left[-\frac{\eta}{\sqrt{1-\eta^2}}\left(\pi - arctan\frac{2\eta\sqrt{1-\eta^2}}{1-2\eta^2}\right)\right] & \left(0 \le \eta \le \frac{1}{\sqrt{2}}\right) \\ exp\left(-\frac{\eta}{\sqrt{1-\eta^2}}arctan\frac{2\eta\sqrt{1-\eta^2}}{2\eta^2-1}\right) & \left(\frac{1}{\sqrt{2}} \le \eta \le 1\right) \\ exp\left(-\frac{\eta}{\sqrt{\eta^2-1}}ln\frac{\eta+\sqrt{\eta^2-1}}{\eta-\sqrt{\eta^2-1}}\right) & (\eta > 1) \end{cases} \quad (7)$$

In the Equation (7): ε is the recovery factor.

In RockyDEM, the tangential force model is set to the Coulomb limit model as shown in equation (8).

$$\mathrm{F_\tau} = -\mu\mathrm{F_n}\frac{\dot{\mathrm{s}}_\tau}{|\dot{\mathrm{S}}_\tau|} \quad (8)$$

In the Equation (8): F_τ is the tangential force; μ is the friction coefficient; and S_T is the tangential component of the relative velocity.

SolidWorks software is used to simplify and model the conveying and soil-removing device.

The simplified device mainly consists of two parts: the casing consists of screen and baffle plate, the screen is 1915 mm long and wrapped around the spiral conveying shaft in a positive octagonal shape, and the round hole screen is arranged in a T-shaped arrangement; the baffle plate is divided into front and rear baffle plate, support plate and upper baffle plate; the outer diameter of the spiral blade is 304 mm, the spiral shaft is 114 mm in diameter and the shaft length is 2400 mm. The diameter of the spiral blade is 304 mm, the diameter of the spiral shaft is 114 mm, and the length of the shaft is 2400 mm. The speed of the screw conveyor shaft is set to 1600 r/min by reviewing the literature (*Tian et al, 2018*) and combining with the actual situation.

The material model settings are shown in Table 1 (*Schulz et al, 2019; Kovacs A et al, 2017*).

Table 1

Material model settings

Project Name	Model Type	Vertical Aspect Ratio	Horizontal Aspect Ratio	Number of surfaces	Length range
Soil	Irregular Polyhedra	1.5	1	24	1~2 mm
Corn stalks	Cylindrical	10	1	-	50~100 mm

Referring to the relevant literature, the material property parameters and material contact parameters between the conveying soil removal device casing, soil particles and corn stalks particles were determined as shown in Table 2 (*Li et al, 2019*).

Table 2

Material contact parameters

Interaction	Recovery factor / e	Static friction coefficient / s	Rolling friction coefficient / k
Corn stalks-corn stalks	0.3	0.3	0.01
Corn stalks-soil	0.5	0.5	0.05
Corn stalks-casing	0.3	0.45	0.01
Soil-casing	0.6	0.6	0.05
Soil-soil	0.5	0.4	0.4

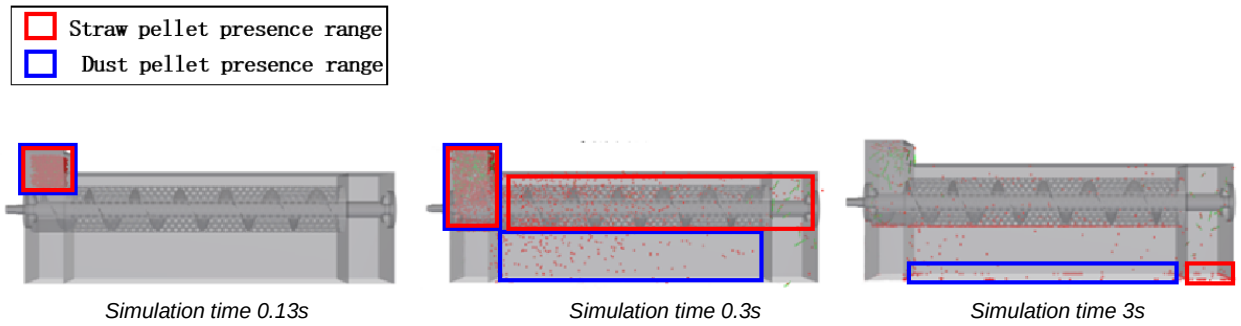

Fig. 3 - Simulation situation under different time steps

The corn stalks-soil mixture feeding time is set to 2 s, and the data collection frequency is 100 points per second. It is known that the machine to be optimized can pick up 1.5~2 t of corn stalks per hour, and the weight ratio of soil to corn stalks is about 1:4. Assuming that the machine picks up 1.8 t of corn stalks per hour, the feeding amount of soil particles is 0.36 t/h, and the feeding amount of corn stalks particles is 1.44 t/h. Figure 4 shows the simulation situation under different time steps, and it can be seen from Figure 3 that the mixture is delivered completely when the total simulation time is 3 s.

Simulation test factors and indicators

In order to study the working performance of the conveying and de-soiling device under different structural parameters, after reviewing the literature, the aperture diameter of the sieve, the pitch and the gap between the blade and the casing were used as the test factors, and the corn stalks loss rate and the de-soiling rate were used as the evaluation indexes of the working performance (*Fu Qiankun et al, 2018*).

According to DB21T 2786-2017 "Technical conditions of biomass solid forming fuels", the corn stalks loss rate of the conveying and soil-removing device should be less than 15% and the soil removal rate should be more than 60%, and the single-factor simulation test was conducted based on this standard. The test results are shown in Figure 4.

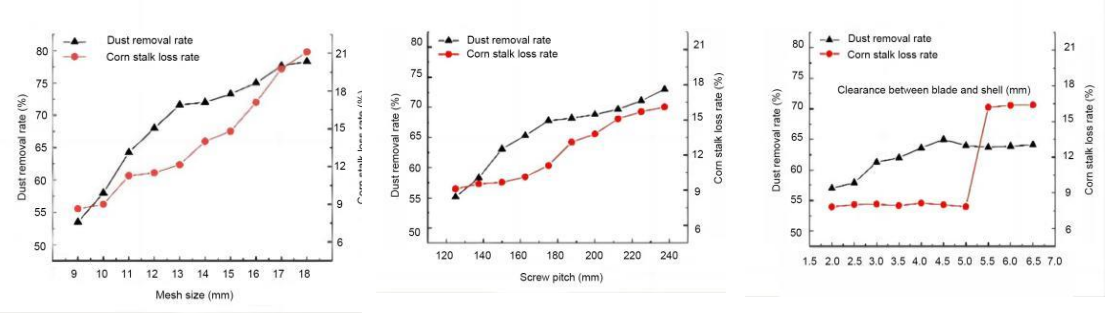

a. Effect of sieve aperture size on soil removal rate and corn stalks loss rate

b. Effect of pitch on the rate of soil removal and corn stalks loss

c. Effect of blade and casing clearance on soil removal rate and corn stalks loss rate

Fig. 4 - Single factor simulation test result

When the simulation is completed, calculate the soil removal rate according to Equation (9).

$$y_1 = \left(1 - \frac{M_y}{M_t}\right) \times 100\% \quad (9)$$

In the Equation (9): M_y is the mass of remaining soil particles, kg; M_t is the total mass of input soil particles, kg.

When the simulation is completed, calculate the corn stalks loss rate according to Equation (10).

$$y_2 = \frac{M_s}{M_j} \times 100\% \quad (10)$$

In the Equation (10): M_s is the lost corn stalks mass, kg; M_j is the total input corn stalks mass, kg.

The simulation analysis of the conveying and soil-removing device shows that: the soil removal rate and corn stalks loss rate increase gradually when the sieve aperture increases; the soil removal rate and corn stalks loss rate increase gradually.

When the pitch increases; the blade shell clearance and the casing increases, and the soil removal takes the lead in increasing and then decreasing. According to DB21T 2786-2017 "Biomass solid forming fuel technical conditions", the range of values is 12~16 mm for the sieve aperture, 150~200 mm for the pitch, and 3~5 mm for the clearance between the blade and the casing.

RESULTS

Results and analysis of single factor test

According to the single-factor simulation test results, the ternary quadratic orthogonal rotating combination test method was used for the characteristic analysis and parameter optimization of the conveying and soil-removing device, and the factor level coding table is shown in the table, and the sieve aperture X_1, pitch X_2, and blade shell clearance X_3 are the actual values of the factors.

Table 3

Coding table of factor level

Code	Sieve aperture / x_1 mm	Pitch / x_2 mm	Blade shell clearance / x_3 mm
+1.682	12	150	3
+1	12.8	160	3.4
0	14	175	4
-1	15.2	190	4.6
-1.682	16	200	5

Experimental results and analysis

The results of the ternary quadratic regression orthogonal rotated combination test are shown in Table 5, with X_1, X_2, and X_3 as factor coded values.

Significance test and regression equation building

The significance test and ANOVA were performed at α=0.05 significance level using Design-Expert data analysis software, and the corn stalks loss rate ANOVA is shown in Table 4 and the soil removal rate ANOVA is shown in Table 5.

Table 4

Analysis of variance

Source	Variance	Degree of freedom	Mean Square	F-value	P-value
Models	392.32	9	43.59	10.91	<0.0001
X_1	78.92	1	78.92	19.76	0.0007
X_2	71.32	1	71.32	17.86	0.0010
X_3	137.82	1	137.82	34.50	<0.0001
$X_1 X_2$	19.03	1	19.03	4.77	0.0480
$X_1 X_3$	0.13	1	0.13	0.031	0.8623
$X_2 X_3$	31.60	1	31.60	7.91	0.0147
X_1^2	3.62	1	3.62	0.91	0.3584
X_2^2	30.13	1	30.13	7.54	0.0166
X_3^2	20.34	1	20.34	5.09	0.0419
Residuals	51.93	13	3.99		
miss drafting	10.77	5	2.15	0.42	0.8236
Error term	41.15	8	5.14		
Total error	444.25	22			

Table 5

Analysis of variance

Source	Variance	Degree of freedom	Mean Square	F-value	P-value
Models	910.30	9	101.14	14.94	<0.0001
X_1	632.95	1	632.95	93.50	<0.0001
X_2	39.40	1	39.40	5.82	0.0313
X_3	144.05	1	144.05	21.28	0.0005
$X_1 X_2$	3.08	1	3.08	0.45	0.5121
$X_1 X_3$	35.28	1	35.28	5.21	0.0399
$X_2 X_3$	6.02	1	6.02	0.89	0.3628
X_1^2	31.77	1	31.77	4.69	0.0494
X_2^2	1.78	1	1.78	0.26	0.6172
X_3^2	15.63	1	15.63	2.31	0.1526
Residuals	88.00	13	6.77		
miss drafting	6.20	5	1.24	0.12	0.9837
Error term	81.80	8	10.23		
Total error	998.30	22			

As can be seen from Table 4, P<0.0001 and F=10.91> F 0.01(9,13)=4.19 for the corn stalks loss rate model indicate that this model is suitable; F=0.42< F 0.05(5,8)=3.69 and P=0.8236>0.05 for the misfit term of this regression equation model, so the model fits well The correlation was high. Among the terms of the model, all of them were significant except for the interaction term X_1X_3 of the sieve aperture and the blade and blade shell clearance and the quadratic term X_1^2 of the sieve aperture. The order of the factors affecting the corn stalks loss rate was blade shell clearance > sieve aperture > pitch.

The regression model of corn stalks loss rate Y obtained after excluding the insignificant term 1 is shown in equation (11).

$$\hat{Y}_1 = 9.52 + 2.4X_1 + 2.29X_2 + 3.18X_3 + 1.54X_1X_2 + 1.99X_2X_3 + 1.38X_2^2 + 1.13X_3^2 \quad (11)$$

As can be seen from Table 5, P < 0.0001 and F = 14.94 > F 0.01(9,13) = 4.19 for the soil removal rate model indicate that the regression is highly significant; F = 0.12 < F0.05 (5,8) = 3.69 and P = 0.9837 > 0.05 for the misfit term indicate that the misfit term is not significant and the model is a good fit.

Since the P-values of sieve aperture (X_1), pitch (X_2), and blade shell clearance (X_3), interaction term of sieve aperture and blade shell clearance (X_1X_3), and quadratic term of sieve aperture (X_1^2) all satisfy P<0.05, it is obtained that X_1,X_2,X_3,X_1X_3,X_1^2 has a significant effect on soil removal rate. According to the F-value analysis, the influence on the soil removal rate from the largest to the smallest is the sieve aperture, blade shell clearance and pitch.

The regression model of soil removal rate Y obtained after excluding the insignificant term 2 is shown in equation (12).

$$\hat{Y}_2 = 60.63 + 6.81X_1 + 1.7X_2 + 3.25X_3 + 2.1X_1X_3 + 1.41X_1^2 \quad (12)$$

Response Surface Analysis

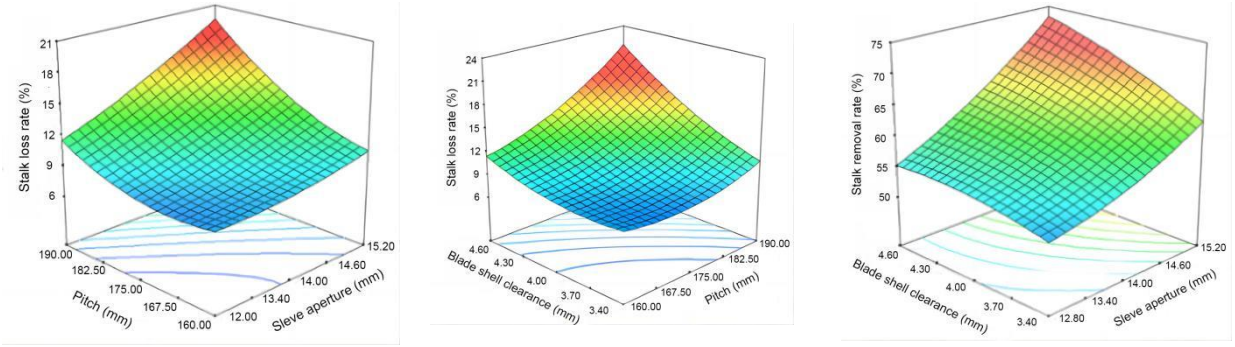

a. The effect of $X_1$and X_2 interactions on Y_1 *b. The effect of the interaction of X_2 and X_3 on Y_1* *c. The effect of X_1 and X_3 interactions on Y_2*

Fig. 5 - Response surface of corn stalk loss rate

As can be seen from Figure 5. When the sieve aperture was fixed, the corn stalks loss rate *Y* shows a gradually increasing trend with the increase of pitch. When the pitch was fixed, the corn stalks loss rate *Y* shows a gradually increasing trend with the increase of sieve aperture. When the blade shell clearance was fixed, the corn stalks loss rate *Y* shows a gradually increasing trend with the increase of pitch. When the pitch was fixed, the corn stalks loss rate *Y* shows a gradually increasing trend with the increase of blade shell clearance. When the pitch was fixed, the corn stalks loss rate *Y* shows a gradually increasing trend with the increase of blade shell clearance. When the clearance between the blade and the casing was fixed, the soil removal rate *Y* gradually increases with the increase of the sieve aperture. When the sieve aperture was fixed, the soil removal rate *Y* gradually increases with the increase of the blade shell clearance and sieve aperture, and the results are consistent with the single-factor test, and the interaction effect of the two factors is obvious. The response surface diagram shows that the corn stalks loss rate is small and the removal rate is high in the range of sieve aperture 12.8~15.2 mm, pitch 160~190 mm, and blade shell clearance 3.4~4.6 mm..

The model is solved optimally using the Optimization-Numerical module in the optimization design software Design-Expert, and the target actual variables are optimized with the constraints as shown in equation (13).

$$\begin{cases} minY_1 \\ maxY_2 \\ 12.8 \le x_1 \le 15.2 \\ 160 \le x_2 \le 190 \\ 3.4 \le x_3 \le 4.6 \end{cases} \quad (13)$$

Applying Design-Expert software to optimize the optimal working parameters: sieve aperture was 15.2 mm, pitch 160 mm, blade shell clearance was 4.6 mm, at this time the corn stalks loss rate is 12.4%, the soil removal rate is 72.8%. Combined with the actual situation to take the sieve aperture was 15 mm, pitch 160 mm, blade and blade shell clearance was 4.5 mm for simulation test verification, simulation results corn stalks loss rate is 13.8%, soil removal rate is 70.3%.

Test bench test verification

The test was carried out with Danyu-311 corn stalks from Heihe County, Jinzhou City, Liaoning Province, with a length of 50-200 mm and a width of 3-15 mm. Portions of corn stalks were randomly selected from the materials to be tested, each with 500±2 g. The corn stalks were weighed after full burning, and the soil content was calculated according to equation (14), and the average soil content was 38%.

According to agricultural machinery test conditions, the average moisture content was measured as 19%.

$$T = \frac{M}{500} \times 100\% \quad (14)$$

Where:

T is the soil content of corn stalks, %; M is the total mass of corn stalks ash and soil after burning, g.

The test apparatus includes: conveying and soil-removing device test bench, optical type tachometer, moisture content measuring instrument, electronic balance (accuracy of 0.01 g), vernier calliper, and timer. The test bench developed by combining the simulation model parameters and simulation optimization results is shown in Figure 6, and its power is provided by a diesel engine.

Fig. 1- Conveying dust removal test device

In order to reduce the error, three repetitive tests were conducted and the test results were averaged. The results are shown in Table 6.

Table 6

Experimental value of evaluation indices at optimal condition

Projects	Corn stalks loss rate/%	Soil removal rate/%
Average value of simulation test	13.8	70.3
Test bench test average	13.2	69.7
Relative Error	4.5	0.8

As can be seen from the table, the error between the test bench verification test results and the simulation test results is small, which proves that the structural parameters optimized by using the discrete element method are reliable and meet the working requirements of actual production.

CONCLUSIONS

(1) Using RockyDEM to establish a discrete element model for simulation tests, the test results show that: screen aperture diameter, pitch and blade and casing clearance have a significant effect on the corn stalks loss rate; the main order of corn stalks loss rate is blade shell clearance > sieve aperture > pitch.

(2) Apply Design-Expert software to optimize the model solution, and get the optimal working parameters: when the sieve aperture was 15.2 mm, the pitch was 160 mm, and the blade shell clearance was 4.6 mm, the corn stalks loss rate was 12.4%, and the soil removal rate was 72.8%.Combine with the actual situation to select the appropriate parameters for simulation verification test: When the screen aperture was 15 mm, the pitch was 160 mm, and the blade shell clearance was 4.5 mm, the corn stalks loss rate is 13.8%, and the soil removal rate is 70.3%.

(3) Based on the simulation and optimization results, a test bench of a conveying and soil-removing device was developed for test verification, and the results showed that when the sieve aperture was 15 mm, the pitch was 160 mm, and blade shell clearance was 4.5 mm, the corn stalks loss rate was 13.2%,and the soil removal rate was 69.7%, which were similar to the simulation test results and the simulation results were reliable. The results of this paper provide a theoretical basis for the selection of structural parameters of the conveying and soil-removing device on the corn stover picking and pelletizing machine.

ACKNOWLEDGEMENT

This research was funded by the Project supported by the National Natural Science Foundation of China （32171900）, Project Supported by Educational Commission of Liaoning Province (01102920015), and the Liaoning Provincial Key R&D Program under Grant (2019JH8/10200019).

REFERENCES

[1] Antypov D, Elliott JA. (2011). On an Analytical Solution for the Damped Hertzian Spring. *Europhysics Letters, 94*(5): 50004. http://doi: 10.1209/0295-5075/94/50004

[2] Cong Hongbin, Yao Zonglu, Zhao Lixin. (2019). Distribution of crop straw resources and its industrial system and utilization path in China. *Journal of Agricultural Engineering, 132-140*. http://doi:10.11975/j.issn.1002-6819.2019.22.015

[3] Fu Qiankun, Fu Jun, Chen Zhi. (2018). Optimization of parameters of straw picking and baling machine with vibration de-soiling operation. *Journal of Agricultural Engineering, 26-33*. http://doi:10.11975/j.issn.1002-6819.2018.08.004

[4] Huo Lili, Zhao L.X., Meng H.B. (2019). Study on the comprehensive utilization potential of crop straw in China. *Journal of Agricultural Engineering: 218-224*. http://doi:10.11975/j.issn.1002-6819.2019.13.026

[5] Kovacs A, Kerenyi G. (2017). Modelling of Corn Ears by Discrete Element Method (DEM) *31st Conference on Modelling and Simulation*. http://doi.org/10.7148/2017-0355

[6] Li Z., Gao Yuhang, Liu P., Li L., De Xuehong. (2019). Discrete element study on the evolution of force chains in the dense forming process of fine branch particles of Salix. *Journal of Solar Energy, 40*(11):3186-3195. http://doi:10.19912/j.0254-0096.2019.11.023

[7] Tian Yang, Lin Jing, Li Baofu. (2018). Design and test of pneumatic straw deep burial return machine conveying device. *Journal of Agricultural Machinery*, (12): 43-51. http://doi: 10.6041/j.issn.1000-1298.2018.12.005

[8] Schulz D., Schwindt N., Schmidt E. (2019). Investigation of the Dust Release from Bulk Material Undergoing Various Mechanical Processes Using a Coupled DEM/CFD Approach. *Powder Technology, 355: 37-56.* http://doi:10.1016/j.powtec.2019.07.005

[9] Ulantuya, Wang Chunguang, Qi Shaohua. (2016). Theoretical model analysis and experiments on spiral conveying of kneaded corn stalks. *Journal of Agricultural Engineering, 32*(22): 26-34. http://doi:10.11975/j.issn.1002-6819.2016.22.003

[10] Wang J.W., Tang H., Wang J.F. (2017). Analysis of the current situation and development of comprehensive utilization of crop straw resources in Northeast China. *Journal of Agricultural Machinery,* (5): 6-26. http://doi:10.6041 /j.issn.1000-1298.2017.05.001

[11] Wang Yongmei, Huang Xiaopeng, Wu Jinfeng. (2017). Flow field simulation analysis of ring die granulator based on POLYFLOW. *Journal of Solar Energy, 38*(12):3419-3425. http://doi:10.19912/j.0254-0096.2017.12.032

ANALYSIS OF VIBRATION CHARACTERISTICS FOR RUBBING MACHINE BASED ON MODAL TEST

/

基于模态试验的揉碎机振动特性分析

Yao YUE, Haiqing TIAN*, Fei LIU, Tao ZHANG, Dapeng LI, Di WANG
College of Mechanical and Electrical Engineering, Inner Mongolia Agricultural University, Hohhot, China
Tel：+86 18347980829；E-mail: hqtian@126.com
DOI: https://doi.org/10.35633/inmateh-68-04

Keywords: *rubbing machine, mechanical vibration, no load test, modal test, whole machine*

ABSTRACT

Aiming at the problems of large vibrations and noise of a working stalk rubbing machine, this paper took the 9R-60 rubbing machine as the research object and used the B&K modal test system and the vibration test system to analyse the modal and no-load conditions of the whole machine. Through analysing modal test data, it was concluded that the first five natural frequencies of the machine were 95.262 Hz, 144.386 Hz, 288.198 Hz, 313.719 Hz and 326.140 Hz. The results showed that spindle rotation had a more significant effect on the vibration than the feed chain rotation; the maximum vibration acceleration occurred at the small motor frame at a spindle speed of 1700 r·min^{-1} and a feed chain speed of 0.65 m·s^{-1}, which was 135.539 m·s^{-2}. The distribution of the amplitude statistical characteristics of the vibration signals follows the normal distribution and belongs to the stationary random process. The vibration was a self-excited vibration of the rotating machinery caused by the rotation of the main shaft and a forced vibration excited by the rotation of the same shaft. The research provides a direction for further research on the vibration characteristics of the rubbing machine under load conditions, and provides a theoretical basis for the subsequent vibration reduction design.

摘要

针对工作状态下揉碎机振动大、噪声大的问题，以 9R-60 揉碎机为研究对象，采用 B&K 模态测试系统与振动测试系统对其模态与空载工况进行分析。通过对模态试验数据的分析，得出其前五阶固有频率分别为 95.262 Hz、144.386 Hz、288.198 Hz、313.719 Hz 和 326.140 Hz。结果表明，主轴转动相比于喂入链转动对揉碎机振动的影响更为明显；在主轴转速 1700 r·min^{-1}、喂入链转速 0.65 m·s^{-1} 时，小电机机架振动加速度最大，为 135.539 m·s^{-2}。振动信号的幅度统计特性分布服从正态分布，属于平稳随机过程。振动是由主轴旋转引起的旋转机械的自激振动和同轴旋转激发的强迫振动。该研究为进一步研究摩擦机在载荷条件下的振动特性提供了方向，并为后续的减振设计提供了理论依据。

INTRODUCTION

As one of the three main grains in China, maize is produced in considerable amounts annually. After harvest, a large number of stalks, which are rich in nutrients, remains. Stalks are an ideal source of feed. In the process of stalk forage, the stalk rubbing machine plays an important role. The rubbing machine can rub maize stalks into filaments, which are closer to the fodder, and have better palatability for cattle and sheep, which is beneficial to the feeding of ruminant livestock. However, the stalk rubbing machine currently on the market generally has problems with large vibrations and high noise, which restricts the popularization and use of the rubbing machine. At the same time, the vibration and noise generated in the feed production process not only pollute the environment but also cause physical and mental harm to workers (*Chen, 2020; Dobie et al., 2008; Li, 2017*). In addition, long-term vibration of the machine causes fatigue damage to the vibrating parts, loosening of screws and other problems (*Lu, 2019*).

Currently, many domestic and foreign studies on the vibration of rubbing machines mainly focus on the vibration characteristics of the main components and parts (*Wang et al., 2018; Lan et al., 2020*), the structure design and test of the machine (*Kakitis et al., 2016*), the modal simulation analysis and the vibration test (*Wang et al., 2010; Yan, 2018*), and suggestions for improvement are put forward based on the test and simulation results. In terms of vibration reduction of other agricultural machinery, domestic scholars have conducted research on the direction of vibration reduction through methods such as vibration tests (*Gao et al., 2017; Zhu et al., 2018; Xu et al., 2014*), modal tests (*Yao et al., 2017; Yao et al., 2018; Zhang et al., 2018*) and modal simulations (*Zhu et al., 2014; Yao et al., 2016; Sun et al., 2014*), and proposed vibration reduction directions such as resonance and dynamic balance. Among foreign

researchers, Tanas et al. obtained the natural frequency and damping parameters of a grain crusher machine through modal tests and combined these parameters to optimize the structure dynamics, thereby reducing the noise value of the whole machine (*Tanas et al., 2018*); Evandro P. da Silva and others carried out modal simulation of a coffee harvester in the empty state and full state and obtained its 20th-order modal frequency. Combined with the stress and displacement simulation results, it was concluded that the main motor of the coffee harvester may cause the fracture of the vibrating parts (*Evandro et al., 2018*). Hoshyarmanesh et al. used experiments and simulations of olive trees to obtain the natural frequency and other related parameters to obtain the best operating parameters, thereby improving productivity (*Hoshyarmanesh, et al., 2017*). This research conducted modal research and experimental exploration from the perspective of the research object, analysed vibration phenomena from multiple angles and used them to provide ideas and theoretical support for subsequent research.

Currently, there are few studies on the vibration of rubbing machines, and the existing research is mostly limited to earlier types of research. Modal test research on large-scale livestock machinery such as rubbing machines is mostly focused on key parts, but modal test research on the whole machine is limited. It is not easy to analyse the response after the system as a whole is subjected to excitation during operation. Based on these results, this paper took the 9R-60- type rubbing machine as an example, carried out a modal test to explore it, and obtained the first five natural frequencies of the whole rubbing machine. Furthermore, vibration tests under no-load conditions were carried out, and the vibrations under different speeds of the spindle and feed chain were analysed by using time domain and frequency domain analysis methods. Combined with the results of the modal test, the vibration characteristics of the rubbing machine under different excitations were obtained.

MATERIALS AND METHODS

Method principle analysis

In physical coordinates, a set of coupled second-order ordinary differential equations is often used to describe the motion of a multi-degree-of-freedom linear vibration system. The physical coordinates are transformed into modal coordinates by using the vibration mode matrix; the ordinary differential equation can be transformed into a set of mutually independent motion equations, each of which has the same structure as a single degree-of-freedom vibration system. This analysis method is called modal analysis.

In modal coordinates, modal parameters (natural frequency, mode shape, modal stiffness, etc.) are usually used to describe the dynamic characteristics of the system. The modal parameters of the system can generally be obtained by analytical calculations or dynamic testing methods.

The differential equation of motion of a damped system with multiple degrees of freedom is then

$$[M]\{\ddot{x}\} + [C]\{\dot{x}\} + [K]\{x\} = \{f\} \quad (1)$$

In the formula, [M] is the mass matrix, [C] is the damping matrix, [K] is the stiffness matrix, {x} is the response vector, and {f} is the force vector.

Under the action of an external force, the motion equation in the form of the state vector of the system is:

$$\begin{bmatrix} C & M \\ M & 0 \end{bmatrix} \begin{Bmatrix} \dot{x} \\ \ddot{x} \end{Bmatrix} + \begin{bmatrix} K & 0 \\ 0 & -M \end{bmatrix} \begin{Bmatrix} x \\ \dot{x} \end{Bmatrix} = \begin{Bmatrix} f \\ 0 \end{Bmatrix} \quad (2)$$

It is assumed that the external force acting on the system is simple and harmonic, that is,

$$\{f\} = \{F\}e^{i\omega t} \quad (3)$$

Then, the response of the physical coordinates and modal coordinates of the system is also simple and harmonic, namely,

$$\{x\} = \{X\}\, e^{i\omega t} \quad (4)$$

$$a_i = \begin{bmatrix} C & M \\ M & 0 \end{bmatrix} e^{i\omega t} \quad (5)$$

Where $a_i = \begin{Bmatrix} \Psi_i \\ s_i\Psi_i \end{Bmatrix}^T \begin{bmatrix} C & M \\ M & 0 \end{bmatrix} \begin{Bmatrix} \Psi_i \\ s_i\Psi_i \end{Bmatrix}$.

The matrix expression of the frequency response function of the multi-degree-of-freedom damped system is derived by the state space method as

$$[H(\omega)] = \sum_{i-1}^{n} \left(\frac{1}{a_i} \frac{\{\Psi_i\}\{\Psi_i\}^T}{i\omega - s_i} + \frac{1}{a_i^*} \frac{\{\Psi_i^*\}\{\Psi_i^*\}^T}{i\omega - s_i^*} \right) \quad (6)$$

Then, the complex frequency is $s_i = -\frac{a_i}{b_i}, b_i = \begin{Bmatrix} \Psi_i \\ s_i\Psi_i \end{Bmatrix}^T \begin{bmatrix} K & 0 \\ 0 & -M \end{bmatrix} \begin{Bmatrix} \Psi_i \\ s_i\Psi_i \end{Bmatrix}$; $\{\Psi_i\}$ is a complex modal vector.

In addition, the relevant theories of the modal assurance criterion (MAC) are also used. The MAC

matrix is the dot product of the vibration mode vectors and is a tool for evaluating the spatial correlation of the modal vectors. Its calculated variable values are between 0 and 1. Its expression is

$$\mathrm{MAC_{ij}} = \frac{(\phi_i^T \phi_j)^2}{(\phi_i^T \phi_i)(\phi_j^T \phi_j)} \quad (7)$$

Where ϕ_i and ϕ_j are the i-th-and j-th-order vectors of the vibration mode matrix, respectively.

If ϕ_i and ϕ_j are estimates of the same vibration mode by the same parameter identification method, i=j. The two modal vectors can be converted to each other according to a certain scale factor, so the values should be close in theory; therefore, the value of the ratio $\mathrm{MAC_{ij}}$ should be close to 1. If different vibration modes are estimated, theoretically, the value is relatively low, and the ratio $\mathrm{MAC_{ij}}$ value should be close to 0.

Modal test

The rubbing machine test bench is composed of a frame, throwing port, spindle rotor, feed inlet, and tooth plates, as shown in Fig. 1. The spindle rotor is located in the rubbing cavity, including the cutter structure, hammers, hammer rack and throwing mechanism; the rubbing chamber, frame, feeding part and throwing port are welded and fixed.

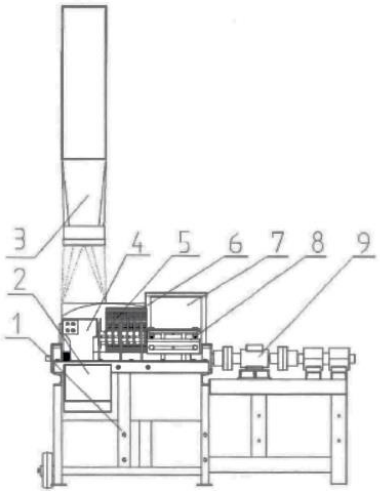

Fig. 1 - Structure diagram of rubbing machine test bench

1. Frame; 2. Lower throwing port; 3. Upper throwing port; 4. Throwing mechanism; 5. Hammer; 6. Tooth plate; 7. Feeding inlet; 8. Cutter structure; 9. Spindle

Due to the large mass and volume of the rubbing machine, the modal test was carried out by adding air spring cushions under the support feet of the machine. The cushion is an elastic element composed of an air chamber, a rubber elastic diaphragm, and a support plate. It is a flexible sealed container with compressed air, which provides resilience and support force by the restoring force of compressed air. As shown in Fig. 2(a), the model chosen is ALJ-51006 of An Lijing ® Company. The five supporting points were arranged on the cushions. At the same time, to make the rubbing machine as free as possible, a rubber pad was added between the machine and the cushions, as shown in Fig. 2(b). During the test, the height of each air spring cushion was measured, an air compression pump was used to inflate the cushions and ensure that each of the cushions had the same height change after inflation, which was 10 mm.

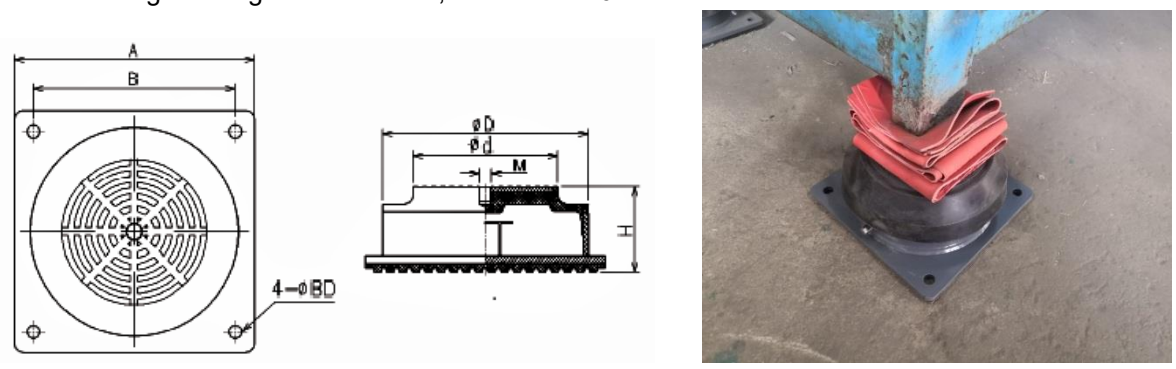

a *b*

Fig. 2 - Structure and working diagram of air spring cushion

To obtain the vibration characteristics of the machine, a force hammer was used to excite the structure. In the pre-tests, better results were obtained when aluminium hammer was used. Therefore, the modal test used an aluminium one.

The test used equipment from the Danish Company B&K, and the MTC Hammer module in the B&K's PULSE 16.0 software was used to collect and analyse data. The relevant models of the test equipment are shown in Tab. 1.

Test Instruments **Table 1**

Instrument	Type
Aluminium hammer	8206-002
Triaxial acceleration sensor	4507Bxyz
Data acquisition instrument	3050-B-060
Data acquisition software	PULSE 16.0
Data post-processing module	Reflex

The test used the single-input single-output method to process the input and output analogue signals through the data acquisition instrument. Here, the input signal was the excitation signal generated by using the roving hammer to knock the measuring points at different positions of the machine, and the output signal was collected by the three-axis acceleration sensor arranged at the fixed point. The data acquisition instrument and PULSE operation software sampled the analogue signal collected by the sensor at a certain time interval, namely discretization was performed. Then, each instantaneous analogue quantity of the discrete-time signal was converted into a digital quantity by an A/D conversion device, that is digitizing the signal, and finally the discrete-time digital signal was obtained. PULSE converted the received time domain digital signal to the frequency domain by FFT and other methods to obtain the frequency response function. The modal parameters of the structure were obtained by the modal parameter estimation algorithm.

Before the test, the data acquisition instrument was connected to the computer through a network cable, and the force hammer and the triaxial acceleration sensor were connected to the acquisition card to complete the hardware connection of the mould test system.

The model used in the test was a three-dimensional wireframe drawing, which compared to its outline is more conducive to analysing data and modal formation in the modal test. Since the test adopted a single reference measurement method and used a roving hammer to excite each measurement point, the theoretical vibration mode was analysed and calculated by finite element software before the reference point was selected, and the position of the node was observed. When placing the sensor, to avoid the modal nodes, select the main connection points, centre points, and boundary points of each part to mark and tap. A total of 48 points were selected for tapping with the hammer icon, as shown in Fig. 3. At the hitting point, the sensor was selected at a connection point on the rack, which is labelled 1 in the figure. The triaxial acceleration sensor was fixed, and the hammer was moved to strike each measuring point to complete the modal test.

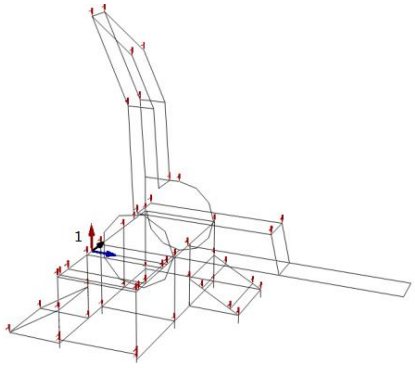

Fig. 3 - Diagram of test points

To ensure that the signal was not distorted after acquisition, the appropriate sampling frequency should be selected before the signal acquisition. Combined with the pre-tests and the working conditions, the sampling frequency was selected as 400 Hz, Lines was set as 400 Hz, and Span was 400 Hz, and Linear was selected as the average method. After the above arrangement and setting, each measuring point was tapped three times in the direction of the plumb weight. Throughout the calculation, a total of 144 taps were made.

Vibration test

After the modal test, the vibration under no load condition was studied. The vibration test instrument used the PULSE system and sensors produced by B&K. One triaxial acceleration sensor and three uniaxial acceleration sensors were arranged on the system to collect vibration data; the data collector received the data collected by the sensor. After analogue-to-digital conversion, it was transferred to the analysis and processing software; PULSE data acquisition analysis and processing software was used for parameter setting during the test process, online signal acquisition, and spectrum analysis of the collected data. The specific parameters of the equipment are shown in Tab. 2.

Equipment parameter table **Table 2**

Instrument	Accuracy	Range
4506-B triaxial acceleration sensor	10mV/m·s-2	700 m·s-2 0.3-3.5k in X,Y and Z directions
4507 single axial acceleration sensor	10mV/m·s-2	700 m·s-2 0.3-6k in each directions
LAN-XI data acquisition front end		
PULSE software		

To fully reflect the overall vibration as much as possible, the three-axis sensor was arranged on the outer sidewall of the machine, namely channels 1, 2, and 3. Channels 1-3 represent the z-direction, x-direction and y-direction where the machine was placed in the Cartesian coordinate system at the angle shown in Fig. 4. The other three single-axis acceleration sensors were arranged above the feed inlet, the small motor frame and the upper part of the rack, which were, channels 4, 5, and 6, as shown in Fig. 4. The uniaxial acceleration sensor and the triaxial acceleration sensor were connected to the data acquisition instrument, and the corresponding channel number was recorded.

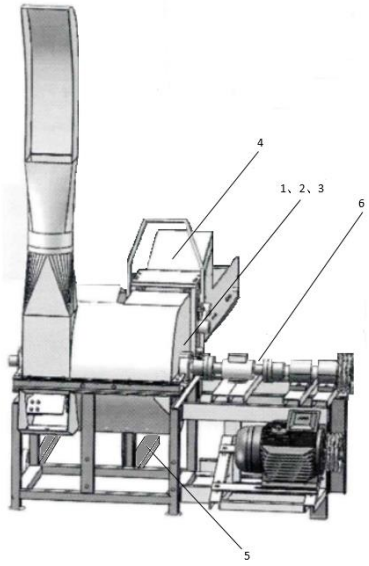

Fig. 4 - Diagram of sensor layout

Before testing, the parameters of the test system were set in the Labshop module of PULSE software. After the setting was completed, the no-load vibration test could be carried out. Referring to the general rules for the design of the rubbing machine rotor in the "Agricultural Machinery Design Manual" and the rotor specifications of this test system, the spindle speed was set to be 1200-1800 r·min^{-1} during the test, and the interval was 100 r·min^{-1}, for a total of 7 groups . The feed chain speed referred to the productivity and other requirements in NY/T509-2015 "Technical Specification of Quality Evaluation for crop Straw rubbing filament Machines", set in the range of 0.35-0.65 m·s^{-1}, with an interval of 0.05 m·s^{-1}, a total of 7 groups. The vibration of the system was tested when the main shaft and the feed chain worked separately and when the two motors drove the main shaft rotor and the feed chain to rotate. Through analysis of single factor test results, it was concluded that when the spindle speed was 1600 r·min^{-1} and the feed chain speed was 0.65 m·s^{-1}, the

frequency of the occurrence of vibration amplitude was higher than for other speeds. Therefore, under the condition of the two motors working separately, when the spindle speed changes, the feed chain speed was set to a fixed value, here 0.65 m·s^{-1}; when the feeding chain speed changed, it would be set to a new fixed value, here 1600 r·min-1. The spindle speed change values were selected as 1400 r·min^{-1}, 1500 r·min^{-1}, 1600 r·min^{-1}, 1700 r·min^{-1} and 1800 r·min^{-1}, and the feed chain speed changed values for 0.45 m·s^{-1}, 0.50 m·s^{-1}, 0.55 m·s^{-1}, 0.60 m·s^{-1}and 0.65 m·s^{-1}, then 9 sets of tests were performed. In this test, the rubbing machine was placed on the softer soil.

RESULTS

Modal test results

The signal collected after exciting the measuring point was processed by the PULSE Reflex module in PULSE, and the frequency response function diagram is shown in Fig. 5.

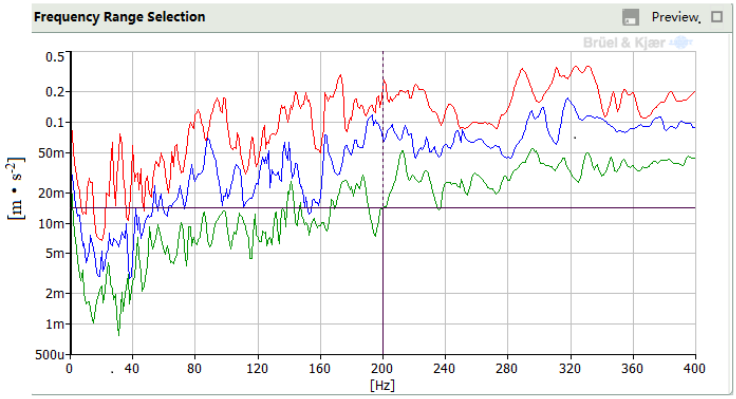

Fig. 5 - Frequency response function

The frequency response function was analysed, and only 40-360 Hz of the test frequency band 0-400 Hz was selected for data analysis to extract modal frequency bands of each order. The test results are shown in Tab. 3.

First 5 natural frequencies **Table 3**

Order	Frequency /Hz	Damping /%
1	95.262	3.154
2	144.386	2.483
3	288.198	1.899
4	313.719	0.851
5	326.140	2.521

Vibration test results

After the vibration test, statistical parameters were used to describe the time domain results of this vibration test. The statistical results of the maximum vibration acceleration in the time domain data obtained in the single factor test are shown in Tab. 4.

Statistical results of time domain maximum of single factor test **Table 4**

Test number	Spindle speed / r·min^{-1}	Feed chain speed / m·s^{-1}	Channel 1 / m·s^{-2}	Channel 2 / m·s^{-2}	Channel 3 / m·s^{-2}	Channel 4 / m·s^{-2}	Channel 5 / m·s^{-2}	Channel 6 / m·s^{-2}
1	1200	0	23.851	78.602	27.336	-24.409	21.574	21.574
2	1300	0	-20.88	-62.516	-22.475	-29.443	79.971	19.723
3	1400	0	-27.587	75.221	-23.082	25.81	-116.811	22.55
4	1500	0	-25.011	-86.79	-31.289	-39.398	-99.567	-26.439
5	1600	0	32.412	-96.549	-34.579	36.393	-123.116	31.627
6	1700	0	-30.761	94.271	35.942	53.027	120.495	36.63
7	1800	0	30.002	92.155	-27.344	-43.764	121.135	38.489
8	0	0.35	9.014	-28.494	11.809	22.392	36.733	-3.89
9	0	0.4	18.85	42.342	12.972	-21.782	26.615	-3.406
10	0	0.45	-10.378	41.784	-13.411	-18.082	35.128	5.056
11	0	0.5	10.533	36.888	-12.17	20.776	35.75	4.419

Test number	Spindle speed / r·min^{-1}	Feed chain speed / m·s^{-1}	Channel 1 / m·s^{-2}	Channel 2 / m·s^{-2}	Channel 3 / m·s^{-2}	Channel 4 / m·s^{-2}	Channel 5 / m·s^{-2}	Channel 6 / m·s^{-2}
12	0	0.55	-11.381	-32.805	-13.059	21.417	35.864	4.298
13	0	0.6	9.42	-45.715	-15.354	24.382	-41.672	-4.965
14	0	0.65	-10.389	-41.186	-14.786	-28.905	44.724	5.109
15	1600	0.45	23.533	102.668	-35.177	41.628	109.148	-32.37
16	1600	0.5	26.434	111.687	41.484	37.658	117.004	37.259
17	1600	0.55	-28.548	79.407	33.541	-44.993	-104.56	37.306
18	1600	0.6	-28.901	-89.006	38.5	46.305	-107.899	31.49
19	1600	0.65	-31.946	86.377	29.376	40.35	113.535	32.008
20	1400	0.65	-33.875	87.619	28.401	50.823	108.875	-28.539
21	1500	0.65	30.836	-74.062	-30.025	-44.825	116.421	-30.548
22	1700	0.65	-35.942	-90.691	-30.159	-53.123	135.539	40.101
23	1800	0.65	38.483	-104.983	37.778	29.902	122.071	35.296

Fig. 6(a) of the stacking histogram shows the amplitude of the corresponding frequency of each measuring point under 23 working conditions. And the distribution of amplitude is shown in Fig. 6 (b).

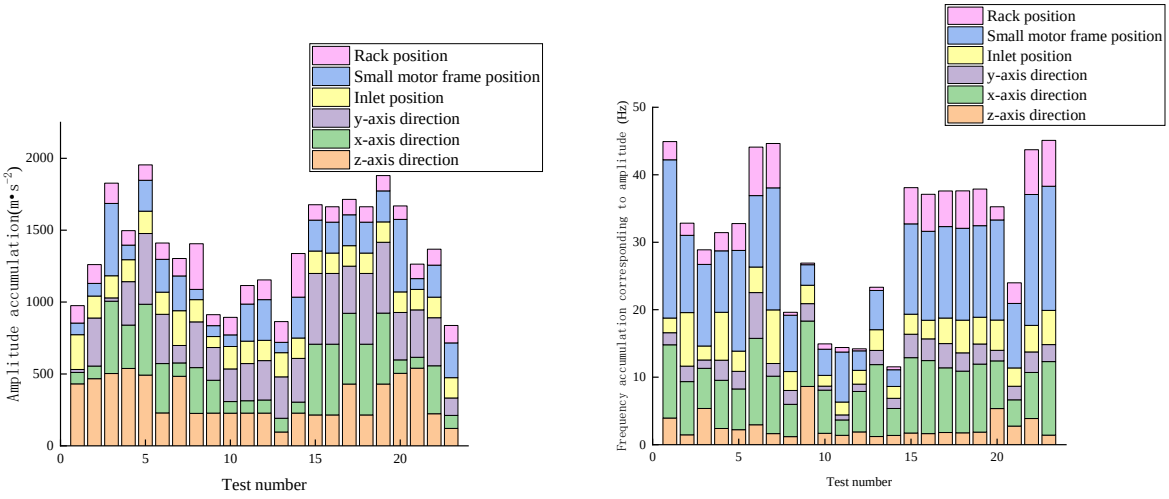

a *b*

Fig. 6 - Frequency domain results stacking histogram

Discussion

The correlation of the model was analysed and its MAC matrix was obtained (*Yao et al., 2017; Su et al., 2021; Sayahkarajy et al., 2018*). It can be seen from Fig. 7 that the MAC value on the main diagonal element of the matrix is equal to 1, while the values outside the element were much less than 1. The MAC value of the same mode shape was 1, indicating that the theoretical mode shapes were correlated; for the smaller values, other than the non-diagonal elements of the matrix, it indicated that the calculated modes of each order were more independent, and the correlation was small, indicating that the test was more effective in extracting the modal parameters of the structure, and the test results had high credibility.

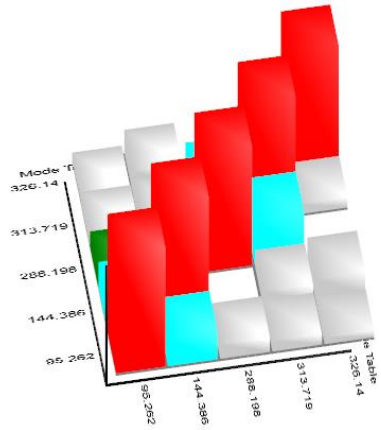

Fig. 7 - MAC matrix chart

By analysing and processing the time domain signal (*Liao et al., 2021*), the result is shown in Fig. 8.

It can be seen from Fig. 8 (a) that the vibration acceleration at each measuring point of the machine when only the spindle rotated (Test No. 1-7) is significantly higher than that when only the feeding chain worked (Test No. 8-14). The results show that the maximum vibration acceleration of the machine is -123.166 $m \cdot s^{-2}$ and the minimum is 19.723 $m \cdot s^{-2}$ when only the spindle rotates. The maximum vibration acceleration is -45.715 $m \cdot s^{-2}$ and the minimum is -3.89 $m \cdot s^{-2}$ when only the feeding chain rotates. It can be seen from Fig.8 (b) that with the increasing spindle speed, the vibration acceleration basically presents a trend of first increasing and then decreasing. It can be seen from Fig. 8 (c) that when two motors work at the same time (Test No. 15-23), the difference between the vibration acceleration value of the rubbing machine and the value when only the spindle rotates is small. Therefore, the influence of the feeding chain rotation on the vibration is less than that of spindle rotation, and spindle rotation is the main vibration cause of the vibration. It can be seen from Fig. 8 (d) that the maximum vibration acceleration (135.539 $m \cdot s^{-2}$) occurs at the small motor frame under the condition of spindle speed 1700 $r \cdot min^{-1}$ and feeding chain speed 0.65 $m \cdot s^{-1}$. On the one hand, the mass of the small motor is larger, on the other hand, the cantilever of the motor frame is fixed on the frame, and the bottom does not contact the ground and other supports, which makes the external force have a longer action torque, so the vibration acceleration at this point is larger than that at other points, and the fatigue and other damage caused by vibration are relatively large.

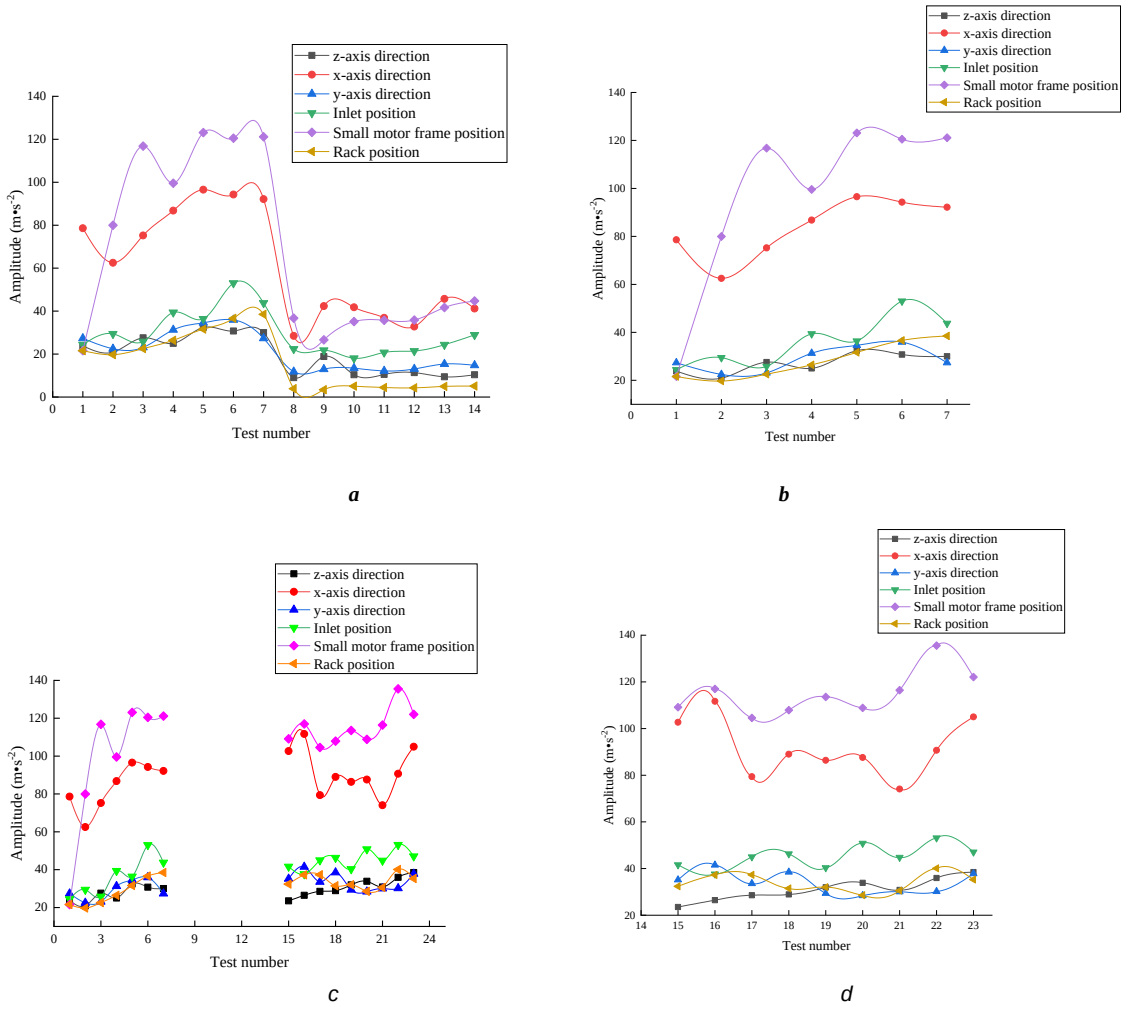

Fig. 8 - Time domain amplitude analysis diagram

By analysing the vibration acceleration data collected from the first three channels, we can get that, as far as the point on the wall of the rubbing chamber is concerned, when the spindle rotates and the feed chain rotates, the vibration of the left and right direction of the machine is obviously stronger than that of the front and rear directions and the up and down directions.

According to the frequency domain results (*Yao et al., 2015*), the range of amplitude frequencies is shown in Fig. 9(a). The frequencies corresponding to the amplitude fall in the centre of the range, which are 125 Hz, 225 Hz, 325 Hz and 75 Hz, account for approximately 0.681% of the total statistical data.

Combined with the results of the modal test, the natural frequencies are 95.262 Hz, 144.368 Hz and 313.719 Hz, which fall in the histogram of 75 Hz, 125 Hz and 325 Hz. It can be inferred that one of the reasons for the vibration of the rubbing machine is the self-excited vibration caused by the rotation of the main shaft. The frequency corresponding to the other amplitudes is 4-21 times the spindle speed frequency under the corresponding working conditions. It can be concluded that spindle rotation is the main cause of forced vibration.

It can be seen from the analysis in Fig. 9(b) that the random vibration signal obeys the Gaussian normal distribution, which is the expected curve form. Therefore, the distribution of the amplitude statistical characteristics of the vibration signals of the six measuring points of the machine approximately obeys the normal distribution, and it can be considered that the vibration under each no-load condition belongs to a stationary random process.

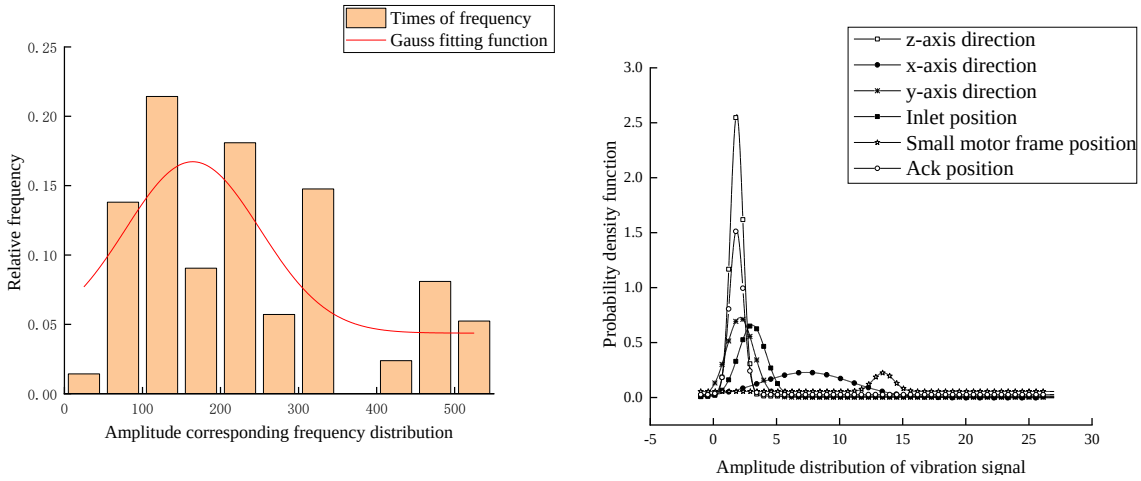

a *b*

Fig. 9 - Distribution diagram

ACKNOWLEDGMENT

The supports of the National Natural Science Foundation of China (NSFC) (No. 51905277) and the Inner Mongolia Special Project for Transformation of Scientific and Technological Achievement (No. 2019CG034), National Natural Science Foundation of China (No. 32071893) for this research are greatly appreciated.

REFERENCES

[1] Chen Q.S., (2020), Focus on prevention and control of noise and hand-arm vibration, and protect workers' health (*关注噪声和手传振动防控*). *Journal of Environmental and Occupational Medicine.* 37(04):334-336. doi: 10.13213/j.cnki.jeom.2020.20099;

[2] Dobie Robert A., (2008), The burdens of age-related and occupational noise-induced hearing loss in the United States. *Ear and Hearing*. 29(4):565-577. doi: 10.1097/AUD.0b013e31817349ec;

[3] Evandro P da Silva; Fábio M da Silva; Ednilton T de Andrade; Ricardo R Magalhães, (2018), Structural static and modal frequency simulations in a coffee harvester's chassis. *Revista brasileira de engenharia agricola e Ambiental.* 22(7): 511-515.

[4] Gao Z.P., Xu L.Z., Li Y.M., Wang Y.D., Sun P.P., (2017), Vibration measure and analysis of crawler-type rice and wheat combine harvester in field harvesting condition. (*履带式稻麦联合收获机田间收获工况下振动测试与分析*) *Transactions of the Chinese Society of Agricultural Engineering*. 33(20):48-55.

[5] Hoshyarmanesh H., Dastgerdi H.R., Ghodsi M., Khandan R., Zareinia K., (2017), Numerical and experimental vibration analysis of olive tree for optimal mechanized harvesting efficiency and productivity. *Computers and electronics in agriculture* 132: 34-48.

[6] Kakitis A., Berzins R., Berzins U., (2016), Cutting energy assessment of hemp straw. *Engineering for Rural Development*, Jelgava, (Latvia), May 25-27. pp: 1255-1259;

[7] Lan Y.Z.; Zhang L., Zhai Z.P., Li Z.W., Li C., (2020), Analysis of the Influences of Structure Parameters on Pneumatic Noise of the Impeller Blower of the Stalk Rubbing Machine. (*结构参数对秸秆揉碎机抛送装置气动噪声的影响分析*) *Journal of Agricultural Mechanization Research*. 42(12):34-38+63. doi: 10.13427/j.cnki.njyi.2020.12.006)

[8] Li T., (2017), Explore the Syrian Industrial Production Vibration Harm and Control Countermeasures. (*工业生产振动的危害及其控防对策研究*) *China Personal Protective Equipment* (02):48-52. doi: 10.16102/j.cnki.cppe.2017.02.011;

[9] Liao Y.T., Qi T.X., Liao Q.X., Zeng R., Li C.L., Gao L.P., (2021), Vibration characteristics of pneumatic rape precision combine direct seeder and its effect on seeding performance. (*气力式油菜精量联合直播机振动特性及对排种性能影响*) *Journal of Jilin University (Engineering and Technology Edition)*, doi: 10.13229/j.cnki.jdxbgxb20210001;

[10] Lu Y.H., (2019), Preface to the topic "study on fatigue in vibration environment". (*振动环境下疲劳问题研究"专题序言*). *Equipment Environmental Engineering.* 16(11):10+9;

[11] Sayahkarajy, M, (2018), Mode shape analysis, modal linearization, and control of an elastic two-link manipulator based on the normal modes. *Applied mathematical modelling* 59: 546-570. https://doi.org/10.1016/j.apm.2018.02.003;

[12] Su H.J., Cui H.M., Li F.Y., (2021), Free Modal Test and Analysis of Air Blown Deep Loose Shovel. (*气吹式深松铲自由模态试验与分析*). *Journal of Agricultural Mechanization Research.* 43(05):212-216+262.

[13] Sun Z.., Wang L., Pan Z.., (2014), Analyses of vibration characteristics of power fan for the 4ztl-1800 pneumatic conveying combine stripper harvester. *Transactions of the ASABE.* 57(3): 693-699.

[14] Tanas W., Szczepaniak J., Kromulski J., Szymanek M., Tanas J., Sprawka M., (2018), Modal analysis and acoustic noise characterization of a grain crusher. *Annals of agricultural and environmental medicine.* 25(3):433-436. Doi:10.26444/aaem/87154;

[15] Wang J.B., Dong H.J., Zhai Z.P., Cheng H.Y., Kang X.Y., Wu Y.M., (2018), Modal Analysis and Structure Optimization of the Rotors of Forage Rubbing and Breaking Machines. (*饲草揉碎机转子模态分析及结构优化*). *Noise and Vibration Control.* 38(05):52-56+61;

[16] Wang J., (2010), *Study on noise of 9R-40 rubbing and breaking machine. (9R-40 型揉碎机噪声分析研究)*. PhD thesis. Univ. Inner Mongolia agricultural, Hohhot, China;

[17] Xu L.Z., Li Y.M., Su P.P., Pang J., (2014), Vibration measurement and analysis of tracked-whole feeding rice combine harvester. (*履带式全喂入水稻联合收获机振动测试与分析*) *Transactions of the Chinese Society of Agricultural Engineering*. 30(08):49-55. doi:CNKI:SUN:NYGU.0.2014-08-006;

[18] Yan P., (2018), *Test research on the performance and vibration of the 9RS-60 stalk rubbing machine*. (*9RS-60 型揉碎机性能试验与振动测试研究*) MSc thesis. Univ. Inner Mongolia agricultural, Hohhot, China;

[19] Yao Y.C., Du Y.F., Zhu Z.X., Mao E.R., Song Z.H., (2015), Vibration characteristics analysis and optimization of corn combine harvester frame using modal analysis method. (*基于模态的玉米收获机车架振动特性分析与优化*). *Transactions of the Chinese Society of Agricultural Engineering.* 31(19):46-53.

[20] Yao Y.C., Song Z.H., Du Y.F., Mao E.R., Zhao X.Y., Zhang W.R., (2016), Optimum seeking of spot weld model on numerical simulation of stress and modal analysis for corn combine harvester frame. (*玉米收获机车架应力及模态数值模拟焊点模型优选*) *Transactions of the Chinese Society of Agricultural Engineering.* 32(24):50-58. doi:CNKI:SUN:NYGU.0.2016-24-007;

[21] Yao Y.C., Song Z.H., Du Y.F., Zhao X.Y., Mao E.R., Liu F., (2017), Analysis of vibration characteristics and its major influenced factors of header for corn combine harvesting machine. (*玉米收获机割台振动特性及其主要影响因素分析*) *Transactions of the Chinese Society of Agricultural Engineering.* 33(13):40-49;

[22] Yao Y.C., Zhao X.Y., Du Y.F., Song Z.H., Yin Y.Y., Mao E.R., Liu F., (2018), Operating modal analysis and test of harvester induced by mass-varying process. (*考虑质量时变的收获机械工作模态分析与试验*) *Transactions of the Chinese Society of Agricultural Engineering* 34(09): 83-94. doi:CNKI:SUN:NYGU.0.2018-09-010;

[23] Zhang J.X., Yang C., Zhang L., Jiang Y.X., Wang C.Y., (2018), Analysis and experiment on strength and vibration characteristics of corn stubble plucking mechanism. (*玉米起茬机构的强度及振动特性分析与试验*), *Transactions of the Chinese Society of Agricultural Engineering*. 34(12):72-78. doi:CNKI:SUN:NYGU.0.2018-12-009;

[24] Zhu L.H., Li Y.M., Tang Z., Xu L.Z., (2018), Vibration Test and Analysis of the All-in-one Machine of Combine Harvester and Baler. (*联合收获打捆复式作业机振动测试与分析*), *Journal of Agricultural Mechanization Research.* 40(03):146-151. doi:10.13427/j.cnki.njyi.2018.03.029;

[25] Zhu S.H., Xu G., Yuan J.Q., Ma J.F., Yi Lidaer Li K., (2014), Influence of implement's mass on vibration characteristics of tractor-implement system. (农具质量对拖拉机悬挂农具系统振动特性的影响), *Transactions of the Chinese Society of Agricultural Engineering.* 30(24):30-37. doi:CNKI:SUN:NYGU.0.2014-24-004.

CONSIDERATIONS ON HEMP STALK HARVESTING USING SPECIALIZED EQUIPMENT
/
CONSIDERAŢII PRIVIND RECOLTAREA TULPINII DE CÂNEPĂ UTILIZÂND UN ECHIPAMENT SPECIALIZAT

Lorena-Diana POPA[1)], Ana ZAICA [2*)], Ancuța NEDELCU [2)], Alexandru ZAICA [2)], Gheorghe MATEI [3)], Margareta NAIE [1)], Georgiana RĂDEANU [4)], Cristina PRECUPEANU [4)]

[1)] Agricultural Research and Development Station Secuieni, Romania;

[2)] National Institute of Research - Development for Machines and Installations Designed for Agriculture and Food Industry, Romania;

[3)]University of Craiova, Romania;

[4)]Ion Ionescu de la Brad" Iaşi University of Life Sciences, Romania

**Correspondence: zaica_ana@yahoo.com*

DOI: https://doi.org/10.35633/inmateh-68-05

Keywords: *industrial hemp; stalks; harvesting; energy indices; cutting*

ABSTRACT

Within the current hemp cultivation technologies, the use of high-performance technical equipment is required for all applied works, and following the concerns regarding diversified and efficient ways of harvesting, INMA Bucharest has created and experimented an innovative technical equipment for harvesting and tying the stalks into sheaves. In order to demonstrate the efficiency of this equipment, the paper presents the experimental results obtained by INMA Bucharest regarding hourly fuel consumption and fuel consumption per hectare. These energetic indices are important in the evaluation of expenses per surface unit, constituting the basis of the economic efficiency evaluation. At the same time, at ARDS Secuieni, in 2021, research was carried out on the influence of the cuttings application and different sowing norms on the agro-productive capacity of the Ratza monoecious hemp variety for stalks and fibre. The obtained results constitute premises in order to optimize some technological links of cultivation at hemp for stalks and fibre, but they also confirmed the fact that fuel consumption per hectare recorded at hemp stalks harvesting was influenced both by the technical characteristics of the equipment used and by the characteristics of the experimented crop.

REZUMAT

În cadrul tehnologiilor actuale de cultivare a cânepei se impune utilizarea unor echipamente tehnice performante pentru toate lucrările aplicate, iar în urma preocupărilor privind modalități diversificate și eficiente de recoltare, INMA București a realizat și experimentat un echipament tehnic inovativ pentru recoltarea și legarea tulpinilor în snopi. În vederea demonstrării eficienței acestui echipament, în cadrul lucrării sunt prezentate rezultatele experimentale obținute de INMA București privind consumul de combustibil orar şi consumul de combustibil la hectar. Acești indici energetici sunt importanți în evaluarea cheltuielilor la unitatea de suprafață, constituind baza evaluării eficienței economice. Concomitent, la SCDA Secuieni, în anul 2021, au fost derulate cercetări privind influența aplicării retezărilor și a diferitelor norme de semănat asupra capacității agroproductive la soiul de cânepă monoică pentru tulpini și fibră Ratza. Rezultatele obținute constituie premise în vederea optimizării unor verigi tehnologice de cultivare la cânepa pentru tulpini și fibră, dar au confirmat și faptul că consumul de combustibil la hectar înregistrat la recoltarea tulpinilor de cânepă a fost influențat atât de caracteristicile tehnice ale utilajului folosit, cât și de caracteristicile culturii experimentate.

INTRODUCTION

In recent years, there has been considerable development in the industrial hemp industry, contributing to the development of the national economy and thus of the world economy. In our country, after 1989, the cultivation of industrial hemp (*Cannabis sativa* L.) experienced a spectacular decline caused, in large part, by the impact of the transition period on the industrial sector, especially on the sector dedicated to stems processing, by the restructuring of the agricultural sector, but also because of the legislation, which included this culture in the category of those from which narcotic substances are extracted. Currently, industrial hemp is no longer a crop prohibited or restricted by law, only that such a plantation must be authorized and monitored by various state institutions, depending on the country in which it is grown. The industrial hemp sector has transformed from a fibre-based processing sector into a more complex industry, including the healthcare, textile, automotive, etc. sectors (*Ceyhan, V. et al., 2022*).

Beyond the impediment related to authorization and monitoring, hemp cultivation brings more than profitable profits to those who invest in it. It is cultivated for its relatively high natural fibre content and for its seeds rich in siccative oil. Among the textile plants of the temperate climate, hemp provides the highest amount of fibre per hectare (2.2 - 5.5 t/ha) (*Trotuş, E. et al., 2020)*. Hemp fibres are durable, resistant, longer than the flax ones and are used in the manufacture of a wide range of textiles, and impregnated with various plastics, they can be used in various fields of the technical industry (*Matthew, R.L., 2020; Trotuş, E. et al., 2020; Stroescu, Ghe. et al., 2021*). Shorter fibres resulting from processing are a very good fuel, but are also used in the manufacture of cellulose, particle board, insulation boards, and which by treatment improve the properties of composites reinforced with such fibres (*Zane, Z. et al., 2020)*.

The cultivation of hemp for seed production is due to the multiple applications in the technical, food, cosmetics and fodder fields. In the literature (*Grégoire, M. et al., 2020*) it is highlighted that it is important that the whole hemp plant can be valued, being known for its multifunctionality.

Combined harvesting systems capable of simultaneously harvesting seeds and stalks have been designed for hemp harvesting, as specified by the authors (*Gusovius, H.-J. et al., 2016*).

Natural fibres have been threatened by the growth of artificial fibre alternatives, so natural fibre industries must remain competitive, must continue technological progress through mechanization, the use of synthetic or natural fertilizers, plant protection chemicals and genetic engineering tools (*Townsend, T. 2020)*.

The production of stalks, respectively of fibre per surface unit is influenced, among other things, by the cultivation technology applied and the genotype used. Agricultural Research and Development Station Secuieni created and homologated monoecious hemp genotypes for stalks and fibre, Dacia-Secuieni and Ratza, and studied different technological links to increase the agro-productive capacity of its genotypes, while maintaining the THC content within legal limits (*Popa, L.D. et al., 2022*).

At INMA Bucharest, following the concerns for the diversification of hemp harvesting equipment, innovative technical equipment for stalks harvesting and sheaf-binding has been designed, developed and tested.

Considering the above mentioned, in the present work both the combined influence between the application of cutting and the seed norm used, on the agro-productive capacity of a monoecious hemp genotype, as well as the hourly fuel consumption, respectively the consumption per unit, were experimented. The results obtained will allow the establishment of some optimal technological links for cultivation, while the knowledge of the energy indices will be useful for the evaluation of expenses per hectare, in order to draw up the expense-income balance, which is the basis of the assessment of economic efficiency.

MATERIALS AND METHODS

The biological material was represented by Ratza monoecious hemp genotype for fibre. This is an energetic variety, homologated in 2016, created following the appearance of a natural mutation in the Alice genotype, followed by isolation and repeated individual selection. The production potential of the variety is 700-800 kg/ha seed and 20.0-25.0 t/ha energetic stalks (*Trotuş, E. et al., 2020*).

In 2021, a monoecious hemp culture for fibre was established in the experimental field of the Agricultural Research and Development Station Secuieni, Neamț, according to (fig. 1), where the combined influence of applied cutting and seed norm on stalk production was studied. The experimental field was of the subdivided plots type, corresponding to the studied factors: factor A = type of cutting, with two graduations (a_1 = NT, uncut, a_2 = T1, cut once); factor B = seed norm, with three graduations (b_1 = 20 kg/ha, b_2 = 40 kg/ha, b_3 = 60 kg/ha).

In autumn, after harvesting the preceding plant, ploughing was carried out at a depth of 25 cm. In the spring, when preparing the seedbed, a levelling was carried out with the disc harrow, followed by a pass with the combine. Taking into account the fact that the species is demanding on the content of nutrients in the soil, complex fertilizers N:P:K 16:16:16 were administered, in the amount of 300 kg/ha.

The crop was established in the last decade of April, the sowing being followed by herbicidation with Aloha, in a dose of 1.5 l/ha. During the vegetation period, specific maintenance works were carried out on the experimental plots. Within the T1 variant, the Secuieni method of cultivating monoecious hemp for seed was applied, which is the subject of the patent (*Găucă, C.*, *Patent no. 115211*). The method consists in the mechanized cutting of plants that have 5-6 nodes formed, 20-30 cm from the ground level, resulting in the development of new shoots with inflorescences, obtaining more uniform crops, but also a reduction in the height of the field (*Trotuş, E. et al., 2015; Gherasim, A., 2017*).

The cut crop will allow the harvesting of hemp for seed directly from the field, with combines for cereals, with the header raised below the point of insertion of the inflorescences, and for hemp for fibre by using technical equipment with devices for cutting and binding the stalks.

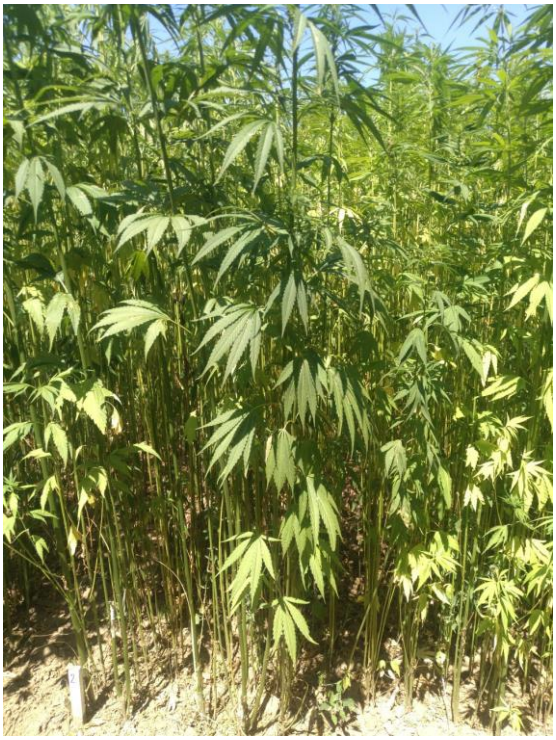

Fig. 1 - Appearance from the culture for fibre

During the course of the experiments, the evolution of the experimental field of monoecious hemp variety Ratza was followed, in the meteorological conditions of the 2020-2021 agricultural year (fig. 2 and fig. 3) and the combined impact of cutting and the seed norm used on the production of stalks.

The 2020-2021 agricultural year is characterized as hot and dry, with the average annual temperature being 9.9°C, being 1.0°C higher than the multiannual average (8.9°C).

In five calendar months, there were quite large deviations of the average monthly temperature, between +1.6°C and +3.6°C, compared to the multiannual average. The low temperatures in April and May, with large temperature alternations from day to night, but also from one day to another, were considered atypical for this period of the year, the monthly deviation being -2.0°C, respectively -0.7 °C compared to the multiannual average.

The amount of precipitation recorded between October 2020 and September 2021 was 399.8 mm, with145.5 mm less than the multiannual amount of 544.3 mm, with the agricultural year falling into the dry category.

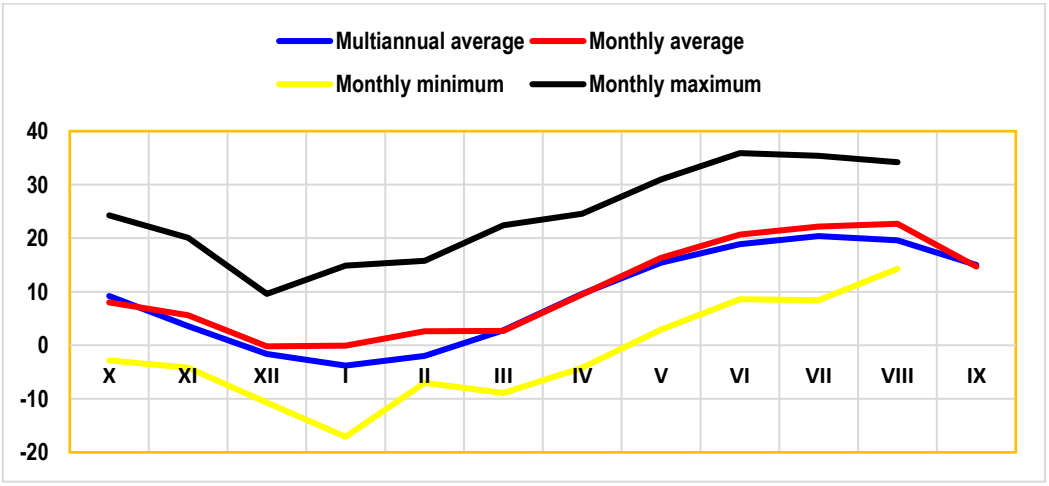

Fig. 2 - The evolution of the minimum, maximum and average temperatures recorded at ARDS Secuieni

The collection of samples from each variant was done manually, in the second decade of August, the experimental data obtained being processed statistically by methods specific to bifactorial experiences. The production increases recorded were assessed by calculating the limit differences (*Leonte and Simioniuc, 2018*).

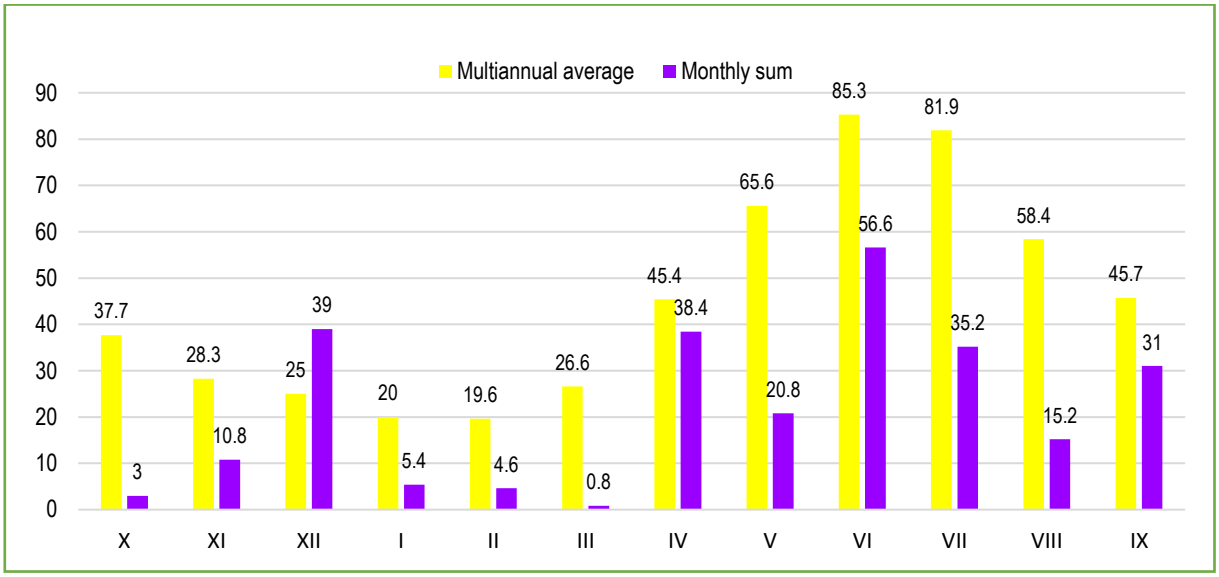

Fig. 3 - Evolution of monthly precipitation recorded at ARDS Secuieni

As a result of collaboration between A.R.D.S. Secuieni and INMA Bucharest was developed an experimental model for harvesting hemp stalks (fig. 4), which performs: stalk cutting, sheaf-binding, loading on the equipment platform and unloading on the ground, on the side of the working system.

Fig. 4 - The experimental model, SRC, for harvesting and binding the hemp stalks

Some of the results of the experiments on the constructive and functional characteristics of the technical equipment for harvesting hemp stalks and sheaf-binding and the observations on the influence of adjustments of working devices on the characteristics of hemp sheaves were presented by (*Nedelcu, A. et al., 2021*). The experiments were performed according to the methodology developed for this technical equipment and the procedures described by (*Vlăduţ, N-V. et al., 2012*).

The determination of the energy indices (working speed, fuel consumption) was done simultaneously with the indices regarding the working quality of the experimental model (actual working width, cutting height, losses on stubble field), *(Chiţoiu, M. et al., 2016; Chiţoiu, M. et al., 2017)*. Fuel efficiency varies by type of fuel and by percent load on the engine (*Grisso, R. D et al., 2004).*

The total fuel consumption in a shift depends on the hourly consumption recorded in each operating mode and the operating time in that mode, according to formula (1):

$$G_s = G_1T_1 + G_2T_2 + G_3T_3 \quad \text{[kg/shift]} \tag{1}$$

Where:

G_s – total fuel consumption in a shift, kg/shift;
G_1 – hourly fuel consumption during actual operation, kg/h
T_1 – actual operating time, h;
G_g – hourly fuel consumption while idling, kg/h
T_g – idling time, h;
G_0 – hourly fuel consumption in steady-state, kg/h
T_0 – steady-state operating time with (low speed), h;
The fuel consumption per hectare of cultivated land, G_{ha}, is determined by relation (2):

$$G_{ha} = \frac{G_s}{W_s} \quad \text{[kg/ ha]} \tag{2}$$

$$W_s = 0.36\, B_l V_l T_1 \text{ [ha/shift]} \tag{3}$$

Where: W_s - working capacity per shift, ha/shift
B_l – working width, m
B_l=1.4 m
V_l – working speed, m/s
Hourly fuel consumption G_1, for each operating mode is determined experimentally by means of a device for determining fuel consumption (accuracy ± 1 g).

G_1, depending on the energy source, can also be calculated with the relation (4):

$$G_1 = c_s P_{tr} \text{ [kg/h]} \tag{4}$$

Where:

c_s - is the specific fuel consumption, kg/ HP h;
P_{tr} – traction power, HP.

Fuel consumption for the innovative hemp stalk harvesting system was calculated based on the specific fuel consumption of the New Holland TD 80D tractor engine used in the experiments.

RESULTS AND DISCUSSION

As mentioned in the fibre crop, different seed norms were experimented, 20 kg/ha, 40 kg/ha, and 60 kg/ha respectively, the corresponding densities, determined at the 6-leaf stage, being shown in figure 5.

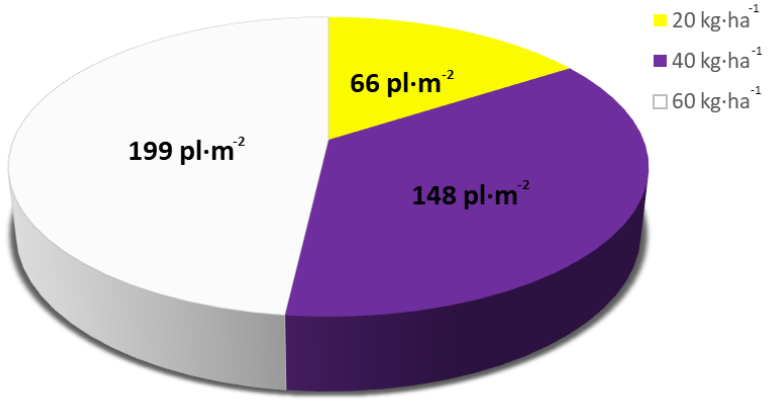

Fig. 5 - The densities corresponding to the seed norms applied in the crop for fibre

In the samples collected from the experience, biometry and agro-productivity determinations were made, depending on the cutting applied and the norm of seed/ha used, the results being summarized in the table below.

As can be seen, there is an inversely proportional relationship between the number of cuttings applied and the height of the plants, a relationship that is also found between the norm of seed applied and the height of the plants. At the same time, plant density/m^2 increases with the use of higher seed norms, while there is a direct correlation between the application of cuttings and the number of shoots formed/m^2. At the same time, the average stem diameter decreases with the application of cutting, respectively with the increase of the seed norm used per surface unit.

Table 1

Biometric and agro-productivity determinations in the harvested samples

Cutting variant	Seed norm, kg /ha	Stalk length, m	No. of plants per m^2, pc.	No. of branches per m^2, pc.	Fibre weight (g)	Fibre content (%)	Average diameter (mm)
NT	20	2.20	76	-	41	29.2	8.0
NT	40	2.10	133	-	29	30.2	6.9
NT	60	2.00	157	-	26	29.3	6.3
T1	20	1.60	60	113	21	27.1	5.6
T1	40	1.30	107	170	14	27.3	4.5
T1	60	1.20	138	192	12	27.2	4.3

According to the table below, the cutting applied to the hemp crop negatively influenced the production of stalks, the results recorded by the variant that was cut (T1 – 6706 kg/ha) being distinctly significant negative compared to the uncut control variant (11286 kg/ha), the difference from this being - 4580 kg/ha (table 2).

Table 2

Influence of cutting on stalk production

No. crt.	Variant	Production			The meaning of the differences
		average ± standard error (kg/ha)	% to the control	differences from the control	
1.	NT	11286 ± 284	100	0	Mt
2.	T1	6706 ± 448	59.42	-4580	00

DL 5% = 1269.1 kg/ha
DL 1% = 2930.8 kg/ha
DL 0.1% = 9326.6 kg/ha

In the course of the experience, the seed norm of 20 kg/ha determined statistically assured production increases at a very significant level in terms of stalk production (1251 kg/ha) compared to the control taken in the study, namely the seed norm of 40 kg/ha (8902 kg/ha), according to the results shown in the table below. The norm of 60 kg/ha registered production results below the level of the control variant, the differences being distinctly significant negative (7932 kg/ha stalks).

Table 3

Influence of seed norm on stalk production

Nr. crt.	Variant	Production			The meaning of the differences
		average ± standard error (kg/ha)	% to the control	differences from the conrol	
1.	20	10153 ± 786	114.06	1251	***
2.	40	8902 ± 1259	100	0	Mt
3.	60	7932 ± 1059	89.10	-970	00

DL 5% = 456.4 kg/ha
DL 1% = 663.8 kg/ha
DL 0.1% = 995.7 kg/ha

The combined influence of the two factors considered in the study (cutting x seed norm) on the production of stalks determined production increases that are not statistically ensured in the case of the NT x 20 combination (186 kg/ha) compared to the control Mt taken in the study - NT x 40 kg/ha (11702 kg/ha), according to Figure 6.

The combinations between the cutting applied and the three experimental norms (T1 x 20 kg/ha, T1 x 40 kg/ha and T1 x 60 kg/ha) determined differences ensured at a statistically significant negative level compared to the control of this experience (NT x 40 kg/ha – 11702 kg/ha).

Stalks productions were negatively influenced by the applied cutting and positively by the seed norm of 20 kg/ha.

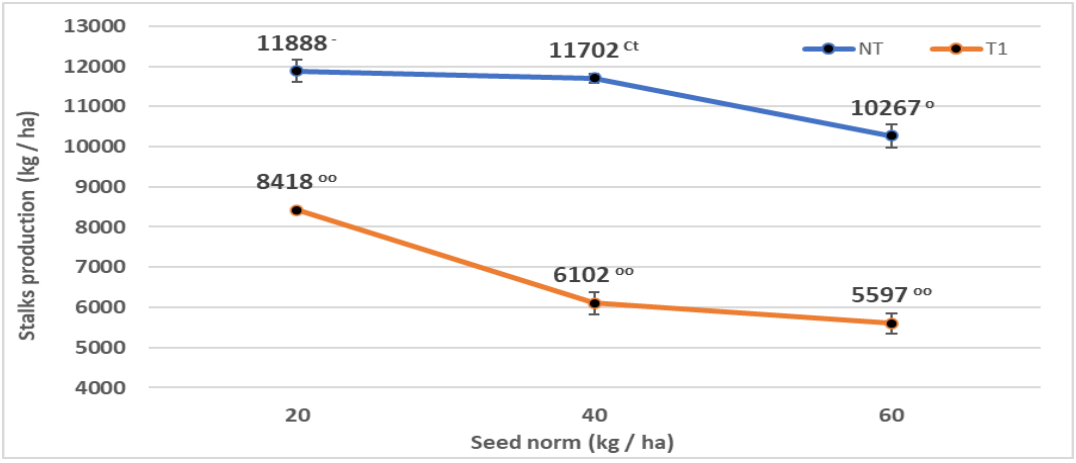

Fig. 6 - Influence of cutting and seed norm combination on stalks production

To determine the hourly fuel consumption, three measurements were made for two operating speeds of the New Holland TD 80D tractor. For the tractor engine used in the experiments, the specific consumption at rated speed was assessed, according to the operator's book:

c_s = 0,200 kg/kW h=0,176 l/CP h.

The values for the traction power consumed, used in the calculation, are presented in Table 4.

To express fuel consumption in litres/h, divide the value determined by relation (4) to diesel density which is 836 kg m^{-3} (0.836 kg/l).

Table 4

Hourly fuel consumption

Working speed, km /h	Power consumed, HP	Calculated average power, HP	Hourly fuel consumption, l/h	Average hourly fuel consumption, l/h
1.75	25.0	25.43	5.50	4.47
	25.5		5.59	
	25.8		5.68	
2.25	28.5	28.33	6.27	4.98
	27.5		6.05	
	29.0		6.38	

The norms of working capacity and fuel consumption for mechanized works for hemp stalk harvesting and binding, performed with the experimental model SRC are presented in Table 5.

Table 5

Fuel consumption per hectare

Working speed, km/h	Working capacity, ha/h	Working capacity per shift, ha/shift	Average hourly fuel consumption, l/h	Fuel consumption per hectare, l/ha
1.75	0.245	1.96	4.47	18.24
2.25	0.315	2.52	4.98	15.81

The work of stalk harvesting and sheaf-binding was carried out on flat land, with a slope of up to 60 and the production recorded for hemp crop was approx. 10 t/ha.

The value of fuel consumption per hectare of 15.81 l/ha, at a crop production of 10 t/ha, obtained with the New Holland TD 80D tractor system + harvesting and sheaf-binding equipment, SRC, compared to the value, 16.5 l/ha, indicated for the harvesting and binding machine JSK 2.1, presented in the work *Ecological agriculture technologies (Samuil, C., 2007)*, is smaller and is due to the high-performance equipment used.

CONCLUSIONS

The cutting applied to the hemp crop, for all three seed norms used, negatively influenced the production of stalks, following the comparison with the control of the experience (NT x 40 kg/ha – 11702 kg/ha); at the same time, the use of a seed norm of 20 kg/ha had a positive impact on stalk production.

The results obtained after testing the equipment presented in the paper demonstrate the fact that the fuel consumption recorded for the harvesting of hemp stalks, having a value of 15.81 l/ha, at a crop production of 10 t/ha, is lower compared to that of the equipment taken as standard JSK 2.1.

The registered results are premises for optimization of some technological links at hemp cultivation and also confirm that the fuel consumption per hectare recorded at hemp stalks harvesting is influenced both by the technical characteristics of the equipment used and by the characteristics of the harvested crop.

ACKNOWLEDGEMENT

The paper has been funded by the ADER 2022 Sectoral Programme, through financing contract no. 25.1.1 /26.09.2019 for the project “ADER 25.1.1 - *Mechanization technology and technical system for harvesting hemp crops*”.

REFERENCES

[1] Ceyhan, V., Türkten, H., Yıldırım, Ç., Canan, S. (2022). Economic viability of industrial hemp production in Turkey. *Industrial Crops and Products*, vol. 176, 114354. https://doi.org/10.1016/j.indcrop.2021.114354

[2] Chiţoiu, M., Voicu, Gh., Paraschiv, G., Moiceanu, G., Vlăduţ, V., Matache, M., Marin, E., Bunduchi, G., Danciu, A., Voicea, I., Găgeanu, I. (2016), Energy consumption of a hammer mill when chopping miscanthus stalks, *Proceedings of the 44 International Symposium on Agricultural Engineering "Actual Tasks on Agricultural Engineering",* pp. 215-224, Opatija – Croaţia;

[3] Chiţoiu, M., Voicu, Gh., Paraschiv, G., Moiceanu, G., Vlăduţ, V., Matache, M., Grigore, I., Bunduchi, G., Voicea, I., Găgeanu, I. (2017), Comparison of energy consumption of a hammer mill during chopping miscanthus stalks and energetic willow, *Proceedings of the 45 International Symposium on Agricultural Engineering "Actual Tasks on Agricultural Engineering",* pp. 259-268, Opatija – Croaţia;

[4] Grégoire, M., Barthod-Malat, B., Labonne, L., Evon, P., De Luycker, E., Ouagne, P. (2020). Investigation of the potential of hemp fibre straws harvested using a combine machine for the production of technical load-bearing textiles*. Industrial Crops and Products*, vol.145, article 111988. https://doi.org/10.1016/j.indcrop.2019.111988

[5] Gusovius H.-J., Hoffmann T., Budde J., Lühr C. (2016). Still special? Harvesting procedures for industrial hemp*. Landtechnik*, 71(1), pp.14–24. DOI:10.15150/lt.2016.3118

[6] Găucă, C. (1999), *Method of Cultivation of Hemp for Seed*. Romania. Patent no. 115211.

[7] Gherasim, A. (2017). Research on improving the cultivation technology at monoecious hemp for fibre for the efficiency of culture (*Cercetări cu privire la îmbunătățirea tehnologiei de cultivare a cânepei monoice pentru fibră în vederea eficientizării culturii*). Doctoral thesis.

[8] Grisso, R. D., Kocher M. F., Vaughan, D. H. (2004). Predicting tractor fuel consumption. *Annual Meeting of the American-Society-of-Agricultural-Engineers,* vol. 20(5), pp. 553-561.

[9] Leonte, C., Simioniuc, V. (2018). Methods and techniques used in agronomic research (*Metode și tehnici utilizate în cercetarea agronomică*). Publishing house "Ion Ionescu de la Brad" Iași.

[10] Matthew, R.L. (2020). *5B* - Bast fibres: hemp cultivation and production*. Handbook of Natural Fibres (Second Edition)*. vol. 1, pp.163-196. https://doi.org/10.1016/B978-0-12-818398-4.00007-4

[11] Nedelcu, A., Ciupercă, R., Popa, L.-D., Mihai, M., Zaica, A., Olteanu, B.-G. (2021). Aspect on Testing the Technical Equipment for Harvesting Hemp Stalks in Sheaves*, Proceedings of International Symposium ISB-INMA TEH- Agricultural and Mechanical Engineering,* 29 October, Bucharest, Romania, pp. 708-713.

[12] Popa, L.D., Buburuz, A.A., Trotuș, E., Vlăduţ, N.-V., Teliban, G.C., Agapie, A.L., Puiu, I., Burducea, M., Melucă, C., Pintilie, P.L., Matei, G. (2022). Recent progress in monoecious hemp variety for seed, obtained in Romania. *Romanian Agricultural Research*, no. 39, pp. 187-194. DII 2067-5720 RAR 2022-171

[13] Samuil, C., (2007). Ecological agriculture technologies (*Tehnologii de agricultură ecologică*). Publishing house Pim, Iaşi, ISBN 973-7967-32-1.

[14] Stroescu, Ghe., Păun, A., Bunduchi, G., Dumitrașcu, A., Olan, M., Epure, M., Dumitru, I., Cristea, M. (2021). Hemp Cultivation in Romania. Present and Future. *International Symposium-ISB-INMA TEH Agricultural and Mechanical Engineering*, 29 October, Bucharest, Romania, pp 558-565.

[15] Townsend, T. (2020). 1B - World natural fibre production and employment. *Handbook of Natural Fibres* (Second Edition), vol.1, pp. 15-36. https://doi.org/10.1016/B978-0-12-818398-4.00002-5

[16] Trotuş, E., Lupu, C., Druțu, A.C., Pochișcanu, S., Găucă, C., Naie, M., Popa, D.L., Leonte, A. (2015). Technologies for cultivating some field plants for the central area of Moldova (*Tehnologii de cultivare a unor plante de câmp pentru zona centrală a Moldovei*). Publishing house „Ion Ionescu de la Brad" Iași.

[17] Trotuş, E., Isticioaia, S.F., Mîrzan, O., Popa, L.D., Naie, M., Lupu, C., Leonte, A., Pintilie, P.L., Buburuz, A.A., Pleşcan, I.D. (2020). *Technologies for cultivating some field plants for the central area of Moldova*. Publishing house „Ion Ionescu de la Brad" Iași, pp. 139-159.

[18] Vlădut, N-V., Matache, M., Voicea, I., Nicolescu, M., Biriş, S., Paraschiv, G., Voicu, Gh., Danciu, A., Persu, C. (2012). *Assisted testing of biotechnical systems (Testarea asistată a sistemelor biotehnice)*, Publishing house "Terra Nostra", Iaşi, Romania, pp.51-54.

[19] Zane, Z., Kukle, S., Kajaks, J., Bake, I. (2020) Effect of ageing on hemp waste/polyethylene composites surface properties, *19th International Scientific Conference Engineering for Rural Development*, Jelgava, 20.-22.05.2020, pp. 204-211, DOI:10.22616/ERDev.2020.19.TF048

DESIGN AND PERFORMANCE TEST OF SPOILER BLADES OF THE DIRECT SEED-METERING DEVICE FOR RICE
/
水稻直播排种器扰流叶片的设计与性能试验

Lin WAN*[1,2], Hongchao WANG[1,2], Gang CHE[1,2], Wensheng SUN[1], Zhengfa CHEN[1] [1]
[1] College of Engineering, Heilongjiang Bayi Agricultural University, Daqing / China;
[2] Key Laboratory of Intelligent Agricultural Machinery Equipment in Heilongjiang Province, Daqing / China
Tel: +86 13555523188; E-mail: wanlin0@yeah.net
DOI: https://doi.org/10.35633/inmateh-68-06

Keywords: *seed-metering device, rice, spoiler blades, design, test*

ABSTRACT
In order to improve air pressure utilization and working performance, the direct seed-metering device for rice was designed with spoiler blades embedded in the air cavity. The study was carried out using theoretical analysis and hydrodynamic methods to obtain the optimum structure of the spoiler blades. Taking the rotating speed of the air cavity, the negative pressure of the air cavity, and the filling height as the test factors, the multiple regression analysis and the response surface analysis were carried out to obtain the best working parameters of the seed-metering device with spoiler blades. The results showed that when the rotating speed of the air cavity was 23.56 r/min, the negative pressure of the air cavity was 4.97 kPa and the filling height was 12.82 cm, the qualified index was 95.21%, the missing index was 3.28% and the multiple index was 1.51%, which was the best seeding performance. Comparing the test with the seed-metering device without spoiler blades, the results showed that the installation of spoiler blades can improve the performance of the seed-metering device under the best working parameters. This study provide a reference for the design of direct seed-metering device for rice.

摘要
为提高气压利用率和工作性能，设计一种在气腔内嵌入扰流叶片的水稻直播排种器。采用理论分析与流体力学方法进行研究，获得了最佳扰流叶片结构。以气腔旋转速度、气腔负压真空度、填种高度为试验因素，进行多元回归分析和响应曲面分析，得到装扰流叶片排种器的最佳作业参数。结果表明当气腔旋转速度为23.56r/min，气腔负压大小为4.97kPa，填种高度为12.82cm时，合格率为95.21%，漏播率为3.28%，重播率为1.51%，排种性能最佳。在最佳工作参数条件下与未安装扰流叶片的排种器进行对比试验，结果表明安装扰流叶片能够提高排种器工作性能。本研究可为水稻直播排种器的设计提供参考。

INTRODUCTION
Rice is one of the main grain crops in China, and it is a staple food for more than half of the global population *(Tian et al., 2022)*. With the acceleration of urbanization and the shortage of rural labor resources, mechanized planting will become an important way of grain production. The level of agricultural machinery in foreign developed countries is relatively high, and rice production has been fully mechanized *(Wan et al., 2019)*. In China, rice is mainly grown in paddy fields, with the main mechanized planting method being machine transplanting *(Chauhan et al., 2015; Yamauchi, 2017)*. Compared with machine transplanting, mechanized direct seeding can reduce the cost without the process of rice transplanting and increase yield per unit area. Therefore, direct seeding of rice is the main development direction for mechanized farming *(Zhang et al., 2018)*.

The performance of the pneumatic seed-metering device decreased due to insufficient utilization of air pressure and the great difference in rice varieties *(Luo et al., 2019; Liu et al., 2018)*. Most scholars use theoretical analysis and structural design methods to solve these problems *(Wu et al., 2020; Yatskul and Lemiere, 2018; Zhang et al., 2021)*. A kind of pneumatic cylinder structure seed-metering device was designed, which can realize the function of one device with multiple rows, and effectively improve the problems of complex pneumatic system and insufficient utilization of air pressure *(Zhang et al., 2015)*.

[1] *Lin Wan, Prof. Ph.D.; Hongchao Wang, Ph.D.; Gang Che, Prof. Ph.D.; Wensheng Sun, Master Degree; Zhenfa Chen, Ph.D.*

According to the principle of side suction seed, a double-cavity structure was designed for rice, which can meet the requirements of direct seeding of conventional rice and hybrid rice. Theoretical analysis of the working process was carried out, and mechanical models were established. The test showed that the seed-metering device has good applicability and uniformity *(Zhang et al., 2016)*.

With the development of computer simulation technology, fluid simulation technology has been more widely used in the research of seed-metering devices. This technology can quantitatively analyze and describe the simulation results *(Li et al., 2021; Gao et al., 2021; Ye et al., 2021)*. With the help of the EDM-CFD simulation method, the working process of the seed-metering device was simulated, and the seed filling performance of different shapes of seeds was analyzed. The design of the seed-metering device was optimized based on the simulation results *(Ding et al., 2018)*. By using the CFD simulation method, the structure of the negative pressure channel was simulated, and the best channel structure was determined. Several independent negative pressure channels control the precision of seed suction, which improves the utilization rate of air pressure and working performance *(Xing et al., 2019)*. At present, a lot of research has been done on the seed-metering device, but few studies have been found on the structure of the air cavity and the flow field in the air cavity of the seed-metering device.

The main objective of this paper is to investigate the effect of different structured spoiler blades on the internal flow field distribution and operating performance of the seeder. The fluent software was used to simulate and analyze the three kinds of spoiler blades, and the optimal structure of the spoiler was determined. The necessity of installing the spoiler blade was verified by a comparative test. A three-factor and the five-level orthogonal experiment was designed to obtain the best working parameters of the pneumatic seed-metering device under the spoiler blades. This study provides guidance and direction for the direct seed-metering device.

MATERIALS AND METHODS

Overall structure and working principle

The direct seed-metering device for rice is mainly composed of spoiler blade, seed-metering plate, directional stirring teeth, and shell, as shown in Fig.1. The negative pressure environment is an enclosed space consisting of a seed-metering plate and base with embedded spoiler blades, rubber brush and bearing. The sprocket is bolted to the base and moves through the drive mechanism, which in turn rotates the air chamber. However, the spoiler blade, rubber brush and bearing remain relatively stationary. Throughout the process, the rice fills the seed storage chamber and is distributed near the suction holes. The rotating process of the air chamber enhances the mobility of the rice by the action of the mixing device, which is more conducive to the adsorption of rice. Depending on the pressure difference between the inside and outside of the air chamber, the rice seeds are sucked onto the seed-metering plate. The scraping adjusting device removes the excess rice seeds and the rubber brush blocks the suction holes. The rice seeds will no longer be sucked by the negative pressure and will fall by its own gravity to the seed delivery tube, ending the seed discharge process.

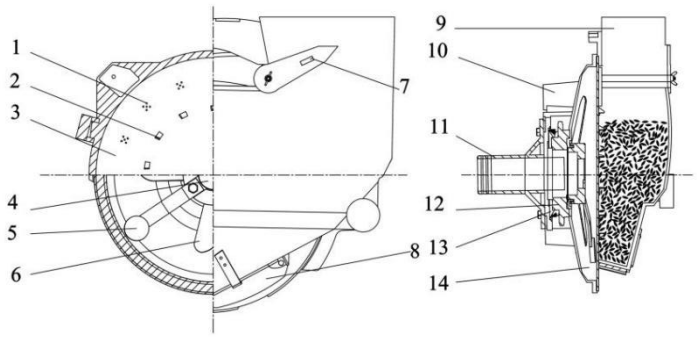

Fig. 1 - Structure of the seed-metering device

1. suction hole; 2. mixing device; 3. seed-metering plate; 4. bearing; 5. rubber brush; 6. spoiler blade; 7. scraping adjusting device; 8. seed unloading device; 9. cover; 10. shell; 11. fan joint; 12. sprocket; 13. washer; 14. base

The spoiler blades

The spoiler blades are installed in the air cavity and rotate relative to the air cavity. As the air chamber turns counterclockwise, the outer ring of the spoiler blades will generate a high linear velocity, driving the surrounding airflow during rotation.

From the simplified Bernoulli's equation, it can be seen that the faster the air flow rate, the lower the pressure, and the larger the air pressure difference at the location of the suction hole, which can improve the air pressure utilization and seed adsorption effect, as shown in equation Eq.(1).

$$p+\rho gh+\frac{1}{2}\rho u^2=C_p \quad (1)$$

Where: p is the pressure (Pa); ρ is the density of the fluid (kg/m^3); g is the acceleration of gravity (m/s^2); h is the height (m); u is the fluid velocity (m/s); C_p is a constant.

The spoiler blades improve the fluidity of the internal flow field of the seed-metering device and increases the pressure difference at the suction holes, thus improving the adsorption performance of the seeds and ensuring that the group of suction holes can evenly absorb the seeds.

Design analysis of three spoiler blade

To investigate the effect of different spoiler blade structures on the internal flow field and the performance of the seed-metering device, three different structures of spoiler blades were designed, as shown in Fig. 2. All three structures were symmetrically distributed in a circular pattern and 3D printed in PLA resin.

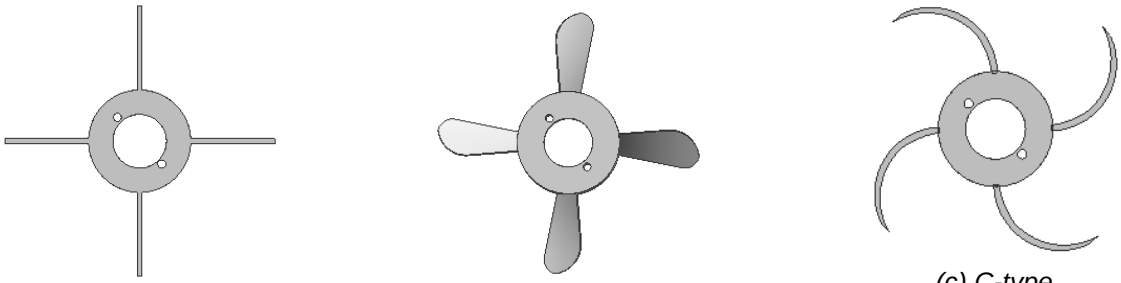

(a) A-type *(b) B-type* *(c) C-type*

Fig. 2 - Structural diagram of three kinds of spoiler blades

The analysis of the three structures of the spoiler blade shows that the A-type spoiler blade is in right-angle contact with the airflow, which has a good spoiler effect, but does not have a significant effect on the airflow guidance. The C-type spoiler blade structure is in right-angle contact with the airflow and has a good inflow effect, but the disturbance effect is not significant. The B-type spoiler blade are designed in a curved form to enhance the flow guidance and contact the airflow at an acute angle, so that the B-type spoiler blades have both flow guidance and spoiler properties. In order to obtain the trajectory of the central air infusion to the outer ring, the starting coordinates of the air mass are assumed to be (R1, 0), and after a period of counterclockwise rotation of the seed-metering plate, the relative equation of motion of the air mass is derived as shown in Eq. (2).

$$\begin{cases} x=R_1\cos(\omega t)-Z\sin(\omega t) \\ y=R_1\sin(\omega t)+Z\cos(\omega t) \end{cases} \quad (2)$$
$$\omega \mathrm{t}\in(0,2\pi)$$

x is the involute abscissa value (mm); y is the involute ordinate value (mm); ω is the angular velocity (rad/s).

The equation shows that the equation of motion of the trajectory of the air mass is an involute with the radius R1 of the base circle. Considering the size of the space in the air cavity and the working efficiency, R1 is designed to be 30 mm and the number of spoiler blade is designed to be 4. To increase the air flow velocity at the group suction holes, the radius of circumferential operation is designed to be 85 mm according to the working principle of the spoiler blade, this position of the suction holes can achieve the best flow velocity and pressure to improve the seeding performance.

Blade design theory

In order to design three types of spoiler blades in a rational way, the analysis of the spoiler blades is based on Schmitz theory. The design of the spoiler blade has to meet the aerodynamic requirements, as illustrated by the B-type spoiler blade. The spoiler blades have an effect on the nearby airflow, causing changes in the flow field within the air cavity and at the cluster suction holes, which can improve the suction performance of the seed-metering device. The air chamber rotates with the sprocket to drive the internal air flow. The spoiler blades come into contact with the air flow inside the chamber and the viscosity of the gas causes a pressure differential to form on the surface of the blades. The forces during the operation of the spoiler blades are shown in Fig. 3.

The simplified formula of L and D is expressed as in the following equation:

$$L = \frac{1}{2}\rho W^2 C_L C dr \tag{3}$$

$$D = \frac{1}{2}\rho W^2 C_D C dr \tag{4}$$

The axial thrust (T) and torque (Q) at the radius of the blade rotation area are shown as follows:

$$dT = N\left(L\cos\phi + D\sin\phi\right) = \frac{1}{2}\rho W^2\left(C_L\cos\phi + C_D\sin\phi\right)KCdr \tag{5}$$

$$dQ = N\left(L\sin\phi - D\cos\phi\right) = \frac{1}{2}\rho W^2 r\left(C_L\sin\phi - C_D\cos\phi\right)KCdr \tag{6}$$

Where: L is the force that raises the blade (N); D is the resistance acting perpendicular to the blade rotation plane (N); C_L is the lift coefficient; C_D is the drag coefficient; ϕ is the inflow angle (°); C is the length of AB (mm); ρ is the air density (kg/m³); W is the relative wind speed (m/s); K is the number of blades; r is the working radius of blade circumference (mm).

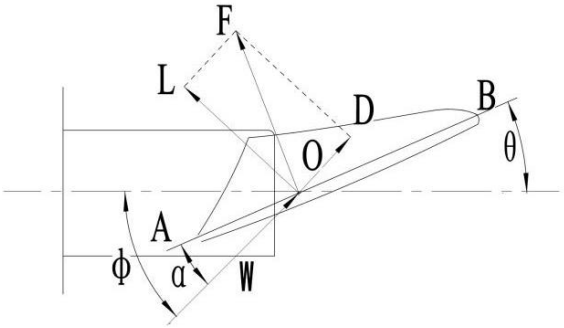

Fig. 3 - Schematic diagram of the spoiler blade

During the relative rotation of the spoiler blades in the air chamber, the pressure on the lower surface is greater than the atmospheric pressure and the pressure on the upper surface is less than the atmospheric pressure, and the airflow at both ends of the blades flows from the high pressure area to the low pressure area. The formation of vortices at the end face of the blade causes the velocity of the flow field corresponding to the group of suction holes to change, increasing the negative pressure difference at the suction holes and improving the seeding performance. Assume that the tangential velocity upstream of the blade is zero and the tangential velocity downstream varies as Δu, as shown in Fig. 4. Then the tangential velocity (U) of the blade is shown as follows:

$$\mathrm{U} = \omega \cdot \mathrm{r} + \frac{\Delta \mathrm{u}}{2} \tag{7}$$

In order to optimize the operating performance of the blades, the value of Δu should be determined by the tip speed ratio of the blades. If friction is neglected and the viscous effect is not considered, the relative speed of the airflow upstream and downstream the blade only changes in direction, and the value does not change.

If the resistance is ignored, the work done by the circumferential force is shown as follows:

$$\mathrm{dP} = \Delta \mathrm{W} \cdot 2\pi\ \rho \mathrm{r}\,\mathrm{dr}\,\mathrm{v}_2 \sin\varphi \cdot \mathrm{r} \cdot \omega \tag{8}$$

$$\mathrm{U} = \omega \cdot \mathrm{r} + \frac{\Delta \mathrm{u}}{2}\ \Delta W = 2W_1 \sin\left(\phi_1 - \phi\right) \tag{9}$$

$$v_2 = W\sin\phi = W_1\cos\left(\phi_1 - \phi\right)\sin\phi \tag{10}$$

Therefore, the power of the blade is as follows:

$$\frac{\mathrm{dP}}{\mathrm{d}\varphi} = 2\pi\rho \cdot \Omega \cdot \mathrm{r}^2 \sin\varphi \cdot \sin\left(2\varphi_1 - 3\varphi\right) = 0 \tag{11}$$

The optimal inflow angle of the relative wind speed is expressed in the following equation:

$$\phi = \frac{2}{3} arcctg\left(\frac{r}{R}\lambda\right) \tag{12}$$

The length of AB and the installation angle of the blade (θ) are expressed in the following equation:

$$C = \frac{16\pi r}{KC_L}\sin^2\left(\frac{arcctg\left(\frac{r}{R}\lambda\right)}{3}\right) \tag{13}$$

$$\theta = \frac{2arcctg\left(\frac{r}{R}\lambda\right)}{3} - \alpha \tag{14}$$

Where: R is the blade spanwise length (mm); α is the angle of attack (°); λ is the blade tip speed ratio.

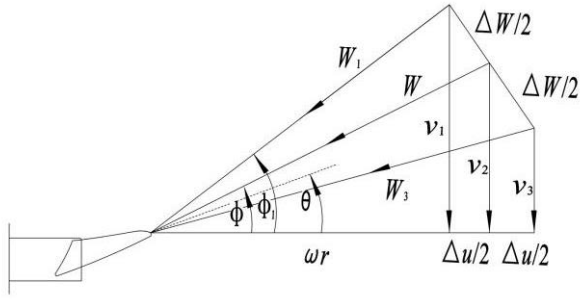

Fig. 4 - Velocity triangles upstream and downstream of the spoiler blade

After theoretical calculation, the installation angle of the spoiler blade is designed as 19° and the length of AB is 51 mm. To consider the working performance and structural balance, the structure coefficient (k_a) can be set, as shown in Fig. 5. The structure coefficient is defined as the ratio of the difference between a certain radius as a reference and the radius of the inner circle, along the direction of increasing blade radius, to the total length of the blade. k_a is expressed in the following equation:

$$k_a = \frac{r_a - r_b}{R} \tag{15}$$

Where: r_a is the radius (mm); r_b is the radius of the inner circle (mm).

The spoiler blades are designed and manufactured as separate components of the seed-metering device and can be delimited by a certain k_a value, divided into an inner and an outer ring along the direction of increasing radius. In order to ensure that the blades have sufficient strength, the blade roots should be kept thick enough. The outer ring of the blade has a high linear velocity, and the Reynolds number of the airflow around the blade is also high, so the curved structure of the blade should be used to increase the gas flow and disturbance, to give full play to the performance of the blade. The k_a =0.5~0.55 range is used as the dividing line, the inner ring area of the blade is dominated by the structural characteristics, the outer ring of the blade is dominated by the maximum air characteristics, so that the design can better maintain the performance of the blade.

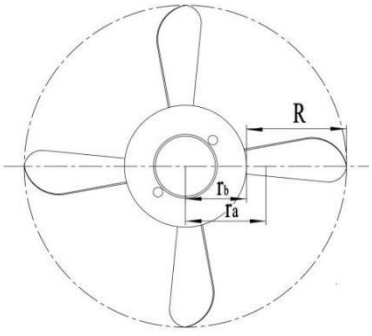

Fig. 5 - Velocity triangles upstream and downstream of the spoiler blade

Experimental material and equipment

The Longjing 31 was selected as the test material. The average moisture content was 22.5% (wet basis) before the test, the weight of 1000 grains was 23.8 g. The experiments were conducted in the Laboratory of Heilongjiang Bayi Agricultural University. The experimental equipment consisted of a belt, motor, rubber tubes, and seed box, as shown in Fig. 6. The direct seed-metering device was installed on a JPS-12 seed-metering device performance test bench. The speed of the locomotive in the field is simulated through the movement of the belt. When the rice falls on the oil belt, the seeds were monitored in real-time through the visual acquisition system. The corresponding data and video were collected to realize the monitoring of the seed-metering process.

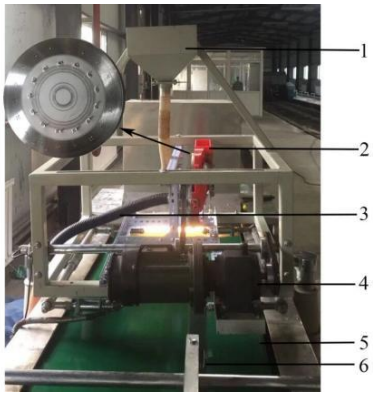

Fig. 6 - Test bench of pneumatic seed-metering device

1. Seed box; 2. seed-metering device; 3. Negative pressure air pipe; 4. Motor; 5. Belt; 6. Oil brush

Experimental design

Simulation test on the flow field of different spoiler blades

According to the structure parameters of the air cavity, the model of the fluid gas cavity was established in the DM module of ANSYS, and the boundary conditions of the inlet, outlet, and wall of airflow were set. The numerical simulations were carried out using an uncoupled implicit solver, choosing the standard k-ε model with an absolute pressure of 101325 Pa. The rotating speed of the air cavity was set at 35 r/min, and the negative pressure of the air cavity was 5 kPa. To quantitatively analyze the simulation effects of the different structures, the average flow velocity data and the average pressure data inside the air cavity for the different sets of suction cross-sections were obtained by means of the post-processing module. To reduce numerical diffusion, a second order windward format was chosen for the calculations and the SIMPLEC algorithm was used for the solution calculations.

Rotation orthogonal combination test

According to the simulation results, the optimal structure of the spoiler blade was selected and applied to the rotation orthogonal combination test. The factor coding levels are shown in Table 1. The optimal combination of parameters was determined through tests, and the interaction between various factors was studied. The experimental design and result are shown in Table 2. In this study, the rotating speed of the air cavity, the negative pressure of the air cavity, and the filling height were represented with codes X_1, X_2, and X_3. The missing index, the qualified index, and the multiple index were taken as output, Y_1, Y_2, and Y_3. According to the actual seeding standard in the field, the qualified index of rice commonly used for direct seeding in holes is 3 to 6 seeds. To ensure the qualified index of operation, agronomic requirements of rice hole diameter is not greater than 50 mm. When the seed-metering device is in a stable state of motion, less than 3 seeds per hole of rice is a missing seed and more than 6 seeds is a reseeding. Each group of experiments was repeated three times, with the average value taken as the test result.

Table 1

Factor level coding table

Code	The rotating speed of the air cavity / r·min^{-1}	The negative pressure of the air cavity / kPa	The filling height / cm
-1.682	14	2.8	6
-1	16.4	3.3	9.6
0	20	4	15
1	23.6	4.7	20.4
1.682	26	5.2	24

RESULTS AND DISCUSSIONS

Analysis of flow field simulation results of different spoiler blades

To study the influence of different structures of the spoiler blade on the internal flow field of the air cavity, the physical model of the corresponding structure was established. Simulation analysis of different structures of spoiler blades was carried out to find the best spoiler blade structure action law. The velocity vector of the flow field in the air cavity was shown in Fig.7.

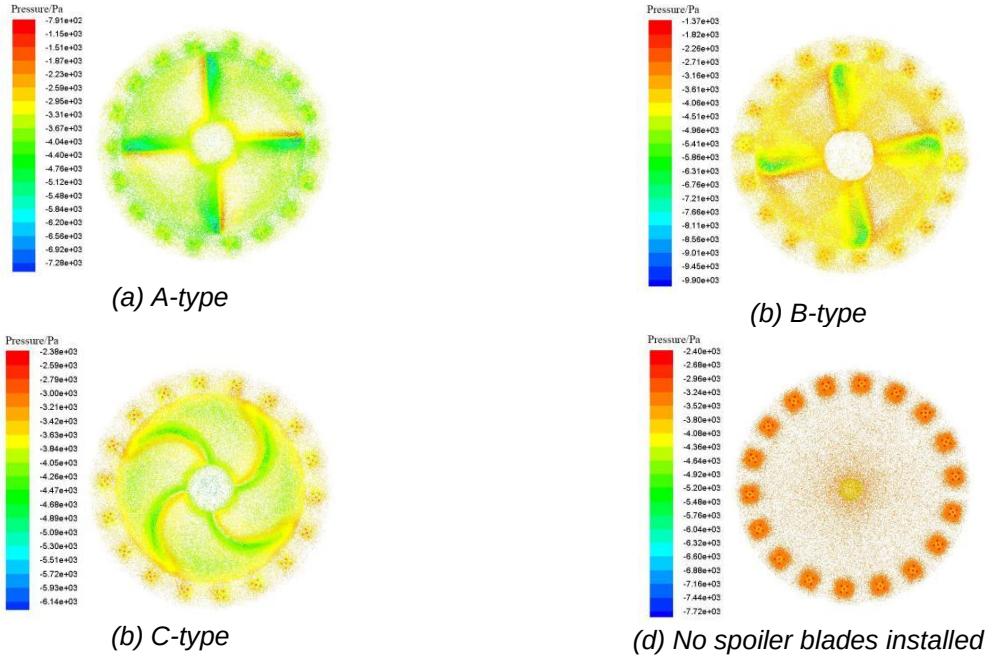

Fig. 7 - Vector diagram of the flow field in the gas cavity

As can be seen from the diagram, the flow field of the different air cavity structures was evenly distributed and stable, with lower pressure values at the group of suction holes than in the surrounding area. The overall pressure and air velocity of the air cavity flow field without the spoiler blade structure was relatively low. In comparison with the simulation of the other three groups of spoiler blades, the spoiler blades can effectively enhance the fluid movement inside the air chamber and increase the air velocity at the group of suction holes, which helps to increase the seed adsorption force and ensure the qualified index. The A-type spoiler blade increase the average pressure inside the air chamber and the air flow velocity at the group of suction holes, but is less effective than B-type and C-type spoiler blades due to the linear structure of the blades and the lack of disturbance. The B-type and C-type were effective in increasing the pressure inside the air chamber and the flow velocity at the suction holes. Due to the curved structure of the B-type and the acute angle of contact with the airflow, the B-type has both inflow and flow disturbance properties. Therefore, a comparative analysis of the structure of the three spoiler blades showed that B-type had a high degree of suitability. The simulation results were consistent with the theoretical analysis. To quantitatively analyze the degree of influence of different spoiler blades on the flow field in the air cavity, the average flow velocity and the average air pressure in the air cavity of different groups of suction hole sections were used as evaluation indicators, and the curves were plotted by processing the simulation data, as shown in Fig. 8.

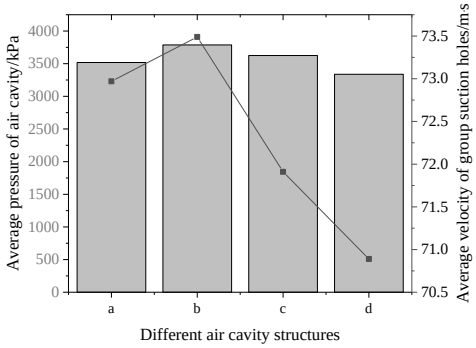

Fig. 8 - Performance curves of different cavity structures

From the simulation results and data graphs, it can be seen that the comprehensive performance of the B-type spoiler blade is optimal, with an average negative pressure of 3787.96 Pa in the air chamber and an average flow velocity of 73.49 m/s at different groups of suction holes, meeting the requirements of direct seeding.

Establishment of the regression model

Multivariate quadratic regression analysis was performed using the Design-Expert software, and the variance analysis of the influence of various factors on evaluating indicators of paddy was obtained, as shown in Table 3. The regression equation of the three groups was highly significant ($p<0.01$). The lack of fit was not significant ($p>0.05$), which indicates the goodness of fit of the regression model. In the results of the variance analysis of the qualified index, the lack of fit P-value was 0.76, indicating that no other factors affect the qualified index. In the results of the variance analysis of the missing index, the lack of fit P-value was 0.11, indicating that no other factors affect the missing index. In the results of the variance analysis of the Multiple index, the lack of fit P-value was 0.06, indicating that no other factors affect the Multiple index. After ensuring that the models were all significant and the misfit terms were not significant, the factor-coded regression equations, excluding the insignificant factors, are shown as follows:

$$Y_1 = 3.9 - 9.37X_2 + 5.57X_1X_3 + 5.51X_1^2 + 8.53X_2^2 \quad (16)$$

$$Y_2 = 92.21 + 4.07X_1 + 6.59X_2 + 7.55X_1X_2 - 10.02X_1^2 - 7.73X_2^2 - 9.72X_3^2 \quad (17)$$

$$Y_3 = 3.89 - 5.19X_1 + 2.79X_2 - 6.64X_1X_2 + 4.51X_1^2 + 6.6X_3^2 \quad (18)$$

By analyzing the result and the P-values of various factors, the effects of these factors on Y_1 ranks in the order: $X_1>X_2>X_3$; on Y_2 ranks in the order: $X_2>X_1>X_3$; in terms of the effect on Y_3 ranks in the order: $X_2>X_1>X_3$.

Table 2

Test scheme and results

Group	X_1	X_2	X_3	Y_1/%	Y_2/%	Y_3/%
1	1	1	1	6.46	88.43	5.11
2	1	1	-1	1.51	95.47	3.02
3	1	-1	1	15.47	81.37	3.16
4	1	-1	-1	14.48	78.58	6.94
5	-1	1	1	4.94	82.84	12.22
6	-1	1	-1	7.9	79.46	12.64
7	-1	-1	1	12.56	83.12	4.32
8	-1	-1	-1	19.71	76.36	3.93
9	1.682	0	0	13.63	84.45	1.92
10	-1.682	0	0	3.84	77.84	18.32
11	0	1.682	0	1.74	91.25	7.01
12	0	-1.682	0	21.85	75.74	2.41
13	0	0	1.682	5.84	83.96	10.2
14	0	0	-1.682	6.84	78.94	14.22
15	0	0	0	6.49	91.74	1.77
16	0	0	0	4.83	92.25	2.92
17	0	0	0	2.94	93.83	3.23
18	0	0	0	3.83	93.83	2.34
19	0	0	0	2.63	94.95	2.42
20	0	0	0	2.85	94.37	2.78
21	0	0	0	1.94	91.87	6.19
22	0	0	0	2.04	92.78	5.18
23	0	0	0	7.78	84.64	7.58

Model interaction item analysis

The qualified index was an important index to evaluate the performance of the direct seed-metering device. Therefore, the research focuses on the analysis of the interaction of various factors on the qualified index, and the response surface was shown in Fig. 9. Figure 9(a) represents the interactive effect of the rotating speed and the negative pressure of the air cavity on the qualified index when the filling height was 15 cm. When the rotating speed of the air cavity was fixed, the qualified index gradually rose with increasing the negative pressure of air cavity, reached a maximum, and then slowly dropped down. When the negative pressure of the air cavity was fixed, the qualified index also gradually rose with increasing the rotating speed of air cavity, reached a maximum, and then slowly dropped down.

The negative pressure of the air cavity had a range of 4.8~5.0 kPa, the rotating speed of the air cavity had a range of 22~24 r/min and the qualified index was optimal. Fig. 9(b) represents the rotating speed of air cavity which was 20 r/min and the interactive effect between the negative pressure of the air cavity and the filling height on the qualified index. When the filling height was fixed, the qualified index gradually rose with increasing the negative pressure of the air cavity, reached a maximum, and then slowly dropped down. When the negative pressure of the air cavity was fixed, the qualified index gradually rose with increasing the filling height, reached a maximum, and then slowly dropped down. The negative pressure of the air cavity had a range of 4.5~4.7 kPa, the filling height had a range of 14~16 cm and the qualified index was optimal. Fig. 9(c) represents the negative pressure of the air cavity which was 4 kPa and the interactive effect between the filling height and the rotating speed of air cavity on the qualified index. When the filling height was fixed, the qualified index gradually rose with increasing the rotating speed of air cavity, reached a maximum, and then slowly dropped down. When the rotating speed of the air cavity was fixed, the qualified index gradually rose with increasing the filling height, reached a maximum, and then slowly dropped down. The rotating speed of the air cavity had a range of 20~22 r/min, the filling height had a range of 14~16 cm and the qualified index was optimal.

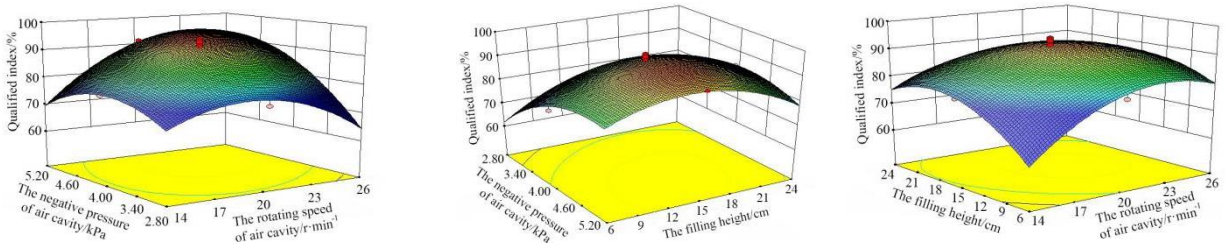

(a) (b) (c)

Fig. 9 - Performance curves of different cavity structures

Table 3

Results of the variance analysis

Source	Missing index			Qualified index			Multiple index		
	Sum of squares	F value	p-value	Sum of squares	F value	p-value	Sum of squares	F value	p-value
Model	684.4	11.2	<0.01	904.7	13.1	<0.01	349.6	4.99	<0.01
X_1	6.14	0.91	0.3	80.76	10.5	< 0.01	131.4	16.9	< 0.01
X_2	414.9	61.3	<0.01	205.1	26.7	< 0.01	36.56	4.7	< 0.01
X_3	2.51	0.37	0.55	14.99	1.95	0.18	5.23	0.67	0.42
X_1X_2	0.81	0.12	0.73	55.81	7.27	*	43.15	5.55	< 0.05
X_1X_3	32.2	4.76	< 0.05	25.88	3.37	0.08	0.34	0.04	0.83
X_2X_3	8.3	1.23	0.28	21.81	2.84	0.11	3.2	0.41	0.53
X_1^2	60.7	8.98	< 0.05	200.9	26.1	< 0.05	40.71	5.23	< 0.05
X_2^2	142.4	21.0	< 0.05	116.8	15.2	< 0.05	1.27	0.16	0.69
X_3^2	19.4	2.87	0.11	188.9	24.6	< 0.05	87.1	11.2	< 0.05
Residual	87.99			99.76			101.1		
lack of fit	54.43	2.59	0.11	24.39	0.52	0.76	68.95	3.43	0.06
Pure error	33.56			75.37			32.2		
Sum	772.4			1004.5			450.7		

From the above analysis, every time the interaction among factors affects the performance of the direct seed-metering device. Optimized parameters were defined by the Design-Expert software version 8.0.6-trail. When the rotating speed of the air cavity was 23.56 r/min, the negative pressure of the air cavity was 4.97 kPa, and the filling height was 12.82 cm, the direct seed-metering device has the overall best performance.

The contrast tests of five groups were carried out according to the optimal parameter combination. The results showed that the performance of the direct seed-metering device can be improved by installing the spoiler blade, as shown in Table 4, which proves the necessity of installing spoiler blades.

Table 4

Contrast test results

Types	Evaluation index		
	Qualified index / %	Missing index / %	Multiple index / %
Spoiler blade installed	93.9	3.6	2.5
No spoiler blade installed	90.5	5.8	3.7

CONCLUSIONS

(1) To further improve the performance of the direct seed-metering device, three spoiler blades with different structures were designed. Through theoretical analysis, it is concluded that the spoiler with a larger upwind angle and curved structure has a better effect on airflow guidance and disturbance.

(2) The CFD method was used to simulate the effect of three different structured spoiler blades on the internal flow field of the direct seed-metering device, and it was concluded that all three types of spoiler blades can improve the flow field. The simulation data showed that the average air pressure in the flow field and the average flow velocity at the suction hole of the B-type spoiler blade were more favorable to the operation, which concluded that the B-type was the most effective.

(3) By optimizing the experimental data, the optimum parameters of the direct seed-metering device are as follows: the rotating speed of the air cavity, 23.56 r/min; the negative pressure of the air cavity, 4.97 kPa; and the filling height, 12.82 cm. Under these conditions, the qualified index is 95.21%, the missing index is less than 3.28% and the multiple index is less than 1.51%.

ACKNOWLEDGEMENT

This work was supported by the National Key R&D Program of China (Grant No. 2018YFD0700601-03); Heilongjiang Bayi Agricultural University Support Program for San Heng San Zong (Grant No. ZRCPY202012); Heilongjiang Bayi Agricultural University Mechanical Engineering Discipline Project.

REFERENCES

[1] Ding, L., Yang, L., Wu, D., Li, D., Zhang, D., & Liu, S. (2018). Simulation and Experiment of Corn Air Suction seed-metering Device Based on DEM-CFD Coupling Method. *Transactions of the Chinese Society for Agricultural Machinery*, vol.49, no.11, pp.48-57.

[2] Farooq, M., Siddique, K. H., Rehman, H., Aziz, T., Lee, D. J., & Wahid, A. (2011). Rice direct seeding: Experiences, challenges, and opportunities. *Soil & Tillage Research*, vol.111, no.2, pp.87-98.

[3] Gao, X., Cui, T., Zhou, Z., Yu, Y., & Song, W. (2021). DEM study of particle motion in novel high-speed seed metering device. *Advanced Powder Technology*, vol.32, no.5, pp.1438-1449.

[4] Li, Z., Zhang, P., Sun, y., Zheng, C., Xu, L., & E, DY. (2021). Discrete particle simulation of gas-solid flow in air-blowing seed metering device. *Computer Modeling in Engineering & Sciences*, vol.127, no.3, pp.1119-1132.

[5] Liu, Q., Cui, T., Zhang, D., Yang, L., Wang Y., He, X., & Wang, M. (2018). Design and experimental study of seed precise delivery mechanism for high-speed maize planter. *International Journal of Agricultural and Biological Engineering*, vol.11, no.4, pp.81-87.

[6] Luo, X., Wang, Z., Zeng, S., Zang, Y., Yang, W., & Zhang, M. (2019). Research progress on mechanized direct seeding technology of rice. *Journal of South China Agricultural University*, vol.40, no.5, pp.1-13.

[7] Tian, L., Ding, Z., Su, Z., Li, L., & Wang, Z. (2022). Design and experiment of rotary precision hill direct seed-metering device for rice. *INMATEH Agricultural Engineering*, vol.66, no.1, pp.311-320.

[8] Wan, L., Wang, H., & Che, G. (2019). Design and Test of Rice Hill-drop seed-metering Device Embedded with Rotating Air Cavity. *Transactions of the Chinese Society for Agricultural Machinery*, vol.50, no.11, pp.74-84.

[9] Wu, Z., Li, M., Lei, X., Wu, Z., Jiang, C., Zhou, L., & Chen, Y. (2020). Simulation and parameter optimization of a centrifugal rice seeding spreader for a UAV. *Biosystems Engineering*, vol.192, pp.275-293.

[10] Xing, H., Zang, Y., Wang, Z., Luo, X., Pei, J., He, S., Xu, P., & Liu, S. (2019). Design and parameter optimization of rice pneumatic seeding metering device with adjustable seeding rate. *Transactions of the CSAE*, vol.35, no.4, pp.20-28.
[11] Yamauchi, M. (2017). A review of iron-coating technology to stabilize rice direct seeding onto puddled soil. *Agronomy Journal*, vol.109, no.3, pp.739-750.
[12] Yatskul. A., & Lemiere, J. (2018). Establishing the conveying parameters required for the air-seeders. *Biosystems Engineering*, vol.166, pp.1-12.
[13] Ye, S., Zheng, D., Li, W., Lu, Q., Yang, Y., Liu, Y., & Xu, B. (2021). Characterization and CFD-DEM modelling of a prismatic spouted bed. *INMATEH Agricultural Engineering*, vol.64, no.2, pp.185-194.
[14] Zhang, G., Zhang, S., Yang, W., Lu, K., Lei, Z., & Yang, M. (2016). Design and experiment of double cavity side-filled precision hole seed-metering device for rice. *Transactions of the CSAE*, vol.32, no.8, pp.9-17.
[15] Zhang, M., Wang, Z., Luo, X., Zang, Y., Yang, W., & Xing, H. (2018). Review of precision rice hill-drop drilling technology and machine for paddy. *International Journal of Agricultural and Biological Engineering*, vol.11, no.3, pp.1-11.
[16] Zhang, S., Xia, J., Zhou, Y., Zhai, J., Guo, Y., Zhang, X., & Wu, H. (2015). Design and experiment of pneumatic cylinder-type precision direct seed-metering device for rice. *Transactions of the CSAE*, vol.31, no.1, pp.11-19.
[17] Zhang, X., Zhu, D., Xue, K., Li, L., Zhu, j., Zhang, S., & Liao, J. (2021). Parameter Optimization and Experiment of Slider-Hole-Wheel Seed-metering Device Based on Discrete Element Method. *INMATEH Agricultural Engineering*, vol.65, no.3, pp.410-420.

PARAMETERS OPTIMIZATION AND EXPERIMENT ON CYCLONE SEPARATION AND CLEANING SYSTEM FOR BUCKWHEAT

/

荞麦旋风分离清选的参数分析与试验研究

Yingshi HUANG [1,2], Weiguo ZHANG*[1,2], Zhongxiao ZHENG [1,2], Chun WANG [1,2], Songke FENG [1,2]
Fuzeng YANG [1,2], Jinfeng GAO[1,2], Baili FENG[1,2] [1]

[1)] College of Mechanical and Electronic Engineering, Northwest A&F University, Yangling, Shanxi 712100, China
[2)] Scientific Observing and Experimental Station of Agricultural Equipment for the Northern China, Ministry of Agriculture and Rural Affairs, Yangling, Shaanxi 712100, China
Tel: +86 18392502024; E-mail: hys893413577@163.com
DOI: https://doi.org/10.35633/inmateh-68-07

Keywords: *buckwheat; cyclone separation and cleaning; orthogonal test; loss rate; cleaning rate*

ABSTRACT

Based on the material characteristics of buckwheat, the cyclone separation and cleaning test bench were designed. The cleaning rate and loss rate of the buckwheat separation and cleaning by the influencing factors of the investigation were studied through single factor and orthogonal tests. The single-factor test results show that the cyclone separation and cleaning performance is better when the speed range of the suction fan is 800~1200 r/min, the speed range of the feeding fan is 600~1200 r/min, and the length range of the suction pipe is 100~250 mm. The regression equation model of the cleaning rate and loss rate was constructed, and the response surface analysis of the test influencing factors and their interaction was carried out. The results show that the speed of the suction fan has the most significant influence on the cleaning rate and loss rate, followed by the speed of the feeding fan and the length of the suction pipe in the separation cylinder has the least effect. By optimizing and solving multi-objective parameters of the regression equation model, reasonable experimental parameters are obtained. The appropriate speed of the suction fan is 1055 r/min, the appropriate speed of the feeding fan is 600 r/min, and the proper length of the suction pipe in the separation cylinder is 175 mm. The cleaning rate and the loss rate of the cyclone separation and cleaning system were 94.78% and 1.67%, respectively.

摘要

本文基于荞麦的物料特性，对荞麦旋风分离清选试验台进行了设计；通过单因素和正交试验研究了试验影响因素对荞麦分离清选的清洁率和损失率的影响规律。单因素试验结果表明：吸杂风机转速范围为800～1200 r/min，喂入风机转速范围为600~1200 r/min，吸杂管长度范围为100 ~250 mm。采用三因素三水平的正交试验，构建了试验影响因素与荞麦分离清选的清洁率和损失率间的回归方程模型，并对试验影响因素及其交互作用进行了响应面分析，结果表明：吸杂风机转速对荞麦分离清选的清洁率和损失率影响最大，喂入风机转速影响次之，分离筒内吸杂管长度影响最小；通过对回归方程模型的多目标参数优化求解，得到了合理的试验影响因素参数：吸杂风机转速为1055 r/min，喂入风机转速为600 r/min，分离筒内吸杂管长度为175 mm；在此工况条件下，荞麦分离清选的损失率为1.67%，分离清选的清洁率为94.78%。

INTRODUCTION

Buckwheat is rich in nutrients and has outstanding medicinal and healthcare functions. It is an internationally recognized economic crop for food and medicine *(Shi, et al., 2015; Hu, 2004; Tae-Gyh. N, et al., 2015)*. Due to the influence of growth characteristics and economic factors, buckwheat in China is mainly cultivated in hilly and mountainous areas with poor natural conditions, irregular plots and large field drops *(Li, et al., 2020; Wang, et al., 2021; Yang, et al., 2021)*. At present, conventional grain combine harvesters with air and screen cleaning devices are primarily used for mechanized buckwheat harvesting and have high terrain flatness requirements, resulting in unsatisfactory cleaning quality in hilly and mountainous areas *(Chen, 2002; Lu, et al., 2020)*.

[1] *Yingshi Huang, M.S. Stud. Eng.; Weiguo Zhang, As. Prof. Ph.D. Eng.; Zhongxiao Zheng, M.S. Stud. Eng.; Chun Wang, M.S. Stud. Eng.; Songke Feng, Prof. Ph.D. Eng.; Fuzeng Yang, Prof. Ph.D. Eng.; Jinfeng Gao, Prof. Ph.D. Eng.; Baili Feng, Prof. Ph.D. Eng.;*

Cyclone separation and cleaning device has been widely used in small grain combine harvesters because of its small size, low cost, stable performance, and low requirements for terrain flatness *(Liao, Q. X., et al., 2015; Liu, D. W., et al., 2016)*.

In recent studies, scholars at home and abroad have mainly researched on grain cyclone separation and cleaning performance *(Huang, 2015)*. *Fuat et al. (2016)* compared the pressure losses at various exit pipe diameters, cylinder heights, cone bottom diameters, and inlet velocities for the conventional and modified design, and designed a new cyclone separation and cleaning model. *Wan et al. (2020)* designed a cyclone separation and cleaning system with replaceable parts, and analyzed the influence of the baffle on the separation performance of rapeseed; they provided a reference for the structural optimization and improvement of the cleaning device for the rapeseed combine harvester. *Zhao et al. (2014)* studied the effect of bucket diameter and bucket length concerning the cyclone body on the separation efficiency by the Fluent method. The loss rate was reduced to 2.2% when the bucket length was 94 mm and the diameter was 196 mm compared to the cyclone separator without a bucket. *Liu, et al., (2015),* designed an air-flowing cleaning unit, and the simulation of the 3D model of the air-flowing field in the cleaning unit was analyzed. The simulation analysis showed that the cleaning device structure and distribution of airflow speed met the design requirements and the cleaning effect well. It improved the efficiency of the micro combine harvester.

Based on the material characteristics of buckwheat, this paper designed the cyclone separation and cleaning test bench for buckwheat. On the self-made test bench, single-factor and orthogonal tests were used to study the influence law of the feeding fan speed, the suction fan speed and the suction pipe length on the cleaning rate and loss rate of the cyclone separation and cleaning of buckwheat.

MATERIALS AND METHODS

Overall structure of the test bench

Since the shell of buckwheat grain is easy to break, the buckwheat grain is easily damaged due to collision and hitting when the buckwheat material is fed by a winnower *(Tomchuk, 2020)*. Therefore, this test bench's buckwheat material feeding method adopted pneumatic feeding. It mainly included centrifugal fans, inverters, height adjustment device for suction inlet, cyclone separator, grain tank and anti-backflow nozzle, as shown in Fig. 1.

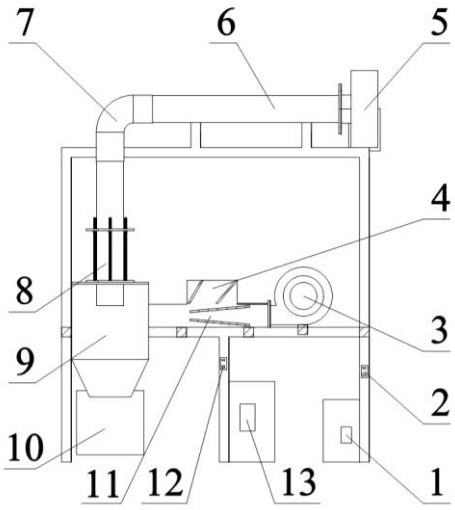

Fig. 1 - Structural diagram of buckwheat cyclone separation and cleaning test bench
1. Feeding frequency converter; 2. Feeding switch; 3. Feeding fan; 4. Feed inlet; 5. Suction fan; 6. Suction pipe; 7. Flexible corner; 8. Height adjustment device of suction inlet; 9. Cyclone separator; 10. Grain box; 11. Anti-backflow nozzle; 12. Suction switch; 13. Suction frequency converter

The materials of buckwheat after passing through the threshing drum mainly include short straws, grains, chaff, dust, leaves and petals, etc., whose quality, density, shape, and size are different, and their suspension speeds in the cyclone separator are also different. The materials are tangentially fed along the wall of the cyclone separator through a feed inlet by the high-speed airflow, generated by the feeding fan. Under the combined action of inertia force and airflow in the cyclone separator, the movement of different component materials in the cyclone separator is also different.

Dust, chaff, short straws and other light impurities with low density are easy to move toward the center of the cyclone separator when suspended in the cyclone separator and are easily discharged from the suction pipe by the updraft generated by the suction fan in the center of the cyclone separator. Buckwheat grains with high density have a large centrifugal force, and they are easy to move to the wall of the cyclone separator, and the updraft speed here is less than its critical suspension speed. So, the buckwheat grains slide down along the wall of the cyclone separator and finally fall into the grain tank from the grain outlet, which realizes the separation and cleaning of the buckwheat material.

The feeding fan can be selected as a YN5-47 centrifugal fan with a rated speed of 2800 r/min, rated flow rate of 1810 m^3/h and total pressure of 790 Pa. Similarly, the suction fan can be selected as the centrifugal fan of YN5-47 which should have an extensive range of airflow velocity adjustment, with a rated speed of 2800 r/min, rated flow of 2250 m^3/h, and total pressure of 940 Pa.

According to the design experience *(Harrison, 1992)* of existing cyclone separators, the specific parameters of the cyclone separator of the test bench are shown in Table 1, and a schematic diagram of the structure is shown in Fig. 2.

Table 1

Size of cyclone separator

Structure parameters of cyclone separator	Size relation	Numerical value(mm)
Cyclone separator diameter, D	D	350
Inlet height, h	(0.3-0.5)D	120
Inlet width, b	(0.2-0.4)D	70
Suction pipe diameter, D_1	0.42D	150
Outlet diameter, D_2	0.57D	200
Separator height, L_1	0.91D	320
Cone length, L_2	0.73D	255
Gross length	1.64D	575

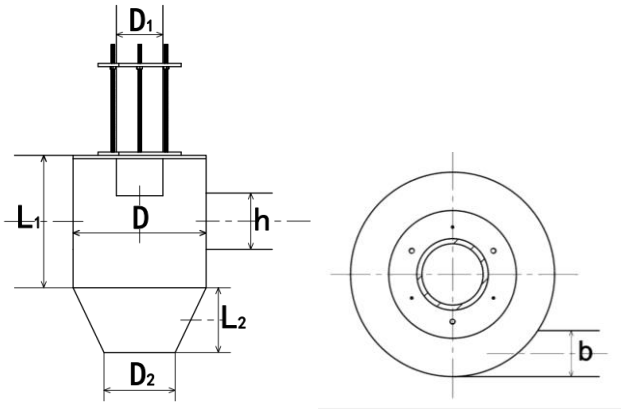

Fig. 2 - Schematic diagram of cyclone separator structure

To prevent the material from being blown backward during the pneumatic feeding *(Li, 2009)*, an anti-backward nozzle is designed in the conveying pipe below the feed inlet. The material can be fed into the cyclone separator smoothly, as shown in Figure 1. The feed inlet diameter D is 35 mm.

Experimental setup

The breed of buckwheat selected for the experiment was Xinong 9979. The cleaning experiment was conducted on the self-made cyclone separation and cleaning test bench, as shown in Fig. 3. To ensure the excellent data repeatability of the experiment, the materials were mixed according to the mass ratio of grain, chaff and stalk 75%：22%：3%. The average moisture content of grain was12.9%, the average moisture content of chaff was 42.1%, and the moisture content of the stalk was 45.5%.

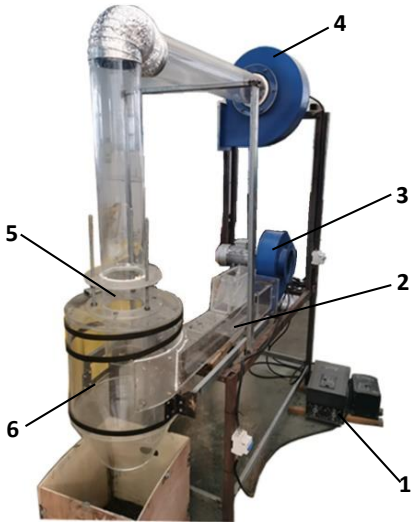

Fig. 3 - Cyclone separation and cleaning test bench
1. Frequency converter; 2. Conveying nozzle; 3. Feeding fan; 4. Suction fan; 5. Suction inlet height adjuster; 6. Cyclone separator

The main performance evaluation indexes of cyclone separation and cleaning test bench are the loss rate and cleaning rate of grain *(Lu, et al., 2016; Liao, et al., 2013; Li, 2006)*. The length of the suction pipe in the cyclone separator, the rotational speed of the suction fan and the rotational speed of the feeding fan were selected as the influencing factors for the loss rate and cleaning rate experiment. The equations of the loss rate and cleaning rate of buckwheat separation and cleaning are as follows:

$$Y_q = \frac{m_2}{m_0} \times 100\% \quad (1)$$

$$Y_s = \frac{m_1 - m_2}{m_1} \times 100\% \quad (2)$$

where, Y_q is the grain cleaning rate, %; Y_S is the grain loss rate, %; m_0 is the total mass of the materials after cleaning, kg; m_1 is the total mass of grains in the materials after cleaning, kg; m_2 is the total mass of the grains after cleaning, kg.

RESULTS

To ensure the test bench's proper functioning, the range of parameter values of the influencing factors was determined by a trial test. The initial examination has shown that the scope of the rotational speed of the feeding fan is 300~1200 r/min, the rotational speed of the suction fan is 400~1600 r/min, and the length of the suction pipe is 0~250 mm.

Single-factor test and analysis of results

The single-factor test of seven levels for the rotational speed of the feeding fan was conducted by setting the suction fan rotational speed at 1200 r/min and the length of the suction pipe in the cyclone separator at 150 mm. Each level of tests was repeated three times with the same input parameters. Based on the above single-factor test, the effect of the rotational speed of the feeding fan on the cleaning rate and loss rate was obtained, as shown in Fig. 4.

Figure. 4 shows that the rotational speed of the feeding fan has little effect on the loss rate and cleaning rate. As the feeding fan rotational speed increases, the cleaning rate of grains decreases slowly, while the loss rate of grains tends to be raised first and then decreases. The reason is that the feeding fan generates tangential airflow, which provides the initial power to rotate and suspend materials when the materials are fed into the cyclone separator. However, with the increase of the rotational speed of the feeding fan and the rise of feeding airflow velocity, the disturbance of the swirling airflow in the cyclone separator increases. The symmetry of the swirling airflow in the cyclone separator decreases, which increases the loss rate of grain and drops of the cleaning rate of gain. Therefore, the feeding fan rotational speed should be in the range of 600~1200 r/min.

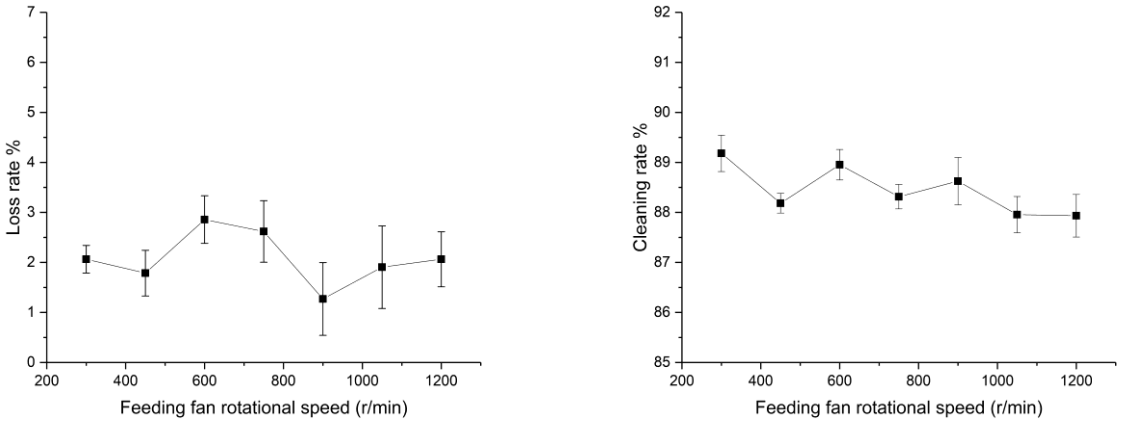

(a) Effect of feeding fan rotational speed on loss rate (b) Effect of feeding fan rotational speed on cleaning rate

Fig. 4 - Effect of feeding fan rotational speed on cleaning performance

The single-factor test of seven levels for the rotational speed of the suction fan was conducted by setting the feeding fan rotational speed at 1200 r/min and the length of the suction pipe in the cyclone separator at 150 mm. Each level of tests was repeated three times with the same input parameters. Based on the above single-factor test, the effect of the rotational speed of the suction fan on cleaning rate and loss rate was obtained, as shown in Fig. 5.

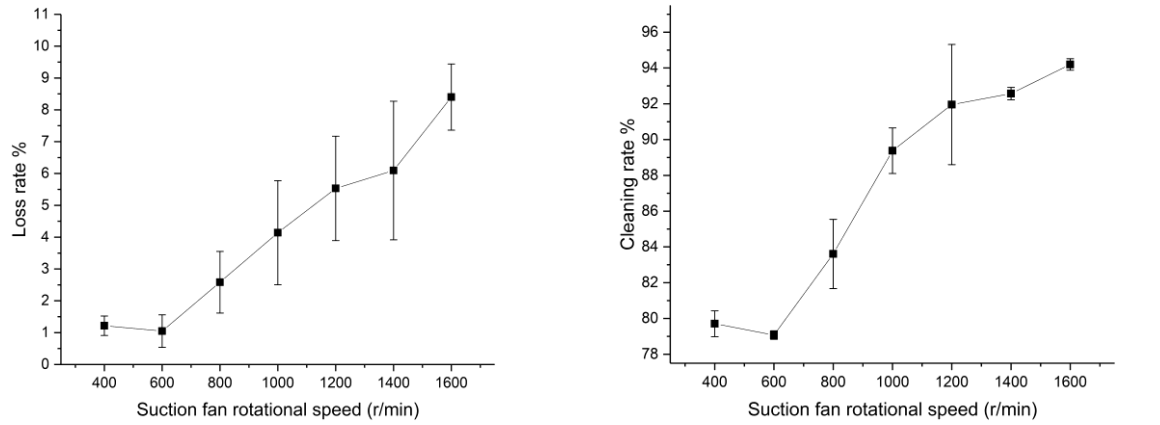

（a）Effect of suction fan rotational speed on loss rate （b）Effect of suction fan rotational speed on cleaning rate

Fig. 5 - Effect of suction fan rotational speed on cleaning performance

Fig. 5 shows that the rotational speed of the suction fan has a significant effect on the loss rate and the cleaning rate. As the rotational speed of the suction fan increases, the velocity of updraft generated by the suction fan increases, the buoyancy of the updraft increases, and the probability of impurities and grains being sucked out by the impurity suction fan increases, and the likelihood of impurities entering into the grain box decreases, which results in the loss rate and the cleaning rate of grain continuing to increase. When the rotational speed of the suction fan exceeds 1200 r/min, the cleaning rate of grain increases slowly, while the loss rate of grain increases significantly. Therefore, the suction fan rotational speed should be in the range of 800~1200 r/min.

The single-factor test of six levels for the length of the suction pipe in the cyclone separator was conducted by setting the suction fan rotational speed at 1200 r/min and the feeding fan rotational speed at 1200 r/min. Each level of tests was repeated three times with the same input parameters. Based on the above single-factor test, the effect of the length of the suction pipe in the cyclone separator on the cleaning rate and loss rate was obtained, as shown in Fig. 6.

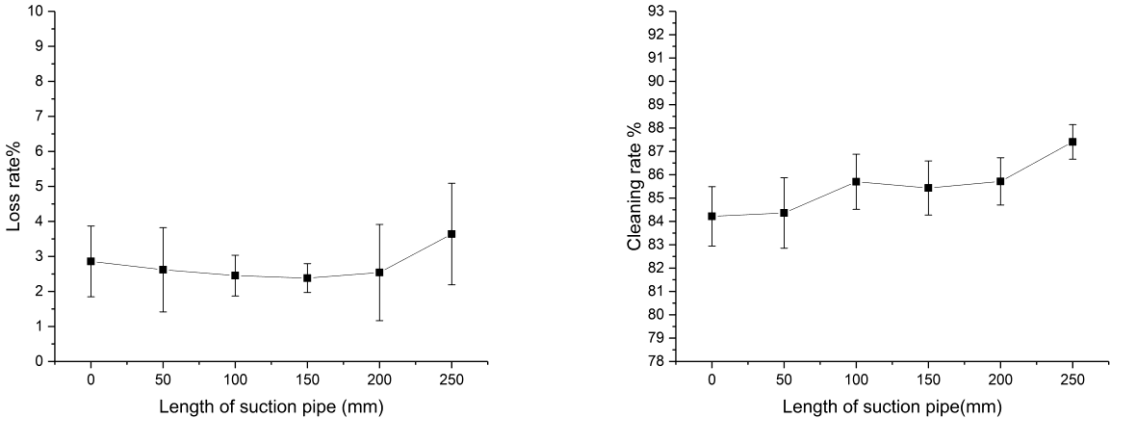

(a) Effect of length of the suction pipe on loss rate (b) Effect of length of the suction pipe on cleaning rate

Fig. 6 - Effect of length of the suction pipe on cleaning performance

Fig. 6 shows that the length of the suction pipe in the cyclone separator has little effect on the loss rate and some influences on the cleaning rate. As the length of the suction pipe in the cyclone separator increases, the grain's cleaning rate increases and the grain's loss rate changes little. When the length of the suction pipe in the cyclone separator exceeds 200 mm, the cleaning rate and the loss rate of grain begin to increase significantly. The reason is that as the length of the suction tube in the cyclone separator continues to grow, the suction inlet is incessantly approaching the feed inlet. More and more airflow generated by the feeding fan are sucked away by suction inlet directly. Therefore, the suction airflow reduces the interference of tangential airflow from the feeding fan on the airflow symmetry in the cyclone separator to increase its cleaning rate. Meanwhile, the grains at the feed inlet are easily sucked away by the suction fan through the suction pipe, increasing the grain loss rate. Therefore, the length of the suction pipe in the cyclone separator should be in the range of 100 mm~250 mm.

Orthogonal test and result analysis

Based on the results of the single-factor test, feeding fan rotational speed X_1, suction fan rotational speed X_2 and length of the suction pipe X_3 were taken as test factors, and the grain loss rate Y_s and the grain cleaning rate Y_q were taken as the evaluation indexes in the trial. The three-factor and three-level response surface method was adopted in the test, and the level codes of the test factors are shown in Table 3.

Coding of factors and levels **Table 3**

Influencing factors	Coding	Coding level		
		-1	0	1
Feeding fan rotational speed（r/min）	X_1	600	900	1200
Suction fan rotational speed（r/min）	X_2	800	1200	1600
Length of suction pipe（mm）	X_3	100	175	250

Response surface analysis tests of 17 groups were carried out (Table 4), and each group of tests was repeated three times.

Experimental methods and results of orthogonal rotational experiment **Table 4**

Number	X_1	X_2	X_3	Y_q	Y_s
1	1	1	0	93.96	7.29
2	-1	1	0	95.63	10
3	1	-1	0	90.98	0.62
4	1	0	-1	91.89	2.92
5	-1	0	-1	93.49	2.5
6	-1	0	1	95.18	5.41
7	1	0	1	93.39	1.46
8	0	1	-1	93.65	6.04
9	0	-1	-1	90.97	0.42
10	0	-1	1	92.94	0
11	0	1	1	94.4	10.42
12	-1	-1	0	93.53	0.83
13	0	0	0	93.39	1.25
14	0	0	0	93.36	1.67
15	0	0	0	93.75	1.25
16	0	0	0	93.75	1.25
17	0	0	0	93.68	2.5

Establishment and test of the regression model of cleaning rate and loss rate

The quadratic regression equation models of *Yq* and *Ys* were established with X_1, X_2 and X_3 as independent variables. The regression equation models were tested for significance by the variance analysis of regression coefficients and F-test. The results are shown in Table 5 and Table 6.

Table 5

Regression equation variance analysis of cleaning rate response surface

Number	Variance source	Quadratic sum	Degrees of freedom	*F* value	*P* value (Prob > *F*)
1	Regression	23.74	9	49.08	< 0.0001
2	X_1	7.24	1	134.66	< 0.0001
3	X_2	10.63	1	197.67	< 0.0001
4	X_3	4.37	1	81.22	< 0.0001
5	X_1X_2	0.19	1	3.60	0.0995
6	X_1X_3	0.009	1	0.17	0.6942
7	X_2X_3	0.37	1	6.92	0.0339
8	X_1^2	0.20	1	3.73	0.0947
9	X_2^2	0.33	1	6.11	0.0427
10	X_3^2	0.42	1	7.86	0.0264
11	Residual error	0.38	7		
12	Lack of fit	0.22	3	1.96	0.2614
13	Error	0.15	4		
14	Sum	24.12	16		
R^2=0.9844; *Adj* R^2=0.9643; Coefficient of variation *C.V*=0.25%					

Table 6

Regression equation variance analysis of loss rate response surface

Number	Variance source	Quadratic sum	Degrees of freedom	*F* value	*P* value (Prob > *F*)
1	Regression	173.98	9	66.98	< 0.0001
2	X_1	5.20	1	18.02	0.0038
3	X_2	127.04	1	440.21	< 0.0001
4	X_3	3.66	1	12.68	0.0092
5	X_1X_2	1.56	1	5.41	0.0529
6	X_1X_3	4.77	1	16.54	0.0048
7	X_2X_3	5.76	1	19.96	0.0029
8	X_1^2	4.02	1	13.92	0.0074
9	X_2^2	19.00	1	65.84	< 0.0001
10	X_3^2	1.10	1	3.82	0.0915
11	Residual error	2.02	7		
12	Lack of fit	0.84	3	0.95	0.4976
13	Error	1.18	4		
14	Sum	176.00	16		
R^2=0.9885; *Adj* R^2=0.9738; Coefficient of variation *C.V*=16.36%					

*Note: * significant (P <0.05) and ** extremely significant (P <0.01).*

According to Table 5 and eliminating the insignificant terms in the regression equation, the regression equation of the cleaning rate *Yq* expressed by coding values was obtained:

$$Y_q = 93.59 - 0.95X_1 + 1.15X_2 + 0.74X_3 - 0.30X_2X_3 - 0.28X_2^2 - 0.32X_3^2 \quad (3)$$

The interaction relationship between the other two influencing factors and their influences on *Yq* were analyzed by setting any factor in Equation (3) at zero level to fit the response surface, as shown in Figure 7.

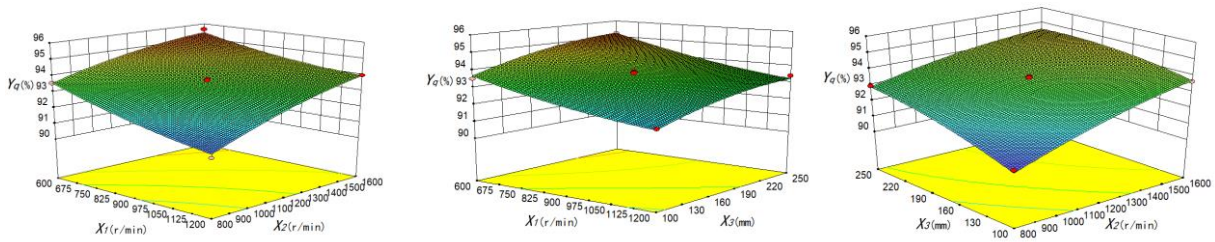

(a) Effect of feeding fan rotational speed and suction fan rotational speed on cleaning rate

(b) Effect of feeding fan rotational speed and length of suction pipe on cleaning rate

(c) Effect of length of suction pipe and suction fan rotational speed on cleaning rate

Fig. 7 - Effects of the interaction of factors on cleaning rate

As can be seen from Fig. 7 (a), when X_3 is 175 mm, *Yq* increases with the decrease of X_1 and the rise of X_2, but the influence of X_1 and X_2 on *Yq* is not significant, which is the same as the result of regression equation variance analysis. As can be seen from the response surface shape of Fig. 7 (b), when X_2 is 1200 r/min, *Yq* increases with the decrease of X_1 and the increase of X_3, but the influence of X_1 and X_3 on *Yq* is also not significant, which is the same as the result of regression equation variance analysis. As can be seen

from the response surface shape of Fig. 7 (c), when X_1 is 900 r/min, X_2 and X_3 have a significant influence on *Yq*, *Yq* increases with the increase of X_3 and X_3. When X_2 increases from 800 r/min to 1600r/min, the effect of X_3 on *Yq* gradually decreases, and when X_3 increases from 100~250 mm, the effect of X_2 on *Yq* reduce progressively.

According to the analysis in Table 6 and eliminating the insignificant terms in the regression equation, the regression equation of the loss rate *Ys* expressed by coding values was obtained:

$$Y_s = 1.58 - 0.81X_1 + 3.98X_2 - 0.68X_3 - 1.09X_1X_3 + 1.20X_2X_3 + 0.98X_1^2 + 2.12X_2^2 \quad (4)$$

The interactional relationship between the other two influencing factors and their influence on *Ys* were analyzed by setting any one factor in Equation (4) at zero level to fit the response surface, as shown in Figure 8.

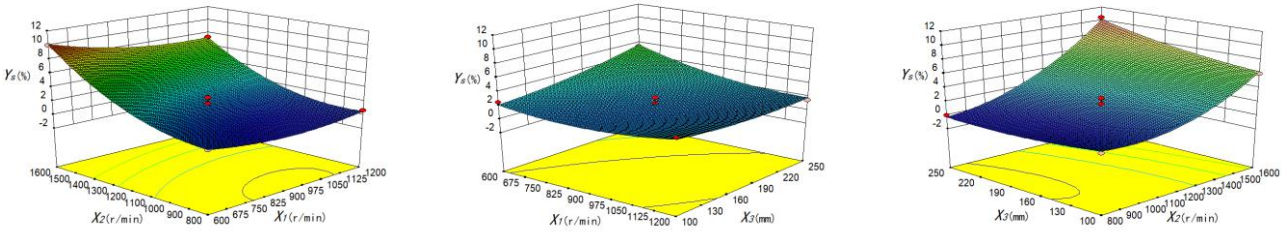

(a) Effect of feeding fan rotational speed and suction fan rotational speed on loss rate

(b) Effect of feeding fan rotational speed and length of suction pipe on loss rate

(c) Effect of length of suction pipe and suction fan rotational speed on loss rate

Fig. 8 - Effects of the interaction of factors on loss rate

As can be seen from Fig. 8 (a), when X_3 is 175 mm, *Ys* increases with the increase of X_2, and the influence of X_1 on *Ys* is not significant, which is the same as the result of regression equation variance analysis that the overall effect of X_1 and X_2 on *Ys* is not significant. As can be seen from the response surface shape of Fig. 8 (b), when X_2 is 1200 r/min, X_1 and X_3 have a significant effect on *Ys*. When X_1 is lower than about 900 r/min, *Ys* increases with the increase of X_3. When the rotational speed exceeds about 900 r/min, the influence of X_3 on *Ys* is not significant. When X_3 is longer than 160 mm, *Ys* increases with the increase of X_1. When the length is shorter than 160 mm, the influence of X_1 on *Ys* is not significant. As can be seen from the response surface shape of Fig. 8 (c), when X_1 is 900 r/min, X_2 and X_3 have an immensely effect on *Ys*, and *Ys* increases with the increase of X_2. When X_2 is higher than about 1000 r/min, *Ys* increases with the rise of X_3. When the rotational speed is lower than about 1000 r/min, the influence of X_3 on *Ys* is not significant. In Figure 14, *Ys*≤0 indicates that the loss rate is 0 at that time.

Parameter optimization and experiment of cyclone separation and cleaning test bench

The influence sorting of three test factors on the test bench is as follows: the rotational speed of the suction fan(X_2), the rotational speed of the feeding fan(X_1) and the length of the suction pipe(X_3). To further determine the suitable parameter combination of influencing factors for test bench, multi-objective parameter optimization was carried out by the regression equation model. Taking the range of values of the test influencing factors as the boundary conditions and taking the minimum loss rate and maximum cleaning rate as the optimization objectives, the mathematical model was as follows:

$$\begin{cases} \max Y_q\left(X_1, X_2, X_3\right) \\ max\, Y_s\left(X_1, X_2, X_3\right) \end{cases} \quad (5)$$

Constraint condition: $\begin{cases} -1 \le X_1 \le 1 \\ -1 \le X_2 \le 1 \\ -1 \le X_3 \le 1 \end{cases}$

The Design-Expert 8.0.5 was used to solve the regression equation model by multi-objective optimization, and the optimal test influencing factor parameters were obtained: X_2 was 1055.86 r/min, X_1 was 600 r/min, and X_3 was 175 mm. Under the optimal parameter combination, the loss rate *Ys* was 1.52%, and the cleaning rate *Yq* was 94.40%.

According to the results of the multi-objective optimal solution and combined with the actual operation requirements of buckwheat cyclone separation and cleaning test bench, the practical test influencing factor parameters were as follows: the rotational speed of the suction fan was 1055 r/min, the rotational speed of the feeding fan was 600 r/min, and the length of the suction pipe in the cyclone separator was 175 mm. Three tests were carried out under the conditions of the test influencing factor parameters through the self-made cyclone separation and cleaning test bench shown in Figure 3. The test results are shown in Table 7. The average cleaning rate was 94.78%, the average loss rate was 1.67%.

Table 7

Experiment results of optimal parameters test

Experimental number	1	2	3	mean
Cleaning rate Y_q（%）	95.43	94.80	94.12	94.78
Loss rate Y_s（%）	1.42	1.68	1.92	1.67

CONCLUSIONS

(1) Based on the material characteristics of buckwheat, the buckwheat cyclone separation and cleaning test bench was built.

(2) The parameter value range of the primary test influencing factors was determined by trial and single-factor tests of the buckwheat cyclone separation and cleaning test bench. The rotational speed range of the suction fan was 800～1200 r/min, the rotational speed range of the feeding fan was 600~1200 r/min, the length range of the suction pipe was 100 mm~250 mm. The quadratic regression equation model was established through an orthogonal test, taking the cleaning rate and the loss rate as performance indicators. The model analysis showed that the rotational speed of the suction fan had the most significant influence on the cleaning rate and the loss rate, followed by the rotational speed of the feeding fan and the length of the suction pipe in the cyclone separator.

(3) The orthogonal experimental results were analyzed by response surface method, and the regression equation model was solved by multi-objective optimization. The rational experimental parameters for the buckwheat cyclone separation and cleaning test bench were determined: the rotational speed of the suction fan was 1055 r/min, the rotational speed of the feeding fan was 600 r/min, and the length of the suction pipe in the cyclone separator was 175 mm. Under this condition, the average cleaning rate was 94.78%, the average loss rate was 1.67%.

ACKNOWLEDGEMENT

This research was conducted at the College of Mechanical and Electronic Engineering, Northwest A&F University, and was supported by a grant from the Key Research and Development Project Plan of Shaanxi Province (No. 2019NY-176), the Agricultural Promote and Practices for Young Scholar of Northwest A&F University (No. 2020-38), the National Key Research and Development Project Plan of China (No. 2016YFD0701804, No. 2020YFD1000805).

REFERENCES

[1] Chen, D. J., Wei, C. M., Xu, J.H., et al., (2002), An improvement on design of a rubber crawler, whole-feeding combine harvester, *Transactions of the Chinese Society for Agricultural Machinery,* issue 01, pp. 115-118+123.

[2] Fuat, T., Irfan, K., Atakan, A., (2016), Effects of geometrical parameters on the pressure drop for a modified cyclone separator, *Chemical Engineering &Technology,* vol. 39, issue 3, pp. 576-581.

[3] Harrison H. P., (1992), Grain separation and damage of an axial-flow combine, *Canadian Agricultural Engineering,* vol. 34, issue 01, pp. 49-53.

[4] Hu, Z. C., (2004), Should strengthen the digestion of key technical facilities and the development of domestic production for buckwheat processing, *Chinese Agricultural Mechanization*, issue 03, pp. 11-13.

[5] Huang, Y., Zhao, M. Q., (2015), Optimization design of performance test of cyclone separator sand sampler based on numerical simulation and wind erosion tunnel experiment, *Transactions of the Chinese Society of Agricultural Engineering*, vol. 31, issue 16, pp. 50-56.

[6] Li Y. M., Xu, L. Z., Lu, L., (2006), Cleaning experiment of rape extractions, *Transactions of the Chinese Society for Agricultural Machinery,* vol. 37, issue 11 pp. 63-66.

[7] Li, Y., Zhu, X. P., (2009), Energy consumption analysis for negative pressure and low-pressure pneumatic conveying systems, *Sulphur Phosphorus & Bulk Materials Handling Related Engineering,* issue 02, pp. 23-26+51-52. doi:10.16341/j.cnki.spbmh.2009.02.008.

[8] Li, M. C., Muneshi M., Eiji I., et al., (2020), Design and performance analysis of a seed metering device for a buckwheat seeder adopting discrete element analysis, *Kyushu University Institutional Repository*, Vol. 65, issue 01, pp. 123-129.

[9] Liao, Q. X., Chen, L., Li, H. T., et al., (2013), Cleaning unit test-bed of extraction components for rape combine harvester, *Transactions of the Chinese Society for Agricultural Machinery,* vol. 44, issue 10 pp. 80-85+79.

[10] Liao, Q. X., Wan, X. Y., Li, H. T., et al., (2015), Design and experiment on cyclone separating cleaning system for rape combine harvester, *Transactions of the Chinese Society of Agricultural Engineering,* vol. 31, issue 14, pp. 24-31.

[11] Liu, D. W., Lu, W., Wang, X. S, et al., (2016), Research status and development trend of cyclone separating cleaning unit of combine harvesters, *Agricultural Equipment & Vehicle Engineering,* vol. 54, issue 05, pp. 8-13.

[12] Liu, Z. H., Zheng, Y. P., Wang, Z. M., et al., (2015), Design on air-flowing cleaning unit of micro rice-wheat combine harvester, *Transactions of the Chinese Society for Agricultural Machinery,* vol. 46, issue 07, pp. 102-108.

[13] Lu, Q., Zheng, D. C., Liu, Y., et al., (2020), Problems and thoughts on mechanized harvesting technology of buckwheat in China, *Agricultural engineering,* vol. 10, issue 01, pp. 6-9.

[14] Lu, W., Liu, D. W., Li, X., et al., (2016), Cyclone separating cleaning test for small-sized rice combine harvester, *Journal of Hunan Agricultural University,* vol. 42, issue 01, pp. 97-101, doi:10.13331/j.cnki.jha u.2016.01.019.

[15] Shi, J. Q., Li, Y. Q., Zhang, Z. W., et al., (2015), Genetic diversity of buckwheat and its wild species, *Journal of Plant Genetic Resources*, vol. 16, issue 3, pp. 443-450, doi:10.13430/j.cnki.jpgr.2015.03.002.

[16] Tae-Gyh. N., Sun, M. L., Ji-Hae P., et al., (2015), Flavonoid analysis of buckwheat sprouts, *Food Chemistry*, Vol. 170, Issue 01, pp. 97-101.

[17] Tomchuk V., (2020), Loss Management when harvesting grain, legume and oilseed crops, *Norwegian Journal of development of the International Science,* issue 50, pp. 54-67.

[18] Wan, X. Y., Liao, Y. T., Yuan J. C., et al., (2020), Parameters analysis and experiment of cyclone separation cleaning system with replaceable parts for rapeseed combine harvester, *Transactions of the Chinese Society for Agricultural Machinery,* vol. 51, issue 02, pp. 202-211. doi:10.6041/j.issn.1000-1298.2020.S2.024.

[19] Wang, J. W., Saddam, H., Lu, Q., et al., (2021), Cleaning performance and optimization of internal and external roller rotary buckwheat thresher, *International Agricultural Engineering Journal*, Vol. 29, issue 02.

[20] Yang, C. Q., Chang, K., Mu L., et al., (2021), Status and trend analysis of buckwheat variety improvement and industrial development, *Crops*, issue 02, pp. 28-34. doi:10.16035/j.issn.1001-728 3.2021.02.004.

[21] Zhao, X. G., Xu, L. M., Gao, L. X., et al., (2014), Simulation of soybean thresher cyclone separating and cleaning system, *Transactions of the Chinese Society for Agricultural Machinery,* vol. 45, issue 01, pp. 80-87.

NUTRIENT DEFICIENCY DIAGNOSIS IN WHOLE HYDROPONIC LETTUCE BASED ON RANDOM FOREST
/
基于随机森林算法的整株水培生菜缺素诊断

Xinyu ZHANG[1,2]; Dandan CAO[1,2]; Minghui WANG[1,3]; Gongpei CUI[1]; Yinggang SHI[1]; Yongjie CUI *[1,3] [1]
[1)] College of Mechanical and Electronic Engineering, Northwest A&F University, Yangling / China;
[2)] Key Laboratory of Agricultural Internet of Things, Ministry of Agriculture and Rural Affairs, Yangling / China;
[3)] Shaanxi Key Laboratory of Agricultural Information Perception and Intelligent Service, Yangling / China
Tel: +86 13720581232; E-mail: agriculturalrobot@nwafu.edu.cn
DOI: https://doi.org/10.35633/inmateh-68-08

Keywords: *hydroponic lettuce, machine learning, feature extraction, deficiency diagnosis*

ABSTRACT
The phenotypic information of lettuce leaves can well reflect its health. In order to diagnose the nutrient deficiency types of hydroponic lettuce accurately, non-destructively and quickly in the mid-growth stage, a method for diagnosis of whole lettuce based on random forest algorithm (RF) was proposed. The images of lettuce under four different conditions, K-deficiency, Ca-deficiency, N-deficiency and Normal, were collected and segmented by Extra-green algorithm. Then, features of color, texture and shape were extracted. A RF classification model for the hydroponic lettuce nutrient deficiency diagnosis was constructed and compared with support vector machine (SVM) and back propagation neural network (BP). RF had the best classification effect among the three methods. The overall classification accuracy was 86.32%, Kappa coefficient was 0.82, and it can provide a basis for the prevention and remedies of lettuce deficiency and the scientific management of nutrient solutions.

摘要
生菜叶片的表型信息可以很好地反映其健康状况。为了准确、无损、快速地诊断水培生菜生长中期的缺素类型，以整株水培生菜叶片图像为研究对象，提出一种基于随机森林算法(RF)的缺素诊断方法。采集缺钾、缺钙、缺氮以及正常 4 种生长条件下的生长中期的水培生菜缺素图像，利用超绿算法分割得到整株水培生菜叶片图像，并提取其颜色、纹理和形状的特征。基于 RF 建立水培生菜缺素诊断模型，并与支持向量机(SVM)和 BP 神经网络(BP)进行对比试验。三种方法中 RF 的分类效果最好,总体分类准确率为 86.32%，Kappa 系数为 0.82，可为水培生菜缺素症防治及采取补救措施以及营养液的科学管理提供依据。

INTRODUCTION
Nutrient solution is the key to the health of crops in the nutrient solution hydroponic plant factory *(He, 2018; Germer et al., 2011; Fang, 2016)*. The difference in its concentration can lead to nutrient deficiency or excess, which will cause the quality and yield of the crop to decline, and even cause disease. In actual agricultural production, the lack of nutrient leads to abnormal growth of crops or even diseases, which is called deficiency disease *(Gillespie et al., 2020; Zhao, 2014)*. Lettuces are one of the most widely planted crops in the hydroponic mode of plant factories; it has high nutritional value and economic benefits. Nutrient deficiency will seriously affect the harvest and sale of lettuce *(Yang et al., 2015)*. Therefore, a timely and accurate method for the diagnosis of nutrient deficiency can provide a basis for the prevention and treatment of hydroponic lettuce nutrient deficiency, and it is of great significance in actual production.

It is a direct and effective method to judge the health status of crops through their leaf feature information. Since the 1980s, many scholars have diagnosed the nutrition and disease of crops by technology of image processing and machine learning, and have made some achievements.

Many scholars have used machine vision to judge the nutritional status of crop leaves by extracting features such as color, texture, and shape *(Mao et al., 2003; Xu, 2013; Flores et al., 2020; Zhang and You, 2017)*. Lu, B. et al. proposed a diagnosis method that combines hyperspectral technology and image color and texture features to identify the disease type and period of lettuce accurately *(Lu et al., 2018)*.

[1] *Xinyu Zhang, M.S. Stud. Eng.; Dandan Cao, M.S. Stud. Eng.; Minghui Wang, M.S. Stud. Eng.; Gongpei Cui, Ph.D. Stud. Eng.; Yinggang Shi, Assoc. Prof. M.S. Eng.; Yongjie Cui, Prof. Ph.D. Eng.*

Yu. et al. established a regression model using hyperspectral technology combined with deep learning to quickly detect the nitrogen content in rape *(Yu et al., 2018)*. Wei, W. S. et al. focused on the development of non-destructive online detection system for leaf vegetables quality detection based on machine vision *(Wei et al., 2018)*. *Mao. et al.* established a predictive model for the nitrogen content of lettuce based on the canopy and spectral reflectance, image features and variable wavelength information by using machine learning *(Mao et al., 2015). Zhang, B. et al.* collected color images of lettuce leaves with different nitrogen levels, extracted their texture and color features, filtered and optimized the image feature vectors, and established a lettuce nitrogen content prediction model with an average error rate of less than 13% *(Zhang et al., 2018)*.

At present, researches on crop nutrition diagnosis mainly focus on cash crops such as rice and rape. There are few studies on the diagnosis of lettuce deficiency. In the existing leaf vegetable disease identification, the leafy vegetables at the mature stage or single leaves are mostly used, which may cause destructive sampling, and is not conducive to remedies. In this study, images of the whole hydroponic lettuce leaves in the mid-growth stage were taken as the research object, collecting images of hydroponic lettuce under K-deficiency, Ca-deficiency, N-deficiency, and Normal. And then, the color, texture and shape features were extracted and randomized. The random forest constructed a diagnosis model, and compared the effects of different methods. The study provided a fast, accurate and non-destructive method for diagnosing the nutrient deficiency of hydroponic lettuce.

MATERIALS AND METHODS

Image acquisition

In November 2020, the planting environment of a plant factory was simulated in an intelligent artificial climate room, and a planting experiment of hydroponic lettuce was designed to obtain images of lettuce in different nutrient deficiency conditions (Shown in Figure 1). The experiment selected the butter lettuce seeds produced by Chinese Vegetable Seed Technology (Beijing) Co.Ltd. Sow the seeds in a seedling tray covered with ceramics and place 2 seeds in each seedling hole. When the lettuce grows to 6 leaves and 1 heart, pull out the seedlings and wrap the roots with a sponge, then, plant them in the cultivation trough. The knop hydroponic formula was used to cultivate 4 types of hydroponic lettuce, which are K-deficiency, Ca-deficiency, N-deficiency and Normal. Throughout the experiment, all environmental parameters of the intelligent artificial climate room were installed referring to the actual conditions of the plant factory, and the pH, EC and liquid temperature of the nutrient solution were monitored continuously to ensure the best level of the planting conditions, so that the growing environment for hydroponic lettuce had always been best. The specific parameters' range is shown in Table 1.

Fig. 1 - Planting experiment of hydroponic lettuce in intelligent artificial climate room

Table 1

Parameters of hydroponic lettuce planting condition

Type	Name	Ranges
Solution Parameters	pH	5.5-6.5
	EC	2-3 dS/m
	Solution Temperature	15-20 ºC
Environmental Parameters	Environmental Temperature	Day 22 ºC Night 18 ºC
	Humidity	70-80% RH
	Illumination Time	24h
	Illumination Type	Red and Blue
	Concentration of CO_2	800 ppm

The hydroponic lettuce images for the experiment were collected by the Lifecam Studio produced by Microsoft. The camera uses a CMOS sensor and it can be connected to a laptop through a USB interface with a maximum resolution of 1280x720. The photo box was built with PVC boards to simulate the shading environment, and that can avoid the influence of red and blue light. The camera was fixed directly above the inside of the photo box, and the vertical distance from the lettuce plant is 50 cm. The white LED light strip was used as a supplementary light source to provide suitable brightness. The entire growth cycle of hydroponic lettuce after planting is generally 30-40 days. In this experiment, there were 36 lettuces in 4 categories including K-deficiency, Ca-deficiency, N-deficiency, and Normal. 1440 lettuce images were collected for follow-up research in the mid-growth stage, that is, within 10-20 days after planting.

It can be seen from Figure 2 that, compared with normal hydroponic lettuce, the overall growth of hydroponic lettuce slowed down in the nutrient-deficient state. The color of K-deficient leaves turns yellow and lighter, the leaves are slightly shrunken, and the tip is accompanied by brown spots; the Ca-deficient leaves have dark brown edges, and the leaves are curled; the N-deficient leaves are smaller, the overall color is lighter, and the stems are slender and soft.

(a) K-deficiency *(b) Ca-deficiency* *(c) N-deficiency* *(d) Normal*

Fig. 2 - Some hydroponic lettuce samples of different nutrient-deficient types under the same growth period

Four kinds of lettuce leaves with different nutrient-deficient types showed different characteristics in color, texture, and shape. Afterwards, pre-treatment and multi-feature extraction were performed on the images of hydroponic lettuce, and recognizing the images of different kinds of lettuce based on the three methods of back propagation neural network (BP), support vector machine (SVM) and random forest algorithm (RF). The classification accuracy of the three models was compared and the best one was selected to realize the diagnosis of nutrient deficiency types. The overall image processing flow is shown in Figure 3.

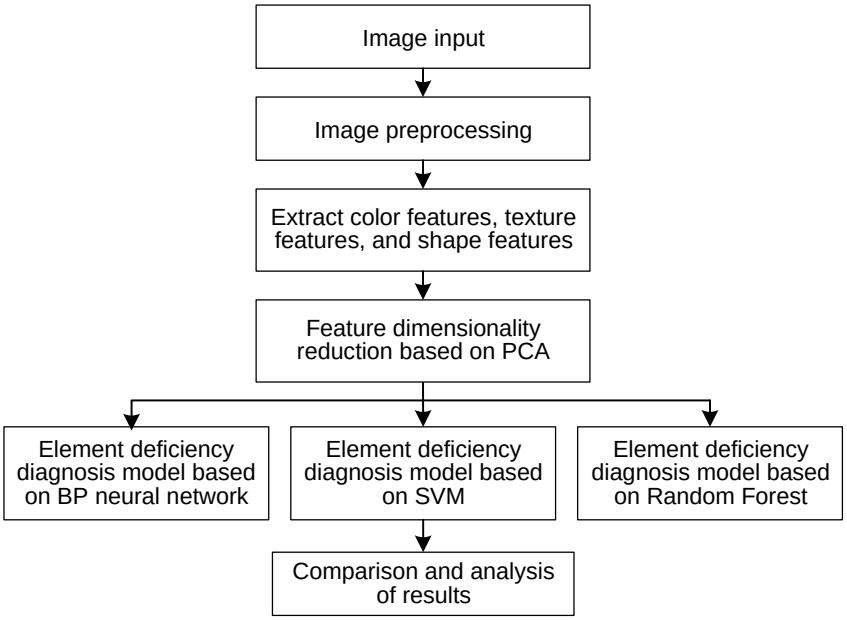

Fig. 3 – The overall flow of image processing

Image feature extraction and optimization

Before the nutrient deficiency diagnosis of the hydroponic lettuce, image enhancement, image segmentation and other pretreatment were performed on the images, and then extracted the color, texture, and shape of the whole lettuce image.

The principal component analysis (PCA) was used to analyze and optimize the all feature data, and the effective parameters were used for the establishment of deficiency diagnosis model.

Image pre-treatment

The pre-treatment of the image can reduce or eliminate irrelevant information of the original image, while retaining useful information, so as to ensure the information reliability of hydroponic lettuce feature extraction, recognition and classification. The specific process is shown in Figure 4. First, the original color image was enhanced by median filtering and histogram equalization. According to the color features of hydroponic lettuce, the Extra-green algorithm was selected to realize the effective segmentation of the hydroponic lettuce leaves, and its gray image and binary image were obtained.

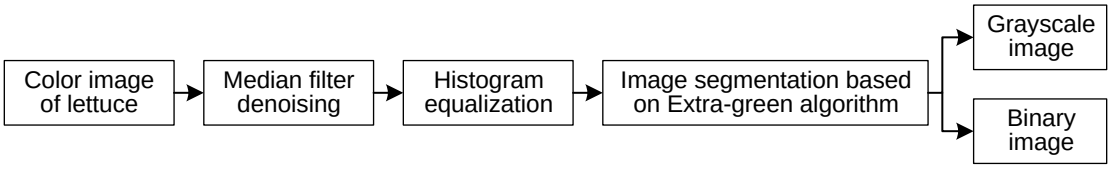

Fig. 4 – Process of image pretreatment

The hydroponic lettuce image segmentation method based on the Extra-green algorithm, which converted the color image in the RGB space into three channels of R, G, and B. When extracting the weight of the G channel, the contrast between the foreground of the green part and the background of the non-green part in the picture was increased. The pixel in the image data was defined as (x, y), and R (x, y), G (x, y), B (x, y) respectively represented the value of the three channels in the RGB color model. Then set the different gray values of the pixels according to equation (1).

$$EXG(x,y)=\begin{cases} 2G(x,y)-R(x,y)-B(x,y) \\ 255, \quad 2G(x,y)-R(x,y)-B(x,y)>255 \\ 0, \quad 2G(x,y)-R(x,y)-B(x,y)<0 \end{cases} \tag{1}$$

For the gray image obtained, the threshold segmentation algorithm was also used to extract the target of hydroponic lettuce leaves from the background. For the image f(x,y) to be segmented, the image segmentation was performed by selecting an appropriate threshold value T and the image g(x,y) was output. The segmentation relationship is shown in equation (2).

$$g(x,y)=\begin{cases} 255, & f(x,y)<T \\ 0, & f(x,y)>T \end{cases} \tag{2}$$

Finally, the image of the hydroponic lettuce leaves can be segmented more accurately, and the result is shown in Figure 5.

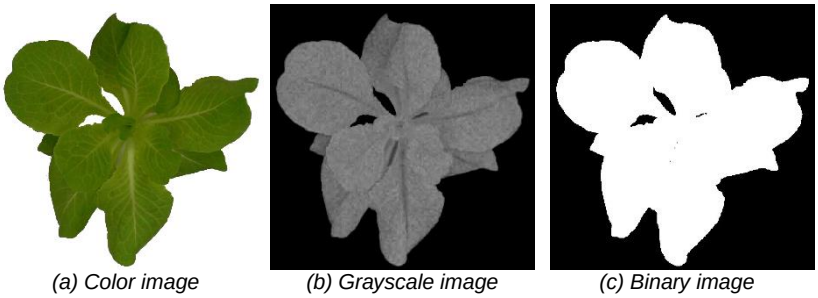

(a) Color image *(b) Grayscale image* *(c) Binary image*

Fig. 5 - Image segmentation result based on Extra-green algorithm

Color feature

Color information can be used as an important feature for judging the types of deficiency in hydroponic Lettuce. As a global descriptor to describe the color features of an image, color moments are often used to represent the correlation properties of colors on image. The effective information of an image is generally concentrated in its low-order moment. The Mean reflects the brightness of the image. The Variance describes the distribution range of colors in an image, and the Skewness shows the symmetry of the image color distribution. The above three can effectively express the color distribution of the image. The mathematical definition is expressed in equation (3).

$$\begin{cases} \mu_i = \frac{1}{N}\sum_{j=1}^{N} p_{i,j} \\ \sigma_i = \left(\frac{1}{N}\sum_{j=1}^{N}\left(p_{i,j}-\mu_i\right)^2\right)^{\frac{1}{2}} \\ S_i = \left(\frac{1}{N}\sum_{j=1}^{N}\left(p_{i,j}-\mu_i\right)^3\right)^{\frac{1}{3}} \end{cases} \quad (3)$$

Where:

$P_{i,j}$ indicates the i-th color component of the j-th pixel of the color image, and N is the number of pixels in the image.

In order to avoid the image of hydroponic lettuce being disturbed by light, the HSV color model, which has little influence on the change of light intensity, was selected to collect low-order moment under the channels of H, S and V. At the same time, combined with the actual situation that the color in the image of hydroponic lettuce is not complex, only the Mean and Variance were used as the feature data to describe the color changes of the image. Partial data are shown in Table 2.

Table 2

HSV color feature of some hydroponic lettuce

Sample name	Mean of H channel	Mean of S channel	Mean of V channel	Variance of H channel	Variance of S channel	Variance of V channel
K-deficiency	0.2496	0.5485	0.0878	0.1289	0.0827	0.1427
Ca-deficiency	0.2041	0.5934	0.1110	0.0622	0.0800	0.1542
N-deficiency	0.2626	0.5373	0.1375	0.1218	0.0787	0.1613
Normal	0.2408	0.5699	0.1560	0.1227	0.0942	0.1548

Texture feature

According to the previous experimental observation, the texture depth and roughness of different types of hydroponic lettuce leaves are different. Therefore, the texture feature is an important indicator for the diagnosis of hydroponic lettuce deficiency. Gray level co-occurrence matrix is usually used to describe texture features. It describes the texture by studying the spatial correlation characteristics of gray levels in the image, and it can intuitively reflect the roughness, depth and similarity of the image. Generally, the texture features of images are usually quantified by calculating the Energy, Entropy, Contrast and Correlation of the grayscale co-incidence matrix in different directions.

Energy can indicate the uniformity of gray distribution and the roughness of texture on the image of hydroponic lettuce. Contrast shows the clarity of hydroponic lettuce leaves and the depth of texture grooves, which can more realistically reflect the image texture features. Entropy expresses the size of texture information on the image of hydroponic lettuce. When the gray level of the image of hydroponic lettuce shows greater randomness, the more complex the image is, the greater the entropy is. Correlation mainly reflects the similarity degree of gray level of hydroponic lettuce image in row direction and column direction. It is calculated by the equation (4).

$$\begin{cases} ASM = \sum_i \sum_j p(i,j)^2 \\ CON = \sum_i \sum_j (i-j)^2 p(i,j) \\ ENT = -\sum_i \sum_j p(i,j)\log(i,j) \\ COR = \left[\sum_i \sum_j (ij)p(i,j) - \mu_i\mu_j\right] / \sigma_i\sigma_j \end{cases} \quad (4)$$

$$\mu_i = \sum_i \sum_j i \cdot p(i,j) \quad \mu_j = \sum_i \sum_j j \cdot p(i,j) \quad \sigma_i^2 = \sum_i \sum_j p(i,j)(i-\mu_i)^2 \quad \sigma_j^2 = \sum_i \sum_j p(i,j)\left(j-\mu_j\right)^2$$

Where:

(i, j) is the gray value of a pixel pair in the image, and $p(i, j)$ is the probability of the gray value appearing in the whole image.

In this study, the values in the four directions of 0°, 45°, 90° and 135° were calculated to represent the texture features of the hydroponic lettuce image, meanwhile, the mean and variance were calculated as the feature information for subsequent research. Partial data are shown in Table 3.

Table 3

Texture feature of some hydroponic lettuce

Sample name	Energy		Entropy		Contrast		Correlation	
	Mean	Variance	Mean	Variance	Mean	Variance	Mean	Variance
K-deficiency	0.6484	0.0112	0.6747	0.0351	0.0469	0.0130	5.3476	0.2418
Ca-deficiency	0.5732	0.0026	0.8394	0.0226	0.0289	0.0080	2.8147	0.0321
N-deficiency	0.5103	0.0182	0.9583	0.0560	0.0812	0.0224	3.6239	0.2176
Normal	0.7892	0.0046	0.4361	0.0175	0.0233	0.0059	9.2589	0.2836

Shape feature

The combination of shape and geometry features can be used as an important basis for distinguishing different types of lettuce deficiency. Based on the boundary feature, the contours of the continuous area of hydroponic lettuce leaves were extracted from the binary image, and then five types of information such as Extent, Eccentricity, Solidity, Thinness ratio and Aspect ratio were extracted to describe the shape features of hydroponic lettuce leaves. Table 4 shows the partial data.

Table 4

Shape feature of some hydroponic lettuce

Sample name	Extent	Eccentricity	Solidity	Thinness ratio	Aspect ratio
K-deficiency	0.4833	0.4252	0.6869	0.0381	1.0441
Ca-deficiency	0.4863	0.7838	0.7182	0.0575	1.3380
N-deficiency	0.3146	0.6336	0.4727	0.0132	1.2285
Normal	0.5840	0.5963	0.7759	0.0796	0.9158

Feature selection based on PCA

PCA is a data processing method that recombines the original variables into a new set of unrelated integrated variables. It uses a few new integrated variables to contain as much of the original data as possible, which reflects the relationship between the original variables and is widely used in data dimensionality reduction processing.

In this study, the 19 original features were extracted from the image of hydroponic lettuce. To avoid a large number of input variables in the establishment of a nutrient deficiency diagnosis model, the principal component analysis was performed to calculate the characteristics of each principal component. The value and contribution rate are shown in Table 5. It can be seen from the results that the eigenvalues of the first six principal components are all greater than 1, and their cumulative contribution rate reaches at 79.376%. Therefore, comprehensively considering the principle of eigenvalue greater than 1 and cumulative contribution rate not less than 80% in the selection of principal components, the first 6 principal components were selected to comprehensively express 19 features.

Table 5

Eigenvalues and contribution rates of principal components

Component	Eigen value			Extraction sums of squared loadings		
	Total	Variance contribution/%	Cumulative variance contribution/%	Total	Variance contribution/%	Cumulative variance contribution/%
1	6.873	36.172	36.172	6.873	36.172	36.172
2	2.610	13.738	49.910	2.610	13.738	49.910
3	1.600	8.421	58.332	1.600	8.421	58.332
4	1.558	8.198	66.529	1.558	8.198	66.529
5	1.440	7.582	74.111	1.440	7.582	74.111
6	1.000	5.265	79.376	1.000	5.265	79.376
7	0.927	4.881	84.257			
8	0.840	4.419	88.675			
9	0.702	3.694	92.369			

Table 5
(continuation)

10	0.495	2.608	94.977			
11	0.287	1.511	96.488			
12	0.248	1.306	97.794			
13	0.145	.765	98.560			
14	0.138	.729	99.288			
15	0.048	.251	99.539			
16	0.044	.233	99.773			
17	0.037	.195	99.968			
18	0.004	.022	99.991			
19	0.002	.009	100.000			

By calculating the load of the 19 features and the eigenvalue of each principal component, the function expressions Y1 to Y6 of the six principal components can be obtained, as shown in equation (5). Z1 ~Z19 respectively represent the mean of H channel, mean of S channel, mean of V channel, variance of H channel, variance of S channel, variance of V channel, mean of energy, variance of energy, mean of entropy, variance of entropy, mean of contrast, variance of contrast, mean of correlation, variance of correlation, extent, eccentricity, solidity, thinness ratio, aspect ratio.

$$
\begin{aligned}
Y_1 &= 0.053Z_1 + 0.0224Z_2 + 0.1454Z_3 + 0.1471Z_4 + 0.1423Z_5 + 0.1024Z_6 + 0.3365Z_7 - 0.3240Z_8 - \\
&\quad 0.3443Z_9 - 0.3577Z_{10} - 0.3454Z_{11} - 0.3528Z_{12} + 0.1811Z_{13} + 0.132Z_{14} + 0.2309\ Z_{15} - 0.0824Z_{16} \\
&\quad + 0.2383Z_{17} + 0.2173Z_{18} + \ 0.0019Z_{19} \\
Y_2 &= -0.0723Z_1 - 0.1068Z_2 - 0.0558Z_3 + 0.1485Z_4 + 0.3825Z_5 + 0.3045Z_6 + 0.1529Z_7 + 0.1755Z_8 + \\
&\quad 0.1392Z_9 + 0.1531Z_{10} \ + 0.1607Z_{11} + 0.1508Z_{12} - 0.1999Z_{13} - 0.1764Z_{14} + 0.4059Z_{15} - 0.0931Z_{16} \\
&\quad + 0.4151Z_{17} + 0.3948Z_{18} - 0.0219Z_{19} \\
Y_3 &= 0.3955Z_1 + 0.3514Z_2 + 0.4879Z_3 - 0.0094Z_4 - 0.2086Z_5 - 0.0056Z_6 - 0.0497Z_7 + 0.1674Z_8 + \\
&\quad 0.0605Z_9 + 0.1293Z_{10} + 0.1749Z_{11} + 0.1635Z_{12} + 0.2576Z_{13} + 0.2892Z_{14} + 0.1289Z_{15} - 0.3696Z_{16} \\
&\quad + 0.0897Z_{17} + 0.0985Z_{18} + 0.0943Z_{19} \\
Y_4 &= -0.3423Z_1 - 0.2982Z_2 - 0.0786Z_3 - 0.424Z_4 - 0.072Z_5 - 0.2841Z_6 - 0.1022Z_7 + 0.0066Z_8 + \\
&\quad 0.0869Z_9 + 0.05614Z_{10} + 0.0209Z_{11} + 0.0433Z_{12} + 0.382Z_{13} + 0.4327Z_{14} + 0.1675Z_{15} + 0.182Z_{16} \\
&\quad + 0.1916Z_{17} + 0.2359Z_{18} + 0.1072Z_{19} \\
Y_5 &= 0.0506Z_1 - 0.0425Z_2 - 0.2737Z_3 + 0.4194Z_4 + 0.3061Z_5 + 0.3756Z_6 + 0.0254Z_7 + 0.1072Z_8 + \\
&\quad 0.0063Z_9 + 0.0592Z_{10} + 0.0872Z_{11} + 0.0766Z_{12} + 0.4228Z_{13} + 0.4567Z_{14} - 0.1501Z_{15} + 0.1132Z_{16} \\
&\quad - 0.1472Z_{17} - 0.1816Z_{18} - 0.0568Z_{19} \\
Y_6 &= -0.2418Z_1 + 0.2325Z_2 + 0.0298Z_3 - 0.0601Z_4 + 0.1428Z_5 + 0.1987Z_6 - 0.0347Z_7 - 0.0594Z_8 + \\
&\quad 0.0403Z_9 - 0.0132Z_{10} - 0.0416Z_{11} - 0.0319Z_{12} - 0.0388Z_{13} - 0.0299Z_{14} - 0.0453Z_{15} - 0.0106Z_{16} \\
&\quad - 0.0715Z_{17} - 0.0772Z_{18} + 0.8933Z_{19}
\end{aligned}
\tag{5}
$$

Random forest

Random forest algorithm (RF) is widely used in data classification because of its advantages of high classification accuracy, fast calculation speed, strong anti-noise ability, and not easy to fall into over-fitting. Its core idea is to integrate multiple unrelated decision trees into a forest. Each decision tree randomly has a replacement sample from the original data set, completes independent learning and calculation, and finally determines the classification result of the random forest based on voting. The random selection of samples and features is the most important feature. The number of decision trees and the number of input feature variables when the nodes of the generated decision tree are split are important parameters that affect the effect of classification. Combining the extracted image feature information of hydroponic lettuce, this paper focused on constructing a random forest algorithm classification model to realize the nutrient deficiency diagnosis in hydroponic lettuce.

RESULTS AND DISCUSSION

The operating environment was Windows 10 system equipped with Intel Core i5-7200U processor, and the recognition algorithm was realized by Matlab and C mixed programming. The classification objects of the model were four types of hydroponic lettuce images including K-deficiency, Ca-deficiency, N-deficiency and Normal. After the features extracted on 1440 original images, rejected some null values, and finally 1424 sets of effective feature data were obtained. Each type of hydroponic lettuce contained 356 sets of feature information, and 200 sets of each type were randomly selected as training samples to form a training set containing 1000 sets of feature information, and 424 sets of feature information were left as a test set.

Results of Random Forest

The important parameters of the model were optimized after multiple experiments by the training set, and finally it was determined that there were 10 decision trees in the RF model, and the number of feature variables K was 6. After training, the model's classification accuracy of the training set reached 94.06%, indicating that the model fully fitted the training data. The 424 sets of test data were used to evaluate the accuracy of the classification results of the model. The classification accuracy of different types of lettuce is shown in Table 6, the confusion matrix of the classification results is shown in Table 7, and the overall classification accuracy of the model was 86.32%, Kappa coefficient was 0.82.

Table 6

Accuracy of diagnostic result on test set

Class	Accuracy /%
K-deficiency	88.68
Ca-deficiency	81.13
N-deficiency	90.57
Normal	84.91

The model had the highest classification accuracy of N-deficient lettuce, which was 90.57%. The classification of Ca-deficient and Normal lettuce was not accurate enough, and the classification accuracy were 81.13% and 84.91%, respectively. Through the confusion matrix, it could be concluded that the misclassified samples of Ca-deficient lettuce were mainly concentrated in K-deficiency and Normal lettuce. The reason may be that in the mid-growth, the leaf curling features of some Calcium-deficient lettuce were not obvious. The dark brown edge of the leaf was long and thin, and might be blurred during leaf segmentation. In the same way, some Ca-deficient images were highly similar to Normal images, which resulted in a large proportion of Normal lettuce that was incorrectly classified as Ca-deficient lettuce.

Table 7

Confusion matrix of diagnostic result on test set

	Predicted Class							
Actual Class	**K-deficiency**		**Ca-deficiency**		**N-deficiency**		**Normal**	
	Number	**Percentage /%**	**Number**	**Percentage /%**	**Number**	**Percentage /%**	**Number**	**Percentage /%**
K-deficiency	94	22.17	6	1.42	3	0.71	3	0.71
Ca-deficiency	7	1.65	86	20.28	4	0.94	9	2.12
N-deficiency	3	0.71	5	1.18	96	22.64	2	0.47
Normal	5	1.18	11	2.59	0	0	90	21.23

Comparison of different methods

In order to further evaluate the classification effect and performance of RF model, it was compared with the SVM and BP models, and the same data were used to judge different types of hydroponic lettuce. The radial basis function was selected as the kernel function to establish the SVM model, and its important parameters such as gamma function g and penalty variable c were optimized through cross-validation. The BP model was constructed with 6 neurons in input layer, 10 neurons in hidden layer and 4 neurons in output layer, the learning rate was 0.02, and the number of iterations was 5000. The functions of hidden layer and output layer were softmax and tradingdx respectively, and the comparison results of the three methods are shown in Figure 6.

The RF model had the best classification effect among the three classification methods. The overall classification accuracy was 86.32%, which was 2.59 and 7.07 percentage points higher than that of SVM and BP, respectively. Kappa coefficient was 0.82, which was 0.04 and 0.10 higher than that of SVM and BP, respectively (Shown in Figure 6). Comprehensive comparison showed that the RF model proposed in this study could diagnose the nutrient deficiency types of hydroponic lettuce more accurately, and had good applicability.

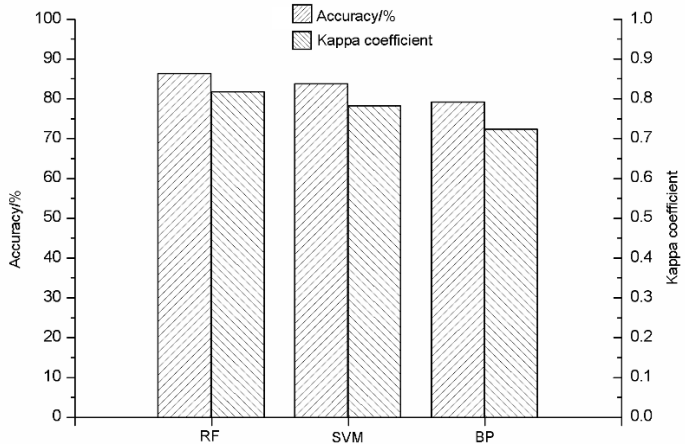

Fig. 6 - Comparison of classification results of different methods

CONCLUSIONS

A method for diagnosing nutrient deficiency in whole hydroponic lettuce based on RF was proposed. Images of the whole hydroponic lettuce in the mid-growth stage were used in the study, the 19 features of three types of leaf color, texture, and shape were extracted, and were reduced to 6 principal component variables by PCA. Then, the diagnosis models were established with RF, SVM and BP. The results showed that RF had the highest classification accuracy, 86.32%, which was 2.59 and 7.07 percentage points higher than that of SVM and BP, respectively. Kappa coefficient was 0.04 and 0.10 higher than that of SVM and BP, respectively.

So, the RF model constructed in this study can diagnose different deficiency types of hydroponic lettuce in the mid-growth stage effectively, and can provide a basis for the prevention and control of hydroponic lettuce deficiency and the efficient management of nutrient solutions in plant factories.

ACKNOWLEDGEMENT

This work was supported by research grants from Shaanxi Key Research and Development Program of China, grant no. 2019ZDLNY02-04.

REFERENCES

[1] Fang, W. (2016). Plant factory industry development and business model in Taiwan (台湾植物工厂产业发展与商业模式). *Agricultural Engineering Technology*, 36(13):17-20. https://doi.org/10.16815/j.cnki.11-5436/s.2016.13.002

[2] Germer, J., Sauerborn, J., Asch, F., de Boer, J., Schreiber, J., Weber, G., &Muller, J. (2011). Skyfarming an ecological innovation to enhance global food security. *Journal of Consumer Protection and Food Safety*, 6(2):237-251. https://doi.org/10.1007/s00003-011-0691-6

[3] Gillespie, D. P., Kubota, C., &Miller, S. A. (2020). Effects of Low pH of Hydroponic Nutrient Solution on Plant Growth, Nutrient Uptake, and Root Rot Disease Incidence of Basil. *Hortscience*, 55(8):1251-1258. https://doi.org/10.21273/HORTSCI14986-20

[4] Gu, Z. F. S., Li, Y. N., Ji, F., &He, D. X. (2019). The sustainable development prospects of artificial light type plant factories (人工光型植物工厂的可持续发展前景). *Agricultural Engineering Technology*, 39(34):22-34. https://doi.org/10.16815/j.cnki.11-5436/s.2019.34.003

[5] Lu, B., Sun, J., Mao, H. P., Yang, N., & Wu, X. H. (2018). Disease recognition of lettuce with feature fusion based on hyperspectrum and image (高光谱和图像特征融合的生菜病害识别). *Jiangsu Journal of Agricultural Sciences*, 34(6):1254-1259. https://doi.org/10.3969/j.issn.1000-4440.2018.06.008

[6] Mao, H. P., Xu, G. L., &Li, P. P. (2003). Extracting and selecting features of leaf images for diagnosing nutrient deficiency diseases in tomatoes (番茄缺素叶片的图像特征提取和优化选择研究). *Transactions of the Chinese Society Agricultural Engineering*, 19(2):133-136. http://www.tcsae.org/nygcxb/ch/reader/view_abstract.aspx?file_no=20030230&flag=1

[7] Mao, H. P., Gao, H. Y., Zhang, X. D., &Kumi, F. (2015). Nondestructive measurement of total nitrogen in lettuce by integrating spectroscopy and computer vision. *Scientia Horticulture*, 184:1-7. https://doi.org/10.1016/j.scienta.2014.12.027

[8] Paulo, F., Zhang, Z., Jithin, M., Nusrat, J., &John, S. (2020). Distinguishing Volunteer Corn from Soybean at Seedling Stage Using Images and Machine Learning. *Smart Agriculture*, 2(03): 61-74. https://doi.org/10.12133/j.smartag.2020.2.3.202007-SA002

[9] Wei, W. S., Xing, Y. Y., Li, Y. Y., Peng, Y. K., &Zhang, W. P. (2018).Online detection and classification system of external quality of leaf for dining hall and family (适于餐厅与家庭的叶菜外部品质在线检测与分级系统). *Transactions of the Chinese Society Agricultural Engineering*, 34(05):264-273. https://doi.org/10.11975/j.issn.1002-6819.2018.05.035

[10] Xu, H. X. (2013). *Study on Nondestructive Detection of Freshness of Post-harvest Spinach Based on Machine Vision and Electronic Nose (基于机器视觉和电子鼻技术的菠菜新鲜度无损检测研究)* [Master dissertation, Jiangsu University]. CNKI. https://kns.cnki.net/KCMS/detail/detail.aspx?dbcode=CMFD&dbname=CMFD201602&filename=1016727760.nh&v=MDExNjBlWDFMdXhZUzdEaDFUM3FUcldNMUZyQ1VSN3VmWU9SdUZ5bm1WTDNQVkYyNkdMUzZHZGJLcjVFYlBJUjg=

[11] Yang, L. Q., Qiu, S. F., Tang, F., Huang, D. F., &Tang, D. Q. (2015). Comprehensive Evaluation for Ornamental Lettuce Based on Principal Component Analysis (基于主成分分析的观赏生菜品质综合评价). *Journal of Shanghai Jiaotong University (Agricultural Science)*, 33(3):53-60. https://doi.org/10.3969/j.issn.1671-9964.2015.03.008

[12] Yu, X. J., Lu, H. D., &Liu, Q. Y. (2018). Deep-learning-based regression model and hyperspectral imaging for rapid detection of nitrogen concentration in oilseed rape (Brassica napus L.) leaf. *Chemometrics and Intelligent Laboratory Systems*, 172(10): 48-55. https://doi.org/10.1016/j.chemolab.2017.12.010

[13] Zhao, D. M. (2014). Common symptoms of vegetable deficiency and prevention methods (蔬菜常见缺素症状及防治方法). *Vegetables*, (11):67-68. https://kns.cnki.net/KCMS/detail/detail.aspx?dbcode=CJFD&dbname=CJFDLAST2015&filename=SCZZ201411032&v=MTY5MzNvOUdab1I4ZVgxTHV4WVM3RGgxVDNxVHJXTTFGckNVUjd1ZlPUnVGeS9uVnIzSk5pN1JkTEc0SDlYTnI=

[14] Zhang, B., Sun, J., Jin, X. M., Li, W. H., Gao, H. Y., &Xiao, L. (2013). Prediction Model of Lettuce Nitrogen Content Based on Color Images. *Information Technology Journal*, 12 (23):7833-7838. https://doi.org/10.3923/itj.2013.7833.7838

[15] Zhang, S. W., Wu, X. W., You, Z. H., &Zhang, L. Q. (2017). Leaf image based cucumber disease recognition using sparse representation classification. *Computers and Electronics in Agriculture*, 134:135-141. https://doi.org/10.1016/j.compag.2017.01.014

TECHNOLOGY OF ADJUSTING THE HEADER HEIGHT OF THE HARVESTER BY MULTI-SENSOR DATA FUSION BASED ON BP NEURAL NETWORK

/

基于 BP 神经网络的多传感器数据融合调节收割机割台高度

Kuizhou JI, Yaoming LI*), Tao Zhang, Shengbo Xia, Junhui Cheng [1]
Key Laboratory of Modern Agricultural Equipment and Technology, Ministry of Education,
Jiangsu University, Zhenjiang 212013, China
Tel:0511-88780048; E-mail: ymli@ujs.edu.cn
Corresponding author: Yaoming Li
DOI: https://doi.org/10.35633/inmateh-68-09

Keywords: *BP neural network, fuzzy control, cutting platform height, multisensor*

ABSTRACT

In this paper, BP neural network is used to collect header height, AMEsim is used to simulate and analyze header height adjustment hydraulic system, and fuzzy PID control is used to adjust header lifting hydraulic cylinder to stabilize header height. The experimental results of harvesting different crops show that under the header height automatic control system, the error between the actual height of crop harvesting and the set height is within 15 mm, and the harvesting effect is good, which can meet the automatic regulation requirements of the header height of the multi crop combine harvester.

摘要

为了提高调节的精度，采用 BP 神经网络多传感器融合处理技术采集割台实时高度，通过 AMEsim 软件对割台高度调节液压系统进行仿真分析，最后采用模糊 PID 控制比例电磁阀调节割台升降液压缸从而稳定割台高度。通过收获油菜、谷子和水稻的试验结果证明：在割台高度自动控制系统下，作物收获的实际高度与设定高度误差在 15mm 以内，收获效果较好，作物割茬高度较为平整，满足多作物联合收获机割台高度自动调控需求。

INTRODUCTION

In the process of multi-crop harvesting, the height of the header is one of the important parameters. If the height of the header is adjusted too large, only part of the plants will be harvested, which may increase the amount of crop loss; if the height of the header is adjusted too small, the straw of harvested grain is too long and may cause the header to clog up or touch the ground, affecting the performance of the harvester. In order to ensure that the height of the header is stable during the harvesting process and reduce the labor intensity of the operator, domestic and foreign engineers and scholars have done relevant researches on the height control of the harvester header *(Tao et al, 2018; Liu et al, 2014; Zheng et al, 2015).*

Hunan Agricultural University *(Liao et al., 2018)* proposed a crop height detection device based on unilateral infrared reflection and a strategy based on fuzzy PID control algorithm to control the height of the header, and used the designed device and system to take rice as the research object. *Yang et al, (2022*), designed an adaptive header height control system. The limitation of traditional PID facing the integral saturation state is analyzed, and a new EVPIVSPID algorithm is proposed and simulated.

Aiming at the problem of low harvesting efficiency caused by the adjustment of the header mainly relying on the experience of the operator when the existing combine harvesters in China are harvesting various crops, this paper designs an automatic control system for the height of the header, and establishes the hydraulic pressure of the multi-crop combine harvester. The relationship model between the telescopic length of the cylinder and the height measured by the sensor, and the collected signals are processed by the BP neural network multi-sensor fusion technology to reduce errors, and the height of the header is regulated by the fuzzy PID control algorithm, so as to be able to achieve cutting in a multi-crop field environment. The automatic control of the table height reduces labor intensity and improves work efficiency.

[1] *Kuizhou Ji, M.S. Stud. Eng.; Yaoming Li, Prof. Ph.D. Eng.; Tao Zhang, M.S. Stud. Eng.;Shengbo Xia M.S. Eng.*

MATERIALS AND METHODS

Design of the profiling device for height adjustment of the header

Fig.1 is a schematic diagram of the height measurement system of the header. The mechanical contact type header height measuring device is mainly composed of a left-right symmetrical profiling plate, a rotating shaft, an angle sensor, a single-chip microcomputer, etc. The structural schematic diagram is shown in Fig. 2:

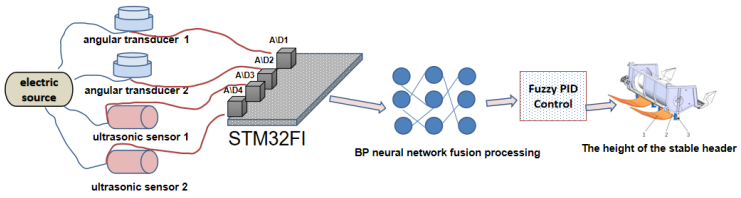

Fig. 1 - Schematic diagram of the header height measurement system

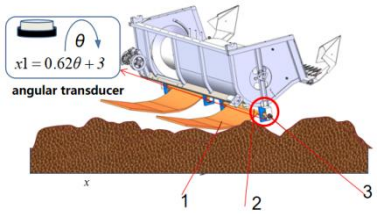

Fig. 2 - Structural Schematic
1. Copy plate; 2. Turn shaft; 3. Angle sensor

After calibration, the relationship between the measured header height *x*1, *x*2 [cm] and the rotation angle θ [°] of the two angle sensors is:

$$x1 = 0.62\ \theta + 3 \tag{1}$$

Non-contact measuring device

The CUM30-M2DV ultrasonic sensor is selected, and ADC3 and ADC4 are used for signal acquisition. The working schematic is shown in Figure 3.

Working principle: The ultrasonic signal is emitted by the ultrasonic transmitter, and the return signal is received by the receiver after the ultrasonic signal touches the ground. The time difference t1 is calculated by the timer function in the controller. Combined with the ultrasonic sound speed calculation formula, the header height K can be calculated:

$$V1 = 331.45 + 0.6T \tag{2}$$

T is the ambient temperature, [°C], which can be measured manually, or a temperature sensor can be installed to meet the time-varying requirements of temperature to reduce the error and obtain the height of the ultrasonic sensor above the ground:

$$K = V1 \times \frac{t1}{2} \tag{3}$$

Among them: K is the distance from the sensor to the field ground, [cm]; $V1$ is the propagation speed of ultrasonic, [cm/s] and $t1$ is the time difference from the transmitted signal to the received signal in seconds.

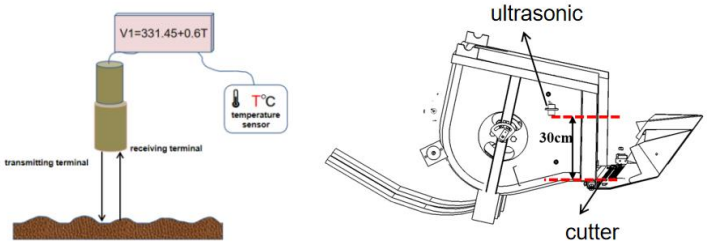

Fig. 3 - Work schematic diagram

Since the ultrasonic sensor is actually installed on both sides of the header, it measures the height of the ultrasonic wave from the ground, and the vertical distance between the ultrasonic wave and the cutting knife is $K0$, $K0$=30 cm, so the actual header height $x3$ and $x4$ obtained by the two ultrasonic measurements are:

$$x3 = K - K0 \tag{4}$$

Multi-sensor data fusion based on BP neural network to adjust the height of harvester header

This project intends to adopt a multi-sensor data fusion processing to adjust the harvester header height technology based on BP neural network. The neural network of the header control system is set as four input points and one output point, and a traditional three-layer network structure is shown in Fig 4 (*Guo et al, 2018; Wang et al, 2022; Qiu et al, 2018)*.

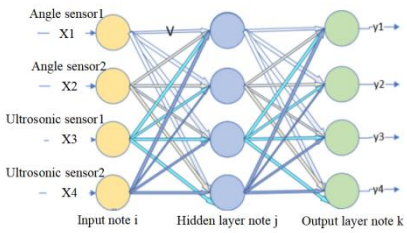

Fig. 4 - Neural network diagram of highly regulated system

The schematic diagram of the fusion processing method based on BP neural network is shown in Fig. 5.

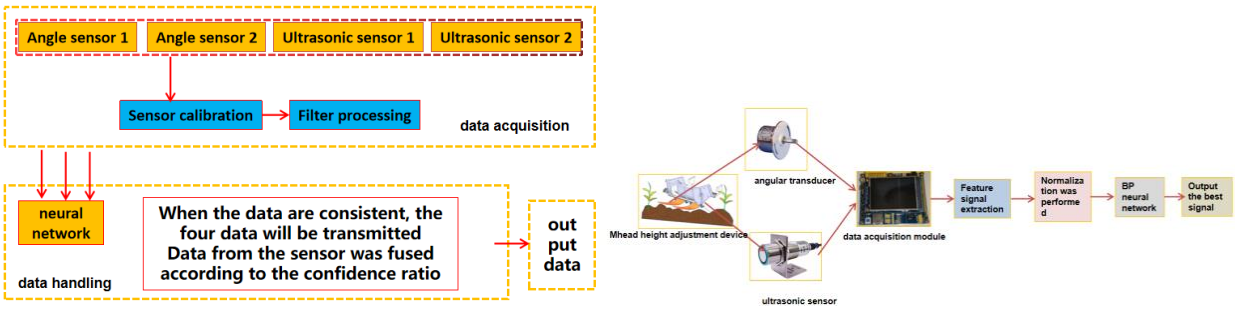

Fig. 5 - Schematic diagram of the fusion processing methods for multiple sensors

In order to obtain an ideal model for the height adjustment control system of the header, a large number of data acquisition and analysis were carried out. In MATLAB, according to the characteristics after filtering the measuring data of ultrasonic sensor and angle sensor, multiple pieces of collected data and multiple pieces of data to be fused at header heights of 10 cm are constructed, including two angle sensors and two ultrasonic sensors. Collect the height data of the header, and finally output the accurate measurement value of the height of the header.

Model establishment

The model of the header height control system is established by Matlab software, which can realize the functions of neural network and fuzzy reasoning (*Erzan et al., 2021)*. The toolbox in this software can realize self-learning of the system to obtain the output value by a lot of training on the established model. In this model, a fuzzy rule corresponding to the input (*x*1, *x*2, *x*3, *x*4) of the four sensors and the output f1 can be implemented. For the calculation from input to output, the intermediate layer is implemented, and the back-propagation algorithm is directly integrated into the inference process in order to obtain accurate output. The whole process can be divided into the following steps:

(1) Use the selected ultrasonic sensor and angle sensor to measure the height regulation state of the header;

(2) Preprocess the collected signals of the four sensors and perform signal feature selection;

(3) These characteristic signals are normalized, and finally the input model of the neural network of the header height control system is obtained. In this paper, the simple and practical Max-min normalization method is used to limit the data processing in the [0,1] interval. Its calculation formula is:

$$X=（x\text{-}xmin)/(xmax\text{-}xmin) \tag{5}$$

x represents the original value, X represents the converted standard value, and $xmin$ and $xmax$ represent the minimum and maximum values of x, respectively.

According to the performance indicators and coefficient calibration of the ultrasonic sensor and the angle sensor, the signals of the four sensors are collected and fused when the height of the header is 10 cm, respectively. The processing sample of BP neural network model in this paper selects the signal value collected when the header height is 10 cm, as shown in Table 1.

The height at 20 cm and 30 cm was also selected as the neural network fit, which was consistent with that at 10 cm, and it was not repeated again.

Table 1

Signal value of header height of 10 cm

Sample number for signal acquisition	1	2	3	4	5	6	7	8	9	10
Angle sensor 1, cm	9.9	10.3	10.1	10.4	9.7	9.8	10.2	9.6	10.0	10.1
Angle sensor 2, cm	10.2	9.9	10.0	10.3	9.6	10.4	10.1	10.2	10.4	9.6
Ultrasonic sensor 1, cm	10.4	10.2	9.7	9.6	10.3	10.5	9.8	10.4	9.4	10.4
Ultrasonic sensor 2, cm	10.3	10.0	10.1	9.8	10.5	9.7	9.9	10.4	10.3	9.6

Neural network model fitting in the header height control system

There are four input points and one output point in the neural network fusion processing of the height control of the header. The four input points represent four sensors. The data collected above are imported into the software for model fitting, and 70% of all data are selected as the training samples, 15% of the data is used as the verification sample, and 15% of the data is used as the test sample.

Fitting process and effect diagram are shown in Fig. 6.

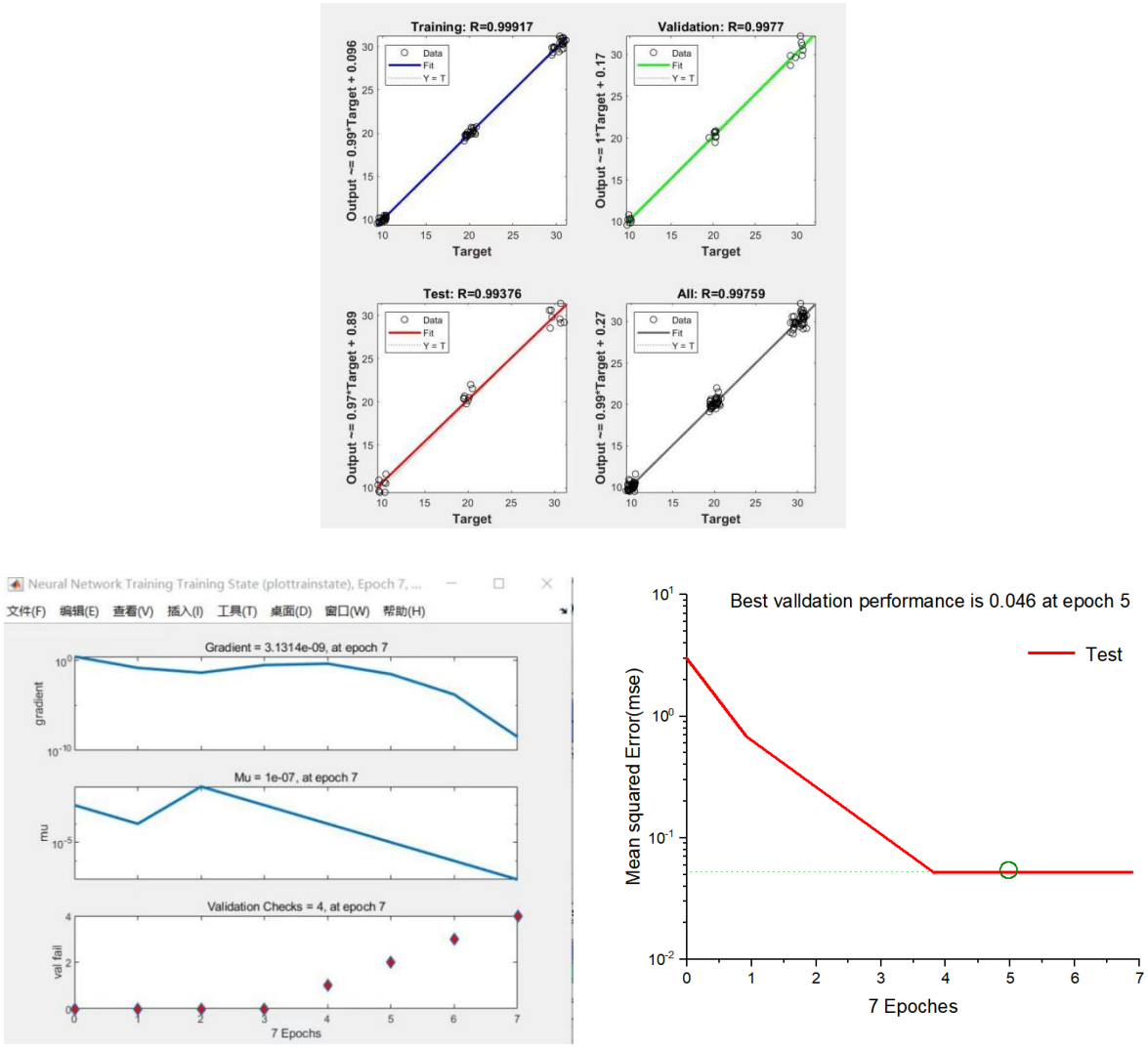

Fig. 6 - Fitting process and effect

The fitting process and effect chart show that the R value of the training sample is 0.99917, the R value of the validation sample is 0.9977, the R value of the test sample is 0.99376, and the overall R value is 0.99759, all of which are infinitely close to 1, indicating that the accuracy of the training model is good. From the BP neural network fitting training error curve, it can be seen that the error continues to decrease after iterative fusion processing, and the validation set and test set also have a good prediction effect, which reflects the BP neural network in adjusting the header.

The practicality of multi-data fusion processing in the height, the fitting error histogram is shown in Fig 7.

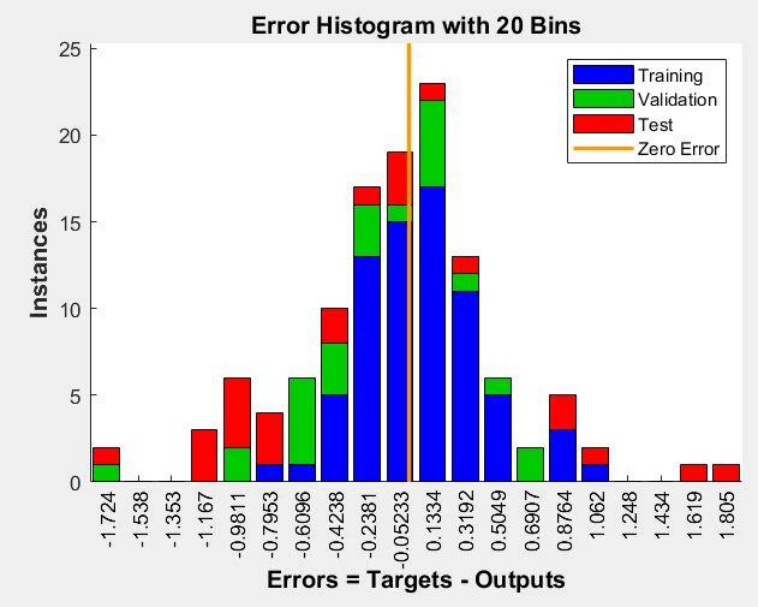

Fig. 7 - Model fit error plot

According to the above model fitting error diagram, the error range of the output results is between -1.742-1.805, and it is mainly concentrated between -0.6096-0.5049. The model training shows that the measured real-time height error range of the header meets the accuracy required.

Modeling and simulation of the hydraulic part of the header height control system using AMEsim software

The modified hydraulic system of the height of the header is simulated and analyzed. It is known that the initial position of the hydraulic cylinder of the header is about 1.5 cm. When the header is raised to the highest level, the displacement of the hydraulic cylinder is about 35 cm. The simulation model and results are shown in Fig. 8. The results show that the designed hydraulic system for the height of the header has a faster response speed, the header can be raised to the highest position within 10 s, and the accuracy is high, which indicates that the designed method is feasible.

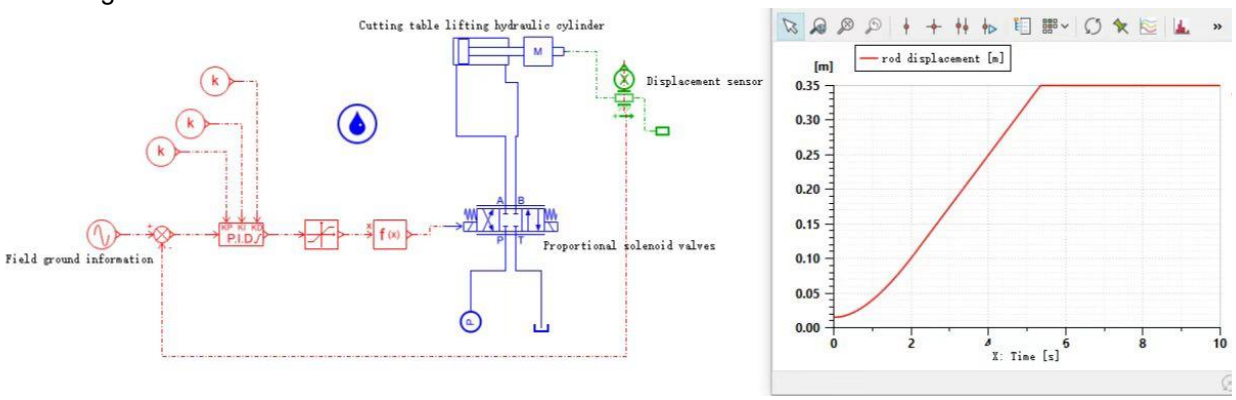

Fig. 8 - Simulation analysis and results of header height hydraulic system

Fuzzy PID design for automatic height adjustment system of multi-crop harvesting header

The real-time height of the header *x* is obtained through the multi-sensor fusion processing of the BP neural network above to obtain a relatively accurate value, and the deviation and deviation change rate are obtained by comparing with the height value of the set header for harvesting crops. In the process, the empirical value of the height of the header suitable for different crops and the reference to the relevant information determine the basic universe of input and output variables. The domain of discourse of E and EC is {-20, 20}, and the domain of discourse of the output variable u is {-5, 5}. It is corrected by fuzzy control theory. The fuzzy subsets of input and output variables are {PB, PS, ZR, NS, NB} *(Xia et al, 2015; Chen et al, 2015; Zhou et al, 2019)*. In order to simplify the calculation process, the membership functions of input distance deviation E and input distance change rate EC all use trigonometric functions. The schematic diagram is shown in Fig. 9:

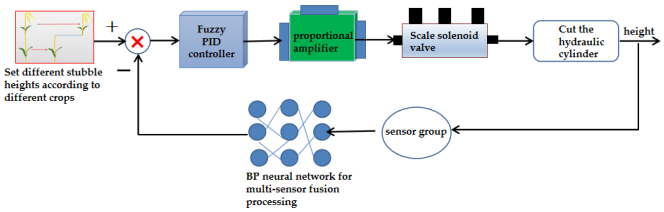

Fig. 9 - Schematic diagram of the header highly fuzzy PID control system

Determination of Header Height Control Transfer Function Model

Generally, in the application of agricultural machinery engineering, the proportional solenoid valve can be regarded as a second-order link, and its transfer function is:

$$\frac{Q(s)}{I(s)} = \frac{k_q k_1 \frac{1}{A_v}}{\frac{s^2}{\omega_h^2} + \frac{2\xi_n s}{\omega_h} + 1} \tag{6}$$

k_q is the flow gain of the electrohydraulic proportional valve m³(S.A), k_q=8.66 × 10⁻⁴, $k1$ is the displacement sensor magnification, k_1 = 9.5, A_v is the effective fluid dynamic area of the main slide valve core, $A_v = 1.06 \times 10^{-2}\ m^2$, ω_h is the natural frequency of the electrohydraulic proportional valve rad/s, take it at 9.5, and ξ_n is the electric-hydraulic proportional valve damping ratio take 6.58.

The transfer function of the proportional solenoid valve driving the hydraulic cylinder to control the height of the header is:

$$G_0(s) = \frac{183.96}{(s^2 + 25.02s + 90.25)k} \tag{7}$$

k is a known constant, $k = \mathrm{x} + 2.65\cos(\beta + 32) - 0.753$.$\beta$ is the initial angle between the conveyor tank and the vertical plane, and x is the lifting height of the header.

Use the graphical user interface in the Fuzzy Toolbox to create a fuzzy control model based on the fuzzy control strategy. In the membership function editor, set the membership function type, basic universe, and the number of fuzzy variable subsets (*Xia et al, 2015)*, as shown in Figure 10.

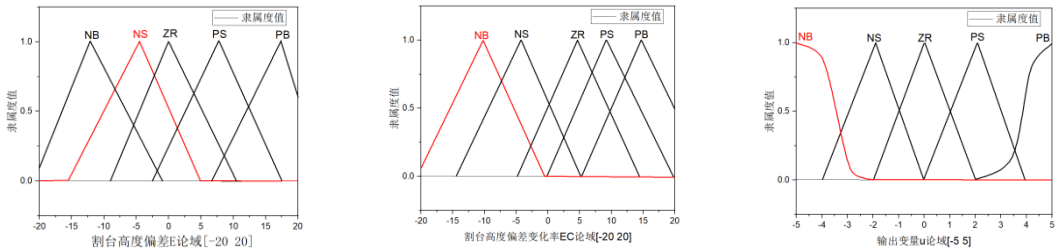

Fig. 10 - Header height, rate of change of height, and membership function plot of output variables

(a) E *(b) EC* *(c) u*

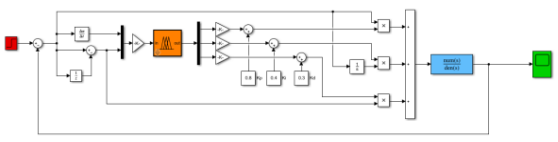

Fig. 11 - Simulation model of fuzzy control

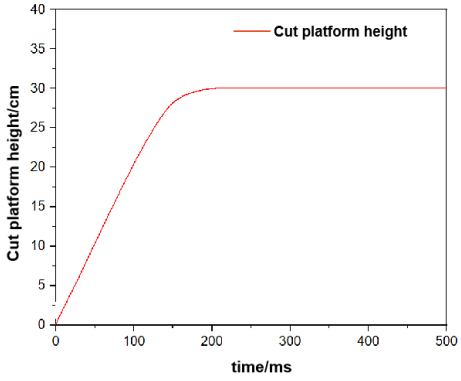

Fig. 12 - Analysis result curve

The simulation model of the fuzzy controller is built in the Matlab/Simulink software, as shown in Fig. 11. Set the simulation time to 0.5 s, simulate the control system, set Kp=0.8, ki=0.4, kd=0.3, and set the height of the header to 30 cm during simulation, that is, the steady-state value of the output of the PID controller is 30 cm, 0.4 s, it is stable and has a fast response speed, which can meet the design requirements of the automatic control system for the height of the header. The analysis results are shown in Fig. 12.

Design of header height data acquisition and output system

The master controller and slave device of the communication system use STM32F1 as the microcontroller. The slave device collects various analog signals or pulse signals through the microcontroller, converts them into digital signals, and sends them to the master controller through the RS485 bus. The overall framework of the RS485 system is shown in Fig. 13.

In 2021, rapeseed, soybean, and rice harvesting experiments will be carried out in Qinghai, Shandong, and Jiangsu, respectively. Due to the large differences in topography of the three fields, they can be used to test the performance of automatic height adjustment of the header. The test model is a 4LZ-5B multi-crop combine harvester, as shown in Fig. 14.

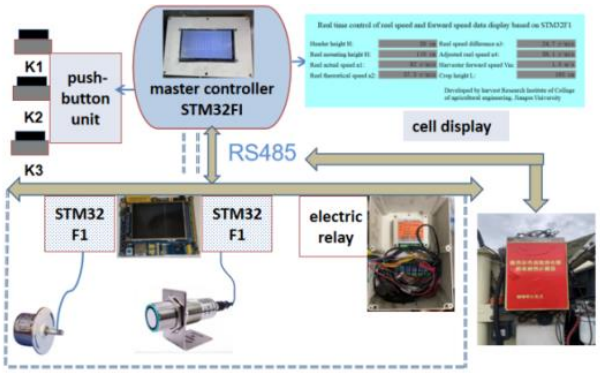

Fig. 13 - Overall framework of the R S 485 system

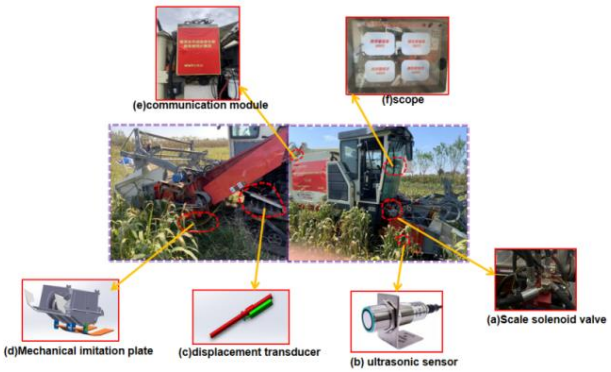

Fig. 14 - Header adjustment device diagram and test diagram

RESULTS

During the field test, the forward speed and direction of the harvester are controlled by the staff, and the height of the header is controlled by the automatic control system. The flagpole is used to set a stop measuring point every 10 meters to measure the height of the header, and the tester uses a tape measure to measure the height of the header from the ground. Table 2 shows the test results when harvesting rapeseed, millet and rice.

Table 2

Test results of combine header height control

test number	Set the height of the cutting table (Rape / Rice / millet) mm	Actual measurement height (Rapeseed / rice / millet) mm	bias in statistics (Rapeseed / rice / millet) mm
1	300/280/210	295.3/275.5/203.0	-4.7/-4.5/-7.0
2	300/280/210	304.8/286.8/212.5	4.8/6.8/2.5
3	300/280/210	296.8/279.5/205.9	-3.2/-0.5/-4.1
4	300/280/210	294.0/276.5/201.7	-6.0/-3.5/-8.3
5	300/280/210	310.6/291.6/217.5	10.6/11.6/7.5
6	300/280/210	295.2/277.3/204.5	-4.8/-2.7/-5.5
7	300/280/210	313.5/294.2/219.6	13.5/14.2/9.6
8	300/280/210	307.4/289.5/215.6	7.4/9.5/5.6

The test results show that when harvesting rape, the error of the height adjustment of the header is less than 13 mm; when harvesting millet, the error of the height adjustment of the header is less than 10 mm, the small error may be because the flatness of the field is high. In the case of rice, there may be many weeds in the field, which affect the accuracy of the sensor measurement, so it exceeds the error of the other two crops when harvesting, but the maximum error does not exceed 15 mm, which meets the harvesting requirements. Therefore, the designed header height control system in this paper can meet the field operation needs of the multi-crop combine harvester.

CONCLUSIONS

(1) Through the BP neural network multi-sensor fusion processing technology, the real-time acquisition value of the header height is obtained, which lays a foundation for the subsequent high-precision and low-error adjustment of the header height.

(2) Carry out the modeling analysis of the mechanical system and the hydraulic system of this harvester to obtain the open-loop transfer function of the header height with respect to the control current, and obtain the response curve of the fuzzy PID control system through Simulink simulation, and the results show that the control system has fast response time and small control error.

(3) The field test of harvesting rapeseed, millet and rice shows that: under the automatic height control system of the header, the error between the actual height of the crop when it is harvested and the set height is within 15 mm, the harvest effect is better, and the height of the crop stubble is relatively flat, satisfying the requirement of automatic control of the height of the combine harvester in the multi-crop growth environment. It also verifies the effect of the fuzzy PID control system designed in this paper in the actual test.

ACKNOWLEDGEMENT

I mainly completed the design of experiments and the writing of papers, Yaoming Li provided funding, and others provided trial assistance. Project source was the Major Science and Technology Innovation Project of Shandong Province: Key technology and Industrialization of intelligent and efficient crawler rape combined harvester (2019JZZY010729).

REFERENCES

[1] Erzan T, EBali E. (2021), Modeling and analysis of an electro-pneumatic brake valve with on-off type solenoid driven by PWM technique. *Journal of the faculty of engineering and architecture of Gazi University*. Vol. 36(3), pp. 1418-1430. Turkey;

[2] Guo W., Yu C., Wang Fu et al (2017). Design and test of ground imitation control system of combine harvester cutter platform (联合收割机割台地面仿形控制系统设计及试验). *Agricultural mechanization Research*, Vol. 39(5), pp. 150-154. Heilongjiang/China.

[3] Hunan Agricultural Machinery and Power Co. LTD (2014). Height adjustment device for semi-feeding harvester (半喂入式收割机的割台作物夹持高度调节装置): 201310630999.3. Hunan/China.

[4] Liu J. (2015) Automatic control system based on o-hydraulic control (基于电液控制的割台高度自动控制系统): China, 201310660343.6. Liaoning/China.

[5] Liao Y., Wu M., Xiang Y. I. (2018). Design and Test of the High Adaptive Regulation System (联合收割机割台高度自适应调节系统的设计与试验). *Journal of Hunan Agricultural University (Natural Science edition)*, Vol. 44(3), pp. 326-329. Hunan/China.

[6] Qiu C. (2018). Multi-sensor data fusion method based on the BP Neural Network. *Changsha Civil Affairs Vocational and Technical College Newspaper*, Vol. 25, 80(02), pp. 131-132. Changsha/China.

[7] Tao J. (2018) Analysis of the research progress of Intelligent Agricultural Machinery and Equipment (*智能化农业机械装备的研究进展分析*). *Southern Agricultural Machinery*, Vol. 7, pp. 8-9. Jiangxi/China.

[8] Wang F., Tang X., Deng L., Li J. (2022). Application of BP neural network to prediction of recovery effect of air-foam flooding in heavy oil. *Petroleum science and technology*.

[9] Xia S., Zhao L. (2015). Multisensor information fusion study of basic BP neural network (基于 BP 神经网络的多传感器信息融合研究). *Computer measurement and Control*, Vol. 23 (5), pp. 1823-1826. Beijing/China.

[10] Xing X., Yao J., Ren J. (2015). Multi-sensor fusion monitoring based on improved adaptive weighting (基于改进的自适应加权的多传感器融合监测). *Computer Measurement and Control*, Vol. 23(12), pp. 3998-4001. Beijing/China.

[11] Yang R., Wang Z., Shang S., et al. (2022). The Design and Experimentation of EVPIVS-PID Harvesters' Header Height Control System Based on Sensor Ground Profiling Monitoring. *Agriculture*, Vol. 12(2), pp. 282. Switzerland. https://doi.org/10.3390/agriculture12020282

[12] Zhou D., Jin C., Ni Y., Zhang G. (2019). Design and test of the high fuzzy control system（高模糊控制系统的设计与测试）. *Jiangsu Agricultural Science*, Vol. 47 (13), pp. 264-267. Jiangsu/China.

[13] Zheng W. (2015). Development status of intelligent agricultural machinery and equipment at home and abroad (国内外智能化农业机械装备发展现状). *Modern Agricultural Machinery*, Vol. 6, pp. 4-8. Zhejiang/China.

DESIGN OF FARMLAND AREA MEASURING INSTRUMENT BASED ON BEIDOU SATELLITE NAVIGATION SYSTEM
/
基于北斗导航系统的农田面积测量仪设计

Liang ZHANG [1 2)], Ming LI [2)], Limin YAO [3)], Jingxin XIE [1)], Xu XIAO [1)], Jingjing HUANG [2)], Jinqi HUANG [2)], Kui FANG *[1)]

[1)]College of Mechanical and Electrical Engineering, Hunan Agricultural University, Hunan, 410125 / China;
[2)]Hunan Agricultural Equipment Research Institute, Hunan Academy of Agricultural Sciences, Hunan, 410125 / China;
[3)] College of Agricultural Engineering and Food Science, Shandong University of Technology, Shandong, 255000 / China
Tel: 18810987071; E-mail: 18810987071@163.com
DOI: https://doi.org/10.35633/inmateh-68-10

Keywords: *BeiDou Navigation Satellite System, farmland area, measuring instrument, triangulation*

ABSTRACT

Farmland area data is one of the important agricultural basic data, which provides parameter basis for the precise operation of agricultural equipment. In order to meet the technical needs of farmers and agricultural machinery operation service billing for acquiring basic information of farmland, this study proposes a farmland area measuring instrument based on the BeiDou Navigation Satellite System. Firstly, the overall design scheme of the measuring instrument, the hardware circuit design scheme and the algorithm design scheme are introduced, and the triangulation area measurement algorithm is emphatically analysed. Finally, the design of this research is applied. The farmland area measuring instrument measures the area of different shapes of farmland and verifies the measurement accuracy. The results show that the average relative error of the measuring instrument for measuring the area of irregularly shaped farmland is 0.7%, which realizes the rapid and high-precision measurement of the area of arbitrarily shaped farmland. It is hoped that this study can provide some reference for the research on the area measurement of farmland in my country.

摘要

农田面积数据是重要的农业基础数据之一，为农业装备实现精准作业提供参数依据。为满足农户和农机作业服务计费等市场对获取农田基本信息的技术需要，本研究提出一种基于北斗卫星导航系统的农田面积测量仪。首先，介绍了测量仪的总体设计方案，硬件电路设计方案和算法设计方案，着重分析了三角剖分面积测量算法设计。最后，应用了本研究的设计。农田面积测量仪测量测量不同形状农田的面积，并验证测量精度。结果表明，测量仪对不规则形状农田面积测量的平均相对误差为 0.7%，实现对任意形状农田面积的快速高精度测量。希望这项研究能为我国农田的面积测量研究提供一定的参考。

INTRODUCTION

Agricultural information technology is the main direction of the development of modern agriculture (*Poppe K. J. et al., 2013*). Farmland area data is an important agricultural basic data *(Yuefeng Du et al, 2019*). Farmland area data provides the basis for agricultural equipment to achieve precise operations, such as precision ploughing, precise fertilization, precise irrigation and precise harvesting *(Xuegeng Chen et al, 2020*).

The current domestic and international farmland area measurement mainly includes:

(1) The tape measure method is only applicable to regular and small-area farmland.

(2) The professional instrument measurement method (total station, etc.) requires professional and skilled operators, complicated calculation, high cost, and is not suitable for farmland area measurement.

(3) The area measuring instruments based on the satellite navigation system are widely used in agriculture (*Dengsheng Zhu et al, 2020*). Researchers at home and abroad have studied the vehicle-mounted farmland area measuring instrument, which calculates the farmland area by recording the length of the track of farm machinery operation and the width of the operation through GNSS (Global Navigation Satellite Systems, GNSS) positioning module/GNSS and AHRS integrated system (*Yunpeng Jing et al, 2019*), but there are errors such as operation track overlap or omission, and the measurement error increases with the increase of operation overlap area or omission;

Yangchun Liu et al. used the third method mentioned above to obtain the farmland area by multiplying the length of the operating trajectory with the width. Because of the overlapping trajectories during the operation, the measured area was larger than the true value, and the experiment showed that the error between the area calculated by this method and the area measured by the tape was generally stable within 3%, which increases with the increase of overlapping trajectories (*Yangchun Liu et al, 2016*).

Binbin Ji et al. used GPS (Global Positioning System, GPS) to measure the trajectory length of agricultural machinery, and used ultrasonic sensors to measure the width of agricultural machinery, and multiplied the trajectory length and width to measure the area of farm machinery operations in real time, and the average error between the area obtained by the device and the actual area was less than 2% (*Binbin Ji et al, 2012*).

Zhixiong Lu et al. used a dual-satellite positioning receiver of GPS and Galileo to improve the positioning accuracy by adaptive filtering algorithm. The area was calculated using the multiplication of track length and width, and the relative error of area measurement was 2.09% (*Zhixiong Lu et al, 2015*).

Hui Liu et al. designed vector buffer algorithm and raster buffer algorithm for agricultural machine operation area measurement, and conducted experiments under three different GNSS positioning accuracy conditions of RTK (Real-Time Kinematic Positioning, RTK), sub-meter level and single-point positioning, respectively and the results showed that GNSS positioning accuracy had significant effects on operation area measurement accuracy. The relative measurement errors of the two algorithms were 0.31% and 0.18%, when RTK positioning was used; 2.43% and 1.44% when sub-meter GNSS positioning was used; 7.20% and 6.31% when single-point GNSS positioning was used. The area measurement accuracy decreases with the decrease of GNSS positioning accuracy (*Hui Liu et al, 2015*).

Researchers at home and abroad have studied handheld farmland area measuring instruments, which measured the coordinates of farmland boundary points and sequentially connected them to obtain farmland areas through the positioning function of GPS. *Zhengjun Qiu et al.* used the GPS positioning function to develop a measuring instrument for farmland area. The farmland area measuring instrument consists of GPS module, microcontroller, keyboard and LCD display, and adopts GPS positioning technology and polygonal farmland area calculation method. The results showed that the measuring instrument can quickly measure the area of farmland the relative error less than 2% (*Zhengjun Qiu et al, 2005*). In this measurement method, the measurement accuracy of the boundary point and distance between the two measurement points will affect the shape of the measurement fitting graph. The closer to the actual farmland, the smaller the measurement error (*Yizhe Sun et al, 2019*). Therefore, the improvement of the boundary point measurement accuracy and the improvement of the shape fitting method will improve the measurement accuracy of farmland area. To sum up, the farmland area measuring instrument has problems such as large overlapping error of measuring area, low accuracy of boundary point measurement, and the farmland shape fitting method needs to be improved.

With the construction of BeiDou Navigation Satellite System ground-based augmentation stations and the development of mobile communication technology (*Guangqi Wang et al, 2018*), high-precision navigation and positioning services were provided (*Sunwen Li et al, 2021*). Triangle is the smallest unit to calculate polygon area, which can be closer to polygon boundary (*Gopi M. et al, 2000*). In this paper, we adopt the BeiDou network differential technology to improve the positioning accuracy of the area measuring instrument, and combined the triangular dissection algorithm to improve the accuracy of polygonal farmland area measurement and eliminate the overlapping error. The hardware design of the farmland area measuring instrument was completed by embedded technology to realize convenient measurement of the area of any shaped farmland.

MATERIALS AND METHODS

The overall design of the farmland area measuring instrument system

The farmland area measuring instrument is mainly composed of BeiDou high-precision positioning module, communication module, Raspberry Pi, HDMI display, power module and virtual keyboard, as shown in Figure 1. The Raspberry Pi is used as the main control board of the farmland area measuring instrument. It is equipped with a 1.2 GHz quad-core Broadcom BCN2837 64-bit ARMv8 processor, and integrates 4 USB2.0 ports and a 40-pin extended GPIO interface. The main control board transmits data through the communication module and the BeiDou high-precision positioning module, collects the latitude and longitude coordinates of the farmland boundary points, and uses the triangulation farmland area calculation algorithm to measure and display the farmland area.

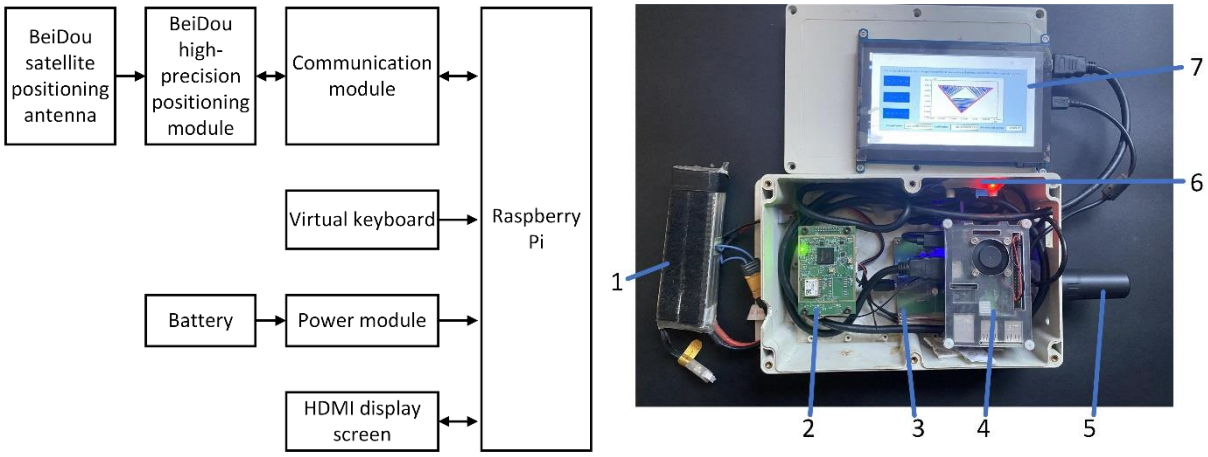

Fig. 1 –General structure of farmland area measuring instrument design
1-Battery; 2-BeiDou high-precision positioning module; 3-Power module; 4-Raspberry Pi; 5-BeiDou satellite positioning antenna; 6-Communication module; 7-HDMI display screen

Hardware design of farmland area measuring instrument

As shown in Figure 2, the farmland area measuring instrument collects the latitude and longitude coordinates of the farmland boundary points, and the positioning error of the boundary points will affect the accuracy of area measurement. Because the MC120M module integrates the single-frequency RTK algorithm, and supports both BeiDou satellite navigation system and the global satellite navigation system, the data update frequency is 1 Hz, the positioning accuracy of MC120M module can reach real-time centimetre level. Therefore, the MC120M is chosen for its accurate positioning, ease of use and low cost. The MC120M module has two power input pins (VCC, V_BACKP) and one power output pin (VCC_RF). The VCC pin is connected to the positive pole of 3.3V power supply, and the GND pin is connected to the negative pole of the power supply to supply power to the module; The V_BCKP pin is connected to 3.3V backup power supply to power the RTC circuit when VCC power failure occurs to ensure the critical information is not lost for hot start function; VCC_RF outputs 3.0V voltage, which can be used to power the antenna; The RF_IN pin is the antenna interface of the module, with built-in 50 ohm impedance matching, which can be directly connected to the multimode antenna; The module comes with its own internal power-on reset circuit, so the RESET_N reset pin is overhung; The TIMEPULSE pin is the second pulse signal output, which is output after several seconds after the module obtains the positioning data, and is used to indicate the positioning status. Therefore, the TIMEPULSE pin is connected to the LED for displaying the positioning status. The TXD and RXD pins are the UART serial port pins of the module, which are respectively connected to the RXD and TXD pins of the communication module, used to communicate with the main control board, and the supported baud rate range is 4800 bps ~ 460800 bps. At startup, the D_SEL pin of the module controls the type of data interface used for communication. When this pin is high or overhung, the UART protocol is chosen. When this pin is low, the SPI protocol is chosen. The UART protocol is selected, so D_SEL is designed to be overhung, and the circuit design is shown in Figure 3.

Fig. 2 - The photos of the operation of collecting the coordinates of the experimental farmland to be measured

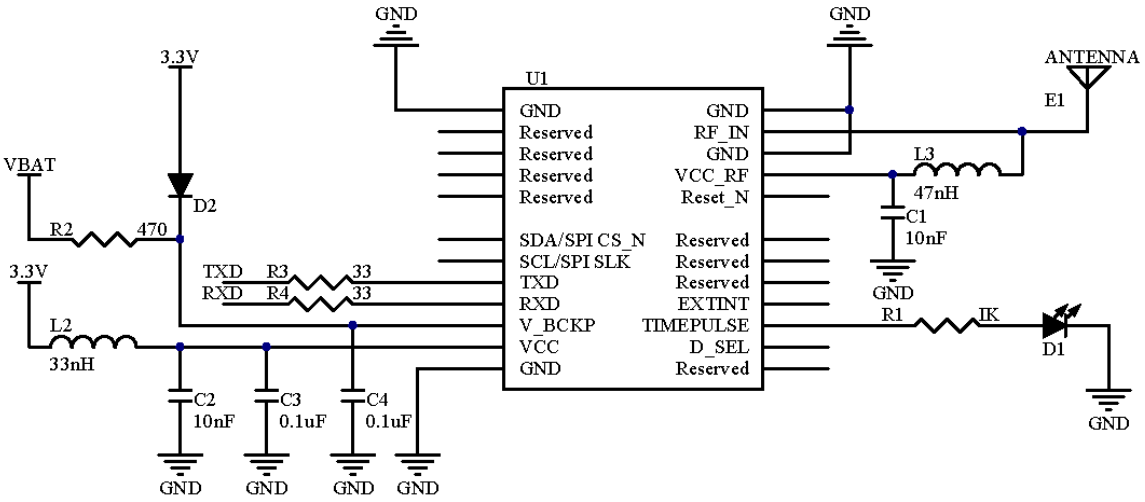

Fig. 3– Design of BeiDou high-precision positioning module circuit of the system

In order to realize the data exchange between the BeiDou high-precision positioning module and the Raspberry Pi, the communication interface circuit of USB to serial port is designed. The CH340T is a USB bus adapter chip used to extend the serial port for the computer or upgrade the serial port devices directly to the USB bus, and it supports full-speed USB device interface and is compatible with USB V2.0. The external circuit components only require a crystal oscillator and capacitors, the circuit design is simple and stable, so the communication interface circuit adopts CH340T chip. The CH340T chip has a built-in USB pull-up resistor, and the UD+ and UD- pins can be connected directly to the USB bus. The clock signal is generated by the built-in inverter through the crystal oscillator frequency stabilization oscillator, so a 12 MHz crystal oscillator is connected between pins XI and XO, and oscillating capacitors C5 and C6 are connected to ground for pins XI and XO, respectively. The CH340T chip supports 5V power supply voltage, VCC pin input external 5V power supply, and V3 pin is connected with power supply decoupling capacitors with capacities of 0.01 μF, 0.1 μF and 22 μF respectively. The data transmission pins TXD and RXD are respectively connected with the RXD and TXD of the MC120M module for data transmission and reception. The design of the communication interface circuit is shown in Figure 4.

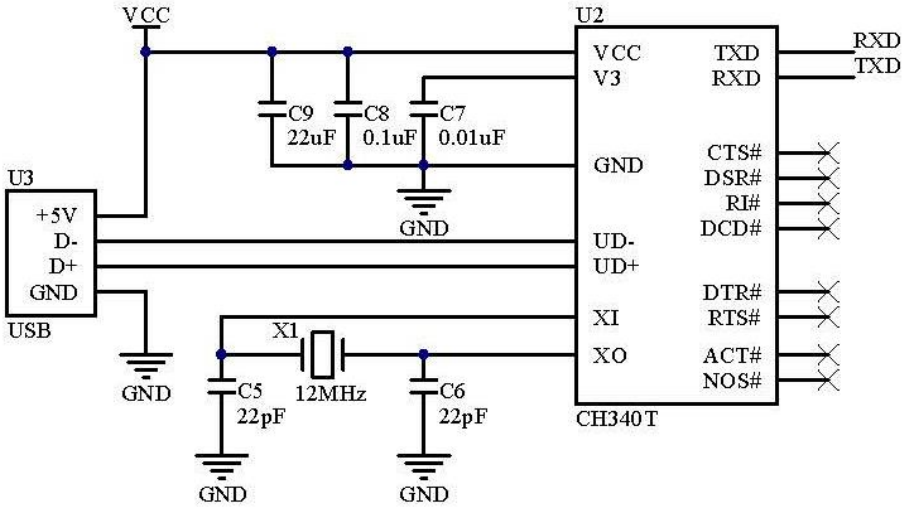

Fig. 4 – Design of communication interface circuit of the system

Algorithm design of farmland area measuring instrument

Using satellite positioning technology to measure the farmland boundary points, the area of the polygon enclosed by the boundary points is the farmland area. The measured farmland is flat dam farmland with a slope of 0° to 6° and suitable slope farmland with a slope of 6° to 25°. Triangle is the smallest unit to

calculate polygon area, which can be closer to polygon boundary. The idea of micro-integration is adopted. Firstly, the undulating polygonal farmland is divided into many triangle areas, which are closer to the local terrain, and then the farmland area is obtained by accumulating the area of each small triangle. The more complex the shape of the farmland, the more undulating the ground, which makes it difficult for the triangle to approach the local terrain, reducing the accuracy of farmland area measurement. The Delaunay triangulation method was used to calculate the farmland area. First, the WGS84 (World Geodetic System (WGS) 1984) coordinate of the farmland boundary points were converted into the Local Cartesian coordinate system, and the discrete boundary points were connected into adjacent and non-overlapping triangles through Delaunay triangulation. The sum of the triangle area is the polygonal farmland area. The triangle can be closer to the complex boundary (The complex boundary composes of more than three lines on different planes that connect in sequence and do not intersect.). Compared with the boundary method, the figure formed by the triangulation algorithm is closer to the actual polygonal farmland, and the measurement error is smaller; compared with the traditional multiplication of width and trajectory, the triangulation algorithm forms adjacent and non-overlapping triangles without overlapping measurement areas. Therefore, the combination of high-precision positioning and Delaunay triangulation method will further improve the accuracy of the farmland area measuring instrument.

The surface of the earth is a curved surface. In order to accurately calculate the farmland area, Gauss projection positive operator is used to expand the curved surface into a plane, and the Krasovsky ellipsoid parameters are used for Gauss projection positive operator, and the WGS84 coordinates of the farmland boundary points are converted into the Local Cartesian coordinate system. Delaunay triangulation makes a finite set of points connected to each other to form a plane formed by a set of adjacent and non-overlapping triangles. Delaunay triangulation is performed on the boundary points of the farmland through the point-by-point interpolation method, and the farmland is divided into a plane formed by a set of triangles, and the area of the farmland is obtained by calculating the sum of triangle area.

The Gaussian coordinates of the boundary points are arranged according to the x and y values from small to large, and a rectangle is established with the points (x_{min}, y_{min}) and (x_{max}, y_{max}) as the diagonal. Based on the diagonal triangle of a half rectangle, the hypotenuse of a right triangle after doubling it according to the similar triangle theorem passes through the point (x_{max}, y_{max}). The base and height of the triangle are expanded, and the expansion principle always maintains that the length of the base of the expanded triangle is greater than the height. As shown in Figure 5, the expanded triangle is symmetrically copied into a triangle enclosing the Gauss coordinate points of the farmland boundary to determine the maximum distribution of the farmland.

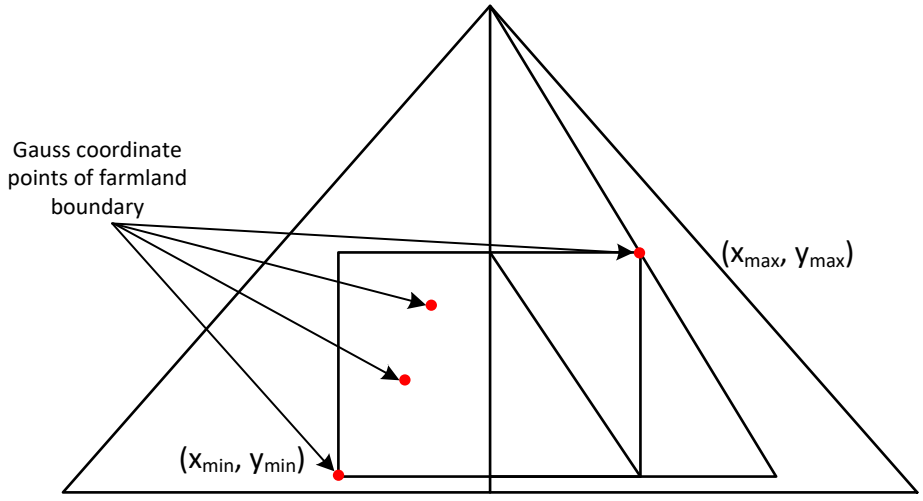

Fig. 5 – The triangle enveloping all points

The point-by-point interpolation to create a triangular mesh: The envelope triangle is put into the temporary triangle list, and the external circles are calculated one by one for the triangles in the temporary triangle list. First, we calculate the external circle of the envelope triangle, as shown in Figure 6. Then, the judgment is made one by one from the point with the x coordinate from small to large. It is found that any point is within the external circle of the enveloping triangle, so the enveloping triangle is not a Delaunay triangle. We save its three sides to the edge buffer array, and delete the enveloping triangle from the temporary triangle list.

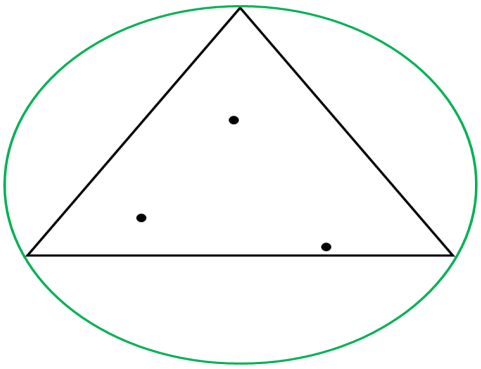

Fig. 6 – The circumscribed circle of enveloping triangle

In the sorted coordinate points, as shown in Figure 7, the point with the smallest x-coordinate value is connected to each edge in the edge buffer array to form three triangles, and the formed triangles are added to the temporary triangle list. As shown in Figure 8, the triangles in the temporary triangle list are traversed to draw the external circle, and the positional relationship between the external circle and the second-smallest point of the x-coordinate value is determined. If the point is on the right side of the circumcircle of the triangle, it means that the triangle is a Delaunay triangle, and the triangle is saved to the list of Delaunay triangles.

If the point is measured to the left of the external circle of the triangle, the triangle will not be judged this time, and it will not be deleted from the temporary triangle list, and the judgement will be made after the next coordinate point is inserted; If the point is inside the external circle of the triangle, the three sides of the triangle are added to the edge buffer array. The point continues to form a triangle with the edge in the edge buffer array and put it in the temporary triangle list, and traverse the positional relationship between each triangle external circle and the next insertion point in the temporary triangle list. All the coordinate points are gradually inserted, and the judgment is carried out in turn. Finally, the triangles related to the three points of the envelope triangle are removed from the list of Delaunay triangles, and the remaining triangles are the triangles formed by the division. As shown in Figure 9, a piece of farmland on the satellite map is divided into many small triangles.

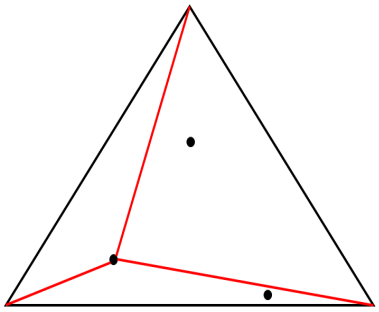

Fig. 7 – The triangles formed by the point inside the triangle and the three sides of the triangle

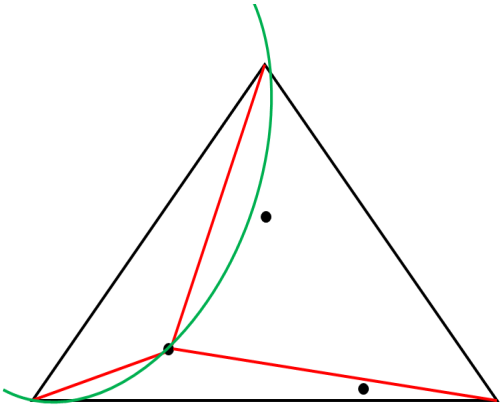

Fig. 8 – The external circle of triangle

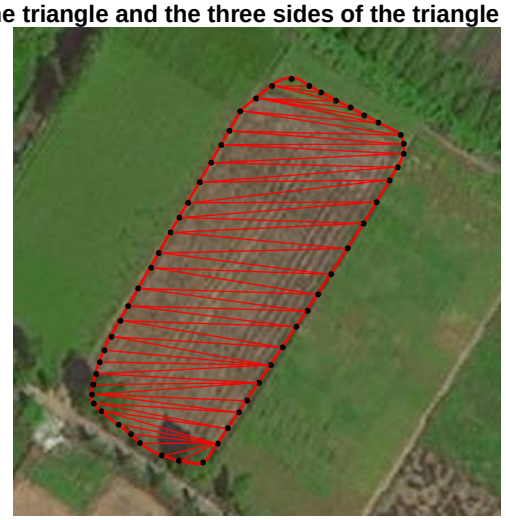

Fig. 9 –The Delaunay triangulation of farmland

The calculation of polygonal farmland area: After the division, the side length of each small triangle is obtained, and the area of each small triangle after division is obtained by Heron formula, and the total area of the farmland is obtained by summing the areas of the divided triangles.

$$S_i = \sqrt{p_i((p_i - a_i)(p_i - b_i)(p_i - c_i))} \quad (1)$$

Where:

S_i is the area of the small triangle. a_i, b_i, c_i are the lengths of the three sides of the small triangle. p_i is the semiperimeter.

$$S = \sum S_i \quad (2)$$

Where: S is the farmland area.

Software design of farmland area measuring instrument

The program adopts modular design to meet the portability of the program. Each functional program includes: BeiDou information collection module, area calculation module, display module and storage module. The flow chart of the program is shown in Figure 10. The BeiDou information collection module reads the positioning information and judges whether the measurement starts. At the beginning of the measurement, the integrity of the positioning information is judged. The latitude and longitude data is obtained and stored by calculating the difference correction number and the original positioning data. When the device measurement is complete, the triangulation area algorithm is run.

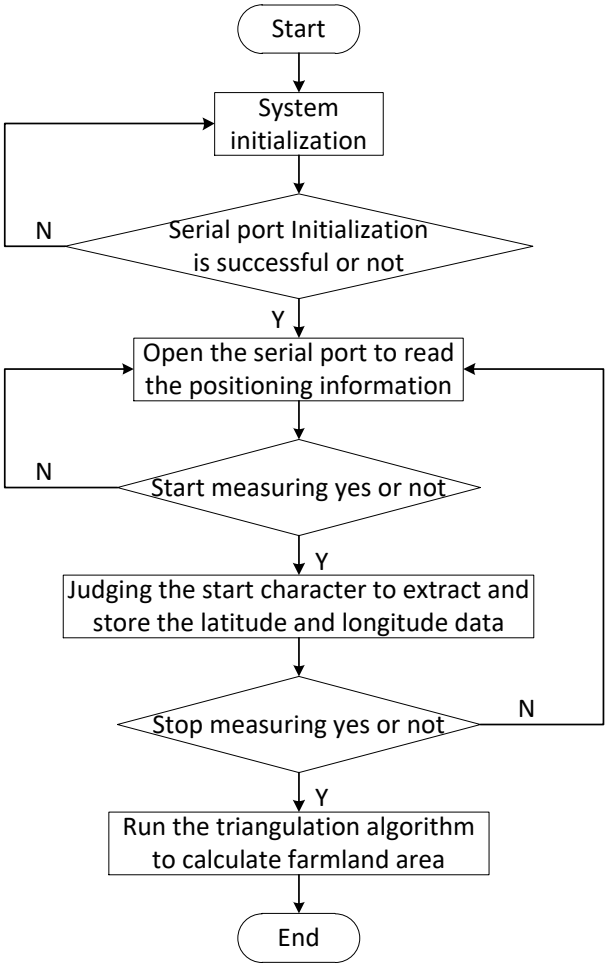

Fig. 10 – The program flow chart of system

After opening the desktop application, click the “measure button” to complete the initialization of the serial port and the BeiDou high-precision positioning module, and then display the differentially calculated high-precision positioning data below the desktop application, as shown in Figure 11.

Then the area measuring instrument starts measuring. When the measurement is finished, click the “End Measurement” button. The triangulation area algorithm implements the area calculation and displays the triangulation map.

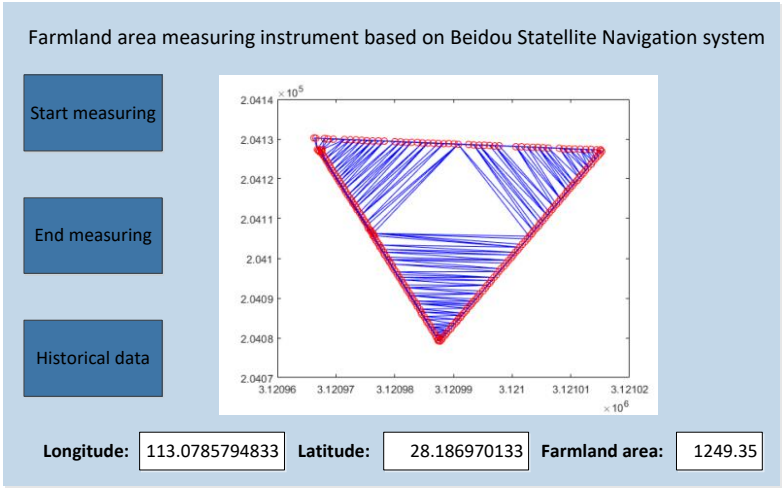

Fig. 11 – The software interface of farmland area measuring instrument

RESULTS

The experimental design of farmland area measurement

In October 2021, the measurement accuracy experiment of the farmland area measuring instrument was carried out in the farmland of Hunan Agricultural Equipment Research Institute near Hunan Agricultural University. The experiment selects square, rectangular, triangular, circular and polygonal plots as the experiment site. The measuring area of the tape is the standard area of the experiment site. The standard areas of the five shape experiment sites (as shown in Figure 12) are: the area of the ABCD square $S_1 = AB \times BC = 50\,m \times 50\,m = 2500\,m^2$; the area of the ABGE rectangular $S_2 = AB \times BG = 50\,m \times 25\,m = 1250\,m^2$; the area of the EBC triangle $S_3 = 0.5 \times EG \times BC = 0.5 \times 50\,m \times 50\,m = 1250\,m^2$; the area of the EFGH circular $S_4 = 3.14 \times OF \times OF = 3.14 \times 25\,m \times 25\,m = 1962.5\,m^2$; the area of the FKCIE polygon $S_5 = 781.25\,m^2 + 468.75\,m^2 + 312.5\,m^2 = 1562.5\,m^2$. The hand-held farmland area measuring instrument walks around the boundary of the experiment site to obtain the field measurement area, and the walking speed is about 1 m/s, and the experiment is repeated five times for each experiment site.

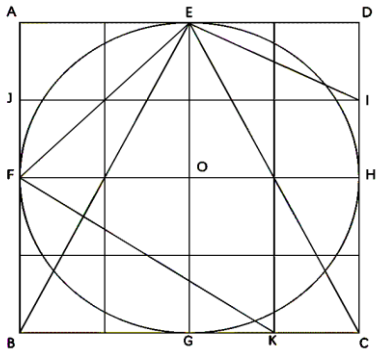

Fig. 12 – The experiment area

Experimental results and analysis

Table 1 shows the data processing results of the standard area, measurement area and relative error of the experiment plot. Figure 13 is the GIS map of the ABEG experimental farmland. Figure 14 is a measurement diagram processed by a triangulation area measurement algorithm. When measuring square, rectangular and circular experiment sites, due to the regular shape, small number of vertices and no sharp vertices, the set of boundary points obtained by the farmland area measuring instrument is accurate, and the average error is 0.5%, 0.516% and 0.556% respectively. When measuring the polygon experimental farmland, due to the irregular shape and many vertices, the boundary points obtained by the farmland area measuring instrument near the polygon vertices are lost. With the increase of polygon vertices the loss of boundary points increases and the average error reaches a maximum of 0.998%. When measuring the triangle experimental farmland, the three vertex angles are all acute angles, the boundary points obtained by the farmland area measuring instrument at the vertex angles are seriously lost, and the average measurement error reaches 0.924%.

Table 1

Comparison of test results of farmland area measuring instrument

Region	Standard area (m^2)	Measurement number	Instrument measurement (m^2)	Difference (m^2)	Relative error (%)	Average relative error (%)
square	2500	1	2498.39	1.61	0.06	0.500
		2	2507.06	7.06	0.28	
		3	2531.64	31.64	1.27	
		4	2486.27	13.73	0.55	
		5	2491.62	8.38	0.34	
rectangular	1250	1	1262.33	12.33	0.99	0.516
		2	1242.37	7.63	0.61	
		3	1245.78	4.22	0.34	
		4	1257.49	7.49	0.60	
		5	1249.50	0.5	0.04	
triangle	1250	1	1279.84	29.84	2.39	0.924
		2	1249.35	0.65	0.05	
		3	1241.61	8.39	0.67	
		4	1258.31	8.31	0.66	
		5	1260.57	10.57	0.85	
circular	1962.5	1	1968.02	5.52	0.28	0.556
		2	1975.47	12.97	0.66	
		3	1972.95	10.45	0.53	
		4	1981.36	18.86	0.96	
		5	1969.40	6.90	0.35	
polygon	1562.5	1	1584.71	22.21	1.42	0.998
		2	1560.48	2.02	0.13	
		3	1568.87	6.37	0.41	
		4	1596.84	34.34	2.20	
		5	1575.45	12.95	0.83	

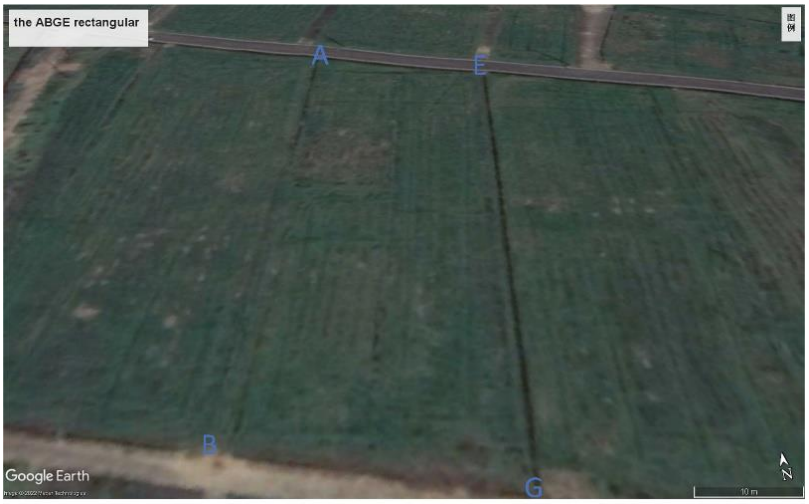

Fig. 13 – The GIS map of the ABEG experimental farmland

The experiment results show that the farmland area measuring instrument can accurately measure the farmland area regardless of the shape of the farmland, and the average error rate of the measurement area is maintained below 0.7%. When measuring polygons with multiple sharp vertices, the measurement error rate increases, and the maximum measurement error does not exceed 2.5, which fully meets the needs of farmland area measurement.

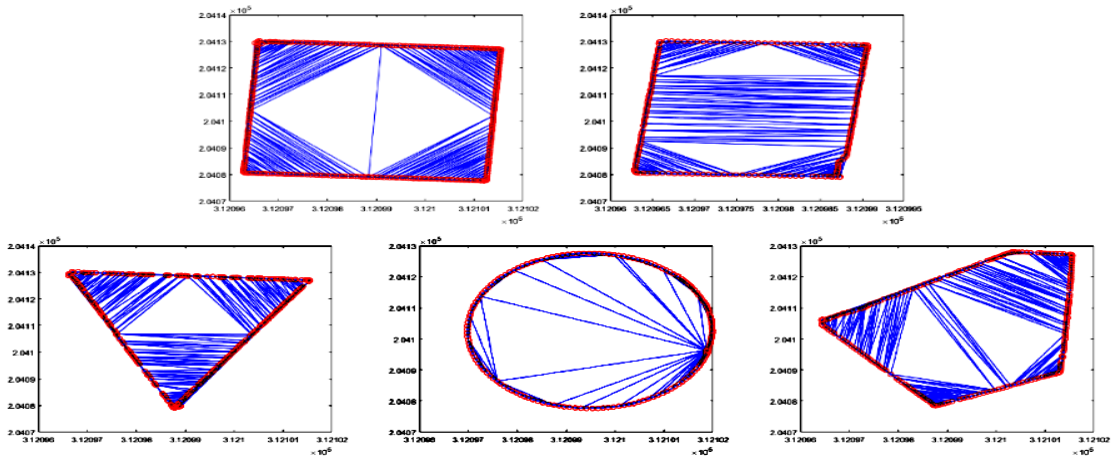

Fig. 14– The area measurement map of farmland

CONCLUSIONS

Based on the BeiDou Navigation Satellite System, this research developed the BeiDou high-precision and communication interface circuit, designed the triangulation farmland area measurement algorithm, and applied the algorithm to the software development of the farmland area measuring instrument. In the area measurement of small-scale farmland, the farmland area measuring instrument based on the BeiDou Navigation Satellite System can accurately measure the farmland area regardless of the shape of the farmland, and the average error of the measurement area is maintained below 0.7%. When the farmland area measuring instrument measures acute-angled triangles and polygonal plots, the measurement error increases, but the measurement does not exceed 2.5%, and the measurement accuracy is significantly improved, which meets the requirements of farmland area measurement. There are also some shortcomings in this study. When measuring the boundary of the plot with acute angle vertices, the measured boundary points at the vertices are seriously lost. In order to reduce the measurement error, in future research, the data update frequency of the BeiDou high-precision positioning module will be increased.

ACKNOWLEDGEMENT

The authors greatly appreciate the careful and precise reviews by anonymous reviews and editors. The study was supported by “Natural Science Foundation of Hunan Province (Grant No.2021JJ40287)” and “Changsha Natural Science Foundation (Grant No.kq2014174)”.

REFERENCES

[1] Binbin Ji, Jun Li, Yuping Yang, Sen Zhang, (2012), A real-time measurement based on GPS which was designed for calculating the harvest area of combine. *Chinese Agricultural Mechanization*, Vol.244, no.6, pp.89-92, China;

[2] Dengsheng Zhu, Hui Fang, Shaoming Hu, Wenquan Wang, Yansuo Zhou, Hongyan Wang, Fei Liu, Yong He, (2020). Development and Application of an Intelligent Remote Management Platform for Agricultural Machinery. *Smart Agriculture*, Vol.2, no.2, pp.67-81, China;

[3] Gopi M., Krishnan S., Silva C.T., (2000), Surface Reconstruction based on Lower Dimensional Localized Delaunay Triangulation. *Eurographics*, Vol.19, no.3, Blackwell Publishers Ltd, Britain, pp.467-478;

[4] Guangqi Wang, Yu Han, Jian Chen, Shubo Wang, Zichao Zhang, Nannan Du, Yongjun Zheng, (2018), A GNSS/INS Integrated Navigation Algorithm Based on Kalman Filter. *IFAC-PapersOnLine*, Vol.51, no.17, Elsevier, Netherlands, pp.232-237;

[5] Hui Liu, Zhijun Meng, Weiqiang Fu, (2012), Overlap and skip evaluation for agricultural machinery operation based on GPS track logs. *Transactions of the Chinese Society of Agricultural Engineering*, Vol.28, no.18, pp.149-154, China;

[6] Hui Liu, Zhijun Meng, Pei Wang, Xueli Wei, Yu Han, (2015), Buffer algorithms for operation area measurement based on global navigation satellite system trajectories of agricultural machinery. *Transactions of the Chinese Society of Agricultural Engineering*, Vol.31, no.7, pp.180-184, China;

[7] Poppe K.J., Wolfert S., Verdouw C., Verwaart T., (2013), Information and Communication Technology as a Driver for Change in Agri-food Chains. *EuroChoices*, Vol.12, no.1, pp.60-65, Britain;

[8] Shuwen Li, Qianxin Wang, Wei Wu, (2021), Analysis of global positioning accuracy of BDS-3 single and dual frequency signals. *Science of Surveying and Mapping*, Vol.46, no.12, pp.67-74, China;

[9] Xuegeng Chen, Haojun Wen, Weirong Zhang, Fochu Pan, Yan Zhao, (2020), Advances and Progress of Agricultural Machinery and Sensing Technology Fusion. *Smart Agriculture*, Vol. 2, no.4, pp.1-16, China;

[10] Yangchun Liu, Yanwei Yuan, Junning Zhang, Fengzhu Wang, Kang Niu, (2016), Design and Experiment of Remote Management System for Subsoiler. *Transactions of the Chinese Society for Agricultural Machinery*, Vol.47, pp.43-48, China;

[11] Yizhe Sun, Ji Li, Bin Liu, Yu Xie, He Gong, (2019), Measurement of agricultural machinery operation area based on improved Alpha Shapes algorithm. *Journal of Chinese Agricultural Mechanization*, Vol.40, no.8, pp.144-148, China;

[12] Yuefeng Du, Shenghui Fu, Enrong Mao, Zhongxiang Zhu, Zhen Li, (2019), Development Situation and Prospects of Intelligent Design for Agricultural Machinery, *Transactions of the Chinese Society for Agricultural Machinery*. Vol.50, no.9, pp.1-17, China;

[13] Yunpeng Jing, Gang Liu, Zhikun Jin, (2019), Topographic survey of farmland based on GNSS dual antenna combined with AHRS. *Transactions of the Chinese Society of Agricultural Engineering*, Vol.35, no.21, pp.166-174, China;

[14] Zhengjun Qiu, Xiafang Ying, Yong He, (2005). A portable instrument for measuring field area based on GPS module. *Journal of Zhejiang University*, Vol.31, no.3, pp.333-336, China;

[15] Zhixiong Lu, Wenjun Zhong, Xiuyong Diao, Shikun Mei, Jing Zhou, Zhun Cheng, (2015), Measurement of field area based on tractor operation trajectory. *Transactions of the Chinese Society of Agricultural Engineering*, Vol.31, no.19, pp.169-176, China.

EFFECT OF LOW-TEMPERATURE ON THE VIBRATION IMPACT COMMINUTION PERFORMANCE OF WHEAT BRAN
/
低温对小麦麸皮振动冲击粉碎性能的影响

Min CHENG*[1)], Yanling SUN[1)], Zhuo CHEN*[2)], Baoguo LIU[1)]
[1)] School of Mechanical and Electrical Engineering, Henan University of Technology, Zhengzhou / China;
[2)] Henan Engineering Research Center of Intelligent Equipment for Grain Processing, Zhengzhou / China
Tel: +86037167756212; E-mail: chengminhappy2006@163.com, zhuocheng1985@sina.com
Corresponding author: Min Cheng, Zhuo Chen
DOI: https://doi.org/10.35633/inmateh-68-11

Keywords: *wheat bran, low-temperature, vibration comminution, LS-DYNA*

ABSTRACT
With the aim of revealing the effects of low temperature on the vibration impact comminution performance of wheat bran, the impact dynamic performance of wheat bran at different temperatures was simulated by using LS-DYNA. According to the impact collision relationship between grinding medium and wheat bran, a three-component numerical calculation model was established. The impact collision dynamic essence of the model was analyzed, and a solution method based on LS-DYNA was proposed. On this basis, the finite element model of the numerical calculation model was obtained. By adjusting the mechanical parameters of wheat bran in the finite element model, the vibration impact comminution performance of wheat bran at different temperatures were analyzed. It is found that the contact force, contact deformation and comminution energy of wheat bran increase with the decrease of temperature, which indicates that low-temperature comminution of wheat bran is more advantageous than room temperature comminution. However, when the temperature drops from - 40 ℃ to - 80 ℃, the above index parameters almost remain, which indicates that it is more economical to apply low-temperature comminution at the temperature range from - 40 ℃ ~ 0°C. This research provided a foundation for the analysis, prediction and optimization of vibration impact comminution performance of wheat bran.

摘要
为揭示低温对小麦麸皮振动冲击粉碎性能的影响，利用LS-DYNA模拟分析了不同温度下小麦麸皮的冲击动力性能。根据振动球磨机的振动冲击粉碎机理，建立了三构件粉碎机理的数值计算模型，分析了模型的冲击碰撞动力学本质，提出了基于LS-DYNA的求解方法。在此基础上建立了粉碎机理数值计算模型的有限元模型。通过调整有限元模型中小麦麸皮的力学参数，比较分析了小麦麸皮在不同温度下的振动冲击粉碎性能。结果发现：随着温度的降低，小麦麸皮的接触力、接触变形和粉碎能量均得到了提高，表明小麦麸皮低温粉碎比室温粉碎更具优势。但当温度从-40℃下降到-80℃时，以上指标参数的变化较小，表明采用-40℃~0℃作为小麦麸皮低温粉碎的温度调节范围更为经济。上述研究为小麦麸皮低温振动粉碎性能的分析、预测和优化奠定了基础。

INTRODUCTION
Wheat bran is a kind of by-product of flour processing, and it is rich in protein, dietary fiber, vitamins, amylase, minerals and other nutrients. Thus, it has various potential applications in food processing industry (*Onipe et al., 2016*), medical care industry (*Elmone, 2021*), biochemistry industry (*Martín-Diana et al., 2021*), etc. The superfine comminution of wheat bran has become an important way for its in-depth development and comprehensive utilization (*Craeyveld et al., 2009; Zhu et al., 2010; Rosa et al., 2013*). At present, the low-temperature vibration comminution technology, which combines the advantages of vibration impact comminution and the advantages of low-temperature comminution, has been preliminarily applied in the superfine comminution of wheat bran. As a result, low-temperature vibration comminution technology has shown excellent comminution performance (*Hemery et al., 2011; Huang et al., 2009*).

[1]Min Cheng, Lecturer Ph.D.Eng.; [1]Yanling Sun, M.Stud.Eng.; [2]Zhuo Chen, Lecturer Ph.D.Eng.; Baoguo Liu, [1]Prof. Ph. D. Eng.

In order to further improve its superfine comminution efficiency, it is necessary to study the effects of low-temperature on the vibration comminution performance of wheat bran.

The factors restricting the low-temperature vibration comminution performance of wheat bran mainly include the motion characteristics of grinding medium and the low-temperature mechanical properties of wheat bran. In order to study the comminution effects of grinding medium movement, researchers simplified the grinding medium in grinding cylinder into single rigid body (*Huang et al., 1997*), grinding medium layer (*Sidor, 2010*), discrete grinding medium group (*Lee et al., 2010; Mishra et al., 2015*) and grinding medium flow (*Yang et al., 2018*) respectively. Researchers also established the rigid dynamics model, hierarchical dynamics model and discrete element model (DEM) of grinding medium. However, these models do not contain crushed objects. Therefore, they cannot be used to comprehensively describe the comminution effects of the grinding medium movement on wheat bran. Moreover, these models cannot be used to simulate and analyze the influences of physical properties of the grinding medium on the superfine comminution performance of wheat bran. This is the main reason why the experimental method is generally used to study the low-temperature vibration comminution performance of wheat bran. Although Hemery (*Hemery et al., 2010*) discovered the influences of low temperature on the mechanical properties and strain energy density of wheat bran and its structural layers by using the tensile test, the relationship between temperature and comminution mechanical properties of wheat bran is still not clear. It is because that the temperature field and the comminution force field belong to different physical fields. Therefore, it is impossible to study the low-temperature vibration comminution of wheat bran by using the existing models of grinding medium.

Due to the rapid progress of computer technology, it is possible to evaluate the low-temperature vibration comminution performance of wheat bran by using nonlinear finite element method. The commercial software LS-DYNA is currently recognized as one of the most outstanding nonlinear finite element simulation software with the functions of explicit analysis and implicit analysis. It has been applied in numerical simulations of material comminution performance in many fields, such as textile (*Barauskas et al., 2007*), wheat stem (*Yuan et al., 2013*), concrete (*Ma et al., 2020*), etc. At present, when LS-DYNA is used to simulate the impact comminution performance of materials, two-dimensional or three-dimensional unilateral impact calculation models of two components are generally adopted (*Barauskas et al., 2007; Yuan et al., 2013; Ma et al., 2020*). In the model, one component is set as a target, and the other component is set as a projectile. However, this model cannot simulate the bilateral comminution effects of grinding medium on wheat bran, such as shear, extrusion and grinding. The other disadvantage of the past work is that this model cannot directly take into account the low-temperature embrittlement effects.

In the current research, a three-component comminution mechanism calculation model which is based on the similarity principle of grinding medium motion was proposed. In the rest of this paper, the model is named as grinding medium-wheat bran-grinding medium model. In order to verify the efficiency of the model, the impact extrusion comminution effects of wheat bran at room temperatures and at low temperatures were simulated and analyzed by adjusting the mechanical parameters of wheat bran. The results showed that the low temperatures have a significant effect on the comminution performance parameters of wheat bran, such as contact force, contact deformation and internal energy, which verifies the reliability of the model.

MATERIALS AND METHODS

Impact dynamics modelling of vibrating ball mill

The results of high-speed camera observation show that the grinding medium of the vibrating ball mill has three motion forms, namely, impact motion, overall rotation and self-rotation (*Gock et al., 1999; Lee et al., 2010*), and the comminution effects such as impact, shear, extrusion and grinding are formed between the adjacent two grinding mediums. Based on the high-speed camera observation results of the grinding medium motion of a vibrating ball mill, the motion diagram of the grinding medium in the grinding cylinder can be obtained, as shown in Fig. 1. It is easy to find that the impact collision contact relationship between the grinding medium group and the grinding cylinder wall is the dynamic essence of the three motions of the grinding medium group. In the superfine comminution process of wheat bran in a vibrating ball mill, the high-speed rotation of a single grinding medium has grinding effects on wheat bran. Meanwhile, the slow revolution of a single grinding medium has grinding and homogenizing effects on wheat bran. Moreover, the impact movement of a single grinding medium forms the impact collision contact relationship between adjacent grinding medium or between grinding medium and grinding cylinder, which has impacting, squeezing or shearing effects on wheat bran.

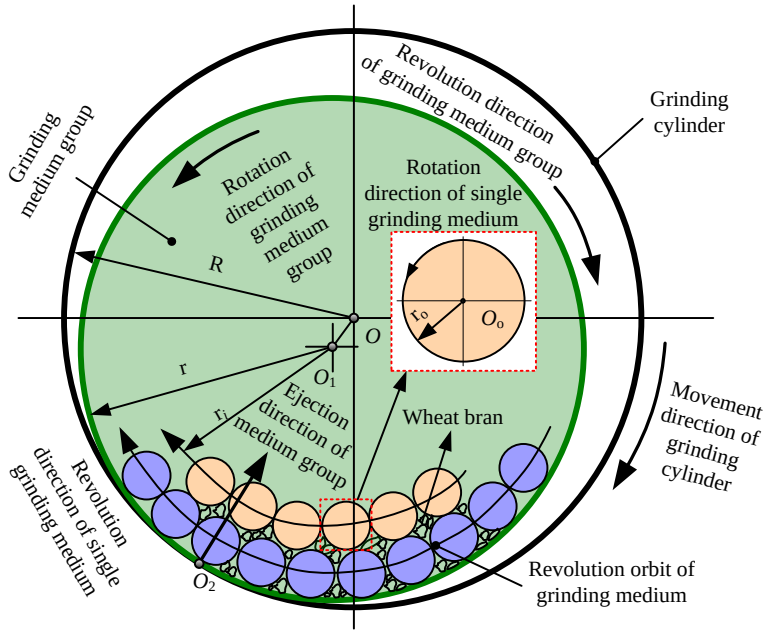

Fig. 1 - Movement of grinding medium in the grinding tube

R —radius of the grinding cylinder of vibrating ball mill; O — the geometric center of the grinding tube; r — radius of the grinding medium group; O_1 — geometric center of the grinding medium group; r_o—radius of the single grinding medium ball; O_O — geometric center of the single grinding medium ball

Ignoring the influences of surrounding grinding medium and wheat bran, and taking any two mutually contacting grinding medium balls and a piece of wheat bran between two adjacent grinding medium layers as shown in Fig. 1, the three-component calculation model named grinding medium - wheat bran - grinding medium can be obtained as shown in Fig. 2. The two grinding balls are labelled as grinding medium 1 and grinding medium 2, respectively. In Fig. 2, s_1 and s_2 represent the distances from the grinding medium 1 and the grinding medium 2 to the contact surface of the wheat bran respectively. O_1 and O_2 are the centroids of the grinding medium 1 and the grinding medium 2 respectively, and the eccentricity is e_{12}. r_1 and r_2 are the radii of the grinding medium 1 and the grinding medium 2 respectively. ω_1 and ω_2 are the rotation velocities of the grinding medium 1 and the grinding medium 2 respectively, and their steering directions are identical. When v_{1r} and v_{2r} represent the impact velocities of the grinding medium 1 and the grinding medium 2 respectively, v_{1c} and v_{2c} can be considered as the revolution velocities of the grinding medium 1 and the grinding medium 2. According to the energy transfer law of the grinding medium in the grinding tube, the directions of v_{1r} and v_{2r} can be considered on the same straight line, but their sizes are different (*Feng et al., 2018*). Due to the different values of v_{1r} and v_{2r}, the impact comminution effect of the grinding mediums on the wheat bran is formed.

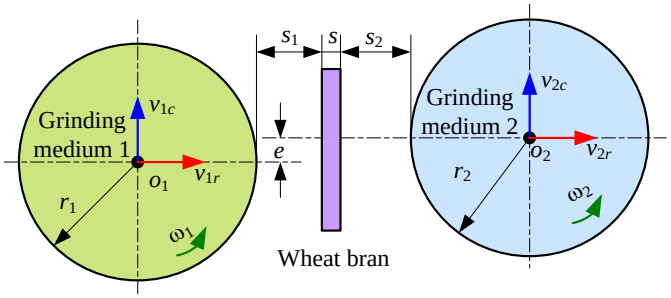

Fig. 2 - Calculation model of vibrating ball mill

According to the relativity principle of motion, the grinding medium 2 can be considered as a fixed state. At this time, only three motions of the grinding medium 1, including impact, revolution and rotation, need to be considered. These three movements produce three kinds of contact forces on the wheat bran. These forces are the high-frequency impact force of the grinding medium impact motion on the wheat bran, the grinding force of the grinding medium revolution motion on the wheat bran, and the grinding force of the grinding medium rotation motion on the wheat bran, respectively. The previous research shows that the impact force of the grinding medium is the primary factor, and the grinding force generated by the rotation and revolution of

the grinding medium is the secondary factor in comminution of wheat brans by vibrating ball mills (*Kostishin et al., 2015*). At this time, the grinding medium 1 can be considered to bear only one impact force in any direction, that is, the grinding medium 1 has only one impact movement in any direction. The rectangular coordinate system xO_1y is established with the geometric center O_1 of the grinding medium 1 as the origin point. The simplified calculation model is shown in Fig. 3. The impact velocity of the grinding medium 1 is v and the impact angle in X direction is α.

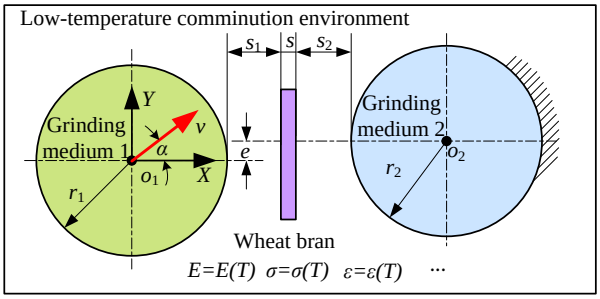

Fig. 3 - Low-temperature calculation model of vibrating ball mill

In actual comminution processes, low-temperature will affect wheat brans and grinding mediums, such as the emergence and propagation of surface cracks, the changes of geometric dimensions and mechanical properties, etc. In fact, in the tensile test of mechanical properties of wheat brans at low-temperature, the effects of changes on surface cracks, geometric dimensions and morphological structure caused by low temperature on wheat bran will be converted into mechanical properties. Therefore, based on the calculation model of the vibrating ball mill, a low-temperature comminution model describing the low-temperature vibration superfine comminution of wheat brans can be obtained, as shown in Fig. 3. In Fig. 3 s represents the thickness of the wheat bran, and $E=E(T)$, $\sigma=\sigma(T)$, $\varepsilon=\varepsilon(T)$ represent the physical relationships between the mechanical parameters of the wheat bran and the comminution temperature. According to Fig.3, the influence of the comminution temperature on the comminution performance of the wheat bran can be analyzed by changing the elastic modulus E, ultimate stress σ and ultimate strain ε of the wheat bran in the comminution model. Thus, it provides an economical and convenient method to study the effects of low-temperature on the vibration comminution performance of wheat bran.

According to the comminution mechanism model shown in Fig.3, the low-temperature vibration comminution of wheat brans is a typical contact collision elastoplastic large deformation problem. Therefore, using nonlinear finite element numerical method to solve this problem has significant advantages. From a mechanics point of view, the most notable technical characteristic of LS-DYNA is that it can solve highly nonlinear problems such as dynamic contact of objects, large deformations, material nonlinearities, and high-speed transient problems such as explosions, impacts, pouring, and material forming (*Menezes et al, 2014*). Therefore, the vibration superfine comminution mechanism of wheat bran under low temperature fully meets the application requirements of LS-DYNA. In this research, the Lagrangian method of LS-DYNA with updated format algorithm is selected to solve the simplified low-temperature vibration comminution mechanism calculation problem of wheat bran.

Finite element modeling and solution setting of low-temperature calculation model

Considering the non-fracture phenomenon and large deformation characteristics of wheat brans in vibration impact experiments, the plate shell unit shell163 is selected for the wheat bran, with the length of 3 mm, the width of 2 mm and the thickness of 80 μm. Fig. 4 shows a set of stress-strain curves of the wheat bran at comminution temperatures of 30 °C, 0 °C, − 40 °C and − 80 °C, respectively (*Cheng et al, 2019*). As shown in Fig. 4, when the stress-strain curve of the wheat bran includes two stages of elastic deformation and plastic deformation, the bilinear BKIN model is selected as the material model; when the stress-strain curve of wheat bran only includes an elastic deformation stage, the Isotropic model is selected as the material model. The input parameters of the bilinear BKIN model of wheat bran include Young's modulus E, density ρ, Poisson's ratio μ, Yield stress σ_s and Tangent modulus E_p. The yield stress σ_s is approximately equal to the elastic stress σ_{ela}, the Poisson's ratio is 0.3, and the tangent modulus $E_p=(\sigma_{max}-\sigma_{ela})/(\varepsilon_{max}-\varepsilon_{ela})$. Moreover, σ_{max} is the ultimate stress, ε_{max} is the ultimate strain, and ε_{ela} is elastic strain. The input parameters of the isotropic model of the wheat bran only include Young's modulus E, density ρ and Poisson's ratio μ. The mechanical and physical parameters of wheat bran identified based on Fig. 4 are shown in Table 1.

The solid unit solid164 with the radius of 2 mm is adopted by grinding medium. The Rigid body model is selected as the material model of the grinding medium. The intervals s_1 and s_2 between the grinding medium and the wheat bran surface are set as 0.5 mm. There is no eccentricity between the two grinding mediums. The wheat bran is discretized with quadrilateral mapping grid, and the grinding medium is discretized with hexahedral mapping grid. The finite element model of the low-temperature calculation model of wheat bran is shown in Fig. 5. After discretization, the element number of the wheat bran is 3600 and the element number of the grinding medium is 16384. The input parameters of the rigid body model of grinding medium include density ρ, Young's modulus E and Poisson's ratio μ. Zirconia ball is selected as the grinding medium, and its material characteristic parameters are shown in row 6 of Table 1. As shown in Table 1, the Young's modulus of zirconia is much higher than that of the wheat bran. Therefore, the rigid body model is suitable for the finite element model of the grinding medium.

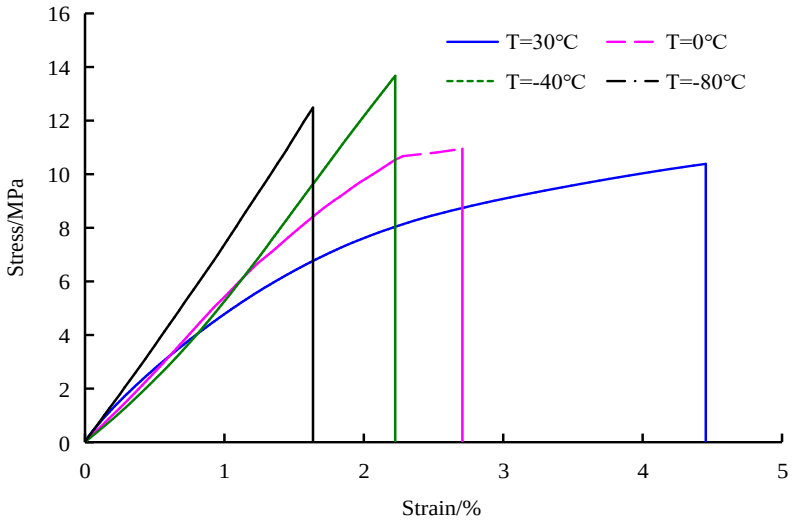

Fig. 4 - Stress-strain curves of wheat bran at different temperatures

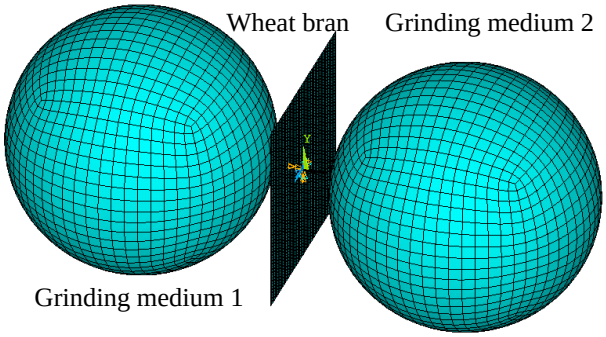

Fig. 5 - Finite element model of Low-temperature calculation model of wheat bran

Table 1

Material characteristic parameters of wheat bran and grinding ball

Name	Temperature	Density ρ	Elastic strain ε_{ela}	Elastic stress σ_{ela}	Young's modulus E	Ultimate strain ε_{max}	Ultimate stress σ_{max}	Tangent modulus E_p	Poisson's ratio μ
	[℃]	[kg/m^3]	[%]	x 10^6 [N/m^2]	x 10^8 [N/m^2]	[%]	x 10^7 [N/m^2]	x 10^8 [N/m^2]	/
wheat bran	30	1250	1.24	6.40	5.00	4.45	1.04	1.40	0.30
	0		1.29	7.12	5.48	2.71	1.10	3.43	
	-40		—	—	6.35	2.23	1.37	—	
	-80		—	—	7.58	1.64	1.25	—	
Zirconia ball	—	5800	—	—	2200	—	—	—	0.23

Furthermore, the movement and rotation degrees of freedom of grinding medium 2 are restrained. The impact velocity and impact angle of grinding medium 1 can be set by defining the velocity components in X and Y directions. The X-direction impact velocity of grinding medium 1 is set as 3 m/s, and the Y-direction

impact velocity is set as 0 m/s. At this time, the impact angle is 0 degree. The eccentricity between the two grinding mediums is 0 mm. At this time, the grinding medium has only impact extrusion grinding effect on the wheat bran. The contact type between wheat bran and grinding medium is automatic face-to-face contact, and the dynamic and static friction coefficients are defined as 0.3. The wheat bran has no fixed boundary and its central node moves along the *X* direction, which is similar to the actual vibration impact grinding. Due to the large deformation and even mesh distortion of the wheat bran in the process of impact collision, hourglass control (0.1) and adaptive mesh control are adopted. In order to ensure the calculation accuracy and convergence speed, five integral points of the wheat bran model are selected.

RESULTS

The contact force, contact deformation and internal energy between the wheat bran and the grinding mediums were selected as evaluation indexes to analyze the effects of low-temperature on the comminution performance of the wheat bran. Fig.6 shows the contact force curves between the wheat bran and the grinding mediums at 30 ℃, 0 ℃, - 40 ℃ and - 80 ℃, respectively. According to Fig. 6, when the grinding temperatures are at 30 ℃, 0 ℃, - 40 ℃ and - 80 ℃, the maximum contact forces generated by the impact extrusion of the wheat bran by the grinding medium 1 are 11.5733 N, 12.8110 N, 16.0461 N and 16.2857 N, respectively. And the disengagement times between the grinding medium 2 and the wheat bran are 0.52 ms, 0.48 ms, 0.47 ms and 0.47 ms, respectively. Compared with the value obtained at 30 ℃, the maximum contact forces of the wheat bran at 0 ℃, - 40 ℃ and - 80 ℃ are increased by 10.69%, 38.65% and 40.72%, respectively. Obviously, when the comminution temperature is - 80 ℃ and - 40 ℃, the grinding time of wheat bran are exactly the same. It can be seen that with the decrease of the grinding temperature, the contact force produced by the grinding medium gradually increases and the contact time gradually shortens. At the same time, it was found that when the comminution temperature decreased from - 40 ℃ to - 80 ℃, the contact force increased only 0.2396 N and the sensitivity was 0.006 N/℃. However, when the comminution temperature decreased from 0 ℃ to - 40 ℃, the contact force increased by 3.2351 N and the sensitivity was 0.081 N/℃. It shows that the effects of the comminution temperature on the contact force is uneven. With the decrease of comminution temperature, the sensitivity of the contact force and the economy of low-temperature comminution keep decreasing. Therefore, it is economical to set the comminution temperature to - 40 ℃.

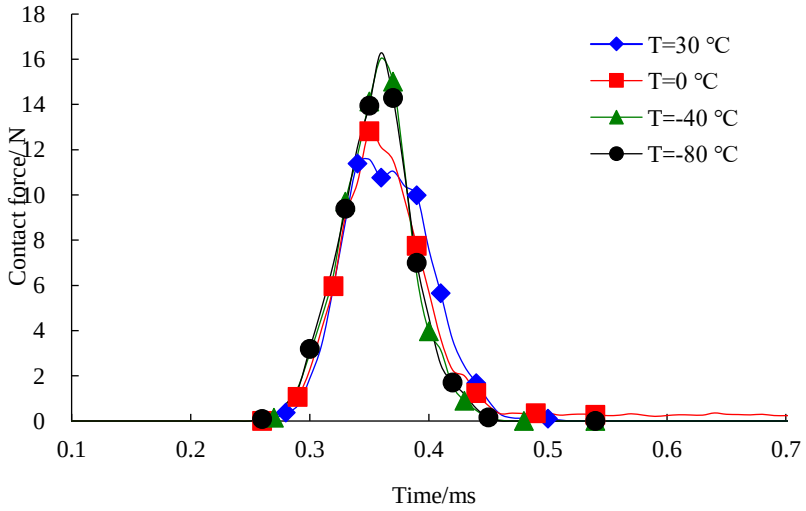

Fig. 6 - Influence of comminution temperature on the contact force of wheat bran

Fig. 7 shows the contact deformation of the wheat bran when the comminution temperatures are at 30 ºC, 0 ºC, - 40 ºC and - 80 ºC, respectively. At this time, the wheat bran has completely disengaged from the grinding medium 2, and the impact extrusion comminution process is over. According to Fig. 7, the contact areas of wheat bran at 30 ºC and 0 ºC are basically the same, and that at - 40ºC and - 80 ºC are also basically the same, but their contact area are less than those at 30 ℃ and 0 ℃. When the comminution temperature was - 40 ºC or - 80 ºC, the contact area of the wheat bran was distorted and overlapped. It can be seen from Fig. 4 that the low-temperature embrittlement of the wheat bran has occurred at the comminution temperatures of - 40 ℃ and - 80 ºC. Theoretically, this phenomenon of distortion and overlap should not occur. It is because that when using LS-DYNA for numerical simulation calculation, the wheat

bran at - 40 °C and - 80 °C is considered as isotropic linear elastic material, and its elastic modulus and ultimate stress are greater than those at 30 °C and 0 °C. It is equivalent to enhancing the comminution resistance of the wheat bran, resulting in smaller contact area and increased distortion of the wheat bran when impacted and extruded.

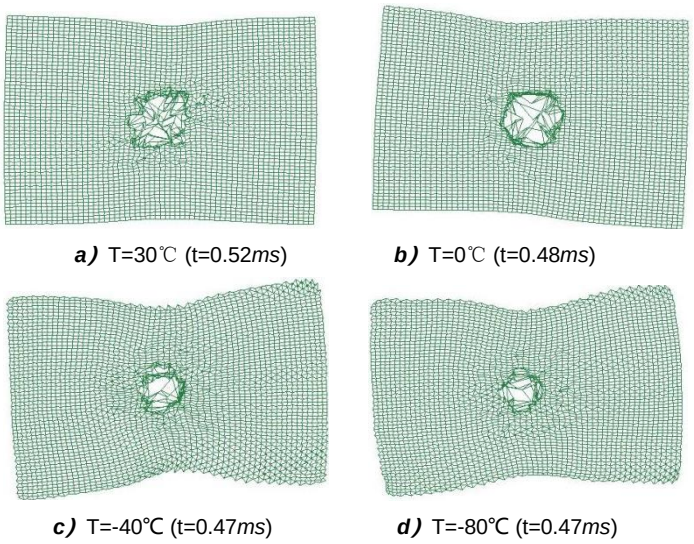

Fig.7 - Influence of comminution temperature on the contact deformation of wheat bran

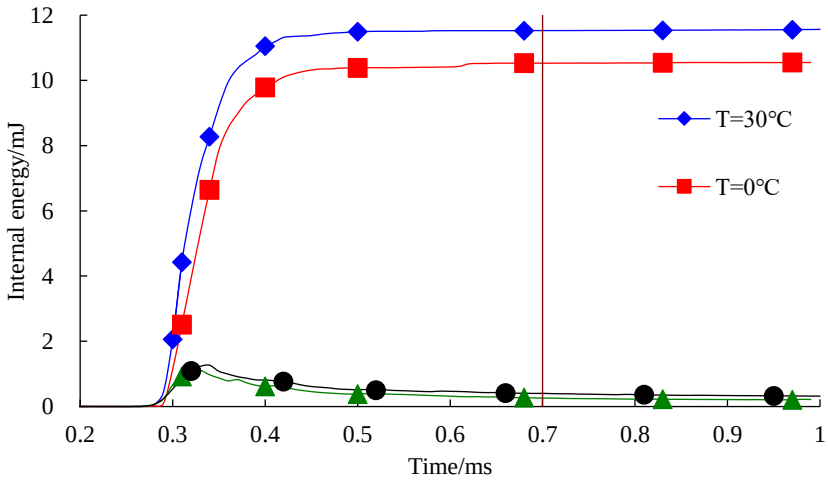

Fig. 8 - Influence of comminution temperature on the internal energy of wheat bran

Fig. 8 shows the internal energy curves of the wheat bran at the comminution temperatures of 30 °C, 0°C, -4°C and -80°C, respectively. Taking the time of 0.7 ms after the completion of the impact extrusion comminution process as an example, according to Fig. 8, the corresponding internal energy at the comminution temperature of 30°C, 0°C, - 40°C and - 80°C are 11.5280 mJ, 10.5280 mJ, 0.2576 mJ and 0.4035 mJ, respectively. Compared with the internal energy of wheat bran at 30°C, the internal energy of wheat bran at 0°C, - 40°C and -80°C decreased by 8.67%, 97.77% and 96.50% respectively. It can be seen that at the same impact velocity, the kinetic energy of the grinding ball is exactly the same, but the energy conversion caused by impact on the wheat bran at different temperatures is different. The internal energy produced at 30 °C and 0°C is much greater than that produced at - 40°C and - 80°C. The internal energy stored at - 40°C is the lowest. It is about 2.23% of that at 30°C. According to the law of energy conservation, the low-temperature comminution consumes most of the kinetic energy of the grinding medium ball as the form of comminution energy of wheat bran. However, the room temperature comminution stores most of the kinetic energy of the grinding medium ball as the form of internal energy, which provides accumulation energy for the next impact comminution. It can be seen that the low-temperature comminution of wheat brans has more advantages than room temperature grinding. At the same time, it was found that the stored internal energy of the wheat bran at - 40°C was less than that at - 80°C, which implies that it was more reasonable to take - 40°C as the low-temperature comminution temperature. However, the tensile breaking strain energy density of the wheat bran

at - 80°C is less than the tensile breaking strain energy density of the wheat bran at - 40°C. It is probably because that the stress mode of the wheat bran during tensile fracture and vibration comminution is different. Therefore, it is not accurate to directly use the tensile fracture strain energy density to describe the low-temperature vibration comminution performance of wheat bran. It is reasonable to take - 40°C ~ 0°C as the temperature regulation range of the low-temperature vibration superfine comminution of wheat bran.

CONCLUSIONS

The three-component numerical calculation model proposed in this paper can completely simulate the vibration impact comminution mechanism of the vibrating ball mill. By adjusting the mechanical parameters of the wheat bran at different temperatures, the effects of low temperature on the vibration impact comminution performance of the wheat bran can be simulated and analyzed.

Low-temperature has a significant effect on the vibration impact comminution performance of wheat bran. Compared with 30°C, the contact force of the wheat bran at - 80°C increased by 40.72% and the internal energy decreased by 96.50%. However, compared with - 40°C, the contact force of wheat bran at - 80°C only increased by 1.31%, and the internal energy increased by 56.64%. The contact area and deformation degree of the wheat bran at - 40°C and - 80°C are basically the same. Therefore, it was more economical to determine - 40°C ~ 0°C as the temperature regulating range of low-temperature comminution of wheat bran.

Based on the explicit nonlinear finite element model, the vibration impact comminution performance of the vibration ball mill can be simulated and analyzed, which provides a method for analyzing the low-temperature vibration superfine comminution performance of wheat bran.

ACKNOWLEDGEMENT

The authors were funded for this project by science and technology research project of Henan (No. 212102110312) and the scientific research foundation for advanced talents of Henan University of Technology (No. 2020BS020).

REFERENCES

[1] Antoine C., Peyron S., Mabille F. et al, (2003). Individual contribution of grain outer layers and their cell wall structure to the mechanical properties of wheat bran. *Journal of Agricultural and Food Chemistry*, Vol.51, Issue7, pp. 2026-2033, USA;

[2] Barauskas R., Abraitiene A., (2007). Computational analysis of impact of a bullet against the multilayer fabrics in LS-DYNA. *International Journal of Impact Engineering*, Vol.34, Issue7, pp.1286-1305, England;

[3] Cheng M., Liu B. G., Cao X. Z., (2018). Discussion on the application of LS-DYNA in superfine grinding of wheat bran. *Grain & Oil Science and Technology*, Vol.1, Issue3, pp.138-144, P.R.C;

[4] Cheng M., Liu B.G., Liu Y.X., (2019). Effect of low temperature on tensile mechanical properties of wheat bran. （低温小对麦麸皮拉伸力学特性参数的影响）. *Transactions of the Chinese Society of Agricultural Engineering (Transactions of the CSAE)*, Vol.35, Issue13, pp.312 - 318, P.R.C;

[5] Craeyveld V.V., Holopainen U., Selinheimo E. et al, (2009). Extensive dry ball milling of wheat and rye bran leads to in situ production of Arabinoxylan oligosaccharides through nanoscale fragmentation. *Journal of Agricultural and Food Chemistry*, Vol.57, Issue18, pp.8467-8473, USA;

[6] Elmone M.A., (2021). Effect of wheat bran on anthropometric measures, serum glucose and lipid profile in type 2 diabetes patients. *Pakistan Journal of Biological Sciences*, Vol.24, Issue3, pp.345-349, Pakistan;

[7] Feng P.Z., Wang X.H., Qiang Y.H. et al, (2008). Energy analysis of mechanical alloying of molybdenum disilicide in a new-type high energy vibrating ball mill. *Journal of China University of Mining & Technology*, Vol.18, Issue3, pp.449-453, P.R.C;

[8] Gock E., Kurrer K.E., (1999). Eccentric vibratory mills - theory and practice. *Powder Technology*, Vol.105, Issue1-3, pp.302-310, Switzerland;

[9] Hemery Y., Mabille F., Martelli M. et al, (2010). Influence of water content and negative temperatures on the mechanical properties of wheat bran and its structural layers. *Journal of Food Engineering*, Vol.98, Issue3, pp. 360-369, England;

[10] Huang H., Pan J., McCormick P., (1997). Prediction of impact forces in a vibratory ball mill using an inverse technique. *International Journal of Impact Engineering*, Vol.19, Issue2, pp.117-126, England;

[11] Huang S., Zhu K.X., Qian H.F. et al, (2009). Effects of ultrafine comminution and freeze-grinding on physico- chemical properties of dietary fiber prepared from wheat bran（超微及冷冻粉碎对麦麸膳食纤维理化性质的影响）. *Food Science*, Vol.30, Issue15, pp.40-44, P.R.C;

[12] Hemery Y., Chaurand M., Holopainen U. et al, (2011). Potential of dry fractionation of wheat bran for the development of food ingredients, Part I: Influence of ultra-fine grinding. *Journal of Cereal Science*, Vol.53, Issue1, pp.1-8, England;

[13] Kostishin V.G., Andreev V.G., Chitanov D.N. et al, (2015). Analysis of the effect of comminution of strontium hexaferrite powders in a vibratory mill on the properties of magnets on their basis. *Physical Science of Materials*, Vol.85, Issue8, pp.91-93, USA;

[14] Lee H., Cho H., Kwon J., (2010). Using the discrete element method to analyze the breakage rate in a centrifugal/vibration mill. *Powder Technology*, Vol.198, Issue3, pp.364-372, Switzerland;

[15] Mishra B.K., Rajamani R.K., (2015). The discrete element method for the simulation of ball mills. *Applied Mathematical Modelling*, Vol.16, Issue11, pp.598-604, USA;

[16] Ma H., Yue C., Yu H. et al, (2020). Experimental study and numerical simulation of impact compression mechanical properties of high strength coral *aggregate seawater concrete. International journal of impact engineering*, Vol. 137, Issue Mar, pp.103466.1-103466.13, England;

[17] Menezes P.L., Lovell M.R., Avdeev I.V. et al, (2014) Studies on the formation of discontinuous rock fragments during cutting operation. *International Journal of Rock Mechanics and Mining Sciences*, Vol.71, Issue 9, pp.131-142, England;

[18] Martín-Diana A.B., Tomé-Sánchez I., García-Casas M.J. et al, (2021). A novel strategy to produce a soluble and bioactive wheat bran ingredient rich in ferulic acid. *Antioxidants*, Vol.10, Issue6, USA;

[19] Onipe O.O., Ideani A.I.O., Beswa D., (2016). Composition and functionality of wheat bran and its application in some cereal food products. *International Journal of Food Science & Technology*, Vol.50, Issue12, pp.2509-2518, England;

[20] Peyron S., Abecassis J, Jeanc. Autran A, et al, (2001). Enzymatic oxidative treatments of wheat bran layers: effects on ferulic acid composition and mechanical properties. *Journal of Agricultural & Food Chemistry*, Vol.49, Issue10, pp.4694-9, USA;

[21] Peyron S., Chaurand M., Rouau X., et al, (2002) Relationship between Bran Mechanical Properties and Milling Behavior of Durum Wheat (Triticum durum, Desf.). Influence of Tissue Thickness and Cell Wall Structure. *Journal of Cereal Science*, Vol.36, Issue3, pp.377-386, England;

[22] Rosa N.N., Barron Cécile, Gaiani C., et al, (2013) Ultra-fine grinding increases the antioxidant capacity of wheat bran. *Journal of Cereal Science*, Vol.57, Issue1, pp.84-90, England;

[23] Sidor J., (2010). A mechanical layered model of a vibratory mill. *Mechanics and Control*, Vol.29, Issue 3, pp.138-148, Singapore;

[24] Yuan Z.H., Li J.W., Tian H. et al, (2013). Simulation and Analysis of the Wheat Stem Lodging. *Advanced Materials Research*, Vol.652-654, pp.1416-1419, P.R.C;

[25] Yang X.L., Wang Y.L., Xia Z.Q. et al, (2018). Numerical simulation and experiment of medium flow energy field in vibrating mill. *International Journal of Modeling, Simulation, and Scientific Computing*, Vol.09, Issue02, pp.627-636, Singapore;

[26] Yokoyama T., Tamura K., Usui H. et al, (1996). Simulation of ball behavior in a vibration mill in relation with its grinding rate: effects of fractional ball filling and liquid viscosity. *International Journal of Mineral Processing*, Vol.44–45, pp.413-424, Netherlands;

[27] Zhu K.X., Huang S., Peng W. et al, (2010). Effect of ultrafine grinding on hydration and antioxidant properties of wheat bran dietary fiber. *Food Research International*, Vol.43, Issue 4, pp.943-948, USA.

STUDY ON THE CHANGE RATE OF THE INDOOR TEMPERATURE OF A SUNKEN SOLAR GREENHOUSE

/

下沉式日光温室温度变化机制的研究

Weiwei CHENG, Zhonghua LIU* [1]
Shanxi Agricultural University, College of Urban and Rural Construction, Taigu/China
Tel: +86-0354-6287420; E-mail: lzh6175305@163.com
Corresponding author: Zhonghua LIU
DOI: https://doi.org/10.35633/inmateh-68-12

Keywords: *sunken solar greenhouse, thermal environment, change rate, wire sensor*

ABSTRACT

A sunken solar greenhouse has a good heat preservation environment. The influence of the general indoor temperature on the temperature of the roots was evaluated. A wireless sensor and U disk recorder were used to determine the indoor temperatures of a single section and multiple sections in a sunken solar greenhouse. The results showed that the temperature change rate was the greatest along the vertical direction of the greenhouse and less along the longitudinal direction of the greenhouse at the moment of opening in the morning and at the moment of strong light at noon. The temperatures in the single cross-section and multiple cross-sections were approximately equal during winter from 00:00 to 8:00 in the morning. These values can be used for calculating theoretically the heat loss in a greenhouse.

摘要

下沉式日光温室温室保温效果较好，室内温度会影响植物根区温度，利用无线传感器和 U 盘记录仪测定室内单截面和多截面的温度值，结果表明:在开启时刻和强光时刻，室内三维方向的温度变化速率由大到小依次为竖向、水平和纵向；冬季 00:00 ~ 8:00，单截面温度值与多截面温度值近似相等，可作为理论公式中计算温室热损失的依据。

INTRODUCTION

The temperature in a solar greenhouse has an obvious diurnal variation pattern and the indoor temperature of a greenhouse can increase by 0.25–3.9°C compared with the open-field temperature *(Wei et al., 2010; Tu et al., 2011)*. *Zhang, (2015),* studied the effects of indoor temperatures and humidity on the growth and fruiting of strawberry and soil-borne diseases in a greenhouse. The results showed that within the range of day at 20–28 °C, night at 5–12 °C and relative humidity of 40%–80%, the combination of temperature and humidity was more beneficial to the growth of strawberry and reduced the occurrence of soil-borne diseases than the individual same temperature and humidity. *Xu, (2018),* conducted an experimental study on the variation of indoor temperature and light in a solar greenhouse in the desert during winter. The results showed that the indoor temperature value fluctuated greatly, and the difference in the indoor temperature between day and night was substantial. The solar greenhouse in the desert could better convert solar energy into heat energy, and the indoor relative humidity was low. Regardless of the weather conditions outdoors, temperature varies in a greenhouse *(Guo and Zhao, 2009)*. In addition, the temperature changes in the vertical direction are more drastic, whilst the changes in temperature distribution in the horizontal direction are more moderate *(Yang XG et al., 2005)*. Considering the internal temperature in the different directions of sunlight in a greenhouse, *Hu et al., (2014),* used a thermometer and wall temperature of a thermistor to measure the sunlight greenhouse and temperature in the east–west central portion of three sections of the greenhouse during the over-wintering stage in the Lishi District. The results showed that the greenhouse temperatures along the vertical, horizontal and longitudinal directions showed regular changes during the day and night. The length of sunshine affected the distribution of the indoor air temperature.

Liu et al., (2013) conducted an experimental study on the characteristics of changes in the indoor air temperature and ground temperature with time and space in a solar greenhouse. The results indicated that indoor air temperature was not evenly distributed in space. *Zhang et al., (2009),* used CFD software to simulate the indoor temperature field of a sunken solar greenhouse during winter.

[1] *Weiwei Cheng, As Lec. Ph.D. Eng.; Zhonghua Liu*, Asoc.Prof.Ph.D. Eng,*

The results showed that the average temperature in the eastern part of the indoor area was lower than those in the western and central parts, and the air temperatures near the indoor wall and ground were higher. *Sun et al., (2020),* also used CFD to study the changes in the internal temperature of a solar greenhouse in different environments. The results demonstrated that ventilation time should be paid attention to in the internal ventilation and dehumidification of a greenhouse during winter to prevent frostbite of crops. *Albright et al., (2001),* proposed a classical model of the indoor temperature and relative humidity in a greenhouse. *Jang et al. (2011),* found that the relationship between crops and the environment in a greenhouse is strong and interactive. *Taki et al., (2016)* found that a high temperature in a greenhouse has a strong impact on crop photosynthesis. This condition affected the crop photosynthetic rate, transpiration rate, intercellular CO_2 concentration and greenhouse output, resulting in economic losses. *Khoshnevisan et al., (2014),* showed that both high and low temperatures inside the greenhouse would affect the quality and quantity of crops planted in the greenhouse. *Cheng et al., (2021),* evaluated the changes in temperature in a sunken solar greenhouse through a single cross-section. In the absence of protective measures, indoor plants would also suffer damage or disease during extreme external temperatures. *Md Shamim Ahamed et al.*, (2020) modelled heating demands in a Chinese-style solar greenhouse using the transient building energy simulation model TRNSYS. *Stefano Morelli et al., (2022)* optimized the temperature field in a greenhouse in order to make it suitable for basil cultivation.

A sunken solar greenhouse is the preferred greenhouse for three-dimensional planting. Previous studies have demonstrated the uneven distribution of indoor temperature in a solar greenhouse. Amongst the various indicators for measuring plant growth, the plant body temperature is the most sensitive factor for the healthy growth of plants, whilst amongst the numerous environmental factors, air temperature is the most synergistic with plant body temperature *(Yu M.H. et al., 2015)*. These two factors have the same trend *(Yu et al., 2015)*. In addition, the matrix temperature of three-dimensional substrate cultivation is also closely related to air temperature *(Shi et al., 2016)*. However, studies have mainly focused on the variation rules of the internal temperature, wall temperature and indoor soil temperature of greenhouses. A qualitative study on the indoor temperature along the horizontal, vertical and longitudinal temperature distribution rate is lacking. However, greenhouses heating is essential to provide favourable climatic conditions for growing plants under cold periods (*Bazgaou A. et al., 2021*). The study of the rate of temperature change in different directions inside the greenhouse can determine the relationship between the rate of change in the three-dimensional direction, thus determining the direction of temperature control, as well as the low and high temperatures, thus providing experimental data support for greenhouse regulation.

MATERIALS AND METHODS

Experimental greenhouse

The experimental greenhouse was a sunken three-dimensional planting solar greenhouse, as shown in Figure 1. The greenhouse faced south with a length of 108 m and a span of 12 m. The sinking depth of the south wall of the greenhouse was 1.2 m, and the width of the south corridor was 1.1 m. The width of the north corridor was 1.2 m. The external height of the back wall of the greenhouse was 4.3 m, and the ridge was 5 m high. The width of the north wall was 6 m at the bottom and 2 m at the top. The main load-bearing skeleton was made of an elliptical steel tube. The frame spacing was 1 m, and the covering material was made of plastic film.

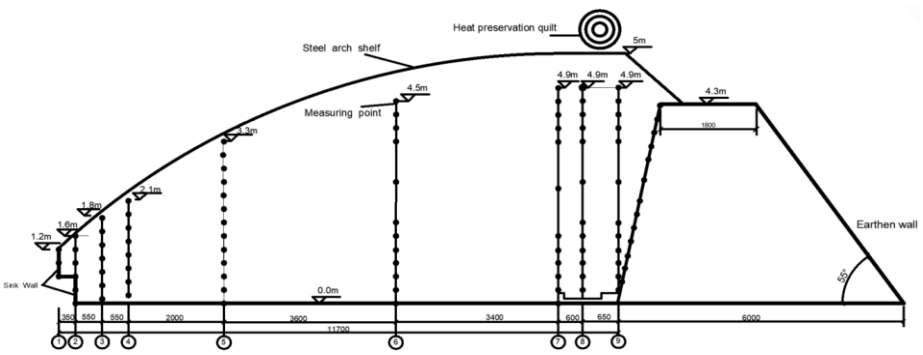

Fig. 1 - Layout of the measuring line and measuring points in the greenhouse

Testing instruments

The indoor temperature and humidity collection instrument in solar greenhouse was the HT59-Li-A1 wireless temperature and humidity collector developed by Shenyang Winen Technology Co., LTD., calibrated by Liaoning Provincial Institute of Metrology Science and coordinated with WG59 gateway and U-disk temperature collection instrument.

The collected temperature and humidity data were transmitted by the wireless temperature and humidity collector to the WG59 gateway through GPRS. The WG59 gateway collected the private network data to the cloud server through the Internet and obtained the data information through mobile phones or computers. Temperature measurement range of the wireless temperature and humidity collection instrument was 40– 85 °C, with an accuracy of ±0.2 °C in the 0–65 °C and ±1 °C in the other temperature range. The transmission period between the wireless temperature and humidity collector and the gateway was 6 min. The data were measured and transmitted continuously for 24 h a day.

The PRECISION Chuang RC-5 temperature recorder and USB automatic data temperature and humidity recorder were adopted. The instrument had a built-in wide temperature CR2032 battery. The recording interval was set to 6 min. The recorder could continuously record for 3 months. The built-in battery was regularly replaced to ensure the continuous operation of the temperature recorder. The temperature range of the recorder was from −30 °C to 70 °C, with accuracy of ±0.5 °C in the temperature range from −20 °C to 20 °C and 1 °C in the other ranges. The USB disk recorder had a built-in NTC thermistor and could store 32000 sets of data.

Test method for single cross-section temperature and humidity in the sunken solar greenhouse

The variation in the indoor air temperature in the horizontal and vertical directions of the greenhouse was substantial, and the rate of indoor temperature in the vertical direction was smaller. When the vertical and horizontal distance changed at the same time, the difference in the temperature in the vertical direction of the indoor temperature was more than 2 times that in the horizontal direction. Therefore, an experimental study on the vertical and horizontal variations of the indoor temperature in the sunken solar greenhouse was firstly carried out; that is, the single cross-section temperature and humidity test. In the test, sensors with smaller spacing were arranged along the vertical and horizontal directions, and the vertical spacing of the measuring points was mostly 300 mm. A total of 96 sensors were arranged. The experiment period was from March 8, 2019 to June 8, 2019 and from August 31, 2019 to December 23, 2019. The temperature and humidity inside the tested greenhouse were tested using the HT59-LI-A1 wireless temperature and humidity tester, and the data were collected at an interval of 6 min.

The cross-section at 30 m from the west wall was selected as the cross-section to be measured, and the coordinate system was established using this cross-section. The intersection point between the indoor ground and the extension line of the sinking wall was 0, and the vertical upward direction was the positive z-axis. The intersection line between the indoor ground and the cross-section was north and was the positive y-axis. The established coordinate system is shown in Figure 1, which illustrates the position of the measuring line. Table 1 provides the heights of the measuring points.

Table 1

Height values of the measured lines and points on the indoor floor (m)

		Line number									
		1	**2**	**3**	**4**	**5**	**6**	**7**	**8**	**9**	**10**
y-coordinate		0	0.4	0.9	1.5	3.5	7	10.5	11	11.7	WALL
Height of measuring point (m)	1	1.2	1.6	1.8	2.1	3.3	4.5	4.9	4.9	4.9	4.3
	2	0.9	1.3	1.5	1.8	3	4.2	4.6	4.6	4.6	4
	3	0.6	1	1.2	1.5	2.7	3.9	4.3	4.3	4.3	3.7
	4		0.7	0.9	1.2	2.4	3.6	4	4	4	3.4
	5		0.4	0.6	0.9	2.1	2.7	3.7	3.7	3.7	3.1
	6		0	0.3	0.6	1.8	1.8	2.7	2.7	2.7	2.5
	7			0	0.3	1.5	1.5	1.5	1.7	1.7	1.9
	8				0.1	1.2	1.2	1.2	1.4	1.4	1.6

Table 1
(continuation)

	Line number									
	1	**2**	**3**	**4**	**5**	**6**	**7**	**8**	**9**	**10**
9					0.9	0.9	0.9	1.1	1.1	1.3
10					0.6	0.6	0.6	0.8	0.8	1.0
11					0.3	0.3	0.3	0.5	0.5	0.7
12					0	0	0	0.3	0.2	0.4

Test for the indoor multi-cross-section temperature in the sunken solar greenhouse

Based on the test results, a number of cross-sectional temperature tests were carried out for indoor temperature, with vertical spacing mainly increased to 600 mm. Six positions were selected horizontally and 7 auxiliary sections were selected along the longitudinal direction to explore the variations along the longitudinal, transverse and vertical indoor temperatures.

The experiment lasted from December 26, 2019 to June 2, 2020. The temperature in the sunken solar greenhouse was measured by a wireless temperature sensor and USB disk temperature recorder. In the cross-sections, the intersection point between the indoor ground and the sinking wall was 0, the y-axis was horizontally oriented to the north, and the z-axis was vertically upward on survey line 1. The vertical direction of the sinking greenhouse was the positive direction of the x-axis along the east direction. Figure 2 and Tables 2 and 3 show the position of the indoor cross-sections and the layout of measuring points on the measuring lines at each cross-section. A U-disk type temperature recorder was installed at 1.5 m outdoor height without shelter to record the outdoor temperature.

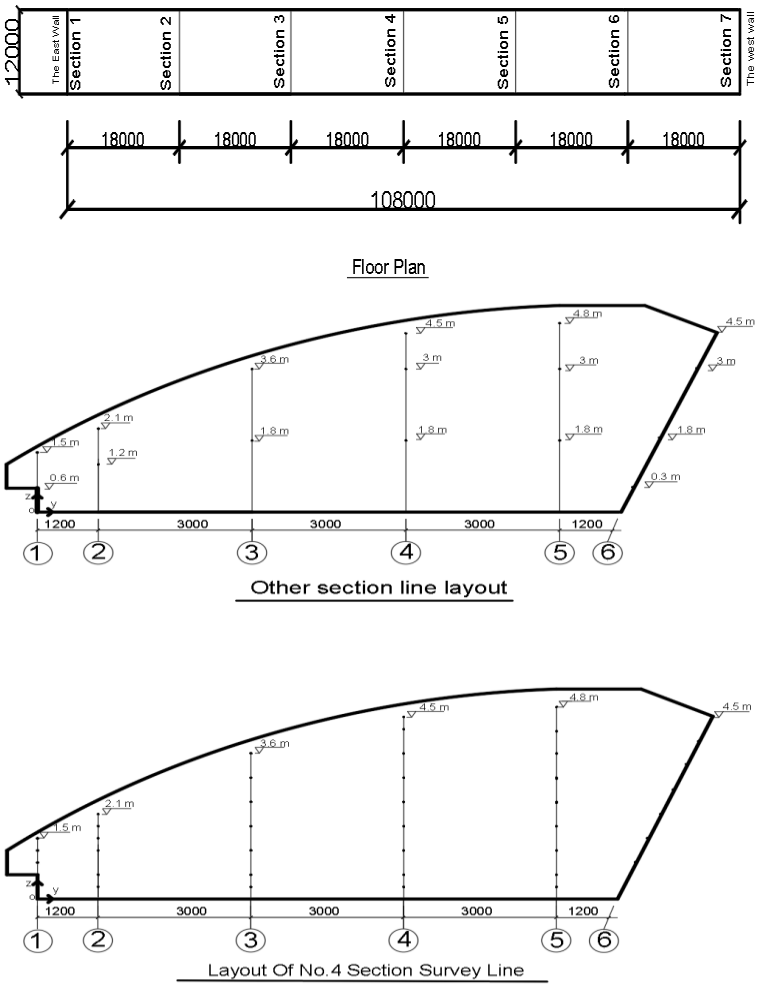

Fig. 2 - Layout of the cross-sectional survey lines and points

Table 2

Layout of the other cross-section survey lines and points (m)

		Line number					
		1	**2**	**3**	**4**	**5**	**6**
y coordinate		0	1.2	4.2	7.2	10.2	墙体
Height of measuring point (m)	1	1.5	2.1	3.6	4.5	4.8	4.5
	2	0.6	1.2	1.8	3	3	3
	3	0	0	0	1.8	1.8	1.8
	4	-	-	-	0	0	0.3

Table 3

Layout of no. 4 cross-section survey line and point (m)

Code number		**Line number**					
		1	**2**	**3**	**4**	**5**	**6**
y coordinate		0	1.2	4.2	7.2	10.2	墙体
Height of measuring point (m)	1	1.5	2.1	3.6	4.5	4.8	4.5
	2	1.2	1.8	3.3	4.2	4.5	3.9
	3	0.9	1.5	3	3.9	4.2	3.3
	4	0.6	1.2	2.4	3.6	3.6	2.7
	5	0.3	0.6	1.8	3	3	2.1
	6	0	0.3	1.2	2.4	2.4	1.5
	7	-	0	0.6	1.8	1.8	0.9
	8	-	-	0.3	1.2	1.2	0.3
	9	-	-	0	0.6	0.6	-
	10	-	-	-	0.3	0.3	-
	11	-	-	-	0	0	-

RESULTS

Distribution of the lowest temperature in a single cross-section during winter

During winter, the earlier the strawberries ripen, the higher the price. Thus, studying the minimum indoor temperature during the flowering and budding period of strawberry in winter is very important to make the harvest early and the strawberry less vulnerable to freezing damage. The lowest outdoor temperature (−12.9°C) was recorded during November–December 2019.

The weather on November 25, 2019 was as follows: clear all day; southwest force, 1–2; sunrise, 7:20; and sunset, 17:13. The shed was opened at 8:28. Given the low room temperature, the quilt was raised to 1/3 span of the greenhouse. All quilts were removed at 9:58, and the upper air outlet was opened for ventilation at 10:15.

The maximum difference in the temperatures at the measuring points on the same measuring line at the same time was 2.9 °C. These points were measuring points 1 and 12 on the measuring line 6. The vertical height difference was 4.5 m, and the change rate of temperature in the vertical direction was 0.64 °C/m. The maximum difference in temperature between the measuring lines at the same time and at the same height was 3.1 °C, and the horizontal distance was 11.7 m. The change rate in the temperature along the horizontal direction was 0.26 °C/m, and the maximum change rate of the temperature in the vertical direction was 11.9 times that in the horizontal direction. Therefore, the temperature distribution in the vertical direction was more uneven than that in the horizontal direction.

During the period from 00:00 to 8:00, the outdoor temperature dropped by 5.4 °C, and the indoor temperature dropped by approximately the same range at each measuring point, with a difference of less than 0.4 °C. The drop in the indoor temperature at each measuring point was 2.4 °C±0.3 °C. Covering using an insulation cotton showed good insulation of the sinking greenhouse. The air temperature in the different areas of the sunken solar greenhouse decreased at the same rate with time at night.

Lowest temperature distribution at the longitudinal multi-section in winter

January 14, 2020 was the coldest day during the winter of 2020, and the lowest outdoor temperature was −19.8 °C. The lowest indoor temperature was recorded at 8:00, and the highest indoor point temperature was determined at 11:48.

The lowest temperature of 86% of the indoor measuring points was lower than 5 °C, which was unfavourable to the growth and development of strawberry. The minimum indoor air temperature of the sunken solar greenhouse varied in the horizontal, vertical and longitudinal directions. This result was consistent with the studies of Sun et al. (2019) and Zhang et al. (2019), but these groups did not study the variation rate of indoor night low temperature in three-dimensional coordinates and the length of the low temperature region.

The maximum difference in temperature was 4.8 °C (the longitudinal horizontal spacing was 90 m) in the measuring points equal to the horizontal distance *y* from the sinking wall and equal to the height *z* of the indoor ground, namely, the measuring points at the same height on the same longitudinal section. The change rate of the lowest indoor temperature at night along the longitudinal maximum temperature difference was 0.053 °C/m. For the measuring points with the same cross-section and height, the maximum difference in temperatures of the measuring points was 2.8 °C (horizontal spacing was 7.2 m), and the change rate in the maximum difference in temperature along the transverse direction was 0.38 °C /m. In the same section and measuring line, the maximum difference in the temperatures of the measuring point was 4.2 °C (the vertical distance was 3.6 m) on the measuring line 3 of section 7. The change rate of the lowest indoor temperature at night along the maximum vertical temperature difference was 1.17 °C/m. Thus, the distribution of the indoor temperature along the vertical height had larger inhomogeneity than that along the longitudinal distribution. In addition, the change rate of the maximum temperature along the height direction in the greenhouse was 13 times that along the longitudinal direction and 3 times that along the horizontal direction. Therefore, studying the variations in the indoor temperature distribution in vertical direction of a sunken solar greenhouse is of great significance.

The temperature drop at each section and each measuring point from 00:00 to 8:00 on January 14, 2020 were calculated. The results showed that points 1, 2, 3, 4, 5, 6 and 7 in the corresponding cross-section dropped by 2.7 °C ± 0.4 °C, 2.7 °C ±0.4 °C, 2.6 °C ± 0.4 °C, 2.5 °C ±0.2 °C, 2.6 °C ±0.3 °C, 2.6 °C ± 0.4 °C and 2.8 °C ±0.3 °C. The differences in the temperature drops at the measuring points on each section were less ≤ 0.8 °C, and the temperature drop of the outdoor measuring points was 5.5 °C in this period. The temperature drops of the measuring point were approximately equal in this period.

Distribution law of maximum temperature in a single cross-section during winter

At 11:48, the outdoor temperature was 9.2 °C. At 11:48, the lowest temperature of the measuring points in the single cross-section was 15.6 °C (2–6 measuring points), and the highest temperature was 34.9 °C (10–6 measuring points). The temperature difference between the two measuring points was 19.3 °C.

The maximum temperature difference of the different measuring points on the same measuring line at the same time was 13.7 °C, and the vertical height difference was 4.5 m. At this time, the vertical variation of the indoor temperature was 3.04 °C/m. The maximum temperature difference of measuring points at different horizontal distances at the same time and height was 14.7 °C and the horizontal distance was 11.7 m. At this point, the indoor temperature changed at 1.25 °C/m in the horizontal direction. The maximum change rate of indoor temperature in the vertical direction was 2.4 times that in the horizontal direction. The temperature distribution in the vertical direction was more uneven than that in the horizontal direction.

Distribution law of maximum temperature at the longitudinal multi-section measuring points in winter

The temperature at 11:48 was the maximum value of 85% of the measurement points, and the maximum temperature of each measurement point occurred between 11:42 and 11:54.

At the same height and horizontal distance, the maximum difference in temperature between the measuring points was 13.2 °C (the horizontal distance between the two sections was 36 m). At this point, the change rate in the maximum difference in the indoor temperatures along the longitudinal direction was 0.37 °C/m. The maximum difference in temperature was 5 °C for the measuring points at the same section and at the same height at different horizontal positions (transverse horizontal distance was 7.2 m). The change rate of the maximum difference in temperatures along the transverse direction was 0.69 °C/m. At the same section and horizontal distance, the maximum difference in temperature of measuring points at different water heights was 14.9 °C (the vertical distance between two measuring points was 3 m). At this point, the indoor temperature changed by 4.97 °C/m along the vertical direction. The change rate of the maximum difference in the indoor temperature along the vertical height was 13.4 times that along the vertical direction and 7.2 times that along the transverse direction.

The change rates of the maximum and minimum temperatures in the greenhouse along the vertical direction were greater than those along the horizontal direction. The change rates of the maximum and minimum indoor temperature along the horizontal direction was greater than that along the vertical direction. Therefore, evaluating the law in the vertical change of the indoor temperature in a sunken solar greenhouse is very important.

CONCLUSIONS

In this paper, the law of the change in indoor temperature and humidity of a sunken solar greenhouse was analysed. The following conclusions were drawn:

(1) From 00:00 to 8:00 in winter, the difference in the temperature drops of the measuring points in the single cross-section was less than 0.4 °C, whilst this difference in the multi-cross section was less than 0.8 °C. The temperature drops of the measuring points were approximately equal at night. These values could be used as the basis for calculating the heat loss in a greenhouse.

(2) Temperature differences were found in the indoor temperatures along the vertical, horizontal and longitudinal directions of the sunken solar greenhouse. The change rate in the indoor temperature in vertical direction was greater than those in the horizontal and longitudinal directions.

ACKNOWLEDGEMENT

The authors appreciate the assistance of Professor Wang Shuangxi and Associate Professor Liu Zhonghua. During the doctoral study, the professors have revised and provided guidance in the experimental scheme many times. They have also reviewed and corrected the manuscript. Their figures and teachings are evident in this work. The authors were in the office at night for the revision and guidance of the experimental scheme. The professors were always available in the campus to revise and make suggestions for the paper. They provided valuable guidance at the greenhouse test site. The authors are deeply grateful for the assistance of the two professors.

REFERENCES

[1] Albright L.D., Gates R.S., Arvanities K.G. et al (2001). Environmental Control for Plants on Earth and In Space. *IEEE Control System Magazine*. 21(5): 28-47.

[2] Bazgaou A., H. Fatnassi, R. Bouharroud et al (2021). Effect of active solar heating system on microclimate, development, yield and fruit quality in greenhouse tomato production, Renew. *Energy* 165: 237–250.

[3] Cheng W.W., He J.L., Liu Z.H. (2021). Evaluating how the temperature changes in a sunken solar greenhouse. *Engenharia Agrícola*. (3):279-285.

[4] Guo H.G., Zhao H. (2009). Effect of sunny and cloudy days on temperature of solar greenhouse with different structure（晴阴天对不同结构日光温室温度影响）. *Journal of Anhui Agricultural Sciences*. 37(28): 13964-13966, 13973.

[5] Hu J.J., Fan GS, Gao Y.J. (2014). Experimental study on air temperature variation characteristics of solar greenhouse during overwintering period (越冬期日光温室空气温度变化特性的试验研究). *Journal of Taiyuan University of Technology*. 45(4): 490-495.

[6] Jang Y., Goto E., Ishigami Y., Mun B. et al (2011). Effects of Light Intensity and Relative Humidity on Photosynthesis Growth and Graft-take of Grafted Cucumber Seedlings during Healing and Acclimatization. *Hortic. Environ.Biotechnol*. 52(4): 331–338.

[7] Khoshnevisan B., Rafiee S., Mousazadeh H. (2014). Application of Multi-layer Adaptive Neuro-fuzzy Inference System for Estimation of Greenhouse Strawberry Yield. *Measurement*. 47 (1): 903–910.

[8] Liu S.M., Xue Q.Y., Li C. (2013). Temporal and spatial variation of air temperature and ground temperature in sunken solar greenhouse (下沉式日光温室气温和土温时空变化特征研究). *Tianjin Agricultural Sciences*. 19(5): 53-57.

[9] Liu S., Zhang L.H., Zhang F. (2009). Research progress on the influence mechanism of heat and humidity environment in solar greenhouse (日光温室热湿环境影响机理研究进展). *Journal of Shandong Jianzhu University*. 24(6): 587-593.

[10] Md Shamim Ahamed, Huiqing Guo, Karen Tanino (2020). Modelling heating demands in a Chinese-style solar greenhouse using the transient building energy simulation model TRNSYS. Journal of Building Engineering 29 : 101114

[11] Shi Y.L., Wang X.F., Wei M. et al (2016) Temperature variation and heat storage and release characteristics of soil wall in solar greenhouse (日光温室土墙体温度变化及蓄热放热特点). *Transactions of the CSAE.* 32(22):214-221.

[12] Stefano Morelli, Filippo Cossio, Danilo Monarca et al (2022). Parametric sweep simulation for greenhouse temperature field optimization: An Italian case study. Energy Reports 8:881–895

[13] Sun S.P., Dong C.Y., Li Z.F. et al (2020). Study on internal temperature change of solar greenhouse under different ambient temperature based on CFD (基于 CFD 的不同环境温度下日光温室内部温度变化研究). *Tianjin agricultural sciences*. 26(10): 43-47.

[14] Taki M., Ajabshirchi Y., Ranjbar S.F. et al. (2016). Heat Transfer and MLP Neural Network Models to Predict Inside Environment Variables and Energy Lost in a Semi-solar Greenhouse. *Energy Build*. 110: 314–329.

[15] Tu M.Y., Jiang G.L., Du J.C., et al (2011). Effects of temperature and humidity inside and outside greenhouse on growth and development of spring shoot and fruit of loquat japonica（温室内外温湿度对枇杷春梢和果实生长发育的影响）. *Southwest China journal of agricultural sciences*. 24(6): 2336-2341.

[16] Wei R.J., Wang C.Y., Fan Z.L (2010). Winter microclimate characteristics and its relationship with macroclimate in solar greenhouse in Shijiazhuang area（石家庄地区日光温室冬季小气候特征及其与大气候的关系）. *Chinese journal of meteorology*, 36(1): 97-103.

[17] Xu H.J., Li Y.R., Cui Y.M., et al (2018). Environmental Testing and analysis of solar greenhouse in hinterland of Xinjiang Hotan Desert (新疆和田沙漠腹地日光温室环境测试与分析). *Transactions of the Chinese Society of Agricultural Engineering*. 34 (suppl.): 60-65.

[18] Xu H.J., Cao Y.F., Li Y.R. et al (2019). Construction and application of solar radiation model in solar greenhouse (日光温室太阳辐射模型构建及应用). *Transactions of the Chinese society of agricultural engineering*. 35(7): 160-169.

[19] Yang X.G., Zhao B.C., Qi Z.G. (2005). Observation and analysis of temperature gradient in solar greenhouse (日光型温室内温度梯度变化的观察与分析). *Journal of Hebei normal university (natural science edition)*. 29(1): 79-84.

[20] Yu M.H., Gao G.L., Ding G.D. et al (2015) Review of plant body temperature research (植物体温研究综述). *Chinese journal of ecology*. 34(12): 3533-3541.

[21] Zhang J.J. (2015). Effects of greenhouse temperature and humidity conditions on growth and fruity and soil-borne diseases of strawberry（温室温湿条件对草莓生长结实及土传病害的影响. *Journal of Northwest S&F university (natural science edition),* 43 (5): 143-148.

[22] Zhang C.K., Wei M., Liu F.S. et al (2019). Unsteady thermal conductivity of soil at night in a downward-digging solar greenhouse (下挖式日光温室夜间土壤非稳态导热过程). *Journal of China Agricultural University.* 24 (1): 108-118.

FRAME STRUCTURE DESIGN AND FINITE ELEMENT ANALYSIS OF CORN COMBINE HARVESTER FOR HILLS AND MOUNTAINS
/
丘陵山地玉米联合收获机车架结构设计与有限元分析

Zhu ZHAO [1,2], Zhongnan WANG [2], Bintong ZHAO [1], Yuqiu SONG [1], Mingjin XIN *[1]
[1] College of Engineering, Shenyang Agricultural University, Shenyang / China;
[2] Liaoning Agricultural Technical College, Yingkou / China
Tel: +86-024-88487119; E-mail: xinmjsynd@163.com
Corresponding author: Xin Mingjin
DOI: https://doi.org/10.35633/inmateh-68-13

Keywords: *Corn harvester, frame, strength analysis, modal analysis, optimization design, stability analysis*

ABSTRACT
In view of high center of gravity and poor stability of traditional corn harvesters, a corn combine harvester frame is designed for hill and mountain operations based on TRIZ theory. The frame supports engine mode of middle engine rear drive, consisting of a front frame and a rear frame. The tail of the front frame is welded under the head of the rear frame. The front frame has reduced height and increased width to allow lower center of gravity and better stability of the whole machine. The left and right longitudinal beams of the front frame have different heights to allow better trafficability of the whole machine. A 3D model is established using SolidWorks software and incorporated with ANSYS software to perform finite element analysis and modal analysis on the frame. It turns out that under full-load bending and full-load torsion conditions, the frame strength and stiffness meet the mechanical performance requirements, and the frame displays fine dynamic characteristics. According to the analysis results, the frame is optimized under the goal of light weight. While the frame strength and stiffness requirements are met, the frame mass is lowered by changing the frame component thickness. After optimization, the entire frame volume is reduced by 14.27%, with mass reduced by 14.3%, and the strength and stiffness conform to the requirements, thus achieving lightweight optimization of the frame. Moreover, the stability analysis of the corn combine harvester shows the overturning angle of uphill is 45.3°, the overturning angle of downhill is 45.7°, and the overturning angle of slope is 40.2°.

摘要
为解决传统玉米收获机重心高、稳定性差等问题，基于 TRIZ 理论设计了一种适合丘陵山地作业的玉米联合收获机车架。该车架适合于发动机中置后驱形式，车架由前框架和后框架组成，前框架尾部焊接在后框架头部之下，前框架高度降低、宽度增加，有利于降低整机重心，提高整机稳定性，前框架左右纵梁高度不同，提高整机的通过性。利用 Solidworks 软件建立三维模型，导入 ANSYS 软件对车架进行有限元分析和模态分析，结果表明在满载弯曲和满载扭转工况下，车架强度和刚度均满足力学性能要求，车架动态特性良好。根据分析结果，以轻量化为目标对车架进行优化，在满足车架强度和刚度要求的前提下，通过改变车架构件板厚的方式实现车架的轻量化，优化后整个车架体积减少 14.27%，质量减少 14.3 %，强度和刚度均符合要求，达到了车架轻量化优化目的，最后整车稳定性分析表明收获机上坡极限倾翻角度为 45.3°，下坡极限倾翻角度为 45.7°，横向极限倾翻角度为 40.2°。

INTRODUCTION

Corn, one of the three major food crops in China, had a planting area of about 4×10^7 hm^2 in 2022. The corn planting area on hills and mountains exceeds 1.2×10^7 hm^2, accounting for a non-negligible proportion *(Wei et al., 2022). D*ue to the limitation of terrain conditions, hills and mountains have far lower level of mechanized corn harvesting than plain areas. Hence, it is of great significance to study and develop corn harvesters for hills and mountains. Hilly land is uneven, with multiple potholes and great slope, which imposes high requirements on the trafficability and stability of corn harvester *(Xu et al., 2021*).

[1] *Zhao Zhu, Ph.D. Stud. Eng.; Wang Zhongnan, Lab.Techo. MA. Eng.; Zhao Bintong, MA. Stud. Eng.; Song Yuqiu, Prof. Ph.D. Eng.; Xin Mingjin, Prof. Ph.D. Eng.*

The frame bears the load impact from various working parts of the corn harvester and receives excitation from the hilly road, playing an important role in determining trafficability and stability of the whole machine.

There are many important theoretical achievements in terms of frame design, mainly focusing on the frame structure optimization. For example, Wu et al. conducted finite element modal analysis on the frame of the hillside orchard transporter, changed the middle beam position based on topology optimization to achieve model improvement (*Wu et al., 2016)*. Zhang et al. modified the rice transplanter frame through goal-driven optimization, with mass decreased by 16.77% after optimization (*Zhang et al., 2014*). Using finite element software, Mohd et al. analyzed the frame stress, deformation and fatigue characteristics under dynamic and static loads to optimize and perfect the local frame structure. There are also some achievements in frame design pattern of corn harvester (*Mohd et al., 2012; Masanori H., 2022; S. Krishna et al., 2014*). For instance, Ma Lina et al. performed function analysis of corn harvester based on axiomatic design, extracted the main structural design parameters of the side beam frame, and then designed the frame using mathematical language (*Ma et al., 2019*). Gong Jingfeng et al. designed a trapezoid frame parametric platform in MATLAB/GUI software environment to perform frame structure design. Nevertheless, these research methods are to optimize the traditional frame structure, without innovative changes in the frame structure, and the frame design process fails to take into account particularity of hill and mountain operations *(Gong et al., 2021)*. Accordingly, it is particularly urgent to design a corn harvester frame for hills and mountains.

This paper bases itself on the TRIZ theory, analyzes the impact of frame installation height of the corn harvester on the stability and trafficability of the whole machine. Adhering to the physical contradiction solving principle and idea, a staggered frame is designed for corn harvester for hills and mountains to increase the whole machine trafficability and stability in hill and mountain operations. To determine the frame structure reliability, stress and deformation of the corn harvester frame are analyzed using ANSYS software under two typical working conditions: full-load bending and full-load torsion, so that frame modal analysis can be made. Lightweight improvement of the frame is performed by optimizing sectional dimension. This research carries practical significance for the development and design of harvester frame for hill and mountain operations.

MATERIALS AND METHODS

Overall frame design based on TRIZ theory

TRIZ represents a new theory that comprehensively and systematically discusses and solves invention-creation problems to achieve technological innovation. It provides scientific principles for humans to obey in the process of invention, creation and technical problem solving *(Zhang et al., 2014; Li et al., 2022)*. According to the TRIZ conflict resolution principle, demand analysis is made on corn harvester frame to innovatively design the corn harvester frame structure for hill and mountain operations, so that whole machine stability is higher.

An effective approach to increase roll stability of the corn harvester is to reduce the height-width ratio of the whole machine. The specific measures are to reduce the height of the center of gravity and increase the wheel base. As an important component of the corn harvester, the frame bears and connects the working parts such as the engine, gearbox, cab, header, peeler and granary. Reduced frame installation height of the whole machine helps lower its center of gravity, but will also reduce the ground clearance and then impair the field trafficability of the whole machine. The frame should be installed both low and high, resulting in conflicts between geometric physical parameters. By solving physical contradictions in TRIZ theory, innovative design of a higher level is possible. The core idea for solving physical contradictions is to separate the two contradictory sides by spatial separation *(Li et al., 2022)*. The recommended invention principles for space separation include 1 division, 2 extraction, 3 local masses, 4 asymmetry, 7 nesting and 17 shift from one-dimension to multi-dimension. Comparison between the above 6 invention principles reveals that, for the innovative frame structure, 1 division, 4 asymmetry and 17 dimension change are more valuable invention principles.

Normally, the frame of corn combine harvester adopts a side-beam trapezoidal frame structure, which is welded by longitudinal beam, cross beam, reinforcing rib, etc. *(Ma et al., 2019)*, as shown in Figure 1(a). According to the segmentation principle, solution 1 is proposed: front and rear frame structure. The conventional side-beam integrated trapezoid frame consists of two parts: the front frame and the rear frame.

The front frame bears the header, engine, transmission, elevator and peeler. The front frame has reduced height and increased width to lower the center of gravity of the whole machine, with roll stability of the whole machine increased; the rear skeleton bears the ear box at a height to maintain grain unloading efficiency of the ear box, as shown in Figure 1(b).

According to the dimension change principle, solution 2 is proposed: the front and rear layered frame. The front and rear frames are arranged in layers, the rear frame head is welded on the front frame tail, and the front frame is installed with engine and gearbox. The engine has greater geometric dimension than the gearbox. By lowering the engine installation position, it is possible to greatly reduce the center of gravity of the whole machine, as shown in Figure 1(c). According to the asymmetry and dimension change principle, solution 3 is proposed: staggered frame structure. The left and right longitudinal beams of the front frame are changed in height so that one longitudinal beam is placed under the front frame beam, while the other longitudinal beam has the same height as the front frame beam, making the cross beam and the form a staggered frame structure, as shown in the Figure 1(d).

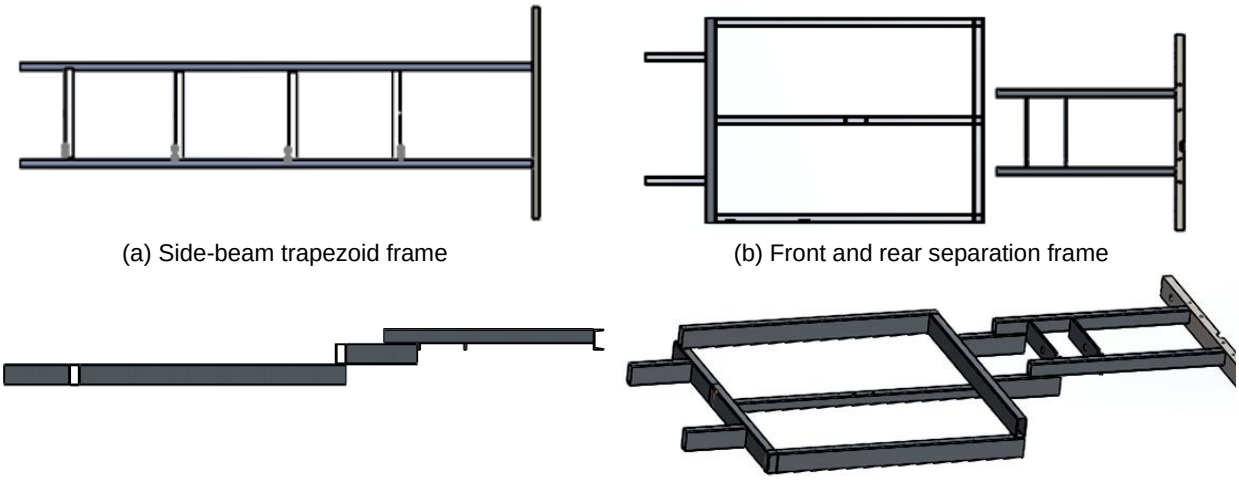

(a) Side-beam trapezoid frame (b) Front and rear separation frame

(c) Front and rear separation layered frame （d）Staggered frame

Fig. 1 - The frame design evolution process of corn harvester

Attach the engine, gearbox, cab, header, peeler, granary and other parts to the frame. The structure of the corn combine harvester is shown in Figure 2.

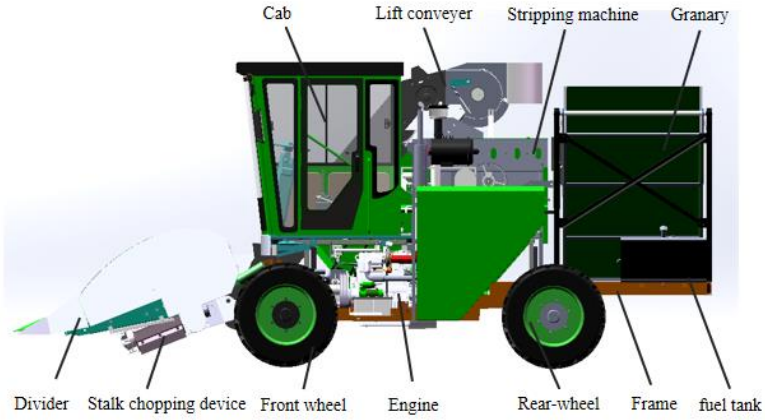

Fig. 2 - The structure diagram of corn harvester for hilly area

Design of main structural parameters of the frame

The frame length has something to do with the front and rear wheelbases. The wheelbase should be decided based on factors such as vehicle performance, loading area and axle load distribution. The shorter, the better. According to the preset whole machine dimension, the wheelbase is initially determined to be 2400 mm, and the frame length is generally1.3~1.7 times that of wheelbase. The frame length (that is, the length of the longitudinal beam) is thus selected as 3900 mm to basically meet the above requirements.

Frame width is the distance between the outer edges after welding of the two longitudinal beams and the cross beam, which is subject to limitation of the wheelbase and the suspension elastic element. Judging from the need for better handling stability, the wider the frame, the better, but too wide frame will make whole machine mass greatly increased, which harms economic and power performance. Accordingly, both aspects need to be taken into consideration.

Based on comprehensive consideration of the body layout, the front frame width is 1140 mm, and the rear frame width is 800 mm. The frame height is the vertical distance between the frame bottom and the frame top, which is 360 mm herein. The frame is made of 45Mn square tube with a rectangular section and a thickness of 6 mm.

Finite element static and modal analysis of the frame

The established Solidworks frame geometry model is imported into ANSYS software, and the frame structure is simplified with the main mechanical properties of the frame structure maintained. The frame is welded by various components, and the component joints are bound by contact to form a rigid connection. The frame material properties are described in Table 1. In this calculation, SOLID 95 element is taken, the element length is 10 mm, and 447,366 elements and 108,222 nodes are derived from mesh division of the frame.

Table 1

Material parameter

Project	parameter	unit
Material	45 Mn	-
Poisson's Ratio	0.28	-
Elastic Modulus	210	GPa
Density	8	$g \cdot cm^{-3}$
Yield Strength	375	MPa
Tensile Strength	620	MPa

Each part assembly on the frame directly acts on the corresponding frame parts with a uniform load *(Wang et al., 2014; Badretdinov et al., 2020)*, and the frame dead-weight can be automatically entered by setting the material density software. The loads required for the calculation and its definitions are illustrated in Table 2.

Table 2

Frame load values and loading modes in the finite element analysis

Name	Load value（N）	Loading mode
Header	8250	uniform load
Engine	3310	uniform load
Transmission	2520	uniform load
Cab	2480	uniform load
Elevator	2575	uniform load
Peeler	5935	uniform load
Granary (full load)	16120	uniform load
Frame dead-weight	5160	inertial load
Total	46350	

Considering working environment and stress conditions of corn harvester for hills and mountains, the constraints of the analysis model are determined: 1) Full constraints are applied at the welding point between the front axle and the left and right longitudinal beams; 2) 5 degrees of freedom are constrained at the two ends of the shaft extending from the rear axle shell, with rotational degrees of freedom released around the axis (*Ali Mohammod et al., 2021)*.

RESULTS AND ANALYSIS

Corn harvester for hills and mountains face relatively complicated operating environment. In view of its operating conditions, two typical working conditions are selected for analysis: the full-load bending condition, which is a working condition of the corn harvester during normal operation; the full-load torsion condition, which is an abominable working condition for corn harvester.

Analysis of the frame under full load bending condition

Under full-load bending condition, when the corn harvester is running at full load, the wheels are in full contact with the ground, the wheels are on the same working plane, and the whole machine is in a balanced state.

Under full-load bending condition, corn harvester for hills and mountains has relatively low operating speed, and the main load on the frame is the static load at full load. To check the structural strength and stiffness of the frame, the full-load bending safety factor is selected as 1.7 *(Wang et al., 2011)*, and the allowable stress of the frame is 220 MPa (375/1.7) now. Under the full-load bending condition, the stress of the corn harvester frame is distributed as shown in Figure 3(a). The overall stress on the frame is small, and the maximum stress on the frame appears at the juncture between the front and middle beams of the front frame, which is 154 MPa and smaller than the allowable material stress of 220 MPa, so frame strength meets the mechanical performance requirements under full-load bending condition.

Under full-load bending condition, the deformation and displacement of the corn harvester frame are distributed as shown in Figure 3(b). The maximum frame displacement appears at the tail beam of the frame, with a value of 4.5 mm. The reason is that it bears the granary weight, with a location far from the frame supporting point. Seen from the overall displacement cloud map, the front frame has greater deformation in the middle, with a value of about 2.9 mm. This relates to the actual load distribution, and conforms to the actual situation. The deformed frame has a safety factor of 2.4 (375/154), indicating good deformation resistance of the frame. In addition, the deformation of the longitudinal beams is symmetrically distributed on the left and right sides of the frame, resulting in a good load ratio of the frame.

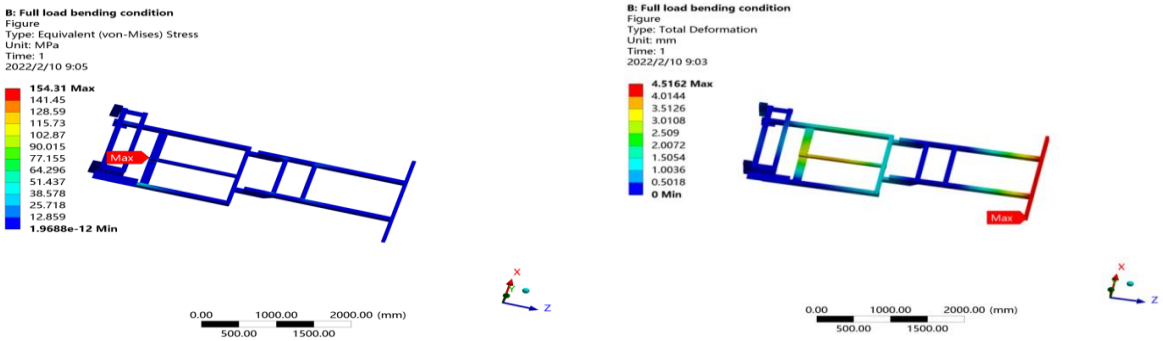

（a）Stress distribution diagram （b）Deformation distribution diagram

Fig. 3 - Full load bending condition

Analysis of the frame under full-load torsion condition

Hilly areas feature complicated terrain, uneven land and widespread potholes. When the corn harvester drives on potholes, the contact point between the wheel and the ground is not on the same plane, with the frame subject to torsional deformation under torsional load. The torsional condition studied herein is when the left front wheel is in the suspended state, and the full load torsional safety factor is selected as 1.3 *(Ma et al., 2019*). The allowable stress of the frame structure is 288 MPa at this time. Under full-load torsion condition, the stress of the corn harvester frame is distributed as shown in Figure 4(a). The maximum frame stress is 246 MPa at the juncture between the front and middle beams of the front frame, and there is greatly increased stress at the left column juncture of the front frame, though smaller than the allowable frame stress. Hence, frame strength meets the mechanical performance requirements under full-load torsion condition.

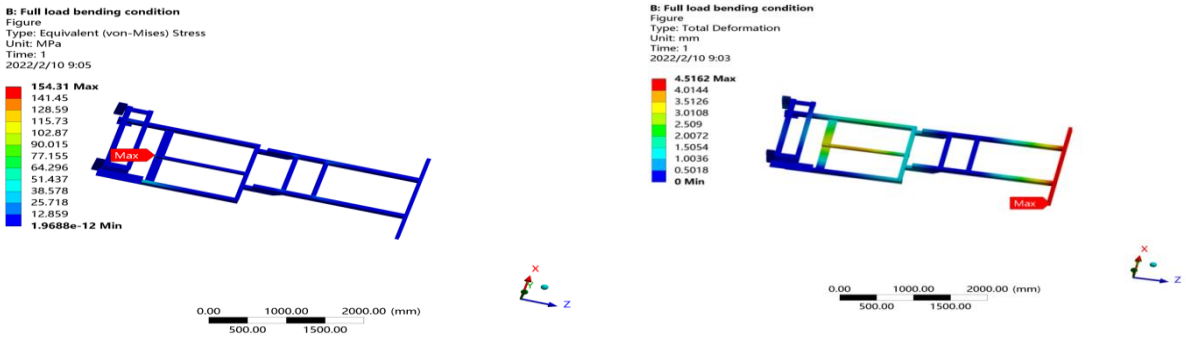

(a) Stress distribution diagram (b)Deformation distribution diagram

Fig. 4 - Full-load torsion condition

Under full-load torsion condition, the deformation and displacement of the corn harvester frame is distributed as shown in Figure 4(b). The maximum frame displacement occurs at the middle beam of the front frame, with a value of 5.1 mm, which is within the allowable range and conforms to the actual stress situation.

Finite element analysis of the frame under the full-load static state indicates that, under full-load bending and torsion conditions, the frame structure strength and stiffness meet the usage requirements. Mastery of the load distribution and weak frame parts under the full-load condition provides a theoretical basis for frame improvement in trial manufacturing.

Modal analysis of the frame

Modal analysis is performed on the corn harvester frame, and the calculated natural frequency is compared with the external frequency to analyze the reliability of the designed frame. Figure 5 displays the first sixth-order modes of the Modal module solved by ANSYS. Solution of the modes takes full-load bending condition as an example. Table 3 lists the sixth-order mode of the frame and its corresponding vibration modes.

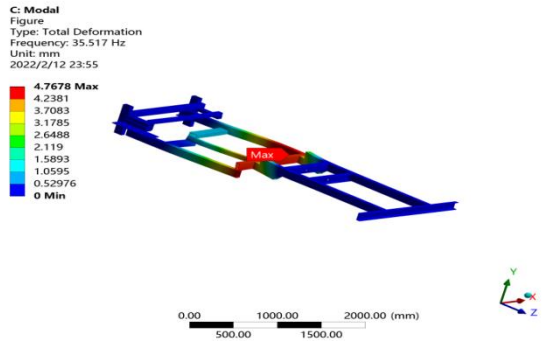

(a) The first-order modal shape diagram

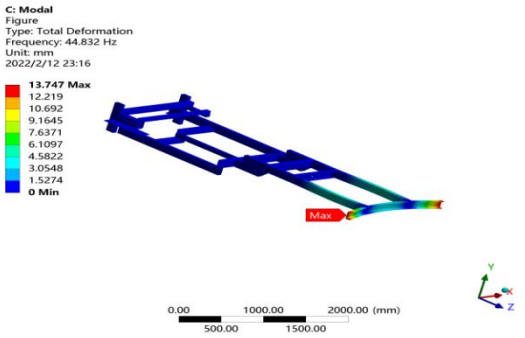

(b) The second-order modal shape diagram

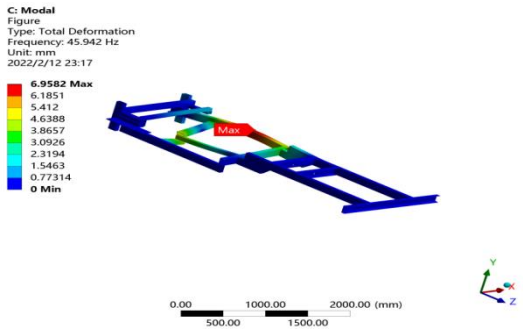

(c) The third-order modal shape diagram

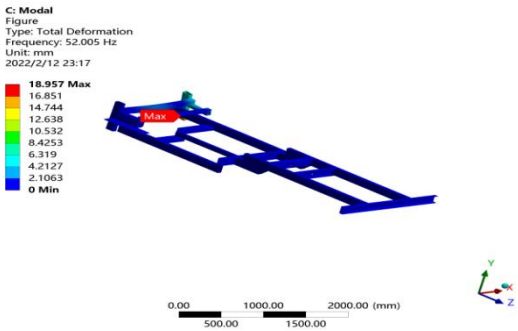

(d) The fourth-order modal shape diagram

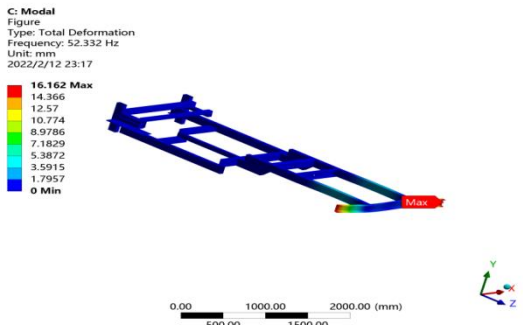

(e) The fifth-order modal shape diagram

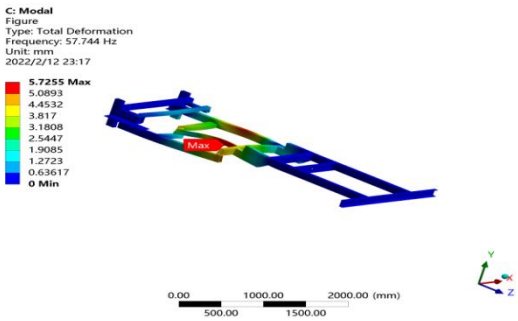

(f) The sixth-order modal shape diagram

Fig. 5 - Sixth-order Modal Shape Diagram of the frame

Seen from vibration mode of each order in Table 3 and Figure 5, the natural frequency of the corn harvester frame is uniformly distributed, displaying reasonable vibration mode. Vibration deformation mostly occurs in the middle of the front frame and the tail of the rear frame. Regarding the great deformation in the middle of the front frame, it is because the front frame bears components like engine, transmission, with the frame heavily loaded. For the great deformation of the frame tail, it is because the outer beam of the compartment at the frame tail is an overhanging beam structure prone to vibration deformation. In addition, other frame parts have relatively small vibration deformation, featuring smooth vibration mode and relatively stable structure.

Table 3

Modal frequency of frame structure

Mode Order	Frequency (Hz)	Vibration mode
1	35.517	Bending vibration
2	44.832	Bending vibration
3	45.942	Bending-torsion combination vibration
4	52.005	Bending-torsion combination vibration
5	52.332	Bending-torsion combination vibration
6	57.744	Bending-torsion combination vibration

The modal analysis result is compared with some important excitation forces of the frame under actual working conditions to analyze rationality of the designed vehicle frame. During normal driving, corn harvester is exposed to road excitation, engine excitation, wheel imbalance excitation and drive shaft excitation. The road excitation frequency is generally within 3 Hz, the wheel unbalance excitation is generally within 5 Hz. The engine speed frequency varies depending on the engine speed, and the engine vibration frequency can be calculated via the following formula *(Huang et al., 2020)*:

$$f = \frac{2nm}{60\,p} \tag{1}$$

Where:

f stands for the engine speed frequency.

n denotes engine speed;

m represents number of engine cylinders;

p stands for the number of engine strokes;

The transporter herein has a four-cylinder four-stroke engine with a maximum speed of 2500 r/min. According to the formula calculation, the engine has a vibration frequency of 83.3Hz under the maximum speed. The engine excitation frequency during normal driving is much lower than the vibration frequency under maximum speed. Modal calculation results reveal that the first sixth-order natural frequencies of the corn harvester frame are all lower than the engine excitation frequency, thus meeting the frame design requirements.

Frame optimization and result analysis

Using ANSYS optimization calculation module, an optimization model with minimal mass is established while strength and stiffness requirements are met. In comprehensive analysis with the maximum deformation under full-load bending condition as the state variable, the optimization goal is to minimize the frame mass, and the optimal design variable is the section geometry parameter of the frame. After 20 iterations, the optimization results are shown in Table 4.

Table 4

Comparison of main parameters before and after price optimization model

Optimization variables	Initial value	Optimization results	Change ratio/%
Volume of car frame U/mm	0.39231×10^{8}	0.33632×10^{8}	-14.27
Maximum deformation of bending condition M/mm	4.5162	5.828	22.51
External beam thickness	6	5.6074	-6.54
Thickness of other beam of frame T/mm	6	4.5459	-24.23

Seen from the optimization results, although the maximum deformation is increased from the original 4.5 mm to 5.8 mm with an increase ratio of 22.51%, it is still within a reasonable range, and the section thickness of each frame beam is greatly reduced. To verify whether the stiffness and strength of the optimized new frame meet the requirements, the material is assigned with new thickness in the optimization scheme and compared with the original frame strength, so that the main performance parameters can be compared before and after the frame model optimization, as shown in Table 5.

Table 5

Comparison of main parameters before and after price optimization model

Frame performance parameters	Before optimization	After optimization	Change amount	Change rate/%
Frame quality / kg	494.82	424.2	-70.62	-14.3
Bending the maximum equivalent stress / MPa	154.31	203.27	48.96	31.7
Maximum amount of bending deformation / mm	4.5162	5.9536	1.4374	31.8
Maximum torsional equivalent stress / MPa	246.73	278.14	31.41	12.7
Maximum torsional deformation / mm	5.1888	6.4365	1.2477	24.04

According to the above table, by optimizing the key frame parts of the corn harvester for hills and mountains, there is a great room for reducing the frame mass. After optimization, the transporter frame mass is reduced by 70.62 kg. Despite the certain increase in maximum deformation and maximum equivalent stress under torsion and bending conditions, the various performance parameters change little, and the results are ideally within a reasonable range. To conclude, this optimization scheme makes it possible to better distribute the frame mass of the corn harvester, which achieves the purpose of light weight to a certain extent and lowers the manufacturing cost.

Stability analysis of the corn combine harvester

The force analysis of a corn harvester moving uphill on a mountainous terrain with a slope φ is shown in Figure 6(a). When the harvester is tilted longitudinally around the point O_2, the moment balance at point O_2 is $\sum M_{O_2} = 0$, then:

$$F_{Z1} = \frac{A_2 G\cos\varphi - hG\sin\varphi}{A} \quad (2)$$

If the corn harvester is to be prevented from tipping longitudinally around the point O_2 when going uphill, then $F_{Z1} \geq 0$, i.e.:

$$A_2 G\cos\varphi - hG\sin\varphi \geq 0 \quad (3)$$

$$\varphi \leq \arctan(\frac{A_2}{h}) \quad (4)$$

The limiting tipping angle for longitudinal tipping of a corn harvester while driving uphill in hilly mountainous terrain is:

$$\varphi_{lim} = arctan(\frac{A_2}{h}) \quad (5)$$

Where:

F_{z1} is the support force on the front wheel;

A is the distance between shafts;

A_2 is the distance distance from the center of gravity of the machine to the slope of the rear axle;

G is the weight of harvester;

h is for the vertical height from the center of gravity to the slope;

φ is for the angle of uphill;

φ_{lim} is for the uphill tipping angle limit.

The value of φ_{lim} can be used to measure the ability of the corn harvester to resist longitudinal tipping when going uphill, and it is related to the distance from the center of gravity of the entire machine to the slope of the rear axle A_2 and vertical height h from the center of gravity to the slope.

The force analysis of a corn harvester moving uphill on a slope with a gradient φ' is shown in Figure 6(b). When the harvester tilts longitudinally around the point O_1, the moment balance at the point O_1 is $\sum M_{O_1} = 0$, then:

$$F'_{z2} = \frac{A_1 G\cos\varphi' - hG\sin\varphi'}{A} \quad (6)$$

If the corn harvester is to be prevented from tipping longitudinally around the point O_1 when going downhill, then $F'_{z2} \geq 0$, i.e.:

$$A_1 G\cos\varphi' - hG\sin\varphi \geq 0 \quad (7)$$

$$\varphi' \leq \arctan(\frac{A_1}{h}) \quad (8)$$

The limiting tipping angle for a corn harvester that tilts longitudinally while driving downhill in hilly mountainous terrain is:

$$\varphi'_{lim} = arctan(\frac{A_1}{h}) \quad (9)$$

Where:

F'_{z2} is the support force on the rear wheel;

A_1 stands the distance from the center of gravity of the entire machine to the front axle slope;

φ' stands for the angle of slope down;

φ'_{lim} stands for the downhill ultimate tipping angle.

The value of φ'_{lim} can be used to measure the resistance of the corn harvester to longitudinal tipping when going downhill, and it is related to the distance from the center of gravity of the entire machine to the front axle slope A_1 and the vertical height h from the center of gravity to the slope.

The force analysis of the entire machine when the corn harvester travels laterally on a mountainous terrain with a slope γ is shown in Figure 6(c). When the harvester is tilted laterally around the point O'_1, the moment balance at point O'_1 is $\sum M_{O'_1} = 0$, then:

$$F_{zo} = \frac{B_2 G cos\gamma - hGsin\gamma}{B_1 + B_2} \quad (10)$$

To keep the corn harvester from tipping laterally around point O'_1 when traveling laterally, $F_{zo} \geq 0$, i.e.:

$$B_2 G cos\gamma - hGsin\gamma \geq 0 \quad (11)$$

$$\gamma \leq \arctan(\frac{B_1}{h}) \quad (12)$$

The limiting tipping angle for lateral tipping of a corn harvester while driving laterally in hilly mountainous terrain is:

$$\gamma_{lim} = arctan(\frac{B_1}{h}) \quad (13)$$

Where:

F_{zo} is the support force on the righr wheel;

B_1 stands the distance from the center of gravity of machine to the slope of the left walking wheel;

B_2 stands the distance from the center of gravity of machine to the slope of the right walking wheel;

γ stands for the rollover angle;

$\gamma_{\lim}$ stands for the lateral ultimate tipping angle;.

The value of $\gamma_{\lim}$ can be used to measure the resistance of the corn harvester to lateral tipping when traveling laterally, and it is related to the distance from the center of gravity of the entire machine to the slope of the left walking wheel B_1 and vertical height h from the center of gravity to the slope.

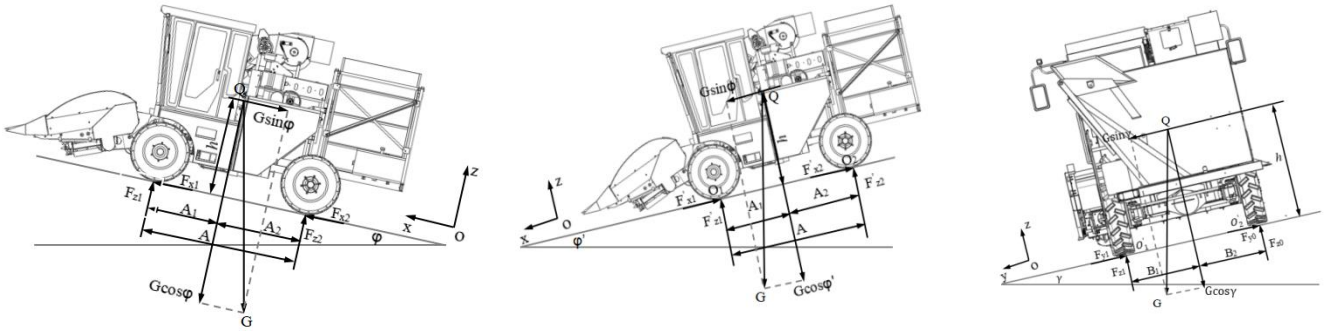

(a)uphill driving (b) downhill driving (c)slope driving

Fig. 6 - The driving force diagram of harvester

The analysis of the anti-tip ability of the corn harvester in mountainous regions shows that the height of the center of gravity and width of the wheelbase of the harvester affect its anti-vertical tipping ability and anti-transverse tipping ability. The height of center of gravity decreases and the wheelbase width increases, and the anti-tip ability of the harvester increases. The 3D model of the entire machine was created in Solidworks software. Assuming that the mass of the operator is 80 kg and the harvester is in the process of driving with a full load in the grain bin, the vertical height h of the center of gravity of the entire harvester from the ground is 1080 mm, the distance from the front axle A_1 is 1110 mm, the distance from the rear axle A_2 is 1090 mm, and the distance from the left wheel B_1 is 913 mm by evaluating the mass property options in SolidWorks software. By substituting the abovementioned parameters into Eqs. (5), (9), and (13), the limit tilting angle of the mountain corn harvester was calculated to be 45.3°, 45.7°, and 40.2° for travelling uphill, downhill, and laterally, respectively.

CONCLUSIONS

This paper designs a corn combine harvester frame for hill and mountain operations, with contributions mainly reflected in three aspects.

(1) Based on the TRIZ innovation theory, analysis is made on the frame effect on the trafficability and stability of the whole machine, and a staggered frame structure is innovatively designed according to the physical contradiction solving principles. Static analysis and modal analysis of the frame is performed using ANSYS software to examine the stress and deformation under the two typical working conditions of full-load bending and full-load torsion. The maximum value appears in the middle of the front frame and the tail beam of the rear frame. As the first sixth-order natural frequencies of the frame are all below the engine excitation frequency, frame design requirements are met.

(2) An optimization analysis is performed with the maximum deformation under the full-load bending condition as the state variable, the minimum frame mass as the goal, and the geometric parameters of the beam section as the variables. The optimization reduces the frame mass by 14.3%, so that lightweight of the frame is possible. In view of complicated environment in hill and mountain operations, it is necessary to further study how to improve stability of the whole machine in the future researches, such as by optimizing the frame material and the frame welding mode.

(3) Based on the stability analysis of the corn combine harvester, it puts forwards the overturning angle of uphill is 45.3°, the overturning angle of downhill is 45.7°, and the overturning angle of slope is 40.2°.

ACKNOWLEDGEMENT

This research was funded by the Project supported by the National Natural Science Foundation of China (51405311) and the results of the work are obtained using the corn harvester for hilly area provided by Fushun Dayi Agricultural Machinery Equipment Co., Ltd.

REFERENCES

[1] Ali Mohammod, Lee Ye Seul, Chowdhury Milon et al, (2021), Analysis of Driving Stability and Vibration of a 20-kW Self-Propelled 1-Row Chinese Cabbage Harvester, *Journal of Biosystems Engineering*, Vol.46, Issue1, pp.48-59, Daejeon /Korea;

[2] Badretdinov I., Mudarisov S., Lukmanov R. et al, (2020), Mathematical Modeling and Study of The Grain Cleaning Machine Sieve Frame Operation, *Inmateh-Agricultural Engineering*, Vol.60, No.1, pp.19-28, Ufa / Russia;

[3] Gong Jingfeng, Shan Dongsheng, Liu Hao et al, (2021), Design and Finite Element Analysis of Parametric Platform for Trapezoidal Frame of Truck (载货汽车梯形车架参数化平台设计及有限元分析), *Machinery Design and Manufacture*, Vol.16, Issue 7, pp.6-9, Wuhan/ P.R.C;

[4] Huang Zhouwei, (2020), Strength Optimization Design of the Frame of a Three-wheeled Transport Vehicle in Greenhouse (某大棚三轮运输车车架强度优化设计), *Agricultural equipment and vehicle engineering*, Vol.59, Issue 6, pp.63-68, Shanghai/ P.R.C;

[5] Krishna S., Narayanan S., Denis Ashok S., (2014), Fuzzy logic based yaw stability control for active front steering of a vehicle, *Journal of Mechanical Science and Technology*, Vol.28, Issue 12, pp.5169-5174, Tamil Nadu /India;

[6] Li Jing, Yuan Heng, Sun Di, Ma Jiachen, et al, (2022), Design of Cassava Seed Cutting Machine Based on TRIZ Theory and Adams (基于 TRIZ 理论与 Adams 优化设计木薯种茎切割机), *Journal of Chinese Agricultural Mechanization*, Vol.56, Issue 2, pp.39-44, Guangxi / P.R.C;

[7] Ma Lina, Wei Junyi, Huang Xiaomao, et al, (2019), Design method of corn harvester frame based on axiomatic design (基于公理化设计的玉米收获机车架设计方法), *Journal of Anhui Agricultural University*, Vol.46, Issue5, pp.894-900, Beijing/ P.R.C;

[8] Masanori Honda, Chikara Kawamura, Isamu Kizaki, et al, (2022), Construction of Design Guidelines for Optimal Automotive Frame Shape Based on Statistical Approach and Mechanical Analysis, *Computer Modeling in Engineering & Sciences,* Vol.128, Issue 2, pp.731-742, Shinchi/Japan;

[9] Mohd Azizi Muhammad Nor, Helmi Rashid, Wan Mohd Faizul Wan M. et al, (2012), Stress Analysis of a Low Loader Chassis, *Procedia Engineering*, Vol.41, Issue C, pp.995-1001, Shah Alam / Malaysia;

[10] Wang Xiagndao, Hu Dongfang, Du Yanping (2014), Finite element analysis and testing of corn harvester chassis frame (玉米收获机底盘车架有限元分析及试验), *Journal of Chinese Agricultural Mechanization*, Vol.35, Issue 2, pp.213-215, Henan / P.R.C;

[11] Wang Zhongqun, Liang Jian, Cao Guangqiao, et al, (2011), Developing agricultural mechanization scientifically and moderately on the hilly lands in the south of China (山地果园轮式运输机车架结构分析与优化), *Chinese Agricultural Mechanize*, Vol.2, Issue 234, pp3-8, Shandong/ P.R.C;

[12] Wei Tianjiao, (2022), Effects of soil salinization on weed community diversity in maize field and maize yield (土壤盐渍化对玉米田杂草群落多样性和玉米产量的影响), *Journal of China Agricultural University*, Vol.27, Issue10, pp.44-53, Jilin / P.R.C;

[13] Wu Weibin, Liao Jingwei, Hong Tiansheng et al, (2016), Analysis and optimization of frame structure for wheeled transporter in hill orchard (山地果园轮式运输机车架结构分析与优化), *Transactions of the Chinese Society of Agricultural Engineering*, Vol.32, Issue 11, pp.39-47, Shandong / P.R.C;

[14] Xu Haigang (2021), Development and Application of Corn Harvester for Hilly Area (丘陵山区玉米收获机研制与应用), *Agricultural Engineering*, Vol.11, Issue 3, pp.102-107, Shandong/ P.R.C;

[15] Zhang Fanglan, Yang Minglang, Liu Weidong, (2014), Study on product innovation based on TRIZ technology and demand evolution theories (基于 TRIZ 技术与需求进化理论的产品创新), *Journal of Nanchang University (Natural Science)*, Vol.38, Issue 2, pp.192-195, Guangxi / P.R.C.

FLUID ANALYSIS AND OPTIMIZATION DESIGN OF SPRAYING PIPE OF INTEGRATED PUMPING AND DISCHARGING FERTILIZER TRUCK
/
抽排一体式施肥车喷洒水管流体分析及优化设计

Bingchuan BIAN, Tao SONG *) [1]
College of mechanical and architectural engineering, Taishan University, Taian, Shandong/ China
Tel: +8605386711808; E-mail: stsong925@163.com
Corresponding author: Tao Song
DOI: https://doi.org/10.35633/inmateh-68-14

Keywords: *Sprinkler pipe, simulation platform, fluid pressure, fluid velocity, flow trace number*

ABSTRACT
According to the flow calculation, the basic structure of the sprinkler pipe of the integrated suction and drainage fertilizer truck was designed. Based on the 3D CAD / CAE Software SolidWorks / flow simulation platform, the structural models of three kinds of sprinkler pipes with different layout forms of outlet pipes were established, and the fluid analysis was carried out. According to the distribution of pressure, velocity and flow trace number in the tube, the optimal structure was obtained.

摘要
根据流量计算设计了抽排一体式施肥车洒水管的基本结构，并基于三维CAD/CAE软件SolidWorks/ Flow simulation 平台，建立出水管不同布置形式的三种洒水管的结构模型，进行流体分析。并根据管内的压力、速度和流动迹线数的分布，得出了最优结构。

INTRODUCTION
The integrated pumping and discharging fertilizer truck is suitable for sucking and transporting from septic tank to rural land, and spraying manure, sewage, and all fluid and semi-fluid substances to the land. The basic principle of fertilizing vehicle is to use engine power to drive the on-board pumping and discharging integrated pump through the power output device connected to the gearbox, so as to realize the suction and discharge of liquid fertilizer. The integrated pumping and discharging fertilizer vehicle is mainly composed of chassis, diesel engine, integrated pump, suction pipeline system, spraying pipeline system and control system. Among them, how to design the structure of the spraying pipeline can ensure that the flow of each branch pipe is equal when the main pipe pressure is equal. Therefore, it is of great significance to the structural design of spraying pipeline.

The research on the spray pipeline system is relatively less, compared with the similar research mainly having the following content.

The spatial pipeline of a power system was studied. The Galerkin method was used to discretize the coupling system composed of conduit and fluid, and the governing equation of the coupling system was established. The finite element method considering the initial stress stiffness is used to numerically calculate the vibration characteristics of the conduit before and after pressurization. The influence of fluid structure interaction on the vibration characteristics of the pipe structure is analysed in detail, and the results are compared with the experimental results (*Chen, 2007*).

The researchers analysed the fluid structure coupling phenomenon of pressure pipeline, established the finite element mathematical model of fluid solid coupling, used the finite element software ADINA to simulate the transition process caused by valve opening and closing, carried out numerical simulation calculation on the fluid solid coupling phenomenon of straight pipe pressure pipeline under different constraint conditions, and carried out modal analysis (*Feng, 2009*).

The researchers studied the cavitation phenomenon in the water pipeline of the heat exchanger test-bed, simulated the cavitation process of the fluid in the pipeline throttling by using the numerical calculation method, and analysed the changes of water content and pressure along the pipeline under different outlet pressure (*Zheng, 2011*).

[1]*Bingchuan Bian, Prof. Ph.D.; Tao Song, associate Prof. Ph.D.*

CFD technology to simulate the three-dimensional flow of a flat inlet water jet propulsion system was used. Based on the flow loss, outflow quality and pressure distribution in the inlet pipe, the influence of five different inlet lip angle schemes on the flow performance of the pipeline is compared and analysed (*Liu, 2011*).

The special water injection pipe was designed. The collar of the water injection pipe adopts the structure of inner boss and special thread structure, so that the inner diameter of the water injection pipe and the coupling is completely consistent, which can effectively eliminate the influence caused by eddy current, prolong the continuous working life of the water injection pipe, increase the water injection volume, increase the formation pressure, and improve the oil recovery. To a certain extent, the frequency of shutdown maintenance is reduced, and the production cost is greatly reduced (*Li, 2013*).

The researchers simulated and analysed three different types of draft tubes based on CFD technology, and revealed the influence of the pier on the internal flow of the draft tube by comparing the velocity distribution and streamline parameters of the draft tube (*Liao, 2016*).

The influence of structural parameters of cooling water pump on characteristics and how to adjust it to achieve the desired effect were studied. ANSYS CFX was used to analyse the flow field of cooling water pumps with different structures to obtain corresponding data for comparative analysis (*Feng, 2017*).

The researchers established a variety of finite element simulation models with different parameters of pipe wall thickness, length, inner diameter and material using ANSYS Workbench analysis software, and analysed the stress-strain characteristics of pipe wall under internal pressure in detail (*Yan, 2018*).

The authors studied the characteristics of velocity field and pressure field of the pressure pipe of tea cleaning machine by means of CFD fluid analysis and simulation software combined with the relevant basic theory of fluid mechanics. By comparing three different sizes of circulating pipes, the influence of different sizes on the pressure field distribution of circulating pipelines is obtained (*Yu, 2019*).

The researchers introduced the main functions of the Fluid Simulation Software SolidWorks flow simulation by simplifying the modelling of the hot air pipeline of rotary kiln and simulating the air flow in the pipeline, and analysed the structural design of the hot air pipeline of the rotary kiln (*Zhang, 2019*).

The authors used COMSOL Multiphysics software to simulate the fluid dynamics of pipelines with different leakage apertures, so as to analyse the pressure and flow variation law of leakage pipelines and leakage openings (*Wang, 2020*).

The computer model was developed to simulate pressure and flow rate distribution along pipes and laterals of pressurized irrigation systems in operation were studied. The software runs in a Windows environment and is capable of simulating irrigation systems having multiple pump stations combined in series and/or in parallel, booster pump stations, parallel pipes and looping pipes (*C.de L.T. de Andrade, 1999*).

The analysis and optimization of a liquamatic fire water monitor with a novel self-swinging mechanism were presented. The design of the self-swinging mechanism has adopted a four-bar linkage driven by an impeller. The Fluent software was used to simulate the internal flow performance of the fire water monitor. In particular, the effects of the cross-sectional shape, diameters of the monitor body, inlet water pressure, and drive set of the self-swinging mechanism on the jet characteristics were analysed (*Hu, 2012*).

An optical particle tracking velocimetry (PTV) technique is proposed in this paper to determine drop velocity, diameter and angle. The technique has been applied to the drops emitted by an isolated impact sprinkler equipped with two nozzles (diameters 3.20 and 4.37 mm) operating at a pressure of 175 kPa (*Bautista Capetillo, 2014*).

The pipes made of plastic materials are generally used in pipelines and the laterals of irrigation systems. Plastic materials such as polyethylene allow significant changes in pipe cross section due to operating pressure, but traditional equations used for determining head loss do not account for this effect. The purpose of this research was to develop an equation for determining friction head loss along elastic pipes (*O. Rettore Neto, 2014*).

The optimal design of sprinkler irrigation systems is a complicated nonlinear programming problem that is related to the performance of the system and meanwhile an economic problem to farmers in developing countries. Ant colony optimization (ACO), a meta-heuristic algorithm with the strategies inspired by foraging ants, was considered. Exactly an Ant Cycle System was proposed to solve this problem. The performance of ACO was compared to that of Genetic Algorithm (GA), and the optimal results were further validated by field tests on four small-scale irrigation systems (*Qin, 2015*).

The dynamical interaction between solids and fluids is a subject of paramount importance in Mechanics with a wide range of applications to engineering problems. It is, however, still a challenging topic of theoretical investigation.

With a view to case studies of dynamical behaviour of rockets, turbines, jets and sprinklers, a treatment was developed that, in the full respect of the principle of conservation of mass and under suitable simplifying assumptions, leads to evaluate the thrusting force exerted by the fluid on the solid (*Giovanni Romano, 2017*).

A multi-objective optimization of a flow straightener in a firefighting water cannon is performed by using the surrogate modelling and a hybrid multi-objective genetic algorithm to increase the jet range of the water cannon. Based on analysis using the three-dimensional Reynolds-averaged Navier-Stokes equations, the optimization is carried with a surrogate model and the radial basis neural network (*Xiang, 2019*).

One of the important parameters in developing dry ice blasting nozzle is the high-speed dry ice pellets. However, many studies focus primarily only on its performance without considering the noise emission that comes from an operating nozzle. In this method, the central composite optimization tool has been used. The two-way mass momentum and energy exchange are successfully modelled using the two-way mass momentum model. As an attempt to theoretically verify the model accuracy, a comparison is conducted on the density, pressure, temperature, as well as Mach number ratios corresponding to various ratios of nozzle area (*Mohamad Nur Hidayat Mat, 2021*).

In this paper, the three-dimensional basic finite element model of the spraying pipe of the integrated pumping and drainage fertilizer truck is established on the platform of SolidWorks / flow simulation. On the basis of fluid finite element analysis, the layout of spray pipe joint is optimized, and a good conclusion is obtained, which has certain reference significance for actual production.

MATERIALS AND METHODS

Mathematical model of spraying pipe of fertilizer truck pipeline parameter design

It is known that the diameter of the main pipe is D104 mm / D114 mm, the internal pressure is 0.15 MPa, the ambient temperature is 20° and the liquid velocity in the main pipe is V_1 = 1 m/s, and the total length is L = 1000 mm. Two pipes are arranged around, and one pipe can be calculated by calculation formula.

The diameter of the branch pipe is designed according to the known conditions.

According to the section average velocity V and cross-section area a, the flow rate is as follows:

$$Q = VA \tag{1}$$

Then the flow rate of the main pipe is equal to the sum of the flow rate of the branch pipe, and the following formula is established:

$$Q_1 = Q_2 \tag{2}$$

There are:

$$V_1 A_1 = n V_2 A_2 \tag{3}$$

Where V_1 is the average cross-section velocity of the main pipe; A_1 is the cross-sectional area of the main pipe; n is the number of branch outlets; V_2 is the average flow velocity of the branch section; A_2 is the cross-sectional area of the main pipe.

Establishment of mathematical model calculation of Reynolds

The Reynolds number of the fluid in a circular pipe is calculated according to the parameters of the known liquid.

$$Re = \frac{\rho V d}{\mu} \tag{4}$$

Where ρ is the density of the liquid, calculated according to the density of water, ρ = 1000 kg/m^3; V is the average velocity; D is the characteristic length (m), where D is the diameter of the circular pipe through which the fluid flows; μ is the viscosity of the fluid, and the viscosity of water at 20^{o}C is μ = 0.001 Pa.s. The critical Reynolds number of the tube is 2300.

If the above parameters are substituted into formula (4), then:

$$Re = \frac{\rho V d}{\mu} = 104000 > Re_{cr} = 2300 \tag{5}$$

It can be seen from the above formula that the fluid in the pipe is turbulent with high Reynolds number.

Mach number calculation

Mach number is the ratio of the characteristic velocity of a fluid to the velocity of sound in the fluid. It is mainly used to measure the compressibility of a fluid.

$$Ma = \frac{V}{C} = \frac{1}{1500} \approx 6.667 \times 10^{-4} < 0.3 \quad (6)$$

Where C is the velocity of sound propagating in the fluid, C = 1500 m/s. According to the above formula, it can be concluded that this fluid is low Mach number fluid flow, and the liquid is incompressible fluid with constant density.

Problem solving

The Reynolds averaged Navier Stokes equations (RANS equations) are used to solve the fluid motion in water pipes. For Newtonian fluids, the following results are obtained:

$$\rho\left(\frac{\partial \mathrm{u}}{\partial \mathrm{t}} + \mathrm{u}\cdot\nabla\cdot\mathrm{u}\right) = -\nabla \mathrm{P} + \nabla\cdot\left(\mathrm{u}\left(\nabla\cdot\mathrm{u} + (\nabla\cdot\mathrm{u})^{\mathrm{T}}\right) - \frac{2}{3}\mu(\nabla\cdot\mathrm{u})\mathrm{I}\right) \quad (7)$$

ρ is the density of the liquid (kg/m³); u is the velocity of the fluid (m/s); t is the time (s); P is the fluid pressure (Pa); T is the temperature (K); μ is the hydrodynamic viscosity (Pa.s); I is the Prandtl mixing length (m).

RESULTS

Fluid numerical analysis

The three-dimensional finite element model of sprinkler pipe of suction and drainage integrated fertilizer truck was established by using SolidWorks / flow simulation software, as shown in Figure 1, and the fluid analysis was carried out. The upper branch pipe at the right end is the fluid inlet, and the left and right sides of the horizontal main pipe are all closed. The thermal condition of the wall is adiabatic and the roughness is 12.5 μm.

According to the length of the main pipe, 11 thin tubes on the horizontal main pipe are fluid outlets, and the outlet spacing is evenly distributed. The distance of the branch pipe is L = 80 mm, n = 11, and the flow rate of liquid in the branch pipe is V_1 = 1.25 m/s. Substituting the parameters into equation (3), the following results are obtained:

$$1\times\pi\times 52^2 = 11\times 1.25\times\pi r_2^{\,2} \quad (8)$$

where r_2 is the radius of branch pipe, r_2 = 14.023 mm, so after rounding, the diameter of nozzle outlet pipeline is D=28 mm / d=34 mm. The nozzle outlet pressure is set to the ambient pressure and set to 0.10325 MPa.

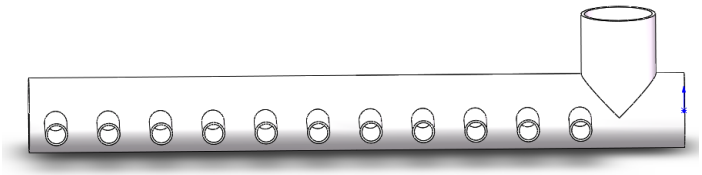

Fig. 1 - Three dimensional model of sprinkler pipe with uniform outlet pipe

The global grid is selected for grid division. After 70 iterations, the flow traces are set as 50, and the baseline diameter is 2 mm. The cloud chart and flow trace of pressure calculation results are shown in Fig. 2, and the nephogram and flow trace of water flow velocity are shown in Fig. 3. The distribution of flow trace number of uniform distribution structure of outlet pipe is shown in Table 1.

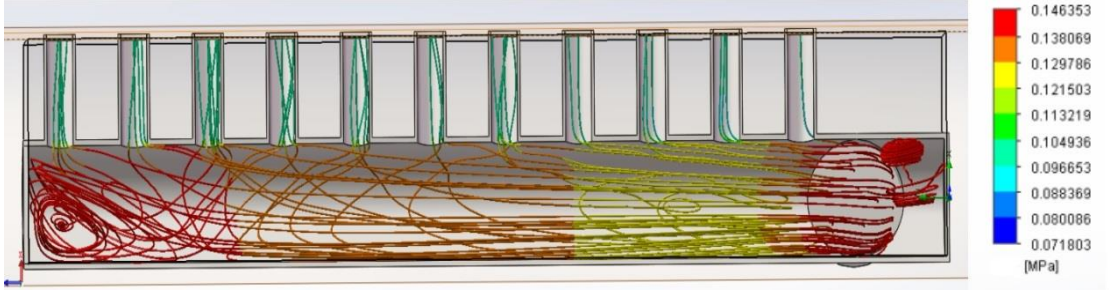

Fig. 2 - Pressure nephogram and flow trace of uniform distribution structure of outlet pipe

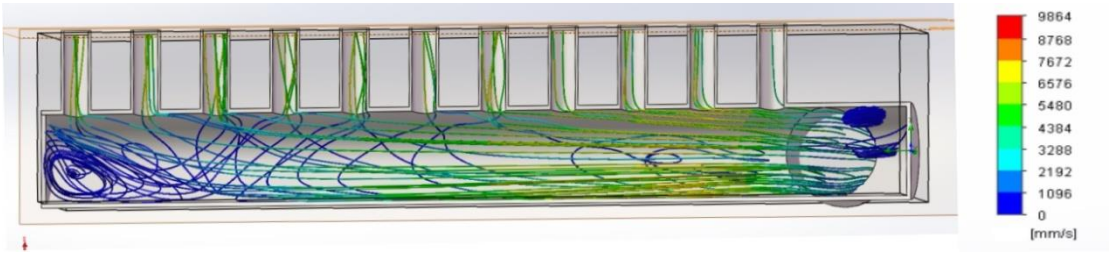

Fig. 3 - Water pipe velocity distribution and flow of uniform distribution structure of outlet pipe

It can be seen from Figure 2 that the water pressure at the inlet of the main pipe is the maximum, and the water pressure gradually decreases with the flow to the middle, and increases to the initial value when it reaches the end of the left main pipe. At the same time, the water pressure at the outlet is lower than that at the inlet. It can be seen from Fig.3 that the water flow velocity at the inlet of the main pipe is the maximum, and the water flow velocity gradually decreases with the flow towards the middle. When it reaches the end of the left main pipe, the flow velocity drops to the lowest; the vortex velocity at the left and right ends of the main pipe is the lowest; at the same time, the water flow velocity at the outlet is lower than that at the inlet.

Table 1

Distribution of the number of flow traces in the uniform structure of outlet pipe

Serial number of outlet pipe (from left to right)	1	2	3	4	5	6	7	8	9	10	11	loss
Number of flow traces	5	4	8	5	5	3	5	2	3	3	1	6

It can be concluded from table 1 that the largest number of flow traces is 8, and the third exit from left to right is 700 cm away from the entrance centre; the least number of flow traces is 1, 60 cm away from the entrance centre, and the number of flow traces at the 8th, 9th and 10th is very small, so the distance is obtained; the number of flow traces is lost by 6, and the loss rate is 12%.

It can be concluded from the above that the number of flow traces in the three-dimensional model with uniform distribution of outlet pipe is more in the distance from the inlet, and less in the near area, that is, the far flow rate is larger, the near flow rate is small, the flow trace loss rate is 12%, and the flow trace efficiency is 88%, which is mainly manifested in the formation of vortices on the left and right sides of the main pipe. It can be concluded from the above that the efficiency of this kind of structure is low, and the flow rate of each outlet is uneven, which affects the average of fertilization effect.

Structural calculation of outlet

Modify the three-dimensional finite element model of sprinkler pipe of fertilizer truck, reduce the number of outlet pipes to 8, start from the main inlet pipe according to the spacing, start from 80 mm, increase by 10 mm each time, and increase until the spacing is 140 mm. The other boundary conditions are analysed as shown in Fig. 4.

Take n = 8, where r_2 is the radius of the branch pipe, and its size remains unchanged, r_2 = 14 mm.

$$1\times\pi\times52^2 = 8\times V_1\times\pi r_2^2 \tag{9}$$

The results show that the velocity of liquid in the branch pipe is V_1 = 1.72 m/s, the number of branch pipes decreases and the velocity increases. The nozzle outlet pressure is set to the ambient pressure and set to 0.10325 MPa.

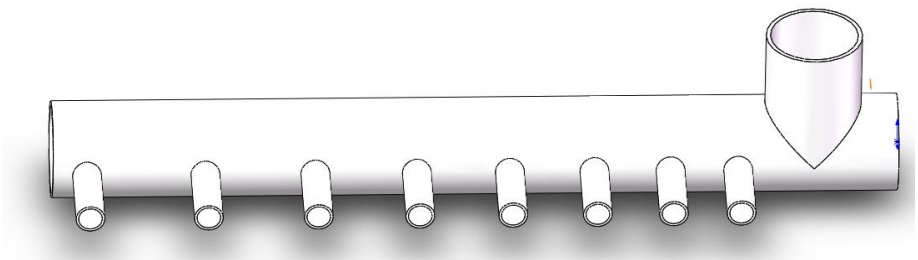

Fig. 4 - Three dimensional model of the structure in which the distribution distance of the outlet pipe increases gradually from the inlet

The global grid is selected for grid division. After 67 iterations, the flow trace is set as 50, and the baseline diameter is 2 mm. The pressure calculation results and flow trace are shown in Fig. 5, and the flow velocity nephogram and flow trace are shown in Fig. 6. The distribution of outlet pipe gradually increases from the inlet, and the structure flow trace distribution is shown in Table 2.

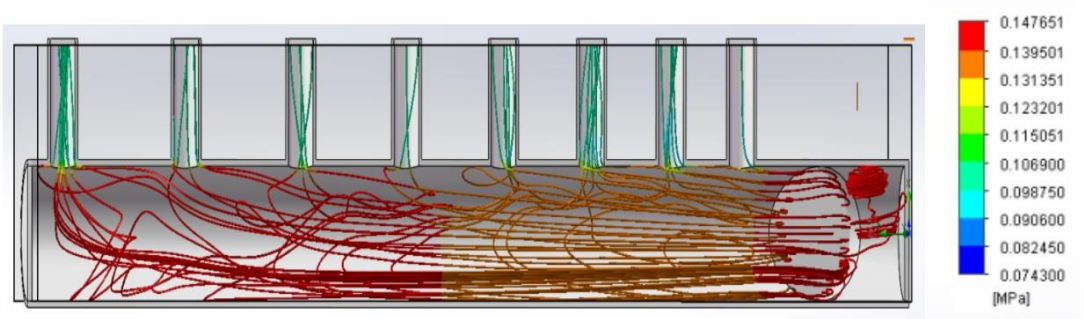

Fig. 5 - Pressure nephogram and flow trace of 3D model with the distribution distance of outlet pipe gradually increasing from the inlet

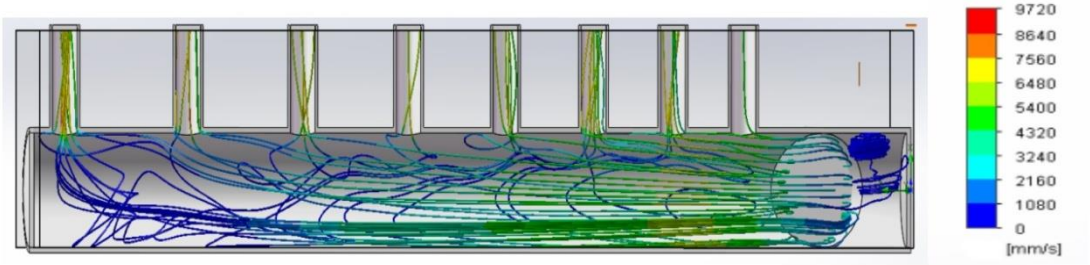

Fig. 6 - Water flow velocity nephogram and flow trace of 3D model with the distribution distance of outlet pipe gradually increasing from the inlet

It can be seen from Fig. 5 that the water pressure at the inlet of the main pipe is the maximum, and the water pressure gradually decreases with the flow to the middle. When it reaches half of the main pipe on the left, the water pressure increases to the initial value. At the same time, the water pressure at the outlet is lower than that at the inlet. It can be seen from Fig. 6 that the water flow velocity at the inlet of the main pipe is the maximum, and with the flow speed gradually decreasing towards the middle, the water flow speed will be the lowest when reaching the end of the left main pipe; there is no eddy current at the left end of the main pipe, and the vortex velocity at the right end is the lowest; at the same time, the water flow velocity at the outlet is lower than that at the inlet.

Table 2

Distribution of water outlet pipe gradually increases from the water inlet to the structure flow trace distribution

Serial number of outlet pipe (from left to right)	1	2	3	4	5	6	7	8	loss
Number of flow traces	14	5	4	2	5	9	6	1	4

It can be concluded from table 2 that the largest number of flow traces is 14, which is at the exit of the first leftmost end, 860 cm away from the entrance centre; the number of flow traces at the eighth outlet is the least, which is 1, 60 cm away from the inlet centre; 4 flow traces are lost, with a loss rate of 8%.

It can be concluded that the distribution of outlet pipe gradually increases from the inlet, and the number of flow traces in the structure model is further from the inlet, and the number is the least close to the entrance. It also shows that the far flow is larger and the near flow is smaller. The loss rate of the flow trace is 8%, and the effective rate of the flow trace is 92%. It can be concluded from the above that the efficiency of this structure is better than that of uniform distribution structure, but there are also vortices, the efficiency is not high, and each outlet flow is not uniform, which will affect the average of fertilization effect.

The distribution of water outlet pipe

Modify the three-dimensional finite element model of sprinkler pipe of fertilizer truck, reduce the number of outlet pipes to 8, start from the main inlet pipe according to the spacing, start from 140 mm, decrease by 10 mm each time, and increase until the spacing is 80 mm and carry out fluid analysis, as shown in Fig. 7. Other boundary conditions remain unchanged and other parameters are the same as those in Fig. 1.

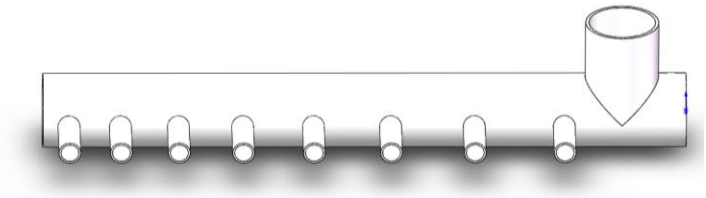

Fig. 7 - 3D model of structure in which the distribution distance of outlet pipe gradually decreases from the inlet

The global grid is selected for grid division. After 72 iterations, the flow trace is set as 50, and the baseline diameter is 2 mm. The pressure calculation results and flow trace are shown in Fig. 8, and the flow velocity nephogram and flow trace are shown in Fig. 9.

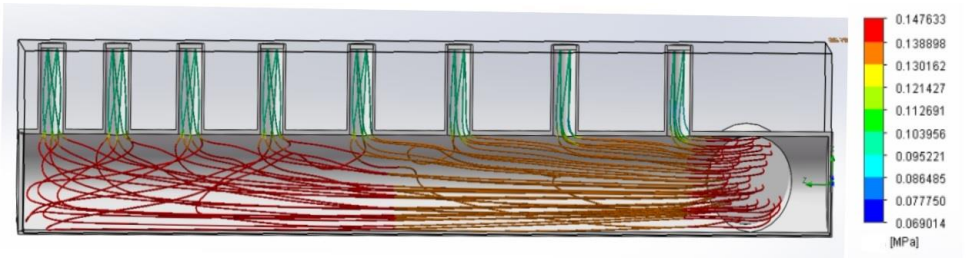

Fig. 8 - Pressure nephogram and flow trace of 3D structure model with the distance of outlet pipe decreasing gradually from inlet

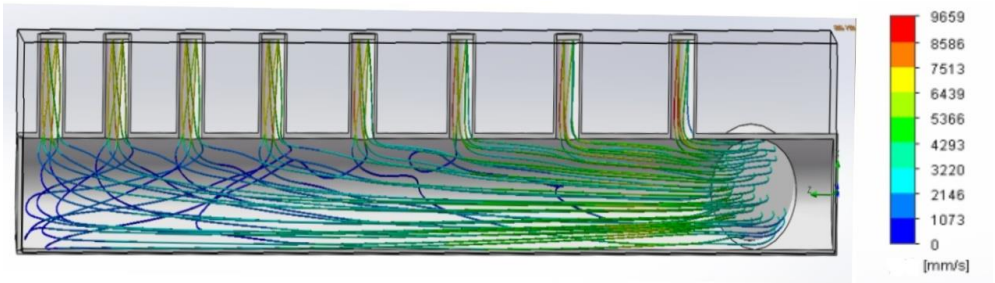

Fig. 9- Flow velocity nephogram and flow trace of 3D model with outlet pipe decreasing gradually from inlet

It can be seen from Fig. 8 that the water pressure at the inlet of the main pipe is the maximum, and the water pressure gradually decreases with the flow to the middle. When it reaches half of the main pipe on the left, the water pressure increases to the initial value. At the same time, the water pressure at the outlet is lower than that at the inlet. It can be concluded from Figure 9 that the water flow velocity at the inlet of the main pipe is the largest, and the flow velocity decreases gradually with the middle flow. When it reaches the end of the left main pipe, the flow velocity will be reduced to the lowest; there is no eddy current at the left end of the main pipe; meanwhile, the water flow velocity of the outlet is lower than the water velocity of the inlet.

Table 3

The distribution of outlet pipe gradually reduces the number of structural flow trace from the inlet

Serial number of outlet pipe (from left to right)	1	2	3	4	5	6	7	8	Loss
Number of flow traces	6	6	6	6	6	6	7	7	0

It can be concluded from table 3 that the highest number of flow traces is 7, which is at the 7th and 8th outlet pipe of the rightmost end, 60 cm away from the inlet centre; the number of flow traces of other outlet pipes are the same, all of them are 6; the number of flow traces is 0, and the loss rate is 0%.

It can be concluded that the number of flow traces of this structural model is relatively average, which also shows that the flow rate of each outlet is almost equal, the loss rate of flow trace is 0%, indicating that the flow efficiency is 100%, and there is no vortex on the left and right sides of the main pipe. To sum up, this kind of structure has the highest efficiency, the average flow rate of each outlet is almost equal, and the fertilization effect is equal, so this structure is finally selected.

CONCLUSIONS

1) Fluid numerical analysis shows that the sprinkler pipe is an important part in the design and manufacturing process of the fertilizer truck. The design of the fertilizer truck mainly focuses on the main pipe size design of the sprinkler pipe and the size design and distribution design of the outlet pipe orifice.

2) Structural calculation of outlet show that the spraying speed and uniformity of liquid fertilizer can be improved effectively by reasonably arranging the position, quantity and diameter of the outlet pipe.

3) The distribution analysis of water outlet pipe shows that the application of fluid finite element analysis method in the design of sprinkler pipe of suction and drainage integrated fertilizer truck can effectively improve the design quality of sprinkler pipe, reduce the blindness in sprinkler design, and improve the economy and accuracy of product design.

ACKNOWLEDGEMENTS

We acknowledge that this work was financially supported by the Shandong Major Agricultural Application Technology Innovation Project "Research, development and integration demonstration of key equipment for rural toilet waste treatment and utilization (No.SD2019NJ017)".

REFERENCES

[1] C. de L.T. de Andrade., R. G. Allen., (1999). SPRINKMOD pressure and discharge simulation model for pressurized irrigation systems. Model development and description. *Irrig Sci*, Issue 18, pp. 141-148, New York / United States.

[2] Capetillo C.B.., Robles O., Salinas H., Playán E., (2014). A particle tracking velocimetry technique for drop characterization in agricultural sprinklers. *Irrig Sci*, Issue 32, pp. 437-447, New York / U.S.A.

[3] Chen X., Zhou W., (2007). Vibration characteristic analysis of pressure pipes with fluid-structure interaction (压力管道流固耦合振动特性分析). *Journal of Rocket Propulsion*, Vol. 33, Issue 5, pp. 27-31, Xian / China.

[4] Feng W., Song L., Xiao G., (2009). Coupling analysis of fluid-structure interaction in pressure pipes based on *ADINA* (基于 ADINA 的压力管道流固耦合分析). *Engineering Journal of Wuhan University*, Vol. 42, Issue 2, pp. 264-267, Wuhan / China.

[5] Hu G., Long M., Liang J., Li W., (2012). Analysis of jet characteristics and structural optimization of a liquamatic fire water monitor with self-swinging mechanism. *International Journal Advanced Manufacturing Technology*, Issue 59, pp.805-813, Guildford / England.

[6] Giovanni R., Raffaele B., Marina D., (2017). Solid-fluid interaction: a continuum mechanics assessment. *Acta Mech*, Issue 228, pp. 851-869, Wien / Austria.

[7] Liao R., (2016). Analysis of the influence of diaphragm pier on the stability of flow in draft tube (隔墩对尾水管内部水流运动稳定性影响分析). *Yangtze River*, Issue 47, pp. 116-119, Wuhan / China.

[8] Liu R., Huang G., (2011). Numerical study on effect of inlet lip on hydrodynamics for water jet propulsion (入口唇角对喷水管道流动性能影响的数值分析). *Ship Building of China*, Vol. 52, Issue 1, pp. 39-46, Shanghai/China.

[9] Li S., Li S., Qin S., (2013). Research and application of water injection pipe with new connection mode (新型连接方式注水管的研制与应用). *Manufacturing informatization*, Issue 4, pp. 111-114, Jiangsu/China.

[10] Mohamad N.H.M., Asmuin N.Z., Basir M.F., Mohammad R.S., Mohd S.M.K., Taufq K.A.K., Marjan G., (2021). Optimizing nozzle convergent angle using central composite design on the particle velocity and acoustic power level for single-hose dry ice blasting nozzle. *Journal of Thermal Analysis and Calorimetry*, Issue 144, pp. 2159-2173, Dordrecht / Hungary.

[11] Neto O.R., Botrel T.A., Frizzone J. A., Camargo A.P., (2014). Method for determining friction head loss along elastic pipes. *Irrig Sci*, Issue 32, pp. 329–339, New York/United States.
[12] Tu Q., Li H., Wang X., Chen C., (2015). Ant colony optimization for the design of small-scale irrigation systems. *Water Resources Manage*, Issue 29, pp. 2323-2339, Beijing/China.
[13] Wang W., Guo J., Zhou C., Zhang J., Huang J., Yao W., (2020). COMSOL Fluid simulation analysis of urban water supply pipeline leakage (城市供水管道泄漏的 COMSOL 流体仿真分析). *China Municipal Engineering*, Issue 2, pp. 36-41, Shanghai/China.
[14] Xiang Q., Xue L., Kim KwangYong., Shi Z., (2019). Multi-objective optimization of a flow straightener in a large capacity firefighting water cannon (大容量火灾中流动矫直机的多目标优化). *Journal of Hydrodynamics*, Vol 31, Issue 1, pp. 137-144, Shanghai/China.
[15] Yan Z.，Chen G.，Xu C., (2018). Simulation study on stress and strain characteristics of fluid pipeline based on finite element model (基于有限元模型的流体管道应力应变特性仿真实验研究). *Research and Exploration in Laboratory*, Vol 37, Issue 7, pp. 110-114, Beijing /China.
[16] Yu P., Gao T., Li M., (2019). Design and optimization of pressure pipe of tea cleaning machine based on CFD fluid analysis technology (基于 CFD 流体分析技术的茶叶清洗机压力管道设计与优化). *Journal of Baoshan University*, Vol 38, Issue 5, pp. 27-31, Yunnan/China.
[17] Zhang B., (2019). Simulation and analysis of rotary kiln hot air pipeline based on SolidWorks (基于 CFD 流体分析技术的茶叶清洗机压力管道设计与优化). *Modern metallurgy*, Vol 47, Issue 5, pp. 60-62, Jiangsu/China.
[18] Zheng C., Zheng Q., Zhou D., Zan S., Sun Y., (2011). Numerical simulation on cavitation of throttle pipe in heat exchanger test-bed (换热器试验台节流管道气蚀现象数值模拟分析). *Refrigeration Air Conditioning & Electric Power Machinery*，Vol 32, Issue 2, pp. 12-15, Zhejiang/China.
[19] Zhu Y., Tang L., XU L., Peng K., Zhang Z., (2017). Design and simulation of wheel foot structure of a composite robot (一种复合式机器人的轮足结构设计及仿真). *Equipment Manufacturing Technology*, Issue 10, pp. 26-28, Guangxi /China.

EQUIPMENT AND EXPERIMENT OF GREENHOUSE HIGH-PRESSURE ATOMIZATION SPRAYING BASED ON PLC

/

基于 PLC 的温室高压雾化喷药设备及试验

Aoqi ZHANG[1)], Qinghai HE[2)], Guohai ZHANG[1,*)], Jitan LIAN[1)], Jia YAO[1)], Xin WANG[1)], Yujie DENG[1)], Xiaohui YANG[1)] [1]

[1)]School of Agricultural Engineering and Food Science, Shandong University of Technology, Zibo, 255000, China
[2)]Shandong Academy of Agricultural Machinery Sciences, Jinan, 250100, China
Tel: +86-15965534882; E-mail: guohaizhang@163.com
DOI: https://doi.org/10.35633/inmateh-68-15

Keywords: *greenhouses, fogging spray, PLC, orthogonal test*

ABSTRACT

Aiming at the problems of the low efficiency of manual pesticide application in the greenhouse, the narrow operating space of plant protection machinery, and the possibility of poisoning the pesticide applicators due to the closed space, a high-pressure atomization spraying equipment for the greenhouse was designed. The spraying equipment adopts two-way communication between PLC and HMI to realize the adjustment of atomization pressure and atomization flow, and the control equipment completes automatic spraying. To determine the best working parameters of the spraying equipment, orthogonal tests were conducted with atomization pressure and atomization nozzle aperture as the test factors and the coefficient of variation of the fog volume distribution as the evaluation index. The optimum combination after parameter optimization was determined to be as follows: atomization pressure of 4 MPa, atomization nozzle aperture of 0.4 mm. The test results under the optimal parameters showed that the spray distribution coefficient of variation was 10.5%, and the uniformity of fog volume distribution was good to meet the requirements of spraying in greenhouses.

摘要

针对温室手动施药效率低、植保机械作业空间狭窄、空间封闭容易造成施药人员中毒等问题，设计了一种温室高压雾化喷药设备。该喷药设备采用 PLC 和 HMI 之间的双向通信实现对雾化压力和雾化流量的调整，控制设备完成自动喷药。为确定喷药设备的最佳工作参数，以雾化压力和雾化喷头孔径为试验因素，以雾量分布变异系数为评价指标，进行了正交试验。获取最优参数组合为雾化压力为 4MPa、雾化喷头孔径为 0.4mm。最优参数下的试验结果表明，雾量分布变异系数为 10.5%，雾量分布均匀性较好，满足在温室大棚内的喷药要求。

INTRODUCTION

The greenhouse is to create a growth environment suitable for crop development under relatively controlled environmental conditions to achieve uninterrupted production of vegetables in all seasons, but the warm, humid greenhouse environment is very likely to cause disease and pest outbreaks, seriously affecting crop growth, yield, and quality (*He, 2020; He, 2018*). The current greenhouse application equipment is mainly semi-automatic rough machinery, spraying process droplet particle size, settling fast, easy to lose from the crop target, resulting in pesticide waste, soil pollution, while the closed, high-temperature greenhouse environment is easy to cause pesticide poisoning of application personnel (*Wang et al., 2021; Guo et al., 2022).*

Therefore, developing spray medicine equipment suitable for greenhouse growing patterns is an urgent need to achieve efficient production, and scholars at home and abroad have conducted a lot of research on spray medicine equipment for greenhouse environments. Some scholars used GPRS communication and control technology to achieve remote control and operation of the fogging machine in the greenhouse cluster (*Qi et al., 2016*). Some scholars used PLC as the controller, the developed greenhouse track application robot travels on the paved track, which initially realizes the automatic control of application in the greenhouse (*Li et al., 2016*). Some scholars have installed the spray nozzles on fixed brackets inside the greenhouse and used relays to automatically control the application time to achieve unmanned automatic applications (*Rowe et al., 2000*).

[1] *Aoqi Zhang M.S. Stud. Eng.; Qinghai He M.S. Eng.; Guohai Zhang, As. Ph.D. Eng.; Jitan Lian, M.S. Stud. Eng.; Jia Yao, M.S. Stud. Eng.; Xin Wang, M.S. Stud. Eng.; Yujie Deng, M.S. Stud. Eng.; Xiaohui Yang, M.S. Stud. Eng.*

Some scholars have designed a greenhouse automatic sprayer that advances and retreats along a rail laid between greenhouse crops (*Alireza Rafiq et al., 2014*). At present, some scholars have designed small spraying robots for greenhouse spraying that use sensors to detect plants and spray them (*Hossein Mosalanejad et al., 2021*).

This paper uses PLC controller as the core. The high-pressure atomization control system is used to control the spraying pressure and spraying time of the equipment. In order to spray automatically and isolate people from drugs in the spraying process, various sensors are adopted to real-time monitor the running status of the equipment, and the water consumption and the alarm of the equipment are recorded after each spraying.

MATERIALS AND METHODS

System design

The greenhouse high-pressure atomization spraying equipment mainly consists of four parts: control system, actuator, sensor module, and auxiliary components. The control system includes PLC controller and HMI touch screen. The actuator includes the inverter, high-pressure atomization pump, electric ball valve, high-pressure atomization nozzle, etc. The sensor modules include pressure sensors, flow sensors, and level sensors. The auxiliary components include medicine tank, water tank, high-pressure fogging pipeline etc.

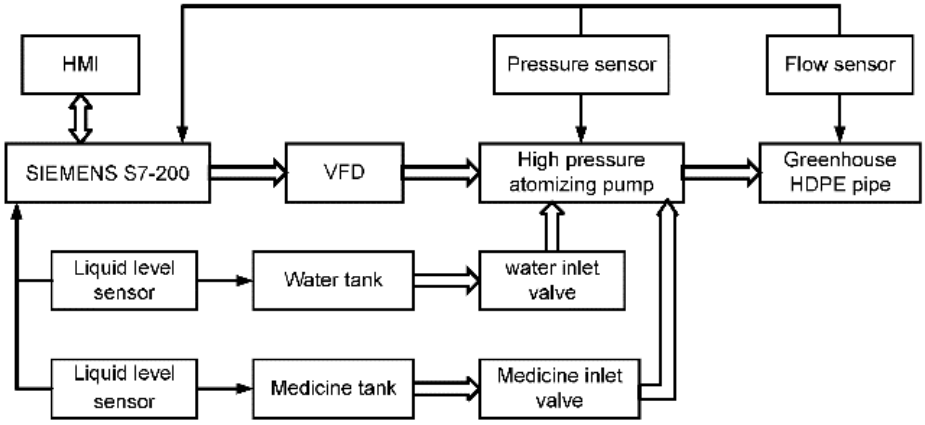

Fig. 1 - Block diagram of high-pressure atomization spraying system

The high-pressure fogging pipeline is arranged over the greenhouse, the pipeline selects 9.52 mm HDPE pipe, and the connection of the pipeline selects quick-connect 180° straight double spray joint, the spacing is 1.5 m, and the connection is made in straight series. High-pressure atomization spraying equipment is equipped with a standard interface for quick docking, and the high-pressure atomization pipeline is equipped with a corresponding docking interface for quick docking with the equipment. Each greenhouse requires only one set of high-pressure fogging pipes to be installed, and one unit can be used for multiple greenhouses, improving the utilization of equipment and reducing purchase costs.

Hardware design

The control system controller is an S7-200 SMART PLC, including a 4-way analogue input/2-way analogue output module, EM AM06. The working performance is more stable and can meet the requirements of the greenhouse site. The touch screen is PI8102-R of WECON, using PIStudio configuration software to write a greenhouse spray control system program, for parameter setting and real-time monitoring, communicating with PLC via RS-485 bus.

The actuator uses the BZ-986-45 high-pressure atomization pump with a power of 5.5KW. It has the advantage of high volumetric efficiency, good uniformity of liquid flow, and can meet high-pressure work. The working principle is: after the power is turned on, the liquid at low water level first enters from the inlet of the pump, generating a vacuum, and then discharges after being pressurized by the pump, and the discharged fluid is conveyed along the line into the spray tube, sprayed from each nozzle on the spray tube under high pressure. Depending on the spray pressure and nozzle type, fog with different droplet diameters is produced.

The performance of the nozzle directly affects the effect of atomized spraying. Select the high-pressure atomization nozzle with excellent atomization effect, stable spraying, and anti-drip. Commonly used nozzles are divided into 9 models from 0 to 8. After experimental testing, the No.4 high-pressure nozzle meets the greenhouse spraying requirements. Through the regulation of pressure, its spraying effect can meet the needs of greenhouse spraying pesticides and foliar fertilizers.

Table 1

Flow rates of different nozzle aperture at different pressures

Nozzle model		Flow rate（L/min）		
Model number	Nozzle aperture	4MPa	5MPa	6MPa
No. 2	0.2mm	0.07	0.08	0.09
No. 3	0.3mm	0.09	0.10	0.11
No. 4	0.4mm	0.22	0.25	0.28
No. 5	0.5mm	0.23	0.26	0.30
No. 6	0.6mm	0.27	0.32	0.38

As the detection part of the whole control system, the sensor element plays a crucial role and is the basis for the decision of the control system, the data acquired by the sensors directly affects the execution of the system actions (*Zhang et al., 2017*). The sensor module of this system mainly includes pressure sensor, flow sensor, and liquid level sensor. The selection is shown in Table 2.

Table 2

Sensor Model

Name of sensor	Model Specification
Pressure sensor	Measuring range: 0~20MPa, Accuracy: 0.5%, Two-wire system, Output: 4~20mA
Flow sensor	WL-LWGB-30 flowmeter, Two-wire system, Output: 4~20mA
Liquid level sensor	Measuring range: 0~1000mm, Accuracy: 0.2%, Two-wire system, Output: 4~20mA

Software design of high-pressure fogging spraying equipment for greenhouse

PLC control program design

The control programming is mainly written in the ladder language under the Siemens programming software STEP 7-Micro/WIN SMART environment. The system workflow is shown in Figure 2.

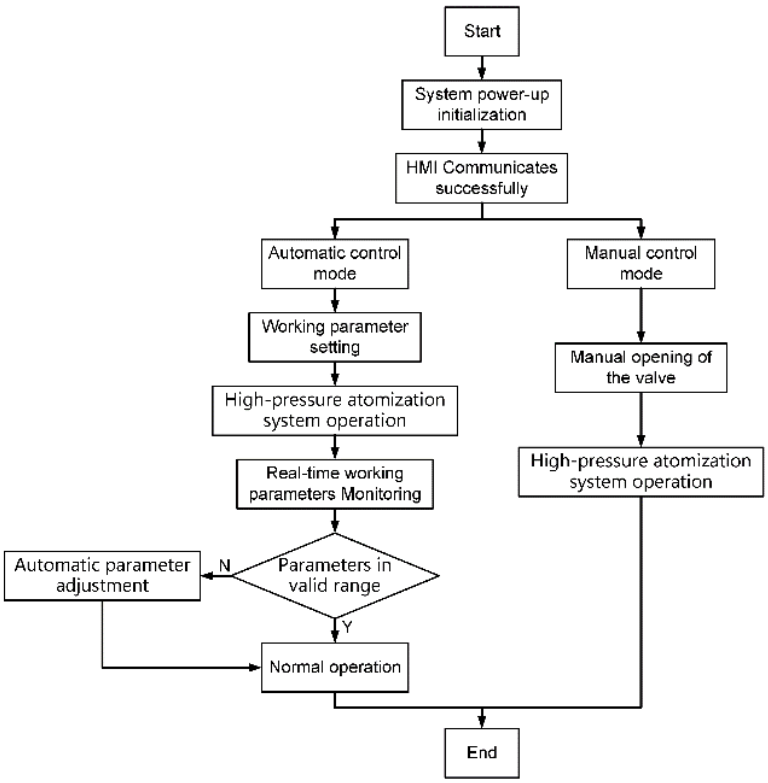

Fig. 2 - Control system workflow

After the greenhouse spraying equipment is started, there are two working modes to choose from, automatic and manual. In the automatic mode, the greenhouse spraying equipment enters the autonomous spraying state. After initialization, the system first reads the liquid level of the medicine tank and water tank and issues an alarm if it is lower than the minimum liquid level.

Set the working pressure, and working time, on the touch screen, the liquid level sensor detects that the liquid level has reached a predetermined value and turns on the spraying, medicine tank, water tank solenoid valve which open at the same time, after mixing water and medicine through the high-pressure pump to reach the nozzle to start the spraying work. The pressure sensor detects whether the pressure is within the set value in real-time, flow sensors measure the total spray volume, and the solenoid valve closes when the set time is reached. After reaching the set time, the solenoid valve closes and the spraying work stops automatically. In manual mode, spraying works by human control. The operator can freely set the equipment spraying pressure, spraying time, solenoid valve flow, and other various parameters to achieve a more accurate spraying effect.

HMI design

The Human Machine Interface (HMI) allows users to observe the operation status of spraying equipment at all times to achieve the purpose of real-time monitoring. Design the equipment operating status interface through the WECON PIStudio configuration software programming environment.

The default state of the system is the interface for setting the operating parameters of the device, as shown in Figure 3. Manual and automatic working modes can be selected in the parameter setting interface. In manual mode set the high-pressure pump pressure, click the spray pump, water valve, and drug valve switch button in turn, and you can carry out spraying work. In automatic mode set high-pressure pump pressure, and atomization time can be automatic spraying.

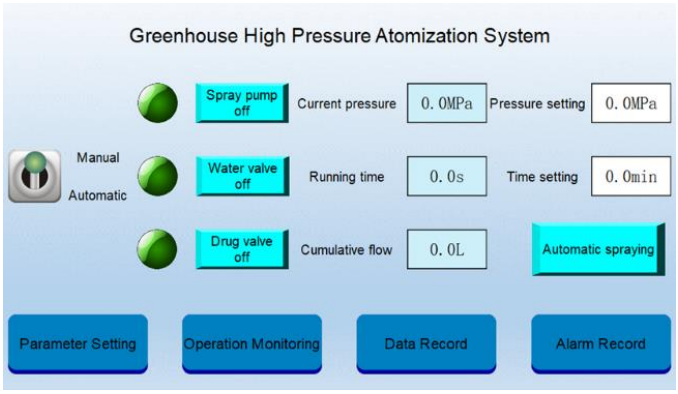

Fig. 3 - Working parameter setting interface

In the system operation monitoring interface, as shown in Figure 4, users can observe the current working pressure of the high-pressure pump, the working status of the solenoid valve of the medicine tank and water tank, as well as the liquid level of the medicine tank and water tank. In the data logging screen, users can view the equipment's past work history. In the alarm logging interface, users can view the contents of the alarms during the operation of the device.

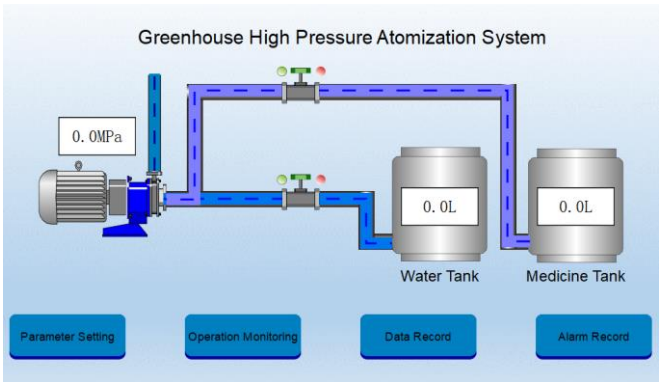

Fig. 4 - Work status monitoring interface

Experimental design

The high-pressure atomization spraying test is conducted according to the relevant national standard JB/T 9782-2014 "Equipment for crop Protection-General test methods". The experiment was conducted in June 2022 in Dongying City, Shandong Province. The greenhouse spans 10 m in the east-west direction and 70 m in the north-south direction, and a green pepper crop with a plant height of 150 cm and a spacing of 40 cm was used as the test object.

Randomly select 6 rows of green peppers in the greenhouse and fix the Water Sensitive Paper on the leaf with a paper clip, adjust the working parameters of the equipment for spraying operations, and collect the Water Sensitive Paper after completion. Fog drop coverage of Water Sensitive Paper was obtained by image processing using DepositScan software. The coefficient of variation of the fog volume distribution is used as an indicator, and the data obtained are analysed to determine the optimal value of each influencing factor.

The coefficient of variation of the fog volume (CV) distribution is an indicator that reflects the uniformity of the fog volume distribution along the axial direction of the fog flow of the nozzle. The smaller the coefficient of variation, the more uniform the distribution of spraying.

The calculation formula is as follows:

$$CV = \frac{S}{\overline{X}} \times 100\% \quad (1)$$

Where:

CV- is the spray distribution coefficient of variation;

S- is the standard deviation of the sample data;

$\overline{X}$- is the mean of the sample data.

RESULTS AND ANALYSIS

Single factor test

The range of the three factors that significantly affect the uniformity of atomization distribution is determined by single-factor tests, and the basis for orthogonal tests to determine the optimal test parameters is laid. The main factors affecting the uniformity of atomization distribution are high-pressure atomization pressure, high-pressure atomization nozzle aperture, and high-pressure atomization time.

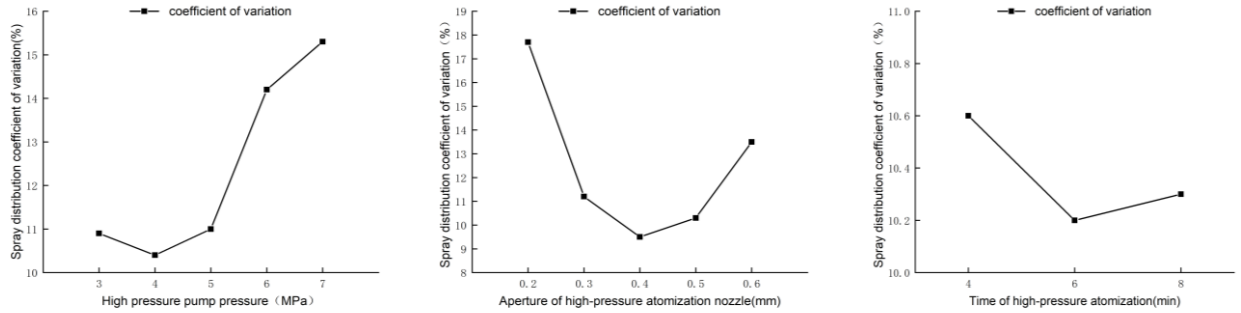

(a) (b) (c)

Fig. 5 - Influence of different factors on the effect of greenhouse fogging spraying

Before the experiment, run the high-pressure atomization pump to empty the air in the HDPE pipe and wait for the system to run stably. High-pressure atomization nozzle aperture selection of 0.4 mm is made, nozzle spacing is 100 cm, high-pressure atomization time is set to 5 min, and high-pressure atomization pressure is set to 3, 4, 5, 6, and 7 MPa respectively. It can be seen from Figure 5-a that with the increase of the atomization pressure, the coefficient of variation of the fog volume distribution increases and decreases. When the fogging pressure is in the range of 3 MPa to 5 MPa, the coefficient of variation is less than 11%, indicating that the fogging spraying effect is better.

High-pressure atomization pressure is set to 4 MPa, nozzle spacing is 100 cm, high-pressure atomization time is set to 5 min, high-pressure atomization nozzle aperture selection of 0.2, 0.3, 0.4, 0.5, 0.6 mm respectively is made. It can be seen from Figure 5-b that with the increase of atomization pressure, the coefficient of variation of fog volume distribution decreases and increases. The coefficient of variation was less than 11% when the nozzle aperture diameter was in the range of 0.3 mm to 0.5 mm, indicating a better fogging application effect.

High-pressure atomization pressure is set to 4MPa, high-pressure atomization nozzle aperture selection of 0.4 mm is made and nozzle spacing is 100 cm. High-pressure atomization time is set to 4, 6, and 8 min respectively. It can be seen from Figure 5-c that the coefficient of variation of the fog volume distribution does not change significantly with the extension of the fogging time. The coefficients of variation of the distributions

were all below 11%, indicating that there was no significant correlation between the coefficients of variation and the fogging time.

Orthogonal experiment

Through the single-factor test, the coefficient of variation of the fog volume distribution did not change significantly with the extension of the atomization time, and the high-pressure atomization pressure and the aperture diameter of the atomization nozzle had a significant effect. The orthogonal test was designed according to the range obtained from the Single factor test, and the levels of each factor were determined as shown in Table 3.

Table 3

Experimental factors and levels

levels	Factors	
	High-pressure atomization pressure (MPa) A	Aperture diameter of the atomization nozzle (mm) B
1	5	0.5
2	4	0.4
3	3	0.3

According to the test scheme, 9 groups of tests were performed, and each group of tests was repeated three times. Take the average value as the test results. And the test results are shown in Table 4.

Table 4

The experiment results

Test number	A (MPa)	B (mm)	Average droplet coverage (%)	Coefficient of variation (%)
1	1	1	45.1	12.1
2	1	2	28.0	11.6
3	1	3	14.7	12.5
4	2	1	38.5	11.4
5	2	2	21.2	10.7
6	2	3	12.4	11.9
7	3	1	24.6	13.2
8	3	2	16.7	12.6
9	3	3	9.9	13.9
Y	k1	36.2	36.7	
	k2	34.0	34.9	
	k3	39.7	38.3	
	R	5.7	3.4	
	better level	A_2	B_2	
	Major and minor factors	A_2B_2		

Analysis of variance was performed using Design Export 12.0 and the results are shown in Table 5.

Table 5

Variance analysis results

Source	SS	DF	MS	F Value	P Value
Model	7.46	5	1.49	156.45	0.0008
A	2.04	1	2.04	214.08	0.0007
B	0.43	1	0.43	44.74	0.0068
AB	0.022	1	0.022	2.36	0.2221
A^2	3.47	1	3.47	363.55	0.0003
B^2	1.50	1	1.50	157.51	0.0011
Residual	0.029	3	9.537×10-3		
Cor Total	7.49	8			

Note: SS is the sum of squares of deviations; DF is the degrees of freedom; MS is the average of the sum of squares of deviations; $P < 0.01$ (extremely significant); $0.01 < P < 0.05$ (significant); $P > 0.05$ (not significant).

It can be seen from Table 5 that A, B, A^2, and B^2 have extremely significant effects on the damage rate ($P<0.01$). Other factors had no significant effect on the damage rate ($P>0.1$).

After removing insignificant terms, the fitted regression equation is:

$$Y = 10.76 - 0.58A - 0.27B + 1.32A^2 + 0.87B^2 \quad (2)$$

Comprehensive range and variance analysis show that the optimal level combination of the uniformity of the distribution of spraying mist in the greenhouse is A_2B_2, and the order of influence on the uniformity of fog volume distribution is A>B. To obtain the optimal operating parameters of the greenhouse fogging spraying equipment, the optimization module in Design-Export 12.0 was used to solve for the optimal parameters with the coefficient of variation of the fog volume distribution as the optimization objective. It can be obtained in the test range, when the high-pressure atomization pressure is 4 MPa, atomization nozzle aperture diameter is 0.4 mm. The test results may obtain the minimum spray distribution coefficient of 10.6%.

With the optimal combination of test parameters, when other parameters remain unchanged, high-pressure fogging pressure is 4 MPa, fogging nozzle aperture is 0.4 mm for greenhouse fogging spray test, the results of the three tests are averaged. The spray distribution coefficient of variation is 10.5%, which is similar to the predicted 10.6%. The results from the experimental analysis are consistent with the actual working results.

CONCLUSIONS

In this study a greenhouse high-pressure fogging spraying equipment based on PLC controller and HMI touch screen was designed. The equipment can complete the manual or automatic spraying work in the greenhouse.

To determine the optimal operating parameters of the equipment, orthogonal tests were conducted with atomization pressure and atomization nozzle aperture as the test factors and the spray distribution coefficient of variation as the evaluation index. Through the range and variance analysis of the spray distribution coefficient of variation, the influence of the factors on the response index is obtained.

Taking the spray distribution coefficient of variation as the optimization goal, the best working parameters are obtained. The best working parameters are: high-pressure atomization pressure 4 MPa, atomization nozzle aperture 0.4 mm, to obtain the spray distribution coefficient of variation 10.5%. The results of the validation tests show that the results from the test analysis are consistent with the actual working results.

ACKNOWLEDGEMENT

The work was supported by the Colleges and Universities of Shandong Province Advantage Discipline Talent Team Cultivation Program Project.

REFERENCES

[1] Alireza Rafiq, Davood Kalantari, Hamid Mashhadimeyghani. (2014). Construction and development of an automatic sprayer for greenhouse. *Inventi Impact Agro Tech*, Vol. 16, No. 2, 36-40.

[2] Guo Na, Tian Subo, Xu Hui et al. (2022). Research progress on precision spraying technology and equipment of protected horticulture (设施园艺植保装备及其精准施药技术研究进展). *Journal of Agricultural Mechanization Research*, Vol. 44, No. 11, 1-10.

[3] Hassan Poorvousooghi Gargari, Rahman Farrokhi Teimourlou, Morteza Valizadeh. (2019). Spray droplet characterization using a piezoelectric sensor through classification based on machine learning. *INMATEH-Agricultural Engineering,* Vol. 59, No. 3, 151-160.

[4] He Xiongkui. (2020). Research progress and developmental recommendations on precision spraying technology and equipment in China (中国精准施药技术和装备研究现状及发展建议). *Smart Agriculture*, Vol. 2, No. 1, 133-146.

[5] He Xiongkui. (2018). Research and development and application of high-efficiency pesticide application equipment and technology for vegetables (蔬菜高效施药装备与技术研发应用). *Vegetables*, No. 8, 1-17.

[6] Hossein Mosalanejad, Saeid Minaei, Alimohammad Borghei, et al. (2021). Navigation, validation and evaluation of four-wheeled robot for greenhouse spraying. *INMATEH-Agricultural Engineering*, Vol. 63, No. 1, 169-178.

[7] Jiang Huanyu, Zhang Lijun, Shi Weinan. (2016). Effects of Operating Parameters for Dynamic PWM Variable Spray System on Spray Distribution Uniformity. *Ifac Papersonline*, Vol. 49, No.16, 216-220.

[8] Kang Feng, Wu Xuanyi, Wang Yaxiong, et al. (2021). Research progress and prospect of pesticide

droplet deposition characteristics (农药雾滴沉积特性研究进展与展望). *Transactions of the Chinese Society of Agricultural Engineering*, Vol. 37, No. 20, 1-14.

[9] Luck J.D., Shearer S.A., Sama M.P. et al. (2015). Control system development and response analysis of an electronically actuated variable-orifice nozzle for agricultural pesticide applications. *Transactions of the ASABE*, Vol. 58, No.4, 997-1008.

[10] Lv Shixiong, Hu Jianing, Ren Zhenhui, et al. (2021). Design of Control System of Variable Flow Target Mist Sprayer Based on PLC (基于 PLC 的可变量对靶弥雾喷药机控制系统设计). *Journal of Agricultural Mechanization Research*, Vol. 43, No. 12, 152-156.

[11] Li Jingzhu, Zhu Fengwu. (2017). Design and experiment of automatic targeting spraying control system based on PLC (基于 PLC 自动对靶喷雾控制系统的设计与试验). *Journal of Chinese Agricultural Mechanization*, Vol. 38, No. 8, 55-58.

[12] Li Liang, Zhang Wenai, Feng Qingchun et al. (2016). System design for rail spraying robot in greenhouse (温室轨道施药机器人系统设计). *Journal of Agricultural Mechanization Research*, Vol. 38, No. 1, 109-112+118.

[13] Mei Yincheng, Qi Lijun, Ji Ronghua et al. (2016). Design and experiment of remote control system of greenhouse self-propelled mist sprayer (温室自走式弥雾机远程控制系统的设计与试验). *Journal of China Agricultural University*, Vol. 20, No. 1, 170-175.

[14] Qi Lijun, Du Zhengwei, Ji Ronghua et al. (2016). Design of remote control system for automatic sprayer based on GPRS in greenhouse (基于 GPRS 的远程控制温室自动施药系统设计). *Transactions of the Chinese Society of Agricultural Engineering*, Vol. 32, No. 23, 51-57.

[15] Rafiq A, Kalantari D, Mashhadimeyghani H. (2014). Construction and development of an automatic sprayer for greenhouse. *Agricultural Engineering International: The CIGR e-journal*, Vol. 16, No.2, 36-40.

[16] Rowe D.E., Malone S., Yates Q.L. (2000). Automated Greenhouse Spray System for Increased Safety and Flexibility. *Crop Science*, Vol. 40, No.4. 1176-1179.

[17] Wang Guobin, Li Xuan, John Andaloro, et al. (2021). Current status and prospects of precise sampling of pesticide droplets (田间农药雾滴精准采样技术与发展趋势). *Transactions of the Chinese Society of Agricultural Engineering*, Vol. 37, No. 11, 1-12.

[18] Wang Lu, Chen Yongcheng, Su Di, et al. (2015). Experimental study on spray distribution uniformity of the spray rod (喷杆式喷雾分布均匀性试验研究). *Journal of Agricultural Mechanization Research*, Vol. 37, No. 10, 193-196+200.

[19] Zhang Jianhua, Wu Jianzhai, Han Shuqing et al. (2017). Research progress and performance analysis of agricultural sensor technology (农业传感器技术研究进展与性能分析). *Agricultural Outlook*, Vol. 13, No. 1, 38-48.

[20] Zou Xuejian, Zang Xiufa, Wang Xiaoyong. (2020). Status and Development Measures of Plant Protection Machinery and Pesticide Application Technique (我国植保机械与施药技术现状及发展措施). *Agricultural Science&Technology and Equipment*, No. 12, 49-50.

DESIGN AND EXPERIMENTAL STUDY OF MOISTURE CONTENT DETECTION DEVICE BASED ON CAPACITIVE METHOD

/

基于电容法含水率检测装置设计与试验研究

Chao HUANG[1)], Shu CHEN[1)], Qing JIANG*[1,2)], Liang-yuan XU[1,2)]
[1)]College of Engineering, Anhui Agricultural University, Anhui/China
[2)]Anhui Province Engineering Laboratory of Intelligent Agricultural Machinery and Equipment, Anhui/China
Tel: +86 0551-65786450; E-mail: jtao@ahau.edu.cn
Corresponding authors: Qing Jang
DOI: https://doi.org/10.35633/inmateh-68-16

Keywords: *Capacitance method, Detection precision, Moisture detection, Parallel-plate moisture content detection device (PPMCDD).*

ABSTRACT

To enable the accurate detection of grain moisture content and improve the efficiency of the drying process, a parallel-plate moisture content detection device (PPMCDD) was developed in this study. Firstly, the detection principle and influencing factors of this device are analyzed. Then the effects of three key factors as distance, thickness, relative area on the accuracy of the device were determined through simulation, and the optimal combination of parameters was obtained through analysis of variance of a regression model and response surface methodology. Finally, a simple test bench is built to verify the effectiveness of PPMCDD by comparative experiment. Through simulation and response surface analysis, the optimal combination parameters are as follows: thickness =1 mm, pacing =19.54 mm, relative area =4023.17 mm2, corresponding to the measured capacitance value of 37.676 pF. By comparative experimental analysis, it is found that the maximal relative error of the moisture content detection device evaluated in this study was 1.58%. The detection error is small, and the device exhibits high accuracy and stability and meets the design requirement.

摘要

为了提高烘干机谷物含水率的检测精度和干燥过程的效率，本研究开发了一种基于电容法的平行板式含水率检测装置(PPMCDD)。首先，根据电容检测原理和影响因素进行了分析，并对平行极板模型进行了初步设计；然后通过仿真确定了距离、厚度、相对面积三个关键因素对装置精度的影响，并通过回归模型方差分析和响应面法得到最佳参数组合；最后通过对比实验验证 PPMCDD 的有效性。通过仿真和响应面分析得到最佳的组合参数为：厚度=1㎜，间距=19.54㎜，相对面积=4023.17㎜2，对应实测电容值为 37.676pF；并且通过对比实验分析，本研究评估的含水率检测装置的最大相对误差为 1.58%。PPMCDD 检测误差小，具有较高的检测精度及稳定性，满足设计要求。

INTRODUCTION

Moisture content is one of the important quality parameters of grain, which is related to the value of the grain. It is of great significance in the grain harvest, processing, storage and trade. When harvesting grain in the field, the grain moisture content is the key index affecting the operational performance and efficiency of the combined harvester. With the rapid development of science and technology, grain output is increasing constantly; however, for various reasons, a large quantity of grain is rendered unusable each year. *Yigit et al., (2018),* reported that defects in the drying process and in the moisture detection technology employed in grain dryers directly lead to the deterioration of many grains, which may develop high moisture content if stored for too long. Geographical location, seasons, and harvesting methods affect the moisture content of grain. If the moisture content exceeds the recommended value because of insufficient drying, the grain is affected by the excess moisture and mildew. Many scholars found that excessive drying can also damage the grain's quality (*Fan et al., 2020; Zambrano et al., 2019; Sosa-Morales et al., 2010)*. Therefore, a rapid and accurate moisture content detection instrument and real-time monitoring can improve the drying process and preserve the quality of grains.

[1] *Chao, Huang, M.S. Stud. Eng.; Shu Chen, M.S. Stud. Eng.;Qing Jiang, Prof. M.S. Eng.; Liangyuan Xu, Prof. Ph.D. Eng.*

Many scholars have made outstanding contributions to the development of moisture detection devices. *Rai et al., (2008),* used the principle of the dielectric constant changing with moisture content to develop a model for measuring moisture content. *Wang et al., (2009),* proposed an online method based on electrical capacitance tomography for the measurement of solid moisture after intermittent drying in a fluidized bed dryer. *Kandala and Puppala, (2013),* employed a parallel-plate capacitance sensor and an impedance meter to determine the average moisture content of peanuts, wheat, and other grains by measuring impedance and the phase angle. *Kim et al., (2000),* studied the effect of the permittivity of rice with moisture content of 11%–27% and wheat with the moisture content of 11%–21% in South Korea and developed a grain moisture meter that uses 10.5-GHz microwave attenuation and water density.

Jiang and Hua, (2009), studied multiple sensing mechanisms and developed an improved back-propagation neural network for the online detection of moisture in corn; the authors developed hardware for a corn moisture detection system using an STM32F103C8T6 microcontroller unit (MCU) as the core. *Casada and Armstrong, (2009),* tested the applicability and accuracy of an edge effect capacitive sensor in measuring grain moisture content. *Mcintosh and Casada, (2008),* studied a fringing field capacitive sensor for measuring the moisture content and temperature of agricultural products.

Laleicke et al., (2018), studied a four-channel planar capacitance sensor and calibrated it on maple veneer. *Fan et al., (2020),* studied the online detection method based on capacitance method through the combination of AD7745 chip and single chip microcomputer, and proved the correlation between capacitance change and moisture content.

The accuracy of grains moisture content detection performed using dryers devices is low because the calculations do not account for individual influential factors. Furthermore, such systems often do not allow for the real-time transmission of information. In this paper, we describe a parallel-plate moisture content detection device (PPMCDD) developed on the basis of capacitance method, which allows for real-time monitoring of the test bench, optimization of structural parameters, performance testing, and calibration of the platform based on individual factors. The consideration of the aforementioned capabilities in the design and development contributed to the device's high accuracy and reliability.

MATERIALS AND METHODS

Measuring Principles and Factors Influencing PPMCDD

Grain moisture detection methods can be divided into two categories: direct detection and indirect detection *(Nelson et al., (2016)*. Direct detection methods include drying measurement and chemical measurement, which are often used for the detection of moisture content in small amounts of grain or laboratory samples. Indirect detection methods include resistance, capacitance, microwave, infrared, nuclear magnetic resonance, neutron, and radiofrequency impedance methods. The PPMCDD presented in this paper employs a design based on the principles of capacitance sensing. Compared with a cylinder-type moisture detection device, the proposed device requires less space, has a simpler structure, is more convenient and cost inexpensive to install, and has fewer requirements for installation related to the surrounding working environment. The basic structure of the PPMCDD consists of two metal plates, as illustrated in Figure 1. The basic formula for calculating the capacitance of the parallel plates is as follows:

$$C = \frac{\varepsilon_0 \varepsilon A}{D} \tag{1}$$

Where:

ε_0 is the permittivity of vacuum (8.85×10^{-15} F/m), ε is the relative permittivity between the two plates, A is relative area of the plates (mm^2), D is spacing between the plates (mm).

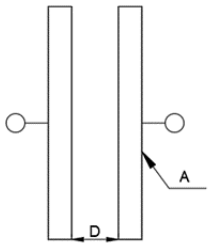

Fig. 1 - The basic structure of parallel plates

To test the performance of the PPMCDD, the composition of the media inserted between the parallel plates can be simplified into the grain, water, and air to facilitate our study. The simplified model is illustrated in Figure 2, and Figure 3 presents the size of the gap between the parallel plates.

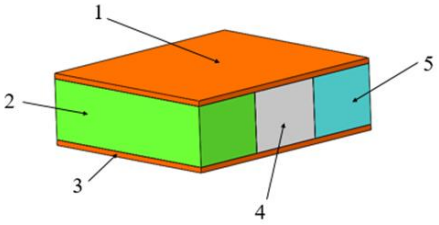

Fig. 2 - Equivalent model of medium between parallel plates

1 - Upper plate; 2 – Grain; 3 - Lower plate; 4 - Air 5 - Water

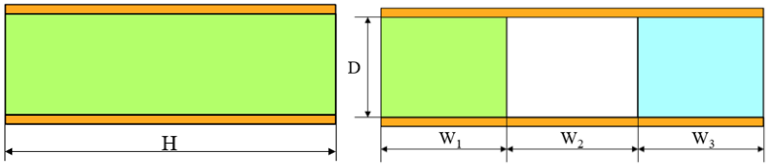

Fig. 3 - Structural dimensions between parallel plates

The three relative permittivity values of the parallel-plate device are ε_1 , ε_2 , and ε_3 , and the corresponding capacitance values of the cavity are C_1, C_2, and C_3. Therefore, the total capacitance of the two plates can be calculated as follows:

$$C = \frac{\varepsilon_0 A}{D}\left(\frac{A_1}{A}\varepsilon_1 + \frac{A_2}{A}\varepsilon_2 + \frac{A_3}{A}\varepsilon_3\right) \quad (2)$$

Where:

A_1, A_2, and A_3 are relative areas of the grain, water, and air media.

The moisture content w of grain is then calculated as follows:

$$w = \frac{m_2}{m_1 + m_2} \times 100\% = \frac{\rho_2 A_2}{\rho_1 A_1 + \rho_2 A_2} \quad (3)$$

Where:

m_1 and ρ_1 are mass and density of the grain in the parallel plate, m_2 and ρ_2 are mass and density of the water in the grain.

Korkua and Sakphrom, (2020), concluded that the density of water is ρ_2=1and the dielectric constant of vacuum is $\varepsilon_0 = 8.85 \times 10^{-12}\,\mathrm{F/m}$. A_3/A represents the pore ratio of the parallel plates and is denoted by e. In the final design of the PPMCDD, A and D are fixed values and are therefore treated as constants. With $k_0 = \frac{\varepsilon_0 A}{D}$, the aforementioned formula (2-3) can be presented as follows:

$$C = k_0\varepsilon_1 + k_0\left(\varepsilon_2 - \varepsilon_1\right)\left(1 - e\right) \times \frac{w\rho_1}{1 + w\left(\rho_1 - 1\right)} + k_0 e\left(\varepsilon_3 - \varepsilon_1\right) \quad (4)$$

According to Eq. (4), the moisture content of grain exhibits a one-to-one correspondence with the capacitance value. From the capacitance, the moisture content of the grain at a given temperature can be calculated. However, because the permittivity between the parallel plates changes with the ambient temperature, a temperature sensor is required and can be used by the MCU to accordingly adjust the dielectric constant. When grain moisture is measured using a PPMCDD, the pore ratio is affected by the bulk density of the grain. Therefore, the bulk density must be accounted for to minimize the effect of the pore ratio on the accuracy of the collected data. To summarize, when the PPMCDD is used to detect grain moisture content, the reported values are affected by the ambient temperature and bulk density of the grain in the sensor. Therefore, in the design and optimization of a sensor, these factors should be considered to maximize the detection accuracy and practicability of the device.

Material Preparation and Test Methods

A national standard drying method (the 105°C constant weight method) was used to measure the moisture content of Anhui 185 indica hybrid rice planted in the vicinity of Lu'an in Anhui province. The main test equipment used comprised Petri dishes, a precision balance, and an electric air-drying oven. The test was conducted as follows. First, clean Petri dishes were placed into an electric blast box, dried for 30 min, and placed into a drying container for cooling. The Petri dishes were weighed using a precision balance; the weight of an empty Petri dish was recorded as M_1. An appropriate amount of rice was placed into each dried Petri dish for weighing. After drying, the rice was weighed, and the weight was recorded as M_2. To ensure the accuracy of the experimental results, the total amount of rice to be measured was evenly divided into three parts, which were dried and measured successively, and the average value of the measurements was recorded.

The Box–Behnken method was used in this test to determine the optimal device parameters for measuring capacitance (*Boateng et al., 2021; Khatib et al., 2021*). The factors considered comprised the plate spacing D (mm), plate thickness H (mm), and relative area A (mm^2). The Box–Behnken method was used to design a three-level test accounting for these factors, and the capacitance measured by the PPMCDD was considered the response value. The influencing factors and their optimal levels were determined through simulation. The optimal levels of each of the factors are presented in Table 1.

Table 1

Factor level table

Order	Independent variable	Value of each factor level		
		1	0	-1
1	Distance (mm)	30	20	10
2	Thickness (mm)	3	2	1
3	Relative area (mm2)	6000	4500	3000

RESULTS

Data processing and analysis

Design-Expert software was used to process the test data of Table 1. The test results are presented in Table 2.

Test results **Table 2**

Source	Sum of squares	df	Sum of mean square	F-value	P-value
model	200.51	9	22.28	45.26	0.0001
X1	52.69	1	52.69	107.04	0.0001
X2	7.16	1	7.16	14.55	0.0066
X3-	0.42	1	0.42	0.86	0.3846
X1X2	1.11	1	1.11	2.26	0.1763
X1X3	20.34	1	20.34	41.33	0.0004
X2X3	6.30	1	6.3	12.8	0.009
X12	10.53	1	10.53	21.4	0.0024
X22	37.94	1	37.94	77.08	0.0001
X32	53.49	1	53.49	108.68	0.0001
Residual	3.45	7	0.49		
Lack of fit	2.34	3	0.78	2.83	0.1703
Pure error	1.10	4	0.28		
Cor total	203.96	16			
R^2=0.9831, *Adj* R^2=0.9614					

[a] *X_1=Thickness (mm), X_2=Distance (mm), X_3=Relative area (mm^2).*

[b] *A p-value <0.01 was considered extremely significant, a p-value ≤0.1 was considered significant, and a p-value >0.1 was considered nonsignificant.*

After nonsignificant factors were removed, the regression equation for the capacitance Y_c was determined:

$$Y_C = 14.36375 - 4.05925X_1 + 0.81333X_2 - 9.42367\times10^{-3}X_3 + 0.05275X_1X_2 + 1.50333\times10^{-3}X_1X_3 + 8.36667\times10^{-5}X_2X_3 - 1.58175X_1^2 - 0.03002X_2^2 - 1.58411\times10^{-6}X_3^2 \quad (5)$$

Where: Y_c is capacitance value (pF), X_1 is plate thickness (mm), X_2 is plate spacing (mm), X_3 is relative area (mm²).

The fitted model accurately described the relationship between measured capacitance and the characteristics of the parallel plates, as indicated by the table 2 results that were significant at $p < 0.01$. The effects of plate thickness ($p = 0.0001$) and plate spacing ($p=0.0066$) on capacitance were extremely significant; however, the effect of relative plate area was nonsignificant ($p = 0.3846$). The calculated coefficient of determination ($R^2 = 0.9831$) and adjusted coefficient of determination ($Adj\ R^2 = 0.9614$) indicate that the proposed model is highly accurate in predicting capacitance.

Optimization of Structural Parameters

The edge effect of a parallel-plate capacitor affects the moisture content detected by the device. The edge effect is mainly caused by changes in the electric field lines from parallel to open lines as the width of the space between the plates increases; the edge effect causes the distribution of the electric field lines to concentrate at the edges of the plates, resulting in additional capacitance. Therefore, optimization of the plate structure is key to minimizing the influence of the edge effect and improving the accuracy of capacitance detection.

The effects of the interactions among plate thickness, spacing, and relative area on capacitance, as determined through the analysis conducted using the Design-Expert software, are presented in Figure 4. The effect of the interaction between plate thickness and plate spacing is nonsignificant; however, the interactions of plate spacing and plate thickness with relative area strongly affect capacitance measurement. As the plate spacing decreases and the plate thickness and relative area increase, the measured capacitance increases.

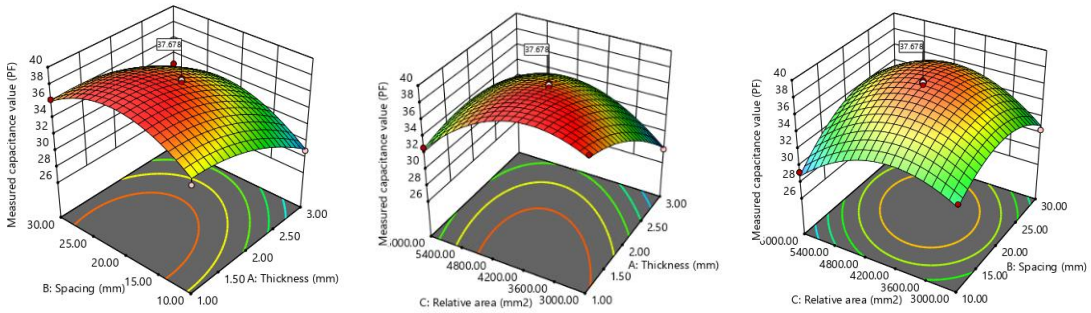

Fig. 4 - Influence of interaction of various factors on capacitance value

According to the regression equation and the response surface diagram presented in Figure 4, the relative area of the parallel plates exerts a nonsignificant effect on capacitance. Nevertheless, a smaller relative area is associated with less friction damage and longer service life. Therefore, the relative area should be minimized. The following optimization model was obtained with consideration given to the edge effect, regression equation, and response surface:

$$\begin{cases} 30 \le Y \le 40 \\ MinA \\ 1 \le D \le 3 \\ 10 < H \le 20 \end{cases} \quad (6)$$

The optimal dimensions of the parallel plates were calculated using the Design-Expert software to be a plate thickness of 1 mm, plate spacing of 19.54 mm, and relative area of 4023.17 mm². The capacitance value corresponding to these parameters is 37.678 pF, as indicated in Figure 5.

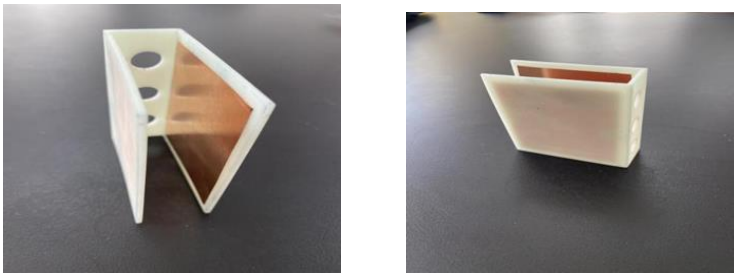

Fig. 5 - Trial-produced parallel-plate structure

Structural Design of PPMCDD

Through the field investigation and theoretical analysis of grain elevators, we determined that the optimal position for a moisture detection device is at the head of the grain elevator. This device position ensures that a sufficient amount of grain enters the sampling box and that the grain sampling is random. Just before the grain enters the detection chamber of the parallel-plate device, the upper polar plate is opened by a push-pull electromagnet to allow the grain to enter. To avoid clogging caused by grain accumulation, a triangular structure is fixed on the upper plate. When the parallel-plate detection cavity is filled with grain, the upper polar plate is closed, and the triangular structure allows the remaining grain to return to the granary without interrupting grain circulation. After the detection cycle is completed, the lower polar plate opens to allow the grain to return to the granary through an inclined chute. Subsequently, the lower polar plate is closed, the upper polar plate is opened, and the next detection cycle begins. This process is illustrated in Figure 6.

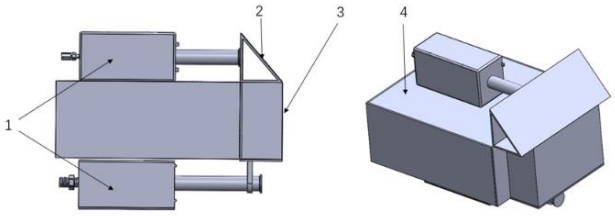

Fig. 6 - Structure diagram of PPMCDD

1 - Push-pull type electromagnet; 2 - Tripod construction; 3 - Detection cavity; 4 - Circuit board seal box

Establishment of Moisture Content Model

Frequency Processing

The change in capacitance between the plates of the parallel-plate device described herein is converted into a change in frequency, and the moisture content of a grain sample is calculated indirectly from this difference in acquisition frequency. The moisture content of the rice was 10%–30%, and the frequency range was 8–40 kHz. The frequencies measured by the parallel-plate sensor indicated that frequency drift had occurred during the moisture detection process. Because of the interference from the motion of the rice and the vibration of the machine during the drying process, the moisture content within the rice becomes unstable after the rice enters the parallel-plate detection cavity, which leads to fluctuations in capacitance and indirectly causes fluctuations in frequency.

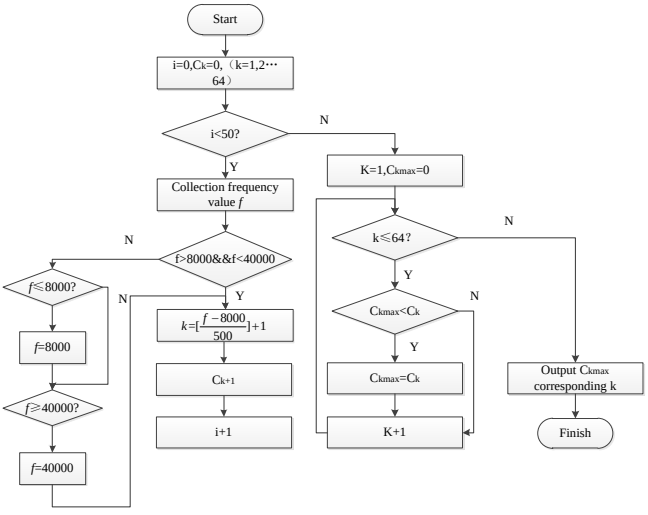

Fig. 7 - Frequency acquisition and processing

On the basis of the aforementioned problems and a study by *Huang et al., (2015),* on fuzzy logic–based multi-input data processing algorithms for nuclear power plant control systems, we implemented feature coding for our device to evaluate frequency. As illustrated in Figure 7, when a set time delay expires, the parallel-plate device measures the frequency. When the frequency is <8 kHz, it is read as 8 kHz, and the coding value is 1. When the measured frequency is >40 kHz, the frequency is read as 40 kHz, and the coding value is 64. When the frequency is in the range of 8–40 kHz, the corresponding coding value is in the range of 1–64. This method can be used to address the problem of frequency drift and improve the measurement accuracy of the parallel-plate device. The frequency coding value is calculated as follows:

$$K = \left[\frac{f - 8}{0.5} \right] + 1 \tag{7}$$

Where:

K is coding value, *f* is the frequency (kHz), [ ] is the integer notation.

Moisture Content Model

In this study, samples of indica hybrid rice (Anhui 185) with various moisture content were obtained from the Lu'an area of Anhui province to test the proposed device. The moisture content of the Anhui 185 rice was 14%–21%, and the rice temperature was between 20°C and 36°C. We used the KETT Grain PM-8188-NEW grain moisture detecting (measurement range: 8%–35%, error: <0.5%) to obtain moisture content measures for each of the rice samples. The rice samples with different moisture content were placed into 20 x 14 mm bags, which were sealed, stored, and labeled with their corresponding moisture content.

Fig. 8 - Calibration experiment diagram

To more accurately simulate the drying environment, we tested the detection of the PPMCDD in an electric air-drying oven, as illustrated in Figure 8. We first adjusted the electrothermal blowing temperature to the minimum temperature required by the experimental design. We subsequently debugged the PPMCDD placed in the drying oven. When the temperature of the oven met the requirements of the experimental design, the rice was placed in the sampling box, and random sampling of the rice was conducted. We observed and recorded the temperature, coding value, and moisture content presented on the display panel, as presented in Table 3.

Table 3

Coded values detected by weight and temperature of rice with different moisture content

Order	Coded values	Weight [g]	Temperature [℃]	Moisture content [%]	Order	Coded values	Weight [g]	Temperature [℃]	moisture Montent [%]
1	50	256	35.3	17.64	31	49	256	25.6	17.89
2	49	260	35.1	17.71	32	51	253	26.9	16.56
3	50	253	34.6	17.58	33	50	254	25.7	17.68
4	50	248	34.4	17.52	34	51	256	29.6	16.57
5	50	255	33.2	17.53	35	51	258	28.4	16.72
6	50	251	32.6	17.45	36	51	259	27.6	16.84
7	50	252	32.3	17.5	37	50	254	27.8	17.09
8	50	258	31.8	17.46	38	51	251	27.3	16.82
9	50	256	31.3	17.25	39	48	253	32.5	18.56
10	50	258	28.9	17.23	40	51	254	35.6	16.52
11	51	254	22.3	16.83	41	54	259	31.6	14.53
12	51	258	21.4	16.78	42	53	257	32.7	14.86
13	51	253	20.4	16.56	43	53	256	31.8	14.95
14	46	259	28.6	20.56	44	51	253	29.6	16.86
15	47	254	21.4	19.78	45	50	251	28.3	17.51
16	47	256	28.3	19.67	46	51	254	27.6	16.59
17	47	253	35.6	19.45	47	49	258	30.8	17.83
18	47	258	32.6	19.23	48	52	256	31.2	16.24
19	47	256	28.9	19.58	49	51	257	30.6	16.55

Order	Coded values	Weight [g]	Temperature [℃]	Moisture content [%]	Order	Coded values	Weight [g]	Temperature [℃]	moisture Montent [%]
0	48	251	27.6	18.98	50	46	259	30.9	20.13
21	49	253	25.6	18.56	51	46	253	32.4	20.23
22	48	252	28.4	18.64	52	47	258	32.7	19.86
23	49	256	27.2	18.13	53	48	260	31.7	18.64
24	49	254	28.3	18.25	54	47	263	29.3	19.61
25	51	253	24.9	16.54	55	51	254	32.5	16.79
26	52	259	26.8	16.23	56	49	259	34.6	17.69
27	51	257	27.6	16.52	57	51	254	33.6	16.62
28	52	256	25.1	15.75	58	48	256	33.8	18.56
29	53	253	26.7	15.45	59	47	257	29.6	19.83
30	53	254	25.4	15.23	60	48	258	28.7	18.67

The temperature range of the oven was 20°C–35°C, and the moisture content of rice samples was between 14%–21%. Each group of samples was measured three times to more accurately evaluate the device's detection ability. Regression equation fitting was performed using Origin software, and the resultant fitting equation is as follows:

$$W = -0.01492G - 0.01372T - 0.72828K + 58.01498 \quad (8)$$

Where: W is the moisture content (%) of the rice, G is the weight indicated by the pressure sensor, T is the temperature displayed by the temperature sensor, K is the frequency coding value.

The coefficient of determination (R^2) of Eq. (8) was 0.981, and the comprehensive error rate was 0.0163. The moisture content of each rice sample was calculated using Eq. (8), and the calculated value was displayed in real-time on the display panel.

Experimental Platform

In this study, Laboratory Virtual Instrument Engineering Workbench (LabVIEW) was used to design an upper computer display panel, grain temperature, weight, and moisture content data were collected by the STM32 MCU and transmitted to the upper computer LabVIEW for display. The panel consisted mainly of three waveform chart displays, a sliding column moisture content display, and a moisture content alarm. The experimental platform is illustrated in Figure 9.

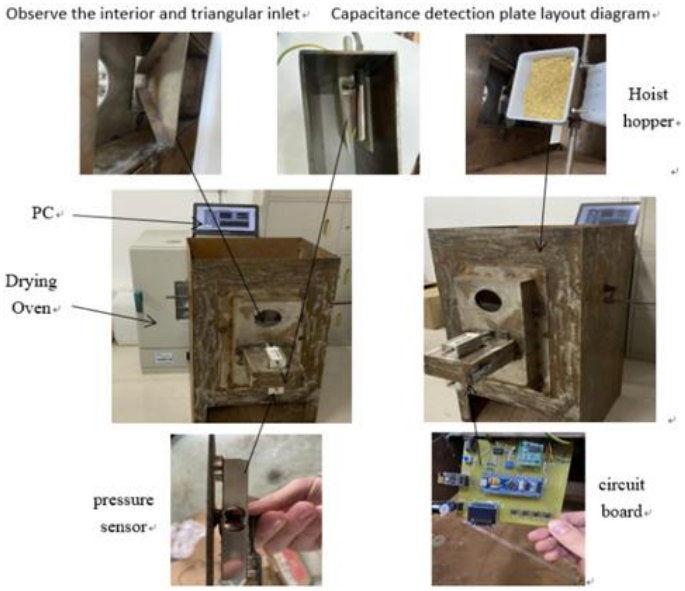

Fig. 9 - Experimental platform

Experimental Verification

To test the reliability of the model, 40 rice samples with 8%–35% moisture content were randomly and successively fallen into the detection chamber through the grain hopper. After data were collected for each sample, the results were compared with values obtained using the international standard drying method. Each sample was tested 10 times, and the average value was used for comparison, as illustrated in Figure 10.

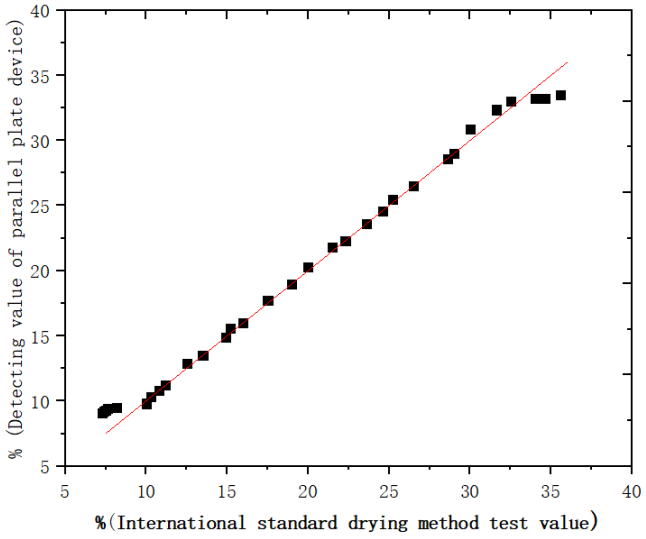

Fig. 10 - Comparison of measured values by drying method and measured values by the detection system

As illustrated in Figure 10, when the moisture content of a sample is 10%–28%, the results obtained using the PPMCDD are generally consistent with those obtained using the international standard drying method. When the moisture content of a sample is >28% or <10%, the results obtained using the device yield large errors in comparison with those obtained using the international standard drying method. Therefore, the moisture detection range of the PPMCDD developed in this study is 10%–28%.

Experimental Analysis

Detection accuracy is a key indicator of a sensor's practical applications. In this study, the PPMCDD and the international standard drying method were used to test rice samples with various moisture content. Test data were collected and analyzed to compare the methods.

The test was conducted at 24°C and 50% relative humidity. The international standard drying method was used to prepare 10 rice samples with moisture contents of 12.45%, 15.12%, 17.45%, 18.53%, 19.63%, 21.34%, 23.65%, 25.19%, 26.58%, and 27.63%. The PPMCDD was used to conduct 10 tests for each sample, and the average value for each set of test data for each sample was calculated, as listed in Table 4. When the moisture content of a rice sample was low, the maximal relative error of the data obtained using the proposed device was also low; when the moisture content of a rice sample was high, the maximal relative error of the corresponding data was also high. However, when the moisture content of the rice sample was >21%, the maximal relative error of the PPMCDD and the international standard drying method was the same, and the maximal relative error of the device was 1.58%, which indicates the great effect of employing the device for moisture content detection.

Table 4

Experimental results of detection of the device

Values measured by standard drying method /%	PPMCDD test value /%	Maximum relative error/%
12.45%	12.29%	1.31
15.12%	14.93%	1.28
17.45%	17.21%	1.35
18.53%	18.27%	1.41
19.63%	19.00%	1.52
21.34%	21.67%	1.53
23.65%	24.02%	1.55
25.19%	25.65%	1.54
26.58%	26.32%	1.58
27.63%	28.06%	1.56

CONCLUSIONS

In this study, a model of capacitance parallel-plate detection was established, and a regression equation for capacitance was derived through a combination of quadratic regression and orthogonal selection. After adjustment for the edge effect, the optimal combination of plate parameters was determined to be a plate thickness of 1 mm, plate spacing of 19.54 mm, and relative area of 4023.17 mm^2, which correspond to a capacitance value of 37.678 pF.

Origin software was used to fit the collected data and obtain the formula for calculating the moisture content of rice. The coefficient of determination (R^2) of the formula was 0.981, and the comprehensive error rate was 0.0163.

This paper takes a test bench that was performed as a static test. The results revealed that the detection range and maximal relative error of the PPMDD were 12%–28% and 1.58%, respectively. The detection error of PPMDD is small, and the accuracy and stability of the device are high.

ACKNOWLEDGEMENT

The authors thank Fund Project: Anhui Province Science and Technology Major Special Project (17030701040) and Anhui Province Engineering Laboratory of Intelligent Agricultural Machinery and Equipment and Anhui Agricultural University for their funding support.

REFERENCES

[1] Boateng, I. D., & Yang, X. M. (2021). Process optimization of intermediate-wave infrared drying: screening by Plackett–Burman; comparison of Box-Behnken and central composite design and evaluation: a case study. *Industrial Crops and Products, Netherlands, 162*, 113287. https://doi.org/10.1016/j.indcrop.2021.113287

[2] Casada, M. E., & Armstrong, P. R. (2009). Wheat moisture measurement with a fringing field capacitive sensor. *Transactions of the ASABE*, *USA*, *52*(5), 1785-1791. https://doi.org/10.13031/2013.29119.

[3] Fan, C. X., Li, Z. G., Jang, T. L., Chen, Z. A., Zhao, B., Liu, Y. C. & Zhou, M. L. (2020). On-line detector of mass flow rate of self-propelled corn silage harvester based on capacitance method. *Journal of Chinese Agricultural Mechanization, China*, (07), 137-142. https://doi.org/10.13733/j.jcam.issn.2095-5553.2020.07.021.

[4] Fan, L., Chai, Z., Wang, Y., Wang, Z., Zhao, P., Li, J. & Huang, L. (2020). A Novel Handheld Device for Intact Corn Ear Moisture Content Measurement. *IEEE Transactions on Instrumentation and Measurement*, *USA*, *69*(11), 9157-9169. https://doi.org/10.1109/TIM.2020.2994603

[5] Huang, Q., Sun, J., Zhang, R., Zhang, Y., Wang, S., Chen, K., & Wang, W. (2015). Study on multi-input processing algorithm research based on fuzzy principle in nuclear power plant instrumentation and control system. *Chinese Journal of Nuclear Science and Engineering*, *China*, *35*(4), 785-789.

[6] Jiang, J., & Ji, H. (2009). Study of Moisture Test for Grain Based on Neural Network and Mechanism of Multi-Sensor. In 2009 International Conference on Computational Intelligence and Software Engineering (pp. 1-4). *IEEE*. https://doi.org/10.1109/CISE.2009.5362610

[7] Kandala, C. V., & Puppala, N. (2012). Capacitance sensors for nondestructive moisture determination in grain, nuts and bio-fuel materials. In 2012 Sixth International Conference on Sensing Technology (ICST) (pp. 42-45). *IEEE*. https://doi.org/10.1109/ICSensT.2012.6461715

[8] Khatib, I., Chow, M. Y., Ruan, J., Cipolla, D., & Chan, H. K. (2021). Modeling of a spray drying method to produce ciprofloxacin nanocrystals inside the liposomes utilizing a response surface methodology: Box-Behnken experimental design. *International Journal of Pharmaceutics, Netherlands, 597*, 120277. https://doi.org/10.1016/j.ijpharm.2021.120277

[9] Kim, K. B., Kim, J. H., Lee, S. S., & Noh, S. H. (2002). Measurement of grain moisture content using microwave attenuation at 10.5 GHz and moisture density. *IEEE Transactions on Instrumentation and Measurement*, *USA*, *51*(1), 72-77. https://doi.org/10.1109/19.989904

[10] Korkua, S. K., & Sakphrom, S. (2020). Low-cost capacitive sensor for detecting palm-wood moisture content in real-time. *Heliyon*, 6(8), e04555. https://doi.org/10.1016/j.heliyon.2020.e04555

[11] Laleicke, P. F., & Kamke, F. A. (2018). A capacitive multi-wavelength sensor for moisture content gradient sensing in wood. Wood Sci. Technol., 52(3), 717-732. https://doi.org/10.1007/s00226-018-0988-z

[12] Mcintosh, R. B., & Casada, M. E. (2008). Fringing field capacitance sensor for measuring the moisture content of agricultural commodities. *IEEE Sensors journal*, *USA*, *8*(3), 240-247. https://doi.org/10.1109/JSEN.2007.913140

[13] Nelson, S. O., & Trabelsi, S. (2016). Historical development of grain moisture measurement and other food quality sensing through electrical properties. *IEEE Instrumentation & Measurement Magazine*, *USA*, *19*(1), 16-23. https://doi.org/10.1109/MIM.2016.7384955

[14] Rai, A. K., Khare, P. K., & Mor, P. (2008). Microprocessor based measurement system for grain moisture. IET-UK International Conference on Information and Communication Technology in Electrical Sciences. https://doi.org/10.1049/ic:20070730

[15] Sosa-Morales, M. E., Valerio-Junco, L., López-Malo, A., & García, H. S. (2010). Dielectric properties of foods: Reported data in the 21st Century and their potential applications. LWT-Food Science and Technology, England, *43* (8), 1169-1179. https://doi.org/10.1016/j.lwt.2010.03.017

[16] Wang, H. G., Senior, P. R., Mann, R., & Yang, W. Q. (2009). Online measurement and control of solids moisture in fluidized bed dryers. *Chemical Engineering Science*, *USA*, *64*(12), 2893-2902. https://doi.org/10.1016/j.ces.2009.03.014

[17] Yigit, E., Sabanci, K., Toktas, A., Ustun, D., & Duysak, H. (2018). Grain moisture detection by using a-scan radar measurement. In 2018 XXIIIrd International Seminar/Workshop on Direct and Inverse Problems of Electromagnetic and Acoustic Wave Theory (DIPED) (pp. 222-224). *IEEE*. https://doi.org/10.1109/DIPED.2018.8543311

[18] Zambrano, M. V., Dutta, B., Mercer, D. G., MacLean, H. L., & Touchie, M. F. (2019). Assessment of moisture content measurement methods of dried food products in small-scale operations in developing countries: A review. *Trends in Food Science & Technology*, England, 88, 484-496. https://doi.org/10.1016/j.tifs.2019.04.006

ENERGY CONSUMPTION EVALUATION OF ROTARY TILLER USING DYNAMIC MODELLING
/
EVALUAREA CONSUMULUI DE ENERGIE A FREZEI AGRICOLE FOLOSIND MODELAREA DINAMICĂ

Ferenc TOLVALY-ROȘCA, Zontán FORGÓ, Judit PÁSZTOR *[1)]
Sapientia Hungarian University of Transylvania, Faculty of Technical and Human Sciences, Târgu Mureş/ Romania;
Tel: +40720399662; *E-mail: pjudit@ms.sapientia.ro*
DOI: https://doi.org/10.35633/inmateh-68-17

Keywords: *rotary tiller, computer simulation, fuel consumption, Matlab Simulink*

ABSTRACT

Tillage is the most energy-intensive agricultural operation. In the actual energy situation it is important to explore and analyze the physical laws of soil cultivation processes, which demand increased energy, at the border of technical- and agricultural sciences. In this paper, the physical phenomena that occur during soil work with a rotary tiller were studied, and the energy requirements were approximated by computer simulation using Matlab Simulink environment. The model used was a simplified solid model of an FPP-1.3 type rotary tiller, used previously in real experiments to determine fuel consumption at various working parameters. The results obtained by the dynamic simulation were compared with the real measurements.

REZUMAT

Prelucrarea solului este cea mai energo-intensivă operație agricolă. În actuala situație energetică, este importantă studierea și analiza legilor fizicii, care caracterizează procesele de prelucrare energo-intensive. În acest articol s-au studiat procesele fizice caracteristice frezării solului și s-a aproximat necesarul de energie utilizând programul de simulare Matlab Simulink. Modelul folosit a fost modelul solid simplificat a frezei de sol tip FPP-1,3, utilizat în anii precedenți în experimente reale care au urmărit determinarea consumului de combustibil pentru diferiți parametri de prelucrare. Rezultatele obținute prin simularea dinamică au fost comparate cu măsurătorile reale.

INTRODUCTION

Tillage is an intervention in the physical condition of the soil, in such a way that the most favorable living conditions are created for the plants. During tillage, ground cultivation and seedbed preparation are carried out. Basic cultivation means turning the soil, while bed preparation means soil shredding, loosening, mixing, surface shaping and compaction below sowing depth *(Marin et al., 2012)*.

The basic aim in tillage operations is always to provide the seedbed required for plant growing, with the least possible number of passes and minimum energy consumption. In order to reduce the number of passes, tillage machines with active tillage tools are preferred *(Cujbescu et al., 2019; Tenu et al., 2012)*.

It is common for the seedbed to be prepared with a rotary tiller, which mixes, but it also shreds, loosens and levels the soil. The rotary tiller's working tools are active, and during towing, they are also driven by the power take-off shaft (the PTO). For this reason, the traction power requirement of the working machine is lower; the sliding losses are also reduced, so the rotary tiller can be also used in moist soil conditions *(Usaborisut et al., 2020; Vlăduţ et al., 2018)*. Cultivation with this type of machine is intensive, creates dust, increases the mineralization process of soil organic matter, and reduces the formation of hardpans *(Catania et al., 2018*; *Chen et al., 2022; Hassan et al., 2018)*.

Many researches deal with the study of the active soil tillage machines. They often visualize the operation by means of mechanical / kinematic models. *Ahmadi I., (2017),* developed a theoretical calculator to determine the torque and power requirement of the rotary tiller. Using an Excel spreadsheet, based on the given mathematical formulas, the performance requirements of some tillage tools can be effectively predicted. Thus, the performance requirements of different tillage machines can be compared. The spreadsheet calculator is also suitable for examining the effect of a selected input working parameter on outputs.

[1] *Ferenc Tolvaly-Roșca, Assoc.prof.*; *Zontán Forgó, Assoc.prof,*; *Judit Pásztor, Lecturer*

Nowadays, studying and modeling of tillage tools is an important part in the development of new agricultural machines. The precise mechanical sizing of a new tool must be carried out before field tests, with modern mathematical-mechanical computer methods.

By computer modeling, the interaction between the tool and the soil, development time and costs can be significantly decreased *(Kuan, 2020; Major and Csanády, 2014; Forgó et al., 2021)*. *Saimbhi et al., (2004),* also used computer modeling methods of the working process in their minimum tillage study, and FEM methods were used for the study of soil compaction *(Ungureanu et al., 2017; Ungureanu et al., 2018)*. With the help of special engineering software, *Tolvaly-Roșca and Pásztor, (2019),* studied the trajectory of the tiller, and the shape and size of the cut soil slices, respectively.

Determining the energy demand for the tilling processes is useful both for the developers and operators of machines. Energy demand is measured in laboratory and field conditions, but it is increasingly common to determine it by computer simulation. When studying the performance requirements of the rotary tiller, it is also important to explore the forces and loads occurring on the blades during operation.

MATERIAL AND METHODS

In the present paper an FPP-1,3 type rotary tiller was studied. In previous years, experiments regarding the real fuel consumption varying the linear speed of the tractor were lead. The results were presented in (*Drunek, 2009)*. Using Autodesk Inventor software, a simplified solid assembly model of the rotary tiller (modeling blades without wear) was built using. The image from Figure 1 was taken a few years later with visible wear signs on the blades. Using the solid subtraction method simulating software, developed and presented in (*Tolvaly-Rosca and Pásztor, 2019*) the cuts for a single blade rotation were simulated, then the dislocated soil volumes for the three different advancing speed (the working speed of the tractor) of the real experiments were determined.

Using the literature *(Sitkei, 1976; Căproiu et al., 1982; Aluko, 2000; Amantayev et al., 2017)* and some new considerations observed after the simulations, the loads and forces acting on a single blade were determined and calculated. The solid model of the rotary tiller was imported to Matlab Simulink environment with similar procedures as those presented in *(Forgó et al., 2021)*. The calculated forces was applied on each blade of the model, and as output of the Simulink simulation, the working trajectories of the blades, and the energy consumption of the tillage process were obtained.

In a next step of the energy evaluation, the results from the simulation and the results obtained earlier upon the field experiments were compared.

The experimental and simulation results were presented and compared.

The FPP-1.3 Type Rotary Tiller

The FPP-1.3 type rotary tiller is intended for the superficial mixing and loosening of the soil, the crushing of clods and the destruction of weeds, the crushing and incorporation of organic fertilizers into the soil of vegetable, viticulture and fruit cultures, especially in greenhouses.

The presented rotary tiller is a suspended agricultural machine; it works in aggregate with the 33 kW tractors. The machine's main organ is the horizontal rotor with blades. The cutter rotor is driven from the tractor's power take-off through a lateral transmission. There are seven flanges on the rotor on which the blades are mounted. Three blades are fixed on the marginal flanges, and six on each of the inner flanges: three are left- and three are right sided. The blades are rigid, curved in an L shape. The rotor is covered by a casing. The casing contributes to the energetic shredding of the soil; it is leveling the processed soil and also has a human protection purpose.

Fig.1 - FFP-1.30 type rotary tiller

The main technical characteristics of the FPP-1.3 type rotary tiller are presented in Table 1.

Table 1

Main technical characteristics of the FPP-1.3 type rotary tiller

Tractor, kW	33
Tractor's PTO speed, rot/min	540
Rotor's spindle speed, rot/min	144–225
Angular speed of the rotor, rad/s	15,07; 16,85; 21,14; 29,55
Working depth, cm	15–20
Working width, m	1,30
Diameter of the rotor, mm	510
Number of flanges	7
Number of the blades on a flange	6 (3 on the external flanges)
Total Number of the blades	36

The Cad Model of the Rotary Tiller

As the energy consumption measuring experiments were made with the FPP-1.3 type rotary tiller, a simplified 3D solid assembly model of the active part of the machine was built. In a first step brand new, unused rotary tiller blades were modeled using Autodesk Inventor (Fig. 2).

Fig. 2 - The real (left) and the 3D solid model (right) of a single blade

Then, using the of modeled blades (a right-handed and a left-handed), a simplified solid assembly model of the active part was built (the shaft with the blade holding discs, the bolts and the nuts) with proper material assignments to obtain a most accurate mass of the working assembly (Fig. 3).

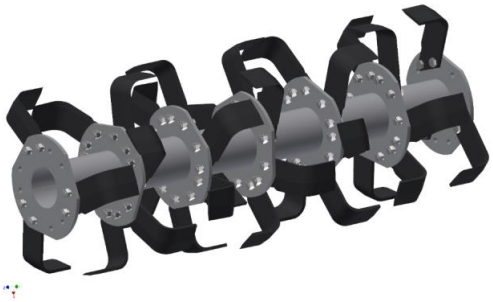

Fig. 3 - The simplified assembly model of the rotary tiller active part

During a single rotation of one blade and according on his relative movement, the solid model of rotary tiller blade was subtracted from the soil block with known volume (Fig. 4).

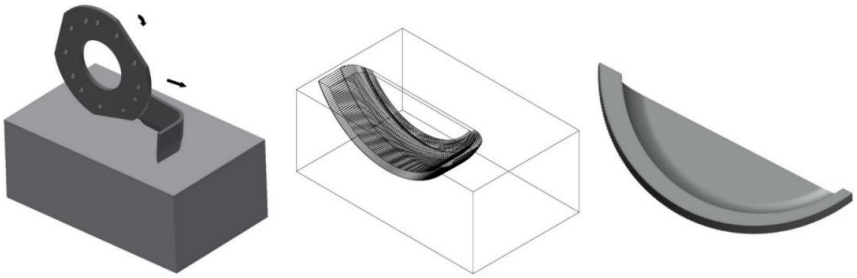

Fig. 4 – Approximating the soil volume thrown by the blade

Left - The cutting simulation model; Middle – The soil with the removed volume; Right – A soil slice

For the cutting simulation, the corresponding three linear advancing speeds and the spindle speed from the real experiments was used (Table 2). Where v_a is the advancing and v_p is the peripheral speed of the blades.

Reading the remained soil volume, and calculating the difference from the initial volume, an approximation of the removed soil volume was calculated and used in the further calculation.

Table 2

Approximation of the directly dislocated soil slice volumes at different advancing speeds

Advancing speed v_a	Angular speed of the rotor ω	Spindle speed of the rotor	Dislocated soil volume V	Peripheral speed of the rotor v_p	v_p/v_a λ
[m/s]	[rad/s]	[rpm]	[mm^3]	[m/s]	[u.l.]
0.50	15.07	146.91	1048942.6	3.843	7.67
0.57	15.07	146.91	1034835.5	3.843	6.76
0.91	15.07	146.91	966676.6	3.843	4.24

In Figure 4 it can be observed that the soil slice thickness (considered in the radial direction to the rotation axis) it is not constant for a single revolution of the blade in the soil. In the deepest point of the cut, the thickness of the soil slice has its maximum value approx. 22.5 mm (after this position the soil is already shredded and loosened, and the rotation tends to throw out the soil, there is no more compression). The thickness of the slice at the start and varies according to increase of the advancing speed, between 10.44–15 mm, and it is larger than the blade thickness (8.2 mm). Based on this observation, a compacting force must be considered, force which is neglected in the literature. This force must vary according the advancing- and rotating speed ratio (**λ**), but also according to the angular position of the blade during the rotation process.

Loads and Forces in the Tilling Process

Determining the forces resulting from the tillage process and the loads on the working machines is a difficult task, since the already existing stresses in the soil can also influence the reaction of the soil on the tillage forces. According to *Rajaram (2018)*, they are also recommended to be included in the models.

To determine the exact mechanical properties of different soils types in a given moment of time can be done relatively easily with modern technical measuring devices. But to evaluate them in a general model is an extremely complex task, as many individually factors are related to strength and deformation properties, such as moisture content and soil composition (*Amantayev et al., 2017; Chen et al., 2017*).

Cultivation with tillers is a very energy-intensive process. In order to study the performance requirement, it is necessary to know the working way of the blade and the characteristics of its interaction with the soil. This mechanical work consists in two main stages:

- The working way of a rotary tiller: the blade penetrates the soil, cuts off a soil slice, accelerates it and throws it away. The thrown piece of soil hits the cover plate, where it further crumbles.

- In our study, the work performed by the rotary tiller is divided into two elementary processes: the separation process of the ground slice and the dislocation process of the soil slice (*Sitkei, 1976*).

In these two stages, according to elementary processes, four type of loads can be considered, with the following forces (Fig. 5):

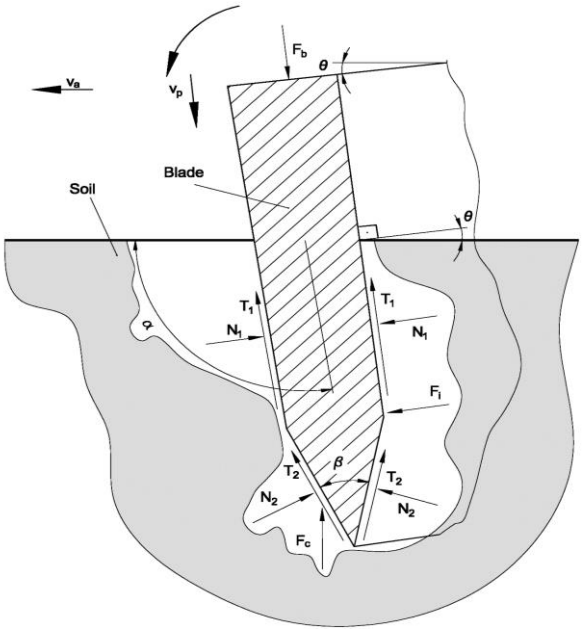

Fig. 5 – Forces acting in the working process

- the frictional forces ($\mathbf{T_1}$ and $\mathbf{T_2}$), acting on the sides of the blade;
- the normal forces ($\mathbf{N_1}$ and $\mathbf{N_2}$), acting on also on the blade sides;
- the compacting force $\mathbf{F_c}$, assumed from the dislocated soil slice model;
- the inertial force $\mathbf{F_i}$, given by the throwing process of the dislocated soil parts.

A fifth force, the cutting force, present most literature, noted here with $\mathbf{F_b}$, is given by the frictional- and normal forces.

The bite forces

The forces acting on the blade are shown in Figure 5. To determine the cutting force (or the bite force in the literature, noted with $\mathbf{F_b}$), blade penetration into the soil is considered as a planar movement, and the blade as a wedge with small thickness *(Aluko and Seig, 2000; Amantayev et al., 2017; Sitkei, 1976)*.

Cutting the soil with the blade is considered a clean cut. The resistance of the wedge is given by the sum of the normal forces **N** and the frictional forces **T** acting on the wedge (Equations 1-4). The occasional concentrated load (stone, root) acting on the edge of the tool is not taken into account *(Sitkei, 1976)*. The value of the cutting force ($\mathbf{F_b}$) is calculated with (7) considering the two active parts of the blade: the cutting force acting along the shorter wedge, the wedge perpendicular tot o advancing direction of the machine, and the cutting force acting along the longer wedge, the one parallel with the advancing direction. The first one noted with $\mathbf{F_{b1}}$ from the moment of the contact with the soil can be considered a constant force and is calculated using (5). The second force, noted $\mathbf{F_{b2}}$, depends on the angle θ, the angle between the soil surface and the direction of the longer (the mounted) blade segment (Fig. 5), and is calculated using (6).

$$N_2 = k_{sh} \cdot A_2 \text{ [N]} \tag{1}$$

$$T_2 = \mu \cdot N_2 = \mu \cdot k_{sh} \cdot A_2 \text{ [N]} \tag{2}$$

$$N_1 = k_p \cdot A_1 \text{ [N]} \tag{3}$$

$$T_1 = \mu \cdot N_1 = \mu \cdot k_p \cdot A_1 \text{ [N]} \tag{4}$$

$$F_{b1} = 2 \cdot k_{sh} \cdot A_{21} \cdot \left(\sin\frac{\beta}{2} + \mu \cdot \cos\frac{\beta}{2}\right) + 2 \cdot \mu \cdot k_p \cdot A_{11} \text{ [N]} \tag{5}$$

$$F_{b2} = \left[2 \cdot k_{sh} \cdot A_{22} \cdot \left(\sin\frac{\beta}{2} + \mu \cdot \cos\frac{\beta}{2}\right) + 2 \cdot \mu \cdot k_p \cdot A_{12}\right] \sin\theta \text{ [N]} \tag{6}$$

$$F_b = F_{b1} + F_{b2} \tag{7}$$

where: μ is the friction coefficient between the soil and the blade and it was chosen from *(Sitkei, 1976)* at a value of 0.61; and β is the wedge angle of the blade, measured at 17°.

The k_{sh} and k_p are the specific resistance to soil deformation [N/m^2] on the sharpened and the parallel surfaces; A_1 is the summed surface of both of the parallel sides of the blade in contact with the soil [m^2], and it is composed from two A_{11} (for the shorter blade part) and two A_{12} (for the longer, mounted blade part) surfaces; A_2 is the active surface formed by the two sharpened surfaces of the blade [m^2], composed also from two sub surfaces two A_{21} and two A_{22}, surfaces of the shorter and respectively the longer blade parts.

The normal (**N**) and frictional (**T**) forces 1 and 2 indices are corresponding to above notations of the surfaces A_1 and A_2.

The inertial force

The inertial force $\mathbf{F_i}$ acting on the blade is given by the lift- and the throw process of the soil slice. The displaced soil's mass is approximated using the solid subtraction method to determine the volumes from Table 2, then using the Equation (8) to obtain the magnitude of the inertial force:

$$F_i = V \cdot \rho_{soil} \cdot a_s \text{ [N]} \tag{8}$$

where: ρ_{soil} is the density of the soil [kg/m^3]; V is the volume of the lifted and thrown soil chip [m^3]; a_s is the displaced soil acceleration [m/s^2].

The compacting force

The compacting force is neglected in the literature. Using solid modeling procedures, can be observed that the thickness of the cut soil slice varying alongside the blade trajectory. Due this fact, we concluded that must be acting a compression force (compacting force), which tends to compress the part of the soil in front of the blade. The exact physical phenomenon is a very complex one; it depends from the soil structure, moisture and cohesion state of the soil. This force also varies with the advancing- and rotating speed ratio (**λ**).

To calculate the soil compaction force **F_c**, the Reece equation from *(Cardei et al., 2019)* was applied to the specific position of the blade. The compression resistance per unit width in case of the rotary tiller's blade is calculated using the Equation (9) considered for a wide blade. The maximum magnitude of the compacting force depends from the width of the blade Equation (10) and the magnitude of **F_c** changes according to the position of the blade Equation (11), but also according to the advancing- and rotating speed ratio (λ). As the differences between the advancing speeds are smaller, we considered that the Reece's equation can be used and the effects of different λ values can be neglected to simplify the calculations. The θ angle of the blade can be seen in Figure 5.

$$f_c = \gamma \cdot a^2 \cdot N_\gamma + c \cdot a \cdot N_c \left[\frac{\text{N}}{\text{m}}\right] \quad (9)$$

$$F_{cmax} = f_c \cdot l \ [\text{N}] \quad (10)$$

$$F_c = F_{cmax} \cdot \sin\theta \ [\text{N}] \quad (11)$$

where: a is the width of the blade [m], γ is the specific gravity of the soil [N/m^3]; c is cohesion of the soil [N/m^2], N_g, N_c are Reece type resistance factors (dimensionless); l is the length of the blade's cutting edge; θ is the angle between the plan containing the blade's edges and the soil surface. According to the literature *(Cardei et al., 2019; Sitkei, 1976):* γ = 14715 N/m^3, c = 150 N/m^2, N_g = 9 and N_c = 5; and from the measurements: a = 82 mm, l = 115 mm.

The calculated **F_c** from Equation (11) was introduced in the Simulink model, and his variation according to the advancing- and the peripheral speed ratio λ was included in the computer model, as these speeds were already included in the computer model's input.

Table 3 contains the magnitude of the calculated forces, determined using Equations (1-11).

Table 3

The magnitude of the forces acting on the blade

F_b	F_i		F_c
[N]	[N]		[N]
F_{b1} = 174.99	v_{a1} = 0.50 m/s	112.55	F_{cmax} = 109.48
F_{b2max} = 309.20	v_{a2} = 0.57 m/s	110.84	
	v_{a3} = 0.91 m/s	103.032	

RESULTS

Field Experiments

Fuel consumption experiments of the rotary tiller were carried out in April 2009 in the greenhouses of the Research - Development Station for Fruit Culture, Băneasa-Bucharest, and were presented in details in *Drunek (2009).*

Energy consumption during working with the cutter was considered the energy stored in the consumed fuel. Fuel consumption when working with the rotary tiller and the idle consumption were measured at three advancing speeds, with working depth of 15 cm and length of 15m, the width of 1.30 m, i.e. on 19.5 m^2.

Fuel consumption of the work was calculated with Equation (12):

$$C_{cl} = C_{cs} - C_{cg}, \ [\text{cm}^3] \quad (12)$$

where: C_{cl} is the fuel consumption of the tillage work [cm^3]; C_{cs} is the fuel consumption when working with the rotary tiller, aggregated with the U445 tractor [cm^3]; and C_{cg} is the idle consumption: tractor running with the three speeds and the FPP-1,30 is idle, suspended over the soil [cm^3].

The total energy obtained burning the fuel Q_{cl} can be calculated using (13):

$$Q_{cl} = C_{cl} \cdot \rho \cdot H, \ [\text{J}] \quad (13)$$

where: ρ – fuel density [kg/m^3]; H - the calorific power of the fuel [J/kg]. In the calculations, the following values were considered: ρ = 820 kg/m^3 and H = 41 MJ/kg (at 15°C).

The Simulink Model

The assembly model of the tiller mechanism, developed using the Autodesk Inventor modeling software, was imported in Matlab Simulink environment. To simplify the simulation method, a single flange was isolated and imported; the loads acting on one single blade were taken into consideration during the simulations. The outcome of that latter is the needed torque in order to do the tilling process with one blade.

As post-simulation work, these time series data are shifted and added accordingly the distribution of the blades on a flange. After determining the needed torque for one flange, the result is multiplied by the number of working flanges: five complete flanges with six blades and two flanges (on the extremities) with only three even distributed blades. For these two flanges the calculated torque is altered accordingly.

As depicted in Figure 6, the mechanism model is extended in order to calculate and to apply the loads raised during the tilling process. Different type of blocks may be identified inside the presented model.

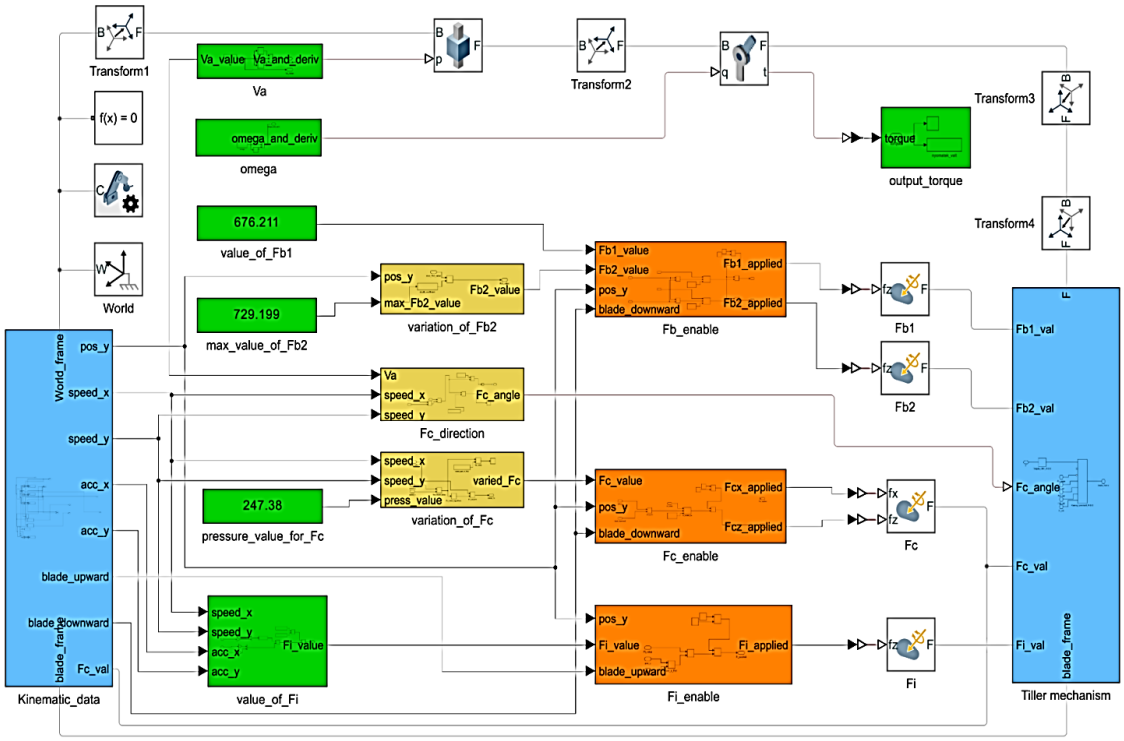

Fig. 6 – The extended model of the tilling mechanism

The blue background block (*Tiller mechanism*) contains the mechanism model and opposite of that, the other blue one (*Kinematic data*) calculates the kinematical parameters of the model regarding the world frame: the displacement, velocity and acceleration of a characteristic point (the tip) of a blade. The left side green blocks are considered the numerical input of the model: the values of the loads calculated based on Equations (5), (6), (8) and (11) are considered. Because the magnitude and direction of the loads must follow certain rules during the flange displacement and rotation (ex. the magnitude the force $\mathbf{F_{b2}}$ is growing from zero the value determined by Equation (6) as the blade penetrates the soil), they are altered by the yellow background blocks. The orange-colored blocks take care for the timing of the forces, they should load the mechanism at particular intervals (ex. the bite force acts only if the blade is moving downward inside the soil), and so these blocks are the enablers for that. During the simulation run, the right-side green block will save the time series torque data, which will be processed after the simulation as presented above.

The presented simulation process was applied using the advancing speed and angular speed values of the rotor from Table 2. The resulting torque's graphs (Fig. 7) are showing an even dispersion for their value during the simulations, so mean torques can be calculated.

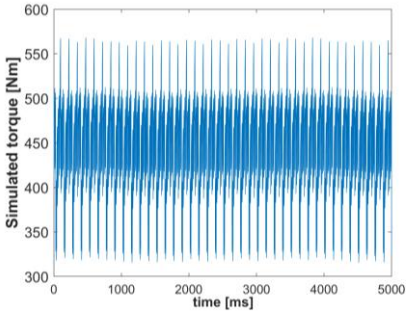

Fig. 7 – The simulated torque's graphs

Taking in account that the field experiments were made below the recommended advancing speed for tractors (0.5–0.9 m/s), the efficiency of the Diesel engine considered at 42% and transmission losses at 5%, the mechanical energy Q_m generated by the burnt fuel can be evaluated. The measured and calculated values regarding the fuel and energy consumption can be seen in Table 4.

Table 4

Fuel consumption and calculated energy values obtained in the field experiment *(Drunek, 2009)*

Working speed V_a	Fuel consumption of the work C_{cl}	Caloric energy Q_{cl}	Mechanical energy Q_m
[m/s]	[cm³]	[J]	[J]
v_{a1}=0.50	18.58	624659.6	231124.052
v_{a2}=0.57	17.58	591039.6	218684.652
v_{a3}=0.91	16.46	553385.2	204752.524

The necessary mechanical energy for the tilling process from the computer simulation is calculated, multiplying the mean torque with the known angular displacement of the rotor. The results are presented in Table 5.

Table 5

Mechanical energy determined by simulations

Working speed V_a	Angular speed of the rotor ω	Mechanical energy (simulation) Q_m	Mechanical energy (experimental) Q_m	Deviation	Total experimental mechanical energy	Simulated mech. energy + experimental idle energy	Deviation
[m/s]	[rad/s]	[J]	[J]	[%]	[J]	[J]	[%]
v_{a1}=0.50	15.07	204053.61	249863.84	-11.7	653492.112	654219.985	-0.12
v_{a2}=0.57		180180.56	236415.84	-17.6	635135.592	609826.456	4.7
v_{a3}=0.91		113602.63	221354.08	-44.5	615084.624	578549.77	7.3

Table 5 is also summarizing the energy values from the simulated mechanical work and the energy used for towing from the field experiments (idle energy). This is necessary to evaluate the predicted total (from simulation) energy compared to the results from the experiments.

The energy values obtained with the simulation, excluding the idle energy consumption, gives the mechanical work's energy requirement. Compared to the similar mechanical energy deduced from the fuel consumption in the field experiments, shows lower values, and they also depend from the advancing speed.

The deviation from the experimentally deduced values varies between -11.7% and -44.5%. As it can be seen in Figure 9, the simulated working energy (orange color), shows also a decreasing tendency compared to the experimental values (gray line).

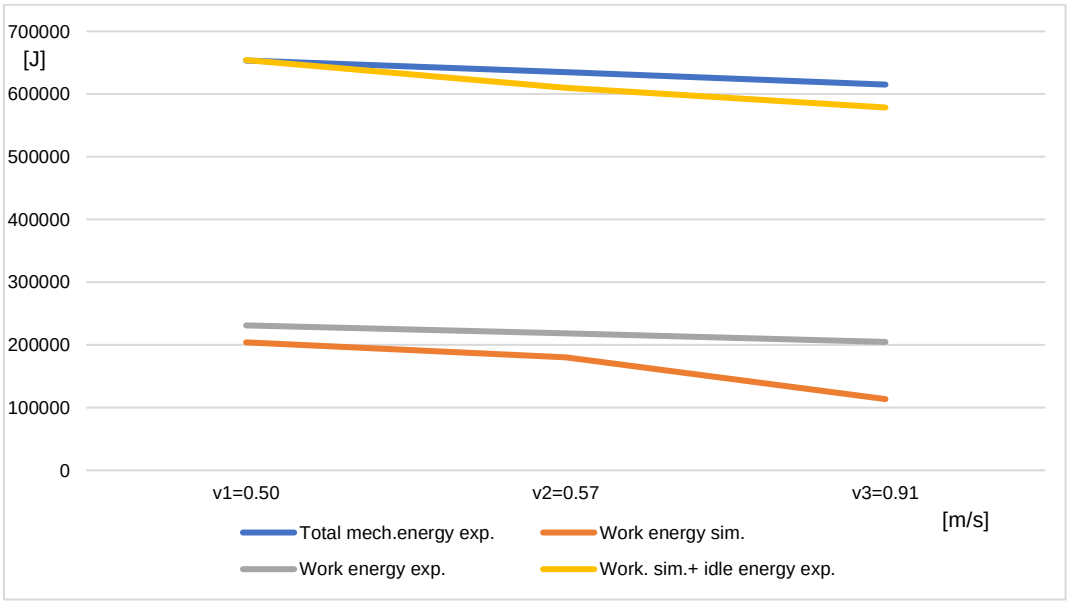

Fig. 9 – Energy consumption comparison graphs

The difference between the two energy increases with the advancing speed. The field experiments contain all the type of losses arising in a real a real working process. The minimum difference of -11.7%, consists in losses not calculated in the simulation (i.e. transmission losses at 5%, tire slipping etc.). But the increase of the difference from -11.7 % to 44.5% may be confusing at a first look.

CONCLUSIONS

The explanation for the increasing value of the deviation between the experimental and simulated working energy, with the increase of the advancing speed, can be found in the literature: considering the rotor a traction wheel, a part of the working energy it is transformed in a pushing energy for the working unit. According to equation of this energy it varies directly proportional with the v_a working speed. It means that the real working energy deduced from the field experiments must be reduced, according to the increase of the advancing speed.

Taking in consideration this phenomenon, it is obvious that the curve of the experimental working energy (gray line) slopes down more steeply. The exact value of this transformation it was not taken in consideration at the time of the experiments, its determination requires new experiments. Regardless to these differences the developed method shows a very good approximation of the energy needs in the rotary tilling process. This can be concluded more accurately following the total energy spent for the whole working process: the blue line from Figure 9 shows the variations of the total mechanical energy deduced in the field experiments, compared to the total energy calculated from simulation and the experimental idle energy (yellow line). It varies between -0.12% and 7.3%, according to the advancing speed variation, and normally also includes the difference given by the transformation of a part of the working energy in a pushing energy of the whole unit. Whit this simulation values a fuel consumption can be predicted and used in field works.

The simulation method developed and applied in this paper to the spading machine in the previous work, was also applied with sufficient precision to the rotary tilling machine. Using CAD modeling methods and numerical simulations, the forces acting during soil processing by tiller were studied and analyzed.

Precise modeling of all physical phenomena that occur during agricultural work is almost impossible to achieve, due to the variety of soil types and the parameters that influence the different soil processing processes. An assessment with sufficient accuracy of fuel consumption for different parameters of the work process for different tillage processes, if it is fast as well, as in the case of the presented method, could be a particularly useful tool in modern agriculture. To predict more precisely the total energy consumption of the whole working process more field experiments need to be done, but even at the present stage of our work, a sufficiently precise prediction of the fuel consumption can be made and used in the real field works.

REFERENCES

[1] Ahmadi I. (2017). A torque calculator for rotary tiller using the laws of classical mechanics. *Soil and Tillage Research*, vol. 165, ISSN 0167–1987, pp.137–143, Netherlands;

[2] Ahmadi I. (2021). Application of MS Excel to Estimate Power Needs of Tillage Tools. *Journal of Agricultural Machinery*, vol. 11, no. 1, ISSN 2423–3943, pp. 123–130, Iran;

[3] Aluko, O.; Seig, D. (2000). An experimental investigation of the characteristics of and conditions for brittle fracture in two-dimensional soil cutting. *Soil and Tillage Research* vol. 57 issue 3, ISSN 0167–1987, pp. 143–157, Netherlands;

[4] Amantayev, M.; Gaifullin, G.; Nukeshev, S. (2017). Modelling of the Soil-Two-Dimensional Shearing Tine Interaction. *Bulgarian Journal of Agricultural Science* 23, no. 5, ISSN 2534-983X, pp. 882–885, Bulgaria;

[5] Cardei P., Muraru S.L., Sfiru R., Muraru V. (2019). General Structure of Tillage Draft Force. Consequences in Experimental and Applicative Researches. *INMATEH - Agricultural Engineering*, vol. 59, no.3, ISSN 2068–2239, pp. 253–262, Bucharest/Romania;

[6] Catania P., Badalucco L., Laudicina V.A., Vallone M. (2018). Effects of tilling methods on soil penetration resistance, organic carbon and water stable aggregates in a vineyard of semiarid Mediterranean environment*. Environmental Earth Sciences*, vol. 77, no. 348, ISSN 1866–6299, pp.1–9, Germany;

[7] Chen, K.; Cai, Z.; Hou, Z.; Qu, C. (2017). An Experimental Device for Measuring Cutting Forces of a Cutting Tool. *Advances in Engineering Research. 5th International Conference on Mechatronics, Materials, Chemistry and Computer Engineering 2017*, vol. 141, ISSN 2352–5401, pp. 1257–1260, Chongqing/China;

[8] Căproiu Șt., Scripnic, V., Babiciu, P., Ciuobotartu., C, Roș, V. (1982*). Agricultural machinery for tillage, sowing and crop maintenance (Mașini agricole de lucrat solul, semănat și întreținere a culturilor),* Didactic and Pedagogic Publishing House (Editura didactică și pedagogică), Bucharest/Romania;

[9] Chen W., Ding Y., Tashi N., Zhu J., Yuan D., Yao K., Xia M., Sun L. (2022). Design and experiment of a vertical rotary tillage machine with fixed-layer fertilization function. *INMATEH - Agricultural Engineering*, vol.67, no. 2, ISSN 2068–2239, pp. 33–40, Bucharest/Romania;

[10] Cujbescu D., Ungureanu N., Vlăduţ V., Persu C., Oprescu R., Gheorghiţă E. (2019). Field testing of compaction characteristics for farm tractor universal 445. *INMATEH - Agricultural Engineering*, vol. 59, no. 3, ISSN 2068–2239, pp. 245–252, Bucharest/Romania;

[11] Drunek (Pásztor) J. (2009). *Researches on the Energy Optmization of the Preparation Works of the Germination Bed in Greenhouses (Cercetări privind optimizarea energetică a lucrărilor de pregătire a patului germinativ în sere),* Phd dissertation, Transilvania University Brașov.

[12] Forgó Z., Tolvaly-Roșca F., Pásztor J., Kovari A. (2021). Energy Consumption Evaluation of Active Tillage Machines Using Dynamic Modelling. *Applied Sciences*, vol.11, no. 14, art. ID 6240, ISSN 2076–3417, pp. 1–17, Switzerland;

[13] Hassan S., Nawi M. A. M., Khor C. Y., Jamalludin M. R., Wan Mohd Faizal Wan Abd Rahim, Ishak M.I., Rosli M. U., Zakaria M. S. (2018). The effect of rotary tiller blade design on soil pulverization. *AIP Conference Proceedings 2030*, 020099, issue 1, ISBN: 978-0-7354-1752-6, pp. 1–5, Vietnam;

[14] Kuan Q., Xiaolong L., Chengmao C., Liangfei F. (2020). Relationship between soil movement and power consumption in a furrow-opening rotary blade. *INMATEH-Agricultural Engineering*, vol. 62, no. 3, ISSN 2068–2239, pp. 55–68, Bucharest/Romania;

[15] Major, T., Csanády, V. (2014). Application of numerical analysis for the design of rotating tool. *Hungarian Agricultural Engineering*, no. 26, HU ISSN 2415–9751, pp. 16–19, Hungary;

[16] Marin E., Pirnă I., Sorică C., Manea D., Cârdei P. (2012). Studies on structural analysis of resistance structure as a component of equipment with active working parts driven to deeply loosen the soil. *INMATEH-Agricultural Engineering*, vol.36, no. 1, ISSN 2068–2239, pp. 13–21, Bucharest/Romania;

[17] Rajaram, G. (2018). *Mechanical Behavior of an Agricultural Soil*. Ph.D. Thesis, Iowa State University, Ames, IA, USA.

[18] Saimbhi, V.S., Wadhwa, D.S., Grewal, P.S. (2004). Development of a Rotary Tiller Blade using Three-dimensional Computer Graphics. *Biosystems Engineering*, vol. 89, issue 1, ISSN 1537–5110, pp.47–58, United States;

[19] Sitkei, G. (1976). *Soil Mechanics Problems of Agricultural Machines*. Franklin Book Programs, New York/ USA.

[20] Tenu I., Carlescu P., Cojocariu P., Rosca R. (2012). *Resource management for sustainable agriculture*. Impact of Agricultural Traffic and Tillage Technologies on the Properties of Soil (Chapter 10), ISBN 978-953-51-0808-5, London/United Kingdom;

[21] Tolvaly-Roșca F., Pásztor J. (2019). Work Process Analysis of the Machines with Working Parts Entrained in Seedbed Preparation Works (Analiza procesului de lucru al mașinilor cu organe de lucru antrenate la lucrările de pregătire a patului germinativ). *INMATEH-Agricultural Engineering*, vol. 58, no. 2, ISSN 2068–2239, pp. 9–16, Bucharest/Romania;

[22] Ungureanu N., Vlăduţ V., Biriş S.Șt. (2017). FEM modelling of soil behaviour under compressive loads. Materials Science and Engineering, vol 163, art. ID 012001, pp. 1–9, doi:10.1088/1757-899X/163/1/012001;

[23] Ungureanu N., Vlăduţ V., Biriș S.Șt., Paraschiv G., Dincă M., Zăbavă B. Ș., Ștefan V., Gheorghiță N. E. (2018). FEM modelling of machinery induced compaction for the sustainable use of agricultural sandy soils, *Proceedings of the 46 International Symposium on Agricultural Engineering "Actual Tasks on Agricultural Engineering"*, ISSN 1848-4425, pp. 201–211, Opatija/Croatia.

[24] Usaborisut, P., Sukcharoenvipharat, W., Choedkiatphon, S., (2020). Tilling tests of rotary tiller and power harrow after subsoiling. *Journal of the Saudi Society of Agricultural Sciences*, vol. 19, issue 6, ISSN 1658-077X, pp. 391–400, Saudi Arabia.

[25] Vlăduţ D.I., Biriş S.Șt, Vlăduţ V., Cujbescu D., Ungureanu N., Găgeanu I. (2018). Experimental researches on the working process of a seedbed preparation equipment for heavy soils, *INMATEH-Agricultural Engineering*, vol. 55, no. 2, ISSN 2068–2239, pp. 27–34, Bucharest/Romania.

ANALYSIS AND CALIBRATION OF PARAMETERS OF WET-VISCOUS PADDY MUD PARTICLES BASED ON THE SLUMP EXPERIMENT

/

基于坍落度试验的湿粘性水田泥浆颗粒离散元参数分析及标定

Zhongyi YU [1)], Wei XIONG[1)], Dequan ZHU[*1,2)], Kang XUE[1)], Shun ZHANG[1)], Fuming KUANG[1)], Jinnan QUE[1)], Xiaoshuang ZHANG[1)], Ben HENG[1)]

[1)] College of Engineering, Anhui Agricultural University, Hefei 230036, China;

[2)] Anhui Province Engineering Laboratory of Intelligent Agricultural Machinery and Equipment, Hefei 230036, China;

[*)] *Corresponding author: Dequan Zhu, E-mail: zhudequan@ahau.edu.cn*

DOI: https://doi.org/10.35633/inmateh-68-18

***Keywords**: Slump test, Mud particles, Response surface methodology, DEM, Parameter calibration*

ABSTRACT

In order to obtain the discrete element contact parameters of wet and viscous paddy field mud particles, an accurate numerical simulation model was constructed. In order to obtain the discrete element contact parameters of wet and viscous paddy field mud particles, an accurate numerical simulation model was constructed.Firstly, the paddy field mud with an average particle size of 0.2 mm was taken as the research object, and the basic physical parameters and rheological behavior laws were obtained through physical measurements and rotational rheological tests. Based on the slump test, combined with the particle scaling theory and Johnson-Kendall-Roberts (JKR) model, and the slump and slump-flow values were taken as response values, the Plackett-Burman test, the steepest climb test and the Box-Behnken test were designed by Design-Expert software to complete the simulation parameters calibration. The optimal significance parameters are as follows: 0.096 J/m^2 for the JKR surface energy of mud, 0.13 for the mud-mud restitution coefficient and 0.6 for the mud-steel static friction coefficient. Finally, the mud slump and fluidity verification tests showed that the relative errors between the simulation values and the physical values of slump and slump-flow are 1.73% and 0.42%, and the average error of torque is 2.47%, and the parameters are accurate and reliable. The calibration method can accurately construct the discrete element model of wet-viscous particles, which provides basic data and technical guidance for the coupling mechanism of paddy machinery-mud.

摘要

为获取湿黏性的水田泥浆颗粒离散元接触参数，构建精准的数值仿真模型。首先，以平均粒径为 0.2 mm 水田泥浆为研究对象，通过物理测定和旋转流变试验，得出基本物理参数和流变行为规律。基于坍塌物理试验，结合颗粒缩放理论和 JKR 接触模型，以塌落度和拓展度为响应值，采用 Design Expert 软件依次设计 Plackett-Burman 试验、最陡爬坡试验和 Box-Behnken 试验,进行仿真参数标定。显著性参数最优值为泥浆 JKR 表面能为 0.096 J/㎡、泥浆-泥浆恢复系数为 0.13 和泥浆-钢静摩擦系数 0.6。最后，水田泥浆塌落和流变验证试验表明，塌落度和拓展度仿真与物理值的相对误差为 1.73%、0.42%，扭矩平均误差为 2.47%，标定参数准确可靠。本文提出的标定方法能够精确地构建湿黏性颗粒-泥浆离散元模型，为机械-泥浆耦合机理提供基础数据和技术指导。

INTRODUCTION

At present, the bed soil with high water content and no surface water is used in rice seedlings in order to cultivate stronger machine-planted rice seedlings, which is in line with the characteristics of rice planting mechanization in southern China (*Li et al., 2018; Ye., 2021*). Compared with ordinary soil, paddy mud is sticky and heavy, with stronger swelling and flow plasticity, leading to adhesion problems of soil-touching parts in the field and seriously affects production efficiency. Due to the complexity of paddy mud structure and the importance of developing soil-touching parts, it is necessary to analyze the interaction coupling mechanism between them. However, the macroscopic physical test cannot prove the microscopic motion law of mud

[1] *Zhongyi Yu, As. M.S. Stud. Eng.; Wei Xiong, Ph.D. Eng.; Dequan Zhu, Prof. Ph.D. Eng.; Kang Xue, As. Ph.D. Stud. Eng.; Shun Zhang, Prof. Ph.D. Eng.; Fuming Kuang, Prof. Ph.D. Eng.; Jinnan Que, As. M.S. Stud. Eng.; Xiaoshuang Zhang, As. M.S. Stud. Eng.;*

particles, and the research is generally carried out using numerical simulation.

Since the finite element method simulates the overall disruptive behavior of the mud in the form of a continuous medium, it is impossible to analyze the movement process of mud particles. The research shows that the discrete element method based on the principle of particle contact mechanics is suitable for soil particle groups with power-law rheological characteristics, especially wet soil or paddy mud with complex composition and rheological properties (*Xu et al., 2003; Tamás K et al., 2013*).

Generally, simulation parameters need to be determined before constructing the discrete element numerical model. The material intrinsic parameters are obtained from references, material contact, and model parameters are obtained by direct measurements or calibration of virtual tests. Due to the limitations of test conditions and methods, it is difficult to obtain accurate contact parameters through actual tests. Most research concentrated on using virtual simulation experiments to obtain the contact parameters of wet and viscous materials, and a large number of virtual calibration simulation experiments have been performed (*Du et al., 2021; Zhang et al., 2022; Wang et al., 2021; Zheng et al., 2021*). An optimization method based on a regression model was established by combining physical experiments, to address the difficult problem of obtaining the contact characteristic parameters used in the DEM model of quinoa grains and for calibrating the parameters of the quinoa DEM model *(Liu et al., 2020).* An accurate clay loam discrete element simulation model was constructed based on the accumulation test, which provided technical support for the research on the dynamics of soil-contacting parts (*Xiang et al., 2019)*. Based on the DEM numerical model, a method for simulations of soil flow properties was proposed using the discrete element method (DEM) (*Qi L. et al., 2019)*. The simulation optimization design experiments and physical experiments were combined to calibrate the parameters of simulated discrete element of buckwheat seeds *(Xu B.et al., 2021)*. The Hertz-Mindlin with bonding contact model was used to calibrate the parameters of soils in Inner Mongolia, and to solve dynamic soil behavior at the contact interface, which makes it difficult to ensure transplanting quality during transplanting (*Zeng et al., 2021)*. Based on the theory of particle scaling, the contact parameters of seeds, powders, and between powders and seeds were calibrated to provide a reference to the discrete element simulation parameter calibration of similar fine particles and powders materials (*Ma et al., 2022)*. The Johnson-Kendall-Roberts (JKR) contact model was applied to construct and calibrate the parameters of wet sand and gravel particles in the screening process, which provided theoretical guidance for studying the modeling of wet particles and improving the screening efficiency (*Zhou JC et al., 2022)*. Although wet material particles have been widely studied by different methods and means, there is still little research on discrete element simulation modeling and parameter calibration of paddy mud with complex components, high water content, and micro-sized particle, and the aforementioned methods are not applicable.

Therefore, the approaches to accurately obtain the contact parameters between the mud particles and that between the mud particles and the working parts on the transplanter were studied. The contact and model parameters of paddy mud simulation were calibrated, combined with the advantages of discrete element technology in the nonlinear simulation of wet granular materials. The findings can be applied to the numerical simulation research of paddy field machinery. Given the large number and small particle size of paddy mud in southern China, particle scaling theory engineering technology is used to enlarge the particles in the original system to reduce the number of discrete units in the model and to carry out effective simulation and calculation (*Li et al., 2019*). In addition, paddy mud is difficult to accumulate due to its good fluidity, the slump test can be used to measure the fluidity and consistency by observing the slumped shape of the mud under the action of self-weight *(Wang et al., 2022; Coetzee, 2017)*. A method combining discrete element virtual simulation and slump physical test was proposed to calibrate wet-viscous mud particles' contact and model parameters based on the particle scaling theory and the JKR contact model. The accuracy of simulation parameters was verified by field test and the fluidity test, in order to build an accurate discrete element numerical model of wet-viscous mud in southern China.

MATERIALS AND METHODS

Basic physical parameters of test materials

The paddy mud samples were collected from Feixi County, Anhui Province, China. The particle volume fraction distribution of mud was determined by Mastersizer 2000 particle analyzer (*Wang et al., 2014*), as shown in Fig.1. The average particle size was calculated to be 0.2 mm. The basic physical parameters of paddy mud were determined through a drying test and mud hydrometer and liquid plastic limit measurement test, which were shown in Table 1.

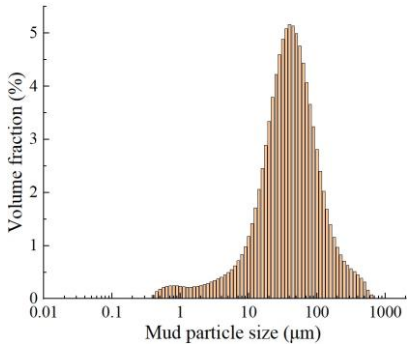

Fig. 1 - Particle size distribution of paddy mud

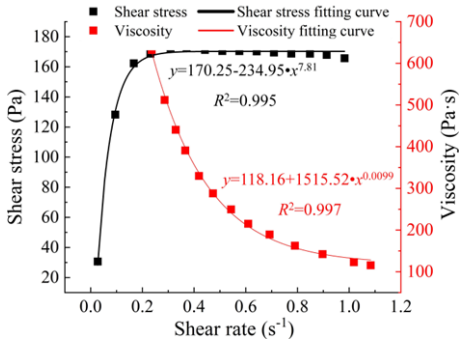

Fig. 2 - Fitting curves of mud at 38% water content

Table 1

Basic parameters of physical mud

Particle size distribution /%			Liquid limit (%)	Plastic limit (%)	Plasticity index (%)	Proportion (g·cm^{-3})	Moisture content (%)
cohesive grain (0-2 μm)	powder grain (2-20 μm)	sand grain (20-2000 μm)					
38.24	19.61	42.61	15.67	26.10	10.43	1.68	38

Experimental study on rheological properties of paddy mud

Rheological tests can describe the rheological behavior of wet and viscous materials (e.g., concrete and mud) and clarify the functional relationship between the characteristic parameters of shear stress or viscosity *(Yang et al., 2017)*. The shear rate-stress and shear rate-viscosity function curves of mud samples with a water content of 38% were obtained via the Brookfield R/S plus rheometer, in order to study the rheological behavior characteristics and parameter change low of paddy mud, as shown in Fig. 2.

In Fig. 2, the shear stress of the sample shows a tendency of increasing with the shear rate, which is consistent with the basic law of rheology. After reaching a certain level, the mud shows a strong shear dilution, leading to a slow decrease in shear stress. As the shear rate increases, the gap between particles increases during the flow of mud, resulting in the decrease of adhesion and the gradual decrease of viscosity. Therefore, the sample mud is a non-Newtonian fluid with power-law rheological characteristics, which is suitable for numerical simulation of the discrete element method *(Sun, 2017)*. The Herschel-Bulkley constitutive equation of the mud sample was fitted, as illustrated in Eq. (1), where τ is the shear stress, τ_0 is the yield stress, K is the viscosity coefficient, D is the shear rate, and n is the flow indicator.

$$\tau = \tau_0 + K \cdot (D)^n \tag{1}$$

Physical test of paddy mud slump

Abrams has proposed that the slump test can characterize the rheological parameters of fluidity and viscosity through the slump and slump-flow of materials *(Sun, 2017)*. The slump test of paddy mud refers to the "Standard for Test Methods for the Performance of Ordinary Concrete Mixtures" *(GB/T 50080-2016, 2016)*, and the test tools and process are shown in Fig. 3.

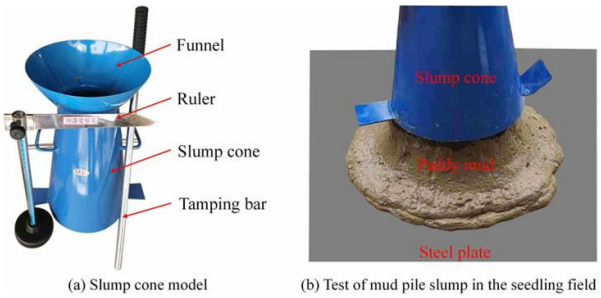

(a) Slump cone model (b) Test of mud pile slump in the seedling field

Fig. 3 - Physical test of mud pile slump

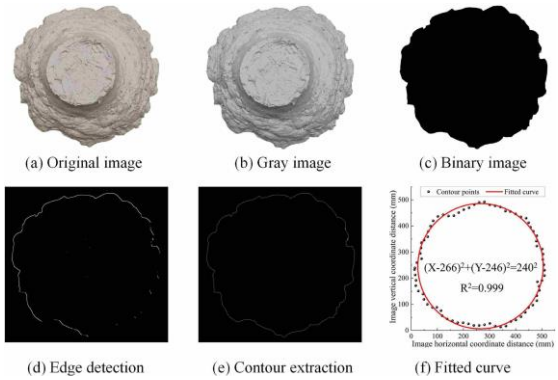

Fig. 4 - Image processing of slump-flow

The average value of 10 test values of 231 mm mud was taken as the measured slump value to reduce the ruler measurement errors.

The grayscale processing, binarization processing, edge detection, and contour extraction sequence were performed on the obtained original image of slump-flow, in order to more accurately measure the slump-flow values of mud piles with uneven surfaces and boundaries. Edge contour pixel points were converted into real coordinate data, and the equation of the circle curve function was fitted. The approximate circle diameter of 480 mm was taken as the slump-flow value, as shown in Fig. 4.

Slump test simulation model modeling

The virtual slump test of paddy mud was performed in EDEM 2018 software, and the model parameters were continuously adjusted until the mechanical behavior and flow states of the model were consistent with reality. It can be considered that the parameters of the discrete element model are consistent with the actual situation *(Zeng et al., 2021)*. The slump and slump-flow values were measured when the velocity of mud particles was approximately zero and no significant flow occurred, as shown in Fig. 5(a). The Hertz-Mindlin (no slip) contact model was chosen as the contact model between mud particles and steel. The mud and steel intrinsic parameters are listed in Table 2 *(Ghosh et al., 2021; Hao et al., 2020)*.

Since the size of paddy mud is micron level, increasing the particle radius or calculation time step is beneficial to improve the simulation efficiency *(Zhang et al., 2022)*.

The calculation formula of Rayleigh time step T_R is shown in Eq. (2).

$$T_R = \frac{\pi R}{(0.163\nu + 0.877)}\sqrt{\left(\frac{\rho}{G}\right)} \tag{2}$$

where R is the particle radius, ρ is the mud density, G is the shear modulus, and ν is the Poisson's ratio of mud.

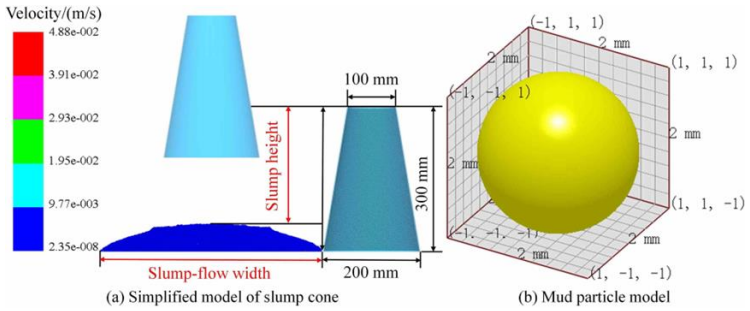

Fig. 5 - EDEM virtual slump test model

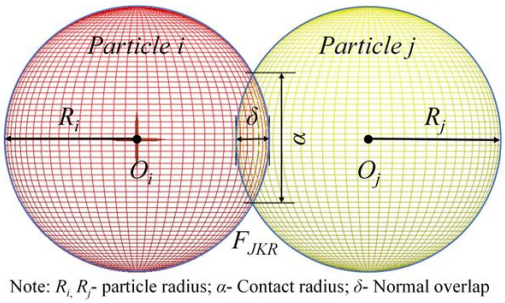

Fig. 6 - Diagram of particles in JKR contact

Table 2

Intrinsic parameters of mud particles and steel

Materials	Poisson's ratio	Density (kg·m^{-3})	Shear modulus (MPa)
Mud	0.5	1680	1
Steel	0.3	7800	7000

Mud particles contact model selection

The paddy mud studied in this paper has a high water content due to long-term soaking, and the adhesion between particles leads to complex and diverse mechanical behaviors of paddy mud. The Hertz-Mindlin with JKR cohesion contact model can better characterize the obvious adhesion and agglomeration between particles due to electrostatic force and water content, which is suitable for moisture-containing materials with significant bonding and agglomeration caused by moisture (*Li et al., 2019; Rojek et al., 2019*), as shown in Fig. 6.

The normal cohesive force of the model, F_{JKR}, relates to the amount of normal overlap δ, interaction parameters, and cumulative surface energy density γ (J/m^2).

The expressions are as follows:

$$F_{JKR} = -4\sqrt{\pi\gamma E^*}\alpha^{\frac{3}{2}} + \frac{4E^*}{3R^*}\alpha^3 \tag{3}$$

$$\delta = \frac{\alpha^2}{R^*} - \sqrt{\frac{4\pi\gamma\alpha}{E^*}} \tag{4}$$

$$\frac{1}{E^*} = \frac{\left(1-\nu_i^2\right)}{E_i} + \frac{\left(1-\nu_j^2\right)}{E_j} \tag{5}$$

$$\frac{1}{R^*} = \frac{1}{R_i} + \frac{1}{R_j} \tag{6}$$

where α is the tangential overlap between the two particles, E^* and R^* are the equivalent radius and equivalent Young's modulus, E_i, ν_i, and R_i are the elastic modulus, Poisson's ratio, and radius of particle i; E_j, ν_j, and R_j are the elastic modulus of particle j.

The separation force $F_{abruption}$ required to separate the two particles depends on the surface tension γ_s and wetting angle θ.

$$F_{abruption} = -2\pi\gamma_s \cos(\theta)\sqrt{R_i R_j} \tag{7}$$

The paddy mud particles were set to spherical particles with a diameter of 2 mm by using the particle contact scaling principle on the calculation capability and simulation model reliability of the software (*Li et al., 2019; Coetzee., 2017; Zhang et al., 2022; Roessler et al., 2018*). A simplified slump cone simulation model was built with the actual size, as shown in Fig. 5. After several simulation pre-tests and physical tests, it was determined that the ascending speed of the slump cone was 0.05 m/s, 0.9 million particles were generated, and the total simulation time was 5 s. The test process is shown in Fig. 7.

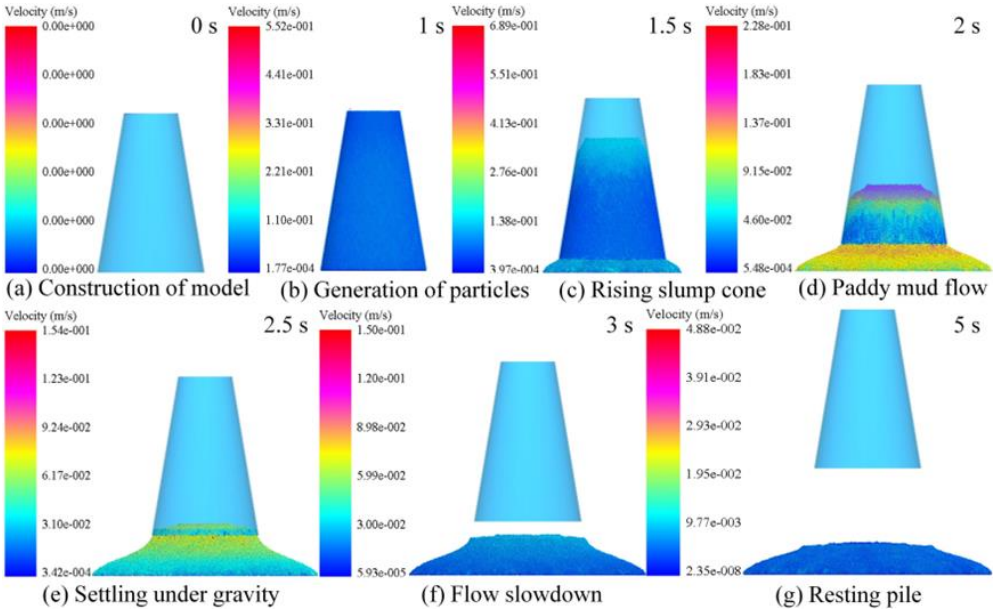

Fig. 7 - The simulation test process of paddy mud's slump and slump-flow

RSM test for simulation parameters calibration

The Plackett-Burman test was performed to identify the parameters with significant influence. Combined with a large number of pre-tests, the eigen parameters of paddy mud were entered into the EDEM 2018 Generic material model database (GEMM), and the range of contact parameters was determined, as shown in Table 3. There were 7 real parameters (H_1 to H_7) and 4 virtual parameters (H_8 to H_{11}) in the simulation test. Each parameter was set to a low and high level, which were represented by codes -1 and +1, respectively.

According to the significant parameters obtained from the Plackett-Burman test, the steepest climb test was designed to reduce the number of tests and find the level ranges of the best response values. The relative errors δ_t between the simulation value and the physical value of the slump or slump-flow were taken as the evaluation indicators, respectively. The calculation formula for the relative errors δ_t is as follows:

$$\delta_t = \frac{\left|Y_t - Y_t'\right|}{Y_t'} \tag{8}$$

where Y_t is the measured value of slump Y_1 or slump-flow Y_2, and Y_t' is the simulation value of slump Y_1' or slump-flow Y_2'.

Table 3

The parameter table of the Plackett-Burman test

Symbol	Simulation parameters	Parameter levels		
		-1	0	1
H_1	Mud-mud restitution coefficient	0.01	0.055	0.1
H_2	Mud-mud static friction coefficient	0.1	0.15	0.2
H_3	Mud-mud rolling friction coefficient	0.05	0.125	0.2
H_4	Mud-steel restitution coefficient	0.1	0.3	0.5
H_5	Mud-steel static friction coefficient	0.2	0.35	0.5
H_6	Mud-steel rolling friction coefficient	0.01	0.055	0.1
H_7	JKR surface energy of mud ($J \cdot m^{-2}$)	0.02	0.06	0.1
H_8, H_9, H_{10}, H_{11}	Virtual parameters	-1	0	1

Box-Behnken test was used to express the second-order regression equation between the significance parameters and response values by response surface methodology (RSM). The high, medium, and low levels of significance parameters were set to +1, 0, and -1. The non-significant parameters take the middle value of each factor in Table 3. The 5 center points were used to estimate the error, and the 17 tests were performed in total. Each set of simulation tests was repeated 3 times, and the average value was recorded as the numerical result of the simulation tests.

RESULTS AND DISCUSSION

Plackett-Burman test

Taking the slump and slump-flow values of paddy mud as the response values, the Plackett Burman test was designed by Design-Expert 12 software. The 13 groups of tests are performed, as shown in Table 4.

Table 4

Scheme and results of Plackett-Burman test

No.	Test factors											Slump Y_1 (mm)	Slump-flow Y_2 (mm)
	H_1	H_2	H_3	H_4	H_5	H_6	H_7	H_8	H_9	H_{10}	H_{11}		
1	-1	-1	-1	-1	-1	-1	-1	-1	-1	-1	-1	265	635
2	1	1	1	-1	-1	-1	1	-1	1	1	-1	249	596
3	-1	1	-1	1	1	-1	1	1	1	-1	-1	252	518
4	-1	1	1	-1	1	1	1	-1	-1	-1	1	247	478
5	-1	1	1	1	-1	-1	-1	1	-1	1	1	262	622
6	1	-1	1	1	-1	1	1	1	-1	-1	-1	248	592
7	1	-1	1	1	1	-1	-1	-1	1	-1	1	244	495
8	-1	-1	1	-1	1	1	-1	1	1	1	-1	253	496
9	-1	-1	-1	1	-1	1	1	-1	1	1	1	258	608
10	1	1	-1	-1	-1	1	-1	1	1	-1	1	255	606
11	1	1	-1	1	1	1	-1	-1	-1	1	-1	246	496
12	1	-1	-1	-1	1	-1	1	1	-1	1	1	237	480
13	0	0	0	0	0	0	0	0	0	0	0	245	505

The significant result of each parameter was obtained, as shown in Table 5 and Fig. 8. It can be seen that the restitution coefficient (H_1) of mud-mud, the static friction coefficient (H_5) of mud-steel, and the JKR surface energy of mud (H_7) have significant effects on the simulated slump and slump-flow, while other simulation parameters have no significant effect on them.

Table 5

Significance analysis of Plackett-Burman test results

Indexes	Sources of variation	Sum of squares	Degrees of freedom	Mean square	*F*-value	*P*-value	Significance ranking
Slump (mm)	Model	670	7	95.71	26.1	0.0035**	
	H_1	280.33	1	280.33	76.45	0.0009**	1
	H_2	3	1	3	0.82	0.4169	5
	H_3	8.33	1	8.33	2.27	0.2062	4
	H_4	1.33	1	1.33	0.36	0.579	6
	H_5	280.33	1	280.33	76.45	0.0009**	1
	H_6	0.33	1	0.33	0.09	0.778	7
	H_7	96.33	1	96.33	26.27	0.0069**	3
	Curvature	37.03	1	37.03	10.1	0.0336*	
	Residual	14.67	4	3.67			
	Total sum	721.69	12				
	R_1^2=0.9786; R_{1adj}^2=0.9411; CV=0.76%; Adeq Precision=15.6911						
Slump-flow (mm)	Model	42471.67	7	6067.38	100.29	0.0003**	
	H_1	705.33	1	705.33	11.66	0.0269*	2
	H_2	8.33	1	8.33	0.14	0.7294	7
	H_3	341.33	1	341.33	5.64	0.0764	5
	H_4	133.33	1	133.33	2.20	0.2118	6
	H_5	40368.00	1	40368.00	667.24	<0.0001	1
	H_6	408.33	1	408.33	6.75	0.0603	4
	H_7	507.00	1	507.00	8.38	0.0443*	3
	Curvature	2024.64	1	2024.64	33.47	0.0044**	
	Residual	242.00	4	60.50			
	Total sum	44738.31	12				
	R_2^2=0.9943; R_{2adj}^2=0.9844; CV=1.42%; Adeq Precision=23.1259						

*Note: **means the item is extremely significant ($P < 0.01$), *means the item is significant ($0.01 \leq P < 0.05$), and $P \geq 0.05$ means the item is insignificant.*

The steepest climb test

Considering the range of three significant parameters, i.e., H_1 (A), H_5 (B), and H_7 (C) obtained from the Plackett-Burman test ($P < 0.05$), each step length of the steepest climb test was set as follows: ΔA was 0.03, ΔB was 0.1, and ΔC was 0.03. The results are shown in Table 6.

With the gradual increase of the significance parameter, the slump and slump-flow gradually decrease, and the relative errors between the real test and the simulation gradually decrease. The relative error of the 4th test was the smallest and less than 5%, which meets the experimental requirements. Therefore, the parameter of the 4th test was chosen to be the intermediate level (0), and the parameter of the 3rd test was chosen as the low level (-1). A set of parameters with equal step length was selected as the high level (+1) for the subsequent response surface design. The low, medium and high levels of parameters A, B and C are 0.07, 0.1, and 0.13; 0.4, 0.5, and 0.6; 0.07 J/m^2, 0.1 J/m^2 and 0.13 J/m^2, respectively.

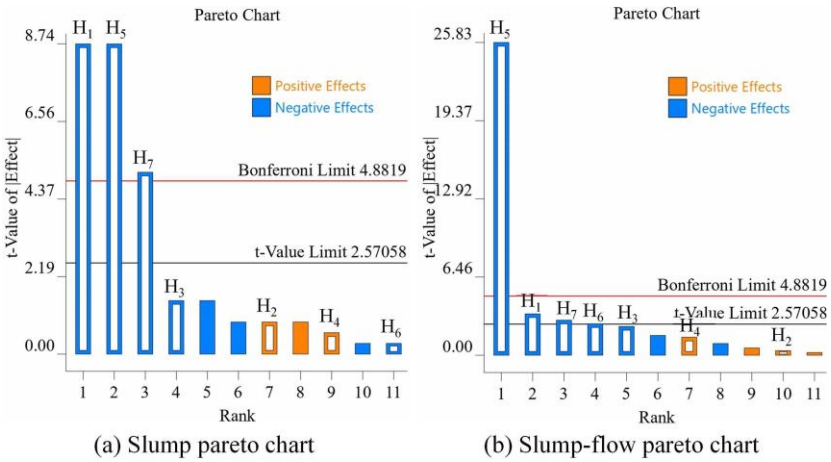

(a) Slump pareto chart (b) Slump-flow pareto chart

Fig. 8 - Slump and slump-flow Pareto chart

Table 6

Scheme and results of steepest climb test

No.	Test factors			Slump Y_1 (mm)	Relative errors δ_1 (%)	Slump-flow Y_2 (mm)	Relative errors δ_2 (%)
	A	*B*	*C*				
1	0.01	0.2	0.01	258	11.69	612	27.50
2	0.04	0.3	0.04	249	7.79	537	11.88
3	0.07	0.4	0.07	245	6.06	503	4.79
4	0.10	0.5	0.10	242	4.76	485	1.04

Note: Parameters A, B, and C are equal to test factors H_1、H_5、H_7, respectively.

Box-Behnken test

Table 7

Design and results of Box-Behnken test

No.	Factors			Slump Y_1 (mm)	Relative errors δ_1 (%)	Slump-flow Y_2 (mm)	Relative errors δ_2 (%)
	A	*B*	*C*				
1	1(0.13)	1	0	236	2.16	474	1.25
2	1	-1	0(0.1)	240	3.90	494	2.92
3	1	0(0.5)	-1	249	7.80	534	11.25
4	1	0	1	236	2.16	468	2.50
5	-1(0.07)	-1	0	242	4.76	498	3.75
6	-1	1(0.6)	0	244	5.63	490	2.08
7	-1	0	-1(0.07)	243	5.19	488	1.67
8	-1	0	1	250	8.23	524	9.17
9	0(0.1)	1	1	237	2.60	470	2.08
10	0	1	-1	243	5.19	492	2.50
11	0	-1	1(0.13)	243	5.19	496	3.33
12	0	-1(0.4)	-1	241	4.33	498	3.75
13	0	0	0	244	5.63	484	0.83
14	0	0	0	243	5.19	486	1.25
15	0	0	0	244	5.63	488	1.67
16	0	0	0	244	5.63	484	0.83
17	0	0	0	244	5.63	486	1.25

Note: Numbers in brackets are the values of test factor levels.

The Box-Behnken test was applied to conduct response surface analysis and find the optimal solution. The values of other non-significant parameters were the same as those in the steepest climbing test. The test protocol and results are shown in Table 7.

Response surface regression modeling and ANOVA

Multiple regression fitting analysis of the slump test results was performed via Design-expert 12 software, as shown in Table 8.

Table 8

ANOVA of the quadratic polynomial model of the Box-Behnken test

Indexes	Source of Variance	Sum of Squares	Degree of freedom	Mean Square	*F*-value	*P*-value
Slump Y_1 (mm)	Model	231.94	9	25.77	78.43	<0.0001**
	A	40.5	1	40.5	123.26	<0.0001**
	B	4.5	1	4.5	13.7	0.0076**
	C	12.5	1	12.5	38.04	0.0005**
	AB	9	1	9	27.39	0.0012**
	AC	100	1	100	304.35	<0.0001**
	BC	16	1	16	48.7	0.0002**
	A^2	0.04	1	0.04	0.13	0.7309
	B^2	48.67	1	48.67	148.14	<0.0001**
	C^2	1.52	1	1.52	4.61	0.0688
	Residual	2.3	7	0.33		
	Lack of fit	1.5	3	0.5	2.5	0.1985
	Pure error	0.8	4	0.2		
	Sum	234.24	16			
	R_1^2=0.9902; $R_1^2{}_{adj}$=0.9776; CV=0.2363%; Adeq Precision=32.9820					
Slump-flow Y_2 (mm)	Model	4463.92	9	495.99	114.96	<0.0001**
	A	112.5	1	112.5	26.08	0.0014**
	B	450	1	450	104.3	<0.0001**
	C	364.5	1	364.5	84.49	<0.0001**
	AB	36	1	36	8.34	0.0234*
	AC	2601	1	2601	602.88	<0.0001**
	BC	100	1	100	23.18	0.0019**
	A^2	337.27	1	337.27	78.18	<0.0001**
	B^2	129.69	1	129.69	30.06	0.0009**
	C^2	337.27	1	337.27	78.18	<0.0001**
	Residual	30.2	7	4.31		
	Lack of fit	19	3	6.33	2.26	0.2234
	Pure error	11.2	4	2.8		
	Sum	4494.12	16			
	R_2^2=0.9933; $R_2^2{}_{adj}$=0.9846; CV=0.4227%; Adeq Precision=40.4883					

*Note: ** and * indicated significance at 0.01 and 0.05 levels, respectively.*

A second-order regression model of the simulated slump Y_1 and slump-flow Y_2 of paddy mud was built, and the significant parameters were obtained. The regression model is expressed as follows:

$$\begin{cases} Y_1 = 243.8 - 2.25A - 0.75B - 1.25C - 1.5AB - 5AC - 2BC + 0.1A^2 - 3.4B^2 + 0.6C^2 \\ Y_2 = 485.6 - 3.75A - 7.5B - 6.75C - 3AB - 25.5AC - 5BC + 8.95A^2 - 5.55B^2 + 8.95C^2 \end{cases} \quad (9)$$

Table 8 shows the model with $P < 0.0001$, indicating the regression models of slump and slump-flow are extremely significant. It can be seen that the quadratic term (B^2), the restitution coefficient (A) of mud-mud, the static friction coefficient (B) of mud-steel, the JKR surface energy of mud (C), and their interaction terms have extremely significant effects on the slump and the slump-flow. The quadratic terms A^2 and C^2 have no significant effect on the slump ($P > 0.05$). The lack-of-fit term $P > 0.05$, the variation coefficient of 0.2363% and 0.4227% are low, indicating the two equations fit well. The coefficients of determination, R_1^2, equals 0.9902, and R_2^2, equals 0.9933; the correction coefficients of determination, $R_1^2{}_{adj}$, equals 0.9776, and $R_2^2{}_{adj}$, equals 0.9846. All of the coefficients are close to 1, indicating the fitting equations are highly reliable. The precisions are 32.982 and 40.4883, respectively, indicating the accuracy of the model is good.

Interaction effect analysis

To explore the interaction effect of three significant parameters on the predicted response values, the interaction term response surface and contour distribution map of the slump and slump-flow were obtained. As shown in Fig. 9, the curvature of the response surface shows that the order of influence of the interaction term is $AC > BC > AB$, where AC refers to the interaction between A and C, and so on.

(1) Analysis of interaction effect on the slump

From Fig. 9(a), the slump decreases with the increase of the mud-mud restitution coefficient, and increases first and then decreases abruptly with the increase of the mud-steel static friction coefficient. However, the response surface varies faster along the direction of the mud-mud restitution coefficient than the direction of the mud-steel static friction coefficient. From Fig. 9(b), the slump decreases sharply with the increase of the mud-mud restitution coefficient and the JKR surface energy of mud, and the effect is significant. From Fig. 9(c), the slump first increases and then decreases sharply with the increase of the mud-steel static friction coefficient, and decreases with the increase of the JKR surface energy of mud.

(2) Analysis of interaction effect on slump-flow

From Fig. 9(d), the slump-flow increases with the increase of the mud-mud restitution coefficient, and decreases with the increase of the mud-steel static friction coefficient. From Fig. 9(e), the mud-mud restitution coefficient and the JKR surface energy of mud increase, the slump-flow rapidly decreases, and the impact is significant. From Fig. 9(f), the slump-flow decreases with the increase of the mud-steel static friction coefficient, and first decreases and then increases with the increase of the JKR surface energy of mud.

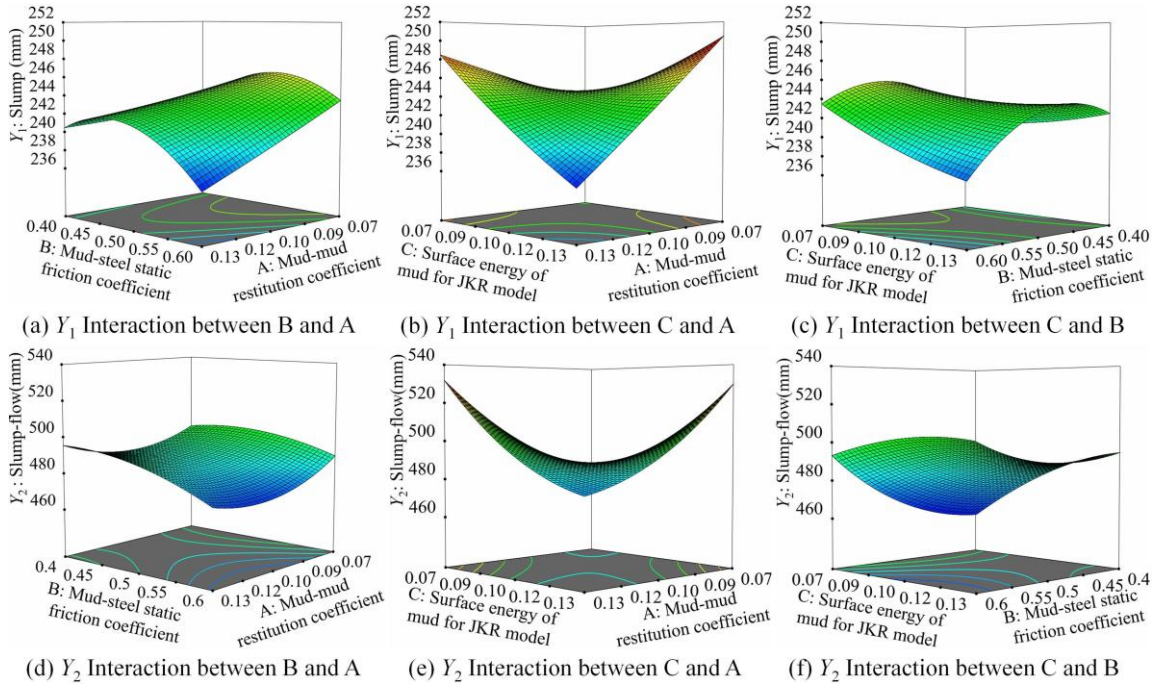

(a) Y_1 Interaction between B and A (b) Y_1 Interaction between C and A (c) Y_1 Interaction between C and B

(d) Y_2 Interaction between B and A (e) Y_2 Interaction between C and A (f) Y_2 Interaction between C and B

Fig. 9 - Effects of interactive factors on slump and slump-flow

Overall, the response surface curve of the mud-mud restitution coefficient (*A*) and the JKR surface energy of mud (*C*) are steepest, indicating they have a more significant impact on the slump and the slump-flow. The result is consistent with that of variance analysis of the regression model.

Determining the optimal parameters

The regression model and simulation parameters were optimized; the measured slump of 231 mm mud and the slump-flow of 480 mm mud were used as the target values for the verification of simulation tests. The corresponding objective and constraint equations are as follows:

$$Obj.\begin{cases} Y_1(A,B,C)=231 \\ Y_2(A,B,C)=480 \end{cases}$$
$$s.t.\begin{cases} 0.07 \le A \le 0.13 \\ 0.4 \le B \le 0.6 \\ 0.07 \le C \le 0.13 \end{cases} \quad (10)$$

A set of optimal solutions that are similar to the actual physical slump and slump-flow data were obtained, and the result data were 0.13 for the mud-mud restitution coefficient, 0.6 for the mud-steel static friction coefficient, 0.096 J/m^2 for the JKR surface energy of mud, and values of the rest non-significant parameters are the same as those in the steepest climbing test. The optimal values of each parameter and response indexes are shown in Fig. 10.

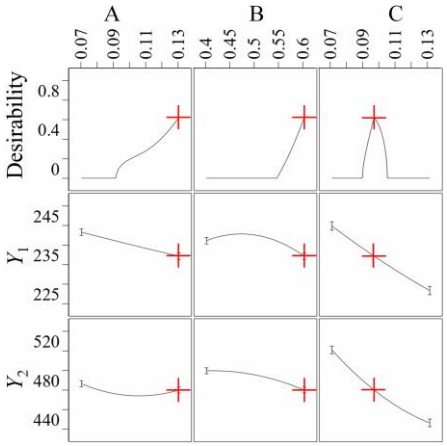

Fig. 10 - Ramp function graph for parameters and response value

Validation test

From Fig. 11, the predicted values of the slump and the slump-flow under the optimal solution of regression fitting are 237 mm and 480 mm, respectively. The mean relative errors are 0.85% and 0.42% with the simulation test results, respectively.

Fig. 12 describes the comparison between the simulated and measured values of the slump and the slump-flow under the optimal parameters. The average relative errors with the simulation test are only 1.73% and 0.42%.

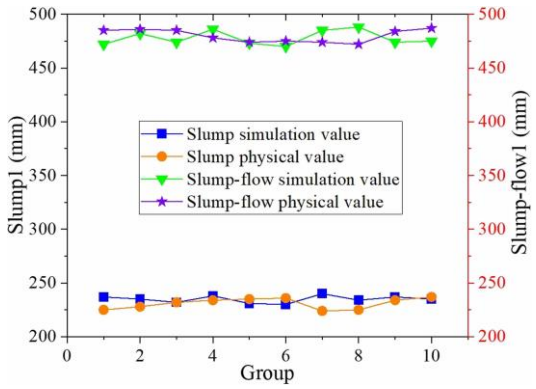

Fig. 11 - Comparison between physical and simulation results of paddy mud slump and slump-flow

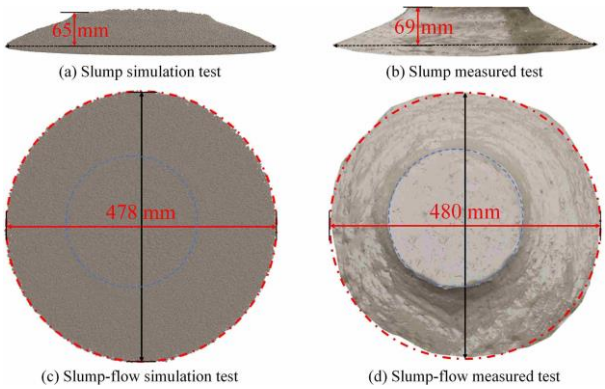

Fig. 12 - Comparison of physical test and simulation test

To further identify the accuracy and rationality of calibrated model parameters, the aforementioned R/S plus rheometer was used to perform the paddy mud fluidity verification test. The target of the test was the rotor blade torque, and the rheological properties of mud were selected as the verification indicator *(Han et al., 2021)*. A simplified model of the rheological test was constructed in EDEM software *(Nan et al., 2020)*. The simulation test was performed on the calibrated optimal parameters, and blade torque data after smooth rotation of mud was derived. The experimental device and simulation test model are shown in Fig. 13.

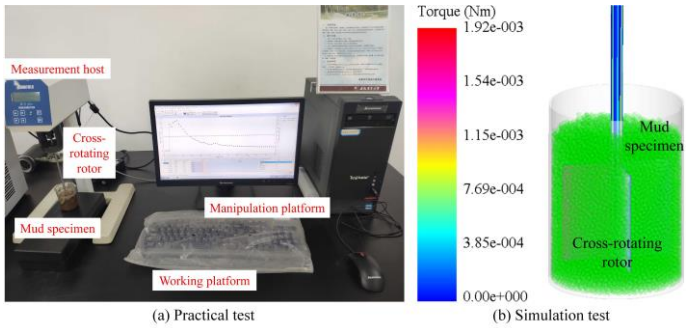

Fig. 13 - The validation test process of paddy mud fluidity

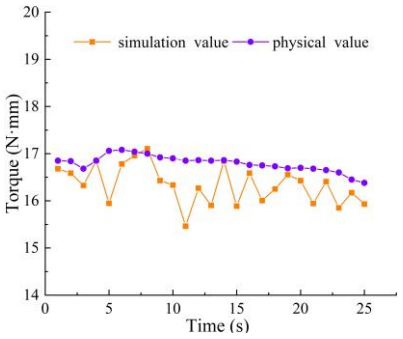

Fig. 14 - Simulation and physical results of paddy mud flow torque

Fig. 14 shows a comparative analysis of the blade torque in mud flow in the measured and simulated values with an average relative error of 2.47%, indicating that the bulk rheological properties of paddy mud in the simulation model are consistent with the actual, and the built discrete element model of wet particles is reliable.

CONCLUSIONS

(1) Taking the paddy field mud in southern China as an example, a method for systematically obtaining the calibration and optimization of discrete element simulation parameters of wet-viscous mud particles is proposed, which is based on the combination of slump physical test and DEM virtual simulation. The method can construct an accurate discrete element simulation model of paddy mud in southern China.

(2) Taking the slump and the slump-flow as the response values, the simulation parameters were calibrated and optimized by significance analysis and response surface method. The optimal parameters were obtained, and the result data were 0.13 for the mud-mud restitution coefficient, 0.6 for the mud-steel static friction coefficient, and 0.096 J/m2 for the JKR surface energy of mud. The remaining non-significant parameters include the mud-mud static friction coefficient is 0.15, the mud-mud rolling friction coefficient is 0.125, the mud-steel restitution coefficient is 0.3 and the mud-steel rolling friction coefficient is 0.055. Finally, the accuracy of the constructed discrete element simulation model of mud particles was verified by the physical slump test and fluidity test. The results of the research can provide basic data and technical support to investigate the rheological behavior and dynamic characteristics of the mud-mechanical components of the paddy field.

(3) The verification tests of paddy mud slump and fluidity show that paddy mud is a non-Newtonian fluid with power-law rheological characteristics. The relative errors between the simulation and physical values of slump and slump-flow are 1.73% and 0.42% respectively. The average relative error of rotational torque is 2.47%, which indicate that the method of parameter calibration and research results are accurate and reliable.

ACKNOWLEDGEMENTS

This work was supported by the Natural Science Foundation of Anhui Province (Grant No. 2208085ME131), Major Science and Technology Project of Anhui Province (Grant No. 202203a06020004), Postgraduate Scientific Research Projects of Universities in Anhui Province (Grant No. YJS20210233), Innovation and Entrepreneurship Training Program for College Students of Anhui Agricultural University (Grant No. X202210364564) and Key common technology research and development projects in Hefei (Grant No. 2021GJ078).

REFERENCES

[1] Coetzee C.J., (2017). Review: Calibration of the Discrete Element Method. *Powder Technology*, No. 310, pp. 104-142.

[2] Du X., Liu C.L., Jiang M. et al., (2021). Calibration of bonding model parameters for coated fertilizers based on PSO-BP neural network. *INMATEH-Agricultural Engineering*, Vol.65, No. 3, pp.255-264.
[3] GB/T 50080-2016., (2016). Standard for test method of performance on ordinary fresh concrete. Ministry of Housing and Urban-Rural Development of the Peoples Republic of China.
[4] Ghosh P., Anan G. K., (2021). Discrete element modeling of cantilever beams subjected to geometric nonlinearity and particle–structure interaction. *Computational Particle Mechanics*, No. 8, pp. 1-15.
[5] Han J.G., Bi Y., Yan P.Y. et al., (2021). Acquisition of Bingham fluid rheology parameters using a coaxial double-cylinder rheometer. *Journal of the Chinese Ceramic Society*, Vol.49, No. 2, pp. 323-331.
[6] Hao J.J., Long S.F., Li J.C. et al., (2020). Effect of granular ruler in discrete element model of sandy loam fluidity in Ma yam planting field. *Transactions of the Chinese Society of Agricultural Engineering*, Vol.36, No. 21, pp. 56-64.
[7] Li J.W., Tong J., Hu B. et al., (2019). Calibration of parameters of interaction between clayey black soil with different moisture content and soil-engaging component in northeast China. *Transactions of the Chinese Society of Agricultural Engineering*, Vol.35, No. 6, pp. 130-140.
[8] Li Y.X., Li F.X., Xu X.M. et al., (2019). Parameter calibration of wheat flour for discrete element method simulation based on particle scaling. *Transactions of the Chinese Society of Agricultural Engineering*, Vol.35, No. 16, pp. 320-327.
[9] Li Z.H., Ma X., Li X.H. et al., (2018). Research Progress of Rice Transplanting Mechanization. *Transactions of the Chinese Society for Agricultural Machinery*, Vol.49, No. 5, pp. 1-20.
[10] Liu F., Li D.P., Zhang T.et al., (2020). Analysis and calibration of quinoa grain parameters used in a discrete element method based on the repose angle of the particle heap. *INMATEH-Agricultural Engineering*, Vol.61, No. 2, pp.77-86.
[11] Ma X.J., Hou Z.F., Liu M., (2022). Calibration of simulation parameters of coated particles and analysis of experimental results. *INMATEH-Agricultural Engineering*, Vol.67, No. 2, pp.233-242.
[12] Nan W.G., Gu Y.Q., (2020). Stress analysis of blade Rheometry by DEM simulations. *Powder Technology*, No. 376, pp. 332-341.
[13] Qi L., Chen Y., Sadek M., (2019). Simulations of soil flow properties using the discrete element method (DEM). *Computers & Electronics in Agriculture*, No. 157, pp. 254-260.
[14] Roessler T., Katterfeld A., (2018). Scaling of the angle of repose test and its influence on the calibration of DEM parameters using upscaled particles. *Powder Technology*, No. 330, pp. 58-66.
[15] Rojek J., Lumelskyj D., Nosewicz S. et al., (2019). Numerical and experimental investigation of an elastoplastic contact model for spherical discrete elements. *Computational Particle Mechanics*, Vol.6, No. 3, pp. 383-392.
[16] Sun G.D., (2017). *Study of the device for seedling mud lifting and conveying on rice paddy field.* South China Agricultural University.
[17] Tamás K., Jóri I.J., Mouazen A.M., (2013). Modelling soil–sweep interaction with discrete element method. *Soil and Tillage Research*, No. 134, pp. 223-231.
[18] Wang L., Hu C., He X.W. et al., (2021). A general modelling approach for coated cotton-seeds based on the discrete element method. *INMATEH-Agricultural Engineering*, Vol.63, No. 1, pp.221-230.
[19] Wang W.P., Liu J.L., Zhang J.B. et al., (2014). Evaluation and correction of measurement using diffraction method for soil particle size distribution. *Transactions of the Chinese Society of Agricultural Engineering*, Vol.30, No. 22, pp. 163-169.
[20] Wang X.Z., Zhang Q.K., Huang Y.X. et al., (2022). An efficient method for determining DEM parameters of a loose cohesive soil modelled using Hysteretic Spring and Linear Cohesion contact models. *Biosystems Engineering*, No. 215, pp. 283-294.
[21] Xiang W., Wu M.L., Lü J.N. et al., (2019), Calibration of simulation physical parameters of clay loam based on soil accumulation test. *Transactions of the Chinese Society of Agricultural Engineering*, Vol.35, No. 12, pp. 116-123.
[22] Xu B., Zhang Y.Q., Cui Q.L.et al., (2021). Construction of a discrete element model of buckwheat seeds and calibration of parameters. *INMATEH-Agricultural Engineering*, Vol.64, No. 2, pp.175-184.
[23] Xu Y., Li H.Y., Huang W.B., (2003). Modeling and methodological strategy of discrete element method simulation for tillage soil dynamics. *Transactions of the Chinese Society of Agricultural Engineering*, Vol. 19, No. 2, pp. 34-38.
[24] Yang H.J., Wei F.Q., Hu K.H. et al., (2017). Effects of mud slurry on flow resistance of cohesionless coarse particles. *Powder Technology*, No. 310, pp. 1-7.

[25] Ye S.Q., (2021). Wet seedling raising technology in paddy field in southern Jiangxi. *Primary Agricultural Technology Extension*, Vol.9, No. 12, pp. 1-5.
[26] Zeng F.D., Li X.Y., Zhang Y.Z. et al., (2021). Using the discrete element method to analyze and calibrate a model for the interaction between a planting device and soil particles. *INMATEH-Agricultural Engineering*, Vol.63, No. 1, pp.413-424.
[27] Zeng Z.W., Ma X., Cao X.L. et al., (2021). Critical Review of Applications of Discrete Element Method in Agricultural Engineering. *Transactions of the Chinese Society for Agricultural Machinery*, Vol.52, No. 4, pp. 1-20.
[28] Zhang P., Zhang H., Li J.M.et al., (2022). Parametric calibration of cotton straw parameters in Xinjiang based on discrete elements. *INMATEH-Agricultural Engineering*, Vol.67, No. 2, pp.314-322.
[29] Zhang P.T., Sun X.J., Zhou X.J. et al., (2022). Experimental simulation and a Rapid reliable calibration method of rockfill microscopic parameters by considering flexible boundary. *Powder Technology*, No. 396, pp. 279-290.
[30] Zheng Z.Q., Zhao H.B., Liu P. et al., (2021). Maize straw cutting process modelling and parameter calibration based on discrete element method (DEM). *INMATEH-Agricultural Engineering*, Vol.63, No. 1, pp.461-468.
[31] Zhou J.C., Zhang L.B., Hu C. et al., (2022). Calibration of wet sand and gravel particles based on JKR contact model. *Powder Technology*, No. 397, pp. 117005.

EXPERIMENTAL RESEARCH ON THREE-LEVEL VIBRATING SCREENING OF BUCKWHEAT BASED ON DISCRETE ELEMENT METHOD
/
基于离散元法的荞麦三级振动筛分试验研究

Bing XU[1], Decong ZHENG [1,2*], Qingliang CUI [1]
[1)] College of Agricultural Engineering, Shanxi Agricultural University, Taigu 030801, / China;
[2)] Research center of Shanxi modern agricultural facilities and equipment, Taiyuan 030031, / China
Tel: +86-0354-6288339; E-mail: zhengdecong@126.com
DOI: https://doi.org/10.35633/inmateh-68-19

Keywords: *buckwheat, classifying screen, amplitude, discrete element, numerical analysis*

ABSTRACT
To improve the operating effect of buckwheat classifying equipment and meanwhile reduce the dependence on tests in the process of operating parameter optimization of the equipment, this paper designed a three-level classifying screen for buckwheat, confirmed the structure and parameters of upper and lower sieves, established a three-level screening discrete element model for buckwheat with the EDEM software, and conducted the numerical simulation for the sieving processes at an amplitude of 24 mm, 28 mm and 32 mm, respectively. The results indicated that when the inclination angle of screen surface was 3°, the vibrational direction angle was 30° and the vibrational frequency was 4.5 HZ, as the amplitude increased, the conveying capacity of the classifying screen increased and at the same time the seed loss rate also increased, of which at 16 s, the loss rate was 0.03%, 0.37% and 1.42%, respectively; the proportion of medium particles in the collecting box of screen overflow was 2.88%, 8.65% and 17.65%, respectively; and the proportion of small particles in the collecting box of screen residue was 0.58%, 6.06% and 19.14%, respectively. Through comprehensive analysis of conveying capacity, screening loss and classifying effect, when the amplitude of the classifying screen was 28 mm, the classifying operating effect was good. This study can provide reference for the design and operating parameter optimization of buckwheat classifying equipment.

摘要
为改善荞麦分级设备作业效果、同时减少设备工作参数优化过程中对试验的依赖。设计了荞麦三级分级筛，确定了上、下筛片的结构及参数，应用 EDEM 软件建立了荞麦三级筛分离散元模型，并对振幅分别为 24 mm、28 mm、32 mm时的筛分过程进行了数值模拟。结果表明：在筛面倾角为3°、振动方向角为30°、振动频率为4.5 HZ 时，随着振幅的增大，分级筛输送能力增加，同时籽粒损失率也增大，16 s 时损失率分别为 0.03%、0.37%、1.42%，筛上物收集箱内中颗粒占比分别为 2.88%、8.65%、17.65%，筛中物收集箱内小颗粒占比分别为 0.58%、6.06%、19.14%。综合分析输送能力、筛分损失、分级效果，分级筛振幅为 28 mm 时分级作业效果较好。本研究可为荞麦分级设备的设计及工作参数优化提供参考。

INTRODUCTION

As one of pseudocereals, buckwheat has abundant nutritional value and powerful medicinal value, and it is an ideal raw material of functional food *(Mazahir et al., 2022; Ahmed et al., 2022; Cao et al., 2022)*. In recent years, rational diet and balanced nutrition have received more and more attention, and buckwheat food has appeared in people's lives in the forms of staple food, convenience food, leisure food, etc., a demand that is gradually increasing *(Ren et al., 2018; Ren et al., 2022)*. With the increase of the market demand for buckwheat food, the better operating effect and efficiency of relevant food processing and raw material handling equipment are requested. The rough grain harvested mechanically usually undergoes preliminary cleaning and de-stone processing to obtain buckwheat seeds, and then buckwheat rice is obtained after the hulling treatment of buckwheat seeds *(Liu, 2014)*. Since buckwheat seeds have various sizes, crisp and fragile kernels and a smaller space between hulls and kernels, screening classification must be performed for

[1] *As Lec .M.S.Eng. Bing XU; Decong ZHENG, Prof. Eng.; Qingliang CUI, Prof. Ph.D. Eng.*
[2] *Decong ZHENG, Prof. Eng. Chief of Research Centre*

buckwheat seeds before the hulling treatment in batches to reduce the broken rate of buckwheat rice in the hulling treatment, and the more the classification, the lower the broken rate of buckwheat rice will be *(Li et al., 2016; Quan et al., 2014)*. The working performance of classifying procedure relates to the quality of buckwheat food, so research and development of efficient multi-level buckwheat screening equipment has great significance to promote the development of buckwheat deep-processing industry.

In recent years, many scholars have researched the cleaning and classification of buckwheat from the aspects of the design and operating parameter optimization of cleaning device, screen surface, etc. Zhang Longxiang et al. designed an air-and-screen cleaning device with pre-cleaning structure, performed numerical simulation tests for buckwheat cleaning processes on the basis of gas-solid coupling technology, and determined the optimum working parameter combination of air blower and vibrating screen, thus providing evidence for the operating parameter optimization of cleaning device *(Zhang, 2020)*. Lu et al. designed an air-and-screen cleaning device used for Buckwheat threshers, and conducted prototype experiments, which showed that when the wind speed of blower was 8 m/s and the vibration frequency of vibrating screen was 25.12 rad·s^{-1}, the cleaning loss rate was 1.96% *(Lu et al., 2022)*. In order to solve the problems of high loss rate and impurity rate in the screening of buckwheat extractions, Fan et al. performed simulated screening tests for 5 different screen surfaces with the EDEM software, and the results revealed that non-planar convex-column screen surface had the best screening effect *(Fan et al., 2022)*. Moreover, taking the threshing material of buckwheat at the harvest time as research object, recently they carried out single factor experiments on cleaning testing platforms for 7 factors that may affect cleaning quality, and screened out the factors that can influence loss rate and impurity rate significantly, thus laying a good foundation for the operating parameter optimization of cleaning device *(Fan et al., 2023)*. To improve the separating effect between buckwheat rice and unhulled buckwheat, Liu Chuang et al. designed a new type of circular sieve plate, and conducted sieve tests, which showed that the screening effect of the new type of circular sieve plate proposed was better than that of traditional circular and triangular sieve plates *(Liu, 2014)*. Quan Yajing et al. conducted an experimental study on buckwheat classification and its influence on the hulling effect, and designed an elongated round hole sieve used in the buckwheat classification from the two aspects of reducing the differential in the classification and changing the hole pattern, in order to perfect the situation of buckwheat classification *(Quan, 2014)*. Aiming at the problems of severe screen hole blocking and low classification efficiency in the process of buckwheat classification, Chang Rong et al. explored the effect of bouncing ball screen cleaning, and investigated the influencing rule of bouncing ball quantity on classification efficiency via tests, which showed that the effect of bouncing ball screen cleaning was remarkable and an appropriate number of bouncing balls could enhance classification efficiency *(Chang et al., 2016)*.

At present, many studies on buckwheat screening mainly focus on two aspects: (1) the cleaning and separation of buckwheat extractions in the harvesting link; and (2) the separation between buckwheat rice and buckwheat hulls as well as unhulled buckwheat in the hulling link. However, there is little research on classification, which is an intermediate link between the above two links. To improve the operating effect of buckwheat classification, this study intended to design the overall structure of buckwheat three-level classifying screen, and confirm the structure and parameters of sieves. It built a three-level vibrating screening model with the discrete element method, and performed the numerical simulation for vibrating screening processes under different amplitudes to determine suitable working parameters.

MATERIALS AND METHODS

The structure and parameters of buckwheat three-level classifying screen

The buckwheat three-level classifying screen consists of rack, electromotor, drive system, crank, connecting rod, feed hopper, suspender, sieve etc., and its overall structure is shown in Figure 1.

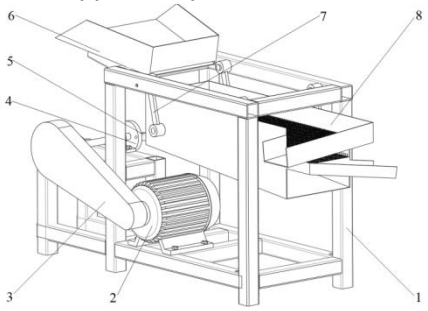

Fig. 1 - The overall structure of buckwheat three-level classifying screen

1- rack; 2- electromotor; 3- drive system; 4- crank; 5- connecting rod; 6- Feed hopper; 7- suspender; 8- sieve

The sieve is comprised of upper sieve, side board, front board, lower sieve, bottom board, discharge chute of screen overflow and discharge chute of screen residue, as shown in Figure 2.

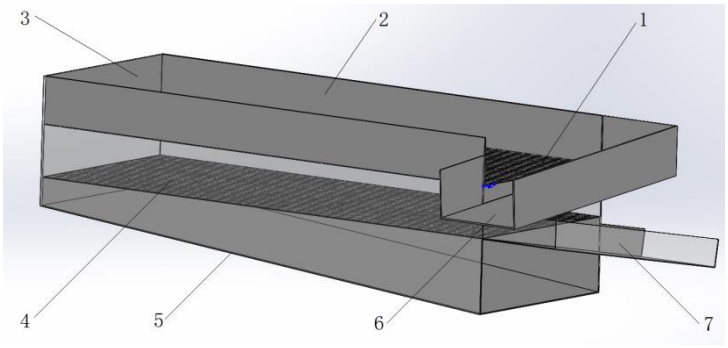

Fig. 2 - Schematic diagram of screen body structure
1- upper sieve; 2- side board; 3- front board; 4- lower sieve; 5- bottom board; 6- discharge chute of screen overflow; 7- discharge chute of screen residue

The upper and lower sieves are both made of stainless steel with the thickness of 0.8 mm, and have the shape of 720 mm×270 mm rectangle. Since the shape and size of sieve aperture as well as its distribution rule on the sieve all have impacts on screening quality, the design of sieve aperture needs to take into account factors such as seed shape, size distribution and classification requirement. The pertinent literature shows that over 90% of buckwheat seeds have a particle size of 3.8 mm~5.0 mm *(Li et al., 2016)*. Thus, this study planned to divide buckwheat seeds into: particle size<4.2 mm, particle size>4.8 mm and 4.2 mm~4.8 mm.

Round stamped sieve was adopted in both upper and lower sieves, the size and distribution of sieve aperture were designed according to GB 3943-83 Type Ⅰ Sieve *(China Academy of Agricultural Mechanization Sciences, 2007)*.

The center of sieve aperture is located at the vertex of equilateral triangle, and the direction of material motion is perpendicular to a side of the equilateral triangle, as shown in Figure 3.

The relevant parameters of the sieve are shown in Table 1.

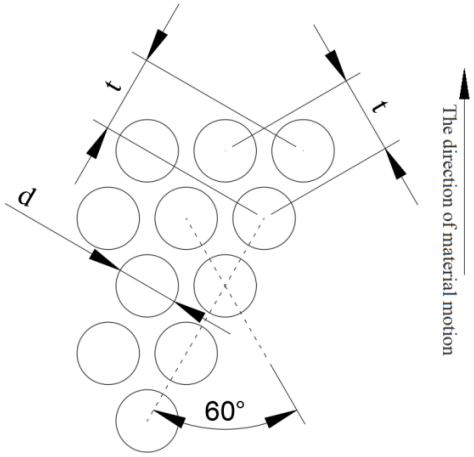

Fig. 3 - The schematic diagram of screen size and distribution

Table 1

Sieve parameters

Sieve	Diameter of sieve pore / d (mm)	Hole spacing / t (mm)	Percentage of screening area / (%)
upper sieve	4.8	6	58
lower sieve	4.2	6	44

The establishment of a discrete element model for the buckwheat three-level vibrating screen

Modeling of screening materials

Buckwheat seeds present a triangular pyramid. As different seeds have different sizes, it is impossible to build a seed group model exactly according to the actual size of all seeds. In order to simplify the modeling process, manual filling was only used to establish models for seeds in three sizes - small, medium and large, and these models were saved as particle template, as shown in Figure 4. The diameter of the three dimensions of all large particles is greater than 4.8 mm, the diameter of the three dimensions of all medium particles is between 4.2 mm and 4.8 mm, and the diameter of the three dimensions of all small particles is less than 4.2 mm.

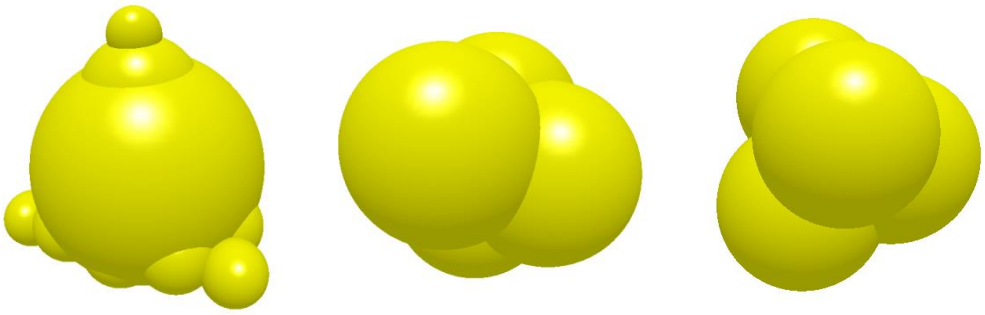

(a) large particle (b) medium particle (c) small particle

Fig. 4 - Particle Models

Establishment of three-level vibrating screening model

The three-dimensional model of sieve was established in accordance with the structure and parameters of the sieve, and it was transformed into STEP format to induct to EDEM. Then, the templates of small, medium and large particles were inducted to EDEM. By referring to relevant literature and our preliminary research, the parameters required in the screening simulation tests were determined and set, as shown in Table 2 *(Zhang et al., 2020; Hou et al., 2019; Xu et al., 2021; Fan et al., 2022; Fan et al., 2021)*.

Table 2

The list of parameters in the screening simulation tests

Parameters	Values
Poisson's ratio of stainless steel	0.29
Shear modulus of stainless steel (MPa)	70000
Density of stainless steel (kg/m^3)	8000
Poisson's ratio of buckwheat	0.3
Shear modulus of buckwheat (MPa)	34.3
Density of buckwheat (kg/m^3)	2540
Buckwheat-buckwheat restitution coefficient	0.2
Buckwheat-buckwheat static friction coefficient	0.532
Buckwheat-buckwheat rolling friction coefficient	0.01
Buckwheat-stainless steel restitution coefficient	0.508
Buckwheat-stainless steel static friction coefficient	0.7
Buckwheat-stainless steel rolling friction coefficient	0.043

The factory of particles in the size of 260 mm×160 mm was established above the upper sieve and near the feeding inlet of the sieve, and it was used to produce the mixed material containing small, medium and large particles in the initial phase of simulation tests. The factory of particles in all simulation tests in this study was set as follows: the type was “dynamic”; the total number of particles in the mixed material was 6,000; the mixed material was produced evenly within 2 s before simulation tests; and the initial velocity of particles at the Z-axis direction was -0.5 m/s. The collecting boxes of screen overflow, screen residue and screen underflow were respectively established in the model. The discrete element model for buckwheat three-level screening is shown in Figure 5.

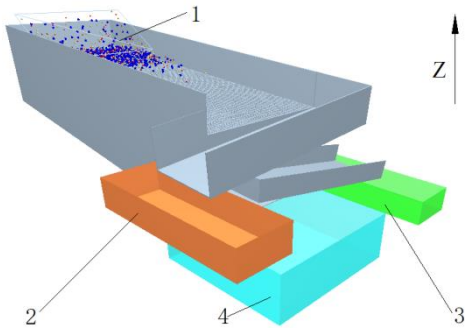

Fig. 5 - Discrete element model for the buckwheat three-level vibrating screen

1- factory of particles; 2- the collecting boxes of screen overflow; 3- the collecting boxes of screen residue; 4- the collecting boxes of screen underflow;

Simulation tests for buckwheat three-level vibrating screening

On the basis of our previous research, the three amplitudes of 24 mm, 28 mm and 32 mm for the classifying screen were determined, and vibrating screening tests were separately performed with the EDEM software. The corresponding installation and vibration parameters of the classifying screen in simulation tests are shown in Table 3.

Table 3

Installation of the classifying screen and vibration parameters

Number	Amplitude / (mm)	Vibrational frequency / (HZ)	Inclination angle of screen surface / (°)	Vibrational direction angle / (°)
1	24	4.5	3	30
2	28	4.5	3	30
3	32	4.5	3	30

The simulated time was set as 16 s in each test, and the interval of data storage was set as 0.25 s in the simulation process. In order to compare and analyze the screening performance of classifying screen under different amplitudes, the EDEM post-processing module was used to establish analog computational domain and statistical domain of the collecting boxes of screen overflow, screen residue and screen underflow in the screening model after screening tests, as shown in Figure 6.

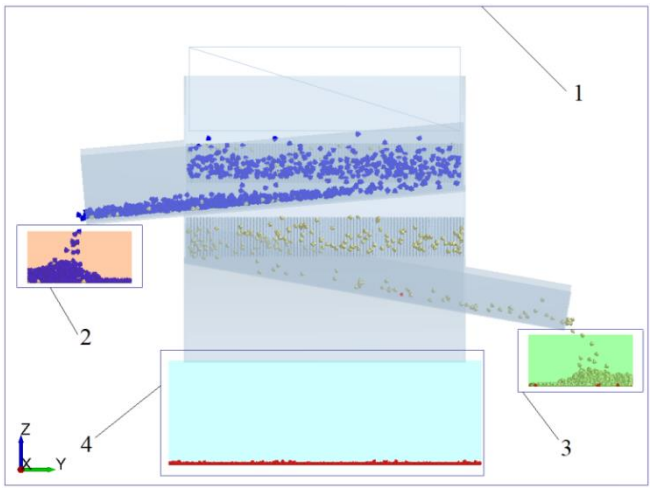

Fig. 6 - Division of statistical domains

1- analog computational domain; 2- statistical domain of the collecting boxes of screen overflow; 3- statistical domain of the collecting boxes of screen residue; 4- statistical domain of the collecting boxes of screen underflow

Evaluation indexes

This study evaluated the screening performance of vibrating screen under three amplitudes from the three aspects of conveying capacity, screening loss and classification effect.

The conveying capacity is related to many factors such as the inclination angle of screen surface, vibrational frequency and amplitude *(Li et al., 2011)*. This study performed qualitative analysis of the conveying capacity only through comparing the total number of particles in the three collecting boxes under different amplitudes in the same time. In the process of vibration classification, due to the interaction among particles as well as between particles and the sieve, some particles fly off the computational domain, leading to the screening loss, and the loss rate is defined as the ratio of lost particles to the total particles produced by the particle factory. The most desirable outcome of classification is that small, medium and large particles fall into the collecting boxes of screen underflow, screen residue and screen overflow, respectively. But some small and medium particles may not complete the screening process because of their insufficient contact with the screen surface in the process of classification, causing that the collecting box of screen overflow contains a certain amount of small and medium particles, and the collecting box of screen residue contains a part of small particles. This study took the ratio of small and medium particles to the total particles in the collecting box of screen overflow and the ratio of small particles to the total particles in the collecting box of screen residue at 16 s as indexes to evaluate the classification effect.

RESULTS

After numerical simulation tests, by entering into the EDEM post-processing module, the dynamic process of simulation tests under the three amplitudes was observed and compared. The distribution of particles in the sieve under the three amplitudes at 16 s is shown in Figure 7.

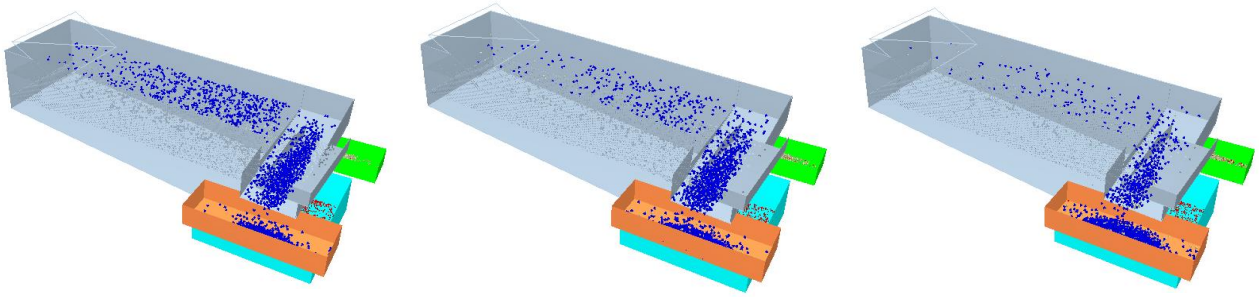

(a) 24 mm (b) 28 mm (c) 32 mm

Fig. 7 - The distribution of particles in the sieve under different amplitudes at 16 s

It can be known from Figure 7 that there were obvious differences in the distribution of particles in the sieve under different amplitudes. The total number of particles outputted in the three collecting boxes under each amplitude at different times was counted, and its changing curve with time was drawn, as shown in Figure 8. The number of particles flown out the analog computational domain in the process of screening was counted, and its changing curve with time was drawn, as shown in Figure 9.

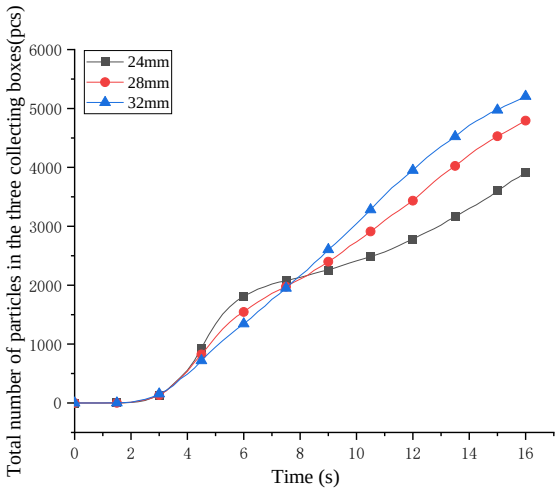

Fig. 8 - The change of the total number of particles in the three collecting boxes under different amplitudes

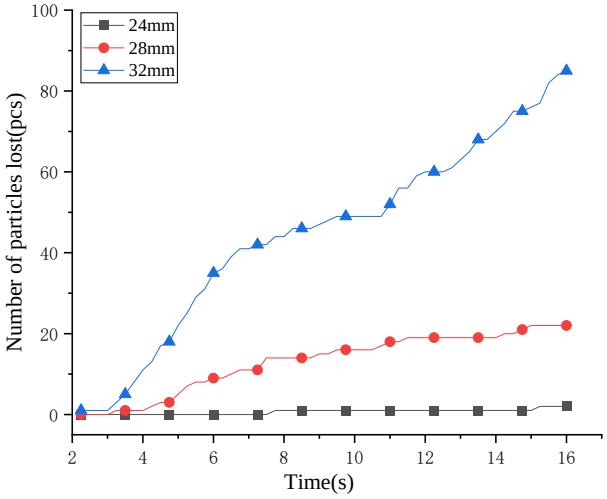

Fig. 9 - The changing curve of particle loss under different amplitudes

It can be seen from Figure 8 that there were no significant differences in the number of particles in the collecting boxes under the three amplitudes before 7.5 s, during which the particle material was moving from the front sieve to the back sieve, while the number of particles in the collecting boxes increased with the increase of amplitude after 7.5, suggesting the increase of conveying capacity. It can be seen from Figure 9 that when the amplitude was 24 mm, particle loss was the least, but when the amplitude was 32 mm, particle loss was the most, and the number of lost particles under the three amplitudes of 24 mm, 28 mm and 32 mm at 16 s was 2, 22 and 85, respectively, with the loss rate of 0.03%, 0.37% and 1.42%, respectively.

The total number of particles in the collecting box of screen overflow and the number of small and large particles contained were counted at different times in the three tests, and their changing curve with time was drawn, as shown in Figure 10. The data of particles outputted in the collecting box of screen overflow at 16 s are shown in Table 4.

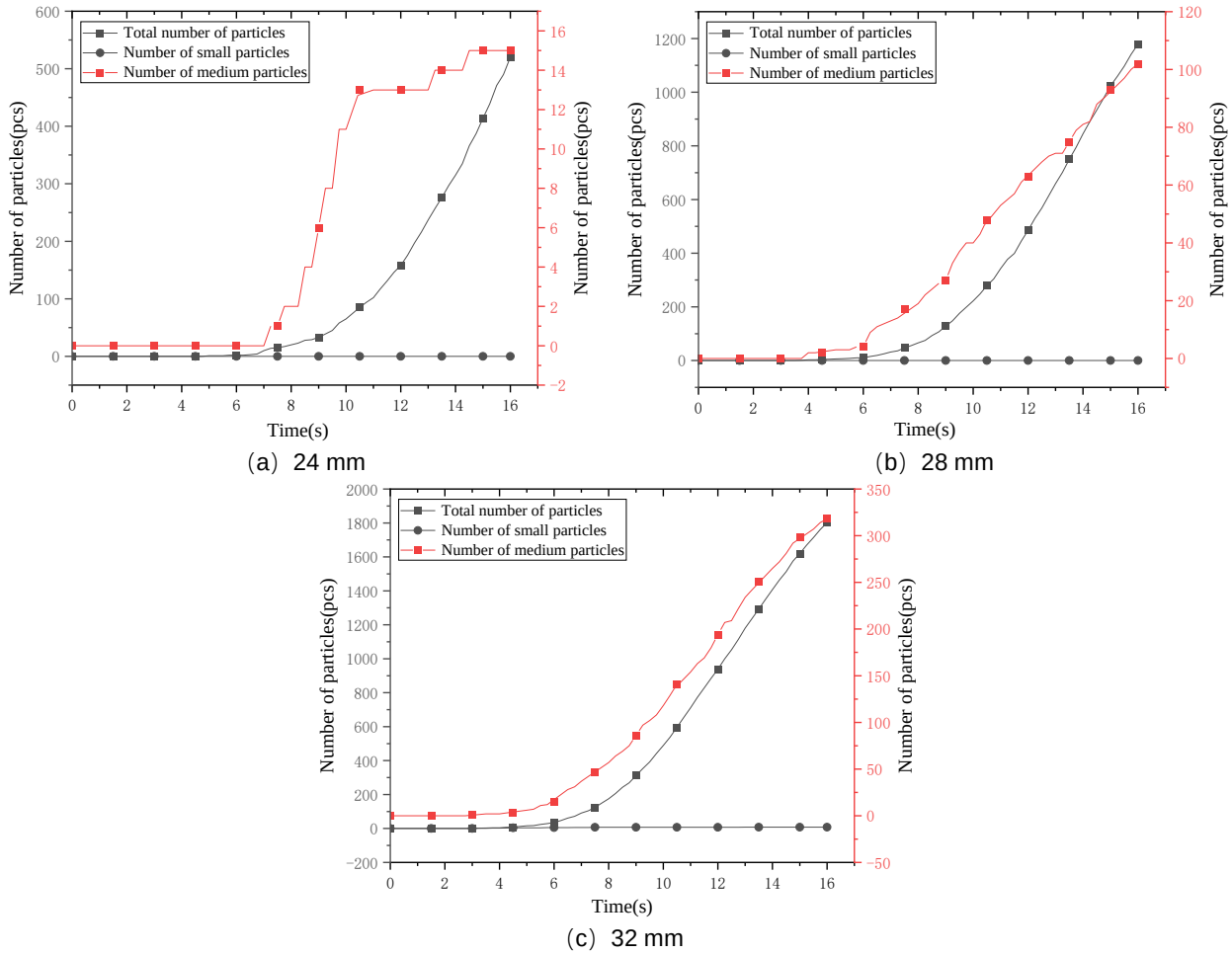

Fig. 10 - The change of particles in the collecting box of screen overflow

Table 4

The number of particles in the collecting box of screen overflow at 16 s

Amplitude mm	Total number of particles pcs	Medium particle		Small particle	
		Number pcs	Proportion %	Number pcs	Proportion %
24	520	15	2.88	0	0
28	1179	102	8.65	0	0
32	1802	318	17.65	8	0.04

It can be known from Figure 10 and Table 4 that there were few small particles in the collecting box of screen overflow under the three amplitudes, but with the increase of amplitude and conveying capacity, the total number of particles in the collecting box of screen overflow increased and meanwhile the number of medium particles that didn't complete the screening process also increased, and the proportion of medium particles in the collecting box of screen overflow at 16 s was 2.88%, 8.65% and 17.65%, respectively.

The total number of particles in the collecting box of screen residue and the number of small particles contained were counted at different times in the three tests, and their changing curve with time was drawn, as shown in Figure 11. The data of particles outputted in the collecting box of screen residue at 16 s are shown in Table 5.

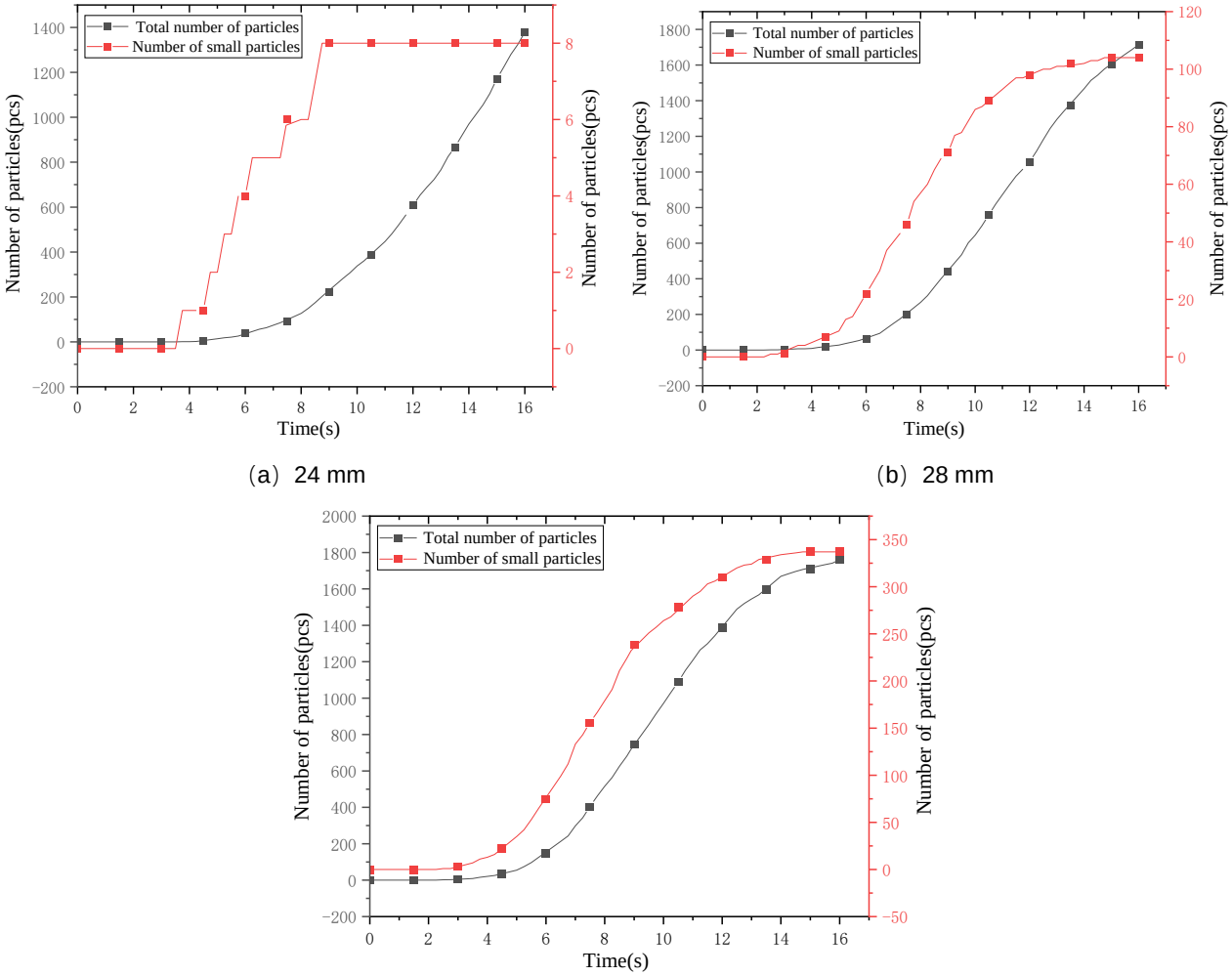

(a) 24 mm (b) 28 mm

(c) 32 mm

Fig. 11 - The change of particles in the collecting box of screen residue

Table 5

The number of particles in the collecting box of screen residue at 16 s

Amplitude mm	Total number of particles pcs	Small particle	
		Number / pcs	Proportion / %
24	1379	8	0.58
28	1715	104	6.06
32	1760	337	19.14

It can be known from Figure 11 and Table 5 that when the amplitude increased from 24 mm to 28 mm, the total number of particles in the collecting box of screen residue increased significantly, while when the amplitude increased from 28 mm to 32 mm, there was no significant increase in the total number of particles in the collecting box of screen residue, but the number of small particles that didn't complete the screening process increased remarkably from 104 to 377, and the proportion of small particles in the collecting box of screen residue at 16 s was 0.58%, 6.06% and 19.14%, respectively.

CONCLUSIONS

(1) According to the requirement of buckwheat classification, this study designed a three-level classifying screen for buckwheat and determined the structure and parameters of upper and lower sieves.

(2) This study established a discrete element model for the buckwheat three-level vibrating screen, and conducted numerical simulation for the classification process under the three amplitudes of 24 mm, 28 mm and 32 mm. The results indicated that when the inclination angle of screen surface was 3°, the vibrational direction angle was 30° and the vibrational frequency was 4.5 HZ, as the amplitude increased, the conveying capacity of the classifying screen increased and at the same time the seed loss rate also increased, of which at 16 s, the loss rate was 0.03%, 0.37% and 1.42%, respectively; the proportion of medium particles in the collecting box of screen overflow was 2.88%, 8.65% and 17.65%, respectively; and the proportion of small particles in the collecting box of screen residue was 0.58%, 6.06% and 19.14%, respectively. Through comprehensive analysis of conveying capacity, screening loss and classifying effect, when the amplitude of the classifying screen was 28 mm, the classifying operating effect was good.

(3) This study is a single factor experiment on amplitude, but the operating effect of classifying screen is related to many factors such as the inclination angle of screen surface, vibrational direction angle and vibrational frequency. This study can lay a foundation for multi-parameter combination optimization in the future.

ACKNOWLEDGEMENT

This research, titled “Experimental Research on Three-Level Vibrating Screening of Buckwheat Based on Discrete Element Method”, was funded by project: “Major Special Projects for the Construction of China Modern Agricultural Industrial Technology System (Grant No. CARS-07-D-2)”.

REFERENCES

[1] Cao R.G., Guo Z.C., Wang L.J., et al., (2022), Processing and Quality Improvement of Buckwheat Noodles: A Review *（荞麦面条加工及品质提升的研究进展）. Food Research and Development*. http://kns.cnki.net/kcms/detail/12.1231.TS.20221014.1907.002.html,Online,pp.1-16, Tianjin/China;

[2] Chang R., Du W.L., Chen W. et al., (2016), Experiment Study of the Influence of Bouncing Ball Screen Cleaning on Buckwheat’s Grading Efficiency (*弹球清筛对荞麦分级效率影响的试验研究*). *Journal of Agricultural Mechanization Research,* Vol.38,Issue 03,pp.187-190+195,Haerbin/China;

[3] Fan R., Cui Q.L., Zhang Y.Q. et al., (2021), Analysis and calibration of parameters of buckwheat grain. *INMATEH - Agricultural Engineering*, Vol. 64, No. 2, pp.467-476, Bucharest/Romania;

[4] Fan R., Cui Q.L., Lu Q. et al., (2022), Experimental study on non-planar screening device for buckwheat threshing material. *INMATEH Agricultural Engineering*, Vol.66, Issue 1, pp.73-80, Bucharest/Romania;

[5] Fan R., Cui Q.L., Lu Q. et al., (2023), Parameter Optimization and Experimental Study of Cleaning Device on Buckwheat Threshing Material（*荞麦混合脱出物清选装置参数优化及试验研究*）. *Journal of Agricultural Mechanization Research*， Vol.45, Issue 05, pp.136-142, Haerbin/China;

[6] Hou H.M., (2019), *Experimental study on cleaning dynamic characteristics of coarse cereals crops harvested by machinery（杂粮作物机械收获清选动力学特性研究）.* PhD Dissertation. Shanxi Agricultural University, Taiyuan/China;

[7] Li H.C., Li Y.M., Tang Z., (2011), Numerical simulation and analysis of vibration screening based on EDEM（*基于EDEM的振动筛分数值模拟与分析*）. *Transactions of the CSAE*, Vol.27, Issue 5, pp.117-121, Beijing/China;

[8] Li J.C., Zhao X.H., Zhao J.C. et al., (2016), Study on physical characteristics of buckwheat seeds（*荞麦籽粒的物理学特性研究*）. *Food and Machinery*, Vol.32, Issue 7, pp.1-4+79, Changsha/China;

[9] Liu C., (2014), Analysis and Experimental Study of the Sieving Performance Parameters in Sieving of Shelled Buckwheat *（荞麦米分离过程中筛分性能参数的分析与试验研究）.* Master thesis. Inner Mongolia Agricultural University, Huhehaote/China;

[10] Lovro S., Matjaž D., Rok K. et al., (2022), Macro/microelements, nutrients and bioactive components in common and Tartary buckwheat (Fagopyrum spp.) grain and stone-milling fractions. *LWT-Food Science and Technology*, Vol.161, 113422. Ed. Elsevier, London/England;

[11] Lu Q., Zheng D.C., Li L.H., et al., (2022), Design and experiment of 5TG-85 buckwheat thresher. *INMATEH Agricultural Engineering*, Vol.66, Issue 1, pp.289-300, Bucharest/Romania;

[12] Mazahir M., Ahmed A., Ahmad A. et al., (2022), Extraction and determination of bioactive compounds and antioxidant activity of buckwheat seed milling fractions. *Food Science and Technology*, Vol.42, pp.1-6, Rio de Janeiro/Brazil;

[13] Quan Y.J., (2014), Experiment Study on Buckwheat Grading and the Shucking Effect Caused by Buckwheat Grading（*荞麦分级及其对荞麦剥壳效果的影响研究*）. Master thesis. Inner Mongolia Agricultural University, Huhehaote/China;

[14] Quan Y.J., Du W.L., Liu C. et al., (2014), The Research on the Influence of Elongated Apertures with Round Screens Grading to Buckwheat Shelling Effect（*长圆孔筛分级对荞麦剥壳效果的影响试验*）. *The Food Industry*, Vol.35, Issue 10, pp.205-208, Shanghai/China;

[15] Ren C.Z., Cui L., He F. et al., (2018), Construction and Development of China Oat and Buckwheat Industrial Technology System *（我国燕麦荞麦产业技术体系建设与发展）. Journal of Jilin Agricultural University*, Vol.40, Issue 04, pp.524-532, Changchun/China;

[16] Ren C.Z., Shan F., Wang M. et al., (2022), Review on the Nutrition and Functionality and the Food Product Development of Buckwheat *（荞麦营养与功能性研究及其产品开发）. Journal of the Chinese Cereals and Oils Association*. Online DOI：10.20048/j.cnki.issn.1003-0174.000001, Beijing/China;

[17] Xu B., (2021). Construction of a discrete element model of buckwheat grain and calibration of parameters. *INMATEH-Agricultural Engineering*, Vol.64, Issue 2, pp.175-184, Bucharest / Romania;

[18] Zhang L.X., (2020), Research and Design of Buckwheat Harvester Cleaning Device Based on FLUENT-EDEM Coupling *（基于 FLUENT-EDEM 耦合的荞麦收获机清选装置研究设计）.* PhD Dissertation. Cheng du University, Chengdu / China;

[19] ***China Academy of Agricultural Mechanization Sciences, (2007), *Agricultural Machinery Design Manual（农业机械设计手册）*. ISBN 9787802333352, China Agricultural Science and Technology Press, Beijing/China.

ANALYZING THE HOMOGENEITY IN THE REDUCTION OF WATER CONTENT DURING THE DRYING PROCESS OF GRAINS USING A FLATBED DRYER MACHINE EQUIPPED WITH A STIRRING MECHANIZATION SYSTEM

/

PEMBUKTIAN HOMOGENITAS PENURUNAN KADAR AIR DI PROSES PENGERINGAN BIJI-BIJIAN MENGGUNAKAN MESIN FLATBED DRYER YANG DILENGKAPI SISTEM MEKANISASI PENGADUKAN

Dandy Z. SJECHLAD, S.A. WIDYANTO, B. PURWANGGONO, M. MUNADI [1]
Department of Mechanical Engineering, Faculty of Engineering, Diponegoro University / Indonesia
Tel:+6281218620214; Email: dsjechlad@gmail.com
DOI: https://doi.org/10.35633/inmateh-68-20

Keywords*: *Flatbed Dryer; Auto stirring; Stirring; Water Content; homogeneity; Uniform

ABSTRACT

Uneven drying is a prominent problem in the performance of Flatbed type grain dryer. An effort to move around the materials during the drying process is needed in order to get a uniformed drying rate. This paper investigates the conditions of an evenly distributed reduction of materials' water content during drying, using a flatbed dryer and a stirring mechanization system. It is found that ≥ 4rpm stirring rotation produces a relatively even drying result after 1 hour, and that there exists a second airflow that leaked due to the stirring process moving around with the motion of the stirrer.

ABSTRAK

Hasil pengeringan yang tidak rata merupakan masalah utama dalam kinerja mesin pengering biji-bijian tipe Flatbed. Diperlukan upaya pengadukan komoditas bahan yang dikeringkan agar laju pengeringannya seragam. Pada penelitian ini akan khusus menginvestigasi kondisi kerataan distribusi penurunan kadar air dari komoditas bahan yang dikeringkan tersebut dengan menggunakan pengering type Flatbed yang dilengkapi sistem pengaduk otomatis. Hasil pengujian menunjukkan di putaran pengadukan ≥ 4rpm, setelah 1 jam pertama pengeringan, kerataan pengeringan yang relatif seragam antar lapisannya. Dibuktikan pula pada hasil pengujian bahwa terdapat aliran udara kedua yang bocor akibat proses pengadukan yang berpindah-pindah mengikuti pergerakan pengaduk.

INTRODUCTION

In order to properly store grains and further process them in methods such as the cracked shells and polishing process, as well as other efforts such as the one concerning the prevention of fungus during long-term storage or shipment (*Muller & Heindl, 2006; Madamba, et al., 1996*), it is necessary for harvested grains to be dried from a 28% - 18% water content *(Chen, et al., 2019*) to a 14% - 13% water content *(Karbassi & Mehdizadeh, 2008*). The drying process is considered very integral, and the bare minimum amount of energy needed to do it is quite large (*Motevali & Chayjan, 2017*), thus constantly making it a subject of concern and sensitivity. Other than the material commodity's starting water content, the drying process itself is dominated by 3 main variables, which consist of Hot Air Velocity, Drying Temperature (*Motevali & Chayjan, 2017*)) (*Dorneles, et al., 2019*) (*Paziuk, et al., 2019*) (*Snezhkin, et al., 2020*) and Ambient Air Humidity *(Chanpet, et al., 2020; Namkanisorn & Murathathunyaluk, 2020; Lira, et al., 2009*). The higher temperature used in drying, the faster the drying rate would be (*Muller & Heindl, 2006)*. However on the other hand, a drying rate this rapid could negatively affect the dried result due to hasty dehydration (the thermal quenching phenomenon)) (*Paziuk, et al., 2019*), especially in the case of seeds (*Snezhkin, et al., 2020*) (*Rogovskii, et al., 2019*). In Indonesia, there has been a restriction on a Flatbed Dryer's maximum limit of the average drying temperature (Indonesia, 2015) to 43^{o} C for grains and soybeans, and 65^{o}C for corn. On the other hand, the higher the air flow rate and the lower the humidity level, the more rapid the drying process is *(Muller & Heindl, 2006)*. Considering that factors of weather, climate, geographical location, as well as day and night conditions are difficult to control, in consequence they greatly affect the humidity of the air around the environment.

[1] *Dandy Z. Sjechlad, Mech. Eng. Stud.; Susilo A. Widyanto, Dr. Lecturer Mech. Eng.; Bambang Purwanggono, Dr. Lecturer Industrial. Eng.; M. Munadi, Dr. Lecturer Mech. Eng*

The emphasis of control variables here will be more dominant on aspects regarding drying air temperature and hot air velocity.

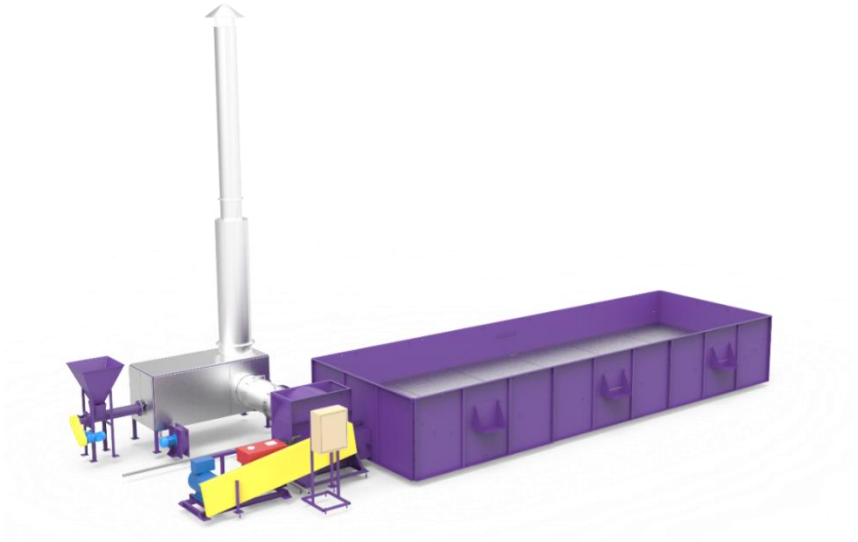

Fig. 1 - Flatbed / Fixed Bed Dryer

Flatbed Dryer or Fixed Bed Dryer is a type of grain / fruit dryer that has simple properties due to its physical form, uncomplicated working principle, sturdy and convenient construction, as well as easy maintenance, (*Teodorov, et al., 2012*) as well as a considerably affordable investment of its manufacture that allows for small to medium batch size applications and for it to be developed directly by farmers *(Noetzel, 2006*). It is constructed as a rectangular chamber separated into two sides horizontally aligned through a perforated dividing screen, with the top part being a reservoir for commodity materials to be dried, and the bottom (plenum space) being a part where the air sourced from the burner is accommodated and distributed. The heat generated by the burner is exhaled by the blower, then directed towards the plenum space, and afterwards flowed out through the dividing perforate screen, penetrating the layer of the material that requires drying while carrying the existing water content.

This type of dryer has generated several flaws. Some of the prominent ones are the uneven and non-uniform result of drying, as well as the heat loss that occurred from unequal distribution of air stream *(Brooker, et al., 1992*) (*Jayas & Muir, 2002*) *(Mellmann & Fürll, 2008*) (*Nagle, et al., 2008*) (*Nagle, et al., 2010*) *(Noetzel, 2006*) (*Ramsey & Fortis, 1984)*, labor intensive, and the lack of process control, instrumentation (Mellmann & Fürll, 2008) and automation function. There is a lot of research that has analyzed the homogeneity of airflow in the plenum space with a scale model testing experiment validated by Computer Fluid Dynamics (CFD). The first method of testing was done by directing the airflow coming from the blower in order to maintain it being linear. Examples of this are through making modifications with chambers/baffles in the plenum area, to get a steady airflow (*Nhi, et al., 2003*) (*Teodorov, et al., 2012*), and through modifying by creating multiple inlet locations that are evenly distributed on all sides (*Roman, et al., 2012*). The second method is done by placing in the plenum area a barrier configuration/screen (*Teodorov, et al., 2012*), a reflector configuration, as well as other varying configurations (*Nagle, et al., 2010*) before the air blows out to the drying chamber, which in consequence will cause the velocity of the air coming out from the plenum space to the commodity material to be more evenly distributed. All tests in this research are done in the effort of producing a uniform airflow coming out from the plenum space. However, all tests except Nagle's research have a drawback where the focus of the research is in the plenum area, instead of the drying chamber where the commodity material itself is being dried. Nevertheless the grain itself is the final subject that must be uniformly dried, and not a homogeneous airflow velocity that comes out of the plenary room.

In contrast to the research discussed above, Nagle's (*Nagle, et al., 2008*) previous research has analyzed a drying process with a Flatbed dryer, which focused on the causative factors in the uneven drying of longan fruits in Thailand. The research did so by dividing the areas in the drying basin into 3 layers resembling large nets, whose position would afterward be moved and horizontally rotated 180^{O} with a big crane. In each respective net, 5 porous sacks which were each written with a number would be filled with longans and combined in one layer with other longans.

This experiment was done by doing various drying trial experiments with inter-layer displacement patterns and horizontal rotation, as well as the positional displacement to the 5 sacks in each layer. The resulting conclusion was that a Flatbed dryer produces uneven drying results with a tendency for the bottom layer, middle layer, and areas near the air intake's base to be even drier than the rest of the commodity's pile.

It was a research that combined both the drying chamber's internal aspect as well as the aspect of plenum space (*Nagle, et al., 2010*), and then was validated with CFD (*Prukwarun, et al., 2013*) with the conclusion that the evenness of the air in the plenary room does not solve the problem of uncontrolled drying rates. It concluded that there is still a need to undergo the process of displacing the materials that are already dry (bottom layer) with the ones that are still relatively undried (upper layer). This process can be done by rotating/stirring the material commodities of the bottom layer, moving them, and afterward replacing them with the ones whose water content is relatively still higher (*Yahya, et al., 2018*).

The concept of this research is in line with other previously-done research in continuously stirring using a stirrer (*Sjechlad, et al., 2019*) which is attached on the drying chamber and operated automatically. This will be a reference used in this paper to test the evenness of reducing water content during the drying process.

MATERIALS AND METHODS

As it was previously discussed in the paper (Sjechlad, et al., 2019)**,** the concept of stirring in this mechanization system was designed to guarantee that the stirring process would happen without having to rely on human resources as stirring labor, which is a factor that naturally increases operational costs. With the exception of one human operator who oversees the overall drying process, the role of human labor is significantly minimized during the drying process except the process of loading/unloading the materials. In addition to being more efficient with a lower production cost rate (due to it having only to rely on a 3phase 2HP electric motor as its driving source) the system was designed to make as little skin contact as possible for the operator involved with the grain. The skin of grains contain very high silica content (Fernandes, et al., 2016) which will cause itching and irritation because of the scratches occurring between human skin with grain skin. Another thing to overcome is minimizing human interaction with dust produced from the drying process.

The solution is designed to utilize the rotational and translational motion of the stirring shaft. The stirring shaft itself continuously rotates at about 4 rpm and is directed following the motion of the translational movement of the shaft at about 0.94 m/min along the long span of the Flatbed dryer (Fig. 2). The shaft diameter is 110 mm. It has a length of 2810 mm, and it has 22 stirring blades of 500 mm length. This stirring mechanism is designed as an attachment to conventional flatbed dryers. This design makes it easy to apply the machine to already widely distributed dryers. In order to be able to thoroughly stir and mix the material to the very depth of its pile, a combination of rotational and translational motion must reach the span of the drying basin's effective length, while the blades must be able to rake until the very bottom of the plenum. Furthermore, stirring is done from the top to minimize resistance. The electric motor drives the stirring shaft in a rotational and translational motion by utilizing a chain along the rail as a medium that is pulled by the gears of the electric motor driving it. Furthermore, as shown in Fig. 3, the dead corner spaces, or in other words areas where the blades cannot reach, must be closed to ensure all grain is touched with the stirrer.

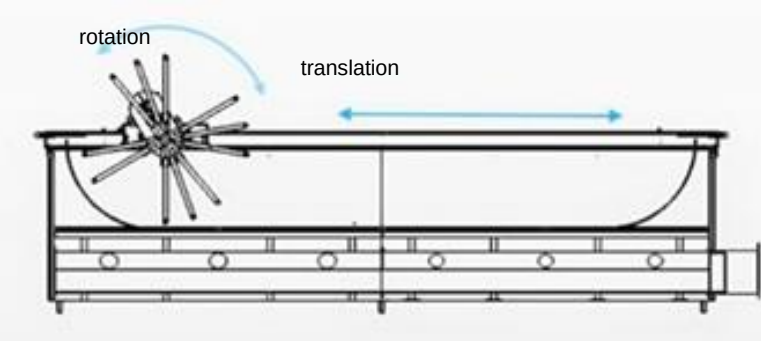

Fig. 2 - Translational and rotational movements in the stirring system

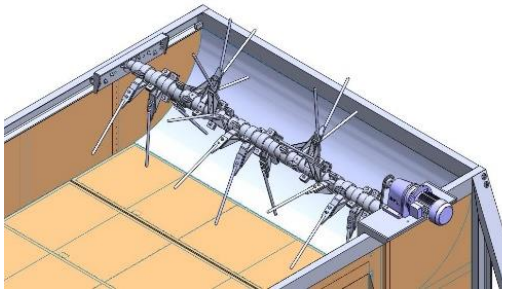

Fig. 3 - Curved wall divider in the Dryer

In this study, it has not been proven that the dried material commodities experience a uniform rate of reduction in water content in each layer and in every part in the drying chamber.

This research has just proven that the drying cost rate is lower than the one belonging to a conventional system that utilized human labor power and answer the problem of labor intensity, lack of process control, instrumentations, and automation functions. The design solution has not been proven able to overcome the main weakness of the Flatbed dryer as has been widely reviewed in previous studies.

The purpose of this paper is to study the evenness of material commodities' drying rate that happen due to stirring. This paper aimed to do this with the above mechanization system where it is expected that the bottom, middle and upper layers will experience drying rates that are relatively the same, so that a uniformed drying rate will be achieved. If this is proven, then this automatic stirring system solution approach may be an answer to the weaknesses of the Flatbed Dryer, which have been widely reviewed in previous studies as being non-uniform in its drying process, and as being prone to heat loss due to uneven flow distribution.

A flatbed dyer of a 7280 mm x 2600 mm x 1100 mm measurement was used as the testing tool. It was equipped with a drying chamber's storage volume of 4.28 m^3. The dried material was grain, and its initial moisture content was in the range of 22.3% - 19.1%, depending on their condition in each test batch. The burner used was of the Husk / Biomass Burner type, and hot air was supplied by a blower. The stirring mechanism was rotated by a 2Hp 3 phase electric motor.

Two types of tests were carried out in a series form. The first tests were carried out 3 times with the aim of observing the homogeneity rate of drying of wet grain with varying rotational speeds. The fourth test was carried out only once with the aim of proving the occurrence of air velocity leaking due to the exposure of the commodity material pile by the movement of the stirring, proving the descent of height in the surface of grain piles due to the stirring, as well as seeing the effect that occurs when the blower speed and/or stirring speed are changed. These are deemed necessary to prove, because without an air breakthrough, the regular air passing through the commodity pile will work harder to bind water in the upper layers (Sarker, et al., 2014). It is necessary then to prove that the drying occurring during the stirring process is a combination of both the movement of commodity materials, and the breakthrough of fresh air that continuously moves according to the movement of the stirrer.

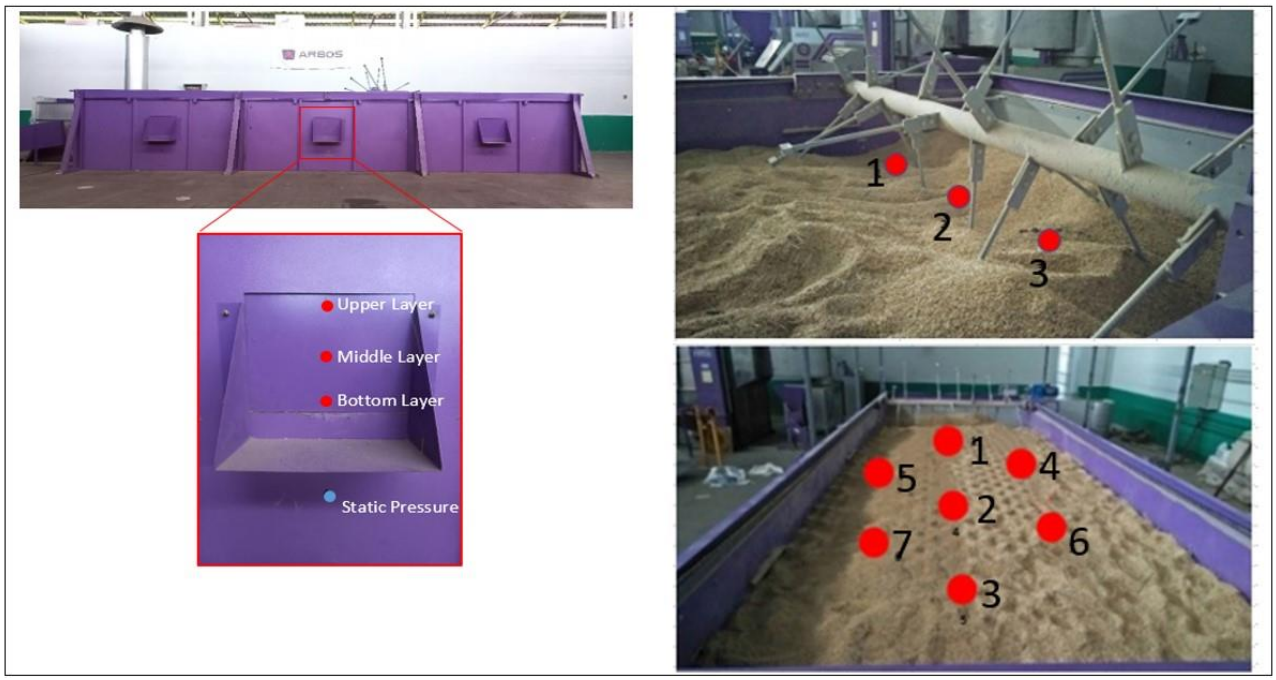

Fig. 4 - Location points for taking specimens and data

The measurement sampling points are shown in Fig. 4 that shows how the temperature was taken at 9 points on the side wall of the drying chamber where each layer is represented by 3 sample points. Moisture test samples were taken at 7 points where the top layer was measured at a depth of 5 cm from the surface of the material, whereas the bottom one was measured at a depth of 5 cm above the bottom of the perforated partition. These measurements were done on the upper, middle and lower layers. Whereas for the duration, the data collection was carried out every 30 minutes, counted starting from the beginning of the test, until the desired moisture content was reached.

RESULTS

The first, second and third tests were carried out using approximately 3.5 tons of wet grain. Each with an initial moisture content of 22.3%, 21.9% and 19.1%. The drying process was carried out using standardized heat of approximately 1549 kJ/Kg, at a static pressure of 10.8 mmH20 and an average blower speed of 4.53 m/s at 1500 rpm rotation. The first test was done with a stirring rotation speed of 2 rpm and with a translational speed of 0.47 m/min, the second test with a rotation 4 rpm/translation 0.94 m/min, and the third test with a rotation 6 rpm/translation of 1.41 m/min (fixed drive gear ratio). Keeping in mind that the purpose of these three tests were to observe the effect of stirring on the evenness of the drying rate, the blower speed was then kept constant according to the manufacturer's settings.

The first test was conducted from 08.00 to 15.00 with an average RH of 55.31% and an average temperature of 32.96^{0}C. In Fig. 5(a) it can be seen that the 2 rpm rotation had not been able to even out the temperature. In fact, over time the difference between the bottom, middle and top layers was getting higher. However, up to 7 hours in the drying process, the maximum average temperature was still below the maximum reference standard, which is a maximum of 43^{0}C (Indonesia, 2015).

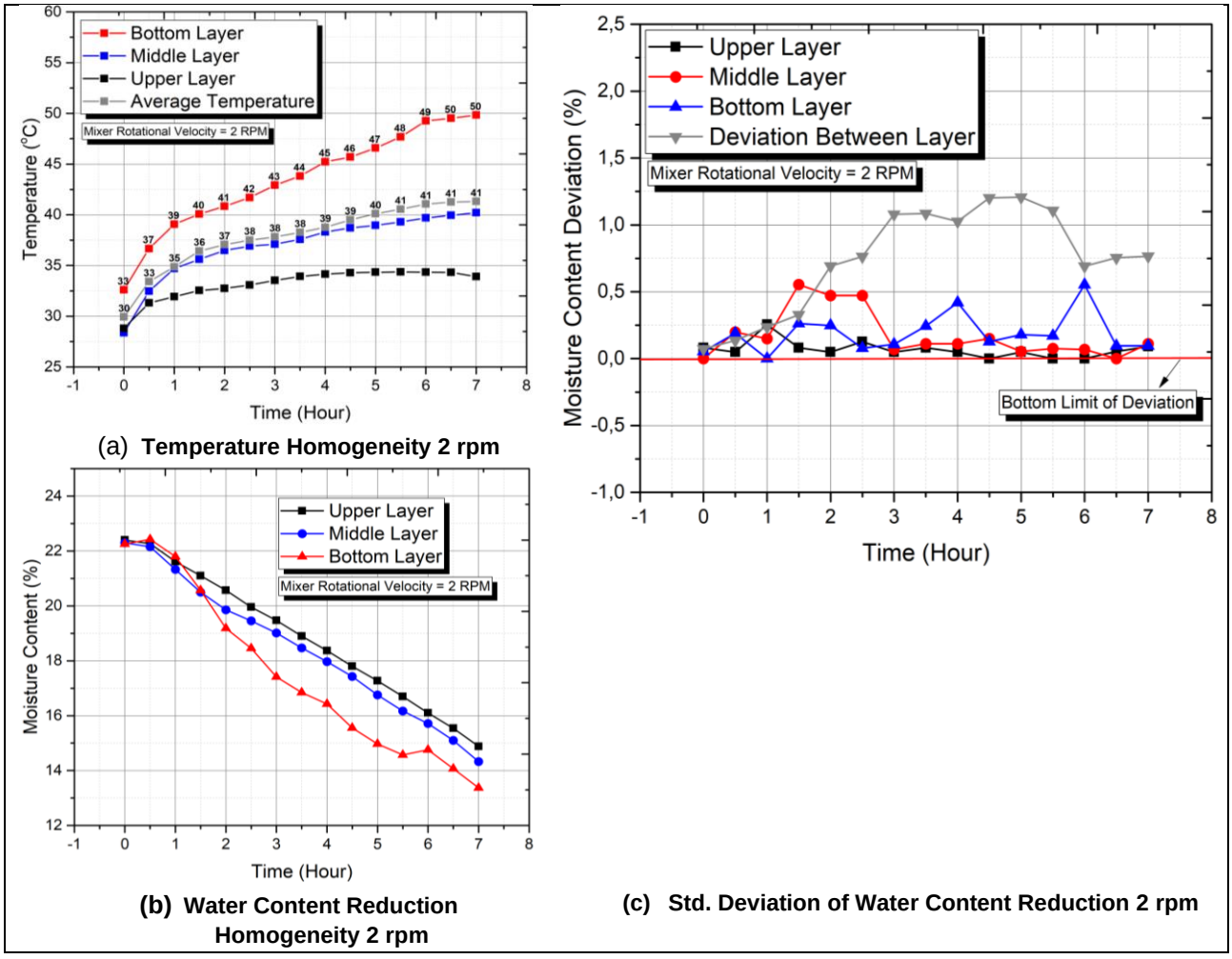

(a) **Temperature Homogeneity 2 rpm**

(b) Water Content Reduction Homogeneity 2 rpm

(c) Std. Deviation of Water Content Reduction 2 rpm

Fig. 5 - The results of the drying test at a stirring rotation of 2 rpm

This 2 rpm stirring rotation itself was also not able to even out the rate of the reduction in water content. In Fig. 5(b), we can see a relative uniformity only in the middle and upper layers. In Fig. 5(c) it can be seen that the std. deviation in the same layer was relatively low (uniform), but the std. deviation of the combined layers (top, bottom and middle average water content) was very high. This means that there was a distance between the layers.

The second test was conducted from 09.00 to 16.00 hours with an average RH of 54.53% at an average temperature of 33.17^{o}C. The test results are shown in Fig.6(a) which shows that with a stirrer rotation of 4 rpm, the temperature could only be evened out in the middle and top layers, the same as in the 2 rpm rotation. Until the end of the drying process, the maximum average temperature was still safely below the maximum reference standard.

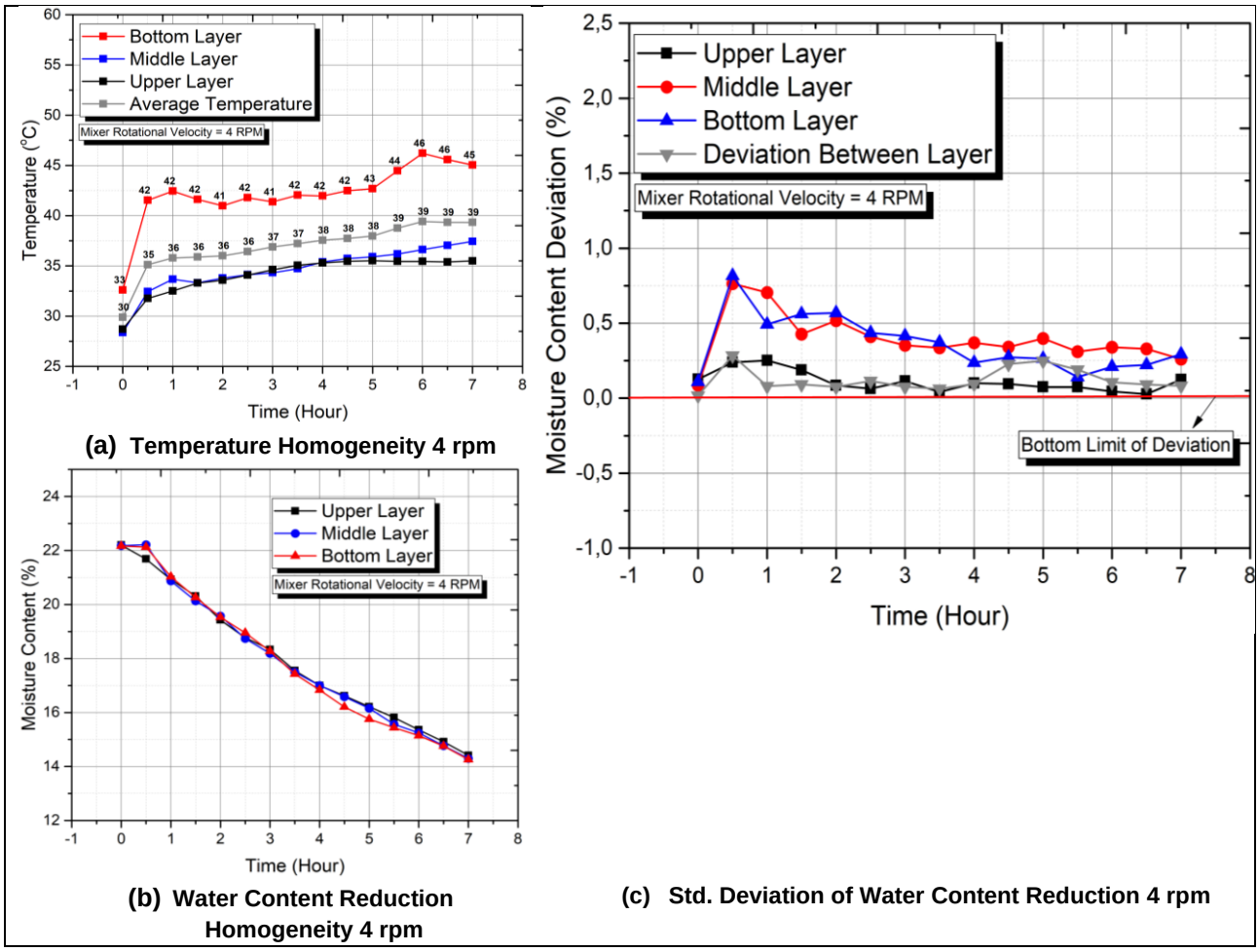

Fig. 6 - The results of the drying test at a stirring rotation of 4 rpm

After 1 hour of processing at 4rpm stirring rotation, one can see a uniform effect of evenness in the reduction of water content. In Fig. 6(c) it can also be seen that the std. deviation of combined layers value was much smaller than the three already relatively small std. deviations of each layer. This can be used as an indicator of the formation of homogeneity in water content reduction throughout the layer as a whole. The oversaturation in airflow was a phenomenon that occurred at the beginning of the process in the lower and middle layers. This could be seen at both the speeds of 2 and 4 RPM in the first 30 minutes. Hot air was not able to bind steam anymore. Instead, it was now only able to heat the layer above, and that condensation-caused steam migrated by diffusion to the layer above it (*Sarker, et al., 2014*) *(Nagle, et al., 2008*).

The third test conducted from 08.30 to 15.30 with an average RH of 55.31% at an average temperature of 32.99°C. At this 6 rpm rotation, a very good effect of a uniform reduction in water content was seen from the start of the process (Fig. 7(b)). It was better than 4 rpm, in Fig. 7(c) is shown that the std. deviation of each layer several times has a very low value, following std. deviation of the combined layers that was already very low. This indicates a better homogeneity process in all layers. In Fig. 7 it can be seen that until the stirring rotation was at 6 rpm, the stirring test had not been able to even out the temperature of all layers. However, this is still considered safe due to the maximum average temperature being still below the maximum reference standard.

The fourth test was carried out using the dry grain from the third test result. The test was to examine if there is a resulting second airflow that is fresh and drier from the outcropping of the stirring effect. The test also verified whether the airflow, as depicted in Fig. 8, was affected by the rotation speed of the stirrer and/or the blower. The test was carried out by measuring 3 points below the stirring shaft and 7 points above the commodity pile. Considering the safety concerns as well as the difficulty of measurement, the collection of the speed data under the stirrer is done by pausing the stirring system for a moment. However, the collection of 7 speed data above the commodity pile was carried out while the stirring process was ongoing.

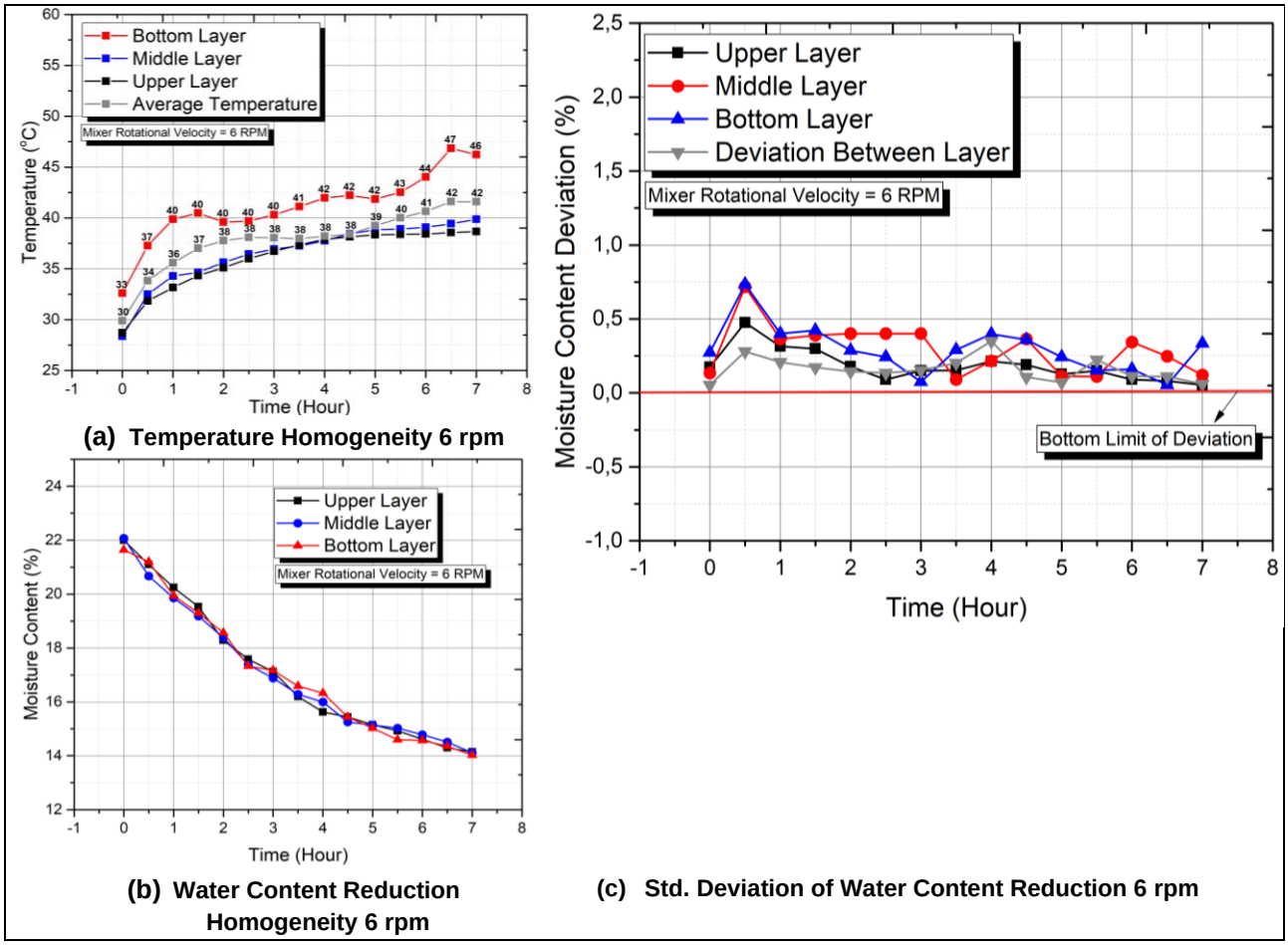

Fig. 7 - The results of the drying test at a stirring rotation of 6rpm

From Fig. 9, one can see that the stirrer's motion is proven to leak air at an amount of almost twice the normal speed of air that penetrates the commodity layer with a difference of about 0.2 m/s.

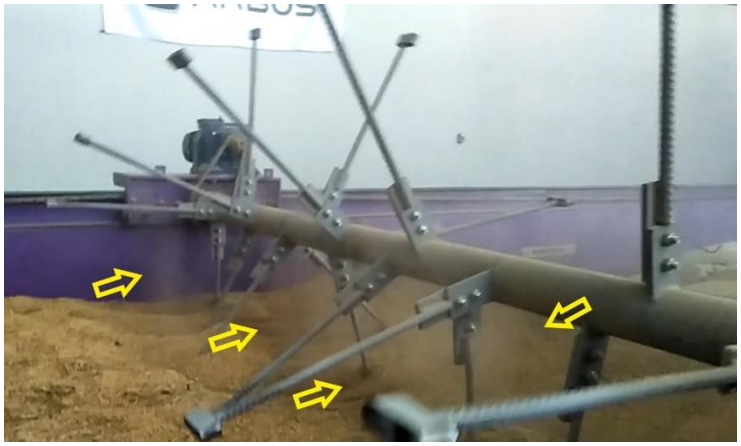

Fig. 8 – Air Velocity experiment

It can also be seen that as the speed of the blower increases, the speed of these two air velocities also increases, although the difference was around 0.2 m/s, it was still visible. This phenomenon appeared similar at the rotational stirring of 2, 4, and 6 rpm.

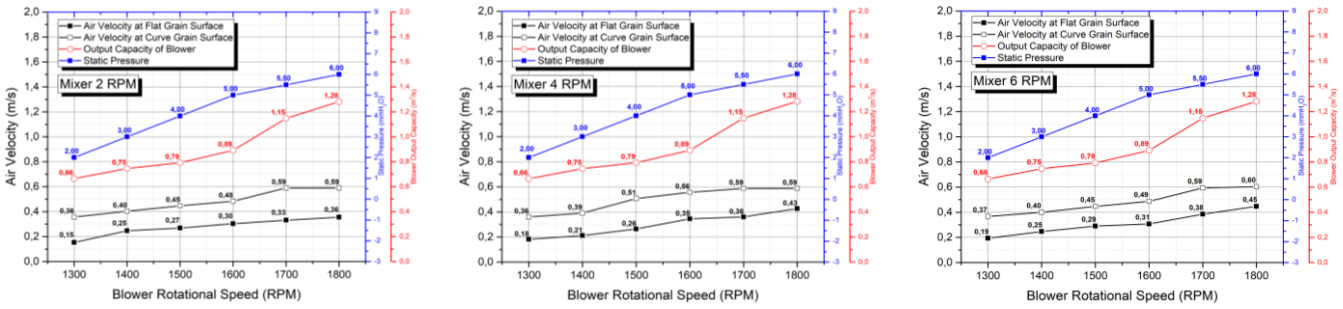

Fig. 9 - The air velocity performances

It can be seen that although the normal air velocity was affected by the blower air velocity, it was not affected by the stirring speed. It can also be seen that the air velocity of the outcrop was affected by the blower's speed and agitation. Meanwhile, normal air velocity, static pressure in the plenum chamber, as well as blower air velocity were not affected by the stirring rotation, and instead by the blower rotation. As can be seen in Fig. 8, with the blower set fixed, the air velocity was normal. The blower's air velocity and static pressure were also relatively constant, while the outcrop air velocity was affected by the stirring cycle.

The fourth test also saw the phenomenon of a decrease in the surface height of the pile due to stirring. Fig. 10(a) shows a descent in the grain's surface flatness face to about 200 mm during the stirring movement, lower than the average surface of the other grains of 325 mm. This lowering in the material's surface appears not to be influenced by the stirring speed, and instead by the configuration of the shape of the stirrer. It can also be seen in Fig. 10(b) that the process of stirring has relatively no influence on changes of either the static pressure in the plenum space, or the speed of airflow penetrating the grain pile's layers.

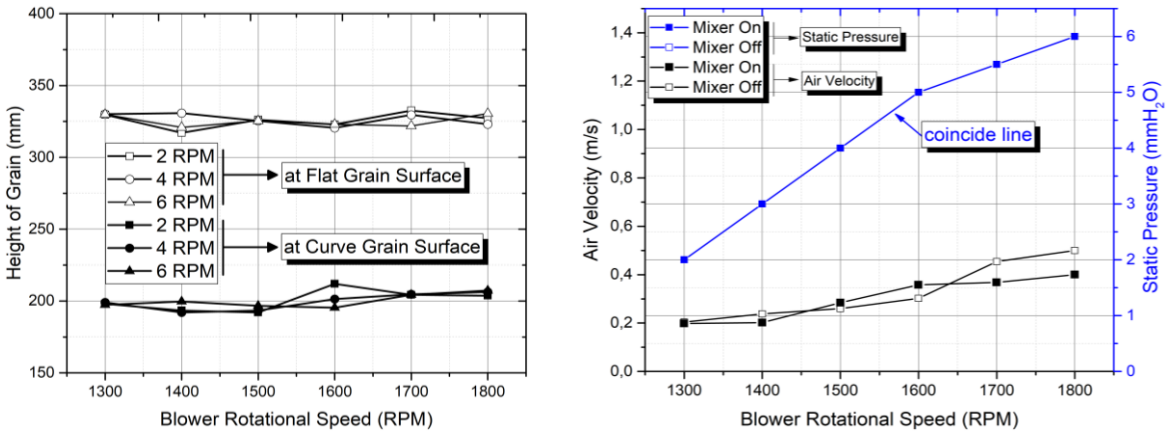

(a) Surface Drop under Stirrer

(b) Distribution of Airflow & Static Pressure due to Stirring

Fig. 10 - The phenomenon of stirring effect

CONCLUSIONS

Through the tests performed with grains, one can see that a stirring mechanism was proven to be able to maintain the evenness of the reduction of water content in all parts of the drying chamber, in order to produce a drying end result with uniformed quality. It has also proven the way these translation and rotational motions were able to replace the role of stirrers to evenly turn over and mix the commodity. The stirring that was done on various rotational speeds up to 6 rpm in this testing was not yet able to even out the grains' drying temperature, particularly in the bottom layer near the perforated dividing screen. However, the acceleration in stirring speed was proven as able to narrow down the temperature difference between the layers, starting from the layer positioned furthest from the source of hot air.

The evenness of stirring can be seen from the std. deviation graphic of interlayer water content reduction. The smaller the value, the more even and uniformed the reduction of water content between the layers. The higher the stirring rotation, the smaller the resulting std. deviation between the layers. During the 2 rpm rotation, one can see the top and middle layer receiving uniformed rate of drying.

However, the drying rate in the furthest bottom layer became faster especially after the 90 minutes' mark. This shows that the rotational speed was not yet optimal due to the evenness between the layers having not yet occurred. This phenomenon is further clarified by the std. deviation between the layers, which became bigger in size after that minute. During the ≥ 4 rpm rotation, one can begin to see the drying rate becoming more uniformed in all layers, particularly after the 1-hour mark since the drying process started. The higher the stirring rate, the quicker the homogenization process of the water content reduction rate started. This was further clarified by the std. deviation graphic, in which one can see that the std. deviation of 4 rpm and 6 rpm stirring rotations between layers where the value was very small and lower than the std. deviation of each layers. However, during the initial drying process under the 4 rpm rotational speed at the middle and a relatively lower layers, we can see a phenomenon of oversaturation happening in the hot airflow, in which hot air was not able to bind steam anymore. Instead, it was now only able to heat the layer above, and that condensation-caused steam migrated by diffusion to the layer above it.

Due to the stirring motion, a second continuous airflow was caused. This airflow occurred because of the outcrop and moved according to the motions of the stirrer, where there was a difference with the even air flow that had penetrated the grain pile, because it could be seen that the air velocity is greater by about 0.2 m/s. This difference was relatively constant, even though the rotations of stirring and/or blower were changed. Due to the displacement of the continuous movement, this second airflow also contributed to evenly aid the drying rate, because the normal air flow that penetrated the grain pile tend to have a higher moisture content than the material commodities in the middle/upper layers, especially in the early stages of drying time.

In the fourth test, one can see that the movement of the stirring rotation had no effect on the static pressure in the plenum chamber, the air velocity that penetrated the grain pile, as well as the air velocity under the stirrer. Instead it can be seen that the blower's rotational speed was the one that had an effect on the increase. The higher the blower speed rotation, the more increased the value. In this test, it was also proven that the stirring process has an effect on the decrease in the surface of the grain pile under the stirring shaft which moved along with the stirring movement. The difference in height was constant even though the stirring speed was variously changed. This shows that the grain pile's height difference was not due to the rotational speed, but the configuration of the shape of the stirrer blades. It was then also proven that the static pressure and the speed of air flow that penetrated the grain pile did not change according to the changes in stirring conditions.

REFERENCES

[1] Brooker, D. B., Bakker-Arkema, F. W. & Hall, C. W., 1992. *Drying and Storage of Grains and Oilseeds.* New York: Van Nostrand Reinhold.

[2] Chanpet, M., Rakmak, N., Matan, N. & Siripatana, C., 2020. Effecy of Air Velocity. Temperature, and Relative Humidity on Drying Kinetics of Rubberwood. Volume 6.

[3] Chen, P., Xu, J., Tang, Y. & M.H., L., 2019. Experiments on Paddy Drying Mechanicm of Far-Infrared Convection Combination in Combine Harvester. *INMAH - Agricultural Engineering,* Volume 59 No. 3, pp. 133-140.

[4] Dorneles, L. d. N. S. et al., 2019. Effect of Air Temperature and Velocity on Drying Kinetics and Essential Oil Composition of Piper Umbellatum L. Leaves. *Industrial Crops and Products,* Volume 142, pp. 0926-6690.

[5] Fernandes, L. J. et al., 2016. Characterization of Rice Husk Ash Produced Using Different Biomass Combustion Techniques for Energy. *Fuel,* Issue 165, pp. 351-359.

[6] Indonesia, S. N. I., 2015. *Standard Nasional Industri Indonesia No. SNI 4412:2015.* Jakarta: s.n.

[7] Jayas, D. S. & Muir, W. E., 2002. The Mechanics and Physics of Modern Grain Aeration Management. In: S. Navarro & R. Noyes, eds. *Aeration System Design.* s.l.:CRC Press Inc., pp. 195-249.

[8] Karbassi, A. & Mehdizadeh, Z., 2008. Drying Rough Rice in a Fluidized Bed Dryer. *J. Agric. Sci. Technol,* Volume 10, pp. 233-241.

[9] Lira, T., Barrozo, M. & Assis, A., 2009. Concurrent Moving Bed Dryer Modelling: Sensitivity of Physicochemical Parameters and Influence of Air Velocity Profiles. *Applied Thermal Engineering,* Issue 29, pp. 892-897.

[10] Madamba, P. S., Driscoll, R. H. & Buckle, K. A., 1996. The Thin-layer Drying Characteristics of Garlic Slices. *Journal of Food Engineering,* Issue 29, pp. 75-97.

[11] Mellmann, J. & Fürll, C., 2008. Drying facilities for medicinal and aromatic plants - Specific energy. *Journal of Medicinal and Spice Plants,* 13(3), p. 127e133.

[12] Motevali, A. & Chayjan, R. A., 2017. Effect of various drying bed on thermodynamic characteristics. *Case Studies in Thermal Engineering,* Volume 10, pp. 399-406.

[13] Muller, J. & Heindl, A., 2006. Drying of Medicinal Plants. pp. 237-252.

[14] Nagle, M. et al., 2008. Effects of operating practices on performance of a fixed-bed convection dryer and quality of dried longan. *International Journal of Food Science and Technology,* 43(11), p. 1979–1987.

[15] Nagle, M. et al., 2010. Improved quality and energy performance of a fixed-bed longan dryer by thermodynamic modifications. *Journal of Food Engineering,* 99(3), pp. 392-399.

[16] Namkanisorn, A. & Murathathunyaluk, S., 2020. Sustainable Drying of Galangal Through Combination of Low Relative Humidity, Temperature and Air Velocity. *Energy Reports,* Issue 6, pp. 748-753.

[17] Nhi, N. T. et al., 2003. Simulation of Airflow in a Flatbed Dryer by Computational Fluid Dynamics: Application for the Drying of Rice in Mekong, Delta, Vietnam. *The Society for Engineering in Agricultural, food, and biological system,* pp. 1-15.

[18] Noetzel, A. M., 2006. Untersuchung Zum Stand Der Technik in der Krautertrocknung Kleiner bis Mittelgrober Anbaubetriebe in der Bundesrepublik Deutschland. *Agrartechnik Witzenhausen.*

[19] Paziuk, V., Petrova, Z., Tokarchuk, O. & Yaropud, V., 2019. Research of Rational Modes of Drying Rape Seed. *INMATEH - Agricultural Engineering,* Volume 58 No. 2, pp. 303-310.

[20] Prukwarun, W., Khumchoo, W., Seancotr, W. & Phupaichitkun, S., 2013. CFD simulation of fixed bed dryer by using porous media concepts: Unpeeled longan case. *International Journal of Agricultural and Biological Engineering,* 6(1), pp. 100-110.

[21] Ramsey, T. R. & Fortis, T., 1984. Improving the Air Flow Distribution in a Batch Walnut Dryer. *American Society of Agricultural and Biological Engineers,* 27(3), pp. 0938-0941.

[22] Rogovskii, I. et al., 2019. Experimental Studies on Drying Conditions of Grain Crops With High Moisture Content in Low-Pressure Environtment. *INMATEH Agricultural Engineering,* 57(1), pp. 141-146.

[23] Roman, F., Strahl-Schafer, V. & Hensel, O., 2012. Improvement of Air Distribution in A Fixed-Bed Dryer Using Computational Fluid Dynamics. *Biosystems Engineering,* Issue 112, pp. 359-369.

[24] Sarker, M., Ibrahim, M. N., Aziz, N. A. & Salleh, P. M., 2014. Energy and Rice Quality Aspects During Drying of Freshly Harvested Paddy With Industrial Inclined Bed Dryer. *Energy Conversion and Management,* Issue 77, pp. 389-395.

[25] Sjechlad, D. Z., Jamari, J. & Widyanto, S., 2019. Auto-Stirring Grains Bed Dryer as an Innovative Efficiency Solution. *ICENIS,* Issue 125.

[26] Snezhkin, Y., V.M., P., O., P. Z. & O.A., T., 2020. Determination of The Energy Efficient Modes for Barley Seeds Drying. *INMATEH Agricultural Engineering,* Volume 61, p. No. 2.

[27] Teodorov, T., Scaar, H., Ziegler, T. & Mellmann, J., 2012. *Homogenization of Airflow in a Fixed-Bed Dryer for Medicinal Plants Based on Computational Fluif Dynamic (CFD).* Valencia, Spain, ResearchGate, pp. 1-7.

[28] Yahya, S. et al., 2018. Drying Performance and Effect of Drying Temperatures on Stress Cracks of Shelled Corn. *MSAE Conference,* pp. 2-7.

ANALYSIS AND OPTIMIZATION TEST OF OPERATION PROCESS OF CLEANING DEVICE OF CORN SEED HARVESTER
/
玉米籽粒收获机清选装置作业机理分析与优化试验

Zedong ZHAO, Xiaohui YANG, Guohai ZHANG *
College of Agricultural Engineering and Food Science, Shandong University of Technology, Zibo 255091, China
Tel: +86-15965534882; E-mail: guohaizhang@163.com
DOI: https://doi.org/10.35633/inmateh-68-21

Keywords: *corn; sieve; mechanics analysis; response surface*

ABSTRACT

Aiming at the current problem of the high rate of impurity and loss in the cleaning device of corn seed harvesters in China, this paper took the cleaning device of 4YZL-6 self-propelled corn seed harvester as a sample and analyzed the movement law of the material on the sieve. Box-Behnken response surface experimental design theory was used for the orthogonal tests. Wind inlet angle, airflow velocity, and crank angular velocity were selected as influencing factors, and the impurity rate and loss rate as the evaluation index of operation quality. A regression mathematical model between each influencing factor and indicator was established, and the model was also integrated and optimized. The optimal parameter combination was obtained as follows: the wind inlet angle was 37.95°, the airflow velocity was 11.3 m/s, and the crank angular velocity was 4.1 r/s. The corresponding impurity rate was 0.87% and the loss rate was 0.34%. Verification tests were conducted on the optimization results, and the test results showed that under the optimal combination of parameters, the impurity rate was 0.89% and the loss rate was 0.35%. The relative errors of each evaluation index and its model prediction were 2.29% and 2.94%, respectively.

摘要

针对目前中国玉米籽粒收获机清选装置含杂率和损失率较高的问题，本文以4YZL-6自走式玉米籽粒收获机清选装置为例，分析了物料在筛子上的运动规律。采用Box-Behnken响应面试验设计理论，以入风角度、风速和曲柄角速度为影响因素，以含杂率和损失率为作业质量评价指标，进行三因素三水平正交试验。建立了各影响因素与指标之间的回归数学模型，同时对模型进行了综合优化。获得最优参数组合为：入风角度37.95°、风速11.3m/s、曲柄角速度4.1r/s，对应的含杂率为0.87%、损失率为0.34%。对优化结果进行验证试验，试验结果表明在最优参数组合下，含杂率为0.89%、损失率为0.35%，各评价指标与其模型预测值的相对误差分别为2.29%和2.94%。

INTRODUCTION

Impurity rate and loss rate are two important indicators of the operational performance of corn seed harvesters, which directly reflect the technical level of the harvester *(Wang et al., 2018; Xu et al., 2019)*. The cleaning device is one of the core components of the corn grain harvester, and its operation effect directly affects the harvesting quality of the whole machine *(Hou et al., 2019)*, so scholars at home and abroad have conducted a lot of research on it.

To improve the efficiency of sieving grain mixtures with flat seeds, sieves with size activators, which have a riffle appearance, were proposed *(Kharchenko et al., 2019)*. Some scholars determined the influence of the deck gap on the distribution of thrashing mass between cleaning and straw walker, keeping the degree of grain crushing limited with GOST *(Alexey et al., 2019)*. Some scholars analyzed the movement state of corn in the airflow field and designed a stepped sieve *(Wang et al., 2020)*. The sieve was designed with a step buffer zone, which allows the seeds to be temporarily retained in the step so that the loss rate was greatly reduced. In addition, some scholars studied the clogging law of the sieve and determined the desorption force of the clogged corn cob shaft on the sieve through experiments *(Cheng et al., 2021)*. Some scholars built a test platform for cleaning based on the cleaning system of the CASE-4099 corn seed harvester. The test platform used a new type of vertical adjustable wind divider and simulation to optimize the operating performance of the cleaning device *(Li et al., 2020)*.

Some scholars presented a mathematical model that characterizes the process of threshing and separation from the threshing machine with an axial flow of a thresher *(Vlădut et al., 2022)*. This study provided a reference for the analysis of corn threshing and separation processes.

The above research provides an important theoretical basis for the design and optimization of the parameters of the cleaning device of the corn seed harvester. However, fewer studies have been conducted to analyze the mechanism of the operating process of the cleaning device of the corn seed harvester. This paper took the cleaning device of 4YZL-6 self-propelled corn seed harvester as a sample and analyzed the movement law of the material on the sieve. A mathematical model between the operating parameters of the cleaning device and the cleaning effect was established through experiments conducted by the Box-Behnken central combination design method. Finally, the optimal combination of the operating parameters of the cleaning device of the corn seed harvester was obtained by optimization. This study can provide a reference for the selection and optimization of parameters for the cleaning device of corn seed harvester.

MATERIALS AND METHODS

Structure and working principle

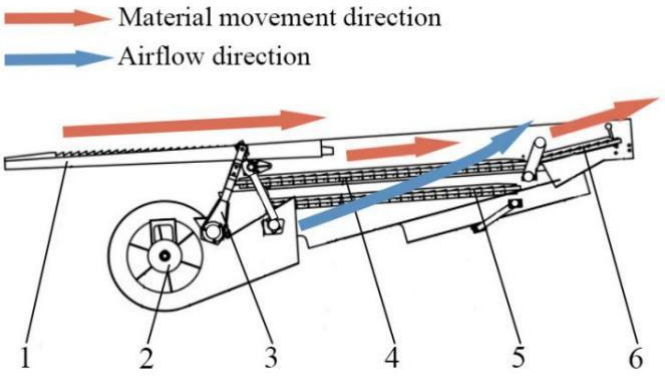

Fig. 1 – Structural diagram of the cleaning device

1.Shaking plate; 2. Centrifugal fan; 3. Crank-link mechanism; 4. Upper sieve； 5. Lower sieve; 6. Tail Sieve

As shown in Fig. 1, the cleaning device of the corn seed harvester is mainly composed of shaking plate, centrifugal fan, crank-link mechanism, upper sieve, lower sieve, and tail sieve. In which, the shaking plate feeds the threshed material to the cleaning device by reciprocating motion. The role of the centrifugal fan is to provide the airflow required for clearing operation and to blow and transport the material during screening by using the difference in physical properties to accelerate the dispersion of the material on the sieve. The crank-link mechanism causes the sieve to perform a planar reciprocating motion, the function of which is to continuously throw and transport the material on the sieve backward. The upper sieve and the lower sieve make use of the size difference between the materials to make the seeds pass through the sieve while the miscellaneous residue is discharged from the tail sieve to realize the separation of corn seeds and miscellaneous residue.

Analysis of the operating mechanism of the cleaning device

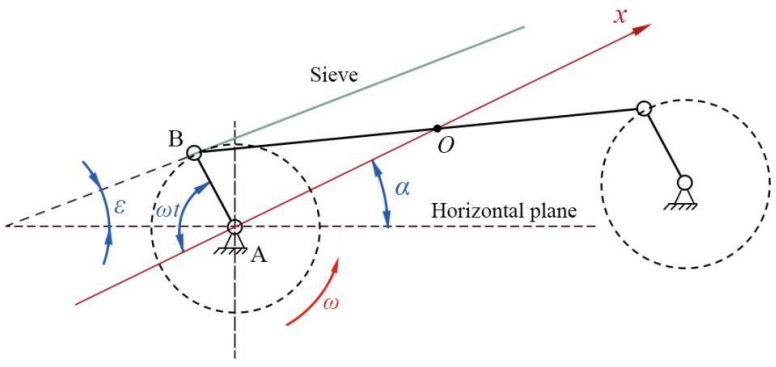

Fig. 2 – Analysis of sieve movement

The cleaning device takes advantage of the difference in suspension speed between corn kernels and redundant debris to achieve separation through high-speed airflow *(Tong et al., 2016; Hou et al., 2020)*. The separation process of the material is mainly carried out on the screen and therefore requires a detailed analysis of the movement process. In this study, the sieve is powered by a crank-link mechanism, and the schematic diagram of its motion is shown in Fig. 2. In the figure, the angle between the sieve and the horizontal plane is ε, the radius of the crank AB is r, and the angular velocity of the crank AB is ω. The crank *AB* rotation center *A* is the coordinate origin, the midpoint of the sieve is *O*. *AO* is the positive direction of the *x*-axis, and the angle between the *x*-axis and the horizontal plane is α. The length of the crank *AB* is much smaller than the length of the connecting rod, and the sieve is supported by a parallel four-bar mechanism, so the movement pattern of each point on the sieve is the same, which can be regarded as the reciprocating linear motion of the sieve along the *OB* direction *(Feng, 2022; Han, 2020)*.

Thus, the acceleration a at any point on the sieve can be represented as follows:

$$a = r\omega^2 \cos \omega t \tag{1}$$

As shown in Fig. 3, when the material is moving along the sieve, the forces acting on the material include the inertial force μ, gravity mg, the normal reaction force N of the sieve, the frictional force f and the airflow thrust P.

The inertial force μ is as follows:

$$\mu = mr\omega^2 \cos \omega t \tag{2}$$

The frictional force f is as follows:

$$f = N \cdot tg\phi \tag{3}$$

According to the gas-solid two-phase flow separation theory *(Li et al., 2022; Ren et al., 2022)*, the airflow thrust P is as follows:

$$P = \frac{1}{2} CA\rho_s v_s^2 \tag{4}$$

Where, μ is the inertia force, N; m is the mass of the material, kg; f is the friction force, N; N is the normal reaction force of the sieve, N; φ is the friction angle between the material and the sieve, (°); P is the airflow thrust, N; C is the material resistance coefficient; A is the material windward area, m^2; ρ_s is the material density, kg/m^3; v_s is the airflow velocity, m/s.

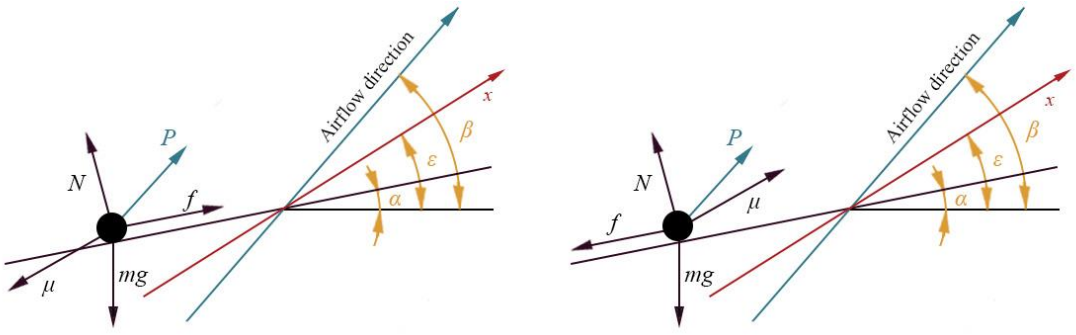

(a) a>0 **(b) a<0**

Fig. 3 – Sketch of material movement

Material slides forward along the sieve

As shown in Fig. 3a, the material and the sieve surface move together, when ωt is in the interval from 0 to π/2 and 3 π/2 to 2π, the acceleration a is positive, the inertia force μ is negative, and the material has the tendency to slide forward along the sieve surface *(Wang, 2022)*. At this point, the material is subjected to the following forces:

$$\begin{cases} N = \mu \sin(\varepsilon - \alpha) + mg\cos\alpha - P\sin(\beta - \alpha) \\ f = \mu\cos(\varepsilon - \alpha) + mg\sin\alpha - P\cos(\beta - \alpha) \end{cases} \quad (5)$$

From Eqs. (2) to (5), it is obtained that:

$$mr\omega^2\cos\omega t(\varepsilon - \alpha + \varphi) = mg\sin(\varphi - \alpha) + \frac{1}{2}CA\rho_s v_s^2\cos(\beta - \alpha + \varphi) \quad (6)$$

The airflow thrust P is determined by the material resistance coefficient C, the windward area of materials A, the density of material ρ_s, and the airflow velocity v_s. So, for the convenience of expression, δ is taken as the adjustment coefficient, and the adjustment coefficient δ varies with the change of airflow thrust P and satisfies the following equation.

$$\frac{1}{2}CA\rho_s v_s^2\cos(\beta - \alpha + \varphi) = (\delta - 1)mg\sin(\varphi - \alpha) \quad (7)$$

Substituting Equation (7) into Equation (6):

$$\frac{r\omega^2}{g}\cos\omega t = \frac{\delta\sin(\varphi - \alpha)}{\cos(\varepsilon - \alpha + \varphi)} \quad (8)$$

Since ωt is in the interval 0 to π/2 and 3π /2 to 2π, cosωt ≤1. Therefore, to make the material slide forward along the sieve, the following formula needs to be satisfied:

$$\frac{r\omega^2}{g} > \frac{\delta\sin(\varphi - \alpha)}{\cos(\varepsilon - \alpha + \varphi)} \quad (9)$$

Material slides backwards along the sieve

When ωt in π/2 ~ 3π/2 interval, the acceleration a is negative, the inertia force μ is positive, and the material has the tendency to slide backward along the sieve (as shown in Fig. 3b). By analogy with equations (5) to (9), the material has to meet the following to slide backward along the sieve.

$$\frac{r\omega^2}{g} > \frac{\delta\sin(\varphi + \alpha)}{\cos(\varepsilon - \alpha - \varphi)} \quad (10)$$

Material thrown off the sieve surface

In the cleaning operation, it is necessary to keep the seeds from leaving the sieve surface. The material is moving by inertia force, when the inertia force μ is along the positive direction of the *x*-axis, the acceleration a is negative, with the increase of $r\omega^2$, the normal reaction force N decreases, the material has the tendency to be thrown away from the sieve surface *(Si, 2017; Zheng, 2020)*. As shown in Fig.4, the sign of the material being thrown away from the sieve surface is N = 0.

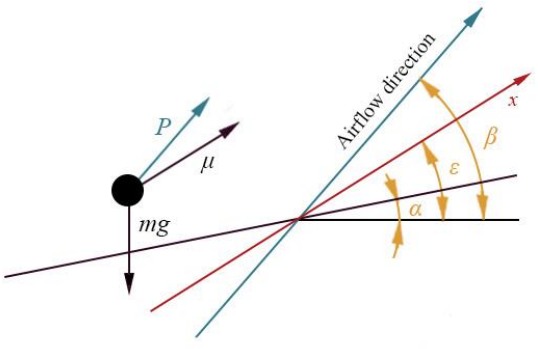

Fig. 4 – Sketch of material movement

At this time, the material is subjected to the following forces:

$$N = mg\cos\alpha - \mu\sin(\varepsilon - \alpha) - \frac{1}{2}CA\rho_s v_s^2\sin(\beta - \alpha) \quad (11)$$

Taking θ as the adjustment coefficient, the adjustment coefficient θ varies with the airflow thrust P and satisfies the following equation:

$$\frac{1}{2}CA\rho_s v_s^2 \sin(\beta-\alpha) = (1-\theta)mg\sin\alpha \tag{12}$$

When the material is thrown away from the sieve, N = 0. The following equations can be obtained by analogy from equations (5) to (9).

$$\frac{r\omega^2}{g} > \frac{\theta\cos\alpha}{\sin(\varepsilon-\alpha)} \tag{13}$$

In order to make full use of the area of the sieve for separation, and make the corn seeds have more chances to fall into the sieve holes, it is necessary to ensure that the material slides up or down along the sieve, while the distance sliding down is greater than the distance sliding up, and is not thrown away from the sieve surface *(Chai et al, 2021; Mu et al, 2020)*.

The following formula needs to be satisfied:

$$\frac{\theta\cos\alpha}{\sin(\varepsilon-\alpha)} > \frac{r\omega^2}{g} > \frac{\delta\sin(\varphi-\alpha)}{\cos(\varepsilon-\alpha+\varphi)} > \frac{\delta\sin(\varphi+\alpha)}{\cos(\varepsilon-\alpha-\varphi)} \tag{14}$$

From the above analysis, the main factors affecting the effect of cleaning are the sieve and the centrifugal fan. Among them, the crank angular velocity affects the magnitude of the inertial and frictional forces. Airflow velocity and wind inlet angle affect the size of airflow resistance. The following orthogonal tests and response surface analysis were conducted on the effects of the three factors, wind inlet angle, airflow velocity and crank angular velocity, on the scavenging effect to determine the optimal combination of parameters.

Experimental design

Based on the analysis of the operating mechanism of the cleaning device of corn seed harvester, wind inlet angle A, airflow velocity B and crank angular velocity C were selected as the test factors. The experiment was conducted using Box-Behnken central combination design method with orthogonal test. The test factors and levels are shown in Table 1.

Table 1

Experimental factors and levels

levels	Factors		
	Wind inlet angle A	**Airflow velocity B**	**Crank angular velocity C**
	[°]	**[m/s]**	**[r/s]**
-1	30	8	4
0	40	12	6
1	50	16	8

As shown in Fig. 5, the test was conducted in Zibo City, Shandong Province, and the harvested corn variety was Zhengdan 958. The physical characteristics at harvest were as follows: the average moisture content of harvested seeds was 32.6%, the average moisture content of stalks was 91.2%, the average moisture content of fruit stalks was 52%, and the mass weight of 100 grains was 39-48 g.

Fig. 5 – Test site

As shown in Fig. 6, the test machine was 4YZL-6 self-propelled corn seed harvester, the size of the machine was 8800×4180×3850 mm, the rated power was 147 kW, and the number of harvested rows was 6. The implement forward speed was 2 km/h, and the flow of material was 60 kg/h. The maximum air volume of the fan of the cleaning device was 10 m^3/s. The amount of corn offcuts fed that the sieve can bear per unit area was 1.5~2.5 $kg/(s \cdot m^2)$. The cleaning device is shown in Fig. 7.

Fig. 6 – Self-propelled corn grain harvester

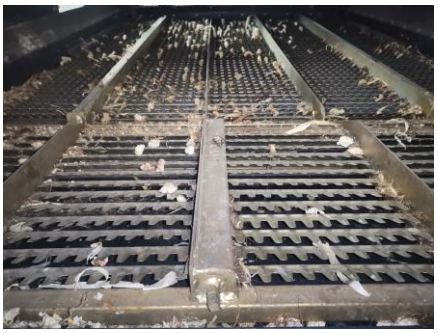

Fig. 7 – Cleaning device

The testing instruments include: tape measure, SN-DHS-20A intelligent moisture tester, electronic stopwatch, electronic balance, TEST0410-2 anemometer, Testo 465 optical tachometer and 3G3JZ-A4007 transducer. The test was conducted according to GB /T 21961-2008 *Test Methods for Corn Harvesting Machinery*. The speed of the harvester was 2.5 km/h during the test, and the average value was taken after each group of tests was repeated three times. Random samples were taken from the grain bins after the test, no less than 2000 g each time, and impurities were selected and weighed. The entire mixture was also collected in the assay area and the seeds were weighed according to the same method. Calculate the impurity rate Y_1 and loss rate Y_2 according to the following equation *(Chen et al. 2019; Geng et al., 2021)*.

Impurity rate Y_1:

$$Y_1 = \frac{w_1}{w_2 + w_1} \times 100\% \tag{15}$$

Loss rate Y_2:

$$Y_2 = \frac{w_3}{w_3 + w_4} \times 100\% \tag{16}$$

where, w_1 is the mass of impurities in the grain box sample, g; w_2 is the mass of seeds in the grain box sample, g; w_3 is the mass of seeds in the sample in the measurement area, g; w_4 is the mass of impurities in the sample in the measurement area, g.

RESULTS AND ANALYSIS

As shown in Table 2, the test protocol consisted of 17 sets of tests, and each set of tests was repeated three times to take the average value as the test results.

Table 2

The experiment results

Test number	Wind inlet [°]	Airflow velocity [m/s]	Crank angular [r/s]	Impurity rate %	Loss rate %
1	-1	-1	0	1.19	0.88
2	1	-1	0	1.31	0.73
3	-1	1	0	1.28	1.03
4	1	1	0	1.31	1.23
5	-1	0	-1	1.04	0.47
6	1	0	-1	1.27	0.49
7	-1	0	1	1.11	1.58
8	1	0	1	0.97	1.85
9	0	-1	-1	1.01	0.32
10	0	1	-1	1.05	0.67
11	0	-1	1	0.90	1.39
12	0	1	1	0.89	2.11
13	0	0	0	0.95	0.71
14	0	0	0	0.87	0.73
15	0	0	0	0.86	0.66
16	0	0	0	0.91	0.68
17	0	0	0	0.87	0.58

Analysis of variance

According to the test results in Table 2, ANOVA is performed on the impurity rate and loss rate. The non-significant items are excluded, and the results are shown in Table 3.

The regression equations of the impurity rate and loss rate are shown in Eqs. (17) to (18).

$$Y_1 = 0.89 + 0.03A - 0.063C - 0.093AC + 0.26A^2 + 0.12B^2 - 0.052C^2 \quad (17)$$

$$Y_2 = 0.67 + 0.22B + 0.62C + 0.095BC + 0.13A^2 + 0.16B^2 + 0.29C^2 \quad (18)$$

As can be seen from Table 3, the *P*-values for both the impurity rate and loss rate models were <0.01, indicating that the regression model was highly significant. Their coefficients of determination R^2 are 0.9848 and 0.9896, respectively, indicating that the changes in response values can be explained by models Y_1 and Y_2. The *P*-values of the model misfit terms for the impurity rate and loss rate were 0.8525 and 0.1561, respectively, which were greater than 0.05, indicating that the error generated by the test was small and the model was reasonable, and model Y_1 and Y_2 could be used to predict the trends of the impurity rate and loss rate.

Table 3

Variance analysis results of impurity removal rate

Source	Y_1					Y_2				
	Sum of Squares	DF	Mean Square	F Value	P Value	Sum of Squares	DF	Mean Square	F Value	P Value
Model	0.44	9	0.49	50.41	<0.0001	4.18	9	2.29	73.72	<0.0001
A	7.2×10^{-3}	1	7.2×10^{-3}	7.43	0.0295	0.041	1	0.041	2.29	0.1737
B	1.8×10^{-3}	1	1.8×10^{-3}	1.86	0.2150	0.37	1	0.37	59.38	0.0001
C	0.031	1	0.031	32.26	0.0008	3.11	1	3.11	493.99	<0.0001
AB	2×10^{-3}	1	2×10^{-3}	2.09	0.1914	0.031	1	0.031	4.86	0.0633
AC	0.34	1	0.34	35.34	0.0006	0.016	1	0.016	2.48	0.1593
BC	6.2×10^{-4}	1	6.2×10^{-4}	0.65	0.4482	0.036	1	0.036	5.73	0.0479
A^2	0.28	1	0.28	288.8	<0.0001	0.076	1	0.076	12.00	0.0105
B^2	0.063	1	0.063	65.50	<0.0001	0.11	1	0.11	17.43	0.0042
C^2	1.1×10^{-2}	1	1.1×10^{-2}	11.87	0.0108	0.36	1	0.36	56.78	0.0001
Residual	6.8×10^{-3}	7	9.7×10^{-3}			0.044	7	0.0063	3.03	
Lack of Fit	1.1×10^{-3}	3	3.7×10^{-3}	0.26	0.8525	0.031	3	0.010	73.72	0.1561
Pure Error	5.7×10^{-2}	4	1.42×10^{-3}			0.013	4	0.003		
Cor Total	0.45	16				4.22	16			

Note: P < 0.01 (extremely significant), 0.01 <P < 0.05 (significant).

Analysis of response Surface

From the analysis of variance of each index in Table 3, it can be seen that the interaction term that has a significant effect on the impurity rate is *AC*, and the interaction term that has a significant effect on the loss rate is *BC*, and the interaction of each factor is shown in Fig. 8.

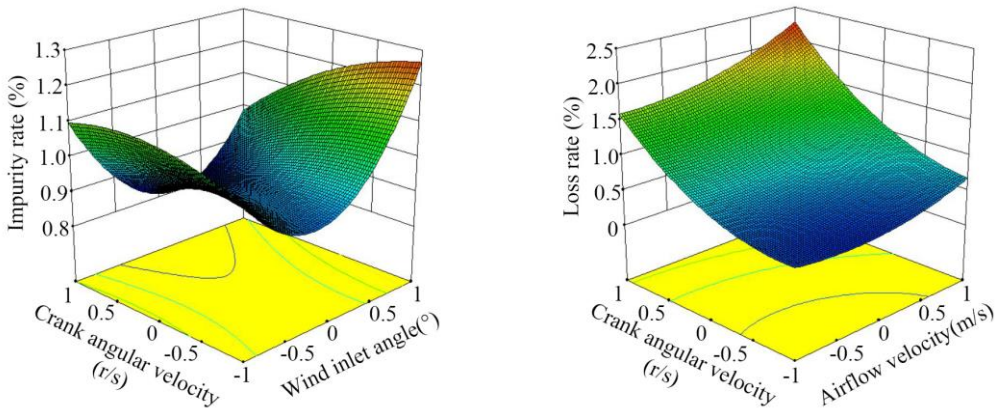

(a) Y_1=(A, 0, C) **(b) Y_2=(0, B, C)**

Fig. 8 – Response surface

Fig. 8a shows the effect of the interaction between the inlet wind angle and the crank angular velocity on the impurity rate when the wind velocity is fixed at 0 level. From the figure, it can be seen that the impurity rate decreases with the inlet wind angle and then rises rapidly. This is because when the inlet wind angle is too small, the angle between the airflow thrust and the sieve is too small, which will cause the debris to stick to the sieve surface, and it is difficult to blow the debris to the back of the sieve through the airflow. When the inlet wind angle is too large, the angle between the airflow thrust and the sieve is too small, which will cause the airflow to blow the debris upward. When the debris hits the shell of the cleaning device, the debris will fall back to the sieve surface and it is difficult to exclude the sieve from the device.

Fig. 8b shows the effect of the interaction between the airflow velocity and the crank angle velocity on the loss rate when the inlet wind angle is fixed at the 0 level. It can be seen from the figure that the loss rate increases with the increase of the crank angle velocity and the airflow velocity. This is because when the airflow velocity is larger, the airflow thrust is also larger and the corn kernels with slightly lighter mass will be thrown off the sieve surface. When the crank angle velocity is larger, the frequency of sieve vibration will be larger, and the corn seeds will be thrown away from the sieve surface more easily.

Parameter optimization and validation

To achieve the best harvesting performance of the scavenging unit, minimum impurity and loss rates are required. Parameter optimization was performed using Design-Expert 10.0 software with the objective function and the objective constraints and variable intervals shown in equation (19).

$$\begin{cases} \min\ y_1(A,B,C) \\ \min\ y_2(A,B,C) \\ s.t.\begin{cases} 30°<A<50° \\ 8m/s<B<16m/s \\ 4r/s<C<6r/s \end{cases} \end{cases} \tag{19}$$

The multi-objective optimization solution of each parameter was performed by Design-Expert10.0, and the optimized results were obtained as follows: the wind inlet angle was 37.95°, the airflow velocity was 11.3 m/s, the crank angular velocity was 4.1 r/s, corresponding to the impurity rate of 0.87% and loss rate of 0.34%.

Table 4

Test results of optimized parameter combination

Items	Impurity rate Y_1 /(%)	Loss rate Y_2 /(%)
Predicted value of model	0.87	0.34
Value of validation test	0.89	0.35
Relative error	2.29	2.94

To verify the accuracy of the model predictions of each indicator, a validation test was conducted in Zibo City, Shandong Province, in September 2022. The optimal combination of parameters obtained from the previous paper was used for the operational parameters, and three sets of parallel tests were designed, and the test results are shown in Table 4. Under the condition of optimal parameter combination, the impurity content of model verification test was 0.87% and the loss rate was 0.34%. The relative errors of each evaluation index and its model predicted value were 2.29% and 2.94%, which were less than 5%, and the parameter optimization results were reliable.

CONCLUSIONS

In this paper, the operating mechanism of the cleaning device of the corn seed harvester was studied. And the optimal operating parameters of the 4YZL-6 self-propelled corn seed harvester cleaning device were derived from the experiment. The specific conclusions drawn from this study are as follows:

1. The principle analysis of the cleaning operation and the force analysis of the operating process were carried out. The factors influencing the cleaning effect are the wind inlet angle, airflow velocity and crank angle velocity.

2. Field trials were conducted using the Box-Behnken test protocol. Wind inlet angle, airflow velocity and crank angle velocity were used as influencing factors, and impurity rate and loss rate were used as evaluation indicators. The optimization model of cleaning device parameters was established by ANOVA and response surface analysis, excluding the insignificant term. The optimal combination of parameters was obtained: the wind inlet angle was 37.95°, the airflow velocity was 11.3 m/s, and the crank angle velocity was 4.1 r/s. The corresponding impurity rate was 0.87% and loss rate was 0.34%.

3. Validation tests were conducted for the optimal parameter combinations. The results of the field validation tests were as follows: the impurity rate was 0.89% and the loss rate was 0.35%, and the relative errors of each index and the model predicted values were less than 5%.

ACKNOWLEDGEMENT

The work was supported by the High Efficiency and Low Loss Single Longitudinal Axial Flow Threshing and Separation Technology and Development of Intelligent Flexible Threshing Device, (Grant No.2021YFD200050204), and the Development of Intelligent Multifunctional Wheat Corn Grain Combine Harvester, (Grant No.2016YF026).

REFERENCES

[1] Buryanov A., Chervyakov I. et al. (2019) Using combines for cleaning grain crops by non-traditional technologies. *INMATEH – Agricultural Engineering*, Volume 59 / No.3 / 2019, pp. 27-32.

[2] Chai, J. (2021). *Design and Experiment of Countersink Screen in Cleaning Device of Maize Combine Harvester* (玉米联合收获机清选装置沉孔筛的设计与试验). Northeast Agricultural University.

[3] Cheng, C., Fu, J., Cen, Z., et al. (2019). Optimization Experiment on Cleaning Device Parameters of Corn Kernel Harvester (玉米籽粒收获机清选装置参数优化试验). *Transactions of the Chinese Society for Agricultural Machinery,* 50 (07):151-158.

[4] Cheng, C., Fu, J., Cen, Z. et al. (2021). Sieve blocking laws and stripping test of corn grain harvester (玉米籽粒收获机清选筛堵塞规律及脱附试验). *Journal of Jilin University,* 51(02):761-771.

[5] Feng, X. (2022) *Study on Working Mechanism and Structural Optimization Design of Cleaning Device in Maize Grain Combine Harvester* (玉米籽粒联合收获机清选装置的工作机理及结构优化设计研究). Northeast Agricultural University.

[6] Geng, D., Sun, Y., Li, H. (2021). Design and experiment of crawler corn harvester for sloping fields (履带式坡地玉米收获机设计与试验). *Transactions of the CSAE*, 37(13):11-19.

[7] Hou, C., Dong, Y., Liu, C et al. (2019) Industry Status and Quality Analysis of Domestic Maize Harvester (我国玉米收获机行业现状及质量分析). *Agricultural Engineering,* 2019, 9(06):20-25.

[8] Hou, J., Xie, F., Liu, D., et al. (2020). Research progress on air screen cleaning device for combined harvester (联合收获机风筛式清选装置研究进展). *Agricultural Engineering and Equipment,* 47(03):12-17.

[9] Han, M. (2020) *Study on the maize threshing and cleaning mechanism with low loss and anti-blocking and its linkage control* (玉米低损防堵脱粒清选机构及其联动控制研究). Jiangsu University.

[10] Kharchenko S., Kovalyshyn S., Zavgorodniy A., et al. (2019). Effective sifting of flat seeds through sieve. *INMATEH – Agricultural Engineering*, Volume 58 / No.2 / 2019, pp. 17-26.

[11] Li, H. (2022) *Research on Walnut Winnowing Based on CFD-DEM Coupling* (基于CFD-DEM耦合的核桃风选研究). Tarim University.

[12] Li, X., Du, Y., Niu, X., et al. (2020). Optimization Design and Experiment of Corn Cleaning Device (玉米清选装置结构优化设计与试验). *Transactions of the Chinese Society for Agricultural Machinery*, 51(S2): 233-242.

[13] Mu, P. (2020) *Research on High Net and Low Loss Cleaning Screen of Corn Grain Harvester* (玉米籽粒收获机械高净低损清选筛研究). Jilin University.

[14] Ren, D., Li, J., Nie, Y., et al. (2022) Design and Experimental Study on Air-suction Hazelnut Picking and Cleaning Machine (气吸式榛子捡拾分选机设计与试验). *Journal of Shenyang Agricultural University*, 53(02):177-186.

[15] Si, Z. (2017). *Design and Test of Multi - roller Combined Harvester Cleaning Device* (多滚筒联合收获机清选装置设计与试验). Jiangsu University.

[16] Tong, S., Shen, Q., Tang, N. et al. (2016). Numerical Simulation and Optimization Experiment of Mixed Flow Field on Longitudinal Axial Flow Cleaning Device (纵轴流清选装置混合流场数值模拟与优化试验). *Transactions of the Chinese Society for Agricultural Machinery*, 47(07):135-142.

[17] Vlădut N.-V., Biris S. St., Cârdei P., et al. (2022) Contributions to the Mathematical Modeling of the Threshing and Separation Process in An Axial Flow Combine. *Agriculture.* 2022, 12, 1520. https://doi.org/10.3390/ agriculture12101520.

[18] Wang, L., Ma, Y., Feng, X. et al. (2020). Design and Experiment of Segmented Vibrating Screen in Cleaning Device of Maize Grain Harvester (玉米籽粒收获机分段式振动筛清选装置设计与试验). *Transactions of the Chinese Society for Agricultural Machinery*, 51(09):89-100.

[19] Wang, Q., Wu, W., Zhu, H. (2018). Design and test of screw cleaning mechanism for corn (玉米螺旋式清选装置的设计与试验). *Transactions of the CSAE*, 34(20): 12-19.

[20] Wang, Y. (2022). *Design of the Cleaning Device for the Peanut Combine Harvester and performance studies* (花生联合收获机清选装置的设计与性能研究). Hebei Normal University of Science & Technology.

[21] Xu, L., Li, Y., Li, Y., et al. (2019) Research progress on cleaning technology and device of grain combine harvester (谷物联合收获机清选技术与装置研究进展). *Transactions of the Chinese Society for Agricultural Machinery*, 50(10): 1-16.

[22] Zheng, Z. (2020). *Simulation Study on the Properties of Collision between the Maize Particles in the Harvest Screening Process* (玉米收获清选中籽粒碰撞特性研究). Northeast Agricultural University.

SIMULATION AND DESIGN ON AIRFLOW DISTRIBUTION CHAMBER OF PNEUMATIC SEED METERING DEVICE
/
气力输送式排种器流场模拟与气流分配室结构设计

Zuoli FU*, Zhiqi ZHENG, Guichuan LI, Yuxiang HUANG, Ruixiang ZHU, and Jinpu HE[1]
Northwest A&F University College of Mechanical and Electronic Engineering, Shaanxi Yangling 712100, China;
Tel:+86 18729045993; E-mail: fuzuoli@nwsuaf.edu.cn
DOI: https://doi.org/10.35633/inmateh-68-22

Keywords: *Seeding, Pneumatic Forming Machine, Computational Fluid Dynamics (CFD), Design*

ABSTRACT
The pneumatic conveying metering technology is used to enhance the filling and clearing capacity of the seed metering device by forming a rotary air flow field inside the airflow distribution. The simulation test results show that the increase of the number of fan blades, the velocity of flow field at different outlets of the seed cleaning area decreases linearly, but the average velocity basically remains unchanged. The flow field velocity in the seed filling area decreased significantly with the increase of fan angle, and the difference between seed filling area and clearing area remains unchanged. When the blade angles in the filling area are the same, the fan blades size has no effect in flow field velocity.

摘要
提出气力输送式排种技术，在排种器内形成旋转气流，增强吸种和清种能力，设计了一种以气流分配室为核心的风送式排种器。试验结果表明随着气流分配室中扇叶数量的增加（7 叶-10 叶）清种区的平均速度呈线性下降趋势，清种区的平均速度保持不变；冲种区速度随着扇叶角度的增加而明显降低，但是冲种区与清种区平均速度差不变，当冲种区扇叶角度一直时，速度与扇叶大小无关。

INTRODUCTION
The seed metering device is an important part of the seeder, and its performance affects the operation quality of the seeder (*Zhai et al, 2016; Zhang et al., 2016*). Pneumatic seed metering device which depends on air suction or pressure can be used directly to seed for improving the success rate in filling and clearing (*Zang et al, 2015; Yuan et al., 2008*). Compared to the mechanical seed metering, the pneumatic seed metering device has advantages in high seeding and adaptation to seeds. So far, it has been applied widely to the seeder for corn, rice, rape and so on (*Cong et al, 2014; Han et al., 2022; Hu et al., 2012; Pasha et al., 2016; Markauskas et al., 2010; Cao et al., 2013; Li et al., 2013*).

The computational fluid dynamics (CFD) and high-speed photography are used to realize the technology upgrade and structural optimization of seed metering device (*Cao et al, 2015; Wang et al., 2021; Hou et al., 2020; Zhang et al., 2015*). Zhang Ying has monitored the process of clearing seeds by high-speed photography, and the technology of active retaining structure was proposed to improve the precision of the seeder (*Zhang et al., 2022*). On the other hand, Li has simulated the flow field of seed metering device of rice, through the bench experiment, optimized the structure of air distribution chamber, and then improved the performance of seed metering (*Chen et al., 2022; Ma et al., 2020; Liu et al., 2012*).

In summary, most studies about structural optimization of pneumatic seed metering device was based on traditional device, and there are little studies on the new structures and new methods. A new study on the pneumatic forming device for seeds has attracted more and more attention. The seed flow is formed in the seed metering device and seed drop tube, through the transportation of air. The clearing capacity of the seed metering device and the precision of seeding are greatly improved.

This study designed a special flow field forming technology inside the device. Through both forward and reverse blades laying out in the area of filling and cleaning seed, the flow parameters of air will change. The negative pressure (-) is close to the filling area, and nearby the cleaning area, the pressure is higher (+). Meanwhile, a part of the flow passes through the area of cleaning with seed, therefore, it can transport the seed outside the device. The theoretical analysis, simulation analysis and the bench experiment of the pneumatic forming device have been completed with both forward and reverse blades. The results show that the structure and number of blades had significant effect on the flow parameters.

[1]*Zuoli Fu, Ph.D. Eng.; Zhiqi Zheng, Ph.D. Eng.; Guichuan Li, M.S. Stud. Eng.; Yuxiang Huang, Prof Ph.D Eng.; Ruixiang Zhu, Prof M.S. Eng; Jinpu He, M.S. Eng.*

MATERIALS AND METHODS

The structure of the pneumatic forming device

The pneumatic forming device includes seed case, forming machine, seed metering wheel and so on, as shown in Fig. 1. The useful flow field is generated inside the forming machine for seed filling and cleaning by installing different numbers of both forward and reverse blades.

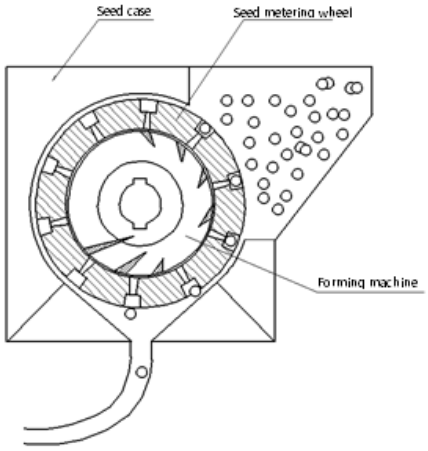

Fig. 1 - Structure of pneumatic forming device

The air flow from the fan enters into the forming machine along tangential direction and forms rotary flow filed. In the function of both forward and reverse blades, the area of negative pressure and high pressure are formed inside the forming machine. When the air flow passes through the forward blades in the forming machine, the negative pressure will be formed nearby the seed filling area, so the suction force on seed is forming, which can improve the filling capacity. When the flow passes through the reverse blades in the forming machine, the high pressure will be formed nearby the cleaning area, so the forming force on seed is forming, which can improve the cleaning capacity.

Principle of the forming machine

The seed flow passes through the seed drop tube quickly, without the impacting between seed and tube, which improves the precision of seeding. At the end of the seed drop tube, the separating device was designed so that the seed would not be blown out of the seed bed. With rotation of the seed metering wheel, it is helpful for seed filling in the function of negative pressure, and seed cleaning in the function of high pressure in the seed metering device.

As shown in Fig. 2, the flow in the forming machine is passing through both forward and reverse blades. The negative pressure will be formed in the function of forward blades near the filling area. And when the flow passes the reverse blades, the high pressure will be formed between blades, which is helpful for seed cleaning.

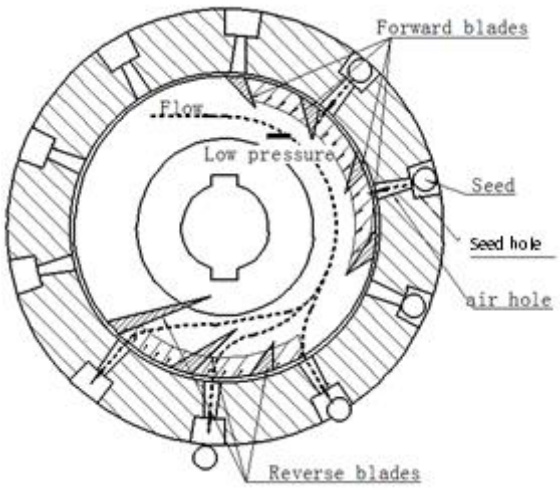

Fig. 2 - The flow in the forming machine

Therefore, the useful flow is mainly determined by the structure of forward blades and reverse blades, including the number and degree of blades, the distance between adjacent blades, and the size of air hole. Fig. 3 shows that the seeds in the filling area are pressed into the seed hole through force effect (F_x), which is formed by the negative pressure.

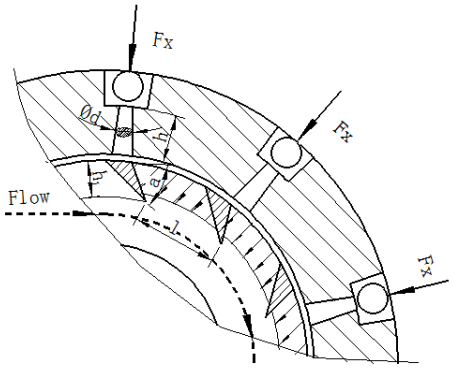

Fig. 3 - The force analysis about seed in the function of flow

As shown in Fig. 3, when the inlet flow parameters are kept invariable, the force in the function of flow is determined by the structure of blades and air hole. Therefore, the Strength of negative flow is related to the height of blade (h_1), the degree of blade (a) and the distance between adjacent blades (l). Meanwhile, the capillary effect will be formed when the flow is passing through the air hole, and the length and diameter (h and d) of the air hole will directly affect the force (F_x) acting on the seed. The parameters of blades and air hole are shown in Table 1.

Table 1

The parameters of blades and air hole

Project	Parameters	Symbol
Blades	Height /mm	h_1
	Degree /°	a
	Distance /mm	l
Air hole	Diameter /mm	d
	Length /m	h

The seed is pressed into the seed hole in the function of negative pressure, and the force is Fx,

$$F_x = P\,{\pi d^2}/{4} - F_{ds} \quad (1)$$

where: F_{ds} is the pressure loss, N; p is the flow pressure intensity, Pa; d is diameter of air hole, m.

The flow velocity has a decisive role on the formation of pressure intensity. When the flow passes through the forward blades with a blade angle, the velocity will decrease.

Simulation and analysis of the flow in the forming machine

The 3D model of the forming machine was built by SOLIDWORKS, and the mesh was generated by GAMBIT. As shown in Fig. 4, the fluid was defined in the blades and the middle area of the forming machine, the surface of the model was wall in soft. The inlet was set at the first forward blade, and the outlet was set at the other blades. The flow could pass through between the blades and the middle of the model in order to form the rotational flow.

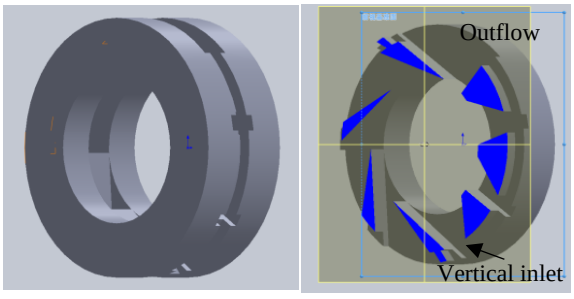

Fig. 4 - The 3D model of forming machine

SIMPLE was used to couple calculation. And air was selected to the flow, which density is 1.29 kg/m^3, and 1.85×10^{-5}Pa.s is for viscosity. The wall is stationary and no slip. Flow velocity is 4 m/s at the vertical inlet and is perpendicular to the face of the inlet. The first blade is inlet, and the others are outlet, which are outflow. The residual precision is10^{-4}.

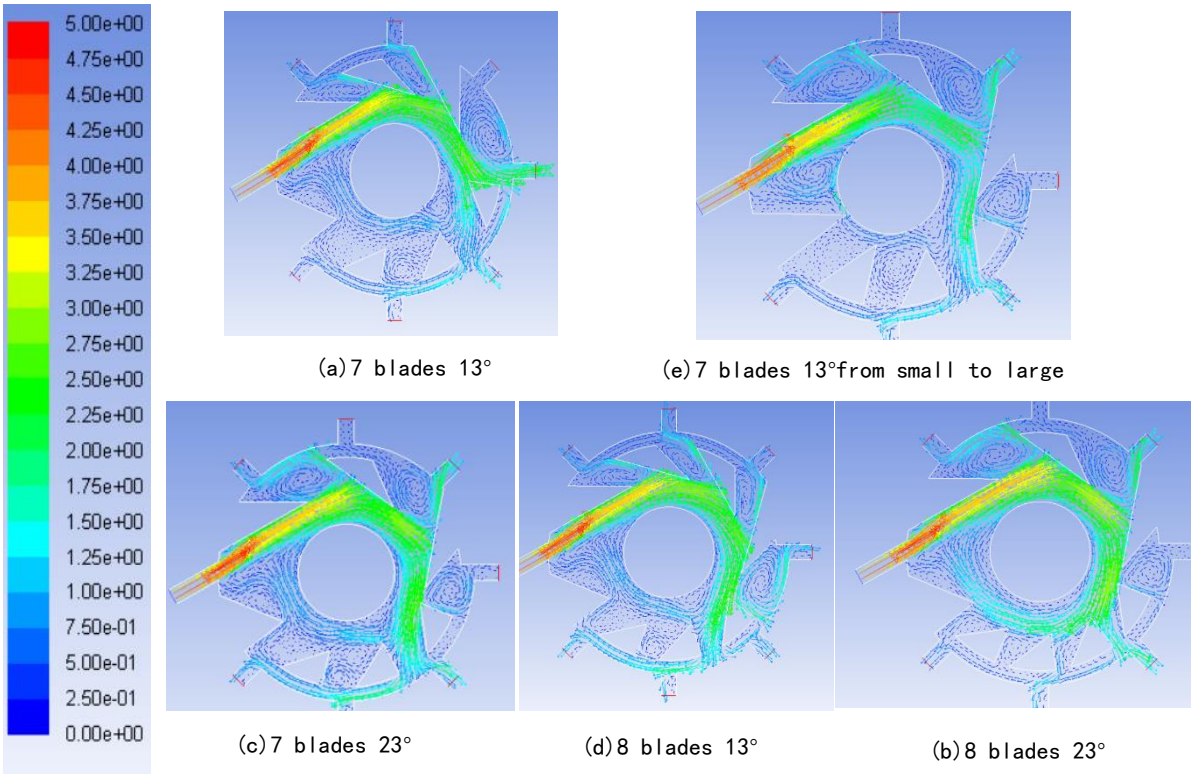

Fig. 5 - The speed vector of different blade structure parameters

Fig. 5 and Fig. 6 show the flow section of the forming machine in different structure parameters of blades, which include the number of blades (7, 8, 10), the angle of blades (10°, 13°) and the size of blades (from big to small). The speed ranges from 0 to 15 m/s.

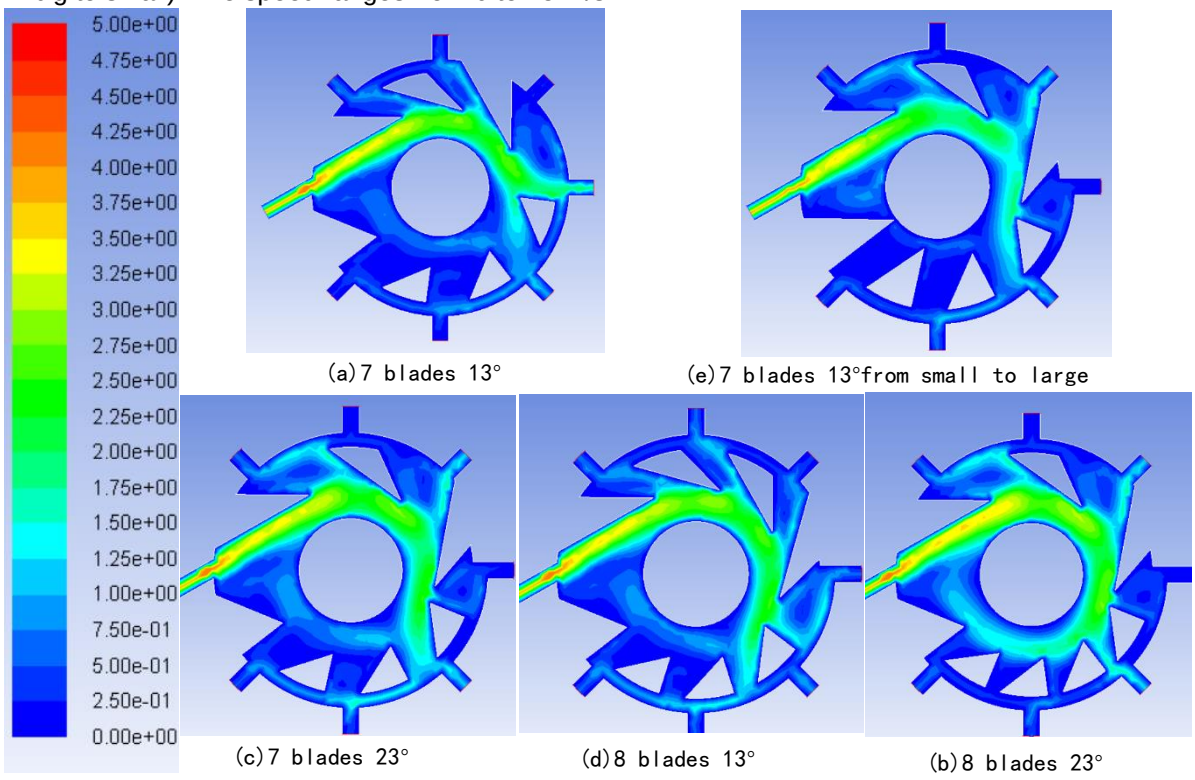

Fig. 6 - The speed cloud of different blade structure parameters

The flow entered into the forming machine from the first forward blades, and rotational flow field was forming in the circular inside.

The flow speed is from 0.7 m/s to 5m/s in the area of forward blades, and the maximum speed was present at the top of the blades, where the hydraulic diameter of the forming machine was the smallest.

The flow speed has a large span in the area of reverse blades, and in the first blade is larger than the others. From fig (c), (d) and (e), the speed in the area of first blade is becoming smaller and smaller when the number of blades is higher.

Two axial symmetric rotational flows with low speed were formed in the middle of the forming machine. At the bottom of the blades, the distance of adjacent blades is smaller and smaller, the speed of the flow increases gradually, and the low pressure forms in the forward blades and the high pressure forms in the reverse blades.

The bench experiment of forming machine

The experimental device is shown in Fig. 7, including the computer, the forming machine, the fan, and the flow velocity sensor, in which, the forming machine was manufactured by 3D printer, the type of speed sensor is AW with a range of 1-10 m/s, and the fan is FH6250 from FEIKE with the precision of 0.05 m/s.

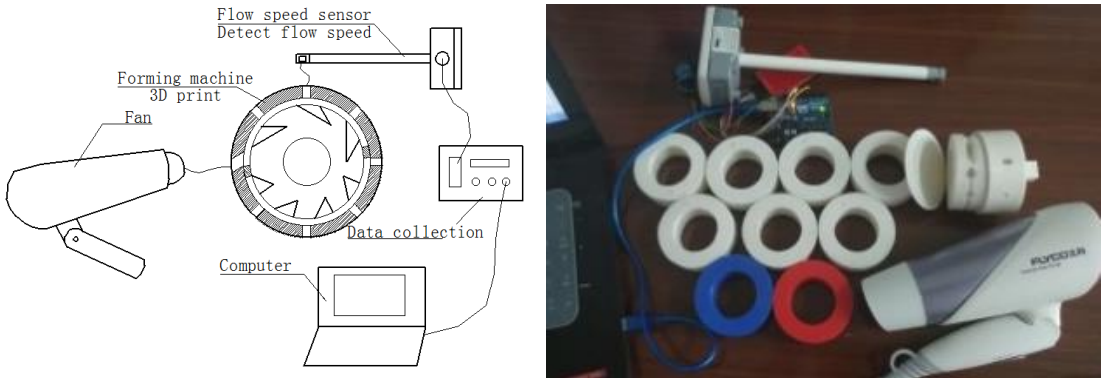

Fig. 7 - The sketch and physical figure of the experiment equipment and program

The different number and arrangement of fan blade structures are used as experiment factors, the parameter of the experiment is the flow velocity at the outlets of the forming machine. Each experiment is repeated three times. As shown in table 2, five different fan blade structure parameters were designed in the experiment.

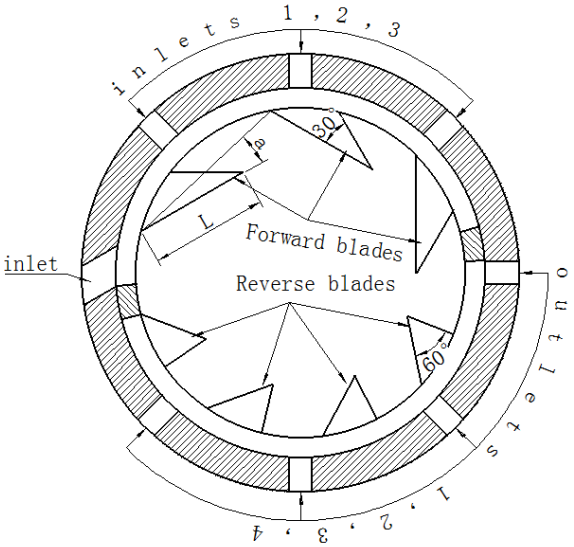

Fig. 8 - Air outlets and inlets numbers of the forming machine

The air outlet number is shown in Fig. 8. During the experiment, the outlet flow velocity is detected by the sensor.

Table 2

Design of experimental factors

The number	blade structure parameters
1	7 blades, 13°
2	7 blades, 23°
3	8 blades, 13°
4	8 blades, 23°
5	7 blades, 13° (from small to large)

RESULTS

The single factor experiment results and analysis

(1) The influence of the number of blades on flow speed

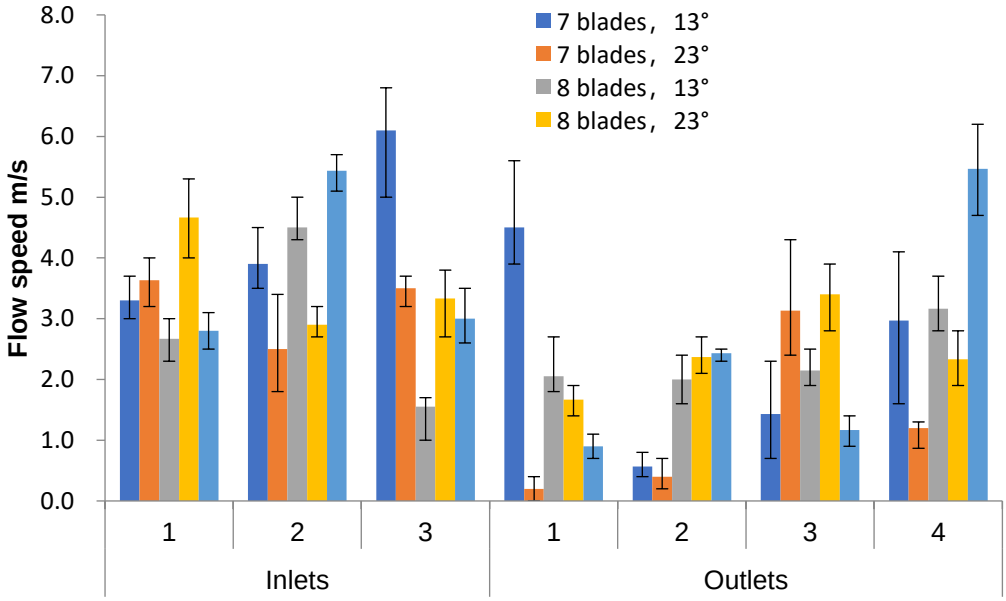

Fig. 9 - The flow speed of measuring point under the condition of different structural parameters of blades

As shown in Fig. 9, the average flow velocity is 4.4 m/s and 2.4 m/s respectively at the inlets and outlets. The closer to the outlet, the greater the speed of the flow, which is basically a linear distribution. It shows that under the function of the forward blades, the negative pressure was generated at the inlets of the forming machine, and the positive pressure was generated at the outlets.

As the flow is formed inside the forming machine, the speed gradually decreases, the negative pressure effect is weakened. When the blade angle is 13°, as the number increases, the average flow velocity is 4.4, 3.6 and 2.9 m/s respectively at the outlets, at the same time, the speeds at the inlets are 2.4, 2.4 and 2.3 m/s respectively. It shows that as the number of blades increases, more flow will pass through the seeding area (inlets) and will be discharged from the cleaning area (outlets). This is because the number of blades at the inlets is increased, and the distance between the two fan blades becomes smaller, which will be covered by more blades, and it is easier to form negative pressure, which is consistent with the theoretical analysis. The special result is that when the blade angle is 13°, when the number of blades is 7, the flow velocity of the nearest inlet is much higher than the other number blades.

(2) The influence of the blade angle on flow velocity

As shown in Fig. 10, the flow velocity at the inlets and outlets is measured, when the number of blades is 7, and the blade angle is 13° and 23° respectively.

In general, the angle of the blade has little effect on the flow velocity at inlets and outlets. However, the increase in the angle of adjacent blades will weaken the negative pressure in the filling area, which will reduce the flow velocity at the inlets. Therefore, increasing the angle of the blades can reduce the absolute flow velocity in the filling area.

(3)The influence of the order of blade on flow velocity

As shown in Fig. 11, the flow velocity at the inlets and outlets is measured, when the number of blades is 7, and the blade angle is 23°, and the order of blades is from small to large and the size of blades is average respectively.

The experiment results show that when the size of the blade is average, the average speeds of the inlets and outlets are 3.7 and 2.4 m/s, respectively. And when the size of the blade is from small to large, the average speeds of the inlets and outlets are 4.4 and 2.5 m/s, respectively. When the blades are arranged in different order, the flow velocity at the inlets varies greatly, increasing by about 18.9%, and there is little difference in speed at the outlets. The reason is that when the inlets blades are arranged from large to small, the size of the fan blade at the end is small, which causes the inlet to be blocked by the blade and the area is too small to generate sufficient negative pressure. Therefore, the highest flow velocity of the No. 4 air outlet is up to 5.5 m/s. As a result, the average flow velocity of the air outlets increases when the size of the blade is from small to large.

In summary, increasing the number of fan blades, the average flow velocity in the cleaning area is approximately linearly reduced, and the average flow velocity in the filling area remains basically unchanged. Increasing the angle of the blades has little effect on the flow velocity difference on the filling and the cleaning operations, but it can reduce the absolute flow velocity. When the blades are arranged in order from large to small, the average flow velocity in the cleaning area decreases.

Experiment results and analysis of multiple factors

Orthogonal experiment with interaction is used to verify the influence of various factors and their interaction on the flow field formation. The experiment factors are the number, angle and arrangement order of the blades. The experiment parameter is the average flow speed at the inlets and outlets. The experiment can get the significance of the influence of each factor on the parameter. The experiment design is shown in Table 4.

Table 4

Multifactor experiment design

factors		A Number	B Angle/°	C Arrangement order
Level	1	7	8	Small to large
	2	8	10	Large to small
	3	10	13	Average

The three-factor orthogonal experiment with interaction is designed through SPSS. The significance analysis of each factor was carried out according to the experiment results, and the results are shown in Table 6. It can be seen from the table that the number of blades, and the interaction between the number and the angle of the blades (AB) have a significant impact on the flow speed of inlets and outlets. Other factors are not significant.

According to the impact on the parameter, the order from largest to smallest is the number of blades, the interaction of the number and angle of the blades, the interaction of the angle and arrangement order of the blades, the arrangement order of the blades, the interaction of the number of blades and the arrangement order, and the angle of blades. Table 5 shows the significance experiment analysis.

Table 5

The variance analysis

Project	Mean square sum	df	Mean square	F	Significance
Modle	4.770[a]	12	0.398	5.238	0.040
A	4.014	2	2.007	26.449	0.002
B	0.034	2	0.017	0.227	0.805
C	0.168	2	0.084	1.105	0.400
AB	0.241	2	1.21	15.89	0.029
AC	0.081	2	0.041	0.534	0.616
BC	0.231	2	0.116	1.523	0.304
Error	0.379	5	0.076		

a. decisive factor = 0.926

CONCLUSIONS

(1) Using the pneumatic conveying metering technology, designed a seed metering device with forming machine. The simulation results show that the filling and clearing ability of the 7 blade 10° forming machine is better than that of other groups of blade structure parameters.

(2) When the blade angle is 10°, as the number increases from 7 blades, 8 blades to 10 blades, the average flow speed of the outlets (cleaning area) is close to linear distribution, and the inlets (seeding area) is basically unchanged. It shows that as the number of blades increases, more flow will pass through the filling area and be discharged from the cleaning area.

(3) Increasing the angle of the blade (10°, 13°) has little effect on the flow rate difference between the filling area and the cleaning area, but it can reduce the absolute flow speed.

(4) When the blade angles in the filling area are the same, the speed has nothing to do with the arrangement order of the blades, but the speed distribution of the cleaning area is related to the size of the blade at the end of the cleaning area. As the size decreases, the speed in the cleaning area increases. The experiment results show that when the blade size is reduced by half, the flow speed increases by about 18.9%.

ACKNOWLEDGEMENT

The authors thank the editing team of Editor Bar for improving the English language fluency of our paper. The work in this paper was supported by the Key Research and Development Program of Shaanxi Province (No.2019NY-175).

REFERENCES

[1] Cao Chengmao, Qin Kuan, Wang Anmin, Sun Yan, Zhou Min, Li Weiya, (2015). Design and Experiment on Rice Hill Seeder with Air-blowing Special Hole and Scoop-wheel (水稻直播机气吹辅助勺轮式排种器设计与试验). *Transactions of the Chinese Society for Agricultural Machinery*, Vol. 46, pp. 66-72, Guangdong/China.

[2] Chen Jin, Yan Yuqiang, Zhang Xuedong, Liu Rui, (2022). Design of control system of speed metering device test-bed based on fuzzy PID (基于模糊 PID 的排种器试验台控制系统设计). *INMATEH-Agricultural Engineering*, Vol. 67, pp. 509-524, Bucharest/Romania.

[3] Cong Jinling, Liao Qingxi, Cao Xiuying, Liao Yitao, Yu Jiajia, Wang Lei, (2014). Seed filling performance of dual-purpose seed plate in metering device for both rapeseed & wheat seed (油菜小麦兼用排种盘的排种器充种性能). *Transactions of the Chinese Society of Agricultural Engineering*, Vol. 30, pp. 30-39, Hubei/China.

[4] Han Jie, Zhuang Yajun, Liu Zeqi, Jin Yachen, Chen Yulong, (2022). Experimental research on performance of multi-mode seed metering device (多模式排种器作业性能实验研究). *INMATEH-Agricultural Engineering*, Vol. 67, pp. 251-258, Bucharest/Romania. https://doi.org/10.35633/inmateh-67-25 https://doi.org/10.35633/inmateh-67-50

[5] Hou Z.W., Dai N.Z., Chen Z., (2020). Measurement of physical parameters of wheatgrass seed and calibration of discrete element simulation parameters (冰草种子物性参数测定与离散元仿真参数标定). *Journal of Agricultural Engineering*, Vol. 36, pp. 46-54, Beijing/China.

[6] Hu W.J., Xia J.F., Zhou Y., Luo C.M., Zhou M.K., Liu Z.Y., (2022). Measurement and Calibration of the Discrete Element Parameters of Coated Delinted Cotton Seeds [J]. *Agriculture*, Vol. 12, pp. 286-294.

[7] Li Ming, Liu Xiaohui, Liao Yitao, Liao Qingxi, (2013). Pneumatic Cylinder-type Centralized Precision Metering Device for Rapeseed (气力滚筒式油菜精量集排器). *Transactions of the Chinese Society for Agricultural Machinery*, Vol. 44, pp. 68-73, Hubei/China.

[8] Liu Jia, Cui Tao, Zhang Dongxing, Yang Li, Shi Song, (2012). Mechanical-pneumatic Combined Corn Precision Seed metering Device (机械气力组合式玉米精密排种器). *Transactions of the Chinese Society for Agricultural Machinery*, Vol. 43, pp. 43-47, Henan/China.

[9] Liu Junjie, Yang Cunzhi, Yang Xu, Xiang Jianting, Cong Peijun, (2015). Performance Analysis of Maize Precision Seed Metering Device and Contrast Test (玉米精量排种器性能分析与对比试验). *Agricultural Science & Technology and Equipment*, pp. 44-47, Henan/China.

[10] Liu, Yueqin; Zhao, Manquan; Hu, Yongwen, (2012). Finite element analysis of airflow field for vacuum chamber in air-suction seed metering device of no-till seeder. *International Conference on Applied Mechanics and Materials*. Sanya, China, Vol. 12, pp. 24-25, Guangdong/China.

[11] Ma W.P., You Y., Wang D.C., (2020). Parameter calibration of alfalfa seed discrete element model based on RSM and NSGA-Ⅱ (基于 RSM 和 NSGA-Ⅱ的苜蓿种子离散元模型参数标定). *Journal of Agricultural Machinery*. Vol. 51, pp. 136-144, Beijing/China.

[12] Markauskas D., Kacianauskas R., Dziugys A., (2010). Investigation of adequacy of multi-sphere approximation of elliptical particles for DEM simulations [J]. *Granular Matter*, Vol. 12, pp. 107-123, Vilnius/Lithuania.

[13] Mei Ting, XieFangping, Li Xu, Wang Xiushan, Mao Licheng, (2014). Adaptability experiment on pneumatic metering device for small-sized seeds (小粒径作物种子气力式排种器适应性试验). *Journal of Hunan Agricultural University (Natural Sciences)*, Vol. 02, pp. 216-220, Hubei/China.

[14] Pasha M., Hare C., Ghadiri M., (2016,). Effect of particle shape on flow in discrete element method simulation of a rotary batch seed coater [J]. *Powder Technology*, Vol. 296, pp. 29-36, Leeds/UK.

[15] Wang Yingbo, Li Hongwen, Wang Qingjie, He Jin, Lu Caiyun, Yang Qinglu, Liu Peng, (2021). Experiment and parameter optimization of seed distributor of mechanical shooting seed metering device (机械排种器排种器的试验与参数优化). *INMATEH-Agricultural Engineering*, Vol. 63, No. 1, pp. 29-40, Bucharest / Romania https://doi.org/10.35633/inmateh-63-03.

[16] Wu M.C., Cong J.L., Yan Q., (2020). Calibration and Experiment of Discrete Element Simulation Parameters of Peanut Seed Particles (花生种子颗粒离散元仿真参数标定与试验). *Journal of Agricultural Engineering*, Vol. 36, pp. 30-38, Beijing/China.

[17] Xing He, Zang Ying, Cao Xiaoman, Wang Zaiman, Luo Xiwen, Zeng Shan, Huang Miao, (2015). Experiment and analysis of dropping trajectory on rice pneumatic metering device (水稻气力式排种器投种轨迹试验与分析). *Transactions of the Chinese Society of Agricultural Engineering*, Vol. 31, pp. 23-30, Guangdong/China.

[18] Zhai Jianbo, Xia Junfang, Zhou Yong, (2016). Design and Experiment of Pneumatic Hybrid Rice Precision Hole Direct Seed Metering Device (气力式杂交稻精量穴直播排种器设计与试验). *Transactions of the Chinese Society for Agricultural Machinery*. Vol. 41, pp. 75-82, Guangdong/China.

[19] Zhang Jing, Li Zhiwei, Liu Haochun, Wu Gang, (2016). Mathematical modelling and validation of seeder's suction-boundary on pneumatic-roller type metering (气力滚筒式排种器种子吸附边界模型及验证). *Transactions of the Chinese Society of Agricultural Engineering*, Vol. 32, pp. 12-20, Hubei/China.

[20] Zhang Shun, Xia Junfang, Zhou Yong, ZhaiJianbo, Guo Yangmin, Zhang Xiumei, Wu Hao, (2015). Design and experiment of pneumatic cylinder-type precision direct seed metering device for rice (气力滚筒式水稻直播精量排种器的设计与试验). *Transactions of the Chinese Society of Agricultural Engineering*, Vol. 31, pp. 11-19, Guangdong/China.

[21] Zang Ying, Xing He, Wang, Zaiman, Luo Xiwen. Cao Xiaoman, Wang Baolong, (2015). Design and Experiment of Shield Device on Rice Pneumatic Metering Device (水稻气力式排种器挡种装置设计与试验). Transactions of the Chinese Society for Agricultural Machinery, Vol. 46, pp. 33-38, Guangdong/China.

RESEARCH ON AGRICULTURAL VEHICLE SAFETY WARNING SYSTEM BASED ON LIDAR

/

基于激光雷达的农业车辆安全预警系统研究

Weiyu KONG [1),2)], Guangrui HU [1)], Shuo ZHANG [1)], Jianguo ZHOU [1)], Zening GAO [1)], Jun CHEN *[1)]

[1)] College of Mechanical and Electronic Engineering, Northwest A&F University, Yangling 712100, China;

[2)] AVIC Zhonghang Electronic Measuring Instruments Co.,ltd., Xi 'an 710119，China

Tel: +86 13572191773; E-mail: chenjun_jdxy@nwsuaf.edu.cn

DOI: https://doi.org/10.35633/inmateh-68-23

Keywords: *Agricultural vehicle, Lidar, Safe distance, Pre-warning*

ABSTRACT

Intelligent agricultural vehicles have been widely used in the process of farming and harvesting in the field, which has brought great convenience to agricultural production. However, there are also safety issues such as accidental collision of agricultural vehicles or other agricultural machinery during operation. The use of sensing technology for the timely and accurate detection and pre-warning of obstacles during the operation of agricultural machinery is critically important for ensuring safety. In this paper, a two-dimensional Lidar is used to detect obstacles in front of tractors with the Density-Based Spatial Clustering of Applications with Noise (DBSCAN) algorithm and the Minimum Cost Maximum Flow algorithm (MCMF). A method to judge whether the obstacle is static or dynamic and a classification model of different security warning levels for obstacles in different states is proposed. Actual vehicle tests were conducted, with static obstacles tested repeatedly, and dynamic obstacles tested at different directions and speeds. The results showed that the overall average warning accuracy rate is 90.5%. Prediction results were robust for obstacles in different states, indicating that this system is able to ensure the safety of agricultural vehicles during their operation and promoted the development of agricultural mechanization.

摘要

智能化农业车辆在田间耕作和收获过程中已广泛使用，给农业生产带来了极大地便利。然而，还存在着在作业过程中农业车辆误撞人或其他农业机械等安全问题。利用传感技术，及时、准确地对作业农业车辆周围的障碍物进行检测和预警就有着重要的作用和意义。本文利用二维激光雷达，结合 DBSCAN 点云聚类算法和最小费用最大流算法对障碍物进行检测和追踪，提出了判断障碍物状态的方法并对不同状态的障碍物提出对应的安全预警级别划分模型。最后进行了实车试验，对静态障碍物进行了多次重复试验，对动态障碍物进行了不同方向不同速度的多次重复试验，整体的预警准确率均值为 90.5%。试验结果表明对不同状态的障碍物均取得了良好的预警效果,推动了农业机械化事业的发展。

INTRODUCTION

With the continuous development of electronic control technology and sensing technology, the degree of automation and intelligence of agricultural machinery and equipment has been continuously improved rapidly. Drones equipped with sensors can estimate crop yields (*García-Martínez et al., 2020*) and electric vehicles work together to harvest (*Loukatos et al., 2021*). They all have brought a lot of convenience to agricultural production. However, accidents frequently occur during the operation of agricultural vehicles. For example, accidents in which tractors collide with obstacles, people, or animals during their operation in the field can be fatal, damage agricultural vehicles, and lead to significant economic losses. The safety production of agricultural vehicles is thus critically important.

Several studies have examined the anti-collision safety pre-warning system in the automotive field. *Jeong et al.* proposed a safety warning information system that can provide warning messages about impending dangers by using a networked vehicle environment, thereby increasing the driver's attention (*Jeong et al., 2015*). Liu et al. proposed a pre-warning algorithm for the vehicle collision avoidance time based on vehicle speed. The algorithm sets different safe collision avoidance times according to different vehicle speeds. Furthermore, it judges whether warnings are needed by comparing the safe collision avoidance time with the time required for the vehicle to collide (*Liu et al., 2017*).

Tak et al. studied a new type of collision warning system that describes the vehicle movement handled by the roadside unit. The proposed collision warning system based on segment information overcomes the limitations of existing collision warning systems (*Tak et al., 2020*). The above research environment is the urban road traffic environment. They all need to install sensors on the vehicle and the vehicle being detected to obtain its information and make an early warning. In the farmland environment, the types of obstacles that appear are random, and may be people or livestock, not necessarily other agricultural vehicles, so they are not suitable for farmland environments.

Few studies have examined anti-collision and safety pre-warning systems in the context of agricultural production and agricultural vehicles. Zhao studied the BDS-based cross-border system for agricultural vehicles involved in soil preparation operations. Guo et al. designed a hierarchical cross-border early warning system with cross-border prediction function. Zhu et al. studied the rollover warning of heavy vehicles (*Zhao, 2019; Guo et al., 2019; Zhu et al., 2011*). Kubota Corporation of Japan developed a classification for the dangerous warning areas for its smart tractors, but the relationship between moving objects and the tractor has not been considered, which has likely caused some unnecessary alarms. Kapilan's research involves automatic accident alerts in the event of a vehicle accident. Once a specific vehicle has an accident, the proposed system will detect it and immediately send an alert containing the required information to a certain registered number (*Kapilan et al., 2020*). It can be seen that the research on the safety early warning of agricultural vehicles is still lacking.

In addition, environmental information perception is an indispensable and important link in the safety early warning system. Perceiving the surrounding environment not only requires detecting obstacles but also tracking and predicting the trajectory of dynamic obstacles. MCMF algorithm has also been widely used in wireless network control load, large-scale resource scheduling, and multi-target tracking (*Sun et al., 2014; Chen et al., 2017; Liang et al., 2019*). It achieved good results, solved the problem of finding the optimal path in the network structure, and can be used to track objects in the point cloud of the Lidar. Cao et al. improved DBSCAN to improve the accuracy of multi-radar perception of the environment of autonomous vehicles (*Cao, Wang, 2016*), However, multiple radars are used and the cost is high.

Asvadi et al. used only a three-dimensional radar and positioning and navigation equipment to detect common static and dynamic obstacles in the urban road environment, and the test results verified the feasibility of this method (*Asvadi et al., 2016*). However, the large amount of 3D Lidar data requires high performance of the processor, which results in high costs and does not meet the requirements of agricultural production. Campos et al. used the machine vision system on the tractor driving in the corn field to detect unexpected obstacles or elements in the video sequence, but this method requires higher ambient light (*Campos Y. et al., 2016*). Corno proposed an adaptive positioning system based on ultrasonic car sensors for the autonomous navigation of agricultural tractors in vineyards, but the accuracy of ultrasonics will change under the influence of temperature (*Corno et al., 2021*). Therefore, two-dimensional Lidar is used to detect obstacles in the farmland environment.

Therefore, in view of the characteristics of the field environment where agricultural vehicles are operating, this paper proposes a two-dimensional Lidar-based classification algorithm for agricultural vehicle safety warning levels. It takes into account the randomness of obstacles movement in the farmland environment. A system is then designed and tested to verify its warning accuracy and assess its applicability. The aim of this system is to reduce the occurrence of accidents during the operation of agricultural vehicles to ensure the safety of production personnel and production equipment as well as promote the development of agricultural mechanization.

MATERIALS AND METHODS

Research platform

The research platform uses the Oubao 4040 tractor. The front wheels of the tractor are turned to the rear wheels to drive. The agricultural vehicle safety pre-warning system is divided into three parts: perception, decision-making, and execution. The sensing part is the UST-20LX two-dimensional Lidar (detection range: 270°; scanning frequency: 0.25 s; angular resolution: 0.25°; HOKUYO Co., Japan) and Xingwang Yuda XW-GI5610 Beidou navigation equipment (sampling frequency: 10 Hz; manufactured by StarNeto Co., Ltd., China). The controller of the decision-making part is personal computer (PC). It is a host computer that is responsible for receiving sensor data, processing data, and making decisions. As the lower computer, Arduino Uno is responsible for receiving the signal from the upper computer to control the actuator.

The executive part is an LED alarm with red, yellow, and green lights and a buzzer. The buzzer can be combined with any colour of light to generate an alarm signal.

The LIDAR sensor is connected to the PC network port through a network cable for network port communication. BDS and PC, upper computer and lower computer are all serial communication devices. The GPIO port of Arduino is connected to the relay to control the on and off of the sound and light alarm. The sensor layout of the system is shown in Figure 1.

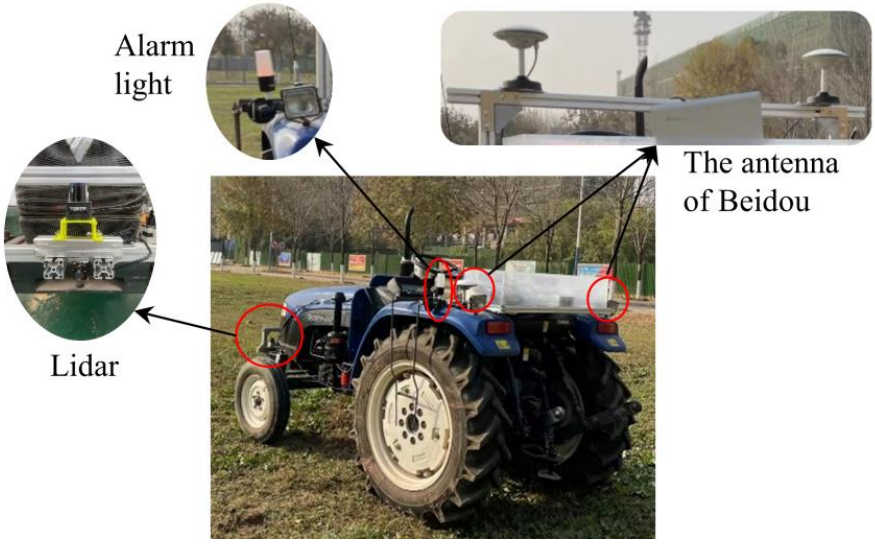

Fig. 1 - Schematic diagram of the overall structure of the system

Coordinate System

The coordinate system shown in Figure 2 is set, namely the tractor coordinate system $X_TY_TZ_T$, the laser coordinate system $X_LY_LZ_L$ and the map coordinate system XYZ.

In the laser coordinate system $X_LY_LZ_L$, the origin O_L of the laser coordinate system is the centre of the laser line emitted by the laser radar, the Y_L axis is pointing to the front of the laser radar along the 135° direction of the laser beam, and the X_L axis is along the 45° direction of the laser beam. Pointing to the right side of the Lidar, the Z_L axis is perpendicular to the plane formed by the X_L axis and the Y_L axis.

The tractor coordinate system $X_TY_TZ_T$ is the mobile station coordinate system of BDS. The position of the coordinate system changes with the movement of the tractor. The origin O_T is the installation position of the mobile station, the X_T axis points to the right along the line connecting the installation positions of the two antennas, the Z_T axis is perpendicular to the ground and upwards, and the Y_T axis is perpendicular to the plane formed by the X_T axis and the Z_T axis.

In the absolute coordinate system XYZ, the starting point of the tractor is taken as the origin O, X, Y, Z axes point to true north, true east, and vertical ground upwards, respectively. First, obtain the coordinates of the tractor in the absolute coordinate system by analysing the BDS data, and then obtain the relationship between the laser coordinate system and the tractor coordinate system from the relative position of the laser radar and the BDS installation.

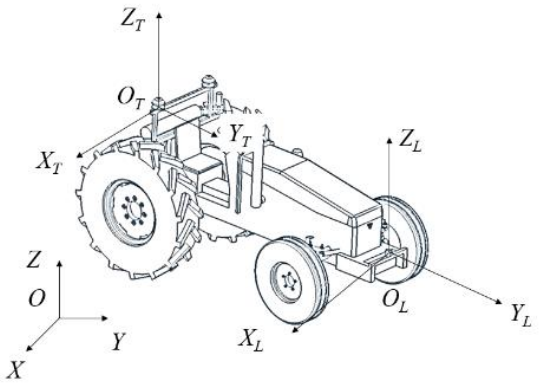

Fig. 2 - Coordinate system

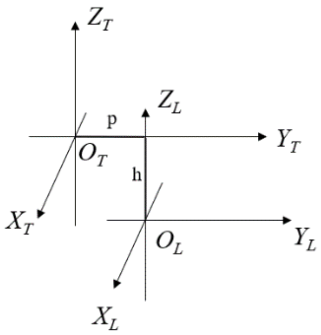

Fig. 3 - The geometric relationship between the laser coordinate system and the tractor coordinate system

As shown in Figure 3, p is the difference between O_T and O_L along the Yaxis; h is the difference between O_T and O_L along the Z axis. Therefore, the conversion relationship between the coordinates (x_L, y_L, z_L) in the laser coordinate system and the coordinates of the tractor body coordinate system (x_T, y_T, z_T) can be obtained as

$$\begin{bmatrix} x_T \\ y_T \\ z_T \end{bmatrix} = \begin{bmatrix} x_L \\ y_L \\ z_L \end{bmatrix} + \begin{bmatrix} 0 \\ p \\ -h \end{bmatrix} \quad (1)$$

$$x_L = \rho \cos\theta \quad (2)$$

$$y_L = \rho \sin\theta \quad (3)$$

The polar coordinates of the Lidar point cloud are converted to coordinates in the plane rectangular coordinate system through formulas (2) and (3). Among them, ρ is the distance between the object detected by the Lidar and the Lidar, and θ is the angle between the laser beam and the 0° line. In addition, the CGCS2000coordinates provided by BDS are converted to Gaussian plane coordinates by Gaussian orthographic projection (*Liu, 2018*).

Lidar point cloud clustering based on DBSCAN

DBSCAN is a density-based clustering algorithm. A clustering category is obtained by classifying closely connected samples into one category (*Yan W Y, et al., 2016*). All of the closely connected samples are divided into different categories, and the final results of all cluster categories are obtained. Therefore, for high-density data such as Lidar point clouds, DBSCAN clustering is used. In addition, compared with other clustering algorithms, DBSCAN has the advantages of not requiring inputs such as the number of clusters and the shape of clusters (*Zhang Y.H., et al., 2017*).

The system uses the point cloud library (PCL) to process point cloud data. First, clusters are searched by checking the Eps neighborhood of each point in the Lidar data. If the Eps neighborhood of point p contains more points than MinPts, then a cluster with p is created as the core object, and objects that are directly accessible from these core objects are iteratively gathered. This process sometimes involves the merging of clusters with reachable density. When no new points are added to any clusters, the process ends. Different colors are then added to the point cloud clusters of different objects. After visualization in Rviz, the approximate shapes and positions of different objects in the point cloud can be intuitively observed (Fig. 4).

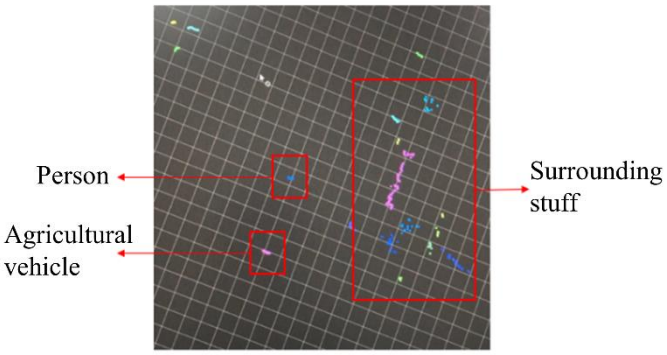

Fig. 4 - Point cloud clustering renderings

Obstacle tracking

To ensure that safety warnings for both static and dynamic obstacles are accurate, the dynamic obstacles need to be tracked to obtain various types of information, such as their movement status. The idea in this research is based on the DeepSort tracking algorithm. It uses Euclidean distance as the position metric (*Buczkowska et al., 2019*) and the MCMF to perform data association and applies them to the laser point cloud to track the objects detected by the laser to prepare for safety pre-warning.

In the position measurement, Euclidean distance is used to evaluate the degree of matching between the state predicted by the Kalman filter and the actual state.

$$\rho=\sqrt{(x_2-x_1)^2+(y_2-y_1)^2} \tag{4}$$

(x_1, y_1) and (x_2, y_2) represents the coordinates of two points, and ρ represents the Euclidean distance between these two points.

The DeepSort algorithm is applied to the image and uses the position of the detection frame for calculation (*Wojke et al., 2017*). For the point cloud data of Lidar, the position of the detection frame is replaced with the coordinates of the point cloud clustering center for calculation. The Kalman filter is used for target motion state estimation, and the MCMF is used for position matching.

For each tracking target, the number of frames a_k since the last detection result that matches the tracking result is recorded. Once the detection result of a target is correctly associated with the tracking result, this parameter is set to 0. The maximum threshold A_{max} is then set for a_k. If a_k exceeds the set maximum threshold, the tracking process for the target is considered to have ended. When the moving object gradually moves outside the detection range of the Lidar, the tracking of the object ends at this time. When an object in a detection result cannot always be associated with the existing tracker, and the prediction results of the target position of the potential new tracker can be correctly associated with the detection result 5 consecutive times, then the judgment result is the appearance of new objects, avoiding the situation of “false alarms” caused by the jitter of the laser point cloud.

Obstacle status judgment

From the data collected by Beidou navigation equipment, the driving speed V_1 of the tractor is analyzed. Analyze and process the Beidou data, and extract the 10th to 12th places of the Beidou data, that is Ve, Vn, Vu. Use equation (5) to calculate the tractor speed, denoted as V_1:

$$V_1=\sqrt{V_e^2+V_n^2+V_u^2} \tag{5}$$

Obtain the trajectory information and speed information of the obstacle through the target tracking algorithm. The speed information is the sub-velocities in the X_L and Y_L directions in the Lidar coordinate system, and the speed vector V_r and distance S_r. Theoretically, when the obstacle relative to the tractor's speed V_r and the tractor's traveling speed V_1 are numerically equal, the obstacle is considered to be stationary; the rest are considered to be moving. However, in actual situations, due to the measurement error and calculation error of the sensor itself, it is impossible for V_r and V_1 to be completely equal in value, so given a threshold k, when:

$$|V_r|-|V_1|<k \tag{6}$$

The obstacle is considered to be stationary; the rest are considered to be moving. The value of k is determined according to the test of the actual equipment, so that the accuracy of static and dynamic judgments are both above 90%, and the final value is 1.1m/s.

Security warning level division algorithm

This security pre-warning level classification algorithm has different classification models for static obstacles and dynamic obstacles. It is divided into three levels: From level one to level three, the degree of danger gradually decreases.

Static obstacle

Taking the tractor as the research object, and establishing the kinematics model of the tractor, as shown in Figure 5. In the process of tractor driving, the influence of factors such as slip, side slip and ground smoothness are not considered. The model is represented by formula (7) ~ formula (10).

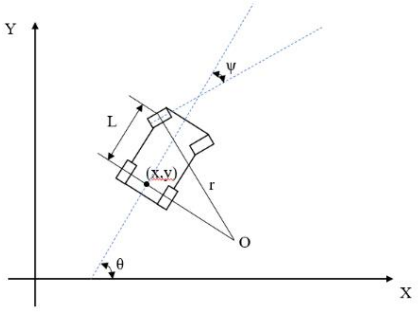

Fig. 5 - Tractor kinematics model

$$\dot{x} = v\cos\theta \tag{7}$$

$$\dot{y} = v\sin\theta \tag{8}$$

$$\dot{\theta}=\omega=\frac{v}{L}\tan\psi \tag{9}$$

$$r = L/\sin\psi \tag{10}$$

where: x and y – the global coordinates of the tractor rear axle center;

θ – The heading angle of the tractor in the global coordinate system (°);

ω – The angular speed of the tractor (rad/s);

v – The driving velocity of the tractor, $v \in (0, v_{max}]$ (m/s);

ψ–The steering angle of the tractor's front wheels (°);

L –The distance between the front and rear wheels of the tractor (m);

r –The turning radius of the tractor (m).

For static obstacles, when the tractor moves forward, the Lidar detects the obstacle, as shown in Figure 6. At this time, the tractor's motion state is estimated according to its kinematics model. $Q(x_k, y_k)$ is the tractor coordinates determined by GNSS at k, and the point $Q'(x_{k+1}, y_{k+1})$ represents the position of the tractor after time ΔT, which is predicted by equation (11).

$$\begin{bmatrix} x_{k+1} \\ y_{k+1} \end{bmatrix} = \begin{bmatrix} x_k \\ y_k \end{bmatrix} + v_k \Delta T \begin{bmatrix} \cos\psi_k \\ \sin\psi_k \end{bmatrix} \tag{11}$$

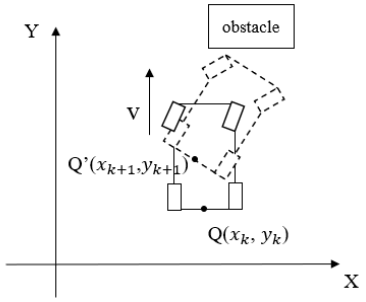

Fig. 6 - Model prediction

When the tractor turns at the maximum turning angle without hitting the obstacle, it is the critical value of turning at this time, that is, the boundary point B of the obstacle is on the trajectory circle where the tractor turns at the maximum turning angle. As shown in Figure 7.

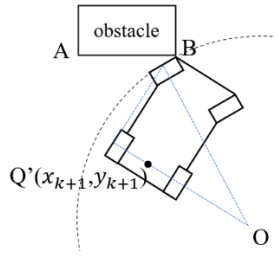

Fig. 7 - Critical condition

From the geometric relationship, the coordinates (a, b) of point O can be obtained, and the circular curve with point O as the center and r as the radius is

$$(x-a)^2+(y-a)^2=r^2 \tag{12}$$

When predicting the trajectory of the tractor, the coordinates of point B(x_B, y_B) are substituted into equation (12) to determine the relationship between point B and point O. As shown in Figure 8, the first-level warning is set to the coordinate of point B within circle 1, the second-level warning is set to the coordinate of point B is within circle 1 and circle 2, and the third-level warning is set to the coordinate of point B is outside circle 2. Among them, circle 2 is concentric with circle 1, and the radius is r+1.

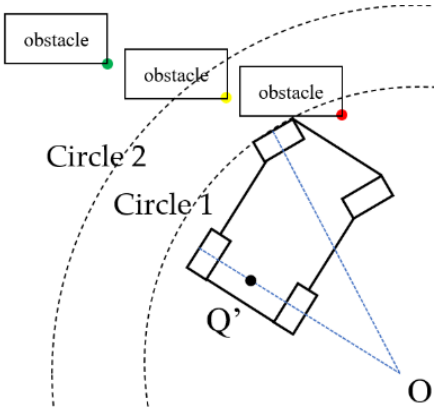

Fig. 8 - Classification of pre-warning levels

Translating it into judging the distance relationship between point B and point O, the following three situations will occur:

$$\sqrt{(x_B-a)^2+(y_B-b)^2}<r \tag{13}$$

$$r<\sqrt{(x_B-a)^2+(y_B-b)^2}<r+1 \tag{14}$$

$$\sqrt{(x_B-a)^2+(y_B-b)^2}<r+1 \tag{15}$$

Then when the coordinate of point B conforms to formula (13), the tractor cannot turn to avoid the obstacle, it is a first-level warning; when the coordinate of point B conforms to formula (14), the tractor can just avoid the obstacle at the maximum turning angle, and it is judged as Second-level early warning; when the coordinate of point B conforms to formula (15), the tractor can avoid the obstacle, and it is judged as a third-level early warning.

Dynamic obstacle

The set safety distance (*Liu et al., 2016*) is the distance required for the tractor to brake to stop. This article sets two levels of safety distance. The first-level safety distance s is the braking distance required for the tractor to decelerate with maximum acceleration. It contains four parts: s_1, s_2, s_3 and s_4. It can be seen from the acceleration change curve in the braking process shown in Figure 9, where s_1 represents the distance traveled by the tractor within t_1 from the time the system sends a signal to the start of the brake. s_2 represents the distance traveled by the tractor within t_2 from the start of the brake action to the time the brake is applied. Therefore, the tractor maintains the initial speed v_1 during the two periods of t_1 and t_2. s_3 represents the distance traveled by the tractor t_3 during the time the brake is applied until the deceleration stabilizes. During t_3, the tractor starts to decelerate, the braking force starts to increase to the maximum, and the deceleration increases. s_4 is the distance traveled by the tractor during the period t_4 when the deceleration is stabilized until the tractor comes to a complete stop. The deceleration reaches its maximum within t_4, and the value remains unchanged to keep the vehicle moving at a constant deceleration. This stage continues until the speed is zero, and the vehicle stops.

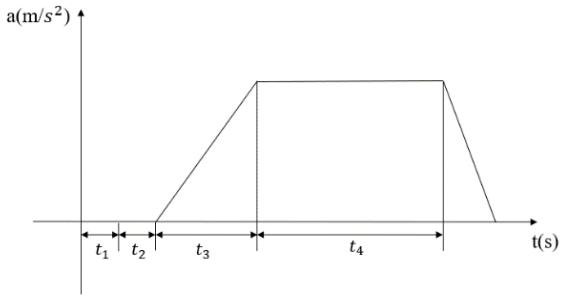

Fig. 9 - Acceleration over time diagram

(1) The above analysis indicates that the tractor moves at a constant speed during t_1 and t_2, thus:

$$s_1 = v_1 t_1 \tag{16}$$

$$s_2 = v_1 t_2 \tag{17}$$

(2) During t_3, the tractor starts to decelerate and the deceleration is increasing. Therefore, the following equation can be used:

$$\frac{dv}{dt} = kt \tag{18}$$

$k = -\frac{a_{\max}}{t_2}$, so $\int dv = \int ktdt$

Since the initial speed of the vehicle at this stage is v_1, so:

$$v_1' = v_1 + \frac{1}{2} k t_3^2 \tag{19}$$

thereby $\frac{ds}{dt} = v_1 + \frac{1}{2} kt^2$, so:

$$\int ds = \int (v_1 + \frac{1}{2} kt^2) dt \tag{20}$$

Initial moment $S = 0$, so:

$$s_3 = v_1 t_3 + \frac{1}{6} k t_3^3 \tag{21}$$

k can then be substituted into the above formula to obtain:

$$s_3 = v_1 t_3 + \frac{1}{6} a_{\max} t_3^2 \tag{22}$$

(3) During t_4, the tractor uses $a_{\max}$ as the deceleration speed to make uniform deceleration motion. At this time, the initial speed is v_1' and the final speed is 0, so:

$$s_4 = \frac{v_1^2}{2a_{\max}} - \frac{v_1 t_3}{2} + \frac{a_{\max} t_3^2}{8} \tag{23}$$

In summary, the expression of s is:

$$s = s_1 + s_2 + s_3 + s_4 \tag{24}$$

$$s = v_1(t_1 + t_2) + \frac{1}{2} v_1 t_3 - \frac{1}{24} a_{\max} t_3^2 + \frac{v_1^2}{2a_{\max}} \tag{25}$$

The second-level safety distance s' is the braking distance required for the tractor to brake at 1/2 of the maximum deceleration. s' also contains four parts: s_1, s_2, s_3 and s_4. The meaning of each section of displacement is the same as the first-level safety distance.

Thus,

$$s' = s_1 + s_2 + s_3 + s_4 \tag{26}$$

$$s' = v_1(t_1 + t_2) + \frac{1}{2}v_1 t_3 - \frac{1}{48}a_{\max}t_3^2 + \frac{v_1^2}{a_{\max}} \tag{27}$$

In the system, t_1 and t_2 are 1.3 s, t_3 is 0.2 s, and a_{max} is 6 m/s^2 according to the actual equipment used.

For dynamic obstacles, the speed V_r of the obstacle relative to the agricultural vehicle is a vector. The forward direction of the agricultural vehicle (i.e. the x direction of the coordinate system) is in the positive direction and vice versa. When the speed is in the positive direction, the obstacle is far away from the agricultural vehicle; thus, no pre-warning is considered. When the speed is in the negative direction, the obstacle is approaching the agricultural vehicle. At this time, the safety warning level is judged.

The collision time is calculated according to the movement state of the agricultural vehicle and the obstacle at the time $t = S_r / V_r$. The distance the tractor travels during this time is $S_t = v_1 t$. S_t is then compared with the two-level safety distance to judge the level. To ensure the unified evaluation of the degree of danger, a pre-warning evaluation index δ is proposed to rank the degree of danger.

Suppose $i = S_t / S$, $j = S_t / S'$

$$\delta = ij \tag{28}$$

δ appears in three situations:

$$\begin{cases} 0 < \delta < 1 \\ j < \delta < i \\ \delta > i \end{cases} \tag{29}$$

When $0<\delta<1$, it is judged as a first-level warning; when $j<\delta<i$, it is judged as a second-level warning; when $\delta>i$, it is judged as a third-level warning.

Real vehicle test

Place static obstacles directly in front of the tractor's forward direction, and through manual tests, determine the position where the tractor cannot go around at the maximum turning angle, the position where the tractor can go around at the maximum turning angle and the distance does not exceed 1m, and the tractor can go around at the maximum turning angle. The positions that pass and the distances differ by more than 1m correspond to the three lines shown in Figure 10. The tractor is driving forward at a speed of 9km/h (±0.8km/h), and the time when the LED warning light is correctly illuminated within each distance is recorded. The experiment was repeated three times for data analysis.

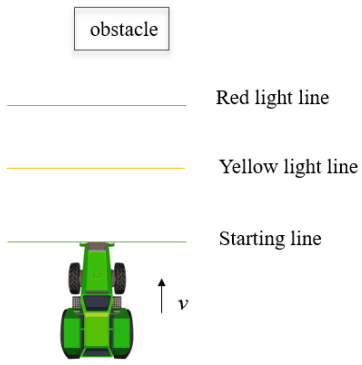

Fig. 10 - Static obstacle test plan

The same site was used to conduct dynamic obstacle tests, and human subjects were used as dynamic obstacles. Tests were conducted both away from and close to the tractor. The tests away from the tractor were conducted as follows: a person walks from the front of the tractor (Figure 11(a)) and the side (Figure 11(b)), including the left and right sides, at a brisk walking speed (1.2–1.4 m•s^{-1}) while staying away from the tractor. The test was run three times in each direction to determine whether the warning light was always green.

The other test was conducted as follows: a person approaches the tractor at a distance from the front walking at a normal speed (1 m/s (±0.3 m•s^{-1})), fast walking speed (2 m/s (±0.3 m•s^{-1})), and jogging speed (3 m/s (±0.3 m•s^{-1})) (Figure 11(c). Tests for each type of speed were repeated three times, and the distance and speed between the person and the tractor when the warning light changes from green to yellow and to red were recorded for data analysis.

(a)Front (b)Side (c) approach

Fig. 11 - Dynamic obstacle test photo

RESULTS AND DISCUSSION

It can be seen from the test results that the early warning accuracy rate of this safety early warning system for static obstacles is over 85.5%, and the early warning effect is good. The green light area has the best effect due to the long distance and long distance, and the error of the Lidar ranging has less influence on it. The yellow light area has the shortest distance. A slight bump of the tractor during driving will cause data instability, which will lead to a decrease in accuracy. Although the distance of the red light area is also short, it is already very close to the obstacle, and the Lidar data error is small, so the accuracy rate has increased.

The test results of static obstacles are shown in the table below.

Table 1

Results of the first test

Times / Result	Correct lighting time / s	Error lighting time / s	Accuracy	Average
Green light area	6.9	0.90	88.5%	85.4%
Yellow light area	1.5	0.30	83.3%	
Red light area	3.8	0.70	84.4%	

Table 2

Results of the second test

Times / Result	Correct lighting time/s	Error lighting time/s	Accuracy	Average
Green light area	6.8	0.8	89.5%	85.7%
Yellow light area	1.8	0.3	85.7%	
Red light area	3.2	0.7	82.1%	

Table 3

Results of the third test

Times / Result	Correct lighting time / s	Error lighting time / s	Accuracy	Average
Green light area	6.5	0.8	89.0%	85.4%
Yellow light area	1.9	0.4	82.6%	
Red light area	3.3	0.6	84.6%	

When dynamic obstacles are far away from the tractor, the warning light is green more than 96.6% of the time, which is consistent with expectation. That is, when the obstacle is far away from the tractor, it is considered safe, and no warning is required.

In 3.4% of the cases, the lights were not turned on correctly because of the effect of the bumpy terrain on the sudden change in tractor speed and the occasional deviation in the speed of BDS.

The test results of people far away from the tractor are shown in Table 4-6:

Table 4

Ahead far away the test results

Times / Result	Correct lighting time / s	Error lighting time / s	Accuracy	Average
The first test	7.9	0	100.0%	98.3%
The second test	8.3	0.2	97.6%	
The third test	7.6	0.2	97.4%	

Table 5

Far away from the left side the test results

Times / Result	Correct lighting time / s	Error lighting time / s	Accuracy	Average
The first test	7.3	0	100.0%	97.9%
The second test	7.5	0.2	97.3%	
The third test	8.1	0.3	96.4%	

Table 6

Far away from the right side the test results

Times / Result	Correct lighting time / s	Error lighting time / s	Accuracy	Average
The first test	7.7	0.1	98.7%	99.6%
The second test	8.4	0	100.0%	
The third test	7.5	0	100.0%	

During the test, the tractor drives forward at the tillage speed of 9 km/h; the first-level safety distance S is 4.3 m, and the second-level safety distance S' is 4.8 m. Based on the results in the above table, 94.4% of the pre-warning distances are consistent with expectations. In the second test of the human subjects walking at normal speeds, S_t when the green light turns to yellow is slightly larger than S', which is caused by the bumps of the tractor during the driving process. In addition, in the test with artificial jogging, the warning light did not appear to be yellow for the first and third repetitions of the test but instead directly changed from green to red. The analysis indicated that the movement of the dynamic obstacles is faster at this time; furthermore, the range of changes in various parameters is greater, the yellow light range is shorter, and there is no yellow light warning. When the dynamic obstacle moves faster, the warning light sends out a red warning signal when the tractor is still far away from the obstacle to provide more time for braking or making a turn. Thus, this system can send out a red warning signal faster based on the speed of the obstacle when the dynamic obstacle is moving rapidly, thus enhancing the safety of operation. To sum up, the pre-warning accuracy of dynamic obstacles is 95.5% for the results of faraway experiment and near experiment. The results of people approaching the tractor are shown in Table 7:

Table 7

Jogging speed test results

	Normal walking speed		Brisk walking speed		Jogging speed	
	Red	Yellow	Red	Yellow	Red	Yellow
The first test	4.16	4.63	3.71	4.46	3.02	-
The second test	3.98	4.82	3.65	4.39	3.14	4.35
The third test	4.03	4.69	3.85	4.55	2.98	-

CONCLUSIONS

This research presents a system suitable for monitoring the surrounding environment of agricultural vehicles that can provide a safety warning and proposes a method to detect obstacles and judge the state of obstacles through Lidar scanning. Different safety pre-warning models are proposed for static and dynamic obstacles. The accuracy of the pre-warning is 90.5% (average value of static obstacle experiment and dynamic obstacle experiment results), and faster obstacles correspond to higher danger and more rapid triggering of alarms.

Compared with previous studies, the parameters of this system can be set according to the actual agricultural vehicles used, which increases its applicability. In addition, this system features a two-level safety distance that can match the degree of danger of different obstacles in more detail. Finally, the motion parameters of obstacles are comprehensively considered rather than simply using distance as the criterion, which improves the accuracy of pre-warning.

However, this study only conducted experimental verification using one type of tractor. Thus, future studies are needed to verify the model using different types of agricultural vehicle tests. Furthermore, the entire safety pre-warning model needs to be modified to accommodate the parameters of different types of agricultural vehicles.

ACKNOWLEDGEMENT

The authors thank the editing team of EditorBar for improving the English language fluency of our paper. The work in this paper was supported by the National Key Research and Development Program (No. 2017YFD0700402), the China Postdoctoral Science Foundation (No. 2019M653764) and the Chinese Universities Scientific Fund (No. 2452018051).

REFERENCES

[1] Asvadi A., Premebi Da C., Peixoto P., et al. (2016). 3D Lidar-based static and moving obstacle detection in driving environments. *Robotics & Autonomous Systems*, pp. 299-311;

[2] Buczkowska S., Coulombel N., et al. (2019). A comparison of Euclidean Distance, Travel Times, and Network Distances in Location Choice Mixture Models. *Networks and Spatial Economics*, vol. 19, no. 4, pp. 1215-1248;

[3] Campos Y., Sossa H. and Pajares G., (2016). Spatio-temporal analysis for obstacle detection in agricultural videos. *Applied Soft Computing Journal*, vol. 45, pp. 86-97;

[4] Cao M.C. and Wang J.M., (2016). Obstacle Detection for Autonomous Driving Vehicles with Multi-Lidar Sensor Fusion. *Journal Of Dynamic Systems Measurement and Control-Transactions of the ASME*, vol. 142, no. 2;

[5] Chen X.X., Wu H., Wu Y.W., et al. (2017), Large-Scale Resource Scheduling Based on Minimum Cost Maximum Flow (基于最小成本最大流量的大规模资源调度), *Journal of Software*, vol. 28, no. 3, pp. 598-610;

[6] Jeong E., Oh C. and Lee G. (2015). Emission evaluation of inter-vehicle safety warning information systems. *Transportation Research Part D: Transport and Environment*, vol. 41, no. 12, pp. 106-117;

[7] Corno M., Furioli S., Cesana P., et al., (2021). Adaptive Ultrasound-Based Tractor Localization for Semi-Autonomous Vineyard Operations. *Agronomy*, vol. 11, no. 2, pp. 287;

[8] García-Martínez H., Flores-Magdaleno H., Ascencio-Hernández R. et al. (2020). Corn Grain Yield Estimation from Vegetation Indices, Canopy Cover, Plant Density, and a Neural Network Using Multispectral and RGB Images Acquired with Unmanned Aerial Vehicles, *Agriculture*, vol. 10, no. 7, pp. 277;

[9] Guo, C.Y., Zhao X., Zhang S., et al. (2019). Design of a cross-boundary warning system for soil preparation based on bds, *INMATEH-Agricultural Engineering*, vol. 59, no. 3, pp. 59-68;

[10] Kapilan K., Bandara S. and Dammalage T., (2020). Vehicle Accident Detection and Warning System for Sri Lanka Using GNSS Technology. in 1st International Conference on Image Processing and Robotics, ICIPRoB 2020, March 6, 2020 - March 8, 2020. *Negombo, Sri Lanka: Institute of Electrical and Electronics Engineers Inc*;

[11] Liang Y.Y., Liu X.H., He Z.Y. et al. (2019). Multiple objects tracking by reliable tracklets. *Signal Image and Video Processing*, vol. 13, no. 4, pp. 823-831;

[12] Liu G.R., Zhou M.Z., Wang L.L., et al. (2016). Control model for minimum safe inter-vehicle distance and collision avoidance algorithm in urban traffic condition. *Automotive Engineering,* vol. 38, no. 10, pp. 1200-5+1176.
[13] Liu M.C., (2018). Research on inspection and obstacle avoidance methods of agro-machinery obstructions (农机障碍物检测与避障方法研究), *Northwest A&F Univ*;
[14] Liu Q., Qiu X.X., Xie L.M., et al. (2017). Anti-collision warning time algorithm based on driving speed of vehicle(基于车速的车辆碰撞预警时间算法), *Transactions of the Chinese Society of Agricultural Engineering*, vol. 33, no. 12, pp. 99-106;
[15] Loukatos D., Petrongonas E., Manes K., et al. (2021). A Synergy of Innovative Technologies towards Implementing an Autonomous DIY Electric Vehicle for Harvester-Assisting Purposes, *Machines*, vol. 9, no. 4, pp. 82;
[16] Sun Q., Huang L.S., Guo W.J., et al. (2014), Content-aware association control in wireless networks. *Journal of Computational Information Systems*, vol. 10, no. 7, pp. 2865-2872;
[17] Tak S., Yoon J., Woo S., et al. (2020). Sectional Information-Based Collision Warning System Using Roadside Unit Aggregated Connected-Vehicle Information for a Cooperative Intelligent Transport System, *Journal of Advanced Transportation*, pp. 1-12;
[18] Wojke N., Bewley A., Paulus D., et al. (2017). Simple online and realtime tracking with a deep association metric. *24th IEEE International Conference on Image Processing*, ICIP 2017, September 17, 2017 - September 20, 2017. Beijing, China: IEEE Computer Society;
[19] Yan W.Y., Salem M., Ahmed S., et al. (2016). Automatic extrajction of highway light poles and towers from mobile Lidar data. *Optics And Laser Technology*, vol. 77, pp. 162-168;
[20] Zhang Y.H., Geng G.H.,Wei X.R.,et al. (2017). Feature extraction of point clouds using the DBSCAN clustering(基于DBSCAN聚类的点云特征提取), *Journal of Xidian University*, vol. 44, no. 2, pp. 114-120;
[21] Zhao X. (2019). Study on the cross-boundary warning system of soil preparation based on BDS (基于BDS的整地跨界预警系统研究), *Northwest A&F Univ*;
[22] Zhu, T.J., Zong C.F., Wu B.S., et al. (2011). Rollover warning system of heavy-duty vehicle based on improved TTR algorithm (基于改进TTR算法的重型车辆侧翻预警系统), *Journal of Mechanical Engineering*, vol. 47, no. 10, pp. 88-94.

EFFECT ON MECHANICAL DAMAGE ON CASTOR GERMINATION AND DAMAGE DETECTION METHOD
/
机械损伤对蓖麻种子发芽影响试验及损伤检测研究

Junming HOU, Enchao YAO, Hongjie ZHU, Weixue HU, Zhaotan REN
Shenyang Agricultural University, College of Engineering / China;
Tel: +86024-88487116; E-mail: junming_hou@163.com
DOI: https://doi.org/10.35633/inmateh-68-24

Keywords: *Castor seed; Mechanical damage; Germination; Image processing*

ABSTRACT
To study the types of mechanical damage for castor seeds and their effects on germination, the image processing method was applied to detect the damage affecting germination. Two typical varieties of castor were selected for test. The type of mechanical damage of castor seeds was taken as the factor, the germination rate and germination vigor index were selected as indicators for one-way analysis of variance. The effects of mechanical damage on the germination of castor seeds were analyzed. Different algorithms were applied to extract the features of cracks and seed shell missing, and the corresponding defect parameters were calculated. The results showed that the effects of mechanical damage on the germination rate, germination potential, germination index, and vigor index of castor seeds were significant. The endosperm damage seriously affected the activity of castor seeds and seriously hindered seed germination. According to the analysis of the shell, some castor seeds cracked or there was incomplete shell damage at the same time, the internal endosperm being also damaged. The actual crack length was compared with the length measured by the ultra-depth of field microscope, which found that the margin of error was about 25% and the better error was 10%. Through the morphological processing, it could completely extract the characteristics of castor seed image without seed shells. The error between the extracted feature area and the measured object area function of the super depth of field microscope is about 10%.

摘要
为了研究蓖麻种子机械损伤类型及其对发芽的影响，并通过图像处理手段对损伤进行检测。选用两种典型材料试验，以蓖麻种子机械损伤类型为因素，以发芽率、发芽势、活力指数等为指标做单因素方差分析，分析机械损伤对蓖麻种子发芽的影响。最后通过不同算法对裂纹与种壳缺失进行特征提取，并计算相应的缺陷参数。研究结果表明，机械损伤对蓖麻种子的发芽率、发芽势、发芽指数及活力指数影响显著；胚乳损伤严重影响蓖麻种子的活性，严重阻碍种子发芽；根据去壳分析，部分蓖麻种子产生裂纹或者种壳不完全损伤的同时，内部胚乳也产生了损伤，从而导致它们与完整蓖麻种子之间发芽率差异显著。将检测实际裂纹长度与超景深显微镜测量长度比较，可以看出误差范围基为25%，比较优异的误差为10%。通过最大类间方差法对种壳缺失的蓖麻种子进行图像分割，并通过形态学处理后，能将种壳缺失蓖麻种子图像的特征完全提取出来，提取到的特征面积与超景深显微镜的实测物体面积功能的误差为10%。

INTRODUCTION
Castor is an important biomass resource oil crop with high oil content, which can produce nylon, lubricants, surfactants, and other products, and has a wide range of applications in high-technology fields such as aviation, navigation, transportation, and pharmaceutical manufacturing (*Li et al, 2018; Sun et al, 2012*). The damage among castors is serous in the process of shelling. The slight deformation or external damage to the seed directly affect its germination rate and the growth of the plant (*Yu et al, 2019*).

The related aspects have been studied by scholars on other materials. Mechanical threshing causes various forms of internal damage to soybean (*Gao et al, 2010*). These damages seriously affect the germination rate of soybean seeds and their germination quality. Related studies have analyzed the relationship between the degree of mechanical damage and germination of maize seeds by different techniques (*Zhang et al, 2014; Junior et al, 2019*). It was found that the damage rate of maize seeds increased and seed viability decreased with the increase in seed water content during mechanical threshing

Hou Junming, AP., Ph.D. Eng.; Yao Enchao, MS. Stud. Eng.; Zhu Hongjie, MS. Stud. Eng., Hu Weixue., MS. Stud. Eng.

(*Gu et al, 2019*). It was deduced that split glumes and cracks led to lower germination potential and germination rate of rice seeds and lower seedling quality. The correlation analysis between plant height and the degree of pressure application was performed (*Song et al, 2019*). Related studies found that mechanical scratching and mechanical shelling process without injuring the inner part of the seeds can promote seed germination and water absorption. When the inner part was injured mechanical damage to some extent will inhibit seedling growth after germination, which also reduce seed dry weight to some extent (*Ju et al, 2018; Ju et al, 2020*). It is clear that when mechanical damage injures the inner part of the seeds, it inhibits seed germination. When the seeds are not injured inside, it can promote seed germination appropriately. When mechanical damage inhibits seed germination, seeds that cannot germinate need to be detected by image processing algorithms. Related studies acquired the defect images by the multispectral computer vision system, which combined with the corresponding traditional algorithm for defect detection. The method can obtain the defect information better and has a high defect detection rate (*Che et al, 2020; Cheng et al, 2018; Luo et al, 2019*). Some studies applied threshold segmentation methods for image segmentation of larger defects, which are good for obtaining larger defect information (*Liu et al, 2017; Diao et al, 2018; Su et al, 2019; Henila et al, 2020*). Edge detection algorithms can be used to obtain edge information and pinpoint edge locations, which also have better edge processing capabilities (*Yang et al, 2021; Sangeetha et al, 2016; Wang et al, 2017; Ju et al, 2020; Han et al, 2020*).

The study first carried out germination test on damaged castor seeds, and detected part of mechanical damage. In this study, castor widely planted in Tongliao region was selected as the research object. The damage types of castor seeds caused by actual shelling were analyzed. The effects of damage types on the germination rate, germination potential, germination index and vigor index of castor seeds were also studied. Finally, image processing algorithm was used to detect the defects of damaged castor seeds.

MATERIALS AND METHODS

Experimental material

Castor capsule was divided into two categories, which are thornless and thorny castors. TongBi No.9 was thorny and ZheBi No.4 was thornless. The material was collected from Tongliao city. Fig. 1 showed the schematic diagram of castor capsule and castor seeds.

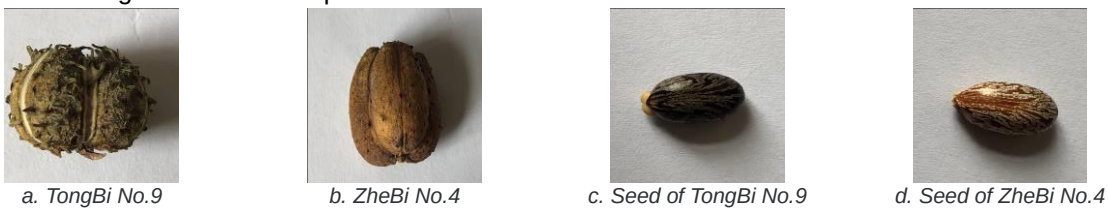

a. TongBi No.9 *b. ZheBi No.4* *c. Seed of TongBi No.9* *d. Seed of ZheBi No.4*

Fig. 1- Castor capsule and castor bean seed

Castor seeds of different damage types

Castor seeds would produce some form of damage in the process of shelling. The damage was based on the actual condition of the material after shelling (*Na et al, 2010*). The castor seed damage characteristics was divided into five cases (Fig. 2).

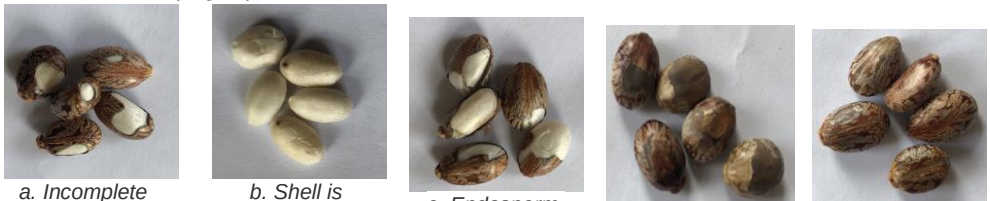

a. Incomplete damage to seed shell *b. Shell is completely damaged* *c. Endosperm injury* *d. Scaling* *e. Crack*

Fig. 2 - Damage characteristics of castor oil seeds

They were shown as following: incomplete damage to the seed shell—castor seeds were missing part of the shell, the missing part to reveal the white endosperm (Fig. 2a). Complete damage to the seed shell-castor seeds were completely missing the shell-the white endosperm was completely exposed (Fig. 2b). Endosperm damage, when the seed shell was missing, the white endosperm was partially cracked or partially broken (Fig. 2c). Scaling-the epidermis of castor seed shell was peeling off (Fig. 2d). The cracking-the surface of castor seed shell was split (Fig. 2e).

Test procedure

Selected mechanically damaged and complete castor seeds (seeds full and similar in size) of 30 each, soak in warm water at 40~50℃ for 5~6 hours to soften the hard shell, so that the seeds absorb enough water to speed up seed germination. They were evenly put on a press cloth on a 60-millimeter petri dish. Each petri dish was filled with 5 milliliters of water, thus forming germination condition. The experiment was repeated three times. In the process of germination and growth, pour the same amount of water over the castor seeds every day. After 24 hours of germination promotion, the germination situation was observed (Seed germination occurs when the bud grows to about 3 millimeters). Then the germination of castor seeds was observed every 24 hours and the number of germinated seeds was recorded for a total of 7 to 9 days. The germination rate, germination potential, germination index, and vigor index were selected to test the quality of mechanically damaged castor seeds, then the effect of mechanical damage on germination was tested (*Li et al, 2018; Joanna et al, 2018; Chiara et al, 2018*).

$$\text{Germination rate } (GP,\%) = \frac{N_{8D}}{N_{TD}} \quad (1)$$

$$\text{Germination potential } (GE,\%) = \frac{N_{4D}}{N_{TQ}} \quad (2)$$

$$\text{Germination index (Gi)} = \sum_{i=1,2...} \frac{N_{Di}}{D_i} \quad (3)$$

$$\text{Vital index } (V_i) = G_i * L \quad (4)$$

Where N_{8D} is the number of seeds germinated after 8 days. N_{TQ} is the total number of seeds per tray. N_{4D} is the number of seeds germinated after 4 days. N_{Di} is the number of seeds germinated on a day i. D_i is the number of days on the day i. L is the length of germinated seedlings.

Statistical analysis for test

The results for each treatment group were three independent replicate trials, then the values for each experiment were expressed as mean± standard deviation (SD). One-way ANOVA method was used to determine the mean of the experimental data and the significance for each index, and the significance of differences between levels was determined according to the Duncan multiple comparison method with a significance level of 0.05.

The results of the germination of castor seed

Take the castor seeds with the missing seed shell of TongBi No.9 as an example, and observe its germination and growth process for 6 days. After 6 days of germination, the number of germinated castor seeds had remained the same, so the growth could be observed for 6 days. Fig. 3 shows the germination and growth of castor seeds with missing seed shells.

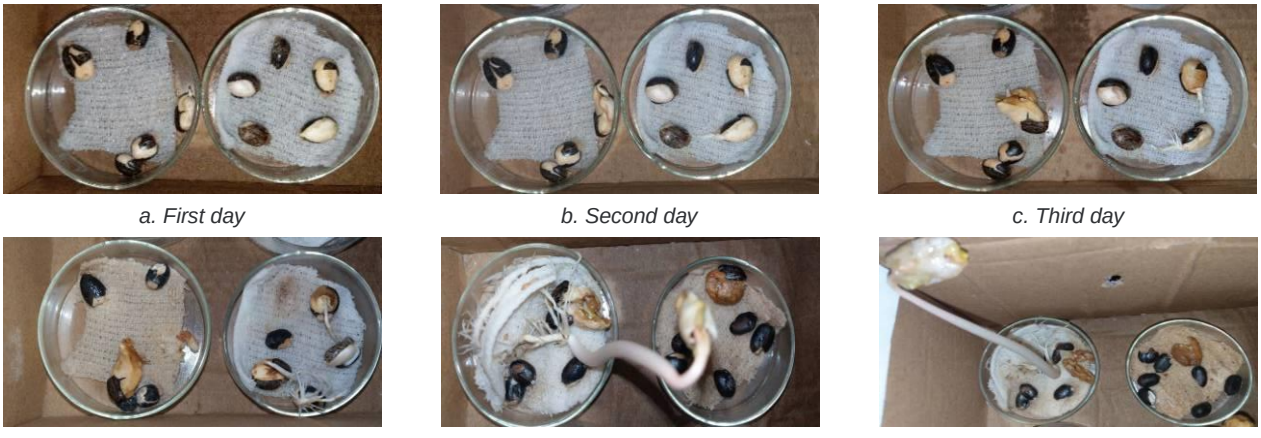

a. First day *b. Second day* *c. Third day*

d. Fourth day *e. Fifth day* *f. Sixth day*

Fig. 3 - Germination and growth of castor seeds with missing shells

Fig. 3(a) shows the germination of castor seeds after one day. One castor seed had germinated and the radicle had grown on 5 mm, exposing the germ.

Fig. 3(b) shows the germination of castor seeds after two days. The germinated seeds already had four grains, but the pre-growth was slow and the radicle length is 8-10 mm. Fig. 3(c) shows the germination of castor seeds after three days, with one seed having grown many radicles. Fig. 3(d) is the growth of four days castor seeds with increasingly developed and dense root systems. Fig. 3(e) and Fig. 3(f) shows the growth of castor seed after five or six days, it had a thick main stem, cotyledons gradually unfolded, cotyledons and root system grew well.

RESULTS AND DISCUSSION

Effect of mechanical damage on germination rate and germination potential

The germination rate and germination potential of seeds were important indicators of seed quality. Fig. 4 shows the statistical graphs of germination rate and germination potential of TongBi No.9 and ZheBi No.4. It could be observed that the germination rate and germination potential of the two varieties seeds had the same distribution. The germination rate and germination potential of each damage type were not different. They were the highest germination rate of complete castor seeds and the lowest germination rate of endosperm damaged castor seeds. It shows that the variety has little effect on germination rate and germination potential.

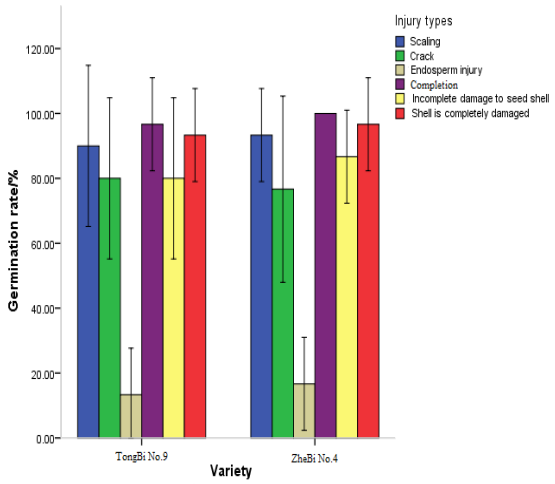

a. Statistics on the germination rate of TongBi No.9 and ZheBi No.4

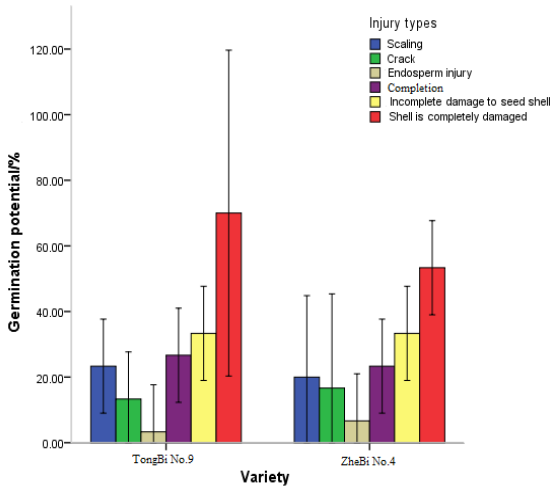

b. Statistics on the germination potential of TongBi No.9 and ZheBi No.4

Fig. 4 - Statistics of the germination rate and germination potential of TongBi No.9 and ZheBi No.4

It could be found that the effect of variety on germination rate and germination potential was not significant. Then the dynamic analysis and table analysis were conducted with TongBi No. 9 as an example. Fig. 5 shows the relationship between germination rate and germination potential of castor seeds under different damage types of TongBi No.9.

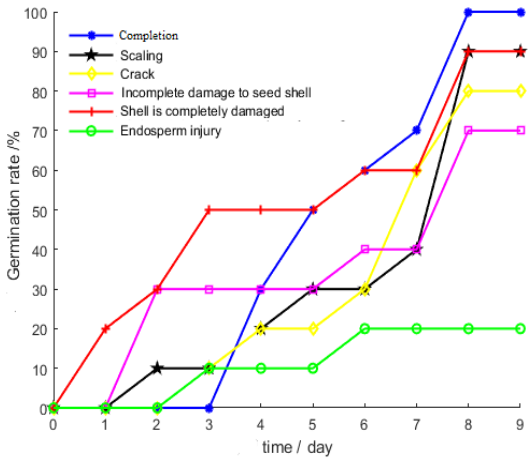

a. Dynamic diagram of germination rate

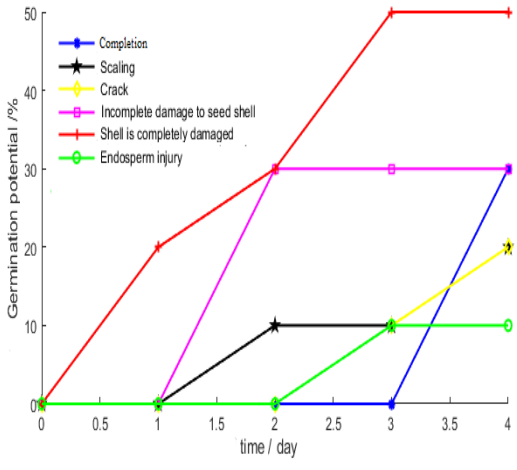

b. Dynamic chart of germination potential

Fig. 5 - Germination rate and germination potential of castor oil seeds

It could be found that castor seeds with partial and complete damage to the seed shell germinated earlier than other castor seeds. They had higher germination potential than other damage types of castor seeds. The growth dynamics of complete, peeled, and cracked castor seeds were similar. In the first three days, the germination was slow, then it became faster. The germination rate of complete castor seeds and peeled castor seeds was not much, while the cracked castor seeds germination rate was about 10% lower than it. Endosperm damage of castor seeds germination was slow and germination rate was not high.

Table 1 showed the effect of the degree on mechanical damage on the germination rate and germination potential of castor seeds. The one-way ANOVA showed that mechanical damage had a significant effect on the germination rate and germination potential of the two varieties. By Duncan's multiple comparisons, the difference in germination rate between incompletely damaged castor seeds and cracked castor seeds was significant. The difference in germination rate between endosperm damaged castor seeds compared with complete castor seeds was highly significant. The difference of germination potential between damaged endosperm castor seeds and complete castor seeds was very significant. The germination rate of castor seeds with incomplete shell damage and cracked castor seeds were both 80%, but the germination potential of castor seeds with incomplete shell damage was 20% higher than that of cracked castor seeds.

It could be found that the germination rate of different damage types of castor seeds was significantly lower compared with complete after six days of germination test under the same environmental conditions. The seed shell damage could accelerate the germination of castor seeds, and endosperm damage seriously affected the germination and growth of castor seeds.

Table 1

Effects of injury characteristics on germination rate and germination potential of castor oil seeds

Injury types	TongBi No.9		ZheBi No.4	
	Germination rate (%)	Germination potential (%)	Germination rate (%)	Germination potential (%)
Completion	96.67±5.77a	26.67±5.77bc	100.0a	23.33±5.77bc
Scaling	90.00±10.00ab	23.33±5.77bc	93.33±5.77ab	20.00±10.00bc
Crack	80.00±5.77b	13.33±5.77cd	76.67±11.55c	16.67±11.55cd
Incomplete damage to seed shell	80.00±10.00b	33.33±5.77b	86.67±5.77bc	33.33±5.77b
Shell is completely damaged	93.33±5.77ab	70.00±20.00a	96.67±5.77ab	53.33±5.77a
Endosperm injury	13.33±5.77c	3.333±5.77d	16.67±5.77d	6.667±5.77d

Note: Duncan's Multiple Range Test method was used for analysis, and different letters in the same column represented significant differences (P<0.05，n=3)

Effect of damage on germination index vigor index

The germination index and vigor index of seeds were important indicators for seed vigor. Fig. 6 shows the statistical graphs of germination index and vigor index of TongBi No. 9 and ZheBi No.4.

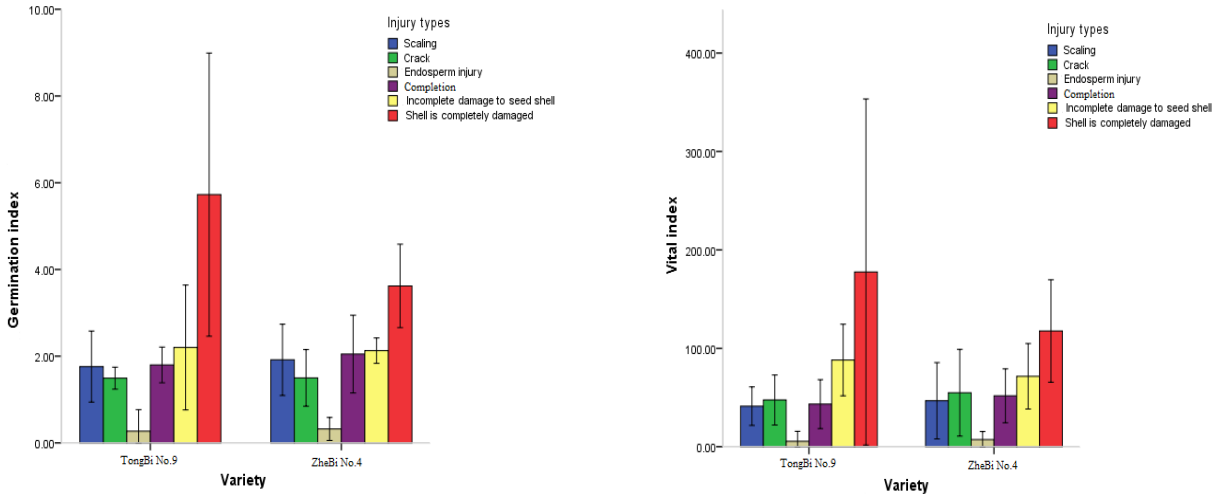

a. Statistics of germination index for TongBi No.9 and ZheBi No.4 *b. Statistics of vitality index for Tong Bi No.9 and ZheBi No.4*

Fig. 6 - Statistics of germination index and vitality index for TongBi No.9 and ZheBi No.4

It could be found that the distribution of seed germination index and vigor index of the two varieties is the same. They are the highest for castor seeds with complete shell damage and the lowest for castor seeds with endosperm damage, which indicated that the difference between varieties on germination index and vigor index was not significant.

As shown in Table 2, the type of damage had a significant effect on the germination index and vigor index of both varieties. By Duncan's multiple comparisons, the difference in germination index between castor seeds with complete shell damage and castor seeds with endosperm damage was significant. The vigor index between cracked castor seeds, completely damaged castor seeds and complete castor seeds was highly significant. The germination index and vigor index of castor seeds with completely damaged seed shell were the highest, with a germination index of 5.73, 2.2 times higher than that of complete castor seeds. The vigor index of completed damaged shell is 177.55. While the germination index and vigor index of damaged endosperm seeds were the lowest, with a germination index of 0.32 and a vigor index of 7.28.

According to the results, the germination index vigor index is the highest when the seed shell is completely damaged. This indicated that its activity is the highest. The effect of endosperm injury on the germination index and vigor index of castor seeds is significant. So, the activity of castor seeds is seriously affected.

Table 2

Effects of damage characteristics on germination index and vitality index of castor oil seeds

Injury types	TongBi No.9		ZheBi No.4	
	Germination index	Vital index	Germination index	Vital index
Completion	1.80±0.17b	43.26±9.99bc	2.05±0.36b	51.74±11.03b
Scaling	1.76±0.33b	41.21±7.91bc	1.92±0.33bc	46.72±15.58b
Crack	1.49±0.10b	47.47±10.23bc	1.50±0.26c	54.85±17.75b
Incomplete damage to seed shell	2.20±0.58b	88.08±14.66b	2.13±0.12b	71.57±13.38b
Shell is completely damaged	5.73±0.31a	177.55±70.79a	3.62±0.39a	117.54±20.96a
Endosperm injury	0.27±0.20c	5.51±4.07c	0.32±0.11d	7.28±3.29c

Note: Duncan's Multiple Range Test method was used for analysis, and different letters in the same column represented significant differences ($P<0.05$, $n=3$)

The reasons for the low germination rate

The castor seed structure is shown in Fig. 7. The cracks and incomplete damage to the seed shell are seed shell breakage, and the germination site of castor seeds in the endosperm. It is known that the germination rate of cracked seeds and seed shells incompletely damaged seeds is 10% lower than the germination rate of castor seeds with completely fallen skin. Therefore, the cracked castor in seed and seed shell incomplete damage castor seeds needed to be dehulled to observe the internal conditions.

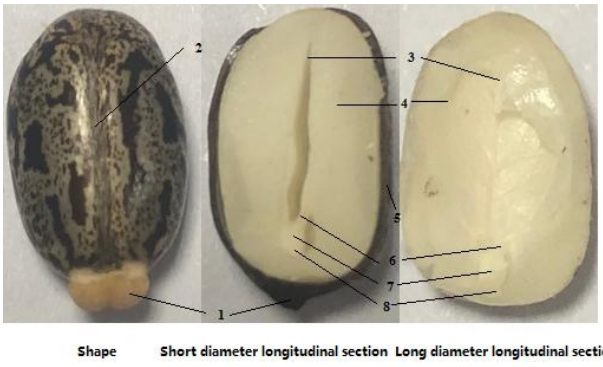

Fig. 7 - Structure of castor seeds

1.Caruncle; 2. Ridge; 3. Cotyledons; 4. Endosperm; 5. Seed shell; 6. Germ; 7. Hypocotyl; 8. Radicle

Fig. 8 shows the interior of the seed shells of both damage types, the small image in the image was a magnified view of the damage inside the defective image. It could be found that there are obvious cracks on the internal endosperm of castor seeds, indicating that the incomplete damage to the seed shell of castor seeds that did not germinate and cracked castor seeds also produced a certain amount of internal damage. The germination test found that when mechanical damage does not hurt castor seed endosperm, so mechanical damage could promote castor seed germination to some extent. When the mechanical damage is produced in castor seed endosperm and internal, mechanical damage would inhibit castor seed germination.

In this study, the number of castor seeds with completely damaged seed shells was less. According to the statistical results, the proportion of damaged castor seeds was less than 10%. The cracked castor seeds and seed shell incomplete damage castor seeds also contained 20-30% of endosperm damage castor seeds. Therefore, cracked castor seeds and castor seeds with incomplete damage to the seed shell were classified as damaged objects in the subsequent classification.

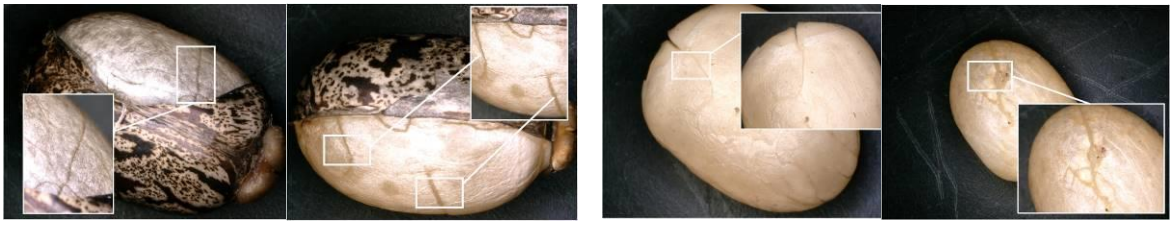

a. Incomplete damage to the interior of the seed shell *b. Cracked castor seed shell inside*

Fig. 8 - Interior of the seed shell of two types of damage

CRACK DETECTION ALGORITHM ON CASTOR SEEDS

Castor seed crack image

The castor seeds of ZheBi No.4 were selected as the test sample. The mechanical damage of castor seeds after shelling was surface cracking. Its common forms of cracking were lateral cracking text, abdominal cracking, and dorsal cracking, as shown in Fig. 9.

a. Lateral crack *b. Abdominal crack* *c. Back crack*

Fig. 9 - Cracks in different parts of castor seeds

Improved Canny algorithm

In this study, the maximum interclass variance method was applied, then the automatic threshold selection method of gradient magnitude histogram to find the low threshold of the image automatically. The gray levels after non-maximum suppression were divided into [0, L-1], and the pixels in the edge map after non-maximum suppression were classified into three classes: C_0, C_1, C_2. The class C_0 was for pixels that were not edge points. The class C_2 was for pixels that were edge points, and class C_1 contains pixels that might or might not be edge points. Set N to be the total number of pixels of modulus i, the number of pixels corresponding to gray level L-1 to be n_i, and P_i to be the probability that the number of pixels of that gray level represents the number of pixels of the whole image.

$$P_i = \frac{n_i}{N} (i=1,2,3....,L\text{-}1) \tag{5}$$

Let C_0 contain pixels with amplitude gradients of [0, 1, ..., k]. C_1 contains pixels with gray levels [k+1, k+2, ..., m]. C_2 contains pixels with gray levels [m+1, m+2, ... , L-1] of pixels, where k and m were low and high threshold values, respectively. The expectation of C_0, C_1, and C_2 were:

$$E_{C_0} = \frac{\sum_i^k i \cdot P_i}{\sum_i^k P_i} \tag{6}$$

$$E_{C_1} = \frac{\sum_{k}^{m} i \cdot P_i}{\sum_{k}^{m} P_i} \tag{7}$$

$$E_{C_2} = \frac{\sum_{m}^{L-1} i \cdot P_i}{\sum_{m}^{L-1} P_i} \tag{8}$$

The expectation for the entire interval was:

$$E = \frac{\sum_{i}^{L-1} i \cdot P_i}{\sum_{i}^{L-1} P_i} \tag{9}$$

The inter-class variance function could be defined as

$$\sigma^2 = (E_{C_0} - E)^2 + (E_{C_1} - E)^2 + (E_{C_2} - E)^2 \tag{10}$$

For a known graph, k and m could be found by the gradient histogram, and the variance in the maximum interclass variance method is denoted by σ^2. The superiority of interclass separability in the mathematical-statistical sense could be judged by maximizing the interclass variance. Therefore, the maximum value of σ^2 could be found, and the values of k and m corresponding to its maximum value are the dividing points of the intervals C_0, C_1, and C_2, which are also the high and low thresholds of the desired Canny operator. The result is shown in Fig.10.

Fig. 10 - Results of the improved algorithm

Calculation of the length of crack defects in castor seeds

Calibration of objects

In this study, a square standard block was used with the upper surface of 1 cm side length to calibrate the object based on the correspondence between the pixel value of the standard block and the actual size. The original image of the calibration block is shown in Fig. 11.

Fig. 11 - Original image of calibration block

Fig. 12 - Actual measured crack length

According to the Canny edge detection, the perimeter pixel of the calibration block was 3526. The crack length pixel obtained by the edge detection algorithm with the Canny operator was 698. The multiple calibrators could make the actual size represented by the pixel more accurate. The values of its multiple calibration blocks are shown in Table 3. As shown in Fig. 12, the actual length of castor seed cracks measured according to the length measurement function of the super depth-of-field microscope was plotted, then the actual length of cracks L1 was measured. The pixel to actual size relationship of the calibration block is calculated by equation (11).

$$A = \frac{l}{P} \tag{11}$$

Where: A is the actual size represented by a pixel value (um·px^{-1}). l is the actual size of the calibration block (um). P is the pixel value of the calibration block (px).

Table 3

Multiple calibration block pixels represent actual size values

	Object description 1	Object description 2	Object description 3
A/um·px^{-1}	11.76	11.68	11.71

When several calibration blocks of pixels representing the actual size were found, the average value was taken to make the calculation easier. The actual length of the crack L_2 was obtained by calculation as 8181 um. The actual crack length detected was compared with the length measured by the ultra-field microscope, the error of which was 23.46%. Fig.13 shows a graph of the crack treatment for recording some of the castor seeds. Table 4 shows the comparison between the actual length of crack detection and the length measured by the deep field microscope for castor seeds.

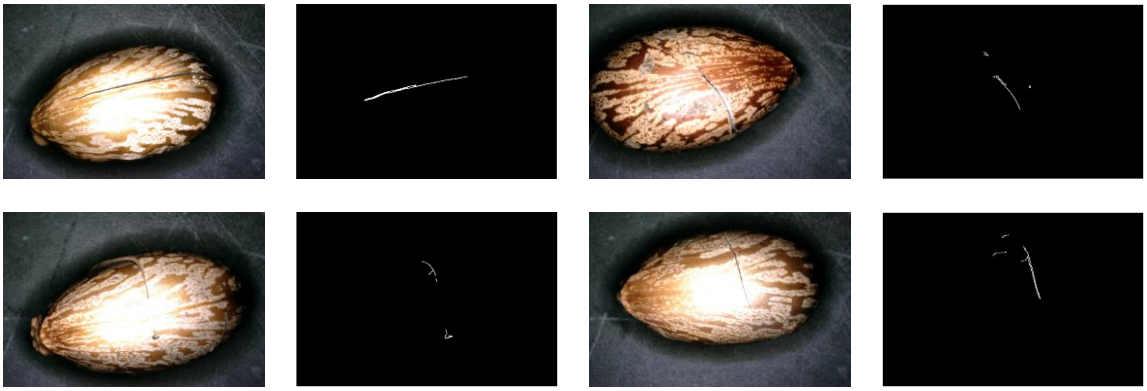

Fig. 13 - Castor seed crack treatment results comparison diagram

Table 4

Surface crack length of castor seeds

Number	Actual crack length/um	Measures length/um	Error/%
1	8181	10688	23.46
2	7258	7971	8.94
3	2076	2686	23.71
4	5177	6871	24.65
5	5083	6144	17.27
6	2073	2654	21.89
7	809	1001	19.18
8	3871	5316	27.18

There were many factors in the process of crack identification that could affect the results. The castor seeds have grayish-white and dark brown or yellowish-brown patterns on the surface, and the cracks were similar in color to the patterns. The computer can incorrectly identify the patterns as cracks in the identification process, which would lead to large errors in the results. The surface of castor seed is curved in the light to produce shadows, projected on the outer contour of the castor seed. The edge of the outer contour is partially covered by shadows, resulting in the detection of its area being smaller than its actual area.

ALGORITHM STUDY OF CASTOR SEEDS WITH SEED SHELLS

Image of castor seeds with missing seed shells

Seed shell loss was a serious problem during the shelling process of castor capsules. It resulted in the breakage and loss of the outer seed shell of castor seeds, exposing the inner white endosperm directly to the air. Fig. 14 shows the image of castor seed after seed shell loss.

Fig. 14 - Lack of castor seeds in shells

Threshold segmentation

In this study, the automatic threshold selection method with the maximum variance between classes was used in image thresholding, which was based on the grayscale distribution of the image. It calculated the grayscale histogram classes of the background and the target under different thresholds by traversing. Then by comparing the variance between the background and the target, the variance was maximized.

Area calibration and calculation

Each parameter of the super deep field microscope was adjusted: the castor seeds were placed directly below the microscope camera, a suitable shooting distance was selected, and the focal length and aperture of the microscope were adjusted to make the sharpest images of the collected castor seed samples. Secondly, a rectangular standard block with an upper surface of 1.1 cm × 0.9 cm was applied in this study to calibrate the object based on the correspondence between the pixel value of the standard block and the actual size. The original image of the area calibration block is shown in Fig.15.

Fig. 15 - Image of area calibration block

Fig. 16 - Absence of actual measured area of the seed shell

After morphological processing, the area pixels of the calibration block were 731108 and the area pixels of the seed shell missing castor seed map obtained with the maximum interclass variance algorithm was 157302. As shown in Fig. 16, the area map was measured with the super deep field microscope device. The actual area of the missing seed shell S_1 was measured, which is 24977950 um^2. The relationship between the pixels of the calibration block and the actual size is calculated according to equation (12).

$$a = \frac{S}{P} \tag{12}$$

Where: a is the actual area size represented by a pixel value ($um^2 \cdot px^{-1}$). S is the actual size of the calibration block (um). P is the pixel value of the calibration block (px). According to the formula, a is 135.411.

The defect area extraction was performed by the maximum interclass variance algorithm for seed shell defective castor seed images with different parts of defects. The different images are enumerated as shown in Fig. 17 below.

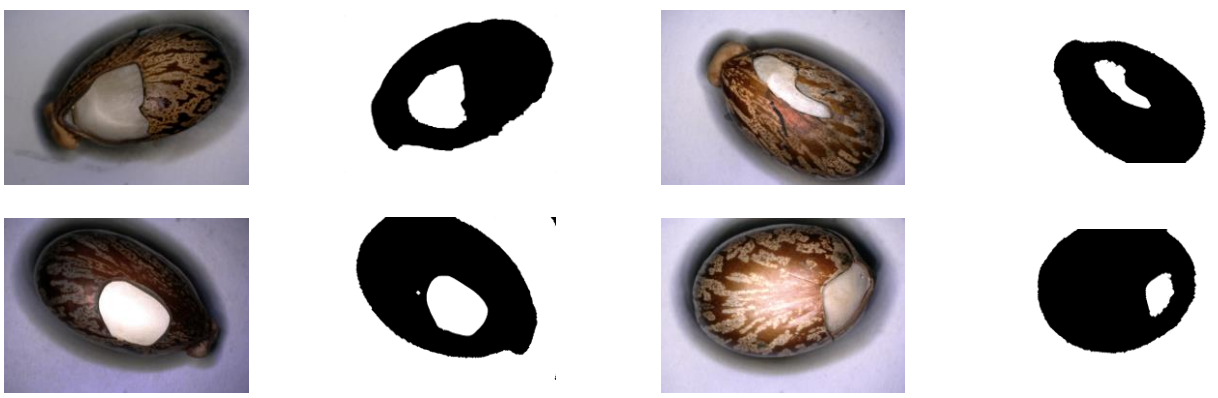

(a) Absence of castor seed image in the seed shell *(b) Processed image* *(a) Absence of castor seed image in the seed shell* *(b) Processed image*

Fig. 17 - Results of castor treatment without castor seeds of different species

Comparison of the missing area of castor seed shell surface **Table 5**

Number	Area of pixels	Actual area / um^2	Measures area / um^2	Error / %
1	157302	21300421	24977950	14.72
2	78983	10695167	10877339	1.68
3	145846	19749153	18130755	-9.38
	608	82330		
4	66235	8968948	11238750	20.20
5	86772	11749883	14332479	18.02
6	61098	8273341	8668171	4.55

From Table 5, it could be calculated that the minimum error of castor seeds with seed shell missing was 1.68% and the larger error was 20.20%. However, seed shell missing defects in the recognition process would have many factors that affect the extraction of defective features, part of which had the phenomenon of skin loss connected with defects, resulting in a smaller detection area than the actual area. The castor seed defects were too close to the edge, which resulted in a smaller detection area than the actual area. The castor seeds had a smooth surface, which would reflect the light.

CONCLUSIONS

The single factor experimental analysis shows that the mechanical damage has a significant effect on the germination rate, germination potential, germination index, and vigor index of castor seeds. The germination rate and germination potential of castor seeds with complete shell damage are the highest, with 93% germination rate and 70% germination potential. The germination rate of castor seeds with incomplete shell damage and cracked castor seeds are both 80%, but the germination potential of castor seeds with incomplete shell damage is 20% higher than that of cracked castor seeds.

It is found that there are two types of damage castor seed internal endosperm, which are single crack and turtle crack. Then the other forms of cracks produced is the same. The endosperm damage germination rate is 20%, which seriously affected the germination rate of castor seed and its germination quality. The cracked castor seed and seed shell incompletely damaged castor seed germination rate was 10% lower than the germination rate of intact castor seeds.

Comparing the detection of the actual crack length with the length measured by the super deep field microscope, it could be found that the error range was basically around 25%, and the better error was around 10%. The image segmentation of castor seeds with missing seed shells by the maximum variance method and the morphological processing could completely extract the features of seed shell missing castor seed images. The error between the extracted feature area and the actual measured object area function of the super-field microscope is around 10%.

ACKNOWLEDGEMENT

This research is supported by the National Natural Science Foundation of China, China (51457312), the authors thank relevant scholars for their assistance in the literature.

REFERENCES

[1] Che W.K., Sun L.J., Zhang Q., Tan W.Y., Ye D.D., Zhang D., Liu Y.Y., (2018), Pixel based bruise region extraction of apple using Vis-NIR hyperspectral imaging. *Computers & Electronics in Agriculture*, Vol.146, pp.12-21;

[2] Cheng L., (2018), *Apple surface defect detection research based on improved particle swarm optimization algorithm. Food & Machinery*, Vol.34, Issue 03, pp.141-145.;

[3] Chiara L.P., Dana Z., Agata L., Daniela B., Fabio P., Pietro F., Brijesh T., Paula B., Cullen P.J., (2018), Plasma activated water and airborne ultrasound treatments for enhanced germination and growth of soybean. *Innovative Food Science & Emerging Technologies*, Issue 49, pp.13-19;

[4] Diao Z.H., Diao C.Y., Yuan W.B., Wu Y.Y., (2018), Threshold segmentation algorithm for wheat diseased spot based on improved fuzzy edge detection. *Transactions of the Chinese Society of Agricultural Engineering*, Vol.34, Issue 10, pp. 147-152;

[5] Gao L.X., Li X.F., Jie X., Na X.J., Zhang W., Du X., (2010), Effects of internal mechanical damage on germination of soybean. *Transactions of the Chinese Society for Agricultural Machinery*, Vol.41, Issue 10, pp.63-66+102;
[6] Gu R.L., Huang R., Jia G.Y., Yuan Z.P., Ren L.S., Li L., Wang J.H., (2019), Effect of mechanical threshing on damage and vigor of maize seed threshed at different moisture contents. *Journal of Integrative Agriculture*, Vol.18, Issue 07, pp.1571-1578;
[7] Han Y., Chu Z., Zhao K., (2020), *Target positioning method in binocular vision manipulator control based on improved canny operator. Multimedia Tools and Applications*, Vol.79, pp.9599-9614.;
[8] Henila M., Chithra P., (2020), Segmentation using fuzzy cluster-based thresholding method for apple fruit sorting. *IET Image Processing*, Vol.14, Issue 16, pp.4178-4187;
[9] Joanna P., Agnieszka S., Agnieszka S., Piotr Y., Michal K., Malgorzata B., Dariusz A., (2018), Effects of atmospheric pressure plasma jet operating with DBD on Lavatera Thuringia L. seeds' germination. *PLOS ONE*, Vol.13, Issue 04, pp.1-12;
[10] Ju S., Bo K., Chla B., (2020), Breaking combinational dormancy of Rhus javanica L.seeds in South Korea: Effect of mechanical scarification and cold-moist stratification. *South African Journal of Botany*, Vol.133, pp.174-177;
[11] Ju S.C., Lee C.H., (2018). Effect of germination and water absorption on scarification and stratification of kousa dogwood seed. *Horticulture Environment & Biotechnology*, Vol.59, Issue 03, pp.1-10;
[12] Ju Z.Y., Xue Y.J., Zhang W.X., Zhai C.Y., (2020), Pomegranate Disease Spot Detection Algorithm Based on Adaptive Threshold Prewitt. *Transactions of the Chinese Society of Agricultural Engineering*, Vol.36, Issue 08, pp.135-142;
[13] Junior F.G., Cicero S.M., Vaz C., Lasso P., (2019), X-ray microtomography in comparison to radiographic analysis of mechanically damaged maize seeds and its effect on seed germination. *Acta Scientiarum Agronomy*, Vol.41, pp. e42608;
[14] Li J.W., Zhou R.W. Zhou R.S., Zhang X.H., Yang S.Z., (2018), Atmospheric-pressure plasma-treated water for seed germination and seedling growth of mung bean and its sterilization effect on mung bean sprouts. *Innovative Food Science & Emerging Technologies*, Issue 53, pp.36-44;
[15] Li J.Z., Zhang B.X., Wang W.N., Hou X.Y., Liu H.G., Yang Y.F., Tang D.Y., Wang G.M., (2018), Research progress in breeding and cultivation of castor in China. *Bulletin of Agricultural Science and Technology*, Issue 10, pp.198-200,2;
[16] Li Y.N., Sun J., Ding Q.S., Liu Y.Y., Ding W.M., (2015), Effects of glumes and cracks on seed germination and seedling growth of hybrid rice. *Hybrid Rice*, Vol.30, Issue 04, pp.71-74;
[17] Liu L.B., Cheng X.L., Dai J.G., Lai J.C., (2017), Adaptive Threshold Segmentation of Cotton Field Canopies Image Based on Logical Regression Algorithm [J]. *Transactions of the Chinese Society of Agricultural Engineering*, Vol.33, Issue 12, pp.201-208;
[18] Liu Y.X., Su B.F., Wang C., Mi Z.W., Wang F.Y., (2019), Leaf area estimation method based on three-dimensional point cloud. *Transactions of the Chinese Society for Agricultural Machinery*, Vol.50, Issue 12, pp.240-246+254;
[19] Luo W., Zhang H., Liu X., (2019), Hyperspectral/Multispectral Reflectance Imaging Combining with Watershed Segmentation Algorithm for Detection of Early Bruises on Apples with Different Peel Colors. *Food Analytical Methods*, Vol.12, Issue 05, pp.1218-1228;
[20] Sangeetha D., Deepa P., (2016), FPGA implementation of cost-effective robust Canny edge detection algorithm. *Journal of Real-Time Image Processing*, Vol.16, pp.957-970;
[21] Song Y.Q., Jiao J.K., Wu L.Y., Chi B.W., Chen T.Y., Zhang B.F., Lu C.Z., Xin M.J., (2019), Effects of mechanical compression on emergence and growth of garlic seed flap. *Transactions of the Chinese Society of Agricultural Engineering*, Vol.35, Issue 05, pp.26-32;
[22] Wang G., Tse P.W., Yuan M., (2017), Automatic internal crack detection from a sequence of infrared images with a triple-threshold Canny edge detector. *Measurement Science and Technology*, Vol.29, pp.025403;
[23] Yang Y., Zhao X., Huang M., Zhu Q; (2021), Multispectral image-based germination detection of potato by using supervised multiple threshold segmentation models and Canny edge detector. *Computers and Electronics in Agriculture*, Vol.182, Issue 07, pp.106041;
[24] Yu S.C., Li Y.M., Ma Z., Wang J.T., Hu B.Y., Xu L.Z., Tang Z., (2019), Study on the morphology of grain and cob damage during direct harvesting of maize. *Journal of Agricultural Mechanization Research*, Vol.41, Issue 10, pp.208-212.

IMAGE EVALUATION METHOD FOR ROTARY TILLAGE OPERATION QUALITY
/
面向旋耕作业质量的图像评价方法

Xiudong SUN [1], Yong WANG [2], Yusong CHEN [2], Renyuan SHEN [2], Changxing GENG *[2]
[1]Shanghai Vocational College of Agriculture and Forestry, Shanghai/China;
[2]Robotics and Microsystems Centre, Soochow University, Suzhou/China
Tel: +8618662299889; E-mail: chxgeng@suda.edu.cn
DOI: https://doi.org/10.35633/inmateh-68-25

Keywords: *machine vision; rotary tillage condition detection; residual stubble amount*

ABSTRACT
In the scene of paddy field rotary tillage, a real-time detection method of rotary tillage condition based on machine vision is proposed, and the quality of rotary tillage is evaluated by the index of residual stubble. The residual root stubble is selected as the research object, and the root stubble detection method based on the standard deviation of Y component in YCrCb space is proposed to determine the residual root stubble of soil after rotary tillage, which is divided into three levels: less root stubble, medium root stubble, and more root stubble. Finally, the accuracy of the algorithm is verified by field test and questionnaire survey. On the basis of manual evaluation, the accuracy rate of the working condition is 83.6 %, which provides a more accurate basis for the real-time adjustment of the control strategy for the unmanned operation of agricultural machinery in the field, and realizes the rotary tillage quality from qualitative evaluation to quantitative evaluation, and lays the foundation for the data of rotary tillage quality.

摘要
在面向水田旋耕作业场景中，提出基于机器视觉的旋耕工况实时检测方法，以残余根茬量的指标来评价旋耕质量。选取残余根茬量为研究对象，提出基于 YCrCb 空间 Y 分量的标准差的根茬量检测方法来判断旋耕后土壤的残余根茬量，分为三个等级：根茬量较少、根茬量中等、根茬量较多；最终以现场试验和问卷调查的形式验证算法的准确性。在人工评判的基础上，该工况的准确率为 83.6%，这对大田农机无人化作业的控制策略的实时调整提供较为准确的依据，实现对旋耕质量从定性评价到定量评价的转换，为旋耕质量数据化奠定基础。

INTRODUCTION

In the traditional rotary tillage operation mode, manual observation of the quality of rotary tillage operation is time-consuming and labor-intensive, and there is a certain degree of subjectivity. Therefore, the automatic operation of paddy field agricultural machinery needs to have the function of automatic inspection of the operation quality of rotary tillage operation conditions. Scholars have studied the effects of different soils on crops *(Huifeng Wang et al., 2019; Yong Liu et al., 2016; Giulia Bondiet al., 2018; Bruno Vizioli et al., 2021)*, and there are different studies from the planting stage to the harvesting stage *(Guilherme Adalberto Castioni et al., 2018; Rituparna Saikia et al., 2020; Lotfollah Abdollahi et al., 2015)*. From a qualitative point of view, scholars first proposed the concept of soil surface roughness *(Gerard Govers et al., 2000)*, and then proposed a soil surface roughness index based on the standard deviation of the sampling height measurement describing the vertical component of the roughness *(Bertuzzi, P. et al.,1990; Chi-hua Huang et al.,1992; Grant, C.D. et al.,1992)*. From the perspective of quantitative analysis, scholars improve the measurement quality by using high-precision instruments and technologies, such as using laser sensors to scan the contour of the soil surface *(Yi Qiu et al., 2020; Daniele Pochi et al., 2010)* and using unmanned aerial vehicles to carry cameras and imaging technology to evaluate the quality of cultivation *(Roberto Fanigliulo et al., 2020; Naveed Anwar et al., 2018)*. If the simulation experiment is only conducted in the laboratory, very good results will be obtained whether using laser sensors or cameras. However, in the field operation environment, there are many uncertainties, so the quantitative analysis of rotary tillage quality is more challenging *(Cezary Kaźmierowski et al., 2015)*.

The purpose of this paper is to evaluate the working conditions of rotary tillage in paddy field. By selecting the perception of working conditions of residual stubble as the research object, the automatic detection algorithm of residual stubble of rotary tillage is studied.

---

[1] *Xiudong Sun, As. Prof. Ms.Eng.;*
[2] *Changxing Geng, As. Prof. PhD.Eng.; Yong Wang, Ms. Stud. Eng.; Yusong Chen, Ms. Stud. Eng.; Renyuan Shen, Ms. Stud. Eng.;*

MATERIAL AND METHODS

Experimental equipment

In this experiment, a Kubota M854k tractor with a speed of 2 m/s and a rated power of 85 horsepower is used, and a rotary tiller with a working width of 2.2 m on the rear suspension. On the tractor, Advantech's MIC-7700 industrial computer and Intel Real Sense D435i depth camera are independently built. The camera parameters are shown in Table 1. The camera collects color images and depth images in real time, and the obtained image data is transmitted to the industrial computer; the industrial computer runs a homemade software system to analyze the image data. The specific installation method is shown in Figure 1. The industrial computer is installed under the tractor seat. The camera is installed above the rear of the tractor with a height of 2.45 m, and its optical axis is installed at 35°with the ground, as shown in Figure 2, where AB is the ground, AC is the distance from the camera axis to the ground, BC is the camera installation height of 2.35 m, the angle between AC and AB is the angle between the camera axis and the ground is 35°.

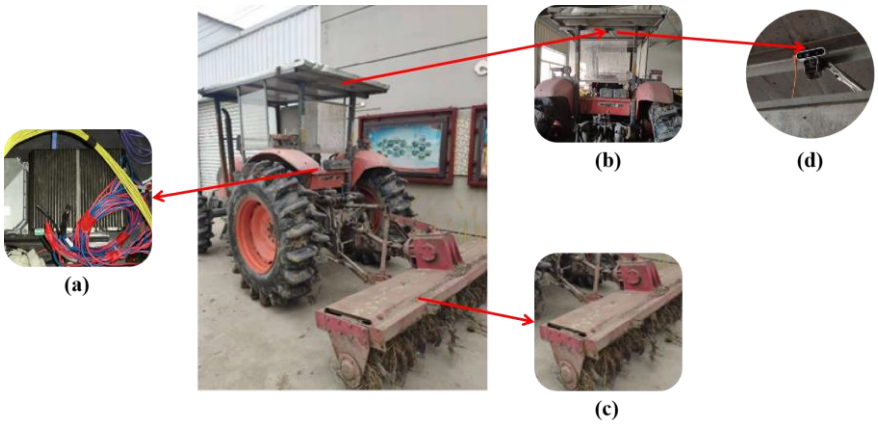

Fig. 1 - Tractor for experiment

(a) Industrial computer; (b) Camera installation location; (c) Rotary tiller; (d) Camera installation location;

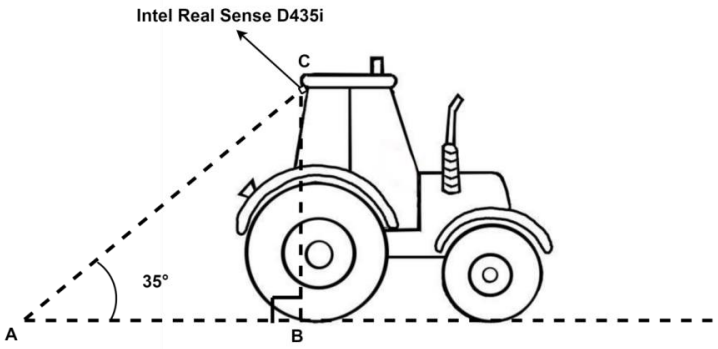

Fig. 2 - The camera is installed on the tractor.

Table 1

Camera parameters

The camera specifications	Parameter index
Use environment	Indoor and outdoor
Depth detection range (m)	0.2 m - 10 m
Color camera resolution (frames)	1920 * 1080 / 90 fps
Depth camera resolution (frames)	1280 * 720 / 30 fps
Shape size (length * width * height)	90 mm * 25 mm * 25 mm

Test scenarios and data collection

This test site is in Changshu Guli town, Wuqiu village, at national modern agriculture (rice and wheat) demonstration base, as shown in Figure 3. The tractor is performing rotary tillage.

A total of 14732 images of normal operation, good quality, uneven tillage depth, and different residual stubble are collected for the operation scene of rotary tillage after rice harvest. The images are divided into different operation conditions for analysis. The image acquisition frequency is 10 frames per second, and the size is 1280 * 720 pixels. As shown in Figure 4, the depth map of the corresponding image is retained for the detection of the depth information of the rotary tiller.

Fig. 3 - Rotary tillage scene

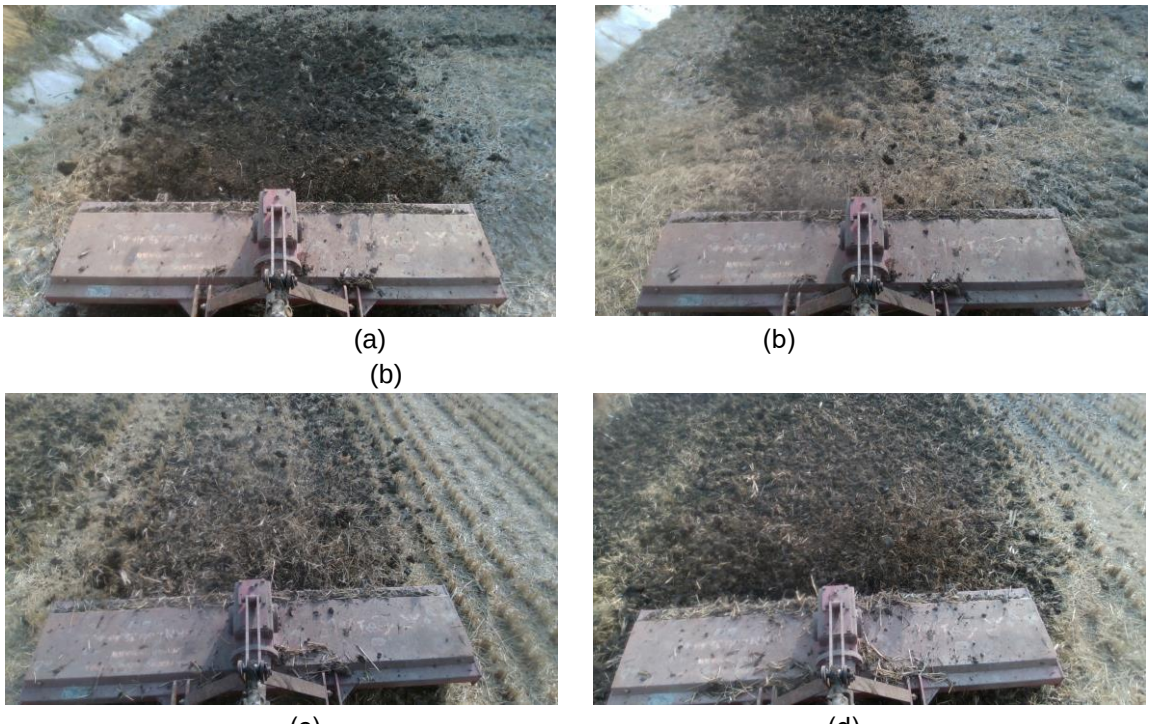

Fig. 4 - Images of different rotary tillage operations

(a) Good quality; (b) More root stubble; (c) Medium root stubble; (d) Less root stubble

Detection of rotary tillage residual stubble based on image understanding

- ROI selection

Figure 5 shows that the upper part of the image is mainly land completed by rotary tillage, and the lower part is mainly the rotary tillage machine. The selection of region of interest (ROI) needs to exclude the rotary tiller part and retain the stubble part of the soil after rotary tillage. In the process of tractor operation, the rotary tiller may oscillate slightly, so the rotary tillage area cannot be accurately determined by the position of rotary tillage machine. It can be seen from the analysis of the rotary tillage image that the position of the newly-cultivated area in the image is basically in the trapezoidal part near the upper end of the image, so the 400 * 400 pixels area in the middle of the top of the original image can be used as ROI.

Fig. 5 - ROI region diagram of rotary tillage image

- Image analysis of rotary tillage based on YCrCb color space

The typical image of rotary tillage working condition is shown in Figure 6(a). The left area is the cultivated land, and the right area is the uncultivated land (full of stubble). The horizontal line y = 200 (satisfying the condition of color difference) is extracted from the original image (taking the right upper corner of the image as the coordinate origin, the transverse x axis and the longitudinal y axis), and the line profile method is used to analyze the RGB values of all pixels on the horizontal line. The histogram of the color distribution of the line section is shown in Figure 6(b), and the values of the three components are close in both cultivated and uncultivated areas, so the RGB color space is not applicable. However, there are great differences in brightness characteristics, and the color space separated by brightness and color can be used. As shown in Figure 6(c), the brightness component Y has a wide distribution and approximate bimodal characteristics, which is conducive to the threshold segmentation of different semantic regions. Therefore, the Y component in YCrCb space is suitable for the study of the difference between soil and root stubble characteristics.

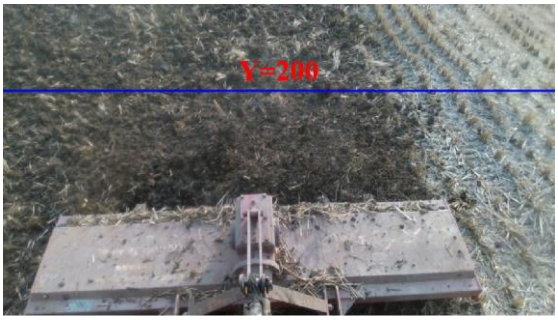

(a)

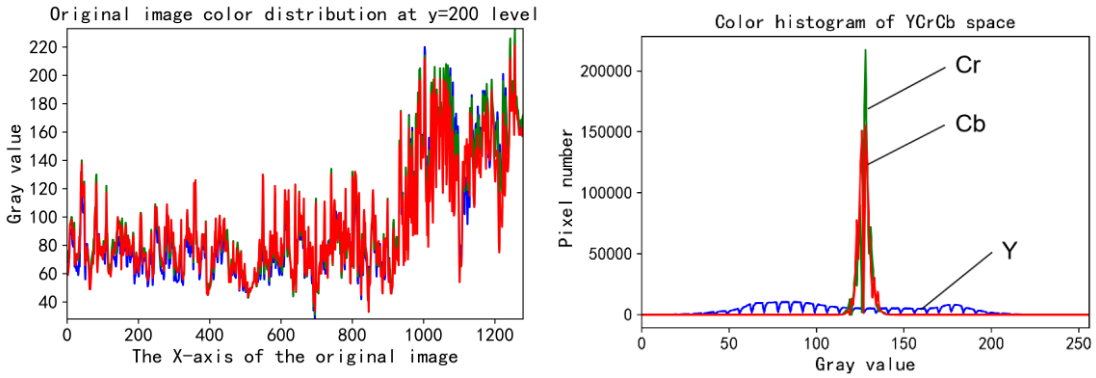

(b) (c)

Fig. 6 - Typical images of rotary tillage and their horizontal distribution histograms

(a) Original image; (b) The original map in the y = 200 horizontal line color distribution (red, green and blue three color curves respectively represent the value of R, G, B three components); (c) YCrCb color space color histogram

Taking the image of rotary tillage after harvesting in machine-transplanted paddy field as the research object, 40 rotary tillage images with less residual stubble, medium number of stubble and more stubble judged by human eyes are selected respectively. Mean m and standard deviation σ are used to describe the characteristics of the image at this time, as shown in Equation 1 and Equation 2. The mean and standard deviation of ROI in Y-component gray image are analyzed, and the statistical results are shown in Table 2.

$$m = \sum_{i=0}^{N-1} K_i \, P(K_i) \quad (1)$$

$$\sigma = \sqrt{\sigma^2} = \sum_{i=0}^{N-1} (K_i - m)^2 \, P(K_i) \quad (2)$$

where:

Ki -- a possible gray value in the image

P(Ki) -- the frequency of the gray value in the image

N -- the number of possible gray values

m -- the mean value in Equation (1).

Table 2

Statistical parameter distribution

Type of parameters	Less root stubble	Medium root stubble	More root stubble
Mean value	62.06	86.10	85.33
Standard deviation	16.36	27.44	34.07

According to the Table 2, soil and stubble have significant differences in the value of Y component. It can be seen from Figure 7 that the greater the standard difference, there is more stubble. Therefore, a root stubble detection method based on the standard deviation of Y component in YCrCb space is proposed for real-time detection of rotary tillage residual root stubble. Through the standard deviation data in Table 2, the residual stubble of rotary tillage can be divided into three grades, less, medium and more, as shown in Table 3.

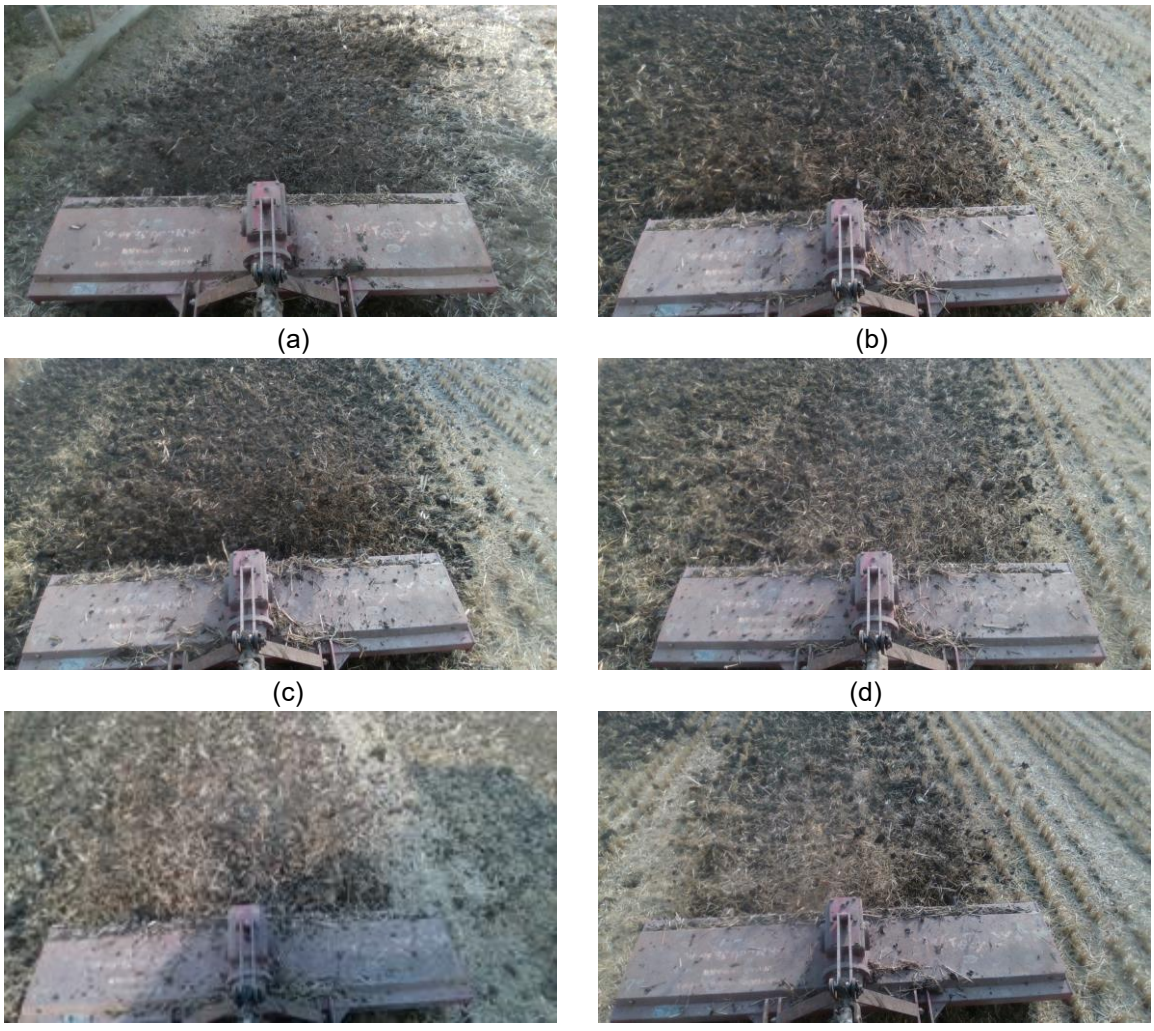

(a) (b) (c) (d) (e) (f)

Fig. 7 - Typical pictures and standard deviation of different stubble after tillage

(a) σ = 16.486. (b) σ = 18.076. (c) σ = 25.424. (d) σ = 26.548. (e) σ = 36.498. (f) σ = 34.191;

Table 3

Classification Criteria of Stubble Quantity Based on Standard Deviation

Root stubble amount	Less	Medium	More
Standard deviation	Less than 20	20-30	Greater than 30

RESULTS

In order to verify the accuracy of the algorithm, this paper has double verification. In this paper, a field test was carried out. The test site was located at the national demonstration base of modern agriculture in Guli Town, ChangShu, on 30 January 2021. By analyzing the image data of rotary tillage collected by camera, the algorithm is used to determine the stubble quantity. As shown in Figure 8, Figure 8(a) is the paddy field before rotary tillage, and Figure 8(b) is the paddy field after rotary tillage. In order to make the artificial evaluation representative, the staff of Suzhou Agricultural Machinery Extension Station were invited to carry out artificial evaluation on the root stubble amount of field operation. In order to reduce the subjectivity of manual evaluation, 40 agricultural machinery extension station technicians with rich experience in rotary tillage were invited to evaluate the stubble quantity and tillage depth uniformity of field operation. The 40 technicians are distributed as follows, as shown in Table 4.

(a) (b)

Fig. 8 - Paddy fields before and after tillage

(a) Before tillage; (b) After farming;

Table 4

Distribution law of 40 technicians in agricultural machinery extension stations

Subordinate institutions	**All personnel are located in agricultural extension stations in Suzhou**			
Professional title	Senior engineers	Engineers	Assistant engineers	No
	9	18	6	7
Direction of engagement	Agricultural machinery promotion	Agricultural machinery management	Agricultural machinery education	Agricultural mechanization
	35	3	1	1
Work experience	0 year - 5 years	6 years -10 years	10 years – 15 years	Over 15 years
	14	8	3	15
Degree of understanding rotary tillage	Don't understood	Far understood	Understood	Very well understood
	12	19	6	3

Assessment results of rotary tillage residual stubble

A total of 500 images were randomly selected from the collected images, and the results of the algorithm detection were compared with those of the manual evaluation to calculate the proportion of the images with the same judgment in the total. As shown in Table 5, the results are divided into three levels: less, medium and more. The number of manual evaluation results, the number of algorithm evaluation results and the number of consistent judgment results are counted respectively. The results of each evaluation are averaged, and the accuracy rate is the number of images with consistent results divided by the number of images obtained by manual evaluation. The proportion of the quantitative evaluation results based on standard deviation consistent with the manual evaluation is 83.6%.

Table 5

Statistics of area, perimeter and area-perimeter ratio

Root stubble amount	Artificial evaluation (picture)	Algorithm evaluation (picture)	Consistent results (picture)	Accuracy rate (%)
Less	142	147	127	87.3
Medium	261	248	204	79.3
More	97	105	97	89.7
Grand total	500	500	418	83.6

Figure 9 is a typical picture in which the method proposed in this paper is inconsistent with the artificial evaluation. In Figure 9(a), the standard deviation of the Y component is 37.536. The standard deviation of Figure 9(b) is 29.561. According to the method in this paper, the result is that the amount of stubble is medium, but the result of artificial evaluation is that the amount of stubble is more. Figure 9(a) is a typical situation at the boundary of two qualitative factors because it is located at the edge of farmland and is greatly disturbed by external factors.

(a) (b)

Fig. 9 - The Images with inconsistent results obtained by algorithm evaluation and manual evaluation

(a) σ = 37.536; (b) σ = 29.561;

Considering that the artificial evaluation also has certain subjectivity, 20 pictures with different root stubble are extracted according to the algorithm, as shown in Figure 10.

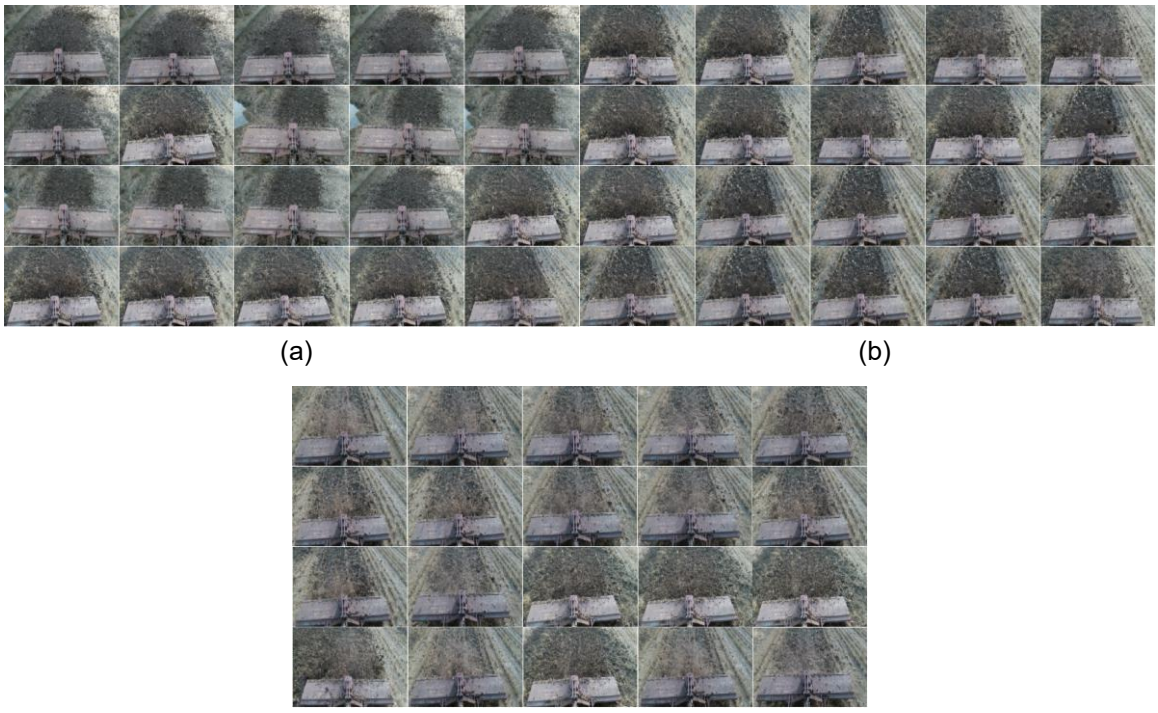

(a) (b)

(c)

Fig. 10 - Randomly selected rotary tillage images

(a) Less stubble; (b) Medium stubble; (c) More root stubble;

The result measured by the algorithm in Figure 10(a) is that the root stubble is less, the result measured by the algorithm in Figure 10(b) is that the root stubble is medium, and the result measured by the algorithm in Figure 10(c) is that the root stubble is more. After the pictures were randomly disrupted and the number of pictures at three levels was not informed, the questionnaire survey results of 40 technicians in agricultural machinery extension stations were obtained through the form of questionnaire survey, as shown in Figure 11. The average results of the three levels of less stubble, medium stubble and more stubble were 18, 21 and 21. The data that obviously deviate from the algorithm results are excluded from the evaluation results of the 40 agricultural extension station technicians, that is, the data that the evaluation results of the 40 agricultural extension station technicians for each grade are satisfied between 10 and 30 are retained. Finally, only 27 agricultural extension station technicians are satisfied with the evaluation results.

The specific results are shown in Figure 12, and the average results of the three grades of less stubble, medium stubble and more stubble are 20, 21 and 19, respectively.

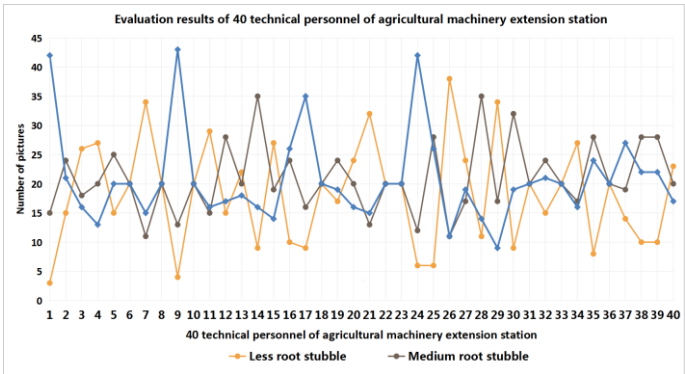

Fig. 11 - 40 agricultural machinery extension station technical personnel evaluation results

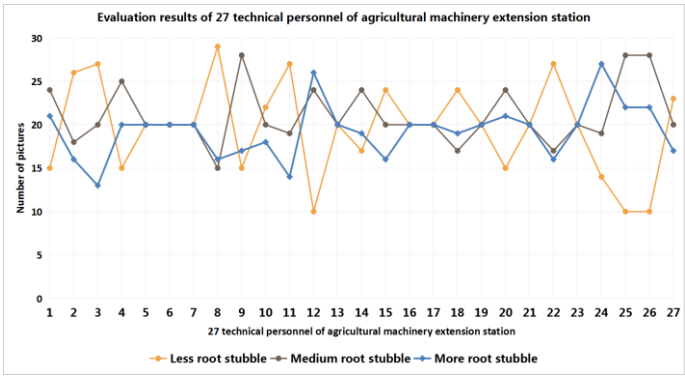

Fig. 12 - 27 agricultural machinery extension station technical personnel evaluation results

After considering the results of artificial evaluation and algorithm evaluation, combined with the results of technical personnel evaluation, it can be seen that the rotary tillage stubble detection method proposed in this paper has high reliability and can replace the artificial to evaluate the rotary tillage stubble in real time. The reasons are as follows. (1) Table 5 calculates the accuracy of algorithm evaluation based on manual evaluation, and the accuracy is 83.6 %. In order to ensure the reliability of the algorithm, this paper uses the form of questionnaire survey to collect the evaluation results of 40 agricultural machinery extension station technicians. The images evaluated by them are all different levels of images obtained by the algorithm, such as the average values of the evaluation results of Figure 11 and Figure 12 are basically consistent with the results obtained by the algorithm, and the error is within the acceptable range. (2) From Figure 11 and Figure 12, it can be seen that on the basis of algorithm evaluation, in the broken line diagram of three different situations of rotary tillage stubble obtained by manual evaluation, the data of three different situations fluctuate greatly, which is the disadvantage of manual evaluation, and the algorithm in this paper will reduce the disadvantages of manual evaluation, and the evaluation of rotary tillage operation conditions is relatively fair. (3) Whether the results obtained by the algorithm or the results obtained by manual evaluation, there will be an unhandled critical value, as shown in Figure 9. Therefore, for the critical value, both cannot be accurately judged, so it can be ignored, and the error is within an acceptable range.

CONCLUSIONS

In this paper, a real-time detection method of rotary tillage condition based on machine vision is proposed for paddy field rotary tillage operation condition, and the accuracy of the algorithm is verified by analyzing the index of rotary tillage residue. The root stubble amount detection method based on standard deviation in the Y component gray image of YCrCb space was used to determine the residual root stubble amount of soil after rotary tillage. After experimental analysis, the root stubble amount was divided into three grades by using two standard deviation thresholds. Finally, the accuracy of the algorithm is verified by field experiments and questionnaires. The results showed that on the basis of artificial evaluation, the accuracy rate of rotary tillage residue was 83.6 %. Based on the actual situation, the method proposed in this paper can replace manual automatic detection of working conditions. The deficiency is that the accuracy of the algorithm will decrease when the tractor is performing rotary tillage at the edge of the farmland or at the intersection of two different stubble quantities (such as the number of stubbles between a small amount and a medium amount), which is a problem to be solved in the later stage. In the detection of residual stubble in rotary tillage, the interference caused by possible shadows was not considered, and this situation needs to be taken into account in order to improve the environmental adaptability of the algorithm. To solve the above two problems, the accuracy of the algorithm will be improved. Scholars have also done little research on the quality evaluation of rotary tillage, so this paper has not been compared with the research done by other scholars.

ACKNOWLEDGEMENT

This study was supported by a National Key Research and Development Program of China (No. 2016YFD0700600).

REFERENCES

[1] Abdollahi, L., Hansen, E. M., Rickson, R.J., Munkholm, L. J., (2015). Overall assessment of soil quality on humid sandy loams: Effects of location, rotation and tillage. *Soil and Tillage Research. 145,* 29-36. https://doi.org/10.1016/j.still.2014.08.009

[2] Anwar, N., Izhar, M. A., Najam, F. A., (2018). Construction Monitoring and Reporting using Drones and Unmanned Aerial Vehicles (UAVs). *In Proceedings of the 10th International Conference on Construction in the 21st Century (CITC-10), Colombo, Sri Lanka, 2-4*. https://doi.org/10.1007/978-3-319-40379-3_12

[3] Bertuzzi, P., Rauws, G., Courault, D., (1990). Testing roughness indices to estimate soil surface roughness changes due to simulate rainfall. *Soil Tillage Res.17,* 87-99. https://doi.org/10.1016/0167-1987(90)90008-2

[4] Bondi, G. L., Creamer, R., Ferrari, A., Fenton, O., Wall, D. (2018). Using machine learning to predict soil bulk density on the basis of visual parameters: Tools for in-field and post-field evaluation. *Geoderma an International Journal of Soil Science.* https://doi.org/10.1016/j.geoderma.2017.11.035

[5] Castioni, G. A., Cherubin, M. R., Menandro, L. M. S., Sanches, G. M., Bordonal, R. D. O., Barbosa, L. C., Franco, H.C.J, Carvalho, J. L. N., (2018). Soil physical quality response to sugarcane straw removal in Brazil: A multi-approach assessment. *Soil and Tillage Research. 184,*301-309. https://doi.org/10.1016/j.still.2018.08.007

[6] Cezary K., Jakub C., Sławomir K., Cierniewski, J., Jasiewicz, J., Wyczałek, M., (2015). M. Soil surface roughness quantification using DEM obtained from UAV photogrammetry. *In Geomorphometry for Geosciences, Adam Mickiewicz University in Pozna'n-Institute of Geoecology and Geoinformation. International Society for Geomorphometry: Tokyo, Japan*. https://doi.org/10.13140/RG.2.1.4811.8889

[7] Govers, G., Takken, I., Helming, K., (2000). Soil roughness and overland flow. *Agronomie.20,* 131-146. https://doi.org/10.1051/agro:2000114

[8] Grant, C.D., Dexter, A.R., Huang, C., (1990). Roughness of soil fracture surfaces as a measure of soil microstructure. *Eur. J. Soil Sci. 41,* 95-110. https://doi.org/10.1111/j.1365-2389.1990.tb00048.x

[9] Huang, C. H., Bradford, J. M., (1992). Applications of a laser scanner to quantify soil microtopography. *Soil Sci. Soc. Am. J. 56,*14-21. https://doi.org/10.2136/sssaj1992.03615995005600010002x

[10] Liu, Y., Wang, H. F., Zhang, H., Karsten Liber. (2016). A comprehensive support vector machine-based classification model for soil quality assessment. *Soil & Tillage Research, 155*, 19-26. https://doi.org/10.1016/j.still.2015.07.006

[11] Pochi, D., Roberto F. L., (2010). Testing of soil tillage machinery. *Soil Biology. pp.147-168*. https://link.springer.com/chapter/10.1007%2F978-3-642-03681-1_10

[12] Qiu, Y., Chen, Z., Hou, Z. f., Liu, H. Y., Guo, F., Nianzu Dai, N. Z., (2020). Investigation on data collection and fractal characteristics of soil surface roughness. *INMATEH Agricultural Engineering. 16(2),* 135-142. https://doi.org/10.35633/inmateh-61-15

[13] Roberto F. L., Francesca A., Simone F., Pochi, D., Federico P., Laura F., Renato G., Corrado C., (2020). Light Drone-Based Application to Assess Soil Tillage Quality Parameters. *Sensors (Basel, Switzerland).20(3)*. https://doi.org/10.3390/s20030728

[14] Saikia, R., Sharma, S., Thind, H. S., Singh, Y., (2020). Tillage and residue management practices affect soil biological indicators in a rice-wheat cropping system in north-western India. *Soil Use and Management. 36(1)*. https://doi.org/10.1111/sum.12544

[15] Vizioli, B., Cavalieri-Polizeli, K. M. V., Tormena, C. A., (2019). Effects of long-term tillage systems on soil physical quality and crop yield in a Brazilian Ferralsol. *Soil and Tillage Research. 209,*104935. https://doi.org/10.1016/j.still.2021.104935

[16] Wang, H. F., Zhang, H., Liu, Y. (2018). Using a posterior probability support vector machine model to assess soil quality in Taiyuan, China-Science Direct. *Soil and Tillage Research, 185,* 146-152. https://doi.org/10.1016/j.still.2018.08.013

AUTOMATIC SYSTEM AND METHOD FOR IMPROVING AERIAL SPRAY DROPLET PENETRATION
/
提高航空喷雾雾滴穿透性的方法和自动系统研究

Zhiwei TIAN [1,2], Xinyu XUE [3], Famin DUAN [1], Sen YAO [1,2], Wei MA*[1]
[1] Institute of Urban Agriculture, Chinese Academy of Agricultural Sciences, Chengdu / China;
[2] Chengdu National Agricultural Science and Technology Center, Chengdu / China;
[3] Nanjing Research Institute for Agricultural Mechanization, Ministry of Agriculture and Rural Affairs, Nanjing / China
Tel: 8613521210452; E-mail: mawei03@caas.cn
DOI: https://doi.org/10.35633/inmateh-68-26

Keywords: *aerial application, unmanned aerial vehicle (UAV), droplet penetration, spray system optimization*

ABSTRACT
When UAVs apply a pesticide at different speeds, droplet deposition area and canopy vortex area are not at the same location, which prevents droplets from depositing on the backside of leaves and lower part of plants in canopy vortex, and affects spray quality and pests and diseases control effect. To shorten the distance between the two areas and improve droplet penetration, a method for adjusting nozzle inclination angle based on droplet force analysis and tests was proposed in this paper. According to the obtained model, an automatic nozzle angle adjustment system was developed from hardware and software. The experimental results showed that the number of droplets deposited on the entire leaf increased by 21.58% when UAV spraying with the system mounted. The average number of droplets on the front side of the leaf increased by 14.44% while 66.05% was on the backside of the leaf with the system mounted. This indicates that the method and system proposed have a significant impact on improving the UAV spray penetration.

摘要
无人机以不同速度施药时，液滴沉积区和冠层涡流区不在同一位置，导致液滴无法沉积在叶片背面和植物下层，影响喷雾质量和病虫害控制效果。为了弥补两区域之间的间距并提高液滴渗透率。本文基于液滴受力分析和试验，提出了一种调整喷嘴倾角的方法。发现最佳喷管角度(y)与无人机飞行速度(x)的关系为：$y = -0.367x^2 + 6.2932x - 0.8438$，$R^2 = 0.8333$. 根据该模型，从硬件和软件上开发了自动喷嘴角度调整系统。结果表明，安装该系统的无人机喷洒后，沉积在整个叶片上的液滴数量增加了 21.58%，叶片正面平均液滴数增加了 14.44%，而叶片背面的液滴数量增加了 66.05%。这表明所提出的方法和系统对提高无人机喷雾穿透能力有显着影响。

INTRODUCTION
In the past decade, small rotor UAVs have been widely used in pesticide application, covering staple food crops, oil crops and cash crops (*Xue et al., 2020*). During the pesticide application, rotors often provide lift force for the UAV body while generating strong downwash airflow (*Fan et al., 2019*). When the airflow spreads to the crop canopy, it would swing plants seriously and form a canopy vortex. As shown in Figure 1, the plants in the vortex sway, and their leaves turn over, which is a specific spray characteristic of a small plant protection UAV (*Wei et al., 2021*).

Theoretically, the canopy vortex is helpful to promote droplet penetration by blowing crop canopy dispersing, and increasing the number of droplets deposited on the backside of leaves and the lower part of plants, and give a positive effect on pests and diseases control, because some crop pests and diseases, such as powdery mildew, rice planthoppers, and cotton aphids, are mainly parasitic on the lower parts of plants and the back of leaves. The more droplets deposited on these target areas, the more chance the diseases and pests are exposed to pesticides. It is indispensable to ensure a perfect control effect (*Qin et al., 2018*). On the other hand, more droplets falling on the target area means fewer droplets are lost, the effective spray is important for avoiding excessive application of pesticides and protecting the environment.

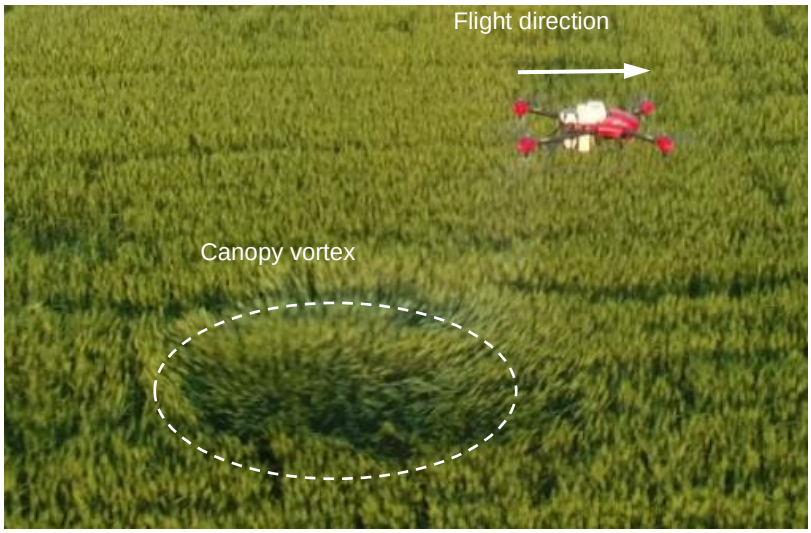

Fig. 1 - Crop canopy vortex caused by rotor downwash airflow

For these reasons, understanding the canopy vortex features and making full use of them is a potential research topic. To some extent, it decides UAV spray quality. Some researchers have investigated the distribution characteristics of the canopy vortex and its influence on droplet deposition. Based on field tests, *Li Jiyu et al., (2018),* found that the obvious canopy vortex of multi-rotor UAVs has a significant promotion on the droplet distribution. The number of droplets deposited under flight with a large-size canopy vortex was 1.5 times more than those with a small-size vortex and 7 times more than the flight without a canopy vortex (*Guo et al., 2019*). So, it is believed that the canopy vortex should be taken seriously, and this area is regarded as the target area where the droplets should be sprayed (*Lan et al., 2018*). However, the canopy vortex is not always effective in improving the deposition performance of droplets. We carried out many spray experiments under different UAV operating parameters in 2018 and 2019 (*Tian et al., 2020a*). The results showed that the positive effect of canopy vortex on droplet penetration is not constant, and it varied with operating parameters greatly. To figure out the reasons, our team extracted the canopy vortex area at different UAV flight speeds based on machine vision technology and compared their distribution characteristics in 2020 (*Tian et al., 2020b*). According to the research results and spray process observation, it was concluded that the downwash airflow can only improve the droplet penetration effectively when three conditions are met: (i) the droplets can travel to the crop canopy, (ii) the airflow is strong enough to sway the crop canopy and make leaves turn over, and (iii) the final deposition area of droplets have to be at the same location with the canopy vortex area, so droplets can fall on the leaves back and the lower part of plants in time when crop canopy sway.

The small plant protection UAV often flies at a low-altitude manner of less than 5 m, so it is easy to form a canopy vortex as airflow is still strong even coming to crop canopy. On the other hand, nozzles of many UAVs are amounted below the rotors. The downward airflow from rotors would transport droplets to the crop canopy. Therefore, the conditions of (i) and (ii) are easy to be met, while (iii) mentioned above is difficult in the practical spray. When UAV is hovering, the droplet deposition and canopy vortex areas are both located directly below the UAV body and overlap with each other (*Yang et al., 2018*). When it moves quickly, during the time droplets and airflow travel down to the crop canopy, UAV has moved forwards a distance, which makes the two areas look like they have a lag relative to the location of the drone (*Yang et al., 2018*). Due to particle weight differences, the velocity attenuation rate of airflow and droplets are different when they move in the air (*Chen et al., 2017*). There is a much velocity loss for airflow but less for droplets. At the same falling height, airflow takes more time. So, there is a distance gap between the droplet deposition area and canopy vortex area when they reach crop canopy. The droplet deposition area is ahead of the canopy vortex area, which weakens the positive effect of canopy vortex on droplet penetration.

In this paper, a method by adjusting nozzle spray angle was proposed based on droplet force analysis to eliminate the gap between the droplet deposition and the canopy vortex areas. Then, the relationship between optimal nozzle angles and different flying speeds was studied through experiments. And based on the results, an automatic system was developed for nozzle angle adjustment. Finally, the spray performance of the UAV equipped with the system was tested.

MATERIAL AND METHODS

METHOD ANALYSIS OF ADJUSTING NOZZLE SPRAY ANGLE

Force analysis of droplet under different nozzle angle

UAV flight speed is the main reason causing a lag of the canopy vortex and droplet deposition areas (*Tian et al., 2020c*). There are different lag distances between the two areas at different speeds, while the flight height has a little contribution to it. In practical pesticide application, the UAV flight height is usually constant around 2 m, while the flight speed setting varies within the range of 1~8 m/s in the existing researches (*QIN et al., 2017*). As a result, our focus is on how to improve the positional relationship between the canopy vortex and the droplet deposition area at different UAV flying speeds. As analyzed in the INTRODUCTION, the canopy vortex is behind the droplet deposition area. As shown in Figure 2, it is necessary to move the canopy vortex forward or move the droplet deposition area backward to make the two areas at identical location. The canopy vortex is determined by the rotor wind field and is related to the UAV body structure and flight principle, which was difficult to be changed. Therefore, optimizing the spray system and making the droplet deposition area move backward to minimize the distance a is a valuable method.

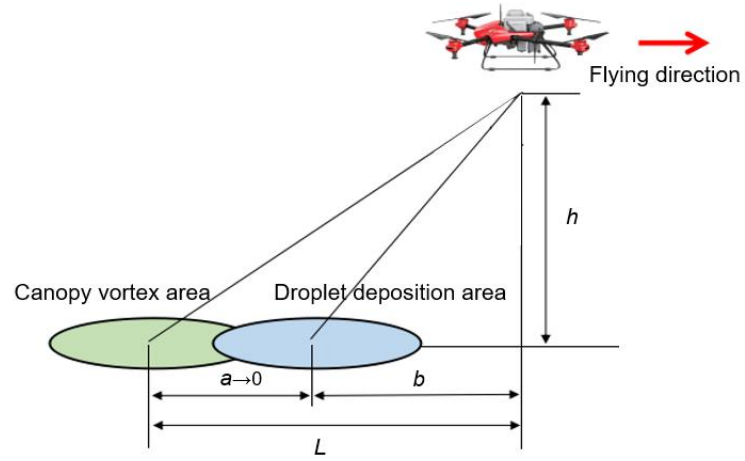

Fig. 2 - Distribution of canopy vortex and droplet deposition area

P20 (Guangzhou Jifei Technology Co., Ltd.), the commonly used electric four-rotor plant protection UAV in China, was a subject in this research. The effective spray width of P20 is 3 m, four centrifugal nozzles are assembled under each rotor, and the spray volume can be set from 0 to 15 L·ha^{-1} with a load capacity of 10 kg. Flying speed can be configured from 1 to 12 m·s^{-1}. The RTK provides high-precision positioning and navigation with an accuracy of a centimeter.

Centrifugal nozzle has a better atomization effect compared with traditional nozzles. The liquid is atomized by a centrifugal disc with high rotation speed and sprinkled under the centrifugal force. Droplet movement is mainly affected by G (Gravity), F_a (Centrifugal force), F_w (Pressure force of downwash airflow), and F_f (Air resistance). As shown in Figure 3(a), when the nozzle is installed downwards as normal, G and F_w are downward, and F_a is distributed tangentially along the edge of the disc. The direction of F_f is opposite to the droplet movement. In Figure 3(b) when the nozzle tilts backward, the force of G, F_w, and F_f on the droplet is consistent with the vertical condition, but the direction of centrifugal force F_a changes.

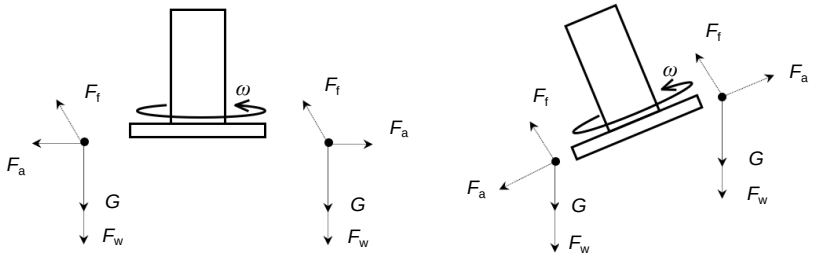

(a) Downwards nozzle (b) Backwards nozzle

Fig. 3 - Force analysis on droplet under different nozzle angles

The centrifugal force on the droplet in front of the nozzle tilts downwards. Its vertical downward component can further promote the droplet falling. The centrifugal force on the droplet behind the nozzle tilts upwards.

Its horizontal backward and vertical upward components can help the droplet move more distant backward, as these force components increase the droplet falling time. Therefore, a proper backward nozzle inclination angle would make part of droplets move backward, making up the distance between the canopy vortex and the droplet deposition areas. At the same time, it would help to promote some droplets depositing downward.

Statistical analysis on nozzle angle and flight speed

Different flight speeds should match the corresponding nozzle inclination, which is determined by droplet distribution characteristics. In many researches, CFD (Computational Fluid Dynamics) was used to simulate downwash airflow distribution and droplet deposition. However, it is difficult to make sure the simulation results are close to practical conditions because of model choices and parameters setting (*Parra H.G. et al., 2019*). In this paper, field tests were conducted to investigate the optimal nozzle angle of each UAV flight speeds.

A framework was designed and installed at the rotor arm to achieve nozzle angle adjustment. Before the UAV taking off different nozzle angles were set manually, and when the spraying tests were finished, the optimal nozzle angle was evaluated through droplet deposition information on the backside of plant leaves. Taking usual operating parameters as a reference, the flight height is constant at 2 m while the operating speeds are 3, 4, 5, and 6 m/s, respectively. When the nozzle angle of P20 is greater than 45°, part of the droplets would be lifted to air and cause droplet loss. On the other hand, the pre-experiments showed that small angle divisions have no obvious distinction in droplet deposition. Based on these factors the nozzle angle was set to 0°, 10°, 20°, 30°, and 40° under each speed. There are 20 group tests in total and each test has 3 repetitions.

Experiments were carried out at 10 a.m. on December 4th, 2019, at the test field of Nanjing Institute of Agricultural Mechanization, Ministry of Agriculture and Rural Affairs. During the test, meteorological data was recorded by a Kestrel 4500 Environmental Meter (Nielsen-Kellerman, USA). The air temperature was 22.4~25.6°C, the relative humidity was 41.3%~ 55.3%, and the wind speed was within 1.9 $m \cdot s^{-1}$. The spray liquid is an Allure Red aqueous solution with a ratio of 5%. As shown in Figure 4a, on a flat ground 10 sampling rods were arranged in two rows, the vertical and horizontal distance between them was 60 cm. Paper cards were fixed on the sampling rods 40 cm away from the ground. The front side of the paper card represents the front side of the plant leaf, while the backside was the back of a leaf. UAV's flying route was consistent with the long axis of the sampling rod, and it was located in the middle of rows. The route length was 50 m. To avoid the influence of unstable airflow during the acceleration and deceleration phase of the drone, sampling rods were put in the middle of the flying route. For each flight, the spray liquid was added to 8 L to maintain the UAV attitude constant. The spray volume was set to 12 $L \cdot hm^{-2}$ while the droplet size was 120 μm. After each flight was completed, paper cards were collected into ziplock bags for storage. They were taken to Lab and scanned into images with a resolution of at least 600 dpi. Finally, images were analyzed through ImageJ (National Institutes of Health, USA) to obtain droplet deposition information, including droplet number per unit area and droplet size (Shown in Figure 4c).

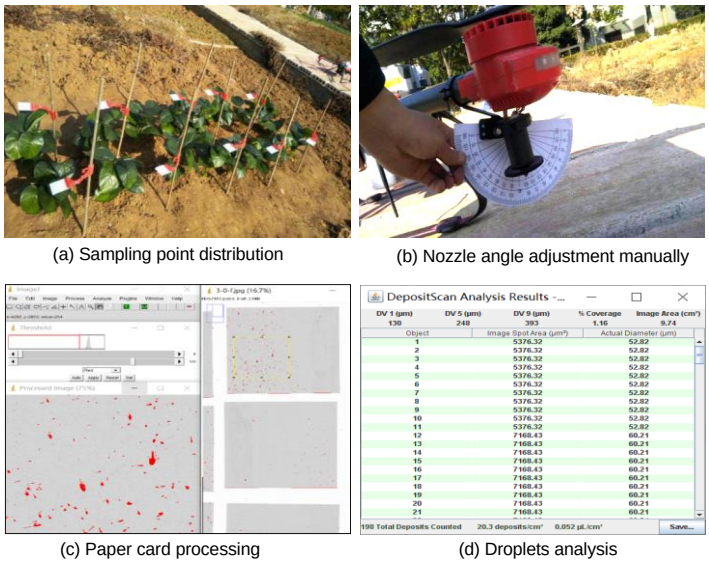

(a) Sampling point distribution (b) Nozzle angle adjustment manually

(c) Paper card processing (d) Droplets analysis

Fig. 4 - Test site and droplets analysis

The number of droplets deposited on the backside of the leaf at 10 sampling points was averaged to get the droplet deposition levels of this test. One-way ANOVA was used to analyze the influence of different spray angles on the number of droplets deposited on the back of the leaves. The results are shown in Table 1, P-value=2.52E-05<0.01, and F=28.154>Fcrit=4.301, indicating that in the case of α=0.05, there is a significant difference in the number of droplets deposited under different spray angles.

Table 1

Variance analysis

Source of difference	SS	df	MS	F	P-value	F crit
Between groups	1768.167	1	1768.167	28.15416	2.52E-05	4.30095
Within-group	1381.667	22	62.80303			
Total	3149.833	23				

For each flight speed, the optimal nozzle angle was screened out based on the droplet number of leaf back. When the drone is hovering, the nozzle is vertically downward and has no adjustment, so the beginning point of the line was connected with the origin coordinate to estimate the nozzle angle curves when UAV speed is less than 3 m/s, and to meet the angle adjustment requirements of UAV acceleration period, as shown in figure 5. Finally, a regression analysis based on the quadratic polynomial was adopted to describe the relationship between UAV flight speed (x / m·s^{-1}) and optimal nozzle angle (y / °).

The model is expressed as:

$$y = -0.367x^2 + 6.2932x - 0.8438,\ R^2 = 0.8333 \quad (1)$$

R^2 is the correlation coefficient, the closer the value of R^2 is to 1, the better the fitting effect of the model and the stronger the linear correlation between the two variables.

The fitting line shows that the optimal nozzle angle increases first and then sees a decreasing trend with UAV flight speed increase. When the drone sprays at different flying speeds, the spray effect of adjusting the nozzle angle are better than that without adjusting the nozzle inclination (nozzle angle is 0 degrees)

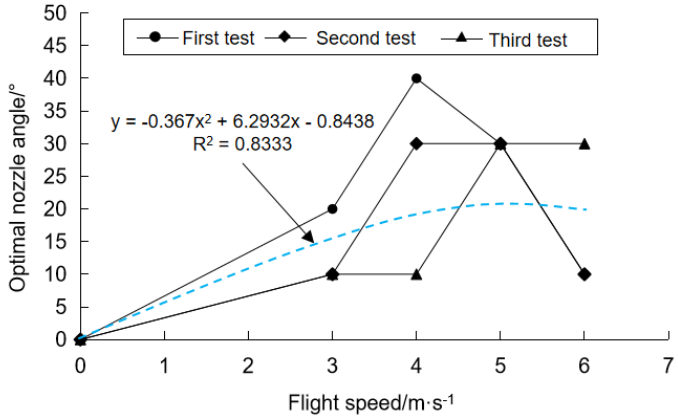

Fig. 5 - Relationship between fight speed and optimal nozzle angle

DEVELOPMENT OF AUTOMATIC NOZZLE ANGLE ADJUSTMENT PLATFORM

Hardware of control system

To achieve automatic adjustment of nozzle angle in real-time a system was designed. The optimal nozzle inclination varies with different operating speeds of UAV, so in this system, the flying speed needs to be collected firstly. And then the best nozzle angle is calculated according to the model in figure 5. Finally, the nozzle was driven to the expected position through the servo motor.

Arduino Uno was used as a controller, because this module is small in size, light in weight, low in cost, and it has been used widely in agricultural intelligent control scenarios. The working voltage is 5V and powered by two rechargeable lithium-ion batteries. The NEO-6M GPS module collects UAV flight speed in real-time. The size of the module is 31.5×25.5×8.2 mm, the collecting accuracy of speed is 0.01m·s^{-1}. The servo motor of RB-65PG was used to change the nozzle angle, with the control accuracy of 0.24°, and the maximum torque can reach 0.8 N·m. E103-W02 WiFi module can perform remote communication. This module's effective communication distance is 350 m.

Crop fields are broken down into small pieces in many provinces of China except Xinjiang and Neimeng. These small fields have different crops and owners, which limits UAV flying distance and more than 80% of UAV single flying route is within 200 m. Therefore, the communication distance of WiFi module is enough to cover UAV flying range. An LCD screen was also installed to help debug and read system parameters.

At the beginning, the controller reads UAV speed through the GPS module and calculates the optimal nozzle angle according to the model. Then the signal is sent to the servo motor through PWM and the servo motor drives the nozzle to the expected angle. At the same time, the current UAV flight speed and nozzle angle are displayed on an LCD screen. This data is also sent to the cloud for monitoring. The controller compares the deviation between the current nozzle angle and the optimal one continuously and changes the nozzle angle in real-time. As shown in Figure 6, all modules are integrated into the control box. IDE was used as platform to code and run the C program.

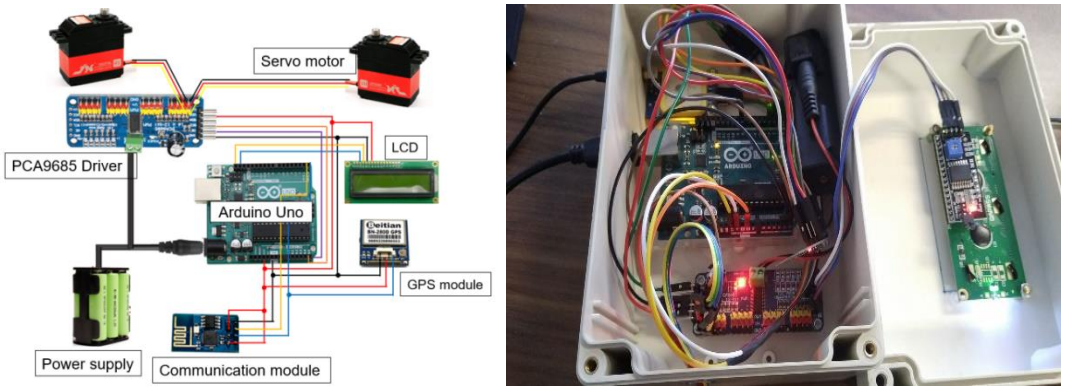

Fig. 6 - Hardware structure of nozzle angle adjustment system

However, the continuous adjustment will make the system too sensitive and frequent-shaking to spray stably. As a result, the model in figure 5 was dispersed and shown in Table 2. The error between the expected nozzle angle and the current one is changing with time.

Table 2

Nozzle angle controlling method

Speed scope (x / m·s^{-1})	Nozzle angle (y / °)
0 ≤ x < 1.5	5
1.5 ≤ x < 2.5	10
2.5 ≤ x < 3.5	15
3.5 ≤ x < 4.5	18
4.5 ≤ x < 5.5	21
5.5 ≤ x < 6.5	24
6.5 ≤ x < 7.5	25
x ≥ 7.5	26

Spray data monitoring platform

Monitoring the system parameters is helpful to detect its working status and prevent some failures ahead of time. An Android APP was developed based on App Inventor, an Android programming framework launched by Google. App Inventor not only has the advantages of easy development and high efficiency but also has a network database allowing clients access to data at any time.

The APP has two performances, one is reading and displaying current UAV speed and nozzle angle from the cloud. APP sends a GET request to cloud server through URL and API reading code, then receives JSON text. The text is parsed to the current system data. The second one is sending data to the cloud. This part could control the nozzle angle remotely. When the UAV speed is constant the nozzle angle can be set manually instead of frequent adjustment automatically. Clicking the mode button to choose manual mode, and entering a number within 0-45 can configure a nozzle angle. This data would be sent to the cloud and request writing through the URL and API writing code, waiting for the nozzle angle control system to read and execute.

The APP interface for system monitoring is shown in Figure 7. In this project, ThingSpeak was adopted as a cloud to connect the nozzle angle adjustment system and the client's APP. It can collect and stores sensor data through APP and API codes, additionally, ThingSpeak also supports data export access.

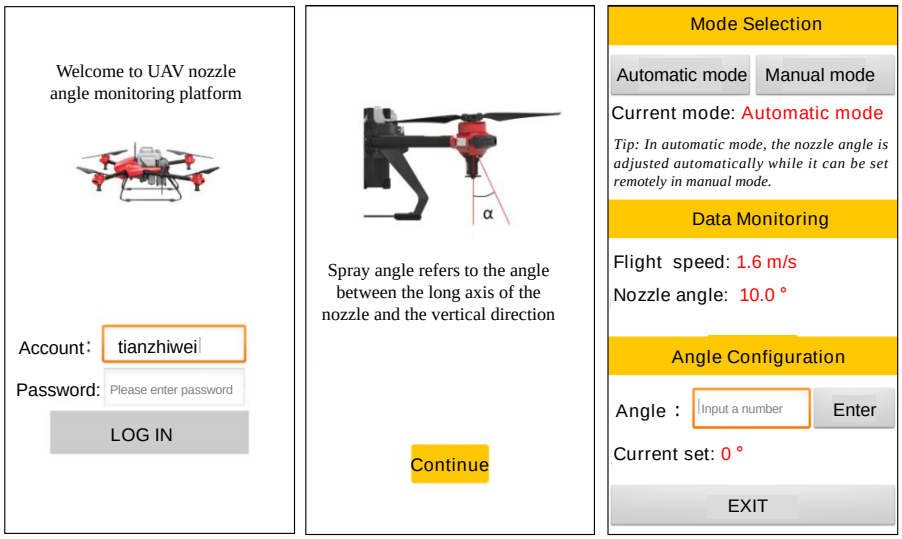

（a）Login interface （b）Introduction interface （c）Working interface

Fig. 7 - APP of nozzle angle adjustment system

DROPLET PENETRATION TESTS BASED ON THE ANGLE ADJUSTMENT SYSTEM

In order to learn about how does the nozzle adjustment system affects spray quality and verify whether the system has a positive effect on droplet penetration, it was needed to collect and analyze the number of droplets deposited on the front and backside of leaves.

Experiments were carried out at 2:00 pm on November 16th, 2020, in the rape field of the Hetian Agricultural Machinery Service Cooperative in Gaochun District, Nanjing. The test field was 300 m×80 m in size. At that time, the plants were in the seedling stage with an average height of 10 cm, their leaves were too small to attach sampling paper cards. Therefore, the test method was as same as that carried out before, including sampling points distribution, the way UAV spray, and droplet deposition data analysis.

Fig. 8 - Experimental scene

RESULTS

As shown in Figure 9a, regardless of whether the nozzle inclination adjustment system is installed or not, the number of droplets deposited on the front side of leaves decreased gradually with UAV flight speed increase. When the drone moved forward quickly, downwash airflow was weakened severely, the optimal meeting-point position of the downwash airflow from 4 rotors would lift. In this case, it not only doesn't promote droplet deposition but also has a "rolling-up effect", which rolls droplets up to the air. On the other hand, when the drone is flying at high speeds, the wind field is weak and sweeps across the plant canopy slightly, it can't overturn leaves and has a limited promotion effect on droplet penetration. When the system was installed, the number of droplets increased significantly. The faster the drone moves forwards, the more obvious the increase in the number of droplets.

As for the backside of the leaf, the droplet number of flight with the system was more than that without system installed for each speed. As shown in figure 9b, as flight speed increases, the number of droplets sees a dropping trend, which is the same as the condition of the front side of the leaf. When the drone flies slowly, the canopy vortex area is concentrated and in an elliptical shape, the plants in vortex sway seriously. When it flies fast the canopy vortex area is distributed in long strips, and plants sway slightly. From figure 9b it could be observed that the droplet number on the leaves' back is much more than others when UAV flying at 3 m/s, which indicates the concentrated canopy vortex is important for increasing droplet deposition on the backside of leaf. After the nozzle angle adjustment system was installed, the droplet number of 3 m/s increased more, because the strong downwash airflow under slow flight speed can sway plants and overturn leaves. At the same time, the backward nozzle helps droplets fall on this area in time, unlike the previous condition when droplet often falls on other areas. The results also imply flying speed of UAVs should not be too fast during pesticide application.

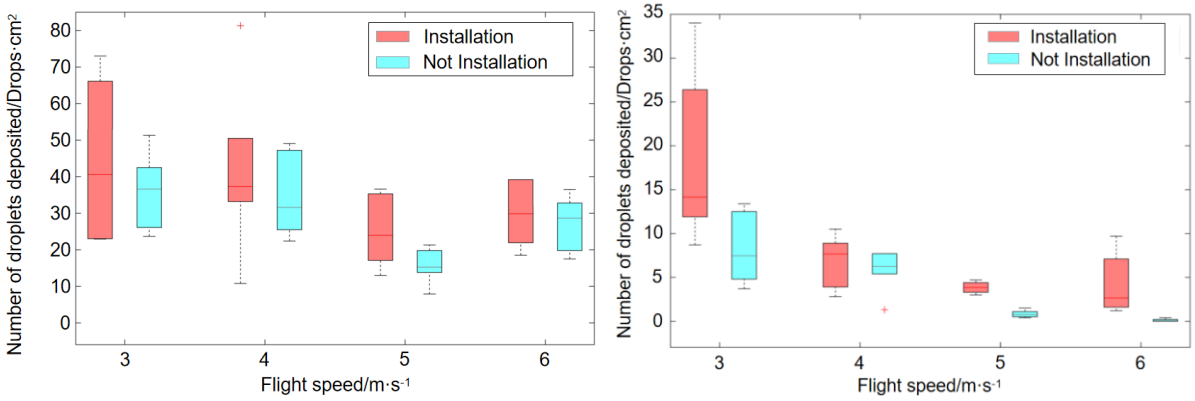

(a) Front side of leaf (b) Back side of leaf

Fig. 9 - Comparison of number of droplets deposited with and without the system installed

The number of droplets deposited on the front and backside of leaves was summed to have the total droplet number on one leaf. As shown in Table 3, the droplet number on the entire leaf increased by 21.58% after the nozzle angle adjustment system was installed.

Table 3

Comparison of number of droplets deposited before and after system installation

Flying speed /m·s^{-1}	Droplets deposited on the front side of leaf/Drops·cm^{-2}		Droplets deposited on the backside of leaf/Drops·cm^{-2}		Number of droplets deposited on whole leaf/Drops·cm^{-2}	
	Without system	With system	Without system	With system	Without system	With system
3	36.13	38.38	8.22	18.22	44.35	56.6
4	34.57	41.73	6.90	7.31	41.47	49.04
5	20.55	24.98	2.83	3.85	23.38	28.83
6	27.32	30.6	1.08	2.22	28.40	32.82
Average	29.64	33.92	4.76	7.90	34.40	41.82

Droplet number increased by 27.62%, 18.25%, 23.31%, and 15.56% respectively at flight speeds of 3, 4, 5, and 6 m·s^{-1}. Droplets number for the front side of the leaf was 29.64/cm^2 on average when UAV was spraying without the system, and 33.92/cm^2 when the system was installed, which increased by 14.44%. Without the system, the number of droplets deposited on the leaf back was 4.76/cm^2 on average, while 7.90/cm^2 with the system, this data increased by 66.05%. These results showed that the spray performance of UAVs with a nozzle angle adjustment system improved greatly, and the method and system proposed in this paper can improve the droplet penetration effectively.

CONCLUSIONS

When plant protection UAV applies pesticide at different speeds, droplet deposition and canopy vortex areas are not at the same location, which prevents droplets from depositing on the backside of the leaf and lower layer of the plant, and affects spray quality and pests and diseases control effect. In order to bridge the gap between the two areas and improve droplet penetration, in this paper, the method of adjusting the nozzle inclination angle was analyzed and tested firstly. It was found that the relationship between UAV flight speed(x) and optimal nozzle angle(y) was expressed as: $y = -0.367x^2 + 6.2932x–0.8438$, $R^2 = 0.8333$. Based on this model an automatic nozzle angle adjustment system was developed from hardware and software. The results showed that the number of droplets deposited on the entire leaf increased by 21.58% when the UAV spraying with the system was installed. The average number of droplets on the front side of the leaf increased by 14.44% while 66.05% was on the backside of the leaf after the system was installed. These results proved the nozzle angle adjustment system has a positive effect for improving droplet penetration, and the spray performance of UAVs with nozzle angle adjustment system also improved greatly.

During the UAV spray process, the flight height is usually rarely changed. However, to improve the operation efficiency, the flight speed setting varies greatly, it has been reported in the range of 1~8 $m \cdot s^{-1}$. Based on this fact the system developed in our project only considered the impact of UAV flight speed on the distance between crop canopy vortex area and droplet deposition area. However, flight height has a slight influence on the distance between the two areas, because changes in height would change the time that airflow and droplet flow need to spread to the crop canopy. Although flight speed is the primary factor; it would be more indicated if factors like flight height is also considered before designing a nozzle angle adjustment system.

On the other hand, the droplet deposition area and the canopy vortex area are easily affected by crosswinds, they may be located obliquely behind the UAV. Some research reported that when the crosswind speed was 1.1-7.0 m/s, the cumulative drift rate of droplets was between 13.0% and 56.2%, so the industry standard stipulated plant protection UAV can only apply pesticide when crosswind speed less than 3 m/s (*T/CCPIA 019-2019*). Following the standard, the aerial spray should be stopped when the wind speed is too fast to prevent the droplets from drifting into the air. If this rule is followed well by growers, the system will not face the challenge mentioned above.

ACKNOWLEDGEMENT

The authors thank the experts for editing our paper. We gratefully acknowledge the Local Finance Special Fund of Chengdu Agricultural Science and Technology Center (NASC2020KR05), Science and Technology Innovation Project Fund of Chinese Academy of Agricultural Sciences (ASTIP-2020-003), and the Science and Technology Innovation Project Fund of Chinese Academy of Agricultural Sciences (ASTIP-2020-001). We also thank the anonymous reviewers for their critical comments and suggestions to improve the manuscript.

REFERENCES

[1] Chen S.D., Lan Y.B., Bradley K.F., Li J.Y., Liu A.M., Mao Y.D. (2017). Effect of wind field below rotor on distribution of aerial spraying droplet deposition by using multi-*rotor UAV. Transactions of the Chinese Society for Agricultural Machinery.* 48(8): 105-113.

[2] Fan Jiarong, Zhaohui, Feng Ya'nan et al. (2019). Effects of Rotor Wheelbase on Downwash Flow Aggregation and Wind-resistance. *Mechanical Science and Technology for Aerospace Engineering* 38(12):1966-1974.

[3] Guo S., Li J. Y., Yao W. X., Zhan Y. L., Li Y. F. & Shi Y. Y. (2019). Distribution characteristics on droplet deposition of wind field vortex formed by multi-rotor UAV. *PLoS ONE*, 14(7), 22-34.

[4] Lan Y. B., Wang L. L. & Zhang Y. L. (2018). Application and prospect on obstacle avoidance technology for agricultural UAV. *Transactions of the CSAE*, 34(9), 104-113.

[5] Li J. Y., Lan Y. B. & Shi Y. Y. (2018). Research progress on airflow characteristics and field pesticide application system of rotary-wing UAV. *Transactions of the CSAE*, 34(12): 104-118.

[6] Parra H.G., Morales V.D.A. & Garcia E.E.G. (2019). Multiphase CFD simulation of photogrammetry 3D model for UAV crop spraying. *World Conference on Information Systems and Technologies*, 4, pp. 812-822. Springer, Cham.

[7] Qin W. C., Xue X. Y., Zhang S. M., Gu W. & Wang B. K. (2018). Droplet deposition and efficiency of fungicides sprayed with small UAV against wheat powdery mildew. *Int J Agric & Biol Eng*, 11(2): 27-32.

[8] Qin Weicai. (2017). *Research on spraying parameters optimization for single-rotor plant protection UAV*. Zhenjiang: Jiangsu University.
[9] T/CCPIA 019-2019, *Specification for Safe Application of Pesticide by Crop Protection UAS*.
[10] Tian Z. W., Xue X. Y., Cui L. F., Chen C., Peng B., & Liu B. (2020). Comparison of droplet deposition characteristics and cotton aphid control effect of plant protection UAV working during the day and night. *Transactions of the CSAE*, 36(5), 69-77.
[11] Tian Z.W., Xue X.Y., Xu Y., Yang F.B. & Sun Z. (2021). Effect of Plant Protection UAVs Downwash on Crop Canopy. *Transactions of the Chinese Society for Agricultural Machinery*, 52(1):40-48.
[12] Tian Zhiwei. (2020). *Optimization Design of Operating Parameters and Spraying System of Multi-rotor Plant Protection UAV Against Cotton Aphid*, Beijing, Chinese Academy of Agricultural Sciences.
[13] Wei X., Li J., Long B., Hu X., Wu H. & Li H.. (2021). Method for vortex shape retrieval and area calculation based on convex hull algorithm. *IEEE Access*, 9, 2706-2714.
[14] Xue X. Y., Gu W., Xu Y., Sun Z.& Lan Y. B. (2020). Review on current state of agricultural UAS regulations and standards. *Transactions of the Chinese Society for Agricultural Machinery*, 51(10), 1-10.
[15] Yang F.B., Xue Xi.Y., Cai C. & Zhou Q. Q. (2018). Effect of down wash airflow in hover on droplet motion law for multi-rotor unmanned plant protection machine. *Transactions of the CSAE*, 34(2), 64-73.
[16] Yang Z. L., Ge L. Z., Qi L. J., Cheng Y. F. & Wu Y. L. (2018). Influence of UAV rotor downwash airflow on spray width. *Transactions of the Chinese Society for Agricultural Machinery*, 49(1), 116-122.

TEST AND ANALYSIS OF MECHANICAL PROPERTIES OF BUCKWHEAT STEM DURING HARVEST
/
荞麦茎秆机械收获力学性质测试与分析

Yanqing ZHANG, Qingliang CUI*, Can WANG, Hongbo LI, Zhiyong ZHANG [1]
College of Agricultural Engineering, Shanxi Agricultural University, Taigu/China
Tel: +86-0354-6288339; E-mail: qlcui@126.com
DOI: https://doi.org/10.35633/inmateh-68-27

***Keywords*:** *mechanical property, mechanical harvest, test, buckwheat stem*

ABSTRACT
Buckwheat crops are subjected to complex stress during harvest. And there are problems such as large deformation, severe brokenness, and high energy consumption of stems during the mechanical harvesting, such as cutting, transporting, threshing, separating and cleaning. In this study, the mechanical properties of buckwheat stem during mechanical harvesting were tested, including tensile, bending, shearing and dynamic cutting, and the effects of moisture content, stem position and working parameter on their mechanical properties were analyzed. The test results showed that the tensile strength, elastic modulus, cutting stress and unit area cutting energy of stem with higher moisture content were significantly greater than those of stem with lower moisture content (P<0.05). The flexural modulus and bending strength of stem with higher moisture content were significantly lower than those of stem with lower moisture content (P < 0.05). The flexural modulus, bending strength, shear strength, cutting stress and unit area cutting energy decreased gradually with the stem height increasing. The cutting parameters had significant effects on the mechanical properties of stem (P<0.05), and the cutting mechanical properties first decreased and then changed steadily with the average cutting speed increasing. The cutting stress gradually decreased with the blade oblique angle increasing, but the unit area cutting energy decreased first and then increased. The average cutting speed and blade oblique angle of buckwheat stem are recommended to be 0.75-1.0 m/s and 30º, respectively. This research can provide basic data for the design of the buckwheat harvesting machinery.

摘要
荞麦作物在机械收获切割、输运、脱粒分离和清选等作业环节，其茎秆会受到复杂应力作用，存在茎秆受力变形大、破碎严重、耗能大等问题。本文测试了荞麦茎秆在机械收获过程中的力学性质，包括拉伸、弯曲、剪切和动态切割力学性质，并分析了含水率、茎秆部位和相关工作参数对其力学性质的影响。试验结果表明：较高含水率的荞麦茎秆拉伸强度、弹性模量、切割应力和单位面积切割功耗均显著大于较低含水率的荞麦茎秆（P＜0.05）；但较高含水率的荞麦茎秆弯曲模量和抗弯强度显著小于较低含水率的荞麦茎秆（P＜0.05）。随着茎秆离地高度的增大，其弯曲模量、抗弯强度、剪切强度、切割应力和单位面积切割功耗均逐渐减小。切割工作参数（平均切割速度和刀片斜角）对荞麦茎秆的切割应力、单位面积切割功耗影响显著（P＜0.05），随着平均切割速度的增大，切割力学性质参数呈现先减小后平稳变化的规律，而随着刀片斜角的增大，切割应力逐渐减小，而单位面积切割功耗先减小后增大，荞麦茎秆的平均切割速度和刀片斜角建议分别选取 0.75-1.0 m/s 和30°。本研究为荞麦低损高质收获机械关键部件设计提供了基础数据。

INTRODUCTION
Buckwheat, an annual or perennial herb, belongs to a dicotyledonous plant in the *Polygonaceae* family. It originated in China and has a long cultivation history and a large planting area. Buckwheat grains are rich in a variety of biologically active ingredients, which have anti-tumor and anti-oxidant effects after consumption *(Xiang et al., 2013; Wang et al., 2010)*. In recent years, lots of scholars have conducted preliminary explorations on buckwheat harvesting technology and machinery *(Zhang et al., 2019; Wang et al., 2020)*.

[1] *Yanqing Zhang, As Prof. Ph.D. Eng.; Qingliang Cui*, Prof. Ph.D. Eng.; Can Wang, Prof. Ph.D. Eng.; Hongbo Li, Prof. Ph.D. Eng.; Zhiyong Zhang, Prof. Ph.D. Eng.*

Buckwheat mechanical harvesting methods mainly include combined harvesting and segmented harvesting, and the corresponding machines include combine harvesting machinery, swather and pickup machinery. The problems such as high impurity content in grains and high energy consumption of these machines are mainly caused by severely damaged stems *(Lu et al., 2020)*. The research on the mechanical properties of crops is the basis for the innovative design of mechanical harvesting equipment. Therefore, it is urgent to study the mechanical properties of buckwheat stems to optimize the design parameters of harvesting equipment and improve its performance.

Many scholars have conducted a large number of biomechanical tests on the stems of wheat, rice and other crops, and have achieved excellent results. *Zhao et al.* conducted tensile tests for forage stems and measured the maximum tensile load, stress, strain, elastic modulus and other mechanical characteristics, which provided basic data for the design of its harvesting machines *(Zhao et al., 2009)*. *Esehaghbeygi A. et al.* found that the correlation between the elastic modulus, bending strength and moisture content of the wheat stems, and these results can not only evaluate the lodging resistance of wheat stem but also provide a reference for the design of wheat harvester headers *(Esehaghbeygi et al., 2013)*. A study on *energycane* stem showed that selecting appropriate cutting parameters can reduce power consumption *(Mathanker et al., 2015)*. Research about millet stem presented that different cutting speeds and blade oblique angles have a great influence on cutting mechanical properties (*Zhang et al., 2018; Zhang et al., 2020*). Buckwheat stems are different from rice, wheat and other stems. The high moisture content of buckwheat stems makes them break easily during the harvest period, and the lignin content of the bottom stem is high and makes it difficult to cut. However, there was an extreme shortage of machines suitable for buckwheat harvesting. Testing the mechanical properties of buckwheat stem is the premise of designing machinery and equipment, which can obtain the design parameters for improving the performance of the buckwheat harvester.

In this research, the tensile, bending, shearing and dynamic cutting mechanical properties of buckwheat stem were studied, and the effects of different stem positions, moisture content and cutting technical parameters on its mechanical properties were analyzed. These results can provide a reference for the design and optimization of key components of buckwheat mechanical harvesting.

MATERIALS AND METHODS

Materials and Test equipment

Heifeng No.1 buckwheat was randomly collected in the test field of buckwheat planting in Taigu County, Shanxi Province, China (112º55′ E, 37º43′ N). The bending test was carried out in the buckwheat field, and the other mechanical properties tests were conducted in the laboratory. After harvesting, the stems were made samples in time and put into sealed bags. Simultaneously, the moisture content (w.b.%) of the stem was measured by the standard method (*ASABE, 2008*).

The test equipment used for tensile and shearing tests was a 5544 universal material testing machine (Instron, United States) with a maximum load of 2 kN. The test tools used for bending tests were spring dynamometers and rulers. The self-made cutting test bench was used for stem dynamic cutting tests (*Zhang et al., 2020*).

Tensile test

Buckwheat stems are hollow tubes. The stress concentration phenomenon is easy to occur at the clamping parts of the stem when it was fastened by the tensile fixture, which leads to inaccurate test results. So the test methods for physical and mechanical properties of wood were used to make tensile test samples *(China National standardizing committee, 2009).* The shape of the sample was similar to a cuboid, and its length, width, and thickness are *p*, *q*, and *r*, respectively, which were measured by the vernier caliper before the tensile test. And the sandpapers were put into the clamping part of the tensile fixture to increase friction and prevent the stem from slipping. The tensile loading rate was set at 2 mm/min. The tensile force and displacement were recorded by the testing machine, and the tensile strength and elastic modulus were calculated as follows:

$$\sigma = \frac{F_t}{q\mathrm{r}} \tag{1}$$

$$E = \frac{\sigma}{\varepsilon} \tag{2}$$

σ is the tensile strength, [MPa]; F_t is the Maximum tensile force [N]; E is the elastic modulus [MPa]; q is the width of the stem sample, [mm]; r is the thickness of the stem sample, [mm]; ε is the strain, %.

Bending test

The stem bending test was carried out in the field. The straight stems without disease and insect pests were randomly selected, a ruler was set vertically near the stem, and the measured stem position (distance from the ground was *a,* Fig.1b) was marked. The stem was hooked by the spring dynamometer. The field test picture is shown in Fig. 1a.

a. The field test b. The test schematic diagram

Fig. 1 - Bending test of buckwheat stem in field

According to the method in literature (*A. Ince S. et al.,2005; Esehaghbeygi A. et al., 2013*), pull the stem at a slow and uniform speed in the horizontal direction to the point of deflection *ω*（*ω*=50 mm）, and the pulling force F_B (N), the distance from stress point to the ground L(mm), the distance between the stem axis and the surface of stem *y* (mm) in the pulling direction, the inner diameter of stem stress point *d* (mm) and the outer diameter of stem stress point D (mm) were measured. The test schematic diagram is shown in Fig. 1b. The flexural modulus E_b [GPa], moment of inertia *I* (mm^4), bending strength σ_b [MPa] and the flexural stiffness $E_b I$（Nm^2）were calculated as follows:

$$E_b = \frac{F_B L^3}{3\omega I} \quad (3)$$

$$I = \frac{\pi D^4 (1-\alpha^4)}{64} \quad (4)$$

$$\alpha = \frac{d}{D} \quad (5)$$

$$\sigma_b = \frac{F_B L y}{I} \quad (6)$$

Shearing test

The collected buckwheat stems were made into 70 mm length samples, the midpoint of stem internode and node were used as the shearing point, and the outer diameter of stem midpoint was measured before the test. The shearing fixture was installed on the mechanical testing machine and the shearing speed was set to 5 mm/s. After the shearing tests, the stem wall thickness was measured. The maximum shear force F_s and shear energy W_s can be recorded by the mechanical testing machine and the shear strength was calculated as follows:

$$\tau = \frac{F_s}{A} \quad (7)$$

$$A = \frac{\pi}{4}\left[D^2 - (D-2t)^2\right] \quad (8)$$

where: τ is the shear strength, [MPa]; F_s is the maximum shear force [N]; A is the cross-sectional area of stem [mm^2]; D is the outer diameter of stem [mm]; *t* is the wall thickness of stem [mm].

Dynamic cutting test

The self-made cutting test bench was used to the dynamic cutting test of buckwheat stem (Fig.2). The function of the cutting test bench, the introduction of the testing method and the calculation of data are consistent with *Zhang's* research (*Zhang et al., 2020*). During the dynamic cutting test, the standard type Ⅱ cutter (including the type Ⅱ moving blade and the type Ⅳ guard) commonly used in harvester were selected *(China National standardizing committee, 2009)*, and the blade oblique angle and average cutting speed were set to 0-48° and 0-1.5 m/s, respectively.

The ratio of average cutting speed to feeding speed has a great influence on the re-cutting, missed cutting and one-time cutting performance of stem, and it was set at 1.6 after the initial tests. The adjustment of blade oblique angle is shown in Fig. 3.

Fig. 2 - The dynamic cutting test of buckwheat stem

Fig. 3 - The adjustment of blade oblique angle

RESULTS

Tensile test results of buckwheat stem

The tensile test picture and stress-strain curve of buckwheat stem are shown in Fig. 4a and Fig. 4b, respectively. From Fig.4b, the stem had no obvious yield point, and the stress changed uniformly with the strain increasing until the stem sample broke during the entire tensile test.

a. The tensile test picture

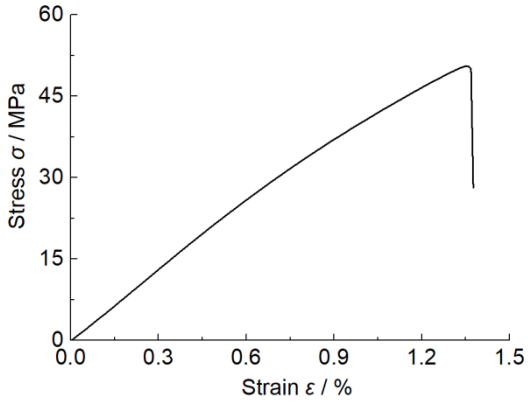

b. Stress-strain curve of stem

Fig. 4 - The tensile test

The effect of moisture content on tensile mechanical properties is shown in Table 1. It can be seen from Table 1 that the range of the maximum tensile force of buckwheat stems was unstable. Since buckwheat stems are biological materials, which may be determined by the number of fibers and their connection mode, the tensile strength and elastic modulus are selected for further analysis in this study. Through multiple comparisons of mean values, the tensile strength and elastic modulus of the stem with higher moisture content were significantly greater than those with lower moisture content (P<0.05). This result indicates that buckwheat stems with lower moisture content are prone to breakage, and it was agreed with the tensile tests of corn stems previously mentioned (*Yu et al.,* 2012).

Table 1

Tensile test results of buckwheat stem

Moisture content [%]	Sample	F_t [N]	σ [MPa]	E [MPa]
57.33	1	135.60	64.64	5858.30
	2	84.62	42.05	4410.15
	3	89.97	50.10	4895.58
	4	77.95	50.06	4647.80
	5	64.93	41.74	4,410.15
	Mean	90.61	49.72A	5017.00A
40.56	1	82.71	37.26	4179.28
	2	87.53	49.81	4069.31
	3	89.01	38.76	4030.39
	4	74.27	43.17	4321.88
	5	86.58	44.54	4123.71
	Mean	84.02	42.71B	4114.91B

Note: Different letters (A, B) represent significant differences in tensile mechanical properties among moisture content (p<0.05).

Therefore, the moisture content of the stem should not be too low when the buckwheat is harvested, otherwise, it will cause serious deformation of the stem and increase the impurity content of the grains.

Bending test results of buckwheat stem

The effects of moisture content and stem position (test site) on the bending mechanical properties are presented in Table 2. Different moisture content and stem position have effects on the moment of inertia, flexural modulus and bending strength of buckwheat stem. For the same stem position, the moment of inertia of stem with higher moisture content was significantly greater than those with lower moisture content (P<0.05), but the flexural modulus and bending strength of stem with higher moisture content were significantly lower than those with lower moisture content (P<0.05). The flexural stiffness of the stem with the moisture content of 75.34% and 63.68% was not significant (P >0.05). For stems with the same moisture content, the moment of inertia, flexural modulus, bending strength, and flexural stiffness of the stem test site at a height of 120 mm from the ground are significantly lower than those of the test site at 60 mm (P<0.05). As a result,, the higher collision point of the stem divider, the easier it is to cause the stem to bend and break off in the working process of the harvester. The height of the collision point between the stem and the stem divider should be reduced as much as possible to avoid stem lodging and grain loss.

Table 2

Bending test results of buckwheat stem

Test site (height from the ground) [mm]	Moisture content [%]	I [mm^4]	E_b [GPa]	σ_b [MPa]	E_b [Nm^2]
60	75.34	46.42 Aa	2.43 Ba	20.64 Ba	0.11 Aa
60	63.68	34.18 B	3.31 A	25.51 A	0.11 A
90	75.34	43.21 a	2.15 a	20.42 a	0.09 ab
120	75.34	32.54 b	1.54b	15.58 b	0.05b

Note: Different letters (A, B) and (a, b) represent significant differences of bending mechanical properties in moisture content and test site, respectively ($p<0.05$).

Shearing test results of buckwheat stem

The shear mechanical properties of buckwheat stem (with the moisture content 76.62%, w.b.) were obtained in Table 3. As shown in Table 3, the cross-sectional area, maximum shear force, shear energy and shear strength of buckwheat stem decreased with the increase of stem height. Through mean multiple comparisons, it was found that there were significant differences in the cross-sectional area and maximum shear force of stem in different positions (P<0.05). For internodes, the shear energy and shear strength of different positions were significantly different (P<0.05). In terms of nodes, the shear energy and shear strength of the 1st stem node were significantly greater than those of the 5th stem node (P<0.05), while the difference between the 2nd and 4th stem nodes was not significant (P>0.05). Meanwhile, the average shear strength of stem internode and node was 11.10 MPa and 15.70 MPa, respectively, and the stem node shear strength was greater than that of stem internode. Buckwheat crops will be impacted and sheared by rod teeth during the threshing process, and this research clarifies the positions of the stem with lower shear strength, which provides help for targeted flexible threshing components.

Table 3

Shearing test results of buckwheat stem

Order from the ground	Internode				Node			
	A [mm^2]	F_s [N]	τ [MPa]	W_s [J]	A [mm^2]	F_s [N]	τ [MPa]	W_s [J]
1	/	/	/	/	26.53a	595.92a	22.46a	1.65a
2	20.55a	383.46a	18.66a	0.84a	25.65a	438.13ab	17.08ab	1.39ab
3	19.92ab	212.09b	10.65b	0.78ab	21.12b	334.00b	15.82b	1.35b
4	19.91ab	160.05bc	8.04bc	0.61b	21.07b	318.87b	15.14b	1.32b
5	17.60b	120.29c	6.83c	0.45c	20.63b	165.31c	8.01c	0.63c

Note: The 1st internode stem is very close to the ground, far less than the stubble height, its mechanical properties do not need to be measured. Different letters (a, b, c) represent significant differences of shearing mechanical properties in stem position, respectively ($p<0.05$).

Dynamic cutting results of buckwheat stem

The average cutting speed and blade oblique angle were set to 1 m/s and 30°, respectively, and the stem dynamic cutting test was carried out to analyze the differences between the moisture content and stem position on its cutting mechanical properties. The test results are shown in Fig.5. In the case of the moisture content, the cutting stress and unit area cutting energy of stem had the same trend, and both increased with the increase of moisture content. The reason is that the increase of stem moisture content leads to increased stem toughness *(Wang et al., 2020).* In Fig.5, it was found that the regression fitting equation of stem moisture content and cutting mechanical properties showed a quadratic function relationship, and the fitting accuracy was greater than 0.92. It can predict its cutting mechanical properties according to the stem moisture content. These results provide a reference for selecting the appropriate moisture content of buckwheat stem to reduce its cutting force and cutting energy during harvest. For the stem position, the change rule of cutting mechanical properties of buckwheat stem is basically the same as that of shear mechanical properties, and the cutting stress and unit area cutting energy decreased with the increase of stem height. Similarly, the unit area cutting energy of the 2nd internode from the ground was significantly greater than that of the 4th internode (P<0.05), and there was a significant difference in cutting stress between the 2nd internode and the other internodes of the stem (P<0.05), which is due to the higher lignin content and mechanical strength of the bottom stems *(Li et al., 2011).*

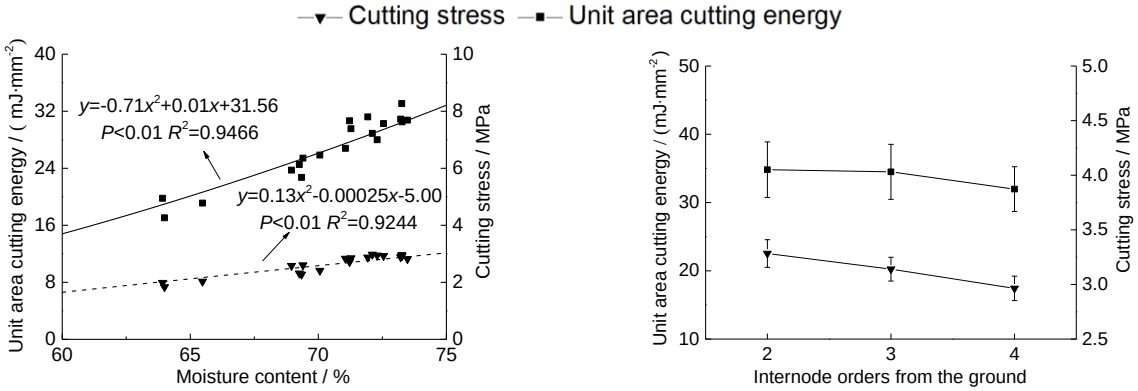

Fig. 5 - Variation of cutting mechanical properties under different stem position and moisture content

Similarly, the maximum cutting force and cutting energy decreased with the stem height increasing, and the differences were significant (P<0.01). The maximum cutting force, cutting energy and cross-sectional area of the stem were regressed, and the fitting equation is shown in Fig. 6. The accuracy of the fitting model is greater than 0.92, and these results provide a basis for choosing a suitable cutting height to reduce the cutting force and power consumption of the buckwheat stem.

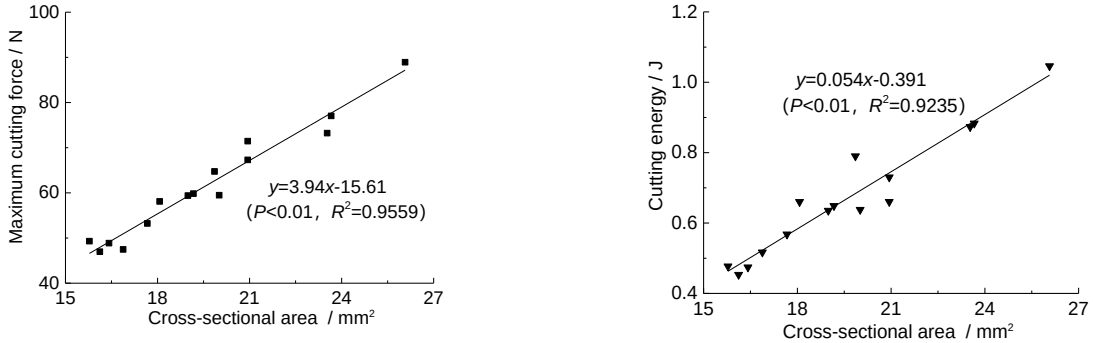

Fig. 6 - Correlation between cross-sectional area, cutting force and cutting energy

Cutting is the primary working process of buckwheat harvesting machinery *(Igathinathane, 2010)*, and the cutting parameters have a great influence on its cutting mechanical properties, especially cutting speed and blade oblique angle *(Johnson et al., 2012; Mathanker, et al., 2015).* In this paper, dynamic cutting experiments with different average cutting speeds and blade oblique angles were carried out, and the results are shown in Fig. 7.

As can be seen in the first picture of Fig.7, the cutting stress and unit area cutting energy of stem first decreased and then remained unchanged with the increase of average cutting speed when the blade oblique angle was 30°, and the cutting mechanical properties at a cutting speed of 0.5 m/s were significantly greater than those at a cutting speed of 0.75-1.5 m/s.

The conclusion of the study is consistent with that of *Zhang's* research about the millet stalk *(Zhang. et al., 2020),* and the average cutting speed should be greater than 0.75m/s to reduce the cutting force and cutting energy. However, relevant studies had shown that too fast cutting speed will cause increased vibration of the cutting header and additional energy consumption, and the average cutting speed should not be too large *(Ji. et al., 2017)*. So, this paper suggests that the average cutting speed should be kept at 0.75-1.0 m/s when the buckwheat is to be harvested.

The effect of blade oblique angle on cutting mechanical properties was tested at an average cutting speed of 1.0 m/s. From the second picture in Fig.7, the cutting stress decreased with the increase of the blade oblique angle, which is because the sliding cutting can reduce the cutting force of the stem. The larger blade oblique angle, the larger sliding cutting angle, and the more significant sliding cutting function on the stems *(Song. et al., 2015)*. Nevertheless, the unit area cutting energy decreased first and then increased with the increase of blade oblique angle, and it was the smallest when the blade oblique angle was 30°. This is due to the fact that the blade cutting displacement increased, and the frictional power consumption between the blade and the stem increased significantly when the blade oblique angle increased to a certain extent *(Pang. et al., 1982)*. In general, the increase of blade oblique angle will reduce the cutting stress and unit area cutting energy to a certain extent, but a too large blade oblique angle may cause the larger energy consumption or the stalk to be unable to be clamped and cut *(Pang. et al., 1982)*. Therefore, this study recommends that the blade oblique angle should be about 30° for buckwheat stem cutting.

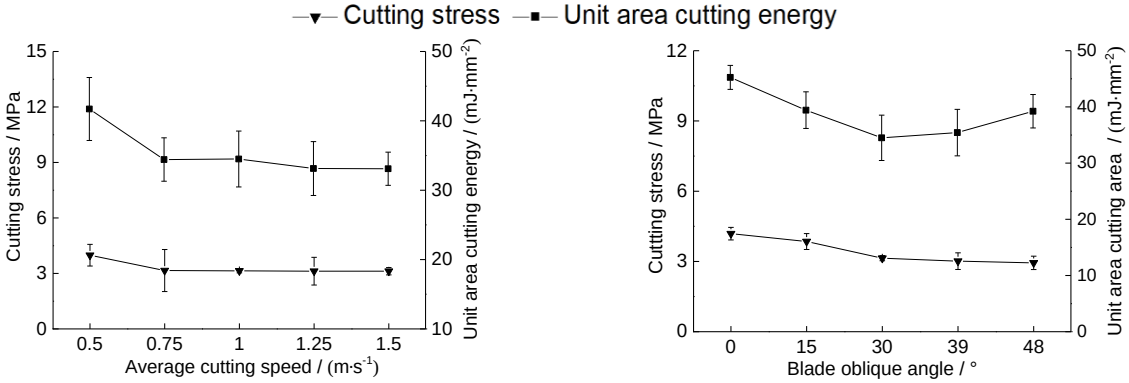

Fig. 7 - Variation of cutting mechanical properties in different average cutting speeds and blade oblique angles

CONCLUSIONS

The tensile, bending, shearing and dynamic mechanical properties of buckwheat stem during mechanical harvesting were tested, and the following conclusions were obtained:

(1) The moisture content had a significant effect on the tensile mechanical properties of the stem. The lower moisture content of the stem had small tensile strength and elastic modulus and was easy to break.

(2) The moisture content and stem position had significant effects on the bending and dynamic cutting mechanical properties of the stem. The bottom stem with lower moisture content had higher bending strength, flexural modulus and cutting stress, and was not easy to bend and cut.

(3) The stem position had a significant effect on the shearing mechanical properties of the stem, and the shear strength and shear energy of the stem in the upper position were significantly smaller than those in the lower position.

(4) The average cutting speed and blade oblique angle have a great influence on the cutting mechanical properties of the stem. This research suggests that the cutting speed and blade oblique angle of buckwheat stems should be 0.75-1 m/s and 30°, respectively.

ACKNOWLEDGEMENTS

Thanks to the financial support provided by the Doctoral Research Project of Shanxi Province (SXYBKY2019048), the Science and Technology Innovation Fund Project of Shanxi Agricultural University (2020BQ11) and the National Key Research and Development Project of China (2016YFD0701801).

REFERENCES

[1] A. Ince S. et al., (2005), Bending and shearing characteristics of sunflower stalk residue, *Biosystems Engineering*, Vol. 92, Issue 2, pp.175-181, Ed. Elsevier, San Diego/USA;

[2] ASABE Standards, 2008. S358.2. Moisture Measurement-Forages. American Society of Agricultural and Biological Engineers, St. Joseph, MI, Spokane/USA;

[3] Esehaghbeygi A., (2013), Bending and Shearing Properties of Wheat Stem of Alvand Variety, *World Applied Sciences Journal*, Vol. 6, Issue 8, pp.1028-1032, Islamabad/Pakistan;

[4] Igathinathane C., (2010), Corn stalk orientation effect on mechanical cutting. *Biosystems Engineering*, Vol. 107, Issue 2, pp. 97-106, Ed. Elsevier, San Diego/USA;

[5] Ji J.T., (2017). Analysis of minimum amplitude points and optimization of connection position for header of micro grain combine (微型谷物联合收割机割台最小振幅点分析及挂接点优化), *Transactions of the Chinese Society of Agricultural Engineering*, Vol. 33, Issue 12, pp. 28-33, Beijing/ P.R.C.;

[6] Li Y.M., (2011), Experiments and analysis on mechanical property of corn stalk reciprocating cutting (玉米茎秆往复切割力学特性试验与分析), *Transactions of the Chinese Society of Agricultural Engineering*, Vol.27, Issue 1, pp.160-174, Beijing/P.R.C.;

[7] Lu Q., (2020), Problems and thoughts on mechanized harvesting technology of buckwheat in China (我国荞麦机械化收获技术问题与思考), *Agricultural Engineering*, Vol. 10, Issue 1, pp.6-9, Beijing/P.R.C.;

[8] Mathanker S.K., (2015), Effect of blade oblique angle and cutting speed on cutting energy for energycane stems. *Biosystems Engineering*, Vol. 2015, Issue 133, pp. 64-70, Ed. Elsevier, San Diego/USA;

[9] Pang S.H., (1982), Theory of sliding cutting and the choice of its angle (关于滑切理论与滑切角的选用). *Journal of Huazhong Agricultural College*, Vol. 1982, pp. 64-69, Wuhan/P.R.C.;

[10] Song Z.H., (2015), Experiment on cutting characteristics of cotton stalk with double supports (棉花秸秆双支撑切割性能试验), *Transactions of the Chinese Society of Agricultural Engineering*, Vol.31, Issue 8, pp.37-45, Beijing/P.R.C.;

[11] Wang B.A. et al., (2020), Test and analysis of cutting force of highland barley in mature stage (成熟期青稞茎秆切割力的测试与分析), *Journal of Gansu Agricultural University,* Vol. 55, Issue 2, pp.201-207, Lanzhou/ P.R.C.;

[12] Wang J.W., (2020), Cleaning performance and optimization of internal and external roller rotary buckwheat thresher, *International Agricultural Engineering Journal*, Vol. 29, Issue 2, pp.174-181, Bangkok/Thailand;

[13] Wang J.W., (2020), Design and threshing outputs study of internal and external rotary roller buckwheat thresher, *INMATEH Agricultural Engineering*, Vol. 60, Issue 1, pp.173-182, Bucharest / Romania; https://doi.org/10.35633/inmateh-60-20

[14] Wang W., (2010), Advances in chemical constituents of Tartary buckwheat and its bioactivities (苦荞麦化学成分及生物活性研究进展), *Rain Fed Crops*, Vol. 30, Issue 6, pp.419-423, Shenyang/ P.R.C.;

[15] Xiang D.B., (2013), Research progress on buckwheat cultivation (荞麦栽培研究进展), *Crops*, Vol. 2013, Issue 3, pp.1-6, Beijing/ P.R.C.;

[16] Yu Y. et al., (2012), Experimental study on tensile properties of corn straw (玉米秸秆拉伸特性的试验研究), *Transactions of the Chinese Society of Agricultural Engineering*, Vol. 28, Issue 6, pp.70-76, P.R.C.;

[17] Zhang J., (2019), Design and finite element analysis of buckwheat threshing device, *Journal of Chinese Agricultural Mechanization*, Vol. 40, Issue 7, pp.7-12, Nanjing//P.R.C.;

[18] Zhang Y.Q., (2018), Effects of stem region, moisture content and blade oblique angle on mechanical cutting of millet stems, *INMATEH-Agricultural Engineering*, Vol. 55, Issue 2, pp.105-112, Romania;

[19] Zhang Y.Q., (2020), Simulation and Test of Cutting Mechanical Characteristics of Millet Stalk Based on ANSYS/LS-DYNA, *INMATEH-Agricultural Engineering*, Vol. 61, Issue 2, pp.143-150, Bucharest / Romania. https://doi.org/10.35633/inmateh-61-16

[20] Zhao C.H., (2009), Experiment on stalk mechanical properties of legume forage and grasses (豆禾牧草茎秆的力学特性试验), *Transactions of the Chinese Society of Agricultural Engineering*, Vol. 25, Issue 9, pp.122-126, Beijing / P.R.C.;

[21] ***Ministry of Industry and Information Technology, (2009), *Agricultural machinery-cutter bars-part 3: knife sections, ledger plates and knife backs, GB/T 1209.3-2009*, China Machine Press, Beijing/P.R.C.;

[22] ***Ministry of Industry and Information Technology, (2009), *General requirements for physical and mechanical tests of wood, GB/T 1928-2009*, China Machine Press, Beijing / P.R.C.

DESIGN AND TEST OF TRACTION COMBINED MACHINE FOR SUBSOILING AND LAND PREPARATION
/
牵引式深松整地联合作业机设计与试验

Jingyu LI, Sihao ZHANG, Pengfei ZHANG, Wenjun WANG *)
School of Agricultural Engineering and Food Science, Shandong University of Technology, Zibo/China;
Tel: +86-15550326189; E-mail: wjwang2016@163.com
Corresponding author: Wenjun Wang
DOI: https://doi.org/10.35633/inmateh-68-28

Keywords: *conservation tillage, subsoiler, soil crushing, stalks mulching, variable fertilization, hydraulic control system*

ABSTRACT
In order to solve the problems of crop residue clogging, poor soil crushing and low operation efficiency under the stalks mulching condition, the traction combined machine for subsoiling and land preparation was designed. The optimization test was carried out to optimize the stalk cutting device and the soil crushing device under stalk mulching condition. The optimization test used a randomized complete block design, consisting of 10 treatments, in a 5 × 2 factorial arrangement. Each treatment included the combination of coulter types (8W, 13W, 18W, 25W and NW) and soil crushing roller types (with blade angle and without blade angle). The results showed that the combination of the fluted coulters with 8 waves and the soil crushing roller with blade angle was optimal. Finally, the verification test of the whole machine was carried out to evaluate the performance, and the results showed that the average value of subsoiling depth was 35.8 cm, the stability coefficient of subsoiling depth was 93.9% and the soil crushing rate was 53.7%. This research provides an important reference for the structure design of the large multi-functional combined machine for conservation tillage.

摘要
为解决秸秆覆盖条件下深松作业缠绕堵塞严重，以及作业效率低等问题，研制了牵引式深松整地机，包括新型切茬松土装置、仿形碎土装置、液压控制系统和变施肥控制系统。通过田间优化试验探究全量秸秆覆盖条件下新型切茬松土装置和仿形碎土装置对整机性能的影响，试验因素包括耕刀类型（8W, 13W, 18W, 25W and NW）和碎土轮类型（有叶片倾角和无叶片倾角两种），优化试验结果表明，8 波纹的犁刀与带叶片角的碎土辊组合使用效果最佳。最后进行了整机田间验证试验，结果表明：平均深松深度为35.8 cm，深松稳定系数为93.9%，土壤破碎率为53.7%，该研究为保护性耕作条件下的大型深松整地联合作业机设计提供参考。

INTRODUCTION
In the past 30 years, the long-term use of small-scale mechanical rotary tillage instead of deep plowing has caused soil compaction, severe wind and water erosion, poor drought and waterlogging resistance, difficulty in deep rooting of crops, and frequently crop lodging in autumn, seriously endangering food production (*Daraghmeh et al., 2019; Qi et al., 2020; Qu et al., 2021*). Conservation tillage has been described as one of the key solutions to these problems. Research results in recent years have shown that the use of conservation tillage mode, including stalk returning, subsoiling and no-tillage planting, is an effective method to improve the ecological environment, increase soil water storage capacity and fertility, and maintain sustainable agricultural development (*Wang et al., 2016; Issaka et al., 2019; Mondal et al., 2019*). Subsoiling refers to the soil loosening operation that exceeds the normal plow depth, destroying the hard plough pan, increasing water storage capacity and improving the growth environment of crops (*Guo et al., 2021*). Especially for deep root crops, subsoiling is an important technology to increase production (*Qi et al., 2018*).

The subsoiler creates a "virtual and solid coexistence" tillage layer structure that is different from traditional plowing. The subsoiling breaks the plough pan and only loosens the soil without turning it, establishing a suitable growing environment and improving the ability to resist drought and soil erosion. Practice has proved that subsoiling technology has strong pertinence and obvious effect on mitigating spring drought and soil erosion during the rainy season in northern China (*Zhang et al., 2018*).

With the application and popularization of high-power tractors, agricultural machinery has generally developed in the direction of large-scale and combined operations, which are characterized by large subsoiling depth, high work efficiency, and good work quality (*Celik et al., 2012; Prathuang et al., 2018; Jiang et al.,*

2020). Therefore, it is necessary to develop the combined machine for subsoiling and land preparation to overcome the serious soil compaction caused by the repeated operation of small-scale machines.

In addition, the traditional subsoiling machine works well in the cropland without mulch, but the operating effect is significantly reduced in the cropland with mulch (*Jia et al., 2017; Wang et al., 2021*). Under the stalk mulching condition, the phenomenon of crop residue clogging will occur during subsoiling operation, especially when the straw cover ratio reaches more than 90%, the working resistance caused by straw blocking increases by more than 20% (*He et al., 2018*). In addition, the subsoiler will squeeze the upper soil to uplift the surface soil during subsoiling operation, forming a large number of soil blocks. The large gaps between these soil blocks will cause the moisture to disperse quickly (*Feng et al., 2018*). Therefore, it is necessary to develop a subsoiling machine that can adapt to the cropland mulched stalk and stubble, and solve the problems of crop residue clogging and poor soil crushing under the condition of stalk mulching.

In order to solve the above problems, we designed the traction combined machine for subsoiling and land preparation, which can perform several operations in a single pass, reduce the number of passes of the agricultural machine on the cropland and improve work efficiency. The field optimization test was carried out to optimize the parameters of the key components and evaluate the machine performance under stalk mulching condition.

MATERIALS AND METHODS

General design of traction combined machine for subsoiling and land preparation

The traction combined machine for subsoiling and land preparation is mainly composed of four functional modules: stalk cutting and topsoil loosening, subsoiling, variable fertilization and land preparation. The four modules are reasonably configured and work independently to achieve the combined operation. The whole structure of the machine is shown in Fig. 1.

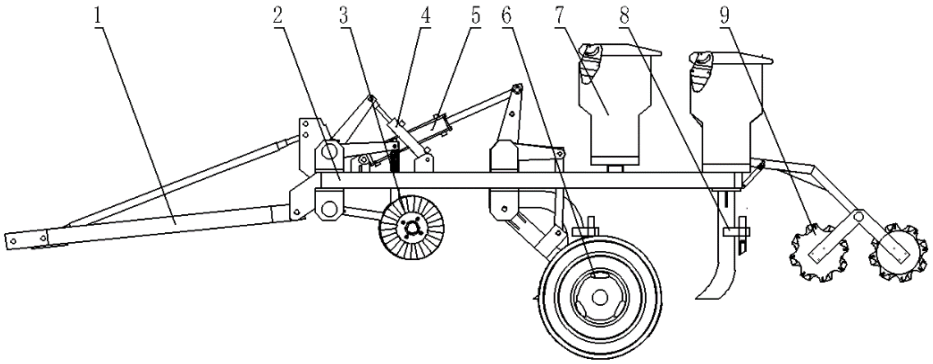

Fig. 1 - Whole structure of the machine

1-Traction frame; 2-Main frame;3-Stalk cutting device; 4-Stalk cutting device cylinder; 5-Land wheel cylinder; 6-Land wheel; 7-Fertilizer box; 8-Subsoiler; 9-Soil crushing device

The main frame was composed of three beams: front beam, middle beam and rear beam. Seven sets of stalk cutting devices were hinged on the front beam. The subsoilers were fixed to the middle beam and the rear beam. The land wheels were hinged on the middle beam to control the lifting of the whole machine. The soil crushing devices were hinged on the rear beam. The stalk cutting devices were controlled by stalk cutting device cylinder, and the land wheels were controlled by land wheel cylinder. The main technical parameters of the whole machine are shown in Table 1.

Table 1

Main technical parameters of the machine

Parameter	Value
Overall dimension, L×W×H (mm×mm×mm)	5800×4640×1500
Working rows	7
Row spacing (mm)	600-700
Power requirements (kW)	88.2-132.3
Working speed (km/h)	3-5
Maximum subsoiling depth (mm)	40
Mass (kg)	1300

Design of the hydraulic control system

In order to reduce the work intensity of the operator, the hydraulic control system was designed. The working principle of the hydraulic control system is shown in Fig. 2. The hydraulic control system was divided into two independent parts: the hydraulic control system of land wheels (Fig. 2A) and the hydraulic control system of stalk cutting devices (Fig. 2B). The hydraulic oil of the entire system came from the tractor.

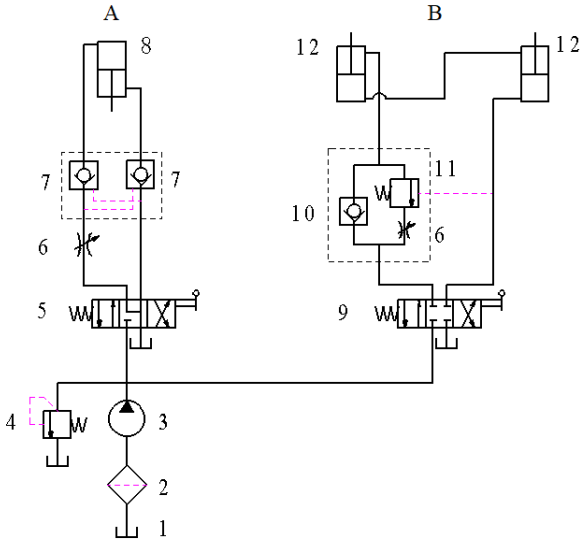

Fig. 2 - Working principle of the hydraulic control system.

1-Hydraulic fluid chamber; 2-Filter; 3-Oil pump; 4-Overflow valve; 5-Hand-operated direction valve with Y-type median function; 6-Throttle valve; 7-Pilot operated check valve; 8-Land wheel cylinder; 9-Hand-operated direction valve with O-type median function; 10-Check valve; 11-Sequence valve; 12-Stalk cutting device cylinder

(1) Whole structure design

The hydraulic control system of land wheels is shown in Fig. 3a. The switching between work state and transport state of the whole machine is realized by the land wheel cylinder. The switching between transport state and working state of the whole machine should meet two conditions: the height of the subsoiler tip from the cropland is more than 300 mm under transport state and the subsoiler tip is 400 mm below the cropland at the maximum working depth. The switching process of the two states is shown in Fig.3. The solid line outline in Fig. 3b indicates the transport state of the whole machine. At this time, the height of the machine from the cropland is maximum and the land wheel cylinder is at the maximum stroke. The dotted line outline in Fig. 3b indicates the maximum working depth of the machine.

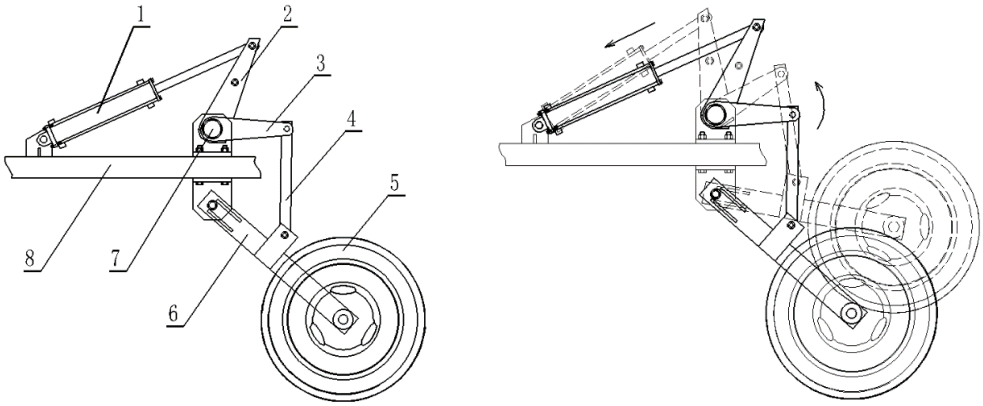

a. Structure diagram *b. State switching process*

Fig. 3 - Structure of the hydraulic control system of land wheels

1-Land wheel cylinder; 2-Main swing arm; 3-Lifting swing arm; 4-Linkage; 5-Land wheel; 6-Wheel frame; 7-Rotating shaft; 8-Frame of whole machine

In order to adapt to the no-till cropland with a large amount of straw mulch, the stalk cutting device with a symmetrical double-coulter was designed, as shown in Fig. 4a. The device can cut the long stalks and weeds to avoid the tangling and clogging of subsoiler, and can also play the role of loosening the topsoil.

The lifting of the stalk cutting devices is controlled by the stalk cutting device cylinder, as shown in Fig. 4b. The device can float up and down around the rotating shaft during the work process. The spring can maintain the stalk cutting and topsoil loosening pressure of the coulter. When the coulter encounters hard stalk or soil, the upward pressure acted on the coulter increases, and the stalk cutting devices float upward. At this time, the pressure of the spring gradually increases until the hard stalk or soil is chopped. So, the stalk cutting devices float with the undulation of the cropland surface to prevents damage caused by excessive stress.

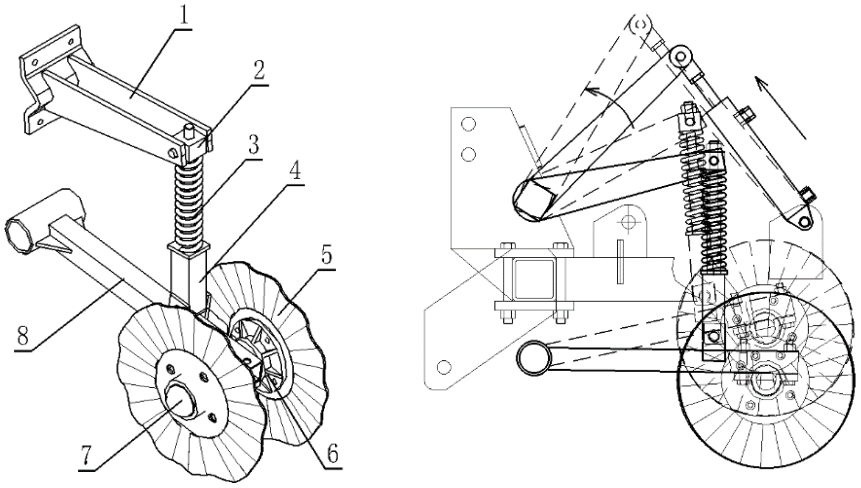

a. Structure diagram *b. working process*

Fig. 4 - Structure of the hydraulic control system of stalk cutting devices

1-Upper swing arm; 2-Pressure rod; 3-Spring; 4-Pressure rod tube; 5-Coulter; 6-Bearing seat; 7-Dust cap; 8-Lower swing arm

(2) Hydraulic actuators design

The working pressure of the hydraulic transmission system could be selected according to the maximum load in the load diagram of the actuator, or according to the type of the machine. The working pressure of the hydraulic system in general agricultural machine was 10-16 MPa, so the maximum pressure selected in this research was 16 MPa.

The hydraulic actuators included the land wheel cylinder and the stalk cutting device cylinder, so it was necessary to calculate the body diameter and rod diameter of two types of hydraulic cylinders.

The maximum mass of the whole machine that the land wheel cylinder needs to overcome was 1300 kg, and the cylinder load was the largest when it reached the maximum stroke, which was about 3 times the weight of the whole machine, that was, F=39000 N. Then the working area of the land wheel cylinder was:

$$A = \frac{F}{p} = \frac{\pi(D^2 - d^2)}{4} \quad (1)$$

where: D is body diameter, m; F is load, N; p is system pressure, Pa; d is rod diameter, m, d = 0.4D.

Substitute p and F into the formula (1) to get D=70 mm. According to the standard specification of hydraulic cylinder, the selected body diameter was D=63 mm, so the selected rod diameter was d =25 mm for the land wheel cylinder.

For the stalk cutting device cylinder, the load was the maximum pressure of coulters. The pressure of a coulter required 1946 N (*Wang et al., 2012*), which was the basis for calculating the pressure of hydraulic cylinders. In the paper, there were seven sets of double coulters and two cylinders in the whole machine, so the load of each cylinder was 13622 N respectively. Similarly, the formula (1) could be used to determine that the body diameter was 40 mm and the rod diameter was 16 mm for the stalk cutting device cylinder.

For the land wheel cylinder and the stalk cutting device cylinder, the rod strokes should not exceed 500 mm and 300 mm respectively, and the time required for lowering or raising was 20 s. The flow rate could be calculated by the following formula.

$$Q = \frac{\pi}{4} \cdot D^2 \cdot \frac{S}{t} \quad (2)$$

where, Q is the maximum flow rate of hydraulic cylinder, m^3/s; S is the stroke of hydraulic cylinder, m;

t is the time required for lowering or raising, s.

Substituting D, S, and t into the formula (2), it was obtained that the flow rate was 11.8 L/min for the land wheel cylinder and 4.5 L/min for the stalk cutting device cylinder.

Design of the variable fertilization control system

The variable fertilization software run on PIC18F2682, the single chip microcomputer (micro control unit) collected the speed sensor signal to calculate the forward speed of the machine, and controlled the speed of stepper motor according to the fertilization formula to implement variable fertilization. The working principle of variable fertilization control system is shown in Fig. 5.

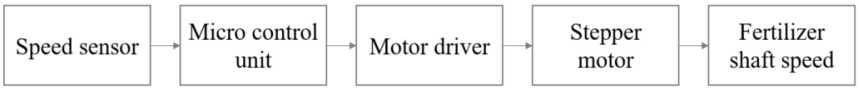

Fig. 5 - Schematic of the variable fertilization control system

The forward speed and the speed count-pulse meet the following formula:

$$v = \frac{I}{N} \cdot \pi D \times 3.6 \quad (3)$$

where, v is the forward speed of the machine, km/h; I is the number of speed pulses per unit time, s^{-1}; N is the number of magnets on the wheel hub used for counting; D is the diameter of the wheel used for counting, m.

The fertilizing amount should meet the following formula:

$$q = \frac{1}{6} vBQ \times 10^{-4} \quad (4)$$

where, q is the fertilizing amount per unit time of each fertilizer apparatus, kg/min; B is the row spacing of fertilizing operation, B=0.65 m; Q is the fertilizing amount per hectare, kg/hm^2.

The fertilizing amount per unit time of each fertilizer apparatus q and the rotation speed of the fertilizing shaft n meet the following formula:

$$q = kn + b \quad (5)$$

where, n is the rotation speed of the fertilizing shaft, r/min; k and b are the constant coefficient, k=0.032, b=0.1935.

Substituting formula (5) into formula (4), we can get:

$$n = (\frac{1}{6} vBQ \times 10^{-4} - b)/k \quad (6)$$

According to formula (6), the rotation speed of the fertilizing shaft can be changed automatically with the forward speed just by inputting Q value into the system before operation. The system can input different Q values according to the requirements of different regions or plots for fertilizer.

Design of the soil crushing device

The soil crushing device is arranged behind the subsoiler to finely break the surface soil after subsoiling. The soil crushing device designed is shown in Fig. 6a, including two soil crushing rollers, which can achieve profiling on the cropland surface around the rotation points 1 and 2.

The surface of the soil crushing roller is evenly distributed with blades, and each blade rolls into the soil gradually with the rolling of the roller. According to the twisting direction of blades, the soil crushing roller can be divided into the roller with left-rotation blades (Fig. 6b) and the roller with right-rotation blades (Fig. 6c). Two type rollers are combined into the soil crushing device, which can further crush and suppress the surface soil to form a flat seed bed. With reference to rod-type spiral soil crushing roller, the blade angle of the soil crushing roller is 15°.

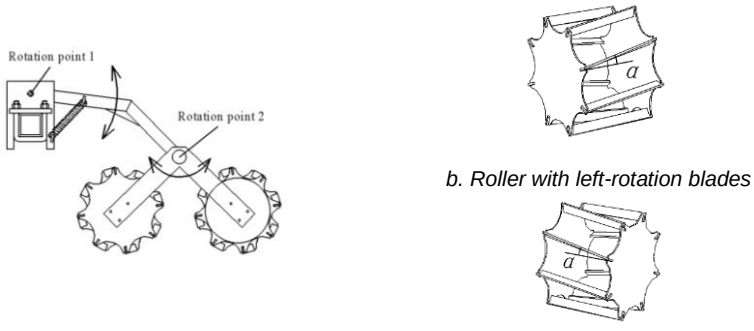

a. Profiling principle *b. Roller with left-rotation blades* *c. Roller with right-rotation blades*

Fig. 6 - Structure of the soil crushing device. Note: α is the blade angle of the soil crushing roller.

Test plot

The field test was conducted in the test field at Shandong University of Technology, Zibo, China. The last crop of the test plot was corn, the stubbles and stalks were left on the cropland after harvesting in autumn. The field test consisted of two parts: optimization test and verification test.

Test scheme and method

(1) Optimization test

The traction came from the Deere 1404 tractor, and the working speed was about 0.9 m/s in the optimization test. The different coulters and different soil crushing rollers were selected to test. The coulters had five levels: four fluted coulters (with 8, 13, 18, 25 waves) and one flat coulter (without wave), which were named as 8W, 13W, 18W, 25W and NW, respectively. The soil crushing rollers had two levels: with blade angle (α=15°) and without blade angle (α=0°). So there were 10 treatments in the optimization test. The test indicators were the stalk cutting rate and soil crushing rate. The test area was 100 m long and 50 m wide. For each treatment, one coulter and one soil crushing roller were selected to work on the test plot.

Measurement of stalk cutting rate: All the stalks touched by the coulter were collected and counted. The stalk cutting rate was calculated according to the following formula.

$$T = \frac{a}{a+b} \times 100\% \tag{7}$$

where, T is the stalk cutting rate, %; a is the number of stalks cut; b is the number of stalks uncut.

Measurement of soil crushing rate: Randomly take 10 measuring points with an area of 0.5 m×0.5 m to measure the quality of the soil block with the longest side less than 4 cm and the total quality of all soil block, respectively. The soil crushing rate was calculated according to the following formula, and the average value was taken as the final result.

$$C = \frac{G_a}{G} \times 100\% \tag{8}$$

where, C is the soil crushing rate, %; G_a is the quality of the soil block with the longest side less than 4 cm, kg; G is the total quality of all soil block, kg.

(2) Verification test

The purpose was to verify the operating performance of the whole machine under optimal parameter combination conditions, including subsoiling performance, soil crushing performance and fertilizing performance. The corresponding test indicators were the subsoiling depth and the stability coefficient of subsoiling depth, the soil crushing rate, the variation coefficient of fertilizing amount in each row and the variation coefficient of total fertilizing amount. The set theoretical subsoiling depth was 35 cm, and the presupposed fertilizing amount was 150, 400, 800 kg/hm^2 respectively. The whole machine worked back and forth once in the test plot with 100 m long.

Subsoiling performance: In the measurement area, 5 points were randomly selected for each row to measure the subsoiling depth. The stability coefficient of subsoiling depth ε was calculated by the following formula.

$$\varepsilon = 1 - \sqrt{\frac{\sum(h_i - \bar{h})^2}{n-1}} / \bar{h} \times 100\% \tag{9}$$

where, ε is the stability coefficient of subsoiling depth, %; h_i is the subsoiling depth at the i-th point, mm; $\bar{h}$ is the average value of subsoiling depth, mm; n is the number of measured points.

Soil crushing performance: Randomly take 10 measuring points with an area of 0.5 m×0.5 m for each row to measure. The measurement method is the same as that described in the optimization test. The soil crushing rate was calculated according to the formula (8) and the average value was taken as the final result.

Fertilizing performance: The fertilizing performance test was carried out when the machine was parked. All 7 rows were tested, and the measurement time was 30 s each time, repeated 5 times. The variation coefficient of fertilizing amount in each row ζ_r and the variation coefficient of total fertilizing amount ζ_t were calculated by the following formulas:

$$\zeta_r = \sqrt{\frac{\sum(Q_i - \overline{Q_r})^2}{k-1}} / \overline{Q_r} \times 100\% \tag{10}$$

$$\zeta_t = \sqrt{\frac{\sum(Q_j - \overline{Q_t})^2}{m-1}} / \overline{Q_t} \times 100\% \quad (11)$$

where, ζ_r is the variation coefficient of fertilizing amount in each row, %; Q_i is the fertilizing amount for the i-th row, g; $\overline{Q_r}$ is the average value of the fertilizing amount of the each row, g; k is the number of measurements; ζ_t is the variation coefficient of total fertilizing amount, %; Q_j is the value of total fertilizing amount for the j-th time, g; $\overline{Q_t}$ is the average value of total fertilizing amount of the each time, g; m is the number of rows.

The field test site is shown in Fig. 7.

a. Physical prototype *b. Operation process*

Fig. 7 - Field test site

RESULTS AND DISCUSSION

Optimization test

The data of optimization test were processed and analyzed using SPSS version 19.0 statistical software (SPSS Inc., Chicago). The analysis of variance (ANOVA) of each variable with their means, level and F test results are shown in Table 2.

The effect of coulter types on the stalk cutting rate was not significant (P≥0.05) (Table 2). The results showed that the stalk cutting rate was 97.7%-99.2%, which means the stalk cutting device with double-row coulter could effectively cut stalks covering the cropland, regardless of the coulter types. The reason was that the hydraulic control system gave a large downforce during operation, which is enough to cut the straw by different types of coulters.

Table 2

Statistical analysis of the different factors and their interactions

Factors	Variables	
	Stalk cutting rate (%)	Soil crushing rate (%)
Coulter types (F1)		
NW	99.2a	33.7e
8W	98.4a	52.5a
13W	97.7a	47.0b
18W	98.1a	43.3c
25W	97.9a	40.8d
Soil crushing roller types (F2)		
With blade angle	/	46.7a
Without blade angle	/	40.2b
F-test		
F1	0.35ns	614.23**
F2	/	54.31**
F1×F2	/	3.28*

*Note: 8W, 13W, 18W, 25W and NW respectively represent four fluted coulters (with 8, 13, 18, 25 waves) and one flat coulter (without wave). Means followed by the same letter in the column do not differ significantly by LSD's test (p≥ 0.05). **significant at 1% probability (p < 0.01). *significant at 5% probability (p < 0.05). ns: non-significant (p≥ 0.05). F-test is any statistical test in which the test statistic has an F-distribution under the null hypothesis.*

The effects of coulter types and soil crushing roller types on soil crushing rate were both very significant ($P<0.01$), and there was a significant interaction between the two factors ($P<0.05$) (Table 2).

The soil crushing rate of NF was the smallest (33.7%) in all treatment. The soil crushing rate of 8W, 13W, 18W and 25W were 55.8%, 39.5%, 28.5%, 21.1% higher than that of NF respectively (Table 2, Fig. 8). With the increase of the number of waves for the fluted coulter, the soil crushing rate gradually decreased. The reason was that the surface soil was loosened by the double-row fluted coulter before the subsoiling operation, it was not easy to form large soil blocks on the surface during subsoiling operation. The smaller the number of waves, the larger the range of soil loosening, which would cause more disturbance of the surface soil and the less likely to form large soil blocks. For the NF coulter, its main function was to cut the stalk, and the soil loosening performance was poor, so it was easier to form large soil blocks than fluted coulters. Wang et al. reported that a different working width resulted in a different soil disturbance width, and a narrower tool created less soil disturbance normally (*Wang et al., 2018*). Zeng et al. also got the same conclusion (*Zeng et al., 2018*).

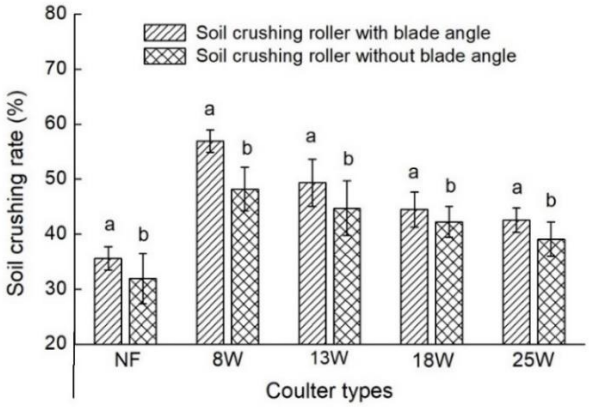

Fig. 8 - Effect of coulter types and soil crushing roller types on soil crushing rate

Note: The same letters over bars indicate groups which were not significantly different (P≥0.05)

The soil crushing roller with blade angle had a better soil crushing effect, and its soil crushing rate was 16.2% higher than that without blade angle (Table 2, Fig. 8). The reason was that the blade angle could ensure the blades gradually entered the soil, and there be sufficient shear force to cut large soil blocks during this process. Compared with the soil crushing roller without blade angle, the combined action of the soil crushing rollers with left-rotation blades and right-rotation blades made the leakage area less. In addition, the special profiling structure could make the double soil crushing roller to move close to the cropland surface, making the soil more finely broken.

For subsoiling operations, a higher soil crushing rate could effectively reduce soil moisture loss (*Borek et al., 2018*), so the combination of the fluted coulters with 8 waves (8W) and the soil crushing roller with blade angle was optimal.

Verification test

The test results of subsoiling performance obtained are shown in Table 3. It can be seen that the average value of subsoiling depth was 35.8 cm, slightly larger than the theoretical subsoiling depth of 35 cm, and the stability coefficient of subsoiling depth was 93.9%, which met the design requirements of the China National Standard No. GB/T 24675.2-2009 ($\varepsilon \geq 85\%$).

Test results of subsoiling performance **Table 3**

Row	Measuring point (cm)					Row average value (cm)	Total average value (cm)	Stability coefficient ε (%)
	1	2	3	4	5			
Row 1	41.0	35.2	36.1	40.1	35.2	37.5		
Row 2	37.5	40	33.2	37.9	39.5	37.6		
Row 3	38.3	37.2	36.7	34.5	30.6	35.5		
Row 4	32.3	36.6	33.4	31.4	33.2	33.4	35.8	93.9
Row 5	38.2	37.3	39.5	37.9	40.5	38.7		
Row 6	34.4	33.7	35.2	30.5	33.9	33.5		
Row 7	35.2	31.6	34.7	36.4	32.4	34.1		

The test results of soil crushing performance obtained are shown in Table 4. It can be seen that the soil crushing rate met the design requirements of the China National Standard No. GB/T 24675.2-2009 (C≥30%).

Table 4

Test results of soil crushing performance

Row	Row 1	Row 2	Row 3	Row 4	Row 5	Row 6	Row 7	Average
Soil crushing rate *C* (%)	54.3	43.4	60.7	58.9	62.4	51.2	45.2	53.7

The test results of fertilizing performance obtained are shown in Table 5. It can be seen that the fertilizing amount can be adjusted in the range of 150-800 kg/hm^2. With the increase of the fertilizing amount, the variation coefficient of fertilizing amount in each row increases, while the variation coefficient of total fertilizing amount decreases. Both test indicators met the design requirements of the China Agricultural Industry Standard No. NY/T1003-2006 (ζ_r≤13%, ζ_t≤7.8%).

Table 5

Test results of fertilizing performance

Presupposed value (kg/hm^2)	800	400	150
$\overline{Q_r}$ (g)	2195.2	1192.5	404.8
ζ_r (%)	4.1	7.6	11.2
$\overline{Q_t}$ (g)	13171.1	7155.3	2429
ζ_t (%)	3.3	3.2	1.5

CONCLUSIONS

The traction combined machine for subsoiling and land preparation was designed, including the new stalk cutting device with double-row coulter, the soil crushing device with profiling structure, the hydraulic control system and the variable fertilization control system. The machine can complete the functions of stalk cutting and topsoil loosening, subsoiling, variable fertilization and land preparation in one operation, solving the problems of crop residue clogging, poor soil crushing and low operation efficiency in the cropland covering stalks.

The field optimization test was carried out to evaluate the effects of coulter types and soil crushing roller types on the machine performance. The results showed that the combination of the fluted coulters with 8 waves (8W) and the soil crushing roller with blade angle was optimal.

The results of field verification test showed that all performances met the design requirements of the relevant standards. This research provides an important reference for the structure design of stalk cutting device and soil crushing device for conservation tillage. The large multi-functional combined machine is the developing direction of agricultural equipment in the future.

ACKNOWLEDGEMENT

This work was supported by the National Natural Science Foundation of China (Grant No. 52005307).

REFERENCES

[1] Borek L., Bogdal A., Ostrowski K., (2018), The effect of subsoiling on changes of compaction and water permeability of silt loam, *Rocznik Ochrona Srodowiska*, vol.20, pp.538-557.

[2] Celik A., Raper R.L., (2012), Design and evaluation of ground-driven rotary subsoilers, *Soil and Tillage Research*, vol.124, pp.203-210.

[3] Daraghmeh O.A., Petersen C.T., Munkholm L.J., Znova L., Obour P.B., Nielsen S.K., Green O., (2019), Impact of tillage intensity on clay loam soil structure, *Soil Use and Management*, vol.35, no.3, pp.388-399.

[4] Feng X.M., Hao Y.B., Latifmanesh H., Lal R., Cao T.H., Guo J.R., Deng A.X., Song Z.W., Zhang W.J., (2018), Effects of subsoiling tillage on soil properties, maize root distribution, and grain yield on Mollisols of Northeastern China, *Agronomy journal*, vol.110, no.4, pp.1607-1615.

[5] Guo M.J., Li J.Y., Li J., Qi J.R., Zhang X.Y., (2021), Changes of soil structure and function after 16-year conservation tillage in black soil, *Transactions of The Chinese Society of Agricultural Engineering*, vol.37, no.22, pp.108-118.

[6] He M., Gao H.W., Dong P.Y., Cui D.J., Zhao W.G., (2018), Sub-soiling experiment on double cropping and conservation tillage adopted area, *Transactions of the Chinese Society for Agricultural Machinery*, vol.49, no.7, pp.58-63.
[7] Issaka F., Zhang Z., Zhao Z.Q., Asenso E., Li J.H., Li Y.T., Wang J.J., (2019), Sustainable conservation tillage improves soil nutrients and reduces nitrogen and phosphorous losses in maize farmland in southern China, *Sustainability*, vol.11, no.8, pp.2397.
[8] Jia H.L., Jiang X.M., Yuan H.F., Zhuang J., Zhao J.L., Guo M.Z., (2017), Stalk cutting mechanism of no-tillage planter for wide/narrow row farming mode, *International Journal of Agricultural and Biological Engineering*, vol.10, no.2, pp.26-35.
[9] Jiang X.H., Tong J., Ma Y.H., Sun J.Y., (2020), Development and verification of a mathematical model for the specific resistance of a curved subsoiler, *Biosystems Engineering*, vol.190, pp.107-119.
[10] Mondal S., Chakraborty D., Das T.K., Shrivastava M., Mishra A.K., Bandyopadhyay K.K., Aggarwal P., Chaudhari S.K., (2019), Conservation agriculture had a strong impact on the sub-surface soil strength and root growth in wheat after a 7-year transition period, *Soil and Tillage Research*, vol.195, pp.104385-104385.
[11] Prathuang U., Kittikhun P., (2018), Performance of combined tillage tool operating under four different linkage configurations, *Soil and Tillage Research*, vol.183, pp.109-114.
[12] Qi H., Li C.F., Zhao M., Jiang Y., (2020), Developments and prospects of conservation tillage in the dryland of northern China, *Crops*, vol.36, no.2, pp.16-19.
[13] Qi J.Y., Wang X., Pu C., Ma S.T., Zhao X., Xue J.F., Zhang H.L., (2018), Research advances on effects of conservation tillage practice on soil nitrogen component, *Transactions of The Chinese Society of Agricultural Engineering*, vol.34, pp.222-229.
[14] Qu Y., Pan C.L., Guo H.P., (2021), Factors affecting the promotion of conservation tillage in black soil - The case of Northeast China, *Sustainability*, vol.13, no.17, pp.9563.
[15] Wang B., Xu J.G., Li W.H., (2021), Design and experiment on bionic vibrant subsoiler for corn fields in northern China, *Journal of Agricultural Mechanization Research*, vol.43, no.5, pp.104-108.
[16] Wang H.L., Zhang W., (2012), Optimization design on stubble-cutting disc with ripples of no-tillage planter, *Journal of Agricultural Mechanization Research*, vol.34, no.10, pp.102-105.
[17] Wang Q. Zhu L.T., Li M.W., Huang D.Y., Jia H.L., (2018), Conservation agriculture using coulters: Effects of crop residue on working performance, *Sustainability*, vol.10, no.11, pp.4099.
[18] Wang Z.Q., Wang W.X., Li X., Li W.C., Guo J.L., Tang M.J., Fang R., (2016), Development status of subsoiling at home and abroad under conservation tillage, *Journal of Agricultural Mechanization Research*, vol.38, no.6, pp.253-258.
[19] Zeng Z.W., Chen Y., (2018), The performance of a fluted coulter for vertical tillage as affected by working speed, *Soil and Tillage Research*, vol.175, pp.112-118.
[20] Zhang F.L., Ren Y.W., Lu C.J., Yu Y.F., Wu M.Q., Luo Y., Zhang Z.Y., Yang L., (2018), Effects of subsoiling on soil physical properties and crop yields, *Hubei Agricultural Sciences*, vol.57, pp.46-48.

EXPLORING THE SOCIAL SUSTAINABILITY OF RUBBER FARMERS – INDIVIDUAL FARMERS PERSPECTIVE

/

สำรวจความยั่งยืนทางสังคมของชาวสวนยาง — มุมมองของเกษตรกรรายบุคคล

Kajohnjak NUANPHROMSAKUL[1)], Lucian-Ionel CIOCA[2)], Singha CHAVEESUK[1)], Wornchanok CHAIYASOONTHORN[1)]

[1)] KMITL Business School, King Mongkut's Institute of Technology Ladkrabang, Bangkok 10520, Thailand

[2)] Lucian Blaga University of Sibiu, Faculty of Engineering, Industrial Engineering and Management Department, Emil Cioran, Street, no. 4, 550025, Sibiu, ROMANIA

Tel: (+66-02-329-8460); E-mail: singha.ch@kmitl.ac.th

DOI: https://doi.org/10.35633/inmateh-68-29

Keywords: *Social Sustainability, Sustainability, Rubber Farmers, Satisfaction, Loyalty, Brand Image*

ABSTRACT

This research was geared towards analyzing the factors that influence the social sustainability of rubber farmers from an individual perspective. The research was driven by the fact that in Thailand, rubber farmers are still underprivileged and lack knowledge of marketing, finance, technology, business, and economic opportunities. The research adopted a model that evaluated the relationship between study variables with a focus on their effect on social sustainability. A quantitative methodology was adopted, where the data was collected from 436 individual rubber farmers in Thailand. The proposed model and constructs were evaluated using reliability and validity tests and CFA fitness. The data analysis utilizes structural equation modeling. The findings indicated that social sustainability was directly and significantly influenced by brand image and loyalty factors. Additionally, it was found to be indirectly influenced by satisfaction and trust. The research recommended that improvement in the brand image of the rubber farmers in states both locally and internationally would result in increased business sustainability.

บทคัดย่อ

งานวิจัยนี้มุ่งสู่การวิเคราะห์ปัจจัยที่มีอิทธิพลต่อความยั่งยืนทางสังคมของชาวสวนยางในมุมมองของแต่ละคน การวิจัยได้รับแรงหนุนจากข้อเท็จจริงที่ว่าเกษตรกรชาวสวนยางในประเทศไทยยังคงด้อยโอกาสและขาดความรู้ด้านการตลาด การเงิน เทคโนโลยี ธุรกิจ และโอกาสทางเศรษฐกิจ การวิจัยได้นำแบบจำลองที่ประเมินความสัมพันธ์ระหว่างตัวแปรการศึกษาโดยเน้นที่ผลกระทบต่อความยั่งยืนทางสังคม วิธีการเชิงปริมาณถูกนำมาใช้ โดยรวบรวมข้อมูลจากเกษตรกรชาวสวนยางในประเทศไทยจำนวน *436* ราย แบบจำลองและโครงสร้างที่เสนอได้รับการประเมินโดยใช้การทดสอบความน่าเชื่อถือและความถูกต้องและความเหมาะสมของ *CFA* การวิเคราะห์ข้อมูลใช้แบบจำลองสมการโครงสร้าง ผลการวิจัยพบว่าความยั่งยืนทางสังคมได้รับอิทธิพลโดยตรงและอย่างมีนัยสำคัญจากภาพลักษณ์ของแบรนด์และปัจจัยความภักดี นอกจากนี้ยังพบว่าได้รับอิทธิพลทางอ้อมจากความพึงพอใจและความไว้วางใจ การวิจัยชี้ให้เห็นว่าการปรับปรุงภาพลักษณ์ของเกษตรกรชาวสวนยางในรัฐทั้งในประเทศและต่างประเทศจะส่งผลให้ธุรกิจมีความยั่งยืนเพิ่มขึ้น

INTRODUCTION

The rubber farmers, a large group of people in Thailand, are still underprivileged, and they lack knowledge of marketing, finance, technology, business, and economic opportunities. Furthermore, they are facing several problems, such as losses from low product prices, high production costs, and natural disasters. Social sustainability depends on recognizing and managing corporate effects on people, both beneficial and detrimental. However, many problems have affected the livelihoods of rubber farmers and the activities of the farmer institutions, and the government has been required to resolve the issues of rubber prices every year as follows: "More than 200 rubber farmers from Surat Thani Province gathered to submit the letter to the Prime Minister through the provincial governor." They demand that the rubber price be set at 80 baht per kilogram. They are also compelled to gather again if there is no progress within seven days" (*Manager, 2014*). Additionally, "The leader of Trang Province's small rubber farmer network claimed that he would discuss with other leaders of rubber farmers in all 14 southern provinces on Jan. 12 so that they could conclude their demands proposed to the government if the policy is not effective" (*Thairat Online, 2016*).

The rubber farmer institutes' request for government assistance demonstrated a lack of resilience and capacity to function independently of the government and tackle issues bedeviling the farmers. Besides, the world rubber price situation has been volatile and uncertain. The prices of natural rubber depend on the price in the futures market and the speculation of market investors.

In the situation of global rubber production in 2015, there were 28 rubber-producing countries with a total of 77.60 million rai, and the total production was 12.0 million tons (*Office of Agricultural Economics, 2015*). Thailand is the no. 2 country with the most rubber plantation areas (the rubber plantation area in Thailand is 22,176,714 million rai, followed by Indonesia (*Rubber Research Institute, The Rubber Authority of Thailand, 2017*). Moreover, Thailand produces and exports the most natural rubber in the world, at a rate of 4,473,370 tons annually, with an annual export of 3,749,456 tons (*Rubber Research Institute, 2014*). Based on these statistics, this research is focused on developing a framework and model proposition for the social sustainability of the rubber farmer institute. When the rubber farmer institutes are stable and sustainable under a successful model of establishment, it will result in gathering members, products, dividends, working capital, brainstorming, and the concept of activity. It will not only create a stable and sustainable situation for natural rubber prices but also affect the livelihood of rubber farmers. It also strengthens the social sustainability of rubber farmer institutes.

MATERIALS AND METHODS

Sustainability aspect in rubber farming

Sustainable development refers to the development strategy that manages all resources, whether they are natural, human, financial, or physical resources, to create wealth, well-being, and complete happiness. Sustainable development depends on correct and proper environmental management. In short, the development is within ecological limits. Sustainable development is, according to the World *Commission on Environment and Development, (1990)*, when development satisfies demands of the situation devoid of jeopardizing the potential for the unborn generations to gratify their expectations. Sustainable development is essential for enhancing individual wellbeing because it can encourage adequate management of public resources. Additionally, it establishes a sustainable financial system independent of external interventions and offers a strong environmental quality so that people may utilize natural resources effectively, particularly when used as a base for production to support economic growth (*Brundtland Commission, 1987*).

Dey et al., (2020), reasoned that sustainable development is integrated development as a whole. It aims to harmoniously gather and combine all variables in a balanced manner, even in a diverse context of economic differences; it can be considered development according to the competitiveness based on their resources, society, and environment, which must be emphasized to consistently respond to the needs of relevant people in their social and cultural contexts (*Suksanchananun et al., 2020; Slusarczyk et al., 2016; Kot & Brzezinski, 2015*).

Aaker, (2014), noted that brand loyalty is the positive view and satisfaction of the consumer with a product. Consumers have a tendency to frequently buy the products as a result of this notion. In contrast, *Chaudhuri, (1999),* indicated that brand loyalty occurs when the consumer continues to purchase a particular brand's products over another. It occurs when the consumer is satisfied with the quality of the products. *Haque, (2013),* and *Das, (2014),* stated that brand loyalty is the consumer behavior that they maintain when purchasing a particular product. The same goes for *Schiffman and Kanuk, (2010)*. However, the marketing strategy plays a crucial role in brand loyalty since brand loyalty should be built otherwise the consumer will purchase other brands. Previous research suggests that image of the brand is also linked to customer loyalty as well as perceived value. For instance, *Jung et al., (2020),* conducted a study on sustainable ad initiates in the conventional apparel industry and customers loyalty to the brand. The finding revealed that sustainable marketing activities resulted in brand image, trust, and satisfaction positively. When applied to rubber cooperatives, the study sought to ascertain the loyalty of rubber farmers to the collective, and if they will prefer alternatives or operate their farms individually.

Robinson and Barlow (1959) define a brand image as the self-image of the institute and organization that people connect in their minds. They can perceive and gain from direct experience or word of mouth. *Jefkins, (1993),* explained that brand image is the overall impression of the organization that the people can recognize as a positive image. The element of brand image proposed by *Wijaya, (2013),* has been adopted as one of the frameworks since it is relevant to the sustainable model of the rubber farmer institute registered as a juristic person. The elements of brand image were demonstrated as follows: (1) brand identity refers to the name, logo, color, slogan, tagline, and vision; the personality of the executive; or typeface of the institute/group of rubber farmers. (2) Brand personality refers to the institute/group's disposition of the rubber farmer. (3) Activity refers to the income, profit, satisfaction, management, and administration of an institute/group in terms of training and the participation of rubber farmers, and so forth. *Pool et al., (2016),* studied the association of brand image and perceived value utilizing Structural Equation Modeling technique.

According to *Fehrenbach* and *Herrando*, *(2021)*, a consumer's perception of value depends on how pleased they are with the service/product. It is divided into two types: the perceived value of a product and the perceived value of quality. *Petrick*, *(2002),* reasoned that the instrument that had been used to measure the perceived value could merely indicate that tangible results were discernible from utilizing the product or service. Perceived value can be developed as a primary differentiating tool to preserve competitive advantage. Perceived value is one of several aspects that influence client happiness and trust in marketing, according to numerous studies (*Anderson et al., 1992; Chen & Lin, 2015*). Other studies show that by assessing sustainability and consumer intents, perceived value can be used as a metric for marketing success (*He et al., 2022; Brychko et al., 2022; Muangmee et al., 2021; Rahardja et al., 2021; Lakatos et al., 2021*). Assessing customer's perception of the value of the service and the product can be used as a metric or indicator of perceived value. What value do members of the rubber association place on the group? How valuable do members consider the group in running and maintaining their rubber farms? These are important questions that need clarification.

Skowron, (2020), noted that satisfaction refers to a result of participating in an activity that leads to a positive attitude towards that activity; a negative attitude can indicate dissatisfaction. Prior research on the notion of satisfaction, classified it into two types: positive and negative feelings (*Jiang et al., 2021; Kuan et al., 2020*). The positive feeling produces a sense of pleasantness, but this type of pleasantness is different. To explain this, the feeling of pleasure can make other favorable feelings. The positive and negative feelings as well as the complicated feeling can create the concept of satisfaction (*Di Castro et al., 2018*). *Gerdt et al., (2019),* identified an association where sustainability and customer satisfaction were linked and mediated by ranking. Additionally, the findings reveal that the link varies depending on the sustainability metric used. *Chaudhuri and Holbrook, (2001),* averred that trust is the inclination where individual customers trust the capacity of the brand towards accomplishing its objectives. Trust comes from the words, actions, and commitment of a person or institute. *Alam and Yasin, (2010),* explained that trust is the expectation that a person can rely on other persons. Trust can refer to the anticipation of positive results including risk and uncertain results. According to *Schurr and Ozanne, (1985)*, trust fosters positive sentiments toward suppliers and increases client loyalty. It also aids members in projecting their future interactions (*Deheshti et al., 2016*). In uncertain situations, trust boosts competitiveness, lowers search and transaction costs, and minimizes opportunism (*Nazari et al., 2015*). According to *Reast, (2005)*, trusted brands will fare better than their rivals' less reliable competition. Similarly, rubber associations and cooperatives that provide satisfaction to members are more likely to be trusted, and provide satisfaction to members.

Conceptual framework

Figure 1 illustrates the study model based on a survey of the extant literature.

The research hypotheses are presented next.

- H1: The brand image of the rubber farmers has a positive influence on customers' perceived value.
- H2: The brand image of the rubber farmers' group positively influences the loyalty of the members to the group.
- H3: The brand image associated with the rubber farmers' group positively and significantly influences the adoption of sustainability practices by its members.
- H4: The perceived value of the rubber farmers' group positively influences members' satisfaction with the group activities.
- H5: Trust in the rubber farmers' group positively influences member satisfaction.
- H6: The perceived value of the rubber farmers' group positively influences trust by members of the collective.
- H7: Satisfaction with the rubber farmers' group has a positive effect on the loyalty of the members to the group.
- H8: Trust in the rubber farmers' group positively influences the loyalty of the members to the group.
- H9: Loyalty of the group members towards the policies of the rubber farmers' group positively impacts the adoption of sustainability practices.
- H10: The impact of independent variables on sustainability is significantly moderated by loyalty.

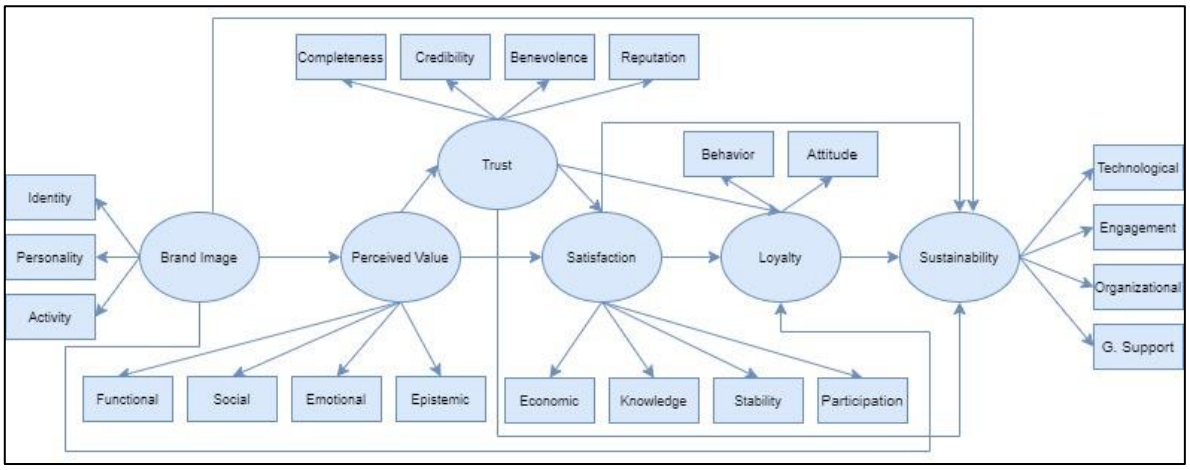

Fig. 1 - Conceptual framework

Population and sample size

The research adopted a quantitative survey design, using primary data from individual rubber farmers in Thailand. This research aimed to create a model of sustainability for rubber farmers who were individual farmers. According to *Dejchanchaiwong et al., (2019)*, there are 535 rubber farmers' groups in Thailand, with a combined membership of 112,556. This served as the research population. *Krejcie and Morgan, (1970),* recommended a sample size of 384 for a population size equal to or greater than 100,000. This number is considered as being statistically relevant. The researchers distributed 600 copies of the questionnaire to accommodate the large study universe available to the researchers. Of the 600 copies of the questionnaire shared with the respondents, 487 were returned, representing a response rate of approximately 81%. After validating the returned copies, removing those partially completed and those missing information considered critical, 436 were considered fit for analysis.

The rubber farmers were categorized into three groups:

(1) The group of rubber farmers in the advanced or developed stage.

(2) The group of rubber farmers in the developing stage.

(3) The group of rubber farmers in the initial stage.

The instrument for data collection for the survey was a structured questionnaire using close-ended questions. The closed-ended questions were utilized to ask respondents to choose from distinct sets of responses. The data collection process included the following steps; the research was authorized by the King Mongkut's Institute of Technology Ladkrabang's Research Ethics Committee, Thailand, and was assigned the code EC-KMITL_64_050. The Ethics Committee granted the study an exemption waiver following the guidelines of the Helsinki Declaration. The researchers affirm that all respondents voluntarily have provided explicit consent to take part in the study. There was no information on the questionnaire that might be used to identify responders.

RESULTS AND DISCUSSION

Demographic characteristics

The demographic variables evaluated include gender, age, period of rubber farming and the rubber products produced. Most of the respondents evaluated were male (72%) while the females were the minority (28%). The highest age group was 31 – 40 years (37%) while the lowest group was 50+ years (12%). For the farming period, the majority indicated having farmed for 6 – 10 years (50%) while for the rubber products, the majority indicated having 20 – 50 kgs (54%). The data are summarized in Table 1. Table 2 and Figure 2 also present the findings and model evaluation.

Demographic data of respondents **Table 1**

Variables	Values	n	%
Gender	Male	312	0.72
	female	124	0.28
Age	20-30	82	0.19
	31-40	163	0.37
	41-50	137	0.31
	50+	54	0.12
Farming period (years)	0-5	57	0.13
	6-10	217	0.50

	11+	162	0.37
Rubber Products (kg)	0-20	72	0.17
	20-50	237	0.54
	50+	127	0.29

Table 2

Model Evaluation

Path Relationships			Factor Loadings	Cronbach's alpha	Composite Reliability	AVE
BI	→	Loyalty	0.878			
BI	→	Acti	0.81			
BI	→	Pers	0.893	0.782	0.927	0.927
BI	→	Iden	0.718			
Loyalty	→	Beh	0.795			
Loyalty	→	Atti	0.792	0.827	0.872	0.982
Perceived	→	Epis	0.869			
Perceived	→	Emo	0.87	0.782	0.892	0.967
Perceived	→	Soc	0.77			
Perceived	→	Func	0.7			
Satisfaction	→	Par	0.893			
Satisfaction	→	Stab	0.868	0.872	0.972	0.628
Satisfaction	→	Know	0.842			
Satisfaction	→	Eco	0.83			
Sustainability	→	GovS	0.726			
Sustainability	→	Org	0.84			
Sustainability	→	Enga	0.897	0.852	0.897	0.762
Sustainability	→	Tech	0.748			
Trust	→	Comp	0.709			
Trust	→	Cre	0.916	0.871	0.971	0.762
Trust	→	Ben	0.857			
Trust	→	Rep	0.799			

Discriminant validity, as shown in Table 3, was also used to assess the constructs' validity. To make sure that each notion for the latent variable is distinct from other latent variables, discriminant validity is used. The Fornell-Larker criteria demand that all constructs must have an AVE square root value that is greater than their correlation with other latent constructs, indicating that the discriminant validity was attained.

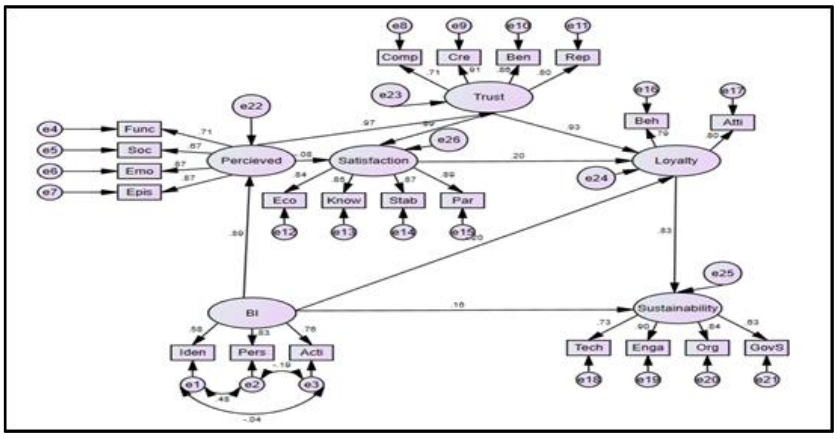

Fig. 2 - Empirical Results

Table 3

Discriminant Validity

	1	2	3	4	5	6
BI	0.828					
Loyalty	0.618	0.927				
PV	0.728	0.789	0.829			

	1	2	3	4	5	6
Satisfaction	0.835	0.756	0.772	0.854		
Sustainability	0.872	0.729	0.872	0.761	0.792	
Trust	0.836	0.863	0.723	0.792	0.773	0.872

Empirical results

The empirical findings of the investigation of the correlation between the various study variables are presented in this section. The results are summarized in Table 6, for both direct and indirect effects.

Table 4

Empirical Results

	Path Relationships					Estimate	S.E.	C.R.	P
	Direct Effects								
H1	BI	→	Perceived			.774	.212	3.648	***
H2	BI	→	Loyalty			-.163	.175	-.929	.353
H3	BI	→	Sustainability			.129	.110	1.173	.024
H4	Perceived	→	Satisfaction			-.087	.289	-.300	.765
H5	Trust	→	Satisfaction			.935	.262	3.565	***
H6	Perceived	→	Trust			1.091	.063	17.251	***
H7	Satisfaction	→	Loyalty			.179	.082	2.187	.029
H8	Trust	→	Loyalty			.789	.182	4.333	***
H9	Loyalty	→	Sustainability			.803	.132	6.098	***
	Indirect Effects								
H10	BI	→	Loyalty	→	Sustainability	.672	.283	6.811	***
	Satisfaction	→	Loyalty	→	Sustainability	.028	.189	1.872	***
	Trust	→	Loyalty	→	Sustainability	.427	.897	5.278	0.002
	Satisfaction	→	Trust	→	Loyalty	.719	.236	3.852	***

The results of the study indicated that brand image bears a strong and positive effect on perceived value ($\beta = 0.774$, $p<0.05$) confirming hypothesis 1 of the study. The brand image was deemed to have a negative and insignificant influence on loyalty ($\beta = -0.163$, $p>0.05$), hence rejecting hypothesis 2. Brand image has a positive and significant effect on sustainability ($\beta = 0.129$, $p<0.05$) confirming hypothesis 3 of the study. Perceived value was determined to have a negative and insignificant effect on satisfaction ($\beta = -0.087$, $p>0.05$) hence rejecting hypothesis 4. Trust was shown to have a positive and significant effect on satisfaction ($\beta = 0.935$, $p<0.05$) confirming hypothesis 5 of the study. Perceived value was seen to have a positive and strong effect on trust ($\beta = 1.091$, $p<0.05$) confirming hypothesis 6 of the study. Satisfaction was revealed to positively and significantly affect loyalty ($\beta = 0.179$, $p<0.05$) confirming hypothesis 7 of the study. Trust was found to have a positive and significant effect on loyalty ($\beta = 0.789$, $p<0.05$) confirming hypothesis 8 of the study. Loyalty was confirmed to have a positive and significant effect on sustainability ($\beta = 0.803$, $p<0.05$) confirming hypothesis 9 of the study. In addition, the researchers also evaluated the mediating role of loyalty. The research showed that brand image, customer satisfaction, and trust were all significantly mediated by loyalty when it came to the adoption of sustainability in rubber farming.

The research indicated that loyalty is a crucial element in bringing about aspects of sustainability of individual farmers. The respondents believed when there is loyalty, there is the sustainability of the concerned aspect. For this study, the loyalty of customers regarding the rubber farmers would increase the associated sustainability. The aspects of loyalty considered in this case are behavior and attitude. Loyalty referred to the commitment and obligation between the rubber farmer members that willingly participate in the activities of the group. It leads to a positive relationship and encourages the members to maintain their commitment. It is the result of brand loyalty that the consumer has towards the product and service and the result of a source of inspiration that the consumers can gain. For this reason, the consumers not only continue to purchase the brand's products but also promote the product. Furthermore, the result can bring confidence in executives and staff as well as the supplier to become a partnership.

If there is brand loyalty—a collection of favorable evaluations and unwavering convictions about a certain brand, the consumers continuously purchase the same brand. In addition to the aspects above, trust and satisfaction were found to have a significant and indirect influence on sustainability. In this case, loyalty was considered the mediating factor. In other words, satisfaction and trust would influence loyalty, and in turn rubber farmers sustainability. In this case, satisfaction was considered and found to be an important aspect in improving the sustainability of the respondents.

CONCLUSIONS

This study sought to identify characteristics that, from a personal standpoint, affect the viability of rubber farmers. The research developed and adopted a comprehensive model that was considered suitable to evaluate the sustainability aspect. The model considered sustainability as the endogenous variable. Brand image, perceived value, contentment, trust, and loyalty made up the external factors. Important conclusions were developed after the examination of the findings. These include that brand image is important to sustainability, and satisfaction is important to sustainability. Rubber farmers groups in Thailand can leverage on the results to understand the needs of their members by understanding the relevance of the brand image, perceived value and build trust which can lead to sustainability of the group.

For the model evaluation, model chi-square, root mean square error of approximation (RMSEA), comparative fit index (CFI), root mean square residue, adjusted goodness of fit (AGFI), and the goodness of fit (GFI) were among the fitness factors that were assessed. The following results were obtained; RFI = 0.923, GFI = 0.902, TLI = 0.948, NFI = 0.937, CFI = 0.957, IFI = 0,958 which satisfied the required threshold of >0.900. AGFI = 0.867 satisfied the required minimum threshold of >0.800. The Chi-square/df = 2.941 satisfied the required threshold for <5.00. The RMSEA = 0.067 which satisfied the required threshold of <0.08. These thresholds were suggested by *Andersson et al., (2022)*, *Byrne, (1994), Schumacker and Lomax, (2004),* and *Kline R.B., (2015)*. The satisfaction of these thresholds confirmed that the data and study constructs fitted well with the model.

In addition to the model fitness tests, the reliability and validity of the constructs utilized in the research were also assessed. Standardized factor loadings and the average variance were used to assess the validity. Reliability was evaluated using composite reliability and Cronbach's α. To measure the validity, factor loadings ranged from 0.70 to 0.916, while the values for AVE ranged from 0.628 to 0.982. These values, according to *Hair et al., (2010),* and *Ghozali, (2014),* should be above 0.5, this threshold requirement was satisfied. The composite reliability ranged from 0.872 to 0.972, while Cronbach's α values ranged from 0.782 to 0.871. The required threshold is that the values should be above 0.7, the requirement that was met (*Khalid, 2021*).

Kaojan, (2003), asserted that satisfaction is a positive feeling that the employees have towards their profession. This feeling can arouse the feeling of appreciation, enthusiasm, determination, and the morale of the employee work. All these feelings have impacted the effective work and the organization's success. The features of a service are sometimes best identified by customer satisfaction. The executive must survey consumer satisfaction towards the product and service because the results can reveal the attitude and comments of the consumers on the product and service. Thus, the providers can offer services that meet the need of each aspect of the consumers. Consumer satisfaction is a significant variable in evaluating the quality of service. If any providers can offer a service that meets the need and expectations of the consumers, the consumers continue to get the same service. The quality of service depends on the place, equipment the personality of the staff, the creditability of the service, the willingness of the staff as well as the ability to provide service with reliability and compassion. One measure of a service business' performance is employee satisfaction. Giving precedence to employee satisfaction is as crucial as consumer satisfaction. If the employees are fulfilling the desires of their career, they can perform their tasks effectively and that leads to consumer satisfaction and the success of the business.

The research also revealed that loyalty, trust, and satisfaction significantly influenced the sustainability of rubber farmers. Brand image is a critical and significant factor for the improvement of sustainability. The improvement in the brand image of the rubber farmers in states both locally and internationally would result in increased business sustainability. In this case, brand image referred to the positive perception of the rubber farmer institutions that are cooperating so that the memberships, non-memberships, and other people can recognize the products and the organization. Satisfaction was considered and found to be an important aspect in improving the sustainability of the respondents. The aspects of satisfaction that are critical in improving sustainability include economics, knowledge, stability, and participation. When there is loyalty, there is the sustainability of the concerned aspect.

To this study, the loyalty of customers regarding the rubber farmers' institutes would increase the associated sustainability. Future studies can consider the influence of loyalty towards attracting new members to the farmers' cooperative and foster a sustainable relationship between the government and farmers cooperatives. Future studies can also replicate the study in other cooperative groups to ascertain the consistency of the results. A limitation of the study was that respondents were virtually always self-selected. That is, no matter how often they are reminded or what incentives are provided, not everyone who receives a survey will respond. This limitation was minimized by following up with reminders to the respondents. There were also response accuracy issues. This was however, limited to 51 copies of the questionnaire. This did not significantly affect the results.

ACKNOWLEDGEMENT

The authors highly appreciate the thorough and detailed reviews provided by anonymous reviewers and editors, who contributed immensely to the improved final output quality.

REFERENCES

[1] Aaker D. (2014). *Aaker on branding: 20 principles that drive success*. Morgan James Publishing, New York/USA.

[2] Alam, S.S., & Yasin, N.M. (2010). What factors influence online brand trust: evidence from online tickets buyers in Malaysia. *Journal of Theoretical and Applied Electronic Commerce Research*, *5*(3).

[3] Andersson, B., Luo, H., & Marcq, K. (2022). Reliability coefficients for multiple group item response theory models. *British Journal of Mathematical and Statistical Psychology*, *75*(2), 395–410.

[4] He, K., Oláh, J., & Hasan, M. (2022). The influence of psychological ownership and social support on organizational resilience: the mediating role of organizational identity. *Journal of Business Economics and Management*, *23*(3), 650–667. https://doi.org/10.3846/jbem.2022.16571

[5] Brychko, M., Bilan, Y., Lyeonov, S., & Streimikiene, D. (2022). Do changes in the business environment and sustainable development really matter for enhancing enterprise development? *Sustainable Development*. https://doi.org/10.1002/sd.2410

[6] Byrne B.M. (1994). *Structural equation modeling with EQS and EQS/Windows: Basic concepts, applications, and programming.* Thousand Oaks, Sage, California/USA.

[7] Chaudhuri, A., & Holbrook, M. B. (2001). The Chain of Effects from Brand Trust and Brand Affect to Brand Performance: The Role of Brand Loyalty. *Journal of Marketing*, *65*(2), 81–93.

[8] Chen, S. C., & Lin, C. P. (2015). The impact of customer experience and perceived value on sustainable social relationship in blogs: An empirical study. *Technological Forecasting and Social Change*, *96*, 40–50.

[9] Deheshti, M., Adabi Firouzjah, J., & Alimohammadi, H. (2016). The Relationship between Brand Image and Brand Trust in Sporting Goods Consumers. *Annals of Applied Sport Science*, *4*(3), 27–34.

[10] Dejchanchaiwong, R., Kumar, A., & Tekasakul, P. (2019). Performance and economic analysis of natural convection-based rubber smoking room for rubber cooperatives in Thailand. Renewable Energy, 132, 233-242.

[11] Dey, P. K., Malesios, C., De, D., Chowdhury, S., & Abdelaziz, F. B. (2019). The Impact of Lean Management Practices and Sustainably-Oriented Innovation on Sustainability Performance of Small and Medium-Sized Enterprises: Empirical Evidence from the UK. *British Journal of Management*, *31*(1), 141–161.

[12] Di Castro, V. C., Hernandes, J. C., Mendonça, M. E., & Porto, C. C. (2018). Life satisfaction and positive and negative feelings of workers: a systematic review protocol. *Systematic Reviews*, *7*(1).

[13] Fehrenbach, D., & Herrando, C. (2021). The effect of customer-perceived value when paying for a product with personal data: A real-life experimental study. *Journal of Business Research*, *137*, 222–232.

[14] Gerdt, S. O., Wagner, E., & Schewe, G. (2019). The relationship between sustainability and customer satisfaction in hospitality: An explorative investigation using eWOM as a data source. *Tourism Management*, *74*, 155–172.

[15] Ghozali I. (2014). *Structural Equation Modeling, Metode Alternatif dengan Partial Least Square (PLS),* 4th edition. Badan Penerbit Universitas Diponegoro, Semarang/Indonesia.

[16] Hair, J.F., Black W.C., Babin B.J., & Anderson R.E. (2010). *Multivariate data analysis*, 7th ed. Pearson Prentice Hall, New Jersey/USA.

[17] Jiang, X., Ji, L., Chen, Y., Zhou, C., Ge, C., & Zhang, X. (2021). How to Improve the Well-Being of Youths: An Exploratory Study of the Relationships among Coping Style, Emotion Regulation, and Subjective Well-Being Using the Random Forest Classification and Structural Equation Modeling. *Frontiers in Psychology*, 12.
[18] Kaojan, P. (2003). *The satisfaction of parents towards the secondary school management in the elementary school: Ubon Ratchathani Primary Educational Service Area Office*. (Master's thesis) Faculty of Education, Ubon Ratchathani Rajabhat University, Ubon Ratchathani/Thailand.
[19] Khalid, B. (2021). Entrepreneurial insight of purchase intention and co-developing behavior of organic food consumption. *Polish Journal of Management Studies*, *24*(1), 142–163.
[20] Kline R.B. (2005). *Principles and practice of structural equation modeling*, 2nd ed. Guilford Press, New York/USA.
[21] Kot, S., & Brzezinski, S. (2015). Market orientation factors in sustainable development and corporate social responsibility. *Asian Journal of Applied Sciences*, 8(2), 101-112.
[22] Krejcie, R.V., & Morgan, D.W., (1970). Determining Sample Size for Research Activities. Educational and Psychological Measurement.
[23] Kuan, M. Y., Wang, J. H., Liou, Y. C., & Peng, L. P. (2020). Exploring the Association between Life Perceptions and Emotional Profiles in Taiwan: Empirical Evidence from the National Well-Being Indicators Survey. *International Journal of Environmental Research and Public Health*, *17*(12), 4209.
[24] Lakatos, E. S., Nan, L. M., Bacali, L., Ciobanu, G., Ciobanu, A. M., & Cioca, L. I. (2021). Consumer Satisfaction towards Green Products: Empirical Insights from Romania. *Sustainability*, *13*(19), 10982.
[25] Manager Online (2014). *Surat rubber farmers assembled to claim the rubber price*. [Online], Available from: https://mgronline.com/south/detaiF9570000141505 [accessed 20 June 2021],
[26] Muangmee, C., Kot, S., Meekaewkunchorn, N., Kassakorn, N., & Khalid, B. (2021). Factors Determining the Behavioral Intention of Using Food Delivery Apps during COVID-19 Pandemics. *Journal of Theoretical and Applied Electronic Commerce Research*, *16*(5), 1297–1310.
[27] Nazari E., Ghasemi B., & Saeidi S.S. (2015). Explain the relationship between green brand image, green satisfaction and green trust and factors affecting on green brand equity. *Bulletin of the Georgian National Academy of Sciences*, Vol.9, pp. 487-94.
[28] Pool K.A., Pool M.K., & Taghipourian M.J. (2016). Customer satisfaction through corporate reputation: The mediating role of perceived value*. International Journal of Humanities and Cultural Studies,* Vol.3, no.2, pp. 1424-1434.
[29] Rahardja, U., Hongsuchon, T., Hariguna, T., & Ruangkanjanases, A. (2021). Understanding Impact Sustainable Intention of S-Commerce Activities: The Role of Customer Experiences, Perceived Value, and Mediation of Relationship Quality. *Sustainability*, *13*(20), 11492.
[30] Reast, J. D. (2005). Brand trust and brand extension acceptance: the relationship. *Journal of Product & Brand Management*, *14*(1), 4–13.
[31] Rubber Authority of Thailand Act, B.E. 2560. 2017. *Rubber Authority of Thailand Annual Report 2017*. [Online], Available from: http://online.pubhtml5.eom/sibs/humw/#pM. [accessed 20 June 2021],
[32] Rubber Authority of Thailand Act. 2017. Rubber Research Institute: Hot Issue. [Online], Available from: https://library2.parliament.go.th/ebook/content-issue/25 5 9/hi25 59-032. pdf [accessed 20 June 2021],
[33] Schumacker R.E. & Lomax R.G. (2004). *A beginner's guide to structural equation modeling*, Second edition. Lawrence Erlbaum Associates, Mahwah, NJ/USA.
[34] Schurr, P. H., & Ozanne, J. L. (1985). Influences on Exchange Processes: Buyers' Preconceptions of a Seller's Trustworthiness and Bargaining Toughness. *Journal of Consumer Research*, *11*(4), 939.
[35] Skowron, L., Gąsior, M., & Sak-Skowron, M. (2020). The Impact of a Time Gap on the Process of Building a Sustainable Relationship between Employee and Customer Satisfaction. *Sustainability*, *12*(18), 7446.
[36] Slusarczyk, B., Smolag, K., & Kot, S. (2016). The supply chain of a tourism product. *Actual Problems of Economics*, *179*(5), 197–207.
[37] Suksanchananun, W., Chaiyasoonthorn, W., & Chaveesuk, S. (2020). The impact of supply chain management competencies on the rice community enterprises. *Polish Journal of Management Studies*, *22*(1), 531–544.
[38] Thairat Online (2016). The rubber farmers in Trang has threatened to starve in protest for speed up the solution. [Online]. Available from: https://www.thairath.co.th/content/560843 [accessed 20 June 2021].

[39] Wijaya B.S. (2013). Dimensions of brand image: A conceptual review from the perspective of brand communication. *European Journal of Business Management*, Vol.5, pp. 55-65.
[40] ***Office of Agricultural Economics 2015. *Agricultural Statistics of Thailand (2015)*. [Online], Available from: http://www.oae.go.th/assets/portals/l/files/ebook/yearbook58.pdf [accessed 5 July 2021].

DESIGN AND EXPERIMENTS OF A LAYERED FERTILIZER SHOVEL FOR MAIZE
/
玉米分层施肥铲设计与试验

Xin DU[1, 2)], Cailing LIU[1*)], Meng JIANG[1)], Hao YUAN[1)], Lei DAI[1)], Fanglin LI[1)], Zhanpeng GAO[1)]
[1)] College of Engineering, China Agricultural University, Beijing 100083/ China;
[2)] School of Mechanical Engineering, Jiangsu Ocean University, Lianyungang 222005/ China
Tel: 0086-010-62737502; E-mail: cailingliu@163.com
Corresponding author: Cailing Liu
DOI: https://doi.org/10.35633/inmateh-68-30

Keywords: *Point-applied fertilization; Layered fertilization; Shovel; Box-Behnken design*

ABSTRACT
A layered fertilizer shovel is designed to achieve double layer fertilization in response to the current problem of large fertilizer efficiency loss in one-time banding application. The key structural parameters of the layered shovel were designed and the working speed V, the distance L_1 between the banding fertilizer discharging pipe and the point-applied fertilizer discharging device and the distance L_2 between the fertilizer distribution plate and the point-applied fertilizer discharging device were determined as the main factors affecting the layered distance h. A quadratic regression model between factors and indicators was established by single-factor test and response surface analysis. With the layered distance h=10 cm as the optimization target, the predicted value of layered distance h is 10 cm when V, L_1 and L_2 are 2.7 km/h, 15.3 cm and 18.2 cm, respectively, and the simulation test is conducted to verify the combination of the parameters obtained from the optimization solution, and the simulated value of layered distance h is 9.9 cm, which is a small error compared with the predicted value. The field test was conducted under the optimal combination of parameters, and the results showed that the layered distance h was 9.1 cm at the working speed V of 2.7 km/h, and the relative error was 8.1% compared with the simulation value, which can be considered as a high reliability of the simulation test, and the simulation test can accurately simulate the distribution of fertilizer particles in the real environment in the field. When the working speed V is 1.8-5.4 km/h, the distribution range of layered distance h is 8.0-9.5 cm, which can meet the agronomic requirements of fertilizer layered application.

摘要
针对目前肥料一次性条施存在肥效损失大的问题，设计了一种分层施肥铲，实现双层施肥。对分层施肥铲的关键结构参数进行了设计，确定作业速度 V、条施肥排肥管与穴施肥排肥器间距离 L_1 和分肥板与穴施肥排肥器间距离 L_2 为影响分层距离 h 的主要因素。通过单因素试验和响应面分析建立因素和指标间的二次回归模型。以分层距离 h=10 cm 为优化目标，得到作业速度 V、条施肥排肥管与穴施肥排肥器间距离 L_1 和分肥板与穴施肥排肥器间距离 L_2 分别为 2.7 km/h、15.3 cm 和 18.2 cm 时，分层距离 h 预测值为 10 cm，对优化求解得到的参数组合进行仿真试验验证，得到分层距离 h 仿真值为 9.9 cm，与预测值相比误差较小。在最优参数组合下进行田间试验，结果表明作业速度 V 为 2.7 km/h 时，分层距离 h 为 9.1 cm，与仿真值相比相对误差为 8.1%，可认为仿真试验可信度高，仿真试验可准确模拟肥料颗粒在田间真实环境下的分布情况。当作业速度 V 为 1.8-5.4 km/h 时，分层距离 h 的分布范围为 8.0-9.5 cm，可满足肥料分层施用的农艺要求。

INTRODUCTION
Maize is the largest and most productive food crop in China, and plays a leading role in the country's food production and food security (*Li et al.*, *2017*). As China's per capita arable land continues to decrease, increasing yields has become the only way to ensure food security and people's livelihood (*Liu et al.*, *2018*). In order to ensure high crop yields, farmers apply chemical fertilizers in large quantities while causing serious surface pollution and fertilizer waste, which restricts the sustainable development of agricultural production Zhang *et al.*, *2021*). In order to improve crop yield and fertilizer use efficiency, a lot of research has been carried out by scholars at home and abroad (*He et al.*, *2014*).

Xin Du, Ph.D. Stud.; Cailing Liu, Prof. Ph.D.; Meng Jiang, Ph.D. Stud.; Hao Yuan, Ph.D. Stud.; Lei Dai, Ph.D. Stud.; Fanglin Li, Ph.D. Stud.; Zhanpeng Gao Ph.D. Stud.*

Farmers used to apply fertilizer in a one-time banding fertilization at a distance of 5-10cm from the seed row and 10cm deep when sowing maize (as shown in Figure 1), some of the fertilizer is in the soil far from the roots and the root system is very inefficient, the released nutrients are not absorbed and used in time, the excess fertilizer nutrients leave the cultivated soil due to runoff, leaching or gaseous loss, thus causing groundwater or atmospheric pollution (*Ye et al.*, *2010; Zhu et al., 2013; Chen et al., 1995*). In recent years, there has been widespread interest in the root zone application pattern (as shown in Figure 1). It has been found that when fertilizer is point-applied in a single burrow 5-10 cm away from the plant and 10 cm deep at the time of sowing, ammonia volatilization and run-off losses from urea granules are significantly reduced, thus greatly improving the utilization of nitrogen fertilizer (*Cao et al.*, *1984; Savan et al., 1980*). Zhou et al. found that a single root-zone point application under monopoly furrow with full film cover was beneficial to the concentration of nitrogen in the soil tillage layer, improving the efficiency of nitrogen use by summer maize and promoting the accumulation of dry matter and yield of summer maize (*Zhou et al.*, *2020*). Jiang et al. found that a one-time root zone point application of urea increased yield by 9.8% and 8.8%, respectively, and the apparent nitrogen fertilizer utilization rate increased by 12.4% and 8.3%, respectively, compared with a one-time banding application of urea and farmers' customary split application of nitrogen, so a one-time root zone point application of urea can achieve the effect of slow-release fertilizer and improve the utilization rate of nitrogen fertilizer (*Jiang et al., 2018*; *Jiang et al.*, *2019; Jiang et al., 2018; Jiang et al., 2018*). Zhang et al. used indoor simulations to investigate the nutrient transport patterns of nitrogen, phosphorus and potassium under the point application conditions of urea, ammonium polyphosphate and potassium chloride compound fertilizers (*Zhang et al.*, *2020*). He found that the nitrification of ammonium nitrogen under fertilizer cavity application conditions was inhibited by the high concentration of nutrients in the fertilizer interval, thus delaying the conversion of ammonium nitrogen to nitrate nitrogen, which is an important reason for the sustained and efficient supply of nitrogen in the root zone primary application technique. Guo et al. showed that full inter-plant point application increased plant yield by 3.70%, above-ground biomass by 3.56% and N and P nutrient accumulation by 11.24% and 19.44% compared with open-row strip application (*Guo et al.*, *2020*). Wang et al. believes that most crops have a low proportion of inter-root soil in the total volume of farm soil, and the nutrients absorbed by the root system mainly come from the soil around the root zone (*Wang et al.*, *2013*). Fertilizer application in the root zone is the best way to match the dynamic range of fertilizer nutrient diffusion with the dynamic range of root extension, which has a significant effect on weight loss and efficiency.

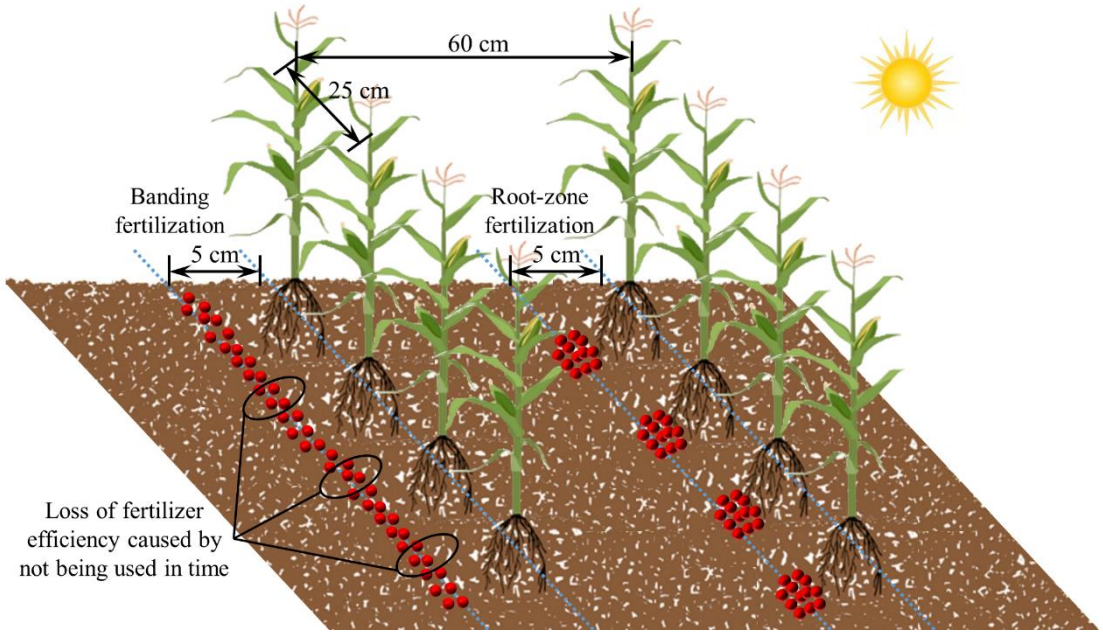

Fig. 1 – Agronomic diagram of banding and root zone fertilizer application

Studies have shown that the most active root system of maize plants is at 10 cm before and after the pulling stage, the most active root system is at 20 cm before and after the spitting stage, and the dry weight of the root system in the depth range of 0-20 cm accounts for more than 80% of the total dry weight of the root system from the trumpet stage to the finishing stage (*Guan et al.*, *2006*). The root system is most active within 20 cm of the horizontal distribution.

At present, a single application of fertilizer at a depth of 10 cm only ensures efficient uptake of fertilizer by the maize plant around the time of nodulation. In order to ensure an efficient supply of fertilizer during all growth periods of the maize plant, this study was based on the agronomic basis of the growth and development of the maize plant root system and its fertilizer uptake pattern, and the fertilizer was applied to the soil in two layers (as shown in Figure 2). The upper layer of fertilizer is 10 cm deep to meet the nutritional requirements of the maize plant before the nodulation stage, and since the horizontal distribution of the root system is much less than 25 cm (the theoretical spacing of the maize plant) at this time, the fertilizer granules are point-applied 5 to 10 cm from the plant. The lower layer of fertilizer was applied at a depth of 20 cm to meet the nutritional requirements of the maize plant after the nodulation stage, when the horizontal distribution of the root system at a depth of 20 cm is almost equal to 25 cm (the theoretical spacing of the maize plant), so the fertilizer granules were applied in banding 5 to 10 cm from the plant rows.

In order to realize the above fertilizer application pattern, this study designed a layered fertilizer shovel. The structure and parameters of the layered fertilizer shovel were investigated by discrete element simulation experiments with the objective of layered distance, and the optimal combination of structural parameters was optimized and field trials were conducted in order to provide a research basis for the maize stratified fertilizer application device.

STRUCTURE AND WORKING PRINCIPLE

The structure of the internal pneumatic-filled maize precision seed rower is shown in Figure 2 and consists mainly of a fertilizer tank, fertilizer feeder, fertilizer supply tube, fertilizer point-applied device, layered plates, shovel body and shovel tip. The fertilizer point-applied device transforms the continuous flow of fertilizer from the fertilizer feeder into a fertilizer pile and discharges it, the detailed principle of which has been described in previous studies (*Du et al.*, 2022).

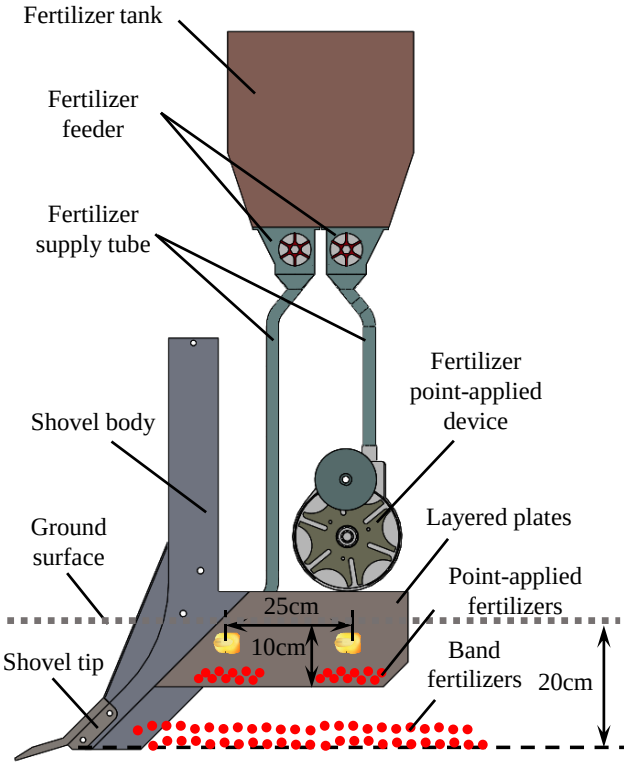

Fig. 2 – Schematic diagram of the structure and principle of the layered fertilizer application unit

When working, fertilizer particles flow out of the fertilizer tank through the fertilizer feeder of the outer groove wheel and flow into the fertilizer shovel and the fertilizer point-applied device respectively under the guidance of the fertilizer supply tube. The soil is destroyed by the action of the shovel tip and the shovel body to form a 20 cm deep trench, the fertilizer particles flowing into the shovel fall into the deep trench in the form of banding application. The soil flows back into the trench by its own gravity and buries the fertilizer particles. Due to the existence of the layered plate, the soil cannot completely flow back and will form a 10 cm deep shallow trench. The fertilizer particles form a fertilizer pile gathered by the action of the point-applied device and are discharged into the shallow trench. Finally, the soil completely flows back to bury the shallow trench.

MATERIALS AND METHODS

Soil model and simulation model construction

According to the literature, the properties of soil particles are usually nucleated, flaky, striped and blocky, as shown in Figure 3(a) to (d) (*Ma et al., 2019; Ding et al., 2018; Wang et al., 2017)*. The smaller the particle size of the soil, the more time consuming the simulation will take. In order to improve the computational efficiency and save simulation time, four types of spherical particles with a radius of 4 mm are used: nuclei, flakes, strips and blocks. The Poisson's ratio, shear modulus and density of the soil particles are 0.3, 1×10^6 Pa and 2600 kg/m^3, respectively. The coefficient of restitution, static friction and rolling friction between soil particles are 0.6, 0.14 and 0.33, respectively.

A soil box of length, width and height 1200 mm x 400 mm x 450 mm is modelled in EDEM (as shown in Figure 3(e)). The tillage layer was set at a depth of 300 mm and was randomly filled with 64078 nucleated particles, 64077 flake particles, 64074 strip particles and 64071 block particles. The fertilizer shovel was plowed to a depth of 200 mm and made of 65Mn with Poisson's ratio, shear modulus and density of 0.427, 1×10^6 Pa and 7820 kg/m^3, respectively. The coefficient of restitution, static friction and rolling friction between the fertilizer shovel and soil particles were 0.6, 0.14 and 0.33, respectively.

The triaxle dimensions of the fertilizer granules were 4.08 mm x 3.97 mm x 3.89 mm, with equivalent diameters and sphericity of 3.98 mm and 0.975. A single sphere particle with a diameter of 3.98 mm was created in EDEM to simulate fertilizer particles with Poisson's ratio, shear modulus and density of 0.3, 1×10^6 Pa and 2600 kg/m^3 respectively. The coefficient of restitution, static friction and rolling friction between fertilizer particles were 0.509, 0.176 and 0.033, respectively. The coefficient of restitution, static friction and rolling friction between fertilizer particles and soil particles were 0.1, 0.5 and 0.1, respectively. The coefficient of restitution, static friction and rolling friction between the fertilizer granules and the fertilizer shovel were 0.47, 0.42 and 0.095, respectively. The total simulation time was set to 10 s, the Rayleigh time step was $2.5\text{x}10^{-6}$ s, the grid size cell was 2.5 times the minimum particle radius and the data was recorded at 0.01 s intervals.

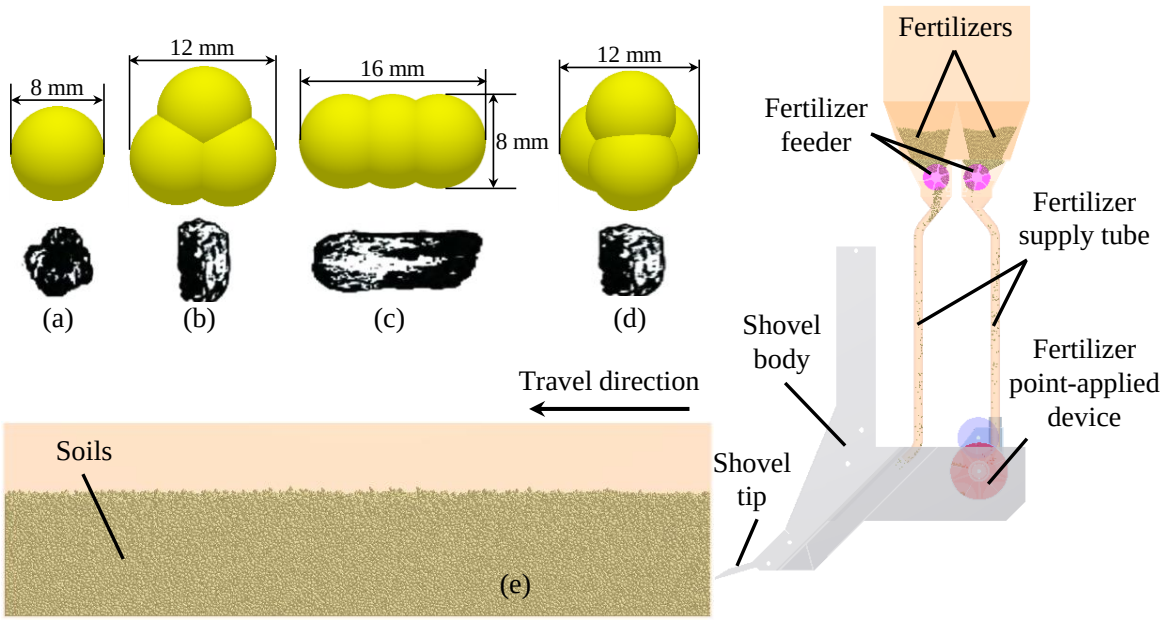

Fig. 3 – Soil particle model

Soil contact model

To better represent the strain relations in soils, researchers at the University of Edinburgh, UK, have proposed a model that considers both nonlinear elasto-plastic deformation and bonded contact, with the inter-particle normal force-displacement relationship shown in Figure 4 (*Subhash et al., 2014*). When loaded with an external force, the overlap δ of the 2 particles increases and the strain relationship changes according to the loading curve. When an external force is unloaded, the overlap of the 2 particles δ decreases and the strain relationship follows the unloading/reloading curve and will continue to follow the unloading/reloading curve when reloaded by any external force before the 2 particles are separated. The bonding force between the particles is characterized when f_n is less than 0. When the bonding force decays to the extreme value f_{min} the bonding between the particles disappears and will thereafter gradually decrease to the initial contact force f0 between the 2 particles in accordance with - $k_{adh}\delta^n$.

The main model parameters to be considered for the application of the EEPA model in EDEM include the initial contact force f0, the habitual contact surface energy Δγ, the contact plasticity ratio λp, the non-linear curve power index n, the adhesion branching curve power index *x* and the tangential stiffness factor ξ_{tm}. For reference (*Wang et al.*, 2017; *Janda et al.*, 2016), each parameter was set to f_0=0，$\Delta\gamma$=50，λ_p=0.7，n=1.5，x=5，ξ_{tm}=0.28571.

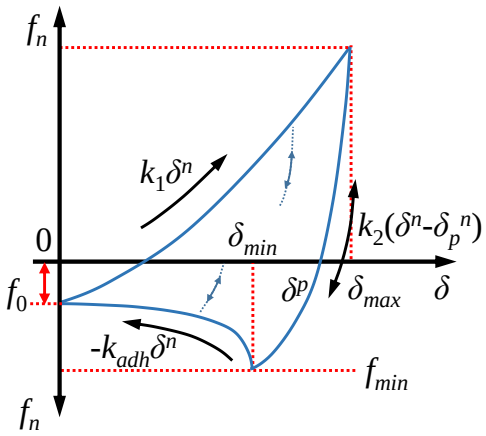

Fig. 4 – Normal contact force-displacement curve

Experimental design and experimental indicators

In this paper, the inter-layer distance (as shown in Figure 5) is selected as the test index. The inter-layer distance is the vertical distance between the banding-applied fertilizer layer and the point-applied fertilizer layer, which is calculated by selecting the middle of the fertilizer layer as the measurement point after the layering operation, using the ground as the coordinate reference point, and measuring the longitudinal coordinate values of the banding-applied fertilizer layer and the point-applied fertilizer layer respectively, and then subtracting them to obtain the fertilizer strip layering distance *h*. Each group of tests is repeated three times to obtain the average value.

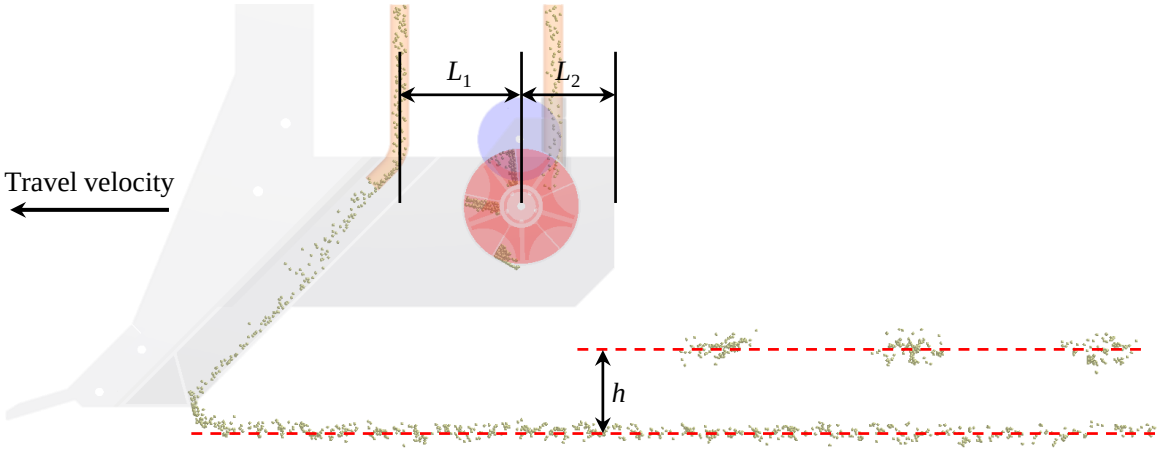

Fig. 5 – Inter-layer distance measurement chart

RESULTS

Operating speed V

A single-factor test was designed with a distance L_1 between banding fertilizer discharge pipe and point-applied device and a distance L_2 between the fertilizer layered plate and the point-applied device of 13 cm and 16 cm, and operating speeds *V* of 1.8, 2.7, 3.6, 4.5 and 5.4 km/h. The results of the test are shown in Figure 6.

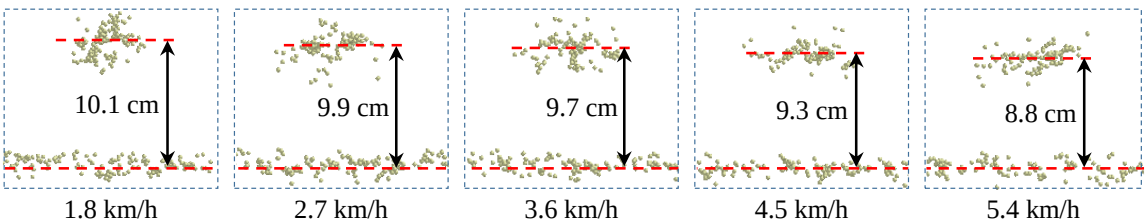

Fig. 6 – Plot of interlayer distance *h* against operating speed *V*

As can be seen from Figure 6, the interlayer distance *h* decreases with the increase of operating speed *V*. When the operating speed *V* is 1.8 km/h, the maximum interlayer distance *h* is 10.1 cm, and when the operating speed *V* gradually increases to 5.4 km/h, the interlayer distance *h* gradually decreases to 8.8 cm. As the soil is fluid, after the trencher has opened the soil out of the deep trench, the soil in the cultivated layer, which is not covered by the layered plates, will flow back into the trench by gravity. At the same time the soil is viscoelastic and flows back slowly, so when the operating speed V increases, some of the soil particles do not flow back into the furrow in time resulting in a reduction in the distance h between the layers of fertilizer particles.

Distance L_1 between banding fertilizer discharge pipe and point-applied device

A single-factor test was designed with operating speeds *V* and a distance L_2 between the fertilizer layered plate and the point-applied device of 3.6 km/h and 16 cm, and a distance L_1 between banding fertilizer discharge pipe and point-applied device of 12, 13, 14, 15 and 16 cm. The results of the test are shown in Figure 7.

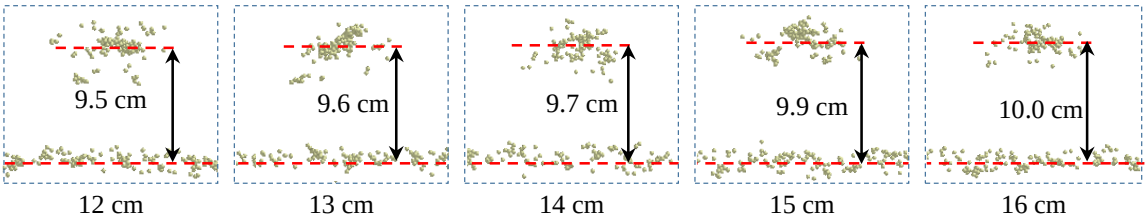

Fig. 7 – Plot of interlayer distance *h* against distance between banding fertilizer discharge L_1 pipe and point-applied device

As can be seen from Figure 7, the interlayer distance *h* increases with the increase of the distance L_1 between banding fertilizer discharge pipe and point-applied device, and the minimum interlayer distance *h* is 9.5 cm when the distance L_1 between banding fertilizer discharge pipe and point-applied device is 12 cm. When the distance L_1 between banding fertilizer discharge pipe and point-applied device gradually increases to 16 cm, the distance *h* between layers gradually increases to 10.0 cm. The larger the L_1 the more time the tilled soil has to flow back into the furrow under the influence of gravity, and conversely the smaller the distance *h* between the layers of fertilizer particles.

Distance L_2 between the fertilizer layered plate and the point-applied device

A single-factor test was designed with operating speeds *V* and a distance L_1 between banding fertilizer discharge pipe and point-applied device of 3.6 km/h and 13 cm, and a distance L_2 between the fertilizer layered plate and the point-applied device of 12, 14, 16, 18 and 20 cm. The results of the test are shown in Figure 8.

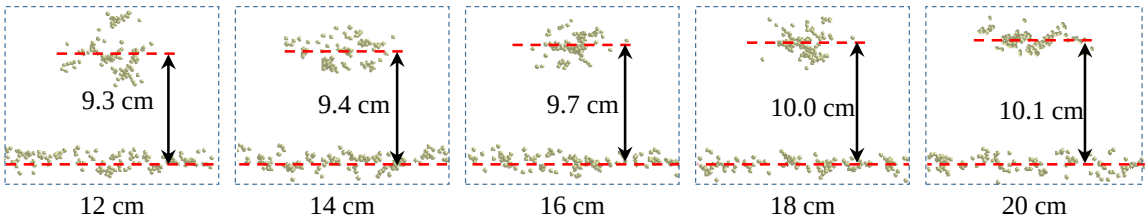

Fig. 8 – Plot of interlayer distance *h* against distance L_2 between the fertilizer layered plate and the point-applied device

As can be seen from Figure 8, the interlayer distance *h* increases as the distance L_2 between the fertilizer layered plate and the point-applied device increases, and the minimum interlayer distance is 9.3 cm when the distance L_2 is 12 cm. When the distance L_2 between the fertilizer layered plate and the point-applied device is gradually increased to 20 cm, the distance *h* between layers is gradually increased to 10.1 cm. The greater the distance between the fertilizer layered plate and the point-applied device, the more time the fertilizer particles have to fall into the furrow, otherwise the upper layer of fertilizer particles will have a larger vertical distribution and affect the stability of the distance *h* between the layers of fertilizer particles.

Box-Behnken design

Based on the results of the above single-factor test, the scope of work for each influencing factor and the factor codes were determined as shown in Table 1. A response surface test was designed to investigate the influence pattern of the interaction between factors on the indicators, with 17 treatment groups in the test protocol, and the test results are shown in Table 2. To further analyze the effects of the factors and interactions between factors on the test indicators, multiple regressions were fitted to the test results using Design-Expert 8.0.6 to establish a quadratic regression model between the test indicators and the factors, and the results of their significance tests are shown in Table 3.

The results of the ANOVA in Table 3 show that the quadratic regression model for the layered distance *h* between fertilizers is highly significant and the misfit term is not significant, indicating that the model is highly accurate and the regression equation fits well with the actual situation. The factors affecting the layered distance are, in descending order, the operating speed *V*, the distance L_1 between banding fertilizer discharge pipe and point-applied device and the distance L_2 between the fertilizer layered plate and the point-applied device. The interaction between the *V* and L_2, L_1 and L_2 had a significant effect on the layered distance *h*.

Table 1

Box-Behnken test factor coding

Codes	Factors		
	V/ km/h	L_1/ cm	L_2/ cm
-1	1.8	14	16
0	3.6	15	18
+1	5.4	16	20

Table 2

Box-Behnken test program and results

No.	Test factors			Test indicators
	V/ km/h	L_1/ cm	L_2/ cm	*h*/cm
1	1.8	14	18	9.93
2	5.4	14	18	9.35
3	1.8	16	18	10.03
4	5.4	16	18	9.55
5	1.8	15	16	9.90
6	5.4	15	16	9.48
7	1.8	15	20	10.08
8	5.4	15	20	9.50
9	3.6	14	16	9.65
10	3.6	16	16	9.86
11	3.6	14	20	9.85
12	3.6	16	20	9.93
13	3.6	15	18	9.92
14	3.6	15	18	9.85
15	3.6	15	18	9.89
16	3.6	15	18	9.86
17	3.6	15	18	9.88

The quadratic regression equation between each test factor and the test indicator is

$$h = -6.690 + 0.124V + 1.554L_1 + 0.459L_2 + 0.014VL_1 - 0.011VL_2 - 0.01L_1L_2 - 0.038V^2 - 0.041L_1^2 - 0.004L_2^2 \quad (1)$$

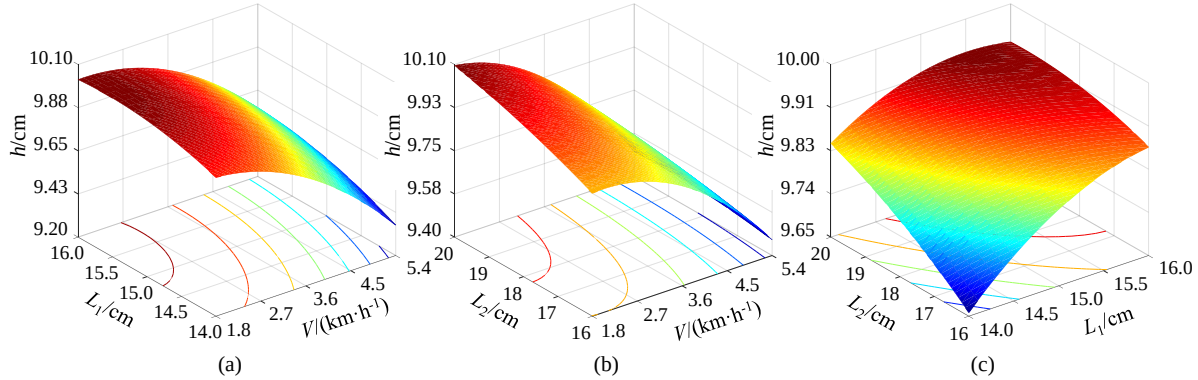

Fig. 9 – Effect of factor interactions on layered distances *h*

To visually analyze the effect of factor interactions on the rate of missed seeding, response surface plots were drawn as shown in Figure 9. As can be seen from Figure 9(a), there is a maximum layered distance *h* for a minimum operating speed *V* and a maximum distance L_1 between banding fertilizer discharge pipe and point-applied device. From Figure 9(b), it can be seen that there is a maximum layered distance *h* for a minimum operating speed *V* and a maximum distance L_2 between the fertilizer layered plate and the point-applied device. From Figure 9(c), it can be seen that a maximum value of layered distance *h* exists at the maximum distance L_1 between banding fertilizer discharge pipe and point-applied device and at the maximum distance L_2 between the fertilizer layered plate and the point-applied device.

Table 3

Analysis of variance table

Source of variation	Square	df	*F* value	*P* value
Model	0.6915	9	131.99	<0.0001*
V	0.5305	1	911.20	<0.0001*
L_1	0.0435	1	74.75	0.0001*
L_2	0.0276	1	47.43	0.0002*
$V L_1$	0.0025	1	4.29	0.0770
$V L_2$	0.0064	1	10.99	0.0128*
$L_1 L_2$	0.0042	1	7.26	0.0309*
V^2	0.0645	1	110.76	<0.0001*
L_1^2	0.0072	1	12.31	0.0099*
L_2^2	0.0011	1	1.91	0.2095
Residual	0.0041	7		
Lack of Fit	0.0011	3	0.48	0.7149
Cor Total	0.6956	16		

Notes：*Shows that the term is significant (i.e., $P < 0.05$).

In order to accurately find the optimal combination of parameters for each factor, the quadratic regression model established with the layered distance *h*=10 cm as the final optimization objective, combined with the boundary conditions, is solved optimally for multiple factors with the function objective and constraints as

$$\begin{cases} h = 10\ \text{cm}(V, L_1, L_2) \\ \text{s.t.} \begin{cases} 1.8\ \text{km/h} \le V \le 5.4\ \text{km/h} \\ 14\ \text{cm} \le L_1 \le 16\ \text{cm} \\ 16\ \text{cm} \le L_2 \le 20\ \text{cm} \end{cases} \end{cases} \quad (2)$$

The optimized solution was carried out using Design-expert 8.0.6 and the predicted layered distance *h* was 10 cm for the operating speed *V*, the distance L_1 between banding fertilizer discharge pipe and point-applied device and the distance L_2 between the fertilizer layered plate and the point-applied device for 2.7 km/h, was 15.3 cm and 18.2 cm respectively. The simulated value of the layered distance *h* is 9.9 cm, which is a small error compared to the predicted value.

Field trials

To verify the accuracy of the simulation tests and the performance of the field work, based on the optimal combination of working parameters determined from the above tests, a layered fertilizer application shovel was designed and machined and tested at different operating speeds (as shown in Figure 10). The fertilizer was applied at a depth of 10 cm (upper layer) and 20 cm (lower layer), with the upper layer applied in holes at a theoretical spacing of 25 cm and a theoretical application rate of 2.5 g per hole, and the lower layer applied in strips at a rate of 500 kg/hm^2, using Stanley slow-release compound fertilizer granules (N-P_2O_5-K_2O 15-15-15), with the results shown in Table 4.

Table 4

Fertilizer layered distances at different operating speeds

Operating speed *V* (km/h)	Upper depth h_1 (cm)	Lower depth h_2 (cm)	layered distance *h* (cm)
1.8	9.8	19.3	9.5
2.7	10.1	19.2	9.1
3.6	10.4	19.3	8.9
4.5	10.7	19.4	8.7
5.4	11.2	19.2	8.0

From Table 4, it can be seen that the layered distance *h* gradually decreases with increasing operating speed, and when the operating speed *V* is greater than 4.5 km/h, the stratification distance h decreases sharply. The layered distance *h* is 9.1 cm at an operating speed *V* of 2.7 km/h. The relative error compared to the simulation value is 8.1%, which can be considered a high degree of confidence that the simulation test can accurately simulate the distribution of fertilizer particles in the real environment in the field. When the operating speed *V* is 1.8 to 5.4 km/h, the distribution of the layered distance *h* ranges from 8.0 to 9.5 cm, which meets the agronomic requirements for fertilizer stratification.

(a) (b)

Fig. 10 – Operating speed adaptation results

CONCLUSIONS

A layered fertilizer application shovel was designed to achieve a double layer of fertilizer, with the upper layer at a depth of 10 cm and the lower layer at a depth of 20 cm, in response to the current problem of large losses in fertilizer efficiency with a single strip application.

The key structural parameters of the layered shovel were designed and the operating speed *V*, the distance L_1 between banding fertilizer discharge pipe and point-applied device and the distance L_2 between the fertilizer layered plate and the point-applied device were identified as the main factors influencing the layered distance *h*.

With the layered distance *h*=10 cm as the optimization target, the predicted value of *h* is 10 cm when the *V*, L_1 and L_2 are 2.7 km/h, 15.3 cm and 18.2 cm respectively. The simulated value is 9.9 cm, which is a small error compared to the predicted value.

The results of the field test with the optimal combination of parameters show that the *h* is 9.1 cm at the *V* of 2.7 km/h, with a relative error of 8.1% compared to the simulated value, which can be considered a high degree of confidence that the simulation test can accurately simulate the distribution of fertilizer particles in the real environment in the field. When the *V* is 1.8~5.4 km/h, the *h* is 8.0~9.5 cm, which can meet the agronomic requirements of fertilizer stratification application.

ACKNOWLEDGEMENT

This work was financially supported by National Key Research and Development Plan of China (2017YFD0700703).

REFERENCES

[1] Cao, Z., De Datta, S. K., Fillery, I. R. P. (1984). Nitrogen-15 balance and residual effects of Urea-N in wetland rice fields as affected by deep placement techniques. *Soil Science Society of America Journal*, *48*(1), 203-208. http://doi.org/https://doi.org/10.2136/sssaj1984.03615995004800010037x.

[2] Chen, Z., Yuan, F., Yao, Z., et al. (1995). The movement and leaching loss of NO_3—N in profile of Chao soil in Beijing (北京潮土NO_3—N在土体中的移动特点及其淋失动态). *Journal of Plant Nutrition and Fertilizers,* (02), 73-81.

[3] Ding, S., Bai, L., Yao, Y., et al. (2018). Discrete element modelling (DEM) of fertilizer dual-banding with adjustable rates. *Computers and Electronics in Agriculture*, *152*, 32-39. http://doi.org/10.1016/j.compag.2018.06.044.

[4] Du, X., Liu, C., Jiang, M., Yuan, H. (2022). Design and development of fertilizer point-applied device in root-zone. *Applied Engineering in Agriculture*, *38*(3), 559-571.
[5] Guan, J., Liu, K., Guo, X. (2006). Advances of research on maize root system architecture. (玉米根系构型的研究进展) *Journal of Maize Sciences* (06), 162-166.
[6] Guo, Y., Yin, H., Chang, F., et al. (2020). Inter-plant hole application of fertilizer: effect on yield and nutrient absorption of summer maize (株间穴施对夏玉米产量和养分吸收的影响) *Journal of Agriculture*, *10*(03), 43-48.
[7] He, P., Xu, X., Qiu, S., et al. (2014). Yield response and economic analysis of fertilizer application in maize grown in North China (我国北方玉米施肥产量效应和经济效益分析) *Journal of Plant Nutrition and Fertilizers*, *20*(06), 1387-1394.
[8] Janda, A., Ooi, J. Y. (2016). DEM modeling of cone penetration and unconfined compression in cohesive solids. *Powder Technology*, *293*(SI), 60-68. http://doi.org/10.1016/j.powtec.2015.05.034.
[9] Jiang, C., Lu, D., Zu, C., et al. (2018). One-time root-zone N fertilization increases maize yield, NUE and reduces soil N losses in lime concretion black soil. *Scientific Reports*, *8*(1). http://doi.org/10.1038/s41598-018-28642-0.
[10] Jiang, C., Lu, D., Zu, C., Zhou, J., Wang, H. (2018). Root-zone fertilization improves crop yields and minimizes nitrogen loss in summer maize in China. *Scientific Reports*, *8*(1). http://doi.org/10.1038/s41598-018-33591-9.
[11] Jiang, C., Ren, X., Wang, H., et al. (2019). Optimal nitrogen application rates of one-time root zone fertilization and the effect of reducing nitrogen application on summer maize. *Sustainability*, *11*(10), 2979. http://doi.org/10.3390/su11102979.
[12] Jiang, C., Wang, H., Lu, D., et al. (2018). Single fertilization of urea in root zone improving crop yield, nutrient uptake and use efficiency in summer maize (一次性根区穴施尿素提高夏玉米产量和养分吸收利用效率) *Transactions of the Chinese Society of Agricultural Engineering*, *34*(12), 146-153.
[13] Li, K., Yuan, W., Zhang, W., et al. (2017). Research status and development trend of corn fertilizing technology and fertilizing machine. *Journal of Agricultural Mechanization Research*, *39*(01), 264-268.
[14] Liu, J., Ning, J., Kuang, W., et al. (2018). Spatio-temporal patterns and characteristics of land-use change in China during 2010-2015. *Acta Geographica Sinica*, *73*(05), 789-802.
[15] Ma, Y., Wang, A., Zhao, J., et al. (2019). Simulation analysis and experiment of drag reduction effect of convex blade subsoiler based on discrete element method. (基于离散元法的凸圆刃式深松铲减阻效果仿真分析与试验) *Transactions of the Chinese Society of Agricultural Engineering*, *35*(03), 16-23.
[16] Savant, N. K., De Datta, S. K. (1980). Movement and distribution of ammonium-N following deep placement of urea in a wetland rice soil. *Soil Science Society of America Journal*, *44*(3), 559-565. http://doi.org/https://doi.org/10.2136/sssaj1980.03615995004400030025x.
[17] Subhash, C. T., John, P. M., Jin, S., J., F. C., Jin, Y. O. (2014). Micromechanical analysis of cohesive granular materials using the discrete element method with an adhesive elasto-plastic contact model. *Granular Matter*, *16*(3).
[18] Wang, H., Zhou, J. (2013). Root-zone fertilization——a key and necessary approach to improve fertilizer use efficiency and reduce non-point source pollution from the cropland, *Soils*, *45*(05), 785-790.
[19] Wang, X., Hu, H., Wang, Q., et al. (2017). Calibration method of soil contact characteristic parameters based on DEM theory (基于离散元的土壤模型参数标定方法) *Transactions of the Chinese Society for Agricultural Machinery*, *48*(12), 78-85.
[20] Ye, Z., Chu, G., Ye, J., et al. (2010). A comparison of mobility and availability of granular and fluid phosphate fertilizers in calcareous soils under laboratory conditions (固、液态磷源在石灰性土壤中的移动性及其对土壤有效磷含量影响的研究) *Journal of Plant Nutrition and Fertilizers*, *16*(06), 1433-1438.
[21] Zhang, L., Song, H., Chen, X., et al. (2020). Primary study on nutrient migration under hole fertilization in soils (穴施条件下肥料养分在土壤中迁移规律的初步研究) *Soils*, *52*(06), 1145-1151.
[22] Zhang, W., Yang, S., Sun, D., et al. (2021). Effects of straw mulching and nitrogen reduction on the distribution of soil nitrogen and groundwater nitrogen pollution (秸秆覆盖与氮减施对土壤氮分布及地下水氮污染影响) *Environmental Science*, *42*(02), 786-795.
[23] Zhou, C., Li, Y., Chen, P. (2020). Effects of Single Application of Fertilizer on Yield and Nitrogen Utilization of Mulching Summer Maize (一次性施肥模式对覆膜夏玉米产量与氮素利用的影响) *Transactions of the Chinese Society for Agricultural Machinery*, *51*(10), 329-337.
[24] Zhu, Z., Jin, J. (2013). Fertilizer use and food security in China (保障我国粮食安全的肥料问题) *Journal of Plant Nutrition and Fertilizers*, *19*(02), 259-273.

RECOVERY OF RESIDUAL SLUDGE FROM A WASTEWATER TREATMENT PLANT. IMPACT OF SLUGE-SOIL MIXTURE ON THE GROWTH OF TOMATO SOLANUM *LYCOPERSICUM* L.

/

استرداد الحمأة الناتجة من محطة معالجة مياه الصرف الصحي. تأثير مزيج التربة والحمأة على نمو الطماطم SOLANUM *LYCOPERSICUM* L.

OUADAH Sahraoui [1)], MAATOUG Mhamed *[1)], SOUDANI Leila[1)], CHAFAA Meriem[1)], MAATOUG Z. Zakaria[1)]
Laboratory of Agro-biotechnology and Nutrition in Semi-arid Areas
University of Tiaret, Algeria
Tel: +21346256125; E-mail: maatoug_m@univ-tiaret.dz
Corresponding author: Maatoug Mhamed
DOI: https://doi.org/10.35633/inmateh-68-31

Keywords: *Sewage sludge, soil physico-chemical characteristics, tomato growth, heavy metal, risk.*

ABSTRACT

Sewage sludge is used as a fertilizer in agriculture to rehabilitate deteriorated soils and replace artificial fertilizers. Sludge can be utilized to improve soil characteristics, promote microbial life, and increase plant production where it includes the primary nutrients and organic matter. The current study investigated the impact of the treatment of sewage sludge on the physico-chemical characteristics of the soil, and also on the growth of tomato (Solanum lycopersicum). The experiment consists of using a sludge-soil mixture, with different fractions of sewage sludge: soil control (0% sludge) and 20%, 40%, 60%, 100% of sludge. Biometric measurements (height, stem diameter and number of leaves) were performed on the tomato. The results showed good fertilizing properties of a sludge/soil mixture with the 60% sludge fraction. However, the tomato that grew on the 40% fraction had better growth and high foliage compared to the plants on the other fractions. The spreading of sludge provides a soil amendment and an additional supply of nutrients for tomatoes. The use of 40% fraction of sludge spreading for the cultivation of this plant can maintain better soil fertility while reducing the risk of heavy metal accumulation. Indeed, the 40% fraction of sludge has concentrations which are: 86±0.40 mg/kg for copper, 294 ±0.40 mg/kg for zinc and 50±5.9 mg/kg for lead, lower than the limits recommended by the European directives.

ملخص

الكلمات المفتاحية: حمأة الصرف الصحي ، الخصائص الفيزيائية والكيميائية للتربة ، نسبة 40٪ ، نمو الطماطم ، المعادن الثقيلة ، المخاطر

تستخدم حمأة الصرف الصحي كسماد في الزراعة لإعادة تأهيل التربة المتدهورة واستبدال الأسمدة الصناعية. يمكن استخدام الحمأة لتحسين خصائص التربة، وتعزيز حياة الكائنات الحية المتواجدة في التربة، و كذا زيادة المحصول النباتي للإحتوائها على العناصر الغذائية الأولية والمواد العضوية. تهدف الدراسة الحالية إلى دراسة تأثير معالجة حمأة الصرف الصحي على الخصائص الفيزيائية والكيميائية للتربة، وكذلك على نمو الطماطم (*Solanum lycopersicum L.*). تتمثل التجربة في استخدام خليط التربة مع الحمأة بنسب مختلفة من الحمأة، حيث استعملنا التربة الخالصة (أي 0٪ الحمأة) و 20٪ من الحمأة ، 40٪ ، 60٪ ، 100٪ من نسب الحمأة. تم إجراء القياسات الحيوية (الطول وقطر الساق وعدد الأوراق) على الطماطم. أظهرت النتائج خصائص تسميد جيدة لخليط الحمأة / التربة بنسبة 60٪ من الحمأة. ومع ذلك ، فإن الطماطم التي نمت على الجزء 40٪ كان لديها نمو أفضل وأوراق شجر عالية مقارنة بالنباتات في الأجزاء الأخرى. يوفر انتشار الحمأة تعديلًا للتربة وإمدادًا إضافيًا بالمواد المغذية لنمو للطماطم. يمكن أن يؤدي استخدام نسبة 40٪ من انتشار الحمأة لزراعة هذا النبات إلى الحفاظ على خصوبة التربة بشكل أفضل مع تقليل مخاطر تراكم المعادن الثقيلة. في الواقع ، يحتوي جزء 40٪ من الحمأة على تركيزات هي: 86 ± 0.40 مجم / كجم للنحاس ، 294 ± 0.40 مجم / كجم للزنك و 50 ± 5.9 مجم / كجم للوزن ، أقل من الحدود الموصي بها من قبل المعايير الأوروبية.

INTRODUCTION

The disposal of sewage sludge, a primary product of wastewater treatment plants, is a challenge. On the one hand, sewage sludge is environmentally harmful, but on the other side, it can be used as a fertilizer in organic farming *(Jarde, 2002; Soudani et al., 2017).*

The sludge treatment and disposal account for around half of the expenses of running sewage treatment plants. Traditional sludge disposal techniques, such as landfill, incineration, and ocean disposal, have a number of drawbacks. Sludge landfilling and incineration both have significant environmental consequences due to groundwater contamination and the creation of global warming gases *(Scholz, 2016; Eid et al., 2017).*

The use of treated sludge in agriculture can greatly reduce the cost of disposal, protect the environment, cut prices when compared to commercial fertilizers, offer critical plant nutrients, and increase soil fertility *(Zhao et al., 2012).*

Organic additions are required to improve soil fertility and productivity in arid land due to the low organic matter concentration *(Hussein, 2009; Eid et al., 2017).* For that it is hypothesized that urban sludge can improve organic matter in agricultural soil, hence enhancing plant growth and reducing the volume of sewage sludge produced. The content of the added sludge, including the organic matter and soil physio-chemical parameters, are related to the observed changes in soil chemical properties after the addition of the sludge *(Kidd et al., 2007; Tejada et al., 2016; Eid et al., 2017).*

De Sousa et al (2022) evaluated the impact of sewage sludge on soil fertility, nutrition and yield of sugarcane in three successive crops. Results showed that waste sludge increased pH and base sum, reduced exchangeable aluminum and improved soil chemical conditions. Sugarcane yield increased after SS rates and decreased with each crop cycle.

However, *Sabbahi et al (2022)* examined the presence of helminth eggs and protozoan cysts in samples of dried sewage sludge collected from ten sewage treatment plants (WWTPs) located in eight governorates of Tunisia. Based on morphological criteria, protozoan cysts were detected in all composite samples of dried sludge (N = 116) from the treatment plants studied; the content of all the dried sewage sludge samples examined was below WHO (2006) and US EPA (2003) recommendations and therefore the sludge could potentially be reused in agriculture. Sludge samples were taken from five municipal sewage treatment plants located in the largest industrial area in southern Poland to determine the ecological risk from heavy metals in sludge. This risk was assessed by calculating the potential ecological risk factor (ER), the risk index (RI), the risk assessment code (RAC), the individual contamination factor (ICF), the global risk (GRI) as well as the Individual Ecological Risk (IER) and Global Ecological Risk (GER).

The results found showed that the highest ecological risk was posed by Zn, Cd and Ni, while in the case of their total concentrations, by Cd and Hg. The results obtained confirm that the quantitative determination of the total content of heavy metals in sewage sludge is not a sufficient criterion in the assessment of the ecological risk that these elements pose to the natural environment and living organisms *(Tytla, 2020*).

The purpose of this study is to determine the impact of the application of various fractions of urban sludge from the Tiaret wastewater treatment plant on the properties of the soil, and on the development of tomato cultivation in a mixture of sludge-ground.

MATERIALS AND METHODS

In this experiment, soil samples were taken from a 25 cm layer. On the other hand, a dried sewage sludge was collected from the wastewater treatment plants of Bouchekif (Wilaya of Tiaret, Algeria).

The ground sludge was mixed with agricultural soil in proportions of 0% sludge for control soil, fraction of 20% sludge, 40% sludge, 60% sludge and 100% (0% soil). The different fractions were cultured in registered pots. Note that the residual sludge from this treatment plant does not have any treatment before its use in agricultural spreading.

Tomato seeds were grown on these pots in semi-controlled culture conduction (daytime temperature of 25°C, nighttime temperature of 10°C, and 60% humidity). During germination of tomato seeds, operations of depressing the young plants were carried out in order to reduce the density of the plants in the pot. The pot experiment was conducted in a completely random block design with 60 replicates for each treatment. Plants were watered manually daily with tap water. For additional investigation, soil mixture samples were air-dried, powdered, and sieved at 2 mm. The pH was measured in soil-water extracts *(Jackson, 1958).* The texture examination was carried out according to Robinson Khon's instructions. The wet oxidation method was used to determine organic matter in the soil mixture, while the micro-Kjeldahl method was used to determine total Kjeldahl nitrogen and the Drouineau method was used to determine active lime; the procedure involved

reacting the soil with ammonium oxalate and then determining unreacted oxalate by back-titration with potassium permanganate. Trace metals (Cu, Zn, and Pb) were analyzed using an Atomic Absorption Spectrophotometry after being digested with a nitric acid mixture *(Carter et Gregorich, 2008*). The number of tomato leaves was recorded, the height growth, and circumference were measured once per month.

RESULTS AND DISCUSSION

Soil/sludge mixture physico-chemical properties

One of the main goals of this study is to determine the impact of sewage sludge on the physico-chemical properties of the soil. The current study found that the application of sewage sludge changed the parameters of agricultural soil. The chemical characteristics of the soil were dramatically improved by increasing the sludge application rates (Tab 1, 2).

Table 1

Physico-chemical characterization of the different sludge fractions (Mean ± SD)

Level of Factor	N	pH	Total limestone (%)	Active limestone (%)	C%	Organic matter (%)	EC (mS/cm)	CEC (cmol/kg)	N (%)	C/N
Sludg 100% (B)	60	8.24±0.06	37.12±0.08	23.16±0.05	12.03±0.02	20.70±0.04	5.20±0.08	26.67±0.44	1.30±0.02	9.27±80.17
Sludg 20% (B1)	60	7.18±0.06	22.13±0.08	14.07±0.05	2.30±0.07	3.96±0.12	1.36±0.04	19.16±0.18	0.24±0.01	9.74±0.52
Sludg 40% (B2)	60	7.82±0.02	24.45±0.05	16.35±0.05	5.88±0.07	10.12±0.13	2.21±0.04	19.16±0.18	0.62±0.01	9.56±0.16
Sludg 60% (B3)	60	7.61±0.02	27.46±0.05	20.84±0.07	9.16±0.10	15.76±0.17	3.56±0.06	24.10±0.03	0.96±0.02	9.52±0.16
Ordi Soil (T)	60	7.36±0.39	26.15±0.06	19.14±0.09	0.63±0.05	1.09±0.09	0.92±0.03	18.34±0.38	0.06±0.01	11.03±10.62

The physico-chemical properties obtained for the mixtures show that the pH value is the same. In this respect, *Parkpain et al., (2000),* found that acidic soils had a higher pH than neutral soils after the addition of sludge, whereas neutral soils had no change.

According to the findings of other researchers, the electrical conductivity increases when the dose is increased *(Dridi et Toumi, 1999; Pisson, 2000; Korboulewsky et al. 2001; Boutmedjet, 2004; Bipfubusa et al, 2006; Amadou, 2007; Bahri et al. Annabi, 2011; Guerf, 2012).*

In modified substrates, the CEC appears to be increasing. *Epstein et al. (1976)* discovered that adding sludge compost raises CEC and that this increase is proportional to the dose given. An increase in the CEC of the soil increases the potential pool of nutrients available to plants (cations) while decreasing the loss of ETM, which are preferentially fixed on the adsorbing complex rather than transferred to the soil solution *(Mazen et al 2010; Eid et al., 2017).*

The addition of residual sludge has also aided in the improvement of maximum values in organic matter, which has increased from 1.09± 0.09 % in T (100% soil) to 3.96±0.12%, 10.12 ± 0.13% and 15.76±0.17 % in B1, B2, and B3 respectively (Tab 1), and thus in organic carbon. This is in line with findings from earlier investigations *(Hussein, 2009; Mazen et al., 2010; Soudani et al., 2017; Eid et al., 2017).*

Several authors had also discovered that the sludge had significantly increased the amount of organic carbon in the soil as well as the amount of azote in the soil *(Dridi et Toumi, 1998; Korboulewsky et al, 2001; Bipfubusa et al., 2006; Bahri et Annabi, 2011; Guerf, 2012).*

The B3 substrate, which contains 60% sludge, is particularly rich in organic matter, according to *Baize (1988)* categorization. The compost enhanced the organic matter content and cation exchange capacity of the soil substantially. *Guerrero et al. (2001)* discovered that when sewage sludge was added to the soil, total soil organic carbon rose.

Organic matter is a source of plant nutrients, and the progressive mineralization of organic matter provides plants with bioavailable ions. The C/N ratio in all substrates is close to 10, which has a non-depressive effect on the plants since it operates directly on the soil biology and does not generate mineral nitrogen blockages *(Glemas, 1980).*

Houot, (2009), Annabi et Bahri, (2011), noted that the C/N ratio here implies strong biological activity. The addition of sludge tends to raise trace element concentrations; however, they were present in low concentrations in the various substrates and do not exceed the AFNOR standard's permissible levels (1985).

The quantities of zinc, lead, and copper measured in the altered substrates are similar to those found in sludge, indicating that the soil has a significant fixing potential. These findings are comparable to those of *(Antolin et al., 2005; Mazen et al., 2010; Nogueira et al., 2013; Soudani et al., 2017; Eid et al., 2017)*, who found that soil levels of Zn, Pb, and Cu are directly proportional to sludge spread dosages.

These high Cu and Zn concentrations are similar to those reported by *Eid et al. (2017)*, although they are greater than *Gattullo et al. (2017)* 's average values of 128 mg/kg (Cu) and 302 mg/kg (Zn). The zinc values in our study were sharply increased and are now given with non-toxic values. Zn is less linked to organic matter than other ETM, according to *Bhogal et al. (2003)* and *Moffett et al. (2003)*, and thus would be less influenced by sludge decomposition (Fig. 1).

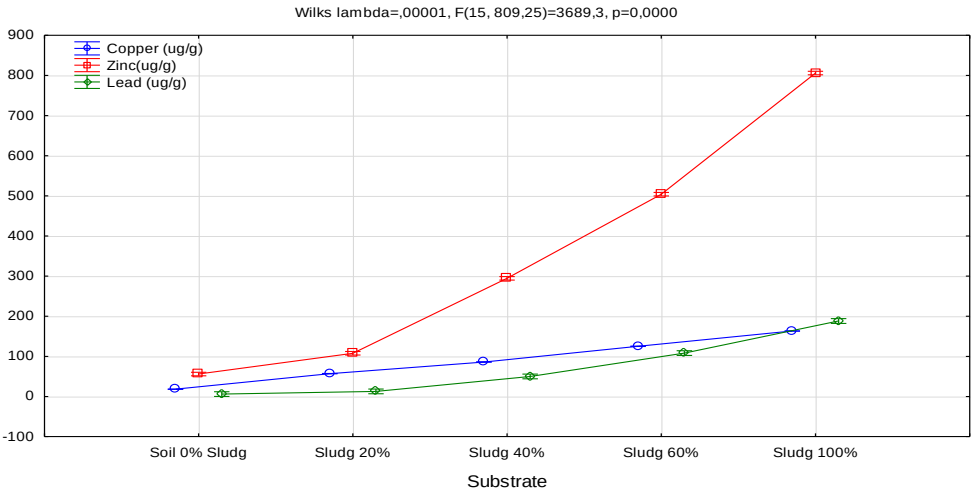

Fig. 1 - Evolution of heavy metals Pb, Zn, Cu as a function of different substrate fractions

Indeed, the 40% fraction of sludge has concentrations which are: 86±0.40 mg/kg for copper, 294 ±0.40 mg/kg for zinc and 50±5.9 mg/kg for lead, lower than the limits recommended by the European directives, which are respectively: 50-140 mg/kg, 150-300 mg/kg and 50-300 mg/kg Pb.

Texture has a direct relationship with hydrodynamic parameters in particular permeability, water storage capacity and porosity as well as cation exchange capacity. The samples analyzed are composed of several fractions dominated much more by silts and sands. It can be concluded that the samples used in this experiment have a sandy silty texture which favors the dynamics and the entrainment of heavy metals at depth. The comparison between the different textures shows that there are no significant differences between the size fractions and the doses of sludge applied, which is in agreement with the work of *Gallardo et al., (1987)*, or they report that changes in physical properties are only obtained for high dose applications.

The sludge used in this experiment consists of the following fractions in order of decrease: the silty fractions then the sandy fractions and lastly the clay fractions. In conclusion, this sludge has a sandy loam texture (Table 2).

Table 2

Characterization of the particle size distribution in the different sludge fractions (Mean ± SD)

Substrate	N	Clay (%)	Fine silt (%)	Coarse silts (%)	Fine sands (%)	Coarse sands (%)
fraction1 (100% raw sludge)	60	11.95±0.09	41.06±0.09	14.49±0.09	22.72±0.09	9.79±0.08
fraction 2 (20% sludge)	60	8.53±0.22	31.75±0.29	26.09±0.24	15.82±0.30	17.80±0.55
fraction 3 (40% sludge)	60	9.93±0.19	38.70±3.86	23.82±0.08	17.49±0.20	9.56±0.13
fraction 4 (60% sludge)	60	11.12±0.05	40.40±0.11	18.82±0.18	20.89±0.14	8.77±0.10
fraction 5 (100% raw soil)	60	2.19±0.11	6.22±0.09	59.15±0.39	6.85±0.30	25.58±0.36

Growth and productivity of Solanum lycopersicum tomato in sludge-soil mixture

Biometric measurements of *Solanum lycopersicum* plants in soil mixed with sewage sludge at a proportion of 0 (control), 20, 40 and 60% (60 replicates for each) are shown in table 3.

After two months of growing, the survival rate of tomato plants was around 85%. In general, biometric measurements had increased with increasing proportion of sludge in mixtures. The results compared to a control based on agricultural soil, show that the tomato grows very significantly in the three mixtures, however this growth is very remarkable in the mixture with 40% sludge (Table 3).

Plants grown on the 40% mud mix had a maximum final height of 78.50 cm, a maximum leaf count of 32.00 and a maximum stem diameter of 6.00 cm. In the case of plants grown on the control soil, much lower maximum results were recorded: 36.20 cm for the height, 12.00 for the number of leaves and 2.30 cm for stem diameter.

The impacts of sludge on improving soil aggregation and the contribution of organic matter in improving soil chemical characteristics, increasing soil water retention, and, as a result, providing vital nutrients for plant growth, could explain why sludge application increases plant productivity *(Antolin et al., 2005; Hussein, 2009; Soudani et al., 2017).*

Moreover, *Mendoza et al., (2006),* found that the agricultural use of sewage sludge increased the morphological characteristic of sorghum plants.

Al-Saikhan et al., (2020), had demonstrated good growth of lettuce and cucumbers on arid soil fertilized with municipal sludge, considered as a source of fertilizer due to its high contents of organic matter and available nitrogen and phosphorus; he had also found limited absorption of the heavy metals.

Table 3

Biometric parameters of tomatoes grown in different sludge fractions (Mean±SD)

Biometric parameters of Tomato	N	Mean±SD	Min	Max
TH Stem_Soil (cm)	60	35.73±0.32	35.00	36.20
TH Stem_ Sludg (cm)	60	64.50±0.86	63.00	65.70
TH Stem_ Sludg 20% (cm)	60	49.49±5.85	5.00	50.80
TH Stem_ Sludg 40% (cm)	60	77.58±0.50	76.50	78.50
TH Stem_ Sludg60% (cm)	60	68.04±0.63	66.80	69.00
Diam COL_ soil (cm)	60	1.99±0.19	1.60	2.30
Diam COL_ Sludg (cm)	60	6.59±0.27	6.00	7.10
Diam COL_ Sludg20% (cm)	60	3.17±0.22	2.70	3.50
Diam COL_ Sludg40% (cm)	60	5.74±0.19	5.30	6.00
Diam COL_ Sludg 60%(cm)	60	4.26±0.21	3.80	4.60
Nbr Leav_soil	60	9.87±1.61	5.00	12.00
Nbr Leav_Sludg	60	20.65±1.38	17.00	23.00
Nbr Leav_Sludg20%	60	13.28±1.17	11.00	15.00
Nbr Leav_Sludg 40%	60	28.93±1.53	27.00	32.00
Nbr Leav_Sludg 60%	60	20.57±12.84	17.00	118.00

Interaction: Waste sludge – Soil – Tomato

In order to study the effect of the supply of residual sludge, from a wastewater treatment plant of the Ain Bouchekif station, on the physico-chemical characteristics of the soil, on the one hand and on the physiology of the tomato on the other hand; a canonical correspondence analysis (CCA) was performed, taking these parameters into account. The result of this CCA is shown in Figure 2.

Two dimensions can be interpreted:

- F1 which represents 95.03% of the point clouds (95.03% of the information can be explained in this dimension).

- F2 which represents 4.7% of the point clouds can be explained in this axis.

On the positive side of the F1, one can find: Pure sludge and the 40% sludge fraction correspond with better growth of the tomato. This mixture: soil-sludge is rich in organic matter, in nitrogen with good electrical conductivity. This explains why sewage sludge has high fertilizing values for tomato (phosphorus, nitrogen and

calcium oxide) and organic matter. A rapid enrichment in mineral nitrogen is observed in the 60% fraction favoring the rapid growth of the plant.

Indeed, the solid fraction of the effluents constitutes a potential of fertilizing organic and mineral matter. However, this potential undergoes notable spatio-temporal variations *(Bahri et al, 1987).* In the young *Eucalyptus camaldulensis Dehnh* plants grown in three fractions of soil-sludge mixtures (20%, 40% and 60%), the biometric values (heights and diameters of the stems, number of leaves) of the plants in all the sludge mixtures were higher than those of control plants (100% soil). The mixture, which contained 60% sludge, gave the best result *(Soudani et al, 2017).* For tomato, the 40% fraction is best.

Also on this side, an interaction between the rate of silt and pure sludge fractions and 60% is observed. The higher the percentage of mud, the greater the quantity of silt.

However, the 60% mixture presents a risk of pollution by heavy metals, in particular the Pb, which requires monitoring before any use of these soils in agriculture.

Akintola et al., (2019), showed the efficiency and ability of *Adansonia digitata L* to accumulate and distribute heavy metals in its tissue parts. Thus, a difference in the concentrations in mg/Kg of Pb (28.22; 19.58), Zn (76.22; 48.06) and Cu (55.68; 26.45) in the soil, before and after planting *Adansonia digitata L*, clearly significant was observed. Along the same axis, on the negative side, one can find: ordinary soil and the 20% sludge fraction correspond to a fairly high pH and mineralization of organic matter (a fairly high C/N ratio due to the drop in mineral nitrogen in this section). In fact, the electrical exchange capacity CEC is related to the pH, it is the nutrient retention capacity of the soil at alkaline pH. The texture of the soil is loamy and the rate of limestone (total and active) is high.

Also on this side, an interaction between the rate of silt, pure sludge fractions and 40% is observed. Indeed, the higher the percentage of sludge, the greater the amount of silt.

In the F2 axis, positive side, the projection of the information on this axis makes it possible to define the correspondence of the 40% fraction and the rate of clays and silt (fine and coarse). It should be noted that the texture of the soil-sludge mixture is strongly influenced by the condition of the environment, in particular the long-term climate factor. *Fahd-Rachid (1993)* showed that an increase in the organic matter content, in certain mineral elements (P and Ca), in the cation exchange capacity and in the pH were observed in a field of stony sandy soil mixed with the incorporation of sewage sludge or urban compost and grown in temperate regions, after 18 years of experimentation. On a practical level, the use of composts and sludge helps maintain the stock of humus in the soil. Isohumic coefficients are between 0.08 and 0.20 for sludge and between 0.28 and 0.33 for composts.

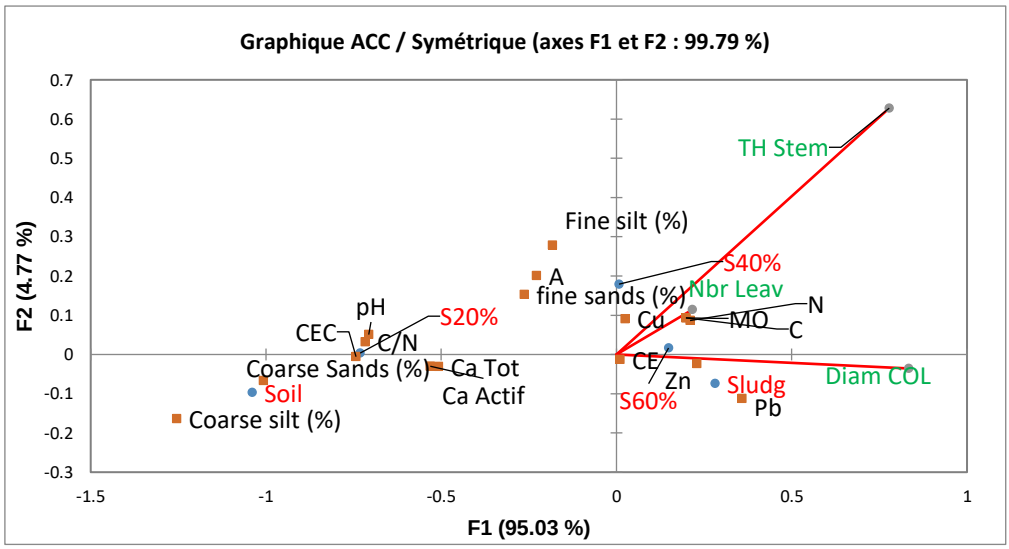

Fig. 2 - Relation: sludge-soil-plant by Canonical Correspondence Analysis (CCA)

CONCLUSIONS

The agricultural benefits of sewage sludge application are enormous, especially when added to low-organic-matter soils like those in Tiaret, Algeria. The effects of varied sewage sludge application rates (0, 20, 40, and 60%) on selected soil parameters and tomato plant growth were explored in this study.

The current study's findings show that using sewage sludge in agriculture can improve soil properties/fertility, provide critical plant nutrients, and increase crop productivity. In this study, sewage sludge was applied to agricultural soil and resulted in a significant increase in soil organic matter content and, as a result, crop output. Sludge at a 60% rate is useful in increasing soil characteristics and fertility. In the 40% mixture, tomato plants treated with sludge exhibited superior development and a high number of leaves. Plant development was improved by the mud, yet there were no negative effects on plant health.

The CCA has made it possible to define the beneficial aspect of the spreading of residual sludge from urban treatment plants for tomatoes. An increase in the growth in height and in diameter of the seedlings is remarkable in the 40% sludge fraction, compared to the seedlings grown in the ordinary soil and the substrate of 20% sludge. This means that the addition of sludge constitutes a satisfactory fertilization in nitrogen and organic matter. However, the residual load of nitrogen and heavy metals can present a risk of contamination of the water table by nitrates and also a risk of soil pollution by heavy metals. The cultivation of plants that bio-accumulate these pollutants is strongly recommended before any use of these soils for other crops.

Agricultural land application of sewage sludge would be an environmentally benign solution to traditional disposal issues, reducing the requirement for commercial fertilizers and, as a result, protecting our environment. Proper environmental protection management, concentrating on the potential dangers of heavy metal pollution, can sustain the benefits of wastewater for soil fertility and sludge spreading. More research is needed to track the accumulation of heavy metals in soil and to look into the pre-treatment of sewage sludge before it is applied to agricultural land. Additionally, future research should investigate the use of sludge spreading rates (40%) to maintain better soil fertility while reducing the risk of sludge buildup and heavy metal pollution of soils. Additionally, trace metals in fruits and vegetables should be carefully monitored.

It should be noted that Algerian (Executive Decree No. 2006-138), European and World Health Organization (86/278/EEC) directives have been established relating to the use of sewage sludge by farmers as fertilizer, in order to avoid harmful effects on the environment and human health, by ensuring that the nutritional needs of plants are taken into account and that the quality of the soil and surface and ground water is not compromised.

REFERENCES

[1] AFNOR., *(1985), Norme Française NU44-041, Matières fertilisantes, Boues des ouvrages des eaux usées urbaines, Détermination et spécification.*

[2] Akintola, OO., Aderounmu, AF., Abiola, IO., & Bodede, IA., (2019), Remediation potential of Baobab (Adansonia digitata L.) Seedlings grown in sewage sludge contaminated by Heavy Metals. *Journal of Applied Sciences and Environmental Management, vol.23, no. 9,* ISSN 1119-8362, pp. 1691-1697, Negira.

[3] Al-Saikhan,MS., El-Sayed, AB and Babeker, & MY., (2020), Study of Sewage Sludge Use for the Cultivation of Plants and its Effects on Soil Properties in Al Ahsa. *The Scientific Journal of King Faisal University*, vol.21, no.2, pp.1-7, Saudi Arabia.

[4] Amadou, H., (2007), *Modélisation du séchage solaire sous serre des boues de stations d'épuration urbaines.* Thèse de Doctorat. Université Louis Pasteur-Strasbourg 1/ France.

[5] Antolin, M.C., Pascual, I., Garcia, C., Polo, A., & Sanchez-Diaz, M., (2005), Growth, yield and solute content of barley in soils treated with sewage sludge under semi-arid Mediterranean conditions. *Field Crops Research*, vol.94, no. 2, pp. 224–37.

[6] Bahri, A., Houmane, B., (1987), Effet de l'épandage des eaux usées traitées et des boues résiduaires sur les caractéristiques d'un sol sableux de Tunisie. *Science du sol,* vol.25, no. 4, ISSN: 0011-9164, pp. 267-278.

[7] Bahri, H., Annabi, M., (2011), Effet des boues urbaines sur la mouillabilité et la stabilité structurale d'un sol cultivé. *Étude et Gestion des Sols,* vol.18, no. 3, pp. 7-15.

[8] Baize, D., (1988), Les formations crayeuses redistribuées du Jovinien et les sols qui en sont issus. *Sci. Sol,* vol.26, no. 2, pp. 113-116.

[9] Bhogal, A., Nicholson, F.A., Chambers, BJ., & Shepherd, MA., (2003), Effects of past sewage sludge on heavy metal availability in light textured soils: implications for crop yields and metal uptakes. *Environmental Pollution,* vol.12, no. 1, pp. 413-423.

[10] Bipfubusa, M., N'Dayegamiye, A., & Antoun, H., (2006), Evaluation des effets des boues mixtes fraiches et de leurs composts sur les rendements des cultures et leur nutrition minérale. *Agrosols,* vol.17, no. 1, pp. 65-72.

[11] Boutmedjet, A., (2004), *La valorisation des boues résiduaires urbaines en plantation forestière dans la zone aride.* Thèse de Magister. Université Kasdi Merbah de Ouargla / Algérie.

[12] Carter, M.R., Gregorich, E.G., (2008), Soil Sampling and Methods of Analysis. *NW, USA: Canadian Society of Soil Science, Taylor and Francis Group, CRC Press*

[13] de Souza, A. A. B., Ramos da Silva, W., Nascimento, C. W. A. D., da Silva, Y. J. A. B., & Biondi, C. M. (2022). Residual effects of alkalized sewage sludge application on soil quality and sugarcane yield. *Archives of Agronomy and Soil Science*, 1-13. https://doi.org/10.1080/03650340.2022.2106369.

[14] Dridi, B., Toumi, C., (1999), Infuence d'amendements organiques et d'apport de boues sur les propriétés d'un sol cultivé. *Etude et gestion des sols,* vol.6, no. 1, pp. 7-14.

[15] Eid, E.M., Alrumman, S.A., El Bebany, A.F., Hesham, A., Taher, M.A., & Fawy, K.F., (2017), The effects of different sewage sludge amendment rates on the heavy metal bioaccumulation, growth and biomass of cucumbers (*Cucumis sativus L.). Environmental Science and Pollution Research,* vol.24, no. 19, pp.16371-82.

[16] Epstein, E., Taylor, JM., & Chaney RL., (1976), Effects of sewage sludge and sludge compost applied to soil on some soil physical and chemical properties. *Journal of Environmental Quality,* Vol.5, no.1, pp. 422-426.

[17] Fahd-Rachid, A., (1993), *Effet à long terme d'apports continus de déchets urbains sur les caractéristiques du sol. Conséquences sur les propriétés de la matière organique en relation avec sa teneur en lipides.* Thèse de Doctorat en Sciences agronomiques. Montpellier, ENSA/France.

[18] Gallardo-Laraa, F., Nogales, R., (1987), Effect of the application of town refuse compost on the soil-plant system: *A review. Biological Wastes*, vol.19, no. 1, pp. 35-62.

[19] Gattullo, C.E., Mininni, C., Parente, A., Montesano, F.F., Allegretta, I., & Terzano, R., (2017), Effects of municipal solid waste- and sewage sludge-compost-based growing media on the yield and heavy metal content of four lettuce cultivars. *Environmental Science and Pollution Research*, vol.24, no. 32, pp. 25406–25415.

[20] Glemas, P., (1980), Fertilisation boue, gadoue, composts de finition fabrication et caractéristique. *Revue cultivar,* vol.13, no. 2, pp. 44-51.

[21] Guerf, Z., (2012), *Impact de l'utilisation des boues résiduaires sur les propriétés physico-chimique des sols de la haute Vallée de la Medjerda willaya de Souk Ahras*. Thèse de Magister. Université Badji Mokhtar d'Annaba /Algérie.

[22] Guerrero, FD., Davey, RB., & Miller, RJ., (2001), Use of an allele-specific polymerase chain reaction assay to genotype pyrethroid resistant strains of *Boophilus microplus* (Acari: Ixodidae). *Journal of Medical Entomology*, vol.38, no. 1, pp. 44-50.

[23] Houot, S., Cambier, P., Benoit, P., Deschamps, M., Jaulin, A., Lhoutellier, C., & Barriuso, E., (2009), Effet d'apports de composts sur la disponibilité de micropolluants métalliques et organiques dans un sol cultivé. *Étude et Gestion des Sols,* vol.16, pp. 255-274.

[24] Hussein, A.H.A., (2009), Impact of sewage sludge as organic manure on some soil properties, growth, yield and nutrient contents of cucumber crop. *Journal of Applied Sciences*, vol.9, no. 8, pp. 1401– 11.

[25] Jackson, M.L., (1958), *Soil Chemical Analysis*. N.J., USA: Prentice-Hall Inc., Englewood Cliffs. 498p.

[26] Jarde, E., (2002), *Composition organique des boues résiduaires des stations d'épuration lonaines; caractérisation moléculaire et effets de la biodégradation.* Thèse de doctorat en Sciences de l'Univers. Université Henri Poincaré, Nancy I / France.

[27] Kidd, P.S., Dominguez-Rodriguez, M.J., Diez, J., & Monterroso, C., (2007), Bioavailability and plant accumulation of heavy metals and phosphorus in agricultural soils amended by long-term application of sewage sludge. *Chemosphere*, vol.66, no. 8, pp. 1458–67.

[28] Korboulewsky, N., Masson, G., Bonin, G., Massiani, C., & Prone, A., (2001), Effets d'un apport de compost de boues de station d'épuration dans un sol d'un vignoble du Sud de la France. *Étude et Gestion des Sols,* vol.8, no. 3, pp. 203 – 210.

[29] Mazen, A., Faheed, F.A., & Ahmed, A.F., (2010), Study of potential impacts of using sewage sludge in the amendment of desert reclaimed soil on wheat and Jews mallow plants. *Brazilian Archives of Biology and Technology*, vol.53, no. 4, pp. 917–30.

[30] Mendoza, J., Garrido, T., Castillo, G., & Martin, N.S., (2006), Metal availability and uptake by sorghum plants grown in soils amended with sludge from different treatments. *Chemosphere,* vol.65, no. 11, pp. 2304 –12.

[31] Moffett, BF., Nicholson, FA., Uwakwe, NC., Chambers, BJ., Harris, JA., & Hill TCJ., (2003), Zinc contamination decreases the bacterial diversity of agricultural soil. *FEMS Microbiology Ecology,* vol.43, pp. 13-19.

[32] Nogueira, T.A.R., Franco, A., He, Z., Braga, V.S., Firme, L.P., & Abreu-Junior, C.H., (2013), Short-term usage of sewage sludge as organic fertilizer to sugarcane in a tropical soil bears little threat of heavy metal contamination. *Journal of Environmental Management*. 114:168–77.

[33] Parkpain, P., Sreesai, S., & Delaune, R.D., (2000), Bioavailability of heavy metals in sewage sludge-amended Thai soils. *Water, Air and Soil Pollution*, vol.122, pp. 163-182.

[34] Pisson, C., (2000), *Impact de l'épandage agricole des boues résiduaires urbaines sur la qualité des productions céréalières en particulier sur l'aspect des éléments traces métalliques. Mémoire d'Ingénieur*. Ecole Nationale de la Santé Publique, Paris /France.

[35] Sabbahi, S., Ben Ayed, L., Trad, M., Berndtsson, R., & Karanis, P. (2022). Parasitological Assessment of Sewage Sludge Samples for Potential Agricultural Reuse in Tunisia. *International Journal of Environmental Research and Public Health*, *19*(3), 1657. doi: 10.3390/ijerph19031657

[36] Scholz, M., (2016), Sludge treatment and disposal. In: *Wetlands for Water Pollution Control*. Ed. 2 nd edition. Amsterdam, Elsevier. pp. 157-168.

[37] Soudani, L., Maatoug. M., Hermann, H., Mykola, K., Oliver, W., Christin, M., & Nadia, B., (2017), Fertilization value of municipal sewage sludge for Eucalyptus camaldulensis plants. *Biotechnology Reports*, vol.13, pp. 8-12.

[38] Tytła, M. (2020). Identification of the chemical forms of heavy metals in municipal sewage sludge as a critical element of ecological risk assessment in terms of its agricultural or natural use. *International Journal of Environmental Research and Public Health*, *17*(13), 4640. doi: 10.3390/ijerph17134640

[39] Tejada, M., Rodriguez-Morgado, B., Gomez, I., Franco-Andreu, L., Benitez, C., & Parrado, J., (2016), Use of biofertilisers obtained from sewage sludges on maize yield. *European Journal of Agronomy*, vol.78, pp. 13–9.

[40] Zhao, X.L., Mu, Z.J., Cao, C.M., & Wang, D.Y., (2012), Growth and heavy-metal uptake by lettuce grown in soils applied with sewage sludge compost. *Communications in Soil Science and Plant Analysis,* vol.43, no .11, pp. 1532-41.

Regulatory texts of the official journals

[41] Council Directive 86/278/EEC of 12 June 1986 on the protection of the environment, and in particular of the soil, when using sewage sludge in agriculture. https://eur-lex.europa.eu/legal-content/FR/TXT/?uri=celex:31986L0278

[42] Executive decree no. 06-104 of February 28, 2006 establishing the nomenclature of waste, including special hazardous waste.www.joradp.dz

DETERMINATION OF SOME PHYSICAL AND MECHANICAL PROPERTIES OF ONION / 洋葱基本物理力学特性测定

Hongguang YANG, Bing WANG, Fengwei GU, Feng WU, Yanhua ZHANG, Zhichao HU* [1]
Nanjing Institute of Agricultural Mechanization, Ministry of Agriculture and Rural Affairs, Nanjing, 210014/China
Tel: +86-025-84346256; E-mail: 1432245697@qq.com
DOI: https://doi.org/10.35633/inmateh-68-32

Keywords: *onion, bulb, cauloid, physical properties, mechanical properties*

ABSTRACT

Lack of sufficient knowledge about the physical and mechanical properties of onion can result in higher waste during harvesting and post-harvesting. The objective of this work was to determine some physical and mechanical properties of onion cultivated in China. These properties include linear dimensions, mass, shape index, pull-out force, compression and shear forces. The mean longitudinal diameter of bulb (BLD), transverse diameter of bulb (BTD), bulb weight (BW), pull-out force of bulb (BPF), depth of the bulb buried in the soil (BSD), bulb shape index (BSI), diameter of cauloid (CD), circumferential distribution of root systems (RCD), longitudinal length of root systems (RLL) and weight of root systems (RW) were 78.1±9.6 mm, 89.6±10.1 mm, 333.0±101.7 g, 43.9±21.6 N, 35.7±8.7 mm, 1.2±0.1, 15.3±3.7 mm, 89.2±19.7 mm, 42.9±10.0 mm and 0.8±0.4 g. In the study of mechanical properties of onions, the maximum compression force (MCF) required for compression deformation 10 mm of bulb was 462.2 N, and the maximum shear failure force (MSF) required for shearing of cauloid was 113.8 N. The results of the research will be very useful in the design and optimization of harvest and postharvest machines with reduced waste and damage.

摘要

由于对洋葱基本物理力学特性缺乏充分认知，经常会在收获和产后加工处理时产生较高的浪费。本研究的目标是确定中国栽培洋葱的一些基本物理力学特性。这些特性主要包括线性尺寸、重量、形状、起拔力、压缩力和剪切力。试验结果表明，洋葱鳞茎纵向平均直径、横向平均直径、重量、起拔力、入土深度、形状指数、假茎直径和根系周向分布直径、长度及重量分别为 78.1±9.6 mm、89.6±10.1 mm、333.0±101.7 g、43.9±21.6 N、35.7±8.7 mm、1.2±0.1、15.3±3.7 mm、89.2±19.7 mm、42.9±10.0 mm 和 0.8±0.4 g。力学特性试验表明，洋葱鳞茎压缩变形 10mm 所用压缩力平均值为 462.2N，洋葱假茎剪切破坏所用剪切力平均值为 113.8 N。研究结果对于设计优化洋葱收获和产后加工机械及减少损伤浪费有重要价值。

INTRODUCTION

Onion is one of the most economically important vegetable crops grown in China (*Ren et al, 2021; Wang et al, 2021*). The scientific name of it is Allium cepa L. which belongs to the family of Liliaceae. Although it has only been cultivated in China for more than 100 years, it is widely grown in different parts of the country (*Yang et al, 2019*). China, India, United States, Iran, Egypt and Russia are the main producers of onions in the world (*Zhang et al, 2022; Bisen et al, 2013*). China is the largest onion growing country in the world with the production of 23.7 million tons in 2020 under the area of 1.1 million ha (Data from the FAOSTAT database of the Food and Agricultural Organization (FAO) of the United Nations).

The physical and mechanical properties of agricultural products are very important. Lack of sufficient knowledge about the physical and mechanical properties of agricultural products can result in higher waste of them (*Jahanbakhshi et al, 2018*). Meanwhile, a detailed understanding of these can better design and optimize the relevant production and processing machinery. For example, *Jahanbakhshi et al.,* (*2018*), studied the physical and mechanical properties of carrot. *Kibar and Öztürk,* (*2008*), studied the physical and mechanical properties of soybean under different moisture content. Wang et al. (*Wang et al, 2019*) tested the tensile properties of Nagafu apple, Crisp pear, Tainong mango and long eggplant. *Li et al.*, (*2018*) reported that the mechanical properties and microstructure of potato peels. *Jithender et al.,* (*2017),* studied the physical and mechanical properties of pomegranate fruit and aril.

[1] *Hongguang Yang, MS.Eng.; Bing Wang, MS.Eng.; Fengwei Gu, MS.Eng.; Feng Wu, Prof.; Yanhua Zhang, MS.Eng.; Zhichao Hu *, Prof..*

Sagsoz and Alayunt, (*2001*), analysed the several methods for measuring the modulus of elasticity of onion bulb. *Cakir et al.,* (*2001*), tested the compression properties of onion bulbs. *Essa and Gamea,* (*2003*), tested the physical and mechanical properties of onion bulbs. *Bahnasawy et al, (2004*), estimated the physical and mechanical properties of the most popular cultivars (Giza 6, Beheri and Giza 20) of onion in Egypt. *Dabhi and Patel,* (*2017*), estimated the physical and mechanical properties of Talaja Red onion cultivar. *Karthik et al, (2016*), studied the physical, frictional and mechanical properties of the three popular onion varieties (Satara Garva, Arka Kalyan and Bangalore rose) in India.

Numerous studies have been carried out on the physical and mechanical properties of different agricultural products. However, there are few reports on the physical and mechanical properties of onion cultivated in China. It is due to the lack of much knowledge about the physical and mechanical properties of onion in China and how to reduce its waste as well as design and optimize the required harvesting and post-harvesting machinery. This study aims to contribute to fill this research gap. The main objective of this study is to investigate some physical and mechanical properties of bulbs, roots and cauloids of onion plants. These properties include linear dimensions, mass, shape index, pull-out force, compression and shear forces.

MATERIALS AND METHODS

Determination of some physical properties and pull-out force of onion

The test was conducted in the vegetable planting base in Ulanqab City of Inner Mongolia Autonomous Region of China. The planting pattern of onion is bed planting. There are eight rows in a bed. The bed width is 1300 mm and the distance is 1900 mm. The row spacing of onion on the bed is 15 mm and the plant spacing is 17 mm. The soil type is sandy loam (artificially improved soils). The mean soil compaction and moisture content at depths of 0 cm to 5 cm are 1093.3 kPa and 10.3% respectively. The mean soil compaction and moisture content at depths of 5 cm to 10 cm are 1213.3 kPa and 12.8% respectively.

The onion was planted in the middle of May. The variety is Red Hydrangea. It is a long-day variety with bright purplish red skin which has a growth period of about 170 days and plant height of 60 cm to 70cm. This variety of onion is widely cultivated in China, especially the northern part of the country. The test field and planting pattern of onion are shown in Figure 1.

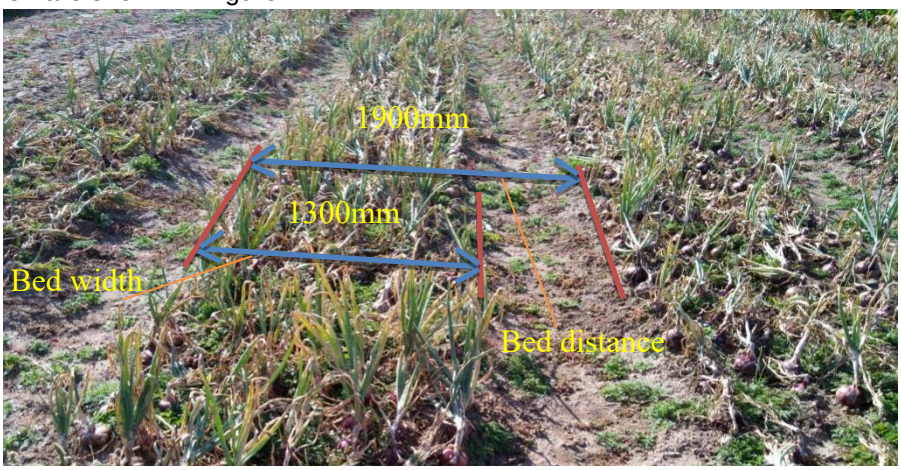

Fig. 1 - Test field and planting pattern of onion

The test instruments for this study are electronic digital display vernier caliper (Model: Guilin, manufacturer: Guilin Guanglu Measuring Instrument Co., Ltd., measuring range: 0 mm to 150 mm, measurement accuracy: 0.01 mm), electronic balance (Model: NS, manufacturer: Fuzhou HUAKE Electronic Instruments Co., Ltd., measuring range: 0 kg to 6 kg, measurement accuracy: 0.1 g), electronic hanging scale (Model: OCS-L, manufacturer: Hangzhou Tianchen Scale Equipment Co., Ltd., measuring range: 0.2 kg to 30 kg, measurement accuracy: 0.01 kg), steel ruler (Model: GWR, manufacturer: Ningbo Great Wall Precision Industrial Co.,Ltd., measuring range: 0 mm to 300 mm, measurement accuracy: 1 mm).

In this experimental study, the main measurement objects of onion plants mainly include the mean longitudinal diameter of bulb (BLD), transverse diameter of bulb (BTD), bulb weight (BW), pull-out force of bulb (BPF), depth of the bulb buried in the soil (BSD), bulb shape index (BSI), diameter of cauloid (CD), circumferential distribution of root systems (RCD), longitudinal length of root systems (RLL) and weight of root systems (RW).

As shown in Figure 2, BLD is the distance between the onion crown and the point of root attachment to the onion. BTD is the maximum width of the onion bulb in a plane perpendicular to the BLD. BSD is the depth at which onion bulb grow under the soil. CD is the diameter of 2 cm away from the junction of onion crown and cauloid. RCD is the diameter of the circumferential distribution of root systems measured after onion bulbs are pulled out. RLL is the maximum length of root systems measured after onion bulbs are pulled out. RW is the weight of root systems measured after onion bulbs are pulled out. BW is the weight of a single onion bulb. BPF is the force used to pull-out the bulb form the soil.

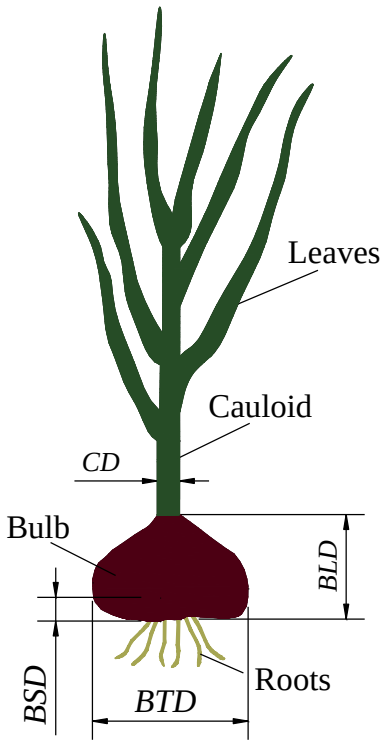

Fig. 2 - Schematic diagram of onion plant

In addition, BSI is used to evaluate the shape of onion bulbs and it is calculated according to the equation (1). The onion bulb is considered an oval if the BSI >1.5, on the other hand, it is considered spherical if the BSI <1.5 (*Cakir et al, 2016*).

$$BSI = \frac{BTD}{BLD} \tag{1}$$

During the experiment, 50 onion plants were randomly selected as the test object. Firstly, the BPF in natural growth of onion plants during harvest was measured by electronic hanging scale. Then, vernier caliper, electronic balance and steel ruler were used to measure and calculate the BLD, BTD, BW, BPF, BSD, BSI, CD, RCD, RLL and RW. Finally, the measured data were statistically analysed by MS-Excel.

Determination of compression properties of onion bulb

As we all know, the most commonly used mechanical properties of agricultural products is compression characteristics. Compression damage is the main reason for the loss of agricultural products. Therefore, the compression test of onion bulb was carried out. However, because the bulb has its own shape (composed of layers of fleshy scales), it is heterogeneous and isotropic. It cannot be made into regular sample (a cylindrical or a square shape), but can only be compressed as a whole.

Onion bulbs were taken from the test field. The mean moisture content of bulb is 88.9%. The compression test of bulb was carried out by electronic universal testing machine (Model: UTM6503, manufacturer: Shenzhen SUNS Technology Stock Co., Ltd., measuring range: 0 kN to 5 kN). The indenter of the testing machine is round, with a diameter of 100 mm and a thickness of 20 mm. The testing machine and some onion bulbs for testing are shown in Figure 3.

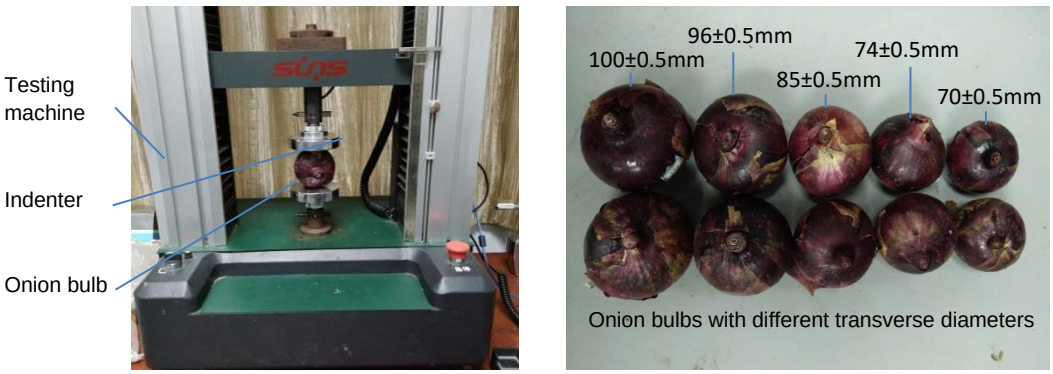

Fig. 3 - Compression test and some onion bulbs

Taking the BTD and the compression speed (CS) of the testing machine as the test factors, the maximum compression force (MCF) of 10 mm compression deformation of bulb is the test index. The quadratic general rotary unitized test was carried out. There are 13 groups of tests in total. According to the measured transverse diameter of onion bulb (mostly concentrated in 70 mm-100 mm, accounting for more than 85% of the total) and the compression test of relevant agricultural products (Aprilia *et al, 2021*), the test factor code and value are designed as shown in Table 1. Through the analysis of the test results, the influence law of the BTD and CS on the MCF is revealed. In order to facilitate the analysis of test results, the coded values of BTD and CS are recorded as A and B respectively.

Table 1

Factors and levels of compression test

levels	Factors	
	BTD	CS
	[mm]	[mm/min]
-1.414	70±0.5	10
-1	74.4 (74±0.5)	23.2 (23)
0	85±0.5	55
1	95.6 (96±0.5)	86.8 (87)
1.414	100±0.5	100

Determination of shear properties of onion cauloid

The shear properties of onion cauloids which were taken from the experimental field were tested by universal testing machine. The testing machine and some onion cauloids for testing are shown in Figure 4. Among them, the effective working width of the cutter of testing machine is 25 mm, the height is 23 mm, the thickness is 3 mm, and the height of the cutter tip is 10 mm. The effective length of onion cauloid samples are 80±0.5 mm. The CD, the moisture content (MC) of onion cauloid and the shear speed (SS) of the testing machine are selected as the test factors. The maximum shear failure force (MSF) is selected as the test index. Three-factor and three-level orthogonal test was carried out.

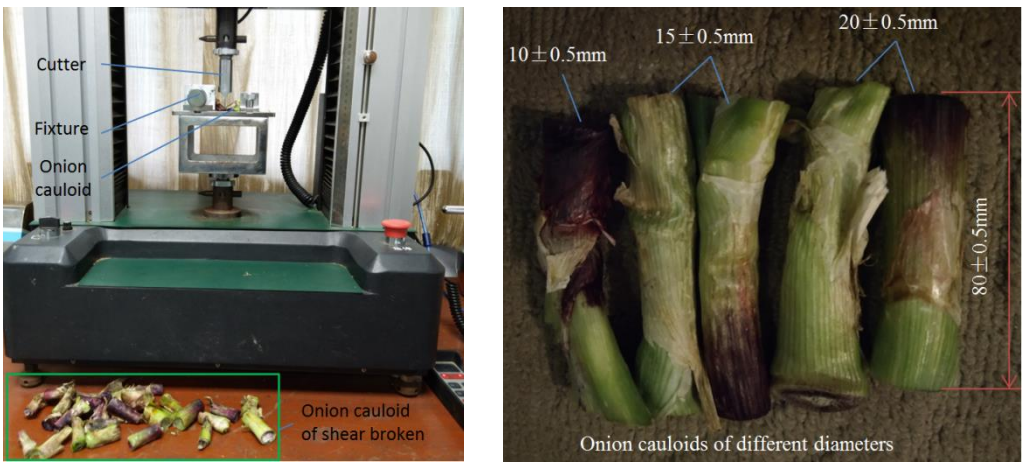

Fig. 4 - Shear test and some onion cauloids

The moisture content of onion cauloid on the sampling day was taken as level 1. The moisture content after one day and two days of natural drying was regarded as level 2 and level 3. Through actual measurement, the mean moisture content of cauloid on the day of sampling, natural drying for one day and two days is 88.9%, 74.0% and 68.5%, respectively. At the same time, according to the measurement of cauloid diameter in the experimental field (mostly concentrated in 10 mm-20 mm, accounting for more than 75% of the total) and relevant shear characteristic tests (*Xin et al, 2020*), the arrangement of each factor is shown in Table 2. An $L_9(3^4)$ orthogonal table was established, in which C, D, and E are the coding values of each factor level.

Table 2

Factors and levels of shear test

levels	Factors		
	CD	MC	SS
	[mm]	[%]	[mm/min]
1	10±0.5	68.5	10
2	15±0.5	74.0	20
3	20±0.5	88.9	30

RESULTS

Determination of some physical properties and pull-out force of onion

Figure 5 shows the mean values, maximum, minimum, standard deviation (SD) and coefficient of variation (CV) of the BLD, BTD, BW, BPF, BSD, BSI, CD, RCD, RLL and RW.

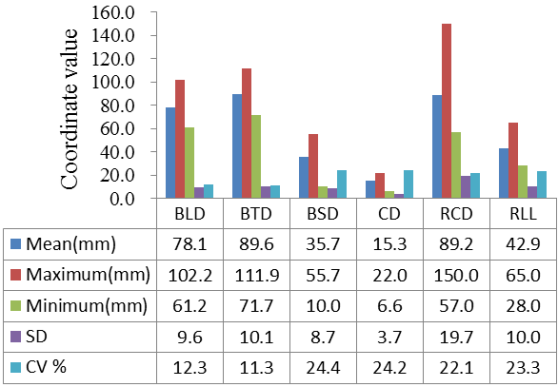

	BLD	BTD	BSD	CD	RCD	RLL
Mean(mm)	78.1	89.6	35.7	15.3	89.2	42.9
Maximum(mm)	102.2	111.9	55.7	22.0	150.0	65.0
Minimum(mm)	61.2	71.7	10.0	6.6	57.0	28.0
SD	9.6	10.1	8.7	3.7	19.7	10.0
CV %	12.3	11.3	24.4	24.2	22.1	23.3

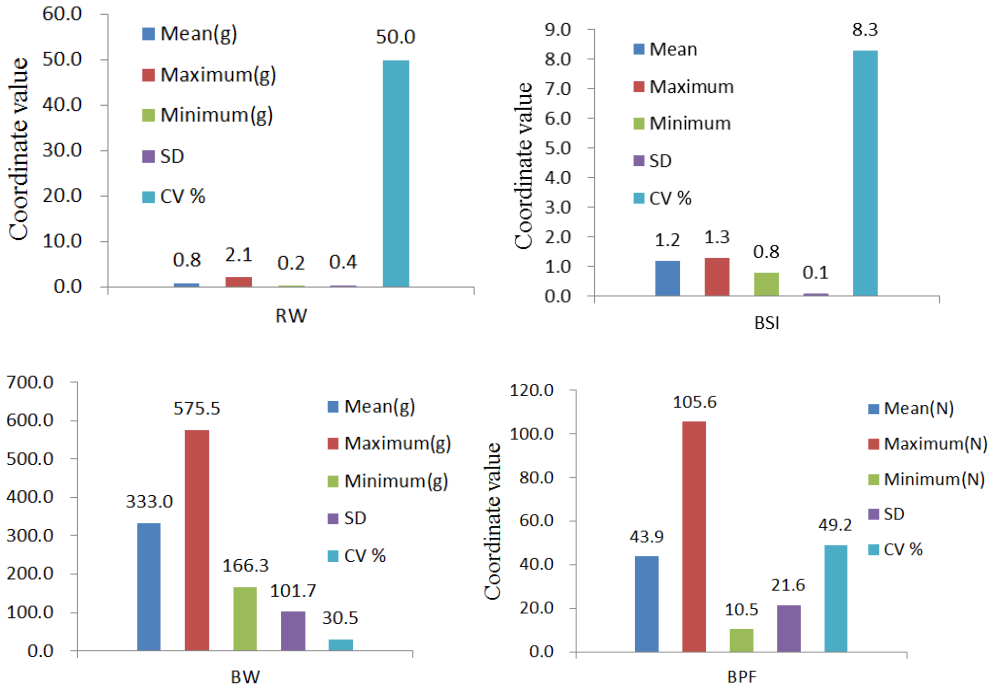

Fig. 5 - Mean values, maximum, minimum, SD and CV of onion

As can be seen from Figure 5, the mean of the BLD, BTD, BW, BPF, BSD, BSI, CD, RCD, RLL and RW are 78.1±9.6 mm, 89.6±10.1 mm, 333.0±101.7 g, 43.9±21.6N, 35.7±8.7 mm, 1.2±0.1, 15.3±3.7 mm, 89.2±19.7 mm, 42.9±10.0 mm and 0.8±0.4 g, respectively. According to the equation (1), the onion bulb is considered an oval if the shape index > 1.5, on the other hand, it is considered spherical if the shape index <1.5. Hence, it indicated that the onion bulb of Red Hydrangea was a spherical in shape. And the CV of the BLD value was higher than that of BTD. This result was in agreement with those reported by Bahnasawy et al. (*Bahnasawy et al, 2004*) and Dabhi et al. (*Dabhi et al, 2017*). During the pull-out test, it was found that the cauloids of several onion plants were broken. The reason may be that the force required to pull-out onion bulb exceeds the breaking force limit of cauloid. It can be seen that it was difficult to harvest onions in the natural growth state by direct extraction, and some auxiliary excavation work was necessary (*Kumawat et al, 2022; Joshi et al, 2020*).

Determination of compression properties of onion bulb

The compression test results are shown in Table 3. When the bulb compression de-formation is 10 mm, the mean value of MCF measured in 13 groups of tests is 462.2 N, the standard deviation is 45.0, and the coefficient of variation is 9.7%. The analysis of variance of test results is shown in Table 4.

Table 3

Test scheme and results of compression test

Test No.	1	2	3	4	5	6	7	8	9	10	11	12	13
A	1	1	-1	-1	-	1.414	0	0	0	0	0	0	0
B	1	-1	1	-1	0	0	-	1.414	0	0	0	0	0
***MCF* [N]**	502.6	505.4	510.2	417.0	412.5	492.6	494.4	529.7	455.9	437.2	437.3	374.5	439.6

Table 4

Analysis of variance of compression test

Source	**Sum of squares**	***d***	**Partial correlation**	***F*-value**	***P*-value**	**Significance**
A	4708.31	1	0.72	7.69	0.03	**
B	2461.27	1	0.60	4.02	0.09	*
A^2	1035.41	1	0.44	1.69	0.24	
B^2	12242.11	1	0.86	20.01	0.00	***
AB	2304.00	1	-0.59	3.77	0.09	*
Regression	22036.06	5	F_2=7.20			
Residual	4283.47	7				
Lack of fit	341.17	3	F_1=0.12			
Pure Error	3942.30	4				
Correlation total	26319.52	12				

Note: The critical value of significant judgment $F_{0.1}(1,7)=3.59$, $F_{0.05}(1,7)=5.59$, $F_{0.01}(1,7)=12.25$, $F_{0.1}(5,7)=2.88$, $F0.05(5,7)=3.97$, $F_{0.01}(5,7)=7.46$, $F_{0.1}(3,4)=4.19$, $F_{0.05}(3,4)=6.59$, $F_{0.01}(3,4)=16.69$.

** indicates that the factors have some influence on the test index ($0.05 < p \leq 0.1$),*

*** indicates that the factors have a significant influence on the test index ($0.01 < p \leq 0.05$),*

**** indicates that the factors have a very significant influence on the test index ($p \leq 0.01$).*

From Table 4, it can be seen that F_2 =7.20>$F_{0.05}$ (5, 7) = 3.97 and F_1 = 0.12<$F_{0.1}$ (3, 4) = 4.19. The regression equation and lack of fit are credible under the condition of 95% confidence level. The regression coefficient analysis showed that the first item *B*, interaction item *AB* have some influence, first item *A* has a significant influence, square item B^2 has a very significant influence. From the results of analysis of variance, it can be seen that the influence order of various factors on MCF is *A* > *B*.

Set one of the factors to the zero level for single factor effect analysis. The results are shown in Figure 6. When CS is zero, MCF increases with the increase of BTD, and the two meet the linear relationship. When BTD is zero, MCF first decreases and then increases with the increase of CS, and the two meet the quadratic polynomial relationship.

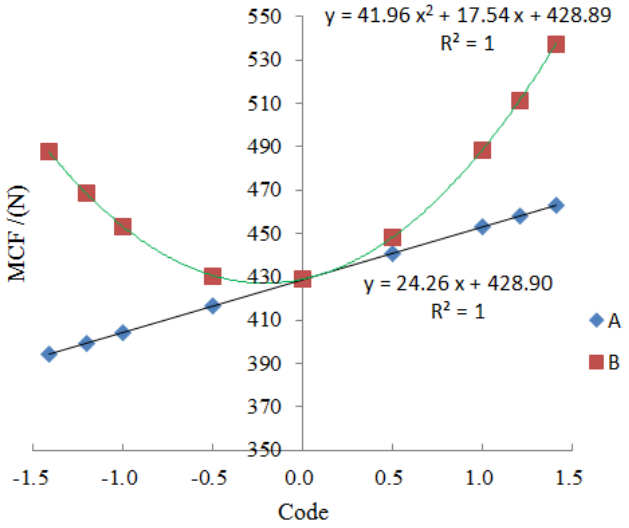

Fig. 6 - Single factor effect

It can be seen from table 4 that the interaction of the two factors has a significant impact on the test index. As shown in Figure 7, it is a three-dimensional response surface diagram of the interaction of two factors. As can be seen from Figure 7, when the value of CS is certain, MCF increases with the increase of BTD. When the value of BTD is certain, MCF first decreases slowly and then increases rapidly with the increase of CS.

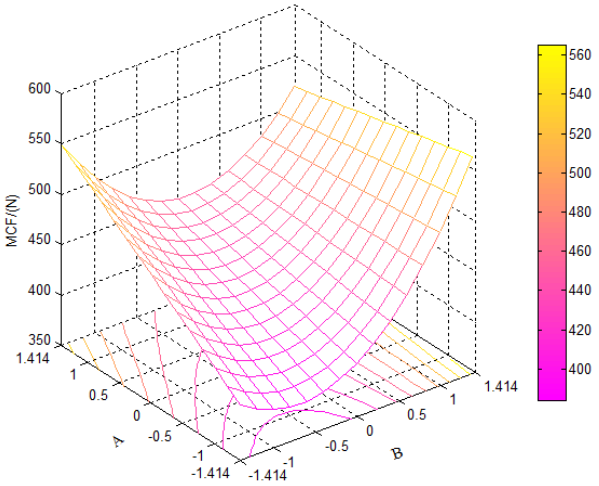

Fig. 7 - Interaction effect of two factors

Determination of shear properties of onion cauloid

The shear test results are shown in Table 5. The range analysis and analysis of variance of the test results are shown in Figure 8 and Table 6.

Table 5

Test scheme and results of shear test

Test No.	Factors				MSF [N]
	C	*D*	*E*	Empty column	
1	1	1	1	1	105.6
2	1	2	2	2	82.7
3	1	3	3	3	73.2
4	2	1	2	3	143.7
5	2	2	3	1	133.3
6	2	3	1	2	87.0
7	3	1	3	2	163.0
8	3	2	1	3	127.3
9	3	3	2	1	108.1

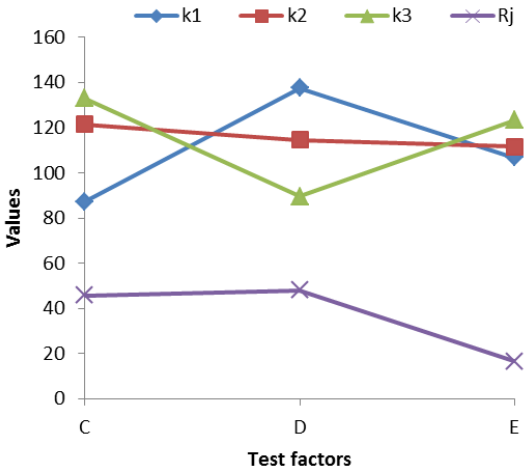

Fig. 8 - Range analysis of test results

Table 6

Analysis of variance

Indexes	Variance Source	Sum of Squares	Free Degree	*F*-Value	*p*-Value	Significance
MSF	*C*	3381.25	2	88.31	0.011	**
	D	3458.00	2	90.32	0.011	**
	E	433.15	2	11.31	0.081	*
	Error	38.29	2			

Note: The critical value of significant judgment $F_{0.01}(2,2) = 99.00$, $F_{0.05}(2,2) = 19.00$, $F_{0.1}(2,2) = 9.00$.
** indicates that the factors have some influence on the test index ($0.05 \le p < 0.1$),*
*** indicates that the factors have a significant influence on the test index ($0.01 \le p < 0.05$),*
**** indicates that the factors have a very significant influence on the test index ($p < 0.01$).*

From the results of range analysis and analysis of variance, it can be seen that the influence order of various factors on MSF is *D>C>E*. The mean value of MSF measured in 9 groups of tests is 113.8N, the standard deviation is 27.0, and the coefficient of variation is 23.7%. The mean shear strength of onion cauloid is 0.64 MPa. Obtaining the shear strength of onion cauloid is the key basis for the design of onion topper and combine harvester (*Yang et al, 2019; Joshi et al, 2020*).

At the same time, the results showed that the higher the moisture content of onion cauloid, the smaller the force to cut it. This result was in agreement with the reported shear characteristics of potato seedlings by Xin et al. (*Xin et al, 2020*). The main reason may be that when the moisture content is high, the stem is brittle and the force required to cut it is small.

CONCLUSIONS

This work focuses on some physical and mechanical properties of Red Hydrangea cultivar of the onions. The physical properties of the mean BLD, BTD, BW, BPF, BSD, BSI, CD, RCD, RLL and RW were 78.1±9.6 mm, 89.6±10.1 mm, 333.0±101.7 g, 43.9±21.6N, 35.7±8.7 mm, 1.2±0.1, 15.3±3.7 mm, 89.2±19.7 mm, 42.9±10.0 mm and 0.8±0.4 g. The shape of the onion bulbs may be considered spherical. The mechanical properties were the compression properties of onion bulb and the shear properties of onion cauloid. The maximum forces required for compression deformation 10 mm of the onion bulb was 462.2 N. The maximum forces required for shearing of the onion cauloid was 113.8 N, and the mean shear strength of cauloid was 0.64 MPa. The influence order of various factors on MCF was transverse diameter of the bulb and compression speed. The influence order of various factors on the MSF was moisture content, diameter of the cauloid and shear speed.

This study makes up for the lack of research on the basic physical and mechanical properties of onion cultivated in China, and can provide a reference for optimization design of harvesting and post-harvesting machines. However, the current research is only carried out for one variety of onion. In the next step, our research group will select multiple onion varieties for comparative research, and strive to form a basic database of physical and mechanical properties of Chinese onion.

ACKNOWLEDGEMENT

This research was funded by the Agricultural Science and Technology Innovation Programme (ASTIP) of the Chinese Academy of Agricultural Sciences (CAAS), grant number 31-NIAM-02; The Central Public Interest Scientific Institution Basal Research Fund, grant number S202110-02.

REFERENCES

[1] Aprilia, G., Triawan, F., Saville, R. (2021), Crispness measurement of potato crisps by single specimen using compression test. IOP Conference Series: *Materials Science and Engineering*, vol. 1098, no. 062100.

[2] Bahnasawy, A., El-Haddad, A., El-Ansary, M., et al, (2004), Physical and mechanical properties of some Egyptian onion cultivars. *Journal of Food Engineering*, vol. 62, pp. 255-261.

[3] Bisen, D., Kudnar, N. (2013), The production, export and catchment areas market of onion in Indian agriculture. *Research Expo International Multidisciplinary Research Journal*, no. 3, pp. 39-44.

[4] Cakir, E., Alayunt, F., Kurpinar, E. (2001), Dimensional analysis of mechanical behaviour of some onion varieties. *Journal of Biological Sciences*, no. 1, pp.925-928.

[5] Dabhi, M., Patel, N. (2017), Physical and mechanical properties of Talaja Red onion cultivar. *Bioprocess Engineering*, no. 1, pp. 110-114.

[6] Essa, A., Gamea, G. (2003), Physical and mechanical properties of bulb onions. *Misr Journal of Agricultural Engineering*, vol. 20, pp.661-676.

[7] Jahanbakhshi, A., Abbaspour-Gilandeh, Y., Gundoshmian, T. (2018), Determination of physical and mechanical properties of carrot in order to reduce waste during harvesting and post-harvesting. *Food Science & Nutrition*, no.6, pp.1898-1903.

[8] Jithender, B., Vyas, D., Abhisha, S., et al, (2017), Determination of physical and mechanical properties of pomegranate (Var. bhagwa) fruit and aril. *International Journal of Current Microbiology and Applied Sciences*, no. 6, pp.879-885.

[9] Joshi, S., Sathe S., Joshi, S., et al, (2020), Design, development and FEA of 3-point actuated digging and conveyor system for self-propelled onion harvester. *International Journal of Engineering and Technical Research*, no.9, pp.888-891.

[10] Karthik, S., Kumar, S., Palanimuttu, V. (2016), Engineering properties of some Indian onion cultivars. *International Journal of Agriculture Sciences*, no. 8, pp.1613-1617.

[11] Kibar, H., Öztürk, T. (2008), Physical and mechanical properties of soybean. *International Agrophysics*, vol. 22, pp. 239-244.

[12] Kumawat, L., Raheman, H. (2022), Mechanization in onion harvesting and its performance: a review and a conceptual design of onion harvester from Indian perspective. *Journal of the Institution of Engineers (India): Series A*, vol. 103, pp. 295-304.

[13] Li, J., Ma, Y., Tong, J., et al, (2018), Mechanical properties and microstructure of potato peels. *International Journal of Food Properties*, vol. 21, pp.1395-1413.

[14] Ren, F., Zhou, S. (2021), Phenolic components and health beneficial properties of onions. *Agriculture*, vol. 11, no. 872.

[15] Sagsoz, S., Alayunt, F. (2001), Comparison of some methods to determine the modulus of elasticity of some onion varieties. *Journal of Biological Sciences*, no. 1, pp.798-800.

[16] Wang, J., Zheng, D., Cui, Q., et al, (2019), Study on tensile mechanical property and microstructure of fruit and vegetable peels. *INMATEH Agricultural Engineering*, vol. 59, pp.227-236.

[17] Wang, R., Zhou, L., Ren, X., et al, (2019), Optimization technology of layer mesh belt hot air drying of onion (洋葱带式热风干燥工艺优化). *Science and Technology of Food Industry*, vol. 42, pp.195-201.

[18] Xin, Q., Lv, Z., Liu, L., et al, (2020), Experimental study on maximum shear force per unit diameter of potato seedlings at mature stage (成熟期马铃薯秧的单位直径最大剪切力试验研究). *Journal of Agricultural Mechanization Research*, vol. 42, pp.176-180, 195.

[19] Yang, H., Wang, B., Peng, B., et al, (2019), Performance test and parameter optimization of net-chain type onion harvester. *International Agricultural Engineering Journal*, vol. 28, pp. 248-256.

[20] Zhang, S., Yang, H., Hui, L., et al, (2022), Status and trends of onion (Allium cepa L.) research based on bibliometric analysis (基于文献计量分析洋葱研究热点与趋势). *Journal of China Agricultural University*, vol. 27, pp.118-134.

STUDY ON FEATURE EXTRACTION OF PIG FACE BASED ON PRINCIPAL COMPONENT ANALYSIS

/

基于主成分分析的猪脸特征提取研究

Hongwen YAN*, Zhiwei HU, Qingliang CUI [1]

College of Information Science and Engineering, Shanxi Agricultural University, Taigu/China

Tel: +86-0354-6288165; E-mail:yhwhxh@126.com

DOI: https://doi.org/10.35633/inmateh-68-33

Keywords: *PCA, eigenface, feature extraction, intelligent management of pig breeding, identification*

ABSTRACT

Individual identification and behavioural analysis of pigs is a key link in the intelligent management of a piggery, for which the computer vision technology based on application and improvement of deep learning model has become the mainstream. However, the operation of the model has high requirements to hardware, also the model is of weak interpretability, which makes it difficult to adapt to both the mobile terminals and the embedded applications. In this study, it is first put forward that the key facial features of pigs can be extracted by Principal Component Analysis method first before the eigenface method is adopted for verification tests to reach an average accuracy rate of 74.4%; the key features, for which the most identifiable ones are in turn, respectively, face contour, nose, ears and other parts of the pigs, can be visualized, and this is different from the identification features adopted in manual identification. This method not only reduces the computational complexity but is also of strong interpretability, so it is suitable for both the mobile terminals and the embedded applications. In some way, this study provides a systematic and stable guidance for livestock and poultry production.

摘要

生猪个体识别和行为分析是猪场智能管理的关键环节，以深度学习模型应用和改进为主计算机视觉技术已成为其主流，但模型运行对硬件要求高、可解释性不强，难以适应移动端和嵌入式应用，本研究提出首先采用 PCA 方法提取生猪脸部主要特征，并采用特征脸方法进行验证实验，取得 74.4%的平均准确度，对其主要特征可视化，最具有辨识度的特征依次为生猪脸部轮廓、鼻子、耳朵和其他部分，与人工识别采用的辨识特征不一致，该方法减少了运算量，可解释性强，适合移动端和嵌入式应用，有利于对畜禽生产提供系统、稳定的指导。

INTRODUCTION

Individual identification and behavioural analysis of pigs is an important link in the intelligent management of pigs. Compared with the traditional RFID (Radio Frequency Identification) management method that does not conform to the concept of welfare breeding, computer vision technology which mainly focuses on the application and improvement of deep learning model, has become the mainstream in the intelligent management of pigs. Tu Shuqing et al. *(Tu et al., 2021)* explored a PIGMS R-CNN (Region Convolutional Neural Networks) framework based on mask scoring R-CNN (MS R-CNN) to segment the adhered part in images for pig groups, to separate the recognition and location of pig groups, and to integrate the Feature Pyramid Network (FPN) as the feature extraction network to obtain the feature map of the input image, with a network structure reaching 101 layers. Zhang Jianlong *(Zhang et al., 2021)* et al. modified DenseNet201, Resnet152 V2, Xception and MobileNet V2 into a multi-output regression CNN (Convolutional Neural Network) and performed drills on the modelling data. The modified Xception was selected as the optimal estimation model. In order to improve the real-time performance of the model, Residual learning structure, whose MSE (Mean Squared Error) reaches 0.092, was introduced. Chen Cheng *(Chen et al., 2020)* et al. used the deep learning algorithm with few layers of cyclic neural network to identify pigs' preference for objects. Through the full connection layer and Softmax classifier, the preference was identified, achieving a good identification accuracy rate. CNN and LSTM (Long Short Term Memory) network were combined to identify pigs' aggressive behaviours, and the accuracy reached 97.2%, though its operating efficiency was only 15 fps.

[1] *Hongwen Yan*, As. Ph.D. Prof. Eng.; Zhiwei Hu, Lect. Ph.D. Eng.; Qingliang Cui, Prof. Ph.D. Eng.*

In order to increase the model's interpretability and controllability, Mathieu Marsot *(Marsot et al., 2020)* adopted a cascade classifier with Haar features and used the activation-like graphs generated by Grad-CAM to know how the neural network learns to distinguish parameters intuitively, with the accuracy rate of 320 test images reaching 83%. These provide some reference for the interpretability of the deep learning model.

Though the deep learning model as listed above has achieved a high identification accuracy, its high requirements for hardware makes it difficult to adapt to the mobile terminals and embedded applications. In addition, the model is of weak interpretability, thus promotion drills of indicators of the model largely depend on luck, and they are random, so it is difficult to form systematic, stable guidance for its application in agricultural production. Although some scholars *(Marsot et al., 2020)* have carried out exploratory researches on its interpretability, systematic research results have not been formed yet.

Therefore, in this study, the principal component analysis method is used first to extract the features of the most important parts for identification of individual pigs before the extracted features are used as input for eigenface method to identify the pigs. PCA (Principal Component Analysis) is a method to analyse multivariate statistical distribution by eigen quantity first proposed by Karl Pearson *(Pearson K, 1901)* in 1901. In 1991, Turk *(Matthew et al, 1991)* perfected and supplemented it and applied it to the field of facial feature extraction. PCA method, which has been continuously improved, has been widely used in dimension reduction *(Yan et al, 2017)*, feature extraction, data visualization and pattern recognition *(Shi et al., 2006; Li et al., 2015; Wang et al., 2009)*. In the field of image processing, PCA method is also called Karhunen-Loève transformation. Data goes through PCA process so that the orthogonal projection data in low dimensional space may have the maximum variance. In accordance with the biggest variance form, the theory of minimum square error refers to getting new coordinates for all the sample points, so as to make the sum of the distance from all the sample points to the new axis base minimum. In accordance with the minimum error form, PCA refers to finding the linear projection with the lowest average projection cost of the data. According to the theory of signal processing, the bigger the signal variance is, the smaller the noise variance is *(Hu G.S., 1997; Gonzalez, 2007; Cofer, 2007)*. Therefore, after the original data is reduced from dimension *n* to dimension *k*, if the sample variance in each dimension is large, it is an ideal projection.

This method has low requirements to hardware conditions of equipment, and it is with strong interpretability, also the controllability of the model is strong, so it can support the mobile terminals and embedded applications in the intelligent management of pigs.

MATERIALS AND METHODS

Sample collection

As shown in Fig. 1, the experimental materials of this study were collected on a small farm in Wujiazhuang, Taigu County, Shanxi Province, China (112º53′E, 37º42′N), and the sampling date was in March 2018. Pictures of a total of 10 pigs were collected, the samples in each category were divided into training set and test set according to the ratio of 1:1, including 515 training samples, and 500 test samples. These pigs all belong to the same breed, which is named Big York pig, and the faces of the pigs of the same breed are indistinguishable for the human eye, as shown in Fig. 1, this is also an important factor for many researchers to use computer to identify the pig. Using machine vision method can extract the characteristics of each pig, so as to identify its identity.

Fig.1 - Pig Samples

The computer used in the experiment is configured with 64-bit windows system, Intel Core i7-6700, 8GB memory, 6GB video memory capacity, and Program development uses Python V3.5 version language.

Principle of pig face feature extraction by PCA

In principal component analysis, each principal component is determined according to the following principles. Firstly, PCA needs to find the linear transformation matrix *p*, so that *p* shall be put on the left and get multiplied by matrix *x*, where each row of *x* is a sample and each column is a feature of the sample. Secondly, *x* is projected into a new space to obtain matrix *y*, as shown in Equation 1.

$$y=p\,x \tag{1}$$

where: *x* represents sample matrix, the number of rows represents the number of samples, and each column represents a feature, [dimensionless];

p represents the transformation matrix found by PCA method, [dimensionless];

y represents the new matrix after dimension reduction, [dimensionless].

When PCA is applied to extract the facial features of pigs, first, the pixel matrix of each image of pig face need to be represented as a row vector, then all the row vectors shall be stored in the matrix. Supposing that the number of images of pig face is *m*, and the length of them is of *i* pixels, and the width is of *j* pixels, a matrix A（*m, n*) with *m* rows and *n* columns is generated to store the data of pig face, where *n* is the product of *i* and *j*. It can be known from A's generation process that the images of pig face are shown horizontally in a row with pixel as the unit. Pixels, which can be understood as a feature of the sample, are formally represented as a column. The number of pixels is the same with the number of columns, and dimension reduction means to represent the original images with fewer columns. All images of pig faces are processed in this way, and they are represented in the matrix A (*m, n*), in which *n* is the number of all pixels in an image. In the matrix A (*m, n*), every row represents an image of pig face (generated randomly for testing purposes here), and the solution process of the matrix for its principal component is shown in Fig. 2.

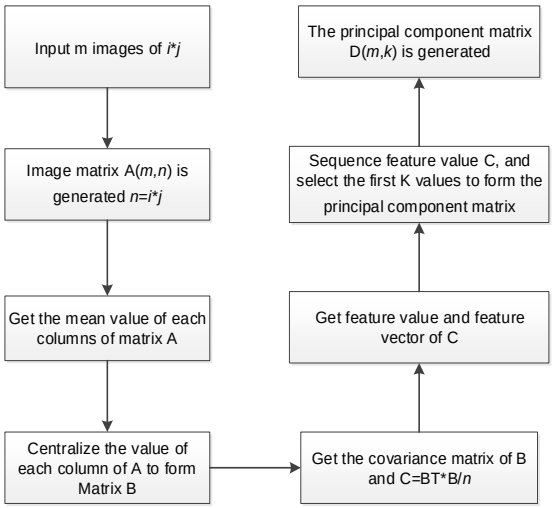

Fig. 2 - Flowchart for solving the principal component matrix

Determination of number of facial features of pigs' to be extracted by PCA

After PCA processing, the dimensions of pig face data will be reduced, thus the amount of information in the original data will be reduced accordingly. The reduction of the amount of information is positively related to the number of dimensions reduced. How to determine the number of dimensions to be reduced, or how to determine the appropriate value of *k*, is the first problem to be solved in applying PCA method. According to the calculation process of principal component analysis, it can be seen that the data is reduced from dimension *n* to dimension *k*. Adopting the form of minimum error means to project the original data with *k* vectors to minimize the projection distance. *k* can also be determined by using a formula or by taking the test method. Equation (2) can be used to determine the value of *k*.

$$\frac{\frac{1}{m}\sum_{i=1}^{m}\|x^{(i)}-x_{appro}^{(i)}\|^2}{\frac{1}{m}\sum_{i=1}^{m}\|x^{(i)}\|^2}\leq a \tag{2}$$

where:

m represents number of features, [a];
$x^{(i)}$ represents original sample points, [a];
$x_{appro}^{(i)}$ represents projection sample points, [a];
a represents data loss ratio, [dimensionless].

In Equation (2), the numerator value represents the mean square error of projection, and the denominator represents the sum of variance. In practical application, a can be 0.05 in accordance with the empirical rule. In this study, the value of *k* was determined by experiment. If *k* is the same as in the original dimension, 100% information is retained; if *k* is 0, that means 0% information is retained. The retained information of the original data after PCA extraction of the key features can be represented by the ratio of the sum of selected eigenvalues to the sum of all eigenvalues, as shown in Equation (3)

$$\eta = \frac{\gamma_1 + \cdots + \gamma_k}{\gamma_1 + \cdots + \gamma_n} \quad (3)$$

where: r represents the proportion of information retained after dimension reduction, [dimensionless];
h represents the i[th] eigenvalue, [a].

PROCESS FOR PCA PIG FACE FEATURE EXTRACTION

Determination of number of features of pig face *k*

To be able to reduce the data from dimension *n* to dimension *k*, PCA needs to find *k* vectors for projecting the original data. According to the minimum square error theory, the smaller the sum of the distance between the original point and the projection point is, the more completely the data after dimension reduction can represent the data before dimension reduction. In general, the bigger the number of principal components is, the more complete the retained information is. The completeness represented by different numbers of principal components can be quantitatively expressed by the sum of variance percentages of different numbers of principal components. The percentage of population variance can reflect the degree of similarity between the extracted features and the original data. The higher the percentage of variance is, the better the original data is reconstructed. For this reason, in this paper, the relationship between the different numbers of principal components and the sum of variance interpretation rate of each component is studied at first, and the relationship curve is as shown in Fig. 3.

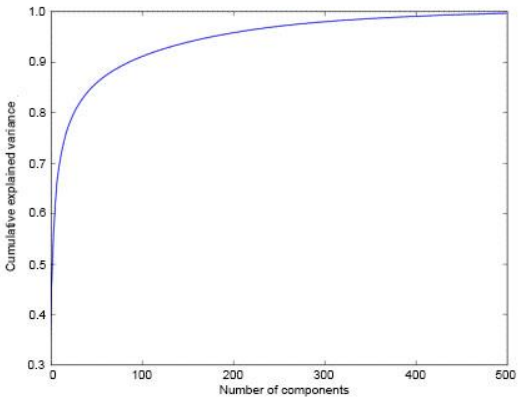

Fig. 3 - The relationship between the number of principal components selected by PCA and the amount of information retained

In Fig. 3, the horizontal axis represents the number of different principal components ranging 1~500, while the vertical axis represents the sum of variance interpretation rate of each principal component. In the optimal conditions, the sum of variance interpretation rate of each principal component is 1, that is, the information originally input is completely reconstructed. With the number of principal components increasing, the sum of variance interpretation rate increases and eventually reaches a smooth and steady state. According to the empirical principle, the interpretation rate of population variance shall be 95% at least. As can be seen in Fig. 3, at the moment, the number of principal components was selected as 300.

RESULTS AND DISCUSSION

Visual analysis of results

In order to reflect the data distribution of the original data after the key features are extracted by PCA more intuitively, in this study, the first two principal components among the 300 principal components of each input image data were visualized and their scatter diagrams were drawn. The results are as shown in Fig. 4.

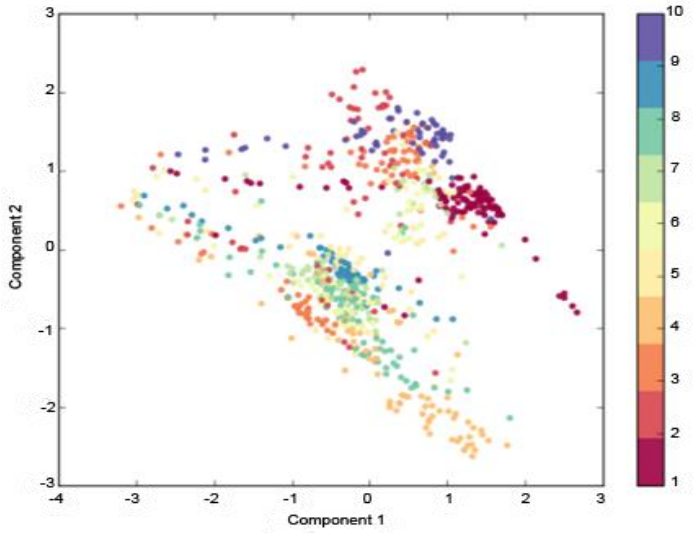

Fig. 4 - Visualization of the first two principal components

In Fig. 4, each point represents a pig sample, and points of different colours represent different individual pigs, multiple dots of the same colour represent different facial images of the same pig. The horizontal axis shows the value of principal component 1, while the vertical axis shows the value of principal component 2. In Fig. 4, it can be seen that, though the points of different colours overlap in part, the sample points of the same colour are basically clustered together; the distribution areas of individual pigs of different identities are different, while the overall distribution of the individual pigs of the same identity is in an adjacent area. Fig. 4 shows that the key features extracted by PCA processing do not lose the category information of pig data, while the pig image information that needs to be processed in subsequent applications is significantly reduced, which has a positive effect on the time efficiency of subsequent algorithms.

The features extracted from images of pig face by PCA can be used as the feature selector for identification of individual pigs. As pigs have rich facial features, different principal components may represent different parts of the pig face in images. To understand different features represented by different principal components intuitively, this study visualized the first 24 features among 300 principal components, and the results are shown in Fig. 5.

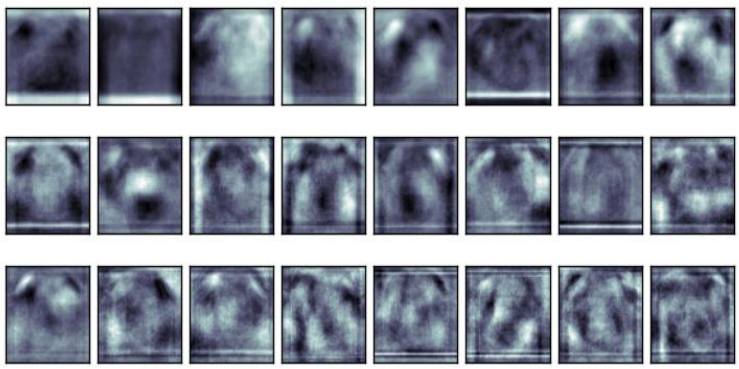

Fig. 5 – Eigenface of the first 24 principal components

As can be seen in Fig. 5, the first principal component extracted shows the contour feature of pig face, which is its most identifiable biological feature. For the second principal component, the feature of pig nose is extracted. For the third principal component, the feature of pig ears is extracted. For other principal components, the features of different parts of pigs are extracted, and the eigenvectors representing the principal components of each feature are in an orthogonal state.

The visualized results show that the pig face contains the most abundant biological feature information, different proportions of which can be seen in nose, ears and other parts of the pig body. In the intelligent management of pigs, facial contour may be considered. Are the features used to distinguish individual pigs on the farm consistent with the experimental results? According to the four experienced farmers from Wujiazhuang, Taigu County, Shanxi Province, the sequence of markers used by farmers to distinguish pigs in their daily management is as shown in Table 1.

Table 1

Markers used by farmers to distinguish pigs in their daily management

Index	Facial contour	Nose	Ears	Non-biological information
Farm A	3	4	2	1
Farm B	4	3	2	1
Farm C	3	4	2	1
Farm D	4	3	2	1

From Table 1, it can be seen that after the features on images of pig face are extracted by PCA method, the extracted facial features of pigs are almost totally different from the features for identification adopted by farmers in their daily management. For the four breeding farms, what they would select first for distinguishing pigs is marks other than biological features, such as earmarking and RFID, and second is ear features, while in the third and fourth places, nose features or external contour are adopted, since it is difficult to distinguish the biological features of pigs with human eyes. However, with the principal component analysis method, the distinguishable biological features of pigs can be extracted. Therefore, compared with manual identification, it has a much higher identification capability.

To further verify that after the pig face images go through PCA processing, the key features extracted shall be used to identify pigs, for the ten categories of pigs as mentioned above, PCA method was first used for feature extraction before the eigenface method was adopted for individual pig identification; finally, the accuracy rate as well as the overall accuracy rate for the identification of each category of pigs is statistically analysed. The accuracy rate of each category is obtained by dividing the number of pigs correctly identified among the category of pigs participating in the identification by the total number of the pigs of the same category participating in the identification. The overall accuracy rate for identification is obtained by summing the values of all the identification accuracy rates of each category before the mean value is obtained, as shown in Equation (4).

$$accuracy = \frac{x_{i.1}}{x_{i.1}+x_{i.0}} \quad (4)$$

where: $x_{i.1}$ represents the number of pigs of category *i* correctly identified, [a];

$x_{i.0}$ represents the number of pigs of category *i* wrongly identified, [a].

The identification accuracy rates of the ten categories of pigs in the experiment are as shown in Table 2.

Table 2

PCA recognition results

Category	Sample number set in tests	Accuracy rate（%）
1	40	86.7
2	38	92.9
3	64	96.3
4	46	94.4
5	58	100
6	50	65

Category	Sample number set in tests	Accuracy rate（%）
7	46	33
8	50	55
9	52	33
10	58	87.5
Mean value	50	74.4

With facial features of pigs extracted by PCA method, the eigenface space is generated. On this basis, identification is implemented. The overall identification rate of pig face images reached 74.4%, which was a little low. The main reason lies in that in the images collected, the illumination difference is obvious. For pig images obtained in poor lighting (too dark and too light) conditions, the accuracy rate of eigen method is low. Table 2 shows that for pigs of the 5th category, the accuracy rate reached 100%, while for pigs in the 7th and 9th categories, the accuracy rates were only 33%. Significant difference is observed. Observing the images in Category 5, it was found that with the highest identification accuracy, the images of pig faces are with sufficient illumination, and the front of the face is captured in the facial profiles, while in Categories 7 and 9, side face of pigs is captured. It shows that this method for identification is greatly influenced by both illumination and posture of pigs.

CONCLUSIONS

In this study, for 1,015 photos taken for 10 pigs representing 10 identities of pigs, the principal component analysis method was adopted to extract the distinguishable features on the faces of pigs, and eigenface method is used for verification tests with the extracted features employed. The conclusions of the tests are as follows:

(1) The facial features of 10 pigs were extracted by the PCA method, and the face contour, nose, ears and other parts of pigs were sequenced in turn according to their distinguishable degrees.

(2) The features extracted by the algorithm are different from those used by farmers in their daily management.

(3) The experiment for individual identification of pigs by using the eigenface method shows that pig face features extracted by PCA method are highly distinguishable.

(4) The accuracy rate of eigenface method adopted for pig face identification is greatly influenced by both the angle that pigs face to the camera and the illumination conditions for image taking. When pigs face directly to the camera, the accuracy rate is high; though with other postures, the accuracy rate may be low. Normal illumination can also improve the accuracy rate. This study provides important experimental evidence for the data collection of pig faces.

ACKNOWLEDGEMENTS

This research, titled ‘Study on Feature Extraction of Pig Face Based on Principal Component Analysis’, was funded by the National Key Research and Development Plan of China (2016YFD0701801), the Shanxi Province Basic Research Program Project (Free Exploration) (Grant No.20210302124523, 202103021224149, 202103021223141), the Doctor Scientific Research Foundation of Shanxi Agricultural University (2020BQ14). The authors are grateful and honoured to have obtained support from the Key Laboratory of Biomechanics.

REFERENCES

[1] Chen C., Zhu W.X., Juan S., et al., (2020), Recognition of aggressive episodes of pigs based on convolutional neural network and long short-term memory. *Computers and Electronics in Agriculture*, Vol.169, ISSN:01681699, pp.105166, Oxford/England;

[2] Chen C., Zhu W.X., Oczak M., et al., (2020), A computer vision approach for recognition of the engagement of pigs with different enrichment objects. *Computers and Electronics in Agriculture*, Vol.175, ISSN:01681699, pp.105580, Oxford/England;

[3] Cofer, (2007), *Fundamentals of Information Theory*, Mechanical Industry Press, pp.7-12, ISBN: 9787111220404, Beijing/China;

[4] Hu G.S., (1997), *Digital Signal Processing-Theoretical Algorithms and Implementation,* Tsinghua University Press, pp.374-379, ISBN：9787302297574, Beijing/China;

[5] Gonzalez, (2007), *Digital image processing*, Publishing House of Electronics Industry, pp.338-339, ISBN：9787121368981, Beijing/China;

[6] Li K.L., Zhang Y.X., Liu L.L., (2015), Palmprint recognition based on improved PCA and support vector machine. *Computer Science,* Vol.42, Supplement (2), ISSN：1002-137X, pp.146-150, Chongqing / China;

[7] Marsot M., Mei J.Q., Shan X.C., et al., (2020), An adaptive pig face recognition approach using Convolutional Neural Networks. *Computers and Electronics in Agriculture*, Vol.173, ISSN:01681699, pp.105386, Oxford / England;

[8] Pearson K., (1901), On lines and planes of closest fit to systems of points in space. *Philos Mag*, Vol.9, Issue 2, ISSN:14786435, pp.559 -572, London / England;

[9] Shi Y.X., Cai Z.X., Wang X.W., (2006), Face recognition technology based on improved PCA algorithm and Fisher linear discriminant. *Journal of Chinese Computer Systems,* Vol.9, pp.1731-1736, Shenyang/ China;

[10] Tu S., Yuan W., Liang Y., Wang F., Wan H., (2021), Automatic Detection and Segmentation for Group-Housed Pigs Based on PigMS R-CNN. *Sensors,* Vol.21, Issue 9, ISSN: 14243210, pp.3251, Basel / Switzerland;

[11] Turk M., Pentland A., (1991), Eigenfaces for Recognition. *Journal of Cognitive Neuroscience,* Vol.3, Issue 1, ISSN: 0898929X, pp.71-86, Cambridge / US;

[12] Turk M., Pentland A., (1991), Face Recognition Using Eigenfaces. *IEEE Computer Society Conference on Computer Vision and Pattern Recognition*, ISSN: 1063-6919, pp.1:586-591, Hawaii / USA*;*

[13] Wang Q.G., Li J.W., (2009), Improved PCA Algorithm with Local Structure Preservation. *Pattern Recognition and Artificial Intelligence,* Vol.22, Issue 3, ISSN：1003-6059, pp.388-392, Heifei/ China;

[14] Yan R.H., Peng J.Y., Wen D.S., (2017), The relationship between PCA and 2DPCA. *Computer Science,* Vol.44, Issue 11, ISSN: 1002-137X, pp.202-206+216, Chongqing / China;

[15] Zhang J.L., Zhuang Y.R., Ji H.Y., Teng G.H., (2021), Pig Weight and Body Size Estimation Using a Multiple Output Regression Convolutional Neural Network: A Fast and Fully Automatic Method. *Sensors*, Vol.21, Issue 9, ISSN：14243210, pp.3218, Basel/ Switzerland.

DESIGN AND EXPERIMENT OF COMB-BRUSH AIR-SUCTION COMPOSITE FLAX CAPSULE HARVESTING TEST BENCH

梳刷气吸复合式亚麻（胡麻）蒴果收获试验台设计与试验

Fulong XU[1,2)], Junlin HE *[1)], Yuehua WANG[1)], Jiaojiao LI[1)]

[1)]College of Agricultural Engineering, Shanxi Agricultural University, Taigu/China;
[2)]Shanxi Limin Industrial Co, Taigu/China;
Tel: +86-0354-6288400; E-mail: hejunlin26@126.com
DOI: https://doi.org/10.35633/inmateh-68-34

Keywords: *Harvesting test bench; Harvesting methods; Comb-brush air-suction; Flax capsule*

ABSTRACT

In view of the problem of plant entanglement threshing roller in the process of mechanized flax harvesting, a comb-brush air-suction composite flax capsule harvesting test stand was designed based on the harvesting method of harvesting capsules independently and then breaking the capsules to thresh them. The following four parameters were selected as experimental factors: the shape of comb tooth cross-section, the rotational speed of comb roller, the relative speed of machine travel and the air volume of centrifugal fan. The following four indicators were chosen as the experimental indicators: capsule removal rate, capsule breakage rate, capsule collection rate and plant winding rate. A four-factor and three-level orthogonal test was conducted. The results showed that the optimal combination of test factors was as follows: the shape of comb tooth cross-section was rectangular, the rotational speed of the brush roller was 90 rad/min, the speed of machine travel relative to the plant was 80 mm/s and the air volume of centrifugal fan was 6000 m³/h. Under the condition of better experiment parameters combination, the capsule removal rate was 96.45%, capsule shell breaking rate was 98.79%, capsule collection rate was 95.65% and flax plants winding rate was 2.52%. The comb-brush air-suction composite flax capsule harvesting test bench provided the feasibility scheme for the problem of plant winding thresher roller and capsule collection.

摘要

针对亚麻（胡麻）机械化收获过程中植株缠绕脱粒滚筒问题，基于先独立收获蒴果、再对蒴果破壳脱粒的收获方式，设计了一种梳刷气吸复合式亚麻（胡麻）蒴果收获试验台。以梳齿截面形状、梳刷滚筒转速、机具行进相对速度、离心式通风机风量为试验因素，以蒴果脱尽率、破壳率、收集率、植株缠绕率为试验指标，进行四因素三水平正交试验。正交试验结果表明：较优试验因素组合梳齿截面形状为矩形、梳刷滚筒转速为 90 rad/min、机具相对植株行进速度为 80 mm/s、离心风机风量为 6000 m³/h；在较优试验因素组合作业条件下，蒴果脱尽率为 96.46%、蒴果破壳率为 98.91%、蒴果收集率为 95.66%、植株缠绕率为 2.52%。梳刷气吸复合式亚麻（胡麻）蒴果收获试验台提供了解决亚麻（胡麻）植株缠绕滚筒和蒴果收集问题的可行性方案。

INTRODUCTION

At present, foreign flax mechanized harvesting mode mainly consists of two-stage harvesting and combined harvesting, among them, the two-stage harvesting is mainly to harvest flax firstly and then lay it in the field for 2~3 days, then it is picked up and harvested by traction or self-propelled combined harvester with pick up function. Meanwhile, foreign flax harvesting equipment has high intelligence level, complex operation control system and high price, which are not suitable for a wide application of Chinese flax mechanized production equipment (*Dai., 2020*). Currently, in China, research on flax harvesting is mainly based on full-feed and half-feed harvest, for example, the machine was designed for separating and cleaning different components of flax threshing material in the harvest period (*Dai et al., 2019; 2020*). The full feeding type flax thresher is designed for the problem of small flax seed, easy winding stem and poor feeding fluidity (*Shi et al., 2019*). According to the agronomic requirement of flax retting production, the 5YF-150 traction flax retting and threshing machine was designed (*Zhang et al., 2008*). In order to realize the goal of flax picking, threshing and laying, a traction type flax threshing machine was designed (*Zhao et al., 2010*). In view of the problems such as small land area, narrow roads, difficult transportation, difficult transfer and difficult operation of the large

[1] *Fulong Xu,As.M.S.Stud.;Junlin He,Prof.Ph.D.Eng.;Yuehua Wang,As.M.S.Stud.;Jiaojiao Li,As.M.S.Stud.*

combine harvester, flax stalk is easy to be wound and blocked, difficult to feed and so on, the crawler type flax combine harvester be applied to hilly and mountainous areas was designed (*Shi et al., 2021*). There are problems both in terms of winding the threshing roller when feeding the plant and blocking the sieve plate when cleaning the material due to complex impurities, therefore the plant twining roller is an urgent problem to be solved in mechanized flax harvesting (*Xu et al.,2021*).

Aimed at the aforementioned problem of plant winding roller in mechanized flax harvesting, the purpose of this study is to design a flax capsule harvesting test bench based on the methods that the flax capsule was harvested independently first and then threshed.

MATERIALS AND METHODS

Experiment materials, conditions and equipment

Fig. 1 - Comb-brush air-suction composite flax capsule harvest test bench

The mature blue flax plants with 15.33% moisture content were selected as test materials, it is also called perennial root flax (*Linum perenne* L.*var.sibiricum* Planch.) which is a perennial herb of flax genus in flax family, its plant and capsule characteristics are similar to flax. The test site was chosen in the Mechanical Design Laboratory of the College of Agricultural Engineering, Shanxi Agricultural University. Test equipment includes the comb-brush air-suction composite flax capsule harvesting test bench (Fig. 1 -), electric air blowing drying oven, electronic balance (precision 0.01 g). The experimental data processing software includes Microsoft office Excel 2019 and Statistical Analysis System 9.1.

Overall structure and working principle of experiment equipment

The working parts of the test bench mainly include brushing device, collection system, power system, delivery system and control system. It mainly consists of machine frame, brush roller, protective cover of brush roller, V belt, big belt wheel, small belt wheel, variable speed belt wheel, plant conveyor guide rail, plant holding device, centrifugal fan, electromagnetic variable-speed motor, three-phase asynchronous motor, stepper motor and other structures. (Fig. 2 -)

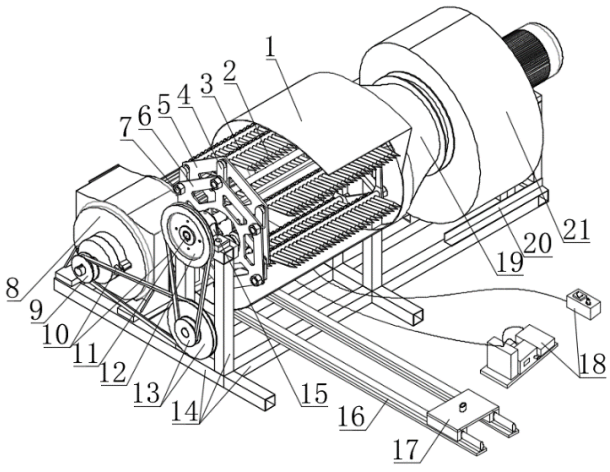

Fig. 2 - Comb-brush air-suction composite flax capsule harvesting test bench

1-Brush roller protection cover; 2-Comb tooth; 3-Comb tooth rack; 4-Fittings; 5-Active hexagonal disc; 6-Driven hexagonal disc; 7-Driven shaft; 8-Motor; 9-Small pulley; 10-The belt; 11-Roller shaft; 12-The big belt wheel; 13-Variable speed pulley; 14-Machine frame; 15-Bearing; 16-Conveying guide rail; 17-Holding device; 18-The controller; 19-Fan interface; 20-Fan frame; 21-Centrifugal fan

When the test bench is working, the brush roller rotates under the power which is output from the motor through the belt drive to the brush roller shaft via the variable speed pulley. The comb teeth of the brushing roller does parallel movement under the constraint of the parallel four-bar mechanism, the translating comb teeth act on the clamped plants of the conveyor rail. The plant keeps close contact with the comb tooth under the wind power action of the centrifugal fan, which is beneficial for the plant be brushed better. Under the protection of the brush roller protection cover, the removed capsule falls into the protective cover or rests on the surface of the comb tooth, under the action of the centrifugal fan with specific wind pressure, capsules are collected to a specified position, at the same time, under the strong wind force of the centrifugal fan, there is a large impact force between the capsule and the fan blade, therefore, the collected capsule material belongs to the semi-threshing material which is conducive to the subsequent stage of capsule breaking and threshing.

The main technical parameters of the comb-brush air-suction composite harvesting test bench of flax capsule are listed in Table 1.

Table 1

Main technical parameters of comb-brush air-suction composite flax capsule harvesting test bench

Technical parameters	Value	Units
Whole machine size (length× width× height)	1335×870×750	mm
Working width	570	mm
Rotational speed of roller shaft	0-139	rad/min
Length of comb tooth	140	mm
Clearance of comb tooth	4	mm
Power of centrifugal ventilator	3000	W
Pressure of centrifugal ventilator	1210-998	Pa
Air volume of centrifugal ventilator	6000-7640	m^3/h
Power of motor	2200	W
Transmission ratio	1:9	/

Dynamics analysis of main components

Analysis of the process of capsule being brushed

The comb-tooth flax capsule brush roller is mainly composed of active hexagonal disc AB (original actuator), driven hexagonal disc DC (actuator), connecting piece BC (actuator), frame AD, comb tooth frame, driven shaft, roller shaft and other structures, all of which also constitute a parallel four-bar mechanism (Fig. 3 - a, c). The comb tooth of the brush roller does parallel movement under the constraint of the parallel four-bar mechanism, the comb gap are designed for 4 mm, the comb teeth are designed with a certain angle to the horizontal direction (α=10°). The action direction of the parallel moved comb teeth on the plant is certain, the phenomenon of the plant winding roller is avoided. The motion tracks of the comb tooth frame, driven shaft and comb tooth of the parallel four-bar mechanism are S_1, S_2 and S_3 (Fig. 3 - b, c), they all move in circles (*Xu et al., 2021*). Take point A as the origin of coordinates and establish the coordinate system (Fig. 3 - c), the motion trajectory equation of the comb tooth tip as follows. This allows a better understanding of the working principle of the device and the movement of the capsule.

$$\begin{cases} x = \overline{BE}\cos\alpha + \overline{AB}\cos\theta + v_R t = \overline{BE}\cos\alpha + \overline{AB}\cos\omega t + v_R t \\ y = \overline{BE}\sin\alpha + \overline{AB}\sin\theta = \overline{BE}\sin\alpha + \overline{AB}\sin\omega t \end{cases} \quad (1)$$

Taking the derivative of equation (1) with respect to time, the velocity equation of the comb tooth can be obtained as follows.

$$\begin{cases} v_x = -\omega\overline{AB}\sin\omega t + v_R \\ v_y = \omega\overline{AB}\cos\omega t \end{cases} \quad (2)$$

Where:

α is the angle between the comb tooth and the horizontal direction; θ is the rotational angle of the brush roller (independent variable); ω is the uniform rotational speed of the brush roller, [rad/min]; V_R is the moving speed of the test bench relative to the plant, [m/s]; $\overline{AB}$ is the distance between the center of the shaft hole of the active hexagonal disc and the axis of the roller, [m]; $\overline{BE}$ is the length of the comb tooth, [m].

To do a stress analysis of the capsule during the brushing process (Fig. 3 - b), mg is the gravity of the capsule itself, F_N is the supporting force of the comb tooth, F_f is the friction of the comb teeth. The capsule is subjected to centripetal force in the +x region as shown in Formula (3), So the capsule is attached to the surface of the comb tooth; The capsule is not subjected to centripetal force in the -x region and rolls freely along the inclination angle of the comb teeth.

$$F_r = mg\sin\alpha + fmg\cos\alpha = m\frac{v_r^2}{r} \quad (3)$$

Where:

m is the mass of capsule, [kg]; f is the dynamic friction coefficient of comb teeth; v_r is the centripetal speed of the comb tooth, [m/s]; r is the distance between the comb tip and point A, [m].

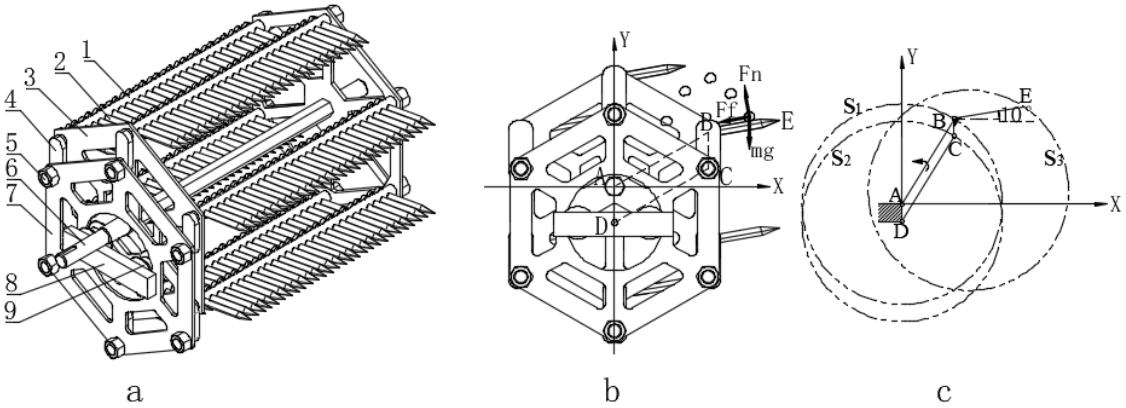

Fig. 3 - Structure diagram and motion trail diagram of parallel four-bar mechanism

1-Comb tooth rack; 2-Comb tooth; 3-Active hexagonal disc; 4-Connections; 5-Driven shaft; 6-Roller shaft; 7-Driven hexagonal disc; 8-Slot wheel carrier; 9-Slot wheel

Analysis of the process of capsule being collected

To do the following analysis according to the different situations in the collection process, the coordinate system was established with the centre of mass of the capsule as the origin. Fig. 4 - a shows that after the capsule is removed, it bounces up in the air between the brush device and the protective cover, the capsule is mainly affected by the wind force of the fan and its own gravity, the equilibrium equation is shown in equation (4); Fig. 4 - b shows the capsule falling on the surface of the comb teeth after being removed, the capsule is mainly affected by the centrifugal fan's wind force, its own gravity, the friction of the comb tooth, the support force of the comb tooth, the equilibrium equation is shown in equation (5); Fig. 4 - c shows the situation in which the capsule falls on the surface of the brush roller guard after being removed, the capsule is mainly affected by the wind force of fan, the gravity of the capsule itself, the friction of the protective cover, the support force of the protective cover, the equilibrium equation is shown in equation (6). In Fig. 4 -a, b, c, V represents the capsule motion velocity vector. According to the above stress analysis, the capsule in the air between the brush device and the protective cover has the least resistance, so it is the easiest to collect, the capsule on the surface of the protective cover is next, the capsule on the comb tooth surface of the brush device is slightly difficult to collect, and the capsule outside the protective cover cannot be collected because it is not in the air duct. These forces are an important basis for designing the structure and strength of the test bench.

$$\begin{cases} F_x = F_{\mathrm{AF}x} + F_{\mathrm{FW}} = ma_x \\ F_y = F_{\mathrm{AF}y} + mg = ma_y \end{cases} \quad (4)$$

$$\begin{cases} F_x = F_{f1} + F_{\mathrm{AF}x} + F_{\mathrm{FW}} = ma_x \\ F_y = F_{\mathrm{f2}} + F_{\mathrm{AF}y} + F_1 = ma_y \\ F_z = F_{\mathrm{f3}} + F_{\mathrm{AF}z} = ma_z \end{cases} \quad (5)$$

$$\begin{cases} F_x = F_f + F_{\mathrm{AF}} + F_{\mathrm{FW}} = ma_x \\ F_y = F_1 + mg = ma_y \end{cases} \quad (6)$$

Where:

F_{AF} is the air resistance to the capsule, [N]; F_{FW} is the force of the centrifugal fan to the capsule, [N]; F_{f} is the frictional resistance to the contact surface of the capsule, [N]; F_1 is the support force on the contact surface of the capsule, [N]; a is the acceleration of the capsule, [m/s^2]; m is the mass of the capsule, kg; x, y, and z indicates the direction of the coordinate axis.

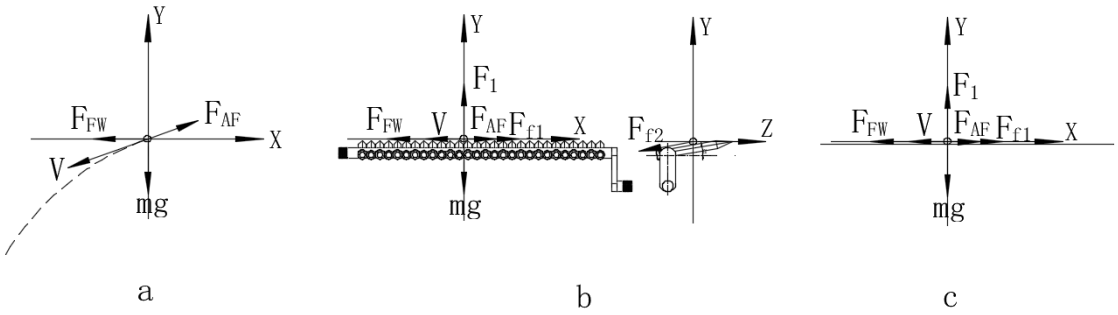

Fig. 4 - Schematic diagram of flax capsule collection process

Experiment design

Determination of experimental factors and its control methods

According to the bench test results of the comb-tooth flax capsule brush test bench (*Xu et al., 2021*), combined with the structure arrangement and working principle of comb-brush air-suction composite flax capsule harvesting test bench, the following four experimental factors were selected, comb tooth cross section shape *A*, brush roller rotational speed *B*, speed of the machine moves relative to the plant *C*, centrifugal fan air volume *D*, the experimental factors and levels are shown in Table 2. The shape of the comb tooth cross section is controlled by installing different the comb tooth with cross section shapes, the brush roller rotational speed by adjusting the motor speed to control, the speed of the machine moves relative to the plant and is controlled by adjusting the speed of the stepper motor on the guide rail, the air volume of the centrifugal fan is controlled by adjusting the size of the fan inlet.

Table 2

Experiment factors and levels

Levels	Shape of comb tooth cross section	Rotational speed of roller shaft	Relative speed of the machine	Air volume of centrifugal ventilator
	/	[rad/min]	[mm/s]	[m³/h]
	A	***B***	***C***	***D***
-1	rectangular	44	80	2000
0	circular	67	140	4000
1	diamond	90	200	6000

Determination of experimental index and its calculation methods

According to the bench test results of the comb-tooth flax capsule brush test bench (*Xu et al., 2021*), combined with the structure arrangement and working principle of comb-brush air-suction composite flax capsule harvesting test bench, the following four test indexes were selected, capsule removal rate is Y_1, capsule breaking rate is Y_2, capsule collection rate is Y_3, plant winding rate is Y_4. The test bench requires the plant winding rate as small as possible, and other test indicators as large as possible.

The calculation formula of each test index was shown in the following formula.

$$Y_1 = \frac{M - M_1}{M - M_2} \times 100 \quad (7)$$

$$Y_2 = \frac{M_3 - M_4}{M_3} \times 100 \quad (8)$$

$$Y_3 = \frac{M_3}{M - M_1} \times 100 \quad (9)$$

$$Y_4 = \frac{M_5}{M} \times 100 \quad (10)$$

Where:

M is the total weight of the flax plant before being brushed, [g]; M_1 is the weight of the flax plant after being brushed, [g]; M_2 is the weight of the flax plant after excluding all capsules, [g]; M_3 is the total weight of the capsules that are collected by the fan outlet, [g]; M_4 is the weight of the unbroken capsules that are collected by the fan outlet, [g]; M_5 is the weight of the flax plant wrapped around the brush roller, [g].

RESULTS AND ANALYSIS

Bench test

Experiment scheme and results

Orthogonal experiments with four factors and three levels were designed according to the orthogonal table with $L^9(3^4)$ to study the significance of the influence of each experimental factor to the each experimental index. A total of 9 groups of experiments were conducted, and each group of experiments was repeated three times to take the average value, each test index was calculated according to formula (7)~(10) for each test. The factors and levels of the orthogonal test were shown in Table 2, and the orthogonal test scheme and results were shown in Table 3, and Table 3 was made based on Table 2.

Table 3

Experiment scheme and results

Test number	Levels of experiment factors				Experiment index			
	A	*B*	*C*	*D*	Y_1[%]	Y_2[%]	Y_3[%]	Y_4[%]
1	1	1	1	1	98.19	97.42	94.45	1.79
2	1	0	0	0	97.37	97.25	82.87	4.21
3	1	-1	-1	-1	96.30	95.57	30.13	0.36
4	0	1	0	-1	94.39	96.16	28.73	0.00
5	0	0	-1	1	96.92	97.53	95.63	0.38
6	0	-1	1	0	97.62	98.06	89.63	0.17

Table 3 (continuation**)**

Test number	Levels of experiment factors				Experiment index			
	A	*B*	*C*	*D*	Y_1[%]	Y_2[%]	Y_3[%]	Y_4[%]
7	-1	1	-1	0	97.68	98.15	90.30	0.93
8	-1	0	1	-1	96.45	96.23	30.05	0.00
9	-1	-1	0	1	95.85	97.99	94.67	0.00

Experiment data analysis

According to the range analysis results (Table 4), the optimal experimental factors combinations of capsule removal rate, breaking rate, collection rate and plant winding rate respectively were $A_1B_0C_1D_0$, $A_{-1}B_1C_1D_0$, $A_{-1}B_{-1}C_{-1}D_1$ and $A_{-1}B_{-1}C_{-1}D_{-1}$. The effects of various factors on the capsule removal rate, breaking rate, collection rate and plant winding rate respectively were in the following order: *D>C>A>B*, *D>A>B>C*, *D>C>A>B*, *A>D>B>C*.

Table 4

Range analysis of orthogonal experiment

Analysis item	Y_1[%], Capsule removal rate				Y_2[%], Capsule shell breaking rate			
	A	*B*	*C*	*D*	*A*	*B*	*C*	*D*
K_1	97.28	96.75	97.42	96.99	96.75	97.24	97.24	97.65
K_0	96.31	96.92	95.87	97.55	97.25	97.01	97.13	97.82
K_{-1}	96.66	96.59	96.97	95.72	97.46	97.21	97.08	95.87
Range	0.97	0.32	1.54	1.84	0.71	0.24	0.15	1.84
Optimal solution	$A_1B_0C_1D_0$				$A_{-1}B_1C_1D_0$			
P&S factors	*D>C>A>B*				*D>A>B>C*			
K_1	69.15	71.16	71.38	94.92	2.12	0.91	0.66	0.73
K_0	71.33	69.52	68.75	87.60	0.18	1.53	1.77	1.77
K_{-1}	71.68	71.48	72.02	29.64	0.30	0.17	0.56	0.12
Range	2.52	1.96	3.26	65.28	1.94	1.36	1.21	1.65
Optimal solution	$A_{-1}B_{-1}C_{-1}D_1$				$A_{-1}B_{-1}C_{-1}D_{-1}$			
P&S factors	*D>C>A>B*				*A>D>B>C*			

Note: K_i is the average of the corresponding results when the level number on any column is i (i=1,0,-1).

Because each index optimal working condition was different, the comprehensive weighted scoring method was adopted to give consideration to the gains and losses of each index. According to the experience and practical requirements, since the experiment bench mainly solves the problem of plant winding and capsule collection, the capsule collection rate was related to the work efficiency of the test bench, it is considered that capsule removal rate, collection rate and plant winding rate were equally important, and the weights were 0.3 respectively. Since the collected capsules have to go through the subsequent breaking and threshing process regardless of the breaking degree, so the breaking rate was not the most important in this experiment, and the weight was given to 0.1. According to the comprehensive weighted scoring value, the range analysis of the test results was carried out (Table 5). It showed the optimal working parameters combined of the test bench as follows: the shape of the comb tooth cross section was rectangular, the rotational speed of the comb roller was 44 rad/min, the speed of machine travel relative to the plant was 80 mm/s, the air volume of the fan was 6000 m^3/h.

Table 5

Comprehensive weighted score range analysis results

Analysis item	Experiment factors			
	A	***B***	***C***	***D***
K_1	58.97	59.83	60.17	67.12
K_0	59.96	59.17	58.57	64.79
K_{-1}	60.15	60.09	60.24	47.17
Optimal solution	$A_{-1}B_{-1}C_{-1}D_1$			

Note: K_i is the average of the corresponding results when the level number on any column is i (i=1,0,-1).

According to the results of the variance analysis (0), none of the experiment parameters had significant effect on the capsule removal rate.

Table 6

Variance analysis of orthogonal experiment

Index	Variance Sources	*DF*	*Anova SS*	*Mean Square*	*F* value	*P* value
Y_1[%] Capsule removal rate	***A***	2	4.39	2.20	0.60	0.5610
	B	2	0.47	0.24	0.06	0.9380
	C	2	11.42	5.71	1.55	0.2386
	D	2	16.02	8.01	2.18	0.1422
	Model	8	32.31	4.04	1.10	0.4084
	Error	18	66.20	3.68	R^2=0.328 Coeff var=1.98	
	Sum	26	98.51			
Y_2[%] Capsule shell breaking rate	***A***	2	2.39	1.19	4.72	0.0225
	B	2	0.30	0.15	0.59	0.5651
	C	2	0.11	0.06	0.22	0.8026
	D	2	18.46	9.23	36.56	<0.0001
	Model	8	21.26	2.66	10.52	<0.0001
	Error	18	4.55	0.25	R^2=0.82 Coeff var=0.52	
	Sum	26	25.81			
Y_3[%] Capsule collection rate	***A***	2	33.69	16.85	0.81	0.4613
	B	2	19.96	9.98	0.48	0.6273
	C	2	53.76	26.88	1.29	0.2998
	D	2	23025.30	11512.65	551.99	<0.0001
	Model	8	23132.74	2891.59	138.64	<0.0001
	Error	18	375.41	20.86	R^2=0.98 Coeff var=6.46	
	Sum	26	23508.15			

Index	Variance Sources	*DF*	*Anova SS*	*Mean Square*	*F* value	*P* value
Y_4[%] Flax plants winding rate	***A***	2	21.19	10.60	3.71	0.0449
	B	2	8.31	4.15	1.45	0.2602
	C	2	3.87	1.93	0.68	0.5212
	D	2	12.54	6.26	2.19	0.1406
	Model	8	45.90	5.74	2.01	0.1049
	Error	18	51.48	2.90	R^2=0.47 Coeff var=193.96	
	Sum	26	97.38			

Note: P<0.05(significant,); P<0.01(highly significant,**)*

According to the results of the capsule brushing test in the early stage (*Xu et al., 2021*), the optimal clearance of comb teeth selected in this test was 4 mm, when different shapes of comb teeth cross section are installed under this clearance, the capsule can be brushed off and the capsule removal rate is very high. The effects of comb tooth cross section shape, centrifugal fan air volume and other factors on capsule breaking rate respectively were significant, extremely significant and insignificant. This is because the capsule is in direct contact with the comb tooth, the impact force between the capsule and the fan blade and the collection box is also different for the different wind force of the centrifugal fan. Therefore, the degree of capsule breaking is different due to the different shapes of the comb tooth cross section and different fan air volume. The influence of the air volume of centrifugal ventilator and other factors on capsule collection rate respectively was extremely significant and insignificant, this is because the capsule is mainly collected by the fan, so the greater the air volume of the fan, the better the collection effect of the capsule. The effects of comb tooth cross section shape and other factors on plant winding rate respectively were significant and insignificant. This is due to the direct contact between the plant and the comb teeth, the damage degree of the plant is different with different shapes of the comb teeth cross section, this results in the different plant winding rates.

Experimental Verification

Under the conditions of the optimal experiment parameters combination, the test bench was tested and verified, and the test verification results are shown in 0. The capsule removal rate was 96.45%, the capsule breaking rate was 98.79%, the capsule collection rate was 95.65%, and the plant winding rate was 2.52%. The results indicating that the combing, collection and anti-entanglement effects of the test bench were better.

Table 7

Experiment results of the test bench verification test

Test index	Test number			Average value
	1	2	3	
Y_1[%], Capsule removal rate	98.13	94.75	96.48	96.45
Y_2[%], Capsule shell breaking rate	98.76	99.48	98.12	98.79
Y_3[%], Capsule collection rate	93.46	97.15	96.35	95.65
Y_4[%], Flax plants winding rate	2.72	2.86	1.99	2.52

CONCLUSIONS

In this paper, the comb-brush air-suction composite flax capsule harvesting test bench was designed, on the basis of the harvesting methods of obtaining flax's capsule firstly and then breaking and threshing it. Single-factor tests and multi-factor orthogonal tests of each test factor were conducted to analyse the significant differences in the effects of each test factor on each test index and the order of effects, the results of the orthogonal test showed that the combing, collecting and anti-entanglement effects of the test bench were good. It provides a feasible solution to solve the problem of plant winding thresher roller in the process of mechanized flax harvesting and avoid the phenomenon of flax broken straw blocking the sieve hole. The test bench has a compact structure, easy to install and disassemble, and reasonable transmission.

The flax capsule material collected by the test bench is semi-threshing material, with little straw in the material, which is conducive to subsequent shell breaking and threshing of the capsule. It provides the basis of components and theoretical reference for the innovative design of flax harvester. It lays a theoretical basis and data basis for the design of comb-brush air-suction composite flax capsule harvesting device. So there are great prospects for application.

ACKNOWLEDGEMENT

This research was supported by the science and technology Innovation Fund project of Shanxi Agricultural University (Zdpy201802 and Zdpy201906).

REFERENCES

[1] Dai F., (2020), *Study on separation and cleaning mechanism and key technology of flax threshing material (胡麻脱粒物料分离清选机理与关键技术研究)*. PhD dissertation, Gansu Agricultural University, Lanzhou/China;

[2] Dai F., Zhao W. Y., Liu G.C., Zhang S.L., Shi R J, Wei B. (2019), Design and test of separating and cleaning machine for flax threshing material (胡麻脱粒物料分离清选机设计与试验), *Transactions of the Chinese Society for Agricultural Machinery*, Beijing/China, vol.50, issue 8, pp.140-147;

[3] Dai F., Zhao W.Y., Song X.F., Shi R.J., Liu G.C., Wei B. (2020), Parameters optimization and test on separating and cleaning machine for flax threshing material (胡麻脱粒物料分离清选作业机参数优化与试验), *Transactions of the Chinese Society for Agricultural Machinery*, Beijing /China, vol.51, issue 7, pp.100-108;

[4] Du X.B., He J.L., He Y.Q., Fang D W. (2020), Design and experiment of eccentric swing combing device for Cerasus humilis, *INMATEH-Agricultural engineering*, Bucharest/ Romania, vol.60, issue1, pp.89-98;

[5] Fang D.W., He J.L., He Y.Q., Du X B, Yi M, Jing Y, Du J J. (2019), Design and experimental of comb - tooth Cerasus humilis picking test bench (梳齿式钙果采摘试验台的设计与试验) *Journal of Gansu Agricultural University*, Lanzhou/China, Vol.54, Issue 5, pp. 212−218+231;

[6] Li D.P., Liu F., Zhao M.P., Yue Y., Zhang T., Lin Z. (2019). Structure design and performance test of pneumatic precision seed metering device for millet (气力式谷子精量排种器结构设计及性能试验), *Journal of China Agricultural University*, Beijing/China, vol.24, issue 11, pp.141-151;

[7] Shi R.J., Dai F., Zhao W.Y, Zhang S. L., Zhang F. Wi, Liu X. L. (2019), Design and test of full feed type flax thresher (全喂入式胡麻脱粒机的设计与试验), *Journal of China Agricultural University*, Nanjing/China, vol.24, issue 8, pp.120-132;

[8] Shi R J, Dai F, Liu X. L., Zhao W. Y., Zhai J. F., Zhang F. W., Qin D. G. (2021), Design and test of crawler-type hilly and mountainous flax combine harvester (履带式丘陵山地胡麻联合收割机设计与试验), *Transactions of the Chinese Society of Agricultural Engineering*, Beijing/China, vol.37, issue 05, pp.59-67;

[9] Xu F L, He J L, Du X B, Fang D W, He Y Q, Yi M. (2021), Design and test of comb brush test bed for flax capsule (梳齿式亚麻蒴果梳刷试验台的设计与试验), *Journal of Gansu Agricultural University*, Lanzhou / China, vol. 56, issue 03, pp.159-167+175;

[10] Xie J. H., Tang W., Chao S. L., Han Y. J., Zhang Y., Ynag Y. X., Li K.J. (2020), Design and test of compound type residual film recovery machine with tooth chain (齿链复合式残膜回收机设计与试验), *Transactions of the Chinese Society of Agricultural Engineering*, Beijing/China, vol. 36, issue 1, pp.11-19;

[11] Zhang L. M., Cao H. F., Gong Y. F., & Gao L. H. (2008), Research and design of traction flax thresher of 5YF-150 (5YF-150 型牵引式亚麻翻麻脱粒机的研究设计), *Agricultural mechanization research*, Harbin / China, issue 9, pp.78-80;

[12] Zhao W. C., Gong Y. F., Zhang L. M. (2010), Design of traction type flax thresher (牵引式亚麻脱粒机的设计), *Agricultural machinery*, Beijing/China, issue 11, pp.71-72.

EFFECT OF TINE FURROW OPENER ON SOIL MOVEMENT LAWS USING THE DISCRETE ELEMENT METHOD AND SOIL BIN STUDY

/

基于 EDEM 仿真与土槽试验的移动式开沟器土壤扰动规律研究

Chengyou SONG[1)], Xiangcai ZHANG[*1)], Hui LI[2)], Yuchun LV[1)], Yonggang LI[1)], Xianliang WANG[1)], Zhongcai WEI[1)], Xiupei CHENG[1)]

[1)]School of Agricultural and Food Science, Shandong University of Technology, Zibo (255000), China;
[2)]Shandong Academy of Agricultural Machinery Sciences, Jinan (250010), China
Tel: +86-15169235925; E-mail: zxcai0216@163.com
Corresponding author: Xiangcai Zhang
DOI: https://doi.org/10.35633/inmateh-68-35

Keywords: *tine furrow opener, discrete element, soil disturbance, high-speed photography*

ABSTRACT

The mechanism of furrow opener-soil interaction plays an important role in analyzing the process of no-till planting furrow opener. In order to study the disturbance effect of the furrow opener on the loam soil, firstly, the three-dimensional model of the furrow opener was established by using SolidWorks. Secondly, the 3D discrete element model of furrow opener-soil interaction was established by EDEM software. Combined with the indoor soil bin test bench and high-speed camera technology, the micro-disturbance and macro-disturbance behavior of the furrow opener on soil at different positions, speeds and operating depths were compared and analyzed. The results showed that, the disturbance range of soil was decreased with the increase of the distance between the furrow opener and the soil. At different locations, the disturbance range of soil from large to small was the surface layer, the shallow layer and the middle layer. Under the conditions of three different layouts of furrow openers, through the comparison of the soil trench test and the simulation test, it was determined that the furrow openers in a staggered layout would be beneficial to reduce the degree of soil disturbance. In the trenching process, the soil movement velocity was decreased with the increase of the distance between the soil and the furrow opener, and the distribution curves of the same-speed soil particles were basically consistent with the curves of the furrow opener. The average velocities of soil particles with different velocities and depths in different directions were the surface layer, the shallow layer and the middle layer. However, there were differences in the maximum velocities of soil particles in different directions. By comparing the data obtained from the simulation test and the soil bin test, it was found that the parameters obtained from the simulation and the test were basically consistent, and it was determined that the discrete element simulation could simulate the soil disturbance behavior of the furrow opener more accurately. The relative errors of cross-sectional area of the front furrow opener and the rear furrow opener were 2.48 % and 5.2 %, respectively. The relative errors of the dynamic soil rate of the front furrow opener and the rear furrow opener were 0.25 % and 5.12 %, respectively.

摘要

开沟器—土壤之间的相互作用机理对于分析开沟器的免耕作业过程有着重要的作用。为研究开沟器对土壤的扰动作用，首先利用 SolidWorks 建立开沟器三维模型；其次使用 EDEM 软件建立开沟器-土壤相互作用的三维离散元模型。结合室内土槽试验台以及高速摄像技术，对比分析不同位置、不同速度、不同作业深度下开沟器对土壤的微观扰动以及宏观扰动行为。结果表明，土壤的扰动范围会随着与开沟器之间距离的增大而逐渐减小；不同位置土壤的扰动范围由大到小依此为表层、浅层、中层。在开沟器 3 种不同布局方式的条件下，通过对土槽试验和仿真试验的对比，确定开沟器以相互交错的布局方式，会有利于减小土壤的扰动程度。在开沟过程中，土壤的运动速度会随着与开沟器之间距离的增大而逐渐减小，土壤颗粒的等速度分布曲线与开沟器的切土刃口弧线基本吻合；不同速度、不同深度的土壤颗粒在不同方向上的平均速度由大到小均为表层、浅层、中层；但土壤颗粒在不同方向上的最大速度存在着差异。通过对仿真试验与土槽试验获得的数据进行对比，发现仿真与试验获取的各项参数基本一致，确定离散元仿真能够较准确的模拟开沟器对土壤的扰动行为；前排开沟器和后排开沟器的沟型截面积相对误差分别为 2.48%、5.2%，前排开沟器和后排开沟器的动土率相对误差分别为 0.25%、5.12%。

INTRODUCTION

As the key tillage component of no-tillage drill *(Zhang et al., 2016)*, furrow opener is conducive to forming a good seedbed environment. At the same time, the tine furrow opener is an important ditching component in the process of sowing and trenching. Soil disturbance process has always been a complex process, which is mainly affected by the difference of soil spatial distribution, the dynamics of tillage components, and the movement and breakage of soil itself *(Fang et al., 2016; Fang et al., 2016)*. Therefore, it is extremely difficult to analyze the behavior of furrow opener on soil disturbance. And the traditional test method cannot accurately describe the micro-disturbance movement of soil caused by the furrow opener during the tillage process.

In recent years, researchers have mainly analyzed soil-tillage component interactions through simulation software. At present, the main methods commonly used include finite element method (FEM) and discrete element method (DEM). The finite element method (FEM) studies the material as a continuum, but it is difficult to simulate the disturbance behavior of soil and the interaction between the soil and the furrow opener *(Abo-Elnor et al., 2004; Fielke, 1999; Tagar et al., 2015)*. The discrete element method (DEM) can be used to simulate the *macroscopic and microscopic* deformation of granular objects and research materials, allowing the formation and destruction of contact between granular materials *(Huang et al., 2016)*. Domestic and foreign scholars have conducted extensive research on the operating characteristics of furrow openers based on discrete element method (DEM) *(Barr et al., 2020; Chen et al., 2013; Matin et al., 2014; Ucgul et al., 2015; Ucgul et al., 2017; Wang et al., 2021; Wang et al., 2022; Zhang et al., 2007)*. For example, *Yu et al., (2009),* used the DEM to study the opening process of the furrow opener, analyzed the working resistance of the furrow opener under different conditions, and proved the feasibility of using the discrete element method (DEM) to analyze the operating process of the furrow opener by comparing the actual test results with the simulation results. *Ucgul et al. (2014)* used different discrete element contact models to simulate the furrow opener in the case of non-cohesive soil and cohesive soil respectively, and verified the reliability of the discrete element method (DEM). By using the discrete element method (DEM), *Gou et al. (2012)* found that when the operating depth was fixed, with the increase of operating speed, the vertical force of the furrow opener increased slightly, while the horizontal working resistance increased greatly. Through the discrete element simulation, *Liu et al. (2021)* determined that under the condition of a certain width of the furrow opener, with the increase of the sowing depth and the angle of penetration, the working resistance was on the rise, and the angle of penetration had the greatest influence on the working resistance. Under the condition of a certain angle of penetration or sowing depth, with the increase of the width of the furrow opener, the working resistance did not change significantly. Through simulation, *Zhao et al. (2017)* determined that the working resistance of the furrow opener increased with the increase of soil moisture content under a certain depth, and the change of soil disturbance by the furrow opener was not obvious under the condition of constant depth and moisture content. The existing researches mainly focused on the macro-disturbance behavior of soil and the effects of individual furrow opener on soil, but there lacks the exploration of micro-disturbance behavior of soil under different conditions, also the law of soil disturbance and the interaction effect of tine furrow openers need further study.

Therefore, the objective of this study was to analyze the disturbance behavior of the farmland soil by the tine furrow opener, and the soil bin test bench was used to carry out the ditching test with the comprehensive utilization of DEM and high-speed camera during the tillage process. It focused on the study of the disturbance process of seedbed and the interaction effects between adjacent furrow openers. The micro-disturbance movement and macro-disturbance behavior of the soil was also analyzed under different operating conditions (different furrow depths, different operating speeds, different position relationship of furrow openers and different layout method), that can provide experimental basis for the design and optimization of the structure of the furrow opener and the layout of the tine furrow opener.

MATERIALS AND METHODS

Description of tine furrow opener

As the soil touching parts, the tine furrow opener directly comes in contact with the soil, and the structure parameters of the furrow opener affects the seedbed environment during the seeding operation. Rake angle (α) and penetration clearance angle (β) were the main operating parameters. The researches showed that the rake angle (α), edge of tine furrow opener and the ground surface, will raise the soil layer and go against the operation of inserting into the soil when the rake angle is too large, will make the shovel tip of the furrow opener too long and reduce the strength when the rake angle is too small *(Jia et al., 2020; Liu et al., 2021; Manuwa et al., 2012; Singh et al., 2016; Ucgul et al., 2014; Yao et al., 2009)*. The penetration clearance angle (β),

between the bottom of the furrow opener and the ground surface, will affect the quality of backfilling soil when the angle is too large, and the small angle will reduce the penetration performance *(Jia et al., 2020; Zhang et al., 2016)*. Therefore, the tine furrow opener, shown in Fig. 1, was designed as the test part to analyze its effects on soil disturbance, and its structure diagram was shown in Fig. 1. The height of the furrow opener (h) was 540 mm, the length of the shovel handle (L) was 100 mm, the width of the furrow opener (d) was 40 mm *(Zhang et al., 2016)*, the rake angle (α) was 55° *(Yao et al., 2009)*, and the penetration clearance angle (β) was 5°.*(Wang et al., 2021)*

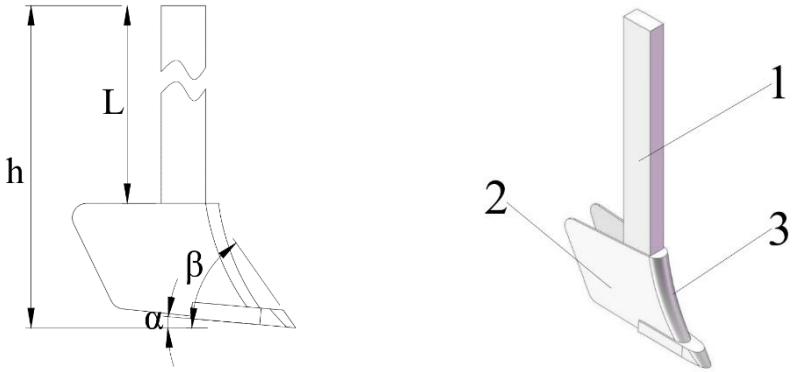

Fig. 1 - Structure parameter diagram of furrow opener

1 – Shovel handle; 2 – Retaining plate; 3 – Cutting edge

h: Height of the furrow opener; L: Length of the shovel handle; α: Rake angle; β: Penetration clearance angle

Site and equipment description

The indoor experiment was carried out in the laboratory of the Conservation Tillage Innovation Team, Shandong University of Technology. The soil bin test bench with control the system for adjusting parameters was used to analyze ditching experiment, and the structure of the soil bin test bench was designed by Conservation Tillage Innovation Team (Fig. 2b). The soil bin test bench was mainly composed of frame, mobile device, lifting device and control system. The mobile device adopted the form of sliding block and linear cylindrical guide rail to realize the linear movement of the device. The lifting device, mounted on the moving beam, controlled the ball screw through the stepper motor to achieve the upper and lower displacement of the sliding table. The control system was mainly composed of intelligent serial screen, Arduino controller, photoelectric limit switch sensor and speed encoder. The technical parameters of the soil bin test bench were shown in Table 1.

Input the corresponding control signal to the control the system through the touch screen, and transmitted the obtained signal to the stepper motor driver to control the stepper motor to rotate forward and reverse at the expected speed. At the same time, the stepper motor transmitted the power to the moving beam through the sprocket-chain mechanism, which drove the moving beam to move horizontally along the cylindrical guide rail. The lifting system was mounted on the moving beam and moved laterally with the moving beam, and the mounting plate of the tillage parts on the lifting system moved up and down with the movement of the ball screw mechanism. The control signal can control the rotation of the motor at the top of the lifting system, which in turn drove the mounting plate of the tillage component to move up and down with the ball screw mechanism to realize the adjustment of the working depth. The schematic diagram of the control system was shown in Fig. 2c.

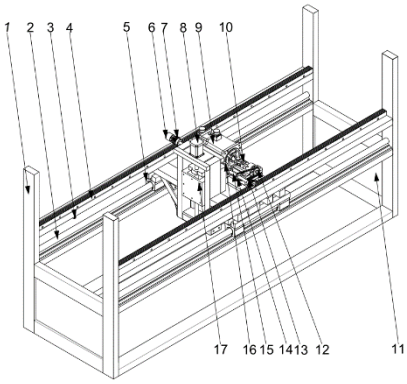

(a) Schematic diagram of soil bin structure

(b) Actual diagram of soil bin structure

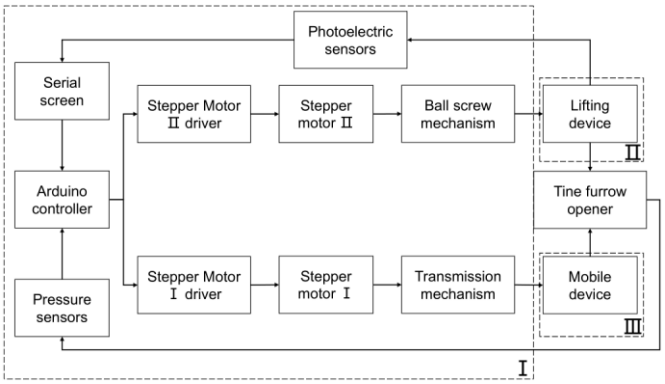

(c) Schematic diagram of the control system

Fig. 2 - Soil bin test bench

1 – Frame; 2 – Linear cylindrical guide; 3 – Photoelectric sensors; 4 – Rack; 5 – Slider; 6 – Speed encoder; 7 – Gear; 8 – Stepper Motor Ⅱ; 9 – Stepper Motor Ⅰ; 10 – Drive shaft Ⅰ; 11 – Acrylic sheet; 12 – Driving wheel; 13 – Chains; 14 – Driven wheel; 15 – Drive shaft Ⅱ; 16 – Bearing housing; 17 – Lifter; Ⅰ – Control system; Ⅰ –Mobile device; Ⅲ – Lifting device

Table 1

Technical parameters of test bench

Projects	Parameter
Machine size (m)	8×1×1
Horizontal velocity (m·s^{-1})	0-1.62
Maximum traction (N)	649
Lifting displacement (mm)	0-300
Maximum lifting force (N)	13572

There are different types of furrow opener arrangements. According to the different crops and the structure of the planter, the furrow openers were arranged on the planter in single-row (Fig. 3b) and multi-row configurations (Fig. 3a). In order to analyze the effect of furrow openers on soil disturbance and the interaction between multiple furrow openers, the position of the furrow openers needed to be adjusted during the trenching process.

In order to simulate the ditching process of no-tillage planter, the suspension bracket, made up of aluminum profiles and angular codes, were fixed on the lifting device, and the angular codes were used to connect aluminum profiles. Then the test tine furrow openers can be mounted on the suspension bracket by U-shaped bolt respectively. The suspension bracket, which may contain multiple beams according to experiment requirements, was shown in Fig. 3. Before the test, it was necessary to set the motion parameters (operation speed and operation depth) of the tillage parts through the touch screen according to the experimental design, and the position of each furrow opener needed to be installed according to the arrangement requirements.

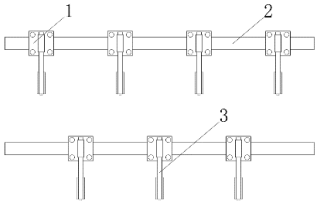

(a) Multi-row furrow opener layout

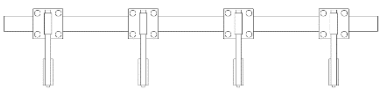

(b) Single-row furrow opener layout

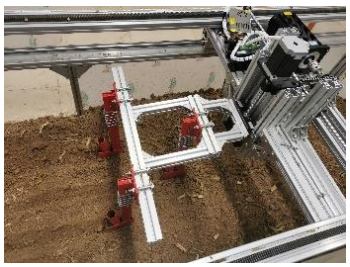

(c) Connection diagram of furrow opener

Fig. 3 - Layout diagram of furrow opener

1 – Fixtures; 2 – Rack; 3 – Furrow opener

During the experiment, in order to ensure that the soil parameters in the soil bin were close to the soil environment of the farmland, the tillage tool was used to loosen the soil and the soil was compacted. Then the appropriate amount of water was sprayed on the treated soil surface, and the ploughing tools were used to loosen the soil again when the water went deep into the soil. Each treatment was repeated three times before the ditching experiment. The soil texture in the soil bin was loam. The samples of test soil in soil bin were used to measure the moisture content by oven drying method and GZX-9146MBE dryer. The soil bulk density was measured by weight method. Soil aggregates analyzer (TPT-100) was used to measure the proportions of soil water-stable aggregates of the test soil by wet-sieving method. Soil conditions of the soil bin were included in Table 2.

Table 2

Technical parameters of test bench

Soil type	Depth (cm)	Soil moisture content (%)	Soil dry bulk density ($g \cdot cm^{-3}$)	Proportions of soil water-stable aggregates				
				> 5 mm	5-2 mm	2-1 mm	1-0.5 mm	<0.5 mm
Loam	0-3	11.36	1.258	12.3	23.6	22.4	30.5	11.2
	3-6	14.57	1.274	10.2	32.5	14.6	27.5	15.2
	6-10	17.13	1.293	9.98	27.8	29.7	23.4	9.12

When the speed of the seeder is too large, the operating performance of the seed rower will be reduced *(Ballel.Z., Moayad, 2009; Liu et al., 2009; Yao et al., 2007)*. In order to ensure the stability of the seed rower, the operating speed selected for this test was 1 m/s, and the operating speeds of 0.8, 1.2 m/s were selected as the control experiment. According to the agronomic requirements *(Wang, 2014)*, the trenching depth of this experiment was 50 mm, and the trenching depth of 100 mm was selected as the control experiment. During the experiment, the OSG030 - 790UM high-speed camera, with the time resolution of 790 frames/s, was used to record the ditching process of the furrow opener. And the AMCAP software was used to obtain the dynamic video at a specific location. The high-speed camera was perpendicular to the forward direction of the furrow opener, and its layout was shown in Fig. 4. Kinovea software was used to post-process the recorded video to obtain the required image and analyze the disturbance behavior of the furrow opener on the soil during the trenching process.

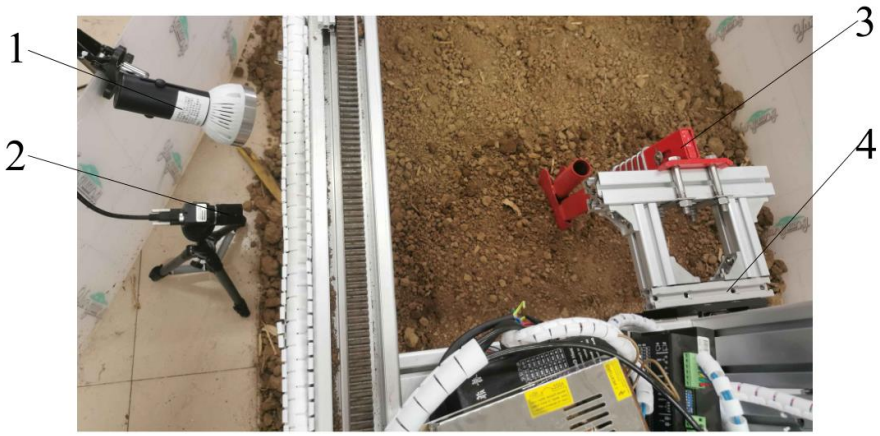

Fig. 4 - Location and schematic of high-speed camera

1 – Fill light; 2 – High-speed camera; 3 – Furrow opener; 4 – Fixtures

Measurements

After the ditching experiment, the measuring tool was used to measure the ridge height (*df*), soil dumping width (T), soil cutting width (W_{fs}), and operating depth (t) after tillage. In order to ensure the accuracy of the test data, the measurements of each ditching line were carried out at three positions, and the required data were obtained by calculating the average value. All the tests were replicated for five times.

The cross-sectional area (S) of seeding furrow type and the soil disturbance rate (D) can be used as evaluation indexes to analyze the effect of furrow opener on soil disturbance. After the end of the soil bin test, soil cutting width (W_{fs}), operating depth (*t*), ridge height (*df*) and soil dumping width (T) were measured by using the ruler, as shown in Fig. 5.

Fig. 5 - Soil disturbance parameters after soil ditching

T: Soil dumping width; df: Ridge height; t: Operating depth; W: Width of furrow opener; Wfs: Soil cutting width

The cross-sectional area (S) of soil disturbance was calculated by formula (1)*(Manuwa et al., 2012; Zhang et al., 2016)*, and the soil disturbance rate (D) was calculated by formula (2)*(Yao et al., 2020)*

$$S=\frac{w+w_{fs}}{2}t \quad (1)$$

Where:

S is the cross-sectional area of furrow opener, cm^2; *W* is the width of furrow opener, cm; W_{fs} is the width of soil, cm; *t* is the operating depth, cm.

$$D=\frac{W_{fs}}{d}\times 100\% \quad (2)$$

Where:

D is the soil disturbance rate, %; W_{fs} is the width of soil, cm; d is the row spacing between furrow openers, cm, here 4 cm is taken.

Data analysis

After the simulation of opening operation, soil cutting width (W_{fs}) and operating depth (t) were measured by the clipping function of the EDEM simulation software. Then, according to Eq. (1) and (2), the cross-sectional area (S) of soil disturbance and the soil disturbance rate (D) were calculated, respectively, and compared with the test data obtained from the soil bin test. The relative error between the simulation results and the test results was calculated, which was defined as the percentage of the absolute difference between the simulation results and the test results.

Discrete element simulation test

In order to ensure the feasibility of the simulation, the following assumptions were made for the simulation process:

(1) The actual soil was simplified to a sufficient number of particles and certain quality and parameters were given to the soil particles.

(2) Hertz-Mindlin (no slip) contact model was selected for particle contact model.

(3) Tillage process was the process of furrow opener acting on soil particles at a certain speed.

Modeling of furrow opener

According to the simplification principle of numerical simulation, the furrow opener was simplified to remove the components unrelated to the operating process. The 3D model of the furrow opener was designed using SolidWorks according to the scale of 1:1 (Fig. 1), and imported into the Geometry item of EDEM in .igs format. The material properties of the furrow opener were set as the material was 45 steel, the density was 7865 kg/m^3, Poisson's ratio was 0.3, and the shear modulus was 7.9×10^{10}Pa *(Gou et al.,2012)*.

Soil particle modeling

Because the smaller the simulated soil particles are, the slower the simulation speed is and the larger the computer memory is occupied, the soil particles in the simulation are generally much larger than the actual soil particles *(Gao et al., 2022; Mak et al., 2012; Yuan et al., 2021)*. In order to improve the accuracy of the simulation of soil particles, the soil particles with a radius of 5 mm were selected in this paper *(Wang et al., 2017)*. Hertz - Mindlin (no slip) contact model was set as the contact model between soil particles, the soil density was 2550 kg/m^3, the Poisson's ratio was 0.38, and the shear model was 1.0×10^6 Pa. The accumulation angle test of soil particles was carried out, as shown in Fig. 6. The simulated accumulation angle test used a steel pipe with a radius of 15 mm, which contained 5000 soil particles. The steel tube was moved vertically upward at a uniform velocity of 0.01 m/s *(Wang et al., 2020; Wang et al., 2017)*, the simulation ended when all

particles stopped moving. The soil accumulation angle was measured using the protractor function in the EDEM software, and the comparison with Fig. 6b showed that the simulated soil particles basically matched the soil parameters in the soil bin.

(a) Simulation test (b) Soil bin test

Fig. 6 - Accumulation angle test

EDEM modeling

The contact parameters between soil particles and furrow opener were shown in Table 3 *(Fang et al., 2016; Ucgul et al., 2014; Yu et al., 2020)*. According to the operating condition of wheat no-till planter in the field and the requirement of simulation test, the virtual soil bin was established in EDEM. The basic size (length × width × height) of the soil bin was set as 2000 mm × 1000 mm × 130 mm, 350000 soil particles were generated. According to the proportion of the soil height of each layer, the number of soil particles in the surface layer, the shallow layer, the middle layer, the deep layer and the lower layer of the furrow opener were set to 60000, 60000, 60000, 60000 and 110000 respectively. The simulation time step was 20%, and the grid cell was 2.5 times of the minimum soil particle size. The established virtual soil bin simulation model was shown in Fig. 7.

Table 3

Contact parameters of discrete element simulation

Parameter	Numerical value
Soil particle radius, R1 (mm)	5
Soil density, ρ (kg·m^{-3})	2550
Soil Poisson's ratio, μ	0.38
Soil shear modulus, G (Pa)	1.0×10^{6}
Furrow opener density, ρ_1 (kg·m^{-3})	7865
Furrow opener Poisson 's ratio, μ_1	0.3
Shear modulus of the furrow opener, G_1 (Pa)	7.9×10^{10}
Soil-soil recovery coefficient	0.6
Soil-furrow opener recovery coefficient	0.6
Soil - soil static friction coefficient	0.6
Static friction coefficient of soil-furrow opener	0.6
Soil-soil dynamic friction coefficient	0.4
Dynamic friction coefficient of soil – furrow opener	0.05

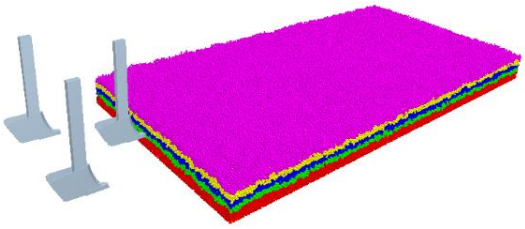

Fig. 7 - Virtual soil bin model

RESULTS AND DISCUSSION

Analysis of soil disturbance state

In order to analyze the disturbance behavior of soil particles at different depths, the soil was divided into five layers: the surface layer, the shallow layer, the middle layer, the deep layer and the lower layer of the furrow opener. Except the lower layer of the furrow opener, the depth of each layer was 25 mm, as shown in Fig. 8. In order to understand the disturbance behavior of the furrow opener on the soil during the trenching process, the forward direction and the vertical direction of the furrow opener were analyzed. Fig. 8a showed the longitudinal section of soil distribution, which was mainly used to analyze the disturbance behavior of soil caused by the furrow opener in the forward direction. Fig. 8b showed the transverse section of soil distribution, which was mainly used to analyze the disturbance behavior of soil caused by the furrow opener in the vertical forward direction.

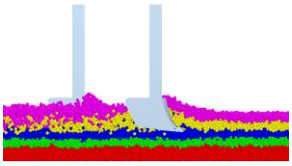
(a) Longitudinal section of soil distribution

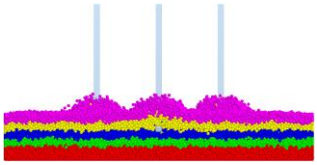
(b) Transverse section of soil distribution

Fig. 8 - Soil distribution

Mechanism analysis of soil disturbance

In the simulation process, the process of soil disturbance by the furrow opener was shown in Fig. 9. At 0.05 s, the front row furrow opener shovel tip completely entered the soil. At 0.22 s, the front row furrow opener completely entered the soil. At 0.3 s, the rear row furrow opener shovel tip completely entered the soil. At 0.47 s, the rear row furrow opener completely entered the soil. At 1 s, the front row furrow opener was in the middle of the trenching process. And at 1.25 s, the rear row furrow opener was in the middle of the trenching process.

It can be seen from Fig. 9 that in the trenching process of the furrow opener, the disturbance degree of the surface soil was the largest, followed by the shallow soil, followed by the middle soil, and the disturbance degree of the deep soil was the smallest. When the shovel tip of the furrow opener entered the soil (0.05, 0.3 s), the shallow soil and the middle soil started to move under the extrusion and shearing action of the shovel tip, respectively. The shallow soil pushed the surface soil upward to make it slightly elevated at the surface, while the middle soil moved downward to squeeze the deep soil and restrict its movement. When the furrow opener completely entered the soil (0.22 s, 0.47 s), under the cutting action of the furrow opener, the soil moved forward and upward with the furrow opener, expanding the longitudinal disturbance range of the soil. Under the pressing action of the retaining plate and the cutting edge, the soil moved forward with the furrow opener and moved to both sides, which increased the lateral disturbance range of the soil. As the furrow opener continued to work (1, 1.25 s), the shear force between the soils will reach the limit of the shear strength. At this time, the soil will undergo shear failure, and a fan-shaped soil fragmentation contour will be formed on the surface, and the contour will gradually expand to both sides along the direction perpendicular to the retaining plate as the furrow opener advanced. Based on the interaction between the shear effect of the cutting edge and the soil, the broken soil was further broken by the extrusion of the retaining plate. At this time, the movement of soil became more complex. Part of the soil moved forward and on both sides under the compression of the furrow opener, while the other part of the soil moved backward along the retaining plate through the friction with the furrow opener, and fell back to the ground under the action of gravity to backfill the seed trench. Comparing the disturbance of the front row and rear row furrow openers on the soil, it can be seen that at the same position, the disturbance behaviors of the front row and rear row furrow openers on the soil were basically the same.


0.05 s 0.22 s 1 s

Fig. 9a - Soil disturbance process under high-speed camera

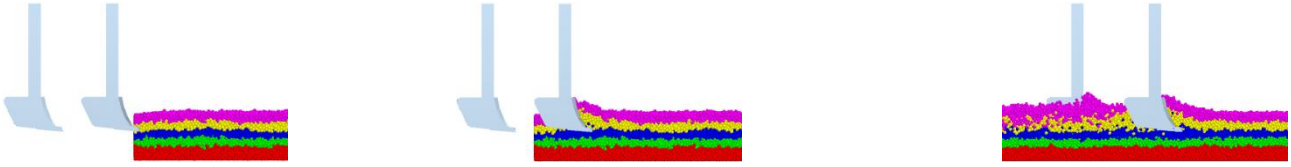
0.05 s 0.22 s 1 s

Fig. 9b - Longitudinal disturbance section of the front row furrow opener

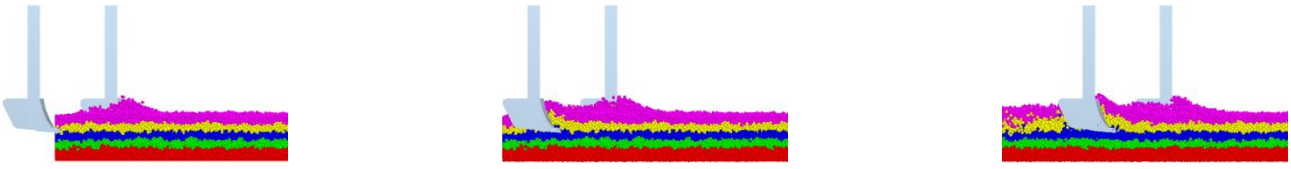
0.3 s 0.47 s 1.25 s

Fig. 9c - Longitudinal disturbance section of the rear row furrow opener

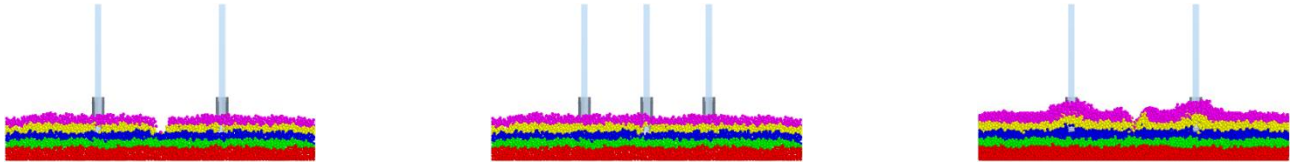

Fig. 9d - Longitudinal disturbance section of the front row furrow opener

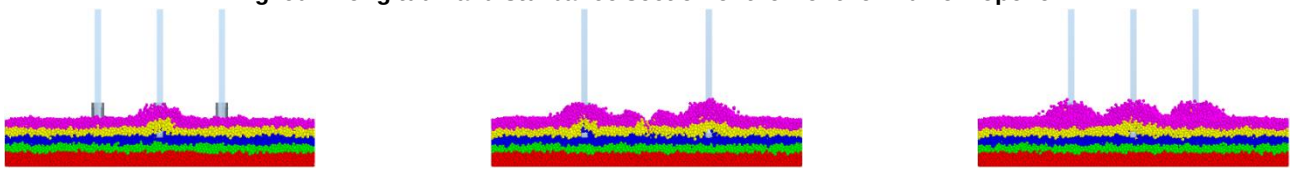

Fig. 9e - Longitudinal disturbance section of the rear row furrow opener

Analysis of soil disturbance state at different positions

In order to study the effect of the distance between adjacent furrow openers on soil disturbance, the soil at 1 s position was analyzed between horizontally and vertically (Fig.9). According to the disturbance of the soil in the transverse and longitudinal directions by the furrow opener, the 0 mm position of the profile was the transverse and longitudinal center of the front furrow opener. The longitudinal profile interval was 50 mm, and the transverse profile interval was 100 mm. The soil disturbance at different positions was shown in Fig.10.

It can be seen from Fig. 10a that the longitudinal disturbance degree of the furrow opener to the soil gradually decreased with the increase of the horizontal distance between the soil and the furrow opener. At the position 50 mm away from the furrow opener, the degree of soil disturbance gradually decreased, and the reduction degree of soil disturbance range was the lowest in the middle layer, followed by the shallow layer, and finally the surface layer. The degree of soil disturbance tended to stabilize at position 100 mm and above from the furrow opener. The main reason was that the influence of the soil by the force of furrow opener was decreased with the increase of the distance between the soil and the furrow opener.

It can be seen from Fig. 10b that the horizontal disturbance degree of the furrow opener to the soil gradually decreased with the increase of the longitudinal distance between the soil and the furrow opener. In the longitudinal center position of the furrow opener (0 m), the uplift of the soil by the furrow opener was small. At the center of the furrow opener shovel handle (100 mm), the soil was subjected to the pressing force and shearing force of the retaining plate, and was lifted to both sides along the forward direction of the furrow opener, which expanded the lateral disturbance range of the furrow opener. At the furrow opener tip position (200 mm), the soil received the strongest force from the tip, so the soil was lifted the most at this position. With the increasing distance between the soil and the furrow opener (300 mm), the amplitude of soil uplift gradually decreased. The main reason was that the squeezing and shearing effect of the furrow opener on the soil and the interaction between soil and soil were decreased with the increase of the distance between the soil and the furrow opener.

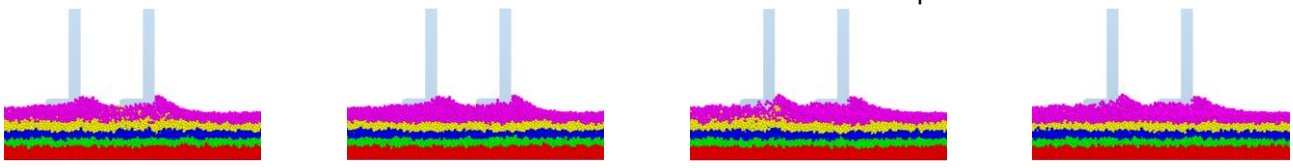

Fig. 10a - Longitudinal disturbance section of the furrow opener

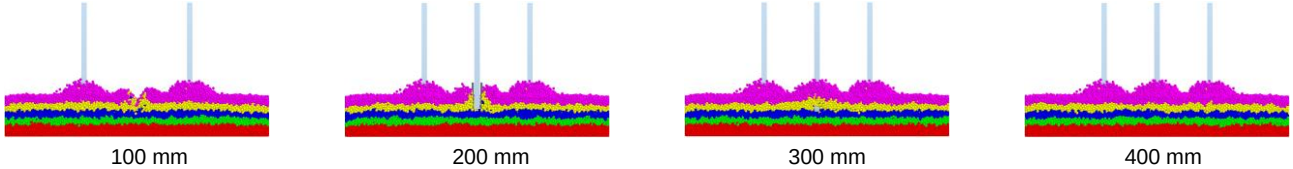

Fig. 10b - Transverse disturbance section of the furrow opener

Analysis of soil disturbance state at different operating depths

In order to analyze the soil disturbance caused by furrow opener under different operating depths, the soil disturbance of the furrow opener at 100 mm operating depth was selected for comparative analysis.

On the basis of Fig. 9, the soil at 1 s and 1.25 s was transversely and longitudinally examined to observe the disturbance of the front and rear furrow openers on the soil.

Fig. 11a showed that when the operating depth was 100 mm, the disturbance degree of the shallow soil was the largest, followed by the surface soil and the middle soil, and the deep soil was the smallest. The shallow soil was lifted upward by the squeezing action of the shovel handle, the shearing action of the cutting edge and the interaction between soil and soil, pushing the surface soil to move and making it slightly elevated at the surface. At the same time, the surface soil moved forward and upward under the squeezing action of the shovel handle, which increased the longitudinal disturbance range of the soil.

Fig. 11b showed that when the operating depth was 100 mm, the lateral disturbance range of soil was significantly larger than that when the operating depth was 50 mm. The main reason was that with the increase of the operating depth, the scope of action on the soil was also expanded. At this time, the soil was not only subjected to the shearing force of the cutting edge and the acting force between soil and soil, but also the shearing force and extrusion force of the shovel handle on the soil. The deep soil started to move under the squeezing and shearing action of the shovel tip. The downward movement of the deep soil squeezed the deep soil to restrict its movement, while the upward movement of the deep soil pushed the surface, shallow and middle soil to make it slightly elevated at the surface. Therefore, under certain conditions, the lateral disturbance range of soil will expand with the continuous increase of the depth of the furrow opener.

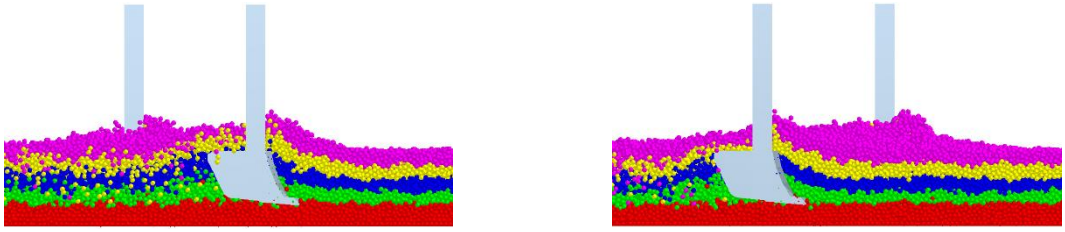

Fig. 11a - Longitudinal disturbance section of the furrow opener

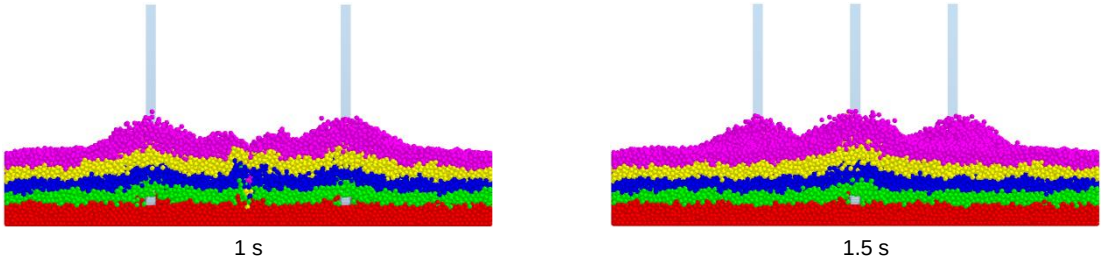

Fig. 11b - Transverse disturbance section of the furrow opener

Analysis of soil disturbance state under different layouts

In order to study the state of soil disturbance caused by the furrow opener under different arrangements, the arrangement modes of a single furrow opener and three furrow openers in parallel were selected. On the basis of Fig. 9, the soil at 1 s position was dissected laterally to observe the disturbance state of soil caused by the furrow opener.

It can be seen from Fig. 12a that ridge height was lower than that in Fig. 9e when only a single furrow opener was used. The main reason was that when a single furrow opener was used for trenching operation, the soil will only be subjected to the squeezing and shearing action of the furrow opener and the interaction between soil and soil, and will not be affected by other furrow openers, so the soil will be lifted to a lesser extent.

It can be seen from Fig. 12b that the ridge height was higher than that in Fig. 9e when three furrow openers were parallel. The main reason was that when the three furrow openers were in parallel, the soil was not only subjected to the extrusion and shear of the furrow opener and the interaction between soil and soil, but also subjected to the extrusion of the adjacent furrow openers, which made the soil lifted to a larger extent.

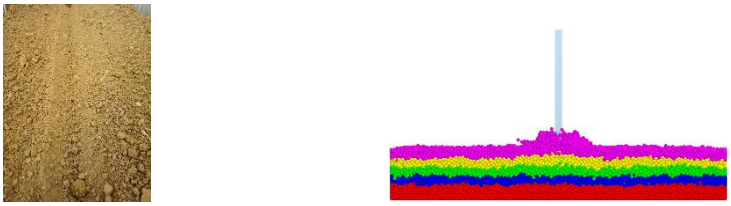

Fig. 12a - The disturbance of single furrow opener on the soil

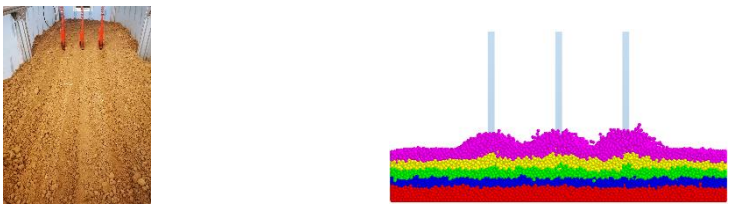

Fig. 12b - Disturbance of parallel furrow openers on the soil

Analysis of soil movement state

Analysis of soil overall movement state by furrow opener

In order to study the influence of the furrow opener on the soil movement state under different depths at different times, three positions were selected to analyze the movement velocity at different moments: the furrow opener tip into the soil (0.05, 0.3 s), the furrow opener completely into the soil (0.22, 0.47 s) and the furrow opener located in the middle of the trenching process (1, 1.25 s).

According to the color distribution of Fig. 13a, the middle soil moved forward and upward under the action of the shovel tip when the shovel tip entered the soil, and the surface soil and the shallow soil were lifted upward under the action of the middle soil. At this time, the velocity of the middle soil was the fastest, followed by the shallow soil, and least in the surface soil. When the furrow opener completely entered the soil, the soil particles with movement velocity were the most in the surface layer, followed by the shallow layer and the least in the middle layer. The closer the soil was to the furrow opener, the greater the velocity of movement, and the distribution curves of the same-speed soil particles were basically consistent with the curves of the furrow opener. At this time, the shallow soil and the middle soil were rose upward along the direction perpendicular to the shovel tip and the cutting edge. Under the extrusion and cutting action of the furrow opener and the disturbance of the shallow soil and the middle soil, the surface soil moved forward and upward. When the furrow opener was in the middle of the trenching process, the movement of the soil in front of the furrow opener was not much different from that when the furrow opener was completely in the soil. When the soil moved forward, it was also moved backward along the retaining plate through friction with the furrow opener, and fell back to the ground under the action of gravity to backfill the seed trench. As can be seen from Figure 13b, the movement of the soil during tillage of the rear row furrow opener was basically the same as the tillage process of the front row furrow opener.

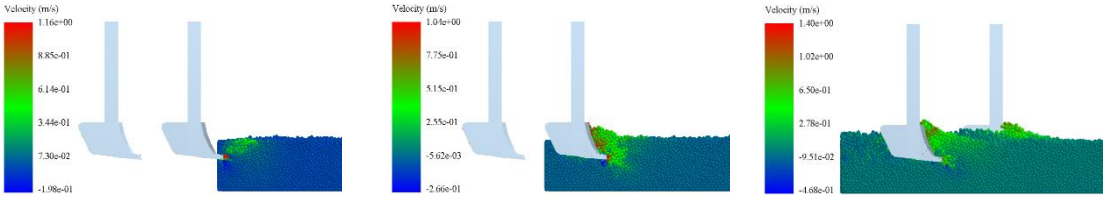

0.05 s 0.22 s 1 s

Fig 13a - Analysis of the whole movement state of soil by front row furrow opener

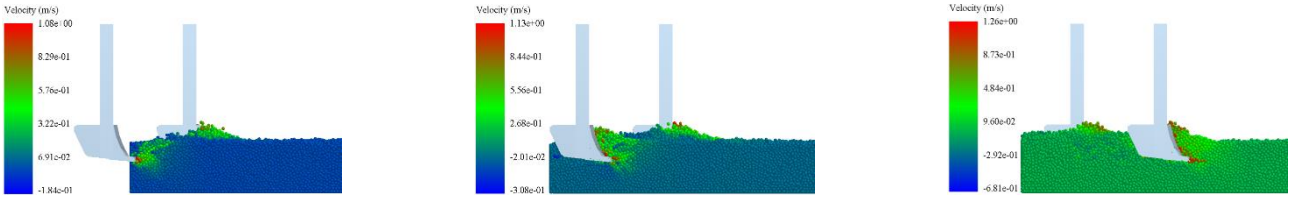

0.3 s 0.47 s 1.5 s

Fig 13b - Analysis of the whole movement state of soil by rear row furrow opener

Analysis of soil particle motion at different velocities

In order to analyze the movement state of each soil layer under different speeds of furrow opener, the operating speeds were selected as 0.8, 1 and 1.2 m/s to obtain the average horizontal, vertical and lateral speeds of the surface layer, the shallow layer and the middle layer, as shown in Fig. 14.

It can be seen from Fig. 14 that during the ditching process, the average velocities of soil at different depths were varied with the advance of the furrow opener. When the operating speed was 0.8 m/s, in the x-direction, the average velocities of the surface layer, the shallow layer and the middle layer were 0.010216, 0.006969 and 0.002948, respectively. In the y-direction, the average velocities of the surface layer, the shallow layer and the middle layer were 0.00135, 0.001133 and 0.000617, respectively. In the z-direction, the average velocities of the surface layer, the shallow layer and the middle layer were 0.003678, 0.001867 and 0.000799,

respectively. When the operating speed was 0.8 m/s, the average speeds from large to small were the surface layer, the shallow layer and the middle layer (Fig. 14a). When the operating speed was 1 m/s, in the x-direction, the average velocities of the surface layer, the shallow layer and the middle layer were 0.014108, 0.008219 and 0.003365, respectively. In the y-direction, the average velocities of the surface layer, the shallow layer and the middle layer were 0.0012896, 0.000995 and 0.000856, respectively. In the z-direction, the average velocities of the surface layer, the shallow layer and the middle layer were 0.004341, 0.002103 and 0.000807, respectively. When the operating speed was 1 m/s, the average speeds from large to small were the surface layer, the shallow layer and the middle layer (Fig.14b). When the operating speed was 1.2 m/s, in the x-direction, the average velocities of the surface layer, the shallow layer and the middle layer were 0.01808, 0.01052 and 0.003596, respectively. In the y-direction, the average velocities of the surface layer, the shallow layer and the middle layer were 0.001658, 0.001353 and 0.000868, respectively. In the z-direction, the average velocities of the surface layer, the shallow layer and the middle layer were 0.005327, 0.00286 and 0.001222, respectively. When the operating speed was 1.2 m/s, the average speeds from large to small were the surface layer, the shallow layer and the middle layer (Fig. 14c). At the same speed, the velocities of soil particles at different depths were different due to the extrusion, shear and interaction between soil and soil. As the operating speed of the furrow opener changed, the speed of the soil at the same depth in different directions will change accordingly.

It can be seen from Fig. 14 that the average velocities of the soil particles changed rapidly after the front row of furrow opener was completely inserted into the soil, and then tended to stabilize. In the x-direction, the average velocities of the surface layer, the shallow layer and the middle layer were significantly different, with the surface soil velocity being the largest, followed by the shallow soil, and the middle soil being the smallest. In the y-direction, the variation curves of average velocities of the surface layer, the shallow layer and the middle layer were basically the same. In the z-direction, the average velocities curves of the surface layer, the shallow layer and the middle layer were basically the same, and the change of the surface soil velocity was the most obvious.

The movement speeds of soil were analyzed under different times, different depths and different speeds. When the operating speed was 0.8 m/s, in the x-direction, the movement speed of the middle soil was the largest, while the movement speed of the shallow soil was slightly lower than that of the middle soil, and the movement speed of the surface soil was the smallest. In the y-direction, the movement speed of the shallow soil was the largest, and the difference between the movement speed of the surface soil and the middle soil was small. In the z-direction, the movement speed of the surface soil was the largest, and the difference between the movement speed of the shallow soil and the middle soil was small. When the operating speed was 1 m/s, in the x-direction, the movement speed of the shallow soil was the largest, and the difference between the movement speed of the surface soil and the middle soil was small. In the y-direction, the movement speed of the shallow soil was the largest, and the difference between the movement speed of the surface soil and the middle soil was small. In the z-direction, the movement speed of the middle soil was the largest, while the movement speed of the shallow soil was slightly lower than that of the middle soil, and the movement speed of the surface soil was the smallest. When the operating speed was 1.2 m/s, in the x-direction, the movement speed of the middle soil was the largest, the movement speed difference between the surface and the middle soil was small, and the movement speed of the shallow soil was the smallest. In the y-direction, the movement speed of the shallow soil was the largest, the movement speed difference between the shallow and the middle soil was small, and the movement speed of the surface soil was the smallest. In the z-direction, the movement speed of the middle soil was the largest, and the movement speed difference between the surface and the shallow soil was small, and the movement speed of the shallow soil was the smallest.

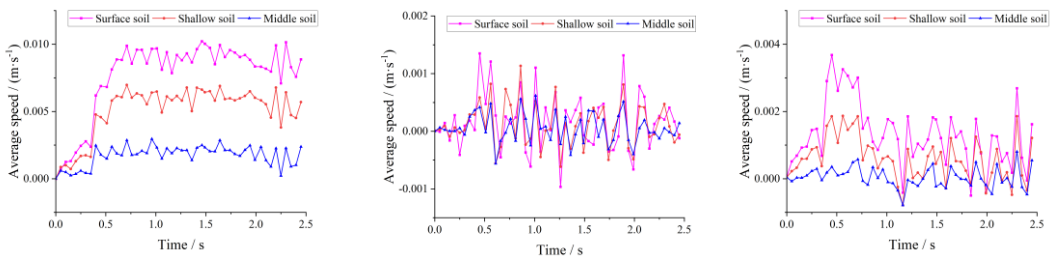

Average velocity in x-direction Average velocity in y-direction Average velocity in z-direction

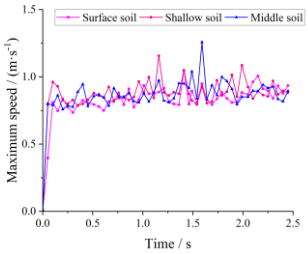

Maximum velocity in x-direction

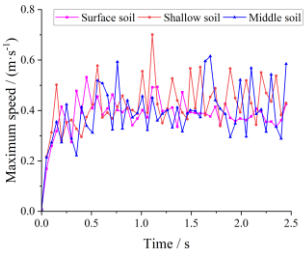

Maximum velocity in y-direction

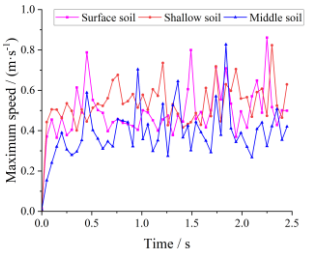

Maximum velocity in z-direction

(a) Operating speed of 0.8 m/s

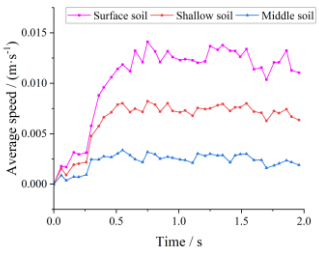

Average velocity in x-direction

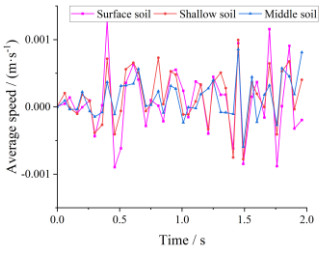

Average velocity in y-direction

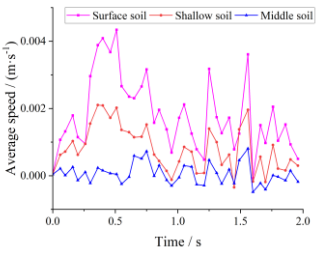

Average velocity in z-direction

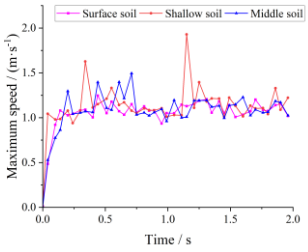

Maximum velocity in x-direction

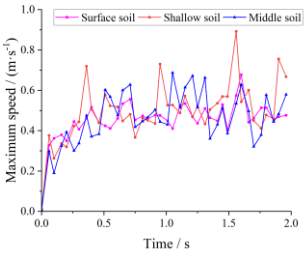

Maximum velocity in y-direction

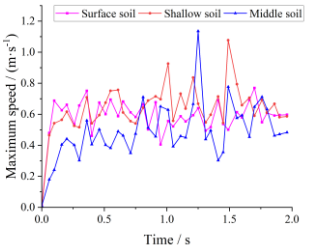

Maximum velocity in z-direction

(b) Operating speed of 1 m/s

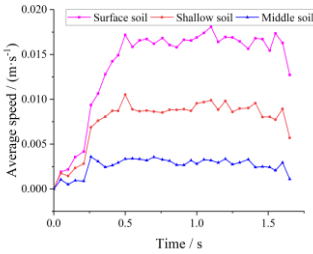

Average velocity in x-direction

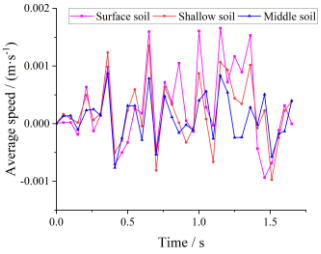

Average velocity in y-direction

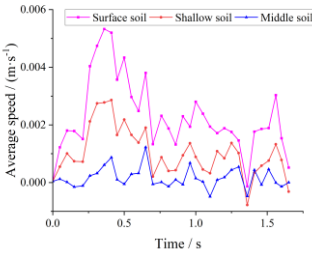

Average velocity in z-direction

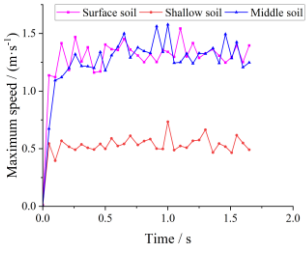

Maximum velocity in x-direction

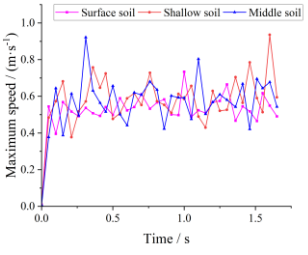

Maximum velocity in y-direction

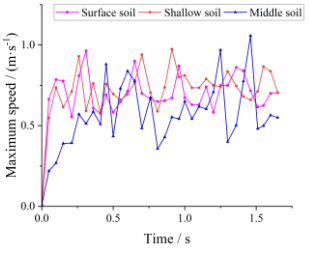

Maximum velocity in z-direction

(c) Operating speed of 1.2 m/s

Fig. 14 - Movement speed of soil at different speeds and depths

Analysis of soil disturbance effect

The data obtained from simulation and soil bin test were calculated separately, and the relative errors between the simulation and test results were calculated, as shown in Table 4.

Table 4

Soil disturbance effect analysis

Parameter	Front row simulation value	Front row test value	Relative error (%)	Rear row simulation value	Rear row test value	Relative error (%)
Ridge height (cm)	1.99	2	0.5	1.99	2.05	2.93
Dumping width (cm)	15.71	16.01	1.87	18.08	18.87	4.19
Cutting width (cm)	11.17	11.2	0.27	13.13	13.84	5.13
Operating depth (cm)	3.42	3.5	2.29	4.64	4.7	1.28
Cross-sectional area (cm^2)	25.94	26.6	2.48	39.74	41.92	5.2
Soil disturbance rate (%)	27.93	28	0.25	32.83	34.6	5.12

It can be seen from Table 4 that the experimental data of soil disturbance parameters, such as ridge height, soil dumping height, soil cutting height, operating depth and cross-sectional area of furrow opener, were slightly larger than the simulation data. Among them, the relative error of the cross-sectional area of the rear row furrow opener was the largest, which was 5.2%, and the relative error of the soil disturbance rate of the front row trench opener was the smallest, which was 0.25%. It showed that the simulation results can accurately reflect the disturbance of the soil during the trenching process of the furrow opener.

It can be seen from Table 4 that the parameters of the front row furrow openers were smaller than those of the rear row furrow openers. The reason may be that during the trenching process of the rear furrow openers, the soil moved to both sides under the action of the retaining plate, and filled back the seed furrow cultivated by the front row furrow opener under the action of gravity, making the data of the seed furrow cultivated by the front row furrow opener smaller. The disturbance process of the furrow opener to the soil provided a way of thinking about the layout of the furrow opener.

CONCLUSIONS

(1) The macro-disturbing mechanism and micro-disturbing state of soil in trenching process were analyzed by combining discrete element simulation with high-speed camera and soil bin test. The range of soil disturbance decreased with the increase of the distance between the soil and the furrow opener, and the range of soil disturbance at different locations from large to small was the surface layer, the shallow layer and the middle layer. The degree of soil disturbance by the furrow opener varied at different operating depths. At the operating depth of 50 mm, the degree of soil disturbance from large to small was the surface layer, the shallow layer and the middle layer. At the operating depth of 100 mm, the degree of soil disturbance from large to small was the shallow layer, the surface layer, the middle layer and the deep layer. Through the test comparison of three different layout methods of furrow openers, it can be seen that taking the layout of interlocking furrow openers was conducive to reducing the degree of soil disturbance, so determining a reasonable layout of furrow openers was conducive to reducing the disturbance effect of furrow openers on the soil.

(2) The velocity of soil movement gradually decreased with the increase of distance between the soil and the furrow opener, and the distribution curves of the same-speed soil particles were basically consistent with the curves of the furrow opener. The average velocities of the soil in different directions under different operating speed conditions were basically the same, from large to small was the surface layer, the shallow layer and the middle layer. At the same operating speed, soil particles under different depths were squeezed and sheared by the furrow opener, also the interactions between soil and soil were different, that resulted in the different movement speeds of soil particles. At the same depth of the soil, with the increase of the speed of the furrow opener, the speed in different directions also increased. Under different operating speed conditions, the maximum speed of soil in different directions was quite different.

(3) The discrete element simulation can accurately simulate the soil disturbance process in the trenching process. By comparing the test data obtained from simulation and test, it was found that the data obtained from simulation and test were basically consistent. The relative errors of the cross-sectional area of the front furrow opener and the rear furrow opener were 2.48% and 5.2%, respectively. The relative errors of the soil disturbance rate of the front furrow opener and the rear furrow opener were 0.25% and 5.12%, respectively.

ACKNOWLEDGEMENTS

This work was financially supported by the National Natural Science Foundation of China (Grant No. 51805300).

REFERENCE

[1] Abo-Elnor, M., Hamilton, R., & Boyle, J. T. (2004). Simulation of soil–blade interaction for sandy soil using advanced 3D finite element analysis [J]. *Soil and Tillage Research*, *75*(1): 61-73. https://doi.org/10.1016/s0167-1987(03)00156-9.

[2] Ballel.Z.Moayad. (2009). effects of biomimetic surface designs on furrow opener performance [j]. *journal of bionic engineering*, *6*(03): 280-289.

[3] Barr, J., Desbiolles, J., Ucgul, M., & Fielke, J. M. (2020). Bentleg furrow opener performance analysis using the discrete element method [J]. *Biosystems Engineering*, *189*: 99-115. https://doi.org/10.1016/j.biosystemseng.2019.11.008.

[4] Chen, Y., Munkholm, L. J., & Nyord, T. (2013). A discrete element model for soil–sweep interaction in three different soils [J]. *Soil and Tillage Research*, *126*: 34-41. https://doi.org/10.1016/j.still.2012.08.008.

[5] Fang, H. M., Ji, C. Y., Chandio, F. A., Guo, J., Zhang, Q. Y., & Arslan, C. (2016). Analysis of soil dynamic behavior during rotary tillage based on distinct element method (基于离散元法的旋耕过程土壤运动行为分析) [J]. *Transactions of the Chinese Society of Agricultural Machinery*, *47*(03): 22-28. https://kns.cnki.net/kcms/detail/11.1964.s.20160118.1043.008.html

[6] Fang, H. M., Ji, C. Y., Tagar, A. A., Zhang, Q. Y., & Guo, J. (2016). Simulation analysis of straw movement in straw-soil-rotary blade system (秸秆-土壤-旋耕刀系统中秸秆位移仿真分析) [J]. *Transactions of the Chinese Society of Agricultural Machinery*, *47*(01): 60-67. https://kns.cnki.net/kcms/detail/11.1964.s.20151113.1140.012.html

[7] Fielke, J. M. (1999). Finite element modelling of the interaction of the cutting edge of tillage implements with soil [J]. *Journal of Agricultural Engineering Research*, *74*(1): 91-101.

[8] Gao, Z. H., Shang, S. Q., Xu, N., & Wang, D. W. (2022). Parameter calibration of discrete element simulation model of wheat straw-soil mixture in Huang Huai Hai production area [J]. *INMATEH-Agricultural Engineering*, *66*(1): 201-210.

[9] Gou, W., Ma, R. C., Yang, W. Y., Fan, G. Q., Lei, X. L., Hui, K., & Yang, H. Z. (2012). Design of opener on no-till wheat seeder (小麦免耕播种机开沟器的设计) [J]. *Transactions of the Chinese Society of Agricultural Engineering*, *28*(S1): 21-25.

[10] Huang, Y. X., Hang, C. G., Yuan, M. C., Wang, B. T., & Zhu, R. X. (2016). Discrete element simulation and experiment on disturbance behavior of subsoiling (深松土壤扰动行为的离散元仿真与试验) [J]. *Transactions of the Chinese Society of Agricultural Machinery*, *47*(07): 80-88. https://kns.cnki.net/kcms/detail/11.1964.s.20160517.0944.002.html

[11] Jia, H. L., Meng, F. H., Liu, L. J., Shi, S., Zhao, J. L., & Zhuang, J. (2020). Biomimetic design and experiment of core-share furrow opener (芯铧式开沟器仿生设计与试验) [J]. *Transactions of the Chinese Society of Agricultural Machinery*, *51*(04): 44-49+77.

[12] Liu, L. J., Yang, X. J., Li, C. R., Liu, Y. C., & Liu, D. S. (2009). Design of 2BMG - 24 no-till wheat planter (2BMG-24 型小麦免耕播种机设计) [J]. *Transactions of the Chinese Society of Agricultural Machinery*, *40*(10): 39-43.

[13] Liu, R., Li, Y. J., Liu, C. X., & Liu, L. J. (2021). Design and experiment of shovel type wide seedling belt oat seeding furrow opener (铲式宽苗带燕麦播种开沟器设计与试验) [J]. *Transactions of the Chinese Society of Agricultural Machinery*, *52*(09): 89-96. https://kns.cnki.net/kcms/detail/11.1964.S.20210726.0948.004.html

[14] Mak, J., Chen, Y., & Sadek, M. A. (2012). Determining parameters of a discrete element model for soil–tool interaction [J]. *Soil and Tillage Research*, *118*: 117-122. https://doi.org/10.1016/j.still.2011.10.019.

[15] Manuwa, S. I., Ademosun, O. C., & Adesina, A. (2012). Regression equations for predicting the effect of tine width on draught and soil translocation in moderately fine textured soil [J]. *Journal of Environmental Science and Engineering B*, *1*(6B): 820-825.

[16] Matin, M. A., Fielke, J. M., & Desbiolles, J. M. A. (2014). Furrow parameters in rotary strip-tillage:

Effect of blade geometry and rotary speed [J]. *Biosystems Engineering*, *118*: 7-15. https://doi.org/10.1016/j.biosystemseng.2013.10.015.

[17] Singh, S., Tripathi, A., & Singh, A. K. (2016). Effect of furrow opener design, furrow depth, operating speed on soil characteristics, draft and germination of sugarcane [J]. *Sugar Tech*, *19*(5): 476-484. https://doi.org/10.1007/s12355-016-0499-x.

[18] Tagar, A. A., Changying, J., Adamowski, J., Malard, J., Qi, C. S., Qishuo, D., & Abbasi, N. A. (2015). Finite element simulation of soil failure patterns under soil bin and field testing conditions [J]. *Soil and Tillage Research*, *145*: 157-170. https://doi.org/10.1016/j.still.2014.09.006.

[19] Ucgul, M., Fielke, J. M., & Saunders, C. (2014). 3D DEM tillage simulation: Validation of a hysteretic spring (plastic) contact model for a sweep tool operating in a cohesionless soil [J]. *Soil and Tillage Research*, *144*: 220-227. https://doi.org/10.1016/j.still.2013.10.003.

[20] Ucgul, M., Fielke, J. M., & Saunders, C. (2015). Defining the effect of sweep tillage tool cutting edge geometry on tillage forces using 3D discrete element modelling [J]. *Information Processing in Agriculture*, *2*(2): 130-141. https://doi.org/10.1016/j.inpa.2015.07.001.

[21] Ucgul, M., Saunders, C., & Fielke, J. M. (2017). Discrete element modelling of tillage forces and soil movement of a one-third scale mouldboard plough [J]. *Biosystems Engineering*, *155*: 44-54. https://doi.org/10.1016/j.biosystemseng.2016.12.002.

[22] Wang, J., Jiang, K. L., Yu, F., Chen, Z. H., Yu, Y. J., & Lai, Q. H. (2021). The simulation design and experiment of reverse ditcher for small grain coffee cultivation based on discrete element method (基于离散元法的小粒咖啡种植逆转开沟器的仿真与设计) [J]. *Journal of Agricultural Mechanization Research*, *43*(01): 62-69. https://doi.org/10.13427/j.cnki.njyi.2021.01.012.

[23] Wang, J. Z., Sun, W., Wang, H. C., Zhang, H., & Liu, X. L. (2021). Research of long wing and sharp angle opener (尖角长翼型开沟器的研究) [J]. *Journal of Agricultural Mechanization Research*, *43*(11): 64-70. https://doi.org/10.13427/j.cnki.njyi.2021.11.012.

[24] Wang, L. M., Fang, S. Y., Cheng, H. S., Meng, H. B., Shen, Y. J., Wang, J., & Zhou, H. B. (2020). Calibration of contact parameters for pig manure based on EDEM (基于 EDEM 的猪粪接触参数标定) [J]. *Transactions of the Chinese Society of Agricultural Engineering*, *36*(15): 95-102.

[25] Wang, S. J. (2014). Analysis on advantages and techniques of wheat planting in Shandong Province (山东省小麦种植优势分析及技术探析) [J]. *Agricultural development and equipment*, (10) 110. https://kns.cnki.net/kcms/detail/32.1779.th.20141031.1611.096.html

[26] Wang, W. W., Song, J. L., Zhou, G. A., Pan, B. T., Wang, Q. Q., & Chen, L. Q. (2022). Simulations and experiments of the seedbed straw and soil disturbance as affected by the strip-tillage of rowcleaner (Dem) [J]. *INMATEH Agricultural Engineering*, *66*(1): 49-61. https://doi.org/10.35633/inmateh-66-05.

[27] Wang, X. L., Hu, H., Wang, Q. J., Li, H. W., He, J., & Chen, W. Z. (2017). Calibration method of soil contact characteristic parameters based on DEM theory (基于离散元的土壤模型参数标定方法) [J]. *Transactions of the Chinese Society of Agricultural Machinery*, *48*(12): 78-85. https://kns.cnki.net/kcms/detail/11.1964.s.20170718.1412.026.html

[28] Yao, W. Y., Zhao, D. B., Xu, G. F., Chen, M. Z., Miao, H. Q., & Diao, P. S. (2020). Design and experiment of anti-blocking device for strip to row active corn no-tillage seeding (条带对行主动式玉米免耕播种防堵装置设计与试验) [J]. *Transactions of the Chinese Society of Agricultural Machinery*, *51*(S2): 55-62+71.

[29] Yao, Z. L., Gao, H. W., Li, H. W., & Wang, X. Y. (2009). Effect of different structural no-till openers on soil resistant force (不同结构免耕开沟器对土壤阻力的影响) [J]. *Journal of Agricultural Mechanization Research*, *31*(07): 30-34.

[30] Yao, Z. L., Gao, H. W., Wang, X. Y., & Li, H. W. (2007). Effect of three furrow openers for no-till wheat seeder on crop growth performance (小麦免耕播种机开沟器对作物生长的试验研究) [J]. *Transactions of the Chinese Society of Agricultural Engineering*, (07): 117-121.

[31] Yu, C. C., Wang, Q. J., Li, H. W., He, J., Lu, C. Y., & Liu, H. (2020). Design and experiment of spiral-split sowing strip cleaning device (螺旋切分式种带清理装置设计与试验) [J]. *Transactions of the Chinese Society of Agricultural Machinery*, *51*(S2): 212-219.

[32] Yu, J. Q., Qian, L. B., Yu, W. J., Pan, S. Q., Fang, Y., & Fu, H. (2009). DEM analysis of the resistances applied on furrow openers (开沟器工作阻力的离散元法仿真分析) [J]. *Transactions of the Chinese*

Society of Agricultural Machinery, *40*(06): 53-57.

[33] Yuan, P. P., Li, H. W., Jiang, G. J., He, J., Lu, C. Y., & Huang, S. H. (2021). Design and experiment of straw cleaning device for wide narrow maize no-tillage sowing strip in drip irrigation area (滴灌区宽窄行玉米免耕播种带秸秆清理装置设计与试验) [J]. *Transactions of the Chinese Society of Agricultural Machinery*, *52*(06): 43-52. https://kns.cnki.net/kcms/detail/11.1964.S.20210408.1333.009.html

[34] Zhang, R., Li, J. Q., Zhou, C. H., & Xu, S. C. (2007). Simulation of dynamic behavior of soil ahead of the bulldozing plates with different surface configurations by discrete element method (推土板表面形态对土壤动态行为影响的离散元模拟) [J]. *Transactions of the Chinese Society of Agricultural Engineering*, (09): 13-19.

[35] Zhang, X. C., Li, H. W., Du, R. C., Ma, S. C., He, J., Wang, Q. J., Chen, W. Z., Zheng, Z. Q., & Zhang, Z. Q. (2016). Effects of key design parameters of tine furrow opener on soil seedbed properties [J]. *International Journal of Agricultural*, *9*(3) 14.

[36] Zhao, S. H., Tan, H. W., Zhang, X. M., Liu, H. J., Cao, X. Z., & Yang, Y. Q. (2017). Design and numerical simulation of new acute angle opener (新型锐角开沟器的设计及数值模拟) [J]. *Journal of Agricultural Mechanization Research*, *39*(11): 44-48+58. https://doi.org/10.13427/j.cnki.njyi.2017.11.008.

DESIGN AND EXPERIMENT OF KEY PART OF 2ZXS-2 CANTALOUPE TRANSPLANTER
/
2ZXS-2 哈密瓜移栽机的关键部件设计与试验

Dejiang LIU[1,2)], Yan GONG[1*)], Yingchun ZHU[2,3)], Kehen YAO[1)], Xiao CHEN[1)], Guo WANG[1)], Xiao ZHANG[1)]

[1)] Nanjing Institute of Agriculture Mechanization, Ministry of Agriculture and Rural Affairs, Nanjing 210014, China
[2)] Western agricultural research centre, Chinese Academy of Agricultural Sciences, Changji 831199, China
[3)] Zhengzhou Fruit Research Institute, Chinese Academy of Agricultural Sciences, Zhengzhou 450009, China
Tel: +86 025-84346227; E-mail:gongyan@caas.cn
DOI: https://doi.org/10.35633/inmateh-68-36

Keywords: *Cantaloupe transplanter; mechanism design; field experiment*

ABSTRACT

Aiming at the trouble of low survival rate of cantaloupe seedling in hyperthermia, drought and dry land in Turpan region of China, the existing transplanting machine is the key to mechanized and non-destructive transportation and planting of large plants of young tender melon seedlings, root water injection, and precise soil piling in planting holes, and other technical difficulties. The design of mulch film planting cantaloupe transplanter for laying pipes belts and membranes, watering and transplanting, which can complete rotary tillage, spreading drip irrigation belts, laying mulch and covering the soil around the membrane, transplanting pot seedlings on the membrane, and water injection at the bottom. This machine puts the water injection pipeline under the inner side of the transplanter, and through the multi-point linkage electric control, the seedling preservation water is injected into the bottom of the seedlings pot while the seedlings are transferred, which not only ensures the survival rate of the melon seedlings, but also an accurate piling of the planting hole is realized. The technology of transplanting with water and piled soil for planting holes effectively solved the technical problems of mechanized transplanting of cantaloupe under high temperature and arid climate conditions in Turpan. After the cantaloupe seedlings were transplanted in dry land, the probability of survival was more than 96.9% after seven point five hours of drip irrigation. Operating efficiency can reach 0.067 hectares per hour, eight times as much as manual transplanting. The speed of transplanting machine is about 1.1 m/s, the quality of transplanting rate was 93.26 percent. The operating standards of these transplanters meet the agronomic requirements for transplanting cantaloupe.

摘要

针对现有新疆吐鲁番地区高温干旱，瓜苗旱地移栽成活率低等问题，现有移栽机对于大株型幼嫩瓜苗的机械化无损输送及栽植、根底注水、种植穴精准堆土等关键技术难题，设计哈密瓜铺管铺膜坐水移栽机，实现了一个作业流程即可完成旋耕、铺滴灌带、铺地膜及膜边覆土、钵苗膜上移栽、根底注水、种植穴堆土及镇压的机械化复式作业。该机具创新设计的坐水系统将注水管路置于鸭嘴栽植器的内侧下方，通过多点位联动机电控制，在移苗的同时将保苗水注入钵苗根底，不仅确保了瓜苗成活率，并且大幅提高了水分利用率；通过覆土滚筒与鸭嘴栽植器的运动耦合设计，实现了种植穴的精准堆土。坐水移栽技术与种植穴堆土技术有效解决了吐鲁番等地高温干旱气候条件下进行哈密瓜机械化移栽的技术难题，旱地移栽后 7.5 小时进行滴灌的瓜苗成活率超过 96.9%。田间试验表明，机械化作业效率可达 0.067 公顷/人/小时，较人工作业提高 8 倍以上。机具作业速度为 1～1.1m/s 左右，移栽合格率为 93.26%，满足哈密瓜移栽农艺要求。

INTRODUCTION

In these years, with the change of China's agricultural structure layout, the planting scale of cantaloupe has been expanding and there is a lack of matching mechanized special equipment. Then, many transplanting machines are used for pepper, tomato, cabbage and other vegetables (*Bao, 2020; Chen Jianneng, 2015*). Because the characteristics of different regions in China vary greatly, the cantaloupe planting areas have strict requirements on planting conditions, especially in the light, soil, rain and other environments. The agronomic requirements for growing cantaloupe in the eastern and western parts of China are quite different. In order to reduce the obstacle and harm of continuous cropping of cantaloupe, it is necessary to spray the roots of cantaloupe seedlings.

In the arid areas of western China, cantaloupe is planted with agricultural film covering technology. Generally, pipe is first laid, film is laid and then transplanted. These processes are usually carried out manually with a large amount of labour. In actual planting, in order to avoid dehydration of seedlings due to high temperature, a certain amount of water is often injected into the root of seedlings when transplanting, and finally the survival rate of transplanting can be guaranteed.

According to the cantaloupe transplanting order, the newly transplanted cantaloupe seedlings untill the transplanting completed, then unified irrigation water. Take the planting area of 5 ha as an example, each machine and tool operate at 1.67 ha/day, a 5 hectares transplant takes 2.9 days to complete. If it is waited for 5 hectares of transplanting to be completed before watering the transplanted seedlings, it is inevitable that the first transplanted seedlings will not survive due to dehydration. If you want to solve this problem, you can first fill the soil with water before transplanting, but it will lead to excessive soil moisture, resulting in heavy soil viscosity, which makes it difficult for the transplanting machine to enter the operation. Therefore, the root irrigation of cantaloupe seedlings at the same time of transplanting can effectively improve the survival probability of cantaloupe seedlings.

Early in the 1960s, dry land transplanting machinery has begun to be researched in China, but did not develop quickly (*Jin Liyu, 2021; Jin Xin, 2018*). Since the 1970s, China has begun to develop bare seedling transplanting machine, originally used for beet transplanting; used in the vegetable transplanters. After the 1980s, semi-automatic transplanting machinery structure gradually improved, functional adaptability was stronger, but developed foreign transplanting machine, having a cost that is too high, is not suitable for China's transplanting technology agronomic requirements. China's transplanting machine development started late, the effective combination of agricultural machinery and agronomy is not high, the structure and function are relatively simple. In the early 21st century, China's semi-automatic transplanting machinery began to be widely used, but the cantaloupe water transplanting machinery is rarely studied. (*Liu Cunxiang, 2013; Lu Yongtao, 2011*).

Therefore, this paper designed a water cantaloupe seedlings transplanter with water injection function can realize transplanting at the same time with soil table irrigation. The machine’s operation process can complete soil rotary tillage, drip belt, mulching film, film and soil, bowl seedling film transplanting, root water injection (water), planting hole soil and ballast mechanized double operation.

MATERIALS AND METHODS

Whole structure and working principle - Whole structure

2ZXS-2 type cantaloupe seedlings water transplanting machine with water injection function mainly consists of duck beak transplanting device, transmission system, film covering mechanism, water injection mechanism, CAM mechanism, frame and other components. The 3D assembly drawing is shown in Figure 1 below. The working principle of the transplanting machine is as follows: the seedlings are fed into the duckbill transplanting device by the seedling tray. The transplanting device is driven by the multi-rod mechanism to complete the work of opening, planting and rotating, and then the suppression wheel is overlaid to complete the transplanting operation. Main working parts: duck-head planter, multi-rod drive mechanism and seedling feeding plate. The two-dimensional final assembly drawing is shown in Figure 1, and its appearance is shown in Fig. 2.

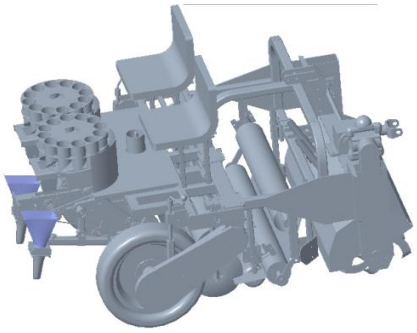

Fig. 1 – Overall cantaloupe transplanter

Fig. 2 – Appearance

The transplanter and the tractor are connected by three-point suspension system, relying on the driving wheel and the ground to roll power, and then the power is transmitted through the transmission system to each key component.

The duckbill transplanter puts the cantaloupe seedlings into the seedling tray, and then keeps the duckbill mouth of the duckbill transplanter upward through the linkage mechanism. The transplanter has two duckbill funnels, and the cam mechanism drives and controls the opening and closing of the duckbill funnels. When working, the operator on the machine will put the transplanted seedlings into the seedling tray, and the seedling dispenser will feed the distributed seedlings into the rotator of the transplanting device. After the transplanting rotator is turned to the lower part of the dispenser and inserted into the soil, the duck-billed funnel will be opened, and a certain amount of water will be injected at the same time. After the melon seedlings fall, the duck-billed funnel will be kept open and will be pulled out of the soil through the rotation of the dispenser and then closed, waiting for the seedlings to be cast again. The opening and closing of the duck-billed funnel are controlled by the CAM mechanism. The soil covering wheel located at the back of the dispenser compresses the soil on both sides of the root of the melon seedlings, which plays the role of burying soil and compacting. (*Li Hua, 2017; Li Ge, 2003; Lu Zhijun, 2017; JB / T 10291, 2013*).

Transplanting agronomic qualification

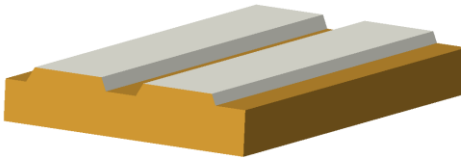

Fig. 3 - Ridging Cantaloupe double membrane cultivation agronomy

The technical data of transplanting machine for Hami melon in northwest arid areas are shown in table1.

Table 1

Transplanting machine technical parameter table

No.	Project	Technical parameters
1	Version	2ZXS-2
2	Form of power	by tractor
3	Horse power of tractor	≥40
4	Membrane width	350-450 (mm)
5	Adjustable planting width	85, 90, 95 (cm)
6	Adjustable water injection	60-100 (ml/hole)
7	Outline dimensions L × W × H	2250 x 1500 x 1800 (mm)
8	Machine weight/kg	700~ 750 kg

Design analysis of key mechanisms - Chain drive design of the planting mechanism

The duck-bill transplanting mechanism is a key part of the whole transplanter. The transplanter mechanism is a crank-link - CAM mechanism. The assembly drawing of the transplanting machine is shown in Figure 1, and the duck-bill transplanting mechanism is shown in Figure 4. Before the cantaloupe transplanter operation, which should match well transplanting speed and forward speed and seeding speed match, avoid injured cantaloupe seedlings, seedling clip and seedling belt phenomenon (*Shao Yuanyuan, 2019; Tang Qing, 2016; Wu Jun, 2016; Wu Jun, 2012*).

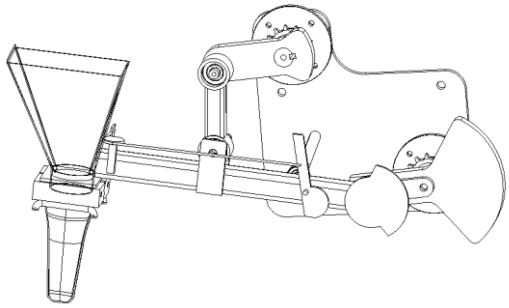

Fig. 4 - 3D image of transplanter

The “duck mouth” actuated by the CAM drives the crank connecting rod mechanism to move, and the cam-to-connecting rod power transmission ratio is calculated as follows:

$$i = i_{\omega} \frac{z_2}{z_1} = \frac{n_1}{n_2} \quad (1)$$

where: i - Transmission box reducer reduction ratio;

Z_1, Z_2 - Number of teeth of the sprockets in the planter drive system;

n_1, n_2 -Power speed of the seedling mechanism and crank speed , [r/min].

The crank angle speed depends on the transplanting operation speed of 4.8 rad/s, take the delivery agency for cantaloupe seedlings speed is 0.59 rad/s, and the transmission ratio i_ω , choose 10 speed reduction gear. According to the above selection data and transmission ratio 0.12, the number of gears driven by two cams is calculated: z_2=15, z_1=18.

Field testing - *Test site and test method*

The test site was selected in Turpan, China, and the test time was March 2022. The main measuring instruments were clocks, tape measures, soil moisture content tester, etc. According to the transplanting conditions of Hami melon planted in the arid areas of northwest China, the relevant parameters of the machine and tools were set in advance to match the operation speed, seeding speed and transplanting row spacing and plant spacing. In this experiment, the row spacing of planting cantaloupe is 45 cm, while the plant spacing is 40 cm. The field debugging test diagram is shown in Figure 5.

Fig. 5 - Transplanting machine operation test site

Test methods

Dry cantaloupe transplanting machine belongs to the technology and method of transplanting machine in dry area, so, we take reference to the standard “transplanter in dry land” and manufacturer's standard Q/HY·J0324—2019 “Melon transplanter” including the relevant provisions of the test method for conducting the transplanting operation (*Wang Yongwei, 2018; Wu Wei, 2013; Xue Dangqin, 2013; Xu Gaowei, 2019; Yu Xiaoxu, 2014*). The cantaloupe transplanting effect test was carried out in the planting season of Turpan Cantaloupe, China. This experiment analysed the influence of operation speed on evaluation index of transplanting effect under different moisture content soil (*Zhao Xiaowei, 2014; Zhang Xiaolong, 2017*).

The corresponding index detection methods are shown as follows in Table 2.

Table 2

The corresponding index detection methods

No.	Index	Computational formula	Terms explanation
1	Seedling lodging rate	$T = \frac{N_{DF}}{N}$	T - Seeding lodging rate, [%]; N_{DF} - Lodging point number, [-]; N - The total number of points determined, [-].
2	Repeat planting rate	$D = \frac{N_{CZ}}{N}$	D - Heavy planting rate, [%]; Ncz - Heavy planting point number, [-].
3	Missing planting rate	$M = \frac{N_{LZ}}{N}$	M - Missing planting rate, [%]; N_{LZ} - The number of missing holes, [-].
4	Injury seedling rate	$W = \frac{N_{SM}}{N}$	W - Injury seedling rate, [%]; N_{SM} - number of injury seedling, [-].
5	Transplanting qualified rate	$Q = \frac{N_{HG}}{N}$	N_{HG}=N-(2N_{CZ}+N_{DF}+N_{LZ}+N_{SM}) Q-Transplanting qualified rate, [%].

RESULTS

Land plots with different moisture content were selected for the test (22.5%, 20.3%, 18.1%, 16.2%), at the beginning of the transplanting test, the seedlings being transplanted at a 0.8 m/s, 1 m/s, 1.2 m/s, 1.4 m/s operation speed; the repeat planting rate, lodging rate, missing planting rate and seedling damage rate were determined respectively, and the transplant quality rate was calculated. The specific test data is shown in Table 3.

Transplanting operation quality indices at different operating speeds **Table 3**

Soil rate of water content [%]	Machine speed [m/s]	Transplant quality evaluation parameters				
		Repeat planting rate [%]	Lodging rate [%]	Missing planting rate [%]	Seedling damage rate [%]	Transplanting quality rate [%]
22.5	0.8	1.21	1.61	1.23	2.23	93.72
	1.0	1.68	1.26	1.17	2.63	93.26
	1.2	1.13	2.23	1.16	3.11	92.37
	1.4	1.92	1.95	1.75	3.05	91.33
20.3	0.8	1.77	1.71	3.77	2.23	90.52
	1.0	1.53	1.32	1.65	2.61	92.89
	1.2	1.66	2.21	2.32	2.94	90.87
	1.4	2.28	2.36	3.61	2.81	88.94
18.1	0.8	2.30	2.13	4.37	2.15	89.05
	1.0	1.92	1.96	2.65	1.92	91.55
	1.2	1.78	2.75	2.25	2.96	90.26
	1.4	3.21	3.46	3.69	2.55	87.09
16.2	0.8	3.41	4.23	5.17	2.03	85.16
	1.0	3.95	2.86	3.44	1.44	88.31
	1.2	3.86	3.71	3.16	2.88	86.39
	1.4	4.12	4.43	4.52	2.61	84.32

According to the experimental data, recorded in the above table 3, the data in the table was analysed. Test data shows that, it can be seen significantly that when the dry land transplanter operation with different moisture content, the machine speed increased, the damage rate and lodging rate of the transplanting seedlings became larger, the repeated transplanting rate and the leakage rate became smaller and then increased, the transplanting qualified index showed a weak trend, when the machine speed was 1 m/s. The evaluation index of transplanting effect is the best, the damage rate is the lowest, and the qualified rate of transplanting is the highest at this time, 93.26. Therefore, the matching speed was set as the best agronomic parameter of the machine.

CONCLUSIONS

(1) According to the Xinjiang Turpan melon planting mode and agronomic requirements, based on the existing transplanting methods for the mechanized non-destructive transportation and planting of large young melon seedlings, root water injection, planting hole accurate soil piling and other key technical problems, the innovative water injection system places the water injection pipe, which put in the inside of the transplanter, through multi-point linkage electromechanical control, the water for the seedling is injected into the bottom of the pot while removing seedlings, not only to ensure the survival rate of the melon seedlings, but also to greatly improve the water utilization rate; the design of the cover roller achieves the accurate soil accumulation of planting holes.

(2) In this paper, a cantaloupe transplanting machine with water injection is designed, which can complete rotary tillage, pipe and film laying, transplanting, water injection, soil covering and other processes at one time to meet the agronomic requirements of cantaloupe planting in arid areas. Through the adaptability test study in Turpan, China, it can effectively solve the phenomenon that cantaloupe seedlings wither and die due to delayed water injection after transplantation. After transplanting, the survival probability can be up to 98%, and the transplanting efficiency can also reach 0.067 ha/h/person. When the transplanting speed is 1 m/s, the best transplanting qualified rate is 93.26%, which meets the agronomic requirements of transplanting cantaloupe in arid areas and can improve the theoretical data support for transplanting cantaloupe in arid areas.

ACKNOWLEDGEMENT

This research was supported by the China Agriculture Research System (CARS-25), Xinjiang Uygur Autonomous Region focuses on research and development (2022B02025-4).

REFERENCES

[1] Bao, X., Zhao, X., He, J., et al, (2020), Design and performance test of plowing and rotary tillage combined machine. *INMATEH-Agricultural Engineering*, Vol.60, Issue 1, pp. 213-222.

[2] Chen Jianneng, Xia Xudong, Wang Ying, et al. (2015) Motion differential equations of seedling in duckbilled planting nozzle and its application experiment. *Transactions of the CSAE*, 31(3): pp 31－39.

[3] Jin Liyu. (2021). *Design and experiment of planting mechanism of pepper pot transplanting machine 辣椒钵育移栽机栽植机构设计与试验*, Heilongjiang Bayi Agricultural University.

[4] Jin Xin, Ji Jiangtao, Liu Weixiang et al. (2018). Structural optimization of duckbilled transplanter based on dynamic model of pot seedling movement (基于钵苗运动动力学模型的鸭嘴式移栽机结构优化). *Transactions of the CSAE*, 34(9): pp. 58－67.

[5] Liu Cunxiang, Li Xiaohu, Yue Xiuman, et al. (2013). The status quo and development trend of dryland transplanters in my country 我国旱地移栽机的现状与发展趋势. *Journal of Agricultural Mechanization. Research*, 34(11), pp. 249-252.

[6] Lu Yongtao, Li Yaxiong, Li Bin, et al. (2011). Analysis on the status quo of transplanting machines and transplanting technology at home and abroad (国内外移栽机及移栽技术现状分析). *Xinjiang Rural Mechanization*, (3), pp. 29-32.

[7] Li Hua, Cao Weibin, Li Shufeng, et al. (2017). Development of 2ZXM-2 fully automatic vegetable plug seedling film-laying transplanter. *Transactions of the CSAE* 33(15), pp. 23-33.

[8] Li Ge, Ai Li Hasimu, Kang Xiusheng, et al. (2003). Parameter optimization of the spiral cover drum of the film planter (地膜播种机螺旋覆土滚筒的参数优化). *Transactions of the CSAE*, 19(6), pp. 135-138.

[9] Lu Zhijun, Shan Yiyin, Wang Jie et al. (2017). Research status of vegetable transplanting equipment and prospects of pot seedling transplanting equipment 蔬菜移栽装备研究现状和钵苗移栽装备展望. *Chinese Journal of Agricultural Mechanization Chemistry*, 38 (11), pp. 30-34.

[10] Ministry of Industry and Information Technology of the PRC Republic of China. (2014). JB / T 10291-2013 Dryland Planting Machinery (旱地栽植机械). Beijing: *Machinery Industry Publishing House*.

[11] Shao Yuanyuan, Liu Yi, Xuan Guantao, Gao Xuemei, Han Xiang, Wang Yongxiang. (2019). Design and simulation analysis of multi-function duck mouth vegetable transplanting machine (多功能鸭嘴式蔬菜移栽机设计与仿真分析). *China Agricultural Machinery Chemical News*, 40 (11), pp. 09-12, 34.

[12] Tang Qing, Wu Chongyou, Yuan Wensheng, et al. (2016). Structural design of soil-covering suppression device for rape blanket seedling high-speed transplanter 油菜毯状苗高速移栽机覆土镇压装置结构设计. *Chinese Journal of Agricultural Machinery Chemistry*, 37(3), pp. 20-22.

[13] Wu Jun, Tang Qing, Yuan Wensheng, et al. (2016). Design and parameter optimization of ditching and suppression components of rapeseed blanket seedling transplanter 油菜毯状苗移栽机开沟镇压部件设计与参数优化. *Chinese Journal of Agricultural Engineering*, 32(21), pp. 46-53.

[14] Wu Jun, Yu Wenyi, Zhang Min et al. (2012). Design and test of Z Y-6 (2ZY-6 型油菜毯状苗移栽机设计与试验). *Journal of Agricultural Machinery*, 51 (12), pp. 95-103

[15] Wang Yongwei, He Chaoliang, Wang Jun, et al. (2018). Dryland vegetable bowl seedlings automatic transplanting machine planting Performance test 旱地蔬菜钵苗自动移栽机栽植性能试验. *Journal of Agricultural Engineering*, 34 (3), pp. 19-25.

[16] Wu Wei, Sun Songlin, Xiao Mingtao. (2013). The status quo and development trend of transplanting machinery in my country. Agricultural Technology and Equipment, (12), pp. 7-8.

[17] Xue Dangqin, Hou Shulin, Zhang Jia Xi. (2013). Research progress and development trend of dryland transplanting machinery in my country (我国旱地移栽机械的研究进展与发展趋势). *Chinese Journal of Agricultural Machinery Chemistry*, 34(5), pp. 8-11.

[18] Xu Gaowei. (2019). Research on the key components of the double-row salvia transplanter on a large ridge film and the design of the whole machine *Northeast Agricultural University*.

[19] Yu Xiaoxu, Zhao Yun, Chen Baocheng et al. (2014). Development status and prospects of transplanting machinery (移栽机械发展现状与展望). *Journal of Agricultural Machinery*, 45(8), pp. 44－53.

[20] Zhao Xiaowei, Guo Hui, Zhang Jing, et al. (2014). The status quo and development trend of dryland transplanter in Xinjiang (新疆旱地移栽机的现状及发展趋势). *Xinjiang Rural Mechanization*, (4), pp. 25-29.

[21] Zhang Xiaolong, Woodlin, Wu Chongyou et al. (2017). Design and experimental study of duck-mouth bowl seedling transplanting machine. *Agricultural mechanization research*, 3 (3), pp. 134-143.

A REAL-TIME DETECTION MODEL FOR IDETIFICATION OF CITRUS DURING DIFFERENT GROWTH STAGES IN ORCHARDS
/
一种实时检测模型在果园不同生长阶段的柑橘识别

Changgao XIA *[1)], Wanlei NI [1)], Kun JIANG [1)], Xiaofan LI [2)] [1]
[1)] School of Automotive and Traffic Engineering, Jiangsu University, Zhenjiang 212013, China
[2)] School of Management, Jiangsu University, Zhenjiang 212013, China
Tel: 13815171208; E-mail: xiacg@ujs.edu.cn
Corresponding author: Changgao Xia
DOI: https://doi.org/10.35633/inmateh-68-37

Keywords: *Full growth cycle citrus, Deep learning, Detection, YOLOV-V5*

ABSTRACT
In order to solve the problem of citrus full growth cycle identification in complex scenes, this paper proposed a multi-scale detection model of citrus whole growth cycle in orchard environment. The weighted bi-directional feature pyramid network (BiFPN) is used to combine multiple feature information of high resolution and low-resolution feature layers, and the feature information is extracted by the depth-separable convolution and lightweight New-C3 module. The results show that the average accuracy of the multi-scale detection model proposed in this paper was 91.35%, 92.89%, 94.12%, 90.39% in the young citrus, expanding citrus, ripe citrus and full growth cycle citrus, and the average detection time was 92.60 FPS/s under 1920×1080 image pixels, which meets the real-time detection requirements of citrus orchard.

摘要
为了解决复杂场景下柑橘的全生长周期识别问题，本文提出了一种果园环境下柑橘全生长周期的多尺度检测模型。采用加权双向特征金字塔网络（BiFPN）来融合高分辨率和低分辨率特征层的多项特征信息，且通过深度可分离卷积和轻量型 New-C3 模块实现特征信息的提取。结果表明，本文提出的多尺度检测模型在生长期、膨果期、成熟期和全生长周期柑橘的平均精度为 91.35%，92.89%，94.12%，90.39%，在 1920×1080 图像像素下的平均检测时间为 92.60 FPS/s，满足果园柑橘的实时检测要求。

INTRODUCTION
In recent years, the production of citrus and other fruits has steadily ranked first in the world. As a result, China has gradually become one of the important fruit-producing countries in the world *(Zhao et al., 2016).* Throughout the citrus planting and management process, fruit farmers are the main labour force in orchards, and labour costs account for 50% to 70% of the total input costs. Real-time detection technology can accurately identify citrus at different growth stages, which is one of the important means to realize the fine management of orchards *(Wang et al., 2013; Zhang et al., 2002).*

In the recognition of citrus at different growth stages, there are complex scene problems such as citrus overlap, branches and leaves shading, site influence, light conditions, and the colour and volume of citrus can change with its different growth stages, which can greatly reduce the accuracy of citrus recognition. In the early days, researchers at home and abroad explored many target detection algorithms, and these recognition methods were used to accomplish recognition detection by extracting feature information such as the colour and shape of fruits *(Yu et al., 2013; Kurtulmus et al 2011; Zhao et al., 2016)*. However, these methods can only detect fruits at specific growth stages, and using the same model to detect fruits at different growth stages is not satisfactory *(Illingworth et al., 1988)*. *Rakun et al., (2011),* used colour segmentation to separate the fruit from the background in order to overcome the influence of light conditions and partial fruit occlusion. By analysing three different features (colour, texture and 3D space) of possible regions, the detection rate of fruits was improved. However, the detection effectiveness of this method is greatly reduced when there are more small targets in the image. The recognition effect of the above method is highly dependent on the environment and influenced by the lighting conditions. When the detected fruits are small, dense, or the colour features are similar to the background, it is difficult to extract the feature information, resulting in lower detection accuracy.

[1] *Changgao Xia, Prof. Ph.D. Eng.; Wanlei Ni, M.S. Stud. Eng.; Kun Jiang, M.S. Stud. Eng.; Xiaofan Li, M.S. Stud Eng.*

Since the 1980s, machine learning has been widely applied in the direction of agriculture *(Tanima et al., 2020).* Many machine learning theories have been applied to fruit recognition in orchards, such as Canny, HOG (Histogram of Oriented Gradient), and SVM (Support Vector Machine) methods to extract fruit features and train the features, and then use the trained model to predict the location and class of new input features. *Kelman et al., (2014),* used the Canny edge detection operator to extract all the contour information in the image and construct the 3D contour feature function of Apple, and then used this function to screen all the contour information in the image to identify apple. After experimental analysis, this function can identify 94% of the apples. But a branch or leaf with a convex surface similar to the contour of an apple resulted in 14 percent of false positives. *Ji et al., (2012),* used SVM+HOG classifier to classify bagged apples and ordinary apples, achieving 89% detection accuracy for bagged apples. However, the average detection time of this algorithm is 352ms, which makes it impossible to implement this algorithm in real-time system, and the average error rate is 11% due to leaf occlusion. *Zhuang et al., (2018),* proposed a robust detection algorithm based on monocular vision system to identify citrus fruits. Combined with Otsu threshold, morphological operation, watershed transformation of marker control and other methods, the potential citrus region was located from the colour map, and then the local texture information was extracted from the potential region. Finally, SVM was used to make the final decision. The results showed that the recall rate of citrus was greater than 0.86, but the detection time was 0.53s. In summary, the method of machine learning for fruit recognition has low accuracy and is easily disturbed by the complex environment of the orchard.

In recent years, convolutional neural network has been rapidly developed in the field of target recognition *(Liu et al.,2020; Zheng et al., 2021)*, and more and more researchers worldwide have applied those recognition algorithms to orchard crop recognition and achieved remarkable results.

Tian et al., (2019), proposed a method using DenseNet to improve YOLO-V3 model for detecting apples during different growth stages. The DenseNet method is used to process the lower resolution feature layers in the YOLO-V3 network, which can effectively enhance feature propagation, promote feature reuse and improve network performance. Experiments showed that the F1 scores of apples in the young apple, expanding apple, ripe apples and full growth apple were 0.832, 0.841, 0.864, and 0.817. Respectively, the average detection time under the image with a resolution of 3000×3000 was 0.304s. This method can complete the study of the entire growth cycle of apples, but the recognition accuracy and average detection time still need to be further improved. *Wang et al. (2021)* used the pruned YOLO-V5s model to identify apples. The experiments showed that the apple recall, accuracy, F1 score and false detection rate of small fruits reached 87.6%, 95.8%, 91.5%, and 4.2%. The average detection time per image is 8ms, and the model size is only 1.4MB, but the model is not good for the recognition of occluded apple fruit. *Lyu et al., (2022),* proposed a lightweight YOLOv5-CS model to identify and count green citrus in natural environment. The model uses the CBAM attention mechanism to optimize the convolutional and detection layers, while using CIoU (Complete Intersection over Union) loss function and cosine annealing algorithm to strengthen the model, and finally implant the model into a mobile device. The results show that the mAP@0.5 of the YOLOv5-CS model for green citrus is 98.23%, the recall rate is 97.66%, the inference speed of detecting pictures on the server is 0.017s, and the inference speed on Nvidia Jetson Xavier NX is 0.037s. In the follow-up research, the citrus at different growth stages can be studied. *Huang et al., (2021),* improved the YOLO-V5s model using the CBAM attention mechanism and adaptively fused features, and then pruned the model to reduce the model size. The experiment was carried out on a self-made citrus dataset, the detection accuracy was 93.32%, and the processing speed of the edge computing device was 180ms/frame.

To sum up, those neural network recognition model has the advantages of high detection accuracy and fast detection speed in the detection of orchard crops. However, the above studies are not effective in detecting multi-size orchard crops and dense scenes. Meanwhile, the full growth cycle of citrus fruits has not been studied. Therefore, this paper constructs a multi-scale detection model for the whole growth cycle of citrus in the orchard environment, and explores the recognition problems in complex scenes such as citrus with different sizes, different colours, overlapping citrus, and occlusion of branches and leaves. In this paper, the following two structural optimizations are carried out for the YOLO-V5m model:

(1) Optimization of the YOLO-V5m neck network using a weighted bi-directional feature pyramid network (BiFPN).
(2) Deeply separable convolution and lightweight New-C3 modules are proposed to replace the conventional convolution and C3 modules for feature information extraction.

The research results show that the YOLOV5_L model has the advantages of high detection accuracy, fast detection speed, and small model size. Firstly, the adopted weighted bidirectional feature pyramid network fuses multiple feature information from high-resolution and low-resolution feature layers to enhance the recognition accuracy of the model for citrus. Secondly, the lightweight module used optimizes the YOLO-V5 network structure, which greatly reduces the model size.

MATERIALS AND METHODS

Image data preprocessing

In this study, the collection site of citrus images was located in Jiangxinzhou citrus picking garden, Zhenjiang City, Jiangsu Province. The collected images contain orchard scenes such as unobstructed, branches occlusion, leaves occlusion, branches, and leaves occlusion and citrus overlapping. In order to identify full growth cycle citrus, there are 500 original images were collected for each growth stage, and the three growth stages formed a total original dataset of 1500 images.

In this paper, data augmentation methods such as Mosaic, Augment HSV, and Random affine were used to increase the richness of the dataset. First, the Mosaic data enhancement method is used to randomly select four images and randomly scale them, and then randomly stitch them together, which greatly increases the richness of the dataset. Second, the Augment HSV method is used to randomly adjust the chroma, saturation, and lightness of the image to increase the diversity of the image. Finally, random affine swaps are performed via the Random affine method. In this paper, the above image enhancement methods greatly enriched the types and sizes of images. The original 500 pictures in each growth stage were expanded to 1500 pictures, and the total datasets reached 4500 pictures. After that, 150 images are randomly taken as the test dataset in each growth stage, and the remaining 4050 images are used as the training set to train the model. The rich dataset makes the network more robust.

Basic model selection

The YOLO-V5 network improves the network structure and training methods on the basis of the YOLO-V4 network and improves the detection performance of the model. In the model image processing method, as show in Fig.1, YOLO-V5 uses the adaptive image scaling function to process the original images of different sizes and obtain various scaling coefficients, then selects the smallest coefficient to multiply with the length and width of the original image, and finally adaptively adds the least black edge to the original image to reduce the redundant information, which reduces the computation and improves the detection speed in the inference process.

YOLO-V5m is a lightweight detection model designed for mobile devices, which is difficult to accurately detect small targets and perform deeper feature fusion in complex orchard environments. The young citrus contains a large number of small citrus, and as the tool moves during the shooting of citrus, the citrus in the distance will become smaller and there will be pixel distortion, which makes the fusion of feature information very difficult. To address these issues, this paper optimizes the YOLO-V5m model to strengthen the detection of small targets and the fusion of multi-scale feature maps.

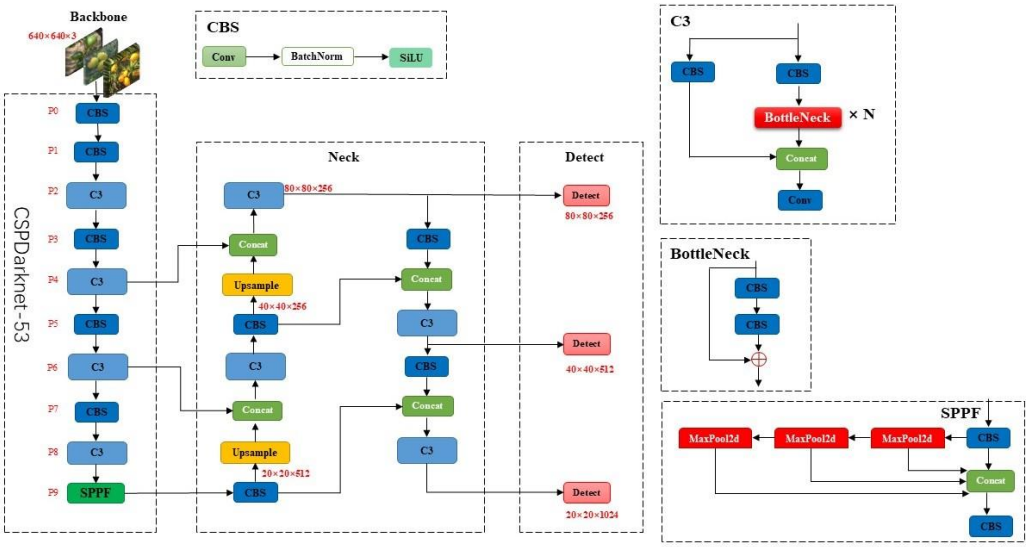

Fig. 1 - Structure of Yolo-V5 model

Model design of weighted bi-directional feature pyramid network (BiFPN)

The orchard environment is very complex, the citrus is small and there is pixel distortion in the distant citrus as the shooting tool moves. the YOLO-V5m model cannot extract the feature information of this part of the citrus, which leads to many missed and wrong detections. To this end, this paper proposes an optimized YOLO-V5m model based on a weighted bi-directional feature pyramid network *(Tan et al., 2020)* (BiFPN) structure, which enhances the fusion of feature information. As shown in Fig.2, the main idea of the BiFPN network structure is divided into two parts: one is efficient bidirectional cross-scale connectivity, efficient bidirectional cross-scale connection, and the other is the fusion of weighted feature maps. For bidirectional cross-scale connectivity, this network structure is equipped with bottom-up and top-down bidirectional channels. Different scale feature layers use upsample and convolution with a stride of 2 to adjust the resolution, so as to achieve high resolution. The fusion of high-resolution and low-resolution feature layers, and adding lateral connections between the original input and output nodes of the same feature, fuses more clementine feature information at a very low computational cost.

Since the input feature layers of different scales have different resolutions and contain different amounts of feature information, the input feature layers of different scales contribute unevenly to the output feature layers. In order to solve this problem, the BiFPN network structure needs to weigh the different scale feature layers during the feature layer fusion. Equation (1) is a fast normalized fusion method.

The ReLU activation function ensures that a small value is used to ensure the stability of the value. In order to further improve the efficiency, the Depthwise Separable Convolution is used here for feature fusion, and the batch normalization layer and the ReLU activation layer are added after each convolution operation.

$$O = \sum_i \frac{\omega_i}{\varepsilon + \sum_j \omega_j} I_i \tag{1}$$

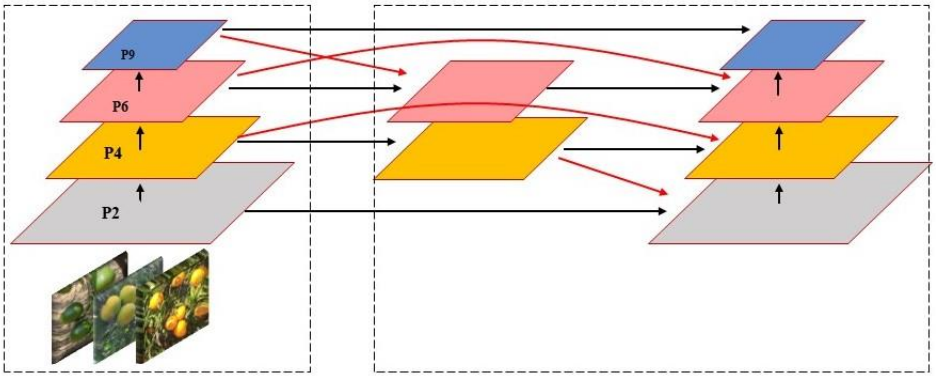

Fig. 2 - BiFPN feature network

Model design of light

Depthwise Separable Convolution

The YOLO-V5m model uses Standard Convolution (CBS) for the extraction of feature information, which causes the network to generate a large number of parameters. The characteristics of citrus fruits are relatively single and do not require too many parameters to fit the data. To this end, this paper proposes a feature extraction module based on Depthwise Separable Convolution (DWC) to optimize the YOLO-V5m model. Depthwise Separable Convolution is a lightweight network structure, which has the advantages of less number of parameters and lower operational cost compared with standard convolution. As shown in Fig.3, the Depth-Separable Convolution consists of two parts: Depthwise Convolution and Pointwise Convolution. One convolution kernel is responsible for one channel, and the number of feature map channels generated during the convolution process is exactly the same as the number of input channels. The point-by-point convolution is actually a 1×1 convolution, which plays two roles in the depth-separable convolution: first, it allows the depth-separable convolution to freely change the number of output channels; the other is to output the channel-by-channel convolution. feature layer for channel fusion.

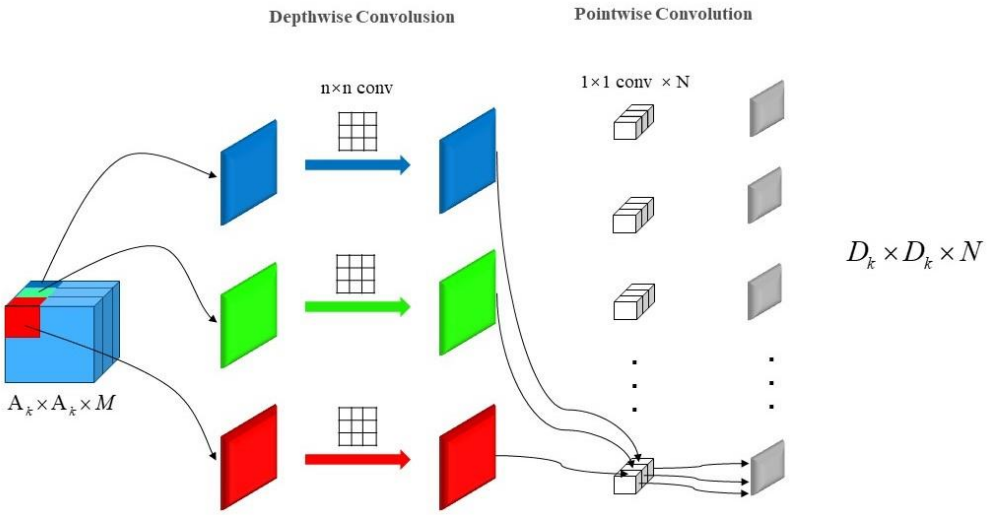

Fig. 3 - Depthwise Separable Convolution model

In terms of computational performance, the Depthwise Separable Convolution has been greatly improved compared to the standard convolution. Assuming that, the size of the input feature map is $A_k \times A_k \times N$, the size of the output feature map is $D_k \times D_k \times M$, and the size of the convolution kernel is *nxn*. The standard convolution layer operates the input feature map of each channel using the convolution kernel before outputting, and the computational volume is as follows:

$$C_{std} = D_k \times D_k \times M \times N \times n \times n \tag{2}$$

Depthwise Separable Convolution is first performed channel-by-channel and then point-by-point convolution, which is computed as:

$$N_{std} = D_k \times D_k \times M \times n \times n + D_k \times D_k \times M \times N \tag{3}$$

from the above equation, the ratio of the DWC to the standard convolution as:

$$\frac{N_{std}}{C_{std}} = \frac{D_k \times D_k \times M \times n \times n + D_k \times D_k \times M \times N}{D_k \times D_k \times M \times N \times n \times n} = \frac{1}{N} + \frac{1}{n^2} \tag{4}$$

In general, both N and n are greater than 1. From equation (4), the computational efficiency of the Depth Separable Convolution is better than that of the standard convolution.

New-C3 model

As shown in Fig.1, the C3 module of the YOLO-V5m model is the main module for learning the residual features. The structure of the C3 module is divided into two branches, one uses multiple Bottleneck stacks and 3 standard convolutional layers, the other passes through a basic convolution module, and finally, the two branches are concated. The standard convolution process is "convolution" - "batch normalization" - "non-linear activation", which generates a large number of parameters and increases the computational effort. In order to streamline the network structure, reduce the computation and decrease the model inference time, this paper proposes a lightweight New-C3 module for learning the residual features.

Compared with C3, the biggest change of the New-C3 module is to use NewBottleNeck to replace the original BottleNeck. As shown in Fig.4, the New-C3 module is a phased convolution module that uses Depthwise Separable Convolution and NewConv convolution instead of standard convolution to obtain more feature maps and eliminates redundant features. The function of NewConv is to reduce the number of channels with similar feature maps during the convolution process. For these repeated channels, using standard convolution calculation will consume a lot of computing power. NewConv is also divided into two branches, one uses the standard convolution unit to obtain the first part of the channel, the other one uses the Depthwise Separable Convolution on the first part of the channel to obtain the remaining part of the channel, and the

other uses the Depthwise Separable Convolution to obtain all channels. Finally, the two parts of the channel are spliced, which reduces the amount of calculation and avoids the appearance of duplicate channels.

The NewBottleNeck module structure is also divided into two branches and is greatly affected by the Stride. For the case of Stride=1, in one branch, a NewConv is used as an extension layer to increase the number of channels, and then the NewConv module is used to reduce the number of channels to match the number of channels in the Shortcut layer. In the other branch, Depthwise Separable Convolution is used for feature extraction, and the number of channels is matched. Finally, the outputs of the two branches are connected using Shortcut. For Stride=2, between the two NewConv of the first branch, a Depthwise Separable Convolution with Stride=2 is used for connection, and Depthwise Separable Convolution and standard convolution unit are used on the other side for feature extraction. Finally, the outputs of the two are connected by shortcut. This model structure can obtain more feature maps while reducing the size and number of parameters of the model.

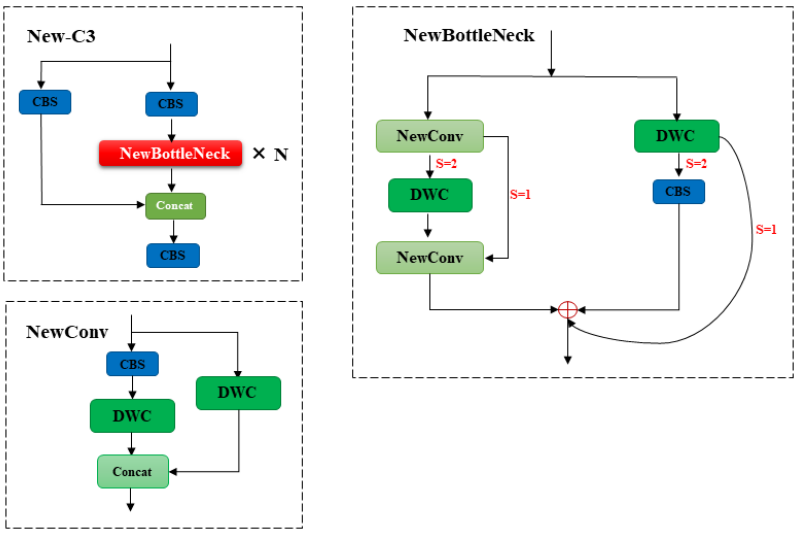

Fig. 4 - New-C3 model

RESULTS

Evaluation indicators

The precision P, recall R, average precision (AP), F1 Score are selected in the field of target detection. Accuracy indicates the probability of successful prediction among the predicted targets. Recall indicates the probability of successful prediction among the targets to be predicted. The average accuracy AP represents the cumulative sum of accuracy and recall under different confidence thresholds. F1 is a composite performance indicator that reconciles accuracy and recall, and the more F1 converges to 1, the better the overall performance of the model. In this paper, the threshold value is set to 0.5, and the prediction is considered successful if the intersection ratio between the measured target and the real target is greater than 0.5.

Precision:

$$P = \frac{TP}{TP + FP} \tag{5}$$

Recall:

$$R = \frac{TP}{TP + FN} \tag{6}$$

Average Precision:

$$AP = \sum_{K=i}^{N} P(k)\Delta R(k) \tag{7}$$

F1:

$$F_1 = \frac{2PR}{P + R} \tag{8}$$

Ablation Experiment

In this paper, based on the YOLO-V5m model, each optimization part was compared separately, and a series of ablation experiments were performed on the data sets of various growth stages of citrus to test the performance of the model. The specific experimental results are shown in Table 1.

The following results can be observed from the data in Table 1:

(1) Full growth cycle citrus

The average accuracy of YOLO-V5m in full growth cycle citrus was 87.54%. When using only BiFPN optimization, the average accuracy increases by 3.14%, the number of parameters increases by 2.29M, and the detection speed decreases by 13.2PFS/s. In order to reduce the number of parameters and speed up the detection speed of the model, this paper improves the lightweight network structure for feature extraction and fusion. The parameter amount of the model is reduced to 9.23M, and the detection speed is increased to 92.6PFS/s, which greatly improves the detection speed, and the AP is improved the average accuracy by 2.85%.

(2) Young citrus

The average precision of YOLO-V5m was 88.64% for citrus in the young citrus. When only BiFPN was added, the model accuracy increased by 3.08%. After combining the BiFPN and DG model, the most significant improvement in average accuracy was increased by 2.71%.

(3) Expanding citrus

The average accuracy of YOLOv5m in expanding citrus was 90.23%. When only using BiFPN optimization, the average accuracy increased by 2.79%. After combining the BiFPN and DG model, the most significant improvement in average accuracy was increased by 2.66%.

(4) Ripe citrus

The average precision of YOLO-V5m in ripe citrus was 91.24%. When only using BiFPN optimization, the average accuracy increased by 3.34%. After combining the BiFPN and DG model, the most significant improvement in average accuracy was increased by 2.88%.

It was found that the following two improvements were made in this paper relative to the baseline YOLO-V5m model. Firstly, after adding the optimization of the network using BiFPN showed that the AP values of expanding citrus, ripe citrus, and full growth cycle citrus increased significantly. BiFPN enables the model to efficiently realize the bidirectional cross-scale connection of feature layers and weighted feature fusion, as also a weighted fusion of feature information of different resolutions. The large size and fruit color of expanding citrus differ slightly from the surrounding environment. At the ripe citrus, the citrus volume is large, and the fruit color is significantly different from the surrounding environment. Therefore, the BiFPN structure can obtain more volume and color features, so that the model can better recognize the citrus in the expanding citrus and ripe citrus. When using both the BiFPN and DG model to optimize the YOLO-V5m model, the model has achieved a good detection for citrus at all growth stages, but both improvements will make the model parameter quantity increase and reduce the model detection speed.

Table 1

Model Ablation Experiment Analysis Results

Citrus Stage	BiFPN	DG	AP / %	FPS / s	Parameters (M)
Full growth cycle citrus			87.54	71.40	19.91
	√		90.68	58.20	22.20
	√	√	90.39	92.60	10.68
Young citrus			88.64	71.40	19.91
	√		91.72	58.20	22.20
	√	√	91.35	92.60	10.68
Expanding citrus			90.23	71.40	19.91
	√		93.02	58.20	22.20
	√	√	92.89	92.60	10.68
Ripe citrus			91.24	71.40	19.91
	√		94.58	58.20	22.20
	√	√	94.12	92.60	10.68

Influence of data category

In order to verify the influence of data categories on the detection performance of the model, the YOLOV5_L model was used in this paper to analyse the citrus data sets of the young citrus, expanding citrus, ripe citrus, and full growth cycle citrus. The obtained F1 score is shown in Table 2, and the P-R curve is shown in Fig.5. The P-R curve is an important index to evaluate the detection results of the identification model, and the area enclosed with the coordinate axis is the AP value. It is generally believed that the closer the P-R curve of the model is to the upper right corner of the coordinate axis, the better the performance of the model. The F1 score of the full growth cycle citrus data set was 0.845, which was lower than 0.017 in the young citrus, 0.063 in the expanding citrus, and 0.067 in the ripe citrus, and the P-R curve is at the lower left of each growth stage, indicating the detection performance of this model for the full growth cycle of citrus significantly lower than that of citrus at different growth stages. This is because of the wide variety of data for full growth cycle citrus and the inconsistency of citrus growth characteristics at each growth stage, so the detection difficulty is greatly increased during the data enhancement process of the model and the training process of the model. Among the individual growth stages, due to the small size of the young citrus and the similar colour to the surrounding environment, the F1 scores in the young citrus were significantly smaller than those in the expanding and ripe citrus, and the P-R curve was at the lower left of the expanding and ripe citrus. The F1 score and the P-R curve of the fruit in the expanding citrus are slightly lower than those of the fruit in the ripe citrus because the size of the fruit in the expanding citrus is the same as that in the ripe citrus, but the colour is between green and yellow, which is slightly similar to the surrounding branches and leaves. YOLOV5_L model has the best recognition effect on ripe fruits, which is due to the large size of ripe fruits and the colour characteristics that are different from the colour of the surrounding branches and leaves, so this model has the best effect on the detection of ripe citrus.

Table 2

F1 Scores of Citrus Detection Models in Several Categories

Class	F1
Young citrus	0.862
Expanding citrus	0.908
Ripe citrus	0.912
Full growth cycle citrus	0.845

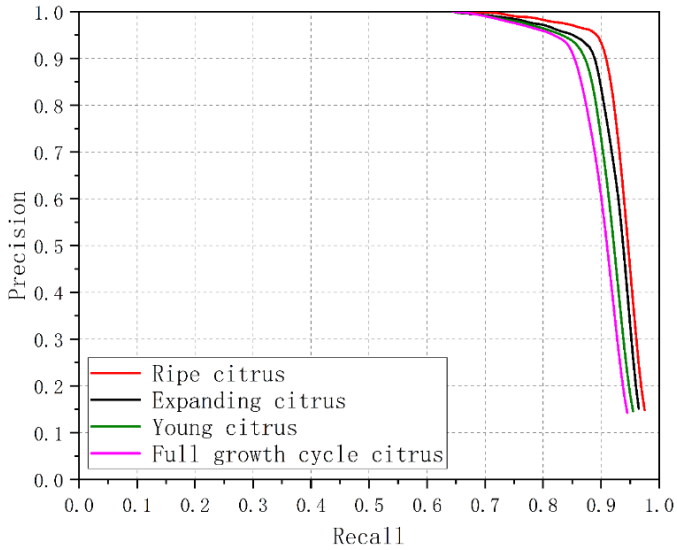

Fig. 5 - P-R Curves of Citrus Detection Models in Several Categories

Comparison of different algorithms

In this section, in order to further the superiority of YOLOV5_L model for citrus recognition effect. The YOLOV5_L model is compared with YOLO-V5s with faster detection speed and smaller memory; YOLO-V4, Faster R-CNN model with higher accuracy but slower detection speed.

The comparison results are shown in Table 3. From Table 3, it is found that the YOLOV5_L model has superior performance in detection accuracy with an AP of 90.39%, which is 2.71%, 3.07%, and 4.07% higher compared to Faster R-CNN ResNet50, YOLO-V4, and YOLO-V5s. This is because the full growth cycle citrus dataset contains a large number of small green citrus, large green citrus, and large yellow citrus. The YOLOV5_L model adds an optimized feature fusion network based on BiFPN, so it has more recognition ability for the above mentioned full growth cycle citrus. In terms of detection speed, this paper proposes a lightweight network structure for feature information extraction and fusion, and the experimental results show that the detection speed is improved to 92.60 FPS/s, which is 2.80 times, 2.42 times, and 1.02 times higher compared with Faster R-CNN ResNet50, YOLO-V4, and YOLO-V5s. In terms of model size, the model size of YOLOV5_L model is reduced to 10.68MB, which is much smaller than other models and can be flexibly deployed in low-memory devices.

Table 3

Performance Results from Different Object Detection Algorithms.

Models	AP %	FPS / s	Size / MB
Faster R-CNN ResNet50	87.68	33.12	314.06
YOLO V4	87.32	38.20	236.48
YOLO V5s	86.32	90.91	14.41
YOLOV5_L	90.39	92.60	10.68

CONCLUSIONS

Firstly, this paper uses a weighted bidirectional feature pyramid network structure to fuse feature layers with different resolutions, so that the model learns more feature information during the training process. The experimental results show that the multi-scale detection model of the citrus full growth cycle in an orchard environment constructed in this paper has better detection accuracy compared with previous detection networks. On the one hand, the network has good detection performance in detecting citrus with different degrees of shading and overlapping; on the other hand, the network has a good detection effect even in the growth period when the citrus is small and the colour characteristics of citrus are similar to those of citrus leaves. The future work is to apply the model proposed in this paper to computer devices with mobile platforms and to track and identify the fruits to realize the yield assessment of citrus in orchards and really apply the model.

ACKNOWLEDGEMENT

I mainly completed the design of experiments and the writing of papers, Changgao Xia provided funding, and others provided trial assistance. Project source was the Major Science and Technology Innovation Project of China: Research and development of high-torque reserve diesel engine and multi-point power output transmission for hilly and mountain tractors (1621120014).

REFERENCES

[1] Huang, H., Huang, T., Li, Z., Lyu, S., & Hong, T. (2021). Design of Citrus Fruit Detection System Based on Mobile Platform and Edge Computer Device. *Sensors*, 22(1), 59.

[2] Illingworth, J., & Kittler, J. (1988). A survey of the Hough transform. *Computer vision, graphics, and image processing*, 44(1), 87-116.

[3] Ji, W., Zhao, D., Cheng, F., Xu, B., Zhang, Y., & Wang, J. (2012). Automatic recognition vision system guided for apple harvesting robot. *Computers & Electrical Engineering*, 38(5), 1186-1195.

[4] Kurtulmus, F., Lee, W. S., & Vardar, A. (2011). Green citrus detection using 'eigenfruit', color and circular Gabor texture features under natural outdoor conditions. *Computers and Electronics in Agriculture*, 78(2), 140-149.

[5] Kelman, E. E., & Linker, R. (2014). Vision-based localisation of mature apples in tree images using convexity. *Biosystems Engineering*, 118, 174-185.

[6] Liu, L., Ouyang, W., Wang, X., Fieguth, P., Chen, J., Liu, X., & Pietikäinen, M. (2020). Deep learning for generic object detection: A survey. *International journal of computer vision*, 128(2), 261-318.

[7] Lyu, S., Li, R., Zhao, Y., Li, Z., Fan, R., & Liu, S. (2022). Green Citrus Detection and Counting in Orchards Based on YOLOv5-CS and AI Edge System. *Sensors*, 22(2), 576.

[8] Rakun, J., Stajnko, D., & Zazula, D. (2011). Detecting fruits in natural scenes by using spatial-frequency based texture analysis and multiview geometry. *Computers and Electronics in Agriculture*, 76(1), 80-88.

[9] Tanima, D., Ranjit, K., Bhar, L. M. (2020) Application of Machine Learning Techniques with GARCH Model for Forecasting Volatility in Agricultural Commodity Prices[J]. *Indian Society of Agricultural Statistics*, 74(3), 187-194

[10] Tian, Y., Yang, G., Wang, Z., Wang, H., Li, E., & Liang, Z. (2019). Apple detection during different growth stages in orchards using the improved YOLO-V3 model. *Computers and electronics in agriculture*, 157, 417-426.

[11] Tan, M., Pang, R., & Le, Q. V. (2020). Efficientdet: Scalable and efficient object detection. In *Proceedings of the IEEE/CVF conference on computer vision and pattern recognition* (pp. 10781-10790).

[12] Wang, Q., Nuske, S., Bergerman, M., & Singh, S. (2013). Automated crop yield estimation for apple orchards. In *Experimental robotics* (pp. 745-758). Springer, Heidelberg.

[13] Wang, D., & He, D. (2021). Channel pruned YOLO V5s-based deep learning approach for rapid and accurate apple fruitlet detection before fruit thinning. *Biosystems Engineering*, 210, 271-281.

[14] Yu, Z., Cao, Z., Wu, X., Bai, X., Qin, Y., Zhuo, W., ... & Xue, H. (2013). Automatic image-based detection technology for two critical growth stages of maize: Emergence and three-leaf stage. *Agricultural and forest meteorology*, 174, 65-84.

[15] Zhao, Y., Gong, L., Huang, Y., & Liu, C. (2016). A review of key techniques of vision-based control for harvesting robot. *Computers and Electronics in Agricultur*e, 127, 311-323.

[16] Zhang, N., Wang, M., & Wang, N. (2002). Precision agriculture—a worldwide overview. *Computers and electronics in agriculture*, 36(2-3), 113-132.

[17] Zhao, C., Lee, W. S., & He, D. (2016). Immature green citrus detection based on colour feature and sum of absolute transformed difference (SATD) using colour images in the citrus grove. *Computers and Electronics in Agriculture*, 124, 243-253.

[18] Zhuang, J. J., Luo, S. M., Hou, C. J., Tang, Y., He, Y., & Xue, X. Y. (2018). Detection of orchard citrus fruits using a monocular machine vision-based method for automatic fruit picking applications. *Computers and Electronics in Agriculture*, 152, 64-73.

[19] Zheng, C., Chen, P., Pang, J., Yang, X., Chen, C., Tu, S., & Xue, Y. (2021). A mango picking vision algorithm on instance segmentation and key point detection from RGB images in an open orchard. *Biosystems engineering*, 206, 32-54.

RESEARCH AND SIMULATION ANALYSIS OF PEANUT COMBINED HARVESTER EXCAVATING DEVICE
/
花生联合收获机挖掘装置研究与仿真分析

Baiqiang ZUO[1)], Shuqi SHANG[1)], Xiaoning HE[1)], Zenghui GAO[2)], Wei LIU[3)], Chunxiao ZHANG[1)], Zhenjia MA[1)], Dongwei WANG*[1)]

[1)] Qingdao Agricultural University, College of Mechanical and Electrical Engineering / China;
[2)] Xinjiang Agricultural University, College of Mechanical and Electrical Engineering / China;
[3)] Shandong Yuanquan Mechanical Co / China
Tel: +86-0532-58957391; E-mail: 200701031@qau.edu.cn
DOI: https://doi.org/10.35633/inmateh-68-38

Keywords: *peanut combine harvester, digging shovel, optimization, simulation analysis, experiment*

ABSTRACT
For the peanut combine harvester excavation process resistance, poor soil crushing effect and poor reliability of the problem, the excavation shovel optimization needs improvement. Firstly, a mechanical model of the resistance of the excavation shovel was established to investigate the key factors affecting the degree of resistance of the excavation shovel. Next, the design of the main parameters of the excavation shovel was done to determine the range of values of the main factors affecting the peanut excavation shovel. EDEM software was used to simulate and analyse the excavation process and to explore the influence law of excavation shovel parameters on the resistance. Improvements were made to the excavation shovel, discrete element simulation tests were used to demonstrate that the optimized excavation device had better resistance reduction and soil crushing than the original device. By designing a three-factor, three-level orthogonal simulation test, the best parameters for the excavation shovel were obtained: the shovel surface inclination is 20°, the excavation depth is 131mm, and the shovel surface width is 277mm. Field trials were conducted under the optimal combination of parameters to test the reliability of the improved digging shovel. Compared with the operating effectiveness of the original machine, the result was improved to some extent. It proves that the optimized design of excavating shovel is reasonable and can improve the operation effect of peanut harvester.

摘要
针对花生联合收获机存在挖掘作业过程阻力大、碎土作业效果差以及可靠性差的问题，对挖掘铲进行优化改进。首先建立挖掘铲阻力力学模型，探究影响挖掘铲阻力大小的关键因素。其次对挖掘铲的主要参数进行设计，确定影响花生挖掘铲的主要因素的取值范围。利用EDEM 软件对挖掘过程进行仿真分析，探明挖掘铲参数对阻力的影响规律。对挖掘铲进行改进，利用离散元仿真试验证明了优化后的挖掘装置的减阻和破碎土壤效果优于原装置。通过设计三因素三水平正交仿真试验，得出挖掘铲最佳的参数组合：铲面倾角为 20°，挖掘深度为 131mm，铲面宽度为 277mm。在最优参数组合下进行田间试验，检验 131 改进后挖掘铲的可靠性。与原机作业效果对比，效果得到一定提高。证明挖掘铲优化设计合理，能够改善花生收获机的作业效果。

INTRODUCTION
Peanut is one of China's important economic and oilseed crops (*Wang et al., 2021; Li et al., 2018; Wang et al., 2017*). In recent years, peanut planting area is increasingly expanding. The consequent problem faced has been the harvesting of peanuts, so there is a need to further improve the machine harvesting rate of peanuts (*Chen et al., 2017; Shang et al., 2008*). As the basic link of peanut harvester, excavating device has a great influence on the operation quality of the harvester. As the excavation device penetrates deep into the soil, the magnitude of its resistance has an essential effect on the power loss (*Shi et al., 2015; Zhang et al., 2015; Wang et al., 2010; Chen et al., 2005*).

The excavation device is one of the key technologies to reduce the leakage rate and is also an important measure to reduce the resistance, increase the soil breakage rate and reduce the loss. In recent years, to realize the reduction of resistance and consumption in the excavation device of harvesters, scholars at national level and abroad have conducted more research on the excavation device of root crops and solved the problem from several aspects of research and analysis (*Hou et al., 2021*). Kang et al. conducted experimental tests on vibratory excavation shovels and found that the increase in vibration frequency and decrease in amplitude facilitated the improvement of excavation performance and also facilitated the separation of soil from the shovel surface.

Natenadze designed a vibrating shovel to improve the effectiveness of digging in hard soils. The relation between the technology and the design parameters of the vibration excavation shovel is analysed theoretically, and the parameters are optimized (*Natenadze, 2020)*. Wang et al. designed an ultrasonic vibration soil cutting and digging device (*Wang et al., 2020)*. The test verified that the device could achieve resistance reduction but could not reduce machine energy consumption. Zhang C et al designed a wedge-shaped self-lubricating deep loose shovel (*Zhang et al., 2021*). Self-lubricating inlaid pastes were installed on the wedge-shaped sides of the handle and tip to reduce the friction coefficient on the contact surface with the soil and reduce the tillage resistance. This device consumed considerable power and had low working reliability. The excavation and gripping device of the peanut combine harvester has a compact structure. It is difficult to reduce the drag of the excavation device by adding a vibration mechanism or other devices. Therefore, it is necessary to optimize the parameters of the digging shovel to achieve the best operation effect.

In this paper, the main parameters of the peanut digging shovel are studied and analysed by conducting a kinetic analysis of the shovel. The operation process of the excavation shovel was simulated and analysed using EDEM software. After the improvement of the excavation device, the optimal working parameters of the excavation shovel were determined through tests. The results of the field trials verified the reliability of the improved digging device. The content of the study can provide a theoretical basis for subsequent research on peanut digging shovels.

MATERIALS AND METHODS

Analysis of shovel resistance under ideal conditions

From the crop's point of view, the digging device has a root shovelling as well as lifting effect on the peanut plant. From the soil's point of view, the excavation process has actually a cutting action on the soil. Without considering the physical and mechanical properties of soil, the mechanical analysis of the excavating shovel, soil and peanut was carried out. The mechanical model is relatively simple due to the lack of research on the complex properties of the soil. The forces include the resistance f_1 to the movement of the soil-peanut agglomerates along the shovel surface and the edge cutting resistance f_2 of the digging shovel. Therefore, in the ideal state, the resistance model of the excavation shovel is:

$$f = f_1 + f_2 = mg\tan(\alpha+\varphi) + k_r A \quad (1)$$

where:

m indicates the mass of peanut-fruit-soil mixture, (kg); g denotes the gravitational acceleration, (m/s^2); α denotes the angle of inclination of the shovel surface, (°); φ indicates the angle of friction between the peanut-soil mixture and the digging shovel; k_r denotes excavation specific resistance, (N/m^2); A denotes the cross-sectional area of the soil on the surface of the excavation shovel, (m^2).

It can be seen that, under ideal conditions, the shovel face inclination and soil conditions are the key factors affecting the digging resistance. The greater the inclination of the shovel surface, the easier it is for the digging shovel to enter the soil. However, the total resistance of excavation also increases with the increase of angle, so it is necessary to design the shovel face inclination angle reasonably. Excavation resistance and soil are closely related. Sandy loam plots with high water content have correspondingly low shear resistance and labour-saving excavation.

Analysis of factors influencing excavation resistance

As shown in Fig 1(a), In order to obtain the expression of the traction force on the excavation shovel, each force acting on the excavation shovel is decomposed along the horizontal direction. The balanced equation can be written as:

$$F_1 = N_0\sin\alpha + \mu N_0\cos\alpha + C_a S\cos\alpha + kb\cos\alpha \quad (2)$$

where:

F indicates the digging resistance, (N); F_1 denotes the traction force, (N); k indicates the cutting resistance of the soil per unit width, (N/m); b indicates the width of the excavation shovel, (m); α denotes the tilt angle of the shovel surface, (°); N_0 denotes the normal load on the excavation shovel surface, (N); C_a indicates the soil adhesion parameter; S denotes the area of the shovel surface of the excavator, (m^2); μ denotes the coefficient of friction between the peanut and fruit soil agglomerates and the shovel surface.

The soil of the peanut planting site is uniform in texture and does not cause the dulling of the shovel blade of the excavation shovel, so the cutting resistance of the soil is negligible (*Deng et al., 2014*).

According to Newton's second law, the expression for the resistance of a digging shovel can be derived as:

$$F = F_1 - kb\cos\alpha = N_0\sin\alpha + \mu N_0\cos\alpha + C_a S\cos\alpha \tag{3}$$

As shown in Fig 1(b), mechanical analysis was carried out on excavated objects (soil, peanuts, etc.) from the shovel surface.

The mechanical equations in the horizontal and vertical directions were established.

$$\begin{cases} C_a S\cos\alpha + N_0(\mu\cos\alpha + \sin\alpha) - N_1(\sin\beta + \mu_1\cos\beta) - (CS_1 + F_b)\cos\beta = 0 \\ G + C_a\sin\alpha + N_0(\mu\sin\alpha + \cos\alpha) - N_1(\cos\beta + \mu_1\sin\beta) + (CS_1 + F_b)\sin\beta = 0 \end{cases} \tag{4}$$

where:

N_1 denotes the normal load on the excavation shovel surface, (N); G indicates the gravity of the fruit and soil mixture on the excavation shovel, (N); β indicates the inclination angle of the front failure surface, (°); S_1 denotes the area of the front shear failure surface, (m²); F_b denotes the inertial force of the excavated object, (N); μ_1 denotes the soil-to-soil friction coefficient.

Combining Eq. 3 and Eq. 4, the mechanical model expression for the excavation resistance is obtained after simplification.

$$F = \frac{G}{Z} + \frac{CS_1 + F_b}{Z(\sin\beta + \mu_1\cos\beta)} + \frac{C_a S}{Z(\sin\alpha + \mu_1\cos\beta)} \tag{5}$$

Of which:

$$Z = \left(\frac{\cos\alpha - \mu\sin\alpha}{\sin\alpha + \mu\cos\alpha} + \frac{\cos\beta - \mu_1\sin\beta}{\sin\beta + \mu_1\cos\beta}\right) \tag{6}$$

A schematic diagram of the geometric relations established for each parameter of the excavation system is shown in Fig 1(c).

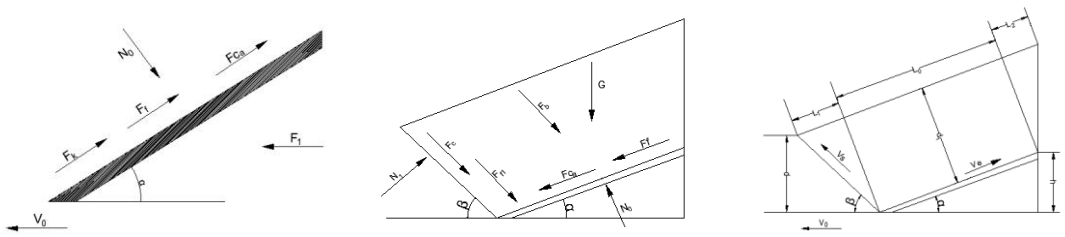

(a) (b) (c)

Fig. 1 - Mechanical and geometrical parameters of excavation device analysis diagram

The expressions for the gravity of the excavated object G, the inertial force of the excavated object F_b, and the area of the shovel surface S_1 can be derived from the analysis as follows:

$$\begin{cases} G = \rho g b d\ \dfrac{\sin(\alpha+\beta)}{\sin\alpha}\left(L + \dfrac{d\cos\beta}{2\sin\beta\cos\alpha}\right) \\ S_1 = \dfrac{bd}{\sin\beta} \\ F_b = \rho b d v_0^2 \dfrac{\sin\alpha}{\sin(\alpha+\beta)} \end{cases} \tag{7}$$

In summary, the working resistance of the excavation shovel is closely related to the physical and mechanical properties of the soil and the structural parameters of the excavation shovel, to provide a theoretical basis for the selection of subsequent test factors for the optimization of excavator structure parameters.

Design of the main parameters of the excavation shovel

Design of shovel face inclination

When the machine works forward, the force of the object on the shovel is shown in Fig 2.

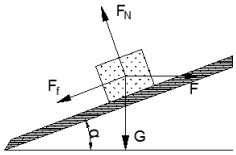

Fig. 2 - Shovel surface force analysis

Through the mechanical model, the following equation is established:

$$\begin{cases} F\cos\alpha - F_f - G\sin\alpha = 0 \\ F_N - G\cos\alpha - F\sin\alpha = 0 \\ F_f = \mu F_N \end{cases} \quad (8)$$

where:

F indicates the force required to move the excavated object along the shovel, (N); F_N denotes the reaction force of the excavation shovel on the soil, (N); G indicates the gravity of the excavated object, (N); F_f denotes the friction between the excavation shovel and the soil, (N); μ denotes the coefficient of friction of the soil on the excavation shovel, (N); α indicates the tilt angle of the shovel surface, (°).

The solution gives:

$$\alpha \le \arctan\frac{F - \mu G}{\mu F + G} \quad (9)$$

Through the theoretical analysis of excavation shovel resistance, it is necessary to ensure that the shovel surface inclination is less than the theoretical analysis value α. If the shovel surface angle is set too large, it will cause an increase in digging resistance and energy consumption (*Xu et al., 2022*). Comprehensive consideration, the digging device shovel face inclination was set at 15 to 25 °.

Digging deeper into the design

Based on the theoretical analysis of the resistance of excavating shovel, it is concluded that the force of excavating shovel is directly proportional to the excavation depth. As the excavation depth continues to increase, the resistance also rises sharply. According to the preliminary investigation and the relevant literature, the bearing depth of peanuts in the suitable harvest period is about 80~120mm. The applicability of excavating shovels needs to be improved as far as possible to ensure that the excavation operation loss rate and fruit leakage rate are the lowest. The excavation depth was determined to be 125mm ~ 145mm.

Design of shovel face width

At present, the main peanut production areas mainly adopt the ridge planting mode, needing to determine the width of the digging shovel according to the combination of peanut planting agronomy. The mean value of the distribution range of peanut results is BS, and the deviation of its distribution is B_1 (the standard distribution B_1 takes the value of 54mm), and there is a certain deviation value B_2 (generally takes the value of 30mm) when the machine is moving.

$$B = \frac{X + B_S + B_1 + B_2}{n} \quad (10)$$

Through literature review and preliminary investigation, combined with theoretical analysis, the width of excavating shovel is determined to be 250 ~ 300mm.

Simulation model construction

On a micro level, excavation operations are a complex process. The theoretical analysis cannot directly analyse the excavator shovel force; the actual field experiment cannot observe the working process of

excavating shovel, and the soil movement state cannot be obtained. Therefore, the discrete element simulation method investigates the excavation shovel's operating mechanism. Analysing the interaction between the shovel and the soil provides a fundamental theoretical basis for the design of the excavation shovel.

Soil particle model

In the discrete element modelling of soil, spherical particles with a single diameter should not be used; otherwise, the accuracy and reliability of simulation results will be seriously affected. The actual soil particle size is measured by the test, considering that the simulation results will not be affected. The soil particle size was set to 3mm, and four soil particle models were established. Soil parameters were set as in Table 1.

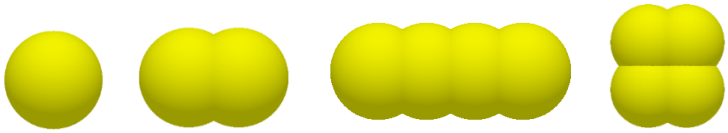

Fig. 3 - Soil particle model

Table 1

Soil parameters

Test parameters	Unit	Numerical value
Soil Density	Kg/m^3	1540
Soil Poisson's ratio	/	0.3
Soil shear modulus	Pa	1*10^8

Excavation device model

The excavation shovel was modelled using Solidworks software and imported into EDEM software. The material of the peanut excavation device is 65Mn steel with a density of 7810kg/m^3. Its model and parameter settings are shown in Fig 4.

(a) (b)

Fig. 4 - Excavation device model and parameter setting

Peanut Monopoly Model

According to the actual investigation, the ridge top width and bottom width of peanut were set as 450mm and 600mm, respectively. The model length was set to 1500 mm to reduce the simulation time. The peanut monopoly was modelled using Solidworks and then imported into EDEM software. Based on field conditions and existing soil particle simulation studies, the Hertz-Mindlin with Bonding model has less influence on the interaction between soil particles and was selected as the soil interparticle contact model (*Hang et al., 2017; Horabik et al., 2008; Mak et al., 2012; Ucgul et al., 2014*). The particle factory dynamically generates soil particles, which settle, pile up and bond to form peanut ridges. The model is shown in Fig 5 and the model contract parameters are shown in Table 2.

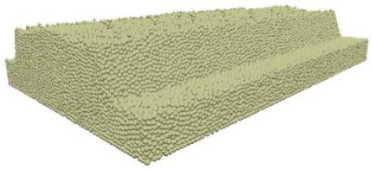

Fig. 5 - Peanut Monopoly Model

Table 2

Model contact parameter

Contact Model	Restitution Coefficient	Static Friction Coefficient	Rolling Friction Coefficient
Soil—Soil	0.56	0.31	0.15
Soil—65Mn	0.16	0.47	0.2

Simulation test analysis

To see the relation between the movement of the excavation shovel and the soil particles, three moments of the simulation process were taken to analyse the movement state of the soil, as shown in Fig 6.

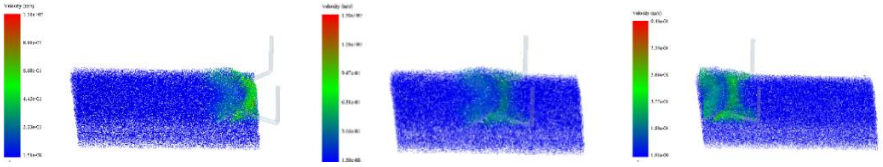

(a) (b) (c)

Fig. 6 - Overall view

According to the analysis of Fig 6, the different colours of the dominant bands in the graph represent soil particles of different velocities. When the digging shovel first touches the soil, the soil particles gain a certain speed and are displayed in green. However, because the shovel's contact with the ground is too small, the soil still has an overall blue state. As the digging shovel gradually enters the earth, the soil above the front of the shovel is disturbed more and more, and the speed becomes larger and larger. As the shovel surface continues to move forward, the soil particles begin to be thrown backward, at which point the velocity of the particles is increasing. When the soil is thrown to the ground, the speed becomes stationary again and starts settling.

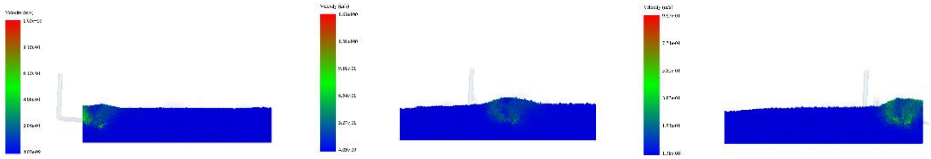

(a) (b) (c)

Fig. 7 - Cross-sectional view

The simulation is processed using the Clipping function to further observe the movement of the soil. It can be seen that the soil acquires a greater velocity when the tip of the excavation shovel enters the soil, indicating that the soil is more disturbed by the excavation shovel at this time. As the digging shovel undergoes movement, the direction of the velocity of the soil particles in the middle shovel surface area gradually changes to the vertical direction. This indicates that the soil starts to move upwards, which causes it to build up on the shovel surface and is an important cause of congestion. The amount of congestion then influences the change in excavation resistance.

Influence of different operating parameters on digging resistance

According to the existing research content of previous papers, the influence of shovel surface inclination, excavation depth, shovel surface width, and operating speed on the working resistance is studied. After Origin treatment, more intuitive resistance variation rules were explored to lay a theoretical foundation for the subsequent optimization of excavating shovel.

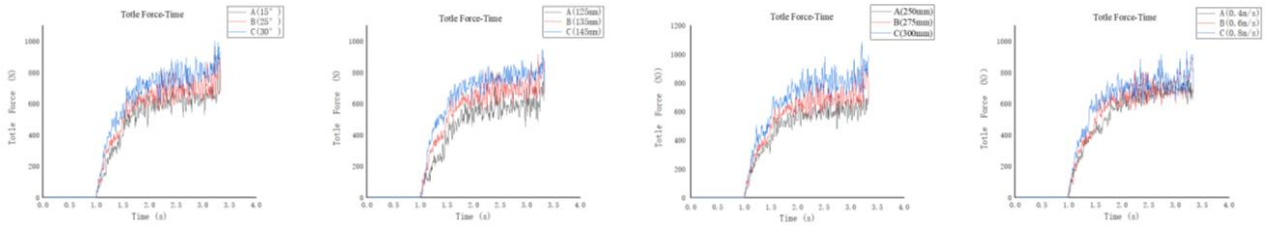

(a) (b) (c) (d)

Fig. 8 - Digging resistance comparison

Figure 8 (a, b, c, d) indicates the variation law of resistance at different shovel surface inclinations, different digging depths, different shovel surface widths, and different operating speeds, respectively. Excavation resistance increases with the increase of shovel surface inclination, excavation depth, and shovel surface width, and the change of resistance is more pronounced. When the speed of the machine is changed, the resistance of the excavation is not obvious. Therefore, the effect of working speed on drag can be ignored.

Optimization and improvement of excavation device

Through the theoretical and simulation analysis in the previous section, the influencing factors on shovel resistance were determined, and the interaction characteristics of "shovel-soil" were analysed at the microscopic level. In order to further reduce the resistance of the excavation shovel and improve the ground-breaking effect, a Fence bar excavation shovel is designed. The high-water content of the soil results in high cohesion. Therefore, this form is used to destroy the cohesion between the soils, further break the soil and reduce the adhesion of the soil to the shovel surface. In order to ensure that the peanut-soil through the bump on the crushing soil effect is better, the fence bar spacing is set to 20mm. Its structure is shown in Fig. 9.

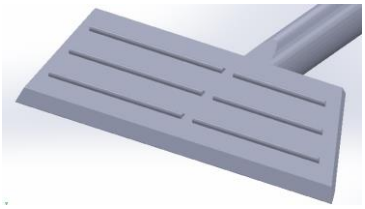

Fig. 9 - Grate excavation shovel

RESULTS

Test comparison of excavation device before and after improvement

After saving the changed excavation shovel in STL format, it was imported into EDEM for simulation test. Five sets of tests were designed to compare the two excavation devices' resistance and soil breaking rate. The excavation resistance was solved for the average value based on the data plots, and the soil fragmentation rate was derived from the number of bonds before and after the test. The data is shown in Table 3.

Table 3

Comparison of test data

Test number	Excavation resistance		Soil fragmentation rate	
	Original excavation shovel	Fence bar excavation shovel	Original excavation shovel	Fence bar excavation shovel
1	724.13	652.71	52.12	62.37
2	809.25	715.94	49.34	61.24
3	715.64	649.55	53.66	64.03
4	653.71	576.35	55.91	64.91
5	824.63	734.63	50.62	61.71

By comparing the data, the improved excavation device works better than the former, which proves the practical design.

Multi-factor test

The problem of resistance to the excavation shovel and the damaging effect on the soil were investigated. The test factors are the shovel surface inclination, digging depth, and width. Excavation resistance and soil fragmentation rate were selected as test indicators. Box-Behnken tests were conducted using the response surface method, and each set of tests was repeated three times to determine the best combination of parameters for the excavation device. The test factors and codes are shown in Table 4.

Table 4

Experimental factors and levels

Factor level	-1	0	1
Shovel face inclination	15	20	25
Digging Deeper	125	135	145
Width of shovel surface	250	275	300

The experimental design scheme and results are shown in Table 5.

Table 5

Test plan and results

Serial number	X_1 Shovel face inclination	X_2 Digging Deeper	X_3 Width of shovel surface	Y_1 Excavation resistance	Y_2 Soil fragmentation rate
	°	mm	mm	%	%
1	20	135	275	673	64.62
2	20	125	300	673	63.91
3	25	135	300	761	64.01
4	20	135	275	675	64.51
5	15	125	275	607	62.15
6	15	135	250	600	62.17
7	15	135	300	692	63.52
8	20	145	250	722	62.39
9	25	145	275	790	63.62
10	20	135	275	661	64.13
11	20	135	275	664	64.43
12	20	145	300	815	64.23
13	20	125	250	603	62.11
14	15	145	275	716	62.56
15	25	135	250	646	63.07
16	20	135	275	668	64.46
17	25	125	275	671	63.41

Regression analysis and significance test

Based on the experimental protocol and results, the data was analysed by multiple regression fitting using Design-Expert 13 software. A full-factor coded mathematical regression model was established with shovel surface inclination, excavation depth, and shovel face width as independent variables and excavation shovel resistance and soil fragmentation rate as objective functions.

(1) Excavation resistance response surface regression model:

$$Y_1=668.2+31.63X_1+61.13X_2+46.25X_3+2.5X_1X_2+5.75X_1X_3 +5.75X_2X_3-0.35X_1^2+28.15X_2^2+6.9X_3^2 \quad (11)$$

(2) Soil fragmentation rate response surface regression model:

$$Y_2=64.43+0.46X_1+0.15X_2+0.74X_3-0.05X_1X_2-0.1X_1X_3 -0.01X_2X_3-0.73X_1^2-0.76X_2^2-0.51X_3^2 \quad (12)$$

Analysis of variance and significance tests were performed on the established response surface regression models. The regression model ANOVAs for excavation shovel resistance and soil fragmentation rate is shown in Table 6 and Table 7.

Table 6

Analysis of variance for mining resistance

Sources	Squares	DF	MS	F value
Model 1	48091.79	9	83.04	< 0.0001
X_1	6786.13	1	105.46	< 0.0001
X_2	24420.50	1	379.49	< 0.0001
X_3	13530.13	1	210.26	< 0.0001
X_1X_2	72.25	1	1.12	0.3245
X_1X_3	100.00	1	1.55	0.2526
X_2X_3	110.25	1	1.71	0.2319
X_1^2	2.69	1	0.0419	0.8437
X_2^2	2857.27	1	44.40	0.0003
X_3^2	118.27	1	1.84	0.2173
Residual	450.45	7		
Lack of Fit	345.25	3	4.38	0.0939
Pure Error	105.20	4	R^2	0.9907
Cor Total	48542.24	16	Adj R^2	0.9788

Note: highly significant (P<0.01); significant (P<0.05).

According to the analysis of Table 5, the P of this model is less than 0.001, and the value of the misfit term is more than 0.05, indicating that the established model has a high degree of fit. The coefficient of determination was 0.9907, showing only 0.0193 variations, and the predicted value error of the model was close to the field experiment value. The experimental factors in the table significantly influence the equation, and the model can be used for parameter optimization of the excavation unit.

Table 7

Soil fragmentation rate analysis of variance

Sources	Squares	DF	MS	F value
Model 2	12.79	9	21.20	0.0003
X_1	1.72	1	25.66	0.0015
X_2	0.1861	1	2.77	0.1397
X_3	4.40	1	65.55	< 0.0001
X_1X_2	0.0100	1	0.1491	0.7108
X_1X_3	0.0420	1	0.6267	0.4545
X_2X_3	0.0004	1	0.0060	0.9406
X_1^2	2.25	1	33.58	0.0007
X_2^2	2.46	1	36.63	0.0005
X_3^2	1.08	1	16.09	0.0051
Residual	0.4694	7		
Lack of Fit	0.3360	3	3.36	0.1362
Pure Error	0.1334	4	R2	0.9646
Cor Total	13.26	16	Adj R2	0.9191

Note: highly significant (P<0.01); significant (P<0.05).

According to the analysis of Table 6, the P of the model is less than 0.001, and the value of the misfit term is more than 0.05, indicating that the established model has a high degree of fit. The test factors significantly affect the equation, and the order of influence of the three parameters on the soil crushing impact is: shovel face inclination > shovel face width > excavation depth. The model can be used for parameter optimization of the excavation unit.

Response surface analysis

The data was processed using Design-Expert 13 software to obtain the response surfaces of factor interactions on excavation resistance and soil fragmentation rate.

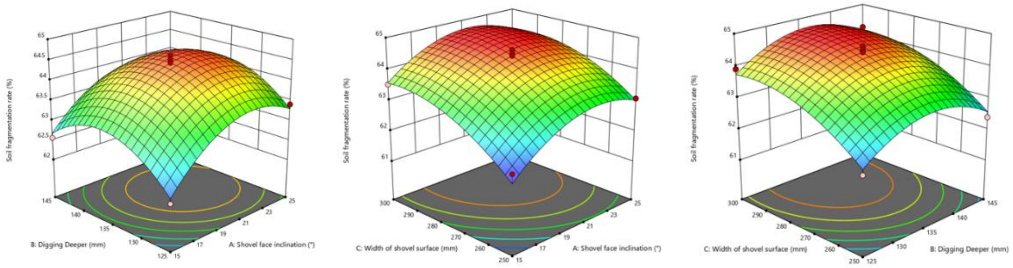

(a) (b) (c)

Fig. 10 - Response surface of the effect of factor interactions on excavation resistance

From Fig 10(a), it can be seen that the width of the shovel face remains the same. The digging depth is 125~135mm, and the digging resistance increases sharply after a slow increase. The digging resistance rises steadily with the shovel face inclination. From Fig 10(b), it can be observed that the excavation depth remains the same. With the shovel surface inclination increase and shovel face width, the digging resistance tends to rise. The width of the shovel surface influences the digging opposition. From Fig 10(c), it can be observed that the shovel face inclination angle remains constant. As the digging depth increases, the digging resistance increases slowly and then rises sharply. When the shovel surface width increases from 250mm to 300mm, the digging resistance rises steadily.

In a comprehensive analysis, the increase in shovel surface width and excavation depth leads to an increase in the weight of soil on the shovel surface. An increase in shovel surface inclination leads to a rise in congestion, leading to an increase in digging resistance. Therefore, taking as small a value as possible is essential to ensure that the digging resistance is not too high.

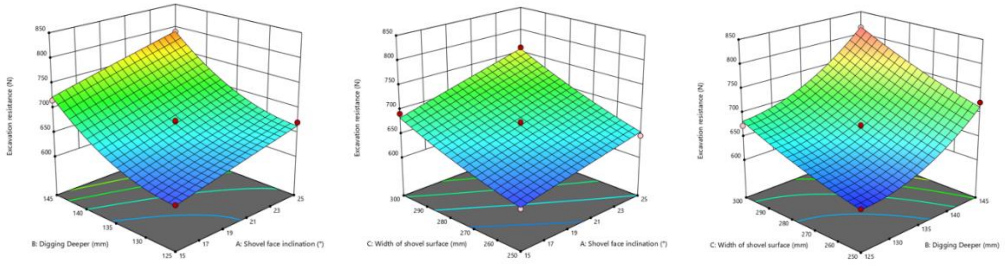

(a) (b) (c)

Fig. 11 - Response surface of the effect of factor interactions on soil fragmentation rate

From Fig. 11(a), it can be observed that the width of the shovel surface remains the same. With the increase of shovel surface inclination and excavation depth, the soil fragmentation rate shows a trend of increasing and decreasing. From Fig 11(b), it can be observed that the excavation depth remains the same. The soil fragmentation rate rises sharply in the range of 250~287mm at the shovel surface, after which the trend does not change significantly. Soil fragmentation rate increases with shovel surface inclination and then slightly decreases. From Fig 11(c), it can be observed that the shovel surface inclination angle remains constant. Soil fragmentation rate increases continuously with the width of the shovel surface and increases and then decreases with the excavation depth. Comprehensive analysis shows that the rise in shovel surface width and shovel surface inclination increases the soil contact area and causes the soil to break up. The increased tendency of the shovel surface raises the height of dirt falling from the back end of the shovel face, making it easier to break up the soil.

Optimization analysis of excavation device parameters

To achieve the best operational performance of the excavation unit, the influencing index parameters need to be minimized. The two indicators are considered together, and the operating parameters are optimized in a targeted manner.

The objective function and constraints are expressed in Equation (13).

$$\begin{cases} Y_1 = F\left(X_1、\ X_2、\ X_3\right) \to \min \\ Y_2 = F\left(X_1、\ X_2、\ X_3\right) \to \max \\ s.t. \begin{cases} -1 \le X_1 \le 1 \\ -1 \le X_2 \le 1 \\ -1 \le X_3 \le 1 \end{cases} \end{cases} \tag{13}$$

Optimization analysis of the best combination of results was performed using Design-Expert 13. The optimal working parameters include shovel surface inclination, digging depth, and shovel surface width of 20°, 131mm, and 277mm, respectively. The digging resistance and soil fragmentation rate were 583N and 64%, respectively.

Field trials

The optimal operating parameters of the excavation shovel were derived after simulation tests of the excavation unit. Field trials were conducted based on the optimal operating parameters obtained from the tests to further verify the operational effectiveness of the fence bar excavation shovel.

Fig. 12 - Field trials

The test results are shown in Table 8.

Table 8

Field trial data

Serial number	Peanut loss rate	
	Fence bar excavation shovel	Original excavation shovel
1	1.25	1.75
2	1.09	1.62
3	1.19	2.07
4	0.97	1.85
5	1.35	1.96
Average value	1.17	1.85

CONCLUSIONS

(1) In order to explore the main factors affecting the excavation resistance, a mechanical model of the excavation device was established. Through theoretical analysis, the influencing factors and their value range are determined.

(2) To further explore the excavation operation, a discrete element simulation model was constructed. The change law of excavation motion and excavation resistance is analysed by experiments.

(3) In order to obtain the optimal working parameters of the excavation shovel, the orthogonal test of three factors and three levels was carried out. Analysis of the test results yielded the best combination of operating parameters: shovel surface inclination of 20°, digging depth of 131 mm, and shovel surface width of 277 mm. Field trials were conducted under optimal operating parameters, and the results showed that the peanut loss rate was reduced by 0.68% and the improved digging shovel was reasonably designed.

ACKNOWLEDGEMENT

This research was funded by Modern Agricultural Industrial Technology System Project (CARS-13) and Shandong Provincial Key Science and Technology Innovation Engineering Project (2021CXGC010813).

REFERENCES

[1] Chen Zhihua, Li Yaoming, Sun Xingzhao, (2005). Dynamic analysis and experiment of peanut excavating shovel（花生挖掘铲动力学分析与试验）, *Transactions of the Society for Agricultural Machinery,* Vol.36, Issue 11, pp. 59-63.

[2] Chen Zhongyu, Gao Lianxing, Chen Charles et al., (2017). Status and development analysis of peanut harvesting mechanization technology in China and America（中美花生收获机械化技术现状与发展分析）, *Transactions of the Society for Agricultural Machinery,* Vol.48, Issue 4, pp. 1-21.

[3] Deng Weigang, Wang Chunguang, Sun Hong et al, (2014). Construction of mechanical model of potato excavator（马铃薯挖掘机挖掘铲力学模型构建）, *Agricultural Mechanization Research*，Vol.36, Issue 01, pp. 84-86.

[4] Hang C, Gao X, Yuan M, et al. (2018). Discrete element simulations and experiments of soil disturbance as affected by the tine spacing of subsoiler. *Biosystems Engineering*, 168: 73-82.

[5] Horabik J, Wiącek J, Parafiniuk P. et al. (2020), Calibration of discrete-element-method model parameters of bulk wheat for storage. *Biosystems Engineering*, 200: 298-314;

[6] Hou Jialin, Chen Yanyu, Li Yuhua, et al, (2021). Design and experiment of shovel - sieve combined scallion excavating, shaking and cleaning device（铲筛组合式大葱挖掘抖土疏整装置设计与试验）, *Transactions of the CSAE*, Vol.37, Issue 18, pp. 29-39.

[7] Kang W S, Halderson J L, Goodyear J D, (1991). A two-row vibratory potato digger[J]. *Paper-American Society of Agricultural Engineers (USA)*, 1991.

[8] Li Guanghui, Wang Xingjun, Shi Suhua, et al., (2018). Research status and prospect of fresh food peanuts in China（我国鲜食花生研究现状及展望）, *Chinese Journal of Oil Crops*，Vol.40, Issue 4, pp.604-607.

[9] Mak J, Chen Y, Sadek M A, (2012). Determining parameters of a discrete element model for soil-tool interaction[J]. *Soil&Tillage Research*, Vol.118:117-122.

[10] Natenadze N. The design and theoretical justification of a vibratory digger shovel[J]. Mechanization in agriculture & Conserving of the resources, 2016, 62(1): 9-11.

[11] Shang Shuqi, Zhou Yalong, Wang Xiaoyan, et al., (2008). Comparative experimental study on operating performance of three peanut harvesters（三种花生收获机的作业性能对比试验研究）. *Transactions of the CSAE*，Vol.24, Issue 6, pp. 150-153.

[12] Shi Chao, Yang Ranbing, Shang Shuqi, (2015). Finite element statics analysis of peanut harvester excavating device based on UG（基于 UG 的花生收获机挖掘 装置有限元静力学分析）, *Agricultural mechanization Research*, Vol.37, Issue 1, pp. 18-21.

[13] Ucgul M, John M F, Chris S, (2014). 3D DEM tillage simulation:validation of a hysteretic spring (plastic) contact model for a sweep tool operation in a cohesionless soil[J]. *Soil&Tillage Research,* Vol.144:220-227.

[14] Wang Bokai, Yu Zhaoyang, Hu Zhichao, et al., (2021). Numerical simulation and experiment of the flow field of the three-air air separation system of peanut picker（花生捡拾收获机三风系风选系统流场数值模拟与试验）, *Transactions of the Society for Agricultural Machinery,* Vol. 52, Issue 11, pp. 103-114.

[15] Wang Bing, Hu Zhichao, Peng Baoliang, et al., (2017). Optimization of operation parameters of spring finger screen structure of peanut combined harvester with half feeding four rows（半喂入四行花生联合收获机弹指筛结构运行参数优化）, *Transactions of the CSAE,* Vol.33, Issue 21, pp. 20-28, Nanjing/ P.R.C;

[16] Wang Dongwei, Wang Jiasheng, (2020). Design and test of soil cutting and excavating device based on ultrasonic vibration（基于超声振动的土壤切削挖掘装置设计与试验）, *Transactions of the Society for Agricultural Machinery,* Vol.51, Issue 11, pp. 85-92.

[17] Wang Hongli, Zhang Wei, (2010). Finite element analysis of deep loose shovel based on Pro E and ANSYS（基于 Pro E 和 ANSYS 的深松铲有限元分析）, *Agricultural Mechanization Research*, Vol.32, Issue 12, pp. 33-36.

[18] Xu Xing, Chen Shiguo, Hu Lihua, (2022). Design and Analysis of Excavation Mechanism of Prince Ginseng Harvester（太子参收获机挖掘机构设计及分析）, *Chinese Journal of Agricultural Mechanization,* Vol.43, Issue 08, pp. 32-39.

[19] Zhang Chong, Fan Xuhui, Wang Huze, et al, (2021). Structural design and drag reduction test of wedge-shaped self - lubricated deep loose shovel（楔形自润滑深松铲的结构设计与减阻试验）, *Agricultural Mechanization Research*, Vol.43, Issue 02, pp. 78-83.

[20] Zhang Hai-Liang, Zhao Feng-qin, (2015). Static analysis of excavating shovel based on ANSYS（基于 ANSYS 的挖掘铲静力分析）, *Agricultural technology and equipment*, Vol.5, 55 pp. 13-15.

MECHANICAL PROPERTIES AND MICROSTRUCTURE ANALYSIS OF TPA IN APPLE PULP BASED ON DIFFERENT LOADING SPEEDS
/
基于不同加载速度的苹果果肉TPA力学特性与微观结构分析

Bingyao JIANG[1)], Juxia WANG*[1)], Yifan WANG[1)], Tao LI[1)], Chen LI[1)], Xinhui WU[1)], Yulei ZHAN[1)]
[1)] College of Agricultural Engineering, Shanxi Agricultural University, Taigu 030801 / China
Tel: +86-18634418916; E-mail: wangjuxia79@163.com
DOI: https://doi.org/10.35633/inmateh-68-39

Keywords: *TPA mechanical test, Microstructure, Voronoi model, Plastic damage model*

ABSTRACT
In order to enrich the apple quality evaluation system, TPA mechanical tests were carried out on Fuji, Guoguang and Golden delicious apple pulp at 10 loading speeds of 0.01, 0.1, 0.5, 1, 2, 5, 9, 13 and 17 mm/s, and the mechanical characteristic parameters of pulp were obtained. The effects of loading speed on pulp hardness, elasticity, cohesiveness, chewiness and resilience were analysed. The microstructure of pulp of different varieties pulp was observed by laser confocal microscope. Based on the Voronoi model of pulp tissue structure, the compression test was simulated to construct the relationship between microstructure and mechanical properties. The results showed that the loading speeds had a certain effect on the cohesiveness and chewiness, and had a linear relationship with the cohesiveness of Guoguang variety and the chewiness of Golden delicious. The microstructure of pulp directly determines its mechanical properties, the smaller the roundness of cells and pores, the greater the hardness, cohesiveness, chewiness and resilience. Using Abaqus for compression test simulation, the maximum deviation of stress is 4.3%, which proves that the model is effective and the accuracy is improved. The results provide technical parameters for mechanical system improvements for apple during harvesting, storing and transporting and perfect evaluation system of apple texture.

摘要
为了丰富苹果品质评价体系，选用 0.01, 0.1, 0.5, 1, 2. 5, 9, 13, 17 mm/s 10个加载速度，对富士、国光、金冠苹果果肉进行了TPA力学试验，获得果肉力学特性参数，分析加载速度对果肉硬度、弹性、内聚性、咀嚼度、回复性的影响；采用激光共聚焦显微镜对不同品种果肉微观结构进行观测，得到不同品种组织结构差异；基于果肉组织结构的Voronoi模型模拟仿真压缩试验，构建微观结构与力学特性的联系。结果表明，加载速度对内聚性、咀嚼度有一定影响，与国光品种内聚性、金冠品种内聚性、咀嚼度成线性关系；果肉微观结构直接决定了其力学特性，细胞及孔隙圆形率越小，硬度、内聚性、咀嚼度、回复性越大；运用Abaqus软件进行压缩试验仿真，应力最大值偏差度为4.3%，证明模型有效，且精确度提升。研究结果为苹果采收、贮藏、运输等相关机械系统的改善提供数据支持，完善苹果贮运品质评价体系。

INTRODUCTION
Apple has rich nutritional value and is the second largest fruit species in China, with an annual output of one million tons *(Li et al., 2021)*. The evaluation of apple quality mostly adopts sensory evaluation, instrumental analysis and other methods to realize the difference comparison of characteristic parameters such as fruit hardness, brittleness, chewiness and moisture content *(Yogesh et al., 2017).* Many studies have shown that the difference in fruit quality is closely related to its microstructure. For example, Hou *(Hou et al., 2016)* analysed the mechanical properties of apple on the basis of puncture and compression experiments, combined with the observation of laser confocal microscope to obtain the pulp cell structure, and realized the prediction of the quality of fruit pulp. Yang *(Yang, 2019)* constructed the macro and micro models of dried apple pulp slice, carried out experimental verification, and analysed the drying characteristics of apple pulp slice under different conditions. Fan *(Fan, 2017)* observed the cell structure of 'Ruiyang' and 'Ruixue' by scanning electron microscope, obtained the content changes of pulp cell wall materials and components,

[1] *Bingyao JIANG, M.S. Stud. Eng.; Juxia WANG, A.P. Ph.D. Eng.; Tao LI, M.S. Stud. Eng.; Tao CHEN, M.S. Stud. Eng.; Xinhui WU A.P. Ph.D. Eng.; Yulei ZHANG, M.S. Stud. Eng.*

which provided a reference for apple quality evaluation and genetic breeding from the perspective of cytology. Wang *(Wang et al., 2020)* studied the quality of freeze-dried apple pulp slices, analysed the effects of polysaccharide and its concentration on the quality and microstructure of freeze-dried apple slices. Wang *(Wang et al., 2020)* observed the microstructure of apple peel and studied the relationship between its mechanical properties and microstructure. Bu *(Bu et al., 2020)* constructed the model of apple, constructed the plastic damage model of apple pulp through the test data, carried out the simulation test, which proved that the model was reasonable and accurate. To sum up, the parameters such as peel breaking force, pulp hardness and brittleness can evaluate the texture of apple, the microstructure of pulp tissue is closely related to the texture of apple. At present, there are few studies on the simulation of tissue microstructure based on geometric parameters *(Bu et al., 2020)*, which still stay in obtaining the relevant parameters of peel and pulp through experiments and the stage of simulation *(Hou et al., 2016)*. The purpose of this study is to: (1) Measure the TPA mechanical parameters of the same variety of apple pulp under different loading speeds, study the effect of loading speeds on the mechanical parameters, so as to provide data support for the improvement of the harvest, transportation and storage of apple. (2) The effect of pulp tissue on fruit substantive parameters was studied through the analysis of TPA mechanical parameters of different varieties of pulp, so as to provide reference for consumers' selection. (3) The microstructure of different apple varieties was observed, the Voronoi model of microstructure was constructed, the mesh was divided based on the Voronoi model in the Abaqus simulation analysis, the three-dimensional model of pulp tissue was established, and the relationship between the mechanical properties of TPA and its microstructure was analysed to verify the effectiveness of the model.

MATERIALS AND METHODS

Test materials

Fuji, Golden delicious and Guoguang apples were selected from Fruit Tree Research Institute of Shanxi Academy of Agricultural Sciences in October 2019. The apples with regular shape, similar size, no diseases and pests and no obvious defects were selected. The electronic balance hc31 produced by Huachao High Tech Institute was used to measure the single apple quality, and the digital vernier caliper produced by Dongguan Sanliang measuring tools Co., Ltd. was used to measure the transverse and longitudinal diameter of apple. Measure the circumference of the equator with a tape measure to obtain various parameters of the fruit, as shown in Table 1.

Quality and geometric dimensions of different varieties of apples **Table 1**

Varieties	Mass	Transverse diameter	Longitudinal diameter	Circumference at equator
	[kg]	[mm]	[mm]	[mm]
Fuji	195.6±31.3a	75.7±5.0a	62.0±5.5a	249.5±12.4a
Guoguang	120.0±24.2b	67.0±4.8b	51.4±4.1b	218.8±15.4b
Golden delicious	161.0±16.9c	72.4±2.5c	62.7±3.3a	236.0±7.7c

It can be seen from Table 1 that there are significant differences in the quality and geometric dimensions of different apple varieties. Fuji varieties have the largest parameters, followed by Golden delicious varieties and Guoguang varieties, indicating that Fuji varieties have the largest fruit and Guoguang varieties have the smallest size.

TPA mechanical test instruments and methods

Cut an apple into two halves along the radial direction, take samples at the equator of the apple with a cylindrical mold with a diameter of 1 cm. Take two samples on each half. Select two sharp blades, fix them at an interval of 1 cm, keep the two blades parallel to each other, cut the sample, and obtain a cylindrical sample with regular shape and 1 cm height for subsequent test.

TPA mechanical tests were conducted on the prepared cylindrical sample using TA-XT plus texture analyser (SMSTA.XTPlus, UK) which can measure load 0.001 to 295 mm and show the kinematic course of the force size, the sample deformation amount, and a test curve real-time. During the test, P50 probe is selected. The speed before measurement is 3 mm/s and the speed after measurement is 3 mm/s. The loading speeds are 0.01, 0.1, 0.5, 1, 2, 5, 9, 13 and 17 mm/s. For one loading speed, 10 samples from five apples are selected for repeated test. Analyse the test data and obtain the force time curve, as shown in Fig.1.

According to the force time curve, five parameters of hardness, elasticity, cohesiveness, chewiness and resilience can be calculated. Hardness is the maximum force in the first compression process on the curve. Elasticity is the ratio of the time difference between anchor 4 and anchor 5 to the time difference between anchor 1 and anchor 2. Cohesiveness is the ratio of the area under the curve of anchor 4 and anchor 6 to the area under the curve of anchor 1 and anchor 3. Chewiness is the product of hardness, cohesiveness and elasticity. Resilience is the ratio of the area under the curve of anchor 2 and anchor 3 to the area under the curve of anchor 1 and anchor 2.

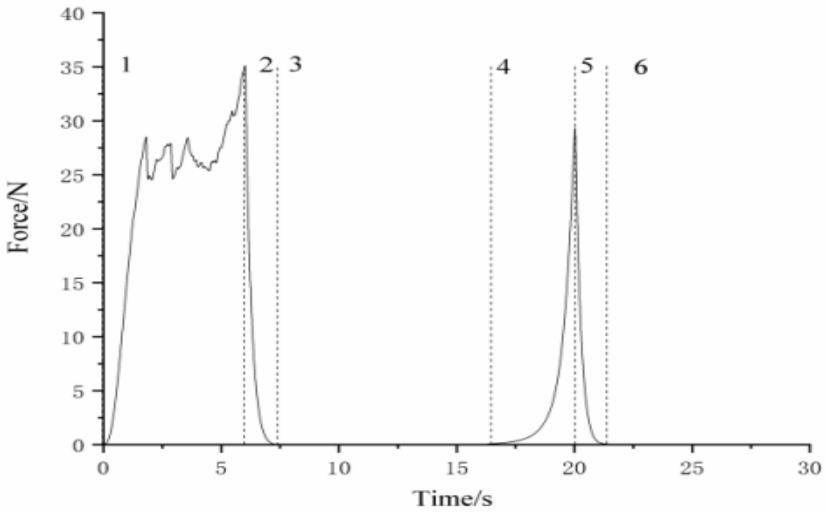

Fig. 1 - Force time curve

Instruments and methods for observing the microstructure of apple pulp

Cut out as thin as possible disc-shaped pulp tissue on the prepared cylindrical sample with a blade *(Li et al., 2020)*, soak it in Congo red dye with a concentration of 5% for 20 minutes, take it out after discoloration, wash it in deionized water, place it on the slide, absorb excess water, cover the slide, and observe the microstructure with a laser confocal microscope, 488 nm argon ion laser irradiation is selected to excite fluorescence, and the observation time shall not exceed 5 minutes to avoid the influence of tissue dehydration curl on the results *(Pipintakos et al., 2021)*. 10 apples were selected from each variety, and 10 disc-shaped tissues were taken from each apple for analysis *(Sheppard, 2021)*.

Compression test simulation

The first compression process in TPA mechanical test is used for data analysis and simulation. The stress and strain obtained from the test are nominal stress and nominal strain *(Jiang et al., 2021)*. In order to accurately describe the change of the sample in the process, it is necessary to calculate its real stress and real strain. The calculation formula is as follows *(Zhan et al., 2021)*:

$$\varepsilon_{true} = \ln(1+\varepsilon_{nom}) \quad (1)$$

$$\sigma_{true} = \sigma_{nom}(1+\varepsilon_{nom}) \quad (2)$$

Where: ε_{nom} is the nominal strain, %; ε_{true} is the true strain, %; σ_{nom} is the nominal stress, MPa; σ_{true} is the true stress, MPa.

In order to characterize the damage of the sample, a plastic damage model is constructed, and the relevant parameters of the plastic stage required for the simulation are calculated by using Sidoroff's energy equivalence principle. The calculation formula is as follows *(İynen et al., 2021)*:

$$\varepsilon^{in} = \varepsilon - \varepsilon_0^{el} \quad (3)$$

$$\varepsilon_0^{el} = \frac{\sigma}{E_0} \quad (4)$$

$$\varepsilon^{pl} = \varepsilon^{in} - \frac{d}{1-d}\varepsilon_0^{el} \quad (5)$$

$$d = 1 - \sqrt{\frac{\sigma}{E_0 \varepsilon}} \quad (6)$$

Where: ε^{in} is inelastic strain, %; ε_0^{el} is Elastic strain under the initial stiffness E_0, %; ε^{pl} is plastic strain; d is the damage factor.

The Voronoi model is constructed by MATLAB, the Voronoi model is imported into AutoCAD as a template for meshing, and the three-dimensional model of pulp is established. Then the three-dimensional model is imported into Abaqus for compression test simulation. According to authors *(Lv et al., 2017)*, combined with the test data, the apple pulp density is 8.4E-10 tonne/mm3, the elastic modulus is 5 MPa, the initial elastic modulus is 3.5 MPa, and the Poisson's ratio is 0.35. Through the simulated compression test, the maximum stress is obtained by outputting the stress-strain curve. Compared with the parameters obtained from the test, the accuracy of the model is analysed.

Data and image processing

Origin2017 is used to draw the force time curve, locate the anchor and calculate the area under the curve, using SPSS13.0 carries out difference analysis on mechanical characteristic parameters of pulp, linear fitting with loading speed and difference analysis on Euclidean geometric structural parameters of pulp tissue, taking 95% confidence interval *(Jiang, 2021)*.

Image J is used to process the image and extract the geometric parameters of cells. As shown in Fig.2, convert the image into 8-bit gray image, adjust the threshold to make the red fill the cells and pores, keep the contour clear, and extract the geometric parameters *(Sun et al., 2020)*.

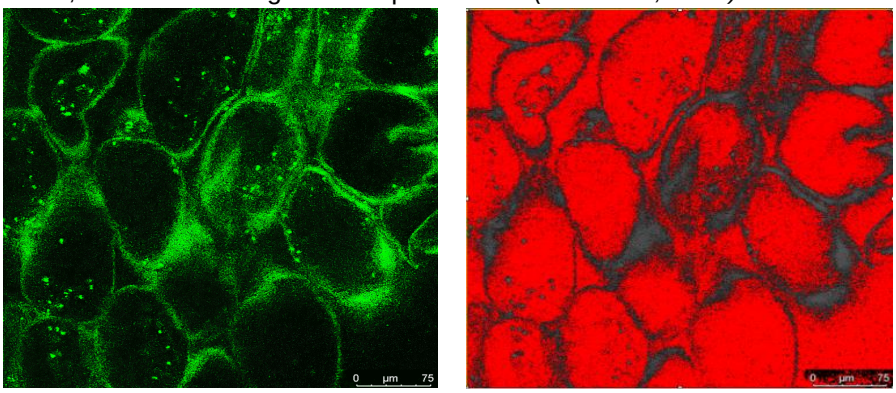

(**a**) (**b**)

Fig. 2 - (a) Fuji pulp laser confocal image; (b) Fuji pulp laser confocal image after image J processing

RESULTS

Analysis of TPA mechanical characteristic parameters of pulp

With the increase of loading speed, the impact of the indenter on the pulp increases and the resistance increases, resulting in the increase of three parameters related to the tightness of pulp tissue: hardness, cohesiveness and chewiness, which is consistent with the situation shown in Fig. 3. Among them, Fuji variety has close pulp tissue, the greatest resistance, hardness, cohesiveness and chewiness, and Guoguang variety has the opposite. There was no significant difference in elasticity among different varieties, indicating that they had the same elasticity under small shape variables. The resilience is related to the tightness of pulp tissue binding and the size of intracellular turgor. Among different varieties, Fuji variety has the largest resilience while Guoguang has the smallest, reflecting that the resilience is less affected by the tightness of pulp tissue binding than the parameters of hardness, cohesiveness and chewiness.

Analysis of TPA mechanical characteristic parameters of pulp under different loading speeds. The differences of the mechanical characteristic parameters of the pulp of the same variety of apple under different loading speeds are analysed, and the ratio between the cases with significant differences and all cases is set. The result is the influence rate of loading speeds on the mechanical characteristic parameters of the pulp *(Zhang et al., 2018)*, and the results are shown in Table 2. It can be seen from Table 2 that different loading speeds have a great impact on the pulp cohesiveness of the three varieties of apple, with an average value of 0.578, which has a certain impact on the hardness, chewiness and resilience, with an average value of 0.4, 0.385 and 0.326 respectively, which basically has no impact on the pulp elasticity, indicating that the change of loading speeds have a certain impact on the degree of pulp tissue binding. Fuji varieties are closely combined with tissues and have the strongest ability to resist the change of loading speed, so the change of loading speed has the least influence on various mechanical characteristic parameters of Fuji varieties. The tight degree of tissue binding of Golden delicious varieties is between Fuji

varieties and Guoguang varieties, but the change of loading speed has the greatest impact on the mechanical properties of Golden delicious varieties, indicating that the mechanical properties of Golden delicious varieties pulp are more vulnerable to the influence of different loading speeds during storage and transportation, and its tissue binding mode may be more vulnerable to the change of loading speed.

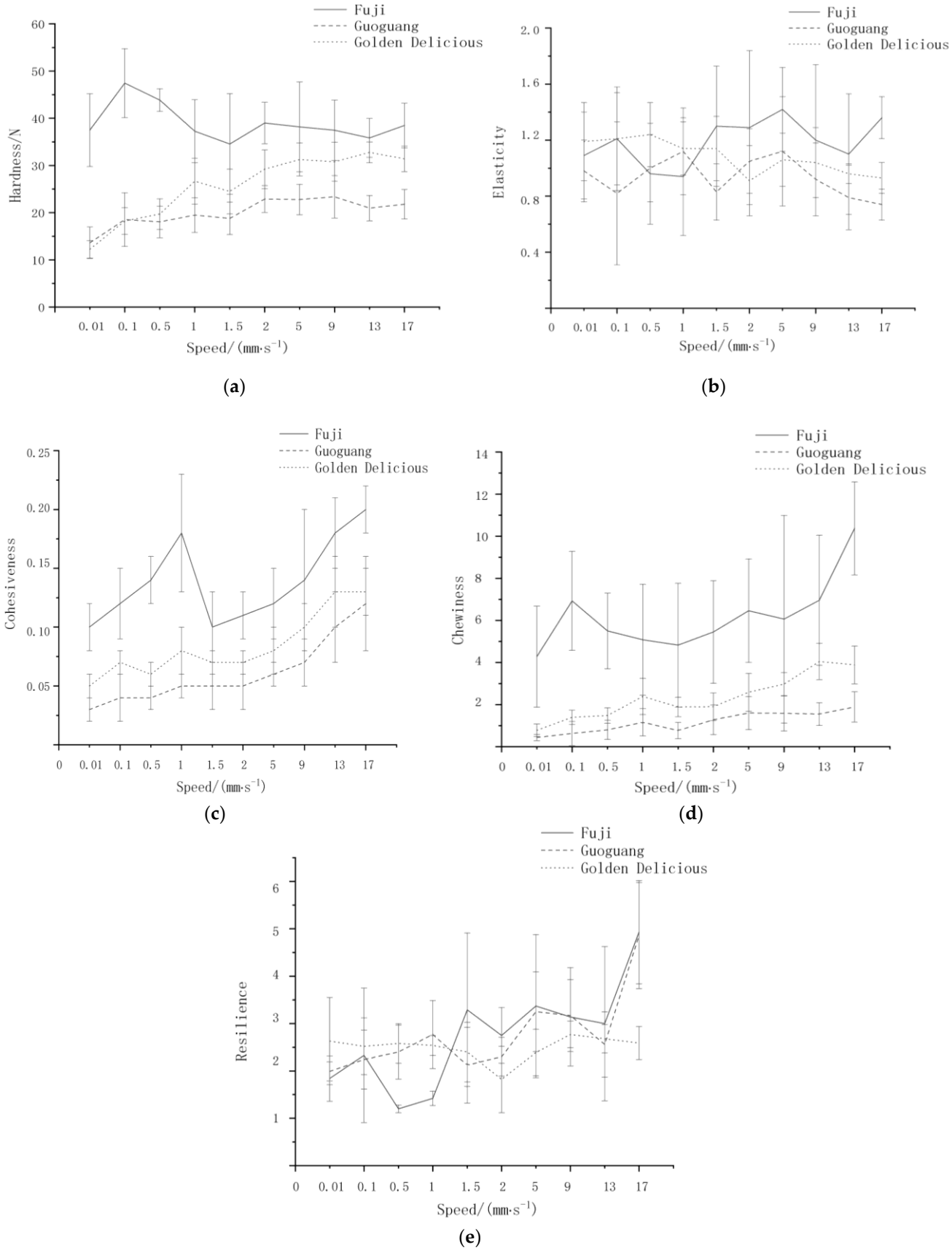

Fig. 3 - (a) Hardness; (b) Elasticity; (c) Cohesiveness; (d) Chewiness; (e) Resilience

Table 2

Effects of different loading speeds on TPA mechanical parameters of apple pulp

Varieties	Hardness	Elasticity	Cohesiveness	Chewiness	Resilience
Fuji	0.267	0.089	0.444	0.222	0.4
Guoguang	0.333	0.156	0.667	0.333	0.289
Golden delicious	0.6	0.156	0.622	0.6	0.289

Note: The closer the influence rate is to 1, the greater the influence of loading speed on the mechanical parameters of TPA in apple pulp.

Prediction ability of loading speed on mechanical parameters of apple pulp. In order to analyse the prediction ability of different loading speeds on the mechanical characteristic parameters of apple pulp, the univariate linear model is used to fit them, and the fitting equation is:

$$y = \beta x + k \tag{7}$$

Where: y is the mechanical characteristic parameter of apple pulp including cohesiveness, chewiness, resilience; β is the fitting coefficient; x is the loading speed, mm/s; k is the intercept.

The determination coefficients of univariate linear regression model with different loading speeds and pulp mechanical characteristic parameters are shown in Table 3.

Table 3

Determination coefficients of univariate linear regression model between loading speed and mechanical characteristic parameters of pulp

Varieties	Hardness	Elasticity	Cohesiveness	Chewiness	Resilience
Fuji	0.059	0.025	0.097	0.122	0.216
Guoguang	0.264	0.021	0.521	0.325	0.127
Golden delicious	0.386	0.147	0.557	0.619	0.001

Note: The closer the influence rate is to 1, the greater the influence of loading speed on the mechanical parameters of TPA in apple pulp.

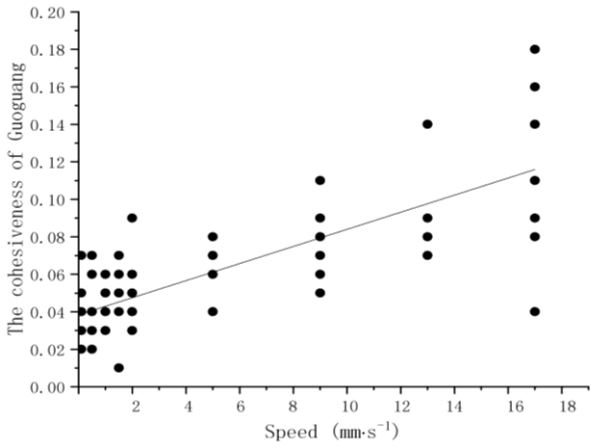

(a)

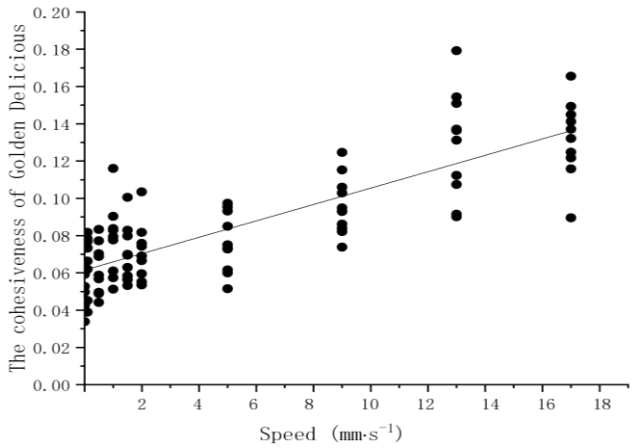

(b)

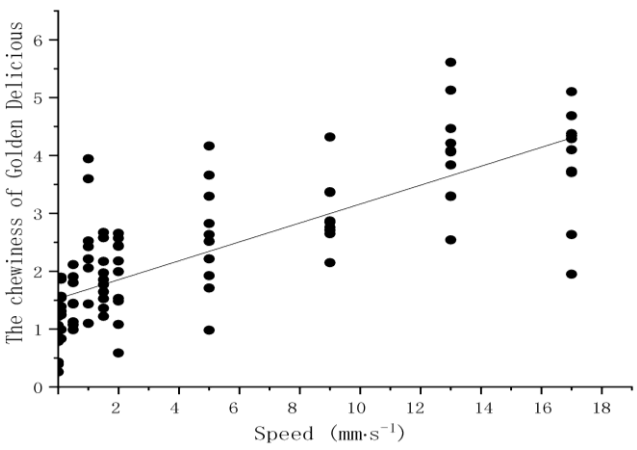

(c)

Fig. 4 - (a) Guoguang cohesiveness; (b) Golden delicious cohesiveness; (c) Golden delicious chewing

It can be seen from Table 3 that the loading speed is used to predict the cohesiveness of Guoguang varieties, and the determination coefficient of linear regression model R^2=0.521 (p<0.05). The loading speed is used to predict the cohesiveness and chewiness of Golden delicious varieties. The determination coefficients of linear regression model R^2=0.557 (p<0.05) and R^2=0.619 (p<0.05), indicate that the loading speed has a certain impact on the cohesiveness, cohesiveness and chewiness of Guoguang varieties and has the ability of prediction *(Fu, 2021)*. The results are basically the same as the effects of different loading speeds on the mechanical parameters of apple pulp. The image of linear regression equation between loading speeds and Guoguang variety cohesiveness, Golden delicious variety cohesiveness and chewiness is shown in Fig. 4. The linear regression equation between different loading speed and Guoguang variety cohesiveness is $y=0.0046x+0.038$, with Golden delicious variety cohesiveness is $y=0.0044x+0.062$, and with Golden delicious variety chewiness is $y=0.163x+1.572$.

Analysis of mechanical characteristic parameters of pulp of different varieties. The differences of pulp mechanical characteristic parameters of different varieties of apples under the same loading speed are analysed. The influence rate of varieties on pulp mechanical characteristic parameters is shown in Table 4. It can be seen from Table 4 that different varieties have a great impact on pulp hardness, cohesiveness and chewiness, and basically have no impact on elasticity and resilience, indicating that there are great differences in the tightness of pulp tissue and cells between varieties. Combined with the changes of TPA mechanical parameters of pulp, the image analysis results show that, compared with the three parameters of hardness, cohesiveness and chewiness which are affected by the combination degree of pulp tissue, the difference of resilience among varieties is small, which is less affected by the tightness of pulp tissue and varieties.

Table 4

Influence rate of different varieties on mechanical parameters of apple pulp

Varieties	Hardness	Elasticity	Cohesiveness	Chewiness	Resilience
0.01	0.667	0	1	1	0
0.1	0.333	0	1	0.667	0
0.5	1	0.333	0.333	1	0.667
1	1	0	0	1	0.667
1.5	1	0.667	1	1	0
2	0.667	0	1	0.667	0
5	1	0.333	1	1	0
9	0.667	0	1	1	0
13	1	0	1	0.667	0
17	0.667	1	0.667	1	0.333

Note: The closer the influence rate is to 1, the greater the influence of loading speed on the mechanical parameters of TPA in apple pulp.

Morphological analysis of apple pulp

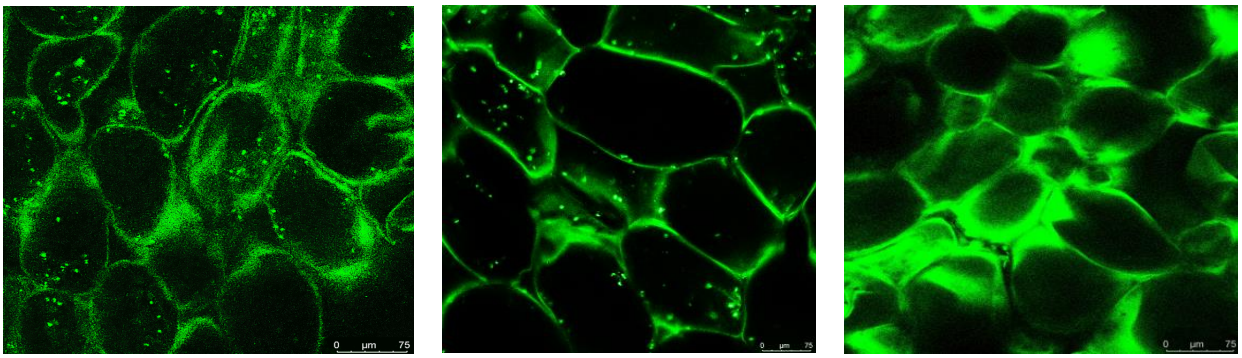

(**a**) (**b**) (**c**)

Fig. 5 - (a) Laser confocal image of Fuji pulp tissue; (b) Laser confocal image of Fuji pulp tissue; (c) Laser confocal image of Fuji pulp tissue

Microstructure of pulp of different varieties. Fig. 5 is a laser confocal image of apple pulp tissue. It can be seen from Fig. 5 that the apple pulp tissue cells are connected by the cell wall, which is mixed with irregular polygonal areas. The pulp tissue cells and pores of Guoguang apple are larger than those of Fuji

and golden delicious varieties. In Fig. 5 (a), the pulp cells of Fuji varieties are mostly oval, one end is sharp, and the cells are closely connected. Fig. 5 (b) the area and perimeter of pulp cells of Guoguang varieties are large, and the binding length between cells is short. In Fig. 5 (c), there are many round cells in the pulp of golden delicious varieties, and the cells are closely bound, but the connection length is small and the pores are less. The connection modes of tissue cells of the three varieties are different, and the histomorphological parameters are also different.

Euclidean geometric morphological parameter analysis of pulp cells and pores. Image J is used to calculate the area, perimeter, equivalent diameter and circularity of cells and pores, ignoring the characteristics of cells and pores with straight lines at the edge of the picture. The roundness rate is a shape parameter. The smaller it is, the rounder the cell is. The calculation formula is as follows:

$$\gamma = \frac{C^2}{4\pi S} \tag{8}$$

Where: γ is circularity; C is the perimeter, μm; S is the area of cells or pores, μm^2.

The Euclidean geometric morphological parameters of cells and pores of pulp tissues of different apple varieties are shown in Table 5. It can be seen from Table 5 that the area, perimeter and equivalent diameter of pulp tissue cells of different apple varieties are the largest in Guoguang variety, indicating that Guoguang variety has the largest pulp tissue cells. The area, perimeter and equivalent diameter of pulp tissue cells of Guoguang varieties were significantly different from those of the other two varieties (p<0.05). The roundness rate of pulp tissue cells of the three varieties was the smallest in Guoguang variety and the largest in Fuji variety. There was a significant difference in the roundness rate between the three varieties (p<0.05), indicating that the pulp tissue cells of Guoguang variety were round and there were few connections between cells. It can also be seen from Table 5 that the area, perimeter and equivalent diameter of pulp tissue pores of Guoguang varieties are greater than those of Fuji and Golden delicious varieties, indicating that the pulp tissue pores of Guoguang varieties are the largest. The area, perimeter and equivalent diameter of pulp tissue pores of Guoguang varieties were significantly different from those of Golden delicious (p<0.05), but not from Fuji varieties. The round rate of pulp tissue pores of Fuji varieties was higher than that of Guoguang and Golden delicious varieties, which reflected that the round rate of pulp tissue pores of Guoguang varieties was the lowest. There was significant difference between Fuji and the other two varieties in the pore roundness rate of pulp tissue (p< 0.05), indicating that Fuji has longer connecting distance and more contact between pulp tissue cells. In conclusion, Fuji variety has the largest cell and pore roundness rate, long connection distance and tight combination, while Guoguang variety has the smallest cell and pore roundness rate and less cell connection. Hardness, cohesiveness, chewiness and resilience are in direct proportion to the tightness of pulp tissue. Combined with the analysis results of pulp mechanical parameters, the pulp tissue structure directly determines the texture parameters.

Table 5

Euclidean geometric morphological parameters of Apple tissue cells and pores

Organization	Varieties	Area [μm^2]	Perimeter [μm]	Equivalent diameter [μm]	Circularity
Cells	Fuji	9374.91±2237.95ab	110.86±14.27a	96.64±18.09a	0.11±0.01a
	Guoguang	36532.54±10730.10b	201.31±59.42b	157.09±24.62b	0.08±0.02c
	Golden delicious	9828.16±2418.73a	111.01±19.11a	94.48±15.10a	0.10±0.02b
Pore	Fuji	4593.77±3047.03a	82.09±20.31a	65.06±26.92a	0.15±0.01a
	Guoguang	9011.71±4293.68b	93.58±28.92a	69.35±20.48a	0.07±0.04b
	Golden delicious	4925.27±2364.63a	84.90±16.23b	67.30±12.30a	0.09±0.11b

Note: Different lowercase letters represent the same Euclidean geometric morphological parameters of cells or pores of different varieties, with significant differences.

Simulation analysis of pulp mechanical test process

Voronoi model of apple pulp tissue. According to the cell area, 7477 Fuji pulp tissue cells, 2737 Guoguang pulp tissue cells and 10175 golden delicious pulp tissue cells can be distributed in a given square area of 10000 μm x10000 μm. The Voronoi model of Fuji pulp tissue cells *(Zheng et al., 2021)* is constructed by MATLAB. In order to facilitate analysis, the cell area is enlarged by 10 times in equal proportion, imported into AutoCAD, and the Voronoi model is adjusted according to the pulp tissue

structure of Fuji varieties *(Xing et al., 2021)*. The adjusted model ensures that the pulp tissue structure is similar to the actual observation. The geometric model of pulp tissue structure is shown in Fig. 6 (a). The three-dimensional model of pulp tissue structure is constructed by using AutoCAD and imported into Abaqus. The mesh is divided based on the adjusted Voronoi model. The obtained model is shown in Fig. 6 (b).

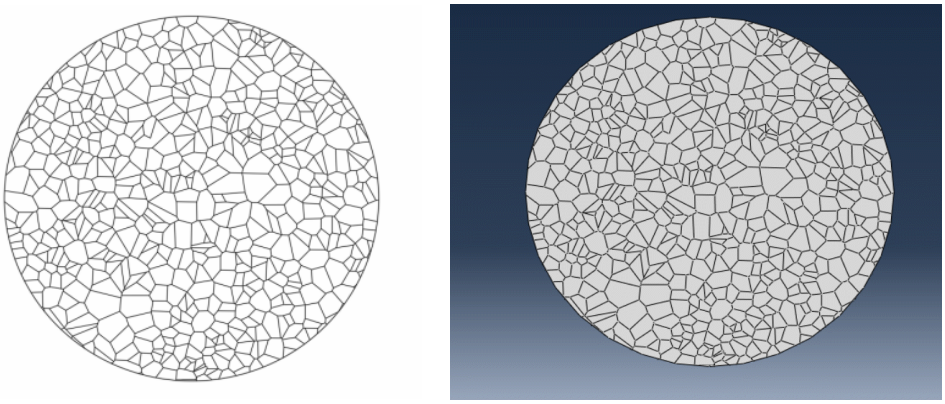

(a) (b)

Fig. 6 - (a) Voronoi model; (b) Mesh generation

Voronoi model of apple pulp tissue. Using Abaqus, set the parameters of the three-dimensional model according to the mechanical properties of Fuji apple pulp, select the elastic, plastic and density parameters to build the plastic damage model, use the adjusted Voronoi model as the basis for grid division, select the loading speed of 1 mm/s, and output the displacement stress curve, as shown in Fig. 7. The simulation results are in good agreement with the test results. In the TPA mechanical test, the maximum stress value at the speed of 1 mm/s is 0.46 ± 0.02 MPa, and in the simulation, the maximum stress value is 0.48 MPa. The relative deviation between the two is 4.3%, which is lower than the deviation of the existing simulation test, indicating that the model can better simulate the damage of apple pulp during compression. Based on the analysis of the first compression in TPA mechanical test, the pulp plastic damage model is constructed, and the simulation test is carried out to ensure the effectiveness of the model. The grid division method is refined. Voronoi model similar to the microstructure of apple pulp is adopted and adjusted according to the microstructure observation results, so as to make the model closer to the real microstructure of apple pulp and effectively improve the accuracy.

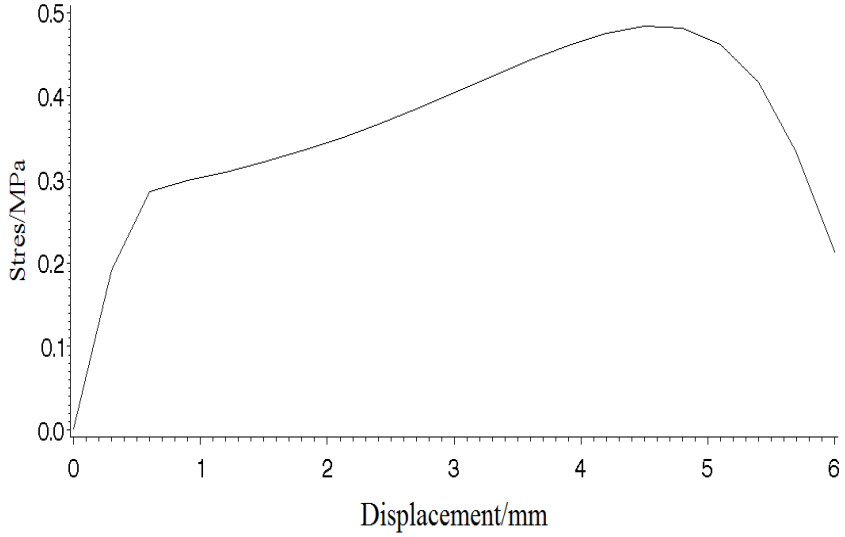

Fig. 7 - Displacement stress curve

CONCLUSIONS

(1) TPA mechanical tests were carried out on the pulp of three apple varieties at different loading speeds, and the differences of mechanical properties of the pulp of the same apple variety under different

loading speeds were analysed. The results showed that there were differences in the mechanical properties parameters of the same apple variety under different loading speeds, and the loading speed had the greatest influence on the cohesiveness, with an average value of 59.1%. Hardness, chewiness and resilience have a certain impact, with an average of 40%, 38.5% and 32.6% respectively, which has no effect on elasticity. Among the three varieties, Fuji variety has the least influence on various mechanical characteristic parameters by the change of loading speed, and has the strongest ability to resist fruit damage caused by the change of loading speed.

(2) The results showed that under the same loading speed, there were differences in the mechanical parameters of different apple varieties. The varieties had a great influence on the chewiness, hardness and cohesiveness, with the average values of 90.01%, 80.01% and 80% respectively. Among the 10 loading speeds, the mechanical parameters of apple at the speeds of 1.5 and 17 mm/s were most affected by the varieties, and the difference of fruit damage was also the largest.

(3) The microstructure of apple pulp was observed by laser confocal microscope. The rounder the pulp cells, the smaller the connection between cells, the looser the structure and the smaller the mechanical characteristic parameters. Among the three varieties of apple, Fuji has the highest rate of pulp tissue cells and pore roundness, the highest hardness, cohesiveness, chewiness and resilience, and Guoguang has the lowest rate of pulp tissue cells and pore roundness, Hardness, cohesiveness, chewiness and resilience were the smallest, and the correlation between Euclidean geometric parameters of pulp tissue and mechanical properties was established.

(4) According to the observation image of Fuji variety pulp microstructure, the Voronoi model of pulp tissue structure is constructed. The plastic damage model is established by using the parameters obtained from the first compression test in TPA mechanical test. The Voronoi model is used for grid division, and Abaqus finite element simulation is carried out. The deviation between the simulation results and the actual test results is 4.3%. The model is effective and has high precision. It can be used for mechanical test analysis of whole apple TPA.

ACKNOWLEDGEMENT

This research, titled ‘MECHANICAL PROPERTIES AND MICROSTRUCTURE ANALYSIS OF TPA IN APPLE PULP BASED ON DIFFERENT LOADING SPEEDS’, was funded by the National Natural Science Foundation of China (11802167), the Shanxi Province Key Research and Development Program (202102020101012), the applied basic research of Shanxi Province (201801D221297), the Doctor Scientific Research Foundation of Shanxi Agricultural University (2017YJ15), the applied basic research of Shanxi Province (201901D211364), the Doctor Scientific Research Foundation of Shanxi Agricultural University (2017YJ16) and the Excellent Doctor Scientific Research Foundation the Excellent Doctor Foundation of Work Reward for Shanxi Province (SXYBKY201754). The authors are grateful and honoured to have obtained support from the Key Laboratory of Biomechanics.

REFERENCES

[1] Bu, L.X., Hu, G.R., Chen, C.K., Sugirbay, A., & Chen, J. (2020). Experimental and simulation analysis of optimum picking patterns for robotic apple harvesting. *Scientia Horticulturae*, *Amsterdam/Netherlands, 261*: 1-9. https://doi.org/10.1016/j.scienta.2019.108937

[2] Fan, X.G. (2017). Cytological studies on texture difference in fruit development of 'Ruiyang', 'Ruixue' and their parents. Maste Dissertation, *Orthwest A&F University, Xianyang/China.*

[3] Fu, H. (2017). *Apple impact bruising mechanism and targeted shake-and-catch harvesting for fresh market apples in trellis trained trees* (苹果碰撞损伤机理和局部对靶振动采收方法研究). PhD Dissertation, *Zhejiang University*, *Hangzhou/China*.

[4] Hou, J.M., Sun, Y.H., Chen, F.Y., Yu, L.B., Mao, Q., Mao, L., Wang, L., Guo, X.L., & Liu, C. (2016). Analysis of microstructures and macrotextures for different apple cultivars based on parenchyma morphology. *Microscopy research and technique*, *Hoboken/USA, 79*(4), 304-312. https://doi.org/10.1002/jemt.22631

[5] İynen, O., Kadir, Ekşi, A.K., Akyıldız, H.K, & Özdemir, M. (2021). Real 3D turning simulation of materials with cylindrical shapes using ABAQUS/Explicit. *Journal of the Brazilian Society of Mechanical Sciences and Engineering*, Rio/*BRAZIL, 43* (374): 1-18. https://doi.org/10.1007/s40430-021-03075-5

[6] Jiang, N. (2021). Research on cell counting based on density estimation and its applications in microscopic image (基于密度估计的细胞计数方法及其在显微图像中的应用研究). PhD Dissertation, *Zhejiang University*, *Hangzhou/China*.

[7] Jiang, J.Q., Xu, R.Q., Qiu, Z.J., Zhan, X.B., Wang, Y., & Cheng, G.M. (2021). Egg-shaped elasto-plastic constitutive modelling for over-consolidated clay (超固结土的蛋形弹塑性本构模型). *Journal of Zhejiang University (Engineering Edition)*, *Hangzhou/China, 55*(08), 1444-1452. https://doi.org/10.3785/j.issn.1008-973X.2021.08.005

[8] Li, C.H., Tian, Y.F., & Yan, S.G. (2020). Laser Scanning Confocal Microscopy and Its Application (激光扫描共聚焦显微成像技术与应用). *Experimental science and technology*, *Chengdu/China, 18*(04), 33-38. https://doi.org/10.12179/1672-4550.20190257

[9] Li, S.J., Yuan, X.Y., Xu, Y., Li, Z.Z., Feng, Z.Z., X., Yue, X. & Paoletti, E. (2021). Biogenic volatile organic compound emissions from leaves and fruits of apple and peach trees during fruit development. *Journal of Environmental Sciences*, *Beijing / China, 108*(10), 152-163. https://doi.org/10.1016/j.jes.2021.02.013

[10] Lv, Y.X., Li, H.B., Zhu, X.H., & Liu, W.J. (2017). Discrete element method simulation of random Voronoi grain-based models. *Cluster Computing*, New York/USA*, 20*(1): 335-345. https://doi.org/10.1007/s10586-016-0705-3

[11] Pipintakos, G., Hasheminejad, N., Lommaert, C., Bocharova, A., & Blom, J. (2021). Application of Atomic Force (AFM), Environmental Scanning Electron (ESEM) and Confocal Laser Scanning Microscopy (CLSM) in bitumen: A review of the ageing effect. *Micron*, Oxford/England, 147: 1-14.

[12] Sheppard, C.J R. (2021). Structured illumination microscopy and image scanning microscopy: a review and comparison of imaging properties. *Philosophical Transactions of the Royal Society A,* London/England, *379*: 1-15. https://doi.org/10.1098/rsta.2020.0154

[13] Sun, Q., Zhang, M.T., & Huo, B. (2020). Analyses on cytoskeleton structure basing on confocal microscope (基于激光共聚焦显微镜的细胞骨架结构分析). *Scientia Sinica (Physica, Mechanica & Astronomica)*, *Beijing/China, 50*(09), 176-188.

[14] Wang, H.O., Wang, Q.J., Yan, Q.J., Jiang, Y., Zhou, F., & Hua, C. (2020). Effects of polysaccharide impregnating treatment on the quality and microstructure of vacuum freeze-dried apple slices. *Food and Fermentation Industries*, *Beijing/China, 46*(16), 43-48+55. https://doi.org/10.13995/j.cnki.11-1802/ts.022821

[15] Wang, J.X., Jiang, B.Y., Xu, S.H., Cui, Q.L., & Zheng, D.C. (2020). Research on the contribution ratio of apple peel puncture behaviour to fruit firmness. *INMATEH-Agricultural Engineering*, *Bucharest/Romania, 60*(1), 163-172. https://doi.org/10.35633/inmateh-60-19

[16] Xing, N., Wan, J.Q, Li, J.G., Liang, Z.X., Yang, F., & Leng, Z.Z. (2019). Effects of different drying methods on the quality and microstructure of apple slices (不同干燥方法对苹果片品质及微观结构的影响). *Food and fermentation industry*, *Beijing/China, 45*(16), 148-154. https://doi.org/10.13995/j.cnki.11-1802/ts.021131

[17] Yang, X.S. (2019). *Study of microscopic model and drying characteristics of apple slices (苹果片干燥微观模型研究与干燥特性分析)*. Master Dissertation, Orthwest A&F University, Xianyang/China.

[18] Yogesh, Dubey, A.K., Arora, R.R., & Mathur A. (2021). Fruit Defect Prediction Model (FDPM) based on Three-Level Validation. *Journal of Nondestructive Evaluation*, USA*, 40*(2), 1-12. https://doi.org/10.1007/s10921-021-00778-6

[19] Zhan, H.J., Xu, S.H., Wang, Y.D., & Wang, H. (2021). On fracture locus of corroded steel plates with nominal fracture strain and corrosion morphology. *Journal of Constructional Steel Research*, Oxford / Netherlands*, 184*: 1-13. https://doi.org/10.1016/J.JCSR.2021.106828

[20] Zhang, J., & Gan, L.P. (2018). Analysis and experimental study on anisotropic mechanical properties of apple pulp. *Hebei agricultural machinery*, Shijiazhuang / China*,* (02), 59-60. https://doi.org/10.15989/j.cnki.hbnjzzs.2018.02.040

[21] Zheng, Z.G., Wang, Z.L., Feng, Q., Yuan, S., & Wang, J.X. (2016). A method of polycrystal finite element modelling based on Voronoi diagram (一种基于 Voronoi 图的多晶体有限元建模方法). *Journal of Guangxi University (Natural Science Edition)*, Nanning / China*, 41*(02), 460-469. https://doi.org/10.13624/j.cnki.issn.1001-7445.2016.0460

EXPERIMENTAL STUDY AND ANALYSIS OF SMALL CORN HARVESTERS ON LODGED CORN IN HILLY AREAS
/
小型玉米机在丘陵山区收获倒伏玉米的试验研究与分析

Qiankun FU [1, 2]; Jun FU *, [1, 2]; Zhi CHEN [2, 3]; Luquan REN [1, 2]
[1)] Key Laboratory of Bionic Engineering, Ministry of Education, Jilin University / China;
[2)] College of Biological and Agricultural Engineering, Jilin University / China
[3)] Chinese Academy of Agricultural Mechanization Sciences / China
Tel: 86-431-85095760; E-mail: fu_jun@jlu.edu.cn
DOI: https://doi.org/10.35633/inmateh-68-40

Keywords: *corn harvest, corn lodging, corn harvester header, crawler, harvest loss, hilly areas*

ABSTRACT
In the harvest of lodged corn in hilly areas, over low position of corn ears and large slope of the land caused severe losses. The comprehensive performance of loss reduction and terrain adaptability was studied on three small corn harvesters. The tested harvesters were 4-row 4YZP-4Y wheeled harvester, 2-row 4YZLP-2C crawler harvester and 2-row 4YZLP-2C-AF crawler harvester that equipped with spiral lifers. The results showed the all-speed corn ear loss and grain loss of the 4YZP-4Y harvester were 55.6% and 57.6% lower than the 4YZLP-2C harvester, while those of the 4YZLP-2C-AF harvester was 23.2% and 17.3%. lower than the 4YZLP-2C harvester. The all-height corn ear loss and grain loss of the 4YZP-4Y harvester was 35.2% and 56.6% lower than the 4YZLP-2C harvester, those of the 4YZLP-2C-AF harvester was 19.9% and 24.9% lower than the 4YZLP-2C harvester. Smaller header width and larger roller compacted area of the 4YZLP-2C harvester were main factors that caused harvest loss. Wider harvester header, auxiliary feeding devices and smaller roller compacted area were key methods to reduce the harvest loss of lodged corn in hilly areas. This study provides technical scheme and design references for harvesters on lodged corn in hilly areas.

摘要
在丘陵山区倒伏玉米的收获中，过低的果穗位置和较大的地面坡度造成了严重的收获损失。本研究对三种小型玉米收获机进行了玉米收获损失和地形适应性的综合性能试验。试验所用玉米收获机机型分别为4 行4YZP-4Y 型轮式收获机、2 行 4YZLP-2C 履带式收获机和安装了螺旋提升器的 2 行 4YZLP-2C-AF 型履带式收获机。试验结果表明，在不同作业速度下，与 4YZLP-2C 收获机相比，4YZP-4Y 收获机的果穗损失和籽粒损失分别低了 55.6%和 57.6%，4YZLP-2C-AF 型收获机分别降低了 23.2%和 17.3%；在不同割台高度下，与 4YZLP-2C 收获机相比，4YZP-4Y 收获机的果穗损失和籽粒损失分别降低了 35.2%和 56.6%，4YZLP-2C-AF 型收获机分别降低了19.9%和24.9%。较小的割台宽度和较大的地面碾压面积是造成4YZLP-2C 履带式收获机收获损失的主要原因。增大割台宽度，加装辅助喂入装置以及缩小地面碾压面积是减小丘陵地区倒伏玉米收获损失的关键措施。本研究为丘陵地区倒伏玉米收获中收获机的适应性研究提供技术支撑和设计参考。

INTRODUCTION

Lodging is one of the main factors that caused corn yield reduction all over the world (*Flint-Garcia et al., 2003*). A lot of researches have been made on the causes of corn lodging. Due to these researches, insufficient application of nitrogen fertilizer, excessive planting density, and unreasonable field irrigation would aggravate lodging (*Berry et al., 2021, Wang et al., 2020*). Physically, it was the suboptimal structure that leads to the failure and fracture of corn stalk (*Ma et al., 2014*). Therefore, many studies predicted lodging resistance of corn stalk with the structural strength. For example, the rind penetrometer resistance (RPR) and the stalk crushing strength (SCS) were considered as important indicators to characterize the lodging resistance of corn (*Albrecht et al., 1986, Seegmiller et al., 2020*). Robertson et al. (*2016*) believed that the stalk flexural stiffness better represent the stalk strength than the RPR and SCS according to the beam theory. Guo et al. (*2018*) and Cook et al. (*2019*) individually designed testing devices to measure the bending forces, horizontal deformations and bending angle of corn stalks in the field.

Lodging may occurr in the milky or wax ripeness stages of corn growth because of terrible weathers like strong winds and rainstorms (*Martinez-Vazquez 2016*). This kind of lodging has small impact on yield, but it brought great difficulties to harvesting (*Wang et al, 2021*). At present, most studies about late-stage lodging focused on the inducement investigation, lodging detection, and lodging area measurement. Unmanned aerial vehicles imagery, remote sensing, and high-throughput micro-phenotyping were employed to quantify the lodging areas and lodging severity (*Zhang et al., 2018, Wilke et al., 2019*). During harvest, ears on lodged corn were mostly lifted by headers with longer snouts and picked with narrow-spaced units (*Yang et al., 2016*). Xue et al. (*2018*) tested the harvest loss of lodged corn with different lodging conditions and found the loss was mainly caused by ear falling. Different from picking ears in corn harvesting, short-stem crops such as rice, wheat and soybean were gathered with whole plant due to their small size and the easiness in threshing (*Paulsen et al., 2014*). These crops were harvested by lowering the harvester headers and slowing down the speed (*Phetmanyseng et al., 2019*). Lodged sugarcane was gathered with stalk lifters. Chains or spiral blades were applied to lift the canes (*Bai et al., 2020*). However, there is no in-depth experimental study and theoretical analysis on the working conditions and technical difficulties in lodged corn harvest, including the application adaptability of different harvesters and headers.

Moreover, in the vast hilly areas like Southern and Northeast China, large harvesters are difficult to operate due to the small plot area, large land slope and poor road conditions (*Wang et al., 2012, Liu et al., 2021*). Only small harvesters could be used for the harvesting of corn in these areas. Machines with crawler were considered to be most suitable for farmwork in hilly areas because of their good traction performance, lower groundpressure, and excellent climbing ability (*Molari et al., 2012*). However, rare study was made on the adaptability of small corn harvesters in hilly areas, eapecially when the working condition was exacerbated by lodging.

This study is aimed to explore the adaptability of small harvesters on lodged corn and analyze the reasons for harvest loss in the hilly areas. A 4-row wheeled corn ear harvester (4YZP-4Y), a 2-row crawler corn ear harvester (4YZLP-2C), and a self-modified 2-row crawler corn ear harvester with spiral auxiliary feeding lifters (4YZLP-2C-AF) were employed and compared on the harvest loss under different working parameters on a land with large slope. The reasons for grain loss were analyzed with structural and operational parameters of harvester headers. This study provides technical scheme and design references for harvesters on lodged corn in hilly areas.

MATERIALS AND METHODS

Materials

- **Terrain conditions**

The plot for test was located in Changpaozi Village (E 125.341020, N 43.146970), Yitong Manchu Autonomous County, Jilin Province. It was in the hilly area of the transition from Changbai Mountain to Songliao Plain. The plot covered an area of 2.19 hectares. The maximum distance in the east-west direction was 210 m and that in the north-south direction was 190 m. The maximum altitude difference of the selected land was about 30 m, and the slope was between 7° to 10° according to the contour map, as is shown in Figure 1. The contour map was obtained from software LocaSpaceViewer 4 that development by Beijing Three Dimensional Vision Technology Co., Ltd.

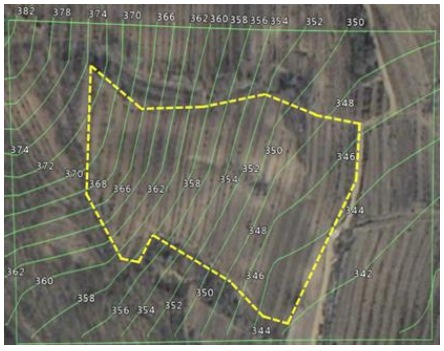

Fig. 1 - Contour distribution of tested plot (unit: m).

- **Corn lodging survey**

The morphology of corn used in the test is shown in Figure 2. The lodging occurred in Aug 27, 2020 to Sep 8, 2020, about 40 days before the test. Ridging was adopted in the land preparation before planting.

The investigations before test showed that the residual ridge height was 83 mm, the top width was 232 mm, the bottom width was 387 mm, and the ridging distance was 650 mm. As can be seen in Figure 2, most stalks lodged on the ground were cross to the ridge with an angle of 45° to 135°.

Before test, 5 plots covered 10 m × 10 m were randomly selected for the lodging investigation. The statistics was carried out according to the morphology of corn stalks. The lodging was divided into root lodging and stalk lodging. For root lodging corn, the included angle between corn stalk and the ground was measured. The heights of stalk breaking point were recorded for the stalk lodging corn.

Fig. 2 - Lodging conditions of corn stalks in the test plot.

- **Corn harvesters**

Three types of small corn harvester were selected for the test, as shown in Figure 3. The first was the 4YZP-4Y 4-row wheeled corn harvester (Figure 3a), the second was the 4YZLP-2C 2-row crawler corn harvester (Figure 3b). They were both manufactured by Shandong Juming Agricultural Machinery Co., Ltd. The same corn picking units were equipped on them with different rows according to their operating width. The third harvester was the 4YZLP-2C-AF crawler corn harvester (Figure 3c) that modified from the 4YZLP-2C harvester with spiral auxiliary stalk lifters, the structure diagram of 4YZLP-2C-AF harvester is shown in Figure 4. The main structural and technical parameters of the three corn harvesters are shown in Table 1. Among the parameters, the roller compacted area was calculated with the ratio of total width of the wheels or the crawlers to the harvester header width.

(a) **(b)** **(c)**

Fig. 3 - Working scene of the 3 corn harvester in the test.

(a) – the 4YZP-4Y 4-row wheeled corn harvester, (b) – the 4YZLP-2C 2-row crawler corn harvester, (c) – the 4YZLP-2C-AF corn harvester equipped with spiral auxiliary stalk lifters.

Table 1

Structural and technical parameters of 3 corn harvesters used in the test

Corn Harvester Model	Overall Dimension [mm×mm×mm]	Engine Power [kW]	Travel Mechanism	Header Width [mm]	Header Rows	Header Inclination [°]	Roller compacted area [%]
4YZP-4Y	8130×2850×3550	147	Wheel	2550	4	10°-30°	27.4
4YZLP-2C	5310×1750×2680	48	Caterpillar	1510	2	10°-30°	37.1
4YZLP-2C-AF	5870×1750×2680	48	Caterpillar	1730	2	10°-30°	32.4

The 4YZLP-2C-AF harvester lifted lodged corn stalks with spiral lifters. Its power was provided by the axle of stalk shredder with the chain transmission system. Gearboxes were applied to transfer the power to the spiral lifters. The specific parameters of the refitted working parts are as follows: the outer diameter of the spiral lifter was 150 mm; the inner diameter of the spiral lifter was 50 mm; the pitch of the spiral lifter was 150 mm; the length of the spiral part was 1500 mm; the inclination angle of the spiral lifter was 30° which consistent with the header; the speed of the spiral lifter was 300 r/min (*Fu et al., 2022*).

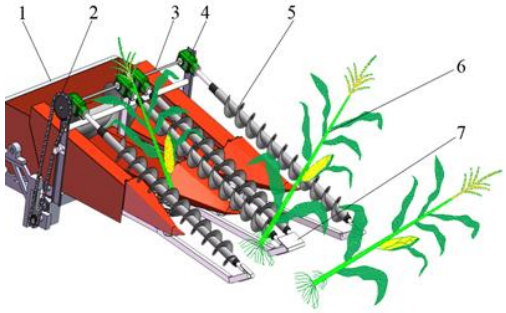

Fig. 4 - Structure diagram of the 4YZLP-2C-AF corn harvester.
1 – Corn harvester header; 2 – Chain transmission system; 3 – Horizontal shaft; 4 – Gearbox; 5 – Spiral lifter; 6 – Corn plant; 7 – Crop divider.

Test Factors

- **Harvester forward speed**

Harvest loss was directly related to the forward speed of corn harvester. The standard speed of the corn harvesters in this test was 0.55 m/s to 1.1 m/s. In the harvest of the lodged corn, the corn headers may be blocked by the stalks. So the forward speed of harvesters was tested lower than the standard speed. The test speeds were 0.3 m/s, 0.5 m/s, 0.7 m/s, 0.9 m/s and 1.1 m/s, while the average height of corn headers were controlled at 80 mm.

- **Header height**

The header height was a key factor that influence the harvest loss of lodged corn. As the land slope may cause inconsistent of height between different sides of the headers, the average header height was adopted, as shown in Figure 5 and the following equation:

$$h = (h_L + h_R)/2 \text{ [mm]} \quad (1)$$

where:

h was the average header height, h_L was the height of the left side, h_R was that of the right side.

Also, the height differences between right and left sides of the corn headers were compared to see their relationship with the land slope and the harvest loss. To test the effect of land slope on the header height differences, harvesters were driven along contour lines with the same direction. Before harvesting, the headers were set to the target height with the hydraulic control system. The actual height of the outermost snouts on both sides were measured respectively. For the 4YZP-4Y and 4YZLP-2C harvesters, the measuring points of the headers were at the tip of snouts on the outermost sides. For the 4YZLP-2C-AF harvester, the measuring points were at the tip of crop dividers. According to the height of corn ears that shown in Table 2, the target header average heights were determined to be 40 mm, 80 mm, 120 mm, 160 mm and 200 mm, respectively. In this test, the forward speed of the corn harvesters was 0.5 m/s.

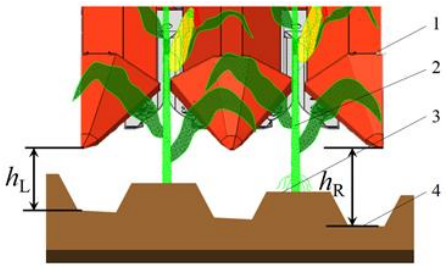

Fig. 5 - Measure method of the average header height.
1 – Corn header; 2 – Corn plant; 3 – Ridge top; 4 – Ridge bottom.

Metrics and test methods

- **Ear loss rate**

In the harvest of lodged corn, grain loss was mainly in the form of corn ear dropping (*Xue et al., 2018*). So, the ear loss rate was taken as the first experimental metrics in this test. To keep consistency of the test area, the working distance of the 4YZLP-2C harvester and the 4YZLP-2C-AF harvester was 20 m, and that of the 4YZP-4Y harvester was 10 m. After harvesting, corn ears left on the ground were collected and counted. The total number of corn ears was determined by the residual roots on the ground. The ratio of dropped ears and the total number of corn plants was the ear loss rate. Each trial was repeated for 3 times.

- **Grain loss mass**

Grain loss mass was the mass of detached kernels on the ground. It did't consist kernels on the dropped corn ears. It indicated the harvest loss that could not be recovered with human hands as these kernels scattered on the ground dispersedly. It could be compensated by picking up grains manually after harvesting. In this metrics, an area of 1 m^2 was randomly selected after harvesting to collect the kernels on the ground. After removing the stalk segments, all grains scattered on the ground except the ones attached on corn cobs were collected. Each trial was repeated for 3 times.

RESULTS AND DISCUSSION

Lodging morphology

The statistical results of lodging morphology are shown in Table 2. It can be seen that the lodging was serious. Most of the lodging was on corn root. A small part of lodging was caused by stalk breaking.

Table 2

Statistics result of lodging morphology in the test field

Term		Total Lodging Rate [%]	Root Lodging Rate [%]	Root Lodging Angle [°]	Stalk Lodging Rate [%]	Stalk Lodging Height [mm]	Corn Peduncle Height [mm]
Sampling Plot	1	92.3	83.6	11.4	8.7	366.5	201.27
	2	87.7	80.3	9.5	7.4	427.1	163.85
	3	94.5	88.2	10.8	6.3	345.4	186.59
	4	93.6	89.9	15.2	3.7	410.6	254.18
	5	99.2	98.4	13.7	0.8	455.2	216.64
Average		93.46±3.70	88.08±6.17	12.12±2.05	5.38±2.82	400.96±39.98	204.51±30.33

The lodging angles of the rood lodged stalks were large. As the corn ears were lower than their peduncles because of self-weight, most corn ears were below 200 mm. For the stalk lodged corn, the fracture points were mostly at the third or fourth internode of the stalks. These internodes borne large forces under the combined function of root anchorage and the wind (*Albrecht et al., 1986*). The upper part corn stalks would fall to the ground after stalk lodging. It made corn ears difficult to pick in their inverted orientation.

Header height

Figure 6 shows the height of harvester headers on different sides. The height on different sides of the harvester headers showed no clear regularity. But the fluctuation amplitude and standard deviation of the 4YZP-4Y wheeled harvester was much larger than that of the 4YZLP-2C crawler harvester and the 4YZLP-2C 2-row crawler harvester. Considering the harvesters had same mechanical connection between header and frame, it could be drawn that the factor affecting height difference was the bumping of headers rather than the plot slope (*Liu et al., 2021*). As the 4YZP-4Y wheeled harvester had a wider header, its fluctuation amplitude would be larger when they have same fluctuation angle. The fluctuation of corn headers would cause miss picking of corn ears in lodging situation. Therefore, in hilly areas, the harvester headers width should be limited within a reasonable scope to avoid header fluctuation.

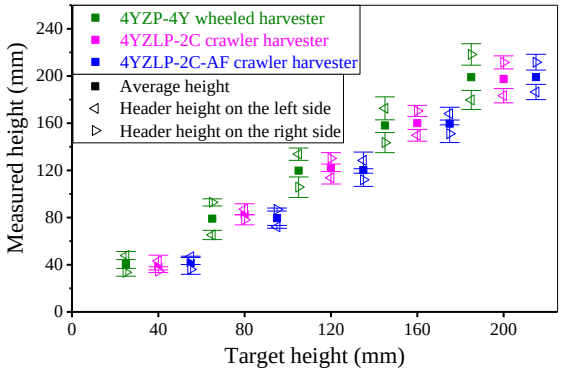

Fig. 6 - Statistics of headers' height at different target height.

Effect of harvest speed

The corn ear loss and grain loss mass of the corn harvesters in dealing with the lodged corn at different travel speeds are shown in Figure 7.

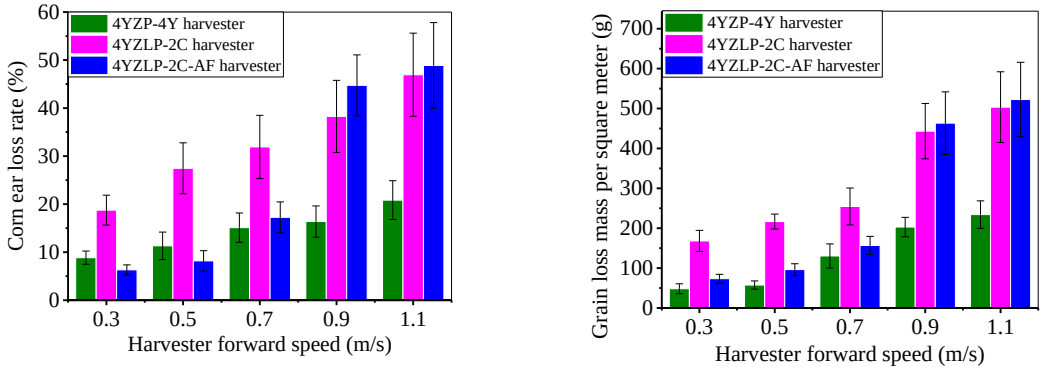

(a) **(b)**

Fig. 7 - Ear loss rate and grain loss mass per square meter of the 3 corn harvesters at different forward speed.

(a) – corn ear loss rate; (b) – grain loss mass per square meter

It can be seen from Figure 7 that the corn ear loss and grain loss of the harvesters increased obviously when the forward speed got higher. Among them, the corn ear loss rate of the 4YZP-4Y harvester, 4YZLP-2C harvester and the 4YZLP-2C-AF harvester increased from 8.85%, 18.76% and 6.31% to 20.84%, 46.95% and 48.89%, while the grain loss mass per square meter of them increased from 48.32, 168.14 and 73.54 g/m^2 to 234.10, 503.55 and 522.56 g/m^2 respectively. The increasing was consistent with the conclusion of Paulsen et al. (*2014*).

The lodged corn would stack in the front of harvester headers in harvesting. They would be pushed forward instead of being rolled down by the stalk rolls (*Xue et al., 2018*). As a result, the corn ears would be miss-picked and dropped to the ground. The all-speed corn ear loss rate of the 4YZP-4Y harvester and the 4YZLP-2C-AF harvester were lower than the 4YZLP-2C harvester with the percentage of 55.6% and 23.2%. It can be inffered that the width of the 2-row harvester header was too small to hold the corn plant when the harvester moved perpendicular to the lodging direction, as shown in Figure 8(a) and 8(b). However, the spiral lifters on the 4YZLP-2C-AF harvester could help to lift the stalks and feed them to the corn picking position, as shown in Figure 8(c). That was why the corn ear loss of the 4YZLP-2C-AF harvester lower than the 4YZLP-2C harvester. The corn ear loss rate of the 4YZLP-2C-AF harvester increased sharply when the forward speed got higher than 0.7 m/s. It indicated that the spiral lifter mached well with the header at low speed. When the harvester forward speed got higher, the stalk fquantity exceeded the dealing capacity of the spiral lifters. The spiral lifters would cause severe loss when they did't mach well with the deeding of lodged corn.

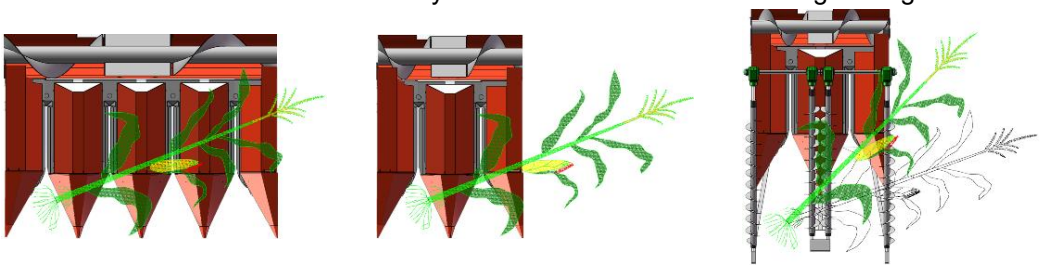

(a) **(b)** **(c)**

Fig. 8 - Corn ear picking process on different corn harvester headers.

(a) – 4YZP-4Y harvester header; (b) – 4YZLP-2C harvester header; (c) – 4YZLP-2C-AF harvester header

Figure 7(b) showed the grain loss increased with the harvester speed, just like the corn ear loss. A small part of grains on the ground were induced by the impact between corn ears and the harvester header working parts (*Fu et al., 2019*). More grain loss were caused by the roller compact on wheels or crawlers. Among the harvesters, the grain loss of the 4YZP-4Y harvester was the lowest at all time, while the 4YZLP-2C-AF harvester had low grain loss at low speed. The all-speed grain loss of the 4YZP-4Y harvester and the 4YZLP-2C-AF harvester were lower than the 4YZLP-2C harvester with the percentage of 57.6% and 17.3%. The conclusion was just the same as the study of Shauck et al. (*2011*) that wider header could reduce harvest loss. The dropped corn ears would be rolled by the wheels or the crawlers, and the grains would be threshed, which made up a larger part of grain loss, as shown in Figure 9.

Meanwhile, the crawler harvesters would cause unrecoverable loss because of the larger roller compacted area compared to the wheeled harvesters. Therefore, even the crawler machines were more adaptive in the hilly areas, the crawler harvesters were not competent in the lodged corn harvesting.

Fig. 9 - Kernels detached after the rolling of corn harvesters.

Effect of header height

The ear loss rate and grain loss per square meter of the corn harvesters at different harvester header heights are shown in Figure 10.

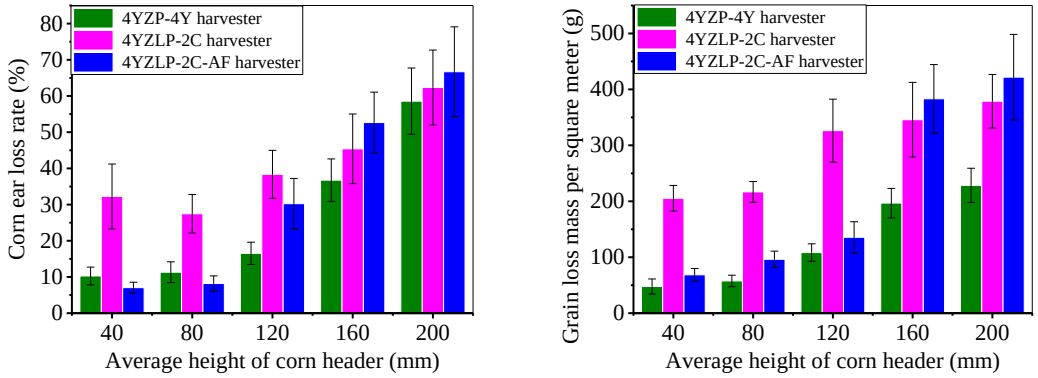

(a) **(b)**

Fig. 10 - Corn ear loss rate and grain loss mass of the 3 corn harvesters at different header heights.

(a) – corn ear loss rate; (b) – grain loss mass per square meter

It can be seen from Figure 10 that the corn ear loss and grain loss of the 3 harvester increased significantly when the harvester header got higher. Among them, the corn ear loss rate of the 4YZP-4Y harvester, the 4YZLP-2C harvester and the 4YZLP-2C-AF harvester increased from 10.28%, 32.25% and 7.05% to 58.57%, 62.35% and 66.71%, while the grain loss mass per squre meter increased from 47.68, 205.33 and 68.63 g/m^2 to 228.51, 378.81 and 421.95 g/m^2, respectively. The all-height corn ear loss rate and the grain loss mass per square meter of the 4YZP-4Y harvester was lower than that of the 4YZLP-2C harvester with the percentages of 35.2% and 56.6%. Those of the 4YZLP-2C-AF harvester was 19.9% and 24.9% lower than the 4YZLP-2C harvester.

After lodging, the corn ears were too low for the working parts of the headers to pick up. The results in Figure 10 showed corn harvester headers even couldn't pick the ears smoothly when they were a little lower than the corn ear position. It was necessary to reserve a height to make sure the ears be rolled down by the working parts of corn harvester headers, or they would be left to the bottom of corn headers (*Lopes et al., 2002*). Particularly, the corn ear loss rate of the 4YZLP-2C-AF harvester was the lowest when the header worked at low positions. But it became the highest when the corn header got higher. It was indicated that the additional mechanical kinematics aggravated corn ear loss when the corn stalks were not fed with the whole plant. Just as Yang et al. (*2016*) verified that the direct contact between corn ears and working components may cause high loss rate. The corn ear loss of the 4YZP-4Y harvester increased largely when the header got higher. It might be the jigging motion of its header that caused miss picking of corn ears, as indicated in Figure 6.

The changes of grain loss showed strong consistency with corn ear loss. The dropped corn ears would be rolled by the harvester to thresh the grains. Although the corn ear loss could be retrieved by picking up manually, it still need to be reduced.

The above analysis showed harvesters had different adaptability when dealing with the lodged corn in hilly areas. Even the 2-row 4YZLP-2C crawler harvesters had better trafficability in hilly area, it was still not qualified for the harvest of lodged corn because of the small header width and the limited stalk lifting ability. The larger roller compacted area even made the grain loss more serious. The 2-row 4YZLP-2C-AF crawler harvester that equipped with spiral lifter could reduce the corn ear loss by lifting stalks and help with the feeding. For the 4-row 4YZP-4Y harvester, the larger header width could reduce corn ear loss, and smaller roller compacted area of the wheels could reduce the grain loss caused by the rolling corn ears. But it should be pointed out that the jigging motion would increase corn ear loss when of the 4YZP-4Y harvester header stayed at higher positions. As a conclusion, application of wider harvester header and auxiliary feeding devices and reduce the roller compacted area were key methods to reduce the harvest loss of lodged corn in hilly areas.

CONCLUSIONS

Harvesting test on three types of corn harvester showed the 4-row 4YZP-4Y wheeled harvester and the 2-row 4YZLP-2C-AF crawler harvester that equipped with spiral lifters were more adaptive than the 2-row 4YZLP-2C crawler harvester for the harvesting of lodged corn in hilly areas. The all-speed corn ear loss rate and grain loss mass of the 4YZP-4Y harvester was lower than the 4YZLP-2C harvester with the percentage of 55.6% and 57.6%, while those of the 4YZLP-2C-AF harvester was lower than the 4YZLP-2C harvester with 23.2% and 17.3%. The all-height corn ear loss rate and grain loss mass of the 4YZP-4Y harvester was lower than the 4YZLP-2C harvester with the percentage of 35.2% and 56.6%, while those of the 4YZLP-2C-AF harvester was lower than the 4YZLP-2C harvester with 19.9% and 24.9%.

Even the 2-row 4YZLP-2C crawler harvesters had better trafficability in hilly area, it was still not qualified for the harvest of lodged corn. The small header width and the limited stalk lifting ability restricted its ear picking capacity on lodged corn. The larger roller compacted area even made the grain loss more serious. Fitting wider harvester headers, applying auxiliary feeding devices and reducing the roller compacted area were key methods to reduce the harvest loss of lodged corn in hilly areas.

ACKNOWLEDGEMENT

This research was funded by the National Natural Science Foundation of China, grant number 52105257 and Major State Research Development Program of China, Grant No. 2017YFD0700302.

REFERENCES

[1] Albrecht, K.A., Martin, M.J., Russel, W.A., Wedin, W.F., & Buxton, D.R., (1986), Chemical and in vitro digestible dry matter composi-tion of maize stalks after selection for stalk strength and stalk-rot resistance, *Crop Science*, WI/USA, vol.26, pp.1051–1055. https://doi.org/10.2135/cropsci1986.0011183X002600050043x

[2] Bai, J., Ma, S., Wang, F., Xing, H., Ma, J., & Wang, M., (2020), Performance of crop dividers with reference to harvesting lodged sugar-cane, *Sugar Tech*, Basel/Switzerland, vol.22, pp.812-819. https://doi.org/10.1007/s12355-020-00829-8

[3] Berry, P.M., Baker, C.J., Hatley, D., Dong, R., Wang, X., Blackburn, G.A., Miao, Y., Sterling, M., & Whyatt, J.D., (2021), Development and application of a model for calculating the risk of stem and root lodging in maize, *Field Crops Research*, Amsterdam/Holland, vol.262, No.108037. https://doi.org/10.1016/j.fcr.2020.108037

[4] Cook, D.D., Chapelle, W., Lin, T.C., Lee, S. Y., Sun, & W., Robertson, D.J., (2019), DARLING: a device for assessing resistance to lodging in grain crops, *Plant Methods*, Amsterdam/Holland, vol.15, No.102. https://doi.org/10.1186/s13007-019-0488-7

[5] Flint-Garcia, S.A., Jampatong, C., Darrah, L.L., & McMullen, M.D., (2003), Quantitative trait locus analysis of stalk strength in four maize populations, *Crop Science*, WI/USA, vol.43, pp.13-23.

[6] Fu, Q., Fu, J., Chen, Z., Han, L., & Ren, L., (2019), Effect of impact parameters and moisture content on kernel loss during corn snap-ping. *International Agrophysics*, Lublin/Poland, vol.33, pp.493-502. https://doi.org/10.31545/intagr/113490

[7] Fu, Q., Fu, J., Chen, Z., Zhao, R., & Ren, L, (2022), Design and experimental study of a spiral auxiliary feeding device for lodged corn on a combine harvester, *Journal of the ASABE*, MI/USA, vol.1, pp.31-38. https://doi.org/10.13031/ja.14580

[8] Guo, Q., Chen, R., Sun, X., Jiang, M., Sun, H., Wang, S., Ma, L., Yang, Y., & Hu, J., (2018), A non-des tructive and direc-tion-insensitive method using a strain sensor and two single axis angle sensors for e valuating corn stalk lodging resistance, *Sensors*, Basel/Switzerland, vol.18, No.1852. https://doi.org/10 .3390/s18061852

[9] Liu, Z., Zhang, G., Chu, G., Niu, H., Zhang, Y., & Yang, F., (2021), Design matching and dynamic perf ormance test for an HST-based drive system of a hillside crawler tractor, *Agriculture*, Basel/Switzerlan d, vol.11, No.466. https://doi.org/10.3390/agriculture11050466;

[10] Lopes, G.T., Magalhaes, P.S.G., & Nobrega, E.G.O., (2002), Optimal header height control system for combine harvesters, *Biosystems Engineering*, Amsterdam/Holland, vol.81, pp.261-272. https://doi.org/ 10.1006/bioe.2001.0016;

[11] Ma, D., Xie, R., Liu, X., Niu, X., Hou, P., Wang, K., Lu, Y., & Li, S., (2014), Lodging-related stalk chara cteristics of maize varieties in China since the 1950s, *Crop Science*, WI/USA, vol.54, pp.2805-2814. ht tps://doi.org/10.2135/cropsci2014.04.0301;

[12] Martinez-Vazquez, P., (2016), Crop lodging induced by wind and rain, *Agricultural and Forest Meteorology*, Amsterdam/Holland, vol.228–229, pp.265–275.

[13] Molari, G., Bellentani, L., & Guarnieri, A., (2012), Performance of an agricultural tractor fifitted with rubber tracks, *Biosystems Engineering*, Amsterdam/Holland, vol.111, pp.57–63;

[14] Paulsen, M.R., Pinto, F.A.C., & Sena, D.G., Zandonadi, R.S., Ruffato, S., Costa, A.G., Ragagnin, V.A., Danao M.G.C., (2014), Measurement of combine losses for corn and soybeans in Brazil, *Applied Engineering in Agriculture*, MI/USA, vol.30, pp.841-855. https://doi.org/10.13031/aea.30.10360;

[15] Phetmanyseng, X., Senthong, P., Chay, B., & Shu, F., (2019), Combine harvesting efficiency as affected by rice fifield size and other factors and its implication for adoption of combine contracting service, *Plant Production Science*, Oxford/UK, vol.22, pp.68-76. https://doi.org/10.1080/1343943X.2018.1561196;

[16] Robertson, D.J., Lee, S.Y., Julias, M., & Cook, D.D., (2016), Maize stalk lodging: flexural stiffness predicts strength, *Crop Science*, WI/USA, vol.56, pp.1711-1718. https://doi.org/10.2135/cropsci2015.11.0665;

[17] Shauck, T.C., & Smeda, R.J., (2011), Factors influencing corn harvest losses in Missouri, *Crop Management,* MO/USA, vol.10. https://doi.org/10.1094/CM-2011-0926-01-RS;

[18] Seegmiller, W.H., Graves, J., & Robertson, D.J., (2020), A novel rind puncture technique to measure ri nd thickness and diameter in plant stalks, *Plant Methods*, Amsterdam/Holland, vol.16, No.44. https://do i.org/10.1186/s13007-020-00587-4;

[19] Wang, K., Xie, R., Ming, B., Hou, P., Xue, J., & Li, S., (2021), Review of combine harvester losses for maize and influencing factors, *International Journal of Agricultural and Biological Engineering*, Beijing/ China, vol.14, pp.1-10. https://doi.org/10.25165/j.ijabe.20211401.6034;

[20] Wang, Q., Xue, J., Zhang, G., Chen, J., Xie, R., Ming, B., Hou, P., Wang, K., & Li, S., (2020), Nitrogen split application can improve the stalk lodging resistance of maize planted at high density, *Agriculture*, Basel/Switzerland, vol.10, No.364. http://dx.doi.org/10.3390/agriculture10080364;

[21] Wang, Y., Liu, Y., & Yang, F., (2012), Development and test of tiny remotely controlled electric tractor for green houses (温室微型遥控电动拖拉机的研制与试验), *Transactions of CSAE*, Beijing/China, vol.28, pp.23-29;

[22] Wilke, N., Siegmann, B., Klingbeil, L., Burkart, A., Kraska, T., Muller, O., Doorn, A., Heinemann, S., & Rascher U., (2019), Quantifying lodging percentage and lodging severity using a UAV-based canopy h eight model combined with an objective threshold approach, *Remote Sensing*, Basel/Switzerland, vol.1 1, No.515. https://doi.org/10.3390/rs11050515;

[23] Xue, J., Li, L., Xie, R., Wang, K., Hou, P., Ming, B., Zhang, W., Zhang, G., Gao, S., Bai, S., Chu, Z., & Li, S., (2018), Effect of lodging on maize grain losing and harvest efficiency in mechanical grain harves t (倒伏对玉米机械粒收田间损失和收获效率的影响), *Acta Agronomica Sinica*, Beijing/China, vol.44, pp. 1774-1781. https://doi.org/10.13597/j.cnki.maize.science.20200617;

[24] Yang, L., Cui, T., Qu, Z., Li, K., Yin, X., Han, D., Yan, B., Zhao, D., & Zhang, D., (2016), Development and application of mechanized maize harvesters. *International Journal of Agricultural and Biological Engineering*, Beijing/China, vol.9, pp.15-28. https://doi.org/10.3965/j.ijabe.20160903.2380;

[25] Zhang, Y., Du, J., Wang, J., Ma, L., Lu, X., Pan, X., Guo, X., & Zhao, C., (2018), High-throughput micro-phenotyping measurements ap-plied to assess stalk lodging in maize (Zea mays L.), *Biological Research*, Amsterdam/Holland, vol.51, No.40. https://doi.org/10.1186/s40659-018-0190-7;

FEASIBILITY ANALYSIS OF FLUTED ROLLER DISPENSER APPLICATION FOR PRECISION FERTILIZATION
/
SOONRULLDOSAATORI RAKENDATAVUS TÄPPISVÄETAMISEL

Lillerand TORMI*[1)], Reinvee MÄRT[1)], Virro INDREK[1)], Olt JÜRI[1)] [1]
[1)] Estonian University of Life Sciences / Estonia;
Tel: +372 7313 317; E-mail: tormi.lillerand@emu.ee
Corresponding author: Tormi Lillerand
DOI: https://doi.org/10.35633/inmateh-68-41

Keywords: *Agriculture 4.0, smart farming, volumetric dispenser, blueberry cultivation, granular fertilizer*

ABSTRACT
With depleting resources, it is essential to increase the application of Agriculture 4.0 principles and technologies. Blueberry cultivation includes various operations, one of them being fertilization. To precisely discharge the correct amount of fertilizer, a volumetric dispenser utilizing a straight fluted roller could be considered as an option. The aim of this research is to verify whether such a dispenser could be used for precision fertilization with solid granular fertilizers. The output of the dispenser was measured on different conditions with three NPK fertilizers. Based on statistical analysis, the required 10% discharge uniformity cannot be achieved and it is necessary to modify the dispenser or use another one.

LÜHIKOKKUVÕTE
Järjest kahanevate ressurssidega on ülioluline tõsta ja kiirendada Põllumajandus 4.0 põhimõtete ning tehnoloogiate rakendamist. Kultuurmustikate kasvatamine kätkeb endas mitmesuguseid operatsioone, üks neist on väetamine. Soovitud koguse täppisväljutamiseks võib võimalikuks lahenduseks pidada sirgsoonrulliga mahtdosaatorit. Antud uurimuse eesmärk on selgitada välja, kas tuntud väljakülviseade on kasutatav granuleeritud väetisega täppisväetamiseks. Dosaatori väljundit mõõdeti erinevatel tingimustel kolme NPK väetisega. Statistilise analüüsi põhjal saab väita, et väljakülvi ühtlust 10% piires ei võimalik saavutada ning dosaatorit on tarvis kas modifitseerida või kasutada teist.

INTRODUCTION

Cultivation of low-bush blueberries (Vaccinium angustifolium Ait.) on depleted peat fields is seen as an economically profitable way to reduce greenhouse gas emissions (*Vahejõe et al., 2010*). However, the peat fields are commonly located in remote areas where workforce is scarce. Therefore, the mechanization and automation of technological operations is essential. Traditional agricultural machinery is intended to be used on mineral soils, which restricts its use on peat fields, as the traditional machinery may be too heavy (*Olt et al., 2013*). This creates a need for autonomous robots which are manufactured for use on peatlands. Notably the automation of the technological operations is also more efficient than mechanization (*Virro et al., 2020*).

Cultivation of blueberries requires several technological operations (*Olt et al., 2013*): soil preparation, planting, plantation maintenance, fertilization, plant protection, harvesting, post-harvesting processing, and cutting back the plants or carrying out rejuvenation pruning. From the list of technological operations above, fertilization is particularly important, as it may increase the yield from 3 to 8 times (*Vahejõe et al., 2010*). In order to achieve high yield, one must consider the issues of economic loss and potential environmental pollution due to excessive fertilization and plant's nutritional disorders due to excessive or insufficient fertilization (*Chang et al., 2016*). Thus, precision agriculture plays an enormous role in the sustainable development of the cultivation system (*Chen et al., 2014*) and furthermore, precision fertilization is a key to economic and environmental success.

For effective and sustainable fertilization, suitability of machinery is essential. Evolution of machinery used for fertilization has been significant and in constant improvement. This has narrowed down the acceptable tolerances for fertilizer spread and discharge uniformity. Initially commonly used centrifugal spreaders provided approximately 30% uniformity (*Boson et al., 2016*).

[1] *Tormi Lillerand, M.S. Stud. Eng.; Märt Reinvee, Lecturer Ph.D Eng; Indrek Virro, M.S. Stud. Eng.; Jüri Olt, Prof. DSc. Eng.*

After improvement and further development of such spreaders, 15% uniformity has been achieved (*Bulgakov et al., 2021*). Major improvements have been done based on mathematically modelling the trajectory of fertilizer particles (*Olt & Heinloo 2009*). With computer-aided engineering software, which are based on discrete element method, more complex and precise simulations are being introduced (*Liedekerke et al., 2009*). This results in centrifugal disc spreaders providing less than 10% deviation from the target discharge rate (*Bulgakov et al., 2021*). This is acceptable for example for grain cultivation, but in some cases, such as blueberry cultivation, regardless of improved uniformity and enhanced control over discharge, broadcast fertilization with centrifugal-type disc spreader is not feasible and is unacceptable in terms of sustainable cultivation. Blueberry bushes are cultivated in rows (*Arak et al. 2020*), which means that applying fertilizer only for a row would have significant advantages compared to broadband spreading. More suitable is a spreader based on roller with outer grooves, often referred as a fluted roller dispenser, which has gained significant popularity and is considered very efficient when cultivating in rows (*Lv et al., 2012).* Such dispensers are simple, easy to manufacture, lightweight and compact (*Kuş et al., 2021*), capable of providing discharge uniformity usually between 10% and 20%, where better than 20% is considered acceptable and better than 10% is considered good (*Huang et al. 2018*). Due to the plantation pattern on the blueberry field, there are bare spots (*Soots et al. 2021*) between plants. Applying fertilizer to such spots would not only encourage weed growth on the field but also contaminate and simply waste fertilizer (*Olt et al., 2013*). Instead of simply applying fertilizer for the whole row, spot application has a significant effect to save up fertilizer costs, increase yield and decrease weed growth (*Chang et al., 2016*).

On the global scale the recommended fertilization rate for low-bush blueberries varies to a large extent. The recommended rate of nitrogen (N) in Canada (*Lafond, 2000)* is significantly higher than rates that have shown highest yield in Estonia (*Albert et al., 2011*). These locations differ by their latitude which implies differences in the length of vegetation period and climate condition. Moreover, meteorological conditions have shown to have the greatest impact on low-bush blueberry yield (*Parent et al., 2020*) and fertilization should take the length of vegetation period into account, as excessive amount of nitrogen during autumn fertilization may impede the lignification of shoots, which then are susceptible to frost damages (*Paal et al., 2004*). Therefore, the dispenser must allow fertilization rate adjustment while maintaining precision. However, the variety of granular fertilizers with significant differences in granule shape and size (*Lillerand et al., 2021)* add further complexity to the technical requirements of dispensing automation.

The aim of this paper is to clarify suitability of a common straight fluted roller dispenser for precision fertilization application by evaluating its precision in terms of agrotechnical and economic requirements, fulfilling 10 % discharge deviation criteria from determined target fertilization rate, while using three widely available granular fertilizers for low-bush blueberry.

MATERIALS AND METHODS

A commercially available volumetric dispenser was selected (Fig 1.), based on fluted roller design. Such a dispenser was considered due to its fairly simple construction, low price, versatility and longevity (*Huang et al., 2018, Bangura et al., 2020, Kuş et al., 2021*). In addition, such dispensers have proven themselves to be accurate enough in the grain seed sowing applications (*Kuş et al., 2021*). The roller is divided into grooves, with volume dependent on the radius of the flute and length of the roller. Rotating the roller by corresponding number of degrees results in output of a single groove while a revolution results in output of single grooves multiplied by number of grooves.

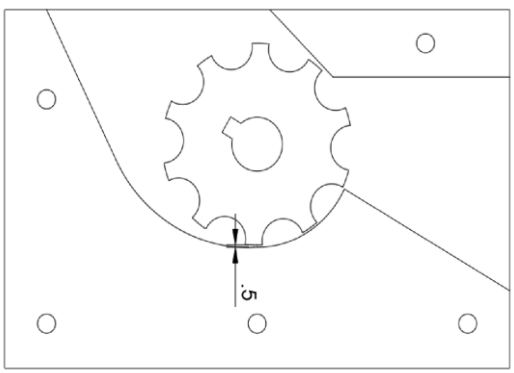

Fig. 1 - Simplified cross-section of the volumetric dispenser

In the study, a straight fluted roller (Fig 2.) was selected with 10 grooves, each of them with volume of 2.048 cm^3. With altering roller parameters such as flute diameter, shape, length and angle, the discharge rate is affected (*Liping et al., 2018, Kuş et al., 2021*). Using an optimal roller that ensures uniform discharge can result in saving up to 40% from fertilizer costs (*Bangura et al., 2020*). The number of flutes and their diameter is selected according to required discharge rate in time and considering size of the particles *(Gujar et al., 2018*).

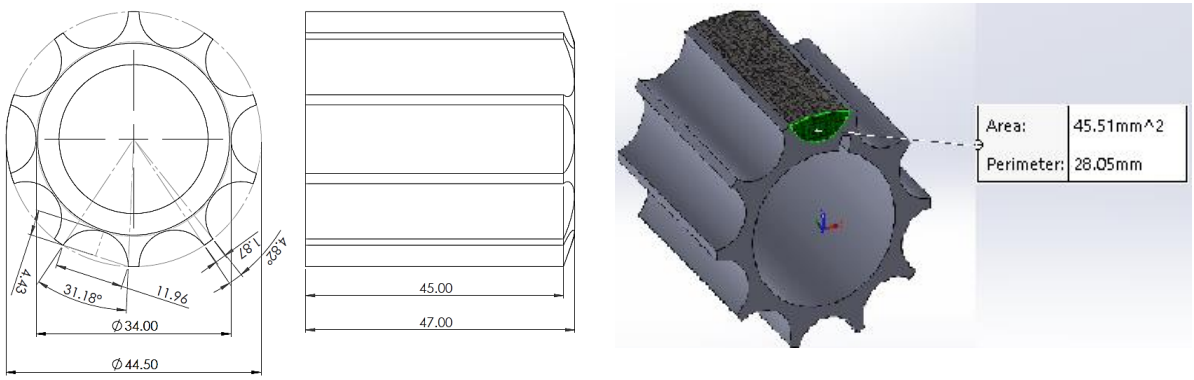

(**a**) (**b**)

Fig. 2 - The selected fluted roller (Lillerand et al., 2021)

(a) measurements of the roller; (b) cross-section area of its groove

As seen in Fig. 3 and Fig. 4 the groove is never fully filled due to irregular placement and granulometric variations of fertilizer particles. In this case, the empty volume should be defined as porosity, where the porous part consists of the empty gaps between the fertilizer granules. Porosity is variable not only between different fertilizers but also within a single fertilizer and therefore, average porosity must be taken into account. It must be assumed that the fertilizer particles are spherical (*Valius & Simutis, 2009*). To express porosity:

$$\Phi=\frac{V_p}{V_s}=\frac{V_s-V_f}{V_s}=1-\frac{V_f}{V_s} \quad (1)$$

where:

V_p – volume of pores; V_s – volume of a groove; V_f – volume of granules in groove, with m_f.

Equation 1 reveals that by knowing discharged volume V_0, e.g. volume of groove and measured weight of discharged fertilizer m_f from it, the porosity can be easily found. To presume that granular fertilizer particles are with similar diameter spheres, then porosity is expressed:

$$\Phi=1-\frac{V_t}{V_s}=1-\frac{\pi}{6}n\left(\frac{d}{a}\right)^3 \quad (2)$$

where:

n - number of granules in cube with side length of a; d – diameter of granules.

It can be presumed that the number of granules in volume V_s = a^3 depends on their positioning. Theoretically it can be expressed if their placement is regular:

$$n=\frac{a}{x}\cdot\frac{a}{y}\cdot\frac{a}{z}=\frac{a^3}{xyz} \quad (3)$$

where:

x, y, z on Eq.3 is distance between granules in direction according to their X, Y and Z axis.

By combining equation 3 with 2:

$$\Phi=1-\frac{\pi d^3}{6xyz} \quad (4)$$

When observing two situations, with dense and sparse positioning, then porosity can be expressed:

$$\Phi_s=1-\frac{\pi}{6}\approx 0.48=48\% \quad (5)$$

$$\Phi_d = 1 - \frac{\pi\sqrt{2}}{6} \approx 0.26 = 26\% \quad (6)$$

This indicates that theoretically the porosity doesn't depend on the size of particles, but only on how they are positioned. From measuring the length, width and thickness of fertilizer granules, it is clear that the dimension is not constant and varies greatly. Therefore, to define the diameter of the particles, geometric mean d_m is used. To measure porosity directly in the dispenser, computed tomography device Yxlon FF35 CT was used. The porosity was measured from the corresponding groove, straight before discharging the fertilizer in 10 repetitions for each fertilizer, resulting in mean average porosity 48% for Substral, 59% for Agro NPK and 68% for Agro Organic.

The output of such dispensers is affected not only by the parameters of the roller or the granulometric parameters of a specific fertilizer, but also by the gap between the roller and dispensers' bottom flap (*Huang et al., 2018*). Every time the roller is being rotated, the moving particles can be divided in two separate layers: forced moving layer and influenced layer. Particles in the first layer rotate along with the roller while particles in the influenced layer are being dragged along by friction and interlocking between the particles (*Huang et al., 2018*). In addition, motion of the particles in the influenced layer is affected by friction between particles and the dispenser shell, including the adjustable bottom flap. Adjusting the gap to minimum, it results in less drag but too small gap can result in seized dispenser, crushed particles or even damaged dispenser. Too large gap creates greater drag, which decreases discharge uniformity (*Huang et al., 2018*). Therefore, the optimal gap was chosen based on granulometric properties of 3 fertilizers in this research scope (*Lillerand et al. 2021*), considering the mean average of the geometric mean diameters of the particles in the sample sets. Using the Industrial Computed Tomography device Yxlon FF35 CT, the measured gap was 4.38 mm (Fig 4.) which was fixed and remained the same through all the experiments carried out.

Fig. 3 - Straight fluted roller with a filled groove

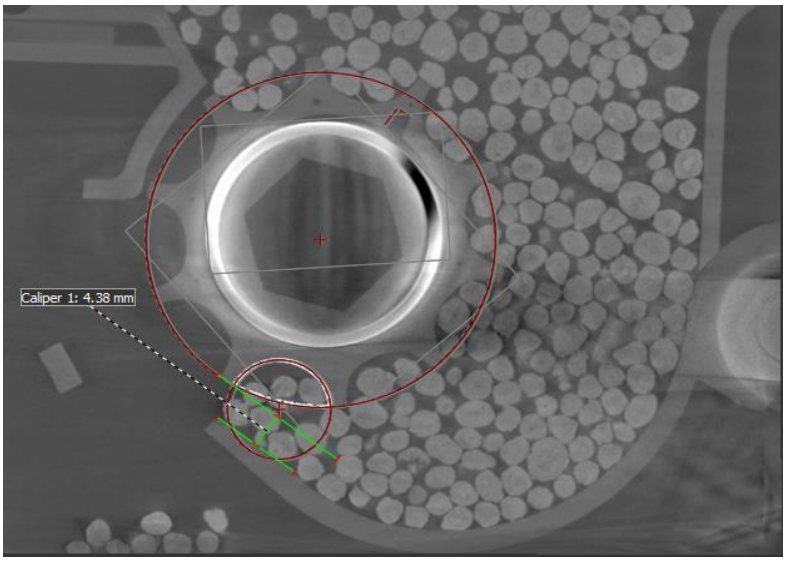

Fig. 4 - Dispenser cross-sectional view

4.38 mm gap measured between the roller and adjustable bottom flap

The necessity of using different fertilizers during the vegetation period comes from that for spring and autumn fertilization, different fertilizers are required due to different concentration of minerals, where in spring growth is stimulated and in autumn the plant receives minerals to enhance its resistance against the cold (*Paal et al., 2004*). As provided in table 1, concentration of nitrogen can vary up to 3 times. Taking examples from other similar research papers (*Bangura et al., 2020, Huang et al., 2018.*), the size of a sample set was 100 granules per fertilizer. For all three fertilizers, length, width and thickness of 100 particles were measured with a digital caliper Mahr 16 EWRi. Mean geometric diameter of 100 particles varies by 15%, sphericity varies by 21% and bulk density varies by 25%. This creates an additional requirement for the dispenser to be simultaneously suitable for three significantly different fertilizers (Fig 5.).

Table 1

Properties of blueberry fertilizers in scope

Fertilizer	N	P	K	E_f	$d_{m,100}$	φ	γ
	[%]	[%]	[%]	[€·g^{-1}]	[mm]	[-]	[kg·m^{-3}]
Agro NPK	12	6	24	0.0026	4.29	0.90	1030
Agro Organic	4	3	8	0.0016	3.64	0.74	775
Substral	5	15	30	0.0062	3.68	0.93	950

Fig. 5 - Examples of used fertilizers
(a) Agro Oranic; (b) Substral and (c) Agro NPK

Opposed to other similar research where the fertilizer discharge on field is measured in time (*Gujar et al., 2018, Huang et al., 2018, Bangura et al., 2020, Kuş et al., 2021*) in this study a different approach has been selected due to spot application. The number of discharged grooves is controlled by the feedback from the encoder attached to the fluted roller. Therefore, it is essential to clarify and establish the best possible discharge uniformity from a single groove. The output of the selected 10 groove fluted roller dispenser with bottom flap gap adjusted to 4.38 mm was measured respectively: output of single groove in 10 repetitions, output of full revolution in 10 repetitions, for each fertilizer. Each time the output was weighted with analytical scale Kern ABJ 220-4NM (Fig 6.), creating a dataset that was used for predicting the output based on the required number of grooves to be emptied.

Fig. 6 – Kern ABJ 220-4NM analytical scale (*Lillerand et al., 2021*)

Average groove discharges ($\underline{m_g}$) of a single groove and the full revolution of the grooved roller were compared in order to understand if the mass of multiple consecutive groove discharges differs from the mass of a single groove discharge. As the grooved roller had 10 grooves, the discharged mass of a full revolution was multiplied by the factor of 0.1 in order to make the values comparable with the discharge mass of a single groove. Normality of data was evaluated with Shapiro-Wilk test. As the distributions did not significantly differ from normal distribution ($p > 0.171$ in all cases), two-sample t-test was used to compare the $\underline{m_g}$ of the single groove and full revolution conditions.

A novel approach was used to determine the discharging precision. Usually discharge uniformity in time unit is used to evaluate the discharging precision (*Gujar et al., 2018, Huang et al., 2018, Bangura et al., 2020, Kuş et al., 2021*). In the current study discrete values of single grove discharges were combined to calculate the distribution of fertilization rates. Discharging precision was evaluated by setting the target fertilization rate Q_t [g·plant $^{-1}$], calculating the number of groove discharges η_c, and then calculated fertilization rates Q_c were found using η_c and measured m_g values.

Nitrogen rates resulting in high yield in an Estonian low-bush blueberry fertilization experiment (*Albert et al., 2011*) were used to set Q_t value. The average of the two N rates with highest yield, Q_{tN} = 1.6 g plant $^{-1}$, was then divided by the fertilizer's N concentration (table 1) to calculate the Q_t for each fertilizer (table 2).

The number of groove discharges η_c was calculated:

$$\eta_c = \frac{Q_t}{\underline{m_g}} \tag{7}$$

The η_c values were rounded to the nearest integer and are denoted as η_t. Then, the number of possible combinations C that can be obtained with η_t and the quantity of m_g data was found:

if $\eta_t < 10$, then:

$$C = \frac{n!}{(\eta_t!(n-\eta_t)!)} \tag{8}$$

if $\eta_t > 10$, then:

$$C = \frac{n!}{(x!(n-x)!)} \cdot \frac{n!}{(y!(n-y)!)} \tag{9}$$

where: $n = 10$, $10x + y = \eta_c$, $x = \{1, 2, ..., 9\}$ and $y = \{0, 1, ..., 9\}$.

For each fertilizer all C combinations of m_g data were obtained with a custom MATLAB script. Combinations of m_g data, denoted as m_c, were then used to calculate Q_c:

$$Q_{c_i} = m_{c_i} \cdot \eta_t, \ [g \cdot plant^{-1}] \tag{10}$$

where: $i = \{1, 2, ..., C\}$.

Table 2

Parameters of discharging precision evaluation

Fertilizer	Q_t	$\underline{m_g}$	η_t	C
	[g·plant $^{-1}$]	[g]	-	-
Agro NPK	13.3	2.705	5	252
Agro Organic	40.0	1.730	23	5400
Substral	32.0	2.664	12	450

Targeted (E_t) and calculated (E_c) fertilizer expenses were calculated as follows:

$$E_t = Q_t \cdot E_f, \ [€] \tag{11}$$

$$E_c = \underline{Q_c} \cdot E_f, \ [€] \tag{12}$$

where:

$\overline{Q_c}$ is the average calculated fertilization rate, and E_f is fertilizer's unit expense €·g^{-1} (table 1).

RESULTS

In the case of Agro NPK the differences of average groove discharges between the single groove ($\underline{m_g}$ = 2.705 g) and full revolution ($\underline{m_g}$ = 2.672 g) conditions were not statistically significant, $t(18) = 0.21$, $p = 0.836$. Similarly, in the case of Agro Organic the differences of average groove discharges between the single groove ($\underline{m_g}$ = 1.730 g) and full revolution ($\underline{m_g}$ = 1.955 g) conditions were not statistically significant,

t(18) = 1.64, p = 0.119. In contrast, in the case of Substral the differences of average groove discharges between the single groove ($\underline{m_g}$ = 2.664 g) and full revolution ($\underline{m_g}$ = 2.377 g) conditions were statistically significant, t(18) = 2.97, p = 0.008.

In all cases the Q_c values fall in the range of the minimum and maximum fertilization rates (Fig 7.) providing the highest yield in the experiment of Albert et al. (*Albert et al., 2011*). However, in the case of Agro Organic and Substral the calculated rate is significantly different from the target, where with Organic the fertilizer is potentially wasted and with Substral, the fertilization is significantly below target rate. With fertilizer Organic the actual cost per plant is also higher than the target is. The fertilization rates provided in the experiment of Albert et al. (*Albert et al., 2011*) do not consider modern agricultural machinery capabilities or the precision fertilization principles and simply provide the data for fertilization rates that the plant can handle without damaging and providing the greatest yield.

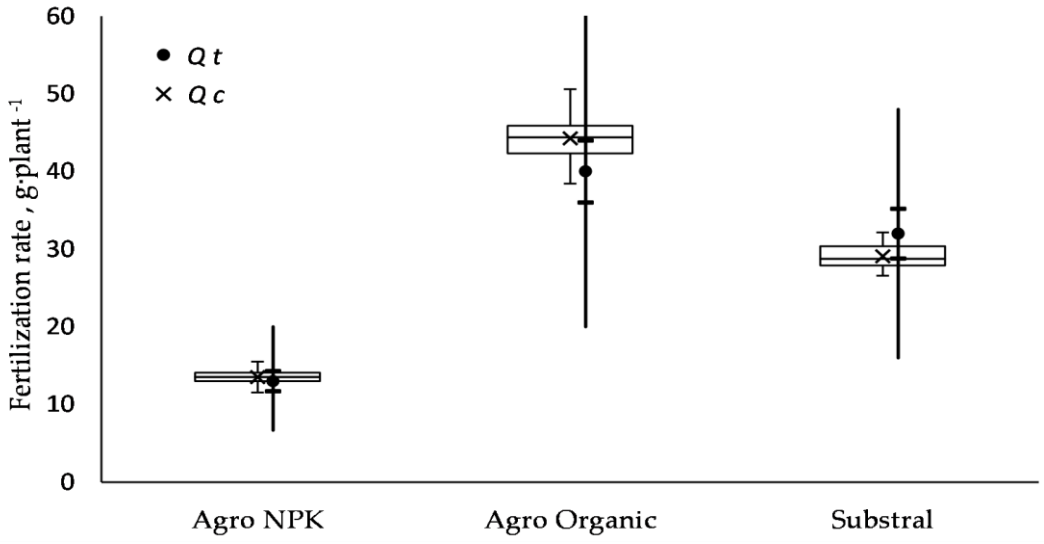

Fig. 7 - Targeted (Q_t) and calculated (Q_c) fertilization rates

Boxplots represent distribution of Q_c, the lines next to boxplots cover the range of two highest yielding fertilization rates in Albert et al., (2011) with target rate Q_t and 10% deviation tolerance for it

By adding the 10% discharge deviation requirement to the target fertilizer rate, only with Agro NPK the dispenser meets the requirements. For Agro Organic, the calculated discharge rate is rather near the upper 10% limit from the target rate and for Substral, the calculated discharge rate is near the bottom 10% limit. In some cases, the discharge rate is out of the 10% tolerance limits. This indicates that in terms of precision farming and precision fertilization, the dispenser is not meeting the requirements (*Huang et al., 2018*).

Discharging excessive fertilizer has effect on increased weed growth and environmental contamination, which both inhibit yield and profit from the blueberry cultivation (*Olt et al., 2013*). Provided in the research of Albert et al. (*Albert et al., 2011*) and Paal et al. (*Paal et al., 2004*)., it is rather preferred to fertilize below the target than above it, as over-fertilization has greater effect on the yield than under-fertilization.

In addition to plant health, yield and environmental aspects, there is also an economical aspect. Due to the vast increase in the prices of available fertilizers, the significance of precision in fertilization process becomes progressively dominant. On a blueberry field of 25 ha area and 1 by 1 m^2 plotting, with technological paths and infrastructure, fertilization of over 200 000 plants can result in excessively spent 1400 € when using one of the three fertilizers (Organic) studied in the paper. Moreover, in the long run additional issues may rise from the inability to predict precise quantity of fertilizer for the whole vegetation period (table 3). This is especially important considering the instabilities in supply chains.

Table 3

Target of fertilizer cost per plant, calculated cost, difference between target and calculated

Fertilizer	E_t	E_c	E_c - E_t
	[€·plant $^{-1}$]	[€·plant $^{-1}$]	[€·plant $^{-1}$]
Agro NPK	0.035	0.035	-0.001
Agro Organic	0.065	0.072	-0.007
Substral	0.197	0.179	0.018

The suitability of a selected common straight fluted roller dispenser for precision fertilization, using three widely available granulated low-bush blueberry fertilizers, is assessed by corresponding to agrotechnical and economic requirements. Firstly, the agrotechnical requirements are met, as these are robust and perhaps outdated. The agrotechnical requirements reflect the capabilities of the previous generations of agricultural machinery and do not allow to apply the full potential of machinery in the Agriculture 4.0 framework, as the paradigm of precision has obtained stricter tolerances. Further research is needed to determine the agrotechnical requirements for precision fertilization in the context of increased potential of the machinery. Secondly, the economic requirements are heavily influenced by fertilizer's parameters (unit cost, nutrient composition, granulometric and mechanical parameters) and agrotechnical requirements (need to adjust the fertilization rate during the vegetation period). The selected common fluted roller dispenser managed to achieve acceptable fertilization rate only in the case of one of the three fertilizers (Fig 7.). This is an insufficient result, as the dispenser is expected to achieve precision regardless of the fertilizer's parameters. Fertilizer must be chosen considering the needs of the plant not by the capabilities of the dispenser, therefore the dispenser design needs to be altered to support precise discharging of various fertilizers.

The total deviation of a fluted roller dispenser's output is incremental and depends on the number of required grooves (*Bangura et al., 2020*). By reducing the necessary number of dispensed grooves, decreasing porosity in a groove and increasing discharge uniformity, better results can be expected. The design and optimization are advised to be done by using discrete element method-based simulation software, as trial and error approach is ineffective and time consuming and may require over 20 iterations considering a single fertilizer (*Huang et al., 2018*). Alternative design, verified by discrete element method simulations is most likely to enhance the results and provide a design fulfilling the requirements for all three fertilizers.

CONCLUSIONS

Due to the fact that different fertilizers with different chemical, mechanical and granulometric properties are used during the vegetation period, key requirement to the dispenser is compatibility with all the fertilizers simultaneously, providing accurate and consistent output. The aim of this paper was to clarify suitability of a commercially available common straight fluted roller dispenser for precision fertilization application. This was done by evaluating its precision in terms of agrotechnical and economical requirements while using three widely available granular fertilizers for low-bush blueberry. It was found that the selected dispenser when used with one of the three fertilizers is suitable and accurate enough to support both, the agrotechnical and economical requirements. While in the case of the remaining two fertilizers, the agrotechnical requirements are met, but the conceptual requirements and economic aspects involve risks due to inability to precisely meet the targeted fertilization rates. In conclusion, practical tests and data analysis revealed that in current state, the commercially available dispenser is not suitable for precision fertilization applications and further development is required by mainly designing a suitable roller for the fertilizers in the scope.

REFERENCES

[1] Albert, T., Karp, K., Starast, M., Moor, U., & Paal, T. (2011). Effect of fertilization on the lowbush blueberry productivity and fruit composition in peat soil. *Journal of Plant Nutrition*, 34(10), 1489–1496. https://doi.org/10.1080/01904167.2011.585205

[2] Arak, M., & Olt, J. (2020). Technological Description for Automating the Cultivation of Blueberries In Blueberry Plantations Established on Depleted Peat Milling Fields. *Rural Development 2019*, 2019(1), 98–103. https://doi.org/10.15544/rd.2019.024

[3] Bangura, K., Gong, H., Deng, R., Tao, M., Liu, C., Cai, Y., Liao, K., Liu, J., & Qi, L. (2020). Simulation analysis of fertilizer discharge process using the Discrete Element Method (DEM). *PLOS ONE*, 15(7), e0235872. https://doi.org/10.1371/journal.pone.0235872

[4] Boson, E.S., Verniaev, O.V., Smirnov, I.I., Sultan-Shach, E.G. 2016. *Theory, Construction and Calculation of Agricultural Machines: Vol 1.*, Scientific Publisher, 314 pp. ISBN: 9789383692378.

[5] Bulgakov, V., Adamchuk, O., Pascuzzi, S., Santoro, F., & Olt, J. (2021). Experimental research into uniformity in spreading mineral fertilizers with fertilizer spreader disc with tilted axis. *Agronomy Research*, 19(1), 28–41. https://doi.org/10.15159/AR.21.025

[6] Bulgakov, V., Adamchuk, O., Pascuzzi, S., Santoro, F., & Olt, J. (2021). Research into engineering and operation parameters of mineral fertiliser application machine with new fertiliser spreading tools. *Agronomy Research*, 19(Special Issue 1), 676–686. https://doi.org/10.15159/AR.21.040

[7] Chang, Y. K., Zaman, Q. U., Farooque, A., Chattha, H., Read, S., & Schumann, A. (2017). Sensing and control system for spot-application of granular fertilizer in wild blueberry field. *Precision Agriculture*, 18(2), 210–223. https://doi.org/10.1007/s11119-016-9457-6

[8] Chen, C., Pan, J., & Lam, S. K. (2014). A review of precision fertilization research. *Environmental Earth Sciences*, 71(9), 4073–4080. https://doi.org/10.1007/s12665-013-2792-2

[9] Gurjar, B., Sahoo, P. K., & Kumar, A. (2017). Design and development of variable rate metering system for fertilizer application. *Journal of agricultural engineering*, 54(3), 12-21.

[10] Huang, Y., Wang, B., Yao, Y., Ding, S., Zhang, J., & Zhu, R. (2018). Parameter optimization of fluted-roller meter using discrete element method. *International Journal of Agricultural and Biological Engineering*, 11(6), 65–72. https://doi.org/10.25165/j.ijabe.20181106.3573

[11] Kuş, E. (2021). Seed Damage Test for Roller-Type Device Designed at Different Flute Helical Angles. *Uluslararası Tarım ve Yaban Hayatı Bilimleri Dergisi*, 7(3), 495–502. https://doi.org/10.24180/ijaws.938870

[12] Lafond, J. (2000). Fertilization in Wild Blueberry Production. Wild Blueberry Production Guide in a Context of Sustainable Development.

[13] Liedekerke, P., Tijskens, E., & Ramon, H. (2009). Discrete element simulations of the influence of fertiliser physical properties on the spread pattern from spinning disc spreaders. *Biosystems Engineering*, 102(4), 392–405. https://doi.org/10.1016/j.biosystemseng.2009.01.006

[14] Lillerand, T., Virro, I., Maksarov, V. V., & Olt, J. (2021). Granulometric Parameters of Solid Blueberry Fertilizers and Their Suitability for Precision Fertilization. *Agronomy*, 11(8), 1576. https://doi.org/10.3390/agronomy11081576

[15] Liping, Z., Lixin, Z., & Weiqiang, Z. (2018). Fertilizer feeding mechanism and experimental study of a spiral grooved-wheel fertilizer feeder. *Journal of Engineering Science and Technology Review*, 11(6), 107–115. https://doi.org/10.25103/jestr.116.14

[16] Lv, H., Yu, J., & Fu, H. (2013). Simulation of the operation of a fertilizer spreader based on an outer groove wheel using a discrete element method. *Mathematical and Computer Modelling*, 58(3–4), 842–851. https://doi.org/10.1016/j.mcm.2012.12.017

[17] Olt, J., & Heinloo, M. (2009.). On the formula for computation of flying distance of fertilizer's particle under air resistance. *Journal of Agricultural Science*, 20(2), 25–34.

[18] Olt, J., Arak, M., & Jasinskas, A. (2013). Development of mechanical technology for low-bush blueberry cultivating in the plantation established on milled peat fields. *Agricultural Engineering*, 45(2), 120–131.

[19] Paal, T., Starast, M., & Karp, K. (2004). Influence of different fertilisers and fertilising frequency on the developing of seedlings of Vaccinium angustifolium. *Botanica Lithuanica*, 10(2), 135–140.

[20] Parent, S. É., Lafond, J., Paré, M. C., Parent, L. E., & Ziadi, N. (2020). Conditioning machine learning models to adjust lowbush blueberry crop management to the local agroecosystem. *Plants*, 9(10), 1–21. https://doi.org/10.3390/plants9101401

[21] Soots, K., Lillerand, T., Jogi, E., Virro, I., & Olt, J. (2021). Feasibility analysis of cultivated berry field layout for automated cultivation. *Engineering for Rural Development*, 20, 1003–1008. https://doi.org/10.22616/ERDev.2021.20.TF222

[22] Thielke, Dipl.-Wirtsch.-I., Kemper, Dipl.-I., & Frerichs, S. (2015). Simulation of agricultural processes using the discrete element method. *Scientific Proceedings III International Scientific and Technical Conference "Agricultural Machinery"*, 1, 21-24.

[23] Valiulis, G., & Simutis, R. (2009). Modeling of Continuous Fertilizer Granulation-drying Circuit for Computer Simulation and Control Purposes. *In ICINCO-SPSMC,* 98-103.

[24] Virro, I., Arak, M., Maksarov, V., & Olt, J. (2020). Precision fertilisation technologies for berry plantation. *Agronomy Research*, 18(Special Issue 4), 2797–2810. https://doi.org/10.15159/AR.20.207

DESIGN AND EXPERIMENT OF CAM-LINKAGE SELF-CLEANING FERTILIZER APPARATUS
/
凸轮顶板自清式排肥器的设计与试验

Yize SHI [1, 2], Jiajia YU[1, 2], Muhua LIU [1, 2], Gaoliang ZHANG [1, 2], Fan LU[1], Zhangxing QIN [1, 2], Peng FANG[1, 2], Xiongfei CHEN[*1, 2] [1]

[1)] Jiangxi Provincial Key Laboratory of Modern Agricultural Equipment, Nanchang 330045, China;
[2)] College of Engineering, Jiangxi Agricultural University, Nanchang 330045, China;
Tel: +8617307006979; E-mail: 121686212@qq.com
Corresponding author: Xiongfei Chen

DOI: https://doi.org/10.35633/inmateh-68-42

Keywords: *Fertilizer apparatus, cam-linkage, compound fertilizers, self-cleaning device, moisture content*

ABSTRACT

Aiming at the poor performance and low efficiency of moist fertilizers, a cam-linkage self-cleaning fertilizer apparatus is designed. The cam-linkage mechanism matched with the self-cleaning device is applied to scrape off the residuals, and the structural parameters of flute cam in the wheel are obtained by using the polar equations. The physical characteristics of Stanley compound fertilizer, Kingenta compound fertilizer and Kingenta dual-effect nitro-fertilizer are analyzed to build the discharging model and obtain the key parameters, such as the wheel diameter, the groove number. The trajectory of fertilizer is introduced for the scraper plate. To evaluate the performance, a full factorial experiment including fertilizer types, moisture content and rotating speed is conducted, taking the discharging and coefficient of variation as the evaluation indicators. The results show that in the rotation of 10-50 r/min, the cam-linkage self-cleaning fertilizer apparatus could discharge compound fertilizers with a moisture content less than 8%, and the coefficient of variation is 0.12% -8.21%. In addition, the relationship between the rotating speed and the discharging has the linear relationship, and the determination coefficient R^2 are more than 0.974. This study helps promoting the deep fertilization technology and equipment in southern rice region.

摘要

针对高湿南方稻区肥料颗粒吸湿粘附堵塞排肥器，影响深施肥作业效果及效率的问题，基于凸轮顶板自清的技术思路，设计了一种凸轮顶板自清式排肥器。建立了凹槽凸轮的极坐标方程及排肥速率数学模型，明确了该排肥轮直径、料槽数量等结构参数；通过开展颗粒肥料运动轨迹分析，获得了清肥刮板结构参数；借助人工气候箱模拟江西省早、中、晚稻种植的温度和湿度，开展了排肥器内颗粒肥料吸湿试验，获得了颗粒肥料含水率的范围；并以史丹利复合肥、金正大复合肥和金正大硝基双效肥为试验材料，肥料类型、肥料含水率和排肥轮转速为试验因素，以排肥量及其变异系数为评价指标，开展了排肥器工作性能试验。试验结果表明：排肥器转速在 10~50r/min 条件下，不同含水率（2%、4%、6%、8%）的 3 种供试肥料的排肥速率与排肥轮转速均呈线性关系，决定系数 R^2 大于 0.974，3 种供试肥料随着含水率增加，排肥速率变异系数均呈增大趋势，变化范围为 0.12~8.21%；影响排肥性能的显著因素由大到小为排肥轮转速、含水率、肥料种类、肥料种类和含水率的交互作用、含水率和排肥轮转速的交互作用。因此，该排肥器在 10~50r/min 转速条件下可适用于含水率不高于 8%的吸潮颗粒肥料稳定排施，可为高湿南方稻区水稻种植同步深施肥机具的研制提供核心部件。

INTRODUCTION

The average discharging of nitrogen fertilizer in rice planting is 180 kg/hm^2 in China *(Bai, 2018, Randive et al., 2021)*, which is more than 75% of the worldwide average *(Tajamul et al., 2022; Ludemann et al., 2022)*. However, the utilization rates of nitrogen, phosphorus and potassium fertilizers is low, which are 30%~35%, 10%~25% and 35%~50%, respectively *(Sichul, 2021, Yu et al., 2022)*. Studies show that the deep fertilization is a great method of increasing efficiency and decreasing cost *(Jelle et al., 2018; Kakar et al., 2019)*. Compared with the scattering fertilization on the soil surface, *(Alameen et al., 2019; Siddique et al., 2020)*, it can also reduce the environmental pollution *(Jabbar et al., 2022; Paul et al., 2022)*, promote the utilization rate

[1]*Yize Shi, Master, Jiajia Yu, Ph.D. Lecturer; Muhua Liu, Ph.D., Professor; Gaoliang Zhang, Lecturer; Fan Lu, Master; Zhangxing Qin, Master; Peng Fang, Ph.D. Lecturer; Xiongfei Chen, Ph.D., Associate Professor.*

and rice product *(Rebecca et al., 2022; Tang et al., 2019),* and reduce the volatilization and loss. Deep fertilization is achieved by fertilization equipment *(Liu et al., 2022).* Researchers of agricultural companies, such as Kubota Agricultural Machinery (Suzhou) Co, Ltd, Yanmar Agricultural Machinery (China) Co, and Ltd and Huanan Agricultural University are researching deep fertilization equipment for rice planting and are manufacturing many agricultural machines.

Fertilizer apparatus is the key to develop deep fertilization for rice planting, and its performance will influence the uniformity, stability and adaptability of fertilization. Most fertilizer apparatuses such as outer-fluted wheel fertilizer apparatus perform well in northern drylands *(Tan et al., 2020; Liu et al., 2021),* and poorly with bonding and blockage in southern paddy field *(Uspensky et al., 2021; Xiao et al., 2021)*. The reasons may be that: the granular fertilizer is a pore structure with a great surface energy, which is easy to absorb moisture and bond in the fertilizer apparatus *(Liu et al., 2021.* Once the fertilizer powder blocks the fertilization wheel and stops running, the efficiency would be affected. To solve this problem, many fertilizer apparatuses are studied *(Sugirbay et al., 2020; Liu et al., 2021; Du et al., 2021),* and few applications are found in rice planting.

Aiming to the blockage and bonding of fertilizer apparatuses in the southern region, a cam-linkage self-cleaning fertilizer apparatus is designed. The structure of cam-linkage self-cleaning is analyzed, and then the experiment is carried out to perform the discharging of moist fertilizer. The results show that the fertilizer apparatus could promote the application of deep fertilization in rice planting.

MATERIALS AND METHODS

Cam-Linkage Self-Cleaning Fertilizer Apparatus

The structure of cam-linkage self-cleaning fertilizer apparatus is composed of the upper shell, lower shell, flute cam, linkage, wheel, transmission shaft, discharging plate, cleaning brush and scraper plate, as shown in Figure 1. The wheel with two flute cams is installed in the transmission shaft, and the linkage with the top plate is fixed into the flute cam. Then the cleaning brush is located to clean the extra fertilizer out of the grooves, and the plate discharges the fertilizer into the shell after work. The scraper plate is installed in the lower shell to clean the residues sticking in the wheel, and the lower shell is locked with the upper shell.

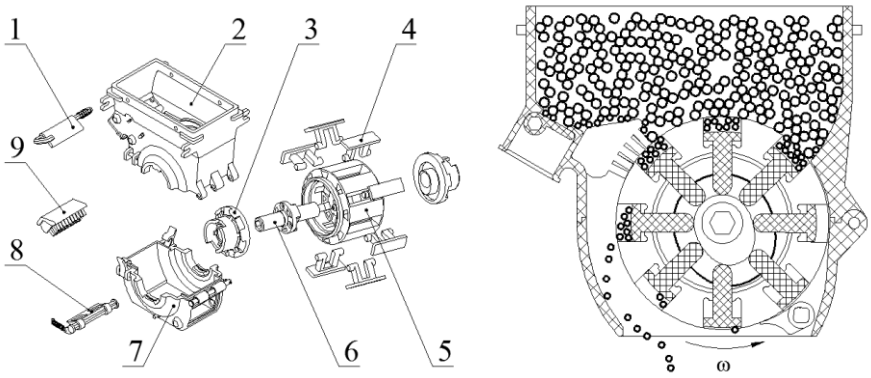

a. Structure of the fertilizer apparatus b. Fertilization process

Fig. 1 - Structural diagram of the cam-linkage self-cleaning fertilizer apparatus
1. Discharging plate 2. Upper shell 3. Flute cam 4. Linkage 5. Fertilization wheel 6. Transmission shaft 7. Lower shell 8. Scraper plate 9. Cleaning brush

The transmission shaft rotates to drive the wheel, and then the linkage moves with the flute cam. When the top plate of linkage moves down to change the volume of grooves in the wheel, the fertilizers in the box will be filled. When the linkage moves the deepest, the cam-linkage mechanism is in the near angle of repose stage, and the extra fertilizers out of grooves are cleaned by the brush. In this way, the grooves are full of fertilizers, and the cam-linkage mechanism is in the far angle of repose stage. The top plate of linkage pushes out the fertilizers, and the apparatus discharges the fertilizers, and then the cam-linkage mechanism runs into the lift stage. Finally, the scraper plate cleans the residuals, and the cam-linkage mechanism keeps running in the return stage. Thus, he fertilizer apparatus works with “filling-transporting-discharging-cleaning” as shown in Figure 2, and the cam-linkage mechanism works as “near angle of repose-far angle of repose-lift-return”.

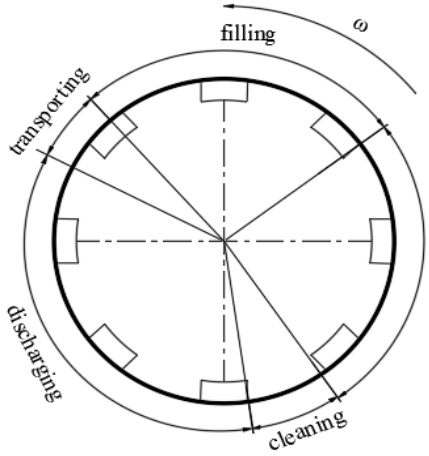

Fig. 2 - Operating process of the flute cam

Parameters of Cam-Linkage Mechanism

Flute cam: The performance of fertilizer apparatus would be influenced by the structural parameters, and the discharging would be influenced by the filling process. Figure 3 shows the near angle of repose θ_1, and θ_1 i 3π/4. The scraper plate is installed in the far angle of repose θ_3 to cover the single groove, and θ_3 is π/9. The wheel discharges the fertilizers in the return stage θ_2 with 5π/9, and the lift stage θ_4 is 7π/12 to prepare for filling.

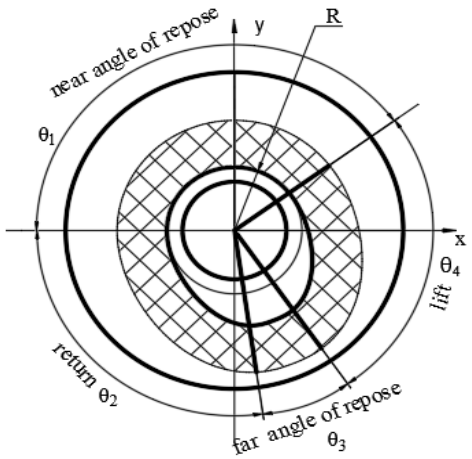

Fig. 3 - Structural parameters of the cam-linkage mechanism

A four-stage analysis of the structure of the flute cam is conducted to analyze the movement without impact. The semi-diameter of the base circle in the flute cam *R* is 15 mm, and the width *d* is 10 mm, the curve of the flute cam is thus established with quantic polynomial equations (1).

$$\begin{cases} \rho_1 = 25 & \theta_1 \in \left(0, \frac{3}{4}\pi\right) \\ \rho_2 = -131.58\theta_2^5 + 410.23\theta_2^4 - 346.21\theta_2^3 \\ \quad -59.638\theta_2^2 + 191.12\theta_2 - 62.318 + 25 & \theta_2 \in \left(\frac{3}{4}\pi, \frac{47}{36}\pi\right) \\ \rho_3 = 33 & \theta_3 \in \left(\frac{47}{36}\pi, \frac{17}{12}\pi\right) \\ \rho_4 = 33 - (59.516\theta_4^5 - 764.64\theta_4^4 + 3559.2\theta_4^3 \\ \quad -7777.7\theta_4^2 + 8106.2\theta_4 - 3245.7) & \theta_4 \in \left(\frac{17}{12}\pi, 2\pi\right) \end{cases} \quad (1)$$

where ρ_1 is the displacement between the origin and the point of near angle of repose, mm; θ_1 is the near angle of repose of the cam, rad; ρ_2 is the displacement equation between the origin and the point of the lift stage, mm; θ_2 is the motion angel of the lift in the cam, rad; ρ_3 is the displacement between the origin and the point

of the far angle of repose, mm; θ_3 is the far angle of repose of the cam, rad; ρ_4 is the displacement equation between the origin and the point of the return stage, mm; θ_4 is the motion angel of return in the cam, rad.

Fertilization wheel: The theoretic discharging speed required by agronomy and the real discharging speed of fertilizer apparatus are calculated as follows:

$$\begin{cases} Q_s = \dfrac{Q_t B v}{10} \\ Q_s = \dfrac{\rho \lambda w h l Z N n}{60} \end{cases} \quad (2)$$

where Q_s is the theoretic discharging speed, g/s; Q_t is the theoretic quantity of fertilization in a unit area, kg/hm^2; v is the forward speed of tractor, m/s; B is the operating width of fertilization, m; Q_m is the real discharging speed in a unit area, g/s; ρ is the bulk density of granular fertilizer, kg/m^3; λ is the filling coefficient; w is the width of the groove, m; h is the depth of the groove, m; l is the length of the groove, m; Z is the groove number of the fertilization wheel; N is the number of fertilizer apparatuses in the tractor, and n is the rotation of the fertilization wheel, r/min.

Q_t can be obtained by Eq. (3).

$$Q_t = \frac{\rho \lambda w h l Z N n}{6 B v} \quad (3)$$

The operating width B and the forward speed v are determined by the tractor, thus the groove length l, the groove number Z, the fertilizer apparatus number N, and the filling coefficient λ have an inverse ratio relationship with the rotating speed n. Since n and Z are influenced by the wheel diameter D, and Z would increase when enlarging D. In the same operational conditions, λ can increase by lowering n.

Stanley compound fertilizer, Kingenta compound fertilizer and Kingenta dual-effect nitro-fertilizer are selected as the experimental materials, and the test parameters as shown in Table 1. The results show that the average size of the fertilizer granular is 4.24mm×3.82mm×3.45mm, and the angle of repose is 30.02° with 90.46% sphericity. The bulk density of Stanley compound fertilizer is the greatest with 867.86 kg/m^3, and Kingenta compound fertilizer has a small bulk density with 819.11 kg/m^3. Therefore, the filling volume of grooves is obtained, and D is 113 mm. To make the linkage move fluently, the width and depth of straight grooves are 20 mm and 8 mm, respectively.

Table 1

Physical and mechanical characteristics of different fertilizers

Name	Length/ mm	Width/ mm	Depth/ mm	Sphericity/ %	bulk density/ kg·m^3	angle of repose/ °
Stanley compound fertilizer	4.25	3.82	3.29	89.12	867.86	29.41
Kingenta compound fertilizer	4.20	3.72	3.34	89.08	819.11	28.84
Kingenta dual-effect nitro-fertilizer	4.27	3.92	3.73	93.19	832.62	31.82

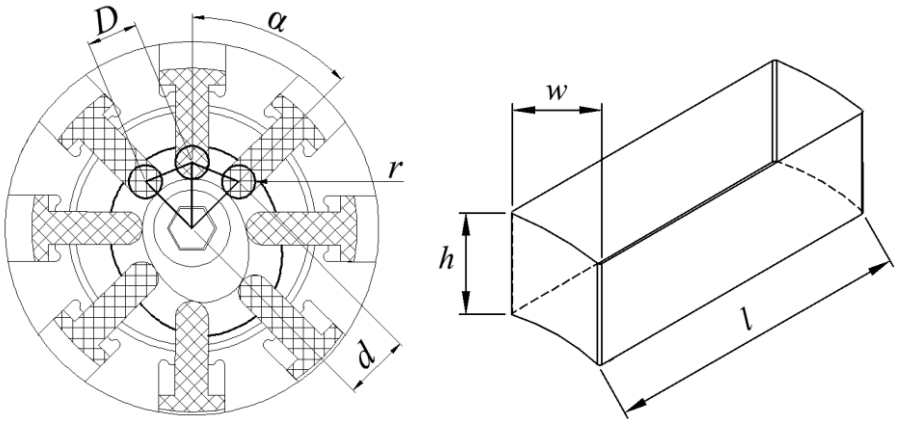

a. Diagram of fertilization wheel b. Groove structure

Fig. 4-Structure of the fertilizer groove

Since the groove number Z had a relationship with the bottom radius of the linkage r, Z was *8* according to Eq. (4):

$$\begin{cases} D = 2d\sin\dfrac{\alpha}{2} \\ \alpha = \dfrac{2\pi}{Z} \\ 2r < \mathrm{D} \\ \mathrm{Z}\arcsin\dfrac{r}{d} < \pi \end{cases} \quad (4)$$

where D is the distance between the two bottom balls of linkage, mm; α is the angle between two linkages, rad; d is the central distance between the ball and transmission shaft, mm; r is the bottom radius of linkage, mm.

Scraper plate: To clean the residual fertilizers in the top plate of the wheel, the scraper plate is installed on the lower shell with a spring, and the hollow curve surface is designed to reduce the bonding of moist fertilizer as shown in Fig. 5. When the linkages push the moist fertilizers out from the grooves, the scraper plate scrapes the residuals to stop the blockage. When the residuals are cleaned and dropped into the outlet, the discharging is uniform, and the filling performance is stable in the next operation.

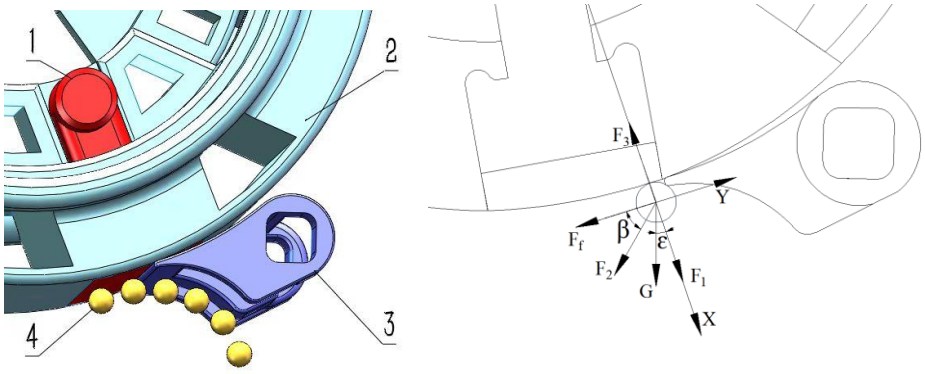

Fig. 5 - Force analysis of bonding fertilizer on the self-cleaning device
1. Linkage 2. Fertilization wheel 3. Scraper plate 4. Bonding fertilizers

To acquire the structural parameters of scraper plate, the force analysis of moisture fertilizer in the top plate is conducted, including the gravity G, the support force from the top plate F_1, the force from the scraper plate F_2, the adhesion force between the bonding fertilizer and the top plate F_3, and the frictional force between the top plate and fertilizers F_f. The following formula can be obtained:

$$\begin{cases} F_1 = \mathrm{m}\omega^2\mathrm{r} \\ F_\mathrm{f} = F_3 - G\cos\varepsilon - F_1 - F_2\sin\beta \end{cases} \quad (5)$$

where:

F_1 is the support force from the top plate, N; F_2 is the force from the scraper plate, N; F_3 is the adhesion force between the bonding fertilizer and the top plate, N; F_f is the frictional force between the top plate and fertilizers, N; ε is the angle between G and F_1, °, and β is the angle between F_f and F_2, °.

To reduce the second adhesion of the scraper plate, the trajectory of the bonding fertilizer is conducted according to Eq. (6). The curve surface of self-cleaning device is designed as Fig. 6.

$$\begin{cases} \mathrm{x}_0 = V_1\cos\varepsilon * \mathrm{t} + \dfrac{1}{2\mathrm{m}}F_2\cos\ (\varepsilon+\beta) * \mathrm{t}^2 \\ \mathrm{y}_0 = V_1\sin\varepsilon * \mathrm{t} + \dfrac{1}{2\mathrm{m}}F_2\cos\ (\varepsilon+\beta) * \mathrm{t}^2 + \dfrac{1}{2}\mathrm{gt}^2 \end{cases} \quad (6)$$

where:

x_0 is the horizontal displacement of fertilizer, m; y_0 is the vertical displacement of fertilizer, m; t is the dropping time, s; m is the mass of fertilizers, kg; V_1 is the velocity of fertilizers, m•s^{-1}, F_2 is the force from the scraper plate, N; ε is the angle between G and F_1, °, and β is the angle between F_f and F_2, °.

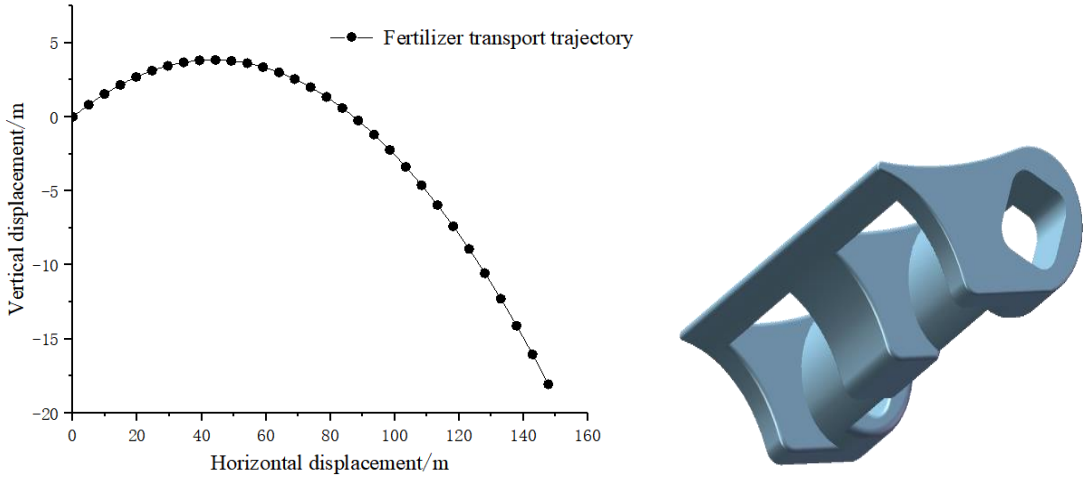

Fig. 6 - Structure of self-cleaning device

Moisture content: To require the moisture content of fertilizers during working, the temperature and humidity parameters of Jiangxi province from 2010-2019, and the data of nine counties including Poyang, Nanchang, Guixi, Yichun, Nancheng, Yongfeng, Gi'an, Suichuan and Ningdu from March to August are collected as shown in Table 2.

Table 2

Average temperature and humidity from March to August in Jiangxi Province's counties (2010-2019)

	March		April		May		June		July		August	
	Temperature /°C	Humidity /%	Temperature /°C	Humidity /%	Temperature /°C	Humidity /%	Temperature /°C	Humidity /%	Temperature /°C	Humidity /%	Temperature /°C	Humidity /%
Poyang	12.9	76.3	18.6	75.8	23.4	76.1	26.7	79.0	29.8	74.6	29.9	72.0
Nanchang	13.0	78.8	19.0	77.3	23.7	77.6	27.0	78.6	30.3	70.2	29.9	70.0
Guixi	13.2	77.6	18.7	78.5	23.4	78.9	26.6	81.7	29.7	75.1	29.5	74.8
Yichun	12.7	81.8	18.4	80.8	22.7	82.0	26.4	80.7	28.8	78.1	28.5	77.2
Nancheng	13.2	78.6	18.9	77.5	23.4	78.3	26.8	79.1	29.3	72.2	29.1	72.9
Yongfeng	13.0	82.5	19.0	80.7	23.3	81.5	26.8	80.1	29.3	74.7	28.9	75.7
Gi'an	13.8	82.3	19.8	80.2	24.0	81.6	27.5	79.1	30.1	72.0	29.7	73.4
Suichuan	14.2	79.8	20.0	77.8	24.0	80.1	27.3	80.2	29.6	72.1	28.8	75.2
Ningdu	14.2	78.6	19.6	77.9	23.8	79.6	27.1	77.6	28.9	73.3	28.5	73.6
Average value	13.36	79.59	19.11	78.50	23.52	79.52	26.91	79.57	29.53	73.59	29.20	73.87

The sowing times of early, middle and late rice are from March to April, May to June and July to August, respectively. The acquired average temperatures are 16.30°C, 25.20°C and 29.30°C respectively, and the average humidity of early, middle and late rice are 79.10%, 79.60% and 73.80% respectively.

To this end, the moist fertilizers in the apparatus are obtained by setting the average temperature and humidity in the growth chamber for 24 hours. The moisture content is tested by using the Karl-Fischer titration method with three republications, as shown in Table 3.

The results show that the initial moisture content of fertilizers from the nylon bag has a great difference between 0.553%~2.307%, while the moisture content still increases in different sowing temperatures and humidity. The moisture content of fertilizers below the surface 0-1cm and in the cleaning brush is higher than other fertilizers. The greatest moisture content is 4.166% below the surface 0-1cm, at the temperature of 29.30°C and the humidity 73.80%, thus the moisture content of fertilizers is introduced experimentally.

Moisture content of fertilizers in different positions of box **Table 3**

Mass of fertilizers	Sample position	Moisture Content %		
		Temperature 16.30°C and Humidity79.10%	Temperature 25.20°C and Humidity 79.60%	Temperature 29.30°C and Humidity73.80%
Full Box (20kg)	Initial value	1.633~2.307	1.098~2.033	1.544~2.022
	Below the surface 0~1 cm	3.300	3.291	4.166
	Below the surface 1~3 cm	1.912	2.389	3.561
	Below the surface more than 3 cm	2.063	1.394	2.911
	Cleaning brush	1.894	1.368	3.735
Half Box (10kg)	Initial value	1.808~2.224	0.998~1.406	0.764~1.534
	Below the surface 0~1 cm	3.220	1.282	1.830
	Below the surface 1~3 cm	2.478	1.358	1.367
	Below the surface more than 3 cm	2.233	1.169	0.859
	Cleaning brush	2.107	1.196	0.985
Shallow Box (0.85kg)	Initial value	0.553~1.230	0.875~1.098	1.265~1.651
	Below the surface 0~1 cm	1.394	2.275	2.272
	Below the surface 1~3 cm	0.946	1.241	1.769
	Below the surface more than 3 cm	0.934	1.19	1.675
	Cleaning brush	0.988	0.994	1.877

Stanley compound fertilizer, Kingenta compound fertilizer and Kingenta dual-effect nitro-fertilizer are introduced to test the performance of the cam-linkage self-cleaning fertilizer apparatus, and JYC-412 growth chamber, WKT-C20 Karl-Fischer titration equipment and the weighing system are conducted in the experiments, as shown in Figure 7.

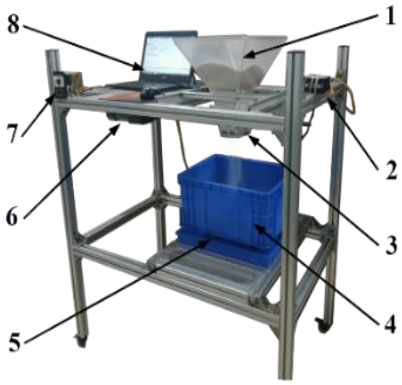

Fig. 7 - Test platform of the fertilizer apparatus

1. Fertilizer box 2. Hall speed sensor 3. Cam-linkage self-cleaning fertilizer apparatus 4. Collecting case 5. Weighing sensor 6. Adjustable speed motor 7. Frequency converter 8. Weighing system

To test the performance and application of fertilizer apparatus, three kinds of fertilizers in different moisture contents and the rotating speeds are used in the full-factor experiment, as shown in Table 4. The above fertilizers were treated with four moisture contents of 2%, 4%, 6% and 8%. Karl Fischer titration is introduced to test the moisture content, and the discharging of fertilizer apparatus in the weighing system was obtained in 1 minute with 4 repetitions.

Test factors and levels **Table 4**

No.	Factors		
	A Types	B Moisture content , %	C Rotating speed , r·min^{-1}
1	Stanley compound fertilizer	2.00	10.00
2	Kingenta compound fertilizer	4.00	20.00
3	Kingenta dual-effect nitro-fertilizer	6.00	30.00
4	——	8.00	40.00
5	——	——	50.00

According to GB/T9478-2005, the discharging and coefficient of variation are employed as the evaluation index

$$\begin{cases} q = \dfrac{\sum_{i=1}^{j} q_i}{j} \\ CV = \dfrac{\sqrt{\dfrac{1}{j-1}\sum (q_i - q)^2}}{q} \times 100\% \end{cases} \quad (7)$$

where q is the discharging, g; q_i is the amount in 1 minute of i times, g; j is the repetitions, and CV is the coefficient of variation of fertilizers, %.

RESULTS

Effect of the Discharging and Coefficient of Variation

The result showed that the fertilizer apparatus could discharge three different fertilizers with 2-8% moisture content, and the discharging increased with the increase of rotating speed from 10 r/min to 50 r/min. The range of discharging per minute is 602.64-3494.50 (Figure 8a~c), which can meet the agronomic requirement of discharging 30-60 kg per 667 m^2 in the field. When the rotating speed was lower than 40 r/min, the discharging was stable. However, when the rotating speed reached 50 r/min, only the discharging of Kingenta dual-effect nitro-fertilizer still had the same trend, while the others decreased. It indicates that greater rotating speed and higher moisture contents could increase the discharging, and the uniformity is worse. The reason is that the diameters and bulk density of moist fertilizers change, and the fertilizers are damaged into powder and adhered in the wheel.

In addition, the coefficient of variation of discharging increases with the increase of moisture content (Figure 8d~f), only the coefficient of variation of discharging Kingenta compound fertilizer is fluent in 10-50 r/min rotating speed, and the others change greatly. Especially in the case of 8% moisture content and 50 r/min rotating speed, the trend of coefficient of variation is the same as the discharging. For discharging Stanley compound fertilizer, Kingenta compound fertilizer and Kingenta dual-effect nitro-fertilizer under this apparatus, the minimum values of coefficient of variation are 0.16%, 0.12% and 0.28%, respectively, and the maximum values are 8.21%, 2.14% and 3.75% respectively. The results are better than the outer-flute fertilization wheel fertilizer apparatus. Consequently, the cam-linkage self-cleaning fertilizer apparatus could discharge no more than 8% moisture content of compound fertilizers with 10-50 r/min rotating speeds.

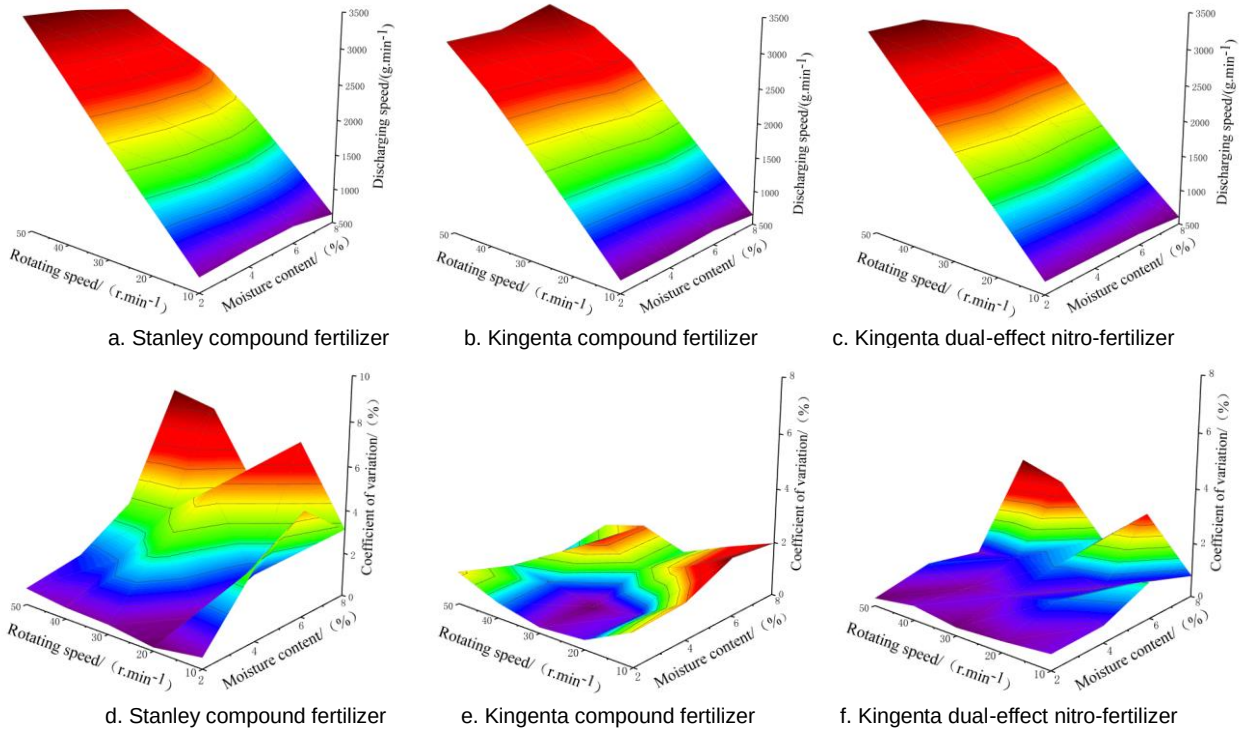

a. Stanley compound fertilizer b. Kingenta compound fertilizer c. Kingenta dual-effect nitro-fertilizer

d. Stanley compound fertilizer e. Kingenta compound fertilizer f. Kingenta dual-effect nitro-fertilizer

Fig. 8 - The performance of fertilizer apparatus in different moisture contents and rotational speeds

The variance analysis shows that the fertilizer types, the moisture content, the rotating speed, the interaction between the fertilizer types and the moisture content, the interaction between the moisture content and the rotating speed, all have a significant influence on discharging, as shown in Table 5. The sequence of influencing factors is as follows: the rotating speed, the moisture content, the types, the interaction between the types and the moisture content, the interaction between the moisture content and the rotating speed.

Table 5

Analysis

Error source	Square sum	df	Mean square	F	Sig.
Model	4.987E+007	35	1.425E+006	298.42	＜0.0001**
Kinds	1.302E+005	2	65075.62	13.63	0.0001**
Moisture content	6.064E+005	3	2.021E+005	42.33	＜0.0001**
Rotating speed	4.867E+007	4	1.217E+007	2548.36	＜0.0001**
Interaction between types and moisture content	1.761E+005	6	29352.23	6.15	0.0005**
Interaction between types and rotating speed	18781.62	8	2347.70	0.49	0.8500
Interaction between moisture content and rotating speed	2.684E+005	12	22363.21	4.68	0.0006**
Interaction between types, moisture content and rotating speed	1.146E+005	24	4774.99		
Total	2.852E+008	60			
Correct total	4.999E+007	59			

Mathematical Model of Discharging

To figure out the effect between the rotating speeds and the discharging with 2-8% moisture content fertilizers on this fertilizer apparatus, the linear equations are fitted (Figure 9) and the determination coefficients R^2 are more than 0.974 (Table 6). The results show that the rotating speed controls the discharging of moist fertilizers, and the moisture content reaches 8%. The discharging decreases as the damage and bonding increase and the fitting curve is still parallel. This indicates that the discharging with three kinds of compound fertilizers has a linear relationship in 10-50 r/min rotating speed and 2-8% moisture content. This fertilizer apparatus can adapt different fertilizers, and is easy to adjust the rotating speeds to control the discharging in applications. This conclusion is the same as the experimental results.

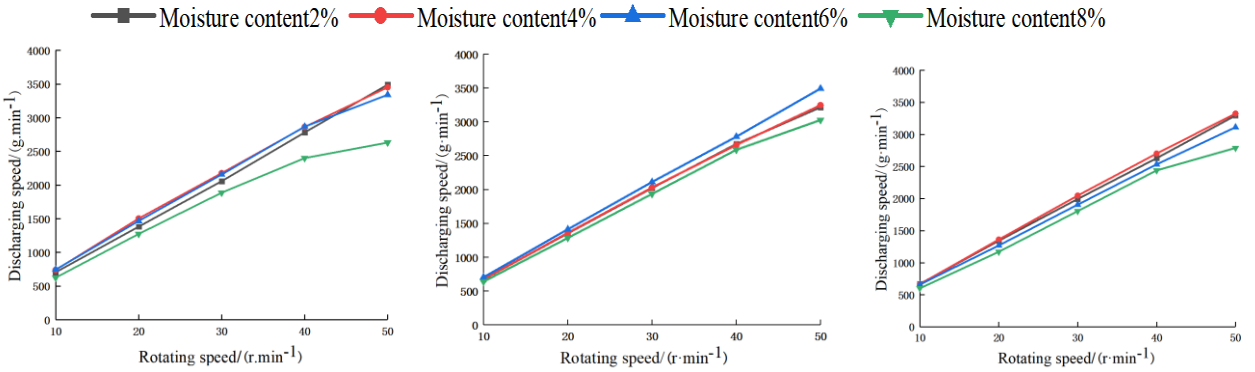

a. Stanley compound fertilizer b. Kingenta compound fertilizer c. Kingenta dual-effect nitro-fertilizer

Fig. 9 - Relationship between the discharging speed and the rotating speed

Table 6

Linear relationship of discharging different fertilizers between discharging and rotating speeds

Moisture content / %	Stanley compound fertilizer		Kingenta compound fertilizer		Kingenta dual-effect nitro-fertilizer	
	Equations	Determination coefficient/R^2	Equations	Determination coefficient / R^2	Equations	Determination coefficient/R^2
2.00	$y=69.72x-7.8$	0.999	$y=64.02x+68.68$	0.998	$y=65.37x+26.1$	0.999

Table 6

(continuation)

Moisture content / %	Stanley compound fertilizer		Kingenta compound fertilizer		Kingenta dual-effect nitro-fertilizer	
	Equations	Determination coefficient/R^2	Equations	Determination coefficient / R^2	Equations	Determination coefficient/R^2
4.00	$y=67.82x+112.72$	0.998	$y=64.44x+62.56$	0.999	$y=66.58x+24.12$	0.999
6.00	$y=65.94x+137.34$	0.995	$y=69.44x+19.38$	0.999	$y=61.69x+46.22$	0.999
8.00	$y=51.38x+222.16$	0.974	$y=60.75x+74.1$	0.995	$y=56.44x+68.56$	0.991

CONCLUSIONS

(1) A new cam-linkage self-cleaning fertilizer apparatus is designed for discharging the moist fertilizer in southern rice region, aiming to solve the bonding and blockage problem of traditional fertilizer apparatus. The polar coordination equations of the cam-linkage mechanism are built to determine the parameters of the flute cam. The mathematical model of discharging is analyzed to obtain the wheel diameter and groove number, and the self-cleaning device is designed for scraping the residual fertilizers.

(2) The results show that the fertilizer apparatus can discharge less than 8% moisture content compound fertilizers, and the sequence of influencing discharging speed are: the rotating speed, the moisture content, the fertilizer types, the interaction between the fertilizer types and the moisture contents, the interaction between the moisture contents and the rotating speeds.

(3) The experimental results show that the fertilizer apparatus can discharge 2-8% moisture content under different compound fertilizers (Stanley compound fertilizer, Kingenta compound fertilizer and Kingenta dual-effect nitro-fertilizer) in 10-50 r/min rotating speeds. The coefficient of variation of discharging increases with the increase of moisture content, and the range changes from 0.12% to 8.21%. Furthermore, the discharging has a linear relationship with the rotating speed, and the determination coefficient R^2 is more than 0.974.

ACKNOWLEDGEMENT

This research is supported by National Science Foundation (Grant No. 52165030), Jiangxi Provincial Key Development Research Foundation (Grant No. 20201BBF61009) and Jiangxi Provincial Agricultural Machinery Equipment Application Industrial Technology Research Systems (Grant No. JXARS-21).

REFERENCES

[1] Alameen, A. A., Al-Gaadi, K. A., & Tola, E., (2019). Development and performance evaluation of a control system for variable rate granular fertilizer application. *Computers and Electronics in Agriculture.* Vol 160, pp. 31-39. England.

[2] Bai, Y. L. (2018). The situation and prospect of research on efficient fertilization（高效施肥技术研究的现状与展望）. *Scientia Agricultura Sinica*, Vol 51, pp. 2116-2125. Beijing/China.

[3] Du, X., Liu, C. L., Jiang, M., Yuan, H., Dai, L., Liu, F. L., (2021). Design and Experiment of Inclined Trapezoidal Hole Fertilizer Point-applied Discharging Device（倾斜梯形孔式穴施肥排肥器设计与试验）. *Transactions of the Chinese Society for Agricultural Machinery*, Vol .52, pp. 43-53. Beijing/China.

[4] Jelle, V. L., Alicia B., Speratti, L. G., Bram, G., (2018). Precision for Smallholder Farmers: A Small-Scale-Tailored Variable Rate Fertilizer Application Kit. *Agriculture*, Vol. 8, pp. 318-324. Switzerland.

[5] Jabbar, M. K., Ali Sbti, A. M., (2022). Study of Reducing Chemical Fertilizers and Enhancing by Organic and Biological Fertilizers for Cowpea Crop. IOP Conf. Series: *Earth and Environmental Science*, England.

[6] Kakar, K., Nitta, Y., Asagi, N., Komatsuzaki, M., Shiotau, F., Kokubo, T., Xuan, T.D. (2019). Morphological analysis on comparison of organic and chemical fertilizers on grain quality of rice at different planting densities. *Plant Production Science*, Vol .22, pp. 510-518. JAPAN

[7] Liu, M. H.,Shi, Y.Z.,Chen, X.F., Yu., J.J., Liu,J.A., Liu,Z.P., Xia.,H.Y., Qin.,Z.X., Zhang.,Q.L. (2022) *A kind of synchronous deep fertilization rice hole directing machine China*, ZL202220914466.2. China.

[8] Liu, H. N., Li, T., Zhao, H. Y., Li. J., Lei, X. L., Ren, W. J., (2021). Design and experiment of screw-type feeding device of air-assisted centralized fertilizer application device（气送式集中排肥器螺旋排肥装置的改进与试验）. *Journal of China Agricutural University*, Vol. 26, pp. 150-161. Beijing/China.

[9] Liu, X. D., Hu, R., Wang, D. H., Lu B., Wang, W. C., Ding, Y. C., (2021). Optimization and Test of Fertilizer Apparatus Based on Granular Fertilizer Movement Model (基于颗粒肥料运动模型的排肥器优化与试验). *Transactions of the Chinese Society for Agricultural Machinery,* Vol. 52, pp. 85-95. Beijing/China.

[10] Liu, D. Z., Zhou, Y., Zhang, G. Z., Zhang, M.Y., KE, H. B., Yang. Q. J., (2021). Design and Experiment of Pneumatic Double-side Fertilizer Devices for Ratoon Rice（再生稻气送式双侧施肥装置的设计与试验研究）. *Journal of Agricultural Science and Technology,* Vol. 23, pp. 77-85. Beijing/China.

[11] Ludemann, C. I., Gruere, A., Hefer, P., & Dobermann, A., (2022). Global data on fertilizer use by crop and by country. *Scientific data*, Vol. 9. England.

[12] Paul, B., Patnaik, U., Sasidharan, Murari, K. (2022). Fertilizer Use, Value, and Knowledge Capital: A Case of Indian Farming. *Sustainability*, Vol .14. Switzerland.

[13] Randive, K., Raut, T., & Jawadand, S. (2021). An overview of the global fertilizer trends and India's position in 2020*, Mineral Economics*, Vol .34, pp. 371-384. Switzerland

[14] Rebecca, T., Suduan, G., James, E. A., Dong, W. (2022). Carbon and Nitrogen Dynamics Affected by Drip Irrigation Methods and Fertilization Practices in a Pomegranate Orchard. *Horticulturae*, Vol. 5, Switzerland.

[15] Sichul, L. (2021). Recent Advances on Nitrogen Use Efficiency in Rice. *Agronomy*, Vol.11, Switzerland.

[16] Siddique, I.A., Al Mahmud, A., Hossain, M., Islam, M.R., Singh, U. (2020). Movement and retention of NH4-N in wetland rice soils as affected by urea application methods, *Journal of Soil Science and Plant Nutrition*, Vol. 20, pp. 589-597. Switzerland

[17] Sugirbay, A. M., Zhao, J., Nukeshev S.O., Chen, J. (2020). Determination of pin-roller parameters and evaluation of the uniformity of granular fertilizer application metering devices in precision farming. *Computers and Electronics in Agriculture*, Vol.179, England.

[18] Tajamul, H., Nurda, H., Mukhtar, A., Charassri, N., Saowapa, D. (2022). Impact of Nitrogen Application Rates on Upland Rice Performance, Planted under Varying Sowing Times. *Sustainability*, Vol. 14, Switzerland.

[19] Tang, H., Wang, J. W., Xu, C. S., Zhou, W. Q., Wang, J. X., Wang, X. (2019). Research progress analysis on key technology of chemical fertilizer reduction and efficiency increase（化肥减施增效关键技术研究进展分析）. *Transactions of the Chinese Society for Agricultural Machinery*, Vol. 50, pp. 1-19. Beijing/China.

[20] Tan, Y., Xie, F. P., Xiao, M. T. (2020). Design and simulation test of an eccentric ejection fertilizer apparatus（偏心弹射式排肥器设计与仿真试验）. *Journal of Chinese Agricultural Mechanization*, Vol. 41, pp. 26-32. Jiangsu/China.

[21] Uspensky, I. A., Fadeev, I. V., Alekseev V., Filippov, V. P. (2021). Modeling the Effect of Fertilizers on the Dynamics of Moisture Contours at Drip Irrigation. *Engineering Technologies and Systems*, Vol. 31, pp. 97-108. Russian Federation.

[22] Xiao, W. L., Liao, Y. T., Shan, Y. Y., Li, M. L., Wang, L., Liao, Q. X. (2021). Design and Experiment of Quad-screw Double-row Fertilizer Apparatus for Rape Seeding Machine（油菜直播机四头螺旋双行排肥器设计与试验）. *Transactions of the Chinese Society for Agricultural Machinery*, Vol .52, pp. 68-78. Beijing/ China.

[23] Yu, X., Keitel, C., & Zhang, Y. Wangeci, A. N., Dijkstra, F. A. (2022). Global meta-analysis of nitrogen fertilizer use efficiency in rice, wheat and maize*, Agriculture, Ecosystems & Environment,* Vol. 338, pp.371-384. Netherlands.

LOW POWER CONSUMPTION MONITORING METHOD OF AGRICULTURAL GREENHOUSE ENVIRONMENT BASED ON WIRELESS SENSOR NETWORK

/

基于无线传感器网络的农业温室环境的低功耗监测方法

Bing ZHANG[1,2)]

[1)] Institute of Information Engineering, Suqian College, Suqian, 223800, China;

[2)] Jiangsu Province Engineering Research Center of Smart Poultry farming and Intelligent Equipment, Suqian, 223800, China

DOI: https://doi.org/10.35633/inmateh-68-43

Keywords: *Wireless sensor; Agricultural greenhouse; Low power consumption monitoring; Network node; Communication protocol; Abnormal data*

ABSTRACT

In order to improve the reliability of wireless sensor networks and reduce the power consumption in the monitoring process, the low power consumption monitoring method of agricultural greenhouse environment based on wireless sensor networks is studied. The terminal node of wireless sensor network is constructed by using CO_2 sensor, temperature and humidity sensor and illumination sensor. In the sensor network layout stage, in order to reduce the node power consumption, considering the number of nodes and network coverage, the cuckoo search algorithm is used to optimize the node layout model. The communication module uses Low Energy Adaptive Clustering Hierarchy (LEACH) protocol to transmit the environmental data collected by the terminal node to the monitoring center. The cluster head link is selected in LEACH protocol to save energy. After receiving the environmental data collected by the terminal node, the monitoring center uses multi-dimensional data to identify and locate abnormal environmental data according to the correlation between multi-modal data streams in the same node, so as to realize the environmental monitoring of agricultural greenhouse. The experimental results show that the data transmission of the research method is stable and reliable, and the node's power consumption in the process of internal environment monitoring of the research object is effectively reduced.

摘要

为了提高无线传感器网络的可靠性并减少监视过程中的功耗，研究了基于无线传感器网络的农业温室环境的低功耗监测方法。无线传感器网络的末端节点是使用 CO2 传感器，温度和湿度传感器和照明传感器构建的。在传感器网络布局阶段，为了减少节点功耗，考虑到节点和网络覆盖范围，杜鹃搜索算法用于优化节点布局模型。通信模块使用 Leach 协议将终端节点收集的环境数据传输到监视中心。簇头链接在 Leach 协议中选择以节省能源。在收到终端节点收集的环境数据之后，监视中心使用多维数据根据同一节点中的多模式数据流之间的相关性来识别和定位异常的环境数据，以实现对农业监测的环境监视温室。实验结果表明，研究方法的数据传输是稳定且可靠的，并且节点在内部环境监测过程中的功耗有效地减少了。

INTRODUCTION

With the rapid development of protected horticulture in China in recent years, by 2015, the total area of agricultural greenhouse in China has exceeded 2.08 million hm^2 (*Pisanu et al. 2020*), of which the cultivated area of protected vegetables in the North has exceeded 1.25 million hm^2. At the same time, with the development of information technology, traditional agriculture is gradually transitioning to fine agriculture (*Li et al., 2021*). Among them, intelligent technologies such as sensors, wireless networks, information processing and decision-making service are gradually applied to the effective management of agricultural greenhouses (*Chan et al., 2019*). Especially in recent years, the development and application of Internet of things communication technology at home and abroad have effectively reduced the complexity (*Honeycutt et al., 2021*) of information transmission in the agricultural greenhouse and promoted the development process of intelligent management of agricultural greenhouse. The normal growth of crops requires appropriate temperature and humidity. Once the environment in the agricultural greenhouse is not well controlled, it is easy to lead to crop yield reduction (*Rosa et al., 2020*), and even disease and death. Therefore, it is of great significance to study an effective and energy-saving environmental monitoring method for agricultural greenhouse.

At present, the monitoring methods of greenhouse include manual control and wired monitoring. The manual control method requires users to have strong perception of the environment. If the control is not appropriate, the time and labor cost will be too high, which will cause huge economic losses.

For the wired monitoring method, *Koroak et al.* designed a low power consumption environmental monitoring and soil moisture measurement system based on Ultra High Frequency Radio Frequency Identification (UHF RFID) (*Koroak et al. 2019*), which used Radio Frequency (RF) technology to monitor the data such as temperature, light, relative humidity and weight moisture content in the soil, providing a simple, cost-effective solution for monitoring and controlling plant growth in modern agriculture. However, the wired monitoring method realizes the regulation of the greenhouse environment by arranging complex wires and related control equipment in the greenhouse, which makes it inconvenient for crops to sow and fertilize, and the wires are often broken in production activities. With the rapid development of Internet of things technology, wireless sensor network technology is applied to greenhouse monitoring, omitting the wiring link, avoiding the problems encountered in traditional greenhouse, and meeting the requirements of real-time monitoring of greenhouse environmental factors. Therefore, Abdulkarem et al. combined wireless sensor network technology with monitoring system (*Abdulkarem et al., 2019*), which improved the defects of manual control method and wired monitoring method, but there was a problem of high node power consumption.

Based on this, the low power consumption monitoring method of agricultural greenhouse environment based on wireless sensor network is researched in this paper. Wireless sensor network is a comprehensive technology integrating multiple disciplines. It can monitor the crop growth, soil, diseases and pests and other information in agricultural greenhouse in real time, facilitate the smooth development of seed collection, irrigation and pest control, and facilitate managers to understand the information in greenhouse in the control room. Through real-time dynamic monitoring, it can promote the level of agricultural management in China to be more intelligent and networked.

MATERIALS AND METHODS

The overall structure of monitoring method

The whole network of low power consumption monitoring methods of agricultural greenhouse environment based on wireless sensor network in the actual monitoring process is composed of monitoring center and ZigBee network. Figure 1 shows the details.

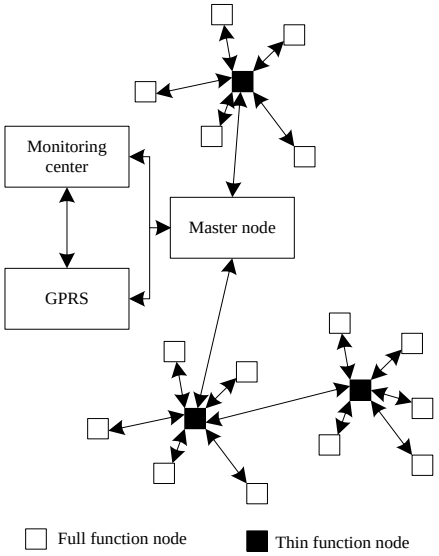

Fig. 1 - Overall structure of low power consumption monitoring method for agricultural greenhouse environment based on wireless sensor network

The overall structure of the low power consumption monitoring method of agricultural greenhouse environment based on wireless sensor network is a hierarchical network structure. The sensor terminal node is at the bottom, followed by ZigBee master node (Coordinator) and monitoring center. The monitoring center is a computer, which is used to display the environmental monitoring data of agricultural greenhouse and send commands to the network. ZigBee network is responsible for collecting environmental data of agricultural greenhouse. It is composed of ZigBee master node and ZigBee terminal node (*Shan et al. 2019*). The terminal node is a sensor star network composed of a full function node and a thin function node.

The full function node collects the environmental data uploaded by the terminal equipment and transmits it to the thin function node. The thin function node integrates and uploads the data and sends the integrated environmental data to the ZigBee master node. There must be a ZigBee coordinator in each wireless sensor network, which is responsible for initiating the network, managing and maintaining it, including assigning network address to newly added devices, joining and leaving nodes, distribution and update of network security key, etc. In order to prevent nodes from joining any network, resulting in uneven power consumption distribution of network nodes, the network is divided into several small star networks, and each star network is defined as a group. The central node of the star network integrates the environmental information of the agricultural greenhouse uploaded by the terminal equipment, and then sends the integrated environmental data of the agricultural greenhouse to the ZigBee master node. There are two ways to connect ZigBee network with the monitoring center. Generally, the coordinator can be directly connected with the monitoring center through serial port. When it is not convenient for the monitoring center to use on site for a long time, GPRS can be used to send the environmental data of agricultural greenhouse to the monitoring center connected with GPRS receiving device.

The monitoring center needs to monitor the working status and health of the sensor node, display the source address of all data, the environmental data of agricultural greenhouse collected by the sensor and the change trend of the data (*Grace and Manju, 2019*), and adjust the work task of the node accordingly. The health status of nodes includes the remaining energy, the working status of sensors and communication components. By monitoring the sensor status, the work cycle of sensor nodes can be adjusted in time and tasks can be reassigned, so as to reduce the application power consumption of wireless sensor networks, avoid premature failure of nodes and prolong the life of the whole network. At present, the residual energy information of nodes is mainly judged by the working voltage of nodes. If the voltage value is too low, the reliability of the node reading sensor data will also be reduced. Therefore, it is necessary to prolong the sleep time of the node with too low voltage and reduce the sampling frequency.

Deployment of terminal node in wireless sensor network

Structure design of terminal node in wireless sensor network

In the process of low power consumption monitoring of agricultural greenhouse environment, the sensor terminal node is at the bottom of wireless sensor network, and its function is mainly completed by the sensor node based on Internet of things data transmission. The sensor node uses ARM Cortex M3 Series MCU (STM32F103R) as the core microprocessor to communicate with the sensor module and wireless communication module. Figure 2 is the structural block diagram of the sensor node. Lithium battery is used for independent power supply, and time-sharing multiplexing of multi-channel sensors is supported for environmental data acquisition of agricultural greenhouse. The backplane provides Flash chip (W25Q64BV) and writes the collected environmental data of agricultural greenhouse as required. The reserved Universal Asynchronous Receiver/Transmitter (UART) communication interface can realize wired reading of node data and avoid the loss of environmental data of agricultural greenhouse caused by insufficient power and poor wireless communication quality. Considering the low transmission power of wireless communication module NRF24L01 and serious plant shielding in the agricultural greenhouse environment, the power adjustable RF amplification chip RFX2401C is used for power amplification to ensure that the wireless transmission can achieve the required transmission power in the agricultural greenhouse environment.

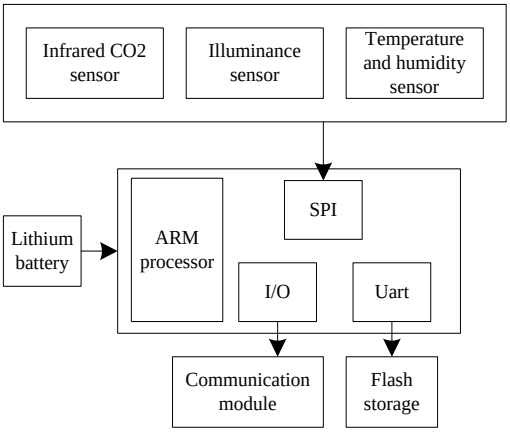

Fig. 2 - Node structure of wireless sensor network

The sensor node comprises a power supply battery, a CO_2 sensor and corresponding circuit parts, which are encapsulated in a waterproof box with the size of (8×8×4.5) cm^3. In order to prevent the high humidity environment in the agricultural greenhouse environment from affecting the internal infrared carbon dioxide sensor and measuring circuit (*Saban et al., 2021*), the waterproof breathable membrane made of EPTFE material is used at the vent hole of the outer wall for waterproof and breathable treatment. The air after waterproof treatment will not affect the measurement of the internal infrared carbon dioxide sensor. At the same time, the condensation phenomenon caused by the large temperature difference between day and night in the agricultural greenhouse environment is avoided. The temperature and humidity sensor, illumination sensor and wireless communication antenna are exposed outside the shell to realize the accurate measurement of environmental factors of agricultural greenhouse and wireless transmission of data.

Considering the semi enclosed environment of agricultural greenhouse, the minimum volume fraction of CO_2 in daytime can reach 2×10^{-4} below, and accurate CO_2 concentration measurement directly affects the decision-making gas fertilizer irrigation of greenhouse agriculture. The traditional electrochemical sensor (such as MG811) has a high detection lower limit (4×10^{-4}) and large power consumption (1.2W), which cannot meet the lower limit of measurement of closed agricultural greenhouse and cannot work independently for a long time, so they are not suitable for the design requirements of sensor nodes in wireless sensor networks. At the same time, due to the complex application environment of agricultural greenhouse, the injected methane and other gas components released by chemical fertilizer and soil greatly limit the availability of semiconductor CO_2 sensors (*Haque et al., 2020*). On the premise of considering the cost performance, S300 infrared CO_2 sensor designed based on direct absorption method is selected as the sensor node to measure the CO_2 concentration in agricultural greenhouse. Compared with electrochemical and semiconductor sensors, it ensures higher measurement accuracy and lower detection limit.

According to the variation range of environmental temperature and humidity of agricultural greenhouse and the demand of low-cost miniaturization design, SHT15 temperature and humidity sensor is selected as the sensor node to measure the temperature and humidity in the greenhouse, and the corresponding nonlinear correction is carried out to improve its detection accuracy. BH1750FVI digital illuminance sensor is used to measure the illuminance. The measurement center wavelength is 560 nm, which is in the visible range. The measurement results have high resolution, and the measurement range is 1～65 535 lx.

Node deployment model

In the deployment of wireless sensor nodes, increasing the number of sensors is usually used to improve the network coverage in the agricultural greenhouse environment. However, deploying too many sensors will produce a large number of redundant nodes, resulting in data transmission conflicts, waste of resources and the instability of the network. Therefore, in order to achieve the purpose of low power consumption monitoring, the number of nodes and network coverage are considered at the same time in the layout stage of sensor networks.

The coordinate system is established with the center point of the greenhouse area as the origin, and the east direction as the positive direction of the x-axis of the coordinate axis. Because the greenhouse is usually built in a flat area, excessive gradient difference in the greenhouse will affect the uniformity of the temperature in the greenhouse, so the influence of height factor is not considered, and only the plane is assumed. Assuming that each sensor in the wireless sensor network has the same communication radius and sensing radius (*Rienzo et al., 2020*), let $w=\{w_1, w_2, w_3, \cdots w_n\}$ be a set of wireless sensors, (x_i, y_i) be the coordinate of any wireless sensor node w_i in the set, and (x_j, y_j) be the coordinate of any point w_j in the environmental monitoring area of agricultural greenhouse, then the Euclidean distance from node w_i to point w_j is defined as *(Mabrouki J et al., 2019)*:

$$d(w_i, w_j)=\sqrt{(x_j-x_i)^2+(y_j-y_i)^2} \quad (1)$$

The environmental monitoring area a of agricultural greenhouse is discretized into a grid point, point K with coordinate (x, y), to judge whether point K is covered by sensor node w_i, which can be expressed by equation (2):

$$P(K,w_i)=\begin{cases}1, d(w_i,p_j)\le r\\ 0, \text{otherwise}\end{cases} \quad (2)$$

In formula (2), r represents the radius of the detection area. For any coordinate point (x,y), as long as there is a sensor node in node B so that $F_{\text{cov}}(x,y,b_i)=1$, b_i represents the total number of sensor nodes in the current area, it means that the point is covered by at least one sensor node, and the joint measurement coverage $F_{\text{cov}}(B)$ of the node set is:

$$F_{\text{cov}}(B)=\left(1-\prod_{b_i\in B}\left(1-F_{\text{cov}}(x,y,b_i)\right)\right)\times\phi \quad (3)$$

Where ϕ represents the coverage correction value, the coverage correction value is generally 0.75.

After simplifying small grid points into grid points, the coverage of wireless sensor network is defined as the proportion of the number of discovered grids to the total number of grids (*Fakhri et al., 2020*), that is:

$$F_a=\sum_{x=1}^{m}\sum_{y=1}^{n}F_{\text{cov}}(B)\times\frac{1}{m\times n} \quad (4)$$

In order to use the optimization algorithm to solve the problem of optimal deployment of wireless sensor networks for environmental monitoring of agricultural greenhouse, the network coverage objective function and constraints are defined as follows:

$$\begin{cases}\overline{F}=m\times n\times\dfrac{1}{\sum_{x=1}^{m}\sum_{y=1}^{n}F_{\text{cov}}(B)}\\ m\le h_m\\ n\le h_n\\ F_{\text{cov}}(B)\ge 1\end{cases} \quad (5)$$

The cuckoo search algorithm is used to solve the objective function. The goal of the research is to maximize the function. It is expected to obtain wider coverage, so as to improve the monitoring capability of the network. After deploying the wireless sensor network node, the communication protocol is used to realize the transmission of agricultural greenhouse environmental monitoring data between the wireless sensor network node and the monitoring center.

Communication protocol

The improved LEACH communication protocol is adopted in the process of environmental monitoring of agricultural greenhouse. The traditional LEACH protocol randomly divides the area distributed by the sensors into pieces. In each piece, a node with sufficient energy is randomly selected as the cluster head node through the algorithm to communicate with the outside world.

The operation of LEACH protocol is divided into two rounds, and each round is divided into two parts: establishment stage and stability stage *(Rezvani et al., 2020*). The establishment stage is self-organized into clusters. In each round, the nodes become the cluster head node with the probability of $G_i(t)$. After becoming the cluster head node, they broadcast messages, and the node receiving the information sends a join request to the cluster head node, and the cluster sends back the confirmation information; In the stable stage, the cluster head node collects the information sent from the members in the cluster, and then sends it to the sink node after processing, which circulates in turn. $G_i(t)$ is calculated as follows:

$$G_i(t)=\begin{cases}k\times\dfrac{1}{N-k^*\left(o\bmod(\frac{N}{k})\right)}, H_i(t)=1\\ 0, H_i(t)=0\end{cases} \quad (6)$$

In equation (6), k is the expected value of the node becoming the cluster head node, t is time, mod is residual function, o is the current number of rounds, N is the number of nodes in the network, and $H_i(t)$ is the prediction function (*Ge X et al., 2019*).

In the process of environmental monitoring of agricultural greenhouse, LEACH protocol does not need to randomly select cluster heads, but only needs the reliability of data transmission and the robustness of communication network. Therefore, the protocol needs to be improved to adapt to the specific application of environmental monitoring of agricultural greenhouse. LEACH protocol selects cluster heads through G probability (*Khan et al. 2021*), which will consume part of the energy of nodes. In the improved protocol, there is no need to poll to select cluster heads. Therefore, after selecting cluster heads for the first time, it is no longer necessary to run the algorithm, so as to save energy.

According to the energy dissipation model of LEACH protocol, the energy attenuation of sending data and receiving data in wireless sensor networks are as follows:

$$\begin{cases} S_{Tx} = S_{Tx-elec}(l) S_{Tx-amp}(l,d) \\ S_{Rx}(l) = S_{Rx-elec}(l) = lS_{elec} \end{cases} \quad (7)$$

where, S_{elec} represents the energy consumption of transceiver circuit of wireless sensor network, d represents the distance between nodes, and l represents the number of data bits to be launched or accepted. S_{Tx} represents the energy attenuation of the data sent by the sensor network, S_{Rx} represents the energy attenuation of the data received by the sensor network, $S_{Tx-elec}$ represents the energy consumption of the sending circuit, $S_{Rx-elec}$ represents the energy consumption of the receiving circuit, and S_{Tx-amp} represents the energy consumption of the sending current.

According to the design requirements of wireless sensor network for monitoring the environment of agricultural greenhouse, the protocol assumes that each agricultural greenhouse has n_i $(i=1,2,3,\cdots,k)$ nodes, and $g(0 \le g \le 1)$ is the success prediction probability of the base station, that is, at this time, the node needs to send prediction data to the greenhouse cluster head. According to the judgment of the cluster head, if it is the probability of g, it will not send, and if it is the probability of $(1-g)$, it will send fusion data.

According to the description, the energy consumption of cluster head nodes in a single agricultural greenhouse cluster is:

$$S_{CH} = lS_{elec}(n_i - 1) + lS_{DA}n_i + lS_{elec} + l(1-p)d_{toBS}^4 \quad (8)$$

where, S_{DA} represents the energy consumption of environmental detection data fusion in agricultural greenhouse, and d_{toBS}^4 represents the distance from the node to the base station.

The energy consumption of non-cluster head nodes in each round is:

$$S_{non-CH} = lS_{elec} + ld_{toCH}^2 \quad (9)$$

Where, d_{toCH}^2 is the distance from the node to the cluster head.

The energy consumption of an agricultural greenhouse cluster in each round is:

$$S_C = S_{CH} + (n_i - 1) S_{non-CH} \quad (10)$$

Then the energy consumption of wireless sensor network nodes in the whole greenhouse base in one round is:

$$S_{to} = \sum_{i=1}^{s} \left[n_i \left(2S_{elec} + S_{DA} + d_{tpCH}^2 + (1-g) \right) d_{tpBS}^4 \right] \quad (11)$$

Identification and location of abnormal data in wireless sensor networks

Abnormal data identification

In the process of environmental detection of agricultural greenhouse, the measured value of wireless sensor network should accurately reproduce the actual environmental characteristics of agricultural greenhouse. Therefore, the measured value $c_j(t_i)$ shows slow fluctuation within a certain range in a stable

agricultural greenhouse environment (*Picallo et al. 2021*), but there will be obvious deviation in a short time in case of abnormality. If $c_j(t_i)$ satisfies equation (12), the measured value may be abnormal data:

$$\left| c_j(t_i) - \frac{Q_{ej}(t) + Q_{nj}(t)}{2} \right| > \gamma^2 \tag{12}$$

where: t is the corresponding sampling time of the wireless sensor network node; $Q_{ej}(t)$ represents the mathematical expectation of the measured value of the sensor in the agricultural greenhouse environmental monitoring area, $Q_{nj}(t)$ represents the mathematical expectation of the measured value in the agricultural greenhouse monitoring area under general conditions, which is derived from the measured data in the same period over the years; It is generally believed that $Q_{nj}(t)$ is a constant in a stable environment. The values of $Q_{ej}(t)$ and $Q_{nj}(t)$ in different environments are different, which should be determined according to the environmental monitoring data set of agricultural greenhouses, and γ represents the variance of sampling data.

In addition, when the wireless sensor itself fails (energy is exhausted or damaged and cannot work normally), it may continuously produce the same readings at different sampling times (Bai et al. 2019), that is:

$$c_j(t_i) = c_j(t_{i-1}) \tag{13}$$

The above two cases are called the judgment conditions to judge whether the sensor reading is abnormal, and on this basis, the abnormal probability $P_j(t_i)$ of single-mode data flow is calculated:

$$P_j(t_i) = P_j(t_{i-1}) + r \cdot u^2 \tag{14}$$

The single-mode anomaly probability $P_j(t_i)$ is an accumulated value. The probability of anomaly at sampling time t_i is expressed in $P_j(t_i)$, the probability of anomaly at previous sampling time t_{i-1} is expressed in $P_j(t_{i-1})$, the number of times meets the judgment conditions is expressed in constant u, and r represents the radius of the detection area. If the reading $c_j(t_i)$ continuously meets the judgment conditions at several sampling times, u increases gradually from 0. At this time, $P_j(t_i)$ and u have an exponential relationship. If $c_j(t_i)$ does not meet the judgment conditions, u, $P_j(t_{i-1})$ and $P_j(t_i)$ are cleared at the same time. When $c_j(t_i)$ meets the judgment conditions, the accumulation starts again.

In the process of environmental monitoring of agricultural greenhouse, a variety of sensors can be integrated in the wireless sensor network to collect multimodal data streams at a certain sampling time and generate multiple groups of $P_j(t_i)$ values. However, it is not accurate to judge the cause of data anomaly only through a single-mode data flow, and it needs to fuse multi-mode data flow for analysis and judgment. The multi-mode anomaly probability $P_T(t_i)$ can be calculated from multiple groups of single-mode anomaly probability $P_j(t_i)$ values:

$$P_T(t_i) = \sum_{j=1}^{m} \varsigma_j \cdot P_j(t_i), \left(\sum_{j=1}^{m} \partial_j = 1 \right) \tag{15}$$

Where, the weight coefficient is expressed by ς_j. Considering that there may be differences in $P_j(t_i)$ values of different data, some are larger and some are relatively smaller, in order to balance the impact of different $P_j(t_i)$ on $P_T(t_i)$, ς_j of data with fast fluctuation frequency and large amplitude is set to a larger value to improve the sensitivity of the algorithm; On the contrary, ς_j is set to a smaller value to effectively avoid misjudgment due to individual data. Considering that ς_j is related to the fluctuation range of the data, its value can be consistent with the standard deviation ratio of the data in proportion (*Rosero-Montalvo et al., 2020*).

Abnormal source location

When the $P_T(t_i)$ value of a sensor node in the wireless sensor network reaches the threshold $C_{th} = \sum_{j=1}^{m} \partial_j \cdot \frac{Q_{ej}(t) + Q_{nj}(t)}{2}$, it is considered that the agricultural greenhouse environment of the node may be abnormal. Considering the differences of multimodal data sets and the robustness of methods, it is inappropriate to set C_{th} as a fixed value, and the value of C_{th} should be related to the statistical characteristics of the data set and highlight different influence factors. Therefore, C_{th} is set as the weighted average of the mean value of the cube, which not only reflects its correlation with all data sets, but also ensures that there are differences between different data sets; In order to confirm the source of the anomaly, spatial correlation needs to be used for verification. When a node detects its own suspected abnormality, it sends a request message to its adjacent node through the wireless channel and receives the $P_T(t_i)$ value of the adjacent node. According to the Laida Criterion (*Zhou et al., 2020*), if the $P_T(t_i)$ value of the node meets $|P_T(t_i) - \psi| < \gamma\varepsilon$ (ψ and ε are the mean and standard deviation of $P_T(t_i)$ value of the neighbor node respectively), it is considered that the error comes from the random error in the process of the event, and the state of this node is consistent with that of the neighbor node; If not, it is considered that the state of this node is inconsistent with that of the adjacent node, and there is a fault or measurement error. γ needs to be taken according to the specific situation, but generally, the event process can be regarded as a Bernoulli process in which the random variable conforms to the normal distribution, so the random variable can be simplified into a random variable with standard normal distribution:

$$p = P\left(\frac{|P_T(t_i) - \psi|}{\varepsilon} \geq \gamma\right) = 2 - 2\Phi(\gamma) \quad (16)$$

Where: $\Phi(\gamma)$ represents the standard normal distribution. By looking up the table, we can find that when $\Phi(\gamma) > 0.975$, $p < 0.05$; when γ is about greater than 1.96, $\Phi(\gamma) > 0.975$, it can take $\gamma = 2$. The specific judgment conditions of abnormal source are as follows:

If $c_j(t_i) \neq c_j(t_{i-1})$ and $|P_T(t_i) - \psi| < 2\varepsilon$, it is considered that significant environmental changes have occurred in the agricultural greenhouse;

If $c_j(t_i) = c_j(t_{i-1})$ and $|P_T(t_i) - \psi| \geq 2\varepsilon$, the sensor is considered to have failed;

If the above conditions are not met, it is considered that there may be measurement errors. It is necessary to further detect the possible measurement errors and screen out the data with measurement errors.

RESULTS

In order to verify the application effect of the low power consumption environmental monitoring method for agricultural greenhouse based on wireless sensor network in the actual environmental monitoring process, a large strawberry greenhouse is selected as the research object. During the test, the plant is in the mature stage. The solar greenhouse is a column less arched roof greenhouse with an area of 250×8 m^2, with a height of about 3 m. The canopy is covered with straw curtain at night to achieve the effect of thermal insulation at night. The method in this paper is used to monitor the internal environment of the research object. In the process of monitoring, in order to avoid the generation of antenna gain, the same antenna is used at the transmitting end and the receiving end. The antenna direction of the transmitting and receiving node is the same, and the height from the ground is greater than 0.5 m. The monitoring sensor device is shown in Figure 3.

Considering the indoor environmental area of the shed and the monitoring range of the sensor, 83 sensors are placed in the whole shed with the first sensor coordinate (0,0) as the origin, and each sensor device is 6 meters apart. The host computer software monitors and records the wireless signal strength (RSSI) in real time.

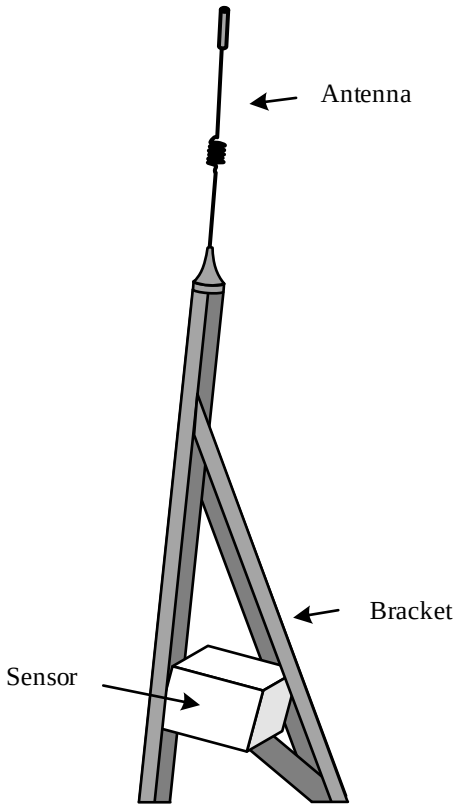

Fig. 3 - Monitoring sensor device

The experimental time is October 2021, and the sampling data are all taken from the sampling results on the first day. The experimental parameter settings are shown in Table 1.

Table 1

Experimental Parameter Setting

Parameter	Numerical value
m	250
n	8
d	6
ϕ	0.75
Sensitivity	2mV/V
Temperature resolution	0.01°C
Carbon dioxide concentration resolution	0.01ppm
Illumination resolution	0.1lx

Actual monitoring results

Using the method in this paper to monitor the internal environmental information of the research object, the data can be easily presented through the monitoring interface of the monitoring center. Taking carbon dioxide concentration, temperature and illumination as examples to test whether this method can work normally and whether the performance of this method can meet the needs of environmental monitoring of the research object. The test is on one day. The carbon dioxide concentration, temperature and illuminance information in the experimental object are monitored every 1 hour, and the deviation results are obtained by comparing with the actual environmental information.

The comparison of the measured data is shown in Table 2.

Table 2

- Monitoring results of internal environmental information of the research object

Time	Carbon dioxide concentration		Temperature		Illuminance	
	Monitoring value / ppm	Deviation/ %	Monitoring value / ℃	Deviation/ %	Monitoring value/ lx	Deviation / %
0:00	359	0.16	12.2	0.11	897	0.02
1:00	362	0.15	11.8	0.09	898	0.01
2:00	360	0.17	11.9	0.04	897	0.03
3:00	359	0.07	11.9	0.02	898	0.00
4:00	361	0.09	12.1	0.07	898	0.01
5:00	357	0.12	12.7	0.05	902	0.05
6:00	301	0.16	14.3	0.10	924	0.05
7:00	225	0.18	15.6	0.12	938	0.08
8:00	199	0.22	18.0	0.04	957	0.06
9:00	192	0.15	19.8	0.07	962	0.07
10:00	194	0.24	21.5	0.02	967	0.09
11:00	182	0.26	23.6	0.09	981	0.04
12:00	179	0.20	23.9	0.04	984	0.02
13:00	181	0.14	23.8	0.05	982	0.00
14:00	183	0.18	23.6	0.08	975	0.01
15:00	196	0.21	22.4	0.03	966	0.05
16:00	205	0.17	20.7	0.14	920	0.03
17:00	229	0.15	18.0	0.08	903	0.04
18:00	268	0.13	16.1	0.05	900	0.02
19:00	327	0.22	15.7	0.00	898	0.00
20:00	346	0.20	15.3	0.02	897	0.01
21:00	358	0.16	14.4	0.07	897	0.00
22:00	359	0.14	13.2	0.02	897	0.00
23:00	359	0.11	12.3	0.05	897	0.01

By analyzing the monitoring data in Table 2, it can be obtained that there is a certain error among the carbon dioxide concentration, temperature, illumination and other data obtained by using the method in this paper to monitor the internal environment of the research object and the actual environmental data, but the error is relatively small. Among them, the carbon dioxide concentration error is the largest, which is basically controlled between 0.10% and 0.25%; the temperature error shall be controlled between 0.00% and 0.15%; the illuminance error is the smallest, which is basically controlled below 0.10%. The above error values are within the allowable range, which shows that this method can effectively achieve the purpose of internal environmental monitoring of the research object. At the same time, the monitoring data obtained in Table 1 are transmitted through ZigBee wireless sensor network, which also shows that the data transmission of wireless sensor network used in this method is stable and reliable.

Performance test of wireless sensor network

The construction and application performance of wireless sensor networks are the key to the performance of the method in this paper. Therefore, the changes of wireless signal strength, packet loss rate and monitoring error of the wireless sensor network built in this method under different wireless communication distances are analyzed. The results are shown in Figure 4.

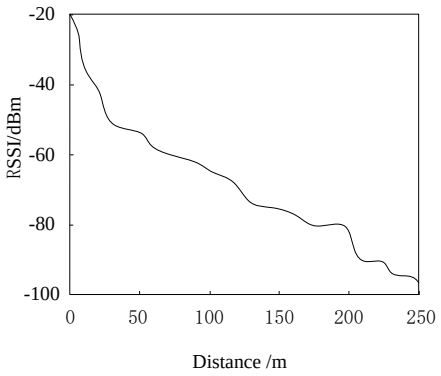

(a) Wireless signal strength

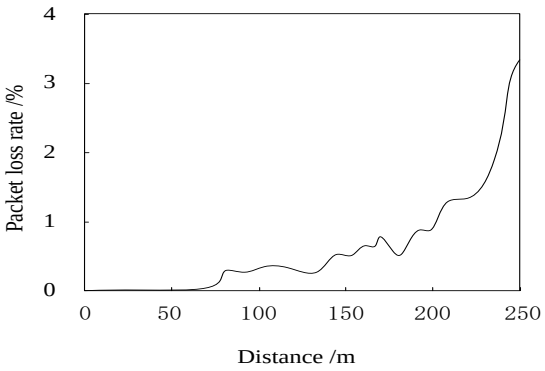

(b) Packet loss rate

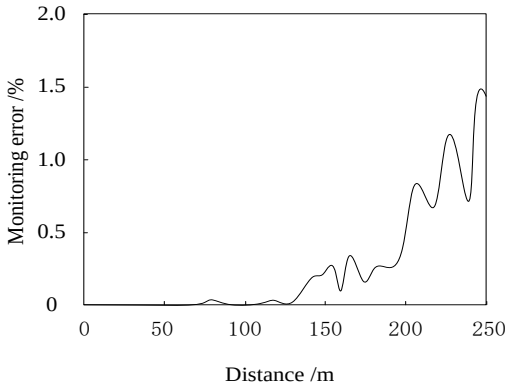

(c) Monitoring error

Fig. 4 - Performance test results of wireless communication

Figure 4 (a) shows the change trend of the received wireless signal strength value with the increase of transmission distance. Through analysis, it can be seen that the wireless signal strength value gradually decreases with the increase of wireless communication distance. When the transmission distance is within 0-25 m, the wireless signal strength value changes obviously, rapidly reducing from – 20 dBm to about – 50 dBm. With the further increase of wireless communication distance, the wireless signal strength shows a relatively slow change trend. When the wireless communication distance reaches 200 m, the wireless signal strength decreases to about - 80 dBm. When the wireless communication distance is higher than 200 m and reaches 250 m, the decline range of wireless signal strength increases to about – 95 dBm. The test results accord with the theoretical relationship that the wireless signal strength changes with the increase of wireless communication distance.

Figure 4 (b) shows the relationship between the packet loss rate of internal environment monitoring data transmission of the research object and the increase of wireless communication distance. The analysis shows that when the wireless communication distance is less than 75 m, the packet loss rate of environmental monitoring data transmission is basically controlled at about 0%; as the wireless communication distance increases, the packet loss rate of environmental monitoring data transmission tends to increase gradually. When the wireless communication distance reaches 200 m, that is, when the wireless signal strength value is lower than -80 dBm, the packet loss rate of environmental monitoring data transmission is always controlled within 1%, and the rate of increase is relatively gentle; When the wireless communication distance is higher than 200 m, the increase in the packet loss rate of environmental monitoring data transmission fluctuates significantly, from 1% to about 3.3%. The data retransmission caused by the increase of the packet loss rate means that the power consumption of the sensor node energy is further increased, and the service life is shortened.

Figure 4 (c) shows the variation relationship of environmental information monitoring error with the increase of wireless communication distance. Through analysis, it can be seen that when the wireless communication distance is within 125 m, the fluctuation of monitoring error is relatively stable, basically controlled at about 0%, and the monitoring accuracy is high; When the wireless communication distance is between 125 and 200 m, the monitoring error will fluctuate slightly, which is basically controlled within 0.5%;

When the wireless communication distance is higher than 200 m, the monitoring error is accompanied by large fluctuation.

Based on the above analysis, it can be concluded that using the method in this paper to monitor the internal environmental information of the research object has better information transmission performance.

Comparison of power consumption

The power consumed by the internal environmental monitoring of the research object before and after using the method in this paper is compared. The results are shown in Figure 5.

By analyzing Figure 5, it can be seen that before adopting the method in this paper, the average power consumption of nodes in the process of monitoring the internal environment of the research object is about 64 W; After using the method in this paper, the node power consumption of the internal environment monitoring of the research object is about 37 W, which is 36% lower than before. This shows that using this method can effectively reduce the node power consumption in the process of internal environment monitoring. This is because in the deployment stage of sensor nodes, the number of nodes and network coverage are considered at the same time to prevent data transmission conflict and resource waste. At the same time, LEACH protocol is optimized in the process of node communication so that it does not need to randomly select cluster heads, so as to save energy.

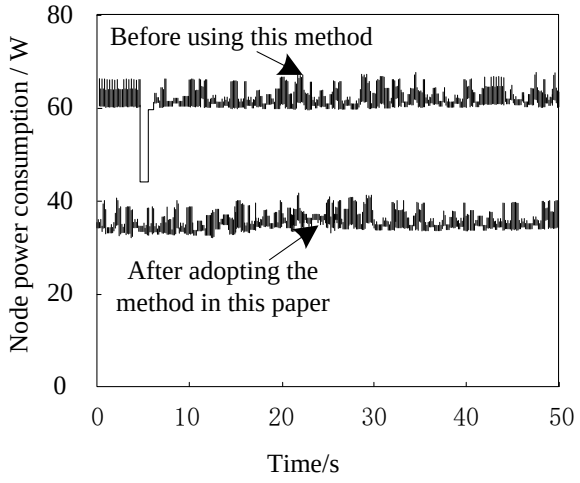

Fig. 5 - Comparison results of power consumption

CONCLUSIONS

According to the needs of environmental monitoring of modern agricultural greenhouse, the low power consumption monitoring method of agricultural greenhouse environment based on wireless sensor network is studied. This method can efficiently monitor the environmental parameters of agricultural greenhouse, including temperature, humidity and light intensity, and has the characteristics of low power consumption, high reliability and stable power supply. Because the research focus of this method is to improve the reliability of wireless sensor networks and reduce the power consumption in the monitoring process, we should further improve the routing protocol and improve the real-time and stability of wireless sensor networks in the future.

ACKNOWLEDGEMENT

The research is supported by: Suqian Science & Technology Plan Program, Research on Key Technologies of precision planting in smart greenhouse (Grant No. L202109). Supported by Jiangsu Sci&Tech Program: Research and Development of Key Technologies for Green and Intelligent Breeding of White Feather Broilers (Grant No. BE2021354)

REFERENCE

[1] Abdulkarem, M., Samsudin, K., Rokhani, F. Z., Rasid, M. (2019). Wireless sensor network for structural health monitoring: a contemporary review of technologies, challenges, and future direction. *Structural Health Monitoring*, 19(2), 147592171985452.

[2] Bai, X., Wang, Z., Sheng, L., Wang, Z. (2019). Reliable data fusion of hierarchical wireless sensor networks with asynchronous measurement for greenhouse monitoring. *IEEE Transactions on Control Systems Technology*, 27(3), 1036-1046.

[3] Chan, K. L., Mo, C., Shin, K. Y., Im, Y. H., Yoon, S. W. (2019). A study of the effects of enhanced uniformity control of greenhouse environment variables on crop growth. *Energies*, 12(9), 1749.
[4] Fakhri, A. B., Gharghan, S. K., & Mohammed, S. L. (2020). Power reduction based on sleep/wake scheme in wireless sensor network for patient's vital sign monitoring system. *Technology Reports of Kansai University*, 62(4), 1669-1685.
[5] Grace, R. K., Manju, S. (2019). A comprehensive review of wireless sensor networks-based air pollution monitoring systems. *Wireless Personal Communications*, 108(4), 2499-2515.
[6] Haque, M. E., Asikuzzaman, M., Khan, I. U., Ra, I. H., Shah, S. (2020). Comparative study of IoT-based topology maintenance protocol in a wireless sensor network for structural health monitoring. *Remote Sensing*, 12(15).
[7] Honeycutt, W. T., Kim, T., Ley, M. T., Materer, N. F. (2021). Sensor array for wireless remote monitoring of carbon dioxide and methane near carbon sequestration and oil recovery sites. *RSC Advances*, 11(12), 6972-6984.
[8] Khan, Z., Khan, M. Z., Ali, S., Abbasi, I. A., Huang, J. (2020). Internet of things-based smart farming monitoring system for bolting reduction in onion farms. *Scientific Programming*, 2021(7), 1-15.
[9] Koroak, I., Suhadolnik, N., Pleterek, A. (2019). The implementation of a low power environmental monitoring and soil moisture measurement system based on UHF RFID. *Sensors*, 19(24), 5527.
[10] Li, K., Xie, Z., Zeng, D., Li, W. & Xia, C. (2021). Power cable vibration monitoring based on wireless distributed sensor network. *Procedia Computer Science*, 183(10), 401-411.
[11] Liu, B., Yang, R., Xu, M., & Zhou, J. (2021). A chaotic elite niche evolutionary algorithm for low power consumption clustering in environment monitoring wireless sensor networks. *Journal of Sensors*, (3), 1-12.
[12] Picallo, I., Lopez-Iturri, P., Astrain, J. J., Aguirre, E., Falcone, F. (2021). Basketball player on-body biophysical and environmental parameter monitoring based on wireless sensor network integration. *IEEE Access*, PP (99), 1-1.
[13] Pisanu, T. Garau, S., Ortu, P., Schirru, L. & C Macciò. (2020). Prototype of a low-cost electronic platform for real time greenhouse environment monitoring: an agriculture 4.0 perspective. *Electronics*, 9(5), 726.
[14] Rezvani, M. E., Abyaneh, H. Z., Shamshiri, R. R., Balasundram, S. K., Mahns, B. (2020). IoT-based sensor data fusion for determining optimality degrees of microclimate parameters in commercial greenhouse production of tomato. *Sensors*, 20, 6474.
[15] Rienzo, M. D., Rizzo, G., Iilay, Z. M., & Lombardi, P. (2019). SeisMote: a multi-sensor wireless platform for cardiovascular monitoring in laboratory, daily life, and telemedicine. *Sensors* (Basel, Switzerland), 20(3).
[16] Rosa, R. L., Dehollain, C., Livreri, P. (2020). Advanced monitoring systems based on battery-less asset tracking modules energized through RF wireless power transfer. *Sensors* (Basel, Switzerland), 20(11).
[17] Rosero-Montalvo, P. D., Erazo-Chamorro, V. C., VF López-Batista, MN Moreno-García, & Peluffo-Ordóez, D. H. (2020). Environment monitoring of rose crops greenhouse based on autonomous vehicles with a WSN and data analysis. *Sensors*, 20(20), 5905.
[18] Saban, M., Aghzout, O. A., Rosado, A., Medus, L. D., Casans, S. (2019). Sensor node network for remote moisture measurement in timber based on Bluetooth low energy and web-based monitoring system. *Sensors*, 21(491), 16.
[19] Shan, W., Jin, X., Meng, X., Yang, X., Xu, Z., Gu, Z., et al. (2019). Dynamical monitoring of ecological environment quality of land consolidation based on multi-source remote sensing data. Nongye Gongcheng Xuebao / *Transactions of the Chinese Society of Agricultural Engineering*, 35(1), 234-242.
[20] Zhou, C., Luo, X., Huang, T., Zhou, T. (2020). Function matching of terminal modules of intelligent furniture for elderly based on wireless sensor network. *IEEE Access*, PP (99), 1-1.
[21] Mabrouki J, Azrour M, Dhiba D, et al. (2021). IoT-based data logger for weather monitoring using Arduino-based wireless sensor networks with remote graphical application and alerts [J]. *Big Data Mining and Analytics*, 4(1): 25-32.
[22] Ge X, Han Q L, Zhang X M, et al. (2019). Distributed event-triggered estimation over sensor networks: A survey [J]. *IEEE transactions on cybernetics*, 50(3): 1306-1320.

MECHATRONIC SYSTEM USED IN THE LABORATORY FOR COMPLEX ANALYSIS APPLIED AND USED IN INDUSTRY
/
SISTEM MECATRONIC UTILIZAT IN LABORATOR PENTRU ANALIZE COMPLEXE APLICATE ȘI UTILIZATE ÎN INDUSTRIE

Iulian ILIE
National Institute of Research in Mechatronics and Measurement Technique, Bucharest / Romania
E-mail: iuliancefin@yahoo.com
https://doi.org/10.35633/inmateh-68-44

Keywords: *measurement, control, mechatronic, positioning*

ABSTRACT
Equipment and methods for microfabrication and micro measurements are under constant development. There are a multitude of possibilities to connect and control equipment for control and measurements adapted with the development of Industry 4.0. Using the terms Internet of Things, 3D printing, virtual reality, augmented reality, collaborative robots, microfabrication, etc. and related applications are common in daily research and innovation activity. This paper presents the construction of a mechatronic system and the measurement procedures used in the working mode. Experimental results and their interpretation as well as the final conclusions of this paper are presented. The mechatronic system is intended for use in the main fields such as automotive, aeronautics, robotics, agriculture and others.

REZUMAT
Echipamentele și metodele pentru microfabricație și micromăsurări sunt în continuă dezvoltare. Există o multitudine de posibilități de a conecta și de a controla echipamente pentru control și măsurări adaptate o dată cu dezvoltarea Industriei 4.0. Utilizarea termenilor Internet of Things, printare 3D, realitate virtuală, realitate augmentată, roboți colaborativi, microfabricație, etc. și a aplicațiilor aferente sunt comune în activitatea zilnică de cercetare și inovare. Această lucrare prezintă construcția unui sistem mecatronic și procedurile de măsurare utilizate în modul de lucru. Sunt prezentate rezultate experimentale și interpretarea acestora precum și concluziile finale ale acestei lucrări. Sistemul mecatronic este destinat utilizării în principalele domenii, cum ar fi cel auto, aeronautic, agricultură, robotică și altele.

INTRODUCTION

In the research activity in the field of mechatronics, a precise method of measurement is necessary in order to carry out conclusive tests. The development of manufacturing processes is correlated with the four identified industrial revolutions: the first industrial revolution took place at the end of the 18th century and the beginning of the 19th century; the second industrial revolution begun at the end of the 19th century; the third industrial revolution begun in the second half of the 20th century; and the fourth industrial revolution begins with the 3rd millennium (*Vinitha K. et al., 2020*).

The mechatronic system presented in this paper is intended for the improvement of mechanical microfabrication (*Brousseau et al., 2010; Razali et al., 2013; Quaglia G. et al., 2020*) techniques, namely: micro-milling, micro-drilling, micro-turning, micro-rectification, micro-polishing, micro-polishing and water jet abrasive micro-machining, etc. Also, the mechatronic system is intended to improve microforming techniques: microforging, microextrusion, microstamping and microhydroforming, microforming (*Xu J. et al., 2021; Raja P. et al., 2021*), etc.

Globally, there is an ongoing concern for microfabrication, especially for its manufacturing methods/processes. One of the most popular microfabrication processes is microforming.

Recently, in Europe, the concept of micro-nano manufacturing technologies (MNMT) was used due to the difficulty to delimit the fields of micro technologies and nano technologies. An example is The Center of Micro/Nano Manufacturing Technology (MNMT-Dublin - https://www.mnmt-dublin.org/) and INCDMTM laboratories (*www.incdmtm.ro*) used in the daily research and innovation activity (*Gheorghe et al., 2022*).

The paper aims to present a mechatronic system *(Ivanov D., 2021)* that is intended for use in the laboratory and in the industrial environment and improves the quality of positioning and measurement in the

field of mems correlated with the reduction of working time. The approach to the measurement systems and the procedures used is, lately, built on Industry 4.0 (*Oztemel et al., 2020; Zheng et al., 2021; Ghobakhloo M., 2020*) and IoT (*Kiran D.R., 2017*) concepts in order to control the mechatronic system from distance and watch the measurement process through virtual reality applications, augmented reality (*Tan et al., 2022*) or robots or collaborative robots (*Böckmann et al., 2021; Patange et al., 2022*). An important aspect of various industries' approaches to data use is data protection and cyber security (*Martin et al., 2017*).

MATERIALS AND METHODS

The mechatronic system is based based on a hexapod platform with controller (*Gauthier et al., 2011*) presented in Figure 1 and uses for measurements a transducer with (Figure 3, position 4) and a renishaw probe (Figure 5, position 2) with a ruby ball stylus.

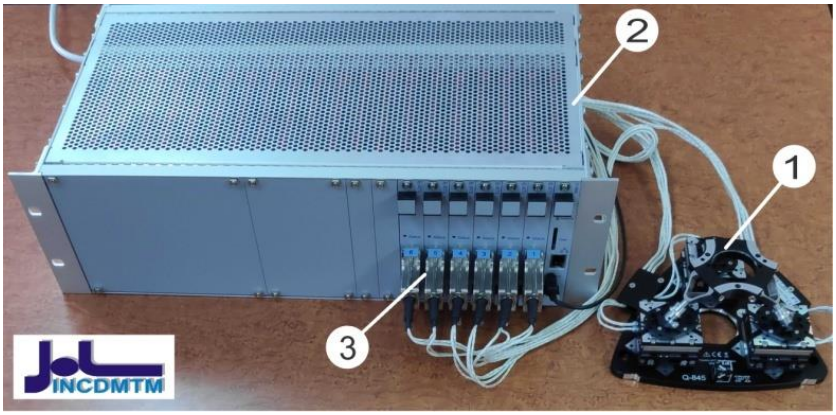

Fig. 1 - Mechatronic system used in the laboratory for complex analysis applied in industry

1-Motion platform with six degrees of freedom; 2- Kinematic controller; 3-Connection plugs for controller and motion platform

The main characteristics motion platform are: ±7 mm travel range in X and Y, and ±5 mm in Z; ±7° rotation range in θX, θY, and ±8° in θZ; 10 N load capacity, center mounted.

The main characteristics motion platform are: ±7 mm travel range in X and Y, and ±5 mm in Z; ±7° rotation range in θX, θY, and ±8° in θZ; 10 N load capacity, center mounted.

The Renishaw probe have a 10 cm feeler and it has a force of 0.07–0.08 N.

The transducer has 10 mm measurement range and 1 μm resolution.

For analysis and interpretation regarding the microgeometry topography of the structures surfaces (*Garcia et al., 2020*) for the measured parts analysed in presented paper is used Atomic Force Microscope from INCDMTM CERTIM Laboratory and presented in Figure 2. The movement accuracy is at the nanometer level and allows the system to amplify the displacement > 2000 times.

Fig. 2 - AFM Microscope, NTEGRA Probe NanoLaboratory NT – MDT

1 – base unit; 2 – measurement head; 3 – vibrations isolation system; 4 – optical system visualization

Following the scanning of 50 × 50 µm surfaces, different topographic parameters could be analysed (roughness, surface asymmetry, flattening coefficient), which provide information related to the surface quality of the measured part. In this way it was possible to characterize in detail the structure of the surfaces.

The determined topographic parameters (roughness-Ra, maximum height-h_{max}, height in 10 points-Rz, asymmetry of the surface-Ssk, flattening coefficient-Ska) following the AFM study provide information related to the analysed surfaces.

The asymmetry index Rsk evaluates the degree of asymmetry of a distribution and characterizes, together with the flattening index Ska, the shape of the distribution (illustrated as a histogram). The Ssk asymmetry index is negative or positive as the survey distribution is asymmetric to the left or to the right, respectively. A symmetrical distribution, such as the normal distribution, has zero asymmetry.

The flattening coefficient Ska is part of the indices of appreciation of the shape of a distribution. A high flattening index shows a distribution with large “tails” (far from average categories are present), while a low flattening index shows a distribution in which fewer far from average categories are present. In the case of a distribution close to the normal distribution, the flattening coefficient is around 3. Based on this result, the excess E is defined as the difference between the flattening coefficient and three. For E> 0, the distribution is called leptokurtic (the height of the curve is higher compared to normal), and for E <0, it is called platykurtic (the curve is flattened). If E = 0, the distribution is mesokurtic. Excessively large data sets tend to have a distinct peak near the mean. Low excess data sets tend to have a flat maximum near the average rather than a sharp peak. A uniform distribution would be the extreme case.

The method for measurement with mechatronic system using the transducer and renishaw probe with stylus is using the contact point by positioning the with motion platform and controller. The measurement are made in 4 point and repeated 10 times for each measurement point. The relation used for result determine is:

$$\overline{y} = \frac{\sum_{i=1}^{10} p_i}{10} \text{ [mm]} \quad (1)$$

The measurement procedure for mechatronic system is presented in the next 5 figures and we can see the contact point realized. The measurement can be done in industry like automotive, agriculture, aeronautical etc.

In Figure 3 is presented the mechatronic system and linear transducer in the active measurement of a cylindrical probe.

In Figure 4 is presented the mechatronic system and linear transducer in the active measurement of a automotive industry probe.

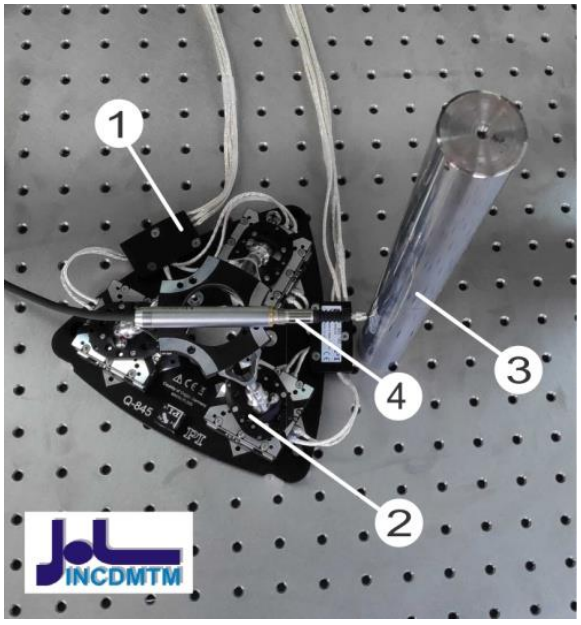

Fig. 3 - Measurement process with mechatronic system and transducer – view 1

1- drive motor for movement and positioning platform; 2- movement and positioning platform; 3 - measured part; 4- linear transducer

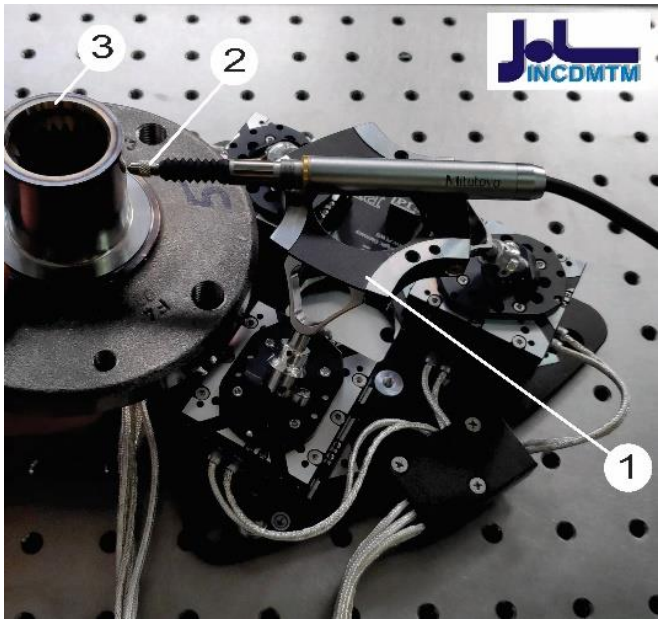

Fig. 4 - Measurement process with mechatronic system and transducer – view 2

1-movement and positioning platform; 2- linear transducer; 3-measured part

In Figure 5 is presented the mechatronic system and stylus probe in the active measurement of a 3D prototyped probe made of plastic material powder.

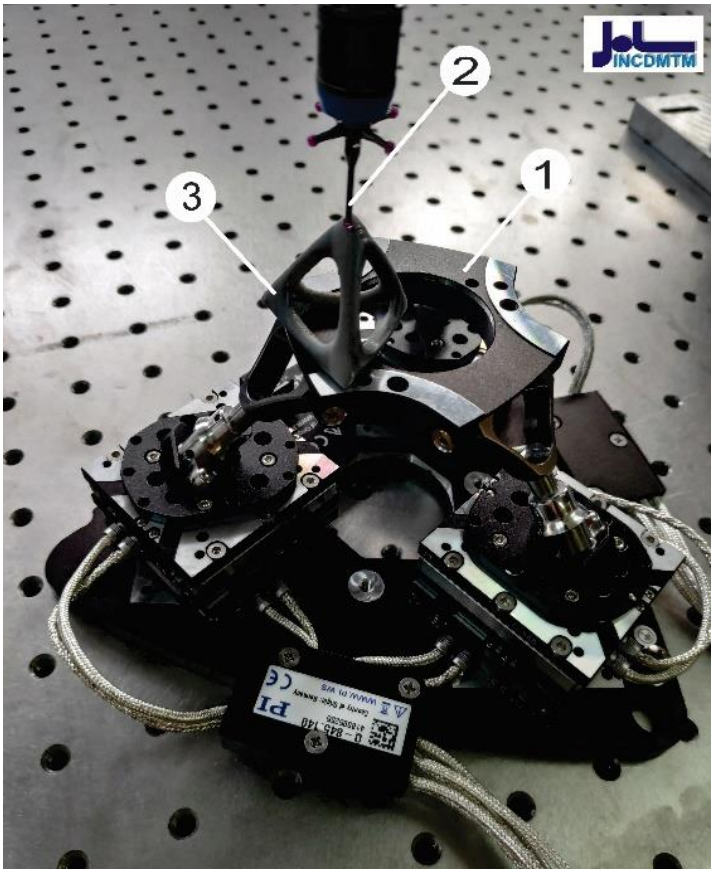

Fig. 5 - Measurement process with mechatronic system and probe stylus – view 1
1-Movement and positioning platform; 2- 3D stylus probe; 3- 3D printed plastic probe for measurement

In Figure 6 is presented the mechatronic system and stylus probe in the active measurement of a 3D prototyped probe made of metal material powder.

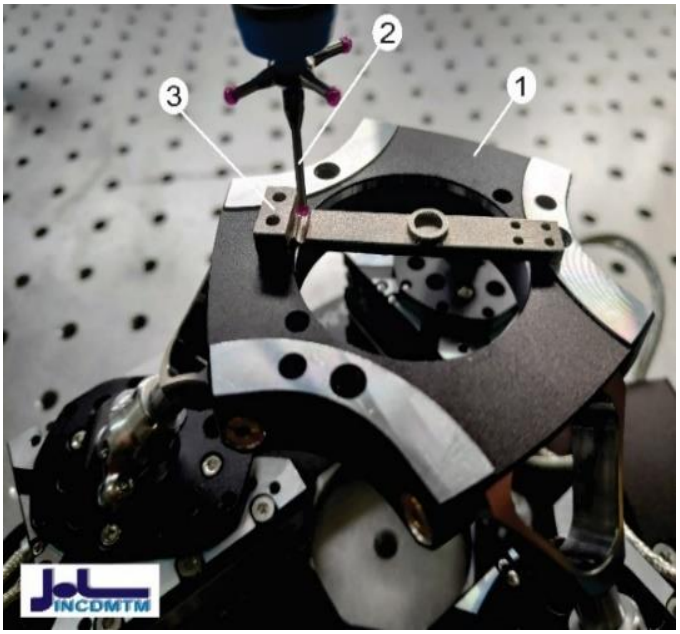

Fig. 6 - Measurement process with mechatronic system probe stylus – view 2
1-Movement and positioning platform; 2- 3D stylus probe; 3- 3D printed metal probe for measurement

In Figure 7 is presented the mechatronic system and stylus probe in the active measurement of automotive industry probe.

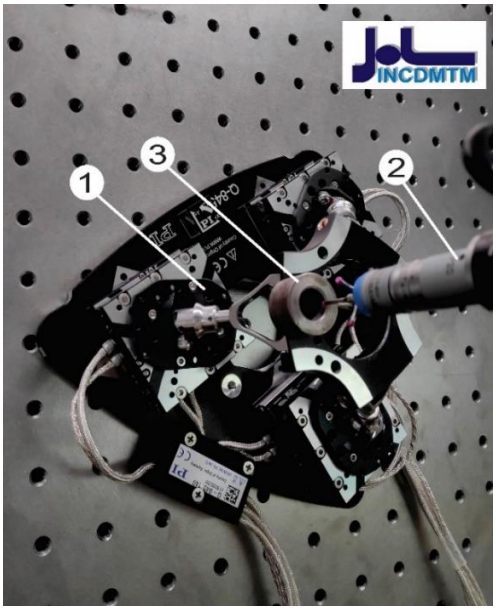

Fig. 7 - Measurement process with mechatronic system probe stylus – view 3
1-Movement and positioning platform; 2- 3D stylus probe; 3- Measured part

RESULTS

The results for analysis and interpretation on the microgeometry topography of the structures surfaces for the measured parts analysed are presented in Table 1 and Figures 8-10, which present the values of the main topographic parameters determined experimentally and their calculated average value for the measured part.

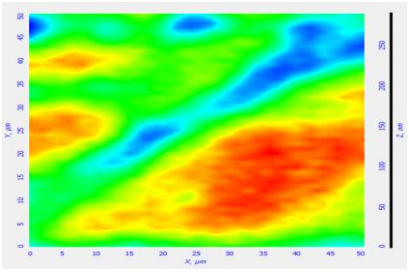

(*a) the scanned 2D surface*

Amount of sampling	2601
Max	358.251 nm
Min	0 nm
Peak-to-peak, Sy	358.251 nm
Ten point height, Sz	179.681 nm
Average	167.593 nm
Average Roughness, Sa	99.9529 nm
Second moment	201.026
Root Mean Square, Sq	111.014 nm
Surface skewness, Ssk	0.2145
Coefficient of kurtosis, Ska	-1.44054
Entropy	6.86163
Redundance	-14.5328

(b) determined topographical parameters

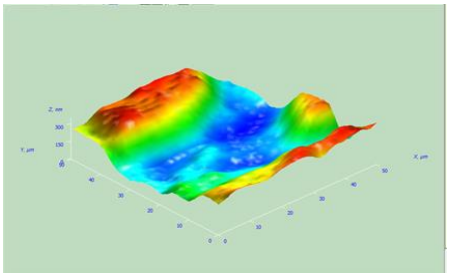

(c) the scanned surface transformed into 3D

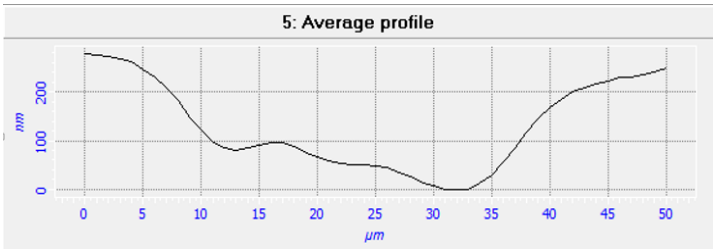

(d) the average profile in the X direction

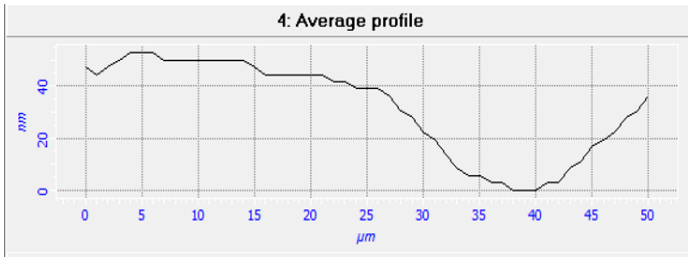

(e) the average profile in the X direction

Fig. 8 - Surface analysis of area 1 on the part measured using AFM

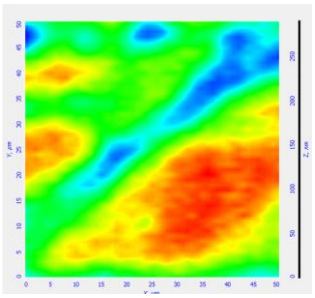

(a) the scanned 2D surface

Amount of sampling	2601
Max	288.823 nm
Min	0 nm
Peak-to-peak, Sy	288.823 nm
Ten point height, Sz	148.855 nm
Average	169.075 nm
Average Roughness, Sa	55.8775 nm
Second moment	181.65
Root Mean Square, Sq	66.4111 nm
Surface skewness, Ssk	-0.279015
Coefficient of kurtosis, Ska	-0.847434
Entropy	6.45144
Redundance	-16.6243

(b) determined topographical parameters

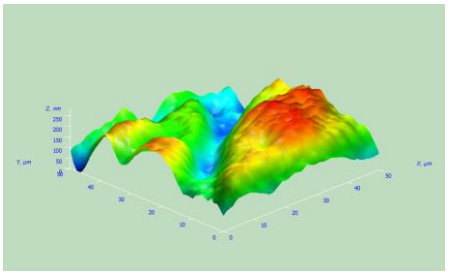

(c) the scanned surface transformed into 3D

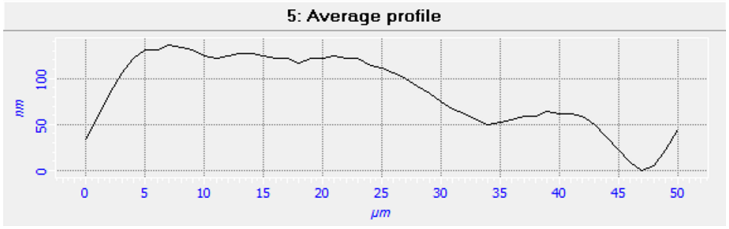

(d) the average profile in the X direction

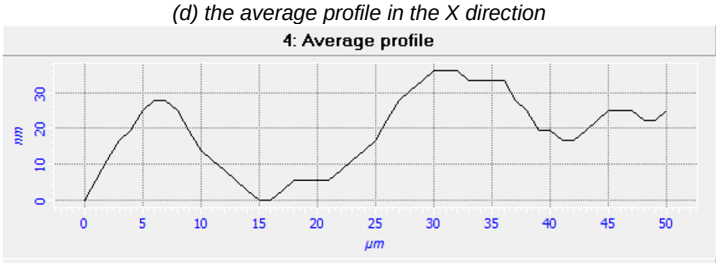

(e) the average profile in the X direction

Fig. 9 - Surface analysis of area 2 on the part measured using AFM

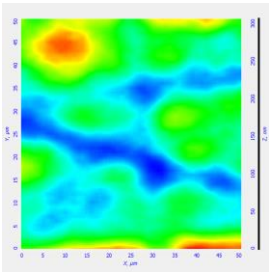

(a) the scanned 2D surface

Amount of sampling	2601
Max	305.486 nm
Min	0 nm
Peak-to-peak, Sy	305.486 nm
Ten point height, Sz	151.632 nm
Average	117.3 nm
Average Roughness, Sa	46.8714 nm
Second moment	131.17
Root Mean Square, Sq	58.7044 nm
Surface skewness, Ssk	0.664095
Coefficient of kurtosis, Ska	-0.0103481
Entropy	6.31535
Redundance	-15.4212

(b) determined topographical parameters

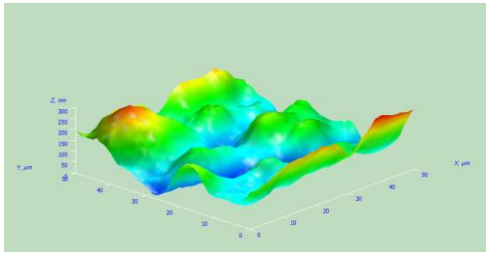

(c) the scanned surface transformed into 3D

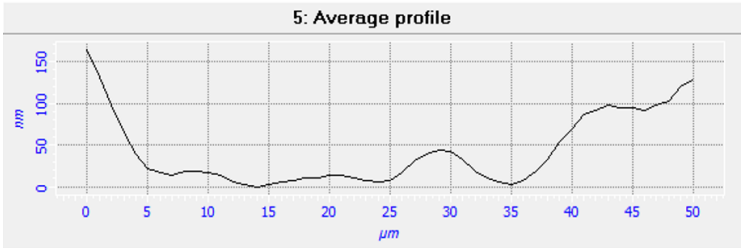

(d) the average profile in the X direction

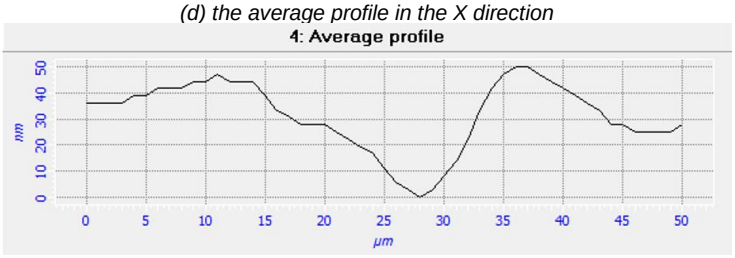

(e) the average profile in the X direction

Fig. 10 - Surface analysis of area 3 on the part measured using AFM

Table 1 presents the results of the surface analysis of measured piece.

Table 1

The average of the selected parameters for 3 measured areas

Analysed zone	Ra (nm)	h_{max} (nm)	Ssk	Ska
Area 1	99.95	358.25	0.21	-1.44
Area 2	55.87	288.82	-0.27	-0.84
Area 3	46.87	305.48	0.66	-0.01
Average calculated value	**67.56**	**317.52**	**0.20**	**-0.76**

The results of measurement tests are presented in Table 2.

Table 2

Measurement 4 points 10 times

Number of measurement	Point 1 [µm]	Point 2 [µm]	Point 3 [µm]	Point 4 [µm]
1	596	700	801	898
2	603	696	802	900
3	600	696	801	905
4	602	698	798	904
5	604	703	796	896
6	603	705	797	898
7	600	705	797	900
8	595	697	800	899
9	597	700	801	904
10	601	702	800	902
$\overline{y} = \frac{\sum_{i=1}^{10} p_i}{10}$	600.10	700.20	799.30	900.60

According to Table 2, for the set of 10 measurements performed on 4 contact points, there is a similar variation for repetability. For point 1, there is a variation between 595 µm and 604 µm resulting $\overline{y} = \mathbf{600.10}\,\overline{y}$ µm. For point 2, there is a variation between 696 µm and 705 µm resulting $\overline{y} = \mathbf{700.20}\,\overline{y}$ µm. For point 3, there is a variation between 796 µm and 802 µm resulting $\overline{y} = \mathbf{799.30}\,\overline{y}$ µm. For point 4, there is a variation between 896 µm and 902 µm resulting $\overline{y} = \mathbf{799.30}\,\overline{y}$ µm.

CONCLUSIONS

In conclusion, considering all the measurements and analysis presented and prepared as a result of the experimental research carried out in the metrologically certified laboratories of the National Institute for Research-Development in Mechatronics and Measurement Technique in Bucharest, the mechatronic system is validated for metrological and industrial use in technical fields of automotive, agricultural, aeronautics, robotics etc. and in all manufacturing industries.

Future research and concept development, starting from the presented mechatronic system, are highlighted below:

- Research on the development of a virtual application for mechatronic system;
- Research for improved protection of the human operator;
- Research to improve the speed and stability of the mechatronic system;
- Research on the mapping of the workspace so that we can accurately identify, at any time, the position of the analysed parts at a defined time.

ACKNOWLEDGEMENT

This work was supported by the project "Increasing INCDMTM performance and international involvement by supporting expertise in advanced mechatronic technologies - PERFORM-MECH", financed by The Ministry of Research, Innovation, and Digitalization, in the framework of Programme 1 – Development of the national research and development system, Sub-programme 1.2 – Institutional Performance – Projects for financing excellence in Research, Development and Innovation, Contract no. 3PFE/2021.

The author is grateful to INCDMTM Bucharest. Design Execution and testing parts was an extremely delicate process due to its innovative character and precision of execution. For this reason, was preferred to make them on specialized 3D printing equipment, existing in the CERMISO center from INCDMTM Bucharest. In this sense, an EP - M250 Shining 3D equipment was used for 3D metal printing and a JCR 1000 Dual Sicnova equipment for 3D plastic printing. Access to these modern technologies has greatly facilitated the process of adapting the elements mentioned above to the executed mechatronic system, eliminating costs and additional time generated by the classic casting technology.

REFERENCES

[1] Akhtar Razul Razali, Yi Qin, (2013). A Review on Micro-manufacturing. Micro-forming and their Key Issues. *Procedia Engineering*, Vol. 53, pp. 665-672, ISSN 1877-7058. https://doi.org/10.1016/j.proeng.2013.02.086.

[2] Böckmann, Sönke, Igor Titov, and Martina Gerken, (2021). Extraction of Soil Solution into a Microfluidic Chip. *AgriEngineering*, Vol.3, no. 4. pp. 783-796. https://doi.org/10.3390/agriengineering3040049

[3] Brousseau, E. B., Dimov, S. S., & Pham, D. T., (2010). Some recent advances in multi-material micro- and nano-manufacturing. *International Journal of Advanced Manufacturing Technology*, Vol. 47(1-4), pp.161-180. doi:10.1007/s00170-009-2214-5.

[4] Garcia, R. (2020). Nanomechanical mapping of soft materials with the atomic force microscope: Methods, theory and applications. *Chemical Society Reviews*, Vol. 49(16), pp.5850-5884. doi:10.1039/d0cs00318b.

[5] Gauthier, M., (2011). Microhandling strategies and microassembly in submerged medium. *Robotic microassembly*, pp. 189-224. doi:10.1002/9780470634417.ch5.

[6] Gheorghe, G; Sorin-Ionut, B; Ilie, I; Veronica, D; (2022) Is Romania Ready for the Development of Smart Industry 4.0?. *Innovations in mechatronics engineering*. pp. 293-304. doi 10.1007/978-3-030-78170-5_26

[7] Ghobakhloo, M., (2020). Industry 4.0, digitization, and opportunities for sustainability. *Journal of Cleaner Production*, Vol. 252, doi:10.1016/j.jclepro.2019.119869.

[8] Ivanov, D., Tang, C. S., Dolgui, A., Battini, D., & Das, A., (2021). Researchers' perspectives on industry 4.0: Multi-disciplinary analysis and opportunities for operations management. *International Journal of Production Research*, Vol. 59(7), pp. 2055-2078. doi:10.1080/00207543.2020.1798035.

[9] Kiran D.R. (2019). Internet of Things. Production Planning and Control. pp. 495-513, ISBN 9780128183649. https://doi.org/10.1016/B978-0-12-818364-9.00035-4.

[10] Martin E., Thomas D., Hristo A., (2017). The Evolution of the V-Model: From VDI 2206 to a System Engineering Based Approach for Developing Cybertronic Systems. *14th IFIP International Conference on Product Lifecycle Management (PLM)*. pp. 382-393, ff10.1007/978-3-319-72905-3_34ff. ffhal-01764166f

[11] Oztemel, E., & Gursev, S., (2020). Literature review of industry 4.0 and related technologies. *Journal of Intelligent Manufacturing*, Vol. 31(1), pp. 127-182. doi:10.1007/s10845-018-1433-8.

[12] Patange, Abhishek & R, Jegadeeshwaran & Bajaj, Naman & Khairnar, Apoorva & Gavade, N., (2022). Application of Machine Learning for Tool Condition Monitoring in Turning. *Sound & Vibration*. Vol. 56, pp. 127–145. 10.32604/sv.2022.014910.

[13] Pradeep Raja, C., & Ramesh, T., (2021). Influence of size effects and its key issues during microforming and its associated processes – A review. *Engineering Science and Technology, an International Journal*, Vol. 24(2), pp. 556-570. doi:10.1016/j.jestch.2020.08.007.

[14] Quaglia, Giuseppe, Carmen Visconte, Leonardo Sabatino Scimmi, Matteo Melchiorre, Paride Cavallone, and Stefano Pastorelli, (2020). Design of a UGV Powered by Solar Energy for Precision Agriculture. *Robotics* 9, Vol. 1: 13. https://doi.org/10.3390/robotics9010013

[15] Tan, Yi, Wenyu Xu, Shenghan Li, and Keyu Chen, (2022). Augmented and Virtual Reality (AR/VR) for Education and Training in the AEC Industry: A Systematic Review of Research and Applications. *Buildings*. Vol. 12(10), 1529. https://doi.org/10.3390/buildings12101529

[16] Vinitha, K., Ambrose Prabhu, R., Bhaskar, R., & Hariharan, R., (2020). Review on industrial mathematics and materials at industry 1.0 to industry 4.0. *Materials Today: Proceedings*, Vol. 33, pp. 3956-3960. doi:10.1016/j.matpr.2020.06.331.

[17] Xu, J., Wang, X., Wang, C., Yuan, L., Chen, W., Bao, J., . . . Guo, B., (2021). A review on Micro/Nanoforming to fabricate 3D metallic structures. *Advanced Materials*, Vol. 33(6). doi:10.1002/adma.202000893.
[18] Zheng, T., Ardolino, M., Bacchetti, A., & Perona, M., (2021). The applications of industry 4.0 technologies in manufacturing context: A systematic literature review. *International Journal of Production Research*, Vol. 59(6). pp. 1922-1954, doi:10.1080/00207543.2020.1824085.
[19] https://incdmtm.ro/?lang=en
[20] https://www.mnmt-dublin.org/

COMPARATIVE ANALYSIS OF THE IDLE MOVE LENGTH WHEN MAKING T-TURNS BY A MOUNTED MACHINE TRACTOR UNIT IN A FIELD OF IRREGULAR SHAPE
/
СРАВНИТЕЛЕН АНАЛИЗ НА ДЪЛЖИНАТА НА НЕРАБОТНИЯ ХОД ПРИ ИЗВЪРШВАНЕ НА ГЪБОВИДНИ ЗАВОИ ОТ НАВЕСЕН МАШИННО-ТРАКТОРЕН АГРЕГАТ В ПОЛЕ С НЕПРАВИЛНА ФОРМА

Krasimir TRENDAFILOV*[1)], Galin TIHANOV[2)]

[1)] Trakia University – Stara Zagora, Faculty of Technics and Technologies – Yambol, Department of Mechanical Engineering / Bulgaria;
[2)] Trakia University – Stara Zagora, Faculty of Agriculture, Department of Agricultural Engineering / Bulgaria
Tel: +359 887 708 603; E-mail: krasimir.trendafilov@trakia-uni.bg
DOI: https://doi.org/10.35633/inmateh-68-45

Keywords: *T-turns, idle move length, motion of a machine-tractor unit, field of irregular shape*

ABSTRACT
The productivity of machine-tractor units depends on the length of the idle move performed in the headland. Analytical dependences for determining the length of the idle move when making T-turns by a machine-tractor unit with a mounted machine in a field of irregular shape have been specified in the article. Five types of T-turns have been considered in two variants – open turn and closed turn. Each of them is carried out in two directions of motion. A total of 20 variants of turns have been described. The methodology for determining the idle move length for a specific machine-tractor unit consisting of a tractor and a mounted row seeder has been demonstrated. It has been established that the idle move of the machine-tractor unit had the smallest length when the direction of making the turn is from right to left. For three of the studied turns, the idle move length in open and closed turns is the same when travelling from right to left. Right-to-left open and closed T-turns have been shown to provide the same idle move length of the unit in the headland, which is the smallest compared to the other turns.

РЕЗЮМЕ
Производителността на машинно-тракторните агрегати зависи от дължината на неработния ход извършван в ивицата за завиване. В статията са посочени аналитични зависимости за определяне на дължината на неработния ход при извършване на гъбовидни завои от машинно-тракторен агрегат с навесна машина в поле с неправилна форма. Разгледани са пет вида гъбовидни завои в два варианта – отворен завой и затворен завой. Всеки от тях се извършва в две направления на движение. Общо са описани 20 варианта на завои. Демонстрирана е методиката за определяне на дължината на неработния ход за конкретен машинно-тракторен агрегат съставен от трактор и навесна редова сеялка. Установено е, че неработният ход на машинно-тракторния агрегат е с най-малка дължина когато посоката на извършване на завоя е отдясно наляво. За три от изследваните завои дължината на неработния ход при отворени и затворени завои е еднаква при движение отдясно наляво. Доказано е, че отворените и затворените гъбовидни завои извършвани отдясно наляво осигуряват еднаква дължина на неработния ход на агрегата в ивицата за завиване, която е най-малка в сравнение с останалите завои.

INTRODUCTION
The idle move length performed by a machine-tractor unit in the field had an effect on its productivity. In most mechanized operations turns in the headland had the greatest share among idle moves *(Sabelhaus et al., 2013*). It has been found in a study by Bochtis and Sorensen (2009) that turns comprised 5.27 % and 6.48 % of the total distance travelled the machine-tractor unit (*Bochtis et al., 2009*). When the machine needs to be stocked on the field, for example with liquid fertilizer, the distance travelled by the unit for making turns is the second longest idle distance after the distance travelled to the loading station. It is 14 – 42 % of the idle moves or an average of 29 % (*Jensen et al., 2015*).

Therefore, minimizing the length of moves and the time for making them will have a positive effect on the productivity of machine-tractor units. This can be done by an appropriate choice of turns in the headland and a method of making the working moves. In order to minimize the time for making turns and servicing the machine on the field (loading and unloading of materials and crop), the orientation (angle) of moves, the order of making moves and the types of turns among them are to be optimized. The angle between the direction of the working moves and the field border has an effect on the number and length of moves of the machine-tractor unit, the number of turns and the positions where the unit can be serviced (*Spekken de Bruin, 2013*).

To optimize the trajectory of machine-tractor units on the field, graphical and functional methods are used. The graphical method makes use of simple forms such as circles, arcs and lines to present the trajectory of motion. In the methods based on functions, the trajectory of motion is presented as equations of spirals, clothoids, etc. (*Khan et al., 2018*).

Determining the length of turns composed of straight lines and arcs of permanent radius only is not precise, since the deflection of the tractor control wheels for reaching the necessary radius of a turn does not happen immediately (*Trendafilov, 2022*). Due to that reason, some researchers use clothoids connecting straight-line areas with curved-line areas of a turn with permanent curve radius, comprising an arc of a circle (*Sabelhaus et al., 2013*). The length of the turn and the width of the headland when using clothoids depend on the forward speed of the machine-tractor unit and the angular speed with which the deflection of its control wheels is carried out. As the speed of the turn increases, its length increases (*Vezirov et al., 2011*).

The actual length of turns cannot be determined analytically, as it is also influenced by factors such as driver skill, soil conditions, interaction between the tractor wheels and the soil, etc. These factors result in extending turns relative to their theoretical length. This additional path travelled by the aggregate cannot be determined analytically and is a stochastic quantity (*Bochtis and Vougioukas, 2008*). Due to the driver's inability to make a perfectly shaped turn and the interaction between soil and machine-tractor unit, there is a difference between the theoretical and the actual length of turns. In some studies, it is 3.6 – 12 % (*Bochtis and Vougioukas, 2008*).

Very often, a geometric model is used to determine the length of turns. The length of a turn is a function of the operating width, the minimum radius of a turn, the angle between the direction of travel and the headland, the number of missed moves when making the turn *(Bochtis et al., 2010; Bochtis and Sorensen, 2009; Spekken et al., 2015*). It is calculated analytically as the sum total of the lengths of straight and curved sections. The shape and length of turns in the headland changes depending on the angle between the direction of motion of the machine-tractor unit when making the operating move and the field border (*Trendafilov, 2021*). With a different value of this angle, turns have different length and require different width of the headland (Trendafilov K., 2020; Trendafilov K. 2021 a, b; Trendafilov K. 2022 a, b).

The type of turn can be automatically selected and its parameters can be determined according to the information about the headland obtained from the navigation system and the type of unit (*Freyberger and Jahns, 2000*). Such a system of motion in the headland can be successfully connected to a device making repeated actions on the machine-tractor unit (for example, control of the tower, the power take-off shaft, hydraulic valves), which allows fully automated turning by the units (*Cariou et al, 2010 a,b*). Automatic turning will allow the operator to focus more on performing the relevant operation (*Freyberger and Jahns, 2000).* During turning at the edge of the field, wheel slip takes place, which impairs the ability to follow a predetermined trajectory. Incorporating a slip estimation mechanism leads to an increase in the operating accuracy of the control system (*Bayar et al., 2016*).

In order to find a fully automated solution and reduce the workload of workers, even to create unmanned machine-tractor units, the motion of the units in the headlands has to be studied with the greatest accuracy (*Cariou et al., 2010*).

The objective of this article is to make a comparative analysis of the length of the idle stroke when making different T-turns in the headland of an irregularly shaped field and to justify the choice of a type of turn and direction of its execution in the field in order to ensure minimum length of the idle moves of the unit.

MATERIALS AND METHODS

Five types of T-turns performed by a machine-tractor unit have been discussed:

- T-turns with straight-line backward move parallel to the field border;
- T-turns with straight-line backward move not parallel to the field border;

- T-turns with arc-shaped backward move;
- T-turns with straight-line move upon entering the headland;
- T-turns with straight-line move upon exiting the headland.

Each of the turns is in two variants - open and closed and is performed in two directions - from left to right and from right to left. A geometric method was used for designing the turns in which turns are represented by lines and arcs of circles with the same radius. Fig. 1 shows the diagrams of some of the turns. The length of the turn is the distance travelled by the unit from point *A* (bringing the machine-tractor unit into transport position at the beginning of the turn) to point *B* (bringing the machine-tractor unit into working position at the end of the turn). Points *A* and *B* are in the centre of the unit, i.e. in the middle of the rear axle of the tractor. The idle run length in the headland includes the length of the turn and the length of straight runs before and after it has been made within the headland.

The headland is determined in two ways depending on the type of unit, the operation performed and the direction of making the turn. When the unit does not need to enter the field when making a turn in order not to damage the plants, for example, when working with perennial plantations and field crops the headland has greater width *E'*. If there are no such restrictions, the headland had smaller width *E*. A stripe with width *E'* is available only in some turns. According to some authors, the headland strip is not necessary when the angle between the direction of motion of the unit and the field border is less than 15° (*Oksanen, 2007*). Others accept that the field has a headland when the angle between the direction of motion and the field border is greater than 10° (*Aurbacher and Dabbert, 2009*).

To compare the length of the idle move in the different turns, calculations have been made about a specific machine-tractor unit composed of tractor Lamborghini Sprint 674-75 and seeder Gaspardo M300 (Fig. 2). The analytical relations given in Table 1 have been used (*Trendafilov, 2020; Trendafilov 2021 a, b; Trendafilov, 2022 a, b*). The designations used on Fig. 1 and in the formulas have the following meanings:

α is the angle between the direction of motion and the border of the field;
point *A* – beginning of the turn;
point *B* – end of the turn;
O – centre of the respective curvilinear motion within the turn;
β – central angle of the respective curvilinear motion;
R – radius of the unit turn;
H – longitudinal base of the tractor;
l_a – kinematic length of the unit;
M – tractor track;
B – operating width of the unit;
E – minimum headland width;
E' – headland width limited by the tractor wheels;
l_g – length of the straight idle move in the headland. When the straight line before and after the turn is of different length, it is denoted respectively:
l_{g1} – length of the straight idle move before the beginning of the turn;
l_{g2} – length of the straight idle move after the end of the turn.

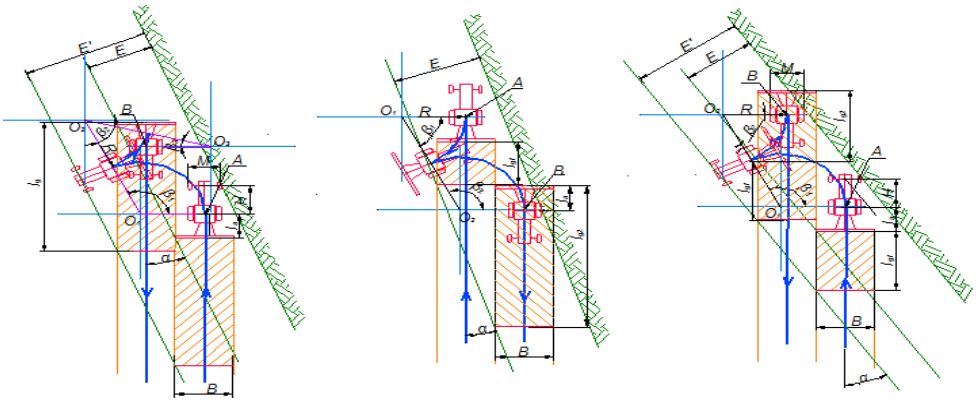

a) *b)* *c)*

Fig. 1 – Diagrams of closed T-turns

a – with arc-shaped backward move and motion from right to left; b – with straight move upon entering the headland and motion form left to right; c – with straight move upon entering the headland and motion from right to left

The machine-tractor unit has the following parameters: Operating width B = 3 m; kinematic length l_a = 3.1 m; radius of turn R = 2 m; longitudinal tractor base H = 2.25 m and tractor track M = 1.34 m. A range of variation of angle α from 10° to 90° has been adopted. Since there are no restrictions for entering the field for the particular unit, the calculations have been made for a headland of width E. The obtained results about the length of the idle move are presented graphically.

Fig. 2 – Machine-tractor unit

Table 1

Analytical relations for determining the length of the idle move when making turns by a machine-tractor unit on a field of an irregular shape *(Trendafilov K., 2020; Trendafilov K. 2021 a, b; Trendafilov K. 2022 a, b)*

Name of the turn	Direction of execution	The idle move length when making T-turns
1	2	3
T-turn with straight-line backward move parallel to the field border		
open turns	left to right 	$l_n = l_T + l_g$ (1) where $l_T = \pi \cdot R + \frac{2R+B}{\sin\alpha}$ (2) $l_g = \frac{2R}{\tan\alpha} - 2l_a$ (3) when $\alpha > \tan^{-1}\left(\frac{R}{l_a}\right)$ (4) $l_g = -\left(\frac{2R}{\tan\alpha} - 2l_a\right)$ (5)
	right to left 	$l_n = l_T + l_g$ (1) where l_T is determined by dependence (2) $l_g = \frac{2R}{\tan\alpha} + 2l_a$ (6)
closed turns	left to right 	$l_n = l_T + l_g$ (1) where $l_T = \pi \cdot R + \frac{2R-B}{\sin\alpha}$ (7) l_g is determined by dependence (6)

	right to left 	$l_n = l_T + l_g$ where l_T is determined by dependence (7) l_g is determined by dependence (3), (4) и (5)	(1)
T-turn with straight-line backward move not parallel to the field border			
open turns	left to right 	For a headland of width *E* $l_n = l_T$ where $l_T = \pi \cdot R + \sqrt{(2R+B)^2 + \left(\frac{B}{\tan\alpha} + 2l_a\right)^2}$	(8) (9)
	right to left 	For a headland of width *E* $l_n = l_T$ where $l_T = \pi \cdot R + \frac{2R+B}{\sin\beta_2}$ The central angle β_2 is determined by the dependence: $\beta_2 = \tan^{-1}\left(\frac{2R+B}{\frac{B}{\tan\alpha} - 2l_a}\right)$ After substituting dependence (11) into (10) for the length of the turn is obtained: $l_T = \pi \cdot R + \sqrt{(2R+B)^2 + \left(\frac{B}{\tan\alpha} - 2l_a\right)^2}$ when $\alpha > \tan^{-1}\left(\frac{B}{2l_a}\right)$ the central angle β_2 is determined by the dependence: $\beta_2 = 180 + \tan^{-1}\left(\frac{2R+B}{\frac{B}{\tan\alpha} - 2l_a}\right)$	(8) (10) (11) (12) (13)
		For a headland of width *E*` $l_n = l_T + 2l_g$ where l_T is determined by dependence (10) $l_g = \frac{(0.5M - R)\cos\beta_2 + R + 0.5B}{\tan\alpha} + (0.5M - R)\sin\beta_2 + l_a$ $l_g = 0$ when $\alpha = \tan^{-1}\left(\frac{(0.5M - R)\cos\beta_2 + R - 0.5B}{(R - 0.5M)\sin\beta_2 - l_a}\right)$	(14) (15) (16)
closed turns	left to right 	For a headland of width *E* $l_n = l_T$ where $l_T = \pi \cdot R + \frac{2R-B}{\sin\beta_1}$ The central angle β_1 is determined by the dependence: $\beta_1 = \tan^{-1}\left(\frac{2R-B}{\frac{B}{\tan\alpha} + 2l_a}\right)$	(8) (17)

After substitution in dependence (17) is obtained:

$$l_T = \pi \cdot R + \sqrt{(2R-B)^2 + \left(\frac{B}{\tan\alpha} + 2l_a\right)^2} \quad (18)$$

(19)

For a headland of width *E`*

$$l_n = l_T + 2l_g \quad (14)$$

where l_T is determined by dependence (17)

$$l_g = \frac{(2R-B)\cdot\sin(\alpha+\beta_1)}{\sin\alpha\cdot\sin\beta_1} + \frac{(0.5M+R)\cdot\cos(\alpha+\beta_1)}{\sin\alpha} - l_a - (0.5B+R)\cdot\cot\alpha \quad (20)$$

when $\alpha > \tan^{-1}\left(\frac{l_a + \sqrt{l_a^2 + (2R-B)B}}{2R-B}\right)$ (21)

$$l_g = \frac{(2R-B)}{\tan\alpha} + \frac{(R-0.5M)\cos\beta_1}{\tan\alpha} - (R-0.5B)\sin\beta_1 + l_a \quad (22)$$

where $\sin\beta_1 = \frac{2R-B}{\sqrt{\left(\frac{B}{\tan\alpha} + 2l_a\right)^2 + (2R-B)^2}}$ (23)

where $\cos\beta_1 = \frac{\frac{B}{\tan\alpha} + 2la}{\sqrt{\left(\frac{B}{\tan\alpha} + 2l_a\right)^2 + (2R-B)^2}}$ (24)

right to left

For a headland of width *E*

$$l_n = l_T \quad (8)$$

where $l_T = \pi \cdot R + \sqrt{(2R-B)^2 + \left(\frac{B}{\tan\alpha} - 2l_a\right)^2}$ (25)

The central angle β_2 is determined by the dependence:

$$\beta_2 = \tan^{-1}\left(\frac{2R-B}{\frac{B}{\tan\alpha} - 2l_a}\right) \quad (26)$$

when $\alpha > \tan^{-1}\left(\frac{B}{2l_a}\right)$ the central angle β_2 is determined by the dependence:

$$\beta_2 = 180 + \tan^{-1}\left(\frac{2R-B}{\frac{B}{\tan\alpha} - 2l_a}\right) \quad (27)$$

For a headland of width *E`*

$$l_n = l_T + 2l_g \quad (14)$$

where

$$l_g = \frac{(R+0.5)\cdot\cos(\alpha+\beta_2) + H\cdot\sin(\alpha+\beta_2)}{\sin\alpha} + (R-0.5B)\cdot\cot\alpha - l_a \quad (28)$$

$$l_g = 0 \text{ with } \alpha = \tan^{-1}\left(\frac{(R-0.5M)\cos\beta_2 + H\cdot\sin\beta_2 - R - 0.5B}{(R-0.5M)\sin\beta_2 + 2l_a - H\cdot\cos\beta_2}\right) \quad (29)$$

T-turn with arc-shaped backward move

open turns — left to right

$$l_n = l_T + l_g \quad (1)$$

where $l_T = \pi R$ (30)

$$l_g = \frac{B}{\tan\alpha} + 2l_a - \sqrt{4R^2 - B^2} \quad (31)$$

$$l_g = 0 \text{ when } \alpha = \tan^{-1}\left(\frac{B}{\sqrt{4R^2 - B^2} - 2l_a}\right) \quad (32)$$

open turns — right to left

$$l_n = l_T + l_g \quad (1)$$

where l_T is determined by dependence (30)

$$l_g = \frac{B}{\tan\alpha} - 2l_a - \sqrt{4R^2 - B^2} \quad (33)$$

$$l_g = 0 \text{ when } \alpha = \tan^{-1}\left(\frac{B}{\sqrt{4R^2 - B^2} + 2l_a}\right) \quad (34)$$

closed turns — left to right

$$l_n = l_T + l_{g_1} + l_{g_2} \quad (35)$$

where l_T is determined by dependence (30)

$$\text{where } l_{g_1} = (R - 0.5M)\frac{\sqrt{4R^2 - B^2}}{2R} - l_a + \frac{R - B + \frac{M \cdot B}{4R}}{\tan\alpha} \quad (36)$$

$$\text{where } l_{g_2} = l_a - (R + 0.5M)\frac{\sqrt{4R^2 - B^2}}{2R} + \frac{R + \frac{M \cdot B}{4R}}{\tan\alpha} \quad (37)$$

$$\text{when } \alpha > 90^\circ - \cos^{-1}\left(\frac{B}{2R}\right) \quad (38)$$

$$l_{g_1} = (R + 0.5M)\frac{\sqrt{4R^2 - B^2}}{2R} - l_a + \frac{R - B - \frac{M \cdot B}{4R}}{\tan\alpha} \quad (39)$$

$$l_{g_2} = (0.5M - R)\frac{\sqrt{4R^2 - B^2}}{2R} + l_a + \frac{R - \frac{M \cdot B}{4R}}{\tan\alpha} \quad (40)$$

when the angle α is greater than that determined by dependence (32) l_T is determined by dependence (30)

$$l_{g1} = l_{g2} = (R + 0.5M)\sin\beta_3 - 2R \cdot \sin\beta_1 - l_a + \frac{(R + 0.5M)\cos\beta_3 + 2R \cdot \cos\beta_1 - R - 0.5B}{\tan\alpha} \quad (41)$$

$$\text{where } \beta_1 = \cos^{-1}\left(\frac{2R - B}{4R \cdot \cos\left(\tan^{-1}\left(\frac{\frac{B}{\tan\alpha} + 2l_a}{2R - B}\right)\right)}\right) - \tan^{-1}\left(\frac{\frac{B}{\tan\alpha} + 2l_a}{2R - B}\right) \quad (42)$$

$$\beta_3 = \cos^{-1}\left(\frac{2R-B}{4R\cdot\cos\left(\tan^{-1}\left(\frac{\frac{B}{\tan\alpha}+2l_a}{2R-B}\right)\right)}\right)+\tan^{-1}\left(\frac{\frac{B}{\tan\alpha}+2l_a}{2R-B}\right) \quad (43)$$

right to left

For a headland of width *E*

$$l_n = l_T \quad (8)$$

where $l_T = \pi R + \frac{B}{\tan\alpha} - 2l_a - \sqrt{4R^2 - B^2}$ (44)

l_T decreases to $l_T = \pi R$ at α determined by dependence (34)

For a headland of width *E*`

$$l_n = l_T + 2l_g \quad (14)$$

where l_T is determined by dependence (44)

$$l_g = \frac{H\cdot B}{2R} - \left(0.5+\frac{M}{4R}\right)\sqrt{4R^2-B^2} - l_a + \frac{R+\frac{M\cdot B}{4R}+\frac{H\sqrt{4R^2-B^2}}{2R}}{\tan\alpha} \quad (45)$$

When the angle α is greater than defined by dependence (32) l_T is determined by dependence (30)

$$l_g = \frac{R-0.5B}{\tan\alpha} + \frac{H\cdot\sin(\beta_1-\alpha)-(R+0.5M)\cos(\beta_1-a)}{\sin\alpha} - l_a \quad (46)$$

$$l_g = 0 \text{ when } \alpha = \tan^{-1}\left(\frac{R-0.5B-(R+0.5M)\cos\beta_1+H\cdot\sin\beta_1}{l_a+(R+0.5M)\sin\beta_1+H\cdot\cos\beta_1}\right) \quad (47)$$

where

$$\beta_1 = \cos^{-1}\left(\frac{2R-B}{4R\cdot\cos\left(\tan^{-1}\left(\frac{\frac{B}{\tan\alpha}-2l_a}{2R-B}\right)\right)}\right)+\tan^{-1}\left(\frac{\frac{B}{\tan\alpha}-2l_a}{2R-B}\right) \quad (48)$$

T-turn with straight-line move upon entering the headland

open turns

left to right

$$l_n = l_T + l_g \quad (1)$$

where l_T is determined by dependence (30)

where l_g is determined by dependence (31)

$l_g = 0$ with α is determined by dependence (32)

When the angle α is greater than defined by dependence (32) the straight-line move l_g is when the unit enters the headland and its length is determined by the dependence:

$$l_g = \sqrt{4R^2-B^2} - \frac{B}{\tan\alpha} - 2l_a \quad (49)$$

	right to left 	For a headland of width *E* $l_n = l_T + l_{g_1}$ where l_T is determined by dependence (30) $l_{g1} = \sqrt{4R^2 - B^2} + \frac{B}{\tan\alpha} - 2l_a$ The straight-line move decreases to $l_{g1} = 0$ at $\alpha = \tan^{-1}\left(\frac{-B}{\sqrt{4R^2 - B^2} - 2l_a}\right)$	(50) (51) (52)
		For a headland of width *E*` $l_n = l_T + l_{g_1} + 2l_{g_2}$ where l_{g1} is determined by dependence (51) $l_{g2} = \frac{R + \frac{M \cdot B}{4R} - B}{\tan\alpha} - \sqrt{4R^2 - B^2}\left(0.5 - \frac{M}{4R}\right) + l_a$	(53) (54)
closed turns	left to right 	$l_n = l_T + l_{g_1} + l_{g_2}$ where l_T is determined by dependence (30) l_{g_1} is determined by dependence (36) $l_{g_2} = l_a - (R + 0.5M)\frac{\sqrt{4R^2 - B^2}}{2R} + \frac{R - B + \frac{M \cdot B}{4R}}{\tan\alpha}$ when condition (38) is fulfilled for angle l_{g1} is determined by dependence (39) l_{g2} is determined by dependence (40) $l_{g2} = 0$ when $\alpha = \tan^{-1}\left(\frac{R - \frac{M \cdot B}{4R}}{\left(0.5 - \frac{M}{4R}\right)\sqrt{4R^2 - B^2} - l_a}\right)$ When the angle α is greater than defined by dependence (56) $l_{g2} = \sqrt{4R^2 - B^2} - 2l_a - \frac{B}{\tan\alpha}$	(35) (55) (56) (57)
	right to left 	$l_n = l_T + l_g$ where l_T is determined by dependence (30) $l_g = \sqrt{4R^2 - B^2} - 2l_a + \frac{B}{\tan\alpha}$	(1) (58)
T-turn with straight-line move upon exiting the headland			
open turns	left to right 	$l_n = l_T + l_{g_1} + l_{g_2}$ where l_T is determined by dependence (30) $l_{g_1} = \frac{R - B + \frac{M \cdot B}{4R} + \frac{H\sqrt{4R^2 - B^2}}{2R}}{\tan\alpha} + \left(\frac{M}{4R} - 0.5\right)\sqrt{4R^2 - B^2} - \frac{H \cdot B}{2R} - l_a$	(35) (59)

<table>
<tr><td></td><td></td><td>$$l_{g_2}=\frac{R+\frac{M\cdot B}{4R}+\frac{H\sqrt{4R^2-B^2}}{2R}}{\tan\alpha}+\left(\frac{M}{4R}+0.5\right)\sqrt{4R^2-B^2}-\frac{H\cdot B}{2R}+l_a$$ (60)
$$l_{g_1}=0 \text{ when } \alpha=\tan^{-1}\left(\frac{R-B+\frac{M\cdot B}{4R}+\frac{H\sqrt{4R^2-B^2}}{2R}}{\frac{H\cdot B}{2R}+l_a-\left(\frac{M}{4R}-0.5\right)\sqrt{4R^2-B^2}}\right)$$ (61)
When the angle α is greater than defined by dependence (61)
$$l_{g2}=\sqrt{4R^2-B^2}+2l_a+\frac{B}{\tan\alpha}$$ (62)</td></tr>
<tr><td></td><td>right to left
  </td><td>$$l_n=l_T+l_g$$ (1)
where $l_T=\pi R+\frac{B}{\tan\alpha}-2l_a-\sqrt{4R^2-B^2}$ (63)
l_T decreases to $l_T=\pi R$ at α determined by dependence (34)
At a larger angle, the unit performs a straight move before exiting the headland with length
$$l_g=\sqrt{4R^2-B^2}+2l_a-\frac{B}{\tan\alpha}$$ (64)</td></tr>
<tr><td>closed turns</td><td>left to right
  </td><td>$$l_n=l_T+l_g$$ (1)
where l_T is determined by dependence (30)
$$l_g=\sqrt{4R^2-B^2}+2l_a+\frac{B}{\tan\alpha}$$ (65)</td></tr>
<tr><td></td><td>right to left
  </td><td>For a headland of width E
$$l_n=l_T+l_{g_2}$$ (66)
where l_T is determined by dependence (63)
When the angle α increases, the length of the straight-line back move decreases and reaches $l_b=0$ when α is determined by dependence (34)
At a larger angle α the unit performs a straight line move before exiting the headland with length
$$l_{g2}=\sqrt{4R^2-B^2}+2l_a-\frac{B}{\tan\alpha}$$ (67)</td></tr>
<tr><td></td><td></td><td>For a headland of width E`
$$l_n=l_T+l_{g_2}+2l_{g1}$$ (68)
where $l_{g1}=\frac{H\cdot B}{2R}-\left(0.5+\frac{M}{4R}\right)\sqrt{4R^2-B^2}-l_a+\frac{R+\frac{M\cdot B}{4R}+\frac{H\sqrt{4R^2-B^2}}{2R}}{\tan\alpha}$ (69)
where α is determined by dependence (38)
$$l_{g1}=\frac{H\cdot B}{2R}-\left(0.5-\frac{M}{4R}\right)\sqrt{4R^2-B^2}-l_a+\frac{R-\frac{M\cdot B}{4R}+\frac{H\sqrt{4R^2-B^2}}{2R}}{\tan\alpha}$$ (70)
where $\alpha>\tan^{-1}\left(\frac{B}{\sqrt{4R^2-B^2}-H}\right)$ (71)</td></tr>
</table>

		l_{g1} is determined by dependence (67) l_{g2} is determined by dependence (64) $l_{g1}=0$ when $\alpha=\tan^{-1}\left(\dfrac{R-\dfrac{M\cdot B}{4R}+\dfrac{H\sqrt{4R^2-B^2}}{2R}}{l_a+\left(0.5-\dfrac{M}{4R}\right)\sqrt{4R^2-B^2}-\dfrac{H\cdot B}{2R}}\right)$ (72)

RESULTS

Since the discussed machine-tractor unit has different parameters from the one for which the relations given in Table 1 have been made, mainly due to its greater kinematic length l_a, for some of the turns the following additions have to be made.

- *For a closed T-turn with arc-shaped backward move when moving from left to right*.

Upon entering the headland, the unit does not make an arc-shaped move to the left, only a straight one. The length of the straight move upon entering the headland is $l_{g1}=0$. However, the length of l_{g2} increases with the value of l_{g1} determined by the formulas, but with the opposite sign. It is recorded as follows:

$$l'_{g2}=\frac{B}{\tan\alpha}+2l_a-\sqrt{4R^2-B^2} \tag{73}$$

The same result is obtained when the values obtained from formulas (37) and (36), as well as from formulas (40) and (39) are deducted, regardless of the fact that l_{g1} is obtained with a negative sign. Therefore, for the length of the straight move upon exiting the headland the following can be denoted:

$$l'_{g2}=l_{g2}-l_{g1} \tag{74}$$

The length of the idle move is determined by the relation:

$$l_n=l_T+l'_{g2}=l_T+l_{g2}-l_{g1} \tag{75}$$

- *For an open T-turn with straight move upon entering the headland and motion from right to left*

At angle α greater than the one determined by relation (52), the straight move l_{g1} is when the unit exits the headland and its length is determined by the relation:

$$l_{g1}=2l_a-\sqrt{4R^2-B^2}-\frac{B}{\tan\alpha} \tag{76}$$

- *For a closed T-turn with straight move upon entering the headland and motion from left to right*

Since the machine-tractor unit had great length l_a, the headland is limited towards the field on the right side of the machine and not by the tractor wheels when making the turn with backward motion. For this reason, there is no straight move l_{g1} upon entering the headland, and the straight move upon exiting the headland has length determined by relation (70).

- *For a closed T-turn with straight move upon entering the headland and motion from right to left.*

The straight move upon entering the headland decreases and becomes $l_g=0$ at:

$$\alpha=\tan^{-1}\left(\frac{B}{2l_a-\sqrt{4R^2-B^2}}\right) \tag{77}$$

At greater angle the straight move is already when the unit exits the headland and is determined by the relation:

$$l_g = 2l_a - \sqrt{4R^2 - B^2} - \frac{B}{\tan\alpha} \quad (78)$$

Fig. 3 and Fig. 4 show the results from the calculations for the different types of turns. It is also seen that the open turns are shorter in length when made from right to left except for the straight backward move turn. The shortest idle move is when making a turn with an arc-shaped backward move and a turn with a straight move upon entering the headland.

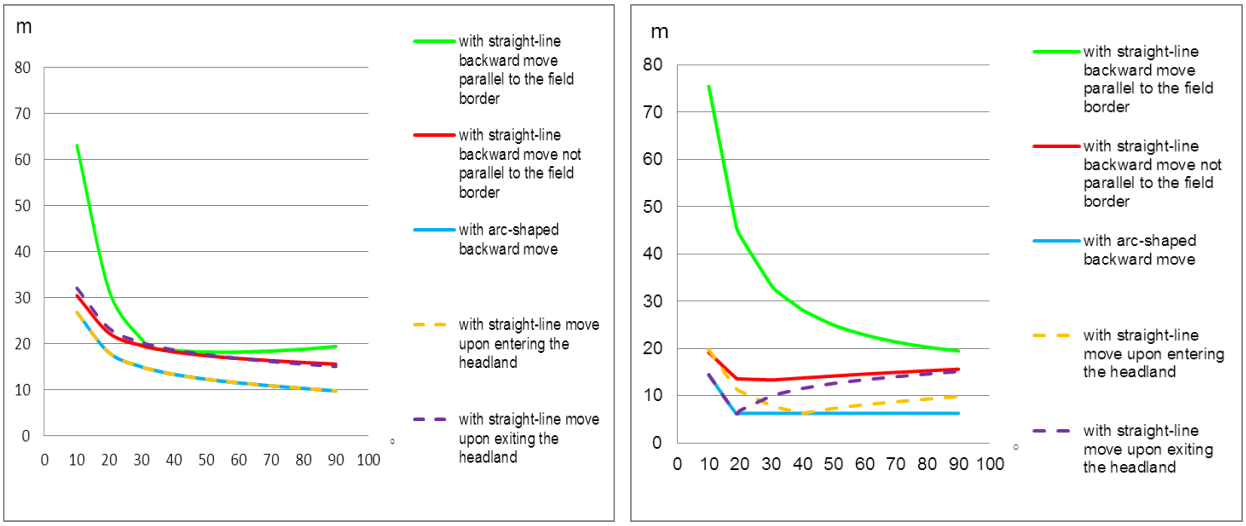

a) *b)*

Fig. 3 – Length of the idle move depending on the angle between the direction of motion of the machine-tractor unit and the field border when making open T-turns and motion in the field:

a) from left to right; b) from right to left

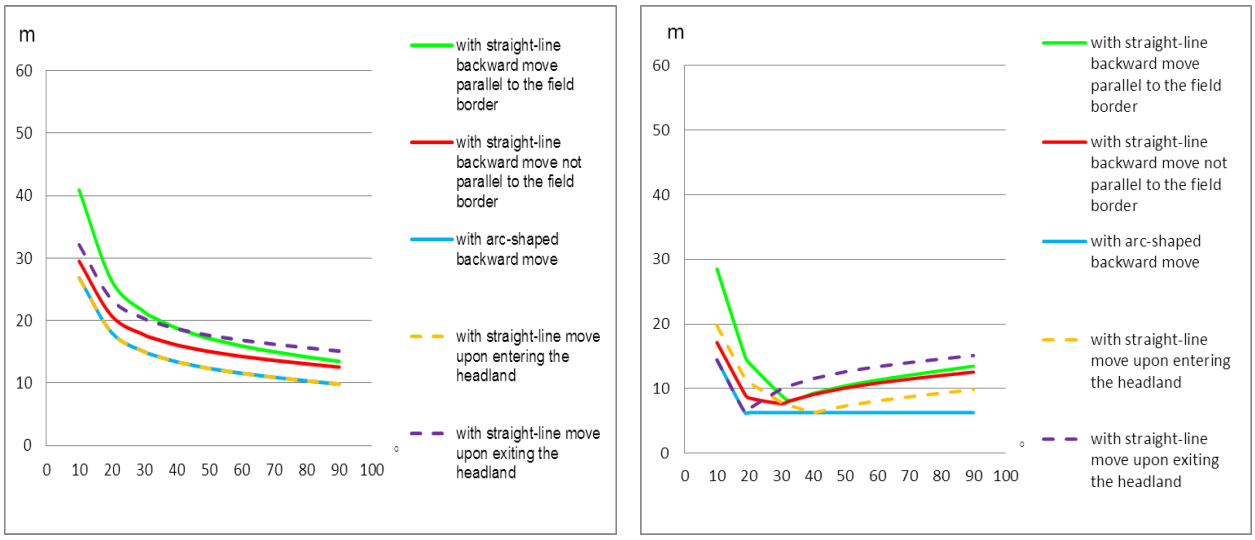

a) *b)*

Fig. 4 – Length of the idle move depending on the angle between the direction of motion of the machine-tractor unit and the field border when making closed T-turns and motion in the field:

a) from left to right; b) from right to left

When making closed turns, the idle move is also shorter in direction from right to left. The difference between the two directions in making the turn is greater at a small angle between the direction of motion and the field border. At a large angle, the difference in the length of the idle move in different directions of the turn decreases and in some turns it is equal at an angle of 90°. Here, as in the case of open turns, the idle move is the shortest when making a turn with an arc-shaped backward move and a turn with a straight move upon entering the headland.

It can also be seen from the figures that in three of the turns, the length of the idle move in open and closed turns is the same in motion from right to left - a turn with an arc-shaped backward move, a turn with a straight move upon entering the headland and a turn with straight move upon exiting the headland.

CONCLUSIONS

The theory for determining the length of the idle move when making various types of open and closed T-turns in the headland of a field with an irregular shape has been supplemented.

It has been established that the idle move of the machine-tractor unit has the smallest length when the direction of making the turn is from right to left.

It has been established that for three of the studied turns, the length of the idle move in open and closed turns was the same when moving from right to left.

Right-to-left open and closed T-turns have been shown to provide the same length of the idle move of the unit in the headland, which is the smallest compared to other turns.

For the practice, it can be recommended to use an open and closed turn with an arc-shaped backward move and a turn with a straight move upon entering the headland, the direction of making the turn should be from right to left. At a small angle between the direction of motion and the field border, a turn with a straight move upon exiting the headland may be used.

The development of the theory for determining the length of the idle move and the width of the headland in a field with an irregular shape can be used to develop an algorithm for automatic selection of a turn and direction of making it depending on the parameters of the unit and the angle between the direction of motion and field border. This will exclude the subjective decision of the operator when choosing motion in the headland, which will result in an increase in the efficiency of agricultural operations performed.

ACKNOWLEDGEMENT

This work was supported by the Bulgarian Ministry of Education and Science under the National Research Programme „Smart crop production" approved by Decision of the Ministry Council № 866 / 26 November 2020.

REFERENCES

[1] Aurbacher J., Dabbert S. (2009). Integrating GIS-based field data and farm modeling in a watershed to assess the cost of erosion control measures: An example from southwest Germany, *Journal of soil and water conservation*, *64* (5), 350-362

[2] Bayar G., Bergerman M., Konukseven E., Koku A. B. (2016). Improving the trajectory tracking performance of autonomous orchard vehicles using wheel slip compensation. *Biosystems engineering*, *146*, 149-164, https://doi.org/10.1016/j.biosystemseng.2015.12.019

[3] Bochtis D. D., Vougioukas S. G. (2008). Minimising the non-working distance travelled by machines operating in a headland field pattern. *Biosystems engineering*, *101*, 1-12. https://doi.org/10.1016/j.biosystemseng.2008.06.008

[4] Bochtis D. D., Sorensen S. G. (2009). The vehicle routing problem in field logistics part I. *Biosystems engineering*, 104, 447-457

[5] Bochtis D. D., Sorensen C. G., Jorgensen R. N., Green O. (2009). Modelling of material handling operations using controlled traffic. *Biosystems engineering*, *103*, 397-408, DOI: 10.1016/j.biosystemseng.2009.02.006

[6] Bochtis D. D., Sorensen C. G., Busato P., Hameed I. A., Rodias E., Papadakis G., Green O. (2010). Tramline establishment in controlled traffic farming based on operational machinery cost. *Biosystems engineering*, 107, 221-231

[7] Cariou C., Lenain R., Thuilot B., Humbert T., Berducat M. (2010 a). Maneuvers automation for agricultural vehicle in headland. *International Conference on Agricultural Engineering*, September 6-8, Clermont-Ferrand, France, 1-10

[8] Cariou, C., Lenain R., Berducat M., Thuilot B. (2010 b). Autonomous maneuvers of a farm vehicle with a trailed implement in headland. ICINCO 2010, *Proceedings of the 7th International Conference on Informatics in Control* Automation and Robotics, Volume 2, Funchal, Madeira, Portugal, 15-18, 109-114

[9] Freyberger F., Jahns G. (2000). Symbolic course description for semiautonomous agricultural vehicles. *Computers and Electronics in Agriculture*, *25 (1-2)*, 121-132, doi:10.1016.SO168-1699(99)00059-9

[10] Jensen M. F., Norremark M, Busato P., Sorensen C. G., Bochtis D. (2015). Coverage planning for capacitated field operations, Part I: Task decomposition. *Biosystems Engineering*, 139, 136-148.

[11] Khan A., Noreen I., Habib Z. (2017). On complete coverage path planning algorithms for non-holonomic mobile robots: survey and challenges. *J Inform Sci Eng*, 33 (1), 101-121

[12] Oksanen T. (2007). Path planning algorithms for agricultural field machines. Helsinki University of Technology Automation Technology Laboratory, *Series A: Research Reports*, 31

[13] Sabelhaus D., Röben F., L. P. M. zu Helligen, Lammers P. S. (2013). Using continuous-curvature paths to generate feasible headland turn manoeuvres. *Biosystems engineering,* 116, 399- 409

[14] Spekken M., Molin J. P., Romanelli, T. L., (2015). Cost of boundary manoeuvres in sugarcane production. *Biosystems engineering*, 129, 112-126

[15] Spekken M., Bruin S. (2013). Optimized routing on agricultural fields by minimizing maneuvering and servicing time. *Precision Agric,*14, 224-244

[16] Trendafilov K. (2020). Determination and analysis of the length of the nonworking move and the width of the headland when making fishtail turns with a rectilinear reverse movement parallel to the boundary of an irregularly shaped field. *Applied Researches in Technics, Technologies and Education*, Volume 8, No 2, 79-87, Doi: 10.15547/artte.2020.02.001

[17] Trendafilov K. (2021 a). Theoretical determination and analysis of the length of the non-working move and the width of the headland when performing fishtail turn with a rectilinear reverse move, which is not parallel to the boundary of a field with an irregular shape, *IOP Conference Series: Materials Science and Engineering* 1031 012005, Doi:10.1088/1757-899X/1031/1/012005

[18] Trendafilov K. (2021 b). Theoretical determination and analysis of the length of the non-working move and of the width of the headland when performing a fishtail turn with a curvilinear reverse move by a machine-tractor unit with a mounted machine in an irregularly shaped field, *IOP Conference Series: Materials Science and Engineering* 1031 012006, Doi:10.1088/1757-899X/1031/1/012006

[19] Trendafilov K. (2021). Movement of machine-tractor units with trailed and semi-mounted machines on an irregularly-shaped field, Monograph. Trakia University Publishing House, Stara Zagora, ISBN: 978-954-338-170-8

[20] Trendafilov K. (2022). Kinematics of a symmetrical machine-tractor unit with a mounted machine in the turning strip in an irregularly shaped field, Monograph. Academic Publishing House "University of Ruse", Ruse, ISBN: 978-954-338-178-4

[21] Trendafilov K. (2022 a). T-turn with straight movement upon entering the headland on an irregularly-shaped field, *Science, education, intellect*, 14, 33-50

[22] Trendafilov K. (2022 b). T-turns with straight movement upon exiting the headland on an irregularly-shaped field. *Science, education, intellect*, 14, 65-85

[23] Vezirov Ch., Atanasov A., Radeva P. (2011). Kinematics of the turns of energy units in the field when moving back and forth. *Scientific papers of the University of Ruse* – 2011, 50, Series 1.1, 29-34

NEURAL NETWORK TESTING FOR SPOT-APPLICATION OF PHYTOSANITARY SUBSTANCES IN VEGETABLE CROPS USING A SELF-PROPELLED ELECTRICAL SPRAYER

/

TESTAREA UNEI REȚELE NEURONALE PENTRU APLICAREA ȚINTITĂ A SUBSTANȚELOR FITOSANITARE ÎN CULTURILE DE LEGUME FOLOSIND O MAȘINĂ DE STROPIT AUTOPROPULSATĂ ELECTRIC

Mihai Gabriel MATACHE *[1)]; Florin Bogdan MARIN [2)], Carmela GURAU [2)], Gheorghe GURAU [2)], Mihaela MARIN [2)], Iuliana GĂGEANU [1)], Alexandru IONESCU [1)]

[1)] INMA Bucharest / Romania;

[2)] University "Dunarea de Jos" of Galati / Romania

E-mail: gabimatache@yahoo.com

DOI: https://doi.org/10.35633/inmateh-68-46

Keywords: *self-propelled electrical sprayer, neural network, spot-application*

ABSTRACT

For negative effects minimization generated by agriculture on the environment, there were established a series of measures regarding the reduction of the amount of fertilizers and phytosanitary substances used. Thus, one of the innovative technologies appeared on the market is represented by the usage of some automated equipment for selective spraying of targeted plants, this way significantly reducing the amount of active substances used. The paper presents the usage of a technique specific to artificial intelligence for identification of target crops and their proper treatment. Thus, was developed a convolutional neural network formed of six neuron layers, which was used for analysis of crop field images recorded with a LOGITECH HD Pro C92.0 video camera. The network was developed in C++ programming language, using function libraries from OpenCV, and has run on a Dell laptop, with Intel i8 processor. Following images analysis and targeted plants identification, from laptop there are sent ON/OFF commands through an Arduino microcontroller toward the electrical microvalves mounted on the nozzles of a self-propelled electric spraying machine having a working width of 8 m, with the purpose of spot-spraying the crop plants and reducing the amount of used substances. In this paper are presented the experiments done for testing the neural network efficiency.

REZUMAT

In scopul minimizarii efectelor negative generate de agricultura asupra mediului s-au stabilit o serie de cerințe privind reducerea cantităților de substanțe fitosanitare și fertilizanți. Astfel, una din tehnologiile inovative apărute pe piață este reprezentată de utilizarea unor utilaje automatizate pentru stropirea selectivă a plantelor țintă, reducându-se astfel semnificativ cantitatea de substanțe active folosite. Lucrarea prezintă utilizarea unei tehnici specifice inteligenței artificiale pentru identificarea culturilor țintă și tratarea acestora corespunzător. Astfel a fost dezvoltată o rețea neuronală convoluțională formată din șase straturi de neuroni, care a fost folosită pentru analizarea imaginilor câmpului de cultură înregistrate de o cameră video LOGITECH HD Pro C92.0. Rețeaua a fost dezvoltată în limbajul de programare C++, folosind librării de funții din OpenCV, și a rulat pe un laptop Dell, cu processor Intel i8. În urma analizei imaginilor și identificării plantelor țintă, din laptop se trimit comenzi de PORNIT / OPRIT printr-un microcontroller Arduino către microvalvele electrice montate pe duzele unei mașini de stropit autopropulsată electric cu o lățime de lucru de 8 m, în scopul stropirii țintite a plantelor de cultură și reducerii cantității de substanțe folosite. În cadrul lucrării se prezintă experimentele efectuate pentru testarea eficienței rețelei neuronale.

INTRODUCTION

In the field of conventional agriculture, inputs of chemical substances have been used to increase production. Unfortunately, the use of a significant amount of chemicals (such as fertilizers or herbicides) involves serious problems related to water contamination, health risks (for workers and food consumers), reduced biodiversity and risks of developing weeds resistant to herbicides.

Smart agriculture involves the objective of continuing to use herbicide chemicals but significantly reducing the amount of chemicals to maintain production efficiency by killing weeds (*Latha A. Poojith et al., 2014; Jianlun Wang et al., 2013; Jianshu Chen, 2013; S.J. Rees et al.*).

In order to achieve this objective, one way is to only administer the substances in the area where it is located spatially and in this way the administration of the herbicide to the plant or the soil is avoided. In a similar case, for the administration of a chemical fertilizer, it would only be administered to the plant.

Image classification is a key component in the field of artificial vision algorithms to develop applications such as: surveillance, traffic monitoring, collision avoidance, face recognition, augmented reality, ocular tracking, medical imaging, agricultural industry, etc.

Classification is a process of assigning a user-defined class to an object in a scene. Some of the classification methods used on the scale are: Bayes-Naiv Classifier, Support Vector Machine (SVM), K-Nearest Neighbors (KNN), Decision Tree, Random Forest, Logistic Regression, Neural Networks and other classifiers (*Jain AK et al., 2000; Ian H. et al., 2005; Cortes C. et al., 1995*). The biggest advantage of these classifiers is their ability to perform classification using relatively low computational resources.

The emergence of classification methods based on neural networks has generally resulted in improved image classification accuracy (*Jain et al., 2000*). Algorithms that work using ANN-based classifier networks offer good performance when working with large datasets consisting of hundreds of classes. A fully connected ANN is a core of modern image classification and detection algorithms. The standard architecture of ANN includes an input layer, few hidden layers and an output layer.

There are various approaches and experimental prototypes for the task of achieving intelligent spraying (Figure 1) (*A. Shinde et al., 2014; A. Perez et al., 2000; Sethy P.K. et al., 2019; Knoll F.J. et al., 2018; Patil J.K. et al., 2017*).

Fig. 1 - Experimental spraying systems (*Knoll F.J. et al., 2018; Patil J.K. et al., 2017*)

Since intelligent spray systems will have a low price, it is need to identify low-cost electronic components for the cameras used in such systems. Also, the evolution of cameras on the market and the appearance of new cameras requires us to develop algorithms that produce similar results, regardless of camera brand, in the same quality class. The artificial vision algorithm testing procedure must take into consideration testing on different cameras but also in specific situations that arise in reality.

Regarding optical errors, systems with artificial vision must take into consideration the treatment of the problem of their elimination, caused by the manufacturing precision of the lenses, which in the medium-priced cameras are made of plastic material and not of glass. The importance for identification applications is accentuated in an artificial vision application because the algorithm may fail as a consequence of distortions. High-quality glass lenses do not cause serious errors and are used in practice in computer vision applications, but they are also many times more expensive than optics used in webcams. Ideal lenses refract light rays accordingly so as not to influence light waves. However, even glass lenses are made by polishing glass, which by default means that each lens has unique properties.

The main types of aberrations that appear either due to optics, but especially due to a wrong focus or due to the large relative movement of some portions of the image, according to several authors (*Cortes C. et al., 1995; M. Mustafa et al., 2007*) are:

• Distortion: pixels are mapped to incorrect locations relative to reality, as is the case when an object is moving at a high-speed relative to the camera;

• Spherical aberration: marginal light rays bend more than those near an optical axis, therefore producing two separate images;

• Field curvature: the actual image plane is curved rather than flat since all paraxial rays converge through a single focal point;

• Chromatic: A refractive index depends on the wavelength leading to the bending of the colours of an individual light beam, consequently causing blurring.

An approximate linear correction algorithm can be created even if the exact error model is not known. In this context, linear correction means that the locations of the pixels are changed by determining the coefficient, the size of which depends on the distance from the optical axis. This can work as a first aid for error minimization, but advanced calibration algorithms use high-order polynomial functions due to the non-linear nature of the distortion.

Probably the most famous calibration algorithm was proposed by Tsai (*Shinde et al., 2014*). In that method, the calibration is performed in two consecutive steps (*Perez et al., 2000; Sethy et al., 2019; Knoll et al., 2018*), first solving the rotation and translation parameters and then the remaining ones. Testing the functioning of algorithms must take into consideration real situations, to avoid malfunctioning or blocking of algorithms (*Patil et al., 2017; Hlaing et al., 2014; Zhao et al., 2009; Garousi et al. al., 2016; Moghadam M.H., 2019; Shen et al., 2009; Frommknecht et al., 2014; Perona et al., 1990*).

MATERIALS AND METHODS

The experimental sprayer model used for the experiments consists of three main electrically driven systems, a self-propelled mobile platform, a boom spraying system and the neural network control system. The first system is a mobile platform driven by a 12 kW variable speed electric motor powered by a three-phase controller that converts the electricity from a 96 VDC Li-ion battery into three-phase variable frequency electricity. The advantages of the platform consist of zero toxic emissions due to electric propulsion, increased mechanical torque even at very low speeds and low weight. The li-ion battery can also be charged from renewable energy sources. The system for spraying and biological protection of plants is mounted on the mobile platform and is also an electrical equipment destined for the distribution of phyto-pathological treatments for vegetable crops, driven by a 3 kW motor powered by a 48 VDC battery.
The main technical characteristics of the electrically driven spraying machine are:

Table 1

Main technical characteristics of the electrically driven spraying machine

Characteristic	U.M.	Value / Characterization
Rear wheels Gauge	mm	1320
Wheelbase	mm	2600
Electric drive motor	kW	12
Li-ion battery	VCC	96
Solution tank capacity	l	400 l
Tank material	-	glass fibre reinforced resin
Pump motor	kW	3
Maximum flow rate of the pump	l /min	86 l/min
Maximum working pressure	bar	20 bar
Line filter	-	with self-cleaning and discharge on hydraulic agitator
Agitation system	-	with hydraulic stirrer
Boom length	m	8
Number of boom sections	-	3
Number of nozzle holder	-	32
Pressure and flow regulator	-	3 way
Capacity of the clean water tank for human operator	l	10
Solution indicator	-	through transparency
Platform structure	-	galvanized steel

In order to achieve the targeted application of phytosanitary substances on crops, microvalves were fitted for each port-nozzle support of the dosing system boom. The solenoid valve coil works in an ON/OFF manner at 12 VDC. The system thus created allows the individual control of each nozzle separately by means of electromagnetic microvalves controlled by a central computer, based on an algorithm to identify cultivated

vegetables using real-time images taken from an RGB video camera, processed using a neural network. After identifying the cultivated plants, the microvalves located above them are commanded so that the substances are applied only to the respective plants.

Fig. 2 – Electric self-propelled spraying machine - experimental model

The neural network used was a multi-layer convolutional neural network (CNN) type that consists of two different types of layers, i.e. convolution layers (c layers) and pooling layers - p layers. C layers and the p layers are alternately connected and form the middle part of the network. As shown in Figure 3, the input image is convolved by successive filtering to produce feature maps in the first layer c. The network architecture used consists of 4 hidden layers and of course an input layer and an output layer. The 4 layers are convolutional, pooling and two fully connected layers. The convolution layer is the building block of the CNN, which bears the main responsibility for the computation. The input layer accepts three-dimensional input, represented by an image in the spatial form of the size (width × height) of the image, but also the third dimension represented by the colour channels (in this case RGB (Red, Green, Blue). A proprietary set of 200 weed images and 100 crop plant images were used for training. The C++ language was used for the development of the program, the library of functions intended for the processing of OpenCV and AI platform Caffe images.

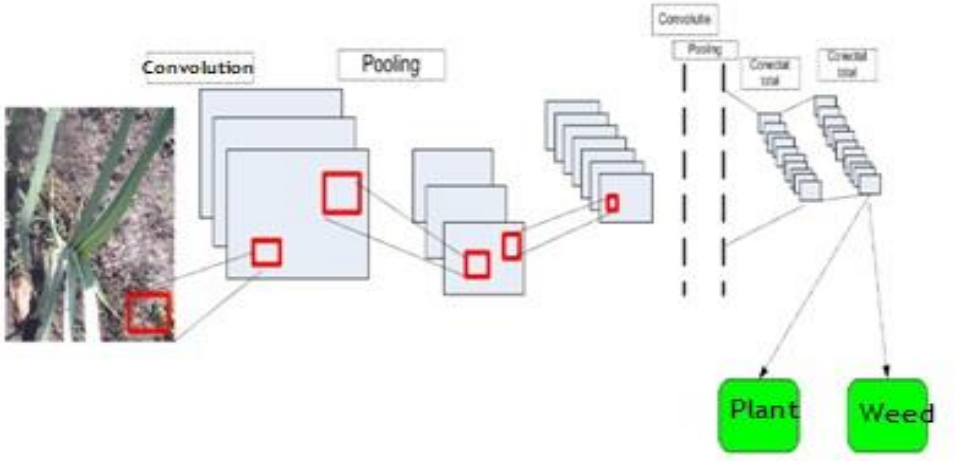

Fig. 3 - The network architecture used

The camera used was a LOGITECH HD Pro C92.0 webcam. The recognition process takes about 100 - 50 ms per image (or 10 - 20 fps) to detect a weed target before a new image is captured and ready for processing, which allows the data to be processed to enable command in real time for real situations.

A laptop receives the data flow from the cameras and, depending on the identification of the weeds, commands the central controller of the machine, connected to the relays for actuating the microvalves of the spray nozzles.

Special problems that appear in the field of image processing are known, but especially in the case of real-time recognition tasks, due to variations in light intensity. If in the case of industrial applications this problem is solved by the fact that in the controlled environment in which artificial vision systems work, the properties of light can be controlled in detail, in the case of applications that work in a natural environment, the light intensity varies during the day in a significant manner.

Various developments have used coating systems to allow the control of light intensity (Figure 4). This method, however, does not allow the elimination of the problem of light intensity variation, because due to the condition that the covering screen must be placed at a distance from the ground in order not to hit the plants, natural light penetrates through this space. This type of system has multiple disadvantages, namely that it needs to be repositioned and adjusted for each crop, and in the case of certain crops it leads to a disadvantageous flow of sprayed substances.

Fig. 4 - Smart spraying system equipped with canopy (*Patil J.K. et al., 2017*)

Identification algorithms should provide high accuracy under all conditions, so they must also be tested for light intensity variability. The following figure shows the stages of testing the robustness of the neural network algorithm.

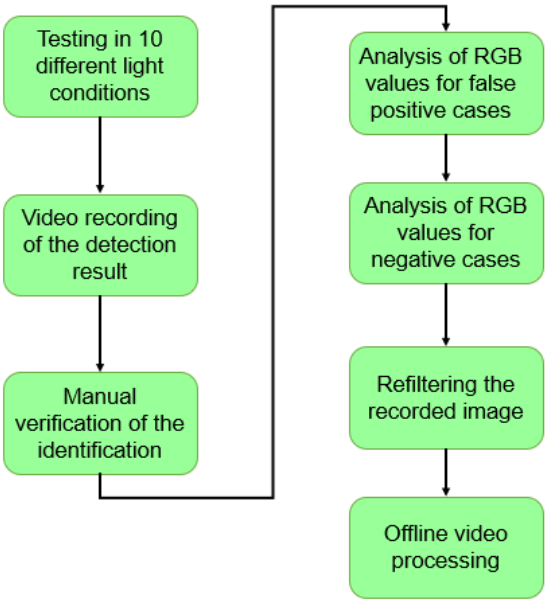

Fig. 5 - The stages of testing the robustness of the algorithm in different lighting conditions

RESULTS

With the experimental model of the spraying machine, the same rows of onion plants were tested for 4 consecutive days, in different luminosity conditions. Although the position relative to the camera for the same plant location is different, in the 10 passes performed, due to the fact that the same trajectory cannot be reproduced every time and because the plants change their position due to weather factors, as well as the fact that plants grow within the 4-day test interval, it is considered useful to test the algorithm in this way to check robustness to brightness variation.

It can be noticed that the capture conditions (height and viewing angle) emulate real situations when the light intensity varies, but also the distance from the camera to the ground due to the appearance of some vertical movements in the machine.

The videos were always captured during daylight hours and the wind speed was very low or zero to avoid the occurrence of technical problems regarding the appearance of drops on the camera. The lux meter used to measure the brightness was LX 1010B.

Table 2

Results obtained from the experiments using the electrically driven spraying machine

No.	Luminosity (lux)	Neural network identification accuracy (%)	False positive (%)
1	5000	92.11	8.12
2	8590	91.98	10.11
3	12456	93.23	9.12
4	45890	91.16	11.12
5	90456	89.16	9.11
6	125600	95.30	7.9
7	130567	91.26	9.67
8	14786	91.36	10.2
9	225786	92.51	11.21
10	250456	91.06	11.12

Testing in different condition

As shown in the figure below (Figure 6), even when dry plant remains appear in the scene, and the crop plant (onion) is partially dry, the algorithm works without causing false-positive identifications.

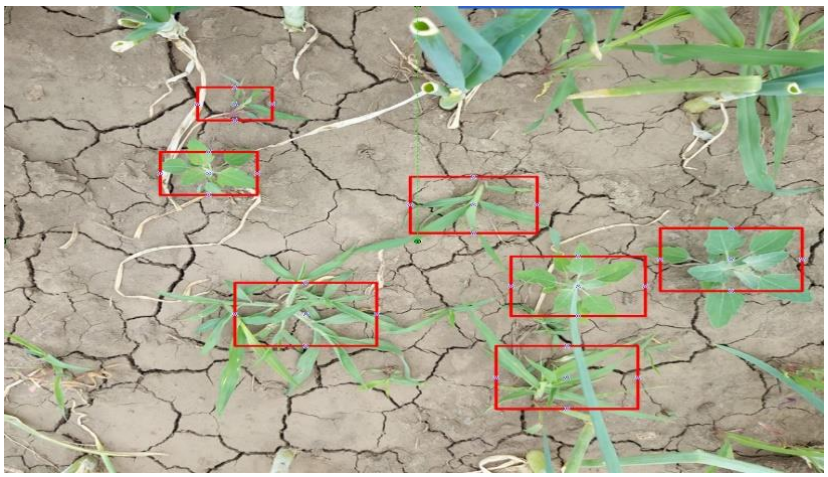

Fig. 6 - Identification in the case of the existence of plant remains

In the figure below (Figure 7) the operation of the algorithm can be seen even in the conditions where, due to a misalignment of the row, the camera is not positioned above the intervals between the rows of plants, but is positioned above the row. This situation occurs frequently in real situations when, due to some technical conditions of the ground, the row is not straight. The developed algorithm works with very good results even in this situation.

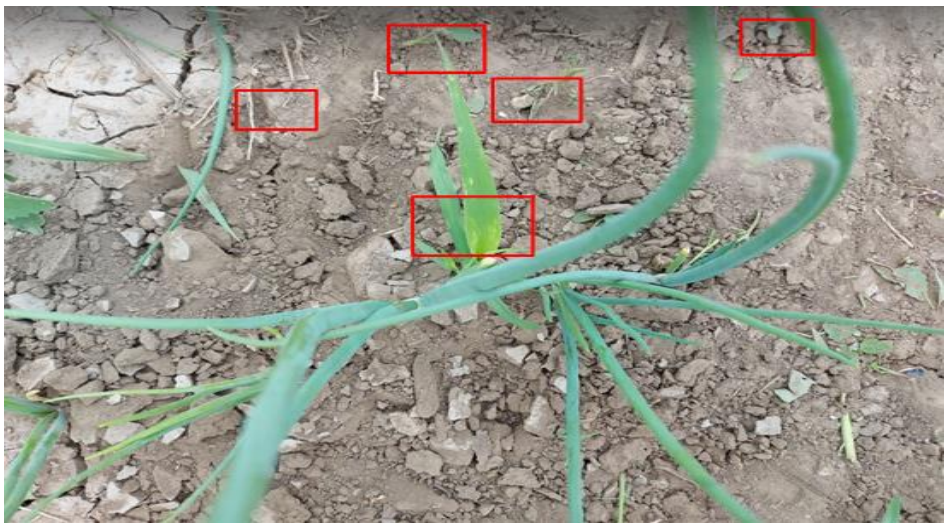

Fig. 7 - Identification in the case when the camera is above the crop plant

For the case when the plant is so close to the camera that a certain portion of it is not in focus, as shown in the figure below (Figure 8), the algorithm has a good detection rate.

Fig. 8 - Identification in the case when a certain area in the scene is out of focus

In the case when the plant is very close to the central area of the camera, as seen in Figure 9, due to the fact that the image is blurred, the weeds are not identified with a very good accuracy. In position 1, the top of the plant is observed to be weakly focused.

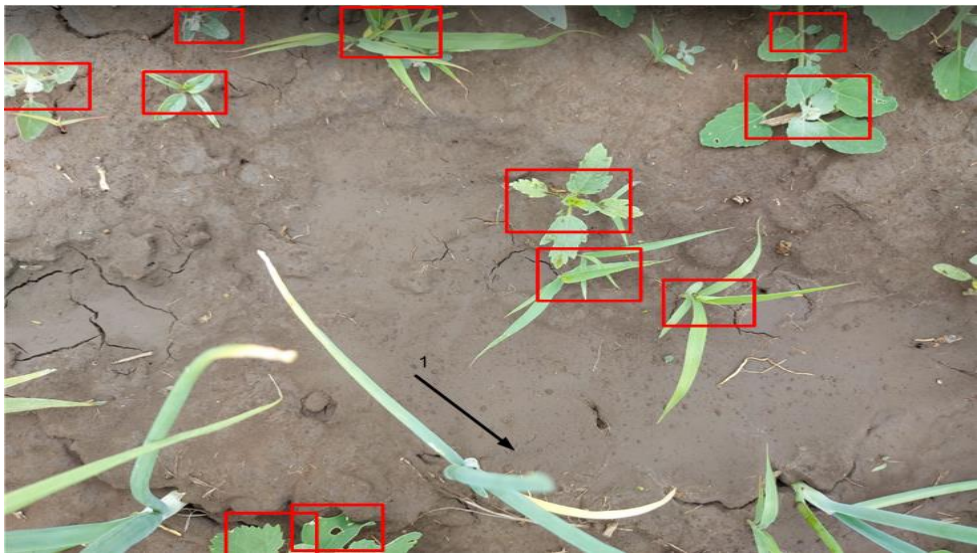

Fig. 9 – Identification in the case when the plant is near the camera

For the case when there are weeds with a considerable length in the scene to be analysed, as is the case below, the algorithm worked with a good detection rate (Figure 10).

Fig. 10 – Identification in the case when the weeds have a considerable length

As shown in the images below (Figure 11), the algorithm developed works for any kind of soil texture, which translates into a distinctly different colour and appearance between tilled, wet or dry soil.

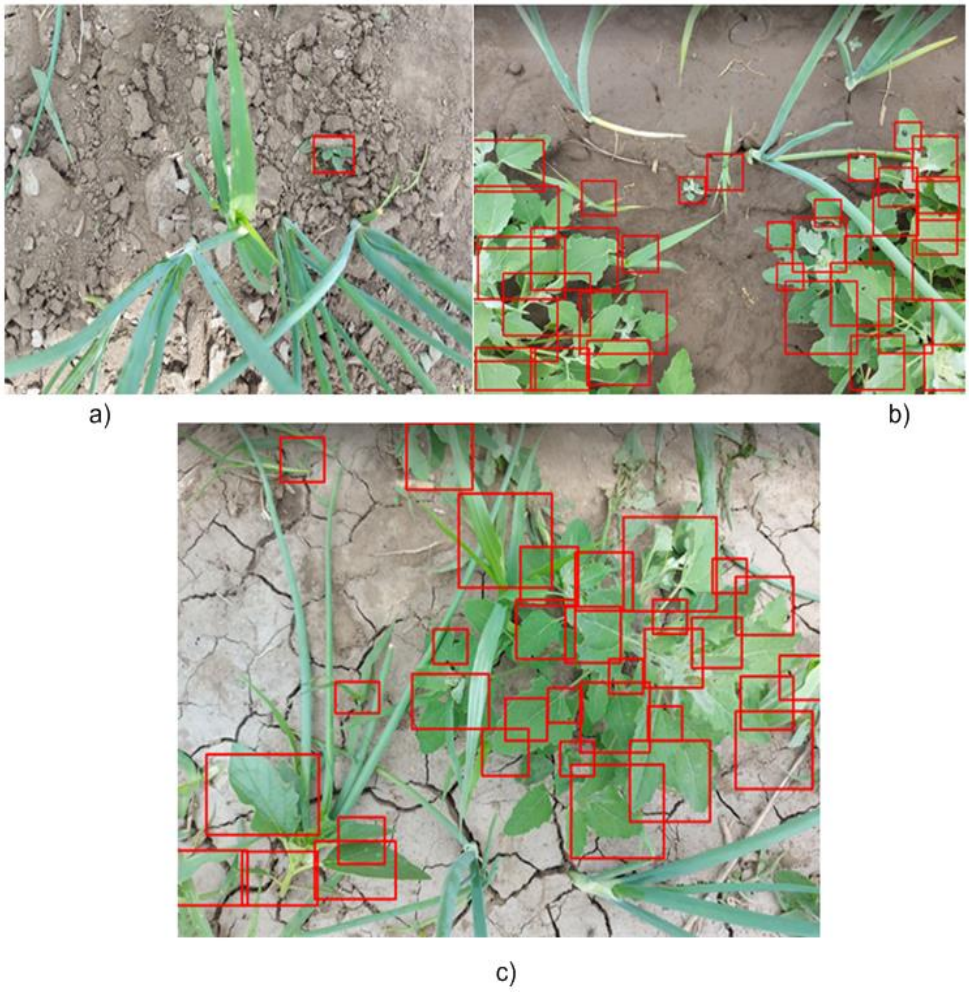

Fig. 11 - Identification of weeds in scenes with different soil texture: a) texture for tilled land, b) texture for wet land, c) texture for arid land

Due to the proximity to the camera of a leaf that occupies a considerable area in the scene, the camera focuses on the nearest considerable area, as is the case below. In the tests considered, there were only 7 positions with this situation, but the detection was at a good rate.

Fig. 12 – Identification in the case when weeds occupy a considerable area in the scene

Night time functionality testing was done to test the capabilities of the algorithm. Unfortunately, due to the artificial lighting and the characteristic of the LED light, the results decrease, and in the areas where there is less light, due to the positioning of the lighting system, it is obvious that the weeds cannot be identified at a high rate. The identification accuracy is 40%.

Fig. 13 - Tests carried out at night using LED lighting

CONCLUSIONS

Following the tests carried out, the following can be stated:

- the neural network algorithm is robust even in conditions of variable luminosity;
- at night, using LED lighting, the identification accuracy partially decreases, especially since the lighting system does not make the image visible in its entirety;
- several situations from reality were taken into consideration, such as: different texture of the soil, weak focus, the existence of plant residues in the scene;
- the algorithm works even if the camera takes information above the plant or above the interval between crop rows.

ACKNOWLEDGEMENT

This work was supported by a grant of the Ministry of Agriculture and Rural Development, contract of sectorial financing, ADER type, no.25.2.2 Research on the design of intelligent horticultural equipment for analysis, prediction and biodynamic action".

REFERENCES

[1] Cortes C, Vapnik V (1995) Support-Vector networks. *Machine Learning 20: 273*

[2] Frommknecht, A.; Effenberger, I. (2014). Texture Based Algorithm for Analysing Defects and Fibre Orientation of Fibre Reinforced Plastics. In: P*roceedings Conference on Industrial Computed Tomography (ICT) 2014: Non-destructive Testing, 3D Materials Characterisation and Dimensional Measurement*; 25th 28th February 2014, Wels, Austria, p. 389-394

[3] Garousi, V., Felderer, M., & Mäntylä, M. V. (2016). The need for multivocal literature reviews in software engineering: complementing systematic literature reviews with grey literature. *EASE 2016: 26:1 – 26:6*

[4] Hlaing S H & Khaing A S (2014). Weed and crop segmentation and classification using area thresholding. *International Journal of Research in Engineering and Technology 3*. 375-382

[5] Ian H, Frank E. (2005). *Data mining: practical machine learning tools and techniques*. Morgan Kaufmann

[6] Jain AK, Duin RPW, Mao J (2000) Statistical pattern recognition: a review. *IEEE Trans. Pattern Analysis and Machine Intelligence 22*: 4–37

[7] Jianlun Wang, Jianlei He, Yu Han, Changqi Ouyang, Daoliang Li. (2013). An Adaptive Thresholding algorithm of field leaf image, *Computers and Electronics in Agriculture*, 2013, 96:23~39.

[8] Jianshu Chen. (2013). *The research on diseases of straw berry image features matching search*. [D]. Beijing: China Agricultural University.

[9] Knoll, F.J.; Czymmek, V.; Poczihoski, S.; Holtorf, T.; Hussmann, S. (2018). Improving efficiency of organic farming by using a deep learning classification approach. *Comput. Electron. Agric., 153*, 347–356.

[10] Latha, A Poojith, Amarnath Reddy B V, Vittal Kumar G; (2014). Image Processing In Agriculture, *International Journal of Innovative Research in Electrical, Electronics, Instrumentation and Control Engineering, Vol. 2, Issue 6*

[11] Moghadam, M. H. (2019). Machine Learning-assisted Performance Testing. *ESEC/SIGSOFT FSE 2019*, 1187–1189

[12] Mustafa M., Hussain A., Ghazali K. and Riyadi S. (2007). Implementation of Image Processing Technique in Real Time Vision System for Automatic Weeding Strategy, in *IEEE International Symposium on Signal Processing and Information Technology*, Giza, Egypt, pp. 632-635

[13] Patil, J.K.; Kumar, R. (2017). Analysis of content based image retrieval for plant leaf diseases using colour, shape and texture features. *Eng. Agric. Environ. Food 10,* 69–78

[14] Perez A., Lopez F., Benlloch J. and Christensen S., (2000). Colour and shape analysis techniques for weed detection in cereal fields, *Computers and Electronics in Agriculture, vol. 25*, pp. 197-212

[15] Perona, Pietro; Malik, Jitendra. (1990). Scale-space and edge detection using anisotropic diffusion. Pattern Analysis and Machine Intelligence, *IEEE Transactions on, Vol. 12, No. 7,* p. 629-639.

[16] Rees S.J., McCarthy C.L., Artizzu X.P.B., Baillie C.P., Dunn M.T. (2009). Development of a prototype precision spot spray system using image analysis and plant identification technology, *Agricultural Technologies in a Changing Climate: The 2009 CIGR International Symposium of the Australian Society for Engineering in Agriculture*. National Centre for Engineering in Agriculture (NCEA), USQ, Toowoomba, QLD, Australia

[17] Sethy, P.K.; Routray, B.; Behera, S.K. (2019). Detection and Counting of Marigold Flower Using Image Processing Technique. In *Lecture Notes in Networks and Systems; Springer: Singapore*, pp. 87–93

[18] Shen, X., Wang, Q., Wang, P., & Zhou, B. (2009). Automatic generation of test case based on GATS algorithm. *GrC 2009*, 496–500

[19] Shinde A. and Shukla M. (2014). Crop detection by machine vision for weed management, *International Journal of Advances in Engineering & Technology, vol. 7*, pp. 818- 826.

[20] Zhao F, Cai C, Huang S, He D & Zhu J. (2009). Weed Seeds Recognition Using Locally Linear Embedding. In: 2009 International Conference on Test and Measurement, 5-6 December, Hong Kong, China, pp. 59-62

POTENTIAL OF MILLED AMARANTH GRAIN PRODUCTS IN PROVIDING FOOD WITH ESSENTIAL MINERAL ELEMENTS
/
ПОТЕНЦІАЛ ПРОДУКТІВ ПОМЕЛУ ЗЕРНА АМАРАНТУ У ЗАБЕЗПЕЧЕННІ ХАРЧОВИХ ПРОДУКТІВ ЕСЕНЦІАЛЬНИМИ МІНЕРАЛЬНИМИ ЕЛЕМЕНТАМИ

Svitlana MYKOLENKO[1)], Svitlana SYTNYK[1*)], Tatiana BOJŇANSKÁ[2)], Eva IVANIŠOVÁ [2)], Ivona JANKO[2)], Andrea HRICOVÁ[3)]

[1)] Dnipro State Agrarian and Economic University, Sergiia Yefremova Str. 25, 49600 Dnipro, Ukraine
[2)] Institute of Food Sciences, Slovak University of Agriculture in Nitra, Slovak Republic
[3)] Institute of Plant Genetics and Biotechnology, Nitra, Slovak Republic
Tel: 0989642684; E-mail: svitlana.mykolenko@hest.ethz.ch

DOI: https://doi.org/10.35633/inmateh-68-47

Keywords: *amaranth grain, milled products, essential mineral elements, food ingredients.*

ABSTRACT
Amaranth grain is a promising pseudocereal, and milled amaranth grain products as ingredients may improve the nutritional value of food products. Twenty amaranth products from different Ukrainian varieties such as Kharkivs'kyi-1, Liera, Sem (Amaranthus hypochondriacus L.), Ultra (Amaranthus hybridus L.), and different milled fractions (flour, middling, coarse seed coat, and fine seed coat) were analysed in this study. Amaranth whole grain has 2-3- and 20-fold content of manganese, iron, copper, zinc, and calcium respectively in comparison to wheat. Flour fractions of the amaranth grain presented a reduced content of magnesium, potassium, calcium, manganese, and iron compared to their content in the whole grain. Studied amaranth grain and the milled products of different varieties revealed a significant (p>0.05) positive (0.47…0.90) correlation between all analysed essential minerals, except molybdenum, which demonstrated 0.46…0.56 correlations with calcium, zinc, potassium, iron, and copper. Milled amaranth grain products such as ingredients in bread, pasta, or cookies formulations at 10…50% substitution of wheat flour, might fulfil the daily requirements in magnesium, manganese, iron, copper, and molybdenum enhancing the nutrition value of the products.

ТЕЗИ
Зерно амаранту є перспективним псевдозлаком, продукти помелу якого можуть використовуватися як інгредієнти, здатні суттєво покращувати мінеральний склад харчових продуктів. Двадцять продуктів переробки зерна амаранту з різних українських сортів, як-от Харківський-1, Лєра, Сем (Amaranthus hypochondriacus L.), Ультра (Amaranthus hybridus L.) та різних фракцій помелу (борошно, крупка, крупні висівки, дрібні висівки) були досліджені на вміст макро- і мікроелементів. Вміст марганцю, заліза, міді, цинку і кальцію в зерні амаранту був вищим в 2-3 і 20 разів порівняно із зерном пшениці. Борошняна фракція зерна амаранту (борошно і крупка) мала знижений вміст магнію, калію, кальцію, марганцю та заліза. Встановлено, що досліджене зерно амаранту різних сортів і продукти помелу мали достовірний (p>0.05) позитивний (0.47…0.90) кореляційний зв'язок між вмістом усіх проаналізованих есенціальних металів, крім молібдену, який корелював на рівні 0.46…0.56 з кальцієм, цинком, калієм, залізом та міддю. Використання здрібнених продуктів зерна амаранту для виробництва хліба, макаронних виробів або печива при 10-50% заміні пшеничного борошна вищого сорту може задовольнити добову потребу людини в магнії, марганці, залізі, міді та молібдені суттєво поліпшуючи біологічну цінність харчових продуктів.

INTRODUCTION
Amaranth is a promising pseudocereal crop still underestimated in XXI century. Amaranth grain presents high nutrition value containing a wide variety of bioactive compounds (*Peter and Gandhi, 2017; De la Rosa et al., 2019*). Micronutrients scarcity is known to provoke the development of alimentary diseases (*White and Broadley, 2009*). Therefore, amaranth grain processed products might also be considered as food ingredients regarding the mineral composition. There are 17 grain amaranth varieties in Ukraine (*Hoptsiy et*

al., 2018). Amaranth grain is known as a source of magnesium, calcium, and iron (*Nascimento et al., 2014; Schmidt et al., 2021*).

Wheat grain, especially wheat patent flour, is scarce in minerals (*Gómez-Galera et al., 2010; Baloch et al., 2014*). To explore functional properties of amaranth grain processed products might be useful to sustain food supply chains for better nutrition (*Kumar et al., 2016; Cotovanu and Mironeasa, 2022*).

High-fibre, high-protein, and high-starch amaranth semolina fractions were classified following the granulometric method by specific differential milling (*Tosi et al., 2001*). Particle size offers valuable information about the quality of amaranth flour depending on milled fractions. The roller milling of amaranth grain allowed producing fractions enriched with nutrients of functional properties to incorporate them as food improvers (*Sakhare et al., 2017; Ramesh and Prakash, 2020*).

Substitution of wheat flour with different types of amaranth grain processed products produced from Ukrainian amaranth grain varieties improved consumer quality of bread and increased the specific volume and crumb porosity, especially when using whole amaranth grain flour of the Kharkivs'kyi-1 variety, defatted flour from amaranth flakes and groats (*Mykolenko et al., 2020*). However, a comprehensive study of the macro- and microelements composition in amaranth grain, particularly made of the Ukrainian varieties, is limited to the best of our knowledge (*Levashova et al., 2018*). The research was aimed to assess essential metal elements as micronutrients in whole grain and milled products of *Amaranthus* L. of different Ukrainian varieties to enhance the nutritional values of food.

MATERIALS AND METHODS

Amaranth grain used in the study was presented by the following Ukrainian varieties: Kharkivs'kyi-1, Liera, Sem (*Amaranthus hypochondriacus* L.), and Ultra (*Amaranthus hybridus* L.) and harvested in 2018–2019 in Ukraine. Dockage-free amaranth grain was used and calibrated by size. Amaranth grain of 9–11% moisture content was grinded in Chopin CD1 Mill (Chopin Technologies, France) to obtain four different amaranth milled products: flour fractions FL (flour) and ML (middling) with a size of less than 160 µm, as

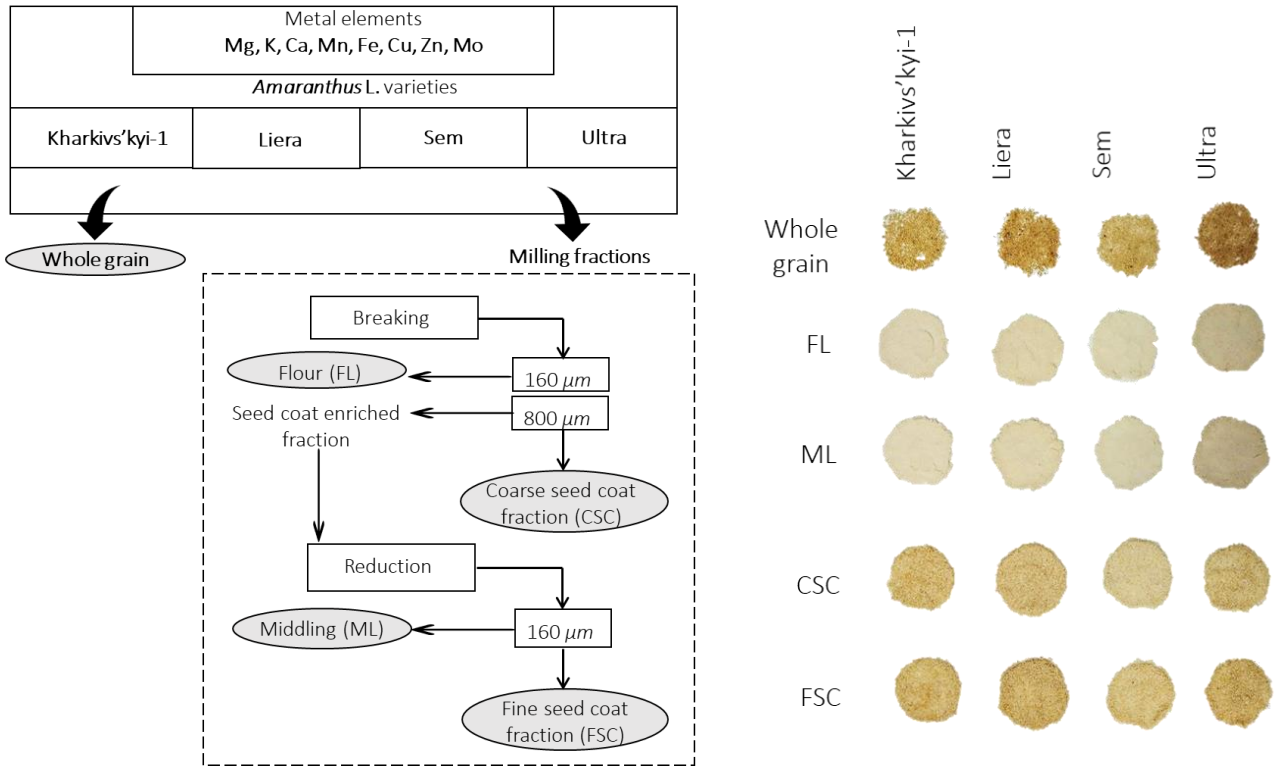

products after the break and grinding rollers, respectively; bran fraction CSC (coarse seed coat) with a size of more than 800 µm after break rollers; bran fraction FSC (fine seed coat) with a size of 160–800 µm after grinding rollers (Fig. 1).

Fig. 1 - Experimental sampling chart (a), amaranth grain and milled products of different varieties (b)

Milled fractions of amaranth grain and whole grain were analysed by the content of metal elements. The samples were mineralized using a microwave pressure splitting system (Ethos one, Milestone, Italy) in a medium with 5 ml of concentrated nitrate acid (69%, chemically pure) and 1 ml of hydrogen peroxide (30%, chemically pure) with the addition of 1 ml of deionized water. The material samples obtained in this way were qualitatively and quantitatively analysed using inductively coupled plasma-optical emission spectrometry (ICP-OES) on the Agilent ICP-OES 720 instrument (Agilent Technologies, Germany) for the content of magnesium, potassium, calcium, manganese, iron, copper, zinc, and molybdenum. The sample evaporates and the element of interest is sprayed at an extremely high argon plasma temperature (~7000°C). ICP-OES is used to detect metals only in liquid samples, and the wavelength is specific to each element, taking into account its atomic mass and concentration intensity. The mineral concentration was expressed in mg per 100 g of dry matter. The moisture content of the samples was determined by AOAC 952.08, 2000 method. A 5 g of the weighed sample was placed in a dryer at 102°C ± 2°C until the sample acquired a constant mass. Statistical processing of experimental data was performed in MS Excel and STATISTICA software. Pearson correlation analysis was performed at $p<0.05$, and cluster analysis was done by the agglomerative hierarchical clustering method (Ward's method).

RESULTS

Table 1 shows the content of macro- and microelements in whole amaranth grain of different varieties. Metal elements could be divided into three groups by their content (mg·100 g^{-1}): <1.0 – molybdenum; 1.0-10.0 – manganese, iron, zinc, copper; 100.0 - 400.0 potassium, calcium, magnesium. In terms of molybdenum, copper, zinc, and magnesium content, whole amaranth grain of Liera and Sem varieties did not differ significantly. The range of molybdenum content was in range of 0.022 - 0.052 mg·100 g^{-1}. Moreover, the whole amaranth grain presented a low concentration of molybdenum, a minor dispersion of its absolute content was depending on the variety, and its maximum accumulation in the seeds reached for the Kharkivs'kyi variety: 0.052 mg·100 g^{-1}.

Table 1

Macro- and microelements in whole amaranth grain

Variety	Mo [mg·100 g^{-1}]	Cu [mg·100 g^{-1}]	Zn [mg·100 g^{-1}]	Mn [mg·100 g^{-1}]	Fe [mg·100 g^{-1}]	K [mg·100 g^{-1}]	Ca [mg·100 g^{-1}]	Mg [mg·100 g^{-1}]
Kharkivs`kyi-1	0.052a	1.2a	2.75a	3.3a	9.6ac	261a	173a	181a
Liera	0.024b	1.2a	3.26b	2.5b	9.4a	382b	185a	270b
Sem	0.022b	1.3a	3.32b	3.1a	8.3b	411c	195b	287b
Ultra	0.040c	1.3a	4.06c	3.5a	10.1c	374b	151c	268b

Note. The mean values of the obtained results are shown, and different letters for each value in the table show statistically significant differences ($p<0.05$).

Copper showed 1.2 - 1.3 mg·100 g^{-1} content in the grain of all the studied varieties. The results of zinc concentrations in the studied grain were corresponding to the optimal range. The manganese content in the whole grain of the amaranth varieties was 2.5 - 3.5 mg·100 g^{-1}; these values were insignificant and met the lowest limit of the threshold for plants: 2.0 - 30.0 mg·100 g^{-1} (*Kabata-Pendias, 2000*). Iron of the studied amaranth grain reached a higher concentration compared to other metal elements of the group including copper and manganese. Its content in the seeds of the studied varieties varied between 8.3 and 10.0 mg·100 g^{-1}, while the optimal content in plant tissues is known to be around 5.0 - 30.0 mg·100 g^{-1}. But there was no significant difference among the varieties. Potassium was concentrated in the whole grain within the range of 261 - 411 mg·100 g^{-1}. Meanwhile, the calcium content in the tested seeds met the range of 151 - 195 mg·100 g^{-1}, when magnesium concentration occurred at 181 - 287 mg·100 g^{-1}.

Table 2 shows the metal elements composition in the milled amaranth grain products. All metal elements content in the bran fractions differed significantly from flour counterparts. At the same time, the fractions represented mainly by perisperm particles (FL and ML) of Liera and Sem varieties showed no difference in manganese, potassium, magnesium, calcium, copper and zinc, calcium, copper, molybdenum, respectively. Flour (FL) of all the varieties of *Amaranthus* L. had a decrease in macroelements (potassium, calcium, magnesium) as well as manganese and iron. On top of that, zinc concentration decreased for Kharkivs'kyi-1, Liera, and Ultra varieties.

The middling fraction ML in all studied varieties presented a relative concentration of magnesium to whole grain. Middling fractions of three varieties showed an increase in potassium, calcium, manganese, iron, zinc,

copper, and molybdenum. The concentration of the essential elements of this fraction for the Liera variety had a decrease in manganese, iron, potassium, zinc, calcium, copper, and molybdenum.

Table 2

Essential macro- and microelements in amaranth milled grain products

Variety	Mn [mg·100 g^{-1}]	Fe [mg·100 g^{-1}]	K [mg·100 g^{-1}]	Mg [mg·100 g^{-1}]	Zn [mg·100 g^{-1}]	Ca [mg·100 g^{-1}]	Cu [mg·100 g^{-1}]	Mo [mg·100 g^{-1}]
Flour (FL)								
Kharkivs`kyi-1	1.5a	4.8a	138a	97a	1.58a	83a	0.7a	0.016a
Liera	2.3b	9.1b	338b	245b	3.12b	165b	1.4b	0.052b
Sem	2.3b	7.1c	338b	239b	3.45c	169b	1.5b	0.027c
Ultra	2.8c	9.2b	261c	200c	2.74d	141c	1.2c	0.016a
Middling (ML)								
Kharkivs`kyi-1	5.1a	18.2a	444a	322a	4.75a	287a	2.1a	0.069a
Liera	3.6b	15.7b	551b	397b	4.54b	270b	1.7b	0.055b
Sem	3.9c	13.6c	583c	411c	4.53b	265b	1.6b	0.050b
Ultra	3.3d	8.7d	253d	187d	2.87c	144c	1.2c	0.019c
Fine seed coat (FSC)								
Kharkivs`kyi-1	4.0a	11.9a	329a	228a	3.56a	187a	1.3a	0.081a
Liera	1.7b	6.3b	246b	182b	2.10b	109b	0.9b	0.021b
Sem	3.7c	10.3c	542c	391c	4.24c	210c	1.7c	0.021b
Ultra	3.6c	7.7d	282d	212d	3.05d	154d	1.2a	0.012c
Coarse seed coat (CSC)								
Kharkivs`kyi-1	4.4a	1.3a	366a	236a	3.71a	233a	1.5a	0.075a
Liera	2.9b	10.0b	464b	303b	3.81ac	218b	1.2b	0.027b
Sem	1.7c	4.2c	232c	159c	1.99b	119c	0.9c	0.015c
Ultra	6.6d	16.9d	255d	437d	3.91c	361d	1.4a	0.006d
Daily intake, mg·100 g^{-1}								
Ukraine	2	17	-	500	15	1200	1	0.07
EPSA	3	19.6	3500	350	14	1000	1.6	0.065
Upper level	-	-	-	250	25	2500	5	0.6

Notes. The mean values of the obtained results are shown, and different letters for each value in the table show statistically significant differences ($p<0.05$). The norm value is calculated for an individual weighing 70 kg

The fine seed coat fraction (FSC) of the Liera variety contained fewer metal elements than the whole grain. Additionally, almost all elements of this fraction for the Ultra variety, except manganese and calcium, decreased drastically too. The FSC of amaranth grain of the Kharkivs'kyi-1 variety showed a higher content of the macro- and microelements compared to the unprocessed grain. A similar trend was for the coarse seed coat (CSC) of the Sem variety, which also had a high content of the studied elements with exception of molybdenum. Moreover, manganese content in middling and coarse bran surpassed the recommended daily intake of 2-3 mg·100 g^{-1}. The middling fraction showed iron in a concentration close to the recommended one, while other milled amaranth grain products concentrated this element at less quantity. The range of the recommended calcium daily intake is 1000 - 2500 mg·100 g^{-1}. This metal content varied from 83 to 361 mg·100 g^{-1} in all the milled fractions. Copper intake in the human body is known to be 1-1.6 mg·100 g^{-1}. The milled products of amaranth varieties mainly included this element up to 1 mg·100 g^{-1}, and its concentration reached 2.0 mg·100 g^{-1} in middling of the Kharkivs'kyi-1 variety. The molybdenum in 100 g of all fractions of amaranth grain of the Kharkivs'kyi-1 variety, except flour, was close to the recommended daily intake.

Table 3 and Figure 2 show a correlation between the content of essential minerals in the amaranth grain and the milled products. All elements, except molybdenum, showed a positive and reliable correlation. For molybdenum, a significant average-strength correlation (0.46...0.56) was characteristic of calcium, zinc, potassium, iron, and copper. Zinc demonstrated the highest level of correlation with essential metals, the presence of which in the amaranth grain and the milled products was associated with magnesium, potassium, calcium, iron, and copper (0.83...0.90), and with manganese at the level of 0.75 at $p<0.05$. Magnesium showed a strong positive correlation with potassium, calcium, and zinc (0.81...0.90), when calcium and iron content correlated with iron

(0.86) and manganese (0.88) respectively. Furthermore, copper showed a weaker correlation (0.69...0.77). Thus, according to the interconnectedness of concentration, essential metals in the amaranth grain and its milled products were arranged in the following order: Zn → Mg, Ca, Fe → K → Mn → Cu → Mo.

Table 3

Correlation matrix of essential minerals in amaranth grain and milled products

Mineral	Mg	K	Ca	Mn	Fe	Cu	Zn	Mo
Mg	1.00	0.81	0.88	0.64	0.77	0.75	0.90	-
K	0.81	1.00	0.73	0.47	0.62	0.71	0.83	0.56
Ca	0.88	0.73	1.00	0.79	0.86	0.77	0.86	0.46
Mn	0.64	0.47	0.79	1.00	0.88	0.69	0.75	-
Fe	0.77	0.62	0.86	0.88	1.00	0.70	0.85	0.53
Cu	0.75	0.71	0.77	0.69	0.70	1.00	0.86	0.55
Zn	0.90	0.83	0.86	0.75	0.85	0.86	1.00	0.51
Mo	-	0.56	0.46	-	0.54	0.55	0.51	1.00

Note. Correlation are statistically significant at p<0.05

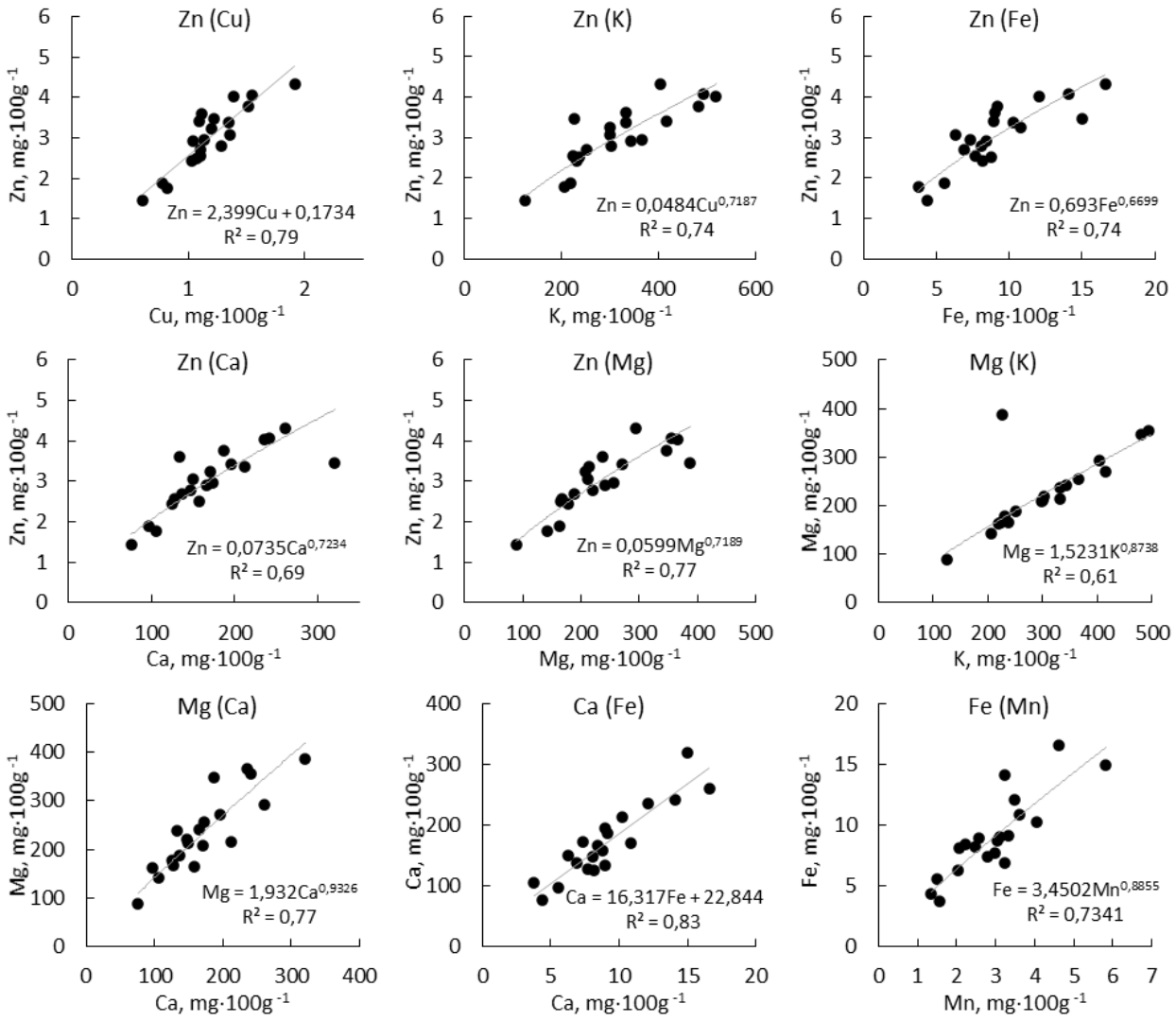

Fig. 2 – Correlation of essential minerals in amaranth grain and milled products

The concentration of zinc, magnesium, and calcium in the whole amaranth grain and the milled products increased with higher copper, potassium, iron, calcium, magnesium, and manganese content. Cluster analysis of

the composition of amaranth grain and the milled products revealed essential metals assembling into three separate clusters (Fig.3).

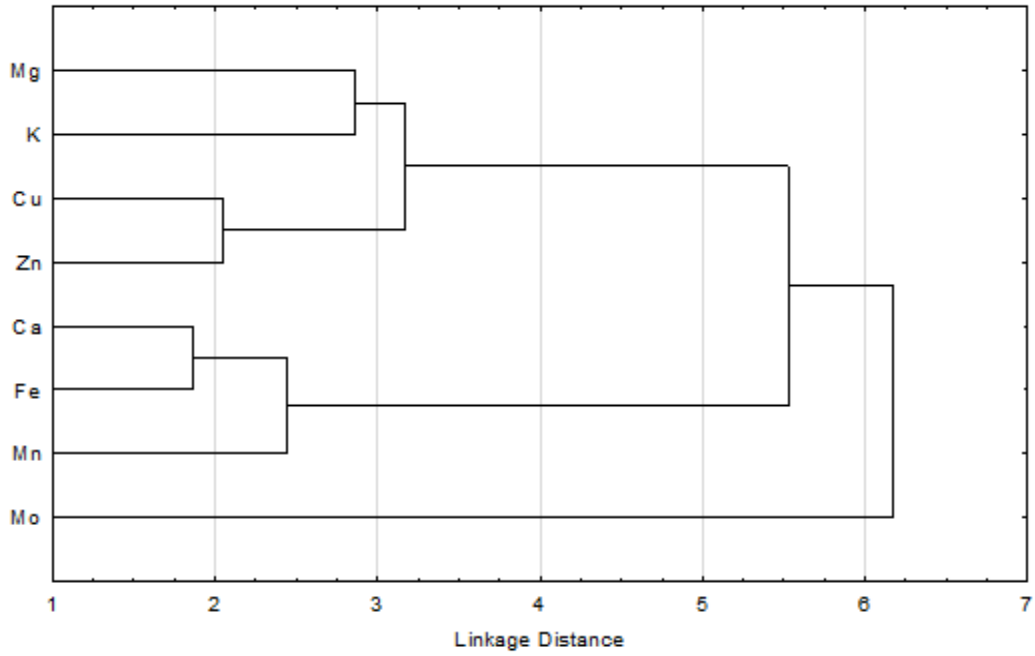

Fig. 3 - Cluster analysis of essential minerals in amaranth grain and milled products

The first cluster included magnesium, potassium, copper, and zinc. The second cluster comprised calcium, iron, and manganese, and its statistical relatedness was higher than in magnesium and potassium. The third cluster was presented by trace element molybdenum with lower concentration capacity, demonstrating a lack of correlation at a reliable level with metals such as magnesium and manganese. According to the level of statistical relatedness of the metal element concentration in amaranth grain and the milled products, the closest pairs were calcium, iron, zinc, and copper, which positively correlated at the level of 0.86 ($p<0.05$).

Table 4 shows a range of essential mineral elements in grain of *Triticum sp.* and *Amaranthus sp.* Amaranth grain of Krepysh, Kizlyarets, Kinelsky, and Yantar varieties were characterized by 2-5-fold content in molybdenum, manganese, potassium, calcium, and magnesium to wheat grain.

Table 4

Content of essential nutritional elements in wheat and amaranth grain

Species	Mo [mg·100 g^{-1}]	Cu [mg·100 g^{-1}]	Zn [mg·100 g^{-1}]	Mn [mg·100 g^{-1}]	Fe [mg·100 g^{-1}]	K [mg·100 g^{-1}]	Ca [mg·100 g^{-1}]	Mg [mg·100 g^{-1}]	Reference
Triticum sp.	0.023 – 0.033	0.14–0.18	0.85–1.36	2.43–3.69	2.11–3.77	278–410	2–3	60–95	*Miroshnichenko et al, 2017*
Amaranthus sp.	-	0.57	4.55	4.42	7.35	552	200	328	*Mota et al., 2016*
Amaranthus hypochondriacus L. var.:									*Fursa et al, 2013*
Voronezhskiy	0.022	1.6	3.1	7.3	51.0	830	474	270	
Krepysh	0.182	3.8	2.4	11.5	47.9	251	425	400	
Kizlyarets	0.223	0.8	2.9	7.1	36.4	738	427	420	
Kinelskiy	0.102	3.6	6.5	12.5	41.6	483	262	191	
Yantar	0.186	1.7	5.5	3.0	28.6	780	337	328	

The copper content in the grain of amaranth varieties (*Fursa et al, 2013*) had a high variability; the Kinelsky variety contained 0.8 mg.100 g^{-1} of this metal, which was less than in the studied raw materials, while another four varieties (Yantar, Kizlyarets, Krepysh, and Voronezhsky) included more copper. Iron content in the grain of all amaranth varieties found by *Fursa et al. (2013)* surpassed the studied varieties as well as results presented by *Mota et al. (2016)*. Nevertheless, amaranth grain of the Liera and the Sem varieties showed the same molybdenum, copper, zinc, and magnesium content. These varieties are known by their similar genotypic

characteristics (*Hoptsiy et al., 2018*). *Mota et al (2016)* showed that amaranth grain had a high content of potassium, calcium, and magnesium compared to the varieties studied in the work. Only copper presented a lower content to the Ukrainian varieties. Copper can exhibit antagonistic interactions with iron and molybdenum (*Agarwala et al., 1989; Palmer and Guerinon, 2009*). However, according to the results of the study, a positive correlation between copper and iron (0.70) took place. But among all essential elements, the correlation between copper and molybdenum content was the lowest (0.55). Zinc promotes the assimilation of copper by plants, being at the same time an antagonist of manganese and iron (*Kabata - Pendias, 2000*). So far, positive correlations between zinc concentration and copper (0.86), iron (0.85), and manganese (0.75) in the amaranth grain and its milled products were revealed.

Biochemical role of magnesium, calcium and potassium in plants has many similarities (*Hauer-Jakli and Tranknen, 2019*). This is consistent with the results of our study, where the correlation between the concentration of magnesium and these minerals was 0.88 and 0.81, respectively. In contrast to wheat grain, the elemental composition of amaranth grain was characterized by higher content of copper, zinc, iron, and magnesium, the increase of which was up to 3-fold. Calcium of the amaranth grain was 20 times higher than its content in the wheat grain. *Kiewlicz and Rybicka (2020)* proved that amaranth grain flakes could better cover recommended intake of calcium, iron, potassium, magnesium, manganese, sodium, and zinc, in particular magnesium and iron, compared with flakes of rye, barley, winter wheat, spelt wheat, buckwheat, corn, quinoa, millet, oats, or rice. All analysed milled fractions (based on the median for the studied varieties of the amaranth grain) provided above 10% of the recommended daily intake for manganese, iron, magnesium, zinc, calcium, copper, and molybdenum when using 100 g of the product a day in accordance with the EPSA directives (Table 5).

Table 5

Covering essential minerals daily intake by amaranth flour and bread, %

Product	[%]	Type of product	Mn	Fe	K	Mg	Zn	Ca	Cu	Mo
Flour	100	Flour	68	37	8	56	19	14	72	29
		Middling	111	67	13	92	29	24	92	72
		Fine seed coat	108	41	8	56	21	15	70	29
		Coarse seed coat	108	48	8	69	24	20	72	29
Wheat bread	100	Flour	101	55	11	83	28	20	107	44
		Middling	165	99	19	136	43	35	136	107
		Fine seed coat	161	61	12	83	31	23	103	43
		Coarse seed coat	161	72	12	102	35	30	107	43
	50	Flour	51	27	6	41	14	10	54	22
		Middling	83	49	9	68	21	18	68	53
		Fine seed coat	80	30	6	42	16	11	52	21
		Coarse seed coat	80	36	6	51	18	15	54	21
	25	Flour	25	14	3	21	7	5	27	11
		Middling	41	25	5	34	11	9	34	27
		Fine seed coat	40	15	3	21	8	6	26	11
		Coarse seed coat	40	18	3	25	9	7	27	11
	15	Flour	15	8	2	12	4	3	16	7
		Middling	25	15	3	20	6	5	20	16

Product	[%]	Type of product	Mn	Fe	K	Mg	Zn	Ca	Cu	Mo
		Fine seed coat	24	9	2	12	5	3	15	6
		Coarse seed coat	24	11	2	15	5	4	16	6
	10	Flour	10	5	1	8	3	2	11	4
		Middling	17	10	2	14	4	4	14	11
		Fine seed coat	16	6	1	8	3	2	10	4
		Coarse seed coat	16	7	1	10	4	3	11	4

Note. The calculation considered the flour and the bread consumption level as 100 and 200 g a day

At the same time, 100 g of middling fractions, fine or coarse seed coat could provide 108-111% of the daily need in manganese. Moreover, the optimal intake of manganese, magnesium, copper, and molybdenum is overtopped when bread produced of 100% amaranth product is introduced into the daily diet at 200 g a day, especially when the middling is used as an ingredient of the formulation. Therefore, it is reasonable to use the milled amaranth grain-derived products in the composite flours, for example, together with wheat flour of the highest grade, which is known to be depleted of the essential minerals. Replacing wheat flour with amaranth one resulted in a significant increase in the intake of manganese and copper (10%); manganese, magnesium, and copper (15%): magnesium, iron, magnesium, copper, and molybdenum (25%). Bran fractions and middling should be introduced into the bread formulations at 10-15% to achieve a similar effect.

Pasta is a popular food based on flour and water all over the world. Wheat flour replacement by the amaranth products at 15% in pasta formulations might cover up to 10% of the manganese recommended intake. But the noticeable mineral improvement of the product occurs if wheat flour is replaced with the amaranth products up to 25%. This makes it possible to meet more than 10% of the daily need in manganese, copper for all the milled products studied, and in iron, magnesium, and molybdenum when using the middling. Considering the absence of gluten and functional properties of amaranth starch, increasing the amaranth flour in pasta up to 50% could deteriorate the quality of the product.

Milled amaranth grain products could significantly improve cookies quality (*Mykolenko and Zakharenko, 2020*). Meanwhile, compared to bread and pasta, the daily intake of cookies is more limited and does not exceed 35 g a day in the common diet. From this point of view, only complete replacement of wheat flour with milled amaranth counterparts may result in the mineral-enriched product. The cookies with amaranth flour can provide 11-15% of magnesium, manganese and copper recommended daily intake, whereas 50% substituted wheat flour by the amaranth middling or the bran fractions would assist 9-11% covering in magnesium, manganese, and copper.

CONCLUSIONS

Amaranth grain presented high content of zinc, magnesium, and calcium which makes this crop a promising improver of the nutritional value of food products. The highest concentration of manganese, iron and zinc occurred in the amaranth grain of the Liera variety, and potassium, calcium, and magnesium accumulated mostly in the grain of the Sem variety. The Kharkivs'kyi-1 variety grain showed the highest molybdenum content among minerals. The amaranth flour was characterized by reduced potassium, calcium, magnesium, manganese, and iron content in comparison to the whole grain. According to interconnectedness, the essential minerals in the amaranth grain and the milled products were arranged in the following order: Zn → Mg, Ca, Fe → K → Mn → Cu → Mo. Wheat-amaranth composite flour in the bread formulations might cover daily intake level of manganese and copper (90-10), manganese, magnesium, and copper (85-15), magnesium, iron, magnesium, copper, and molybdenum (75-25). Bran fractions and middling should be introduced into the bread formulations at 10–25% to achieve a similar effect, while 50% replacement of wheat flour with these amaranth products is needed in the cookie formulations.

ACKNOWLEDGEMENT

This study is based upon the work from COST Action 18101 SOURDOMICS – Sourdough biotechnology network towards novel, healthier and sustainable food and bioprocesses (https://sourdomics.com/; https://www.cost.eu/actions/CA18101/). COST is a funding agency for research and innovation networks. Also, this work was supported by the Ukrainian State Project for Young Scientists of the Ministry of Education and Science of Ukraine (No. 0120U100322).

The authors express their gratitude to Dana Carmen Chira for her kind assistance in data acquisition. Also, the authors are grateful to Olexandr Duda, the President of the Association of Amaranth Producers and Processors, for providing the amaranth grain for the experiments.

REFERENCES

[1] Agarwala, S.C., Chatterjee, C., Sharma, C.P., & Nautiyal, N., (1989). Copper-molybdenum interaction in maize. *Soil Science and Plant Nutrition*, 35 (3), 435–442. doi: 10.1080/00380768.1989.10434776. The Netherlands.

[2] Baloch, F.S., Karakoy, T., Demirbas, A., Toklu, F., Ozkan, H., & Hatipoglu R. (2014). Variation of some seed mineral contents in open pollinated faba bean (Vicia faba L.) landraces from Turkey. *Turkish Journal of Agriculture and Forestry*, 38, 591–602. doi:10.3906/tar-1311-31. Ankara/Turkey.

[3] Cardoso, R.V.C., Fernandes, Â., Gonzaléz-Paramás, A.M., Barros, L., & Ferreira, I., (2019). Flour fortification for nutritional and health improvement: A review, *Food Res Int.*, 125:108576. doi:10.1016/j.foodres.2019.108576. Madrid/Spain.

[4] Cotovanu, I., & Mironeasa, S., (2022). Features of Bread Made from Different Amaranth Flour Fractions Partially Substituting Wheat Flour. *Appl. Sci.,* 12, 897. https:// doi.org/10.3390/app12020897. Basel/ Switzerland.

[5] De la Rosa, A.P., Fomsgaard, I.S., Laursen, B., Mortensen, A.G., Olvera-Martínez, L., & Leon-Rodrigueza A.D., (2009). Amaranth (Amaranthus hypochondriacus) as an alternative crop for sustainable food production: Phenolic acids and flavonoids with potential impact on its nutraceutical quality. *Journal of Cereal Science*, 49 (1), 117–121. https://doi.org/10.1016/j.jcs.2008.07.012. The Netherlands.

[6] Fursa, N.S., Parfenov, A.A., Jurko, Y.A., & Korenskaya, S., (2013). Chromato-mass spectrometry of the component composition of ethanol extraction of seeds of the Voronezhsky Amaranth variety prior to and after extraction by hexane (Хромато-масс-спектрометрия компонентного состава этанольной экстракции семян сорта Воронежский Амарант до и после экстракции гексаном). *Bulletin of Voronezh State University (Бюллетень Воронежского государственного университета).* Series: Chemistry. Biology. Pharmacy 1, 240–247, Voronezh/Russia. (in Russian)

[7] Gómez-Galera, S., Rojas, E., Sudhakar, D., Zhu, C., Pelacho, A.M., … & Christou P., (2010). Critical evaluation of strategies for mineral fortification of staple food crops. *Transgenic Research*, 19 (2), 165–180. doi:10.1007/s11248-009-9311-y. The Netherlands.

[8] Hauer - Jákli, M. & Tränkner, M., (2019). Critical leaf magnesium thresholds and the impact of magnesium on plant growth and photo - oxidative defense: A systematic review and meta-analysis from 70 years of research. *Frontiers in Plant Science*. 10:766. doi: 10.3389/fpls.2019.00766. Lausanne/Switzerland.

[9] Hoptsiy, T.I., Voronkov., M.F., Bobro, M.A., Miroshnichenko, L.A., Limanskaya, S.V., … & Duda Y.V., (2018). *Amaranth: selection, genetics, and prospects of cultivation (Амарант: селекція, генетика та перспективи вирощування),* Monograph (Монографія), Kharkiv/Ukraine.362p. (in Ukrainian)

[10] Kabata - Pendias, A., (2010). *Trace elements in Soils and Plants*. CRC Press. 548p. https://doi.org/10.1201/b10158.Boca-Raton/USA. Boca Raton/USA.

[11] Kiewlicz, J., & Rybicka, I., (2020). Minerals and their bioavailability in relation to dietary fiber, phytates and tannins from gluten and gluten-free flakes. *Food Chemistry* 305: 125452. doi:10.1016/j.foodchem.2019/125452. The Netherlands.

[12] Kumar, K.V., Dharmaraj U., Sakhare, S.D., & Inamdar, A.A., (2016). Effect of grain moisture content during milling on pasting profile and functional properties of amaranth fractions. *J Food Sci Technol*. 53(5):2434-2442. doi: 10.1007/s13197-016-2226-8.The Netherlands.

[13] Levashova, O.L., Tishakova, T.S., Syrova, G.O., & Kovalenko, S.M., (2018). Complex application of amaranth and soya in medicine and food industry. International Trends in Science and Technology. In: *Proceedings of the VI International Scientific and Practical Conference*, 6–8, Warsaw/Poland.

[14] Miroshnichenko, I.M., Makoveychuk, T.I., Mykhalska, L.M., & Schwartau, V.V., (2017). Changes in the elemental composition of winter wheat plants caused by the action of Megafol and retardants. *Regulatory Mechanisms in Biosystems*, 8 (3), 403 –409. doi:10.15421/021762. Dnipro/Ukraine.

[15] Mota, C., Nascimento., A.C., Santos, M., Delgado, I., Coelho, I.,…& Castanheira I., (2016). The effect of cooking methods on the mineral content of quinoa (Chenopodium quinoa), amaranth (Amaranthus sp.) and buckwheat (Fagopyrum esculentum). *Journal of Food Composition and Analysis*, 49, 57– 64. doi.org/10.1016/j.jfca.2016.02.006. The Netherlands.

[16] Mykolenko, S. & Zakharenko, A., (2020). Study of the effect of amaranth and flaxseed flour on the quality of cookies. *Technical Sciences and Technologies*, 1 (19). 228–240. doi: 10.25140/2411-5363-2020-1(19)-228-240. Chernigiv/Ukraine.

[17] Mykolenko, S., Zhygunov, D., & Rudenko, T., (2020). Baking properties of different amaranth flours as wheat bread ingredients. *Food Science and Technology*, 14 (4), 62–71. doi:10.15673/fst.v14i4.1896. Odessa/Ukraine.

[18] Nascimento, A.C., Mota, C., Coelho, I, Gueifão, S., Santos, M., … & Castanheira I., (2014). Characterisation of nutrient profile of quinoa (Chenopodium quinoa), amaranth (Amaranthus caudatus), and purple corn (Zea mays L.) consumed in the North of Argentina: Proximates, minerals and trace elements. *Food Chemistry*, 148, 420–426. The Netherlands.

[19] Orsango, A.Z., Loha, E., Lindtjørn, B., & Engebretsen, I.M.S., (2020). Efficacy of processed amaranth-containing bread compared to maize bread on hemoglobin, anemia and iron deficiency anemia prevalence among two-to-five year – old anemic children in Southern Ethiopia: A cluster randomized controlled trial. *PLoS ONE*, 15(9): e0239192. doi:10.1371/journal.pone.0239192. Cambridge/UK

[20] Palmer, C.M. & Guerinon, M.L., (2009). Facing the challenges of Cu, Fe and Zn homeostasis in plants. Nature Chemical Biology, 5, 333–340. New York/ USA.

[21] Peter, K. & Gandhi, P., (2017). Rediscovering the therapeutic potential of Amaranthus species: A review. *Egyptian Journal of Basic and Applied Sciences*, 4(3), 196–205. doi.org/10.1016/j.ejbas.2017.05.001. The Netherlands.

[22] Ramesh D., & Prakash J., (2020). Nutritional and functional properties of amaranth grain flour fractions obtained by differential sieving. *Progress in Chemical and Biochemical Research*, 3(3), 272–286.doi: 10.33945/SAMI/PCBR.2020.3.10. Iran.

[23] Sakhare S.D., Inamdar A.A., Preetham Kumar K.V., & Dharmaraj U., (2017). Evaluation of roller milling potential of amaranth grains. *Journal of Cereal Science*. Vol.73, 55–61, https://doi.org/10.1016/j.jcs.2016.11.006.Vienna/Austria. The Netherlands.

[24] Schmidt, D., Verruma-Bernardi, M.R., Forti, V.A., & Borges, M.T., (2021). Quinoa and Amaranth as Functional Foods: A Review. *Food Reviews International*, doi:10.1080/87559129.2021.1950175, USA.

[25] Soliman, J.S.A., Amer, A.Y., & Soliman, J.S.A., (2019). Association of zinc deficiency with iron deficiency anemia and its symptoms: results from a case-control study. *Cureus*, 11(1): e3811. doi:10.7759/cureus.3811. San Francisco / USA.

[26] Tosi E.A., Re E., Lucero H., & Masciarelli R., (2001). Dietary fiber obtained from amaranth (Amaranthus cruentus) grain by differential milling. *Food Chemistry* 73(4), 441– 443. doi: 10.1016/S0308-8146(00)00326-5. The Netherlands.

[27] White, P.J. & Broadley, M.R., (2009). Biofortification of crops with seven mineral elements often lacking in human diets – iron, zinc, copper, calcium, magnesium, selenium and iodine. *New Phytologist*, 182 (1), 49–84. doi:10.1111/j.1469-8137.2008.02738.x. Lancaster/UK.

CLASSIFICATION OF DEGRADED SPECIES IN DESERT GRASSLANDS BASED ON MULTI-FEATURE FUSION AND UNMANNED AERIAL VEHICLE HYPERSPECTRAL /

基于多特征融合与无人机高光谱的荒漠草原退化物种分类

Tao ZHANG [1], Fei HAO *[2], Yuge BI [1], Jianmin DU [1], Weiqiang PI [3], Yanbin ZHANG [1], Xiangbing ZHU [1], Xinchao GAO [1], Eerdumutu JIN [1]

[1] Inner Mongolia Agricultural University, Mechanical and Electrical Engineering College, Hohhot / China
[2] Hohhot Vocational College, Mechanical and Electrical Engineering Department, Hohhot / China
[3] Huzhou Vocational and Technical College, College of Mechatronics and Automotive Engineering, Huzhou / China
Tel: 17852092475; E-mail: taozhang626@163.com

DOI: https://doi.org/10.35633/inmateh-68-48

Keywords: *Desert grasslands, Deep learning, Hyperspectral images, Unmanned aerial vehicle, Fine classification*

ABSTRACT

Accurate spatial distribution of grassland degradation indicator species is of great significance for grassland degradation monitoring. In order to realize the intelligent remote sensing grassland degradation monitoring task, this paper collects remote sensing data of three degradation indicator species of desert grassland, namely, constructive species, dominant species, and companion species, through the UAV hyperspectral remote sensing platform, and proposes a multi-feature fusion (MFF) classification model. In addition, vertical convolution, horizontal convolution, and group convolution mechanisms are introduced to further reduce the number of model parameters and effectively improve the computational efficiency of the model. The results show that the overall accuracy and kappa coefficient of the model can reach 91.81% and 0.8473, respectively, and it also has better classification performance and computational efficiency compared to different deep learning classification models. This study provides a new method for high-precision and efficient fine classification study of degradation indicator species in grasslands.

摘要

准确掌握草地退化指示物种的空间分布对草地退化监测有着重要意义。为实现智能化遥感草地退化监测任务，本文通过无人机高光谱遥感平台对荒漠草原建群种、优势种和伴生种三种退化指示物种遥感数据采集，并提出一种多特征融合（MFF）的分类模型。此外，引入垂直卷积、水平卷积和分组卷积机制，进一步减少模型参数量，有效提升模型的计算效率。结果表明，该模型的总体精度和 kappa 系数分别可达 91.81%、0.8473。同时，与不同深度学习分类模型相比，也具有更优的分类性能和计算效率。本研究为草地退化指示物种的高精度、高效率的精细分类提供了一种新方法。

INTRODUCTION

Grassland desertification is one of the ten most serious ecological and environmental problems in the world *(Tang et al., 2016)*. Inner Mongolia Autonomous Region is the province with the largest grassland area in China, with a total grassland area of 87 million hectares, accounting for 73.4% of the land area of the region. However, under the combined influence of global climate change and human factors, more than 90% of the grassland area in the Inner Mongolia Autonomous Region has been severely degraded *(He et al., 2021)*. Grassland degradation will not only lead to ecological problems such as soil erosion, sand and dust storms, a decrease in grassland productivity, and the loss of biodiversity *(Liu et al., 2021; Wang et al., 2020)*, but will also affect the development of local animal husbandry *(Briske et al., 2015)*. Therefore, there is an urgent need for efficient and accurate technology and methods for effective monitoring of desert grasslands, to provide assistance for the restoration and management of desert grasslands.

In recent years, some scholars have applied machine learning to grassland degradation monitoring to classify grassland characteristics. For example, Yang et al. *(2021)* achieved the classification of desert steppe species by constructing a decision tree classification model. However, this machine learning classification method requires manual extraction of a large amount of feature information, which is time-consuming and labor-intensive.

Subsequently, some scholars began to introduce deep learning into the classification task of grassland degradation indicator species to achieve an integrated process from feature extraction to classification. For example, Pi et al. *(2021)* realized the end-to-end classification of grassland degradation indicator species by building a 3D convolutional neural network classification model. However, the constructed model not only has a large number of network parameters but also needs to be improved in classification performance. In the classification of grassland degradation indicator species, the speed of model inference is a necessary factor to improve the efficiency of grassland monitoring. Therefore, it is very important to explore a high efficiency and high precision classification model for grassland degradation indicator species.

Currently, a convolutional neural network (CNN) is a widely used hyperspectral image classification method in hyperspectral image classification *(Liu et al., 2022; Xu et al., 2021)*. CNN is divided into a 1D convolutional neural network (1DCNN), a 2D convolutional neural network (2DCNN), and a 3D convolutional neural network (3DCNN). Since the 1DCNN filter is one-dimensional, it can only extract the spectral features of hyperspectral images *(Hsieh and Kiang, 2020)*; the 2DCNN filter is two-dimensional, so it can only extract the spatial features of hyperspectral images *(Shenming et al., 2022)*; while the 3DCNN filter is three-dimensional, which has one more spectral dimension compared to 2DCNN, so it can extract the spatial-spectral features of hyperspectral images, which usually is better than 1DCNN and 2DCNN in terms of classification performance *(Jung et al., 2022)*. However, 1DCNN, 2DCNN, and 3DCNN ignore the correlation between the pixels to be classified and the neighboring pixels when classifying hyperspectral images.

To address the above problems, this paper uses an unmanned aircraft remote sensing platform to collect data on desert grassland species and proposes a multi-feature fusion (MFF) classification model. The model effectively combines the spatial and spectral features of hyperspectral images, as well as the correlation information between the pixels to be classified and neighboring pixels, which further improves the classification performance of the model. At the same time, vertical convolution, horizontal convolution, and group convolution mechanisms are introduced to further reduce the number of model parameters and effectively improve the computational efficiency of the model. The purpose of this paper is to explore a high precision and high-efficiency method to monitor indicator species of desert grassland degradation, in order to provide help for the management and monitoring of grassland degradation.

MATERIALS AND METHODS

Overview of the study area

The present study area is located on Gegenthala grasslands (111 ° 52′47′ ′ E, 41 ° 46′48′ ′ N) in the Inner Mongolia Autonomous Region, China. The grassland type in this area is *Stipa breviflora* grassland desert, and the vegetation is sparse and low, with a cover of only 15-25% and an average plant height of only 8 cm. The type of climate belongs to a temperate monsoon climate, with an average annual temperature of 3.5 °C and an altitude of 1456 m *(Zhang et al.*, *2022)*. After investigation, there are more than 20 types of vegetation, which can be subdivided into constructive, dominant, and companion species. Here, constructive species are *Stipa breviflora*, dominant species are *Cleistogenes songorica* and *Artemisia frigida*, and companion species are *Neopallasia pectinata*, *Leymus chinensis*, and *Ceratoides latens (Pan et al.*, *2016)*.

Experimental equipment

The instruments used in this study include mainly a hyperspectral imager, a UAV, and a gimbal. Among them, the hyperspectral imager adopts the Pika XC2 hyperspectrometer made by Resonon, USA, with a weight of 2.2 kg. The spectral range of this spectrometer is between 400 and 1000 nm, the maximum number of bands can be set to 447 bands, the spectral resolution is 1.34 nm, and the number of spatial channels is 1600. The Jinan Share HEX-8 eight-rotor UAV was selected, with a professional A3 pro flight control system and dual positioning systems of BeiDou and GPS, which can perform accurate positioning and autonomous route flight. The aircraft has a maximum load of 40 kg and can fly continuously for 30 min at full load with a maximum flight speed of 10 m/s. The gimbal is DJI Ronin-M with a weight of 3.6 kg.

Data collection

Based on local climatic conditions and vegetation growth, data was collected from July 5 to 15, 2019. To reduce the shadow interference, the collection time was between 11:00 and 13:00. At the same time, the weather was ensured to be clear and cloudless and the wind speed was lower than 3.5 m/s. After several flight experiments, the spatial size of the collected hyperspectral images was set at 6062 lines × 1600 samples, and the number of bands was 231; the flight height of the UAV was set at 30 m and the spatial resolution was 2.1 cm at this time.

During the acquisition of 2.5 hm^2 hyperspectral image data, the UAV flew autonomously according to the planned route and set the bypass overlap rate at 55%. Furthermore, three types of vegetation, namely constructive species, dominant species, and companion species, were surveyed in the UAV flight area by arranging 1 m × 1 m sample boxes; Only one type of vegetation was included in a single sample box; the vegetation coverage, latitude and longitude, and type of vegetation were recorded in the sample boxes.

Data processing

The acquired hyperspectral image data were manually checked to remove distorted and overexposed images. Reflectance correction of hyperspectral image data was performed using Spectral Pro software to obtain the reflectance values of the real features, as shown in Figure 1. From the figure, it can be seen that the reflectance values of the last 40 bands fluctuate greatly due to the influence of noise and should be given to be removed, and finally 191 bands are retained. In addition, in order to reduce the subsequent calculation cost and correlation between the bands, the PCA dimensionality reduction algorithm is applied to reduce the number of bands to 15 bands, and this group of bands retains 96.90% of the features of the hyperspectral image.

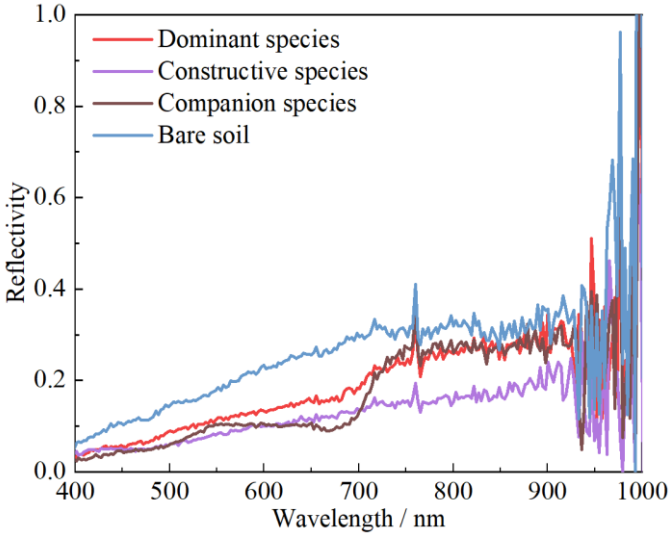

Fig. 1 - Spectral curves of target ground objects

Dataset Production

Taking into account the computational cost, the hyperspectral image data was cropped to a spatial size of 601 lines × 601 samples. Taking into account the data balance problem, the cropped images should contain three feature types: constructive species, dominant species, and companion species. Subsequently, the cropped images were labeled with samples according to the extensive ground survey. Finally, 187482 constructive species samples, 158945 dominant species samples, 3049 companion species samples, and 11725 bare soil samples were obtained, totaling 361201 sample data. This hyperspectral false-color image and ground truth image are shown in Figure 2.

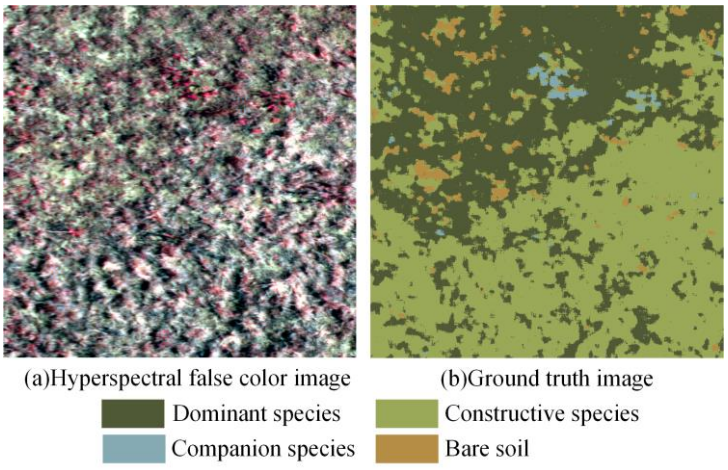

Fig. 2 - Hyperspectral images and ground truth images

ALGORITHM PRINCIPLE

Spatial feature extraction

The spatial feature extraction of hyperspectral images is generally performed using convolution kernels of n × n (n > 1). In Inception-v3 *(Szegedy et al., 2016)*, it is noted that n × n convolution kernels can be replaced by vertical convolution (n × 1) and horizontal convolution (1 × n) to effectively reduce the number of model parameters while ensuring classification accuracy. However, the order of vertical and horizontal convolution also has some influence on the classification performance of the model. In this paper, the dual-branch horizontal vertical convolution (DHVC) module is proposed, see Fig. 3.

In the figure, $\mathbf{X} \in \mathbb{R}^{\mathrm{H\times W\times C}}$ is the input hyperspectral data, $\mathbf{Y} \in \mathbb{R}^{\mathrm{H\times W\times C}'}$ is the output after DHVC spatial feature extraction, H×W is the length and width of the input hyperspectral data, *C* and C' are the number of bands, and 1×1@*C*/8 conv means there are *C*/8 convolution kernels for 1×1, and the rest are the same.

In the DHVC module, the first 1×1 convolution kernel is used to reduce the spectral dimensionality of the input data to reduce the model parameters and computational cost. Subsequently, horizontal convolution (1×3) and vertical convolution (3×1) by two branches are used for spatial feature extraction, and this structure can compensate for the impact on model classification accuracy due to the different order of horizontal and vertical convolution. After the extraction of spatial features from the two branches, the outputs of the two branches are stitched in the channel dimension. At the same time, 1×1 convolution kernels are used to fuse the features across the channels of the spliced data, and the spectral dimension of the data is expanded to C' to obtain the final output $\mathbf{Y} \in \mathbb{R}^{\mathrm{H\times W\times C}'}$, which is set to $C' = 2C$ in this paper. for the two 1×1 convolution kernels, the LeakyReLU activation functions are accessed after them. In addition, group convolution is introduced in horizontal and vertical convolution to reduce the number of model parameters, and the groups are set to C/64.

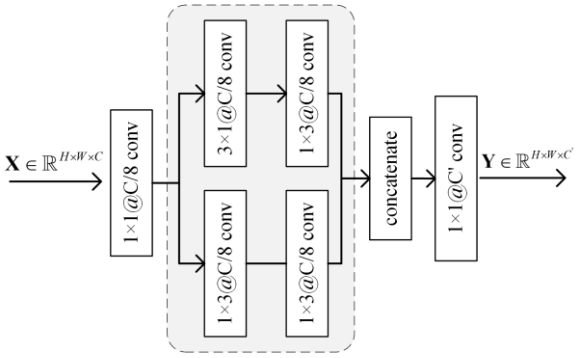

Fig. 3 - Structure of the DHVC module

Spectral feature extraction

The spectral features are extracted on the spectral dimension of individual pixels in the input data block. A 1×1 convolution kernel is equivalent to a linear fitting function, so a 1×1 convolution kernel is used to fit the spectral features. Meanwhile, the LeakyReLU activation function is introduced to activate the fitted spectral features so that they have a nonlinear relationship and can better extract the spectral features. Therefore, the extraction of spectral features can be represented by 1×1@C' conv+LeakyReLU.

Extract of correlation sequence features

In this paper, a correlation sequence feature extraction (CSFE) module is proposed for the extraction of correlation information between the pixels to be classified and the neighboring pixels, see Figure 4.

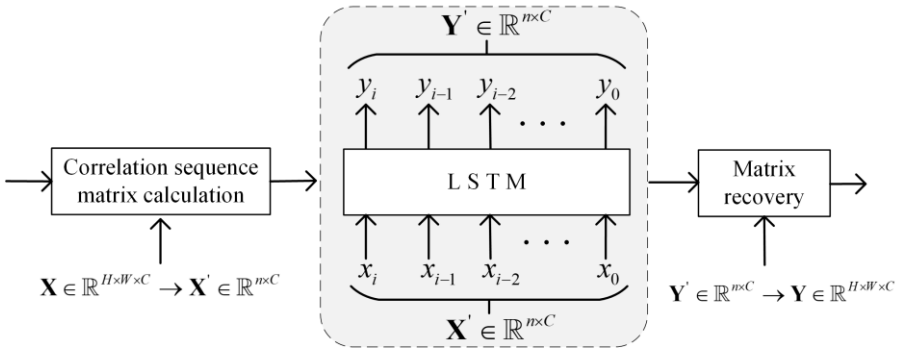

Fig. 4 - Structure of the CSFE module

Assuming that the input hyperspectral data $\mathbf{X} \in \mathbb{R}^{\mathrm{H}\times\mathrm{W}\times\mathrm{C}}$, the correlation size between the pixel to be classified $x_0 \in \mathbb{R}^{\mathrm{C}}$ and the neighboring pixels $x_i \in \mathbb{R}^{\mathrm{C}}, i = 1,2,\ldots,n\ (\mathrm{n} = \mathrm{H}\times\mathrm{W})$ can be calculated by the Euclidean distance function. Then the correlation sequence matrix $\mathbf{X}' \in \mathbb{R}^{\mathrm{n}\times\mathrm{C}}$ is obtained by reordering based on the correlation size from smallest to largest. The correlation sequence is brought into a single-layer long short-term memory (LSTM) network as a temporal sequence for correlation sequence feature extraction, and $\mathbf{Y}' \in \mathbb{R}^{\mathrm{n}\times\mathrm{C}'}$ is obtained. Finally, the pixels in the $\mathbf{Y}'$ matrix are restored to their original positions to obtain $\mathbf{Y} \in \mathbb{R}^{\mathrm{H}\times\mathrm{W}\times\mathrm{C}'}$.

MFF Model Framework

In the MFF model, feature pre-extraction is first performed by a 3×3@64 2D convolution kernel with padding set to 1. Subsequently, it is passed into the joint extraction module of spatial and spectral features and correlated sequence features.

The model is set up with 4 layers of the joint extraction module, and the extracted spatial and spectral features and related sequence features are summed in each layer, and a 2×2 maximum pooling function is used for spatial downsampling between the layers. The spectral feature outputs for each layer are set to 64, 128, 256, and 512, respectively. Finally, a fully connected (FC) layer with 4 neurons is used for the final classification. The structure of this network is shown in Fig. 5, where {64} indicates that the spectral dimension of the module output is 64, and the rest is the same.

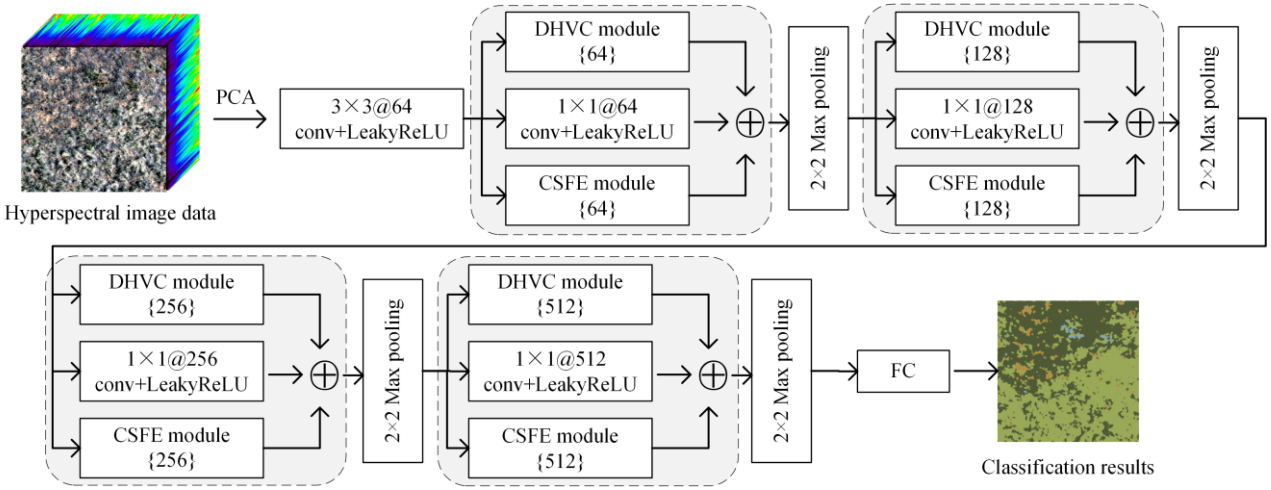

Fig. 5 - Structure of the MFF classification model

EXPERIMENT AND ANALYSIS

This experiment uses the Pytorch framework for model construction. Computer hardware devices are i7-11800H CPU, RTX 3060 graphics card, and 16 GB RAM. The learning rate is set to 0.001, patch to 13, epochs to 10, batch size to 128, and Adam optimization function is selected. In the experiment, 50% of the data is selected as the training set and the rest as the validation set. In addition, the overall accuracy (OA) and the kappa coefficient are selected as the evaluation criteria of the model.

Ablation experiments

To verify the effectiveness of spatial feature extraction, spectral feature extraction and correlated sequence feature extraction of the classification model proposed in this paper, ablation experiments will be analyzed, and the experimental results are shown in Table 1. It can be seen from the table that the classification accuracy of the model extracting only spatial features is the worst, and its OA value is only 87.79%. After adding spectral feature extraction, the OA value of the model is improved by 2.3%, and the kappa is improved by 0.048. The MFF model that simultaneously extracts spatial features, spectral features, and related sequence features have the best classification performance, with an OA of 91.81% and a kappa of 0.8473, indicating the effectiveness of the model proposed in this paper.

Table 1

Analysis of ablation experiments

Spatial features	Spectral features	Correlation sequence features	OA / %	Kappa
√			87.79	0.7663
√	√		90.09	0.8143
√	√	√	91.81	0.8473

RESULTS

Experimental results and analysis

To better evaluate the classification performance of the MFF model proposed in this paper, a total of three classical models, 2DCNN, Resnet18 and Densenet121, were selected for comparison experiments. The experimental results are shown in Table 2, the classification effect is plotted in Fig. 6, and the bold in the table indicates the highest accuracy.

As can be seen in Figure 6, the classification effect map of 2DCNN has the worst performance, the classification effect map of Resnet18 contains too many noise points, and the classification effect map of Densenet121 has too many constructive species identified as dominant species. In general, 2DCNN, Resnet18, and Densenet121 are not good at extracting features from small ground objects such as desert grasslands, while the classification result of the proposed MFF model is closer to the ground truth image and retains the distribution and details of ground objects.

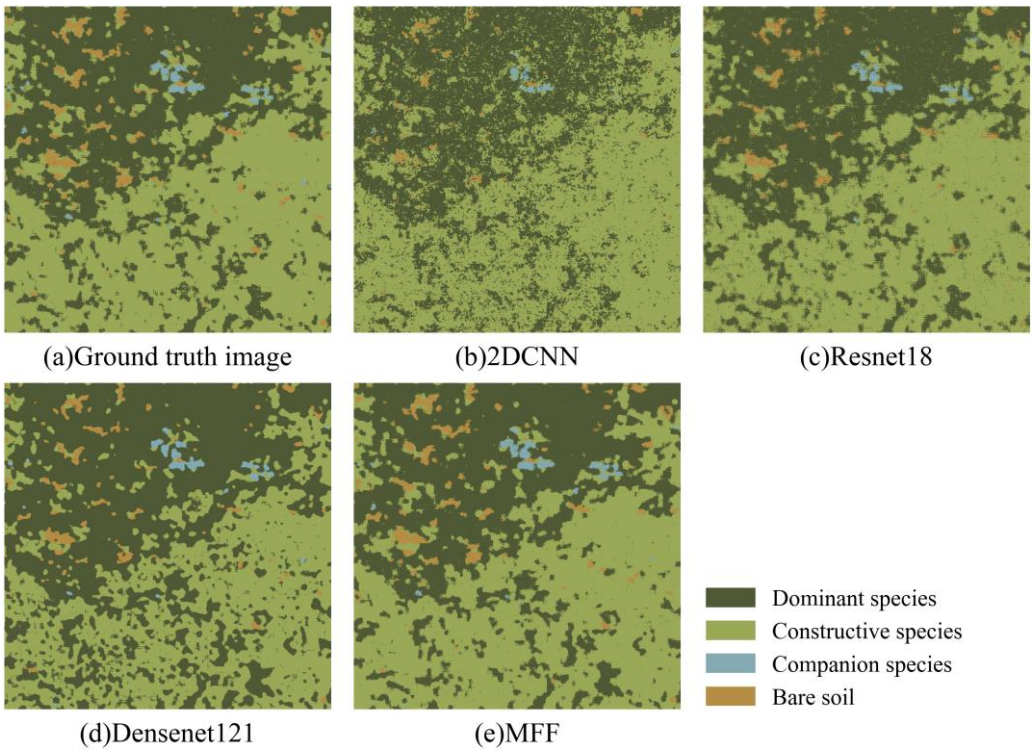

Fig. 6 - Classification effect images of different models

Table 2

Comparison of the classification performance of different models (%)

Category	2DCNN	Resnet18	Densenet121	MFF
Constructive species	82.86	86.70	81.21	**92.28**
Dominant species	77.11	88.07	**97.49**	92.67
Companion species	30.75	48.59	76.59	**78.56**
Bare soil	24.94	40.83	63.48	**75.97**
OA	78.01	85.49	87.76	**91.81**
Kappa	0.5793	0.7269	0.7729	**0.8473**

Efficiency comparison experiment

To further evaluate the computational efficiency of the proposed MFF model, the model parameters, floating point operations (FLOPs), and prediction time are now selected for efficiency evaluation. The comparison model selects 2DCNN, Resnet18, and Densenet121, and the experimental results are shown in Table 3. As can be seen from the table, 2DCNN has the least prediction time and FLOPs, but performs worse in classification performance. The parameter quantity and prediction time of MFF are better than the two classification models of Resnet18 and Densenet121, and the FLOPs are moderate, indicating that MFF has faster model calculation efficiency while ensuring classification accuracy.

Table 3

Comparison of the computational efficiency of different models

Models	Number of participants / M	FLOPs / M	Prediction time / s
2DCNN	5.3	7.3	15
Resnet18	11.2	17.3	67
Densenet121	6.9	134	81
MFF	2.4	18.2	25

CONCLUSIONS

In this paper, we collected data of three types of degradation indicator species in a desert grassland: constructive species, dominant species, and companion species by a UAV hyperspectral remote sensing platform, and proposed a multi-feature fusion (MFF) classification model to achieve high precision and high-efficiency classification performance of fine features in desert grassland. The main findings of this study are as follows:

1) A data set of desert grassland degradation indicator species was established, and a multi-feature fusion (MFF) classification model was proposed, whose overall classification accuracy could reach 91.81% and the kappa coefficient could reach 0.8473.

2) Introduce the idea of spectral correlation and use of LSTM to extract correlation features between long-distance pixels to be classified and neighboring pixels by effective analysis.

3) The analysis of ablation experiments concludes that the classification of spectral features, spatial features, and correlation features of hyperspectral images extracted alone is poor, while the classification performance of joint multi-feature extraction is optimal.

4) Introduce vertical convolution, horizontal convolution, and group convolution mechanisms to further reduce the number of model parameters and effectively improve the computational efficiency of the model. The dual-branch horizontal and vertical convolution (DHVC) module is proposed to compensate for the impact of different back and forward sequences of vertical and horizontal convolution on the classification performance of the model.

5) The overall accuracy of the proposed model is improved by 13.8%, 6.32% and 4.05% compared to three classification models, namely 2DCNN, Resnet18 and Densenet121, respectively.

The effective combination of the MFF model and the hyperspectral remote sensing of the UAV proposed in this paper can effectively achieve the identification and classification study of ground objects of grassland degradation indicator, providing a new method for monitoring grassland degradation. In the future, different feature extraction methods will be considered for joint feature extraction, and the model parameters will be optimized to further improve the classification performance and computational efficiency of the model, to provide a reference for the management of desert grassland.

ACKNOWLEDGEMENT

The research leading to these results received funding from the National Natural Science Foundation of China under Grant Agreement No. 31660137.

REFERENCES

[1] Briske D.D., Zhao M., Han G., et al., (2015), Strategies to alleviate poverty and grassland degradation in Inner Mongolia: Intensification vs production efficiency of livestock systems. *Journal of Environmental Management*, 152, 177-182.

[2] He Y., Li X., Yang X., et al., (2021), The Estimation of Actual and Potential Carbon Sequestration in Typical Steppe in Xilingol County, Inner Mongolia. *Acta Agrestia Sinica*, 29(10), 2274-2285.
[3] Hsieh T., Kiang J., (2020), Comparison of CNN Algorithms on Hyperspectral Image Classification in Agricultural Lands. *Sensors*, 20(6), 1734.
[4] Jung D., Kim J.D., Kim H., et al., (2022), A Hyperspectral Data 3D Convolutional Neural Network Classification Model for Diagnosis of Gray Mold Disease in Strawberry Leaves. *Frontiers in Plant Science*, 13, 837020.
[5] Liu K., Yang M., Huang S., et al., (2022), Plant Species Classification Based on Hyperspectral Imaging via a Lightweight Convolutional Neural Network Model. *Frontiers in Plant Science*, 13, 855660.
[6] Liu Y., Lu C., (2021), Quantifying Grass Coverage Trends to Identify the Hot Plots of Grassland Degradation in the Tibetan Plateau during 2000-2019. *International Journal of Environmental Research and Public Health*, 18(2), 416.
[7] Pi W., Du J., Bi Y., et al., (2021), 3D-CNN based UAV hyperspectral imagery for grassland degradation indicator ground object classification research. *Ecological Informatics*, 62, 101278.
[8] Pan Z., Wang Z., Han G., et al., (2016), Responses of methane fluxes on warming and nitrogen addition in Stipa breviflora desert steppe. *Ecology and Environmental Sciences*, 25(2), 209-216.
[9] Shenming Q., Xiang L., Zhihua G., (2022), A new hyperspectral image classification method based on spatial-spectral features. *Scientific Reports*, 12(1), 1541.
[10] Szegedy C., Vanhoucke V., Ioffe S., et al., (2016), Rethinking the Inception Architecture for Computer Vision. *2016 IEEE Conference on Computer Vision and Pattern Recognition (CVPR)*, Las Vegas, NV, USA, 2818-2826.
[11] Tang Z., An H., Deng L., et al., (2016), Effect of desertification on productivity in a desert steppe. *Scientific Reports*, 6(1), 27839.
[12] Wang Y., Ren Z., Ma P., et al., (2020), Effects of grassland degradation on ecological stoichiometry of soil ecosystems on the Qinghai-Tibet Plateau. *Science of The Total Environment*, 722, 137910.
[13] Xu H., Yao W., Cheng L., et al., (2021), Multiple Spectral Resolution 3D Convolutional Neural Network for Hyperspectral Image Classification. *Remote Sensing*, 13(7), 1248.
[14] Yang H., Du J., (2021), Classification of desert steppe species based on unmanned aerial vehicle hyperspectral remote sensing and continuum removal vegetation indices. *Optik*, 247, 167877.
[15] Zhang T., Du J., Zhang H., et al., (2022), Research on recognition method of desert steppe rat hole based on unmanned aerial vehicle hyperspectral. *Journal of Optoelectronics·Laser*, 33(02), 120-126.

RESEARCH OF NON-RESONANT OSCILLATIONS OF THE "TELESCOPIC SCREW - FLUID MEDIUM" SYSTEM
/
ДОСЛІДЖЕННЯ НЕРЕЗОНАНСНИХ КОЛИВАНЬ СИСТЕМИ «ТЕЛЕСКОПІЧНИЙ ГВИНТ – СИПКЕ СЕРЕДОВИЩЕ»

Lyashuk O.L. [1)], Hevko I.B. [1)], Hud V.Z. [1)], Tkachenko I.G. [1)], Hevko O.V. [1)], Sokol M.O. [2)], Tson O.P. [1)], Kobelnyk V.R.[1)], Shmatko D.Z. [3)], Stanko A.I. [1)]

[1)]Ternopil Ivan Puluj National Technical University, Ukraine;
[2)]Ternopil Volodymyr Hnatiuk National Pedagogical University, Ukraine;
[3)] Dniprovsk State Technical University, Ukraine
E-mail: oleglashuk@ukr.net
DOI: https://doi.org/10.35633/inmateh-68-49

***Keywords*:** *conveyors, mechanical systems, amplitude, resonance, telescopic screw, bulk medium, dynamic process, torsional vibrations*

ABSTRACT

In the article it is substantiated the value of the angular speeds of rotation of the auger screw, which leads to the breakdown of its lateral vibrations. The dependences describing the law of change of amplitude or natural frequency at slowly variable length of the telescopic screw are deduced. Based on the Van der Paul's method, in the developed system differential equations are obtained that determine the laws of change of amplitude and frequency of the wave process in the system of a telescopic propeller. It is established that for nonresonant oscillations for this system the main parameters of bending oscillations are a continuous flow of bulk medium - the screw does not depend on its small torsional oscillations and external periodic perturbation. The analysis of the given regression equations shows that to reduce the torque of the auger it is necessary to reduce the frequency of its rotation and the angle of the conveyor. The constructive diagram and the results of theoretical calculations for assessing the influence of constructive-kinematic parameters on the torque indicators of the telescopic screw conveyor are presented.

РЕЗЮМЕ

В статті обґрунтовано значення кутових швидкостей обертання гвинта шнека, що призводить до зриву його поперечних коливань. Виведено залежності, які описують закон зміни амплітуди чи власної частоти за повільно змінної довжини телескопічного гвинта. На основі методу Ван-дер-Поля, розробленої системи отримано диференціальних рівняння, які визначають закони зміни амплітуди та частоти хвильового процесу в системі телескопічного гвинта. Встановлено, що для нерезонансних коливань для даної системи основні параметри згинальних коливань є суцільний потік сипкого середовища – гвинт не залежать від малих крутильних його коливань та зовнішнього періодичного збурення. Представлено конструктивну схему результати теоретичних розрахунків для оцінки впливу конструктивно-кінематичних параметрів на показники крутного моменту телескопічного гвинтового транспортера.

INTRODUCTION

In order to achieve the required overloading distance, screw conveyors are made prefabricated, assembled and disassembled from separate parts in manual mode or with the help of hydraulic or pneumatic equipment, which makes their design quite expensive and difficult to operate. To improve the operation of screw conveyors and increase their mobility, it is advisable to use the principle of telescope in their designs. Due to the significant angular velocities of the augers in telescopic screw conveyors (up to 800 rpm and above), the existing inhomogeneous inclusions in the reloading material, the asymmetry of the telescopic screw and external perturbations lead to its oscillations, as well as to significant dynamic loads in the auger (*Rogatynskyi et al., 2019; Rogatynskyi et al., 2014; Hevko et.al., 2019*).

Some papers consider the operation mode of an inclined screw conveyor which has a screw operating element with constant parameters incorporated in it (*Pezo et. al., 2015; Mondal, 2018*). The kinematics of grain loading has been investigated based on the motion equations in a screw conveyor. The analysis of loading movement at constant high-speed mode has been analyzed.

The works of *Chen (2009), Fernandez et al., (2011), Sun et.al., (2017), Tian & Cheng, (2018*), provide research findings on flow patterns of bulk materials depending on constructional and kinematic characteristics of screw operating tools, bunker type and solid particles, as well as frictional forces.

The authors developed and patented a number of designs of screw conveyors with rotary casings and also the directions of screw conveyors operational life increase are described in some papers (*Tripathi, et. al., 2015; Roberts, 2015; Mondal, 2018).* Some research is dedicated to the solving of above-mentioned problems, namely the development of energy-saving designs of screw conveyors and choosing their the most efficient parameters and working modes *(Pylypaka et al., 2018; Rogatynskyi et al., 2019; Pylypaka et al., 2019*).

In other articles the influence of the motion of a continuous flow of a loose or viscous medium on the longitudinal or bending oscillations of elastic bodies is studied (*Sokil and Sokil 2017; Bogolyubov and Mitropolsky 1961; Stotsko et al., 2002; Stotsko et al., 2007*). Studies have shown that even a constant velocity of the bulk or viscous medium changes the basic dynamic characteristics of bending and longitudinal oscillations. The telescopic screw system rotates at a significant angular velocity, which means that even minor transverse deformations at some point in time lead to significant stresses. With the relative movement of the bulk medium along the screw, the mathematical model of bending oscillations qualitatively acquires a new form - the appearance in it of a mixed derivative of linear and temporal variables. The working telescopic propeller is an elastic body that rotates, so due to partial wedging, inhomogeneity of the environment and other reasons, it additionally performs more torsional oscillations.

Therefore, the study of these phenomena in the system telescopic screw is a bulk medium during the movement of bulk material makes it possible to pre-select such modes of operation of the conveyor, which make these processes impossible, and thus increase the service life of the conveyor.

MATERIALS AND METHODS

Based on some research results, the maximum relative linear displacements of the outer points of the screw, due to torsional vibrations, are much less linear displacement due to its bending vibrations. (*Rogatynskyi et al., 2019; Hevko et. al., 2018*). Mathematical models of bending oscillations of the studied system assume that torsional oscillations cause a small amount of periodic action on the bent. The main parameters of this action (primarily frequency) can be determined on the basis of the main characteristics of the screw: its running mass, the moment of inertia, elastic characteristics of the material (*Stotsko et al., 2000*) or by partial processing of experimental data (*Topilnysky et al., 2017; Hevko et.al., 2020*).

In some works, the mathematical model of bending vibrations of an elastic body, which rotates along a fixed axis with a constant angular velocity, provided that a continuous flow of a homogeneous medium of zero rigidity moves along it with a constant relative linear velocity, is the system of differential equations (*Hevko et.al., 2018; Hud, 2019*).

$$\begin{aligned}
&(\rho_1+\rho_2)\frac{\partial^2 u}{\partial t^2}+2\rho_2 V\frac{\partial^2 u}{\partial t\partial z}-2(\rho_1+\rho_2)\Omega\frac{\partial w}{\partial t}+\rho_2 V^2\frac{\partial^2 u}{\partial z^2}-\\
&-2(\rho_1+\rho_2)I\Omega\frac{\partial^3 w}{\partial t\partial z^2}+EI\frac{\partial^4 u}{\partial z^4}-(\rho_1+\rho_2)\Omega^2 u=\varepsilon f\left(u,w,\frac{\partial u}{\partial t},\frac{\partial w}{\partial t},\frac{\partial u}{\partial z},\frac{\partial w}{\partial z},...,\frac{\partial^3 u}{\partial z^3},\frac{\partial^3 w}{\partial z^3},\gamma\right)\\
&(\rho_1+\rho_2)\frac{\partial^2 w}{\partial t^2}+2\rho_2 V\frac{\partial^2 w}{\partial t\partial z}+2(\rho_1+\rho_2)\Omega\frac{\partial u}{\partial t}+\rho_2 V^2\frac{\partial^2 w}{\partial z^2}+\\
&+2(\rho_1+\rho_2)I\Omega\frac{\partial^3 u}{\partial t\partial z^2}+EI\frac{\partial^4 w}{\partial z^4}-(\rho_1+\rho_2)\Omega^2 w=\varepsilon g\left(u,w,\frac{\partial u}{\partial t},\frac{\partial w}{\partial t},\frac{\partial u}{\partial z},\frac{\partial w}{\partial z},...,\frac{\partial^3 u}{\partial z^3},\frac{\partial^3 w}{\partial z^3},\gamma\right),
\end{aligned} \tag{1}$$

Where:

$u(t,z), w(t,z)$ - projections of the vector of movement of the point of the central axis with the coordinate z of the telescopic screw at any time t;

Ω is angular velocity of rotation of the screw around the specified axis,

ρ_1, ρ_2 is respectively, the mass per unit length of the body and the moving medium,

EI is its stiffness to bend the screw (*Hud, 2019*)

$f\left(u,w,\frac{\partial u}{\partial t},\frac{\partial w}{\partial t},\frac{\partial u}{\partial z},\frac{\partial w}{\partial z},...,\frac{\partial^3 u}{\partial z^3},\frac{\partial^3 w}{\partial z^3},\gamma\right)$ and $g\left(u,w,\frac{\partial u}{\partial t},\frac{\partial w}{\partial t},\frac{\partial u}{\partial z},\frac{\partial w}{\partial z},...,\frac{\partial^3 u}{\partial z^3},\frac{\partial^3 w}{\partial z^3},\gamma\right)$ - 2π - periodic for $\gamma=\nu t+\gamma_0$ functions that describe the nonlinear components of the reducing force, resistance force and other forces, the maximum value of which is much smaller than the value of the reducing force, as indicated by a small parameter.

The dynamic process of the auger screw depends not only on the force and kinematic ($\frac{\partial\vartheta(z,t)}{\partial t}$, $\frac{\partial^2\vartheta(z,t)}{\partial t^2}$, Ω, V) factors but also on the method of fastening. In the case of slowly adjustable length and corresponding to the movement of the elastic screw in the bearings, the distance between $l(\tau)$ takes the form *(Hud, 2019)*:

$$u(t,z)\big|_{z=0}=\left.\frac{\partial^2 u}{\partial z^2}\right|_{z=0}=0,\quad w(t,z)\big|_{z=0}=\left.\frac{\partial^2 w}{\partial z^2}\right|_{z=0}=0,$$
$$u(t,z)\big|_{z=l(\tau)}=\left.\frac{\partial^2 u}{\partial z^2}\right|_{z=l(\tau)}=0\ w(t,z)\big|_{z=l(\tau)}=\left.\frac{\partial^2 w}{\partial z^2}\right|_{z=l(\tau)}=0. \tag{2}$$

In the mathematical model, the variable length of the screw, $l(\tau)=l_0+\varepsilon k_1 t$, k_1 is constant. This problem is to describe the main parameters of the bending oscillations of the auger screw, provided that the torsional oscillations are described by the dependence (*Hud, 2019)*:

$$\vartheta(t,z)=h\sin\frac{k\pi}{l(\tau)}z\cos\vartheta,\ \vartheta=(\Theta t+\vartheta_0) \tag{3}$$

where h is their amplitude; $\Theta=\frac{k\pi}{l(\tau)}\sqrt{\frac{GJ_0}{I_0}}$, - frequency; ϑ_0 - initial phase; I_0 - running moment of inertia about the neutral axis of the elastic body together with the medium; J_0 - its equatorial moment of inertia; G - shear modulus.

In this problem, it is believed that the bulk medium that moves along the screw does not change the stiffness of bending and torsion, and torsional vibrations of the screw. The most important from a practical point of view are cases of external and internal resonances. As for the resonance caused by external force factors, they can be caused by periodic action at the points of imperfect fixation or the interaction of the telescopic screw and the casing, and others. Restrictions on the amplitude of torsional oscillations of the considered dynamic system, the continuous flow of the medium-elastic screw, allow to build the solution of the boundary value problem Eq. 2, provided Eq. 3 to use the basic ideas of asymptotic methods of nonlinear mechanics to construct a solution of the undisturbed analogue of Eq. 1. (*Lyashuk et al., 2018; Hud, 2019; Hevko et al., 2019*).

$$\begin{aligned}&(\rho_1+\rho_2)\frac{\partial^2 u_0}{\partial t^2}-2(\rho_1+\rho_2)\Omega\frac{\partial w_0}{\partial t}+\rho_2 V^2\frac{\partial^2 u_0}{\partial z^2}-2(\rho_1+\rho_2)I\Omega\frac{\partial^3 w_0}{\partial t\partial z^2}+\\&+EI\frac{\partial^4 u_0}{\partial z^4}-(\rho_1+\rho_2)\Omega^2 u_0=0,\\&(\rho_1+\rho_2)\frac{\partial^2 w_0}{\partial t^2}+2(\rho_1+\rho_2)\Omega\frac{\partial u_0}{\partial t}+\rho_2 V^2\frac{\partial^2 w_0}{\partial z^2}+2(\rho_1+\rho_2)I\Omega\frac{\partial^3 u_0}{\partial t\partial z^2}+\\&+EI\frac{\partial^4 w_0}{\partial z^4}-(\rho_1+\rho_2)\Omega^2 w_0=0\end{aligned} \tag{4}$$

under boundary conditions:

$$u_0(t,z)\big|_{z=j}=\left.\frac{\partial^2 u_0}{\partial z^2}\right|_{z=0}=0,\quad w_0(t,z)\big|_{z=l}=\left.\frac{\partial^2 w_0}{\partial z^2}\right|_{z=l}=0 \tag{5}$$

In order to determine the natural frequency of bending oscillations of the body as a function of the angular and linear velocity of the medium along the elastic body in the form *(Hevko et al., 2020)*

$$\omega_k = \Omega\left(I\kappa_k - 1\right) \pm \kappa_k \sqrt{\Omega^2 I\left(\kappa_k^2 I - 2\right) - \frac{\rho_2 V^2 - EI\kappa_k^2}{\rho_1 + \rho_2}} \tag{6}$$

The obtained ratio makes it possible to determine the influence of nonlinear forces on the dynamic process, as well as the whole set of external and internal factors on the bending oscillations of the auger. Among the analytical methods for studying linear oscillatory systems with concentrated masses, the most convenient for their practical use is the combination of the Bubnov-Galerkin method (*Rogatynskyi et al., 2019*) and Van der Pol (*Lyashuk et al., 2018*) and KBM (Krylov-Bogoliubov-Myitropolskyi) (*Lyashuk et al., 2018; Hevko et al., 2015; Hud et al., 2020*). To solve this problem, the basic idea of the first methods will be extended to the basic system of Eq. 1 under boundary conditions Eq. 2 Based on the Bubnov - Galerkin method and the principle of oscillation frequency in nonlinear systems, for the solution of the perturbed (nonlinear) boundary value problem Eq. 1, Eq. 2 in a form close to the "k" form of dynamic equilibrium, assume that for the perturbed case the parameters h and φ be functions of time:

$$\begin{aligned} u(t,z) &= h(t)(\cos(\kappa z + \omega t + \psi(t)) - \cos(\kappa z - \omega t - \varphi(t)), \\ w(t,z) &= h(t)(\sin(\kappa z + \omega t + \psi(t)) + \sin(\kappa z - \omega t - \varphi(t)). \end{aligned} \tag{7}$$

For complex nonlinear oscillations of the auger, more precisely for their bending component it is obtained:

$$\begin{aligned} \frac{\partial u(t,z)}{\partial t} &= -h(\omega + \frac{d\varphi}{dt})(\sin(\kappa z + \omega t + \varphi) + \sin(\kappa z - \omega t - \varphi)) + \\ &+ \frac{dh}{dt}(\cos(\kappa z + \omega t + \varphi) - \cos(\kappa z - \omega t - \varphi)), \\ \frac{\partial w(t,z)}{\partial t} &= h(\omega + \frac{d\varphi}{dt})(\cos(\kappa z + \omega t + \varphi) - \cos(\kappa z - \omega t - \varphi)) + \\ &+ \frac{dh}{dt}(\sin(\kappa z + \omega t + \varphi) + \sin(\kappa z - \omega t - \varphi)) \end{aligned}, \tag{8}$$

where the index k indicates the form of dynamic equilibrium.

According to the main idea of the Van der Paul's method, dependencies that relate the derivatives of the desired functions are obtained:

$$\begin{aligned} -h\frac{d\varphi}{dt}(\sin(\kappa z + \omega t + \varphi) + \sin(\kappa z - \omega t - \varphi)) + \frac{dh}{dt}(\cos(\kappa z + \omega t + \varphi) - \cos(\kappa z - \omega t - \varphi)) = 0, \\ h\frac{d\varphi}{dt}(\cos(\kappa z + \omega t + \varphi) - \cos(\kappa z - \omega t - \varphi) + \frac{dh}{dt}(\sin(\kappa z + \omega t + \varphi) + \sin(\kappa z - \omega t - \varphi)) = 0. \end{aligned} \tag{9}$$

Therefore, by differentiating the dependencies of Eq. 9, taking into account the derivatives of the desired functions, we are get:

$$\begin{aligned} \frac{\partial^2 u(t,z)}{\partial t^2} &= -\frac{dh}{dt}\omega(\sin(\kappa z + \omega t + \varphi) + \sin(\kappa z - \omega t - \varphi)) + \\ &+ h\omega(\frac{d\varphi}{dt} + \omega)(\cos(\kappa z + \omega t + \varphi) - \cos(\kappa z - \omega t - \varphi)), \\ \frac{\partial^2 w(t,z)}{\partial t^2} &= \frac{dh}{dt}\omega(\cos(\kappa z + \omega t + \varphi) - \cos(\kappa z - \omega t - \varphi)) - \\ &- h\omega(\frac{d\varphi}{dt} + \omega)(\sin(\kappa z + \omega t + \varphi) + \sin(\kappa z - \omega t - \varphi)). \end{aligned} \tag{10}$$

The obtained dependences in the base are substituted into the system of differential equations Eq. 1 taking into account Eq. 3, it is obtained:

$$\begin{aligned} -\frac{dh}{dt}\omega(\sin(kz + \omega t + \varphi) + \sin(kz - \omega t - \varphi)) + h\omega\frac{d\varphi}{dt}(\cos(kz + \omega t + \varphi) - \cos(kz - \omega t - \varphi)) = \varepsilon\tilde{f}(h, x, \psi, \vartheta), \\ -h\frac{d\varphi}{dt}(\sin(\kappa z + \omega t + \varphi) + \sin(\kappa z - \omega t - \varphi)) + \frac{dh}{dt}(\cos(\kappa z + \omega t + \varphi) - \cos(\kappa z - \omega t - \varphi)) = 0, \end{aligned} \tag{11}$$

$$\frac{dh}{dt}\omega(\cos(\kappa z+\omega t+\varphi)-\cos(\kappa z-\omega t-\varphi))-h\omega\frac{d\varphi}{dt}(\sin(\kappa z+\omega t+\varphi)+\sin(\kappa z-\omega t-\varphi))=\varepsilon\tilde{g}(a,z,\psi,\gamma,\vartheta).$$

where $\varepsilon\tilde{f}(h,x,\psi,\gamma,\vartheta),\varepsilon\tilde{g}(h,z,\psi,\gamma,\vartheta)$ - correspond to the values according to the function:

$$f_1\left(u,w,\frac{\partial u}{\partial t},...,\frac{\partial^3 w}{\partial z^3},\gamma\right)+2(\rho_1+\rho_2)\frac{\partial\vartheta(z,t)}{\partial t}\frac{\partial w}{\partial t}+2(\rho_1+\rho_2)I\frac{\partial\vartheta(z,t)}{\partial t}\frac{\partial^3 w}{\partial t\partial z^2}+2(\rho_1+\rho_2)\Omega\frac{\partial\vartheta(z,t)}{\partial t}u+(\rho_1+\rho_2)\frac{\partial^2\vartheta(z,t)}{\partial t^2}w$$

$$f_2\left(u,w,\frac{\partial u}{\partial t},...,\frac{\partial^3 w}{\partial z^3},\gamma\right)-2(\rho_1+\rho_2)\frac{\partial\vartheta(z,t)}{\partial t}\frac{\partial u}{\partial t}-2(\rho_1+\rho_2)I\frac{\partial\vartheta(z,t)}{\partial t}\frac{\partial^3 u}{\partial t\partial z^2}-2(\rho_1+\rho_2)\Omega\frac{\partial\vartheta(z,t)}{\partial t}w(\rho_1+\rho_2)\frac{\partial^2\vartheta(z,t)}{\partial t^2}u \quad (12)$$

where, $u(t,z)$, $w(t,z)$, $\vartheta(t,z)$ functions are described by relations Eq. 3, Eq. 8.

If the right-hand side of the basic system of differential equations satisfies the specified condition, then this relation takes the form:

$$\begin{aligned}&\int_0^l\int_0^{2\pi}\tilde{f}(h,z,\psi,\gamma,\vartheta)(\sin(\kappa z+\psi)+\sin(\kappa z-\psi,\gamma,\vartheta))dzd\psi=\\&=\int_0^l\int_0^{2\pi}\tilde{g}(h,z,\psi,\gamma,\vartheta)(\cos(\kappa z+\psi)-\cos(\kappa z-\psi)dzd\psi,\\&\int_0^l\int_0^{2\pi}\tilde{f}(h,z,\psi,\gamma,\vartheta)(\cos(\kappa z+\psi,\gamma,\vartheta)-\cos(\kappa z-\psi,\gamma,\vartheta)dzd\psi=\\&=\int_0^l\int_0^{2\pi}\tilde{g}(h,z,\psi,\gamma,\vartheta)(\sin(\kappa z+\psi)+\sin(\kappa z-\psi))dzd\psi,\end{aligned} \quad (13)$$

The obtained system of differential equations Eq. 12 with conditions that follow from the main idea of the Van der Paul's method, allows determining the laws of change of amplitude and frequency of the wave process *(Hevko et al., 2020)*:

$$\begin{aligned}\frac{dh}{dt}&=-\frac{1}{2\pi\omega l(\rho_1+\rho_2)}\int_0^l\int_0^{2\pi}\tilde{f}(h,z,\psi,\gamma,\vartheta)(\cos(\kappa z+\psi)-\cos(\kappa z-\psi))d\psi dz,\\\frac{d\theta}{dt}&=\omega+\frac{1}{2h\pi\omega l(\rho_1+\rho_2)}\int_0^l\int_0^{2\pi}\tilde{f}(h,z,\psi,\gamma,\vartheta)(\sin(\kappa z+\psi)+\sin(\kappa z-\psi))d\psi dz,.\end{aligned} \quad (14)$$

In the system of differential equations Eq. 14 the subintegral functions, and the right parts are periodic by arguments ψ,γ,ϑ, which can have non-resonant and resonant oscillations in the screw auger. Based on this, non-resonant oscillations of the amplitude and frequency of bending oscillations of the telescopic auger are described by the dependences *(Hevko et al., 2020)*:

$$\begin{aligned}\frac{da}{dt}&=\frac{-\varepsilon}{8\omega\pi^2 l}\int_0^l\int_0^{2\pi}\int_0^{2\pi}\int_0^{2\pi}\tilde{f}(h,z,\psi,\gamma,\vartheta)\sin\frac{\pi}{l}z\cos\psi dzd\psi d\gamma d\vartheta,\\\frac{d\psi_1}{dt}&=\omega-\frac{\varepsilon}{8\omega\pi^2 hl}\int_0^l\int_0^{2\pi}\int_0^{2\pi}\int_0^{2\pi}\tilde{f}(h,z,\psi,\gamma,\vartheta)\sin\frac{\pi}{l}z\sin\psi dzd\psi d\gamma d\vartheta\end{aligned} \quad (15)$$

Thus, with 2π periodicity in the phase of forced vibrations and the phase of torsional vibrations of the auger screw of subintegral functions it follows that for non-resonant oscillations the system is considered where the main parameters of bending oscillations of the system are continuous flow of bulk medium. However, the amplitude of these vibrations depends on the elastic characteristics of the screw material, which affect the natural frequency, viscoelastic friction forces, the method of fastening, but also on the angular velocity of its rotation.

For different angular velocities of the screw rotation, the time variation of the amplitude of damped oscillations is presented, provided that the elastic properties of the material of the auger screw satisfy the nonlinear technical law of elasticity, and the viscous friction force is proportional to the speed in the degree of motion of the points.

In this case, differential equations Eq. 15 are transformed to the form:

$$\frac{dh}{dt}=-\frac{k_1(\omega)^{s-1}}{(\rho_1+\rho_2)\pi}h^s;\quad \frac{d\psi}{dt}=\omega-\frac{\bar{k}_1 EI}{(\rho_1+\rho_2)}h^2-(\frac{\pi}{l})^2\frac{\rho_2}{8\omega(\rho_1+\rho_2)}V^2. \quad (16)$$

RESULTS AND DISCUSSION

In fig. 1 and fig. 2, for different values of the parameters of the system "telescopic screw as a bulk medium" is shown the change in time of the amplitude and frequency of the damping oscillations of the screw.

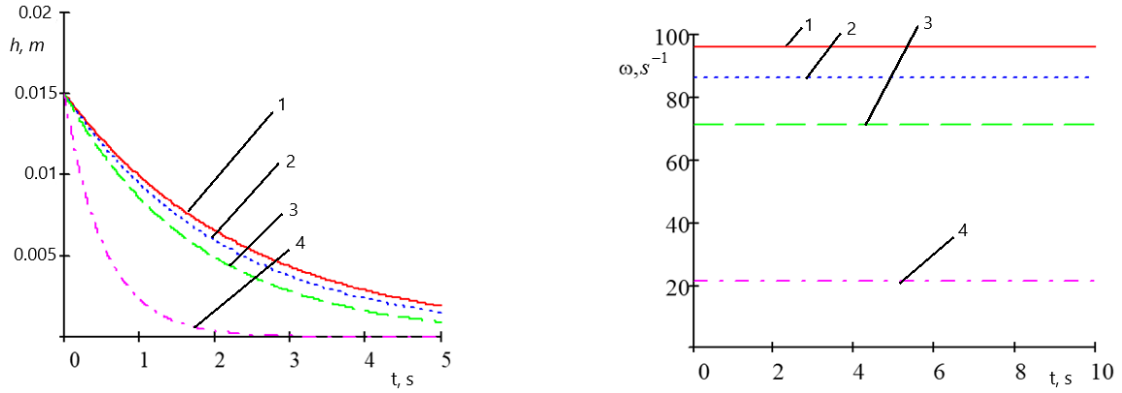

a) 1– $\Omega_1 = 0 rad/s$; 2– $\Omega = 10 rad/s$; 3 – $\Omega = 25 rad/s$; 4– $\Omega = 75 rad/s$

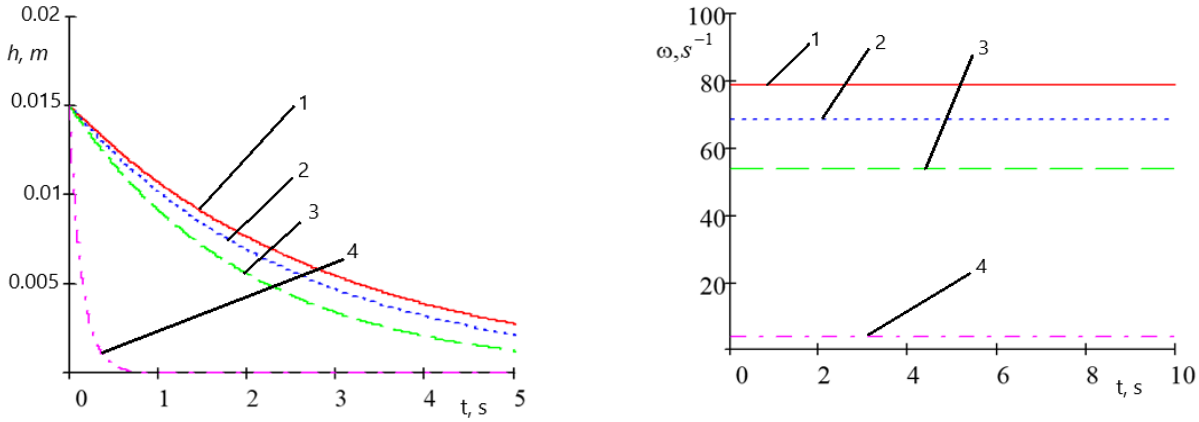

b) 1 – $\Omega_1 = 0 rad/s$; 2– $\Omega = 10 rad/s$; 3– $\Omega = 25 rad/s$; 4– $\Omega = 75 rad/s$

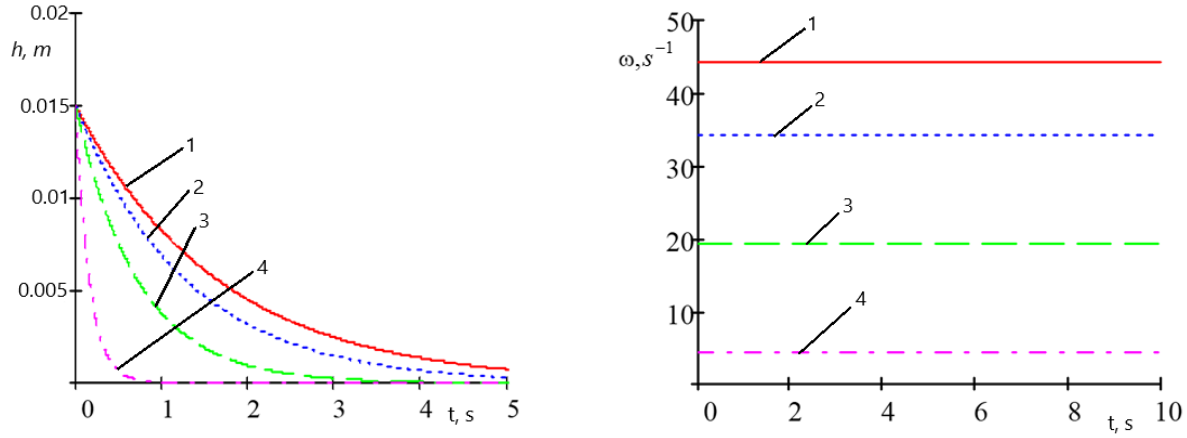

c) 1 – $\Omega_1 = 0 rad/s$; 2– $\Omega = 10 rad/s$; 3– $\Omega = 25 rad/s$; 4– $\Omega = 40 rad/s$

c) ------- $\Omega_1 = 0 s^{-1}$; ····· $\Omega = 10 s^{-1}$; – – – – – $\Omega = 25 s^{-1}$; –·–·– $\Omega = 40 s^{-1}$

Fig. 1 - Laws of change of amplitude of damped oscillations and natural frequency of the telescopic screw without environment ($\rho_2 = 0$ kg/m) at various angular speeds of its rotation at $I = 6 \cdot 10^{-6}$ kg m²;

$E = 2,06 \cdot 10^{11}$ N/ m²: *a) l = 6 m; $\rho_1 = 10$ kg / m; б) l = 6 m; $\rho_1 = 15$ kg / m; в) l = 8 m; $\rho_1 = 15$ kg / m*

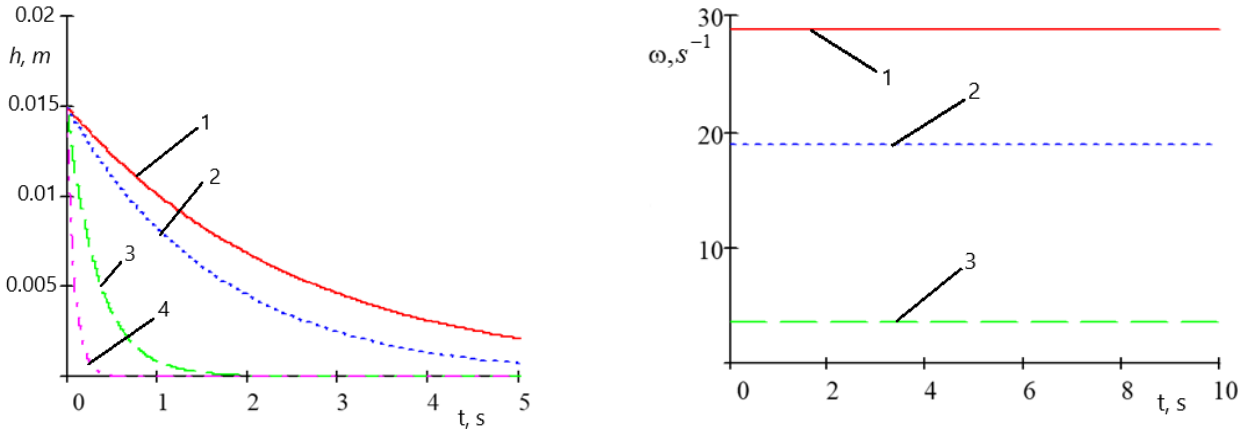

a) $1-\Omega_1 = 0 rad/s;\ 2-\ \Omega = 10 rad/s;\ 3-\ \Omega = 25 rad/s;\ 4-\Omega = 28 rad/s$

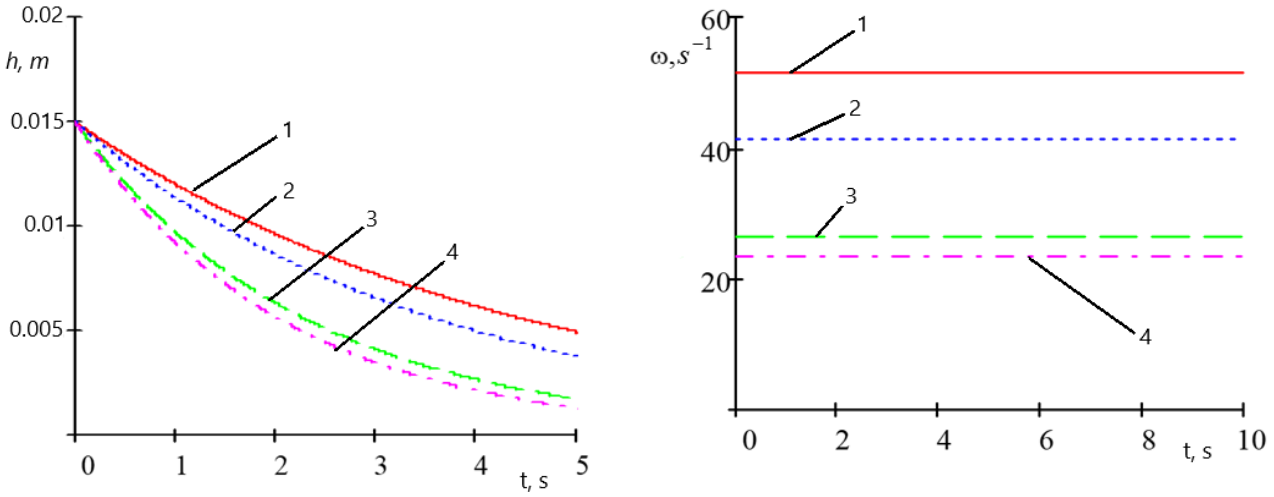

b) $1-\ \Omega_1 = 0 rad/s;\ 2-\Omega = 10 rad/s;\ 3-\ \Omega = 25 rad/s;\ 4-\Omega = 28 rad/s$

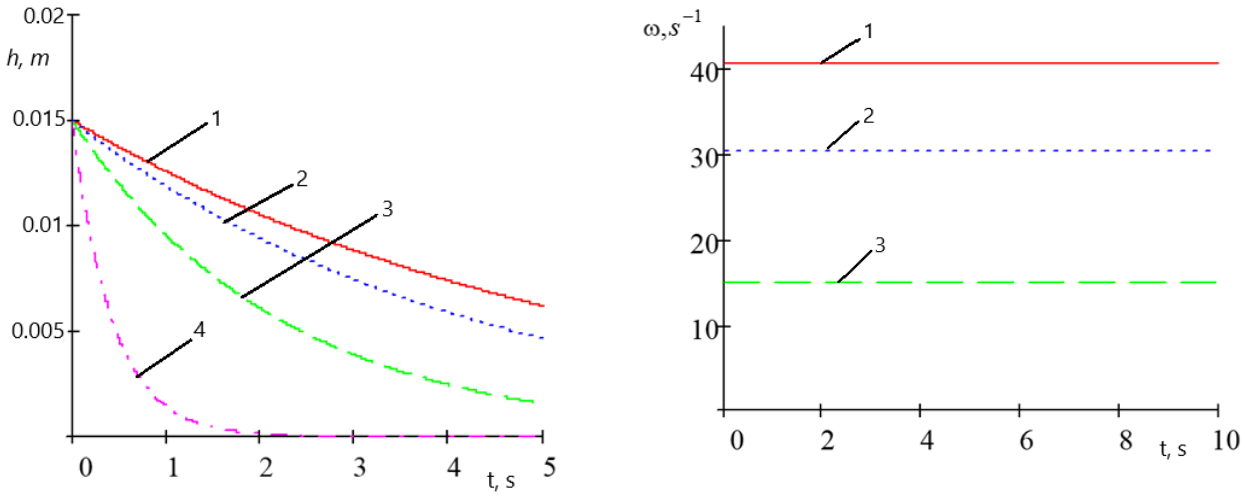

c) $1-\Omega_1 = 0 rad/s;\ 2-\Omega = 10 rad/s;\ 3-\Omega = 25 rad/s;\ 4-\Omega = 38 rad/s$

Fig. 2 – Laws of change of amplitude of damped oscillations and natural frequency of the telescopic screw at different angular velocities of its rotation and different quantities of relative motion of the medium at

ρ_1 =15 kg/m; $I = 6 \cdot 10^{-6}$ kg m ²; V = 5 m/s; $E = 2.06 \cdot 10^{11}$ N/m²*:*

a) ρ_2 =20 kg/m*; l* = 8 m*; b)* ρ_2 =20 kg / m*; l* =6 m*; c)* ρ_2 = 40 kg/m*; l* =6 m

In fig. 1 and fig. 2, it can be seen that the failure of oscillations occurs at Ω = 100 rad/s (Fig. 1.a), Ω= 80 rad/s (Fig. 1.b) and Ω = 45 rad/s (Fig. 1.c); Ω = 30 rad/s (Fig. 2.a), Ω = 55 rad/s (Fig. 2.b) and Ω = 40 rad/s (Fig. 2.c). It is established that at certain values of angular velocities of the auger screw the failure of its transverse oscillations occurs for larger values of running mass of the propeller.

The obtained results reflect the dynamic processes in the screw under the condition of slowly changing its length. The obtained dependence Eq.16 describes the law of change of amplitude or natural frequency at slowly variable length of the telescopic screw. Figure 3 shows the laws of change of these parameters for a telescopic propeller without a bulk medium, and in Fig. 4 with bulk medium.

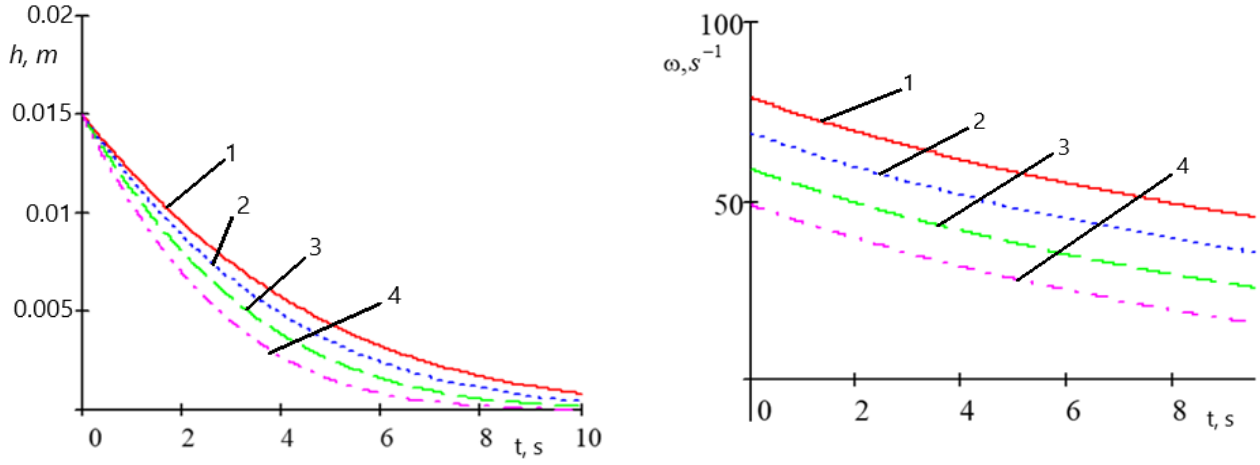

a) $1-\Omega_1=0\,\text{rad/s};\ 2-\Omega=10\,\text{rad/s};\ 3-\Omega=25\,\text{rad/s};\ 4-\Omega=30\,\text{rad/s}$

Fig. 3 – Change of amplitude-frequency characteristic of the telescopic screw at slowly variable length

at: $\rho_1=15$ kg/m; $\rho_2=0$ kg/m; $I=6\cdot10^{-6}$ kg·m²; $E=2.06\cdot10^{11}$ N/m²; v = 5 m/s; l = 6 + 0.2t

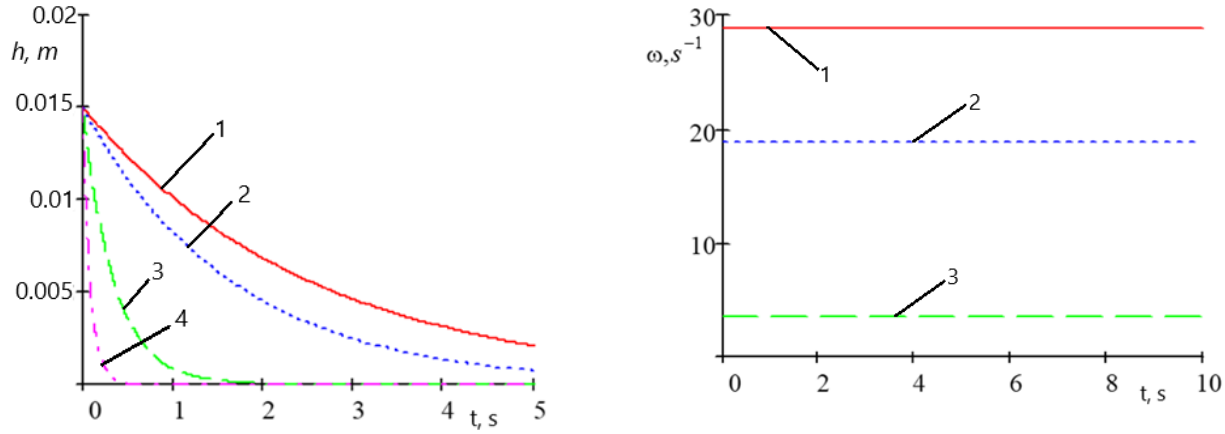

a) $1-\ \Omega_1=0rad/s;\ 2-\Omega=10rad/s;\ 3-\Omega=20rad/s;\ 4-\Omega=30rad/s$

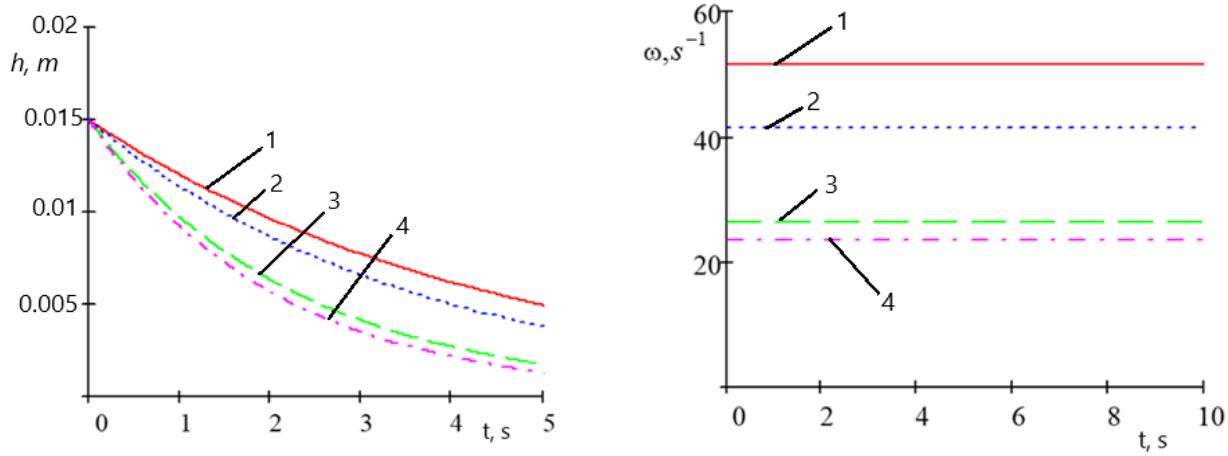

b) $1-\ \Omega_1=0rad/s;\ 2-\Omega=10rad/s;\ 3-\Omega=20rad/s;\ 4-\Omega=30rad/s$

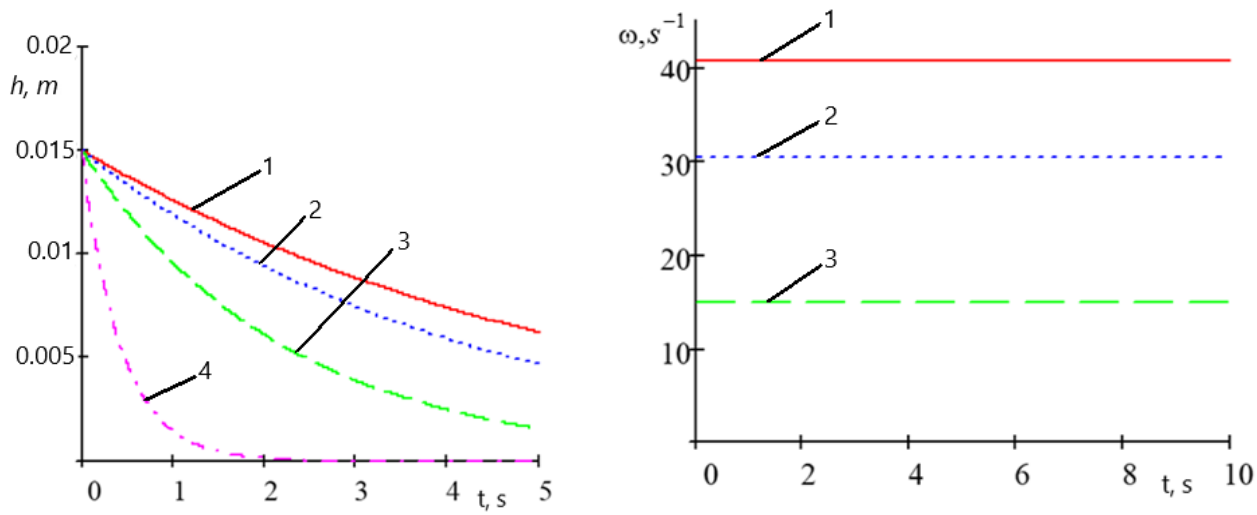

c) $1-\Omega_1=0 rad/s;\ 2-\Omega=10 rad/s;\ 3-\Omega=20 rad/s;\ 4-\Omega=30 rad/s$

Fig. 4 – Change of amplitude-frequency characteristic of the system "telescopic screw as a bulk medium" at different quantities of movement of the last and variable length of the screw at $\rho_1=15$ kg/m; l = 6 + 0.2t;

V=5 m/s; $I=6\cdot10^{-6}$ kg·m ²; $E=2.06\cdot10^{11}$ N/m²: *а)* ρ_2 =15 kg/m; *б)* ρ_2 =20 kg/m; *в)* ρ_2 =30 kg/m

The presented graphical dependences show that with the elongation of the telescopic screw the frequency of its oscillations decreases over time, and the main results obtained for the case of its constant length can be used for the case of slowly variable length. However, from a theoretical point of view, it is also important to study the system in the so-called resonance zone, or more precisely when passing the resonance.

To confirm the theoretical assumptions, an experimental setup was designed and manufactured, which is shown in Fig. 5 (*Hud et. al., 2019*).

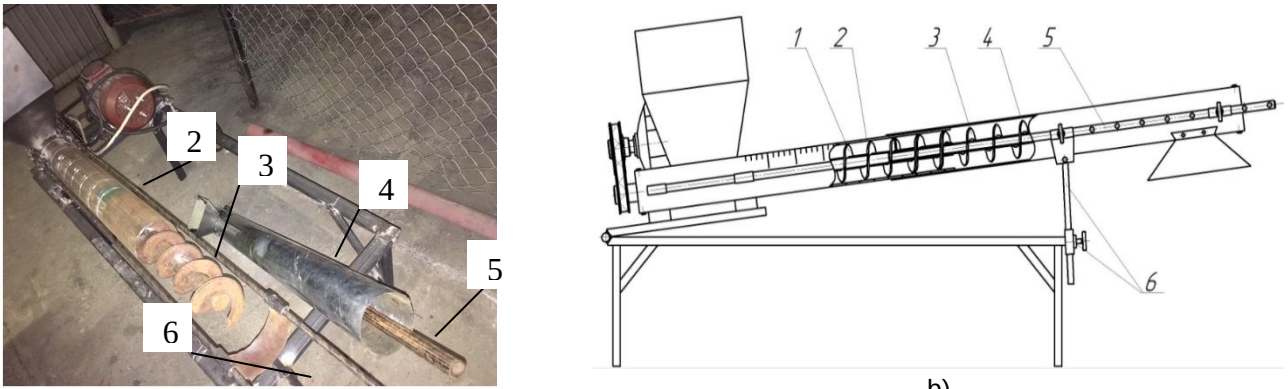

a) b)

Fig. 5 – Stand to study the characteristics of telescopic screw conveyors: a) general view; b) structural scheme

1) screw axial motion in the axial direction of the screw section; 2) part of the casing is fixed in the axial direction; 3) screw moving in the axial direction of the screw section; 4) part of the casing moving in the axial direction; 5) guides; 6) support for adjusting the height of the material

In the experimental setup, the outer diameter of the auger is 97 mm; inner diameter of the fixed branch pipe - 100 mm; external - 107 mm; the inner diameter of the movable pipe is 109 mm. The movable pipe is made of galvanized sheet, and therefore it contains a connecting seam and ovals and irregularities along the entire length, which affected the speed of twisting and untwisting of the telescopic part of the screw conveyor.

To determine the influence of structural and kinematic parameters (auger speed, auger elongation length and angle of the conveyor) on the torque of the auger drive during transportation of corn, wheat and feed, full-factor experiments were performed and regression equations were derived:

- during transportation of corn:

$$T_{(n_s,l,\gamma_1)} = -12.91 + 1.18 \cdot 10^{-2} n_s + 17.33l + 3.8 \cdot 10^{-2} \gamma_1 - 4.46 \cdot 10^{-3} n_s l + \\ + 2.9 \cdot 10^{-6} n_s^2 - 1.73l^2 - 4.6 \cdot 10^{-4} \gamma_1^2; \quad (17)$$

- during transportation of wheat:

$$T_{(n_s,l,\gamma)} = -13.59 + 1.23 \cdot 10^{-2} n_s + 18.77l + 3.99 \cdot 10^{-2} \gamma_1 - 4.68 \cdot 10^{-3} n_s l + \\ + 3.05 \cdot 10^{-6} n_s^2 - 1.84l^2 - 4.83 \cdot 10^{-4} \gamma_1^2; \quad (18)$$

- during transportation of compound feed:

$$T_{(n_s,l,\gamma)} = -11.53 + 1.05 \cdot 10^{-2} n_s + 15.95l + 3.412 \cdot 10^{-2} \gamma_1 - 4 \cdot 10^{-3} n_s l + \\ + 2.63 \cdot 10^{-6} n_s^2 - 1.53l^2 - 4.12 \cdot 10^{-4} \gamma_1^2. \quad (19)$$

The analysis of the given regression equations shows that to reduce the torque of the auger it is necessary to reduce the frequency of its rotation and the angle of the conveyor. Based on the regression equations Eq. 17-19, the graphical dependences of the torque value are constructed, which are shown in Fig. 6.

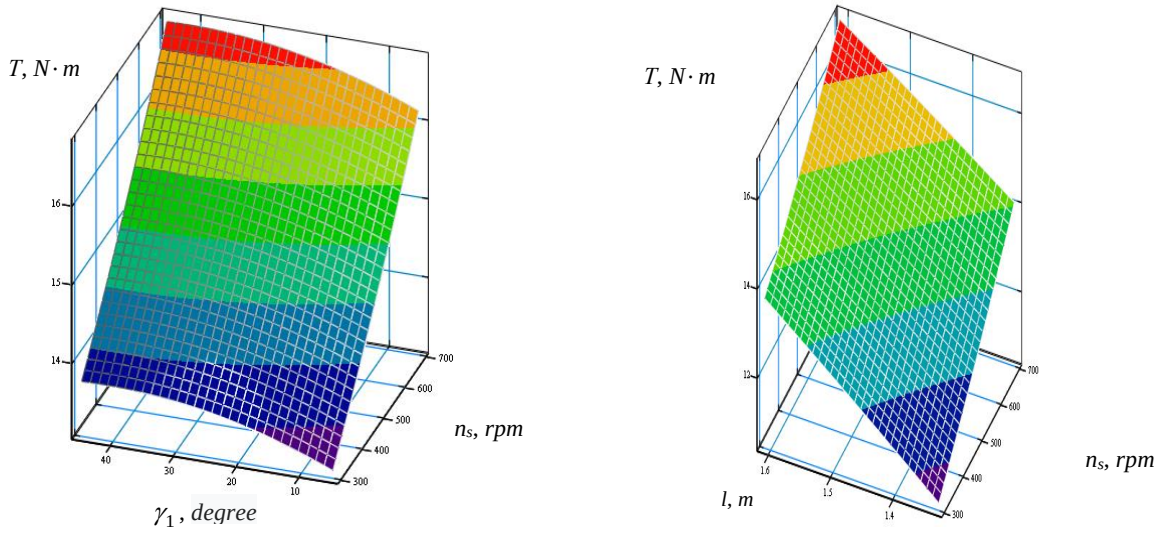

Fig. 6 – Response surface (a, b) dependence of the torque on the drive of the telescopic screw conveyor during corn overload from: a) $T = f(n_s;\gamma_1)$ at $l = 1.61$ m; b) $T = f(n_s;l)$ at $\gamma_1 = 45$ degrees

From (fig. 6) the analysis of the given regression equations shows that to reduce the torque of the auger it is necessary to reduce the frequency of its rotation and the angle of the conveyor. It is experimentally established that the biggest problem in telescopic screw conveyors is to maintain the same gap between the casing and the spiral in different sections of the telescope, which significantly affects the rolling of the movable part of the auger on the stationary and the appearance and magnitude of torsional and bending vibrations.

CONCLUSIONS

It has been established that at certain values of the angular velocities of rotation of the auger screw, its transverse oscillations are disrupted: for large values of the linear mass of the screw or medium, the disruption of oscillations takes place at lower angular velocities; for auger screws of large lengths, the breakdown of oscillations takes place at lower angular speeds of rotation. Dependences are derived that describe the law of variation of the amplitude or natural frequency for a slowly variable length of the telescopic screw. It was found that with lengthening of the telescopic screw the frequency of its oscillations comes with time, and the main results obtained for the case of its constant length can be used for the case of slowly variable length.

It is seen that with increasing auger speed, auger elongation length and conveyor angle, the torque on the auger drive increases and the maximum torque of 17.51 N.m is reached during wheat transportation. The

maximum torque on the drive of the telescopic screw conveyor, auger for transportation of corn and compound feed is 16.75 N.m and 15.02 N.m, respectively, and the minimum - 9.94 N.m and 8.93 N.m. Increasing the speed of the auger n_s, from 300 rpm up to 700 rpm leads to an increase in torque on the auger drive to 35%. The increase in the angle of the conveyor from 5 to 45 degrees gives an increase in torque to 4.1%, and increasing the length of the elongation of the auger from 1.33 to 1.61 m leads to an increase in torque by 24.4%.

REFERENCES

[1] Bogolyubov N.N., Mitropolsky Yu. A., (1961), Asymptotic methods in the theory of nonlinear oscillations, *Gordon and Breach,* New York / USA.

[2] Chen L.Q., (2009), Nonlinear parametric vibration of axially moving beams: asymptotic analysis and differential quadrature verification. *Journal of Physics: Conference*, series 181, pp.1–8, DOI:10.1088/1742-6596/181/1/012008.

[3] Fernandez J. W., Cleary P. W., Mcbride W., (2011), Effect of screw design on hopper draw dawn by a horizontal screw feeder. In *Seventh International Conference on CFD in the Mineral sand Process Industries CSIRO*, 9–11 December, pp. 1–6, Melbourne /Australia.

[4] Hevko B., Lyashuk O., Sokil M., Skyba O., Marunych O., Shmatko D.,(2018), Dynamics of auger working body of a multifunctional conveyor, *Bulletin of the Karaganda University: Series Mathematics*, vol. 89, no.1, pp. 105-113, Karaganda / Kazakhstan.

[5] Hevko B.M., Hevko R.B., Klendii O.M., Buriak M.V., Dzyadykevych Y.V., Rozum R.I., (2018), Improvement of machine safety devices, *Acta Polytechnica, Journal of Advanced Engineering*, Vol.58, no.1, pp. 17-25, ISSN 1210-2709, Praha / Czech Republic.

[6] Hevko I., Lyashuk O., Sokil M., Slobodian L., Hud V., Vovk Yu., (2019), Resonant oscillation of vertical working part of conveyer-loader, *Bulletin of the Karaganda University: Series Physics*, vol. 94, no. 2, pp.73–81, ISSN / EISSN 2518-7198 / 2518-7198, Karaganda / Kazakhstan.

[7] Hevko I.B., Dyachun A.Ye., Hud V.Z., Rohatynska L.R., Klendiy V.M., (2015), Investigation of the stability of the torsorial vibrations of a screw conveyer under the influence of pulse forces, *INMATEH - Agricultural Engineering*, vol. 45, no.1, pp.77-86, ISSN 2068 – 2239, Bucharest / Romania.

[8] Hevko I.B., Hud V.Z., Rohatynsky R.M., Lyashuk O.L., Pik A.I., Huryk O.Y., (2020), The research of the resonant oscillations of the system telescopic screw is a bulk environment caused by external periodic forces, *INMATEH - Agricultural Engineering*, vol. 60, no 1, P. 29-39, ISSN 2068 – 2239, Bucharest / Romania.

[9] Hevko, R.B., Zalutskyi S.Z., Hladyo Y.B., Tkachenko I.G., Lyashuk O.L., Pavlova O.M., Pohrishchuk B.V., Trokhaniak O.M., Dobizha N.V., (2019), Determination of interaction parameters and grain material flow motion on screw conveyor elastic section surface, *INMATEH - Agricultural Engineering*, vol. 57, no.1, pp. 123-134, ISSN 2068 – 2239, Bucharest / Romania.

[10] Hud V., Hevko I., Lyashuk O., Hevko O., Sokil M., Shust I., (2020), Research of resonance vibrations of the system «Telescopic screw — bulk medium» caused by torsional vibrations. *Bulletin of the Karaganda University. Series Physics*, vol. 98, no. 2, pp. 119–126, ISSN / EISSN 2518-7198 / 2518-7198, Karaganda / Kazakhstan.

[11] Lyashuk O., Sokil M., Vovk Y., Gupka A., Marunych O., (2018), Torsional oscillations of an auger multifunctional conveyor's screw working body with consideration of the dynamics of a processed medium continuous flow. *Ukrainian Food Journal*, vol. 7, no. 3, pp. 499–510, Kyiv / Ukraine.

[12] Lyashuk O.L., Sokil M.B., Klendiy V.M., Skyba O.P., Slobodian L.M., (2018), Mathematical model of bending vibrations of a horizontal feeder-mixer along the flow of grain mixture, *INMATEH - Agricultural Engineering*, vol. 55, no.2, pp.33-42, ISSN 2068 – 2239, Bucharest / Romania.

[13] Mondal D., (2018), Study on filling factor of short length screw conveyor with flood-feeding condition. *Mater. Today Proc.*, vol.5, pp.1286–1291, ISSN 1359-6454, London / United Kingdom.

[14] Pezo L., Jovanovic A., Pezo M., Colovic R., (2015), Modified screw conveyor-mixers – discrete Element modelling approach, *Advanced Powder Technology*, vol. 26, pp. 1391–1399, ISSN 0921-8831, Netherlands.

[15] Pylypaka S., Klendii M., Kremets T., Klendii O., (2018), Particle motion over the surface of a cylinder, which performs translational oscillations in a vertical plane. *Engineering Journal*, vol. 22, no. 3, pp. 83–92, ISSN 0125 - 8281, Bangkok / Thailand.

[16] Pylypaka S.F., Nesvidomin V.M., Klendii M.B., Rogovskii I.L., Kresan T.A., Trokhaniak V.I., (2019), Conveyance of a particle by a vertical screw, which is limited by a coaxial fixed cylinder, *Bulletin of the Karaganda University. «Mathematics» series*, vol. 95, no. 3, pp.129-139, ISSN / EISSN 2518-7198 / 2518-7198, Karaganda / Kazakhstan.

[17] Roberts A.W., (2015), Bulk solids: Optimizing screw conveyors, *Chemical Engineering*, vol. 122, no.2, pp. 62-67, Praha / Czech Republic.

[18] Rogatynskyi R.M., Hevko I.B., Liashuk A.L., Hud V.Z., Diachun A.E., Melnychuk A.L., Slobodyan L.M., (2019), Prospective screw conveyors: structures, calculation, research, *TNTU*, 212 pp, Ternopil / Ukraine.

[19] Rogatynskyi R. M., Hevko I. B., Diachun A. E., (2014), Scientific and Applied Fundamentals for Creation of Screw Transport and Technological Mechanisms, Ternopil, 280 pp, Ternopil / Ukraine.

[20] Sokil B.I., Sokil M.B., (2017), Forced oscillations of flexible tubular bodies, along which a continuous flow of medium moves, *Bulletin of the National University "Lviv Polytechnic" Dynamics, strength and design of machines and instruments*, vol.866, pp.60-65, Lviv / Ukraine.

[21] Stotsko Z, Sokil B, Topilnytskyi V. (2002), Effect of structural and kinematic parameters of vibration machines on the increase in intensity of volume processing, *All-Ukrainian Scientific and Technical Journal of Vibration in Engineering and Technology*, vol. 4, 25, pp.46-52.

[22] Stotsko Z, Sokil B, Topilnytskyj V. (2007), Complex mathematical model and optimization of vibration volumetric treatment for surfaces of machine parts, *Journal of Achievements in Materials and Manufacturing Engineering*, vol. 24, pp. 283-290.

[23] Stotsko Z, Sokil B, Topilnytskyj V. (2000), Nonlinear parametric model of machine masses, vibrations, volume vibrations and vibrations. *Kwartalnik Naukowo – Techniczny Maszyny dzwigowo – transportowe*, vol. 3, pp. 50-62.

[24] Sun X.X., Meng W.J., Yuan Y., (2017), Design method of a vertical screw conveyor based on TaylorCouette-Poiseuille stable helical vortex, *Advances in mechanical engineering*, vol.9, no.7.

[25] Tian Y., Cheng Q. and others, (2018), Research on the Principle of a New Flexible Screw Conveyor and Its Power Consumption, *Applied Sciences*, vol. 8 no 7.

[26] Topilnysky V, Rebot D, Sokil M, Velyca O, Liaskovska S, Verkhola I, Kovalchuk R, Dzyubyk L., (2017), Modeling the dynamics of vibratory separator of the drum type with concentric arrangement of sieves, *Eastern – European Journal of Enterprise Technologies*, vol 2, no 7, pp. 26-35.

[27] Tripathi N., Sharma A., Mallick S., Wypych P., (2015), Energy loss at bends in the pneumatic conveying of fly ash, *Particuology*, vol. 21, pp. 65-73.

[28] Viktor Hud (2019), The dynamic processes during the telescopic screw transporters work, *Scientific Journal of TNTU*, vol. 95, no 3, pp. 34–40, ISSN: 2522-4433, Ternopil / Ukraine.

DESIGN AND EXPERIMENT OF A THREE-RIDGE SIX-ROW PEANUT COMBINE HARVESTER BASED ON DEEP INTEGRATION OF AGRICULTURAL MACHINERY AND AGRONOMY
/
基于深度农机农艺融合的三垄六行花生联合收获机的设计与试验

Zenghui GAO[1)], Shuqi SHANG[1,2)], Nan XU[3)], Dansong Yue[2)], Jinming Zheng[4)], Dongwei WANG [2*)]

[1)] Xinjiang Agricultural University, College of Mechanical and Electronic Engineering, Xinjiang, China
[2)] Qingdao Agricultural University, College of Mechanical and Electronic Engineering, Shandong, China
[3)] Shandong Agricultural University, College of Mechanical and Electronic Engineering, Shandong, China
[4)] College of Engineering, Nanjing Agricultural University, Nanjing, 210095, China
*Tel: 13869881615; *) Corresponding author E-mail: w88030661@163.com*
DOI: https://doi.org/10.35633/inmateh-68-50

Keywords: *Integration of agricultural machinery and agronomy; clamping and collection; Semi-feeding picking fruit; mechanical analysis; low-damage harvesting*

ABSTRACT

In order to improve the efficiency of peanut harvesting in China, realize the deep integration of agricultural machinery and agronomy in peanut production and promote the development of peanut industry. According to the research on peanut planting agronomy and plant biological characteristics, this paper focuses on the analysis of the clamping and collecting scheme of the three-ridge six-row peanut combine harvester, and designs the structure of the clamping and collecting device to solve the situation that the peanut clamping and collecting process is prone to congestion under large feeding volume. By analysing the forces on the peanut plant, the structure of the core fruit picking device has been designed, and the factors and parameters affecting the effectiveness of the peanut picking operation have been optimised through experimental research using the peanut leakage and crushing rates as indicators. The whole machine structure of the three-ridge six-row peanut combine harvester was designed to ensure that the peanut combine harvester can complete the processes of harvesting, digging, clamping and conveying, soil removal, collecting, fruit picking, cleaning and fruit collection at one time. Finally, through field tests on the three-ridge six-row peanut combine harvester, it was verified that the peanut leakage rate was 1.92% and the crushing rate was 0.84% at different forward speeds, and all of them were congested, which met the national peanut harvesting standards.

摘要

为提高我国花生收获效率，实现花生生产农机农艺的深度融合，促进花生产业的发展。根据花生种植农艺及植株生物特性的研究，本文重点解析了三垄六行花生联合收获机的夹持归集方案，设计了夹持归集装置的结构，解决了在大喂入量情况下花生夹持归集过程易拥堵的情况；通过对花生植株进行受力分析，解析了摘果核心装置结构，以花生的破碎率、漏摘率为指标，试验分析得出了影响花生摘果作业效果的因素及参数范围。对三垄六行花生联合收获机整机结构进行了设计，确保花生联合收获及可以一次性完成扶禾、挖掘、夹持输送、去土、归集、摘果、清选、集果等工序。最终通过对三垄六行花生联合收获机进行田间试验验证得出机具在不同的前进速度下，花生的漏摘率为 1. 92%，破碎率为 0. 84%，且均未出现拥堵的情况，符合国家花生收获的标准。

INTRODUCTION

Peanut is the world's major cash crop and oil-bearing crop, but also one of the main cash crops exported by China (*Shang et al., 2005*). China's peanut planting area is of nearly 4.75 million hectares, accounting for more than 20% of the world's total peanut planting area, ranking second in the world for many years (*Gao L. et al., 2017*). But regarding the current level of mechanized joint harvesting of peanuts in China, whether compared to foreign harvesting levels or harvesting levels of other domestic food crops and major cash crops, there is a big gap, seriously hampering the rapid and healthy sustainable development of China's peanut industry (*Wang S. et al., 2022*).

[1] *Zenghui Gao, Ph.D. Stud. ; Shuqi Shang, Prof. ; Nan Xu, Ph.D. Stud. ; Dansong Yue, lectr. ; Jinming Zheng, Ph.D. Stud. ; Dongwei Wang, Prof.*

In recent years the peanut planting pattern gradually standardized, became large-scale and industrialized, which to a certain extent prompted the development of peanut harvesting machinery to large, efficient direction (*Wang B.et al., 2018*). Europe and the United States and other countries for peanut machinery research than China much earlier, peanut cultivars and China's peanut varieties differ greatly, the United States peanut is mostly prostrate peanut, using a two-stage harvesting method, through the peanut digging placement machine digging out the peanut plants laid in the field, after drying, the use of picking joint harvester to complete picking, fruit picking, cleaning and collection operations (*USDA, 2021*). The typical peanut digging and laying harvesters in the United States include a series of peanut harvesters produced by KMC, 9997 and 2110 traction peanut combine harvesters produced by Amadas (*Amada 2021*). The two models can harvest 4 rows and 6 rows of peanuts at the same time. These machines can simultaneously complete the peanut excavation, transportation, soil removal, flip the plants and lay them for drying, peanut excavation and harvesting loss rate can be steadily controlled within 2%. Typical peanut picking combine harvester is divided into two types, respectively, traction type peanut picking combine harvester and self-propelled peanut picking combine harvester. The representatives of traction type are KMC3376-6 and KMC3374-4 traction type picking combine harvester produced by KMC; the representatives of self-propelled type are 9900SP and 9970SP self-propelled peanut picking combine harvester produced by Amadas (*Tian, 2017*). For vertical peanuts planted in other developed countries, the combined harvesting method of one-time excavation, clamping collection, soil removal, fruit picking, cleaning, fruit collection and other processes is mostly adopted. This method generally adopts chain clamping trajectory device, which has high reliability and good clamping stability (*Ferezin E. et al., 2018; Leszczynski N. et al., 2011*). At present, foreign peanut harvesting machinery is developing in the direction of large-scale, machine-electric-hydraulic integration, intelligence and high efficiency (*Hu et al., 2010*). China gradually began to combine the actual situation of the country's peanut planting research and development of more efficient and applicable peanut harvesting machinery, with representative harvesting machinery. Qingdao Agricultural University developed 4HQL-2 type whole-feed peanut combine harvester and 4LH-2 type semi-feed self-propelled peanut combine harvester, Dongtai Machinery produced 4HBL-2 type peanut combine harvester and 4HB-2A type peanut combine harvester (*Hu et al., 2010*). The current semi-feed peanut combine harvester has been commonly promoted and applied, but there is still a lot of room for improvement with respect to China's peanut combine harvester regarding the adaptability and harvesting efficiency (*Hu et al., 2010*).

At present, China's peanut combine harvester has gradually developed from a single ridge double row harvesting to two ridge four rows, greatly improving the efficiency of peanut harvest. Taking into account the characteristics of peanut harvesting mostly in the rainy season, combined with the requirements of peanut harvesting standards, in order to further enhance the harvesting efficiency of peanuts, to achieve a rush harvest, the high-efficiency three-ridge six-row peanut combine harvesting machinery suitable for China's peanut plant agronomic requirements and characteristics was designed. The machine can complete the excavation, clamping collection, soil removal, fruit picking, cleaning, fruit collection and other processes at one time under the condition of large feeding capacity, and ensure that there is no congestion of clamping collection in the process, with low crushing and leakage rates.

MATERIALS AND METHODS

Agronomic Plant Biological Characterization Study of Peanut Planting

China's land area is large, the climate varies greatly, the soil moisture content and soil quality in different areas are different, so the peanut planting methods are also very different (*Wang S. et al., 2019)*. The current peanut planting can be broadly divided into flat planting, ridge planting and high ridge planting. The ridge method is conducive to plant ventilation and light, and also helps the peanut reasonable dense planting, improve the soil's drought resistance and moisture retention performance, to ensure high peanut yield and high quality. At present, most of the main peanut production areas in China use a ridge of two rows of mulching ridge peanut planting method. Figure 1 shows the actual production of one ridge and two rows of peanut ridge planting mode schematic diagram, ridge height H for 100 mm ~ 150 mm, row spacing S for 200 mm ~ 250 mm, ditch width M for 150 mm ~ 200 mm, ridge distance D for 700 mm ~ 800 mm, ridge top width L_1 for 500 mm ~ 550 mm, ridge bottom width L_2 for 600 mm ~ 650 mm.

There are many types of peanut varieties in China, and with the continuous maturation of breeding technology, peanut varieties are increasing (*Wang B. et al., 2022)*. Based on the morphological characteristics of peanut plants, peanuts can be divided into: erect type, semi-prostrate type and prostrate type. Currently,

most of the peanuts promoted and planted in China are the upright type, and the peanuts planted in large areas in the main peanut production are Luhua series and Yuhua series. The four peanut plants that are most widely and commonly planted are Luhua 12, Jihua 18, Yuhua 40 and HuaYu 33 each with 50 plants for geometric measurements, and the dimensions are shown in Table 1.

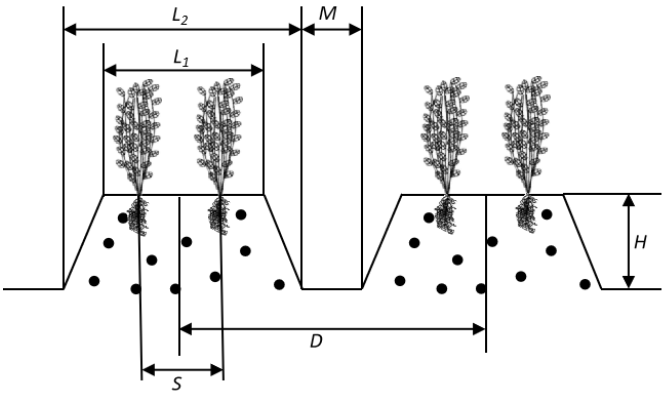

Fig. 1 - Planting pattern of one ridge and two rows peanut

Plant height: measuring the height of peanut plants in their natural state to provide a basis for studying the clamping position.

Plant width: measuring the width of the plant in its natural state, to provide a basis for the design of the crop supporting device.

Root length, width and height: measuring the natural length of the root system of peanut plants to provide a basis for the study of the design of the fruit picking pair of rollers (*Hu et al., 2017)*.

Average number of pods: Measure the average number of pods of each peanut plant to provide a basis for the design of the structure and movement parameters of the peanut picking device.

Table 1

Geometric dimensions of peanut

Species	Average plant height/mm	Average plant width/mm	Average root length/mm	Average root width/mm	Average root height/mm	Average number of pods/mm
Luhua 12	463.45	199.7	129.97	85.44	130.14	43
Jihua 18	476.39	202.5	128.34	87.67	125.43	38
Yuhua 40	447.68	195.6	130.76	83.54	126.93	40
HuaYu 33	420.63	193.3	133.78	93.91	120.09	36

Structural design of the whole machine of three-ridge six-row peanut combine harvester

Combined with the peanut harvesting process, the overall structure of the machine is shown in Figure 2, which mainly consists of the grubbing device, digging device, clamping and conveying device, soil removal device, collecting device, fruit picking device, cleaning device, fruit collection device and other parts.

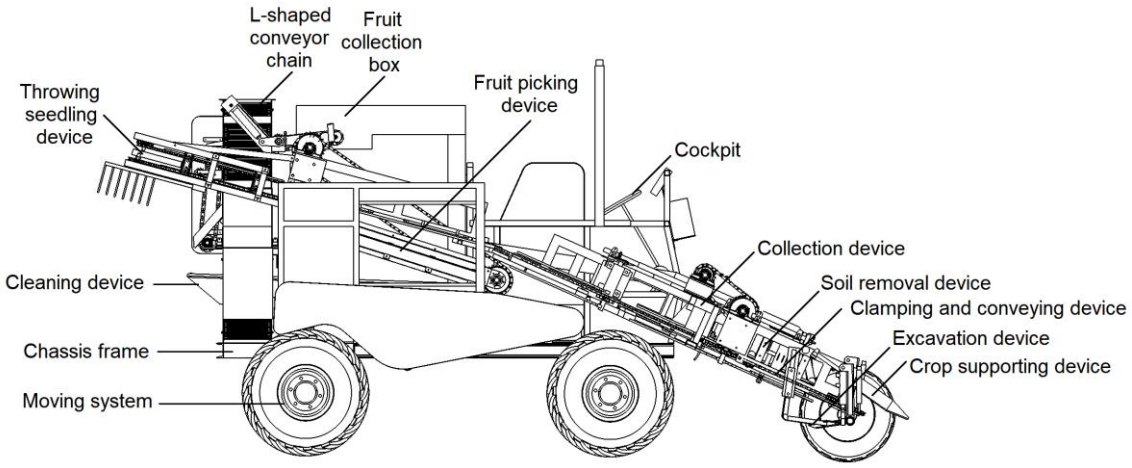

Fig. 2 - Structure diagram of three-ridge six-row peanut combine harvester

When the three-ridge six-row peanut combine harvester is in operation, the peanut plants to be harvested are separated from the peanuts in other rows by a three-pair crop clamping device, and the holding device rotates in the direction of the peanut plants to be harvested, that is, rotating to the inside, and the peanut plants are raised and gathered in the middle position. At the same time, the digging shovel will break the main root of the peanut and loosen the soil under the action of the forward force of the machine. With the cooperation of the crop supporting device and the digging device, the peanut plant moves backward according to the inertia and enters the clamping chain in turn. In the process of clamping and conveying, the soil removal device will follow the peanut to carry out the left and right reciprocating beating action, and remove the soil and impurities on the root system of the peanut plant. After that, the three-row peanuts will be gathered in the middle and sent to the fruit picking section, the roots of peanut plants will enter the picking roller device under the clamping and conveying of the clamping chain. The picking roller drives the picking boards, and picks the pods on the peanut roots by rotating the brush. The peanuts fall to the cleaning parts under the action of gravity, and the heavier soil blocks and other impurities are sieved out through the reciprocating motion of the parts. At the same time, the lighter boards and membranes are blown out with the blower to complete the secondary impurity removal operation. After cleaning, the peanut pods will enter the fruit box driven by the L-shaped conveyor belt. The fruit box is equipped with a hydraulic device, which can tilt the box to facilitate subsequent bagging operations. After the picking operation is completed, the podded peanut plant is conveyed backward with the clamping conveyor chain, and finally thrown into the field through the guide rail and the seedling guide device with the clamping chain as the power.

Design of key devices for three-ridge six-row peanut combine harvester

The peanut clamping and collecting device is the key core component of the three-ridge six-row peanut combine harvester, which plays a vital role in the transmission efficiency of peanut plants (*Leszczynski N.,2011; Gao Z. et al., 2023; Yang et al., 2010)*. The current peanut harvesting ridge two-row clamping device is relatively mature, and the structure and motion parameters are able to complete the operation better; the structure of the collecting device should be able to realize the collection of six rows of peanuts into the same conveying chain without congestion. Combined with the analysis of the literature for the aggregation components, the final choice of the highly reliable clamping chain type conveying, the conveying route was designed as shown in Figure 3.

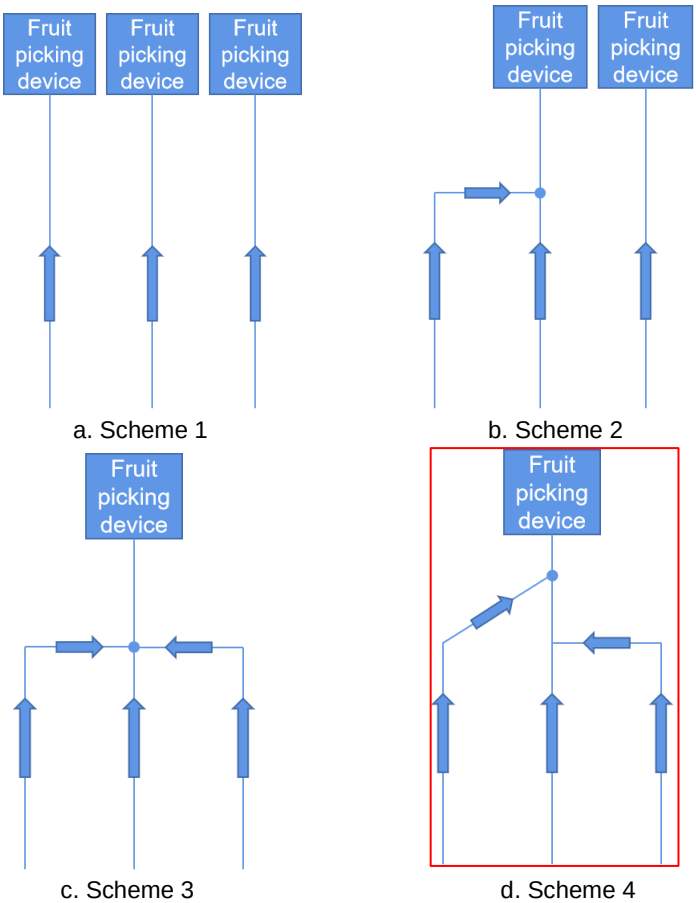

Fig. 3 - Design of peanut clamping conveying scheme

In scheme 1 and scheme 2, the clamping and conveying device sends peanuts into the picking device according to 1 and 2 ways respectively. The peanut picking efficiency is high and the picking effect is relatively good. However, the large peanut combine harvester is equipped with two or more sets of fruit picking devices, which makes the whole machine structure and transmission become quite complex, and it is not convenient for the simplification of the machine. Scheme 3 and scheme 4 only need to configure a set of fruit picking device, and the fruit picking effect and fruit picking efficiency are not as good as in the first two schemes. However, by adjusting the structure and motion parameters of the fruit picking device, the crushing rate and leakage rate of peanut fruit picking can be effectively reduced, and the effect of peanut fruit picking can be improved. Among them, in scheme 3 peanuts are collected at the same position, which is easy to cause congestion of peanut vines during transportation, while scheme 4 can effectively alleviate congestion, so scheme 4 clamping collection path is finally determined.

The structure of the clamping and collecting device is shown in Figure 4. The device mainly completes the processes of crop supporting, digging, clamping and conveying, and tapping the root system to remove soil, etc. (*Chen et al., 2020; Zhai et al., 2020)*. It is composed of three parallel and identical structures, and after completing the series of processes, it is collected and conveyed to the fruit picking operation. The overall layout of the structure is reasonable. In order to increase the adjustment range of the chain and avoid congestion in the process of conveying, the double floating adjustment method is adopted. At the same time, in order to adapt to the different agronomy of peanut planting in different regions of China, the design of automatic adjustment device of ridge width is more applicable to the ridge distance of peanut planting in different regions.

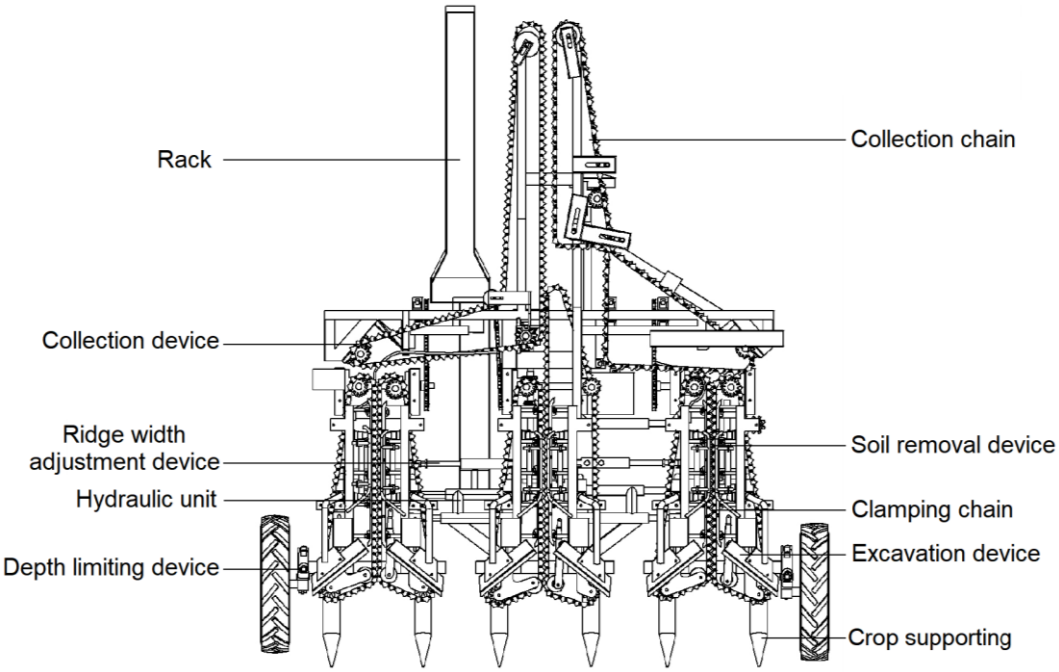

Fig. 4 - Structure diagram of clamping and collecting device

At present, there are two kinds of picking methods for peanut combine harvester: half feeding picking method and full feeding picking method. (*Wang et al., 2022)*. Semi-feeding means that the peanut plant seedlings and vines are transported in the direction opposite to the machine's operating speed under the clamping action of the chain, and the plant roots enter the fruit picking device. The pulling force of the chain on the vine of the plant and the brushing force of the pod picking device (pod picking board) on the roots pull the peanut pods down from the root system to complete the harvest, which is applicable to the harvesting of dried peanuts and freshed peanuts.

The full feeding method is to feed the peanut plant into the fruit picking drum and separate the plant from the pods through fruit shaking and fruit stroking, mostly used for dried peanuts harvesting, when harvesting fresh peanuts, this method has a greater impact on the peanut crushing rate and lower harvesting efficiency. Therefore, the final selection of semi-fed pod picking method, picking device as shown in the Figure 5.

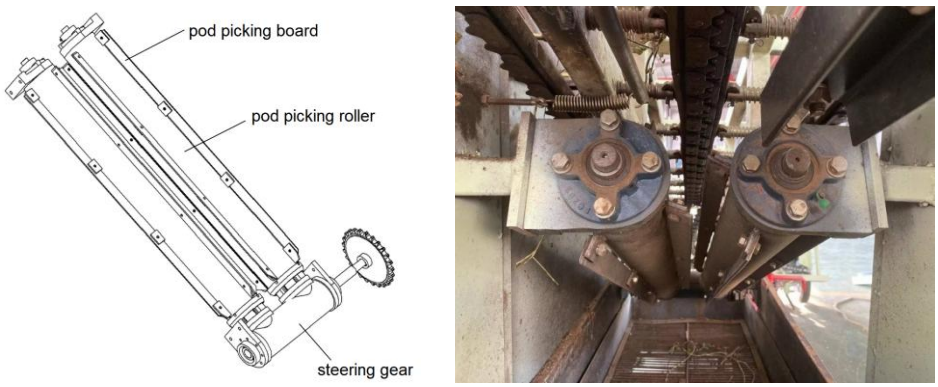

Fig. 5 - Fruit picking pair of rollers structure diagram

Analysis of peanut plant stresses during fruit picking

During the whole pod picking process, the peanut plant is not only subjected to the tension of the clamping and conveying chain, but also the root system and peanut pods are also subjected to the centrifugal force and impact force generated during the brushing of the boards on the roller. The force of the peanut plant when beated by one side of the picking board is analysed, as shown in Figure 6.

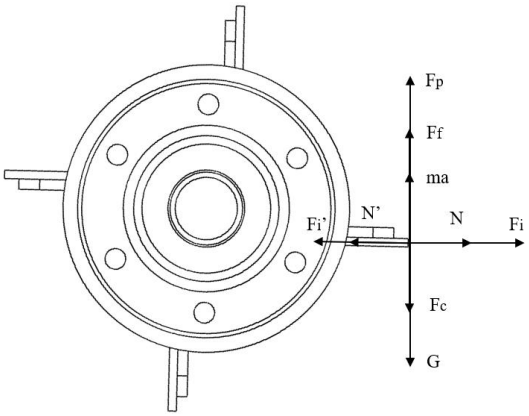

Fig. 6 - Stress of peanut plants during fruit picking

The forces applied to the peanut plant during the fruit picking process yielded.

$$\begin{cases} F_i + N = F_i' + \mathrm{N}' \\ F_p + F_f + ma = F_c + G \end{cases} \quad (1)$$

where: Fi—Centrifugal force of peanut pods slapped by picking boards, N;

F_i'—Centrifugal force of peanut pods slapped by picking boards on the other side, N;

F_p—Pull of peanut plant by clamping chain, N;

F_f—Peanut pod picking leaf friction, N;

ma—The inertial force of peanut pods, N;

F_c—Impact force of peanut pods when slapped by picking boards, N;

G—Peanut plant gravity, N.

The centrifugal force on the peanut pods is $F_c = mw^2R$, w is the rotational speed of the fruit picking pair of rollers. R is the radius of rotation of the fruit picking pair of rollers. Organizing the equation yields,

$$F_p = F_c + mg - \mu N - ma \quad (2)$$

As can be seen from the formula, the speed of the fruit picking pair of rollers directly affects the size of the impact force on peanuts, and is proportional; at the same time, as the speed continues to increase, the clamping conveyor chain will increase the pull force on the plant, excessive rotation speed will cause peanut plants to be pulled off, the speed of the pod picking rollers needs to be further determined by experimentation.

At present, most peanut picking institutions in China mainly pick peanuts after drying, mainly because after drying the fibres in the shell become hard, at this time they can withstand a stronger impact force, not easy to cause peanuts crushing, making it easier to improve the peanut harvesting rate. However, due to the fragility of freshed peanut shell fibers, the peanut pods can withstand less impact force when the peanuts are picked. If the speed of the fruit picking blade is too fast or the brushing force is large in the brushing process, it will lead to crushing peanut pods; while when the speed of the fruit picking blade is too slow or the brushing force is small, it will make the peanuts not be completely picked, and then this will lead to an increase in the peanut leakage rate. Therefore, the impact test on peanut pods and analysis of test data were performed to provide a theoretical basis for the design of the structure and parameters of the subsequent peanut picking device.

Test Method and Result Analysis

The test material was peanut pods at harvest time, and Luhua 12, Jihua 18, Yuhua 40 and HuaYu 33, which are the most widely planted in China, were selected as the main research subjects. Taking the peanut sowing time as the starting point, the peanut harvesting period is about 148 days. The test samples of each variety consist of 10 plants, and the moisture content is measured. Based on this, the impact force range that peanut pods can bear is measured.

After determining the test samples, a test bench was used to conduct impact tests on 40 peanut plants. The peanut plants were fixed on the clamping conveyor chain according to the actual clamping height at the time of harvesting, and the impact plate was driven to rotate and brush the peanut root system by adjusting the engine speed. The peanut pods were impacted by the impact plate and fell downward in the form of a parabola, ensuring that each peanut pod is hit only once. Combine the engine speed, calculate the speed of pod picking board according to the speed ratio, and count the crushing rate of 4 kinds of peanuts under different impact speed.

The maximum rotational speed that peanuts can bear on the day of harvest was measured by experiment. According to the broken situation of peanuts at different rotational speeds, the quantitative relationship between peanut crushing rate and the speed of picking roller was obtained. The test results are shown in Table 2.

Table 2

Crushing rate of peanut at different rotational speeds

Peanut varieties	Water content/%	Peanut crushing rate at different speeds/%				
		450 r/min	500 r/min	550 r/min	600 r/min	650 r/min
Luhua 12	54.47	0.03	0.84	1.47	1.84	2.32
Jihua 18	58.35	0.05	0.92	1.66	2.02	2.65
Yuhua 40	52.41	0.01	0.81	1.25	1.96	2.21
Huayu 33	55.82	0.03	0.76	1.38	1.89	2.58

From the above table, it can be derived that at peanut speed of 450 r/min, peanut pods began to crush, and as the speed continues to increase the rate of breaking peanut pods also increased, when the speed reached 650 r/min, four kinds of peanuts crushing rates are more than China's peanut picking industry standard (NY/T-993-2006), so it was determined that the impact speed of peanut pods can withstand a range of 450 r/min ~ 650 r/min, the distance between the two fruit picking rollers is 190mm.

The maximum impact speed that the peanut pods can withstand can be calculated by the formula:

$$v = \frac{2\pi D}{60} \cdot n \tag{3}$$

That is, the maximum impact velocity range of peanuts under suspension is 8.95 m/s~12.93 m/s.

RESULTS

By means of the actual harvesting of the whole machine in the field, the structure and parameters of the optimized clamping and gathering and fruit picking devices were used to adapt to different planting patterns and feeding volumes of different ridge widths, and important indexes such as leakage rate, crushing rate and productivity were measured during the operation of the whole three-ridge six-row peanut combine harvester.

Test material

The average height of the root system was 130.14 mm, width 85.44 mm and length 129.97 mm. The weight of 100 fruits was about 212.76 g. The soil moisture content of the trial field was 10.7% during the harvest period, and the planting pattern was one ridge and two rows.

Test Method

The test equipment is a three-ridge six-row peanut combine harvester equipped with a designed and optimized clamping and collection scheme and a picking device structure and motion parameters, electronic scale.

Eighteen plots were randomly selected in the test field, each 50 m long, with a three-ridge width (2.1 m) as the standard for the test. The leakage rate, crushing rate and harvesting efficiency of the peanut combine harvester at different speeds were measured, and the average value of each test group was taken and recorded accordingly.

After the test, the leakage of pods on the peanut plant, the crushing rate of peanut pods in the fruit collection box and the productivity of the peanut harvester as a whole were measured. The congestion in the clamping and collecting part of the peanut combine harvester was observed during each group of tests.

Fig. 7 - Field test verification

Analysis of results

The feeding amount of peanuts is controlled by controlling the forward speed of the machine. From table 6.1, it can be seen that with the continuous increase of the forward speed of the machine, the missing picking rate and crushing rate of peanuts also increase. The specific experimental data are shown in figures 8 and 9. In the whole test process, there was no congestion at the clamping collection, which proved that the optimized clamping collection speed was reasonable. The maximum forward speed of three-ridge six-row peanut combine harvester is 0.7 m / s, which is consistent with the results of preliminary field experiment.

Table 3

Harvesting effects of three-ridge six-row peanut combine at different speeds

Machine advance speed/m•s^{-1}	Average missed pick rate/%	Average crushing rate/%	Productivity/hm^2•h^{-1}	Congestion
0.3	0.00	0.00	0.23	Not available
0.4	0.02	0.01	0.30	Not available
0.5	0.67	0.34	0.38	Not available
0.6	1.53	0.90	0.45	Not available
0.7	2.79	1.63	0.53	Not available
0.8	4.88	2.21	0.61	Not available

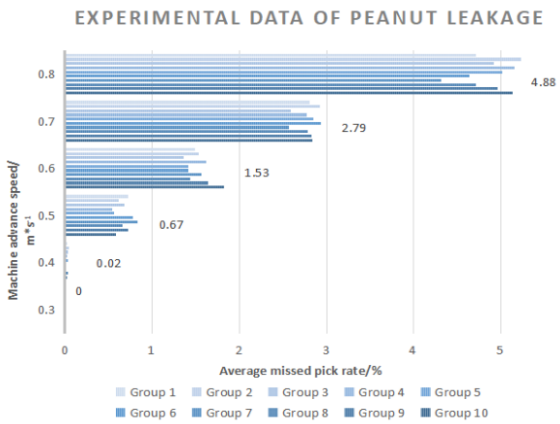

Fig. 8 - Experimental data of peanut leakage

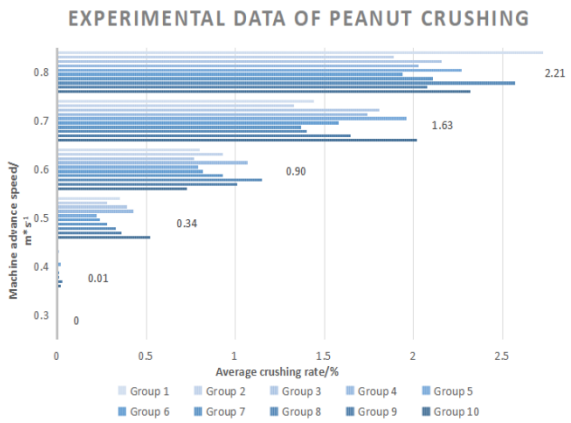

Fig. 9 - Experimental data of peanut crushing

Under the condition of ensuring the harvesting efficiency of peanut combine harvester, 10 sets of validation tests were conducted after setting the forward speed of the machine at 0.6 m/s. The final experimental results are shown in Table 4.

Table 4

Test results of three-ridge six-row peanut combine harvester

Projects	Test results	Technical Requirements
Missed pick rate	1.92%	5%
Crushing rate	0.84%	2%
Congestion	Not available	/
Productivity	0.45 hm^2/h	/

The field test results found that the performance of the three-ridge six-row peanut combine harvester harvesting has been able to meet the technical requirements. Moreover, there was no peanut plant congestion in all 10 trials, which proved that the combine harvester could ensure normal and efficient operation under the condition of large feeding volume. The field test proved that the machine is better than the national standard in various indicators while ensuring harvesting efficiency.

CONCLUSIONS

The article studied the agronomic and biological characteristics of peanut planting and determined the peanut planting pattern of one-ridge two-row of mulch ridge culture crop. 50 plants of each of the 4 peanut varieties most widely and commonly grown in China were selected and their plant height and width, root length, width and height, and average number of pods were measured to provide theoretical support for the design of structural and movement parameters of the peanut picking device.

Through comparison and experimental verification, the structure design scheme of clamping and collecting device of the three-ridge six-row peanut combine harvester was determined. Through mechanical analysis and experimental research, the motion parameters of the picking device were determined.

The overall design of the three-ridge six-row peanut combine harvester was completed, and the field test was carried out. The feeding amount of peanuts was controlled by controlling the forward speed of the machine, and the average leakage rate, crushing rate, productivity and congestion of the harvester were obtained. The operation effect of the whole machine was the best at 0.6 m/s, and 10 sets of verification tests were carried out. There was no congestion of peanut plants, and the combine harvester could ensure normal and efficient operation.

ACKNOWLEDGEMENT

We acknowledge that this work was financially supported by Key R&D plan of Shandong Province "Creation of key components of high-performance sowing and harvesting and intelligent work tools" (2021CXGC010813).

REFERENCES

[1] Chen M., Zhai X., Zhang H., Yang R., Wang D., Shang S., (2020). Study on control strategy of the vine clamping conveying system in the peanut combine harvester. *Computers and Electronics in Agriculture*, UK, Vol. 178, 105744. https://doi.org/10.1016/j.compag.2020.105744.

[2] Ferezin E., Silva R., Santos A D. (2018). Development of an electrohydraulic drive system for the vibrating conveyor belt of the peanut digger-inverter [J]. *IEEE Transactions on Industry Applications,* Vol. 58, Issue S1, pp. 13-21.

[3] Gao L., Chen Z., Charles C., C.L. Butts, (2017). Evolution of peanut harvesting mechanization technology in the United States and its enlightenment to China (*美国花生收获机械化技术衍变历程及对中国的启示*). *Transactions of the Chinese Society of Agricultural Engineering*, Vol. 33, Issue 12, pp. 1-9.

[4] Gao Z., Shang S., Wang D., He X., Xu N., Zheng J., Zhou Z., Liu B., (2023). Design and test of fruit picking device for three ridges and six rows peanut combine harvester (*三垄六行花生联合收获机摘果装置设计与试验*). *Journal of Agricultural Mechanization Research*, Vol. 45, Issue 3, pp. 176-181.

[5] Hu Z., Wang B., Yu Z., Peng B., Zhang Y., Tan L., (2017). Design and test of semi-feeding peanut picking test bench. *Transactions of the Chinese Society of Agricultural Engineering*, Vol. 33, Issue 17, pp. 42-50.

[6] Hu Z., Wang H., Wang J., Hu L., Tian L., Zhong T. (2010). 4HLB-2 type semi-feeding peanut combine harvester test (*4HLB-2 型半喂入花生联合收获机试验*). *Transactions of the Chinese Society of Agricultural Machinery*, Vol. 41, Issue 4, pp. 79-84.

[7] Leszczynski N. (2011). The influence of working parameters of a carrot harvester on carrot root damage [J]. *Maintenance and Reliability*, Issue 1, pp. 35-41.

[8] Shang S., Liu S., Wang F., Jiang Y., Hua W. (2005). Research status and progress of peanut production machinery (*花生生产机械的研究现状与进展分析*). *Transactions of the Chinese Society of Agricultural Machinery*, Vol. 3, pp. 143-147.

[9] Tian L. (2017). Study on the mechanism of peanut orderly strip harvest (*花生有序条铺收获机理研究*). Master Thesis, *Qingdao Agricultural University*, Qingdao / Shandong.

[10] Wang B., Gu F., Cao M., Xie H., Wu F., Peng B., Hu Z. (2022). Analysis and Evaluation of the Influence of Different Drum Forms of Peanut Harvester on Pod-Pickup Quality. *Agriculture*, Vol. 12, Issue 6, 769. https://doi.org/10.3390/agriculture12060769

[11] Wang B. (2018). Study on fruit picking mechanism and screening characteristics of four-row semi-feeding peanut (*四行半喂入花生联合收获摘果机理与筛选特性研究*). *PhD thesis*, Chinese Academy of Agricultural Sciences, Haidian / Beijing.

[12] Wang S., Ji J., Geng L. (2019). Design of sieve-roll combined peanut pods cleaning device. *INMATEH - Agricultural Engineering*, Vol. 59, Issue 3, pp. 141-150.

[13] Wang S., Hu Z., Chen Y., Wu H., Wang Y., Wu F., Gu F. (2022). Integration of agricultural machinery and agronomy for mechanised peanut production using the vine for animal feed. *Biosystems Engineering*. Vol. 219, pp. 135-152. https://doi.org/10.1016/j.biosystemseng.2022.04.011.

[14] Yang R., Shang S. (2010). Design and experiment of flexible clamping device for peanut combine harvester (*花生联合收获机柔性夹持装置设计与试验*). *Transactions of the Chinese Society of Agricultural Machinery,* Vol. 41, Issue 8, pp. 67-71.

[15] Zhai X., Chen M. (2020). Load spectrum compilation of vine clamping and conveying system of peanut combine harvester (*花生联合收获机秧蔓夹持输送系统载荷谱编制*). *Transactions of the Chinese Society of Agricultural Machinery*, Vol. 51, Issue S1, pp. 261-266 + 363.

[16] ***Amadas Industries. Machinery for Agriculture [EB/OL]. (2021-12) [2022-1-9]. https: // amadas.com/agriculture/#Peanuts.

[17] ***Kelley Manufacturing Co. Peanut Equipment [EB/OL]. (2021-12) [2022-1-9]. https://www.kelleymfg.com/product-category/equipment/peanut/.

[18] ***United States Department of Agriculture. Foreign Agricultural Service [EB/OL]. (2021-12)[2022-1-8].https://apps.fas.usda.gov/psdonline/app/index.html#/app/adv Query.

CALIBRATION OF SOIL DISCRETE ELEMENT CONTACT PARAMETER IN RHIZOME MEDICINAL MATERIALS PLANTING AREA IN HILLY REGION
/
丘陵山地根茎类中药材种植区土壤离散元参数标定

Bin CHEN[1)], Yan LIU[1)], Qingxu YU[1)], Xiaobing CHEN[1)], Youyi MIAO[1)], Yuanxiu HE[2)], Jiahao CHEN[3)], Jingchao ZHANG*[1)]

[1)] Nanjing Institute of Agricultural Mechanization, Ministry of Agriculture and Rural Affairs, Nanjing / China;
[2)] NanJing XiaoZhuang University, Nanjing / China;
[3)] HeFei Normal University, Hefei / China;
Tel: +86 025-84346278-60; E-mail: zhangjingchao@caas.cn
DOI: https://doi.org/10.35633/inmateh-68-51

Keywords: *rhizome medicinal materials; hilly region; soil discrete element parameters; calibration; soil-machine interaction*

ABSTRACT

Aiming at the lack of accurate and reliable discrete element simulation parameters in the study of the soil-machine interaction mechanism and the design of machinery in the planting areas of rhizomes in hilly mountainous areas, EDEM software was used to calibrate the parameters. The soil angle of repose test was used to calibrate the contact parameters between soil particles, and the soil sliding test was used to calibrate the contact parameters between soil and machinery. The Box-Behnken optimization method was used to establish the multiple regression model of the angle of repose and the sliding angle, and the optimal contact parameters between soil particles were obtained by solving the model. The optimal combination of contact parameters was used to conduct tests on the angle of repose and soil sliding angle and the errors between the simulation and physical tests were 3.94% and 3.66%, respectively. In order to further verify the accuracy of the calibrated and optimized discrete element model parameters, the rotary tillage ridge field test and the simulation test were used for comparative analysis, and the relative errors of the simulated test results and the field test results for ridge height, ridge top width, and ditch bottom width were obtained, respectively. 4.45%, 6.96%, 8.56%, the error is within the acceptable range. The rotary tillage and ridging effects are consistent in simulation and field tests, confirming the accuracy and reliability of the calibration of soil parameters.

摘要

针对丘陵山区根茎类中药材种植区土壤-机械互作机理研究以及机具设计缺乏准确可靠的离散元仿真参数的问题,采用 EDEM 软件进行参数标定。采用土壤休止角试验校准土壤颗粒之间的接触参数，采用土壤滑动试验校准土壤与机械之间的接触参数。采用 Box-Behnken 优化方法建立了静止角和滑动角的多元回归模型，通过解算模型得到土壤颗粒间的最佳接触参数。以最优组合进行堆积角试验和滑落角试验，仿真试验和物理试验之间的误差分别为 3.94%、3.66%。为进一步验证标定优化的离散元模型参数的准确性，采用旋耕起垄田间试验和仿真试验进行对比分析，获取垄高、垄顶宽、沟底宽仿真试验结果与田间试验结果的相对误差分别为 4.45%、6.96%、8.56%，误差在可接受范围内。仿真试验和田间试验旋耕起垄效果基本一致，验证了土壤参数标定的准确可靠。

INTRODUCTION

Chinese medicinal materials are a characteristic economic crop. In recent years, Chinese medicinal materials planting has become a pillar industry for rural revitalization. In China, the planting area of Chinese medicinal materials is about 5,864 thousand hectares *(Chen et al., 2021)*. However, the comprehensive mechanization rate of Chinese medicinal materials is only 16.87% *(Huang Luqi, 2021)*. Among them, rhizome medicinal materials have the most diverse varieties and highest production, while their production is also most labor-intensive and has the least mechanization rate *(Zhao et al., 2012)*. In order to improve the mechanization level of rhizome medicinal materials production, it is necessary to study the soil-machine interaction mechanism in planting area.

1 Bin Chen, ENGR; Yan Liu, Pro; Qingxu Yu, PHD student; Xiaobing Chen, Pro; Youyi Miao, ENGR; Yuanxiu He, BSC student; Jiahao Chen, BSC student; Jingchao Zhang, ENGR.

The discrete element method (DEM) has become an important means to study the mechanism of soil-machine interaction *(Ucgul et al., 2020)*. Different types of soil lead to differences in the performance of soil-mechanical interactions *(Chen et al., 2013).* When modeling different types of soil, it is necessary to select an appropriate soil contact model and accurately calibrate the relevant model parameters according to the specific conditions of the soil to ensure the authenticity of the simulation test. Aitkins et al. explored DEM contact parameters of highly viscous soil particles by combining hysteretic spring and linear cohesion models, calibrated the coefficients of static friction and rolling friction, and verified accuracy of parameter calibration through field tests and simulation of ditching *(Aikins. et al., 2021)*. Xing et al. used the Hertz-Mindlin with JKR contact model in the simulation software extended discrete element model (EDEM) to calibrate key model parameters of lateritic soils in Hainan Province, China and obtained contact parameters between lateritic soil particles and between the soil and 28MnB5 plates. They also verified these parameters through tests of soil breakage resistance *(Xing et al., 2020)*. Taking soil around tubers during potato harvesting period as research objects, Li et al. calibrated the soil discrete element contact parameters through accumulation test and shear crushing test. The relative error between the simulation results and the actual measured values was 1.37% *(Li et al., 2022)*. Meanwhile, some scholars calibrated DEM parameters of specific soil according to research demands, including ploughed soil in a cotton field *(Song et al., 2021),* no-till soil in a winter wheat-corn rotation system *(Tian et al., 2021)*, grapevine anti-freezing soil *(Ma et al., 2020)*, covering soil on whole plastic film with mulching on double ridges *(Dai et al., 2019)*, and wet clayey paddy soil *(Ding et al., 2017)*. However, there is no research into the calibration of soil discrete element parameters in the planting area of rhizome medicinal materials in hilly region.

By combining simulation and physical tests, the discrete element parameters between soil and machine were calibrated. The angle of repose tests of soil could be conducted to calibrate contact parameters between soil particles and sliding tests of soil were conducted to calibrate contact parameters between soil and machinery. Furthermore, multivariate regression models of the contact parameters with the angles of repose and sliding were established, thus obtaining the optimal combination of contact parameters. Moreover, field tests and simulation were performed based on the self-developed rotary tillage and ridging machine to determine accurate and reliable DEM parameters of soil.

MATERIALS AND METHODS

Test materials

The test soil samples were collected from a planting area of *Fritillaria thunbergii* (Xinfeng Town, Dafeng District, Yancheng City, Jiangsu Province, China) (120°47′48″ N, 33°28′88″ E). The soil samples were collected in late May 2022, which was consistent with the harvesting period of *Fritillaria thunbergii*. Because *Fritillaria thunbergii* is a shallow-rooted crop, soils at the depth of 0~20 cm were taken as the research object. The field soil was sampled using the five-point sampling method, and test instruments were utilized to determine measure intrinsic parameters including the density, hardness, and moisture content. Afterwards, a cutting ring (100 cm^3) and an electronic balance (NS-3200A, measurement range of 0 to 3200 g, and precision of 0.001 g) were used to measure the soil density. A hardness meter of soil (TYD-2, measurement range of 100 kg, and precision of 0.5%) was employed to measure soil hardness in the plough layer. An electro-thermostatic blast oven (DHG-9076A, measurement range of 50 to 300 °C) was adopted to measure the average soil moisture content. The simulation parameters including shear modulus and Poisson's ratios of soil and steel components were derived from relevant literature (*Xing et al., 2020; Dai et al., 2019*). The specific parameters are listed in Table 1.

Table 1

Intrinsic physical parameters in DEM simulation of soil

Parameter	Value
Soil hardness [kPa]	1263.5
Soil moisture content	18.65%
Soil density [$kg \cdot m^{-3}$]	1250
Soil Poisson's ratio	0.4
Soil shear modulus [Pa]	1×10^6
Steel density [$kg \cdot m^{-3}$]	7.85×10^3
Steel Poisson's ratio	0.3
Steel shear modulus [Pa]	7×10^7

Physical tests of soil

The physical testing apparatus for the angle of repose of soil is shown in figure 1a. The apparatus consisted of a lifting test bench, a steel cylinder, and a steel plate. The steel cylinder had a height of 240 mm, a diameter of 80 mm, and a length-diameter ratio of 3:1, and its bottom was in contact with the steel plate (500 mm × 400 mm). The steel cylinder was filled with soil. Then, a KD-2768 hoisting machine was used to lift the cylinder at a constant rate of 0.02 m/s, which allowed soil particles to fall from the bottom of the cylinder and accumulate on the steel plate. After finishing each test, a digital display angle ruler (Kapro992, with a measurement range of 0° to ± 225°, and a precision of 0.05°) was used to measure the angle of repose θ from four directions (figure 1b) and the mean value in all four directions was taken as the value of the angle of repose of soil in the test. The test was repeated five times and the mean value was calculated. In this way, the angle of repose θ of soil was found to be 35.77°, with a standard deviation of 1.23° and a coefficient of variation (CV) of 3.44%.

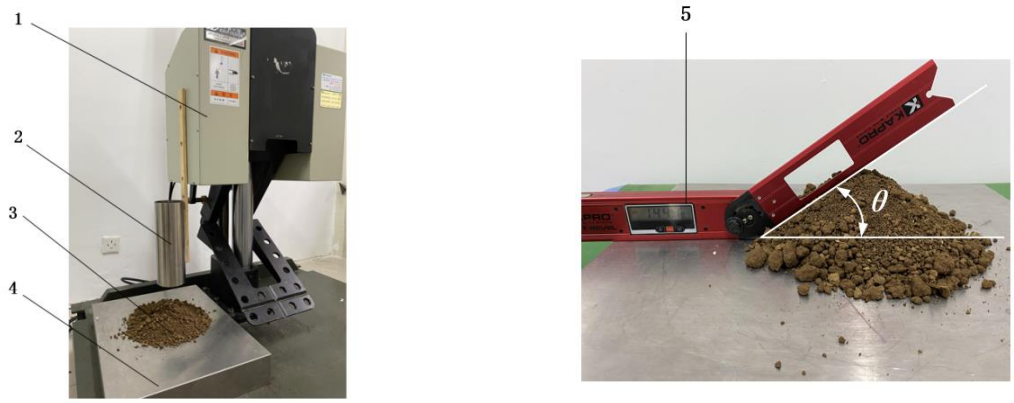

(a) Test bench for measuring the angle of repose of soil (b) Measurement of the angle of repose

Fig. 1 - Physical test of soil repose angle

1-Lifting test bench; 2 - Steel cylinder; 3 - Soil mound; 4 - Steel plate; 5 - Digital display angle ruler

The sliding tests of soil are shown in figure 2a. The test equipment comprised an inclined test bench, a steel box, a steel ring (Φ 154 mm × 30 mm), and a digital display angle ruler. The steel box was placed on the inclined test bench and leveled using the digital display angle ruler. The steel ring was put in the middle at the top of the steel box. Then, the electronic balance was used to weigh 100 g of soil, which were uniformly distributed around the steel ring. Afterwards, the steel ring was removed, and the inclined test bench was rotated around the y-axis at 2 °/s. The rotation was stopped when the soil began to slide. Under the condition, the digital display level ruler was used to measure the angle between the x-axis of the inclined test bench and the horizontal plane, that is, the sliding angle γ (Figure 2b). The test was repeated five times and the mean value was taken as the test result. In this way, the sliding angle γ of soil was found to be 22.4°, with a standard deviation of 0.41° and a CV of 1.35%.

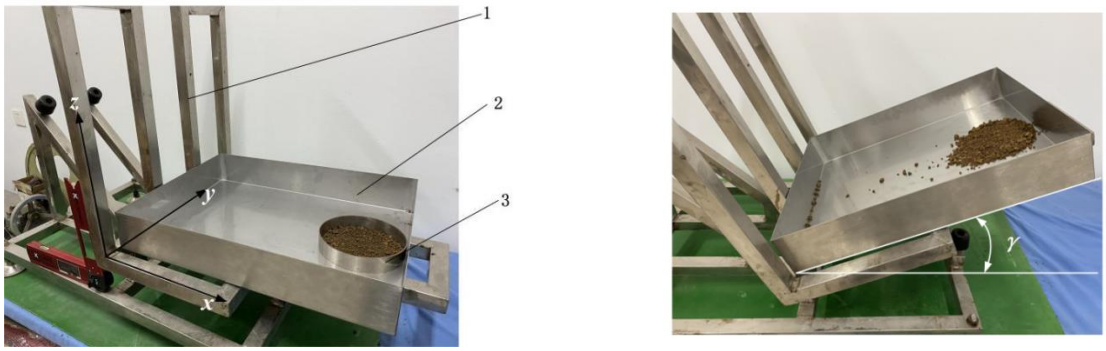

(a) Test bench for measuring the sliding angle of soil (b) Measurement of the sliding angle

Fig. 2 - Physical test of soil sliding angle

1- Inclined test bench; 2 - Steel box; 3 - Steel ring

DEM simulation of soil

(1) Determination of value ranges of parameters to be calibrated

The intrinsic parameters and simulation scale of soil and steel components were input to the EDEM software. Test factors and their value ranges in simulation were determined based on the GEMM (generic

EDEM material model) database and the literature (*Aikins. et al., 2021; Tian et al., 2021; Song et al., 2021*). The value ranges of factors A (the coefficient of restitution of soil particles), B (coefficient of static friction of soil particles), C (the coefficient of rolling friction of soil particles), D (JKR surface energy), E (coefficient of restitution between soil and steel), F (the coefficient of static friction between soil and steel), and G (the coefficient of rolling friction between soil and steel) are 0.15 to 0.75, 0.2 to 1.16, 0.05 to 0.25, 0.01 to 2.8 J/m^2, 0.05 to 0.65, 0.3 to 0.9, and 0.05 to 0.25, respectively.

(2) Establishment of the simulation model

According to the simulation scale, the built-in spherical particle elements of EDEM were used to establish the soil model and set the radius of soil particles and the magnifying power of spherical diameter as 5 mm and 0.95 to 1.05, respectively *(Shi et al., 2017)*. The three-dimensional (3-d) models of the test benches for the angle of repose tests and sliding tests of soil were built using SolidWorks, saved as .x_t format, and imported in EDEM. As shown in Figure 3 and Figure 4, the simulation models were simplified: only the cylinder and steel plate were reserved in the angle of repose tests of soil and only the steel box was reserved in the sliding tests, whose sizes were same as those of the cylinder, steel plate, and steel box in the physical tests of soil. The cylinder in the angle of repose tests was lifted at 0.02 m/s and the steel box in the sliding tests was rotated at 2 °/s, all consistent with those in the physical tests of soil. The intrinsic parameters of soil and steel components were set as Table 1. The Hertz-Mindlin with JKR contact model was selected for soil particles, and the Hertz-Mindlin non-sliding contact model was selected for soil particles and steel components. The time step in Rayleigh analysis was set to 20%. In addition, the interval for data storage, gravitational acceleration, and grid cell size were 0.01 s, 9.81 m/s^2, and 2.5 times the average radius of particles, respectively.

After completing the simulation, the model was adjusted to the front view and images were captured. In order to avoid the result error caused by human measurement, the repose angle measurement adopts the method of image processing (Figure 4). The image was captured as 804×804 pixels and imported into MATLAB. Firstly, the RGB original image was converted into a binary image, and the left half of the binary image was obtained by image segmentation. Then the boundary curve was extracted by edge detection, and the fitting line was further obtained. The angle between the fitting line and the horizontal plane is the repose angle. The slip angle was obtained by measuring the angle between the flat plate and the horizontal plane by CAD software.

(a) Simulation model of the angle of repose test of soil

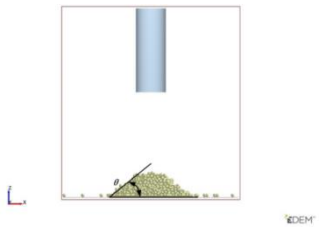

(b) Simulation results of the angle of repose

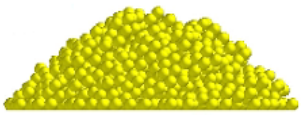

(c) RGB original image

(d) binary image

(e) half of the binary image

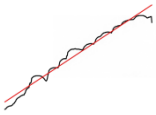

(f) boundary curve and fitting line

Fig. 3 - Simulation of the angle of repose of soil

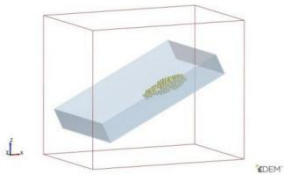

(a) Simulation model of the sliding angle test of soil

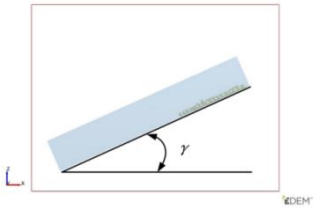

(b) Simulation results of the sliding angle

Fig. 4 - Simulation of the sliding angle of soil

(3) Arrangement of simulation

The contact parameters (A, B, C, and D) of soil particles were calibrated by conducting simulation on the angle of repose of soil, and those between soil and steel (E, F, and G) were calibrated through simulation

of the sliding angle. At first, the steepest ascent experiments were designed to shrink the ranges of values of parameters, to approach the optimal values with greatest accuracy. In the simulation, the parameter values were increased at the designed steps and the corresponding angles of repose and sliding of soil in the simulation were recorded and analyzed.

Parameters were set to three levels (high, intermediate, and low which were separately expressed as +1, 0, and −1) according to results of the steepest ascent experiments and the Box-Behnken test design. The error was estimated using five central points in the tests, in which 29 and 17 groups of simulation were separately conducted on the angles of repose and sliding of soil, during which these were measured for specimens in each group and were recorded. Then, analysis of variance (ANOVA) was applied to the simulation results and the multivariate regression analysis was used to obtain regression models. By using the parameter optimization module in Design-Expert, the established models were optimized taking the repose and sliding angles of soil as the objectives, so as to determine the optimal solutions. Thereafter, the simulation results were verified.

Test verification of rotary tillage and ridging work

(1) Field tests of rotary tillage and ridging work

The rotary tillage and ridging machine mainly consisted of a caterpillar chassis, a suspension system, a gear reducer, a chain driving system, a rotary tillage and ditching device, a ditch-cleaning shovel, a ridge roller, and a rack. The whole machine is shown in Figure 5a and the main technical parameters are listed in Table 2. The tests were conducted in the planting area of *Fritillaria thunbergii* (Xinfeng Town, Dafeng District, Yancheng City, Jiangsu Province) after harvest.

Main technical parameters of the whole machine **Table 2**

Parameter	Value
Overall machine size [mm × mm × mm]	4950 × 2030 × 2020
Total mass [kg]	2618
Matched power [kW]	36.8
Knife-cylinder speed [rpm]	230
Rotational speed of ridge roller [rpm]	85

According to the test method stipulated in the Rototill combine equipment Part 2: Rototill scarifying-paring-ridging machine (JB/T8401.2-2017), the machine was driven in a field. This formed three complete ridges and two half ridges. The forward speed, rotational speed of rotary blades, tillage depth of the machine, and rotational speed of the ridge roller were 0.5 m/s, 230 rpm, 220 mm, and 85 rpm, respectively. Field tests are shown in Figure 5b. The measurement devices included a leather measuring tape, a steel measuring tape, and a digital display level ruler (KAPRO-985D with a measurement range of 0 to 180°, and a precision of 0.1°). The sections with the length of 20 m in the middle of the three complete ridges were taken as the data measurement ranges. The ridge height, top width of ridges, and bottom width of ditches were measured by using the five-point sampling method and then they were recorded.

(a) Test prototype

(b) Operation effect

(c) Measurement of ridge height

(d) Measurement of top width of ridges and bottom width of ditches

Fig. 5 - Field tests of rotary tillage and ridging work

(2) Simulation of rotary tillage and ridging work

The geometries module in EDEM was used to establish the soil-bin model measuring 2100 mm × 2100 mm × 400 mm, and SolidWorks was adopted to build the 3D model of the rotary tillage and ridging machine. The models were simplified and then imported in EDEM (figure 6). Soil particles were set using the calibrated and optimized parameters, and the Hertz-Mindlin non-sliding contact model was applied between the soil and rotary tillage ridging parts. Based on relevant research results and combining with the simulation scale, the radius of soil particles was magnified to 10 mm, which can effectively save simulation resources and improve the simulation efficiency (*Dai et al., 2019*).

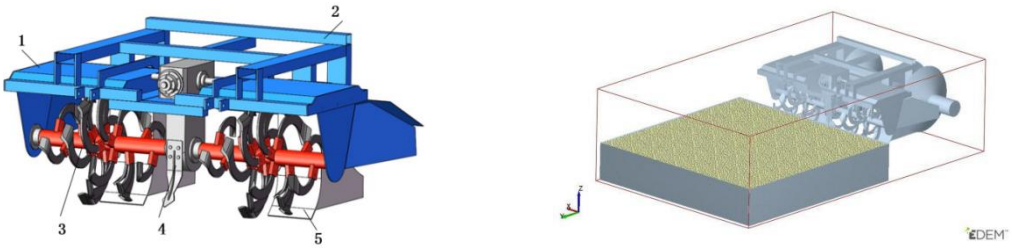

(a)3-d model of the rotary tillage and ridging machine (b)DEM model of rotary tillage and ridging work

Fig. 6 - Simulation models of rotary tillage and ridging machine and work
1- Cover plate; 2 - Rack; 3 - Rotary blade; 3 - Small front plough; 3 - Trenching shovel

The rotational speed of rotary blades, forward speed of the machine, tillage depth, and rotational speed of the ridge roller were the same as those in the field tests. After simulation, the ridge height (h), top width of ridges (l_1), bottom width of ditches (l_2) was measured at five points in the stable working stage and their averages were calculated, as shown in figure 7. The deviations were calculated using equation 1.

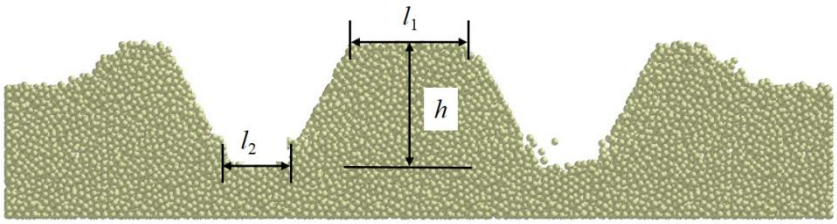

Fig. 7 - Measurement in the simulation of rotary tillage and ridging work

$$\delta = \frac{|\eta' - \eta|}{\eta} \times 100\% \quad (1)$$

where η' and η represent the simulation and field test results of the ridge height, top width of ridges, and bottom width of ditches, respectively.

RESULTS

Results of the steepest ascent experiments

The steepest ascent experiments were conducted taking the JKR surface energy, contact parameters of soil particles, and contact parameters between soil and steel as test factors. The relative errors of the actual repose and sliding angles with the simulation results were calculated. Simulation results of the angle of repose are listed in Table 3.

Table 3

Results of steepest ascent experiments of the angle of repose

Serial Number	Parameter A	Parameter B	Parameter C	Parameter D [J·m^{-2}]	Angle of repose θ [°]	Relative error
1	0.15	0.2	0.05	0.01	9.83	-72.52%
2	0.3	0.44	0.1	0.7	33.93	-5.14%
3	0.45	0.68	0.15	1.4	37.52	4.89%
4	0.6	0.92	0.2	2.1	40.05	11.97%
5	0.75	1.16	0.25	2.8	90	151.61%

In the third group of tests, the relative error of the angle of repose is the minimum of 4.89%, so it is determined that the optimal interval is approximated to the third group of parameters.

Therefore, the subsequent Box-Behnken tests were conducted by taking the parameter values in the third group as the intermediate level, and those in the second and fourth groups as the low and high levels. Simulation results of the sliding angle are listed in Table 4. In the second group of tests, the relative error of the sliding angle is minimized, so the optimal interval is found to be approximated to the second group of parameters. Hence, the subsequent Box-Behnken tests were conducted by taking the parameter values in the second group as the intermediate level, and those in the first and third groups as the low and high levels.

Table 4

Results of steepest ascent experiments of the sliding angle

Serial Number	Parameter E	Parameter F	Parameter G	Sliding angle γ [°]	Relative error
1	0.05	0.3	0.05	16.88	-24.64%
2	0.2	0.45	0.1	23.77	6.12%
3	0.35	0.6	0.15	27.15	21.21%
4	0.5	0.75	0.2	32.12	43.39%
5	0.65	0.9	0.25	37.35	66.74%

Box-Behnken test results of the angle of repose

Table 5 lists the Box-Behnken test results of the angle of repose. The multivariate regression model between the angle of repose θ of soil particles and various contact parameters was constructed using Design-Expert based on the test results and the polynomial equation is shown as equation 2.

Table 5

Box-Behnken test results of the angle of repose

Serial Number	Parameter A	Parameter B	Parameter C	Parameter D [J·m^{-2}]	Angle of repose θ [°]
1	-1 (0.3)	-1 (0.44)	0 (0.15)	0 (1.4)	32.15
2	1 (0.6)	-1	0	0	36.1
3	-1	1 (0.92)	0	0	36.85
4	1	1	0	0	36.99
5	0 (0.45)	0 (0.68)	-1 (0.1)	-1 (0.7)	32.16
6	0	0	1 (0.2)	-1	39.65
7	0	0	-1	1 (2.1)	41.27
8	0	0	1	1	37.6
9	-1	0	0	-1	34.73
10	1	0	0	-1	35.7
11	-1	0	0	1	37.45
12	1	0	0	1	39.78
13	0	-1	-1	0	37.12
14	0	1	-1	0	38.56
15	0	-1	1	0	37.83
16	0	1	1	0	39.65
17	-1	0	-1	0	35.08
18	1	0	-1	0	38.97
19	-1	0	1	0	37.98
20	1	0	1	0	38.82
21	0	-1	0	-1	32.92
22	0	1	0	-1	35.8
23	0	-1	0	1	37.81
24	0	1	0	1	39.2
25	0	0	0	0	36.16
26	0	0	0	0	36.86
27	0	0	0	0	36.24
28	0	0	0	0	36.43
29	0	0	0	0	36.01

$$\theta = 36.34 + 1.01A + 1.09B + 0.7C + 1.85D - 0.95AB + -0.76AC + 0.34AD + 0.095BC - 0.37BD - 2.79CD - 0.19A^2 - 0.14B^2 + 1.58C^2 + 0.25D^2 \quad (2)$$

The coefficient of determination R^2, corrected determination coefficient A_{dj} R^2, and CV of the regression equation are 0.9541, 0.9083, and 1.81%, respectively. The result implies that the regression model has a high degree of fitting and favorable correlations, so it can be used for further analysis. By ANOVA in regression of test results (Table 6), the regression model is found to have $P < 0.0001$, which indicates that the model is very significant and can be used to estimate the angle of repose of soil.

Among these four test factors, A, B, C, and D all have significant influences on the angle of repose of soil, and they are listed (in ascending order) as B, D, A and C according to their significance. AB and AC have a significant effect on the angle of repose, CD has an extremely significant effect on the angle of repose, and the interaction of other factors is not significant. Except for C^2 that has extremely significant influences of the angle of repose, quadratic items of other factors have insignificant influences.

Table 6

ANOVA of the regression equation of the angle of repose of soil

Sources of variation	Sum of squares	Degree of freedom	Mean square	F	P
Model	130.07	14	9.29	20.81	< 0.0001
A	12.24	1	12.24	27.42	0.0001
B	14.34	1	14.34	32.13	< 0.0001
C	5.84	1	5.84	13.08	0.0028
D	40.89	1	40.89	91.58	< 0.0001
AB	3.63	1	3.63	8.13	0.0128
AC	2.33	1	2.33	5.21	0.0386
AD	0.46	1	0.46	1.04	0.3261
BC	0.036	1	0.036	0.081	0.7803
BD	0.56	1	0.56	1.24	0.2836
CD	31.14	1	31.14	69.74	< 0.0001
A2	0.22	1	0.22	0.5	0.4913
B2	0.12	1	0.12	0.28	0.6073
C2	16.11	1	16.11	36.08	< 0.0001
D2	0.4	1	0.4	0.9	0.3599
Residual	6.25	14	0.45		
Lack of Fit	5.82	10	0.58	5.42	0.0589
Pure Error	0.43	4	0.11		
Cor Total	136.32	28			

The regression model of the angle of repose was optimized using the parameter optimization module in Design-Expert and taking the angle of repose of 35.77° as the objective. The resulting sets of solutions were used to simulate and verify the angle of repose. By doing so, a set of optimal solutions enabling a shape similar to that in physical tests was obtained, including A (coefficient of restitution of soil particles) of 0.57, B (coefficient of static friction of soil particles) of 0.85, C (the coefficient of rolling friction of soil particles) of 0.15, and D (JKR surface energy) of 1.05 J/m^2.

Box-Behnken test results of the sliding angle

Table 7 lists the Box-Behnken test results of the sliding angle. According to the test results, Design-Expert was used to establish the multivariate regression model of the sliding angle γ with various contact parameters of soil particles and the polynomial equation is expressed as equation 3.

Table 7

Box-Behnken test results of the sliding angle

Serial Number	Parameter E	Parameter F	Parameter G	Sliding angle γ [°]
1	-1 (0.05)	-1 (0.3)	0 (0.1)	18.66
2	1 (0.35)	-1	0	18.56
3	-1	1 (0.6)	0	23.16
4	1	1	0	23.13
5	-1	0 (0.45)	-1 (0.05)	14.95
6	1	0	-1	14.23
7	-1	0	1 (0.15)	23.62
8	1	0	1	23.89
9	0 (0.2)	-1	-1	10.15
10	0	1	-1	18.11
11	0	-1	1	24.37
12	0	1	1	23.89
13	0	0	0	22.04
14	0	0	0	21.7
15	0	0	0	21.63
16	0	0	0	22.06
17	0	0	0	22.29

$$\gamma = 21.94 - 0.072E + 2.07F + 4.79G + 0.017EF + 0.25EG - 2.11FG - 0.51E^2 - 0.55F^2 - 2.26G^2 \quad (3)$$

The coefficient of determination R^2, corrected determination coefficient A_{dj} R^2, and CV of the regression equation are 0.9963, 0.9915, and 1.83%, respectively, indicative of a high goodness of fit and close correlations in the regression model, so it can be used in subsequent analysis. Through ANOVA in regression of test results (Table 8), the regression model is found to have P < 0.0001, which indicates that the model is very significant and can be used to estimate the sliding angle of soil. Among the above three test factors, F and G have extremely significant influences while E exerts no significant influences on the sliding angle of soil; FG has extremely significant influences on the sliding angle, while the interaction of other factors exerts insignificant influences. E^2 and F^2 have significant influences while G^2 has extremely significant influences on the sliding angle of soil.

Table 8

ANOVA of the regression equation of the sliding angle of soil on steel components

Sources of variation	Sum of squares	Degree of freedom	Mean square	F	P
Model	261.29	9	29.03	207.81	< 0.0001
E	0.042	1	0.042	0.3	0.6003
F	34.24	1	34.24	245.07	< 0.0001
G	183.65	1	183.65	1314.53	< 0.0001
EF	0.00123	1	0.00123	0.00877	0.928
EG	0.25	1	0.25	1.75	0.227
FG	17.81	1	17.81	127.47	< 0.0001
E2	1.1	1	1.1	7.9	0.0261
F2	1.29	1	1.29	9.27	0.0187
G2	21.5	1	21.5	153.87	< 0.0001
Residual	0.98	7	0.14		
Lack of Fit	0.68	3	0.23	3.01	0.1577
Pure Error	0.3	4	0.075		
Cor Total	262.26	16			

By using the parameter optimization module in Design-Expert, the regression model of the sliding angle was optimized taking the sliding angle of 22.4° as the objective. The resulting sets of solutions were used to simulate and verify the sliding angle. In this way, a set of optimal solutions enabling a shape similar to that in physical tests could be obtained, including E (coefficient of restitution between soil and steel) of 0.09, F (coefficient of static friction between soil and steel) of 0.5, and G (coefficient of rolling friction between soil and steel) of 0.09.

Test verification results of the repose and sliding angles

To verify the accuracy of the contact model of soil and the calibration results of contact parameters, DEM simulation was carried out on the repose and sliding angles and the test results are shown in Figure 8 and Figure 10. Each test was repeated for five times.

The angle of repose of soil was 37.18° and the sliding angle of soil on the steel was 23.22°. Compared with the physical tests, the errors were separately 3.94% and 3.66%, indicating the accuracy and reliability of the calibrated parameters.

(a) Physical test of the angle of repose of soil (b) Simulation of the angle of repose of soil

Fig. 8 - Comparison of physical tests and simulation of the angle of repose of soil

(a) Initial sliding state (b) Complete sliding state

Fig. 9 - Physical tests of the sliding angle of soil. (a) Initial sliding state; (b) Complete sliding state

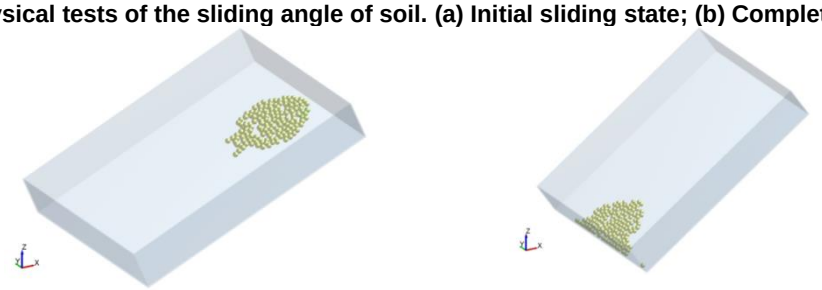

(a)Initial sliding state; (b)Complete sliding state

Fig. 10 - Simulation of the sliding angle of soil. (a) Initial sliding state; (b) Complete sliding state

Simulation of rotary tillage and ridging work

Figure 11 shows the rotary tillage and ridging process of the rotary tillage and ridging machine under the optimal combination of calibrated contact parameters between soil particles and geometries. The 0.4 s before simulation covered the contact process between rotary tillage and ridging components and soil, and soil particles migrated under action of rotary blades at 0.4 s; from 0.4 to 1.6 s, soil particles were cut and smashed under the action of rotary blades and thrown to the bonnets and soil-retaining boards in both sides with the high-speed rotation of the shaft of rotary blades; at 2.8 s, the rotary tillage and ridging machine was in complete contact with the soil particles, and the soil particles below the soil-retaining boards were extruded to ridges under the action of the ridge roller; from 2.8 to 4.0 s, the rotary tillage and ridging machine tended to work steadily and obvious ridges were formed on the soil surface.

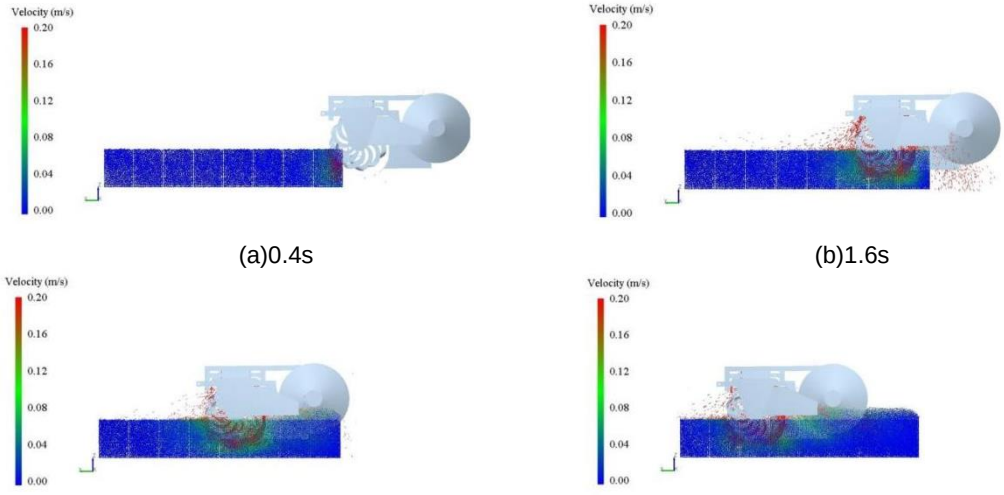

(a)0.4s (b)1.6s

(c)2.8s (d)4.0s

Fig. 11 - Simulation of rotary tillage and ridging work

Field test and simulation results of rotary tillage and ridging work are displayed in Table 9. The ridge height, top width of ridges, and bottom width of ditches in the field tests are 334.6, 326.3, and 158.8 mm, respectively; while those in simulation are 319.7, 303.6, and 145.2 mm. The two have relative errors of 4.45%, 6.96%, and 8.56% (all less than 10%), indicative of the accuracy of the simulation. The test results show that after calibrating and optimizing DEM model parameters using the multivariate regression model based on the JKR contact model and combining with value ranges of physical parameters recommended by the GEMM database of EDEM, rotary tillage ridging parts move in a same way in the simulated soil model as that in the field tests. The result indicates that the calibration and optimization of relevant contact parameters are reliable and effective.

Table 9

Comparison of simulation and field test results of rotary tillage and ridging work

Parameter	Field test result	Simulation result	Relative error
Ridge height [mm]	334.6	319.7	4.45%
Top width of ridges [mm]	326.3	303.6	6.96%
Bottom width of ditches [mm]	158.8	145.2	8.56%

CONCLUSIONS

The soil in the planting area of *Fritillaria thunbergii* was taken as the research object. The Hertz-Mindlin with JKR model was selected as the contact model to calibrate contact parameters between soil particles and between soil and steel through the combination of physical tests and simulation. The optimal combination of parameters was determined, which was verified by comparing field tests and simulation of rotary tillage and ridging work. The main conclusions obtained are as follows:

The multivariate regression model of the angle of repose was established using the Box-Behnken optimization method taking the coefficient of restitution of soil particles, the coefficient of static friction and the coefficient of rolling friction, and JKR surface energy of soil particles as test factors and the simulated angle of repose as the evaluation index of tests. Through optimization, the coefficients of restitution of soil particles, static friction and rolling friction, and JKR surface energy of soil particles were 0.57, 0.85, 0.15, and 1.05 J/m^2, respectively. Under the optimal solution, the simulated angle of repose is 37.18°, which has a relative error of 3.94% with the physical tests.

Soil sliding tests were conducted to calibrate and optimize the coefficients of restitution, static friction and rolling friction between soil and steel. Taking the sliding angle of soil as the evaluation index of tests, the multivariate regression model of the sliding angle was established using the Box-Behnken optimization method. Through optimization, the coefficients of restitution, static friction and rolling friction between soil and steel were obtained as 0.09, 0.5, and 0.09, respectively. The simulation result of the static sliding friction angle in the optimal solution is 23.22°, which has a relative error of 3.66% with the physical tests.

To verify the accuracy of the calibrated and optimized DEM model parameters, field tests and simulation of rotary tillage and ridging work were conducted and compared. The simulation can characterize soil migration in the rotary tillage and ridging process. The measurement results of the ridge height, top width of ridges, and bottom width of ditches in the simulation show errors of 4.45%, 6.96%, and 8.56% compared to those in field tests, that is, all relative errors are below 10%, within an acceptable range. The result indicates that simulation model of soil shares consistent physico-mechanical properties with the actual soil, verifying the accuracy and reliability of calibration results of DEM simulation parameters and the research method on planting area soil of rhizome medicinal materials. The research explored the method for systematic calibration and optimization of physical parameters of soil in DEM simulation and established the accurate DEM simulation model for planting area soil of rhizome medicinal materials in hilly region. It can provide theoretical basis and technical support for soil - machine interaction research and machine design.

ACKNOWLEDGEMENT

This research was funded by Institute-level basic scientific research business expenses project of the Chinese Academy of Agricultural Sciences (S202101-03, S202218, S202219). We greatly appreciate the careful and precise reviews by the anonymous reviewers and editors.

REFERENCES

[1] Aikins, K. A., Ucgul, M., Barr, J. B., Jensen, T. A., Antille, D. L., Desbiolles, J. M. (2021). Determination of discrete element model parameters for a cohesive soil and validation through narrow point opener performance analysis. *Soil and Tillage Research*, Elsevier/Amsterdam, Vol.213, ISSN 0167-1987, 105123.

[2] Chen, Y., Munkholm, L. J., Nyord, T. (2013). A discrete element model for soil–sweep interaction in three different soils. Soil Tillage Res, 2013, 126, 34-41. *Soil and Tillage Research*, Elsevier/Amsterdam, Vol.126, pp.34-41.

[3] Chen, Y.; Zou, J.; Sun, H.; Qin, J.; Yang, J. (2021). Metals in traditional Chinese medicinal materials (TCMM): A systematic review. *Ecotoxicology and Environmental Safety*, Elsevier/Amsterdam, Vol.207.

[4] Dai, F.; Song, X.; Zhao, W.; Zhang, F.; Ma, H.; Ma, M. (2019). Simulative Calibration on Contact Parameters of Discrete Elements for Covering Soil on Whole Plastic Film Mulching on Double Ridges (全膜双垄沟覆膜土壤离散元接触参数仿真标定). *Transactions of the Chinese Society of Agricultural Engineering*, Chaoyang / Beijing, vol. 50 No. 2, ISSN 1002-6819, pp. 49-56+77.

[5] Ding, Q.; Ren, J.; Belal, E.; Zhao, J.; Ge, S.; Li, Y. (2017) DEM Analysis of Subsoiling Process in Wet Clayey Paddy Soil (湿粘水稻土深松过程离散元分析). *Transactions of the Chinese Society of Agricultural Engineering*, Chaoyang / Beijing, vol. 48 No. 3, ISSN 1002-6819, pp. 38-48.

[6] Huang, L. (2021). National Chinese Medicinal Materials Production Statistics Report (2020). Shanghai Science and Technology Press: Shanghai, China.

[7] Li, Y.; Fan, J.; Hu, Z.; Luo, W.; Yang, H.; Shi, L.; Wu, F. (2022) Calibration of Discrete Element Model Parameters of Soil around Tubers during Potato Harvesting Period. *Agriculture*, MDPI/Basel, Vol.12.

[8] Ma, S.; Xu, L.; Yuan, Q.; Niu, C.; Zeng, J.; Chen, C.; Wang, S.; Yuan, X. (2020) Calibration of discrete element simulation parameters of grapevine anti-freezing soil and its interaction with soil-cleaning components (葡萄藤防寒土与清土部件相互作用的离散元仿真参数标定). *Transactions of the Chinese Society of Agricultural Engineerin*g, Chaoyang / Beijing, vol.36, No.1, ISSN 1002-6819, pp. 40-49.

[9] Shi, L.; Zhao, W.; Sun, W. (2017). Parameter calibration of soil particles contact model of farmland soil in northwest arid region based on discrete element method (基于离散元的西北旱区农田土壤颗粒接触模型和参数标定). *Transactions of the Chinese Society of Agricultural Engineering*, Chaoyang / Beijing, vol.33, No.21, pp. 181-187.

[10] Song, S.; Tang, Z.; Zheng, X.; Liu, J.; Meng, X.; Liang, Y. (2021). Calibration of the discrete element parameters for the soil model of cotton field after plowing in Xinjiang of China (新疆棉田耕后土壤模型离散元参数标定). *Transactions of the Chinese Society of Agricultural Engineering*, Chaoyang / Beijing, vol.37, No.20, pp. 63-70.

[11] ***The Ministry of Industry and Information Technology of the People's Republic of China. *Rototill combine equipment Part 2: Rototill scarifying-paring-ridging machine: JB/T 8401.2-2017*; Machinery Industry Press: Beijing,

[12] Tian, X.; Cong, X.; Qi, J.; Guo, H.; Li, M.; Fan, X. (2021). Parameter Calibration of Discrete Element Model for Corn Straw-Soil Mixture in Black Soil Areas (黑土区玉米秸秆-土壤混料离散元模型参数标定). *Transactions of the Chinese Society of Agricultural Engineering*, Chaoyang/Beijing, vol. 52 No.10, pp.100-108+242.

[13] Ucgul, M.; Saunders, C. (2020). Simulation of tillage forces and furrow profile during soil-mouldboard plough interaction using discrete element modelling. *Biosystems Engineering*, Elsevier/Amsterdam, Vol.190, pp.58-70.

[14] Xing, J.; Zhang, R.; Wu, P.; Zhang, X.; Dong, X.; Chen, Y.; Ru, S. (2020). Parameter calibration of discrete element simulation model for latosol particles in hot areas of Hainan Province (海南热区砖红壤颗粒离散元仿真模型参数标定). *Transactions of the Chinese Society of Agricultural Engineering*, Chaoyang / Beijing, vol.36, No.5, pp. 158-166.

[15] Zhao, Z.; Guo, P.; Brand, E. (2012). The formation of daodi medicinal materials. *Journal of Ethnopharmacology*, Elsevier/Amsterdam, Vol.140, pp.476-481.

INVESTIGATION OF THE TRACTOR PERFORMANCE WHEN BALLASTING ITS REAR HALF-FRAME

/

ДОСЛІДЖЕННЯ ТЯГОВИХ ПОКАЗНИКІВ ТРАКТОРА ПРИ БАЛАСТУВАННІ ЙОГО ЗАДНЬОЇ ПІВРАМИ

Volodymyr BULGAKOV[1)], **Roman ANTOSHCHENKOV**[2)], **Valerii ADAMCHUK**[3)], **Ivan HALYCH**[2)], **Yevhen IHNATIEV**[4)], **Ivan BELOEV**[5)], **Semjons IVANOVS***[6)]

[1)]National University of Life and Environmental Sciences of Ukraine,
[2)]State Biotechnological University, Kharkiv, Ukraine,
[3)]Institute of Mechanics and Automation of Agricultural Production of the National Academy of Agrarian Sciences of Ukraine, Ukraine,
[4)]Dmytro Motornyi Tavria State Agrotechnological University, Ukraine,
[5)]Angel Kanchev" University of Ruse, Bulgaria,
[6)]Latvia University of Life Sciences and Technologies, Latvia
Correspondence: *Tel.+37129403708, e-mail: semjons@apollo.lv*
DOI: https://doi.org/10.35633/inmateh-68-52

Keywords: *machine and tractor aggregates, traction indicators, half-frame, ballasting, capacity*

ABSTRACT

When designing and determining the potential technical capabilities and characteristics of the tractor, the so-called traction calculation is carried out. The aim of the work is to study regularities of changes in the traction and coupling characteristics of a tractor with an articulated frame depending on the size of the ballast, the presence of dual wheels and other parameters, using the KhTZ-242K tractor as an example. The numerical solution of the deduced mathematical model made it possible to obtain graphical dependences of the change in the main traction and coupling characteristics of the tractor KhTZ-242K depending on the mass of the tractor, which varied from 8600 kg to 10100 kg by changing the ballast mass. The maximum tractive power of the tractor on single wheels without a ballast is 121 kW, which is achieved at a speed of 12 km·h^{-1}, and on single wheels with a ballast 122 kW, at a speed of 15 km·h^{-1}. This, in its turn, greatly affects the productivity and fuel efficiency of the aggregate.

АНОТАЦІЯ

При конструюванні та визначенні потенційних технічних можливостей і характеристик трактора важливе значення має, так званий тяговий розрахунок. В результаті теоретичних досліджень отримано закономірності зміни тягово-зчіпних характеристик трактора з шарнірно зчленованою рамою в залежності від величини баласту та наявності здвоєних коліс. Проведене числове рішення отриманої математичної моделі дозволило отримати графічні залежності зміни основних тягово-зчіпних характеристик трактора ХТЗ-240К в залежності від маси трактора, яка змінювалася від 8600 кг до 10100 кг шляхом зміни маси баласту. Максимальна тягова потужність колісного трактора ХТЗ-240К на одинарних колесах без баласту становить 121 кВт, що досягається за швидкості 12 км·г$^{-1}$, а на одинарних колесах із баластом N_{kr} =122 кВт – при швидкості 15 км·г$^{-1}$.

INTRODUCTION

When designing and determining the potential technical capabilities and characteristics of the tractor, the so-called traction calculation is carried out *(Artiomov et al., 2021; Blundell and Harty, 2004).* As investigations have shown, high traction and fuel economic indicators of the tractor can be reached only in the case of an optimal ratio of its main parameters, which are initially determined by calculation at the design stage *(Cviklovic et al., 2021; Artiomov et al., 2021; Bulgakov et al., 2016)*. Their interrelation, to a greater extent, characterizes the main operational qualities of tractors *(Adamchuk et al., 2016; Bulgakov et al., 2020; Bulgakov et al., 2022).*

The analysis of some works showed that for the traction calculation of the tractor the following basic parameters are necessary: the total and the structural mass; the maximum operating power of the engine; the transmission gear ratios and the estimated gear speeds (*Adamchuk et al., 2016*; *Blundell and Harty, 2004; Bulgakov et al., 2019)*.

Vibrations of the elements of the machine and tractor aggregates lead to a deterioration in the fulfilment of the agrotechnical requirements because of nonstraightness of the trajectory of movement, over-compaction of the soil, etc. To reduce the vibrations of tractors and agricultural machines, the following measures are justified: the use of elastic elements in the transmission of the tractors; an active hitch with a pneumohydraulic elastic element; elastic fastening of the working bodies of the agricultural machines; installation of damping elements between the frames; the use of dual / triple wheels; ballasting, etc. With an increase in the weight of the tractor, the contact area of the wheel (caterpillar) with the field surface should also increase in such a way as to reduce the pressure on the soil or keep it at an acceptable level. For technological adaptation, reduction of vibrations of the elements of the wheeled tractors and increasing their productivity, it is recommended to install a ballast.

Ballasting of tractors is carried out mainly by installing removable ballast weights in front of the tractor frame on a special bracket and on the disks of the rear wheels, as well as an additional set of front and rear wheels, or only the rear ones. Sometimes on some models (Terrion 5280, Terrion 7360), weights are also installed on the front wheel disks *(Cviklovic et al., 2021; Artiomov et al., 2021; Ivanovs et al., 2020; Beloev et al., 2015)*.

Accordingly, when designing a tractor, the maximum value of the operating weight should be chosen in such a way that, when the tractor is operating on unpeeled stubble of cereal crops at the lowest operating speed and the rated traction load, the slippage of the movers does not exceed the allowed rate, which is set in the regulatory documents. This rate has the following permitted limits: 18% – for the tractors with a wheel configuration 4K2; 16% – for the tractors with a wheel configuration 4K4 and 5% – for the caterpillar tractors. Tractor ballasting in order to improve the traction characteristics was studied in *(Galych et al., 2021; Galych, 2018; Ivanovs at al., 2018)*. However, the existing design features of tractors require a more accurate determination of their traction properties, depending on the size of the ballast.

The aim of the work is to study regularities of changes in the traction and coupling characteristics of a tractor with an articulated frame depending on the size of the ballast, the presence of dual wheels and other parameters, using the KhTZ-242K tractor as an example.

MATERIALS AND METHODS

During the conducted experimental studies of the traction dynamics of the tractor, vibrations of the tractor half-frames along three axes were studied depending on the speed of the movement and load, taking into account ballasting of the rear half-frame of the tractor and two sets of the wheel systems (single and dual tires). The KhTZ-242K tractor was chosen as the object of research (Fig. 1).

Fig. 1 - Object of experimental research (tractor KhTZ-242K)

The tractor during the research was equipped with an inertial measuring device (IVP-1) *6*, which was installed on the first half-frame of the tractor; inertial measuring device (IVP-2) *7* which was installed on the second half-frame of the tractor; the wheel dynamics sensors *8*, which are located in the centre of rotation; electronic dynamometer *9*. Communication between the sensors, inertial measuring devices and the computing module takes place via CAN bus *5*. The measuring system was powered by a gel lead-acid AGM battery. The data of the research results are stored on the storage medium in the computing module *1*, which is controlled by console 2. A GPS *3* navigation receiver is connected to the module. Location of sensors on the tractor is shown in Fig. 2.

The dynamic sensors *1, 2, 7, 8* were installed on the axes of rotation of the wheels. The vibration of the first half-frame of the tractor was determined by IVP-1 *4*, respectively, for the second half-frame IVP-2 *6*. These sensors cannot be located in the centres of mass of the tractor half-frames *3* and *9*; therefore, the methodology for the compensation of the error in the location of the sensors, described in (*Galych et al., 2021*, *Galych, 2018)*, was used, which determined the actual accelerations in the centres of mass of the tractor half-frames. The navigation receiver antenna *5* is located on the tractor cab symmetrically to the longitudinal axis. The tractor is equipped with ballast *10* weighing 1500 kg, which is located on the second half-frame of the tractor. The traction force was measured by an electronic dynamometer *11*.

In experimental investigations there was used the measuring system VSDEMM for fixing the dynamics and energy of mobile machines (*Artiomov et al., 2021; Galych et al., 2021)*. This measuring system relates to the technical means of operational control and diagnostics, and it is designed to determine the kinematic, dynamic, power and energy characteristics of the mobile machines and their elements during the road, field and bench tests (*Galych, 2018*).

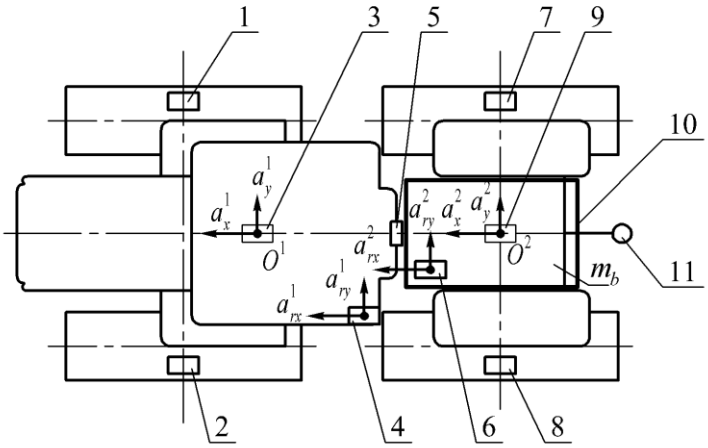

Fig. 2 - Layout of sensors on the tractor

1, 2, 7, 8 – the wheel dynamics sensors (front left, front right, rear left, rear right);
3 – centre of gravity of the first half-frame of the tractor; 4 – IVP-1; 5 – the GPS receiver antenna; 6 – IVP-2;
9 – centre of gravity of the second half-frame of the tractor; 10 – the –ballast; 11 – the traction force sensor

To carry out theoretical studies, a diagram of a tractor with an articulated frame, equipped with a ballast, was drawn up (Fig. 3).

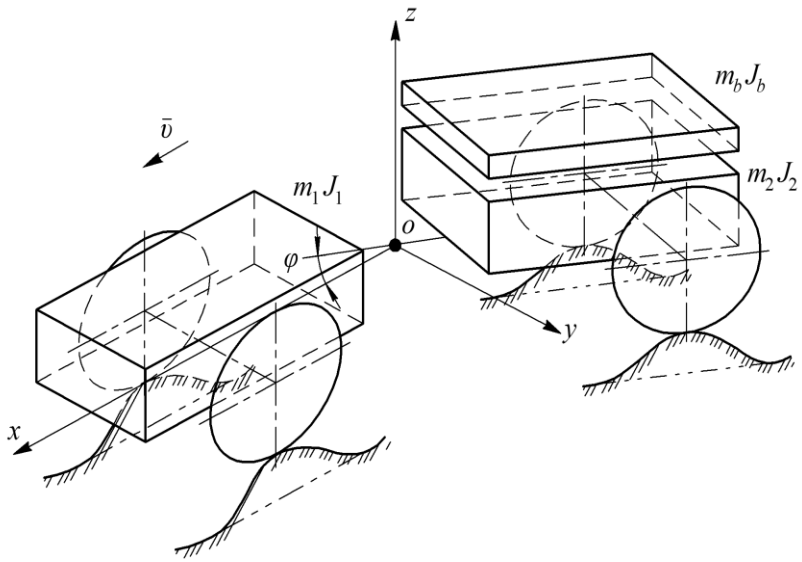

Fig. 3 - Scheme of a tractor with an articulated frame, equipped with a ballast on the rear half-frame

m_b *– weight of the ballast;* J_b *– the reduced moment of inertia of the ballast*

When compiling a mathematical model of the effect of the ballast upon the traction-scene properties, the tractor traction balance equation was used, which, with steady motion on a horizontal surface, has the form *(Werner, 2012; Yahya et al., 2004; Bulgakov et al., 2020; Bulgakov et al., 2019)*:

$$P_k = P_{kr} + P_f \text{ , N,} \tag{1}$$

where P_k – the tangential traction force on the rim of the driving wheel;

P_{kr} – the traction force on the hook of the tractor;

P_f – the rolling resistance force.

The traction indicators of the tractor are determined for the following modes of operation: from the nominal – $M_{\text{d.nom}}$ up to the maximum torque $M_{\text{d.max}}$ for the range of the working gears (*Adamchuk et al., 2016*).

The tangential traction force is determined:

$$P_k = M_d \cdot U_{\text{tr}} \frac{\eta_{\text{tr}}}{r_{\text{kd}}} \text{ , N,} \tag{2}$$

where U_{tr} – the transmission ratio;

η_{tr} – coefficient of efficiency of the transmission;

r_{kd} – the dynamic radius of the wheel, m.

However, we use a model of the wheel that takes into account the dependence on pressure and speed; then the dependence of the rolling resistance force will take the form:

$$P_f = \left(\frac{P}{P_0}\right)^{\alpha} \left(\frac{P_Z}{P_{Z0}}\right)^{\beta} P_{Z0} \cdot \left(A + B|v| + Cv^2\right), \tag{3}$$

where P , P_0 – the actual and the nominal pressure in the tire;

P_Z , P_{Z0} – the actual and the nominal load onto the wheel;

α , β , A , B , C – the approximating coefficients.

The rolling resistance force is determined through the sum of the rolling resistances for each of the wheels of the tractor separately, taking into account the pressure in the tire, the load onto the wheel and the travel speed:

$$P_f = \sum_{i=1}^{2}\sum_{j=1}^{2}\left(\left(\frac{P_{ij}}{P_{0ij}}\right)^{\alpha} \left(\frac{P_{Zij}}{P_{Z0ij}}\right)^{\beta} P_{Z0ij} \cdot \left(A + B\left|v_{Cij}\right| + Cv_{Cij}^2\right)\right), \text{ N} \tag{4}$$

Taking into account (1), the formula for determining the tangential traction force (2) and the rolling resistance force (3), the traction force on the tractor hook is determined from the expression:

$$P_{\text{kr}} = M_d \cdot U_{\text{tr}} \frac{\eta_{\text{tr}}}{r_{\text{kd}}} - \sum_{i=1}^{2}\sum_{j=1}^{2}\left(\left(\frac{P_{ij}}{P_{0ij}}\right)^{\alpha} \left(\frac{P_{Zij}}{P_{Z0ij}}\right)^{\beta} P_{Z0ij} \cdot \left(A + B\left|v_{Cij}\right| + Cv_{Cij}^2\right)\right), \text{ N} \tag{5}$$

The theoretical speed of movement is determined (without considering the slipping of the driving wheels):

$$\upsilon_t = \omega_d \cdot \frac{r_{kd}}{U_{tr}} \text{ , m·s}^{-1}. \tag{6}$$

The actual speed of movement takes into consideration slipping of the driving wheels:

$$\upsilon_d = \upsilon_t \left(1 - \delta\right) \text{ , m·s}^{-1}, \tag{7}$$

where δ – slipping of driving wheels.

The hook power (the power on the hook) is determined from the expression:

$$N_{\text{kr}} = P_{\text{kr}} \cdot \upsilon_d \text{ , W,} \tag{8}$$

or in an expanded form:

$$N_{\text{kr}} = \left(M_d \cdot U_{\text{tr}} \frac{\eta_{\text{tr}}}{r_{\text{kd}}} - \sum_{i=1}^{2}\sum_{j=1}^{2}\left(\left(\frac{P_{ij}}{P_{0ij}} \right)^{\alpha} \left(\frac{P_{Zij}}{P_{Z0ij}} \right)^{\beta} P_{Z0ij} \right) \cdot \left(A + B\left|v_{Cij}\right| + Cv_{Cij}^2 \right) \right) \times$$
$$\times \omega_d \cdot \frac{r_{kd}}{U_{tr}} (1-\delta), \text{ W.} \quad (9)$$

Equation (9), obtained as a result of theoretical studies, in contrast to the known ones, makes it possible to simultaneously determine the influence of the type of movers, air pressure in the tires and ballasting upon the theoretical traction characteristic of the tractor, and the fuel consumption.

RESULTS

Using the results of the theoretical research and methodology (*Galych et al., 2021; Bulgakov et al., 2022)*, a numerical solution of the mathematical model (9) was carried out. Due to ballasting the mass of the tractor during its numerical modelling varied from 8600 kg to 10100 kg (tractor KhTZ-240K). As a result, the dependence of slipping of tractor's driving wheels upon the mass m_t of the tractor and tractive effort was obtained:

$$\delta = -459.9 + 0.1415m_t - 0.00178P_{\text{kr}} - 1.459 \cdot 10^{-5} m_t^{\,2} +$$
$$+1.391 \cdot 10^{-7} m_t P_{\text{kr}} + 2.342 \cdot 10^{-7} P_{kr}^2 + 5.058 \cdot 10^{-10} m_t^{\,3} + \quad (10)$$
$$+6.69 \cdot 10^{-12} m_t^{\,2} P_{\text{kr}} - 2.4466 \cdot 10^{-11} m_t P_{\text{kr}}^2 + 3.811 \cdot 10^{-12} P_{\text{kr}}^3.$$

A graphical display of dependence (10) of slipping of tractor's driving wheels upon the mass of the tractor and the tractive effort is shown in Fig. 4.

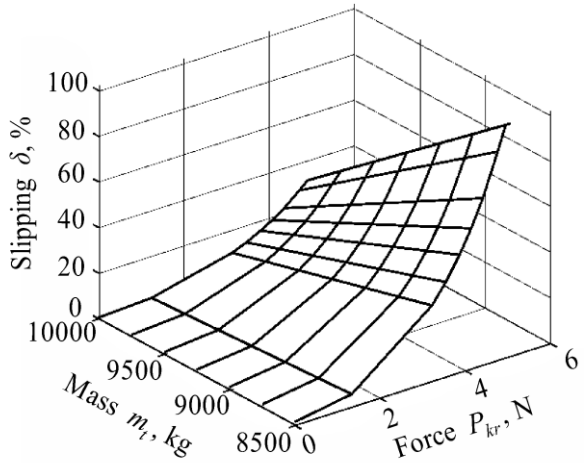

Fig. 4 - Dependence of slipping of the driving wheels δ of the tractors of the KhTZ-240K series upon mass m_t of the tractor and tractive effort P_{kr}

The analysis of the obtained dependence showed that an increase in the weight of the tractor by 1500 kg leads to a decrease in the wheel slip of the tractor from 5.9 to 1.8% at P_{kr} = 13000 N, from 33.5 to 10.3% at P_{kr} = 32000 N, and from 41.8 to 15.9% at P_{kr} = 35300 N (Fig. 4), etc. ballasting leads to the improvement of the traction class tractor.

Next, dependence of the rolling resistance force of the tractor wheel on the load onto the wheel G_k and the speed of movement were determined, which has the form:

$$P_{\text{kf}} = 1255 + 739.7\upsilon + 60.08G_k + 171\upsilon^2 + 35.42\upsilon G_k - 0{,}0505G_k^2 -$$
$$-3.588 \cdot 10^{-14}\upsilon^3 + 8.186\upsilon^2 G_k - 0.026\upsilon G_k^2 + 0.00085G_k^3. \quad (11)$$

A graphical representation of the dependence of the rolling resistance of the tractor wheel on the load onto the wheel and the speed of movement is shown in Fig. 5.

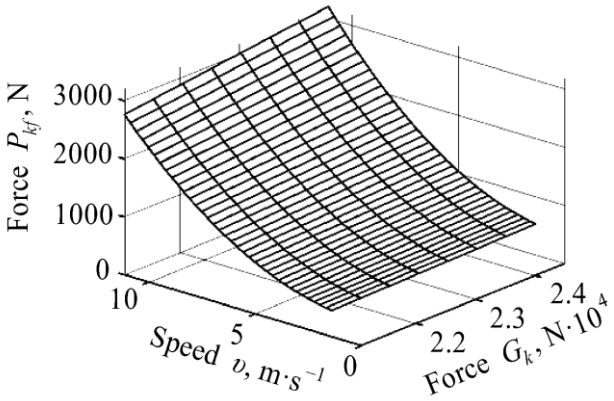

Fig. 5 - Dependence of the rolling resistance force G_k of the tractor wheel on the load onto the wheel and the speed of movement υ

The analysis shows that the lowest rolling resistance force of the tractor wheel P_{kf} = 458 N is observed for the speed of movement υ = 1.38 m·s^{-1} and the load on the wheel G_k = 21070 N (Fig. 3). When the load onto the wheel is increased to 24500 N, P_{kf} increases to 530 N. At the speed of movement υ = 2.8 m·s^{-1} – P_{kf} = 568 N, and it increases to 657 N when the tractor is ballasted. The maximum value of the rolling resistance force of the tractor wheel $P_{kf\,max}$ = 2764 N at υ = 11.1 m·s^{-1} and G_k = 21070 N; and increases to $P_{kf\,max}$ = 3199 N (for a ballasted tractor).

With further solution of the obtained dependence (9), there was established a dependence of the power that is spent for rolling the tractor wheel from the load onto the wheel G_k and the speed of movement υ, which has the form:

$$N_{\text{kf}} = 7842 + 8250\upsilon + 375.5G_k + 3206\upsilon^2 + 437.4\upsilon G_k - 0.3917G_k^2 + \\ +494.2\upsilon^3 + 153.5\upsilon^2 G_k - 0.3242\upsilon G_k^2 + 0.006646G_k^3. \quad (12)$$

A graphical representation of the dependence of the power that is spent on rolling the tractor wheel is shown in Fig. 6.

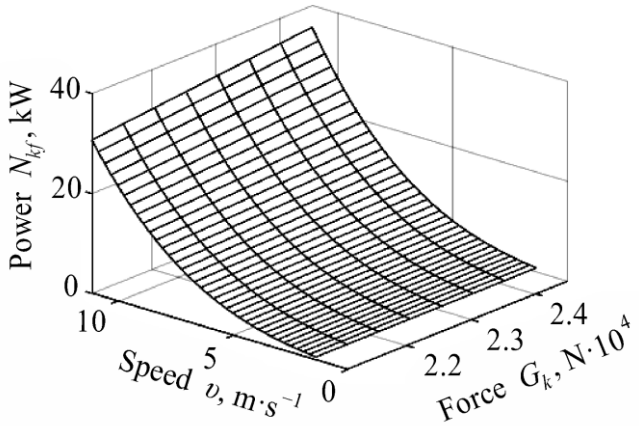

Fig. 6 - Dependence of the power which is spent for rolling the tractor wheel on the load onto the wheel G_k and the speed of movement υ

After examination of Fig. 8 we can say that the minimum power that is spent for rolling the tractor wheel is N_{kf} = 0.63 kW for the speed of movement υ = 1.38 m·s^{-1} and the load on the wheel G_k = 21070N (Fig. 8), and it increases up to N_{kf} = 0.91 kW with an increase in load onto the wheel up to 24500 N. For the operating speed of the sowing aggregate υ = 2.8 m·s^{-1}, the power is N_{kf} = 1.51 kW (for a tractor without a ballast) and N_{kf} = 1.82 kW (for a tractor with a ballast). At the maximum travel speed of 11.11 m·s^{-1}, for a tractor without a ballast, 30.7 kW is spent for the wheel rolling, and for a tractor with a ballast, 35.5 kW.

The dependence of the tractor rolling resistance force on mass m_t and the speed of movement υ, has the form:

$$P_f = 5019 + 2959\upsilon + 204.3G_k + 683.8\upsilon^2 + 141.7\upsilon G_k - 0.2023G_k^2 - \\ -6.346\cdot10^{-15}\upsilon^3 + 32.74\upsilon^2 G_k - 0.105\upsilon G_k^2 + 0.003432G_k^3. \quad (13)$$

A graphical representation of the dependence of the tractor's rolling resistance force on mass m_t and the speed of movement is shown in Fig. 9. Analysing the obtained dependence (9), it can be seen that the minimum value of the tractor rolling resistance force is P_f = 1832 N at υ = 5 km·h^{-1} and m_t = 8600 kg. At the operating speed υ = 10 km·h^{-1}, the rolling resistance force of the tractor is P_f = 2272 N (at m_t = 8600 kg), and an increase in the tractor weight by 1500 kg increases the rolling resistance to 2630 N. The maximum value of the tractor rolling resistance force is $P_{f\,max}$ = 11056 N (at m_t = 8600 kg) and $P_{f\,max}$ = 12798 N (at m_t = 10100 kg) (Fig. 7).

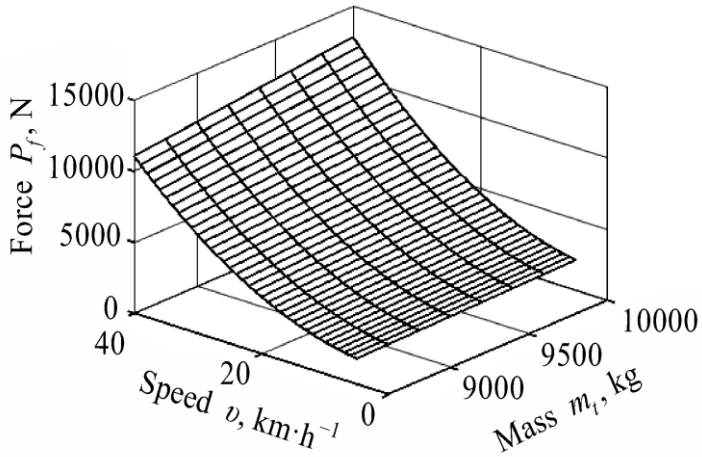

Fig. 7 - Dependence of the tractor rolling resistance force on mass m_t and the speed of movement υ

Next, the dependence of the power that is spent for rolling the tractor was determined, which has the form:

$$N_f = 3.137\cdot10^4 + 3.3\cdot10^4\upsilon + 1502G_k + 1.283\cdot10^4\upsilon^2 + 1750\upsilon G_k - \\ -1.567G_k^2 + 1977\upsilon^3 + 614.1\upsilon^2 G_k - 1.297\upsilon G_k^2 + 0.02658G_k^3. \quad (14)$$

A graphical display of the dependence of the power that is spent for rolling the tractor on the mass m_t and the speed of movement υ is shown in Fig.8.

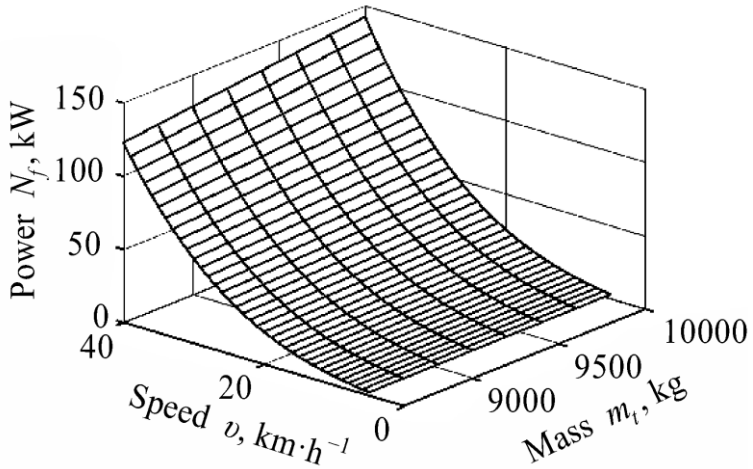

Fig. 8 - Dependence of the power which is spent for rolling the tractor on the load onto the wheel G_k and the speed of movement υ

The analysis shows that the power that is spent for rolling the tractor at a speed of υ = 10 km·h^{-1} and m_t = 8600 kg is equal to N_f = 2.2 kW. It increases to N_f = 2.6 kW with an increase in the tractor weight by

1500 kg (Fig. 10). The minimum power that is spent for rolling the power tool without a ballast is $N_{f\,min}$ = 1.8 kW. Ballasting raises this value to N_f = 2.1 kW. The maximum value of the power that is spent for rolling the power tool without a ballast is N_f = 110 kW, with a ballast – N_f = 127.9 kW. There was determined the dependence of the tractive power of the KhTZ-242K tractor on the mass of the ballast and the traction force on the hook (Fig. 9).

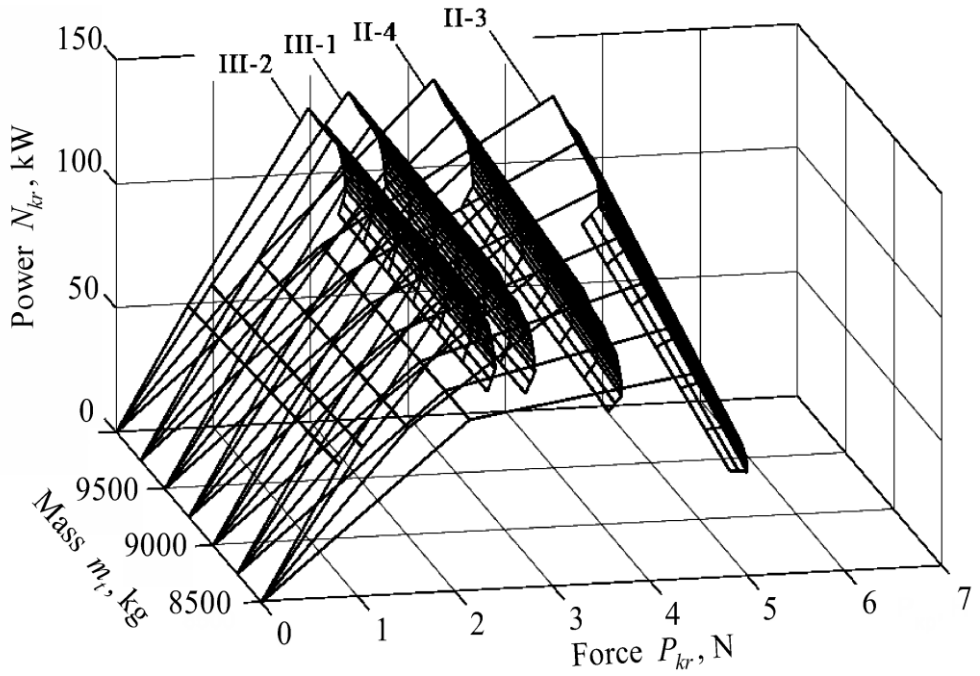

Fig. 9 - Dependence of the tractive power of the KhTZ-242K tractor on the mass of the ballast and the traction force on the hook

The analysis of Fig. 11 shows that the traction power N_{kr} = 113 kW is developed by the tractor without a ballast in the III-2 gear with the traction force on the hook P = 20698 N, and the installation of the ballast leads to an increase in the traction power N_{kr} = 115 kW with a decrease in the traction force on the hook to 19755 N. Accordingly, for transmission III –1 – N_{kr} = 118 kW, P = 24770 N for a tractor without a ballast and N_{kr} = 121 kW, P = 23927 N with a ballast. The maximum tractive power of the tractor is achieved in the II-4 gear and is N_{kr} =120 kW at P=33179 N, and with the ballast installed N_{kr} = 122 kW at P = 32677 N. In the II-3 gear the installation of the ballast increases the traction power by 31% from 82 kW to 108 kW.

Thus, the maximum tractive power of the tractor on single wheels without a ballast 121 kW is achieved at a speed of 12 km·h^{-1}; on single wheels with a ballast N_{kr} = 122 kW – at speed υ = 15 km·h^{-1}. The lowest value of slippage was observed for the KhTZ-242K tractors on dual wheels with a ballast installed. However, at the traction forces over 60 kW, slippage of the gearbox clutch was observed during testing. The highest value of slippage is observed for tractors in standard setting on single wheels without a ballast. To confirm the obtained theoretical results, experimental studies were conducted, and the traction power of the KhTZ-242K tractor was determined (Fig. 10).

The analysis of the graphical results of experimental studies showed that for a KhTZ-242K wheeled tractor on single wheels without a ballast, the maximum traction power N_{kr} =121 kW is achieved at a translational speed $\upsilon = 12$ km·h^{-1}, the traction efficiency η_t =0.68, and traction force on the hook P = 30.2 kN.

The maximum traction power of 122 kW for a tractor on single wheels with a ballast (Fig. 10, b) is achieved at a speed of 15 km·h^{-1}, a traction efficiency of 0.68, and a traction force on the hook of 29 kN. The maximum allowed value of slipping of the tractor wheels is achieved with a traction force on the hook of 45 kN. The tractor KhTZ-242K on dual wheels without a ballast develops maximum tractive power of 121 kW at a speed of 14.5 km·h^{-1}, traction efficiency of 0.68 and traction force on the hook of 32 kN. However, 15% slippage of the tractor wheels is achieved with a traction force on the hook of 42 kN.

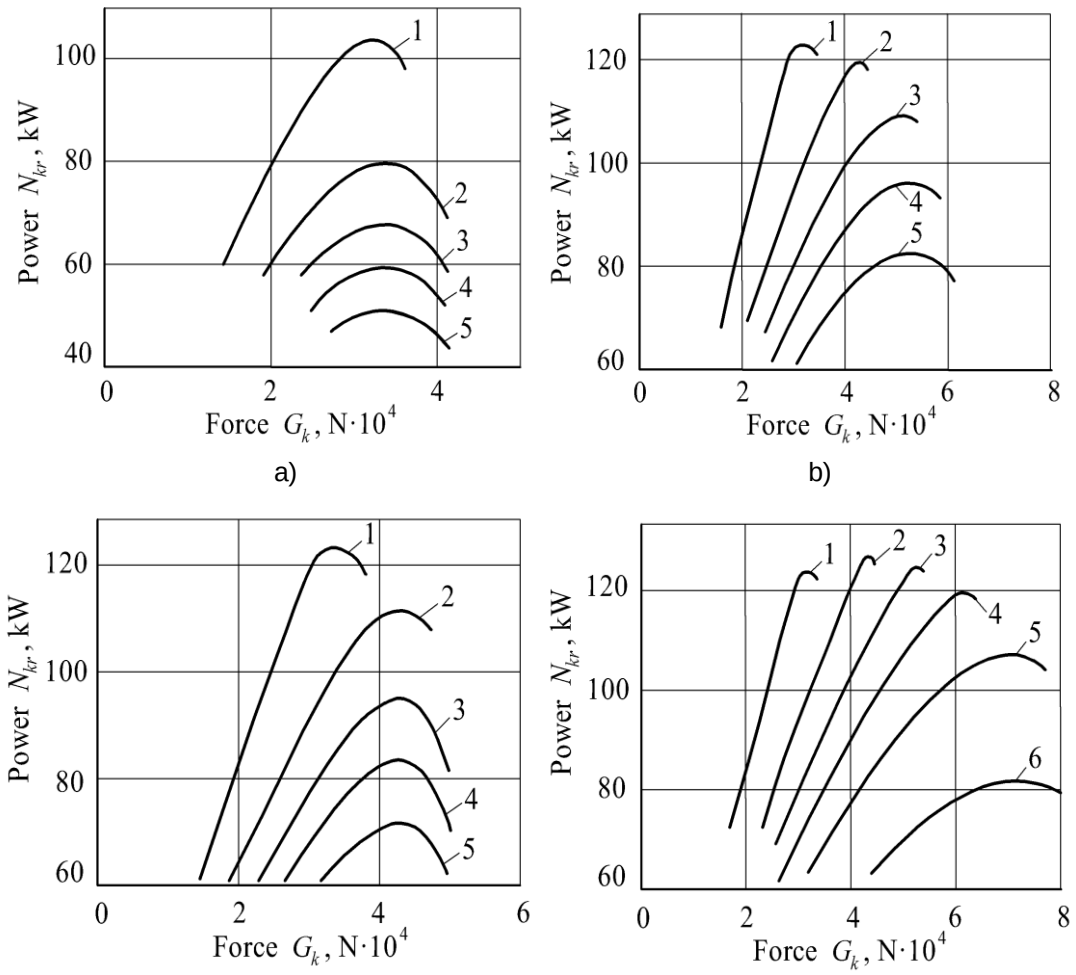

Fig. 10 - Traction power of the KhTZ-242K tractor

a – single wheels without a ballast; b – single wheels with a ballast; c – twin wheels without a ballast; g – dual wheels with a ballast; on gears: 1 – II-4; 2 – II-3; 3 – II-2; 4 – II-1; 5 – I-4; 6 – I-3

The use of twin wheels and a ballast allows the tractor to develop a maximum traction power of 126 kW at a speed of 11...15 km·h^{-1}, a traction efficiency of 0.72 and a hook pull of 35...45 kN. The maximum value of the wheel slip according to agrotechnical requirements of 15% is achieved with a traction force on the hook of 60 kN. However, it is not recommended to operate the tractor with pulling forces over 60 kN, as the reliability of its units is reduced. At tractive forces over 45 kN, the tractors of the KhTZ-240K series without a ballast with single or dual wheel systems are prone to galloping.

CONCLUSIONS

When conducting theoretical research, regularities were obtained for changing the traction and coupling characteristics of a tractor with an articulated frame, depending on the size of the ballast and the presence of dual wheels.

The numerical solution of the deduced mathematical model made it possible to obtain graphical dependences of the change in the main traction and coupling characteristics of the tractor depending on the mass of the tractor, which varied from 8600 kg to 10100 kg by changing the ballast mass.

The maximum tractive power of the tractor on single wheels without a ballast is 121 kW, which is achieved at a speed of 12 km·h^{-1}, and on single wheels with a ballast N_{kr} = 122 kW, at a speed of v = 15 km·h^{-1}. Which, in its turn, greatly affects the productivity and fuel efficiency of the aggregate.

As a result of the analysis of the experimental data of the traction tests, it is recommended to equip the KhTZ-240K tractor with a ballast, weighing 1500 kg, to reduce slipping. For light soils and the spring work the twin wheel systems are recommended.

REFERENCES

[1] Adamchuk V., Bulgakov V., Nadykto V., Ihnatiev Y., Olt J. (2016). Theoretical research into the power and energy performance of agricultural tractors. *Agronomy Research*. Vol. 14 (5), pp. 1511-1518, Tartu / Estonia.

[2] Artiomov N., Antoshchenkov R., Antoshchenkov V., Ayubov Abdulmelik. (2021) Innovative approach to agricultural machinery testing. *Engineering for Rural Development*. Vol.20. pp. 692-698, Jelgava / Latvia.

[3] Beloev H., Borisov B., Adamchuk V., Petrychenko I. (2015). Theory of movement of the combined seeding unit. *Agriculture and Agricultural Science Procedia*, vol. 7, pp. 21-26, Amsterdam / Netherlands.

[4] Blundell M, Harty D. (2004). The Multibody System Approach to Vehicle Dynamics. 518 p., Amsterdam / Netherlands.

[5] Bulgakov V., Adamchuk V., Arak M., Nadykto V., Kyurchev V., Olt J. (2016). Theory of vertical oscillations and dynamic stability of combined tractor-implement unit. *Agronomy Research*. Vol. 14(3), pp. 689–710, Tartu / Estonia.

[6] Bulgakov, V., Aboltins, A., Ivanovs, S., Beloev H., Nadykto V., Ihnatiev Ye. (2022). Theory of Movement of Machine-Tractor Unit with Trailer Haulm Harvester Machine. *Applied Sciences* (Switzerland), Vol.12, article 3901, Basel / Switzerland.

[7] Bulgakov V., Pascuzzi S., Beloev H., Ivanovs S. (2019), Theoretical investigations of the headland turning agility of a trailed asymmetric implement-and-tractor aggregate. *Agriculture.* Vol. 9(10), article 224, Basel / Switzerland.

[8] Cviklovic V., Srnanek R., Hruby D., Harnicarova M. (2021). The Control Reversing Algorithm for Autonomous Vehicles with PSD-Controlled Trailers. *Acta Technologica Agriculturae*. Vol. 4, pp. 187-194, Nitra / Slovakia.

[9] Galych I., Antoshchenkov R., Antoshchenkov V., Lukjanov I., Diundik S., O. Kis. (2021). Estimating the Dynamics of a Machine-Tractor Assembly Considering the Effect of the Supporting Surface Profile. *Eastern-European Journal of Enterprise Technologies*. Vol. 7(109). № 1, pp. 51-62., Kharkiv / Ukraine.

[10] Galych I., (2018). Results of experimental researches of tractor fluctuations KhTZ-242K. 20. *TEKA. Commission of motorization and energetics in agriculture.* Vol 18. № 4. pp. 35-40, Lublin-Rzeszow / Poland.

[11] Ivanovs S., Bulgakov V., Nadykto V., Ihnatiev Ye., Smolinskyi S., Kiernicki Z. (2020). Experimental study of the movement controllability of a machine-and-tractor aggregate of the modular type. *INMATEH – Agricultural Engineering*. Vol. 61, No.2, pp. 9–16, Bucharest / Romania.

[12] Ivanovs, S., Bulgakov, V., Nadykto, V., Kuvachov, V. (2018). Theoretical investigation of turning ability of two-machine sowing aggregate. *Engineering for Rural Development,* vol. 17, pp.314–322, Jelgava / Latvia.

[13] Werner R. (2012). Dynamic modeling and path tracking control for a farm tractor towing an implement with steerable wheels and steerable drawbar. *Commercial Vehicle Technology*, Proceedings of Symposium, 13-15 March 2012, pp. 241-250, Kaiserslautern / Germany.

[14] Yahya A., Zohadie M., Kheiralla A., Gew S., Wee E. (2004). Precision system for mapping terrain trafficability, tractor-implement performance and tillage quality. *Proceedings of the 7th International Conference on Precision Agriculture and Other Precision Resources Management*. 25-28 July 2004, pp. 23-41, Minneapolis / USA.

EXPERIMENTAL INVESTIGATIONS OF THE OPERATION OF ELEMENTS OF THE EQUIPMENT FOR CASSETTE-LESS BREEDING OF THE GRAIN MOTH

/

ЕКСПЕРИМЕНТАЛЬНІ ДОСЛІДЖЕННЯ РОБОТИ ЕЛЕМЕНТІВ КОМПЛЕКТУ ОБЛАДНАННЯ ДЛЯ РОЗВЕДЕННЯ ЗЕРНОВОЇ МОЛІ БЕЗ ВИКОРИСТАННЯ КАСЕТ

Volodymyr BELCHENKO[1)], Nonna PISHCHANSKA[1)], Volodymyr BULGAKOV[2)], Semjons IVANOVS[3*)]

[1)]Engineering and Technology Institute "Biotechnica", Ukraine;

[2)]National University of Life and Environmental Sciences of Ukraine, Ukraine;

[3)]Latvia University of Life Sciences and Technologies, Latvia

**Correspondence*: *Tel.+37129403708, e-mail: semjons@apollo.lv*

DOI: https://doi.org/10.35633/inmateh-68-53

Keywords: *grain moth, Trichogramma, cassette-less, technology, temperature, humidity, eggs, imago.*

ABSTRACT

Increasing the production efficiency of Trichogramma of guaranteed biological quality by creating promising biotechnologies, based on the optimization of the parameters of technobiocenosis, is an urgent scientific and practical problem. There have been developed elements of a set of equipment by the method of cassette-less breeding of the grain moths for industrial production of Trichogramma. Experimental and analytical studies were carried out of the impact of the main biological indicators upon the quality of production of an entomological preparation of Trichogramma. The impact of the main factors of technocenosis upon the viability and productivity of the grain moths has been studied by using a cassette-less production technology. The developed technological scheme for cassette-less cultivation of the grain moth and the use of recommendations for industrial production of Trichogramma will increase the output of biolaboratories by 10-15% while obtaining a Trichogramma of guaranteed biological quality.

АНОТАЦІЯ

Розроблено елементи комплекту обладнання методом розведення зернової молі без використання касет для промислового виробництва трихограми. Проведено експериментальні та аналітичні дослідження впливу основних біологічних показників на якість виробництва ентомологічного препарату трихограми. Досліджено вплив основних факторів техноценозу на життєздатність та продуктивність зернової молі під час використання технології виробництва без використання касет. Розроблена технологічна схема для розведення зернової молі без використання касет та дотримання рекомендацій щодо промислового виробництва трихограми дозволять збільшити на 10-15% продуктивність біолабораторій, при цьому буде отримана трихограма гарантованої біологічної якості.

INTRODUCTION

One of the effective ways of using the biological method of protecting plants, mainly the field and vegetable crops, is the use of local species of entomophages by the method of their seasonal colonization. It is carried out by releasing artificially bred individuals of a species, common for the place of application. Most massively used in Ukraine and other European countries is the egg-eater Trichogramma. An increase in the scale and efficiency of the use of Trichogramma can be achieved by the development and implementation of more modern technologies, based on the creation of a unified set, characterized by balanced mechanization, decrease in the amount of manual labour, reduction in the cost and decrease in the technological operations, used during the production cycle *(Rudyk et al., 2013; Belchenko et al., 2000; Buse et al., 2015; Krutyakova et al., 2020*).

As a result of analysis of the existing technologies, the following urgent tasks were identified: – improvement of technology and technical means throughout the entire cycle of production of grain moth and Trichogramma; – maximum reduction in the number of modifications of the equipment, used in the production cycle; – solution of a problem of efficient layout of laboratories of various production capacities; – creation of an element base of machines, instruments and devices to ensure resuscitation of the network of biofactories and biolaboratories that

existed before. Elements of a set of equipment were created by the method of cassette-less breeding of the grain moth for industrial production of Trichogramma *(Marsh & Trenham, 2008)*. This method provides for a cycle of technological operations (infection, maintenance, release and collection of the imago) in a single apparatus, which allows to reduce the number of technological operations, the labour costs, and dust emission. Thus cultivation of the grain moths in a large quantity makes it possible to abandon the traditional cassette-box technology and move on to building entomological production facilities of a new generation *(Ghosh, Haldar & Mandal, 2014)*.

Preliminary research showed that introduction of a cassette-less technology for breeding the grain moths and Trichogramma, in contrast to the existing equipment, will increase the level of mechanization and automation of the technological operations by up to 20%, reducing the metal consumption of the created equipment by up to 15% *(Morales-Ramos, Rojas, & Shapiro-Ilan, 2014; Dortel et al., 2013, Marus et al., 2022)*.

The aim of the work is to study the dynamics of the grain moth cultivation using a set of equipment for the production of Trichogramma according to a cassette-less technology.

MATERIALS AND METHODS

The installation for cassette-less breeding of the grain moth allows one to combine in a single volume the technological processes, such as infection of the grain, the development of caterpillars, pupae and emergence of the imago. The installation allows mechanization of the processes of «loading – unloading» the grain, its mixing and ventilation. It consists of a cylindrical container with vertical perforated tubes, located inside for the moth exit and the grain cooling, a mixing device in the form of a driven auger, and a fan, which are switched on by signals from a temperature control sensor, located in the working volume (Fig. 1). The traditional method consists in infecting the grain in open pallets, manually mixing it, which are closed with tight lids before the butterflies leave and turn into cassettes. The rotation speed of the screw was 24 rpm, atmospheric pressure was maintained inside.

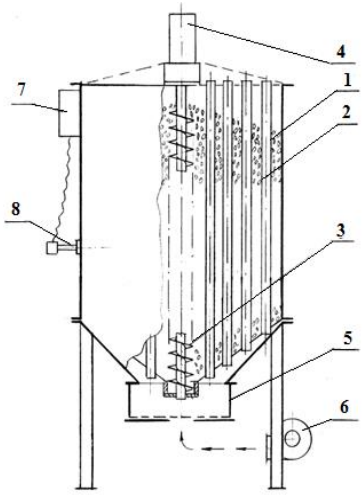

Fig. 1 - A scheme of the installation for cassette-less breeding of the grain moth

1 – motor-reducer, 2 – moth conduit, 3 – auger, 4 – electric drive, 5 – receiving cage, 6 – fan, 7 – temperature controller, 8 – temperature sensor

To ensure the technological temperature and humidity parameters of the process, as well as to synchronize the output of the imago, mechanical mixing and ventilation of the grain are provided. The capacity of the installation is 1.5 kg of the grain moth eggs per cycle. The experimental samples of the technological equipment ensure maintenance of the microclimate parameters for breeding Trichogramma by the method of intensive air exchange between the multiplier and the room where the pre-set microclimate parameters are maintained within the range of temperature t from 22 to 28° C and relative humidity φ from 75 to 85%. In the production area itself, it is planned to use a displacement ventilation scheme. Air humidification is effected by using water vapour. A high degree of synchrony in the Trichogramma development is achieved by ensuring uniform distribution of the fields of abiotic factors that characterize the technocenosis in the working volume: the temperature, relative humidity, illumination, and so on *(Isaev et al., 2008)*.

To ensure uniform distribution of the microclimate parameters in the container itself, as well as to remove the volatile metabolites, a constant movement of the air mass and a high intensity of air exchange are maintained. The air movement is directed along the surface of the plates with the host eggs. The excretion of metabolites makes it possible to reduce the stress level of the individuals due to the increased density of population retention, as well as to prevent the development of pathogenic microflora in the working area. Illumination of low intensity and uniform over the entire area of the working zone contributes to uniform distribution of the entomophagy individuals over the working surface.

The design of the working area suggests a possibility to select the Trichogramma individuals by the search and flight activity. That is, there is excluded a possibility of direct transfer of the Trichogramma specimens from the container for the exit of the imago directly into the plates with the laid eggs of the host. To this end, the plates are placed in such a way that they do not have direct contact with the walls of the main chamber. Considering that the equipment is aimed at the use of an entomophage in the industrial production, particular attention was paid to the convenience of its use. So the maintenance of the working area (introduction of the prepared plates with the host eggs into the main chamber, introduction of the Trichogramma of the parent generation, extraction of the biomaterial, cleaning of the working area from contamination) is carried out through the side wall of the main chamber. The cycle of the technological process is carried out within 42 – 50 days.

The prepared grain moth eggs, weighing 1 g per 1 kg of grain, are introduced into the installation by evenly scattering them over the surface of the grain cone. On the surface of the grain cone two control cards are placed with 10 mg of the grain moth eggs on each in order to monitor the regeneration dynamics of the larvae and establish the starting date of the grain infection, the date of which should coincide with the rebirth of at least 80% of the larvae.

For 5 days the moisture content of the grain is determined (if necessary, bringing it to the nominal value), and the auger is turned on. When controlling *t* of grain, the measurement is made at 5 points of the grain chamber, and the average value is determined. After 15 days, when the larvae pass over into the pupa, the percentage of the grain infection is determined. During the period of the imago emergence it is continued to control *t* and the grain moisture, which are decisive for the technological cycle of the grain moth production; ventilation is continued without mixing.

The development of Trichogramma begins with the application of a feeder egg to the working plates, after which a block of the plate is placed in the multiplier container and a revived Trichogramma is introduced in a definite amount. Within two days the infection process should take place under hygrothermal conditions that are optimal for specific types of Trichogramma and a corresponding geographical area. To prepare the trichogram for a diapause induction, the general quality indicators of the parental generation of Trichogramma are preliminarily assessed: the number of parasitized eggs, the rebirth, sex index.

RESULTS AND DISCUSSION

The conducted laboratory investigations of the cycle of cassette-less breeding of the grain moth made it possible to determine the dynamics of changes in the temperature of the grain and air (Fig. 2), and relative humidity (Fig. 3). The grain temperature during the period of the grain moth colonization (1-7 days) increases quite smoothly and reaches approximately 28° C. At the same time the air temperature fluctuates slightly at the level of 25° C. The relative humidity of the air in the room remained within the regulated limits ($\varphi \approx 80\%$), the air temperature (Δt) increased by more than 8° C. This difference may reach 12° C, but during this period, in addition to the fan, the auger also works, which makes it possible to keep the temperature of the grain within the limits stipulated by the regulations. The relative humidity of the air during this period decreases, which is caused by an increase in the temperature of the room *(Bespalov, Belchenko & Leshishak, 2015)*.

In our experiment φ decreased below the regulated value by 5%. The cassette-less grain moth breeding equipment is distinguished by a more uniform temperature field of the grain in the working area, determined by the following components: blowing air with optimal temperature through the moth conduits, evenly spaced over the volume, for growing the grain moths, which ensures convective heat removal; a significant reduction in the amount of grain in the boundary layer, in contrast to the cassette-box technology; by mixing the nutrient medium

with an auger mechanism, which ensures regular movement of each individual grain both in the vertical and horizontal directions. The most stressful period are the first five days of obtaining the imago (Fig. 4).

Its implementation is complicated by the fact that the screw mechanism does not work, but Δt gradually decreases from the maximum.

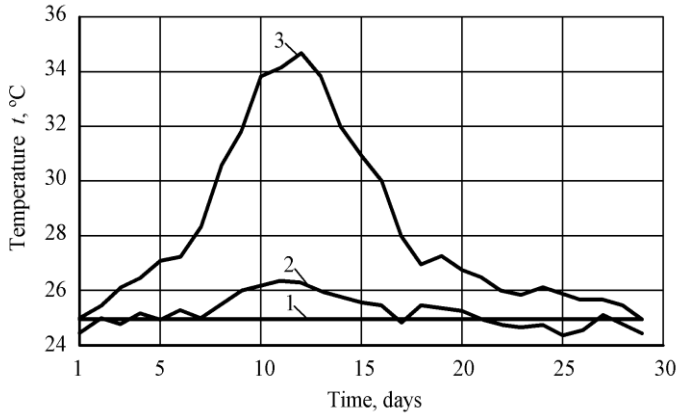

Fig. 2 - Dynamics of the air and grain temperature changes during the grain moth breeding cycle

1 – set temperature; 2 – air temperature; 3 – grain temperature

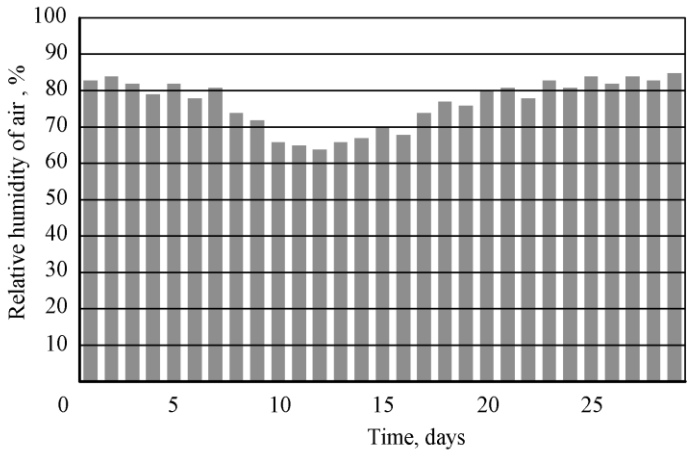

Fig. 3 - Dynamics of changes in the relative humidity of the air, during grain moth breeding cycle

Processing of the results obtained according to the output of the imago (y, r) made it possible to obtain an equation in the form of a polynomial of the 6th degree:

– for the modular kit:

$$y = 0.0003 \cdot x^6 - 0.025 \cdot x^5 - 0.9584 \cdot x^4 - 17.01 \cdot x^3 + 137.44 \cdot x^2 - 379.47 \cdot x + 383.33 \quad (1)$$

– for the equipment of the cassette-less production:

$$y = 4 - 0.5 \cdot x^6 - 0.0042 \cdot x^5 + 0.1591 \cdot x^4 - 3.0715 \cdot x^3 + 27.887 \cdot x^2 - 64.053 \cdot x + 106.39 \quad (2)$$

Where: y – mass (weight) of the imago of the grain moth, g;

x – term, days.

The approximation confidence factor (R^2), showing the degree of compliance of the trend model with the original data, is: – for the modular kit 0.9067; – for the equipment of the cassette-less production 0.9806. It can be concluded that the obtained models correspond to the natural experiment with a satisfactory error.

The conducted studies made it possible to analyse the dynamics of obtaining eggs with various technologies of breeding the grain moths (Fig. 5). The release of the imago during the cassette-free breeding takes place in a shorter period of time *(Belchenko & Pishchanska, 2018)*.

Processing the results before obtaining the egg (y, g) made it possible to obtain an equation in the form of polynomials of the 6th degree:

– for the modular kit:

$$y = -2 - 0.5 \cdot x^6 + 0.0015 \cdot x^5 - 0.0462 \cdot x^4 + 0.5718 \cdot x^3 - 2.7717 \cdot x^2 + 12.368 \cdot x - 7.5513 \quad (3)$$

$R^2 = 0.9954$;

– for the equipment of the cassette-less production:

$$y = 3 - 0.5 \cdot x^6 - 0.0029 \cdot x^5 + 0.1184 \cdot x^4 - 2.2817 \cdot x^3 + 19.508 \cdot x^2 - 51.037 \cdot x + 46.834 \quad (4)$$

$R^2 = 0.963$;

Where: y – mass of the eggs of the grain moth, g;

x – term, days;

R^2 – the approximation confidence factor.

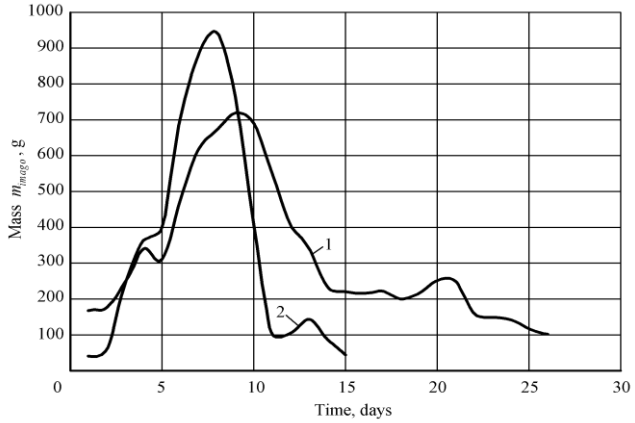

Fig. 4 - Dynamics of grain moth imago production, using a cassette and a cassette-less technologies

1 – modular kit; 2 – installation of cassette-less breeding of grain moth

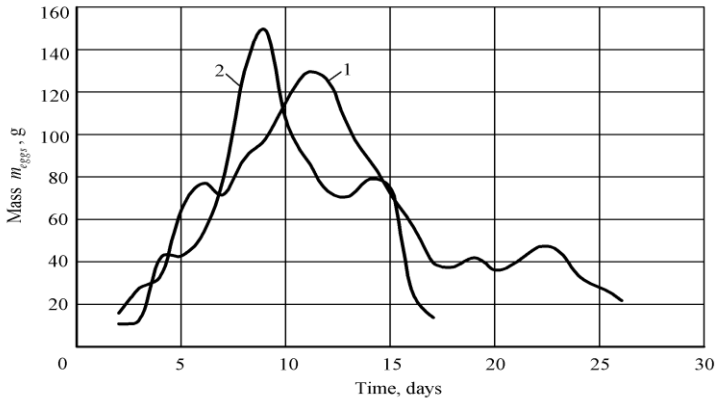

Fig. 5 - Dynamics of the grain moth egg production, using a cassette and a cassette-less technologies

1 – modular kit; 2 – installation of cassette-less breeding of grain moth

When growing the grain moths in a large volume, 80% of the egg production was achieved in 17 days, and the remaining 20% in the following 7 days. Taking into account that the production of the grain moth is seasonal, it is advisable to stop the cycle on the 17-18th day and, at the expense of the time saved, increase the number of cycles per season. This approach will improve the efficiency of the equipment used. The resulting dependencies can be used to determine the busy time of the equipment used.

Approbation was carried out – the equipment is able to work, and its use ensures an increase in the output of the semi-automated and mechanized technological operations up to 23%, a decrease in the metal consumption up to 14%, compared to the existing one. The results were also implemented – an experimental sample of a set of equipment, based on the cassette-less breeding of the grain moth for industrial breeding of Trichogramma was created.

CONCLUSIONS

1. The cassette-less grain moth breeding equipment is distinguished by a more uniform temperature field of the grain in the working area, determined by the following components: blowing air with an optimal temperature for breeding the grain moths (t = 20-22° C and φ = 70-80%) through the moth conduits, evenly spaced over the volume, which ensures convective heat removal; reduction in the amount of grain which is in the boundary layer with the air of the working area by almost 3 times, compared to the cassette-box technology; mixing of the nutrient medium by an auger mechanism, which ensures regular movement of each individual grain both in a vertical and a horizontal direction.

2. The industrial cycle of breeding the grain moths in a large volume can be reduced by 10-12 days, in comparison with the cassette technology, while receiving 80% of the total amount of the egg production. Taking into account that the grain moth production is seasonal, it is advisable to stop the cycle on the 17th-18th day of the imago emergence and, at this expense, to increase the number of cycles per season. The shortened technological cycle will increase the efficiency of the equipment used by 20%.

REFERENCES

[1] Belchenko V., Pishchanska N., (2018). Information model as a basic element of creating biotechnological systems for growing entomocultures. *Abstracts of reports of IX congress of Ukrainian Entomological Society,* pp. 17–18, Kyiv / Ukraine.

[2] Belchenko V., Honcharuk O., Senichev M., (2000). Cultivation of insects is on an industrial basis. Collection of scientific works. *The Republican Entomological Conference is dedicated to the 50th anniversary of the Ukrainian Entomological Society*, pp. 89-90, Kyiv / Ukraine.

[3] Bespalov I., Belchenko V., Leshishak A., (2015), Basic principles of creating entomological productions. *Collection of scientific works «Protection of plants»,* 39, pp. 144–151, Minsk / Belarus.

[4] Buse J., Šlachta M., Frantisek X., Sladecek F.X.J., Pung M., Wagner T., Entling M., (2015). Relative importance of pasture size and grazing continuity for the long-term conservation of European dung beetles. *Biological Conservation,* 187, pp. 112–119, Montpellier / France.

[5] Dortel E., Thuiller W., Lobo J.M., Bohbot H., Jay-Robert J.P., (2013). Potential effects of climate change on the distribution of Scarabaeidae dung beetles in Western Europe. *Journal of Insect Conservation,* 17(5), pp. 1059–1070, Springer / Switzerland.

[6] Ghosh S., Haldar P., Mandal D.K., (2014). Suitable food plants for mass rearing of the short-horn grasshopper Oxya hyla (Orthoptera: Acrididae). *Eur. J. Entomol.,* 111(3), pp. 448–452, Ceske Budejovice / Czeh Republic.

[7] Isaev O., Starchevskyi I., Bespalov I., Belchenko V., Voblyi P., (2008). *Installation for the production of grain moth.* Ukrainian patent UA 83571, Kyiv / Ukraine.

[8] Krutyakova, V., Molchanova, O., Bulgakov, V., Rucins, A., (2020). Experimental investigation of ways to increase efficiency of breeding grain moth. *Engineering for Rural Development,* 19, pp. 1168-1174, Jelgava / Latvia.

[9] Marus, O., Golub, G., Yarosh, Y., Karpiuk, N., (2022). Estimation of electrostatic field influence on quality indicators of grain moth eggs for production *Trichogramma*. *Engineering for Rural Development,* 21, pp. 244-249, Jelgava / Latvia.

[10] Marsh D., Trenham P., (2008). Current Trends in Plant and Animal Population Monitoring. *Conservation Biology,* 22 (3), pp. 647–655, London / UK.

[11] Morales-Ramos J., Rojas M., Shapiro-Ilan D., (2014). *Mass Production of Beneficial Organisms: Invertebrates and Entomopathogens.* Elsevier Inc. 244 p. ISBN: 9780128221068, London / UK.

[12] Rudyk L., Targonya V., Grogulenko D., Belchenko V., Molchanova O., (2013). Industrial biotechnology of the production of the entomological preparation Brakon for biological protection of plants*. Techniques and technologies of agricultural industry,* 12 (59), pp. 29–33, Kyiv / Ukraine.

EFFECTS OF IRRIGATION AND NITROGEN FERTILIZATION ON SOIL NA$^+$ IN ROOT ZONE AND SALT-TOLERANT RICE YIELD

/

水氮调控对根层土壤 Na^+ 及耐盐水稻产量的影响

Jin LI[1)], Xiaolin FAN[2)], Xianmin WANG[1)], Risheng CHEN[1)], Gangshun RAO[1)], Tingting DUAN[1*)] [1]

[1)] Guangdong Ocean University, Zhanjiang, Guangdong, 524088, China

[2)] South China Agricultural University/Environment Friendly Fertilizer Engineering Technology Research Center, Guangzhou, 510642, China

[*]*Corresponding authors. Email: duan_1257@126.com*

DOI: https://doi.org/10.35633/inmateh-68-54

Keywords: *Irrigation, N fertilization, Saline-sodic soil, Na$^+$, sea rice, Yield*

ABSTRACT

The cultivation of salt-tolerant rice (sea rice) along beaches has become an effective measure for the restoration and utilization of saline-sodic land, so this paper studies the effects of irrigation and nitrogen fertilization on soil Na$^+$ in root zone and sea rice yield, and provides a scientific basis for planting sea rice. A pot experiment (two-factor split plot) of sea rice with salt stress (10 g NaCl/kg soil) was carried out. The main plot consists of three types of irrigation methods: flooding irrigation (F), intermittent irrigation (I), and controlled irrigation (C). The subplots are three types of nitrogen fertilizers: urea (U), controlled-release urea (R), and mixed fertilizer (M) with U and R. The results showed: (1) The soil water-soluble Na$^+$ of MI was significantly smaller than that of other treatments with NaCl, but the Ca^{2+}/Na$^+$ and Mg^{2+}/Na$^+$ were opposite. (2) The nitrogen uptake and dry weight of rice of MI were significantly larger than those of other treatments with NaCl, and were respectively 23% and 32% higher than UI, 49% and 16% higher than MF, 56% and 38% higher than UF, 75% and 61% higher than RI, 76% and 50% higher than RF. (3) The sea rice yield of MI was increased by 105%, 154%, 262%, 338%, and 428% compared with MF, RF, UF, RI, and UI, respectively. Therefore, the MI can effectively reduce the Na$^+$ and increase the Ca^{2+}/Na$^+$ and Mg^{2+}/Na$^+$ in root layer soil, and promote the nitrogen absorption and production of sea rice. So the article recommends that M and I methods should be adapted to plant sea rice on coastal saline-sodic soil.

摘要

【目的】近年来，种植耐盐水稻（海水稻）已成为沿海滩涂及盐碱地修复与利用的有效措施，但针对海水稻的水肥管理配套技术研究还较少。本文开展了水氮调控对根层土壤 Na$^+$ 及海水稻产量影响的研究，为优化海水稻的水氮管理提供科学依据。【方法】在加氯化钠(10g/kg)高盐胁迫下，采用两因素裂区设计进行海水稻盆栽试验。主处理是施肥量相等的普通尿素（U）、控释尿素（R）、混合氮肥（M）3 种氮肥；副处理为淹水灌溉（F）、间歇灌溉（I）、控制灌溉（C）3 种灌水方式。另设未加 NaCl 的无盐对照，共 10 个处理。【结果】（1）MI 处理的土壤水溶性 Na$^+$ 在水稻生育期内基本保持不变，且显著小于其它加盐处理的，而其它加盐处理的 Na$^+$ 均呈增加趋势；MI 处理的土壤 Ca^{2+}/Na$^+$ 和 Mg^{2+}/Na$^+$ 随着水稻生长期的延长显著增大，且在水稻孕穗期和成熟期时，显著大于其它加盐处理的。（2）MI 处理的海水稻吸氮量和干重显著大于其它加盐处理的，分别比 UI 高 23%和 32%，比 MF 高 49%和 16%，比 UF 高 56%和 38%，比 RI 高 75%和 61%，比 RF 高 76%和 50%。（3）水氮调控对海水稻的产量影响显著。MI 的产量分别比 MF 提高 105%，比 RF 提高 154%，比 UF 提高 262%，比 RI 提高 338%，比 UI 提高 428%。【结论】MI 处理能有效降低耕层土壤中的水溶性 Na$^+$，而提高水溶性 Ca^{2+}/Na$^+$ 和 Mg^{2+}/Na$^+$，减轻根层土壤 Na$^+$ 对海水稻的危害，促进海水稻的氮素及生物量累积，增加海水稻产量。因此，本文建议在 NaCl 危害较重的滨海盐渍地上种植海水稻，应采用控释尿素与尿素混合施肥，并综合间歇式浇灌的水肥管理模式。

INTRODUCTION

Soil salinization is a serious problem facing agriculture all over the world *(Liang et al., 2018).* There are 950 million hm^2 of saline-sodic land in the world, in which 100 million hm^2 of saline-sodic land and 2.34 million hm^2 of tidal flats are in China *(Chen et al., 2018)*. There are nearly 200,000 hm^2 of saline-sodic land along the beach in Guangdong, in which a tidal flat area of 100,000 hm^2 is in Zhanjiang, and accounts for 1/2 of the coastal tidal flat area of Guangdong. In addition, there is a coastal saline land of 40,000 hm^2 in Zhanjiang.

[1] *Jin Li, associate professor; Xiaolin Fan, professor; Xianmin Wang, professor; Risheng Chen, chair professor; Gangshun Rao, lecturer; Tingting Duan, associate professor.*

Under the dual pressure of salinization of cultivated land and scarcity of water resources, growing saline-alkali-tolerant crops on saline-sodic land and beaches to ensure the food security and quantity of cultivated land has become an urgent agricultural problem *(Wang et al., 2018)*. In recent years, saline-alkali-tolerant rice (sea rice) as a pioneer crop is planted for the development and utilization of beaches and saline-sodic land, which has become an effective measure for the restoration and utilization of saline-sodic land and provides a new way to solve the problem of food security *(Chen et al., 2018).*

At present, sea rice is suitable for growing in coastal soil with salinity below 0.6%, and it needs to be diluted with fresh water to below 1% for irrigation. Therefore, reducing the total concentration of Na^+ in the rice root layer soil is still the key to the normal growth and yield of seawater rice *(Chen et al., 2018).* Irrigation and fertilization is the most important agronomic measure in agricultural activities. And both compressed salt by water and fertilizer supply should be taken into consideration in the irrigation and fertilization of saline-sodic land. Unreasonable fertilization and irrigation will lead to accumulation of soil salt, which cannot reduce salt and increase yield. Therefore, the reasonable regulation of water and fertilizer is an important measure to reduce the Na^+ and other salt content in coastal saline soil and increase crop yields quality *(Lima et al., 2020).* Numerous studies have shown that the use of comprehensive water and fertilizer control technology for saline-sodic soils can achieve good salt control and yield increase effects *(Lima et al., 2019).* However, researches on sea rice in coastal areas are currently mostly focused on the selection and breeding of high-yield salt-tolerant sea rice varieties, but lack of supporting sea rice water and fertilizer management technology. Therefore, the production of sea rice on the coastal saline-sodic land is limited. At the same time, there is low water and nitrogen utilization rate, which causes water resources and environmental problems *(Bao et al., 2019).*

Rice is the crop with the largest amount of nitrogen fertilizer in China *(Huang et al., 2019)*. The application of nitrogen fertilizer plays a decisive role in the yield of rice. Among them, controlled-release nitrogen fertilizer reduced salinity in soil because of the slow release of nutrients, so it can effectively regulate the soil salinity of saline-sodic soils *(Qi et al., 2019).* Therefore, this paper studies the water and nitrogen regulation modes of different irrigation methods (continuous flooding irrigation, intermittent irrigation, controlled irrigation) and fertilizers (urea and controlled-release urea, etc.) under high salt stress of NaCl (10 g/kg), and study its influence on the Na^+ and other salts in root zone soil and the yield of sea rice. In anticipation of optimizing the water and nitrogen management mode of sea rice, it provides a scientific basis for the efficient restoration and utilization of coastal saline-sodic land.

MATERIALS AND METHODS

Test soil: soil taken from the cultivated layer (0-20 cm) of the rice breeding base of Guangdong Ocean University (N21°8′54″, E110°18′14″). Its pH is 6.52, bulk density is 1.25 g/cm^3, organic matter is 29.08 g/kg, alkali hydrolyzed nitrogen is 77.67 mg/kg, available phosphorus is 29.01 mg/kg, and available potassium is 52.33 mg/kg. After the soil sample is air-dried and crushed, it is passed through a 10-mesh sieve (2.00 mm), fully mixed, and 400 g of NaCl is added and mixed evenly, and then packed into a barrel (inner diameter 28 cm, height 60 cm), 40 kg per barrel.

Test crops: The "sea rice 86" series variety HR86401 provided by Prof. Risheng Chen's group from Guangdong Ocean University was used as the test rice. The rice is salt-tolerant rice, which can grow normally on coastal saline soil with a total salt content of 0.6%, and its root is mainly distributed within 25 cm of the soil surface. The rice seedlings are cultivated in a sterile incubator to 3 true leaves stage, and seedlings with the same growth are selected and transplanted into the test barrel.

Test fertilizer: Nitrogen fertilizer was provided by Environmental Friendly Fertilizer Engineering Technology Research Center in Guangdong. Including vegetable oil-coated controlled release urea (N≥43.0%, 3-4 months fertilizer validity period), ordinary urea (N≥46.0%), and mixed nitrogen fertilizer made by mixing 30% N urea and 70% N controlled release urea. Phosphate fertilizer is single superphosphate (P_2O_5≥16%). Potash fertilizer is potassium chloride (K_2O≥60%).

The experiment was carried out in the glass greenhouse of the Institute of Agricultural Biotechnology of Guangdong Ocean University from November 26, 2020, to March 26, 2021. A two-factor split zone design is adopted. The main treatments are different irrigation methods, namely continuous flooded irrigation (F), intermittent irrigation (I), and controlled irrigation (C). Side treatments are 3 kinds of nitrogen fertilizers, which are ordinary urea (U), controlled release urea (R), and mixed nitrogen fertilizer (M). The nitrogen, phosphorus and potassium fertilizers of each treatment are mixed with the soil as a base fertilizer and applied at one time. The fertilization rates of the treatments were all 0.72 g N, 0.48 g P_2O_5, and 0.64 g K_2O, that is, 1.57 g of urea,

1.71 g of controlled release urea, 1.64 g of mixed nitrogen fertilizer, 3.00 g of single superphosphate, and 1.07 g of potassium chloride were applied according to the treatment design per barrel. In addition, the flooded irrigation treatment without adding NaCl and applying urea was used as a control treatment (CK). There were 10 treatments in total; each treatment was repeated in 5 barrels, and 6 seedlings were planted in each barrel.

Irrigation method: The F treatment is to maintain a 2 cm water layer in the barrel. The I treatment is to stop the irrigation after watering to the 2 cm water layer, and the water surface is naturally dried before watering, cyclically. The C treatment is continuous precision irrigation, and maintains 80%-100% of the soil field water holding capacity by weighing and adding water.

Collection of soil and plant samples: The sea rice seedlings were transplanted on November 26, 2020, and the first soil sample was collected in the middle of the rice green-returning stage (December 26, 2020). A soil drill was used to collect the 0-25 cm root layer soil in the barrel, and the collection was repeated 5 times (5 barrels/treatment). After removing stones and plant roots from the soil samples, they were passed through a 2 mm sieve and were air-dried for testing. On January 5, 2021, the second sampling was conducted during the mid-tillering stage of rice, and soil and plant samples were collected. Separate the above-ground parts and roots of rice for sampling, and gently wipe the leaves with wet gauze. The roots were washed with deionized water and then blotted dry with absorbent paper. Measure the fresh weight first, and then dry it at 75°C to a constant weight after curing (105°C, 30 min), then measure its dry weight, and store it after crushing for testing. On January 30, 2021, the third soil and plant samples were collected at the middle of the rice booting stage. On March 26, 2021, soil samples were collected and the rice was harvested, and the yield was measured when the rice was mature.

Determination of plants and soil samples: After the plant samples were digested with H_2SO_4–H_2O_2, the nitrogen content was determined with Full Automatic Azotometer (Shanghai Yihong NKY6120) *(Lu, 2000).* Use the German STEP soil salinity detector (PNT300 type) to regularly monitor the soil electrical conductivity (EC) of the 0-25 cm deep root layer in the barrel. The alkaline hydrolysis diffusion method was used to determine the soil alkaline hydrolysis nitrogen content *(Lu, 2000)*. Use atomic absorption spectrophotometer (Japan Shimadzu AA-7000) to determine water-soluble sodium (Na^+), calcium (Ga^{2+}), magnesium (Mg^{2+}) ion content in soil (Lu, 2000). Count the number of effective panicles per pot, the number of grains per panicles, the grain ripening percentage, and the weight of thousands of grains per pot to calculate the yield per pot.

$$Yield\ (g/pot) = \frac{E(piece/pot) \times G\ (piece/pot) \times P\ (\%) \times W\ (g)}{1000 \times 100} \quad (1)$$

E means effective panicles number (piece/pot), *G* means grain number per panicles (piece/pot), *P* means grain ripening percentage (%), *W* means thousand-grain weight (g) *(Liu et al., 2017)*.

Use Excel 2007 and SPSS 22.0 software for data processing.

RESULTS

Dynamics of soil electrical conductivity under different water and nitrogen regulation modes

As shown in Figure 1, different water and nitrogen control treatments have significant effects on root zone soil electrical conductivity (EC).

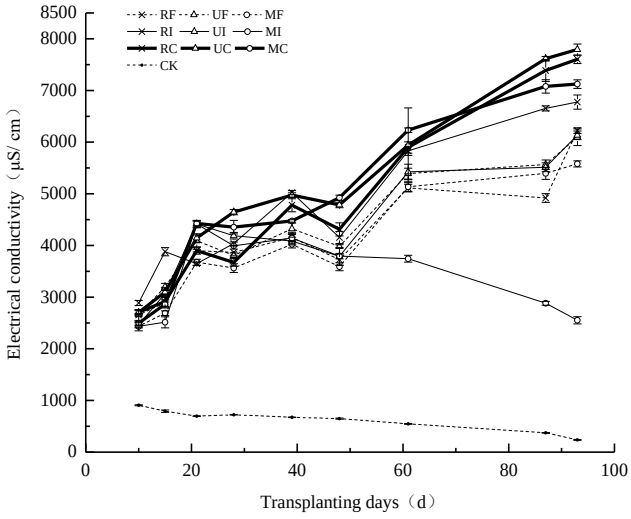

Fig. 1 - Soil EC under different irrigation and N fertilization modes

Among them, the CK treatment showed a slow decline with the increase of the number of rice transplanting days, and it was significantly lower than the treatments with NaCl. The MI treatment first increased and then decreased, and other treatments showed an upward trend. There was basically no difference in soil EC of treatments with NaCl during 0-40 days, and the difference began to be obvious after 40 days, and the C treatments (RC, UC, MC) were significantly larger than the other treatments. RI was significantly greater than UI, MI, and F treatments (RF, UF, MF), while MI was the smallest and significantly smaller than other treatments with NaCl.

Dynamics of soil water-soluble Na^+ content under different water and nitrogen regulation modes

It can be seen from Figure 2 that different water and nitrogen control treatments have significant effects on the water-soluble Na^+ content of root layer soil. Among them, CK remained basically unchanged in each growth period of rice and was significantly lower than that treated with NaCl. MI was basically unchanged and significantly smaller than other treatments with NaCl. Except for CK and MI treatments, other treatments showed an increasing trend throughout the rice growth period. And C treatments were significantly larger than I (RI, UI, MI) and F treatments. UF, RI and UI were significantly larger than MF and RF in booting stage and maturity stage.

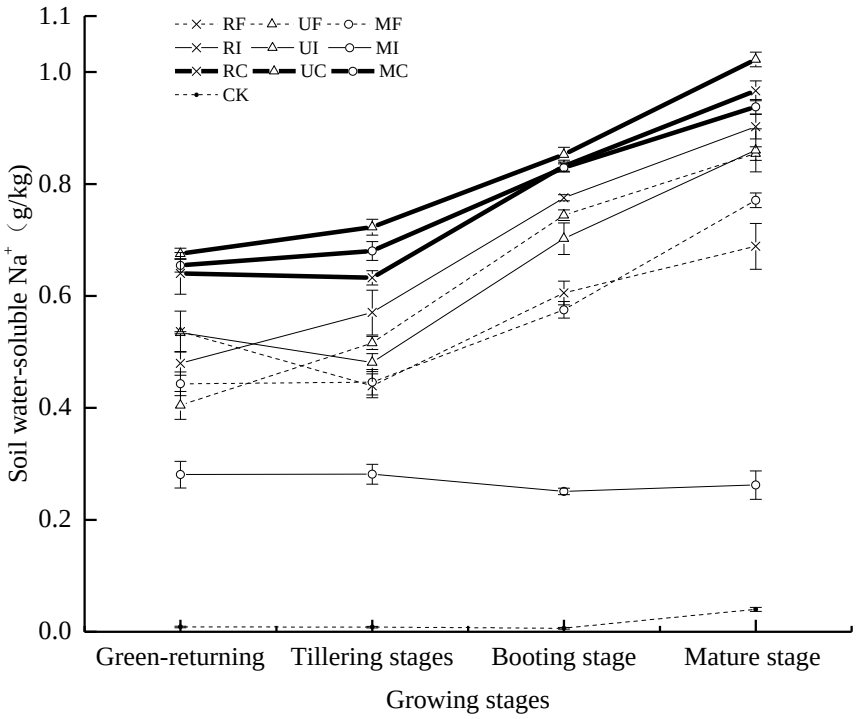

Fig. 2 - Soil water-soluble Na^+ under different irrigation and N fertilization modes

Effects of water and nitrogen regulation modes on the ratio of water-soluble salt ions in soil

It can be seen from Table 1 and Table 2 that there was basically no difference in water-soluble Ca^{2+}/Na^+ and Mg^{2+}/Na^+ in the root soil of the NaCl-added treatments except MI in each growth period of the rice. The MI increased significantly with the extension of the growth period, and it was significantly larger than other treatments with NaCl at the booting and maturity stages of rice. During the whole growing period of rice, the Ca^{2+}/Na^+ and Mg^{2+}/Na^+ of CK were significantly higher than those treated with NaCl.

Table 1

Soil water-soluble Ca^{2+}/Na^+ under different irrigation and N fertilization modes

Treatment	Ca^{2+}/Na^+			
	Green-returning	Tillering stage	Booting stage	Mature stage
RF	0.034bB	0.094bAB	0.124cA	0.080cAB
UF	0.033bA	0.044bA	0.074cA	0.070cA
MF	0.033bA	0.051bA	0.083cA	0.071cA
RI	0.048bA	0.064bA	0.086cA	0.087cA
UI	0.038bA	0.061bA	0.076cA	0.079cA

Treatment	Ca^{2+}/Na^{+}			
	Green-returning	Tillering stage	Booting stage	Mature stage
MI	0.055bC	0.125bBC	0.206bAB	0.219bA
RC	0.022bA	0.099bA	0.102cA	0.077cA
UC	0.017bA	0.071bA	0.098cA	0.074cA
MC	0.021bA	0.078bA	0.098cA	0.072cA
CK	0.542aC	1.589aB	3.372aA	0.854aBC

Note: Different lower case letters in a column indicate significant difference among treatments at the 5% level. Different capital letters in a row indicate significant difference among the same treatment for different growth stages at the 5% level.

Table 2

Soil water-soluble Mg^{2+}/Na^{+} under different irrigation and N fertilization modes

Treatment	Mg^{2+}/Na^{+}			
	Green-returning	Tillering stage	Booting stage	Mature stage
RF	0.069bcB	0.233bcA	0.293bcA	0.201cA
UF	0.081bcB	0.108dAB	0.197cA	0.162cAB
MF	0.082bcB	0.126cdAB	0.238cA	0.178cAB
RI	0.120bA	0.163bcdA	0.217cA	0.219cA
UI	0.104bB	0.152bcdAB	0.216cA	0.198cAB
MI	0.137bC	0.314bB	0.516bAB	0.564bA
RC	0.044cB	0.208bcdA	0.252cA	0.196cA
UC	0.050bcB	0.218bcA	0.251cA	0.184cA
MC	0.052bcB	0.196bcdA	0.243cA	0.200cA
CK	1.287aC	3.940aB	8.435aA	2.125aBC

Note: Different lower-case letters in a column indicate significant difference among treatments at the 5% level. Different capital letters in a row indicate significant difference among the same treatment for different growth stages at the 5% level.

Effects of water and nitrogen regulation modes on soil alkali-hydrolyzable nitrogen

As shown in Table 3, the soil alkali-hydrolyzable nitrogen contents of all treatments in the rice green-returning stage were significantly greater than those in the tillering stage, booting stage and maturity stage. From the tillering stage to the maturity stage of rice, the soil alkali-hydrolyzable nitrogen of R (RF, RI, RC) treatments showed an increasing trend, and that of U (UF, UI, UC), CK, MF and MC remain basically unchanged, while that of MI showed a significant downward trend. During the whole rice growth period, the soil alkali-hydrolyzable nitrogen of CK was significantly smaller than the treatments with NaCl or there was no significant difference from them.

Table 3

Soil alkali-hydrolyzable nitrogen content under different irrigation and N fertilization modes

Treatment	Soil alkali-hydrolyzable nitrogen (mg/kg)			
	Green-returning	Tillering stage	Booting stage	Mature stage
RF	154.13 bcA	57.59 dD	77.19 bcC	108.52 aB
UF	143.73 cA	64.12 cdB	56.62 dB	66.54 deB
MF	159.70 bcA	52.63 dB	66.54 cdB	67.99 dB
RI	144.70 cA	60.01 dC	109.61 aB	108.64 aB
UI	158.97 bcA	89.53 abB	85.41 bB	86.87 bcB
MI	168.89 abA	79.85 bcB	70.17 bcdBC	55.17 eC
RC	155.34 bcA	80.57 bcC	105.01 aB	109.13 aB
UC	177.36 aA	102.35 aB	107.68 aB	81.30 cC
MC	173.49 aA	86.62 abC	106.47 aB	98.96 abBC
CK	143.97 cA	60.25 dB	55.89 dB	54.20 eB

Note: Different lower case letters in a column indicate significant difference among treatments at the 5% level. Different capital letters in a row indicate significant difference among the same treatment for different growth stages at the 5% level.

Effects of water and nitrogen regulation modes on nitrogen uptake of sea rice

As shown in Figure 3, the nitrogen uptake of F, I, and CK-treated rice all increased significantly with the growth of rice. However, C treated rice have no significant changes in nitrogen uptake, and all die at the maturity stage without nitrogen accumulation. In the tillering stage, the nitrogen uptake of UF, MI, CK treated rice was significantly greater than that of other treatments. At the booting stage, CK was significantly higher than that of the treatments with NaCl. The nitrogen uptake of UF, MF, I treatments were greater than other treatments with NaCl. At maturity stage, MI and CK were significantly larger than that of other treatments. MI was 23% higher than UI, 49% higher than MF, 56% higher than UF, 75% higher than RI, and 76% higher than RF.

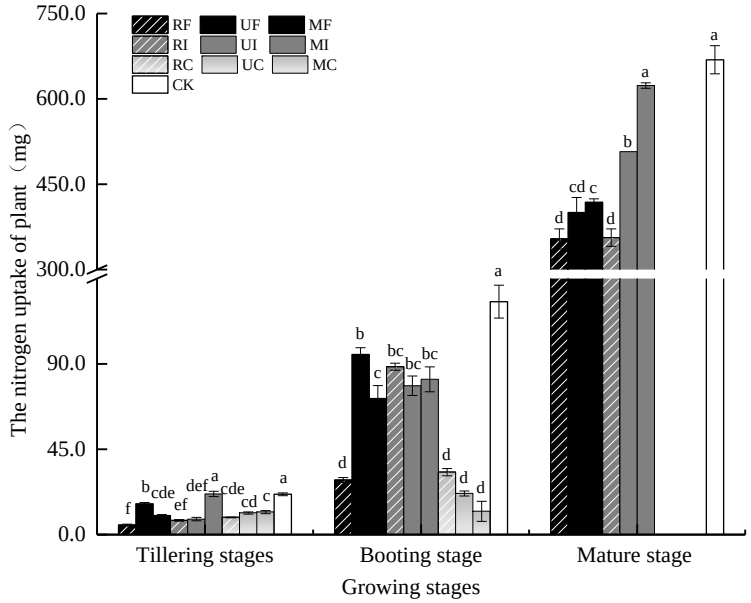

Fig. 3 - The nitrogen uptake of single plant under different irrigation and N fertilization modes

Note: Different lower case letters in a column indicate significant difference among treatments for the same growth stage.

Effects of water and nitrogen regulation modes on the dry matter of sea rice

As shown in Figure 4, the dry weight of rice treated with F, I, and CK increased significantly with the extension of the growth period.

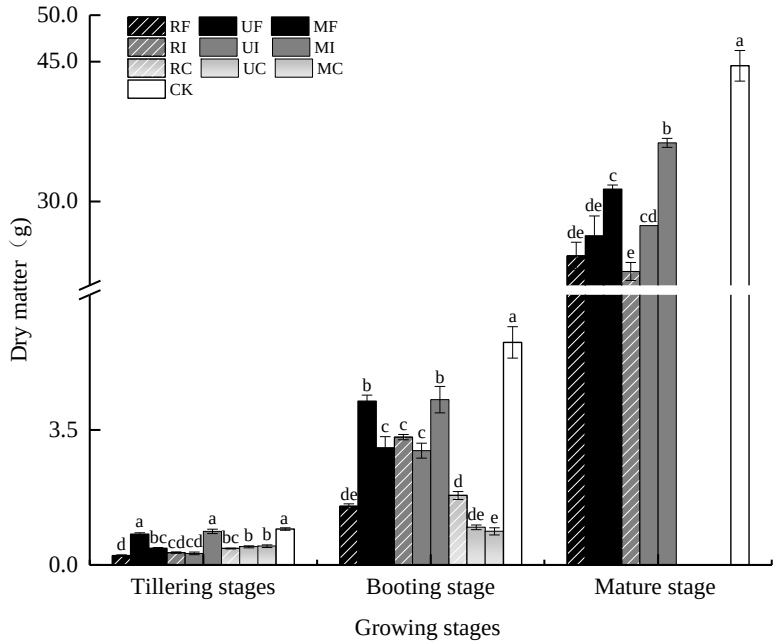

Fig. 4 - Effects of different irrigation and N fertilization on the dry weight of rice

Note: Different lower case letters in a column indicate significant difference among treatments for the same growth stage.

The C-treated rice grew slowly before the booting stage, and all died at the maturity stage. In the tillering stage, the dry weight of rice treated with UF, MI and CK were significantly greater than that of other treatments. At the booting stage, CK was significantly larger than that treated with NaCl. The UF and MI are significantly larger than other treatments with NaCl. Finally, CK was significantly larger than the NaCl-added treatments, and MI was significantly larger than other NaCl-added treatments at the maturity stage, and it was 16% higher than MF, 32% higher than UI, 38% higher than UF, 50% higher than RF, and 61% higher than RI.

Effects of different water and nitrogen regulation modes on sea rice yield and its components

It can be seen from Table 4 that different water and nitrogen control treatments have significant effects on rice yield and its constituent factors. Under continuous flooded irrigation condition, the sea rice yield of MF was significantly greater than that of RF and UF. Similarly, the yield of MI was significantly greater than that of RI and UI in the inter-irrigation treatments. The sea rice treated with C all died at the maturity stage, so there was no yield. The yields of MI and CK were significantly greater than that of other treatments, and the yield of MI was 10% higher than CK, 105% higher than MF, 154% higher than RF, 262% higher than UF, 338% higher than RI, and 428% higher than UI.

Table 4

Effects of different irrigation and N fertilization on rice yield and its components

Treatment	Effective panicles	Grain number per panicles	Grain ripening percentage (%)	Thousand-grain weight (g)	Yield (g/pot)
RF	54	113	85	18.72	97.45 cd
UF	18	239	86	18.41	68.27 de
MF	60	126	87	18.81	120.37 bc
RI	45	79	85	18.45	56.50 de
UI	30	97	89	18.32	47.29 e
MI	60	234	91	18.95	247.22 a
RC	0	0	0	0	0
UC	0	0	0	0	0
MC	0	0	0	0	0
CK	80	261	95	18.74	224.17 a

Note: Different lower case letters in a column indicate significant difference among treatments at the 5% level.

DISCUSSION

Soil electrical conductivity is closely related to soil salinity, and there is a linear relationship between the soil EC and salinity *(Nocco et al., 2019).* Therefore, soil EC can better reflect soil salinity. The EC of CK treatment showed a slow downward trend, and the water-soluble Na^+ remained basically unchanged, and both were significantly lower than that treated with NaCl. This is because CK did not add NaCl, and it absorbed NH_4^+, PO_4^{3-}, K^+, Ca^{2+}, Mg^{2+} plasma in the soil with the continuous growth of sea rice *(Manohara et al., 2020).* Except for MI, the EC and Na^+ of the treatments with NaCl showed an upward trend. This is because the test soil in this experiment has a higher organic matter content (29.08 g/kg). After NaCl is added to the soil, the organic colloid adsorbs a large amount of free Na^+ and other salt-alkali ions. The organic matter continues to decompose with repeating irrigation, and releasing Na^+ plasma, which causes the content of soil EC and water-soluble Na^+ to increase *(El-Shazely, 2021).* The EC of MI increased first and then decreased, and the water-soluble Na^+ remained basically unchanged. This is because the inter-irrigation method leaches the soil soluble salt into the lower layer of the soil *(Hu and Gao, 2018).* The mixed fertilization with the controlled-release urea (CU) and urea is beneficial to the nitrogen absorption and growth of sea rice during the whole growth period. Sea rice absorbs more salt ions, and controlled-release urea controls the release of nitrogen, so slowing the soil EC of MI. The results show that the soil EC and water-soluble Na^+ treated with F and I are less than those treated with C. This is because a large amount of watering can dilute the soil salt concentration, and leach Na^+ plasma below the soil root layer *(Hu and Gao, 2018).* Control irrigation treatments are less watered, which is 80%-100% of the soil field water holding capacity. Salt ions cannot be fully leached into the underlying soil, and water evaporates quickly. Salt ions accumulate to the upper layer of the soil along with the water vapor surface, leading to the increase of soil EC and water-soluble Na^+ in the root layer *(Sarwar et al., 2020).*

In saline soil, high Ca^{2+}/Na^{+} and Mg^{2+}/Na^{+} play an important role in alleviating the toxicity of mono-salt to plants, and increasing the Ca^{2+}/Na^{+} and Mg^{2+}/Na^{+} in the soil can effectively reduce the toxicity of Na^{+} to crops. The higher the Ca^{2+}/Na^{+} and Mg^{2+}/Na^{+}, the lower the Na^{+} toxicity in the soil *(Zhang et al., 2018).* The results showed that the Ca^{2+}/Na^{+} and Mg^{2+}/Na^{+} of MI showed a significant increasing trend. The reason may be that as the irrigation time increases, Ca^{2+} and Mg^{2+} in the soil are gradually dissolved, or replaced by Na^{+}, NH_4^{+} plasma from the soil *(Zhang et al., 2018).* However, Na^{+} is absorbed by sea rice or leached into the lower layer of the soil, resulting in a relative decrease in Na^{+} in the root layer of soil, and a relative increase in Ca^{2+} and Mg^{2+}. Therefore, Na^{+} is less toxic to MI-treated sea rice than other NaCl-added treatments. This article only studied the soil salt content of the root layer (25 cm) where the HR86401 sea rice root is mainly distributed but did not involve the salt ion status of Na^{+}, Ca^{2+}, Mg^{2+} in the soil profile below 25 cm. And it is a pot experiment, which is quite different from the salt leaching and migration status in the field. Therefore, it is necessary to further study the rule of water and salt transportation and salt leaching status of the soil profile by different irrigation and fertilization managements in field production. And verify the growth and yield of MI-treated sea rice in the field.

The soil alkali-hydrolyzable nitrogen content of each treatment at the rice green-turning stage was significantly greater than that at the tillering stage, booting stage and maturity stage. This is because sea rice absorbs the nitrogen in soil during the growth process, and the plant accumulates nitrogen. This was verified by the increase in the amount of nitrogen absorbed by sea rice in each treatment with the extension of the growing season (Figure 3). From the tillering stage to the maturity stage of rice, the soil alkali-hydrolyzable nitrogen of R treatments showed an increasing trend. This is because controlled-release urea slowly releases nitrogen into the soil for plant absorption and utilization in the middle and late stages of sea rice growth *(Hou et al., 2019).* The soil alkali hydrolyzable nitrogen of MI and CK showed a decreasing trend because the sea rice treated with them absorbed more nitrogen than other treatments (Figure 3).

Nitrogen fertilizer is one of the indispensable nutrients for the growth of rice. Nitrogen plays an important role in promoting the growth and yield of rice *(Liu et al., 2021).* The sea rice of MI and CK absorbs more nitrogen, which is conducive to its growth. Therefore, it grows fast and grows well. In the tillering stage, booting stage and maturity stage, the dry weight of MI and CK sea rice was higher than that of other treatments (Figure 4). The growth of sea rice treated with CK is better because no NaCl is added, and the sea rice is not affected by salt damage. The sea rice of MI grows well, and the biomass accumulation is more than that of other treatments with NaCl. This may be because the nitrogen supply rule of the M treatments (30% urea and 70% controlled release urea) conforms to the nitrogen demand law of sea rice. Nitrogen can be supplied by 30% urea in the early growth period, and it can be supplied by 70% controlled release urea in the middle and late growth period. It may also be because I treatments leached soil soluble Na^{+} into the lower layer of the soil *(Hu and Gao, 2018),* the root layer (25 cm) where the rice roots are mainly distributed has low soil Na^{+} content, and relatively high Ca^{2+}/Na^{+} and Mg^{2+}/Na^{+}. Therefore, single Na^{+} is less toxic to sea rice, which is beneficial to the normal growth of sea rice.

The formation of crop yield is essentially a process of dry matter accumulation and distribution, which usually depends on its yield components *(Sarker et al., 2015).* The dry weight, effective panicle number, panicle grain number, grain ripening percentage and thousand-grain weight of MI and CK were all higher than those of other treatments. Therefore, their final yield is also significantly greater than that of other treatments. There was no significant difference in yield between MI and CK (Table 4). This may be because Na^{+} salt stress has an inhibitory effect on the carbon metabolism and yield of rice *(Zhang et al., 2018),* which affects the formation of sea rice yield components. But the sea rice of CK has no salt stress effect. At the same time, the inter-irrigation method can reduce the water-soluble Na^{+} content of the root layer soil, and Ca^{2+}/Na^{+} and Mg^{2+}/Na^{+} are higher. Single sodium damage had little effect on sea rice treated with I. In addition, mixed fertilization is more suitable for the nitrogen demand of sea rice during the growth process, which is beneficial to the absorption and transformation of nitrogen, the formation of grains and increases the thousand-grain weight *(Samarajeewa et al., 2005)*. So the thousand-grain weight of sea rice grains treated with MI was the highest under the combined effect of mixed fertilization and inter-irrigation, which contributed the most to its yield. Therefore, this article recommends that the mixed fertilization with the controlled-release urea (CU) and urea as well as intermittent irrigation management should be adopted when planting sea rice on coastal saline-sodic land where NaCl is the main hazard. It is beneficial to increase the production of sea rice. However, this article does not involve field experiments and the physiological and biochemical mechanism of the mixed fertilization and inter-irrigation mode to increase the yield of sea rice. This content needs further research.

CONCLUSIONS

(1) The soil EC of CK was significantly lower than the treatments with NaCl, and that of MI was significantly smaller than the other treatments with NaCl. The root layer soil Na^+ of MI was significantly smaller than that of other treatments with NaCl. The root layer soil Ca^{2+}/Na^+ and Mg^{2+}/Na^+ of MI increased significantly with the growth of sea rice, and they were significantly larger than those of other treatments with NaCl at the booting and maturity stages.

(2) The nitrogen uptake and dry weight of rice treated with F, I, CK increased significantly with the growth of rice. However, those treated with C did not change significantly, and all of them died at the maturity stage. At the maturity stage of rice, the nitrogen uptake and dry weight of MI and CK were significantly greater than those of other treatments, and those of MI were respectively 23% and 32% higher than those of UI, 49% and 16% higher than those of MF, 56% and 38% higher than those of UF, 75% and 61% higher than those of RI, 76% and 50% higher than those of RF.

(3) Irrigation and nitrogen fertilization have significant effects on the yield and its constituent factors of sea rice. The yield of sea rice treated with M was significantly higher than that treated with R or U fertilization alone under F and I irrigation. The yield of MI is significantly larger than that of other treatments with NaCl, and was 105% higher than that of MF, 154% higher than that of RF, 262% higher than that of UF, 338% higher than that of RI, and 428% higher than that of UI, respectively. Therefore, this paper recommends that controlled-release urea and urea mixed fertilization integrated intermittent irrigation should be used when planting sea rice on coastal saline-sodic soils, which can effectively reduce the water-soluble Na^+ in the root layer soil, thereby the Ca^{2+}/Na^+ and Mg^{2+}/Na^+ of soil can be increased, the toxicity of Na^+ to sea rice can be controlled, and promote nitrogen absorption and biomass accumulation of sea rice, and finally to increase the yield of sea rice grown on saline-sodic land.

ACKNOWLEDGEMENTS

This work was supported by National Natural Science Fund of China (NSFC32000164), China Agricultural Research System (nycytx-33-07), Construction Project of Environmental Friendly Fertilizer Engineering Technology Research Center in Guangdong (CCZX-A100), Science and Technology Special Fund of Guangdong Province (2020A03019, 2021A05226), Oceanic Economy Development Special Fund of Ministry of Natural Resources in Guangdong Province (GDNRC[2021]38).

REFERENCES

[1] Bao, Y., Huang, L., Li, Y., Wang, M., Liang, Z. (2019). How different nitrogen application rates affect yield composition and nitrogen uptake of rice (Oryza sativa L.) in a saline-sodic paddy field. *Polish Journal of Environmental Studies,* Vol. 28, pp. 553-564. Poland.

[2] Chen, Y.S., Wang, P., Wang, K.X., Chen, N., & Zhao, L. (2018). The strategic choice of sea rice industry development in China (我国海水稻产业发展的战略选择). *Journal of Ocean University of China*, Vol. 1, pp. 50-54. Shandong/China.

[3] El-Shazely, M.A. (2021). Effectiveness of the size of organic matter used in the reclamation of saline sodic soil. *Journal of Soil Sciences and Agricultural Engineering,* Vol. 12, pp. 51-60. Egypt.

[4] Hou, P., Xue, L., Zhou, Y., Li, G., Yang, L., Xue, L. (2019). Yield and N utilization of transplanted and direct-seeded rice with controlled or slow-release Fertilizer. *Agronomy Journal,* Vol. 111, pp. 1208-1217. United States.

[5] Hu, Y.T., Gao, J. (2018). The dynamic changes of soil salinity in different growth periods of rice growing along the yellow river in Shaanxi province under well water irrigation (井水灌溉条件下沿黄盐碱地水稻种植不同生育期土壤盐度动态变化). *Land Development and Engineering Research,* Vol. 3, pp. 57-62. Shannxi/China

[6] Huang, M., Fan, L., Zou, Y. (2019). Contrasting responses of grain yield to reducing nitrogen application rate in double- and single-season rice. Scientific Reports, Vol.9, pp. 92. England.

[7] Liang, W., Ma, X., Wan, P., Liu, L. (2018). Plant salt-tolerance mechanism: A review. *Biochemical and Biophysical Research Communications,* Vol. *495*, pp. 286-291. United States.

[8] Lima, G.S.D., Pinheiro, F.W., Dias, A.S., Gheyi, H.R., Soares, L.A.D.A., Silva, S.S.D. (2019). Growth and production components of West Indian cherry cultivated with saline waters and potassium fertilization. *The Brazilian Journal of Agricultural and Environmental Engineering,* Vol. 23, pp. 250-256. Brazil.

[9] Lima, G.S.D., Pinheiro, F.W.A., Gheyi, H.R., Soares, L.A.D.A., Silva, S.S.D. (2020). Growth and post-harvest fruit quality of West Indian cherry under saline water irrigation and potassium fertilization. *Caatinga Magazine,* Vol. 33, pp. 775-784. Brazil.

[10] Liu, T., Chen, W., Wang, Y.F., Wu, W., Sun, C.M., Ding, J.F., Guo, W.S. (2017). Rice and wheat grain counting method and software development based on Android system. *Computers and Electronics in Agriculture,* Vol. 141, pp. 302-309. England.

[11] Liu, Y., Wang, H., Jiang, Z., Wang, W., Xu, R., Wang, Q., Zhang, Z., Li, A., Liang, Y., Ou, S., Liu, X., Cao, S., Tong, H., Wang, Y., Zhou, F., Liao, H., Hu, B., Chu, C. (2021). Genomic basis of geographical adaptation to soil nitrogen in rice. *Nature,* Vol. 590, pp. 600-605. England.

[12] Lu, R.K. (2000). Soil agricultural chemical analysis method (土壤农业化学分析方法). Beijing: China Agricultural Science and Technology Press. 156-221. Beijing/China

[13] Manohara, K.K., Morajkar, S., Shanbagh, Y. (2020). Genetic analysis of grain yield and its associated traits in a set of diverse salt tolerant rice genotypes under coastal salinity condition. *Journal of Cereal Research,* Vol. 12, pp. 290-296. Indian.

[14] Nocco, M.A., Ruark, M.D., Kucharik, C.J. (2019). Apparent electrical conductivity predicts physical properties of coarse soils. *Geoderma*, Vol. 335, pp. 1-11. Netherlands

[15] Qi, H., Ma, R., Shi, C., Huang, Z., Liu, S., Sun, L., Hu, T. (2019). Novel low-cost carboxymethyl cellulose microspheres with excellent fertilizer absorbency and release behavior for saline-alkali soil. *International Journal of Biological Macromolecules,* Vol. 131, pp. 412-419. NETHERLANDS.

[16] Samarajeewa, K.B.D.P., Kojima, N., Sakagami, J.I., Chandanie, W.A. (2005). The Effect of different timing of top dressing of nitrogen application under low light intensity on the yield of rice (Oryza sativa L.). *Journal of Agronomy and Crop Science,* Vol. 191, pp. 99-105. Germany.

[17] Sarker, S.C., Ali, M.H., Biswas, P.K., Chakraborty, R., Amin, R., Khandker, S. (2015). Contribution of nitrogen and methods of weeding on the yield components and yield of hybrid Boro rice (HEERA 4). *European Academic Research,* Vol. 2, pp. 16046-16060. Romania.

[18] Sarwar, G., Schmeisky, H., Hussain, N., Malik, M.A., Manzoor, M.Z., Zafar, A., Murtaza, G. (2020). Impact of compost to produce rice-wheat crops from saline sodic soil. *Journal of Pure and Applied Agriculture,* Vol. 5, pp. 11-19. Pakistan.

[19] Wang, H., Takano, T., Liu, S.K. (2018). Physiological adversity resistance of sea rice to salinity stress. *Agronomy,* Vol. 8, pp.205. United States.

[20] Zhang, Y.H., Fang, J.P., Wu, X.B., Dong, L.Y. (2018). Na^+/K^+ balance and transport regulatory mechanisms in weedy and cultivated rice (Oryza sativa L.) under salt stress. *BMC Plant Biology,* Vol. 18, pp. 375. England.

[21] Zhang, T.B., Zhan, X.Y., He, J.Q., Feng, H., Kang, Y.H. (2018). Salt characteristics and soluble cations redistribution in an impermeable calcareous saline-sodic soil reclaimed with an improved drip irrigation. *Agricultural Water Management,* Vol. 197, pp. 91-99. Netherlands.

DESIGN AND TEST OF HYDRAULIC DRIVEN SYSTEM FOR SMALL MULTIFUNCTIONAL AGRICULTURAL CHASSIS
/
小型多功能农用底盘液压驱动系统的设计与试验

Xiaolian LÜ[1,2], Xiaohu CHEN[3], Huijuan ZHANG[1], Xiaorong LÜ[3*] [1]

[1] Nanjing Research Institute for Agricultural Mechanization, Ministry of Agriculture and Rural, Nanjing, Jiangsu, 210014, China
[2] College of Machinery and Automotive Engineering, Chuzhou University, Chuzhou, Anhui, 239000, China
[3] College of Machinery & Electronics, Sichuan Agricultural University, Yaan, Sichuan, 625014, China
*E-mail: lxrxj2008@163.com
DOI: https://doi.org/10.35633/inmateh-68-55

Keywords: *Agricultural chassis; Hydraulic drive system; AMESim; Simulation analysis; Performance test*

ABSTRACT

In view of the problems of the output power and operation, when the multi-function machine in hilly and mountainous areas driving in the field, the hydraulic control drive system of small multi-function agricultural hydraulic chassis is designed. The key components of the hydraulic drive system were selected and matched. The hydraulic system simulation model was established in AMESim simulation analysis software, and the dynamic analysis of the hydraulic system operation under different conditions is carried out. The simulation analysis results show that the hydraulic system has a large impact and vibration when it is started instantaneously, and the hydraulic system has smaller impact and vibration when it is started stably. It is consistent with the actual working state of the hydraulic chassis. Under the two starting controls, the maximum flow of the hydraulic pump is 50L/min, the motor torque is about 440N · m, and the motor stable pressure is 6Mpa, the motor speed is 96 r/min, which is within the bearing range of the hydraulic components. The simulation output parameters are basically consistent with the theoretical calculation results, and meeting the design requirements. The chassis performance test results show that the maximum crossing height of the chassis is 200mm, the crossing width is 300mm, the maximum deviation of high-speed straight driving is 2.57m, it can stably pass 20° slope, and the operation is stable and the steering is flexible. All performance parameters can better meet the requirements of chassis operation in hilly and mountainous areas.

摘要

针对丘陵山地多功能作业机在田间行驶中在输出动力及操作中存在的问题，设计了一种履带式小型多功能农用液压底盘的液压控制驱动系统。对液压驱动系统关键元件进行了选型与参数匹配，利用AMESim仿真分析软件建立了液压系统仿真模型，对不同条件下液压系统作业状况进行了动态分析，仿真分析结果可知，瞬时启动时，液压系统有较大冲击及震荡，稳定启动时，液压系统波动小、几乎无冲击及震动，与液压底盘的实际工作状况一致，两种启动控制下变量泵流量最大值为50L/min时，马达扭矩约为440N.m，马达稳定时压力为6Mpa，马达转速为96r/min，均在液压元件的承受范围之内，且仿真输出的参数与理论计算结果基本一致，符合设计要求。通过底盘作业性能试验结果可知，底盘最大跨越高度为200mm，跨越宽度为300mm，高速直线行驶最大偏移量为2.57m，可稳定通过20°坡度，且操作平稳，转向灵活，各项性能参数均能较好地满足丘陵山地底盘作业要求。

INTRODUCTION

At present, agricultural machinery is developing rapidly, but it is only suitable for large and flat areas. In hilly and mountainous areas, due to the great undulates and complex conditions of the ground, ordinary agricultural machinery has insufficient adaptability to the terrain, poor vehicle stability, which affects the work quality of the machinery. Therefore, it is necessary to effectively solve the adaptability, controllability and stability of chassis operation of agricultural machinery to improve the level of agricultural mechanization in hilly and mountainous areas *(Wang et al., 2022; Wu et al., 2022, Chen, 2021)*. The hydraulic drive system uses hydraulic oil to drive the drive wheel rotating to achieve the walking function. The complex mechanical transmission links are omitted, so that the transmission system is simplified and the transmission efficiency is improved. Moreover, the hydraulic drive operation is easy, the maintenance and overhaul are convenient, which is very consistent with the operation requirements in hilly and mountainous areas *(Ling 2017; Gupta et al., 2019; Hu et al., 2019; Yermek et al., 2019)*.

Xiaolian Lü, Prof.; Xiaohu Chen, M.S. Stud; Huijuan Zhang, Associate researcher; Xiaorong Lü, Prof..

Therefore, hydraulic drive technology is widely used in walking machinery *(Suslov et al., 2020; Zhang 2017; Gradl et al., 2016)*. In recent years, scholars have done a lot of research on the application of hydraulic technology in the walking system of agricultural machinery *(Nie et al., 2020; Andrzej et al., 2016; Hu et al., 2018; Sachin 2018; Kumar et al., 2021; Gonzalez et al., 2016)*. *Kodrič and Pehan (2020)* designed a simple and effective hydraulic management system by using a small IC diesel engine to provide power for the hydraulic pump, which is composed of basic valves, electrical sensors and switches. The system can predict and analyze the important working conditions of the machine. *Zhang et al., (2022)* designed a hydrostatic chassis drive system for a large plant protection machine. The system realizes the prevent slip and rotation of the plant protection machine through the combination of the hydraulic drive system and the diverter valve. The designed hydraulic chassis of the plant protection machine has good driving stability. *Hu and Zhang (2018)* designed rice transplanted with an entirely hydraulic chassis. The chassis is driven by a single pump driving four motors, and a diverter valve is set to prevent wheel slipping. *Fan et al., (2018)* designed an output system based on hydraulic transmission for operation in hilly and mountainous areas, and the performance of the hydraulic system were verified through the hydraulic system simulation and prototype test. The hydraulic system technology has been applied in agricultural machinery, but few hydraulic chassis are suitable for operation in hilly and mountainous areas. On the basis of the existing hydraulic chassis research, this paper designs a kind of hydraulic drive system of tracked multi-functional agricultural hydraulic chassis suitable for hilly and mountainous areas, in order to improve the adaptability, flexibility and drive performance of the walking system of hilly and mountainous work tools, and meet the needs of the development of agricultural mechanization in hilly and mountainous areas.

MATERIALS AND METHODS

STRUCTURE AND WORKING PRINCIPLE

The structure of the chassis hydraulic drive system is shown in Figure 1. The system adopts shunt transmission mode. Part of the power output of the engine is sent to the hydraulic pump to drive the walking wheel, and other part of the power is transmitted to the rear power output shaft to provide power for the agricultural machinery. The traveling drive system is supplied with oil by the double-pump. The drive wheels are driven rotation by the hydraulic motor to realize the traveling and steering functions of the chassis. The operating handle controls the steering and speed of the motor by controlling the direction change and opening of the reversing valve, and realizes the forward, backward, and variable-speed driving of the chassis.

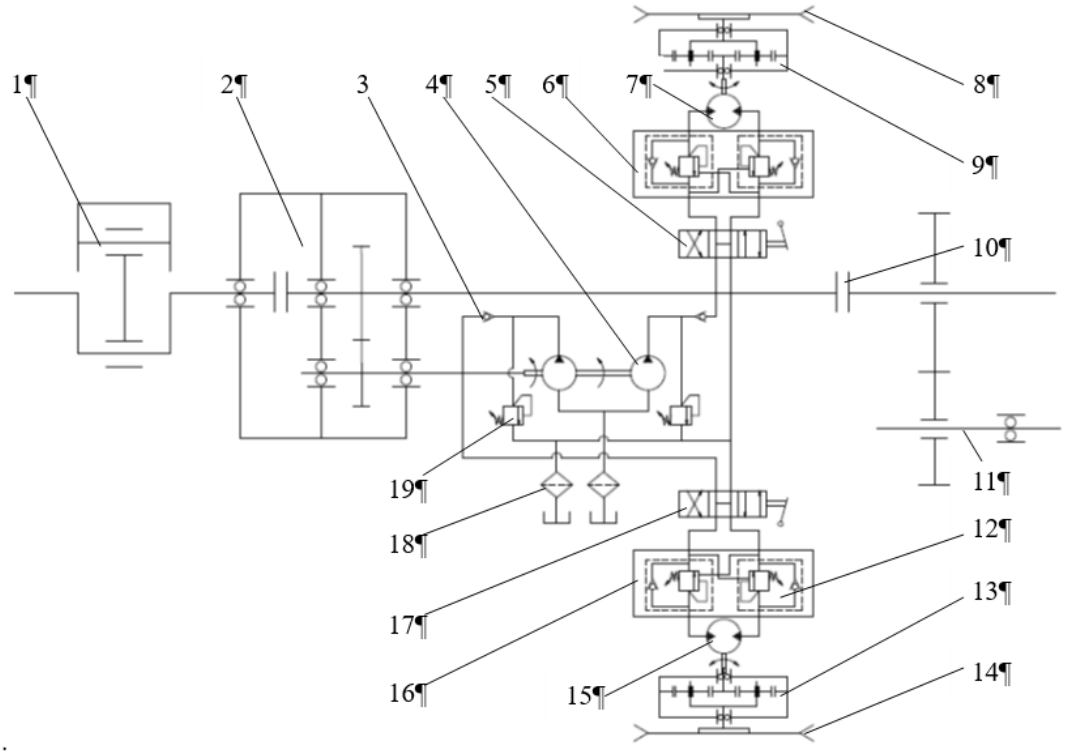

Fig. 1 - Schematic diagram of chassis hydraulic drive system

1. Diesel engine; 2. Transfer case; 3. One way valve; 4. Double-pump; 5. 17. Reversing valve; 6. 16. Self -locking device; 7. 15. Hydraulic motor; 8. 14. Drive wheel; 9. 13. Brake; 10. Clutch; 11. Rear output shaft; 12. One way sequence valve; 18. Oil filter; 19. Overflow valve

When the hydraulic system is working, the outputs power of the engine drives the pump to provide pressure oil for oil circuits by the transfer case. In order to prevent the impact of hydraulic oil backflow on the pump, the pressure oil inflows the reversing valve through the one-way valve. The operating handle on the chassis controls the reversing and opening of the corresponding reversing valve. When the operating handles on both sides are pushed forward, the chassis moves forward. When the operating handles are pushed backward, the chassis moves backward. The opening of the reversing valve can be adjusted by the operating handle to change the motor flow. The greater the valve opening, the greater the motor flow, the faster the motor speed, the higher the chassis speed. The smaller the valve opening, the smaller the motor flow, the slower the motor rotation speed, the slower the chassis speed. When the opening of the two control handles in the same direction is different to achieve the steering function. When the left and right control handles are reversed, the left and right tracks of the chassis will reverse the differential steering to achieve the in-situ steering. The self-locking device of the hydraulic drive system is composed of two one-way sequence valves. Two one-way sequence valves are two way self-locking. When the operating handle of the directional valve is in the middle position, the pressure oil of the pump output directly returns to the oil tank through the interior of the directional valve, and the two one-way sequence valves are in a self-locking state, the hydraulic motor is locked. In order to improve the safety and braking effect of the system, wheel side brakes are installed on the inner side of the drive wheels to achieve the effect of auxiliary braking on the chassis.

SELECTION OF MAIN COMPONENTS OF HYDRAULIC SYSTEM

The designed small multi-function agricultural hydraulic chassis is suitable in the hilly and mountainous areas operations, and can drive various suspended small agricultural machines and tools for farming, sowing, harvesting and other operations by the rear power output. The main technical parameters of the agricultural hydraulic chassis are shown in Table 1.

Table 1

Hydraulic crawler chassis vehicle technical parameters

Index	Unit	Parameter value
Chassis mass (m)	kg	420
Diesel engine power (Pw)	kw	13.4
Diesel engine revs (n)	r/min	1250
Drive wheel radius (r)	mm	175
Working pressure (P)	MPa	7
Operating speed (V)	km/h	0-6
Maximum climbing degree	°	20

The selection of hydraulic motor shall meet the requirements of maximum operating parameters during chassis operation. During the operation of hydraulic motor, the working pressure, speed range, operating torque, efficiency, installation conditions, etc. shall be considered. The determination of influencing factor coefficients of main technical parameters can be obtained to consult manual or refer to experience values *(Chen et al., 2020; Yang and Zhu, 2010)*.

Calculation of motor driving torque:

$$T_p = F_T \times r \tag{1}$$

In the formula: T_p—Motor torque, N.m; F_T—Traction force, N; r—Radius of driving wheel, mm.

$$\begin{cases} F_T = F_q - F_f \\ F_q \leq F_\varphi \\ F_f = f \times G_s \end{cases} \tag{2}$$

F_q—Tangent driving force, N; F_f—Rolling resistance, N; F_φ—Adhesion, N; G_s- Chassis weight, N; f—Rolling resistance coefficient, (0.06~0.07).

$$\begin{cases} F_\varphi = \varphi \times G_\varphi \\ G_\varphi = G_s \end{cases} \tag{3}$$

G_φ—Adhesion weight, N; G_s—Chassis weight, N; φ—Adhesion coefficient, (0.9~1.1).

The motor torque can be obtained by solving equations (1), (2) and (3).

$$T_p \geq G_s(\varphi - f) \times r = 749.1 \text{ N.m} \tag{4}$$

φ—Adhesion coefficient, (0.9~1.1); f—Rolling resistance coefficient, (0.06~0.07); r—Radius of driving wheel, mm.

The displacement of hydraulic motor, V_{gm}, is:

$$V_{gm} = \frac{2\pi T_g}{\Delta P \times \eta_{mm}} \geq 373.4 \text{ mL/r} \quad (5)$$

T_g—Driving torque of single motor, N.m; ΔP—Motor pressure difference, MPa; η_{mm}—mechanical efficiency of motor, (0.9~0.99).

According to the chassis speed, the motor speed is determined as:

$$n_m \geq \frac{V}{2\pi r} = \frac{1.67 \times 60}{0.175 \times 2 \times \pi} = 91.2 \text{ r/min} \quad (6)$$

In the formula: V—Maximum speed of chassis, m/s; r—Radius of driving wheel, mm.

According to the calculation results, the OMV500 radial piston quantitative motor is selected, the maximum working pressure is 16MPa, displacement is 518mL/r, and speed is 170 r/min.

Since the chassis adopts the pump control principle, two pumps are required to control two hydraulic motors respectively. The selection of hydraulic pump is mainly based on its maximum working pressure and flow (*Yang and Zhu, 2010; Liu et al., 2019)*. The maximum working pressure of the hydraulic pump is determined by the maximum working pressure of the hydraulic motor, namely:

$$P_P \geq P_1 + \sum \Delta P = 16.5 \text{ MPa} \quad (7)$$

In the formula: P_p—Maximum working pressure of hydraulic pump, MPa; P_1—Maximum working pressure of hydraulic motor, MPa; $\sum \Delta P$—Total pipeline loss from the outlet of hydraulic pump to the inlet of hydraulic motor, (0.2~0.50) MPa.

Maximum flow of the double-pump:

$$q_{vp} \geq K \sum q_{Vmax} = K \frac{V_{gm} \times n}{1000} = 44.27 \text{L/min} \quad (8)$$

In the formula: K—leakage coefficient of the system, (1.1~1.3); q_{Vmax}—Maximum flow of hydraulic motor, L/min; V_{gm}—Motor displacement, ml/r; n—Motor speed, r/min.

Based on theoretical calculation and comprehensive consideration, the CBZ2050/2050 BF plunger type double-pump is selected, the rated flow is 50 L/min.

The inner diameter of the hydraulic oil pipe is related to the pipe material and the speed of oil pressure in the pipe. When the flow rate is constant, the larger the inner diameter is, the slower the flow rate is, the less the pressure loss of the oil circuit is, and the smaller the inner diameter is, the faster the flow rate is, the larger the pressure loss is *(Yang and Zhu, 2010)*.

The calculation formula of tubing diameter is:

$$d \geq 4.61 \sqrt{\frac{q}{V}} = 18.82 \quad (9)$$

In the formula: d—Inner diameter of oil pipe, mm; q—Oil pipe flow, L/min; V—flow rate of oil in oil pipe, (2.5-7.6) m/s.

According to theoretical calculation and comprehensive consideration, the inner diameter of hydraulic oil pipe is 20mm. The 34SH-L20H-W three position four-way directional valve is selected, and the nominal diameter is 20mm, the nominal pressure is 20MPa. The DBW10B2-5X/10-6EG24N9K4 relief valve is selected, and the nominal diameter is 10mm, the maximum set working pressure is 10MPa. The S10A1 tubular one-way valve is selected, and the opening pressure is 0.05MPa, the nominal pressure is 10MPa.

SIMULATION ANALYSIS OF HYDRAULIC SYSTEM

According to the overall scheme of hydraulic drive system of the chassis, the AMESim simulation software is used to establish the hydraulic drive system simulation model of chassis (*Liang and Su, 2015*), as shown in Figure 2.

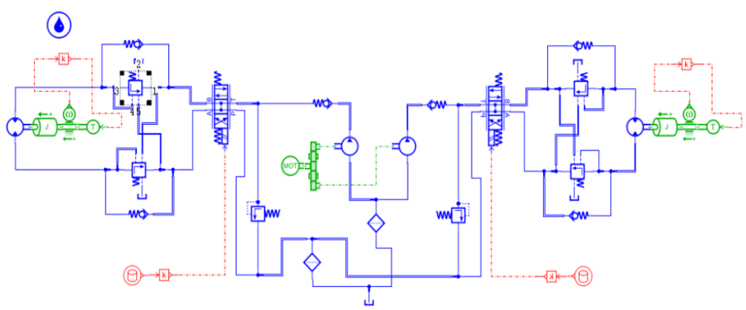

Fig. 2 - Hydraulic system simulation model

The basic performance parameters of the main components of the hydraulic drive system are set as follows: according to the system requirements, the engine power is 13.4kW, the speed is 1250r/min, the hydraulic pump flow is 50mL/r, the speed is 2000r/min, the motor displacement is 518 mL/r, the rated speed is 170r/min, and the overflow pressure of the overflow valve is 10MPa.

In the simulation process, the step signal and slope signal are used to simulate the control of the controller to the hydraulic drive system. The step signal simulates the operation of the quick start system. The signal is set as stop for 2s, forward instantaneous open, forward stable operation for 6s, instantaneous close, stop for 2s, reverse instantaneous open, reverse stable operation for 6s, instantaneous close, and stop operation. The control signal is shown in Figure 3 (a). The slope signal simulates the operation of the smoothly starts system. The signal is set as stop for 1s, forward direction starts to open at a constant speed, and reaches the maximum opening in 1s, forward stable operation for 5s, starts to close at a constant speed, and it is completely closed in 1s, stop for 2s, reverse direction starts to open at a constant speed, and increases to the maximum opening in 1s, reverse stable operation for 5s, starts to close at a constant speed, and it is completely closed in 1s, and stops the operation. The control signal is shown in Figure 3 (b).

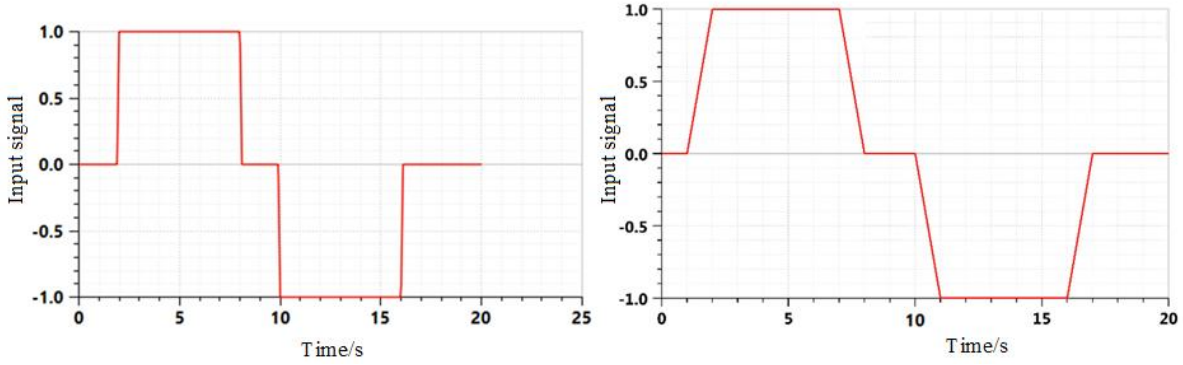

(a) Step signal (b) Ramp signal

Fig. 3 - Hydraulic pump control signal

Under the step signal, the simulation operation of the hydraulic drive system is shown in Figure 4, and under the slope signal, the simulation operation of the hydraulic drive system is shown in Figure 5.

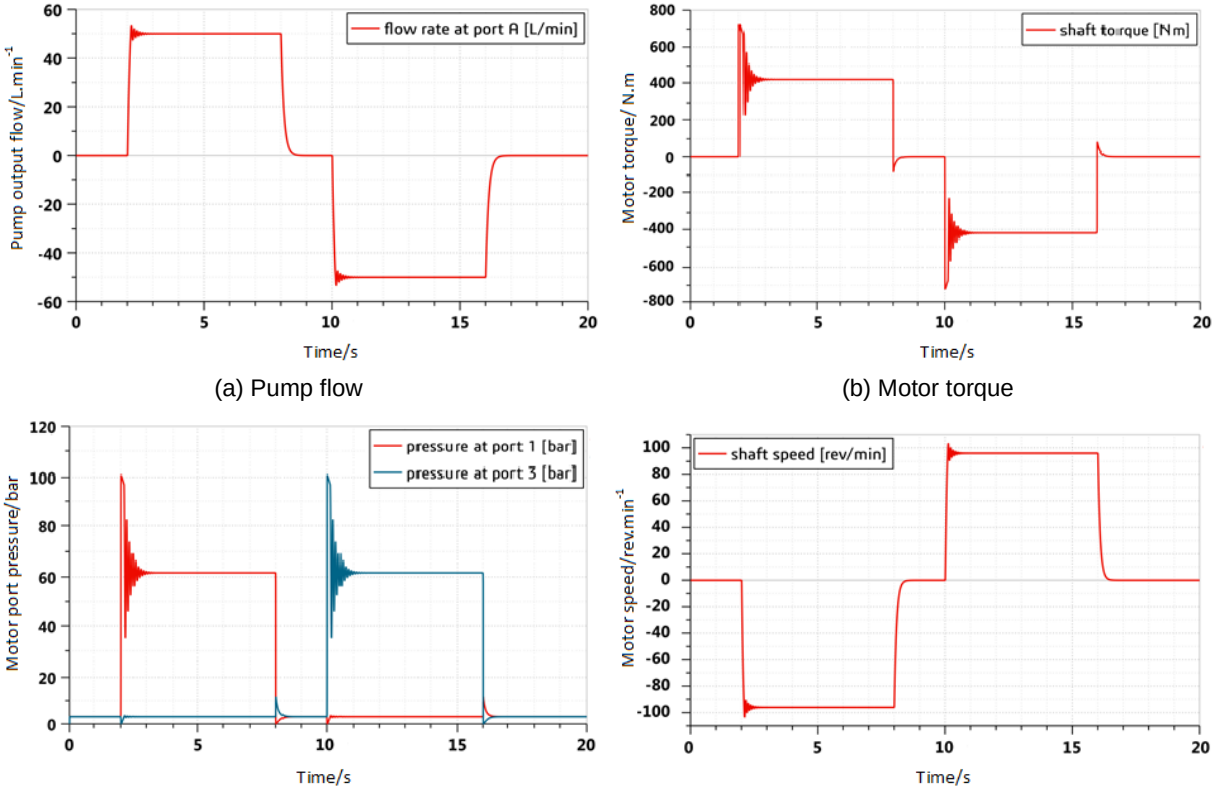

(a) Pump flow (b) Motor torque

(c) Motor pressure (d) Motor speed

Fig. 4 - Operating status of hydraulic components under Step signal

It can be known from the simulation results that: as shown in Figure 4, when instantaneous opening the hydraulic system, the output flow of the hydraulic pump is stabilized at about 50L/min after a short fluctuation. As the hydraulic oil fast flows into the hydraulic motor to generate the instantaneous pulse impact, the motor torque rises instantaneously to reach of about 700N, and it enters a stable state of about 440N.m after a short period oscillation. The port 1 of the motor is a forward oil inlet, and the port 3 is a reverse oil inlet. The pressure changes of the two oil ports are similar, but there is a difference in the opening time. Due to the impact of instantaneous opening, the pressure of the hydraulic system will reach 10MPa of maximum safe pressure of the system.

After a short oscillation period, it will enter a stable state, stabilized at the working pressure of about 6MPa. The motor speed rises instantaneously to the maximum speed about 100r/min, and reaches a stable speed about 96r/min after a short oscillation. It can be concluded that the chassis speed is of about 6.3 km/h at this time, which meets the maximum speed of the chassis of 6 km/h, and meets the design requirements. When the system is closed instantaneously, the output flow of the hydraulic pump is zero instantaneously, and the hydraulic motor stops with the less impact. The pressure at the two oil ports of the motor drops rapidly with a short and small pressure oscillation, and the hydraulic motor speed drops to 0 instantaneously.

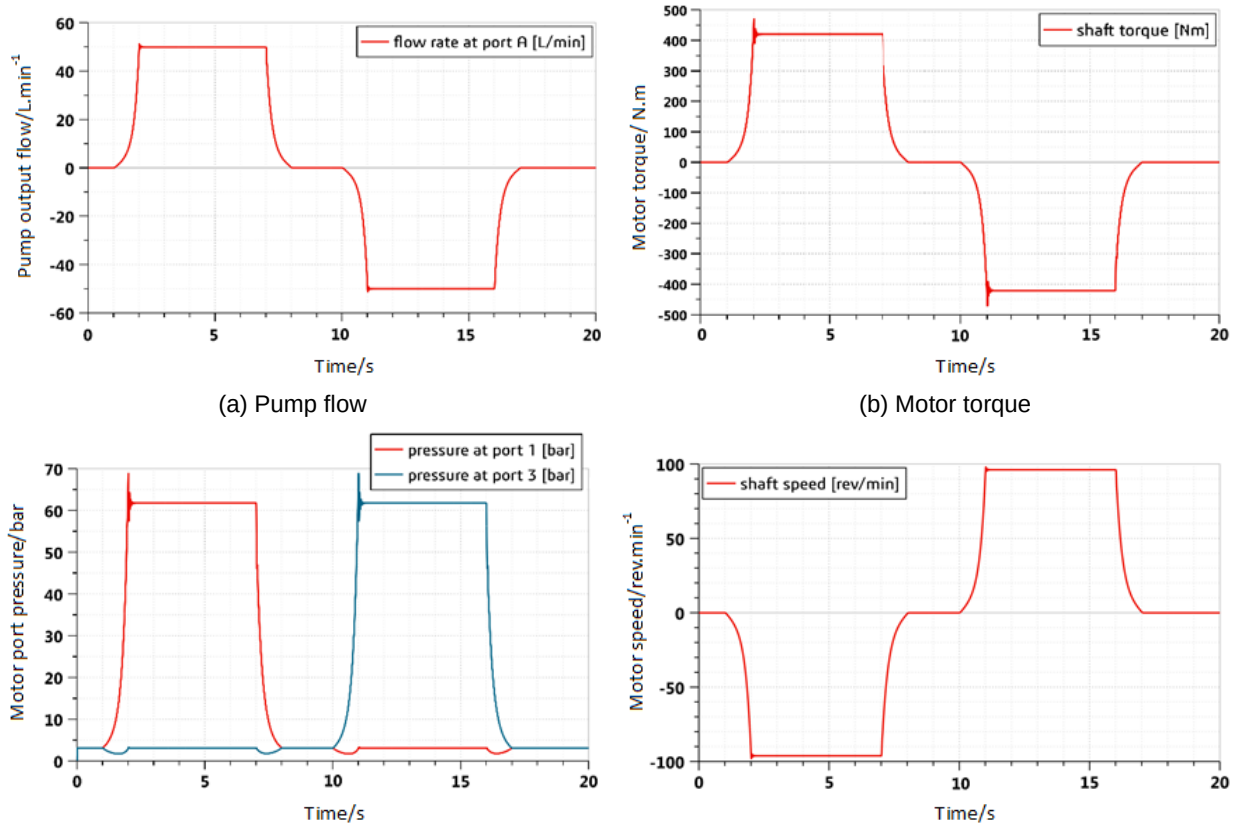

(a) Pump flow (b) Motor torque

(c) Motor pressure (d) Motor speed

Fig. 5 - Operating status of hydraulic components under Ramp signal

As shown in Figure 5, when the steady opening the hydraulic system, the flow of the hydraulic pump can be smoothly transited, stabilized at about 50L/min, and there is no impact and oscillation in the whole process. The motor torque rises steadily, and then there is a small fluctuation, and then it is stabilized at about 400N.m. The pressure changes of motor oil port 1 and oil port 3 are similar, but there is a difference in the opening time. They all gradually and steadily rise to the peak value of about 7MPa. After a small pressure oscillation, they are stabilized at about 6MPa. The motor speed rises steadily at 96r/min. When the system is closed, the output flow of the hydraulic pump is 0 instantly, and the motor torque, the pressure of the two oil ports of the motor, and the motor speed are all steadily reduced to 0. In the actual operation process, when the controller is slowly pushed to the maximum opening, the hydraulic chassis starts smoothly with almost no vibration, and the chassis is in good working state.

Materials and methods of performance test

According to GB/T 3871《Test Methods for Agricultural Wheeled and Tracked Tractors》, the operating performance of the chassis hydraulic drive system is tested through the chassis trafficability, high-speed driving straightness, climbing performance and steering performance.

The chassis trafficability is to test the performance of the chassis through vertical obstacles and horizontal trenches. The accelerator is fully opened, and the chassis is observed to climb over vertical obstacles and drive through horizontal trenches. Each condition is tested three times, one pass is considered as qualified, and data is recorded. When testing the straightness of high-speed driving, first make a reference line, then make a vertical line according to the reference line, and mark 100m from the starting point reference line as the end point. The chassis drive straight from the starting point to the end point at 5km/h constant speed, and the vertical deviation from the calibration line are measured. Tested 6 times, record the test data, and calculate the average value. The deviation of the chassis on the flat road cannot exceed 6m. As the operating gradient in hilly and mountainous areas is generally not more than 15°, the maximum gradient for the climbing performance test is 20°. The climbing performance test is carried out for 4 different gradients of 5°, 10°, 15° and 20°. At a stable climbing speed, each gradient is tested three times, and it is qualified if it passes two tests. During the steering performance test, test the steering effect in the field and on the hard ground. Push the left and right control levers in the opposite direction to drive the two hydraulic motors to rotate relatively, and test the effect of reverse differential in-situ steering.

RESULTS

The chassis performance test states are shown in Figure 6. The chassis trafficability test effects are shown in Figure 6(a) and 6(b). When the chassis is in good working state, the maximum height of crossing vertical obstacles reaches 200mm, and the width of crossing ditches reaches 300 mm, which can better meet the requirements of the chassis trafficability. The driving straightness test results are shown in Figure 6 (c) and Table 2. The maximum deviation of the vehicle in straight line driving is 2.57m, and the average deviation is 2.06m. The deviation is within the allow range of high-speed driving straightness of the chassis, which meets the design requirements. The results of climbing performance test are shown in Figure 6 (d) and Table 3. The chassis has good climbing capacity and good trafficability, which is suitable for operation in hilly and mountainous areas and meets the design requirements. The steering of the hydraulic chassis is mainly to check whether the steering radius of the chassis meets the design requirements and whether it is suitable for steering in a narrow space. During the test, the chassis steers flexibly and can meet the needs of steering in chassis operation. The use of bilateral reverse differential steering can achieve arbitrary adjustment of the steering radius and in-situ steering. The steering effect is shown in Figure 5 (e) and (f).

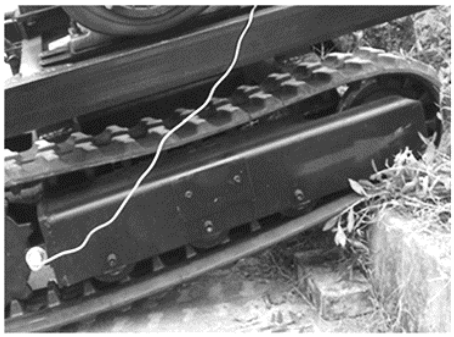

(a) Crossing vertical obstacles

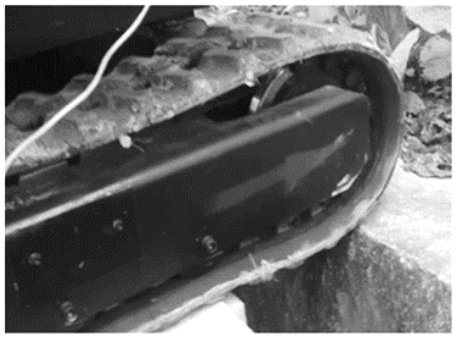

(b) Crossing horizontal ditch

(c) Driving straightness

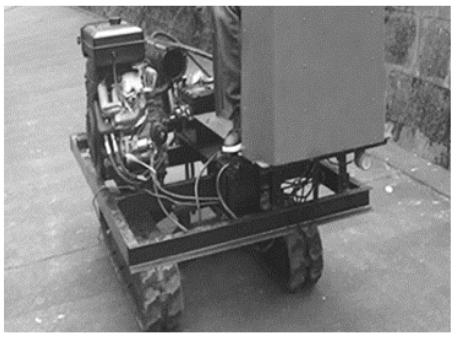

(d) Climbing performance

(e) Steering performance in the field

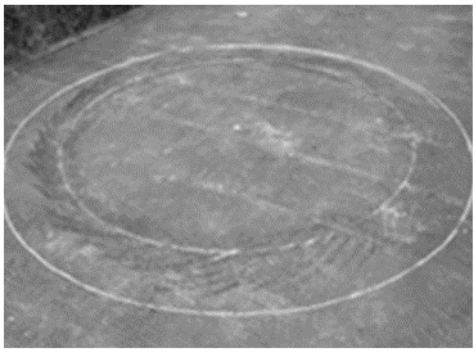

(f) Steering performance on the road

Fig. 6 - Hydraulic chassis performance test

Table 2

Offset test results

NO.	Speed (km/h)	Offset (m)
1	5.0	1.54
2	5.0	2.57
3	5.0	1.78
4	5.0	2.33
5	5.0	1.96
6	5.0	2.15
Average offset (m)		2.06

Table 3

Test of climbing

NO.	Speed(km/h)	Slope(°)	Chassis trafficability
1	3.0	6	Fast and stable passing
2	3.0	10	Fast and stable passing
3	1.5	15	Slow and stable passing
4	1.5	20	Slow and stable passing

CONCLUSIONS

(1) On the basis of the research on the current situation of the agricultural hydraulic chassis in hilly and mountainous areas, the overall design of the hydraulic drive system of the chassis is carried out. The designed hydraulic drive system uses the controller to control the rotation speed of the motor to realize the variable speed driving of the chassis. At the same time, it can control the differential driving of the chassis tracks to achieve arbitrary adjustment of the chassis steering radius and in-situ steering. It effectively solves the existing problems in the adaptability, controllability, and stability of agricultural machinery in hilly and mountainous areas.

(2) According to the overall scheme of hydraulic drive system of the chassis, the AMESim simulation software is used to establish the hydraulic drive system simulation model of chassis. It can be known from the simulation results, when the instantaneous startup the hydraulic system, the system flow, motor pressure, torque and speed will have a transient impact, with large fluctuations, and can cause great damage to the system if it is in this working state for a long time, when the stable startup the hydraulic system, the system flow rises steadily with almost no impact, and the torque, pressure and speed of the motor increase steadily with little fluctuation, without impact and shock. The motor peak pressure is about 7Mpa, and it is stable at about 6Mpa after a small fluctuation. The chassis starts more stably with less vibration, which has a good protection effect on the hydraulic motor. In addition, when the system is stable under the control of two signals, the maximum flow of the hydraulic drive system is 50L/min, the motor torque is about 440N.m, the motor pressure is 6Mpa, and the motor speed is 96r/min, which is consistent with the working states of the hydraulic chassis in the actual operation process.

(3) The chassis performance tested results shown that the designed chassis has good trafficability, the maximum crossing height reaches 200mm and the crossing width reaches 300mm. The maximum deviation of the chassis is 2.57m and the average deviation is 2.06m when stably and high speed driving at 5km/h, which meets requirements of high-speed driving straightness. The chassis has good climbing performance, and can stably passing the 20° slope, adapting to the climbing performance of the chassis in hilly and mountainous areas. In addition, the chassis is stable in operation, flexible in steering, and can achieve in-situ steering. The operation effect can better meet the chassis operation requirements.

ACKNOWLEDGEMENTS

The study was supported by the Key Laboratory of Modern Agricultural Equipment, Ministry of Agriculture and Rural, P.R.China (HT20200702), and the Sichuan Innovation Team of Chinese National Modern Agricultural Industry Technology System (SCCXTD-2023-20).

REFERENCES

[1] Andrzej, G., Jarosław, A., and Piotr, K. (2016). Analysis of the kinematic characteristic of the test stand for various steering for the hydraulic driven working attachment. *Procedia Engineering*, Vol. 136, pp. 3-7. Netherlands.

[2] Chen, P. M., Yang, L. H., Wu, S. H., Deng, Y. G., Wang, Y. Q., Yan, B. (2020). Hydraulic motor torque and speed calculation selection (液压马达扭矩及转速推算选型). *Agricultural Equipment & Technology*, Vol. 46, pp.19-22. Jiangsu/ China.

[3] Chen, S. Q. (2021). Problems and Countermeasures in the Development of Agricultural Mechanization in Hilly and Mountainous Area (丘陵山区农业机械化发展存在的问题与对策). *Agriculture Mechanization Research*, Vol. 2, pp. 39-40. Jiangxi/China.

[4] Fan, Y. K., Mao, E. R., Zhu, Z. X., Xie, B. (2018). Design and Experiment of Hydraulic Multi-point Power Output System for Hilly and Mountain Tractors (丘陵山地拖拉机液压多点动力输出系统设计与试验). *Transactions of the Chinese Society for Agricultural*, Vol. 49, pp. 484-492. Beijing/China.

[5] Gonzalez, D. O., Martin-Gorriz, B.; Berrocal, I. I., Hernandez, B. M., Garcia, F. C., Sanchez, P. M. (2016). Development of an automatically deployable roll over protective structure for agricultural tractors based on hydraulic power: Prototype and first tests. *Computers and Electronics in Agriculture*, Vol. 12, pp. 46-54. England.

[6] Gradl, C., Scheidl, R., Scheidl, R. (2016). Sensorless position control with a hydraulic stepper drive-concept, compression modeling and experimental investigation. *Mechatronics*, Vol. 35, pp. 91-101. England.

[7] Gupta, S., Khosravy, M., Gupta, N., Darbari, H., Patel, N. (2019). Hydraulic System Onboard Monitoring and Fault Diagnostic in Agricultural Machine. *Brazilian Archives of Biology and Technology*, Vol. 62. Brasil.

[8] Hu, K., Zhang, W. Y. (2018). Design and simulation for driving system and steering system of hydraulic chassis of rice transplanter. *Advances in Mechanical Engineering*, Vol. 10, pp. 1-11. United States.

[9] Hu, K., Zhang, W., Qi, B., Li, K., Yan, W. (2019). Application and development of hydraulic chassis in the field of agricultural machinery (液压底盘在农业机械领域的应用与发展). *Jiangsu Agric. Sci.*, Vol 47, pp. 259-263. Jiangsu/China.

[10] Hu, K., Zhang, W., Yu, S., Qi, B. (2018). Design and research of full hydraulic chassis drive system for high-speed rice transplanter (高速插秧机全液压底盘驱动系统设计研究). *Mod. Manuf. Eng*, Vol.10, pp.141-145. Beijing/China.

[11] Kodrič, M., Pehan, S. (2020). Hydraulic Transmission of Agricultural Machine Appropriate for Treating Extreme Steep Farmland Terrains. *Technical Gazette*, Vol. 27, pp. 718-724. Croatia

[12] Kumar, S., Tewari, V., Bharti, C.K., Ranjan, A. (2021). Modeling, simulation and experimental validation of flow rate of electro-hydraulic hitch control valve of agricultural tractor. *Flow Measurement and Instrumentation*, Vol. 82. England.

[13] Liang, Q and Su, Q. (2015). AMESim computer simulation guide. Beijing, China: Machine Press, 2015.

[14] Ling, J. (2017) Application status and trend of hydraulic technology in modern agricultural machinery (液压技术在现代农业机械中的应用现状与趋势). *South Agricultural Machinery*, Vol. 6, pp. 59-60. Jiangxi/China.

[15] Liu, Z. G., Li, R. C., Li, Z. P. (2019). Design of Hydraulic Transmission System for Self-propelled Sprayer's Chassis (自走式喷雾机底盘液压传动系统设计). *Machine Tool & Hydraulic*, Vol. 47, pp.72-75. Guangdong/China.

[16] Nie, Y. Y, Wu, Y. L, Li, C. S, Xu, W. L. (2020). Design and test of hydraulic chassis of high ground clearance sprayer(高地隙喷药机液压底盘的设计与试验). *Nanfang Agric*, Vol. 1, pp, 10-12. Jiangxi/China.

[17] Sachin, P. (2018). Design and Optimization of Hydraulic Farm Tractor Trolley. International Journal of Research in Engineering, *Science and Management*, Vol. 1, pp. 299-302. India

[18] Suslov, N. M., Davydov,S. Ya., Suslov, D. N., Chernukhin, S. A. & Velikanov, V. S. (2020). Thermal Calculation of the Hydraulic Drive for a Dragline Walking Mechanism. Refractories and Industrial Ceramics, Vol. 2, pp.15-17. Russia.

[19] Wang, X. W., Yuan, S. Q., JIA, W. D. (2022). Current situation and development of agricultural mechanization in hilly and moun-tainous areas. *Journal of drainage and irrigation machinery engineering (JDIME)*, Vol. 40, pp. 535-540. USA.

[20] Wu, H. Z, Niu, P., Xie Y. J, Xia, F., Wang M. M. (2022). Present Situation and Suggestions of Agricultural Mechanization in Southwest Hilly and Mountainous Areas (西南丘陵山区农业机械化发展现状及建议). *Agriculture and Technology*, Vol. 42, pp. 68-70. Jilin/China.

[21] Yang, P. Y. and Zhu, F. Y. (2010). *Brief Manual for Hydraulic System Design*. Beijing, China: Machine Press.

[22] Yermek, A., Yerbol, S., Alexander, Y., Bauyrzhan, Z., Erbolat, K. (2021). Study of the hydraulic technology in smart agrian machines for cleaning shaft wells in the mobile unit. *International Journal of Agricultural Resources, Governance and Ecology*, Vol. 17, pp: 211-224. Switzerland.

[23] Zhang, C. L., Li, C. P., Zhao, C. Z., Li, L., Gao, G. L., Chen, X. Y. (2022). Design of Hydrostatic Chassis Drive System for Large Plant Protection Machine. *Agriculture*, Vol. 12, pp 1118. Switzerland.

[24] Zhang, X. F. (2017). Review on Development of Hydraulic Driving Walking Machine (行走机械液压技术的国内外发展综述). *Fluid Power Transmission and Control*, Vol. 3, pp. 1-11. Shanghai/China.

DESIGN AND TEST OF AUTOMATIC CONTROL SYSTEM FOR HEADER HEIGHT OF COMBINE HARVESTER

/

联合收获机割台高度自动控制系统的设计与试验

Mingjian RUAN [1, *)], Hanlu JIANG [2)], Haili ZHOU [3)], Jun YE[1)], Jinpeng HU[4)] [1]

[1)] College of Mechanical and Electrical Engineering, Zhejiang Industry Polytechnic College, Shaoxing/ China;
[2)] Chinese Academy of Agricultural Mechanization Sciences Group Co, Ltd, Beijing/ China;
[3)] Key Laboratory of Transplanting Equipment and Technology of Zhejiang Province, Hangzhou/ China;
[4)] College of Agricultural Engineering, Jiangsu University, Zhenjiang/ China;
Email: ruanmingjian@163.com
DOI: https://doi.org/10.35633/inmateh-68-56

Keywords: *Combine harvester, header height, profiling mechanism, automatic control, gray prediction*

ABSTRACT

Aiming at the problems of poor applicability of traditional header height detection mechanism, poor stability and large lag of automatic control system of combine harvesters, an automatic control system of header height of combine harvester was designed, which mainly included the profiling mechanism, controller, proportional valve, manual operation handle and display module. The profiling detection mechanism was composed of angle sensor, profiling plate, torsion spring and other structures. The key structural parameters of the profiling mechanism were determined by using the Adams simulation software and its working performance was verified. The gray prediction PID algorithm of header height was used to reduce the lag of the control model. The control system detected the height of the header from the ground through the profiling mechanism. After being processed by the controller, the height of the header was changed by adjusting the expansion of the header oil cylinder. The field test results showed that the working performance of the header automatic control system was stable. Under the working conditions of preset header height of 100 mm and 200 mm, the average deviation of the control system was within 21 mm, which met the real-time control demand of header height during the normal operation of the combine harvester. This research could provide intelligent design methods of combine harvesters.

摘要

针对传统联合收获机割台高度检测机构适用性差、自动调控系统稳定性不佳与滞后性大的问题，设计了一种联合收获机割台高度自动控制系统，主要包括随地仿形机构、控制器、比例阀、手动操作手柄和显示模块等。随地仿形检测机构由角度传感器、仿形板、扭簧等结构组成，利用 Adams 仿真软件确定了仿形机构关键结构参数并验证了其工作性能，建立了联合收获机割台高度与传感器信号之间的关系模型，采用割台高度灰色预测 PID 控制算法减小控制模型滞后性，控制系统通过仿形机构检测割台离地高度，经控制器处理后，通过调整割台油缸伸缩量实现割台高度变化。田间试验结果表明，割台自动调控系统工作性能稳定，在预设割台高度 100㎜ 及 200㎜ 工况下，控制系统调节的平均偏差均在 21㎜ 内，满足联合收获机正常作业时割台高度实时调控需求。本研究可为联合收获机的智能化设计提供参考。

INTRODUCTION

The combine harvester is one of the key links in job production. With the continuous maturity of joint harvest equipment, the direction of automation and intelligence has gradually become an important development direction (*Bomoi et al., 2022; Golpira et al., 2022; Kim et al., 2021; Mirmahdi et al., 2021*). The automatic control of the header height is an important aspect. As an important parameter in the operation process of the actual harvester (*Shukla et al., 2021; Shojaei et al., 2021*), the height of header is easy to cause ear loss and grain loss too high, and the increase of stubble height will significantly improve the operating power consumption of the cultivator and increase the operating cost. When the header height is low, it is easy to touch soil and cause machine failure (*Ni et al., 2021*).

[1] *Mingjian Ruan, Lecturer. Eng.; Hanlu Jiang, Ph.D. Eng.; Haili Zhou, Lecturer. Ph.D. Eng.; Jun Ye, Lecturer. Eng.; Jinpeng Hu, Ph.D. Stud. Eng.*

At present, the height control of the header of the combine mainly depends on the manual driving experience. The operation effect and efficiency vary from person to person, and the manipulator has strong manipulation intensity after working for a long time.

In order to reduce the strength of the driver, and improve the efficiency of the combine harvester, domestic and foreign scholars have carried out a large number of research on the height automatic control system of the combined harvesting machine header. *Yang et al., (2018*) arranged three pairs of ultrasonic sensors at the bottom of the cutting stage to achieve non-contact measurement of the ground height from the ground, the measurement effect is susceptible to the influence of the stubble and soil block. *Wei et al., (2017*) and *Geng et al., (2020*) designed contact mechanical feeler mechanism respectively. The mechanical change was converted into electrical signal output by angle sensor, thereby controlling the ground imitation action, but did not consider the latency of the system during the actual job. *Yang et al., (2022*) designed the ground profiling monitoring mechanism and the header height feedback mechanism based on the angle sensor, and the height error of cutting stubble was not more than 2 cm, which showed a stable control effect.

Aiming at the above problems, this paper designed a set of automatic control system for header height of combine harvester. The current height of the header was detected in real time by profiling mechanism and the mathematical model of the header height and angle sensor signal was established. The header height can be adjusted automatically by adjusting the stroke of the header cylinder. The field verification test was carried out, and the reliability of the height adaptive regulation system of the header was evaluated, which provided a reference for the intelligent design of the combine harvesters.

MATERIALS AND METHODS

Overall structure

The automatic header height control system provided the operator with manual and automatic operation modes. The manual operation handle was used to control the lifting of the header during manual operation. The manual operation handle was equipped with a manual and automatic mode switch. The manipulator can complete the switching of the working mode according to the actual needs. The automatic control system was mainly composed of profiling detection mechanism, header lifting cylinder, manual operating handle and other modules. The overall structure of header height automatic control system is shown in Figure 1.

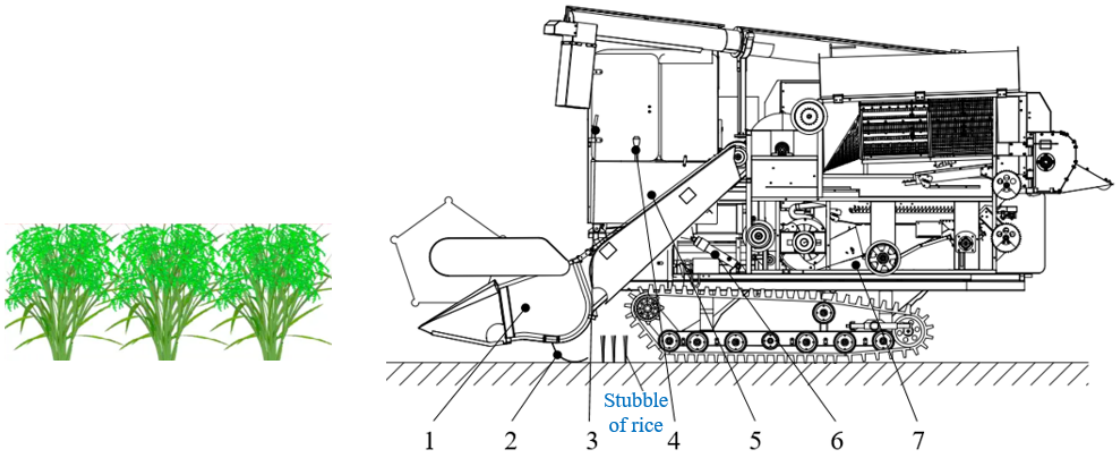

Fig.1 - The overall structure of automatic control system for header height

1. Header of combine harvester; 2. Profiling detecting mechanism; 3. Industrial display screen; 4. Manual operating handle; 5. Controller; 6. Header lifting cylinder; 6. Proportional valve

Working Principle

The profiling detecting mechanism was symmetrically installed on one side of the header, and the fluctuation of the ground was converted into voltage signal output through the angle sensor. The controller was a Bortron Selindro hydraulic controller specially designed for intelligent equipment of agricultural machinery, which was equipped with CAN bus interface communication function. The lifting of the header was controlled by a hydraulic system, and the hydraulic valve is a proportional solenoid valve, which can control the position of the hydraulic cylinder more accurately. The automatic header height control system detected the height of the header from the ground through the profiling mechanism. The controller output the control signal to the proportional valve according to the current header height. The proportional valve changed the hydraulic oil to

push the header lifting cylinder to expand and contract, so as to adjust the header height to the set range. When the profiling mechanism detected that the current header height was greater than the upper limit of the set range, the controller output a signal to energize the electromagnet on the right side of the proportional valve, and the proportional valve spool moved to the right. The piston rod of the header cylinder shrank under the hydraulic oil pressure, and the header dropped; When the profiling mechanism detected that the current header height was less than the lower limit of the set range, the controller output a signal to energize the solenoid on the left side of the proportional valve, the proportional valve spool moved to the left. The header cylinder piston rod extended under the hydraulic oil pressure, and the header rose. The working principle of header height control is shown in Figure 2.

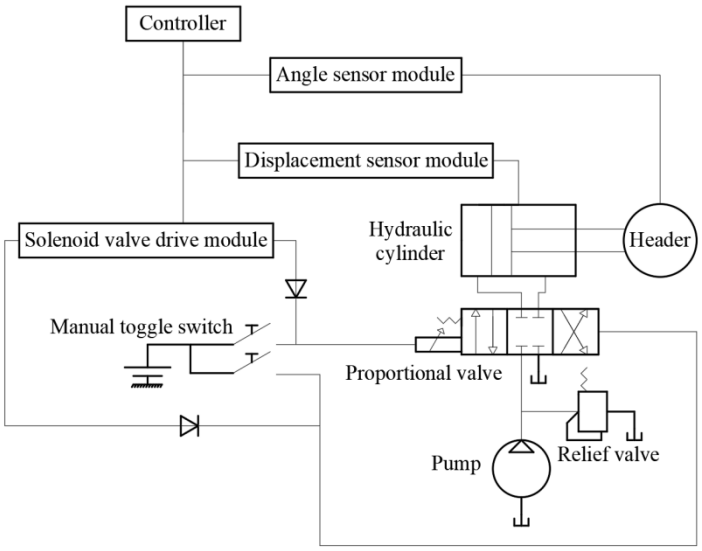

Fig. 2 - Working principle diagram of header height control

Profiling mechanism design

In order to measure the height of the combine header, a header height profiling mechanism was designed. In this section, the structure design of the profiling mechanism is carried out, and the structural parameters were optimized and its operation performance was verified through the multi-body dynamics simulation software Adams. The profiling detection mechanism for header height was mainly composed of profiling plate, torsion spring, angle sensor, mounting frame and other structures, as shown in Figure 3. The profiling plate was always in contact with the ground under the torsion spring pressure and its own gravity. The end of the profiling plate and the angle sensor were respectively fixed with the shaft through set screws. During operation, with the fluctuation of the ground, the profiling plate rotated around the axis, thus driving the sensing shaft of the angle sensor to rotate. Therefore, change of the header height can be obtained according to the angle sensor detection signal.

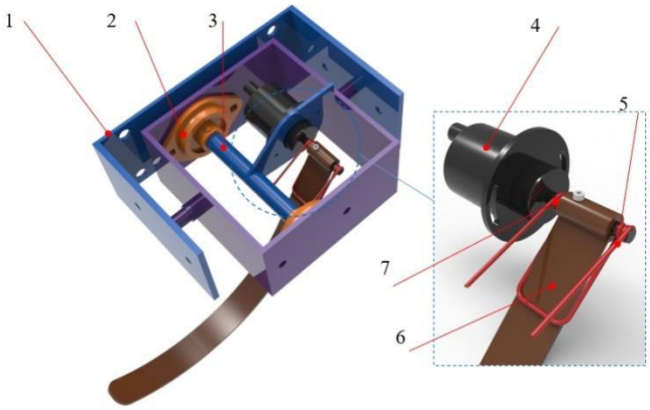

Fig.3 - Profiling mechanism structure diagram

1. The mounting frame; 2. Mounting flange; 3. Pin shaft; 4. Angle sensor; 5. Torsional spring; 6. Profiling plate; 7. Shaft

When the combine harvester is going backwards, a large contact force is produced with the soil by using straight profiling plate. Therefore, the grounding part of the profiling plate of the profiling mechanism was designed to be a combination of "straight line-arc curve". According to the actual operation experience of the operator, when the combine harvester is harvesting crops such as rice and wheat, the stubble height is generally controlled to be within the range of 50-300 mm *(Wang et al., 2015)*. Therefore, in order to ensure that the profiling mechanism can detect the header height within this range, the profiling plate was designed with a length of 110 mm for the straight part, a radius of 200 mm for the arc of the curved part, and an arc angle of 90°. Considering the influence of the structural strength of the profiling plate and debris such as field stones on the detection accuracy of the profiling mechanism, the width of the profiling plate was set to 32 mm and the thickness was set to 4 mm.

When the combine harvester reverses, the linear profiling plate will produce a large contact force with the soil, which will easily cause deformation or even destruction of the profiling mechanism. Therefore, the grounding part of the profiling plate of the profiling mechanism was designed as a combination of "straight arc curve". According to the actual operation experience of the operator, the height of stubble is generally controlled within 50-300 mm when harvesting rice, wheat and other crops with the combine harvester. Therefore, in order to ensure that the profiling mechanism can detect the header height within this range, the profiling plate was designed as a straight part with a length of 110 mm, a curved part with an arc radius of 200 mm and an arc angle of 90 °. Considering the influence of the structural strength of the profiling plate and sundries such as stones in the field on the detection accuracy of the profiling mechanism, the width of the profiling plate was set to 32 mm and the thickness was set to 4 mm.

LAT216 high-precision digital angle sensor was selected as the angle sensor in the profiling mechanism, with a range of 0-120 ° and a linear output of 0-5 V analog voltage signal to meet the requirements of the profiling mechanism designed to detect the stubble height.

ADAMS Simulation

The profiling mechanism designed should be able to detect the height of the header close to the undulating ground. The interaction between profiling plate and mounting frame, header and soil involves multi-body dynamics theory. In order to verify whether the profiling mechanism can meet the above functions, Adams multi-body dynamics simulation software was used to optimize the structural parameters of the profiling mechanism.

The multi-body dynamics model shown in Fig. 4 was established in the Adams software. In order to improve the efficiency of the simulation experiment, the profiling mechanism was simplified when establishing the simulation model *(Vahedi et al., 2021)*. The simplified model consisted of the header, mounting frame, profiled plate and ground. The ground model material was selected as soil, which set the density as 7.801×10^{-6}kg/mm^3, the Young's modulus as 2.07×10^5N/mm^2, the Poisson's ratio as 0.29, and the profiling mechanism material was set to ordinary carbon steel. After the model was established, the rotation pair was added to the mounting frame and profiling plate. A moving pair was added on the header and mounting frame, and a translational drive was added on the moving pair. The set drive speed was set to 1 m/s, and the profiling mechanism moved forward when simulating work. A spring flexible connection was added between the profiling plate and the mounting frame to analog the spring. The simulation model is shown in Figure 4. The simulation time was set to 5 s, and the step size was 0.01.

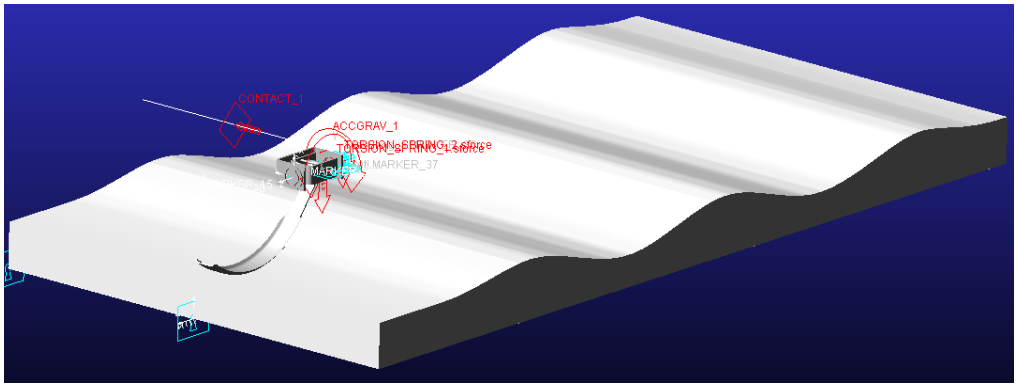

Fig. 4 - Adams simulation model of the profiling mechanism

In order to verify the ground copying ability of the profiling mechanism designed and determine the optimal torque of the torsion spring, the torsion spring torque was took as the influencing factor. We took four levels of torsion spring torque as 0 (no torque applied), 15 N·mm, 25 N·mm, 35 N·mm, and recorded the displacement curve of the Y-axis direction of the centroid point of the profiling plate. The corresponding displacement curve is shown in Figure 5.

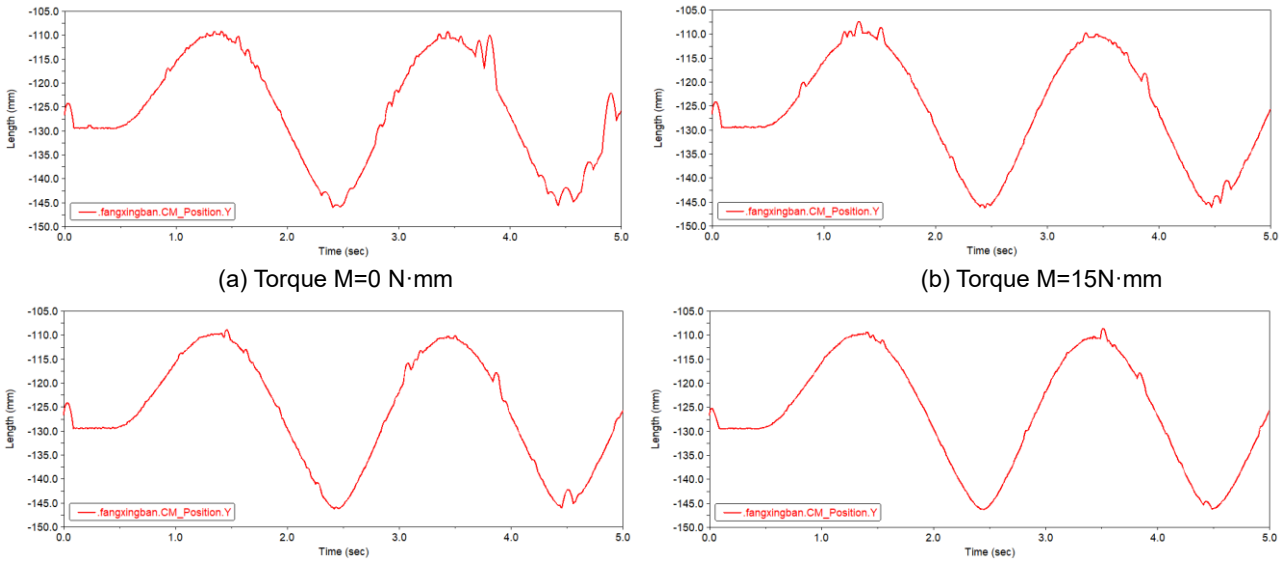

(a) Torque M=0 N·mm (b) Torque M=15N·mm

(c) Torque M=25·N·mm (d) Torque M=35·N·mm

Fig. 5 - Displacement curves of Y-axis of centroid of profile plate under different torques

Analyzing the results shown in Figure 5, it is found that when the profiling plate was not affected by the torque of the torsion spring, there was a significant fluctuation in the displacement of the profiling plate's centroid in the Y-axis direction. With the increase of the torque of the torsion spring, the fluctuation decreased. When the torque is 35N·mm, the fluctuation decreased significantly. Considering that increasing the torque of the torsion spring will increase the resistance and cause the profiling mechanism to sink during wet field operation, the torque of the torsion spring is determined to be 35N·mm. Combined with the size parameters of the profiling mechanism, through the calculation formula (1) of the torsion spring, it was finally determined that the wire diameter of the torsion spring was 2 mm, the pitch diameter was 18 mm, and the effective number of turns was 6.

$$M = PR = \frac{Ed^4\alpha}{3660nD} \quad (1)$$

where: the P is load, N; R is the force arm length, mm; E is the elastic modulus, MPa; d is a line diameter, mm; α is the torsion angle, °; n is the number of effective turns of spring; D is the middle diameter of the spring, mm.

Automatic Regulation Strategy

The height regulatory system of the header needs to adjust distance between header and ground according to the ground undulation, and the choice of the highly regulated strategy of the header will directly affect the control performance of header. Because the height detection and profiling mechanism of the header designed in this paper is installed behind the cutter, the highly regulated process has the characteristics of nonlinearity and time lag, easy to be interfered by external factors. Traditional PID control effect is relatively poor. In order to improve control accuracy and stability, the header height is regulated using a gray prediction PID control algorithm, and the advantages of information-based gray prediction and easy-to-real PID control techniques were combined, and the parameters of the PID controller were adjusted online according to the prediction error and the change rate of the error output by the header height control system.

Calibration of profiling mechanism

This section first studied the relationship model between the header height of the combine harvester and the sensor signal. In order to establish the function relation between the output signal of the angle sensor

of the profiling mechanism and the actual header height, the calibration test of the profiling mechanism was carried out. The header height was changed by manually adjusting the operating handle, and the height of the cutting knife from the ground was measured, that is the header height, with a tape measure, and the output voltage value of the angle sensor corresponding to different header height was recorded. Since the output of the angle sensor was linear, the relationship between the deflection angle of the copy plate and the output voltage is as follows:

$$U = k_1 \cdot \beta \tag{2}$$

where:

U is the output voltage of the angle sensor, V;
β is the rotation angle of the profiling plate, (°);
k_1 is the calibration factor of voltage and angle.

According to the test calibration, the relationship model between the header height and the rotation angle of the copy plate is as follows:

$$H = k_2 \cos\beta + c \tag{3}$$

where: H is the header height, m; k_2 is the calibration coefficient between the header height and the rotation angle of the profiling plate; c is a constant. From this, the functional relationship between the output voltage of the angle sensor and the header height is calculated, as in formula (4).

$$H = k_2 \cos\frac{U}{k_1} + c \tag{4}$$

Gray prediction PID controller

Usually, the gray model is represented by GM (M, N), where *M* represents the order of the model equation, and *N* represents the number of variables in the model equation (*Nurcan et al., 2021)*. The establishment of the grey prediction model of header height in this paper was based on the most widely used GM (1, 1) model. The sampling period is 0.5 s, the length is *n=4*, and the prediction step is *p=5*. Each sampling was brought into the formula (4) to obtain the height of the header $H^{(0)}(t)$, and the original sequence can be obtained as:

$$H^{(0)} = \{H^{(0)}(1), H^{(0)}(2), H^{(0)}(3), H^{(0)}(4)\} \tag{5}$$

The header heights were all positive, so the regularization was not required *(Cai Muzhen et al, 2021)*. The original sequence was accumulated, and then the accumulated generated sequence was obtained.

$$H^{(1)} = \{H^{(1)}(1), H^{(1)}(2), H^{(1)}(3), H^{(1)}(4)\} \tag{6}$$

Where:

$$H^{(1)}(k) = \sum_{m=1}^{k} H^{(0)}(m) \quad (k = 1, 2, 3, 4)$$

Background values: $z^{(1)}(k)$:

$$\begin{cases} k = 2, z^{(1)}(2) = 0.5(H^{(1)}(1) + H^{(1)}(2)) \\ k = 3, z^{(1)}(3) = 0.5(H^{(1)}(2) + H^{(1)}(3)) \\ k = 4, z^{(1)}(4) = 0.5(H^{(1)}(3) + H^{(1)}(4)) \end{cases} \tag{7}$$

References get the development coefficient *a* and grey input *u (Asgari et al., 2021)*:

$$a = \frac{C \cdot D - E}{F - C^2} \tag{8}$$

$$u = \frac{F \cdot D - C \cdot E}{F - C^2} \tag{9}$$

Where:

$$\begin{cases} C = \sum_{k=2}^{4} z^{(1)}(k) \\ D = \sum_{k=2}^{4} H^{(0)}(k) \\ E = \sum_{k=2}^{4} z^{(1)}(k) \cdot H^{(0)}(k) \\ F = \sum_{k=2}^{4} (z^{(1)}(k))^2 \end{cases} \quad (10)$$

After the above parameters are obtained, the predicted value of the header height after p steps is obtained $H^{(0)}(4+p)$:

$$H^{(0)}(4+p) = \left[H^{(0)}(4) - \frac{u}{a} \right] e^{-ap}(1-e^{-a}) \quad (11)$$

The header height automatic control system detected the height of the header from the ground through the profiling mechanism. After the gray prediction, the control deviation e (t) was obtained by comparing the height with the given height. The PID control algorithm was used to calculate the system output. The control system drives the electromagnetic reversing valve through the solenoid valve drive module to control the expansion and contraction of the header hydraulic cylinder, thus realizing the automatic control of the header height. The control principle was shown in Figure 6.

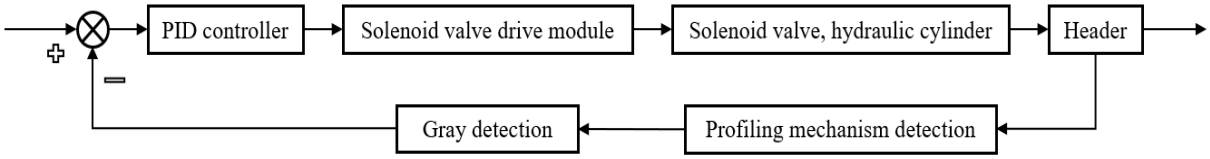

Fig. 6 - Schematic diagram of gray prediction PID control of header height

Matlab Simulink analysis

In order to further verify the proposed header height control strategy, optimize the working parameters of the header height automatic control system, and observe the dynamic response of the system in real time, a simulation model was built in the Matlab Simulink module, which is shown in Figure 7.

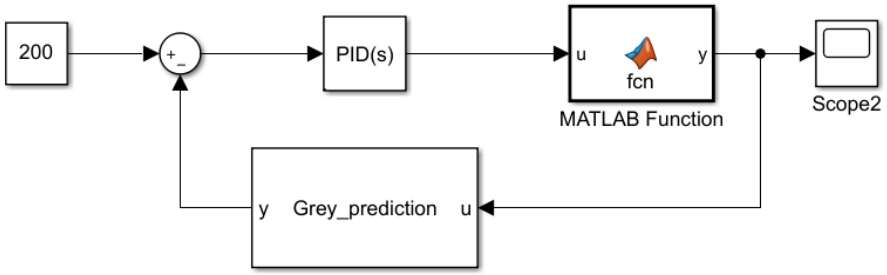

Fig.7 Simulation model of header height regulation in Matlab

In the simulation process, the setting time was 5 s, and the sampling time was 0.01 s. After calculation optimization, when the proportional coefficient K_p=1.57, the integral coefficient K_i=0.78, the differential coefficient K_d=0.8, and the input was 200 mm, the maximum output value of the PID controller was 210.6 mm, the steady state value was 194.7 mm, and the overshoot was 5.3%, the stabilization time was 0.9 s, the response speed was fast, and the overshoot is small, which can meet the design requirements of the automatic control system for the header height, The step response curve is shown in Figure 8. It can be seen that the control effect of the gray prediction PID control technology was significantly better than that of the PID control technology, the response time was relatively short, and the overshoot was relatively small, thus improving the control stability of the header height and obtaining a good control effect.

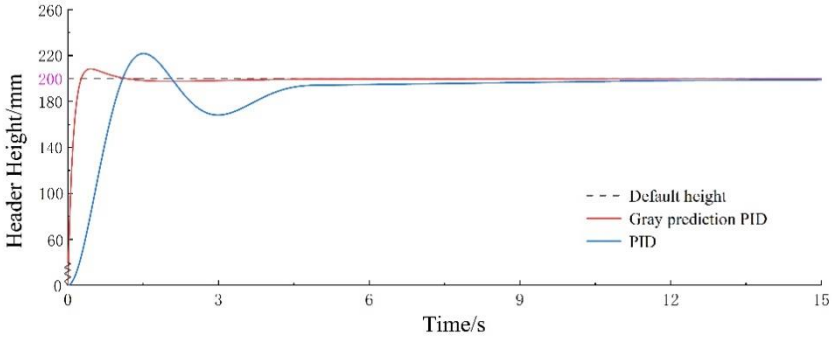

Fig. 8 - Step response curve of gray prediction PID control

Control system programming

The input signal of the automatic control system of the header height included 2 analog signals (2 profiling mechanisms), and the output signal consisted of 2 electromagnetic reversing valves and 1 electromagnetic relief valve. The flow chart of the automatic control system for the header height is shown in Figure 9.

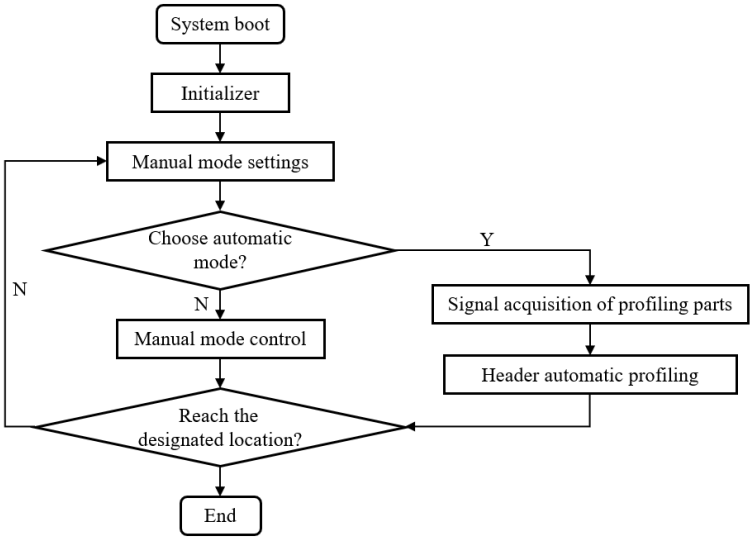

Fig. 9 - The header height control flow chart

When the system startup, the operator initialized the header height in manual mode and set the ideal header height range. In the automatic mode, the profiling mechanism performed signal monitoring, and after eliminating the wrong data, the current header height was obtained according to the functional relationship between the detection data of the profiling mechanism and the header height, and the predicted value of the header height was obtained according to the gray prediction model of the header height.

Compared with the given value, after analysis and processing by the controller, the on-off of the solenoid valve was controlled after the operation and amplification of the solenoid valve drive module, so as to realize the automatic regulation of the header height. When the header height was higher than the upper limit of the set range, the oil cylinder of the header was drive to lower position to reduce the header height. When the header height was lower than the limit of the set range, the oil cylinder of the header was driven to increase the header height.

RESULTS

On November 10, 2021, the field test of automatic control of the header height was carried out at Dafeng farm, Yancheng City, Jiangsu Province. The experimental rice varieties were Jiangfeng NO.1. The properties measured before harvesting were shown in Table 1. The test site is shown in Figure 10.

Table 1

Properties of experimental wheat crops

Project	Natural height	1000-grain weight	Grass to valley ratio	Production
/	[cm]	[g]	/	[kg/hm^2]
Value	76	39	1.28	8000

Fig.10 - Field experiment site of combine harvester

During the experiment, after the combine harvester entered a stable operation state, the manual/automatic control switch of the header height to the automatic state was pushed, and the header height was regulated by the automatic control system. The display terminal collected and saved the header height information in real time.

In the test, two sets of header heights were set 100 mm and 200 mm, respectively, and the harvesting was 10 meters under the automatic control mode of the header height. During the harvesting process, the software recorded the header height in real time. After harvesting, each sampling position was set every 0.5 meters along the forward direction of the harvester, and 5 sampling points were set along the vertical direction of the harvester through each sampling position. With a total of 100 sampling points, the height of the stubble after harvesting, representing the actual height of the header was measured.

The actual measured header height was compared with the set header height to evaluate the automatic control system of header height. The test data are shown in Fig.11.

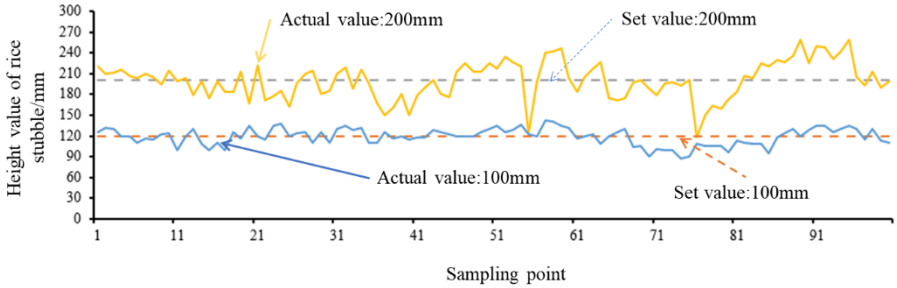

Fig. 11 - The actual stubble height when the height of the header was set to 100 mm or 200 mm

The test results show that when the header height was set to 100 mm, the average height of the actual stubble was 104.6 mm, the average deviation was 14.7 mm, and the maximum deviation was 31 mm. When the header height was set to 200 mm, the average actual stubble height was 192 mm, the average deviation was 20.6 mm, and the maximum deviation was 43 mm. The test results showed that the designed automatic control system for the header height has strong reliability under different setting of the header height. In general, the average deviation between the actual header height and the set header height can be controlled within 21 mm, which met the needs of field work.

CONCLUSIONS

1) Aiming at the problem that the header height of the domestic combine harvester mainly depends on manual operation by manual experience, a set of adaptive control system for the header height of the combine harvester was designed in this study, which provides users with two modes of manual operation mode and automatic control mode. The research on the height control of the harvester header provides a reference.

2) In order to detect the header height, a profiling mechanism was designed, and the parameters of the torsion spring were optimized by Adams simulation. At the same time, the simulation proves that the designed profiling mechanism can detect the header height closely to the undulating ground.

3) In order to realize the automatic control of the header height, the geometric relationship of the combine harvester header was analyzed, and the header height control model based on the grey prediction algorithm was established. The field test results show that the error between the actual header height and the set header height is within 21 mm, which meets the field operation requirements of the combine harvesters.

ACKNOWLEDGEMENT

The work was sponsored by Natural Science Foundation of Zhejiang Province (No: LQ20E050003), the Research Initiation Fund of Zhejiang Sci-Tech University (No: 1113293261009) and the Jiangsu Postgraduate Research and Practice Innovation Program (No: KYCX22_3678).

REFERENCES

[1] Asgari, S., MirhoseiniNejad, S., Moazamigoodarzi, H., Gupta R., Zheng, R., Puri, I. K. (2021). A gray-box model for real-time transient temperature predictions in data centers. *Applied Thermal Engineering*, Vol. 185, 116319. England.

[2] Bomoi, M. I., Nawi N. M., Aziz, S. A., Kassim, M. S. M. (2022). Sensing Technologies for Measuring Grain Loss during Harvest in Paddy Field: A Review. *Agri Engineering*, Vol. 4, 292-310. Switzerland.

[3] Golpira, H., Sola-Guirado, R. R. (2022). Data-Driven Simulator: Redesign of Chickpea Harvester Reels. *Agriculture*, Vol. 12, 264. Iran.

[4] Geng, A. J., Zhang, M., Zhang, J., Zhang, Z. L., Gao, A., Zheng, J. L. (2020). Design and Experiment of Automatic Control System for Corn Header Height (玉米收获机割台高度自动调控系统设计与试验). *Transactions of the Chinese Society for Agricultural Machinery*. Vol. 51, 118-125. Beijing/China.

[5] Kim, W. S., Lee, D. H., Kim, T., Kim, Y.-J., Sim, T. (2021). Weakly supervised crop area segmentation for an autonomous combine harvester. *Sensors*, Vol. 21, 4801. Korea.

[6] Mirmahdi, E., Shirazi, O. G. (2021). Installation of suitable sensors for object detection and height control on combine harvester. *SSRG Int. J. Mech. Eng.*, Vol. 8, 12-19. India.

[7] Ni, Y., Jin, C., Chen, M., Yuan, W., Qian, Z., Yang, T., Cai, Z. (2021). Computational model and adjustment system of header height of soybean harvesters based on soil-machine system. *Computers and Electronics in Agriculture,* Vol. 183, 105907. England.

[8] Nurcan, E., Deniz Köksal, C. (2021). Determination of financial failure indicators by gray relational analysis and application of data envelopment analysis and logistic regression analysis in BIST 100 Index. *Iranian Journal of Management Studies,* Vol.14, 163-187. Iran.

[9] Shukla, P., Mehta, C. R., Agrawal, K. N., Potdar R. (2021). Studies on operational frequencies of controls on self-propelled combine harvesters in India. *Journal of Agricultural Engineering*, Vol. 58, 101-111. Italy.

[10] Shojaei, K. (2021). Intelligent coordinated control of an autonomous tractor-trailer and a combine harvester. *European Journal of Control*, Vol. 59, 82-98. Iran.

[11] Vahedi, A., Jamali, A. (2021). Constraint optimization of nonlinear McPherson suspension system using genetic algorithm and ADAMS software. *Journal of Vibration and Control,* 10775463211026036. England.

[12] Wei, L. G., Che, Y., Wang, F. Z., Li, W. (2017). Design and Experiment of the Ground Profiling Control System of Combine Header (联合收割机割台地面仿形控制系统设计及试验). *Journal of Agricultural Mechanization Research.* Vol. 39, 150-154. Heilongjiang/China.

[13] Yang, Ranbing, Wang, Zhichao, Shang, Shuqi, et al. (2022). The Design and Experimentation of EVPIVS-PID Harvesters' Header Height Control System Based on Sensor Ground Profiling Monitoring. *Agriculture*, Vol. 12, 282. Switzerland.

[14] Yang, Y. H. (2007). Research of header height automatic controlling system based on ultrasonic sensor (基于超声波传感器的割台高度自动控制系统研究). Northwest A&F University. Shanxi/China.

[15] Zhu, L. H., Zhao, C., Dai, J. (2021). Prediction of compressive strength of recycled aggregate concrete based on gray correlation analysis. *Construction and Building Materials*, Vol. 273, 121750. England.

ADAPTIVE NEURO-FUZZY MODEL FOR THE CONTROL SYSTEM OF THE CLINKER GRINDING PROCESS IN BALL MILLS IN CEMENT FACTORIES
/
MODEL ADAPTIV NEURO-FUZZY PENTRU SISTEMUL DE CONTROL AL PROCESULUI DE MACINARE A CLINKERULUI IN MORILE CU BILE DIN FABRICILE DE CIMENT

George IPATE[1)], Cristian CIOBANU[1)], Paula TUDOR*[1)], Iuliana GAGEANU[2)], Dan CUJBESCU[2)], Florentina MANAILA[1)]

[1)] Universities Polytechnic Bucharest, Faculty of Biotechnical Systems Engineering / Romania

[2)] National Institute for Research-Development of Machines and Installations Designed for Agriculture and Food Industry - INMA Bucharest / Romania

E-mail: puiu.ipate@gmail.com, ghvoicu_2005@yahoo.com

DOI: https://doi.org/10.35633/inmateh-68-57

Keywords: *adaptive neuro-fuzzy, ball grinding plants, clinker cement, learning models*

ABSTRACT

The main goal of this study was to create a model for the development of a decision support system for the cement grinding process in ball mills, including the data acquisition, processing and analysis subsystems, based on intelligent hardware and software technologies. The paper presents a model based on the techniques proposed and developed with the application of fuzzy logic and artificial neural networks. The simulation results of the proposed models in the Matlab environment are also presented. Testing and verification of data obtained with the proposed inference model were performed by comparing with experimental data.

REZUMAT

Scopul principal al acestui studiu a constat în realizarea unui model de dezvoltare a unui sistem suport de decizie pentru procesul de măcinare a cimentului în morile cu bile, inclusiv subsistemele de achiziție, prelucrare și analiză a datelor, bazate pe tehnologii hardware și software inteligente. Lucrarea prezintă un model bazat pe tehnicile propuse și dezvoltate cu aplicarea logicii fuzzy și a rețelelor neuronale artificiale. Sunt prezentate și rezultatele simulărilor modelelor propuse în mediul Matlab. Testarea și verificarea datelor obținute cu modelul de inferență propus au fost efectuate prin comparare cu datele experimentale.

INTRODUCTION

The realities are such that there are specific industrial processes that can be characterized by a certain degree of uncertainty in the decision-making process. The basic problem in the automation of industrial processes is the acquisition and structuring of data for the purpose of training intelligent systems. The procedure for training decision systems requires a fairly large volume of data, and the effectiveness of this training directly depends on the quality and quantity of data used. If, under the conditions of the continuous production process, the amount of acquired data is not a problem, then ensuring its quality depends directly on the qualification and experience of the human operator. It should be noted that specific industrial processes can be characterized by the variation of their parameters throughout the technological process. Thus, the task of intelligent decision-making systems consists in making decisions that would ensure the precision of the parameters of the production process within the limits specified by the quality requirements. Insufficient data on the state of the technological process can cause a drastic decrease in the accuracy of quality parameters.

The hypothetical-deductive methodology was used in the research works. The argumentation for the use of this method emerges from the experimental nature of the studied processes and from the possibility of experimental verification of the correctness of the hypotheses and assumptions formulated during the research process. As part of the research, the analysis of the collected statistical data was carried out, with the aim of generalizing the studied process. The elaborated researches are based on mathematical analysis, numerical methods, the theory of fuzzy sets, the theory of artificial neural networks, data acquisition techniques and the design of numerical circuits (*Amaral et al., 2022*).

The capacity of high-tech computer to process large amounts of data quickly provides researchers with a unique occasion to study problems that are too expensive, time consuming, or practically impossible to approach. In this way, researchers can obtain optimal answer that justify experimental reality within a reasonable amount of time. The term adaptive system refers to an interdependent system composed of interconnected entities that cooperate to adapt and self-organize to environmental conditions. Studies in the field of adaptive hardware architectures offer a variety of new solutions and means of addressing different problems related to the methods of organization and efficient operation of systems. The basis of adaptive hardware systems is the collaborative functional components or entities. The system adaptation process can be done through software or hardware. Software adaptation can generally be achieved through a functional change at the application level. Hardware adaptation, as opposed to software adaptation, represents a more profound change in the internal organization of the computing architecture of an embedded system.

Ciobanu and Scrieru, (*2016*), proposed the application of the fuzzy regulation method for the automated control of the wastewater treatment process. In order to obtain a quasi-optimal regulation, a classic PID controller was used and then the Fuzzy controller was implemented in which they were included in the rule base with compound premises, which reflect a situation composed of two variables that simultaneously act on the wastewater flow and its variation to determine the amount of recycled sludge. *Vikram*, (*2014*), presents the results of designing and analysing the functioning of one fuzzy logic control system on the compressor motor of the air conditioning system to control its speed. Analysis was performed using simulations in Simulink. The comparison with a classic bipositional model used in the experiments shows that the energy saved is significant, between 36.29 and 41% for different operating regimes. *Carbune V.,* (*2020*), presents some innovative solutions in the form of embedded hardware systems for use in the research and development of intelligent decision support systems. Intelligent, reconfigurable command and control solutions in the microwire casting process are presented, which have been designed as a flexible set of tools that can be reconfigured for new conditions or even new industrial processes. *Taylan and Karagözoglu,* (*2009*), present in their research a new approach in the design of a FIS based on neural networks to evaluate the school results of students. They mention that fuzzy systems have achieved admirable results in solving various classes of problems. The method they developed uses a neural network augmented fuzzy system to improve some of its characteristics, such as the ability to change or be changed easily according to the situation, rapidity and ability or willingness to change in order to suit different conditions, known as the adaptive inference system (ANFIS).

The aim of the work incorporate the development of new system for prospect the knowledge of the human expert, the development of adaptive neural network controller for the research of the process of making important choices and the construction of a computer program that can arrange and sort large amounts of data, and take important decisions based on the data in industrial applications. The following research objectives are derived from the proposed purpose: a) Examining of the general aspects of self-organizing neuro-fuzzy systems; b) Research, elaboration and growing or becoming stronger or more advanced of decision support procedure and rules under conditions of uncertainty; c) Designing adaptive hardware and software architectures for hybrid decision-making systems.

MATERIALS AND METHODS

Recent progress in the field of artificial intelligence and the optimization of computational software techniques have opened up new opportunities for researchers in the field. The learning methods are based on such paradigms of intelligent computing as: artificial neural networks, decision trees and neuro-fuzzy systems, which are successfully applied to solve various problems in different fields (*Amaral et al., 2022; Ciobanu and Scrieru, 2016; Vikram 2014; Cărbune, 2020; Taylan and Karagözoglu, 2009; Baqui, 2012*).

Since cement crushing systems are nonlinear and time-varying MIMO (Multiple Input Multiple Output) systems, fuzzy logic controllers appear to be in the greatest measure the choices for controlling these. By the same token, considering the human perception of the composition and dimensions of the material is vague and subjective, the theory of fuzzy logic is well suited to describe it linguistically according to the state of the variables dependent on the mineral composition.

The knowledge inference mechanism is the basic element of an expert system that ensures the knowledge process by applying reasoning rules and strategies on the basis of facts. Knowledge is based on three fundamental concepts *(Stefenon et al., 2020; Taylan, 2006)*:

1. Facts – represent primary information that describes the elements of the domain;
2. Rules – describe how facts can be used;

3. Reasoning strategies – describe how the rules can be used.

Knowledge processing involves the definition of storage structures and processing methods, which ensure the realization of reasoning. As a result, specific structures are used for the storage and use of knowledge *(Lin and Lee, 1991).*

The inference mechanism in a fuzzy system consists of three stages. In the first step, the numerical values of the inputs are mapped by a membership function according to the degree of membership in the respective fuzzy sets. This operation is called fuzzification. In the second step, the fuzzy system evaluates the inference rules according to the weights of the inputs. In the third step, the resulting fuzzy values are transformed back into numerical values. The given operation is called defuzzification (*Ciobanu and Scrieru, 2016; Carbune, 2020; Taylan and Karagözoglu, 2009; Freksa, 1994; uk.mathworks.com*).

A fuzzy logic way is used to achieve the desired set of rules based on the input and output data sets and the membership functions. To generate the ANFIS structure, we need to specify the cluster radius, which indicates the extent of influence of the cluster. Consider a collection of n data points $\{x_1,...,x_n\}$ in an M-dimensional space. Since each point is a candidate to be the centre of the cluster, the density measure of the data point xi is defined by the equation (*Taylan and Karagözoglu, 2009*):

$$D_i = \sum_{j=1}^{n} \exp\left(-\frac{\|x_i - x_j\|^2}{(r_a)^2}\right) \quad (1)$$

where, r_a is a positive constant. Data points near the first x_{c1} cluster centre will have significantly reduced density measures.

In principle, the shape of the membership functions is less important than the number of curves and their placement (*Taylan, 2006*). We proposed the form of sigmoidal and three-curve/segment membership functions to adequately cover the required range of input values. In analytical form, it is presented as follows:

$$\mu(x; a_k, c_k) = \frac{1}{1+e^{-a_k(x-c_k)}} \quad (2)$$

where, to define the parameters of the member function, a vector of the form $[a_1\ c_1\ a_2\ c_2]$ is created. Membership values are calculated for each input value in x.

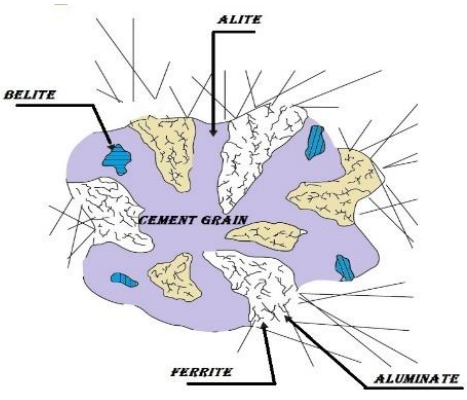

Fig. 1 – The chemical composition of the clinker (adapted from *Schumacher and Juniper, 2013*)

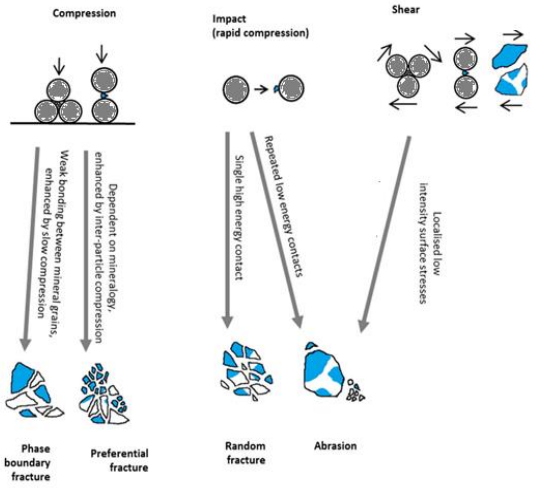

Fig. 2 – Mechanisms of particle breakage - the links between contact events (force application) and the result of breakage (adapted from *Litlle et al., 2017*)

Portland cement is a fine powder produced by grinding Portland cement clinker (more than 90%), a limited amount of gypsum (dehydrated calcium sulphate - $CaSO_4 .2H_2O$, which controls the setting time) and other minor constituents that can be used to vary the properties of the final cement (*Schumacher and Juniper, 2013*). Portland cement clinker is a sintered material (granules with a diameter of 5–25 mm) produced by heating a homogeneous mixture of raw materials in a furnace to a sintering temperature of about 1450 °C for modern cements. The resulting clinker is made up of four main minerals, which mostly give resistance to crushing, presented in Table 1 (*Labahn and Kohlhaas, 1983*). Figure 2 shows the mechanisms of breaking particles - the links between contact events (force application) and the result of breaking *(Little et al., 2017).*

Table 1

Composition of cement granules by mass fraction (%)

% (mass)	Alite	Belite	Aluminate	Ferrite
	C3S	**C2S**	**C3A**	**C4AF**
maxim	**80**	**30**	**15**	**15**
minim	**40**	**0**	**7**	**4**
average	**60**	**15**	**11**	**8**

Following the study of the industrial cement grinding process in the ball mill led by an experienced operator, the idea of developing and implementing an intelligent fuzzy command and control system for the clinker grinding process in the ball mills was put forward. In order to estimate the possibility of achieving the control of the grinding process, the efficiency of the ordering process and the real-time control of the particle sizes, the approach that would use the intelligent techniques was proposed. Fuzzy logic methods and algorithms are implemented in command and control processes either separately or combined with other intelligent methods and techniques (*Cărbune, 2020)*.

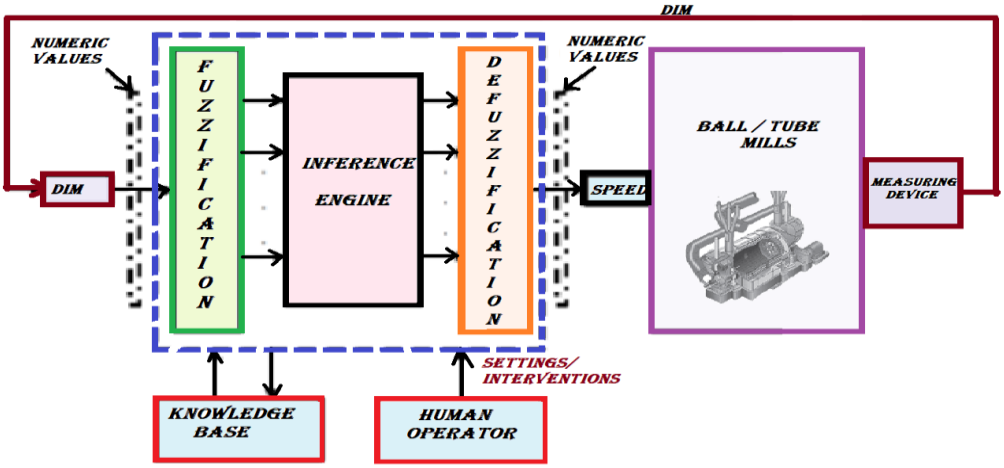

Fig. 3 – The structure of the intelligent command and control system of the grinding process

Practically, two grinding systems are used for the preparation of raw materials for the manufacture of clinker: wet and dry. In the dry system, the raw materials are dosed in the proportions necessary to obtain the desired chemical composition and supply either a rotary ball mill or a vertical axis (roller) mill. The raw materials are dried in advance with the residual process gases taken from the combustion furnace. The objective of the grinding process is for the bulk of the product to be smaller than 75 µm (*Schumacher and Juniper, 2013*). The product from the mill is pneumatically mixed to ensure that it has a well-homogenized chemical composition and is then stored in silos until needed. The fineness of the final product, the amount of gypsum added and the amount of additional additives are all varied to result in the desired quality of each of the final cement products (*Labahn and Kohlhaas, 1983*).

The conceptual structure of the intelligent fuzzy command and control system of the particle grinding process in the ball mill is presented in Figure 3. The system can have a fuzzy intelligent (or neural) control block in its composition. The connection between the control block and the technological system is made with the help of the data acquisition block. At the initial stage of knowledge base collection and testing, the presence of a human operator is required in the decision-making loop to control the comminution process and ensure particle quality parameters. Initially, the most important system variables that can be used in the control process were determined: Dim – particle size; SPEED – rotation speed of the ball mill. The SPEED control variable is an essential one in managing the grinding technological process. In figure 3 the intelligent control subsystem is represented with a block of fuzzy type. A special problem in the construction of fuzzy systems is related to the choice of membership functions (*Cărbune, 2020)*.

Experimental investigations were carried out on samples of Portland cement clinker with a medium phase composition: Alite - C3S 60%; Belite-C2S 17%; Aluminates C3A 10%; Ferrites 5%; CaO 1%. The phase composition was determined by X-ray diffraction. The grinding of the above-mentioned material was carried out on a steel ball mill (drum diameter 280 mm and height 120 mm), filled with steel balls, the diameter of which is 30 mm.

The number of revolutions of the mill was cc 72.5% of the critical speed, which ensures optimal conditions for reducing the size of the clinker grains. The chosen diameter of the mill reduces the risk of the material going up to the feed mouth. Experiments were performed with a mill loading of 55% balls and a particle loading of 100%. The grinding procedure was carried out in 15 batches, with and without chemically active substances, and the cement samples were collected at different time periods. Particle size distribution was determined with the Mastersizer 2000E laser by sieving for 60 seconds. Figure 4 shows the cumulative size distribution curves according to the mass fraction of particles larger than the mesh size of the sieve (passing through the sieve). The data were classified into three groups as follows:

- data for training the model "Prob87", "Prob88", "Prob89" and "Prob95";
- data for testing the "Prob97", "Prob98", "Prob113" and "Prob114" model;
- data for checking the model "Prob116", "Prob117", "Prob118" and "Prob119".

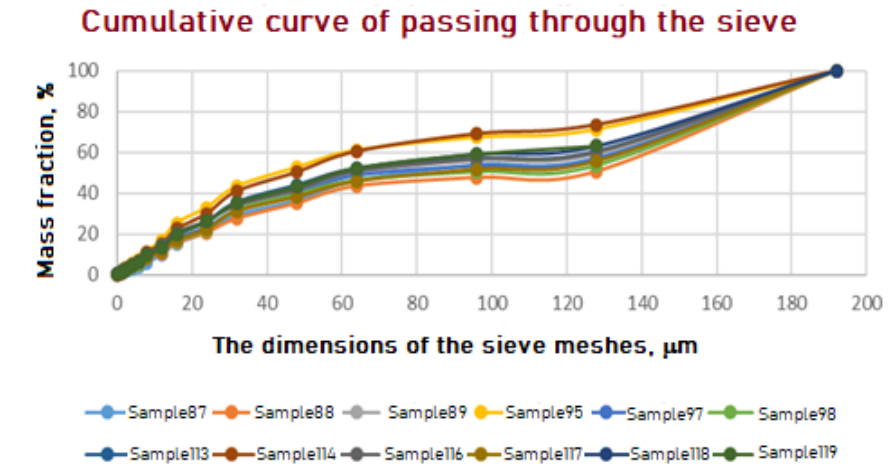

Fig. 4 – Experimental data – cumulative curves of mass fractions smaller than the mesh size of the sieve

The characteristic parameter (x_{50}) of the distributions was obtained by calculation with the weighted average method and is presented in Table 2:

$$x_{50} = \frac{\sum_{i=1}^{n} w_i \cdot x_i}{\sum_{i=1}^{n} wi} \quad (3)$$

where:

x_{50} = weighted average; n = number of terms to be averaged; w_i = weight of fraction i; x_i = average particle size of fraction w_i.

Table 2

Characteristic size x_{50} [µm] of distributions by particle size

Sample	87	88	89	95	97	98	113	114	116	117	118	119
$D_{50[\mu m]}$	66.1	118.8	174.9	119.9	59.3	104.9	127.7	97.3	64.1	94	118.5	92.2

The study of the material's resistance to size reduction based on the obtained values, i.e. the existence of the Rehbinder effect, clearly shows that the addition of chemically active substances does not significantly influence the size reduction rate. However, when the optimal ball mill operating conditions are reached, the chemically active substances become responsible only for the occurrence of the Rehbinder effect *(Little et al., 2017)*.

RESULTS

In this study, three cluster centres were determined for the given 181 data set. The number of fuzzy rule sets would be equal to the number of cluster centres, each representing the cluster feature, as shown in figure 5. Fuzzy rules and fuzzy reasoning are the backbone of fuzzy inference systems, which are the most important modelling tools based on fuzzy sets (*Taylan, 2006*). Fuzzy reasoning is an inference procedure that derives conclusions from the set of fuzzy If-Then rules and known facts. Fig. 6 shows the reasoning procedure for a first-order Sugeno fuzzy model. Since each rule has a clear output, the total result is obtained by a weighted average, thus avoiding the time-consuming process.

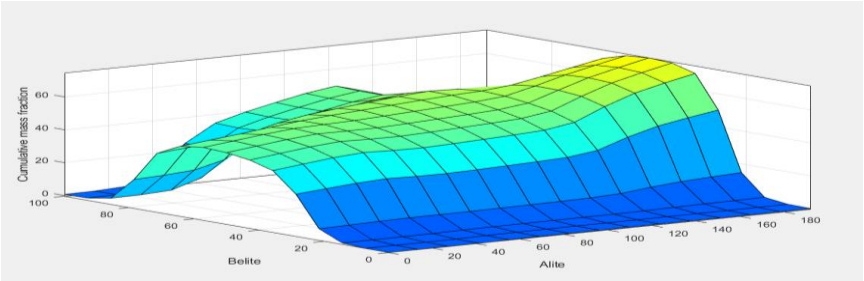

Fig. 5 - The control action surface after training the input data

The input parameters of the ANFIS adaptive inference system taken into account are the mineral compositions, Alite (C3S), Belite (C2S), Aluminate (C3A), Ferrite (C4AF), and the result is the "cumulative particle size distribution (DIM)". These imprecise attributes are called fuzzy linguistic variables and are used to characterize the chemical composition of the product. These linguistic variables are imprecise, vague and incomplete fuzzy terms. They are entered and expressed by fuzzy linguistic values, such as "unsatisfactory (A1), average (A2), good (A3)", as shown in Fig. 7.

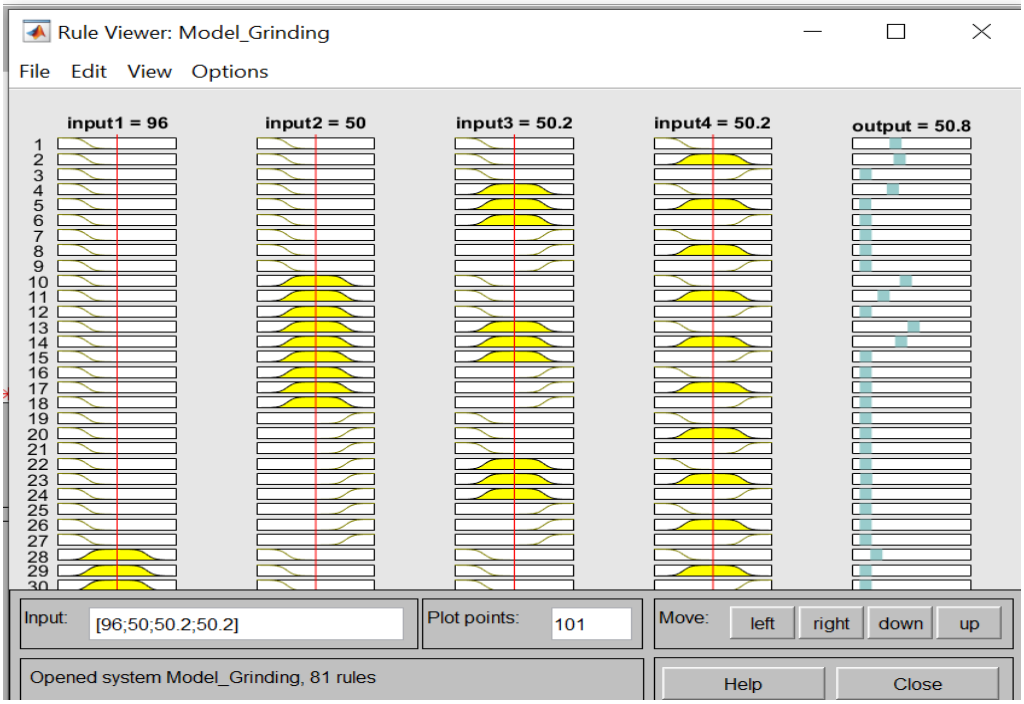

Fig. 6 - Fuzzy procedure for the Sugeno model of the output quantity

Fuzzy rules are mathematical relations that map input relations to output relations and are constituted by fuzzy linguistic variables and their term sets (*Taylan, 2006; uk.mathworks.com*). Fuzzy If-Then rules are known as fuzzy implications or fuzzy conditional statements which are widespread in our daily language expressions. Fuzzy rules are the backbone of an ANFIS model. E.g.: "IF the Alite fraction (C3S) of the slag is good and the Belite fraction (C2S) is medium and the Aluminate fraction (C3A) is medium and the Ferrite fraction (C4AF) is medium THEN DIM will be medium" is a complete rule that defines the relations between the input and output linguistic variables.

Rule 1: If C3S is A1 and C2S is A2 and . . . and C4AF is A2
Then f 1 = p1 C3S + q1 C2S + .. · + m1 C4AF + r1
Rule 2: If C3S is A2 and C2S is Ai and .. . and C4AF is A5
Then f 2 = p2 C3S + q2 C2S + · · · + m2 C4AF + r2
……

Rule n: If C3S is An and C2S is An and . . . and C4AF is An
Then f n = Pn C3S + qn C2S + · · · + mn C4AF + rn

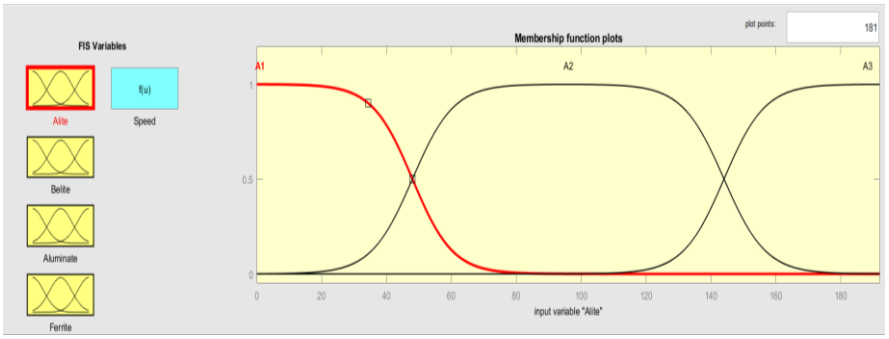

Fig. 7 – Adjusted member functions of the "Alite" input variable

Architecture of hybrid and adaptive learning neuro-fuzzy inference system. Figure 8 shows the architecture of the neural network structure. Calculating the parameters of the MF membership function (or fitting them) is facilitated by a gradient vector, which provides a measure of how well the ANFIS is modelled with the input/output data for a given set of parameters. Once the MFs are established, several optimization methods can be applied to adjust the parameters and reduce the error (typically defined by the sum of the squares of the difference between the actual-measured and desired outputs). The parameters associated with MF will change through the learning process *(Carbune, 2020; Taylan and Karagözoglu, 2009).*

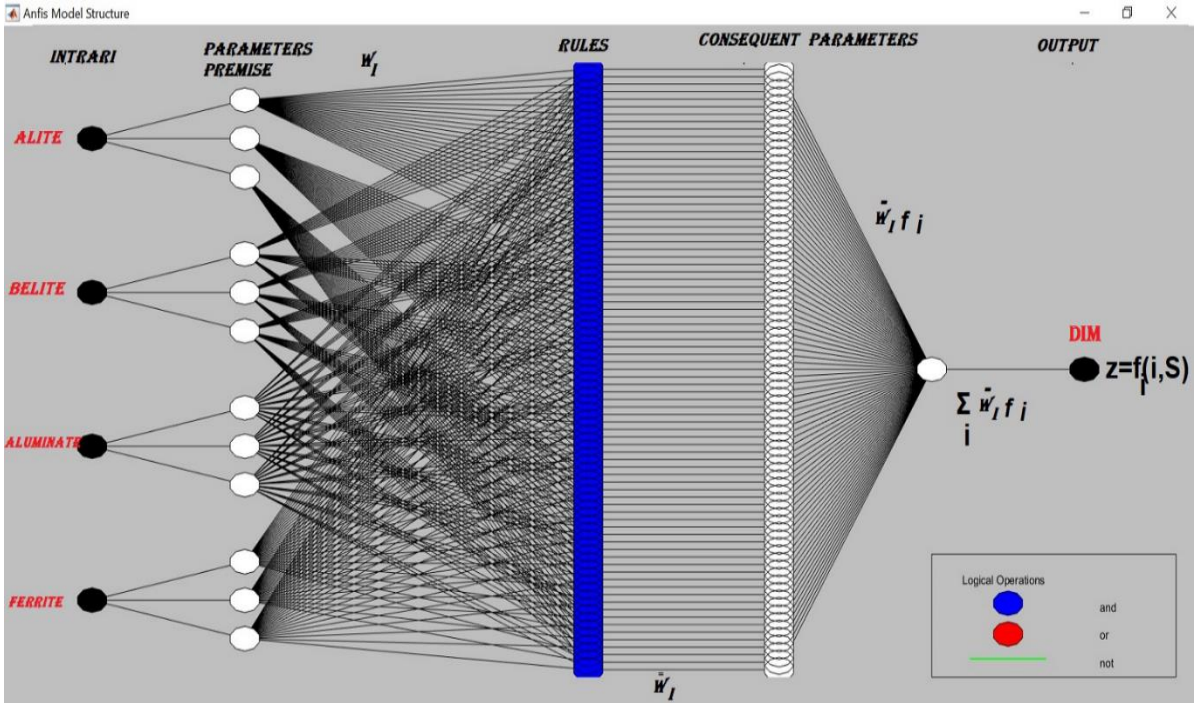

Fig. 8 – ANFIS architecture for a Sugeno fuzzy model with four inputs and one output

The only node in the last layer of the neural network is a fixed node, which calculates the total output as the summation of all input signals calculated by the equation *(Taylan and Karagözoglu, 2009):*

$$z = \sum_i \overline{w}_i \cdot f_i = \frac{\sum_{i=1}^{n} w_i \cdot f_i}{\sum_{i=1}^{n} wi} \quad (4)$$

From the ANFIS architecture shown in Figure 8, it is observed that when the values of the premise parameters are fixed, the total output can be expressed as a linear combination of the consistent parameters. In symbols, the output z can be rewritten as the equation:

$$z = (\overline{w}_1.C3S) \cdot p_1 + (\overline{w}_1.C2S) \cdot q_1 + \cdots + (\overline{w}_1.C4AF) \cdot m_1 + (\overline{w}_1.)r_1 + \cdots + (\overline{w}_n.C3S) \cdot p_n + (\overline{w}_n.C2S) \cdot q_n + \cdots + (\overline{w}_n.C4AF) \cdot m_n + (\overline{w}_n.)r_n \quad (5)$$

which is linear in the consistent parameters, p_1, p_2, q_1, q_2, r_1, and r_2.

To train the designed neural network, the hybrid optimization method was chosen, which uses a combination of back propagation and least squares regression to adjust the FIS parameters.

After the completion of the training process, the details about the status of this process and the accuracy of the neural network operation algorithm are presented. As a result of this stage, graphs are generated that describe the operation mode and performance of the developed artificial neural network (see figure 9).

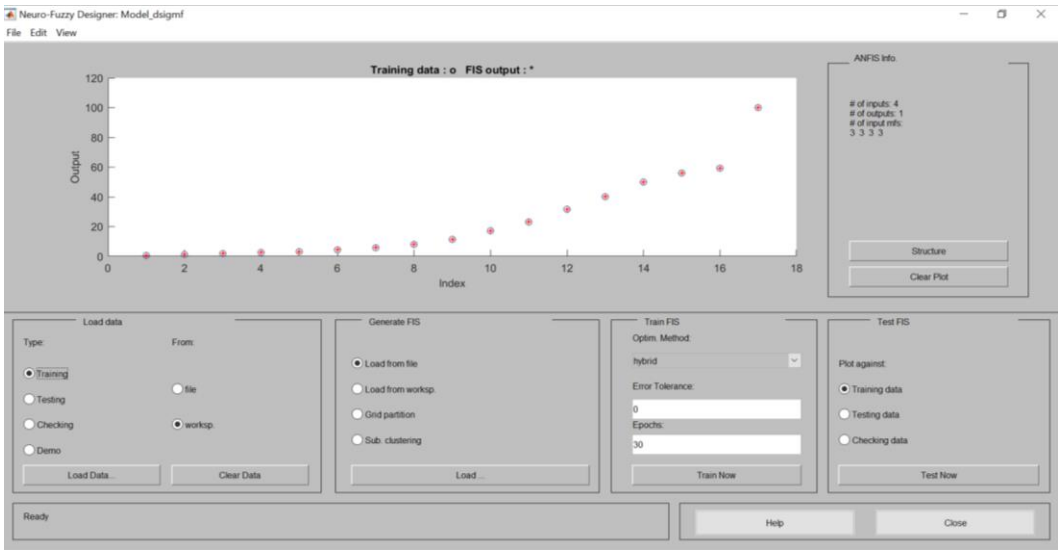

Fig. 9 - Displaying training data in the Neuro-Fuzzy Designer application

The neural network of the designed control system is made up of 193 nodes, with a total number of 453 parameters, of which 405 are linear parameters and 48 are non-linear parameters. For the 17 values of the training data, the network uses a number of 81 fuzzy rules.

Validate the model using the verification and test data set. Model validation is the process by which the input vectors from the input-output data sets are presented to the trained FIS model to see how well the ANFIS model predicts the corresponding data set of values of exit. When the test and training data are fed into the ANFIS adaptive interference system, it is expected that the selected FIS model has associated parameters such that there is minimal error between the model data and the test data. The basic idea behind using a test data set for model validation is that after a certain point in training, the model starts to overfit the training data set. The learning convergence and ANFIS parameters for the training and testing data sets can be seen in figures 10 - 12. The minimum error was 5.43506 e-05, and the final value was 0.000217096.

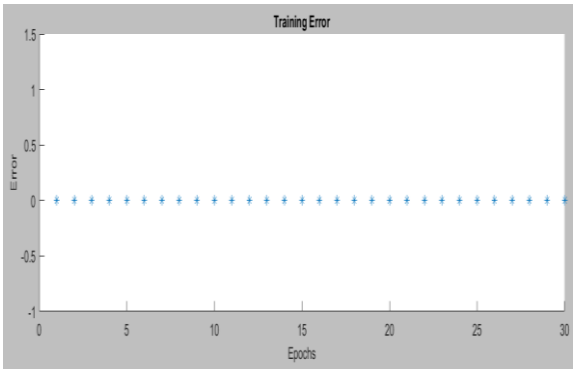

Fig. 10 – Convergence of learning for the training data set

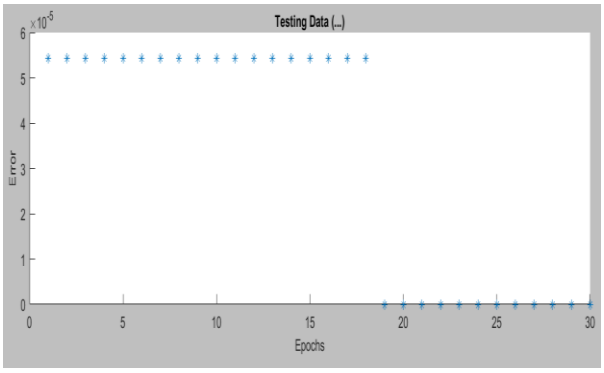

Fig. 11 – Convergence of learning for the test data set

In principle, the model error for the test data set tends to decrease as training occurs until the point where overfitting begins, and then the model error for the test data increases sharply. After loading the verification data set and choosing the variant in which ANFIS will generate a FIS with four inputs having 4 Linguistic Terms (a base of 81 rules), the convergent training of fig. 12. To eliminate this problem, as seen in fig. 13 -14, data are used to identify each input-output parameter used to check model validation. This data set contains all the necessary representative characteristics of the assessment tools. Note its output variable consisting of 17 different values (singleton), each of which is optimized during training. In this case, the linear option was chosen for the member function.

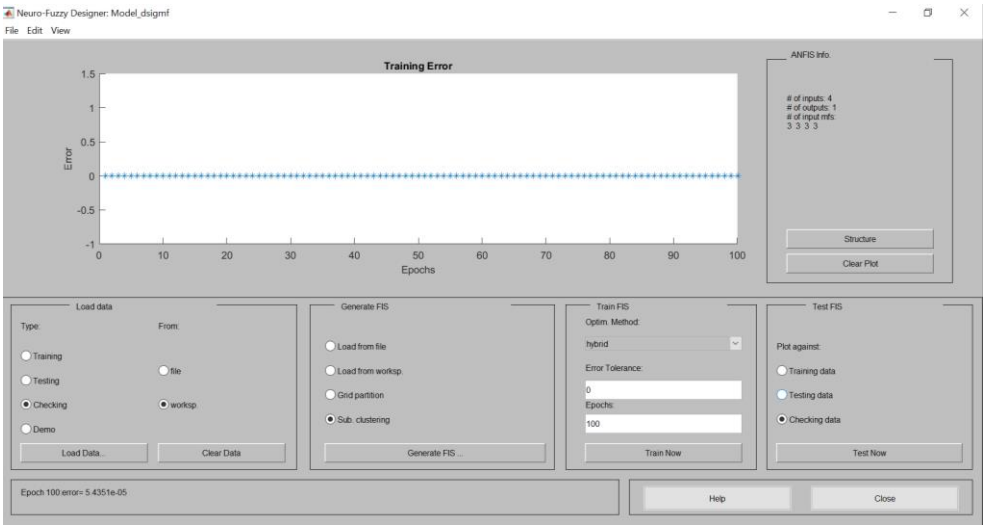

Fig. 12 – Convergence of learning for the test data set to validate the model

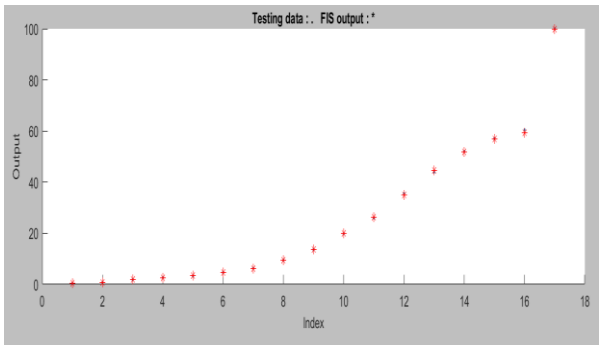

Fig. 13 – Testing the data obtained with the ANFIS model

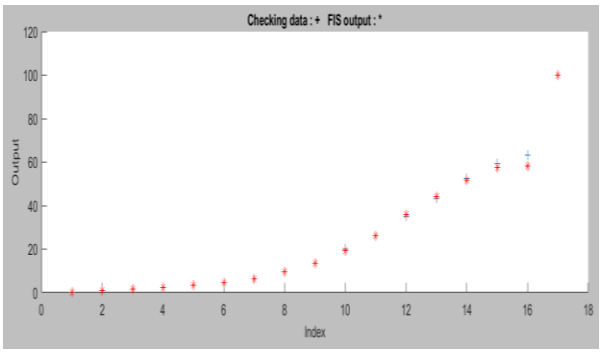

Fig. 14 – Checking the data obtained with the ANFIS model

As many authors have pointed out (*Baqui, 2012; Stefenon et al., 2020; Taylan, 2006; Lin and Lee, 1991; Elkan, 1994*), conventional system analysis techniques are not suitable to deal with a humanistic system, whose behaviour is strongly influenced by human judgment, perception and emotions. This belief gives rise to the concept of linguistic variables as an alternative approach to modelling human thought. Since the convergence errors are both very small, we assume that ANFIS has captured the essential components of the underlying dynamics, and the training data contains the effects of initial conditions that may not be easily explained by the essential components identified by ANFIS.

CONCLUSIONS

One reason for using fuzzy regulation is that it is more appropriate in regulating non-linear processes. If a fuzzy regulator or generally a non-linear one is in principle able to regulate a non-linear process, it is a problem that depends on the chosen inputs of the regulator. When controlling nonlinear processes, fuzzy controllers should outperform conventional controllers. This applies as long as we have additional knowledge about the nonlinearity of the process.

Clearly, we can argue that the information in a neuro-fuzzy control system is usually superficial, both statically and dynamically, but that the numerical parameters can be adjusted during a learning process, which implies a quick adaptation to environmental change and, consequently, to an obvious economic benefit.

A particularly important problem facing the design of an adaptive neuro-fuzzy inference system application is the choice of training, testing and validation datasets. The main way to improve the quality of neuro-fuzzy systems is to choose an appropriate training data set. The more we move from the representation of human knowledge about clearly delimited problems to the representation of concepts related to open domains, the more we will have to overcome certain rigidities of classical formal approaches. The great advantage of control systems with neural networks, the ability of machine learning, can be illustrated by the response of these controllers, very similar to that of much more complicated systems, justifying its choice for applications, considering the similar performances.

REFERENCES

[1] Amaral T.G., Crisóstomo M, Pires V.F. (2022). Adaptive neuro-fuzzy inference system for modelling and control*, IEEE Xplore, Conference: Intelligent Systems, 2002. Proceedings. 2002 First International IEEE Symposium*, Vol. 1, 67-72, https://doi.org/10.1109/IS.2002.1044230.

[2] Ciobanu, N., Scrieru N. (2016). Automated control procedures and algorithms of the wastewater treatment process, *Engineering Meridian, No.3,* Technical University of Moldova (Procedee și algoritmi de control automatizat ale procesului de epurare a apelor uzate, *Meridian Ingineresc, No.3*, Universitatea Tehnica a Moldovei), https://ibn.idsi.md/ro/vizualizare_articol/48308.

[3] Vikram, S.J. (2014). *Design and analysis of fuzzy logic model for the control of compressor motor speed of an air conditioning system*, Dissertation Thesis, Thapar University, Patiala;

[4] Cărbune, V. (2020). *Adaptive hardware architectures for neuro-fuzzy systems with self-organization*, Doctoral Thesis, Technical University of Moldova, Chisinau, http://repository.utm.md/handle/5014/11705.

[5] Schumacher, G., Juniper, L. (2013). Chap.15 - Coal utilisation in the cement and concrete industries, *The Coal Handbook: Towards Cleaner Production, Vol. 2* in Woodhead Publishing Series in Energy, 387-426, https://doi.org/10.1533/9781782421177.3.387.

[6] Labahn, O., Kohlhaas, B. (1983). *Cement Engineers' Handbook*, Bauverlag GmbH, Berlin, https://www.academia.edu/8989358/Cement_Engineers_Handbook.

[7] Glasnovic, A., Hraste, M. (1982). The grinding equation in the investigation of the coarse dispersing system of cement, *Cement and Concrete Research, 12,* 415-424, https://doi.org/10.1016/0008-8846(82)90056-4.

[8] Taylan, O., Karagözoglu, B. (2009). An adaptive neuro-fuzzy model for prediction of student's academic performance, *Computers & Industrial Engineering, Vol. 57*, pp. 732–741, https://doi.org/10.1016/j.cie.2009.01.019.

[9] Little, L., Mainza, A.N., Becker, M., Wiese, J. (2017). Fine grinding: How mill type affects particle shape characteristics and mineral liberation, *Minerals Engineering, Vol. 111*, pp. 148-157, https://doi.org/10.1016/j.mineng.2017.05.007.

[10] Baqui, M.N. (2012). *Fuzzy decision model for a smart grid*, Dissertation Thesis, North Dakota State University of Agriculture and Applied Science Fargo, North Dakota, http://hdl.handle.net/10365/19396.

[11] Stefenon. S.F., Freire. R.Z., Coelho. L.S., Meyer. L.H., Grebogi. R.B., Buratto. W.G., Nied. A. (2020). Electrical insulator fault forecasting based on a wavelet neuro-fuzzy system, *Energies, 13(2), 484*, https://doi.org/10.3390/en13020484.

[12] Taylan, O. (2006). Neural and fuzzy model performance evaluation of a dynamic production system, *International Journal of Production Research, 44(6), 1093–1105,* https://doi.org/10.1080/00207540500362070.

[13] Lin, C.T., Lee, C.S.G. (1991). Neural-network-based fuzzy logic control and decision system, *IEEE Transactions on computers, vol. 40(12*), pp. 1320–1336. https://doi.org/10.1109/12.106218;

[14] Elkan, C. (1994). The Paradoxical Success of Fuzzy Logic, *IEEE Expert, vol. 9, no. 4*, pp. 3-49, https://doi.org/10.1109/64.336150.

[15] Freksa, C. (1994). Fuzzy Logic: An Interface between Logic and Human Reasoning*, IEEE Expert, Vol. 9*, pp 20-21.

[16] ***Difference between two sigmoidal membership functions*, *dsigmf* function syntax, https://uk.mathworks.com/help/fuzzy/dsigmf.html.

IDENTIFICATION SYSTEM OF TOMATO LEAF DISEASES BASED ON OPTIMIZED MobileNetV2
/
基于改进 MobileNetV2 的番茄叶部病害识别

Shengqiao XIE[1, 2)], Yang BAI[*1)], Qilin AN[2)], Jian SONG[1)], Xiuying TANG[2)], Fuxiang XIE[1)]
[1)] College of Mechatronic and Vehicle Engineering, Weifang University / China;
[2)] College of Engineering, China Agricultural University / China
Tel: 17864302980; E-mail: baiyang19891014@163.com
DOI: https://doi.org/10.35633/inmateh-68-58

Keywords: *deep learning, tomato, foliar disease identification, artificial Intelligence, agriculture, mobile applications*

ABSTRACT
Crop diseases have an important impact on the safe production of food. Therefore, the automated identification of pre-crop diseases is very important for farmers to increase production and income. In this paper, a tomato leaf disease identification method based on the optimized MobileNetV2 model is proposed. A dataset of 20,400 tomato disease images was created based on tomato disease images taken from the greenhouse and obtained from the PlantVillage database. The optimized MobileNetV2 model was trained with the dataset to obtain a classification model for tomato leaf diseases. The average recognition accuracy of the model is 98.3% and the recall rate is 94.9%, which is 1.2% and 3.9% higher than the original model, respectively, after experimental validation. The average prediction speed of the model for a single image is about 76 ms, which is 2.94% better than the original model. To verify the performance of the optimized MobileNetV2 model, it was compared with the Xception, Inception, and VGG16 feature extraction network models using migration learning, respectively. The experimental results show that the average recognition accuracy of the model is 0.4 to 2.4 percentage points higher than that of the Xception, Inception, and VGG16 models. It can provide technical support for the identification of tomato diseases, and is also important for plant growth monitoring under precision agriculture.

摘要
农作物病害威胁粮食的安全生产。因此，农作物前期病害的自动化识别对农民增产增收十分重要。本文提出了一种基于优化 MobileNetV2 模型的番茄叶部病害识别方法。基于从温室拍摄及 PlantVillage 数据库获取的番茄病害图像，创建了一个包含 20400 张番茄病害图像数据集。用数据集对优化的 MobileNetV2 模型进行训练，获得了番茄叶部病害的分类模型。经试验验证，该模型的平均识别准确率为 98.3%，召回率为 94.9%，比原模型分别提高了 1.2%和 3.9%。该模型对单张图片的平均预测速度约为 76ms，比原模型提高了 2.94%。为验证优化的 MobileNetV2 模型的性能，分别与使用迁移学习的 Xception、Inception、VGG16 特征提取网络模型进行了比较。试验结果表明，该模型的平均识别准确率比 Xception、Inception、VGG16 模型高出了 0.4 ~2.4 个百分点。可为番茄病害的识别提供技术支持，同时对精准农业下的植物生长监控具有重要意义。

INTRODUCTION

The healthy and stable development of the tomato industry is of great significance to the development of the national economy and the increase in income of farmers. However, in recent years, due to changes in cultivation systems and inadequate plant protection measures, the variety and extent of tomato diseases have been increasing (*Xiong Y. et al., 2020*). There are five common diseases of tomatoes, including late blight, grey mould, powdery mildew, spotted blight and yellowing varroa virus. Efficient identification and control of tomato leaf diseases can significantly reduce the damage caused by the disease and contribute to increased tomato yields (*Liu J. et al., 2020*). How to accurately and effectively identify crop diseases is an important area of research. A great deal of work has been done in the field of disease identification (*Xiao M.H. et al., 2020*), which can effectively identify the type and severity of crop diseases.

With the rapid development of computer vision and artificial intelligence, deep learning technology is becoming more and more important in the field of image recognition (*Too E. et al., 2019*). Convolutional Neural Networks (CNN) have a strong self-learning capability and are typical of deep learning techniques.

CNN can learn a large amount of knowledge through abstract analysis of data to achieve fast and accurate classification (*Jiang P. et al., 2019*). Compared with traditional neural networks, CNN has a strong ability to adapt and generalize. CNN reduces the number of parameters by sharing weights, thus significantly reducing the computational effort. The research method used in this study is the CNN.

In recent years, deep learning technology has been gradually applied in agriculture, which has led to further improvements in the accuracy and efficiency of crop disease identification (*Hu W. et al., 2020*). Zhao et al. used a deep learning approach to extract cotton foliar disease characteristics such as wilt, brown spot, and horn spot. The average test accuracy of the trained model on the test set was 93.5% (*Zhao L. et al., 2021*). Venkatesh et al. proposed a fine-tuned MobileNet convolutional neural network model based on deep learning and used for the classification of strawberries and cherries. The average recognition accuracy of the model is 98.60% and the loss rate is about 0.38% after experimental testing (*Venkatesh N. et al., 2021*). Zeng et al. proposed a method for citrus disease detection based on GANs data enhancement and Inception_v3 model. Zeng trains InceptionV3 model with 14056 images. The test accuracy of the model reached 92.6%, which is 20% higher than the model trained on the original image dataset (Zeng, Q. et al., 2020). Lv et al. designed a novel feature extraction model called DMS-Robust AlexNet based on AlexNet model. New model combines the advantages of multi-scale convolution and dilated convolution to improve feature extraction. The training accuracy of the model is 98.8% (*Lv M. et al., 2020*). An Xception-based method for medicinal plant identification was proposed by Roopashree et al. The average recognition accuracy of the method on the DeepHerb dataset was 97.5% (*Roopashree, S. et al., 2021*). Zhang et al. proposed an improved maize leaf disease diagnosis model based on GoogLeNet. The improved GoogLeNet model has significantly less number of parameters than the VGG and AlexNet models. After experimental testing, the improved GoogLeNet model achieved an average recognition accuracy of 98.9% (*Zhang H. et al., 2018*). Wang et al. proposed a Dense-MobileNet network-based image classification method for image classification of animals. The average recognition accuracy of the model was 96% after experimental testing (*Wang W. et al., 2020*).

Research on crop foliar disease identification has focused on machine learning and deep learning. However, the methods that have been applied to crop disease identification rarely balance accuracy and efficiency (*Liu B. et al., 2020*). In view of the above, a lightweight convolutional neural network-based method for tomato leaf disease identification is proposed in this paper.

MATERIALS AND METHODS

IMAGE ACQUISITION

The images used in the experiment were partially collected from a tomato greenhouse in Huai Gang, Shan County, Shandong Province (34°48'22"N, 116°59'13"E). The collection time is February 3 and February 4, 2021 from 8:00-11:00 am and 14:00-17:00 pm. The tomato variety is West Pink 3. The image acquisition device is Redmi note7. A total of 3000 images of tomato leaves were collected, including late blight, leaf mold, powdery mildew, blotch, yellowing varroa virus and healthy images. The image resolution is 3000 x 4000 pixels and the format is jpg. To enrich the experimental data, some tomato leaf images were selected from the PlantVillage database (Hassan S. et al., 2021). Some of the images are shown in Fig. 1.

(a) Healthy (b) Late blight (c) Leaf mold (d) Powdery mildew (e) Blotch (f) Yellow varroa virus

Fig. 1 - Example of tomato leaf image

AUGMENT DATA

To reduce the experiment running time, the original image was resized to 500 × 500 pixels by Python programming. A random selection of 2400 images from tomato leaf images was used as the test set. To better extract tomato leaf features and avoid overfitting in training, image expansion is performed on the dataset (Chen X. et al., 2020). In this case, the original image is flipped 180 degrees. The image brightness is transformed to between 0.8 and 1.2 of the original image brightness.

Gaussian noise with a variance of 0.02 is added to the image. Transform the chromaticity of the image to 120% of the original image chromaticity of the tomato leaves. A total of 18,000 images were augmented. The dataset contains a total of six categories of tomato leaf late blight, leaf mold, powdery mildew, blotch disease, yellow varroa virus and healthy images. The number of images included in the dataset is shown in Table 1.

Table 1

The number of images included in the dataset

Disease	Original dataset	Augmented dataset	Training dataset	Validation dataset	Test dataset
Late blight	1200	1800	2200	400	400
Leaf mold	1200	1800	2200	400	400
Powdery mildew	1200	1800	2200	400	400
Blotch	1200	1800	2200	400	400
Yellow varroa virus	1200	1800	2200	400	400
Healthy	1200	1800	2200	400	400

OPTIMIZED MOBILENET

MobileNetV2 network is a lightweight neural network proposed by Google for embedded devices such as cell phones. Its core idea is depthwise separable convolution (*Bi C. et al., 2020*). Using depth wise separable convolution can reduce the parameters of the model and realize the light weight of the model. The MobilenetV2 model uses the bottleneck residual block structure (*Chen J. et al., 2020*). The structure of bottleneck residual block is shown in Fig 2. Boosting is performed using 1x1 convolution before the 3x3 network structure. Dimensionality reduction is performed using 1x1 convolution after 3x3 network structure. Dilation first, then compression, is better than convolving directly with a 3x3 network.

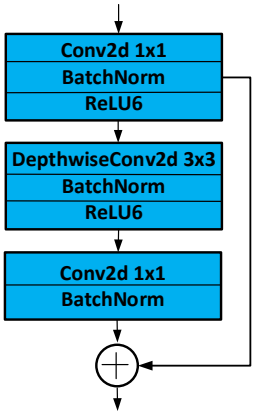

Fig. 2 - The structure of bottleneck design

1) BNECK BLOCK

Although bottleneck residual block as the main structure of MobileNetV2 model is beneficial for model accuracy, this design may lead to information loss and gradient confusion. Short connections in the inverse residual block can affect the gradient back propagation (Sun J. et al., 2020). To address the limitations of the bottleneck residual block module, the size and number of convolutional kernels were fine-tuned and a new Bneck block structure was proposed. The Bneck block structure introduces deep convolution, which can reduce the computational effort of the model. To ensure short connections for high-dimensional features, the position of the 3x3 convolution was adjusted, as shown in Fig. 3. The Bneck block structure first up-dimensions the input feature map using a 3x3 convolution, then extracts features from the feature map using a 1x1 convolution kernel, and finally down-dimensions the feature map using a 3x3 convolution. When stride=1, a shortcut branch exists to connect the input to the output, as shown in Fig. 3(a). When stride=2, there is no shortcut branch, as shown in Fig. 3(b).

The Bneck block structure does not construct short connections between bottleneck layers, but between higher dimensional features, as shown in Fig. 3(b). Wider short connections help to pass more information from the input tensor to the output tensor and thus have more gradients to pass back. The linear bottleneck layer helps to avoid zeroing of features, which in turn leads to information loss. Therefore, an activation function is not added after the 3x3 convolution used for dimensionality reduction. The H-swish activation function is added after the 1x1 convolution and the first 3x3 convolution.

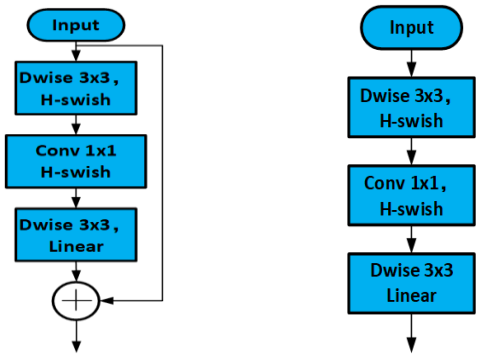

(a) stride=1 block (b) stride=2 block

Fig. 3 - The structure of Bneck design

To further improve the model recognition accuracy, the output of the optimized MobileNetV2 network is batch normalized. A dropout layer with a p-value of 0.5 is added after batch normalization to keep some of the network nodes from working in order to prevent the model from overfitting. A global average pooling layer was added behind the dropout layer to replace the fully connected layer, significantly reducing the model parameters. Finally, a Softmax classifier is added for the classification of images. The newly generated network consists of two main parts. The first part is the pre-training module, which is used to extract image features. The second part is an extension layer that extracts high-dimensional features for image classification.

2) ACTIVATION FUNCTION

The main role of the activation function in neural networks is to enhance the nonlinear modelling capability of the network (*Zhang S. et al., 2019*). It is only after adding the nonlinear activation function that the deep neural network has the ability to learn nonlinear mapping in layers. The original MobileNetV2 model uses the $ReLU$ activation function. The $ReLU$ activation function can be expressed by Equation (1).

$$ReLu(x) = \max(0, x) \tag{1}$$

From Equation (1), it can be seen that $ReLU$ saturates when x is less than zero, while when x is greater than zero, there is no saturation problem. Therefore, $ReLU$ is able to keep the gradient from decaying when x is greater than zero, thus alleviating the gradient disappearance problem. However, as the training progresses, some of the inputs fall into the hard saturation zone, resulting in the corresponding weights not being updated. Similar to sigmoid, the mean value of the output of $ReLU$ is greater than zero.

To further improve the recognition accuracy of the model, the *h-swish* function is chosen to replace the $ReLU$ activation function of the original MobileNetV2 model. The h-swish function can be represented by Equation (2).

$$h\text{-}swish[x] = x\frac{ReLU6(x+3)}{6} \tag{2}$$

The activation function h-swish is unbounded, lower bounded, smooth, and non-monotonic. From Equation (2), it can be seen that the value of the *h-swish* function can be taken to be negative. The *h-swish* function has a wider range of values and stronger convergence performance than the $ReLU$ function.

3) LOSS FUNCTION

The loss function is an important tool to measure the gap between the network output and the target (*Liu B. et al., 2020*). The cross-entropy loss function can better solve the problem of too slow update of the loss function weights. Therefore, this paper uses the cross-entropy loss function in the loss layer. The cross-entropy loss function can be represented by Equation (3).

$$loss = -\left[\frac{1}{n}\sum_{x}\left[y\ln a + (1-y)\ln(1-a)\right]\right] \tag{3}$$

Where, x is the number of samples, y is the actual number of labels, a is the predicted output, and n is the total number of samples.

4) OPTIMIZER FUNCTION

The parameter update of the Adam optimizer is not affected by the scaling transformation of the gradient (*Yuan Y. et al., 2021*). Its parameters are well interpreted and usually require only minor adjustments. Adam

Optimizer is able to automatically adjust the learning rate. Therefore, the Adam optimizer was chosen. The initial learning rate of the model is set to 0.001.

5) THE OVERALL STRUCTURE OF THE OPTIMIZED MOBILENETV2

The optimized MobileNetV2 model contains 7 Bneck blocks, 2 convolutional layers, 2 global average pooling layers, 1 dropout layer, and 1 fully connected layer. The model uses a linear bottleneck and inverted residuals structure to optimize the network, reducing the model by about 2 million parameters. The parameters of the model are shown in Table 2. The technical route for tomato foliar disease identification is shown in Fig. 4.

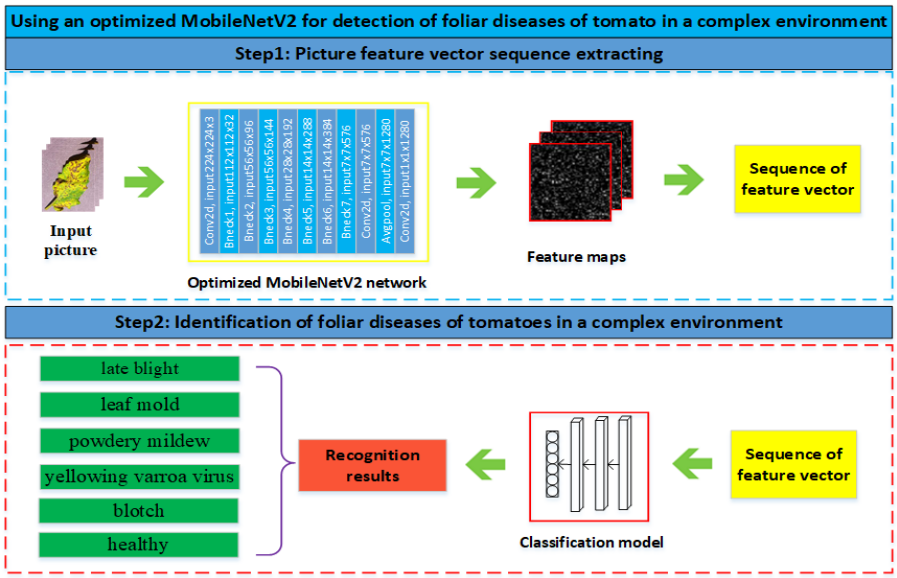

Fig. 4 - Technical route of identification of foliar diseases of tomatoes

Table 2

Relevant parameters of the MobileNetV2 model

Operator	Input	Output	*t*	*c*	*n*	*s*
conv2d 3x3	224×224×3	112×112×32		32	1	2
Bneck	112×112×32	56×56×96	2	16	1	2
Bneck	56×56×96	56×56×144	6	24	1	1
Bneck	56×56×144	28×28×192	6	32	3	2
Bneck	28×28×192	14×14×288	6	64	3	2
Bneck	14×14×288	14×14×384	6	96	4	1
Bneck	14×14×384	7×7×576	6	160	4	2
Bneck	7×7×576	7×7×960	6	320	2	1
conv2d	7×7×960	7×7×1280		1280	1	1
Avgpool	7×7×1280	1×1×1280			1	
conv2d	1×1×1280	1×1×1280		k	1	
Avgpool/dropout	1×1×1280	1×1×1280				
Dense	1×1×1280	1×1×6				

In the table, *t* represents the expansion multiplier, *c* represents the number of output channels, *n* represents the number of repetitions, and *s* represents the stride size.

EXPERIMENT AND ANALYSIS

TRAINING DETAILS

1) EXPERIMENTTAL PLATFORM

The experimental platform is shown in Table 3.

Table 3

Experimental platform

Equipment	Specifications
System	Windows10
Language	Python3.8
Framework Cuda10.0	Tensorflow2.3.0
CPU	Inter Xeon E5-2609 v4@1.70GHz
RAM	32G
GPU	NVIDIA GeForce GTX 1080(8G)

2) BATCH SIZE AND EPOCHS

In this paper, the tomato leaf dataset contains a total of 20,400 images from six categories. 2400 images were randomly selected as the test set. The training set and validation set are divided in a ratio of 4:1.

3) DIVISION OF THE DATA SET

The values of the batch size were set to 6, 12, and 24. The experimental comparison shows that the model is most stable when the value of batch size is 6. When epochs exceed 40, the loss convergence is no longer significant, so the number of training rounds of the model was set to 40.

EVALUATION INDICATORS

There are various evaluation indicators for disease identification models. Different evaluation metrics are selected to evaluate the model performance from different perspectives (Shi C. et al., 2020). In this paper, the accuracy, precision, recall and specificity are chosen as evaluation metrics. The calculated expression is as follows.

$$accuracy = \frac{TP + TN}{TP + TN + FP + FN} \tag{4}$$

$$precision = \frac{TP}{TP + FP} \tag{5}$$

$$recall = \frac{TP}{TP + FN} \tag{6}$$

$$specificity = \frac{TN}{TN + FP} \tag{7}$$

Here, TP and FN represent the number of correct and incorrect predictions for positive samples, respectively. TN and FP represent the number of negative samples correctly predicted and incorrectly predicted, respectively.

RESULTS AND ANALYSIS

The master model chosen for this study is the optimized MobileNetV2. The network models of the control group were InceptionV3, Xception and VGG16, respectively. Different models were trained separately with the same data set in the same experimental setting. Each model was iterated 40 times. The training model was saved once every 5 iterations. The optimal model was selected by comparing the performance of each model. The training results of the model are shown in Fig. 5.

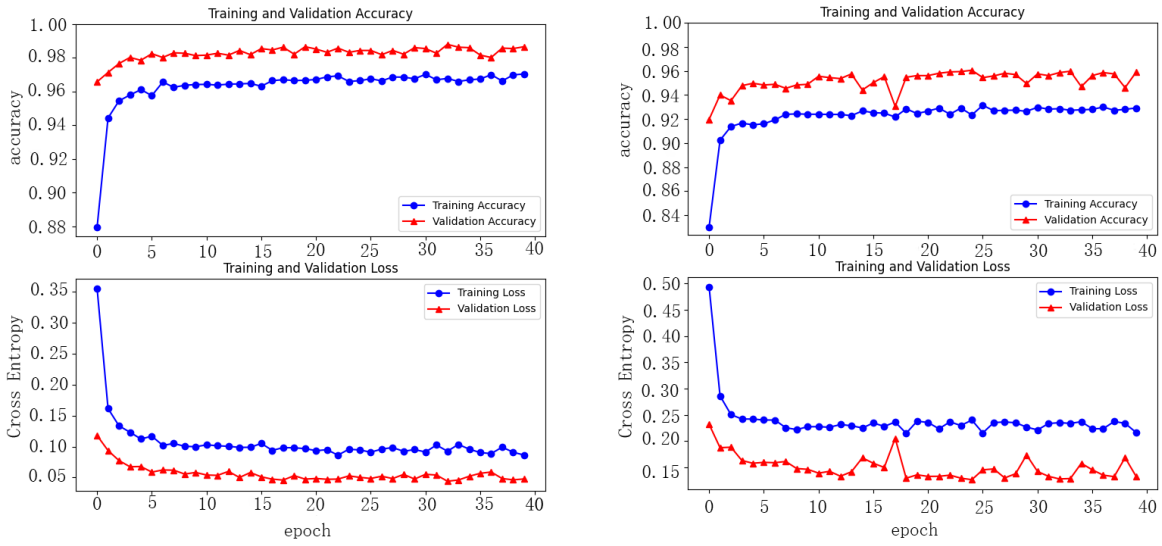

(a) Optimized MobileNetV2, above is the accuracy and below depicts the loss of the model

(b) Inception, above is the accuracy and below depicts the loss of the model

Fig. 5 - Comparison of the highest recognition accuracy and loss value of each model

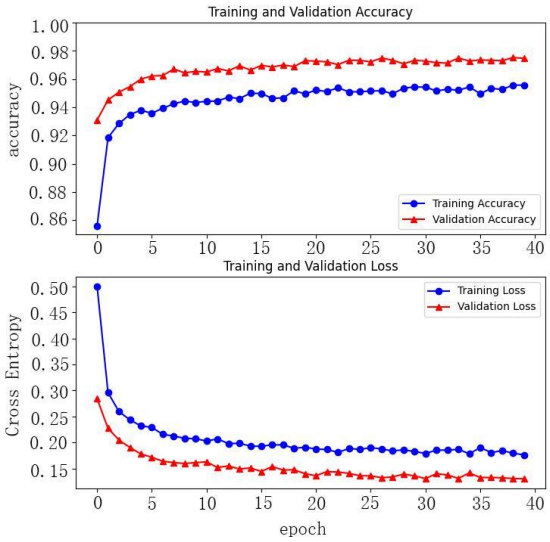

(c) Xception, above is the accuracy and below depicts the loss of the model

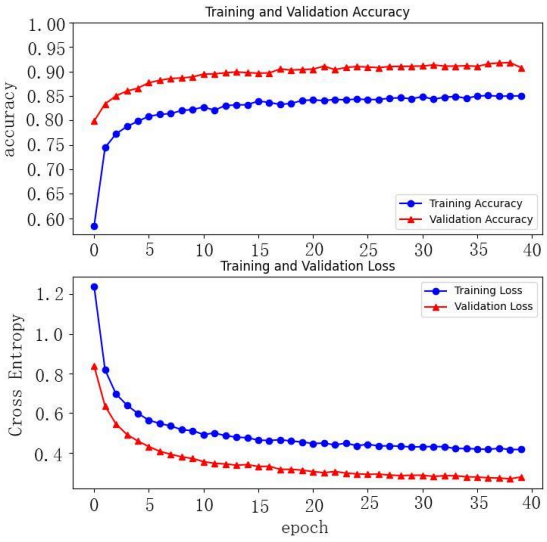

(d) VGG16, above is the accuracy and below depicts the loss of the model

Fig. 5 - Comparison of the highest recognition accuracy and loss value of each model

As can be seen from Fig. 5, the optimized MobileNetV2 model proposed in this paper achieved high training accuracy and low loss values in tomato disease classification. The training accuracy and loss values of the model on the training set are 96.31% and 0.1071, respectively. The training accuracy and loss values of the MobileNetV2 model on the validation set are 98.27% and 0.0562, respectively. In terms of model convergence, the MobileNetV2 model converges the fastest and basically converges in about 10 iterations. Compared with Inception, Xception and VGG16, the optimized MobileNetV2 model can train the optimal model in the shortest time. The VGG16 model converges the slowest and basically tends to converge after about 30 iterations. By comparing the accuracy and loss curves of each model, it can be found that the loss of the model on the training set is slightly higher than that on the validation set, and the accuracy on the training set is slightly lower than that on the validation set.

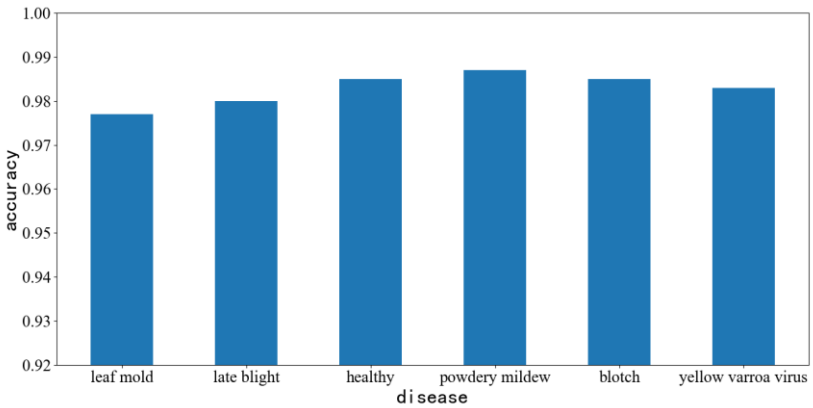

Fig. 6 - Recognition accuracy of the proposed algorithm for different behaviours

Fig. 6 shows the test categories and the corresponding accuracies for optimizing MobileNetV2 on the test set. As can be seen from Fig. 6, tomato powdery mildew was identified with the highest accuracy of 98.7%. The lowest identification accuracy of 97.7% was obtained for tomato leaf blight. The identification accuracy of all six types of tomato leaf diseases was above 97%. Fig. 7 shows the recall, precision and specificity of the optimized MobileNetV2 for the identification of different tomato foliar diseases. As can be seen from Fig. 7, the optimized MobileNetV2 model has the highest recognition accuracy and recall rate for tomato downy mildew, mainly because tomato downy mildew is distinctly different from other diseases.

The lowest accuracy and recall was for tomato leaf mold, mainly because the disease characteristics of tomato leaf mold and late blight are similar, and tomato leaf mold is easily misdiagnosed as late blight.

Especially in the early stages of the disease, the two diseases are extremely similar and difficult to distinguish. The recall and precision of the model for six tomato diseases identification were between 92% and 97%, while the specificity was above 98%. The average recall, precision and specificity of the model for six tomato diseases identification were 95%, 94.9% and 98.9%, respectively. After experimental testing, the average prediction speed of the model for a single image is about 76 ms. The experimental results show that the proposed optimized MobileNetV2 model can consistently identify leaf diseases of tomato.

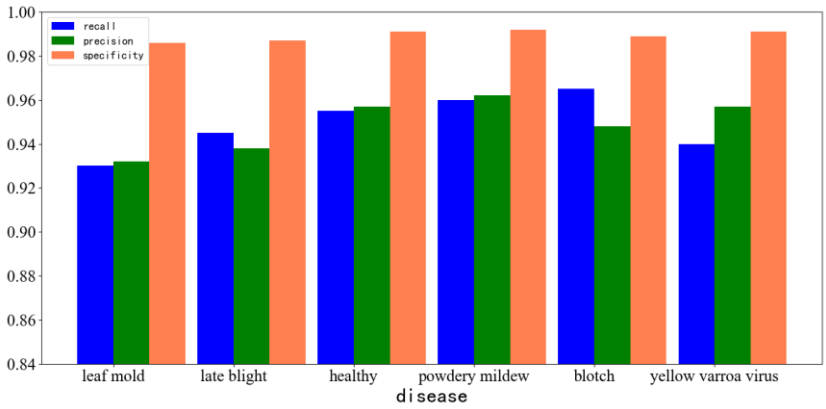

Fig. 7 - The recall, precision and specificity of different disease by proposed algorithm

In this paper, networks such as Inception, VGG16, and Xception are used as control groups to extract image features. The recognition results of different feature extraction networks are compared to verify the effectiveness of the performance of the optimized MobileNetV2 model. The classification models trained by different feature extraction networks were tested with a test set. The test results are shown in Fig. 8.

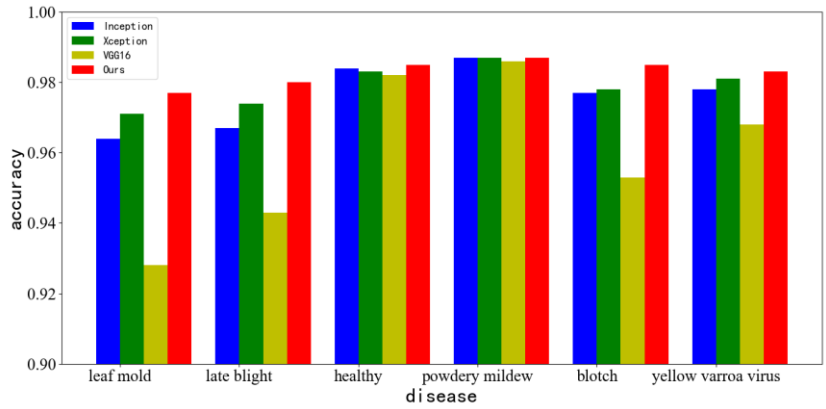

Fig. 8 - Diseases recognition result based on different feature extraction networks

As seen in Fig. 8, the average recognition accuracy of Inception, Xception, and VGG16 models on the test set for the six diseases was 97.6%, 97.9%, and 96%, respectively. The optimized MobileNetV2 model has an average recognition accuracy of 98.3%, which is 2.4%, 0.7% and 0.4% higher than the VGG16, Xception and Inception models, respectively. The test results showed that the VGG16 model had the lowest specificity of 97.4%. The optimized MobileNetV2 model has the highest specificity of 98.9%, which is 1.5% higher than the VGG16 model. The recall rates of the Inception, Xception, and VGG16 models were 92.9%, 93.8%, and 88.6%, respectively. However, the optimized MobileNetV2 model had the highest average recall rate of 94.9% for the six diseases. The optimized MobileNetV2 model has an average recognition accuracy and recall rate of over 90% for six diseases on the test set, which indicates that the model better balances the two evaluation metrics of model accuracy and recall rate.

Fig. 9 shows the results of our method and the MobileNetV2 model for tomato disease identification. According to the analysis of the experimental results, although the recognition accuracy of the MobileNetV2-based recognition method for tomato downy mildew was close to that of our method, the optimized

MobileNetV2 model was significantly more accurate than the MobileNetV2 model for the remaining five diseases.

The average recognition accuracy of the optimized MobileNetV2 model is 98.3%, which is 1.2% higher than the original model. The average recall of this model is 94.9%, which is 3.9% higher than the original model. The average prediction speed of the optimized MobileNetV2 model for a single image is about 76 ms, which is 2.94% better than the original model. Our proposed method has a better classification recognition effect than the original model.

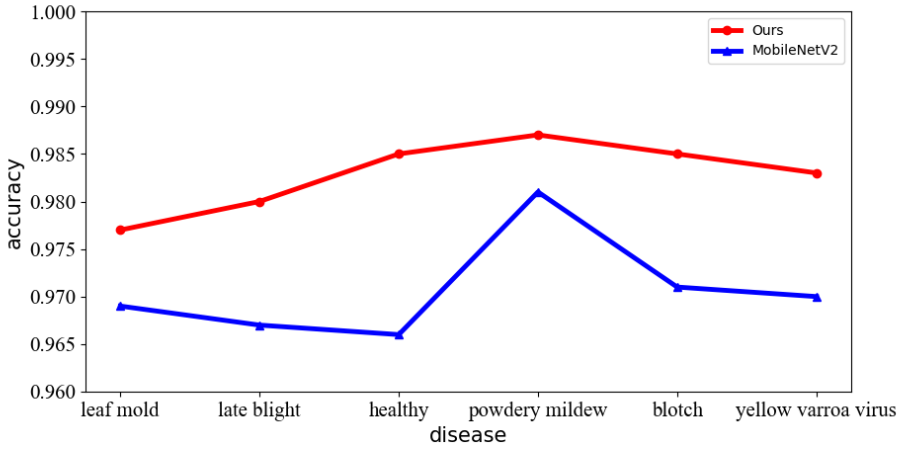

Fig. 9 - Diseases recognition result of our method and MobileNetV2

CONCLUSIONS

In this paper, it was proposed to apply lightweight convolutional neural networks to identify six different leaf diseases of tomato based on deep learning techniques. Based on the MobileNetV2 model, the model has been improved to further adapt to the needs of miniaturization and fast computation of the network model. A new Bneck block structure is proposed for the improvement of MobileNetV2 model. The output of the model was normalized and followed by the addition of a Dropout layer. Replacing the fully connected layer with a global average pooling layer substantially reduces the model parameters. The optimized MobileNetV2 model has an average recognition accuracy of 98.3% and a recall rate of 94.9%, which are 1.2% and 3.9% higher than the original model, respectively. The average prediction speed of the model for a single image is about 76 ms, which is 2.94% better than the original model. Comparison tests with Inception, Xception, and VGG16 models show that the improved MobileNetV2 model has higher average recognition accuracy and recall, and better balances recognition accuracy, recall, and memory requirements consumed for running. The model is minimally affected by factors such as light intensity, weather changes, indicating that the model has good robustness. The optimized MobileNetV2 model can provide a technical reference for the identification of tomato leaf diseases and is important for the remote diagnosis of plant diseases under precision agriculture.

ACKNOWLEDGEMENT

This research was jointly supported by the Shandong Province Key R&D Program(2019GNC106144)

REFERENCES

[1] Bi, C., Wang J., Duan Y., Fu B., Kang J., Shi Y. (2020). MobileNet Based Apple Leaf Diseases Identification," *Mob. Netw. Appl*, Aug. 2020, doi: 10.1007/s11036-020-01640-1.

[2] Chen, J., Zhang D., Nanehkaran, Y. A. (2020). "Identifying plant diseases using deep transfer learning and enhanced lightweight network," Multimed. *Tools Appl.*, vol. 79, no. 41–42, pp. 31497–31515, Nov. 2020, doi: 10.1007/s11042-020-09669-w.

[3] Chen, X., Zhou, G., Chen, A., Yi, J., Zhang, W., Hu, Y. (2020). "Identification of tomato leaf diseases based on combination of ABCK-BWTR and B-ARNet," *Comput. Electron. Agric.*, vol. 178, p. 105730, Nov. 2020, doi: 10.1016/j.compag.2020.105730.

[4] Hassan, S. M., Maji, A. K., Jasiński, M., Leonowicz, Z., Jasińska, E. (2021). "Identification of Plant-Leaf Diseases Using CNN and Transfer-Learning Approach," *Electronics*, vol. 10, no. 12, p. 1388, Jun. 2021, doi: 10.3390/electronics10121388.

[5] Hu, W., Fan, J., Du, Y., Li, B., Xiong, N., Bekkering, E. (2020). "MDFC–ResNet: An Agricultural IoT System to Accurately Recognize Crop Diseases," *IEEE Access*, vol. 8, pp. 115287–115298, 2020, doi: 10.1109/ACCESS.2020.3001237.

[6] Jiang, P., Chen, Y., Liu, B., He, D., Liang, C. (2019). "Real-Time Detection of Apple Leaf Diseases Using Deep Learning Approach Based on Improved Convolutional Neural Networks," *IEEE Access*, vol. 7, pp. 59069–59080, 2019, doi: 10.1109/ACCESS.2019.2914929.

[7] Liu, B., Tan, C., Li S., He J., Wang H. (2020). "A Data Augmentation Method Based on Generative Adversarial Networks for Grape Leaf Disease Identification," *IEEE Access*, vol. 8, p. 11, 2020.

[8] Liu, J., Wang, X. (2020). "Tomato Diseases and Pests Detection Based on Improved Yolo V3 Convolutional Neural Network," *Front. Plant Sci.*, vol. 11, p. 898, Jun. 2020, doi: 10.3389/fpls.2020.00898.

[9] Lv, M., Zhou, G., He, M., Chen, A., Zhang, W., Hu, Y. (2020). "Maize Leaf Disease Identification Based on Feature Enhancement and DMS-Robust Alexnet," *IEEE Access*, vol. 8, pp. 57952–57966, 2020, doi: 10.1109/ACCESS.2020.2982443.

[10] Roopashree, S., Anitha, J. (2021). "DeepHerb: A Vision Based System for Medicinal Plants Using Xception Features," *IEEE Access*, vol. 9, pp. 135927–135941, 2021, doi: 10.1109/ACCESS.2021.3116207.

[11] Shi, C., Xia, R., Wang L. (2020). "A Novel Multi-Branch Channel Expansion Network for Garbage Image Classification," *IEEE Access*, vol. 8, pp. 154436–154452, 2020, doi: 10.1109/ACCES S.2020.3016116.

[12] Sun, J., Yang, Y., He, X., Wu, X. (2020). "Northern Maize Leaf Blight Detection Under Complex Field Environment Based on Deep Learning," *IEEE Access*, vol. 8, pp. 33679–33688, 2020, doi: 10.1109/ACCESS.2020.2973658.

[13] Too, E. C., L, Y. J., Njuki, S., L, Y. C. (2019). "A comparative study of fine-tuning deep learning models for plant disease identification," *Comput. Electron. Agricult.*, vol. 161, pp. 272–279, Jun. 2019, doi: 10.1016/j.compag.2018.03.032.

[14] Venkatesh, N. Y., Hegde, S. U. (2021). "Fine-tuned MobileNet Classifier for Classification of Strawberry and Cherry Fruit Types," *in 2021 International Conference on Computer Communication and Informatics (ICCCI)*, Coimbatore, India, Jan. 2021, pp. 1–8. doi: 10.1109/ICCCI50826.2021.9402444.

[15] Wang, W., Li, Y., Zou, T., Wang, X., You, J., Luo, Y. (2020). "A Novel Image Classification Approach via Dense-MobileNet Models," Mob. Inf. Syst., vol. 2020, pp. 1–8, Jan. 2020, doi: 10.1155/2020/7602384.

[16] Wu, Y., Xu, L., Goodman, E. D. (2021). "Tomato Leaf Disease Identification and Detection Based on Deep Convolutional Neural Network," *Intell. Autom. Soft Comput.*, vol. 28, no. 2, pp. 561–576, 2021, doi: 10.32604/iasc.2021.016415.

[17] Xiao, M., Ma, Y., Feng, Z., Deng, Z., Hou, S., Shu L., Lu, Z. (2018). "Rice blast recognition based on principal component analysis and neural network," *Comput. Electron. Agric.*, vol. 154, pp. 482–490, Nov. 2018, doi: 10.1016/j.compag.2018.08.028.

[18] Xiong, Y., Liang, L., Wang, L., She, J., Wu, M. (2020). "Identification of cash crop diseases using automatic image segmentation algorithm and deep learning with expanded dataset," *Comput. Electron. Agricult.*, vol. 177, p. 105712, Oct. 2020, doi: 10.1016/j.compag.2020.105712.

[19] Yuan, Y., Xu, Z., Lu, G. (2021). "SPEDCCNN: Spatial Pyramid-Oriented Encoder-Decoder Cascade Convolution Neural Network for Crop Disease Leaf Segmentation," *IEEE Access*, vol. 9, pp. 14849–14866, 2021, doi: 10.1109/ACCESS.2021.3052769.

[20] Zeng, Q., Ma, X., Cheng, B., Zhou, E., Pang, W. (2020). "GANs-Based Data Augmentation for Citrus Disease Severity Detection Using Deep Learning," *IEEE Access*, vol. 8, pp. 172882–172891, 2020, doi: 10.1109/ACCESS.2020.3025196.

[21] Zhang, S., Zhang, S., Zhang, C., Wang, X., Shi, Y. (2019). "Cucumber leaf disease identification with global pooling dilated convolutional neural network," *Comput. Electron. Agric.*, vol. 162, pp. 422–430, Jul. 2019, doi: 10.1016/j.compag.2019.03.012.

[22] Zhang, X., Qiao, Y., Meng, F., Fan, C., Zhang M. (2018). "Identification of Maize Leaf Diseases Using Improved Deep Convolutional Neural Networks," *IEEE Access*, vol. 6, pp. 30370–30377, 2018, doi: 10.1109/ACCESS.2018.2844405.

CHANGES IN ELECTROLYTE TRANSMITTANCE AT 254 nm ACCORDING TO THE STATE OF HEALTH OF LEAD ACID BATTERIES

CAMBIOS EN LA TRANSMITENCIA DEL ELECTROLITO A 254nm SEGÚN EL ESTADO DE SALUD DE LAS BATERÍAS DE PLOMO

Edwin García QUINTERO[1)], Jose Alfredo PALACIO-FERNÁNDEZ *[1,2)]
[1)] Universidad de Antioquia; TESLA research group, Medellín Colombia
[2)] Instituto Tecnológico Pascual Bravo; *GIIAM* research group, Medellín Colombia
[*)] *Corresponding author, E-mail: jose.palaciof@udea.edu.co, josealpa@pascualbravo.edu.co*
DOI: https://doi.org/10.35633/inmateh-68-59

Keywords: *Electronic Load, Data acquisition, power-IGBT, Battery management, lead acid battery*

ABSTRACT
The estimation of the state of health (SOH) of lead-acid batteries for electrical energy storage is an important factor when planning their replacement and energy management. There are many methods to calculate this parameter. The novelty of this work is that it employs an optical method that produces compelling results showing the variation of the UVC transmittance of the electrolyte when the battery has different SOH levels, which is a novel alternative to the existing one of ampere counting, which is also experimented within this work.

RESUMEN
La estimación del estado de salud (SOH) de las baterías de plomo-ácido para almacenamiento de energía eléctrica es un factor importante a la hora de planificar su reposición y gestión energética. Hay muchos métodos para calcular este parámetro. La novedad de este trabajo es que emplea un método óptico que produce resultados contundentes mostrando la variación de la transmitancia UVC del electrolito cuando la batería tiene diferentes niveles de SOH, lo cual es una alternativa novedosa a la existente de conteo de amperios, que también es experimentado en este trabajo.

INTRODUCTION

Currently, the global problem linked to the increase of greenhouse gases in the atmosphere such as, for example, the average CO_2 content in the earth's atmosphere, which has increased from 390 ppm in 2011 to approximately 410.19 ppm as of 2018, causing an increase in the temperature of the earth's atmosphere, has manifested itself to a greater degree. This alarming increase in both CO_2 content and its corresponding temperature rise along with finite oil and gas resources have forced mankind to face a challenge and a new opportunity to find different energy sources such as renewable energy sources *(Olia et al., 2019*), but these sources involve new research to facilitate their positioning. This is how renewable energy sources go hand in hand with battery energy storage systems, which are one of the critical elements that allow the adoption of generation based on renewable sources. A considerable amount of research activities is devoted to the field of batteries, especially with the aim of reducing production costs, increasing their reliability and performance *(Ospina Agudelo, Zamboni, & Monmasson, 2021*). One of the main indicators that quantify battery performance is known as State of Health (SOH). This indicator is obtained by comparing the current total capacity value of the battery with its initial value *(Rezvanizaniani et al., 2014; Olabi et al., 2021)*.

The estimation of SOH and other battery performance indicators is a broad research topic with great relevance for all integrated power systems involving batteries of different technologies (*Wong et al., 2017; Dey et al., 2014*), especially for their energy management and for battery replacement planning. This can be done by experimental analysis or by modelling, the experimental analysis can be by direct or indirect measurement (*Xiong et al., 2018*).

Hard sulfation is one of the most frequently cited causes of reduced battery performance. In a lead-acid battery, lead sulphate (PbSO4) is formed at both electrodes as a natural product of the chemical discharge reaction. This presents a number of problems, the first of which is the fact that some of the active materials become locked up within the inactive lead sulphate, causing a decrease in available capacity (*Suozzo, 2008*).

[1] *Edwin García Quintero, Ph.D.; Jose Alfredo Palacio-Fernández, Ph.D. (c)*

Among the experimental methods, the impedance measurement of the battery has been investigated, which increases as the battery wears out or loses its initial current capacity. The internal resistance of the battery does not belong to the external parameters of the battery, strictly speaking, the internal resistance is one of the inherent characteristics of the battery. Most battery management systems take internal resistance parameters as auxiliary parameters for battery condition estimation both to determine the state of charge (SoC) as well as SOH (*Wang et al., 2020; Gaouzi et al., 2021*). Another method is the counting of charge cycles, which is widely employed in the calculation of SOH of laptop batteries, there are also destructive methods in which the battery is uncovered to internally analyse the state by techniques such as Raman spectroscopy, X-ray diffraction, electron microscopy in which changes in the internal structure are looked at Xiong research *(Xiong et al., 2018*).

One of the indirect experiments for SOH calculation and which has good accuracy, besides being the most employed to compare the performance of other methods for SOH calculation, is ampere counting, which, to obtain the remaining capacity for charging or discharging, requires long-term monitoring and memorization of the battery current. It is an indispensable process, which costs a lot of time and energy, and the remaining capacity is highly dependent on the high-precision current sensor used to reduce the accumulated error (*Berecibar et al., 2016; Rezvanizaniani et al., 2014*). The SOH therefore represents the ratio of the current maximum battery capacity to the maximum capacity before first use and is given in percentages as expressed by equation (1) *(Ng et al., 2009*).

$$SOH(k) = \frac{Q_{\max}(k)}{Q_{\max\_new}} \tag{1}$$

where Q_{max} is the current maximum capacity of the battery in Amperes/hours (Ah) and Q_{max_new} is the maximum capacity in Ah when the battery was new.

The amperage count, which gives the current capacity at cycle K of charging or discharging, is defined by equations (2) and (3) (*Rezvanizaniani et al., 2014*).

State of charge during charging:

$$SoC = SoC_0 + \frac{1}{Q_{\max}(k)} \int_0^t |I| dt \tag{2}$$

State of charge during discharge:

$$SoC = SoC_0 - \frac{1}{Q_{\max}(k)} \int_0^t |I| dt \tag{3}$$

Where SoC is the state of charge of the battery, which increases to the maximum capacity as it is charged according to equation (2) or discharged according to equation (3), SoC_0 is the initial state of charge of the battery and is the nominal capacity at the k charge or discharge cycle.

The discharge process at the experimental level, can be performed by means of an electronic load to which the current rate (I) demanded from the battery can be varied and discharged at different rates (*Wong et al., 2017*).

The value of the integration time *t*, changes in each charge discharge cycle and goes up to a value in which the voltage of the battery reaches 10.5 v.

Different characteristics of the battery can be used to identify its SOH, such as capacity and internal resistance, but these are an evaluation and judgment rather than an accurate measurement (*Ng et al., 2009*).

On the other hand, none of the investigated methods perform analysis by transmittance or absorbance of light in any part of the spectrum in which a variation in the transmittance of the battery electrolyte due to the variation of the battery SOH is observed. Investigations of UVC ultraviolet light are quite widespread, for example in virus disinfection or deactivation processes (*Bhardwaj et al., 2021*). The most common UVC light sources for many decades have been mercury discharge lamps, especially low-pressure mercury vapour lamps, with a strong emission peak at 254 nm, which is close to the absorption of RNA (*Heßling et al., 2020*).

Low-pressure mercury lamps are very selective at 254 nm and can be seen in blue in Fig. 1 (*Takeda et al., 2021*).

Although relevant studies on SOH in batteries have been performed by different methods, no research has been found that relates the reduction of transmittance in the electrolyte of a battery to the prolonged time of use (SOH).

In this study, a method of measuring the SOH of liquid electrolyte lead-acid batteries by counting amperes is designed and constructed in parallel, from a data acquisition system connected to an electronic load that allows manipulating or regulating the battery discharge current, and by means of charge and discharge cycles with thirteen battery decay points or total amperes counting for different SOH and relate it to the percentage of transmittance detected by a sensor at the frequency of 254 nm emitted by a UVC radiation.

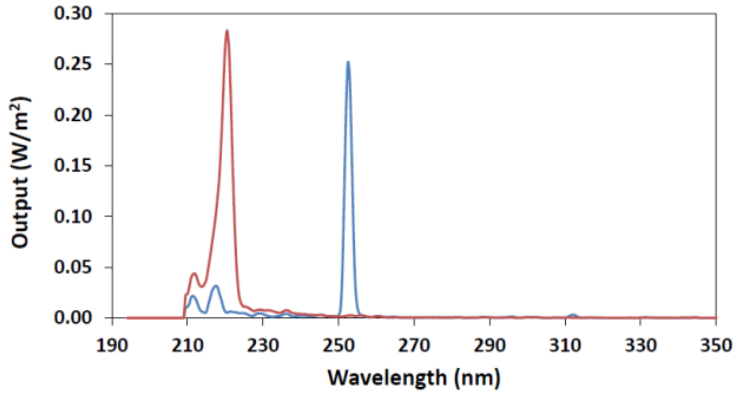

source.

Fig. 1 - Spectral discharge (W m-2) from a 55-W UV-C (254 nm, low-pressure mercury lamp (blue line) and 250 W 222 nm Krypton Chloride excimer lamp (red line) (*Takeda et al., 2021*).

The main objective of this research is to determine the relationship between the SOH measured from a current measurement system that allows the calculation of the total charge of the battery after several charge and discharge cycles, compared with the percentage of transmittance of the electrolyte of 4 lead acid batteries of 42 Ah and 12 V, discharged from 100% of SOH (42 Ah) until it presents 30.5% which is taken as the limit percentage of experimentation due to the long-time of final wear of the batteries of the maximum capacity

MATERIALS AND METHODS

Measurement system of the electrical variables

The embedded system performs permanent monitoring of the current to count the amperes consumed until the voltage drops to a certain value where the electronic load as implemented by *Garcia & Palacio, 2020* (*García Quintero & Palacio-Fernández, 2020*), cannot supply the programmed current or the voltage of the active battery reaches approximately 10.5 volts as deep discharge. And the charging process is started again to fulfil a complete cycle. The scheme implemented to charge and discharge the battery under the above conditions is shown in Fig. 2. In this, the electronic charge control measures the voltage across a 100 W, 1 Ohm resistor connected to the output of the IGBT emitter, the battery current is in proportion to the measured voltage. When the battery is discharging the voltage between collector and emitter is reduced to keep the voltage across the RL resistor constant and therefore the current through it as well. The AO comparator serves as a control element on the IGBT gate voltage, which in turn increases or decreases the VCE voltage in the case of discharge. The embedded system captures the current and adjusts the operational amplifier voltages according to the desired current, the analogue to digital conversion resolution used in the data acquisition with the Arduino to record the tests was 10 bits.

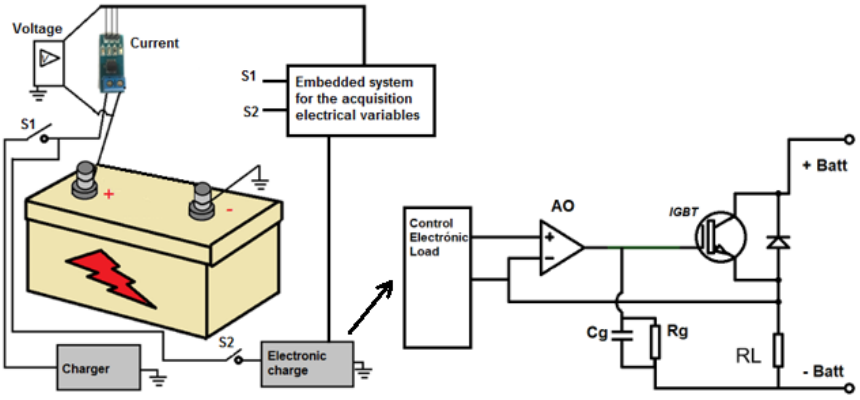

Fig. 2 - General schematic of the experimental set-up

The electronic load (fig. 3.a) maintains an almost constant current around 6 Ah (fig.4) and drops a little at the end of the load when the measured voltage is approximately 10.5 volts. The data are obtained from a data acquisition system (Fig. 3.b) consisting of an embedded system based on Arduino Nano, with storage system in microSD and by serial communication with the PC using Matlab®; in addition to a voltage divider system isolated by operational amplifiers that allow measuring voltages higher than 5 volts and lower than 22 volts.

Fig. 3 - a) Electronic load power system and b) Data acquisition system

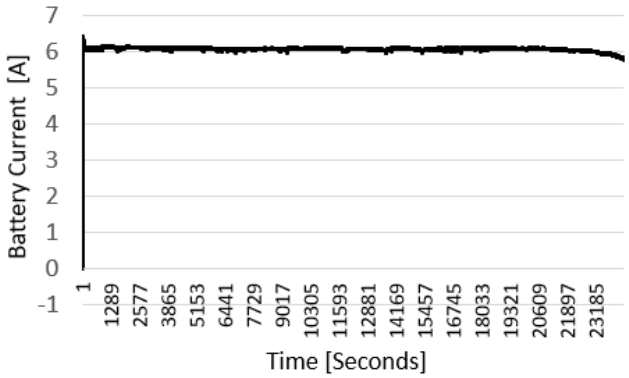

Fig. 4 - Battery discharge current curve taken by the Hall effect sensor.

The developed work considered the analysis for four batteries, whose maximum initial capacity when new is 42 Ah (Ampere-hours). The data are acquired by means of an embedded system and the electronic load is designed from an IGBT as a power control element.

Discharge cycles are performed with a depth of discharge (DoD) of 100%, taking as a base of 100% when the battery drops to a voltage of 10.5 volts. Discharge current was performed at rates of 14.2% of maximum rated capacity, and interleaved discharges of 5% of rated capacity to match the C20 standard which is stated as the maximum load divided by 20, which allows recording the value of the load in the previous cycle of charging and discharging at a higher current.

Discharge tests, as mentioned above, are performed at rates of C3 or 14.2% of the maximum battery capacity. In the case of the 42 Ah batteries, the discharge was performed at 6 amps. It should be noted that this ratio is maintained regardless of the state of health (SOH) by the discharges performed in each cycle, the amperage count is performed by securing the current in the electronic load through the data acquisition system and using equation (1) the SOH is obtained.

Measurement of UVC

Repeat measurements are taken during the same experimental run that is, they are the measurements taken in each cell in the same run of the experiment, while replicate measurements are taken during identical but separate experimental runs, which are taken in the same SOH run, but for cells 2 to 5 of the battery electrolyte, it is monitored that the electrolyte level during the tests is always above the level of the electrodes.

Fig. 5 shows the internal system of the camera implemented for the transmittance measurement that allows to pass through the electrolyte. It consists of a two wire SHT10 digital interface sensor, which allows measuring temperature values in the range 10°C to 80°C with an accuracy of ±0.5°C; a UVC lamp with a narrow spectral range maximized at 254 nm, a quartz cuvette containing the electrolyte to be measured and a 254 nm UVC sensor. The chamber is closed during measurements. The distance between the lamp and the electrolyte is 0.5 cm, and between the electrolyte and the sensor is 1 cm.

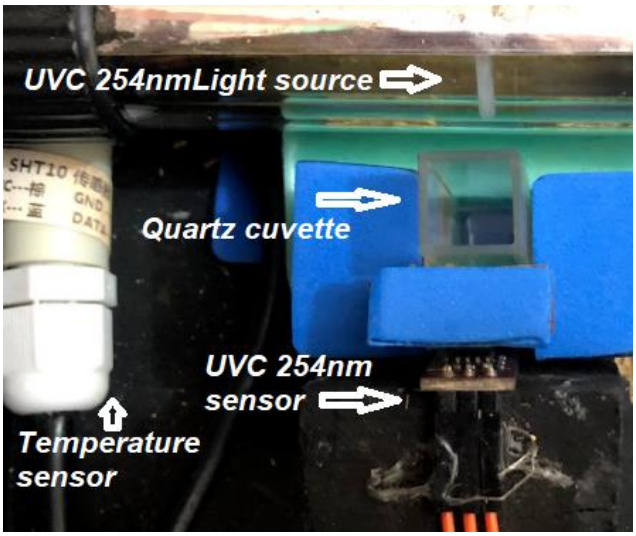

Fig. 5 - Chamber for 254 nm UVC transmittance measurement

RESULTS

The temperature range in which the UVC-254 nm measurements were taken was between 5°C and 30°C, to determine if this variation influences the UVC-254 measurements for each state of charge, an analysis of both values was performed for all the states of charge worked (See Fig. 6) (Each combination corresponds to a test of the SOH in each of the cells during the wear process.). And it was obtained by statistical analysis that the correlation and the P-value (which indicates whether a statistical value is possible from a certain null hypothesis) show that there is no relationship between the variables for the interval investigated.

If P is less than the significance level (the default value is =0.05), the corresponding correlation in R is considered significant, in this case the correlation was close to zero (0.0803) and the value gave a value of 19% indicating no relationship or no significance of the correlation between the variables for which there is then no dependence between the variables analysed (Temperature and UVC-254). And the subsequent analysis is performed without considering the temperature parameter for the range of 25°C to 30°C.

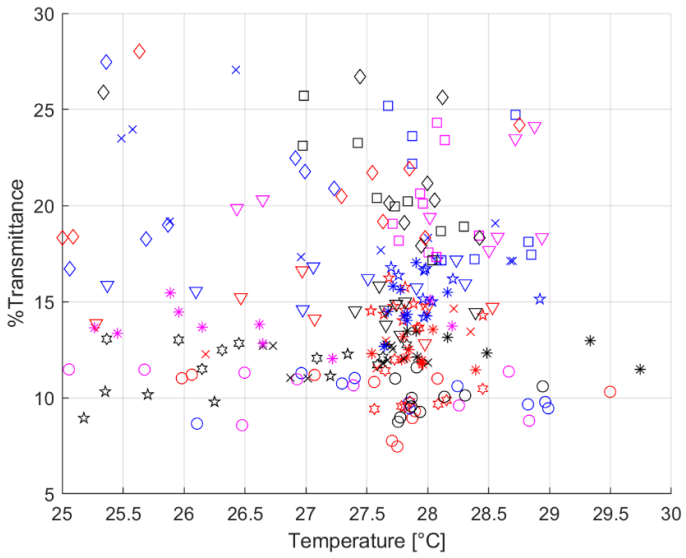

Fig. 6 - Dispersion of the points tested for transmittance and temperature around the measurement chamber.

The other aspect to consider when collecting transmittance samples for each state of charge is to ensure that the battery is at 100% charge since there is a relationship between the transmittance of a discharged battery and a charged one.

Fig. 7 shows the maximum variation of the UVC-254 nm transmittance when the battery is charged and discharged for each of the 4 cells tested, when the battery health state was at 57.62%.

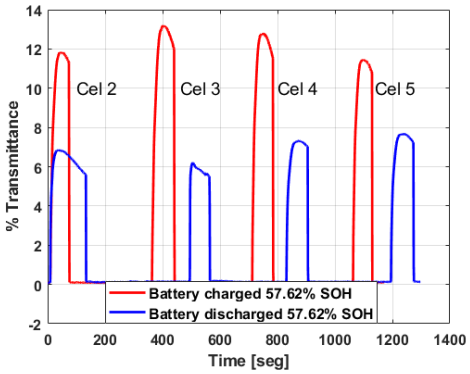

Fig. 7 - Values for % transmittance in a charged and discharged battery electrolyte

The study was performed on 4 batteries of 42 Ah which were subjected to continuous charge and discharge cycles to reduce the capacity or SOH, the depth of discharge was 100% taking as total discharge when the battery presented 10.5 V, the discharge cycles were performed at a rate of 14.2% of the maximum capacity (6 A) during several cycles, until reaching SOH values of: 30.5%, 32.9%, 40%, 49.8%, 52.6%, 57.6%, 71%, 79.5%, 86.2%, 94.8%, 95.7%, 99.2%, and 100%. Four replicates were performed for each battery represented by each of the cells (the cells at the ends of the battery were not taken into account to avoid the error of their contact with the plastic container) and five replicates were performed per replicate (for a total of 260 measured data). The distribution of the values obtained for all the data and for the data with the averaged replicates are shown in Figs. 8 and 9, respectively.

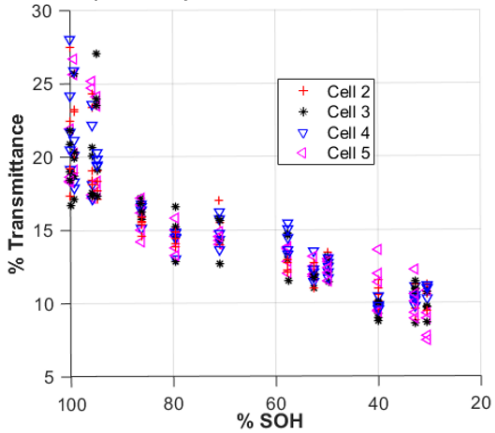

Fig. 8 - Distribution of the point cloud for each of the SOH measurements for each of the reported transmittance percentages

Although the average values at different health states for each cell overlap (Fig. 9.a), the transmittance values between health state ranges decrease as the batteries lose their health state, becoming well defined in health state ranges, as shown enclosed in black ovals in Fig. 9.b; even between these ranges the transmittance values do not overlap, making this novel method a powerful tool for qualitatively and quantitatively determining the loss of lead-acid battery life.

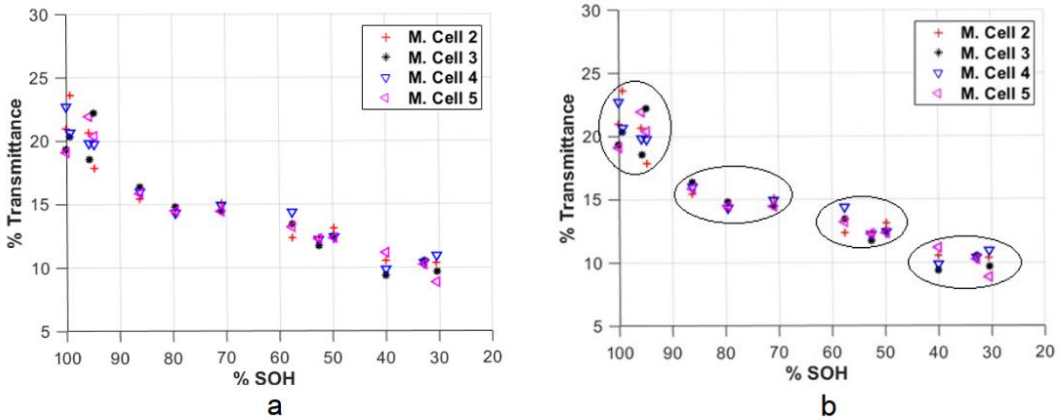

Fig. 9 - Averaged values of the 5 repetitions for SOH with the respective transmittance reported

The average transmittance values of the 13 SOH points measured in their different replicates and repetitions are shown in Table 1. This table shows the variation between the values for the battery with minimum SOH or maximum wear analysed (Group 1) and the values for the same battery when it was new (Group 4).

Table 1

Transmittance value for all the replicates and replicates tested separated and the tested replicates separated by groups

SOH	Group	Transmittance
[%]		[%]
30.5	1	9.97
32.9		10.41
40		10.26
49.8	2	12.61
52.6		12.14
57.6		13.35
71	3	14.75
79.5		14.47
86.2		15.91
94.8	4	20.06
95.7		20.26
99.2		25.75
100		20.54

CONCLUSIONS

The SOH measurement system addressed in this work has not been seen developed by other researchers in any reference found, presenting it as a new methodology for SOH measurement; moreover, the results are conclusive observing that as the battery ages, the electrolyte presents a variation in its concentration that opposes the passage of UVC light, no water is added to the electrolyte so as not to bias the SOH measurement. Although the relationship of the decrease in transmittance with SOH is not linear, they present well determined variations for SOH ranges worked.

ACKNOWLEDGEMENT

Part of the resources of this project has been financed by the Tesla research group of the Univeridad of Antioquia and the direction of technology and innovation of the Institución Universitaria Pascual Bravo.

REFERENCES

[1] Berecibar, M., Gandiaga, I., Villarreal, I., Omar, N., Van Mierlo, J., & Van Den Bossche, P. (2016). Critical review of state of health estimation methods of Li-ion batteries for real applications. *Renewable and Sustainable Energy Reviews*, 56, 572–587. https://doi.org/10.1016/j.rser.2015.11.042

[2] Bhardwaj, S. K., Singh, H., Deep, A., Khatri, M., Bhaumik, J., Kim, K. H., & Bhardwaj, N. (2021). UVC-based photoinactivation as an efficient tool to control the transmission of coronaviruses. *Science of the Total Environment*, 792, 148548. https://doi.org/10.1016/j.scitotenv.2021.148548

[3] Dey, S., Ayalew, B., & Pisu, P. (2014). Combined estimation of State-of-Charge and State-of-Health of Li-ion battery cells using SMO on electrochemical model. *Proceedings of IEEE Workshop on Applications of Computer Vision*. https://doi.org/10.1109/VSS.2014.6881140

[4] Gaouzi, K., El Fadil, H., Rachid, A., Lassioui, A., El Idrissi, Z., & Giri, F. (2021). Sampled-Data Observer for Estimating the State of Charge, State of Health, and Temperature of Batteries. *Electric Power Components and Systems*, 48(19–20), 2168–2180. https://doi.org/10.1080/15325008.2021.1913262

[5] García Quintero, E., & Palacio-Fernández, J. A. (2020). Development of an electronic load applied to the characterization of electric batteries. *International Journal of Engineering Research and Technology*, 13(5), 973–977. https://doi.org/10.37624/ijert/13.5.2020.973-977

[6] Heßling, M., Hönes, K., Vatter, P., & Lingenfelder, C. (2020). Ultraviolet irradiation doses for coronavirus inactivation – review and analysis of coronavirus photoinactivation studies. *GMS Hygiene and Infection Control*, 15, 1–8. https://doi.org/10.3205/DGKH000343

[7] Ng, K. S., Moo, C. S., Chen, Y. P., & Hsieh, Y. C. (2009). Enhanced coulomb counting method for estimating state-of-charge and state-of-health of lithium-ion batteries. *Applied Energy*, 86(9), 1506–1511. https://doi.org/10.1016/j.apenergy.2008.11.021

[8] Olabi, A. G., Onumaegbu, C., Wilberforce, T., Ramadan, M., Abdelkareem, M. A., & Al – Alami, A. H. (2021). Critical review of energy storage systems. *Energy*, 214, 118987. https://doi.org/10.1016/j.energy.2020.118987

[9] Olia, H., Torabi, M., Bahiraei, M., Ahmadi, M. H., Goodarzi, M., & Safaei, M. R. (2019). Application of nanofluids in thermal performance enhancement of parabolic trough solar collector: State-of-the-art. *Applied Sciences* (Switzerland), 9(3). https://doi.org/10.3390/app9030463

[10] Ospina Agudelo, B., Zamboni, W., & Monmasson, E. (2021). *Application domain extension of incremental capacity-based battery SoH indicators*. Energy, 234, 121224. https://doi.org/10.1016/j.energy.2021.121224

[11] Rezvanizaniani, S. M., Liu, Z., Chen, Y., & Lee, J. (2014). *Review and recent advances in battery health monitoring and prognostics technologies for electric vehicle (EV) safety and mobility*. Journal of Power Sources, 256, 110–124. https://doi.org/10.1016/j.jpowsour.2014.01.085

[12] Suozzo, B. (2008), *Lead acid battery aging and state of health diagnosis*. B.S. thesis, The Ohio State University.

[13] Takeda, F., Janisiewicz, W., Short, B., Leskey, T., & Stager, A. (2021). Ultraviolet-C (UV-C) for disease and pest management and automating UV-C delivery technology for strawberry. *Acta Horticulturae*, 1309(April), 533–541. https://doi.org/10.17660/ActaHortic.2021.1309.76

[14] Wang, P., & Zhu, C. (2020). Summary of Lead-acid Battery Management System. *IOP Conference Series: Earth and Environmental Science*, 440(2). https://doi.org/10.1088/1755-1315/440/2/022014

[15] Wong, Y. W., Chong, L. W., Rajkumar, R. K., Leng, W. Y., & Rajkumar, R. K. (2017). A new state-of-charge estimation method for valve regulated lead acid batteries. *Journal of Engineering Science and Technology*, 12(3), 584–595.

[16] Xiong, R., Li, L., & Tian, J. (2018). Towards a smarter battery management system: A critical review on battery state of health monitoring methods. *Journal of Power Sources*, 405(5), 18–29. https://doi.org/10.1016/j.jpowsour.2018.10.019

DESIGN AND TEST OF KEY COMPONENTS OF BIOCHAR RETURN MACHINE BASED ON ROCKY
/
基于 Rocky 的生物炭还田机关键部件设计与试验

Dezhi REN [1,2,3], Luji ZHANG [2], Wanyuan HUANG [2] Huiting CHENG [2], Tian'yi HE [1,3] Jun MENG *[1,3],
[1] Agronomy College of Shenyang Agricultural University, Shenyang 110866, China
[2] Engineering College of Shenyang Agricultural University, Shenyang 110866, China
[3] Key Laboratory of Biochar and Soil Improvement, Ministry of Agriculture and Rural Affairs, P. R. China, Shenyang 110866, China
Tel: +86 15309898525; E-mail: mengjun1217@syau.edu.cn
DOI: https://doi.org/10.35633/inmateh-68-60

Keywords: *Biochar return, Key component design, Rocky, Simulation analysis*

ABSTRACT
To realize the integrated technology of biochar return to the soil, the key components of the biochar discharge system applicable to the biochar return machine were designed, and the force analysis of the return shovel was carried out to obtain the main working parameters affecting the effect of biochar return. Single factor and multi factor simulation tests were conducted with the coefficient of variation of biochar content uniformity as evaluation indexes, and outlet distance, conduit diameter, baffle angle as influencing factors. The data were processed and parameters were optimized using Design-Expert, and the results were optimized and experimentally verified. The validation results showed that the optimal parameters obtained from the simulation data could obtain the best results of biochar return to the field. Therefore, the procedures of this study can be used for the integrated technology of biochar return.

摘要
为实现生物炭还田一体化技术，设计了适用于生物炭还田机上的排炭系统关键部件，并对还田铲进行了受力分析，得到影响生物炭还田效果的主要工作参数。单因素和多因素的仿真试验将炭量均匀性变异系数作为评价指标，将出口距离、导管直径和挡板夹角作为影响因素，利用 Design-Expert 处理数据并优化参数，优化结果并试验验证。实验结果显示，炭量均匀性变异系数与模型的模拟数据有很好的一致性。因此，本研究的程序可用于生物炭还田一体化技术。

INTRODUCTION
Biochar return is an important way of comprehensive utilization of straw (*Zhang, et al., 2019; Liu, et al., 2018; Wei, et al., 2021*). The current method of returning biochar to the soil is to spread the biochar on the surface of the soil and then mix the biochar with the soil using a rototiller, which is extremely labor-intensive and does not allow the biochar to mix evenly with the soil, making the return effect poor (*Cheng, et al., 2016*). The development of simulation technology has greatly reduced the cost of mechanical design. Discrete Element Method (DEM) is a numerical technique for predicting the behavior of bulk solids; it can help shorten (and improve) the design processes for agricultural machinery and their components. Discrete Element Models have been widely used in agriculture, for example, to simulate the working process of agricultural machinery, to predict the wear of machine components, to optimize structural parameters, etc. Therefore, an agricultural machine dedicated to biochar return to the field is designed to improve the efficiency and effectiveness of biochar return to the field using the DEM, and to provide a reference for industrialized equipment for biochar return.

Most of the current research on biochar return is to investigate the effect of mixing biochar and soil on the soil and the growth of various crops, but there is little research on how to return and how to improve the return effect. In the field of agricultural engineering, similar to biochar return technology, there are deep loosening and fertilizing technology and no-till seeding technology. Liu Lijing et al. designed a kind of full-layer fertilization shovel for corn subsoiling and simulated the working process of the shovel by EDEM (*Liu, et al., 2021*).

Zhao Shuhong et al. designed an interactive layered subsoiler based on discrete element simulation of the action of deep loosening shovel on soil (*Zhao, et al., 2021*). According to the agronomic requirements of straw fertilization, Liu Zhongze et al. designed a straw deep burying and returning machine, which can be used for straw fertilization, mulching, ridge beating and soil breaking (*Liu, et al., 2021*). Hu Hong et al., in order to solve the blocking problem in rice-wheat cropping system in the middle and lower reaches of the Yangtze River region, developed a broad width and precision minimal-tillage wheat planter (*Hu, et al., 2016*). Sukhbir Singh et al. studied the effect of different types of openers at different depths and speeds on soil penetration resistance, ridge height, specific draft, soil disturbance and germination rate (*Sukhbir Singh, et al., 2017*). Yang Qinglu et al. designed a corn layered fertilization device analyzed its working process by using the discrete element method (*Yang, et al., 2020*). Wang Chaoqun et al. designed a no-tillage planter with smashing straw and fertilization to solve the problem of suspension seed and hanging seedling in no-tillage seedling machinery (*Wang, et al., 2018*).

In summary, at this stage, there is no machinery designed and manufactured specifically for the characteristics of biochar materials, so this paper studies and designs the key components of biochar return machinery. DEM software Rocky simulation biochar return work process, in this study a Hertzian spring-dashpot model using the DEM was used to model the movement path of particles to measure the effect of biochar return. The structure of components was optimized and the range of main operating parameters was determined based on simulation results. The main parameters affecting the effect of biochar return to the field were determined by Box-Behnken Design, and finally the optimized parameters were obtained and validation tests were conducted.

MATERIALS AND METHODS

Complete machine and key component design

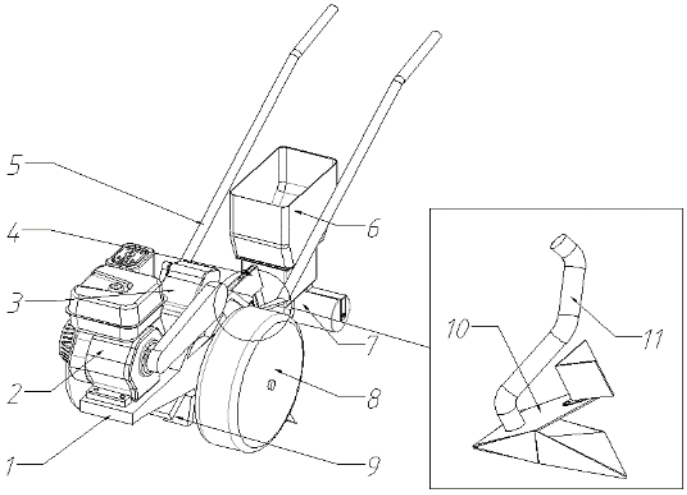

Fig. 1 - Diagram of the whole machine of biochar return machine

1—Mainframe; 2—Gasoline Engine; 3—Transmission; 4—Adjustment Rack; 5—Armrests; 6—Material Box; 7—Mulch Wheel; 8—Traveling wheels; 9—Paddle Wheel; 10—Trenching and Return Shovel; 11—Guide Tube

The whole structure of the biochar return machine is shown in Fig. 1. The working process of the biochar return machine can be divided into three parts: trenching, biochar discharge and soil mulching. The trenching shovel is installed under the connection frame, and the depth of biochar return is changed by the adjustment frame. The whole machine moves forward to drive the paddle wheel to loosen the soil, and the rear return shovel opens out the return ditch to complete the ditching operation. The biochar particles enter the conduit from the material box and flow into the lower shovel surface along the conduit. The mulching wheel at the rear of the machine mulches the returned soil, completing the ditching, biochar discharge and mulching operation.

The key components of the biochar return machine are the components of the biochar discharge system, including the material box, biochar discharger, guide pipe and trenching shovel, which are mainly designed and optimized around the trenching shovel. The main function of the trenching shovel is to open the trench and disperse the biochar particles, so that the biochar particles can be evenly distributed in the soil after returning to the soil. The whole shovel can be divided into three parts: upper shovel, lower shovel and baffle plate, as shown in Fig. 2.

The upper shovel is responsible for trenching and has a through-hole on the shovel face to fit the conduit. The lower shovel is responsible for dispersing the particles, and the shovel surface is equipped with a diversion groove that changes with the position of the upper shovel through-hole, so that the biochar particles can be evenly distributed within the working width of 240 mm after passing through the lower shovel. The upper and lower shovels are equipped with baffles on both sides to prevent the particles from being blown apart. The main structural parameters of the trenching return shovel include: through-hole diameter *R*, which is the same as the diameter of the guide tube; thickness *h*; shovel surface width *B*, which refers to the total longitudinal length of the upper shovel; shovel surface angle *β* and width *H*.

Fig. 3 shows the force diagram of the return shovel, in which the traction force is in balance with all the resistance during the uniform speed operation. According to the force analysis in the figure, the equilibrium equations in the vertical and horizontal directions can be obtained as Equation (1) (2):

$$F_x : F + nN_b(\mu_0 \cos\delta + \sin\delta) = f_{p1}\cos\alpha + N_0 \sin\alpha + N_1 \sin\delta + f_{p2}\cos\delta \quad (1)$$

$$F_y : f_{p1}\sin\alpha + N_1\cos\delta + n\mu_0 N_b \sin\delta = G + N_0\cos\alpha + f_{p2}\sin\delta + nN_b\cos\delta \quad (2)$$

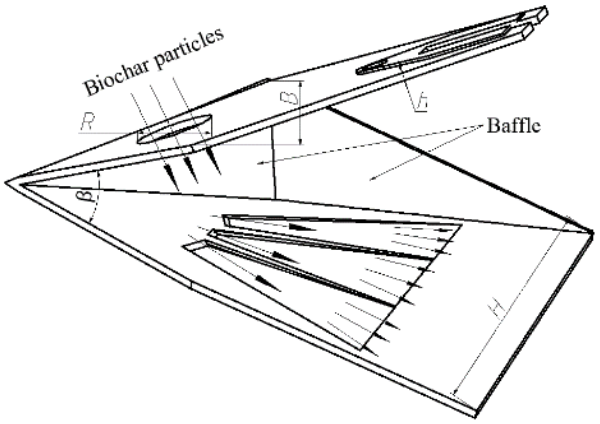

Fig. 2 - Trenching and return shovel

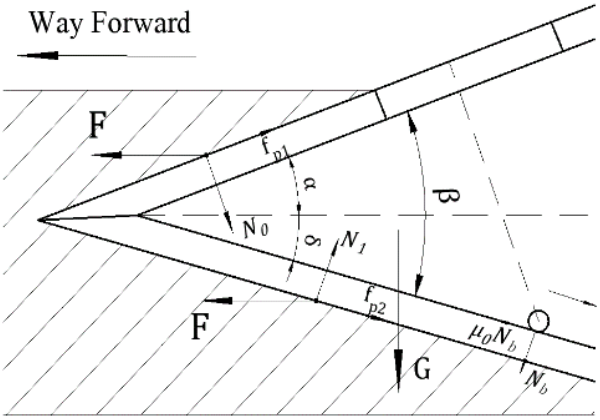

Fig. 3 - Force diagram of return shovel

Where: *G* is the overall gravitational force on the return shovel; *F* is the traction force on the shovel, in the same direction as the forward direction; μ_0 is coefficient of rolling friction between biochar and shovel surface; f_{p1},f_{p2} are the frictional resistance of the soil on the upper and lower shovel surfaces, respectively; N_0,N_1 are the pressure of the soil on the upper and lower shovel surfaces respectively; *α* is the angle between the upper shovel and the horizontal plane; *δ* is the angle between the lower shovel and the horizontal plane; N_b is the pressure of biochar particles on the return shovel; *n* is the number of biochar particles on the lower shovel surface.

Where the pressure generated by the soil on the shovel surface refers to the soil-metal friction mechanism, at relatively low sliding speed (less than 2m/s), the frictional resistance f_p between the metal and the soil is linearly related to the positive pressure *N* between the two, as shown in Equation (3) (*Yao, et al., 1988*). Where *C'*, *A* are empirical constants, *v* is the sliding velocity, Φ_a is the external friction angle of the soil, for loamy soils with different water content, the reference range of the above coefficients are taken as shown in Table 1. From the parameters in the table, the frictional resistance of the soil to the metal becomes larger with increasing speed, but if the speed is below a certain threshold value, the frictional resistance is 0. The reference coefficient was chosen for a moisture content of 17.5% with reference to the characteristics of agricultural soils in the northeast. In addition, since the mass of individual biochar particles is very small, the effect of biochar on the return shovel is neglected, and the Equation (4) can be obtained by combining the Equations (1) to (3).

Table 1

Coefficient reference values

Coefficient	Water content (%)				
	10.0	12.1	17.5	21.8	25.0
C'	30.28	28.11	29.31	26.60	25.31
$tg\Phi_a$	0.3038	0.3177	0.2958	0.2310	0.2553
A	18.38	2.67	24.56	14.72	22.17

$$f_p = C' + A \cdot \ln v + tg\phi_a \cdot N \quad (3)$$

Let $k = C' + A \cdot \ln v$:

$$F = \sum_{i=0}^{1} [(k_i + 03N_i)\cos\beta_i + N_i \sin\beta_i] \quad (4)$$

Where:

β_0 stands for α; β_1 stands for δ; the value of k depends on the sliding speed v;

The formula for calculating the sliding velocity of the shovel surface and the soil is as in Equation (5).

$$v_i = \frac{2v_c}{\cos\beta_i} \quad (5)$$

Where, v_c is the whole machine forward velocity. Comprehensive Equation (3) to Equation (5) can be seen: the smaller the angle of α and δ, the smaller the sliding speed between the soil and the metal, the smaller the frictional resistance; the greater the forward velocity, the greater the resistance of the soil by the components. In the actual mechanical design requirements, the resistance of the parts in the work should be minimized without affecting the normal operation of the mechanism, but the angle of α and δ is not as small as possible: the size of α will affect the performance of soil entry, too small will lose the loosening effect; δ is too small will make it difficult for the biochar particles to slide down from the lower shovel surface, thus affecting the effect of biochar return. Comprehensive consideration: In order to maintain the effect of loosening soil, refer to the design of deep loosening shovel entry angle of agricultural machinery design manual, take α=20° (*Chinese Academy of Agricultural Mechanization Sciences Group., 2007).* In order to maintain a certain speed of biochar particles during sliding, δ = 15° was taken.

Discrete element method simulation

The discrete element software *Rocky* provides the data needed to specifically predict the behavior of particles in agricultural equipment. A three-dimensional model of the biochar return machine was built using the mechanical design software *SolidWorks*, and a simulation model of the biochar return machine was built by *Rocky* to determine key parameters based on the analysis of simulation results. The discrete element simulation requires reasonable determination of various simulation parameters to reflect the real working process. Choosing a suitable mechanical contact model can get reliable analysis results. Since the physical characteristics of biochar particles are similar to those of organic fertilizer, the *Hertzian Spring Dashpot* model was selected as the normal force model, the *JKR* model as the adhesion force model, and the *Linear Spring Coulomb Limit* model as the tangential force model based on the research of discrete element method analysis of organic fertilizer particle application process *(Liu, et al., 2021; Zhao, et al., 2021)*. The material contact parameters are shown in Table 2.

According to the theory of discrete element contact model, the recovery coefficient affects the calculation of normal damping force, while the static/rolling friction coefficient affects the calculation of tangential damping force.

Table 2

Material interaction coefficient

Material Interaction	Recovery coefficient	Static Friction	Dynamic Friction
Biochar- Biochar	0.6	0.6	0.1
Biochar- Steel	0.6	0.6	0.256

The material selected for this test was corn straw biochar supervised by Shenyang Agricultural University Biochar Engineering Technology Research Center, as shown in Fig. 4. According to the theory of discrete element method, when the non-spherical degree of particles is less than 10%, the effect of setting non-spherical particles on the simulation analysis results is minimal, so Biochar particles are established, the shape type is set to spherical particles, the particle sphere diameter is set to 2 mm, 3 mm and 4 mm, and the

three sizes of particles are 1/3 each (*Zhao, et al., 2018*). Import the 3D model of key components into *Rocky* software and set the particle entrance position.

The remaining simulation parameters were as follows: simulation time of 5 s, simulation accuracy of 0.05 s/time, particle generation time of 2 s, and particle mass flow rate of 50 g/s. A slot was added at the end of the shovel to quantify the distribution of biochar particles after the simulation, and the simulation model is shown in Fig. 5.

Fig. 4 - Corn straw biochar pellets

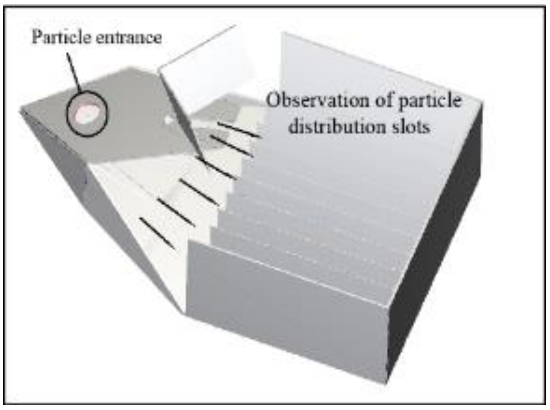

Fig. 5 - Biochar return simulation model

Test design of single factor tests

The key of biochar return technology is how to mix the biochar soil uniformly. In the same depth of soil layer, the uniformity of biochar distribution in the soil will directly affect the return effect, so the coefficient of variation of biochar content uniformity was chosen as the measure of simulation effect. After the simulation test, 12 consecutive sections of 20 mm each were taken within the working width of 240 mm, as shown in Fig. 6.

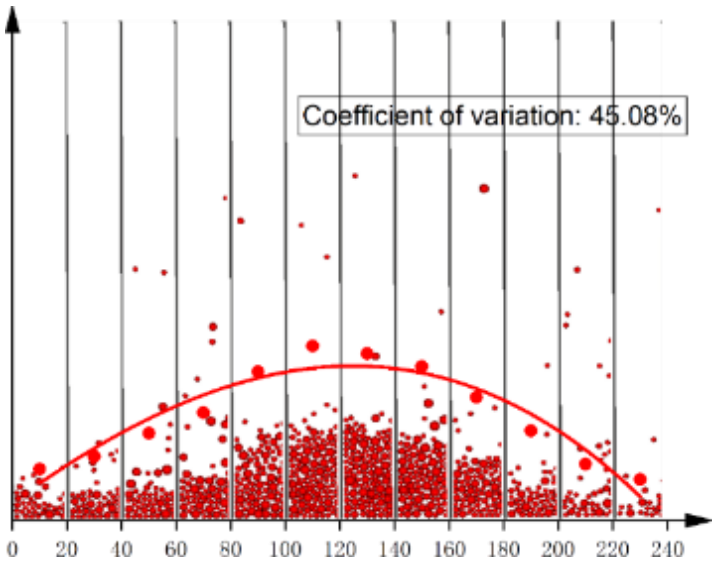

Fig. 6 - Observation trough

The number of biochar particles per section x_i was recorded separately, and the coefficient of variation of biochar content uniformity c_v of the test was:

$$c_v = \sum_{i=1}^{n} \frac{\sqrt{\frac{1}{n-1}(x_i - \bar{x})^2}}{\bar{x}} \tag{6}$$

The coefficient of variation equation is defined as the standard deviation divided by the mean, and in the above equation, *n-1* represents the numerator sample standard deviation. Since the number of particles has been determined before the simulation, i.e., the overall mean is determined, the sample standard deviation is chosen.

From the definition of coefficient of variation, it can be seen that the smaller the value of c_v, the smaller the dispersion of the sample data, given a fixed mean value. The smaller the coefficient of variation of biochar content uniformity represents the more uniform distribution of biochar particles after returning to the soil, and the better the effect of biochar return.

Test design of multi-factor tests

A multi-factor simulation analysis was conducted to investigate the effect of the interaction of various factors on the effect of biochar return to the soil. The Box-Behnken response surface method with three factors and three levels in Design-Expert software was selected for the experimental arrangement. The parameter ranges were obtained based on the results of the single-factor test, and the test factors were coded as shown in Table 3.

Table 3

Factor level coding table of the tests

Levels	Factors		
	Outlet distance x_1[mm]	Conduit diameter x_2[mm]	Baffle angle x_3[°]
-1	65	25	10
0	70	30	20
1	75	35	30

RESULTS

Results and analysis of single factor test

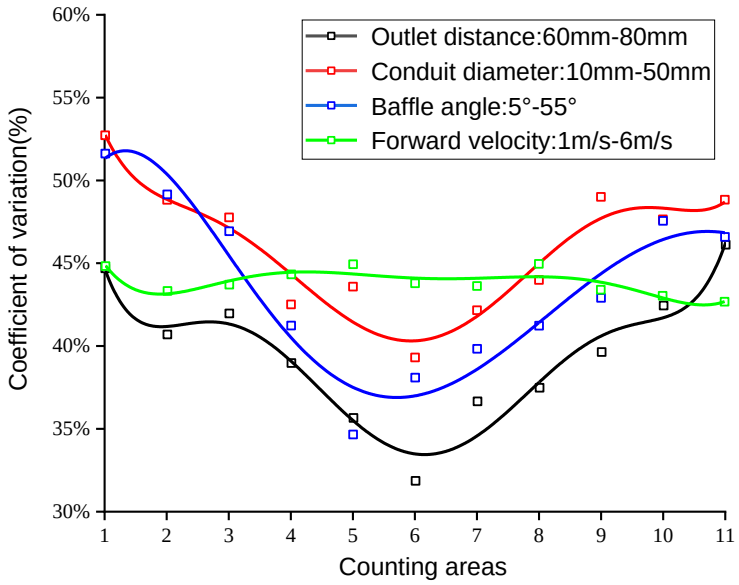

Fig. 7 - Coefficient of variation values at different factor levels

According to the main working parameters of the key components of the structure design, the outlet distance, conduit diameter, forward velocity and baffle angle were selected as the factors for the single-factor test. In order to study the effect of each factor on the return effect, the following ranges of each parameter were obtained: outlet distance 60 mm-80 mm; conduit diameter 10 mm-50 mm; forward velocity 1 m/s-6 m/s; baffle angle 5°-55°. The middle value of each parameter range was taken as the fixed value when other factors were varied, and four groups of mean tests were done, each group eleven times, and the test results are shown in Fig. 7. The test results showed that the values of outlet distance, conduit diameter and baffle angle individually varied significantly on the coefficient of variation of biochar content uniformity under the same conditions of other factors.

The coefficients of variation of conduit diameter and baffle angle were larger at the very small values, and the coefficients of variation of outlet distance and baffle angle were smaller near the median values. In addition, the coefficient of variation was almost not affected by the change of forward velocity. Based on the results of the single-factor test, the outlet distance, conduit diameter and baffle angle were selected as the test factors for the multi-factor simulation test, and the value range of each parameter was further narrowed.

Results and analysis of the Box-Behnken response surface test

The Box-Behnken surface response design test protocol and results are shown in Table 4. The significance test of the test results was performed by using *Design-Expert* software, and the ANOVA on the coefficient of variation of biochar content uniformity was obtained as shown in Table 5. The test results showed that the significant value of model R_1 was $P<0.001$, and the misfit term was $P>0.05$, which indicated that the regression equation test of this multi-factor test reached high significance and the fit was good. Therefore, the results of this test can be further analyzed and optimized. The polynomial regression equation obtained after removing the non-significant term is shown in Equation (7).

Table 4

Experiment scheme and results

Test No.	Factors and levels			Coefficient of Variation R_1[%]
	Outlet distance x_1[mm]	Conduit diameter x_2[mm]	Baffle angle x_3[°]	
1	70	30	20	40.38
2	65	35	20	30.14
3	70	35	30	35.30
4	70	30	20	40.38
5	70	30	20	40.38
6	75	25	20	33.56
7	65	30	30	31.27
8	70	30	20	40.38
9	65	30	10	31.59
10	70	30	20	40.38
11	65	25	20	29.40
12	75	30	30	37.60
13	75	30	10	39.12
14	70	35	10	37.65
15	75	35	20	40.20
16	70	25	30	33.49
17	70	25	10	34.45

Table 5

Significance test result

Source	R_1: Coefficient of Variation				
	SS	df	MS	*F*	*P*
Model	265.70	9	29.52	165.83	<0.0001
A	98.56	1	98.56	553.65	<0.0001
B	19.19	1	19.19	107.79	<0.0001
C	3.32	1	3.32	18.62	0.0035
AB	8.70	1	8.70	48.88	0.0002

Source	R_1: Coefficient of Variation				
	SS	df	MS	*F*	*P*
AC	0.36	1	0.36	2.02	0.1980
BC	0.48	1	0.48	2.71	0.1435
A^2	58.87	1	58.87	330.70	<0.0001
B^2	49.01	1	49.01	275.31	<0.0001
C^2	14.28	1	14.28	80.23	<0.0001
Residual	1.25	7	0.18		
Lack of Fit	0.99	3	0.33	5.11	0.0744
Pure Error	0.26	4	0.064		
Cor Total	266.94	16			

$$R_1 = 40.48 + 3.51X_1 + 1.55X_2 - 0.64X_3 + 1.47X_1X_2 - 3.74X_1^2 - 3.41X_2^2 - 1.84X_3^2 \quad (7)$$

According to the regression equation, the response surface plots of the three factors on the coefficient of variation were drawn as shown in Fig. 7. The ANOVA and response surface plot analysis showed that the three factors of outlet distance x_1, conduit diameter x_2, and baffle angle x_3 all had significant effects on the coefficient of variation individually, and there was a significant interaction between outlet distance and conduit diameter, but the remaining two interaction effects were not significant, which was due to the fact that the effect of baffle angle on the coefficient of variation was actually controlled by controlling the sliding velocity of biochar particles, and in the reference values of α and δ have been given in the design of the return shovel, and the baffle angle $\beta = \alpha + \delta$. In the single-factor test, the coefficient of variation has the minimum value at $\beta = 30°$. Combined with the analysis of the multi-factor test data, the baffle angle will independently affect the return effect, and the baffle angle should be made to tend to 30°. The outlet distance affects the drop position of biochar and the diameter of the conduit affects the mass flow rate of particles per unit time, and both of them affect each other, and in a given range, the coefficient of variation is greatly reduced when the outlet distance is small and the diameter of the conduit tends to 30 mm.

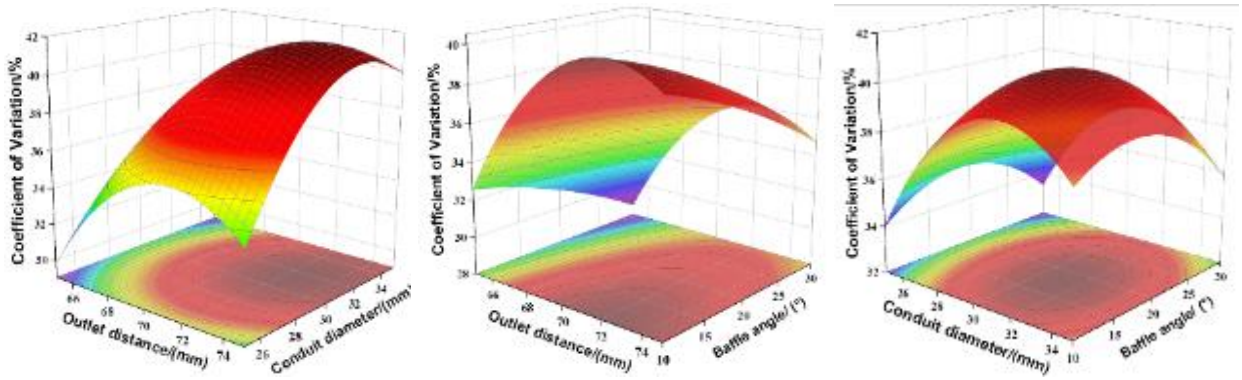

Fig. 8 - Multi-factor Response Surface Plot

Parameter optimization

Parameter optimization of experimental data by *Design-Expert* software, the lower the coefficient of variation of biochar content uniformity, the better the effect of biochar return, and in order to make the baffle angle tend to 30°, set the optimal solution criteria as follows:

$$\begin{cases} \min(R_1) \\ s.t. \begin{cases} 65mm \le x_1 \le 75mm \\ 25mm \le x_2 \le 35mm \\ x_3 \to 30^\circ \end{cases} \end{cases} \quad (8)$$

The optimal solution is obtained as: x_1=65.19 mm, x_2=25.29 mm, x_3=30°, R_1=28.622%. Considering the mechanical design and machining process, the actual parameter values were obtained as 65.20 mm outlet distance, 25.30 mm conduit diameter and 30° baffle angle.

Validation tests

The optimized parameters of the key components of the biochar return machine were obtained by discrete element simulation tests. To verify the reliability of the simulation test, the key components of the biochar discharge system were processed and fabricated according to the designed structural parameters and validation test was conducted. The test was conducted on January 20, 2022 at the test site of Shenyang Agricultural University Hougang Experimental Base, Shenyang, Liaoning Province. The machine was put into the test soil tank with low-speed gearing, as shown in Fig. 8, and the number of particles per 20 mm interval in the working width at a certain forward distance was recorded at the end of the machine work, as shown in Figure 9. The coefficient of variation of biochar content uniformity in the low-speed gear can be calculated as 26.44%, and the average relative error with the theoretical optimum value is 7.80%.

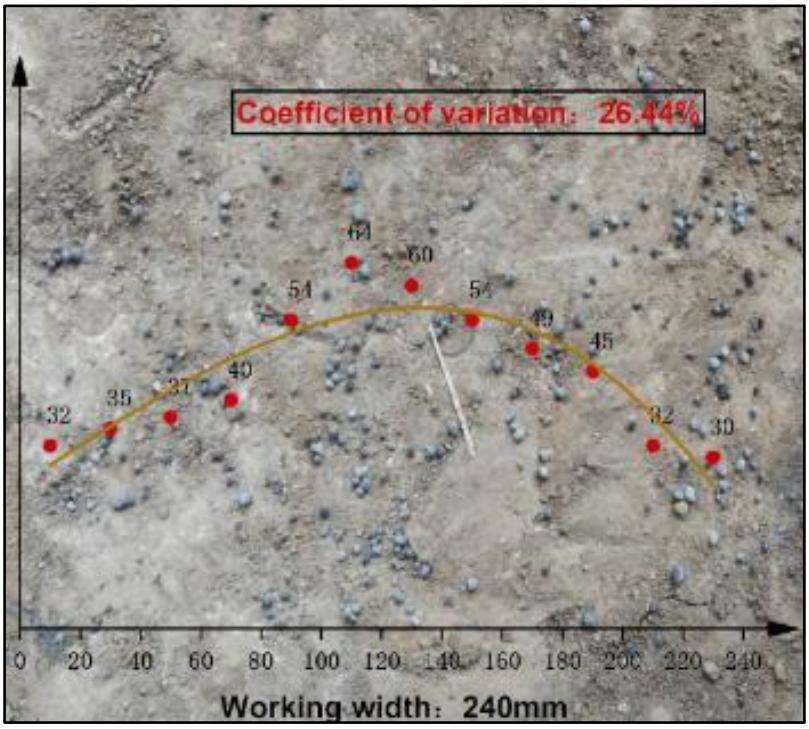

Fig. 10 - Top view of particle distribution

CONCLUSIONS

(1) To realize the integrated technology of biochar return to the soil, this paper designs the key components of the biochar discharge system applicable to the biochar return machine, which can evenly return the biochar to the soil and provide beneficial effects to the root systems of various crops.

(2) Single factor and multi factor tests were conducted by the discrete element simulation software *Rocky*. The range of the main working parameters and the optimal parameters affecting the return effect were obtained. Significance tests and response surface analysis showed that all three factors had significant effects on the biochar return effect, and there was a significant interaction between outlet distance and conduit diameter.

(3) Based on the optimal combination of working parameters: 65.20 mm outlet distance, 25.30 mm conduit diameter and 30° baffle angle, key components were fabricated and tested. The test showed that the best return effect was achieved with the working parameters, and the coefficient of variation of biochar content uniformity could reach 26.44%.

ACKNOWLEDGEMENT

This research was funded by the Project supported by the Science and technology program project of Liaoning Province (2021-MS-232).

REFERENCES

[1] Cheng Xiaoyi, Meng Jun, Huang Yuwei, Lliang Hao, E Yang, He Tianyi, Lan Yu., (2016), Effect of Biochar on Root Growth, Absorption of Nitrogen and Maize Yield. *Journal of Shenyang Agricultural University*, Vol.47, Issue 2, pp.218-223.http://doi:10.3969/j.issn.1000-1700.2016.02.015

[2] Hu Hong, Li Hongwen, Li Chuanyou, Wang Qingjie, He Jin, Li Wenying, Zhang Xiangcai (2016), Design and experiment of broad width and precision minimal tillage wheat planter in rice stubble field (稻茬田小麦宽幅精量少耕播种机的设计与试验), *Transactions of the Chinese Society of Agricultural Engineering*, Vol.32, Issue 4, pp.24-32, http://doi:10.11975/j.issn.1002-6819.2016.04.004

[3] Liu Lijing, Ma Chao, Liu Zhongjun, (2021), EDEM-based simulation and experimental research on the effect of full-layer fertilization shovel in corn subsoiling, *Transactions of the Chinese Society for Agricultural Machinery*, https://kns.cnki.net/kcms/detail/11.1964.s.20210831.1044.006.html

[4] Liu Xiaosheng, Lu Haiying, Cui Hongbiao, Hu Youbiao., (2018), Field application of straw biochar and its environment risk: A review (秸秆生物炭还田应用及环境风险综述), *Jiangsu Agricultural Sciences*, Vol.46, Issue 24, pp.28-35, http://doi:10.15889/j.issn.1002-1302.2018.24.007;

[5] Liu Zhongze, Zhou Weiyan, Lu Haopeng,Cao Xingqiao, Meng Bing., (2021), Design of Straw Deep Buryingand Returning Fertilizer, *Agricultural Science＆Technology and Equipment PhD dissertation*, Issue 4, pp.21-22, Shenyang /P.R.C;

[6] Mechanization Sciences Group. (2007) Agricultural Machinery Design Manual, *China Agricultural Science and Technology Press*, Beijing/P.R.C;

[7] Sukhbir, Singh, Ashok Tripathi, A. K., Singh., (2017), Effect of Furrow Opener Design, Furrow Depth, Operating Speed on Soil Characteristics, *Draft and Germination of Sugarcane*, Vol.19, Issue 5, pp.476-484.http://doi:10.1007/s12355-016-0499-x

[8] Wang Chaoqun, Cao Chengmao, Qin Kuan, Liao Yishan, Guo Yibo, Fan Yakui, Ma Shilong., (2018), Design and experiment of no-tillage planter with smashing straw and fertilization, *Journal of Anhui Agricultural University*, Vol.45, Issue 6, pp.1154-1159, http://doi:10.13610/j.cnki.1672-352x.20190102.021

[9] Wei Yongxia, Xiao Jingping, Wang He, Shi Yun, Liu Hui., (2020), Continual Influences of Applying Biochar on Soil Improvements in Sloping Farmland of Black Soil Region in Northeast China , *Transactions of the Chinese Society for Agricultural Machinery*, Vol.52, Issue 3, pp.305-314, http://doi:10.6041/j.issn.1000-1298.2020.S1.020;

[10] Yang Qinglu, Huang Xingyuan, Wang Qingjie, Li Hongwen, Wang Yingbo, Wang Lanyue., (2020), Structure Optimization and Experiment of Corn Layered Fertilization Device , *Transactions of the Chinese Society of Agricultural Machinery*, Vol.51, Issue S1, pp.175-185, http://doi: 10.6041/j.issn.1000-1298.2020.S1.020;

[11] Yao Yusu, Zeng Dechao., (1988), Investigation on the Relationship Between Sliding Speed and Soil-Metal Friction, *Transactions of the Chinese Society of Agricultural Machinery*, Issue 4, pp.33-40, Beijing/P.R.C;

[12] Zhang Weiming, Chen Wenfu, Meng Jun, Jin Liang, Guo Wei, Zhao Hongliang., (2019), Study of Straw-Biochar on Utilization Potential, Industry Model and Developing Strategy in Northeast China, *Scientia Agricultura Sinica*, Vol.52, Issue 14, pp.2406-2424.http://doi:10.3864/j.issn.0578-1752.2019.14.003

[13] Zhao Shiwei., (2018), Discrete Element Investigation of Physical and Mechanical Properties of Granular Materials, *South China University of Technology*, Guangdong/China;

[14] Zhao Shuhong, Liu Hanming, Yang Chao, Yang Luoluo, Gao Lianlong, Yang Ruiqian., (2021), Design and Discrete Element Simulation of Interactive Layered Subsoiler with Maize Straw Returned to Field, *Transactions of the Chinese Society for Agricultural Machinery*, Vol.52, Issue 3, pp.75-87. http://doi:10．6041 /j．issn.1000-1298.2021.03.008

DISCRETE ELEMENT SIMULATION AND EXPERIMENT OF OPPOSED DOUBLE HELIX OUTER SHEAVE FERTILIZER DISCHARGER

/

对置双螺旋外槽轮排肥器离散元仿真与试验

YuBing WANG [1)], Fang LIANG [1,2*)], Fei XU [1)], Weihong DENG [1)], Yizhe YU [1)]

[1)]College of Engineering, Huazhong Agricultural University, Wuhan 430070, China;

[2)]Key Laboratory of Agricultural Equipment in Mid-lower Yangtze River, Ministry of Agriculture and Rural Affairs, Wuhan 430070, China;

Tel: +8618771938723; E-mail: liangfang101@sina.com

DOI: https://doi.org/10.35633/inmateh-68-61

Keywords: *outer grooved wheel fertilizer distributor, opposed double helix, fertilizer discharge uniformity, discrete element simulation, bench test*

ABSTRACT

Aiming at the pulsation problem of traditional external grooved wheel fertilizer distributor, an opposed double spiral external grooved wheel fertilizer distributor is designed, and the design and analysis of opposed double spiral grooved wheel parameters are carried out. In order to obtain the parameters of the grooved wheel with the best fertilizer discharge effect, the movement process of fertilizer particles in the opposite double spiral external grooved wheel fertilizer distributor was analyzed through discrete element simulation. Using the combination of discrete element simulation and bench test, a simulation orthogonal experiment was carried out on the influence of the rotational speed of the opposed double spiral sheave, the radius of the groove section, the working length of the sheave and the spiral angle of the sheave on the variation coefficient of fertilizer discharge uniformity. The result shows that the factors affecting the uniformity of fertilizer discharge are: trough wheel working length > trough wheel rotational speed > trough wheel helix angle > trough wheel groove radius, and the groove wheel working length of 50 mm, trough wheel rotational speed of 30 r/min, trough wheel spiral lift angle of 45° and groove radius of 10 mm are the optimal combination of structural parameters for fertilizer discharge effect, and the coefficient of variation of uniformity of fertilizer discharge under this combination of parameters is 3.08%. The actual fertilizer discharge performance was verified by bench test. The results show that the variation coefficient of fertilizer discharge uniformity under the parameter combination is 3.99%, and the deviation from the simulation test is 0.91%. The reliability of the discrete element simulation of the fertilizer discharge performance of the opposed double spiral external grooved wheel fertilizer discharger is verified.

摘要

针对传统外槽轮排肥器的脉动性问题，设计了一种对置双螺旋外槽轮排肥器，进行了对置双螺旋槽轮参数设计分析。为获取排肥效果最佳的槽轮参数，通过离散元仿真分析了肥料颗粒在对置双螺旋外槽轮排肥器中的运动过程，运用离散元仿真和台架试验相结合的方式，开展了对置双螺旋槽轮转速、凹槽截面半径、槽轮工作长度和槽轮螺旋升角对排肥均匀度变异系数的影响仿真正交试验，试验结果表明，影响排肥均匀度的因素主次为：槽轮工作长度>槽轮转速>槽轮螺旋升角>槽轮凹槽半径，排肥效果最优的结构参数组合为：槽轮转速30r/min，凹槽半径10mm，槽轮工作长度50mm，槽轮螺旋升角45°，该参数组合下排肥均匀度变异系数为3.08%。通过台架试验来验证其实际排肥性能，结果表明，该参数组合下的排肥均匀度变异系数为3.99%，与仿真试验偏差为0.91%，验证了离散元仿真研究对置双螺旋外槽轮排肥器排肥性能的可靠性。

INTRODUCTION

At present, there are many types of fertilizer dischargers available for fertilizer application operations in China (*Lv., 2014*), and the outer groove wheel dischargers are widely used in fertilizer strip application because of their simple structure and good versatility (*Pan., 2016*).

Most of the common external groove wheel fertilizer eliminators open a certain number of grooves in the cylindrical surface. With the rotation of the groove wheel, the fertilizer is discharged. There is pulsation in the process of fertilizer discharge from adjacent grooves, which affects the uniformity of fertilizer discharge (*Zhang X.C., 2019*).

Through discrete element simulation and bench test, domestic and foreign scholars establish the relationship between the geometric parameters of the outer sheave (sheave diameter, number of grooves, groove radius and groove shape), motion parameters (sheave speed) and the amount and uniformity of fertilizer discharge, so as to optimize the sheave parameters.

Zhu Qingzhen et al. studied the effects of the number of grooves, the radius of the grooves, the effective working length of the grooves and the shape of the groove section on the uniformity of fertilizer discharge by using the combination of simulation and bench for the traditional outer grooved fertilizer discharger (*Zhu et al., 2018*). *Dun Guoqiang et al.* optimized the structure parameters of the fertilizer tongue of the outer groove wheel fertilizer discharger through the discrete element method, and improved the uniformity of the fertilizer discharge flow of the fertilizer discharge tongue (*Dun et al., 2018*). *Wang Botao et al.* used discrete element simulation and bench test to study the influence of the working length of the outer sheave, the speed of the fertilizer discharge shaft, and the opening angle of the fertilizer discharge tongue on the fertilizer discharge amount (*Wang et al., 2017*).

In order to reduce the pulsation of fertilizer discharge, related scholars replaced the traditional straight sheave with oblique sheave and spiral sheave, and optimized its structural parameters (*Gao G.B., 2019*). *Yang Zhou et al.* studied the effects of sheave speed, groove radius and sheave helix angle on fertilizer discharge through discrete element simulation and bench test (*Yang et al., 2018*). *Qi Xingyuan et al.* designed a fertilizer discharger with two rows of fertilizer discharge teeth arranged alternately, which can effectively reduce the fluctuation of fertilizer discharge (*Qi et al., 2016*). *Liu Dezhu and others* designed a staggered inclined groove adjustable outer groove wheel fertilizer discharge device, which has better stability and uniformity than the straight groove wheel (*Liu et al., 2021*).

Spiral outer sheave can reduce the pulsation of fertilizer discharge (*Zhang et al., 2020*). However, due to the action of screw conveying, the fertilizer is transported to one end, and the fertilizer falling belt is not centered when the fertilizer falls into the bottom of the ditch through the fertilizer guiding pipe. In order to solve this problem, this paper designs an opposed double helix outer sheave fertilizer discharger, and uses discrete element simulation to establish the sheave speed, groove radius, sheave working length and the relationship between the helix angle of the sheave wheel and the fertilizer discharge performance, so as to realize the centering of the bottom of the groove and improve the uniformity of fertilizer discharge.

MATERIALS AND METHODS

THE STRUCTURE AND WORKING PRINCIPLE OF THE OPPOSITE DOUBLE HELIX OUTER GROOVE WHEEL FERTILIZER DISCHARGER

The sheave is one of the core parts of the fertilizer distributor (*Zuo et al., 2016*). The opposed double helix outer sheave fertilizer discharger is mainly composed of left and right fertilizer volume regulators, left and right retaining rings, left and right blocking collars, left and right rotating shafts, fertilizer discharge tongues, opposed double helix sheaves, B-type pins, fertilizer shell, fertilizer outlet and other parts, as shown in Fig. 1. The left and right rotating shafts are respectively fixed on the left and right sides of the fertilizer discharge shell by tightening screws, and are arranged concentrically with the opposite double helical sheaves. Compared with the traditional straight sheave, the sheave adopts helical tooth grooves with the same rotation direction on the left and right sides and oppositely arranged.

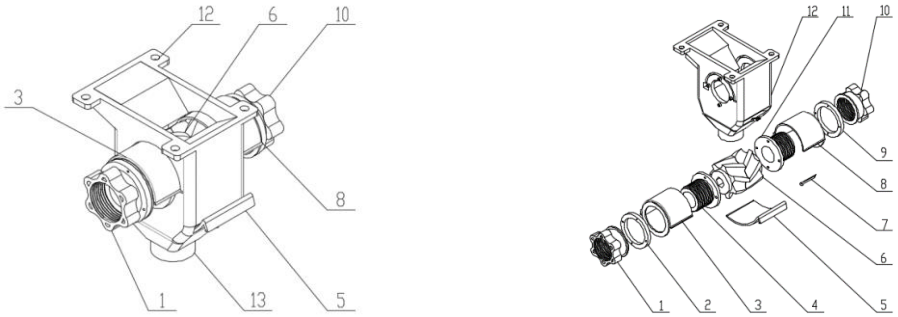

Fig. 1 - Schematic diagram of the structure of the opposite double helix outer groove wheel fertilizer discharger

1- Left fertilizer volume adjuster; 2- Left retaining ring; 3- Left blocking collar; 4- Left rotating shaft; 5- Fertilizer discharge tongue; 6- Opposite double helical sheave; 7- B-type pin; 8- Right blocking collar; 9- Right Retaining ring; 10- Right fertilizer amount adjuster; 11- Right rotating shaft; 12- Fertilizer housing; 13- Fertilizer outlet

During fertilizer discharge, the fertilizer particles enter the fertilizer discharge shell from the fertilizer discharge box by their own gravity, the fertilizer discharge shaft drives the opposite double helix sheave to rotate, and the fertilizer particles are driven by the rotating opposite double helix sheave, and are filled into the spiral groove (*Nukeshev et al., 2016*). With the rotation of the opposite double helical groove wheel, the fertilizer particles turn to the end of the fertilizer discharge tongue, and are automatically discharged from the fertilizer discharge port of the fertilizer discharge shell under the action of its own gravity (*Su et al., 2015*). By turning the left and right fertilizer volume adjusters to drive the left and right blocking collars to move to change the effective working length of the opposed double helical groove wheels to adjust the fertilizer discharge volume, the opening angle of the fertilizer discharge tongue can also be changed by adjusting the position of the B-type pin to adjust the amount of fertilizer discharged.

PARAMETER DESIGN OF OPPOSITE DOUBLE HELIX EXTERNAL SHEAVE

Because the opposed double helix outer groove wheel fertilizer discharger is further optimized and improved based on the traditional outer groove wheel fertilizer discharger, the external groove wheel seed metering device in the agricultural machinery manual should be used as a reference when designing its structural parameters. Referring to the structural parameters of the existing outer sheave fertilizer discharger, the maximum effective working length of the opposed double helical sheave is 60 mm, and the radius of the sheave is 30 mm. The structure diagram is shown in Fig. 2.

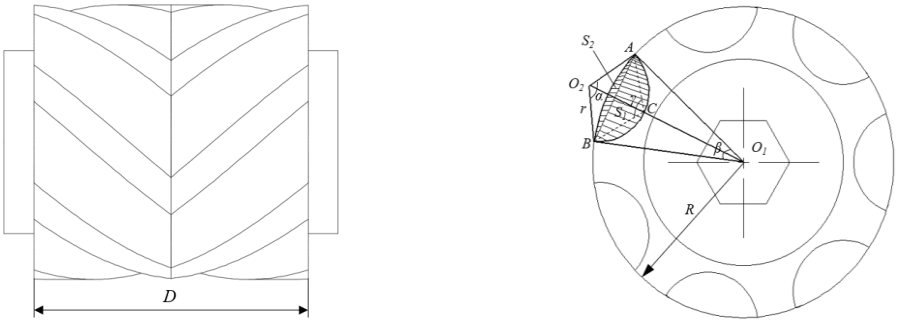

Fig. 2 - Schematic diagram of the structure of opposed double spiral grooved wheels

The groove section of the opposed double helix outer sheave was circular arc, the number of grooves was chosen to be 7, and the groove section area could be calculated by Eq. (1).

$$S = S_1 + S_2 = \frac{R^2}{8}(\beta - \sin\beta) + \frac{1}{2}r^2\sin^2\frac{\alpha}{2}(\alpha - -\sin\alpha) \quad (1)$$

The opposed double helical sheave needs to be driven by the fertilizer discharge shaft to rotate, and moves continuously in the helical groove under the action of various forces. During the fertilizer discharge process, the fertilizer particles located in the spiral groove are not only subject to the normal pressure F_N of the spiral groove, but also to the tangential friction force f_s generated by the contact between the fertilizer particles and the spiral groove. The resultant force of the two is F, and the resultant force F can be decomposed into the axial force F_2 parallel to the axis direction and the axial force F_1 perpendicular to the axis direction. The force acting on the fertilizer particles is shown on the left side of Fig. 3.

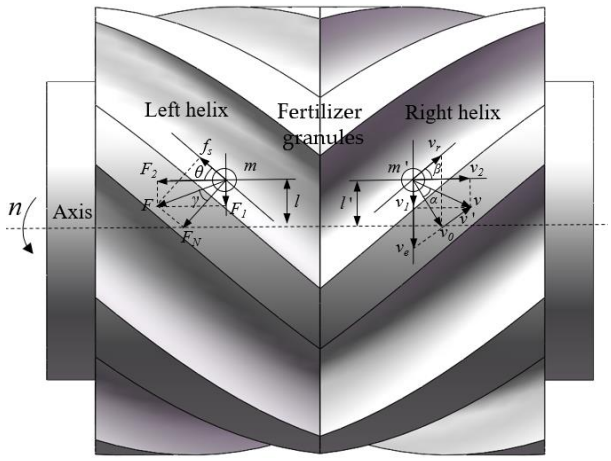

Fig. 3 - Force and Velocity Analysis of Fertilizer Particles in Helical Sheave

It can be seen from Fig. 3 that the angle between the normal pressure F_N and the resultant force F is the friction angle γ, and the helical line is replaced by an oblique line, then θ represents the helix angle of the opposing double helical sheave, and the friction angle γ is determined by the tangential direction. Caused by the friction force f_s, the expression formula of each parameter is as follows:

$$\begin{cases} F = \sqrt{F_1^2 + F_2^2} = \sqrt{f_s^2 + F_N^2} \\ F_1 = F\cos(\theta + \gamma) \\ F_2 = F\sin(\theta + \gamma) \end{cases} \quad (2)$$

In Eq. (2), F is the resultant force of the opposing double helical grooves acting on the fertilizer particles, N; f_s is the tangential friction force generated by the contact between the fertilizer particles and the helical groove, N; F_N is the normal pressure of the spiral groove on the fertilizer particles, N; F_1 is the axial component force, N; F_2 is the circumferential component force, N; θ is the helix angle of the opposed double helix groove wheel, °; γ is the friction angle between the opposed double spiral groove wheel and the fertilizer grain, °(*KIM et al., 2008*).

As can be seen from Eq. (2), when the fertilizer particles move in the groove of the opposed double spiral groove wheel, the axial and circumferential components of resultant force on the fertilizer particles vary with the distance between the fertilizer particles and the axis, with the increase of the spiral angle, the opposed double spiral sheave gradually becomes straight sheave, the pulsation of fertilizer discharge is increased. The proper selection of the spiral angle of the sheave has a direct effect on the force acting on the fertilizer particles in the opposed double spiral groove, being the key to achieving even fertilizer discharge.

In the same way, treating the fertilizer particles inside the spiral grooves as a mass point *m*, the velocity of this mass point was analyzed as shown in Fig. 3, right side.

The movement of fertilizer particles in the opposite double helical grooves is driven by the fertilizer discharge shaft, the implicated velocity v_e is that the linear velocity of the particle is perpendicular to the axis direction, and the relative velocity v_r is parallel to the helix direction. In the ideal case without considering friction, the absolute velocity is v_0. However, in practice, the velocity v' generated by friction will deviate from the ideal absolute velocity v_0. The deviation angle is α, and the actual absolute speed after the deviation is v. At the same time, it can also be decomposed into circumferential speed v_1 and axial speed v_2, which can be expressed as Eq. (3).

$$\begin{cases} \vec{v}_0 = \vec{v}_e + \vec{v}_r \\ \vec{v} = \vec{v}_1 + \vec{v}_2 = \vec{v}_0 + \vec{v}' \end{cases} \quad (3)$$

The circumferential speed v_1 and axial speed v_2 decomposed by the actual absolute speed v can be expressed as Eq. (4):

$$\begin{cases} v_1 = v\cos(\alpha + \beta) \\ v_2 = v\sin(\alpha + \beta) \end{cases} \quad (4)$$

Through trigonometric transformation, it can be obtained:

$$\begin{cases} v_e = \omega l = \dfrac{\pi n l}{30} \\ v = \dfrac{v_0}{\cos\alpha} = \dfrac{v_e\cos\beta}{\cos\alpha} \\ v_1 = \dfrac{\pi n l}{30}\dfrac{\cos\beta}{\cos\alpha}\cos(\alpha + \beta) \\ v_2 = \dfrac{\pi n l}{30}\dfrac{\cos\beta}{\cos\alpha}\sin(\alpha + \beta) \end{cases} \quad (5)$$

In formulas (3) to (5): v_e is the implicated speed, m/s; v_r is the relative speed, m/s; v_0 is the ideal absolute speed, m/s; v' is the speed due to friction, m/s; v is the actual absolute speed, m/s; v_1 is the circumferential speed, m/s; v_2 is the axial speed, m/s; n is the rotational speed of the opposed double helical sheave, r/min;

The ω is the angular velocity of the opposing double helical sheave, rad/s; l is the distance from the fertilizer particle to the axis, mm; α is the angle at which the actual absolute velocity deviates from the theoretical velocity, °. β is the helix angle of the opposing double helical sheave, ° (*Zha et al., 2020*).

According to the above formula, the velocity variation of fertilizer particles in the groove of the opposed Double Helix grooved wheel is related to the spiral angle of the grooved wheel, the distance of fertilizer particles from the axis and the rotation speed of the grooved wheel.

DISCRETE ELEMENT SIMULATION TEST

With the popularity of the discrete element method in the field of agricultural engineering, it has been gradually used by more and more people in scientific research (*Coetzee et al., 2011*; Pasha *et al., 2016*). In this paper, the process of fertilizer discharge of opposed double spiral external grooved wheel fertilizer discharger is analyzed by means of discrete element software EDEM2018, and the method of combining discrete element simulation with bench test is used, the effect of relative parameters of opposed double helix external grooved wheel on its fertilizer discharge performance was studied (*Hu et al., 2016*; *Liu et al., 2017*).

Establishment of discrete element simulation model

Discrete element model of fertilizer discharge device

The created opposed double helix outer groove wheel fertilizer discharge device model is mainly composed of a fertilizer discharge box, a mounting plate, a fertilizer discharge shaft, an opposed double helix outer groove wheel fertilizer discharger and a fertilizer discharge port, as shown in Fig. 4.

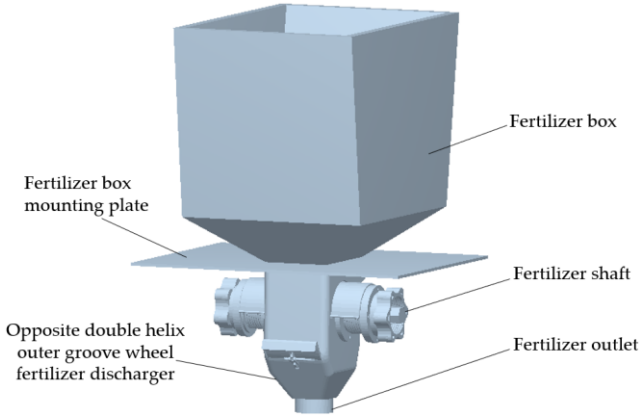

Fig. 4 - Discrete element model of fertilizer discharging device with opposite double helix outer groove wheel

Discrete Element Model of Fertilizer Particles

It was simulated the fertilizer rejection process of fertilizer in a counter placed double spiral outer slot wheel fertilizer remover by discrete element method, and the closer the selected fertilizer grain shape and size were to the true values, the more reliable the fertilizer rejection test results were (*Yuan et al., 2014*; *Yang et al., 2020*; *Ma et al., 2013*). Relevant literature shows that fertilizer grains have a higher sphericity and tend to be greater than 90% (*Coskun et al., 2006*; *Liu et al., 2018*; *Su et al., 2015*). In this paper, 50 grains each of urea, composite and organic fertilizers, which are commonly used fertilizers, were selected to measure their dimensions such as length, width and thickness, and the equivalent diameter and sphericity of the fertilizer grains are available from equations (6) and (7).

$$D=\sqrt[3]{LKH} \tag{6}$$

$$\varphi=\frac{D}{L} \tag{7}$$

In Eqs. (6) and (7): D is the equivalent diameter of fertilizer granules, mm; L is the length of fertilizer granules, mm; K is the width of fertilizer granules, mm; H is the thickness of fertilizer granules, mm; φ is the sphericity of fertilizer granules, % (*Van et al., 2009*).

It was measured that the sphericity of three fertilizer particles, urea, compound fertilizer and organic fertilizer, was high, 97.67%, 96.45% and 95.48%, respectively, which can be approximated as spherical (*Yang et al., 2019*), and combined with the relevant dimensions of the three fertilizers, a ball with a diameter of 3.30 mm was selected as the three-dimensional discrete element model of fertilizer particles in this experiment.

Discrete Element Contact Model

Although fertilizer particles are prone to deliquescence, they are solid and dry granules in the actual fertilization process and do not stick to each other. In order to accurately simulate the fertilization process, Hertz-Mindlin (no slip) was used as the contact model between the fertilizer particles and the fertilization device with the opposite double helix outer sheave (*Chen et al., 2011*; *Zhu et al., 2019*; *Marigo et al., 2015*). The manufacturing material of the opposed double helix outer groove wheel fertilizer spreader is resin. By referring to the relevant literature, the simulation parameters of the relevant materials are determined as shown in Table 1 (*Wang et al., 2017)*.

Table 1

Simulate material and contact mechanics parameters

Parameter	Property	Value
Fertilizer granules	Poisson's ratio	0.25
	Shear modulus/Pa	1.0×10^{7}
	Density (kg m^{-3})	1320
Fertilizer	Poisson's ratio	0.4
	Shear modulus/Pa	1.0×10^{6}
	Density (kg m^{-3})	3500
Fertilizer Granules and Fertilizer Granules	Crash recovery factor	0.11
	Static friction coefficient	0.3
	coefficient of kinetic friction	0.1
Fertilizer Granules & Fertilizers	Crash recovery factor	0.41
	Static friction coefficient	0.32
	coefficient of kinetic friction	0.18

Method for measuring the coefficient of variation of fertilizer uniformity

The test evaluation index selected in this paper is the coefficient of variation of uniformity of fertilizer discharge. Select areas with stable fertilization within the simulated fertilizer ditch area, use the Grid Bin Group function to select a stable fertilization area in the simulated fertilizer ditch area and set up 6 (120mm×200mm×50mm) fertilization monitoring areas with a total length of 1200 mm, and number each area in turn. It is convenient to perform quality statistics on the fertilizer particles in each area after the simulation is over, and according to the formula (8) to (10), the coefficient of variation of the uniformity of fertilizer discharge can be calculated.

$$\bar{m} = \frac{1}{n}\sum m_i \tag{8}$$

$$s = \sqrt{\frac{1}{n-1}\sum (m_i - \bar{m})^2} \tag{9}$$

$$\delta = \frac{s}{\bar{m}} \times 100\% \tag{10}$$

In formulas (8) to (10), The $\bar{m}$ is the average mass of fertilizer particles in the monitoring area, g; The m_i is the quality of fertilizer particles in the i monitoring area, g; n is the number of monitoring areas, n=6; s monitoring area Standard deviation of the total mass of the inner fertilizer particles, g; δ denotes the coefficient of variation of the uniformity of fertilizer discharge, %; δ is inversely proportional to the fertilizer discharge stability and uniformity of the fertilizer discharge device with double spiral outer grooved wheel (*Zhu et al., 2018)*.

RESULTS

Simulation Orthogonal Test and Result Analysis

Test design

Import the model of opposed double spiral external grooved wheel fertilizer discharger into EDEM. A non top shell with a length of 3000 mm, a width of 200 mm and a height of 20 mm is set at the 120 mm position at the lower end of the fertilizer discharge port, the fertilizer spreader being located on the central axis of the housing, it is used to simulate fertilizer ditch and observe the distribution of fertilizer on the ground. In order to simplify the simulation motion setting, the shell (simulating the ground) is set here to move the conveyor belt at the speed of 0.5 m/s, and the fertilizer discharge device is stationary to simulate the fertilizer discharge process. Put the established particle factory directly above the fertilizer discharge box and generate 12000 particles in total at the speed of dynamically generating 6000 particles per second through normal distribution. Set the starting time of the opposed double helix sheave to two seconds after starting to generate fertilizer particles. Set the total simulation time to 18 s and the time step to 18.122% of the Rayleigh time step.

Through the analysis of the relevant parameters of the opposed double helix external grooved wheel affecting the fertilizer discharge effect, combined with the working principle of the opposed double helix external grooved wheel fertilizer discharge device, this paper selects the rotating speed of the grooved wheel, the groove radius, the working length of the grooved wheel and the spiral rising angle of the grooved wheel as the experimental factors, and determines that the diameter of the opposed double helix grooved wheel is 60 mm, the number of spiral grooves is 7 and the forward speed of the machine is 0.5 m/s to design the orthogonal test. The levels of selected test factors are shown in Table 2.

Table 2

Test factor level table

Level	Sheave speed （A）/ r/min	Groove radius (B)/mm	Sheave working length(C)/mm	Null List	Sheave helix angle （D）/°
1	15	9.5	20		45
2	20	10	30		50
3	25	10.5	40		55
4	30	11	50		60

Simulation analysis of movement process of fertilizer particles

From the beginning of the simulation, the fertilizer particles continue to fall from the particle factory within 0~3 seconds, and finally all fall into the fertilizer box. In order to study the movement process of fertilizer particles in the opposed double spiral external grooved wheel fertilizer discharge device, it is convenient to directly analyze the movement track and velocity change of fertilizer particles. According to the movement path of fertilizer particles, the whole process of fertilizer discharge was divided into zones, it is divided into five areas: AB (fertilizer box area), BC (fertilizer housing), CD (slot wheel area), EF (fertilizer tongue area) and GH (fertilizer mouth area). The speed of fertilizer particles is colored to distinguish between the maximum speed of red, yellow, and green which represents the minimum value. The distribution of fertilizer particle velocity in the process of fertilizer discharge is shown in Fig. 5.

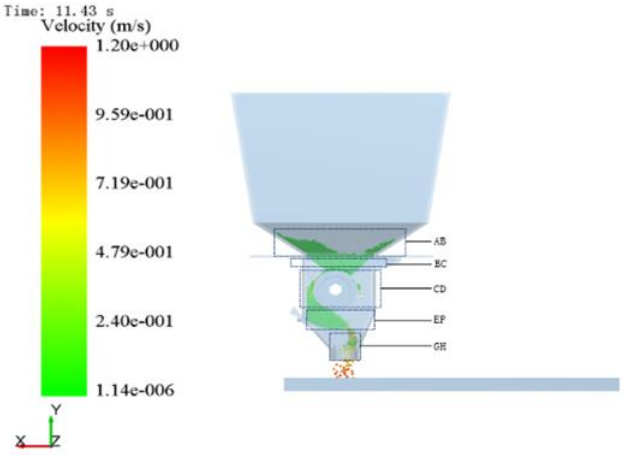

Fig. 5 - Fertilizer particle velocity distribution map

Under the action of its own gravity, the fertilizer particles generated by the particle factory fall into the fertilizer box and enter the fertilizer discharge box of the opposite double helix outer groove wheel fertilizer discharger, and move to the fertilizer discharge tongue under the rotation of the opposite double helix groove wheel. Through the continuous rotation of the groove wheel, the fertilizer continues to accumulate at the fertilizer discharge tongue, and under the action of gravity, it falls to the fertilizer discharge port to complete the fertilizer discharge.

In order to further analyze the movement law of fertilizer particles in the opposite double helix outer groove wheel fertilizer discharge device during the fertilizer discharge simulation process, the Manual Selection function in EDEM is used to select a single fertilizer particle for research. The selected fertilizer particle number is No. 5994. Taking this as the object, analyze its motion trajectory and speed change, as shown in Fig. 6.

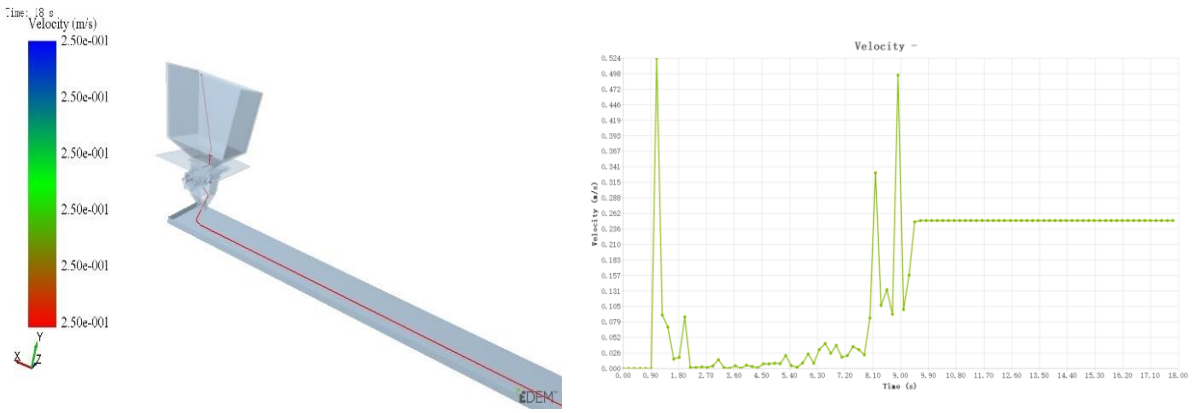

a. Motion trajectory diagram of selected fertilizer particles *b. The selected fertilizer particle velocity change curve*

Fig. 6 - Movement trajectory and speed change diagram of selected fertilizer particles

It can be seen from Fig. 6 that the created particle factory produces fertilizer particles No. 5994 at 0.9 s, and falls to the AB fertilizer box area by its own gravity. Within 0.9~1.2 s, the speed of No. 5994 fertilizer particle increases first and then decreases, reaching a maximum value of 0.524 m/s at 1.0 s. Within 1.2~2.7 s, the particle is in the AB area, and the velocity fluctuates with the accumulated fertilizer particles. Within 2.7~7.8 s, the particle entering the BC fertilizer box area, the speed does not change much and shows a slight fluctuation state. Within 7.8~8.5 s, the particles enter the CD opposed double helix sheave area. Driven by the sheave, the speed first increases and then decreases. The maximum value was reached at 8.2 s, which was 0.341 m/s. Within 8.5~8.9 s, the particles entered the EF fertilizer tongue area, and the speed first increased and then decreased, but the fluctuation was not large. Within 8.9~9.2 s, the particles Entering the GH fertilizer discharge area, the speed still increases first and then decreases, and reaches the maximum value at 9.1 s, which is 0.498 m/s. Within 9.2 s to the end of fertilizer discharge, the particles fall on the simulated ground, and the speed increases, after reaching 0.25 m/s, do a uniform motion to complete the whole process of fertilization.

Test Results and Analysis

The L_{16} (4^5) orthogonal test table was selected for the test by consulting the data to analyze the influence of the selected test factors on the coefficient of variation of fertilizer discharge uniformity (*Siemens et al., 2016)*. The fertilizer discharge simulation test process is shown in Fig. 7, and the experimental design and results are shown in Table 3.

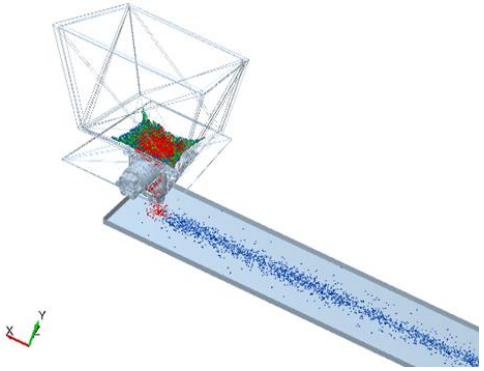

Fig. 7 - Fertilization simulation test process

Table 3

Experimental Design and Results

Test number	A	B	C	Empty column	D	Fertilization uniformity coefficient of variation (%)
1	1	1	1	1	1	6.08
2	1	2	2	2	2	13.25
3	1	3	3	3	3	11.44
4	1	4	4	4	4	6.13
5	2	1	2	3	4	11.54
6	2	2	1	4	3	6.21
7	2	3	4	1	2	5.22
8	2	4	3	2	1	9.86
9	3	1	3	4	2	12.14
10	3	2	4	3	1	3.08
11	3	3	1	2	4	7.89
12	3	4	2	1	3	12.74
13	4	1	4	2	3	3.86
14	4	2	3	1	4	6.43
15	4	3	2	4	1	7.20
16	4	4	1	3	2	5.17
K_1	9.225	8.405	6.338	7.618	6.555	
K_2	8.208	7.243	11.183	8.715	8.945	
K_3	8.963	7.938	9.968	7.808	8.563	
K_4	5.665	8.475	4.573	7.920	7.998	
Very poor	14.24	4.93	26.44	4.39	9.56	
Factor Primary - Secondary	C>A>D>B					
Best plan	$A_4B_2C_4D_1$					

The simulation test results show that the optimal structure parameters for the fertilizer discharge effect of the opposed double helix outer groove wheel fertilizer discharger are: the rotation speed of the grooved pulley is 30 r/min, the cross-sectional radius of the groove is 10 mm, the working length of the grooved pulley is 50 mm, and the Helix Angle of the grooved pulley is 45°. The primary and secondary order of the factors influencing the uniformity of fertilizer discharge is: the working length of the grooved pulley, the rotating speed of the grooved pulley, the helix angle of the grooved pulley, and the cross-sectional radius of the groove.

In order to further understand the importance of the test parameters of the opposed double spiral external grooved wheel fertilizer ejector on the fertilizer discharge performance, the test results are analyzed by variance, and the results are shown in Table 4.

Table 4

Variance analysis

Source of variation	Deviation sum of squares	Degrees of freedom	Sum of mean squares	F	Salience
A	31.686	3	10.562	2.403	*
B	3.866	3	1.289	0.293	
C	114.041	3	38.014	8.648	**
D	2.8	3	0.933	0.215	
error	13.186	3			

*Note: * Significant impact (F0.01>F>F0.05); ** The impact is very significant (F>F0.01)*

It can be seen from Table 4 that the working length of the opposed double spiral grooved wheel has a very significant effect on the fertilizer discharge effect, and the rotating speed of the grooved wheel, the spiral rising angle of the grooved wheel and the groove section radius have no significant effect on the fertilizer discharge effect.

BENCH TEST

Based on the above simulation orthogonal test results, the structural model of opposed double helix external grooved wheel fertilizer ejector under the horizontal combination of the optimal structural parameters when the rotating speed of the grooved wheel is 30 r/min, the groove section radius is 10 mm, the working length of the grooved wheel is 50 mm and the spiral rising angle of the grooved wheel is 45 ° is manufactured. The actual fertilization effect is verified by means of bench test verification.

Test Materials and Devices

The test site of this bench is Hubei Zhongxuan Agricultural Intelligent Technology Co., Ltd, and the time is August 10, 2020. Using the SL6003D printer made by Zhongrui Technology Company to process the opposed double spiral external grooved wheel fertilizer discharger (resin material). The compound fertilizer produced by Stanley Chemical Fertilizer Co., Ltd. was used as the test material, and the self-built test-bed, as shown in Fig. 8.

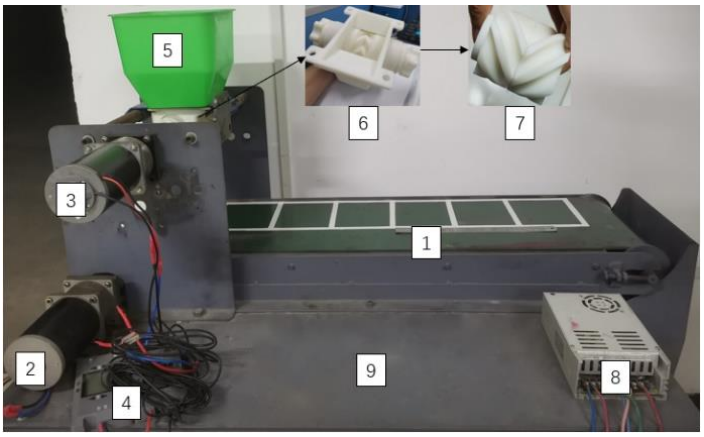

Fig. 8 - Physical map of the structure of the fertilizer test bench

1- Conveyor belt; 2- Conveyor motor; 3- Fertilizer motor; 4- Speed regulator; 5- Fertilizer box; 6- Opposite double spiral outer groove wheel fertilizer discharging device; 7- Opposite double spiral groove wheel; 8- Motor Controller; 9- Test Bench

Test plan

During the bench test, set the forward speed of the conveyor belt as 0.5 m/s, the rotating speed of the sheave as 30 r/min, and the distance between the fertilizer discharge port and the conveyor belt as 120 mm. Use white tape to delineate six grid areas on the conveyor belt, the inner size of each grid is 200 × 220 (mm), and number them. After fertilizer discharge, use a brush to collect the fertilizer particles in the grid into sealed bags. If the fertilizer particles just fall on the frame of the tape, then use the “record the top, not the bottom, the left and not the right” principle to collect. The fertilizer collected in each grid is weighed using an electronic balance. Then make statistics on the mass distribution law of fertilizer particles on the conveyor belt. Calculate the coefficient of variation of the uniformity of fertilizer discharge by the formula, repeat the test five times and get the mean.

Analysis of test results

Through the bench test, the variation coefficients of fertilizer discharge uniformity measured in five repeated tests were 3.71, 4.20, 5.21, 3.14 and 3.69 (%) respectively, and the average value was 3.99%. The test results show that the test results of the opposed double spiral external grooved wheel fertilizer ejector are slightly lower than the simulation test results. Considering that the fertilizer granules and fertilizer discharger models in the simulation are inevitably different from the actual ones. Therefore, it can be considered that the simulation test results are basically consistent with the bench test results. It is further verified that it is reliable to study the fertilizer discharge process of the opposed double helix outer groove wheel fertilizer discharger through discrete element simulation software.

CONCLUSIONS

In this paper, an opposed double spiral external grooved wheel fertilizer distributor is designed, the fertilizer discharge can be controlled by changing the working length of the sheave through the fertilizer regulator on the left and right sides. Replacing traditional straight grooved sheave with opposed double spiral grooved sheave. At the same time, the pulsation of fertilizer discharge is reduced, the fertilizer belt falling into the ditch bottom can be centered, and the fertilizer discharge effect is improved. The structural parameters of the opposed double spiral sheave are optimized through discrete element simulation and bench test. The influence of the rotating speed of the opposed double spiral sheave, the radius of the groove section, the working length of the sheave and the spiral angle of the sheave on the uniformity of fertilizer discharge was investigated, the optimal structure parameters of the opposed double spiral sheave are obtained.

ACKNOWLEDGEMENT

The authors would like to thank the general project of the National Natural Science Foundation of China, the study on the buried mechanism, drag reduction and efficiency increase of rape straw returning to the field by crushing rotary tillage (approval No. 52175233), and also thank the teachers and students of the college for their guidance and help.

REFERENCES

[1] Coetzee C J, Lombard S G, (2011), Discrete element method modelling of a centrifugal fertiliser spreader. *Biosystems Engineering*, 109(4): 308-325.

[2] Chen J, Zhou H., Zhao Z., Li Y.M., (2011), Study on the movement law of rice population in vibrating seed tray based on EDEM [J]. *Journal of agricultural machinery*, 42 (10): 79-83 + 100.

[3] Coskun M., Yalcin L., Ozarslan C., (2006), Physical properties of sweet corn seed (Zea mayssaccharata Sturt)[J]. *Journal of Food Engineering*, 74(4) : 523—528.

[4] Dun G.Q., Yu C.L., Yang, Y.Z. et al, (2018), Discrete element simulation and parameter optimization of fertilizer discharge tongue of external grooved wheel fertilizer ejector [J]. *Journal of Hunan Agricultural university* (natural science edition) ,44 (06): 661-665.

[5] Gao G.B , (2019), *Design and test of key components of air driven rice side deep fertilization device* [D]. Northeast: Northeast Agricultural University.

[6] Hu Y.G., Yang Y.C., Xiao H.R. et al, (2016), Simulation and parameter optimization of centrifugal fertilization process of tea garden fertilizer applicator [J]. *Journal of agricultural machinery*, 47 (05): 77-82.

[7] Kim Y.J., Kim H.J., Ryu K.H. et al, (2008). Fertiliser application performance of a variable-rate pneumatic granular device for rice production [J]. Biosystems Engineering, 100(4): 498-510.

[8] Lv H., (2014), Study on new optimization design method of external grooved wheel fertilizer ejector [D] Changchun: Jilin University.

[9] Liu D.Z., Zhou Y., Zhang G.Z. et al, (2021), Design and experimental study on air assisted double-sided fertilization device for ratooning rice [J] China Agricultural Science and technology guide, 23 (06): 77-85.

[10] Liu C.L., Li Y.N., Song J.N. et al, (2017), Performance analysis and test of centrifugal disc spreader based on edem [J] Journal of agricultural engineering, 33 (14): 32-39.

[11] Liu Z.D., Wang Q.J., Liu, C.G. et al, (2018), Design and experiment of cavity disc precision hole fertilization device [J] Journal of agricultural machinery, 49 (10): 137-144 + 355.

[12] Ma Z., Li Y.M., Xu, L.Z. et al, (2013), Review on particle motion in agricultural engineering [J]. *Journal of agricultural machinery,* 44 (02): 22-29.

[13] Marigo M. , Stitt E.H. , (2015), Discrete element method (DEM) for industrial applications: comments on caliberation and validationfor the modelling of cylindrical pellets[J]. KONA Powder and Particle Journal, 32: 236—252.

[14] Nukeshev S.O., Romanyuk N.N., Yeskhozhin K.J. et al, (2016) Methods and results of the research of the fertilizer distributor of cutter-ridger-fertilizer[J]. *Herald of Science of S. Seifullin Kazakh Agro Technical University*, 3, 138–145.

[15] Pan S.q., Zhao Y.X., Jin L. et al, (2016), Design and experimental study of external grooved wheel fertilizer ejector of 2BFJ-6 variable rate fertilizer applicator [J]. *China Journal of agricultural chemistry*, 37 (01): 40-42.
[16] Pasha M, Hare C, Ghadiri M. et al, (2016), Effect of particle shape on flow in discrete element method simulation of a rotary batch seed coater. *Powder Technology*, 296: 29-36.
[17] Qi X.Y., Zhou Z.Y., Yang, C. et al, (2016), Design and test of key components of pneumatic variable rate fertilizer applicator in paddy field [J]. *Journal of agricultural engineering*, 32 (06): 20-26 + 316.
[18] Su N., Xu T.S., Song L.T., (2015) Variable rate fertilization system with adjustable active feed-roll length[J]. *International Journal of Agricultural & Biological Engineering*, 8(4): 19—26.
[19] Siemens M.C., Gayler R.R., (2016) Improving seed spacing uniformity of precision vegetable planters. *Applied Engineering in Agriculture*, 32(5):579-587.
[20] Van L.P., Tijskens E, Ramon H, (2009), Discrete element simulations of the influence of fertiliser physical properties on the spread pattern from spinning disc spreaders [J]. *Biosystems Engineering*, 102(4) : 392 — 405.
[21] Wang B.T., Bai L., Ding S.P. et al, (2017), Simulation and experimental study on the influence of key working parameters of external grooved wheel fertilizer ejector on fertilizer discharge [J]. *China Journal of agricultural chemistry*, 38 (10): 1-6 + 23.
[22] Wang B.T., (2017), Working process simulation and parameter optimization of external grooved wheel fertilizer ejector based on discrete element method [D]. *Northwest University of agriculture and forestry science and technology*.
[23] Yang Z., Zhu Q.C., Sun J.F. et al, (2018), Study on fertilizer discharge performance of external grooved wheel fertilizer discharge device based on EDEM and 3D printing [J]. *Research on agricultural mechanization*, 40 (05): 175-180.
[24] Yuan J., Liu Q.H., Liu, X. et al, (2014), Simulation of multi fertilizer mixing and optimization of mixing chamber structure in proportional variable rate fertilization [J]. *Journal of agricultural machinery,* 45 (06): 125-132.
[25] Yang Q.L., Huang X.Y., Wang, Q.J. et al, (2020), Structural optimization and experiment of spatial layered fertilization device for maize [J]. *Journal of agricultural machinery*, 51 (S1): 175-185.
[26] Yang Q.L., Li Z.H., Li H.W. et al, (2019), Numerical analysis of particle motion of centralized fertilizer separation device based on CFD-DEM [J]. *Journal of agricultural machinery*, 50 (08): 81-89.
[27] Zhang X.C., (2019), *Optimal design of external grooved wheel fertilizer ejector and influence of key working parameters on fertilizer discharge performance* [D] Nanjing: Nanjing Agricultural University.
[28] Zhu Q.Z., Wu G.W., Chen L.P. et al, (2018), Effect of structural parameters of grooved wheel on fertilizer discharge performance of straight grooved wheel fertilizer ejector [J]. *Journal of agricultural engineering*, 34 (18): 12-20.
[29] Zhang J.Q., Liu G., Hu, H. et al, (2020), Effect of control sequence of bivariate spiral external grooved wheel fertilizer ejector on fertilizer discharge performance [J]. *Journal of agricultural machinery*, 51 (S1): 137-144.
[30] Zuo X.J., Wu G.W., Fu W.Q. et al, (2016), Design and experiment of air driven precision fertilization device for rice lateral depth [J]. *Journal of agricultural engineering*, 32 (03): 14-21.
[31] Zha X.T., Zhang G.Z., Han Y.H. et al, (2020) Structural optimization and performance evaluation of blocking wheel-type screw fertilizer distributor [J]. *Agriculture*, 11(3): 248.
[32] Zhu Q.Z., Wu G.W., Chen L.P. et al, (2019), Structural design and optimization of elastic seed plate of wheat wide seedling belt spreader [J]. *Journal of agricultural engineering*, 35 (01): 1-11.

CALIBRATION OF THE DISCRETE ELEMENT PARAMETERS AND EXPERIMENTAL VERIFICATION OF THE OIL SUNFLOWER PLUG SEEDLING POTS
/
油葵穴盘苗钵体离散元参数标定与试验验证

Fandi ZENG[1)], Xuying LI*[1)], Hongbin BAI[1)], Ji CUI[1)], Xuening LIU[2)], Yongzhi ZHANG[1)]
[1)]Inner Mongolia Agricultural University, College of Mechanical and Electrical Engineering, Hohhot/China;
[2)] Taiyuan Agricultural Technology Extension Service Centre, Taiyuan/China
Tel: +86-0471-4309215; E-mail: zfd19508@163.com
DOI: https://doi.org/10.35633/inmateh-68-62

Keywords: *Plug seedling pot, Drop impact test, Collision impact force, Hertz-Mindlin with bonding model*

ABSTRACT

The movement of plug seedlings and the pots damage mechanism are deeply studied during the planting process, and the planting components are optimized. The Tekscan pressure distribution measurement system was used to measure the mechanical characteristics of the drop impact between the whole plug seedlings and the pots. The relative error between the collision impact force of the plug seedlings and the collision impact force of the pot is less than 20%. Therefore, a drop impact test using the pot allows the whole plug seedling to be characterized. The Hertz-Mindlin with bonding model was used to build a simulation model of the pot based on essential physical parameters. The Plackett-Burman test and the steepest climbing test determined the significant parameters and optimal intervals affecting the collision impact force: the rolling friction coefficient between the pot and pot was 0.35~0.38, the bond stiffness was 0.2~0.6 MN·m^{-3}, and the bond radius was 1.56~1.98 mm. Finally, the Box-Behnken test was performed and the quadratic regression model of the collision impact force was developed. Taking the collision impact force with a drop height of 350 mm as the target, the optimal solution is obtained: the rolling friction coefficient between the pot and pot was 0.35, the bond stiffness was 0.53 MN·m^{-3}, and bond radius 1.97 mm. The average value was used for other insignificant influence parameters. The simulation results are compared with the physical test, and the relative error is 3.65%. Therefore, the pot model established by this simulation parameter can represent the actual drop impact of the pots.

ABSTRACT

为深入研究栽植过程穴盘苗的运动规律和钵体的破损机理，进而优化栽植部件。本文采用 Tekscan 压力分布测量系统对整株穴盘苗与钵体的跌落碰撞力学特征测定，得到穴盘苗的碰撞冲击力与钵体的碰撞冲击力相对误差小于20%，可得采用钵体的掉落碰撞特性可以表征实际的穴盘苗。然后基于本征参数建立钵体的粘结模型，通过 Plackett-Burman 试验和最陡爬坡试验，确定了影响碰撞冲击力的显著性参数和最优区间：钵体-钵体的动摩擦系数为 0.35 ~0.38、粘结刚度为 0.2~0.6 MN•m^{-3} 和粘结半径为 1.56 ~1.98 mm；最终对显著性参数进行了 Box-Behnken 试验，建立了碰撞冲击力与仿真参数的二阶回归模型，并以跌落高度为 350mm 的钵体碰撞冲击力为目标进行寻优，得到最优解：钵体-钵体的动摩擦系数0.36，钵体的粘结刚度0.22 MN•m^{-3} 和粘结半径1.66 mm，相对误差为 3.65%，即采用此仿真参数建立的穴盘苗钵体模型，能表征实际穴盘苗钵体的跌落碰撞力学特性。

INTRODUCTION

Transplanting seedlings can use natural light and heat resources to improve crop quality, increase crop yield and create favourable conditions for high crop yield, which has obvious advantages in open field planting and mulch seeding *(Yang et al., 2018; Zhao et al., 2020)*. The roots of the plug seedlings are mixed and absorb the nutrients in the matrix, forming a pot with a particular strength elasticity to facilitate transplanting in the field *(Han et al., 2019; Wen et al., 2021)*. The movement of the plug seedlings and the damage mechanism of the pot is a very complex system that can seriously affect the quality and efficiency of the transplanting process.

[1] *Fandi Zeng, Ph.D. Stud. Eng;*[1]**Xuying Li, Pro. Ph.D. Eng;* [1]*Hongbin Bai, M.S. Stud. Eng.;* [1]*Ji Cui, M.S. Stud. Eng.;*
[2] *Xuening Liu, M.S. Assistant agronomist;* [1] *Yingzhi Zhang, Ph.D., Associate professor*

Many scholars have focused on research into the damage rate of plug seedlings and the optimization of critical components. *Ryu et al., (2001),* studied the effect of the structural parameters of the seedling gripper on the success of seedling extraction and the loss of quality of potted seedlings. *Jiang et al.,(2017)*, studied the effects of the matrix ratio, water content, and pot quality on seedling extraction and the matrix breakage success rate. *Yang et al., (1991)*, studied the influencing factors of the operational performance of the sliding needle cylinder seedling gripper and analysed the influence of the degree of disc root and the water content of the matrix on the success rate of seedling extraction. *Mao et al., (2021)*, designed a seedling pickup device composed mainly of a conveying device, a feeding device, a seedling clamping device, and an automatic control system. The use of aerodynamically blowing out the seedlings and the end effector significantly reduces the damage rate of the seedlings. *Tian et al., (2022)*, modelled matrix particles of different materials based on the elastic-plastic contact model (ECM) in EDEM to study the interaction between the steel needle and the matrix. Using the response surface method, we investigate changes in matrix loss with different needle diameters, insertion depths, and insertion and grasping speeds. *Liu et al., (2016)*, established a mechanical model for the stage of seedling taking and planting. Combined with the test of the pressure resistance characteristics of the pot, the relevant parameters of the pot suitable for mechanized transplanting were obtained. According to *Jin et al., (2018)*, the high-speed photographic analysis of the collision movement process of the planting device and the seedlings falling to the bottom of the planter established the dynamic model of each stage. *Gao et al., (2017)*, established seedling matrix particle models of various materials based on the extracellular cohesion matrix (ECM) cohesion model and then studied the relationship between the steel needle and the seedling matrix. It is not easy to accurately describe the movement of plug seedlings and pot damage by conventional methods. The discrete element method considers the influence and distribution of physical parameters on particle flow. The velocity and displacement of each particle are solved by Newton's second law and the dynamic relaxation method *(Han et al., 2019; González-Montellano et al., 2012)*. It is especially suitable for studying nonlinear problems such as the pot damage mechanism.

Because there is a multidirectional and complex force chain network between the particles of the pots, it is necessary to input exact simulation parameters to obtain accurate simulation results. At present, individual parameters are mainly measured, but rarely are the parameters of the pot measured in a more comprehensive physical test. In this study, T562 oilseed sunflower plug seedlings were used to study the mechanical characteristics of the drop impact of the whole plug seedling and the pot using the Tekscan pressure distribution measurement system. The Hertz-Mindlin with bonding model was used to build a simulation model of the pot based on essential physical parameters. Taking the collision impact force with a drop height of 350 mm as the target, the PB, steep climb, and Box-Behnken tests were carried out to calibrate the simulation parameters. Simulated collision impact forces are compared with actual collision impact forces to verify the reliability of the model. This study provides a basis for studying the movement of plug seedlings and the pot damage mechanism.

MATERIALS AND METHODS

Test material

In this test, T562 oil sunflower plug seedlings were grown by Inner Mongolia Heyuan Agricultural Technology Corporation. The seedling matrix consisted of grass carbon, vermiculite, and pearlstone with a mass ratio of 3:1:1 *(Zeng et al., 2021)*. The age of the seedlings was 30 d. The water content was 58.78~62.47% by the drying method. The oil sunflower seedlings grew normally, with well-developed root systems knotted together with the seedling matrix to form a strong and flexible pot, as shown in Figure 1.

Fig. 1 – Oil sunflower plug seedlings at the planting stage

Physical test of drop impact between the pots and the whole plug seedlings

As shown in Figure 2, the drop impact test between the plug seedling and the steel plate is composed mainly of a seedling gripper, frame, handle, 5250 flexible thin film network tactile pressure sensor, and computer. The 5250 flexible thin film network tactile pressure sensor, handle, and I-Scan System data processing system make up the Tekscan pressure distribution measurement system *(Hunston, 2002)*. The flexible thin film network tactile pressure sensor is a matrix-based thin film pressure sensor consisting of 2 very thin polyester films. The sensor size is 245.9×245.9 mm, the spatial resolution is 3.2/cm^2, the pressure measurement range is 0~0.179 MPa, and the scanning frequency is 0~100 Hz, as shown in Figure 3. A flexible thin film network tactile pressure sensor was placed at the centre of the seedling gripper for testing *(Agins et al., 2003; Yang et al., 2016)*. During the test, the flexible thin film network tactile pressure sensor sweeps each sensing point and then measures the pressure resistance of each force sensing point. Numerical analysis is performed to convert data on contact stress, contact area, and peak contact stress and generate the corresponding distribution clouds *(Chevalier et al., 2010; Mei, 2021)*.

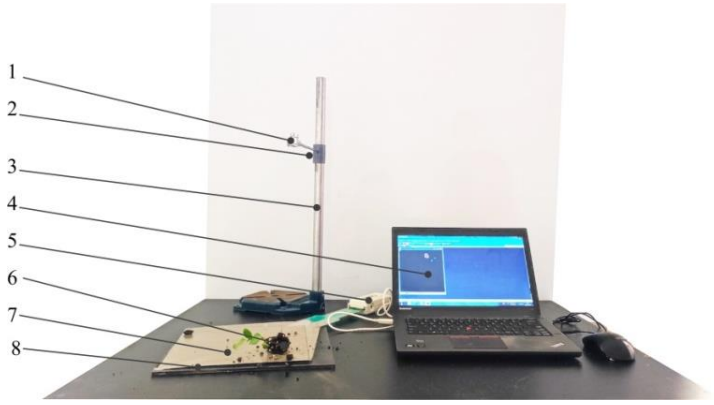

Fig. 2 – Drop impact test on oil sunflower plug seedlings

1. Seedling gripper. 2. Fastening bolts. 3. Frame. 4. Computer and I-Scan System data processing system. 5. Handle. 6. Plug seedlings. 7. 5250 flexible thin film network tactile pressure sensor. 8. The steel plate.

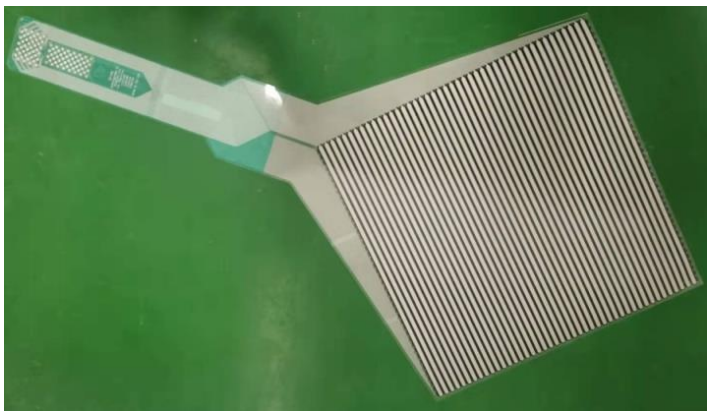

Fig. 3 – 5250 flexible thin film network tactile pressure sensor

The sensor should be calibrated and zeroed before the test. The whole plug seedlings and the pots are dropped against the steel plate at different heights. The steel has a density of 7850 kg/m^3, a Poisson's ratio of 0.3, a shear modulus of 7.0 x 10^{10} Pa, and a thickness of 5 mm. The drop height (h) is the distance from the bottom of the pot to the test plane (Figure 4a).

The test is divided into two main cases, as shown in Figure 4. A steel plate is placed on the test plane, a flexible film network tactile pressure sensor is arranged on it, and the drop impact test of the plug seedling at different drop heights is carried out; The collision between the pot and the steel plate retains the 20 mm stem above the pot so that the seedling gripper can hold the pot. The pots carried out drop impact at different drop heights. This process was repeated in each group several times, and the final value of the average was calculated.

(a) (b)

Fig. 4 – Comparison of whole plug seedlings and pots

a) holding position of the plug seedling; b) whole plug seedling and pot

Determination of the basic parameters of the pot

The mass, density, and other essential parameters of the pot of the T562 oil sunflower plug seedlings are shown in Table 1.

Table 1

Basic physical parameters of the pots

Parameters	Value
Physical dimensions(Top surface × Bottom surface × Height) [mm×mm×mm]	40×20×45
The pot volume [cm^3]	42
Mass [g]	15
Density [kg/m^3]	357

Determination of the restitution coefficient

The restitution coefficient measures the ability of a plug seedling to recover its original shape after a collision and is an essential parameter for analysing changes in the movement of plug seedlings *(Ma et al., 2020)*.The free-falling collision method determined the restitution coefficient of collision between the pot and the steel plate. When the pot falls onto the steel plate, the restitution coefficient *e* is the ratio of the relative velocity of the pot to the steel plate after the collision to the relative velocity before the collision.

$$e= v_2/v_1 \quad (1)$$

Where v_1 and v_2 are the velocities of the pot before and after the collision, m/s.

The pot is under the action of gravity during the falling process. The kinetic energy theorem obtains the normal velocity of the pot before the collision.

$$v_1=\sqrt{2gh_1} \quad (2)$$

Normal velocity after collision:

$$v_2=\sqrt{2gh_2} \quad (3)$$

Therefore,

$$e=\frac{|v_2|}{|v_1|}=\sqrt{\frac{h_2}{h_1}} \quad (4)$$

where v_2 is the normal velocity before the collision, m/s; v_1 is the normal velocity after the collision, m/s; h_1 is the drop height before the collision, mm; and h_2 is the maximum height of the bounce after the collision, mm.

The pots with well-wrapped roots were selected for marking to facilitate the high-speed camera shooting, collision, and rebound effect. The distance between the high-speed camera lens and the test surface was 2000 mm. The marker point of the plug seedling pot fell freely from a height of 350 mm to the steel plate collision and bounced up.

Determination of the restitution coefficient

As shown in Figure 5, the CNY-1 type inclinometer was placed on the horizontal plane *(Zhang et al., 2018)*. The pot was broken up and placed in the cylindrical container to form the cylindrical pot block. The lower surface of the cylindrical container bonded to the test plane of the inclinometer. The inclinometer was turned anticlockwise until the pot was seen to slide. The rotation was stopped, and the angle of the inclination display was recorded at this point.

The static friction coefficient between the pot and pot was calculated from Equation 5. This process was repeated in each group several times, and the final value of the average was calculated. Therefore, the static friction coefficient between the pot and pot is 0.75~0.92; the static friction coefficient between the pot and steel is 0.7~0.88.

$$\mu = \tan \varphi \quad (5)$$

where: μ is the static friction coefficient, and φ is the angle indicated when the pot is about to slide in the plane of determination of the inclinometer, (°).

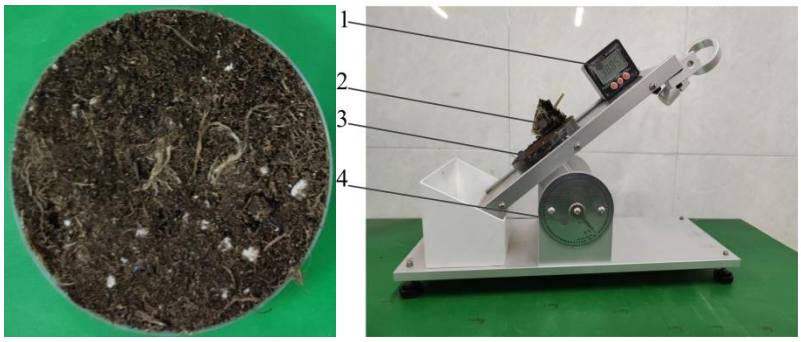

Fig. 5 – Static friction coefficient test between the pot and pot
a) cylindrical pot block; b) static friction coefficient test device

Establishment of the pot contact model

The geometric characteristics of the particles are irregular in the pot, with small holes forming between the particles. The position of the pot particles changes when the pot collides with a vital component of the transplanter *(Ma et al., 2021; Wang, 2016)*. The Hertz-Mindlin with bonding model was chosen as the contact model between the pot's movement and the damage mechanism. In this paper, spherical particles were used as the base particles for the pot model. The particle radius is set to 1.3 mm. The total number of particles was 2587, and the bonding bonds were 42027. The time step was 1%. The data storage time interval is 0.0001 s. The total movement time was 1.6 s. A physical and discrete element simulation model of the plug seedling pot is shown in Figure 6.

Fig. 6 – Physical and discrete element simulation model of the pot

The Hertz-Mindlin with bonding model is based on 5 microscopic parameters: normal bond stiffness S_n, tangential bond stiffness S_t, normal ultimate stress σ_{max}, tangential ultimate stress τ_{max}, and bond radius R_b *(Xiong et al., 2018; Zhang et al., 2019)*. To improve the efficiency of the operation, the bond stiffness and ultimate stress of the pot particles are equal so that $S_n = S_t$ and $\sigma_{max} = \tau_{max}$. The bond radius R_b is usually 1.2~2 times the radius of the particle. Through many drop impact simulations, the initial ranges of the parameters of the discrete element model of the pot, including the bond stiffness, ultimate stress, and bond radius, are 0.2-1.2 MN·m^{-3}, 0.06-0.16 MPa, and 1.56-2.60 mm.

Establishment of the discrete element model of the pot drop impact

First, a discrete element model of dropping impact between the pot and the steel plate was established based on the physical test. Then, the pot particle coordinates were copied into the particle factory data file "Particle_Cluster_Data.txt." The basic information about the pot particles was written into "Particle Replacement prefs.txt." Import the API file "Particlereplacement_v2_x64.dll" with the particle factory into EDEM 2018.

Finally, the parameters were set according to the relevant test scheme, and a simulation was carried out. The discrete element model of the collision between the pot and the steel plate is shown in Figure 7.

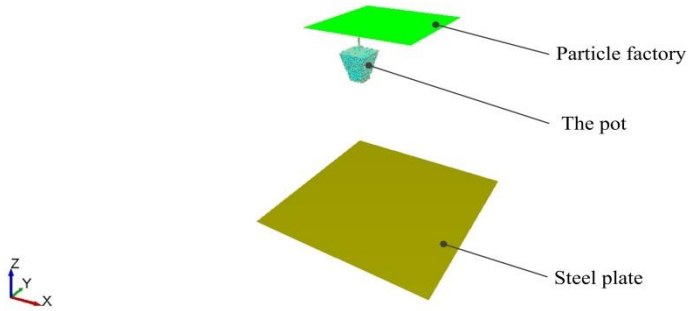

Fig. 7 – Discrete element model of the pot drop impact

RESULTS

Determination of collision impact mechanics between the whole plug seedling and the pot

Analysis of the contact stress distribution characteristics between the whole plug seedling and the pot

The whole oil sunflower plug seedlings and pots were subjected to drop impact tests at different heights. The flexible film network tactile pressure sensor and the I-Scan System data processing system obtained the contact stress and its distribution of the collision between the whole seedling and the pot, as shown in Figure 8. The dark blue area is low stress, the red area is high stress, and the colourless area has a contact stress of 0 kPa. The high stress is located approximately in the centre of the contact area, and the stress values decrease from the centre to the edge of the contact area. As the drop height increases, the low-stress distribution decreases significantly. It is gradually distributed toward the edge of the contact area, while the high-stress distribution gradually increases.

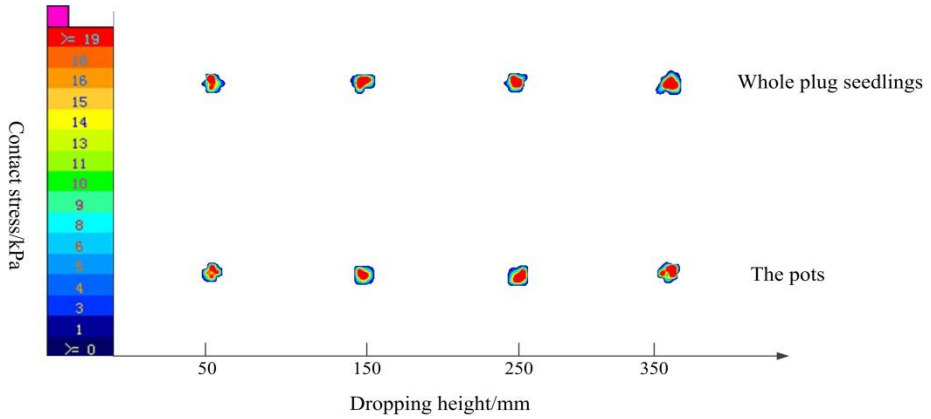

Fig. 8 – Typical stress distribution of dropping impact between whole plug seedlings and the pots

Comparing the collision impact force of the whole plug seedlings and the pots

The I-Scan System is used to process the data to obtain the average contact stress and contact area for a drop impact of an oil sunflower plug seedling. The product of the average contact stress (P) and the contact area (A) is the collision impact force *(Wu et al., 2012)*, as shown in Equation (6).

$$F=P\times A\times 10^{-3} \quad (6)$$

where F is the collision impact force, N; A is the contact area, mm^2; and P is the average contact stress, kPa.

As shown in Table 2, the relative error between the collision impact force of the plug seedlings and the collision impact force of the pot is less than 20%. Therefore, a drop impact test using the pot allows the whole plug seedling to be characterized. It provides support for the discrete element simulation.

Table 2

Comparison of collision impact forces

Type	Dropping height/mm			
	50 mm	150 mm	250 mm	350 mm
Collision impact force of the whole seedlings[N]	4.63	5.37	6.39	7.68
Collision impact force of the pot[N]	3.95	4.75	5.64	6.84
Relative error[%]	14.69	11.55	11.74	10.94

Restitution coefficient test results

The collision process of the pot was recorded with a PCO.dimax S4 high-speed camera. The distance in the horizontal direction is 400 mm, and the displacement in the vertical direction is 700 mm in the image post-processing software TEMA. The vertical displacement curve is shown in Figure 9.

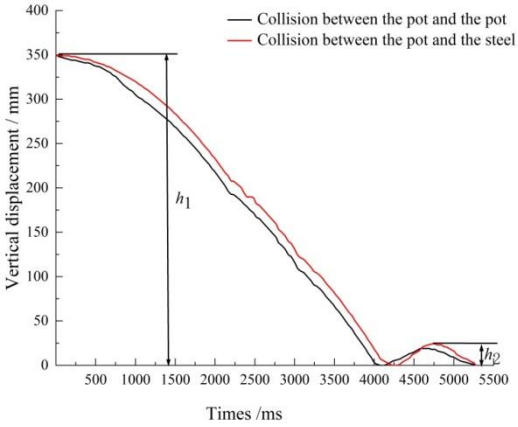

Fig. 9 – Vertical displacement curve

This process was repeated in each group several times, and the final value of the average was calculated. The restitution coefficient between the pot and the pot is 0.26~0.48; the restitution coefficient between the pot and the steel is 0.17~0.24.

Significance parameter selection and analysis of results

The Plackett-Burman experimental design was carried out using Design-Expert 8.0.6 software. The restitution coefficient between the pot and the pot, and the friction coefficient between the pot and steel were determined by high-speed photography and an inclinometer. Additional parameters were consulted in the relevant literature *(Cui et al., 2022; Feng, 2016; Gao, Xie, et al., 2017; Tong et al., 2019)*. A Plackett-Burman test was conducted to identify the parameters that would have significant effect on the collision impact force. Respectively, the maximum and minimum values of the 11 parameters were coded as levels +1 and -1 in Table 3. A total of 12 sets of tests were carried out, with each set being averaged several times to determine the collision impact force. The Plackett-Burman test design and results are shown in Table 4.

Table 3

The Placket - Burman test parameters table

No.	Test parameters	Low level (-1)	High level (+1)
X_1	Poisson's ratio of the pot	0.3	0.44
X_2	Shear strength of the pot [MPa]	1.04	1.76
X_3	the restitution coefficient between the pot and the pot	0.26	0.48
X_4	the static friction coefficient between the pot and pot	0.75	0.92
X_5	the rolling friction coefficient between the pot and pot	0.35	0.43
X_6	the restitution coefficient between the pot and the steel	0.17	0.24
X_7	the static friction coefficient between the pot and steel	0.7	0.88
X_8	the rolling friction coefficient between the pot and steel	0.26	0.3
X_9	Bond stiffness[MN·m^{-3}]	0.2	1.2
X_{10}	Ultimate stress[MPa]	0.06	0.16
X_{11}	Bonding radius[mm]	1.56	2.6

Table 4

The Placket - Burman test design and results

No.	X_1	X_2	X_3	X_4	X_5	X_6	X_7	X_8	X_9	X_{10}	X_{11}	Collision impact force [N]
1	1	1	-1	1	1	1	-1	-1	-1	1	-1	5.39
2	-1	-1	-1	1	-1	1	1	-1	1	1	1	15.11
3	-1	1	1	1	-1	-1	-1	1	-1	1	1	9.86

4	1	1	-1	-1	-1	1	-1	1	1	-1	1	18.14
5	1	-1	1	1	-1	1	1	1	-1	-1	-1	6.33
6	1	-1	1	1	1	-1	-1	-1	1	-1	1	13.7
7	1	-1	-1	-1	1	-1	1	1	-1	1	1	10.91
8	-1	-1	-1	-1	-1	-1	-1	-1	-1	-1	-1	5.82
9	-1	-1	1	-1	1	1	-1	1	1	1	-1	6.38
10	1	1	1	-1	-1	-1	1	-1	1	1	-1	11.54
11	-1	1	1	-1	1	1	1	-1	-1	-1	1	4.35
12	-1	1	-1	1	1	-1	1	1	1	-1	-1	6.99

Determination of the optimal interval

As shown in Table 5, the rolling friction coefficient between the pot and pot (X_5), bond stiffness (X_9), and bond radius (X_{11}) have a significant effect on the collision impact force of the pot. Therefore the steepest climb test was carried out for parameters X_5, X_9, and X_{11}. To further limit the range of parameter values, the relative error between the simulated collision impact force and collision impact force obtained from the physical test (F=6.84 N) was used as the evaluation index, and the average value was used for all insignificant influence parameters. The design and the result of the steepest climb test are shown in Table 6. The results showed that the rolling friction coefficient between the pot and pot (X_5) was 0.35~0.38, the bond stiffness (X_9) was 0.2~0.6 MN·m^{-3}, and the bond radius (X_{11}) was 1.56~1.98 mm.

Table 5

Placket - Burman parameters significant analysis

Parameters	Stdized effect	Sum of Square	Contribution rate/%	Significance ranking
X_1	2.92	25.52	11.98	4
X_2	-0.33	0.33	0.15	10
X_3	-1.7	8.67	4.07	5
X_4	0.04	0.0047	0.002253	11
X_5	-3.18	30.34	14.24	3
X_6	-0.52	0.81	0.38	8
X_7	-0.68	1.37	0.64	6
X_8	0.45	0.61	0.29	9
X_9	4.87	71.05	33.35	2
X_{10}	0.64	1.24	0.58	7
X_{11}	4.94	73.11	34.32	1

Table 6

The test design scheme and results of the steepest climb

No.	Parameters X_5	Parameters X_9	Parameters X_{11}	Collision impact force	Relative error
	[-]	[MN·m^{-3}]	[mm]	[N]	[%]
1	0.35	0.2	1.56	5.81	15.06
2	0.37	0.4	1.77	7.67	12.13
3	0.38	0.6	1.98	9.08	32.75
4	0.40	0.8	2.19	13.32	94.74
5	0.41	1.0	2.40	10.86	58.77
6	0.43	1.2	2.60	8.73	27.63

Collision impact force-simulation parameter regression model establishment

The rolling friction coefficient between the pot and pot X_5, bond stiffness X_9 and bond radius X_{11} were used as test factors. The collision impact force is the response value, and the Box-Behnken module is used to design a 3-factor, 3-level orthogonal test. The test factors and levels are shown in Table 7. A total of 17 tests were carried out and repeated in each group multiple times, and the final value was the average.

Table 7

Test factors and levels

Factors	The level of coding		
	-1	0	+1
The rolling friction coefficient between the pot and pot X_5	0.35	0.37	0.38
Bond stiffness X_9[MN·m^{-3}]	0.2	0.4	0.6
Bonding radius X_{11}[mm]	1.56	1.77	1.98

As shown in Table 8, Design-Expert 8.0.6 software was used to perform multiple regression analyses on the test results of the collision impact force. A quadratic regression model of the rolling friction coefficient between the pot and pot (X_5), bond stiffness (X_9), and bond radius (X_{11}) was established, as shown in Equation 7.

$$\begin{cases} F=9.52-0.57\times X_5+0.45\times X_9-0.40\times X_{11}+2.13\times X_5X_9+ \\ 1.82\times X_5X_{11}-1.51\times X_9X_{11}+1.81\times X_5^2-1.17\times X_9^2-0.44\times X_{11}^2 \end{cases} \quad (7)$$

where:

F is the collision impact force, N; X_5, X_9, and X_{11} are the rolling friction coefficients between the pot and pot, bond stiffness (MN·m^{-3}) and bond radius (mm), respectively.

Table 8

Box-Behnken test design and results

No.	Test factor level value			Collision impact force
	X_5	X_9	X_{11}	[N]
1	0	0	0	9.68
2	-1	0	1	9.67
3	1	-1	0	6.82
4	0	-1	1	8.62
5	-1	0	-1	13.53
6	-1	-1	0	11.97
7	0	-1	-1	6.99
8	0	1	-1	10.24
9	1	0	1	11.92
10	-1	1	0	9.26
11	0	0	0	9.53
12	0	0	0	9.87
13	1	0	-1	8.49
14	0	0	0	9.46
15	0	0	0	9.08
16	1	1	0	12.64
17	0	1	1	5.84

The analysis of variance (ANOVA) results for the above quadratic regression model of collision impact force. The coefficient of determination of the regression Equation R^2=0.9699 and the corrected coefficient of determination adjusted R^2=0.9312 are close to 1, and the coefficient of variation CV=5.60%, so the confidence level of the obtained regression equation is high. The lack of fit P=0.051>0.05 indicates that the regression equation fits well and can better reflect the relationship between collision impact force F and X_5, X_9, and X_{11}.

Table 9

The analysis of variance (ANOVA) on the collision impact force model

Source	Sum of Squares	Freedom	Mean Square	*F* Value	*P* value
Model	65.42	9	7.27	25.05	0.0002**
X_5	2.6	1	2.6	8.96	0.0201*
X_9	1.6	1	1.6	5.52	0.0511
X_{11}	1.28	1	1.28	4.41	0.0738
X_5 X_9	18.19	1	18.19	62.69	<0.0001**
X_5 X_{11}	13.29	1	13.29	45.79	0.0003**
X_9 X_{11}	9.09	1	9.09	31.33	0.0008**
X_5^2	13.86	1	13.86	47.77	0.0002**
X_9^2	5.72	1	5.72	19.72	0.003**
X_{11}^2	0.8	1	0.8	2.76	0.1409
Residual	2.03	7	0.29		
Lack of Fit	1.69	3	0.56	6.51	0.051
Pure Error	0.35	4	0.086		
Cor Total	67.45	16			

*Note: * indicates significant (p<0.05), ** indicates highly significant (p<0.01)*

Selection and verification of optimal parameters

With the optimization module of Design-Expert 8.0.6 software, the collision impact force (*F*=6.84 N) of the physical test measured drop height of 350 mm was used as the target. The software calculated the optimal solution: the rolling friction coefficient between the pot and pot was 0.35, the bond stiffness was 0.53 MN·m^{-3}, and bond radius 1.97 mm. The average value was used for other insignificant influence parameters. The Poisson's ratio was 0.37, and the shear modulus was 1.4 MPa. The restitution coefficient between the pot and the pot was 0.37. The static friction coefficient between the pot and the pot was 0.84, the restitution coefficient between the pot and the steel was 0.21, the static friction coefficient between the pot and the steel was 0.79, the rolling friction coefficient between the pot and steel was 0.28, and the ultimate stress was 0.11MPa. The simulation results are compared with the physical test, and the relative error is 3.65%. Therefore, the pot model established by this simulation parameter can represent the actual drop impact of the pots.

CONCLUSIONS

(i) The Tekscan pressure distribution measurement system was used to measure the mechanical characteristics of the drop impact between the whole plug seedlings and the pots. The relative error between the collision impact force of the plug seedlings and the collision impact force of the pots is less than 20%.

(ii) The Plackett-Burman test and the steepest climbing test determined the significant parameters and optimal intervals affecting the collision impact force: the rolling friction coefficient between the pot and pot was 0.35~0.38, the bond stiffness was 0.2~0.6 MN·m^{-3}, and the bond radius was 1.56~1.98 mm.

(iii) The Box-Behnken test was performed on the significance of the parameters, and the quadratic regression model of the collision impact force was developed. Taking the collision impact force with a drop height of 350 mm as the target, the optimal solution was obtained: the rolling friction coefficient between the pot and pot was 0.35, the bond stiffness was 0.53 MN·m^{-3}, and bond radius was 1.97 mm. The average value was used for other insignificant influence parameters. The simulation results were compared with the physical test, and the relative error was 3.65%. Therefore, the pot model established by this simulation parameter can represent the actual drop impact of the pots.

ACKNOWLEDGEMENT

This project was funded by National Natural Science Foundation of China (NSFC) (32160423) and the Natural Science Foundation of the Inner Mongolia Autonomous Region of China (2020MS05055).

REFERENCES

[1] Yang, Q. Z., Xu, L., Shi, X. Y., Ibrar, A., Mao, H. P., Hu, J. P., & Han, L. H. (2018). Design of seedlings separation device with reciprocating movement seedling cups and its controlling system of the full-automatic plug seedling transplanter. *Computers and Electronics in Agriculture, 147*, 131-145. https://doi.org/10.1016/j.compag.2018.02.004

[2] Zhao, X., Zhang, X. S., Wu, Q. P., Dai, L., & Chen, J. N. (2020). Research and experiment of a novel flower transplanting device using hybrid-driven mechanism. *International Journal of Agricultural and Biological Engineering, 13*(2), 92-100. https://doi.org/10.25165/j.ijabe.20201302.5187

[3] Han, L. H., Francis, K., Mao, H. P., & Hu, J. P. (2019). Design and tests of a multi-pin flexible seedling pick-up gripper for automatic transplanting. *Applied Engineering in Agriculture, 35*(6), 949-957. https://doi.org/10.13031/aea.13426

[4] Wen, Y. S., Zhang, L. A., Huang, X. M., Yuan, T., Zhang, J., Tan, Y., & Feng, Z. (2021). Design of and experiment with seedling selection system for automatic transplanter for vegetable plug seedlings. *Agronomy, 11*(10), 2031.

[5] Ryu, K. H., Kim, G. Y., & Lee, H. H. (2001). Development of a robotic transplanter for bedding plants *Journal of Agricultural Engineering Research, 78*(2), 141-146.

[6] Jiang, Z. H., Hu, Y., Jiang, H. Y., & Tong, J. H. (2017). Design and force analysis of end-effector for plug seedling transplanter. *Plos One, 12*(7), 1-15.

[7] Yang, Ting, K. C., & Giacomelli, G. A. (1991). Factors affecting performance of sliding-needles gripper during robotic transplanting of seedlings. *Applied Engineering in Agriculture, 7*(4), 493-498.

[8] Mao, H. P., Ma, G. X., Han, L. H., Jian, P. H., Gao, F., & Liu, Y. (2021). A whole row automatic pick-up device using air force to blow out vegetable plug seedlings. *Spanish Journal of Agricultural Research, 18*(4). https://doi.org/10.5424/sjar/2020184-17003

[9] Tian, Z. W., Ma, W., Yang, Q. C., Yao, S., Guo, X. Y., & Duan, F. M. (2022). Design and experiment of gripper for greenhouse plug seedling transplanting based on EDM. *Agronomy, 12*(7). https://doi.org/10.3390/agronomy12071487

[10] Liu, J. D., Cao, W. B., Tian, D. Y., Ouyang, Y. N., & Zhao, H. Z. (2016). Optimization experiment of transplanting actuator parameters based on mechanical property of seedling pot（基于苗钵力学特性的自动移栽机执行机构参数优化试验）. *Transactions of the CSAE, 32*(16), 32-39.

[11] Jin, X., Ji, J. T., Liu, W. X., He, Y. K., & Wu, D. X. (2018). Structural optimization of duckbilled transplanter based on dynamic model of pot seedling movement（基于钵苗运动动力学模型的鸭嘴式移栽机结构优化）. *Transactions of the CSAE, 34*(09), 58-67.

[12] Gao, G. H., Wang, K., & Sun, X. N. (2017). Verification for EDEM simulation of process of jacking tray-seedling by steel needle in grafting machine and parameter optimization（嫁接机钢针顶起穴盘苗过程EDEM模拟验证及参数优化）. *Transactions of the CSAE, 33*(21), 29-35.

[13] Han, B., Shen, D. S., Guo, C., Liu, Q., Wang, X., & Song, C. B. (2019). Design and experiment of adjustable end-effector of cabbage seedlings（可调节式甘蓝钵苗取苗末端执行器设计与试验）. *Transactions of the CSAM, 50*(11), 111-120.

[14] González-Montellano, C., Fuentes, J. M., Ayuga-Téllez, E., & Ayuga, F. (2012). Determination of the mechanical properties of maize grains and olives required for use in DEM simulations. *Journal of food engineering, 111*(4), 553-562. https://doi.org/10.1016/j.jfoodeng.2012.03.017

[15] Zeng, F. D., Li, X. Y., Li, X., Su, Q., & Zhang, Y. Z. (2021). Experiment and analysis of high-speed photographic techniques for throwing motion of seedlings（基于高速摄影技术穴盘苗抛投运动试验与分析）. *Journal of China Agricultural University, 26*(09), 168-176.

[16] Hunston, M. (2002). Innovative thin-film pressure mapping sensors. *Sensor Review, 22*(4), 319-321.

[17] Agins, H. J., Harder, V. S., Lautenschlager, E. P., & Kudrna, J. C. (2003). Effects of sterilization on the Tekscan digital pressure sensor. *Med Eng Phys, 25*(9), 775-780. https://doi.org/10.1016/s1350-4533(03)00119-x

[18] Yang, L. J., Zhang, Y., Liu, D. H., Xu, B. P., & Liu, C. X. (2016). Early recognition for dairy cow lameness based on pressure distribution measurement system（基于压力分布测量系统的奶牛跛行早期识别）. *Transactions of the CSAM, 47*(S1), 426-432.

[19] Chevalier, T. L., Hodgins, H., & Chockalingam, N. (2010). Plantar pressure measurements using an in-shoe system and a pressure platform: a comparison. *Gait Posture, 31*(3), 397-399. https://doi.org/10.1016/j.gaitpost.2009.11.016

[20] Mei, Y. (2021). *Research on the bionic mechanism and coupled bionic design method of green tire pattern structure* [Doctor's thesis], Jiang Su University.

[21] Ma, Y. H., Song, C. D., Xuan, C. Z., Wang, H. Y., Yang, S., & Wu, P. (2020). Parameters calibration of discrete element model for alfalfa straw compression simulation（苜蓿秸秆压缩仿真离散元模型参数标定）. *Transactions of the CSAE, 36*(11), 22-30.

[22] Zhang, T., Liu, F., Zhao, M. Q., Ma, Q., Wei, W., Qi, F., & Peng, Y. (2018). Determination of corn stalk contact parameters and calibration of discrete element simulation（玉米秸秆接触物理参数测定与离散元仿真标定）. *Journal of China Agricultural University, 23*(04), 120-127.

[23] Ma, G. X. (2021). *Study on enhancement mechanism of low loss seedling picking in biochar and air ejection-package clamping pick-up device* [Doctor's thesis], JiangSu University.

[24] Wang, Y. Y. (2016). *Key technologies of vegetable plug seedlings transplanting based on machine vision and simulation test* [Ph.D. dissertation Doctor's thesis], Jilin University.

[25] Xiong, P. Y., Yang, Z., Sun, Z. Q., Zhang, Q. Q., Qing, H. Y., & Wei, Z. Z. (2018). Simulation analysis and experiment for three-axis working resistances of rotary blade based on discrete element method（基于离散元法的旋耕刀三向工作阻力仿真分析与试验）. *Transactions of the CSAE, 34*(18), 113-121.

[26] Zhang, L. F., Song, X. F., Zhang, X. K., Zhang, F. Y., Cheng, W. W., & Fei, D. (2019). Simulation and experiment on mechanical characteristics of kneading and crushing process of corn straw（玉米秸秆揉丝破碎过程力学特性仿真与试验）. *Transactions of the CSAE, 35*(09), 58-65.

[27] Wu, J., Guo, K. Q., Ge, Y., & Wang, Y. Y. (2012). Contact pressure distribution characteristics of Korla pear fruit at moment of drop impact（香梨果实跌落碰撞时的接触应力分布特性）. *Transactions of the CSAE, 28*(01), 250-254+300.

[28] Cui, Y. J., Wei, Y. Z., Ding, X. T., Cui, G. P., He, Z., & Wang, M. H. (2022). Design and experiment of adjustable spacing end-effector based on cylindrical cam（基于圆柱凸轮的株距可调式取苗末端执行器设计与试验）. *Transactions of the CSAM, 53*(01), 104-114+122.

[29] Feng, T. X. (2016). *Optimization design and test research of plug seedings end-effector in greenhouse* [Master's thesis], Beijing University of Technology.

[30] Gao, G. H., Xie, H. F., & Wang, T. B. (2017). EDEM simulation and experiment of pullout force of protected vegetable harvester（设施蔬菜收获机拉拔力学性能 EDEM 仿真与试验）. *Transactions of the CSAE, 33*(23), 24-31.

[31] Tong, J. H., Shi, H. F., Wu, C. Y., Ding, Y. H., Zhao, X., & Wang, R. Y. (2019). Simulation and test of seedling pot grabbing by spade end-effector（穴盘移栽指铲式末端执行器苗钵基质抓取仿真与试验）. *Transactions of the CSAM, 50*(08), 107-116.

ASPECTS REGARDING THE COMPACTION OF CARDBOARD WASTE IN VERTICAL PRESSES WITH DISCONTINUOUS FLOW

/

ASPECTE PRIVIND COMPACTAREA DEȘEURILOR DIN CARTON ÎN PRESE VERTICALE CU FLUX DISCONTINUU

Gheorghe VOICU[1)], Mircea-Bucur LAZEA*[2)], Gabriel-Alexandru CONSTANTIN[1)], Paula TUDOR*[1)], Elena-Madalina STEFAN[1)]

[1)] University POLITEHNICA of Bucharest / Romania; [2)] CCR RO Waste Management Systems / Romania

Tel: +40724715585; E-mail: paulavoicu85@yahoo.com; +40753044289; E-mail: mircealazea2005@yahoo.com

DOI: https://doi.org/10.35633/inmateh-68-63

Keywords: *compaction, vertical press, cardboard waste, multiple stages, resisting force, energy consumed*

ABSTRACT

The paper analyses the compaction of cardboard waste in vertically stationary presses, the stages of making the bale of material and the forces resistant to the displacement of the cardboard pressing plate at each stage of compaction, the relationship between the piston stroke and the pressing forces, as well as the partial and total energy consumption of compaction. Some clarifications are made regarding the correlation between the piston stroke and the compaction time, respectively the forces resistant to compaction. A link shall also be established between the volume of pressed material and its mass, so that the final density of the bale of material can be specified.

ABSTRACT

Lucrarea analizează compactarea deșeurilor din carton în prese vertical staționare, etapele realizării balotului de material și forțele rezistente la deplasarea plăcii de presare a cartoanelor în fiecare etapă a compactării, relația dintre cursa pistonului și forțele de presare, precum și consumul de energie partial și total al compactării. Se fac unele precizări legate de corelația dintre cursa pistonului și timpul de compactare, respectiv forțele rezistente la compactare. De asemenea, se stabilește o legătură între volumul de material presat, masa acestuia, astfel încât să se poată preciza densitatea finală a balotului de material.

INTRODUCTION

There are many companies that collect paper and cardboard waste in Romania, but there are few companies that process it for recycling and re-use. Therefore, the integrated process of recovery and recycling of cardboard includes several stages and operations, when we think about using cardboard waste for other purposes than a primary source of heat.

Recycle and reuse of cardboard is a common method of solid waste management which can be easily transformed into other objects, especially for large packaging (*Esmieo, Shaklawon and Ali Shanab, 2018*). Cardboard recycling means the reprocessing and reuse of thick sheets or rigid multi-layered paper primarily for the packaging of large products, including primarily cardboard boxes, but also other categories. First of all, the municipality is responsible for transporting the cardboard to the final disposal site outside the waste site, but the cardboard collectors also have an interest in passing these categories of waste to processors and recyclers (*Esmieo, Shaklawon and Ali Shanab, 2018; Naveen and Sivapullaiah, 2020; Kumar and Agrawal, 2020*).

Recycled cardboard and paper waste, recovered from municipal waste mixtures, can be a good source both for obtaining energy and for treating waste water (from which suitable filters can be made), increasing sustainability and the circular economy in the circuit of recovery and recycling of paper and cardboard (*Peretz et al., 2021*). This waste can also be an important source of cellulosic biomass, used as a substrate for cellulase production, by treatment with sulfuric acid (*Al Azkawi, Sivakuma, Al Bahr, 2018*).

Studies have been carried out to see if cardboard waste can be used as a partial substitute for aggregates to produce lighter, greener and cheaper building bricks in advanced research in the field of innovative sustainable building materials (*Ahmad et al., 2018*).

The results showed, however, that using cardboard as a partial substitute for aggregates leads to obtaining bricks with low strength, which can only be used for non-load-bearing interior walls.

In the recovery of cardboard waste, compacting it to form larger bales that can be stored for a longer period and transported more easily is a basic operation. This can be done with the help of presses, vertical or horizontal, stationary or movable, with continuous or discontinuous flow, of different capacities. In this way, the costs of storage, transport and disposal are thus greatly reduced due to the regular shape of the bales and the increased volumetric mass in relation to the volumetric mass of bulk cartons (*Lazea M.B. et al., 2021*).

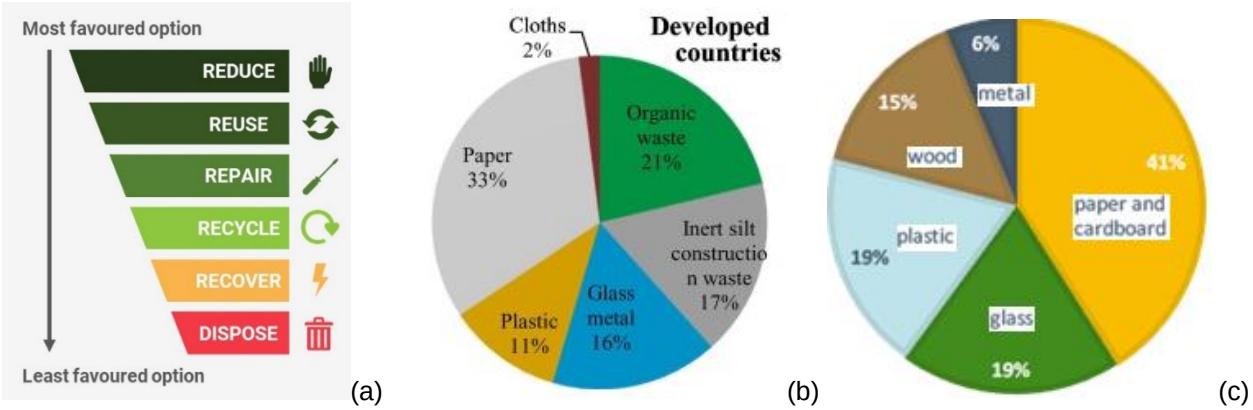

(a) (b) (c)

b) Municipal waste composition ; c) Packaging waste composition (*Collectors, 2020*)

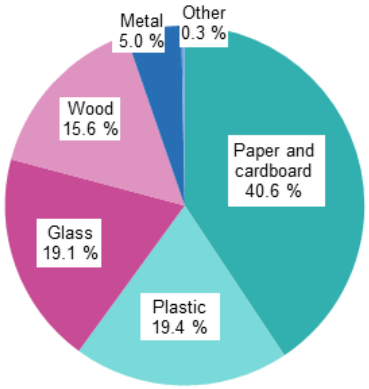

(d)

d) Packaging waste generated by packaging material, (*Eurostat, 2019*)

Fig. 1 – Options in waste management (a) and the composition of municipal waste, respectively packaging, according to several sources (b, c, d)

According to Eurostat (2019), in the EU the participation of paper and cardboard waste in the total waste generated by the recovery from the packaging of products and goods of any nature is about 40.6%, while plastic has a participation of only 19.4%. Finally, the pertinent conclusion can be drawn that paper and cardboard waste is an important raw material for a variety of products, in the most diverse fields of activity. The technological processes of recycling those wastes can lead to the production of composite materials, cellulose nanofibers and nanocrystals, light bricks, porous carbon, bioethanol, hydrogen and biofuel. However, the most feasible and economical would be their use in the production of cellulosic nanomaterials (nanofibers and nanocrystals) (*Ozola et al., 2019*).

As part of mitigating the problem of increasing amounts of paper (and cardboard) waste generated that end up being deposited at municipal waste dumps or being burned, in their paper, *Osamwonyi, Okokpujie and Dirisu,* (*2018*), proposed the design of a horizontal waste paper baler. Design parameters included maximum compression force (10 KN), piston rod travel distance, respective piston stroke (609 mm), time of a work cycle (9 minutes) and hydraulic system pressure.

The conclusion was that such compacting presses can be designed and made according to local needs, in different sizes and according to the nature of the waste that should be compacted and baled.

This work aims to present some information regarding the behaviour of packaging cardboard waste in the process of compaction and baling in stationary vertical presses, with fixed volume, with a discontinuous work process, both in terms of bale formation stages, but also of energy consumption in stages.

MATERIALS AND METHODS

Cardboard waste that occurs in various processes, or from the packaging of relatively large products, needs to be compacted before being sent to recycling for reuse. Their compaction can be done in stationary vertical presses with discontinuous flow or in horizontal presses with continuous flow. The compaction process takes place in several stages, because it is necessary to reduce the dimensions of the volume of material introduced into the press and to compact a large amount of waste, the volume of the pressing chamber being fixed. So, by pressing the first volume of material introduced into the press, it is reduced in volume sufficiently to add another volume of material, relatively identical to the first, followed by compaction in the second stage and again the addition of another volume of material, followed by of further compaction until the press chamber can no longer receive material due to the increase in the density of the material introduced sufficiently long and the force resisting compaction over the force made by the hydraulic piston.

In our experiments, we used a vertical press, with discontinuous flow, PP 1207 (Strautman, Germany), which can develop a maximum force of 50 tf, having a pressing chamber fed from the front by means of a sliding door (fig. 2).

Fig. 2 - Baler press PP-1207 for experiments and the tied bale obtained after compaction/baling

The cartons used in the experiments were recovered from the store network and were of various sizes and shapes, in several layers. There was no analysis of their structure and no prior sorting.11.5 kg of cardboard waste was initially introduced into the pressing chamber, the volume being calculated based on the transverse dimensions of the pressing chamber and the height of the chamber at the moment the cartons are touched by the pressure plate, which is about 0.2 m^3. The data of the experiments carried out are shown in Table 1, the bale formation taking place in seven relatively identical stages, in terms of the amount of material added to the baling chamber and the way of working. It should be noted that the maximum working capacity and performance of the machine specified by its technical book have not been reached.

Moreover, no initial processing of the cartons was carried out, they were not shredded and their dimensions were not reduced, so they were placed in the pressing chamber in accordance with the free volume of the chamber which allowed the introduction of equal amounts of cartons.

RESULTS

Having available the data from Table 1 (*Lazea et al, 2021*), the variation curves of the resistant forces were drawn graphically (in Excel) according to the displacement of the compaction plate, for all the 7 samples mentioned before, so that the resulting bale had about 80.5 kg.

It is found that the variation of the resisting force with the displacement of the pressure plate does not follow a predetermined trajectory, even if in principle it is an upward-sloping curve, the resisting force depending on the random placement of the cartons in the press chamber, with gaps unevenly distributed between the inserted cartons in the press.

There are several similar curves, the maximum resistance force registering very close values mainly due to the way the hydraulic circuit of the press is made.

Table 1

Variation of pressure forces with compaction piston displacement for the seven samples *(Lazea et al., 2021)*

Time, (s)	P1		P2		P3		P4		P5		P6		P7	
	V= 0.2 m³ m = 11.5 kg		V= 0.4 m³ m = 23 kg		V= 0.6 m³ m = 34.5 kg		V= 0.8 m³ m = 46 kg		V= 1.0 m³ m = 57.5 kg		V= 1.2 m³ m = 69 kg		V= 1.3 m³ m = 80.5 kg	
	Displacement (mm)	Force (daN)	Displacement (mm)	Force (daN)	Displacement (mm)	Force (daN)	Displacement (mm)	Force (daN)	Displacement (mm)	Force (daN)	Displacement (mm)	Force (daN)	Displacement (mm)	Force (daN)
1	183	457	233	258	231	153	183	193	236	128	246	148	183	278
2	231	633	271	912	270	914	237	258	267	390	277	410	221	932
3	385	705	347	980	342	982	336	372	336	458	346	478	297	985
4	523	742	432	992	422	992	529	416	418	510	428	530	382	997
5	645	772	523	980	510	981	630	521	479	563	489	583	473	985
6	810	960	595	967	602	962	725	586	555	631	565	602	545	972
7	958	955	671	968	668	961	802	632	626	766	636	646	621	973
8	1099	968	758	966	748	965	868	662	692	802	702	701	708	971
9	1244	980	824	967	817	968	902	706	760	861	770	782	774	972
10	1323	979	896	967	892	968	950	803	838	912	848	893	846	972
11			975	966	991	970	1026	852	905	983	915	978	925	971
12			1035	977	1042	975	1111	876					985	982
13			1234	977	1302	977	1194	921					1184	982
14							1235	961						
15							1278	979						
Energy, J	**673**		**1544**		**1536**		**1292**		**1065**		**1027**		**1554**	

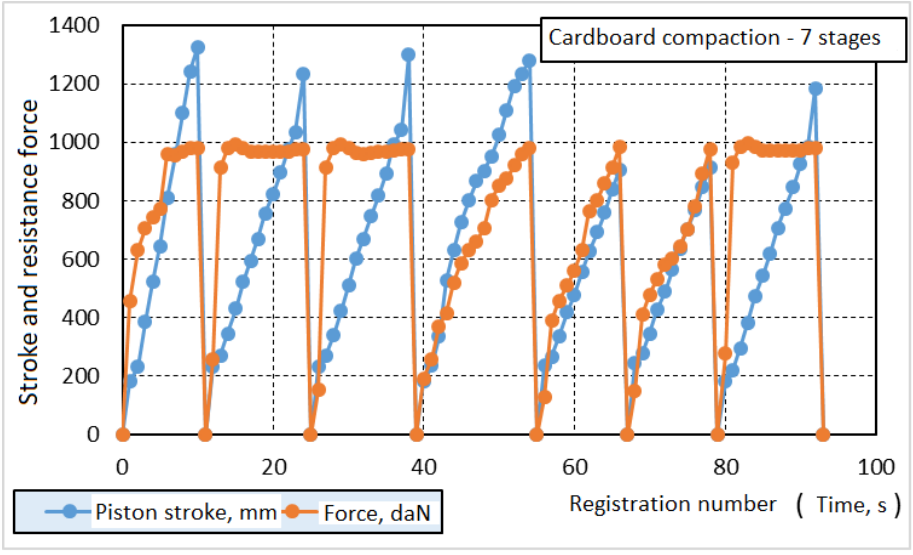

Fig. 3 - Pressure forces and displacement of the pressure plate when compacting cardboards

From the analysis of the data in the table and the graphs in fig.3, it is observed that the displacement of the pressure plate reaches relatively high values not only at the first stages of compaction, but also in the final

phase of compaction, even if the highest displacement value has been reached at the first compression (about 1323 mm), the stroke from which the records of the force resistant to compaction begin, having minimum values of about 183-236 mm. The values of the resistance to compaction force are between 977 - 983 daN, which means that at higher values the resistance sensor in the hydraulic circuit is activated and it gives a signal to retract the pressure plate.

Based on the graphs drawn in the MS Office Excel program, the areas under the force-displacement curves (fig. 4) were determined, which represent the energy consumed in each stage of the compaction process, and its values are presented at the bottom of table 1.

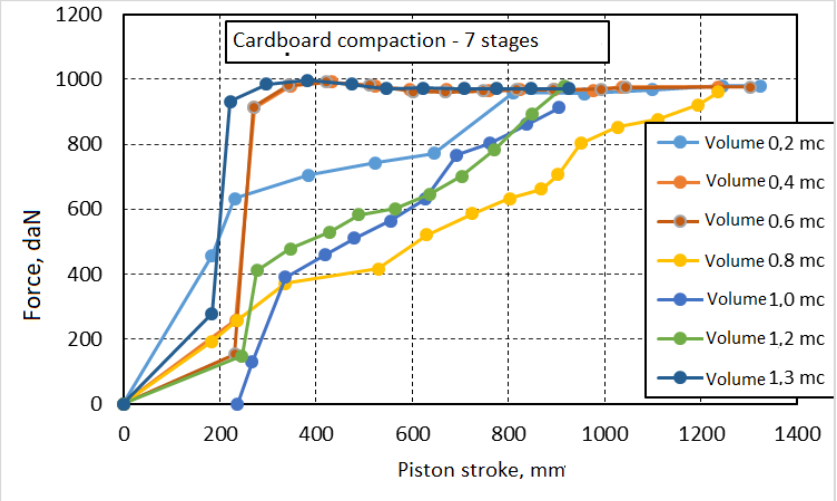

Fig. 4 - Force variation – displacement when loading the press with pressed cardboard in 7 similar stages

It is found that the lowest energy consumption is during the first compaction, when there is a small amount of cartons inside the press, in the following stages the energy consumed increases with the amount of cartons added and with the parameters of the process – force – displacement. However, the placement of the cartons in the press premises also has a determining role, this having a random character.

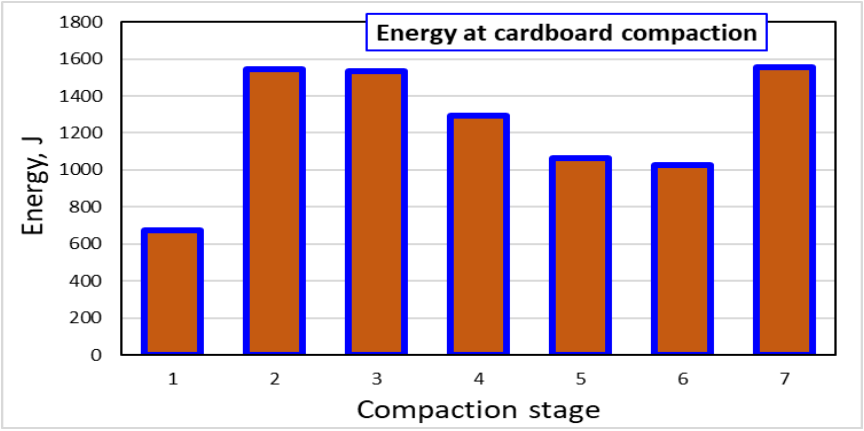

Fig. 5 - Variation of energy when compacting cartons in the 7 stages of compaction

In the separate representation of the stroke of the pressure plate, simultaneously for the 7 stages of compression, the upward slope of the stroke is better observed in correlation with the increment time, which was set to 1 second (fig.5).

At the same time, even if the trend is clearly linear (as shown by the values of the regression coefficient ($R^2 \geq 0.9723$), the plate movement speed is not a constant one, depending on the resistance encountered during compaction and on the random placement of the cartons, and the circuit hydraulically adjusts the speed according to the sensed force. It is found that the speed has values between 69 mm/s (stages 5 and 6) and 135.7 mm/s (at the first stage of compaction). Practically, the actual compaction starts from the moment the material is detected by the pressure plate in its downward stroke.

The data records show the constancy of the volume of cardboard waste introduced/added to the press chamber at each stage of compaction, i.e. the constant increase of the amount introduced.

Based on the volume of material in the press chamber and its bulk volume (placed in the press chamber), the constancy of the density of the material is also observed (fig.8).

In Table 1 and figures 5-7, it can be seen the variation of the pressing force during the seven stages of compacting the cartons until the moment of tying the bale, as well as the variation of the stroke of the piston (pressing plate) and the energy consumed in the process.

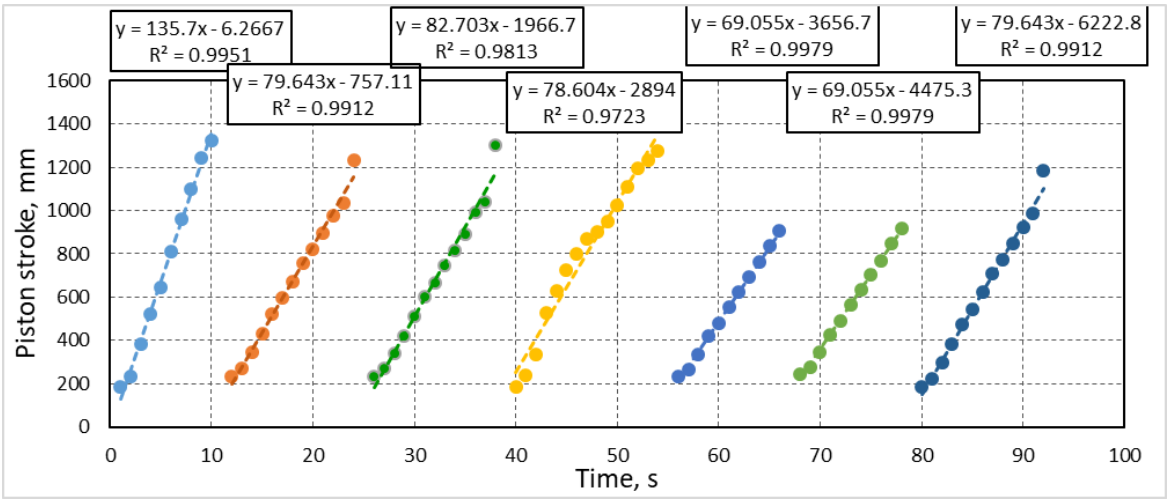

Fig. 6 - The variation of the stroke of the pressure plate when compacting the cartons in the 7 stages

From the regression analysis of the experimental data, respectively of the compaction force with the stroke of the pressure plate, a different variation is found in the seven stages of bale formation, which does not have to be the same every time. This is due to several factors, which are also random: the type and thickness of the cartons, the way they are placed in the pressing chamber, the differentiated arrangement front-back, respectively left-right, the moment the cartons are touched by the pressing plate, etc.

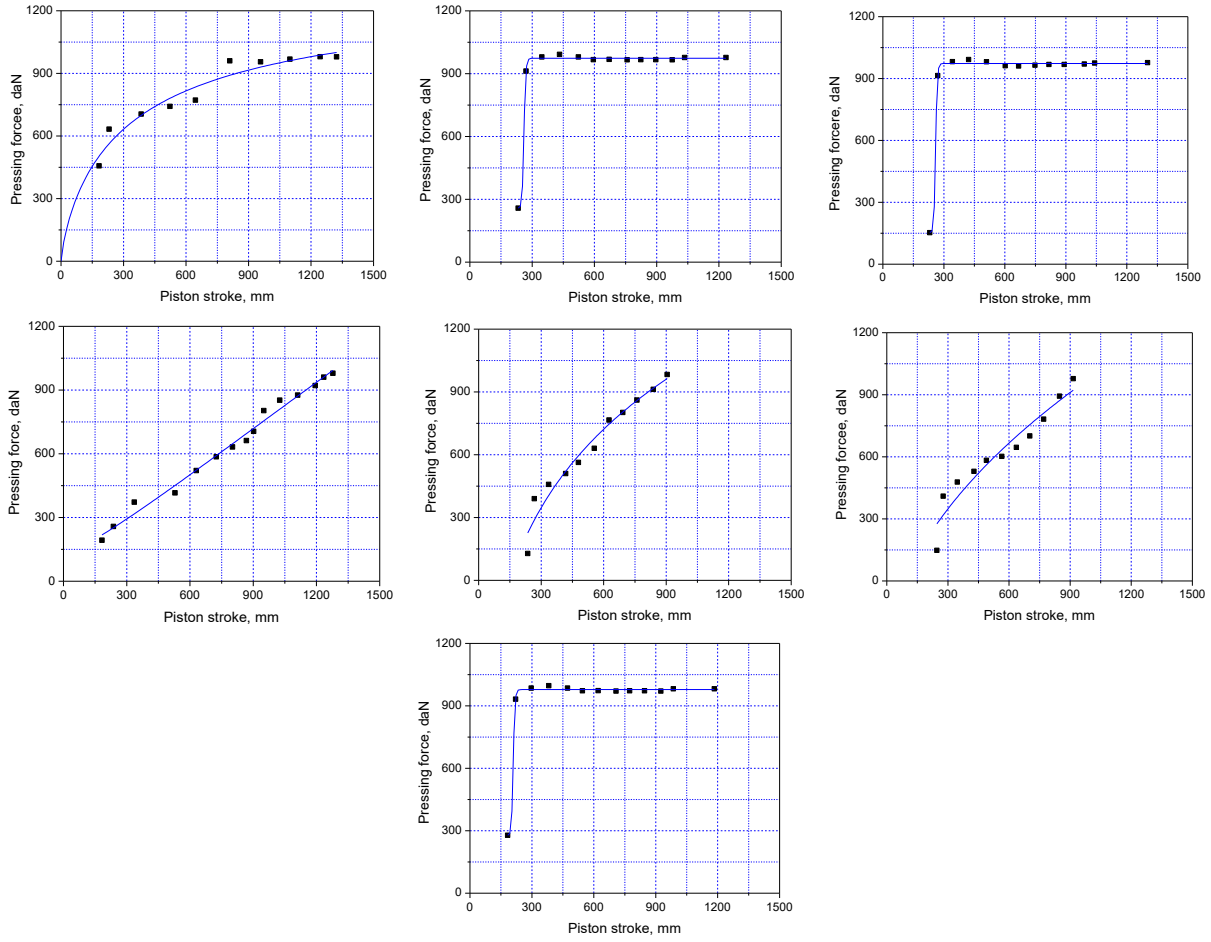

Fig. 7 – The variation of the pressing force with the stroke of the piston, in the 7 stages of compaction

Table 2

Values of the parameters of the logistic regression equation (1) and of the coefficient of determination R^2

	P1	P2	P3	P4	P5	P6	P7
A_1	-0.264	257.218	152.533	122.696	-2107.177	-403.804	277.32
A_2	1347.083	973.364	972.818	7825.699	12500.324	95556.463	978.36
x_o	349.572	260.650	259.457	7202.908	178492.12	$3.7 \cdot 10^6$	209.78
p	0.796	60.794	64.289	1.192	0.250	0.514	50.80
R^2	0.980	0.998	0.999	0.988	0.959	0.920	0.998

$$y = A_2 + \frac{A_1 - A_2}{1 + \left(\frac{x}{x_o}\right)^p} \quad (1)$$

The regression analysis carried out shows a logistic correlation, according to the relation (x), between the compaction resistance force and the stroke of the pressing plate. Although the stroke of the pressing plate shows a linear correlation with the pressing time, we could tend to say that the pressing force has a similar correlation. Yes, this is valid for portions, for areas of the press room (on its vertical), but overall the regression shows us a very good logistic correlation, as said before.

This is represented by the high values of the correlation coefficient R^2, which has very high values (between 0.920 and 0.999), even if looking at the graphs we could say that they are not true, but the analysis program used (Microcal OriginPro 8.0) validated the values presented, together with the coefficients and values of the relationship parameters (1) (see Table 2).

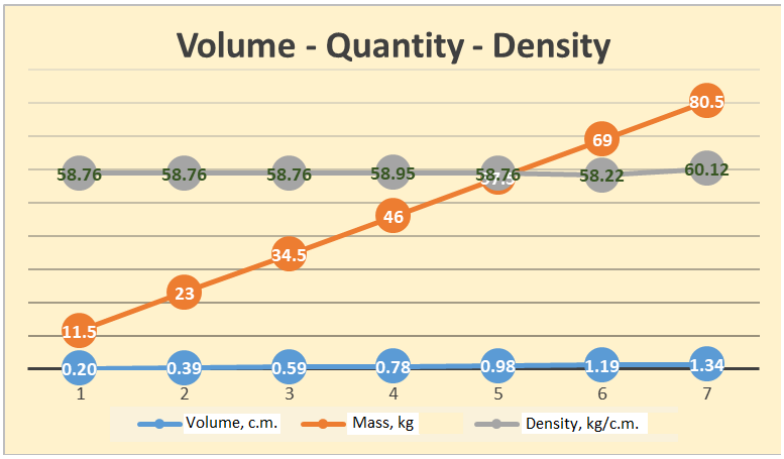

Fig. 8 - The variation of the amount of material, the volume and the density at the initial moments of the compaction stages of cardboard waste

Figure 6 clearly shows the linear variation of piston stroke with press time (having a constant step of 1 second), even though the slope of the line changes depending on the amount of material in the press chamber and the resistive force encountered by it. It should be mentioned here that the characteristics of the cartons in the pressing room and their (random) placement influence both the characteristics of the regression lines and the changes in the pressing resistance force.

A bale is formed in several successive stages (7 stages), in which the machine is successively fed with a relatively close amount of material in terms of volume and mass, in each feeding stage. Therefore, the mass of the final bale is the sum of the masses of the seven consecutively added charges, while the volume of the bale depends on the pressure with which the material is pressed and the resistance of the previously formed bales, and found in the discharge channel. From fig. 8 it is found that the density of the bale increases with each stage of the process, in the end the volumetric mass of the bale can reach values of around 60-70 kg/m^3.

CONCLUSIONS

The elucidation of the movement of the working parts of these mechanisms is necessary for a good understanding of their operation, but especially in order to redesign and improve their functional parameters for an operation without loss of material and with low energy consumption.

From the studies carried out, it was sought to determine the relationship between the pressure applied to the material (waste) in the compaction chamber and the density (densification) of the material.

The dynamic simulation brought results that can be verified in reality, regarding the mechanical behaviour of the studied components.

From the authors' determinations, the maximum compaction/pressing force in each of the seven stages of cardboard waste bale formation has values below 1000 daN, while the total compaction energy is around 8.0-9.0 kJ.

In the future, a complex analysis of the compaction equipment must be made, this being necessary for a system with dynamic data, taking into account the influence of the chassis on the movement of the active parts, referring here to the compaction of waste in the space of municipal waste collection machines, either selected/sorted or unselected.

ACKNOWLEDGEMENT

This research was supported, among others, by Executive Unit for Financing Higher Education, Research, Development and Innovation, UEFSCDI, under the PNCDI III – Programme 2, sub-programme 2.1., as follows partially from: submission code PN-III-P2-2.1-PTE-2019-0446, funding contract no. 53PTE/23.09.2020, project title “Hydrophilic auto-chassis for high energy efficiency operation of interchangeable equipment intended for performing public utility work”, acronym ASHEUP, research direction 3.Econano-technologies and advanced materials, subdomain Advanced materials and submission code PN-III-P2-2.1-PED-2019-4123, funding contract no. 380PED/23.10.2020, project title “Multifunctional hexa-rotors tricopter for precision farming”, acronym 4.0-MHRT, project domain 1.Bioeconomics, subdomain 1.1.

REFERENCES

[1] Ahmad A., Rahman M., Khalil A., Adil M., Khan M. (2018). Efficient Use of Waste Cardboard in Construction Material, *4th Conference on Sustainability in Process Industry (SPI-2018)*, 2018, Peshawar, Pakistan, pag.23-27, https://www.researchgate.net/publication/340938347.

[2] Al Azkawi A.S., Sivakuma, N., Al Bahr S. (2018). Bioprocessing of cardboard waste for cellulase production, *Biomass Conversion and Biorefinery*, 8, 597–606, https://doi.org/10.1007/s13399-018-0309-7.

[3] Esmieo M., Shaklawon M., Ali Shanab O. (2018). Feasibility Study of Cardboard Waste Recycling, *First Conference for Engineering Sciences and Technology*, https://doi.org/10.21467/proceedings.4.38.

[4] ***Eurostat, Packaging waste statistics - Statistics Explained, European Commission - European Union, https://ec.europa.eu/eurostat/statistics-explained/index.php?title=Packaging_waste _statistics&oldid=559603 (accessed 01 October 2022).

[5] Kumar A., Agrawal A. (2020). Recent trends in solid waste management status, challenges, and potential for the future Indian cities – A review, *Current Research in Environmental Sustainability*, vol. 2, https://doi.org/10.1016/j.crsust.2020.100011.

[6] Lazea M.B., Voicu Gh., Constantin G.A., Tudor P., Zabava B.S. (2021). Some aspects regarding compaction of plastic bottles in stationary vertical presses, *Engineering for Rural Development*, Jelgava, Vol. 20, pp. 174–180, (171143), https://doi.org/10.22616/erdev.2021.20.tf036.

[7] Naveen B.P., Sivapullaiah P.V. (2020). Solid Waste Management: Current Scenario and Challenges in Bengaluru, *Sustainable Sewage Sludge Management and Resource Efficiency*, 146 p. https://doi.org/10.5772/intechopen.90837.

[8] Ozola Z.U., Vesere R., Kalnins S.N., Blumberga D. (2019). Paper Waste Recycling. Circular Economy Aspects, *Environmental and Climate Technologies*, 23(3), 260-273, https://doi.org/10.2478/rtuect-2019-0094.

[9] Osamwonyi I., Okokpujie I.P., Dirisu J.O. (2018). Development and performance analysis of horizontal waste paper baling machine, *International Journal of Mechanical Engineering and Technology (IJMET)*, 9(10), pp. 84–101, http://iaeme.com/Home/issue/IJMET?Volume=9&Issue=10.

[10] Peretz R., Mamane H., Wissotzky E., Sterenzon E., Gerchman Y. (2021). Making cardboard and paper recycling more sustainable: Recycled paper sludge for energy production and water-treatment applications, *Waste and Biomass Valorisation.* 12(3), 1599–1608, https://doi.org/10.1007/s12649-020-01117-y.

[11] ****Collectors, Paper and packaging waste (P&PW),* 2020, https://www.collectors2020.eu/the-project/about-collectors/

RESEARCH AND ANALYSIS OF BIONIC GOLDEN CICADA PEANUT DIGGING SHOVEL
/
仿生金蝉花生挖掘铲的研究与分析

Baiqiang ZUO[1)], Shuqi SHANG[1)], Xiaoning HE[1)], Zelong Zhao[1)], Dongjie LI[1)], Wei LIU[2)], Xu LI[1)],) Dongwei WANG*[1)]
[1)] Qingdao Agricultural University, College of Mechanical and Electrical Engineering / China;
[2)] Shandong Yuanquan Mechanical Co / China
Tel: +86-0532-58957391; E-mail: 200701031@qau.edu.cn
DOI: https://doi.org/10.35633/inmateh-68-64

Keywords: *bionic, design, discrete element model, simulation, test*

ABSTRACT
In order to reduce the high resistance problem during peanut digging shovel operation and improve the soil loosening effect, a bionic peanut digging shovel was designed according to the streamlined profile of the head of the golden cicada, and the range of values of the digging operation parameters was analyzed. A discrete element model was developed to verify that the operational resistance of the bionic excavation shovel is lower than that of the flat shovel. The reliability of the simulation test was confirmed by conducting a resistance test on the excavation shovel through a soil trench test. A three-factor, three-water orthogonal combination test was designed to determine the optimal operating parameters of the excavation shovel: the bevel angle of the shovel blade was 55°, the digging depth was 130 mm, and the width of the shovel face was 309 mm. The paper can provide a reference for designing and optimizing peanut-digging shovels.

摘要
为了减少花生挖掘铲作业时阻力大的问题，提高土壤松动效果。根据金蝉头部的流线型轮廓，设计了一种仿生花生挖掘铲，并分析了挖掘作业参数的取值范围。建立离散元模型，验证仿生挖掘铲的作业阻力低于平面铲。通过土槽试验，对挖掘铲进行阻力测试试验，验证仿真试验的可靠性。设计三因素三水正交组合试验，确定挖掘铲的最佳作业参数：铲刃斜角为 55°，挖掘深度为 130㎜，铲面宽度为 309㎜。该文可为花生挖掘铲的设计与优化提供参考。

INTRODUCTION
The peanut-digging shovel is a critical component of the peanut harvester, and the operational effectiveness of the peanut-digging shovel determines the quality and efficiency of the harvest (*Jiang et al., 2021; Yang et al., 2019*). The magnitude of the resistance during the operation of the excavation device also has an important impact on the power loss (*Zhang et al., 2021*). The design and optimization of peanut digging shovels can reduce the working resistance and soil ability to dig shovels into improving the functional quality of the peanut harvester (*Shi et al., 2015*).

To reduce resistance and consumption, many scholars have conducted relevant research on excavation devices for root crops. Foreign scholars conducted anatomical tests on mole cricket and studied the drag reduction performance of mole cricket body structure and pointed out that mole cricket forefoot was more developed (*Godwin R J, 2007; Mouazen A M et al., 1999)*. Tillmann W et al. applied some bio-non-smooth forms to metal tribology, and through test analysis, the friction and bonding effects of metal surfaces with bio-non-smooth forms were improved *(Tillmann W et al., 2017).* Lang Chong created a Panax ginseng seedling digging shovel based on pangolin claw toes and scales and demonstrated its excellent soil-breaking ability and clay reduction effect using discrete element tests (*Lang et al., 2020*). Li Changming Shen studied and designed a bionic peanut-digging shovel using the forefoot of mole crickets as a bionic prototype and proved its excellent drag reduction effect through tests (*Li et al., 2020*). Wang Yujing et al. used the discrete element method to simulate the excavation of a new bionic excavation shovel. The results showed that the excavation shovel has a higher soil fragmentation rate and a lower excavation resistance (*Wang et al., 2017*). Therefore, the design optimization of agricultural machinery mechanisms through the theory of bionics has an excellent operational effect.

In this paper, from the perspective of bionics, based on the streamlined curve of the head profile of the golden cicada, a mathematical model of the fitted curve is established, and a peanut-digging shovel imitating the head profile curve of the golden cicada is designed.

The working resistance of the bionic excavation shovel was verified to be lower than that of the flat shovel by discrete element test and soil trench test. According to the agronomy of peanut planting, the bionic digging shovel operation parameters were optimized and analyzed.

MATERIALS AND METHODS

Design of bionic digging shovel

Related studies have shown that shovel shapes have different disturbance effects on the soil and the resistance they are subjected to. The concave shovel has the highest resistance, and the convex shovel is slightly better than the flat shovel, but the curvature of the convex shovel is difficult to determine (*Fan, 2020*). Yang Ranbing designed a streamlined excavation shovel, and only theoretical analysis was conducted without testing its practical effects (*Yang, 2009*). Based on the digging ability of the golden cicada, its head profile has a good effect of loosening soil and reducing climbing resistance. A bionic peanut-digging shovel is designed for its streamlined head profile to explore the possibility of its drag reduction further.

Golden Cicada Contour Line Extraction and Fitting

Using a 3D scanner, the information on the outer contour of the golden cicada is collected and processed to obtain a 3D model of the golden cicada.

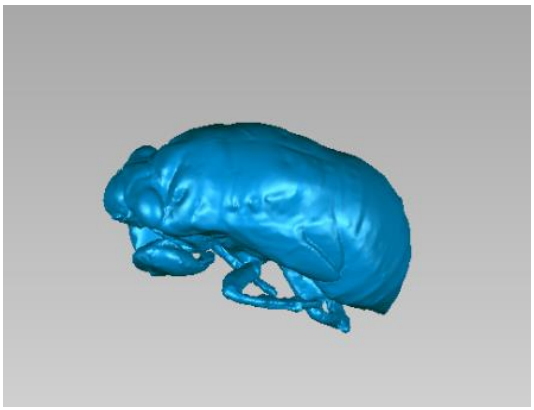

Fig. 1 - Golden Cicada 3D Scanning Model

Import the scanned model of the golden cicada into SolidWorks and use the software to generate a clear and complete profile curve of the head of the cicada. The angle is evenly divided into 12 coordinate points, and the information on the left point is recorded, as in Table 1.

Table 1

Golden Cicada head profile coordinate points

Serial number	1	2	3	4	5	6	7	8	9	10	11	12
x	122.81	132.00	141.72	152.35	164.13	177.20	191.54	206.94	223.07	239.63	256.42	273.34
y	189.10	203.47	217.54	230.89	243.25	254.23	263.47	270.83	276.43	280.60	283.69	286.03

The extracted coordinate points are imported into MATLAB software for processing, and the fitted curves of the coordinate points are obtained. The nth-order polynomial is chosen for fitting the curve equation, and the index of simulation evaluation accuracy can be expressed as the correlation coefficient R^2 of the fitted curve equation.

The equations of the fitted curves are shown in Table 2.

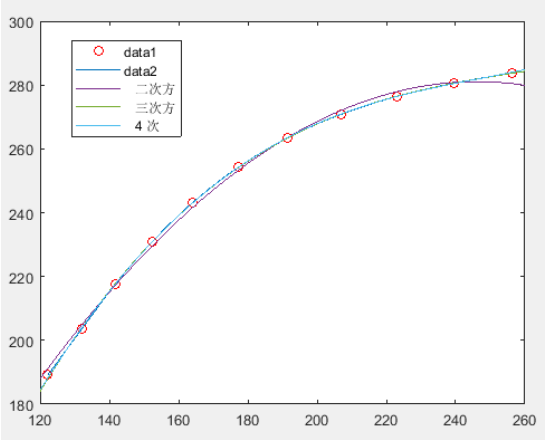

Fig. 2 - Golden cicada head profile fitting curve

Table 2

Curve fitting equation		
Fitting the model	**Fitting equation**	**Correlation coefficient R^2**
quadratic polynomial	$y = -0.0059 * x^2 + 2.9 * x - 74$	0.9970
Third order polynomial	$y = 2.7e^{-05} * x^3 - 0.021 * x^2 + 5.7 * x - 2.4e^2$	0.9999
Fourth order polynomial	$y = 6.7e^{-08} * x^4 - 2.4e^{-05} * x^3 - 0.007 * x^2 - 1.7e^2$	0.9999

A more considerable R^2 value indicates a higher accuracy of the fitted curve equation. In the case of the same precision, the lower-order equation is preferred to facilitate the subsequent bionic design. The final third-order polynomial was used as the correct equation for the head profile curve of the golden cicada.

Bionic excavation shovel model

Select the spline curve in SolidWorks software and find the equation-driven angle. The obtained fitted equation is imported, and the appropriate scale is adjusted. The bionic digging shovel model is shown in Fig 3.

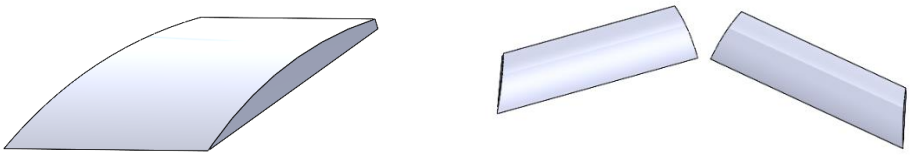

Fig. 3 - Bionic excavation shovel 3D model

Design of working parameters of excavation shovel

Bevel angle of shovel blade

The size of the angle of the shovel blade determines the cutting performance of the excavation shovel on the soil when it enters the ground. To ensure that the environment is cut smoothly and slides away along the edge, improve the self-cleaning ability of the excavation shovel. The bevel angle γ of the shovel surface should satisfy the following:

$$\begin{cases} Q = PQ\cos\gamma \\ T = R\tan\varphi \\ R = P\sin\gamma \end{cases} \quad (1)$$

Conditions for generating slip cuts:

$$Q > T \tag{2}$$

The solution gives:

$$\gamma < 90^{\circ} - \varphi \tag{3}$$

Where:

γ indicates the bevel angle of shovel blade, (°) ;

ϕ denotes the angle of friction between the rootstock and the soil on the shovel blade, (°) ;

T denotes the frictional force of the rootstock and soil sliding backward, (N).

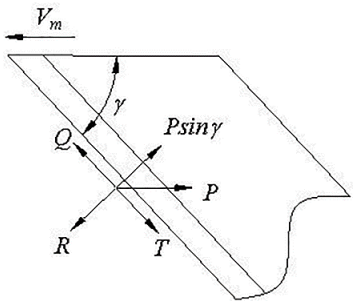

Fig. 4 - Slip-cutting force analysis of shovel blade

The larger the angle of the shovel blade, the larger the digging shovel area, resulting in increased digging resistance; The smaller the digging shovel, the smaller the shovel blade, which is prone to fracture and breakage problems (*Wang et al., 2019*). According to the relevant literature study (Wang et al., 2012), the shovel blade bevel angle range was determined to take the value of 55~65°.

Width of shovel surface

The width of the body of the excavation shovel should be greater than or equal to the width of the distribution of peanut roots in the soil. The width of the shovel body is also related to the planting row spacing, plant spacing, deviations in the forward direction of the digging operation, and irregular deviations of the monopoly. The width of the shovel should be reduced as much as possible on the premise of ensuring the clearance rate of peanut pods to achieve a certain drag reduction effect. The analysis determined that the width of the shovel face is 300~350 mm.

Digging Deeper

Spektor M test studied the nonlinear relationship between the forward resistance and the digging depth in the process of soil cutting by the shovel (*Spektor M., 1981*). The digging resistance becomes continuously more significant with increasing digging depth, ensuring that other parameters remain unchanged (*Chen et al., 2005*). Consider peanut results in a depth of between 80 and 120 mm. It is essential to both reduce the rate of peanut loss and ensure that the digging resistance is as low as possible. Determine the excavation depth of 130~150 mm.

Discrete element model selection

The interaction between the excavation shovel and the soil is a complex movement process. The actual soil trench test could not observe the soil's movement to the excavation shovel. Therefore, the relationship between the action of the excavation shovel and the soil is studied from a macroscopic point of view through discrete element simulation.

Discrete element model selection

The research object of this paper is the soil-excavation shovel system; combined with the actual working condition of the peanut harvester, the contact model is chosen as Hertz-Mindlin with the Bonding model. The model can bond two adjacent soil particles together by a binding force that can withstand tangential and normal displacements.

Soil model construction

In literature (*Chen et al., 2013；Ucgul et al., 2015*), soil particles are set into more than 10 mm spheres. The research shows that the radius of soil particle model is too large, which will affect the calculation accuracy of simulation (*Mark J et al., 2012*). In this paper, in order to control the simulation time in a reasonable range, the soil particle model was developed into spherical particles with a particle size of 3 ~ 5 mm.

As shown in Fig 5, simulated soil tanks with a length of 2000 mm, a width of 800 mm and a height of 400 mm were used to generate soil particles using EDE's particle factory. After all, the particles settle and stabilize, the excavation shovel is imported into EDEM for simulation, and the resistance of the excavation shovel is solved.

Table 3

Basic parameters of discrete element simulation

Parameters	Numerical value
Soil particle density（kg/m^3）	1540
Soil Poisson's ratio	0.32
Soil shear modulus (Pa)	1*10^8
65Mn density（kg/m^3）	7810
65Mn Poisson's ratio	0.29
Elastic modulus of 65Mn (Pa)	8*10^{10}
Coefficient of restitution between soil particles	0.56
Coefficient of static friction between soil particles	0.31
Coefficient of dynamic friction between soil particles	0.15
Coefficient of restitution between soil and excavation shovel	0.16
Coefficient of static friction between soil and excavation shovel	0.47
Coefficient of dynamic friction between soil and excavation shovel	0.20

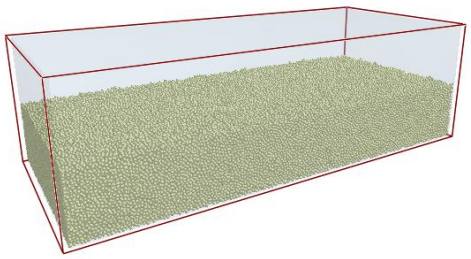

Fig. 5 - Soil model

Simulation test and result analysis

After importing the bionic digging shovel and flat shovel into the model and setting their parameters, start the simulation operation. After the test is completed, the schematic diagram of the simulated motion at three different moments is intercepted. It can be analyzed that there are some differences in the action of the two excavation shovels on the soil during the simulation.

During the operation of the bionic excavation shovel, the speed of the soil does not vary much and tends to be in a steady state. And the velocity of soil particles around the flat excavation shovel increased significantly. The disturbance effect of the bionic digging shovel is better than that of the flat digging shovel.

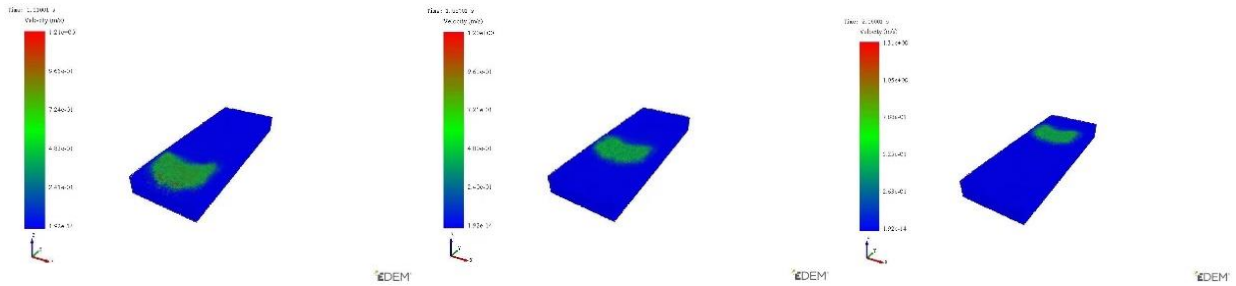

Fig. 6 - Bionic digging shovel

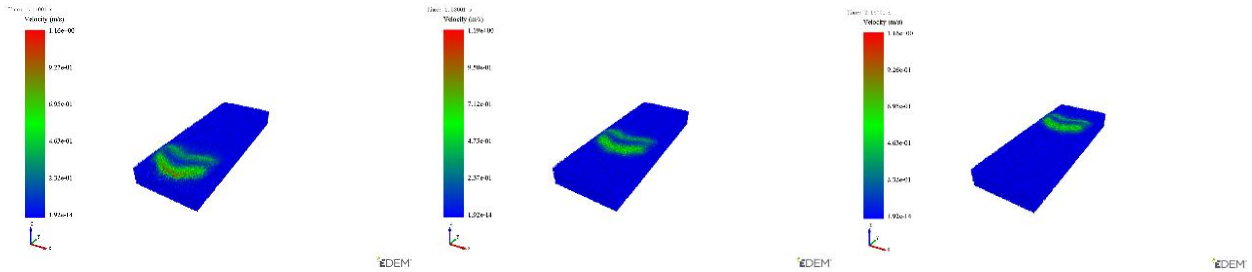

Fig. 7 - Flat excavation shovel

In order to analyze more directly the relationship between the action of the excavation shovel and the soil, the magnitude of the excavation resistance was derived by post-processing, as shown in Fig 8.

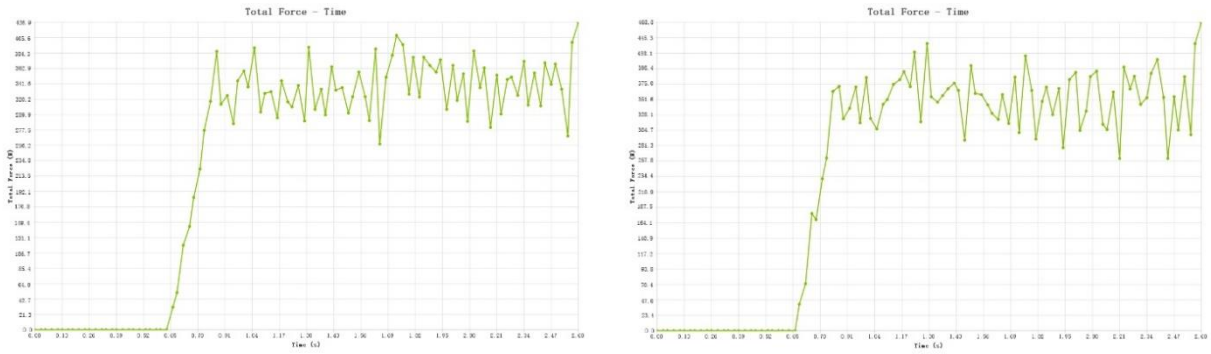

(a) Bionic digging shovel (b) Flat excavation shovel

Fig. 8 - Excavation resistance diagram

According to the digging resistance diagram, it can be analyzed that the bionic digging shovel has a specific resistance reduction ability. The average resistance of the bionic digging shovel was 331.42, and the moderate digging resistance of the flat shovel was 349.73, with a reduced rate of 5.2%. Changing the operating parameters of the excavation shovel and conducting several tests have proven that the bionic excavation lowering ability is better than that of the flat excavation shovel.

Soil Trough Test

Through simulation tests, it was concluded that the bionic excavation shovel has a particular resistance reduction ability. However, the simulation test has some differences from the actual test. Therefore, the soil trough test bed is used to further explore the resistance of bionic excavation shovel and plane shovel. Bionic digging shovel and flat digging shovel size take 1:1 for design. Conduct several tests and take the average value according to the digging resistance change data graph, as shown in Table 4.

Fig. 9 - Soil Tank Test Stand

Table 4

Comparison of soil tank test data

Serial number	Bionic digging shovel	Flat shovel	Resistance reduction rate
1	471.13	515.27	8.6%
2	424.46	476.31	10.9%
3	409.62	454.96	10.%
4	474.17	522.83	9.3%

The resistance reduction rate of the bionic excavation shovel was obtained from the measured resistance difference by the soil trench test. In the actual test, the measured digging resistance value was higher than the simulated test value due to the soil condition and the shovel handles into the soil.

However, the comparison of test data proved the reliability of the simulation test and the resistance reduction effect of the bionic excavation shovel.

RESULTS

Bionic excavation shovel operation parameters optimization test

The drag reduction effect of the bionic digging shovel was verified by simulation and soil trench test. To further determine the optimal combination of parameters for the excavation unit, the shovel blade bevel angle, digging depth, and shovel face width are the test factors, and the digging resistance is selected as the test index. The Box-Behnken test was conducted using the response surface method, and each group of tests was repeated three times to obtain the average value. The test factors and codes are shown in Table 5.

Table 5

Experimental factors and levels

Factor level	—1	0	1
Bevel angle of shovel blade	55	60	65
Digging Deeper	130	140	150
Width of shovel surface	300	325	350

The experimental design scheme and results are shown in Table 6.

Table 6

Test plan and results

Serial number	X1 Bevel angle of shovel blade °	X2 Digging Deeper mm	X3 Width of shovel surface mm	Y1 Excavation resistance %
1	60	140	325	446.61
2	55	150	325	489.41
3	60	150	300	487.82
4	60	140	325	442.37
5	55	140	300	401.27
6	65	130	325	439.26
7	65	140	350	503.76
8	65	150	325	505.92
9	60	140	325	451.42
10	60	140	325	442.37
11	60	130	350	455.79
12	55	130	325	415.37
13	60	150	350	534.62
14	60	140	325	439.62
15	55	140	350	460.62
16	65	140	300	427.86
17	60	130	300	414.36

Analysis of test results

The data were analyzed for ANOVA using Design-Expert 13 software; the results are shown in Table 7. The regression equation between the excavation resistance and the three factors is also established.

Table 7

Analysis of variance for mining resistance

Sources	Squares	DF	MS	F value
Model 1	20817.06	9	33.32	< 0.0001
X_1	1516.08	1	21.84	0.0023
X_2	10730.39	1	154.58	< 0.0001
X_3	6242.91	1	89.94	< 0.0001
X_1X_2	13.62	1	0.1962	0.6712
X_1X_3	68.48	1	0.9865	0.3537
X_2X_3	7.21	1	0.1039	0.7567
X_1^2	48.07	1	0.6926	0.4328
X_2^2	1926.63	1	27.76	0.0012
X_3^2	223.06	1	3.21	0.1161
Residual	485.91	7		
Lack of Fit	400.68	3	6.27	0.0542
Pure Error	85.22	4	R2	0.9772
Cor Total	21302.96	16	Adj R2	0.9479

Note: highly significant (P<0.01); significant (P<0.05).

P-values for the excavation resistance model were less than 0.001, with highly significant differences; the F and P values of the corresponding misfit terms were 6.27 and 0.0542, respectively, which were both

greater than 0.05, and there was no significant difference in the misfit terms. The quadratic regression equation fitted by the model is consistent with the actual one and can predict the test results better.

Response surface plots were established to visually analyze the relationship between the influences of the three factors on the test indexes, as shown in Fig 10.

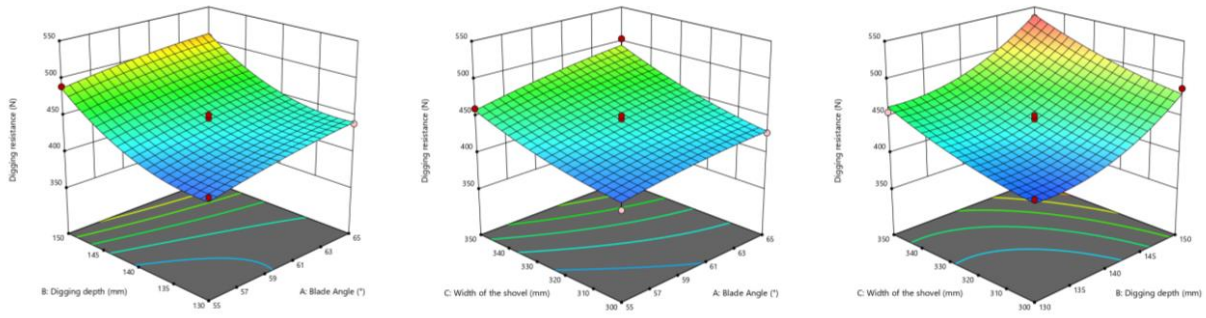

(a) (b) (c)

Fig. 10 - Response surface of the effect of factor interactions on excavation resistance

From figure 10(a), it can be analyzed that the digging resistance increases with the increase of the shovel face inclination. The digging depth is 130~138 mm, the digging resistance rises slowly, and after exceeding 138 mm, the resistance increases sharply. Figure 10(b) can be analyzed: the digging resistance increases with shovel face width and blade inclination angle. Still, the digging resistance is more obviously affected by the shovel face width factor. Figure 10(c) shows that the increase in shovel face width and digging depth cause a sharp rise in resistance. Comprehensive analysis shows that the inclination angle of the shovel blade will lead to a slight increase in the shovel surface area but has little influence on the resistance; the drag resistance is significantly affected by the rise of the excavation shovel surface and excavation depth. Therefore, the effect of the three on the digging resistance needs to be considered comprehensively to reduce the digging resistance as much as possible.

Optimized design of excavation unit

The optimization solution module of Design Expert data analysis software is used to optimally solve the regression equation model for one of the established indicators. The optimum working parameters of the excavation device are: the bevel angle of the shovel blade is 55°, the excavation depth is 130 mm, and the width of the shovel surface is 309 mm. And the excavation resistance is 399.29 N at this time.

To verify the accuracy of the predictions of the described model, soil trench tests were carried out for analysis using the above optimal combination of working parameters, and the results are shown in Table 8.

Table 8

Analysis of test results

Projects	Test average (N)	Model optimization value (N)	Relative Error (%)
Excavation resistance	407.54	399.29	2.0

Due to the influence of the uncertainty of the test, resulting in a relative error of 2%, the bionic excavation shovel operating parameters are reasonably designed.

CONCLUSIONS

(1) The mathematical fitting model was obtained after processing by extracting the coordinates points of the golden cicada's head profile. And a bionic peanut-digging shovel was designed according to the fitted equation.

(2) The discrete element model is established, and the simulation test concludes that the drag reduction effect of the bionic excavation shovel is better than that of the flat excavation shovel. Soil tank tests further verified the reliability of the simulation results.

(3) Three factors and three levels of tests were designed to determine the optimal working parameters of the excavation shovel: the bevel angle of the shovel blade is 55°, the digging depth is 130 mm, and the width of the shovel face is 309 mm. This study may provide a reference for the optimal design of peanut digging shovel.

ACKNOWLEDGEMENT

This research was funded by Modern Agricultural Industrial Technology System Project (CARS-13) and Shandong Provincial Key Science and Technology Innovation Engineering Project (2021CXGC010813).

REFERENCES

[1] Chen Y, Lars J M, Tavs N. (2013). A discrete element model for soil-sweep interaction in three different soils [J]. *Soil & Tillage Research*, 126: 34－41.

[2] Chen Zhihua, Li Yaoming, Sun Xingzhao. (2005). Dynamic analysis and experiment of peanut excavating shovel（花生挖掘铲动力学分析与试验）, *Transactions of the Society for Agricultural Machinery,* Vol.36, Issue 11, pp. 59-63.

[3] Fan Yu. (2020). *Research on potato digging mechanism and design of biomimetic shovel based on discrete element method (基于离散元法的马铃薯挖掘机理研究及仿生铲设计).* Master dissertation, Shenyang Agricultural University. China National Knowledge Internet.

[4] Godwin R J. (2007). A review of the effect of implement geometry on soil failure and implement forces [J] *Soil and Tillage Research,* 97 (2):331-340.

[5] Jiang Yanjin, Chen Lidong, Li Guofang et al, (2021). Research progress of peanut harvester excavating device（花生收获机挖掘装置的研究进展）, *Journal of Hebei Normal University of Science and Technology*, Vol.35, Issue 4, pp. 59-63.

[6] Lang Chongchong, Xu Lulu, Pan Wujian et al. (2020), Design and finite element analysis of bionic excavating shovel for Panax Notoginseng seedlings（三七种苗仿生挖掘铲设计与有限元分析）, *Chinese Journal of Agricultural Mechanization,* Vol.41, Issue 9, pp. 88-94

[7] Li Changming. (2020). *Design and analysis of bionic mole cricket groundnut digging shovel*（仿生蝼蛄花生挖掘铲的设计与分析）, Master dissertation, Shenyang Agricultural University, *China National Knowledge Internet.*

[8] Mark J., Chen Y., Sadek M.A. (2012). Determining parameters of a discrete element model for soil-tool interaction [J]. *Soil & Tillage Research*, 118:117-122.

[9] Mouazen A M, Nemenyi M. (1999) Tillage tool design by the finite element method: Part 1. Finite element modelling of soil plastic behavior [J]. *Journal of Agricultural Engineering Research,* 72（1):37-51.

[10] Shi Chao, Yang Ranbing, Shang Shuqi. (2015). Finite element statics analysis of peanut harvester excavating device based on UG. （基于 UG 的花生收获机挖掘装置有限元静力学分析）, *Agricultural mechanization research,* Vol.37, Issue 1, pp. 18-21

[11] Spektor M. (1981), Principles of soil-tool interaction [J]. *Journal of Terramechanics,* 18(1):51-65.

[12] Tillmann W., Stangier D, Lopes-Dias N.F. et al. (2017). Adjustment of friction by duplex-treated, bionic structures for Sheet-Bulk Metal Forming [J]. *Tribology International,* 111: 9-17.

[13] Ucgul M., John M.F., Chris S. (2015). Three dimensional discrete element modeling (DEM) of tillage: accounting for soil cohesion and adhesion [J]. *Biosystems Engineering*, 129: 298－306.

[14] Wang Fangyan, Sun Guangquan, Shang Shuqi. (2019). Development of 4CL-1 self-propelled combined harvest machine for green onion (4CL-1 型自走式大葱联合收获机的研制), *Transactions of the CSAE,* Vol.35, Issue 24, pp. 39-47

[15] Wang Jiasheng, Shangshu Banner. (2012). Development and experiment of self-propelled double row combined carrot harvester (自走式双行胡萝卜联合收获机的研制及试验), *Transactions of the CSAE,* Vol.28, Issue 12, pp. 38-43

[16] Wang Yujing, Wang Yicai, Liu Ziwen et al. (2017). Simulation analysis of new bionic excavating shovel based on discrete element method（基于离散元法的新型仿生挖掘铲的仿真分析）, *Chinese Journal of Agricultural Mechanization,* Vol.38, Issue 3, pp. 23-26

[17] Yang Li, Dai Kejie, Zhang Tong et al, (2019). Design and optimization of excavating shovel for peanut harvest（花生收获挖掘铲设计及优化）. *Agricultural engineering*, Vol.9, Issue 7, pp. 80-83.

[18] Yang Ranbing. (2009). *Design and Experimental study on Main equipment of HQL-2 peanut Combined Harvester (HQL-2 型花生联合收获机主要装置的设计与试验研究)*. Master dissertation, Shenyang Agricultural University. *China National Knowledge Internet.*

[19] Zhang Hailiang, Zhao Fengqin. (2012). Static analysis of excavating shovel based on ANSYS（基于 ANSYS 的挖掘铲静力分析）, *Agricultural technology and equipment*, Vol.5, pp. 13-15.

CALIBRATION AND EXPERIMENTS OF THE DISCRETE ELEMENT SIMULATION PARAMETERS FOR RICE BUD DAMAGE
/
水稻种芽损伤离散元仿真参数标定与试验

Xiangqian DONG*, Huina ZHENG, Xuan JIA, Yonglei LI, Jiannong SONG, Jicheng WANG [1]
China Agricultural University, College of Engineering, Beijing / China
Tel:0086-010-62737502; E-mail: dxq0558@126.com
Corresponding authors: Xiangqian Dong
DOI: https://doi.org/10.35633/inmateh-68-65

Keywords: *Rice bud; Seed bud cutting; Discrete element method; Parameter calibration*

ABSTRACT *Rice buds are easily bruised or broken during sowing, which affects the seedling rate, and the discrete element simulation of rice buds lacks an accurate model in this process. The EDEM simulation software was used to calibrate the parameters of the discrete element simulation model for different states of rice bud seeds damage. The Hertz-Mindlin model was used to simulate the accumulation of rice bud seeds. Through a series of tests, the interspecific static friction factor was 0.644, and the rolling friction factor was 0.062. The normal contact stiffness and tangential contact stiffness were determined for the bud germination state and the 1-3 mm bud length state, respectively, by using the meta-particle function to build rice seed sprouts and applying the bonding model to conduct Box - Behnken response surface tests for shear damage of rice seed sprouts. Finally, experiments were carried out with a hole-belt-type seed meter. The results showed that under different belt speeds, the relative error between the measured value and the simulated value of the rice bud damage rate was not more than 0.9%, indicating that the calibration parameters were accurate and reliable.*

摘要

水稻在播种过程中种芽易被碰伤或折断影响成苗率，且此水稻种芽离散元仿真缺乏准确模型。以不同状态水稻芽种为研究对象，利用 EDEM 仿真软件开展水稻种芽损伤离散元仿真模型参数标定研究。应用 Hertz - Mindlin 模型进行水稻芽种堆积仿真试验，通过一系列试验，确定了水稻芽种颗粒种间静摩擦因数为 0.644，种间滚动摩擦因数为 0.062。利用 meta-particle 功能建立水稻芽种并应用 Hertz - Mindlin with bonding 粘结模型开展水稻种芽剪切破坏离散元单因素和 Box - Behnken 响应曲面试验，确定了破胸状态与芽长 1-3mm 状态时法向接触刚度分别为 1.07×10e+08N/m、8.99×10e+07N/m，切向接触刚度分别为 9.05×10e+07Pa、8.24×10e+07Pa。采用型孔带式排种器进行了试验验证，结果表明，在不同带速条件下，水稻种芽损伤率实测值与仿真值的相对误差不大于 0.9%，说明标定参数准确可靠。

INTRODUCTION

When sowing rice seedlings, it is necessary to germinate the seeds. Research shows that it is suitable to sow rice seeds in a bud germination state or when the bud length reaches 1~3 mm. Germinated rice seeds differ from dry-based moisture-content rice seeds in terms of morphology, water content and mobility, and rice bud seeds are a more structurally complex agricultural material. Structurally, rice bud seeds consist of two parts: the rice matrix, which includes the brown rice and the rice husk, and the buds, which are developed from the endosperm by consuming nutrients in the embryo. Differences in physical properties due to differences in composition. Rice bud seeds are subject to pressure and impact from outside and between seeds during the sowing process. If the force is too great, the buds will be damaged, and the rice seedling emergence rate will be affected. Therefore, it is necessary to analyse the rice matrix and bud attachment force.

In recent years, EDEM, a simulation software based on the discrete element method (DEM), has been widely used to study agricultural equipment. The accuracy of the model building and the various material parameters in DEM simulations is crucial to the simulation process.

Xiangqian Dong, SE.Ph.D. Eng; Huina Zheng, M.S. Stud. Eng; Xuan Jia, Ph.D.Stud. Eng; Yonglei Li, Assoc. Prof.Ph.D. Eng; Jiannong Song, Prof.ph.D. Eng; Jicheng Wang, ST.

Therefore, DEM models and contact parameters for materials such as buckwheat seeds (*Xu et al., 2021*), mixed biomass sawdust (*Xun et al., 2022*), wheat straw-soil mixtures (*Gao et al., 2022*), king grass (*Huan et al., 2022*) and sunflower seed particles (*Wang et al., 2022*) had been extensively investigated by many scholars.

Some scholars have also used discrete element numerical simulation methods to research on rice seed-metering devices, mainly for modelling and simulation analysis of dry rice seeds. Rice dry seeds (*Zhang et al., 2020*) were filled by a bonded polymerisation model formed by spherical particles with different filling radii. The optimum filling particle radius was sought by stacking angle tests. Lu et al. (*Lu et al., 2018*) constructed a DEM for rice bud seeds and calibrated the main contact parameters of the discrete element for rice bud seeds at different water contents. In this model, the buds are integrated with the matrix. The above studies mainly focused on the dry rice seeds or the matrix and bud as one rice bud seed to build simulation models; none of them analysed the connection force between the matrix and bud.

The Hertz-Mindlin with bonding model can simulate the breakage and fracture of crops during harvesting and processing and is widely used in the field of agricultural material modelling (*Shaikh et al., 2021; Zhang et al., 2022*). Coetzee et al. (*Coetzee et al., 2013*) measured the material properties of grapes through a series of experiments, modelled a bunch of grapes using the bonding model in the discrete element approach, and used a simplified corer model to simulate a peeler to separate the fruit from the stalk.

Yitao Liao et al. (*Liao et al., 2020*) developed a basic contact model and bonding model for forage rape stalks at the Carex stage and calibrated them using stacking angle and shear force. Du et al. (*Du et al., 2021)* trained Bonding models for calibrated envelope fertilizers by uniaxial compression actual and simulation tests and full-factor tests with PSO-BP neural networks. Zhang et al. (*Zhang et al., 2022*) used a BPM model to calibrate a simulation model of the water chestnut peeling and dicing process.

In this paper, discrete element models (DEM) were constructed for rice bud seeds in the bud germination state and the bud lengths of 1 mm, 2 mm and 3 mm. The Hertz-Mindlin model was applied to simulate rice shoot seed stacking, and the main influencing factors were selected to determine the basic contact parameters. The accuracy of the DEM and the parameters calibrated was verified in a bench test using a type-hole belt seed-metering device. The results of the study can provide a new idea for discrete element modelling of rice bud seeds and provide a theoretical basis for analysing the movement, stress state and breakage of rice bud seeds during mechanized seeding in order to provide a database for the optimal design of operational parameters of rice precision seed dispensers.

MATERIALS AND METHODS

The DEM model of rice bud seeds

Randomly take 100 grains of Jing Gangruanzhan from Jiangxi province and measure the length, width and thickness with vernier callipers. Then, ten seeds of each of the three-dimensional dimensions of the broken breast and sprouted state were selected and placed flat, and the image acquisition of the rice sprouted seeds was carried out as shown in Figure 1(a).

The contours were extracted and combined to determine the location of the broken breast and buds, and the Hertz - Mindlin model was used to establish four states of broken breast, bud length 1 mm, 2 mm, and 3 mm, as shown in Figure 1(b). The last three states are represented in one model, with different numbers of particles selected according to the bud length. The radius and X-directional coordinates of the ball are determined in the XZ plane, and the Y-directional coordinates are defined in the XY plane when modelling the rice matrix. The coordinate values are determined according to the number of particles and the coordinate formula. The optimal solution is selected based on the computational efficiency and the degree of model fit. Finally, there is a gap between the bud and matrix particles to prepare for the subsequent addition of bonding bonds in the shear model.

（a）Status of rice bud seeds (b) Rice bud seeds contour and particle distribution in DEM

Fig. 1 - Rice bud seeds

Stacking angle of rice bud seeds

Rice sprout seeds with surface moisture suitable for sowing were selected for the stacking test using the sidewall collapse method. The Jing Gangruanzhan mentioned above was selected as the test material, and the right side of the rice bud seeds collapsed to form the stacking angle during the test. After all the seeds were stationary, the front view of the seed pile was taken with a high-definition camera, and the pile images were grayscale processed and binarized. The image boundary pixel points were extracted and fitted by Matlab, as shown in Figure 2(a). Three replicate tests were conducted at one-hour intervals, and the average pile-up angle for the physical test of rice shoot seeds was obtained as 41.41°.

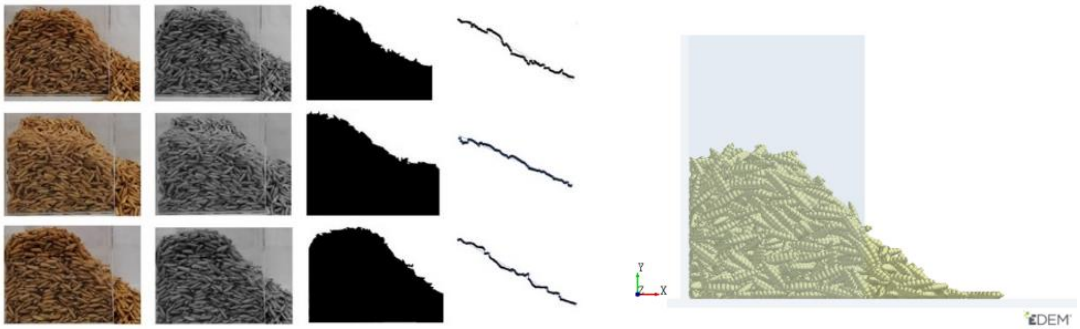

(a) Edge contour extraction process of stacking angle （b）Angle of repose simulation model for rice bud seeds

Fig. 2 - Stacking angle of rice bud seeds

The model was drawn in EDEM software according to the actual single-sided extractable topless cube dimensions. Polygon virtual planes were created at the top of the cube for the dynamic generation of 1000 rice bud seeds at a rate of 1500/s. Rice bud seeds were established according to the DEM above, and the number ratios matched the actual test ratios. In order to ensure that the particles fall quickly, the initial falling speed of particles is set to 1 m/s. After the particles are generated and stabilized, the right baffle is set to be lifted upward with a speed of 1 m/s. The simulated particles collapse from the right side to finally form a stable pile of particles, the model is shown in Figure2(b), and the parameters are set as shown in Table 1.

Table 1

Parameters of angle of repose simulation model for rice bud seeds

Parameter	Poisson's ratio	Real density	Shear modulus	Collision recovery factor with rice bud seeds	Coefficient of static friction with rice bud seeds	Coefficient of rolling friction with rice bud seeds
	—	[kg/m^3]	[Pa]	—	—	—
Rice bud seeds	0.25	1060	1.08e+08	0.46	0.42-0.7[a]	0.04-0.1[a]
Plexiglass	0.23	1200	2.35e+08	0.5	0.24	0.22

Note: a indicates that this item is a test variable, as below.

Shear force of rice bud (actual)

The goal was to obtain the mechanical properties between the rice matrix and the seed bud. First, a tool probe sheared the joint between the matrix and the seed bud on an XT plus texturizer (stable micro systems, UK) close to the side of the matrix. Then, the maximum load of shear damage during loading was recorded as a reference value. Clamp the rice substrate by hand with a pair of sharp-jaw pliers held in place by a homemade jig. Adjust the platform and jig position so that the part of the substrate attached to the seed shoot is directly below the probe, as shown in Figure 3(a).

Two kinds of conventional rice, Jing Gangruanzhan and Feng Yu8, and three kinds of hybrid rice, Tai You398, Hua Zhongyou1 and Yi You2108, were selected. Prefabricated bud species of different states were selected with stainless steel A/MORS probes (thickness 0.3 mm, width 7 mm) and loaded at a speed of 5×10e-4 m/s with a drop distance of 10 mm. The test was repeated ten times for each species in different states, the average value of the maximum shear force was counted, and the coefficient of variation was less than 0.25. It can be seen from Figure 3(b) that although there were differences in the shear force between the rice matrix and bud connection part in different states of different varieties, the shear force was the largest when each variety is in the bud germination state. On the other hand, the shear force tends to be the same and less than the bud germination state when the bud length is 1-3 mm.

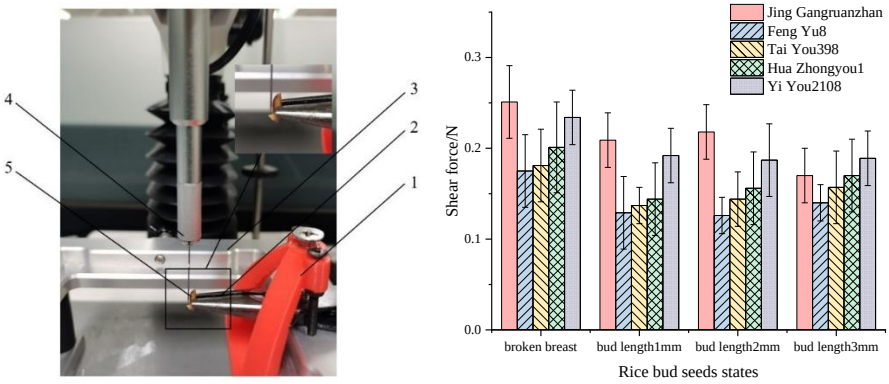

（a）Shearing failure test of rice bud seeds （b）Results of shear force for rice bud seeds

Fig. 3 Shearing failure tests and results of rice bud seeds

1– Fixture; 2– Sharp-jaw plier; 3– Platform; 4–Tool probe;5– Rice bud seed

Shear force of rice bud (simulation)

The rice matrix and buds were modelled separately and combined into rice bud seeds using the meta-particle function, and the contour model was consistent with the above. Based on the Hertz-Mindlin model, the Hertz-Mindlin with bonding model was used to simulate the problems of material fragmentation and fracture by adding inter-particle bonding between the rice matrix and buds. The contact radius R_B is 30% of the physical radius R, and the bond radius is 1.2~2.0 times of the contact radius. The bond is broken when the shear force between the particles reaches the set limit force, and the bond no longer exists between the damaged matrix and buds, which can be used for the simulation study of the damage process of rice seed buds. The particles were used to simulate rice bud seeds, and the bond was broken when the shear force experienced between the particles reached the set limit force. The schematic diagram of particle bonding is shown in Figure 4(a).

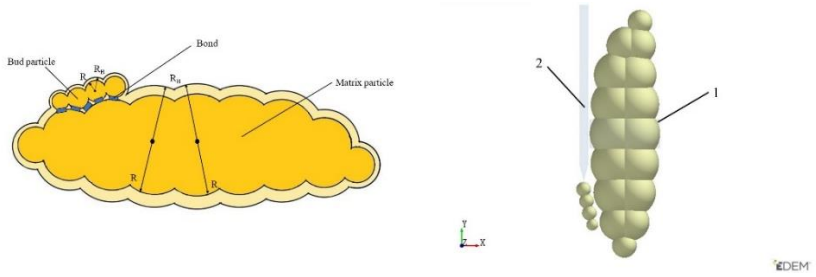

（a）Particle bonding schematic （b）Shearing failure simulation model of rice bud

Fig. 4 Shearing failure test of rice bud seeds

1– Thin-walled cylinder; 2– Tool probe

A particle factory was established to generate a rice bud seed, and the coordinates of the matrix particle and bud particle were extracted. Then the tool model was created by the 3D software SOLIDWORKS and imported into EDEM. Finally, a thin-walled cylinder with a radius of 1.21 mm was created in EDEM to fix the rice bud seed at the centre of the rice matrix. The tool motion speed was the same as the actual one, and the direction was vertical downwards. A simulation model of the shear damage of the buds was created, as shown in Figure 4 (b), and a fixed time step of 3% was set for the simulation calculation. The primary contact parameters of the simulation model are shown in Table 2.

Table 2

Parameters of shearing failure simulation model and bonding for rice bud

Type	Parameter	Values
Tool	Density/(kg·m^{-3})	7850
	Poisson ratio	0.3
	Shear modulus/GPa	7.9
Tool-Rice bud seeds	Coefficient of restitution	0.42
	Coefficient of static friction	0.52
	Coefficient of rolling friction	0.01
Bonding parameters	Normal contact stiffness	10^6~10^{8a}
	Tangential contact stiffness	10^6~10^{8a}
	Critical normal stress	10^6~10^{8a}
	Critical tangential stress	10^6~10^{8a}

RESULTS

Design and analysis of stacking angle response surface tests

The most important factors influencing the stacking angle are the interspecies static friction factor X_1 and the interspecies rolling friction factor X_2 by the Plackett Burman pre-test. The steepest climb test is conducted for the screened main factors to determine the optimal value proximity area. To obtain the optimal contact parameter combinations, a central composite test design was applied to Design-Expert. The stacking angle tests were performed for 11 sets of parameter combinations, of which three sets were central horizontal repetition tests. The factor coding values are shown in Table 3, and the experimental design scheme and results are shown in Table 4.

Table 3

Coding of simulation test factor

Code	-1.414	-1	0	1	1.414
X_1	0.42	0.46	0.56	0.66	0.7
X_2	0.04	0.049	0.07	0.091	0.1

Table 4

Design and results of center compound test

Test No.	X_1	X_2	Stacking angle θ/°	Relative error δ/%
1	-1	-1	37.43	9.61
2	1	-1	38.15	7.87
3	-1	1	39.49	4.64
4	1	1	51.14	23.5
5	-1.414	0	39.45	4.73
6	1.414	0	44.96	8.57
7	0	-1.414	37.53	9.37
8	0	1.414	46.34	11.9
9	0	0	40.4	2.44
10	0	0	40.97	1.06
11	0	0	40.58	2

Table 5

Analysis of variance in regression model of response surface optimization test for stacking angle

Source	Sum of square	df	Sum of mean square	F-value	P-value
model	178.29	5	35.66	42.82	0.0004**
X_1	50.81	1	50.81	61.02	0.0006**
X_2	94.59	1	94.59	113.59	0.0001**
X_1X_2	29.87	1	29.87	35.86	0.0019**
X_1^2	2.37	1	2.37	2.85	0.1523
X_2^2	1.49	1	1.49	1.79	0.2391
Residual	4.16	5	0.8328		
Lack of fit	3.99	3	1.33	15.68	0.0605
Pure error	0.1698	2	0.0849		

*Note: * indicates that this item has significant effect on the result (P≤0.05),*
** * indicates that this item has extremely significant effect on the result (P≤0.01).*

As shown in Table 5 of the ANOVA results, the regression model P=0.0004, the lack of fit P=0.0605, the coefficient of determination R^2 =0.9772, and the coefficient of determination was close to 1, indicating that the regression equation was a good fit. From Table 5, it can be seen that X_1, X_2 and X_1X_2 had highly significant effects on the stacking angle of rice bud seeds, X_1^2 and X_2^2 had insignificant effects on the stacking angle of rice bud seeds, and the effects were ranked from most significant to least: X_2, X_1 and X_1X_2. The stacking angle response surface is shown in Figure 5.

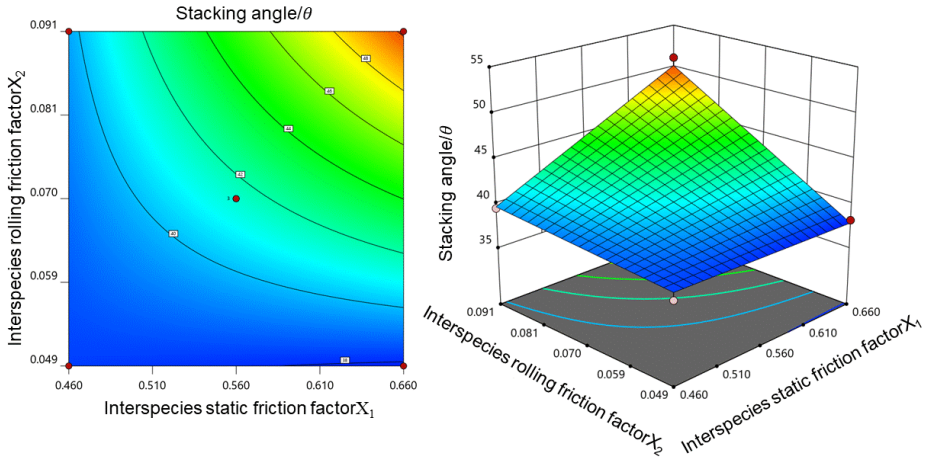

Fig. 5 - Response surface of stacking angle

The stacking angle (θ) regression model with the interspecies static friction factor X_1 and interspecies rolling friction factor X_2 was developed by fitting a binary regression to the data in Table 5 and removing the insignificant factors, as shown in equation (1).

$$\theta = 66.93 - 65.88x_1 - 564.92x_2 + 1301.09x_1x_2 \quad (1)$$

Design and analysis of response surface tests for bonding parameters

According to the Hertz - Mindlin principles with the bonding model, the bond breakage between the particles is the result of a combined effect. The bond radius of 0.5 mm and the order of magnitude of normal contact stiffness, tangential contact stiffness, critical normal stress, and critical tangential stress were determined based on the single-factor pre-test. Box - Behnken Design (BBD) of rice buds shear simulation tests were performed using the parameter values in Table 6 and the bonding parameter values determined in the previous section. The bonding parameters were coded as shown in Table 6. A total of 27 sets of simulations were conducted, with three replications set at the central level. The experimental design and simulation results are shown in Table 7.

Table 6

Coding of bonding parameters

Code	X_3	X_4	X_5	X_6
	[N/m]	[N/m]	[Pa]	[Pa]
-1	0.30×10e+08	0.37×10e+08	0.05×10e+06	0.05×10e+06
0	1.10×10e+08	1.07×10e+08	1.05×10e+06	1.05×10e+06
1	1.90×10e+08	1.77×10e+08	2.05×10e+06	2.05×10e+06

Table 7

Response surface test design and results of bonding parameters

Test No.	X_3	X_4	X_5	X_6	Shear force / [N]
1	-1	-1	0	0	0.0706
2	1	-1	0	0	0.31
3	-1	1	0	0	0.0441
4	1	1	0	0	0.43
5	0	0	-1	-1	0.2552
6	0	0	1	-1	0.2546
7	0	0	-1	1	0.251
8	0	0	1	1	0.256
9	-1	0	0	-1	0.034
10	1	0	0	-1	0.411
11	-1	0	0	1	0.034
12	1	0	0	1	0.416
13	0	-1	-1	0	0.239
14	0	1	-1	0	0.1726
15	0	-1	1	0	0.239
16	0	1	1	0	0.1788
17	-1	0	-1	0	0.0339

18	1	0	-1	0	0.4170
19	-1	0	1	0	0.034
20	1	0	1	0	0.414
21	0	-1	0	-1	0.238
22	0	1	0	-1	0.1746
23	0	-1	0	1	0.239
24	0	1	0	1	0.1788
25	0	0	0	0	0.2636
26	0	0	0	0	0.2518
27	0	0	0	0	0.2729

Table 8

Analysis of variance in regression model of response surface optimization test for shearing force

Source	Sum of square	df	Sum of mean square	F-value	P-value
model	0.4006	14	0.0286	26.35	<0.0001**
X_3	0.3843	1	0.3843	353.91	<0.0001**
X_4	0.0020	1	0.0020	1.88	0.1949
X_5	4.941e-06	1	4.941e-06	0.0046	0.9473
X_6	4.563e-05	1	4.563e-05	0.0042	0.9494
$X_3 X_4$	0.0054	1	0.0054	4.94	0.0462*
$X_3 X_5$	2.403e-06	1	2.403e-06	0.0022	0.9633
$X_3 X_6$	6.250e-06	1	6.250e-06	0.0058	0.9408
$X_4 X_5$	9.610e-06	1	9.610e-06	0.0089	0.9266
$X_4 X_6$	2.560e-06	1	2.560e-06	0.0024	0.9621
$X_5 X_6$	7.840e-06	1	7.840e-06	0.0072	0.9337
X_3^2	0.0026	1	0.0026	2.42	0.1458
X_4^2	0.0081	1	0.0081	7.45	0.0183*
X_5^2	0.0005	1	0.0005	0.5040	0.4913
X_6^2	0.0006	1	0.0006	0.5407	0.4763
Residual	0.0130	12	0.0011		
Lack of fit	0.0128	10	0.0013	11.45	0.0829
Pure Error	0.0002	2	0.0001		

The analysis of variance for the model data is shown in Table 8. The effect of X_3 on shear force of rice buds was significant within the range of different numerical levels of bonding model parameters described in Table 8. X_3X_4 had a significant effect on the shear force, while the rest of the interaction terms did not have a significant effect on shear force; the secondary term X_4^2 had a significant effect on the shear force, while the rest of the secondary terms did not have a significant effect. Figure 6 shows the effect of the interaction between X_3 and X_4 on the shear force. The X_3 effect surface curve is steeper than the X_4 direction, indicating a more significant effect on the X_3 shear force than X_4.

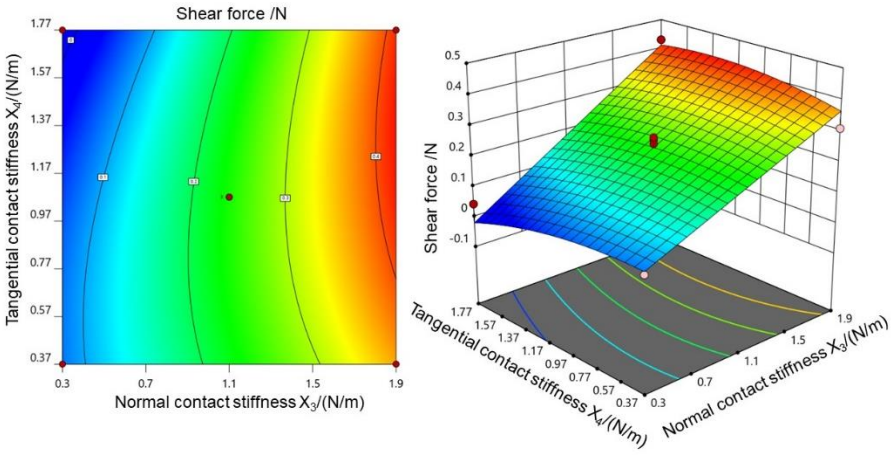

Fig. 6 - Response surface of shearing failure

For the obtained test results, Design-expert software was applied to fit the test results to a multiple regression analysis. For the regression model obtained, the final regression model for shear was obtained by excluding the non-significant term at P>0.05 from the ANOVA, as shown in equation (2).

$$f = 0.02 + 0.154x_3 + 0.042x_4 + 0.065x_3x_4 - 0.062x_4^2 \quad (2)$$

The fitted multiple regression model P<0.0001 indicated that the shear force was highly significant concerning the fitted quadratic regression equation. The coefficient of determination of the fitted model R^2 = 0.9619, R^2_{adj} = 0.9549, and the accuracy of the model in Design-expert was 38, indicating that the quadratic polynomial regression equation was a good fit. The shear force values obtained from the actual shear test were substituted into equation (2) to obtain multiple sets of optimised solutions for simulation. In the case of approximately the same shear displacement, a set of bonding parameters with the closest shear force values in the simulation test and the actual shear test were selected: bond radius of 0.5 mm, normal contact stiffness of 1.07×10e+08N/m, tangential contact stiffness of 9.05×10e+07N/m, critical normal stress of 1.87×10e+05Pa, critical tangential stress of 1.82×10e+05Pa. A comparison of the simulated and measured shear curves is shown in Figure 7.

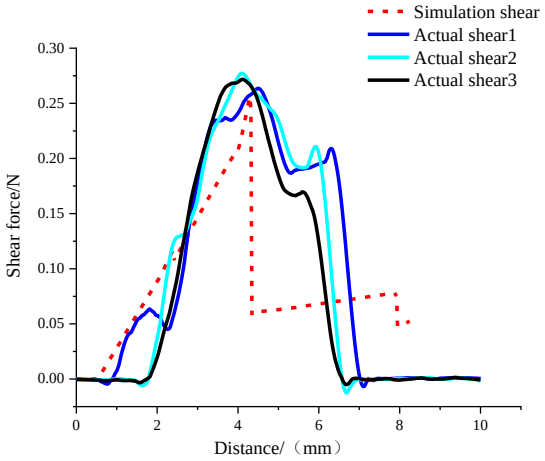

Fig. 7 - Force-displacement curve of shearing failure for simulation-test

The same method was used to calibrate the optimum parameters for rice seeds with bud lengths of 1-3 mm: bond radius of 0.5 mm, normal contact stiffness of 8.99 x10e+07 N/m, tangential contact stiffness of 8.24x 10e+07 N/m, critical normal stress of 1.24 x10e+05 Pa and critical tangential stress of 6.49 x10e+05 Pa.

Bud damage test verification

To further verify the reliability of the DEM and simulation parameters for rice bud seeds, a type-hole belt seed-metering device was built for bench tests. The measured and simulated values of the bud damage rate were compared at belt speeds of 0.05, 0.08, 0.11, 0.14 and 0.17 m/s, respectively, using the bud damage rate as the test index. The Jing Gangruanzhan calibrated above was selected for a bench test, with the seed box made of acrylic and the belt made of PVC, as shown in Figure 8 (a).

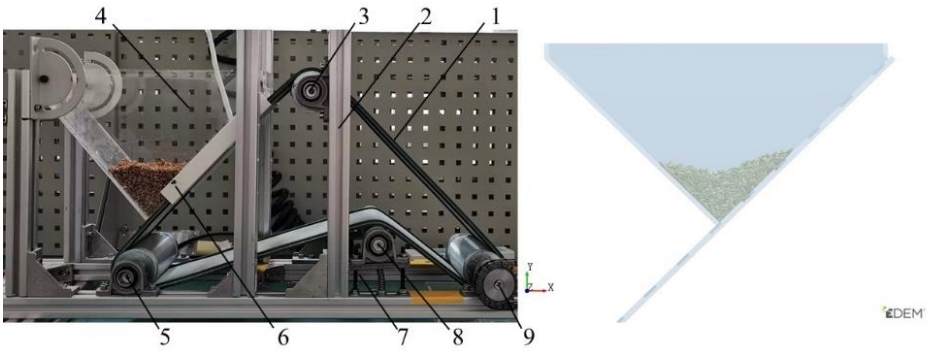

（a）Bench test （b）Simulation test

Fig. 8 - Verification test

1– Type hole belt; 2– Frame; 3– Slave roller I; 4– Seed box; 5– Slave roller II; 6– Guide support slot; 7– Tensioning device; 8– Tensioning roller; 9– Active rollers

For the experiment, 10000 rice bud seeds of Jing Gangruanzhan were prepared and placed in the seed box, and 500 seeds were randomly selected to count the number of different rice states to determine the overall proportion. The controller was switched on and off, the movement was stopped after 10 s, and 500 seeds were randomly selected to count the damage rate of rice buds. The seed-metering device mainly relies on the principle of circulating friction of the seed layer to drive rice bud seed filling. After the seeds entered the hole, they remained stationary with the belt in a stable state. The main force and damage to the buds occurred mainly in the seed-filling process, so the seed-filling process was simulated only. In order to reduce the amount of simulation calculation, the seed box and belt were scaled according to a specific ratio based on the actual test, and the number of simulated rice bud seeds was 1000. The calibrated and measured contact parameters were imported into the discrete element software EDEM. The simulation test was conducted under the same conditions as the bench test to count the number of broken bonds. The simulation test is shown in Figure 8 (b).

Figure 9 shows the measured and simulated values of the bud damage rate at different belt speeds. From Fig.9, the measured and simulated values of bud damage rate increased with the increase of belt speed, and the maximum error between them did not exceed 0.9%.

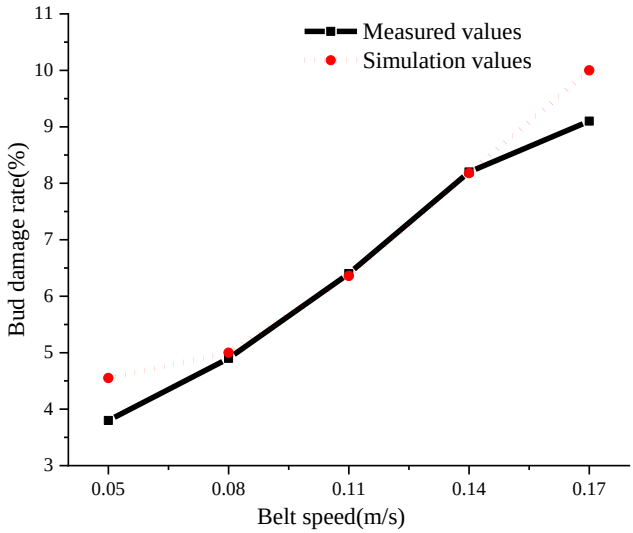

Fig. 9 - Measured and simulated values of damage rate of buds at different belt speeds

CONCLUSIONS

The physical stacking test of rice bud seeds was carried out using the sidewall collapse method. The stacking angle images were processed using MATLAB to obtain edge profiles, which were linearly fitted to obtain a mean stacking angle of 41.41°. A central composite experimental design was applied to Design-Expert to produce an optimized solution. The parameters were 0.644 for the static friction factor between rice bud seeds and 0.062 for the rolling friction factor between seeds. The model was built using the calibrated parameters to simulate the stacking angle, and the relative error between the simulated and measured values was 0.17%.

A Box-Behnken response surface test was carried out to establish a regression model between shear force and two significant parameters: normal contact stiffness and tangential contact stiffness, using the broken chest state of Jing Gangruanzhan as an example. Optimal parameter combinations were in order: 1.07x10e+08 N/m, 9.05x10e+07 N/m. The parameter combinations were 8.99x10e+07 N/m and 8.24x10 e+07 N/m when the same method was used to calibrate bud lengths of 1-3 mm.

A type-hole belt seed-metering device was built for bench testing and simulated in EDEM software for test analysis. The results showed that the maximum error between the measured and simulated values of the bud damage rate did not exceed 0.9% at different belt speeds. Therefore, this DEM of rice bud seeds, contact parameters and bonding parameters between the matrix and buds can be used for discrete element simulation tests.

ACKNOWLEDGEMENT

This research was supported by Technology for the Economy 2020 (2020YFF0426562-2).

REFERENCES

[1] Bing Xu, Yanqing Zhang, Qingliang Cui, Shaobo Ye, Fan Zhao., (2021), Construction of a discrete element model of buckwheat seeds and calibration of parameters, *INMATEH Agricultural Engineering*, Bucharest/Romania, vol.64, no.2, ISSN, pp.175-184.

[2] Corné J. Coetzee, Stephanus G. Lombard., (2013), The destemming of grapes: Experiments and discrete element modelling, *Biosystems Engineering*, vol.114, no.3, ISSN, pp.232-248.

[3] Fangyuan Lu, Xu Ma, Suiyan Tan, Lintao Chen, Lingchao Zeng, Pei An., (2018), Simulative calibrate and experiment on main contact parameters of discrete elements for rice bud seeds (水稻芽种离散元主要接触参数仿真标定与试验), *Transactions of the Chinese Society for Agricultural Machinery*, Madison/Wisconsin, vol.49, no.2, ISSN, pp.93-99.

[4] Guozhong Zhang, Liming Chen, Haopeng Liu, Zhao Dong, Qinghong Zhang, Yong Zhou., (2022), Calibration and experiments of the discrete element simulation parameters for water chestnut (荸荠离散元仿真参数标定与试验), *Transactions of the Chinese Society of Agricultural Engineering*, Madison/Wisconsin, vol.38, no.11, ISSN, pp.41-50.

[5] Lei Zhang, Yibin Zhai, Jianneng Chen, Zhien Zhang, Shouzhi Huang., (2022), Optimization design and performance study of a subsoiler underlying the tea garden subsoiling mechanism based on bionics and EDEM, *Soil &Tillage Research*, Netherlands, vol.191, no.3, ISSN, pp.183-192.

[6] Rongfang Zhang, Wei Jiao, Jilei Zhou, Bing Qi, Hu Liu, Qianqian Xia., (2020), Parameter calibration and experiment of rice seeds discrete element model with different filling particle radius (不同填充颗粒半径水稻种子离散元模型参数标定), *Transactions of the Chinese Society for Agricultural Machinery*, Madison/Wisconsin, vol.51, no. S1, ISSN, pp.227-235.

[7] Sher Ali Shaikh, Yaoming Li, Zheng Ma, Farman Ali Chandio, Mazhar Hussain Tunio, Zhenwei Liang, Kashif Ali Solangi., (2021), Discrete element method (DEM) simulation of single grouser shoe-soil interaction at varied moisture contents, *Computers and Electronics in Agriculture,* Netherlands, vol.191, no.1, ISSN, pp.106538.

[8] Shuai Wang, Zhihong Yu, Aorigeleo, Wenjie Zhang., (2022), Study on the modelling method of the sunflower seed particles based on the discrete element method, *Computers and Electronics in Agriculture,* Netherlands, vol.65, no.3, ISSN, pp.183-192.

[9] Tao Jiang, Chongyou Wu, Qing Tang., (2018), Simulation study of wheat straw cutting based on ANSYS and EDEM (基于 ANSYS 和 EDEM 的小麦茎秆切割仿真研究), *Jiangsu Agricultural Sciences*, Madison/Wisconsin, vol.46, no.17, ISSN, pp.231-234.

[10] Xin Du, Cailing Liu, Meng Jiang, Hao Yuan, Lei Dai, Fanglin Li, Zhanpeng Gao., (2021), Calibration of bonding model parameters for coated fertilizers based on PSO-BP neural network, *INMATEH Agricultural Engineering*, Bucharest/Romania, vol.65, no.3, ISSN, pp.255-264.

[11] Xiaolong Huan, Decheng Wang, Yong You, Wenpeng Ma, Lu Zhu, Sibiao Li., (2022), Establishment and calibration of discrete element model of king grass stalk based on throwing test, *INMATEH Agricultural Engineering*, Bucharest/Romania, vol.66, no.1, ISSN, pp.19-30.

[12] Xun Gong, Xuewei Bai, Haibo Huang, Fengyu Zhang, Yuanjuan Gong, Desheng Wei., (2022), DEM parameters calibration of mixed biomass sawdust model with multi-response indicators, *INMATEH Agricultural Engineering*, Bucharest/ Romania, vol.65, no.3, ISSN, pp.183-192.

[13] Yitao Liao, Qingxi Liao, Yu Zhou, Zaiteng Wang, Yajun Jiang, Fang Liang., (2020), Parameters calibration of discrete element model of fodder rape crop harvest in bolting stage (饲料油菜薹期收获茎秆破碎离散元仿真参数标定), *Transactions of the Chinese Society for Agricultural Machinery*, Madison/Wisconsin, vol.51, no.6, ISSN, pp.73-82.

[14] Zenghui Gao, Shuqi Shang, Nan Xu, Dongwei Wang., (2022), Parameter calibration of discrete element simulation model of wheat straw-soil mixture in Huang Huai Hai production area, *INMATEH Agricultural Engineering*, Bucharest/Romania, vol.66, no.1, ISSN, pp.201-210.

INFLUENCE OF OPERATING PARAMETERS ON THE MILLING QUALITY OF LONG-GRAIN WHITE RICE

/

تأثير عوامل التشغيل على جودة الضرب للأرز طويل الحبة

Mahmoud AWAD, Osama FOUDA, Solaf ABD EL-REHEEM, Fatma ABD EL GAWAD, Mokhtar COTTB, Mahmoud OKASHA [*1]

Agricultural Engineering Research Institute (AEnRI), Agricultural Research Center (ARC), Giza 12611/ Egypt

Tel: +20-1003133841; E-mail: mahmoudokasha1988@yahoo.com

Corresponding author: Mahmoud Okasha

DOI: https://doi.org/10.35633/inmateh-68-66

Keywords: *Broken rice percentage; Milling process; Head rice yield; Whitening degree*

ABSTRACT

The current study aimed to test and evaluate sheets' different perforation shapes, brake angles, and milling durations to improve the quality of long-grain white rice from an abrasive milling machine. The investigated parameters of head rice yield, broken rice percentage, whitening degree, and rice bulk temperature were influenced by five sheets with five perforated shapes (horizontal, vertical, inclined, 1 mm round holes, and 1.5 mm round holes), three brake angles (0, 45, and 90º), and four milling durations (60, 70, 80, and 90 s). The results showed that the horizontal rectangular perforated sheet resulted in the highest value of head rice yield and the lowest value of broken rice. On the other hand, the vertical rectangular perforated sheet resulted in the highest whitening degree, followed by the inclined rectangular perforated sheet. The round holes (1.0 mm and 1.5 mm diameter) are not recommended for the long-grain whitening process because of the resulting high values of broken kernels, rice bulk temperature after the whitening process, and lower values of whitening degree. The brake angle of 90º resulted in the highest value of broken rice for all studied perforated sheets used in this study. This study recommended that the optimum operating conditions were using the horizontal rectangular perforated sheet, zero degree brake angle and milling duration of 80 s.

الملخص

تهدف الدراسة الحالية إلى اختبار وتقييم شبكات التبييض ذات اشكال الثقوب المختلفة وزوايا الفرامل وفترات الطحن المختلفة لتحسين جودة الضرب للأرز الأبيض طويل الحبة. تناولت هذه الدراسة تاثير كلا من شبكات تبييض ذات خمس أشكال للثقوب (أفقية، رأسية، مائلة، ثقوب دائرية 1 مم، وفتحات دائرية 1.5 مم)، وثلاث زوايا فرامل (0، 45، 90 درجة) وأربع فترات طحن (60، 70، 80، 90 ثانية) على نسبة الأرز السليم، ونسبة الأرز المكسور، ودرجة التبييض، ودرجة حرارة الأرز. أظهرت النتائج أن الشبكة المثقبة الأفقية المستطيلة أظهرت أعلى قيمة للأرز السليم وأدنى قيمة الأرز المكسور. وعلى الجانب الأخر، نتج عن الشبكة المثقبة المستطيلة الرأسية أعلى درجة تبييض، تليها الشبكة المثقبة المستطيلة المائلة. لا ينصح باستخدام الشبكات ذات الثقوب المستديرة (باقطار 1.0 مم و 1.5 مم) لعملية التبييض للأرز طويل الحبة بسبب القيم العالية الناتجة للحبوب المكسورة ودرجة حرارة كتلة الأرز بعد عملية التبييض والقيم المنخفضة لدرجة التبييض. أدت زاوية الفرامل البالغة 90 درجة إلى الحصول على أعلى قيمة للأرز المكسور لجميع أشكال الشبكات المثقبة المستخدمة في هذه الدراسة. أوصت هذه الدراسة بأن ظروف التشغيل المثلى كانت باستخدام الشبكة المثقبة الأفقية المستطيلة وزاوية الفرملة الصفرية ومدة الطحن 80 ثانية

INTRODUCTION

Rice (*Oryza sativa* L.) is presently the world's most important cereal grain, with one-fourth of the population depending on it as major stable food. By 2050, rice demand is expected to double as the global population grows (*Ray et al., 2013*), especially after the shortage of wheat supply chains caused by the Russian-Ukrainian war. Egypt is one of the world's major rice-producing countries, producing about 4,893,507 Mg (*FAOSTAT, 2020*). Rice production has expanded in recent years to meet the rise in human demand. Paddy (rough) rice includes two layers that cover a rice kernel; the inner layer is the bran, and the outer layer is the hull or husk. The husk is inedible, and bran diminishes the rice luster; hence, they must be removed from the paddy. The rice milling process is defined as removing the rice kernel's husk (hulling) and bran layer (polishing), making the rice edible (endosperm) and free from impurities. In addition, the milling process is

[1] *Solaf Abd El-Reheem, Senior Researcher; Mahmoud Awad, Senior Researcher; Fatma Abd El Gawad, Senior Researcher; Mokhtar Cottb, Senior Researcher; Mahmoud Okasha, Researcher*

essential because it enhances rice's nutritional, cook time, and sensory qualities (*Dhankhar, 2014*). Rice milling is a routine practice for the post-harvest processing of rice grains. Still, broken rice production during milling is an inescapable and global problem (*Zeng et al., 2022*). Moreover, rice milling plays a key role in determining rice quality, and assessing the appearance quality is an efficient method to differentiate the milling degree (*Ren et al., 2021*).

Most consumers in Egypt prefer well-milled rice with no bran remaining on the endosperm; thus, this procedure must be carried out carefully to prevent extreme kernel breakage and to promote paddy recovery. Consequently, great benefits will be gained by reducing the broken rice rate in white rice during rice milling. Losses during the milling process are classified as quantitative and qualitative losses. Quantitative or physical losses are manifested by low milling recovery.

In contrast, qualitative losses are manifested by a high percentage of broken grains or low head rice recovery in the milled product, especially in long-grain varieties, because of their low hardness compared to short-grain varieties (*Radwan, 2001*). Head rice yield (HRY) often differs from the moisture content (MC) at which rice is harvested (*Siebenmorgen et al., 2007*). Furthermore, many factors influence HRY during the milling process, including preharvest weather conditions, grain moisture content at harvest, techniques of paddy drying, alterations in grain moisture content after drying, storage conditions for paddy, and milling equipment (*Abayawickrama et al., 2017*).

Drying is a post-harvest process that greatly affects rice milling yield and overall quality by lessening paddy rice's moisture content to an appropriate level. Rice's moisture content should be lowered from 22 to 14% at harvest to roughly 13% for storage to diminish the rates of respiration and mold growth and inhibit fungi and insect growth. In fact, milling caused some kernels to break, even in rice lots that have been harvested, dried, and stored with intense care (*Mukhopadhyay and Siebenmorgen, 2018*). In the same trend, rough paddy grains must be dried to a moisture content below 14% (w.b.) for safe storage, whereas the optimal moisture content of paddy for milling remains between 13% and 14% (w.b.) (*IRRI, 2013*). In addition, rice kernels are subjected to intensive thermal and mechanical stresses during milling, which might break or damage some kernels. Some parameters, such as the paddy characteristics, whitening machine type, and environmental factors, influence the rice kernel breakage and damage during the milling process (*Afzalinia et al., 2004*).

Removing all the bran in one whitening operation leads to significant breakage and decreases total rice recovery. Hence, most modern rice mills use multi-pass whiteners because multi-pass whitening produces higher rice mill recovery, increasing head rice yield and reducing broken rice percentage. Therefore, some systems were suggested to get the best rice quality (*Tangpinijkul, 2010*). Using three abrasive-type whiteners with a friction whitener as a polisher kept the minimum breakage of rice and the least milling cost, and its output kept the most acceptable appearance and marketability (*Afzalinia et al., 2004*). Head rice yield (HRY) for long and extra-long grain rice was higher with abrasive milling (61–75%) compared to friction milling (10–60%) (*Kalpanadevi et al., 2019*). Thus, it was the most effective rice milling system for the tested variety and region.

A Satake whitening machine model TM–05 was used to white medium-grain (Mutsuhonami variety) using four rotor speeds (810, 1020, 1310, and 1500 rpm, respectively) for a 40 s whitening period. The results reported that a rotor speed of 810 rpm resulted in under-milling, whereas a rotor speed of 1500 rpm resulted in over-milling (*Bekki and Kunze, 1988*).

Long and tiny rice kernels were more susceptible to breakage than wide short kernels during milling (*Seguy and Clement, 1994*). The milling duration has an effective effect; an increase in duration increases the milling degree and which in turn reduces the head rice yield (*Puri et al., 2014*). In the same trend, Eliçin et al. (2022) studied the influence of rice milling duration on head rice yield (HRY), and their results revealed that rice milling duration is a crucial factor in head rice yield, where increasing the rice milling time from 10 to 25 s decreased the head rice yield by 9.13%. Matthews et al. (1970) evaluated the breakage for both medium-grain and long-grain rice. The results revealed that most breakages ensued in the first 10 s of milling. Removing the bran continued at a decreasing rate throughout the milling duration. The polishing duration could be extended to around 150 s without increasing breakage significantly over that which occurred in the first 10 s of the milling duration. Also, approximately 65 to 73% of the bran was removed in the first 20 s of the milling period for all tested varieties (four long-grain varieties and one medium-grain variety). The rate of bran removal was as much as 4 times higher in the first 20 s than in the next 20 s of the milling period (*Velupillai and Pandey, 1987*). Moreover, excessive milling increases energy consumption (*Ahmad et al., 2017*).

The horizontal whitening machine was developed in Japan after World War II and is well-appropriate to the short-grain Japanese rice varieties. Nevertheless, its introduction in Asia and other Far East countries has

been delayed because sensitive adjustments are necessary to acclimate medium and long-grain varieties (*Soepardjo, 1981*).

Thus, from that time until now, many researchers and investigators have worked on this machine to improve its efficiency and long-grain white rice quality. Therefore, this study aimed to improve long-grain white rice quality by reducing broken rice percentage and increasing the whitening degree and head rice yield by suggesting some shapes of perforated sheets and milling durations to suit the long-grain rice variety in Egypt.

MATERIALS AND METHODS

Rice crop

Egyptian long-grain rice *Indica* type (Giza 181 variety), freshly harvested with an average moisture content of 16% (w.b.), was used in this experiment. The laboratory trials were carried out at the laboratory of Rice Mechanization Center (RMC), Kafr El-Sheikh, Egypt. The rice samples were cleaned of impurities, immature kernels, and foreign materials and stored at 1 ºC in a cooler to avoid moisture loss. At the beginning of the experiment, rough rice samples were taken from the cooler and mixed manually. The samples were dried under shade to the desired moisture content suitable for hulling and whitening (14% ± 0.5% w.b.).

The rice hulling machine

The rubber roll huller Yanmar (model ST–50) was used in this study to hull paddy rice samples and get brown rice for the whitening experiments. The huller comprises two rubber rolls with diameters and lengths of 110Ø × 50 mm, respectively. One has a fixed position, and the other is adjustable to get the desired clearance between the two rolls. The clearance between the two rolls was adjusted to be 2/3 the thickness of the grain (*Radwan, 1994*). The grain feed rate of 1 kg min^{-1} was kept constant, and when the rough rice was fed between the two rolls and then caught under rubber pressure, the husk was stripped off. The resulting brown rice was separately discharged in receptacles and collected in a pan for whitening. The huller was manually cleaned of trapped grains before and after the hulling of each sample.

The rice whitening machine

In this experiment, Satake whitening laboratory machine (model TM–05, Satake Co., Tokyo, Japan) was used to polish the brown rice resulting from the hulling machine. The machine has a capacity of 0.2 kg and a 0.4 kW built-in motor, and it comprises an abrasive roll (emery stone) operating in a cylindrical metal perforated screen. The brown rice fed into the free space between the perforated sheet and the abrasive roll. The abrasive operation removes the bran layers from the grain to produce white rice.

The perforated sheets

The perforated sheets keep the rice grains in contact with the stone's surface, thus allowing bran separation, and, at the same time, its rough surface helps peel the bran layer by friction. Wire netting with suitable mesh size and wire diameter, if compared to the perforated sheets, provides more effective abrasive action and allows more space for the bran to pass through. On the other hand, the perforated sheets reduce the risk of breaking the grains; thus, both materials have advantages and disadvantages (*FAO, 1981*).

In the horizontal whitening machine, three rows of adjustable steel brakes are installed over the cylindrical housing length that can be adjusted from zero to 90 (radial). These adjustable brakes direct the position of the rice grain inside the machine during the whitening process to get optimum whitening efficiency. The optimal brake change angle depends on the variety of rice being processed. This point remains crucial in the machine's operation, which requires an experienced operator. When the inclination is set at zero degree, the resistance pieces give minimum resistance and minimum thrust to the moving grain so that the grain moves along the direction of the slots. When the inclination is set at 45°, the resistance pieces give maximum thrust and medium resistance to the grain. When the inclination is set at 90°, the resistance pieces give maximum resistance but no thrust to the moving grain (*Satake, 1983*).

Rice whitening trial

Five sheets with five perforation shapes (two round holes with diameters of 1.0 mm and 1.5 mm and three rectangular perforations, namely horizontal, vertical, and inclined rectangular with dimensions of 25 mm length and 1.5 mm width, as shown in Figs. 1 and 2, four whitening durations (60, 70, 80, and 90 s) and three steel brake angles (0, 45, and 90º) were used in this study. Samples of 150 grams each were processed in

one pass (Satake, 1992). All the milled rice grains were carefully removed from the machine and collected in a pan to determine the temperature of the resulting white rice immediately. The broken rice was separated from the head rice and weighted. The head rice portions were taken for color analysis. The whitening machine was manually cleaned of trapped grains before and after processing each sample.

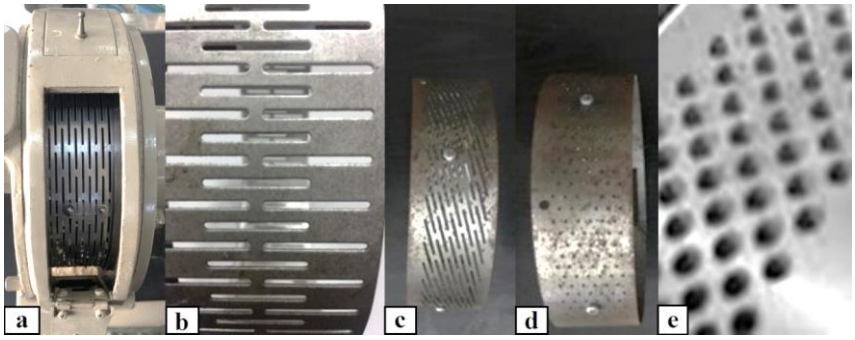

Fig. 1 – Sheets with different perforations shapes *(a) the horizontal rectangular sheet (parallel to rice direction), (b) the vertical rectangular sheet (perpendicular to rice direction), (c) the inclined rectangular sheet, (d) round holes 1.0 mm, and (e) round holes 1.5 mm*

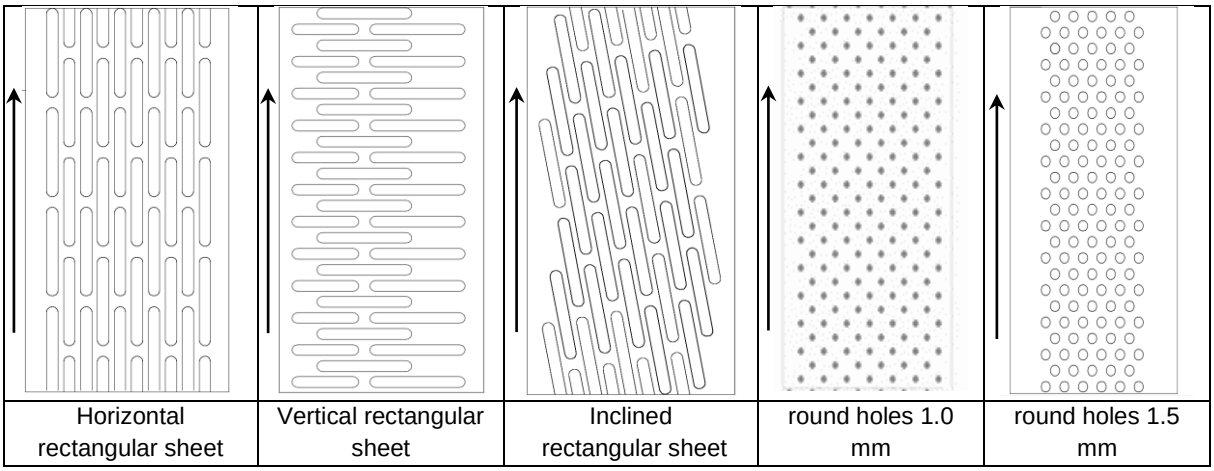

Fig. 2 – The different perforated sheets used for the whitening machine (arrow refers to rice direction)

Measurements

Measurements of rice's dimensions, moisture content, and temperature

One hundred rice grains were randomly selected from the tested variety in this study to determine the mean grain dimensions (length "L", width "W" and thickness "Th"). The mean dimensions were measured by a digital caliper. The paddy sample's moisture content (MC) was determined using a 25 g paddy sample placed in an air oven at 130º C for 16 h (*Matouk et al., 2000*). The resulting moisture content represents the average of three replicates. The bulk temperature of the rice was immediately determined at the end of each trial. The discharged white rice was received in an insulated glass cylinder. A digital multimeter model (A.W. SPERRY DM–8600) with a temperature range from -30 to 400 °C and +0.5% accuracy was used to measure a one-point temperature. The meter prop (K–type thermocouple) was inserted through the rice bulk until reaching a constant reading.

Measurements of milling quality

In order to determine the milling quality of each sample, three calibration parameters were considered, i.e., head rice yield, broken rice percentage, and whitening degree (*Siebenmorgen, et al., 2006*).

a. Head rice yield (HRY)

The head yield is defined as the mass percentage of rough rice that remains head rice after milling (*Siebenmorgen, et al., 2006*). The milled grain that is three-quarters or larger than its original size is considered a whole grain (*Egyptian Standard, 1992*).

b. Broken rice percentage

The broken percentage was calculated in Eq. (1), according to (*Gbabo and Ndagi, 2014*).

$$P = \frac{W_b}{W_s} \cdot \omega \quad (1)$$

where P is the broken percentage, [%]; W_b is the weight of the broken kernels, [g]; and W_s is the total weight of the sample, [g.]

c. Whitening degree

A digital whiteness meter (model C–300, Kett Electric Co., Japan) with a resolution of 0.1% and measuring range of 5–70 was used to measure the whitening degree of milled rice for each treatment.

The measuring principle for this meter depends on the amount of reflected light from the whitened rice surface (photo-diode).

Statistical analysis

Analysis of variance (ANOVA) was done to determine the influence of perforated sheet shape, milling duration, and brake angle on all the dependent variables. The regression analysis was also done to get some relationships between the parameters, and the regression equations are shown in Figs. 3–6 in the results and discussion section.

RESULTS AND DISCUSSION

Grain dimensions

The results of one hundred rice grains from the Egyptian long-grain variety (Giza 181) chosen for the study showed that the mean grain dimensions (length “L”, width “W” and thickness “Th”) were 9.28, 2.52, and 2.02 mm, respectively. The corresponding results for the brown rice grain were 7.42, 2.32, and 1.76 mm, respectively. These results were used to adjust the clearance of the huller machine to obtain a good efficiency of the huller and help select the perforated sheet suit for long-grain rice varieties.

Effect of sheets’ different perforations shapes, brake angles, and milling durations on head rice yield

Five sheets with five perforation shapes were suggested and evaluated to recommend the optimum one for improving long-grain rice quality in terms of head rice yield, broken rice percentage, and whitening degree. Fig. 3 shows the effects of the sheets’ different perforation shapes, brake angles, and milling durations on head rice yield. As shown in the figure, in case of using a 1.0 mm round holes sheet resulted in recording the lowest head rice yields (57.66, 58.54, 60.56, and 62.60%) at 90º brake angle and milling durations of 90, 80, 70, and 60 s, respectively, followed by 1.5 mm round holes. This result may be attributed to the thin rice kernels sometimes lining up in the holes and causing them to break. On the other side, the highest head rice yields (75.57, 74.88, 73.67, and 72.77%) were obtained by using the horizontal rectangular perforated sheet (parallel to the rice direction) at zero degree brake angle and the same milling durations, respectively, followed by the inclined rectangular perforated sheet and the vertical rectangular perforated sheet at the same brake angle. The statistical analysis showed that the perforated sheet shape significantly affected the head rice yield.

Regarding the effect of brake angle on head rice yield, it can also be seen in Fig. 3 that increasing the brake angle from zero to 90º decreases the head rice yield at all shapes of perforated sheets and milling durations under this study. Increasing brake angle from zero to 90º decreased head rice yield from 65.66–62.60%, 74.47–71.47%, 75.57–73.02%, 74.47–72.47%, and 74.87–72.78% at 60 s milling duration for 1 mm round holes, 1.5 mm round holes, horizontal, vertical, and inclined sheets, respectively.

Involving the effect of milling duration on head rice yield, as shown in Fig. 3, increasing milling duration decreased head rice yield for all perforated sheets and brake angles. Where increasing the milling duration from 60 to 90 s, decreased head rice yield from 65.66–60.66%, 74.47–70.77%, 75.57–72.77%, 74.47–71.11, and 74.87–72.27% at zero brake angle for 1 mm round holes, 1.5 mm round holes, horizontal, vertical, and inclined sheets, respectively.

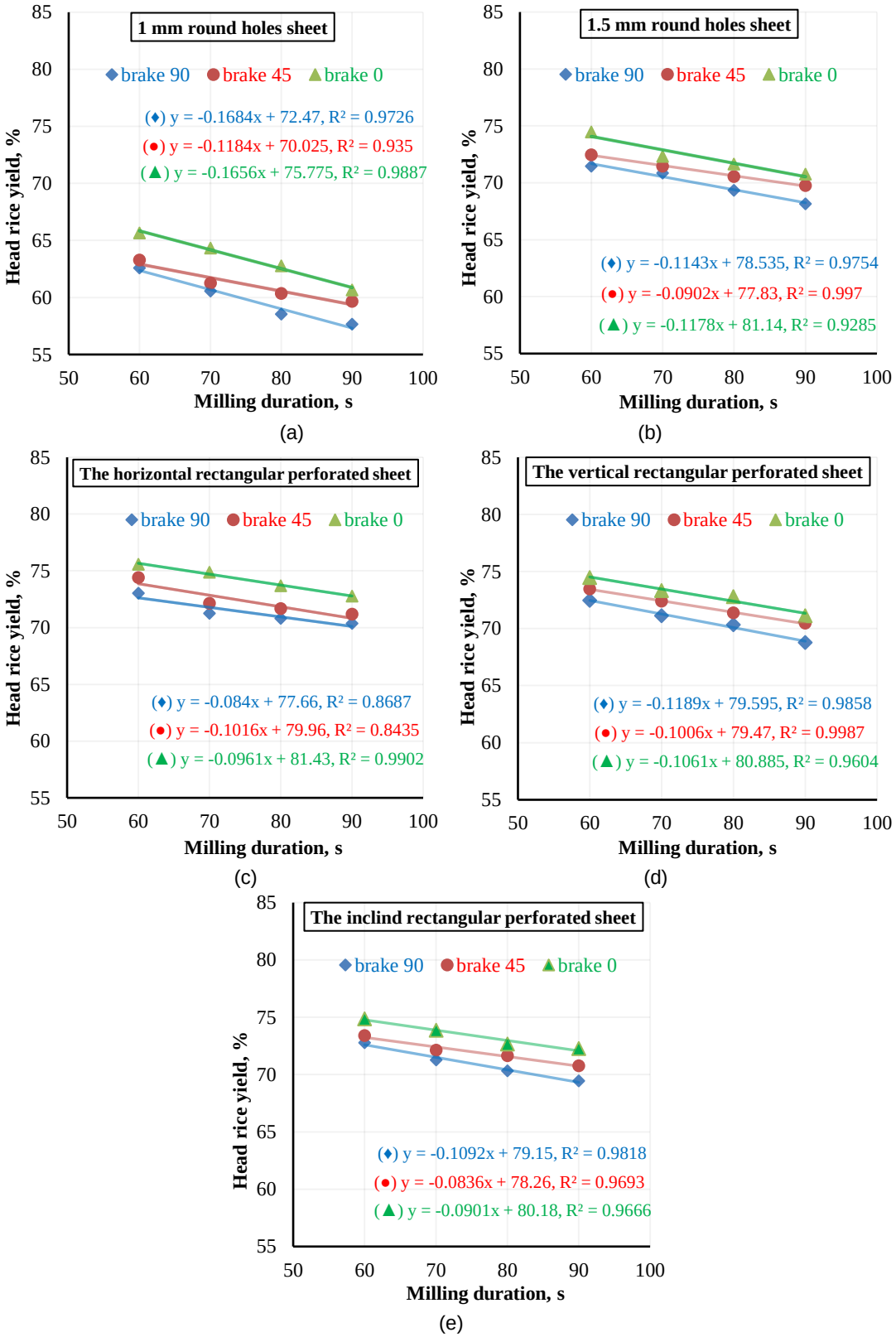

Fig. 3 – Effect of milling durations, brake angles and sheets' different perforations shapes

(a) 1 mm round holes sheet, (b) 1.5 mm round holes sheet, (c) the horizontal rectangular sheet, (d) the vertical rectangular sheet, (e) the inclined rectangular sheet on head rice yield

Effect of sheets' different perforations shapes, brake angles, and milling durations on broken rice percentage

Fig. 4 shows the effect of perforated sheet shape on broken rice percentage. As shown in the figure, in the case of using a 1 mm round holes sheet resulted in obtaining the highest percentage of broken rice (32.30, 31.36, 29.34, and 27.33%) at 90º brake angle and milling durations of 90, 80, 70, and 60 s, respectively, followed by 1.5 mm round holes sheet at the same brake angle. On the other hand, using the horizontal

rectangular perforated sheet resulted in recording the lowest percentages of broken rice (17.73, 17.13, 16.12 and 15.13%) at zero degree brake angle and milling durations of 90, 80, 70, and 60 s, respectively, followed by the inclined rectangular perforated sheet and the vertical rectangular perforated sheet. The statistical analysis revealed that the effect of perforated sheet shape on broken kernels percentage was highly significant.

Concerning the effect of brake angle on broken rice percentage, Fig. 4 reveals that increasing brake angle increased broken rice percentage at all shapes of perforated sheets and milling durations. Increasing brake angle from zero to 90° increased broken rice percentage from 24.30–27.33%, 16.83–18.22%, 15.13–17.20%, 15.51–17.53%, and 15.83–17.23% at 60 s milling duration for 1 mm round holes, 1.5 mm round holes, horizontal, vertical, and inclined sheets, respectively.

Relating the effect of milling duration on broken rice percentage, as shown in Fig. 4, increasing milling duration increased broken rice percentage for all perforated sheets and brake angles. Where increasing the milling duration from 60 to 90 s, increased broken rice percentage from 24.30–29.30%, 16.83–19.17%, 15.13–17.73%, 15.51–18.80, and 15.83–18.23% at zero brake angle for 1 mm round holes, 1.5 mm round holes, horizontal, vertical, and inclined sheets, respectively.

In addition, Fig. 4 shows that most of the rice breakage occurred in the first 60 s of the milling process for all the perforated sheets and brake angles, but the whitening process could not be finished because the white rice's appearance was not good yet.

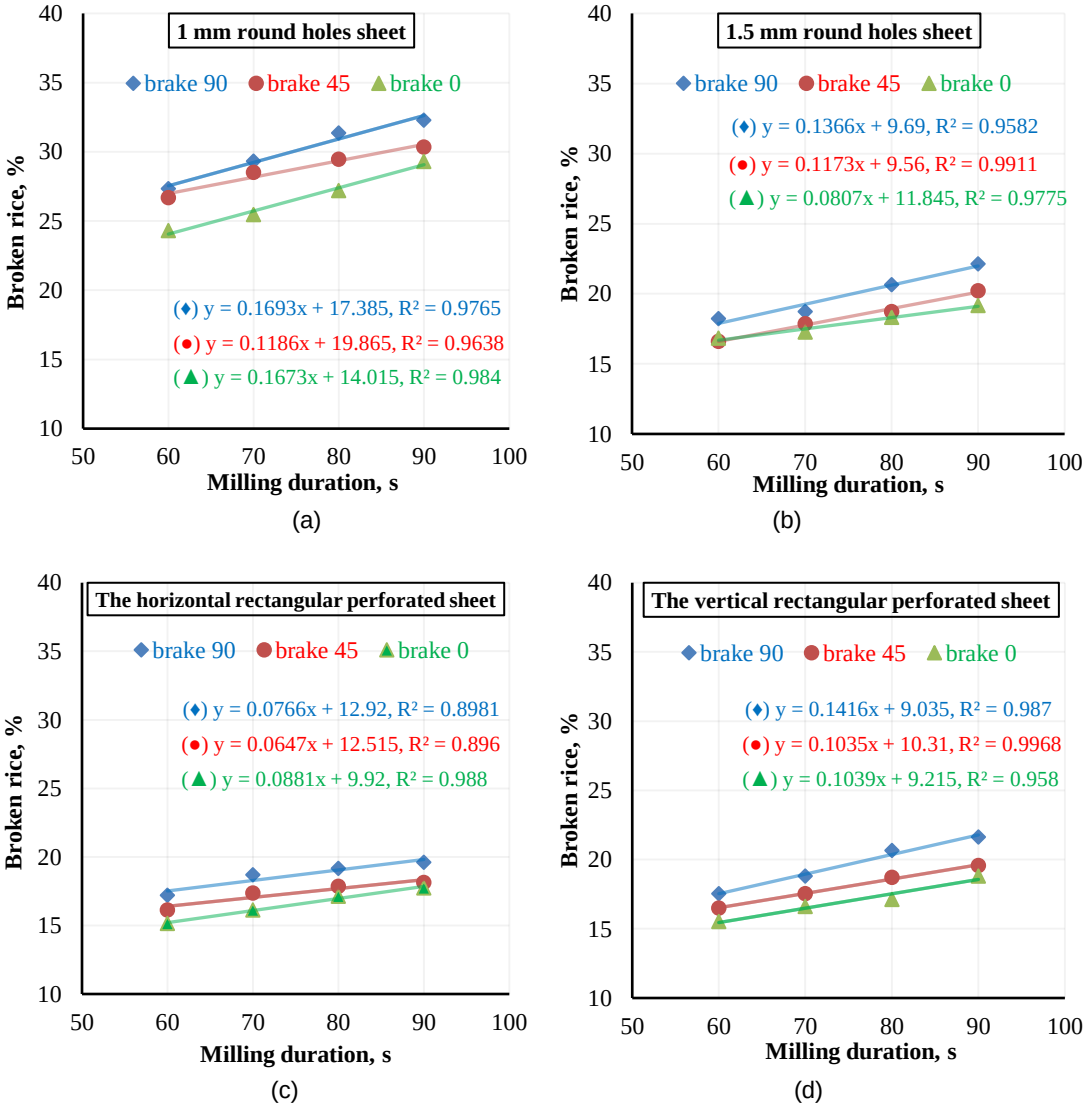

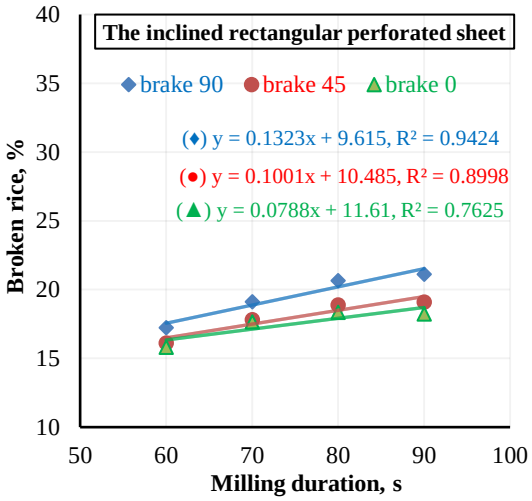

(e)

Fig. 4 – Effect of milling durations, brake angles and sheets' different perforations shapes

(a) 1 mm round holes sheet, (b) 1.5 mm round holes sheet, (c) the horizontal rectangular sheet, (d) the vertical rectangular sheet, (e) the inclined rectangular sheet on broken rice percentage

Effect of sheets' different perforations shapes, brake angles, and milling durations on rice whitening degree

Fig. 5 illustrates the influence of the different perforated sheet shapes on the rice whitening degree. As depicted in the figure, using a sheet with 1 mm round holes yielded the lowest levels of whitening at all milling durations and brake angles. Where the lowest levels of whitening were 27.77, 26.57, 25.77, and 25.23 unit, recorded at zero degree brake angle and milling durations of 90, 80, 70, and 60 s, respectively, followed by the horizontal rectangular perforated sheet. This could be attributed to the difficulty of rice bran passing through the small holes of the perforated sheet, making the whitening process difficult. Contrary to this, the vertical rectangular perforated sheet resulted in the highest values of whitening degree (38.70, 38.40, 37.73, and 37.12 unit) at 90° brake angle and milling durations of 90, 80, 70, and 60 s, respectively, followed by the inclined rectangular perforated sheet and 1.5 mm round holes sheet.

The statistical analysis indicated that the effect of the perforated sheet shape is highly significant on the whitening degree for all the parameters under study.

Regarding the effect of brake angle on whitening degree, it can also be seen in Fig. 5 that increasing the brake angle from zero to 90° increased the whitening degree at all shapes of perforated sheets and milling durations. Increasing brake angle from zero to 90° increased the whitening degree from 25.23–27.13 unit, 29.77–35.13 unit, 28.45–33.30 unit, 31.45–37.12 unit, and 32.57–36.35% at 60 s milling duration for 1 mm round holes, 1.5 mm round holes, horizontal, vertical, and inclined sheets, respectively. The 90º brake angle is recommended compared to zero degree, in the case of whitening degree only, because the angle of 90º yielded a good appearance of white rice. The choice between 90º and 45º brake angle depends upon the choice between the lowest broken rice percentage and the good appearance of white rice.

Concerning the effect of milling duration on whitening degree, as shown in Fig. 5, increasing milling duration increased the whitening degree for all perforated sheets and brake angles. Where increasing the milling duration from 60 to 90 s, increased whitening degree from 25.23–27.77 unit, 29.77–32.23 unit, 28.45–30.13 unit, 31.45–33.13 unit, and 32.57–34.55% at 60 s milling duration for 1 mm round holes, 1.5 mm round holes, horizontal, vertical, and inclined sheets, respectively.

Furthermore, Fig. 5 reveals that the whitening process could continue until the 80 s because the appearance of white rice seems so good now. In addition, there is no difference in the whitening degree for white rice at 80 s and 90 s and at a brake angle of 90º, where the whitening degrees were 38.40 and 38.70 unit for the vertical rectangular perforated sheet, 38.15 and 38.46 unit for the inclined rectangular perforated sheet, 37.47 and 37.88 unit for 1.5 mm round holes, and 35.17 and 35.60 unit for the horizontal rectangular perforated sheet. This means that the 80 s whitening duration is enough to get high-quality white rice with less broken rice percentage compared to the 90 s whitening duration, which may take more power without significant improvement in the quality of the resulting rice.

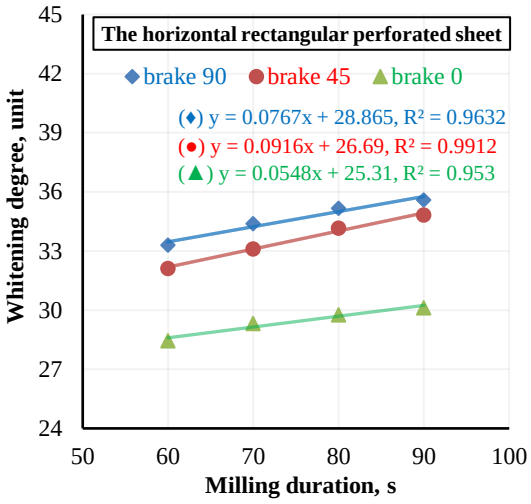
The horizontal rectangular perforated sheet
brake 90
brake 45
brake 0
(♦) y = 0.0767x + 28.865, R² = 0.9632
(●) y = 0.0916x + 26.69, R² = 0.9912
(▲) y = 0.0548x + 25.31, R² = 0.953
Whitening degree, unit
Milling duration, s

(a)

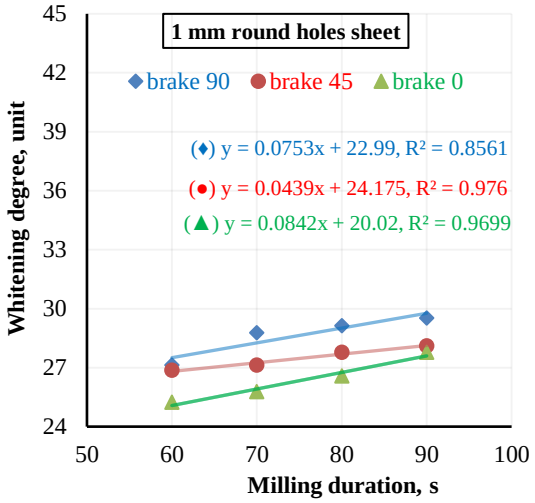
1 mm round holes sheet
brake 90
brake 45
brake 0
(♦) y = 0.0753x + 22.99, R² = 0.8561
(●) y = 0.0439x + 24.175, R² = 0.976
(▲) y = 0.0842x + 20.02, R² = 0.9699
Whitening degree, unit
Milling duration, s

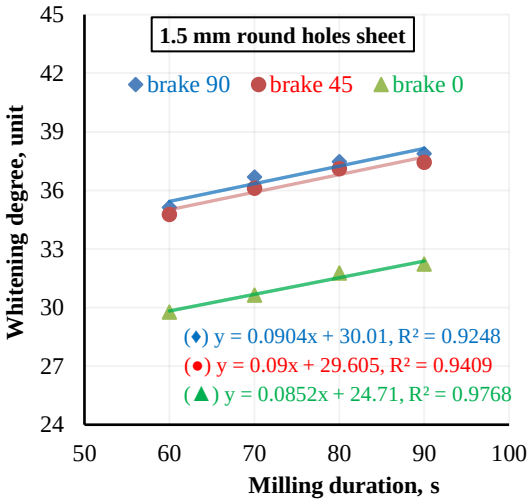
1.5 mm round holes sheet
brake 90
brake 45
brake 0
(♦) y = 0.0904x + 30.01, R² = 0.9248
(●) y = 0.09x + 29.605, R² = 0.9409
(▲) y = 0.0852x + 24.71, R² = 0.9768
Whitening degree, unit
Milling duration, s

(b)

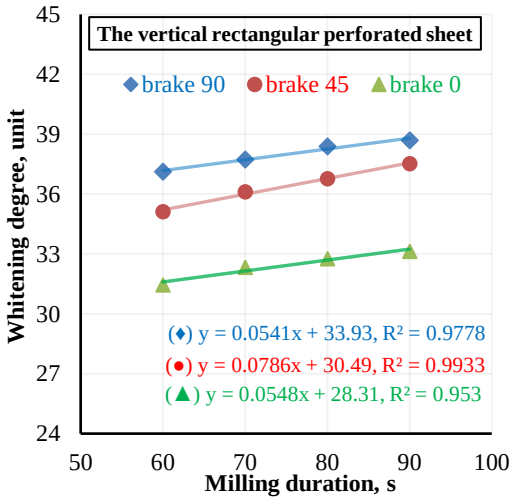
The vertical rectangular perforated sheet
brake 90
brake 45
brake 0
(♦) y = 0.0541x + 33.93, R² = 0.9778
(●) y = 0.0786x + 30.49, R² = 0.9933
(▲) y = 0.0548x + 28.31, R² = 0.953
Whitening degree, unit
Milling duration, s

(c)

(d)

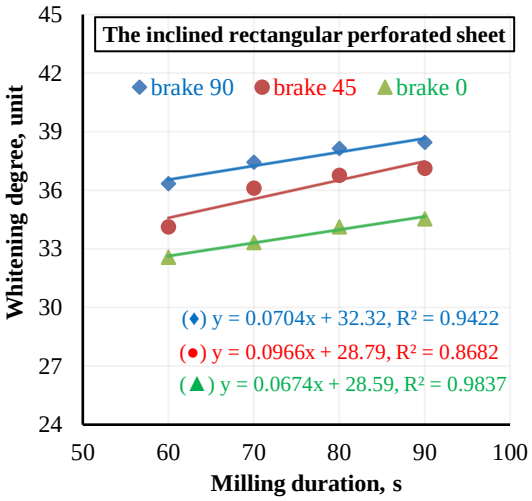

(e)

Fig. 5 – Effect of milling durations, brake angles and sheets' different perforations shapes

(a) 1 mm round holes sheet, (b) 1.5 mm round holes sheet, (c) the horizontal rectangular sheet, (d) the vertical rectangular sheet, (e) the inclined rectangular sheet on whitening degree

Effect of sheets' different perforations shapes, brake angles, and milling durations on white rice bulk temperature

The effect of perforated sheet shape on the white rice bulk temperature is shown in Fig. 6. The obtained data revealed that using a sheet with 1 mm round holes resulted in the highest rice temperatures (32.73, 32.32, 31.13, and 30.15 ºC) at 90° brake angle and milling durations of 90, 80, 70, and 60 s, respectively. The high temperatures could be attributed to the high friction caused by the jam of brown rice and bran, which could not pass through the small holes of the perforated sheet. This jam and high temperature explain the low rice quality in terms of highly broken percentage and low whitening degree when using this shape of perforated sheet. On the opposite side, using the horizontal rectangular perforated sheet resulted in the lowest rice temperatures (29.13, 28.15, 27.55, and 26.45 ºC) followed by a 1.5 mm round holes sheet at the same levels of milling duration and zero degree brake angle.

Regarding the effect of brake angle on rice bulk temperature, Fig. 6 shows that increasing the brake angle from zero to 90° increased rice bulk temperature at all shapes of perforated sheets and milling durations. Increasing brake angle from zero to 90° increased rice bulk temperature from 29.25–30.15 ºC, 27.33–28.25 ºC, 26.45–27.65 ºC, 28.65–29.65 ºC, and 28.25–29.85 ºC at 60 s milling duration for 1 mm round holes, 1.5 mm round holes, horizontal, vertical, and inclined sheets, respectively. Furthermore, statistical analysis revealed that the brake angle significantly affected white rice bulk temperature. The gradients in rice bulk temperature explain the effect of friction action between rice grains and both the whitening stone and the perforated sheet beside the grains themselves. Whenever the rice bulk temperature rises causes increased exposure to thermal stress and easily breaks during the whitening process.

Concerning the effect of milling duration on rice bulk temperature, Fig. 6 illustrates that increasing the milling duration increased rice bulk temperature at all shapes of perforated sheets and milling durations. Increasing the milling duration from 60 to 90 s, increased rice bulk temperature from 29.25–31.55 ºC, 27.33–29.35 ºC, 26.45–29.13 ºC, 28.65–30.55 ºC, and 28.25–30.55 ºC at 60 s milling duration for 1 mm round holes, 1.5 mm round holes, horizontal, vertical, and inclined sheets, respectively. In addition, statistical analysis showed that the milling duration significantly affected white rice bulk temperature.

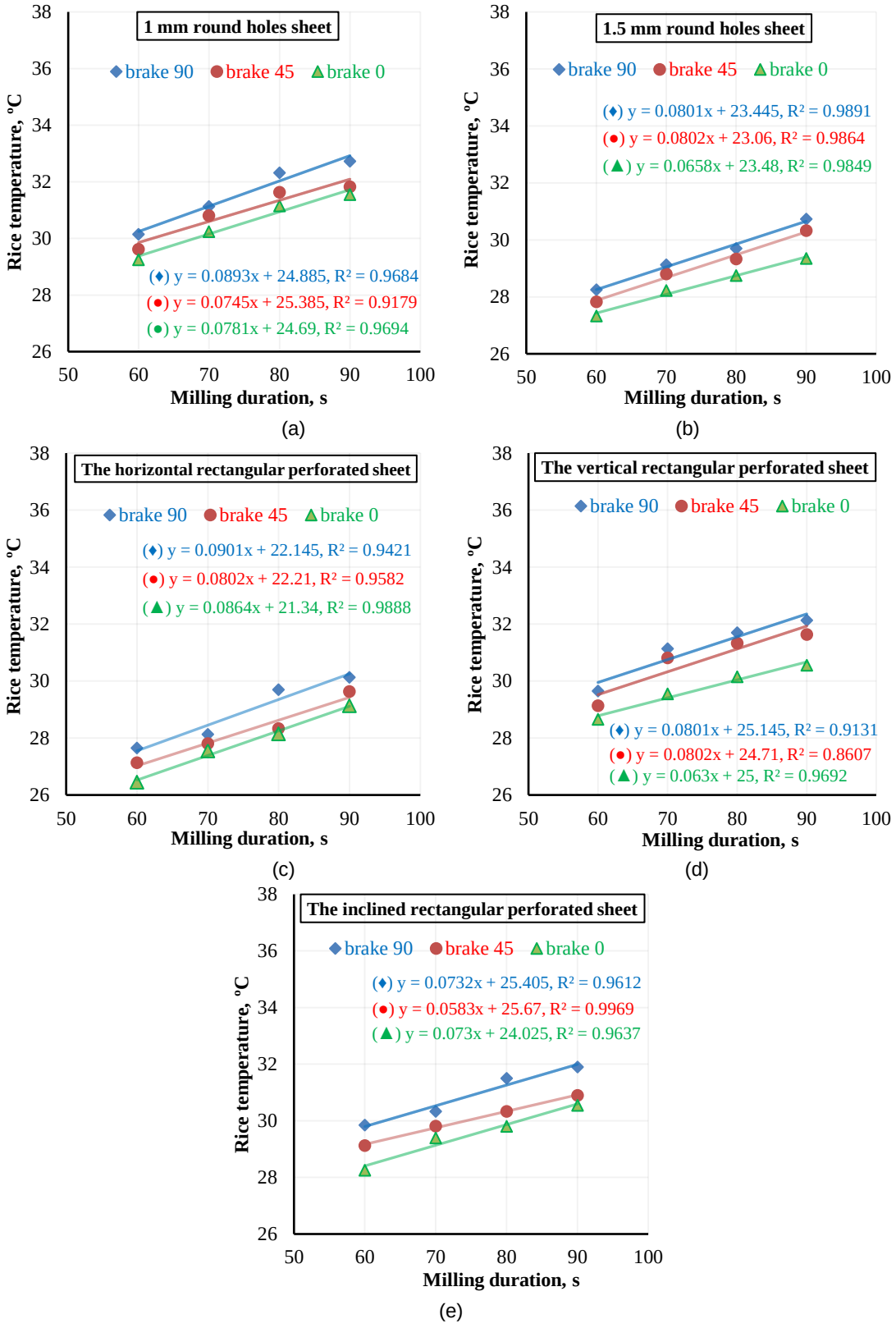

Fig. 6 – Effect of milling durations, brake angles and sheets' different perforations shapes

(a) 1 mm round holes sheet, (b) 1.5 mm round holes sheet, (c) the horizontal rectangular sheet, (d) the vertical rectangular sheet, (e) the inclined rectangular sheet on rice bulk temperature

CONCLUSIONS

The study aimed to test and evaluate five shapes of perforated sheets, three brake angles, and four milling durations to enhance the quality of long-grain white rice resulting from an abrasive milling machine. The results revealed that using a 1 mm round holes sheet resulted in the lowest head rice yields, the highest percentage of broken rice, the highest rice temperature, and the lowest values of whitening degree at all milling durations and brake angles. The best head rice yields and lowest percentage of broken rice were obtained

using the horizontal rectangular perforated sheet at zero degree brake angle followed by the inclined rectangular perforated sheet. The vertical rectangular perforated sheet resulted in the highest values of the whitening degree at all milling durations and 90º brake angle, followed by the inclined rectangular perforated sheet. The horizontal rectangular perforated sheet resulted in the lowest rice temperature, followed by a 1.5 mm round holes sheet at all milling durations and zero degree brake angle. Most of the kernel breakage occurred during the first 60 s, but the processing could not be finished because the appearance of white rice was not good yet. Therefore, the processing could be continued for at least 80 s to get a good appearance of white rice. The brake angle of 90º resulted in the highest broken rice percentage for all studied perforated sheets used in this study. Thus, based on our priorities, the horizontal rectangular perforated sheet is recommended due to its ability to record the highest head rice yield and the lowest broken rice percentage and temperature; it also accomplished an acceptable whitening degree.

ACKNOWLEDGEMENT

The authors would like to thank the Agricultural Engineering Research Institute (AEnRI), Agricultural Research Center (ARC), Giza, Egypt.

REFERENCES

[1] Abayawickrama, A. S. M. T., Reinke, R. F., Fitzgerald, M. A., Harper, J. D. I., & Burrows, G. E. (2017). Influence of high daytime temperature during the grain filling stage on fissure formation in rice. *Journal of Cereal Science*, *74*, 256–262. https://doi.org/10.1016/j.jcs.2017.02.013

[2] Afzalinia, S., Shaker, M., & Zare, E. (2004). Comparison of different rice milling methods. *Canadian Biosystems Engineering/Le génie des biosystèmes au Canada*, *46*, 363–366..

[3] Ahmad, U., Alfaro, L., Yeboah-Awudzi, M., Kyereh, E., Dzandu, B., Bonilla, F., Chouljenko, A., & Sathivel, S. (2017). Influence of milling intensity and storage temperature on the quality of catahoula rice (oryza sativa, L.). *LWT - Food Sci Technol*, *75*,386–392. https://doi.org/10.1016/j.lwt.2016.09.014

[4] Bekki, E., Kunze, O. R. (1988). Flash drying and milling techniques for high moisture brown rice. *Transactions of the ASAE*, 31, 1828–1834. St. Joseph, Michigan.

[5] Dhankhar, P. (2014). Rice milling. *IOSR Journal of Engineering*, *4*(5), 34–42. doi: 10.9790/3021-04543442

[6] Egyptian Standard. (1992). *The Egyptian Organization for Standardization and Quality Control*. UDC.633018003,258. Rice. Egypt.

[7] Elicin, A. K., Esgici, R., & Sessiz, A. (2022). The effect of rice milling time and feed rate on head rice yield and color properties. *International Journal of Agriculture, Environment and Food Sciences*, *6*(4), 585–591.https://doi.org/10.31015/jaefs.2022.4.11

[8] FAO. (1981). *Rice milling equipment, operation and maintenance. FAO agricultural services bulletin*. Food and agriculture organization of the United Nations. Rome. Italy.

[9] FAOSTAT. (2020). Food and Agriculture Organization of the United Nations. FAOSTAT Available at http://faostat.fao.org/site/339/default.aspx. Accessed 10 September 2022.

[10] Gbabo, A., Ndagi, B. (2014). Performance evaluation of a rice mill developed in NCRI. *International Journal of Engineering Research*, *3*(8), 482–487. http://repository.futminna.edu.ng:8080/jspui/handle/123456789/13426

[11] IRRI. (2013). *Trends in global rice consumption: Rice today*. Manila, Philippines: International Rice Research Institute.

[12] Kalpanadevi, C., Singh, V., & Subramanian, R. (2019). Impact of physicochemical properties on duration and head rice yield during abrasive and friction milling of rice. *Journal of Food Science and Technology*, *56*(8), 3900–3909. https://doi.org/10.1007/s13197-019-03861-z

[13] Matouk, A. M., Shalaby, M. T., & El-Kholy, M. M. (2000). Effect of heat treatment on some physical quality and cooking characteristics of milled rice. Paper presented at the first Mansoura conference. Oct. 2000. Mansoura Univ. Mansoura, Egypt.

[14] Matthews, J., Abadie, T. J., Deobald, H. J., & Freeman, C. C. (1970). Relation between head rice yields and defective kernels in rough rice. *Rice Journal*, *73*, 6–12. Raleigh, NC 27625, USA.

[15] Mukhopadhyay, S., Siebenmorgen, T. J. (2018). Effect of airflow rate on drying air and moisture content profiles inside a cross-flow drying column. *Drying Technology*, *36*(11), 1326–1341. https://doi.org/10.1080/07373937.2017.1351453

[16] Puri, S., Dhillon, B., & Sodhi, N. S. (2014). Effect of degree of milling (Dom) on overall quality of rice—a review. *International Journal of Advanced Biotechnology and Research*, *5*(3), 474–48.
[17] Ray, D. K., Mueller, N. D., West, P. C., Foley, J. A., & Hart, J. P. (2013). Yield trends are insufficient to double global crop production by 2050. *PLOS ONE*, *8*(6), e66428. https://doi.org/10.1371/journal.pone.0066428.
[18] Radwan, S. M. (1994). Long grain milling machine under Egyptian condition. Ph.D. Thesis, Dept. of Agric. Mech., Mansoura Univ., Mansoura, Egypt.
[19] Radwan, S. M. (2001). The potential energy consumption for milling some Egyptian rice varieties. *Misr Journal of Agricultural Engineering*, *18*(3), 537–551.
[20] Ren, H., Qi, S., Zhang, L., Wang, L., Huang, J., Yang, H., Ren, C., & Zhou, W. (2021). Variations in the appearance quality of brown rice during the four stages of milling. *Journal of Cereal Science*, *102*, 103344. https://doi.org/10.1016/j.jcs.2021.103344
[21] Satake. (1983). Construction and function of abrasive roll type rice whitening machine and friction roll type rice whitening machine. Satake Engineering Co., Ltd. Tokyo, Japan.
[22] Satake. (1992). Instruction manual for rice whitening machine TM-05. Satake Engineering Co., Ltd. Tokyo, Japan.
[23] Seguy, J., Clement, G. (1994). Behaviour of rice during processing. *Journal of Agriculture Research and Development*, 16, 38–46.
[24] Siebenmorgen, T. J., Bautista, R. C., & Counce, P. A. (2007). Optimal harvest moisture contents for maximizing milling quality of long- and medium-grain rice cultivars. *Applied Engineering in Agriculture*, *23*(4), 517–527. doi: 10.13031/2013.23476
[25] Siebenmorgen, T. J., Matsler, A. L., & Earp, C. F. (2006). Milling characteristics of rice cultivars and hybrids. *Cereal Chemistry*, *83*(2), 169–172. https://doi.org/10.1094/CC-83-0169
[26] Soepardjo, S. (1981). Grain post-harvest processing technology. Southeast Asia cooperative post-harvest research and development program. Searca. Los Banos, Philippines.
[27] Tangpinijkul, N. (2010). Rice Milling System. International Training Course on Post-harvest Technology and Processing of Agricultural Crops. 14 November - 4 December 2010. Manhattan Klongluang Hotel, Pathum Thani, Thailand.
[28] Velupillai, L., Pandey, J. P. (1987). Color and bran removal in rice processing. American Society of Agricultural Engineers St. Joseph, Michigan 49085-9659. USA.
[29] Zeng, Y., Mao, B., Jia, F., Han, Y., & Li, G. (2022). Modelling of grain breakage of in a vertical rice mill based on DEM simulation combining particle replacement model. *Biosystems Engineering*, *215*, 32–48. https://doi.org/10.1016/j.biosystemseng.2021.12.022

A NEW SEED DRILL FOR PLANTING PEAS ON A RAISED-BED

/

سطارة جديدة لزراعة البسلة على مصاطب

Mahmoud AWAD, Osama FOUDA, Solaf ABD EL-REHEEM, Adel AL-GEZAWE, Mokhtar COTTB, Mahmoud OKASHA*[1]

Agricultural Engineering Research Institute (AEnRI), Agricultural Research Center (ARC), Giza 12611/ Egypt

Tel: +20-1003133841; E-mail: mahmoudokasha1988@yahoo.com

Corresponding author: Mahmoud Okasha

DOI: https://doi.org/10.35633/inmateh-68-67

Keywords: *Seed drill; Specific energy; Seeds damage; Germination ratio; Pea yield*

ABSTRACT

Until now, the traditional method for planting pea seeds is manual because of the scarcity of planting machines. Therefore, this study aims to provide and evaluate a new seed drill for planting pea seeds on a raised bed in silt-clay loam soil. This seed drill consists of the frame, seeds hopper, seed metering device, transmission system, and covering unit. Laboratory tests on pea seeds were conducted to determine the seeds' physical and mechanical properties. Field trials were carried out under the following parameters; four forward speeds (0.79, 0.98, 1.28, and 1.64 m s^{-1}), three disc cell capacities (1, 2, and 3 seeds per cell), two different cells shapes (circular, and a rectangle with semicircle end), and three distances between rows (7.5, 10, and 15 cm) to assess the performance of the seed drill on fuel consumption, specific energy, slip ratio, seeds damaged, germination ratio, plants number per hill, longitudinal scattering, and pea pods yield. The results revealed that the optimum performance of the seed drill was achieved at a forward speed ranging from 0.79 to 0.98 m s^{-1}, using a disc cell capacity of 2 seeds, a circular cell shape, and a distance between rows of 10 cm.

الملخص

لا تزال حتى الآن زراعة بذور البازلاء في مصر بالطريقة التقليدية (يدويا) بسبب قلة الآلات المخصصة للزراعة. لذلك ، تهدف هذه الدراسة إلى توفير وتقييم سطارة جديدة لزراعة بذور البازلاء على مصاطب في تربة طينية. حيث تتكون السطارة من الاطار وقادوس البذور وجهاز تلقيم البذور ونظام النقل ووحدة التغطية. أجريت الاختبارات المعملية على بذور البازلاء لتحديد الخصائص الفيزيائية والميكانيكية للبذور. أجريت التجارب الحقلية وفقًا للمعايير التالية ؛ أربع سرعات أمامية (0.79 ، 0.98 ، 1.28 ، 1.64 م ث$^{-1}$) ، ثلاث سعات لخلية القرص (1 ، 2 ، 3 بذور لكل خلية) ، شكلين مختلفين للخلايا (دائري ، ومستطيل بنصف دائرة فى نهايته) ، وثلاث مسافات زراعة بين الصفوف (7.5 ، 10 ، 15 سم) لتقييم أداء السطارة على استهلاك الوقود ، والطاقة النوعية ، ونسبة الانزلاق ، والبذور التالفة ، ونسبة الإنبات ، وعدد النباتات في كل جورة، والتشتت الطولي ، وانتاجية البازلاء. أوضحت النتائج أن الأداء الأمثل للسطارة تم تحقيقه بسرعة أمامية تتراوح من 0.79 إلى 0.98 م ث$^{-1}$ ، باستخدام سعة خلية القرص بذرتين لكل خلية، وشكل الخلية الدائري ، ومسافة الزراعة بين الصفوف 10 سم.

INTRODUCTION

Pea (*Pisum sativum* L.) is one of the extremely crucial legume species (*Krizmanić et al., 2020*); it is a fundamental source of high-quality proteins, micronutrients, starch, phenolic compounds, dietary fibers, and antioxidants (*Yu et al., 2021*). Pea seeds are smooth or wrinkled; the weight of 100 seeds ranges from 10 to 36 g. Pea plants up to 80 per square meter at 3 to 5 cm depth, about 10 cm apart in rows (*Garden peas production, 2011*). The peas' seeds are sown directly in the soil by 10 kg of seeds at an area of 1000 square meters at a depth of 2 to 3 cm, with a plant spacing of 7 to 10 cm (*Burt, 2008*). Furthermore, sown pea seeds in hills with a space of 15 cm apart in rows using two seeds per hill and thinned the hill to one plant 15 days after germination. In addition, adjusted input seeds accurately in the rows at control depth and spacing, and the seeds were covered with soil and provided proper compaction of the seed (*Zaki et al., 2017*).

The manual planting method of seeds has numerous disadvantages; for example, it causes low seed placement, spacing efficiencies, severe backache for the farmer, and decreases the crop field's active area (*Kyada and Patel, 2014*). Moreover, *Vimal et al. (2015)* manufactured a multi-purpose sowing machine suitable for various seeds and small farms with lower operating costs. The influence of planting speed on the seed accuracy of metering devices was studied. Their results found that higher planting speeds led to more hills without seeds, an inaccurate distance between hills, and increased average spacing (*Khan et al., 2017*). A seeder for planting grains on ridges and flat lands was developed. The results reported that the distance between plants, uniformity of seed distribution, and the ratio of seed emergence are the most common characteristics to assess the performance of the seeder (*Olaoye and Bolufawi, 2001*).

[1] *Mahmoud Awad, Senior Researcher; Osama Fouda, Senior Researcher; Solaf Abd E l-Reheem, Senior Researcher; Adel Al-Gezawe, Senior Researcher; Mokhtar Cottb, Senior Researcher; Mahmoud Okasha, Researcher*

Afify, (2009), developed a seed drill feeding device suitable for planting medical and aromatic seeds in hills between rows of 40 cm, four operating speeds, and four distances between hills. The results revealed that the optimal distance between hills was 30 cm to obtain a high yield of seeds of 340 kg ha^{-1} and low specific energy of 7.24 kWh tonne^{-1}. Furthermore, a high germination ratio of 95.37% and a high field efficiency of 89.41% at a forward speed of 3.13 km h^{-1}. A manual multi-crop seeder was developed and evaluated, and the results indicated the seeder had field capacity and field efficiency of 0.39 ha h^{-1} and 76.3%, respectively. Also, the percentage difference between the seed damage was 1.32%, 2.32%, and 3.54% for soybean, maize, and cowpea, respectively, at the average distance between hills of 40.8 cm and a depth of 3.98 cm (*Adekanye and Akande, 2015*).

Moreover, a prototype planter was manufactured for planting wheat seeds on a wide-width row. The results recommended that the optimum seed planting performance was achieved at an operating speed of 4.36 km h^{-1}, a metering cell capacity of 8 seeds. The operation under the previous parameters recorded low energy consumption of 1.26 kWh ha^{-1}, a high grain yield of 1.22 tonnes ha^{-1}, and a high germination ratio of 97.78% (*Awad, 2016*).

Finally, because of the lack of machines that plant pea seeds on terraces in Egypt, the current study aims to provide and evaluate the performance of a new seed drill for planting pea seeds on a raised bed and determine the optimum operating conditions for the seed drill under this study.

MATERIALS AND METHODS

The description of the seed drill

Figure 1 shows the seed drill's photography view, elevation, and side views. All seed drill parts were manufactured and modified at a local workshop in El-Zahaira Village, El-Snbellaween City, Dakahlia Governorate, Egypt. The seed drills' overall dimensions are 150 × 120 × 100 cm (length, width, and height). The total weight of the seed drill is 1.96 kN. The seed drill consists of a frame with L-shaped iron section with dimensions of 140 × 40 × 5 cm (L × W × H), with a thickness of 6 mm. Three-point hitch made of iron plates with a thickness of 2 cm and a width of 10 cm; it was manufactured according to (*ASABE standard, 2003*). The hitch pin is 2.5 cm in diameter, the upper-hitch point is at the height of 60 cm from the lower-hitch point, and the lower-hitch point is at the height of 65 cm from the ground. The seeds hopper is made of an iron sheet with a thickness of 2 mm. It has a trapezoid shape and a slope angle of 70° on two sides, which is more than the repose angle of pea seeds (25.0°–28.7°), according to (*Khan et al., 2017*). The maximum capacity of the seeds hopper is 50 kg. Figure 2 presents the seed metering device, which consists of seven feeding discs made of Teflon with a thickness of 5 cm; on the periphery of the feeding disc, the seed cells were formed in two different shapes and dimensions. The diameter of the feeding disc was about 16 cm. The feeding disc diameter was calculated according to Eq. (1) as follows:

$$Dm = \frac{Dw}{Gr} \quad (1)$$

where Dm is the diameter of the feeding disc [cm], Dw is the ground wheel diameter of the seed drill [cm], and Gr is the gear ratio.

The number of cells on the circumference of the feeding disc was calculated according to (*Khan et al., 2017*), as follows in Eq. (2).

$$Number\ of\ cells\ = \frac{\pi\ \times\ Diameter\ of\ seeder\ ground\ wheel\ (cm)}{Gear\ ratio\ \times\ Intra\ row\ spacing\ of\ seeds\ (cm)} \quad (2)$$

According to equation (2), the number of cells is (6 cells/disc). The cell of seeds was manufactured at three disc cell capacities (one "C1 cell volumetric capacity of 0.42 cm^3", two "C2 cell volumetric capacity of 0.63 cm^3", and three "C3 cell volumetric capacity of 1.26 cm^3" seeds per cell) and two different cell shapes (circular "S1" and a rectangle with semicircle end "S2", as shown in Fig. (2). Each disc was fixed inside the iron case as a cylinder shape with internal and external diameters of 16.1 and 17.0 cm, respectively. The top of the iron case has a hole with a diameter of 21 mm to enter the seeds from the hopper to the disc cells, but on the other side, the bottom has a hole to flow the seeds into the seed tube and consequently to the seedbed. All the feeding discs were installed on an iron shaft with a length of 150 cm and 30 mm in diameter. Each end of the feeding shaft was mounted in a standard cast iron pillow block bearing UCP206, and the shaft took its movement from the ground wheel. The transmission unit consists of two gears. The first gear is fixed on the seed drill's wheel shaft and has 45 teeth with a diameter of 20 cm. The second gear is fixed on the feeding shaft and has 14 teeth with a diameter of 6 cm. The motion transmits at different diameters from 48.0 cm to 16.0 cm of the ground wheel at a ratio speed of discs shaft of 1:3, this ratio adding accurately the numbers of

hills related to the peripheral speed of the ground wheel. A control bar made of iron with a length of 120 cm and a width of 2 cm has holes in equal distances of 2.5 cm and was used to control and adjust the rows' distances. Seven shares with dimensions of 6.0 × 2.5 cm (L × W) are attached in the control bars' holes to cut the soil with the desired depth of 3.0 cm to ease the pea seeds' sown in the recommended depth. At the top of each share is a pipe with a diameter of 2.5 cm and a length of 4.0 cm to install the seeds' tubes. Seven seed tubes made of PVC with a length of 35 cm and a diameter of 2.54 cm are attached between the seed metering device and the shares to ensure the correct positioning of the seed in the allotted place. A chain with a length of 2 m was used as a covering unit to cover the hills with soil after executing the seeding operation. The seed drill is mounted at the rear of a 32 kW tractor (Daedong D4351, 4WD with a fuel tank capacity of 43.5 liters) as a power source to execute all field experiments in this study.

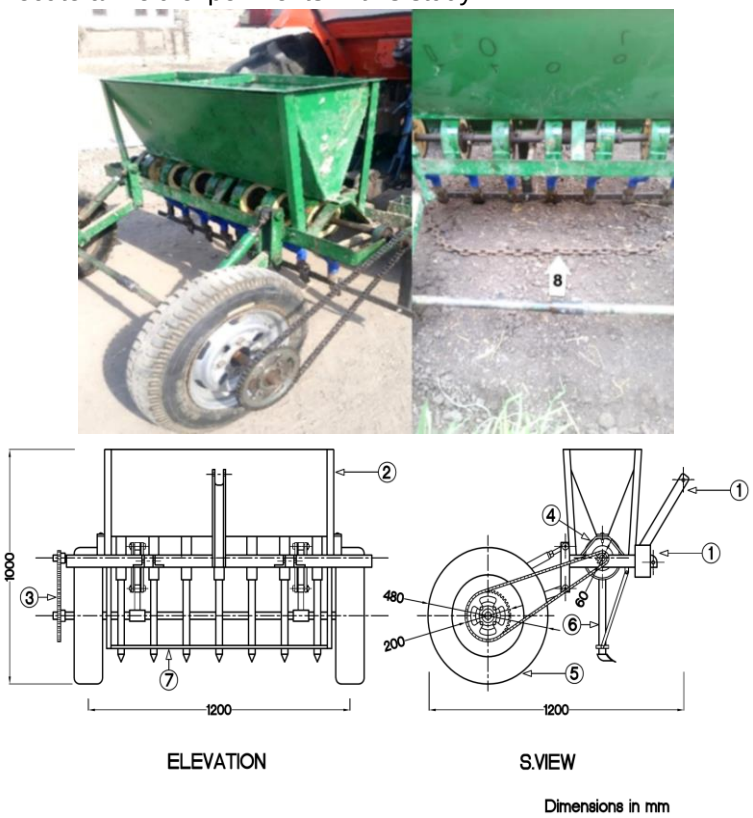

Fig. 1 – Photo, elevation and side views of the seed drill

1 – Three-point hitch; 2 – Seeds hopper; 3 – Chain drive transmission system; 4 – Seed metering device; 5 – Ground wheel; 6 – Seed tube; 7 – The control bar of the planting depth and distance between rows; 8 – Covering unit (chain)

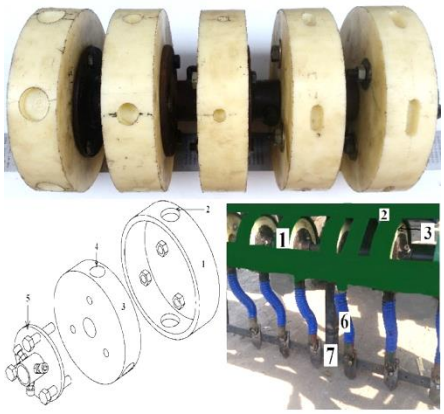

Fig. 2 – The seed metering device

1 – The disc's case; 2 – The seed input hole; 3 – The cell's disc; 4 – The cell of seeds; 5 – The assembly unit; 6 – The seeds' tubes; 7 – The shares

Field trials

The field trials were carried out during the winter season of 2021 in an area of about 1.6 ha after the maize crop. The trials were arranged at four forward speeds of 0.79, 0.98, 1.28, and 1.64 m s^{-1}, three disc cell capacities of one "C1", two "C2", and three "C3" seeds per cell, two cells shapes of circular "S1", and a rectangle with semicircle end "S2", and three distances between rows of 7.5 "D1", 10 "D2", and 15 cm "D3".

The trial area was divided into 216 plots; each plot had a length of 50 m and a width of 1.2 m to assess the seed drill's performance under the studied variables. The field experiments were executed at an average soil moisture content of 14% (dry basis) and an average seeding depth of 3 cm. All treatments were replicated three times in a randomized complete block design. The trials were executed on Master B variety of pea at a farm in El-Zahaira Village (31°28'21.23" E, longitude; 30°55'7.66" N, latitude; and 11 m altitude), Dakahlia Governorate, Egypt. The seed drill sows seven rows with different distances of 7.5, 10, and 15 cm between rows on a terrace that top width is 90 cm, the terrace's total width is 120 cm, and 8.4 cm between the hills in the row, as shown in Fig. (3). The mechanical analysis of the experimental soil was carried out at the Soil, Water, and Environment Research Institute (SWERI), Agricultural Research Center (ARC), Egypt. The experimental soil's texture is silt-clay loam with clay, silt, fine sand, and coarse sand percentages of 35.15, 42.60, 18.42, and 3.83%, respectively.

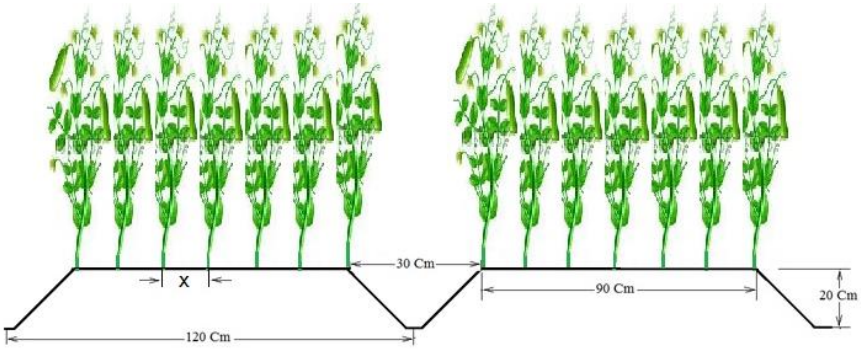

Fig. 3 – Sketch of the terraces' dimensions

Measurements

Measurements on pea seeds before sowing

Laboratory tests were conducted on pea seeds before the sowing operation to determine some physical and mechanical properties of Master B variety pea seeds. An electronic digital caliper with an accuracy of 0.01 mm was used to measure the seeds' dimensions. A graduated cylinder with a volume of 500 cm^3 was used to measure the volume of the investigated seeds to obtain true and bulk density. An electronic digital balance with an accuracy of 0.01 g was used to determine the mass of the seeds' samples to calculate bulk density. A digital coefficient of friction device with an accuracy of 0.01 degrees was used to measure the coefficient of friction of pea seeds on a metal sheet surface. The pea seed's repose angle was measured using an angle of repose tester to measure the angle between the base and slope of cone-formed seed mass. In order to estimate seed damage and germination ratio, five kilograms of pea seeds were sorted manually, and the percentage of damaged seeds was calculated. After that, the remaining pea seeds were put into the hopper, and the ground wheel was rotated to receive the seeds into a packet at the end of the seed tube. Then, the seeds were sorted, and the percentage of damaged seeds was calculated.

Furthermore, five hundred pea seeds were germinated to calculate the actual germination ratio before passing the pea seeds through the seed metering device. The actual germination ratio of seeds was calculated according to (*Yehia, 1993*), as follows in Eqs. (3–5).

All treatments were replicated five times, and the average of the obtained results is presented in Table (1).

$$Actual\ germination\ percent = Germination\ percent\ of\ unsound\ seeds - (visible\ seed\ damage\ [\%] + invisible\ seed\ damage, [\%]) \quad (3)$$

$$Visible\ seed\ damage\ (\%) = \frac{Weight\ of\ damaged\ seeds\ (g) \times 100}{Total\ weight\ of\ seeds\ (g)} \quad (4)$$

$$Invisible\ seed\ damage\ (\%) = \frac{No.\ of\ shoots\ \times\ 100}{Total\ No.\ of\ seeds} \quad (5)$$

.**Table 1**

Some physical properties of pea seeds

Characters / Variety	Static friction coefficient (SFC)	Mass of 100 seeds [g]	Bulk density [g cm^{-3}]	The average diameter of the seeds [mm]	Angle of repose	Moisture content [%, d.b.]
Master B	0.38	18.62	1.10	6.7	28.9°	9.26

Measurements on the seed drill

The measurements were performed on the seed drill, such as actual field capacity (ha h^{-1}), fuel consumption (l h^{-1}), specific energy (kWh ha^{-1}), and wheel slip ratio. The theoretical field capacity (TFC) was determined as follows in Eq. (6)

$$TFC = \frac{W \times S \times 1000}{10000} \quad (6)$$

where TFC is the theoretical field capacity [ha h^{-1}], W is the seed drill's width [m], and S is the seed drill's forward speed [km h^{-1}]

The actual field capacity (AFC) was determined according to (*Srivastava et al., 1993*), as follows in Eq. (7).

$$AFC = \frac{1}{T} \quad (7)$$

where AFC is the actual field capacity [ha h^{-1}], T is the total actual operation time per hectare [h ha^{-1}] (T = Tm + Tt + Tp), Tm is maintenance and lubrication time [h ha^{-1}], Tt is turning time [h ha^{-1}], and Tp is parasitic time [h ha^{-1}]

The fuel consumption rate was measured according to (*Elsbaay and Hegazy, 2016*), as follows in Eq. (8).

$$FCR = \frac{FCV}{1000} \times \frac{60}{OT} \quad (8)$$

where FCR is the fuel consumption rate [l h^{-1}], FCV is the fuel consumption volume [ml], and OT is the operating time [min]

The specific energy (SE) was calculate according to (*Hunt, 1983*), as follows in Eq. (9).

$$SE\ (kWh\ ha^{-1}) = \left(\frac{FCR \times \rho f \times LCV}{3600}\right) \times \left(\frac{427 \times \eta th \times \eta mec}{75 \times 1.36 \times AFC}\right) \quad (9)$$

where SE is specific energy [kWh ha^{-1}], FCR is fuel consumption rate [l h^{-1}], ρf is fuel density [0.85 kg l^{-1} for diesel], LCV is lower calorific value of fuel [10000 kcal kg^{-1}], 427 is thermo-mechanical equivalent [J $kcal^{-1}$], ηth is engine thermal efficiency [≈ 35% for diesel engines], ηmec is engine mechanical efficiency [≈ 80% for diesel engines], and AFC is actual field capacity [ha h^{-1}].

The slippage ratio indicates the power loss due to the load. The slippage was determined according to (*ASABE standard, 2003*), as follows in Eq. (10).

$$S\ (\%) = \left(1 - \frac{Va}{Vo}\right) \times 100 \quad (10)$$

where S is the slippage [%], V_a is the actual speed of the loaded tractor in the field [km h^{-1}], and V_o is the tractor's speed without load on the concrete surface [km h^{-1}]

The seed drill sliding was determined as follows in Eq. (11).

$$S_m\ (\%) = \left(\frac{d1 - d2}{d2}\right) \times 100 \quad (11)$$

where S_m is the seed drill sliding [%], d1 is the actual distance for 10 revolutions of the seed drill wheels [m], and d2 is the theoretical distance for the same revolutions number of seed drill wheels [m]

Measurements on the crop growth

The crop yield is a function of some crop characteristics. Some characteristics are directly measured after sowing before irrigation operation, and the others are after germination and harvesting of the crop. The characteristics measurements include the number of seeds in the hills, seeds damaged, seed germination, longitudinal scattering, and crop yield.

Seeds' numbers in the hill were estimated after the sowing operation, and the number of seeds in each hill was determined manually by counting seeds in each hill at random.

In order to determine the percentage of seeds damaged, the seeds hopper was filled with pea seeds, and at the end of each seed tube, a plastic packet was fixed. The seed drill was operated in the field under different working speeds; all the seeds from each plastic packet were collected, the seeds damaged were counted and weighted, and the percentage of the seeds damaged was calculated, as follows in Eq. (12).

$$Percentage\ of\ seed\ damaged\ (\%) = \frac{W1}{W2} \times 100 \quad (12)$$

where W_1 is the weight of the seeds damaged [g], and W_2 is the total weight of the outlet seeds [g].

The seed germination ratio was calculated according to (*Safdary et al., 2020*), as follows in Eq. (13).

$$Seed\ germination\ ratio\ (\%)\ = \frac{N1}{N2} \times\ 100 \tag{13}$$

where N_1 is the number of seeds germinated in hills, and N_2 is the total number of seeds in hills.

The longitudinal scattering was measured in the intra-row spacing between 20 hills after two weeks from seeding pea seeds to determine the longitudinal scattering of seed placements statistically by standard deviation according to (*Steel and Torrie, 1980*), as follows in Eqs. (14–15).

$$sd = \sqrt{\frac{\Sigma(x - x^{-})^2}{n - 1}} \tag{14}$$

$$CV\ (\%) = \frac{sd}{x^{-}} \times 100 \tag{15}$$

where sd is the standard deviation, x is the distance between hills in a row [cm], x^{-} is the average distance [cm], n is the number of readings, and CV is the coefficient of variation in a row from an average distance [%]. Coefficients of variation under 10% are regarded as excellent; furthermore, values under 20% are regarded as generally acceptable for most field applications, according to (*Coates, 1992*).

The pea pod yield (kg ha^{-1}) was estimated by collecting the pea pods from five random areas for each treatment with an area of 1.0 m × 1.2 m, and the average of the pea pod yield was estimated and recorded.

RESULTS AND DISCUSSION

Effect of forward speed on fuel consumption

Figure 4 shows the influence of forward speed on fuel consumption during the seeding operation. The obtained results revealed that increasing forward speed significantly increased fuel consumption rates. Increasing the forward speeds from 0.79–0.98 m s^{-1}, 0.98–1.28 m s^{-1}, and 1.28–1.64 m s^{-1} increased fuel consumption rates from 3.75–3.96 l h^{-1}, 3.96–4.13 l h^{-1}, and 4.13–4.25 l h^{-1}, respectively. Furthermore, the lowest fuel consumption rate of 3.75 l h^{-1} was recorded at the lowest forward speed of 0.79 m s^{-1}. In contrast, the highest fuel consumption rate of 4.25 l h^{-1} was recorded at the highest forward speed of 1.64 m s^{-1}.

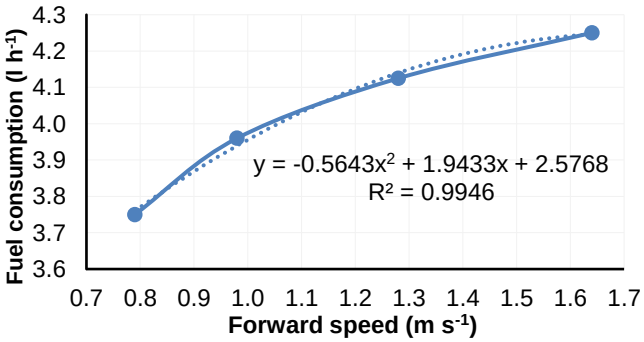

Fig. 4 – Effect of forward speed on fuel consumption

Effect of forward speed on specific energy

Figure 5 shows the influence of forward speed on specific energy. The results revealed that increasing the forward speed decreased specific energy. Increasing forward speed from 0.79–0.98 m s^{-1}, 0.98–1.28 m s^{-1}, and 1.28–1.64 m s^{-1} decreased specific energy by percent of 13.91%, 20.20%, and 18.40%, respectively. This may be attributed to the increased field capacity for high forward speeds. Whereas the highest specific energy of 7.25 kWh ha^{-1} was recorded at a forward speed of 0.79 m s^{-1}. On the other side, the lowest specific energy of 4.06 kWh ha^{-1} was recorded at a forward speed of 1.64 m s^{-1}.

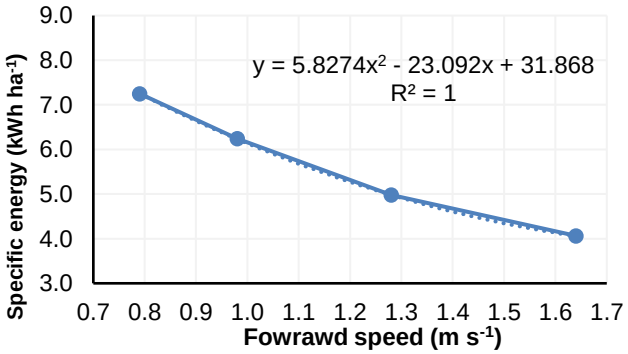

Fig. 5 – Effect of forward speed on specific energy

Effect of forward speed on slip ratio of the tractor and the seed drill

Figure 6 presents the slip ratio of the tractor and the seed drill wheels under the studied forward speeds. The data show that increasing the forward speed gave reasonable rates of increase in slip ratio. Increasing the forward speeds from 0.79–0.98 m s^{-1}, 0.98–1.28 m s^{-1}, and 1.28–1.64 m s^{-1} increased the tractor's slip ratio percentages by 6.50, 5.35, and 4.71%, respectively. On the other side, the seed drill's slip ratio increased by percent of 5.26, 7.32, and 4.65%, respectively, at the same forward speeds. This increment may be attributed to the increase in draft force. The slip ratio should be less than 15% for the seed drill with the tractor. Accordingly, the best operating forward speed is ranged from 0.79 to 1.64 m s^{-1} for executing the seeding operation:

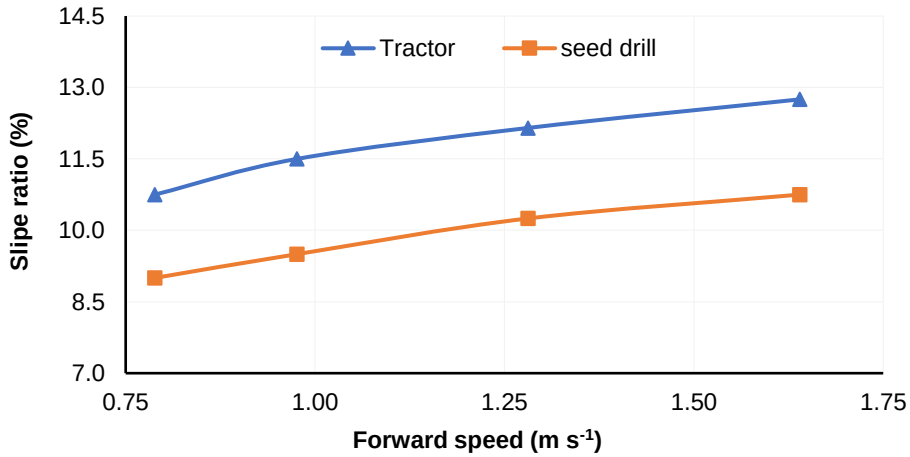

Fig. 6 – Effect of forward speed on slip ratio

Factors affecting crop growth and production

Effect of forward speed, cell shape, and disc cell capacity on the number of seeds per hill

Table (2) shows the influence of forward speed, cell shape, and disc cell capacity on the number of seeds per hill. The results revealed that at forward speeds of 0.79 and 0.98 m s^{-1}, the actual number of seeds per hill equals the number of cell capacities, and at the same time, increasing the forward speed from 0.98 to 1.64 m s^{-1}, the number of seeds decreased by 16.5%. This may be attributed to the increased forward speed, which in turn reduced the time required to fill the cells with the required number of seeds. Nevertheless, the maximum average number of seeds per hill with a disc cell capacity of 3 seeds was recorded at operating forward speeds ranging from 0.79 to 0.98 m s^{-1}. In contrast, the minimum average number of seeds per cell results from a disc cell capacity of 1 seed with an operating forward speed of 1.64 m s^{-1}.

On the other hand, regarding the effect of the different cell shapes, the results indicated that the number of seeds per hill was not affected by the different cell shapes.

Table 2

The average number of seeds per hill

Forward speed [m s^{-1}]	C_1		C_2		C_3	
	S_1	S_2	S_1	S_2	S_1	S_2
0.79	1.00	1.00	2.00	2.00	3.00	3.00
0.98	1.00	1.00	2.00	2.00	3.00	3.00
1.28	1.00	1.00	1.67	1.67	2.67	2.67
1.64	0.67	0.67	1.67	2.00	2.67	2.33

Effect of forward speed, cell shape, and disc cell capacity on seeds damage percentage

Figure 7 shows the influence of operating forward speed, cell shape, and disc cell capacity on seed damage percentage. Concerning the effect of the forward speed on seed damage percentage, increasing the forward speed from 0.79–0.98 m s^{-1}, 0.98–1.28 m s^{-1}, and 1.28–1.64 m s^{-1}, increased seed damage percentage from 2.08–2.28%, 2.28–2.45%, and 2.45–2.58%, respectively at using disc cell capacity of three seeds (C3) and circular cell shape (S1). At the same time, the corresponding values using a rectangle with a semicircle end cell shape (S2) increased from 2.40–2.53%, 2.53–2.67%, and 2.67–2.75%, respectively.

Regarding the effect of cell shape on seed damage percentage, the results revealed that using a circular cell shape (S1) increased seed damage percentages compared with using a rectangle with a semicircle end cell shape (S2). Whereas using a rectangle with a semicircle end cell shape (S2) at the disc cell capacity of three seeds (C3) increased seed damage percentage by percent of 13.33, 9.88, 8.24, and 6.18% at operating forward speeds of 0.79, 0.98, 1.28, and 1.64 m s^{-1}, respectively.

Concerning the effect of disc cell capacity on seed damage percentage, the results indicated that increasing disc cell capacity from one (C1) to three (C3) seeds increased the seed damage percentage. Increasing disc cell capacity from C1–C3 using circular cell shape (S1) increased seed damage percentage by percent of 30.29, 31.58, 32.24, and 31.00% at operating forward speeds of 0.79, 0.98, 1.28, and 1.64 m s^{-1}, respectively. The corresponding percentages using a rectangle with a semicircle end cell shape (S2) were 35.00, 34.00, 33.71, and 31.64% at operating forward speeds of 0.79, 0.98, 1.28, and 1.64 m s^{-1}, respectively.

The maximum seed damaged percentage of 2.75% was obtained at the forward speed of 1.28 m s^{-1}, the disc cell capacity of three seeds (C3), and the cell's shape as a rectangle with a semicircle end (S2). In contrast, the minimum seed damaged percentage of 1.45% was obtained at the forward speed of 0.79 m s^{-1}, the disc cell capacity of one seed (C1), and the cell's shape as circular (S1).

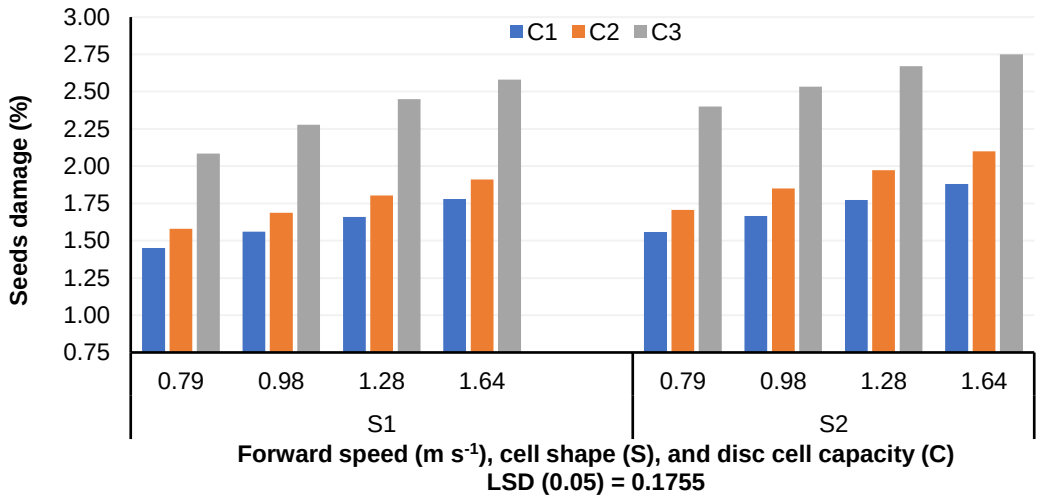

Fig. 7 – Effect of forward speed, cell shapes, and disc cell capacity on seeds damage percentage

Effect of forward speed, cell shape, disc cell capacity, and distance between rows on germination ratio of pea seeds

Laboratory germination percentage is not affected by passing pea seeds through the seed metering unit. Figure 8 presents the data concerning the germination ratio in the field. The data revealed that increasing forward speed decreased the germination ratio percentages. Increasing forward speed from 0.79–0.98 m s^{-1}, 0.98–1.28 m s^{-1}, and 1.28–1.64 m s^{-1} decreased germination ratios by percent of 1.00, 2.00, and 1.00%, respectively, using a circular cell shape (S1), disc cell capacity of three seeds (C3), and distance between rows of 7.5 cm (D1). On the other hand, the traditional method for pea seeds germination ratio recorded 88.90%. The highest germination ratio percentages were recorded at the forward speed of 0.79 m s^{-1} compared to the other forward speeds.

Regarding the effect of cell shape on the germination ratio of pea seeds, the results showed insignificant differences when using a circular shape (S1) or a rectangular with a semicircle end (S2) at different distances between rows.

Concerning the influence of disc cell capacity on the germination ratio percentage, the results indicated that increasing disc cell capacity from one to three seeds (C1–C3) increased the germination ratio at different forward speeds and cell shapes. Whereas increasing disc cell capacity from one to three seeds (C1–C3) increased germination ratios percent by 2.56, 2.55, 2.55, and 2.55%, at forward speeds of 0.79, 0.98, 1.28, and 1.64 m s^{-1}, respectively, at a circular cell shape (S1), and distance between rows of 7.5 cm (D1). At the same time, the corresponding percents at a rectangular with a semicircle end were 1.18, 2.55, 2.56, and 2.55%, respectively. The highest germination ratios percentages were achieved using the disc cell capacity of three seeds (C3).

Involving the effect of distance between rows on the germination ratio percentage, Figure 8 reveals that the germination ratio percentages were 93.44, 96.23, and 95.28% at distances between rows of 7.5, 10, and

15 cm, respectively, at a forward speed of 0.79 m s^{-1}, a circular cell shape (S1), and disc cell capacity of three seeds (C3). The results revealed that the maximum germination ratios percentages were recorded at a distance between rows of 10 cm compared with distances between rows of 7.5 and 15 cm.

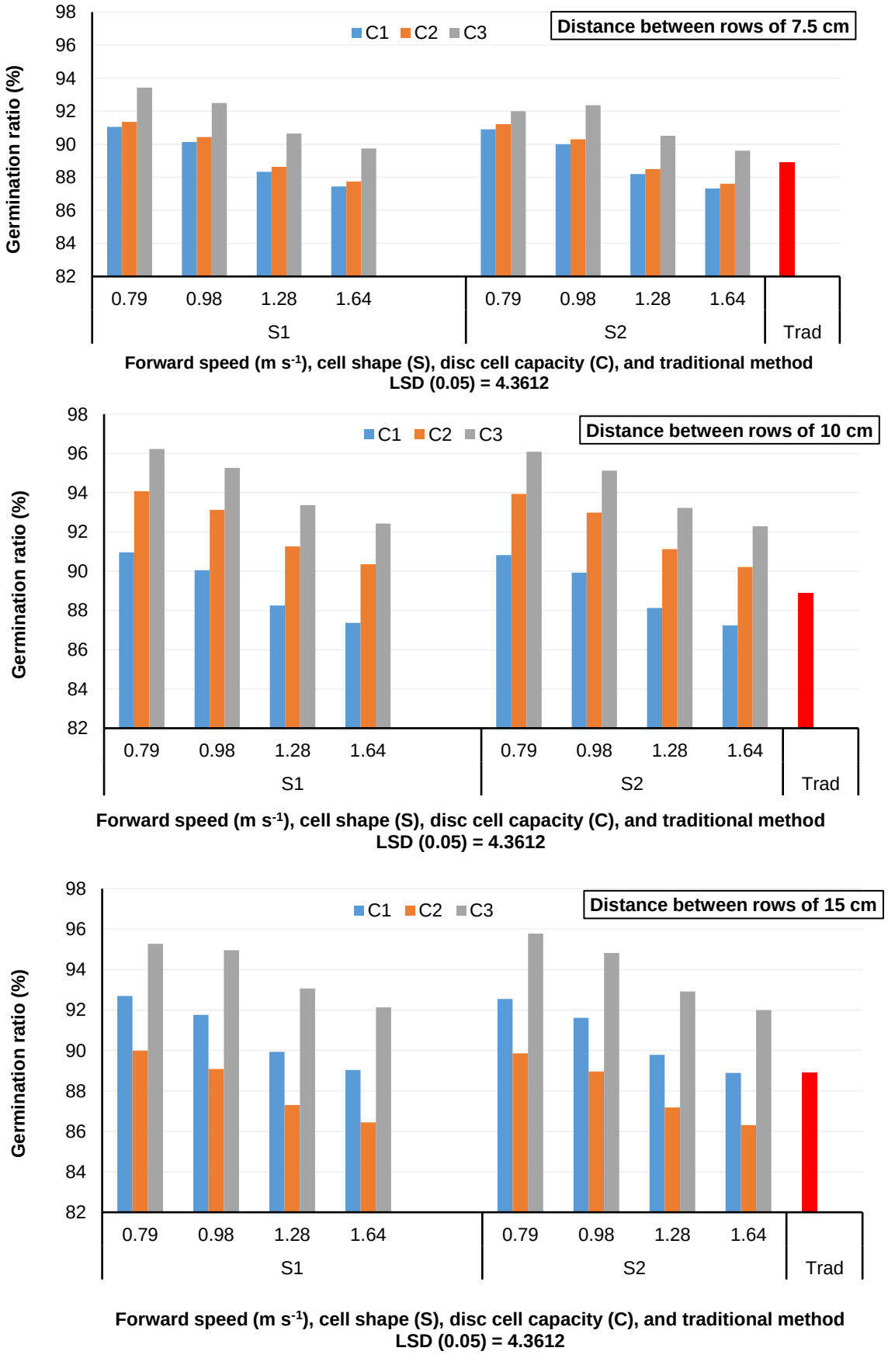

Fig. 8 – Effect of forward speed, cell shape, and disc cell capacity on germination ratio

Effect of forward speed, cell shape, and disc cell capacity on longitudinal scattering

Figure 9 illustrates the influence of forward speed, cell shape, and disc cell capacity on longitudinal scattering. Increasing forward speed increased longitudinal scattering at any cell shape and disc cell capacity. It can be observed that increasing the forward speed from 0.79–0.89 m s^{-1}, 0.89–1.28 m s^{-1}, and 1.28–1.64 m s^{-1} increased the longitudinal scattering from 12.5–14.0%, 14.0–15.6%, and 15.6–17.0%, respectively, at using disc cell capacity of one seed (C1), and a circular cell shape (S1). This may be due to more slips occurring at high operating forward speeds; moreover, high forward speeds generate more vibrations during seeding operating, which increases the seeding uniformity variation coefficient. These results are in harmony with *Liu et al. (2017)*, who stated that the coefficient of variation of seed spacing increased with increasing forward speed. In the same trend, *Sun et al. (2020)* reported that the seeding uniformity variation coefficient increases when the operating forward speed is higher or lower than 0.8 m s^{-1}.

Concerning the effect of the cell shape on longitudinal scattering, the results indicated that using a rectangular with a semicircle end (S2) compared with a circular cell shape (S1) increased longitudinal scattering values at any forward speed and cell shape. Using a rectangular with a semicircle end (S2) compared with a circular cell shape (S1) increased longitudinal scattering from 18.0–19.9%, 19.5–21.0%, 20.9–22.0%, and 22.0–22.5%, respectively, when using disc cell capacity of three seeds (C3).

Regarding the influence of disc cell capacity on longitudinal scattering, the results revealed that increasing disc cell capacity from one to three seeds per cell (C1–C3) led to increasing longitudinal scattering at any forward speed and cell shape. Increasing disc cell capacity from one to three seeds (C1–C3) increased longitudinal scattering from 12.5–18.0%, 14.0–19.5%, 15.6–20.95, and 17.0–22.0% for forward speeds of 0.79, 0.98, 1.28, and 1.64 m s^{-1}, respectively in case of using a circular cell shape (S1). Furthermore, the corresponding values in the case of using rectangular with a semicircle end (S2) increased from 13.0–19.9%, 14.0–21.0%, 15.0–22.0%, and 15.5–22.5%.

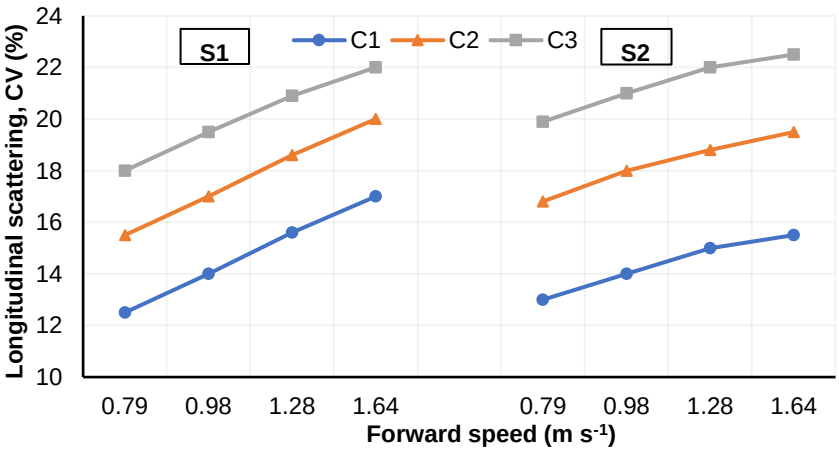

Fig. 9 – Effect of forward speed, cell shape, and disc cell capacity on longitudinal scattering

Effect of forward speed, cell shape, disc cell capacity, and distance between rows on the pea pods yield

Figure 10 shows the effect of forward speed, cell shape, disc cell capacity, and distance between rows on pea pods yield. The results revealed that increasing forward speed decreased the pea pod's yield at any cell shape, disc cell capacity, and distances between rows. Increasing the forward speed from 0.79–1.64 m s^{-1} decreased pea pods yield by a percent of 3.9% because the number of seeds damaged in the hill decreased the plant's growth.

Concerning the influence of cell shape on pea pods yield, the results indicated that using a semicircle end cell shape (S2) compared with a circular cell shape (S1) decreased the yield by a percent of 5.12% because of the increase in the number of seeds damaged. Concerning the effect of disc cell capacity on pea pods yield, the disc cell capacity of 2 seeds (C2) recorded the highest yield value compared with the disc cell capacity of one and three seeds (C1 and C3) at any forward speed, cell shape, and distance between rows.

Regarding the influence of the distance between rows on pea pods yield, the results indicated that distance between rows of 10 cm (D2) recorded the highest yield compared with distances between rows of 7.5 and 15 cm because of suitable seed numbers and distances between rows decreased the competition between the plants, which in turn leads to obtain the highest values of pea pods yield.

Consequently, the highest yield value of 1.22 tonnes ha^{-1} was recorded at a forward speed of 0.79 m s^{-1} and using a cell capacity of 2 seeds (C2).

In contrast, the traditional planting method recorded an average pea pods yield of 0.94 tonnes ha^{-1}. Finally, using the seed drill at a forward speed ranging from 0.79 to 0.98 m s^{-1} with the disc cell capacity of two seeds (C2) and the shape of a circular cell (S1) at a distance of 10 cm between rows (D2) is recommended under this study.

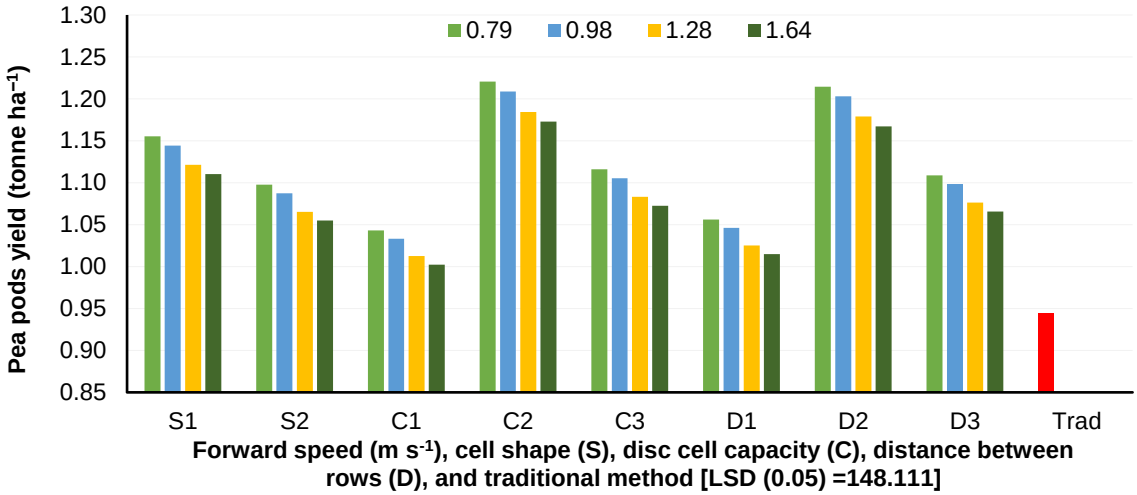

Fig. 10 – Effect of forward speed, cell shape, disc cell capacity, and distance between rows on the pea pods yield

CONCLUSIONS

This study assessed the performance of a new seed drill for planting pea seeds on a raised bed and compared its results with the traditional seeding method; moreover overcomes the shortage of both laborers and the machines that sow pea seeds on a raised bed. The results revealed that the lowest fuel consumption rate and slip ratio was achieved at an operating forward speed of 0.79 m s^{-1}. The lowest seed damage percentage of 1.45% and lowest longitudinal scattering of 12.5% were recorded at a forward speed of 0.79 m s^{-1}, a circular cell shape (S1), and a disc cell capacity of one seed (C1). Furthermore, the highest germination ratio of 96.23% was obtained at a forward speed of 0.79 m s^{-1}, a circular cell shape (S1), disc cell capacity of three seeds (C3), and a distance between rows of 10 cm (D2). The highest pea pod yield was achieved at a forward speed of 0.79 m s^{-1} and disc cell capacity of two seeds (C2). Based on the previous results, it is recommended to operate the seed drill at a forward speed ranging from 0.79 to 0.98 m s^{-1}, using the disc cell capacity of 2 seeds (C2), a circular cell shape (S1), and a distance between rows of 10 cm (D2) to achieve the optimum performance for this seed drill.

ACKNOWLEDGEMENT

The authors would like to thank the Agricultural Engineering Research Institute (AEnRI), Agricultural Research Center (ARC), Giza, Egypt.

REFERENCES

[1] Adekanye, T.A., Akande, A.M. (2015). Development and Evaluation of a Manual Multi-crop Seeder for Peasant Farmers. *Elixir Agriculture, 86*, 35095–35101. https://eprints.lmu.edu.ng/id/eprint/664

[2] Afify, M.K. (2009) Development of seed drill feeding device to suit planting in hills. *Misr Journal of Agricultural Engineering, 26*(2), 561–579. http://dx.doi.org/10.21608/mjae.2009.108893

[3] ASABE standard (2003). *Three-Point Free-Link Attachment for Hitching Implements to Agricultural Wheel Tractors*; ASABE Standard no. S217.12; American Society of Agricultural and Biological Engineers: St. Joseph, MI, USA, 2003.

[4] ASABE Standard (2003). *General Terminology for Traction of Agricultural Traction and Transport Devices and Vehicles*; ASABE Standard no. S296.5 (R2018); American Society of Agricultural and Biological Engineers: St. Joseph, MI, USA, 2003.

[5] Awad, M.A. (2016). Fabricated Prototype of Raised-Bed Planter for Wheat. *Journal of Soil Sciences and Agricultural Engineering*, *7*(12), 921–927. https://dx.doi.org/10.21608/jssae.2016.40547

[6] Coates, W. (1992). Performance evaluation of a pendulum spreader.*Trans of the ASAE*, *8*(3), 285–288

[7] Elsbaay, A.M., Hegazy, R.A. (2016). Alternative Fuel Consumption Measurement Device for Multipurpose Farm Machinery Use. *Misr Journal of Agricultural Engineering, 33*(4), 1187–1206.

[8] Garden peas production (2011). *Plant Production Department of Agriculture, Forestry and Fisheries*, Republic of South Africa, Communication Services Private Bag X144, Pretoria 0001. P. 24.

[9] Hunt, D. (1983). *Farm power and machinery management 8th Ed*., Iowa State Univ., Press Ames, USA. Ames, Iowa USA, 364–368.

[10] Burt, John (2008). Growing snow peas and sugar snaps in Western Australia. State of Western Australia. ISSN: 0726-934X. https://agric.wa.gov.au/n/1046

[11] Khan, K., Moses, S. C., Kumar, A. & Kumar, D. (2017). Design a Seed Metering Wheel for Sowing Pigeon Pea Seeds. *International Journal of Current Microbiology and Applied Sciences, 6*(7), 4291–4299. https://doi.org/10.20546/ijcmas.2017.607.445.

[12] Krizmanić, G., Tucak, M., Brkić, M., Marković, M., Jovanović, V., Cupić, T. (2020). The impact of plant density on the seed yield and the spring field pea's yield component. *Agriculture*, *26*(1), 25–31. https://doi.org/10.18047/poljo.26.1.4

[13] Kyada, A. R., Patel, D.B. (2014). Design and development of manually operated Seed seeder machine. 5th International and 26th All India Manufacturing Technology, Design and Research Conference December 12th–14th IIT Guwahati, Assam, India 591–597

[14] Liu, Q.W., He, X.T., Yang, L., Zhang, D.X., Cui, T., Qu, Z., Yan, B., Wang, M., Zhang, T. (2017). Effect of travel speed on seed spacing uniformity of corn seed meter. *International Journal of Agricultural and Biological Engineering*, *10*(4), 98–106. http://dx.doi.org/10.25165/j.ijabe.20171004.2675.

[15] Olaoye, J. O., Bolufawi, S. J. (2001). Design, fabrication and performance of a multi-purpose row planting machine. *Journal of Sustainable Agriculture and the Environment*, *3*(1), 7–20.

[16] Safdary, A. J., Ahamdi, A. J., Habibi, N., Rahmani, Z., & Rasooli, S. (2020). The effect of different treatments on seed dormancy breaking and germination inducing in Louisiana variety of okra (Abelmoschus esculentus L.). *International Journal of Innovative Research and Scientific Studies*, *3*(3), 187–193. https://doi.org/10.53894/ijirss.v3i4.45.

[17] Steel, R. G. D., Torrie, J. H. (1980). Principles and procedures of statistics, a biometrical approach. 2nd Edition, McGraw-Hill, New York, USA, pp. 20–90.

[18] Sun, D., Cui, Q., Zhang, Y., Hou, H. (2020). Performance test of the 2bde-2 type millet fine and small-amount electric seeder. *INMATEH-Agricultural Engineering*, *60*(1), 129–136. https://doi.org/10.35633/inmateh-60-15.

[19] Srivastava, A.K., Goering, C.E., Rohrbach, R.P., Buckmaster, D.R. (1993). Engineering principles of agricultural machines. ASAE Textbook No. 6, Published by the ASAE. St. Joseph, MI 49085-9659 USA, 35–38.

[20] Vimal, V. M., Madesh, A., Karthick, S. & Kannan, A. (2015). Design and fabrication of multi-purpose sowing machine. *International Journal of Scientific Engineering and Applied Science*, *1*(5), 27–34.

[21] Yehia, I. (1993). Design of a seed drill attached to a power tiller. MSc. Thesis. Fac. of Agric. Ain Shams Univ., Egypt.

[22] Yu, B.Y., Xiang, D.Q., Mahfuz, H., Patterson, N. & Bing, D. (2021). Understanding starch metabolism in pea seeds towards tailoring functionality for value-added utilization. *International Journal of Molecular Sciences*, *22*(16), 8972. https://doi.org/10.3390%2Fijms22168972

[23] Zaki, H. M., Mahmoud, A. M., Abd El-Ati, Y. Y., Hammad, A. M. & Sayed, R. M. (2017). Studies on pea (*Pisum sativum* L.) growth and productivity under agroforestry system: 2. Yield and seed quality of pea under alley cropping system with two types of trees. *Journal of Basic and Applied Research in Biomedicine, 3*(1), 1–9.

INVESTIGATION OF THE DECOMPOSITION PATTERN OF CORN STRAW IN COLD LAND UNDER DIFFERENT FIELD RETURN METHODS
/
寒地玉米秸秆腐解规律的探究

Wenlong LI[1)], Jiahao YANG[1)], Wenting JIN[3)], Liuxuan MA[*1)], Yiyuan GE[1)], Jinbo ZHANG[*1,2)], Yuqi ZHUANSUN [1)]

[1)] College of Mechanical Engineering, Jiamusi University, Jiamus 154007, China;

[2)] Wuzhou College, School of Mechanical and Chemical Engineering, Guangxi 543002, China;

[3)] Chinese Academy of Agricultural Mechanization Sciences Group Co.,Ltd, Beijing 100083, China

Tel: +86-13504771669; E-mail: 208033021@stu.jmsu.edu.cn

DOI: https://doi.org/10.35633/inmateh-68-68

Keywords: *corn straw; straw decomposition pattern; return depth; interaction; return conditions*

ABSTRACT

In order to explore the best parameters for the decomposition of corn straw for return to the field under extremely cold temperature conditions in northeast China, an orthogonal test was used to test the decomposition of corn straw and to analyse the effects of factors such as straw return depth, straw return amount, straw stalk part and decomposer concentration on the decomposition efficiency of corn straw. The results showed that the most significant effect on the decomposition efficiency of cold land corn straw was the amount of straw returned to the field, followed by the concentration of decomposer and the depth of straw returned to the field, and the least effect was the straw part. Among them, the amount of straw returned to the field showed a negative correlation on the decomposition efficiency of cold land corn straw; the concentration of decomposer, the depth of straw returned to the field and the straw part showed a positive correlation on the decomposition efficiency of cold land corn straw.

摘要

为了探索中国东北地区在极寒温度条件下玉米秸秆腐解还田的最佳工作方式，采用正交试验法对玉米秸秆进行腐解试验，分析了秸秆还田深度、秸秆还田量、秸秆茎部位、腐解剂浓度等因素对玉米秸秆腐解率的影响。结果表明，对寒地玉米秸秆腐解率的影响最为显著的是秸秆还田量，其次是腐解剂浓度、翻埋深度，影响最小的是秸秆部位。其中秸秆还田量对寒地玉米秸秆腐解率呈现负相关关系；腐解剂浓度、翻埋深度、秸秆部位对寒地玉米秸秆腐解率呈现正相关关系。

INTRODUCTION

The Three Rivers Plain is located in the northeast border of China and is an important part of the Northeast Plain, one of the three major black soil areas in the world. The climate is mild and humid in summer and cold and dry in winter, with large temperature differences throughout the year (*Liang et al., 2022*). At the same time, Heilongjiang is also a major corn producing region in China, with large amounts of corn straw and abundant corn straw resources after the autumn harvest. In the past, farmers burned corn straw in their fields, with the attendant air pollution problems and fire risks, causing this disposal method to be banned (*Sun, 2015*). Under these conditions, straw return to the field has become the main disposal method and has had an important impact on farm production. In addition, straw returns play an important role in maintaining soil fertility and improving the amount of humus in the soil. It was found that corn straw is rich in nitrogen, phosphorus, potassium and other nutrients for crop growth (*Wang et al., 2013*). In order to improve the efficiency of the use of straw and reduce the waste of resources, a series of methods for the comprehensive use of straw have been proposed, of which straw fertilization is currently the most rapidly developing straw utilization (*Li et al., 2021*). It was found that by controlling the amount of corn straw returned to the field at 4500 KG per hectare and applying a decomposer, the straw decomposed at a higher rate and the following year's corn yield increased more（*Yang et al., 2013*）.

---

[1] *Wenlong LI, Master Degree; Liuxuan MA*, Professor(Corresponding author); Jiahao YANG, Master Degree; Yiyuan GE, Professor; Yuqi ZHUANSUN, undergraduate;*

[2] *Jinbo ZHANG*, Professor(Corresponding author);*

[3] *Wenting JIN, Ph.D Stud;*

Rapid decomposition of cold land corn straw is closely related to crop protection tillage, and there have been studies on the decomposition law and mechanism of cold land straw in China, but there are few studies on the decomposition characteristics of cold land corn straw with additional application of decomposer, and there is also a lack of studies on the decomposition efficiency of corn straw. An orthogonal test design was used to study the decay effect of corn straw decay under different combinations of factors, using the decomposition efficiency of corn straw as the analysis index, to analyze the decomposition efficiency of corn straw and to provide technical and management theoretical guidance for the decomposition of corn straw in cold areas.

MATERIALS AND METHODS

OVERVIEW OF THE TEST AREA

The test was conducted at the Experimental Center of Jiamusi University (130°22'08 "E, 46°48'35 "N, 81.2 m above sea level), which is the hinterland of the Three Rivers Plain formed by the confluence of the Songhua, Heilong and Ussuri rivers, with a climate type belonging to typical temperate continental monsoon climate with high winds and low precipitation in spring, warm and rainy summer, cool climate in autumn and cold and long winter (*Liu et al., 2022*). The soil of the area is black, that is homogeneous humus, a clayey soil with good properties and high fertility. Soil capacity is the ratio of the mass of a unit volume of soil to the mass of the same volume of water in the field in its natural basal state, with clayey soils having a capacity of 1.0~1.5 g/cm^3. The lower the soil capacity and the higher the organic matter content, the better the structural properties. The soil capacity of the test area was 1.25~1.35 g/cm^3.

Table 1

Test environmental factors

Meteorological factors	Oct. 2021	Nov. 2021	Soil freezing period				Apr. 2022	May. 2022
			Dec. 2021	Jan. 2022	Feb. 2022	Mar. 2022		
Average max temperature [K]	286.15	274.15	261.15	261.15	266.15	277.15	287.15	294.15
Average min temperature [K]	272.15	264.15	250.15	249.15	253.15	265.15	274.15	280.15
Average wind velocity [m/s]	2.33	2.83	2.11	1.89	2.53	2.22	3.08	2.25
Total rainfall [mm]	13.82	68.41	6.05	4.39	10.21	13.68	74.69	4.7
Average relative humidity [%]	52.84	77.20	64.26	66.35	65.96	61.97	44.97	54.45

Methods

Multi-factor orthogonal experimental design

In this test, an orthogonal test design method using Design-Expert V8.0.6 software was used to comprehensively analyze the factors affecting the effectiveness of straw decomposition and return to the field (*Qi et al., 2021*). The survey showed that the amount of straw used for straw return should be controlled at about 3750-4500 kg of fresh straw and 1500-3000 kg of dry straw per 1 ha area of field; the amount of fresh straw can be increased to about 6000-6750 kg for plots with good soil fertility level; the amount of fresh straw should be reduced to about 3000-3750 kg for plots with poor soil fertility level (*Yao, 2014*).

The amount of straw used to return to the field is too large and affected the normal growth of the crop seedlings. In combination with the size of the test plots, which were each 0.25 m x 0.25 m, the amount of straw was set at three levels of 30 g, 40 g and 50 g. The corn straws with a more consistent length of corn stalks were selected, and roots and leaves were removed. The treated straws were divided into five equal parts from the top to the roots and represented by numbers 1 to 5 in the upper (top), upper middle, middle, lower middle and lower part (roots) (*Yu et al., 2012*), and three levels were selected 2, 3 and 4.

The organic material ferment produced by Shandong Junde Biotechnology Co., Ltd. was chosen as the straw decomposer, which contains a variety of beneficial microorganisms such as Bacillus, Bacillus, Actinomyces, Saccharomyces, Xylella, Lactobacillus and Photosynthetic bacteria to promote the decomposition of straw; the decomposition agent concentration was set at three levels of 7.5%, 10% and 15%. The straw return depth was set to 0.1 m, 0.15 m and 0.2 m. With the decomposition efficiency of corn straw as the objective of the experimental study, the $L_9(3^4)$ orthogonal test factor level was selected, as shown in Tables 2 and 3.

Table 2

Factor levels of orthogonal tests

Level	Test factors			
	A. Straw amount	B. Straw stalk part	C. Decomposer concentration	D. Straw return depth
	[g]		[%]	[m]
Ⅰ	30	2	15%	0.1
Ⅱ	40	3	10%	0.15
Ⅲ	50	4	7.5%	0.2

Table 3

Orthogonal test design table $L_9(3^4)$

Test treatment	Test factors			
	A. Straw amount	B. Straw stalk part	C. Decomposer concentration	D. Straw return depth
	[g]		[%]	[m]
1	Ⅰ（30）	Ⅰ（2）	Ⅰ（15%）	Ⅰ（0.1）
2	Ⅰ（30）	Ⅱ（3）	Ⅱ（10%）	Ⅱ（0.15）
3	Ⅰ（30）	Ⅲ（4）	Ⅲ（7.5%）	Ⅲ（0.2）
4	Ⅱ（40）	Ⅰ（2）	Ⅱ（10%）	Ⅲ（0.2）
5	Ⅱ（40）	Ⅱ（3）	Ⅲ（7.5%）	Ⅰ（0.1）
6	Ⅱ（40）	Ⅲ（4）	Ⅰ（15%）	Ⅱ（0.15）
7	Ⅲ（50）	Ⅰ（2）	Ⅲ（7.5%）	Ⅱ（0.15）
8	Ⅲ（50）	Ⅱ（3）	Ⅰ（15%）	Ⅲ（0.2）
9	Ⅲ（50）	Ⅲ（4）	Ⅱ（10%）	Ⅰ（0.1）

Measurement index

The nylon mesh bag method was used to determine the decomposition efficiency as follows: the length of straw was fixed at 0.1~0.12m, and the straw was packed into 40 mesh nylon mesh bags (size 0.3 m×0.2 m) and numbered according to the arrangement in Table 3, and six replicate tests were conducted for each group, and buried at a predetermined depth according to the preset in the test program, as shown in Figure 1. Spraying different concentrations of organic material decomposer for the nylon mesh bag before burial according to the test program was performed to ensure full contact between straw and organic material decomposer. The nylon mesh bags were sprayed with different concentrations of organic matter maturing agent prior to burial in accordance with the trial protocol to ensure that the straw was in full contact with the organic matter maturing agent and buried in the ground for 8 months. In addition, each test plot was spaced greater than 0.15 m apart to avoid interference between the two test groups, which could affect the test results.

a Depth of straw return 0.1m

b Depth of straw return 0.2m

Fig. 1 - Return depth limit

a Electric blast dryer

b Drying straw number

Fig. 2 - Thermostatic drying

The straw decomposition efficiency was tested by removing the nylon mesh bag, separating the soil from the straw residue, rinsing the straw residue, drying it with an electric blast dryer, at a constant temperature

of 358.15 K, cooling it to room temperature and then weighing it, and calculating the straw decomposition rate R_d using the weight loss method (*Yu et al., 2015; Wang et al., 2020*). The specific calculation formula is:

$$R_d = (W_i - W_f)/W_i \times 100\% \quad (1)$$

where: W_i - initial dry weight of straw;
W_f - dry weight of straw decay residue.

Data processing

The orthogonal test was performed using the visual analysis method with the following steps:

$$k_i = K_i/s \quad (2)$$

Where:

K_i- the sum of the test results corresponding to the level number i on any column;
k_i- the arithmetic mean of the test results obtained at level i for any of the upper column factors
S - the number of occurrences of each level on any column was taken as 3.

$$R = max\{k_1, k_2, k_3\} - min\{k_1, k_2, k_3\} \quad (3)$$

Where:

R - the extreme difference

If each test factor has no effect on the test index, the values of k_i under each factor should be equal; on the contrary, the presence of a certain difference in the value of k_i under each factor indicates that the test factor has an effect on the test index. The magnitude of the value of k_i is used to determine the degree of influence of each test factor level on the test index, and the magnitude of the R value is an important basis for determining the degree of influence of factors on the test index (Yang et al., 2021).

RESULTS AND ANALYSIS

In Table 4, the decomposition efficiency data presented in the test results are the average values of decomposition efficiencies for six replicate tests (six bags buried simultaneously under the same conditions to ensure the same replicate test conditions).

Analysis of extreme differences

The extreme difference values were calculated for each level of each factor (see Table 4). It can be seen that the extreme difference R_A of straw return amount is 28, the extreme difference R_B of straw part is 3.14, the extreme difference R_C of decomposer concentration is 13.63, and the extreme difference R_D of straw return depth is 6.4. The larger the extreme difference value of the factor, the greater the effect of the level change of the factor on the test results. Among the factors selected in this experiment, the extreme difference values of straw return amount were much higher than those of the other factors, i.e., straw return amount had the greatest effect on the degree of straw decay. Straw part had the least effect on straw decomposition efficiency, decomposer concentration had the second highest effect on straw decomposition efficiency, and straw return depth had the third highest effect on straw decomposition efficiency. Numerically, the main order of the factors was: straw return amount > decomposer concentration > straw return depth > straw part.

Table 4

Results of orthogonal test

Test treatment	Test factors				decomposition efficiency
	A. Straw amount	B. Straw stalk part	C. Decomposer concentration	D. Straw return depth	
	[g]		[%]	[m]	[%]
1	Ⅰ（30）	Ⅰ（2）	Ⅰ（15%）	Ⅰ（0.1）	56
2	Ⅰ（30）	Ⅱ（3）	Ⅱ（10%）	Ⅱ（0.15）	53.1
3	Ⅰ（30）	Ⅲ（4）	Ⅲ（7.5%）	Ⅲ（0.2）	51.9
4	Ⅱ（40）	Ⅰ（2）	Ⅱ（10%）	Ⅲ（0.2）	35.4
5	Ⅱ（40）	Ⅱ（3）	Ⅲ（7.5%）	Ⅰ（0.1）	23.4
6	Ⅱ（40）	Ⅲ（4）	Ⅰ（15%）	Ⅱ（0.15）	39.3
7	Ⅲ（50）	Ⅰ（2）	Ⅲ（7.5%）	Ⅱ（0.15）	15.5
8	Ⅲ（50）	Ⅱ（3）	Ⅰ（15%）	Ⅲ（0.2）	36.4
9	Ⅲ（50）	Ⅲ（4）	Ⅱ（10%）	Ⅰ（0.1）	25.1
K_1	161	106.9	131.7	104.5	
K_2	98.1	112.9	113.6	107.9	

Test treatment	Test factors				decomposition efficiency
	A. Straw amount	B. Straw stalk part	C. Decomposer concentration	D. Straw return depth	
	[g]		[%]	[m]	[%]
K_3	77.0	116.3	90.8	123.7	
k_1	53.67	35.63	43.9	34.83	
k_2	32.7	37.63	37.87	35.97	
k_3	25.67	38.77	30.27	41.23	
R	28.0	3.14	13.63	6.4	
Order of factors	A>C>D>B				
Optimal condition combination	$A_1B_3C_1D_3$				65.5

Influence analysis of factors

According to the characteristic of "balanced and dispersed, neat and comparable" of the orthogonal test, the trend curves of each factor on the decomposition efficiency of straw are plotted as follows.

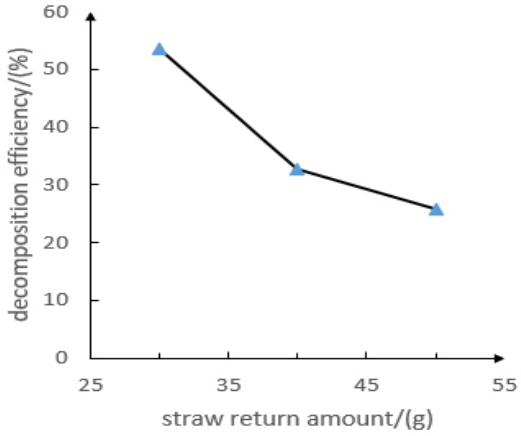

(a) Plot of straw amount versus decomposition efficiency

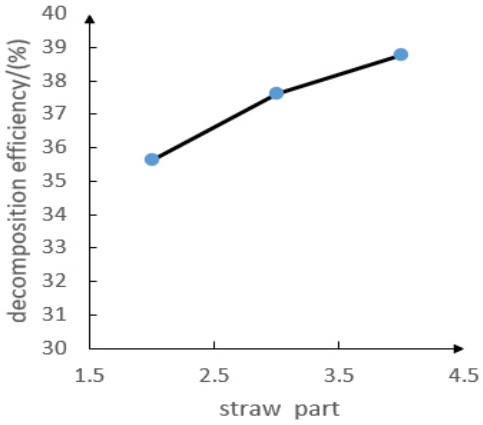

(b) Plot of straw part versus decomposition efficiency

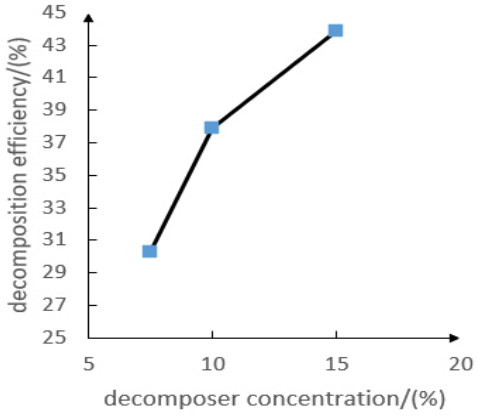

(c) Plot of decomposer concentration versus decomposition efficiency

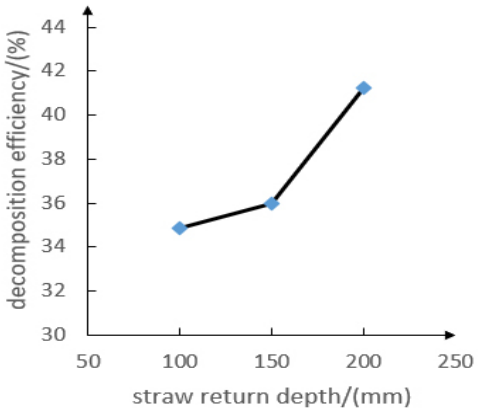

(d) Plot of straw return depth versus decomposition efficiency

Fig. 3 - Factor-indicator relationship curve

From Fig. 3-(a) it can be seen that: the overall trend of straw decomposition efficiency decreased with the increase of straw return amount. This is because straw decomposition is mainly through the decomposition of microbial colonies in the soil, and with the increase in the amount of straw, the amount of remaining straw after decomposition increases, making the soil more porous and affecting the subsequent crop planting. This suggests that straw decomposition is not favored when the amount of straw is high. In terms of the rate of change, the straw decomposition efficiency showed a decreasing trend with the increase in the amount of straw.

The decomposition efficiency decreased by 20.97% from 53.67% to 32.7% when the amount of straw changed from 30 g to 40 g, which is a significant decrease; and when the amount of straw changed from 40 g to 50 g, the decomposition efficiency decreased from 32.7% to 25.67%, which is a 7.03% decrease and a slower decrease. *Wang Hanpeng et al., (2018*), analyzed that the decomposition efficiency of returned straw decreased with the increase of returned straw at different straw return amounts.

From the trend of the curve in Fig. 3-(a), it can be inferred that there is also an optimum amount of straw required for straw decomposition in black soil. The curve path of straw decomposition efficiency with straw amount cannot be clearly given due to the number of straw amount levels in this experiment; however, it can be inferred that the peak decomposition efficiency may occur near the straw amount of 30 g, that is around 4800 kg of straw per hectare of land returned to the field. In view of the significance of the effect of straw amount on the effect of straw decomposition, and considering that the environmental factors and climatic factors in Northeast China differ greatly from those in other regions, the range of suitable straw amount for straw decomposition can be further studied.

From Fig. 3-(b) it can be seen that: With the change of straw part, the closer the straw part is to the root, the higher the moisture content of the straw and the straw decay rate shows an increasing trend, but the trend is slower. The straw decomposition efficiency increased by 2% from 35.63% to 37.63% when the straw parts were shifted down from the middle to the middle, with a slow upward trend; The straw decomposition efficiency increased by 1.14% from 37.63% to 38.77% when the straw parts were shifted down from the middle to the lower middle, with a slower increasing trend. *Cai Lijun et al., (2019),* analyzed the decomposition pattern of different parts of corn straw, and the overall decomposition efficiency of different parts of straw was highest in leaves, followed by stalks, and the rachis was the most difficult to decompose. From the trend of the curve in Fig. 3-(b), it can be inferred that: the decomposition efficiency of corn straw showed an increasing trend as the straw parts became closer to the roots and the water content of the straw became higher (*Yu et al., 2012*). Therefore, considering the characteristics of rainfall in Northeast China, corn straw should be returned to the field for decomposition as early as possible after the corn harvest to ensure a high decomposition efficiency.

From Fig. 3-(c) it can be seen that: the decomposition efficiency of corn straw showed an increasing trend with the increase of decomposer concentration. The decomposition efficiency of corn straw increased from 30.27% to 37.87% when the concentration of decomposer increased from 7.5% to 10%, an increase of 7.6% and an obvious upward trend; when the decomposer concentration increased from 10% to 15%, the decomposition efficiency of corn straw increased from 37.87% to 43.9%, an increase of 6.03%, and the increasing trend became slower. *Fan Zuowei et al., (2021)*, experimentally analyzed that inoculation of corn straw with microbial decomposition solution could effectively promote the rate of straw humification and rapid accumulation of effective nutrients in the soil. From the trend of the curve in Fig. 3-(c), the effect of different decomposer concentrations on the increase of straw decomposition efficiency was significant. However, when the concentration of decomposer is too high, it will increase the number of remaining colonies in the soil and root burn will occur, which will affect the subsequent crop planting. Therefore, the concentration and dosage of the decomposer should be controlled in the straw decomposition and return operation.

From Fig. 3-(d) it can be seen that: the change of straw decomposition efficiency showed an increasing trend with the increase of straw return depth. *Wang Jinwu et al., (2017),* summarized and analyzed that the depth of corn straw returned to the field should be greater than 0.18 m to basically meet the straw decay degradation requirements. From the decomposition change amplitude, the straw decomposition efficiency increased from 34.83% to 35.97% when the return depth was increased from 0.1 m to 0.15 m, up 1.14%, with a slow rising trend; the straw decomposition efficiency increased by 5.26% from 35.97% to 41.23% when the return depth was increased from 0.15 m to 0.2 m, which was a significant increase. The straw decomposition efficiency was 41.23% at a return depth of 0.2 m. It can be inferred from the rate of change of the curve: when the return depth is less than 0.1 m, the straw decomposition efficiency is influenced by the environment and the decomposition rate is low. It is speculated that the highest straw decomposition efficiency of corn straw may occur in the range of 0.15~0.2 m tillage depth.

Experimental validation

To validate the results of the optimal design, the optimal combination of factor parameters was averaged in repeated tests to derive the error between the derived and optimal solution. The results of the validation tests are shown in Table 5.

Table 5

Test validation results

Test number	Test conditions		Decomposition efficiency [%]
1	straw return amount A_1 :	30g	62.2
2	straw stalk part B_3 :	Lower Middle	62.0
3	decomposer concentration C_1 :	15%	63.2
4	straw return depth D_3 :	0.2m	62.6
5			61.4
Average value			62.3
Percentage error			4.89%

The results of the validation tests show that: at a straw amount of 30 g, a straw part of the middle and lower part, a decomposer concentration of 15% and a turning depth of 0.2 m, the average decomposition rate of corn straw was 62.3%, with an error of 4.89% between the optimized result of 65.5%. The small error between the indicator validation test and the optimization results is less than 5%, indicating that the results obtained from the target optimization design are reliable.

CONCLUSIONS

1) The amount of straw had the most significant effect on the straw decomposition efficiency. In the range of straw amount set in this experiment, the decomposition efficiency of straw was negatively correlated with the amount of straw, which was 53.67% when the amount of straw was 30 g, and 25.67% when the amount of straw was 50 g. When carrying out the return operation, it is important to keep the amount of straw returned to the field to around 3500 kg per hectare of land in order to achieve the best possible replacement.

2) Under the incubation conditions, the concentration of decomposer has an important effect on straw decay. The decomposition efficiency of straw showed a positive correlation with the increase of decomposer concentration, when the decomposer concentration was 7.5%, the decomposition efficiency was 30.27%; when the decomposer concentration was 15%, the decomposition efficiency was 43.9%. In this test, the test material is straw stalks, which are difficult to decompose. In field practice, the actual degree of decomposition of the straw is higher than the test data because the straw leaves and stalks are mixed and deeply broken by machinery. When returning the straw to the field, the concentration of the decomposer and the amount of spraying can be increased according to the crushing of the straw in order to achieve a better decomposition effect.

3) In the combination of factors and levels selected in this experiment, the effect of straw return depth on straw decomposition efficiency showed a positive correlation, when the return depth was 0.1 m, the decomposition efficiency was 34.83%; when the return depth was 0.2 m, the decomposition efficiency was 41.23%. Therefore, the straw return depth should be controlled within the range of 0.15 m to 0.2 m. The return depth can be adjusted according to the conditions in the field to achieve good decomposition.

4) In this experiment, the straw part had the least effect on straw decomposition efficiency. Under the level of straw part set in this experiment, the straw decomposition efficiency showed a positive correlation with the straw part, when the straw part was the upper middle part, the straw decomposition efficiency was 35.63%; when the straw part was the lower middle part, the straw decomposition efficiency was 38.77%. Therefore, straw return should be done as early as possible after the corn harvest. The straw return operation should be carried out as early as possible after the maize harvest, when the straw has a high water content, which helps it to decompose.

Discussion

Corn is grown in all the planting area of the Heilongjiang Reclamation Region, in the first, second, third, fourth and fifth cumulus zones (*Zhang et al., 2014*), spread over 12 locations in the east and west of Heilongjiang Province, with marked differences in soil properties between the regions (*Liu et al., 2019*). In addition, the timing of the corn harvest and the form of straw return vary from region to region, with differences in straw decomposition time, degree of shredding and depth of turning and burying. Considering that all of the above factors can affect the effect of straw decomposition and return to the field, it should be applied and promoted in a reasonable manner, taking into account all the local influencing factors, and establishing a straw decomposition and return model that is appropriate to the local situation.

ACKNOWLEDGEMENT

The authors greatly appreciate the careful and precise reviews by anonymous reviewers and editors. This research was supported by the 2022 Central Government-led Local Science and Technology Development Special Project (No. ZYYD2022JMS005); Project of Excellent Innovation Team Construction for Basic Scientific Research Business Expenses of Heilongjiang Provincial Higher Education Institutions (No. 2021-KYYWF-0639); Project funded by Heilongjiang University Student Innovation and Entrepreneurship Training Program (No. 202210222024).

REFERENCES

[1] Cai, L. J., Zhao, G. F., Liu, J. Q., Gai, Z. J., Du, J. X., Guo, Z. H. & Zhang, J. T. (2019). Study on the characteristics of straw decay in different parts of maize and its influencing factors. *Maize Science,* (02), 113-119. http://doi.org/10.13597/j.cnki.maize.science.20190216.

[2] Fan, Z. W., Chen, S. M., Li, Y. Y., Gao, Y. S., Dou, J. J., Hou, Z. H., Liu, H. T. & Wu, H. Y. (2021). Study on the application effect of decomposing bacterial agents on maize straw under different methods of returning to the field. *Maize Science,* (02), 109-116. http://doi.org/10.13597/j.cnki.maize.science.20210217.

[3] Li, C. J., Sun, T. & Zhang, X. Y. (2015). Effect of straw rots on the degradation rate and soil physicochemical properties of maize straw in cold land. *North China Journal of Agriculture* (S1), 507-510.

[4] Li, W. L., Ma, X. B., Zhang, J. B. & Yang, C. H. (2021). Comprehensive treatment and effective utilization of crop straw. *China Science and Technology Information,* (16), 41-42.

[5] Liang, A. Z., Zhang, Y., Chen, X. W., Zhang, S. X., Huang, D. D., Yang, X. M., Zhang, X. P., Li, X. J., Tian, C. J., McLaughlin, Neil B. & Xiang, Y. (2022). Study on the development status and effectiveness of conservation farming in the black soil area of Northeast China. *Geoscience,* (08), 1325-1335. http://doi.org/10.13249/j.cnki.sgs.2022.08.001.

[6] Liu, S. D., Wang, C., Zhang, W. & Wang, H. Y. (2019). Experimental study on the decomposition pattern of maize straw in Heilongjiang Reclamation Area. *Agricultural Mechanization Research,* (08), 186-190. http://doi.org/10.13427/j.cnki.njyi.2019.08.032.

[7] Liu, Y. N., Wu, K. N., Li, X. L. & Li, X. (2022). A study on land type classification at provincial scale based on black land conservation objectives: the case of Heilongjiang Province. *Geoscience* (08), 1348-1359. http://doi.org/10.13249/j.cnki.sgs.2022.08.003.

[8] Qi, J. T., Tian, X. L., Liu, K., Li, M. S., Zheng, T. Z., Li, G. & Fan, X. H. (2021). Influence of maize straw return in black soil area on the infiltration performance of soil water in mixed tillage. *Journal of Agricultural Engineering* (01), 141-147.

[9] Sun, X. Y. (2015). Research on the hazards of straw burning and comprehensive utilization. *Green Technology* (03), 222-224.

[10] Wang, A. L. (2013). Problems and countermeasures of corn straw returning to the field. *Modern Agricultural Science and Technology,* (07), 241+243.

[11] Wang, H. P., Jing, D. X., Zhou, R. J. & Fu, J. F. (2018). Effects of maize straw return volume on soil properties, straw decay and maize blight. *Maize Science,* (06), 160-164+169. http://doi.org/10.13597/j.cnki.maize.science.20180627.

[12] Wang, J.W., Tang, H. & Wang, J. F. (2017). Analysis of the current situation and development of comprehensive utilization of crop straw resources in Northeast China. *Journal of Agricultural Machinery*, (05), 1-21.

[13] Wang, L., Wang, F.L., Duan, T.T. & Liang, X.G. (2020). Study on the decomposition pattern of maize straw returned to the field in Heilongjiang Province. *Agricultural Mechanization Research,* (09), 24-31. http://doi.org/10.13427/j.cnki.njyi.2020.09.005.

[14] Yang, T. R., Zhao, J. H., Yang, L., Peng, Y. P. & Zhou, H. P. (2021). Analysis of optimal yield percolation irrigation technology combinations for maize based on orthogonal tests. *Xinjiang Agricultural Science,* (09), 1585-1593.

[15] Yang, Z. X., Zhou, H. P., Guan, C. L., Xie, W. Y. & Che, L. (2013). Effectiveness of straw rotting agent in corn straw return. Shanxi Agricultural Science (04), 354-357.

[16] Yao, W. H. (2014). An analysis of the benefits and technical requirements of returning corn straw to the field. *Modern Agriculture*, (04), 41. http://doi.org/10.14070/j.cnki.15-1098.2014.04.010.

[17] Yu, H., Gu, Y., Liang, X. H. & Wu, C.S. (2015). Study on the decomposition pattern of maize straw and functional diversity of soil microorganisms. *Journal of Soil and Water Conservation,* (02), 305-309. http://doi.org/10.13870/j.cnki.stbcxb.2015.02.057.

[18] Yu, Y., Lin, Y., Mao, M., Wang, W. M., Tian, F., Pan, J. M. & Ying, Y. B. (2012). Experimental study on the tensile properties of maize straw. *Journal of Agricultural Engineering,* (06), 70-76.

[19] Yu, Y., Mao, M. & Pan, J. M. (2012). Study of moisture content characteristics and tensile properties of different parts of maize straw. *China Agricultural Mechanization,* (04), 75-77.

[20] Zhang, T. Q., Wang, Y., Wang, R. J., Wang, H. & Jiang L. J. (2014). Overview of maize cultivation in Heilongjiang Reclamation Area. *Jilin Agriculture,* (03), 30.

DESIGN AND IMPLEMENTATION OF SHEEP TARGET EXTRACTION ALGORITHM BASED ON MACHINE VISION
/
基于机器视觉的羊只目标提取算法设计与实现

Lili NIE, Linwei LI, Fan JIAO, Haina JI, Zhenyu LIU *) [1]
College of Information Science and Engineering, Shanxi Agricultural University, Taigu, Shanxi / China
Tel: 13593101646; E-mail: lzysyb@126.com
Corresponding author: Liu Zhenyu
DOI: https://doi.org/10.35633/inmateh-68-69

Keywords: *image segmentation, sheep, object extraction, watershed algorithm*

ABSTRACT

In order to improve the quality of sheep foreground object segmentation, images are segmented using the watershed algorithm in combination with a growing region algorithm, and the pixel-by-pixel comparison of segmentation is optimized to reduce the processing time. Compared with other algorithms, the optimized watershed algorithm can achieve more complete target extraction, and its processing time is improved by over 50%. Moreover, the optimized watershed algorithm has the optimal overall image quality indicators. This algorithm can provide a reference for the real-time extraction of the activity state of sheep.

摘要

为改善羊只前景目标分割的质量，结合分水岭算法与生长区域算法对图像进行分割，优化分割的逐像素比较，改进运算时间。改进后的分水岭算法较其它算法目标提取更完整，较其它六种算法处理时间提升 50%以上，各项图像质量指标总体最佳。该算法为实时地提取羊只活动状态提供了一定的借鉴和参考。

INTRODUCTION

Sheep breeding is a vital part of animal husbandry. To meet the development needs, intelligent sheep breeding has become an inevitable trend. Machine identification technology has been increasingly used in the breeding industry to achieve more scientific and convenient management of sheep breeding, which has significantly facilitated the transformation and modernization of the breeding industry *(Ma et al., 2021)*. Target object segmentation is an essential technology in machine vision technology *(Xue et al., 2021)*. The foreground recognition of sheep targets based on image processing technology lays a solid basis for the automatic detection of sheep behaviour while being the premise of this detection, and the image segmentation algorithm can effectively increase the accuracy of foreground target recognition. Thus, the image processing technology was used in this paper to identify the foreground target of sheep in order to analyse the characteristics of different segmentation algorithms.

Extensive research on machine vision technology has been conducted worldwide. *(Qin et al., 2021)*, proposed a cow target extraction algorithm based on correlation filtering and edge detection. The average overlap rate between the targets extracted by the algorithm and the real results was 92.93%, suggesting that the algorithm can be effective in accurate target extraction. *(Zhang et al., 2017)*, proposed a sheep foreground image extraction algorithm based on the superpixel image segmentation algorithm and the FCM clustering algorithm, which extracted the outline of the sheep image and automatically measured the body size parameters. Rare studies have been conducted on image segmentation in the animal husbandry abroad. *(Cao et al., 2021)*, extracted wheat lodging using a hybrid algorithm combining watershed algorithm and adaptive threshold segmentation. *(Muhammad et al., 2018)*, used the optimized HSV and watershed to detect red ripe tomatoes, which shows good application potential in picking robots. *(Chen et al., 2021)* used traditional computer vision to identify livestock at different growth stages. In brief, machine vision technology has been extensively used in the production of the breeding industry, and the sheep breeding industry has been less involved. In this paper, a sheep target extraction algorithm that integrates morphology and watershed algorithm is proposed for sheep target extraction.

[1] *Nie Lili, M.S. Stud.; Li Linwei, Lecturer M.S.; Jiao Fan, M.S. Stud.; Ji Haina, M.S. Stud.; Liu Zhenyu, Prof. Ph.D.*

MATERIALS AND METHODS

Image acquisition and processing

The experimental data were collected at the base of Shanxi Agricultural University, Taigu District, Jinzhong City, Shanxi Province, and 10 adult sheep were selected and placed in stalls with a size of nearly 6m×4.2m×2m. A smart camera is used as a shooting tool. Fig. 1 presents a schematic diagram obtained through the system acquisition. Fig. 2 presents a single image collected by shooting. Fig. 3 gives a representative image of four different poses selected from the 188 image data for batch processing.

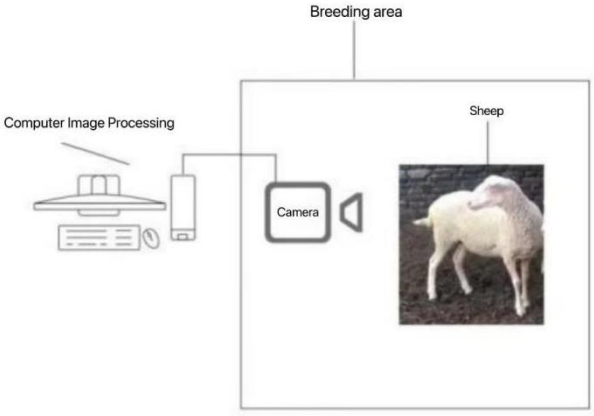

Fig. 1 – Schematic diagram of acquisition system

Fig. 2 – The effect of sheep data acquisition

a) ***b)*** ***c)*** ***d)***

Fig. 3 – Original picture of sheep in four poses

a) Standing; b) Lying on the side; c) Eating; d) Forelimbs bent

When processing an image, the first step is to gray the image, in order to remove the miscellaneous and useless information in the original colour image, simplify the image matrix, and speed up the image processing. The specific operation method of graying processing: read the image, extract the R colour channel grayscale of the colour image, remove a lot of unnecessary information in the colour image, that is, make the RGB values equal, and then the image is converted to gray. When shooting and recording sheep, the original image is too large due to its complex colour and large amount of information, which will reduce the processing speed. The transformed gray image simplifies the matrix in the original colour image, that is, R=G=B, and the equivalent is the gray value. The gray value is 0-255. The gray image is obviously smaller than the colour image, and the processing speed of gray image is faster.

Using linear spatial filtering method, the output pixel is the weighted sum of the input neighbourhood pixels. The use of linear filtering is mainly to improve the image quality, enhance the image recognition, and eliminate a series of interferences such as high-frequency noise. In addition, linear filtering can also enhance the image edge and linearity, and de-blur at the same time. Sobel operator of edge detection is used to convolve the image in vertical and horizontal directions respectively.

To achieve better segmentation results in the image segmentation process, grayscale processing, linear filtering, gradient transformation, and morphological operations should be performed on the image.

When increasing the segmentation effect, it is considered trying the edge detection operator, and comparing the segmentation effects using the Sobel operator, the Laplacian operator, the Laplacian Gaussian operator, as well as the Prewitt operator. The gradient images based on different operators are presented in Fig. 4, and the final segmentation results are compared in Fig. 5. Comparing the images of the segmentation results of different filtering algorithms, the difference in the segmentation results is very small. The four filtering algorithms have good applicability to the watershed segmentation algorithm, and the filtering effect of the Laplacian-Gaussian operator is the best.

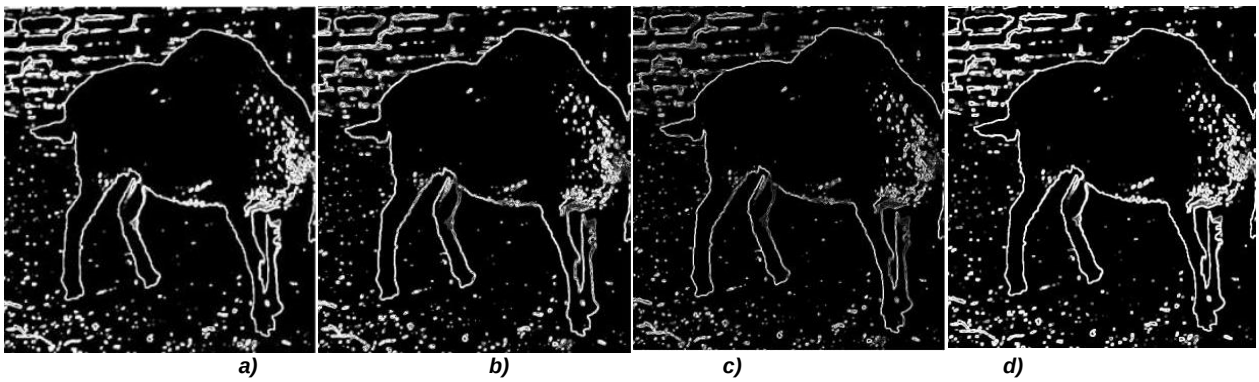

a) b) c) d)

Fig. 4 – Gradient image based on different operators:
a) Sobel operator; b) Laplacian operator; c) Laplace Gaussian operator; d) Prewitt operator

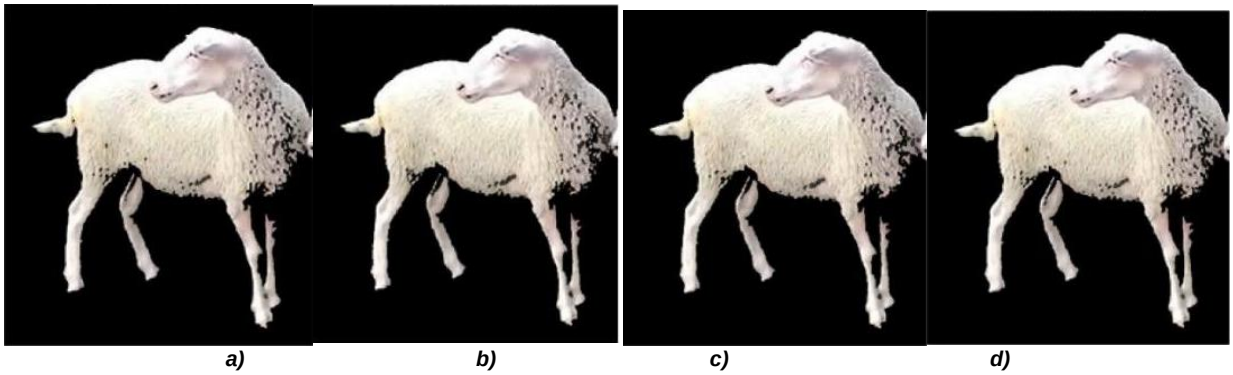

a) b) c) d)

Fig. 5 – Segmentation result graph based on different operators
a) Sobel operator; b) Laplacian operator; c) Laplace Gaussian operator; d) Prewitt operator

Sheep target extraction based on an optimized watershed algorithm

Using the watershed algorithm to process the sheep image shows an advantage that it can process the weak edge perfectly. Moreover, using the method of marking the image for segmentation can reduce the segmentation of the image area with small noise and correct the over-segmentation. The traversal is performed to extract the area where the sheep is located, and then the watershed algorithm is operated to segment the image. Fig. 7(b) illustrates the effect of extracting sheep from the background.

The segmentation result obtained using morphology alone is depicted in Fig. 6(a), which can completely segment the sheep subject, whereas some image data may not be stuck to the background. The segmentation result achieved using the growth region method alone is presented in Fig. 6(b). The sheep subject can be more accurately extracted, whereas there will be noise inside, thus making the segmented sheep target incomplete.

a) b)

Fig. 6 – Separate segmentation result
a) Morphology; b) Growth area

The overall design idea, combining the advantages and disadvantages of the above two methods, is to use the growing region algorithm to outline the accurate outline of the sheep, then adopt the morphological method to fill in the noise part in the middle of the sheep body, and finally combine the largest area object extracted using the two methods to extract the final sheep part.

(1) Local adjustment. Morphological algorithms do not just use simple erosion and dilation, but use composite operations (e.g., erosion, dilation, negation, reconstruction, and local maxima) to further refine the segmentation results. The morphological operations aiming to remove non-target boundaries are conducted.

(2) Specific combination process. Sheep segmented by morphological and growth area methods are treated in three categories below: (a) the part divided by both algorithms: directly judged as the sheep part; (b) the part judged as sheep by morphology and judged as noise by growth area method is judged as sheep; (c) Finally the extracted largest area object is used to extract the final sheep.

The comparison of segmentation results according to the above watershed algorithm and the optimized algorithm is shown in Fig. 7. Compared with the watershed algorithm, the optimized algorithm is more complete in target extraction, which proves the effectiveness of the optimized algorithm for target extraction, which further improves the image processing results and improves the accuracy.

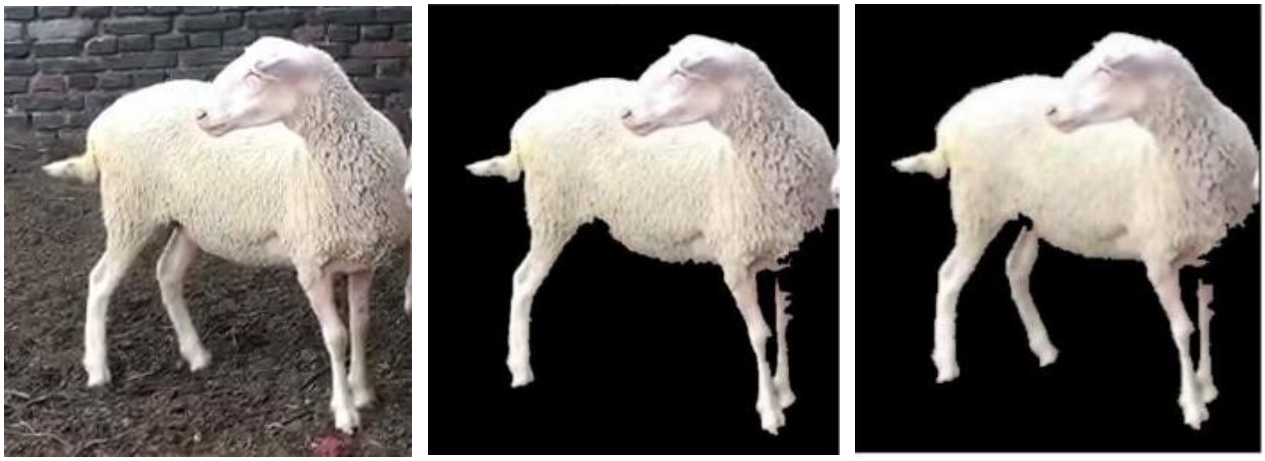

a) *b)* *c)*

Fig. 7 – Comparison of results before and after improvement

a) Original drawing; b) Watershed algorithm; c) Optimized watershed algorithm

Batch time optimization

To further select the optimal algorithm for sheep extraction, the maximum inter-class variance method (OTSU), the wavelet algorithm, the support vector machine (SVM), the optimal histogram entropy method (KSW), the global threshold method, and the optimized watershed algorithm are used to process batch images of 188 sheep image data. The pixel-by-pixel comparison in the process of judging sheep is optimized by the built-in function, and the cycle is reduced by vector calculation in the process of calculating the average assessment index. Moreover, the processing time reduces significantly.

Fig. 8 presents a flow chart of extracting sheep targets before and after time optimization.

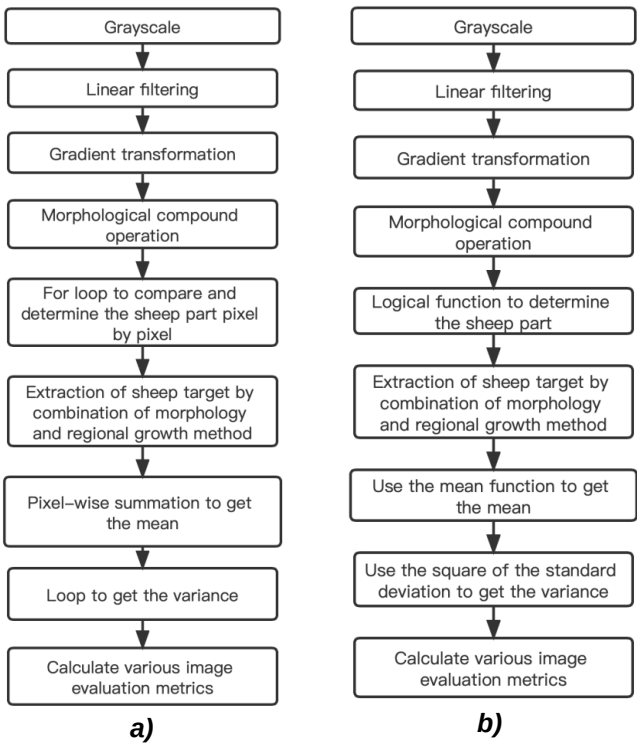

Fig. 8 – Flowchart of extracting sheep targets before and after time optimization

Assessment indicators

Reasonable assessment of image quality has a very important application value, so the quality of the generated segmentation results is assessed through an objective assessment *(Huang et al., 2021)*. Based on the assessment indicators of a single image feature, the following six are selected:

(1) *Mean*. It is the arithmetic mean of the luminance values of all pixels in the image, and the calculation method is expressed in Equation (1).

$$\mu = \frac{1}{M \times N} \sum_{i=1}^{M} \sum_{j=1}^{N} P(i, j) \tag{1}$$

where:

$P(i,j)$—pixel value at point (i,j);

$M \times N$—size of image.

(2) *Standard deviation*. It expresses the degree of dispersion of pixel gray levels from the image mean *(Zhang et al., 2014)*, which is written as Equation (2):

$$\sigma = \sqrt{\frac{1}{M \times N} \sum_{i=1}^{M} \sum_{j=1}^{N} (P(i, j) - \mu)^2} \tag{2}$$

(3) *Information entropy*. Image entropy is a vital indicator to measure the richness of image information. The size of the entropy value indicates the average amount of information involved in the image. The information entropy of an image is defined as Equation (3):

$$E = -K \sum_{i=1}^{n} p_i \log p_i \tag{3}$$

where:

K—A proportional constant corresponding to the chosen unit of measurement;

p_i—The probability that the gray value of a pixel in the image is i.

(4) *Spatial frequency*. It can indicate the overall activity level of an image space, including spatial row frequency RF and spatial column frequency CF, which are respectively defined as Equation (4) and Equation (5):

$$RF = \sqrt{\frac{1}{M \times N} \sum_{i=1}^{M} \sum_{j=1}^{N} [P(i, j) - P(i, j-1)]^2} \tag{4}$$

$$CF = \sqrt{\frac{1}{M \times N} \sum_{i=1}^{M} \sum_{j=1}^{N} [P(i, j) - P(i-1, j)]^2} \tag{5}$$

The spatial frequency is the root mean square of RF and CF, which is written as Equation (6):

$$SF = \sqrt{CF^2 + RF^2} \tag{6}$$

(5) *Variance*. It can indicate the dispersion of the gray level of the respective pixel in the image relative to the average gray level. It can also be used to assess the amount of image information to a certain extent. It is calculated as Equation (7):

$$D(X) = E\left\{[X - E(X)]^2\right\} \tag{7}$$

(6) *Contrast*. It is the ratio of the black and white of the image, i.e., the gradient level from black to white. The larger the ratio, the more gradient levels from black to white will be, and the richer the color expression will be. It is calculated as Equation (8):

$$C = \sum_{\delta} \delta(i, j)^2 P_{\delta}(i, j) \tag{8}$$

where:

$\delta(i,j) = abs(i-j)$—The grayscale difference between adjacent pixels;

$P_{\delta}(i,j)$—The distribution probability of the grayscale difference between adjacent pixels.

RESULTS

Comparison of the effect of segmentation algorithms

Through the comparison of wavelet transform, OTSU algorithm, SVM algorithm, optimal histogram entropy method and global threshold method, the optimal improved watershed algorithm is obtained. As depicted in Fig. 3, the images of four postures of upright, side lying, eating, and forelimb bending are selected for the representative analysis. The OTSU algorithm should be implemented on the targets to be processed respectively, and the effect is relatively poor. Fig. 9 illustrates the extracted image. Since the wavelet transform is a frequency domain operation, it is not sensitive to noise, and Fig.10 presents the segmented image. The SVM algorithm adopts the regional segmentation method to distinguish the image into foreground and background images. Subsequently, the feature vector is extracted as the SVM training sample for the image segmentation, as illustrated in Fig. 11. As depicted in Fig.12 the optimal histogram entropy method performs segmentation by maximizing the entropy of the segmented image *(Cheng et al., 2018)*. The global threshold method is an iterative process, and the segmentation results are illustrated in Fig.13.

a) ***b)*** ***c)*** ***d)***

Fig. 9 – OTSU algorithm

a) Standing; b) Lying on the side; c) Eating; d) Forelimbs bent

a) ***b)*** ***c)*** ***d)***

Fig. 10 – The wavelet transform

a) Standing; b) Lying on the side; c) Eating; d) Forelimbs bent

a) ***b)*** ***c)*** ***d)***

Fig. 11 – The SVM algorithm

a) Standing; b) Lying on the side; c) Eating; d) Forelimbs bent

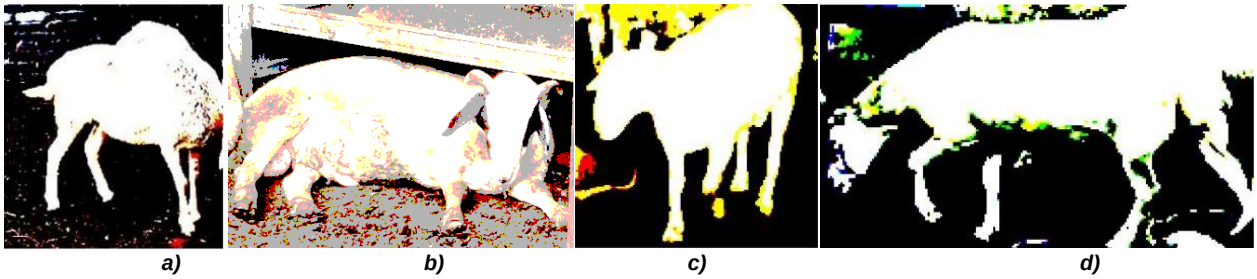

a) ***b)*** ***c)*** ***d)***

Fig. 12 – KSW algorithm

a) Standing; b) Lying on the side; c) Eating; d) Forelimbs bent

a) *b)* *c)* *d)*

Fig.13 – Global threshold method

a) Standing; b) Lying on the side; c) Eating; d) Forelimbs bent

a) *b)* *c)* *d)*

Fig. 14 – Watershed improvement algorithm

a) Standing; b) Lying on the side; c) Eating; d) Forelimbs bent

Compared with other algorithms, the optimized watershed algorithm (Fig.14) handles noise better while more effectively outlining the foreground target area making it more obvious.

Time comparison of segmentation algorithms

For multiple image data, the time average comparison is shown in Table 1 after 7 segmentation algorithms. Compared with other algorithms, the optimized watershed algorithm achieves an improvement rate of higher than 50%, which suggests that the optimized watershed algorithm is highly applicable to batch processing time.

Table 1

Comparison of the mean time of batch image processing

Segmentation algorithm	Operation hours	The improvement rate of the processing time of the optimized watershed algorithm compared with different algorithms
	[s]	[%]
OTSU algorithm	0.4530	59.38%
Wavelet transform	1.0156	81.88%
SVM algorithm	0.4491	59.02%
KSW algorithm	0.6306	70.82%
Global threshold method	0.4253	56.73%
Watershed algorithm	1.1307	83.73%
Watershed improvement algorithm	0.1840	0%

Comparison of image quality indicators for segmentation algorithms

Table 2 presents the average comparison of different image quality indicators of 188 images after segmentation using six algorithms. To be specific, the segmentation effect of wavelet transform is relatively poor, which results in a completely black state, so some image quality indicators of the wavelet transform result are invalid. The analysis of different quality indicators in Table 2 reveals that the smaller the standard deviation and variance of the target extraction results, the wider the gray distribution of the image will be; the larger the information entropy, the richer the information involved in the image will be; the smaller the mean, the lower the brightness will be; the smaller the spatial frequency, the smaller the overall activity level; the smaller the contrast, the less colour expression. In general, the assessment indexes of the segmentation results based on the optimized watershed algorithm are better than those of other algorithms in terms of target extraction.

Table 2

Image quality assessment

Segmentation algorithm	OTSU algorithm	Wavelet transform	SVM algorithm	KSW algorithm	Watershed algorithm	Watershed improvement algorithm
Mean	65.2505	69.0906	65.4993	109.9486	60.6109	54.8811
Standard deviation	85.1338	46.9962	81.5149	98.7614	83.4112	78.2767
Information entropy	0.8585	0.3567	3.1449	1.3190	0.7987	3.0794
Spatial frequency	51.8825	25.3765	51.6625	63.7363	52.6317	32.2580
Variance	85.1331	46.9958	84.5142	98.7606	83.4105	78.2761
Contrast	0.0661	0.0250	0.0628	0.0649	0.0596	0.0349

CONCLUSIONS

The watershed algorithm is prone to over-segmentation. Accordingly, the watershed algorithm is usually combined with different algorithms to increase the processing effect when used to process images. In this paper, a growing region algorithm is introduced into sheep target extraction, and a sheep target extraction algorithm is developed based on a combination of the watershed algorithm. As revealed by the experimental results, the optimized algorithm achieves the optimal recognition for the sheep foreground target, and the segmentation results are more complete. The segmentation results are compared with those of the OTSU algorithm, the wavelet transform algorithm, SVM, the KSW method, and the global threshold method through image quality assessment, and the overall assessment index is the best, suggesting that the optimized algorithm can be effective in accurately extracting sheep targets. The optimized algorithm exhibits high applicability. For batch image processing of multiple images, the average processing time is 0.1840 s, marking an increase of higher than 50% than the processing time of the other six algorithms.

The optimized watershed segmentation algorithm improves the quality of target extraction, simplifies, and accelerates the processing of sheep images, and has promotion value in agriculture and animal husbandry. Machine vision technology has been used in all walks of life, and its extensive application has significantly improved the living standard of human beings. With the improvement of productivity and automation level, machine vision will play wider roles.

ACKNOWLEDGEMENT

The authors would like to thank all the funding projects for their support in this study:

Project No. 20210302124497, Youth Scientific Research Project of Shanxi Provincial Basic Research Program, Research on Animal Individual and Posture Recognition Based on Machine Vision, 2022.01-2024.12.

Project No. 31772651, National Natural Science Foundation of China, Research on the mechanism of inactivation of airborne pathogens in closed livestock and poultry houses by the synergistic effect of high-voltage pulsed electric field, 2018.01-2021.12.

Project No. XK19201, "Teaching and Research Management" Fund of School of Information Science and Engineering, Shanxi Agricultural University, 2019.09-2021.09.

REFERENCES

[1] Chen, C., Zhu, W., & Norton, T. (2021). Behaviour recognition of pigs and cattle: Journey from computer vision to deep learning. *Computers and Electronics in Agriculture*, Vol. 187, pp. 106255, Jiangsu/China.

[2] Cheng, Q., Dong, L., Xiao, D., & Gui, J. (2018). Recognition of Wheat Spike from Field Based Phenotype Platform Using Multi-Sensor Fusion and Improved Maximum Entropy Segmentation Algorithms. *Remote Sensing*, Vol. 10, pp. 246, Hefei/China.

[3] Cao, W., Qiao, Z., Gao, Z., Lu, S., & Tian, F. (2021). Use of unmanned aerial vehicle imagery and a hybrid algorithm combining a watershed algorithm and adaptive threshold segmentation to extract wheat lodging. *Physics and Chemistry of the Earth*, Vol. 123, pp. 103016, Beijing/China.

[4] Huang, Y., Zhong, M., Zhang, T., Liu, Y., Yang, X., (2021). Overview of Image Quality Evaluation Methods Based on Objective Evaluation (基于客观评价的图像质量评估方法综述). *Computer Knowledge and Technology*, Vol. 17, pp. 92-94, Tianjin/China.

[5] Ma, C., Chen, X., (2021). Application and Development of Machine Vision Technology in Agricultural Fields (机器视觉技术在农业领域的应用及发展). *Ningxia Journal of Agri. and Fores. Sci. & Tech*, Vol. 62, pp. 65-70+2, Ningxia/China.

[6] Muhammad, H., Ting, Z., Han, L., & Ahmed, S. (2018). Mature Tomato Fruit Detection Algorithm Based on improved HSV and Watershed Algorithm. *IFAC PapersOnLine*, Vol. 51, pp. 431-436, Beijing/China.

[7] Qin, L., Zhang, X., Dong, M., Yue, S., (2021). Target Extraction of Moving Cows Based on Multi-feature Fusion Correlation Filtering (基于多特征融合相关滤波的运动奶牛目标提取). *Transactions of the Chinese Society for Agricultural Machinery*, Vol. 52, pp. 244-252, Shaanxi/China.

[8] Xue, F., Wang, Y., Li, Q., (2021). Research progress of livestock behaviour recognition based on computer vision technology (基于计算机视觉技术的牲畜行为识别研究进展). *Heilongjiang Animal Science and Veterinary Medicine*, pp. 33-38, Inner Mongolia/China.

[9] Zhang, L., (2017). Study on Sheep's Body Size Measurement Based on Cross-angle Computer Vision (基于跨视角机器视觉的羊只体尺参数测量方法研究). *Doctoral dissertation, Inner Mongolia Agricultural University*, Inner Mongolia/China.

[10] Zhang, X., Li, X., Li, J., (2014). Validation and Correlation Analysis of Metrics for Evaluating Performance of Image Fusion (融合图像质量评价指标的相关性分析及性能评估). *ACTA AUTOMATICA SINICA*, Vol. 40, pp. 306-315, Jilin/China.

DESIGN AND RESEARCH OF A CUTTING BLADE FOR CORN STALKS BASED ON A BIONIC PRINCIPLE
/
基于仿生原理的玉米秸秆切割刀片的设计与研究

Zhu ZHAO [1,2], Zhongnan WANG [2], Bintong ZHAO [1], Yuqiu SONG [1], Mingjin XIN *[1]
[1] College of Engineering, Shenyang Agricultural University, Shenyang / China;
[2] Liaoning Agricultural Technical College, Yingkou / China
Tel: +86-024-88487119; E-mail: xinmjsynd@163.com Corresponding author: Xin Mingjin
DOI: https://doi.org/10.35633/inmateh-68-70

Keywords: *Bionic blade, ant, mandible teeth, corn stalk, finite element analysis, cutting test*

ABSTRACT
The ant (Pheidole megacephala, Fabricius) has a unique and hard mandibular structure to cut branches and crush hard food. Inspired by this special geometric structure of the mandibular teeth, a stereoscopic microscope was used to view the image of the mandible of the ant. The Origin and AutoCAD software were used to obtain the outer profile of the mandibular teeth of the ant. The outer profile of the ant's mandibular teeth was fitted and expressed by five-order polynomial function. According to the analysis of the profile curve of the maxillary teeth, the fourth tooth is the most convex and the sharpest. The fourth tooth of the ant plays a key role in its feeding process, therefore, the structural parameters of the fourth maxillary tooth were selected as bionic elements for bionic blade design. To compare the cutting performance of the bionic and ordinary flat blades, the performance of bionic blade and the ordinary blade were conducted by using ANSYS software, the cutting force-deformation characteristics were tested using the Rapid TA practical texture analyser. The results of the element simulation showed that the mechanical properties of bionic blade were better than those of the ordinary blade. The results of the cutting experiments indicated that under the loading speed of 5 mm/s, the maximum cutting force of the bionic blade was 137.51 N, which is 12.17 % lower than that of the ordinary flat blade. The average cutting force of the bionic blade was 96.56 N, which is 11.58 % lower than that of the ordinary flat blade. The cutting energy consumption of the bionic blade was 9.68 J, which is 11.92 % lower than that of the ordinary flat blade. Under the loading speed of 10 mm/s, the maximum cutting force of the bionic blade was 143.88 N, which is 10.37 % lower than that of the ordinary flat blade. The average cutting force of the bionic blade was 101.03 N, which is 9.77 % lower than that of the ordinary flat blade. The cutting energy consumption of the bionic blade was 10.14 J, which is 9.95 % lower than that of the ordinary flat blade. The experimental results suggested that the bionic blade can effectively reduce the cutting force and energy consumption; thus, the bionic blade is more suitable for cutting stalks. These results will be helpful in the development of cutting elements for cutting and chopping of corn stover and other processing machinery.

摘要
蚂蚁(Pheidole megacephala, Fabricius)具有独特而坚硬的上颚结构，可以切割树枝和粉碎坚硬的食物。受到这种特殊的上颚齿几何结构的启发，我们用体式显微镜来观察蚂蚁的上颚齿结构，利用 Origin 软件和 AutoCAD 软件获得蚂蚁上颚齿的外轮廓曲线，用五阶多项式函数拟合和表示蚂蚁上颚齿的外轮廓曲线。根据上颚齿的轮廓曲线分析，得出蚂蚁上颚第 4 齿最为凸出和尖锐，在其取食过程中起着关键作用，因此，选择蚂蚁上颚第四齿的结构参数作为仿生刀片设计的仿生元素。为了比较仿生刀片和普通平刃刀片的切削性能，运用 ANSYS 软件对普通平刃刀和仿生刀片进行有限元静力学分析，采用 Rapid TA 实用型分析仪对其切削力-变形特性进行了测试。有限元仿真结果表明，仿生刀片的力学性能更优，切削实验结果表明，在 5mm/s 的加载速度下，仿生叶片的最大切削力为 137.31 N，比普通平刃刀片的最大切削力降低了 11.70%，仿生刀片的平均切削力为 96.56 N，比普通平板刀片的平均切削力低 11.58%，仿生刀片的切削能耗为 9.67 J，比普通平板刀片的切削能耗低 11.28%。在 10mm/s 的加载速度下，仿生叶片的最大切削力为 143.88N，比普通平刃刀片的最大切削力降低了 10.37%，仿生刀片的平均切削力为 101.03 N，比普通平板刀片的平均切削力低 9.77%，仿生刀片的切削能耗为 10.14J，比普通平板刀片的切削能耗低 9.95%。实验结果表明，该仿生刀片能有效降低切削力和能耗，仿生刀片更适合切割玉米茎秆。该研究将有助于玉米秸秆切割刀具和其他加工机械的开发。

---

[1] *Zhao Zhu, Ph.D. Stud. Eng.; Wang Zhongnan, Lab.Techo. MA. Eng.; Zhao Bintong, MA. Stud. Eng.; Song Yuqiu, Prof. Ph.D. Eng.; Xin Mingjin, Prof. Ph.D. Eng.*

INTRODUCTION

Cutting corn stalk is an important link in the working process of the corn harvester *(Jia et al., 2022)*. The cutting blade of the corn harvester determines the cutting quality of the corn stalk *(Zhao et al., 2022)*. At present, the cutting blade used in the corn harvesters mainly use flat blades, which are characterized by high cutting resistance, high energy consumption, and poor stubble quality (*Ma et al., 2020; Xu et al., 2021*). Therefore, there is a need to develop a cutting blade with low cutting resistance, low energy consumption, and high cutting quality.

Bionics is an interdisciplinary subject that bridges biology and engineering. By studying the structure, function, and operating principle of organisms, and applying these principles to engineering, it is possible to develop devices and machines with superior performance. It also provides researchers with new ideas and methods for improving the performance of cutting blades (*Chen et al., 2021; Zhang et al., 2022*). Studies on the cutting behaviour of various animals have produced several important theoretical results. The geometric structure and morphological outline of chewing mouthparts can help reduce cutting resistance during the predation and improve cutting quality. Massah et al. designed a corrugated blade based on the *Armadillidium vulgare* body surface geometrical shape. The experimental results showed that in wet soil, the corrugated blade resulted in the lowest drag force (*Massah et al., 2020*). Zhang et al. designed a bionic root cutter based on the contour curve model of the jaw of *Prosopocoilus astacoides*. The trial results showed that the effect of installing the bionic root cutter was better than that of an ordinary triangular root cutter (*Zhang et al., 2022*). Zhao et al. designed a bionic cutting blade that could reconstruct the multi-segment and serrated structure of locusts' mouthparts. The test results showed that the bionic cutting device could reduce the cutting torque and power consumption by 26.6-31.6 % and 21.9-26.1 %, respectively (*Zhao et al., 2020*). Tong et al. found that the contour curve of their incisors was close to the standard arc when studying the mouthparts of *Otidognathus davidis Fair* larvae. Based on this structure, a bionic cutting blade was designed. When cutting cabbage, the energy consumption of the bionic cutting blade was reduced by 12.8 % and the cutting performance was increased by 12.5 % (*Tong et al., 2017*). Tian et al. designed a hemp harvester blade based on the morphological characteristics of the incisors of the Longhorn beetle's mandible. They built a self-made double-acting blade cutting test bench to comparatively test the cutting of the bionic and ordinary blades. The average maximum cutting force and energy consumption of the bionic blade were reduced by 7.4 % and 8.0 %, respectively, and the bionic blade resulted in a significant reduction in resistance and consumption (*Tian et al., 2017*). Jia et al. designed a bionic saw blade inspired by the special geometric structure of incisors. The cutting force test showed that the bionic saw blade could lead to a noticeable reduction in cutting force and energy consumption (*Jia et al., 2013*).

The ant is one of the most widespread and abundant insect species on Earth (*Paul et al., 2003*). Ants have a unique and hard mandible structure that enables them to exert a large bite force to transport food, cut branches and leaves at high speed, and crush hard food (*Lei et al., 2016*). In this study, the ant's mandible was used as a bionic prototype, and its shape and structure were integrated into the design of the corn harvester's cutting blade. A stereoscopic microscope was used to access the ant's mandible image, and Origin and AutoCAD software were used to plot the ant's mandible characteristic curve. After analysing the maxillary teeth profile curve, the structural parameters of the fourth maxillary tooth of the ant were selected as the bionic elements for the bionic blade design. The bionic blade was made of metal and constructed using 3D printing technology. Corn stalk cutting tests were performed on a Rapid TA practical texture analyser to investigate the cutting capacity of the bionic blade against the ordinary flat blade in terms of cutting force and energy consumption.

MATERIALS AND METHODS

Observation and motion analysis of the ant mandible microstructure

The ant species selected in this experiment was *Camponotus japonicus*. Samples were collected from a farmer's corn planting base in Yingkou City, Liaoning Province, China. Scanning electron microscopy is the simplest and most effective method for observing microstructure and surface topography. A research-grade NSZ818 stereo microscope developed and manufactured by Ningbo Yongxin Optics Co., Ltd. was used in this experiment. The ant specimen was placed under the microscope for observation, the external structure and digital photograph of the ant sample is shown in Figure 1.

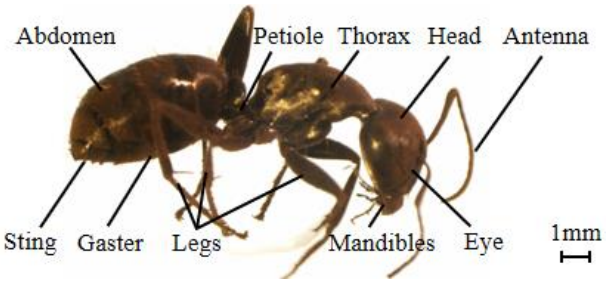

Fig. 1 - External structure of the ant sample

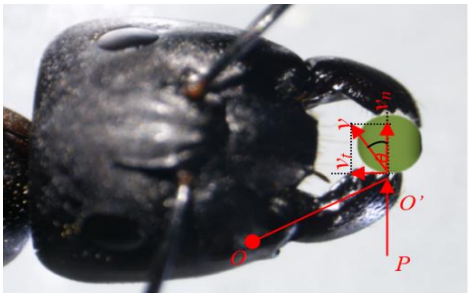

Fig. 2 - Ant occluding force vector diagram

Moreover, the focus knob was manually adjusted to focus on the ant's mandible. The lower jaw was observed moving around point *O*, and the bite force was detected at the end of the upper jaw. The direction of the absolute movement velocity of the upper jaw was neither vertical nor parallel to the cutting edge of the upper jaw. The movement of the ant's lower jaw results in sliding cutting. The absolute velocity was decomposed to obtain the normal and tangential velocities, as shown in Figure 2.

Based on Figure 2,

$$\tan\theta = \frac{v_t}{v_n} \tag{1}$$

Where: v_t is the tangential velocity, m/s; v_n is the normal velocity, m/s; θ is the angle between the absolute and normal velocities, that is, the slip cutting angle, °.

According to Gollum's constant theorem,

$$P^3 S = C \tag{2}$$

Where: P is the normal force required for test cutting depth, g; S is the tangential slip, mm; C is constant.

The Gollum constant theorem states that the greater the tangential slip, the lower the cutting force when the blade cuts into the same depth of material. In addition, the cutting angle is smaller during slip cutting, resulting in a lower cutting force.

Extraction of the ant maxillary tooth contour curve

The mandible was observed to have five teeth with a relatively uniform size and distribution. The anterior and lateral parts of the right mandible were viewed under a stereoscopic microscope, as shown in Figure 3.

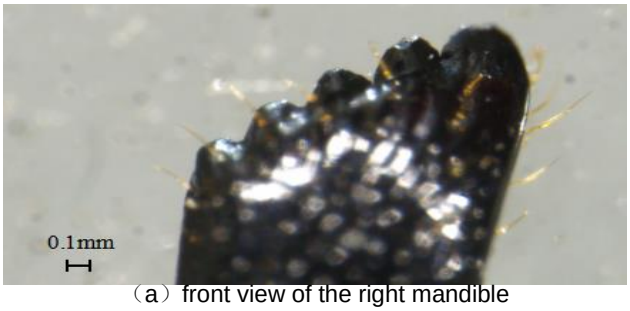

（a）front view of the right mandible

(b) side view of the right mandible

Fig. 3 - Digital photograph of the ant's mandible

To extract the ant maxillary tooth contour curve, Adobe Illustrator software was first used to convert the bitmap into a high-fidelity vector diagram, and all the geometric feature contour points of the teeth were extracted from the ant's mandible. To distinguish the target image from the image background, the vector image was binarized to plot a binarized image. AutoCAD software was used for further adjustment and plotting, which was used to extract the outline of the ant's maxillary tooth structure. Each black pixel in the image represents a two-dimensional variable, which is specified by coordinates. The extracted boundary image is shown in Figure 4. The image outline is clear and complete in the figure and is basically the same as the outline of the original image.

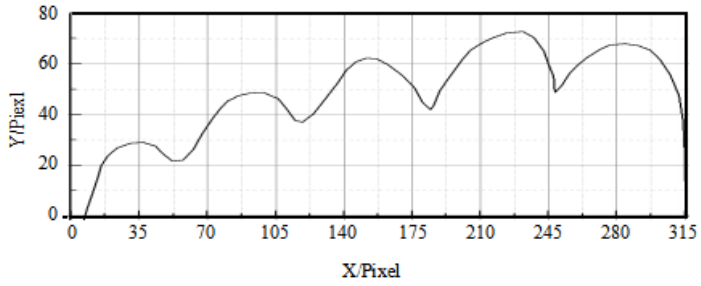

（a）front view of the right mandible

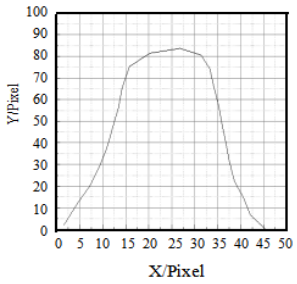

(b) side view of the right mandible

Fig. 4 - Extracted contour line of the ant's mandible teeth

Fitting of the ant maxillary tooth contour curve

The ant maxillary tooth contour curve is relatively complex and difficult to express by a function. To analyse the extracted contour more clearly so that the curve can be expressed accurately, the edge curve of the ant's mandible structure was divided into 5 parts, each corresponding to a peak respectively, as shown in Figure 5.

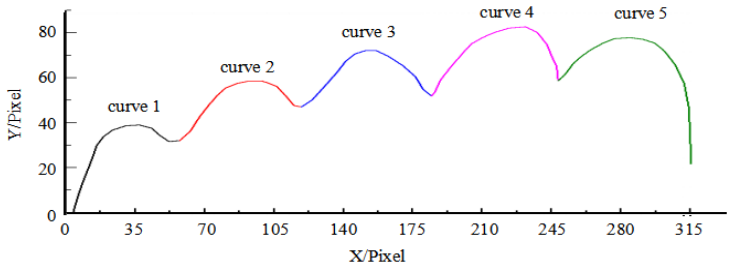

Fig. 5 - Division of extraction curves

Origin software was used for curve fitting, and the least squares method was used to fit each part of the curve. After several attempts, the quintic polynomial function was used to express the contour curve. The function contains 6 parameters, and the fitting equation is expressed as follows:

$$y(x) = Intercept + B_1x + B_2x^2 + B_3x^3 + B_4x^4 + B_5x^5 \quad (3)$$

The fitting results are listed in Table 1:

Curve parameters of the tooth **Table 1**

Parameter	Curve 1	Curve 2	Curve 3	Curve 4	Curve 5
Intercept value	3.18238	918.76187	-134094.10855	342796.87567	-2.27507E6
Intercept standard error	0.13316	183.29073	46153.1945	95347.91022	897390.81551
B_1 value	18.64683	-1066.19397	101804.68471	-216847.35946	1.24004E6
B_1 standard error	0.81429	210.53776	34731.86361	60858.72139	492869.99951
B_2 value	-21.34275	488.22202	-30873.75448	54804.52792	-270226.71585
B_2 standard error	1.56171	95.70713	10445.25828	15529.73055	108232.94174
B3 value	12.13237	-109.45358	4674.85109	-6917.09543	29429.51638
B_3 standard error	1.25171	21.52506	1569.23089	1980.36319	11878.80257
B_4 value	-3.47791	12.03206	-353.40152	435.98646	-1601.79382
B_4 standard error	0.43884	2.39568	117.7696	126.20193	651.58614
B_5 value	0.38642	-0.52015	10.66953	-10.9788	34.85725
B_5 standard error	0.05578	0.10559	3.53224	3.21527	14.29048
Adj.R^2	0.9932	0.9836	0.9955	0.99821	0.98548

A curve fitting variance R^2 closer to 1 indicates a better curve fitting effect and a more realistic fitted function. Table 1 shows that the fitting variances R^2 of all five curves exceed 0.98, indicating a fairly high degree of curve fitting. As observed, the quintic polynomial fitting satisfies the fitting requirements. The side contour curve of the ant's mandible structure was the quintic polynomial function. The result of the fitting is shown in Figure 6, and the fitting equation is expressed as follows:

$$y(x) = 0.13383 + 0.58579x - 0.15297x^2 + 0.29687x^3 - 0.05684x^4 + 0.00282x^5 \quad (4)$$

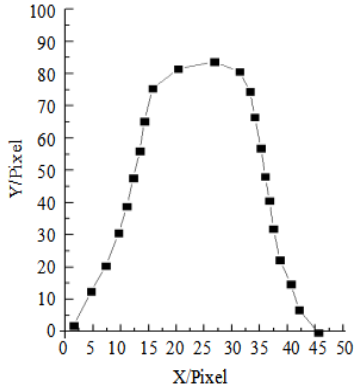

Fig. 6 - Fitted curve of mandible side contour

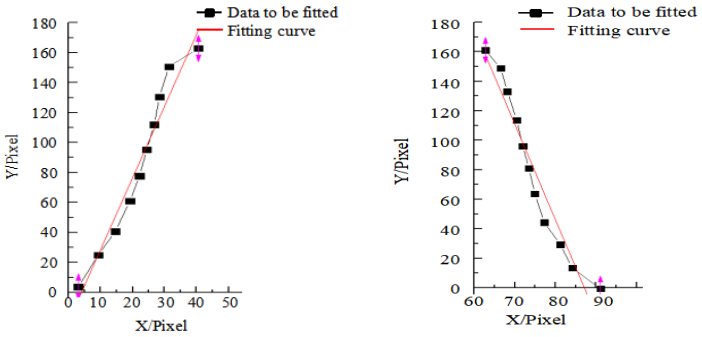

(a) left contour curve (b) right contour curve

Fig. 7 - Fitted line of the mandible side contour

The curve fitting variance R^2 is 0.96513 and it satisfies the fitting requirements. To reduce the machining difficulty of the cutting blade and maintain the bionic character, the least square method was used to fit the left and right contour parts of the curve, as shown in Figure 7. The fitting equation of the left contour curve is expressed as Equation (5), in which the fitting variance R^2 is 0.951563 and the slope is 2.392. The fitting equation of the right contour curve is expressed as Equation (6), in which the fitting variance R^2 is 0.93423, and the slope is -3.23448.

$$y(x) = -2.35631 + 2.392x \quad (5)$$

$$y(x) = 32.42474 - 3.23448x \quad (6)$$

If the accuracy requirements are not high, a straight line can also be used to approximate the upper and lower contour curves of the ventral teeth to simplify the processing technique. The angle between the upper and lower contour lines is 38°.

Analysis of the ant mandible contour curve

The second derivative reflects the slope change rate, and the image of the function is the concave and convex shape of the function (*Zhang et al., 2018*). The second derivative function is obtained for the five fitting polynomial functions, and the graph is plotted for comparative analysis, as shown in Figure 8. Based on Figure 8, the second derivative function of curves 1-5 are generally less than 0. Similar rules apply to curve 1 and curve 2. The second derivative of curve 1 and curve 2 fluctuates between positive and negative values. For curve 3, it begins to decrease at the beginning and increases at the end. Curve 4 and curve 5 have the same rules, it is generally less than 0. The second derivative of the function may reflect the bending direction of the plane curve. When it is greater than, less than, or equal to 0, the image is concave, convex, or neither, respectively. Since the shapes of curve 5 protrude outward, this indicates that the cutting area between the teeth and material is enlarged during cutting, thereby increasing the sliding cutting angle and improving the cutting efficiency, which is conducive to ant feeding. Furthermore, the teeth corresponding to curves 1–5 play a key role in the ant feeding process.

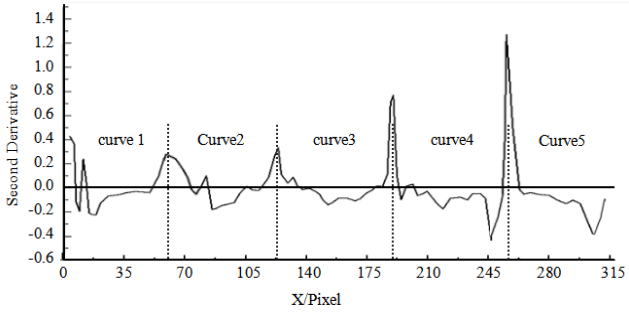

Fig. 8 - Second derivative of the fitted curves with

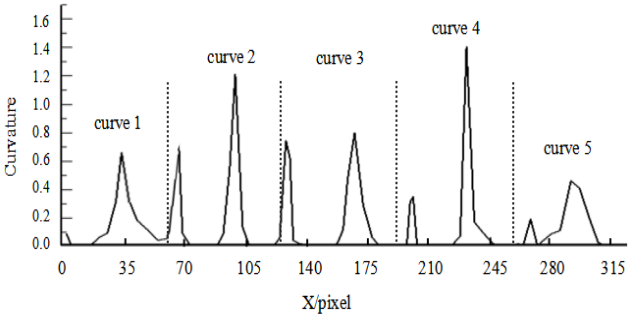

Fig. 9- Curvature of fitted curves with mandible

Curvature is a measure of the degree of non-planarity of the geometry, which can represent the degree of bending of the curve. The greater the curvature, the greater the degree of bending of the curve. The second derivative of the fitted contour curve was calculated, and the curvature of the fitted function was plotted, as shown in Figure 9.

Based on Figure 9, curve 4 has the largest curvature, followed by curves 2 and 3, and curves 1 and 5 have the smallest curvatures. This means that the teeth corresponding to curve 4 are the sharpest and most convex, and therefore the most suitable for cutting. Therefore, in this study, the structural parameters of the fourth tooth of the ant mandible are selected as bionic elements for bionic blade design.

Design and machining of the bionic blade

For comparative analysis, the same structural parameters were used for the bionic blade as in the case of the ordinary flat blade (i.e., *a*=180 mm; *b*= 55 mm; *c*=10 mm; *d*=10 mm; α= 38°). The cutting edge of the bionic blade is represented by the contour curves of the fourth teeth of the ant mandible. Comparing the design of the flat and bionic blades, the difference between the blades is mainly in the cutting edge, as shown in Figure 10. Due to the complex structure of the bionic blade, the blade was made via 3D printing to accurately express the bionic elements (*Chaturvedi et al., 2019*). The BLT-T320 metal 3D printer produced by Xi'an Bright Laser Technologies Co., Ltd. was selected, and the 3D printing material was 316L stainless steel made of fine metal powder.

At a test temperature of 24.8 ℃, the material tap density was measured to be ≥ 4.75 g/cm^3, the tensile strength was 586–649 MPa, the yield strength was 265–382 MPa, and the elastic modulus range was 205–265 GPa. Using direct metal laser sintering technology, the laser beam combines the metal powder layer and fusion point to form the blade. After processing, the bionic blade is clear and complete, with a smooth blade surface. The 3D printed blade is shown in Figure 11.

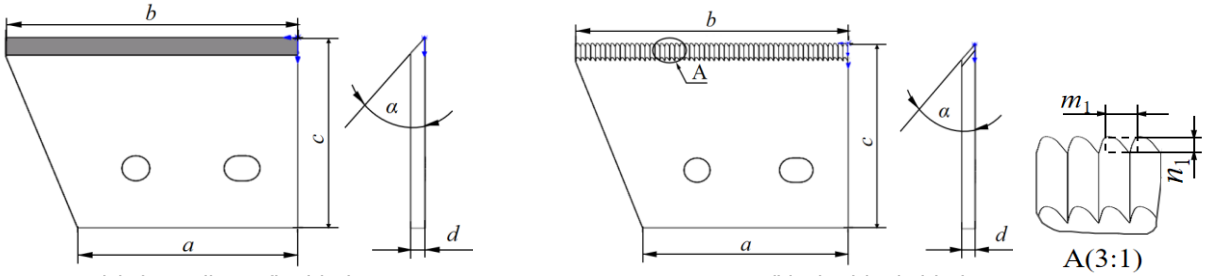

(a) the ordinary flat blade (b) the bionic blade

Fig. 10 - Structural mode of the blades

(a) the ordinary flat blade (b) the bionic blade

Fig. 11 -Samples of the blade

Finite element analysis of the blades

The reliability of the blade directly affects the working efficiency of the device when cutting the stalks. A finite element analysis of the ordinary flat blade and the bionic blade were conducted, and the software used was ANSYS 2020. Defined as the structural steel, the material of the ordinary flat blade and the bionic blade was evaluated; the material properties of the ordinary flat blade and bionic blade were described in Table 2. A finite element analysis was conducted on the blade after being meshed.

Material parameter **Table 2**

Parameters	Value	Units
Structural steel	0.3	-
Elastic Modulus	2.0×10^5	MPa
Density	7.85×10^3	Kg/m^3
Yield Strength	305	MPa

Cutting performance test

The texture analyser is immune to human error, has objectivity, can improve data authenticity, stability, and repeatability, and can be used to measure the material's mechanical properties, such as tissue structure characteristics and cutting resistance. The cutting performance test of the blade was performed with the Shanghai TengBa Rapid TA practical texture analyser, as shown in Figure 12.

Fig. 12 -Test system

When the blade moves down to cut the corn stalks, the configured software system automatically records the cutting resistance and time, cutting resistance and displacement, and time and displacement curves of the blade. In this experiment, the loading speed of 5 mm/s and 10 mm/s were selected for the cutting performance test to analyse the effects of the conventional flat blade and the bionic blade on corn stalk cutting. The test sample is taken from the corn test field of Shenyang Agricultural University. The corn stalk is cut in the same condition and with an average moisture content of 73.8 %.

RESULTS AND ANALYSIS

Analysis of Finite element of blades

As it is shown in Fig. 13, the maximum stress on the ordinary flat blade (33.345 MPa) and the bionic blade (26.526 MPa) are observed at the threaded hole on the right side. Compared with that of the flat blade, the maximum stress of the bionic blade is 20.45% lower. The maximum stress on the ordinary flat blade and the bionic blade are considerably less than 355 MPa. Thus, the strength of the blades meets the requirements of mechanical properties. Furthermore, the total deformation of the ordinary flat blade and bionic blade is 6.1549×10-3 and 4.8942×10-3, respectively. Compared with that of the flat blade, the total deformation of the bionic blade is 20.48% lower. Accordingly, within the safe range, the deformation resistance of the ordinary flat blade and bionic blade are satisfactory, and the bionic blade is more suitable than the ordinary flat blade.

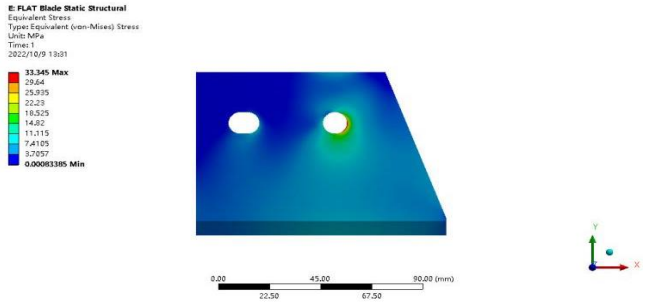

(a) Stress nephogram of the ordinary flat blade

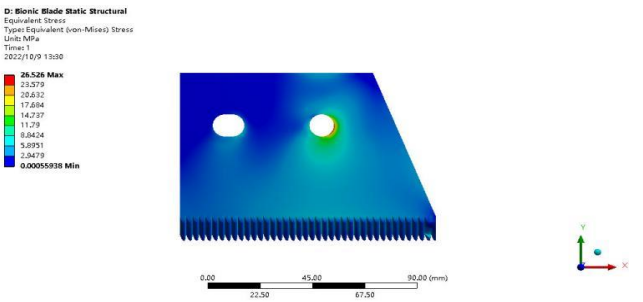

(b) Stress nephogram of the bionic blade

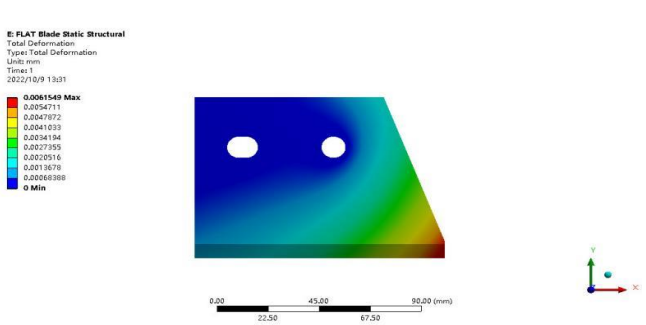

(c) Total deformation nephogram of the ordinary flat blade

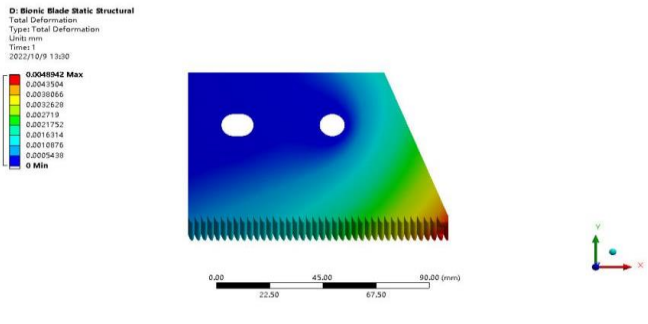

(d) Total deformation nephogram of the bionic blade

Fig. 13 - Results of Finite element analysis of blades

Analysis of the blades on the corn stalk cutting force

Cutting force is a key factor that reflects the cutting efficiency. The relationship between cutting force and displacement is shown in Figure 14.

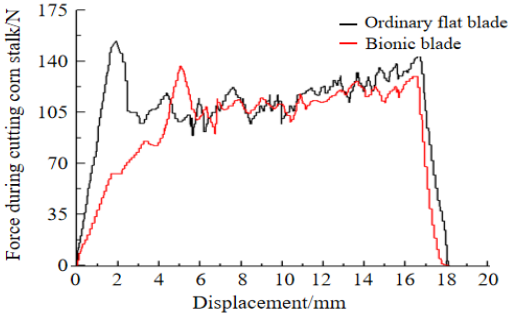

Fig. 14 - Relationship between the cutting force and displacement

When a normal flat blade was used, the cutting force rapidly increased during the displacement from zero to 2 mm. Then, the force decreased and remained in a vibration state that lasted almost until the end of the cutting operation. Toward the end of the cutting process, the forces increased again, reached a maximum, and then promptly dropped to zero. For the bionic blade, the cutting force increased slowly, and the vibration state persisted until the end of cutting. For the bionic blade the cutting force increased from zero to 1 mm and from 4 to 6 mm during the displacement. The maximum forces when cutting corn stalks with the two types of blades are different. The maximum forces in the experiments are listed in Table 3.

Table 3

Maximum force during cutting corn stalk

Loading speed/ mm·s^{-1}	No.	Maximum cutting force/N	
		Ordinary flat blade	Bionic blade
5	1	149.24	131.13
	2	153.52	138.87
	3	167.29	142.83
	4	164.13	140.34
	5	159.11	136.28
	6	150.38	134.22
	7	147.79	133.58
	8	152.57	141.21
	Average	155.50	137.31
10	1	151.83	138.49
	2	158.03	141.35
	3	170.57	151.54
	4	167.62	152.78
	5	165.25	140.17
	6	155.74	142.03
	7	156.81	137.08
	8	158.33	147.62
	Average	160.52	143.88

Under a loading speed of 5 mm/s, the maximum cutting forces of the flat blade and bionic cutter were 155.50 N and 137.31 N, respectively. Compared with that of the flat blade, the maximum cutting force of the bionic blade was 11.70% lower. Under a loading speed of 10 mm/s, the maximum cutting forces of the flat blade and bionic cutter were 160.52 N and 143.88 N, respectively. Compared with that of the flat blade, the maximum cutting force of the bionic blade was 10.37% lower.

The average cutting force when cutting the corn stalk using the ordinary and bionic blades are shown in Figure 15. Under a loading speed of 5 mm/s, the average cutting forces of the ordinary flat and bionic blades were 109.21 N and 96.56 N, respectively. Compared with that of the ordinary flat blade, the average cutting force of the bionic blade was 11.58 % lower. Under a loading speed of 10 mm/s, the average cutting forces of the ordinary flat and bionic blades were 111.97 N and 101.03 N, respectively. Compared with that of the ordinary flat blade, the average cutting force of the bionic blade was 9.77 % lower. This indicates that the bionic blade can reduce the cutting force. There is a statistically significant difference between the data of the four groups at the 0.05 level, indicated by the letters a, b, c and d. The standard deviation of the average cutting force of the ordinary flat blade is larger than that of the bionic blade, indicating that the average force of the bionic blade is similar.

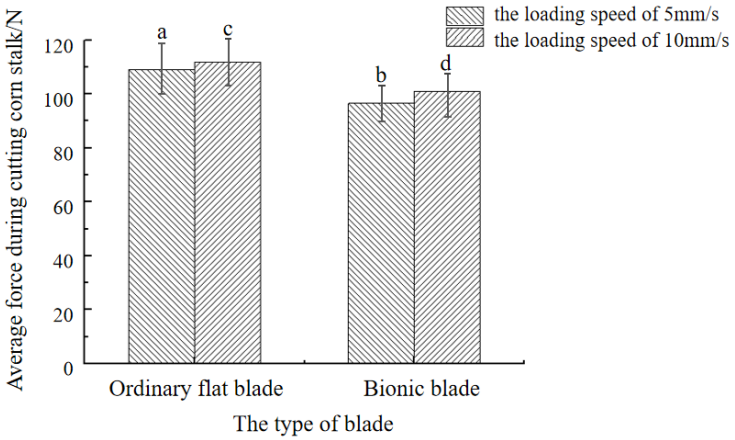

Fig. 15 - Average cutting force

When cutting the straw husk, the required cutting force is 63–83 %, and the cutting force was greater at the beginning and end of cutting. The maximum cutting force of the cutting process was often instantaneous. The greater the instantaneous cutting force, the easier it is to damage the blade during cutting. The maximum transient cutting force of the bionic blade was lower than that of the ordinary flat blade. This means that the cutting of the bionic blade is gentler than that of the ordinary flat blade. The bionic blade can effectively reduce the instantaneous maximum cutting force, which is closely related to the shape of the bionic blade. The evenly distributed tooth edges increase the sliding cutting angle of the bionic blade and improve the cutting performance.

Analysis of energy consumption during cutting

Energy consumption during cutting is an important factor that reflects the cutting quality. The force–displacement curve can be plotted when the blade cuts the corn stalk at a constant speed. The energy consumption during cutting can be calculated from the area between the cutting force curve and the displacement axis. The average energy consumption of the different types of blades during cutting is shown in Table 4. The average energy consumption for cutting a single corn stalk is shown in Figure 16.

Table 4

Energy consumption during cutting corn stalk

Loading speed/ mm·s^{-1}	No.	Energy consumption /J	
		Ordinary flat blade	Bionic blade
5	1	10.28	9.37
	2	10.76	9.72
	3	11.88	10.12
	4	11.35	9.82
	5	11.03	9.56
	6	10.58	9.55
	7	10.35	9.35
	8	10.95	9.88
	Average	10.90	9.67

Loading speed/ mm·s^{-1}	No.	Energy consumption /J	
		Ordinary flat blade	Bionic blade
10	1	10.50	9.90
	2	11.10	9.89
	3	12.11	10.74
	4	11.59	10.69
	5	11.46	9.831
	6	10.96	10.11
	7	10.98	9.60
	8	11.36	10.33
	Average	11.26	10.14

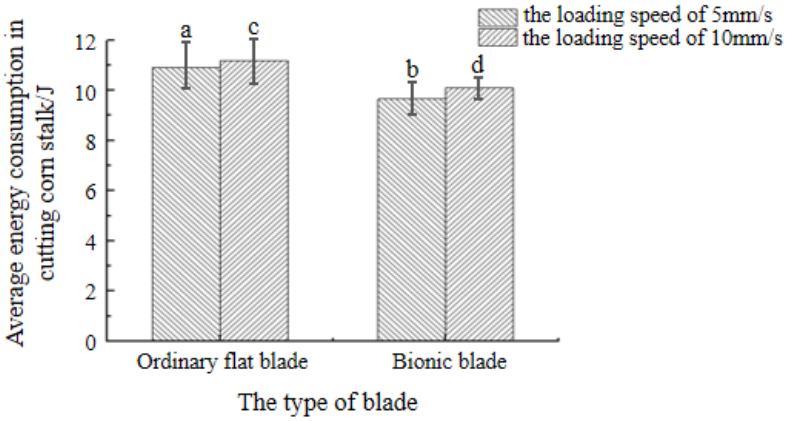

Fig. 16 - Average energy consumption during cutting

Under a loading speed of 5 mm/s, the average power consumption of the flat and bionic blades was 10.90 and 9.67 J, respectively. Compared with the flat blade, the average power consumption of the bionic blade was 11.28% lower. Under a loading speed of 10 mm/s, the average power consumption of the flat and bionic blades was 11.26 and 10.14 J, respectively. Compared with the flat blade, the average power consumption of the bionic blade was 9.95% lower. Due to the different blade types, the average energy consumption during cutting were significantly different. The bionic blade consumed less energy than the flat blade. Therefore, the bionic blade is more suitable for cutting stalks than the flat blade.

CONCLUSIONS

(1) Inspired by the unique geometric structure of ant mandibular teeth, based on the microscopic photography technology and image processing technology to obtain information about the profile curve of the ant mandibular teeth, up to the palate of the profile tooth curve fitting, our analysis concluded that the fourth tooth of the ant mandibular is the most prominent and sharpest, and can be used as a bionic prototype to design and manufacture a new type of bionic blade. Moreover, to carry out finite element static analysis of blades, ANSYS software was applied. The results corroborated the strength and stiffness of the designed bionic blade were better than those of the ordinary flat blade.

(2) To compare the cutting performance of the bionic and the ordinary flat blade, the bionic and ordinary flat blade were manufactured using metal 3D printing technology. The cutting performance of the bionic blade and the ordinary flat blade was tested using the Rapid TA practical texture instrument. Under a loading speed of 5 mm/s, the maximum cutting force of the bionic blade is 11.70 % lower than that of the ordinary flat blade, and the average cutting force of the bionic blade is 11.58 % lower than that of the ordinary flat blade. The average energy consumption of the bionic blade is 11.28 % lower than that of the plain blade during cutting. Under a loading speed of 10 mm/s, the maximum cutting force of the bionic blade is 10.37 % lower than that of the ordinary flat blade, and the average cutting force of the bionic blade is 9.77 % lower than that of the ordinary flat blade. The average energy consumption of the bionic blade is 9.95 % lower than that of the plain blade during cutting. The results show that the bionic blade can effectively reduce the cutting force and energy consumption and is more suitable for cutting corn straw.

(3) In this study, the cutting force and power consumption of the two blades were tested only at quasi-static velocity. Therefore, the cutting performance of the bionic blade at dynamic speed should be further investigated in future research.

ACKNOWLEDGEMENT

This research was funded by the scientific effort of Liaoning Agricultural Technical College (Lnz202216).

REFERENCES

[1] Chaturvedi A, Bhatkar S, Sarkar PS, et al., (2019), 3D geometric modelling of aluminium based foam using micro computed tomography technique, *Materials Today: Proceedings*, Vol.18, Issue 7, pp. 4151-4156, Mumbai / India;

[2] Chen Pan, Xu Pengfei, (2021), Simulation analysis and mechanism study on drag reduction of “Bionics” groove（"仿生学"沟槽减阻仿真分析及机理研究）. *Aeroengine*, Vol.47, Issue 2, pp. 28-32, Shen Yang / P.R.C;

[3] Jia Honglei, Li Changing, Zhang Zhihong et al., (2013), Design of bionic saw blade for corn stalk cutting. *Journal of Bionic Engineering*, Vol.10, Issue 4, pp.497-505, Ji Lin / P.R.C;

[4] Jia Honglei, Tan Hewen, Ma Zhongyang et al., (2022), Design and experiment of the straw breaking and diversion device for maize harvesters (玉米收获机断秸导流装置设计与试验). *Transactions of the Chinese Society of Agricultural Engineering,* Vol.38, Issue 4, pp.12-23, Ji Lin / P.R.C;

[5] Lei Yanyuan; Lv Lihua; Shi Qingxing, et al., (2016), Morphological and ultrastructural observation of mandibles of two invasive fire ants（两种火蚁与黑头酸臭蚁上颚形态及其超微结构观察）, *Journal of Environmental Entomology*, Vol.38, Issue 6, pp.1199-1204, Guangzhou / P.R.C;

[6] Ma Pengbo, Li Liqiao, Wen Banqin et al., (2020), Design and parameter optimization of spiral-dragon type straw chopping Test Rig. *Int J Agric & Biol Eng*, Vol.13, Issue 1, pp.47-56, Shi Hezi/ P.R.C;

[7] Massah Jafar, Hassanpour Fatemeh, Roudbeneh Zeinab Hassanpour et al., (2020), Experimental investigation of bionic soil-engaging blades for soil adhesion reduction by simulating Armadillidium vulgare body surface. *INMATEH-Agricultural Engineering*, Vol.60, Issue 1, pp. 99-106, Bucharest / Romania.

[8] Paul J., Roces F. et al., (2003), Fluid intake rates in ants correlate with their feeding habits, *Journal of Insect Physiology*, Vol.49, Issue 4, pp.347-357, Würzburg / Germany;

[9] Tian Kunpeng, Li Xiangwang, Shen Chen, et al., (2017), Design and test of cutting blade of cannabis harvester based on longicorn bionic principle (天牛仿生大麻收割机切割刀片设计与验), *Transactions of the Chinese Society of Agricultural Engineering,* Vol.33, Issue5, pp. 56－61, Nan Jing / P.R.C;

[10] Tong Jin, Xu Shun et al., (2017), Design of a bionic blade for vegetable chopper, *Journal of Bionic Engineering*, Vol.14, Issue 1, pp.163-171, Ji Lin / P.R.C;

[11] Xu Kai, Ge Yanyan, Xiao Maohua et al., (2021), Design of a straw picking and cutting device. *Int J Agric & Biol Eng*, Vol.14, Issue 6, pp.93–98, Shan Dong / P.R.C;

[12] Zhang Anlun, Teng Guowei, Zhao Haiwu et al., (2018), Video background modelling algorithm with low complexity based on the minimum second derivative (基于最小二阶导数的低复杂度视频背景建模算法), *Journal of Optoelectronics Laser,* Vol.29, Issue 8, pp. 858-864, Shanghai / P.R.C;

[13] Zhang Chenyang, Ding Bing, He Zhongqiang et al., (2022), Kinematics analysis and optimization of rotary multi-legged bionic robot (转盘式多足仿生机器人的运动学分析及优化). *Chinese Journal of Engineering Design*, Vol.29, Issue 3, pp.327-338, Shang Hai / P.R.C;

[14] Zhang Xuening, You Yong, Wang Decheng et al., (2022), Design and experiment of a combined root-cutting and ditching device, *INMATEH-Agricultural Engineering*, Vol.66, Issue 1, pp.383-392, Bucharest / Romania.

[15] Zhao Jiale, Guo Mingzhuo, Lu Yun et al., (2020), Design of bionic locust mouthparts stubble cutting device. *Int JAgric & Biol Eng*, Vol.13, Issue 1, pp. 20-28, Ji Lin / P.R.C;

[16] Zhao Zhu, Wang Zhongnan, Zhao Bintong et al., (2022), Designing a longitudinal hob-type stalk chopping device for corn combine harvester, *INMATEH-Agricultural Engineering*, Vol.67, Issue 2, pp.41-52, Bucharest / Romania.

RESEARCH ON THE ACCUMULATION AND TRANSFER OF HEAVY METALS FROM THE SOIL TO BERRIES (BLUEBERRIES - *Vaccinium myrtillus L.* and RASPBERRIES - *Rubus idaeus*)
/
CERCETĂRI PRIVIND ACUMULAREA ŞI TRANSFERUL METALELOR GRELE DIN SOL ÎN FRUCTE DE PĂDURE (AFINE - Vaccinium myrtillus L. ŞI ZMEURĂ - Rubus idaeus)

Mihaela NIȚU, Augustina PRUTEANU*), Iuliana GĂGEANU
National Institute of Research – Development for Machines and Installations Designed for Agriculture and Food Industry – INMA Bucharest / Romania
E-mail: pruteanu_augustina@yahoo.com
DOI: https://doi.org/10.35633/inmateh-68-71

Keywords: *heavy metals, berries, contamination, pollution*

ABSTRACT
The current study has investigated the accumulation and transfer coefficient for three heavy metals (Cu, Pb, Zn) found in the contaminated soil with three concentrations (c1=1.5%, c2=3.0%, c3=4.5%, c4=6.0%), obtained by mixing the three metals, in blueberry and raspberry fruits. The pots in which the shrubs were planted were loaded with fertile soil which was mixed and homogenized in turn with each of the three solutions of different concentrations. The highest accumulation in blueberry fruits was recorded for zinc, then copper and the lowest for lead, while for raspberries the highest results was recorded for zinc, then lead and the lowest for copper. The findings are valid for all four concentrations used. The transfer coefficient decreases as the concentration of heavy metals increases, thus for high heavy metal concentrations, the values of the transfer coefficient are very low, and for small heavy metal concentrations in the soil, the values for the transfer coefficient are higher. From the assessment of accumulation and transfer of heavy metals to berries (blueberries and raspberry) grown in the contaminated soil, it was concluded that all concentrations of the copper, lead and zinc mix have shown a low risk for human consumption.

REZUMAT
În acest studiu, s-a investigat acumularea si coeficientul de transfer a trei metale grele (Cu, Pb, Zn) din solul contaminat cu patru concentrații (c_1=1.5%, c_2=3.0%, c_3=4.5%, c_4=6.0%) obținute prin amestec din cele trei metale, in fructul de afin si zmeur. Ghivecele în care au fost plantați arbuștii au fost încărcate cu pământ fertil care a fost amestecat și omogenizat pe rând cu fiecare dintre cele trei soluții de concentrații diferite. Cea mai mare acumulare in fructele de afin a fost observată pentru zinc, apoi cupru si cea mai mica pentru plumb, iar in fructele de zmeur pentru zinc, cupru si cea mai mica pentru plumb. Constatările sunt valabile pentru toate cele patru concentrații folosite. Coeficientul de transfer scade pe măsură ce concentrația de metale crește, astfel încât la concentrații mari de metale valorile coeficientului de transfer sunt foarte mici, iar la concentrații mici de metale în sol valorile coeficientului de transfer sunt mai mari. Evaluarea acumulării și transferului metalelor în fructul fructelor crescute în sol contaminat a concluzionat că toate concentrațiile în amestec de cupru, plumb și zinc au prezentat un risc scăzut pentru consumul uman.

INTRODUCTION

Environmental pollution, implicitly that of agricultural soils, with heavy metals is a current topic that concerns humanity. Toxic metals in the soil come from different sources, such as: household waste landfills, agricultural sources, industrial emissions, urban emissions and bedrock. The accumulation of heavy metals in the soil causes the pollution of agricultural soils, with consequences on the quality of fruits and vegetables as well as on human health *(Jolly et al., 2013; Huang et al., 2014, Pruteanu et al., 2019)*.

Fruits and vegetables are often consumed because they are an important source of food, being rich in bioactive compounds (tannins, anthocyanins, antioxidants), vitamins, minerals, proteins, carbohydrates and fibres necessary for human health *(Huang et al., 2014)*. They accumulate heavy metals in both edible and non-edible parts *(Cherfi et al., 2014)*. Heavy metals are necessary for the efficient functioning of biological systems, as long as their concentration in fruits and vegetables is balanced, in order not to produce a series of metabolic disorders *(Fawad et al., 2017)*. In this sense, heavy metal concentrations and nutritional intake from fruits and vegetables are important for maintaining human health *(Balčiauskas et al., 2022)*.

The soil-to-plant transfer factor is an important component due to human exposure to metals through the food chain. The accumulation of metals from soil, water or air in the vegetative organs of plants depends on the properties of metals and the exposure time of metals, absorption rates in different plant tissues and transfer between tissues, plant growth and metabolism parameters, metal partition coefficients between the compartments of the soil-plant system. The transfer factor differs depending on the type of metal, the plant species, but also on the type of soil *(Jolly et al., 2013, Cardei et al., 2021)*.

In the paper written by *Qihang et al., (2021),* the authors studied the geochemical characteristics of heavy metals in blueberries and soil for the Majiang area of Guizhou, China. As methods they used field survey, sampling and indoor analysis, and as benchmarks they relied on national standards for soil pollution risk control on agricultural land. The results showed that the content of heavy metals exceeds the standards only in the lower layer of the soil, without substantially affecting blueberry growth. In fruits, the content of heavy metals did not exceed the concentrations in the standard, which proved that the fruit was safe for consumption.

Also, in the research of *Rusinek et al., (2008)*, the content of heavy metals (Pb, Cd, Cu, Zn, Fe, Mn) was analysed in areas not exposed to pollution (Skierbieszów Landscape Park) and in polluted areas (Rejowiec Cement Factory) for blueberries, raspberries and wild strawberries harvested in the Lublin region. The results showed that, among the berries studied, blueberry had the lowest content of Pb, Zn, Fe, Mn, wild strawberries had a high content of Pb, Zn and Mn, and the content of cadmium was high for all the berries analysed.

Wieczorek et al., (2010), analysed the concentrations of heavy metals (Pb and Cd) in berries (blackberry, raspberry, blueberry, wild strawberry) and wild-harvested hazelnuts as well as in fruit (blackberry, raspberries, blueberries) and hazelnuts harvested from plants grown in orchards in North Eastern Poland. In addition, Pb, Cd concentrations were determined in surface soil samples from the sites where the fruits were collected. It was found that the highest acceptable concentrations based on Polish standards for Pb and Cd were not exceeded in the berries. In wild berries, Pb was undetectable, and in those from orchards, Pb had values of 290 µg/kg. The concentration of Cd varied between 6 and 49 µg/kg wet weight for wild fruits and values up to 72 µg/kg wet weight for orchard fruits. For the soil samples, Pb and Cd had values between 3.2 - 14.9 mg/kg. *Zeiner et al., (2018),* analysed the content of Al, Cd, Cr, Ni and Pb in cranberries, blueberries and rosehips harvested from an unpolluted area in Croatia. The results showed that Cd and Cr were not detected in the samples, and Ni concentrations were mainly lower than 25 mg/kg, in a range comparable to the data from the specialized literature. The consumption of these berries in terms of Cd, Cr and Ni does not present any danger to health, while rosehips contain Pb and Al above the limit allowed in the fruits.

In another paper, the concentrations of 13 elements (Al, Ca, Cd, Cr, Cu, Fe, K, Mg, Mn, Na, Ni, Pb and Zn) were determined for several samples of cultivated and wild blueberry fruits. The authors analysed the total metal content after mineralization using plasma optical emission spectrometry. The results showed that high concentrations of Ca, Na, Mg, Mn and Zn were found in wild blueberries. Also, the concentrations of Cu, Cr, Fe and Ni were found to the same extent, both in wild and cultivated plants. Very high concentrations of Fe and Cd were identified in cultivated blueberries. The efficiency of metal extraction varied depending on their form (fresh or dried) for both blueberry types - wild or cultivated *(Dróżdż et al., 2018).*

In order to determine the transfer of heavy metals from soil to fruits, *Roba et al., (2016)* studied the concentration of four heavy metals (Zn, Cu, Pb, Cd) in raspberries, gooseberries and black currants grown in the gardens of the Ferneziu district residents from Baia Mare mining area (Romania). Due to the different absorption capacity of heavy metals, the concentrations varied for the analysed fruits as follows: Zn > Cu > Pb > Cd. *Lere, B. K. et al., (2021),* focused on the levels of heavy metals in water, soil, fruits and vegetables from three farms located in Nigeria. Water, soil, fruit and vegetable samples were randomly collected, processed and analysed for heavy metals. The concentration of heavy metals in soil was found to be the highest for Fe (57.30–63.51) mg/kg and the lowest was observed for Cu (0.45–1.45) mg/kg. High levels of Pb (0.02–0.03) mg/l, Cd (0.07–0.1) mg/l and Fe (3.23–3.42) mg/l were determined in the irrigation water. In fruits and vegetables, average metal concentration showed significant variation, with Fe having the highest concentration (7.82 mg/kg) in most farm samples. The health risk assessment of heavy metals in fruit and vegetable samples indicated that all metals were within the hazard limit of less than 1, except for Cd.

In their work, *Cui, Y.-J. et al., (2004)* measured the contamination levels of soils and vegetables with cadmium (Cd), lead (Pb), zinc (Zn) and copper (Cu), as well as the factors of transfer (TF) from soil to vegetable plants but also the risk of these heavy metals for health. The results of the research showed that both the soils and the vegetables in two villages in China, one located at 1500 m and another 500 m away from a smeltery

were heavily contaminated, compared to another village located 50 km away from the smeltery. The intake of lead and cadmium from vegetables represented a high risk for the health of local residents (1.44 - 13.5 for Pb) and (3.87 - 7.42 for Cd).

The paper presents the transfer coefficient and the accumulation from the soil in berries (blueberries and raspberries) for the mixture obtained from three heavy metals (Cu, Pb, Zn), at different concentrations (c1 = 1.5%, c2 = 3.0%, c3 = 4.5%, c4 = 6.0%).

MATERIALS AND METHODS

Raspberry (*Rubus idaeus*) and blueberry (*Vaccinium myrtillus L.*) fruits were chosen for this study, because they are rich in antioxidants. Raspberries belong to the *Rosaceae* family and are a bushy, perennial shrub with creeping shoots and straight stems. The fruit, called raspberry, is red, has a sour taste and a pleasant smell. Raspberries can be consumed fresh or industrially processed. The bioactive compound that can be extracted from raspberries is xylitol, beneficial for the prevention of dental caries *(Ardelean et al., 2008)*. Blueberries belong to the *Ericaceae* family and are a bushy, branchy subshrub with a long-branched stem. The fruit called blueberry is a blue, round berry with a pleasant sweet and sour taste *(Ardelean et al., 2008)*.

Blueberry and raspberry cuttings were planted in pots with soil contaminated using mixtures of heavy metals (copper, zinc and lead) in different concentrations, in order to identify the concentrations of heavy metals absorbed during plant growth.

Ten kg of soil was homogenized with 500 ml of heavy metal mixture (Cu, Zn, Pb) for each concentration of 1.5%, 3.0%, 4.5% and 6.0%. The solutions with the following concentrations 1.5, 3.0, 4.5 and 6.0 % were individually prepared in the laboratory. Copper sulphate, lead acetate and zinc sulphate were used as reagents, and distilled water as solvent. To obtain the mixtures of solutions with Cu, Pb, Zn for each of the concentrations of 1.5, 3.0, 4.5 and 6.0% that were individually prepared, equal parts were taken from each solution, element and concentration, and mixed until reaching homogeneity. Heavy metal loading was performed only when the shrubs were planted, without additional loading until harvest.

The control sample was obtained by planting berry shrubs using uncontaminated soil. The soil moisture was maintained at constant levels during the experiments by watering the berry shrubs.

The physico-chemical properties of the soil used in the experiments were: moisture 15%, pH 5.8; phosphorus 0.4%, potassium 0.8%, nitrogen 1.8%.

The experiments were carried out in a specially arranged and controlled space, between March and July 2020. The fruits subjected to the analysis were harvested when they were fully ripe. Images during the experiments are presented in Figure. 1.

a

b

Fig. 1 - Aspects during the research on blueberries (a) and raspberries (b)

The determination of Cu, Pb, Zn from the contaminated soil and from the studied berries was carried out by spectrophotometry (flame atomic absorption).

The transfer coefficient assesses the degree of bioavailability of metals from soil to plants and is a valid function of soil and plant properties. The coefficient was calculated as a ratio between the concentration of a metal (Cu, Pb, Zn) in the fruit and the concentration of the metal in the soil *(Bassey et al., 2014)*.

Based on dry weight, metal concentration in soil and plants was calculated. Thus, the transfer factor (tf) was calculated according to the formula below:

$$tf = \frac{C_{plant}}{C_{soil}} \quad (1)$$

where: C_{plant} and C_{soil} represent metal concentration (with Cu, Pb, Zn) in plants and soil *(Jolly et al., 2013)*.

Values of the transfer factor lower than 0.1 show that the plant does not accumulate metals in its tissues; however, values of the transfer factor above 0.2 show that the plant accumulates metals, requiring careful monitoring of the environment *(Khan et al., 2009; Sponza et al., 2002)*.

RESULTS

Figure 2 shows the results regarding the content of heavy metals (Cu, Pb, Zn) in soil samples contaminated with mixed solutions of different concentrations (1.5%, 3.0%, 4.5%, 6.0%), as well as in uncontaminated soil.

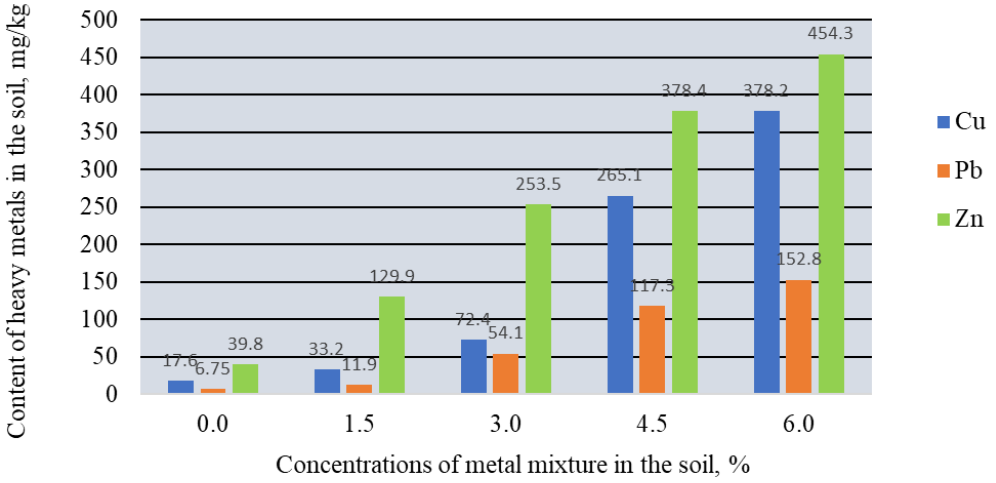

Fig. 2 - The content of heavy metals in the soil

It can be observed that, for all three heavy metals, their concentration in the soil increases progressively, depending on the increase in the concentration of the solutions, the highest concentrations being found for Zn.

Figures 3 and 4 show the results regarding the content of heavy metals (Cu, Pb, Zn) found in the raspberry and blueberry samples for different concentrations (1.5%, 3.0%, 4.5%, 6.0%), as well as in the control sample.

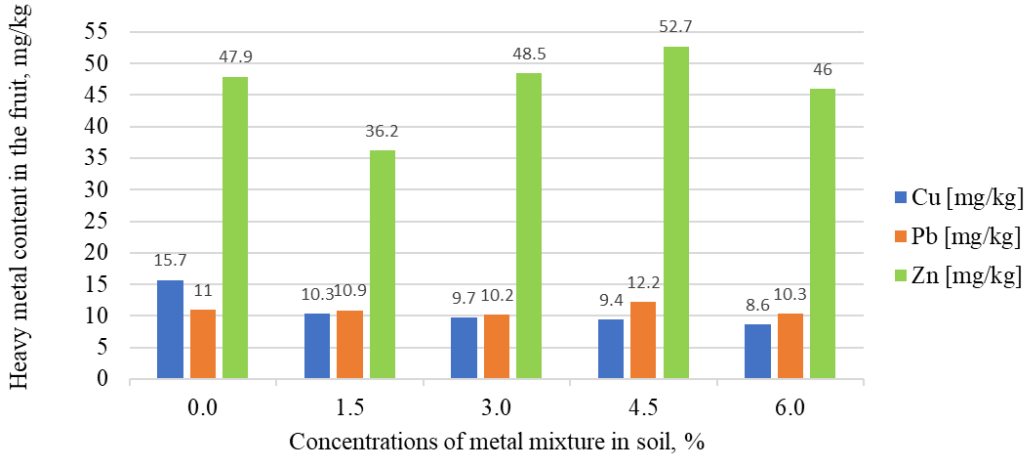

Fig. 3 - The content of heavy metals in raspberry

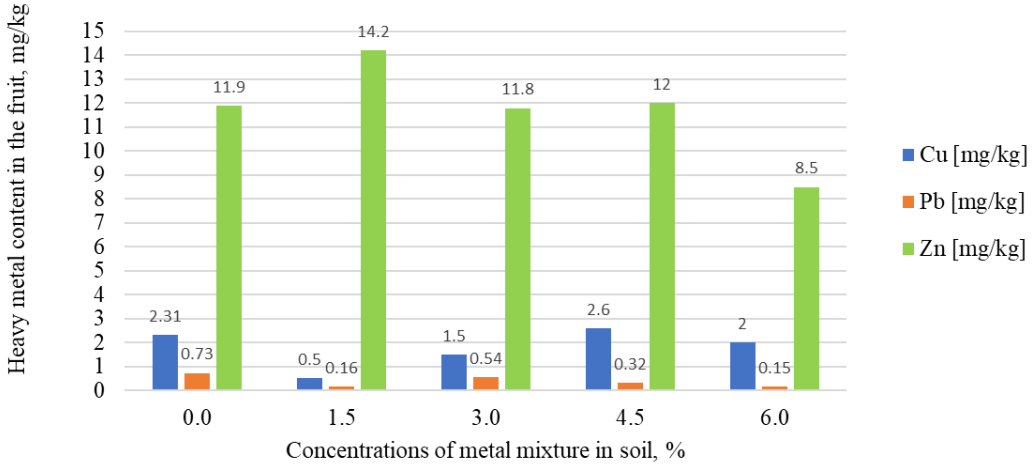

Fig. 4 - The content of heavy metals in blueberries

Analysing figures 3 and 4 for the different concentrations of metals in the soil and their transfer in the studied fruits, it was found that:

a. for raspberries:

- as the concentration of Cu in the soil increases, it decreases in the fruit;
- for Pb, at low concentrations in the soil, the accumulation in the fruit increases progressively, and at the maximum concentration in the soil (6%), it is lower;
- Zn has the highest concentrations in the fruit. For concentrations of 1.5% (36.2 mg/kg), 3% (48.5 mg/kg) and 4.5% (52.7 mg/kg), the Zn content increases gradually, and for the concentration of 6% (46 mg/kg) in the soil, it decreases in the fruit;
- in the control sample, with uncontaminated soil, all three studied metals are present in the fruit.

b. for blueberries:

- in the case of Cu, the content is progressively increasing in fruits for the first three concentrations, while at the maximum concentration of 6% in the soil, the Cu content decreases in the fruit;
- in the case of Pb, values are low, with a value of 0.54 mg/kg for a concentration of 3%;
- Zn has the highest concentrations in the fruit. The content in fruits varies as follows: a concentration of 1.5% translated into 14.2 mg/kg, 3% to 11.8 mg / kg, 4.5% to 12 mg/kg and the concentration of 6% to 8.5 mg/kg;
- for the control sample, all 3 metals were detected in blueberries and raspberries, and the Zn concentration has higher values that could endanger health.

Also, for all the metals studied, at a concentration of 3%, values close to those of the control sample were found.

The transfer factor (tf) values of heavy metals from soil to fruit are graphically shown in Figures 5 and 6.

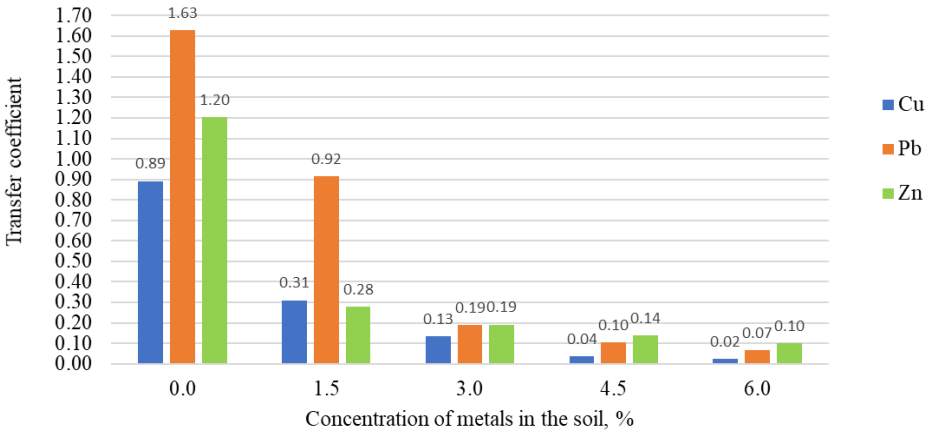

Fig. 5 - The transfer coefficient of heavy metals in raspberries

Analysing Figure 5, the results of the raspberry transfer factor show that:

- for the control sample it has values close to 1 in the case of copper and zinc and values greater than 1.5 for lead;
- for the concentration of the metal mixture of 1.5% in the soil, values of the transfer factor of 0.3 were found for copper and zinc, the transfer coefficient for lead tending towards 1 (0.92);
- for the other concentrations of heavy metal mixture in the soil (3%, 4.5%, 6%), the values of the transfer factor are very low for all metals, tending to 0 (tf = 0.02 for Cu at the concentration of 6% in the soil).

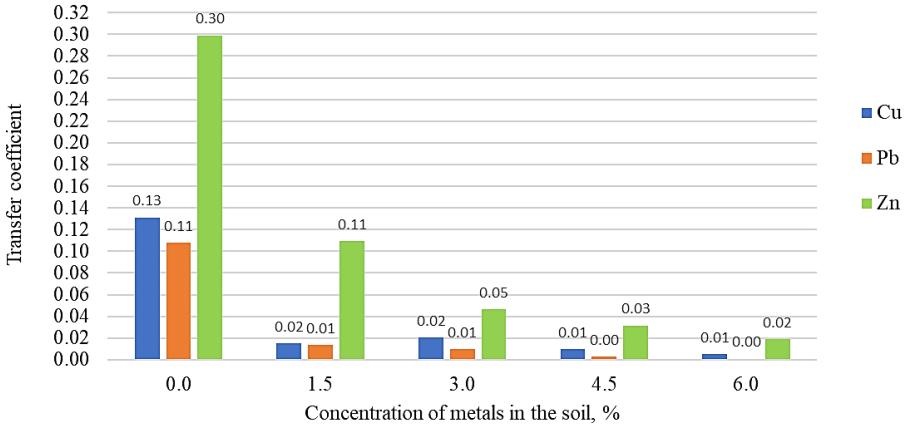

Fig. 6 - The transfer coefficient of heavy metals in blueberries

Analysing Figure 6, the results of the transfer coefficient in blueberries, show the following:

- for the control sample the values of the transfer factor are below 0.3 for all three metals;
- for all other concentrations of the mixture of heavy metals in the soil, the values of the transfer factor are very small (for concentrations of 4.5% and 6%, for Pb, the tf value = 0).

Therefore, it can be considered that for the berries studied, the higher the initial concentration of heavy metals in the soil, the weaker the bioaccumulation.

CONCLUSIONS

For the berries studied, an increase tendency in the amount of heavy metal accumulated in the fruit can be observed, along with the increase in the concentration of the heavy metal mixture in the soil.

The accumulation of heavy metals in berries has revealed that the order of accumulation of metals in fruits is Zn>Pb>Cu for raspberry and Zn>Cu>Pb for blueberries. The highest accumulation among the studied metals is that of zinc for both berries. Lead is below the limit of the control sample, for both berries, this meaning that with the high concentrations the absorption capacity of the heavy metal in the soil decreases, which could lead to explanations related to the possibility that the plants develop protection mechanisms.

Considering the two berries grown applying various concentrations of metal mixture in the soil, a decrease tendency in the transfer coefficient of each heavy metal from the soil to the plant is noticed as the concentration of the mixture increases from 1.5% to 6.0%. Therefore, the bioaccumulation capacity of metals in fruits is small, but the accumulation of metals may have occurred at the level of the other vegetative parts of the shrubs (root, stem, branches and leaves).

Taking into account that forest fruits are rich in antioxidants and are highly appreciated by consumers, the bioaccumulation of heavy metals in fruits is an important aspect that was investigated in this work to evaluate the impact of soil contamination on fruits and can be further explored to develop mathematical models and finding some patterns for the accumulation of heavy metals in the soil and in plants/fruits.

ACKNOWLEDGEMENT

The work has been funded by the Sectoral Programme MADR – ADER 2019-2022, ADER 25.4.1. Technology for obtaining biofertilisers and/or bioinsecticides for ecological production systems, Ctr. no. ADER 25.4.1/24.09.2020 and MRID, Programme 1 - Development of the national research-development system, 1.2 - Institutional performance - Projects for financing excellence in RDI, Ctr. no. 1PFE/30.12.2021.

REFERENCES

[1] Ardelean, A., Mohan, Gh. (2008). *Medicinal Flora of Romania*. All Publishing, Bucharest.

[2] Balčiauskas, L., Ežerinskis, Ž., Stirkė, V., Balčiauskienė, L., Garbaras, A., Remeikis, V. (2022). The elemental composition of small mammals in a commercial orchard–meadow system. *Chemosphere, Volume 296*, 134 – 148. https://doi.org/10.1016/j.chemosphere.2022.134048

[3] Bassey, F.I., Iwegbue, C.M.A., Obi-Iyeke, G.E., Tesi, G.O., Rotu, A.R., Gobe, O.A., Tsafe, A.I. (2014). Heavy metals in soils and tomatoes grown in urban fringe environment in Asaba, Delta State, Nigeria. *Nigerian Journal of Basic and Applied Science, 22*, 27-31. https://doi.org/10.4314/njbas.v22i1.5

[4] Cârdei P., Tudora C., Vlăduț V., Pruteanu A., Găgeanu I., Cujbescu D., Bordean D*, Ungureanu N*, Cristea O. (2021). Mathematical model to simulate the transfer of heavy metals from soil to plant, *Sustainability 2021, vol. 13(11), 6157*, DOI: 10.3390/su13116157

[5] Cherfi, A., Abdoun, S., Gaci, O. (2014). Food survey: levels and potential health risks of chromium, lead, zinc and copper content in fruits and vegetables consumed in Algeria. *Food Chem Toxicol,* 70, 48–53. https://doi.org/10.1016/j.fct.2014.04.044

[6] Cui, Y.-J., Zhu, Y.-G., Zhai, R.-H., Chen, D.-Y., Huang, Y.-Z., Qiu, Y., Liang, J.-Z. (2004). Transfer of metals from soil to vegetables in an area near a smelter in Nanning, China. *Environment International* Volume 30, Issue 6, 785-791. https://doi.org/10.1016/j.envint.2004.01.003

[7] Dróżdż, P., Šėžienė, V., Pyrzynska, K. (2018). Mineral Composition of Wild and Cultivated Blueberries. *Biological Trace Element Research*, 173–177. https://doi.org/10.1007/s12011-017-1033-z

[8] Fawad, A., Hidayat, U., Ikhtiar, K. (2017). Heavy metals accumulation in vegetables irrigated with industrial influents and possible impact of such vegetables on human health. *Sarhad Journal of Agriculture, Volume 33, Issue 3*, 489-502. http://dx.doi.org/10.17582/journal.sja/2017/33.3.489.500

[9] Huang, Z., Pan, X.-D., Wu, P.-G., Han, J.-L., Chen, Q. (2014). Heavy metals in vegetables and the health risk to population in Zhejiang, China. *Food Control,* 36, 248-252. https://doi.org/10.1016/j.foodcont.2013.08.036

[10] Jolly, Y. N., Islam, A., Akbar S. (2013). Transfer of metals from soil to vegetables and possible health risk assessment. *Springer Plus,* 2, 385–391. https://doi.org/10.1186/2193-1801-2-385

[11] Khan, S., Farooq, R., Shahbaz, S., Khan, M.A., Sadique, M. (2009). Health risk assessment of heavy metals for population via consumption of vegetables. *World Applied Sciences Journal,* 6(12), 1602-1606.

[12] Lere, B. K., Basira, I., Abdulkadir, S., Tahir, S. M., Ari, H. A., Ugya, Y. A. (2021). Health risk assessment of heavy metals in irrigated fruits and vegetables cultivated in selected farms around Kaduna metropolis, Nigeria. *Egyptian Journal of Basic and Applied Sciences,* Vol.8, Issue 1, 317-329. https://doi.org/10.1080/2314808X.2021.1992956

[13] Nedelescu, M., Baconi, D., Neagoe, A., Iordache, V., Constantinescu, P., Ciobanu, A. M., Vardavas, I. A., Stan, M., Vinceti, M., Tsatsakis, M. A. (2017). Environmental metal contamination and health impact assessment in two industrial regions of Romania. *Science of the Total Environment,* 580, 984–995.

[14] Pruteanu A., Bordean D-M., Vlăduţ V. (2019). Accumulation of heavy metals in vegetables grown on contaminated soils, Proceedings of the 47th International Symposium on Agricultural Engineering "Actual Tasks on Agricultural Engineering", pp. 135-146, 2019, ISSN 1333-2651, Opatija - Croaţia

[15] Roba, C., Roşu, C., Pişţea, I., Ozunu, Al., Baciu, C. (2016). Heavy metal content in vegetables and fruits cultivated in Baia Mare mining area (Romania) and health risk assessment. *Environ Sci Pollut,* 23, 6062–6073. https://doi.org/10.1007/s11356-015-4799-6

[16] Rusinek, E., Sembratowicz, I., Ognik, K. (2008). Content of selected metals in forest fruits depending on the harvest site. *Roczniki Panstwowego Zakladu Higieny,* 59(2), 155-161.

[17] Qihang, L. Chaofeng, L., Heng, W., Xiao W., Yuansheng, L., Ruidong, Y., Xuefeng W (2021). Geochemical Characteristics of Heavy Metals in Soil and Blueberries of the Core Majiang Blueberry Production Area. *Bulletin of Environmental Contamination and Toxicology*, 57–64. https://doi.org/10.1007/s00128-020-03007-4

[18] Sponza, D., Karaoglu, N. (2002). Environmental geochemistry and pollution studies of Aliaga metal industry district. *Environment International,* 27, 541-553. https://doi.org/10.1016/S0160-4120(01)00108-8

[19] Wieczorek, J., Pietrzak, M., Osowski, A., Wieczorek, Z. (2010). Determination of lead, cadmium, and persistent organic pollutants in wild and orchard-farm-grown fruit in northeastern Poland. *Journal of Toxicology and Environmental Health, Part A,* Vol.73, 1236-1243. https://doi.org/10.1080/15287394.2010.492009

[20] Zeiner, M., Cindrić I. J. (2018). Harmful Elements (Al, Cd, Cr, Ni, and Pb) in Wild Berries and Fruits Collected in Croatia. *Toxics,* 6(2), 318-328. https://doi.org/10.3390/toxics6020031

ANALYSIS OF THE PERFORMANCE OF A PLASTIC MULCH PUNCHING MACHINE
/
ANALISIS KINERJA MESIN PELUBANG MULSA PLASTIK

Mustaqimah MUSTAQIMAH *[1)], Muhammad ANAS MUFTI [1)], Ramayanty BULAN [1)], Oscar HARIS [2)]
[1)] Department of Agricultural Engineering, Faculty of Agriculture, Syiah Kuala University, Indonesia
[2)] Department of Automotive Industrial Engineering Technology, Boash Indonesia Digital Polytechnic, Indonesia
Tel: +62 921-6484-6042; E-mail: mustaqimah@unsyiah.ac.id
DOI: https://doi.org/10.35633/inmateh-68-72

Keywords: *agriculture machinery, appropriate technology, perforation machinery, rotational speed*

ABSTRACT
This study aims to determine the performance of a plastic mulch hole making machine and its electrical power requirements. The study begins by providing speed variations on the engine sprocket, calculating the working capacity of the machine, and analysing the power requirements of the electric motor. The results showed that the engine sprocket could perform an optimal rotation speed for punching holes in plastic mulch. Most holes were created in the treatment with a rotational speed of 70 rpm, 16 holes per 5 m of plastic mulch. Overall, the performance of the plastic mulch punching machine has been able to provide fixes in making holes in mulch plastic. Of the three treatments, the speed variations of the plastic mulch punching machine provided perforations with the criteria of perfect and partial perforation. The highest percentage of ideal perforation was found in the treatment with a rotational speed of 29 rpm, 86%, and the lowest was found in the treatment with a rotational speed of 25 rpm, 9.3%. The coefficient of determination between the rotational speed of the machine and the performance of the machine to punch holes in the plastic mulch can be modelled by a polynomial equation.

ABSTRAK
Penelitian ini bertujuan untuk mengetahui unjuk kerja mesin pembuat lubang mulsa plastik dan kebutuhan daya listriknya. Penelitian diawali dengan memberikan variasi kecepatan pada engine sprocket, menghitung kapasitas kerja mesin, dan menganalisis kebutuhan daya motor listrik. Hasil penelitian menunjukkan bahwa sproket mesin dapat melakukan kecepatan putaran optimal untuk lubang pelubangan mulsa plastik. Lubang terbanyak tercipta pada perlakuan dengan kecepatan putar 70 rpm, 16 lubang per 5 m mulsa plastik. Hasil kinerja mesin pelubang mulsa plastik telah mampu memberikan perbaikan pada mulsa plastik. Dari ketiga perlakuan variasi kecepatan pada mesin pelubang mulsa plastik memberikan perforasi dengan kriteria perforasi sempurna dan sebagian. Persentase perforasi ideal tertinggi terdapat pada perlakuan dengan kecepatan putar 29 rpm sebesar 86%, dan terendah pada perlakuan dengan kecepatan putar 25 rpm sebesar 9.3%. Koefisien determinasi antara kecepatan putar mesin dan kinerja mesin dalam melubangi plastik mulsa dapat dimodelkan dengan persamaan polinomial.

INTRODUCTION

Mulch is a material to cover the soil so that moisture and soil temperature as a medium of plants maintain stability, suppress weed populations and diseases, and avoid splashing rainwater directly onto the ground surface, resulting in erosion (*Tinambunan et al.*, 2014). The use of mulch provides several benefits in terms of biological, physical, and chemical aspects of the soil. Mulch can physically maintain a more stable soil temperature (*Utomo and Agus Suryanto*, 2013). Mulching on land can also prevent water loss through evaporation (*Pribadi et al.*, 2014). The use of mulch can also provide benefits, such as saving water use by reducing the rate of evaporation from the land surface, reducing soil temperature fluctuations (*Marliah*, 2011). Mulch can be divided into two, namely organic mulch and inorganic mulch (*Helyanto*, 2015). Mulches increase soil temperature, delay soil moisture loss, and check weed growth, which are the key factors contributing to production (*Ramakrishna et al.*, 2006; *Bucki and Siwek*, 2019). Coloured plastic mulches affect soil temperature and plant growth (*Ibarra-Jiménez et al.*, 2011; *Torres-Olivar et al.*, 2016). Plastic mulching could significantly increase crop yield and water use efficiency (*Gao et al.*, 2019). The efficiency of water use of plastic mulching was significantly higher than that of straw mulching (*Li et al.*, 2018).

Silver metallic plastic mulch is a plastic mulch that has two different surfaces (*Cahyono*, *2005*). Plastic mulch can also affect the use of sunlight. The reflected light from plastic mulch will have an impact on the process of photosynthesis because all sides of the leaf are evenly exposed to sunlight (*Darmawan et al.*, *2014*). The use of silver metallic plastic mulch gives the best effect on all parameters observed because of the colour of silver mulch; this type can reflect light that can be useful in the photosynthesis process so that more carbohydrates are formed (*Sudjianto and Krestiani*, *2009*). The difference in soil temperature between treatments without mulch and straw mulch in the morning was not different, but silver metallic plastic mulch showed higher soil temperatures (*Hamdani*, *2009*). High soil temperature can reduce humidity around plants so it can inhibit the emergence of diseases caused by bacteria (*Kusuma and Zuhro*, *2015*).

The creation of agricultural equipment and machinery is a basic step in the realization of efficiency and increasing agricultural productivity and quality. Agriculture mechanization aims to improve land and labour efficiency, save energy and resources (seeds, fertilizer and water, and equipment) to increase the effectiveness, productivity, and quality of agricultural products, reduce the workload of farmers, and increase farmer income and welfare (*Cebro and Sitorus*, 2019; *Sitorus et al.*, 2018; *Bulan et al.*, 2019; *Sitorus et al.*, 2019). Therefore, *Harahap et al.* (2020), have designed a mulch plastic punching machine to make it easier for farmers. They no longer have to manually dig the soil mulch. It has sizes of 100 × 80 × 60 cm^3. The initial design of a mulch plastic perforating machine used a sprocket transmission system that had 15 serrations. The results of the percentage of plastic mulch perforation using 15 tooth sprockets are 50%. The results are still low and further research needs to be done to obtain a higher percentage of the initial design of the plastic mulch perforating machine.

In addition, *Khazimov et al.* (2018), developed dual-action equipment for mulching soils and planting vegetable seedlings pulled by a four-wheeled tractor. The capacity of this machine can reach 0.4 ha/day or 271 seedlings/min with a speed of more than 2 km/h. Also, *Lawrence et al.* (2007), developed a dibbling machine for plastic mulch using a pneumatic method driven by a tractor's hydraulic system from a 4-wheeled tractor. This equipment has outstanding performance, but unfortunately, it will not be appropriate with aspects of land conditions and its economy if applied in Indonesia.

Hence, two additional speed variations were given in this study to obtain a higher percentage of perforated plastic mulch for small-scale perforation machinery. Each speed was obtained by giving variations in the size of the sprocket on different engine transmissions. This study uses a variation of a sprocket that has 36 serrations and a sprocket that has 42 serrations. The sprocket that has 36 serrations found that the rotational speed of the eye is 29 rpm and a sprocket that has 42 serrations is 25 rpm. Each sprocket was given three repetitions to see the results of the percentage of mulch plastic perforated by the holes punched.

MATERIAL AND METHODS

Plastic mulch hole puncher machine

This research was carried out at the UPTD Mekanisasi Pertanian in Indrapuri, Department of Agriculture, Aceh Besar Regency, Indonesia. Equipment and materials in this research are mulch plastic perforator, stopwatch, hand digital tachometer, clamp meter, mechanical devices, stationery supplies, and mulch plastic. The research began by studying the mechanism of action of a mulch plastic perforator. The next step is to give a variation of the sprocket in the plastic mulch hole transmission system to obtain three variations of speed. Speed measurements are carried out using a tachometer in the maker of the hole and are found at three different speeds. Each speed treatment was carried out three repetitions of work using 5 m of plastic mulch in each repetition. Of the three treatment speeds result two perforation criteria, namely, the perfect and partial holes. The measurement technique of electric motor power is to measure the available current and amperage of an electric motor using a clamp meter. Three treatments were measured for electric motor power at three different variations in the speed of the holes punched. Measurement of amperage on an electric motor is measured by clamping meter on the electric motor cable until a number appears on the digital screen.

The working mechanism of the plastic mulch hole-making machine carried out in this test starts from the initial roll of mulch paired through the clamp shaft. After that, the plastic mulch is put into the hole puncher roll. In the holes, the puncher roll occurs, the plastic mulch hole perforation process occurs. In the next step, the mulch plastic returns to the clamp shaft and goes to the pulling roll. This towing roll rolls back the hollow plastic mulch. The pinch shaft is used to suppress the mulch because it is easier to perforate. The description of the plastic mulch hole puncher machine designed by *Harahap et al.* (2020) is shown in Figure 1. The previous perforating machines were optimized for their performance in this study.

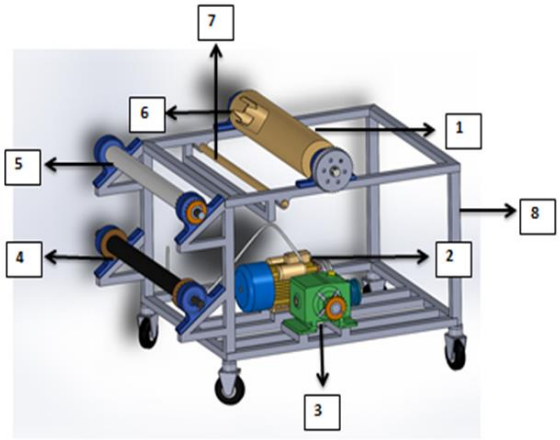

1-Hole puncher roll
2-Electric Motor
3-Gear box
4-Plastic mulch initial rollers
5-Plastic mulch rolling roll
6-Hole puncher blade
7-Plastic mulch clamp shaft
8-Main framework

Fig. 1 – Isometric of plastic mulch hole puncher machine

Determination of hole puncher speed

The effect of variations in rotational speed was investigated using a chain-sprocket transmission system. The sprocket that receives power from the engine has three variations in the number of gears. From the variations in the number of serrations on the sprocket, three different velocity eye holes are found. This speed determination aims to obtain the optimal rotational speed for the eye holes. Each speed is 25 rpm, 29 rpm, and 70 rpm. All speeds are obtained from a variation of the sprocket. First, a rotational speed of 25 rpm uses a sprocket that has the greatest number of serrations (42 serrations). It follows by 29 rpm and 70 rpm; they have 35 and 15 serrations. Figure 2 shows the transmission of the sprocket with a different number of serrations.

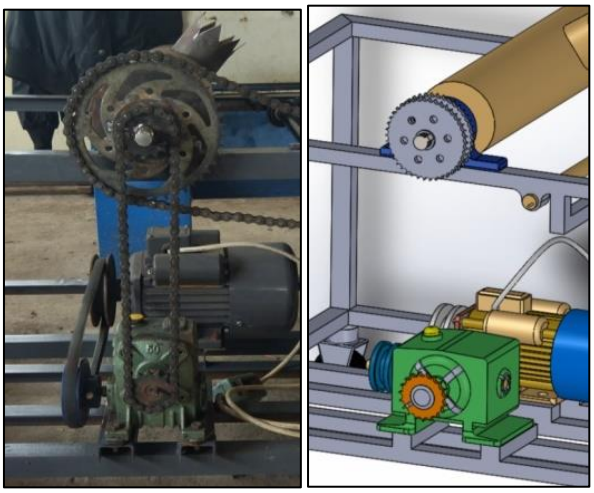

Fig. 2 – The transmission in the machine

RESULTS

Performance of plastic mulch hole puncher machine

Based on the results of the plastic mulch perforation test in the field, the plastic mulch perforation machine conducted by the study was able to perforate the plastic mulch with two quality results, namely a perfectly perforated and partially perforated plastic mulch. Plastic mulch holes puncher blades have been able to perforate flexible plastic mulch according to the research by *Shrefler and Brandenberger* (2014). Plastic mulch is shown to be a low-density polyethylene produced by the process of ethylene polymerization by using very high pressure. It requires a sharp knife to perforate plastic mulch.

Table 1 shows that the results of perfect perforation using 25 rpm have the lowest percentage of perfect perforation, which is equal to 9.3%. While the highest yield is obtained using 29 rpm, namely 86%. Using 29 rpm is said to be the best treatment because it produces the highest percentage of perfect holes. Meanwhile, the spaces between the holes found in the three treatments met the requirements for the planting space of chili. They are not less than 50 cm × 50 cm, but also not more than 65 cm × 65 cm. Spacing patterns must be considered because they can affect the level of competition between plants in terms of water, nutrients, and sunlight (*Hatta*, 2011). The optimal planting distance will provide good growth so that plants can use more sunlight and nutrients (*Sohel et al.*, *2009*).

Table 1

Percentage of perfectly perforated plastic mulch

Rotational speed (rpm)	Total holes	Total perfect holes	Duration (s)	Space between the holes (cm)
25	42	4	50	60
29	42	36	35	60
70	48	24	10	50

Table 2 shows that the average percentage value of partially perforated plastic mulch using 29 rpm is the lowest of the three treatments. Its percentage value is only 14%. The 29 rpm perforation velocity can be sure to be in normal speed when perforating the plastic mulch, so this speed is very suitable to be used. While using 70 rpm speed resulted in 50%, and the highest average percentage of partial perforation was found using 25 rpm, which was 90.6%. Based on the test results, no part of the mulch plastic is perforated even at low speed. The sharpness of the perforated blades of plastic mulch greatly influences the perforation process as in the research on the performance of the garbage chopping machine that has been carried out by *Juardin, (2017)*. The blade is cut by slicing from the base to the tip and may not all meet the rubbish field, and the blade has a tenuous gap, and the sharpness of the blade is still not good. The narrow gap distances are adjusted to improve the blade and are modified to become an edge crusher-type blade.

Table 2

Percentage of partially perforated plastic mulch

Rotational speed (rpm)	Total holes	Total partial holes	Duration (s)	Space between the holes (cm)
25	42	38	50	60
29	42	6	35	60
70	48	24	10	50

Machine capacity of plastic mulch hole puncher machine

The highest hole puncher working capacity is using 70 rpm, which is 576 holes/hr, and the least is using 25 rpm, which is 100 holes/hr. It can be supposed that increasing rotational speed will increase machine capacity. The comparison graph of the working capacity of the hole puncher can be seen in Figure 3. Based on research conducted by *Kharisma* (2014), on the disc mill machine, the higher the value of the rotation speed of the machine used, the longer the starch time successfully extracted is. Rotational speed affects the size and fineness of the particles. This has similarities in this study, namely the higher the speed of the hole puncher, the higher the results of the capacity of the hole puncher, and the speed of the hole puncher also affects the hole perforation produced (Figure 3). The faster the hole puncher rotation, the more holes are produced.

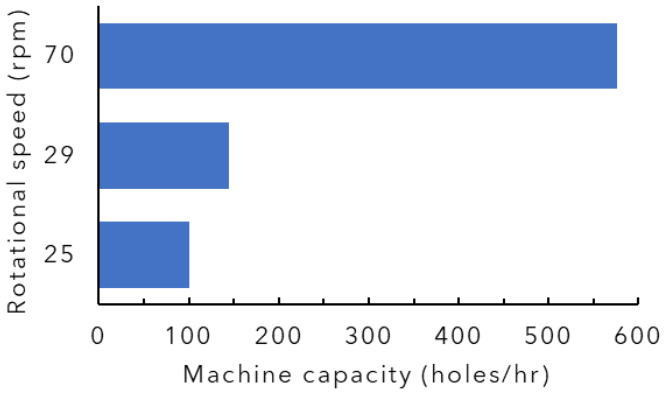

Fig. 3 – Work capacity of hole puncher machine

Correlation of rotation speed with total number of holes

The results of the rotational speed of the engine sprocket and the total plastic perforation of the mulch are shown in Figure 4. It is known that the results of mulch plastic perforation have a positive relationship with the rotational speed of the sprocket by means of a polynomial equation. Thus, the determination value of the graph above shows that the value of mulch punching results has a very close relationship with the rotational speed of the sprocket.

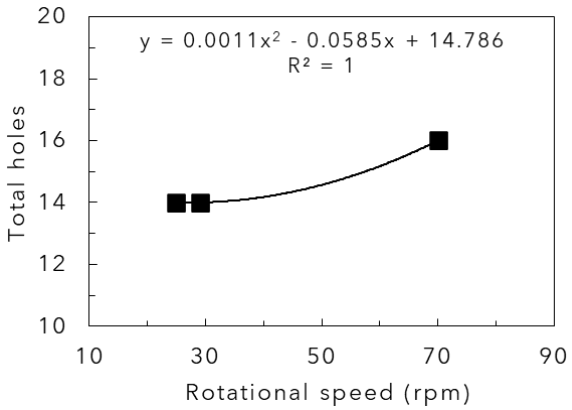

Fig. 4 – Observation results of engine sprocket rotation speed and plastic mulch punching results

Machine power consumption

Based on Figure 5 is performed the comparison of electric motor power requirements above; the electric motor power requirements using 25 rpm is 986.92 watts, then using 29 rpm is 1076 watts and using 70 rpm is 1516 watts. The highest electrical power requirement is at 70 rpm and the lowest is at 25 rpm. There are differences in electrical power requirements due to differences in the speed of the hole puncher. The higher the turning speed of the hole puncher, the higher the electric power needed.

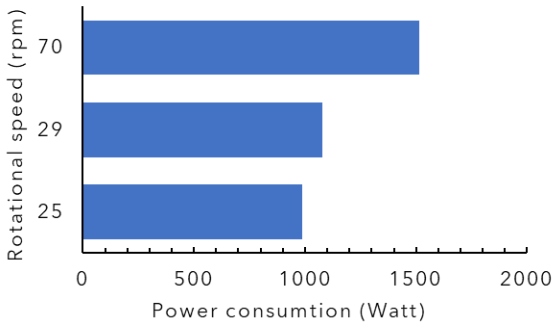

Fig. 5 – Comparison graph of electric motor power requirements

CONCLUSIONS

The increasing performance of the plastic mulch punching machine has been tested and presented in this study. Of the three treatments, the variation in speed on the mulch plastic perforating machine can provide a perforation with the criteria for perfect perforation and partial perforation. The engine sprocket can meet the optimal rotation speed for plastic mulch perforations. In this study, the optimal speed was found using 29 rpm because it has a high percentage of perfect perforation. The higher the speed of the engine sprockets, the more holes are produced by the machine. Most holes were produced using 70 rpm, namely up to 16 holes per 5 meters of mulch plastic. The highest percentage of perfect perforation is in a speed treatment of 29 rpm that is 86% and the lowest is in treatment of a speed of 25 rpm that is 9.3%. The coefficient determination between the rotational speed and machine performance positively correlates with the polynomial equation. The mulch plastic perforating machine that is used still has the disadvantages that there are parts of the mulch plastic that cannot be perforated as a whole, and the machine should be able to use other punching methods to improve the results of the mulch plastic perforation.

REFERENCES

[1] Bucki, P., Siwek P. (2019). Organic and non-organic mulches–impact on environmental conditions, yield, and quality of Cucurbitaceae. *Folia Horticulturae*, 31(1). 129-145.

[2] Bulan, R., Yasar M., Nata Y., Sitorus A. (2019). Design and construction of chopper machine AE02-type for oil palm frond. *INMATEH - Agricultural Engineering*, 57(1). 165-172.

[3] Cahyono, B. (2005). *Kacang Panjang (Teknik Budidaya dan Analisis Usaha Tani)*. *CV. Aneka Ilmu. Semarang. dengan Penambahan Effective Microorganism*, 10. 77-87.

[4] Cebro, I. S., Sitorus A. (2019). Performance evaluation of a hand tractor to climbing sloping land. *International Journal of Scientific and Technology Research*, 8(7). 781-785.
[5] Darmawan, I. G. P., Nyana I. D. N., Gunadi I. G. A. (2014). *Pengaruh penggunaan mulsa plastik terhadap hasil tanaman cabai rawit (Capsicum frutescens L.) di luar musim di Desa Kerta*. *Jurnal Agroekoteknologi Tropika*, 3(3). 148-157.
[6] Gao, H., Yan C., Liu Q., Ding W., Chen B., Li Z. (2019). Effects of plastic mulching and plastic residue on agricultural production: A meta-analysis. *Science of the Total Environment*, 651. 484-492.
[7] Hamdani, J. S. (2009). *Pengaruh jenis mulsa terhadap pertumbuhan dan hasil tiga kultivar kentang (Solanum tuberosum L.) yang ditanam di dataran medium*. *Jurnal Agronomi Indonesia*, 37(1).
[8] Harahap, A., Syafriandi S., Mustaqimah M., Afriadi A. (2020). *Rancang Bangun Mesin Pelubang Plastik Mulsa*. *Jurnal Ilmiah Teknologi Pertanian Agrotechno*, 5(1). 14-19.
[9] Hatta, M. (2011). *Pengaruh tipe jarak tanam terhadap anakan, komponen hasil, dan hasil dua varietas padi pada metode SRI*. *Jurnal Floratek*, 6(2). 104-113.
[10] Helyanto, J. (2015). "*Pengaruh sistem olah tanah dan pemberian mulsa bagas pada lahan tebu PT. GMP ratoon ke-3 terhadap populasi dan biomassa cacing tanah serta populasi dan keanekaragaman mesofauna tanah*." In.: Skripsi
[11] Ibarra-Jiménez, L., Lira-Saldivar R. H., Valdez-Aguilar L. A., Lozano-Del Río J. (2011). Colored plastic mulches affect soil temperature and tuber production of potato. *Acta Agriculturae Scandinavica, Section B-Soil & Plant Science*, 61(4). 365-371.
[12] Kharisma, N. (2014). "*Pengaruh Kecepatan Putar (RPM) Disc Mill Terhadap Keseragaman Ukuran Butiran Gula Semut*." In.: Skripsi. Universitas Lampung. Lampung
[13] Khazimov, Z. M., Bora G. C., Khazimov K. M., Khazimov M. Z., Ultanova I. B., Niyazbayev A. K. (2018). Development of a dual action planting and mulching machine for vegetable seedlings. *Engineering in Agriculture, Environment and Food*, 11(2). 74-78.
[14] Kusuma, A., Zuhro M. (2015). *Pengaruh varietas dan ketebalan mulsa jerami padi pada pertumbuhan dan hasil tanaman tomat (Lycopersicum esculentum Mill.)*. *J. Agrotechbiz*, 2(1). 1-10.
[15] Lawrence, M. J., Buckmaster D. R., Lamont W. J. (2007). A pneumatic dibbling machine for plastic mulch. *Applied Engineering in Agriculture*, 23(4). 419-424.
[16] Li, Q., Li H., Zhang L., Zhang S., Chen Y. (2018). Mulching improves yield and water-use efficiency of potato cropping in China: A meta-analysis. *Field crops research*, 221. 50-60.
[17] Marliah, A. (2011). *Pengaruh pemberian pupuk organik dan jenis mulsa organik terhadap pertumbuhan dan hasil kedelai (Glycine max (L.) Merrill)*. *Jurnal Floratek*, 6(2). 192-201.
[18] Pribadi, G. Y., Roviq M., Wardiyati T. (2014). '*Pertumbuhan dan produktivitas sawi pak choy (Brasica rapa L.) pada umur transplanting dan pemberian mulsa organik*', Brawijaya University
[19] Ramakrishna, A., Tam H.M., Wani S.P., Long T. D. (2006). Effect of mulch on soil temperature, moisture, weed infestation and yield of groundnut in northern Vietnam. *Field crops research*, 95(2-3). 115-125.
[20] Shrefler, J., Brandenberger L. (2014). "Use of plastic mulch and row covers in vegetable production." In.: Oklahoma Cooperative Extension Service
[21] Sitorus, A., Fauzi A., Ramadhan G., Hasan A. R., Karyadi A. (2019). "Conceptual design of harvesters knife for Chinese spinach (ipomoea reptans Poir.): CAD approach." In *Proceedings - 2018 4th International Conference on Computing, Engineering, and Design, ICCED 2018*, 7-12.
[22] Sitorus, A., Hermawan W., Setiawan R. P. A. (2018). "Design and performance of combine corn transplanter powered by hand tractor." In *3rd International Conference on Computing, Engineering, and Design, ICCED 2017*, 1-5.
[23] Sohel, M., Siddique M., Asaduzzaman M., Alam M., Karim M. (2009). *Varietal performance of transplant aman rice under different hill densities*. *Bangladesh Journal of Agricultural Research*, 34(1). 33-39.
[24] Sudjianto, U., Krestiani V. (2009). *Studi pemulsaan dan dosis NPK pada hasil buah melon (Cucumis melo L)*. *Jurnal Sains dan Teknologi*, 2(2). 1-7.
[25] Tinambunan, E., Setyobudi L., Suryanto A. (2014). '*Penggunaan Beberapa Jenis Mulsa Terhadap Produksi Baby Wortel (Daucus carota L.) Varietas Hibrida*', Brawijaya University
[26] Torres-Olivar, V., Valdez-Aguilar L. A., Cárdenas-Flores A., Lira-Saldivar H., Hernández-Suárez M., Ibarra-Jiménez L. (2016). Effect of colored plastic mulch on growth, yield and nutrient status in cucumber under shade house and open field conditions. *Journal of Plant Nutrition*, 39(14). 2144-2152.
[27] Utomo, R. R., Agus Suryanto S. (2013). *Penggunaan mulsa dan umbi bibit (G4) pada tanaman kentang (solanum tuberosum l.) varietas granola*. *Jurnal Produksi Tanaman*, 1(1).

REVIEW ON DRYING PROCESSES AND DAMAGE PROTECTION MECHANISM OF LIQUOR YEAST
/
白酒酵母干燥工艺及损伤保护机制综述

Yue-jin YUAN[1)], Feng-kui XIONG*[1)], Jing-yu LI[2)], Ying-ying XU[1)], Xu-tong ZHAO[1)] [1]

[1)] College of Mechanical & Electrical Engineering, Shaanxi University of Science & Technology, Xian, Shaanxi / China;

[2)] College of Land and Environment, Shenyang Agricultural University, Shenyang, Liaoning/ China

Tel: +8618011140260; E-mail: xfk763101899@126.com, 763101899@qq.com

Corresponding author: Feng-kui Xiong

DOI: https://doi.org/10.35633/inmateh-68-73

Keywords: *Liquor yeast drying process; drying damage mechanism; drying protection strategy; cell membrane perforation.*

ABSTRACT

From the perspective of liquor brewing technology, the quality of liquor yeast undoubtedly determines the quality of liquor products, but the problems such as inconvenient storage, difficult transportation and easy deterioration of liquid liquor yeast greatly restrict the development of liquor industry. Aiming at this problem, the author firstly summarized the research status of drying technology, damage mechanism and protection strategy of white spirit yeast. Then, on the basis of studying the damage mechanism of yeast in the drying process of yeast, the optimization of drying process and the formulation of protective strategies of yeast were discussed. Finally, new research methods are proposed from three perspectives: optimal design of drying process, damage mechanism and protection strategy.

摘要

从白酒酿造工艺出发，白酒酵母的品质无疑决定了白酒产品的质量，但液态白酒酵母储存不便、运输困难、易变质等问题，极大地制约了白酒行业的发展。 针对这一问题，作者首先总结了白酒酵母的干燥工艺、损伤机理和保护策略的研究现状。然后，在研究白酒酵母干燥过程中酵母损伤机理的基础上，对干燥工艺的优化和酒酵母保护策略的制定进行了研究展望。最终分别从干燥工艺优化设计、损伤机制和保护策略三个角度，提出了新兴的研究方法。

INTRODUCTION

There were countless beautiful poems about Liquor in ancient times of China, so Liquor culture is undoubtedly one of the treasures of traditional Chinese culture. At the same time, the liquor industry is also one of the main sources of the national economy (*Wang D. et al., 2019*). However, the inconvenience of transportation and storage of liquid liquor yeast greatly restricts the development of my country's liquor industry (*Jorgensen H., 2009*). Therefore, it is the key to promote the development of the liquor industry to first study the damage protection mechanism of liquor yeast drying, then optimize the drying process, and finally improve the survival rate and efficiency of liquor yeast drying.

The drying of microorganisms represented by liquor yeast is essentially different from ordinary drying of fruits and vegetables. Drying of fruits and vegetables, only needs to consider conventional factors such as drying efficiency and the taste, colour, and shelf life of the dried product, while drying of microorganisms such as liquor yeast must also be considering the biological activity, rehydration survival rate, biological function and other unique factors of the dry product (*Huan-Qin Li et al., 2021*). Therefore, it is particularly important to study the damage mechanism of its drying from the molecular scale, and then formulate an effective protection strategy and optimize the drying process. In the field of drying containing microorganisms, the commonly used drying processes are vacuum drying, freeze drying, fluidized bed drying and spray drying.

In view of the contradiction between the survival rate and efficiency of microbial drying, this paper summarizes the previous researches in-depth and concisely from the drying process, damage mechanism and protection strategy of liquor yeast. Finally, on this basis and in combination with the existing technology, three research directions of microbial drying such as white wine yeast in the future were put forward.

[1] *Yue-jin Yuan., Prof. Ph.D.; Feng-kui Xiong., Ph.D.; Jing-yu Li., MSA.; Ying-ying Xu., Prof. Ph.D.; Xu-tong Zhao., MSE.*

1. Review on the mechanism of drying damage of liquor yeast

Understanding the damage mechanism of liquor yeast drying is the basis for formulating drying protection strategies and optimizing drying processes. It is generally believed that thermal damage, dehydration damage, oxidative damage, osmotic pressure damage and shear damage are the typical damage mechanisms of yeast drying (*Spreutels, L. et al., 2014*).

1.1. Dehydration damage

The water content in microbial cells is about 80-90%, which often exists in the form of bound water and free water, which is not only an indispensable part of biological reaction, but also a necessary component to maintain biological macromolecular structure and fluidity (*Ball P.J.C.R., 2008*). Among them, bound water refers to the water combined with cell components, accounting for about 4.5% of the total water, and its loss is the core cause of cell dehydration damage (*Santivarangkna C. et al., 2007*). Previous studies have shown that dehydration damage is inevitable for microorganisms in drying. On the one hand, because the moisture content of microorganisms dried products is generally required to be less than 7% for long-term preservation (*Peighambardoust S.H. et al., 2011*), but the minimum water content to maintain microorganisms physiological state is 33.33%. When the dry water content is less than 33.33%, it is bound to be quickly inactivated due to dehydration damage. On the other hand, because the cell water loss is not strictly in the order from free water to bound water, but when the water content is lower than 22.3%, the bound water in the cell begins to lose.

A large number of studies have shown that the loss of bound water reduces the stability of the microbial cell substructure, especially the decrease in the fluidity and selective permeability of the cell membrane, which is the main reason for the inactivation of dehydration damage (*Golowczyc M.A. et al., 2011*). Because the cell membrane is the main place for the exchange of substances between microorganisms and the outside world, its unique fluidity and selective permeability have become necessary conditions to maintain the survival of microorganisms. The cell membrane is composed of a phospholipid bilayer, and it is the interaction between phospholipid molecules, water molecules and adjacent phospholipid molecules through hydrophobic interaction, chemical bonds and hydrogen bonds, which ensures the fluidity and selective permeability of the cell membrane. However, the loss of bound water greatly increases the force between phospholipid molecules, resulting in an increase in the lateral stress between the phospholipid bilayers, resulting in a gel phase of the cell membrane and a decrease in cell fluidity, eventually leading to cell death. Many studies have shown that the water content of gel phase transition in microbial cell membrane is about 16.67% (*Santivarangkna C. et al., 2008*). With the continuous loss of water and the increase of transverse stress, the polar head of phospholipid molecules in the bilayer aggregates and nucleates, while the non-polar hydrophobic groups are exposed to the periphery to form Inverse Hexagonal Phase (as shown in Fig. 1) (*Gong P. et al., 2014*). The formation of the anti-hexagonal phase will completely destroy the selective permeability of the cell membrane, so that the substances inside and outside the cell membrane can freely enter and exit the cell, and even the cell membrane will rupture and collapse, resulting in the death of a large number of microorganisms (*Moayyedi M. et al., 2018*). Current studies have shown that the moisture content of Inverse Hexagonal Phase transition in microbial cell membrane is about 10.8%. The relationship between Survival rate of yeast and water content of liquor yeast in the process of traditional drying has shown in Fig. 2.

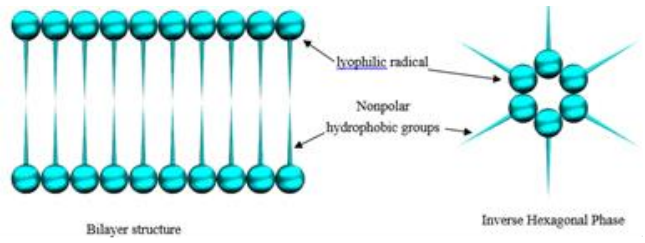

Fig. 1 - The phospholipid bilayer and its inner hexagonal shape

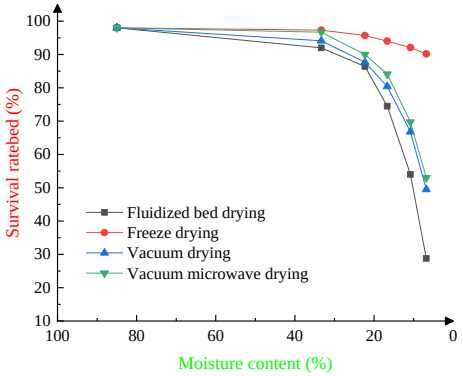

Fig. 2 - Inactivation by desiccation and dehydration damage in sake yeasts

Comparing the change curves of yeast moisture content and fermented rehydration survival rate under each traditional drying process in Fig. 2, then it is not difficult to find that the yeast survival rate has dropped sharply near the points where the moisture content is 22.3%, 16.67% and 10.8%. With the loss of water, the cytoplasm will continue to thicken, and at the same time, the aggregation density of macromolecules in the cytoplasm will continue to increase. When the cytoplasmic viscosity more than the1014 Pa·s, it will degenerate into a metastable with free molecular arrangement and solid physical properties (*Fonseca F. et al., 2016*). This phenomenon is often referred to as the glass transition, and the temperature at which the transition occurs is often referred to as the glass transition temperature. Glass transition could maintain the stability of microbial intracellular structure and inhibit the further occurrence of microbial dehydration damage. However, the water content in the microbial cells is inversely proportional to the glass transition temperature, that is, as the drying progresses, the water content in the bacteria decreases, and the glass transition temperature increases instead. When the moisture content of liquor yeast is 22.3%, the glass transition temperature-Tg=52-58°C, so the glass state is extremely difficult to form during the Liquor yeast drying process.

Studies by Sachie Fujii, a scholar from Yamamoto University in Japan, show that dehydration damage will decrease with the decrease of drying rate (*Sachie Fujii et al., 2014*). Therefore, the author believes that in reducing dehydration damage, the key moisture content point (22.3%) could be used as the conversion point, and the combination drying process and parameters of high and low drying rates are adopted before and after.

1.2. Thermal damage inactivation

Thermal damage inactivation is also one of the main reasons for microbial inactivation in the process of drying. Many studies have shown that heating can damage the functional structures and components of microorganisms, such as cell wall, cell membrane, ribosome, RNA, protein, enzyme and so on. The critical injury temperature of each cell structure is shown in Fig. 3 (*Cebrián G et al., 2019*).

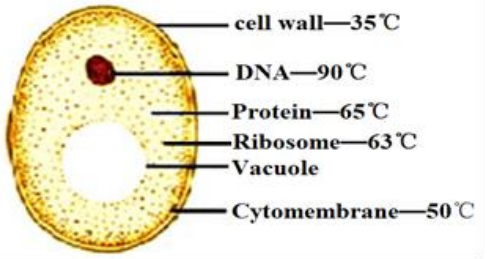

Fig. 3 - Schematic diagram of the critical temperatures for each structure of liquor yeast

The higher the drying temperature, the higher the drying efficiency of microorganisms, which is more conducive to enterprise mass production (*Russell A.D., 2003*). However, the drying temperature is too high, which will increase the thermal damage of the cells, resulting in a large number of microbial deaths. It is generally believed that the drying temperature of microorganisms represented by liquor yeast should be controlled within the range of 60-90°C (*Huang S. et al., 2017*). Based on the above analysis, the author believes that in order to ensure the efficiency and survival rate of microbial drying at the same time, the moisture content should be equal to 33.33% as the transposition point. The drying temperature higher than 70°C should be used in the early stage to improve the drying efficiency, and then the drying temperature below 50°C should be used to ensure the drying survival rate of microorganisms.

1.3. Osmolality damage

With the loss of water, the concentration of cytoplasm will increase, which first leads to the increase of osmotic pressure on the outside of the cell before the glass transition, then causes the cell to contract and separates the cell membrane from the cell wall, and finally leads to the osmotic damage and inactivation of microorganisms. At the same time, in the process of rehydration of liquor yeast dry products, if the rehydration speed is too fast or the osmotic pressure on both sides of the cell membrane is too high, the microbial cells will expand rapidly and excessively, thereby causing osmotic damage and inactivation of the microbial cells (*Meneghel J. et al., 2017*). The authors believe that the reconstruction of osmotic pressure balance on both sides of cell membrane is the essence of solving the problem of cell osmotic damage and inactivation during microbial drying. Loading edible compatible media into bacteria instead of water molecules to combine with cell membranes and other cell structures is the most direct and effective protection method.

1.4. Shear damage

Now studies have shown that although atomization might cause shear damage to microorganisms in the process of spray drying, the direct fatality rate is very low, which is mainly due to the inactivation of microorganisms in the later stage of drying (*Broeckx G. et al., 2016*). Shear damage occurs in the atomization process of spray drying and different atomization methods, nozzle structure size, spray parameters and so on would have a great impact on the degree of shear damage inactivation.

1.5. Oxidative damage

The reactive oxygen species produced during drying can combine with the ribosome, protein and cell membrane of microbial cells, and then resulting in microbial cell damage. The latest study proposed that the oxidative damage of cell membrane lipid is an important cause of cell membrane damage (*Dijkstra A.R. et al., 2014*). Under normal conditions, microorganisms could produce antioxidant enzymes to eliminate free oxygen, but in the drying process, the normal metabolic activities of microorganisms are greatly restricted, so they could not produce enough enzymes to eliminate the active free oxygen accumulated in the environment, finally resulting in oxidative damage inactivation (*Ghandi A. et al., 2012*).

2. Protection mechanisms were reviewed

The current research usually takes the time as the clue and divides the protection strategy into three parts: pre-treatment before drying, adding protective agent and optimizing drying process parameters.

2.1. Optimization of culture conditions and stress treatment

The optimization of culture conditions and stress treatment are the core components of microbial pre-treatment before drying, in which the optimization of culture conditions mainly includes two parts: the optimization of culture parameters and the optimization of culture medium. According to the treatment conditions, stress treatment is mainly divided into heat shock, acid stress and salt stress.

The optimization of culture medium usually includes five steps: primary selection of basic medium, optimization of basic medium, single factor drying experiment of additives, single factor experiment of optimization of culture parameters and response surface analysis. The evaluation indicators are generally set as the growth of yeast and the rehydration survival rate of dry particles.

In the process of culturing microorganisms, the optimization of culture parameters is usually based on the pH of the medium, culture time, culture temperature, environmental humidity, and rotational speed as variables. Then, using the growth amount and survival rate of microorganisms as evaluation indicators, the culture orthogonal test is carried out, and finally the response surface analysis is completed.

2.1.1. Optimization of liquor yeast culture conditions

In the selection of basic medium for drying liquor yeast, current research is mainly focused on YEPD medium, YPD medium, yeast complete medium, yeast basic medium, soybean sprout medium and potato medium (*Senz M. et al., 2015*). Most of them have carried out a large number of experimental studies, and all think that YEPD medium and yeast complete medium are the best basic culture medium for liquor yeast. The author also added the rehydration survival rate, glass transition temperature and particle size distribution of the dried particles as evaluation indicators on the basis of the original experiment, and carried out a new experimental optimization. The results showed that YEPD medium was more suitable as the basic culture medium for liquor yeast than the complete yeast medium.

In the aspect of medium additive optimization, at present, it is mainly to optimize the types and dosage of four kinds of additives: carbon source, nitrogen source, inorganic salt and auxin (*Lin J. et al., 2013*). The main carbon sources are glucose, fructose, lactose, sucrose and soluble starch. The nitrogen sources are beef extract, yeast extract, peptone, NH_4N0_3, $(NH_4)_2SO_4$ and soybean sprouts. The main inorganic salts are KH_2PO_4, $CaCl_2$, $MgSO_4$, NaCl and $ZnSO_4$. The auxins are mainly VB_2, inositol, VB_1, nicotinamide and calcium pantothenate. The commonly optimized method is single factor test to determine the OD600 value of the culture as evaluation indexes, and then take response surface analysis to complete the optimal selection.

On the optimization of liquor yeast culture parameters, the current research mainly focuses on single-factor experiment optimization research on culture temperature, rotation speed and pH. Among them, the culture temperature is the main reason that affects the growth of microorganisms (*Pichler H. et al., 2001*). Too high or too low temperature will have a great impact on the growth of liquor yeast.

Most studies showed that the growth of liquor yeast increased at first and then decreased in the temperature range of 28-32℃ and reached the maximum at 30℃ (*Shiroma S et al., 2014*). The culture rotation speed indirectly affects the growth of liquor yeast by affecting the oxygen content of the culture. If the rotation speed is too low, the yeast will grow slowly, and if the rotation speed is too high, the bacteria will burst. A large number of studies have shown that the optimal speed of liquor yeast culture is 180 r/min.

At present, almost all researches on the optimization of culture conditions in microbial drying only take the culture growth as the evaluation index, and few studies combine the rehydration survival rate, particle size distribution, and glass transition temperature of the dried particles as the evaluation index. This is undoubtedly a defect of the current research, so it could be optimized in the follow-up research.

2.1.2. Stress processing

In the face of adversity, microorganisms could use innate defence mechanisms to produce protective cellular components to enhance their own tolerance to adverse environments (*Lv Y.J. et al., 2014*). Stress treatment is a method to use the characteristics of microorganisms to expose them to adversity to activate the stress system to produce protective components and reduce the drying damage rate of microorganisms (*Su J. et al., 2011*). Common stress treatment methods include heat shock, acid stress and salt stress. Among them, in addition to activating the stress system, heat shock can also induce the production of specific heat shock proteins in microbial cells to repair damaged proteins and DNA in the bacteria, and the heat shock parameters are usually 58 ℃, 15-30 min. Acid stress is a process in which microorganisms can regulate the amount of proton pump of F0F1-ATP enzyme and amino acid decarboxylation metabolism to promote the production of stress protein (GSP) and chaperone protein, repair and degrade damaged DNA or protein, maintain intracellular PH balance and proton transfer characteristics, and treat liquor yeast in the environment with pH ≤ 4 (*Silva J. et al., 2005*). Salt stress is a process that induces the accumulation of intracellular compatible substances (such as trehalose, glycine, etc.), balances the osmotic pressure inside and outside of microorganisms, and resists osmotic damage in the drying process (*Peighambardoust S.H. et al., 2011*).

2.2. Extracellular protection of proteins and enzymatic treatment

Protein is one of the two most important microbial drying protectants, which mainly acts outside the microbial cell membrane (*Khem S. et al., 2016*). By filling the gap between the cell membrane and the cell wall, at the same time reacting with both at the molecular scale to form chemical bonds or hydrogen bonds, the molecular movement rate could be reduced, which ultimately slows down the rate of damage to the cell membrane and cell wall and prevents the cell wall from collapsing (*Morgan C. et al., 2006*).

Enzyme treatment can promote protein cross-linking or semi-cross-linking reaction, and further overcome the damage of electrostatic interaction between microorganisms and proteins. However, excessive cross-linking reaction will lead to the reduction of the space between microorganisms and the decrease of the water migration rate, which will lead to the increase of the viscosity of the microbial feed (*Gaspar A.L.C. et al., 2015*).

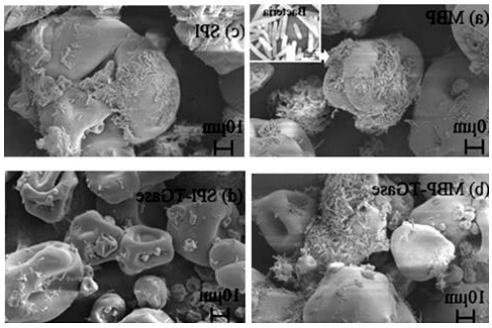

Fig. 4 - The effect of protein and bacterial action on this
(*Gong P. et al., 2018*)

Protective proteins used in microbial drying are often divided into two categories: acidic and alkaline. According to the liquor brewing process and the principle of acid stress treatment, the pH of liquor yeast culture solution is 3-5 and the cells are negatively charged. According to the characteristics of yeast and the principle of pH-PI (*Malhotra A et al., 2004*), it could be inferred that in the acidic culture medium, the liquor yeast has a negative charge, and the acid (alkaline) protein has a negative (positive) charge.

According to the charge principle, it could be inferred that the alkaline protein with positive charge could protect better on liquor yeast cerevisiae with negative charge than the acidic protein with negative charge (*Gottenbos B. et al., 2001*). In view of the verification of this theory, *Gong Pimin et al.* of Harbin Institute of Technology carried out a drying experiment comparative of Liquor yeast cell with bovine milk basic protein (MBP) and acid soybean protein isolate (SPI). The complex morphology of cell protein was observed by scanning electron microscope, as shown in a and c of Fig. 4 (*Gong P. et al., 2018*). Comparing the picture *a* and *c*, it is obvious that MBP can recombine with bacteria better. Finally, it had proved that the combination of the above charge and PH-PI theory is suitable for the drying of microorganisms.

Modern studies have shown that the enzymatically treated protected protein produces a cross-linking reaction to provide more sites for protein and bacterial binding, and at the same time, the secondary structure would change, to result in an increase in hydrophobicity. Ultimately, the protein and the bacterial cells are better combined, which plays a role in enhancing the drying protection effect of the protein on the microorganisms. Gong Pimin (*Gong P. et al., 2019*) et al also carried out TGase treatment experiments on the above two drying experiments, and the complex morphology of bacterial protein was observed by scanning electron microscope as shown in *b* and *d* of Fig. 4. Comparing *b, d* with *a, c* is not difficult to find TGase enzyme treatment could enhance the recombination of protein bacteria and enhance the protective effect of protein.

2.3. Intracellular protection studies with loading compatibility media

As an extremely important intracellular protective agent for microbial drying, disaccharide accumulation in microorganisms can better reduce microbial drying damage and improve drying survival rate. At present, a large number of studies have shown that trehalose is the best protective disaccharide, and has been used as a protective agent in the field of microbial drying on a large scale (*Câmara et al., 2019*). In terms of the protective mechanism of trehalose to microorganisms, there are two hypotheses: "water substitution" and "glassy state" (*Santivarangkna C. et al., 2008*). Trehalose can only play its protective function in microbial cells, while in the drying process microbial cells are dormant and couldn't synthesize trehalose. At the same time, due to the selective permeability of the cell membrane, macromolecular substances such as trehalose and antioxidant enzymes cannot directly enter the microbial cells. Therefore, how to load macromolecular protective agents into cells without damaging the cell membrane has become a hot research topic.

The methods of loading macromolecular substances into microbial cells mainly include co-cultivation method, electroporation method and particle gun method (*Ali Shamsaie et al., 2007*). Among them, the co-cultivation method is the most commonly used method in actual production. The principle is to co-cultivate macromolecular substances with microorganisms for a long time, and enter the microorganism cells through the phagocytosis of the cell membrane. Although this method has low cost and little damage to microorganisms, the co-cultivation time is generally 1-3 weeks, the efficiency is too low, and the macromolecular substances phagocytosed into cells are often uneven (*Feng S. et al., 2015*). Electroporation is a method in which macromolecules such as trehalose and antioxidant enzymes are loaded into microbial cells by using an externally enhanced electric field to change the permeability of the cell membrane. This method greatly improves the loading efficiency, but there are three inherent problems: difficult to control the electric field parameters, excessive irreversible damage to the cell membrane, and polarized and uneven distribution of the loaded substance in the cell (*Saswati Mishra et al., 2020*). The particle gun method is a method in which the particles attached to the trehalose bio-macromolecule are shot by the particles and injected into the bacteria at the high speed. Although this method is highly efficient and simple to control, the damage to the microbial cell membrane is too great, which will cause a large number of inactivation, so it is hardly used in practice.

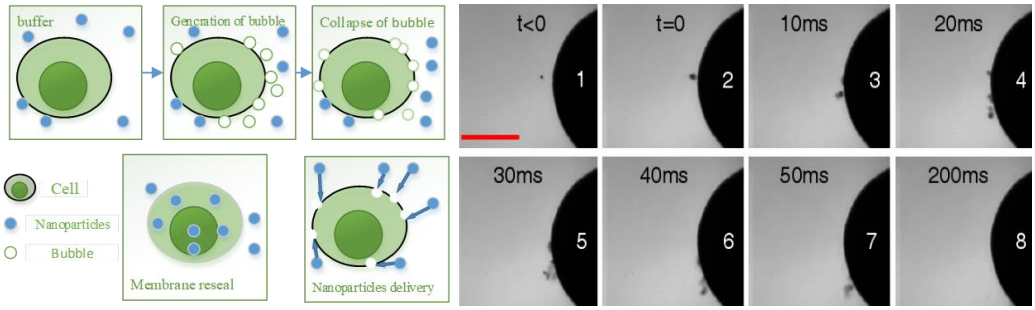

Fig. 4- Ultrasonic perforation process

Ultrasound perforation is an emerging technology that is widely used in high-end medical fields. First, it uses the sound pore effect produced by the ultrasonic wave to stimulate the continuous violent contraction and explosion of the tiny bubbles around the cell membrane, resulting in a reversible pore structure on the cell membrane surface. At the same time, it uses ultrasonic energy to stimulate macromolecular substances such as trehalose and antioxidant enzymes to move at a high speed in a monodisperse state. Finally, the high-speed moving biological macromolecules quickly enter into the cell and distribute evenly through the reversible pore structure formed by the cell membrane (the process is shown in Fig. 4) (*Caixia Jia et al., 2021*). Compared with the above three loading methods, ultrasonic piercing load technology has the advantages of high efficiency, low damage failure rate and uniform load distribution. Therefore, this technology has great potential for development.

3. Review on drying Technology of liquor yeast

It is undoubtedly the ultimate goal of microbial market-oriented large-scale drying to improve the rehydration survival rate and rate of microbial drying at the same time. Therefore, it is particularly important to compare the commonly used liquor yeast drying processes and design the optimal drying process by combination.

The commonly used liquor drying process and its cost and drying survival rate is shown in Table 1.

Table 1

Comparison of cost and typical survival rate of traditional drying technology

Drying process	Cost of equipment (%)	Production cost (%)	Survival of dry products (%)
Freeze drying	100	100	≥90
Vacuum drying	52.2	51.6	49.5
Vacuum microwave	65.4	53.8	53
Spray drying	12	20	44.3
Fluidized bed drying	8.8	17.9	28.8

3.1. Freeze drying

The principle of freeze-drying is as follows: firstly, the yeast liquid with protective agent is rapidly frozen in a freeze dryer at-80 °C under atmospheric pressure, and then vacuum to make the air pressure ≤ 6 mbar to quickly reduce the vapour pressure of water in the cell, and finally make the frozen water sublimate and transfer quickly (as shown in Fig. 6) (*Dimitrellou D. et al., 2016*). From the point of view of the damage mechanism, because it is carried out in the environment of vacuum, low temperature and no shear, the main ways of cell damage and inactivation are dehydration damage and osmotic damage. The damage mainly occurs in the damage to the cell structure during the formation of intracellular ice crystals and the damage to the cell membrane caused by the hyperosmotic environment during water sublimation. Due to the single mechanism of freeze-drying damage, the rehydration survival rate of dried microorganisms is generally more than 90%. However, its equipment structure is complex (the structure diagram is shown in Fig. 7) and precise and the energy consumption of vacuum pumping and freezing is extremely high, so its equipment and use costs are the highest in traditional drying. At the same time, freeze-drying also has the defects of long drying time and intermittent drying, so it is not suitable for the optimization of combined drying process (*Romano N. et al., 2016*).

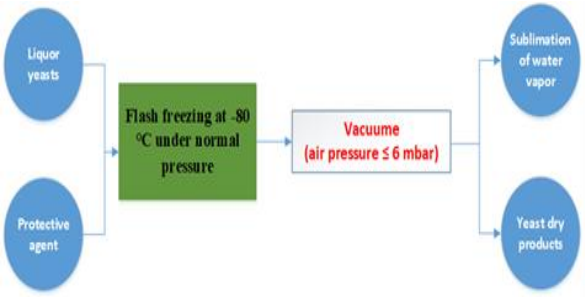

Fig. 6- freeze drying flow chart

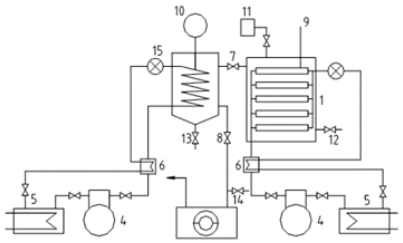

1. Freeze drying box, 2. Condenser, 3. Vacuum pump, 4. Refrigeration compressor, 5. Water cooler, 6. Heat exchanger, 7 8 12 15. Valve, 9 10. Temperature monitor, 11. Vacuum gauge, 13 14. Express

Fig. 7 schematic diagram of integrated freeze-dryer structure

3.2. Vacuum drying versus vacuum microwave drying

Vacuum drying is a kind of drying process, which reduces the vapour pressure of water in bacteria and reduces the drying temperature by vacuuming. Different from non-vacuum high temperature drying, medium temperature vacuum drying could reduce the drying temperature of microorganisms below 50 °C by controlling the vacuum, to reduce the occurrence of thermal damage to death (*Foerst P. et al., 2012*). Therefore, dehydration damage is the main cause of inactivation of microorganisms in it. Although the higher vacuum reduces the drying temperature and makes the rehydration survival rate of liquor yeast generally higher than 45%, it also reduces the heat and mass transfer efficiency, which increases the drying time and high drying cost. Therefore, it is not suitable for enterprise mass drying of yeast alone.

Vacuum microwave drying is essentially an optimization and improvement of vacuum drying process, which uses microwave generator to replace the traditional radiation heat source of vacuum drying. It takes advantage of the high heat transfer efficiency of microwave in vacuum to improve the drying efficiency of ordinary vacuum drying; at the same time, the characteristics of microwave heating from intracellular to extracellular have used to improve the drying survival rate of microorganisms. Finally, the efficiency and quality of vacuum drying have improved at the same time. However, it still does not overcome the problem that it is difficult to produce continuously in large quantities (*Ambros S. et al., 2018*). Therefore, it could be used as one of the alternative processes for combined drying process design.

3.3. Spray drying

Spray drying is an extremely efficient drying process. The drying process is as follows: first, the feed liquid composed of microorganisms, protective agents, carriers, etc. is transported to the spray head by a pump to be dispersed into countless fine droplets. Then, the droplets are allowed to fall freely under the combined action of spray pressure, fluid force and gravity. Finally, in the process of falling, heat and mass transfer occurs in contact with hot air to complete the drying of microorganisms. According to the different flow directions of hot air and materials, spray drying is usually divided into convection drying, co-current drying and mixed-flow drying (as shown in Fig. 8) (*Vega-Mercado H. et al., 2001*).

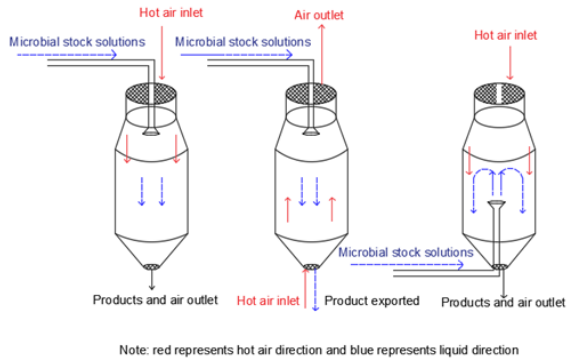

Fig. 8 - Spray drying classification

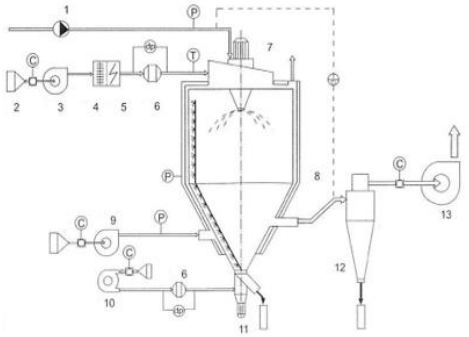

1. Feed pump, 2 6. Filter, 3 9. Fan feeders, 4. Steam heaters, 5. Electric heaters, 7. Nebulizers, 8. Drying column, 10. Air pump, 11. Gas sweep device, 12. Cyclone separator.

Fig. 9 - Schematic of the parallel flow drying column structure

In convection drying, the material and the airflow go in the opposite direction, which can prolong the residence time of the droplets in the drying tower and reduce the height of the drying tower. However, the outlet temperature is the highest and it is in direct contact with the drying particles, so it is only suitable for the drying of non-biologically active materials. In the co-current drying, the droplets first contact with the high temperature air and the material is always in a low wet bulb temperature environment. Only when the drying reaches the stage of decreasing the speed of drying, the material is in direct contact with the air close to the outlet temperature. This process greatly reduces the thermal damage and deactivation of materials, so it is suitable for the drying of active substances such as microorganisms. Although mixed flow drying combines the characteristics of convection and co-current drying, the sprinkler is easy to block upward, so it is rarely used.

The drying of droplets in the co-current drying has divided into four stages: atomization, constant speed drying, slow speed drying, and separation of particles and gases (*Broeckx G. et al., 2016*). Among them, in the atomization stage, the microorganisms are mainly subjected to shear damage. In the constant-speed drying stage, the droplets are in contact with hot air, and the moisture on the particle surface can maintain the gas-liquid two-phase balance.

The direct contact of microorganisms is the lower wet bulb temperature, and the microorganisms are mainly subjected by dehydration and osmotic damage. In the slow drying stage, the moisture on the particle surface cannot maintain the gas-liquid two-phase balance, and the microorganisms directly contact with the high-temperature air and finally reach the outlet temperature. The microorganisms are mainly subjected by dehydration and heat damage. In the dry product particle and gas separation stage, the larger particles remain at the bottom of the tower, and the tiny particles are separated by the cyclone. Thus, it could be seen that the inactivation of microorganisms mainly occurs in the third and fourth stages.

Compared with other traditional drying, spray drying has the advantages of low cost, high drying efficiency and continuous production. Although the survival rate of microbial rehydration after drying is slightly lower, it is one of the potential drying technology to replace freeze-drying, and it is one of the current research hotspots of microbial drying. Therefore, it could be used as the core process of combined drying process design.

3.4. Fluid bed drying

Fluidized bed drying is a drying process of atomizing and spraying the microbial suspension on the dry carrier particles, and then placing it on the fluidized bed to adjust the heat and mass transfer by adjusting the flow of the hot air to change its movement in the hot air. This process has high drying efficiency and low cost, but the rehydration survival rate of the dried product is extremely low, so it is generally not used for microbial drying independently, but is often combined with other processes as an auxiliary drying process.

3.5 Emerging drying technologies

Spray-freeze-drying is a new drying process improved by adding spray module on the basis of freeze drying. The basic principle is the same as freeze-drying, which mainly includes three steps: microbial liquid atomization, refrigerant contact solidification and vacuum low-temperature sublimation (*Ishwarya S.P. et al., 2015*). The material size was reduced by adding spray module, thus the efficiency of freeze-drying is greatly improved. However, the equipment and operating cost is 3 times higher than that of freeze-drying, so it is only suitable for small-scale drying of high-value bioactive substances.

Electrospray drying is a drying process, which uses electrostatic action to optimize the spray head of spray drying, and its characteristics are consistent with the traditional spray drying. The electrostatic spray can not only avoid shear damage, but also refine the droplets, and finally improve the rehydration survival rate of spray-dried particles. However, the electrostatic effect is greatly affected by the properties of the microbial feed liquid, so it could only be applied to the drying of microorganisms with specific electrical properties.

The microwave freeze-drying process is a drying process based on freeze-drying, replacing the original heat source with a microwave generator to improve heat and mass transfer. However, microwaves in high vacuum will stimulate plasma generation, causing uneven heating of microorganisms and additional damage to microorganisms. Therefore, the process is not yet mature and could only be used for small batch production.

4. Summary of current research status and future perspectives

4.1. Summary of current research status

Current research on the mechanism of microbial drying damage inactivation. At the cellular scale, firstly, a set of relatively complete damage inactivation principles has derived from the five macroscopic dimensions of dehydration, heat, oxidation, shear, and osmotic pressure. Then, the characteristics of each damage mechanism is reviewed in detail. Finally, based on the damage mechanism, the commonly used drying processes are analysed in a targeted manner. At the scale of cell substructure, firstly, the damage analysis is carried out, and the specific principle and sequence of the effect of each damage inactivation mechanism on each cell substructure is obtained. Then, the main damage sites for drying inactivation of microorganisms is sorted as follows: cell membrane > intracellular protein > ribosome > cell wall. Overall, the current research has established a relatively complete theory of cell injury inactivation mechanism at the macroscopic and cellular substructure scales.

In terms of microbial drying protection, the current research was carried out from three aspects: pre-treatment before drying, addition of protective agents and optimization of drying process parameters. Firstly, from the two dimensions of culture conditions and stress treatment, the pre-treatment before drying was studied by means of basal medium optimization, additive optimization, culture parameter optimization, and stress treatment.

Then, the protective mechanism of adding protective agent was studied from the two dimensions of extracellular protection of enzyme-treated protein and intracellular protection of loaded compatible mediators.

The current research regards the drying process of microorganisms. Firstly, based on the microbial drying damage mechanism and protection strategy, the advantages and disadvantages of each common drying process was analysed. Then, combined with the microbial drying protection strategy, a number of emerging drying processes were combined and optimized. Finally, the survival rate and efficiency of drying of microorganisms such as liquor yeast were improved.

4.2. Outlook

On the damage mechanism and protection strategy of microbial desiccation, there is no report on molecular scale research. For example, the intracellular protection mechanism of trehalose, there are still two hypotheses of "water replacement" and "Glass transition". Therefore, advanced instruments and optimized detection method would be used to conduct molecular-scale research on it in the later stage.

The preliminary idea is that, firstly, the advanced ultrasonic perforation loading technology would be transferred to the drying protection research of liquor yeast, and silver nanoparticles, trehalose and catalase would be loaded into the cells and evenly distributed. Then, the liquid chip, fluorescent probe and field emission transmission electron microscope would be combined to build a microbe observation platform at the molecular scale. Finally, the molecular-scale observation and research on the drying damage and protection mechanism of liquor yeast would be realized.

In terms of drying process optimization, the combined design of drying process can be carried out on the basis of comparative analysis of traditional processes, combined with the characteristics of damage mechanism of microbial drying under each drying process.

The preliminary idea is that, firstly, an innovative combination of spray drying, vacuum microwave drying and fluidized bed drying is carried out in principle, and the combined drying process of spray + vacuum + vibration + microwave is optimized. Then, the damage mechanism of microorganisms in the new combined drying process is further studied at the molecular scale. Finally, the emerging combined drying protection strategies and equipment are optimized in a targeted manner.

ACKNOWLEDGEMENT

This work was supported by the National Natural Science Foundation of China [No. 51876109] and the Key Project of International Science and Technology Cooperation Program for Shaanxi Province [No.2020KWZ-015].

REFERENCES

[1] Ali Shamsaie, Magdalena Jonczyk, Jennifer D. Sturgis, J. Paul Robinson, Joseph Irudayaraj. (2007). Intracellularly grown gold nanoparticles as potential surface-enhanced Raman scattering probes. *Journal of biomedical optics*, 12(2), 20502.

[2] Ambros S., Foerst P., Kulozik U. (2018). Temperature-Controlled Microwave-Vacuum Drying of Lactic Acid Bacteria: Impact of Drying Conditions on Process and Product Characteristics. *Journal of Food Engineering*, 224, 80-87.

[3] Ambros S., Hofer F., Kulozik U. (2018). Protective Effect of Sugars on Storage Stability of Microwave Freeze-Dried and Freeze-Dried Lactobacillus Paracasei F19. *Journal of Applied Microbiology*, 125 (4), 1128-1136.

[4] Ball P.J.C.R. (2008). Water as an Active Constituent in Cell Biology, *Chemical Reviews*, 108, 74-108.

[5] Broeckx G., Vandenheuvel D., Claes I.J. et al. (2016). Drying techniques of probiotic bacteria as an important step towards the development of novel pharmabiotics. *International journal of pharmaceutics*, 505 (1-2), 303-318.

[6] Caixia Jia, Jianmin Shi, Yao. (2021). Plasma Membrane Blebbing Dynamics Involved in the Reversibly Perforated Cell by Ultrasound-Driven Microbubbles. *Ultrasound in medicine & biology*, 47(3), 733-750.

[7] Câmara A.D.A., Maréchal P-A, Tourdot-Maréchal R. et al. (2019). Dehydration stress responses of yeasts *Torulaspora delbrueckii*, *Metschnikowia pulcherrima* and *Lachancea thermotolerans*: Effects of glutathione and trehalose biosynthesis (Article). *Food Microbiology*, 79, 137-146.

[8] Dimitrellou D., Kandylis P., Kourkoutas Y. (2016). Effect of Cooling Rate, Freeze-Drying, and Storage on Survival of Free and Immobilized Lactobacillus Casei Atcc 393. LWT - *Food Science and Technology*, 69, 468-473.

[9] Dijkstra A.R., Setyawati M C, Bayjanov J.R. et al. (2014). Diversity in Robustness of Lactococcus Lactis Strains during Heat Stress, Oxidative Stress, and Spray Drying Stress. *Applied and Environmental Microbiology*, 80 (2), 603-611.

[10] Feng S., Li Z., Chen G., Lin D., Huang S., Huang Z., Li Y., Lin J., Chen R., Zeng H. (2015). Ultrasound-mediated method for rapid delivery of nano-particles into cells for intracellular surface-enhanced Raman spectroscopy and cancer cell screening. *Nanotechnology*, 25(6), 65101.

[11] Foerst P., Kulozik U., Schmitt M. et al. (2012). Storage Stability of Vacuum-Dried Probiotic Bacterium Lactobacillus Paracasei F19. *Food and Bioproducts Processing*, 90 (2), 295-300.

[12] Fonseca F., Meneghel J., Cenard S. et al. (2016). Determination of Intracellular Vitrification Temperatures for Unicellular Micro Organisms under Conditions Relevant for Cryopreservation. *Plos One*, 11, e0152939.

[13] Gaspar A.L.C., De Góes-Favoni S.P. (2015). Action of Microbial Transglutaminase (Mtgase) in the Modification of Food Proteins: A Review. *Food Chemistry*, 171,315-322.

[14] Ghandi A., Powell I.B., Howes T. et al. (2012). Effect of Shear Rate and Oxygen Stresses on the Survival of Lactococcus Lactis during the Atomization and Drying Stages of Spray Drying: A Laboratory and Pilot Scale Study. *Journal of Food Engineering*, 113 (2): 194-200.

[15] Golowczyc M. A., Silva J., Teixeira P. et al. (2011). Cellular Injuries of Spray-Dried Lactobacillus Spp. Isolated from Kefir and Their Impact on Probiotic Properties. *International Journal of Food Microbiology*, 144, 556-560.

[16] Gong P., Di W., Yi H. et al. (2019). Improved viability of spray-dried Lactobacillus bulgaricus sp1.1 embedded in acidic-basic proteins treated with transglutaminase. *Food chemistry*, 281, 201-212.

[17] Huan-Qin Li, Hu Li, Xin-Yuan Zhou, Ying-Jia Shen, Jian-Qiang Su. (2021). Distinct patterns of abundant and rare subcommunities in paddy soil during wetting–drying cycles, *Science of The Total Environment,* 785, 14729.

[18] Huang S., Vignolles M-L, Chen X. D. et al. (2017). Spray Drying of Probiotics and Other Food-Grade Bacteria: A Review. *Trends in Food Science & Technology*, 63, 1-17.

[19] Ishwarya S.P., Anandharamakrishnan C., Stapley A.G.F. (2015). Spray-freeze-drying: A novel process for the drying of foods and bioproducts. *Trends in Food Science & Technology*, 41 (2), 161-181.

[20] Jorgensen H. (2009). Effect of Nutrients on Fermentation of Pretreated Wheat Straw at very High Dry Matter Content by Saccharomyces cerevisiae. *Appl Biochem Biotechnol,* 153, 44–57.

[21] Khem S., Small D.M., May B.K. (2016). The Behaviour of Whey Protein Isolate in Protecting Lactobacillus Plantarum. *Food Chemistry*, 190, 717-723.

[22] Lv Y-J., Wang X., Ma Q. (2014). Proteomic analysis reveals complex metabolic regulation in Saccharomyces cerevisiae cells against multiple inhibitors stress. *Applied microbiology and biotechnology*, 98, 5, 2207-2221.

[23] Lin J., Zheng W., Tian Y., Wang G., Zheng T. (2013). Optimization of culture conditions and medium composition for the marine algicidal bacterium Alteromonas sp. DH46 by uniform design. *Journal of Ocean University of China*, 12(3), 385-391.

[24] Malhotra A., Coupland J.N. (2004). The Effect of Surfactants on the Solubility, Zeta Potential, and Viscosity of Soy Protein Isolates. *Food Hydrocolloids*, 18 (1), 101-108. doi: 10.1016/S0268-005X(03)00047-X.

[25] Meneghel J., Passot S., Cenard S. et al. (2017). Subcellular Membrane Fluidity of Lactobacillus delbrueckii subsp. bulgaricus under Cold and Osmotic Stress. *Applied Microbiology and Biotechnology*, 101, 6907-6917.

[26] Moayyedi M., Eskandari M.H., Rad A.H.E. et al. (2018). Effect of Drying Methods (Electrospraying, Freeze Drying and Spray Drying) on Survival and Viability of Microencapsulated Lactobacillus Rhamnosus Atcc 7469. *Journal of Functional Foods*, 40, 391-399.

[27] Morgan C., Herman N., White P. et al. (2006). Preservation of Micro-Organisms by Drying; a Review, *Journal of Microbiological Methods*, 66 (2), 183-193.

[28] Peighambardoust S.H., Golshan Tafti A., Hesari J. (2011). Application of Spray Drying for Preservation of Lactic Acid Starter Cultures: A Review. *Trends in Food Science & Technology*, 22, 215-224.

[29] Pichler H., Gaigg B., Hrastnik C., Achleitner G., Kohlwein S.D., Zellnig G. Perktold A., Daum G., (2001). A subfraction of the yeast endoplasmic reticulum associates with the plasma membrane and has a high capacity to synthesize lipids, *European Journal of Biochemistry*, 268(8), 2351-2361.

[30] Romano N., Schebor C., Mobili P. (2016). Role of mono- and oligosaccharides from FOS as stabilizing agents during freeze-drying and storage of *Lactobacillus delbrueckii subsp. Bulgaricus*. *Food Research International*, 90, 251-258.
[31] Russell A.D. (2003). Lethal Effects of Heat on Bacterial Physiology and Structure, *Science Progress*, 86 (1-2), 115-137.
[32] Sachie Fujii, Yuichi Sakamoto, Tamami Aso, Turkan Aktas. (2014). Noriko Yoshimoto & Shuichi YamamotoDrying of Yeasts—Factors Affecting Inactivation During Drying, *Drying Technology: An International Journal*, 29:16, 1981-1985.
[33] Santivarangkna C., Higl B., Foerst P. (2008). Protection mechanisms of sugars during different stages of preparation process of dried lactic acid starter cultures, *Food Microbiology*, 25 (3), 429-44.
[34] Santivarangkna C., Wenning M., Foerst P. et al. (2007). Damage of Cell Envelope of Lactobacillus Helveticus during Vacuum Drying. *Journal of Applied Microbiology*, 102 (3), 748-756.
[35] Senz M., Van Lengerich B., Bader J. et al. (2015). Control of Cell Morphology of Probiotic Lactobacillus Acidophilus for Enhanced Cell Stability during Industrial Processing. *International Journal of Food Microbiology*, 192, 34-42.
[36] Shiroma S., Jayakody L.N., Horie K., Okamoto K., Kitagaki H. (2014). Enhancement of Ethanol Fermentation in Saccharomyces cerevisiae Sake Yeast by Disrupting Mitophagy Function. *Applied and environmental microbiology*, 80, 1002-1012.
[37] Silva J., Carvalho A.S., Ferreira R. et al. (2005). Effect of the pH of Growth on the Survival of Lactobacillus Delbrueckii Subsp. Bulgaricus to Stress Conditions During Spray-Drying. *Journal of Applied Microbiology*, 98 (3), 775-782.
[38] Spreutels L., Haut B., Chaouki J., Bertrand F., Legros R. (2014). Conical spouted bed drying of Baker's yeast: Experimentation and multi-modeling. Food Research International, 62, 137-150.
[39] Su J., Yang X., Zhou Y., Zheng T. (2011). Marine bacteria antagonistic to the harmful algal bloom species Alexandrium tamarense (Dinophyceae). *Biological Control*, 56(2), 132-138.
[40] Vega-Mercado H., Marcela Góngora-Nieto M. (2001). Advances in dehydration of foods. *Journal of Food Engineering*. 49 (4): 271-289.

CONSIDERATIONS REGARDING THE VIBRATIONS TRANSMITTED TO THE OPERATOR BY AN AXIAL FLOW HARVESTER COMBINE
/
CONSIDERAŢII PRIVIND VIBRAŢIILE TRANSMISE OPERATORULUI DE O COMBINĂ CU FLUX AXIAL

BIRIŞ S.Şt.[1)], CONSTANTIN A-M.[2*)], ANGHELACHE D.2*), GĂGEANU I.[2)], CUJBESCU D.[2)], NENCIU F.[2)], VOICEA I.[2)], MATEI Gh.[3)], POPA L.D.[4*)], DUȚU M.F.[1)], UNGUREANU N.[1*)], ŻELAZIŃSKI T.[5)], PERIŞOARĂ L.[1)], FODOREAN G.[2)]
[1)] University „Politehnica" Bucharest / Romania; [2)]INMA Bucharest / Romania; [3)]University from Craiova / Romania;
[4)]ARDS Secuieni / Romania; [5)]Warsaw University of Life Sciences / Poland
E-mail: marin.anamaria26@gmail.com; dragos1989anghelache@gmail.com; nicoletaung@yahoo.com
DOI: https://doi.org/10.35633/inmateh-68-74

Keywords: *combine, amplitude, nomogram, frequency*

ABSTRACT
Vibrations are dynamic phenomena occurring in elastic or quasi-elastic media after a local excitation and becoming manifested by propagating the excitation within the medium in the form of some elastic oscillations. Thus, depending on the phenomenon dynamics, there can be met vibrations with low variation frequencies, characteristic to the mechanical structures, structures in constructions and earthquake waves, as well as vibrations with high variation frequencies. The vibration measuring is performed on a straw cereal harvesting machine with an axial threshing apparatus ("CASE IH") in two conditions: in a stationary position and during work, by using transducers for each of the main working parts of the harvester: thresher, header (stripper), chassis and operator's chair. On the basis of the values of longitudinal, cross and vertical accelerations, measured at various frequencies in the two operating conditions of the harvester (at stationary and during work), the effect of the vibrations is established on each of these parts and, finally, cumulated, the vibrations sent to the operator's chair, the nomograms following to be traced and to be established the range with the limits up to which these are not dangerous for the operator's health.

REZUMAT
Vibraţiile sunt fenomene dinamice care iau naştere în medii elastice sau cvasielastice în urma unei excitaţii locale şi care se manifestă prin propagarea excitaţiei în interiorul mediului sub forma unor oscilaţii elastice. Astfel, în funcţie de dinamica fenomenului se întâlnesc vibraţii cu frecvenţe de variaţie scăzute, caracteristice structurilor mecanice, structurilor din construcţii şi undelor seismice, precum şi vibraţii cu frecvenţe mari de variaţie. Măsurarea vibraţiilor se realizează pe o combină de recoltat cereale păioase cu aparat de treier axial (CASE IH), în două condiţii: la staţionar şi în lucru, utilizându-se traductori pentru fiecare din principalele organe de lucru ale combinei: batoză, heder, şasiu şi scaunul operatorului. Pe baza valorilor acceleraţiilor longitudinale, transversale şi verticale măsurate la diferite frecvenţe în cele două condiţii de funcţionare a combinei (la staţionar şi în lucru) se stabileşte efectul vibraţiilor asupra fiecărui dintre aceste organe şi în final, cumulat, vibraţiile transmise la scaunul operatorului, urmând să se traseze nomogramele şi să se stabilească domeniul cu limitele până la care acestea nu sunt periculoase pentru sănătatea operatorului.

INTRODUCTION

Agriculture provides food, raw materials for other industries and employment opportunities. As a consequence, given the key role of agriculture in global economy, safety and health of its employees are regarded to be of major importance (*Benos L. et al, 2020*).

Vibrations are dynamic phenomena that arise in elastic or quasi-elastic environments following a local excitation and which are manifested by the propagation of the excitation inside the environment in the form of elastic oscillations (*Brăcăcescu C. et al., 2017; Postelnicu et al., 2017; Vlădut V. et al, 2013; Vlădut V. et al, 2014; Vlădut V. et al, 2021*) and they can produce a wide variety of different effects to the machine operators. The effects on the operator exposed to a high vibration level for a longer period of time are usually permanent in character and are therefore considered to be an occupational disease leading to invalidity (*Goglia V. et al, 2006*). Vibration is a complicated movement for the human body to react to, and some factors including vibration magnitude, frequency, duration time, input position, etc., are especially significant to the effects. It

appears that some environmental elements, including light, heat and noise, are also relative to the effects of vibration (British Standards 6481, 1987; *ISO 2631/1, 1985; Brüel & Kjaer, 1984*; *Liang X.C. et al, 2018*).

Frequent exposure to vehicle-and equipment-induced whole body vibration (WBV) is common in agriculture, mining, construction and many other heavy industries. In agriculture, specifically, WBV exposure is highly prevalent during operation of machinery and transport vehicles (*Yung M. et al, 2018*).

Combine harvesters have been playing an important role in modern agricultural production in recent years, their working process is divided into the cutting of the crop and recovering grains from the field, separating grains from the greater crop parts such as straw and separating grains from material-other-than grain (MOG), then collecting cleaned grains in a tank for temporary storage or directly in a bags (*Hamed A.R., 2016*).

Whole-body vibration (WBV) is defined as vibration occurring when a greater part of the body weight is supported on a vibrating surface. WBV principally occurs in vehicles and wheeled working machines, such as combine harvesters. In most cases exposure to WBV occurs in a sitting position and the vibration is then primarily transmitted through the seat pan, but also through the seatback (*Rahmatalla S. et al, 2011*).

Biodynamics of seated human subjects has been a topic of interest over the years, and a number of mathematical models have been established. The concept of absorbed energy was discussed in the mid-1960's by a group of scientists who presented results from investigations which indicated that the subjective experience of vibration is related to the amount of vibration energy absorbed by the body (*Szczepaniak J. et al, 2014*).

Whole body vibration is a reflection of the comfort limitations of agricultural machinery and is subjectively assessed by their drivers or passengers. The effects of mechanical vibration are determined by the frequency of vibrations, magnitude, directions and duration of time. Humans have different sensations of vibration and different parts of the human body resonate at different frequencies. Whole body vibration (WBV) exposures are often predominant in the fore-aft (x) or lateral (y) axis among off-road agricultural vehicles. However, as the current industry standard seats are designed to reduce mainly vertical (z) axis WBV exposures, they may be less effective in reducing drivers' exposure to multi-axial WBV (*Kim H. et al, 2018*).

The European Directive 2002/44/CE on the minimum health and safety requirements regarding the exposure of workers to the risks arising from vibrations impose specific requirements for the safety of workers exposed to mechanical vibrations (*Matache M.G. et al, 2020*). Through this directive two exposure indicators for whole-body vibration have been defined:

- the daily exposure limit value standardised to an eight-hour reference period shall be 1.15 m/s^2 or, at the choice of the Member State concerned, a vibration dose value of 21 m/s1.75;
- the daily exposure action value standardised to an eighthour reference period shall be 0.5 m/s^2 or, at the choice of the Member State concerned, a vibration dose value of 9.1 m/s1.75.

Fig.1 - The ortogonal measuring directions that effect driver WBW, (*Vlăduţ V. et al, 2021*)

Long-term exposure to WBV can be connected with an increased risk of numerous diseases affecting the back, digestive, circulatory and nervous systems, sexual and urinary systems. The exposure to WBVs at work clearly relates also to the increased risk of lumbar pains, the pain of the sciatic nerve and disorders of lumbar intervertebral discs as well as musculoskeletal symptoms in the area of the neck and shoulders. WBV can also cause the loss of tenderness in the limbs as well as skeletal and gastrointestinal disorders. Some symptoms of disorders may also appear in the form of fatigue, insomnia and tremor.

Apart from health effects, exposure to vibrations may impair the performance of operators, particularly in activities with high demands on accuracy that are characteristic of the operation of forest machines as well as harvesters (*Luboš S. and Václav M., 2022*).

MATERIALS AND METHODS

In order to measure the vibrations occurring at the stationary and during the working process on the combine, the longitudinal, transverse and vertical accelerations are measured, corresponding to the three directions of measurement: *x*, *y* and *z*. These accelerations (their size), as well as the frequencies at which they manifest, are measured by means of accelerometers glued to the main parts of the combines that produce vibrations, such as: the threshing apparatus, the chassis and the header to those with axial flow. Subsequently, the vibrations transmitted by these working parts to the seat of the combine and thus to the operator who leads the combine are measured, in order to be able to determine how and the value with which they affect his health.

The establishment of the main requirements and of the measurement points is made taking into account the work conditions, the interaction between the working parts and the field as well as between the constructive elements of the combine, its operating regime, or other requirements. The measurement points where the transducers (accelerometers) are to be placed shall be established either by analytical methods or by using modeling (the finite element method).

Transducers (accelerometers) are mounted on flat surfaces, if possible without inclinations, as close as possible to the working part whose vibrations are intended to be measured. They are not mounted directly on these working parts because most of the working parts of the combine that produce vibrations are in motion: the central conveyor, the cleaning system, the rotor, etc.

The main purpose of the measurements is to determine to what extent the vibrations produced by the main parts of the combine affect the health of the person serving it. For this purpose, the vibrations transmitted to the support of the combine seat are measured (figure 2).

Fig. 2 - Transducers mounted on the combine seat

In order to measure the vibrations produced by the CASE-IH 2388 axial flow harvester (figure 3, 4), the vibrations transmitted by its main working parts to the operator's seat were determined.

The vibrations transmitted to the operator's seat represent the vibrations produced by the threshing cylinder, the header and the other parts of the harvester, transmitted through the chassis to the operator's cab and then from the platform to the seat.

The measurements were done using Bruel & Kjaer type accelerometers, an analog amplifier device, DAP 2400 data acquisition system (*Broch J.T, 1980*), and a laptop, measuring longitudinal, transverse and vertical accelerations for the two operating conditions in which significant vibrations occur: at stationary and at work (when harvesting wheat).

Fig.3 - CASE-IH combine, front view

Fig.4 – CASE-IH combine, perspective view

RESULTS

Vibrations were measured on the chassis, header and thresher on the three orthogonal (x, y, z) axes, during motion and in stationary position. It was found that the level of vibrations transmitted did not endanger the health of the human operator.

The following accelerations were measured for the thresher:

Table 1

Acceleration values measured for the thresher

f [Hz]			1	1.25	1.6	2	2.5	3.15	4	5	6.3	8	10	12.5	16	20	25	31.5	*40*	50	63	80
CASE - IH	thresher *s*	L	0.011	0.006	0	0	0	0	0.016	0.04	0.03	0.02	0.02	0.02	0.008	0.02	0.02	0.07	0.03	0.06	0.17	***0.68***
		T	0	0	0	0	0	0	0	0	0	0.03	0.15	0.16	0.03	0	0.04	0.33	0.1	0.46	2.89	***3.12***
		V	0	0	0	0	0	0	0.05	0.05	0.05	0.03	0.06	0.07	0.05	0.04	0	0.73	0.08	0.18	0.96	***2.75***
	thresher *w*	L	0.06	0.05	0.03	0.02	0.02	0.016	0	0.04	0.14	0.016	0.02	0.03	0.01	0.02	0.02	0.02	0.06	0.03	0.06	***0.16***
		T	0.08	0.08	0.03	0.03	0.03	0.02	0	0	0.02	0.05	0.18	0.08	0.04	0.05	0.12	0.21	0.16	0.55	***2.32***	2.21
		V	0.06	0.08	0.05	0.07	0.08	0.08	0.05	0.05	0.03	0.05	0.06	0.06	0.06	0.08	0.03	0.25	0.08	0.21	0.88	***1.75***

**s - stationary position, w - while working*

Figure 5 shows the longitudinal accelerations-a_x, the range of dangerous frequencies being between 1 and 3.15 Hz. The maximum measured accelerations were:

- CASE-IH combine in stationary position: 0.68 m/s at 80 Hz > 24h;
- CASE-IH combine while working: 0.16 m/s at 80 Hz > 24h,

which means that the operator can work without his health being affected, while the combine is working or in stationary position, for 24 hours.

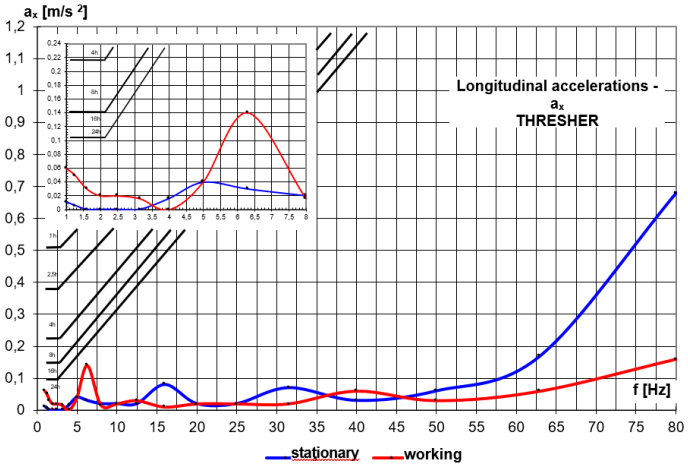

Fig. 5 - Thresher longitudinal accelerations, CASE-IH combine in stationary position and while working

Figure 6 shows the transverse accelerations - a_y, the range of dangerous frequencies being between 1 and 3.15 Hz. The maximum measured accelerations were:

- CASE-IH combine in stationary position: 3.12 m/s^2 at 80 Hz > 24h;
- CASE-IH combine while working: 2.32 m/s^2 at 63 Hz > 24h;

which means that the operator can work without his health being affected, while the combine is working or in stationary position, for 24 hours.

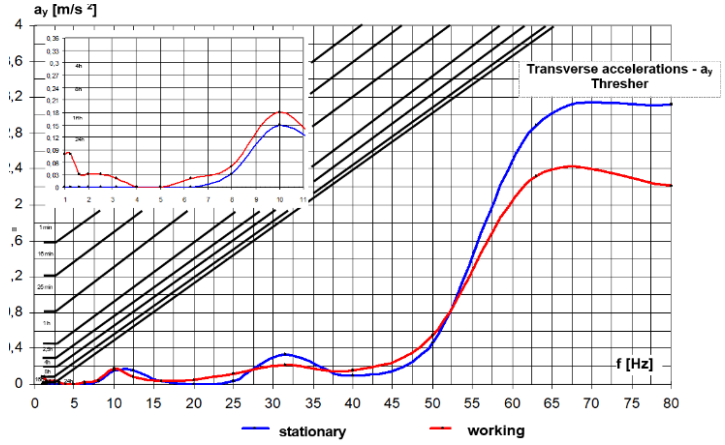

Fig. 6 - Thresher transverse accelerations, CASE-IH combine in stationary position and while working

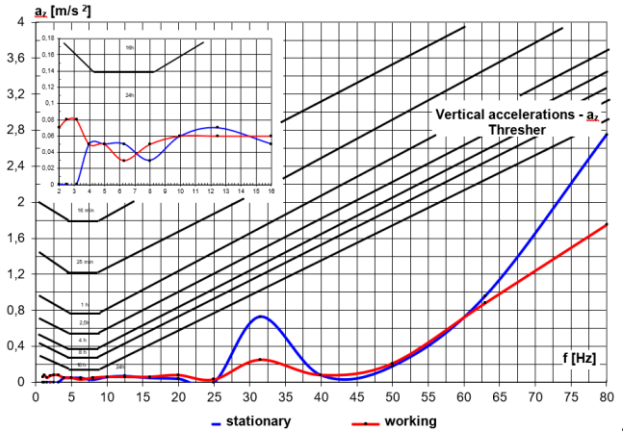

Fig. 7 - Thresher transverse accelerations, CASE-IH combine in stationary position and while working

Figure 7 shows the vertical accelerations – a_z, the range of dangerous frequencies being between 2.5 and 10 Hz. The maximum accelerations were:

- CASE-IH combine in stationary position: 2.75 m/s^2 at 80 Hz > 24h;
- CASE-IH combine while working: 1.75 m/s^2 at 80 Hz > 24h,

which means that the operator can work without his health being affected, while the combine is working or in stationary position, for 24 hours.

For the **CHASSIS**, the following accelerations were measured:

Table 2

Acceleration values measured for the chassis

f [Hz]			1	1.25	1.6	2	2.5	3.15	4	5	6.3	8	10	12.5	16	20	25	31.5	*40*	50	63	80
CASE - IH	Chassi	L	0	0	0.005	0.007	0.007	0.008	0.017	0.028	0.03	0.012	0.014	0.014	0.014	0.034	0.029	0.037	0.033	0.047	0.10	*0.21*
		T	0	0	0	0	0	0	0	0	0	0	0	0	0.018	0.018	0	0.23	0.06	0.31	0.71	*2.04*
		V	0	0	0	0	0	0.008	0.03	0.037	0.03	0	0.034	0.034	0.034	0.034	0.037	0.22	0.06	0.34	0.22	*0.97*
	Chassi	L	0.07	0.066	0.044	0.051	0.058	0.025	0	0.045	0.018	0.026	0.028	0.03	0.035	0.028	0.03	0.04	0.03	0.07	0.12	*0.28*
		T	0.09	0.065	0.065	0.065	0.038	0.038	0.038	0.021	0	0	0.19	0.08	0.06	0.13	0.04	0.12	0.12	0.49	1.0	*2.37*
		V	0.09	0.08	0.10	0.18	0.24	0.11	0.06	0.05	0.04	0.06	0.11	0.07	0.07	0.13	0.05	0.18	0.05	0.12	0.28	*0.45*

**s - stationary position, w - while working*

Figure 8 shows the longitudinal accelerations - a_x. The maximum measured accelerations were:

- CASE-IH combine in stationary position: 0.21 m/s^2 at 80 Hz > 24h;
- CASE-IH combine while working: 0.28 m/s^2 at 80 Hz > 24h,

which means that the operator can work without his health being affected, while the combine is working or in stationary position, for 24 hours.

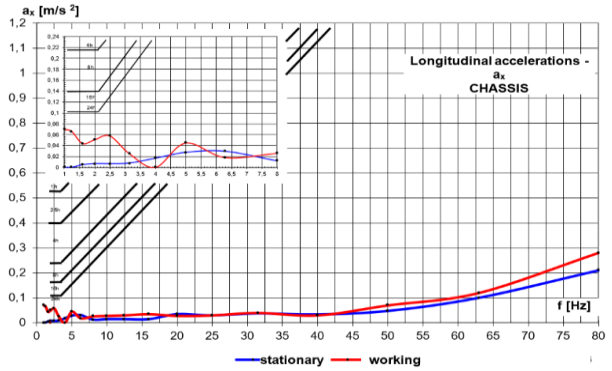

Fig. 8 - Chassis longitudinal accelerations, CASE-IH combine in stationary position and while working

Figure 9 shows the transverse accelerations - a_y, the range of dangerous frequencies being between 1 and 3.15 Hz. The maximum measured accelerations were:

- CASE-IH combine in stationary position: 2.04 m/s^2 at 10 Hz > 24h;
- CASE-IH combine while working: 2.37 m/s^2 at 10 Hz > 24h;

which means that the operator can work without his health being affected, while the combine is working or in stationary position, for 24 hours.

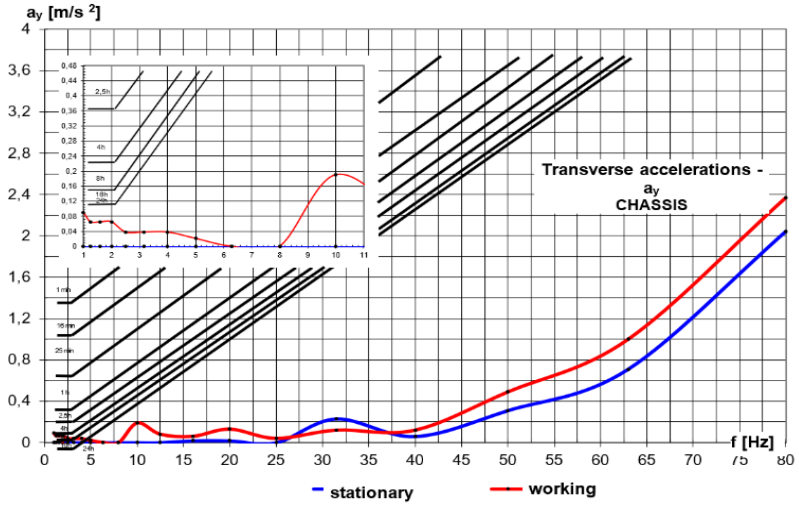

Fig. 9 - Chassis transverse accelerations, CASE-IH combine in stationary position and while working

Figure 10 shows the vertical accelerations - a_z, the range of dangerous frequencies being between 2.5 and 10 Hz. The maximum accelerations were:

- CASE-IH combine in stationary position: 0.97 m/s^2 at 80 Hz > 24h;
- CASE-IH combine while working: 0.24 m/s^2 at 2.5 Hz ≤ 16h,

which means that the operator can work without his health being affected, while the combine is working or in stationary position, for 24 hours.

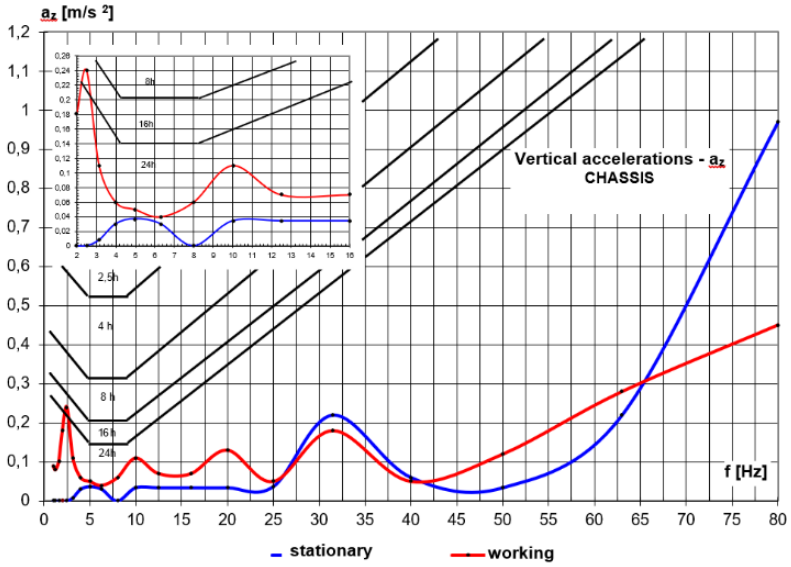

Fig. 10 - Chassis vertical accelerations, CASE-IH combine in stationary position and while working

For the **HEADER,** the following accelerations were measured:

Table 3

Acceleration values measured for the header

f [Hz]			1	1.25	1.6	2	2.5	3.15	4	5	6.3	8	10	12.5	16	20	25	31.5	*40*	50	63	80
CASE - IH	Header s	L	0	0	0	0	0	0.01	0.03	0.025	0.03	0.02	0.02	0.02	0.01	0.02	0.023	0.06	0.05	0.09	0.12	*0.32*
		T	0	0	0	0	0	0	0.01	0.02	0.025	0.037	0.2	0.2	0.03	0.07	0.08	0.24	0.11	0.22	0.31	*0.53*
		V	0	0	0	0	0	0.023	0.08	0.02	0.02	0.06	0.22	*0.25*	0.05	0.08	0.08	0.34	0.15	0.3	0.3	*0.51*
	Header w	L	0.06	0.06	0.04	0.03	0.05	0.03	0.05	0.02	0.03	0.02	0	0.02	0.02	0.02	0.02	0.04	0.06	0.09	0.21	*0.27*
		T	0.05	0.07	0.10	0.07	0.05	0	0	0.04	0.04	0.04	0.15	0.05	0.05	0.17	0.08	0.43	0.13	0.41	0.34	*0.62*
		V	0.13	0.15	0.14	0.11	0.11	0.07	0.08	0.06	0	0.07	0.16	0.07	0.08	0.19	0.08	0.22	0.21	0.43	0.47	*0.59*

**s -stationary position, w - while working*

Figure 11 shows the longitudinal accelerations - a_x, the range of dangerous frequencies for this type of acceleration being between 1 and 3.15 Hz. The maximum measured accelerations were:

- CASE-IH combine in stationary position: 0.32 m/s^2 at 80 Hz > 24h;
- CASE-IH combine while working: 0.27 m/s^2 at 80 Hz > 24h,

which means that the operator can work without his health being affected, while the combine is working or in stationary position, for 24 hours.

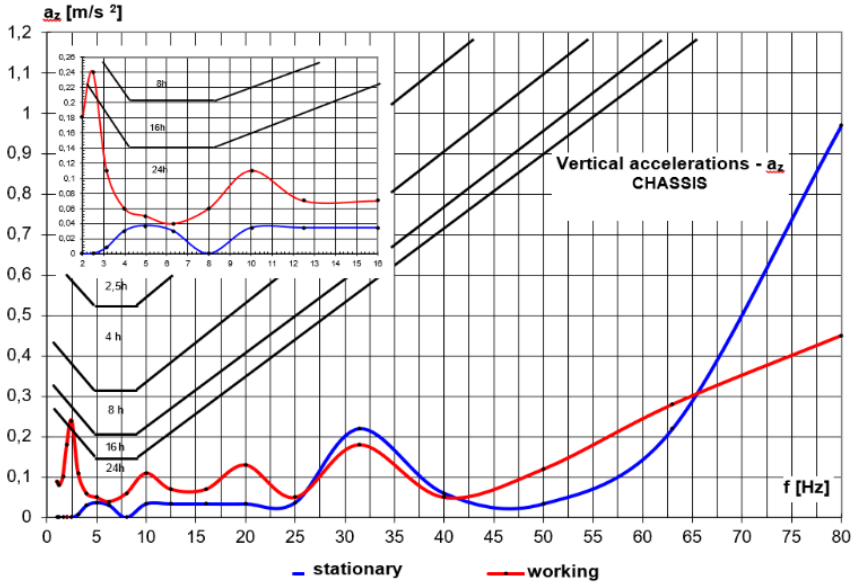

Fig. 11 - Chassis vertical accelerations, CASE-IH combine in stationary position and while working

Figure 12 shows the transverse accelerations - *ay*, the range of dangerous frequencies being between 1 and 3.15 Hz. The maximum measured accelerations were:

- CASE-IH combine in stationary position: 0.53 m/s^2 at 80 Hz > 24h;
- CASE-IH combine while working: 0.62 m/s^2 at 80 Hz > 24h;

which means that the operator can work without his health being affected, while the combine is working or in stationary position, for 24 hours.

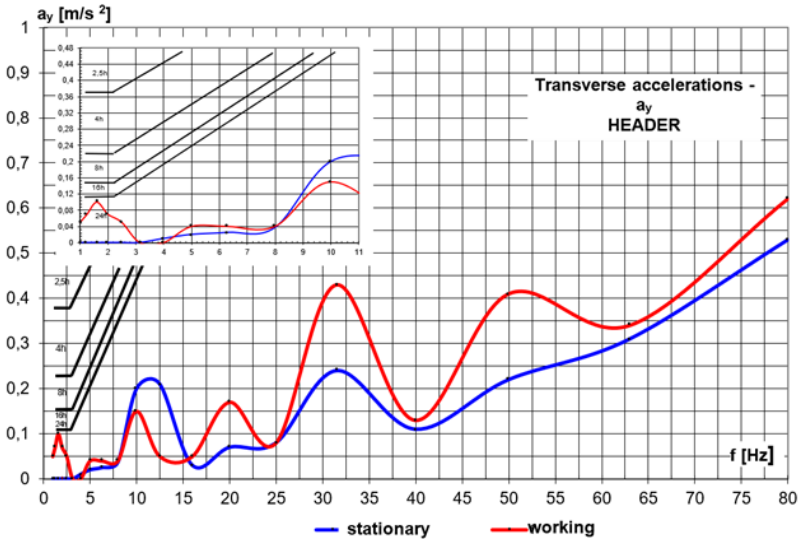

Fig.12 - Header transverse accelerations, CASE-IH combine in stationary position and while working

Figure 13 shows the vertical accelerations - a_z, the range of dangerous frequencies being between 2.5 and 10 Hz. The maximum accelerations were:

- CASE-IH combine in stationary position: 0.25 m/s^2 at 12.5 Hz ≤ 16h;
- CASE-IH combine while working: 0.59 m/s^2 at 80 Hz > 24h,

which means that the operator can work without his health being affected, while the combine is working or in stationary position, for 24 hours.

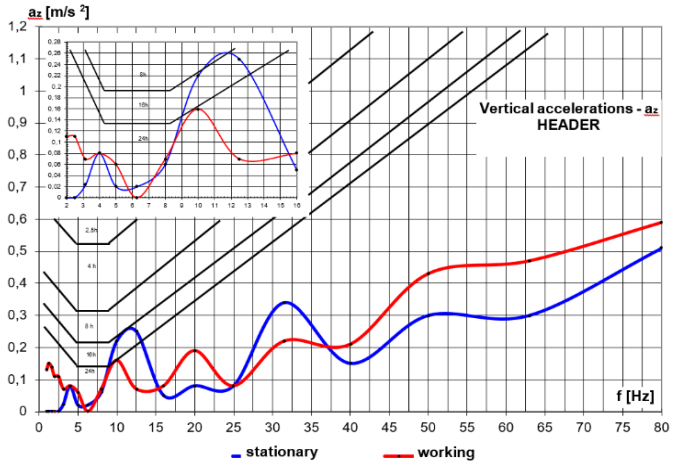

Fig.13 - Header vertical accelerations, CASE-IH combine in stationary position and while working

For the **SEAT**, the following accelerations were measured:

Table 4

Acceleration values measured for the seat

f [Hz]			1	1.25	1.6	2	2.5	3.15	4	5	6.3	8	10	12.5	16	20	25	31.5	*40*	50	63	80
CASE-IH	Seat s	L	0.007	0.007	0.008	0.008	0.011	0.015	0.016	0.018	0.019	0.018	0.036	0.036	0.036	0.04	0.05	0.21	0.08	*0.42*	0.07	0.08
		T	0.007	0.008	0.01	0.012	0.012	0.014	0.014	0.026	0.058	0.07	0.022	0.031	0.17	0.16	0.11	*0.23*	0.08	0.09	0.07	0.11
		V	0.023	0.028	0.026	0.029	0.03	0.05	0.05	0.05	0.06	0.06	0.10	0.09	0.08	0.09	0.11	0.32	0.13	*0.43*	0.17	0.24
	Seat w	L	0.09	0.09	0.06	0.04	0.05	0.04	0.05	0.04	0.04	0.06	0.06	0.07	0.05	0.07	0.07	0.13	0.08	*0.47*	0.08	0.11
		T	0.10	0.10	0.07	0.04	0.04	0.06	0.14	0.08	0.10	0.09	*0.28*	0.13	0.22	0.28	0.21	0.16	0.08	0.10	0.12	0.11
		V	0.17	0.18	0.17	0.014	0.16	0.16	0.09	0.07	0.07	0.09	0.11	0.10	0.12	0.14	0.13	0.18	0.12	*0.34*	0.16	0.19

**s - stationary position, w - while working*

Figure 14 shows the longitudinal accelerations - a_x, the range of dangerous frequencies for this type of acceleration being between 1 and 3.15 Hz. The maximum measured accelerations were:

- CASE-IH combine in stationary position: 0.42 m/s^2 at 50 Hz > 24h;
- CASE-IH combine while working: 0.47 m/s^2 at 50 Hz > 24h,

which means that the operator can work without his health being affected, while the combine is working or in stationary position, for 24 hours.

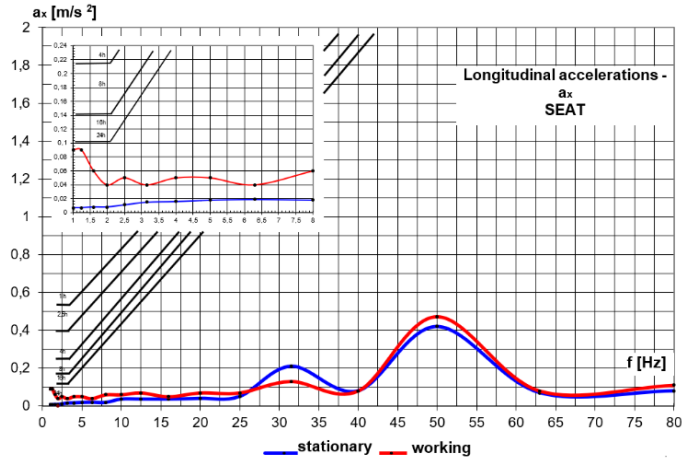

Fig. 14 - Seat longitudinal accelerations, CASE-IH combine in stationary position and while working

Figure 15 shows the transverse accelerations - a_y, the range of dangerous frequencies being between 1 and 3.15 Hz. The maximum measured accelerations were:

- CASE-IH combine in stationary position: 0.23 m/s^2 at 31.5 Hz > 24h;
- CASE-IH combine while working: 0.28 m/s^2 at 10 Hz > 24h;

which means that the operator can work without his health being affected, while the combine is working or in stationary position, for 24 hours.

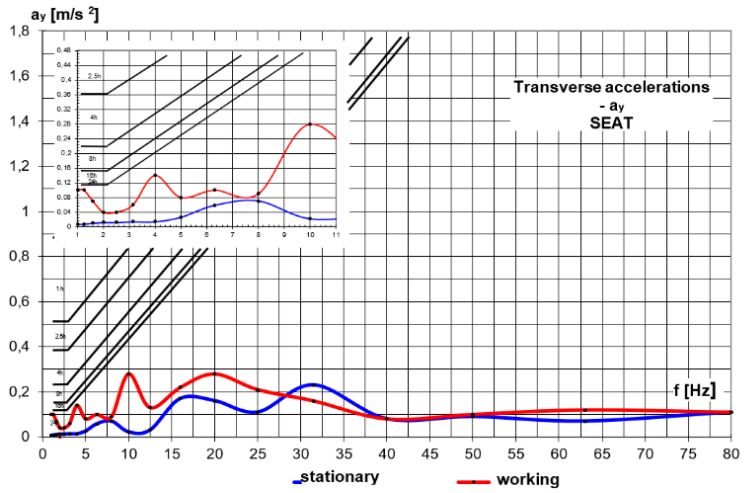

Fig. 15 - Seat transverse accelerations, CASE-IH combine in stationary position and while working

Figure 16 shows the vertical accelerations - a_z, the range of dangerous frequencies being between 2.5 and 10 Hz. The maximum accelerations were:

- CASE-IH combine in stationary position: 0.43 m/s^2 at 50 Hz > 24h;
- CASE-IH combine while working 0.34 m/s^2 at 50 Hz > 24h,

which means that the operator can work without his health being affected, while the combine is working or in stationary position, for 24 hours.

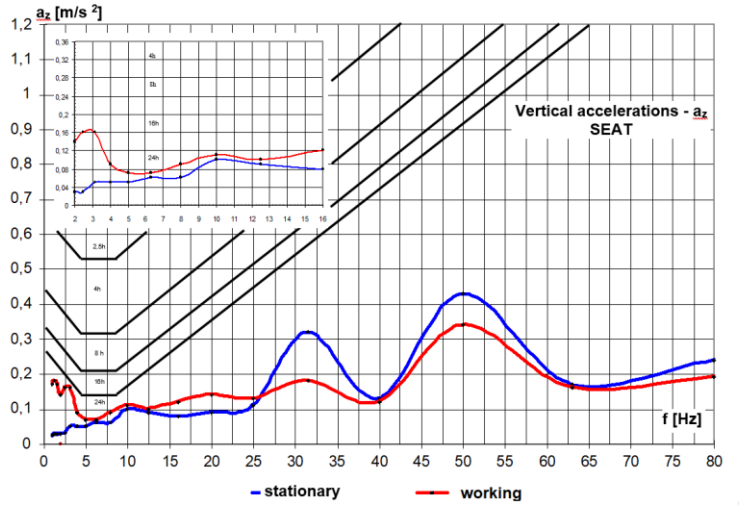

Fig.16 - Seat vertical accelerations, CASE-IH combine in stationary position and while working

CONCLUSIONS

The final value of the vibrations is represented by the value of the vibrations transmitted by the thresher, chassis, and header parts to the seat, because those vibrations directly affect the operator's health.

Following the graphs corresponding to the values of the accelerations on the nomograms, for the SEAT, it results:

- longitudinal accelerations maximum values– a_x (fig.14), were:
  - stationary: 0.42 m/s^2 at 50 Hz;
  - working: 0.47 m/s^2 at 50 Hz,
- transverse accelerations maximum values– a_y (fig.15), were:
  - stationary: 0.23 m/s^2 at 31.5 Hz;
  - working: 0.28 m/s^2 at 10 Hz,
- vertical accelerations maximum values– a_z (fig.16), were:
  - stationary: 1.10 m/s^2 at 40 Hz;
  - working: 0.34 m/s^2 at 50 Hz.

From the nomograms and measurements, it results that for the CASE-IH combine it is possible to work without issues for over 24 hours, continuously, without the vibrations affecting the health of the operator.

ACKNOWLEDGMENT

This work was supported by a grant of the Romanian Research and Innovation Ministry, through Programme 1 – Development of the national research-development system, sub-programme 1.2 – Institutional performance – Projects for financing excellence in RDI, contract no. 1 PFE / 2021

REFERENCES

[1] Benos L., Tsaopoulos D., Bochtis D. (2020). A Review on Ergonomics in Agriculture. Part II: Mechanized Operations, *Applied Sciences,* vol.10

[2] Brăcăcescu C., Vlăduţ V., Sorică E., Popescu S., Sorică C., (2017). Considerations regarding vibrating platforms electromagnetically driven. *Proceedings of the XIV-th International Conference „Acoustics and vibration of mechanical structures* , pp. 271-278, Timişoara/Romania

[3] Goglia V., Gospodaric Z., Filipovic D., Djukic I. (2006*).* Influence on operator's health of hand-transmitted vibrations from handles of a single-axle tractor, *The Annals of Agricultural and Environmental Medicine,* Vol.13, No.1, pp. 33–38

[4] Hamed A.R. (2016), Whole Body Vibration Exposure During Operation of Rice Combine Harvester under Egyptian Field Conditions, *Journal of Soil Sciences and Agricultural Engineering*, Vol. 7, No.12, pp.961–971, Mansoura University, Egypt

[5] Jens Trampe Broch (1980), *Mechanical vibration and shock measurements,* Vol.2*,* Bruel&Kjae, ISBN-10: 8787355361

[6] Jens Trampe Broch (1984), *Mechanical Vibration and Shock Measurements*, K. Larsen & Son A/S, vol.2, Denmark

[7] Kim J.H., Dennerlein J.T., Johnson P.W. (2018). The effect of a multi-axis suspension on whole body vibration exposures and physical stress in the neck and low back in agricultural tractor applications, *Applied ergonomics*, Vol.68, pp.80-89

[8] Liang X.C., Chen J., Wang Z. (2018). Research on the vibration of mini tiller, *INMATEH-Agricultural Engineering,* Vol.56, No.3, pp.17-24

[9] Luboš S., Václav M. (2022). Whole Body Vibrations during Fully Mechanised Logging, *Forests*, Vol.13, No.4, pp. 630

[10] Matache M.G., Munteanu M., Dumitru D.N., Epure M. (2020). Evaluation of hand transmitted chainsaw vibrations during wood cutting, *TE-RE-RD 2020, E3S Web of Conferences,* Vol*.* 180

[11] Rahmatalla S., DeShaw J. (2011). Effective seat-to-head transmissibility in whole-body vibration: Effects of posture and arm position, *Journal of Sound and Vibration – Elsevier*

[12] Sorică E., Vlăduţ V., Cârdei P., Sorică C., Brăcăcescu C. (2017). Comparative analysis of the noise and vibration transmitted to the operator by a brush cutter, *Proceedings of the XIV-th International Conference „Acoustics and vibration of mechanical structures"*, Springer Proceedings in Physics, pp.165-172

[13] Szczepaniak J., Tanas W., Kromulski J. (2014). Vibration energy absorption in the whole-body system of a tractor operator, *Annals of Agricultural and Environmental Medicine*, vol.21, No.2, pp. 399-402

[14] Vlăduţ V., Biris S.S., Bungescu T., Herişanu N. (2013*), Influence of Vibrations on Grain Harvesters Operator." Applied Mechanics and Materials*, Vol. 430, Trans Tech Publications Ltd, pp.290-296

[15] Vlăduţ V., Biris S.S., Petre A.A., Voicea I., Cujbescu D., Ungureanu N., Matei GH., Popa D., Boruz S., Constantin A-M., Vasile C. (2021*),* Comparative study of vibrations in apparatus combinations tangential threshing, *Annals of the University of Craiova - Agriculture, Montanology, Cadastre Series,* Vol. 51, No.2, pp.615-627

[16] Vlăduţ V., Pirnă I., Florea C., Popescu C., Brătucu Gh., Kabas O., Păunescu D. (2014). Influence of the vibration amplitude on the quality of shredded medicinal vegetal material subjected to sorting, *Proceedings of the 42 international symposium on agricultural engineering "Actual Tasks on Agricultural Engineering",* pp. 273-282, Opatija - Croaţia

[17] Yung M., Tennant LM., Milosavljevic S., Trask C. (2018). The Multisystem Effects of Simulated Agricultural Whole Body Vibration on Acute Sensorimotor, Physical, and Cognitive Performance, *Annals of Work Exposures and Health*, Vol.62, No.7, pp. 884–898

EXPERIMENTAL RESEARCH REGARDING THE ACHIEVEMENT OF AN EQUIPMENT DESIGNED FOR CHOPPING WOODY WASTE

/

CERCETĂRI EXPERIMENTALE PRIVIND REALIZAREA UNUI ECHIPAMENT DESTINAT TOCĂRII RESTURILOR VEGETALE LEMNOASE

Lucretia POPA[1*)], Viktor TROKHANIAK[2*)], Ana-Maria CONSTANTIN[1)], Ciprian MIRON[1)], Ana ZAICA[1)], Cătălin PERSU[1)], Augustina PRUTEANU[1)], Ana Maria NICOLAU[3)]

[1)]National Institute of Research, Development for Machines and Installations Designed for Agriculture and Food Industry – INMA Bucharest / Romania; [2)]National University of Life and Environmental Sciences of Ukraine, Kyiv, Ukraine

[3)] POLITEHNICA University of Bucharest / Romania

E-mail: lucretia_popa@yahoo.com;

DOI: https://doi.org/10.35633/inmateh-68-75

Keywords: *tree branch chopper, chopping process, power consumption, fuel material, wood waste*

ABSTRACT

This article presents the results obtained through experimental research carried out with a machine for shredding woody plant residues (twigs, vine ropes), residues obtained from dry or green cuttings, in fruit or wine plantations. The obtained shredding is intended for utilization in the form of compost or biofuel (pellet type). The machine was designed and made by a group of researchers from INMA Bucharest, with the aim of developing the machine system made available to farmers, for mechanized work in small and medium-sized fruit plantations. The sizes of the fractions of the wood fragments resulting from the chopping process, their humidity and volumetric weight were determined. Using as raw material greener or drier branches, with dimensions between 10-45 mm, with an adjustment of the chopping drum at an average speed of 1400 rpm and an average speed of the conveyor chain of 0.425 m/s, wood chips with different sizes between 4-16 mm were obtained, the proportions varying from 13% to 16%. The average working capacity of the equipment was approx. 14.2 mc/h. Research will continue to determine the energy indices of the machine designed and made at INMA Bucharest, and the results will be presented in another article.

REZUMAT

Acest articol prezintă rezultatele obţinute în cadrul unor cercetări experimentale efectuate cu o maşina de tocat resturi vegetale lemnoase (crengi, coarde de viţă de vie), resturi obţinute din tăierile în uscat sau în verde, în plantațiile pomicole sau viticole. Tocătura obținută este destinată valorificării sub formă de compost sau biocombustibil (de tip peleţi). Maşina a fost proiectată şi realizată de către un grup de cercetători din INMA București, cu scopul dezvoltării sistemei de mașini pusă la dispoziția fermierilor, pentru efectuarea de lucrări mecanizate în plantațiile pomicole de dimensiuni mici şi mijlocii. Au fost determinate dimensiunile fractiilor lemnoase rezultate în urma procesului de tocare, umiditatea acestora şi masa volumică. Utilizând ca materie primă crengi mai verzi sau mai uscate, cu dimensiuni cuprinse între 10-45 mm, cu un reglaj al tamburului de tocare la o turație medie a de 1400 rot/min şi la o viteza medie de avans a benzii transportoare de cca.0.425 m/s, s-a obținut o tocătură lemnoasă cu diferite dimensiuni cuprinse între 4 şi 16 mm, proporțiile variind de la 13% la 16%. Capacitatea medie de lucru a echipamentului a fost de cca.14.2 mc/h. Cercetările vor continu pentru a determina indicii energetici ai maşinii proiectată şi realizata la INMA Bucureşti, iar rezultatele vor fi prezentate într-un alt articol.

INTRODUCTION

On a global level, as mentioned in the Green Deal pact, there are preoccupations for the recovery of waste in order to reduce pollution, to maintain a green planet, to reduce the carbon footprint and to reach in 2050 the target of 0 (zero) polluting emissions. Reducing energy consumption is another objective for which in-depth research is being done, in order to use renewable energy sources instead of conventional ones, which have been used indiscriminately and which can be exhausted, so the planet and the entire humanity would suffer. For these reasons, research is being carried out in all areas that could bring a favourable contribution to the fulfilment of these objectives (*Jasinskas et al, 2017*; *Kopac et al, 2003; Caba, 2019)*.

[1] *Lucretia Popa, Ph.D.Eng.; Viktor Trokhaniak, Ph.D.Eng., Assoc.Prof., Ana-Maria Constantin, Ph.D Stud.Eng.; Ciprian Miron, Eng., Ana Zaica, Eng.; Cătălin Persu, PhD.Stud.Eng; Augustina Pruteanu, PhD.Eng.; Ana-Maria Nicolau, PhD.Eng*

Biomasses from agriculture could be used as a dry fuel, when harvested at maturity with about 85% dry matter by baling or chopping, or as a humid fuel with up to 60% dry matter, when harvested before maturity with a chopper, conserved by ensiling and mechanical dehydration before thermic use. To characterize both fuels from different crops chopped with a theoretical cutting length of 4 mm, particle-size-distribution, bulk density and an apparent density as well as nutrient contents and ash fusibility are determined. Wood chips (10 and 20 mm cutting length) have been investigated by *Stulpnagel, (1998)*.

Every year, in orchard plantations or in vineyards, pruning branches in autumn or spring, can offer biomass which can be chopped using special machines. To be profitable, these machines must have high-performances, in order to obtain wood chips at a low cost.

Chopped woody residues can be used to obtain compost or pellets. Pellets are a source of alternative energy and can be obtained from agricultural and forestry materials such as: sawdust, branches, scraps of boards or other wooden scraps, leaves, straw, sunflower or corn stalks, soybeans, etc. The pellet production line also includes biomass chopping or shredding equipment (*Mady, 2015*). The importance of using pellets has determined the performance of numerous researches both on how to obtain them and on the benefits of using them. In the last period, wood pellets are increasingly used, because they are a less polluting source of energy, having less greenhouse gas emissions, and also a renewable fuel, replacing fossil fuels (*Jasinskas et al., 2017; Nedelcu A., 2020; Supin, 2015; Gageanu, 2019)*.

Hamzah et al., (2017), analysed the wood pellets and torrefied wood pellets (named black pellets) as compared to coal and the conclusion was that torrefaction improves the fuel properties of wood pellet similar to coal. Torrefied biomass is more brittle than raw biomass and has a higher carbon content.

Compost is considered one of the best natural and organic fertilizers, obtained by decomposing plant biomass, and chopped branches can also be part of its composition (*Ciuperca et al., 2022; Lixandru et al., 2021; Stefan et al, 2020; Stefan et al, 2021)*

Some researchers have carried out experimental research of a chopper equipment for shredding residual wood branches, in order to improve its technical and technological performance. For this purpose, they implemented sensors and transducers on the equipment to record the evolution of the mechanical and hydraulic parameters. (*Cristescu et al., 2021)*.

Researchers from Poland have developed and tested an innovative system for controlling the variable feeding of equipment for chopping woody plant residues with low power engine. Fuel consumption in the case of the pilot system equipped with an adaptive feeding system was optimized, compared to the constant feeding system. The favourable effects of the tested systems have been demonstrated *(Warguła Łukasz et al, 2022). Wargula et al., (2018),* designed and realized a research stand that allowed both the analysis of the constructive and functional characteristics of the chopper, as well as the evaluation of the wood chopping process. The research carried out by this research team was valuable because it brought important information regarding the factors and their influence on the wood chips shape produced after chopping, as well as the influence on the energy consumption used in the chopping process. Important conclusions could be drawn that lead to the improvement of the work process of this equipment, taking into account that it is influenced by the orthotropic properties of the chopped material, which has an inhomogeneous structure.

Lyashenko et al., (2022), tested a wood branch chopper under specific conditions and obtained certain results that made it possible to provide instructions for its operation as well as its adaptation to the conditions of small plantations in individual fruit orchard.

Taking into account the importance of research in order to diversify and improve machinery for chopping wood waste, especially branches, researchers from INMA Bucharest have proposed a technology and equipment, the use of which will lead to obtaining wood chips, a technology that will contribute to reducing pollution environment and use wood chips as an organic fertilizer or mulch.

The main objectives of this research are: to justify the technology of using tree branch waste; to choose the optimal working parameters for the developed chipper, which is used in the technological process of chopping tree branches and to analyze the effect of the forward speed of the conveyor and the rotation speed of the chopping rotor on the size of wood chips.

MATERIALS AND METHODS

The research carried out had as preliminary stages the analysis of the state of the art worldwide, followed by the design and realization of the experimental model for the equipment designed to chopp wood tree branches, acronym TRL (*Popa et al, 2022a; Popa at al, 2022b)*.

The existing research infrastructure within the Research-Development-Innovation laboratories, the Execution Section and the Testing Department was used for the realization and the execution of the project, as well as for the experiments (https://www.erris.gov.ro/System-of-designing-execution-and-optimising-the-technical-equipment-and-technologies; https://www.erris.gov.ro/research-infrastructure-for-agriculture-forestry-and-food-industry). The design was carried out using SolidWorks, 3D design software, which made it possible to obtain the 2D execution documentation and manufacture the experimental model within the execution department of the research institute. Using this software the time for development was reduced, and the quality of the final product was higher. Tests under real working conditions, by simulation of the working process have been done. 3D Solidworks ensure product quality while reducing prototyping and physical testing costs. The main assemblies of the machine are presented in figure 1.

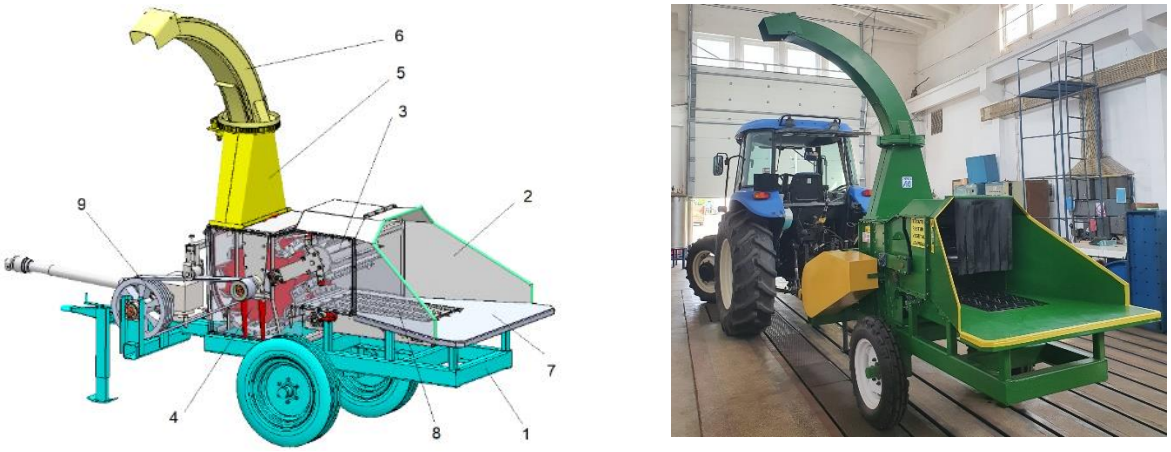

a) Machine Design b) Experimental model

Fig. 1 - Technical equipment for wood waste chopping

1 – infrastructure; 2 – assembled housing; 3 – wood drive drum; 4 – chopping drum; 5 – intermediate section; 6 – material discharge basket; 7 – loading platform; 8 – conveyor chain; 9 – mechanical transmission; 10 – hydraulic transmission (Source: Popa et al., 2022b)

The equipment consists of welded assemblies and elements in series production (gear motor, transmission chains, bearings, wheels, hydraulic cylinders, hydraulic components, removable fasteners: screws, nuts, washers, Grower flat washers and so on). The “core” of the equipment is the chopping drum, which is different from the constructive solutions currently in production. The knives are disposed staggered, to improve the cutting process. The knives are made by a special steel, HARDOX 500, characterized by very good resistance to shocks and deformations.

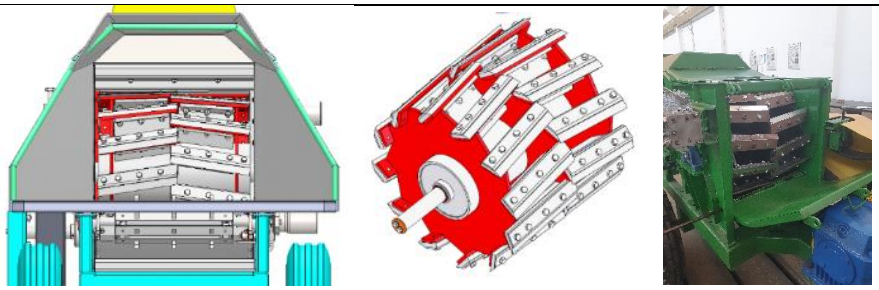

Fig. 2 - Chopping drum with staggered knives

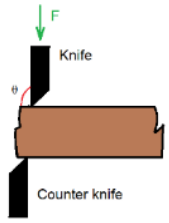

Fig. 3 - Chopping process

The chopper is also equipped with a counter-knife, realized by the same special steel. Together they work like scissors, under the acting force and inertia force. The cutting of the branches is done transversely, the size of the chips depending on the speed of the scraper conveyor, of the type with scrapers arranged on chains with special sprockets.

Before the experiments, the machine was put into operation empty, so that the preliminary adjustments could be made. Experimental research was carried out in November 2022, on the research platform in the INMA enclosure. The purpose of the research was the analysis of the degree of shredding of chopped branches, at certain functional parameters of the machine. The resistant moment was also registered, when the machine worked without load and under load.

To register the resistent effort at the chopping drum, a data acquisition system type MGCplus – HBM (Hottinger-Baldwin-Messtechnik)(Fig.4a) was used. A moment transducer type T 4WA -S3 (Fig.4b), a connecting system interface (Fig.4c), an acquired data setup interface (fig.4d) and a softwere CatmanEasy for data acquisition were used.

c)

d)

c)

d)

Fig. 4 – Data acquisition system

Rotational speeds of the feed drum and of the chopper drum have been measured using a digital tachometer (Fig.5), which allows the operator to make revolutions per minute (RPM's) and speed (m/min) measurements. It offers a high accuracy (0.005%) up to 1 m distance (without contact).

A vibratory sieve shaker AS 200 Basic was used to separate the material into fractions (Fig.6). (*https://www.retsch.com/products/sieving/sieve-shakers/as-200-tap/*). Each vibratory sieve shaker of the series AS 200 is equipped with an electromagnetic drive that is patented by RETSCH (EP 0642844). This drive produces a 3D throwing motion that moves the product to be sieved equally over the whole sieving surface.

The advantage: high stress capacity, extremely smooth operation and short sieving times with high separation efficiency. The moisture and volumicetric weight were also analysed, using a Moisture Analyzer, MB120 AM (*https://us.ohaus.com/en-US/Products/Balances-Scales/Moisture-Analyzers/MB45/Moisture-Analyzer-MB45-AM*) (Fig.7)

Fig. 5 – Digital tachometer

Fig. 6 – Vibratory sieve shaker AS 200 Basic

Fig. 7 – Moisture analyzer

Volumetric weight (ρ_v) is a property of vegetable materials, in the form of chopped or ground, which defines the weight of fragments (m_f) of chopped plants related to the whole volume they occupy (relation 1). The total volume (V_t) occupied consists of the volume of the fragments and the volume of the voids between the fragments.

$$\rho_v = \frac{m_f}{V_t} \quad [kg/m^3] \qquad (1)$$

RESULTS AND DISCUSSIONS

The experiments were performed using branches obtained from trees, green and dry branches, having dimensions between 10-45 mm (Fig.8a,b,c).

a)

b) c)

Fig. 8 – The woody plant material used for experiments

Feeding drum rotational speed was measured and noted, as it can be seen in Fig.9. The rotational speed was also measured for the drum chopper. Feeding drum has been set using the hydraulic distributor and also a hydraulic drossel, and the quantity of chopped wood material was collected on a tarp and weighted.

The tests have been repeated for 3 speeds of the conveyor chain that supplies the shredder with wood branches, (0.425; 0.375; and 0.325 m/s), to check the behaviour of the shredder and the machine productivity.

Fig. 9 – Aspects during the work parameters recording

After the chopping process was finished, the chopped wood material was collected and the sizes of the chopped fractions, the volumetric weight of the material collected by dimensional fractions were determined and then the percentage of each dimensional fraction was calculated. The moisture content was determined. Three samples of 1500 g each, collected randomly, were analysed, precisely to ensure accuracy in the processing and interpretation of the results obtained from the experimental tests, and the data thus obtained were tabulated and graphically represented.

Fig. 10 – Aspects regarding the collected chopped material and its analysis

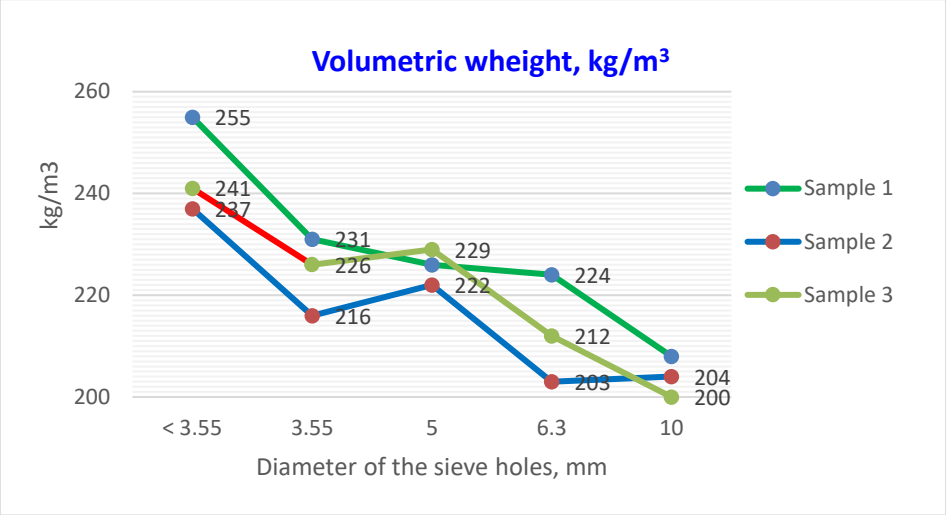

Fig. 12 – Volumetric weight for three samples

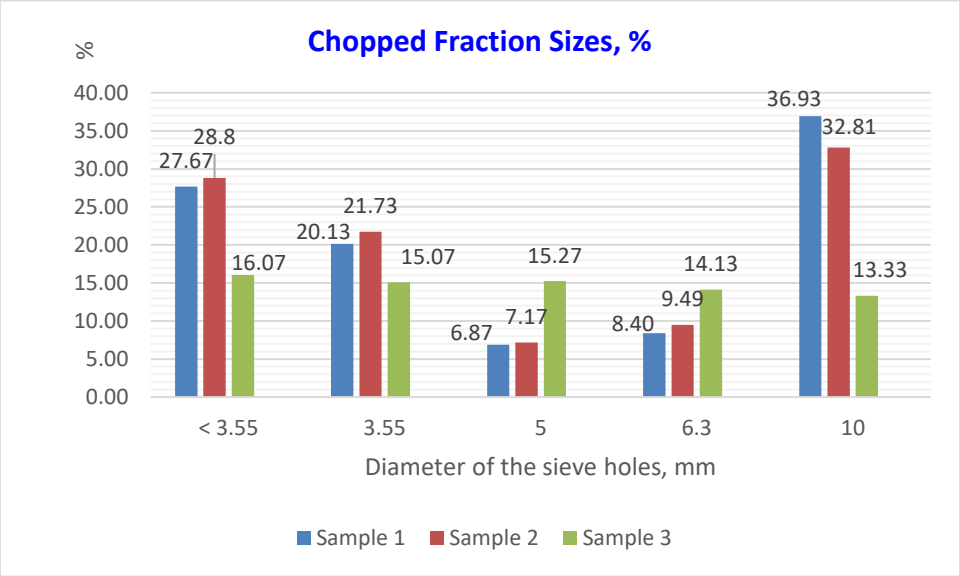

a) For each sample

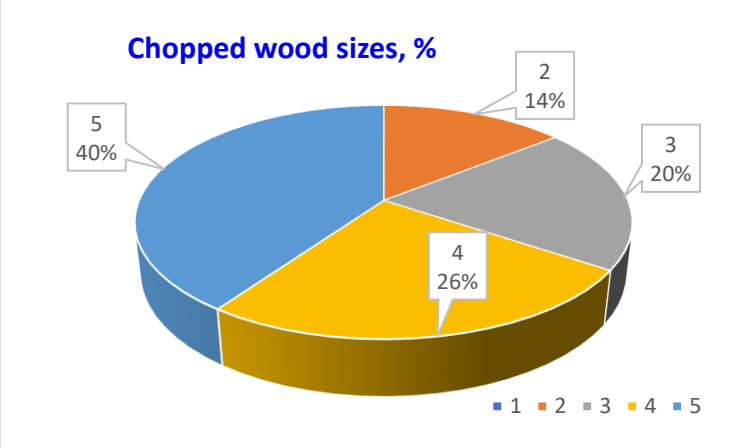

b) Average of the three samples

Fig. 13 – Chopped wood fraction sizes, %

1 – Rejection < 3.55 mm; 2 – Ø3.55 sieve holes; 3— Ø5 sieve holes; 4 – Ø6.3 sieve holes; 5 - Ø10 sieve holes

The moisture content for each chopped wood fraction was determined and the results are presented in the following graphs.

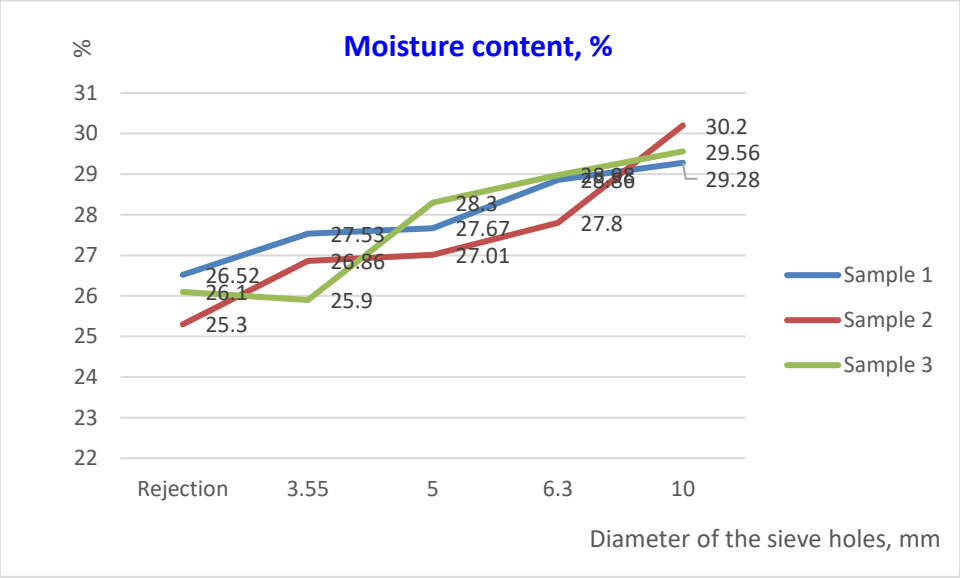

Fig. 14 – Moisture content for chopped wood fraction, %

Chopping drum is acted by a mechanical transmission, where the movement is taken from the tractor's power take-off shaft, through a cardan, then transmitted through a conical group to a belt transmission, whose multiplication ratio is i=3.2, and finally multiplying the rotational speed of the chopper.

The rotational speed of the chopping drum can be variable, depending on the nominal speed of the tractor engine. During these experiments, with the help of the equipment described in the previous chapter, the moment resistant to the chopping rotor was recorded for 4 nominal revolutions of the tractor engine (500 rpm; 900 rpm; 125 rpm and 1500 rpm). The determinations were made when the equipment works unloaded, and the research will be continued with the recording of the resistant moment when the equipment is loaded. The results are presented in the following graphs.

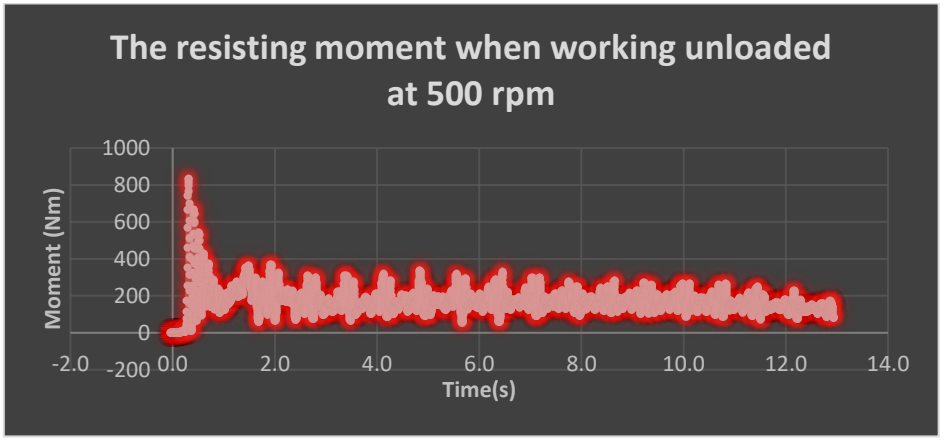

a)

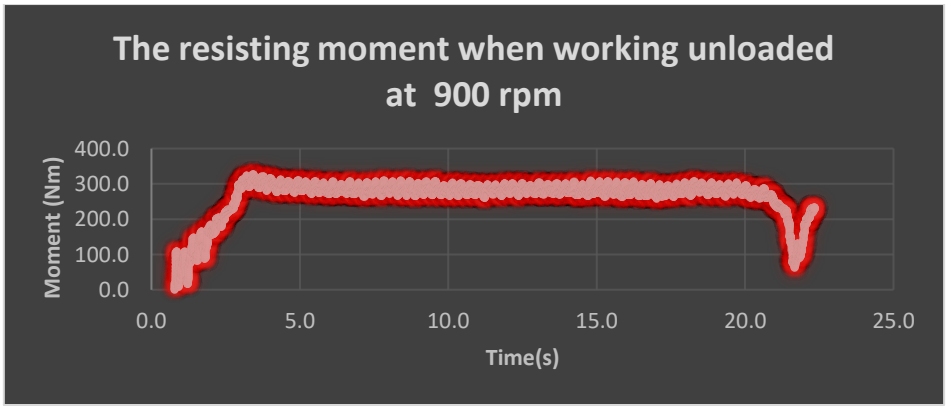

b)

c)

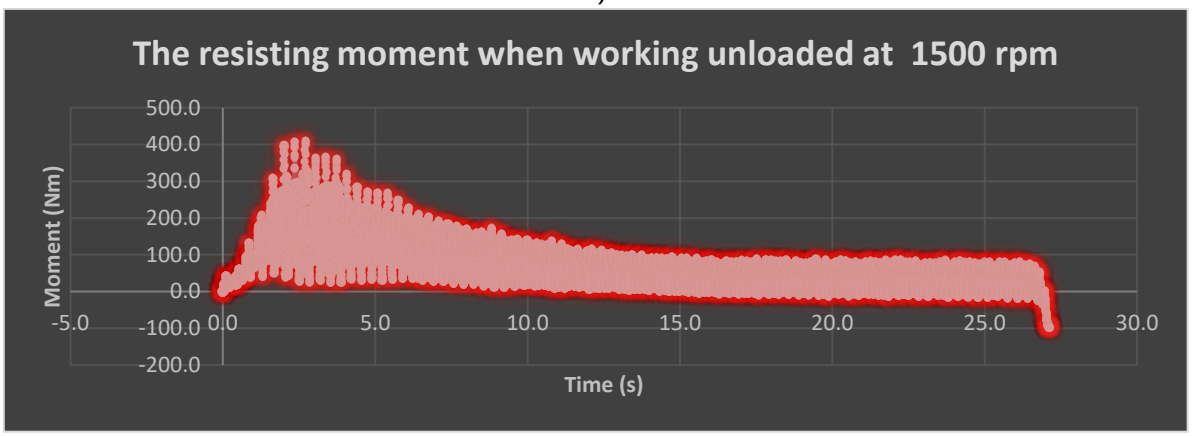

d)

Fig. 15 – Resisting moment when working unloaded

Taking into consideration the experiments performed, a working average capacity was obtained, the values being as in Table 1.

Table 1

Working capacity of the equipment TRL-0

	Measure unit	Sample 1	Sample 2	Sample 3	**Average**
Working capacity	m^3/h	14.2	14.1	14.3	**14.2**

CONCLUSIONS

Not all chopping equipment provide good results if they are used in different conditions and using different wood residues and not all chopping machines are suitable for use on different plantations. It depends on the wood characteristics (moisture content, stress resistance, branch dimensions etc.).

Productivity depends a lot on the shape of the branches, the processed material not being homogeneous. The experiments performed did not aim at determining the performance characteristics of the car, but its functionality.

Research has shown that the machine produces wood chips with dimensions between 4 and 16 mm, those collected on sieves with a hole diameter of 3.55 mm as well as those collected on a sieve with a hole diameter of 10 mm being in a larger proportion than the other two.

The measurement of the moment resistant to the chopping rotor when working unloaded cannot measure the required power, for the optimization of the energy source in the aggregate, respectively the tractor engine power, but these data were collected to see the magnitude of the moment of inertia at start-up and the required surplus power for putting the machine into operation, in case of overload.

Other energetic and performance parameters of the machine will be carried out in a later stage of the research, when in-depth research will be undertaken, using several species of wood, and several variables will be set to different values (advance speed of the conveyor belt, rotation of the chopping rotor)

It is necessary to conclude that appropriate adjustments of the working parts of the machine can lead to obtaining the desired performances.

The productivity depends on the wood physical characteristics which also determines the resistance to cutting and can vary greatly. The moisture contend influences the cutting resistance. The drier the material is, the higher the cutting resistance. In this experiments poplar was used, which is relatively light in weight, has good strength in both tension and compression and provides rigidity, toughness and insulating properties.

ACKNOWLEDGEMENTS

This research was funded by the Romanian Research, Innovation and Digitalization Ministry - MCDI, within the National Research-Development Programme, subprogramme 1.2 – Institutional Performance – Projects for financing excellence in RDI, contract no. 16PFE and Project: PN 19 10 01 05 - Integrated management of work in farms, vineyards and orchards, contract no. 5 / 07.02.2019.

REFERENCES

[1] Caba, I.L.; Laza, E.A.; Constantinescu, M.; Radu, O.D.; Boiu-Sicuia, O.A.; Popescu, C. (2019). Experimental research on the knife blades used to cutting and shredding fibrous fodder. *INMATEH – Agricultural Engineering,* Vol.59 (3), pp.263-276, Bucharest / Romania

[2] Ciupercă R., Constantin A.M., Zaica A., Ştefan V. (2022). Recovery of solar thermal energy and energy from the composting process. *INMATEH Agricultural Engineering,* Vol.68 (3), pp.896-906. 10.35633/inmateh-68-89

[3] Cristescu, C.; Drumea, P.; Dumitrescu, C.; Matache, G. (2012). Experimental testing to measure operational performances of a chopper equipment used for recycling waste wood. 12th International Multidisciplinary Scientific Geoconference, SGEM 2012, Vol. IV, pp.701-708. Bulgaria

[4] Găgeanu, I.; Cârdei, P.; Matache, M.; Voicu, Gh. (2019). Researches on the statistical modelling of the processes of pelleting biomass, testing classic powder compaction models. *INMATEH Agricultural Engineering*, Vol.59 (3), pp.119-124, Bucharest / Romania.

[5] Hamzah, N., Zandi, M., Tokimatsu, K., Yoshikawa, K. (2017). Woody biomass characterization for 100 MegaWatt-hours (MW) power generation. *8th International Conference on Applied Energy (ICAE).* Vol.105, pp.413-418. 10.1016/j.egypro.2017.03.334

[6] Kopac, J.; Sali, S.; (2003). Wood: an important material in manufacturing technology. *Journal of materials processing technology.* Vol.133. pp.134-143

[7] Jasinskas, A.; Kucinskas, V.; Jotautiene, E.; Ziemelis, I. (2017). Assessment of wild cherry (*Prunus avium l.*) chopping and utilization for biofuel and investigation of chaff properties. *16th International Scientific Conference: Engineering for Rural Development*. pp.641-646. 10.22616/ERDev2017.16.N127.

[8] Lixandru M., Fendrihan S., Ştefan V. (2021). Correlation between fertilization, carbohydrate content and frost resistance of vineyards (Corelația dintre fertilizare, conținutul de carbohidrati și rezistența la înghet, la cultura de vita de vie), *Proceedings of ISB-INMATEH 2021*, pp.48-53

[9] Lyashenko, S.; Gorbenko, O.; Kelemesh, A.; Kalinichenko, A.; Stebila, J.; Patyka, V.; (2022). Non-Waste Technology for Utilization of Tree Branches. *Applied Sciences-Basel-MDPI*. Vol.12, Issue 17, Art.no.8871. Poland. 10.3390/app12178871

[10] Mady M.A., Abdel-Hadi M.A., Abd-Allah Y.E., Ali M.F. (2015). A study on some engineering parameters of cutting and chopping machine for agricultural wastes. *Misr J. Ag. Eng*., 32 (4): 1775-1800

[11] Nedelcu A., Ciuperca R., Zaica A., Stefan V., (2020). Influence of forage harvester chopping equipment on characteristics of chips, *Engineering for Rural Development*. Jelgava, 20-22 May 2020, pp.1319-1324, 10.22616/ERDev.2020.19.TF330

[12] Popa, L., Constantin A.M.; Miron I.C.; Stefan V. (2022a). The current stage of the construction of technical equipment for chopping woody plant residues. A review. *Proceeding of International Symposium ISB-INMA-THE'2022*, pp.12-17, Bucharest/ Romania

[13] Popa, L.; Ciupercă, R.; Ştefan, V.; Constantin A.M.; Miron, C.; Zaica, A. (2022b). Integrated technology and technical equipment for chopping vegetable residues resulting from trimming in orchards/vineyards. *Fruit Growing Research*, Vol. XXXVIII, 2022. pp.84-89

[14] Saracoglu, N.; Gunduz, G.; (2009). Wood Pellets-Tomorrow's Fuel for Europe. *Wood Pellets—Tomorrow's Fuel for Europe*. pp.1708-1718. 10.1080/15567030802459677

[15] Stulpnagel, R. (1998). Investigations for a physical and chemical description of different biomasses for energy. *Biomass for energy and industry*. pp.831-834

[16] Supin, M. (2015). Wood pellet global market development. *Wood processing and furniture manufacturing challenges on the world market and wood-based energy goes global.* pp.255-260

[17] Ştefan V., David L., Ciuperca R., Zaica A., Nedelcu A., Suvac A., (2020). Experimental testing of a helical drum for compost distribution, *9th International Conference on Thermal Equipment, Renewable Energy and Rural Development*, *TE-RE-RD*, 2020, Volume 180, Art.03027. doi: 10.1051/e3sconf/202018003027

[18] Ştefan V., Zaica A., Adrian Iosif. (2021). Research on the uniformity degree of solid organic fertilizers distribution, *INMATEH - Agricultural Engineering*, vol.65, no.3, pp.495-504

[19] Warguła Ł., Kukla M., Krawiec P. (2022). Directions of Development of adaptive systems to the operating conditions of mobile wood chopping machines with low power engines. *25th Polish-Slovak Scientific Conference on Machine Modelling and Simulations (MMS 2020). MATEC Web Conf.* Volume 357, Art. No.04002. Slovakia. https://doi.org/10.1051/matecconf/202235704002

[20] Wargula, L.; Adamiec, JM; Walus, KJ; Krawiec, P. (2018). The characteristics analysis of torque and rotation speed of working unit of branch grinder - introductory research. *MATEC Web of Conferences* 157, 01021. https://doi.org/10.1051/matecconf/201815701021

[21] https://www.erris.gov.ro/System-of-designing-execution-and-optimising-the-technical-equipment-and-technologies;

[22] https://www.erris.gov.ro/Research-infrastructure-for-agriculture-forestry-and-food-industry

TEACHING STRATEGIES AND STUDENTS' ACADEMIC PERFORMANCE IN AGRICULTURE STUDIES: THE MEDIATING EFFECT OF TEACHERS' SELF-EFFICACY
/
教学策略与农学学生学习成绩:教师自我效能的中介作用

Muddassar SARFRAZ [1], Nicolae-Valentin VLĂDUŢ [2], Lucian-Ionel CIOCA [3,4], Larisa IVASCU [*4,5]

[1] School of Management, Zhejiang Shuren University, Hangzhou / China

[2] National Institute of Research, Development for Machines and Installations Designed for Agriculture and Food Industry – INMA Bucharest / Romania

[3] Department of Industrial Engineering and Management, Faculty of Engineering, Lucian Blaga University of Sibiu, Sibiu / Romania

[4] Academy of Romanian Scientists, Bucharest / Romania

[*5] Department of Management, Faculty of Management in Production and Transportation, Politehnica University of Timisoara, Timisoara / Romania

Tel: 004-0744-263797 ; E-mail: larisa.ivascu@upt.ro

Corresponding authors: Larisa Ivascu

DOI: https://doi.org/10.35633/inmateh-68-76

Keywords: *Motivational Strategies; Instructional Strategies; Self-Efficacy; Student Academic; Performance, Blended Learning*

ABSTRACT

Recognizing the factors that stimulates the student's academic performance requires investigation of different learning strategies that influence teachers' self-efficacy. With the growing diversity of teaching methods, motivational and instructional strategies have gained significant attention, potentially leading educators to use them as the critical benchmark of superior student performance. The primary objective of this study was to analyze the impact of teaching strategies on the academic performance of the students, while considering the mediating role of teachers' self-efficacy. Data was collected from 260 students from different universities and colleges by using the convenience sampling method. The results of the study reveal that motivational and instructional strategies significantly affect the self-efficacy of teachers and the academic performance of students. Teacher self-efficacy mediates the relationship between instructional strategies, motivational strategies, and student academic performance.

摘要

要认识到激励学生学习成绩的影响因素就需要探究影响教师自我效能的不同学习方式。随着教学方法的日益多样化，动机和教学策略受到了极大的关注，可能导致教育学家将其作为优秀学生表现的关键基准。本研究的主要目的是在考虑教师自我效能的中介作用下，分析教学策略对学生学习成绩的影响。采用简单抽样的方法，对不同高校 260 名学生进行问卷调查。研究结果表明，动机与教学策略显著影响教师的自我效能与学生学习成绩。教师的自我效能在教学策略、动机策略和学生学业成绩之间起着中介作用。

INTRODUCTION

In the 21st century, the increase of globalization and the technological advancements have inevitably made education the center of global development. In the current modern period, intense digital changes have led novel academic knowledge to manifold educational borders, emphasizing the need to exhibit superior academic results. Significantly, increasing requirements have inspired the world's pedagogical institutions to respond by innovation, and to promote the academic performance of the students *(Seitzer & Windzio, 2022)*.

Today, the performance of the students has become the backbone of a global knowledge economy. In recent years, high educational competitiveness has meant students had to face considerable work stress *(Jayasankara Reddy et al., 2018)*, which impacted their academic performance. Researches show that this increasing phenomenon has overwhelmed the world's educationalists, who bear the burden of poor student performance *(Trigueros et al., 2020)*. Therefore, based on prior studies, it has become necessary for educationalists to identify the factors that foster the academic performance of the students in today's challenging environment.

In response to the increasing challenges of the 21st century, the academic performance of the students has gained the attention of researchers. Deterioration of student performance has made educationists to adopt

novel approaches to accelerate students' learning *(Abdullah & Bhatti, 2018)*. Previously, several factors have led students to face difficulty in understanding complex contents. However, today's researchers have identified various drivers that influence students' performance (e.g., teachers' efficacy, teaching skills, and student motivation) *(Abbasi et al., 2018)*. Surprisingly, among all the factors, teachers' self-belief plays a fundamental role in overcoming learning challenges, thereby reporting improved educational outcomes *(C. Choi et al., 2019)*. This highlighted role of teachers' self-efficacy raises important questions regarding the performance of the students. Accordingly, this study incorporates the fundamental concept of teachers' self-efficacy, which requires instructors' immediate response and attention.

The teachers' self-efficacy persistently helps students to overcome academic difficulties, and it makes teachers believe in their students' educational success *(Fong et al., 2019)*. Teacher's self-efficacy alludes to the instructors' belief in achieving fruitful learning outcomes *(Bandura, 1977)*. This high self-efficacy encourages teachers to enhance their students learning activities, substantially increasing their performance effectiveness *(Miller et al., 2017)*. Teachers' self-efficacy improves students' performance by adopting high-quality learning approaches. Teachers' inspired strategies are relevant for achieving learning goals (i.e., improved academic performance). Undoubtedly, instructors form the backbone of today's academic system and they play a key role in incorporating effective learning techniques, thus guiding the students in their learning process. Fundamentally, teaching is a far more difficult profession than it appears. Teachers may face difficulties in elevating students' interest in learning. Accordingly, previous research revealed that motivational practices critically enhance teachers' competence and students' academic performance *(Muwonge et al., 2019)*. Instructors adopt motivational strategies to nurture student motivation *(Barni et al., 2019)*. As such, motivational strategies potentially enhance the effectiveness of instructors' teaching and student performance *(Johnson, 2017).*

To shed light on the effectiveness of various strategies, instructional strategies have been identified as the most constructive development of the recent era. With the increase in technological advancement, today's students find it hard to regulate their learning process. As a result, teachers have introduced novel instructional programs and strategies, which help students to achieve their academic goals. Teachers' instructional strategies monitor, guide, and facilitate students' learning by positively influencing their academic performance. Moreover, instructional strategies equip students with the necessary learning competencies, assisting their academic progression. The previous knowledge demonstrates that instructional strategies are highly needed to develop specialized skills, influencing the students' learning performance *(de Boer et al., 2018)*. Indeed, instructional strategies improve students' understanding *(Obergriesser & Stoeger, 2020)*, stimulating positive learning outcomes.

Consequently, the current study analyzes different characteristics that influence teachers' efficiency and students' academic performance. Yet, this topic needs further investigation in the context of motivational and instructional factors *(Khanshan & Yousefi, 2020)*. Concerning the prevailing gap in research, this paper illustrates the effect of teachers' self-efficacy in ensuring the development of institutional strategies, significantly influencing students' academic performance *(Hettinger et al., 2021)*. Based on literature, it is imperative to investigate the role of teachers' self-efficacy in identifying students' needs to improve performance.

Decades of research have underscored the problem that prevented educationists from identifying the factors that strengthen the academic performance of students. However, identifying these factors enables teachers to address all the ambiguities concerning the performance of students. Potentially, achieving educational goals by using strategies leads to positive learning. Accordingly, this research overcomes the limitations in the previous literature by incorporating teachers' efficacy and student learning strategies in a single framework. This study objective is to highlight the factors that improve students' performance. Also, this study investigates the effect of motivational and instructional strategies on the academic performance of students in the context of teachers' self-efficacy. Understanding the impact of teachers' belief in producing positive educational outcomes is critically important for enhancing student performance. The current investigation addresses the literature gap by examining the mediating role of teachers' self-efficacy nexus to strategies (i.e., motivational and instructional) with students' academic performance.

Significantly, in the global educational system, educationists' direct teachers' attention toward achieving academic goals. A student's academic goals hold considerable value in promoting their academic performance. However, to achieve the learning objective, this study is a unique addition that highlights the factors that effectively contribute to student academic performance. It is noteworthy that prior studies have

considered this phenomenon using various constructs (e.g., student achievement, student satisfaction), but in this context, this study is a significant innovation that incorporates the student performance ideology from the perspective of teachers' self-efficacy. Teachers' self-beliefs inspire their strategic choices. This study highlights the teachers' self-efficacy as the directing tool for monitoring instructional and motivational practices. For this reason, this study is an important source to bridge the gap, ultimately leading to the achievement of superior learning outcomes.

Subsequently, the study findings serve as a meaningful guide for school authorities, administrators, educationists, researchers, and policymakers, thus advising them to embrace strategies to boost teachers' self-efficacy and student performance. The continuous use of learning strategies (i.e., motivational and instructional) significantly adds value to students' learning process. This study expects positive results to enhance educational activities. It makes educationists aware of the key strategies that may assist institutions in improving students' performance.

This study consists of six sections. The introduction highlights the research topic, objectives, and study significance. Then, the literature review empirically presents a theoretical framework for the proposed topic. After the hypothesis development in section 2, section 3 explains the research methodology. Similarly, section 4 demonstrates the analysis results, while section 5 illustrates the study findings concerning the previous literature. Lastly, section 6 concludes the study by suggesting future directions and outlining study limitations.

MATERIALS AND METHODS

Increasing globalization has made the world's institutes regard education as the focal point of global activities. In today's world, technological advancements have encouraged institutes to illuminate the need for novel strategies that influence students' performance. Accordingly, section 2 provides a brief overview of the concepts that direct students to achieve superior learning outcomes. Fundamentally, the literature review examines the relationships between different variables. It presents the conceptual definitions of the following terminologies: Motivational Strategies (MS), Student Academic Performance (SAP), Techers' Self-efficacy (TSE), and Instructional Strategies (IS). This section conceptually provides knowledge of these variables in a similar sequence.

Motivational Strategies and Student Academic Performance

Over the years, the wide acceptance of technology has resulted in the development of the education system, requiring teachers to adopt interactive teaching methods. Today, education has become more than just the learning process, as student academic performance has elevated the concern of educationists. In emerging economies, teachers have adopted different techniques to enhance students' learning process. The literature shows that motivational strategies are vital in nurturing students' academic performance *(Lawrence & Hanitha, 2017).*

Therefore, in fostering learning activity, today's education system demands the need for innovative methods, materials, and strategies to boost the learning process. The motivational strategies encourage students to rigorously accomplish their academic goals in the learning activity. Literature shows that motivational strategies help students gain mastery in their learning *(Bal-Taştan et al., 2018)*, potentially influencing the academic performance of the students. In particular, students' goal orientation is an essential construct that predicts student motivation. When a student aims to outperform others, motivational strategies help them gain mastery over challenging tasks. The motivational strategies work as the value belief that leads the students to achieve academic success. In explaining this notion, recent evidence shows that motivational strategies accelerate students' academic success *(Almalki, 2019)*. Teachers' motivational strategies inspire the students to gain mastery over their goals, thus significantly improving their academic performance.

Undoubtedly, a student's motivation is a constant factor in individual academic achievement. Students with high motivation perform well in their studies. The teachers' counseling and guidance boost students' motivation, improving their academic performance. In explaining this notion, one study states that in student learning, motivational strategies significantly predict the student's positive academic results (e.g., performance and achievement) *(Hariri et al., 2021)*. Motivational strategies inspire students to improve their academic performance *(Sivrikaya, 2019)*.

Motivation is an essential element that enables students to sustain themselves in the fast-growing learning environment. However, in this regard, teachers play a significant role in establishing an environment where students are motivated to learn. Indeed, teachers adopt different methods to inspire their students. The teachers' motivational orientation emphasizes adopting strategies that support student learning.

The learning strategies adopted by teachers intrinsically boost students' goals, motivation, and academic performance *(Kokkinos & Voulgaridou, 2018)*. Hence, based on the literature, this paper suggests the following hypothesis:

H1: Motivational Strategies positively and significantly impact student academic performance.

Motivational Strategies and Teacher Self-Efficacy

Significantly, in recent years, various scholars have increasingly directed the pedagogue's attention towards the role of teachers' self-efficacy. This particular focus involves teachers adopting different motivational approaches for structuring the students' learning activities. As pedagogical activities demand superior academic results, higher education has raised the need for adopting novel teaching strategies to enhance the students' learning process. However, today's educationist has prioritized teachers' self-efficacy to increase the effectiveness of the learning strategies. The studies supporting this notion state that increasing self-confidence motivates teachers to direct their teaching process by adopting constructive approaches *(Barni et al., 2019)*. Teachers' self-efficacy drives the educational goals by effectively handling the learning activities. The study states that teachers' motivational perception induces their self-belief in teaching materials, thus forming a significant relationship between teachers' self-efficacy and motivational strategies *(Alexander, 2020)*.

An active learning classroom demands the active participation of the students and the instructor. However, today, many students find it difficult to motivate themselves. In such situations, motivational strategies creating an active learning environment drive the teachers' self-beliefs to assist the students' learning *(Heyder et al., 2020)*. The motivational strategies boost the teachers' confidence. One study states that teachers' self-efficacy is the salient motivational feature that elevates their beliefs in the teaching method *(Burić & Kim, 2019)*. In particular, teachers are individuals who are responsible for regulating the classroom environment. In the classroom setting, teachers' self-efficacy elevates the need for adopting motivational teaching behaviors to improve the students' learning outcomes. The teachers' self-efficacy is the most adopted motivational characteristic that accelerates students' motivation. This educator's perception motivates the students to elevate their performance in different coursework. It stabilizes the student education programs that make learning meaningful *(Burić & Kim, 2019)*.

Consequently, teachers need to adopt different motivational strategies to boost their confidence in teaching methods. The literature confirming this notion undoubtedly theorizes a positive relationship between motivational strategies and teachers' self-efficacy. This paper thereby suggests the following hypothesis:

H2: Motivational Strategies have a positive and significant impact on teacher self-efficacy.

Instructional Strategies and Student Academic Performance

Instructional strategies are the form of procedural knowledge that guides the students in their learning process. It is a profound method of synthesizing knowledge, thus achieving the learning goals. The instructional strategies enable the students to become active learners. Students need guidance in planning their academic activities. In particular, the teachers' designed instructional strategies enhance the individuals' learning experience. In explaining this notion, one study states that the instructional strategies improve the students' performance, thereby leading to them recording a high score in their course evaluation *(Chutinan et al., 2018)*.

Significantly, the instructional strategies help the students to improve their learning outcomes. The learning tactics enhance the performance by profoundly improving the quality of the students' education. One study explains that the instructional strategies foster the students' pedagogical skills, thus enhancing the students learning performance *(Matcha et al., 2019)*. In particular, the instructional strategies greatly emphasize the individuals' quality of teaching. Effective learning strategies nurture the students' learning process, thus contributing to their professional development. The literature implies that the teaching strategies support the individual's learning process, thus improving the students' academic performance *(Inyang, 2019)*.

Indeed, the instructional strategies yield the highest impact on students' learning. The instructional strategies are a good way of structuring the students' learning experience *(Cheng et al., 2019)*. The instructional method inevitably improves the students' competency by prescribing students with the best procedure to complete the work task. One study indicates that teachers use instructional strategies to address the students' difficulties concerning their work tasks (*Timothy et al., 2018*). Indeed, these studies conclude that strategy instructions significantly affect the student learning process. Therefore, this study proposes the following hypothesis:

H3: Instructional strategies positively and significantly impact student academic performance.

Instructional Strategies and Teacher Self-Efficacy

Today's education demands adopting strategies for achieving fruitful academic results. In this regard, teachers proposed instructional strategies make the learning process effective. Instructional strategies enable teachers to organize their learning materials, ideas, and curriculum according to students' needs. It fosters the teaching process by making teachers believe in their teaching methods. One study states that teacher-guiding programs significantly influence self-efficacy *(Khanshan & Yousefi, 2020).* The teacher's self-belief supports the instructional practices *(Poulou et al., 2019)*, substantially encouraging students' autonomy in accomplishing the task (*Miller et al., 2017*).

Undoubtedly, teachers use different instructional strategies for attaining educational goals. The instructional practices enhance the teachers' skills and capabilities, thus making them believe in the teaching methods. One study states that instructional strategies improve teachers' professional skills by adopting constructive learning materials (e.g., videos, notes, and projects) *(Yang, 2017)*. Hence, due to the increasing benefit of instructional strategies, today's education system has been motivated to adopt effective instructional strategies to boost teachers' self-efficacy *(Poulou et al., 2019)*. In the educational setting, teaching strategies have operationalized the teaching methods to influence students' learning. The instructional tactics enable the teachers to feel confident about their abilities, skills, and teaching methods. Based on this statement, the research shows that learning methods and techniques favor student learning by significantly fostering teachers' self-efficacy *(Mahasneh & Alwan, 2018).*

Therefore, instructional practices are an effective way of supporting the learning objective and teachers' efficacy. The modeling of target strategies makes teachers succeed in their efforts, potentially improving their self-efficacy. Teachers' instructional policies enable them to manage the classroom environment by overcoming the educational challenges influencing effective learning. Accordingly, by highlighting the differentiation role of instructional practices, the literature reports that constructive instructional approaches make teachers believe that their teaching holds paramount significance in regulating classroom learning activities *(Suprayogi et al., 2017)*. Indeed, the literature indicated that deploying instructional strategies improves the teachers' self-efficacy. Hence, based on the previous research, this study proposes the following hypothesis:

H4: Instructional Strategies have a positive and significant impact on teacher self-efficacy.

Teacher Self-Efficacy and Student Academic Performance

Over the years, excessive student failure has emerged as a vital concern to educationists, who have demanded an urgent need to improve students' learning performance. Results have shown that in order to reach the learning standards, students' performance needs to be improved *(Ingersoll et al., 2018)*. However, this challenge to enhance students' performance continues to appear at all educational levels. The research reveals that teachers' efficacy plays a significant role in reciprocating these emerging challenges, thereby countering students' low academic performance *(Mosoge et al., 2018)*. Students demand a higher sense of self-efficacy for outperforming in the international market. Indeed, teachers holding a high level of self-belief view their students' failure as a temporary setback, persistently influencing the need for improving the learner's academic performance.

Undoubtedly, self-efficacy significantly relates to the individual's ability to improve academic performance. The teachers' self-efficacy boosts the students' interest in learning activities, thus promoting improved academic results. In this regard, teachers' self-efficacy significantly strengthens students' learning abilities, eventually influencing their academic performance. Students' performance goals depend on the teacher's characteristics. Teachers' self-efficacy encourages the students to achieve the classroom objectives. The literature states that in the classroom environment, the teachers providing adequate teaching resources encourage students to gain academic outcomes (e.g., improved performance) *(Laninga-Wijnen et al., 2018)*. Accordingly, the research shows that teachers' self-confidence inspires students to achieve their goals *(Yerdelen & Sungur, 2019)*.

Significantly, teachers hold a central position in the educational network, potentially improving learners' academic performance. The instructors' self-efficacy fosters the students' academic performance by directing their attention toward goal attainment. Undoubtedly, the role of teachers' self-efficacy has intrigued researchers and scholars, leading them to focus on the effectiveness of teachers' self-belief in encountering difficulties in improving school performance. In explaining this notion, the research states that the teachers' self-perception assists the students learning process, thereby motivating them to improve their academic performance *(Ghaffar et al., 2019)*. In recent years, teachers' self-efficacy has emerged as a growing topic that has gained

the attention of today's practitioners in enhancing the students' performance *(Mok & Moore, 2019; Sarfraz, et al., 2022a)*. The teacher's self-efficacy makes students effectively perform their tasks *(Perera et al., 2019)*. As indicated by the literature, the previous research states that teaching self-efficacy is the prime driver influencing the students' learning process *(Jabeen & Iqbal Khan, 2022; Sarfraz et al., 2022b)*. Indeed, the studies showed that teachers' self-efficacy had gained significant importance in the education sector, thus influencing the students' academic performance. Therefore, based on the prior literature review, this study proposes the following hypothesis:

H5: Teacher Self-Efficacy positively and significantly impacts students' academic performance.

The Mediating Role of Teachers' Self-Efficacy

Motivation is a critical factor that drives individual academic activities. It makes the students feel attached to the learning task without losing interest and enthusiasm. This phenomenon makes the educationist understand that motivation comes from effective teaching practices. Through this phenomenon, various studies have explained the role of teachers' self-efficacy in influencing learners' educational performance. In this regard, one study states that teachers' motivational belief regulates student learning, thereby contributing to their academic development *(Durksen et al., 2017)*. The research on the teachers' efficacy shows a strong positive correlation between motivational strategies, instructors' self-belief, and students' academic performance *(Karimi & Nikbakht, 2019).*

Arguably, students mostly attend those classes that motivate them to participate in classroom activities. Motivation is a profound concept that needs sustainability in students' academic life. Significantly, teachers are the individuals who care about developing an interactive classroom environment. They intend to adopt different motivational strategies to boost the students' learning process. The research states that effective teachers' understanding makes the learning activity meaningful for students (Bal-Taştan et al., 2018). Teachers' motivational perception is an essential factor that allows them to develop motivational strategies for accelerating students' learning activities. Teachers' self-efficacy motivates the students to learn better, substantially inducing better academic outcomes. In explaining this notion, one study reveals that teachers' self-belief and motivational strategy significantly influence educational outcomes (e.g., student performance and achievement) *(Karimi & Nikbakht, 2019)*. Teachers' motivational strategies play a paramount role in influencing student performance. It makes the teacher realize their responsibility regarding the students' learning, thereby increasing their teaching confidence. One study highlights the importance of motivational regulation to empower the teachers' confidence in the teaching materials *(Zhang & Liu, 2019)*.

Similarly, this relation is also encouraged in another study. It shows that teachers' self-efficacy encourages them to adopt novel motivational tools to accelerate student learning performance *(Bal-Taştan et al., 2018)*. It is a fact that teachers' efficacy influences the teachers' choice of strategies, thus influencing superior academic performance. Accordingly, to explain this phenomenon, the research states that the teachers' motivational approaches support an environment that boosts their confidence in learning outcomes (i.e., student achievement and performance) *(Rawahi et al., 2019).* Therefore, the literature concludes that the teachers' motivational strategies facilitate the students' academic activities, which is critical to influencing their learning outcomes.

Indeed, the teachers' self-perception strongly influences the students' performance. However, in recent years, establishing a belief system that enhances the teachers' strategies (e.g., motivational and instructional) has become significant for today's educationists. Student-centered approaches, methodologies, and techniques foster their competence to perform in academics. The teachers' self-belief makes students select courses, activities, and assignments that shape their efforts in recording high academic results. Therefore, the literature shows that teachers' self-efficacy is a profound construct that enhances students' learning needs *(Laninga-Wijnen et al., 2018)*. Notably, instructors' self-efficacy has emerged as a meaningful way of influencing students' learning performance. Overall, education is a significant component that empowers learners to gain knowledge. In gaining educational goals, teachers are the focal figure that inspires students to achieve academic standards. Teachers' high teaching competency fosters students' learning activities. In explaining this notion, the research shows that conducive instructional practices elevate the teachers' self-efficacy, capabilities, and skills, potentially leaving a positive impact on student performance *(Poulou et al., 2019)*. For example, study states that instructional strategies help teachers guide and maintain course activities *(Hurlbut, 2018)*. The teachers' self-efficacy supports a positive learning environment where high-quality instructions increase the effectiveness of the teaching medium. The instructional strategies make complex concepts look easier, thus providing the students with a clear understanding.

Based on this statement, the study indicates that teachers' self-efficacy elevates the need for guiding strategies, influencing the student's academic performance (*Hayat et al., 2020)*. In particular, student performance regulated by the instructional strategies should bring positive academic results (e.g., improved student performance). The teachers' self-belief increases the readiness for the instructional strategies, thus improving the quality of the student outcome *(Khanshan & Yousefi, 2020)*. Therefore, based on the presented literature, this study proposes the following hypotheses:

H5(a): Teacher Self-Efficacy mediates the relationship between motivational strategies and student academic performance

H5(b): Teacher Self-Efficacy mediates the relationship between instructional strategies and student academic performance

The study proposed hypothesis, direct and indirect relationship among variables is presented in Figure 1.

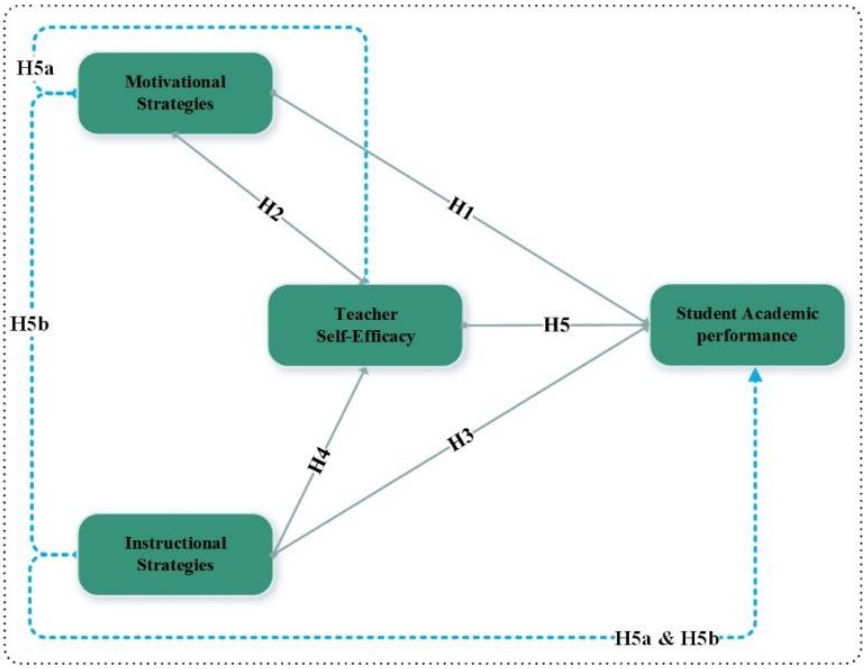

Fig. 1 – Conceptual Model

Research Methodology

The aim of this study was to check the impact of motivational and instructional strategies on students' academic performance during the COVID-19 pandemic. Data was collected from the teachers of higher educational institutes in China. In this study, we have adopted a convenience sampling technique and informed consent was obtained from all participants. A total of 330 questionnaires were distributed to the teachers, between November 2021 to December 2011, but 260 questionnaires were selected for the data analysis. The response rate of the respondents was 78% in this study. Structural equation modeling and a statistical software package for the social sciences (SPSS) were used to test the proposed relationship. We also have checked the common method bias using Harman's single-factor approach. There is no common method bias in this study because the variance extracted by one single factor is 11.843%, less than 50% (*Podsakoff et al., 2003)*.

Motivational Strategies were measured on the 4-item scale, while Instructional Strategies were assessed on the 7-items scale adopted from the study of *Nie et al. (2012).* The sample items include "I make a special effort to give my students creative and imaginative work" and "I give the pupils feedback on their exams or tests." In this study, we have measured Teacher Self-Efficacy on the 5-item scale adopted from *Lazarides & Schiefele (2021).* The sample items include "Respond to difficult questions from your students" and "Implement alternative strategies of knowledge transfer in your classroom." The dependent variable (student academic performance) was assessed on the nine- items scale based on the study of *DuPaul et al. (1991).* The sample items include "Estimate the percentage of written language arts work completed (regardless of accuracy) relative to classmates" and "How frequently does the student accurately follow teacher instructions and/or class discussion during large-group (e.g., whole class) instruction?".

RESULTS

We analyzed the data of 260 participants. Table 1 shows the reliability and validity values of motivational strategies, instructional strategies, teachers' self-efficacy, and student academic performance. All items' factor loading value was higher than 0.6, as suggested by *Hair (2010).* SAP_7 has the lowest factor loading value of 0.669, while SAP_11 has the highest factor loading value of 0.872. *Nunnally et al. (1978)* suggested that the average variance extracted value (AVE) should be higher than 0.5. In this study, all the variables' AVE value was higher than 0.5.

Figure 2 shows the graphical representations of the Measurement Model. The latent constructs were shown in circle shapes, while the items were shown in rectangle shapes.

Table 1

Reliability & Validity Analysis

Construct	Items	Loading	α	CR	AVE
Motivational Strategies	MS_1	0.787	0.877	0.877	0.640
	MS_2	0.812			
	MS_3	0.804			
	MS_4	0.796			
Instructional Strategies	IS_1	0.726	0.920	0.919	0.620
	IS_2	0.774			
	IS_3	0.840			
	IS_4	0.757			
	IS_5	0.817			
	IS_6	0.781			
	IS_7	0.810			
Teacher Self-Efficacy	TSE_1	0.752	0.890	0.890	0.618
	TSE_2	0.819			
	TSE_3	0.834			
	TSE_4	0.723			
	TSE_5	0.796			
Student Academic Performance	SAP_1	0.824	0.952	0.952	0.643
	SAP_10	0.803			
	SAP_11	0.872			
	SAP_2	0.852			
	SAP_3	0.736			
	SAP_4	0.787			
	SAP_5	0.763			
	SAP_6	0.850			
	SAP_7	0.669			
	SAP_8	0.781			
	SAP_9	0.863			

Table 2 shows the value of discriminant validity analysis by using Fornel Larcker & HTMT. The values of the latent constructs were below 0.9 *(Henseler et al., 2015).* Thus, it demonstrates that each latent construct measurement was completely discriminatory concerning one another.

Table 2

Discriminant Validity Analysis (Fornel Larcker & HTMT)

Constructs	1	2	3	4
1. Instructional Strategies	**0.787**	0.486	0.553	0.530
2. Motivational Strategies	0.487	**0.800**	0.534	0.496
3. Student Academic Performance	0.555	0.535	**0.802**	0.514
4. Teacher Self-Efficacy	0.530	0.497	0.517	**0.786**

Table 3

HYPOTHESES TESTING

Hypothesis		Beta	SE	T-Value	P-Value
H1	MS ➔ SAP	0.279	0.066	4.227	***
H2	MS ➔ TSE	0.313	0.077	4.09	***
H3	IS ➔ SAP	0.304	0.07	4.365	***
H4	IS ➔ TSE	0.378	0.077	4.927	***
H5	TSE ➔ SAP	0.217	0.069	3.131	**

***p<0.01, ***p<0.001*

Each of the proposed direct effect paths had a p-value below the accepted threshold of 0.05; they were all determined to be statistically significant. Table 3 describes those motivational strategies has significant relationship with student academic performance (β = 0.279, p < 0.05). H2 states motivational strategies (β = 0.313, p < 0.05) has a significant and positive impact on teacher's self-efficacy. Instructional Strategies has positive and significant impact on student academic performance (β = 0.304, p < 0.05) and teacher self-efficacy (β = 0.378, p < 0.05). So, hypotheses H3 and H4 were accepted. H5, which states that teacher self-efficacy has a positive and significant impact on student academic performance, was accepted in this study (β = 0.217, p < 0.05).

Table 4

Mediation Effect Hypotheses Testing

Hypothesis		Beta	SE	T-Value	P-Value
H5(a)	MS ➔ TSE ➔ SAP	0.068	0.029	2.333	*
H5(b)	IS ➔ TSE ➔ SAP	0.082	0.036	2.293	*

**Indicates significant paths: *p<0.05*

Table 4 shows the results of the mediation analysis. Hypothesis H5(a) states teacher self-efficacy mediates the relationship between motivational strategies and student academic performance. The hypothesis H5(a) was accepted at the (β = 0.068, p < 0.05). H5(b) states teacher self-efficacy mediates the relationship between instructional strategies and student academic performance. The H5(b) was accepted at the (β = 0.082, p < 0.05). Figure 3 shows the results of structural equation modeling.

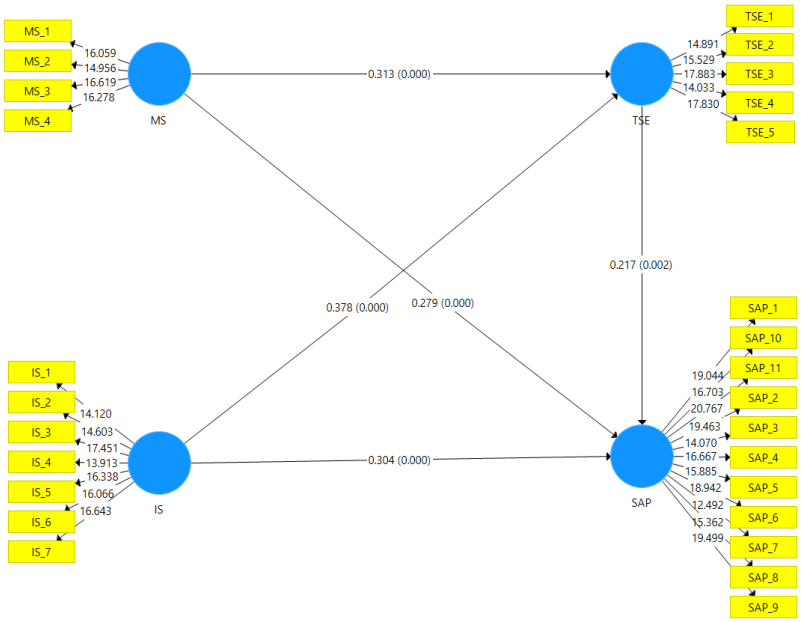

Fig. 2 – Results of Structural Model

Discussion

Education is an activity that demands mastery over the learning activity. Teaching is an activity that involves undertaking knowledge, skills, and models that helps the learners understand and evaluate academic matters. Increasing teachers' self-efficacy fosters their teaching capacity to ensure high-quality learning performances. Indeed, the teachers' self-confidence is a vital construct that influences students' academic outcomes. In this view, this study intends investigated different interdependences that help educators boost students' academic performances. In particular, to analyze the research outcomes, section 5 aims to compare

the study results with the previous findings. This section sheds light on different conceptions that present the teachers' self-efficacy to play a significant role in predicting the students' performance.

In education, the quality of education is only not determined by the teaching skills but also by the motivation that aids student learning. Students cannot perform solely without the support of teachers. One study shows that in enhancing students' performance, the teachers' motivational strategies play an essential role in developing and improving the students' course performance *(Tokan & Imakulata, 2019)*. Among the array of motivational constructs, the teachers' self-efficacy is the strongest predictor of student academic results. Academic self-efficacy makes teachers devise effective instructional practices that enhance student outcomes. Teachers boost students' motivation by providing necessary learning materials that help them outperform others. The teaching guidance and personal characteristics help the students to believe in themselves, which is crucial for accelerating their academic success *(Ghaffar et al., 2019)*. Indeed, referring to these studies, our study also showed similar results. Hence, considering this fact, we have accepted H1 and H2.

In recent years, instructional learning strategies have gained significant research attention in education. In particular, learning strategies are the most significant way of acquiring knowledge and skills. They inspire and encourage the students to participate in the learning activity, thus bringing positive academic outcomes. Today, instructional strategies are the most beneficial instruments for determining students' academic performance. One study states that instructional strategies help the teachers implement effective supporting techniques *(Mahasneh & Alwan, 2018)*, thus improving students' academic performance. At present, the advantages of these tactics have considerably influenced students' learning process. It has made learning meaningful for students, potentially leading to superior academic results. Hence, to achieve the goal of the teaching-learning process, instructional strategies help teachers gain mastery over the learning process. The teaching strategies boost the teachers' morale, thus ensuring the delivery of high-quality teaching to the students *(Poulou et al., 2019)*. Today's learning system emphasizes adopting effective learning methods that enable teachers to confidently become active players in the students' learning process *(Choi et al., 2019)*. Hence, based on this view, our research findings also support and accept the previous literature (i.e., H3 and H4).

Undoubtedly, teachers are the prime executors of teaching functions. In recent years, researchers have proposed that teachers' self-efficacy plays a fundamental role in accelerating students' academic performance. Generally, teachers are the individuals who are responsible for enhancing the students' learning expectations, which, in turn, produces improved academic results. The teachers' self-efficacy motivates the students to achieve a superior performance level. It makes them effectively control their cognition and learning process, thus directly affecting students' goals, inspirations, and performance. In explaining this notion, one study states that teachers' self-efficacy perception affects student learning orientation and performance *(Yerdelen & Sungur, 2019)*. Also, the teachers' self-efficacy supports the implementation of active learning strategies (e.g., motivational and instructional) that influence the students' academic goals and performance. The success of the teaching capabilities increases the teachers' self-perception and confidence in their professional abilities. In this regard, numerous studies have illuminated the role of teachers' self-efficacy in generating and implementing new teaching methods, designs, and strategies for obtaining better students' grades *(Hayat et al., 2020)*. The study states that learning strategies are essential for educators to increase students' academic results *(Ghaffar et al., 2019)*.

In particular, the prior results show a positive relationship between the teachers' efficacy and learning and motivational strategies. Similarly, our study results indicate that motivational and instructional strategies have emerged as a fundamental component in improving students' performance. Hence, in line with the prior evidence, our study results accept and support the previous findings, thus confirming the relationship proposed in H5 and H6. Consequently, our study shows positive and consistent results, thus confirming and verifying all the assumptions made in the previous literature.

CONCLUSIONS

In today's modern era, the continuous technological shift has provided opportunities for global institutions to combat emerging educational challenges. In particular, the extended educational changes have called on worldwide educational institutions to express themselves by devising strategies that drive students' performance. Accordingly, the knowledge-based society demands the need to improve students' performance, specifically related to increasing teachers' self-efficacy. As a result, the world's education institutes benefit by

adopting novel educational strategies (i.e., motivational and instructional) that direct the instructors' attention toward achieving the academic goal.

In particular, teachers' role in learning has recently gained substantial research attention. Teachers strongly contribute to student motivation by devising learning strategies to foster student academic performance. Significantly, teachers' self-efficacy is relevant to students achieving learning goals with the help of planned learning strategies. Hence, this study highlights the relevance of teachers' self-efficacy and student academic performance in the context of motivational and instructional strategies. The literature confirmed that teachers' self-efficacy improves students' learning outcomes.

The study findings suggest that teachers' self-efficacy significantly mediates the relationship between motivational and instructional strategies and student academic performance. The study produced systematic and enduring positive results. The developing effect of educational strategies (i.e., motivation and instruction) is known to have a prolonged impact on effective student performance. However, the literature findings from previous studies confirm a positive and significant relationship between the variables. Additionally, this study posits that these findings provide relevant guidance for future researchers, scholars, institutions, policymakers, and knowledge members (e.g., teachers, students, and administration), directing their attention toward students' academic performance.

ACKNOWLEDGEMENT

This study is supported by the Scientific Research Start-up Fund of Zhejiang Shuren University, PR China (KXJ0122604).

REFERENCES

[1] Abbasi, S., Moeini, M., Shahriari, M., Ebrahimi, M., & Khoozani, E. K. (2018). Designing and manufacturing of educational multimedia software for preventing coronary artery disease and its effects on modifying the risk factors in patients with coronary artery disease. *Electronic Journal of General Medicine*, *15*(3). https://doi.org/10.29333/ejgm/85942

[2] Abdullah, N. A., & Bhatti, N. (2018). Failure in Quality of Academic Performance of Students in Public Sector Schools of Sheikhupura. *Journal of Education and Educational Development*, *5*(2), 289. https://doi.org/10.22555/joeed.v5i2.1655

[3] Alexander, S. (2020). The Relationship among Teachers' Self-Efficacy Beliefs, Student Motivation and Effective Teaching. *UMT Education Review*, *3*(2), 47–64. https://doi.org/10.32350/uer.32.03

[4] Almalki, S. A. (2019). Influence of Motivation on Academic Performance among Dental College Students. *Open Access Macedonian Journal of Medical Sciences*, *7*(8), 1374–1381. https://doi.org/10.3889/oamjms.2019.319

[5] Bal-Taştan, S., Davoudi, S. M. M., Masalimova, A. R., Bersanov, A. S., Kurbanov, R. A., Boiarchuk, A. V., & Pavlushin, A. A. (2018). The Impacts of Teacher's Efficacy and Motivation on Student's Academic Achievement in Science Education among Secondary and High School Students. *EURASIA Journal of Mathematics, Science and Technology Education*, *14*(6). https://doi.org/10.29333/ejmste/89579

[6] Bandura, A. (1977). Self-efficacy: toward a unifying theory of behavioral change. *Psychological Review*, *84*(2), 191.

[7] Barni, D., Danioni, F., & Benevene, P. (2019). Teachers' Self-Efficacy: The Role of Personal Values and Motivations for Teaching. *Frontiers in Psychology*, *10*. https://doi.org/10.3389/fpsyg.2019.01645

[8] Burić, I., & Kim, L. E. (2019). *Teacher self-efficacy, instructional quality, and student motivational beliefs: An analysis using multilevel structural equation modeling*.

[9] Cheng, L., Ritzhaupt, A. D., & Antonenko, P. (2019). Effects of the flipped classroom instructional strategy on students' learning outcomes: a meta-analysis. *Educational Technology Research and Development*, *67*(4), 793–824. https://doi.org/10.1007/s11423-018-9633-7

[10] Choi, C., Lee, J., Yoo, M. S., & Ko, E. (2019). South Korean children's academic achievement and subjective well-being: The mediation of academic stress and the moderation of perceived fairness of parents and teachers. *Children and Youth Services Review*, *100*, 22–30. https://doi.org/10.1016/j.childyouth.2019.02.004

[11] Choi, J., Lee, J.-H., & Kim, B. (2019). How does learner-centered education affect teacher self-efficacy? The case of project-based learning in Korea. *Teaching and Teacher Education*, *85*, 45–57. https://doi.org/10.1016/j.tate.2019.05.005

[12] Chutinan, S., Riedy, C. A., & Park, S. E. (2018). Student performance in a flipped classroom dental anatomy course. *European Journal of Dental Education*, *22*(3), e343–e349. https://doi.org/10.1111/eje.12300

[13] de Boer, H., Donker, A. S., Kostons, D. D. N. M., & van der Werf, G. P. C. (2018). Long-term effects of metacognitive strategy instruction on student academic performance: A meta-analysis. *Educational Research Review*, *24*, 98–115. https://doi.org/10.1016/j.edurev.2018.03.002

[14] DuPaul, G. J., Rapport, M. D., & Perriello, L. M. (1991). Teacher ratings of academic skills: The development of the Academic Performance Rating Scale. *School Psychology Review*, *20*(2), 284–300.

[15] Durksen, T. L., Klassen, R. M., & Daniels, L. M. (2017). Motivation and collaboration: The keys to a developmental framework for teachers' professional learning. *Teaching and Teacher Education*, *67*, 53–66. https://doi.org/10.1016/j.tate.2017.05.011

[16] Fong, C. J., Dillard, J. B., & Hatcher, M. (2019). Teaching self-efficacy of graduate student instructors: Exploring faculty motivation, perceptions of autonomy support, and undergraduate student engagement. *International Journal of Educational Research*, *98*, 91–105. https://doi.org/10.1016/j.ijer.2019.08.018

[17] Ghaffar, S., Hamid, S., & Thomas, M. (2019). The Impact of Teacher's Self-Efficacy on Student's Motivation towards Science Learning. *Review of Economics and Development Studies*, *5*(2), 225–234. https://doi.org/10.26710/reads.v5i2.540

[18] Hair, J. F. (2010). Black, WC, Babin, BJ, & Anderson, RE (2010). *Multivariate Data Analysis*, *7*.

[19] Hariri, H., Hermanto, D., Yayah, E., Rini, R., & Suparman, U. (2021). Motivation and Learning Strategies: Student Motivation Affects Student Learning Strategies. *European Journal of Educational Research*, *10*(1), 39–49. https://doi.org/10.12973/eu-jer.10.1.39

[20] Hayat, A. A., Shateri, K., Amini, M., & Shokrpour, N. (2020). Relationships between academic self-efficacy, learning-related emotions, and metacognitive learning strategies with academic performance in medical students: a structural equation model. *BMC Medical Education*, *20*(1), 76. https://doi.org/10.1186/s12909-020-01995-9

[21] Henseler, J., Ringle, C. M., & Sarstedt, M. (2015). A new criterion for assessing discriminant validity in variance-based structural equation modeling. *Journal of the Academy of Marketing Science*, *43*(1), 115–135.

[22] Hettinger, K., Lazarides, R., Rubach, C., & Schiefele, U. (2021). Teacher classroom management self-efficacy: Longitudinal relations to perceived teaching behaviors and student enjoyment. *Teaching and Teacher Education*, *103*, 103349. https://doi.org/10.1016/j.tate.2021.103349

[23] Heyder, A., Weidinger, A. F., Cimpian, A., & Steinmayr, R. (2020). Teachers' belief that math requires innate ability predicts lower intrinsic motivation among low-achieving students. *Learning and Instruction*, *65*, 101220. https://doi.org/10.1016/j.learninstruc.2019.101220

[24] Hurlbut, A. R. (2018). Online vs. traditional learning in teacher education: a comparison of student progress. *American Journal of Distance Education*, *32*(4), 248–266. https://doi.org/10.1080/08923647.2018.1509265

[25] Ingersoll, R. M., Sirinides, P., & Dougherty, P. (2018). *Leadership Matters: Teachers' Roles in School Decision Making and School Performance*. *42*(13), 13–17.

[26] Inyang, H. (2019). *Teaching Strategies and Academic Performance of Agricultural Science Students in Secondary Schools*.

[27] Jabeen, R., & Iqbal Khan, A. (2022). A Study on Teachers' Sense of Self-Efficacy in Defence Authority Educational Institutions, Karachi, Pakistan. *International Journal of Experiential Learning & Case Studies*, *6*(2). https://doi.org/10.22555/ijelcs.v6i2.38

[28] Jayasankara Reddy, K., Rajan Menon, K., & Thattil, A. (2018). Academic Stress and its Sources Among University Students. *Biomedical and Pharmacology Journal*, *11*(1), 531–537. https://doi.org/10.13005/bpj/1404

[29] Johnson, D. (2017). The Role of Teachers in Motivating Students To Learn. *BU Journal of Graduate Studies in Education*, *9*(1).

[30] Karimi, M., & Nikbakht, E. (2019). Teachers' Efficacy, Identity and Motivational Strategies and their Effects on L2 learners' Achievement. *Advances in Language and Literary Studies*, *10*(5), 20. https://doi.org/10.7575/aiac.alls.v.10n.5p.20

[31] Khanshan, S. K., & Yousefi, M. H. (2020). The relationship between self-efficacy and instructional practice of in-service soft disciplines, hard disciplines and EFL teachers. *Asian-Pacific Journal of Second and Foreign Language Education*, *5*(1), 1. https://doi.org/10.1186/s40862-020-0080-8

[32] Kokkinos, C. M., & Voulgaridou, I. (2018). Motivational beliefs as mediators in the association between perceived scholastic competence, self-esteem and learning strategies among Greek secondary school students. *Educational Psychology*, *38*(6), 753–771. https://doi.org/10.1080/01443410.2018.1456651

[33] Laninga-Wijnen, L., Ryan, A. M., Harakeh, Z., Shin, H., & Vollebergh, W. A. M. (2018). The moderating role of popular peers' achievement goals in 5th- and 6th-graders' achievement-related friendships: A social network analysis. *Journal of Educational Psychology*, *110*(2), 289–307. https://doi.org/10.1037/edu0000210

[34] Lawrence, A. S. A., & Hanitha, T. (2017). A Study on Teachers' Motivational Strategy and Academic Achievement of Higher Secondary Students. *Aarhat Multidisciplinary International Education Research Journal (AMIERJ)*.

[35] Lazarides, R., & Schiefele, U. (2021). The relative strength of relations between different facets of teacher motivation and core dimensions of teaching quality in mathematics-A multilevel analysis. *Learning and Instruction*, *76*, 101489.

[36] Mahasneh, A. M., & Alwan, A. F. (2018). The Effect of Project-Based Learning on Student Teacher Self-Efficacy and Achievement. *International Journal of Instruction*, *11*(3).

[37] Matcha, W., Gašević, D., Uzir, N. A., Jovanović, J., & Pardo, A. (2019). Analytics of Learning Strategies. *Proceedings of the 9th International Conference on Learning Analytics & Knowledge*, 461–470. https://doi.org/10.1145/3303772.3303787

[38] Miller, A. D., Ramirez, E. M., & Murdock, T. B. (2017). The influence of teachers' self-efficacy on perceptions: Perceived teacher competence and respect and student effort and achievement. *Teaching and Teacher Education*, *64*, 260–269. https://doi.org/10.1016/j.tate.2017.02.008

[39] Mok, M. M. C., & Moore, P. J. (2019). Teachers & self-efficacy. *Educational Psychology*, *39*(1), 1–3. https://doi.org/10.1080/01443410.2019.1567070

[40] Mosoge, M. J., Challens, B. H., & Xaba, M. I. (2018). Perceived collective teacher efficacy in low performing schools. *South African Journal of Education*, *38*(2). https://doi.org/10.15700/saje.v38n2a1153

[41] Muwonge, C. M., Schiefele, U., Ssenyonga, J., & Kibedi, H. (2019). Modeling the relationship between motivational beliefs, cognitive learning strategies, and academic performance of teacher education students. *South African Journal of Psychology*, *49*(1), 122–135. https://doi.org/10.1177/0081246318775547

[42] Nie, Y., Lau, S., & Liau, A. (2012). *The teacher efficacy scale: A reliability and validity study*.

[43] Nunnally, J., Barnette, J. J., & Peter, J. P. (1978). Reliability: A review of psychometric basics and recent marketing practices. *Journal of Marketing Research*, *16*(1), 6–17.

[44] Obergriesser, S., & Stoeger, H. (2020). Students' emotions of enjoyment and boredom and their use of cognitive learning strategies – How do they affect one another? *Learning and Instruction*, *66*, 101285. https://doi.org/10.1016/j.learninstruc.2019.101285

[45] Perera, H. N., Calkins, C., & Part, R. (2019). Teacher self-efficacy profiles: Determinants, outcomes, and generalizability across teaching level. *Contemporary Educational Psychology*, *58*, 186–203. https://doi.org/10.1016/j.cedpsych.2019.02.006

[46] Podsakoff, P. M., MacKenzie, S. B., Lee, J.-Y., & Podsakoff, N. P. (2003). Common method biases in behavioral research: A critical review of the literature and recommended remedies. *Journal of Applied Psychology*, *88*(5), 879.

[47] Poulou, M. S., Reddy, L. A., & Dudek, C. M. (2019). Relation of teacher self-efficacy and classroom practices: A preliminary investigation. *School Psychology International*, *40*(1), 25–48. https://doi.org/10.1177/0143034318798045

[48] Rawahi, T. Al, Hassan, N. C., & Ismail, A. (2019). Relationship between Teachers' Motivational Strategies, Self-Efficacy and Beliefs on Students' Academic Achievement at Oman Public Schools. *International Journal of Academic Research in Progressive Education and Development*, *8*(4). https://doi.org/10.6007/IJARPED/v8-i4/6498

[49] Sarfraz, M., Hussain, G., Shahid, M., Riaz, A., Muavia, M., Fahed, Y. S., Azam, F., & Abdullah, M. T. (2022). Medical Students' Online Learning Perceptions, Online Learning Readiness, and Learning Outcomes during COVID-19: The Moderating Role of Teacher's Readiness to Teach Online. *International Journal of Environmental Research and Public Health*, *19*(6), 3520.

[50] Sarfraz, M., Khawaja, K. F., & Ivascu, L. (2022). Factors affecting business school students' performance during the COVID-19 pandemic: A moderated and mediated model. *The International Journal of Management Education*, 100630.

[51] Seitzer, H., & Windzio, M. (2022). *Does Globalization Affect the Performance of Secondary Education Systems? A Coevolution Model of Multiplex Transnational Networks and Educational Performance* (pp. 97–125). https://doi.org/10.1007/978-3-030-78885-8_4

[52] Sivrikaya, A. H. (2019). The Relationship between Academic Motivation and Academic Achievement of the Students. *Asian Journal of Education and Training*, *5*(2), 309–315.

[53] Suprayogi, M. N., Valcke, M., & Godwin, R. (2017). Teachers and their implementation of differentiated instruction in the classroom. *Teaching and Teacher Education*, *67*, 291–301. https://doi.org/10.1016/j.tate.2017.06.020

[54] Timothy, A. M. W. N., Prosper, & Nyamekye, A. D. (2018). Effects of Analogy Instructional Strategy on Students' Performance in Wave Concept. *Journal of Education and Practice*, *9*(5).

[55] Tokan, M. K., & Imakulata, M. M. (2019). The effect of motivation and learning behaviour on student achievement. *South African Journal of Education*, *39*(1), 1–8. https://doi.org/10.15700/saje.v39n1a1510

[56] Trigueros, R., Padilla, A. M., Aguilar-Parra, J. M., Rocamora, P., Morales-Gázquez, M. J., & López-Liria, R. (2020). The Influence of Emotional Intelligence on Resilience, Test Anxiety, Academic Stress and the Mediterranean Diet. A Study with University Students. *International Journal of Environmental Research and Public Health*, *17*(6), 2071. https://doi.org/10.3390/ijerph17062071

[57] Yang, D. (2017). Instructional strategies and course design for teaching statistics online: perspectives from online students. *International Journal of STEM Education*, *4*(1), 34. https://doi.org/10.1186/s40594-017-0096-x

[58] Yerdelen, S., & Sungur, S. (2019). Multilevel Investigation of Students' Self-regulation Processes in Learning Science: Classroom Learning Environment and Teacher Effectiveness. *International Journal of Science and Mathematics Education*, *17*(1), 89–110. https://doi.org/10.1007/s10763-018-9921-z

[59] Zhang, S., & Liu, Q. (2019). Investigating the relationships among teachers' motivational beliefs, motivational regulation, and their learning engagement in online professional learning communities. *Computers & Education*, *134*, 145–155. https://doi.org/10.1016/j.compedu.2019.02.013

EFFECT OF CONTROLLED-RELEASE FERTILIZER ON MAIZE YIELD AND NUTRIENT UPTAKE UNDER A ONE-TIME FERTILIZER LAYERED SYSTEM
/
根区一次性分层施肥对夏玉米产量和养分吸收的影响

Xin DU[1, 2)], Cailing LIU[1*)], Changqing LIU[1, 2)]
[1)] College of Engineering, China Agricultural University, Beijing 100083/ China;
[2)] School of Mechanical Engineering, Jiangsu Ocean University, Lianyungang 222005/ China
Tel: 0086-010-62737502; E-mail: cailingliu@163.com
Corresponding author: Cailing Liu
DOI: https://doi.org/10.35633/inmateh-68-77

Keywords: *Maize yield; Nutrient uptake; Controlled-release fertilizer; one-time fertilizer layered system*

ABSTRACT
Currently, maize production in China suffers from many problems such as excessive fertilizer application, inefficient fertilizer use and insufficient agricultural labour. This research explores the efficient fertilization pattern of maize for fertilizer decrease and yield increase by studying the effect of one-time mechanical point-applied fertilization of controlled-release compound fertilizer in the root-zone, on yield and nutrient uptake. There were six treatments in the application program: 1) no fertilizer (CK); 2) a one-time banding fertilizer application (BDP) 5 cm off the seeds between rows and 10 cm deep; 3) one-time point-applied fertilization (RZF) 5 cm off seed in the row and 10 cm deep; 4) a layered banding application 5 cm off seed, 10 cm and 20 cm deep between rows at a rate of 3:7 (LBD); 5) a 5 cm off seed, 10 cm deep point-applied fertilization, and 20 cm banding application between rows at a rate of 3:7 (LRZ); 6) a fertilizer reduction of 10% between rows at a rate of LRZ (90% LRZ). The results showed that the one-time mechanical layered application of slow-release compound fertilizer (LRZ and LBD) in the root zone increased yields by 11.97% and 11.15%, respectively, compared to the non-layered application of slow-release compound fertilizer (BDP and RZF), and the differences were significant, indicating that mechanical layered application can replace the BDP mode and achieve increased crop yield. The average increase in agronomic efficiency and partial factor productivity of 25.95% and 11.15% for LBD over BDP and 26.10% and 11.97% for LRZ over RZF were significant, indicating that mechanized stratified fertilizer application can significantly improve fertilizer utilization and reduce fertilizer losses and surface source pollution.

摘要
针对夏玉米现有施肥模式下施肥量大、肥效低导致面源污染大、单产低的问题，通过研究分层施肥（上层穴施下层条施）对夏玉米产量和养分吸收的影响，探索减肥增产的玉米高效施肥模式。选用肥料为缓释颗粒肥（N-P_2O_5-K_2O 为 24-6-10），共设 6 个施肥方案，分别为：1)不施肥(CK)；2) 行间偏离种子 5 cm、深 10 cm 一次性条施(BDP)；3) 行间偏离种子 5 cm、深 10 cm 一次性穴施(RZF)；4) 行间偏离种子 5 cm、深 10 cm 和 20 cm 分层条施，且施肥比例为 3：7 (LBD)；5) 行间偏离种子 5 cm、深 10 cm 穴施、20 cm 条施，且施肥比例为 3：7 (LRZ)；6) 减肥 10%行间偏离种子 5 cm、深 10 cm 穴施、20 cm 条施，且施肥比例为 3：7 (90%LRZ)。结果表明，根区一次性机械化分层施用缓释复合肥（LRZ 和 LBD）比不分层施用缓释复合肥（BDP 和 RZF）分别增产 11.97%和 11.15%，且差异显著，说明机械化分层施肥可以代替传统"一炮轰"施肥模式，实现作物增产。LBD 比 BDP 的农学利用率和偏生产力平均增大了 25.95%和 11.15%，LRZ 比 RZF 的农学利用率和偏生产力平均增大了 26.10%和 11.97%，且差异显著，说明机械化分层施肥可以显著提高肥料利用率，减少肥效损失和面源污染。90%LRZ 与 LBD 相比植株高度、茎粗、叶面积、伤流量、根系干物质量和籽粒产量差异均不显著，说明分层穴施肥料是减肥 10%可以实现减肥不减产，节本增效的效果，可为提高作物单产、减少面源污染提高新的研究思路。

Xin Du, Ph.D. Stud.; Cailing Liu, Prof. Ph.D.; Changqing Liu, Ph.D. Stud.*

INTRODUCTION

Maize *(Zea mays L.)* is one of the most widely grown cereal crops globally and the consumption and demand is increasing worldwide as the major source of food, feed, and bio-fuel (*Cassman et al.*, 2003). The cultivated area for maize in China is estimated at 42.42 million ha with yield of about 259.23 million tones' year (*Shemi et al.*, 2021). Therefore, increasing maize productivity has become an important aspect to ensure food security (*Usman et al.*, 2021). However, in order to obtain high yields within short periods, growers often use large amounts of fertilizers, which cause fertilizer losses, wasted resources and challenges to sustainable development of agricultural production (*Luan et al.*, 2020; *Ren et al.*, 2020; *Xu et al.*, 2019). The main reason is that fertilizer application technologies and fertilizer application machinery at national level have lower levels than the level of developed countries in the world (*Shi et al.*, 2020; *Wei et al.*, 2019; *Anstoetz et al.*, 2015).

The conventional fertilizer application mode applies fertilizer in a one-time banding fertilizer at a distance of 5~10cm from the seed row and 10 cm deep at the time of corn sowing, and some conventional fast-acting fertilizers are in the soil far away from the roots with low root efficiency, so that the roots cannot absorb the nutrients released by the fertilizer particles in time, and the excess fertilizer nutrients leave the cultivated soil due to runoff, leaching or gaseous loss, thus causing groundwater or atmospheric pollution (*Ye et al.*, 2010). Recent studies have found that ammonia volatilization and runoff losses are significantly reduced when urea is point-applied to the root zone, greatly improving the utilization of nitrogen fertilizer (*Cao et al.*, 1984; *SavantDe et al.*, 1980). Zhou (*Zhou et al.*, 2020) found that a one-time root zone point-applied application under the furrow full film cover planting method was beneficial to the concentration of nitrogen in the soil tillage layer. Liu (*Liu et al.*, 2017) found that by a single point-applied application of N fertilizer in the root zone of rice, the apparent utilization rate of N fertilizer increased by 22.6%-30.6% and the N loss decreased from 73.0% to 29.7% compared with the previous application. Chen (*Chen et al.*, 2014) proposed a technique of simultaneous lateral deep fertilization of rice, and the results showed that the yield increase ranged from 5.86% to 13.41% compared with manual spreading of fertilizer.

Split fertilization generally uses a combination of base and follow-up fertilizers, which increases the number of fertilization operations, reduces agricultural production efficiency, accelerates soil slumping in the cultivated layer, and is prone to crop damage. The one-time layered fertilizer application technology applies the fertilizer required for the crop growth cycle into the soil in layers at one time with the slow-release fertilizer, which can improve the fertilizer efficiency, completely replace the phased fertilizer application. Wang (*Wang et al.*, 1993) found significant yield increases in maize using stratified ratio fertilization, in addition to improving the efficiency of fertilizer application operations and fertilizer utilization. Wang (*Wang et al.*, 2008) found that wheat yield increased by 27% to 46% using stratified fertilization. Wen (*Wen et al.*, 2017) found that stratified strip application of winter wheat substrate could improve dry matter accumulation and yield. Ma (*Ma et al.*, 2019) found that deep fertilization of summer maize with layered fertilization could effectively improve the water retention performance of deep soil, increase the effective phosphorus content in the lower soil layer, improve maize yield and effectively reduce soil water and phosphorus nutrient losses. Zhang (*Zhang et al.*, 2018) found that deep pine layered fertilization of summer maize significantly increased yield by 7.4% to 13.9%, and observation of root microstructure revealed a significant decrease in the proportion of pith cavity to mid-column area and an increase in the number of root ducts.

Based on the above studies, few studies have been reported on the effects of one-time layered point-applied fertilizer application on maize yield. In this paper, the effects of one-time layered point-applied slow-release compound fertilizer application on yield and nutrient use efficiency of maize through a two-year field experiment were investigated, aiming to provide technical support and theoretical support for weight and yield loss and efficiency of maize production.

MATERIALS AND METHODS

Overview of the test field

The test site is located in XiaoDuzhuang Village, Shenze Town, Shenze County, Shijiazhuang City, Hebei Province, China, at 115°13'48.1" E longitude and 38°12'5.4" N latitude, with an average annual temperature of 12.4 °C, a frost-free period of 188 days, an average annual sunshine duration of 2714.1 h, an average annual rainfall of 489.8 mm, and a temperate continental monsoon climate, with precipitation accounting for 54% of the annual precipitation during the test period (June-September). The precipitations during the test period (June to September) accounted for 54% of the annual precipitations. The previous crop was winter wheat, with a stubble height of 15-20 cm and a straw volume of 0.66 kg/m^2. The soil of the test site was in the transition zone of tidal soil and brown soil, with a soil capacity of 1.37 g/cm^3 and a water content of 23.6%.

Experimental design

Maize seeds used in the experiment were "Zhengdan 958", with 60 cm spacing between rows and 25 cm spacing between plants, and single grain precision sowing. The selected fertilizer was a controlled-release granular fertilizer（24-6-10 for N-P_2O_5-K_2O）with six treatments in the application program: 1) no fertilizer (CK); 2) a one-time banding fertilizer application (BDP) 5 cm off the seeds between rows and 10 cm deep; 3) one-time point-applied fertilization (RZF) 5 cm off seed in the row and 10 cm deep; 4) a layered banding application 5 cm off seed, 10 cm and 20 cm deep between rows at a rate of 3:7 (LBD); 5) a 5 cm off seed, 10 cm deep point-applied fertilization, and 20 cm banding application between rows at a rate of 3:7 (LRZ); 6) a fertilizer reduction of 10% between rows at a rate of LRZ (90% LRZ).

The plot size was 2.4 m × 25 m (4 row zones, 100 plants per row, 400 plants in total), with 3 replications and randomized group arrangement. Field management measures such as pest and weed control and irrigation were consistent among different treatments.

Measurement items and methods

Collection and determination of plant samples

Five plants were randomly selected to measure plant height and stalk diameter (diameter of maize stalk base) at the V5 (fifth leaf collars are visible), V10 (tenth leaf collars are visible), R1 (silks emerge from husks) and R5 (more than 50% of kernels are dented) stages, respectively; five plants were randomly selected to measure plant leaf area at the cob position (single leaf area = leaf length × leaf width × 0.75) at the V10, R1 and R5 stages, respectively.

Collection and determination of soil samples

Root system determination: Five plants were randomly selected at the R1 stage of maize, and the soil was dug out with a 30 cm radius and 30 cm depth, rinsed off the soil with water, and the roots were dried at 80°C for 12 h and weighed for dry weight.

Determination of root injury flow: 5 plants were randomly selected at the V10, R1 and R5 stage, respectively. At 18:00, the stalk was cut horizontally with a sharp blade from a height of 10 cm above the ground and keep the incision flat, was quickly put on the pre-prepared wound fluid collection bag and fastened with a cable tie. The collection belt is an intact transparent sealed bag with dry absorbent cotton inside. It was weighed before use (W_1) and labelled, collected for 12 hours (the wound fluid should not exceed the saturated absorption capacity of absorbent cotton), the collection bag was removed, and weighed again (W_2) to obtain the root wound flow $W= W_2- W_1$.

Production and seed counting

After maturity, maize ears were harvested from the whole plot of each treatment, and the number of harvested ears was calculated and the average number of grains per ear was determined. The 1000-grain weight is based on the average 1000-grain weight of the tested varieties in the first three years. The final grain yield is 85% of the product of the number of ears per hectare, the number of grains per ear and the 1000-grain weight.

Calculation of relevant indicators and statistical methods

Agronomy efficiency (AE, kg/kg) = [yield in fertilized area (kg/hm^2) - yield in the control area (kg/hm^2)]/ nutrient application (kg/hm^2)]

Partial factor productivity (PFP, kg/kg) = yield (kg/hm^2) / nutrient application (kg/hm^2)

SPSS 19.0 software was used for variance analysis, and Duncan's new multiple range method was used to analyse the significant difference between treatments ($P<0.05$), and Origin2018 software was used to draw.

RESULTS

Effect of different fertilizer application methods on maize plant height and stalk diameter

As seen in Figure 1, the one-time mechanical fertilizer application in the root zone increased plant height by 22.09% to 39.73% compared to CK, and the difference was significant. Maize plant height was slightly higher in BDP than in LBD at the V5 stage, but it was basically the same in RZF and LRZ. The plant height of maize in LBD increased from 1.19% to 6.04% compared with BDP at the V10, R1 and R5 stages, and the plant height of LRZ increased from 0.87% to 6.60% compared with RZF, and the difference in plant height between fertilizer treatments increased gradually with time. There was no significant difference in plant height between BDP and LBD, RZF and LRZ at the V5 and V10 stages, and the difference in plant height between maize at the R1 stage gradually appeared, and the plant height at the R5 stage with layered fertilization was significantly greater than that without layered fertilization.

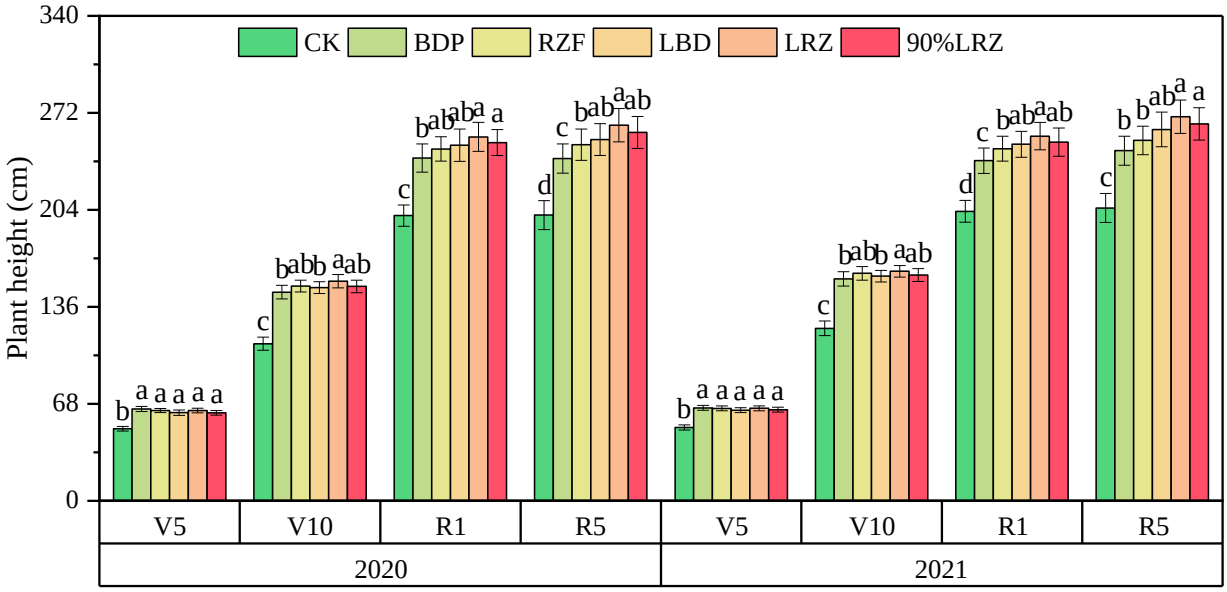

Fig. 1 – Effect of fertilizer application method on maize plant height

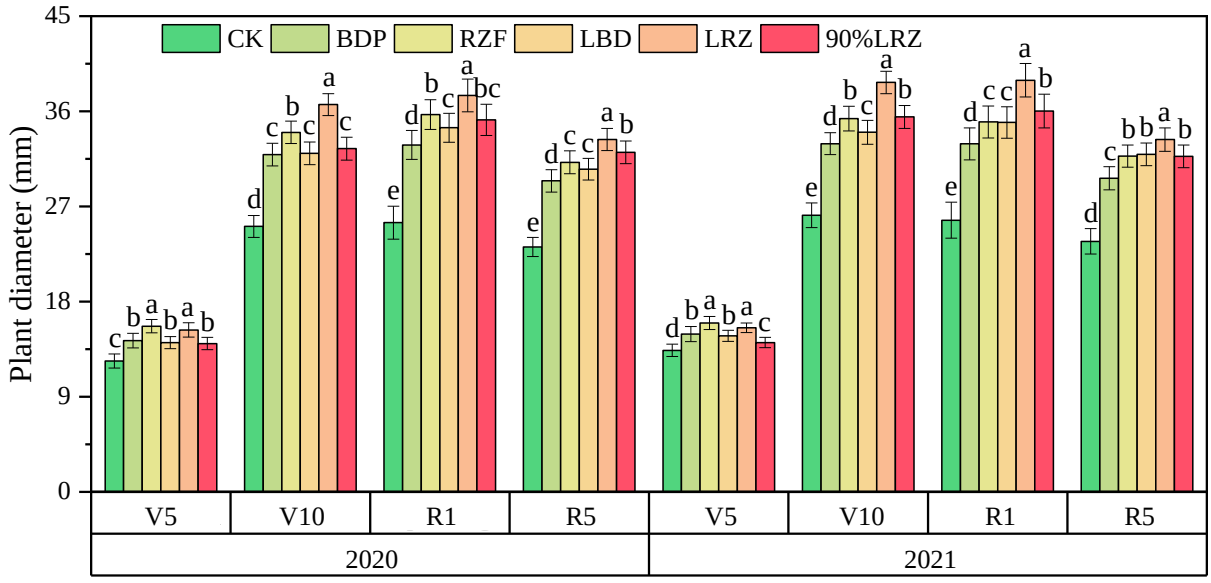

Fig. 2 – Effect of fertilizer application method on maize stalk diameter

As shown in Figure 2, the one-time mechanical fertilization in the root zone increased stalk diameter by 5.46% to 51.53% compared to CK, and the difference was significant. Maize stalk diameter was slightly greater in BDP than in LBD at the V5 stage, but was essentially the same in RZF and LRZ. The stalk diameter of maize in LBD increased from 0.39% to 7.63% compared with BDP at the V10, R1 and R5 stages, and the stalk diameter of plants in LRZ increased from 4.90% to 11.29% compared with RZF. The difference in stalk diameter between different fertilizer treatments increased gradually with time. There was no significant difference in maize stalk diameter between BDP and LBD, RZF and LRZ during the V5 and V10 periods, and the difference in maize stalk diameter gradually appeared during the R1 period, and the stalk diameter of layered fertilizer application during the R5 period was significantly greater than that of non- layered.

Effect of different fertilizer application methods on maize leaf area

As seen in Figure 3, the one-time mechanical fertilizer application in the root zone increased leaf area by 25.78% to 38.79% compared to CK, and the difference was significant. The leaf area of LBD increased by 4.79%~5.09%, 4.40%~4.84% and 3.76%~3.88%, respectively, compared with BDP, and the leaf area of LRZ increased by 4.17%~4.70%, 3.18%~4.96% and 3.76%~3.77%, respectively, compared with RZF at the V10, R1 and R5 stages. The difference in leaf area between different fertilization treatments gradually decreased with time. The leaf area of maize showed significant differences between BDP and LBD, RZF and LRZ during the whole fertility period, and 90% LRZ showed no significant difference in leaf area of maize compared with BDP, indicating that layered fertilization can effectively increase leaf area.

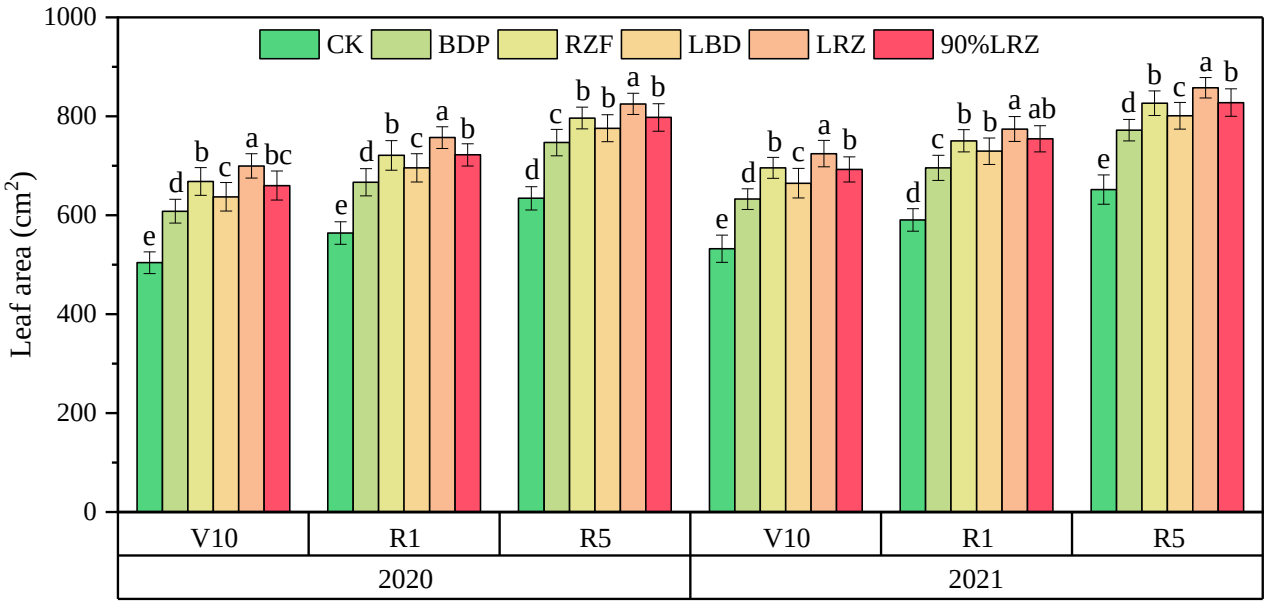

Fig. 3 – Effect of fertilizer application method on maize leaf area

Effect of different fertilizer application methods on maize injury flow

As seen in Figure 4, the one-time mechanical fertilizer application in the root zone increased the injury flow rate by 57.71%~117.17% compared to CK and the difference was significant. Injury flow rate increased by 8.71%~9.29%, 2.20%~7.55% and 12.22%~20.57% in LBD compared with BDP at the V10, R1 and R5 stages, respectively, and increased by 7.12%~7.51%, 7.64%~9.19% and 26.50%~29.38% in LRZ compared with RZF, respectively, and the difference in injury flow rate between different fertilizer treatments gradually increased over time.

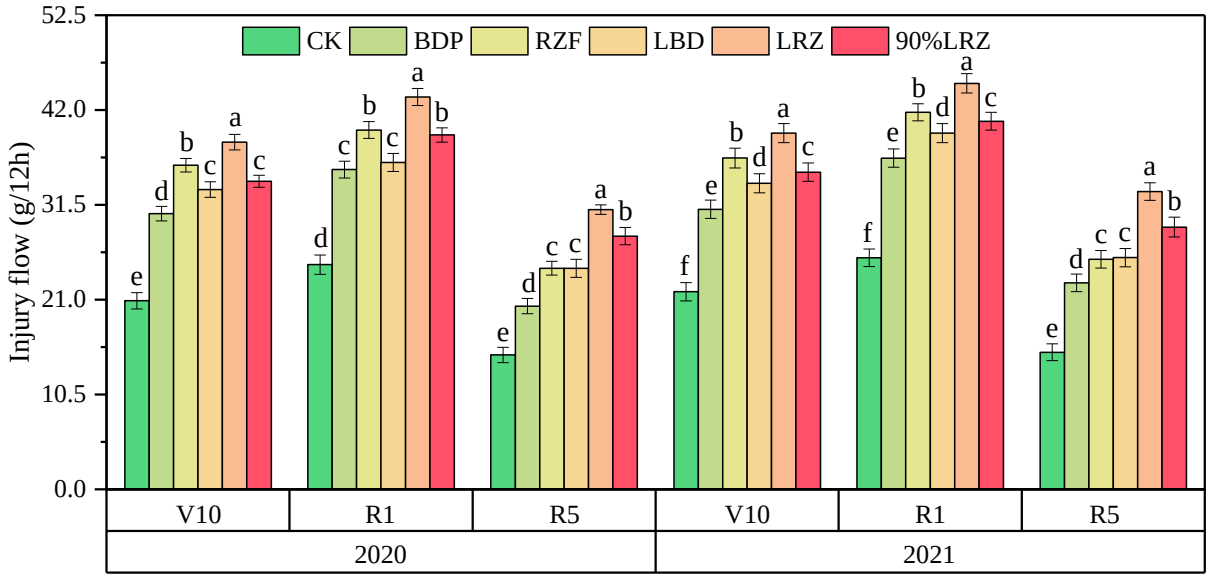

Fig. 4 – Effect of fertilizer application method on maize injury flow

Effect of different fertilizer application methods on maize dry matter mass of root system

As seen in Figure 5, the one-time mechanical fertilization of the root zone increased root dry matter by 161.23% to 189.10% compared to CK, and the differences were significant. The root dry matter increased by 16.18% to 20.41% in LBD compared to BDP and 14.53% to 19.49% in LRZ compared to RZF, and both showed significant differences, indicating that stratified fertilization can effectively increase root dry matter. 90% LRZ showed no significant difference in maize root dry matter compared with LBD and showed significant difference with RZF, indicating that stratified fertilization with upper holes and lower strips could increase root dry matter with reduced fertilizer application.

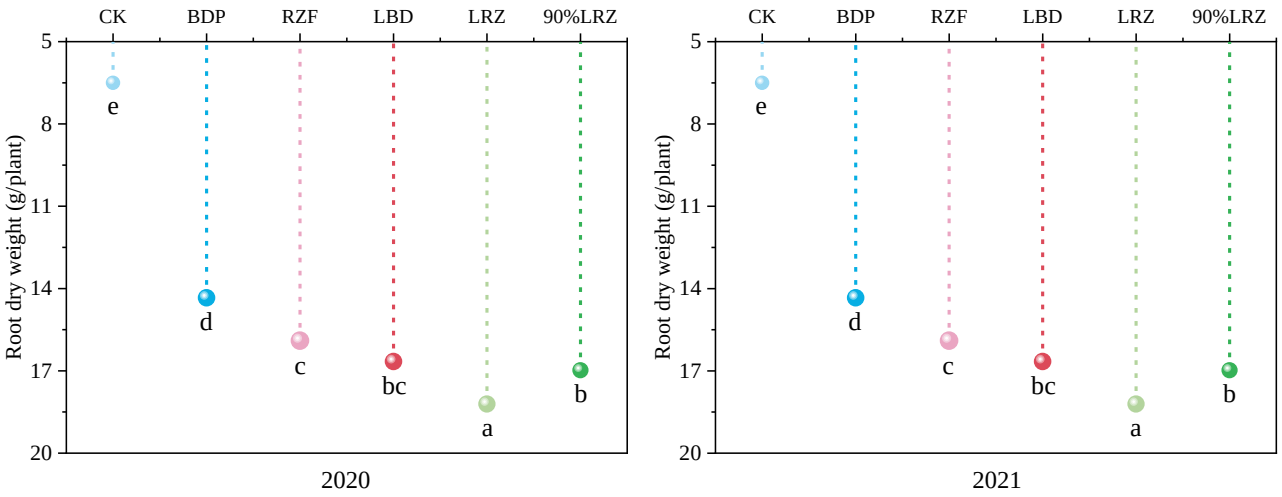

Fig. 5 – Effect of fertilizer application method on maize dry matter mass of root system

Effect of different fertilizer application methods on maize yield and fertilizer utilization

As it can be seen from Table 1, the average 2-year yield of maize under the six treatments ranged from 5700.76 kg/hm^2 to 11216.63 kg/hm^2, and compared with CK, one-time mechanical fertilization in the root zone increased maize yield by 66.87% to 96.76%. LRZ treatment had the highest seed yield and was 11.97% higher than RZF, and LBD was 11.15% higher than BDP seed yield, and all differences were significant, indicating that layered fertilizer application could effectively improve seed yield. Yield in LRZ was reduced by 5.71% when fertilizer application was reduced by 10%. The yield difference between LBD and 90% LRZ was not significant, indicating that the effect of RZF and LBD on yield was not significant when weight loss was 10%, and it can be concluded that fertilizer layered application can reduce fertilizer application but not affect yield.

Table 1

Effect of fertilizer application method on maize yield and fertilizer utilization

Treatment	2020			2021		
	Grain yield (kg/hm^2)	RE (kg/kg)	PFP (kg/kg)	Grain yield (kg/hm^2)	RE (kg/kg)	PFP (kg/kg)
CK	5424.54 e	-	-	5976.98 d	-	-
BDP	9480.52 d	13.796 d	32.247 c	9545.51 c	14.017 d	32.468 c
RZF	9913.85 c	15.270 c	33.721 c	10121.97 b	15.978 c	34.428 b
LBD	10568.02 b	17.495 b	35.946 b	10580.30 b	17.537 b	35.987 b
LRZ	11198.70 a	19.640 a	38.091 a	11234.56 a	19.762 a	38.213 a
90% LRZ	10574.95 b	19.465 a	39.966 a	10576.98 b	19.473 a	39.973 a

As shown in Table 1, the average 2-year agronomy efficiency of maize under the six treatments ranged from 13.906 kg/kg to 19.701 kg/kg, with BDP having the lowest agronomy efficiency of 13.906 kg/kg. RZF, LBD, LRZ and 90% LRZ showed 12.35%, 25.95%, 41.67% and 40.00% increase in agronomy efficiency compared to them, respectively, and all were significantly different. There was no significant difference in agronomy efficiency between LRZ and 90% LRZ compared to each other. LBD could effectively improve the agronomy efficiency of fertilizer by 25.95% compared to BDP, and LRZ improved the agronomy efficiency by 26.10% compared to RZF, indicating that layered fertilizer application could improve fertilizer efficiency and reduce nutrient loss.

As can be seen from Table 1, the average 2-year partial factor productivity of maize under the six treatments ranged from 32.357 kg/kg to 39.970 kg/kg. BDP had the lowest partial factor productivity of 32.357 kg/kg, while RZF, LBD, LRZ and 90% LRZ had 5.31%, 11.15%, 17.91% and 23.53% increase in partial factor productivity compared to them, respectively, and all were significantly different. The partial factor productivity was significantly different between LRZ and 90% LRZ compared to each other. LBD was effective in increasing fertilizer partial factor productivity by 11.15% compared to BDP, and LRZ increased fertilizer partial factor productivity by 11.97% compared to RZF, indicating that layered fertilizer application can increase seed yield with the same amount of fertilizer application.

DISCUSSIONS

The one-time layered application of fertilizer in the root zone compared with conventional unlayered application increased yields by 11.15% to 11.97% on average in 2020 and 2021. This indicates that the layered fertilizer application method can achieve crop yield increase, while there is no significant difference in yield between 90% LRZF and BDP compared to both in 2020 and 2021, indicating that RZF can be used at 10% fertilizer reduction without yield reduction compared to LBD, which improves the fertilizer efficiency utilization. Other scholars have similar findings, such as Gong (*Gong et al.*, 2019) who found that layered bottom application of slow-release fertilizer promoted the growth and development of late summer maize, increased dry matter accumulation in late summer maize. Zhang (*Zhang et al.*, 2017) found that maize leaf area index, dry matter accumulation, yield and N fertilizer utilization efficiency were significantly higher with layered fertilization technology than BDP under the same N application, and yield and N fertilizer partial factor productivity were increased by 5.5% and 7.9%.

The data showed that in 2020 and 2021 LBD had an average increase in agronomy efficiency and partial factor productivity of 25.95% and 11.15% over BDP, and LRZ had an average increase in agronomy efficiency and partial factor productivity of 26.10% and 11.97% over RZF. LRZ had the highest seed yield of 11216.62 kg/hm^2 and the highest agronomy efficiency of 19.701 kg/kg, and the partial factor productivity was second only to 90% LRZ with 38.152 kg/kg. The combined effect of layered fertilizer application and point-applied application, the upper point-applied application of fertilizer allowed the plants to be thick and strong at the seedling stage because fertilizer point-applied application increased the local nutrient supply concentration in the root zone and fertilizer nutrient uptake rate became greater, promoting plant growth and development. The plant height, stalk diameter, leaf area and injury flow rate were the highest in LRZ at the V5, V10, R1 and R5 stages.

The fertilizer application method of upper layer fertilizer point-applied application and lower layer fertilizer banding application makes the spatial distribution pattern of fertilizer particles in the tillage layer soil approximate to a cone platform with small top and large bottom, while the root system of maize plant in the spatial distribution approximate to a cone, so the fertilizer supply is completely concentrated in the coverage of maize plant root system, which avoids nutrient wastage in space, and at the same time promotes deep rooting to avoid plant collapse. Therefore, layered root zone fertilization is currently one of the best fertilizer application methods to improve fertilizer utilization efficiency, as well as a new research idea for improving crop yields.

CONCLUSIONS

The one-time mechanical LRZ and LBD fertilizer application in the root zone increased yields by 11.97% and 11.15%, respectively, compared with BDP and RZF, and the differences were significant, indicating that mechanical layered application can replace the BDP and phased application patterns to achieve increased crop yields. The average increase in agronomy efficiency and partial factor productivity was 25.95% and 11.15% for LBD over BDP and 26.10% and 11.97% for LRZ over RZF, and the differences were significant, indicating that mechanized layered fertilizer application can significantly improve fertilizer utilization and reduce fertilizer losses and surface source pollution.

ACKNOWLEDGEMENT

This work was financially supported by National Key Research and Development Plan of China (2017YFD0700703).

REFERENCES

[1] Cassman, K. G., Dobermann, A., Walters, D. T., Yang, H. (2003). Meeting cereal demand while protecting natural resources and improving environmental quality. *Annual Review of Environment and Resources*, *28*, 315-358.

[2] Shemi, R., Wang, R., Gheith, E. M. S., et al. (2021). Effects of salicylic acid, zinc and glycine betaine on morpho-physiological growth and yield of maize under drought stress. *Scientific Reports*, *11*(1).

[3] Usman, B., Nawaz, G., Zhao, N., et al. (2021). Programmed Editing of Rice (Oryza sativa L.) OsSPL16 Gene Using CRISPR/Cas9 Improves Grain Yield by Modulating the Expression of Pyruvate Enzymes and Cell Cycle Proteins. *International Journal of Molecular Sciences*, *22*(1).

[4] Luan, H., Gao, W., Huang, S., et al. (2020). Substitution of manure for chemical fertilizer affects soil microbial community diversity, structure and function in greenhouse vegetable production systems. *Plos One*, *15*(2).

[5] Ren, H., Cheng, Y., Li, R., et al. (2020). Integrating density and fertilizer management to optimize the accumulation, remobilization, and distribution of biomass and nutrients in summer maize. *Scientific Reports*, *10*(1).
[6] Xu, X., He, P., Pampolino, M. F., et al. (2019). Spatial variation of yield response and fertilizer requirements on regional scale for irrigated rice in China. *Scientific Reports*, *9*.
[7] Shi, Y., Zhu, Y., Wang, X., et al. (2020). Progress and development on biological information of crop phenotype research applied to real-time variable-rate fertilization. *Plant Methods*, *16*(1).
[8] Wei, S., Wang, X., Li, G., et al. (2019). Plant density and nitrogen supply affect the grain-filling parameters of maize kernels located in different ear positions. *Frontiers in Plant Science*, *10*.
[9] Anstoetz, M., Rose, T. J., Clark, M. W., et al. (2015). Novel applications for oxalate-phosphate-amine metal-organic-frameworks (OPA-MOFs): can an iron-based OPA-MOF be used as slow-release fertilizer? *Plos One*, *10*(12).
[10] Ye, Z., Chu, G., Ye, J., et al. (2010). A comparison of mobility and availability of granular and fluid phosphate fertilizers in calcareous soils under laboratory conditions (固、液态磷源在石灰性土壤中的移动性及其对土壤有效磷含量影响的研究) *Journal of Plant Nutrition and Fertilizers*, *16*(06), 1433-1438.
[11] Zhu, Z., Jin, J. (2013). Fertilizer use and food security in China (保障我国粮食安全的肥料问题) *Journal of Plant Nutrition and Fertilizers*, *19*(02), 259-273.
[12] Chen, Z., Yuan, F., Yao, Z., et al. (1995). The movement and leaching loss of NO_3-N in profile of chao soil in Beijing (北京潮土NO_3-N在土体中的移动特点及其淋失动态) *Journal of Plant Nutrition and Fertilizers,* (02), 73-81.
[13] Cao, Z., De Datta, S. K., Fillery, I. R. P. (1984). Nitrogen-15 balance and residual effects of urea-N in wetland rice fields as affected by deep placement techniques. *Soil Science Society of America Journal*, *48*(1), 203-208.
[14] Savant, N. K., De Datta, S. K. (1980). Movement and distribution of ammonium-N following deep placement of urea in a wetland rice Soil. *Soil Science Society of America Journal*, *44*(3), 559-565.
[15] Zhou, C., Li, Y., Chen, P., et al. (2020). Effects of Single Application of Fertilizer on Yield and Nitrogen Utilization of Mulching Summer Maize. (一次性施肥模式对覆膜夏玉米产量与氮素利用的影响) *Transactions of the Chinese Society for Agricultural Machinery*, *51*(10), 329-337.
[16] Liu, X., Chen, X., Wang, H., et al. (2017). Effects and principle of root-zone one-time N fertilization on enhancing rice (*Oryza sativa* L.) N use efficiency (根区一次施氮提高水稻氮肥利用效率的效果和原理) *Soils*, *49*(05), 868-875.
[17] Chen, X., Luo, X., Wang, Z., et al. (2014). Experiment of synchronous side deep fertilizing technique with rice hill-drop drilling (水稻穴播同步侧位深施肥技术试验研究) *Transactions of the Chinese Society of Agricultural Engineering*, (16), 1-7.
[18] Wang, Z., Dong, Y., Yang, K. (1993). Study on the fertilizer practice of corn used layer by layer manuring and according to fertilizer radio in low damp land (低湿耕地玉米分层配比施肥的研究) Journal of Heilongjiang August First Land Reclamation University, (02), 10-14.
[19] Wang, Z., Zhang, X., Chen, S., et al. (2008). Effects of localized irrigation and fertilizing on physiological traits, root distribution and yield of winter wheat (分层施肥及供水对冬小麦生理特性、根系分布和产量的影响). *Acta Agriculturae Boreali-Sinica*, *23*(06), 176-180.
[20] Wen, Y., Wang, D. (2017). Basal fertilization in strips at different soil depths to increase dry matter accumulation and yield of winter wheat. (底肥分层条施提高冬小麦干物质积累及产量) *Journal of Plant Nutrition and Fertilizers*, *23*(05), 1387-1393.
[21] Ma, Y., Wu, M., Guo, X., et al. (2019). Soil water distribution and phosphorus utilization in summer maize field under new tillage and fertilization method (新型耕作施肥方式下夏玉米田土壤水分分布和磷素利用研究) *Journal of Soil and Water Conservation*, *33*(02), 98-102.
[22] Zhang, S., Li, X., Liu, P., et al. (2018). Effects of soil tillage and fertilization on root microstructure and yield in maize (土壤耕作与施肥配合对玉米根系微观结构及产量的影响) *Crops*, (06), 144-148.
[23] Gong, Y., Duan, W., Wang, G., et al. (2019). Effects of layered bottom application of slow-release fertilizer on growth，dry matter accumulation and yield of summer maize. (缓释肥分层底施对夏玉米生长、干物质积累和产量的影响) *Journal of Henan Agricultural Sciences*, *48*(10), 41-46.
[24] Zhang, M., Qiao, J., Gu, L., et al. (2017). Influence of nitrogen fertilizer combined application in different soil layers on growth development and nitrogen use of summer maize. (不同土层氮肥配施方式对夏玉米生长发育及氮肥利用的影响) *Chinese Agricultural Science Bulletin*, *33*(20), 66-70.

MATERIAL CHARACTERISTICS OF VEGETABLE SEEDS WITH SMALL GRAIN SIZE AND DESIGN OF SEED METERING DEVICE
/
小粒径蔬菜种子物料特性研究与排种器的设计

Kaixing ZHANG[1)], Guoliang MA[1)], Jingfeng LI[1,3)], Xiuyan ZHAO[*2)] [1]
[1)] College of Mechanical and Electronic Engineering, Shandong Agricultural University, Shandong / China;
[2)] College of Information Science and Engineering, Shandong Agricultural University, Shandong / China;
[3)] Shandong Provincial Engineering Laboratory of Agricultural Equipment Intelligence, Shandong / China;
Tel: +86 13954895451; E-mail: zhaoxy@sdau.edu.cn
Corresponding author: Xiuyan Zhao
DOI: https://doi.org/10.35633/inmateh-68-78

Keywords: *agricultural mechanization engineering; multiple-grain size; pneumatic; seeder*

ABSTRACT
In order to solve the problems of poor universality and complex structure of the current air-suction precision seed metering device for small vegetable seeds, an air-suction precision seed metering device based on the physical characteristics of small vegetable seeds was developed. The physical characteristics of several typical small vegetable seeds were measured to provide a theoretical basis for the design of air-suction precision seed metering device. Analyzed the force on the seed during seed metering, and used discrete element method to analyze the overall state of the seed at different times in combination with the basic structure. The experiment was designed with the pass rate, replay rate and miss rate as experimental indicators. The regression model was established to obtain the reasonable range of each parameter. The experimental results showed that when the rotary table speed was 28.65 r/min and the working negative pressure was 4.40 kPa, the seeding pass rate of the seed meter was 91.07%, the replay rate was 4.70%, and the missed rate was 4.23%.

摘要
针对目前小粒径蔬菜种子气吸式精密排种器存在的通用性差、结构复杂等问题，设计了一种基于小粒径蔬菜种子物理特性的气吸式精密排种器。测定多种典型小粒径蔬菜种子的物理特性，为排种器的设计提供理论基础，分析排种过程中种子受力情况，结合基本结构运用离散元方法对种子不同时间的整体状态进行分析。以合格率、重播率、漏播率为实验指标，通过正交试验分析得出排种时各参数的合理区间。实验结果表明：当转盘转速为 28.65r/min，工作负压为 4.40kPa 时，排种器排种合格率为 91.07%，重播率为 4.70%，漏播率为 4.23%。

INTRODUCTION
In recent years, with the increase of global vegetable consumption demand, vegetables have become the second largest crop after grains, among which cabbage, rape and other small seed vegetables have the most promotion value, the most extensive planting area and large demand. At present, vegetable planting in most areas of China is mainly based on traditional manual sowing, and the mechanization of vegetable sowing has been at a low level and degree (*Yu et al., 2011; Xia et al., 2008*). Therefore, it is of great significance to study the precision seed metering device for small diameter vegetables for promoting the mechanized production of sowing.

The performance of precision seed metering device directly affects the sowing quality. The air-suction seeder has become the research direction of precision seeder due to its advantages of no seed damage and high operating speed (*Liu et al., 2017; Ding et al.,2018*). *Hensh et al., (2022*), used the electronic metering device to monitor and feed back the seed metering process of the precision seed metering device in real time, reducing missed seeding and improving the precision of seeding quality. *Wang et al., (2022*), have designed a vacuum central cylinder seed metering device, which can realize the replacement of devices with different diameters such as suction holes and stirring, and achieve the effect of high seed suction qualification rate. *Gautam et al., (2019)* based seed metering mechanism provides good seeding uniformity for sowing of

[1] *Kaixing Zhang, Prof. Ph.D.; Guoliang Ma, M.S. Stud.; Jingfeng Li, M.S. Stud.; Xiuyan Zhao, Prof. Ph.D.*

different seeds like okra, cowpea, groundnut etc. at low cost and without creating any environmental hazards. *Karayel et al., (2004),* determined the vacuum negative pressure requirements when sowing different vegetable seeds by exploring a variety of vegetable seeds.

Although the above research has improved the seed metering quality and precision, it has not yet achieved the sowing of multiple-grain size seeds. Based on the research on the physical characteristics of several common small vegetable seeds, this paper designed an air-suction precision seed metering device for small diameter vegetable seeds with adjustable holes to realize the sowing of different diameter seeds; The seed stacking and seed disturbing performance of seed seeder were analyzed in discrete element simulation; Finally, the best operation parameters of seed metering device were obtained through bench test. The seed metering device overcomes the disadvantage that the traditional seed metering device can only sow seeds with the same grain size, greatly improves the universality of the seed metering device, and realizes the sowing of seeds with multiple-grain size.

MATERIALS AND METHODS

Determination of physical parameters of small vegetable seeds

The whole frame

The research objects selected in this paper are six typical small grain vegetable seeds, namely Suzhou Qing, Shanghai Qing, Fast vegetable, pak choi, Chinese cabbage, and Chinese little greens. Through electronic balance, measuring cylinder, vernier caliper, angle of repose tester and other instruments, a thousand seeds weight, density, particle size distribution, angle of repose, and sliding friction angle of six typical small vegetable seeds are measured and analyzed, and the physical characteristics of small grain seeds are fully studied, It can provide guidance and reference for the design of key parameters such as the structure design of seed metering device, the size and distribution of shaped holes (*Zhang et al., 2015;Su et al., 2022*). The six typical small grain vegetable seeds selected are shown in Fig.1.

a) Suzhou Qing b) Shanghai Qing c) Fast vegetable d) pakchoi e) Chinese cabbage f) Chinese little greens

Fig. 1 - The six typical small vegetable seeds

Determination of physical characteristic parameters

Determination of a thousand seeds weight

The study of a thousand seeds weight is helpful to determine the negative pressure value of seed suction, and the electronic balance with an accuracy of 0.001 g is used to measure small vegetable seeds. The determination was carried out in 1000 clean vegetable seeds randomly for weighing and repeated twice. If the weight difference between the two times is more than 5% of the total weight of the sample, weigh the third sample, and select the sample with the smallest difference between the two times to calculate the average value. Take the average value as a thousand seeds weight test value.

Determination of angle of repose of seeds

The angle of repose of seeds can reflect the scattering characteristics and internal friction characteristics of seed materials. The selected measuring instrument is BT-1001 intelligent powder characteristic tester. The experimental instrument and measuring principle diagram are shown in Fig. 2.

a) Angle of repose tester b) measuring principle

Fig. 2 - The intelligent powder characteristic tester and measuring principle

During the measurement, the seeds are stacked on the plane as a cone, and the important parameters for measuring the angle of repose are obtained: the horizontal bottom radius of the material cone, the height of the cone from which the seeds are stacked. The angle of repose is calculated using Eq.(1):

$$\theta' = \arctan\frac{H}{R} \quad (1)$$

where:

θ' is angle of repose, [°]; H is the height of the species cone, [mm]; R is the horizontal bottom circle radius of the material cone, [mm].

Determination of sliding friction angle of seeds

The sliding friction angle of the seed is of great significance to the design of the seed box and the shape design of the seed metering device. During the measurement, 30 groups of 6 types of small vegetable seeds were randomly selected from each type, and 100 seeds were taken from each group and placed on the tester. Slowly shake the handle of the tester to make it more inclined. When the number of seeds to be measured on the tester reaches more than 95%, the inclination angle of the tester was measured, and the data were measured and recorded for many times. Finally, the average value of the measured data was selected.

Determination of seed size

The particle size of the seed has a great influence on the design of the pore size in the later stage. The seeds of the above six typical vegetables are spherical. In this experiment, a vernier caliper with an accuracy of 0.02mm is used to measure the particle size of the seed. Five plump and uniform seeds are selected from each type of seed. The final particle size of the seed is determined by measuring the selected seeds five times and calculating the average value.

Determination of seed density

Seed density is an important factor affecting the suspension characteristics of materials, which is of great significance to the subsequent seed metering structure design and simulation analysis. Put a certain mass of material in the liquid, determine the actual volume of the measured material, and then calculate the volume and mass of the material to calculate the density. The seed density is calculated using Eq.(2):

$$\rho = \frac{m}{v} \quad (2)$$

where: P is the seed density, [g/cm^3]; m is the mass, [g]; v is the volume, [cm^3].

Repeat the test three times for each type of seed, and take the average value as the test value of this density measurement.

The basic parameters of 6 common vegetable seeds obtained from the test are shown in Table 1.

Table 1

Seed test data

Name	Suzhou Qing	Shanghai Qing	Fast vegetable	pakchoi	Chinese cabbage	Chinese little greens
A thousand seeds weight (g)	3.211	2.317	2.089	1.991	3.082	2.749
Angle of repose (°)	26.07	25.65	23.57	24.92	24.39	23.92
Sliding friction angle (°)	21.3	20.5	20.7	21.4	20.6	20.1
Average seed size (mm)	1.71	1.46	1.44	1.41	1.51	1.23
Seed density (g/cm^3)	1.053	0.891	0.880	0.873	0.988	0.927

The overall structure and kinematic analysis of seed feeding process

The whole frame

Air - suction precision seed metering device for small vegetable seeds is shown in the figure Fig. 3. The fixed disc is provided with seed disturbing rod as shown in Fig.4, to stir the seeds close to the seed metering disc, so that the seeds continuously move and surge upward, so as to reduce the friction and adhesion between the seeds and improve the seed filling performance.

One side of the double disc is an air chamber, which is connected with the fan pipe through the air chamber shell, and the other side is a seed chamber. During the operation, the disc rotates, and the seeds leave the negative pressure area with the rotation of the disc. The shaped hole loses the adsorption force on the seeds. The seeds fall into the seed guide tube by their own weight and fall into the seed bed along the seed guide tube, and finally complete seed metering.

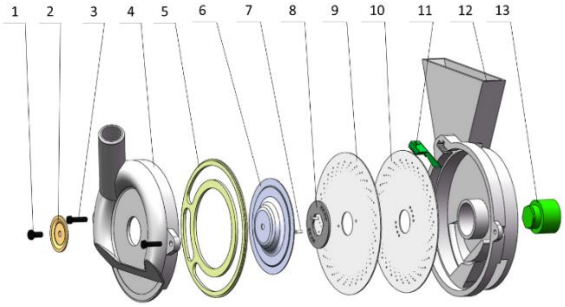

Fig. 3 - Schematic diagram of seed metering device structure

1 - Nut of cover plate; 2 - Cover plate of air chamber shell; 3 - Fix bolts; 4 - Air chamber shell; 5 - Suction pad; 6 - Air cushion pressure plate; 7 - Insert disc bolts; 8 - Fixed insert disc; 9 - Rotating disc; 10 - Fixed disc; 11 - Clearer; 12 - Back cover; 13 - Shaft

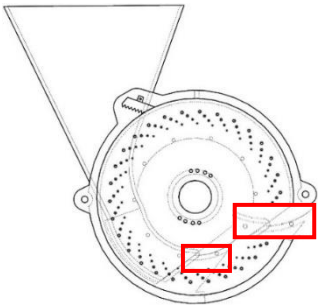

Fig. 4 - Design of the seed disturbing

Design of double discs structure with multiple-grain size

The double disc structure is shown in Fig.5a). The air-suction precision seed metering device is provided with a rotary disc and a fixed disc at the same time. The two discs are rotated axially and oppositely to make the holes with the same diameter on the two discs coincide, and seeds with different seed sizes can be sown.

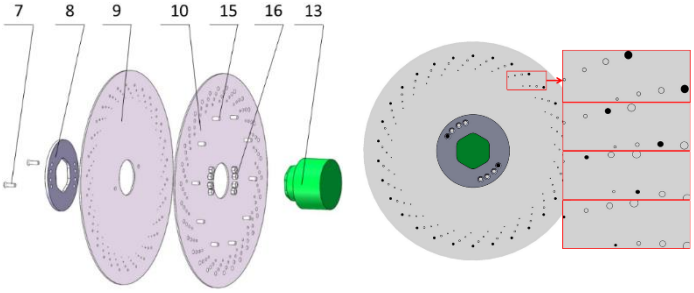

a) Double disc structure *b) Diagram of hole combinations*

Fig. 5 - Schematic diagram of double disc structure

7 - Insert disc bolts; 8 - Fixed insert disk; 9 - Rotating disk; 10 - Fixed disc; 13 - Shaft; 15 - Stir bar; 16 - Hold-down nut

Through theoretical calculation and experience reference, double discs with a diameter of 240mm are selected and made of 1mm stainless steel plates. The distribution of disc shaped holes is shown in Fig.5b). Four kinds of shaped holes A, B, C and D from large to small are set on the two discs. In the four rows of shaped holes on the outside, the black shaped holes indicate that the two disc apertures are connected, while the gray shaped holes indicate that they are not. As the rotating disc rotates clockwise, the corresponding holes are connected in the order of type A holes - type C holes - type B holes - type D holes. In the fixed plug-in disc, the black fixed round hole indicates the fixed position of the plug-in disc bolt.

Kinematic analysis of seed metering process

The seeding process of the seed metering device determines the seeding accuracy of the seed metering device. Ignoring the vibration of the seeder during the seeding process, the seed is approximately regarded as a sphere, and the three-axis Cartesian coordinate system is established with the seed centroid as the origin.

The direction of friction force on the seed is the positive X axis, the direction of centrifugal force is the positive Y axis, and the direction of negative pressure adsorption force is the positive Z axis. Kinematics analysis of the seeding process of the double disc air suction seed metering device is carried out. The process of seed force analysis is shown in Fig.6.

In the process of seed suction, the force on the seed at the hole is balanced. The force analysis of seeds is calculated using Eq.(3):

$$F_p = \sqrt{J^2 + G^2 + F_f{}^2 + 2G\sqrt{J^2 + F_f{}^2}\sin(\theta+\phi)} \cdot \tan\alpha \quad (3)$$

Under the actual working condition, considering factors such as the vibration and friction resistance of the whole machine that affect the seed suction process, and making up for factors such as different seed shapes and sizes and mutual collision and extrusion in the middle, the external condition coefficient K1 is 1.8~2.0 and the seed suction reliability coefficient K2 is 1.8~2.0 according to the mechanical design manual. The negative pressure value of seed at the molding hole is calculated using Eq.(4):

$$P = \frac{4K_1K_2\sqrt{J^2 + G^2 + F_f{}^2 + 2G\sqrt{J^2 + F_f{}^2}\sin(\theta+\phi)} \cdot \tan\alpha}{\pi D^2 \cos^2\alpha} \quad (4)$$

The total speed of seed implantation is calculated using Eq.(5):

$$V_D = \sqrt{V_l^2 + V_c^2 + (gt)^2 + 2V_l\sqrt{(gt)^2 + \left(\frac{zk}{2\pi R}V_l\right)^2}\sin(\gamma+\psi)} \quad (5)$$

where: φ and ψ are auxiliary angles obtained by formula transformation, [°].

When the seed falls on the seed bed, the seed and seed bed will contact and collide to produce rebound, and the plant spacing cannot be guaranteed. In order to reduce the bounce and scattering during seed implantation, a seed guide tube with appropriate curve is selected to make the seed reach the outlet with a larger horizontal velocity to offset the forward speed of the seeder. In order to reduce the variation coefficient of plant spacing of the seed metering device, the rotation speed of the seed metering device can be appropriately reduced under the condition of meeting the seed sowing requirements.

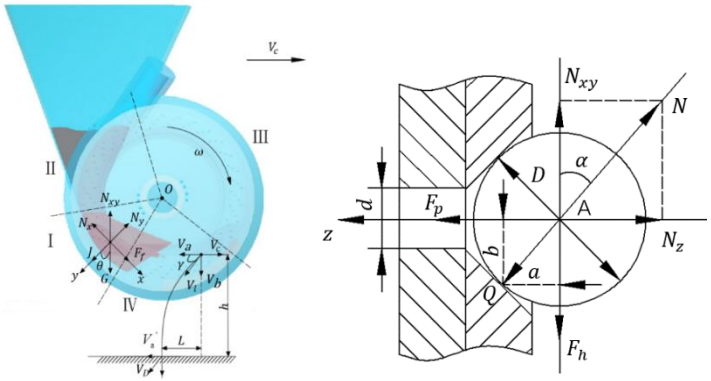

a) XY plane kinematics analysis *b) Z plane kinematics analysis*

Fig. 6 - The process of seed force analysis

Note: In the Figure 6, the notations are:

a) I is seed filling area, II is seed clearing area, III is seed carrying area, and IV is seed feeding area.

b). G is seed gravity, [N]; J - the centrifugal force exerted on the seed, [N]; F_f - the friction force on the seed, [N]; N_x and N_y are the supporting force components of x-axis and y-axis respectively, [N]; N_{xy} - the resultant force of N_x and N_y, [N]; O - the center of the disc; V_a - the horizontal partial velocity when the seed falls off, [m/s]; V_b - the vertical partial velocity when the seed falls off, [m/s]; V_C - the forward speed of the planter, [m/s]; V_l - the linear velocity when the seed falls off, [m/s]; V_D - the speed of seed implantation, [m/s]; H - the seed scattering height, [m]; L - the horizontal displacement of seed, [m]; ω - the rotation angular velocity of seed sucking disc,[rad/s]; θ - the angle between the centrifugal force and the gravity of the seed, [°]; γ - the included angle between V_l and V_a, [°].

Analysis of seed metering device based on discrete element method

Based on the discrete element method, the stacking distribution state of seeds at each time point when they enter the seed box, the movement law of seeds in the seed metering device when they are disturbed and the overall movement trend of the population are analyzed to verify the rationality of the structure design of the air-suction precision seed metering device.

Analysis of Seed Stacking Process

The seed state of the stacking process is shown in Fig.7. The seeds directly hit the seed carrier plate and the bottom of the seed box under the gravity, causing the seeds to bounce. Due to the continuous accumulation of the seeds below, the sliding slope of the upper layer seeds in the seed box keeps getting

longer, the slope angle increases, the friction force on the seeds gets bigger and bigger, the speed of the seeds gradually slows down, and the missile phenomenon gradually weakens. It can be seen from the figures Fig7.a) to d) that the impact force of seed falling is relatively large 7 seconds ago. The bounced seeds fall to the seed support plate under gravity after reaching the highest point, and the seeds fall back to the bottom of the seed box under the effect of the inclined force of the seed support plate. Because the seed support plate is set reasonably, the seeds will not leave the seed support plate. The seeds are always above the seed support plate, so there will be no seed loss; After the seeds continue to fall for 9s, the upper layer seeds in the metering chamber are in a relatively stable state, and the stable state of the upper layer seeds in the seed chamber is more conducive to the adsorption of seeds in the filling stage, reducing the rate of missed seeding. In the Fig.7 f), the seed accumulation in the seed metering device reaches the saturation state, and the seed amount remains constant, and then the seed will be slowly replenished to the air-suction precision seed metering device.

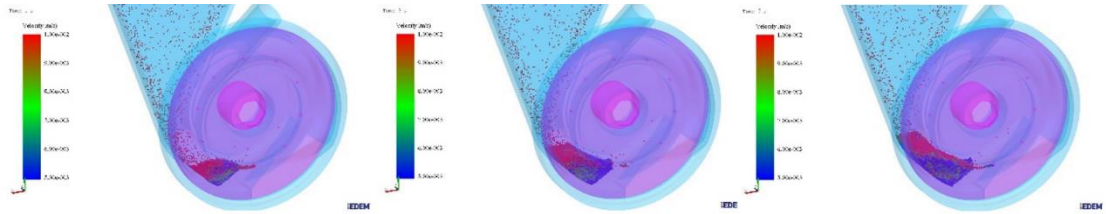

a) 1s seed dropping state *b) 3s seed dropping state* *c) 5s seed dropping state*

d) 7s seed dropping state *e) 9s seed dropping state* *f) 11s seed dropping state*

Fig. 7 - Analysis of seed state in stacking process

Analysis of disturbed seed state

When the seed flows uniformly to the seed filling area under its own gravity, a seed pile is formed in the seed filling area. It can be found in Fig.8 of the seed disturbing process that when the seed disturbing rod contacts the detained seed, the detained seed is pushed by the seed disturbing rod, and the detained seed returns to the upper part of the seed support plate under the force. As the seed disturbing rod rotates out of the seed disturbing tank, part of the seed falls into the seed disturbing tank, but it will never flow out of the seed disturbing tank, and there will be no seed scattering, And the seeds around the seed disturbing rod are obviously stressed and fast. The seed disturbing rod stirs and combs the seeds close to the seed metering disc, making the seeds continuously move upward to reduce the friction and adhesion between the seeds and improve the seed filling capacity.

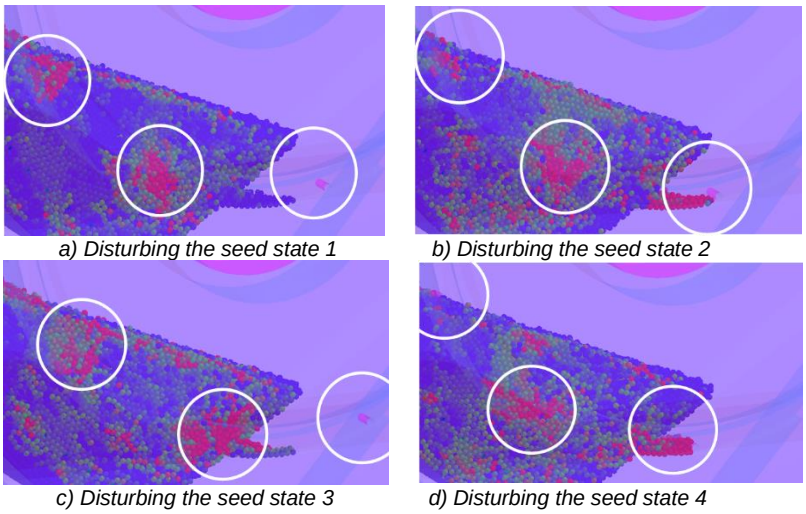

a) Disturbing the seed state 1 *b) Disturbing the seed state 2*

c) Disturbing the seed state 3 *d) Disturbing the seed state 4*

Fig. 8 - Seed disturbing process

RESULTS AND DISCUSSION

Bench Test of Air-Suction Small Vegetable Seeds Metering System

Test material

After theoretical analysis and simulation analysis, in order to verify the reliability and feasibility of air-suction precision seed metering device for small vegetable seeds with multiple-grain size(Li et al., 2018; Shi et al., 2015), a seed metering performance test was conducted in the Seed Metering Performance Laboratory of Shandong Agricultural University, and the variable particle size double disc air-suction precision seed metering device was installed on the JSP-12 seed metering device performance test bench, as shown in Fig.9. The small seed size used in the bench test was Shanghai Qing, with a diameter of about 1.3 mm, 1000 seed weight of 2.317 g, and water content of 4.21%.

Fig. 9 - Seed Meter Performance Tester

1 - High-speed camera; 2 - transmission shaft; 3 - Seed metering device; 4 - Negative pressure tube; 5 - Seed tube

Orthogonal test analysis of velocity and pressure

In order to further explore the interaction and influence of negative pressure and rotating speed on the seed metering performance of the seed metering device, this paper conducted an orthogonal experiment on the seed metering device (*Li et al., 2020*). From previous experience, it can be concluded that when the working pressure (negative pressure) is 3.5~5kPa and the forward speed is 5~9km/h, the seed metering device has high seed metering performance. In this orthogonal experiment, speed and pressure are selected as two factors in the orthogonal experiment. There are 16 groups in total. Each group of experiments is repeated for 3 times. The average value of the data is taken. Each experiment deals with no less than 100 seeds. The experimental results are shown in Table 2.

Orthogonal test results **Table 2**

Test number	Test factors		Evaluation index		
	Forward speed A (km/h)	Work negative pressure, B (kPa)	Missed rate Y1 (%)	Replay rate Y2 (%)	Pass rate Y3 (%)
1	8	4	6.6	3.83	89.57
2	9	3.5	10.83	6.15	83.02
3	5	3.5	9.11	4.97	85.92
4	9	5.5	5.5	9.73	84.77
5	7	4.5	4.05	3.98	91.97
6	5	4.5	5.24	6.2	88.56
7	5	4.5	5.1	6.12	88.78
8	5	3.5	9.22	5.02	85.76
9	9	5.5	5.51	10.05	84.44
10	5	5.5	5.88	10.1	84.02
11	7	5.5	4.32	10.24	85.44
12	7	4.5	4.1	3.95	91.95
13	7	5.5	4.47	10.58	84.95
14	6	5	3.8	6.89	89.31
15	8	5	4.2	6.21	89.59
16	6	4	6.5	3.52	89.98

In order to further study the influence of working pressure and forward speed on missed rate, replay rate and pass rate, the test data was further processed by Design Expert 10.0 software to obtain the response figure of interaction factors (*Gao et al., 2019*). It can be seen from Fig.10 that the interaction factors have a significant impact on the miss rate, replay rate and qualification rate (*Ding et al., 2018*). When the forward speed of the seed metering device is 6~8km/h, that is, the rotating speed is 22~30r/min, and the working pressure is within the range of 4kPa~5kPa, the missed seeding rate and replay rate of the seed metering device are at a low level, while the qualification index is at a high level.

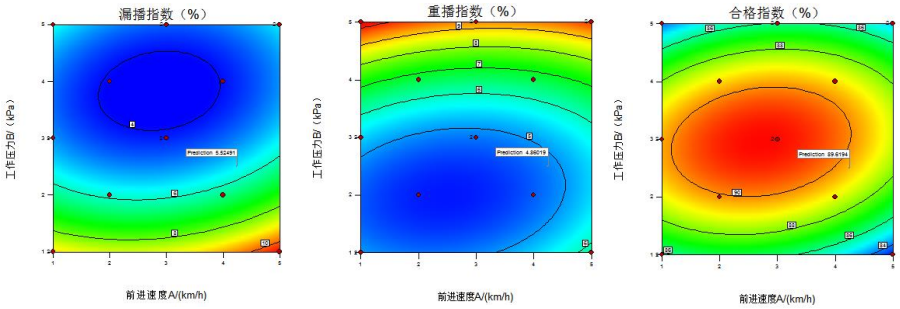

a) missed seeding index b) replay seeding index c) pass seeding index

Fig. 10 - Response figure of interaction factors

Model optimization and verification

In combination with the boundary conditions of various factors, a parametric mathematical model is established for optimal solution. The objective function and constraint conditions are as follows Eq.(6):

$$\begin{aligned} &\max Y_3 = f_3(A,B) \\ &\min Y_1 = f_1(A,B) \\ &\min Y_2 = f_2(A,B) \\ &S.T.\begin{cases} Y_1 \le 8.0\% \\ Y_2 \le 15.0\% \\ Y_3 \ge 80.0\% \\ 6km/h \le A \le 8km/h \\ 4.0kPa \le B \le 5.0kPa \end{cases} \end{aligned} \tag{6}$$

Y_3 in the above equation, namely the qualification index, is the ultimate optimization goal. The regression model is optimized using Design Expert 10.0 to obtain the optimal optimization parameters of the seed metering device: forward speed 7.72 km/h, working pressure 4.37 kPa, at this time, the pass rate is 91.07%, the missed rate is 4.23%, and the replay rate is 4.70%.

Fig. 11 - Optimization test verification

As shown in Figure 11, the optimized theoretical results were tested on the seed metering device performance test bench. Here, the optimized data is adjusted appropriately, the forward speed of the seed metering device is set to 7.72 km/h (the corresponding speed is 28.56 r/min), the working pressure is set to 4.40kPa, and four repeated tests are carried out. The average value of the qualified seed metering index is 91.02%, the average value of the replaying index is 4.71%, and the average value of the missed seeding index is 4.27%. The bench test results are basically consistent with the theoretical analysis results, which can be used as the final optimal working speed.

CONCLUSIONS

(1) The material properties of six typical small vegetable seeds were studied and the main physical parameters of the selected vegetable seeds were determined.

(2) Based on the characteristic parameters of small vegetable size seed material, an air-suction precision metering device for multiple-grain size small vegetable seed was developed. Based on the discrete element theory, the design of seed disturbing rod, seed disturbing slot and seed box is verified and analyzed.

(3) The optimal horizontal range of the operation parameters of the seed metering device is that the rotary table speed is 22~30 r/min, and the working negative pressure is 4~5 kPa. The optimal optimization parameters of the seed metering device system are as follows: the rotational speed is 28.56 r/min, the negative pressure is 4.40 kPa, the pass rate is 91.07%, the replay rate is 4.70%, and the missed rate is 4.23%, meeting the seeding demand.

ACKNOWLEDGEMENT

The study is supported by the Natural Science Foundation of Shandong Province (ZR2021ME181).

REFERENCES

[1] Ding Y., Yang J., Zhang L. et al., (2018) Design and experiment on variable reseeding system for rapeseed precision metering device (油菜精量排种器变量补种系统设计与试验). *Journal of Transactions of the Chinese Society of Agricultural Engineering*, Vol. 34, issue 16, pp. 27-36;

[2] Ding L., Yang L., Liu S. et al., (2018). Design of air suction high speed precision maize seed metering device with assistant seed filling plate (辅助充种种盘玉米气吸式高速精量排种器设计). *Journal of Transactions of the Chinese Society of Agricultural Engineering*, Vol. 34, issue 22, pp. 1-11;

[3] Gao X., Xu Y., He X. et al., (2019). Design and Experiment of Diversion Turbine of Air-assisted High Speed Maize Precision Seed Metering Device (气送式高速玉米精量排种器导流涡轮设计与试验). *Journal of Agricultural Machinery and Technologies*, Vol. 50, issue 11, pp. 42-52;

[4] Gautam P V., Kushwaha H L., Kumar A., (2019). Mechatronics Application in Precision Sowing: A Review. *Journal of Current Microbiology and Applied Sciences*, Vol. 8, issue 4.

[5] Hensh S., Raheman H., (2022). An unmanned wetland paddy seeder with mechatronic seed metering mechanism for precise seeding. *Journal of Computers and Electronics in Agriculture*, Vol. 203, issue 107463;

[6] Karayel D., Barut Z.B., Özmerzi A., (2004). Mathematical Modelling of Vacuum Pressure on a Precision Seeder. *Journal of Biosystems Engineering*, Vol. 4, issue 87;

[7] Li B., (2020). Design and experiment of flow adsorption type soybean seed metering device *(流动吸附式大豆集排精量排种器设计与试验)*. Northeast Agricultural University;

[8] Liu Y., Lin J., Li B. et al., (2017) Design and experiment of horizontal disc seed metering device for maize seeder (玉米播种机水平圆盘排种器型孔设计与试验). *Journal of Transactions of the Chinese Society of Agricultural Engineering*, Vol. 33, issue 8, pp. 37-46;

[9] Li R., (2018). *Design and Experimental Study on the Air Suction Type Electric Driving Corn Precision Metering Device (气吸式电驱动玉米精量排种器设计与试验研究)*. Heilongjiang Bayi Agricultural University;

[10] Shi S., (2015). *Design and experimental study of compressed corn precision seed metering device (气压组合孔式玉米精量排种器设计与试验研究)*. China Agricultural University;

[11] Su W, Chen Z., Lai Q. et al., (2022). Design and Test of Wheel-spoon Type Precision Seed-metering Device for Chinese Herbal Medicine Pinellia ternata (轮勺式半夏精密排种器设计与试验). *Journal of Transactions of the Chinese Society for Agricultural Machinery*, Vol. 53, issue 9, pp. 60－71;

[12] Wang B., Na Y., Liu J., (2022). Design and Evaluation of Vacuum Central Drum Seed Metering Device. *Journal of Applied Sciences*, Vol. 12, issue 2159;

[13] Xia H., Li Z., Niu J. et al., (2008). Dynamic model for metering process for pneumatic roller-type vegetable seeder (气力滚筒式蔬菜穴盘播种机吸排种动力学模型的研究). *Journal of Transactions of the CSAE*, Vol. 24, issue 1, pp. 141-146;

[14] Yu J., Wang G., Xin N. et al., (2011). Simulation Analysis of Working Process and Performance of Cell Wheel Metering Device (型孔轮式排种器工作过程与性能仿真). *Journal of Transactions of the Chinese Society of Agricultural Machinery*, Vol. 42, issue 12, pp: 83-87;

[15] Zhang S., Xia J., Zhou Y. et al., (2015). Design and experiment of pneumatic cylinder-type precision direct seed-metering device for rice (气力滚筒式水稻直播精量排种器的设计与试验). *Journal of Transactions of the Chinese Society of Agricultural Engineering*, Vol. 31, issue 01, pp. 11-19.

CONSTRUCTION OF SPARE PARTS IMPORTANCE EVALUATION FOR CROSS-REGION HARVESTER BASED ON CRITIC AND TOPSIS METHOD

/

基于 CRITIC 和 TOPSIS 方法的跨区收割机备件重要性评估

Weipeng ZHANG, Bo ZHAO*, Yashuo LI, Liming ZHOU, Kang NIU, Hanlu JIANG, Guangrui LI
State Key Laboratory of Soil Plant Machine System Technology, China Academy of Agricultural Mechanization Science Group Co., Ltd. Beijing 100083, China;
Tel: +86-(010)64882659; E-mail: zhaoboshi@126.com
Correspondent author: Bo ZHAO
DOI: https://doi.org/10.35633/inmateh-68-79

Keywords: *Spare parts, Importance evaluation model, Comprehensive evaluation, Service platform*

ABSTRACT

Aiming at the problem of insufficient research on the importance evaluation of agricultural machinery spare parts in the process of cross-region operation of combine harvester, based on CRITIC and TOPSIS, an evaluation model of the importance of spare parts for cross region combine harvesters was established. The CRITIC model was used to calculate the weight of each evaluation index, the weighted TOPSIS evaluation model was used to process the data, and the relative closeness between the spare parts of each harvester to be evaluated and the ideal solution was calculated. Finally, the spare parts resource management decision-making system platform is developed to effectively integrate the spare parts resource allocation. The results show that the model can reasonably and effectively evaluate the important demand degree of combine harvester spare parts, and has a good reference value for the cooperative service of agricultural machinery service vehicles and the priority degree of spare parts loading.

摘要

针对联合收割机跨区作业过程中，农机备件重要度评价研究不足的问题，建立了基于 CRITIC 和 TOPSIS 法的跨区作业联合收割机备件重要度评价模型。运用 CRITIC 模型计算得到各评价指标的权重，运用加权 TOPSIS 评价模型对数据进行处理，并计算各待评价收割机备件与理想解的相对贴近度。建立联合收割机备件重要需求度评价指标体系，最后开发备件资源管理决策系统平台，有效的将备件资源配置进行集成管理，模型能够较合理有效地对联合收割机备件重要需求度进行评价，对农机服务车的协同服务，备件装载优先度有较好的参考价值。

INTRODUCTION

In China, as crops mature seasonally from south to north, the demand for harvesters tends to develop across regions (*Chenbo et al., 2020*). Due to the cross-region operation of combine harvester, its work intensity is high and the machine operation load is heave, which easily leads to a sharp increase in the number of machine failure and a strong demand frequency. After the failure occurs (*Vezirov et al., 2021*), in order to ensure the normal field needs of farmers and the urgent request of the farmers for maintenance (*Xiusheng et al., 2017; Zhengxing et al., 2018*), rapid maintenance and replacement of spare parts is the best solution. In recent years, more and more attention has been paid to the development of optimization technology of agricultural machinery service (*Vlădut et al., 2012; Zhou et al., 2014; Han et al., 2020*).

In the process of maintenance and repair of harvester, spare parts are the key factor for the quick troubleshooting of combine harvester (*Chemweno et al., 2015*). At present, in preventive maintenance (*Yu et al., 2022*) and field maintenance *(Gilev et al., 2019),* relevant research on the maintenance configuration process of spare parts, maintenance personnel and joint optimization of maintenance personnel and spare parts had been carried out by the scholars. Adequate spare parts with high service intensity have better availability for equipment. Spare parts inventory reflects the effectiveness of service execution (*Wang et al., 2021*). For example, intelligent optimization algorithm is adopted to supervise and make decisions on a large number of spare parts. In the evaluation of the importance information of spare parts, the evaluation methods adopted, including AHP hierarchical analysis (*Zandi et al., 2020; Zhang et al., 2021*), CRITIC weight, TOPSIS evaluation (*Rostamzadeh et al., 2018; Wang et al., 2022*) and fuzzy comprehensive evaluation (*Li,et al., 2022*), have been effectively recognized.

Although the above methods have solved the problem of spare parts configuration to a certain extent, there are still shortcomings. The spare parts configuration scheme is directly presented without considering the priority of spare parts configuration.

In view of the above problems, this paper starts with the establishment of the evaluation system of spare parts maintenance demand, combines the Delphi method with the CRITIC method to compare and screen the importance of indicators, and reflects the objectivity of indicators reflected in the actual evaluation value on the basis of fully retaining the subjective intention of experts. An evaluation model of the importance of spare parts based on the weight of Delphi method and the weight of CRITIC method is established. Finally, the importance of spare parts is applied on the platform, and the evaluation results of the importance of spare parts are displayed. This method can determine the priority of spare parts allocation of operation and maintenance service vehicles when the space of service vehicles is limited in emergency service maintenance, and can provide reference for the cross-region operation of combine harvesters and the formulation of spare parts allocation scheme.

MATERIALS AND METHODS

Improve the optimization of spare parts allocation of CRITIC-TOPSIS evaluation model

Problem analysis

As shown in Figure 1, the cross region operation of the combine is a mechanical harvesting method of rice and wheat in the three summer season of China. The cross region operation and maintenance service of the harvester is a process in which the failed agricultural machinery seeks service and maintenance personnel to provide services. However, in the agricultural scene, once the agricultural machinery fails, it is difficult to carry out consignment to the service outlets for maintenance due to the special operation conditions of agricultural machinery. At the same time, the field crops need to be harvested as soon as possible, so effective time processing can improve the speed and efficiency of the entire operation. However, the maintenance process is mostly through reporting to the agricultural machinery enterprises for repair, so that maintenance service vehicles can come to rescue. In the whole transregional maintenance process, the effective allocation of spare parts resources can quickly solve the problem of harvester failures. However, a service vehicle needs to repair multiple faulty agricultural machinery, and the fixed space can only be equipped with a certain number of spare parts. At the same time, the seasonal requirements of transregional operations and the different types of crops lead to different types of demand for spare parts. To avoid the occurrence of spare parts with low configuration importance on the vehicle, it is necessary to evaluate the importance of spare parts. As the harvester is overloaded and continues to operate in transregional operation, the failure problem is mostly vulnerable parts. If the maintenance service vehicle carries reasonable spare parts configuration strategy, combined with the harvester maintenance support force of the agricultural machinery manufacturer, the field emergency repair can be carried out quickly, so as to realize the harvester's reoperation in the field.

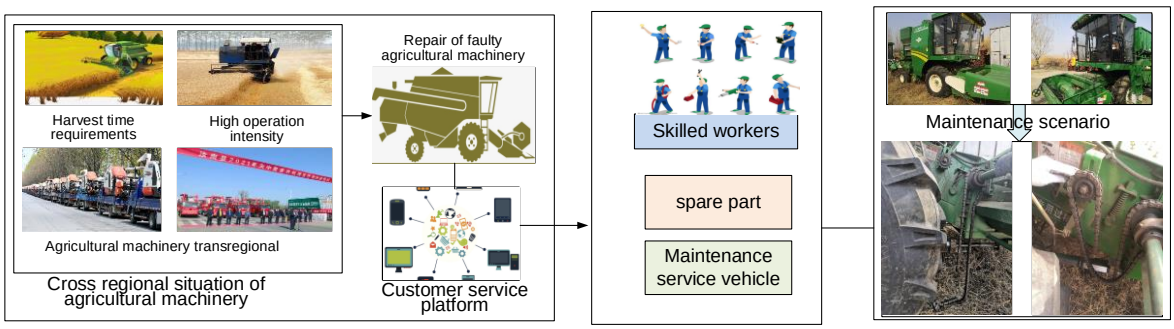

Fig. 1 - Cross region and maintenance scenario of agricultural machinery

Delphi empowerment

Delphi method is a subjective expert opinion evaluation method, which can not only reduce the one-sided caused by experts' personal preferences, but also reflect the differences of opinions among experts. In this paper, the Delphi method is used to give weight to each index in the comprehensive evaluation index system by using experts' knowledge, experience and personal views. The consistency of expert opinions is used as the standard to determine the index weight.

First, use the Delphi method to sort the evaluation element set and calculate the evaluation weight w_{ij} of each factor:

$$w_{ij} = \frac{\sum_{i=1}^{m} v_{ij} \times w_{\exp}}{\sum_{i=1}^{m}\sum_{j=1}^{n} v_{ij} \times w_{\exp}} \quad (1)$$

In formula (1), m is the number of experts; n is the number of evaluation elements; v_{ij} is the evaluation value of each expert on each evaluation element; the weight w_{exp} is the weight of each expert. Thus, we can get the weight vector $W_{DELF}=(w_1,w_2,w_3,w_4)$.

CRITIC empowerment

The multi-index (attribute) comprehensive evaluation method focuses on determining the weight of each evaluation index and evaluating the evaluation object according to the weight of each index. The weight size indicates the importance and influence of the indicator in the evaluation process. Therefore, the objectivity and accuracy of each evaluation index weight directly affect the reliability of the final evaluation results. The existing subjective weighting method relies too much on human factors. The index weights obtained by this weighting method vary from person to person, which makes it difficult to form a unified opinion. The accuracy and credibility of the weighting results are not high. Entropy weight method is a commonly used objective weighting method, which calculates the objective weight according to the difference of each evaluation index, but there is not only difference but also correlation between evaluation indexes. An objective and comprehensive evaluation strategy for the importance of harvester spare parts is particularly important. The specific calculation steps are as follows:

Step 1: Build judgment matrix. Suppose that in an evaluation model, the original evaluation matrix of m evaluation indicators of n evaluation objects is $X = \left(x_{ij}\right)\ n \times m$. Where, x_{ij} is the state value of the i-th evaluation object corresponding to the j-th evaluation index, which is the judgment matrix.

Step 2: Calculate the standard deviation of each index:

$$\sigma_j = \sqrt{\frac{1}{m\text{-}1}\sum_{i=1}^{m}(x_{ij} - \bar{x}_j)^2} \qquad j=1,2,\ldots m \quad (2)$$

In formula (2): σ_j is the standard deviation of evaluation index x_i; $\bar{x}_j$ is the average value of index x_j in m schemes.

Step 3: Build the correlation coefficient matrix. Let the average value of all schemes in index x_i be $\bar{x}_i$. The average value of all schemes in index x_j is $\bar{x}_j$, so the correlation coefficient r_{ij} between index x_i and index X_j is:

$$r_{ij} = \frac{\sum_{i=1}^{n}(x_i - \bar{x}_i)(x_j - \bar{x}_j)}{\sum_{i=1}^{n}(x_i - \bar{x}_i)^2 \sum_{j=1}^{n}(x_j - \bar{x}_j)^2} \quad (3)$$

Step 4: Calculate the information content C_j contained in each indicator, and calculate the comprehensive weight W_{CRITIC} of each indicator. C_i represents the information amount of the indicator in the indicator j system. The calculation formula is:

$$C_j = \sigma_j \sum_{i=1}^{n}\left(1 - r_{ij}\right) \qquad j=1,2,\ldots m \quad (4)$$

In formula (4): σ_j is the standard deviation of evaluation index X_i; r_{ij} is the correlation coefficient between index x_i and index x_j, so the objective weight of the j-th index is:

$$W_{CRITIC} = \frac{C_j}{\sum_{j=1}^{m} C_j} \qquad j=1,2,\ldots m \quad (5)$$

Coupling weight

As shown in Figure 2, in order to avoid ignoring the subjective analysis of indicators because the objective weighting method relies too much on mathematical statistical methods, the comprehensive weight of spare parts configuration is determined by combining CRITIC objective weight W_{CRITIC} and subjective weight Delphi method W_{DELF}. In order to reflect the relative relationship between the weights of various spare parts indicators and the weight proportion in all indicators as much as possible, the multiplier synthesis normalization method is used when coupling the subjective and objective weights. The calculation formula of comprehensive weight is:

$$W = \frac{W_{DELF} W_{CRITIC}}{\sum_{j=1}^{n} W_{DELF} W_{CRITIC}} \tag{6}$$

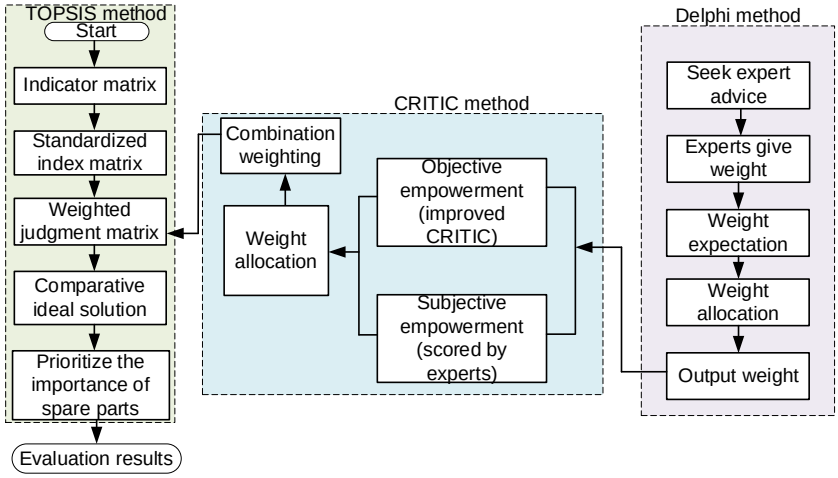

Fig. 2 - Improved CRITIC-TOPSIS evaluation process

Comprehensive evaluation model based on improved TOPSIS

Model building

Suppose there are m alternatives A_1, A_2,…, A_m and n attribute indicators C_1, C_2, …, C_n. x_{ij} is the index value of A_i under C_j ($i=1, 2, \ldots, m$; $j=1, 2, \ldots, n$). The basic steps to improve TOPSIS are as follows.

Step 1: construct the decision matrix X according to the attribute index value.

$$X = \begin{bmatrix} x_{11} & x_{12} & \cdots & x_{1n} \\ x_{21} & x_{22} & \cdots & x_{2n} \\ \cdots & \cdots & & \cdots \\ x_{m1} & x_{m2} & \cdots & x_{mn} \end{bmatrix} \tag{7}$$

Step 2: Calculate the standardized matrix R. In order to eliminate the influence of different data dimensions in the decision matrix, the decision matrix is normalized to obtain a standardized matrix:

$$R = \begin{bmatrix} r_{11} & r_{12} & \cdots & r_{1n} \\ r_{21} & r_{22} & \cdots & r_{2n} \\ \cdots & \cdots & & \cdots \\ r_{m1} & r_{m2} & \cdots & r_{mn} \end{bmatrix} \tag{8}$$

Step 3: Determine the positive and negative ideal schemes H^+ and H^-. The solution process of positive ideal scheme $H^+ = \left[h_1^+, h_2^+, h_3^+ \cdots h_n^+\right]$ and negative ideal scheme $H^- = \left[h_1^-, h_2^-, h_3^- \cdots h_n^-\right]$ is as follows:

When the index type of C_j is benefit type, there are:

$$\begin{cases} h_j^+ = \max\left\{v_{ij} | 1 \leqslant i \leqslant m\right\} \\ h_j^- = \min\left\{v_{ij} | 1 \leqslant i \leqslant m\right\} \end{cases} \tag{9}$$

When the indicator type of C_j is cost type, there are:

$$\begin{cases} h_j^+ = \min\left\{v_{ij} | 1 \leqslant i \leqslant m\right\} \\ h_j^- = \max\left\{v_{ij} | 1 \leqslant i \leqslant m\right\} \end{cases} \tag{10}$$

Step 4: Calculate Euclidean distance. The Euclidean distance calculation involves the Euclidean distance from A_i to D_i^+ and the Euclidean distance from A_i to D_i^-. The specific solution formula is:

$$D_i^+ = \sqrt{\sum_{j=1}^{n}\left(v_{ij} - h_j^+\right)^2} \qquad i=1,2,\ldots,n \tag{11}$$

$$D_i^- = \sqrt{\sum_{j=1}^{n}\left(v_{ij} - h_j^-\right)^2} \qquad i=1,2,\ldots,n \tag{12}$$

Step 5: Calculate the relative closeness.

$$C_i^* = \frac{D_i^-}{D_i^+ + D_i^-} \tag{13}$$

$$C_i^* = \frac{D_i^+}{D_i^+ + D_i^-} \tag{14}$$

Step 6: Determine the relative advantages and disadvantages of the scheme based on C_i^*.

It can be seen from Eq. (13) and Eq. (14) that $C_i^* \in [0,1]$, and the larger the C_i^* obtained from Eq. (13), the better the scheme, while the smaller the C_i^* obtained from Eq. (14), the better the scheme.

Factors influencing the determination of spare parts

In the process of spare parts configuration, the following factors will have an important impact on the determination of spare parts, as shown in Figure 3.

(1) Importance of spare parts. The importance of spare parts refers to the role played by spare parts in the whole operation process of the combine and the extent to which they determine the performance of the operation and body of the combine. The higher the criticality of parts, the greater their impact on the performance of the harvester, and the higher the demand for such spare parts. The criticality of spare parts is an important factor in determining the types of spare parts.

(2) Urgency of spare parts maintenance. The urgency of spare parts maintenance is due to the time requirements for harvesting crops in the field during the operation of the combine, and it also has influence on the efficiency of harvester operators. When the harvester is not urgently repaired, it will indirectly affect its harvesting efficiency and economic costs. According to the regional crops, harvester models and wear and tear conditions, spare parts with urgent requirements for harvester operation should be configured in advance as far as possible. The low loss spare parts can be configured in proper order to improve the utilization rate of spare parts.

(3) Replacement time of spare parts. When the parts of the harvester need to be replaced due to failure. In order to ensure the safe use performance of the harvester, under the condition of large consumption and short replacement time, when replacing spare parts, based on the enterprise knowledge base information, the parts with short replacement time are easy to break, and their configuration priority should be appropriately improved.

(4) Consumption of spare parts. The consumption of spare parts refers to the costs of spare parts, mainly including spare parts purchase costs, storage and maintenance costs, storage damage costs, etc. Annual consumption of a spare part in a region. It can be seen that the greater the annual consumption, the higher the criticality of spare parts.

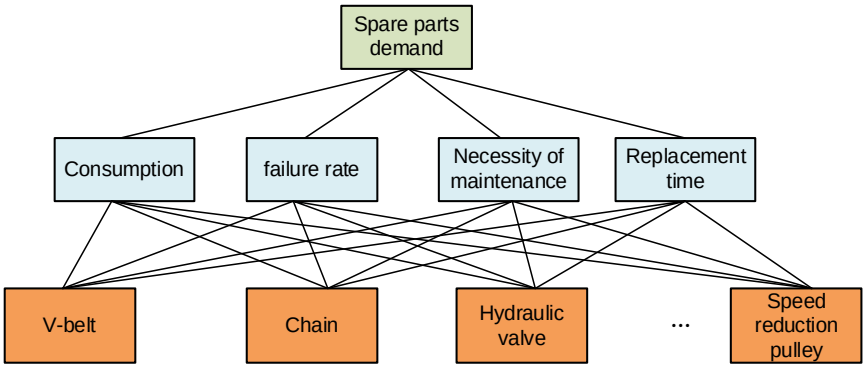

Fig. 3 - Spare parts factor distribution evaluation chart

Spare parts evaluation method

(1) Importance/priority (I). The importance of parts is divided into 10 levels, and the specific scores are shown in Table 1.

Table 1

Scoring method of component importance

Level	Describe	Score
1	Seriously affect the harvester harvest and function realization	10
2	It has a significant impact on the harvest operation and the realization of other functional tasks	9
3	Has a significant impact on harvesting operations and the realization of functional tasks	8
4	It has a slight impact on the harvesting operation and a great impact on the realization of functional tasks	7
5	Has a slight impact on harvesting jobs and affects the realization of functional tasks	6
6	Does not affect harvesting operations, but has significant effects on multiple functions	5
7	It does not affect harvesting operations and only has a minor impact on the implementation of multiple functions	4
8	Harvesting operations are not affected, but the impact on individual functions is significant	3
9	It does not affect harvesting operations and only has a small impact on the implementation of individual functions	2
10	It has no significant effect on the realization of harvesting jobs and functional tasks	1

(2) Fault maintenance emergency (S). After a fault occurs, according to the damage of the parts, the urgency of the need to quickly complete the replacement of spare parts is divided into five levels, the specific score is shown in Table 2.

Table 2

Scoring method of parts maintenance urgency

Level	Describe	Score
1	Seriously affect the work of harvester	5
2	It has great influence on the work of harvester	4
3	It has little effect on the work of the harvester	3
4	Has a slight effect on harvester work	2
5	No effect	1

(3) Replacement time (T). After a harvester fails, the time required for replacement of spare parts can be divided into five levels, and the specific scores are shown in Table 3.

Table 3

Scoring method of replacement time during parts maintenance

Level	Describe/ h	score
1	T>10	5
2	7<T<10	4
3	5<T<7	3
4	3<T<5	2
5	0<T<3	1

(4) Part consumption level/replacement frequency (F). The frequency of failure refers to the frequency of replacement of spare parts due to fault maintenance. The greater the consumption of spare parts, the higher the importance of spare parts maintenance. There are five levels in total, and the specific scores are shown in Table 4.

Table 4

Evaluation method of parts consumption and replacement

Level	Describe	Score
1	Heavy height wearing parts, frequent occurrence, high consumption frequency	5
2	Highly vulnerable parts, frequent occurrence, high consumption frequency	4
3	Moderate wear parts, occasional occurrence, medium consumption frequency	3
4	Low degree wear parts, rare occurrence, high consumption frequency	2
5	Very low wear parts, unlikely to occur, almost zero consumption frequency	1

RESULTS

Case analysis

Through consulting the relevant information that combine harvester spare parts have many kinds, including chain, gear, belt, regulator, belt, control valve, battery, power output assembly, hydraulic valve, moving blade, fixed blade, nozzle and so on. The above parts need to be analyzed in order to determine which spare parts are the most important in the cross-zone operation of the combine. As shown in Figure 5, the first 10 kinds of parts are selected for research to prove the feasibility of the method. The improved TOPSIS algorithm was used to sort the comprehensive benefits of spare parts, obtain the comprehensive evaluation value of the configuration effect of each spare part, and finally analyze and determine the priority of spare parts configuration.

Table 5

Maintenance spare parts data table

Number	Fault information	Name of spare parts	Label
1	The chain rupture	Chain	B1
2	Belt wheel wear	Gear	B2
3	Damage of regulator	Regulator	B3
4	Belt failure	Belt	B4
5	The grain conveying shaft is broken	Bearing	B5
6	Untight seal	Oil seal	B6
7	Control valve damage	Control valve	B7
8	Battery fault	Battery	B8
9	No power idling	Power output assembly	B9
10	The dashboard shows a fault	Dashboard	B10

Firstly, the weight of the value element set of spare parts is determined by coupling weight method. Six experts were invited to evaluate the importance of different value elements. The sum of all factors is a percentage scale, and the results are shown in Table 6.

Table 6

Expert marking table

Assessment element	Expert 1	Expert 2	Expert 3	Expert 4	Expert 5	Expert 6
Importance	40	35	25	35	30	25
Urgency	30	30	25	30	25	32
Replacement time	20	25	40	25	20	20
Consumption	10	10	20	10	25	20

Due to the differences in the credibility of the evaluation of the value factor set among experts, the weights of 6 experts are assigned as w_{exp} = (0.05, 0.05, 2.0, 15, 0.1) according to the expert level and importance. The subjective weight of each evaluation factor is W_{DEL} = (0.3483, 0.2935, 0.2214, 0.1368). The objective weight W_{CRI} was obtained by the weight method of CRITIC as W_{CRI} = (0.2608, 0.1491, 0.3097, 0.2804). According to Equation (6), the coupling weight W can be obtained as follows: W = (0.3760, 0.1812, 0.2839, 0.1589). Secondly, six experts scored each evaluation element of spare parts in turn. The specific scores are shown in Table 7, the comprehensive evaluation matrix of the above parts is:

$$R_1 = \begin{bmatrix} 6 & 5 & 5 & 6 & 5 & 7 \\ 4 & 1 & 3 & 1 & 3 & 2 \\ 5 & 2 & 4 & 3 & 2 & 2 \\ 1 & 1 & 2 & 1 & 1 & 1 \end{bmatrix} \quad R_2 = \begin{bmatrix} 5 & 7 & 8 & 6 & 4 & 8 \\ 3 & 1 & 4 & 2 & 5 & 5 \\ 1 & 2 & 2 & 1 & 4 & 3 \\ 2 & 2 & 1 & 4 & 1 & 2 \end{bmatrix} \quad R_3 = \begin{bmatrix} 7 & 5 & 7 & 4 & 5 & 6 \\ 4 & 4 & 3 & 5 & 3 & 4 \\ 5 & 3 & 5 & 4 & 2 & 4 \\ 2 & 2 & 3 & 2 & 2 & 2 \end{bmatrix}$$

$$R_4 = \begin{bmatrix} 6 & 7 & 6 & 7 & 7 & 8 \\ 4 & 2 & 3 & 2 & 4 & 2 \\ 2 & 4 & 4 & 5 & 4 & 3 \\ 2 & 3 & 3 & 2 & 2 & 1 \end{bmatrix} \quad R_5 = \begin{bmatrix} 6 & 5 & 5 & 6 & 5 & 7 \\ 4 & 1 & 3 & 1 & 3 & 2 \\ 5 & 2 & 4 & 3 & 2 & 2 \\ 1 & 1 & 2 & 1 & 1 & 1 \end{bmatrix} \quad R_6 = \begin{bmatrix} 5 & 7 & 8 & 6 & 4 & 8 \\ 3 & 1 & 4 & 2 & 5 & 5 \\ 1 & 2 & 2 & 1 & 4 & 3 \\ 2 & 2 & 1 & 4 & 1 & 2 \end{bmatrix}$$

Table 7

Priority configuration results of some spare parts

Expert	B1				B2				B3				B4			
	I	S	T	F	I	S	T	F	I	S	T	F	I	S	T	F
Expert1	6	4	5	1	5	3	1	2	7	4	5	2	6	4	2	2
Expert2	5	1	2	1	7	1	2	2	5	4	3	2	7	2	4	3
Expert3	5	3	4	2	8	4	2	1	7	3	5	3	6	3	4	3
Expert4	6	1	3	1	6	2	1	4	4	5	4	2	7	2	5	2
Expert5	5	3	2	1	4	5	4	1	5	3	2	2	7	4	4	2
Expert6	7	2	2	1	8	5	3	2	6	4	4	2	8	2	3	1

Expert	B5				B6				B7				B8			
	I	S	T	F	I	S	T	F	I	S	T	F	I	S	T	F
Expert1	9	4	5	3	9	2	2	3	9	4	4	5	9	3	3	4
Expert2	7	2	4	4	7	3	1	4	7	3	3	3	7	4	2	3
Expert3	5	2	1	3	6	2	4	2	5	4	4	4	5	4	4	5
Expert4	7	4	5	2	7	5	5	2	8	4	4	2	7	4	5	1
Expert5	6	1	3	2	6	4	4	2	6	2	2	2	4	5	3	1
Expert6	7	5	4	1	7	2	4	1	6	5	5	1	6	5	4	1

The priority of spare parts determined by the traditional TOPSIS algorithm and the improved TOPSIS algorithm is compared, as shown in Table 8. In Table 8, the priority of spare parts configuration corresponds to the numbers 1-10 from high to low. It can be seen that the priority of spare parts configuration determined by traditional TOPSIS and improved TOPSIS algorithms is higher for belts, chains, control valves, regulators and oil seals, and lower for gears, bearings, batteries, power take-off assemblies and instrument panels. The priority of spare parts mainly differs from that of gear, battery, power take-off assembly and bearing.

Table 8

Spare parts priority configuration results

Spare part	Traditional TOPSIS		Improve TOPSIS	
	Standardized score	Priority	Standardized score	Priority
Chain	0.0628	10	0.0676	9
Gear	0.0752	9	0.0686	10
Regulator	0.1039	3	0.1033	3
Belt	0.0834	6	0.0846	8
Bearing	0.1088	8	0.11119	7

Spare part	Traditional TOPSIS		Improve TOPSIS	
	Standardized score	Priority	Standardized score	Priority
Oil seal	0.0947	5	0.0953	5
Control valve	0.1192	4	0.1138	4
Battery	0.1105	7	0.1128	6
Power output assembly	0.1177	1	0.1161	1
Dashboard	0.1238	2	0.1261	2

In the traditional TOPSIS algorithm, the priority of gear spare parts configuration is 6. The spare parts configuration priority of bearing is 7, which is higher than that of battery 8. Priority of spare parts configuration of power take-off assembly is 9. The instrument cluster spare parts configuration priority is 10, which is at the end of the priority. In the improved TOPSIS algorithm, the priority of bearing spare parts allocation is 6. The priority of battery spare parts configuration is 7, which is higher than that of gear spare parts configuration 8. Priority of spare parts configuration of power take-off assembly is 9. The priority of spare parts configuration higher than the instrument cluster is 10.

It can be seen from the above analysis that, compared with the traditional TOPSIS, the improved TOPSIS method can better reflect the impact of prioritization, so as to assemble more valuable spare parts in the limited space for service vehicles, provide effective support for the operation and maintenance of service vehicles, and the configuration scheme of spare parts is better.

Development of agricultural machinery spare parts resource management platform

Platform architecture

The platform structure is shown in Figure 4. The platform system of spare parts resource management system can be divided into data layer, platform layer, access layer and application layer from the functional logic. The data layer includes spare parts inventory quantity, repair and replacement records, expert database data, spare parts category classification data, etc. The platform layer is mainly the embodiment of functions, including repair appointment, repair request, repair management, resource allocation, and spare parts management decisions.

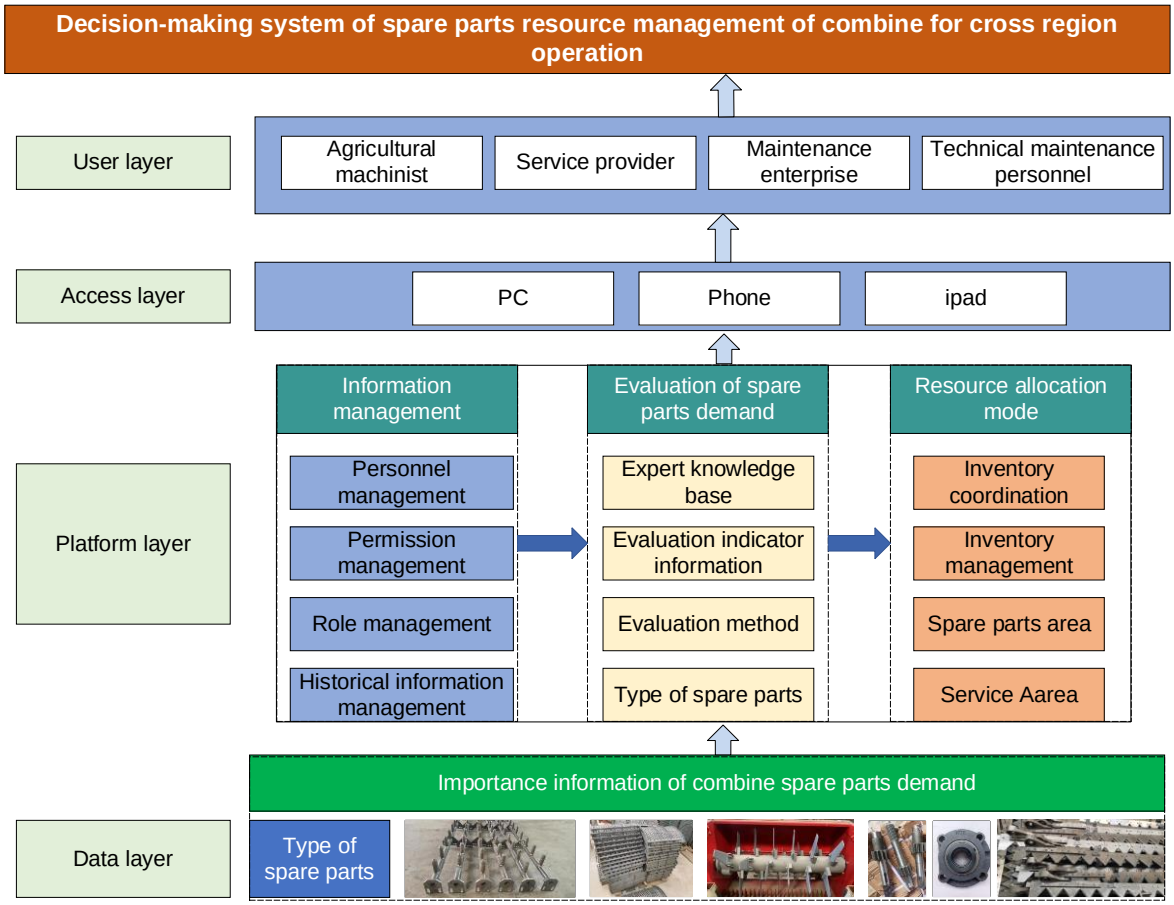

Fig. 4 - Spare parts factor distribution evaluation chart

Importance evaluation of spare parts

As shown in Figure 5, the spare parts data interface can retrieve the data of spare parts from the spare parts information database. Managers can obtain data from experts, click the repair importance evaluation on the data information table, and enter indicator data for calculation. The evaluation results of the repair importance of spare parts can be obtained and saved in the spare parts information. As shown in Figure 6, it is the system display interface.

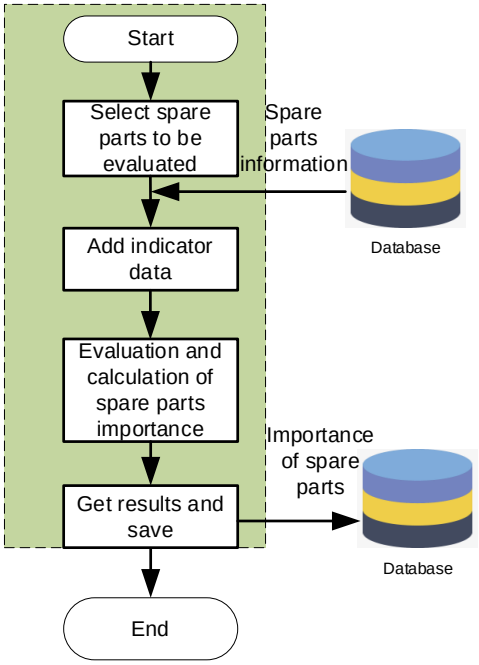

Fig. 5 - Platform system structure diagram of spare parts importance

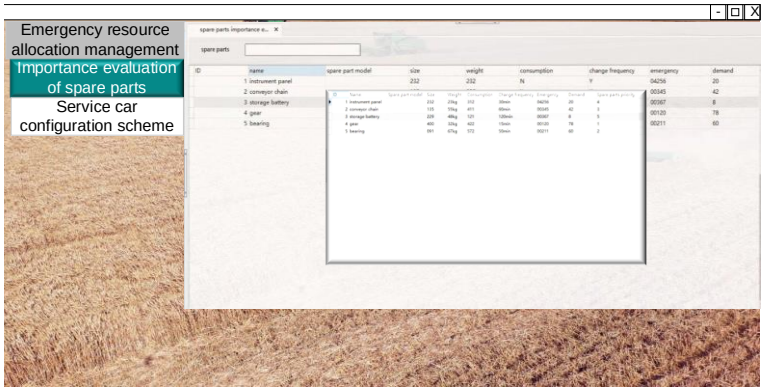

Fig. 6 - Display of spare parts importance evaluation results

CONCLUSIONS

(1) The efficient configuration of spare parts is an important content to improve the level of equipment supportability. On the basis of determining the types of vulnerable spare parts of the combine, the configuration priority of spare parts is studied, and a method for determining the priority of spare parts combined with the improved CRITIC-TOPSIS algorithm is proposed, which can further optimize the configuration scheme of onboard spare parts of the service vehicle, and has a certain role in promoting the precision and standardization of cross-region operation and maintenance service guarantee of the combine harvester.

(2) In this study, based on the establishment of spare parts importance evaluation, the development of the platform system has been expanded, which is convenient for spare parts managers and manufacturers to receive and process data in real-time, achieving a visual effect. At the same time, through the platform system, the importance of spare parts can be evaluated in real-time, and the results of required spare parts can be obtained in real-time.

(3) This study effectively combed the importance of key spare parts for the cross-region operation of the combine. In the later study, the weight, volume and loading capacity of spare parts can be combined to reasonably assemble spare parts for vehicles.

ACKNOWLEDGEMENT

The work was sponsored by the National Key R&D Program Project of China (2020YFB1709603).

REFERENCES

[1] Chen Xiu-sheng, Li Hao, Cao Shu-kun & Wang Dian-zhong. (2017). Study on Intelligent Fault Monitoring System for Corn Combine Harvester.*Proceedings of 2017 3rd International Conference on Applied Mechanics and Mechanical Automation (AMMA2017) ,* pp.181-186. Phuket/Thailand.

[2] Chenbo, X., Guangyou, Y., Lang, L., Jing, L., & Xuehai, C. (2020). Operation faults monitoring of combine harvester based on SDAE-BP. *Transactions of the Chinese Society of Agricultural Engineering (Transactions of the CSAE), 36*(17), 46-53. Wuhan/China.

[3] Chemweno P. K., Pintelon L., & Muchiri P. N. (2015). Evaluating the Impact of Spare Parts Pooling Strategy on the Maintenance of Unreliable Repairable Systems. *IFAC-PapersOnLine, 48*(3), 989-994. doi: https://doi.org/10.1016/j.ifacol.2015.06.212, Celestijnenlaan /Belgium

[4] Gilev S., Zargaryan A., Nesterova E. (2019). Using of electronic field database for analysis of the effectiveness of agricultural technologies. *Proceedings of the International Scientific and Practical Conference "Digital agriculture - development strategy" (ISPC 2019)*, pp.89-92. Yekaterinburg/Russia.

[5] Han J., Hu Y., Mao M., & Wan S. (2020). A multi-objective districting problem applied to agricultural machinery maintenance service network. *European Journal of Operational Research, 287*(3), 1120-1130. doi: https://doi.org/10.1016/j.ejor.2020.05.008, Nanchang/China.

[6] Li F., Ma Y. (2022). Research on the Ranking of Machine Tool Design Elements Based on Analytic Hierarchy Process (基于层次分析法的机床设计元素排序研究), Industrial Design.

[7] Rostamzadeh R., Ghorabaee M. K., Govindan K., Esmaeili A., & Nobar H. B. K. (2018). Evaluation of sustainable supply chain risk management using an integrated fuzzy TOPSIS- CRITIC approach. *Journal of Cleaner Production, 175*, 651-669. doi:https://doi.org/10.1016/j.jclepro.2017.12.071

[8] Vezirov C., Atanasov A., Vladut V., (2021). Calculation of field capacity and fuel consumption of mobile machinery with bunkers, tanks or other containers for agricultural goods. *INMATEH Agricultural Engineering*, Vol.63, Issue 01, pp.19-28. Romania. https://doi.org/10.35633/inmateh-63-02

[9] Vlădut V., Moise V., Biris S.St., Paraschiv G., (2012), Determining the cost matrix of straw cereals combine harvesters according to equipment quality and engine power, *Proceedings of the 40 International Symposium on Agricultural Engineering "Actual Tasks on Agricultural Engineering",* pp. 333-344. Opatija/Croaţia.

[10] Wang R., Lin H., Cheng J., Xu Z., Feng H., Tang Y. (2022). Optimizing the Water Ecological Environment of Mining Cities in the Yangtze River Economic Belt Using the Cloud Model, CV-TOPSIS, and Coupling Coordination Degree. *MDPI(IJERPH), 19*(4), 2469. Switzerland;

[11] Yu V. F., Salsabila N. Y., Siswanto N., Kuo,P.-H. (2022). A two-stage Genetic Algorithm for joint coordination of spare parts inventory and planned maintenance under uncertain failures. *Applied Soft Computing*, 109705. doi: https://doi.org/10.1016/j.asoc.2022.109705. Netherlands

[12] Zandi P., Rahmani M., Khanian M., Mosavi A. (2020). Agricultural Risk Management Using Fuzzy TOPSIS Analytical Hierarchy Process (AHP) and Failure Mode and Effects Analysis (FMEA). *10*(11), 504;

[13] Zhang S., Huang K., Yuan Y. (2021). Spare Parts Inventory Management: A Literature Review. *MDPI(Sustainability), 13*(5), 2460. Switzerland;

[14] Zhengxing Xiao, Qing Jiang, Zhengyong Zhang, Rujin Wang, Liangtu Song, He Huang, Min Wang. (2018). Research on Cleaning Intelligent Control System of Rice and Wheat Combine Harvester. *Proceedings of the 2018 International Conference on Mechanical, Electrical, Electronic Engineering & Science (MEEES 2018)*, pp.168-177. Chongqing/China.

[15] Zhou K., Leck Jensen A., Sørensen C. G., Busato P., Bothtis D.D. (2014). Agricultural operations planning in fields with multiple obstacle areas. *Computers and Electronics in Agriculture, 109*, 12-22. doi: https://doi.org/10.1016/j.compag.2014.08.013, United States.

RESEARCH ON AGENT AND CELLULAR AUTOMATA SIMULATION OF THE HERD EFFECT
/
羊群效应的智能体和元胞自动机模拟研究

Lili NIE, Fan JIAO, Tingting YANG, Zhenyu LIU *) [1]
College of Information Science and Engineering, Shanxi Agricultural University, Taigu,Shanxi/ China
Tel: 13593101646; E-mail: lzysyb@126.com
Corresponding author: Liu Zhenyu
DOI: https://doi.org/10.35633/inmateh-68-80

Keywords: *cellular automata, herd behaviour, movement rules*

ABSTRACT
To investigate the mechanism of the movement law of sheep and theoretically support the study on the herd effect, a herd effect model based on the agent and cellular automata technology is built. The law of the herd effect is defined with the use of PyCharm for simulation, based on the characteristics of the flock tending to the top sheep. The flock activity area falls into several two-dimensional cell space structures, and the grid with the cell state of "sheep" in the cell space structure is considered a type of agent. The model assumed that there are five behaviours, including standing, walking slowly, looking for the leader, random and avoiding collisions in four scenarios. A herd effect model is built, the herd behaviour is simulated, and the simulation results are compared with the actual herd behaviour trajectory. The mean square error between the calculation model and the reality is 1.025. As revealed by the results, the model exhibits effective applicability, so it can better describe the trajectory of real herd behaviour and provide theoretical guidance for the study on the herd effect.

摘要
为揭示羊群的运动规律机制，能够为羊群效应的研究奠定理论依据，构建了基于智能体和元胞自动机技术的羊群效应模型。利用 PyCharm 进行仿真，基于羊群趋向头羊的特点,定义了羊群效应规律，把羊群活动区域分割为若干个二维的元胞空间结构，把元胞空间结构中元胞状态为"羊"的网格看成是一种智能体。模型假设了四种情景下存在站立、慢走、寻找头羊、随机以及避免碰撞五种行为。构建羊群效应模型，对羊群的从众行为进行模拟仿真，并将仿真结果与现实羊群行为轨迹加以比较拟合，计算模型和现实的均方误差为 1.025，结果显示该模型具备了有效的适用性，从而可以较好地描述现实羊群行为轨迹，为羊群效应研究提供理论指导。

INTRODUCTION
Group movement refers to a biological activity in nature *(Lu et al., 2021)*. As intelligent technology of animal husbandry has been continuously updated, the simulation of the herd effect has become a research hotspot. The herd effect represents cattle, sheep and other livestock moving and foraging in groups, following the actions of the leader blindly, and following the respective other in the process. It is also referred to as group psychology, i.e., a phenomenon to consciously imitate the leader. Collective behaviour originates from the interaction between members, sheep show orderly movement in the process of flocking, and the flock naturally tends to follow the leader and walk cooperatively *(Biro D. et al., 2016)*. *Wang et al., (2019),* investigated the feasibility of using animal escape experiments to assist the verification of group simulation models. They provided some references for in-depth research on group behaviour models. *Wang et al., (2021),* built an agent model for simulating fish behaviour. The model assumes three scenarios and eight corresponding fish movement behaviours, thus laying a vital basic of data for fish activity simulation research. *Chang et al., (2011),* built a grid-based Agent group model, dividing the crowd aggregation model into exploration activities, decision-making behaviours, and actions. The Agent group model is capable of accurately simulating crowd behaviour and further studying the law of crowd aggregation. Based on the theory of cellular automata, *Toyama M.C. et al., (2006),* built an Agent-based model, explaining the negative effects of various behavioural characteristics (e.g., gender, speed, perception, herd behaviour, as well as obstacle avoidance behaviour).

[1] *Nie Lili, M.S. Stud.; Jiao Fan, M.S. Stud.;YANG Tingting, M.S. Stud.; Liu Zhenyu, Prof. Ph.D.*

Liu et al., (2022), provided more insights into herd behaviour on crowd evacuation, which contributes to crowd accident management. *(Wagner et al., 1997),* used cellular automata as the research engine of GIS (geographic information systems) to enhance the dynamic spatial modelling ability. According to the advantages of cellular automata simulation in studying more complex systems, it is introduced to the herd effect simulation. The herd effect is clarified by the simulation rules of the herd effect model, and the application of the herd effect in numerous aspects is explored. Through the processing and analysis of the process of the herd effect, the group movement mechanism of sheep is revealed, which lays a theoretical foundation for the study on the herd effect.

MATERIALS AND METHODS

Cellular Automata

Cellular automata (CA), proposed by von Neumann, refers to a method for simulating partial laws and partial associations. A typical cellular automaton is defined on a grid, and the grid at the respective point represents a certain cell and a finite state of motion. The change rules should be suitable for the respective cell and can be performed simultaneously, and finally form the overall evolution trend (*Chang et al., 2011*). In the CA mode, the respective cell distributed in the regular grid takes a finite discrete state, and according to the same functional law, the same changes are made according to the known local law. The evolution of a dynamic system is formed by interactions between a large number of cells.

Agent-based cellular automata modelling theory

Based on a knowledge-based system that interacts with a dynamic environment to perform tasks, an agent is capable of learning and making reasonable decisions in a dynamic environment, and automatically select actions based on task characteristics (*Safa'a Yousef Abu et al, 2021*). Similar to the human brain, Agent can not only perceive environmental information, but also make decisions. The agent can autonomously decide whether to respond to the information from other agents, i.e., the agent system can encapsulate the behaviour.

The agent model for simulating sheep behaviour

The model divides the sheep farm area under study into 20×20 rectangular grids of equal size, the respective grid point represents a set of cell space structure, and the grid points connected together constitute a group of two-dimensional space, that is, the two-dimensional cellular space structure of the sheep farm.

Sheep sensing range

To simulate the sensing range of the sheep agent, it is assumed that in the cell space, the sheep agent is the centre point, the neighbour cell radius of the sensing range is R, and the square formed by the side length is $2R$, which is the sensing range of the sheep agent, as depicted in Fig.1. The induction radius of sheep is around the body length range, and the calculation method is expressed in Equation (1).

$$R = L_f(1 + R_n) \tag{1}$$

where:

L_f—size of sheep;

R_n—random influence factor, the value ranges from 0 to 1.

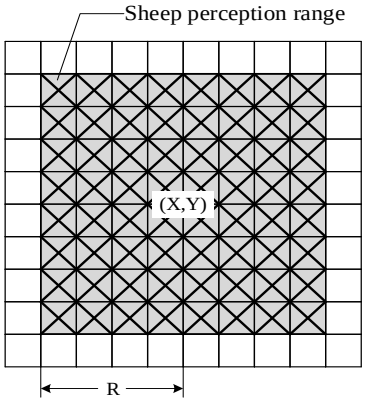

Fig. 1 – Perception range of sheep

Movement direction and step distance

The traditional Agent-CA model uses eight directions as illustrated in Fig. 2 to represent the moving direction of the Agent. Since the above motion method achieves effective results in the simulation of personnel evacuation, this experiment describes sheep behaviour through individual sheep moving direction.

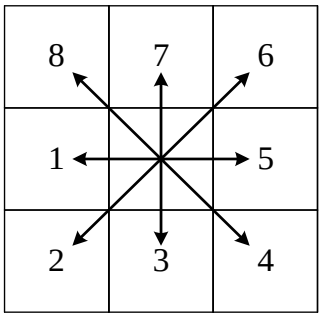

Fig. 2 – Agent movement direction of the traditional model

In this experiment, the movement of sheep in the sheep farm is expressed by combining the movement mode of sheep with the step length. To be specific, the sheep individual represents the centre point, and the square with a side length of $2\Delta_s$ is the movement range of the sheep agent. The correlation between the number of motion directions and the step distance is expressed in Equation (2).

$$n = \left(\frac{2\Delta_s}{a}\right) \times 4 - 4 \tag{2}$$

where:

n—number of directions of motion;

Δ_s—step;

a—grid side length

Gait refers to the coordination relationship between the limbs of animals in time and space during the movement process, i.e., the repetitive sequence and manner of the regular movement and stop of the respective limb. The gait cycle is a complete cycle of a certain foot movement in which the gait movement participates in the movement (*Liu, 2012*). As revealed by the result of the experiment, the average gait cycle of blue sheep walking slowly is 425 ms, the average speed of normal walking on flat ground is 53 cm/s, and the step distance is nearly 27 cm.

The step distance (Δ_s) of the sheep is obtained by Equation (3).

$$\Delta_s = 0.2L_f \tag{3}$$

Model assumptions

According to the relevant research results of group movement, the group movement is divided into four scenarios (*Wang et al., 2019*), as depicted in Table 1.

In the model, when the Agent is in the above four scenarios, it will simulate the sheep to make the corresponding movement behaviour. According to the sheep behaviour data, the corresponding sheep behaviours in the four scenarios assumed by the model are as follows:

① Standing behaviour: The behaviour of the sheep's four hooves coming into contact with the ground to support the body. The sheep agent expressed in the model remains stationary within the sensing range.

② Slow walking behaviour: a group of slow rhythmic symmetrical movements of the ewe. The sheep agent expressed in the model moves to the adjacent grid within the sensing range.

③ Looking for the leader: The sheep senses the leader's direction and moves toward the leader. The sheep agent expressed in the model moves to the most attractive grid within the sensing range.

④ Random behaviour: Since the model does not consider all the influencing factors of the flock activity, it is possible to move in a random direction during the whole flock activity. The sheep agent expressed in the model may move in any direction.

⑤ Collision avoidance behaviour: sheep keep a distance from obstacles to avoid collision. The sheep agent expressed in the model no longer moves to the obstacle.

Table 1

Scenario model assumptions

Scene number(s)	Herd behaviour	Scenario overview
1	standing behaviour; random behaviour	When the small range of activities of the leading sheep and the nearby sheep remains basically unchanged, the behaviour of the sheep is primarily standing behaviour and random behaviour.
2	slow walking behaviour; random behaviour	Sensing the movement of the approaching sheep, the sheep begin to move to the approaching sheep and move with them.
3	looking for leader behaviour; random behaviour	Sensing the movement of the head sheep, the sheep begins to tend to the head sheep, and the behaviour of the sheep is mostly to find the head sheep.
4	avoid collision behaviour; random behaviour	When recognizing that there is an obstacle around, the sheep will not move in the direction of the obstacle, and the behaviour of the sheep at this time is largely to avoid collision.

Movement rules of individual sheep

The movement rule built by the literature (*Goodwin et al., 2006*) is that the agent moves to the grid with the strongest attraction in the vicinity, and randomness is considered when the sheep behaviour rule is being established. In accordance with the response relationship of the sheep agent to the adjacent factors, the probability of the sheep agent moving to the motion area is calculated. On that basis, the final result of the movement of the sheep agent is determined.

The agent movement probability is obtained by Equation (4).

$$prob\_dir_{(D)} = P_{con}^{s}(D) \tag{4}$$

where:

$prob\_dir_{(D)}$—the possibility of the agent moving in the direction D;

$P_{con}^{s}(D)$—attraction probability to D direction in different scenarios.

In the four hypothetical scenarios, when s=*1*, the agent is in the scene of maintaining a small range; when s=*2*, the agent is in following the adjacent scene; when s=3, the agent is in the scene of following the leader; when s=*4*, the agent is in a collision avoidance scenario.

The calculation of the agent's perceived attractiveness probability is shown in Equation (5).

$$P_{con}^{s}(D) = \frac{\sum_{l=1}^{5} \alpha_l^s(D)}{A^s} \tag{5}$$

Where A^s is sum of mesh attraction weight factors in different scenarios; $\alpha_l^s(D)$ is the mesh attraction weight factor for the l behaviour in the D-th direction in the s scene, l is the behaviour, which ranges from 1 to 5, and is represented as standing behaviour, slow walking behaviour, looking for the leader, random behaviour and collision avoidance behaviour. s=1, $\alpha_2^1(D)$, $\alpha_3^1(D)$, $\alpha_5^1(D)$ are all equal to 0; s=2, $\alpha_1^2(D)$, $\alpha_3^2(D)$, $\alpha_5^2(D)$ are all equal to 0; s=3, $\alpha_1^3(D)$, $\alpha_2^3(D)$, $\alpha_5^3(D)$ are all equal to 0; s=4, $\alpha_1^4(D)$, $\alpha_2^4(D)$, $\alpha_3^4(D)$ are all equal to 0.

The sheep agent exhibits different behaviours in four scenarios, and the calculation formula is as follows:

① The effect arising from standing behaviour on the weight factor for grid attraction in all directions.

The standing behaviour is expressed in the model as when there is no movement in the agent's perception area, the sheep agent does not move to other areas.

The calculation formula is Equation (6).

$$\alpha_1^s(D_{stand}) = \alpha_{stand}(s = 1) \tag{6}$$

where:

D_{stand}—Standing direction;

α_{stand}—Attraction weighting factor for the sheep agent to move in situ due to standing behaviour in s-scenario.

② Effect of slow walking behaviour on the weight factor for grid attraction in all directions

The slow walking behaviour is expressed in the model as Agent moving to the adjacent grid within its perception range, and its expression is Equation (7).

$$\alpha_2^s(D_{near}) = \alpha_{near}(s = 2) \tag{7}$$

where:

D_{near}—Approaching the direction of movement of adjacent sheep;

α_{near}—Attraction weighting factor for walking slowly to nearby sheep;

$\alpha_2^s(D_{near})$—The attraction weighting factor that makes the agent move in the D_{near} direction when walking slowly in the s scene.

③ The effect of the behaviour of looking for the leader on the attractiveness weight factor for the grid in all directions

The behaviour of finding the leader is that Agent moves to the location of the leader in its perception area. The calculation formula is Equation (8).

$$\alpha_3^s(D_{main}) = \alpha_{main}(s = 3) \tag{8}$$

where:

D_{main}—The direction of movement to the leader position;

α_{main}—The attractive weight factor for the agent's search for the behaviour of the leader;

$\alpha_3^s(D_{main})$—In the s scene, look for the attractive weight factor that makes the agent move in the direction of D_{main}.

④ Effect of random behaviour on the weight factor for grid attraction in all directions

Random behaviour is expressed as the agent may move in any direction, and its calculation formula is Equation (9).

$$\alpha_4^s(1) = \alpha_4^s(2) = \alpha_4^s(3) = \alpha_4^s(4) = \cdots = \alpha_4^s(n) = \alpha_{ran}(s = 1,2,3,4) \tag{9}$$

where:

n—The number of moving directions of the sheep agent;

α_{ran}—Attraction weight factor for random behaviour;

$\alpha_4^s(1)$~$\alpha_4^s(n)$—Attraction weight factor for the agent to move in the direction 1 ~ n.

⑤ The effect of collision avoidance behaviour on the mesh attraction weight factor in all directions

There are attraction and repulsion effects in the interaction. When there is an obstacle in the perception range of the Agent, it will avoid collision and no longer move in the direction of the obstacle, thus revealing the repulsion effect.

The specific expression is Equation (10).

$$\alpha_5^s(D_{avoid}) = \sum_{i=1}^{5} \alpha_i^s\ (D_{avoid}) = 0(s = 4) \tag{10}$$

where:

D_{avoid}—he direction of the obstacle location;

$\alpha_5^s(D_{avoid})$—Attraction weighting factor for the sheep agent to move in the direction of D_{avoid}.

RESULTS

System accuracy test

Herding behaviour refers to one of the characteristic behaviours of crowd evacuation. The cellular automata model has been extensively used in group evacuation, and the proposed discretization concept provides an effective entry point for the simulation of real herd behaviour on the computer.

The purpose of this experiment is to study the movement state of flock in a limited space. The shooting location is a breeding farm in Baotou, Inner Mongolia, China, with an entity of 20m×20m sheep farms, 15 domesticated sheep in the sheep farm were selected as the experimental objects, and the camera is used to take pictures and videos, and observe in the experiment. In the process from disorder to order, when the flock is in a disordered and mixed state at rest, the leading sheep start to act first, then the number of groups that join the order process increases. Finally, the disordered rest phase gradually turned into an orderly feeding and exercise phase.

The aggregation process is presented in Fig. 3.

a) *b)* *c)*

Fig. 3 – The flock gathering process

PyCharm is a Python IDE that comes with a set of tools to help users improve their productivity while developing in the Python language. The experiment was simulated using PyCharm, with the environment configured as Python=3.8. A 20m×20m sheep farm area is set, twenty sheep in the area were selected as experimental samples. The coordinates of the position point in the area are (x, y) are set, and the parameter values of the model are given: random behaviour is not the main behaviour, so the attraction weight is small, and $\alpha_{ran} = 5$ is defined. The main behaviours of the flock comprise standing, walking slowly, looking for the leader, and avoiding collision. The attraction weight factor for standing behaviour is set as $\alpha_{stand} = 20$, and the attraction weight factor for other behaviours is defined as 25. Each cell represents a solid sheep. The total length of each experiment was 40 s, and the sheep gradually converged to the head through 100 training times. The trajectory results obtained by the model simulation are presented in Fig. 4.

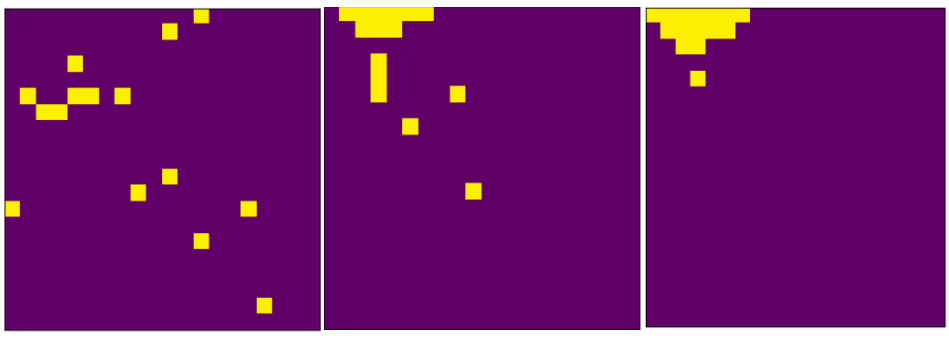

a) *b)* *c)*

Fig. 4 – Simulation process of the herd effect

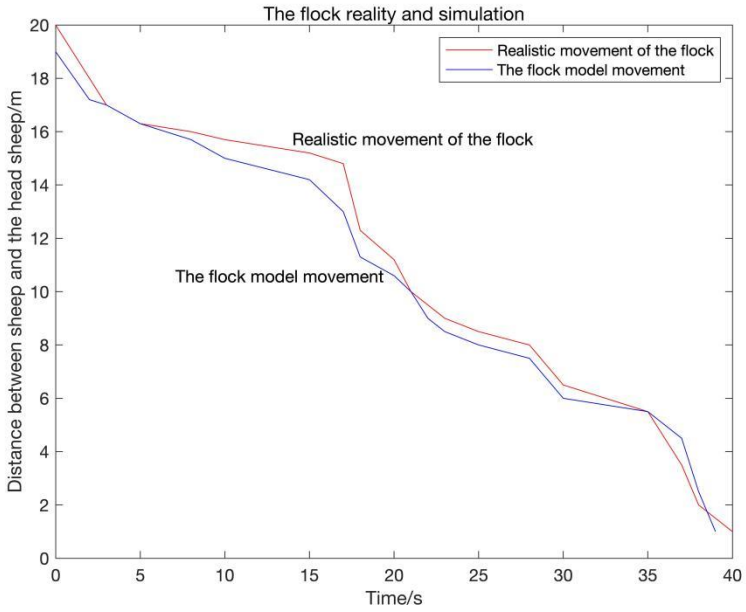

Fig. 5 – Herding reality and model simulation

The distance between the flock and the head sheep is employed as the basis for fitting the model and reality. Through the simulation of the flock model and reality as illustrated in Fig. 5, the mean square error (MSE) between the model and the reality data is obtained as 1.025. Combining the model simulation trajectories in Fig. 3 and 4 with the actual trajectories of the herd effect, the trajectories of the herds tend to be discrete to the leading sheep, and there is a low error. As revealed by the above analysis results, the behaviour of the agent-based herd imitating each other strategy is one of the internal reasons for the formation of herd behaviour.

CONCLUSIONS

In this paper, the agent and the cellular machine are automatically integrated, and a herd effect simulation model is built. The model assumes four scenarios, which consist of keeping a small range, following the approach, following the leader, as well as surrounding obstacles. There are five corresponding behaviours in different scenarios, including standing, walking slowly, looking for a leader, random and avoiding collision. The effect arising from five behaviours on grid attractiveness is analysed, and its moving rules are established by means of random process.

The simulation is performed within the range of sheep activity, and the built Agent model can directly simulate the behaviour pattern of following the leader sheep and the state of the neighbouring cells. The simulation results can reveal the movement law of the herd effect, which confirm that the built Agent model is capable of describing the movement trajectory of the herd behaviour more accurately.

This paper provides a frame of reference for studying the law of movement of biological groups through the herd effect model, which contributes to follow-up research and theoretically guides the study on the herd effect.

ACKNOWLEDGEMENT

The authors were funded for this project by the National Natural Science Foundation of China (NSFC) (No.31772651) and "Teaching and Research Management" Fund of School of Information Science and Engineering, Shanxi Agricultural University (No.XK19201).

REFERENCES

[1] Biro, D, Takao, Sasaki, T. & Portugal S. (2016). Bringing a Time–Depth Perspective to Collective Animal Behaviour. *Trends in Ecology & Evolution*, Vol. 31, pp. 550-562, Britain.

[2] Chang, Q., Dang, H. (2020). Research on Crowd Aggregation Model of Group Events Based on Grid Agent (基于网格 Agent 的群体性事件人群聚集模型研究). *Journal of Chinese People's Public Security University (Science and Technology)*, Vol. 17, pp. 71-74, Beijing/China.

[3] Lu, X., Yuan, W., (2021). Principle of Least Potential Energy in the Cellular Automata Model for Collective Motion of Fish Schools (鱼类群体运动的元胞自动机模型中的最小势能原理). *ACTA AUTOMATICA SINICA*, Vol. 47, pp. 1422-1427, Sichuan/China.

[4] Liu, Y.X., & Mao, Z., (2022). An experimental study on the critical state of herd behaviour in decision-making of the crowd evacuation. *Physica A: Statistical Mechanics and its Applications*, Vol. 595, p.127087, Beijing/China.

[5] Liu, X., (2012). The kinematics analysis of the blue sheep gait in Helan Mountain (贺兰山岩羊步态运动学分析). *Northeast Forestry University*, Heilongjiang/China.

[6] Goodwin R.A., John, Nestler M.J., Anderson J.J., Weber L., Loucks D. (2006). Forecasting 3-D fish movement behaviour using a Eulerian–Lagrangian–agent method (ELAM). *Ecological Modelling*, Vol.192, pp.197-223, U.S.A.

[7] Safa'a Yousef Abu, H., & Ibtehal, N. (2021). An Intelligent Agent Model and a Simulation for a Given Task in a Specific Environment. *American Journal of Artificial Intelligence*, Vol. 5, pp. 1-16, Saudi Arabia.

[8] Toyama M.C, Bazzan A., & da Silva R. (2006). An agent-based simulation of pedestrian dynamics. *Autonomous Agents and Multiagent Systems*, pp. 108-110, Brazil.

[9] Wagner D.F., (1997). Cellular Automata and Geographic Information Systems. *Environment and Planning B: Planning and Design*, Vol. 24, pp. 219-234, U.S.A.

[10] Wang, J., Liu, T., Liu, Z., Xu, H., Zhong, Z., Chai, Y., (2019). Experiments on Animal Evacuation Behaviours and Crowd Virtual Simulations: A Review (动物群体逃生行为实验和群体虚拟仿真研究综述). *Journal of Computer-Aided Design & Computer Graphics*, Vol. 31, pp.218-228, Ningbo/China.

[11] Wang, J., Qi, Z., Sun, S., Zhang, C., (2021). Simulation of fish behaviour in fish pass based on agent and cellular automata (基于智能体和元胞自动机的鱼道内鱼类行为模拟). *Transactions of the Chinese Society of Agricultural Engineering*, Vol.37, pp. 239-248, Hebei/China.

CONSTRUCTION OF PLANT BIOLOGICAL CIRCUIT MODEL FOR STORING MODAL INFORMATION DURING TOMATO GROWTH PROCESS
/
番茄生长过程储存模态信息的植株生物电路模型构建

Ying WANG[1)], Huifei YANG[2)], Ruijie XIE[2)], Zhenyu LIU*[2)]
[1)] College of Agricultural Engineering, Shanxi Agricultural University, Taigu / China;
[2)] College of Information Science and Engineering, Shanxi Agricultural University, Taigu / China
Tel: +86-0354-6288165; E-mail: lzysyb@126.com

DOI: https://doi.org/10.35633/inmateh-68-81

Keywords: *tomato plant, parameter inversion, dielectric characteristics, modal information, circuit model*

ABSTRACT
During the growth and development of tomato plants, its different cells or tissues would store external environmental information and express it in the form of ion transportation. In order to better examine the storage model of tomato plants, the tomato individual tissue and whole plant biological circuit models were closely examined based on the idea of modal theory. According to the parameter inversion theory, in the frequency range of 0.1Hz - 1MHz, the impedance spectrum measurement and dielectric properties of tomato plants in four modal periods of germination stage were carried out. The stages were namely the seedling stage, flowering and fruit setting stage, and fruiting stage respectively. Impedance spectrum fitting was performed with the ZSimpWin software. Then, the biological circuit model of each tissue of tomato plant was obtained. Next, the parameter inversion was used to calculate the value of each element of the biological circuit model. Lastly, the biological circuit model of the tomato plant body in each period was obtained. Through the charging and discharging test of the model of the tomato plant body at each stage, the corresponding parameter value relationship was obtained according to the capacitance characteristics. This would be compared with the component values obtained from the parameter inversion in the model. Results showed that the errors were all less than 4.8%, which verified the rationality of the model. This system acted as a theoretical guidance for the research on the growth and development of tomato and other plants.

摘要
在番茄植株生长发育过程中，不同细胞或组织会对外部环境信息进行储存，并通过离子运输的形式进行表达。为了更好的研究番茄植株的储存模型，用模态理论的思想对番茄个体组织和整体植株生物电路模型进行研究。基于参数反演理论，在 0.1Hz-1MHz 频率范围内，针对发芽期、幼苗期、开花坐果期、结果期四个模态周期的番茄植株进行阻抗谱测量以及介电特性研究，通过 ZSimpWin 软件进行阻抗谱拟合，得出番茄植株各组织生物电路模型，并利用参数反演计算生物电路模型的各元件值，最终得出各时期番茄植株体的生物电路模型。通过对番茄植株体各时期的模型进行充放电试验，根据电容特性得出相应的参数值关系，与模型中参数反演出的元件值对比验证，其误差均小于 4.8%，验证了模型的合理性。本系统为番茄及其他植株生长发育研究提供理论指导。

INTRODUCTION
With the introduction of the modal idea, it was of great significance to introduce this idea to plants. Modality is a processing process that was introduced to plants. Modality could be understood as the change of ion transport in plant cells or tissues under the input of exogenous factors. This resulted in changes in cells, tissues or structures in the process. Tomato is one of the most typical vegetable plants. Under natural conditions, the changes of exogenous factors such as atmospheric electric field and magnetic field would result in an instantaneous potential difference between the top and the root of the tomato during the growth period. This would then drive the soluble ions in the tomato body. Under the influence of an external electrostatic field, this movement would be accelerated in the form of electrostatic induction force. Hence it would form a larger biological current which promoted the movement and absorption of ions and nutrients, thereby, promoting the growth of plants. Ions in tomato acted as electrical signals of tomato plants, which had a remarkably significant effect on tomato growth (*Chen et al., 2010*).

[1] *Ying Wang, M.S. Stud.; Huifei Yang, M.S. Stud.; Ruijie Xie, M.S. Stud.; Zhenyu Liu, Prof. Ph.D.*

As a method of measuring electrical signals in biological tissues, biological circuit models had been utilized in the field of animals and plants. The plant tissue or organ was replaced by a simple biological circuit model. The parameters in the circuit represented the changes in the morphological structure of the plant organ during the growth process. At present, Schwan (*Schwan et al., 2006; Foster et al., 2000*) had established a spherical single-cell dielectric model from the perspective of electric field. With it, he had deduced the calculation method of cell transmembrane potential under the action of a steady electric field. Hodgkin *(Hodgkin et al., 1952)* proposed the equivalent circuit model of the cell membrane by combining the properties of the cell membrane and its ion channels. In the further study on the relationship between cells, resistance and capacitance, Kanai (*Kanai et al., 1983*) obtained a simple cellular RC circuit model by describing the extracellular fluid, cytoplasmic membrane, and cell contents by parallel capacitance and resistance respectively. The circuit model explained the use of dielectric spectroscopy to characterize the dielectric properties of cells principle. According to Yao Chenguo (*Yao et al., 2006*) under the addition of different frequencies of electrical stimulation, the cell circuit model intuitively reflected the influence of cell membrane potential. With the aim of studying the changes between cells or tissues during tomato growth, this paper proposed a plant biological circuit model to store modal information. The modal information stored in plant cells was presented through the biological circuit model. On this basis, combined with the advantages of electrochemical detection, the acquisition of tomato plant health status information could be attained. This would be able to provide help for plant health status diagnosis and promote agricultural development.

PRINCIPLES OF TOMATO PLANT BIOLOGICAL CIRCUIT MODEL

Tomato plant biological circuit model was based on electrochemical impedance spectroscopy (EIS) technique (*Barsoukov et al., 2005*). It uses the electrical impedance imaging of inverse problems in electromagnetic field, the dielectric constant analysis theory of biological tissues (*Li et al., 2020*), and the equivalent circuit to quantitatively evaluate the electrochemical impedance spectrum data, so as to build a tomato plant biological circuit model (*Wang et al., 2019*). Figure 1 showed the impedance chart that reflected the relationship between the real and imaginary parts of impedance. Each parameter value in the impedance circle diagram represented the impedance characteristic of the biological tissue.

The representations of the characteristic parameters R_0, R_∞ and α were as follows:

$$R_0 = x_0 + \sqrt{r^2 - y_0^2} \tag{1}$$

$$R_\infty = x_0 + \sqrt{r^2 - y_0^2} \tag{2}$$

$$\alpha = 1 - \frac{2}{\pi}\arcsin\left(\frac{|y_0|}{r}\right) \tag{3}$$

$$\tau = \frac{\left(\frac{R_0 - Z_i(\omega_i)}{Z_i(\omega_i) - R_\infty}\right)^{\frac{1}{\alpha}}}{j\omega_i} \tag{4}$$

The characteristic parameters can be obtained by the center coordinates (x_0, y_0) and the radius r of the impedance circle. The parameter τ can be obtained by the above calculation, and x_0, y_0 and r can be calculated according to the least square method.

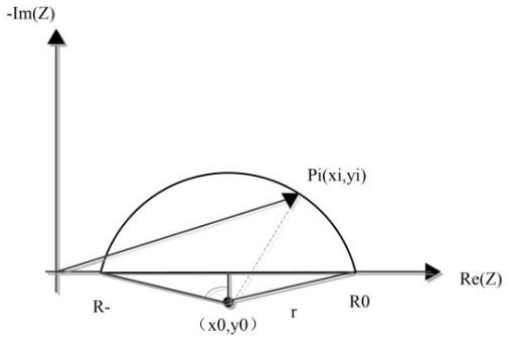

Fig. 1 - Real and imaginary impedance circle diagram

Due to the different external environmental information stored in different biological tissues or structures, the forms of ion transport were different. Hence, the electrical parameters stored in cells were also different. The Cole-Cole theory of bioimpedance established a ternary equivalent circuit model and treated each tissue and organ of a plant as an equivalent circuit (*Wang et al., 2017*) to realize the combination of the ternary equivalent circuit model and the physiology of each plant tissue or organ. Due to the selective permeability of the cell membrane, when a low-frequency AC signal passed through the plant cell, the current would mainly flow from the outside of the cytoplasm. When the frequency gradually increased, the electrical impedance value of the cell membrane would gradually decrease. Electric current passed through the cell membrane to the cell symplast, where it formed a basic parallel circuit of capacitance and resistance (*Lukács et al., 2020*). Therefore, the physiological properties of various tissues or organs of plants could be characterized according to electrical impedance spectroscopy measurements. With the method of parameter inversion, the impedance spectrum curve obtained by the electrical impedance spectrum measurement could be fitted with the basic model. Then, the parameter values in the model can be obtained by the method of parameter inversion.

MATERIALS AND METHODS

Material selection and cultivation

The test samples of plant tomato seeds had utilized tomato plants provided by Shanghai Changzhong Tomato Seed Industry Co., Ltd (Variety: Cooperative 909). They were divided into four different stages. Namely the germination stage, seedling stage, flowering and fruit setting stage, and fruiting stage respectively. In each period, 20 tomato plants in good growth condition were selected for impedance spectroscopy measurement. After the test material was obtained, it would be placed in an incubator. The set temperature of the incubator would be set at 25°C with the humidity at 42%RH and the light at 30000Lx. After the seeds had germinated, they were transferred to room temperature to continue growing.

Impedance spectroscopy

Impedance measurement was performed by adopting the Gamry Framework software installed by the Interface 1000 electrochemical workstation (Gamry, USA) using tomato impedance spectroscopy and parameter setting (*Väinölä et al., 2000; Wang et al., 2019*). By taking 71 frequency points in the frequency range of 0.1Hz - 1MHz (Initial Freq: 1MHz, Final Freq: 0.1Hz), the impedance spectrum data density (Points/Decade) is set to 10 while the AC voltage (AC Voltage, unit: (mV rms)) RMS value is set to 10mV. The default value of electrode active area (Area) is 1. The measured data would be automatically saved to the Gamry Echem Analyst software for analysis through the interface. Then, the impedance spectrum of each tissue would be obtained.

Construction of impedance characteristic model of tomato tissues

Dielectric properties differed between different biological tissues of tomato. Therefore, the model construction of the impedance characteristics of tomato plants would require analysis and examination by sub-organizations, namely tomato plant tissue, roots, stems, branches and leaves all composed of cells. The cell wall was one of the principal substances that made up the cells of each tissue of the plant. Due to the selective permeability of cell membranes, impedance characteristics could be modeled for each cell in plant tissue. In Figure 2(a), R_e represents the resistance of the extracellular fluid, Ce is the capacitance of the extracellular fluid while R_m is the resistance of the cell membrane. Cm refers to the capacitance of the cell membrane, Ri is the resistance of the intracellular fluid, and Ci refers to the parallel capacitance of the extracellular fluid (*Mao et al., 2014*). When the frequency was less than 1MHz, the resistance of the cell membrane would become larger, and the branch where the resistance Rm was located would be regarded as an open circuit. Utilizing the equivalent principle of the circuit, a certain part of the circuit would be simplified, and the volt-ampere characteristics on its port remained unchanged in Figure 2(b). Ri, Re, Cm representing the internal and external fluid resistance and membrane capacitance of biological tissue respectively.

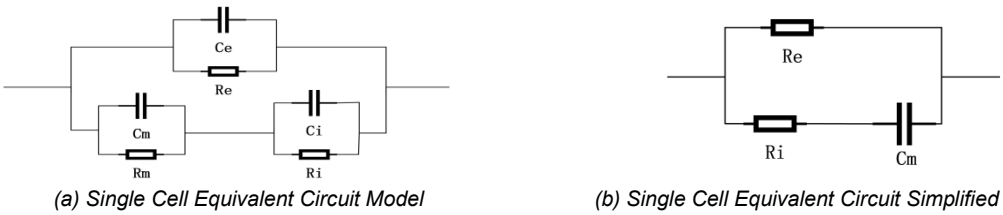

(a) Single Cell Equivalent Circuit Model *(b) Single Cell Equivalent Circuit Simplified Model*

Fig. 2 - A biological circuit model of a single cell in biological tissue

Impedance spectrum fitting

In order to better complete the impedance spectrum fitting process, the model simulation software ZSimpWin was utilized to realize the process (*Rangadhar et al., 2021*). (1) Input the impedance data measured at the roots, stems and leaves of tomato plants into the software to automatically draw the corresponding impedance curves. (2) Select the equivalent circuit model corresponding to each tissue for curve fitting. Next, make corresponding modifications to the model according to the test values. Lastly, compare the test values of each model and determine the equivalent circuit model of each tissue of the plant. (3) According to the determined equivalent circuit model, the corresponding parameter values in the model are obtained through automatic iteration.

Construction of tomato whole plant biological circuit model

Explore the connection between organizations according to the principle of two-port network and equivalent circuit (*Song et al., 2009*). Explore the construction of a biological circuit model of the whole tomato plant and observe how it fitted the biological circuit model. Then, the parameters were inverted to obtain the value of each component. Next, the model would be verified to determine the circuit model of the whole plant. In order to ensure the accuracy of the verification model, impedance spectrum fitting was performed on the four stages of the tomato plant: germination stage, seedling stage, flowering and fruit setting stage, and fruiting stage respectively. Lastly, the ZSimpWin software was utilized to perform model fitting analysis to obtain test values and related parameters. The correctness of the tomato plant biological circuit model would be verified by stages.

RESULTS AND DISCUSSION

Tomato tissue biological circuit model

Impedance spectrum characteristics of tomato tissues

The impedance spectrum curve of each tissue of tomato is shown in Figure 3. From the root Bode plot (Figure 3(b)) it could be observed that the impedance values were higher at frequencies between 100MHz-10kHz (*Rajkai et al., 2005*). When the frequency was between 10kHz-1MHz, the impedance amplitude gradually decreased. By observing Figure 4(d), when the frequency was less than 10kHz, it would belong to the high impedance frequency band. When the frequency was greater than 10kHz but lesser than 1MHz, the impedance amplitude altered from high to low value. From Figure 4(f) can be observed that the impedance of the bottom leaf was the largest followed by the impedance of the parietal leaf in the second place. Lastly, the impedance of the middle leaf would be the smallest. By observing the impedance spectra of roots, stems and leaves, it is discovered that when the current frequency gradually increased, the phase angle gradually reached the highest point first.

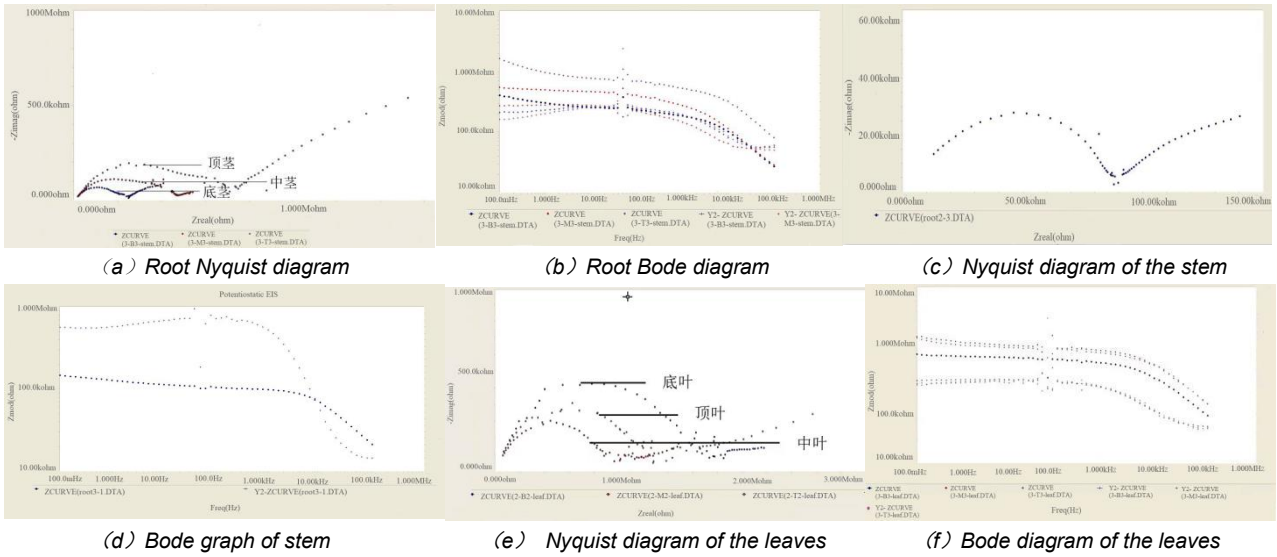

(a) Root Nyquist diagram *(b) Root Bode diagram* *(c) Nyquist diagram of the stem*

(d) Bode graph of stem *(e) Nyquist diagram of the leaves* *(f) Bode diagram of the leaves*

Fig. 3 - Impedance profile of each tissue in tomato

When it was close to the 10kHz frequency point, it would demonstrate an upward trend. According to the analysis curve of the root Nyquist in Figure 4(a) and comparing the four models, the root impedance characteristic model was more in line with the double-DCE model (*Yang et al., 2011; Zhang et al., 2009; Zhang et al., 2005; Wang et al., 2010; Liu et al., 2017*). It could be observed from Figure 4(c) that the impedance

values of the stems of different parts of the tomato plant displayed obvious changes. The result could also be deduced from Figure 4(e). It showed that the impedance values of the leaves of different parts of the tomato plant also had obvious changes. This provided a theoretical basis for the sub-section measurement of tomato stems and leaves (*Xing et al., 2021*).

Construction of biological circuit models of tomato tissues

The ZSimpWin software was utilized to analyze the data measured by the impedance map of each tomato tissue. The R(CR)(CR)) circuit model was fitted with the data measured by the root experiment. The Chisq is 0.0165 when using capacitance C test. Since the time constant of the root impedance spectrum curve was relatively scattered, in the constant phase angle element (CPE) fitting process (*Liu et al., 2012*), R(Q(R(QR))) (Figure 4(a)), the number of iterations of the biological circuit model Iter was 6 with the test value of Chisq at 0.00107. By comparing the test values, it was discovered that the fitting effect of the capacitor C was worse than that of the constant phase angle element CPE. The biological circuit model form of R(Q(R(QR))) was more in line with the actual root impedance characteristics. With the similar root fitting method, the stem R(QR(QR)) biological circuit model in Figure 3(b) possessed the best fitting effect. The leaf R(QR(QR)(CR)) biological circuit model in Figure 3(c) was in line with the actual circuit.

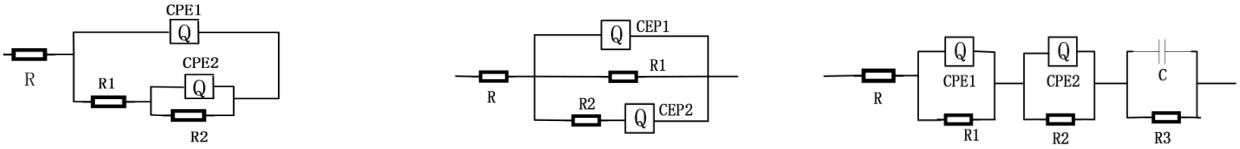

(a) R(Q(R(QR))) biological circuit model *(b) R(QR(QR))biological circuit model* *(c) R(QR(QR)(CR))biological circuit model*

Fig. 4 - Biological circuit model of each tissue in tomato

Establishment of tomato whole plant biological circuit model

Biological circuit model of tomato plants in different periods

In order to further strengthen the accuracy of model validation, impedance spectrum fitting was performed on the four stages of the tomato plant: germination stage, seedling stage, flowering and fruit setting stage, and fruiting stage respectively. The ZSimpWin software was utilized for model fitting analysis, and the test values and related parameters were obtained. At the germination stage of tomato plants, sampling measurements were made to obtain R(Q(R(CR))), R(QR(CR)(CR)), R(QR)(QR)(CR), R(QR)(QR) test values which were 0.0285, 0.00137, 0.00156, 0.00146 respectively. It is proved by referring to relevant data that when the test value is less than 0.01, the fitting effect is good. The smaller the test value, the better the fitting effect. The fitting result is shown in Figure 5. The biological circuit model of the tomato plant at the germination stage was R(QR(CR)(CR)) in Figure 6(a). Similar to the above results, the biological circuit model of the tomato plant body at the seedling stage was R(QR(CR)(CR)). The impedance spectrum model of the plant body at the flowering, fruit setting and fruiting stages was R(Q(R(CR))) in Figure 6(b).

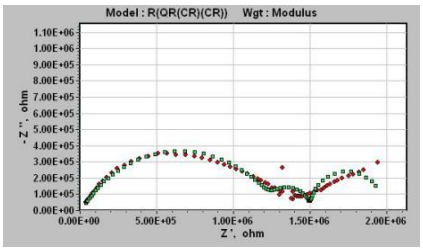

(a) Fitting results of impedance spectrum of tomato plants at germination stage

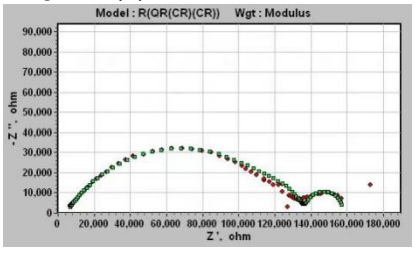

(b) Fitting results of impedance spectrum of tomato plants at seedling stage

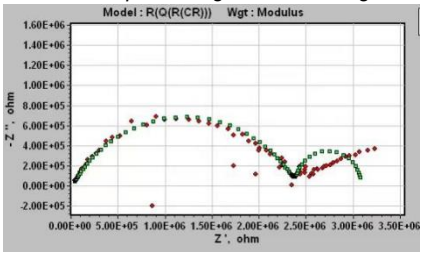

(c) Fitting results of impedance spectrum of tomato plants during flowering and fruit setting

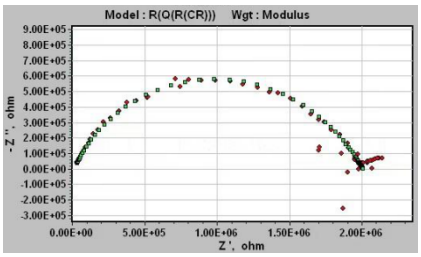

(d) Fitting results of impedance spectrum of tomato plants during the fruiting period

Fig. 5 - Results of fitting of impedance profiles of tomato plants

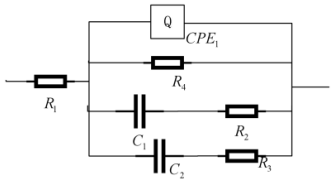

(a) R(QR(CR)(CR)) biological circuit model

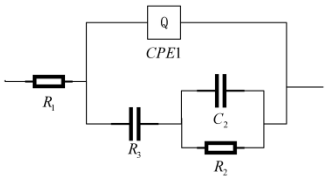

(b) R(QR(CR)(CR)) biological circuit model

Fig. 6 - Biological circuit model of different periods of tomato

Parameter inversion of biological circuit model in different periods of tomato

According to the test value of tomato germination stage ChiSp=0.00137, from the data displayed in Table 1, it could be concluded that the error of each parameter value was less than 0.048. This indicated that the R(QR(CR)(CR)) model was consistent with the impedance characteristics of tomato plants at the germination stage. Similarly, the R(QR(CR)(CR)) model conformed to the impedance characteristics of tomato plants at the seedling stage in Table 2. The R(Q(R(CR))) model was consistent with the impedance characteristics of tomato plants in flowering in Table 3 and fruit-setting and fruiting stages in Table 4.

Table 1

Inversion results of impedance spectrum parameters in germination stage

Parameter	Starting value	Termination value	Error (%)
R(ohm.cm^2)	3089	3089	2.239
Q(S-sec^n/cm^2)	5.72E-10	5.72E-10	4.372
n(0<n<1)	0.660	0.660	1.121
R(ohm.cm^2)	1.97E+03	1.97E+03	1.997
C(F/cm^2)	3.25E-11	3.25E-11	2.110
R(ohm.cm^2)	9.11E+03	9.11E+03	4.754
C(F/cm^2)	6.87E-08	6.88E-08	1.577
R(ohm.cm^2)	3.18E+03	3.18E+03	4.552

Table 2

Inversion results of impedance spectrum parameters in seedling stage

Parameter	Starting value	Termination value	Error (%)
R(ohm.cm^2)	5195	5197	4.718
Q(S-sec^n/cm^2)	2.12E-08	2.12E-08	1.476
n(0<n<1)	0.597	0.597	2.032
R(ohm.cm^2)	1.54E+03	1.54E+03	2.141
C(F/cm^2)	4.99E-11	4.99E-11	4.183
R(ohm.cm^2)	2.32E+03	2.32E+03	3.725
C(F/cm^2)	2.78E-07	2.78E-07	3.725
R(ohm.cm^2)	5.02E+03	5.02E+03	1.529

Table 3

Inversion results of impedance spectrum parameters during flowering and fruit setting

Parameter	Starting value	Termination value	Error (%)
R(ohm.cm^2)	12200	12200	3.952
Q(S-sec^n/cm^2)	5.71E-10	5.71E-10	1.76
n(0<n<1)	0.800	0.800	2.158
R(ohm.cm^2)	2.40E+03	2.40E+03	2.283
C(F/cm^2)	2.90E-07	2.90E-07	3.298
R(ohm.cm^2)	6.80E+03	6.80E+03	1.771

Table 4

Inversion results of impedance spectrum parameters during the result period

Parameter	Starting value	Termination value	Error (%)
R(ohm.cm^2)	10180	10180	3.474
Q(S-sec^n/cm^2)	6.84E-10	6.84E-10	3.327
n(0<n<1)	0.6489	0.6488	4.763
R(ohm.cm^2)	2.76E+03	2.75E+03	3.486
C(F/cm^2)	1.76E-11	1.76E-11	2.423
R(ohm.cm^2)	1.73E+06	1.73E+06	4.135

MODEL VALIDATION

In order to effectively verify the accuracy of the tomato whole plant model, the tomato plants were sampled in four periods. During the verification, the stable voltage of the power supply is 10V, and the frequency is stable at 10Hz. Connect the two ends of the tomato plant to the multimeter. A 10kΩ resistance is connected in series beside the power supply voltage to preliminarily measure the charging and discharging time of tomato plants and determine the charging and discharging time. Then the charge and discharge experiments were completed respectively. Next, an analysis on the charge-discharge situation of the tomato plant within 30 seconds was conducted. Then, the charge-discharge curve was drawn. It was combined with the impedance model at the germination stage and seedling stage of the tomato plant and its charge and discharge conditions. Figure 7(a), 7(b) and Figure 8(a), 8(b) show the average value of charge and discharge at the germination stage and the seedling stage. According to the characteristics of the capacitor, the capacitor was in a short-circuit state at the moment when the capacitor began to charge. Based on the voltage division formula, the voltage across the tomato plant could be calculated separately at the germination stage and the seedling stage. When t=0, V was the voltage across the tomato plant at t=0.

$$V_{(t=0)} = 10V \times \left[\frac{R_1(R_2 \,//\, R_3)}{R_1(R_2 \,//\, R_3) + 10K\Omega} \right] \tag{5}$$

According to formula 5, the resistance value of resistor R_1 in series with two parallel resistors $R_2 \,//\, R_3$ can be found: $R_1(R_2//R_3)$. Since the capacitor is fully charged, the branch where the capacitor is located will form an open circuit. Similarly, according to the voltage division formula, t_1 is the discharge completion time of the capacitor, V' is the voltage across the tomato plant at t = 0, R_1R_4 is the value of the resistors R_1 and R_4 in series, namely:

$$V' = \frac{(10V \times R_1R_2)}{10K\Omega + R_1R_2} \tag{6}$$

According to formula 6, the series resistance value of R_1 and R_4 can be obtained: $R_1 + R_4$, and the value of $R_1(R_2//R_3)$ and $R_1 + R_4$ can be calculated. Then, a comparative analysis was carried out with the values of each element (Table 1, Table 2) inversion of the model parameters to verify the correctness of the equivalent impedance model at the germination stage and seedling stage of the tomato plant. The verification results were displayed in Table 5.

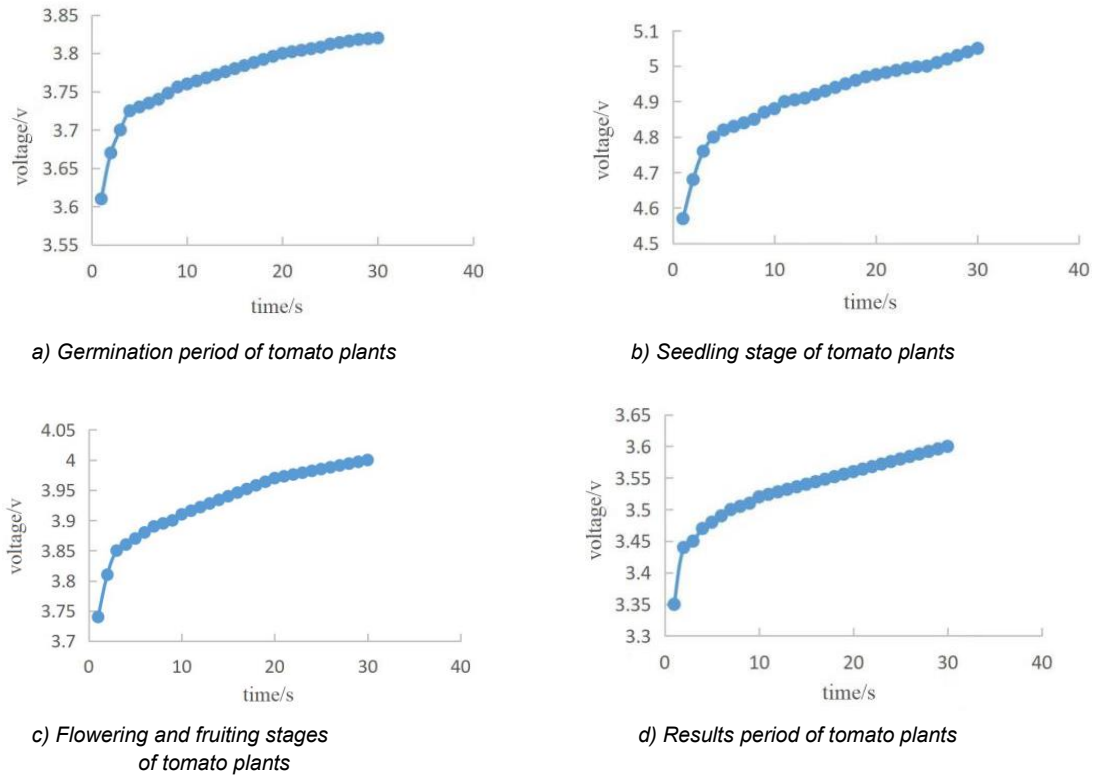

a) Germination period of tomato plants

b) Seedling stage of tomato plants

c) Flowering and fruiting stages of tomato plants

d) Results period of tomato plants

Fig. 7 - Mean charging voltage of tomato plants

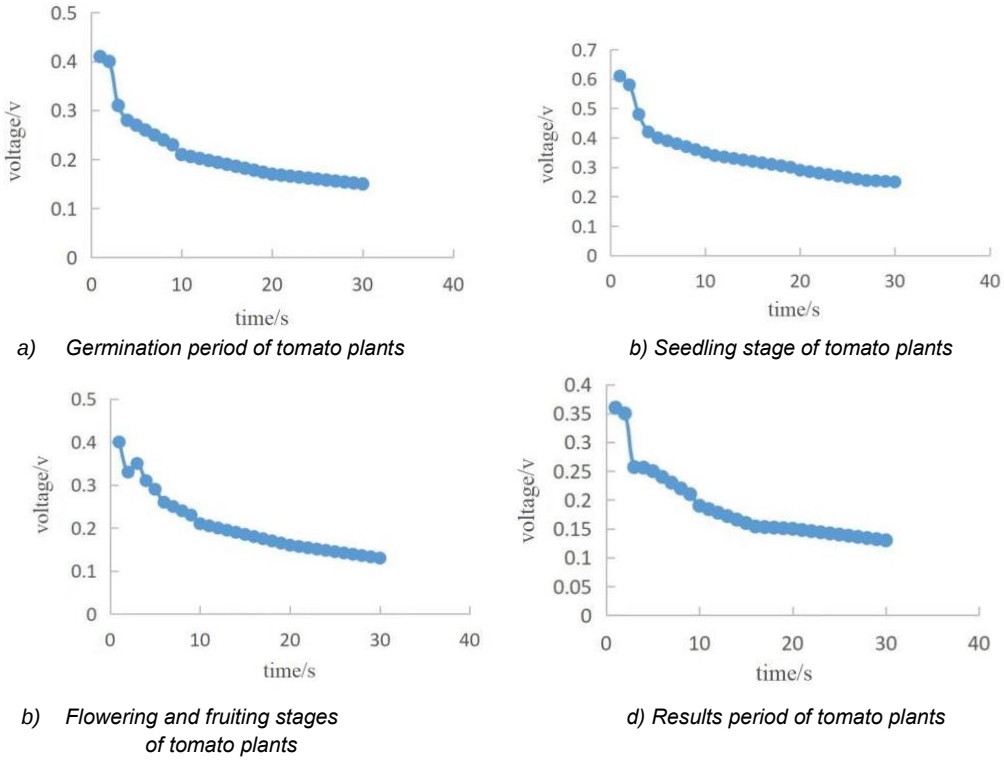

Fig. 8 - Mean discharge voltage of tomato plants

Combine impedance model of tomato plant flowering, fruit setting, fruiting period and its charge and discharge conditions (*Pankaj et al., 2010*). Then compare and analyze with the value of each element inversion of the model parameters in Table 3 and Table 4. to verify the correctness of the biological circuit model at the germination stage and seedling stage of the tomato plant. The verification results were displayed in Table 6.

Table 5

Contrastive analysis of inversion values and measured values of parameters at germination and seedling stages

	Germination stages		Seedling stages	
	$R_1(R_2 // R_3)$	R_1+R_4	$R_1(R_2 // R_3)$	R_1+R_4
Parameter inversion value/Ω	6269	6269	6123	10217
Measurement value/Ω	6075	6129	6330	10725
Error value/%	3.3	2.3	3.2	4.7

Table 6

Comparative analysis of the inversion values and measured values of the parameters at the flowering and fruit setting and fruiting stages

	Fruit setting stages		Fruiting stages	
	R_1+R_2	R_1	R_1+R_2	R_1
Parameter inversion value/Ω	14600	12200	12940	10180
Measurement value/Ω	14100	11900	12430	9860
Error value/%	3.4	2.4	4.0	3.1

By observing the above results, it could be observed that the error between the parameter inversion value and the measured value was less than 4.8%. Within the considered error range, the analysis reviewed that the reason for the error was due to the difference between the capacitive element and the constant phasor element. Then, the accuracy of the tomato plant germination stage, seedling stage, flowering and fruit setting stage, and fruiting stage model could be verified. The conclusions would then be established. The biological circuit model of tomato plant germination stage and seedling stage was R(QR(CR)(CR)), while the biological circuit model of flowering and fruit-setting stage and fruiting stage was R(Q(R(CR))).

CONCLUSIONS

(1) In order to explore the growth and development of tomato plants, this paper proposed to utilize storage modal information as a new method to examine the tomato plants. Due to the differences between different biological tissues or structures, the best choice was to simulate the tissues and organs of each organism with the biological circuit model in physics. The modal information stored in each cell in the plant had its own electrical properties and could be replaced by the equivalent circuit of parallel capacitance and resistance in physics. Therefore, it could transform abstract concepts into concrete models.

(2) By studying the impedance characteristics of tomato plants in different periods, an impedance model was constructed. The ZSimpWin software was adopted to conduct impedance spectrum analysis to discover the optimal biological circuit model. Combined with the theoretical analysis of the two-port network, the connection mode of the biological circuit model of each tissue of the tomato plant was analyzed. The impedance spectrum fitting of the model was then carried out to obtain the results at the germination stage, seedling stage, flowering and fruit setting stage and fruiting stage of the tomato plant. The biological circuit model of the period was obtained, and the component values of each model in each period of the tomato plant were inverted.

(3) During the charging and discharging experiments of tomato plants in different periods, the models of tomato plants in different periods were verified. The results showed that the errors were all less than 4.8%. Through the thorough analysis of the error results, it was discovered that the error was caused by the capacitance element and the differences of constant phasor elements. Hence, the biological circuit model was proved to be reasonable.

REFERENCES

[1] Cao, Y., Repo, T., Silvennoinen, R., Lehto, T., & Pelkonen, P. (2011). Analysis of the willow root system by electrical impedance spectroscopy. *Journal of experimental botany*, 62(1), 351-358.

[2] Chen, S., Li, X., Liu, Y., Tai, P., & Liu, B. (2010). Effect of spatial electric field on soil moisture and barley growth (空间电场对土壤水分和大麦生长的影响). *Transactions of the Chinese Society of Agricultural Engineering*, 26(2), 59-63.

[3] Foster, K. R. (2000). Thermal and nonthermal mechanisms of interaction of radio-frequency energy with biological systems. *IEEE Transactions on Plasma Science*, 28(1), 15-23.

[4] Grosse, C., & Schwan, H. P. (1992). Cellular membrane potentials induced by alternating fields. *Biophysical journal*, 63(6), 1632-1642.

[5] Hodgkin, A. L., & Huxley, A. F. (1952). A quantitative description of membrane current and its application to conduction and excitation in nerve. *The Journal of physiology*, 117(4), 500.

[6] Kanai, H., Sakamoto, K., & Haeno, M. (1983). Electrical measurement of fluid distribution in human legs: estimation of extra-and intra-cellular fluid volume. *Journal of microwave power*, 18(3), 233-243.

[7] Lukács, Z., & Kristóf, T. (2020). A generalized model of the equivalent circuits in the electrochemical impedance spectroscopy. *Electrochimica Acta*, 363, 137199.

[8] Liu Kaiyue, Meng Yu, Lin Shengwei, Cao Yu, Liu Dongyun. (2017). Effects of Drought Stress on Parameters of Electrical Impedance Spectra and Membrane Permeability of Nepeta Leaves (干旱胁迫对荆芥叶片电阻抗图谱参数及膜透性的影响). *Journal of Hebei Agricultural University*, 40(5), 55-59.

[9] Liu Weiqing, Zhou Ming, Liang Zhongguan. (2012). Characteristic simulation and application of constant-phase elements in dye-sensitized solar cells (染料敏化太阳电池中常相角元件特性模拟及应用研究). *Journal of Nanchang Hangkong University (Natural Science Edition)*, 26(03):57-62.

[10] Li Yang, Wang Yongqian, Zhao Pengfei, Wang Nan, Huang Lan, Wang Zhongyi. (2020). Design and experiment of electrical impedance imaging system in plant root zone (植物根区电阻抗成像系统设计与实验). *Journal of Agricultural Machinery*, 51(S1):348-356.

[11] Macdonald, J. R., & Barsoukov, E. (Eds.). (2018). *Impedance spectroscopy: theory, experiment, and applications*. John Wiley & Sons.

[12] Mao Guangjin, Shen Linyong, Zhang Yuhui, Jin Dingyi. (2014). Design and research of bioelectrical impedance measurement experiment. *Industrial Control Computer*, (1), 57-58.

[13] Pradhan, R., Raisa, S. A., Kumar, P., Kalkal, A., Kumar, N., Packirisamy, G., & Manhas, S. (2021). Optimization, fabrication, and characterization of four electrode-based sensors for blood impedance measurement. *Biomedical Microdevices*, 23(1), 1-9.

[14] Pankaj, S. K., Misra, N. N., & Cullen, P. J. (2013). Kinetics of tomato peroxidase inactivation by atmospheric pressure cold plasma based on dielectric barrier discharge. *Innovative Food Science & Emerging Technologies*, 19, 153-157.
[15] Rajkai, K., Végh, K. R., & Nacsa, T. (2005). Electrical capacitance of roots in relation to plant electrodes, measuring frequency and root media. *Acta Agronomica Hungarica*, 53(2), 197-210.
[16] Song Jinyan. (2009). Calculation of two-port network parameters (二端口网络参数的计算). *Science and Technology Information*, (32): 510-511.
[17] Väinölä, A., & Repo, T. (2000). Impedance spectroscopy in frost hardiness evaluation of Rhododendron leaves. *Annals of Botany*, 86(4), 799-805.
[18] Wang Aifang. (2010). Comparative Study on Electrical Impedance and Physiological Indexes of White Bark Pine Seedlings under Drought Stress (干旱胁迫下白皮松苗木电阻抗及生理指标的比较研究). *Hebei Agricultural University*.
[19] Wang Ke, Chen Xuejiao, Xu Xiaowei, Liu Guangqi, Zou Dexu. (2017). Influence of temperature on parameters of Cole-Cole dielectric model of oil-immersed casing (温度对油浸式套管 Cole-Cole 介电模型参数的影响). *Southern Power Grid Technology*, 11(06):42-48.
[20] Wang Yongqian, Zhao Pengfei, Fan Lifeng, Wang Ziyang, Huang Lan, Wang Zhongyi. (2019). Study on compensation and coupling methods in impedance spectroscopy measurement of matrix root zone (基质根区阻抗谱测量中补偿和耦合方法研究). *Journal of Agricultural Machinery*, 50(06):288-298.
[21] Wang, Y. Q., Zhao, P. F., Fan, L. F., Zhou, Q., Wang, Z. Y., Song, C., ... & Wang, Z. Y. (2019). Determination of water content and characteristic analysis in substrate root zone by electrical impedance spectroscopy. *Computers and Electronics in Agriculture*, 156, 243-253.
[22] Xing, D., Chen, L., Wu, Y., & Zwiazek, J. J. (2021). Leaf physiological impedance and elasticity modulus in Orychophragmus violaceus seedlings subjected to repeated osmotic stress. *Scientia Horticulturae*, 276, 109763.
[23] Yao Chenguo, Li Chengxiang, Sun Caixin, MiYan, Mo Dengbin. (2006). Pulse electric field-induced electroporation model of inner and outer membranes and simulation of transmembrane potential. *Chinese Journal of Electrical Engineering,* 26(13): 123-128.
[24] Zhang Gang, Xiao Jianzhong, Chen Duanfen. (2005). Electrical Impedance Spectroscopy Method for Determination of Plant Cold Resistance (测定植物抗寒性的电阻抗图谱法). *Chinese Journal of Plant Physiology and Molecular Biology*, (01): 19-26.
[25] Zhang Jun, Zhao Huijuan, Zhang Gang, Yang Minsheng. (2009). Application of electrical impedance mapping method in determination of cold resistance of Robinia pseudoacacia germplasm resources (电阻抗图谱法在刺槐种质资源抗寒性测定中的应用). *Journal of Plant Genetic Resources*, 10(03): 419-425.

ADULTERATION IDENTIFICATION OF ASTRAGALUS POLYSACCHARIDES BY NIR SPECTROSCOPY COMBINED WITH SIMCA AND PLS-DA
/
近红外光谱结合 SIMCA 和 PLS-DA 鉴别黄芪多糖掺假

Zhao FAN, Zhang JIAWEI *, Zhi JIHAO [1]
College of mechanical and Electronic Engineering, Northeast Forestry University, Haerbin/China
Tel: +86-0450-82190397; E-mail: zjw@nefu.edu.cn

DOI: https://doi.org/10.35633/inmateh-68-82

***Keywords**: Astragalus polysaccharide, Classification, SIMCA, PLS-DA*

ABSTRACT

As a famous Chinese traditional medicine, the Astragalus polysaccharide (APS) market is continually expanding, while the quality of APS cannot be guaranteed. Near-infrared (NIR) spectroscopy has been widely used in the detection of Chinese herbal medicines and traditional Chinese medicine. In this study, NIR spectroscopy was used to identify the adulterants of APS. Prepare adulterated mixtures of APS with 75%, and 50% content, respectively. PLS-DA and SIMCA models were developed for 2-classification of APS, APS mixture (75%+50%), and 3-classification of APS, 75% APS mixture and 50% APS mixture, respectively. In the 2-classification, the correct classification rate of both the calibration set and the test set of the PLS-DA and SIMCA models is 100%. In the 3-classification, the correct classification rates of calibration set and test set for PLS-DA were 97.5% and 96.67%, respectively; the correct classification rates of calibration set and test for SIMCA were 98.33% and 100%, respectively. The study showed that it is feasible to identify adulterated Astragalus polysaccharides using near-infrared spectroscopy.

摘要

黄芪多糖（APS）作为著名的中药，其交易市场越来越大，但其质量却无法保证。近红外光谱已广泛应用于中草药的检测。在这项研究中，近红外光谱被用于鉴别 APS 的掺杂物。制备含量分别为 75%和 50%的掺杂 APS 混合物。PLS-DA 和 SIMCA 模型分别用于 APS、APS 混合物（75%+50%）的 2 级分类和 APS、75%APS 混合物和 50%APS 混合物的 3 级分类。在 2 级分类中，PLS-DA 和 SIMCA 模型的校准集和测试集的正确分类率均为 100%。在 3 级分类中，PLS-DA 的校准集和测试集的正确分类率分别为 97.5%和 96.67%；SIMCA 校准集和测试的正确分类率分别为 98.33%和 100%。研究表明，利用近红外光谱法鉴别掺假黄芪多糖是可行的。

INTRODUCTION

Astragalus polysaccharide (APS) is one of the important active ingredients of *Astragalus (Jin et al., 2014; Yan et al., 2016)*. APS is a brownish-yellow powder with hygroscopic properties, and it is a complex mixture of structure, consisting of hexose acetate, glucose, fructose and other groups. *Astragalus polysaccharide* has antiviral, antitumor, antioxidant and immune enhancing effects *(Fan et al., 2021; Li et al., 2020)*. Yu-ping Zhu et al. found that APS may be used to treat and prevent endothelial cell injury-related diseases *(Zhu et al., 2013)*; Yan-Feng Huang investigated the repairing effect of APS on fatigue, concluding that APS can improve the molecular mechanism of mitochondria *(Yan et al., 2016)*; Kojo Agyemang et al. explored the effect of APS on diabetes *(Kojo et al., 2013)*.

APS has good health effects on the organism, and the trading market of APS is gradually developing and growing. Due to the high requirements of APS for the separation and extraction process, the cost of APS is also high. The price range of APS in the market fluctuates widely, with low price of 10 Yuan/Kg and high price of 300/Kg, Low-priced APS may be adulterated with other substances, such as maltodextrin and rice flour. The common identification methods of APS are physical methods such as taste, color, and dissolution *(Jiang et al., 2020)*, which have large subjective factors and cannot be used as formal judgment criteria in the market; there are also chemical methods such as alcohol precipitation, which are lossy identification and time-consuming. Therefore, it is very important to find a fast, convenient and non-destructive method to identify APS.

[1] *Fan Zhao, AS Lec, Ph.D. Eng.; Jiawei Zhang, Prof. Ph.D.Eng.*

Near-infrared spectroscopy combined with chemometrics can enable nondestructive analysis of many herbal medicines. Linhong Fan et al. used portable NIR spectrometer to evaluate the quality of *Fritillariae cirrhosae (Fan et al., 2022)*, the identification accuracy of sources of different varieties of Fritillariae cirrhosae and the common counterfeits of *Fritillariae cirrhosae* reached 83.33% and 90.91%, respectively. Le Wang et al. used NIR spectroscopy for qualitative and quantitative analysis of *Curcumae Radix* from four botanical origins *(Le et al., 2021)*, models of support vector machine (SVM) and k-nearest neighbors (KNN) achieved the complete discrimination of the four species of Yujin with 100% accuracy. Wenlong Li et.al used near infrared spectroscopy to study the feasibility of detection in the production of traditional Chinese medicine *(Li et al., 2016).* The results showed that NIR spectroscopy was helpful to diagnose the faulty batches in the production of traditional Chinese medicine. However, there are very few studies on the identification of adulterated APS using NIR spectroscopy. This paper attempted to classify APS adulterants based on NIR spectroscopy using SIMCA (Soft Independent Modeling Class Analog) and PLS-DA (Partial least squares Discriminant Analysis).

MATERIALS AND METHODS

Samples

APS was purchased from Evergreen Bioengineering Co., Ltd. of Shanxi Province, China, which provided an analysis report showing that APS was extracted from the roots of Astragalus, passed through 80 mesh sieves, and the index composition of APS was 90.0%. Rice was purchased from a Supermarket in Harbin, Heilongjiang Province, China, it was ground and passed through 80 mesh sieves to obtain the required rice powder.

As the content of APS in adulterants is less than 50%, they can be distinguished by color without the help of NIR spectroscopy; while in the range of 50%-100%, it is impossible to distinguish by eye, which requires the use of NIR spectroscopy to distinguish. Therefore, the content of APS in the adulterants in this paper is only considered between 50% and 100%. APS was mixed with rice powder to form 3 concentrations of APS adulterants, with APS concentrations of 100%, 75% and 50%. The number of samples for each concentration was 60, with a total of 180 samples. The 100% APS was used as category A; the APS mixed with rice flour was used as category B, where the mixture with 75% APS content was used as category B1 and the mixture with 50% APS content was used as category B2. These three categories of APS mixtures are shown in Figure 1, and they are not easily discernible by external appearance.

Category A（100%） Category B1（75%） Category B2（50%）

Fig. 1 - Mixture of *Astragalus Polysaccharides* and rice flour in different concentrations

Spectral acquisition

A portable NIR spectrometer (model: NIRQuest-512) in the wavelength range of 900-1700 nm was used to collect the NIR reflectance spectra of APS adulterants.

Spectral data processing

The K-S (Kennard-Stone) algorithm is commonly used for the partitioning of data sets. The K-S algorithm is based on the principle that all samples are considered as training set candidates, from which the samples are selected in turn to enter the training set. First, the two samples with the farthest Euclidean distance are selected to enter the training set, and then, by calculating the Euclidean distance of each remaining sample to each known sample in the training set, the two samples with the farthest and closest Euclidean distances are found, and these two samples are selected to enter the training set, and the above steps are repeated until the number of samples reaches the requirement *(Morais et al., 2019; Zhang et al., 2017)*. In this study, the K-S algorithm was used to divide the samples of the three categories into calibration set and test set, respectively, in a ratio of 2:1. The number of calibrations set samples for each category was 40 and the number of test set samples was 20.

Because of the large noise at the beginning and end of the acquired spectra, the opening and end bands were removed and the band in the range of 997-1657 nm was used.

Models

SIMCA is a classification method based on Principal Component Analysis (PCA) proposed by Swedish chemists in 1976. It uses a priori classification knowledge to build a PCA model for each category, calculates the distance between the unknown sample and the PCA model, and performs discriminant analysis based on the distance *(Svante et al., 1977)*. The PCA plays a decisive role in the results during the calculation of the SIMCA method.

PLS-DA is often used for classification and discrimination. It is similar to PCA, but PCA is unsupervised analysis, while PLS-DA is supervised analysis *(Abdo et al., 2020)*. The unsupervised analysis method can distinguish between-group differences well when the differences between sample groups are large but within-group differences are small; when the differences between groups are small, the unsupervised analysis method is difficult to distinguish between-group differences. These problems can be well solved by supervised analysis like PLS-DA, which performs modeling under the condition that the number of sample points is allowed to be less than the number of variables.

SIMCA 14.1 software was applied to establish SIMCA and PLS-DA model for 2-classification analysis of A, (B1+B2); 3-classification analysis of A, B1, B2.

RESULTS AND ANALYSIS

Spectral

The average spectral curves of APS mixtures are shown in Fig. 2. It can be seen that the average spectral reflectance of class A is higher than that of classes B1 and B2 overall, while the average spectral curves of the latter two are very close. The overall trend of the A, B1, and B2 spectra is consistent, with a very small absorption near 1200 nm and a larger absorption in the 1450-1650 nm range. It is difficult to visualize the differences between species based on the full spectra of the 3 classes. Therefore, it is necessary to combine chemometric methods to develop classification models for mixtures of different concentrations of APS.

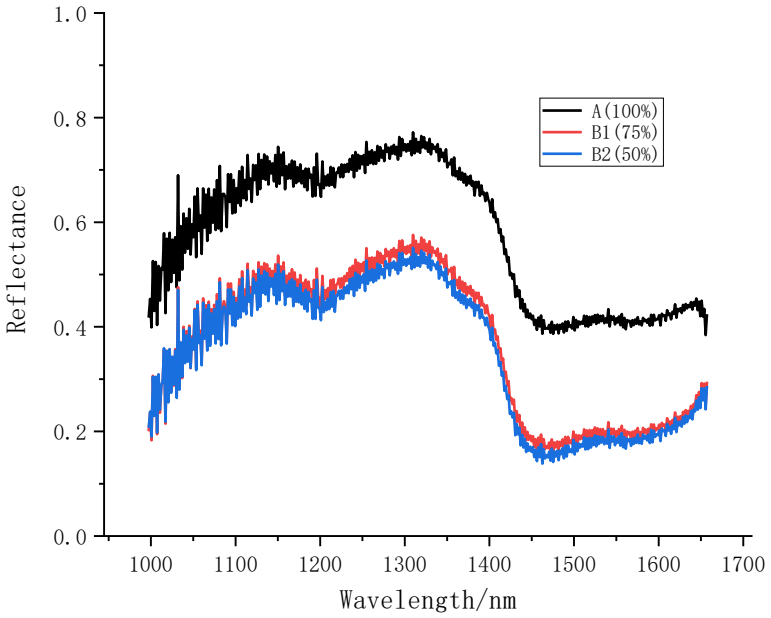

Fig. 2 - Average spectral curves of APS mixtures

2-classification models of A and B

(1) PCA analysis

Twenty samples were extracted from the calibration sets of B1 and B2, respectively, and put together with 40 calibration set samples of class A, as the calibration set of the 2-classification model, and the number of calibrations set samples was 80.

Similarly, the samples of the test set were extracted according to the above method, and the number of test set samples was 40.

All 120 samples of the 2-classifications were subjected to PCA analysis, and R2X (cum) and Q2 (cum) were both 0.995 when the first 2 principal components were taken. R2X (cum) represents the cumulative value of explained variance at the current number of principal components, while Q2 (cum) indicates the total model predictive power at the current number of principal components (*Zhang et al., 2018*). The first 2 principal component score plots are shown in Figure 4(a). The aggregation of the samples in category A is poor, while the aggregation of the samples in category B is better. However, there are individual samples confounded.

(2) PLS-DA Model

The PLS-DA model was built using SIMCA software with 7-fold cross validation (7-fold cross validation), and the values of R2Y (cum) and Q2 (cum), which represent the explanatory degree of the categorical variable Y and the predictive power of the model, respectively *(Du et al., 2021)*, were 0.991 and 0.976. The principal components of the PLS-DA model was 5.

The model was internally validated by the permutation test (permutation test), which randomly changed the order of the categorical variable Y 200 times to obtain different random Q2 values, and the permutation test plot is shown in Figure 3(b). It can be seen that all the points on the left side of R2 and Q2 are lower than those on the right side, and the regression slopes of R2 and Q2 are positive.

VIP (Variable important in projection) is the variable weight value of PLS-DA model variables, which can be used to measure the intensity and explanatory energy of the impact of the differences in the accumulation of each metabolite on the classification discriminations of each group of samples. It is generally considered that variables with VIP>1 may be differential metabolites of the two groups *(Liu et al., 2021)*, and the distribution of VIP predicted values of PLS-DA model is shown in Figure 3(a).

The results of the classification analysis of the correction and prediction sets using the established model are shown in Table 1. The PLS-DA model classifies both the correction and prediction sets with 100% correctness.

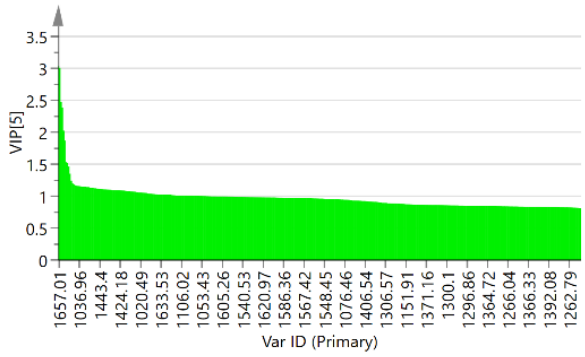

Fig. 3(a) - VIP forecast distribution

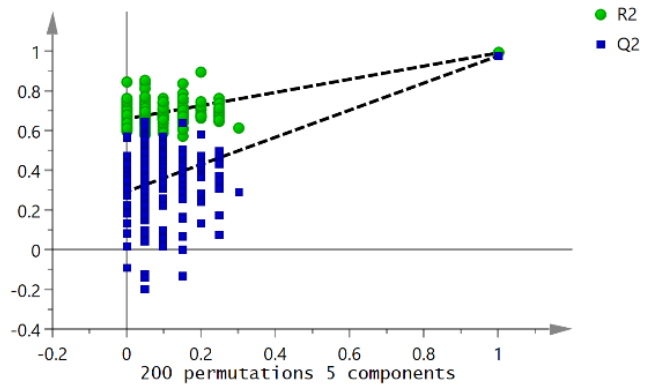

Fig. 3(b) - PLS-DA permutation test

(3) SIMCA Model

SIMCA classification model was established using SIMCA software. Firstly, the PCA models for each class of samples were established separately, and the selected principal component scores were 2 and 3 respectively; then the distances between the predicted samples and the PCA models were calculated, and the predicted samples were classified according to the distances. The results are shown in Table 1. The model classifies 100% of the calibration set and test set samples correctly, and the classification is completely correct.

Table 1

2-Classification results of APS mixtures by SIMCA and PLS-DA

Model	Samples	Class	Members	Correct	A	B
PLS-DA	Correction set	A	40	100%	40	0
		B	40	100%	0	40
		total	80	100%	100%	100%

Table 1

(continuation)

Model	Samples	Class	Members	Correct	A	B
	Test set	A	20	100%	20	0
		B	20	100%	0	20
		Total	40	1000%	20	20
SIMCA	Correction set	A	40	100%	40	0
		B	40	100%	0	40
		total	80	100%	40	40
	Test set	A	20	100%	20	0
		B	20	100%	0	20
		total	20	100%	20	20

3-Classification model of A, B1, B2

All 180 samples of the 3 categories were subjected to PCA analysis, and the R2X (cum) and Q2 (cum) of the first two principal components were both 0.995, and the plots of the scores of the first 2 principal components are shown in Figure 4(b). It can be seen that category A samples are loose and category B1 and B2 samples are more aggregated and have overlapping parts.

The number of samples in the calibration set is 120, which is used to build the SIMCA classification model, and the number of samples in the test set is 60, which is used to verify the reliability of the model.

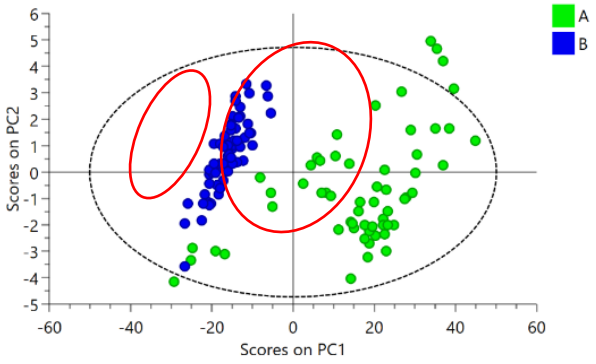

Fig. 4(a) - Principal component score chart

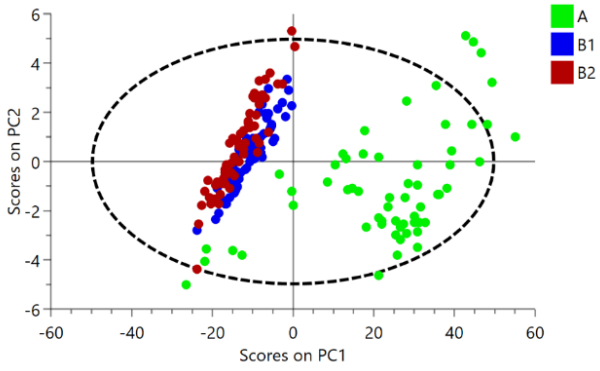

Fig. 4(b) Principal component score chart

(1) PLS-DA model

The PLS-DA classification model was established by using SIMCA software with a master score of 5, and R2Y (cum) and Q2 (cum) were both 0.86 and 0.767, respectively. The replacement test was randomized 200 times, and all the R2 and Q2 on the left side of the obtained replacement test plot were lower than the right side, and the slope was positive, see Figure 5(b). The VIP prediction distribution is shown in Figure 5(a).

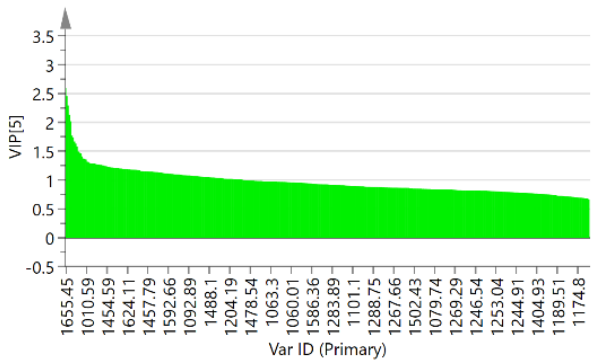

Fig. 5 (a) - VIP forecast distribution

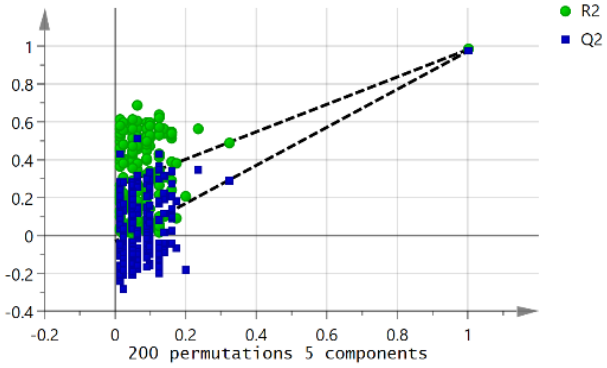

Fig. 5(b) - PLS-DA permutation test

The results of the classification analysis of the calibration set and the prediction set using the established model are shown in Table 2.

When the model classifies the calibration set, 40 samples in A are correctly classified with 100% correct rate; 39 samples in B1 are correctly classified and 1 sample in B1 is classified in B2 with 97.5% correct rate; 38 samples in B2 are correctly classified and 2 samples in B2 are incorrectly classified in B1 with 95% correct rate.

When the model classifies the test set, the 100% of the samples in A were classified correctly. 18 samples in B1 were classified correctly and 2 samples were incorrectly classified in B2, with a 90% correct rate. The samples in B2 were classified correctly with 100%.

(2) SIMCA Model

SIMCA software was used to build A, B1, and B2 SIMCA 3-classification models, and the main score of all three classification models was 2. The classification results of the models on the calibration and test sets are shown in Table 2.

In the calibration set classification results, all 40 samples in A were correctly classified with a 100% correct rate; all 40 samples in B1 were correctly classified with a 100% correct rate; 38 samples in B2 were correctly classified and 2 samples in B2 were incorrectly classified in B1 with a 95% correct rate.

In the test set classification results, all samples A, B1 and B2 were correctly classified with 100% correct rate.

Table 2

3-Classification results of APS mixtures by SIMCA and PLS-DA

Model	Samples	Class	Members	Correct	A	B1	B2
PLS-DA	Correction set	A	40	100%	40	0	0
		B1	40	97.5%	0	39	1
		B2	40	95%	0	2	38
		total	120	97.5%	40	41	39
	Test set	A	20	100%	20	0	0
		B1	20	90%	0	18	2
		B2	20	100%	0	0	20
		total	60	96.67%	20	18	22
SIMCA	Correction set	A	40	100%	40	0	0
		B1	40	100%	0	40	0
		B2	40	95%	0	2	38
		total	120	98.33%	40	42	38
	Test set	A	20	100%	20	0	0
		B1	20	100%	0	20	0
		B2	20	100%	0	0	20
		total	60	100%	20	20	20

Model Comparison

Comparing PLS-DA model with SIMCA model, the results are as follows:

(1) For A and B classification, the correctness of PLS-DA correction set and test set is 100%; The correctness of SIMCA calibration set and test set also reach 100%. PLS-DA and SIMCA performed extremely well in A and B classification, with 100% correct classification rates.

(2) For the A, B1 and B2 classifications, the correction set correctness of PLS-DA and SIMCA is 97.5% and 98.33% respectively; and the test set correctness of PLSA-DA and SIMCA is 96.67% and 100% respectively. SIMCA performed better than PLS-DA in A, B1 and B2 classification.

CONCLUSIONS

This study showed that NIR spectroscopy combined with PLS-DA and SIMCA models can identify APS mixtures. This method has the advantages of simple operation, of being non-destructive and rapid.

(1) APS (100%) and APS mixture (containing both 75% and 50%) were very easy to classify, and the average correctness of the calibration set and test set for all 2-classifition models is 100%.

(2) When the mixture with APS content of 100%, 75% and 50% is classified into 3 categories, the SIMCA model can completely classify the test set correctly, with a correct rate of 100%; while PLS-DA wrongly considered that the two samples with 50% APS content in the test set had 75% APS content, which was correct at 96.67%.

(3) In the 2-classification, SIMCA was as good as PLS-DA, with a 100% correct rate, while in the 3-classification, SIMCA was 100% correct, which was higher than PLS-DA (96.67%), the SIMCA model performs better than PLS-DA.

DECLARATIONS

Fundings This work was supported by the National Key R&D Program of China (Project No. 2020YFC2200800).

Ethics approval (include appropriate approvals or waivers): This article does not include any ethical research on humans or animals.

Declaration of Competing Interest

The authors declare that they have no known competing financial interests or personal relationships that could have appeared to influence the work reported in this paper.

REFERENCES

[1] Abdo H., (2020). Performance of Fluorescence and Diffuse Reflectance Hyperspectral Imaging for Characterization of Lutefisk: A Traditional Norwegian Fish Dish. *Molecules*, vol. 25, no. 1191, Switzerland, doi: 10.3390/molecules25051191.

[2] Du Y., (2021). Serum Metabolomics Study of Papillary Thyroid Carcinoma Based on HPLC-Q-TOF-MS/MS. *Frontiers in Cell and Developmental Biology*, vol. 9, no. February, pp. 1–13, Switzerland, doi: 10.3389/fcell.2021.593510.

[3] Fan L.H., (2022). Quality assessment of Fritillariae cirrhosae using portable NIR spectrometer. *Spectrochimica Acta - Part A: Molecular and Biomolecular Spectroscopy*, vol. 265, p. 120325, England, doi: 10.1016/j.saa.2021.120325.

[4] Fan Y.P., (2012). Effects of Astragalus polysaccharide liposome on lymphocyte proliferation in vitro and adjuvanticity in vivo. *Carbohydrate Polymers*, vol. 88, no. 1, pp. 68–74, England, doi: 10.1016/j.carbpol.2011.11.067.

[5] Jiang X.H., (2020). Comparative Study on the Quality of Astragalus Polysaccharide from Different Sources (不同来源的黄芪多糖产品质量比较研究). *Guangxi Sci.*, vol. 27, pp. 380–386, Guangxi/P.R.C., doi: 10.13656/j.cnki.gxkx.20200924.002.

[6] Jin M.L., (2014). Structural features and biological activities of the polysaccharides from Astragalus membranaceus. *International Journal of Biological Macromolecules*, vol. 64, pp. 257–266, Netherlands, doi: 10.1016/j.ijbiomac.2013.12.002.

[7] Kojo A., (2013). Recent advances in Astragalus membranaceus anti-diabetic research: Pharmacological effects of its phytochemical constituents. *Evidence-based Complementary and Alternative Medicine*, vol. 2013, England, doi: 10.1155/2013/654643.

[8] Le W. et al, (2021). Fast discrimination and quantification analysis of Curcumae Radix from four botanical origins using NIR spectroscopy coupled with chemometrics tools. *Spectrochimica Acta - Part A: Molecular and Biomolecular Spectroscopy,* vol. 254, p. 119626, England, doi: 10.1016/j.saa.2021.119626.

[9] Li W.F., (2020). Characterization and anti-tumor bioactivity of Astragalus polysaccharides by immunomodulation. *International Journal of Biological Macromolecules,* vol. 145, pp. 985–997, Netherlands, doi: 10.1016/j.ijbiomac.2019.09.189.

[10] Li W.L. et al, (2016). A feasibility research on the monitoring of traditional Chinese medicine production process using NIR-based multivariate process trajectories. *Sensors and Actuators B-Chemical*, vol. 231, pp. 313–323, Switzerland, doi: 10.1016/j.snb.2016.03.023.

[11] Liu L.C., (2021). Characterization and identification of different Chinese fermented vinegars based on their volatile components. *Journal of Food Biochemistry*, vol. 45, no. 3, pp. 1–12, United States, doi: 10.1111/jfbc.13670.

[12] Morais C. et al, (2019). Improving data splitting for classification applications in spectrochemical analyses employing a random-mutation Kennard-Stone algorithm approach. *Bioinformatics*, vol. 35, no. 24, pp. 5257–5263, England, doi: 10.1093/bioinformatics/btz421.

[13] Svante W. & Michael S., (1977). SIMCA: A Method for Analyzing Chemical Data in Terms of Similarity and Analogy. *Chemometrics: Theory and application,* ISBN: 9780841203792.
[14] Yan F.H., (2016). Effects of Astragalus Polysaccharides on Dysfunction of Mitochondrial Dynamics Induced by Oxidative Stress. *Oxidative Medicine and Cellular Longevity,* vol. 2016, United States, doi: 10.1155/2016/9573291.
[15] Zhang L.N., (2017). Kennard-Stone combined with least square support vector machine method for noncontact discriminating human blood species. *Infrared Physics and Technology*, vol. 86, pp. 116–119, Netherlands, doi: 10.1016/j.infrared.2017.08.020.
[16] Zhang X., (2018). Determination of bitterness of Andrographis herba based on electronic tongue technology and discovery of the key compounds of bitter substances. *Molecules*, vol. 23, no. 12, pp. 1–13, Switzerland, doi: 10.3390/molecules23123362.
[17] Zhu Y.P., (2013). Astragalus polysaccharides suppress ICAM-1 and VCAM-1 expression in TNF-α-treated human vascular endothelial cells by blocking NF-κB activation. *Acta Pharmacologica Sinica,* vol. 34, no. 8, pp. 1036–1042, Shanghai/P.R.C., doi: 10.1038/aps.2013.46.

CHARACTERISTICS OF COLD BREWED ARABICA COFFEE FROM GUNUNG KARAMAT VILLAGE SUBANG REGENCY AS A RESULT OF DIFFERENT TEMPERATURES AND ROASTING TIME
/
KARAKTERISTIK SEDUHAN DINGIN KOPI ARABIKA ASAL DESA GUNUNG KARAMAT KABUPATEN SUBANG HASIL PERLAKUAN SUHU DAN LAMA PENYANGRAIAN YANG BERBEDA

Doddy Andy DARMAJANA[1)], Rahayu WULANDARI[2)], Diang SAGITA*[1)]
[1)] Research Center for Appropriate Technology, National Research and Innovation Agency / Indonesia
[2)] Department of Food Technology, Pasundan University / Indonesia
Tel: 6285719002251; E-mail: diang.sagita@gmail.com

DOI: https://doi.org/10.35633/inmateh-68-83

Keywords: *Cold brewed, drum type roaster, infrared, roasted bean coffee*

ABSTRACT

Cold brewed coffee has a sweet taste steeping intensity higher than bitter taste and sour taste. One of the flavors of brewing coffee can be affected by the temperature and the roasting time of the equipment used. In this study, cold brewing processes were performed on several Arabica coffee samples obtained from several roasting treatments consisting of three different roasting temperatures (170°C, 180°C, and 190°C) and three levels of roasting times (10, 12, and 15 minutes). The cold brewed in this study has the characteristics of steeping with high acidity intensity, clean aftertaste, the color of the steeping tends to be light brown, and the steeping body was light. The best treatment for roasting was a temperature of 190°C with a roasting time of 10 minutes based on the highest effectiveness value.

ABSTRAK

Kopi seduh dingin memiliki intensitas seduhan rasa manis lebih tinggi daripada rasa pahit dan asam. Cita rasa pada seduhan kopi salah satunya dapat dipengaruhi oleh suhu dan lama waktu penyangraian dari alat yang digunakan. Pada penelitian ini, proses penyeduhan kopi dilakukan pada beberapa sampel Arabika kopi yang diperoleh dari beberapa perlakuan penyangraian yang terdiri dari tiga suhu sangrai yang berbeda (170°C, 180°C, and 190°C) dan tiga tingkat waktu sangrai (10, 12, dan 15 menit). Kopi seduh dingin pada penelitian ini memiliki karakteristik seduhan dengan intensitas keasaman tinggi, clean aftertaste, warna seduhan cenderung coklat muda, dan body seduhan ringan. Perlakuan terbaik untuk penyangraian adalah suhu 190°C dengan waktu penyangraian 10 menit berdasarkan nilai bobot efektifitas tertinggi.

INTRODUCTION

Arabica coffee is included in the coffee beans that have the best quality compared to other types of coffee. This type of coffee is able to produce a distinctive coffee taste and has different biochemical content (caffeine, trigonelline, chlorogenic acid, and sucrose), one of which is based on the area of origin of the coffee beans *(Isnidayu et al., 2020)*. Environmentally Arabica coffee is widely cultivated in areas with an altitude of 610-1830 meters above sea level (MASL), while robusta coffee can be grown in the lowlands, in areas with an altitude of 0-800 MASL *(Darmajana et al., 2022)*. Subang Regency is one of the regions or centers for smallholder Arabica coffee with a total production of 66 tons in 2015-2018 *(Direktorat Jenderal Perkebunan, 2019)*, while in 2019 it increased by 45% with a total production of 120 tons *(Direktorat Jenderal Perkebunan, 2020)*. This production value shows the need for efforts to maintain and increase the productivity of Arabica coffee, especially in Subang Regency in order to be able to compete in the national market, one of which is through processing coffee in the form of coffee powder or processed into cold brewed coffee drinks.

Brewed coffee can have different flavors. The difference in the taste of brewing coffee can be influenced by several factors, one of which is the temperature of the brewing water. Brewing coffee based on the temperature of the brewing water consists of two methods, i.e., high water temperature (hot brewed) and low water temperature (cold brewed) *(Cordoba et al., 2021)*. People in Indonesia generally consume coffee with high water temperatures such as the Aero press, expresso, French press, and *tubruk (Bekti et al., 2019)*.

Cold brewed coffee is a term for serving brewed coffee whose extraction process uses room temperature water or cold water *(Dharmawan, 2017)*, with a serving process that takes 8 to 24 hours *(Cordoba*

et al., 2019). This method has a lower total acidity value, so the resulting taste tends to be sweeter than hot brewed coffee *(Rao and Fuller, 2018)*. The quality of the taste of brewed coffee can be obtained by paying attention to the roasting factor of coffee beans. Roasting can be defined as the process of processing coffee beans that can determine the quality of the coffee drink produced. This process can convert raw coffee beans into processed coffee drinks that have a delicious aroma and taste *(Afriliana, 2018)*. In addition, the quality of the brewed coffee produced can also be influenced by the heating technique or the type of equipment used for roasting.

Roasting machines are generally available in the drum type with a heating system in the form of a fire source originating from LPG gas in direct contact with the rotating cylinder. This equipment is less efficient in roasting because of the large amount of heat lost due to combustion produced from LPG, there is no heating furnace as a coating, so the heat generated is wasted a lot to the environment *(Rusnadi et al., 2018)*. In addition, coffee roasting with an electric heating source is also available, but the roasting time required is longer (34-58 minutes) and the price is relatively expensive for small industrial scales *(Maulina et al., 2022)*. One of the efforts to increase roasting efficiency is to design a roasting machine with an infrared heating source. This machine is more efficient in energy use *(Hidayat et al., 2020)*. However, to determine the efficiency of using a roaster with an infrared is necessary to study further the use of different temperatures and roasting times on the Physicochemical and organoleptic quality characteristics of cold brewed Arabica coffee.

MATERIALS AND METHODS

The main materials used were Arabica coffee beans obtained from Gunung Karamat village, Ciater District, Subang Regency, 12 kg LPG gas, V60 coffee filter paper, buffers pH 4 and 7, standard caffeine, methanol, demineralized water, and distilled water. The main equipment used was the first generation of drum roasting machine developed by *Hidayat et al. (2020)*, digital scales, refrigerator, coffee color tracker, coffee grinder, colorimeter, portable refractometer, oven, TDS meter, pH meter, HPLC, spoon and glass cupping 200 ml.

Sample preparation

The process of making Arabica coffee powder were divided into 5 stages namely, (1) the coffee beans were sorted first; (2) coffee beans roasted in 926 g/batch with treatments roasting temperatures were 170^{o}C, 180^{o}C, 190^{o}C, and roasting times were 10, 12, and 15 minutes; (3) The roasted coffee beans were stored (resting time) at seven days to reduce the carbon dioxide levels that were still lifting after roast; (4) The roasted coffee beans were grinding by using a self-developed coffee grinder (PRTT BRIN) with a medium grinding size; (5) The powder coffee were then sieved using a 20 mesh sieve and stored using zip-lock aluminum foil packaging.

The process of brewing coffee using the cold brewed coffee method was divided into 4 stages, viz. (1) weighing 16 g of coffee powders; (2) The coffee powder were put in a glass jar and 160 ml of cold water (4^{o}C) was added gradually until the coffee powders were submerged; (3) The glass jar containing the soaked coffee was then stored in the refrigerator for 8 hours for the extraction of the coffee process; (4) Arabica coffee that has passed the extraction process was then filtered using a V60 dripper and coffee paper filter to separate the extraction results from the coffee powders.

Physicochemical analysis

The physicochemical analysis evaluated in this study were color (brightness), Total Dissolved Solid, sucrose content, water content, pH, and caffeine content. The color (brightness) of coffee powder was measured using a colorimeter (3NH Technology Co., Ltd., Shenzen, China). The value of TDS brewed coffee was measured by TDS meter (Jinan Huiquan Electronic Co., Ltd., Shandong, China). This test was carried out to see the total dissolved solids expressed in ppm units. The water content of coffee powder was measured using the oven method which refers to SNI 2983:2014 *(BSN, 2014)*, where the coffee powder was dried in the oven for 1 hour, then the sample was weighed. The water content was calculated based on the initial and final weights of the sample. The degree of acidity (pH) was tested using a pH meter (Jinan Huiquan Electronic Co., Ltd., Shandong, China).

The electrode was dipped into the brewed coffee until the pH meter display shows a stable number. The sucrose level indicates the sugar concentration of the brewed coffee. It was measured by using a hand-held Refractometer ATAGO PAL-1 (Atago Co.,Ltd., Tokyo, Japan).

The caffeine content of brewed coffee was measured by using a High-Performance Liquid Chromatography instrument (Agilent Technologies, Inc., California, United States).

Organoleptic taste

Organoleptic test of cold brewed Arabica coffee was performed using the hedonic method (preferred test). The test parameters carried out consisted of attributes of color, aroma, taste, aftertaste, and overall. The sample was evaluated by 25 untrained panelists (barista). There were 27 samples that were evaluated by the panelists and were given a score in the range of 1 to 7 points (1= Really liked, 2= Liked, 3= Somewhat liked, 4= Moderately, 5= Slightly disliked, 6= Disliked, 7= Really disliked).

RESULTS

Total dissolved solid (TDS)

TDS is the amount of substances dissolved in water when the sample is brewed such as organic or inorganic substances *(Borem et al., 2016)*. The results of this study show that the highest TDS value of cold brewed Arabica coffee is 216,06 ppm at 180°C for 15 minutes, while the lowest TDS is 190.39 ppm at 190°C for 10 minutes (Table 1).

Table 1

The data analysis of the physicochemical quality test of cold brewed Arabica coffee

Sample	Color (Lightness)	Total Dissolved Solid (ppm)	pH	Sucrose Content (Brix%)	Moisture Content (% w/w)	Caffeine (%)
170ºC; 10 minutes	44.13	195.87	4.67	1.75	3.18	0.10
170ºC; 12 minutes	41.98	210.48	4.65	1.75	2.49	0.10
170ºC; 15 minutes	38.35	215.90	5.52	1.11	1.80	0.11
180ºC; 10 minutes	43.02	206.01	4.59	1.91	2.75	0.12
180ºC; 12 minutes	41.42	212.92	4.69	1.59	2.21	0.10
180ºC; 15 minutes	38.55	216.06	5.49	1.27	1.92	0.11
190ºC; 10 minutes	43.76	190.39	4.58	1.43	2.73	0.10
190ºC; 12 minutes	40.12	212.65	4.78	1.43	1.85	0.11
190ºC; 15 minutes	37.96	215.35	5.53	1.27	1.61	0.11

This shows that the increasing use of temperature treatment and roasting time results in an increase in the steeping TDS value. According to *Rao et al. (2020)*, although during the roasting process decomposition of compounds occurs which can cause the loss of dissolved solids, new compounds are also formed during the pyrolysis stage which occurs during the dark roasting. In addition, the more intense roasting process can damage the cellular matrix so that the compounds are more easily extracted. The amount of dissolved solids is limited by the use of the brewing water temperature. According to *Cordoba et al. (2019),* the cold brew coffee method has a TDS value that is close to or higher than hot coffee because the extraction temperature is assumed to be the driving force that supports the extraction process of chemical compounds present in coffee powders. This study did not identify specifically the type of solute contained in brewing coffee, so it only measured the overall amount of solute produced in brewing coffee. However, some literature shows that the total dissolved solids content is composed of organic and inorganic substances such as acids, sugars, and salts so that when the salt dissolution is carried out the higher the total dissolved solids value that is read will increase *(Pamungkas, 2016; Nurhayati, 2017)*. In addition, dissolved solids in cold brew coffee can be caffeine, phenol, chlorogenic acid, esters, and organic acids. These compounds contribute to the taste and aroma of the extracted coffee *(Kyroglou et al., 2022)*.

Degree of acidity (pH)

The pH analysis is one of the analytical parameters that can show the concentration of hydrogen ions which states the level of acidity or alkalinity in a solution *(Sudewa and Hadiatna, 2017)*. The pH value of coffee does not represent a sour taste that can be accepted by coffee consumers but is more likely to be used as a parameter of stability and quality of the results of coffee processing such as roasting *(Davids, 2003; Umam, 2017)*.

The results of this study show that the pH value of cold brewed Arabica coffee has the highest value of 5.53 at a temperature treatment of 190°C for 15 minutes, while the lowest pH value is 4.58 at a temperature treatment of 190°C for 10 minutes (Table 1).

The acid contained in coffee when the roasting process undergoes evaporation can cause the acidity of cold brewing Arabica coffee to tend to decrease or the resulting pH value to increase with increasing use of temperature and roasting time. This statement is in accordance with the research results of *Purnamayanti et al. (2017)*, the pH value increases towards a neutral pH value along with the higher and longer the roasting process. This can happen because during the roasting process there are changes in the physical and chemical properties of coffee. According to *Cuong et al. (2014)*, the roasting process will degrade various important compounds found in coffee such as chlorogenic acid, trigonelline, protein, and polysaccharides. These factors can then affect the solubility and availability of organic compounds during coffee brewing so that the pH value of brewing coffee produced can vary.

Sucrose content

Brix value is used as the percentage of dissolved sugar in a solution, higher the value the better taste of brewing coffee *(Maulid et al., 2021)*. This study shows that the highest level of cold brewed Arabica coffee sucrose is 1.91% Brix is found at a temperature treatment of 180°C for 10 minutes, while the lowest is 1.11% Brix is found at a temperature treatment of 170°C for 15 minutes (Table 1). Coffee beans when roasted go through a chemical phase in the form of a caramelization reaction. When passing through this phase, the sugar content in the coffee beans will be degraded and a distinctive coffee taste is formed, but if the coffee beans are exposed to excessive heat, the sugar content in the coffee beans will burn so that the brix% value of brewing coffee produced decreases. This statement can be supported by the literature, which shows that the decrease in the value of Brix in brewed coffee can be caused when the roasting processed coffee beans undergo a caramelization reaction. The reaction can convert sugar monomers into furan and hydroxymethylfurfural, which can cause a decrease in the Brix value in coffee steeping *(Yeretzian et al., 2002; Maulid et al., 2021)*. The Brix value of coffee after roasting will decrease because some of the sucrose undergoes hydrolysis, but some will undergo pyrolysis *(Illy and Viani, 2005; Henrietta, 2020)*.

Moisture content

The water content value shows the amount of water content per unit weight of the material expressed in units of percent on a wet basis or a dry basis to maintain the shelf life of coffee *(Edowai, 2019)*. This study shows that the highest water content of coffee powder is found at a temperature of 170°C for 10 minutes with a water content value of 3.18% w/w, while the lowest water content value is 1.61% w/w at a temperature treatment of 190°C for 15 minutes (Table 1). Roasted coffee beans will go through a water evaporation phase which can cause the water content in the coffee beans to come out due to the help of heat. According to *Setyani et al. (2018)*, the water content of coffee after roasting tends to decrease along with the increase in temperature and duration of roasting of coffee beans. This can happen because the roasting process is related to the rapid propagation of water (diffusion) in the coffee bean cell tissue. Based on the data that had been obtained, the average value of the water content of coffee powders has a value of 1.61-3.18% w/w was indicates that the results obtained have met the quality requirements of SNI 01-3542-2004 for the I and II quality requirements. The water content of powder coffee is not more than 7% w/w *(BSN, 2004)*.

Caffeine content

The concentration of caffeine levels can indicate the strength, body, and bitterness of brewed coffee *(Angeloni al., 2019).* This study showed that the caffeine content of cold brew Arabica coffee did not have a significantly different value. The highest caffeine content was found at 180°C for 10 minutes with a caffeine content of 0.12%, while the lowest caffeine content value was 0.10% at 170°C for 10 minutes (Table 1). The instability of the value of the caffeine concentration in brewing coffee can be influenced by different temperatures and roasting time used and the changes in the physical shape of the roasted coffee beans, one of which is the development of volume in the coffee beans. Research by *Folmer (2012)* and *Kristandi (2018)* shows that the cause of changes in coffee bean caffeine levels during the roasting process is due to structural changes in the cells of the coffee beans. Changes in the structure of coffee beans can determine the increase or decrease in the level of caffeine produced. Based on research data that has been obtained, the average value of cold brewed Arabica coffee has a value of 0.10-0.12%. The caffeine content of cold brewed Arabica coffee, when compared with the value caffeine content of hot brewed coffee has a percentage difference of 89.014-90.610%. The value can be seen in previous research referring to *Rao et al (2020)*, the average value of the caffeine content of hot brewed coffee is 1.035-1.095%.

Organoleptic test result

Aroma Test Analysis in brewing coffee will have different translations from one person to another like in the coffee taste *(Yulia, 2018)*. The hedonic test of the aroma attribute of brewed coffee that the panelists preferred was coffee treated with a temperature of 180°C for 10 minutes, while the panelist not preferred was coffee with a temperature treatment of 180°C for 15 minutes.

The aroma of brewed coffee favored by the panelists has a higher acidity value because the acid compounds that form the aroma and taste in this treatment have not been decomposing much more than coffee that has been roasting for a longer time. According to research *Rao (2014)* and *Amri et al. (2021)* roasting levels of light to medium produce coffee with flavor positive fruity, floral, nutty, and sweet caramel. In addition, the roasting process with a long time will pass through the pyrolysis phase, which can cause various volatile acid compounds as described in *Nopitasari (2010)*, the roasting process of coffee beans at the final stage of pyrolysis occurs degradation of carbohydrate, fat, and protein compounds which can produce volatile acid compounds (formic acid, propanoic acid, acetic acid, and hexanoic acid). According to *Rao et al. (2011)*, a collection of these compounds can only be formed when roasting is carried out. Therefore, when many volatile components dissolve in water during the coffee brewing process, the sharper the coffee brewing fragrance will be.

The color attribute is one of the parameters that can determine the level of panelists' interest in the cold brew of Arabica coffee produced. The hedonic test of the coffee brewing color attribute that the panelists preferred was coffee with a temperature treatment of 180°C for 10 minutes, while the least preferred was coffee with a temperature treatment of 180°C for 15 minutes. Panelists prefer coffee brewed with a brown color rather than dark color. The color of the brewed coffee produced can be influenced because of the increasing use of roasting degrees, so the brewing color of the coffee produced tends to be close to dark brown. This statement is in accordance with the research According to *Vignoli et al. (2014)*, the intensity of the color of the brewed coffee produced is due to the presence of melanoidin compounds. In addition, the color of steeping coffee can be affected by the caramelization reaction due to the presence of caramel compounds that can produce a dark brown color. According to *Kusnandar (2019)*, caramelization reactions are included in reactions that involve simple sugars so that they can give a caramel brown color and form flavor components.

Table 2

The results of the organoleptic quality test analysis of cold brewing Arabica coffee

Sample	Aroma	Color	After-taste	Flavor	Overall
170ºC; 10 minutes	2.93	2.93	2.84	2.85	2.90
170ºC; 12 minutes	3.29	3.15	3.60	3.57	3.39
170ºC; 15 minutes	3.52	3.75	4.91	4.51	4.19
180ºC; 10 minutes	2.77	2.55	3.01	2.85	2.88
180ºC; 12 minutes	3.20	3.00	3.09	3.19	3.17
180ºC; 15 minutes	4.63	3.28	5.27	5.41	4.70
190ºC; 10 minutes	3.33	3.07	3.29	3.28	3.24
190ºC; 12 minutes	2.93	3.37	3.85	3.39	3.40
190ºC; 15 minutes	4.47	3.64	5.16	5.24	4.67

The after-taste attribute aims to give the impression that is sensed by the palate regarding the aroma and taste of brewed coffee after the coffee is swallowed *(SCAA, 2015)*. The assessment of this attribute can be felt as a taste that is left on the base of the tongue when tasting like something is slightly stuck in the throat, or when tasting brewed coffee nothing is left or can be said to be clean (clean) like not drinking coffee *(Yulia, 2018)*. After-taste of cold brewed Arabica coffee that panelists like is coffee with a temperature treatment of 170°C for 10 minutes, while what is not preferred is coffee with a temperature treatment of 180°C for 15 minutes (Table 2). Brewed coffee with a pleasant aftertaste can be felt a few moments after the coffee is swallowed. According to *Budiyanto et al. (2021)*, the after-taste score (preferred by panelists) indicates that there are variations in taste and aroma that give the impression and taste favored by panelists at the end of the test. Research results from *Puspitasari (2020)* show that the longer roasting time has the aftertaste (not favored by panelists) because it detects a sour taste formed by the content of acidic compounds (phenolic acid, chlorogenic acid, and aliphatic acid) increasing so that there is the taste that lingers when the coffee is sipped.

Taste attributes in organoleptic can be done based on the influence, complexity, and quality of the combination of aroma and taste when coffee is sipped in the mouth so that it can involve the entire palate. Non-volatile organic compounds and minerals are flavor-forming compounds that can be produced by the

sense of taste in the liquid phase *(Mulato and Suharyanto, 2012)*. The hedonic test of the coffee brewed taste attribute that the panelists liked was coffee treated with a temperature of 180°C for 10 minutes, while the taste that the panelists did not like was coffee with the treatment 180°C for 15 minutes. The panelist's assessment was quite sensitive to the brewing taste of the coffee produced because the temperature treatment at 180°C for 10 minutes had a higher Brix value and caffeine content than the treatment at 180°C for 15 minutes.

These parameters indicate that the brewed coffee produced has a balanced brewing taste between sweet and bitter tastes. In accordance with the research of *Maulid et al. (2021)*, which shows that the Brix value is used as the percentage of dissolved sugar in a solution, the higher the value, the better the brewed coffee tastes. According to *Sunarharum et al. (2014),* a roasting time that is too long can affect the taste of the coffee produced, namely the dominant charred and bitter taste because, during the roasting process, chlorogenic acid will be broken down into quinine lactic acid, quinine acid, ferulic acid, caffeic acid, and lactone chlorogenic acid which have a sour taste. strong bitterness in brewing coffee. According to *Cordoba et al. (2019)*, cold brew coffee requires a long extraction time so it can cause degradation of compounds and the formation of off-flavor in coffee brewing.

The overall test of cold brewing arabica coffee was carried out with the aim of knowing the panelists' assessment of the observed coffee steeping (aroma, color, taste, and aftertaste). The results showed that overall, the coffee that was liked by the panelists was roasted coffee at 180°C for 10 minutes, while the coffee they disliked the most was coffee roasted at 180°C for 15 minutes. The treatment favored by the panelists resulted in the characteristics of steeping coffee with a higher intensity of acidity, having a pleasant aftertaste or no taste left in the throat, and the color of brewing coffee tended to be light brown. In this study, the results of the assessment by the panelists were in line with the literature from *Amri et al. (2021)*, where roasted coffee with a medium level was preferred because the quality of flavor, clean-up, aroma, and overall was higher than other roasting treatments. In addition, the resulting flavor and aroma character was quite dominated by floral, sugar browning, and slightly fruity.

Effectiveness value

The effectiveness value can be determined based on the effective index method to know the best treatment of temperature and roasting time coffee beans Arabica from Gunung Karamat Village, Subang Regency. The best temperature and roasting time are determined based on the Physicochemical analysis parameters (color, TDS, pH, water content, caffeine content, and sucrose content) and organoleptic (aroma, color, taste, aftertaste, overall). The best treatment in this study was at a temperature of 190°C for 10 minutes because it had the highest effectiveness value of 0.91. This treatment resulted in the characteristics of arabica coffee with a color value of 43.76 L (brightness), TDS brewed coffee 190.39 ppm, pH brewed coffee 4.58, sucrose content of 1.43%Brix, the water content of coffee powder 2.73% w/w, and the caffeine content of cold brewed Arabica coffee is 0,10%. The organoleptic test value of cold brewed Arabica coffee for the color attribute was 3.07 (somewhat liked), the aroma attribute was 3.33 (somewhat like), the taste attribute was 3.28 (somewhat like), the aftertaste was 3.29 (somewhat like), and 3.24 overall (somewhat like). The effectiveness value of cold brewing Arabica coffee as a result of different temperatures and roasting times can be seen in Table 3.

Table 3

Results of analysis of the effectiveness of cold brewing Arabica coffee

Sample	EV	Sample	EV	Sample	EV
170ºC; 10 minutes	0.77	**180ºC; 10 minutes**	0.66	**190ºC; 10 minutes**	0.91
170ºC; 12 minutes	0.60	**180ºC; 12 minutes**	0.66	**190ºC; 12 minutes**	0.55
170ºC; 15 minutes	0.40	**180ºC; 15 minutes**	0.28	**190ºC; 15 minutes**	0.28

Note: EV is effectiveness value

CONCLUSIONS

Based on the research data, the combination of different temperatures and roasting times resulted in the physicochemical quality characteristics of cold brewed Arabica coffee which varied with the TDS (Total Dissolved Solid) value of brewed coffee 190.39-216.06 ppm, pH 4.58-5.53, sucrose content 1.11-1.91 %Brix, and caffeine content 0.10-0.12%. Cold brewing Arabica coffee based on the overall organoleptic test was the most preferred by the panelists in the treatment at 180°C for 10 minutes because the treatment had the characteristics of steeping coffee with high acidity intensity, the aftertaste of the coffee was clean or there was

no taste left in the throat, the brew color tended to be light brown, and the body attribute was light. The best roasting temperature and time can be obtained based on the highest effectiveness value, namely the treatment at 190°C for 10 minutes.

ACKNOWLEDGEMENT

The author would like to thank everyone from the Center for Appropriate Technology Research, National Research and Innovation Agency for the research funds that have been provided, and also to all parties who support the implementation of this research. In addition, the authors would like to thank the Advisory Lecturers and Examiners for the suggestions and inputs that have been given.

REFERENCES

[1] Afriliana, A. (2018). *Latest Coffee Processing Technology [Teknologi Pengolahan Kopi Terkini].* Yogyakarta: CV Budi Utama.

[2] Amri, A.F., Taqiyuddin M., Atmaka W. and Herawati E.R.N. (2021). Physicochemical and sensory characteristics of Arabica coffee Menoreh by cold brew technique [Karakteristik fisikokimia dan sensoris kopi arabika menoreh dengan teknik seduhan cold brew]. *Jurnal Tanaman Industri dan Penyegar.* 8(3): 173-182.

[3] Angeloni G., Guerrini L., Masella P., Innocenti M., Bellumori M. and Parenti A. (2019). Characterization and comparison of cold brew and cold drip coffee extraction methods. *J.Sci Food Agric.* 99(1): 391-399.

[4] Badan Standarisasi Nasional [BSN]. (2004). SNI 01-3542-2004. *Ground coffee [Kopi Bubuk].* Jakarta: Dewan Standarisasi Nasional.

[5] Badan Standarisasi Nasional [BSN]. (2014). SNI 2983:2014. *Instant coffee [Kopi Instan].* Jakarta: Dewan Standarisasi Nasional.

[6] Bekti, W.S., Fibrianto K., Yuwono S.S. and Nur M. (2019). *Indonesian Coffee Science [Sains Kopi Indonesia].* Malang: UB Press.

[7] Borem, F.M., Figueiredo, L.P., Ribeiro, F.C., Taveira, J.H.S., Giomo, G.S. and Salva, T.J.G. (2016). The relationship between organic acid, sucrose, and the quality of specialty coffees. *African Journal of Agricultural Research.* 11(8): 709-717.

[8] Budiyanto, T. Izahar and D. Uker. (2021). Physical characteristics of coffee bean quality and quality of sintaro 2 and sintaro 3 ground coffee with various roast levels [Karakteristik fisik kualitas biji kopi dan kualitas kopi bubuk sintaro 2 dan sintaro 3 dengan berbagai tingkat sangrai]. *Jurnal Agroindustri*. 11(1): 54-71.

[9] Cordoba, N., Moreno F.L., Osorio C., Velasquez S. and Ruiz Y. (2021). Chemical and sensory evaluation of cold brew coffees using different roasting profiles and brewing methods. *Food Research International.* 141: 1-13.

[10] Cordoba, N., Pataquiva L., Osorio C., Moreno F.L.M. and Ruiz R.Y. (2019). Effect of grinding, extraction time and type of coffee on the physicochemical and flavor characteristics of cold brew coffee. *Scientific Reports.* 9(1): 1-12.

[11] Cuong T.V., Ling L.H., Quan G.K. and Tiep T.D. (2014). Effect of roasting conditions on several chemical constituents of vietnam robusta coffee. *Annals of the University Dunarea de Jos of Galati.* 38(2):43-56.

[12] Darmajana, D.A., Hidayat D.D., Indriati A., Sagita D., Rahayuningtyas A., and Sudaryanto A. (2022). Comparative study of changes in physical, mechanical, and colour properties between arabica and robusta coffee beans prior to and after roasting. *AIP Conference Proceedings.* 2493(1): 040008.

[13] Davids, K. (2003). *Home Coffee Roasting, Revised.* Update Edition. Florida: St. Martin's Press.

[13] Dharmawan, A. (2017). Coffee brewing technique: the sensation of fresh cold brewing coffee [Teknik seduhan kopi: sensasi kesegaran kopi cold brewing]. *Warta Pusat Penelitian Kopi dan Kakao (PUSLITKOKA).* 29(1): 14-16.

[14] Direktorat Jenderal Perkebunan. (2019). *Indonesian Plantation Statistics 2018-2020 [Statistik Perkebunan Indonesia 2018-2020].* Jakarta: Direktorat Jenderal Perkebunan.

[15] Direktorat Jenderal Perkebunan. (2020). *National Leading Plantation Statistics 2019-2021 [Statistik Perkebunan Unggulan Nasional 2019-2021].* Jakarta: Direktorat Jenderal Perkebunan.

[16] Edowai, D.N. (2019). Analysis of the chemical properties of Arabica coffee (Coffea Arabica L.) from Dogiyai [Analisis sifat kimia kopi Arabika (Coffea Arabica L.) asal Dogiyai]. *Agritechnology.* 2(1): 16-22.

[17] Folmer, B. (2012). *The Craft and Science of Coffee.* London: Academic Press.

[18] Henrietta, C. (2020). Analysis of the effect of coffee roasting temperature on the characteristics of several types of coffee [Analisis pengaruh suhu penyangraian kopi terhadap karakteristik beberapa jenis kopi]. *Thesis.* Bogor: Department of food science and technology, IPB University.
[19] Hidayat, D.D., Sudaryanto A., Kurniawan Y.R., Indriati A. and Sagita D. (2020). Development and evaluation of drum coffee roasting machine for small-scale enterprises. *INMATEH Agricultural Engineering.* 60(1): 79-88.
[20] Illy A. and Viani R. (2005). *Espresso Coffee: The science of Quality.* Second Edition. London: Elsevier Academic Press.
[21] Isnidayu, A.V., Sukartiko A.C. and Ainuri M. (2020). Sensory attribute indicators for specialty coffee from West Java are based on biochemical components [Indikator atribut sensori kopi specialty asal Jawa Barat berbasis komponen biokimia]. *Jurnal Tanaman Industri dan Penyegar.* 7(1): 1-8.
[22] Kristandi, W. (2018). Factors Affecting Caffeine Levels and Degrees of Acidity in Coffee during Roasting, Grinding and Brewing Processes: Review [Faktor yang mempengaruhi Kadar Kafein dan Derajat Keasaman Pada Kopi selama Proses Pemanggangan, Penggilingan dan Penyeduhan: Review]. *Thesis.* Semarang: Department of food science, Katolik Soegijapranata University.
[23] Kusnandar, F. (2019). *Macro Component Food Chemistry. First Edition [Kimia Pangan Komponen Makro. Cetakan Pertama]*. Jakarta: Bumi Aksara.
[24] Kyroglou, S., Laskari R. and Vareltzis P. (2022). Optimization of sensory properties of cold brew coffee produced by reduced pressure cycles and its physicochemical characteristics. *Molecules.* 27(9): 1-17.
[25] Maulid, M.R., Purwanto E.H., Mardawati E., Harahap B.M. and Saefudin. (2021). Increasing the quality and economy of Arabica coffee through complex roasting [Peningkatan mutu dan keekonomian kopi arabika melalui penyangraian kompleks]. *Jurnal Tanaman Industri dan Penyegar.* 8(1): 19-36.
[26] Maulina, H., Syafriandi and Idkham M. (2022). Test the performance of a coffee roaster using an electric heating element (heater) and an electric motor drive [Uji kinerja mesin penyangrai kopi dengan menggunakan sumber elemen pemanas listrik (heater) dan tenaga penggerak motor listrik]. *Jurnal Ilmiah Mahasiswa Pertanian.* 7(1): 535-542.
[27] Mulato, S. and Suharyanto E. (2012). *Coffee, Brewing, and Health. First Edition* [*Kopi, Seduhan, dan Kesehatan.* Cetakan Pertama]. Jember: Indonesian Coffee and Cocoa Research Institute.
[28] Nopitasari, I. (2010). Processing of Ground Coffee (Arabica and Robusta Mixture) and Quality Changes during Storage [Proses Pengolahan Kopi Bubuk (Campuran Arabika dan Robusta) serta Perubahan Mutunya selama Penyimpanan]. *Thesis.* Bogor: Faculty of Agricultural Technology, IPB University.
[29] Nurhayati, N. (2017). Sensory characteristics of dipped coffee and instant coffee of Robusta and Arabica varieties [Karakteristik sensori kopi celup dan kopi instan varietas Robusta dan Arabika]. *Jurnal Ilmiah Inovasi.* 17(2): 80-85.
[30] Pamungkas, B.T. (2016). Making Fermented Coconut Nira with the Moromi Method as a Substitute for Soy Sauce [Pembuatan Nira Kelapa Fermentasi dengan Metode Moromi untuk Pensubstitusi Kecap Asin]. *Thesis.* Bogor: IPB University.
[31] Puspitasari, R. (2020). The Influence of Coffee Type Composition and Roasting Time on Ground Coffee Characteristics Based on Indonesian National Standards [Pengaruh Komposisi Jenis Kopi dan Lama Penyangraian Terhadap Karakteristik Kopi Bubuk Berdasarkan Standarisasi Nasional Indonesia]. *Thesis.* Palembang: Sriwijaya University.
[32] Purnamayanti, N.P.A., Gunadnya I.B. P., and Arda G. (2017). Effect of temperature and roasting time on the physical characteristics and sensory quality of Arabica coffee (*Coffea arabica L*) [Pengaruh Suhu dan lama penyangraian terhadap karakteristik fisik dan mutu sensori kopi arabika (*Coffea arabica L*)]. *Jurnal Beta*. 5(2).
[33] Rao, N.Z and Fuller M. (2018). Acidity and antioxidant activity of cold brew coffee. *Scientific Reports.* 8(16030): 1-9.
[34] Rao, N.Z., Bhumiratana M.F, Adhikari K. and Chambers E. (2011). Evolution of sensory aroma attributes from coffee beans to brew coffee. *Food Science and Technology.* 44: 2185-2192.
[35] Rao, N.Z., Fuller M. and Grim M.D. (2020). Physiochemical characteristics of hot and cold brew coffee chemistry: the effects of roast level and brewing temperature on compound extraction. *Foods.* 9(7): 1-12.
[36] Rao, S. (2014). *The Coffee Roaster's Companion*. Canada: Scott Rao

[37] Rusnadi, I., Aswan A., Zikri A., Lestari S.P. and Novira A.A. (2018). The prototype rotary type coffee roaster is equipped with a pre-heater [Prototip alat penyangraian kopi tipe rotari dilengkapi pre-heater]. *Jurnal Kinetika.* 9(1): 20-25.

[38] Specialty Coffee Association of America (SCAA). (2015). *SCAA Protocol: Cupping Specialty Coffee.* United States of America: Specialty Coffee Association of America.

[39] Setyani, S., Subeki and Grace H.A. (2018). Evaluation of the defect value and taste of robusta coffee (coffea canephora l.) produced by IKM coffee in Tanggamus district [Evaluasi nilai cacat dan cita rasa kopi robusta (coffea canephora l.) yang diproduksi IKM kopi di kabupaten Tanggamus]. *Jurnal Teknologi dan Industri Hasil Pertanian.* 23(2): 103-114.

[40] Sudewa B. and Hadiatna F. (2017). Evaluation of the FIT0348 Sensor as a means of measuring the potential of Hydrogen (pH) in solution [Evaluasi Sensor FIT0348 sebagai alat ukur potential of Hydrogen (pH) larutan]. *Jurnal Elektro Telekomunikasi Terapan.* 4(2): 570-578.

[41] Sunarharum, W.B., Williams D.J. and Smyth H.E. (2014). Complexity of coffee flavor: a compositional and sensory perspective. *Food Reasearch International.* 62: 315-325.

[42] Umam, K. (2017). The influence of the type of roasting profile and the cold brew brewing method on the characteristics of Bali Kintamani coffee [Pengaruh jenis profil roasting dan metode penyeduhan cold brew terhadap karakteristik kopi bali kintamani]. *Thesis.* Malang: Department of Agricultural Product Technology, Faculty of Agricultural Technology, Brawijaya University.

[43] Vignoli, J.A., Viegas M.C., Bassoli D.G. and Benassi M.de T. (2014). Roasting process affects differently the bioactive compounds and the antioxidant activity of arabica and robusta coffees. *Food Research International.* 61: 279-285.

[44] Yeretzian, C., Jordan A.., Badoud R. and Lindinger W. (2002). From the green bean to the cup of coffee: investigating coffee roasting by on-line monitoring of volatiles. *European Food Research and Tech.* 214: 92-104.

[45] Yulia, F. (2018). Optimization of Roasting for Caffeine Content and Organoleptic Profile of Arabica Coffee (Coffea arabica) with Temperature and Time Control [Optimasi Penyangraian terhadap Kadar Kafein dan Profil Organoleptik pada Jenis Kopi Arabika (Coffea arabica) dengan Pengendalian Suhu dan Waktu]. Thesis. Yogyakarta: Sanata Dharma University.

DESIGN AND ATOMIZATION CHARACTERISTICS OF ELECTRIC CENTRIFUGAL NOZZLE FOR PLANT PROTECTION UNMANNED AERIAL VEHICLES
/
植保无人机电动离心喷嘴设计及雾化特性研究

Rong FAN [1] ; Wei LI [1] ; Zhiming WU [1] ; Bin BU[2]*

[1)] College of Agricultural Engineering, Shanxi Agricultural University, Taigu, 030801/China;
[2)] College of Agriculture, Shanxi Agricultural University (Institute of Crop Science), Taiyuan, 030031/ China
Corresponding author: Bin Bu
Tel: (+86)19103410498; E-mail: 978227369@qq.com
DOI: https://doi.org/10.35633/inmateh-68-84

Keywords: *Plant protection, unmanned aerial vehicles, centrifugal nozzle, structure optimization, atomization characteristics*

ABSTRACT
In order to reduce the drift loss of small droplets sprayed at low altitudes and low volume, a two-channel two-phase electric centrifugal nozzle was designed. The three-dimensional full-size numerical simulation of the flow field in the nozzle was carried out using Fluent software, and the radial distribution characteristics and axial variation of the flow field were studied. The relationships between the motor voltage and the atomizing disc's speed, between the nozzle's inlet pressure and its flow rate were determined. The variations of the droplet size and the droplet spectrum width with the atomizing disc and flow rate were revealed. The results showed that the rotation speed and flow rate were the important factors affecting the droplet's middle diameter and spectrum width. When the rotation speed of atomizing disc was 4000 r/min, the droplet spectrum width exhibited the narrowest, and the middle diameter of the droplet volume was 231.9 μm. The droplet coverage density was higher, meeting the requirements of low-volume aviation spraying control. This study provides a theoretical basis for optimizing nozzle configuration and developing variable spray devices.

摘要
为了减少低空低量喷洒中小雾滴的飘移损失，本文设计了一种双流道两相电动离心喷嘴。通过 Fluent 软件对喷嘴内流场进行三维全尺寸数值模拟，研究了喷嘴稳定喷雾时内流场径向分布特性及轴向变化规律。通过试验明确了电机电压与雾化盘转速、喷嘴入水口压力与其流量间的关系，揭示了雾滴粒径和雾滴谱宽度随喷嘴流量、雾化盘转速的变化规律。结果表明，该电动离心喷嘴可有效改善雾化盘底部液膜分布及喷雾均匀性，提高药液雾化效果。转速和流量是影响雾滴体积中径和雾滴谱宽度的重要因素。当雾化盘转速为 4000r/min 时，雾滴谱宽度最窄，此时雾滴体积中径为 231.9μm，雾滴覆盖密度较高，可满足航空低量喷洒的防治要求。该研究为优化喷嘴构型，研发变量喷雾装置提供了理论基础。

INTRODUCTION
With the development of unmanned aerial vehicles (UAV) technology, agricultural aviation has attracted intense attention *(Wang J. et al., 2019; Huang X. et al., 2020).* UAV have been widely used in crop remote sensing, agricultural monitoring, agricultural plant protection and other fields *(Lan Y. et al., 2017; Sun G. et al., 2018; Dash J. et al., 2017; Tian J. et al., 2017).* Aviation spray application is widely used because of its good operation effect as well as it is not limited by terrain. The plant protection nozzle is one of the key parts of the aviation application system playing a key role in pest control. The efficiency and effect of UAV plant protection can be significantly improved by designing suitable plant protection nozzles and setting reasonable operation parameters.

Low-altitude and low-volume spraying were usually adopted in plant protection UAV. However, the droplet size is small in the case of low-capacity spraying, which might cause drift loss *(Yan X. et al., 2021)*. Intense investigations are focused on UAV's anti-drift loss reduction technology to overcome this problem. *Chen et al.* and *Qi et al.* illustrated the significant impact of flight altitude and flight speed on the average

[1] Rong *Fan, Lecturer, M.S. Eng.;* Wei *Li, Lecturer Ph.D., Eng.;* Zhiming *Wu, A.P., M.S. Eng.*.

[2] Bin *Bu, R.A., M.S., Eng.*.

deposition amount of fog droplets in the target area, so the flight altitude and speed can be used to study the drift reduction strategy further *(Chen D, et al., 2016; Qi H. et al., 2019)*. *Qin et al.* examined the influence of spraying parameters on the deposition distribution of fog droplets in the corn canopy. They believed that when the flight height was 7 m and the transverse spraying range was 5 m, the deposition characteristics and spraying effect of fog droplets were better, and the drift loss was smaller *(Qin W. et al., 2018). Li* revealed the influence of multi-rotor plant protection UAV operation parameters on fog droplet deposition and drift, established a statistical analysis model of fog droplet deposition and drift, and improved the effective utilization rate of pesticides *(Li H. et al., 2021)*.

The above studies focused only on the parameter tuning of the plant protection operation process, while less research has been conducted on spray devices and their characteristics. Electric centrifugal nozzles form mist droplets of different sizes by adjusting the motor voltage and the water outlet pressure to change the velocity and flow of the centrifugal nozzles. The atomization spray is widely used in low-altitude UAV plant protection operations due to its wide width, non-obstinate spray holes, and convenient parameter tuning. However, the application has some problems, such as uneven distribution of droplets, inconsistent atomization, broad droplet spectrum, and easy drift. In this direction, this study focuses on designing a two-channel, two-phase electric centrifugal nozzle, and the spray performance of the nozzle is examined through numerical simulations and solid-state tests for practical applications.

MATERIALS AND METHODS

The structure design of electric centrifugal nozzle for plant protection UAV

In this study, a two-phase, two-channel electric centrifugal nozzle for UAV planting and maintenance was designed to address the above issues. Its overall structure (a) and 3D model (b) are shown in Fig. 1. The nozzle mainly consists of a shell, a gas passage, a steady flow passage, a liquid flow passage, a motor, a mixed flow passage, an atomizing disk, a diverter, a swirling chamber, and other components. The main body of the centrifugal nozzle is connected to the UAV by mounting bracket. The upper end of the steady-state flow chamber is connected to the liquid medicine box by a pipe, and the lower end is connected to the liquid channel. The mixed flow channel and the diverter form a swirl chamber, and the outer part is equipped with an atomization plate. The spinning power of the atomizing disc comes from a motor mounted vertically in the housing.

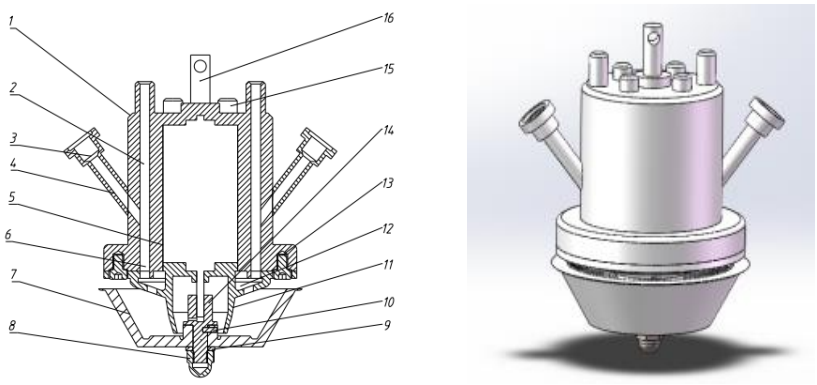

Fig. 1 - Structure diagram and 3D model of centrifugal nozzle

a. Structural diagram b. Three-dimensional model

1. Cover shell; 2. Gas channel; 3. Steady flow chamber; 4. Liquid flow channel; 5. The motor; 6. Mixed channel; 7. Atomization; 8. Cover lock nut; 9. Flat gasket; 10. Cylindrical pin; 11. The shunt; 12. Swirling chamber 13. Cylindrical head screws 14 Sleeve 15 Terminal 16 Installing Supports

Principle of Operation

When the centrifugal nozzle is in operation, the power for the nozzle and the liquid pump is provided by the UAV's DC power generation system. Under the liquid pump action, the liquid flows through the two-sided steady flow chamber into the symmetric tangential flow channel. The airflow under the UAV rotor enters the gas channel. The liquid medicine and air enter the mixing channel, where the liquid is mixed with air, the droplet is broken up. Then they flow into a vortex chamber composed of a tangential flow channel and a diverter. On the one hand, the liquid drug rotates in the vortex chamber, and on the other hand, it advances towards the atomized disk with a certain axial velocity. The motor drives the atomization rotation, and the liquid is ejected under centrifugal action.

Flow field analysis

The flow field of the designed nozzle was analysed by the modern eddy current theory and Computational Fluid Dynamics (CFD). The chosen fluid domain is shown in Fig. 2, and the grid is divided. The VOF and the standard *k-ε* models of the multiphase flow model were selected according to the working conditions of the nozzle. The gas density and viscosity were set to 1.225 kg/m^3 and 1.79e-05 Pa·s, respectively, after the first phase. The second phase liquid density and viscosity were 998.2 kg/m^3 and 0.001003Pa·s, respectively. The gas inlet was set as the pressure inlet, and the total boundary pressure was 101235 Mpa. The liquid inlet was a velocity inlet with a velocity of 1 m/s. The fluid domain of the entire atomized disk was set to a velocity of 3200 rpm.

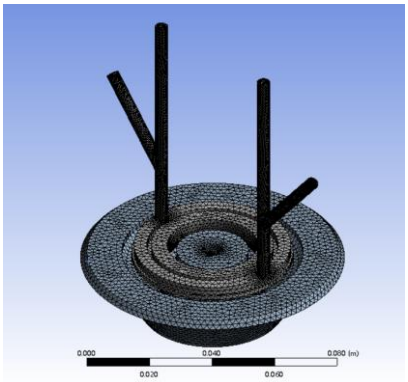

Fig. 2 - Grid division

Nozzle atomization characteristics

In order to solve the problem of the mismatch between the speed, flow rate and nozzle during the application of an electric centrifugal nozzle which is easier to cause the droplet spectrum width, numerical simulations were performed to optimize the nozzle's internal structure. The nozzle was customized based on the optimization results. Combined with the actual production, the experiments were designed to clarify the relationship between the motor voltage and the speed of the atomizing disc, the inlet pressure and the flow rate. It reveals the change in the droplet size and the droplet spectrum width with the flow rate and the atomizing disc speed. It identifies a regular working interval for the designed electric centrifugal nozzle to guide production.

Optimization of nozzle internal structure parameters

The nozzle structure directly affects the spray quality. The velocity at which the nozzle droplet exits directly affects the horizontal displacement of the droplet. Therefore, the drop exit velocity is chosen as the evaluation metric for spray performance. Considering the liquid passage diameter (factor A) and the swirling chamber outlet diameter (factor B) as the main influencing factors, a numerical simulation method was used to optimize the nozzle's internal structure parameters. The nozzle's gas channel diameter was set to 4 mm during the simulation test. Orthogonal tests were performed at 3 levels for factors A and B, respectively, and the resulting test permutations are shown in Table 1. The other parameters were set using the nozzle flow field analysis.

Table 1

Test factors and levels

level	Liquid channel diameter A (mm)	Diameter of swirling chamber outlet B (mm)
1	3	4
2	4	5
3	5	6

Study of atomization properties of the nozzle

Nozzle velocity and flow rate

The velocity and the flow rate are two important parameters in the atomization of an electric centrifugal nozzle. According to the design principle, adjusting the motor's power supply voltage can change the motor's speed, which is the speed of the atomized disk. The flow rate can be changed by adjusting the nozzle inlet pressure. Because of a mismatch problem between speed, flow rate and nozzle, a strobe tester (SW-6500,

accuracy 0.001%) was used in the plant protection spray test bed to examine the corresponding voltage when the speed of the nozzle atomizing disc was 2000, 3000, 4000, 5000, 6000, 7000 r/min, and the relationship between voltage and speed was analysed. The nozzle's inlet pressure was set to 0.2, 0.3, 0.4, 0.5 and 0.6 MPa to measure the nozzle's current flow. The dependence of the flow rate on the inlet pressure was analysed, and a reference was given for using the nozzle.

Droplet size and distribution law

The particle size and the distribution law are the two most important parameters in spray techniques. Particle size refers to the size of each spray droplet forming the spray shape of the nozzle, which is usually measured by the median volume diameter (Dv_{50}). The particle size distribution refers to the fraction of droplets of various sizes in the total number of droplets. It is usually described by the particle size distribution curve or the particle size distribution table. The accurate measurements of the droplet size and the droplet size distribution are important for better control of the spray quality.

This study used a real-time high-speed spray particle size meter (Marvin Spraytec, Fig. 3) to measure the particle size distribution of fog droplets at different speeds and flows. A stable operating range for the centrifugal nozzle was found based on trends in the droplet size and the width of the droplet spectrum. The partial measurements are shown in Fig. 4. The obtained data were used to analyse and calculate the particle size of the droplet forming the scattering spectrum. The test schemes are listed in Table 2.

Fig. 3 - Real-time high-speed spray particle size analyser

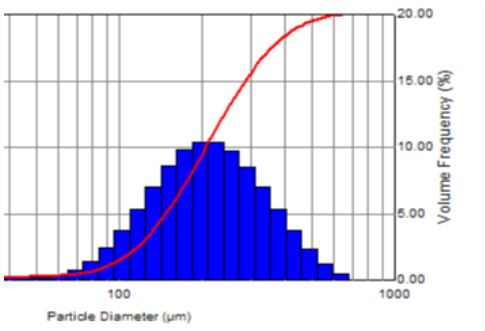

Fig. 4 - Distribution curves of volume diameter and particle size

Table 2

Volumetric medium diameter test scheme of electric centrifugal nozzle

Nozzle flow rate / mL·min^{-1}	800, 1000, 1200
Speed of motor / r·min^{-1}	2000, 3000, 4000, 5000, 6000, 7000, 8000

RESULTS AND ANALYSIS

Simulation of fluid inside the nozzle

The trajectory of the fluid motion is shown in Fig. 5. It is clear from Fig 5a that the liquid phase flows close to the wall. Near the outlet of the liquid channel, the liquid exists as a thin film. The liquid film flows into the vortex chamber under inertial forces and surface tension, as well as the rotor air flow. It is then ejected from the edge of the atomized disc by the centrifugal action of the atomized disc. The flow field's radial distribution exhibits a forced eddy structure at the vortex chamber's profile. The tangential and axial velocities reach their maximum values throughout the basin, as shown in Fig. 5b. Fig. 5c shows the motion path of the fluid in the atomized disk. Under the rotating centrifugal action of the rotating atomization disk, the flow velocity of the droplets increases and presents a helical distribution.

In addition, the horizontal velocity directly affects the spray amplitude. The horizontal velocity of the droplet decreases rapidly to 0 m/s from the initial velocity at which it leaves the atomized disk. Under gravity, the vertical velocity of the droplet increases rapidly from 0 m/s to a certain velocity and then drops at a constant velocity. The droplet's trajectory can reflect the droplet's settling process in the flow field, and the horizontal displacement of the droplet landing site can be obtained. Further analysis shows that the horizontal displacements of mist droplets with different particle sizes differ. At the same height and with the same horizontal initial velocity, the larger the droplet size, the further the droplet moves horizontally.

Depending on the trajectory of the fluid, the entire atomization region is approximately distributed as a hollow conical table, with relatively uniform atomization properties and droplet distribution. It can be seen that the structure can effectively improve the liquid film distribution and spray uniformity, and the atomization effect to a certain extent.

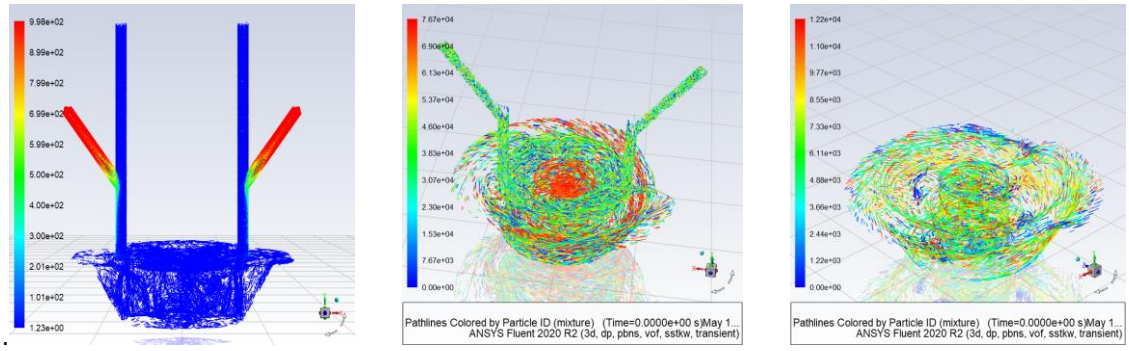

a. Fluid motion trajectory *b. Fluid inside the nozzle* *c. Fluid movement track in atomizing disc*

Fig. 5 - Flow trace diagram of nozzle

Optimization of nozzle internal structure

The nozzle's internal structure was optimized by orthogonal experiments with two factors and three levels. 9 groups of tests were arranged, and the test results are shown in Table 3. The largest speed of fog drops on the edge of the atomizing disc was obtained by test combination A (4 mm), B (5 mm) in No.5, and the test group is preferred. The range analysis shows that the diameter of the nozzle liquid passage and the diameter of the swirling chamber outlet impact the droplet exit velocity, and the influence of the diameter of the swirling chamber inside the nozzle on the droplet exit velocity is significantly greater than the liquid passage diameter.

Table 3

Results and range analysis of the orthogonal test

No.	Factors		The speed of the droplets on the edge of the atomizing disc
	A (mm)	B (mm)	(m/s)
1	3	4	18.4
2	3	5	19.7
3	3	6	18.7
4	4	4	17.9
5	4	5	20.8
6	4	6	17.6
7	5	4	16.6
8	5	5	19.5
9	5	6	17.5
K_1	18.93	17.63	-
K_2	18.76	20.00	-
K_3	17.86	17.93	-
R	1.07	2.37	-

In order to more intuitively reflect the influence law and trend of each diameter on the nozzle exit velocity, the factor level was taken as the horizontal coordinate, and the average droplet velocity on the edge of the atomizing disc was taken as the vertical coordinate to obtain the trend diagram of factors and indicators (Fig. 6). The graphical analysis shows that when B2 is taken, the effect on the exit velocity of the droplet is the greatest. At the same time, A1 and A2 have roughly the same effect on the exit velocity of the droplet. Combining with the test results, the optimal scheme B2A2 is selected, i.e., the diameter of the flow chamber is 5 mm, and the diameter of the liquid channel is 4 mm.

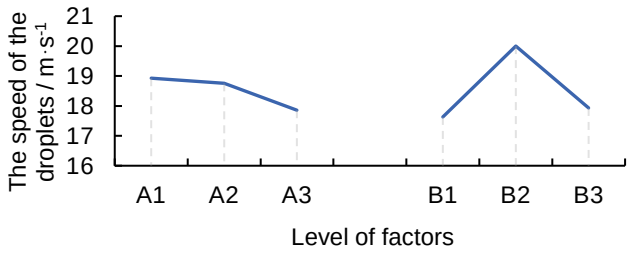

Fig. 6 - Trend chart of factors and indicators

Relationship between atomizing disc speed and voltage, nozzle flow and spray pressure

The strobe was used to test the rotational velocity of the centrifugal nozzle. The voltages corresponding to different rotational velocities were recorded, and the plots of voltage versus rotational velocity were made, as shown in Fig. 7. A positive linear correlation exists between the rotary speed and the voltage. The motor speed increases with the voltage. The spray pressure as a function of the flow rate is shown in Fig. 8. The nozzle flow rate and spray pressure are also approximately linearly and positively correlated with the nozzle flow rate increasing with spray pressure.

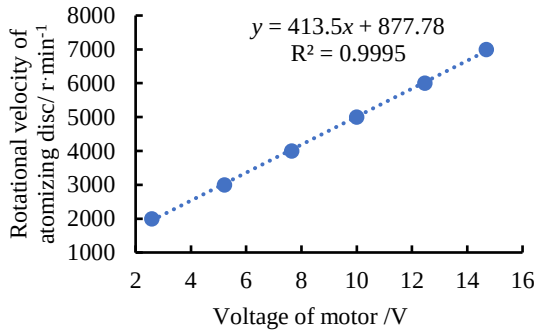

Fig. 7 - Relation between motor speed and voltage

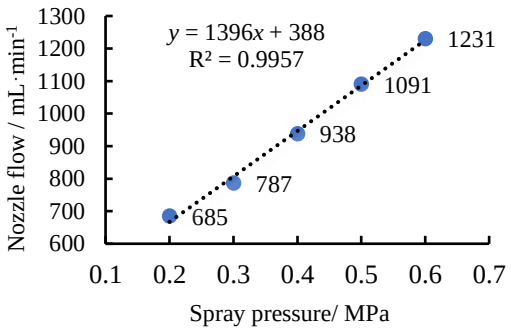

Fig. 8 - Relation between nozzle flow and spray pressure

Droplet size

Fig. 9 shows the atomization disk velocity versus droplet volume diameter for different flow conditions.

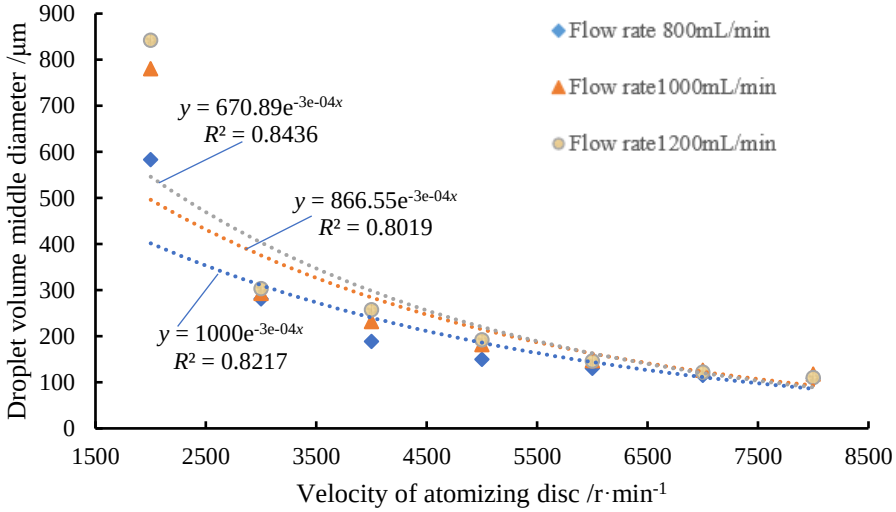

Fig 9 - Relation between atomizing disc speed and droplet volume median diameter under different flow conditions

It shows that at the same flow rate, the droplet size decreases with increasing rotational velocity and exhibits an exponential decline. As the rotational velocity gradually increases from low to high, the

droplet size decreases rapidly. The droplet size decreases slowly when the rotational speed increases to a certain value (above 7000 rpm). At the same rotational speed, droplet size increases with the flow rate, but the range for the change is small. With an increase in the rotational velocity, the particle sizes of fog droplets with different flow rates gradually tend to be the same, indicating that the rotational velocity of the atomizing disc is the main factor affecting the median diameter of the volume of fog droplets.

Distribution law of droplet spectrum width

Table 4 shows the droplet spectrum width under different nozzle flow rates and atomizing disc speeds. It can be seen that under the same flow rate of the nozzle, the droplet spectrum width decreases rapidly at first and then increases slowly with the increase of rotational speed. The spectral droplet width reaches its minimum at a rotation velocity of 4000 r/min. At the same rotational velocity, the spectral width of the droplet increases with the flow rate. However, as the three flow rate levels are similar, the variation of droplet spectrum width is not divided into three obvious levels. Therefore, both the rotation speed and flow rate significantly influence the fog drop spectrum width, and within the flow range of 800~1200 mL/min, the fog drop spectrum width is the minimum when the rotation speed is 4000 r/min.

Table 4

Fog droplet spectrum width of electric centrifugal nozzle

Velocity of motor / r·min^{-1}	Nozzle flow rate / mL·min^{-1}		
	800	1000	1200
2000	1	1.12	1.2
3000	0.89	0.97	0.92
4000	0.76	0.74	0.82
5000	0.77	0.8	0.9
6000	0.8	0.89	0.93
7000	0.85	0.97	0.96

Determination of working parameters of electric centrifugal nozzle

The above analysis shows that the rotation speed and flow rate are the important factors affecting the droplet middle diameter and the droplet spectrum width. The ideal spectral width of droplet size can be obtained by adjusting the speed and flow rate of the atomizing disc. Regulating the motor speed and nozzle flow changes only the motor voltage and spray pressure. According to pest control requirements, the working parameters can be easily adjusted to achieve the best control effect.

If the droplet's particle size is known, the coverage density per unit area can be calculated based on Eq.(1) *(Lan Y. B. et al., 2021)*.

$$f = \frac{6\times10^{-11}}{\pi d^3} \times q \quad (1)$$

Where f is the droplet coverage density (droplets/cm^2); q is the dosage (L/hm^2); d is the droplet particle size (m). According to Eq. (1), the dosage and droplet size directly affect the coverage density. Under low altitude and low dosage, the dosage of rotary wing UAV is generally required to be 15~30 L/hm^2. Due to the influence of plant canopy density, it has a certain vegetation index, and the back of the leaves also requires good coverage. Therefore, the droplet size should not be too large to ensure a good coverage density.

In addition, the aviation low-volume spray volume is small, and the flight height is high; the particle size is too small, easy to evaporate, and easy to produce drift. Droplets with a particle size of less than 100 μm tend to evaporate and drift under high temperatures, humidity, and air flow disturbance. Droplets with a particle size of 300 μm or more have fast settling speed, considerable kinetic energy and are not easy to attach to the leaf surface, resulting in pesticide loss. According to the Biological optimum particle size (BODS), the control effect is the best when the droplet size is between 100 and 300 μm *(Yuan H. et al., 2015)*.

When the droplet size is between 100 and 300 μm, the droplet can be deposited on the target as soon as possible with the rotor downwash air flow to reduce drift.

As shown in Table 4, when the rotation speed is 4000 r/min, the fog droplet spectrum width is the narrowest, and the middle diameter of the fog drop volume is 231.9 μm. If the dosage is 15 L/hm^2, the atomizing disk speed is 4000 r/min, and the droplet volume diameter is 231.9 μm, the fog droplet coverage density can be calculated as 22.95 droplets /cm^2. The droplet coverage density is higher, which meets the requirements of low-volume aviation spraying control.

CONCLUSIONS

(1) The symmetrical two-channel two-phase electric centrifugal nozzle for aviation was developed in this study. This structure can effectively improve the distribution of the liquid film and the uniformity of the spray at the bottom of the atomizing disk and avoid the inhomogeneous and incomplete atomization caused by the one-sided tilt of the water.

(2) The speed of atomizing disc and the nozzle flow rate are the important factors affecting the median diameter and spectrum width of droplet volume. The ideal droplet size and spectral width can be obtained by adjusting the speed and flow rate. When the rotation speed is 4000 r/min, the fog drop spectrum width is the narrowest, and the median diameter of the fog drop volume is 231.9 μm. The fog drop coverage density is higher, meeting the requirements of low-volume aviation spraying control.

(3) The droplet's horizontal velocity directly affects the nozzle's spray amplitude. The trajectory of droplet movement in the air is similar to parabolic motion. At the same height and initial horizontal velocity, the larger the droplet size is in a certain range, the larger the nozzle spray amplitude is.

ACKNOWLEDGEMENT

This research was funded by the Science and Technology Innovation Project of Shanxi Provincial Colleges and Universities (2020L0156) and the "Six New" Project of Shanxi Province Agriculture and Rural areas - Key technologies and equipment research on precision Application of Plant protection UAV. The authors would like to express their gratitude to EditSprings (https://www.editsprings.cn) for the expert linguistic services provided.

REFERENCES

[1] Chen D. S., Lan Y. B., Li J. Y., et al., (2016), Effect of spray parameters of small unmanned helicopter on distribution regularity of droplet deposition in hybrid rice canopy (*小型无人直升机喷雾参数对杂交水稻冠层雾滴沉积分布的影响*), *Transactions of the Chinese Society of Agricultural Engineering*, Vol.32, Issue 17, pp.40-46, Beijing/China.

[2] Dash J. P., Watt M. S., Pearse G. D., et al., (2017), Assessing very high resolution UAV imagery for monitoring forest health during a simulated disease outbreak. *ISPRS Journal of Photogrammetry and Remote Sensing*, Vol.131, pp.1-14.

[3] Huang X. M., Zhang L., Tang L., et al., (2020), Path planning for autonomous operation of drone in fields with complex boundaries (*复杂边界田块旋翼无人机自主作业路径规划*), *Transactions of the Chinese Society for Agricultural Machinery*, Vol.51, Issue 3, pp.34-42, Beijing/China. DOI: 10.6041/j.issn.1000-1298.2020.03.004.

[4] Lan Y. B., Chen S. D. Fritz B. K., (2017) Current status and future trends of precision agricultural aviation technologies. *International Journal of Agricultural & Biological Engineering*, Vol.10, Issue 3, pp.1-17, Beijing/China.

[5] Lan Y. B., Peng J., Jin J., Research status and development of pesticide spraying droplet size (*农药喷雾粒径的研究现状与发展*). *Journal of South China Agricultural University*, Vol.37, Issue 6, pp.1-9, Guangzhou/China.

[6] Li H. Z., (2021) Optimization Design of Spraying System of Plant Protection UAV Based on CFD Theory and Research of Droplet Motion (*基于 CFD 理论的植保无人机喷洒系统优化设计与雾滴运动特性研究*), MSc dissertation. Jilin University, Jilin/China.

[7] Qi H. X., Chen P. C., Lan Y. B., et al., (2019), Experimental Study on Droplet Deposit Distribution of Different Electric UAVs in Rice Fields (*不同电动植保无人机稻田雾滴沉积分布试验研究*). *Journal of Agricultural Mechanization Research*, Vol.41, Issue 9, pp.147-151, Heilongjiang/China.

[8] Qin W., C., Xue X., Y., Zhou L. X., et al., (2014), Effects of spraying parameters of unmanned aerial vehicle on droplets deposition distribution of maize canopies (*无人直升机喷雾参数对玉米冠层雾滴沉积分布的影响*). *Journal of Agricultural Mechanization Research*, Vol.30, Issue 5, pp.50-56, Beijing/China.

[9] Sun G., Huang W. J.， Chen P. F., et al., (2018), Advances in UAV-based multispectral remote sensing applications (*轻小型无人机多光谱遥感技术应用进展*). *Transactions of the Chinese Society for Agricultural Machinery*, Vol.49, Issue 3, pp.1-17, Beijing/China. DOI: 10.6041/j.issn.1000-1298.2018.03.001.

[10] Tian J., Wang L., Li X., et al., (2017), Comparison of UAV and World View 2 imagery for mapping leaf area index of mangrove forest. *International Journal of Applied Earth Observation & Geoinformation*, Vol.61, pp.22-31.

[11] Wang J., Lan Y. B, Yao W. X. et al., (2019), Effects of working height of single-rotor unmanned aerial vehicle on drift and droplets deposition distribution of areca tree (*单旋翼无人机作业高度对槟榔雾滴沉积分布与飘移影响*), *Transactions of the Chinese Society for Agricultural Machinery*, Vol.50, Issue 7, pp.109-119, Beijing/China. DOI: 10.6041/j.issn.1000-1298.2019.07.011.

[12] Yan X. J., Chu S. H., Yang D. B., et al., (2021), Agriculture on the wings of science and technology: plant protection unmanned aerial vehicle (UAV) low-volume spraying technology reduces pesticide use and boosts control efficacy (*给农业插上科技的翅膀:植保无人机低容量喷雾技术助力农药减施增效*), *Journal of Plant Protection*, Vol.48, Issue 3, pp.469-476, Beijing/China.

[13] Yuan H. Z., Wang G. B., (2015), Effects of droplet size and deposition density on field efficacy of pesticides (*雾滴大小和覆盖密度与农药防治效果的关系*), *Plant Protection*, Vol.6, Issue 2, pp.9-6, Beijing/China. DOI: 10.3969/j.issn.0529-1542.2015.06.002

EXPERIMENTAL RESEARCH ON THE SEPARATION PROCESS OF SEEDS AND PULP, FROM THE FRUITS OF SEA BUCKTHORN
/
CERCETARI EXPERIMENTALE ASUPRA PROCESULUI DE SEPARARE A SEMINTELOR ŞI A PULPEI, DIN FRUCTELE DE CATINĂ

Radu CIUPERCA, Alexandra-Liana VISAN*), Augustina PRUTEANU*), Ana ZAICA, Vasilica STEFAN

[1)] National Institute of Research – Development for Machines and Installations Designed for Agriculture and Food Industry – INMA Bucharest / Romania;

E-mail: alexandrion1982@yahoo.com; pruteanu_augustina@yahoo.com
DOI: https://doi.org/10.35633/inmateh-68-85

Keywords: *sea buckthorn seeds, vegetal waste, seed capitalization, vegetal waste separation*

ABSTRACT

In the last period, a sector that has seen an important development in fruit growing is the one dedicated to sea buckthorn crops, respectively the technologies for the valorisation of fruits and food by-products deriving from the technological processes dedicated to these fruits with high human and animal nutritional value. In this paper, the aim is to present the results obtained by implementing innovative technologies for the integrated management of works in agricultural farms, vineyards and orchards, particularly intended for the cultivation of sea buckthorn, through which were tracked the technological parameters achieved by an equipment for the separation of sea buckthorn seeds from the pulp of the fruit, respectively the distribution of the separation fractions from the raw material depending on the working regime (the rotation frequencies of the functional systems) and the sizes of the holes of the separation sieve as well as the energy indices of the equipment. From the analysis of the obtained results, it was concluded that, in order to increase the performance of the experimental equipment, the site sections must include a wider range of hole sizes, it should be equipped with a brush system for their cleaning and improve the box system for collecting the material separated on fractions in order to reduce losses.

REZUMAT

În ultima perioadă, un sector ce cunoaște o dezvoltare importantă în pomicultură este cel destinat culturilor de cătină, respectiv a tehnologiilor de valorificare a fructelor și a subproduselor alimentare ce derivă din procesele tehnologice dedicate acestor fructe cu valoare nutrițională umană și animală ridicată. În cadrul acestei lucrări se urmărește prezentarea rezultatelor obţinute prin implementarea unor tehnologii inovative de management integrat al lucrărilor din ferme agricole, viticole și pomicole, în mod particular destinat culturii de cătină, prin care s-au urmărit parametrii tehnologici realizați de un echipament de separare a semințelor de cătină de pulpa fructului, respectiv distribuția fracțiilor de separare din materia prima în funcție de regimul de lucru (frecvențele de rotaţie ale sistemelor funcţionale) şi dimensiunile găurilor sitei de separare precum şi indicii energetici ai echipamentului. Din analiza rezultatelor obţinute, s-a desprins concluzia că, pentru creşterea performanțelor echipamentului experimentat, trebuie ca secțiunile de site să includă gamă mai largă de dimensiuni ale găurilor, dotarea cu un sistem de perii pentru curățarea acestora şi îmbunătățirea sistemului de cuve pentru colectarea materialului separat pe fracții, în vederea reducerii pierderilor.

INTRODUCTION

Sea buckthorn (*Hippophae rhamnoides* L.) is a unique and valuable multipurpose species currently being cultivated in various parts of the world, Asia: (*Li H, et. al.,2020*), Europa (*Kauppinen S. and Petruneva E., 2014*) and America de Nord (*Li S.C.T. and Schroeder W.R., 1996*).

Buckthorn fruits have a high nutritional level and important medicinal values for human health (*Li S.C.T. and Schroeder W.R., 1996*). Sea buckthorn is also a deciduous shrub considered useful for soil erosion control, reclaiming degraded land, improving wildlife habitat, and protecting farms.

In Europe, sea buckthorn is still a young fruit species, the number of sea buckthorn varieties for the European climate being too low (Finland and Sweden), although it is relatively easy to cultivate. There are many countries where the development of new varieties is sought (Germany).

A common problem is the susceptibility to frost of the male varieties of sea buckthorn, developing well on sandy clay and being a water lover, the effect of irrigation on the growth yield of the plant can be significant (*Höhne Friedrich, 2015*). However, it is exposed to the attack of diseases and pests, the most widespread being fungi and flies that can attack sea buckthorn fruits.

Considerable research is currently being carried out on the properties of sea buckthorn fruits in the pharmaceutical, nutraceutical field (*Ciesarová, Z. et al., 2020; Ursache, F.M. et al., 2017; Suryakumar, G.et al., 2011),* food *(Madawala, S.R.P. et al., 2018; Zeb, A., 2004)* and cosmetic *(Smida, I. et al., 2019; Koskovac, M. et al., 2017*), but also for environmental protection (*Madawala, S.R.P. et al., 2018*).

Research carried out around the world has shown that the leaves, fruits and shoots of the plant contain a series of biologically active substances with an essential role in regulating metabolism (*Rati I. V. et al., 2018*). The main substances present in large quantities in the pulp of sea buckthorn fruits belong to the carotenoid class, the carotenoid content being one of the key characteristics by which sea buckthorn oil is marketed (*Ciesarová, Z. et al., 2020*).

Sea buckthorn seed oil is characterized by a high content of oleic acid (17%), omega-3 (alpha linolenic) and omega-6 (linoleic), important in the regulation of thousands of metabolic functions. In addition, sea buckthorn is a very good source of phytosterols, which play an important role in the prevention of cardiovascular diseases. Another important aspect of promoting sea buckthorn for human health is its high fibre content and the fact that it is considered a unique source of protein.

Sea buckthorn juice is rich in many free amino acids and vitamin C, a total of 18 of the 22 known amino acids found in sea buckthorn fruits, essential in various processes that take place in the human body (*Gâtlan A.-M. and Gutt G., 2021*). The most common product obtained from sea buckthorn is the juice derived from the pulp because it includes all the nutrients of the sea buckthorn, especially the flavonoids with antioxidant properties (*Wojtunik-Kulesza, K. A., et al., 2016; Liu R. et al., 2022*).

The phytochemical and nutritional composition of sea buckthorn fruits differs considerably depending on the species, analysed components, climatic and growing conditions, variations between years, degree of maturation, storage conditions, time of harvesting and last but not least, fruit processing method.

There are three main products that can be obtained through processing, namely: oil obtained from seeds, yellow pigment, and juice obtained from fruits and a secondary one which is the mixture of pulp and peel. Although the total number of publications available, describing the processing of sea buckthorn berries, is quite limited, the processing process of sea buckthorn berries is largely similar to that presented in Fig. 1.

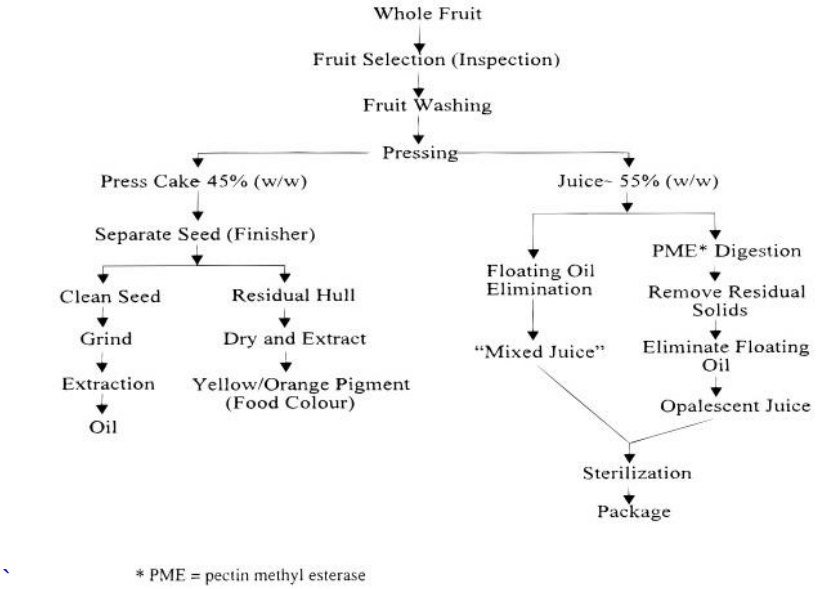

Fig. 1 - Processing of sea buckthorn berries
(*Beveridge T.et al., 1999*)

Tereshchuk L.V. et al., (2019), proposed a scheme of the complex technological flow of sea buckthorn processing is presented. After picking the fruits from the branches, they are washed, the impurities are separated, then they are ground with a disintegrator, the result being 88% pulp+juice and 12% seeds. Further, the seeds are dried, the final percentage being 7.2%, and the pulp+juice are subjected to the centrifugation process, the result being 24.5% juice and 53.5% pulp.

Therefore, sea buckthorn is a valuable plant, with many biologically active compounds with therapeutic functions, which, integrated in the diet, can bring important benefits to human health.

From the point of view of the existing installations and equipment for separating the seeds from the pulp, it can be stated that the offer is not very generous, however, there are several types used for the operation of separating the seeds, either from the raw material in a wet state either after a process of drying it.

Worldwide, there are companies producing complex equipment for separating the seed from the fruit pulp, installations intended especially for processing units with large and very large capacities, which include different separation systems, or individual equipment intended for reduced production.

At the current stage of development of the technique, there are several types of equipment for separating the seeds from the pulp of the buckthorn fruit, made by manufacturers, such as: Milani Estasi ABEVE – Italy; Bucher Industries AG -Switzerland; Diemme S.P.A.- Italy, Murlark-USA; Aslan Machinery – China; ANDGAR FOOD PROCESSING – Canada.

In this scientific paper, it is presented experimental research on the process of separating the pulp from the sea buckthorn seeds, carried out with an equipment designed and manufactured at INMA Bucharest, named: Equipment for separating the pulp from the sea buckthorn seed, symbol: ESSC.

MATERIALS AND METHODS

The determination of the working parameters was carried out using the following measuring and control devices: digital multimeter, electronic thermometer with surface transducer, centrifugal tachometer, electronic balance, vibrating separation device, wattmeter kit.

Three types of functional systems are interconnected within the ESSC composition, such as: Raw material decompaction system - 1; Pulp seed detachment system - 2; Separation system - 3, as shown in the functional scheme, Fig. 3. In addition to the three functional systems, the equipment also includes a frame, item 4, transmission, item 5, vats for the discharge of separated fractions, item 6, access ladder to the feed hopper, item 7, doors visit and access to the separation system, item 8 and the electrical installation, item 9, these components are shown in Fig. 4. Each of these systems performs distinct technological operations that are interconnected to separate the pulp, peels and other impurities from the sea buckthorn seeds, evacuated with the help of the evacuation funnels (B, C, D) of the products resulting from the separation process.

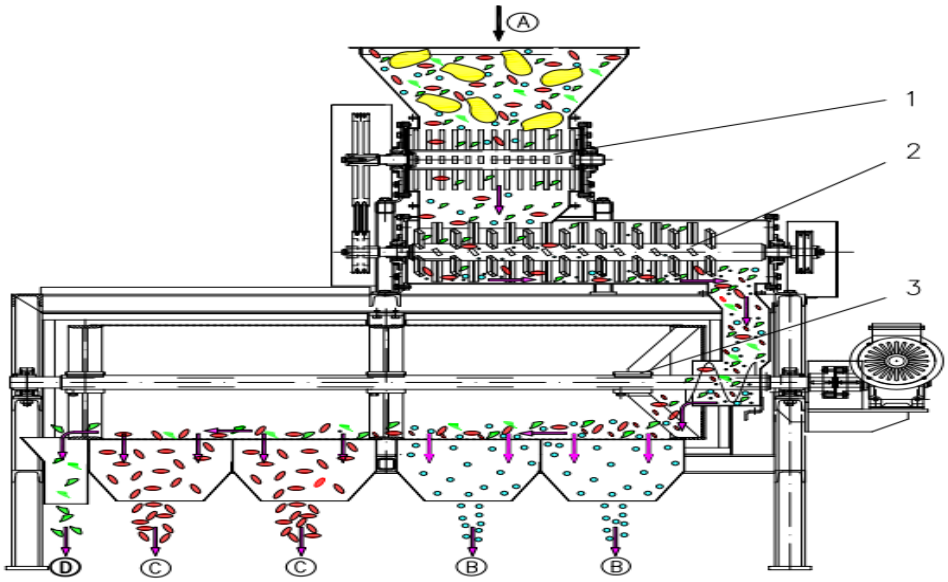

Fig. 3 – The functional scheme and the working principle of the experimentalmodel, ESSC

1 – Raw material decompaction system; 2 – Pulp seeds detachment system; 3 – Separation system; A – feed with dry raw material (mixture of seeds, fruit peels, tails, pulp); B – exhaust fraction smaller than the seeds (fragments of pulp and peels, tails); C – evacuation of sea buckthorn seeds; D – evacuation of fraction larger than the seeds (fragments of pulp and peels)

The main functional characteristics of the ESSC are: total installed power of 2.95 kW; drum speed of raw material decompaction system can vary between 300–400 min^{-1}; the speed of the pulp seed removal system rotor varies between 500–700 min^{-1}.

Characteristics of the sieve separation system: diameter of the sieves, ϕ 400 mm; the active length of the two-section sieve, 2x575 = 1150 mm; sieve rotational speed, 23 min^{-1}; hole sizes for the first separation sieve (*Lxl*= 25x1.8 mm); hole dimensions for the second separation sieve (*Lxl*= 25x2.7 mm).

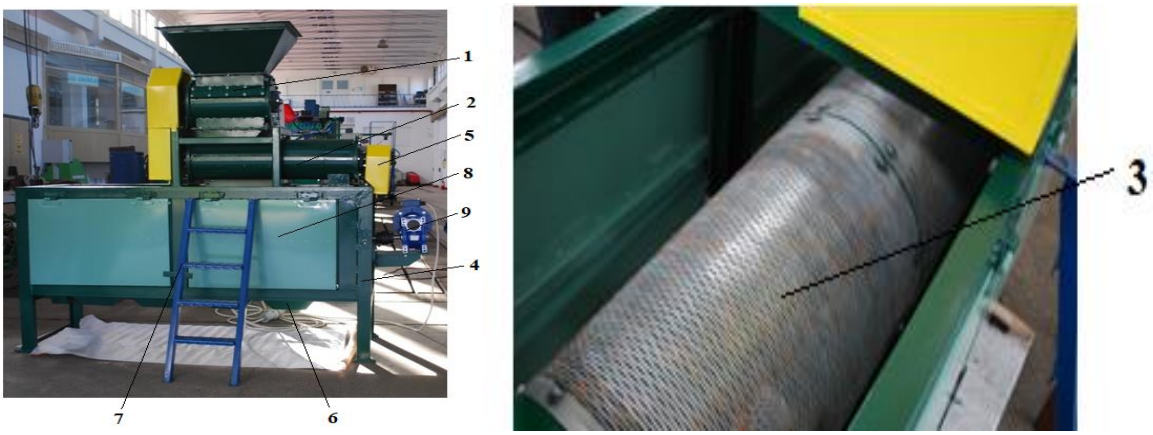

Fig. 4 – The ESSC experimental model tested in laboratory and operating conditions

1 - raw material decompaction system; 2 - pulp seed detachment system; 3 - separation system with circular sieves; 4 - support frame; 5 - transmissions with trapezoidal belts; 6 - exhaust funnels; 7- scale for technical assistance and supervision; 8 - side doors; 9 - electrical drive installation

After adjusting the working parameters, such as the distance between the impactors of the detachment system and its casing, to values between 1.5 -2.5 mm and their inclination angle of approx. 30 degrees, the ESSC equipment was put into operation and fed with raw material in order to separate the seeds from the hawthorn pulp.

During operation, the fractions from the discharge hoppers B, C, D were collected. The seeds, pulp and peels were weighed, the distribution of the separated size fractions being presented in table 2.

The method that is the basis of the process is separating the seeds from the pulp after the mixture has been dried, beforehand, to a humidity below 12%.

In order to evaluate the technological performance of the ESSC equipment and the quality of the separation operation performed on it, a series of stages were completed, based on an experimentation methodology, which includes:

• Stage 1. Extracting the juice from sea buckthorn fruits Fig. 2B, using a juicer Kuvings, model B 1700;

• Stage 2. Drying of the secondary product obtained, consisting of the secondary fraction (pulp + peel) and seeds (fig. 2C), using an oven Memmert, at the temperature of 105^{o}C, for 4 hours;

• Stage 3. Determination of the moisture content of the raw material, Fig. 2D, was made using electronic scale MB 45, the moisture value being 10.8 %;

• Stage 4. Determination of the type dimensions from the dry raw material fractions component, as follows:

Step 1. Weigh a random sample of the by-product, Fig. 2E;

Step 2. Separate the component fractions of the extracted sample into 7 sorts, using 6 sieve sizes, respectively 10; 6.3; 4; 2.8; 2 and 1 [mm], placed on a vibratory separator with a Retsch circular sieve, operating mode: amplitude 50 mm, for 10 minutes, Fig. 2F;

Step 3. Weigh the packaging of the fractions = 5.2 grams, Fig. 2G;

Step 4. Weigh each fraction obtained at each sieve on a Kern model electronic balance, measurement precision of 0.001 g, from which the mass of plastic foil was subtracted, Fig. 2H;

Step 5. Centralise the data obtained according to table 1;

Step 6. Determine the fraction of seeds from the dry raw material mass at 10.8% moisture: pulp+shells = 69.79%; seed = approx. 30.21%, fig. 2 I.

A - Stage 1.
Sea buckthorn fruits to be processed

B – Stage 2.
Extracting the juice from sea buckthorn fruits

C - Stage 3.
Drying the secondary product (pulp+seeds)

D - Stage 4.
Determining the moisture content of the by-product


E – Determination of the mass of the sample


F – Separation of the component fractions from the extracted sample


G– Determining the mass of the package


H- Determination of the mass of the by-product fractions


I–Determination of the percentage of seeds in the pulp

Fig. 2 - Aspects during the preparation of the raw material for experiments

Table 1

Dimensional distribution of fractions from the raw material - Step 5

The amount of raw material separated [g]	Separation sieve hole dimensions [mm]	Distribution of material fractions	
		[g]	[%]
56.7	< 1	0.4	0.705
	1	0.8	1.412
	2	4.2	7.407
	2.8	5.8	10.229
	4	17.9	31.569
	6.3	17.1	30.158
	10	10.5	18.52
TOTAL		**56.7**	**100**

RESULTS

The separation tests were performed for three values of the rotation frequency of the decompaction rotor, respectively detachment rotor. The separation performances of the experimental model were determined by measuring the dimensional distribution of the fractions from the raw material both at the feed (pulp, peels, impurities) and at the exit from the ESSC, respectively of the seed fraction, the values being presented in table 2.

Table 2

Separation parameters of ESSC

Distribution of dimensional fractions in matter before separation [%]	The dimensions of the holes of the separation sieve [mm]	The working rotation frequencies of the decompaction rotor, respectively detachment rotor [min^{-1}]		
		241, respectively 552	402, respectively 920	562, respectively 1288
		Distribution of pulp size fractions, after separation, [%]		
0	**1**	**2**	**3**	**4**
0.705	< 1	3	5	10
1.412	1	5	8	15
7.407	2	12	15	25
10.229	2.8	30	35	35
31.569	4	10	20	7
30.158	6.3	25	10	5
18.52	10	15	7	3

From Table 1, it can be seen that for the sizes of the sieve holes between 0.1…2.8 mm, the distribution of the material before separation is smaller compared to the average distribution of the material after separation. Then, at the sizes of the sieve openings larger than 4 mm to 10 mm, the weight of the distributions is higher before separation and lower after separation.

It is also observed that the distribution of the fractions differs as follows:

- in the material before separation, the distribution is maximum (≈32%), at sieve sizes of 4.0 mm and minimum (≈0.5%) at sizes smaller than 1 mm.

- in the material after separation, the distribution is maximum (≈34%), for sieve sizes of 2.8 mm and minimum (≈6%) for sizes smaller than 1 mm.

Regarding the comparative dimensional distribution of the material fractions after the separation operation depending on the rotation frequencies, table 2, it can be noticed that at small sizes of the sieve holes (1…2.8 mm), the distribution of the material on the fractions increases from the low speed up to high speed. At the larger sizes of the sieve holes (4…10 mm), the distribution of the material into fractions depending on the working rotation frequencies of the decompaction/detachment rotors is different and varies from high percentages of separation to low rotation frequencies at low percentages in the case of high rotation frequencies.

Although the percentage of the last fraction is relatively high, which means that the raw material was not crushed enough, still the seeds were separated from the pulp in a percentage between 85 and 92%.

The degree of separation of the seeds detached from the pulp was approx. 67%, the difference up to 92% being spread in the other fractions, collected by funnels B and C, Fig. 3, due to the fact that the seeds have very varied sizes.

The presence of pulp and peel fractions was also found in the seed collection sections. This fact is caused by the dimensional irregularity of the mentioned fractions, which leads to their separation on several areas of the sieves (B, C), see Fig. 3.

The degree of separation of seeds from the pulp achieved by the equipment can be increased by passing the resulting material through a cyclone with air currents. In this situation, the conclusion was drawn that the equipment must be improved so that the separation system is equipped with sections with sieves with a wider range of sizes at the openings, the differences between them being smaller compared to the existing situation.

It was also found that part of the holes of the sieves got clogged with material, which is why a cleaning brush should be provided. Also, part of the processed material fell outside the collection funnels, therefore some sealing panels will be provided around the sieves.

The values of the intensity and voltage of the electric current were read directly from the converter for different values of the frequency of the current, and the consumed power was calculated with relation 1.

$$P = \sqrt{3} \times U \times I \times \cos\varphi, \ [kW] \quad (1)$$

The characteristics of the electric motors for operating the raw material decompaction system and the seed detachment system are: n_{motor}=920 min^{-1}; P_n= 1.5 kW; I_n= 6.6/3.8 A; U_n= 230/400 V; $\cos\varphi$ = 0.75.

Fig.5 shows some details during the experimental model testing phase in operating mode.

a) Raw material (by-product) supply system

b) By-product separation system

c)

d) Sorts obtained at evacuation

e) Details of the separation process by dimensional fractions

f) Detailed images of the separated fractions at the end of the process

Fig. 5 – Details from the experiments of the ESSC experimental model in operating mode

The values power consumption during the exploitation regime are presented in table 3.

Table 3

Values of ESSC power consumption during the exploitation regime

Work mode (rotational speed of active parts)	Frequency [Hz]	Measured parameter	The value of the measured parameter			
			Sample I	Sample II	Sample III	Average
- decompaction rotor n_1 =241 min^{-1} -detachment rotor n_2 =552 min^{-1}	30	Current intensity, I [A]	3.53	3.47	3.49	3.51
		Current voltage, U [V]	200	199	198	199
		Absorbed power, Pa [kW]	0.916	0.895	0.896	0.902
- decompaction rotor n_1 =402 min^{-1} - detachment rotor n_2 =920 min^{-1}	50	Current intensity, I [A]	2.43	2.44	2.42	2.43
		Current voltage, U[V]	397	398	399	398
		Absorbed power, Pa [kW]	1.27	1.26	1.25	1.16

Experiments were also carried out at speeds higher than 562min^{-1} at the decompaction rotor and 1288min^{-1} at the detachment rotor, but a high percentage of broken seeds was found, which were separated together with the smallest pulp fractions and peels from the separation system, therefore these speeds must be avoided. From the point of view of the energy consumption achieved at the working regimes used, it was found that the range of variation does not exceed 10%. Rotors and determined energy consumptions are not relevant.

However, the energy consumption can vary significantly with the increase in the flow rate of material supply and, implicitly, of separation.

CONCLUSIONS

After carrying out the experiments under operating conditions for the experimental model of the Technical Equipment for the separation of the pulp from the sea buckthorn seed, it was found that this performs the separation sea buckthorn seed pulp in an acceptable percentage and corresponds to the criteria for further processing of the obtained fractions.

The speeds of the decompaction and detachment rotors must be limited to values of approx. 562min^{-1} and at the decompaction rotor at approx. 1288min^{-1}.

In order to improve performance and create a prototype that can be used by processors in the food or phytopharmaceutical industry, the equipment can be improved, respectively the sieve system for separation, so that the sieve sections include a wider range large holes in terms of size (since the experimental model has a sieve of close dimensions), equipping with a system of brushes for cleaning them and a sealed exhaust system to reduce material losses but also better collection of the processed material on fractions.

ACKNOWLEDGEMENT

This work was supported by: Development of the national research-development system, sub-programme 1.2 – Institutional performance – Projects for financing excellence in RDI, contract no. 16PFE and Project: PN 19 10 01 05 - Integrated management of work in farms, vineyards and orchards, contract no.5/ 07.02.2019.

REFERENCES

[1] Beveridge, T., Li, T. S. C., Oomah B. D., Smith, A. (1999). Sea Buckthorn Products: Manufacture and Composition, *J. Agric. Food Chem*., 47, 3480−3488.

[2] Ciesarová, Z.; Murkovic, M.; Cejpek, K.; Kreps, F.; Tobolková, B.; Koplík, R.; Belajová, E.; Kukurová, K.; Daško, L.; Panovská, Z. (2020) Why is sea buckthorn (*Hippophae rhamnoides L*.) so exceptional- A review. *Food Res. Int.*, 133, 109170.

[3] Gâtlan, A.-M. and Gutt, G. (2021), Sea Buckthorn in Plant Based Diets. An Analytical Approach of Sea Buckthorn Fruits Composition: Nutritional Value, Applications, and Health Benefits, *Int. J. Environ. Res*., Public Health, 18, 8986. https://doi.org/10.3390/ijerph18178986].

[4] Höhne, F. (2015), Overview of cultivation technologies and their challenges, *Natural resources and bioeconomy studies,* 31, p.31-35.

[5] Kauppinen, S., Petruneva, E., (2014). Producing Sea Buckthorn of High Quality, *Proceedings of the 3rd European Workshop on Sea Buckthorn*, EuroWorkS2014, October 14-16, Finland

[6] Koskovac, M.; Cupara, S.; Kipic, M.; Barjaktarevic, A.; Milovanovic, O.; Kojicic, K.; Markovic, M. (2017). Sea Buckthorn Oil-A valuable source for cosmeceuticals, *Cosmetics*, 4, 40.

[7] Li, H; Ruan, C; Ding, J; Li J; Wang, L.; Tian X. (2020). Diversity in sea buckthorn (Hippophae rhamnoides L.) accessions with different origins based on morphological characteristics, oil traits, and microsatellite markers. *PLoS ONE 15*(3): e0230356, https://doi.org/10.1371/journal.

[8] Li, S.C.T., Schroeder, W.R., (1996). Sea Buckthorn (Hippophae rhamnoides L.): A Multipurpose Plant-review, *HortTechnology*, Oct./Dec. 1996 6(4), DOI: 10.21273/HORTTECH.6.4.370.

[9] Liu R., Yang Y., Zhao M., Wang Y., Meng X., Yan T., Ho C.-T. (2022) Effect of heat-treating methods on components, instrumental evaluation of color and taste, and antioxidant properties of sea buckthorn pulp flavonoids, *J. Food Sci.*; 87:5442–5454, DOI: 10.1111/1750-3841.16386.

[10] Madawala, S.R.P.; Brunius, C.; Adholeya, A.; Tripathi, S.B.; Hanhineva, K.; Hajazimi, E.; Shi, L.; Dimberg, L.; Landberg, R. (2018). Impact of location on composition of selected phytochemicals in wild sea buckthorn (Hippophae rhamnoides), *J. Food Compos. Anal*., 72, 115–121.

[11] Rati, I. V., Raducanu, D., Cernat, O. E., (2018). Morphological description of sea buckthorn "star" male plant - female plants pollination element (pollinators), Studies and Research, Biology/Studii şi Cercetări, *Biologie*, 27/1, ”Vasile Alecsandri” University Bacău, 44-52.

[12] Smida, I.; Pentelescu, C.; Pentelescu, O.; Sweidan, A.; Oliviero, N.; Meuric, V.; Martin, B.; Colceriu, L.; Bonnaure-Mallet, M.; Tamanai-Shacoori, Z. (2019). Benefits of sea buckthorn (Hippophae rhamnoides) pulp oil-based mouthwash on oral health, *J. Appl. Microbio*l., 126.

[13] Suryakumar, G.; Gupta, A.(2011). Medicinal and therapeutic potential of Sea buckthorn (Hippophae rhamnoides L.), *J. Ethnopharmacol.*, 138, 268–278.

[14] Tereshchuk L. V., Starovoytova K. V., Ivanova S. A., Sergeeva I. Y., (2019). Advances in Social Science, *Education and Humanities Research*, volume 298, p. 407-411.

[15] Tereshchuk, L.V.; Starovoitova, K.V.; Vyushinsky, P.A.; Zagorodnikov, K.A. (2022). The Use of Sea Buckthorn Processing Products in the Creation of a Functional Biologically Active Food Emulsion, *Foods*, 11, 2226. https://doi.org/10.3390/ foods11152226.

[16] Ursache, F.M.; Ghinea, I.O.; Turturică, M.; Aprodu, I.; Râpeanu, G.; Stănciuc, N. (2017). Phytochemicals content and antioxidant properties of sea buckthorn (Hippophae rhamnoides L.) as affected by heat treatment—Quantitative spectroscopic and kinetic approaches, *Food Chem*., 233, 442–449.

[17] Wojtunik-Kulesza, K.A., Oniszczuk, A., Oniszczuk, T., & Waksmundzka-Hajnos, M. (2016). The influence of common free radicals and antioxidants on the development of Alzheimer’s disease, *Biomedicine and Pharmacotherapy*, 78(1), 39–49. https://doi.org/10.1016/j.biopha.2015.12.024.

[18] Zeb, A. (2004). Chemical and Nutritional Constituents of Sea Buckthorn Juice, *Pak. J. Nutr.*, 3, 99–106.

APPLICATION OF OZONE TREATMENT IN AGRICULTURE AND FOOD INDUSTRY. A REVIEW
/
臭氧杀菌技术在农业和食品行业中的应用：综述

Ying WANG[1,2]; Xiao Jun QIAO*[1]; ZhiBin WANG[1]

[1] Information Technology Research Center, Beijing Academy of Agriculture and Forestry Sciences, Beijing/ China;
[2] Nongxin Technology (Beijing) Co., LTD
Tel: +86 01051503650; E-mail: qiaoxj@nercita.org.cn

DOI: https://doi.org/10.35633/inmateh-68-86

Keywords: *Ozone sterilization, Agriculture, Disease, Insect pest, Food industry, Plant protection technology*

ABSTRACT

Ozone is a strong oxidant and strong disinfectant that has a strong anti-pathogenic effect on bacteria, fungi, parasites, and viruses. Because of its advantages such as high reactivity, strong permeability and low residue, the application of ozone is gaining more and more attention, and ozone has been widely used in water treatment, equipment disinfection, public scene disinfection, and other fields. The purpose of this review is to discuss the use of ozone technology for animal and plant protection that can be applied to agriculture, and to emphasize the need for further studies to determine the optimal concentration and application of ozone for different crops so that, in the future, ozone technology can be applied in agriculture to gain a significant competitive advantage and improve product safety.

摘要

臭氧是一种强氧化剂和强消毒剂，对细菌、真菌、寄生虫和病毒有很强的抗病原作用。 由于臭氧具有反应活性高、渗透性强、残留量低等优点，其应用越来越受到重视，臭氧目前已广泛应用于水处理、设备消毒、公共场所消毒等领域。本综述的目的是讨论可应用于农业的臭氧技术在动植物保护中的应用，并强调需要进一步研究以确定不同作物的最佳臭氧浓度和应用，以便在未来在农业中，应用臭氧技术可获得显着的竞争优势，同时提高产品安全性。

INTRODUCTION

Ozone (O_3), an allotropic form of oxygen (O_2), is an unstable colorless gas with a unique smell. Ozone in the atmosphere is usually generated from atmospheric air that has been exposed to a high-energy source, such as ultraviolet radiation or high voltage electrical discharge. Ozone is partially soluble in water and its solubility increases when the partial pressure of the gas increases and the temperature of water decreases. It is an attractive alternative to insecticides and disinfectants because it auto decomposes into oxygen leaving no toxic residues in the environment (*Tiwari et al., 2008*).

The increasing importance of preventing and controlling plant diseases and insect pests in modern agriculture has led to the use of large amounts of insecticides and sterilizing agents to reduce the losses caused by crop diseases and pests. However, chemical pesticides are harmful to the environment and human health, and pesticides are single-targeted to crops, which can cause damage to other crops. Furthermore, the extensive use of chlorine-containing disinfectants in animal husbandry can cause residual problems and may spread harmful microorganisms to humans. In recent years, the focus has shifted more towards economically, environmentally, and socially sustainable development. In agriculture, there is a growing need to find and use methods that are safe for crops and have no adverse impacts on the environment, animals, or humans.

Ozone is an effective bactericide, insecticide, and fungicide that has the advantages of safety, efficiency, and environmental protection. Moreover, ozone can destroy up to 99.9% of pesticide residues and microorganisms commonly found on food because of its potential oxidizing capacity. As an oxidizing agent in organic reactions, ozone is used in many fields, including pulp bleaching, cooling water treatment, and disinfection of medical appliances *(Pandiselvam et al., 2017*). For many years, ozonation technology has been used in Europe to disinfect drinking water and swimming pool water without any problems (*Roustan M, 2008*).

[1] *Ying Wang, M.S.; XiaoJun Qiao, Prof. Ph.D.; ZhiBin Wang, Ph.D.*

In this review, the applications of ozone in agriculture were discussed, with particular attention to experiments and studies that have been reported in scientific papers, and analyze the advantages and constraints of using ozone technology in agriculture. This overview will provide guidelines for further research, the development of new ozone plant protection machinery, and the expansion of its applications in agricultural production.

PRODUCTION OF OZONE

Ozone is very unstable and breaks down quickly into oxygen at room temperature (Figure 1) *(Guzel-Seydim et al., 2004*), so it must be manufactured on site for immediate use (*Brodowska et al., 2018*). Common methods of ozone generation include electrolysis, reaction of elemental phosphorus with water, and radiochemical production. Considering the cost, the most popular methods now are photochemical (ultraviolet light) and corona discharge.

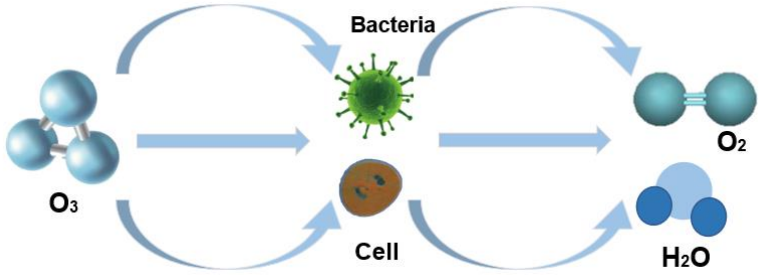

Fig.1 - Action of ozone on cells

Corona (Electrical) discharge method

Corona discharge involves passing dried dust-free air or another oxygen-containing gas mixture through a high-energy electrical field between two electrodes separated by a dielectric material, usually glass. When oxygen passes through the electrical field, the molecules are split apart, forming very active atomic oxygen radicals that can combine with intact oxygen molecules to produce ozone, as shown in the following equations.

An oxygen molecule (O_2) absorbs an electron (e^-) and splits into two oxygen atoms ($2O$).

$$O_2 + e^- \rightarrow 2O \quad (1)$$

Then, each oxygen atom (O) interacts with an oxygen molecule to produce ozone (O_3).

$$2O + 2O_2 \rightarrow 2O_3 \quad (2)$$

The mixture of ozone and gas discharged from an ozone generator contains approximately 1%–3% ozone if dry air is used, and 3%–6% ozone when high-purity oxygen is used as the feed gas (*Patil et al., 2011*).

The corona discharge method has been used widely to produce large amounts of ozone (Figure 2).

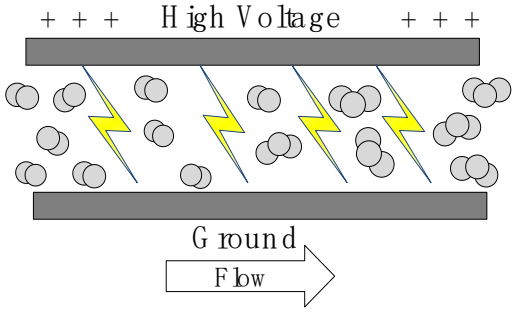

Fig. 2 - Schematic diagram of ozone generation by corona discharge (*Gonçalves, 2009*)**.**

Ultraviolet lamp method

The ozone layer in the Earth's stratosphere is produced by ultraviolet radiation. Therefore, any ultraviolet light with wavelength <200 nm can dissociate oxygen molecules into oxygen atoms and produce ozone. Generally, an ultraviolet lamp with wavelength 140–190 nm can be used to split the oxygen molecules into unstable oxygen radical atoms (photodissociation), thereby starting the process of ozone production, as shown in equations (1) and (2).

The ultraviolet light from the lamp will convert the passing oxygen molecules to ozone (Figure 3). However, the efficiency of this method in generating ozone is very low, so it is best used when only a small amount of ozone is required.

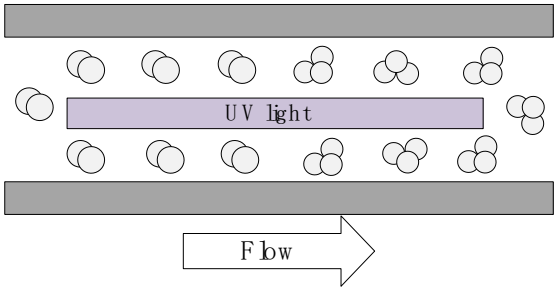

Fig. 3 - Schematic diagram of ozone generation by ultraviolet light *(Gonçalves, 2009)*

The main methods used for ozone generation are described in Table 1.

Table 1

Main methods used to generate ozone (*Cameron, 2012*)

Method	Basis	Advantage	Disadvantage
Corona discharge technology	High voltage; Gas	Fast response; Sufficient materials	High cost; Low ozone concentration; Large noise and electromagnetic interference
Ultraviolet lamp method	UV lamp; Gas	Lower cost; Output hardly affected by humidity	Low efficiency;
Electrochemical Ozone Production	Low voltage direct current	High ozone concentration; Less by-products	Best for water applications

APPLICATION OF OZONE TECHNOLOGY IN AGRICULTURE

Ozone technology has been used in many aspects of agriculture, such as crop pest control, seed treatment, fruit and vegetable storage and preservation, and livestock and poultry farm disinfection and deodorization as has been reported in the literature (Figure 4).

This technology takes advantage of the broad-spectrum, high-efficiency, non-residual sterilization properties of ozone (*Dourado et al., 2019*), and provides a new direction for the development of green agriculture.

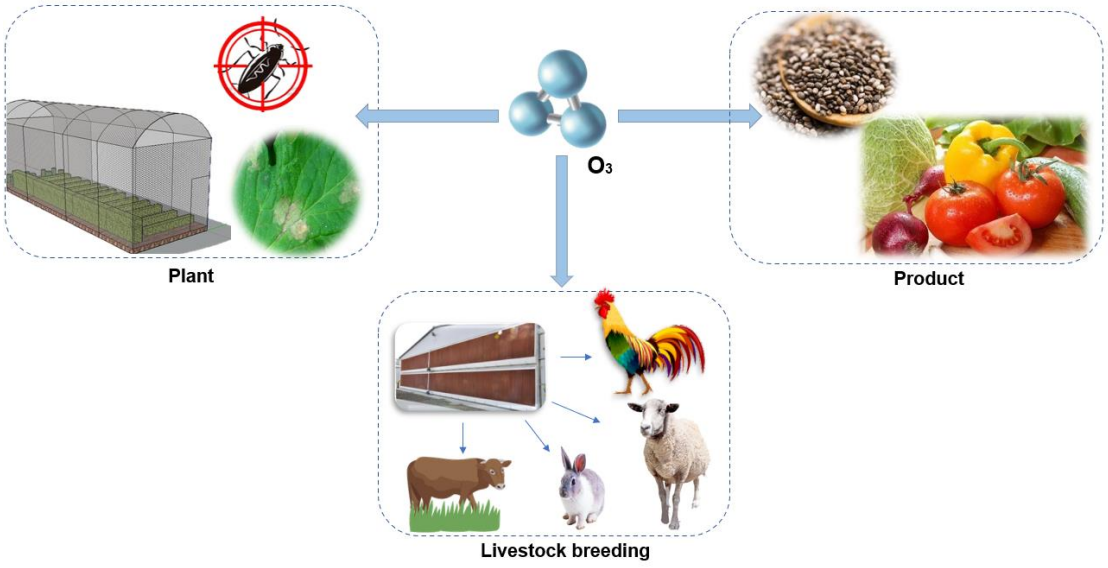

Fig. 4 - Applications of ozone in agriculture reported in the literature

Seed treatment

Seeds are an essential part of agriculture, but they are susceptible to infection in storage and have a high rate of mildew, which often leads to deformed seedlings and dead seeds. Therefore, there is an urgent need to increase grain production by increasing seed germination rates (*Rifna et al., 2019*). Chemical treatments for seeds can cause physiological quality loss. Ozone has many benefits as a substitute for chemicals because it is a strong antimicrobial agent as well as a germination enhancer, which can increase the germination rate of seeds and inhibit the growth rate of surface microorganisms (*Violleau et al., 2008*).

Researchers have studied the effects of ozone treatment on seed germination *(Vazquez-Ybarra J.A.，2015; Abeli T., 2017*). Violleau et al. (*Violleau, 2007*) treated corn seeds with ozone and observed that ozone or oxygen oxidative treatment increased their germination rate. Sudhakar et al. (*Sudhakar et al., 2011*) showed that the application of low doses of ozone in tomato seeds increased the germination rate and produced seedlings with longer roots. Similarly, Normov et al. (*Normov et al, 2020*) found that the roots of ozone-treated maize seeds were twice as long (0.10 m) as the roots of untreated seeds. However, wheat seeds treated with ozone did not show any seminal root length (*Savi G.D., 2014*). Landesmann et al. (*Landesmann et al, 2013*) showed that seeds exposed to 90 parts per billion ozone concentration over a long time exhibited maximum germination when stored at 75% relative humidity and 25°C. Łabanowska et al. (*Łabanowska et al., 2016*) suggested that, at moderate concentrations, ozone has a positive impact on seed grains by prompting the improvement of morphological attributes and enhancing their germination. Lazukin et al. (*Lazukin et al., 2018*) analyzed the morphological characteristics and germination rate of soft spring wheat seeds after treating them with ozone, and found that, although the morphology of the seedlings changed significantly after ozone treatment, seed germination was not affected. Zhang et al. (*Zhang Zhijia, 2019*) used ozone to treat cucumber seeds and showed that low-concentration ozone treatment promoted seed germination, and high-concentration ozone treatment inhibited seed germination. Wu et al. (*Wu et al., 2006*) found that persistent exposure of wheat seeds to ozone gas had unfavorable effects on their germination capacity. Recently, Bataller et al. (*Bataller M, 2020*) confirmed that ozone did not prevent sprouting of Red Scarlet seed potatoes, and showed that the incidence and severity of soft rot (Erwinia ssp.) in inoculated seed potatoes were reduced. They also pointed out that ozone treatment of seeds is a potential alternative to disinfection, but integrated analysis of the seed handling of each crop is required. Mosneaga et al. (*Mosneaga et al., 2020*) treated the seeds of wheat, corn, and beans with ozone, and found that the germination energy increased. They also showed that the growth rate of the ozone-treated wheat was 26 times higher than that of untreated wheat, whereas the growth rate of the ozone-treated corn did not change significantly.

Together, these findings show that the use of ozone to treat seeds before crops are planted can increase the germination rate and inhibit the growth rate of surface microorganisms, confirming that ozone is an effective seed treatment method.

Control of diseases and insect pests

Ozone is a highly active and strong oxidant that is extremely unstable. In the decomposition process, oxygen and free ground state oxygen are released. The free ground state oxygen is also a strong oxidant, which can penetrate the cell wall and oxidize and decompose the oxidase that oxidizes glucose to produce energy for the bacteria, so that the bacteria are inactivated and die. Ozone can directly act on bacteria, fungi, and insects by oxidizing histones, mercaptans, and unsaturated fatty acids, resulting in reduced survival rates and even death (*Komanapalli et al, 1996; Kells et al., 2001*). The feasibility of using ozone to control diseases and insect pests has been the focus of several studies.

Pryor et al. (*Alan Pryor, 1999*) found that ozone reduced the number of root nematodes and bacteria in soil, and increased the yield of tomatoes, strawberries, and carrots. Msayleb et al. *(Msayleb et al., 2011*) studied the killing effect of soil fumigation with ozone gas on nematodes, and showed that ozone was highly lethal to nematodes, whether by gas fumigation or by direct ozonation of samples. Similarly, Mitsugi et al. *(Mitsugi et al., 2017*) proposed the extermination of soil worms and the acceleration of plant growth by the ozone treatment of soil. Veronico et al. (*Veronico P, 2016*) showed that using ozone water to irrigate tomato plants inhibited root nematode production. Mendez et al. (*Mendez and Maier et al., 2003*) reported the efficiency of ozone in controlling insect pests in stored grains. Lemic (*Lemic D., 2020*) demonstrated that ozone had a negative effect on adult wheat weevils, and could cause up to 100% mortality. Lise et al. *(Hansen L.S.,., 2012*) showed that ozonation had great potential as an efficient control method against most insect pests in stored products. In addition to killing insects, ozone can also effectively control crop diseases.

Fujiwara et al. *(Fujiwara and Fujii et al., 2009*) showed that ozone reduced visible physiological disorders in cucumber leaves and had the ability to disinfect powdery mildew, but the concentration of the ozone water that they used was not reported. Hirneisen et al. (*Hirneisen et al., 2011*) treated onion and lettuce with 6.25 ppm ozone for 10 minutes, which reduced the numbers of two different bacteria. Zhang et al. (*Zhang et al., 2011)* found that daily ozone treatment of strawberries for 30 minutes at 0°C inhibited the reduction of ascorbic acid. Lone et al. *(Lone et al., 2019*) reported that ozone techniques had positive results in treating kiwifruit infected with pathogens.

Ozone sterilization for planting in agricultural greenhouses can effectively kill pathogens and the larvae of insect pests. Pesticides have been used for sterilization, disinfection, and pest control in greenhouses, but their repeated use has made pests and pathogens resistant to many pesticides. Furthermore, pesticides can cause widespread pollution of the environment. The use of ozone in greenhouses can control pests and diseases, and does not lead to resistance or cause environmental pollution. The magnitude of reduction in the growth rate of ozone-treated plants appears to depend on the types of pathogens and pests, ozone concentration, and exposure methods and times.

Food preservation

High incidences of foodborne diseases have been associated with contaminated vegetables and fruits, and therefore preventing microbial destruction is essential to achieve the safety and storage stability of food. Traditional processing methods usually sacrifice the sensory attributes and nutritional qualities of the food. The application of chemical fungicides to control post-harvest diseases is increasingly restricted because of concerns about the safety of fungicides and the development of pathogen resistance to many key fungicides. Because consumers increasingly favor fresh foods, alternative technologies are needed to maintain most of the fresh attributes, and ensure the safety and storage stability of food (*Khadre, Yousef et al., 2001*).

Ozone technology provides a new approach to solve the preservation problem of fruits and vegetables. Treating fruits and vegetables with ozone can prolong their storage period, because ozone can kill microorganisms on their surfaces *(Tiwari, Muthukumarappan et al., 2008*) and reduce the breathing intensity of fruits and vegetables, thus slowing the decay process (*Patil S., 2001; Tiwari B.K., 2012*). In 1999, Anglada et al. (*Anglada et al., 1999*) proposed a theoretical mechanism by which ozone destroys ethylene and, subsequently, ozone technology has provided a new way of preserving fruits and vegetables. Muthukumarappan et al. *(Muthukumarappan et al., 2000*) found that the storage life of foods such as beef, chicken, and lamb was prolonged when placed in ozone. Skog et al. (*Skog, 2001*) found that ozone reduced ethylene levels in the air in a cold storage room, and Palou et al. (*Palou et al., 2001*) showed that ozone was effective in removing ethylene from export containers. Karaca et al. (*Karaca et al., 2007*) confirmed that the antiseptic property of ozone was mainly to reduce the production and viability of spores. Wei et al. *(Wei et al., 2011*) studied the effects of ozone treatment on the quality of fresh fruits and the inactivation of natural microflora under different ozone concentrations and concluded that the use of ozone as a disinfectant in the food processing industry needs to be product specific. Venta et al. (*Venta M.B., et al., 2010*) found that the exposure of tomatoes to gaseous ozone not only preserved their sensory attributes but also extended their shelf life. Asokapandian et al. (*Asokapandian Sangamithra, 2018*) used the microbial inactivation effect of ozone to preserve the sensory and nutritive values of foods, and found that even at low concentrations, ozone was very effective against a broad spectrum of microorganisms. Moreover, this method has high practicability, does not leave hazardous residues on food, and because ozone is produced on site, the transportation cost and storage volume of disinfectants are highly reduced.

The efficiency of ozone treatment in reducing microbial counts on fresh produce depends on the ozone dose and on the initial microbial counts/inoculum, as has been demonstrated in many studies (Table 2).

Table 2

Efficiency of ozone treatments against microbial populations on selected fruits and vegetables

Crop	References	State	Treatment(s)	Effect
Carrot	*(Chauhan, 2011)*	Gaseous	9-10ppm/5-15min	*E. coli* decreased by 2.7log CFU;
		Aqueous	10ppm/10min	Yeasts and molds reduced up to 1.92 log CFU
				Standard Plate reduced up to 3.22 log CFU
Tomato	*(Bermúdez-Aguirre, 2013)*	Gaseous	5 ppm/3–15min	*E. coli* decreased by 2.2 log CFU counts
Lettuce	*(Garcia, 2010)*	Aqueous	5ppm/10min	Viable aerobic bacteria and yeast/mold reduced to 1.5 log CFU and 1 log CFU

Crop	References	State	Treatment(s)	Effect
Cucumber	*(Siegel, 1962)*	Aqueous	2.5-5.8 ppm/30min	Psychrotrophic bacteria counts decreased by 1.3 log CFU
Blueberries	*(Bialka, 2007)*	Gaseous	7.9 ppm/32 min	*E. coli* decreased by 2.5 log CFU
		Gaseous	8.9 ppm/32 min	Salmonella decreased by 4.9 log CFU
Apple	*(Yousef, 2001)*	Aqueous	24ppm/1-5min	*E. coli* decreased by 2.6 log CFU
Spinach	*(Klockow P A, 2009; S. M. E. Rahman, 2010)*	Aqueous	5 ppm/0.5-7 min	*E. coli* decreased by 1.22 log CFU
		Gaseous	5-10 ppm/3 days	*E. coli* decreased by 1.8 log CFU

However, ozone can also affect product quality. Sasmita et al. (*Sasmita, 2019*) concluded that the type of ozone treatment and the length of the storage time influenced the texture, color, and weight loss of red cayenne pepper. Together, these findings indicate that the effects of ozone on the sensory (aromatic, color, texture, weight loss) and nutritional (vitamins, antioxidant capacity, biologically active compounds) properties of foods depend on the dosage used.

Disinfection in animal husbandry

The increased awareness of the need to quality control livestock products means the control of livestock and poultry epidemics has become increasingly important. The ability of ozone to disinfect has proven to be very effective in other processes. In breeding environments, bacteria and viruses can breed easily, and ozone technology has a unique role in disinfection and epidemic prevention. Ozone can disperse to every corner of an enclosed space in a short time and instantly kill viruses, bacteria, fungi, and parasites, thereby effectively preventing the infection and transmission of respiratory diseases among livestock and poultry. Ozone also eliminates odors in such spaces and improves the breeding environment (*Vozmilov, Ilimbetov et al., 2016*).

Ozone has 1.5 times the oxidizing potential of chlorine, acts 3000 times faster than chlorine, and does not produce harmful decomposition products (*Troyan, 1989; Horvitz S, 2010*). Restaino et al. *(Restaino et al., 1995*) confirmed the bactericidal action of ozone towards microorganisms, including *Escherichia coli*, a fecal contaminant. Zhu et al. *(Zhu Hanheng et al., 2001*) used ozone in a chicken coop and found that ozone was not only effective in curbing poultry diseases and improving survival rates, but also was pollution- and residue-free, and it provided fresh air for livestock and poultry. Alkoaik (*Alkoaik, 2009*) used an ozone dose of 25 mg/L to treat animal manure and found that it removed the odor; a 66% reduction was observed in a continuous operation. Feng found that ozone directly decomposed ammonia. Reducing ammonia concentrations will only reduce the environmental pollution associated with livestock production but also reduce the incidence of animal diseases *(Feng, 2010*). Di et al. (*Wei Di, 2011*) applied ozone technology to the environmental prevention and control of poultry breeding epidemics and achieved remarkable results. The test results showed that ozone reduced the disease rate of chickens, and the weight of each chicken increased by an average of about 250g. Liu et al. (*Liu Yuhua et al., 2013*) demonstrated a 90% elimination rate of *E. coli* in water by ozone. They turned on the ozone facility at a pig farm and found that ozone broke down 80% of ammonia and 77% of hydrogen sulfide in the air. Lv et al. (*Lv Yanqiu et al., 2018*) found that ozone had a disinfecting effect on both the air and walls in chicken houses. Ozone technology can reduce the use of antibiotics, lower production costs by maintaining clean air quality in chicken houses, and improve the quality of livestock and poultry and their products.

Ozone has numerous potentials to develop the quality of conventional animal husbandry. Compared with traditional disinfection methods that involve spraying insecticides, the broad spectrum of ozone can not only eliminate a variety of pathogens in the environment at the same time but also decompose ammonia, hydrogen sulfide, and other harmful gases and odors in livestock and poultry houses. After sterilization, ozone is converted to oxygen, which increases the oxygen content in livestock and poultry houses and improves the animal living environment.

Other applications

In addition to sterilization and preservation of fruits and vegetables, ozone also is effective in removing pesticide residues in fruits and vegetables. Fruits and vegetables are important components of the human diet, and pesticides are still the main treatment used to control crop diseases. As a result of this treatment, agricultural products often contain significant amounts of pesticide residues (*Jardim and Caldas, 2012*) that can have detrimental effects on human health, including carcinogenesis and abnormal cell development (*Burrows and Canle et al., 2002*).

The elimination of pesticide residues in food to make it safe for human consumption, has been the focus of much research. The efficiency of conventional techniques, such as washing agricultural products with chemicals, depends on, for example, the location of the residues and their water solubility. Such methods do not completely eliminate pesticides *(Lozowicka, Jankowska et al., 2016*). Pesticides are organic compounds, and ozone can react with these compounds by breaking chemical bonds, which produces acids, alcohols, amines, and other small molecules. Most of these products are non-toxic, soluble in water, and can be removed by washing (*Pandiselvam et al., 2017*). Ozone eventually decomposes to oxygen, so the processed products do not contain any harmful residues *(Xiong, 2011*).

Metzger et al. (*Metzger, 2007*) stored waxed navel oranges in an ozone atmosphere and found that malathion (an insecticide) and chlorpyrifos (a pesticide) concentrations were lower (0.18–0.20 ppm [parts per million]) than those in oranges that were stored in air, suggesting that ozone may help reduce such residues on citrus fruits.

Hwang et al. (*Hwang et al., 2001*) showed that mancozeb (a fungicide) residues decreased by 56%–97% and ethylene thiourea was removed completely from fresh apples after ozonated water treatment. Tzortzakis (*Tzortzakis, 2007*) used ozone to treat grapes and strawberries, which inhibited the production of gray mold and effectively prevented fungal diseases in the fruits.

Whangchai et al. (*Whangchai et al., 2011*) suggested that gaseous ozone was more effective than aqueous ozone in degrading chlorpyrifos. Kusvuran et al. (*Kusvuran et al., 2012*) treated the orange matrix with ozone for 5 minutes and were able to remove all chlorothalonil (a fungicide) residues.

Heleno et al. (*Heleno et al., 2014*) concluded that ozone can be used to remove pesticide residues from strawberries without affecting their quality. Balawejder et al. *(Balawejder et al., 2014*) found that the captan (a fungicide) residue was greatly reduced when raspberries and blackcurrants were treated with gaseous ozone.

Karaca (*Karaca, 2019*) found that the butyrate residue was significantly reduced in grapes stored in an ozone-enriched environment (0.64 mg/m−3) but weight loss was less severe for grapes stored in ambient air compared with that for grapes stored in ozone. It was suggested that extra humidification could be done in cold rooms when ozone was used for grape storage.

Wu et al. (*Wu et al., 2019*) showed that the percentage of 10 pesticide residues removed with ozone washing for 15 minutes was significantly higher than it was with ozone washing for 5 minutes. They found the percentage of pesticide residues that was removed depended on the washing solutions and treatment times, as well as the characteristics of the pesticides.

Kusvuran et al. *(Kusvuran et al., 2012)* found that the efficiency of ozone in removing pesticide residues depended on the structural properties of the pesticides and matrices.

Ozone can not only oxidize and degrade pesticide residues on the surfaces of fruits and vegetables, but also can penetrate into the leaves to degrade pesticides. The effects of ozone treatments on the degradation of pesticide residues on the surfaces of fruits and vegetables are shown in Table 3. These findings indicate that ozone cleaning has a significant effect on the removal of pesticide residues.

Table 3

Pesticide degradation by ozone treatment

Fruit/vegetable	References	Pesticide	State	Treatment(s)	Effect (%)
Apple	(Jijun Gong, 2011; Piotr Antos, 2018)	Diphenylamine	Aqueous	16 mg·L^{-1} /20 min	75
		Captan	Gaseous	1 ppm was dosed every 12 h for 1 min up to 84 days	78.9
Citruses	(Kusvuran et al., 2012)	Chlorothalonil	Aqueous	5ppm/10min	100
Strawberry	(Heleno et al., 2014)	Difenoconazole	Gaseous	0.8 mg·L^{-1} /60 min	95
Tomato	(Tawfiq, 2015; Al-Antary, 2018)	Carbosulfan	Aqueous	4 μg·L^{-1}	100
		Myclobutanil	Gaseous	5 ppm /15 min	98
Chili	(Panlop Sintuya, 2018)	Malathion	Aqueous	5.5 g·h^{-1}/30min	68
Carrots	(Lauana Pellanda De Souza, 2018)	Difenoconazole	Aqueous	5 mg·L^{-1}	70.3
			Gaseous	5 mg·L^{-1}	95.3

DISCUSSION

In this review, the current knowledge of the broad social impact of ozone and provided evidence-based data for ozone applications in agriculture was described. Some sterilization methods commonly used in agriculture have adverse effects on human health and the environment, and the use of some chemicals has been restricted. Ozone has the following advantages over conventional agents that can help solve these problems.

High efficiency

Ozone is highly oxidizing and the reaction rate is very fast. At the correct concentrations, ozone can destroy bacterial cells and insect pests within a short time period, thereby eliminating the diseases they cause. Ozone has a broad spectrum and can kill many kinds of pathogens and pests associated with plant diseases, making ozone a highly effective bactericidal and insecticidal reagent.

High cleanliness

Ozone is produced from oxygen in the air. After sterilization, ozone decomposes to oxygen at room temperature because it is extremely unstable. Unlike the traditionally used chemicals, ozone leaves no residue and therefore there is no secondary contamination.

Increased production and improved crop quality

Ozone treatment can significantly improve the safety and quality of fruits and vegetables, including larger fruit, brighter skin surface color, and better flesh taste. Ozone also can degrade pesticide residues on the surfaces of fruits and vegetables, thereby removing harmful chemicals.

Despite the many advantages of ozone, its application in agricultural production still has many limitations. One important aspect is that the concentration of ozone is not easy to control. Although ozone can meet the requirements of agricultural insecticidal sterilization, low ozone concentrations have a limited effect on disease control and high ozone concentrations can lead to electrolyte leakage and membrane damage. At present, it is not possible to precisely control the concentration of ozone released. Furthermore, most of the ozone equipment currently on the market is expensive, which leads to difficulties in promoting ozone technology. Therefore, the development of low-cost ozone sterilization machinery is a good future direction.

CONCLUSIONS

We have argued that ozone sterilization technology has great potential to replace the existing technologies for more sustainable and effective agricultural activities. The ozone characteristics of strong permeability, no residue, and no pollution are the main reasons for the rapid growth of demand for this technology in various fields. The effects of ozone treatments in agriculture depend greatly on the environment and crop types. Some applications of ozone are already in use, whereas other applications require further research to increase trust in the use of ozone. For example, ozone concentrations need to be adjusted according to the tolerance of crops and pests to ozone, so that ozone concentrations are optimized for different environments, different crops, and different pests. Moreover, the influence of high ozone concentrations on crop growth, metabolism, and yield needs to be further clarified. We strongly recommend a planned large-scale experiment to explore the optimal ozone concentrations for use in agriculture.

ACKNOWLEDGEMENT

This study was supported by the National Key R&D Program of China (No. 2020YFD1000300), and the authors are appreciative of the comments from the anonymous reviewers who provided helpful suggestions on improving this paper.

REFERENCES

[1] Abeli T., Guasconi D.B., Mondoni A., Dondi D., Orsenigo S., (2017), Acute and chronic ozone exposure temporarily affects seed germination in alpine plants. *Plant biosystems*, Vol.151, no.2, pp. 304-315.

[2] Achen M., Yousef A.E., (2001), Efficacy of Ozone Against Escherichia coli O157:H7 on Apples. *Journal of Food Science*, Vol.66, no.9, pp. 1380-1384.

[3] Al-Antary T.M., Shaderma A.M., Al-Dabbas M.B., (2018), Ozonation treatment effect on spiked chlorfenapyr pesticide on tomato fruits. *Fresenius Environmental Bulletin*, Vol.2, no.11, pp.7822-7626.

[4] Alkoaik F.N., (2009), Ozone treatment of animal manure for odor control. *American Journal of Environmental Sciences*, Vol.5, no.6, pp.765-771.

[5] Anglada J.M., Crehuet R., Bofill J.M., (1999), The Ozonolysis of Ethylene: A Theoretical Study of the Gas-Phase Reaction Mechanism. *Chemistry A European Journal*, Vol.5, no.6, pp. 1809-1822.
[6] Antos P., Piechowicz B., Gorzelany J., Matlok N., Migut D., Jozefczyk, R., (2018), Effect of Ozone on Fruit Quality and Fungicide Residue Degradation in Apples during Cold Storage. *Ozone: Science & Engineering*, Vol.40, no.6, pp.1-5.
[7] Asokapandian S., Periasamy S., Swamy G.J., (2018), *Fruit Juices*, Chapter 25-Ozone for Fruit Juice Preservation, pp. 511-527.
[8] Balawejder M., Szpyrka E., Antos P., Józefczyk R., Piechowicz B., SadlO S., (2014), Method for reduction of pesticide residue levels in raspberry and blackcurrant based on utilization of ozone. *Ochrona Srodowiska I Zasobów Naturalnych*, Vol.25, no.4, pp.1-5.
[9] Bataller M., Veliz E., Riverol Y., Fernández L.A., Fernández I., (2020), Effect of ozone on sprouting of potato and sugarcane seeds: a sustainable alternative of disinfection. *Ozone Science and Engineering*, Vol.43, no.1, pp.1-10.
[10] Bermúdez-Aguirre D., Barbosa-Cánovas G.V., (2013), Disinfection of selected vegetables under nonthermal treatments: Chlorine, acid citric, ultraviolet light and ozone. *Food Control*, Vol.29, no.1, pp. 82-90.
[11] Bialka K., Demirci A., (2007), Utilization of gaseous ozone for the decontamination of escherichia coli o157:h7 and salmonella on raspberries and strawberries. *Journal of Food Protection*, Vol.70, no,5, pp.1088-1092.
[12] Bialka K.L., Demirci A., (2010), Decontamination of Escherichia coli O157:H7 and Salmonella enterica on Blueberries Using Ozone and Pulsed UV-Light. *Journal of Food Science*, Vol.72, no.9, pp.391-396.
[13] Brodowska A.J., Nowak A., Śmigielski K., (2017), Ozone in the food industry: Principles of ozone treatment, mechanisms of action, and applications: An overview. *Critical reviews in food science and nutrition*, Vol.58, no.13, pp. 2176-2201.
[14] Burrows H.D., Canle L M., Santaballa J.A., Steenken S., (2002), Reaction pathways and mechanisms of photodegradation of pesticides. *Journal of Photochemistry & Photobiology B Biology*, Vol.67, no.2, pp. 71-108.
[15] Cayuela J. A., Vazquez A., Perez A.G., Garcia J.M., (2009), Control of Table Grapes Postharvest Decay by Ozone Treatment and Resveratrol Induction. *Food Science & Technology International*, Vol.15, no.5, pp. 495-502.
[16] Chauhan O.P., Raju P.S., Ravi N., Singh A., Bawa A.S., (2011), Effectiveness of ozone in combination with controlled atmosphere on quality characteristics including lignification of carrot sticks. *Journal of Food Engineering*, Vol.102, no.1, pp. 43-48.
[17] Dajun F., (2010), The effect of ozone disinfection in livestock and poultry house is good (畜禽舍用臭氧消毒效果好), *Hunan Agriculture*, vol.6, pp.22.
[18] Dourado C., Pinto C., Barba, F.J., Lorenzo J.M., Delgadillo I., Saraiva J.A., (2019), Innovative non-thermal technologies affecting potato tuber and fried potato quality. *Trends in Food Science & Technology*, Vol.88, pp. 274-289.
[19] Fujiwara K., Fujii T., Park J., (2009), Comparison of Foliar Spray Efficacy of Electrolytically Ozonated Water and Acidic Electrolyzed Oxidizing Water for Controlling Powdery Mildew Infection on Cucumber Leaves. *Ozone: Science & Engineering*, Vol.31, no.1, pp. 10-14.
[20] Garcia A., Mount J.R., Davidson P.M., (2010), Ozone and Chlorine Treatment of Minimally Processed Lettuce. *Journal of Food Science*, Vol.68, no.9, pp.2747-2751.
[21] Gonçalves A.A., (2009), Ozone: an emerging technology for the seafood industry. B*razilian archives of biology and technology*, Vol.52, no.6, pp. 1527-1539.
[22] Guzel-Seydim Z.B., Greene A.K., Seydim A.C., (2004), Use of ozone in the food industry. *LWT - Food Science and Technology*, Vol.37, no.4 pp. 453-460.
[23] Hanheng Z., (2001), Application of ozone technology in poultry (臭氧技术在家禽中的应用), *China Poultry*, Vol.23, no.7, pp.41.
[24] Hansen L.S., Hansen P., Jensen K.M.V., (2012), Lethal doses of ozone for control of all stages of internal and external feeders in stored products. *Pest Management Science*, Vol.68, no.9, pp. 1311-1316.
[25] Heleno F.F., Queiroz M.E.L.R.D., Neves A.A., Freitas R.S., Faroni L.R.A., Oliveira A.F.D., (2014), Effects of ozone fumigation treatment on the removal of residual difenoconazole from strawberries and on their quality. *Journal of Environmental Science and Health. Part B. Pesticides Food Contaminants and*

Agricultural Wastes, Vol.49, no.2, pp. 94-101.
[26] Hirneisen K.A., Markland S.M., Kniel K.E., (2011), Ozone inactivation of norovirus surrogates on fresh produce. *Journal of Food Protection*, Vol.74, no.5, pp.836-839.
[27] Horvitz S., Cantalejo M.J., Erkan M., Aksoy U., (2010), The Effects of Gaseous Ozone and Chlorine on Quality and Shelf Life of Minimally Processed Red Pepper. *VI International Postharvest Symposium*, pp. 583-589.
[28] Hwang E.S., Cash J.N., Zabik M.J., (2001), Postharvest Treatments for the Reduction of Mancozeb in Fresh Apples. *Journal of Agricultural and Food Chemistry*, Vol.49, no.6, pp. 3127-3132.
[29] Jardim A., Caldas E.D., (2012), Brazilian monitoring programs for pesticide residues in food – Results from 2001 to 2010. *Food Control*, Vol.25, no.2, pp. 607-616.
[30] Jijun Gong, Zhonghai Li, Haiyan Zhong, Jing Tang., (2011), Ozone/ultrasound degradation effect on residual pesticides in commercially available apples. *IEEE - 2011 Semiconductor Conference Dresden: Technology, Design, Packaging, Simulation and Test* (Dresden).
[31] Karaca H., (2019), The Effects of Ozone-Enriched Storage Atmosphere on Pesticide Residues and Physicochemical Properties of Table Grapes. *Ozone Science and Engineering: The Journal of the International Ozone Association*, Vol.41, no.5, pp.404-414.
[32] Karaca H., Velioglu Y.S., (2007), Ozone Applications in Fruit and Vegetable Processing. *Food Reviews International*, Vol.23, no.1, pp. 91-106.
[33] Khadre M.A., Yousef A.E., Kim J.G., (2001), Microbiological Aspects of Ozone Applications in Food: A Review. *Journal of food science*, Vol.66, no.9, pp. 1242-1252.
[34] Klockow P.A., Keener K.M., (2009), Safety and quality assessment of packaged spinach treated with a novel ozone-generation system. *LWT - Food Science and Technology*, Vol.42, no.6, pp. 1047-1053.
[35] Komanapalli I.R., Lau B.H., (1996), Ozone-induced damage of Escherichia coli K-12. *Applied Microbiology & Biotechnology*, Vol.46, no.5-6, pp. 610-614.
[36] Kusvuran E., Yildirima D., Mavruk F., Ceyhanb M., (2012), Removal of chloropyrifos ethyl, tetradifon and chlorothalonil pesticide residues from citrus by using ozone. *Journal of Hazardous Materials*, Vol.241-242, pp. 287-300.
[37] Łabanowska M., Kurdziel M., Filek M., (2016), Changes of paramagnetic species in cereal grains upon short-term ozone action as a marker of oxidative stress tolerance. *Journal of Plant Physiology*, Vol.190, pp. 54-66.
[38] Landesmann J.B., Gundel P.E., Martínez-Ghersa M.A., Ghersa C.M., (2013), Ozone Exposure of a Weed Community Produces Adaptive Changes in Seed Populations of Spergula arvensis. *Plos One*, Vol.8, no.9, pp.1-11.
[39] Lazukin A., Serdukov Y., Pinchuk M., Stepanova O., Krivov S., Lyubushkina I., (2018), Treatment of spring wheat seeds by ozone generated from humid air and dry oxygen. *Research in Agricultural Engineering*, Vol.64, no.1, pp.34-40.
[40] Lemic D., Jembrek D., Baok, R., Ivkovic I.P., (2020), Ozone Effectiveness on Wheat Weevil Suppression: Preliminary Research. *Insects (Basel, Switzerland)*, Vol.10, no.10, pp. 357.
[41] Lone S.A., Sathya R., Davoodbhasha M.A., Srinivasan H., Lee S.Y., (2019), An investigation on the sterilization of berry fruit using ozone: An option to preservation and long-term storage. *Biocatalysis and Agricultural Biotechnology*, Vol.20, pp. 101212.
[42] Lozowicka B., Jankowska M., Hrynko I., Kaczynski P., (2016), Removal of 16 pesticide residues from strawberries by washing with tap and ozone water, ultrasonic cleaning and boiling. *Environmental Monitoring and Assessment*, Vol.188, no.1, pp.51.
[43] Mendez F., Maier D.E., Mason L.J., Woloshuk C.P., (2003), Penetration of ozone into columns of stored grains and effects on chemical composition and processing performance. *Journal of Stored Products Research*, Vol.39, no,1, pp. 33-44.
[44] Metzger C., Barnes J.D., Singleton I., Andrew P., (2007), Effect of low-level ozone-enrichment on the quality and condition of citrus fruit under semi-commercial conditions. *IOA Conference and Exhibition*, Vol 11, pp.1-7, Valencia, Spain.
[45] Mitsugi F., Abiru T., Ikegami T., Ebihara K., Nagahama K., (2017), Treatment of Nematode in Soil Using Surface Barrier Discharge Ozone Generator. *IEEE Transactions on Plasma Science*, Vol,45, no.12, pp. 3076-3081.

[46] Mosneaga A., Nedeff V., Sandu I., Lozovanu P., Sandu I.G., (2020), Utilization of Ozone and Composite Materials in the Seed Treatment to Stimulate the Germination and Growth of Agricultural Crops. *Revista de Chimie -Bucharest- Original Edition*, Vol.71, no.2, pp. 365-370.
[47] Msayleb N., Ibrahim S., (2011), Treatment of Nematodes with Ozone Gas: A Sustainable Alternative to Nematicides. *Physics Procedia*, Vol.21, pp. 187-192.
[48] Muthukumarappan K., Halaweish F., Naidu A.S., (2000), *Natural Food Anti-Microbial Systems*, "Chapter-29 Ozone", CRC Press LLC.
[49] Normov D., Evgenii Chesniuk, Shevchenko A., Normova T., Goldman R., Pozhidaev D., Bohinc T., Trdan S., (2020), Does ozone treatment of maize seeds influence their germination and growth energy? *Acta agriculturae Slovenica*, Vol.114, no.2, pp. 251-258.
[50] Palou L., Smilanick J.L., Crisosto C.H., Mansour M., (2001), Effect of gaseous ozone exposure on the development of green and blue molds on cold stored citrus fruit. *The American Phytopathological Society*, Vol.85, no.6, pp. 632-638.
[51] Pandiselvam R., Sunoj S., Manikantan M.R., Kothakota A., Hebbar K B., (2017), Application and Kinetics of Ozone in Food Preservation. *Ozone: Science & Engineering*, Vol.39, no.2, pp. 115-126.
[52] Patil S., Valdramidis V. P., Tiwari B. K., Cullen P. J., Bourke P., (2011), Quantitative assessment of the shelf life of ozonated apple juice. *European food research & technology*, Vol.232, no.3, pp. 469-477.
[53] Patil S., Smith S.J., (2001), Irradiation and Food Safety. *FOOD TECHNOLOGY*, Vol.58, no.11, pp.48-55.
[54] Pryor A., (1999), Results of two years of field trials using ozone gas as a soil treatment agent. *Annual International Conference on Methyl Bromide Alternatives and Emissions Reductions*.US EPA and USDA San Diego, USA.
[55] Restaino L., Frampton E.W., Hemphill J.B., Palnikar P., (1995), Efficacy of ozonated water against various food-related microorganisms. *Applied and Environmental Microbiology*, Vol.61, no.9, pp. 3471-3475.
[56] Rifna E.J., Ramanan R., Radhakrishnan M., (2019), Emerging technology applications for improving seed germination. *Trends in Food Science & Technology*, Vol.86, pp. 95-108.
[57] Roustan M., Mallevialle J., Jones J.P., (2008), Mass Transfer of Ozone to Water: A Fundamental Study. *Ozone Science & Engineering*, Vol.2, no.4, pp. 337-344.
[58] Rahman S., Tian D., (2010), Inactivation effect of newly developed low concentration electrolyzed water and other sanitizers against microorganisms on spinach. *Food Control*, Vol.21, no.10, pp. 1383-1387.
[59] Sasmita E., Restiwijaya M., Yulianto E., Yuliani F.A., Kinandana A.W., (2019), Effect of ozone technology applications on physical characteristics of red cayenne pepper (Capsicum frutescens L.) preservation. *Journal of physics. Conference series*, Vol.1217, no.1, pp. 12007.
[60] Savi G.D., Piacentini K.C., Bittencourt K.O., Scussel V.M., (2014), Ozone treatment efficiency on Fusarium graminearum and deoxynivalenol degradation and its effects on whole wheat grains (Triticum aestivum L.) quality and germination. *Journal of Stored Products Research*, Vol.59, pp. 245-253.
[61] Siegel S.M., (1962), Protection of Plants Against Airborne Oxidants: Cucumber Seedlings at Extreme Ozone Levels. *PLANT PHYSIOLOGY*, Vol.3, no.37, pp. 261-266.
[62] Sintuya P., Narkprasom K., Jaturonglumlert S., Whangchai N., Peng-Ont D., Varith J., (2018), Effect of Gaseous Ozone Fumigation on Organophosphate Pesticide Degradation of Dried Chilies. *Ozone: Science & Engineering*, Vol.40, no.6, pp. 473-481.
[63] Skog L.J., Chu C.L., (2011), Effect of ozone on qualities of fruits and vegetables in cold storage. *Canadian Journal of Plant Science*, Vol.81, no.4, pp. 773-778.
[64] Souza L.P.D., Lêda R.A.F., Heleno F.F., Pinto F.G., Queiroz M.E.L.R.D., Prates L.H.F., (2017), Ozone treatment for pesticide removal from carrots: Optimization by response surface methodology. Food Chemistry, Vol.243, pp. 435-441.
[65] Stephen A.K., Linda J.M., Dirk E.M., Charles P.W., (2001), Efficacy and fumigation characteristics of ozone in stored maize. *Journal of stored products research*, Vol.37, no.4, pp. 371-382.
[66] Sudhakar N., Nagendra-Prasad D., Mohan N., Hill B., Gunasekaran M., Murugesan K., (2011), Assessing Influence of Ozone in Tomato Seed Dormancy Alleviation. *American Journal of Plant Sciences*, 2011. Vol.2, no.3, pp. 443-448.
[67] Tapp C., Rice R.G., (2012), *Ozone in food processing*, "Wiley", Chapter 4.

[68] Tawfiq M., Al- Antary T.M., Al-Dabbas M.M., Shaderma A.M., (2015), Evaluation of three treatments on carbosulfan removal in tomato juice. *Fresenius Environmental Bulletin*, Vol.24, no.3, pp.733-739.
[69] Tiwari B.K., Muthukumarappan K., (2008), Modelling colour degradation of orange juice by ozone treatment using response surface methodology. *Journal of Food Engineering*, Vol.88, no.4, pp. 553-560.
[70] Tiwari B.K., Muthukumarappan K., (2012), *Ozone in Food Processing*. Chapter 5 "Ozone in Fruit and Vegetable Processing", John Wiley & Sons, Ltd.
[71] Troyan, Jerrold J., Troyan B., Hansen, S. P., (1989), Treatment of microbial contaminants in potable water supplies. Noyes Data Co.
[72] Tzortzakis N., Singleton I., Barnes J., (2007), Deployment of low-level ozone-enrichment for the preservation of chilled fresh produce. *Postharvest Biology and Technology*, Vol.43, no.2, pp. 261-270.
[73] Vazquez-Ybarra J.A., Pena-Valdivia C.B., Trejo C., Villegas-Bastida A., Sanchez-Garcia P., (2005), Promoting growth of lettuce plants (Lactuca sativa L.) with sublethal ozone doses applied to culture medium. *Revista fitotecnia mexicana publ. por la Sociedad Mexicana de Fitogenetica*, Vol.38, no.4, pp.405-413.
[74] Venta M.B., Broche S.S.C., Torres I.F., Pérez M.G., Lorenzo E.V., Rodriguez Y.R., (2010), Ozone Application for Postharvest Disinfection of Tomatoes. *Ozone: Science & Engineering,* Vol.32, no.5, pp. 361-371.
[75] Veronico P., Paciolla C., Sasanell N., Leonardis S.D., Melillo M.T., (2016), Ozonated water reduces susceptibility in tomato plants against Meloidogyne. *Molecular Plant Pathology*, Vol.18, no.4, pp.529-539.
[76] Violleau F., Hadjeba K., Albet J., Cazalis R., Surel O., (2007), Increase of corn seeds germination by oxygen and ozone treatment, *IOA Conference and Exhibition Valencia*, pp. (3-4)1-6, Spain.
[77] Violleau F., Hadjeba K., Albet J., Cazalis R., Surel O., (2008), Effect of Oxidative Treatment on Corn Seed Germination Kinetics. *Ozone: Science & Engineering*, Vol.30, no.6, pp. 418-422.
[78] Vozmilov A.G., Ilimbetov R., Astafev D.V., (2016), The usage of ozone in agriculture technological processes. *2nd International Conference on Industrial Engineering, Applications and Manufacturing (ICIEAM)*, IEEE.
[79] Wei Di., (2011), Experiment of O_3 sterilization and its application in cage breeding (O_3灭菌试验及在舍饲养殖中的应用), *Agricultural Science & Technology and Equipment*, Vol.4, no.202, pp.75-77.
[80] Whangchai K., Uthaibutra J., Phiyanalinmat S., Pengphol S., Nomura N., (2011), Effect of Ozone Treatment on the Reduction of Chlorpyrifos Residues in Fresh Lychee Fruits. *Ozone: Science & Engineering*, Vol.33, no.3, pp. 232-235.
[81] Wu Jiangning, Doan H., Cuenc M.A., (2006), Investigation of gaseous ozone as an anti-fungal fumigant for stored wheat. *Journal of Chemical Technology & Biotechnology*, Vol.81, no.7, pp. 1288-1293.
[82] Xiaona Zhang, Zide Zhang, Lei Wang, Zhenliang Zhang, Jing Li, Congzhi Zhao., (2011), Impact of ozone on quality of strawberry during cold storage. *Frontiers of Agriculture in China*, Vol.5, no.3, pp. 356-360.
[83] Yanqiu Lv, Dongfeng Huang, Xingang Yang., (2018), Ozone Disinfection Test in Chicken House. *Animal husbandry and feed science*, Vol.10, no.02, pp. 97-98.
[84] Yangliu Wu, Quanshun An, Dong Li., Jun Wu, Canping Pan., (2019), Comparison of Different Home/Commercial Washing Strategies for Ten Typical Pesticide Residue Removal Effects in Kumquat, Spinach and Cucumber. *Annals of the American Thoracic Society*, Vol.16, no.3, pp. 1-20.
[85] Yuhua Liu., (2013), Application of Ozone Disinfection Technologies in Livestock and Poultry Breeding. (臭氧杀菌消毒技术在畜禽养殖中的应用), *Agricultural Engineering*, Vol.3 (S1), pp. 45-46+28.
[86] Zhenglong Xiong, Xiang Cheng, Dezhi Sun., (2011), Pretreatment of heterocyclic pesticide wastewater using ultrasonic/ozone combined process. *Journal of Environmental*, Vol.23, no.5, pp. 725-730.
[87] Zhang Zhijia, Liu Hongyan, Zhai Haixiang, Zhang Lina, Jiao Caiju, (2019), Effect of ozone treatment on germination of tomato and cucumber seeds (臭氧处理对番茄和黄瓜种子萌发的影响), *Journal of Northwest A & F University (Natural Science Edition)*, Vol.47, no.9, pp. 98-111.

DESIGN OF AGRICULTURAL PRODUCT COLD CHAIN LOGISTICS SAFETY MONITORING SYSTEM BASED ON INTERNET OF THINGS
/
基于物联网的农产品冷链物流安全监控系统设计

Mengmeng ZHANG[1,2*)], Jiajia REN[1,3)], Qingle QUAN[1)]
[1)]School of Logistics and E-commerce, Henan University of Animal Husbandry and Economy, Zhengzhou, 450044, China
[2)]College of Business Administration, University of the Cordilleras, Baguio City, 2600, Philippines
[3)]School of Management Science and Engineering, Dongbei University of Finance & Economics, Dalian, 116023, China
Corresponding Author: mengmeng_zhang450@163.com
DOI: https://doi.org/10.35633/inmateh-68-87

Keywords: *Internet of things; cold chain logistics; security monitoring; GPS technology; orthogonal basis neural network; multicast greedy forwarding algorithm*

ABSTRACT
In order to improve the safety of cold chain logistics transportation and the accuracy of monitoring results, a design method of agricultural products cold chain logistics safety monitoring system based on the Internet of Things is proposed. The monitoring system includes wireless sensor, embedded and GPS technologies. In order to effectively realize the management of logistics monitoring data, this paper proposes improved Leda criteria to remove outliers in information fusion, and an information transmission method based on multicast greedy forwarding (MGF) algorithm on the basis of traditional management means, thus realizing logistics vehicle monitoring and logistics information tracing. The result shows that the object loss rate of the proposed logistics supervision method is only 1.7%, which is significantly lower than other supervision methods. And the monitoring accuracy of the monitoring method proposed in the study is also significantly higher than other methods, which can achieve effective supervision in the cold chain transport process of agricultural products. The above results show that it is feasible to adopt improved methods to realize the safety monitoring of logistics cold chain transportation, which is of great significance to the external sales of agricultural products and the development of logistics technology.

摘要
为提高冷链物流运输的安全性，提高监测结果的准确性，提出一种基于物联网的农产品冷链物流安全监测系统设计方法，该监控系统中包括了无线传感、嵌入式和 GPS 技术。为了有效实现物流监控数据管理，研究提出改进莱达准则，用以去除信息融合中的异常值，并在传统管理手段基础上提出了基于多播贪婪转发（MGF）算法的信息传输方法，进而实现物流车辆监控和物流信息追溯。在结果中显示，研究提出的物流监管方法的物件丢失率仅为 1.7%，显著低于其余监管方法。并且研究提出的监控方法监控准确率也显著高于其余方法，能够实现农产品冷链运输过程中的有效监管。以上结果表明，采用改进方法实现物流冷链运输的安全监控具有可行性，对农产品的对外销售以及物流技术的发展具有重要意义。

INTRODUCTION
Agricultural products are the necessities for people to live on, and their quality and safety are becoming an increasingly prominent global issue (*Aliakbari et al., 2022*), but the current domestic focus is mainly on the production, processing and sales processes, and the safety issues in the logistics process have not been sufficiently addressed. The supply of agricultural products is still in the traditional storage and transportation mode, and there is insufficient coordination among the operating entities (*Sudrajat et al, 2021*). The lack of supervision by relevant departments in the process of agricultural product circulation, the imperfect cold chain system, and the low refrigerated transportation rate of fresh agricultural products directly lead to serious losses in the process of agricultural product logistics and frequent food safety accidents (*Uluta & Topal, 2021*). This not only seriously affects the health and safety of consumers, but also affects the sustainable development of our country's agriculture. Therefore, it is imperative to strengthen the quality and safety management of agricultural products and study the safety monitoring methods of agricultural cold chain logistics (*Moktadir et al., 2020*).

With the continuous development of logistics technology, how to improve the cold chain technology in the logistics process has become the focus of many scholars. In order to ensure the safety of the logistics cold chain, a large number of studies began to put forward security monitoring system. *Wang et al., (2019),* proposes a real-time monitoring and optimization method for cold chain logistics distribution big data, which combines Odds feature algorithm and BNS feature algorithm, and integrates variance rate and BNS feature value variance and weight to obtain the dynamic characteristics of cold chain logistics distribution big data. The maximum position of the similarity function is obtained according to the dynamic features, and the adaptive weighting and feature selection are determined by the Bhattacharyya coefficient to complete the positioning of the target data in the process of cold chain logistics distribution, , thus realizing the real-time tracking and monitoring of logistics. The simulation results show that the dynamic features obtained by this method have high reliability and high accuracy of target positioning results, but there is a problem of high loss rate of logistics information. *Yu, (2019),* designs a new multi-mode automatic monitoring system for ship logistics information based on wireless network technology. Build a logistics terminal information transceiver as the bottom-end hardware equipment for logistics information monitoring, collect logistics information in time, and prepare a CDMA data core network transmission module based on the wireless network transmission protocol to connect the logistics data terminal transceiver and the current local area network. Build network access protocols between different local area networks, use random codes of monitoring information to ensure local area network carrier synchronization, reduce data transmission barriers, and realize automatic monitoring of multi-mode ship logistics information. The experimental data proves that after the application of the monitoring system, the read-in rate and read-out rate of ship logistics information have been improved, and the data transmission delay has been effectively reduced, but there is the problem of inaccurate monitoring results. *Hu, (2021),* mainly designs the intelligent logistics tracking and supervision system for leather enterprises, and completes the construction of the overall system architecture. Through the comprehensive application of core technologies such as the Internet of Things, sensors, RFID, barcode, GPS/GIS positioning, etc., the logistics tracking process including data collection, comprehensive analysis, query and dynamic monitoring functions has been realized. The structure and realization path of the software system and database are expounded, so as to realize the timely grasp of the dynamic information of leather transportation and logistics. Reference is provided for improving the transportation quality and efficiency of leather enterprise products. However, this method has the problem that the monitoring effect of logistics transportation path is not good.

It can be seen from the current research situation that a large number of scholars have proposed effective methods for the cold chain safety monitoring in the logistics process, but it is worth mentioning that, restricted by traditional monitoring methods, most of the safety monitoring effects are not ideal. For this reason, the research is based on the Internet of Things technology, introduces wireless sensor networks, embedded technology, and at the same time combines GPS positioning technology in the security monitoring to achieve the logistics and transportation monitoring of agricultural products. In order to ensure the safety of cold chain transportation in the logistics and transportation process, a security monitoring system of agricultural cold chain based on the Internet of Things is designed, in order to provide ideas for the sales of agricultural products and the development of logistics and transportation technology.

MATERIALS AND METHODS

Analysis of the cold chain logistics system of agricultural products

Design goals of safety monitoring system

According to the characteristics of the cold chain logistics system of agricultural products, the Internet of Things technology (*Civelek, 2020*) is combined with the cold chain logistics of agricultural products, and it is applied to real-time information collection, real-time control, real-time data storage and analysis, and logistics cargo information management in the process of agricultural cold chain logistics, through the Internet of Things technology to realize the intelligent monitoring of agricultural cold chain logistics, improve the quality and efficiency of agricultural cold chain logistics, and improve the monitoring effect of agricultural cold chain logistics (*Markande et al., 2021*). In addition, in terms of improving the effectiveness of monitoring data, algorithms such as information signature and GF are used to realize data transmission and fusion, to avoid redundancy and complexity caused by data transmission, and to improve data processing effects, realize the automatic processing of agricultural product logistics cargo information, and improve the efficiency and automation level of agricultural product logistics cargo information management.

Design of agricultural product cold chain logistics safety monitoring system

According to the analysis of the composition of the cold chain logistics system of agricultural products and the design goals of the monitoring system, a monitoring system of the cold chain logistics of agricultural products is constructed. Combined with the existing advanced technology, the design scheme of safety monitoring system was formulated, the work flow of the system was designed, and the design of the overall agricultural product cold chain logistics monitoring system was completed.

Overall architecture of agricultural product cold chain logistics safety monitoring system

The design of agricultural product cold chain logistics monitoring system mainly uses wireless sensor technology (*Karunanithy & Velusamy, 2019*), embedded technology and GPS technology (*Chen, 2019*).

Fig.1 is a schematic diagram of the overall architecture of the agricultural product cold chain logistics safety monitoring system.

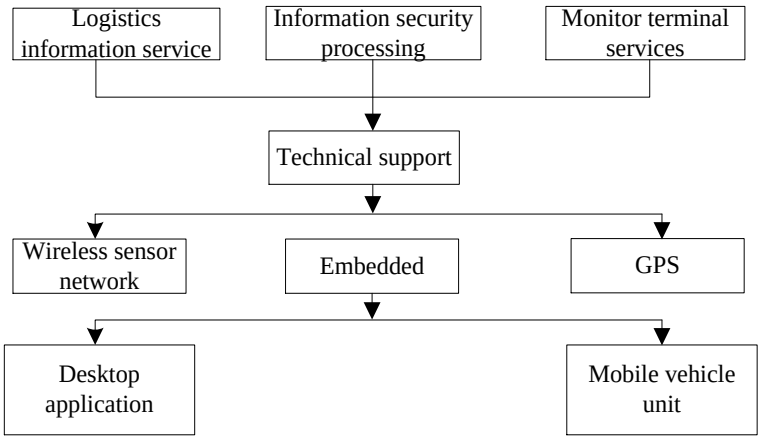

Fig. 1 - Overall architecture of agricultural product cold chain logistics safety monitoring system

Logistics information collection is realized through wireless sensor networks. Sensor nodes can be distributed anywhere in the monitoring area according to the requirements of monitoring or data collection. The coordinator node is connected with the sensor node through wireless communication, which is mainly used to receive the data uploaded by the sensor node, sort and summarize the received data uploaded by each sensor, and upload it to the superior general coordinator, or directly upload the sorted and summarized data to the monitoring center or data center for storage through remote communication.

In order to simplify the development process and improve the overall development efficiency and speed of the system, this paper uses an embedded development board with rich hardware resources as the hardware basis of the agricultural product cold chain logistics monitoring system. Its model is Tiny4412 embedded ARM development board, which has rich interface resources, supports a variety of communication interfaces and protocols, and the main control chip has a strong data processing capability, which can fulfill the data processing capability requirements of various data processing tasks. This paper uses the widely used and easy-to-use Android desktop operating system at this stage as the computer operating system of the embedded development board. The version of Android desktop operating system is Android 4.0, builds the program development environment of Android desktop operating system, and develops the desktop application of agricultural cold chain logistics monitoring system based on Android desktop operating system to meet the functional requirements of real-time acquisition of monitoring information.

The mobile vehicle-mounted unit collects the geographical location information of the logistics vehicle through GPS, collects the logistics information through the wireless sensor network, the monitoring center receives the data and transmits it to the database, uses the GPS to monitor the traveling status of the vehicle, and obtains the logistics transportation path, transit time, refrigerated temperature, and shelf period and other information. Fig.2, is the working principal diagram of the mobile vehicle-mounted unit (*Ejigu et al., 2021*).

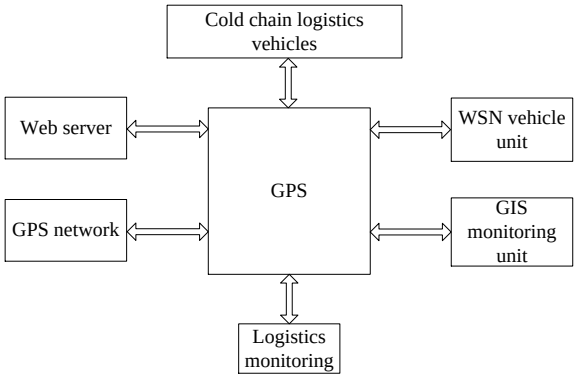

Fig. 2 - Working principal diagram of mobile vehicle-mounted unit

Agricultural cold chain logistics information processing

Collection of logistics information

In the process of collecting agricultural product cold chain logistics information, the data of the cold storage and the data of the refrigerated truck are transmitted to the data center through the corresponding transmission network, so that the data center has all the data in the agricultural product cold chain logistics process. The data center can be a management center established by the government, third-party logistics, or enterprise, etc. It can monitor the cold chain logistics process of all agricultural products it manages, check the status or flow of agricultural products at any time, and realize the traceability of agricultural products. The data center is connected to the outside world, and ordinary consumers can check the production or logistics process of agricultural products at any time through the networked PC or mobile phone to ensure the safety of the purchased agricultural products. If you want to track a certain agricultural product, it is very easy to achieve this because the data center records all the data in the agricultural product logistics process.

In order to ensure the security of logistics information, the security control of logistics information processing stage mainly adopts information signature algorithm. The information signature algorithm can realize the integrity and non-repudiation of information, which refers to the information exchange attached to the information unit, which can protect the information and prevent it from being forged.

The principle of the information signature algorithm is shown in Fig.3.

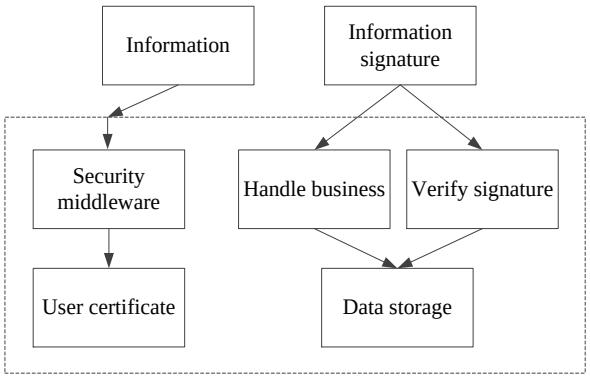

Fig. 3 - Principle of information signature algorithm

Denote the collected logistics information as F_i, the information signature algorithm process is:

$$F_i^* = \frac{\tau_{ij} \times \eta_{ij}}{\sum_{i,j=1}^{N} A_i + B_j} \quad (1)$$

In the formula: F_i^* represents the signed logistics information; N represents the total quantity of the logistics information; A_i and B_j represent the logistics information processing parameters; η_{ij} and τ_{ij} represent the logistics information signature factor, and the signature factor of each logistics information is different.

Logistics information fusion

Orthogonal basis neural network is used to fuse the collected logistics information (*Yousuf & Kadri, 2020*), and the logistics information is represented by a cosine basis function set $X(k)$. In order to make the logistics information general, the orthonormal basis function set is used to approximate any nonlinearity.

The set of transform cosine basis functions $X(k)$ is expressed as follows:

$$X'(k) = \frac{1}{2}\sum_{k=1}^{N}\left(x_k - \bar{x}_k\right)^2 \quad (2)$$

In the formula: $X'(k)$ represents the orthogonal basis function set, which is used as the excitation function of the neural network; x_k and $\bar{x}_k$ represent the orthogonal polynomial.

The topology of the neural network is set to 1 × 3 × 1, that is, an input a, an output $b(a)$, a hidden layer with M orthogonal functions as the excitation function, and the neural network weight is $w_1, w_2, ..., w_m$ (*Hartmann et al, 2019*). The neural network training sample set is a_i, where $i - 1, 2, ..., m$, then the cosine-based neural network output is:

$$b(a_i) = \int_{-\infty}^{\infty} \cos(\theta_k) e^t \times E(k) \quad (3)$$

In the formula: $E(k)$ represents the error function; e^t represents the performance index. The expressions of the two are:

$$E(k) = \int_{t_0}^{t} |h(t)| \cos(\theta_k) \quad (4)$$

$$E(k) = e(D_t) \times \delta(S_t) \quad (5)$$

where: $h(t)$ represents the cosine center loss function; $e(D_t)$ represents the reliability function of the data; $\delta(S_t)$ represents the tolerance function between the data.

The multiple sets of data collected are trained, and the neural network weight vector W is obtained. In order to calculate the result of monitoring information fusion, the average value of all neural network outputs is calculated, and this value is the result of logistics information fusion.

Temperature data abnormal value processing

In the process of transportation and storage of agricultural products, it is necessary to monitor the ambient temperature in real time. However, in actual situations, transfer errors often occur due to abnormal conditions such as measuring instrument failures and sudden changes in ambient temperature, resulting in large errors in the temperature at a certain moment, therefore, it is necessary to deal with outliers of temperature data and reduce the interference items of data fusion. Generally speaking, sensors with equal precision are used to measure the ambient temperature parameters of refrigerated vehicles, so the measured data conform to the normal distribution (*Hasebe et al., 2019*), and the Laida criterion is used to remove bad values with large error values.

Use equal-precision sensors to measure the ambient temperature parameters of the refrigerated truck under test, obtain temperature data $T_1, T_2, ..., T_n$ independently, and calculate its average value:

$$\bar{T} = \frac{1}{n}\sum_{i=1}^{n} T_i \quad (6)$$

Further calculate the residual error:

$$R_E = \frac{1}{\sqrt{1 - \left(K_H^2 + K_H\right)}} \quad (7)$$

In the formula: K_H^2 represents the theoretical error; K_H represents the excess mean square error.

Calculate the standard error according to formula (8):

$$S^2 = R_e - \frac{|R(t)|^2 \times f_s}{|R_c(t)|} \quad (8)$$

In the formula: $|R(t)|^2$ represents the outliers of the original data; f_s represents the dispersion of the data; $|R_c(t)|$ represents the standard deviation error limit.

The outliers are removed according to the improved Laida criterion. If the residual error R_E of a certain measurement value T_i satisfies $|R_E| > 2S$, then T_i is considered to be an outlier with a larger error value and should be removed. After removing the outliers, recalculate the arithmetic mean, residual error, and standard error of the remaining measurement values, and then judge whether the residual error is greater than the standard error, remove new outliers, and so on, until no new outliers appear. When outliers occur, the corresponding sensors should be marked and warned, and technical and physical errors should be found as much as possible so that they can be corrected in time.

In order to determine the temperature of a single sensor at a certain moment during the logistics and transportation of agricultural products, it is necessary to estimate multiple temperature data collected by the sensor in the previous period of time. The L monitoring values $T_{p1}, T_{p2}, ..., T_{pl}$ retained after removing outliers from the improved Laida criterion are equally divided into two groups in chronological order, and the sample averages of the two groups of monitoring values are:

$$\begin{cases} \overline{T_{p1}} = \dfrac{\sum_{i=1}^{n} S_i I_i}{L_n} \\ \overline{T_{p2}} = \sum_{i,j=1}^{n} \left(y_i - y_j \right)^T \end{cases} \tag{9}$$

where: S_i represents the allowable error of the sample mean; I_i represents the sample density; L_n represents the average of all monitoring values; y_i and y_j represent the relative error.

At this point, the standard deviation of $\overline{T_{p1}}$ and $\overline{T_{p2}}$ is:

$$\begin{cases} S_{p1}^2 = \dfrac{1}{L} \sum_{i=1}^{n} \left(T_{pi} - \overline{T_{p1}} \right)^2 \\ S_{p2}^2 = \sum_{i=1}^{n} \left(T_{pi} - \overline{T_{p2}} \right)^2 \end{cases} \tag{10}$$

According to the weighted least squares estimation theory, the local estimation value of a single temperature sensor can be obtained as:

$$\overline{T_p} = S_{pi}^2 / \sum_{i=1}^{n} \max\left(\overline{T_i} \right) \tag{11}$$

Using the variance of the local estimated value $\overline{T_p}$ of a single temperature sensor and the final temperature fusion value $\overline{T_i}$, under the optimal condition of the minimum total mean square error, the weight of each sensor is adaptively adjusted to find the optimal weighted value of each sensor. The larger the variance, the smaller the weight, to minimize the influence of the temperature sensor with larger error on the final temperature fusion value.

Monitoring data upload

The integrated logistics monitoring information is uploaded to the monitoring center or data center for storage and application. This step is mainly realized by the greedy forwarding algorithm. In the greedy forwarding (GF) algorithm, the node selects the node closest to the destination node among its neighbor nodes as the forwarding node until the destination node (assuming that the density of sensor nodes is large enough and there is no empty area problem) (*Wang et al., 2021*). During data upload, the sensor node sends data to multiple reaction nodes, and calculates the optimal transmission path for each reaction node according to the GF algorithm. The transmission path is shown in Fig. 4(a).

The GF algorithm has the best performance in real-time performance, but its energy efficiency is poor. Through the study of Fig. 4(a), it can be found that the same data is transmitted on multiple paths, which is easy to cause waste of energy, so the multicast algorithm is introduced idea, forming a propagation path as shown in Fig. 4(b) (*Raei, 2020*). In this way, only one data packet is transmitted on the common transmission path, which greatly reduces energy consumption.

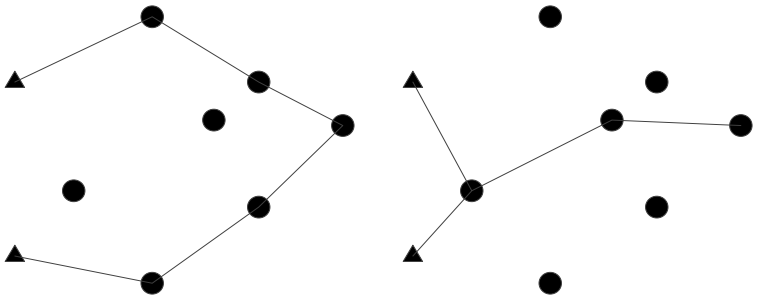

(a) GF algorithm path (b) Improved path

Fig. 4 - Monitoring data upload path

By introducing the idea of multicast to modify the greedy forwarding (GF) algorithm, this paper proposes the multicast greedy forwarding (MGF) algorithm to construct a multicast tree from sensor nodes to its Z destination response nodes. Since only one data packet is transmitted on the common transmission path, in order to shorten the transmission path distance and improve the transmission efficiency, the following constraints are set:

$$\sum_{g\in G}^{N} Z_{gi} \le 1 \tag{12}$$

$$\sum_{g\in G}^{N} Z_{gz}^{\alpha} - \sum_{g\in G}^{N} Z_{gz}^{\beta} = 1 \tag{13}$$

$$H_i \le \sum_{i=1}^{N} J_{iz} < H_j \tag{14}$$

where: H_i and H_j represent the energy cost function between nodes; J_z represents a binary variable that reflects whether node z is the data receiver of the source node, when z is the data receiver, the variable is 1, otherwise it is 0; Z_{gz}^{α} represents a binary variable. When the sensor node sends data to the response node z, and the link connecting the node is on its transmission path, the variable value is 1, otherwise it is 0.

According to the above analysis, the main idea of MGF algorithm is to make the common paths of multicast tree as many as possible (the total transmission paths as few as possible), that is, under the common constraints of formula (12) ~ formula (14), the following objective function is achieved:

$$\min \sum_{z\in Z}^{n} \sum_{g\in G}^{n} Z_{gz}^{\alpha\beta} \tag{15}$$

In order to improve the real-time performance of monitoring data upload, the main method used in this paper is to select the appropriate communication mode of data transmission to improve the communication effect. In the process of design, the system adopts general wireless packet service technology, which is a common mobile communication technology. Now it has been widely used in personal mobile communication services and the application field of Internet of things. It is a common way of data transmission and communication of Internet of things. It has the advantages of many base stations, wide coverage, good communication effect, low price of communicator, simple installation and easy maintenance, etc. It meets the requirements of stable communication and wide coverage of the system, and is suitable for real-time data upload communication in the process of agricultural cold chain logistics.

Logistics vehicle monitoring

The agricultural product cold chain logistics vehicle monitoring process is that after the goods are loaded from the warehouse, they will be transported safely and quickly through various places, and finally the goods will be delivered to the destination for unloading, and the logistics vehicle transportation monitoring will be completed. With the support of the Internet of Things technology, the logistics vehicle monitoring system uses sensing equipment to collect information on vehicle transportation starting points, transportation destinations, vehicle positioning, and cargo information, and transmits the collected data to the monitoring center through the wireless network. The center processes the collected data, realizes the real-time viewing of the tracking track, the scheduling of vehicles, etc., so as to realize the monitoring of logistics vehicles.

The monitoring link of logistics vehicles is mainly divided into three parts: vehicle terminal, server part and monitoring center, and its overall structure is shown in Fig 5. Among them, the main function of the vehicle terminal is information collection, which is controlled by an ARM processor (*Marquez et al., 2020*), integrates GPS positioning module, RFID module, and sensor module to collect various data, and realizes two-way network communication with the server through the transparent transmission mode of the CDMA module. The touch screen module provides simple interaction for the driver. The server part mainly runs in the background to process various data streams. The monitoring center receives the data processed by the server and stores it in the local database, which is convenient for data access and completes the functions of data visualization and user interaction.

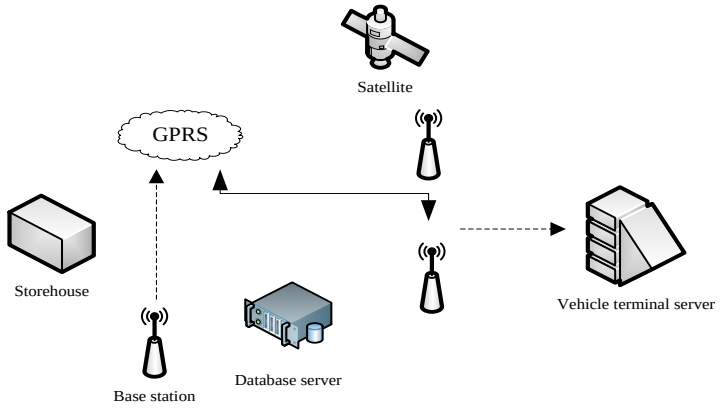

Fig. 5 - Overall architecture of logistics vehicle monitoring

According to Fig. 5, the on-board terminal is installed on the transportation vehicle, mainly used for information collection (longitude, latitude) and cargo label information collection of the transportation vehicle, and transmits the collected data to the monitoring center through the wireless network in real time. Therefore, the vehicle terminal integrates a GPS module, an RFID module and a wireless communication module. Among them, the GPS module used in the vehicle terminal has the advantages of low power consumption, which can realize the ability to quickly locate and track 12 satellites. The chip has built-in 1920 times/frequency hardware, which improves the reception and transmission of satellite signals. The working frequency band of the RFID module is 840 Hz to 960 Hz, and with the cooperation of a standard 8 dBi antenna, the reading distance can reach 10 m. The CDMA wireless communication module is a communication module that integrates communication chips, memory chips, etc. on a circuit board. Based on the CDMA platform integration, it has functions such as sending and receiving short messages, voice calls and data transmission.

Traceability of logistics information

In the cold chain logistics supply chain of agricultural products, several commonly used information representation technologies are one-dimensional code, two-dimensional code, and RFID. Among them, the one-dimensional code contains the name, batch, price and other information of the commodity, has automatic identification function, and the cost is low, but the amount of information is small, it is easily affected by deformation and corrosion, the reliability is average, and it does not have the traceability function; The QR code not only has the function of identification, but can also contain detailed product information, such as item ID, origin code, production date, packaging date, service website, manufacturer's product catalog, etc. In addition, it also has an anti-tampering function.

Manufacturers can generate a QR code after encrypting the code software to prevent logistics companies and retail companies from changing information at will; RFID can be used for product traceability, with waterproof, high temperature resistance, and relatively long reading distance, and other advantages, but the cost is high and the amount of stored information is small (*Kabatiansky, 2019*). Table 1 shows the comparison results of the three identification techniques.

Table 1

Comparison of identification techniques

Information identification technology	Cost	Reliability	With traceability function
One-dimensional code	Lower	Generally,	Does not have
QR code	Lower	Better	Have
RFID	Higher	Better	Have

According to the analysis results in Table 1, and considering the environment and time requirements of products in the cold chain logistics of agricultural products, this paper adopts the combination of two-dimensional code and GPS to realize the traceability of agricultural products. In the field of logistics, traceability can be divided into forward traceability and reverse traceability in terms of time. The product from the factory to the consumer belongs to the forward traceability. In this paper, the cold chain logistics starts from the factory, and the QR code label is attached to the product. The information includes product ID, origin, production date and other information. During the transportation of the product, the refrigerated truck will adjust the temperature according to the transportation requirements of the product, and wireless sensor nodes are installed in the vehicle to monitor the temperature inside the vehicle in real time. The refrigerated truck is also equipped with a GPS positioning system, which can provide real-time information on the location, speed, and current time of the vehicle, and report it to the disposal monitoring center. The product is traceable from the consumer to the factory. Consumers can scan the QR code label of the product with the mobile terminal to obtain the product ID, origin, production date and other information, and query the temperature and humidity information during the transportation of agricultural products through the service website (*Behkami et al., 2019*).

To sum up, the security monitoring system of agricultural product cold chain logistics based on the Internet of Things designed in this paper, the security monitoring system covers all aspects of cold chain logistics transportation. It can not only obtain logistics transportation information in real time, but can also realize the fusion processing of logistics data, to provide reliable monitoring results and improve the monitoring effect of cold chain logistics of agricultural products.

RESULTS

In order to verify the effectiveness of the design method of agricultural products cold chain logistics security monitoring system based on Internet of things, the monitoring results of this method are compared with the cold chain logistics distribution big data real-time monitoring optimization method (method 1) and the design method of ship logistics information automatic monitoring system based on wireless network technology (method 2).

Experimental environment and data settings

The experimental running environment is as follows: Windows 10 operating system, Genuine Intel(R) CPU, 1.73GHz, 8GB memory. After the agricultural product cold chain logistics monitoring system starts to operate, each monitoring node in the carriage starts to collect data, and the coordinator starts to integrate the data uploaded by the monitoring node, the GPS geographic information data and RFID electronic label cargo data obtained by the coordinator, and prepares upload as experimental data.

Analysis of experimental results

(1) Loss rate of logistics information

Taking the loss rate of logistics information as the experimental index, the three methods of agricultural cold chain logistics safety monitoring are compared, and the results are shown in Fig. 6.

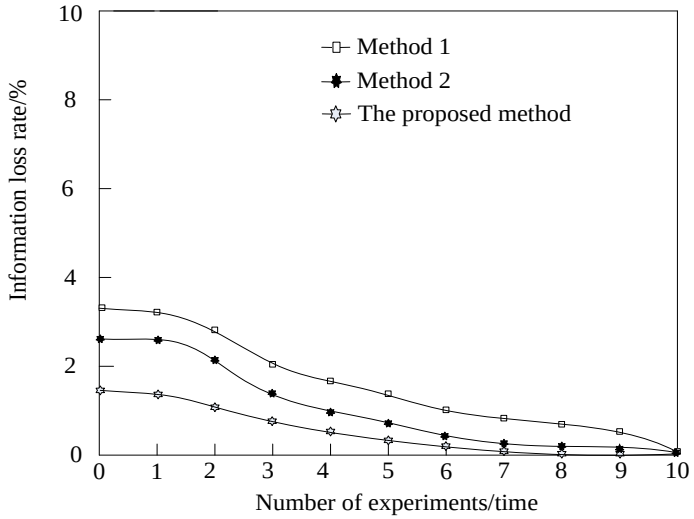

Fig. 6 - Comparison results of logistics information loss rate

According to Fig. 6, with the increase of the number of experiments, the logistics monitoring information loss rate of the three methods shows a downward trend. Among them, the maximum logistics monitoring information loss rate of method 1 is 3.1%, the maximum logistics monitoring information loss rate of method 2 is 2.6%, while the maximum logistics monitoring information loss rate of the proposed method is only 1.7%, and the logistics monitoring information loss rate of the proposed method is always lower than that of method 1 and method 2. The experimental results show that compared with the existing methods, the proposed method greatly reduces the loss rate of logistics information, which fully shows that this method has better security effect. The monitoring results of the proposed method are more comprehensive, can retain more cold chain logistics monitoring information, and provide a more comprehensive reference for agricultural product monitoring.

(2) Tracking effect of logistics vehicle transportation path

Taking the tracking effect of the logistics vehicle transportation path as the experimental index, the safety monitoring effect of the three methods of agricultural cold chain logistics was compared. Fig. 7 shows two distribution lines from the distribution center to the warehouse, and analyzes the line monitoring effects of the three methods.

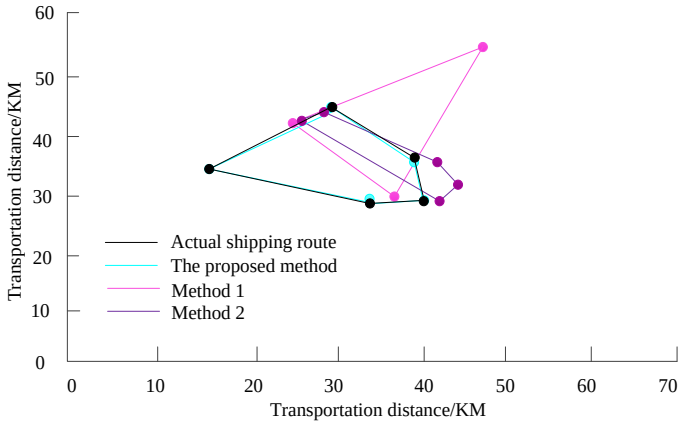

(a) Line 1

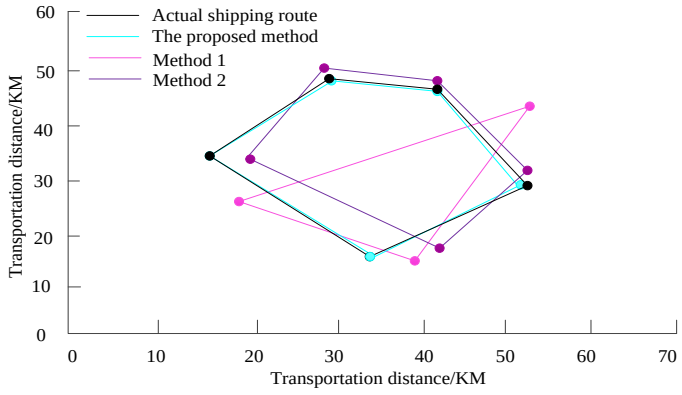

(b) Line 2

Fig. 7 - Tracking effect of logistics vehicle transportation path

According to Fig. 7, when the proposed method is used to track the transportation path of logistics vehicles, the tracking path of both line 1 and line 2 is basically the same as the actual transportation path, while the tracking paths of methods 1 and 2 show varying degrees of deviation. It can be seen that the path tracking effect of the proposed method is better.

(3) Accuracy of monitoring results

Taking the accuracy of the monitoring results as the experimental index, the monitoring effects of the three methods of agricultural cold chain logistics safety are compared, and the comparison results are shown in Fig. 8.

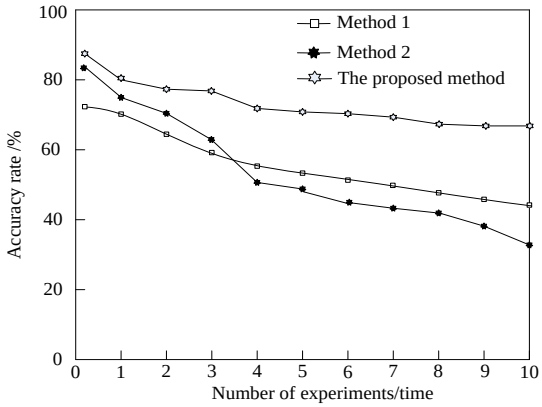

Fig. 8 - Comparison of the accuracy of monitoring results

According to Fig. 8, the accuracy of the monitoring results of the proposed method is always higher than that of method 1 and method 2. Although the accuracy of the monitoring results shows a gradual downward trend, its advantages are still very obvious. By comparison, it can be seen that the highest monitoring accuracy rate is 88%, and the lowest value is 76%, which is higher than the traditional method, which verifies the monitoring effect of the proposed method.

CONCLUSIONS

In order to improve the safety of cold chain logistics transportation and improve the accuracy of monitoring results as the research goals, a design method of agricultural product cold chain logistics safety monitoring system based on the Internet of Things is proposed. With the support of wireless sensing, embedded and GPS technologies, a safety monitoring system for cold chain logistics of agricultural products is designed. It not only improves the accuracy of monitoring results, but also ensures the monitoring effect. The experimental results show that the maximum information loss rate of the proposed method is only 1.7%, the tracking path is basically the same as the actual transportation path, and the monitoring results are more accurate.

ACKNOWLEDGEMENT

The research is supported by: 2022 Henan Science and Technology project "Research on gas sensing technology and modeling method for cold chain logistics Quality perception of fruits and vegetables", (Project No.: 222102110245).

REFERENCES

[1] Aliakbari, A., Komijan, A. R., Tavakkoli-Moghaddam, R, Najafi, E. (2022). A new robust optimization model for relief logistics planning under uncertainty: a real-case study. *Soft Computing*, 26(8), 3883-3901. https://doi.org/10.1007/s00500-022-06823-4

[2] Behkami, S., Gholami, R., Gholami. M., Roohparvar, R. (2019). Precipitation isotopic information: A tool for building the data base to verify milk geographical origin traceability. *Food Control*, 107(2), 106780. https://doi.org/10.1016/j.foodcont.2019.106780

[3] Chen, G. (2019). Application of GPS technology in space geological survey. *Arabian Journal of Geosciences*, 12(23), 1-5. https://doi.org/10.1007/s12517-019-4842-x

[4] Civelek, C. (2020). Evaluation of Internet of Things (IoT) Technology to Be Used as a Precision Agriculture Solution for Turkey's Agriculture. *Fresenius Environmental Bulletin*, 29(7), 5689-5695.

[5] Ejigu, Y. G., Teferle, F. N., Klos, A., Janusz, B., Hunegnaw, A. (2021). Monitoring and prediction of hurricane tracks using GPS tropospheric products. *GPS Solutions*, 25(2), 1-15. https://doi.org/10.1007/s10291-021-01104-3

[6] Hartmann, C., Opritescu, D., Volk, W. (2019) An artificial neural network approach for tool path generation in incremental sheet metal free-forming. *Journal of Intelligent Manufacturing*, 30(2), 757-770. https://www.researchgate.net/publication/310434912

[7] Hasebe Takahiro, Sakuma Noriyoshi, Thorbjrnsen Steen. (2019). The Normal Distribution Is Freely Self-decomposable. *International Mathematics Research Notices*, 2019(6), 1758–1787. https://doi.org/10.1093/imrn/rnx171

[8] Hu, J. H. (2021). Design of intelligent logistics tracking and supervision system for leather enterprises. *China Leather*, 50(11), 40-43+54.
[9] Kabatiansky, G. A. (2019). Traceability Codes and Their Generalizations. *Problems of information transmission*, 55(3), 283-294.
[10] Karunanithy, K., Velusamy, B. (2019). CSDGP: cluster switched data gathering protocol for mobile wireless sensor networks. *IET Communications*, 13(18), 2973-2985. https://doi.org/10.1049/iet-com.2018.6152
[11] Markande, A., Dheeraj, R. (2021). Automated Irrigation System using IOT. *Solid State Technology*, 64(2), 4740-4746. https://www.researchgate.net/publication/356171899
[12] Marquez, R. C., Sarmiento, A., Sanchez-Solano, S. (2020). Implementing Cryptographic Pairings on ARM dual-core Processors. *IEEE Latin America Transactions*, 18(2), 232-240. https://doi.org/10.1109/TLA.2019.9082233
[13] Moktadir, M. A., Rahman, T., Ali, S. M., Nahar, N., Paul, S. K. (2020). Examining barriers to reverse logistics practices in the leather footwear industry. *Annals of Operations Research*, 293(2), 715-746. https://www.researchgate.net/publication/337101862
[14] Raei, M., Ghehsareh, H. R., Galletti, A. (2020). An adaptive sparse kernel technique in greedy algorithm framework to simulate an anomalous solute transport model. *Engineering Analysis with Boundary Elements*, 121(10), 243-254. https://doi.org/10.1016/j.enganabound.2020.10.003
[15] Sudrajat, A., Sudirman, I., Prasetyo, R. (2021). Digitalization of Logistics Processes and Comparison with Several Asian Countries Related to Logistics Information Systems: Propositions of National Logistics System Architecture. *Solid State Technology*, 63(3), 2824-2836. https://www.researchgate.net/publication/348505792
[16] Uluta, A., Topal, A. (2021). A new hybrid model based on rough step-wise weight assessment ratio analysis for third-party logistics selection. *Soft Computing*, 26(4), 2021-2032. https://dl.acm.org/doi/10.1007/s00500-021-06374-0
[17] Wang, X., Li, X., Hou, B., Liu, W., Gao, S. (2021). A greedy algorithm for the fault-tolerant outer-connected dominating set problem. *Journal of Combinatorial Optimization*, 41(7), 1-10. https://link.springer.com/article/10.1007/s10878-020-00668-z
[18] Wang, Y., Zhao, Z. (2019). Cold Chain Logistics Distribution Big Data Real-Time Monitoring Optimization Simulation. *Computer Simulation*, 36(03), 385-388+443.
[19] Yu, L. (2019). Design of multi-mode ship logistics information automatic monitoring system. *Ship Science and Technology*, 41(18), 196-198.
[20] Yousuf, S., Kadri, M. B. (2020). Information Fusion of GPS, INS and Odometer Sensors for Improving Localization Accuracy of Mobile Robots in Indoor and Outdoor Applications. *Robotica*, 39(2), 1-27. https://doi.org/10.1017/S0263574720000351

BENCH TESTS AND PARAMETERS OPTIMIZATION OF ONBOARD SEED COTTON CLEANER
/
机载籽棉预处理机台架试验及参数优化

Yongfei SUN, Lei SHI, Fanting KONG, Qing XIE, Teng WU, Changlin CHEN *[1]
Nanjing Institute of Agricultural Mechanization, Ministry of Agriculture and Rural Affairs, Nanjing, 210014/China
Tel: +86-025-58619528; E-mail: sunyongfei86@163.com
DOI: https://doi.org/10.35633/inmateh-68-88

Keywords: *seed cotton, stripper harvester, cleaner, response surface method, parameter optimization*

ABSTRACT

The working quality of a cotton stripper harvester is limited by the efficiency of onboard seed cotton cleaners. As a basis for research in the design of a cotton stripper harvester prototype, the bench cleaning tests were designed to study the effect of structural and technological parameters on the loss rate and impurities rate of the cleaner. According to the features of different test factors, a combined orthogonal test was applied to determine the best combination of the sawtooth distance, saw cylinder diameter, and cleaning distance. With these parameters fixed, the optimal parameters for the cleaning distance, saw cylinder rotating speed, and brush thickness were obtained using a quadratic-regression rotatable orthogonal test. The best parameter configuration to ensure the cleaning quality of the onboard seed cotton pre-cleaner included the following structural parameters: sawtooth distance of 38 mm and saw cylinder diameter of 340 mm, and technological parameters: rotating speed of 282–288 rpm, clearance of 12.55–14.84 mm, and brush thickness of 8.37–9.69 mm, which decreased the loss rate to less than 10% and the impurities rate to less than 6%. The reliability of the theoretical analysis results was verified by a comparison with experimental results. The experimental results provide a theoretical basis and technical reference for the research and the structural design of seed cotton pre-cleaners.

摘要

针对统收式采棉机作业质量受限于机采籽棉预处理装置清理效率的问题，设计机采籽棉预处理清理作业试验台架。以含杂籽棉为研究对象，研究籽棉清理过程中锯齿间距、锯齿辊直径、锯齿辊转速、排杂棒间距、毛刷厚度等因子对损失率，含杂率的影响，并进行优化分析，确定清理单元结构及工艺的最优组合参数。根据试验因素特点，采用响应面优化设计试验，得到锯齿间距、锯齿辊直径、锯齿辊转速、排杂棒间距的最优参数组合。结果表明：锯齿间距 38 mm，锯齿辊直径 340 mm 时，最优参数组合为锯齿辊转速 282-288 rpm，排杂棒间距 12.55-14.84 mm，毛刷厚度 8.37-9.69 mm，机载籽棉预处理机清选损失率降至 10%以下，含杂率低于 6%。通过试验验证结果可信，可为机采籽棉预处理装置相关研究和结构设计提供理论依据。

INTRODUCTION

Cotton is one of the important cash crops and raw material for textile industry in China. In recent years, the problem of labor shortage has become increasingly prominent, which has seriously limited the development of Chinese cotton industry. Therefore, promoting mechanized cotton picking is an inevitable trend to realize the sustainable development of cotton industry. The mainstream model used in China is the horizontal spindle type cotton picker produced by John Deere and other foreign companies. This type is too large to adapt to the small and medium-sized cotton fields in the Yangtze River and Yellow River basin. Therefore, it can't be popularized in all cotton regions in China. The stripper harvester, which has the advantages of wide range of adaptation and low price, has shown great potential for development. But its shortcomings of high impurity rate have become the main bottleneck hindering its popularization and development. Therefore, it is of great significance to develop an onboard seed cotton cleaner with high efficiency and excellent performance to reduce the seed cotton impurity rate of the stripper harvester and promote the process of cotton picking mechanization in China.

[1] *Sun Yongfei, A.P.; Shi Lei, Prof.; Kong Fanting, MS.Eng.; Xie Qing, MS.Eng.; Wu Teng, MS.Eng.; Chen Changlin*, Prof.*

With the rapid development of the cotton industry, new seed cotton processing technology and equipment have constantly emerged since the Industrial Revolution (*Mao et al., 2017*). The former Soviet Union, the United States, Germany, and other countries are committed to research on related theories, thereby promoting the development of world cotton processing and cleaning technology. Francis et al. proposed a kind of onboard cleaner that primarily uses air flow to separate cotton bolls and seed cotton (*Francis et al., 1969*). Akin et al. designed a cleaning device with adjustable and pre-opening functions. Deutsch introduced onboard seed cotton cleaner with a single-stage cleaning cylinder and a single-stage reclaimed cylinder (Deutsch et al., 1999), whereas Sanderson et al. used an air diverter that is added to the end of the cotton transport pipeline to clean the broken leaves before seed cotton enters the hopper (Sanderson et al., 1990). Patel et al. designed a cotton cleaning device for seed cotton stripper harvesters (*Patel et al., 2002*). Wanjura et al. tested the effect of different intersecting surfaces of the cleaning bar on impurity removal, seed cotton loss, and cotton fiber quality, and optimized the cleaner by establishing a mathematical model and response surface analysis of the impurities rate and loss rate (*Wanjura et al., 2013*). However, most of these research results and equipment have been applied for handpicked seed cotton (*Chen et al., 2015*), and only a few cleaning technology studies have used seed cotton harvested by cotton strippers that contains impurities, like branches and boll shells (*Kazama et al., 2015*). The cleaning of seed cotton harvested by stripper harvesters mainly relies upon the cleaning unit composed of a saw cylinder, brush roller, and cleaning roller. Most of the existing stripper harvesters are equipped with a cleaner consisting of two-stage or multi-stage cleaning units (*Huang et al., 2016*). However, some problems occur with onboard cleaners, such as the incomplete separation of seed cotton and impurities, high loss rate of seed cotton, high power consumption, and poor stability during harvesting.

With the aim of solving these onboard seed cotton cleaner problems, we conducted an experiment on the effects of five factors-sawtooth distance, diameter of the saw cylinder, rotating speed saw cylinder, clearance, and brush thickness-on the loss rate and impurities rate in the seed cotton cleaning process. The structure and operation parameters of the seed cotton cleaning unit were optimized and verified by bench test, which provided a theoretical basis for the design and development of the onboard seed cotton pre-cleaner of the stripper harvester.

MATERIALS AND METHODS

Test Equipment and Material

Test Equipment

A self-designed seed cotton cleaning unit bench was used in the tests. The bench was composed of a feeding bench, power and control system, cleaning bench, and gathering unit, as shown in Figure 1. The cleaning bench was equipped with a replaceable saw cylinder, brush roller, and cleaning bars. The adjustment speed range of the saw cylinder was 0 to 500 rpm and that of the brush roller was 0 to 800 rpm.

Fig. 1 -Seed cotton cleaning bench

1. Gathering unit; 2. Control system; 3. Cleaning bench; 4. Feeding bench

A structural schematic of the seed cotton cleaning bench is shown in Figure 2. We used two kinds of saw cylinder and brush roller combinations. The diameters of the saw cylinder were 420 mm and 340 mm, of the brush roller were 300 mm and 260 mm, respectively. The oval holes were uniformly distributed on the fan area in front of the saw cylinder, which could adjust the clearance between the cleaning bars and saw cylinder. The clearance adjustment was 0-30 mm. The diameter of the cleaning bar was 30 mm. The control system could control the rotating speed of the saw cylinder and brush roller.

The seed cotton and impurities passed through the feed bin and were manually evenly fed into the cleaning bench by the feeding roller. The seed cotton clung to the surface of the saw cylinder under the pressure of the brush. Therefore, the cotton was hooked on the saw cylinder surface and carried into the action range of the brush roller. Then, due to the higher linear speed of the brush roller, it was brushed off the saw cylinder surface and fed into the cotton gathering box. The impurities mixed in the seed cotton were discharged between the clearances of cleaning bars and fell into the impurities gathering box under the action of the centrifugal force of the saw cylinder and counter-acting force of the cleaning bars.

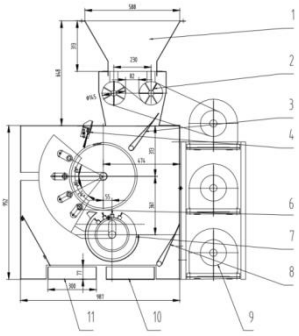

Fig. 2 - Structural schematic of the seed cotton cleaning bench

1. Feed bin; 2. Feeding roller; 3. Overhead baffle; 4. Brush; 5. Saw cylinder; 6. Cleaning bar; 7. Brush roller; 8. Underneath baffle; 9. Motor; 10. Cotton gather box; 11. Impurities gather box.

Test Material

Whole seed cotton, bolls, a few branches and other impurities, which were removed by the stripper harvesters, were manually fed into the onboard seed cotton pre-cleaner for primary cleaning.

The experiments were conducted in October 2020 at the workshop of the Baima Scientific Research and Innovation Experimental Demonstration Base, Nanjing Research Institute for Agricultural Mechanization. Ministry of Agriculture and Rural Affairs (Nanjing, China). The cotton variety was China Cotton 50 and the moisture content was 10.8% (Kong et al., 2021). The seed cotton feed rate was 1 kg/s, which was calculated according to the average cotton yield of 6000 kg/ha and the forward velocity of 4MZ-3 type stripper harvester was 2.8 km/h. Testing samples were selected according to the impurities rate of seed cotton harvested by the 4MZ-3 type cotton stripper harvester, which contained 75% seed cotton, 20% boll shell, 4% branches and 1% cotton leaves. The test materials are shown in Figure 3.

Fig. 3 - Cotton test materials

Test Method

In terms of seed cotton, the cleaning quality is affected by various factors (*Jing et al., 2017*), such as the structural parameters of the cleaning bar and saw cylinder, and technological parameters like the rotating speed of the saw cylinder. In this study, it was experimentally researched on the effect of different structural and technological parameters of the onboard cleaner currently used in cotton stripper harvesters on the loss rate and impurities rate.

Selection of Test Factors

In the cleaning test using an indoor bench, it was studied the influence of different cleaning qualities under different structural and technological parameters (*Hardin et al., 2014*). Because studies on cotton stripper harvesters are in the development stage and research on the cleaning part is still in its infancy, the

sawtooth distance, diameter of the saw cylinder, rotating speed of the saw cylinder, clearance and brush thickness were chosen as the test factors for the experimental studies.

The sawtooth distance is the minimum axial mounting distance between two adjacent U-shaped sawtooth strips. When the sawtooth distance increases, the hooking efficiency of seed cotton decreases, and the effect of hooking on the cotton stick also reduces, which is beneficial for eliminating large impurities. The mounting distance of U-shaped sawtooth strips was divided into four levels in this study: 32, 38, 44 and 50 mm.

The diameter of the saw cylinder is often limited by the machine space. When the diameter of the saw cylinder increases under a constant rotating speed condition, the linear speed and the centrifugal force on the seed cotton caught by the saw cylinder increase. Impurities are more easily separated from the seed cotton by collision with a cleaning bar. In this study, 420 and 340 mm diameters were chosen for the saw cylinder in the seed cotton cleaning bench, according to the processing conditions.

The rotating speed is the rotating speed of the saw cylinder, which is one of the most important parameters that determines the cotton impurities content, clearing loss rate and production efficiency of the saw cylinder. The higher the rotating speeds of the saw cylinder, the larger the centrifugal force generated and the more impurities cleaned. However, a rotating speed that is too high can cause seed cotton to not be fully hooked by the saw and fly out of the saw cylinder. The cleaning effect of the saw cylinder at different rotating speeds was studied. The adjustable range of the rotating speed was 0 to 500 rpm.

Clearance is the saw-to-bar clearance, which is the distance between cleaning bars and the corresponding external diameter of the saw cylinder, in mm. Note that distances between cleaning bars and the corresponding external diameter of the saw cylinder take the same value. Less clearance leads to better performance in terms of impurities removal, but the cotton fiber is more easily damaged.

Brush thickness is the thickness of the nylon brush that can brush seed cotton adhered to the saw cylinder. The adhesive force between the seed cotton and saw cylinder can be changed by changing the brush thickness.

Establishment of Appraisal Indexes

According to cotton harvester operation quality requirements, the impurities rate and loss rate were used as the indexes.

The impurities rate is the percentage of the weight of impurities in the seed cotton mixed with impurities after cleaning. The impurities rate (Z) can be obtained according to:

$$Z = \frac{W_Z}{W_H} \times 100\% \quad (1)$$

where: W_z is the weight of impurities in the seed cotton mixed with impurities after being cleaned

W_h is the total weight of seed cotton mixed with impurities after being cleaned.

The loss rate is the percentage of loss weight of seed cotton entrained in the impurities after being cleaned to the weight of the input seed cotton. The calculation formula of the loss rate (S) is as follows:

$$S = \frac{W_S}{W_C} \times 100\% . \quad (2)$$

where: W_s is the loss weight of seed cotton entrained in the impurities after being cleaned

W_c is the weight of feeding seed cotton.

The sampling methods comply with the Chinese national standards GB/T19818-2005 Seed Cotton Cleaner and GB/T 21397-2008 Cotton Harvester.

Combined Orthogonal Test Arrangement

A number of factors influence the impurities rate and loss rate, such as conditions like the structural and technological parameters. Therefore, after determining the optimum structural parameters of the saw tooth roller with a combined orthogonal test, the technological parameters of the seed cotton cleaning unit bench were optimized using the response surface methodology test method (*Wang et al., 2021; Yang et al., 2021*).

The sawtooth distance (A), diameter of the saw cylinder (B), and cleaning distance (C) were taken as the test factors. The factors and levels are listed in Table 1. According to cotton harvester operation quality

requirements, the impurities rate and loss rate were used as the indexes. The aim of the test was to examine the interaction between *A* and *B.* The sawtooth distance (*A*) was tested at four levels and the other two factors were tested at two levels, so a combined orthogonal table was selected in the test. The sum of the degree of freedom (d_f) of the three factors and interaction was:

$$f_A + f_B + f_B + f_{A\times B} = 1+1+1+1 = 4 \quad (3)$$

The lines of the selected orthogonal table should meet n ≥ 4 + 1 = 5, so $L_8(4^1 \times 2^4)$ was chosen.

Table 1

Factors and levels of orthogonal tests

Factors	Sawtooth Distance (*A*) mm	Diameter of Saw Cylinder (*B*) mm	Clearance (*C*) mm
1	32	340	10
2	38	420	20
3	44	-	-
4	50	-	-

Response Surface Methodology Test Arrangement

The orthogonal test results showed that the diameter of the saw cylinder and other factors have nonlinear effects on the loss and impurities rates. The combined orthogonal test can only reflect the optimal combination of test selection levels. The Box-Behnken response surface test was used to optimize the test to determine the optimized parameters of various factors of the cleaning unit bench (*Omorogie et al., 2017*). The diameter of the saw cylinder is a continuous variable that was obtained by regulation. Other factors that were not involved in the quadratic regression of the orthogonal rotating combinatorial test were fixed as the best level combination of score values in the orthogonal test.

Quadratic regression of the orthogonal rotating combinatorial test of three factors and three levels was conducted according to the Box-Behnken combination principle using Design-Expert software (Stat-Ease, Minneapolis, MN, USA). A total of 17 experiments were conducted on factors influencing the rotating speed *D*: clearance *E* and brush thickness *F*. The experimental factors and level codes are shown in Table 2. The evaluation indexes are as above.

Table 2

Factors and levels of experiments.

Level	Rotating Speed (*D*. rpm)	Clearance (*E*. mm)	Brush Thickness (*F*. mm)
−1	280	10	4
0	340	15	8
1	400	20	12

RESULTS

Combined Orthogonal Test

The loss rate and impurities rate were taken as the appraisal indexes of cleaning quality. The results of the combined orthogonal test and variance calculation for the test of the cleaning quality for each group are shown in Table 3. The analysis of variance (ANOVA) of the loss rate and impurities rate is shown in Table 4.

Table 3

Variance calculation for the loss rate and impurities rate.

No.	*A*	*B*	*A* × *B*	*C*		Loss Rate (%)	Impurities Rate (%)
	1	2	3	4	5	S	Z
1	1	1	1	1	1	25.3	13.1
2	1	2	2	2	2	16.3	11.2
3	2	1	1	2	2	18.4	11.2
4	2	2	2	1	1	19.2	7.4

5		3	1	2	1	2	26.5	15.2
6		3	2	1	2	1	18.3	8.6
7		4	1	2	2	1	26.9	10.5
8		4	2	1	1	2	34.3	9.1
Loss rate	T_1	41.6	97.1	96.3	105.3	89.7	x_i = 185.2 $\sum x_i$ = 4287.38 S_T = 4550.22	y_i =86.3 $\sum y_i$ = 975.31 S_T = 930.96
	T_2	37.6	88.1	88.9	79.9	95.5		
	T_3	44.8	-	-	-	-		
	T_4	61.2	-	-	-	-		
	k_1	20.8	24.275	24.075	26.325	22.425		
	k_2	18.8	22.025	22.225	19.975	23.875		
	k_3	22.4	-	-	-	-		
	k_4	30.6	-	-	-	-		
	S	161.02						
Impurities rate	T_1	24.3	50	42	44.8	39.6		
	T_2	18.6	36.3	44.3	41.5	46.7		
	T_3	23.8	-	-	-	-		
	T_4	19.6	-	-	-	-		
	k_1	12.15	12.5	10.5	11.2	9.9		
	k_2	9.3	9.075	11.075	10.375	11.675		
	k_3	11.9	-	-	-	-		
	k_4	9.8	-	-	-	-		
	Z	12.56	23.46	0.66	1.36	6.3		

A - sawtooth distance; *B* - diameter of the saw cylinder; *C* - cleaning distance; *A* × *B*. interaction between the sawtooth distance and diameter of the saw cylinder; *xi* - sum value of the loss rate; *yi* - sum value of the impurities rate; *T* - sum of test values; S_T - total sum of deviation squares; T_1-T_4 - sums of levels 1-4, respectively; k_1-k_4. averages of levels 1-4, respectively; and *S* - sum of deviation squaresy *A*, *B* and *C* respectively.

Table 4

Analysis of variance (ANOVA) of the loss rate and impurities rate

Source	Loss Rate				Impurities Rate			
	Sum of Squares	*df*	Mean Square	*F* Ratio	Sum of Squares	*df*	Mean Square	*F* Ratio
A	161.02	3	53.67	9.71 **	12.56	3	4.19	1.51
B	10.13	1	10.13	1.83	23.46	1	23.46	8.46 *
A × *B*	6.85	1	6.85	1.24	0.66	1	0.66	0.24
C	80.65	1	80.65	14.60 **	1.36	1	1.36	0.49
e	4.21	1	4.21	$F_{0.95}(3.3)=9.28$ $F_{0.90}(3.3)=5.39$	6.30	1	6.30	$F_{0.95}(3.3)=9.28$ $F_{0.90}(3.3)=5.39$
Crt.e	11.1	2	5.53		8.32	3	2.77	
T	262.84	7	37.55		44.35	7	6.34	

e. error of the empty column; *Crt.e*. corrected error; *T*. sum of the value; d_f. degrees of freedom; * and ** indicate significant differences at $p < 0.1$ and $p < 0.05$, respectively.

Through ANOVA of the loss rate, factors *A* and *C* were significant at the significance level of 0.05. Through ANOVA of the impurities rate, factor *B* was significant at the 0.1 significance level. Interaction item

AB was not significant for either the loss rate or for the impurities rate. The results showed that the sawtooth distance and cleaning distance were the main factors affecting the loss rate and the diameter of the saw cylinder was the main factor affecting the impurities rate. Because the degree of freedom of error in the empty column was only one, interaction between the sawtooth distance and diameter of the saw cylinder was not significantly classified as error when calculating the variance of corrected error.

The best combination of cleaning quality was $A_2B_2C_2$, meaning a sawtooth distance of 38 mm, diameter of saw cylinder of 420 mm, and cleaning distance of 20 mm should be used.

Response Surface Methodology Test

All tests were repeated three times and the average of the three values is reported. The test results of the loss rate and impurities rate are listed in Table 5.

Table 5

Test scheme and results

No.	Rotating Speed *D* (rpm)	Clearance *E* (mm)	Brush Thickness *F* (mm)	Loss Rate *S* (%)	Impurities Rate *Z* (%)
1	340	20	12	22.49	8.92
2	340	15	8	7.71	6.79
3	400	10	8	14.21	7.11
4	340	20	4	18.29	7.97
5	340	15	8	10.11	5.94
6	400	20	8	13.9	7.42
7	340	15	8	9.17	6.42
8	280	15	12	11.27	6.71
9	280	20	8	15.49	6.77
10	280	10	8	7.15	6.19
11	400	15	12	13.15	8.21
12	400	15	4	11.52	8.94
13	340	15	8	12.08	5.69
14	340	15	8	9.03	6.24
15	280	15	4	9.34	7.51
16	340	10	4	13.36	8.79
17	340	10	12	16.59	6.25

Data were analyzed using the statistical software and the results are shown in Table 6, based on different levels of factors.

Table 6

Variance analysis of the loss rate and impurities rate

Evaluation Indexes	Source	Sum of Squares	Mean Square	*F*-Value	*p*-Value
Loss rate (%)	Model	244.16	27.13	13.97	0.0011
	D	11.35	11.35	5.85	0.0462
	E	44.46	44.46	22.90	0.0020
	F	15.10	15.10	7.78	0.0270
	DE	18.71	18.71	9.63	0.0172
	DF	0.02	0.02	0.01	0.9173
	EF	0.24	0.24	0.12	0.7380
	D^2	11.43	11.43	5.89	0.0457

Evaluation Indexes	Source	Sum of Squares	Mean Square	*F*-Value	*p*-Value
	E^2	93.61	93.61	48.21	0.0002
	F^2	47.18	47.18	24.30	0.0017
	Lack of fit	3.10	1.03	0.39	0.7649
	Error	10.49	2.62		
	Total	257.75			
Impurities rate (%)	Model	17.11	1.90	12.42	0.0016
	D	2.53	2.53	16.54	0.0048
	E	0.94	0.94	6.13	0.0424
	F	1.22	1.22	7.95	0.0258
	DE	0.02	0.02	0.12	0.7402
	DF	< 0.0001	< 0.0001	0.01	0.9312
	EF	3.05	3.05	19.90	0.0029
	D^2	0.28	0.28	1.83	0.2177
	E^2	0.67	0.67	4.36	0.0751
	F^2	7.88	7.88	51.50	0.0002
	Lack of fit	0.35	0.12	0.64	0.6289
	Error	0.72	0.18		
	Total	18.18			

The *p*-values of the two models were less than 0.05. All regression equations were significant and error stems were non-significant. The significant determination coefficient (R^2) of the loss rate regression models is 0.9473 and the significant determination coefficient (R^2) of impurities rate is 0.9411, respectively. This means that the regression model accurately reflected the actual situations.

Based on the data in Table 6, two secondary multiple regression equations for the loss rate (*S*) and impurities rate (*Z*) were fitted as follows, respectively:

$$S=9.62+1.19\cdot D+2.36\cdot E+1.37\cdot F-2.16\cdot DE-0.075\cdot DF+0.24\cdot EF-1.65\cdot D^2+4.71\cdot E^2+3.35\cdot F^2 \quad (4)$$

$$Z=6.22+0.56\cdot D+0.34\cdot E-0.39\cdot F-0.068\cdot DE+0.018\cdot DF+0.87\cdot EF+0.26\cdot D^2+0.40\cdot E^2+1.37\cdot F^2. \quad (5)$$

According to the data from Equation (4) and the results in Table 6, it was observed that monomial *E* and quadratic term E^2.F^2 had a significant effect on the loss rate, whereas monomial *D*.*F* interaction *D*.*E* and quadratic term D^2 had a significant effect on the loss rate.

The analysis of variance showed that monomial *D*. interaction *EF*. and quadratic term E^2 had a very significant effect on the impurities rate. The impurities rate was significantly affected by monomial *E*. *F*.

The response surface method (RSM) was used to analyze the effects of the three factors on the loss rate and impurities rate by fixing one factor at a zero level.

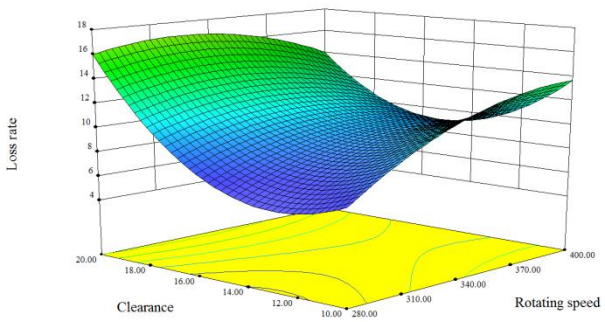

Fig. 4 - Response surface showing the effects of rotation velocity and clearance on the loss rate

To analyze the effect of the interaction between the rotation velocity and clearance on the loss rate, a dual-factor response surface was created, as shown in Figure 4. When the brush thickness was fixed to level zero and the clearance was lower, the loss rate first increased and then tended to remain flat as the rotation increased. These results demonstrated that cotton fiber more easily breaks due to the centrifugal force caused by faster rotation velocities of the saw cylinder (*Tian et al., 2018*). When the centrifugal force continued to increase but was still lower than the break force of intertwining fiber, the loss rate ceased its rapidly increase.

The trend line decreased to a minimum and then increased with an increase in clearance. This occurred mainly because the larger the clearance, the higher the rate of single seed cotton caused by the large hit force and cotton loss, as the saw cannot sufficiently hook seed cotton. When the clearance reaches a certain value, cotton loss and single seed cotton no longer increase accordingly.

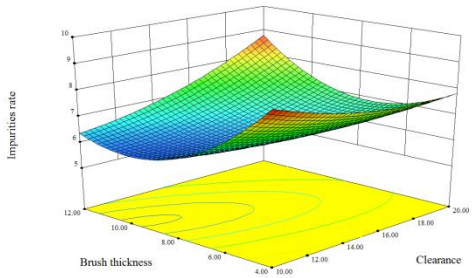

Fig. 5 - Response surface of brush thickness on the clearance impurities rate

When the rotation velocity was fixed to level zero, the impurities rate decreased to a minimum and then increased as the brush thickness increased. It decreased first and then increased with an increase in the cleaning distance. As shown in Figure 5, the impact force of seed cotton generated by the cleaning bar decreased with increasing clearance, and seed cotton was no longer impacted by the cleaning bar to some extent as the clearance increased. Therefore, the impact force of the bar on seed cotton that can separate impurities from cotton increases to maximum and then reduces as the clearance increases. Theoretically, the thicker the brush, the greater the force of seed cotton adhering to the saw cylinder, the more uniform the seed cotton laying. As a result, impurities are easily separated from seed cotton. However, if the brush is too thick, a mixing of impurities and seed cotton may occur, preventing them from being separated effectively.

Based on the test results analysis and model fitting, the experimental parameters were further optimized to guarantee that the loss rate was less than 10% and impurities rate was less than 6%. The scale optimizations were a rotating speed of 282-288 rpm, clearance of 12.55-14.84 mm and brush thickness of 8.37-9.69 mm.

Verification Test

To verify the reliability of the optimized results, a field test was conducted at Baima Scientific Research and Innovation Experimental Demonstration Base, Nanjing Research Institute for Agricultural Mechanization. Ministry of Agriculture and Rural Affairs (Nanjing. China). The optimal structural parameters, which were a sawtooth distance of 38 mm and saw cylinder diameter of 340 mm, were selected as the experimental conditions.

Fig. 6 - Verification test

The results are shown in Table 7. The authentication and predicted values are similar. The test results show that the regression model is reliable and can be used to predict and analyze the technological parameter effect on cotton fiber quality.

Table 7

Experimental scheme and results for prediction verification

No.	Test Scheme			Results	
	Rotating Speed (rpm)	Clearance (mm)	Brush Thickness (mm)	Impurities Rate (%)	Loss Rate (%)
1	285	12	8.5	1.52	9.07
2	285	13	9	0.55	9.37
3	285	13	8.5	0.53	8.91

CONCLUSIONS

In this study, the optimal structural and technological parameters of the cotton stripper pre-cleaner were obtained. The optimal structural parameters of the saw tooth roller were determined using a combined orthogonal test. Then, the technological parameters of the seed cotton cleaning unit bench were optimized using the response surface methodology.

The combined orthogonal test was applied in the bench test using the self-designed test bench. According to the test object, the influences of sawtooth distance, saw cylinder diameter and cleaning distance were investigated. According to the results and analyses of the combined orthogonal test, the best combination of cleaning qualities was a sawtooth distance of 38 mm, saw cylinder diameter of 420 mm, and cleaning distance of 20 mm. The best parameter configuration to maximize the cleaning quality of the onboard seed cotton pre-cleaner included the following structural parameters: sawtooth distance of 38 mm and diameter of the saw cylinder of 340 mm, and the following technological parameters: rotating speed of 282–288 rpm, clearance of 12.55–14.84 mm. and brush thickness of 8.37–9.69 mm, which reduced the loss rate to less than 10% and the impurities rate to less than 6%. The reliability of the theoretical analysis results was verified by comparison with the experimental results, so the findings can provide a theoretical basis and technical reference for research on and the structural design of seed cotton pre-cleaners.

ACKNOWLEDGEMENT

We greatly appreciate the careful and precise reviews by the anonymous reviewers and editors. This research was financially supported by the Agricultural Science and Technology Innovation Program of Chinese Academy of Agricultural Sciences (ASTIP. CAAS. 31-NIAM-05) and the Central Public-interest Scientific Institution Basal Research Fund (S202207).

REFERENCES

[1] Chen Changlin. Shi Lei, Zhang Yutong et al. (2015). Design and experiment of the MQZ-4A type site cotton pre-processor (MQZ-4A 型场地籽棉预处理机的设计及试验研究). *Journal of Chinese Agricultural Mechanization*. Vol. 36, no. 5, pp. 17–19.

[2] Deutsch T.A. (1999). *Lay-Down Bar for a Cotton Cleaner*. Patent. No. US 6159094. USA

[3] Francis J.M., Gable W.T. Jr.; Simpson F.L., Hulseberg P.J. (1969). *Clean-Boll Separator Conveyor for Cotton Harvester*. Patent. No.US 3618761. USA

[4] Huang M., Shi L., Zhang Y. et al. (2016). Optimization experiments of machine-mounted seed cotton pre-treatment apparatus for cotton stripper harvester (统收式采棉机载籽棉预处理装置的优化试验). *Transactions of the Chinese Society of Agricultural Engineering*. Vol 32. no.21, pp. 21-29.

[5] Huang M., Shi L., Yuan J. et al. (2014). Research status on pre-cleaner of cotton harvester (统收式采棉预清理装置研究现状). *Journal of Chinese Agricultural Mechanization*. Vol 35. no. 4.pp. 40–43.

[6] Yang H., Huanxiong Xie*, Hai Wei et al. (2021). Development and testing of soil impurities removing apparatus for potato (马铃薯土杂去除装置研制与试验). *INMATEH-Agricultural Engineering*. Vol. 65, No. 3, pp. 485-494. DOI: https://doi.org/10.356.33/inmateh-65-50.

[7] Hardin I.V., Robert G., (2014). Effect of Seed Cotton Cleaner Speeds on Machine Performance. *In Proceedings of the National Cotton Council Beltwide Cotton Conference. New Orleans. LA. USA*. pp. 584–589.

[8] Jingshan Tiana, Xuyi Zhanga, Wangfeng Zhanga et al. (2017). Leaf adhesiveness affects damage to fiber strength during seed cotton cleaning of machine-harvested cotton [J]. *Industrial Crops and Products*. Vol.107, no.11, pp. 211-216.

[9] Kazama E.H., Ferreira F.M., Silva R.P.D. et al. (2015). Multivariate analysis of fiber characteristics of dense cotton in different harvest systems. *Australian Journal of Crop Science*. Vol.9, no.11, pp.1075-1081.

[10] Kong Fanting, Wu Teng, Chen Changlin et al. (2021). Mechanical properties and construction of constitutive model for compression and stress relaxation of seed cotton (籽棉压缩与应力松弛力学特性及模型构建). *Transactions of the Chinese Society of Agricultural Engineering*. Vol 37. no.7, pp.53-60. DOI: 10.11975/j.issn.1002-6819.2021.07.007.

[11] Mao S., Li Y., Wang Z. et al. (2017). Re-exploration of Developing China's Cotton Industry by Producing High Quality Cotton (再论用"品质中高端"引领中国棉花产业发展). *Agricultural Outlook*. Vol.13. no.04, pp. 40-47.

[12] Omorogie M.O., Naidoo E.B., Ofomaja A.E., (2017). Response surface methodology, central composite design, process methodology and characterization of pyrolyzed KOH pretreated environmental biomass: mathematical modelling and optimization approach. *Modeling Earth Systems & Environment*. Vol.3, no.3, pp.1171–1186.

[13] Patel M.B. (2002). Apparatus and Methods for Stripping Cotton. Patent. No.US 6543091B2. USA

[14] Sanderson L.F., Des Moines I. (1990). Basket Cleaner for a Cotton Harvester. Patent. No.US 5042237. USA

[15] Tian J.S., Zhang X.Y., Zhang W.F. et al. (2018). Fiber damage of machine-harvested cotton before ginning and after lint cleaning. *Journal of Integrative Agriculture*. Vol.17, no.5, pp.8.

[16] Wanjura J.D., Boman R.K., Kelley M.S. et al. (2013). Evaluation of Commercial Cotton Harvesting Systems in the Southern High Plains. *Applied Engineering in Agriculture*. Vol 29, no.3, pp.321-332.

[17] Wang Shengsheng, Chen Pan, Ji Jiangtao et al. (2021). Design and experimental study of flexible threshing unit for Chinese cabbage seeds (大白菜种子柔性脱粒装置设计与试验) Vol. 65. No. 35. pp. 333-344. DOI: https://doi.org/10.35633/inmateh-65-35.

RECOVERY OF SOLAR THERMAL ENERGY AND ENERGY FROM THE COMPOSTING PROCESS
/
RECUPERAREA ENERGIEI TERMICE SOLARĂ ȘI A ENERGIEI TERMICE DIN PROCESUL DE COMPOSTARE

Radu CIUPERCĂ, Ana Maria CONSTANTIN*), Ana ZAICA, Vasilica ŞTEFAN*)
INMA Bucharest / Romania
E-mail: marin.anamaria26@gmail.com; valle_vali@yahoo.com
DOI: https://doi.org/10.35633/inmateh-68-89

Keywords: *biodegradable waste, thermal agent, compost heat recovery, recovery systems*

ABSTRACT
The use of energies from renewable sources, as an alternative to those obtained from fossil fuels, represents a sustained concern in the world scientific environment, this action being a particularly important objective at present, especially in the context of increasingly acute manifestations of the effects of climate change. The recovery and use of thermal energy developed in the composting process of biodegradable and solar waste is a current concern of the research environment in the field. In this paper we want to present some research on the recovery of thermal energy from the two renewable energy sources mentioned in order to use thermal energy for the production of the agent that can be used in the current activity of individual agricultural and livestock farms as well as in households, for the preparation of domestic hot water and heating of living spaces, greenhouses, and solariums. The paper presents the current state of research, some theoretical considerations regarding the thermodynamic phenomena that occur in the thermal energy recovery process, a modulated system for the recovery of thermal energy from the composting process and solar energy, experimentation in real operating conditions, the results and their interpretation and related conclusions.

REZUMAT
Utilizarea energiilor din surse regenerabile, ca alternativă la cele obținute din combustibili fosili, reprezintă una din preocupările susținute ale mediului științific mondial, această acțiune fiind un obiectiv deosebit de important la ora actuală, mai ales în contextul manifestării tot mai acute a efectelor schimbărilor climatice. Recuperarea și utilizarea energiei termice dezvoltată în procesul de compostare a deșeurilor biodegradabile și a celei solare, reprezintă una din preocupările actuale ale mediului de cercetare din domeniu. În această lucrare se prezintă rezultatele cercetărilor obţinute privind recuperarea energiei termice din cele două surse de energie regenerabila menționate, în vederea utilizării acesteia pentru producerea de agent termic care poate fi utilizat în activitatea curentă a fermelor agricole şi zootehnice precum și în gospodăriile individuale, pentru prepararea apei calde menajere și a încălzirii spațiilor de locuit, sere, solarii. În lucrare se prezintă stadiul actual al cercetărilor, câteva considerente teoretice privind fenomenele termodinamice ce se manifesta în procesul recuperării energiei termice, un sistem modulat de recuperare a energiilor termice din procesul de compostare și a celei solare, experimentarea acesteia în condiții reale de funcționare, înregistrarea rezultatelor, interpretarea acestora și concluziile aferente.

INTRODUCTION

This paper discusses the perspective of renewable energy (solar, biomass) in the making of strategies for sustainable development. Such strategies typically involve three major technological changes: energy savings on the demand side, efficiency improvements in energy production, and replacement of fossil fuels by various sources of renewable energy. Consequently, large-scale renewable energy implementation plans must include strategies for integrating renewable sources in coherent energy systems influenced by energy savings and efficiency measures *(Lund H., 2007).*

An important reason for replacing fossil fuels with RE (renewable energy) is to promote ecological sustainability - in particular to minimize further climate change. Nature provides many ecosystem services, such as food provision, fresh water, and climate regulation, but land-intensive RE systems, particularly hydroelectricity and bioenergy, inevitably reduce such service provision *(Moriarty P. et al 2016).*

Although agriculture is responsible for providing people with food, it is one of the sectors that are heavily dependent on fossil fuels, which not only jeopardizes food security but also poses significant risks to its

sustainability and production. Most agricultural practices are generally carried out by burning fossil fuels, which increases the risk of greenhouse gas emissions into the environment. The Consultative Group on International Agricultural Research (CGIAR) notes that agricultural and food chains alone consume about 30% of the world's total energy, and because of the high consumption, this accounts for about one-third (19–29%) of annual greenhouse gas (GHG) emissions. Given concerns about climate change and the damaging impact of fossil fuel prices on production costs, increasing fossil fuel use in the agricultural sector will not be affordable or sustainable. This provides an incentive for the development of renewable energy sources that can supplement and replace fossil fuels *(Gorjian S. et al, 2022).*

Composting is an effective process for treating organic solid waste (OSW). There is a growing interest in recovering and reusing heat from composting, in the context of climate change and fossil fuel depletion. Several literature reviews have been conducted to address the composting process; however, several engineering aspects, including heat estimation, recovery, and utilization, are inadequately addressed in current reviews *(Fan S. et al, 2021).*

Aerobic biodegradation of biomass can release considerable heat, reaching temperatures of up to 65 °C. This heat can be recovered and used for domestic purposes through the implementation of a Compost Heat Recovery System (CHRS) *(Malesani R. et al, 2021).*

According to the blue economy model proposed by *(Pauli G.A., 2010)*, it is necessary to find ways of utilizing physics, chemistry, and biology with renewable materials and sustainable practices just like ecosystems do. In this context, the technologies that mimic processes naturally occurring in ecosystems aim for sustainable economic growth while avoiding the use of non-renewable natural resources and preserving ecosystems by implementing the blue economy model. Green technologies are an example of applying artificial processes for the same purposes. Compost Heat Recovery Systems (CHRS) could be considered a technology that meets the blue economy principles, according to its characteristics (*Malesani R. et al, 2021)*.

A limited number of previous studies have investigated the potential energy content of compost. A recent study reports that during high-temperature phases (~6) of municipal waste composting, on average 1136 kJ kg^{-1} of heat was released. Similar values (961 kJ kg^{-1}) have been reported earlier with an average compost moisture content of 52.7% *(Irvine G. et al, 2010).*

The recovery of solar thermal energy (solar radiation) means the capture of this energy with the help of a technical system and the partial transfer to a solar thermal agent that circulates inside an installation and is generally used for heating, and the difference is ceded to the environment through optical, conductive and convective dispersions. In the renewable energy sector, solar power is the best alternative energy source because it has no harmful effect on the surrounding environment. Solar energy has the potential to meet energy demands in terms of sustainability and quality. The solar energy that falls on Earth's continents is more than 200 times greater than the annual total commercial power currently consumed by humans.

In Europe, the energy of the incident solar rays is 200...1000 W/m2, depending on the latitude, the period of the calendar year, and the climatic conditions. Solar collectors are used to capture this radiant energy of the sun to heat closed spaces, produce hot water, or use it as an energy source in a refrigeration system. Also, the heat obtained can be used to indirectly generate electricity by producing steam and using turbine-generator type systems, or by supplying hot air to Stirling engine-generator type systems. These latter aspects will be discussed in a later chapter *(Maican, 2015).*

Nowadays, the energy originating from photovoltaic sources is used for powerful generators on or off-grid, but it is also used to power small-scale applications such as for isolated embedded systems. Considering all these applications, photovoltaic energy is an interesting source of energy as it is renewable, inexhaustible, pure, and clean to be used in several applications meeting the cost constraints *(Fares M.A et. al, 2017).*

In the published documentation written by *(Shaikh M.R et al, 2017)* it is stated that the previous 10 years are more significant for the per-watt cost of solar energy equipment due to the diminishing availability of renewable energy sources. In the coming years, it will undoubtedly become more affordable and advance as a superior technology in terms of both price and applicability. Earth receives sunshine every day from above (1366 W approx.). This energy source can be used endlessly and is totally free. The primary advantage of solar energy over other conventional power sources is that it can be produced using the tiniest photovoltaic (PV) solar cells, which allow sunlight to be directly transformed into solar energy. In comparison to the cost of various fossil fuels and oils during the past ten years, the most advantageous aspect of solar energy is that it is readily available and free to the general public.

Agriculture and horticulture seek to optimize the capture of solar energy in order to optimize the productivity of plants. Techniques such as timed planting cycles, tailored row orientation, staggered heights between rows, and mixing plant varieties can improve crop yields.

Recovery systems and solar thermal energy have been developed in various types, both from a technical standpoint and the calorific installed power, many of which are equipped with automated monitoring and control of their operation.

The objective of this paper is to present the development and performance evaluation of a pilot-scale compost equipment and the method used for energy recovery.

MATERIALS AND METHODS

The research was carried out on an integrated system, fig.1, which has three component installations, as follows:

- the installation for the recovery and transfer of solar thermal energy, symbolized IRTS - realizes the recovery of solar thermal energy and transfers it to a circuit connected to the public cold water network for heating it for use as domestic hot water.
- the thermal energy recovery facility from the compost symbolized IRTC - carries out the taking over of the hot air from the compost by a fan and its passage through a heat exchanger inside which the transfer of heat from the hot air to the cold water takes place, a phenomenon that leads to its heating for further use, the air used in the exchanger being then introduced back into the composting container;
- the monitoring and automation module, symbolized MMA - performs the control, monitoring, and automation of the modulated system, ordering the use of one or the other of the two thermal energy recovery installations, IRTS or IRTC.

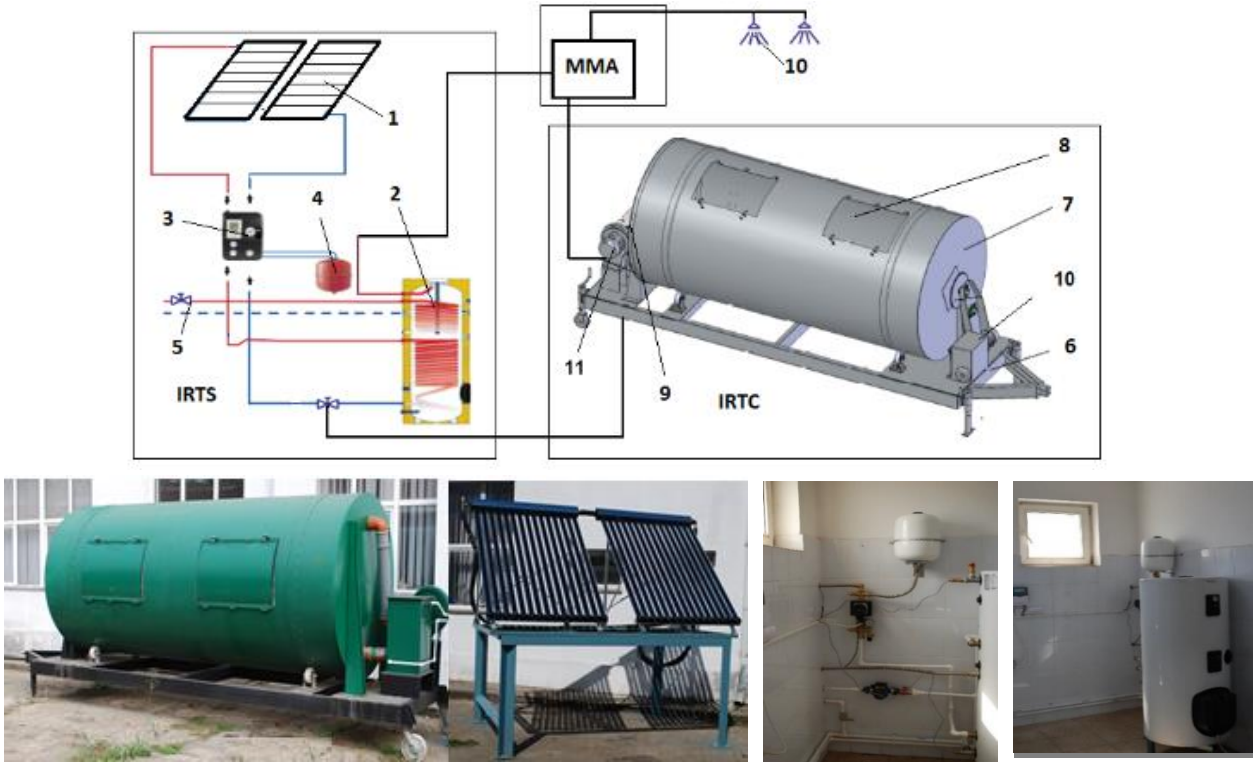

Fig. 1 - Integrated system for recovering solar thermal energy and thermal energy from the composting process

The solar thermal energy recovery installation symbolized IRTS, is mainly composed of two solar collectors (1), a storage tank (boiler) (2), the hydraulic equipment (3), the expansion vessel (4), water circuits (5).

The thermal energy recovery facility resulting from the composting process symbolized IRTC, consists of a frame (6), provided with four rollers on which the composting cylinder (7) rests, two doors (8) for loading-unloading waste /compost, a rear cover (9) equipped with vapor air suction/rejection holes mounted by screws on the frame, a transmission with a gear motor and chain wheels (10) for rotating the composting cylinder in the process of mixing, aeration and discharge of compost, a thermal energy recovery and transfer installation

for the production of domestic hot water (11), consisting of a metal tank, a fan equipped with a frequency converter to regulate the airflow, a copper heating coil.

Technical and functional characteristics of IRTS and IRTC equipment:

- **IRTS**
  - Heating capacity of 650 W/ m^2 (A1 1000 W/ m^2)
  - Ideal flow rate: 2.5 l/min
  - Maximum flow: 18 l/min
  - Maximum power: 1290 W / 4420 Btu
  - Daily heating capacity (Δ40°C): 140-200 l
  - Absorption area: 1.98 m^2
  - Heat-pipe stagnation temperature: 180°C
  - Vacuum tube stagnation temperature: 280°C
  - Required boiler volume: 250 l.
- **IRTC**
  - The volume of the composting cylinder: 10 m^3;
  - Engine power: 3.5 kW;
  - Speed of the composting cylinder: 1.2 min^{-1};
  - Air flow of the fan, adjustable: max. 1790 m^3/h;
  - Fan motor power: 1.5 kW.

1. The recovery process in the installation for the recovery and transfer of solar thermal energy – IRTS

Romania is located in a geographical area with good solar coverage, having 210 sunny days per year and an annual flow of solar energy between 1000 kWh/m^2/year and 1300 kWh/m^2/year. Between 600 and 800 kWh/m^2/year can be captured from this amount of energy.

The potential of using solar energy in Romania is relatively important. There are areas where the annual solar energy flow reaches 1450-1600kWh/m^2/year, in the area of the Black Sea Coast and Dobrogea, as in most southern areas.

The use of solar thermal energy represents the transformation of direct and indirect solar rays into heat or hot water. This heat is produced by capturing the sun's rays by the solar collector, which, through a heat exchanger, heats the water in a boiler. Heated water is used in the kitchen, bathroom or to help heat the home. Thus, by investing in solar energy, the environment can be protected both for our comfort and safety and for future generations *(Solar panels Constanţa).*

Heating load calculation for domestic hot water heating for a solar system

The thermal load required for heating domestic hot water, Q_{acm} can be calculated with equation (1) (*Lund, 2007*):

$$\dot{Q}_{acm} = \frac{m \cdot c_w \cdot (t_b - t_r)}{\pi \cdot 3600} \text{ [kW]} \quad (1)$$

where:

m - the amount of hot water is considered as a daily intake, [kg];

c_w - the specific heat of the water quantity which varies with temperature, [kJ/kg K];

t_b - the temperature of water from the boiler [°C];

t_r - the temperature of the cold water at the inlet, [°C]

π - the length of the hot water heating period considered, [h].

For heating domestic hot water, manufacturing companies recommend the use of solar collectors in different areas depending on the type of collectors and the percentage of annual heat to be provided by those.

For the proposed system we choose solar collectors with vacuum heat tubes, they have the highest capture efficiency. The calculation of the absorbing area S, of the solar collectors for solar sizing is accomplished by the relation (2):

$$S = \frac{\dot{Q}_{acm}}{\dot{Q}_{acm1}} \text{ [m}^2\text{]} \quad (2)$$

where:

Q_{acm1} - average unit thermal load of the solar collectors, [W/m^2].

The number of solar collectors still needed, n_c, is calculated with relation (3).

$$n_c = \frac{S}{s_c} \quad (3)$$

where:

s_c - absorber surface of a solar collector, declared by producer, [m^2] *(Ciupercă R. et al., 2019)*.

2. The process of heat transfer from the composting process

The transfer of thermal energy from the composting process consists of the transfer of heat from the air mixed with steams, sucked from inside the composted material by the fan of the plant and introduced into the premises of a heat transfer system which, in turn, transfers the heat to the cold water which pass through a copper pipe, in the form of a serpentine, which crosses diagonally the transfer tank.

The heat transfer system (fig. 2), which is the subject of research in this work, is a regenerative heat exchanger and the calculation of the transmitted heat is based on a thermal balance relation.

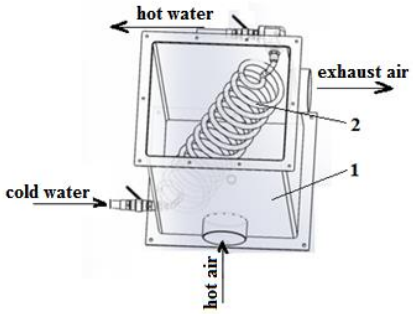

Fig. 2 – Heat transfer system

1-tank; 2- serpentine

Since the installation is thermally insulated and the losses are very small, it is considered that the thermal energy in the form of heat, given by the warm fluid (boiled air from the compost) is equal to the thermal energy transmitted to the cold fluid (cold water from the coil of the installation).

The calculation method for heat transfer in the installation is the classic "LMTD Method" (Log Mean Temperature Difference), which is based on the logarithmic average temperature difference Δt_m *(Fullarton J. W., 1993).*

The heat flow yielded by the warm fluid (air) conforms to the relation (4):

$$Q_1 = m_1 \cdot c_1 \left(t_{f1} - t_{p1}\right) \text{ [W]} \quad (4)$$

where:

m_1 – mass flow rate of hot air, [kg/s];

c_1 – thermal mass capacity of hot air, [J/kg °C];

t_{f1} – temperature of the 1st fluid (warm air from compost), [°C];

t_{p1} – temperature of the outer wall of the pipe, [°C];

The thermal flow received by the cold fluid (cold water) is calculated by the relation (5):

$$Q_2 = m_2 \cdot c_2 \left(t_{f2} - t_{p2}\right) \text{ [W]} \quad (5)$$

where:

m_2 – mass flow rate of cold water, [kg/s];

c_2 - thermal mass capacity of cold water, [J/kg °C];

t_{f2} – temperature of the 2nd fluid (cold water from the pipe), [°C];

t_{p2} – temperature of the inner wall of the pipe, [°C];

The transmitted thermal flow complies equation (6):

$$Q_{tr} = K \cdot A \cdot \Delta t_m \text{ [W]} \quad (6)$$

where:

K – global heat transfer coefficient, [W/m °C];

Δt_m – mean logarithmic temperature difference, [°C].

A – transfer surface, [m^2].

Product $K\,A$ is determined with the relation (7):

$$\frac{1}{K \cdot A} = \frac{1}{\alpha_1 \cdot A_1} + R_p + \frac{1}{\alpha_2 \cdot A_2} \quad (7)$$

where:

α_1 – convection coefficient between the outer wall of the pipe and hot air, [W/ m^2 °C];

α_2 - convection coefficient between the inner wall of the pipe and the cold water in the pipe, [W/ m^2 °C];

A_1; A_2 – the unfolded transfer area of the outside or the inside of the pipe, [m^2]. At small thicknesses of the pipe wall, the two surfaces are considered equal and denoted by A.

R_p – the thermal resistance of the heat exchanger wall is according to the relation (8).

$$R_p = \frac{\delta_p}{\lambda \cdot A_m} \quad (8)$$

where:

δ_p – thickness of the pipe wall, [m];

λ – thermal conductivity of the pipe material, [W/m °C];

A_m – transfer surface deployed on the median thickness of the pipe wall, [m^2];

Thus, the relationship (7) becomes (9):

$$\frac{1}{K} = \frac{1}{\alpha_1} + \frac{\delta_p}{\lambda} + \frac{1}{\alpha_2} \quad (9)$$

Since the two fluids flow in the same direction (equidirection), the average algorithmic temperature difference is calculated with the relation (10):

$$\Delta t_m = \frac{\Delta t_a - \Delta t_b}{\ln \frac{\Delta t_a}{\Delta t_b}} \quad (10)$$

where:

Δt_a; Δt_b – the temperature differences between hot and cold fluids at the ends of the pipe (11).

$$\Delta t_a = t_{f1} - t_{p1}$$
$$\Delta t_b = t_{f2} - t_{p2} \quad (11)$$

To explain the temperatures of the process, the recovery system was considered as a homogeneous cylinder surrounded by two fluids with known temperatures, boundary conditions of the III-rd type *(Coman G. 2000; Leca A., 2000; Miron V. et al, 2006).*

The process consists of three stages of transfer, as follows:

- stage 1, such *as forced thermal convection*, consists of the transfer of heat from the hot air sucked from the composted material to the outer wall of the copper coil that is mounted in the transfer rail;
- stage 2, of the type *of thermal conduction in the variable regime*, consists of the transfer of heat from the outer wall of the coil to its inner wall;
- stage 3, such *as forced thermal convection*, consists in transferring heat from the inner wall of the coil to the cold water circulating inside it.

In these conditions, the relations of the unitary heat flow are written for the three stages, according to the relations (12):

$$Q_1 = \alpha_1 \cdot \pi \cdot d_1 \left(t_{f1} - t_{p1}\right)$$
$$Q_p = \frac{t_{p1} - t_{p2}}{\frac{1}{2 \cdot \pi \cdot \lambda} \cdot \ln \frac{d_2}{d_1}} \text{ [W/m]} \quad (12)$$
$$Q_2 = \alpha_2 \cdot \pi \cdot d_2 \left(t_{p2} - t_{f2}\right)$$

Putting the condition of the unidirectionality of the thermal flux, according to the relation (13):

$$Q_1 = Q_p = Q_2 = Q \tag{13}$$

It follows, the relation (14) for the thermal flux:

$$Q = \frac{t_{f1} - t_{f2}}{\frac{1}{\pi \cdot d_1 \cdot \alpha_1} + \frac{1}{2 \cdot \pi \cdot \lambda} \cdot \ln \frac{d_2}{d_1} + \frac{1}{\pi \cdot d_2 \cdot \alpha_2}} = K\left(t_{f1} - t_{f2}\right) \quad [W/m] \tag{14}$$

in which K has the expression (15):

$$K = \frac{1}{\frac{1}{\pi \cdot d_1 \cdot \alpha_1} + \frac{1}{2 \cdot \pi \cdot \lambda} \cdot \ln \frac{d_2}{d_1} + \frac{1}{\pi \cdot d_2 \cdot \alpha_2}} \quad [\frac{W}{m \cdot {}^oC}] \tag{15}$$

where: d_1 – external diameter of the pipe, [m];

d_2 - the inner diameter of the pipe, [m];

The temperatures on the outer and inner walls of the pipe are according to the relations (16):

$$t_{p1} = t_{f1} - \frac{Q}{\pi \cdot d_1 \cdot \alpha_1} \quad [^oC]$$
$$t_{p2} = t_{f2} + \frac{Q}{\pi \cdot d_2 \cdot \alpha_2} \quad [^oC] \tag{16}$$

Previously written expressions are valid for heat exchange in a second. If fluid 2 (water from the coil) circulates in the transfer medium for a longer time, then the value, according to written relationships, will be amplified with the circulation time. These values, obtained through detailed experimental data, must be amplified with a coefficient because in any moment, following the first second, the temperature of the water in the coil increases with a certain value, the phenomenon being one of the type convections + conduction + forced convection.

In order to determine the water flow circulated in the thermal energy recovery installation, a 2-liter graduated vessel and a wristwatch were used, and for the speed of the air current of the fan a Testovent 4000 type anemometer with a measuring range of 0.4-40 m/s, with the help of which the air current flow was calculated.

The speed of the fan air current was measured on the air return circuit (after exiting the recovery plant and back into the composting container).

Details from the experiments with the plant for the recovery and transfer of thermal energy resulting from the composting process (IRTC) are presented in fig. 3.

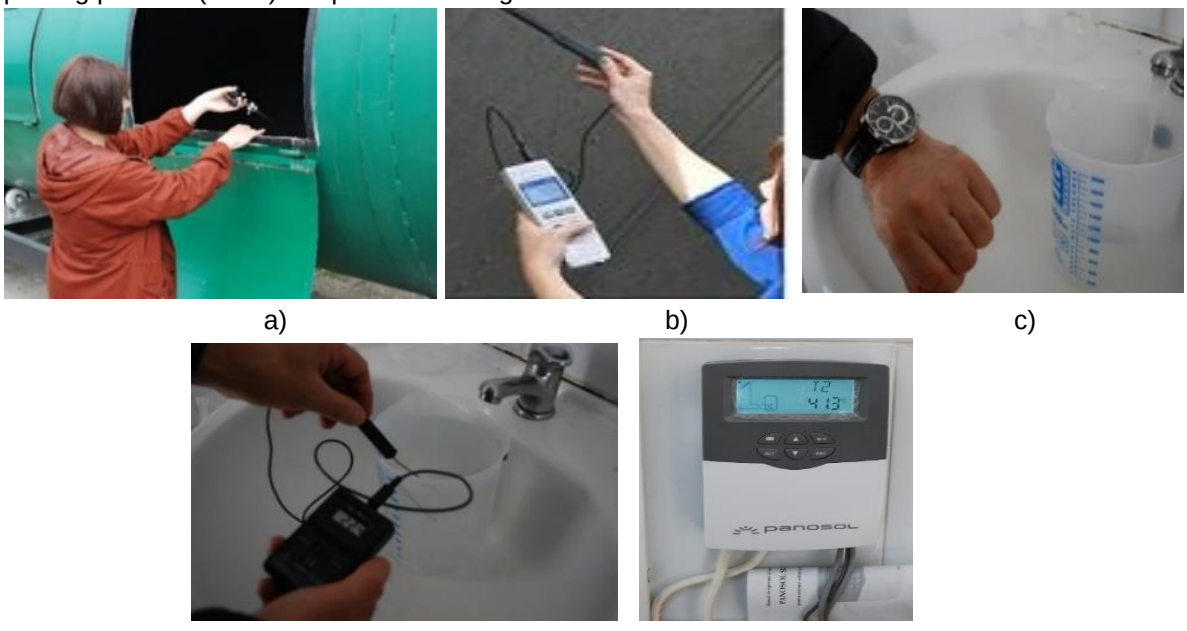

Fig. 3 - Details from the time of the measurements

a-Compost, temperature; b-Airspeed; c-Water flow in the plant; d-Temperature of cold and hot water; e-Temperature in hydraulic circuits for IRTS

RESULTS

➢ Results obtained using the IRTS solar energy recovery system

The measurements were carried out on 4 days, in the time interval 9.30-18.00, hour by hour, the measured parameters being the temperatures of the heating agent and water in various essential points of the installation as well as of domestic hot water to the user.

The graph in fig.4 shows the air temperature and solar radiation recorded during the measurement period.

Input data:

- m - the hot water requirement is 250 l/day or 250 kg/day.
- the average thermal energy required to heat a litre of water is approx. 35W/h;
- t_b = 45 °C - recommended value for the temperature of the hot water in the boiler;
- t_r = 15°C - the average value of the cold water in the public network, at the date of the measurements;
- π = 8h - a value roughly coincides with the average duration in which the solar radiation manifests itself, so with the average duration it can be captured.
- c_w = 4.186 kJ/kg K;
- Q_{acm} = 1290 W.

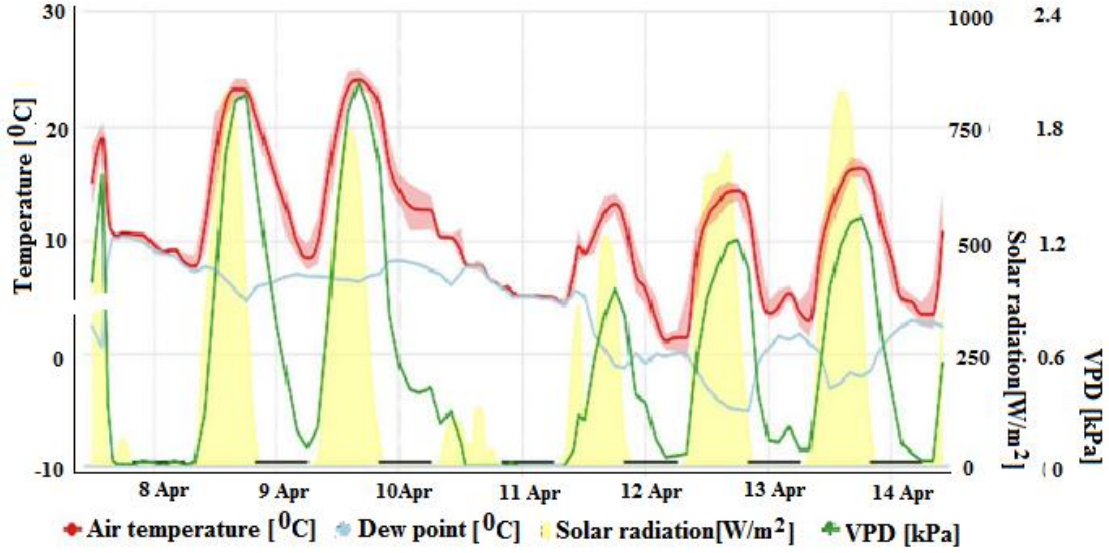

Fig. 4 - Graphic representation of air temperature and solar radiation

VPD - Vapour pressure deficit

Using relation (1), the average temperature in the boiler that the installation can achieve during the experiments, according to the graph in fig. 2, was t_b = 50.5°C.

This temperature is lower than that measured by the thermometer placed on the boiler, in its upper spot, which indicates the maximum. The average temperature in the boiler was close to the one that results in the user, the one presented in Table 4 which is close to the one obtained from the theoretical calculations.

The measured values of the temperatures in the Installation for the recovery and transfer of solar thermal energy - IRTS, corresponding to the mentioned period, are presented in Tables 1-4.

Table 1

Water temperature at the entrance to the storage tank (lower part), T2

Date / Time range of measuring	Temperature, C°									
	9h 30min	10h 30min	11h 30min	12h 30min	13h 30min	14h 30min	15h 30min	16h	17h	18h
*04/08/2022	14.2	16.6	18.2	23.3	31.5	35	38.3	43.6	45.8	46.5
11.04.2022	18.7	20.5	25.3	25.4	26.4	26.9	30.2	32.1	31.4	30.5
12.04.2022	23.5	26.7	30.2	34.7	39.1	41.3	43.7	45.3	45.6	47.3
13.04.2022	29.7	32.7	33.6	35.7	38.1	42.3	44.3	47.6	50.3	50.8

* *Loading the installation with a heating agent and cold water from the public network*

Table 2

The temperature of the heating agent, at the exit from the storage tank (return), T1

Date / Time range of measuring	Temperature, C°									
	9h 30min	10h 30min	11h 30min	12h 30min	13h 30min	14h 30min	15h 30min	16h	17h	18h
*04/08/2022	19.4	25.4	30.6	36	41.5	46.5	47.3	48.4	47.5	46.1
11.04.2022	26.5	28.1	33.3	32.6	33.4	35.9	40.3	43.4	45.5	45.1
12.04.2022	31.3	37.9	42.2	45.4	49.0	51.6	54.6	55.3	55.7	53.2
13.04.2022	37.1	45.2	46.3	52.0	56.2	58.4	60.4	58.9	57.8	54.5

Table 3

The temperature of the water in the storage tank at the top of it

Date / Time range of measuring	Temperature, C°									
	9h 30min	10h 30min	11h 30min	12h 30min	13h 30min	14h 30min	15h 30min	16h	17h	18h
*04/08/2022	19.5	22.5	26.0	34.0	48.0	51.5	53.0	55.0	55.0	55.0
11.04.2022	52.0	52.0	53.0	54.0	54.5	55.0	57.0	57.5	57.5	57.5
12.04.2022	55.0	56.0	56.5	59.0	62.0	64.0	68.5	69.0	69.0	69.0
13.04.2022	67.0	67.0	67.5	69.0	70.0	74.0	76.5	77.0	77.0	77.0

The temperatures measured at the user, for domestic hot water, compared to the temperature in the storage tank (boiler), were measured on 13.04.2022 when the installation reached a normal operating regime.

Table 4

Domestic hot water temperature at the user

Date / Maximum temperature in the storage tank, at the top of it C°	Domestic hot water temperature at the user, C°			
	67.0	69.0	74.0	77.0
13.04.2022	45	46	52	53

- **Results for the IRTC composting process energy recovery system**

- **Preparation of experiments for IRTC**

To carry out the experiments with the installation for the recovery and transfer of the thermal energy resulted in the composting process (IRTC), the following steps have been taken:

- the material for composting was prepared, which consists of manure mixed with fragments of chopped twigs, straw, and dry leaves;

- the composting material was permanently mixed and moistened so that the humidity was adequate, this being checked with the "fist" method;

- the material, prepared according to the previous point, was loaded into the composting container through the two side doors with which it is provided. The amount of material loaded in the quota was about 7m^3;

- the mixing plant was started to homogenize the material, by turning the loaded container. This operation was repeated 5 times a day, 10 min. for each mixing to speed up the composting process.

- measurements of the temperature in the compost were made until it reached values between 55-65^{o}C when the composting process is at its peak. At this moment, the experiments for the recovery of the thermal energy released in the composting process have effectively started;

- the fan of the thermal energy recovery installation and the rotation of the container was put into operation. The fan absorbs hot air from the compost and transfers it to the tank with the transfer coil through which the cold water passes from the public network.

- during the experiments, measurements were made of the temperature from the compost, the hot air from the compost, the cold water from the network, and the resulting domestic hot water.

Using the known data of the transfer system in relations (4-6) and (10-16), in which:

m_1 =0.51 kg/s; c_1 = 1005 J/kg °C; t_{f1} = 62.5 °C; m_2 = 0.039 kg/s; c_2 = 4218 J/kg °C; t_{f2} = 22.5 °C;

δ_p = 0.0005 m; λ_{air} =0.0234 W/m °C; λ_{water} =0.6 W/m °C; λ_{Cu} =397 W/m ^{o}C; d_1 = 0.015 m; d_2 = 0.014 m;

$\alpha_1 = \lambda_{air} / \delta_{air}$ = 0.1872 W/m^2 °C; $\alpha_2 = \lambda_{water} / \delta_{water}$ = 42.86 W/m^2 ^{o}C; δ_{air} = 0.125 m; δ_{water} = 0.014 m;

A = 0.258 m^2

δ_{air} = the thickness of the warm air layer; δ_{water} = the thickness of the water layer.
t_{f2} – average domestic hot water temperature for 4 samples/water flow, according to the values in table 6.

For the recovery and transfer of thermal energy resulting in the composting process (IRTC), the determined values are presented in Table 5-6.

Table 5

Determination of operating parameters

Parameter	Measurement unit	Sample number			
		1	2	3	4
Compost temperature	°C	62	63.5	63	65.5
Fan air flow speed	m/s	35	33.5	34	33.8
Fan airflow	m^3/h	1566	1499	1522	1513

Table 6

Domestic hot water temperature

Parameter	Measurement unit	Water flow in the installation, l/min			
		2.67	3.23	3.65	4.2
Cold water temperature	°C	22.4	22.6	22.5	22.6
Average domestic hot water temperature for 4 samples / water flow	°C	45.5	38.0	33.8	29.2

CONCLUSIONS

Following the experiments of the Installation for the recovery and transfer of thermal energy resulting from the solar installation, IRTS, and from the composting process (IRTC), the following conclusions were drawn:

- When sizing the radiant surface of the panels and the capacity of the boiler, of a thermal energy recovery installation, the estimated amount of water used in a day and its temperature must be taken into account;
- The temperature variations measured in the IRTS facility depend directly on the values of air temperatures and solar radiation and indirectly on the degree of cloud cover and precipitation;
- The values of the hot water temperature at the user are in percentage of approx. 69% of the maximum temperature values in the storage tank, at first use. These values decrease to the extent that the installation is used continuously for a longer time;
- In the IRTS installation, the temperature variations measured for domestic hot water produced by the user depend, in the main, indirectly on the flow rate of the water circulating in the installation and on the temperature of the cold water from the public water network and directly on the temperature of the air in the compost.

ACKNOWLEDGEMENT

This work was supported by Development of the National Research-Development System, subprogramme 1.2 – Institutional Performance – Projects for financing excellence in RDI, contract no. 16PFE and Project: PN 19 10 01 05 - Integrated management of work in farms, vineyards and orchards, contract no. 5/ 07.02.2019.

BIBLIOGRAPHY

[1] Ciupercă, R.; Nedelcu, A.; Popa, L.; Zaica, A.; Ştefan, V.; Anghelet, A. (2019). Intelligent recovery system for solar thermal and heat process composting, *Research People and Actual Tasks on Multidisciplinary Sciences, Proceedings of the Sixth International Conference*, pp.306-310;

[2] Fares, M.A.; Atik., L.; Bachir, G.; Aillerie, M (2017). Photovoltaic panels characterization and experimental testing. *Energy Procedia,* Vol. 119, pp. 945-952, ISSN 1876-6102

[3] Fullarton, J. W. (1993). *VDI-Heat Atlas.* VDI-Verlag GmbH, Düsseldorf, cop. 1993, ISBN 978-3-540-77877-6

[4] Gorjian, S.; Fakhraei, O.; Gorjian, A.; Sharafkhani, A.; Aziznejad, A. (2022). Sustainable Food and Agriculture: Employment of Renewable Energy. *Current Robotics Reports 3*, pp. 153–163

[5] Ismaniza, I.; Roslan, J.; Noor Hidayah, A (2017). Green technology concept and Implementation: a brief review of current development, *Advanced Science Letters,* Vol. 23.9, pp. 8558-8561

[6] Irvine, G.; Lamont, E.R.; Antizar-Ladislao, B. (2010). Energy from Waste: Reuse of Compost Heat as a Source of Renewable Energy*, International Journal of Chemical Engineering,* Vol. 2010, pp. 1-10, DOI:10.1155/2010/627930

[7] Leca A. (2000). *Heat transfer processes (Procese de transfer de căldură).* Technical Publishing House, Bucharest/Romania

[8] Lund, H. (2007). Renewable energy strategies for sustainable development. *Energy,* Vol. 32.6 , pp. 912-919, DOI: 10.1016/j.energy.2006.10.017.

[9] Maican, E., (2015) *Renewable energy systems* / *Sisteme de energii regenerabile*, Printech Publishing House, Bucharest/Romania

[10] Malesani, R.; Pivato, A.; Bocchi, S.; Lavagnolo M.C.; Muraro, S.; Schievano, A (2021). Compost Heat Recovery Systems: An alternative to produce renewable heat and promoting ecosystem services, *Environmental Challenges*, Vol. 4, 100131, ISSN 2667-0100

[11] Miron, V.; Paraschiv, S.; Paraschiv, S. (2006). *Heat transfer.Guidebook/Transfer de căldură. Indrumar,* Publishing House of the Lower Danube University Foundation, Galati/Romania

[12] Moriarty, P.; Honnery, D. (2016). Can renewable energy power the future? *Energy Policy*, Vol. 93, pp. 3-7, ISSN 0301-4215

[13] Pauli, G.A., (2010). *The blue economy: 10 years, 100 innovations, 100 million jobs,* Paradigm Publications

[14] Sai Kumara, Ch. M.; Singh, S.; Gupta, K. M.; Nimdeo, M. Y.; Raushan, R.; Deorankara, V. A.; Kumar, A. T.M.; Rout, K. P.; Chanotiya, C.S.; Pakhale, D. V.; Nannaware, D. A (2022). Solar energy: A promising renewable source for meeting energy demand in Indian agriculture applications. *Sustainable Energy Technologies and Assessments*, Vol. 55, ISSN 2213-1388

[15] Shaikh, M. R.; Shaikh, S.; Waghmare, S.B; Labade, S; Tekale, A. (2017). A review paper or electricity generation from solar energy, *International Journal for Research in Applied Science and Engineering Technology,* Vol.5, DOI: 10.22214/ijraset.2017.9272, ISSN 2321-9653

[16] Fan, S.; Li, A.; Heijne, A.; Buisman, J.N.C.; Chen, W-S. (2021). Heat potential, generation, recovery and utilization from composting: A review, *Resources, Conservation and Recycling,* Vol. 175, 105850, https://doi.org/10.1016/j.resconrec.2021.105850, ISSN 0921-3449

[17] Miron, V. (1999). *Izolatii termice/ Thermal insulations,* Ed. Evrika, ISBN 973- 8052-15-7- 208-7, Braila

[18] *** Solar panels Constanta (Panouri solare Constanta). https://www.panourisolareconstanta.ro/harta-radiatia-solara-in-romania

TEST AND ANALYSIS OF VIBRATION CHARACTERISTICS OF VIBRATION SUBSOILER
/
深松机振动特性试验与分析

Xiangqian DONG*, Huina ZHENG, Chen SU, Yonglei LI, Jiannong SONG, Jicheng WANG [1]
China Agricultural University, College of Engineering, Beijing / China
Tel:0086-010-62737502; E-mail: dxq0558@126.com
Corresponding authors: Xiangqian Dong
DOI: https://doi.org/10.35633/inmateh-68-90

Keywords: *Vibration subsoiler; Phase angle; Amplitude; Eccentricity; Traction*

ABSTRACT

In this paper, the vibration characteristics of the 1ST-460 vibration subsoiler was analyzed. In order to solve the problem of vibration imbalance caused by the vibration component under the action of multiple groups of vibration shovels, the optimal combination mode of the vibration component under the interaction of multiple groups of shovels was obtained. Piezoelectric accelerometers are fixed symmetrically on the frame of the subsoiler to measure the vibration at different positions. TST5910 dynamic signal test and analysis system is used to collect and process the acceleration data. Non-load tests were carried out with different initial eccentric phase angle combination. Results showed that the combination of [0°, 180°, 180°, 0°] (symmetrically up and down staggered vibration) for the eccentric vibration component of four shovels is the optimal initial phase combination, which can lead to the minimum adverse vibration on the frame. Further tests were conducted under different vibrating frequency and amplitude/eccentric with optimal phase combination. The results showed that, when amplitude/eccentricity ratio was 2.0 and 2.5, frequency of vibration was 6.7 and 8.3 Hz, the required traction force of the subsoiler was stable and significantly reduced, which can reduce the harmful vibration on the tractor.

摘要

为研究1ST-460 型振动深松机振动特性，解决在多组振动铲作用下因激振装置的惯性载荷引起的振动不平衡问题，获取多组铲交互作用下激振装置的优化组合方式。采用 TST5910 动态信号测试分析系统对 1ST-460 型振动深松机机架的振动响应特性进行了试验与分析。研究了在不同相位角组合下机架振动位移变化规律和牵引力特性，得到最优起始相位角组合为[0°,180°,180°,0°]；在最优相位角组合下，研究了振动深松机在不同振幅/偏心距比和不同振动频率下的振动特性和牵引力特性，结果表明，当振幅/偏心距比为 2.0 ~2.5，振动频率为 6.7 ~8.3 Hz 时，深松机减阻效果显著且振动影响较小。

INTRODUCTION

Vibrating subsoiling has an advantage of decreasing tillage resistance, but if the vibration of the vibration subsoiler transfers to the tractor, it will cause harmful effect to both the tractor and driver, restricting the popularization of vibration subsoiler (*Yuan et al., 2020; Sun et al., 2018; Qiu & Li, 2000; Cui et al., 2016; Wang et al., 2018; Zhao et al., 2017; Liu et al., 2017*). With the agricultural equipment's modernization and the requirement of agricultural equipment's comfort and the continuously increasing reliability from custom, the study of vibrating deep loosen comfort and reliability, especially the effective way to reduce the bad effect caused by vibration, which is based on the foundation of decreasing the vibrating subsoiling resistance, has practical significance (*Yang et al., 2017*).

Researchers have done quite as much research on the aspects of vibrating drag reduction and vibration characteristics (*Nagasaki et al., 1996; Liu et al., 2017; Sakai et al., 2010*).

Xiangqian Dong, SE.Ph.D. Eng; Huina Zheng, M.S. Stud. Eng; Chen Su, M.S. Stud. Eng; Yonglei Li, Assoc. Prof.Ph.D. Eng; Jiannong Song, Prof.ph.D. Eng; Jicheng Wang, ST.

Radite et al., (2016), studied the application of vibration in reducing the drag of subsoiling, meanwhile, they compared and analyzed the vibration characteristics of different types of subsoiling shovels when doing an operation.

Wang et al., (2020), studied electric–hydraulic control technology to improve the adaptability of the vibrating subsoiler to various soil conditions by adjusting the working pressure of the excitation element. *Hilal et al., (2021),* studied deep loader vibrating and non-vibrating wings and two penetration angles (45°and 55°) in soil at speeds of 2.88, 3.6 and 4.5 km/h. The results showed that the wing vibration had a positive dominance in the Slip, Critical Depth and Depth Stability Ratio, while a negative increase was achieved in the vibration of the driver's seat of agricultural tractors (VDS).

Based on the relevant research results, the vibration characteristics of 1ST-460 vibration subsoiler were studied by using TST5910 dynamic signal test and analysis system. Pre-experiments were carried out on vibration subsoiler with different phase angle combinations, and the initial eccentric phase angle combinations under smaller vibration were obtained. These combinations were tested in soil grooves with different initial phase angles, and the vibration characteristics under different eccentric phase angle combinations were analyzed. Taking the main vibration displacement characteristics and traction characteristics as the optimization indexes, the optimal phase angle combination under the minimum vibration was obtained. Under the optimal phase angle combination, the amplitude/eccentricity ratio and vibration frequency were changed respectively, and the optimal parameter combination was obtained by taking the vibration displacement and traction characteristics as the indexes, so that the optimal combination mode of the vibration components under the interaction of multiple groups of shovels was obtained. In a word, scholars have not studied the vibration characteristics of this kind of combined frame subsoiler, so this paper carried out analysis on the relevant vibration characteristics from this kind of vibration subsoiler with unique structure, as well as the related innovation in the vibration measurement method and treatment, which has certain research value.

MATERIALS AND METHODS

Structure

The structure of model 1ST-460 vibrating subsoiler is shown in Fig. 1. It is mainly composed of gear box, hanger, coupling, vibration components, frame and soil loosening components. The frame connected by the profile is connected by welding, such as the hanger 2 and the frame 5, and the other parts are connected with the frame by anti-loosening bolts and nuts with washers.

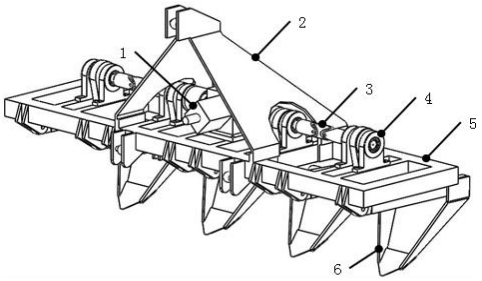

Fig. 1 - 1ST-460 vibration subsoiler

1– Gear box; 2– Hanger; 3– Coupling; 4–Vibration components; 5– Frame; 6–Soil loosening components

Working principle

The machine adopts the active vibration operation mode, the vibration components adopt the eccentric connecting rod excitation device, and the power is transmitted by the rear power output shaft of the tractor, which is connected with the power input shaft of the gear box through the universal joint and the power input shaft of the gear box, and the power is changed by the bevel gear of the reversing box. It is transversely transmitted to the groups II and III of vibration components on both sides, and the connection here is made by a flexible coupling, which allows a certain deviation in the centerline of the two axes. It has the ability to compensate the relative offset of the two axes. Because the working parts of groups I and IV are far apart, the universal coupling is used in the middle transmission part, which allows the two axes to have a large angular offset. The transmission design reduces the positioning accuracy requirements for four groups of vibration components in the installation process, and can achieve simple and reliable transmission, as shown in Fig. 2. The soil loosening components is a frame-type deep-loose shovel, which can reduce the resistance and improve the quality of deep-loose work.

The method to regulate the phase angle

The balance performance and traction resistance of subsoiler will be affected by a different phase angle combination of four groups of vibration shovel. The phase angle is adjusted by universal coupling. The way power is transferred through vibration shovel is shown in Fig. 2. I, II, III and IV, are the four groups of subsoiler shovels respectively. The gear box's output shaft is close to the adjacent vibration component, so it is connected by a double row roller chain coupling (flexible coupling), and between the vibration device and the vibration device is connected by a universal coupling.

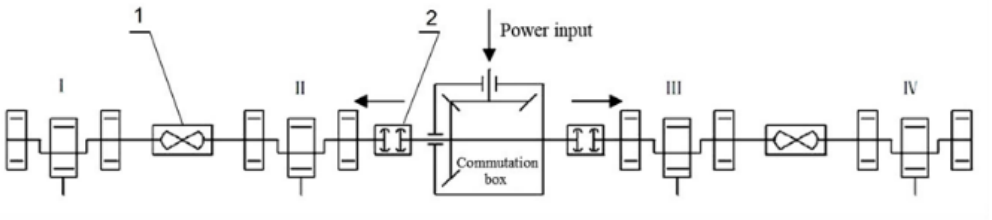

Fig. 2 - Combination configuration of shovels
1– Universal coupling; 2– Hanger Double row roller chain coupling

When adjusting the phase angle between the four groups of vibration components, it is not necessary to disassemble and assemble the shaft and the bearing housing components, the only thing that needs to be done is loosening the locked screw of the universal coupling, disassemble and assemble the universal coupling on the short shaft side. In this way, the relative phase angle between adjacent eccentric vibration components can be adjusted efficiently, the adjustment process is shown in Fig. 3.

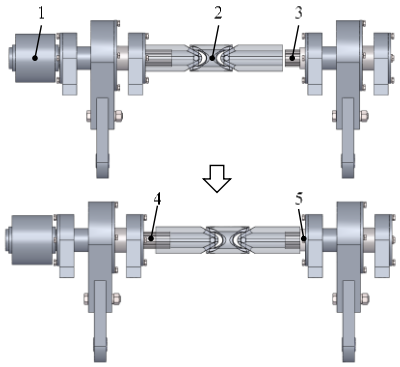

Fig. 3 - Schematic diagram of long and short shaft adjustment method
1- Double row roller chain coupling; 2– Universal coupling; 3– Short shaft; 4– Long shaft; 5– Space

When adjusting the initial phase angle, it is realized by changing the relative rotation teeth of the two sprockets of the roller chain coupling. For every relative rotation of two teeth, the corresponding initial phase angle changes 45°, that is, the first-order initial phase angle is adjusted. The double row roller chain coupling is of KC-4016 type, as shown in Fig. 4, and the starting phase angle of the eccentric sleeve can be adjusted by eight levels with 16 links.

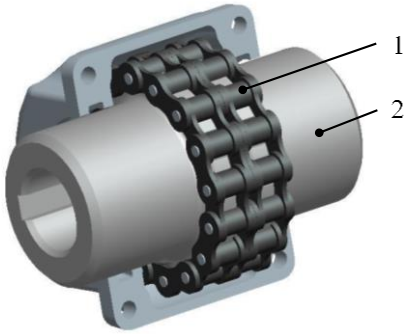

Fig. 4 - Double row roller chain coupling
1– Double row roller chain; 2–Sprocket

The vibration test facility is shown in Fig. 5 (*Wang et al., 2021; Su et al., 2022*). The carrier is used for placing the TST5910 dynamic signal tester and the computer. The traveling wheel of the carrier is a universal wheel, which is connected to the soil bin tester. During the test, the carrier can run both forwardly and backwardly, and one end of the IEPE signal line is connected to the dynamic signal tester, and the other end is connected to the accelerometer.

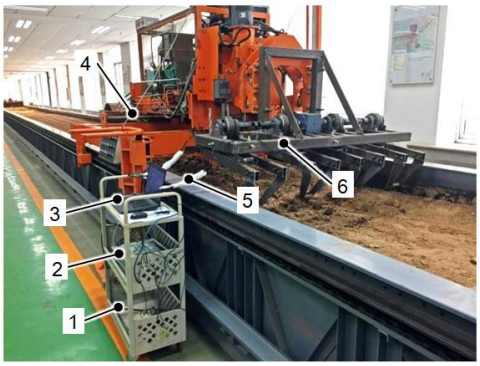

Fig. 5 - Test facility

1– Carrier; 2– Dynamic signal tester; 3– Computer; 4– Soil bin tester; 5– Signal line; 6– Vibration subsoiler

The acceleration curve of each position of the vibrating bulldozer frame was tested by using the TST5910 dynamic signal test and analysis system. The acceleration test adopts the voltage source piezoelectric accelerometer. The vibrating bulldozer is connected behind the soil bin trolley, and the vibrating bulldozer is symmetrical on both sides, so the sensor is only arranged on the left side and the middle position of the bulldozer, which is located in the position of the symmetrical cross section of the loosening parts, where the vibration is caused by the vibration of the loosening parts. In addition, a sensor is placed at the connection between the frame and the parts to measure the vibration of the connecting position, and the sensor is also placed on the force measuring frame. It is used to measure the vibration transmitted to the soil bin trolley. The position of the sensor measuring point is arranged as shown in Fig. 6.

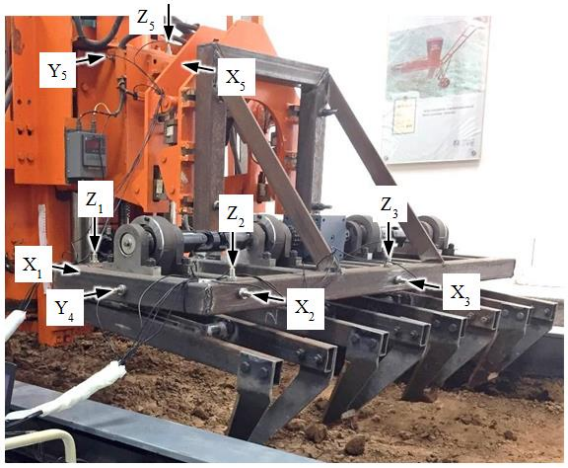

Fig. 6 - Placements of sensors

Test preparation

In the soil bin laboratory of China Agricultural University, the soil of the soil bin was pre-treated before the test. Firstly, the sprinkler function of the TCC electric four-drive soil bin test rig was used to evenly sprinkle the soil needed for the test. The watering operation was repeated three times, after the soil was soaked, and rest for three days. The soil moisture content was checked to ensure that the soil moisture content is wet, and ensure that the soil moisture content is about 18%. The soil was rotated by the 1GQN-125 rotary tiller, and the surface soil was loosened and beaten evenly. The soil after rotary tillage was compacted for three times by using the pressing roller to maintain the rated forward speed. Before the experiment, the soil in the soil bin was sprinkled, rotary ploughed, scraped and compacted, and the soil layers at different depths were sampled and preserved reasonably with a ring knife aluminum box. The soil moisture content and soil bulk density at different depths were measured by drying method, and the soil firmness was measured by SC900 digital soil

compactness meter made by SPECTRUM Company of the United States. The five-point sampling method is used to measure the soil in the soil bin and take the mean value, the measured data are shown in Table 1.

Table 1

Soil condition

Soil depth [mm]	Moisture content [%]	Soil hardness [kPa]	Soil bulk density [g/cm^3]
100	19.4	468.8	1.56
200	18.5	682.8	1.54
350	18.2	1317.6	1.49
Average	18.7	823.1	1.53

The time-domain plot of vibration acceleration. Frequency range chart of vibration acceleration of each measuring point was obtained using the piezoelectric accelerometer, as shown in Figs. 7-8. It can be seen that the acceleration changes violently, there are many clutters, and the change law is not obvious, so it is processed by secondary integration in the dynamic signal test and analysis software system, and the displacement signal was obtained. Effective signal was intercepted and the average value was processed. Stable vibration displacement signal was obtained as shown in Fig. 9. Frequency spectrum was analyzed using TST5910 dynamic signal testing system. Final frequency domain signal of vibration displacement was obtained as shown in Fig. 10. Magnitude of the main vibration amplitude is statistically obtained, which is a relative quantity, not the actual magnitude of vibration displacement, however, it can be used as an indicator to analyze the signal of each test point. The de-averaging of the time domain signals can avoid the peak of the spectrum line at the Frequency 0.

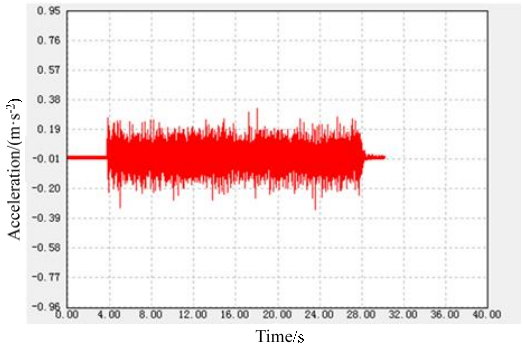

Fig. 7 - Time-domain plot of vibration acceleration

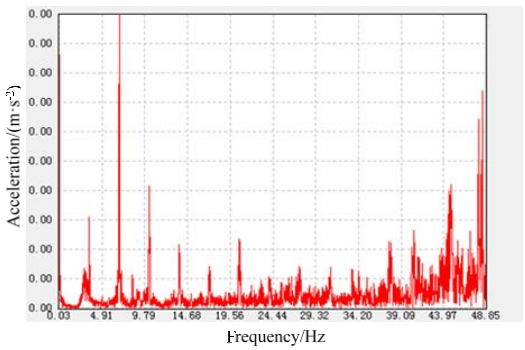

Fig. 8 - Frequency ranges chart of vibration

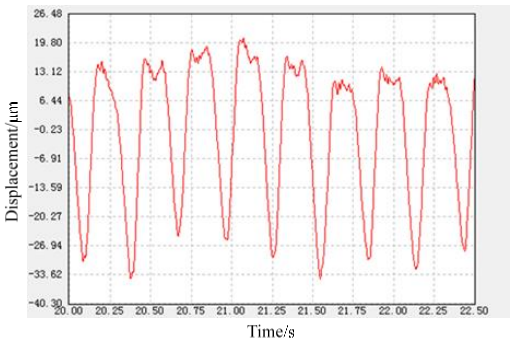

Fig. 9 - Time-domain plot of vibration acceleration

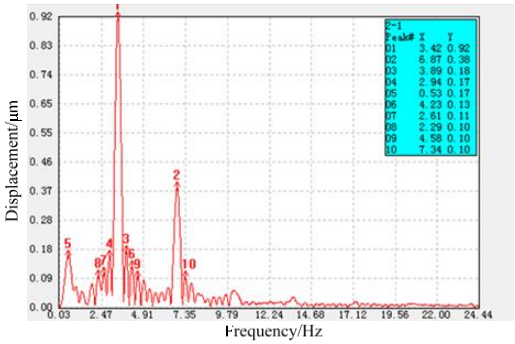

Fig. 10 - Frequency ranges chart of vibration

RESULTS

Different initial phase angle test

The initial phase angle of the fixed loosening shovel I was 0 °, and the other three shovels select the groups with less vibration according to the vibration acceleration reflected by the pre-experiment. Because the combination of different initial phase angles of the four groups of soil loosening components will affect the vibration characteristics of the frame, the soil bin tests with different initial phase angle combinations were carried out to find out the combination of the initial phase angle that caused the minimum vibration of the frame. The experimental phase angle combination is shown in Table 2.

Table 2

Phase angle combination

Number	Phase angle (°)			
	Break shovel Ⅰ	Break shovel Ⅱ	Break shovel Ⅲ	Break shovel Ⅳ
1	0	180	0	180
2	0	180	180	0
3	0	225	315	180
4	0	135	270	270
5	0	180	90	270
6	0	135	225	45
7	0	270	180	90
8	0	0	180	180
9	0	0	0	0
10	\	0	\	\
11	\	0	0	\
12	\	0	180	\

Vibration displacement characteristics

Before the soil loosening test, a no-load test was carried out by setting the traveling speed of the trolley to 0 with the soil shovel away from the soil. By analyzing the vibration data, it is found that the vibration Channel 4 (forward X_2 on the left side of the rear beam) and 5 (vertical Z_3 in the middle of the rear beam) were distorted due to vibration overload, which is not comparable. Fig. 11 shows the vibration data statistics (TST5910 spectrum analysis-real-time spectral peak) of Channel 1 (vertical Z_1 on the left side of the front beam), 2 (forward X_1 on the left side of the front beam), 3 (vertical Z_2 on the left side of the rear beam), 6 (forward Z_3 in the middle of the rear beam), 7 (Y_4 the lateral of the side beam), 8 (vertical Z_5 on the suspension bracket beam), 9 (forward Z_5 on the left side of the suspension bracket beam) and 10 (Y_5 on the side of the suspension bracket beam).

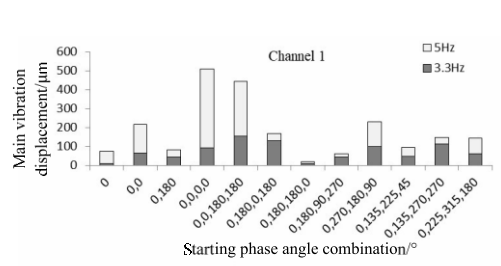

a. Channel 1

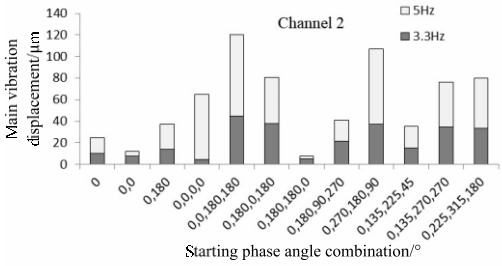

b. Channel 2

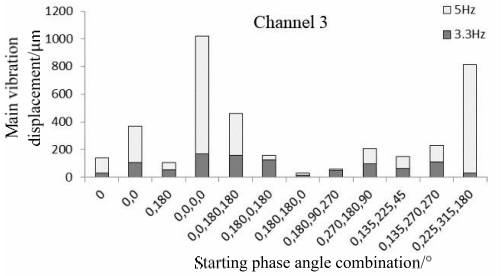

c. Channel 3

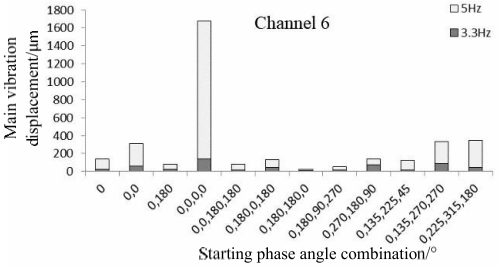

d. Channel 6

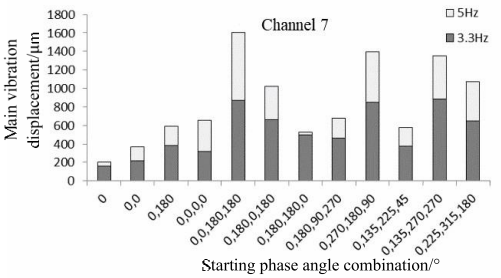

e. Channel 7

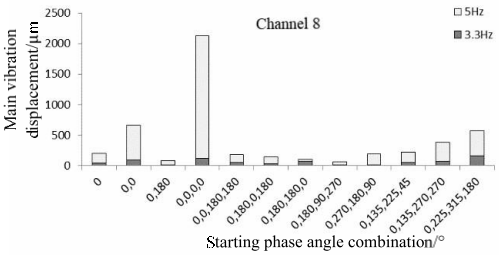

f. Channel 8

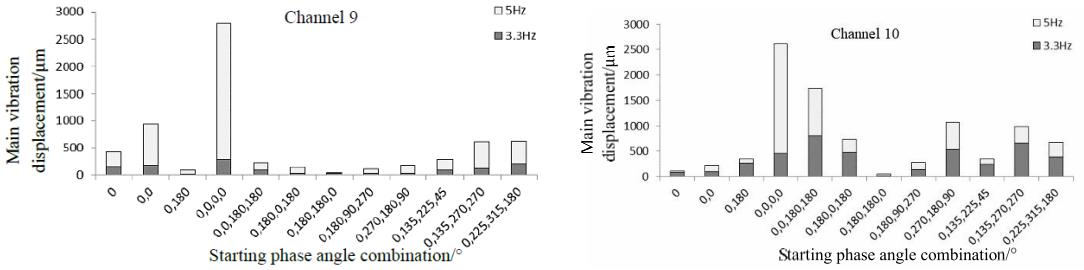

g. Channel 9 **h. Channel 10**

Fig. 11 - Vibration displacement at different positions

As shown in Fig. 11, the vibration displacement in the vertical direction of the rack is larger and the vibration displacement in the positions of channels 1 and 3 (left side of the front beam and left side of the rear beam) is the smallest when the initial phase angle combination is [0°, 180°, 180°, 0°] (symmetrical up and down staggered vibration), otherwise, the vibration displacements of channels 2 and 10 (the left forward direction of the front beam and the side of the suspension bracket frame) are also significantly minimum under that combined condition. In the forward direction, the vibration displacement of Channel 6 and 9 (middle of rear beam, suspension bracket) is smaller under the condition of the combination of initial phase angle [0°, 180°, 180°, 0°] (symmetrical up-down staggered vibration) and [0°, 180°, 90°, 270°] (uniform staggered vibration), otherwise, the vibration displacement of Channel (vertical suspension) is also quite small.

In theory, the lateral vibration displacement should be quite small, but due to the machining error, fit clearance and material deformation, the lateral displacement of staggered vibration is quite large, even larger than the unbalanced initial phase angle combination [0°, 0°, 0°, 0°] condition, as shown in Fig. 11 in Channel 7 (side beam).

Comparing the main vibration displacement of each channel of the four groups of shovel-vibration subsoiler we can see that the vibration displacement of each measuring point is quite small when the initial phase angle is [0°, 180°, 180°, 0°] (symmetrical up-down alternating vibration) and [0°, 180°, 90°, 270°] (uniform alternating vibration). Furthermore, when the initial phase angle combination is [0°, 180°, 180°, 0°], the vertical vibration displacement of the frame is smaller.

Traction characteristics

For the two vibration ways of vibration subsoiler, with the name of symmetrical up-and-down alternating vibration [0°, 180°, 180°, 0°] and uniform alternating vibration [0°, 180°, 90°, 270°] tested in the soil bin to loosen the soil, whose traction force tested in experiments is shown in Fig. 12 from which we can see the percentile values of traction force and the meaning value of symmetrical up-and-down alternating vibration are lower than those of uniform alternating vibration, which shows that the symmetrical up-and-down alternating vibration is more stable and the effect of reducing drag is better.

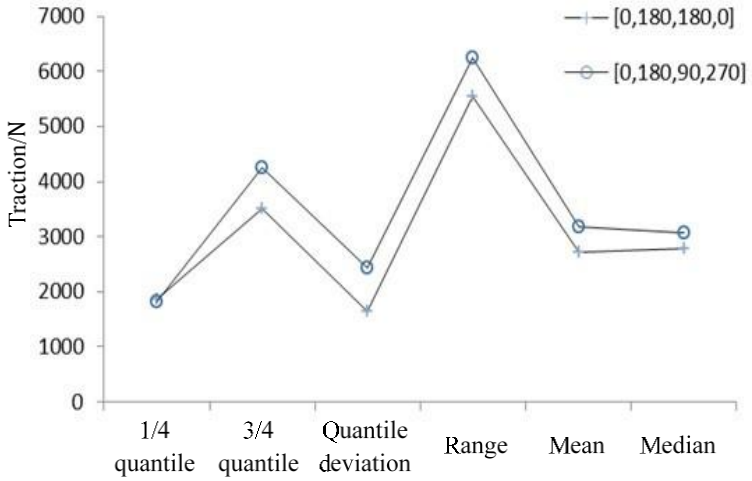

Fig. 12 - Effect of initial phase angle combination of traction

The influence caused by different amplitude/eccentricity ratio on vibration displacement
Method to adjust amplitude/eccentricity ratio

The adjustment of the connecting rod hitch location is shown in Fig. 13.

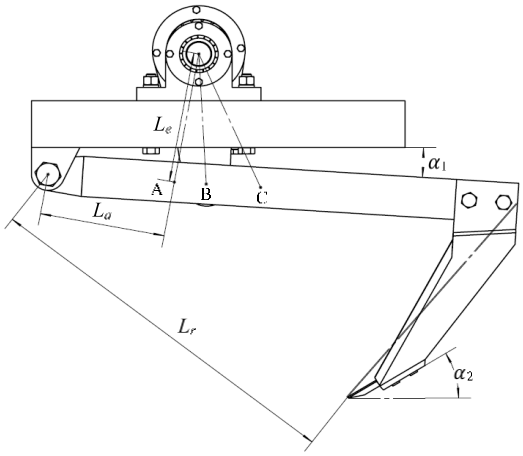

Fig. 13 - Adjustment of connecting rod hitch location

The law of the vibration radius L_r of the shovel tip, the force arm of the connecting rod La and the eccentricity e of the eccentric shaft in exciting parts and amplitude a can be summarized as Equation (1):

$$\frac{L_r}{L_a} = \frac{a}{e} \tag{1}$$

Where, L_r is vibration radius of shovel tip, mm; L_a is the force arm of the connecting rod, mm; a is amplitude, mm; e is eccentricity, mm.

Changing the hitch location between the connecting rod and pull rod (A, B, C in Fig. 14) can change the length of connecting rod arm L_a, and then cause the change of the amplitude. Because the vibration radius Lr of shovel tip is constant, the essence of adjusting connecting rod connection position is changing the length of connecting rod arm La, then cause the change of the amplitude/eccentricity ratio (a/e).

The penetration angle is an important parameter of the loosening operation. If we change it, the resistance of the vibrating soil loosening will be affected, causing the inconsistency of the test. In order to keep the penetration angle into soil unchanged, the length of the connecting rod should be adjusted while changing the position of the connecting rod. Therefore, the connecting rod designed in this paper includes the upper end and the lower end, and connects with different hole positions at the upper end or at the lower end of the connecting rod to get the different connecting rod length.

Vibration displacement characteristics

Under the condition of the different connection position, the amplitude/eccentricity ratio of vibration subsoiler is different. The vibration displacement amplitudes of each channel under the conditions of each connecting hole in the test were measured as shown in Fig. 14.

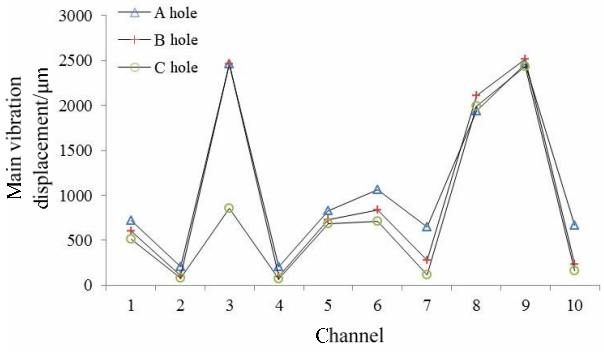

Fig. 14 - Effect of joint position on vibration displacement

For most channels, when connecting rod with B and C holes (amplitude/eccentricity ratio 2.5 and 2.0), the vibration displacement values are similar, and less than hole A (amplitude/eccentricity ratio 3.0), especially

for the data of channels 2, 4, 5, and 10. In the vertical direction (Channel 3) of the rear beam, when the connecting rod is located in the C hole, the corresponding vibration displacement is obviously reduced, while the vibration influence is quite small. So, when the amplitude/eccentricity ratio is 2.0 and 2.5, the required traction force of the subsoiler was stable.

Traction characteristics

As shown in Fig. 15, we can see that when the connecting rod is connected with holes B and C, and there is a small difference in the average traction force. When the connecting rod is connected to the hole A of the pull rod, both the amplitude/eccentricity ratio and the amplitude are the largest, but the connecting rod force arm L_a is the smallest, increasing the force of the connecting rod. When the shovels are working with large amplitude, the shovels advance and retreat greatly, which makes the traction change violently and the operation unstable. It can be seen from Fig. 15, that it is manifested as a sharp increase in the traction difference and range. While doing an operation, to connect the B Hole, C hole, using connecting rod, the traction force change is smaller and the meaning operation is more stable.

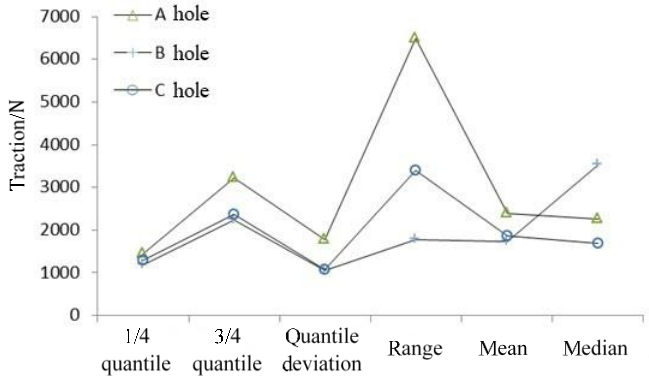

Fig. 15 - Effect of joint position on traction

Influence of different vibration frequency of vibration
Vibration displacement characteristics

The experiment of the combination of initial phase angle [0°, 180°, 180°, 0°] with different rotational speed (vibration frequency) was carried out, when the connecting rod is connected to the C holes. Taking the high frequency vibration into account, some of the measured channel data of the rack would distort, the Vertical Direction Z_5 (Channel 8), the forward direction X_5 (Channel 9) and the lateral direction Y_5 (Channel 10) of trolley suspension frame were measured and analyzed. As shown in Fig. 16, the vibration displacement of each channel is small, the increase of vibration frequency has little effect on the vibration displacement of the frame and trolley suspension, but when the vibration frequency reaches 9.2 Hz, the vibration noise of the structure is great. Therefore, the self-balance effect of symmetrical up-and-down alternating vibration is significant, and the negative effect of its vibration transmission is mainly shown on the great noise caused by the increase of vibration frequency, but the vibration displacement is quite small.

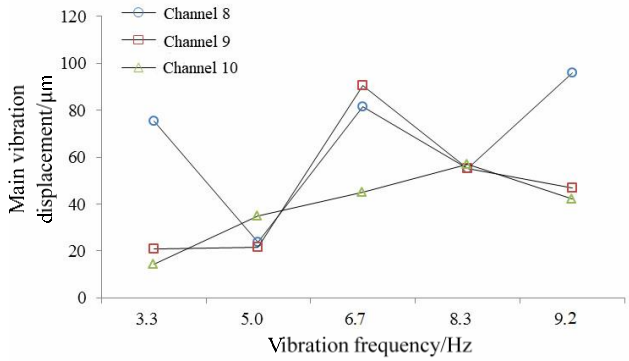

Fig. 16 - Effect of vibratory frequency of vibration displacement

Traction characteristics

Soil loosening tests under non-vibration conditions show that subsoiler is easy to cause soil hilling, as shown in Fig. 17, which will lead to increased tillage resistance.

Fig. 17 - Non-vibrational soil loosening

Deep vibration loosening can reduce the soil hilling phenomenon. With the increase of vibration frequency, the soil hilling phenomenon was gradually weakened and the trend line slope of tillage resistance decreased. When the frequency of the shovels was 0, 5.0, 6.7 and 8.3 Hz, the slope of the traction trend line was 88.234, 66.566, 55.437 and 12.673 respectively, as shown in Fig. 18. It can be concluded that, with the increase of vibration frequency, the traction variance of a subsoiler became smaller and smaller, while the permeability of loose soil increased gradually.

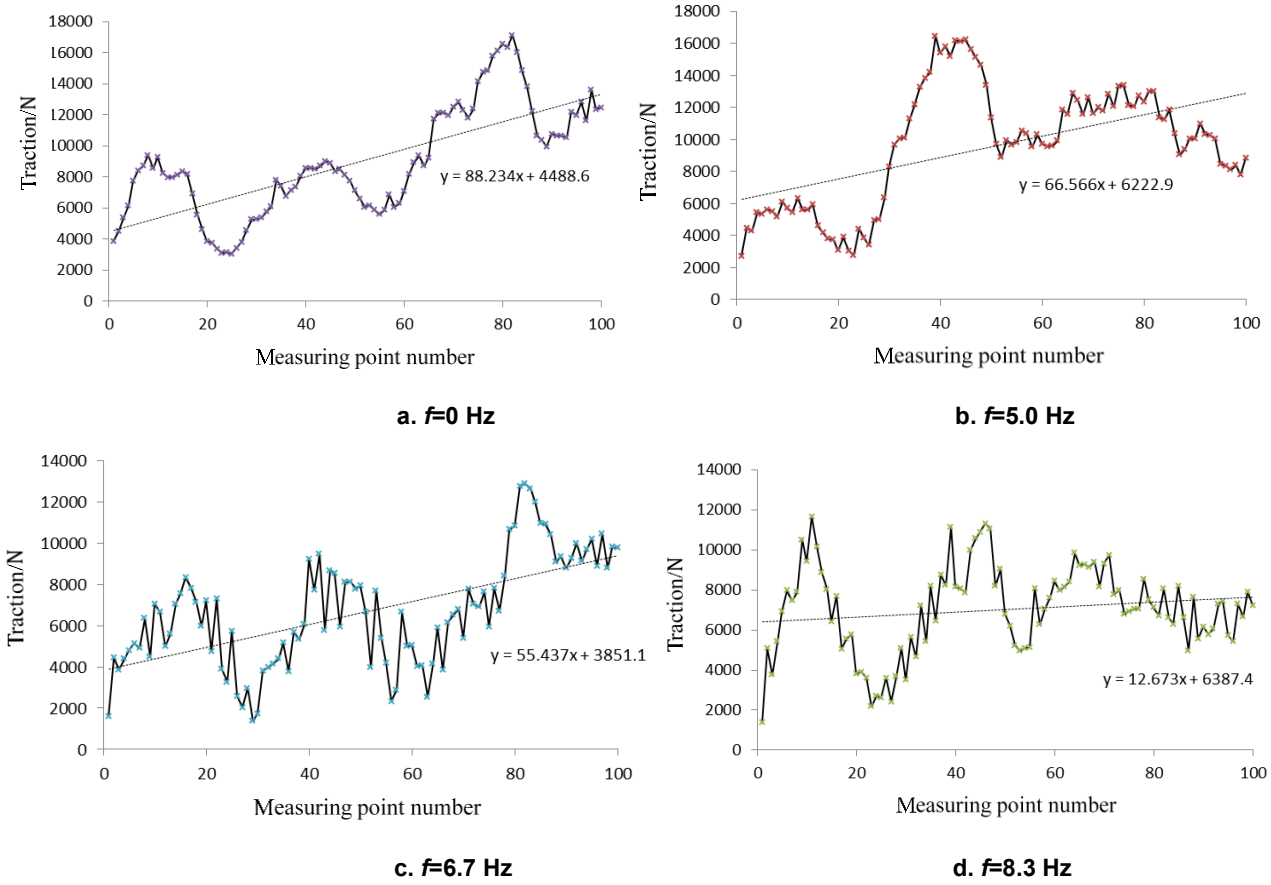

a. *f*=0 Hz **b. *f*=5.0 Hz**

c. *f*=6.7 Hz **d. *f*=8.3 Hz**

Fig. 18 - Variation tendency of traction

As shown in Fig. 19 and Table 3, the traction force of the subsoiler under different frequencies show that the mean value of the traction force decreased significantly as the vibration frequency increased. When the vibration frequency was 6.7 and 8.3 Hz, compared with the traction with non-vibration condition, the average traction force was decreased by 26% and 21% respectively. In addition, when the frequency of vibration loosening was 5.0, 6.7 and 8.3 Hz, the 1/4 percentile values of tractive force decreased by 5%, 25% and 10%, respectively and the tractive percentile difference decreased obviously as the vibration frequency increased, it shows that the variance of traction was reduced and the operation was stable. Therefore, vibration loosening soil using high frequency (*f*=6.7 and 8.3 Hz) was significant to get the effect of obvious drag reduction and small traction force variance, which is helpful to break the hard soil and improve the stability of soil loosening.

Table 3

Traction characteristic value statistics

Frequency	1/4 quantile	3/4 quantile	Quantile deviation	Range	Mean	Median
[Hz]	[N]	[N]	[N]	[N]	[N]	[N]
0	6143	11835	5268	13852	8735	8134
5	5835	12531	6116	13594	9463	9874
6.67	4594	8321	4137	11634	6429	6649
8.33	5516	7967	2863	10028	6897	7135

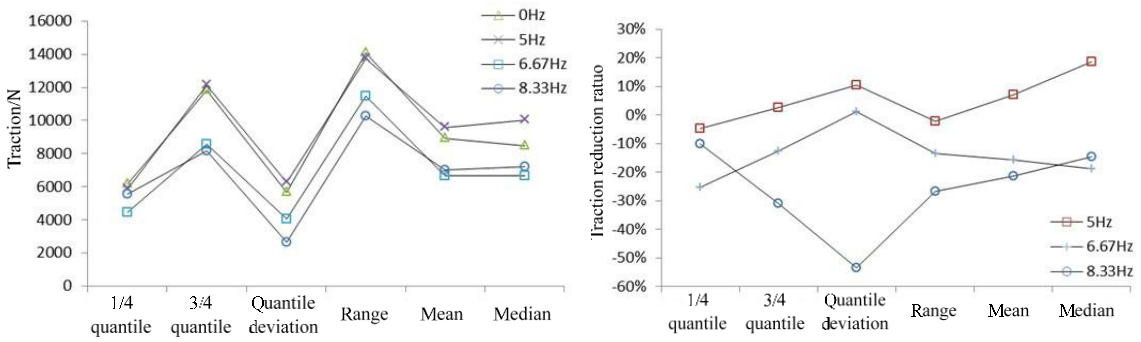

a. Traction **b. Traction reduction ratio**

Fig. 19- Effect of vibratory frequency on traction

CONCLUSIONS

In this paper, the acceleration signal was obtained by vibration acceleration test, and the vibration displacement characteristics were obtained by signal processing. According to the vibration displacement characteristics and traction characteristics, the initial eccentric phase angle combination, amplitude/eccentricity ratio and vibration frequency were selected in turn. The optimization of various parameters was integrated to reduce vibration. The whole research method can provide corresponding reference for the optimization of vibration agricultural machinery.

(1) Using the TST5910 dynamic signal testing system to get vibration displacement data by testing the vibration characteristics of the vibration subsoiler and collecting the vibration acceleration of the measuring point by the piezoelectric accelerometer with a second date treatment of integration, which has good applicability.

(2) Through the test of vibration characteristics and traction force, it can be concluded that the optimum initial phase angle combination of the four groups of shovel-vibration subsoiler was [0°, 180°, 180°, 0°], which caused the best effect of self-balance of symmetrical up-down alternating vibration. Under the condition of optimum initial phase angle combination, using the high frequency vibration and setting amplitude/eccentricity ratio 2.0 and 2.5 to loosen the soil (f=6.7 and 8.3 Hz), the effect of reducing drag is obvious and the influence of vibration is small. The self-balance vibration subsoiler worked stably after optimized, contributing to forming a virtual and real coexisting soil environment after tillage.

ACKNOWLEDGEMENT

This research was supported by China Agricultural University and the 13th Five-Year Plan of the National Key Research and Development Plan (2016YFD0701605).

REFERENCES

[1] Cui T., Shi Z., Yang L., Wang Y., Han D., & Zhang D., (2016). Design and experiment of vibration subsoiler with adjustable spring pre-tightening force (弹簧预紧力可调式振动深松机设计与试验), *Transactions of the Chinese Society for Agricultural Machinery*, vol.47, no.S1, ISSN, pp.96 -102.

[2] Jun Yuan, Jianqun Yu., (2020). Analysis on operational process of self-excited vibrating subsoiler based on DEM-MBD coupling algorithm (基于 DEM-MBD 耦合算法的自激振动深松机仿真分析), *Transactions of the Chinese Society for Agricultural Machinery*, vol.51, no. S1, ISSN, pp.17-24.

[3] Liu C., Li C., Li W., Wang X., Zheng K., Li L., & Hu H., (2017). Design and experiment of 1SZ-180 eccentric vibration subsoiler, *Jiangsu Agricultural Sciences*, vol.45, no.10, ISSN, pp.193-195.
[4] Liu X., & Qiu L., (2017). Experimental design and analysis of an oscillating subsoiler based on LABVIEW. *Journal of Agricultural Mechanization Research*, vol.39, no.2, ISSN, pp.128-132.
[5] Nagasaki Y., Okazaki K., & Miyazaki M., (1996). Development of working system for subsurface tillage. Part 1. Working characteristics of vibrating type whole layer loosening subsoiler, *Bulletin of the Shikoku National Agricultural Experiment Station*, vol.60, no.1, ISSN, pp.89 -104.
[6] Qiu L., & Li B., (2000). Experimental study on the self-excited vibration subsoiler for reducing draft force, *Transactions of the Chinese Society of Agricultural Engineering*, vol.16, no.6, ISSN, pp.72 -76.
[7] Qiang Su, Xuying Li, Fandi Zeng, Junyue Wang, Yongzhi Zhang, Hongbin Bai, Lei Wu., Jie Wang, (2022). Vibration characteristics test and analysis of hanging cup transplanter, *INMATEH Agricultural Engineering*, vol.66, no.1, ISSN, pp.279-288.
[8] Radite P.A.S., Hermawan W., Crosby H. B., Rizkianda A.B., & Mulyana, (2010). Experimental investigation on the application of vibration to reduce draft requirement of subsoiler, *International Agricultural Engineering Journal*, vol.19, no.1, ISSN, pp.31-38.
[9] Sun Y., Dong X., Song J., Wang J., Liu C., & Xu G., (2018). Self-balancing performance and simulation analysis of multi-group vibrating shovels of oscillatory subsoiler (振动深松机多组振动深松铲自平衡性能及仿真分析), *Transactions of the Chinese Society of Agricultural Engineering*, vol.34, no.4, ISSN, pp.92-99.
[10] Sakai K., Hata S., & Nambu S., (2010). Vibration of the tractor body equipped with a 4-shank vibrating subsoiler, *Journal of JSAM*, vol.52, no.3, ISSN, pp.29-35.
[11] Wang Li, Li Shuo, Lv Dianji, Ekhlo Ghay., (2021). Multi-sensor signal acquisition and data processing analysis of combine harvester, *INMATEH Agricultural Engineering*, vol.63, no.1, ISSN, pp.335-344.
[12] Wang Y., Zhang D., Yang L., Cui T., Li Y., & Liu Y., (2018). Design and experiment of hydraulically self-excited vibration subsoiler (液压激振源自激振动深松机深松单体设计与试验), *Transactions of the Chinese Society of Agricultural Engineering*, vol.34, no.11, ISSN, pp.40-48.
[13] Wang Y., Zhang D., Yang L., Cui T., Zhang W., Qi B., Li Y., Zhong X., (2020). Field performance of an electric–hydraulic control system for vibrating subsoiler with flexible tines, Computers and Electronics in Agriculture, vol.172, no.1, ISSN, pp.11-19.
[14] Yousif Y. Hilal, Saad Abdul Jabbar Al-rajabo, Ghazwan Ahmed Dahham., (2021). The effects of vibrating wings subsoiler plow on driver's seat of agricultural tractors and mechanization performance, *Soil & Tillage Research*, vol.205, no.1, ISSN, pp.41-48.
[15] Yang, F., Xu, H., Zhu, J., & Zhang, X., (2017). Method of optimizing the comfort of tractor seat with finite element simulation, *Journal of Chinese Agricultural Mechanization*, vol.38, no.5, ISSN, pp.47-52.
[16] Zhao, S., Wang, J., Wang, F., Zhang, F., & Li, X., (2017). Research status and prospect of agricultural soil vibratory-cutting technology, *Journal of Agricultural Mechanization Research*, vol.39, no.7, ISSN, pp.244-251.

WRITING INSTRUCTIONS

Article Types

Three types of manuscripts may be submitted:

1. **Regular articles:** These should describe new and carefully confirmed findings, and experimental procedures should be given in sufficient detail for others to verify the work. The length of a full paper should be the minimum required to describe and interpret the work clearly (max.10 pages, even number);
2. **Reviews:** Submissions of reviews and perspectives covering topics of current interest are welcome and encouraged (max.12 pages, even number).

Manuscripts should be written in English (American or British usage is accepted, but not a mixture of these) and submitted **electronically** at the following e-mail addresses: ***inmatehjournal@gmail.com***
Please be sure to include your full affiliation and e-mail address (see Sample manuscript)
The authors are responsible for the accuracy of the whole paper and references.
There are allowed 2 papers by each first author.
The text layout should be in single-column format. To avoid unnecessary errors it is strongly advised to use the "spell-check" and "grammar check" functions of your word processor.

Review Process

All manuscripts are reviewed by 2 members of the Scientifically Review Office. Decisions will be made as rapidly as possible and the journal strives to return reviewers' comments to authors in approx.3 weeks.
The editorial board will re-review manuscripts that are accepted pending revision.

NOTE:

Submission of a manuscript implies: that the work described has not been published before (excepting as an abstract or as part of a published lecture or thesis) that it is not under consideration for publication elsewhere.

1. REGULAR ARTICLES

- Manuscripts should be concise, in ***1.15 line spacing***, and should have 2 cm all over margins. The font should be ***Arial 10 pt.*** Ensure that each new paragraph is clearly indicated, using **TAB at 1 cm**.
- Title will be ***Arial 12 pt***. and explicit figures will be ***Arial 9 pt***.
- Text will be written in English.
- Chapters' titles are written by ***Arial 10 pt, Bold, Uppercase*** (e.g. **INTRODUCTION, MATERIALS AND METHODS**), between chapters is left a space for 10 pt. At the beginning of each paragraph, TAB of 1 cm.
- The paper body will be written in ***Arial 10 pt., Justify alignment***.

TITLE ***Arial 12 pt., Uppercase, Bold, Center*** *(in English language)* and ***Bold Italic*** *(in native language).*
Should be a brief phrase describing the contents of the paper. Avoid long titles; a running title of no more than 100 characters is encouraged (without spaces).

AUTHORS ***ARIAL 9, Bold, Centre alignment***
Under the paper's title, after a space (enter) 9 pt., write ***authors' names*** and ***affiliations (Arial 8 pt.-Regular)***
When the paper has more than one author, their name will be followed by a mark (Arabic numeral) as superscript if their affiliation is different. Less than 6 authors.
Corresponding author's name (next row), ***(Arial 8 pt.)***. Should be added also: phone, fax and e-mail information, for the paper corresponding author (***font: 8 pt., Italic***).

KEYWORDS ***(In English)*** about 4 to 7 words that will provide indexing references should be listed (title: ***Arial 10pt, bold italic,*** text ***Arial 10 pt., italic***).

A list of non-standard *Abbreviations* should be added. In general, non-standard abbreviations should be used only when the full term is very long and used often. Each abbreviation should be spelled out and introduced in parentheses the first time it is used in the text. Standard abbreviations (such as ATP and DNA) need not to be defined.
ABSTRACT ***(in English and Native language, Arial 10 pt.)***, the title *bold*; the text of abstract: *italic*) should be informative and completely self-explanatory, briefly present the topic, state the scope of the experiments, indicate significant data, and point out major findings and conclusions. The Abstract should be max.250 words. Complete sentences, active verbs, and the third person should be used, and the abstract should be written in the past tense. Standard nomenclature should be used and abbreviations should be avoided. No literature should be cited.
INTRODUCTION (***Arial 10 pt.)*** should provide a clear statement of the problem, the relevant literature on the subject, and the proposed approach or solution. It should be understandable to colleagues from a broad range of scientific subjects. We should refer to the current stage of researches performed in the field of the paper to be published, by quoting up-to-date specialty studies, preferably published after 2006, excepting certain referential specialty

books/studies, especially papers issued in magazines/journals/conferences/ISI quoted symposia or in other international data bases, which are well known and available.

MATERIALS AND METHODS (***Arial 10 pt.***) should be complete enough to allow experiments to be reproduced. However, only truly new procedures should be described in detail; previously published procedures should be cited, and important modifications of published procedures should be mentioned briefly. Methods in general use need not be described in detail.

RESULTS (***Arial 10 pt.***) should be clarity presented. The results should be written in the past tense when describing findings in the authors' experiments. Results should be explained, but largely, without referring to the literature. Discussion, speculation and detailed interpretation of data should not be included in the Results, but should be put into the Conclusions section.

CONCLUSIONS (***Arial 10 pt.***) The main conclusions drawn from results should be presented in a short Conclusions section. Do not include citations in this section.

Formulae, symbols and abbreviations: Formulae will be typeset in Italics (preferable with the Equation Editor of Microsoft Office 2003) and should be written or marked as such in the manuscript, unless they require a different styling. They should be referred to in the text as Equation (4) or e.g. (4). The formulae should be numbered on the right side, between brackets ***(Arial 10 pt.)***:

$$P = F \cdot v \tag{1}$$

Terms of the equation and the unit measure should be explained, e.g.

P is the power, [W];
F – force, [N];
v – speed, [m/s]

SI units must be used throughout.

Tables should be self-explanatory without reference to the text. The details of the methods used in the experiments should preferably be described in the legend instead of in the text. The same data should not be presented both in table and graph form or repeated in the text.
Table's title will be typed ***Arial 9 pt, Bold, Centered***
In the table, each row will be written Arial 9 pt, single-spaced throughout, including headings and footnotes.
The table should be numbered on the right side, ***Arial 10 pt.***

Figures ***(Arial 9 pt., Bold, Center)***should be typed in numerical order (Arabic numerals). Graphics should be high resolution (e.g.JPEG).Figure number is followed by what represent the figure or graph e.g.:

Fig.1 – Test stand

Legend: ***Arial 8 pt, Italic, Center,*** e.g.:
1 - plansifter compartments; 2- break rolls; 3 – semolina machines; 4 – reduction rolls; 5 – flour

ACKNOWLEDGMENTS (***Arial 10 pt.***) of people, grants, funds etc should be brief (*if necessarily*).

REFERENCES (***Arial 10 pt.***)
(In alphabetical order, in English and in the original publication language).
Minimum 10 references, last 10 years, minimum 3 references from the last 2 years

It can be used "*References*" tool from the *Word Editor*. **APA Style (American Psychological Association)**
https://apastyle.apa.org/style-grammar-guidelines/references/examples

All references must be provided in English
Authors are fully responsible for the accuracy of the references.

References should be **alphabetically**, with complete details, as follows:

Examples:
Books: https://apastyle.apa.org/style-grammar-guidelines/references/examples/book-references

Jackson, L. M. (2019). *The psychology of prejudice: From attitudes to social action* (2nd ed.). American Psychological Association. https://doi.org/10.1037/0000168-000
Kesharwani, P. (2020). *Nanotechnology based approaches for tuberculosis treatment*. Academic Press.
Sapolsky, R. M. (2017). *Behave: The biology of humans at our best and worst*. Penguin Books.

Torino, G. C., Rivera, D. P., Capodilupo, C. M., Nadal, K. L., & Sue, D. W. (2019). *Microaggression theory: Influence and implications*. John Wiley & Sons. https://doi.org/10.1002/9781119466642

In text:

- ***Parenthetical citations***: (Jackson, 2019; Sapolsky, 2017)
- ***Narrative citations***: Jackson (2019) and Sapolsky (2017)

Journal Article:

https://apastyle.apa.org/style-grammar-guidelines/references/examples/journal-article-references

Grady, J. S., Her, M., Moreno, G., Perez, C., & Yelinek, J. (2019). Emotions in storybooks: A comparison of storybooks that represent ethnic and racial groups in the United States. *Psychology of Popular Media Culture*, *8*(3), 207–217. https://doi.org/10.1037/ppm0000185

In text:

- ***Parenthetical citation***: (Grady et al., 2019)
- ***Narrative citation***: Grady et al. (2019)

Conference or Symposium:

https://apastyle.apa.org/style-grammar-guidelines/references/examples/conference-proceeding-references

Duckworth, A. L., Quirk, A., Gallop, R., Hoyle, R. H., Kelly, D. R., & Matthews, M. D. (2019). Cognitive and noncognitive predictors of success. *Proceedings of the National Academy of Sciences*, *USA*, *116*(47), 23499–23504. https://doi.org/10.1073/pnas.1910510116

In text:

- ***Parenthetical citation***: (Duckworth et al., 2019)
- ***Narrative citation***: Duckworth et al. (2019)

Dissertation / Thesis:

https://apastyle.apa.org/style-grammar-guidelines/references/examples/published-dissertation-references

Zambrano-Vazquez, L. (2016). *The interaction of state and trait worry on response monitoring in those with worry and obsessive-compulsive symptoms* [Doctoral dissertation, University of Arizona]. UA Campus Repository. https://repository.arizona.edu/handle/10150/620615

In text:

- ***Parenthetical citations***: (Kabir, 2016; Miranda, 2019; Zambrano-Vazquez, 2016)
- ***Narrative citations***: Kabir (2016), Miranda (2019), and Zambrano-Vazquez (2016)

https://apastyle.apa.org/style-grammar-guidelines/references/examples/unpublished-dissertation-references

Harris, L. (2014). *Instructional leadership perceptions and practices of elementary school leaders* [Unpublished doctoral dissertation]. University of Virginia.

In text:

- ***Parenthetical citation***: (Harris, 2014)
- ***Narrative citation***: Harris (2014)

Patents: Names and initials of authors, year (between brackets), patent title (Italic), patent number,country:

Grant, P. (1989). *Device for Elementary Analyses*. Patent. No.123456. USA.

Legal regulations and laws, organizations:

https://apastyle.apa.org/style-grammar-guidelines/references/examples/iso-standard-references

International Organization for Standardization. (2018). *Occupational health and safety management systems—Requirements with guidance for use* (ISO Standard No. 45001:2018). https://www.iso.org/standard/63787.html

Occupational Safety and Health Administration. (1970). *Occupational safety and health standards: Occupational health and environmental control: Occupational noise exposure* (OSHA Standard No. 1910.95). United States Department of Labor. https://www.osha.gov/laws-regs/regulations/standardnumber/1910/1910.95

In text:

- ***Parenthetical citations***: (International Organization for Standardization, 2018; Occupational Safety and Health Administration, 1970)
- ***Narrative citations***: International Organization for Standardization (2018) and Occupational Safety and Health Administration (1970)

Web references: The full URL should be given in text as a citation, if no other data are known. If the authors, year, and title of the documents are known and the reference is taken from a website, the URL address has to be mentioned after these data.

Citation in text

Please ensure that every reference cited in the text is also present in the reference list (and vice versa).

Do not cite references in the Abstract and Conclusions !.

Unpublished results, personal communications as well as URL addresses are not recommended in the references list.

Making personal quotations (one, at most) should not be allowed, unless the paper proposed to be published is a sequel of the cited paper. Articles in preparation or articles submitted for publication, unpublished, personal communications etc. should not be included in the references list.

Citations style

***Text**:* All citations in the text may be made directly (or parenthetically) as bellow.

- ***single author**:* the author's name (without initials, unless there is ambiguity) and the year of publication:
  "as previously demonstrated *(Brown, 2010)*".
- ***two authors**:* both authors' names and the year of publication: *(Adam and Brown, 2008; Smith and Hansel, 2006; Stern and Lars, 2009)*
- ***three or more authors**:* first author's name followed by "et al." and the year of publication: "As has recently been shown *(Werner et al., 2005; Kramer et al., 2000)* have recently shown ...."

Citations of groups of references should be listed first alphabetically, then chronologically.

Units, Abbreviations, Acronyms

- Units should be metric, generally SI, and expressed in standard abbreviated form.
- Acronyms may be acceptable, but must be defined at first usage.

2. REVIEWS

Summaries, reviews and perspectives covering topics of current interest in the field, are encouraged and accepted for publication. Reviews do not have the requirements for regular articles. However, should include: (*) an introductory chapter, (**) a careful and critical presentation of the relevant aspects of the topic approached and (***) emphasis of the aspects that aren't known and require further research to progress. Reviews should be concise (max. 12 pages).

Edited by: INMA Bucharest
6, Ion Ionescu de la Brad Blvd., sect. 1, Bucharest, ROMANIA
Tel: +4021.269.32.60; Fax: +4021.269.32.73
https:// inmateh.eu
e-mail: ***inmatehjournal@gmail.com***